EPRI
Electric Power
Research Institute

Keywords:
Earthquakes
Site characterization
Hazard assessment
Seismic engineering
Seismology
Geotechnical engineering

Guidelines for Determining Design Basis Ground Motions

Volume 4: Appendices for Laboratory Investigations

Prepared by
ELECTRIC POWER RESEARCH INSTITUTE
in cooperation with the Joint Contractors
(Southern Electric International, Commonwealth Research Corporation,
and Public Service Corporation of New Jersey),
the Nuclear Management and Resources Council,
the U.S. Department of Energy and Sandia National Laboratories.

Guidelines for Determining Design Basis Ground Motions

Volume 4: Appendices for Laboratory Investigations

Procedures currently used to assess the nature of earthquake ground motion in Eastern North America introduce considerable uncertainty to the design parameters of nuclear power plants and other critical facilities. This report examines that issue in-depth and provides an engineering model and guideline for selecting a site and assessing its seismic suitability.

INTEREST CATEGORIES

Nuclear seismic risk, design, and qualification
Advanced light water reactors
Risk analysis; management and assessment
Nuclear plant life extension

KEYWORDS

Earthquakes
Site characterization
Hazard assessment
Seismic engineering
Seismology
Geotechnical engineering

BACKGROUND Eastern North America has sparse earthquake activity with rare occurrences of large earthquakes; thus, little data exists to empirically quantify the characteristics of ground motions. Procedures currently used to estimate ground motion effects in this region introduce considerable uncertainty into the process of developing seismic designs, either due to the procedure's subjectivity or the lack of physical calibration.

OBJECTIVES To develop generic relations for estimating ground motion appropriate for site screening; to develop a guideline for conducting a thorough site investigation needed to define the seismic design basis.

APPROACH The project team specifically considered ground motions resulting from earthquakes with magnitudes from 5 to 8, fault distances from 0 to 500 km, and frequencies from 1 to 35 Hz. To develop generic ground motion relations for Eastern North America, they used theoretical models calibrated against data from earthquakes throughout North America and the world. In these models, the contributions to ground motion, including its variability, were evaluated using physical representations of earthquake processes. Earthquake processes involve the initial generation of seismic energy or waves at the earthquake fault ("source effects"), followed by the propagation of seismic waves through the earth's crust ("path effects"), and finally the modification of seismic waves as they travel through soils near the earth's surface ("site effects"). The team also collected and analyzed extensive geotechnical data at three reference sites. This information provided the basis for developing a guideline to help assess site suitability.

RESULTS This project resulted in an engineering model for estimating earthquake ground motions in Eastern North America. The model considers a wide range of earthquake sizes and site conditions and may be used directly for site screening purposes.

The work also resulted in a guideline for conducting geotechnical and seismic engineering investigations needed to determine the design basis for a site. This guideline is appropriate for investigating a wide range of site conditions and soil depths within and outside Eastern North America.

EPRI PERSPECTIVE Cost-effective seismic regulation of nuclear power plants requires site-specific definition of seismic ground motions. The development of engineering procedures for estimating earthquake ground motion can thus benefit both operating and future plants. For licensing application, these procedures are needed

operating and future plants. For licensing application, these procedures are needed to define the safe shutdown earthquake (SSE). The regulatory guidance found in Section 2.5 of the Standard Review Plan (NUREG 0800) is quite limited in scope and does not reflect the current state of knowledge on earthquake phenomena. With no accepted generic procedures in place, utilities constantly face uncertainty associated with site-specific developments and applications. These factors result in seismic design bases that are excessively conservative and/or contribute to licensing delays, regulatory instability, and high utility costs in the licensing process.

In 1988, EPRI completed a seismic hazard model for the central and eastern United States (NP-4726), including a ground motion model (NP-6074). The present work directly complements NP-4726, while replacing and going significantly beyond the results of NP-6074. The engineering ground-motion model can be used for screening potential sites before conducting extensive site investigations. The guideline provides needed background information to conduct an appropriate geotechnical and seismic engineering investigation of a site for licensing purposes. Additional EPRI reports that provide a basis for the current report include: NP-5577, NP-5875, NP-6304, TR-100409, TR-100410, TR-102261, and TR-102262.

This report is presented in five volumes. Essential background, approach and results are given mainly in Volume 1. Volumes 2, 3, and 4 are appendices containing detailed analyses. Volume 5 (licensed material) contains *Quantification of Seismic Source Effects*, which is summarized in Volume 1, Section 4.

PROJECT

RP3302

EPRI Project Manager: J. F. Schneider

Nuclear Power Division

For further information on EPRI research programs, call
EPRI Technical Information Specialists (415) 855-2411.

Guidelines for Determining Design Basis Ground Motions

Volume 4:
Appendices for Laboratory Investigations

TR-102293
Research Project 3302

Final Report, November 1993

Prepared by
ELECTRIC POWER RESEARCH INSTITUTE
in cooperation with the Joint Contractors
(Southern Electric International, Commonwealth Research Corporation,
and Public Service Corporation of New Jersey),
the Nuclear Management and Resources Council,
the U.S. Department of Energy and Sandia National Laboratories.

Prepared for
Electric Power Research Institute
3412 Hillview Avenue
Palo Alto, California 94304

EPRI Project Manager
J. F. Schneider

Advanced Reactors Development Administration
Nuclear Power Division

DISCLAIMER OF WARRANTIES AND LIMITATION OF LIABILITIES

ORGANIZATION(S) THAT PREPARED THIS REPORT:
ELECTRIC POWER RESEARCH INSTITUTE

ORDERING INFORMATION

Requests for copies of this report should be directed to the EPRI Distribution Center, 207 Coggins Drive, P.O. Box 23205, Pleasant Hill, CA 94523, (510) 934-4212. There is no charge for reports requested by EPRI member utilities.

LIST OF COSPONSORS

Early Site Permit Demonstration Program (ESPDP) Participants

Southern Electric International
42 Inverness Center Parkway
Birmingham, AL 25242

Commonwealth Research Corporation
1400 Opus Place
Downers Grove, IL 60515

Public Service Corporation of New Jersey
80 Park Plaza, 11-A
Newark, NJ 07101

Electric Power Research Institute
3412 Hillview Ave.
Palo Alto, CA 94303

Nuclear Management and Resources Council
1776 Eye Street, Suite 300
Washington, DC 2006

Department of Energy
Office of Nuclear Energy
19901 Germantown, MD 20874

Sandia National Laboratories
1515 Eubank Boulevard Southeast
Albuquerque, NM 87123

PROGRAM PARTICIPANTS

Participants	Affiliation
Project Manager	
Dr. John Schneider	Electric Power Research Institute
Principal Participants	
Dr. Norman Abrahamson	Consultant
Dr. Donald Anderson	CH2M Hill, Inc.
Dr. Gail Atkinson	Consultant
Prof. Carl Costantino	City University of New York
Prof. I.M. Idriss	University of California at Davis
Dr. Robin K. McGuire	Risk Engineering, Inc.
Dr. Robert Nigbor	Agbabian Associates
Dr. Robert Pyke	Consultant
Dr. Walter Silva	Pacific Engineering & Analysis
Dr. Paul Somerville	Woodward-Clyde Consultants—Pasadena
Dr. J. Carl Stepp	Electric Power Research Institute
Prof. Kenneth Stokoe	University of Texas at Austin
Prof. M. Nafi Toksoz	Massachusetts Institute of Technology
Dr. Gabriel Toro	Risk Engineering, Inc.
Dr. Robert Youngs	Geomatrix Consultants
Contributors	
Prof. Keiiti Aki	Consultant
Dr. C. T. Chin	Moh & Associates, Taiwan
Dr. James Chin	University of Southern California
Dr. Shyh-Jeng Chiou	Geomatrix Consultants
Mr. Mark Fuhriman	University of Texas at Austin
Dr. Robert Graves	Woodward-Clyde Consultants
Prof. Robert Herrmann	St. Louis University
Mr. Seon-Keun Hwang	University of Texas at Austin
Mr. Athar Khwaja	University of Texas at Austin
Mr. Joseph Laird	University of Texas at Austin
Mr. David Lapp	Geomatrix Consultants
Mr. Ben T. Lin	Moh & Associates, Taiwan
Mr. Mihalis Madianos	Geomatrix Consultants

Contributors

Dr. Batakrishna Mandal	Massachusetts Institute of Technology
Mr. James McLaren	Woodward-Clyde Consultants
Mr. Bruce Redpath	Redpath Geophysics
Ms. Nancy Smith	Woodward-Clyde Consultants
Ms. Cathy Stark	Pacific Engineering & Analysis
Mr. Robert Steller	Agbabian Associates
Dr. Joseph Sun	Woodward-Clyde Consultants
Dr. Y. T. Gu	City University of New York
Mr. Ernest Heymsfield	City University of New York
Dr. Xiao-ming Tang	Massachusetts Institute of Technology
Mr. Chris Volksen	University of California at Davis
Mr. Donald Wells	Geomatrix Consultants
Mr. Doug Wright	Pacific Engineering & Analysis
Dr. Shen-Chyun Wu	Risk Engineering, Inc.
Ms. Joanne Yoshimura	Consultant

LIST OF CONTRACTORS

Guidelines for Determining Design Basis Ground Motions

TR-102293

Contract	Contractor
RP3302-02	Professor M. Nafi Toksoz Consultant 15 Walsingham St. Newton, MA 02162
RP3302-04	Professor Kenneth Stokoe Consultant 4602 Laurel Canyon Dr. Austin, TX 78731
RP3302-05	Professor I.M. Idriss Consultant P.O. Box 330 Davis, CA 95617-0330
RP3302-06	Dr. Gail Atkinson Consultant 125 Dunbar Road South Waterloo, Ontario N2L 2E8 CANADA
RP3302-07	Dr. Norman Abrahamson Consultant 5319 Camino Alta Mora Castro Valley, CA 94546
RP3302-08	Dr. Paul Somerville Woodward-Clyde Consultants 566 El Dorado St. Pasadena, CA 91101

Contract	Contractor
RP3302-09	Dr. Robin K. McGuire Risk Engineering, Inc. 5255 Pine Ridge Road Golden, CO 80403
RP3302-10	Dr. Walter Silva Pacific Engineering and Analysis 311 Pomona Avenue El Cerrito, CA 94530
RP3302-11	Dr. Robert Pyke Consultant 1076 Carol Lane #136 Lafayette, CA 94549
RP3302-12	Dr. Robert Youngs Geomatrix Consultants 100 Pine Street—10th Floor San Francisco, CA 94111
RP3302-13	Dr. Donald Anderson CH2M Hill, Inc. P.O. Box 91500 Bellevue, WA 98009-2050
RP3302-14	Professor Keiiti Aki Consultant 622 Paseo de la Playa Redondo Beach, CA 90277
RP3302-15	Dr. Joseph Sun Woodward-Clyde Consultants 500 12th Street, Suite 100 Oakland, CA 94607-4014
RP3302-16	Dr. Robert Nigbor Agbabian Associates 1111 South Arroyo Parkway Suite 405 Pasadena, CA 91105
RP3302-18	Prof. Carl Costantino Consultant 4 Rockingham Rd. Spring Valley, NY 10977

ABSTRACT

This report develops and applies a method for estimating strong earthquake ground motion. The emphasis of this study is on ground motion estimation in Eastern North America (east of the Rocky Mountains), with particular emphasis on the Eastern United States and southeastern Canada. Specifically considered are ground motions resulting from earthquakes with magnitudes from 5 to 8, fault distances from 0 to 500 km, and frequencies from 1 to 35 Hz. The two main objectives were: (1) to develop generic relations for estimating ground motion appropriate for site screening; and (2) to develop a guideline for conducting a thorough site investigation needed to define the seismic design basis. For the first objective, an engineering model was developed to predict the expected ground motion on rock sites, with an additional set of amplification factors to account for the response of the soil column over rock at soil sites. The results incorporate best estimates of ground motion as well as the randomness and uncertainty associated with those estimates. For the second objective, guidelines were developed for gathering geotechnical information at a site and using this information in calculating site response. As a part of this development, an extensive set of geotechnical and seismic investigations was conducted at three reference sites. Together, the engineering model and guidelines provide the means to select and assess the seismic suitability of a site.

ACKNOWLEDGMENTS

This project was made possible through extensive support from a great number of institutions and individuals.

For review of draft copies of the report, conducted under an extremely tight schedule, we much appreciate the thoughtful comments by the following individuals: Dr. Michael Bohn, Sandia National Laboratory; Prof. Ricardo Dobry, Rensselaer Polytechnic Institute; Mr. Jeff Kimball, Department of Energy; Dr. Takeji Kokusho, Central Research Institute of Electric Power Industry, Japan; and Dr. Scott Slezak, Sandia National Laboratory.

Field measurements at the reference sites at Treasure Island and Gilroy 2 in California and at Lotung, Taiwan, required considerable logistical coordination and cooperation between institutions and individuals. Major contributions to seismic and other geophysical measurements at Treasure Island and Gilroy 2 were made by Mr. Takashi Kanamori and Mr. Finn Michelson of Oyo Geospace, Mr. Kenji Tanaka of Oyo Corporation, and Mr. Ed Steller of Agbabian Associates. Extensive seismic measurements at Treasure Island and Gilroy 2 were also made by Dr. Ronald Andrus, Mr. Marwan Aouad, and Mr. James Bay of the University of Texas at Austin. Generous support from Mr. Thomas Fumal and Mr. James Gibbs of the U.S. Geological Survey is also acknowledged for their contribution to geologic and seismic logging, respectively, of boreholes at the Gilroy 2 and Treasure Island sites. The following companies assisted the project by providing special equipment used in the measurements: ANCO Engineers, Kinemetrics, Inc., Oyo Corporation, and Redpath Geophysics.

For making arrangements or generously providing access to the reference sites, we are grateful to numerous individuals. We thank Ms. Susan Chang and Dr. Lelio Mejia of Woodward-Clyde Associates for assistance in logistics of drilling at Gilroy 2. Special thanks to Mr. Richard Lake and Mr. Roger Kostenko of Pitcher Drilling Co. for their excellence in drilling and sampling at the Gilroy 2 and Treasure Island sites. Drilling at Lotung, Taiwan, was coordinated expertly by Moh & Associates. We thank Mr. Y. H. Cheng, Deputy Director of the Nuclear Engineering Department at Taiwan Power Co., for helping with access to drilling at the Lotung site owned by Taiwan Power Co. For access to Gilroy 2, we thank Mr. John Belleau, site owner, and Mr. Roger and Ms. Marie Ellissondo, site managers (National 9 Inn). For Treasure Island site access, we thank Mr. Thomas Cuckler and Mr. Donald Brown of the Civil Engineering Department of the Treasure Island Naval Air Station.

Additional data were also generously provided by many individuals and institutions from complementary field measurements at various field test sites. Prof. Pedro de Alba of the University of New Hampshire, Mr. John Egan of Geomatrix Consultants, Prof. Roman Hryciw of the University of Michigan, and Prof. Kyle Rollins of Brigham Young University all generously provided data for our use from other geotechnical studies at Treasure Island. Sponsors of studies that produced these data were the U.S. Naval Air Station and the National Science Foundation. Prof. Pedro de Alba also provided access to boreholes drilled for several of these studies, also sponsored by the National

Science Foundation. Mr. Jeff Kimball of the Department of Energy made it possible to use a collection of geotechnical data from a site at the Savannah River site, South Carolina.

All of the laboratory measurements of dynamic properties of soil samples from the reference sites were performed at the Geotechnical Engineering Center of the University of Texas at Austin (GEC-UT). The large-scale chamber tests used to study field damping measurements were also performed at the GEC-UT. We thank Mr. Ngarkok Lee and Mr. Mark Twede of that institution for their assistance in this work. Further, the assistance of Ms. Teresa Tice-Boggs of the Geotechnical Engineering Center contributed significantly to the success of this work.

Several people assisted in providing and assembling data for the earthquake database used in this project. We appreciate the help of Mr. Phillip Munro of the Geological Survey of Canada for information regarding characteristics of strong-motion instrument sites for data recorded during the 1988 Saguenay, Quebec, earthquake and aftershocks.

Dr. David Boore of the U. S. Geological Survey provided an analysis of the distribution of selected ground motion data recorded on Wood-Anderson seismographs in southern California. Dr. Gail Atkinson provided seismic data and site descriptions from the Eastern Canada Telemetered Seismic Network.

We would like to thank the following people for their participation in various workshops held during the course of the project: Dr. David Boore, Dr. Jon Fletcher, Mr. Thomas Fumal, Mr. James Gibbs, Dr. William Joyner, and Dr. John Vidale of the U.S. Geological Survey; Mr. Scott Ashford, University of California at Berkeley; Ms. Ornella Bonamassa, University of California at Santa Cruz; Dr. David Rodgers, Rogers Pacific Consultants; Mr. Takashi Kanamori and Mr. Finn Michelson of Oyo Geospace; Dr. Clifford Roblee, California Department of Transportation; and Dr. Richard Lee, Westinghouse Savannah River Co. These individuals participated in numerous stimulating discussions that greatly contributed to the final product.

Finally, it is with great appreciation for the financial and managerial support, and, equally important the trust and confidence provided us, that we thank various individuals within and associated with the Department of Energy and utility industry for making the project possible. Special thanks to Ms. Susan Gray, Mr. Murv Little, and Mr. Joseph Santucci of the EPRI Advanced Reactor Program for their generous support, and especially to Ms. Gray for her direction as project manager of the Early Site Permit Demonstration Program. Thanks to Mr. Walter Pasedag of the Department of Energy and Mr. Ajoy Moonka of Sandia National Laboratory; to the Industry Siting Group, especially Mr. Louis Long; to the Nuclear Management and Resources Council (NUMARC), especially Mr. John Ronafalvy; to the Joint Contractors comprised of Southern Electric International, Commonwealth Research Corporation, and Public Service Company of New Jersey, especially Dr. Ninu Kaushal (Commonwealth Edison Co.).

CONTENTS

Volume 4: APPENDICES FOR LABORATORY INVESTIGATIONS

Appendix **Page**

Appendix Page

Appendix **Page**

EXECUTIVE SUMMARY

Introduction

This report develops and applies a method for estimating strong earthquake ground motion. The motivation for this development was the need for a systematic, physically based, empirically calibrated method that can be used to estimate ground motions for input to the design of nuclear power plants and other critical facilities. These ground motions are a function of the earthquake's magnitude and the physical properties of the earth through which the seismic waves travel from the earthquake fault to the site of interest. Procedures currently used to account for these effects introduce considerable uncertainty into the ground motion determination, either due to subjectivity of the procedure or the lack of physical calibration.

The emphasis of this study is on ground motion estimation in Eastern North America (east of the Rocky Mountains), with particular emphasis on the Eastern United States and southeastern Canada. Eastern North America is a stable continental region, having sparse earthquake activity with rare occurrences of large earthquakes. In the absence of large earthquakes within the region of interest, little data exist to empirically quantify the characteristics of ground motions associated with these events. While methods developed in more seismically active areas such as Western North America can be applied to Eastern North America, fundamental differences in the regional geology can lead to variations in ground motion characteristics. Therefore, empirically based approaches that are applicable for other regions, such as Western North America, do not appear to be appropriate for Eastern North America.

Recent advances in science and technology have now made it possible to combine theoretical and empirical methods to develop new procedures and models for estimating ground motion within Eastern North America. Specifically considered are ground motions resulting from earthquakes with magnitudes from 5 to 8, fault distances from 0 to 500 km, and frequencies from 1 to 35 Hz. The results of this report can be used to determine seismic hazards, provided the magnitudes and distances of potential earthquakes are predetermined. In particular, this report is intended for use in site screening as well as detailed characterization of ground motion at a site, such as may be required for structural design.

This study was conducted by a team of experts in seismology, geotechnical engineering, and seismic engineering. The investigations were carried out over a period of approximately 18 months from September 1991 to March 1993. Work included a series of focused workshops with project participants to help achieve consensus recommendations. The project was sponsored by the U. S. Department of Energy (DOE), Sandia National Laboratories, Southern Electric International, Commonwealth Research Corporation, Public Service Company of New Jersey, and the Electric Power Research Institute as part of the DOE's Early Site Permit Demonstration Program. The project was managed by the Electric Power Research Institute.

Objectives

There were two central objectives of the project: (1) to develop generic relations for estimating ground motion appropriate for site screening; and (2) to develop a guideline for conducting a thorough site investigation needed to define the seismic design basis. For the first objective, a set of relations was needed that could be used to predict the expected ground motion on rock or on soil for a future earthquake. The approach was to develop an engineering model consisting of relations appropriate for rock sites and an additional set of amplification factors to account for the response of the soil column over rock at soil sites. For the second objective, a guideline was developed for gathering geotechnical information at a site and using this information in calculating site response. Together, the engineering model and guideline provide the means to select and assess the seismic suitability of a site.

Approach

The method that was used to develop generic ground motion relations in this effort is markedly different from the approach of previous studies. In this study, theoretical models, which have been calibrated against data from earthquakes throughout North America and the world, are used to characterize earthquake ground motion in Eastern North America. In these models, the contributions to ground motion, including its variability, are evaluated using physical representations of earthquake processes. These processes involve the initial generation of seismic energy or waves at the earthquake fault ("source effects"), followed by the propagation of seismic waves through the earth's crust ("path effects"), and finally the modification of seismic waves as they travel through soils near the earth's surface ("site effects"). For a given earthquake magnitude and distance, the source, path, and site each contribute to the observed ground motion, as follows:

- The source controls both the seismic energy generated by rupture of an earthquake fault as well as the accompanying dynamic characteristics.
- The seismic path contributes to ground motion through reflection, refraction, and damping of seismic waves within the earth's crust in response to the various physical properties along the wave path.
- The site contributes to the evolution of seismic waves in much the same way as the path, though on a smaller scale. Site effects are a function primarily of soil depth and type.

The characteristics of the seismic source, path, and site effects form the basis for the parameters in the theoretical models.

The ground motion relations for rock sites were developed using a physically based, empirically calibrated ground motion model. In the model, a wide range of values was assigned to the ground motion parameters. Using the combination of all model parameters and their ranges of values, computer simulations produced hundreds of records of earthquake ground motion for each magnitude and distance considered. While each earthquake simulation represents a possible future earthquake, each earthquake is not equally likely to occur. Therefore, based upon extensive analyses of past earthquakes and comparisons to model predictions, distributions were assigned to the values for all model parameters. The parameter value distributions were based on partitioning their variability into two types: uncertainty, which is due to the lack of knowledge of earthquake characteristics; and randomness, which is due to the inherent variability of those characteristics. Finally, individual parameter weights were combined for each earthquake simulation to produce the appropriate "distribution" of earthquake ground motion for every magnitude, distance, and frequency considered. Together, these distributions constitute a family of functional relations that define the final engineering ground motion model for rock sites. In turn, the engineering model defines ground motion for median levels and associated variability.

To accommodate sites with soil overlying rock (referred to as local site effects), site amplification factors were developed for a range of soil types and depths representative of soil conditions in Eastern North America. The factors were derived by first accumulating data that describe the behavior of various soils during seismic loading. These

data were then used to assess the variability in seismic properties, especially the wave velocity as it changes with depth. In addition, seismic velocity and material damping data were gathered from three reference sites using a variety of field and laboratory techniques. The reference site data were used (1) to improve physical understanding of the dynamic processes of soil response and (2) to assess procedures for measuring the physical properties needed to estimate site effects. The estimation problem is particularly difficult because the seismic properties of soils change depending upon the level of shaking. The resulting "nonlinear" effects generally cause the ratio of soil-to-rock motions (i.e., soil amplification) to decrease as the corresponding rock motion increases. The quantification of these effects through theoretical modeling and comparisons to empirical data resulted in factors that describe the amplification of soils relative to rock for several soil categories. The amplification factors were developed for a wide range of rock motions and are given as median values with variability.

Finally, based upon extensive geotechnical data that were collected at the three reference sites and analyzed as part of this program, a guideline was developed for assessing soil characteristics and site response. This guideline applies to planning and conducting a systematic and thorough geotechnical investigation of soil properties at a potential site. Guidance is also provided for performing dynamic analyses required to determine the response of the soil column to earthquake shaking at (and beyond) the levels of motion of interest to the seismic design.

Conclusions

The engineering ground motion model developed in this study can be used for screening potential sites in Eastern North America before conducting extensive site investigations. However, the application of these procedures to site screening requires information regarding earthquake magnitudes and distances as well as certain site properties such as soil depth and site geology. Magnitudes and distances of potential earthquakes may be derived either probabilistically or deterministically.

The guideline—together with the results of investigations of the three reference sites—provides the means to conduct an appropriate geotechnical and seismic engineering site investigation. In all, this guideline is appropriate for use given a wide range of site conditions and soil depths. While there are certain soil types (e.g., those with liquefaction potential) for which this guideline may not be directly applicable, it may be used widely both within and outside Eastern North America.

The information compiled in this report represents a comprehensive assessment of the nature of earthquake ground motion in Eastern North America. The results incorporate best estimates of ground motion as well as the randomness and uncertainty associated with those estimates for a wide range of earthquake magnitudes, distances, and frequencies. Overall, the results of this study will be useful in performing seismic hazard evaluations and establishing seismic design standards for many years to come.

Organization

The results of this study are presented in five volumes. *Volume I: Methodology and Guidelines for Estimating Earthquake Ground Motion in Eastern North America*, representing the main body of the report, presents the model development and summarizes the key results and conclusions of the study. *Volume II: Appendices for Ground Motion Estimation*, presents the appendices to Sections 2 to 7 of Volume I, and consists primarily of data and details of analyses used to develop the engineering ground motion model and geotechnical guidelines. *Volume III: Appendices for Field Investigations*, and *Volume IV: Appendices for Laboratory Investigations*, present the details of field and laboratory investigations of reference sites; Section 8 of Volume 1 constitutes a summary of these appendices. *Volume V: Seismic Source Effects*, presents separately (as a licensed report) the analyses of the seismic source performed for input to the engineering ground motion model; a summary of this volume is given as Section 4 of Volume 1.

APPENDIX 8.B.1
DYNAMIC PROPERTIES OF UNDISTURBED SOIL SAMPLES FROM TREASURE ISLAND, CALIFORNIA

CONTENTS

APPENDIX 8.B.1
DYNAMIC PROPERTIES OF UNDISTURBED SOIL SAMPLES FROM TREASURE ISLAND, CALIFORNIA

8.B.1.1 Introduction

An investigation of the dynamic properties in shear of undistributed soil samples from Treasure Island, California was conducted. This work was part of an Earthquake Ground Motion Project sponsored by the Electric Power Research Institute (EPRI) and the U.S. Department of Energy (DOE). The dynamic laboratory study was also initiated as part of an earlier EPRI study, No. 3014-4. The soil samples were obtained in November, 1990. The samples were sealed in steel Shelby tubes and transported by automobile to the University of Texas at Austin in January, 1991. Dynamic laboratory testing of the undisturbed samples occurred between February, 1991 and April, 1992.

A total of eight samples was tested. The samples were obtained from depths ranging from 17.5 ft (5.7 m) to 232 ft (70.7 m). Initial properties of the samples are listed in Table 8.B.1-1. The samples range from a silty sand (SM) to a fat clay (CH). Grain size distribution curves for three of the nonplastic samples are given in Figure 8.B.1-1.

To minimize disturbance effects, each sample was extruded from the 3-in. (7.6 cm) diameter sampling tube and hand trimmed to the final specimen dimensions. The dimensions were nominally either 2 in. (5.1 cm) in diameter and 4 in. (10.2 cm) in height or 1.5 in. (3.8 cm) in diameter and 3 in. (7.6 cm) in height. The smaller of the two specimen sizes was used to obtain the larger dynamic strains in testing.

No significant problems were encountered in preparation and testing of the undisturbed clay specimens. However, for the sand specimens, serious problems were encountered during extrusion of the sample due to friction between the soil and inner wall of the Shelby tube. To overcome this problem, both end caps were removed and the sample was allowed free drainage for one day. A four-wheel pipe cutter was then used to cut the Shelby tube into approximately 6 in. segments. These segments were wrapped and placed in a freezer for about one day. No significant expansion of the sample was observed due to freezing. Extrusion and trimmings of the frozen sample was carried out before the sample started to melt. The sample extruded very nicely in the semi-frozen state.

8.B.1.2 Dynamic Laboratory Tests

Resonant column and torsional shear (RCTS) equipment was used to investigate the dynamic characteristics of the intact Treasure Island samples. This equipment is described in detail in Appendix 8.B.1.A. The dynamic characteristics of concern are the shear modulus, G, and the material damping ratio in shear, 8.B.1.D. These parameters were evaluated to determine the influence on them of the following variables:

1. magnitude of isotropic state of stress. Four to seven isotropic pressures were used which ranged from below to above the estimated in situ mean effective stress.
2. time of confinement at each isotropic state of stress. Confinement times at each pressure ranged from 1 to about 3 days.
3. shearing strain amplitude. Strains ranged from the small-strain range, less than 0.001%, to rather large strain amplitudes, strains slightly above 0.2%.
4. numbers of cycles of loading. One to ten cycles of loading were used in the torsional shear test followed by 500 to 1000 cycles in the resonant column test.
5. excitation frequency. Frequencies ranging from 0.1 Hz to about 10 Hz were used in the torsional shear test while the frequency associated with resonance in the resonant column test varied with soil stiffness and ranged from between 20 Hz to about 130 Hz.

Table 8.B.1-1
Initial Properties of Samples Tested From Treasure Island Site

Sample Number	Depth ft (m)	Soil Type (Unified Soil Classification)	LL %	PI %	D_{10} mm	D_{30} mm	D_{60} mm	R_{200}[1] %	Water Content %	Total Unit Weight pcf(g/cm^3)	Void Ratio e	Dia. cm	Height cm	Specific Gravity Gs[2]	Degree of Saturation %
T1	17.5 (5.3)	Silty Sand (SM)	non-plastic		-	-	0.11	66	19.9	120 (1.92)	0.69	5.03	10.07	2.65	76
T2	30 (9.1)	Sand with Silt (SP-SM)	non-plastic		0.10	0.18	0.26	91	21.3	120 (1.92)	0.67	3.78	7.58	2.65	84
T3	60 (18.3)	Fat Clay (CH)	51	26	-	-	-	1	50.2	108 (1.73)	1.34	5.11	10.10	2.70	100[3]
T4	90 (27.4)	Lean Clay (CL)	42	19	-	-	-	3	41.9	113 (1.81)	1.10	5.06	10.15	2.70	98
T5	110 (33.5)	Sand with Silt (SP-SM)	non-plastic		0.13	0..25	0.40	95	21.8	114 (1.83)	0.76	3.75	7.61	2.65	76
T6	130 (39.6)	Sandy Lean Clay (CL)	37	23	-	-	-	38	37	114 (1.83)	1.02	5.13	10.12	2.70	98
T7	170 (51.8)	Sandy Lean Clay (CL)	34	19	-	-	-	31	20.7	128 (2.05)	0.58	5.06	10.17	2.70	96
T8	232 (70.7)	Lean Clay (CL)	48	30	-	-	-	- -	33.3	115 (1.84)	0.95	5.11	9.84	2.70	95

1. R_{200} = Percent of soil sample by weight remaining on #200 sieve
2. Specific Gravity was assumed.
3. Degree of saturation slightly exceeds 100 %.

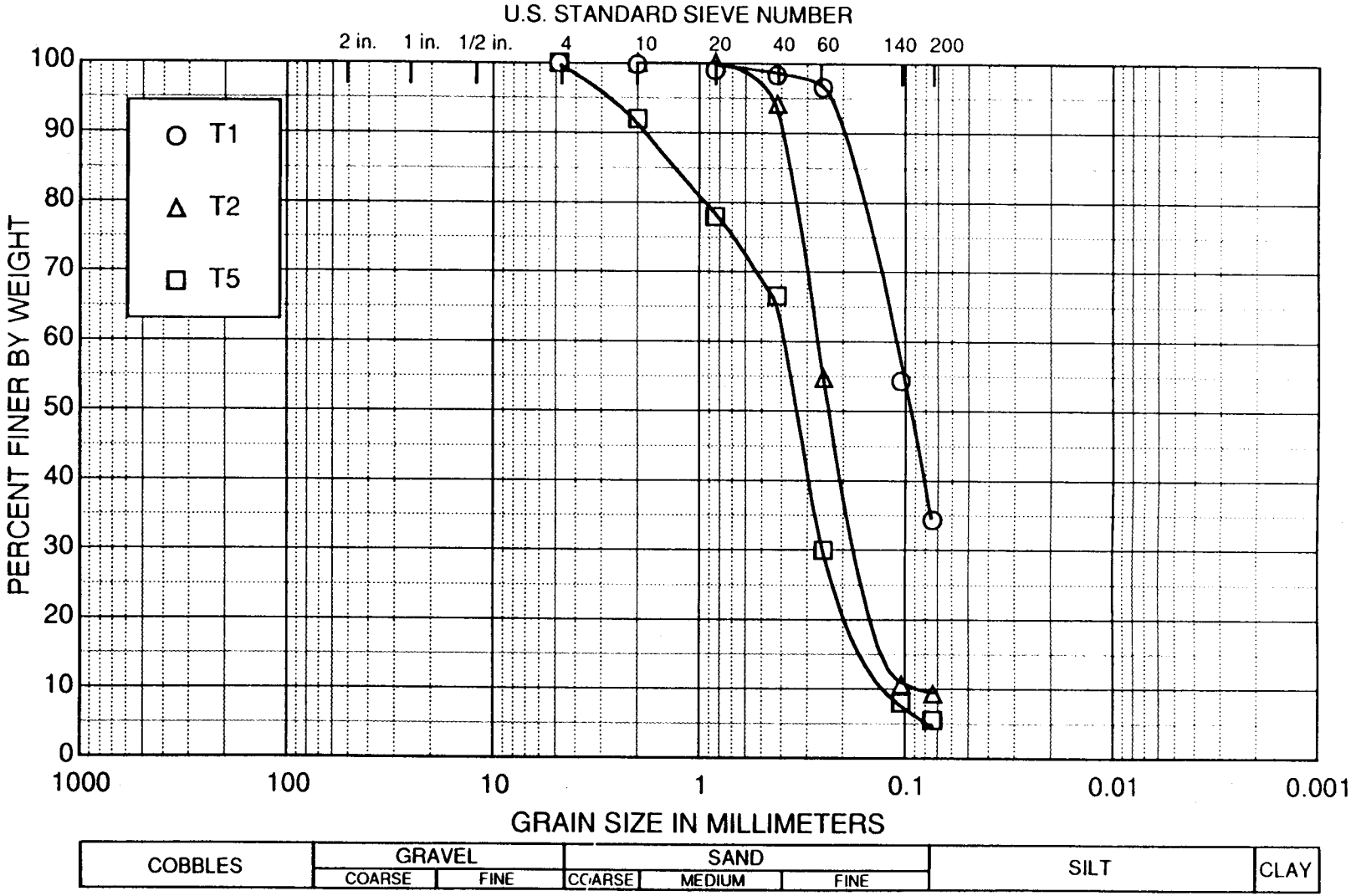

Figure 8.B.1-1
Gradation Curves for Treasure Island Samples

8.B.1.2.1 Testing Program

Before dynamic testing was started, the in situ mean effective stress, σ_m', had to be estimated. This was done at the Treasure Island site by assuming the water table is at a depth of 4 ft (1.2 m), the total unit weight of the soil averages 120 pcf (18.8 kN/m^3), the soil is saturated throughout the profile, and the effective coefficient of earth pressure at rest, K_o', is 0.5. The resulting values of σ_m' for each sample are given in Table 8.B.1-2.

Once σ_m' was estimated, the range in confining pressures over which G and D would be evaluated was determined. Typically, isotropic confining pressures on the order of $0.25\sigma_m'$, $0.5\sigma_m'$, σ_m', $2\sigma_m'$ and $4\sigma_m'$ were selected. Low-amplitude resonant column testing was performed at each confining pressure to determine the influence of time and confining pressure on the small-strain shear modulus, G_{max}, and small-strain material damping ratio, D_{min}. Low-amplitude dynamic tests are defined as those tests in which the resonant amplitude did not exceed 0.001% and typically was considerably below that level.

A summary of all confining pressures at which low-amplitude resonant column tests were performed is given in Table 8.B.1-2. At the estimated in situ mean effective stress, high-amplitude dynamic and cyclic testing was also conducted. This testing is defined as any tests in which the peak shearing strain exceeds 0.001%. This testing was composed of two series of tests. The first involved cyclic torsional (TS) shear testing as illustrated in Figure 8.B.1-2. A complete set of torsional shear tests took about three hours to perform, was performed under drained conditions although no drainage was observed, and involved shearing strains, γ, from less than 0.001% to above 0.05%, depending on the soil stiffness. The majority of the measurements were performed at 0.5 Hz and are labeled as TS1 in Figure 8.B.1-2. However, two sets of TS tests, one at $\gamma \approx 0.001\%$ and one at $\gamma \approx 0.01\%$, were conducted to evaluate the effect of excitation frequency on G and D at those strain amplitudes. In these tests, (denoted as TS2 in Figure 8.B.1-2) one to four cycles of loading was applied at about five different frequencies ranging from 0.1 Hz to about 10 Hz.

After the TS tests were completed, confinement of the sample was continued at σ_m', and a series of high-amplitude resonant column (RC) tests was performed the next day. However, before high-amplitude RC testing commenced, small-strain RC tests were performed to determine if any changes in the soil skeleton had occurred from the TS tests. In essentially all cases, no changes in G_{max} or D_{min} from the TS tests were measured.

Once the small-strain datum was re-established after the TS tests, high-amplitude resonant column testing was conducted to evaluate the influence of strain amplitude on G and D. This series of tests is illustrated in Figure 8.B.1-3. A complete set of resonant column tests took about one hour to perform, was performed under drained conditions just as in the depending on the soil stiffness. In these tests, 500 to 1000 cycles of loading is required at case of the TS tests, and involved shearing strains from less than 0.001% to above 0.1%, each strain measurement.

Upon completion of the high-amplitude RC tests, low-amplitude RC tests were performed to determine if any changes in the soil skeleton had occurred from the high-amplitude tests. In some cases, changes occurred. At that point, confinement of the sample at σ_m' was continued until G_{max} and D_{min} returned to the values before the high-amplitude tests or the change in values was noted before going to the next stage of testing.

The confining pressure was then increased to about $2\sigma_m'$, and low-amplitude resonant column testing was performed for one to several days. For six of the samples, high-amplitude resonant column tests were again performed. Table 8.B.1-2 gives a summary of these tests. In most cases, the pressure was again doubled, and low-amplitude RC testing was repeated.

It should be noted that, in six cases (samples T2, T3, T4, T6, T7 and T8), high-amplitude RC tests were also performed at one or more confining pressures below σ_m'. This was carefully done with only intermediate strain levels generated so as not to disturb the sample before testing at σ_m'.

Table 8.B.1-2
Summary of Resonant Column and Torsional Shear Tests Performed for Treasure Island Samples

Sample Number	Depth ft (m)	Estimated In Situ Mean EffectiveStress, σ_m', psf	Isotropic Test Pressure, psf		
			Low-Amplitude Resonant Column Tests	High-Amplitude Resonant Column Tests	Torsional Shear Test
T1	17(5.3)	835	432, 864, 1728, 3456	864, 1728, 3456	864
T2	30(9.1)	1318	360 ,720, 1440, 2880, 5760	720, 1440, 2880	1440
T3	60(18.3)	2470	648, 1296, 2592, 5184, 10368	1296, 2592, 5184	2592
T4	90(28.5)	3334	576, 1008, 2016, 4032, 8064, 16128	1008, 2016, 4032, 8064, 16128	4032
T5	110(33.6)	4392	576, 1152, 2304, 4608, 9216, 18432, 36864	4608, 18432	4608, 18432
T6	130(39.6)	5158	1440, 2880, 6048, 12096	1440, 2880, 6048	6048
T7	170(51.8)	6694	1008, 2016, 4032, 8064, 16128, 32256	2016, 4032, 8064, 16128	8064
T8	232(44.5)	9075	1440, 2736, 5472, 10800, 21600, 43200	2736, 5472, 10800, 21600	10800

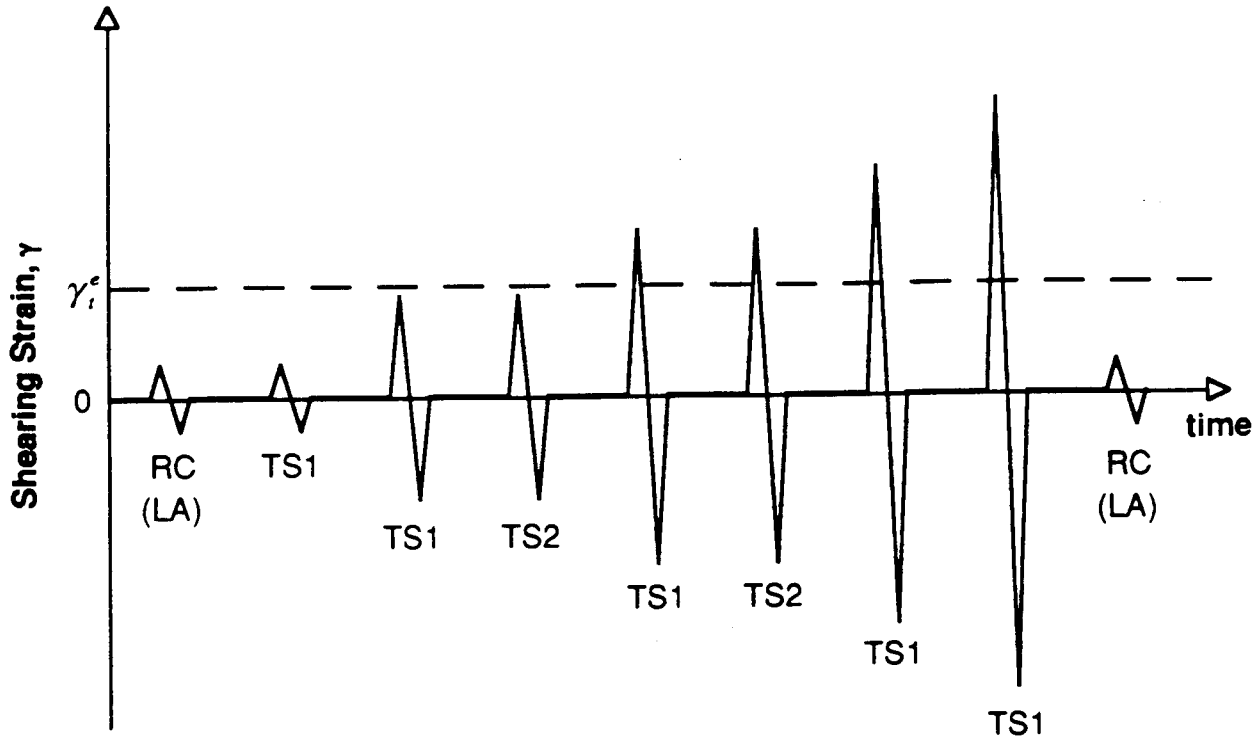

γ_t^e = elastic threshold strain; below γ_t^e, G is constant and equal to G_{max}

RC (LA) = resonant column test at low-amplitudes (strains < 0.001%)

TS1 = torsional shear test in which 1 to 10 cycles are applied at 0.5 Hz

TS2 = torsional shear test in which 4 cycles are applied at each of approximately 5 frequencies between 0.1 to 10 Hz

Figure 8.B.1-2
Testing procedure used in the torsional shear test to investigate the effects of strain amplitude, number of loading cycles, and excitation frequency of undisturbed Treasure Island samples.

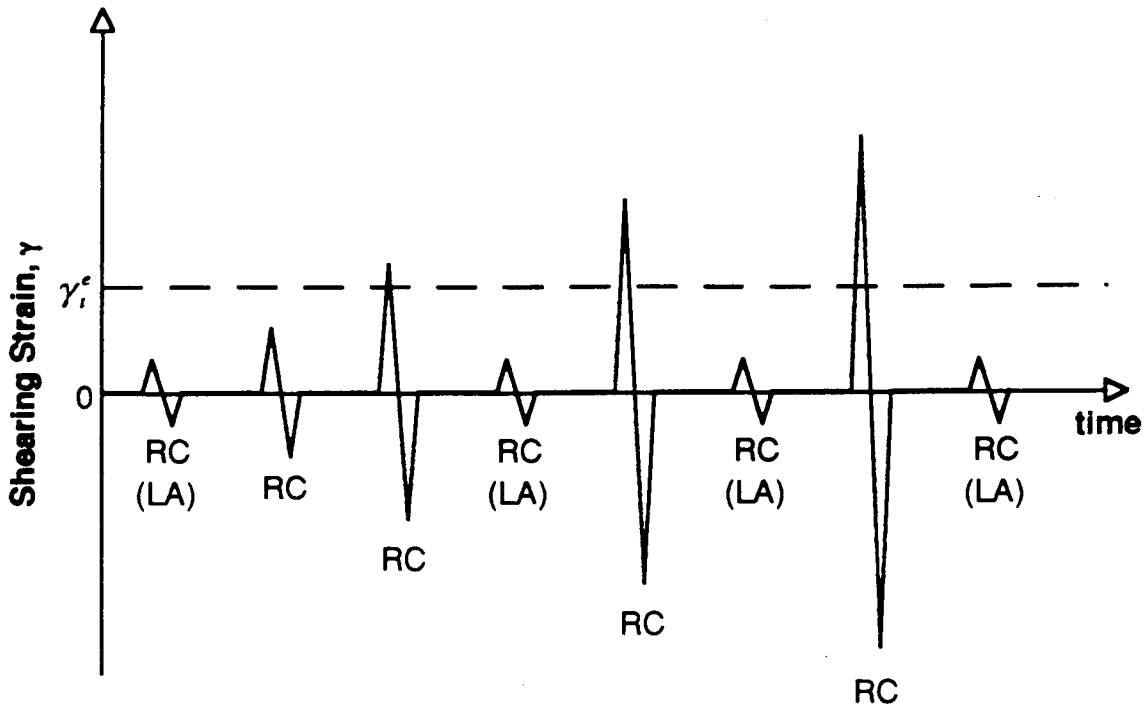

γ_t^e = elastic threshold strain; below γ_t^e, G is constant and equal to G_{max}

RC (LA) = resonant column test at low-amplitudes (strains < 0.001%)

RC = resonant column test in which 500 to 1000 cycles of loading is applied during each measurement

Figure 8.B.1-3
Testing procedure used in the resonant column test to investigate the effect of strain amplitude on G and D of the undisturbed Treasure Island samples.

8.B.1.2.2 Test Results

The results of the RC and TS tests are shown in Appendices 8.B.1.B through 8.B.1.I for the eight Treasure Island samples. Each appendix presents the results for one sample in the following general order (using Appendix 8.B.1.B as the example).

1. Figure 8.B.1.B-1 shows the influence of magnitude and duration of isotropic confining pressure on G_{max} as determined by RC tests.
2. Figure 8.B.1.B-2 shows the influence of magnitude and duration of isotropic confining pressure on D_{min} as determined by RC tests.
3. Figure 8.B.1.B-3 shows the change in void ratio of the sample with magnitude and duration of isotropic confining pressure.
4. Figure 8.B.1.B-4 shows the variation in G_{max} at a confinement time of 1000 minute with effective confining pressure from the RC tests.
5. Figure 8.B.1.B-5 shows the variation in D_{min} at a confinement time of 1000 minutes with effective confining pressure from the RC tests.
6. Figure 8.B.1.B-6 shows the variation in void ratio of the sample at a confinement time of 1000 minutes with effective confinement pressure.
7. Figure 8.B.1.B-7 shows the variation in G with γ at σ_m' from the high-amplitude RC and TS tests.
8. Figure 8.B.1.B-8 shows the variation in G/G_{max} will log γ at σ_m' from the high-amplitude RC and TS tests.
9. Figure 8.B.1.B-9 shows the variation in G with log γ at all tests pressures where high-amplitude RC tests were performed.
10. Figure 8.B.1.B-10 is the normalized (G/G_{max}) version of Figure 8.B.1.B-9.
11. Figures 8.B.1.B-11 through 8.B.1.B-14 are the damping ratio curves which are the companions to the modulus curves given in Figures 8.B.1.B-7 through 8.B.1.B-10.
12. Figure 8.B.1.B-15 shows the effect of excitation frequency on G at $\gamma \sim 0.001\%$ and $\gamma \sim 0.01\%$.
13. Figure 8.B.1.B-16 shows the effect of excitation frequency on D at $\gamma \sim 0.001\%$ and $\gamma \sim 0.01\%$.

8.B.1.3 Discussion of Results

The variation in G_{max} with σ_o' for the eight undisturbed samples tested in this study at the estimated σ_m' and above is shown in Figure 8.B.1-4. The samples should be normally consolidated samples in the pressure range shown if K_o' is reasonably close to 0.5. In fact, results from six of the eight samples show the proper trend. Samples T7 and T8 exhibit the behavior of soils which are still overconsolidated at part or all of the pressures shown. These trends are more easily seen by separating the results into sandy samples and fine-grain samples as shown in Figures 8.B.1-5 and 8.B.1-6, respectively. The trends are further improved by accounting for void ratio variations as shown in Figures 8.B.1-7 and 8.B.1-8. The results from the three sandy samples can be fit with the Hardin (1978) equation as shown in Figure 8.B.1-7 while the Hardin equation also fits the clayey samples as shown in Figure 8.B.1-8. In Figure 8.B.1-8, the moduli for samples T7 and T8 were deleted because they appeared to be overconsolidated at most of the test pressures.

The same set of comparisons for the variation in small-strain material damping ratio, D_{min}, with σ_o' is presented in Figures 8.B.1-9, -10 and -11. In this case, the results fall in a rather narrow range. But D_{min} exhibits more scatter than in the case with G_{max}. The values of D_{min} are also quite low, all less than 2% (or $Q > 25$).

The variation in normalized modulus, G/G_{max}, with log γ for all samples tested in this study at the estimated in situ mean effective stress, σ_m', is presented in Figure 8.B.1-12 for the RC tests, in Figure 8.B.1-13 for the first cycle in the TS test, and in Figure 8.B.1-14 for the combined results. In each case, the results for all samples form a wide band which can be further divided by solid types as follows. The results for the sandy samples are shown in Figures 8.B.1-15 through 8.B.1-17 and for the fine-grained samples in Figures 8.B.1-18 through 8.B.1-20. The sandy soils form a band close to the upper range proposed by Seed and Idriss (1970) for sands. The fine-grained soils form a band considerably above the

upper bound proposed by Seed and Idriss. The results from both the RC and TS tests are compared in Figures 8.B.1-17 and 8.B.1-20 for each soil type. Both types of tests give essentially the same results. It should be noted at this point that all samples are unsaturated and hence any development in pore water pressure due to cyclic loading is significantly inhibited. Therefore, values of G determined at strains above amplitudes on the order of 0.05% do not reflect any reduction which would occur if pore pressures were generated.

Similar results for the variation in material damping ratio with strain amplitude are shown in the remaining figures. Figure 8.B.1-27 shows the variation in D with log γ as determined by RC tests of the sandy soils. The results fall in a rather narrow band which is closest to the lower bound proposed by Seed and Idriss (1970) for sands. Figure 8.B.1-28 shows the same results determined in the first cycle in the TS test. In this case, material damping values are slightly higher in the TS tests than those determined in the RC test at all strains above about 0.003%. This behavior is typical of sandy material with few fines (Kim, 1991). Both results are compared in Figure 8.B.1-29 and expanded versions of the comparisons are presented in Figures 8.B.1-30 through 8.B.1-32.

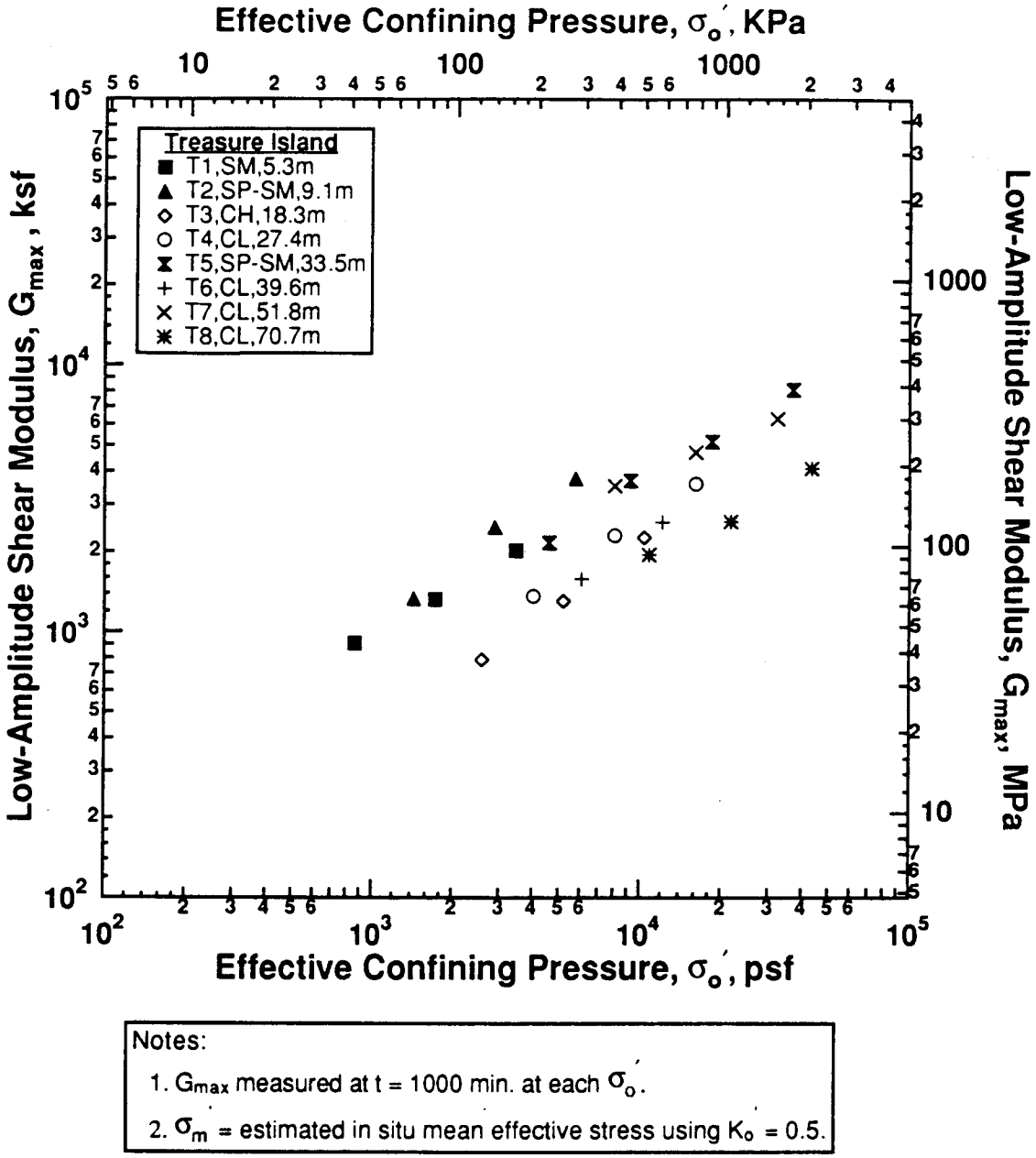

Figure 8.B.1-4
Variation in low-amplitude shear modulus with effective confining pressure from resonant column tests at $\sigma_o' \geq \sigma_m'$ of undisturbed samples from Treasure Island.

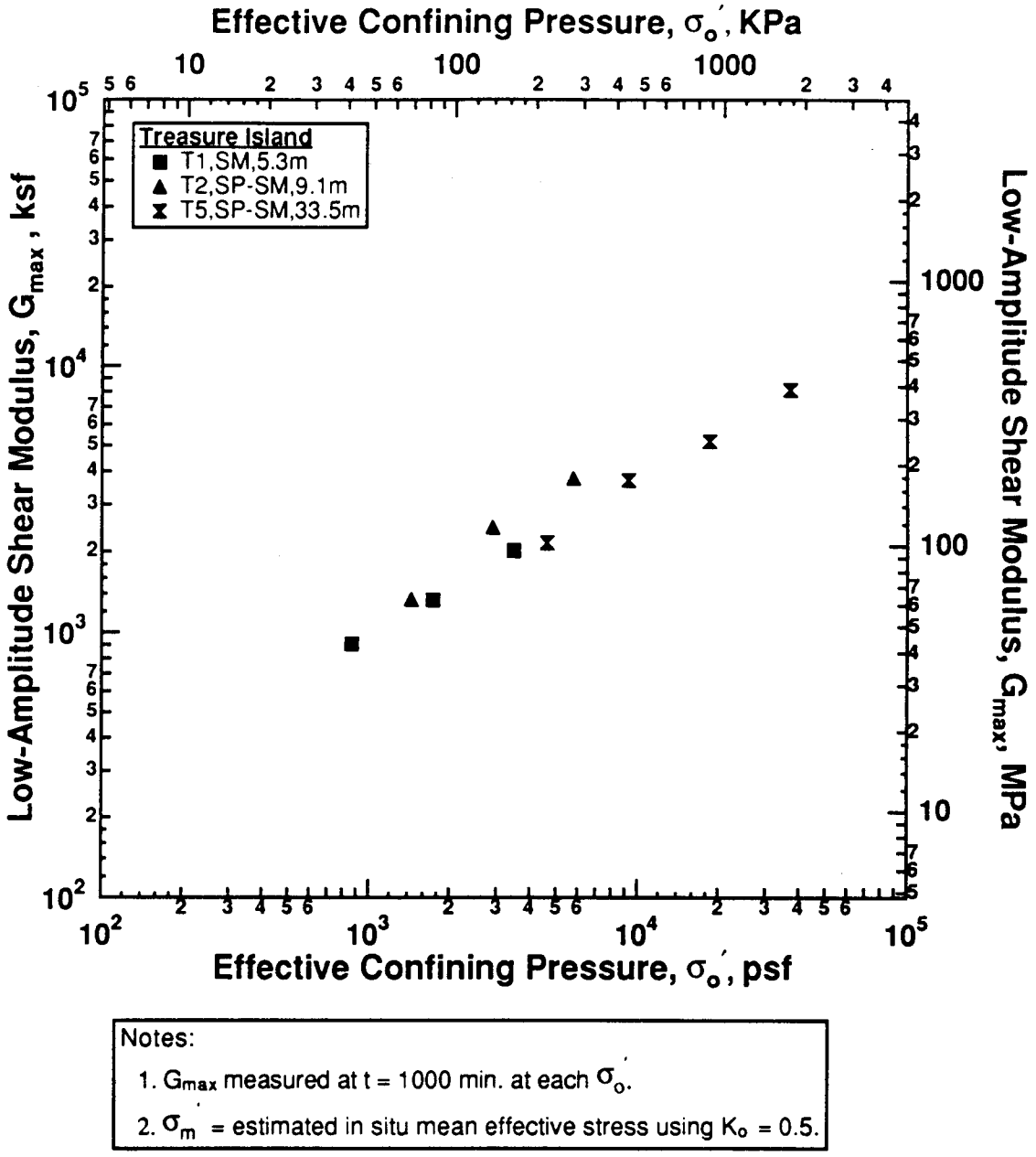

Figure 8.B.1-5
Variation in low-amplitude shear modulus with effective confining pressure from resonant column tests at $\sigma_o' \geq \sigma_m'$ of undisturbed samples from Treasure Island.

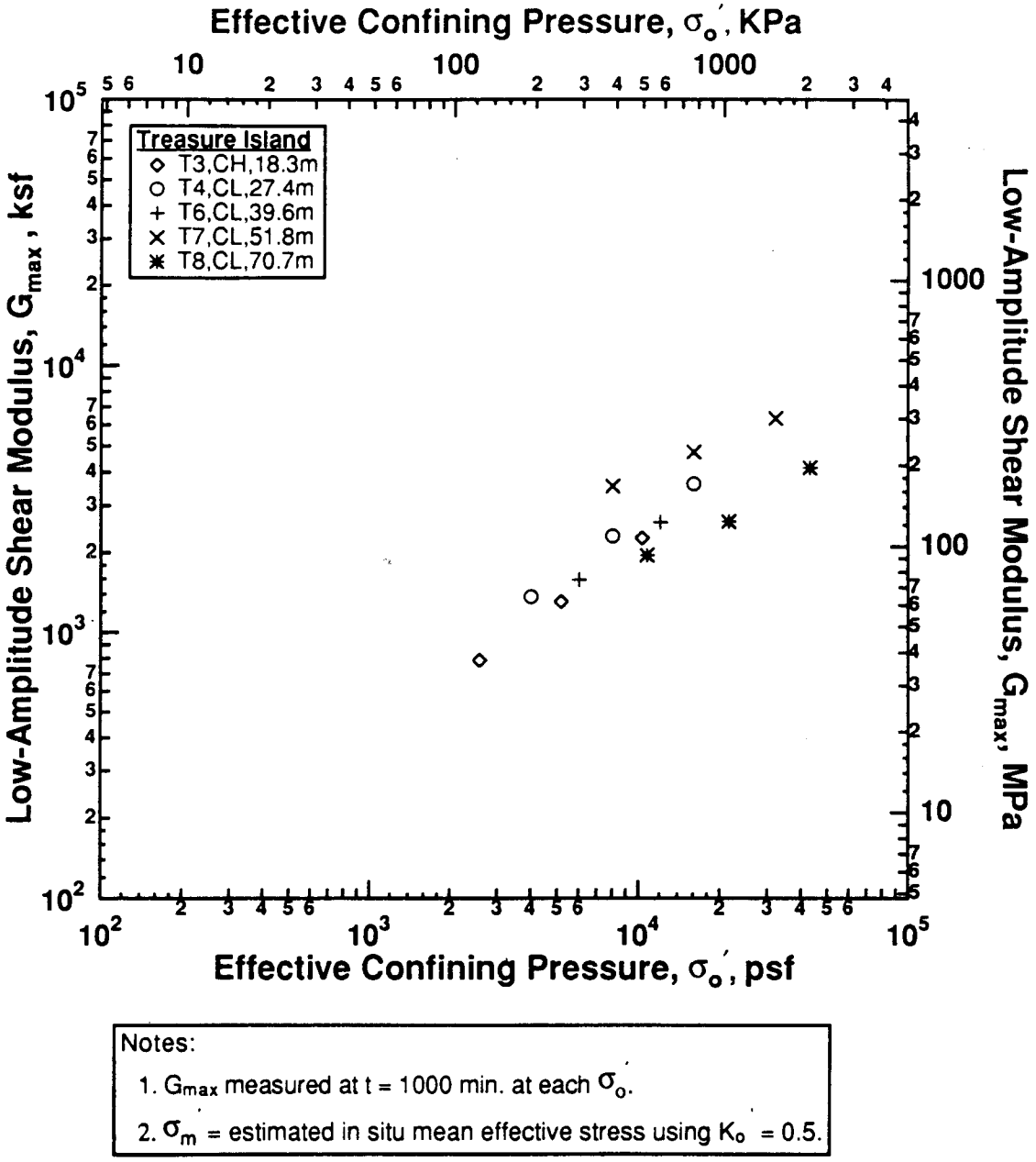

Figure 8.B.1-6
Variation in low-amplitude shear modulus with effective confining pressure from resonant column tests at $\sigma_o' \geq \sigma_m'$ of undisturbed fine-grained samples from Treasure Island.

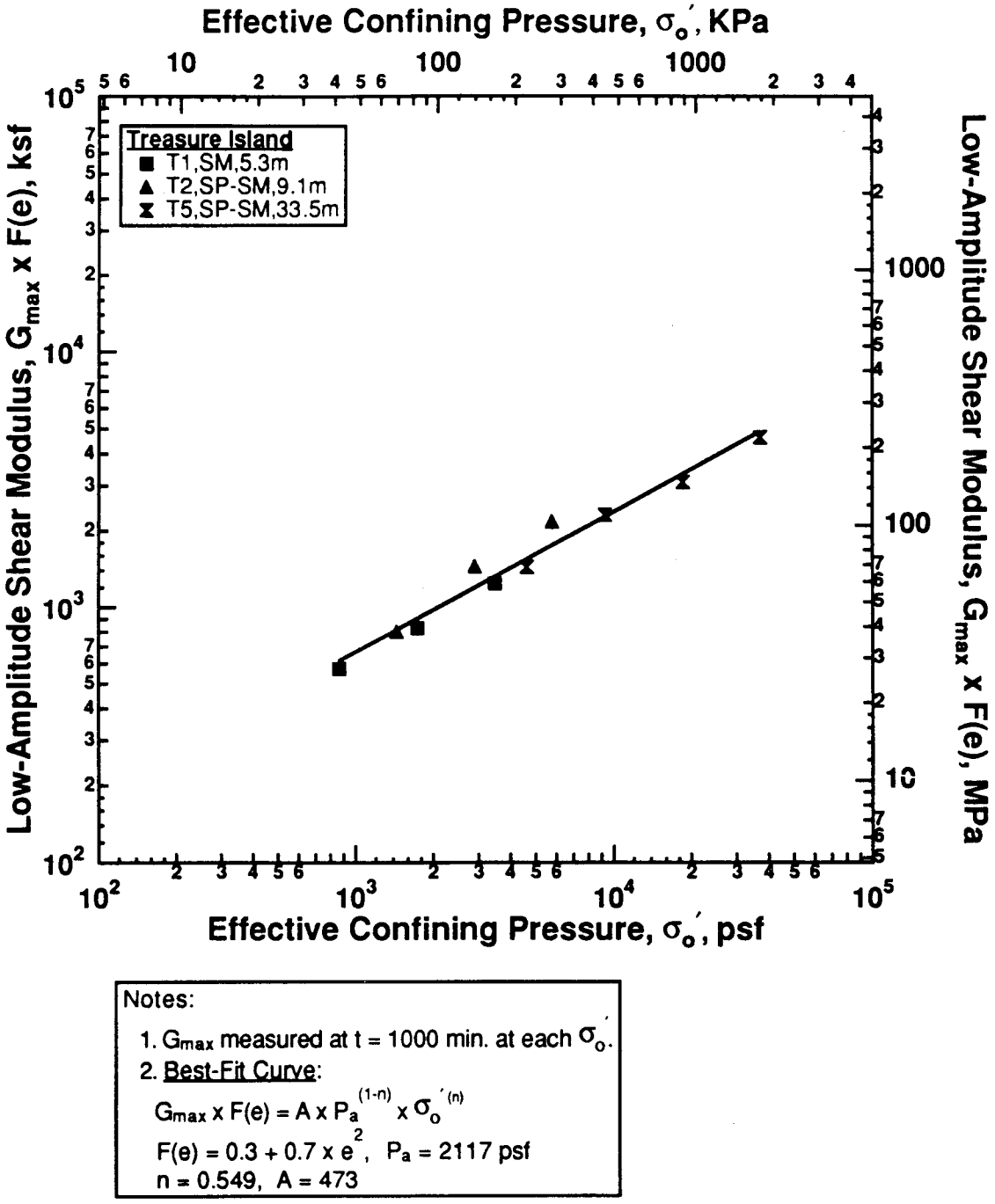

Figure 8.B.1-7
Best-fit curve to log $G_{max} \times F(e)$ – log σ_o' relationship from resonant column tests at $\sigma_o' \geq \sigma_m'$ of undisturbed sandy samples from Treasure Island.

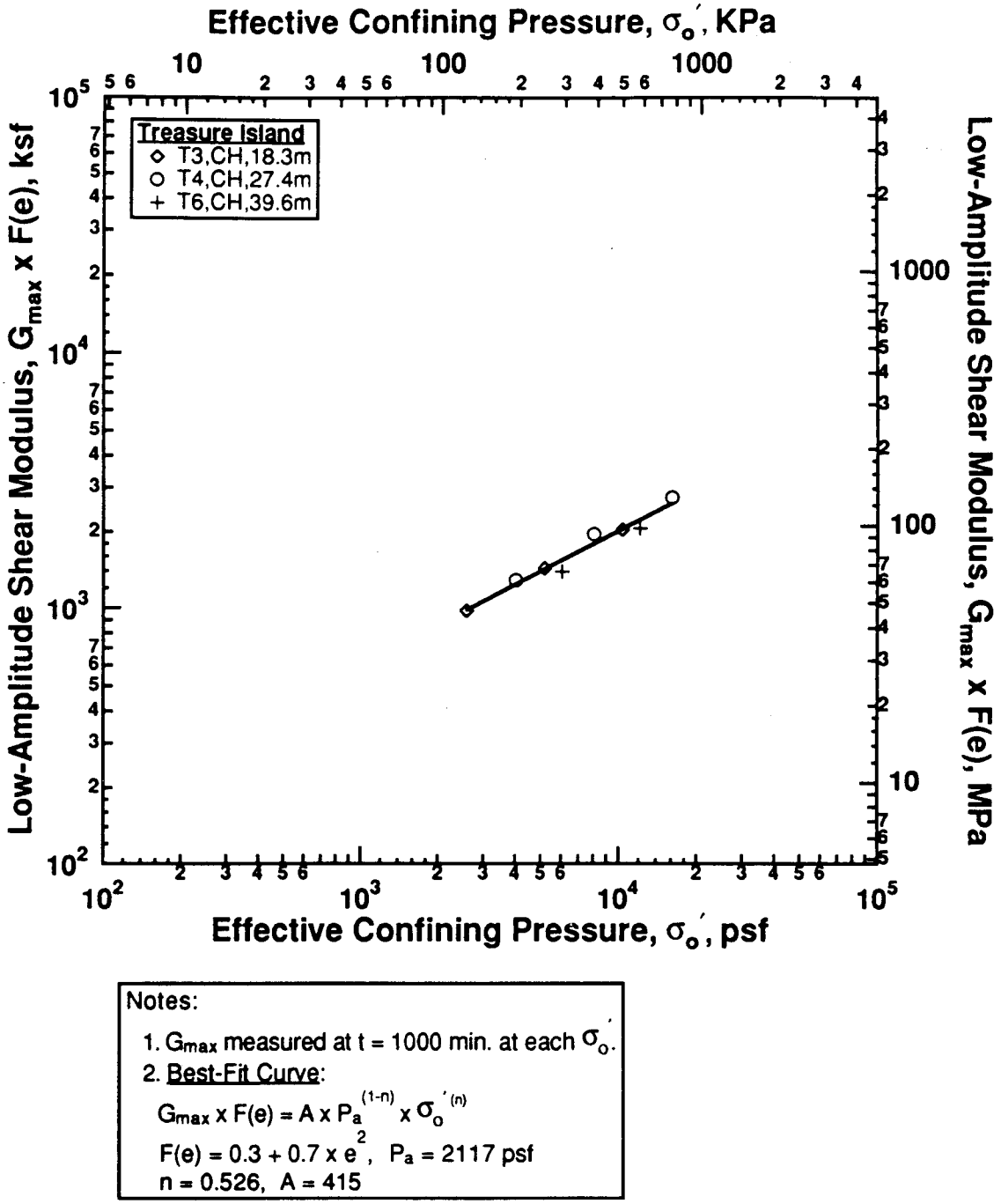

Figure 8.B.1-8
Best-fit curve to log $G_{max} \times F(e)$ – log σ_o' relationship from resonant column tests at $\sigma_o' \geq \sigma_m'$ of undisturbed fine-grained samples from Treasure Island.

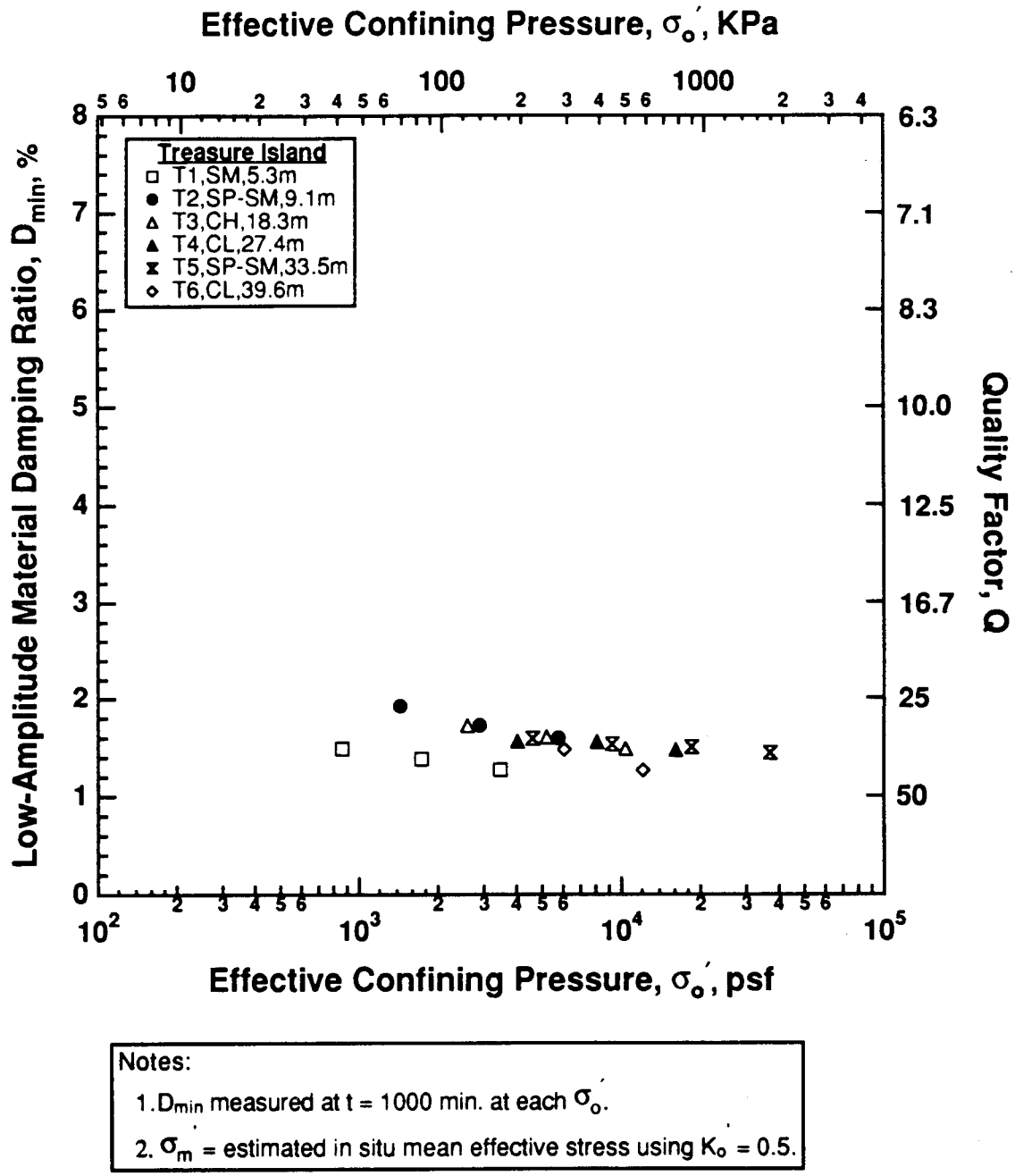

Figure 8.B.1-9
Variation in low-amplitude material damping ratio with effective confining pressure from resonant column tests at $\sigma_o' \geq \sigma_m'$ of undisturbed samples from Treasure Island.

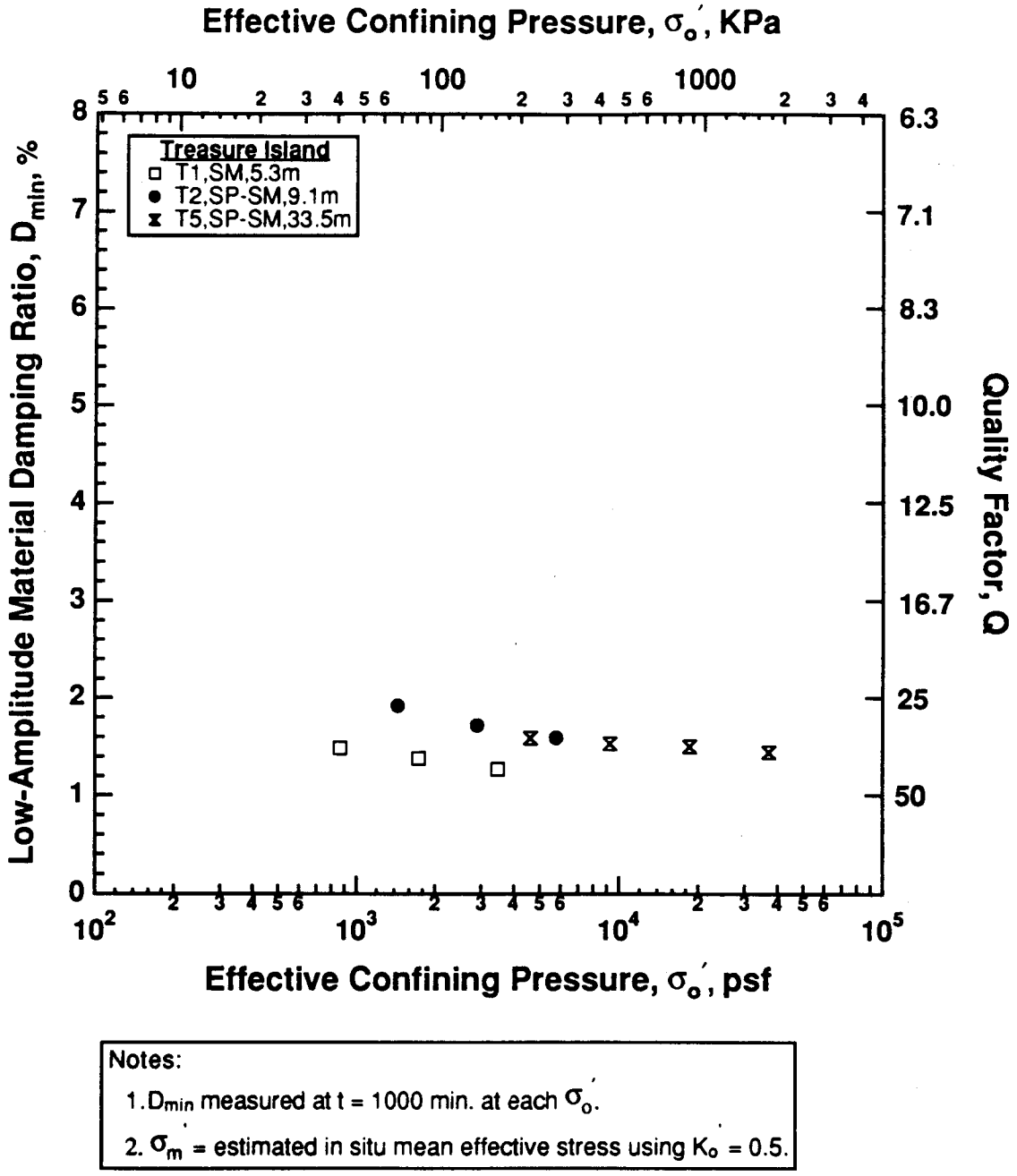

Figure 8.B.1-10
Variation in low-amplitude material damping ratio with effective confining pressure from resonant column tests at $\sigma_o' \geq \sigma_m'$ of undisturbed sandy samples from Treasure Island.

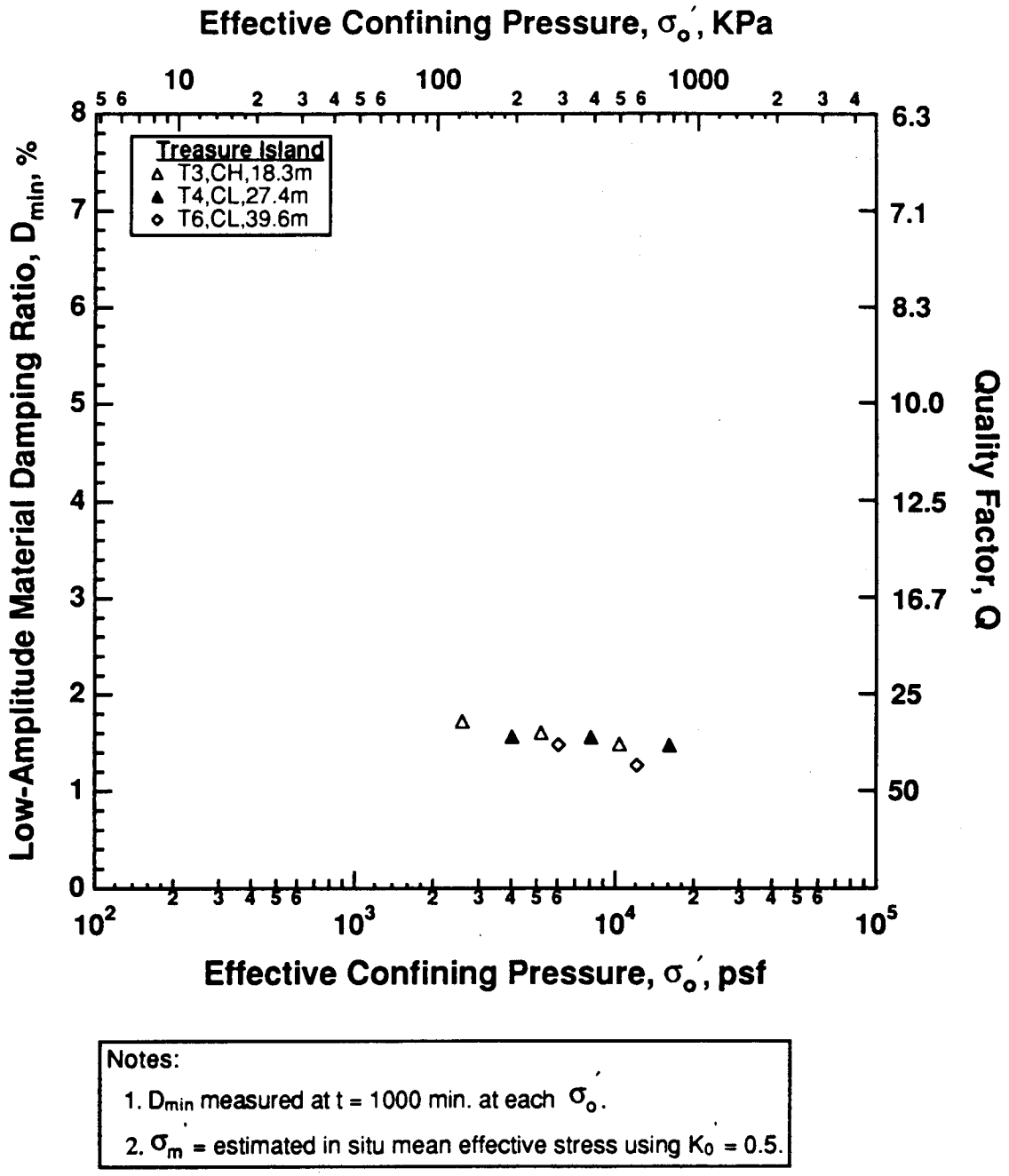

Figure 8.B.1-11
Variation in low-amplitude material damping ratio with effective confining pressure from resonant column tests at $\sigma_o' \geq \sigma_m'$ of undisturbed fine-grained samples from Treasure Island.

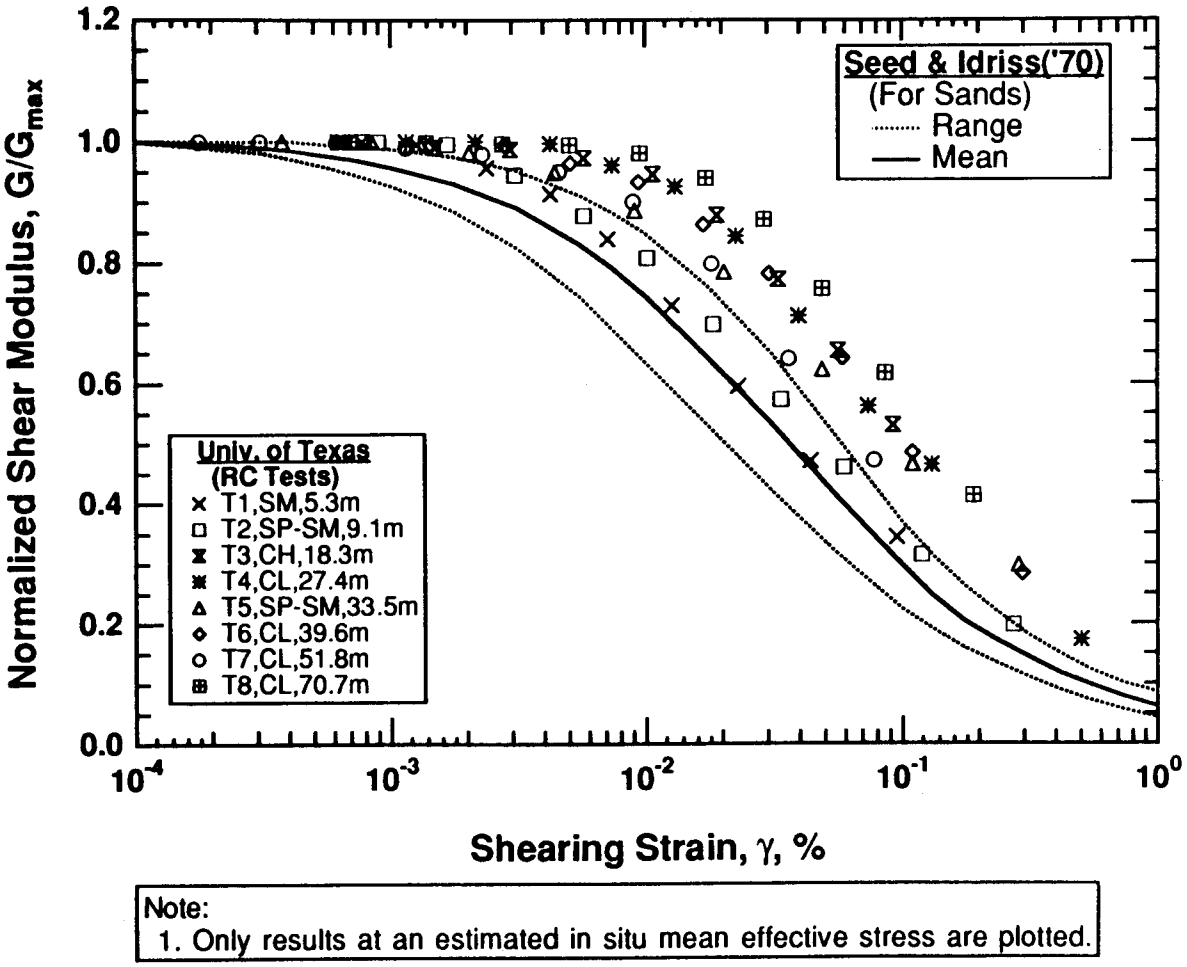

Figure 8.B.1-12
Variation in normalized shear modulus with shearing strain from resonant column tests of undisturbed samples from Treasure Island.

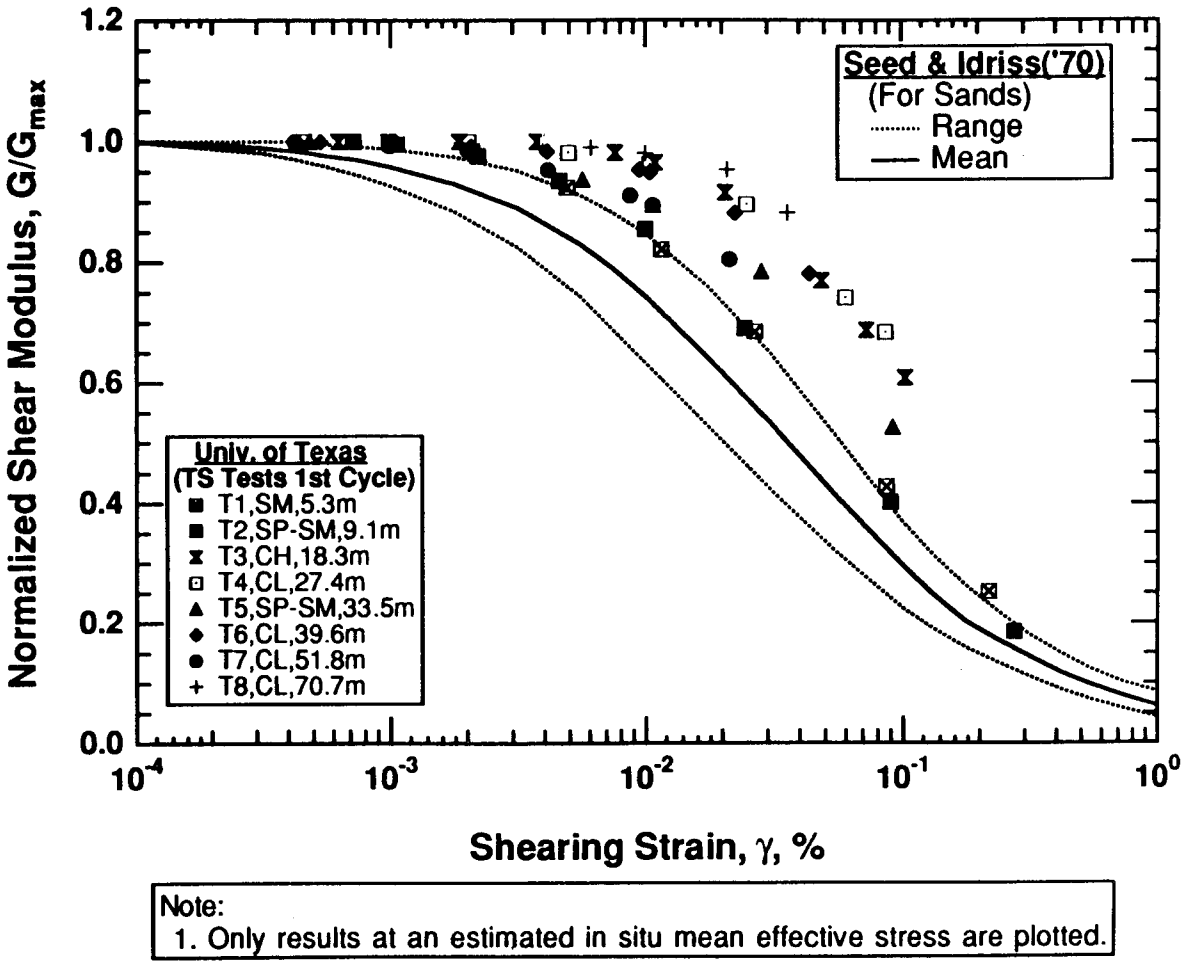

Figure 8.B.1-13
Variation in normalized shear modulus with shearing strain from torsional shear tests of undisturbed samples from Treasure Island.

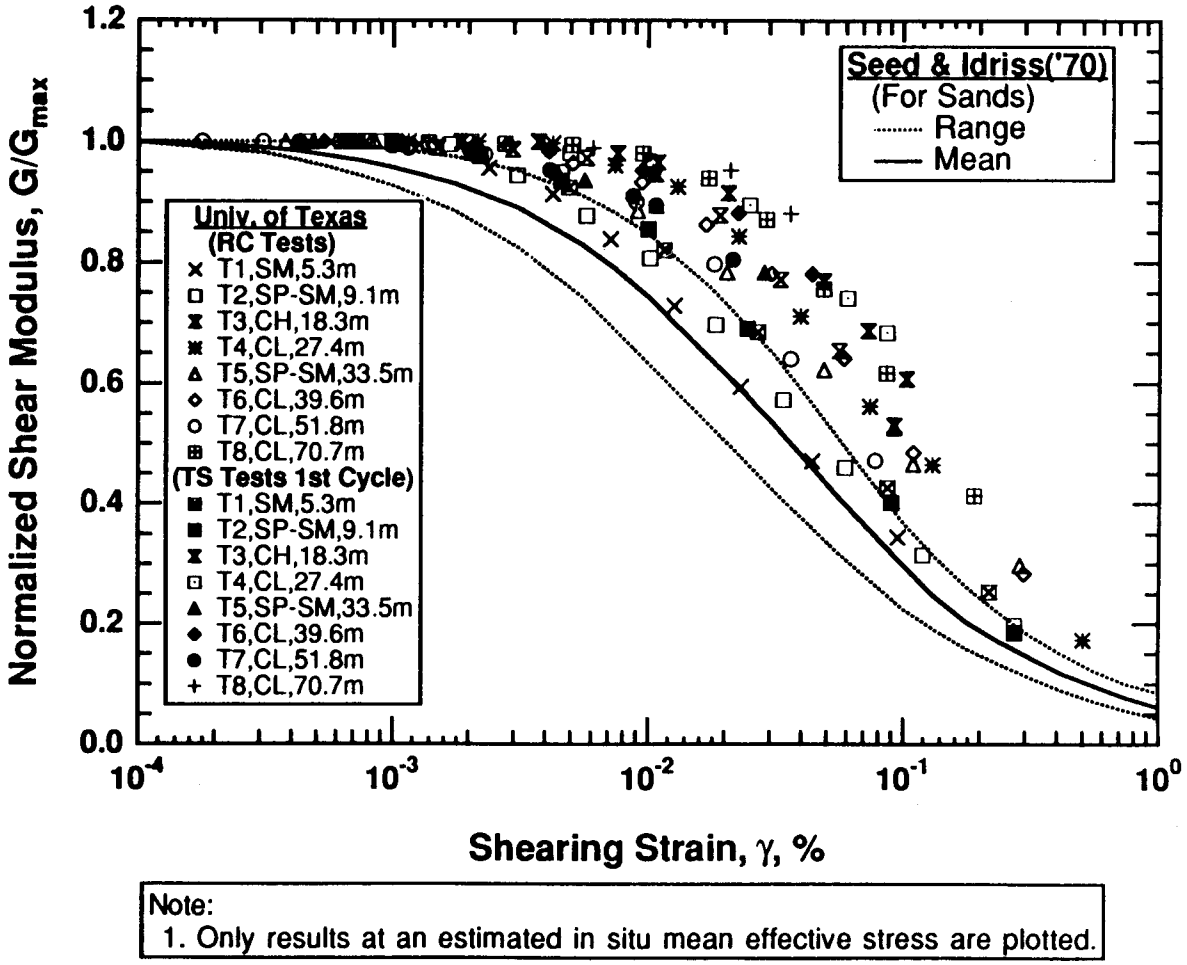

Figure 8.B.1-14
Variation in normalized shear modulus with shearing strain from resonant column and torsional shear tests of undisturbed samples from Treasure Island.

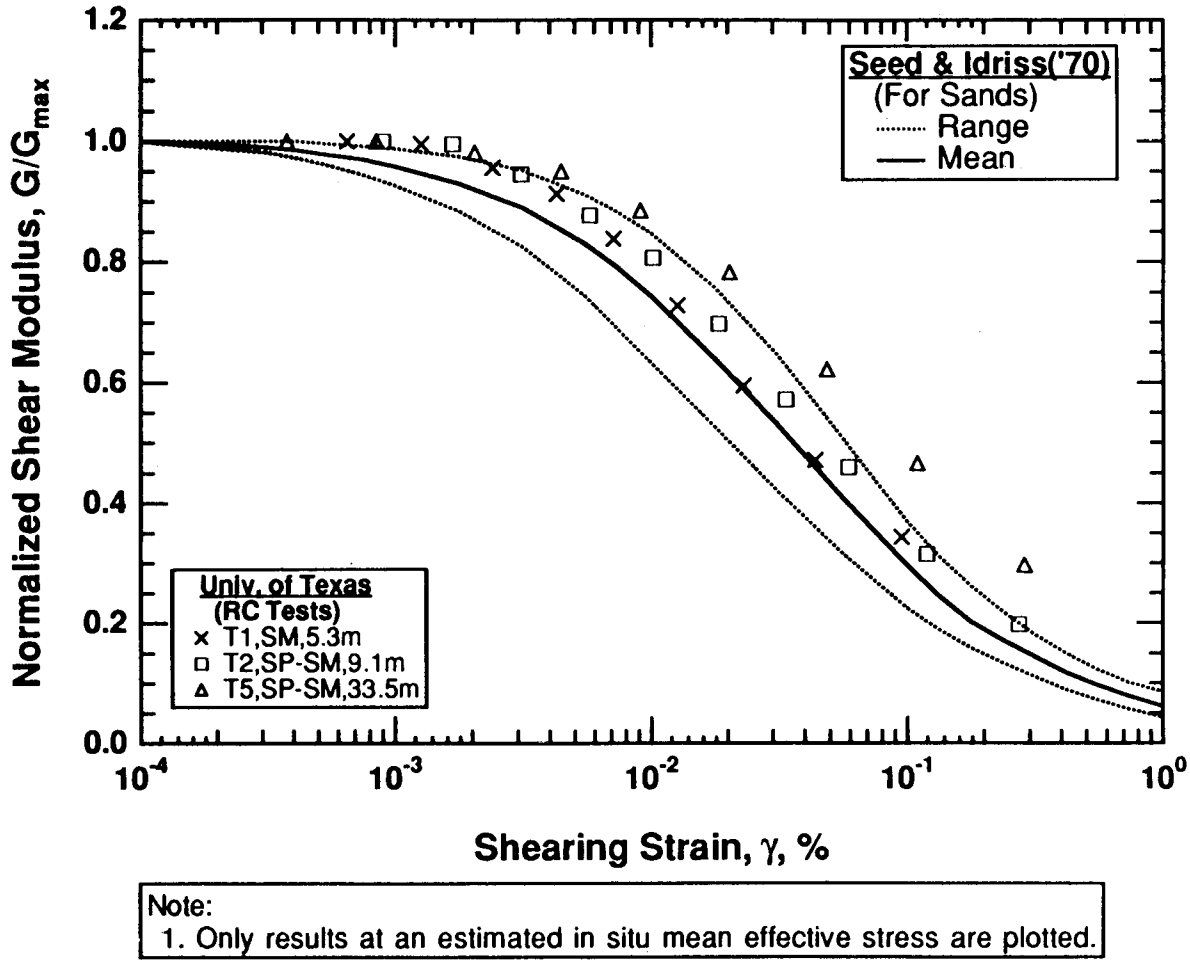

Figure 8.B.1-15
Variation in normalized shear modulus with shearing strain from resonant column tests of undisturbed sandy samples from Treasure Island.

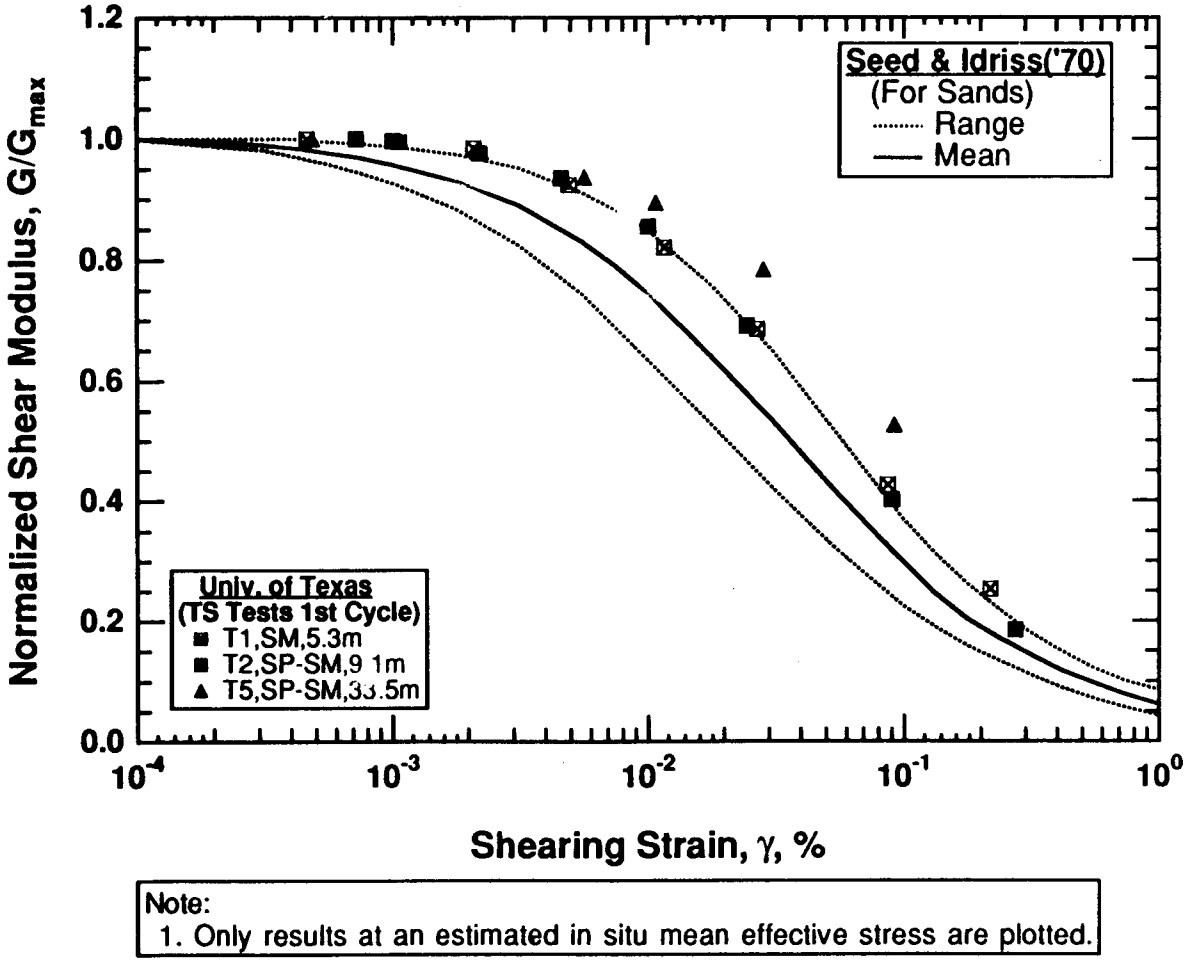

Figure 8.B.1-16
Variation in normalized shear modulus with shearing strain from torsional shear tests of undisturbed sandy samples from Treasure Island.

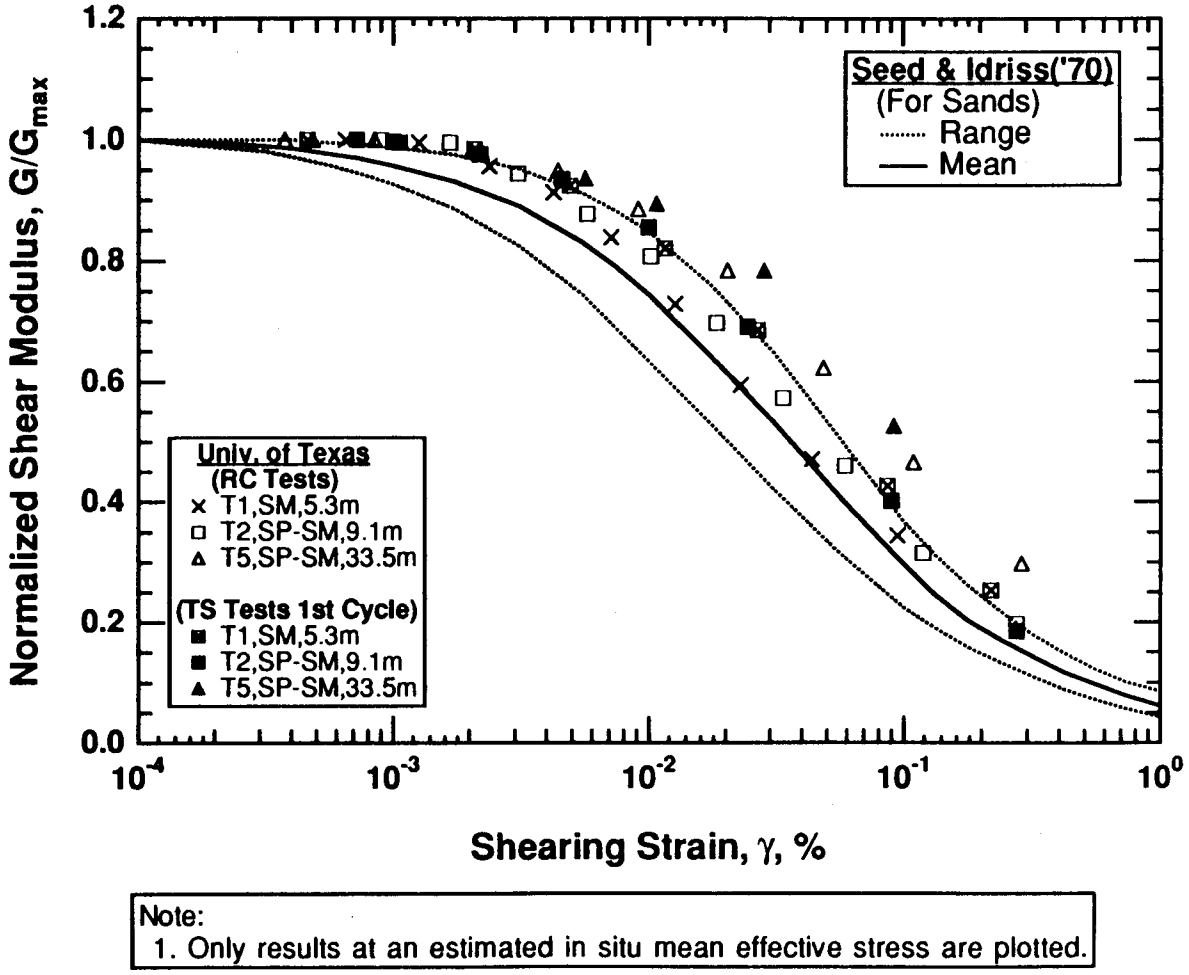

Figure 8.B.1-17
Variation in normalized shear modulus with shearing strain from resonant column and torsional shear tests of undisturbed sandy samples from Treasure Island.

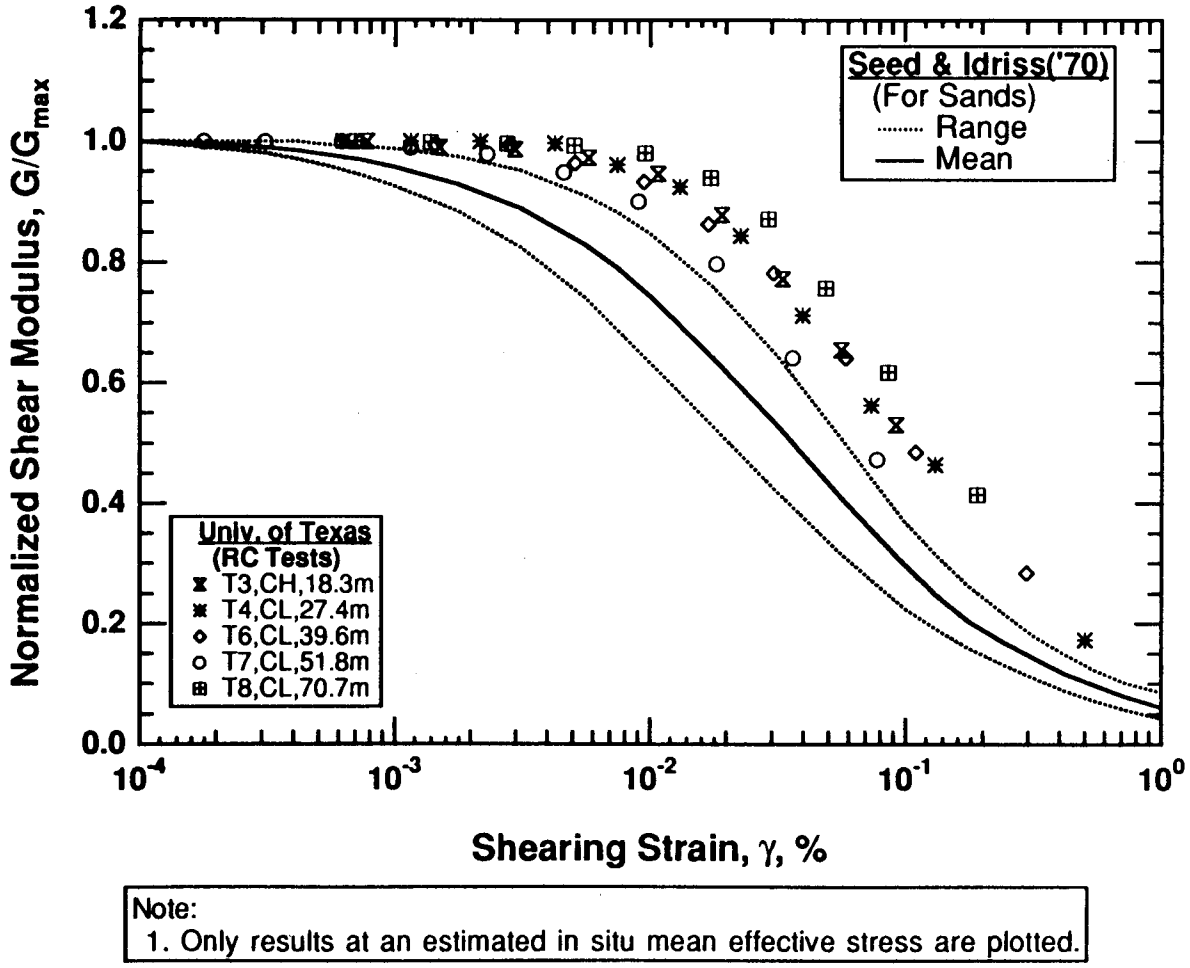

Figure 8.B.1-18
Variation in normalized shear modulus with shearing strain from resonant column tests of undisturbed fine-grained samples from Treasure Island.

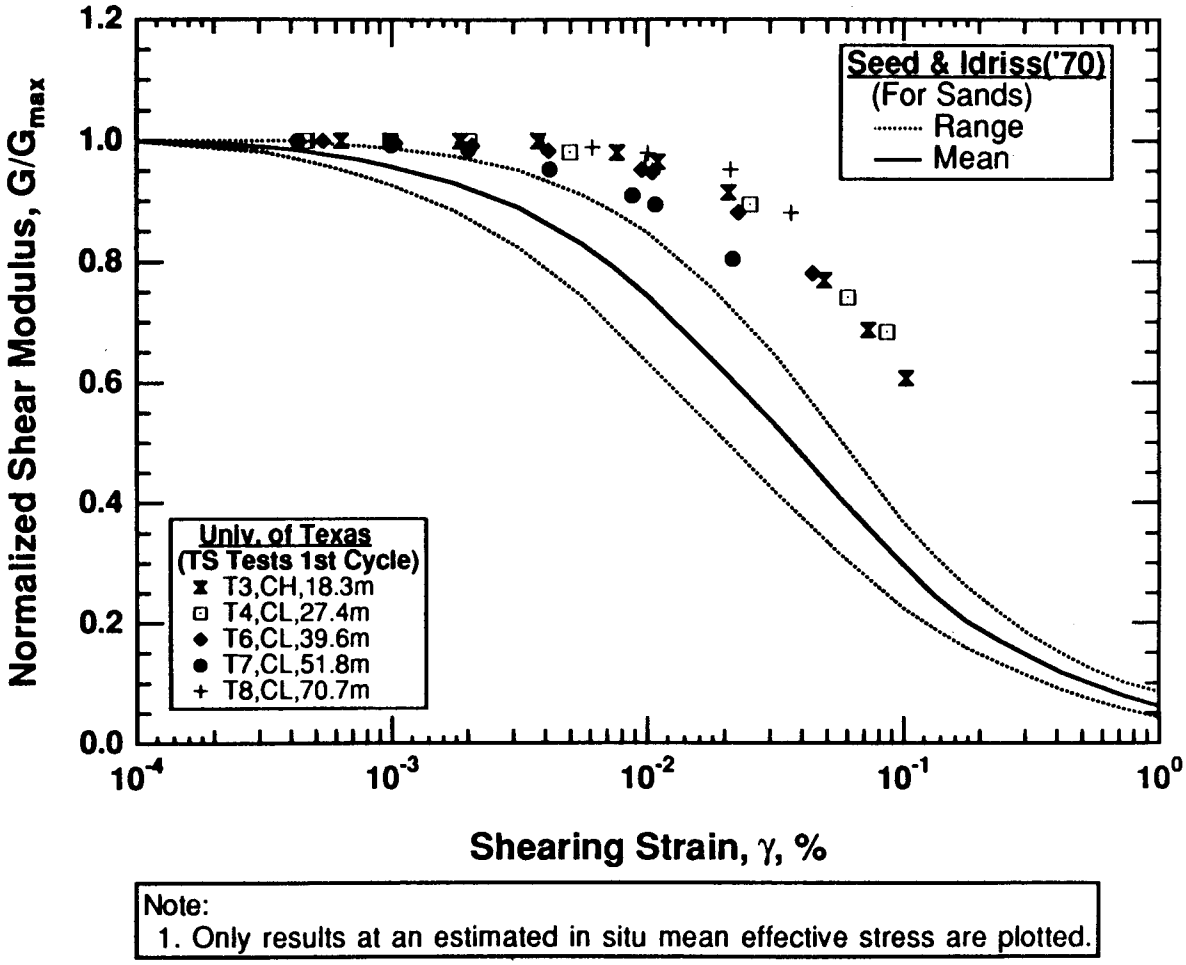

Figure 8.B.1-19
Variation in normalized shear modulus with shearing strain from torsional shear tests of undisturbed fine-grained samples from Treasure Island.

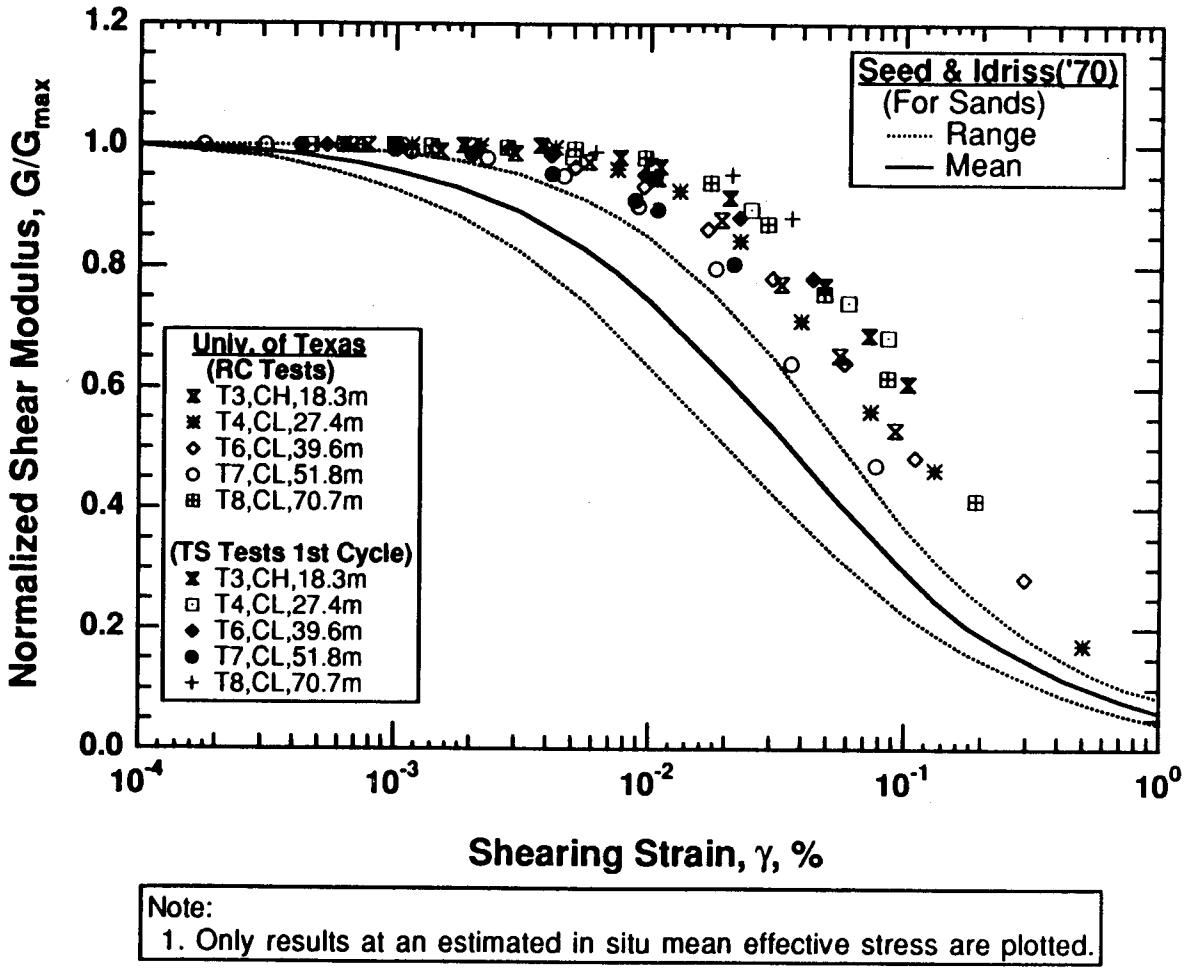

Figure 8.B.1-20
Variation in normalized shear modulus with shearing strain from resonant column and torsional shear tests of undisturbed fine-grained samples from Treasure Island.

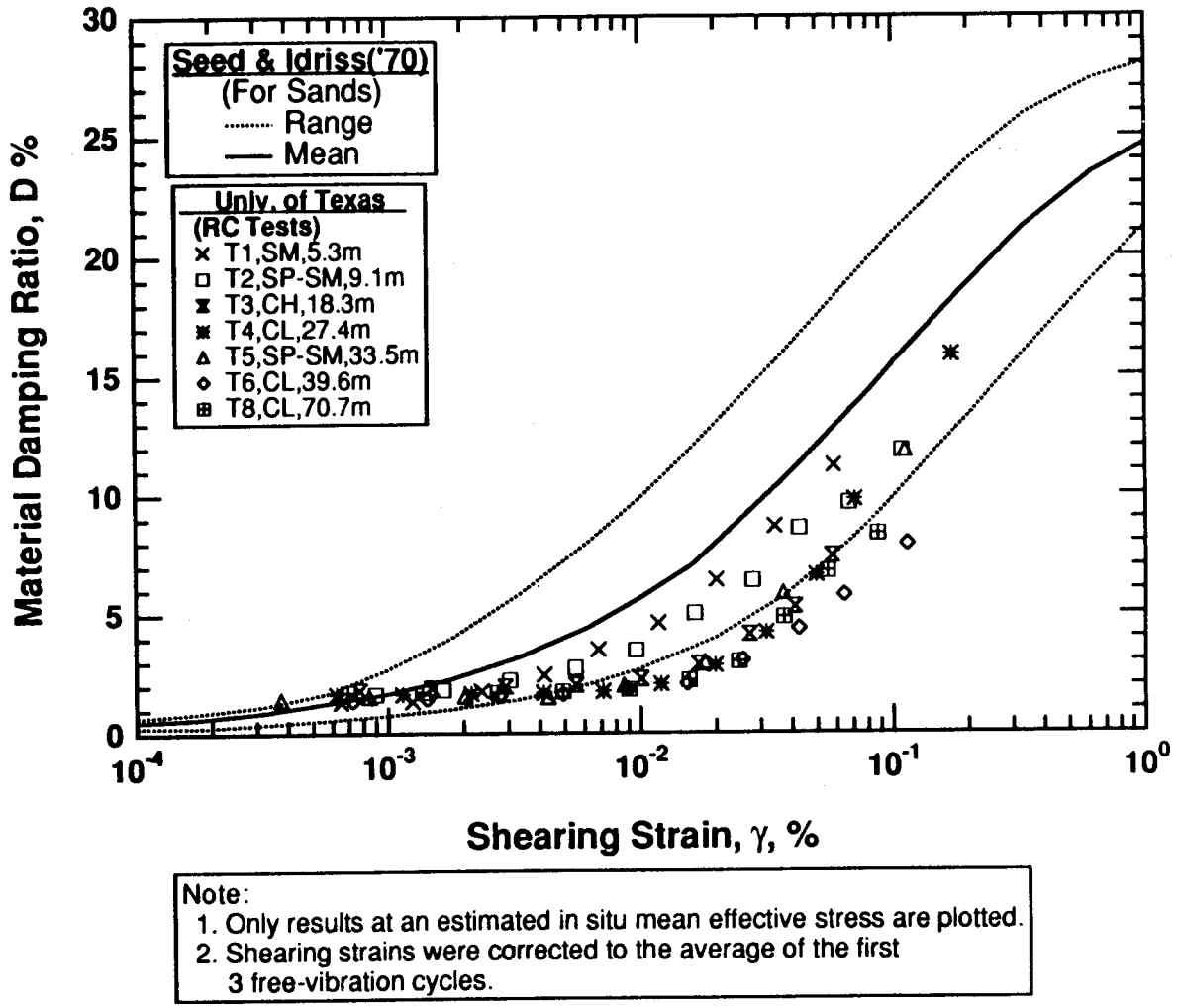

Figure 8.B.1-21
Variation in material damping ratio with shearing strain from resonant column tests of undisturbed samples from Treasure Island.

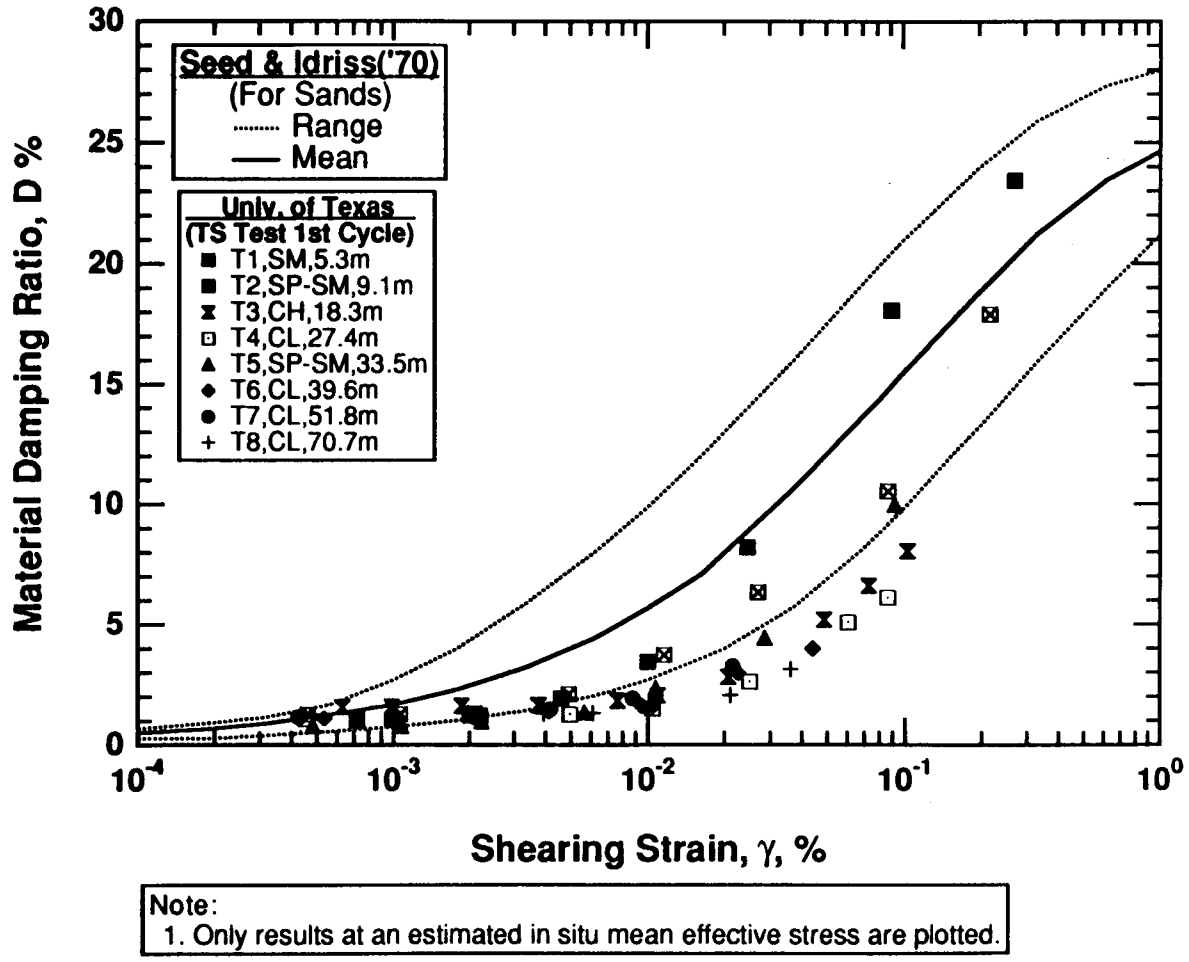

Figure 8.B.1-22
Variation in material damping ratio with shearing strain from torsional shear tests of undisturbed samples from Treasure Island.

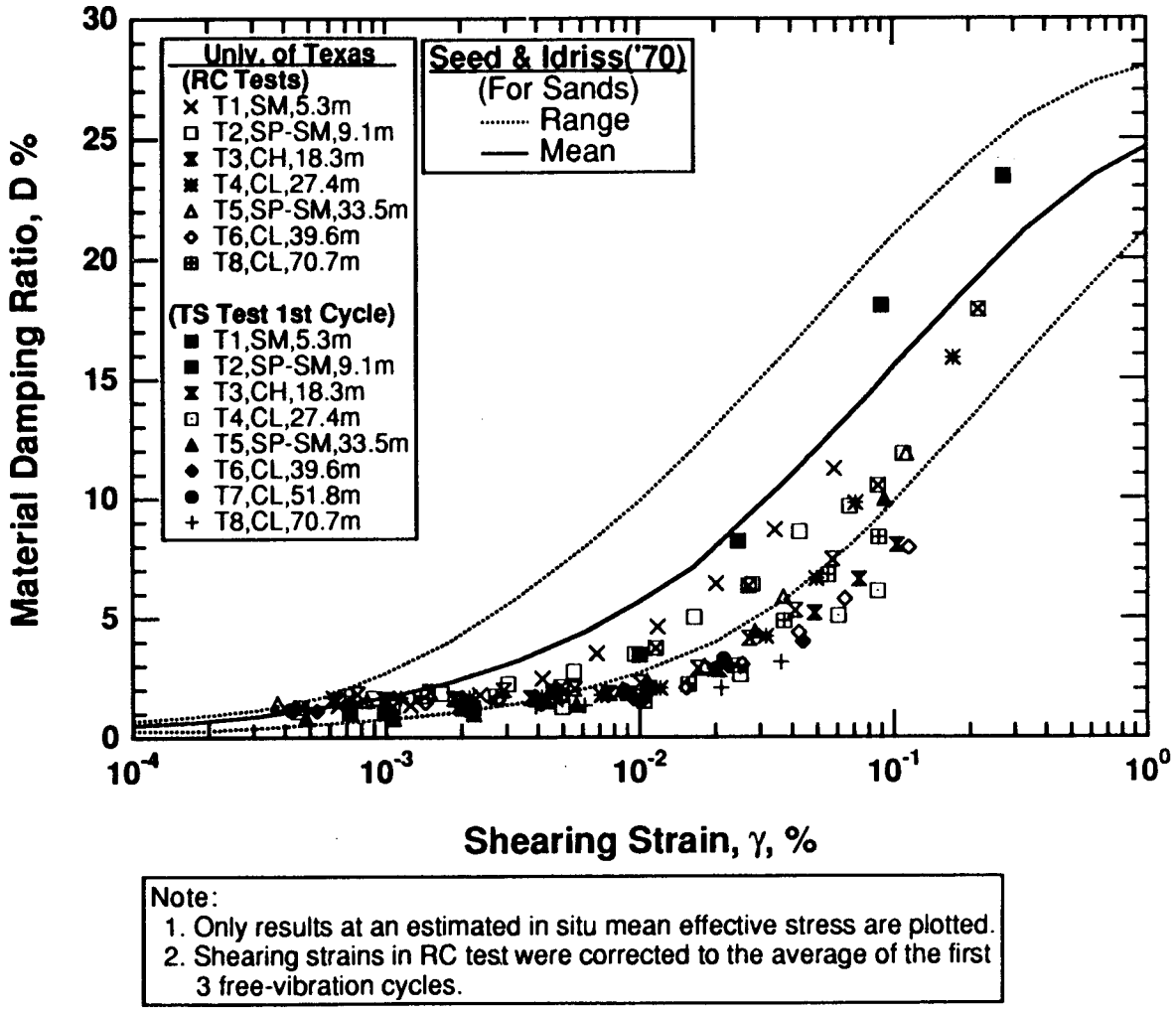

Figure 8.B.1-23
Variation in material damping ratio with shearing strain from resonant column and torsional shear tests of undisturbed samples from Treasure Island.

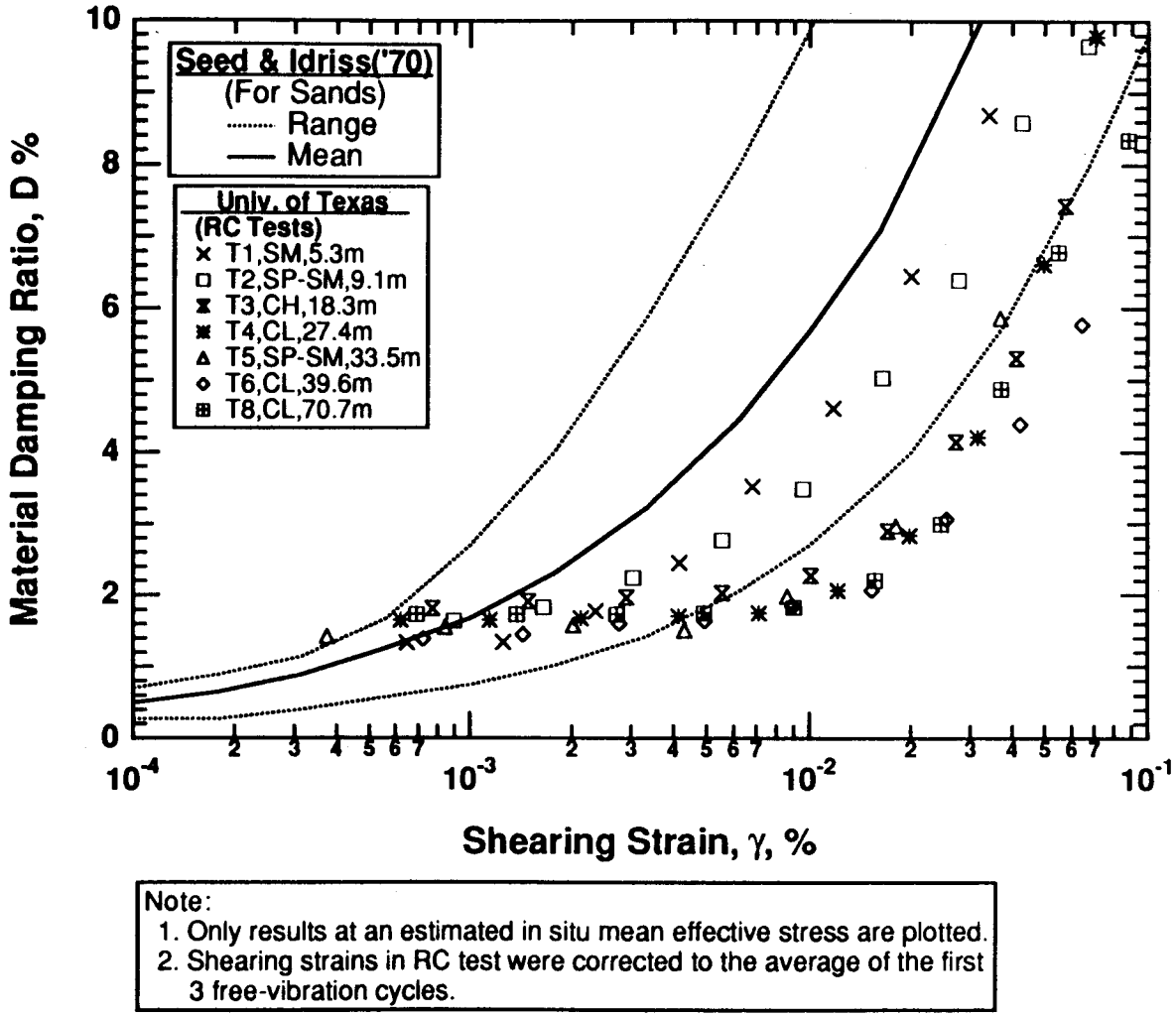

Figure 8.B.1-24
Variation in material damping ratio with shearing strain for $\gamma \leq 0.1\%$ from resonant column tests of undisturbed samples from Treasure Island.

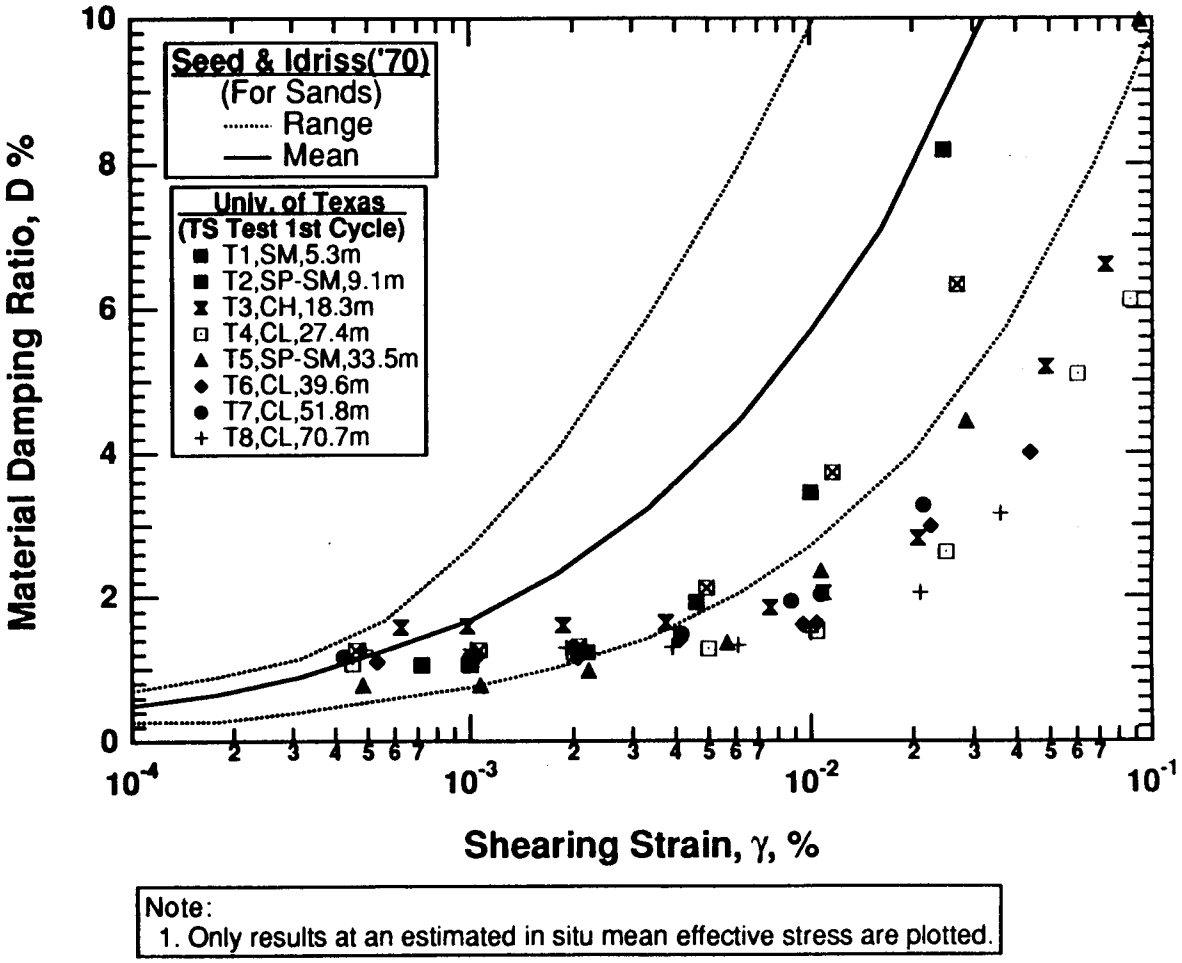

Figure 8.B.1-25
Variation in material damping ratio with shearing strain for $\gamma \leq 0.1\%$ from the first cycle of torsional shear tests of undisturbed samples from Treasure Island.

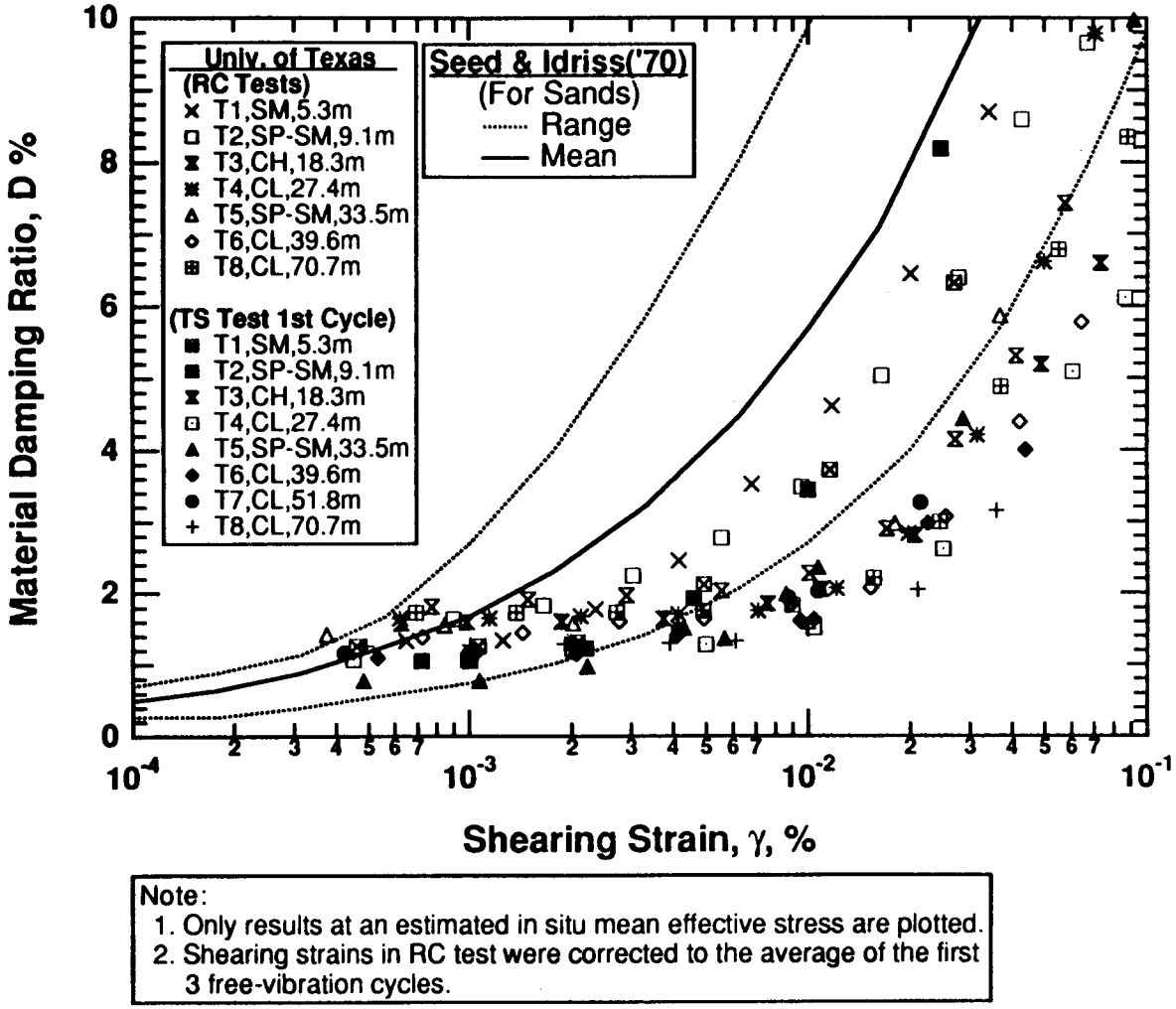

Figure 8.B.1-26
Variation in material damping ratio with shearing strain for $\gamma \leq 0.1\%$ from resonant column and torsional shear tests of undisturbed samples from Treasure Island.

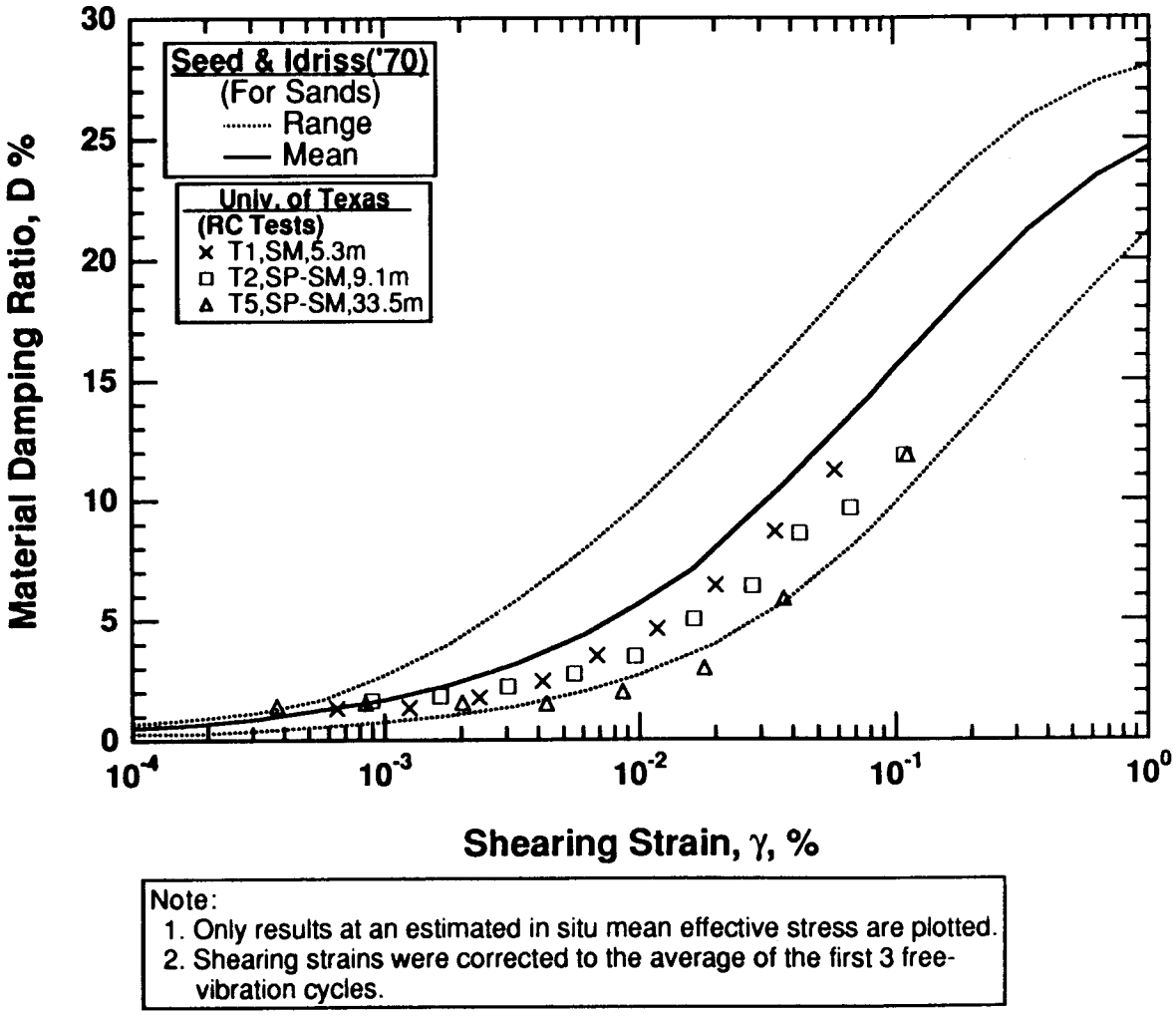

Figure 8.B.1-27
Variation in material damping ratio with shearing strain from resonant column tests of undisturbed sandy samples from Treasure Island.

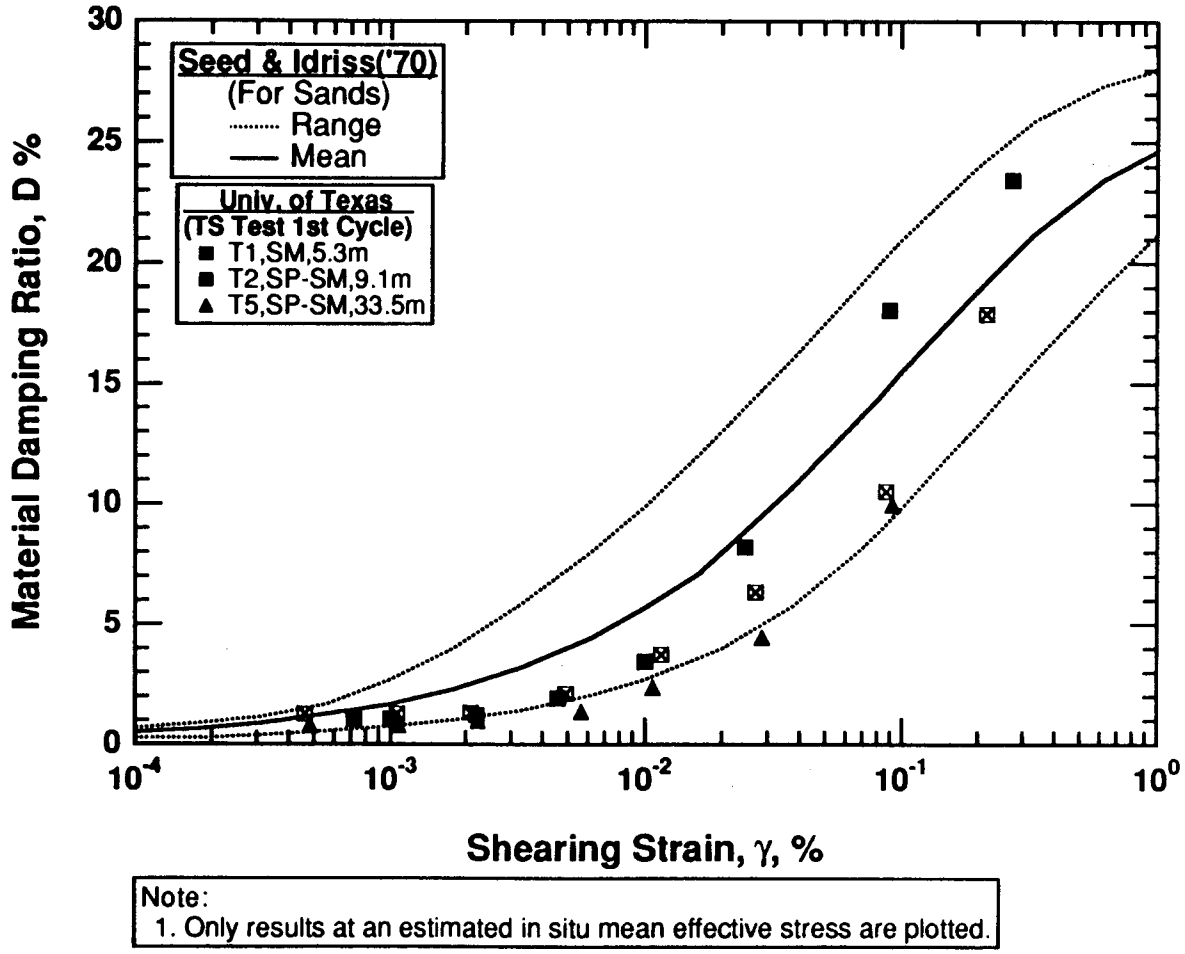

Figure 8.B.1-28
Variation in material damping ratio with shearing strain from torsional shear tests of undisturbed sandy samples from Treasure Island.

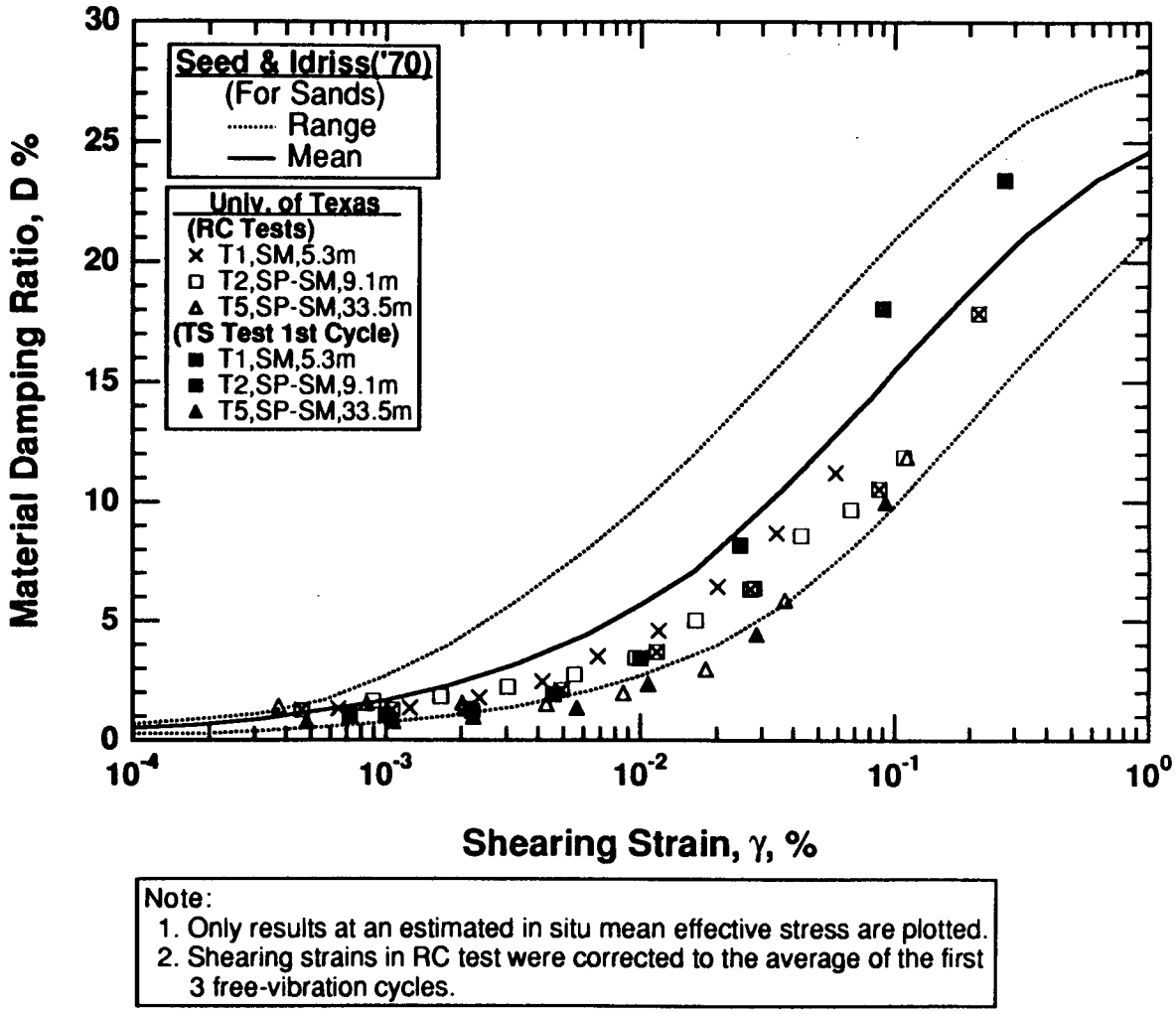

Figure 8.B.1-29
Variation in material damping ratio with shearing strain from resonant column and torsional shear tests of undisturbed sandy samples from Treasure Island.

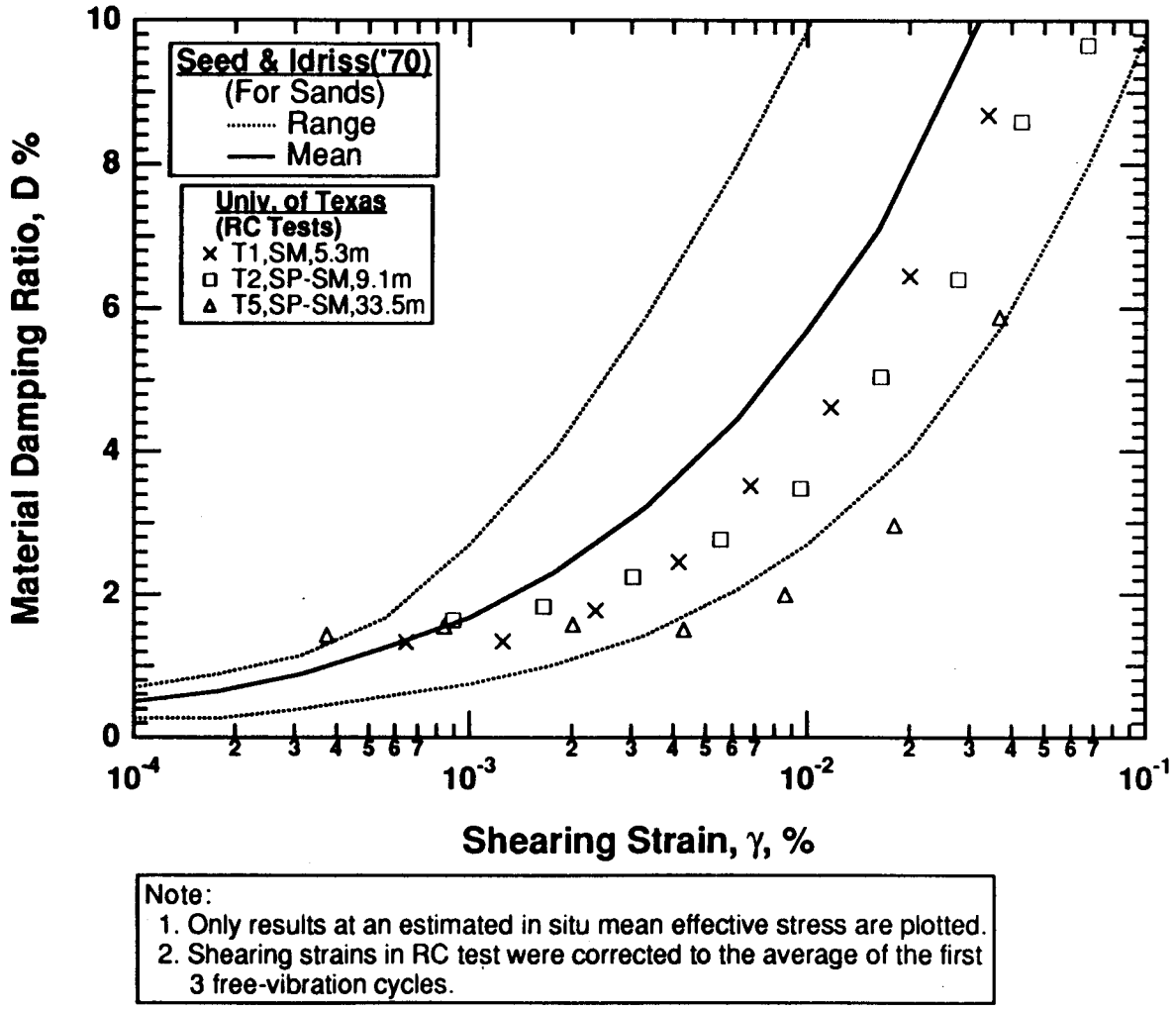

Figure 8.B.1-30
Variation in material damping ratio with shearing strain for $\gamma \leq 0.1\%$ from resonant column tests of undisturbed samples from Treasure Island.

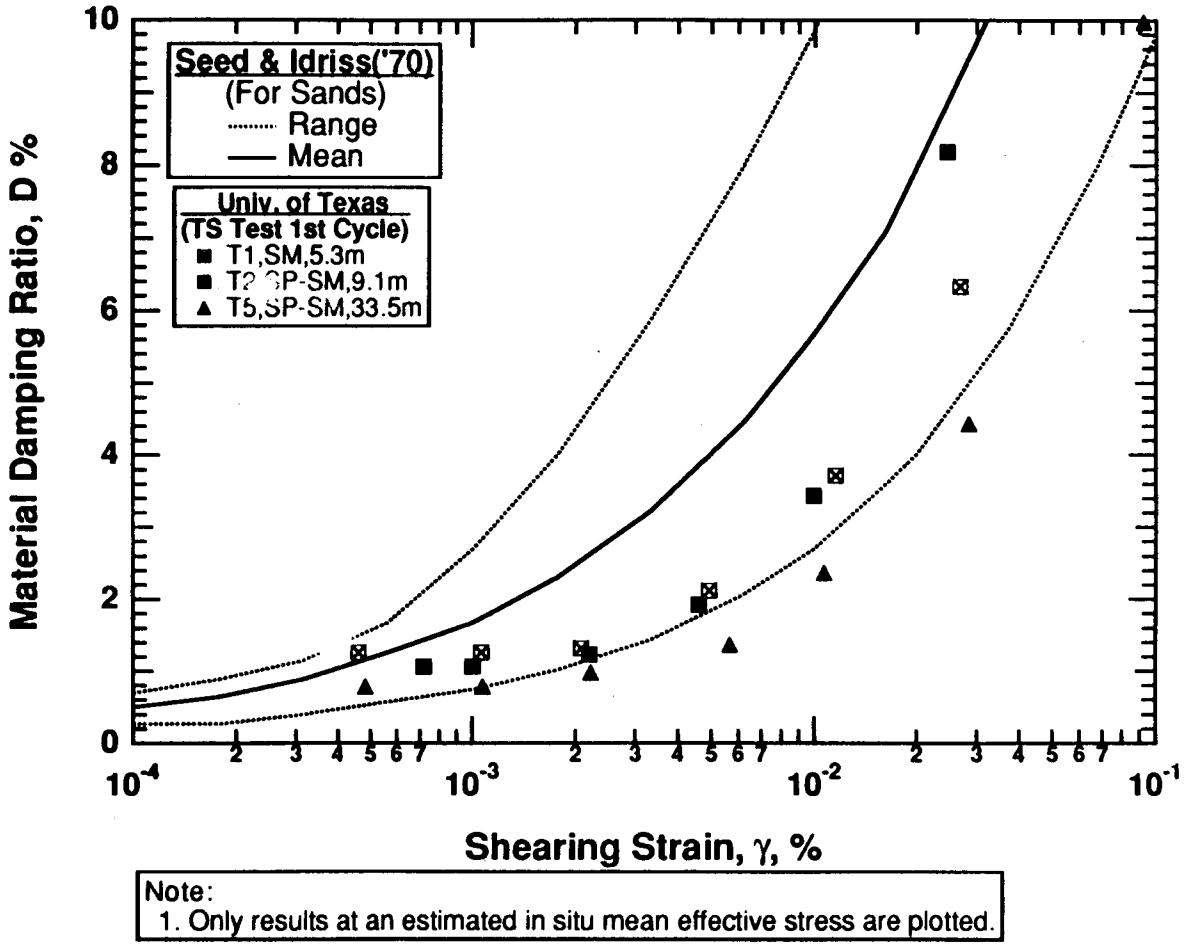

Figure 8.B.1-31
Variation in material damping ratio with shearing strain for $\gamma \leq 0.1\%$ from the first cycle of torsional shear tests of undisturbed sandy samples from Treasure Island.

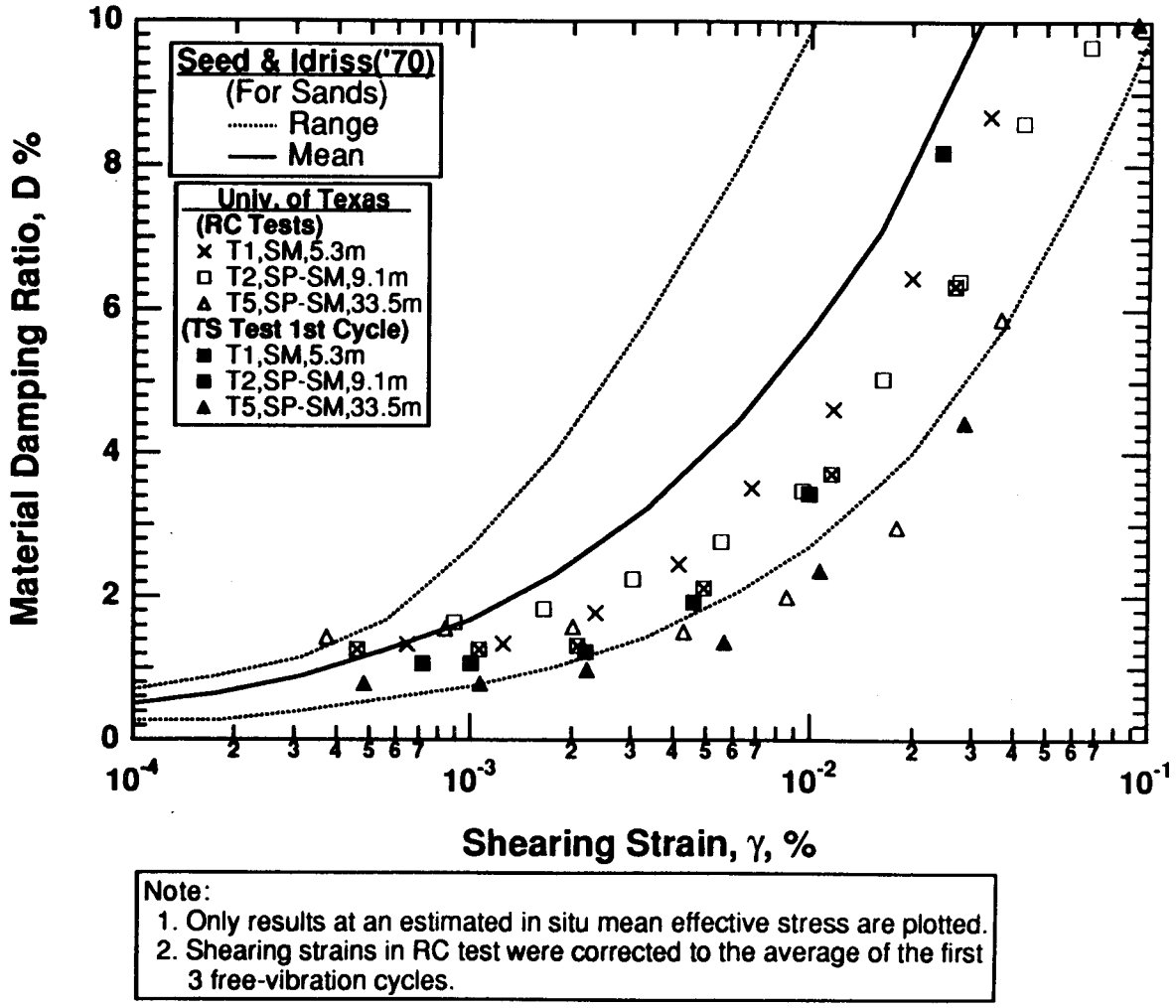

Figure 8.B.1-32
Variation in material damping ratio with shearing strain for $\gamma \leq 0.1\%$ from resonant column and torsional shear tests of undisturbed sandy samples from Treasure Island.

References

Hardin, B.O. (1978), "The Nature of Stress-Strain Behavior for Soils," Proceedings, Geotechnical Engineering Division Specialty Conference on Earthquake Engineering and Soil Dynamics, Vol. 1, ASCE, Pasadena, CA, June, pp. 3–90.

Seed, H.B., and Idriss, I.M. (1970), "Soil Moduli and Damping Factors for Dynamics Response Analysis," Report No. EERC 70-10, Earthquake Engineering Research Center, University of California, Berkeley, September, p. 37.

Kim, D.S. (1991), "Deformational Characteristic of Soils at Small to Intermediate Strains from Cyclic Tests," Ph.D. Dissertation, *Geotechnical Engineering*, Department of Civil Engineering, University of Texas at Austin, August.

APPENDIX 8.B.1.A
TEST EQUIPMENT AND MEASUREMENT TECHNIQUES

8.B.1.A.1 Introduction

Resonant column and torsional shear (RCTS) equipment has been employed in this investigation for measurement of the deformational characteristics (shear modulus and material damping) of intact soil specimens. This equipment has been developed at The University of Texas at Austin over the past two decades (Isenhower, 1979; Lodde, 1982; Ni, 1987; and Kim, 1991). The equipment is of the fixed-free type, with the bottom of the specimen fixed and torsional excitation applied to the top. Both resonant column (RC) and torsional shear (TS) tests can be performed in a sequential series on the same specimen over a shearing strain range from about 10^{-4}% to slightly more than 10^{-1}%. The primary difference between the two types of tests is the excitation frequency. In the RC test, frequencies above 20 Hz are required and inertia of the specimen and drive system are needed to analyze the measurements. On the other hand, slow cyclic loading involving frequencies generally below 5 Hz is performed in the TS test and inertia does not enter data analysis.

8.B.1.A.2 Resonant Column and Torsional Shear Equipment

8.B.1.A.2.1 Overview of RCTS Equipment

The RCTS apparatus can be idealized as a fixed-free system as shown in Fig. 8.B.1.A-1. The bottom end of the specimen is fixed against rotation at the base pedestal, and top end of the specimen is connected to the driving system. The driving system, which consists of a top cap and drive plate, can rotate freely to excite the specimen in cyclic torsion.

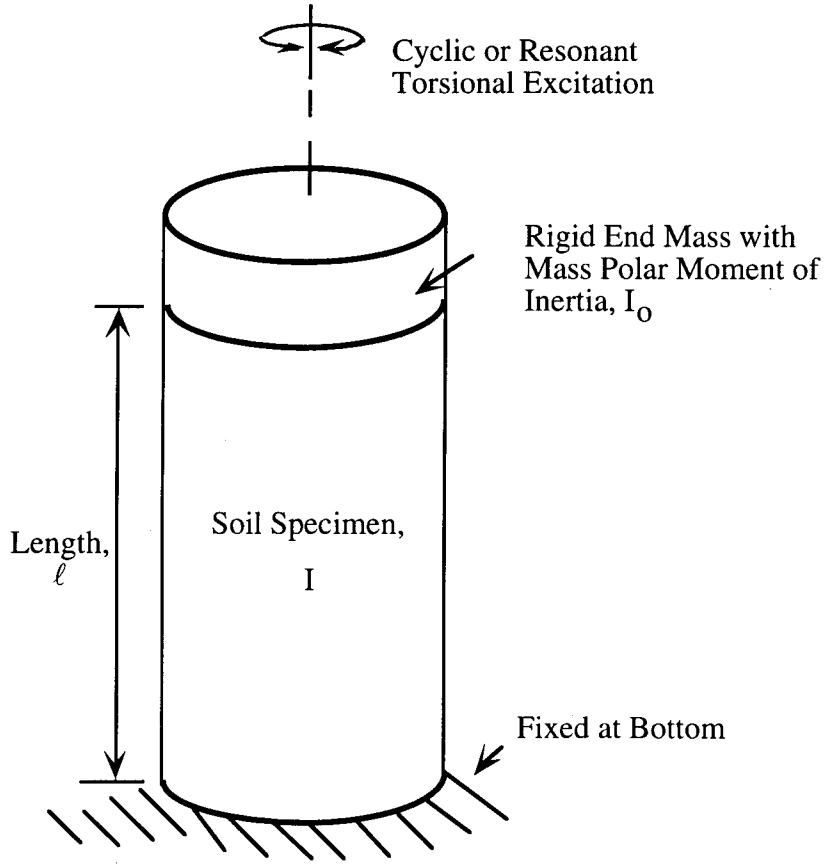

Fig. 8.B.1.A-1
Idealized fixed-free RCTS equipment.

A simplified diagram of a fixed-free resonant column (RC) test is shown in Fig. 8.B.1.A-2. The basic operational principle is to vibrate the cylindrical specimen in first-mode torsional motion. Harmonic torsional excitation is applied to the top of the specimen over a range in frequencies, and the variation of the acceleration amplitude of the specimen with frequency is obtained. Once first-mode resonance is established, measurements of the resonant frequency and amplitude of vibration are made. These measurements are then combined with equipment characteristics and specimen size to calculate shear wave velocity and shear modulus based on elastic wave propagation. Material damping is determined either from the width of the frequency response curve or from the free-vibration decay curve.

The torsional shear (TS) test is another method of determining shear modulus and material damping using the same RCTS equipment but operating it in a different manner. The simplified configuration of the torsional shear test is shown in Fig. 8.B.1.A-3. A cyclic torsional force with a given frequency, generally below 10 Hz, is applied at the top of the specimen. Instead of determining the resonant frequency, the stress-strain hysteresis loop is determined from measuring the torque-twist response of the specimen. Proximitors are used to measure the angle of twist while the voltage applied to the coil is calibrated to yield torque. Shear modulus is calculated from the slope of a line through the end points of the hysteresis loop, and material damping is obtained from the area of the hysteresis loop as shown in Fig. 8.B.1.A-3.

The RCTS apparatus used in this study has three advantages. First, both resonant column and torsional shear tests can be performed with the same set-up simply by changing (outside the apparatus) the frequency of the forcing function. Variability due to preparing "identical" samples is eliminated so that both test results can be compared effectively. Second, the torsional shear test can be performed over a shearing strain range between 10^{-4}% and about 10^{-1}%. Common types of torsional shear tests, which generate torque by a mechanical motor outside of the confining chamber, are usually performed at strains above 0.01% because of system compliance. However, the RCTS apparatus used in this study generates torque with an electrical coil-magnet system inside the confining chamber, thus eliminating the problem with an external motor. The torsional shear test can be performed at the same low-strain amplitudes as the resonant column test, and results between torsional shear and resonant column testing can be easily compared over a wide range of strains. Third, the loading frequency in the torsional shear test can be changed easily from 0.01 Hz to 10 Hz. Therefore, the effect of frequency on deformational characteristics can be conveniently investigated using this apparatus.

The RCTS apparatus consists of four basic subsystems which are: (1) a confinement system, (2) a drive system, (3) a height-change measurement system, and (4) a motion monitoring system. The general configuration of the RCTS apparatus (without the confinement system) is shown in Fig. 8.B.1.A-4. The RCTS apparatus was automated by Ni (1987) so that a microcomputer controls the test, collects the data, and reduces results. Computer-aided subsystems are discussed briefly in the following sections.

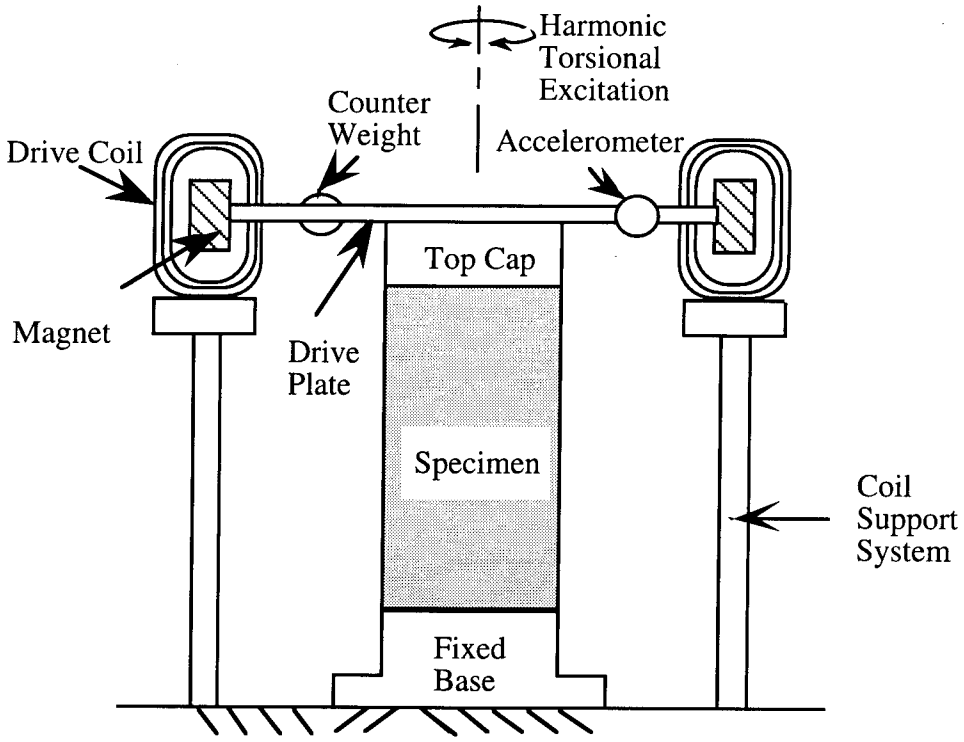

a) Specimen in the Resonant Column Apparatus
(Confinement Chamber Not Shown)

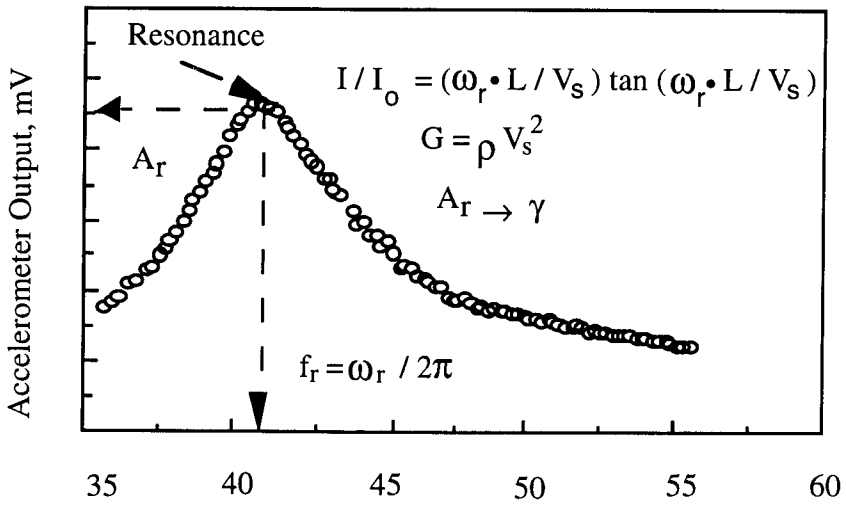

b) Typical Frequency Response Curve

Figure 8.B.1.A-2
Simplified diagram of a fixed-free resonant column test and an associated frequency response curve.

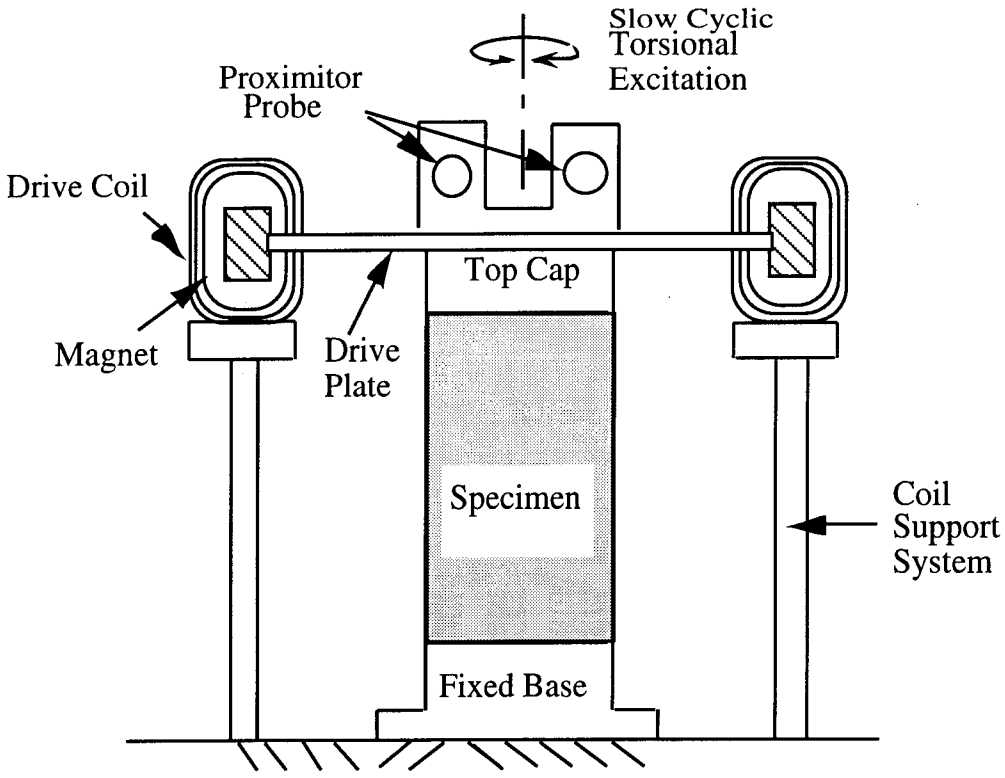

a) Specimen in the Torsional Shear Test Apparatus
(Confinement Chamber Not Shown)

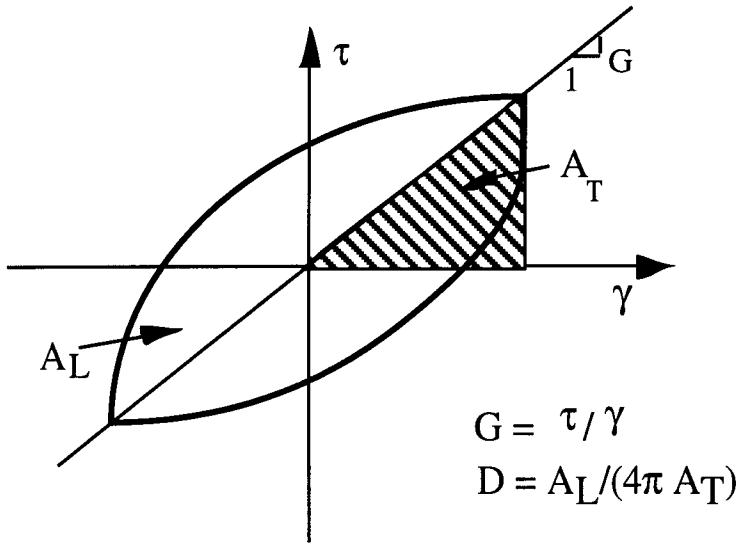

b) Measurement of Shear Modulus and Damping Ratio

Figure 8.B.1.A-3
Configuration of a torsional shear test and evaluation of shear modulus and material damping ratio.

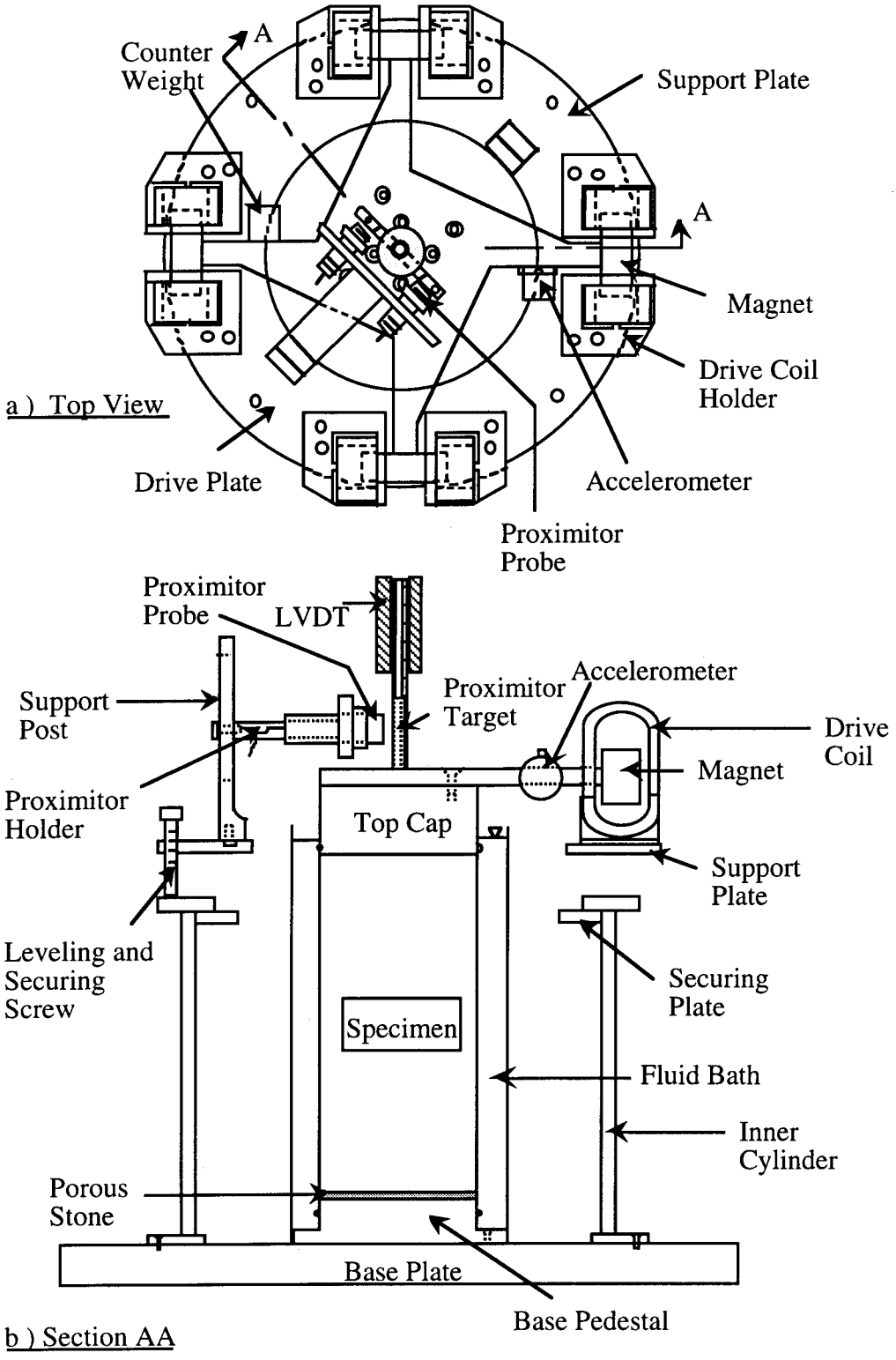

Figure 8.B.1.A-4
General configuration of RCTS equipment (from Ni, 1987).

8.B.1.A.2.2 RCTS Confinement System

The confining chamber is made of stainless steel. A thin-walled (0.6 cm in thickness) hollow cylinder fits into circular grooves machined in 2.5 cm thick base and top plates. Four stainless steel connecting rods (1.28 cm in diameter) are used to secure the base and top plates to the hollow cylinder, and O-rings in the circular grooves are used to seal the chamber. In this configuration, the chamber has been designed to withstand a maximum air pressure of about 200 psi (1379 kPa). To safely test samples at higher confining pressures (pressures on the order of 600 psi (4137 kPa)), the confinement system was modified by adding additional stainless steel rods to secure the cylinder to the top and base plates and reinforcement to the top and base plates.

Compressed air is used to confine isotropically the specimen in the RCTS device. The air pressure to the chamber generally is regulated by a Fairchild M 30 regulator and air supplied to the regulator is filtered. At high confining pressures, additional regulators are used. The soil specimen is sealed in a membrane and pore pressure in the specimen is normally vented to atmospheric pressure.

Inside the confining chamber, the air pressure acts upon a silicon fluid bath which surrounds the sides of the soil specimen. The purpose of the silicon fluid bath is to retard air migration through the membrane and into the specimen to prevent drying of the specimen. Figure 8.B.1.A-5 shows the simplified configuration of the confinement system.

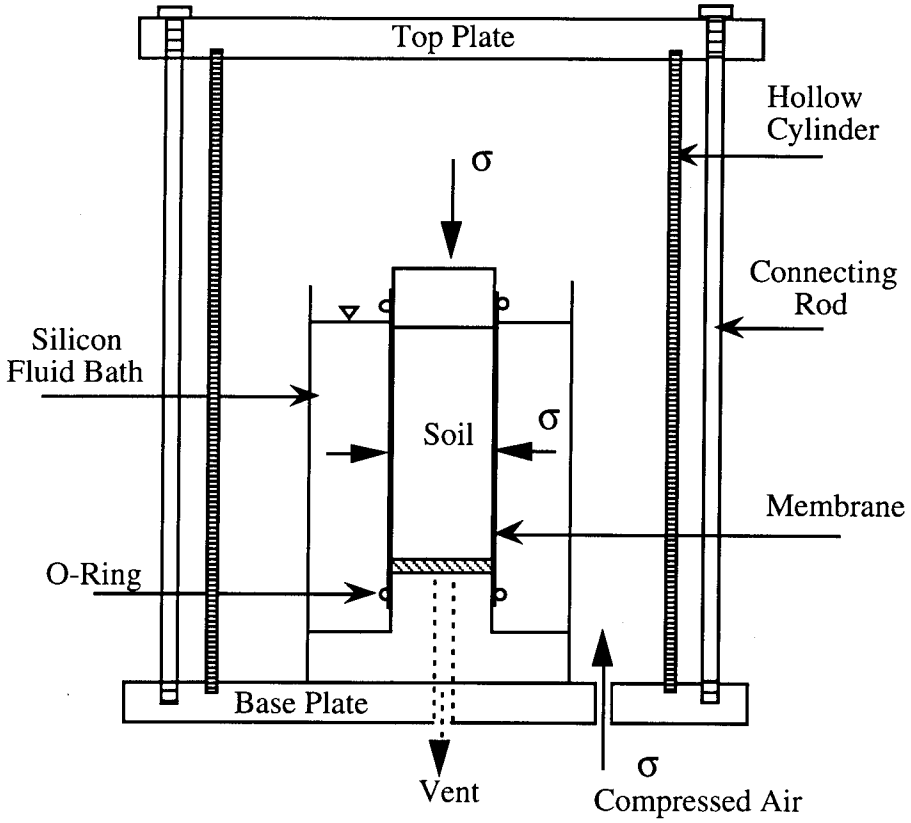

Fig. 8.B.1.A-5
Simplified configuration of confinement system.

8.B.1.A.2.3 Drive System

The drive system consists of a four-armed drive plate, four magnets, eight drive coils, a power amplifier, and a function generator. Each magnet is rigidly attached to the end of one arm of the drive plate as shown in Fig. 8.B.1.A-4. Eight drive coils encircle the ends of the four magnets so that the drive plate excites the soil specimen in torsional motion when a current is passed through the coils. The maximum torque that the drive system can develop depends on the strength of the magnets, size of the drive coils, resistance of the drive coils, size of the space between the magnets and drive coils, length of the arms of the drive plate, and the electrical characteristics of the function generator and power amplifier. For the three drive systems used in this work, the maximum torque was about 0.60 lb-ft (82 N-cm).

A schematic diagram of the drive system is shown in Fig. 8.B.1.A-6. The micro-computer activates a function generator (HP 3314A) to input sinusoidal voltage to the drive coils. In the resonant column (RC) test, the function generator performs frequency sweeps with a constant amplitude while in the torsional shear test, a fixed-frequency N-cycle mode is used. For high-amplitude resonant column and torsional shear (TS) tests, the sinusoidal input current is amplified by a power amplifier (HP 6824A) before going to the drive coils.

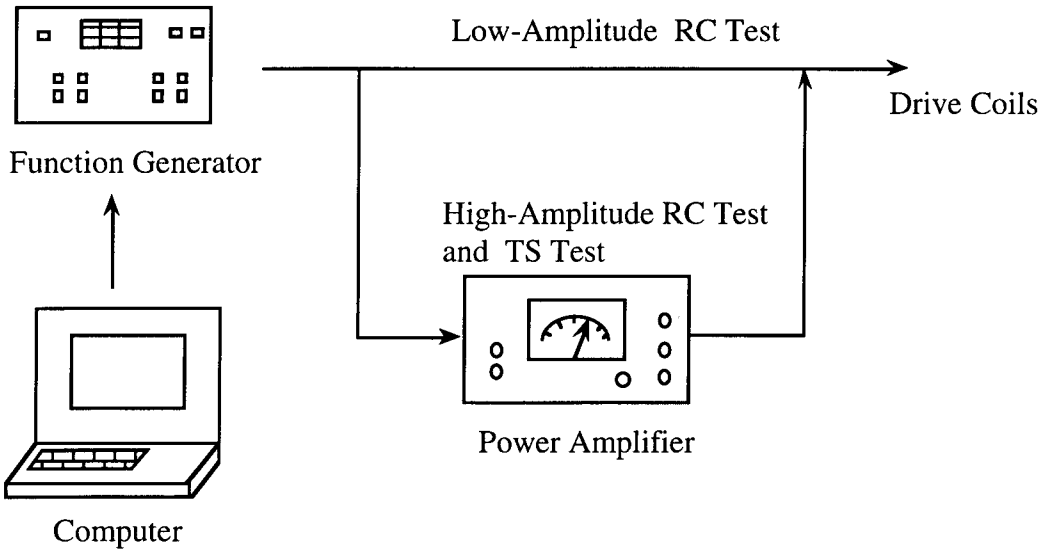

Fig. 8.B.1.A-6
Schematic diagram of the drive system.

8.B.1.A.2.4 Height-Change Measurement System

The height change of the soil specimen is measured to account for the changes in the length and mass of the specimen during consolidation or swell. This measurement is also used to calculate change in the mass moment of inertia, mass density, and void ratio during testing (by assuming isotropic strain under isotropic confinement and constant degree of saturation). The height change is measured by a linear variable differential transformer (LVDT). The height change measurement system consists of an LVDT (CRL Model SH-200-53R), a function generator (HP 3314A), and a digital voltmeter (HP 3456A). The LVDT core is not in contact with the LVDT coil housing so that no friction occurs during RCTS testing.

The output and calibration factor of an LVDT depend on both the frequency and magnitude of the excitation voltage. In this test the computer activates the function generator to generate the input signal in the LVDT coil at a frequency of 500 Hz and a voltage level of 4.77 RMS volts. The output from the LVDT is read with a digital voltmeter. The height change is calculated from the output voltage combined

with the calibration factor. The schematic diagram of the height change measuring system is shown in Fig. 8.B.1.A-7.

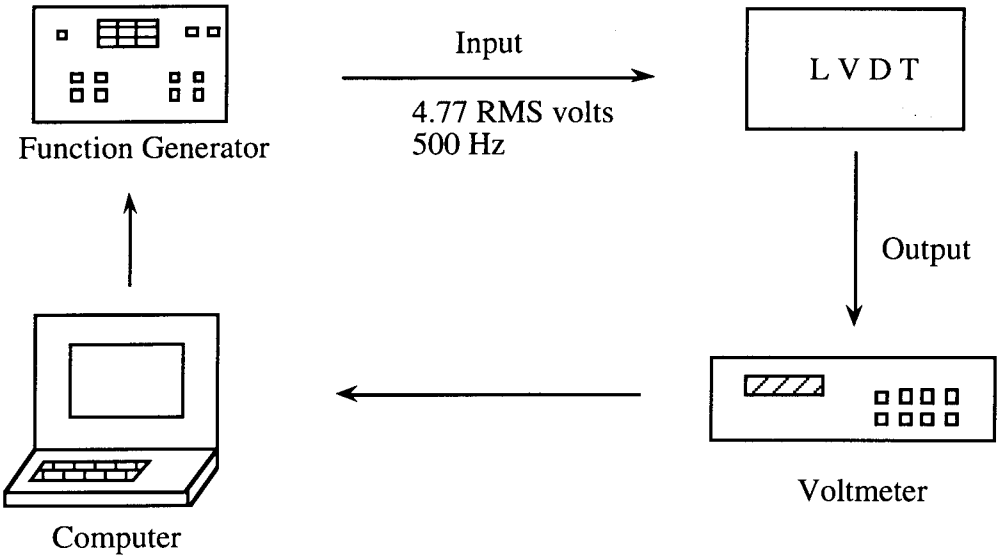

Fig. 8.B.1.A-7
Schematic diagram of the height-change measuring system.

8.B.1.A.2.5 Motion Monitoring System

Dynamic soil properties are obtained in the RC test at the resonant frequency which is usually above 20 Hz while torsional shear testing is used to measure the low-frequency (below 10 Hz) cyclic stress-strain relationship of soil. Because of the different frequencies applied in the resonant column and torsional shear tests, different motion monitoring systems are used.

Resonant Column (RC) Test. The motion monitoring system in the RC test is designed to measure the resonant frequency, shearing strain, and free-vibration decay curve. This system consists of an accelerometer (Columbia Research Laboratory Model 3021), a charge amplifier (Columbia Research Laboratory Model 4102M), a frequency counter (HP 5334A), a digital voltmeter (HP 3456A), and a digital oscilloscope (Nicolet 20929-01). The schematic diagram of the motion monitoring system is shown in Fig. 8.B.1.A-8.

The accelerometer is oriented to be sensitive to torsional vibrations of the drive plate. The charge amplifier conditions the accelerometer output to be linear for all levels of acceleration in the test. The digital voltmeter reads the output voltage from the accelerometer at each frequency which is measured by the frequency counter. The resonant frequency is obtained from the frequency response curve. Once the resonant frequency is obtained, the computer activates the function generator to excite the specimen at the resonant frequency and then suddenly stops the current so that the free-vibration decay curve is recorded by the digital oscilloscope.

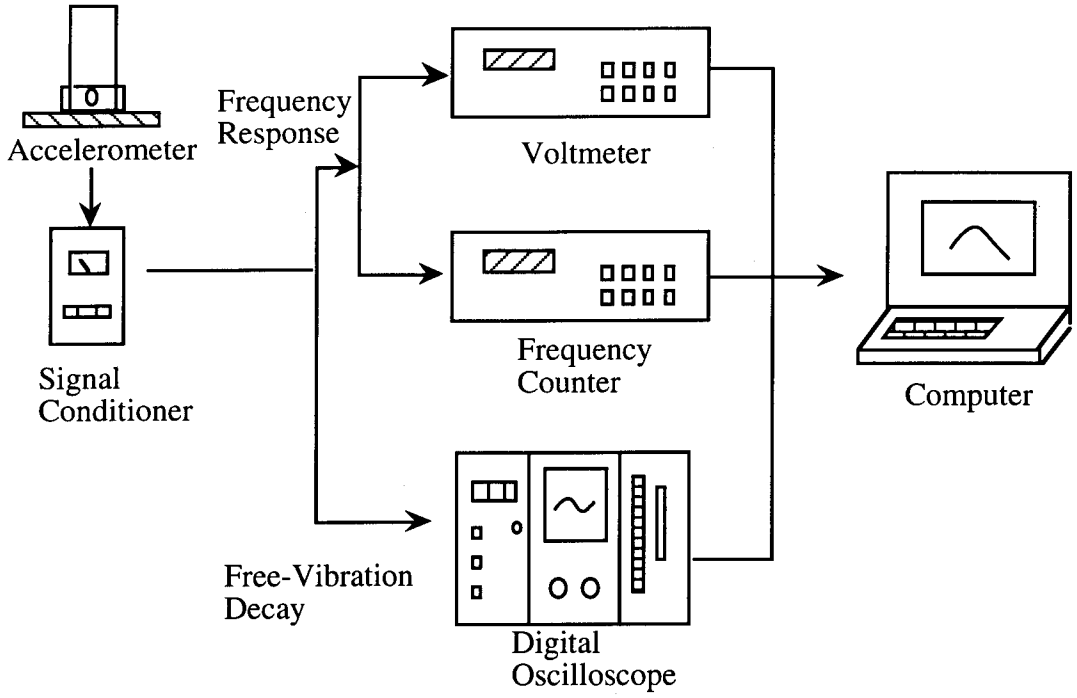

Fig. 8.B.1.A-8
Schematic diagram of the motion monitoring system in the resonant column test.

The resonant frequency of soils are typically in the range of 20 Hz to 300 Hz with this equipment. To test soils effectively over a wide range of stiffnesses, the search for the resonant frequency is performed in two stages, a rough sweep and a fine sweep. During the rough sweep, a fast logarithmic-linear frequency sweep (16 seconds to sweep from 1 to 170 Hz) is used. The fine sweep is then performed to determine an accurate resonant frequency in the neighborhood where the resonant frequency was found in the rough sweep.

Torsional Shear (TS) Test. The motion monitoring system in the TS test (3000 Proximitor System) is used to monitor torque-twist hysteresis loops of the specimen. This system consists of two proximitors (Bentry Nevada M 20929-01), two proximitor probes (Bentry Nevada M 300-00), an operational amplifier (Tektronix TM 504 with AM501), a DC power supply (Lambda M-11-902), a U-shaped target and a digital oscilloscope (Nicolet 20929-01). The U-shaped target is secured to the top of the drive plate, and the two proximitor probes are rigidly attached to the support stand. A schematic diagram of the motion monitoring system in the torsional shear test is shown in Fig. 8.B.1.A-9.

The function of the proximitor probes is to measure the width of the air gap between the target and the probe tip. Because the proximitor probes do not touch the drive plate, no compliance problems are introduced into the measurement. Two probes are used and the operational amplifier subtracts the signal from one probe from the other so that the effect of bending in the specimen toward the probes can be eliminated. The proximitor system is a very effective low-frequency motion monitoring system which does not introduce any compliance problems into the measurement. With the simultaneous measurement of torque, load-displacement hysteresis loops can be determined.

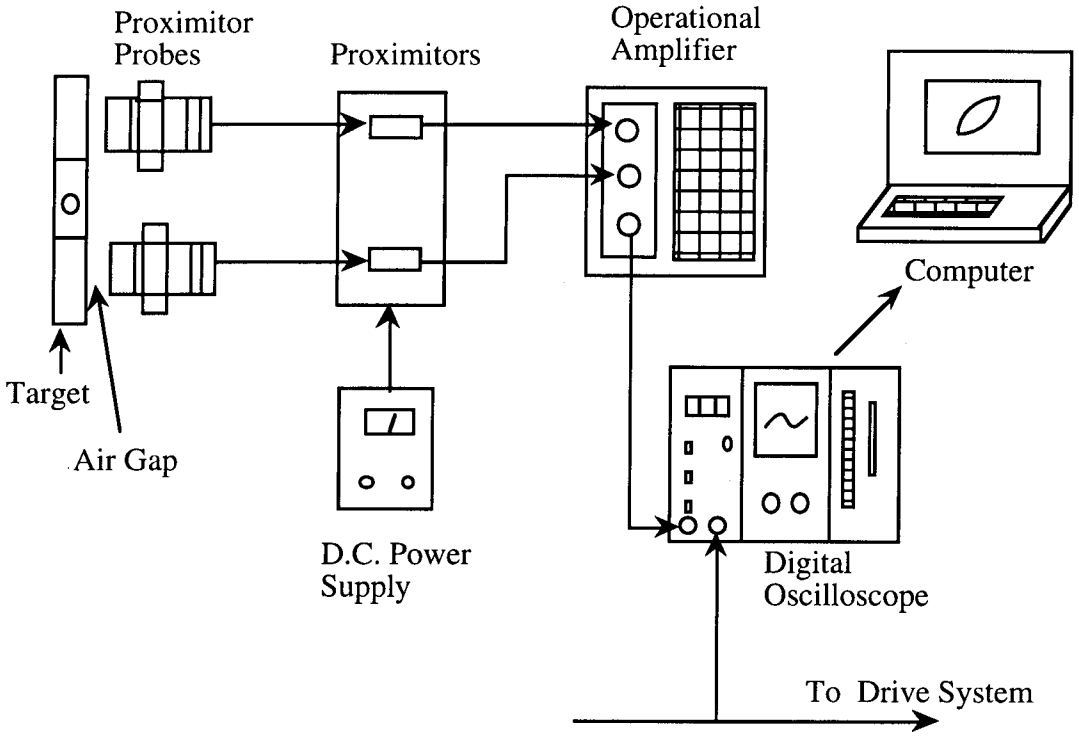

Fig. 8.B.1.A-9
Schematic diagram of the motion monitoring system in the torsional shear test (3000 Proximitor System).

8.B.1.A.3 Method of Analysis in the Resonant Column Test

The resonant column test is based on the one-dimensional wave equation derived from the theory of elasticity. The shear modulus is obtained by measuring the first-mode resonant frequency while material damping is evaluated from either the free-vibration decay curve or from the width of the frequency response curve assuming viscous damping.

8.B.1.A.3.1 Shear Modulus

The governing equation of motion for the fixed-free torsional resonant column test is:

$$\frac{\Sigma I}{I_o} = \frac{\omega_n \bullet l}{V_s} \bullet \tan\left(\frac{\omega_n \bullet l}{V_s}\right) \qquad \text{(8.B.1.A-1)}$$

Where,

ΣI = $I_s + I_m$ + ---
I_s = mass moment of inertia of soil,
I_m = mass moment of inertia of membrane,
I_o = mass moment of inertia of rigid end mass at the top of the specimen,
l = length of the specimen,
V_s = shear wave velocity of the specimen, and
ω_n = undamped natural circular frequency of the system.

The value of I_o is known from the calibration of the drive plate. The values of I_s and l are easily determined from the specimen size and weight. Once the first-mode resonant frequency is determined,

the shear wave velocity can be calculated from Eq. 8.B.1.A-1 by assuming that the resonant circular frequency and ω_n are equal.

As noted above and shown in Fig. 8.B.1.A-2 the resonant circular frequency, ω_r, is measured instead of undamped natural frequency, ω_n, and ω_r is used to calculate shear wave velocity. If the damping in the system is zero, ω_r and ω_n are equal. The relationship between ω_r and ω_n is:

$$\omega_r = \omega_n \sqrt{1-2D^2} \qquad \text{(8.B.1.A-2)}$$

A typical damping ratio encountered in the resonant column test is less than 20 percent, which corresponds to a difference of less than 5 percent between ω_r and ω_n. In this study, the damping measured in the resonant column test was usually less than 10 percent, and ω_r can be used instead of ω_n with less than a two percent error.

Once the shear wave velocity is determined, shear modulus is calculated from the relationship:

$$G = \rho \bullet V_S^2 \qquad \text{(8.B.1.A-3)}$$

where ρ is the total mass density of the soil (total unit weight divided by gravity).

8.B.1.A.3.2 Shearing Strain

The shearing strain varies radially within the specimen and may be expressed as a function of the distance from the longitudinal axis as illustrated in Fig. 8.B.1.A-10. The equivalent shearing strain, γ_{eq} or γ, is represented by:

$$\gamma = r_{eq} * \theta_{max} / l \qquad \text{(8.B.1.A-4)}$$

Where,

r_{eq} = equivalent radius,
θ_{max} = angle of twist at the top of the specimen, and
l = length of the specimen.

Chen and Stokoe (1979) studied the radial distribution in shearing strain to find a value of r_{eq} for the specimen tested in the RCTS equipment to evaluate an effective strain. They found that the value of r_{eq} varied from $0.82*r_0$ for a peak shearing strain amplitude below 0.001% to $0.79*r_0$ for a peak shearing strain of 0.1% for a solid specimen. These values of r_{eq} have been adopted in this study.

In the resonant column test, the resonant period (T_r, seconds), and output voltage of accelerometer (A_c, volts (RMS)) at resonance are measured. Accelerometer output is changed to the displacement by using the accelerometer calibration factor (CF, volts (RMS)/in./sec^2) assuming harmonic motion. The accelerometer displacement is divided by the distance (D_{ac}, inches) between the location of accelerometer and the axis of the specimen to calculate the angle of twist at the top of the specimen (θ_{max}). The shearing strain is then calculated by:

$$\gamma = r_{eq} \frac{A_c \bullet Tr^2}{4\pi^2 \bullet CF} \bullet \frac{1}{D_{ac}} \bullet \frac{1}{l} \qquad \text{(8.B.1.A-5)}$$

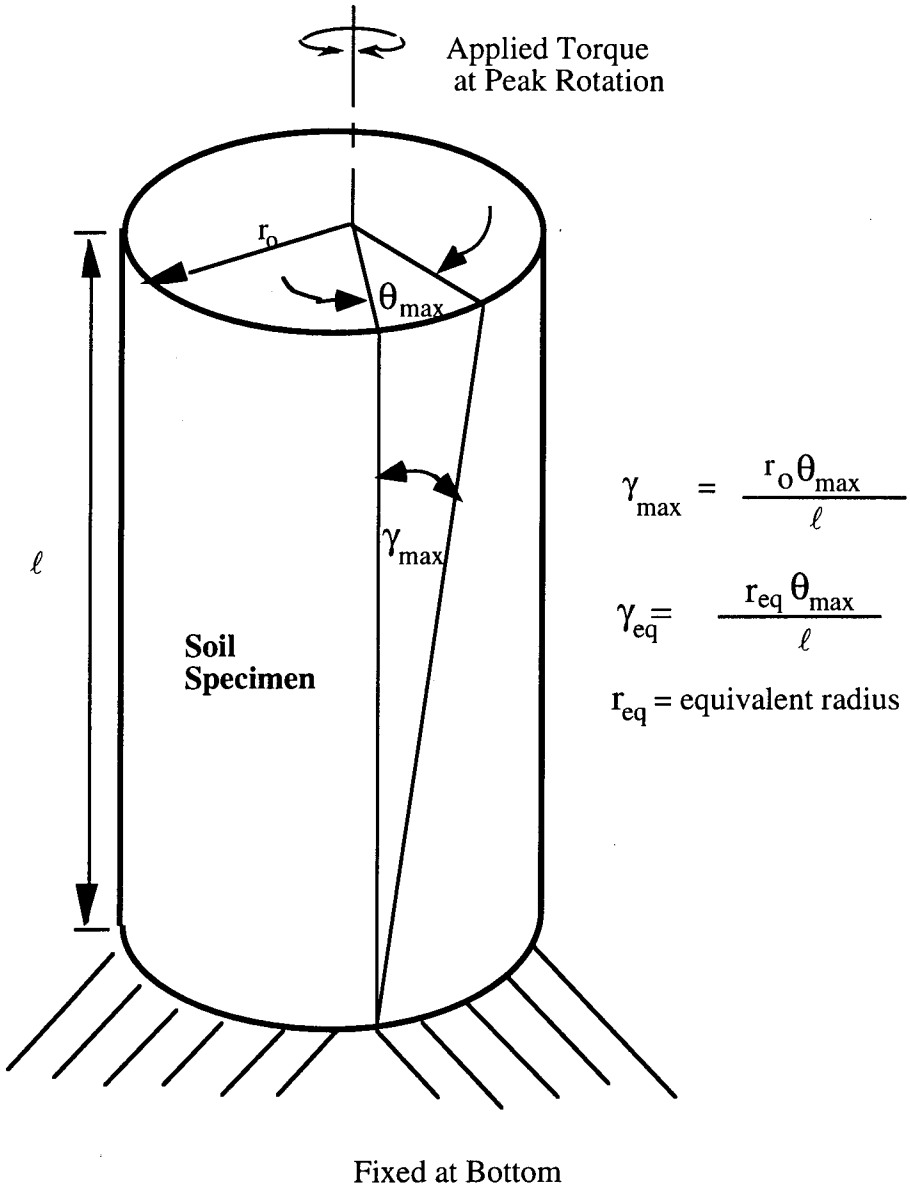

Figure 8.B.1.A-10
Shearing strain in soil column.

8.B.1.A.3.3 Material Damping

In the resonant column test, material damping ratio can be evaluated from either the free-vibration decay method or from the half-power bandwidth method. Each of these methods is discussed below. It is important to note that, in these measurements, the damping measurement includes material damping in the soil plus any damping in the equipment. Calibration of equipment damping is discussed in Section 8.B.1.A.5.

Free-Vibration Decay Method. Material damping in soils can be quite complex to define. However, the theory for a single-degree-of-freedom system with viscous damping is a useful framework for describing the effect of damping which occurs in soil (Richart et al., 1970). The decay of free vibrations of a single-degree-of-freedom system with viscous damping is described by the logarithmic decrement, δ, which is the ratio of the natural logarithm of two successive amplitudes of motion as:

$$\delta = \ln\left(\frac{Z_1}{Z_2}\right) = \frac{2\pi D}{\sqrt{1-D^2}} \qquad \text{(8.B.1.A-6)}$$

Where,

Z_1 and Z_2 = two successive strain amplitudes of motion, and
D = material damping ratio.

The free-vibration decay curve is recorded using an oscilloscope by shutting off the driving force while the specimen is vibrating at the resonant frequency. The amplitude of each cycle is measured from the decay curve, and the logarithmic decrement is then calculated using Eq. 8.B.1.A-6. Material damping ratio is calculated from logarithmic decrement according to:

$$D = \sqrt{\frac{\delta^2}{4\pi^2 + \delta^2}} \qquad \text{(8.B.1.A-7)}$$

A typical damping measurement from a free-vibration decay curve (from a metal calibration specimen) is shown in Fig. 8.B.1.A-11.

In this method, it is not certain which strain amplitude is a representative strain for damping ratio calculated by Eq. 8.B.1.A-7 because strain amplitude decreases during free-vibration decay. In this study, a representative strain amplitude was used as the peak strain amplitude during steady-state vibration for shearing strains below 0.001%. However, at larger strains, the representative strain is smaller than the peak strain, and the average strain determined for the first three cycles of free vibration was used.

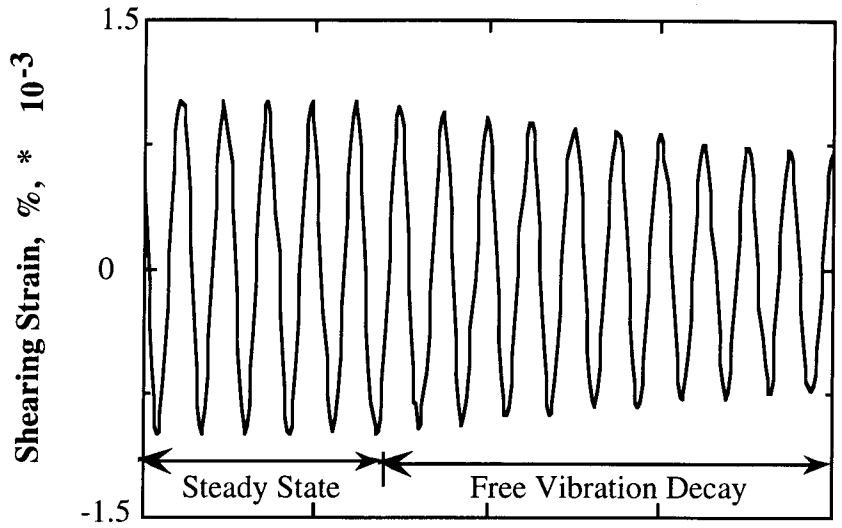

a) Free-Vibration Decay Curve

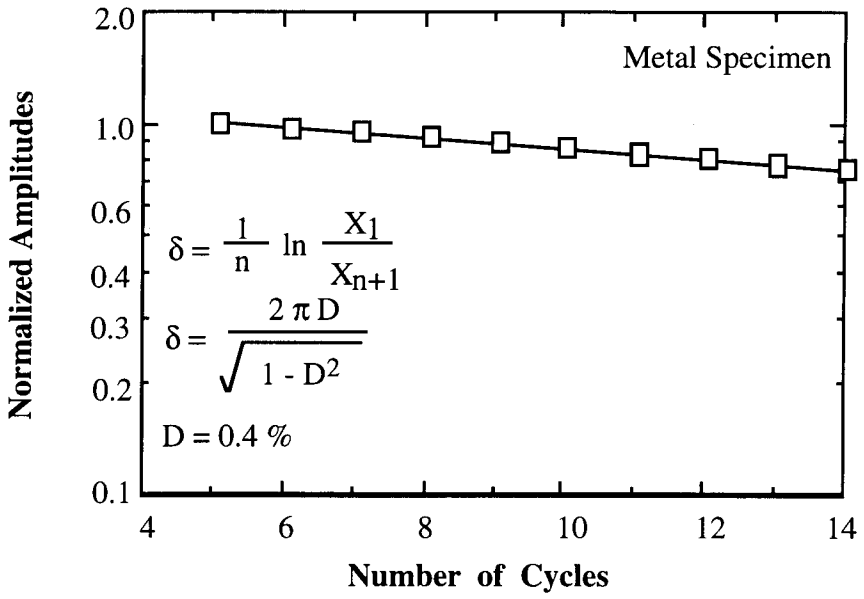

b) Analysis of Free-Vibration Decay Curve

Figure 8.B.1.A-11
Determination of material damping ratio from the free-vibration decay curve using a metal specimen.

Half-Power Bandwidth Method. Another method of measuring damping in the resonant column test is the half-power bandwidth method, which is based on measurement of the width of the frequency response curve near resonance. From the frequency response curve, the logarithmic decrement can be calculated from:

$$\delta = \frac{\pi}{2}\frac{f_2^2 - f_1^2}{f_r^2}\sqrt{\frac{A^2}{A_{max}^2 - A^2}\frac{\sqrt{1-2D^2}}{1-D^2}} \qquad \text{(8.B.1.A-8)}$$

Where,

f_1 = frequency below the resonance where the strain amplitude is A,
f_2 = frequency above the resonance where the strain amplitude is A,
f_r = resonant frequency, and
D = material damping ratio.

If the damping ratio is small and A is chosen as 0.707 A_{max}, which is called the half-power point, Eq. 8.B.1.A-8 can be simplified as:

$$\delta \cong \pi \bullet \frac{f_2 - f_1}{f_r} \qquad \text{(8.B.1.A-9)}$$

Therefore, the damping ratio can be expressed as:

$$D \cong \frac{f_2 - f_1}{2f_r} \qquad \text{(8.B.1.A-10)}$$

A typical damping measurement by the half-power bandwidth method (for a metal calibration specimen) is shown in Fig. 8.B.1.A-12.

Background noise can be a problem in measuring material damping using the free-vibration decay method at strains less than about 0.001%. On the other hand, background noise generally has a smaller effect on the frequency response curve at strains below 0.001%. Therefore, the half-power bandwidth method is preferred to the free-vibration decay method for making small-strain damping measurements. However, at large strains, symmetry in the frequency response curve is no longer maintained, and a serious error can be introduced in the half-power bandwidth method (Ni, 1987). In this study, both types of damping measurements were made at small-strains in an attempt to obtain good data sets while only the free-vibration decay method was used at larger strains (above 0.001%).

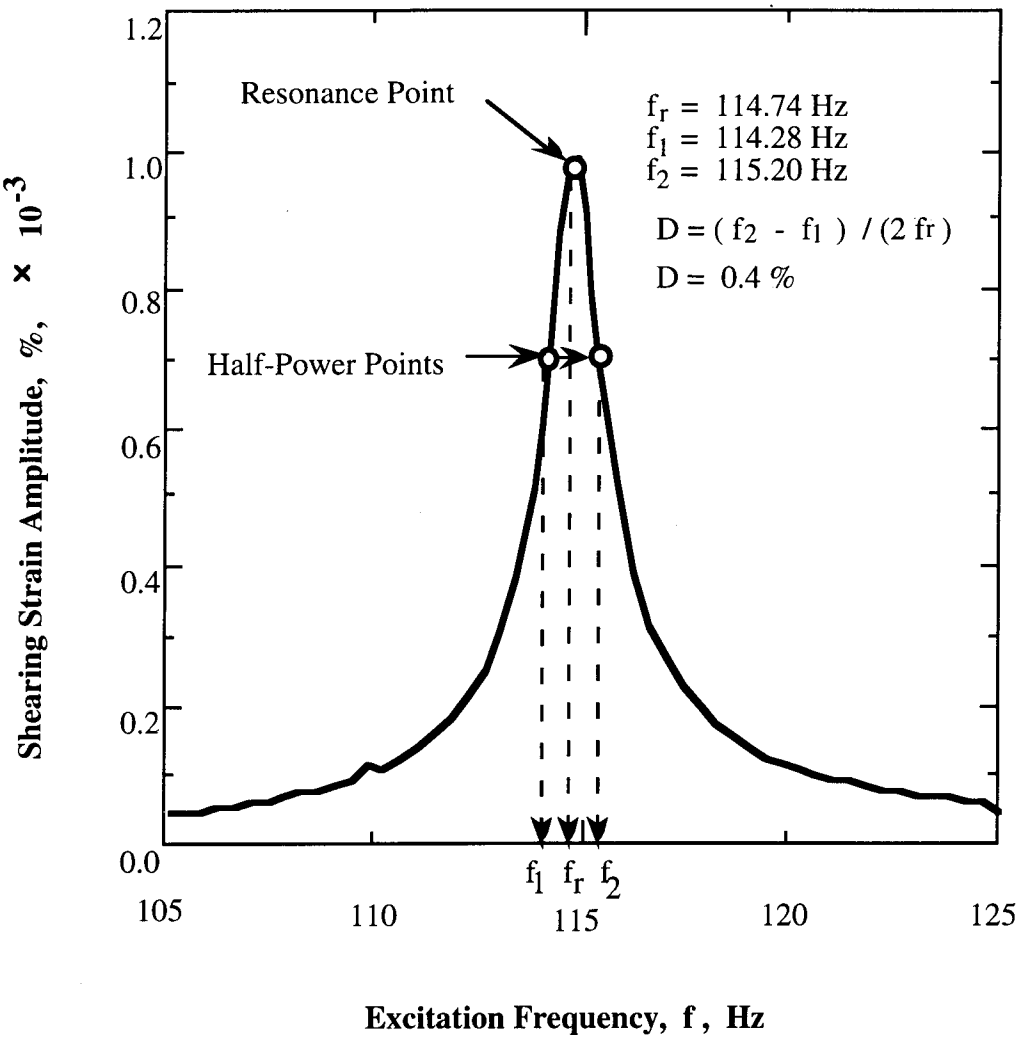

Figure 8.B.1.A-12
Determination of material damping from the half-power bandwidth method using a metal specimen.

8.B.1.A.4 Method of Analysis in the Torsional Shear Test

The torsional shear test is another method of determining the deformational characteristics (modulus and damping) of soil using the same RCTS device. Rather than measuring the dynamic response of the specimen, the actual stress-strain hysteresis loop is determined by means of measuring the torque-twist curve. Shear modulus is calculated from the slope of the hysteresis loop, and the hysteric damping ratio is calculated using the area of the hysteresis loop.

8.B.1.A.4.1 Shear Modulus

Because shear modulus is calculated from the stress-strain hysteresis loop, shearing stress and shearing strain in the torsional shear test need to be defined.

Shearing Stress. Determination of shearing stress in the torsional shear test is based on the theory of elasticity for circular or tubular rods in pure torsion. Assume that pure torque, T, is applied to the top of the specimen. The torque can be calculated from:

$$T = \int_{r_i}^{r_o} \tau_r (2 \pi r) \; r \, dr \qquad \text{(8.B.1.A-11)}$$

where τ_r is the shearing stress at a distance r from the axis of specimen and, r_o and r_i are outside and inside radii, respectively. If the shearing stress is assumed to vary linearly across the radius:

$$\tau_r = \tau_m \bullet (r / r_o) \qquad \text{(8.B.1.A-12)}$$

where τ_m is the maximum shearing stress at $r = r_o$. Eq. 8.B.1.A-12 can be rewritten as:

$$T = \frac{\tau_m}{r_o} \bullet \frac{\pi}{2} \bullet (r_o^4 - r_i^4) = \frac{\tau_m}{r_o} \bullet J_p \qquad \text{(8.B.1.A-13)}$$

where J_p is the area polar moment of inertia. From Eq. 8.B.1.A-13, one can write:

$$\tau_m = r_o \bullet \frac{T}{J_p} \qquad \text{(8.B.1.A-14)}$$

Because shearing stress is assumed to vary linearly across the radius, the average torsional shearing stress is defined as:

$$\tau_{avg} = r_{eq} \bullet \frac{T}{J_p} \qquad \text{(8.B.1.A-15)}$$

The value of r_{eq} is the same value as used in the resonant column analysis for calculation of shearing strain (Section 8.B.1.A.3.2).

The value of applied torque, T, is calculated from the input voltage applied to the drive system, V_T (Volts), and the torque calibration factor, K_T (torque / Volts). Thus, average shearing stress becomes:

$$\tau_{avg} = r_{eq} \bullet K_T \bullet V_T / J_p \qquad \text{(8.B.1.A-16)}$$

Shearing Strain. Calculation of shearing strain in the torsional shear test follows the same procedure used in the resonant column test. The proximitor system directly measures the displacement (instead of acceleration measured in the resonant test). Hence, the angle of twist (θ) is calculated from the proximitor output voltage, V_P (volts), and the proximitor calibration factor, K_P (rad / volt). Shearing strain, γ, is then calculated from:

$$\gamma = r_{eq} \, \Sigma \, K_P \bullet V_P / l \qquad \text{(8.B.1.A-17)}$$

Shear Modulus. Once the stress-strain hysteresis loop is measured, the shear modulus, G, is calculated from the slope of a line through the end points of the hysteresis loop as shown in Fig. 8.B.1.A-13. Thus, the shear modulus is calculated from:

$$G = \tau / \gamma \qquad \text{(8.B.1.A-18)}$$

where τ is peak shearing stress and γ is peak shearing strain.

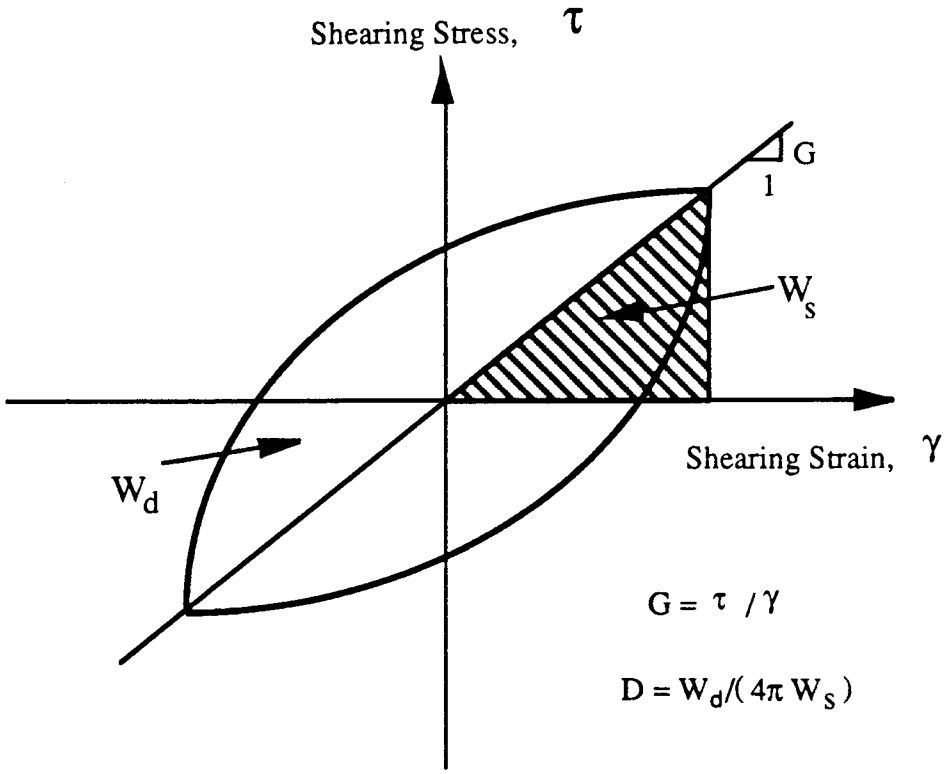

Figure 8.B.1.A-13
Determination of shear modulus and damping ratio in the torsional shear test.

8.B.1.A.4.2 Hysteretic Damping Ratio

Hysteretic damping ratio in the torsional shear test is measured using the amount of energy dissipated in one complete cycle of loading and the peak strain energy stored in the specimen during the cycle.

In the torsional shear test, the dissipated energy is measured from the area of the stress-strain hysteresis loop. The energy per cycle, W_d, due to a viscous damping force, F_d, is:

$$W_d = \int_o^T F_d \bullet \dot{x}\, dt \qquad \text{(8.B.1.A-19)}$$

where $\dot{x}$ is a velocity and T is a period. For simple harmonic motion with frequency of ω, i.e. $x = A \cos(\omega t - \phi)$, W_d become:

$$W_d = \pi c \omega A^2 \qquad \text{(8.B.1.A-20)}$$

From the Eq. 8.B.1.A-20, the viscous damping coefficient can be expressed as:

$$c = W_d / (\pi \omega A^2) \quad (8.B.1.A\text{-}21)$$

The peak strain energy, W_s, stored by the spring is equal to the area under the secant modulus line in Fig. 8.B.1.A-13 and can be written as:

$$W_s = k A^2 / 2 \quad (8.B.1.A\text{-}22)$$

The critical damping coefficient, C_c, is

$$C_c = 2 \bullet \sqrt{k m} = 2 k / \omega_n \quad (8.B.1.A\text{-}23)$$

where k is an elastic spring constant, m is a mass, and ω_n is a natural frequency of system. Using Eq. 8.B.1.A-22, Eq. 8.B.1.A-23 can be rewritten as:

$$C_c = 4 W_s / (\omega_n A^2) \quad (8.B.1.A\text{-}24)$$

Therefore, the damping ratio, D, can be expressed as:

$$D = C / C_c = W_d / (4 \pi W_s) * (\omega_n / \omega) \quad (8.B.1.A\text{-}25)$$

For soils, material damping is often assumed to be frequency independent. Therefore, ω_n / ω is ignored and hysteretic damping is written as:

$$D = \frac{1}{4\pi} * \frac{W_d}{W_s} \quad (8.B.1.A\text{-}26)$$

where W_d is the area of the hysteresis loop and W_s is the area of the triangle as shown in Fig. 8.B.1.A-13.

8.B.1.A.5 Evaluation of RCTS Equipment Compliance With Metal Specimens

To evaluate the RCTS equipment for system compliance, metal specimens were used. The metal specimens were made of brass and aluminum tubes. Eighteen metal specimens of different sizes and materials were used to obtain different resonant frequencies. Details of the metal specimens are presented in Table 8.B.1.A-1. It was assumed that the metal specimens should have (essentially) zero damping and that these specimens should exhibit no effect of frequency on stiffness or damping over the complete range of frequencies used in these tests (from about 0.05 Hz to 400 Hz).

Table 8.B.1.A-1
Metal Specimens Used to Evaluate Equipment Damping Ratio

Specimen Number	Outside Diameter		Inside Diameter		Height		Weight
	inch	cm	inch	cm	inch	cm	gram
1(Brass Tube)	1.000	2.540	0.875	2.223	4.98	12.65	132.35
2(Brass Tube)	0.875	2.223	0.813	2.064	6.96	17.68	79.96
3(Brass Tube)	0.875	2.223	0.813	2.064	8.49	21.56	97.07
4(Brass Tube)	0.750	1.905	0.688	1.746	6.97	17.70	70.72
5(Brass Tube)	0.750	1.905	0.688	1.746	8.49	21.57	85.87
6(Brass Tube)	0.625	1.588	0.563	1.429	6.96	17.68	58.45
7(Brass Tube)	0.625	1.588	0.563	1.429	8.49	21.57	70.94
8(Brass Tube)	0.375	0.953	0.313	0.794	6.94	17.63	33.69
9(Brass Tube)	0.375	0.953	0.313	0.794	8.44	21.45	40.86
10(Brass Rod)	0.313	0.794	0	0	6.92	17.57	74.46
11(Brass Rod)	0.313	0.794	0	0	8.44	21.44	90.30
12(Brass Rod)	0.500	1.270	0	0	7.00	17.78	191.22
13(Brass Rod)	0.750	1.905	0	0	7.00	17.75	429.52
14(Brass Rod)	0.250	0.635	0	0	6.96	17.67	47.53
15(Brass Rod)	1.500	3.810	0	0	7.00	17.78	1731.64
16(Brass Tube)	0.500	1.270	0.438	1.111	6.97	17.71	44.63
17(Brass Tube)	0.500	1.270	0.438	1.111	8.48	21.53	54.29
18(Brass Tube)	1.000	2.540	0.875	2.223	6.97	17.70	178.50

Unit Weight of Brass = 8.49 g/cm^3 (=0.316 lbs/in^3)

Hysteresis loops with one metal specimen measured at a frequency of 0.5 Hz are shown in Fig. 8.B.1.A-14. The stress-strain curve is linear, resulting in no damping as expected. On the other hand, Figs. 8.B.1.A-11 and 8.B.1.A-12 show the damping measurements with the same metal specimen in the resonant column test predict an apparent damping of 0.4% from both the free-vibration decay and half-power bandwidth methods.

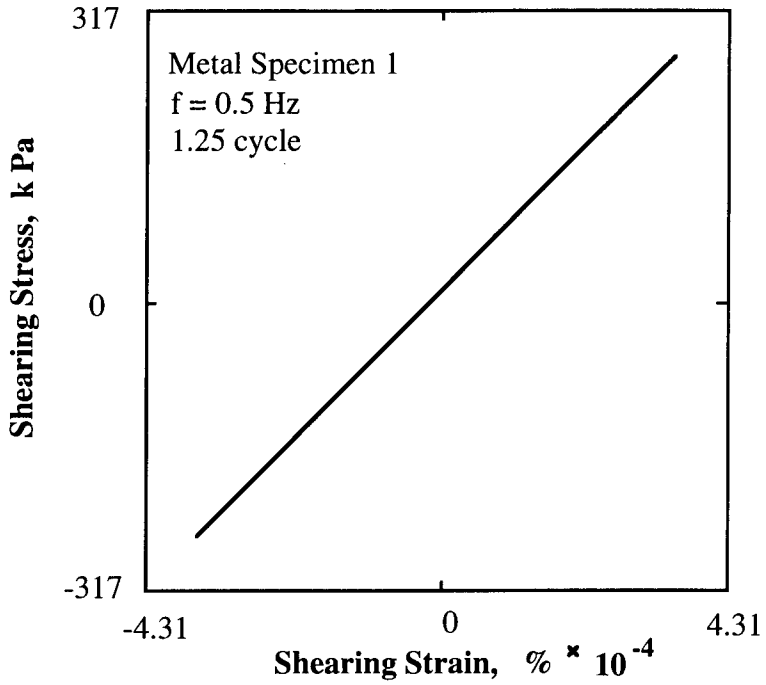

Figure 8.B.1.A-14
Hysteresis loops of metal specimen determined by torsional shear testing at a frequency of 0.5 Hz.

The variations in shear modulus and damping ratio with loading frequency for four of the metal specimens are plotted in Fig. 8.B.1.A-15. The shear modulus of each metal specimen determined from the RCTS equipment is independent of loading frequency as expected. Therefore, shear modulus can be measured properly with RCTS equipment over a wide frequency range without any compliance problem.

On the other hand, the damping ratio measured by the RCTS equipment is affected by the loading frequency. For frequencies less than or equal to 0.5 Hz, damping ratio evaluated by the torsional shear test is essentially zero as expected. In this frequency range, material damping can be evaluated without any equipment correction. For higher frequencies, however, non-zero damping values are obtained with all metal specimens in the torsional shear as shown in Figs. 8.B.1.A-15b and 8.B.1.A-16. In this case the apparent material damping increases significantly as the excitation frequency increases from 1 to 10 Hz. Strain amplitude has little effect on the damping values as shown in Fig. 8.B.1.A-16. These values of apparent material damping are considered to be due to a compliance problem with the complete RCTS system (back-EMF generated by the drive system) and are, therefore, subtracted from all damping measurements in the torsional shear test at the same frequencies when soil specimens are tested.

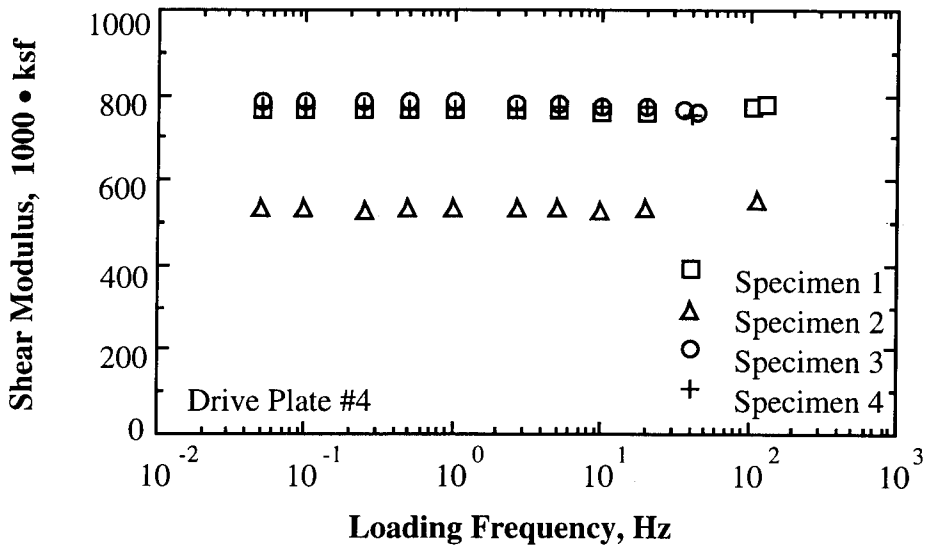

a) Variation in Shear Modulus

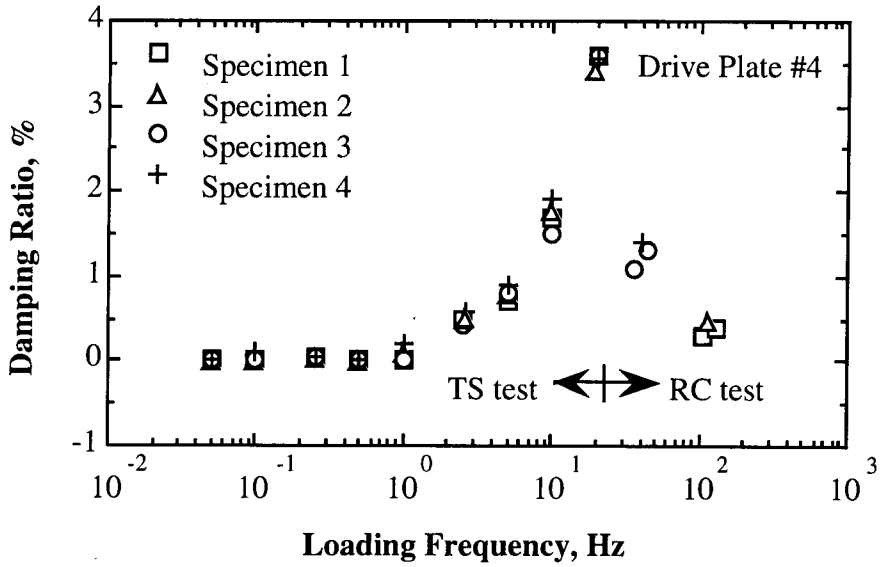

b) Variation in Material Damping Ratio

Figure 8.B.1.A-15
Variation in shear modulus and material damping ratio with loading frequency determined for metal specimens (from Kim, 1991).

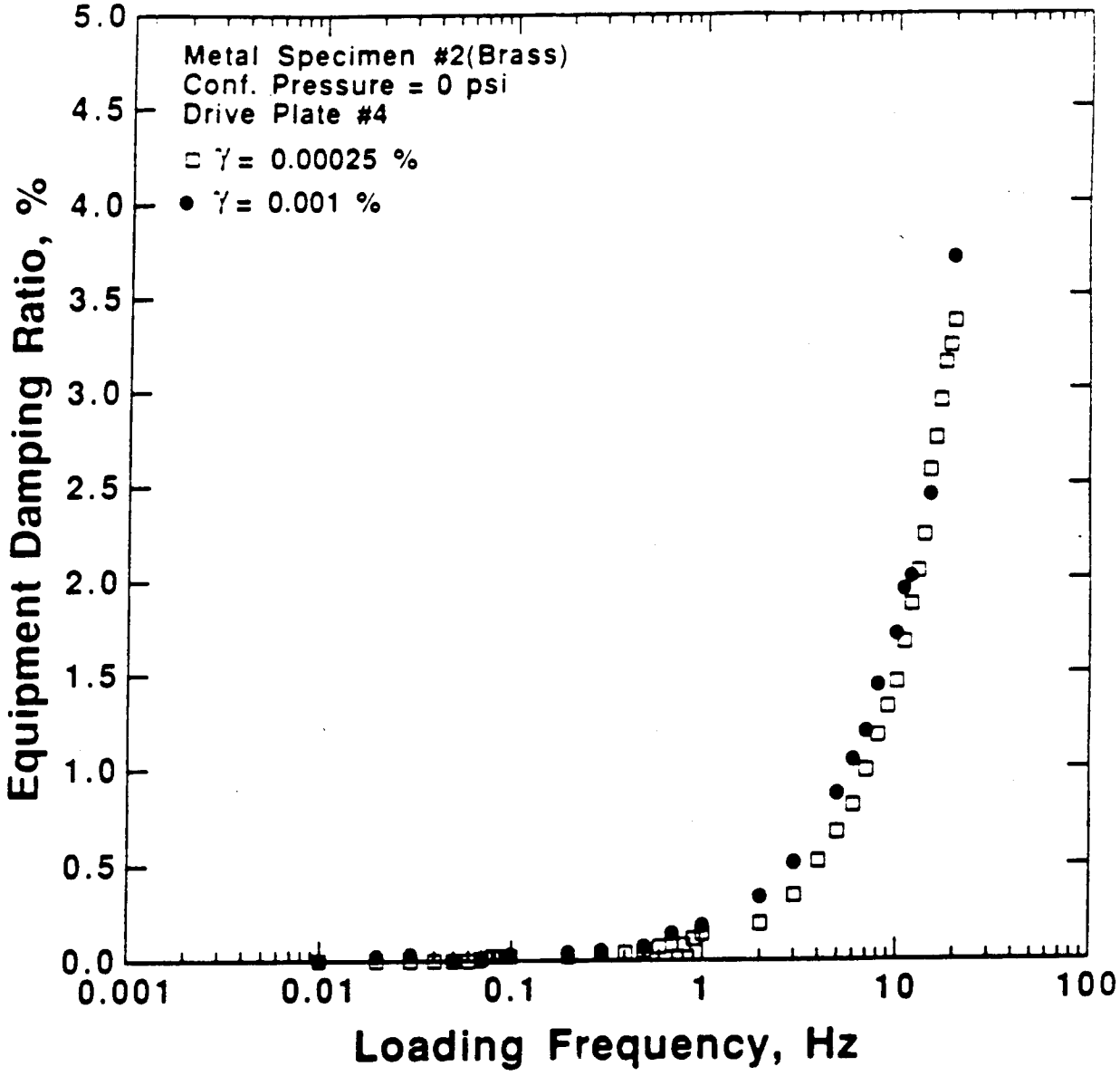

Fig. 8.B.1.A-16
Measured damping ratio for metal specimen #2 in the torsional shear test.

It should be noted that excitation frequencies in the torsional shear test never exceeded 0.1 times the resonant frequency of the soil specimen. This approach was followed so that dynamic amplification did not affect the TS measurements. Even in this case, however, corrections were made for minor dynamic amplification which occurs near 0.1 times the resonant frequency.

In the resonant column test, non-zero damping values were obtained at all resonant frequencies as seen in Figs. 8.B.1.A-15b and 8.B.1.A-17. Equipment damping values ranged from about 3.5% at 20 Hz to about 0.4% at 200 Hz. These resonant frequencies are in the frequency range where all soil testing was conducted. Just as in the TS test, the values of equipment damping measured with the metal specimens were subtracted from the damping measurements in all RC tests with soil specimens at the same resonant frequencies. Strain amplitude had a negligible effect on equipment damping as shown in Fig. 8.B.1.A-18.

Finally, to be sure that coil-magnet interaction was the cause of the equipment damping problem, free-vibration tests were conducted with the RC equipment. In this case, however, all coils were removed which required that the drive plate be excited by hand in free vibration. The resulting tests with drive plate #4 are given in Fig. 8.B.1.A-19 by the solid square symbols. As seen, damping values less than 0.1% were measured. These values are considered to equal zero in this work, indicating the coil-magnet interaction is mainly the cause of the equipment damping.

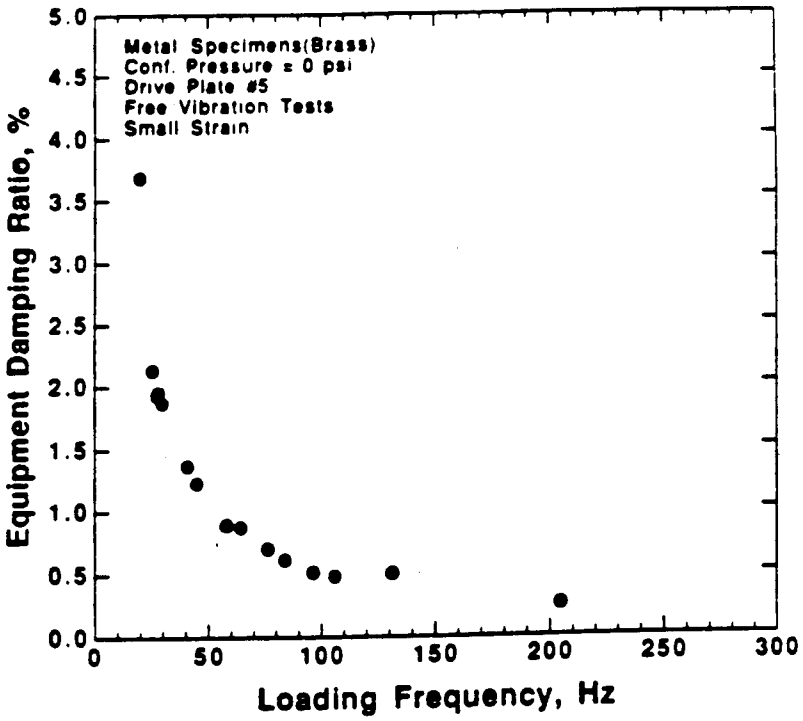

a. Damping from the Free-Vibration Decay Curve

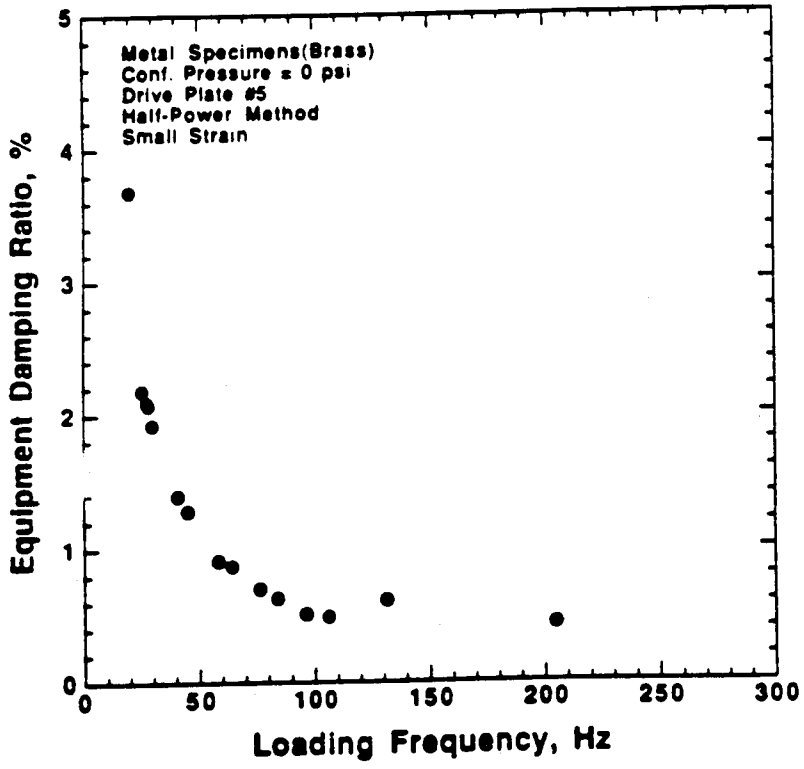

b. Damping from the Half-Power Bandwidth

Figure 8.B.1.A-17
Equipment damping measured in the resonant column test.

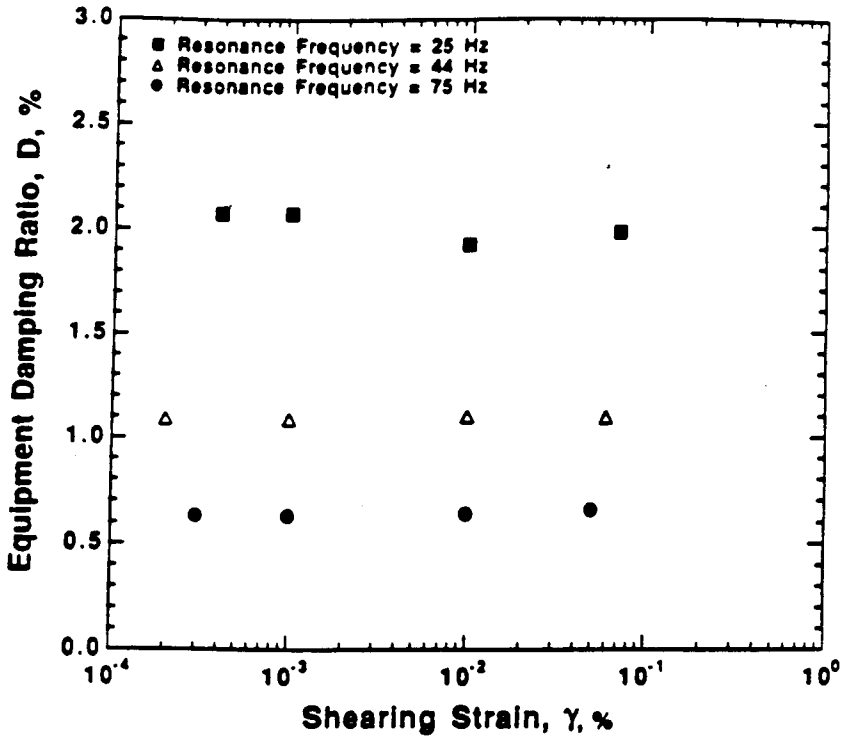

Figure 8.B.1.A-18
Effect of strain amplitude on equipment damping measured in the resonant column test.

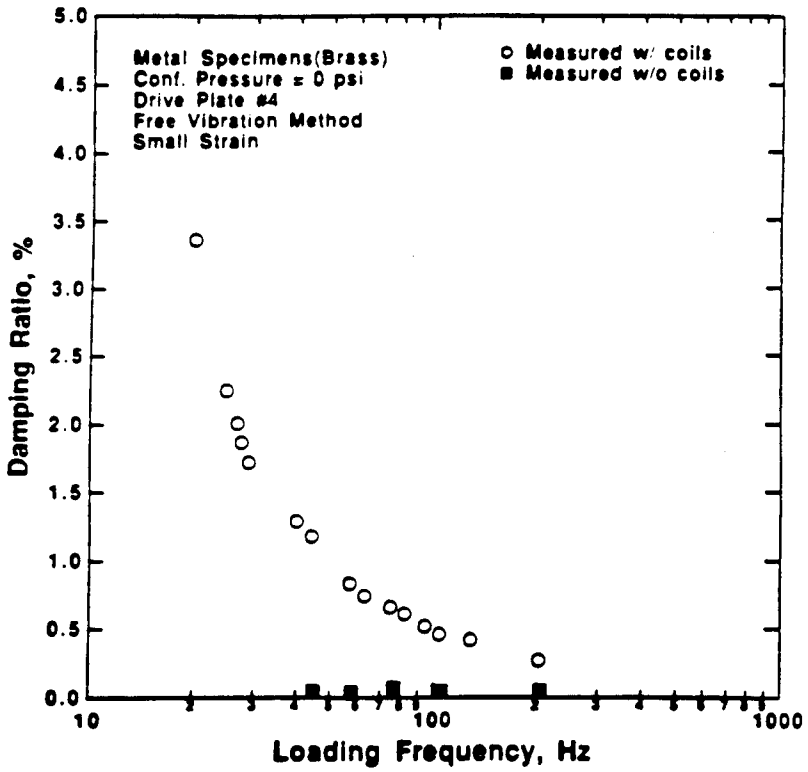

Figure 8.B.1.A-19
Comparison of equipment damping measured in free vibration RC tests with and without the electrical coils.

References

Chen, A.T.F., Stokoe, K.H., II (1979), "Interpretation of Strain Dependent Modulus and Damping from Torsional Soil Tests," Report No. USGS-GD-79-002, NTIS No. PB-298479, U.S. Geological Survey, 46 pp.

Isenhower, W.M. (1979), "Torsional Simple Shear/Resonant Column Properties of San Francisco Bay Mud," Geotechnical Engineering Thesis, GT 80-1, University of Texas, Dec., 307 pp.

Kim, D.-S. (1991), "Deformational Characteristics of Soils at Small to Intermediate Strains from Cyclic Tests," Ph.D. Dissertation, The University of Texas at Austin, 341 pp.

Lodde, P.F. (1982), "Shear Moduli and Material Damping of San Francisco Bay Mud," M.S. Thesis, The University of Texas at Austin.

Ni, S.-H. (1987), "Dynamic Properties of Sand Under True Triaxial Stress States from Resonant Column/Torsional Shear Tests," Ph.D. Dissertation, The University of Texas at Austin, 421 pp.

Richart, F.E., Jr., Hall, J.R., Jr. and Woods, R.D. (1970), *Vibrations of Soils and Foundations*, Prentice-Hall Inc., Englewood Cliffs, New Jersey, 414 pp.

APPENDIX 8.B.1.B
DYNAMIC TESTS OF SAMPLE T1, DEPTH = 17.5 FT (5.3 M)

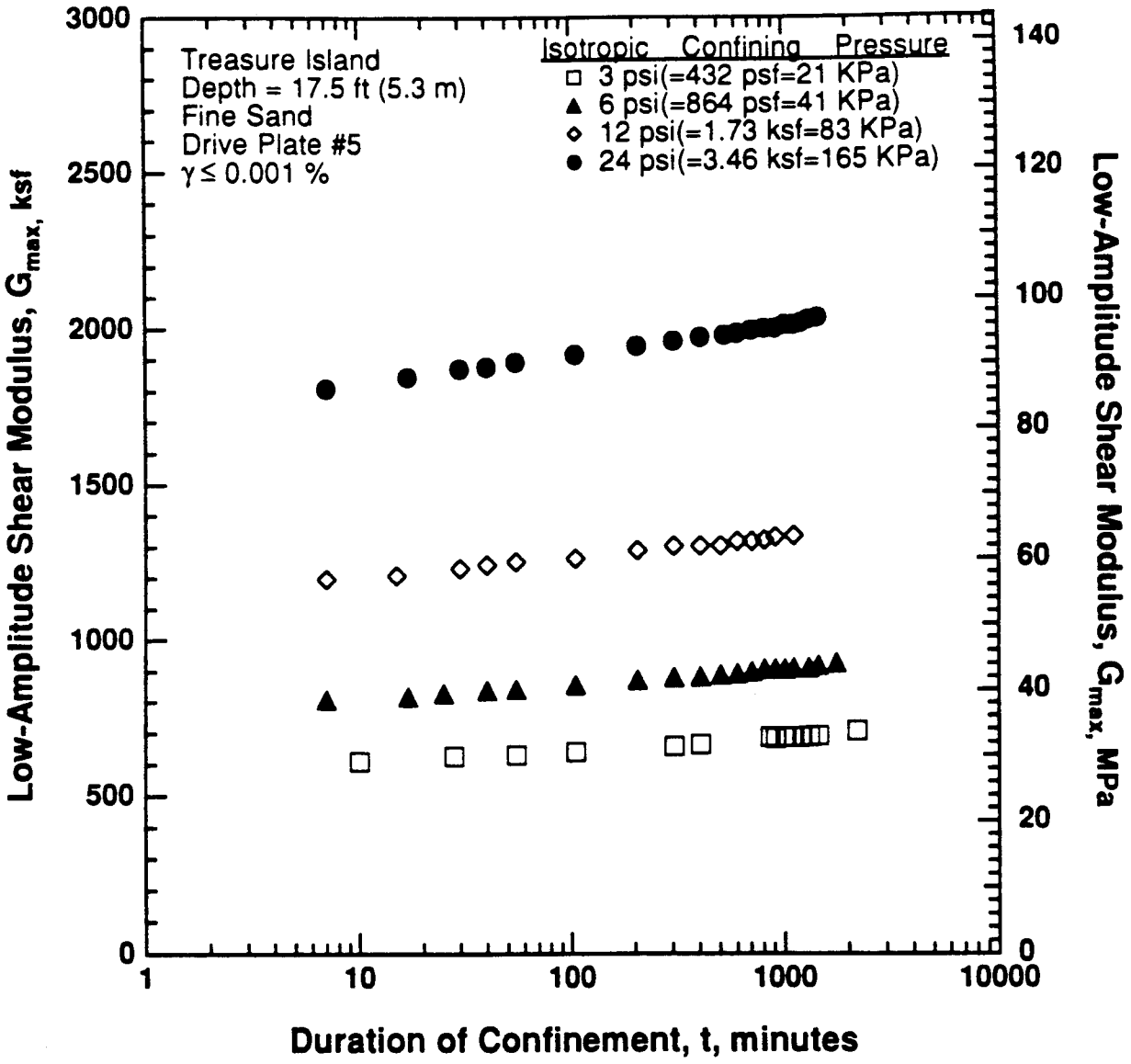

Figure 8.B.1.B-1
Variation in low-amplitude shear modulus with magnitude and duration of isotropic confining pressure from resonant column tests of sample T1.

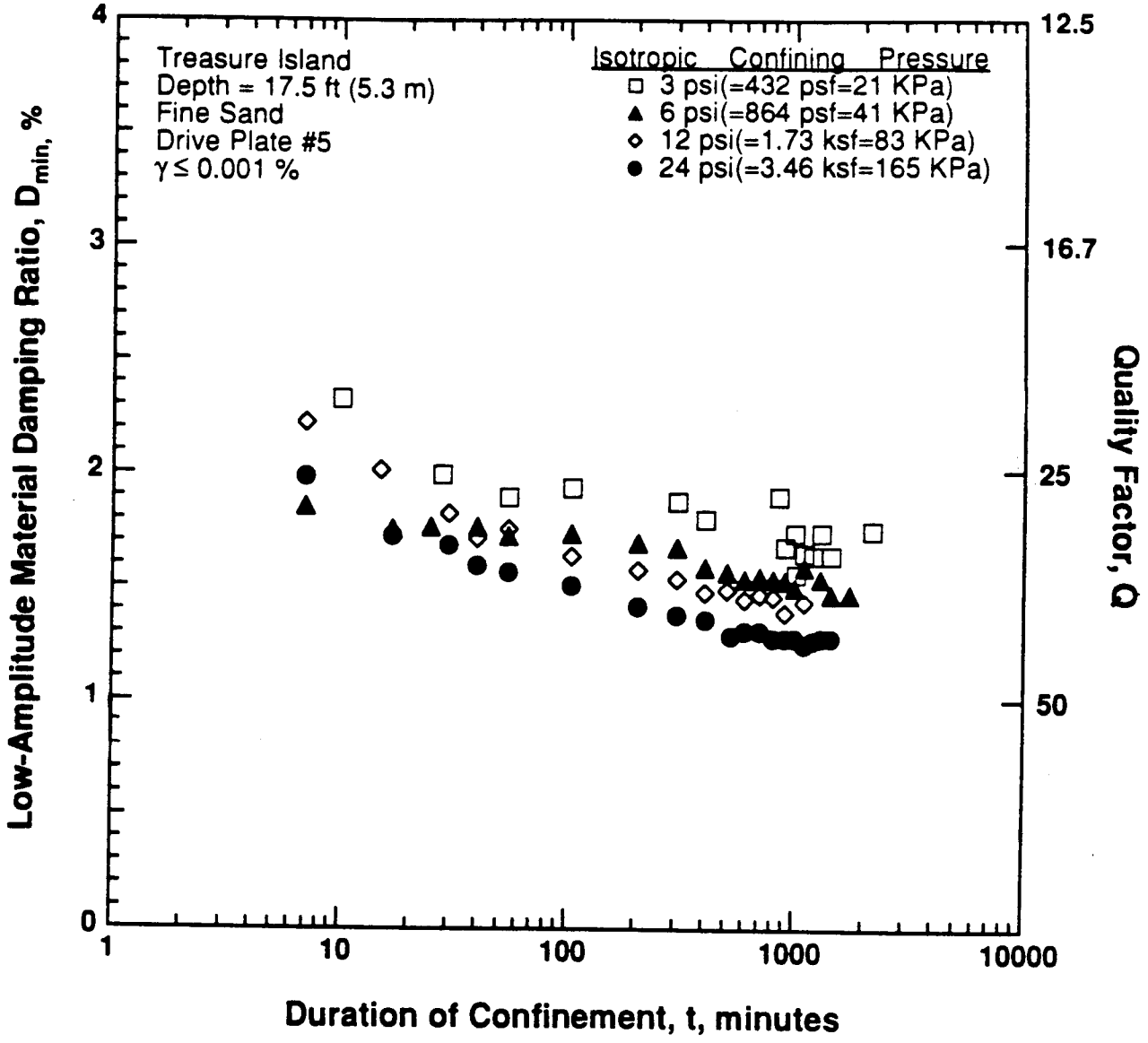

Figure 8.B.1.B-2
Variation in low-amplitude material damping ratio with magnitude and duration of isotropic confining pressure from resonant column tests of sample T1.

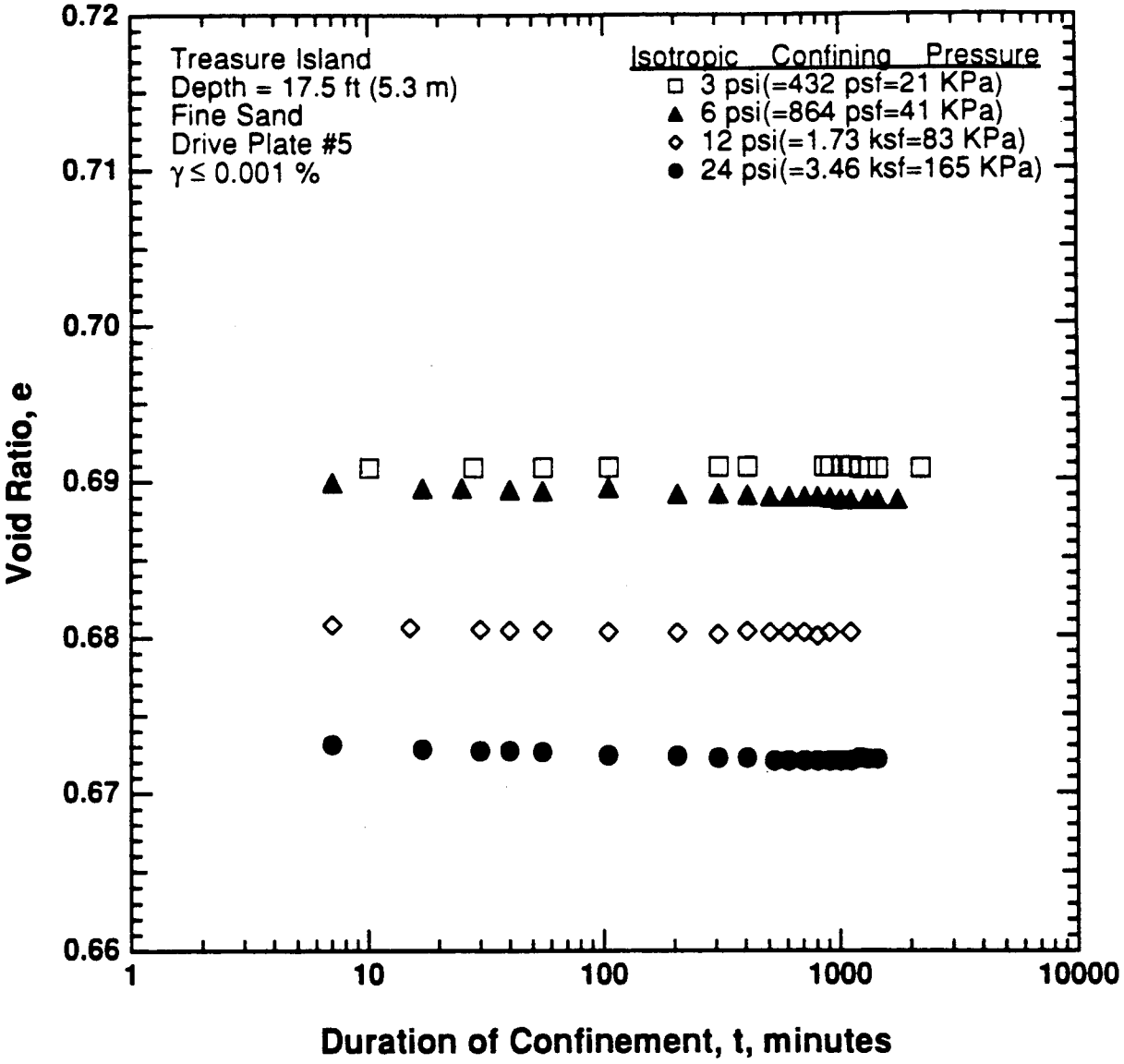

Figure 8.B.1.B-3
Variation in void ratio with magnitude and duration of isotropic confining pressure from resonant column tests of sample T1.

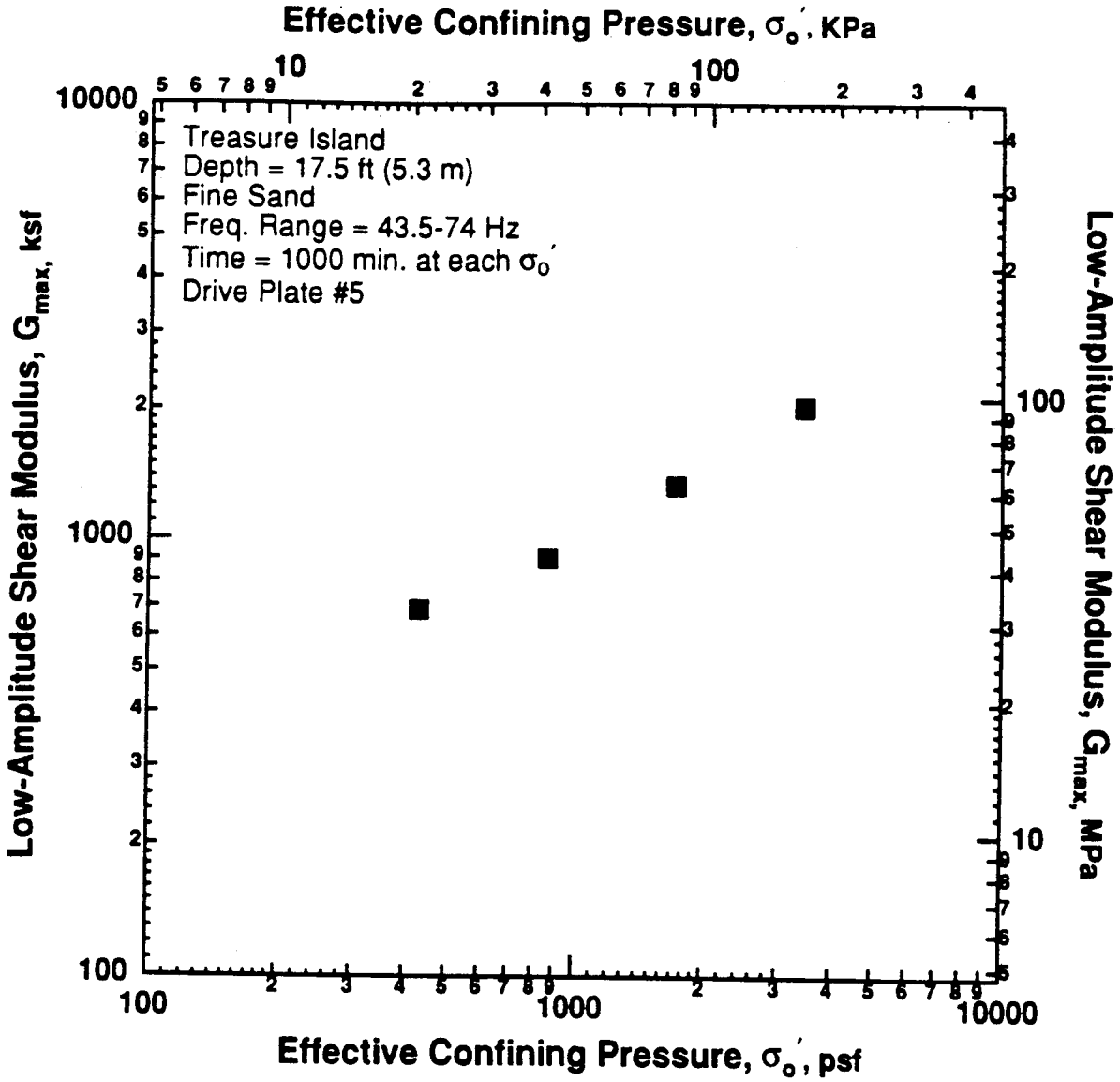

Figure 8.B.1.B-4
Variation in low-amplitude shear modulus with effective confining pressure from resonant column tests of sample T1.

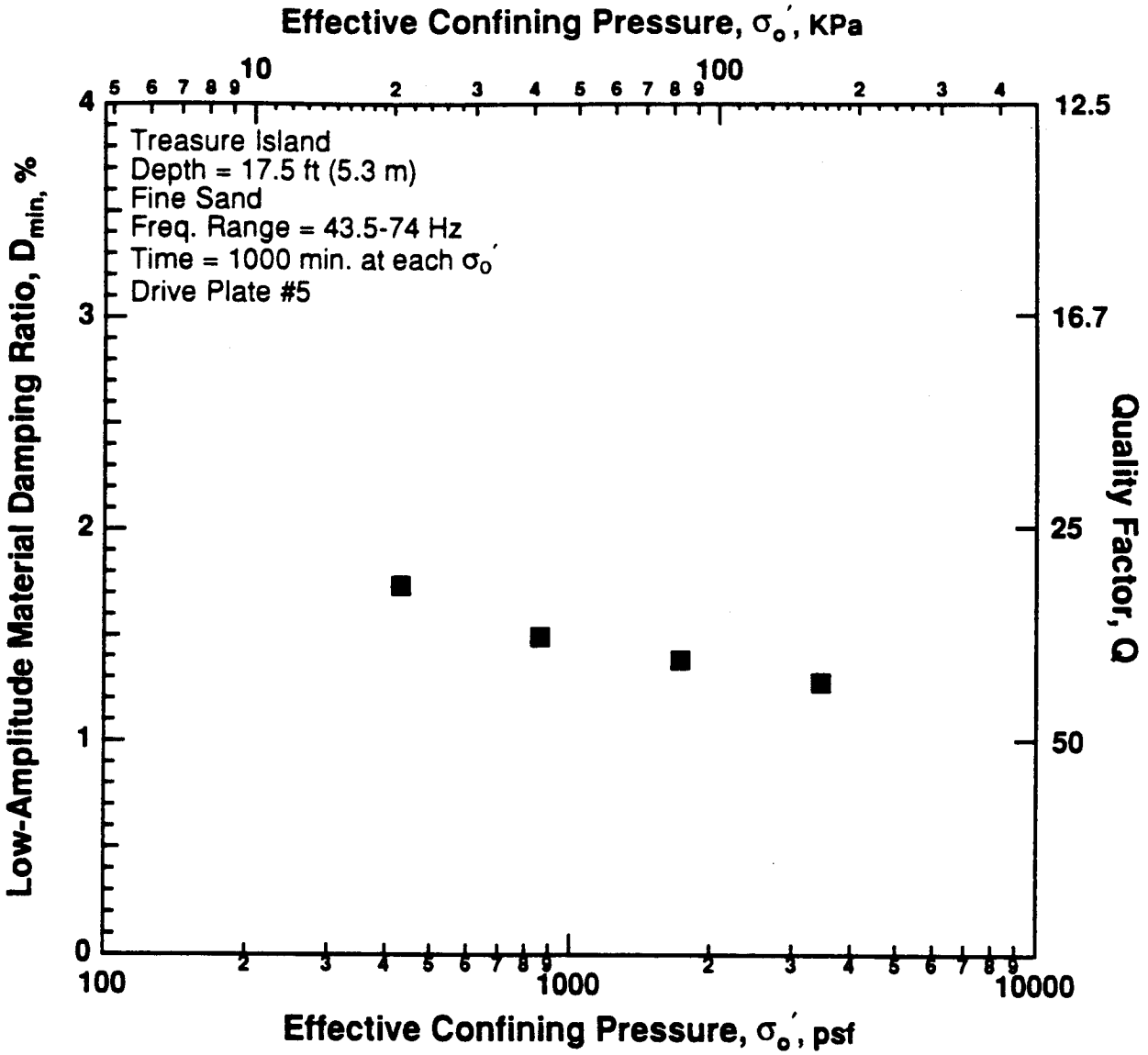

Figure 8.B.1.B-5
Variation in low-amplitude material damping ratio with effective confining pressure from resonant column tests of sample T1.

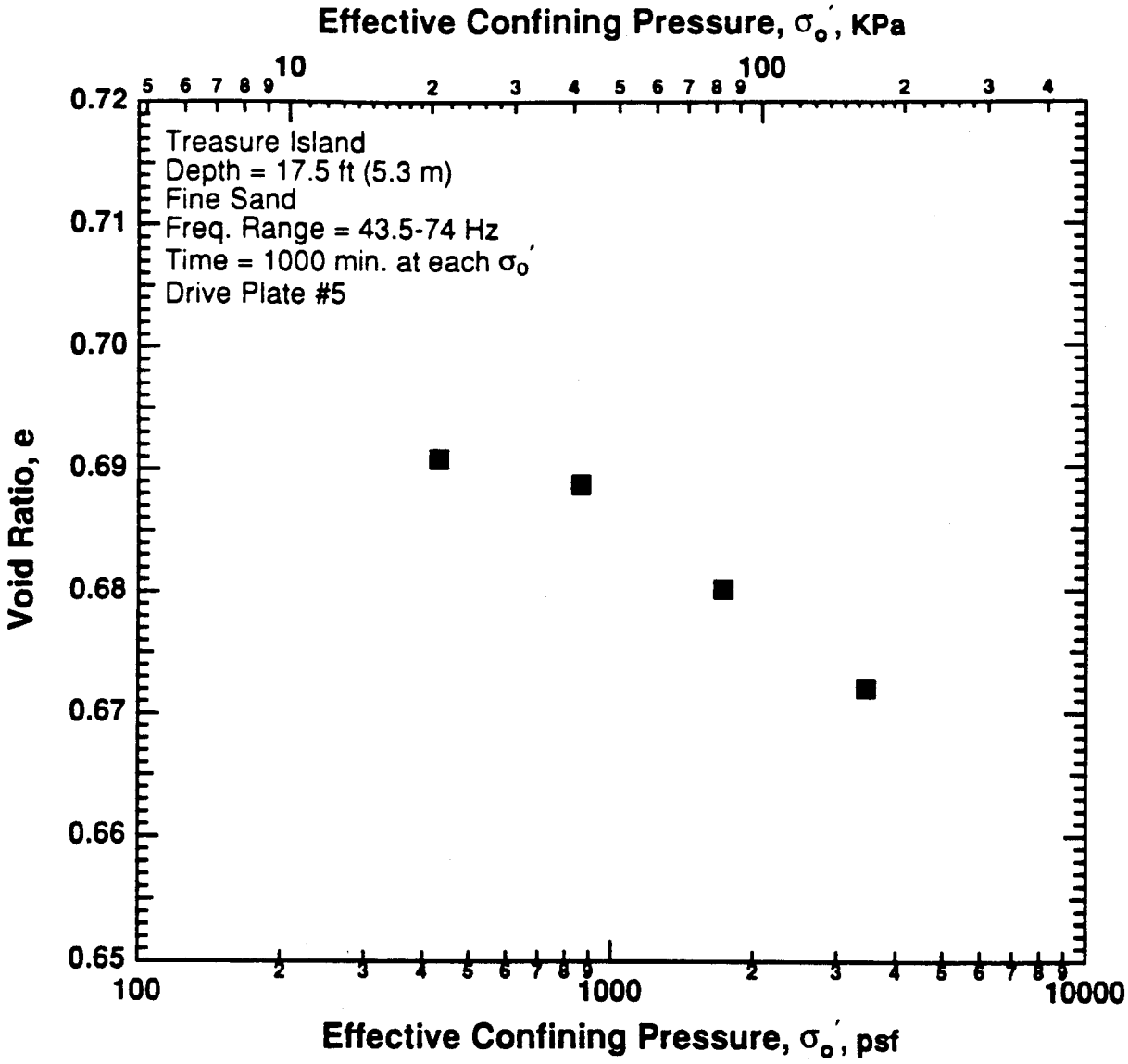

Figure 8.B.1.B-6
Variation in void ratio with effective confining pressure from resonant column tests of sample T1.

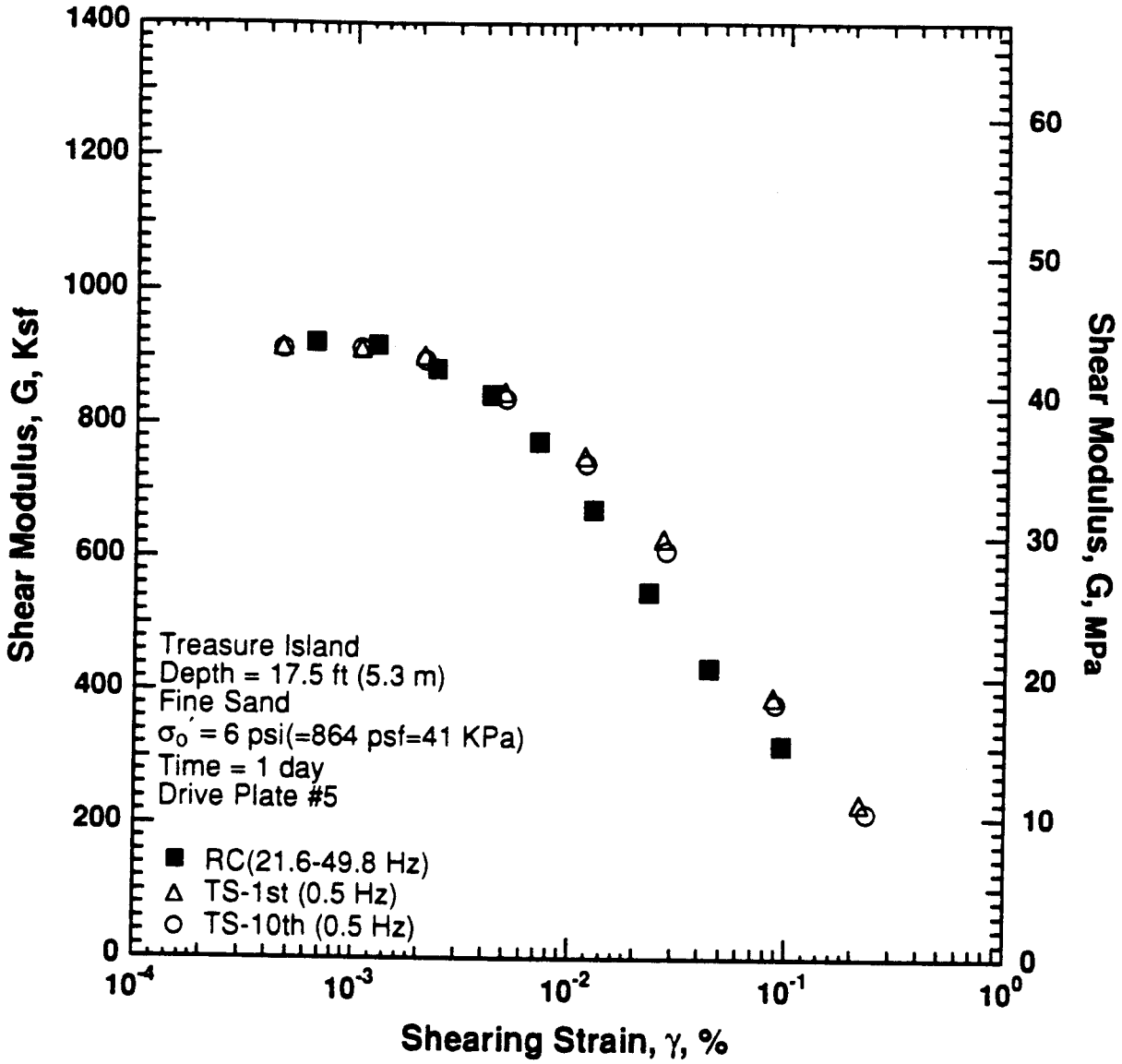

Figure 8.B.1.B-7
Variation in shear modulus with shearing strain at an effective confining pressure of 6 psi (864 psf, 41 kPa) from RCTS tests of sample T1.

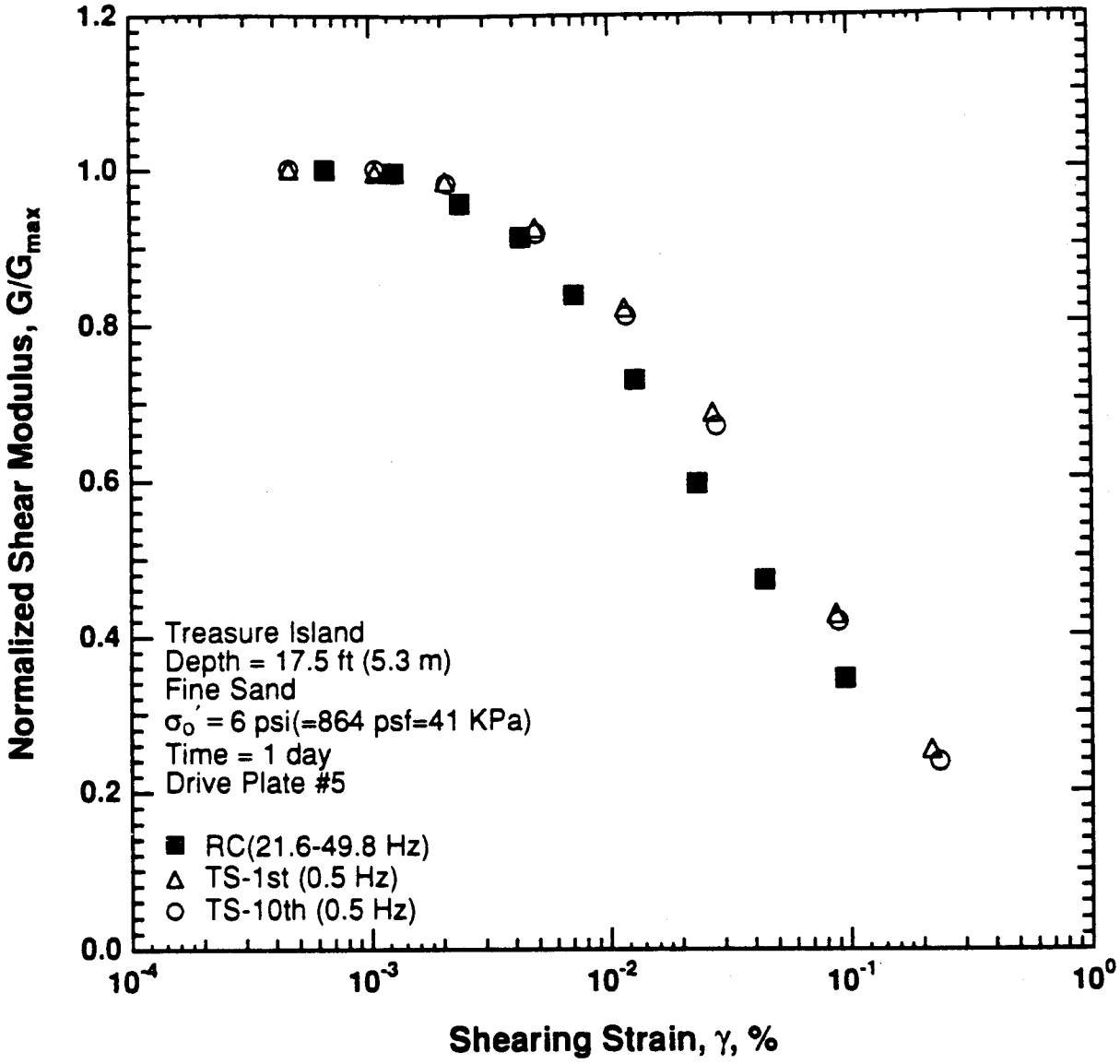

Figure 8.B.1.B-8
Variation in normalized shear modulus with shearing strain at an effective confining pressure of 6 psi (864 psf, 41 kPa) from RCTS tests of sample T1.

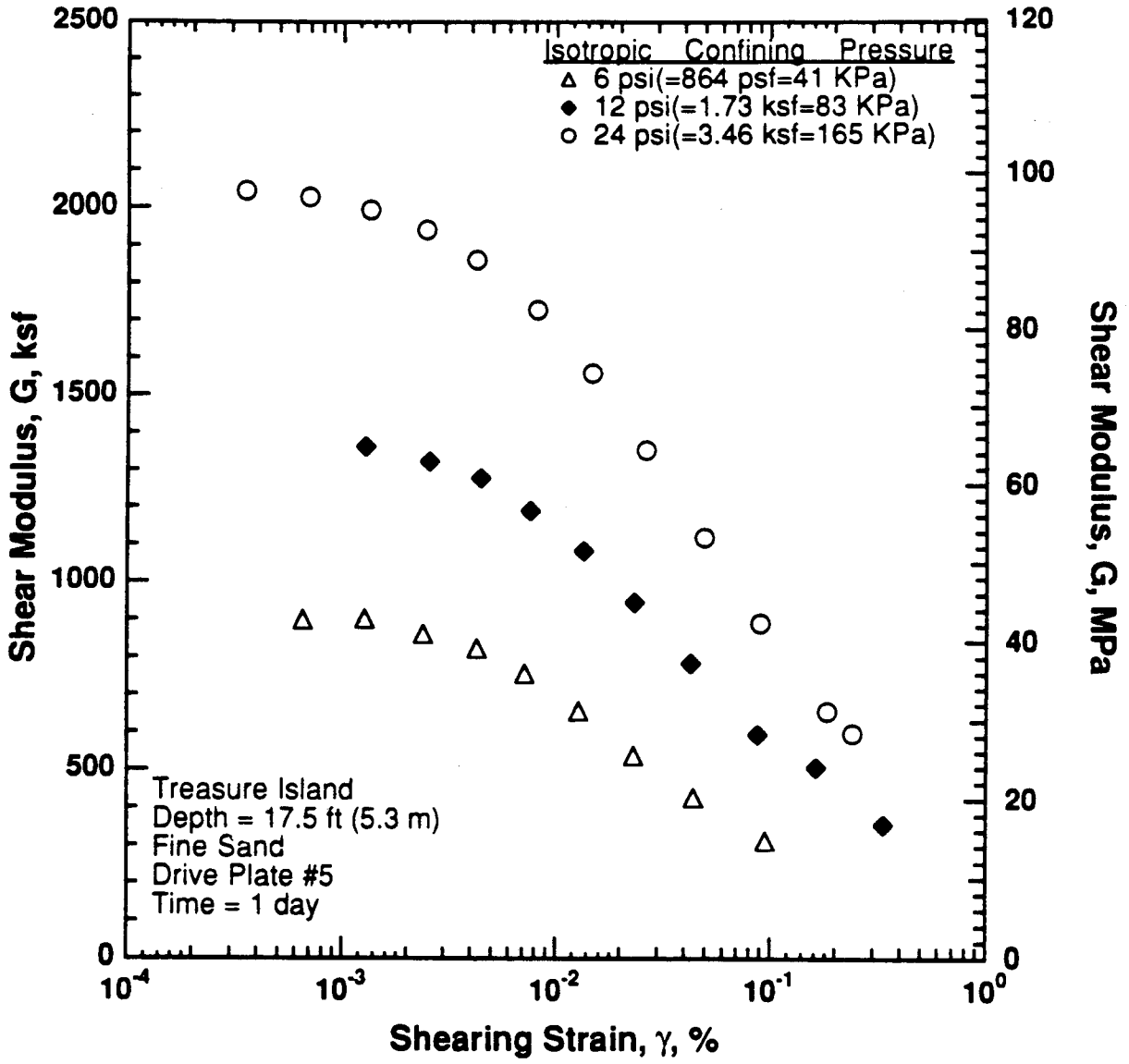

Figure 8.B.1.B-9
Variation in shear modulus with shearing strain and effective confining pressure from resonant column tests of sample T1.

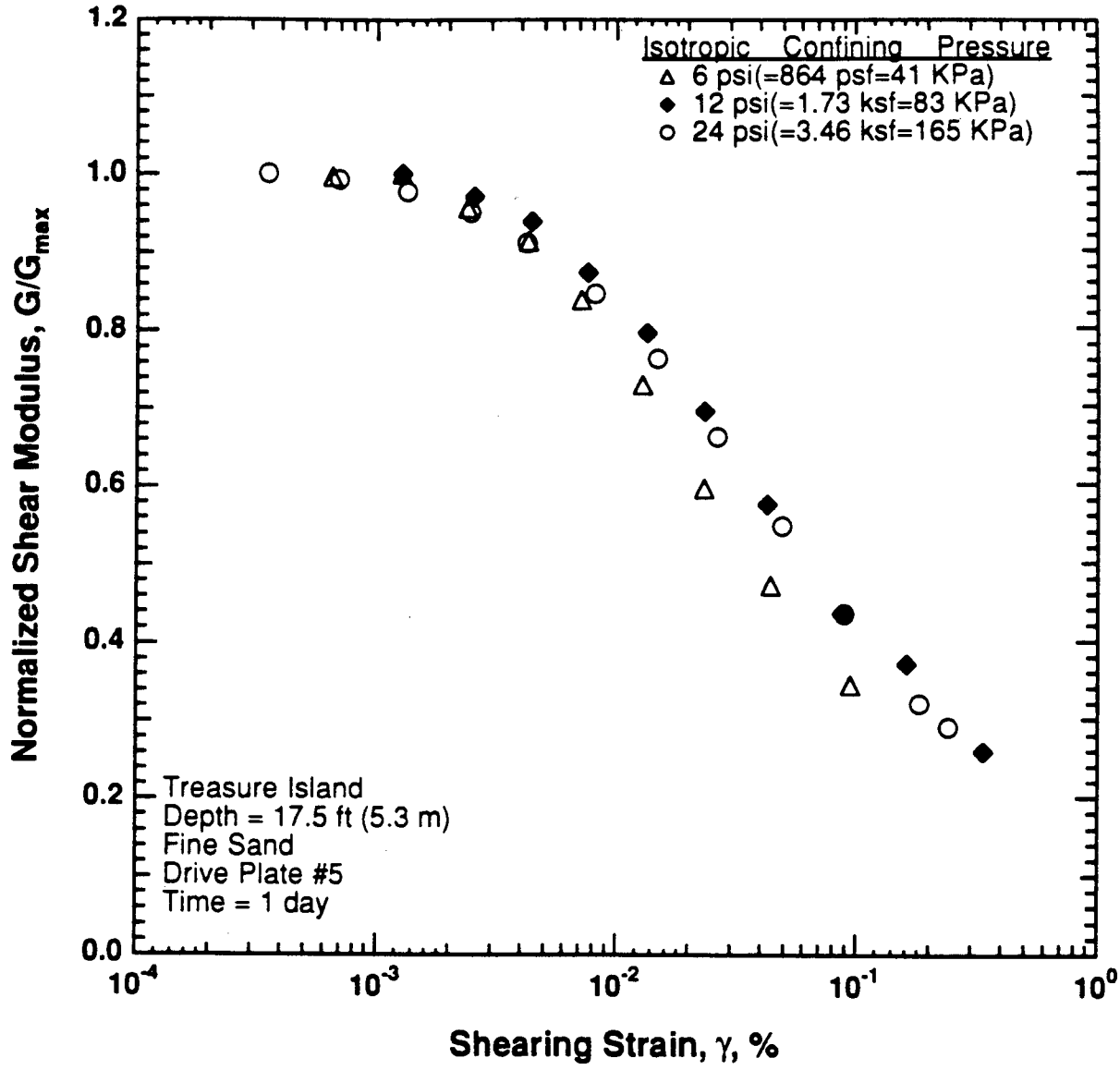

Figure 8.B.1.B-10
Comparison of the variation in normalized shear modulus with shearing strain and effective confining pressure from resonant column tests of sample T1.

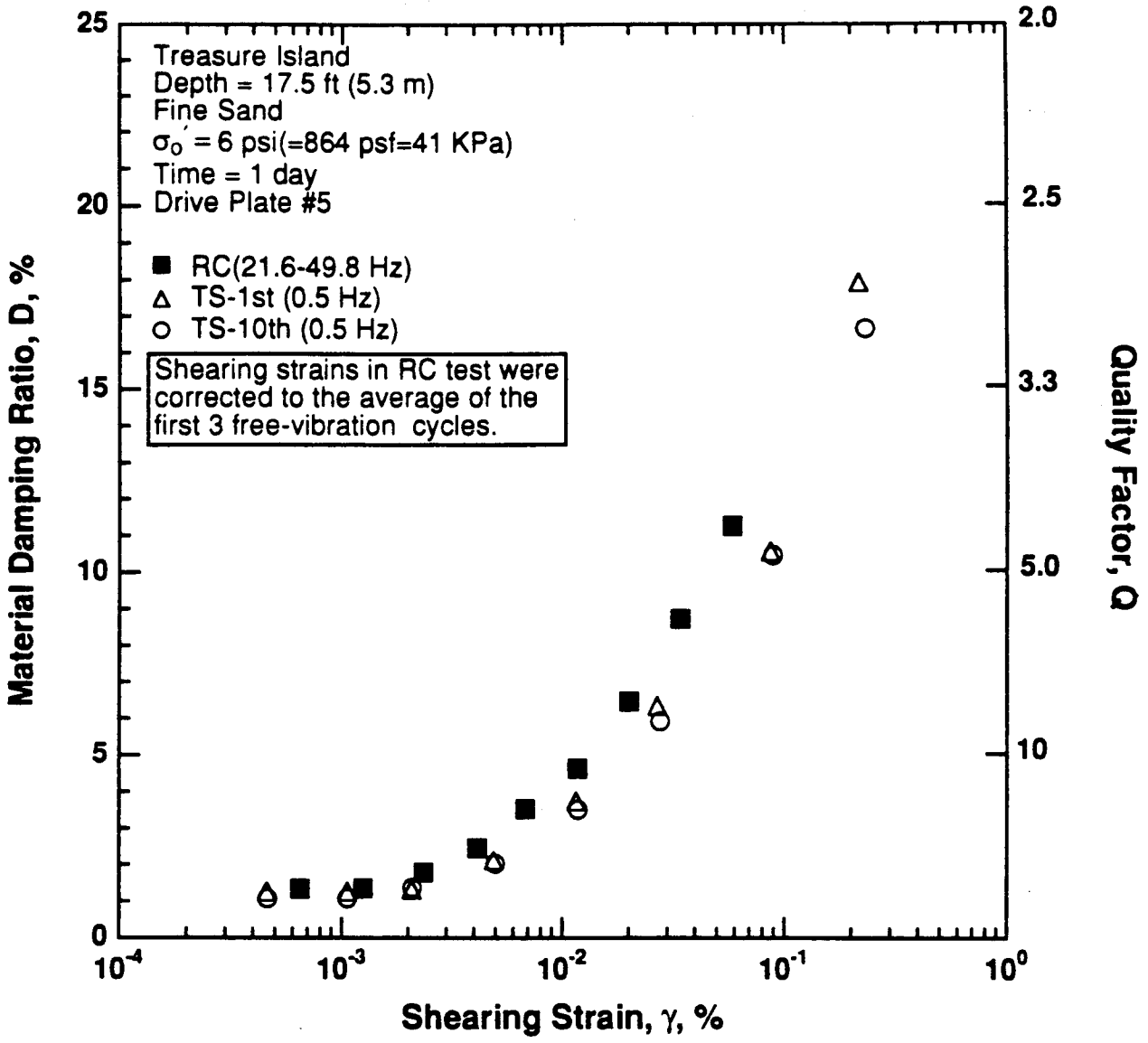

Figure 8.B.1.B-11
Variation in material damping ratio with shearing strain at an effective confining pressure of 6 psi (864 psf, 41 kPa) from RCTS tests of sample T1.

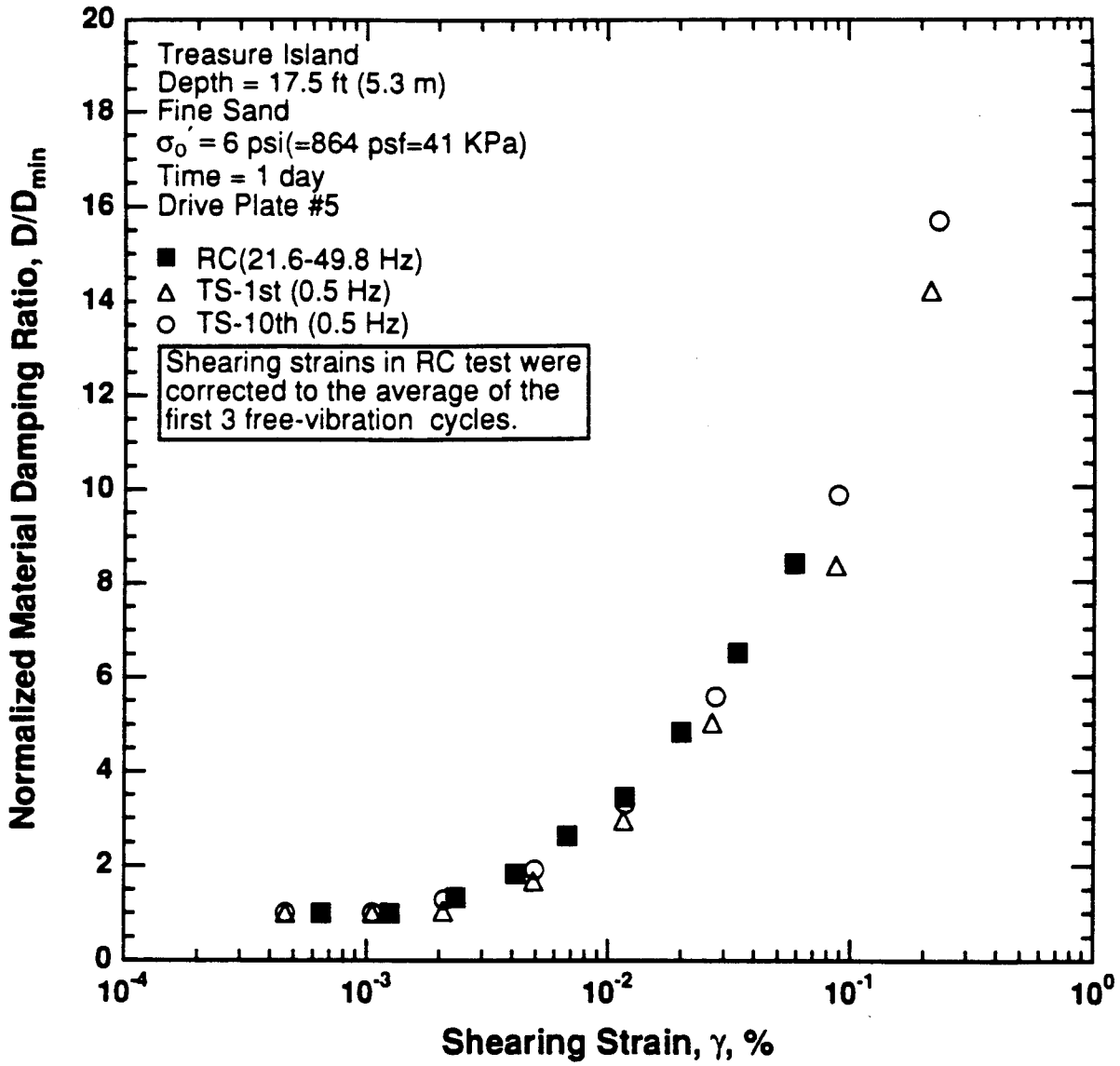

Figure 8.B.1.B-12
Variation in normalized material damping ratio with shearing strain at an effective confining pressure of 6 psi (864 psf, 41 kPa) from RCTS tests of sample T1.

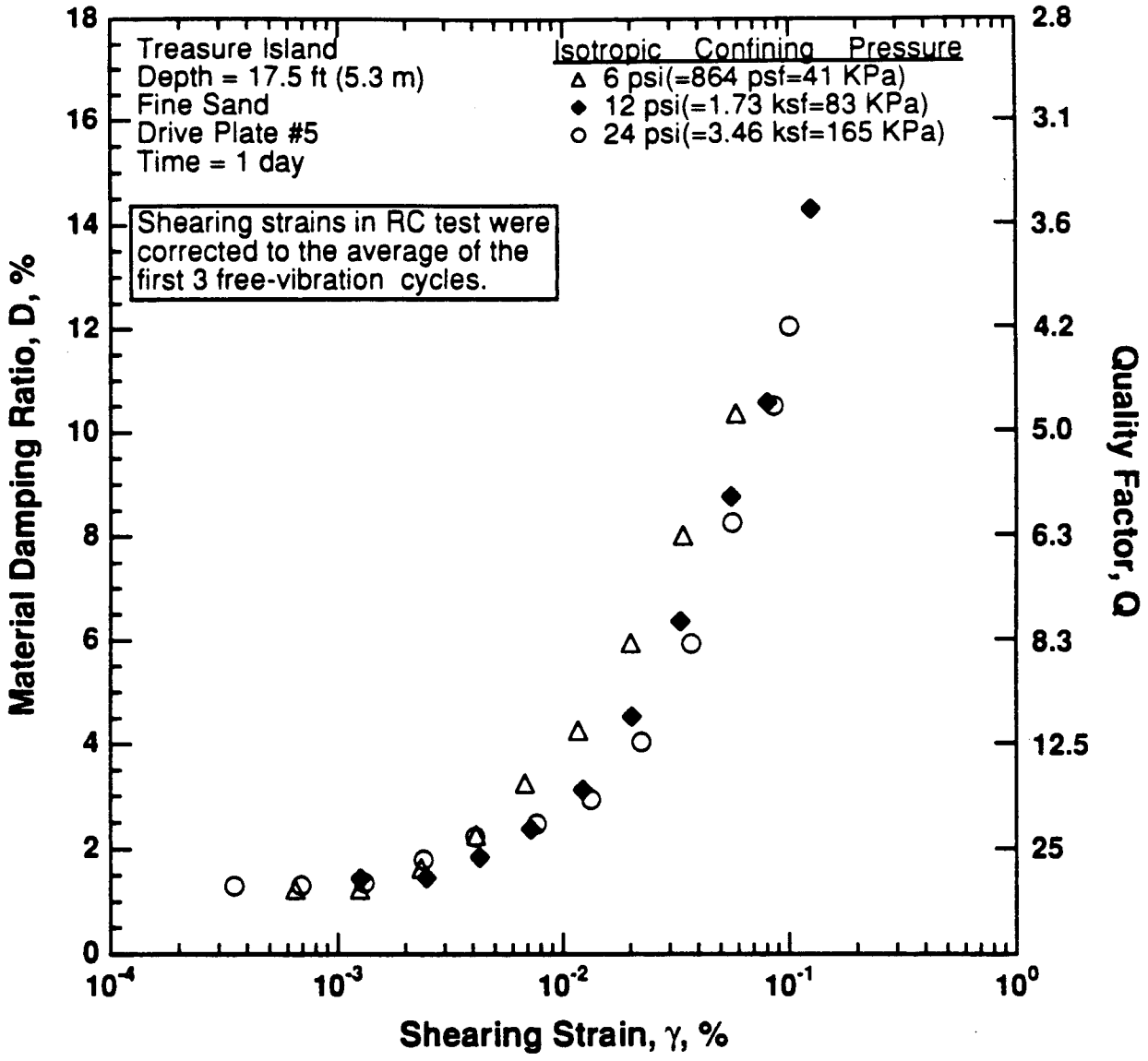

Figure 8.B.1.B-13
Variation in material damping ratio with shearing strain and effective confining pressure from resonant column tests of sample T1.

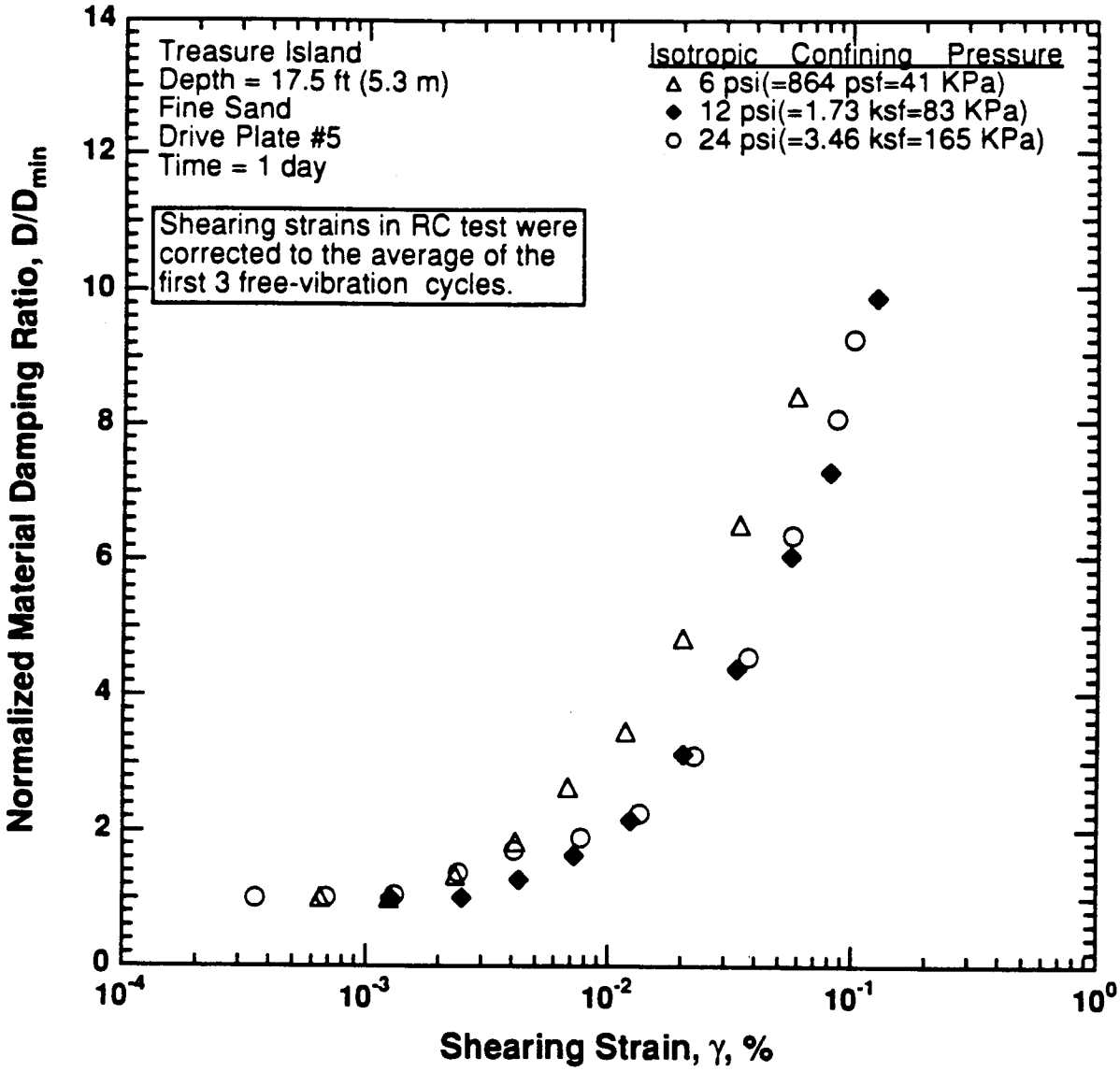

Figure 8.B.1.B-14
Comparison of the variation in normalized material damping ratio with shearing strain and effective confining pressure from resonant column tests of sample T1.

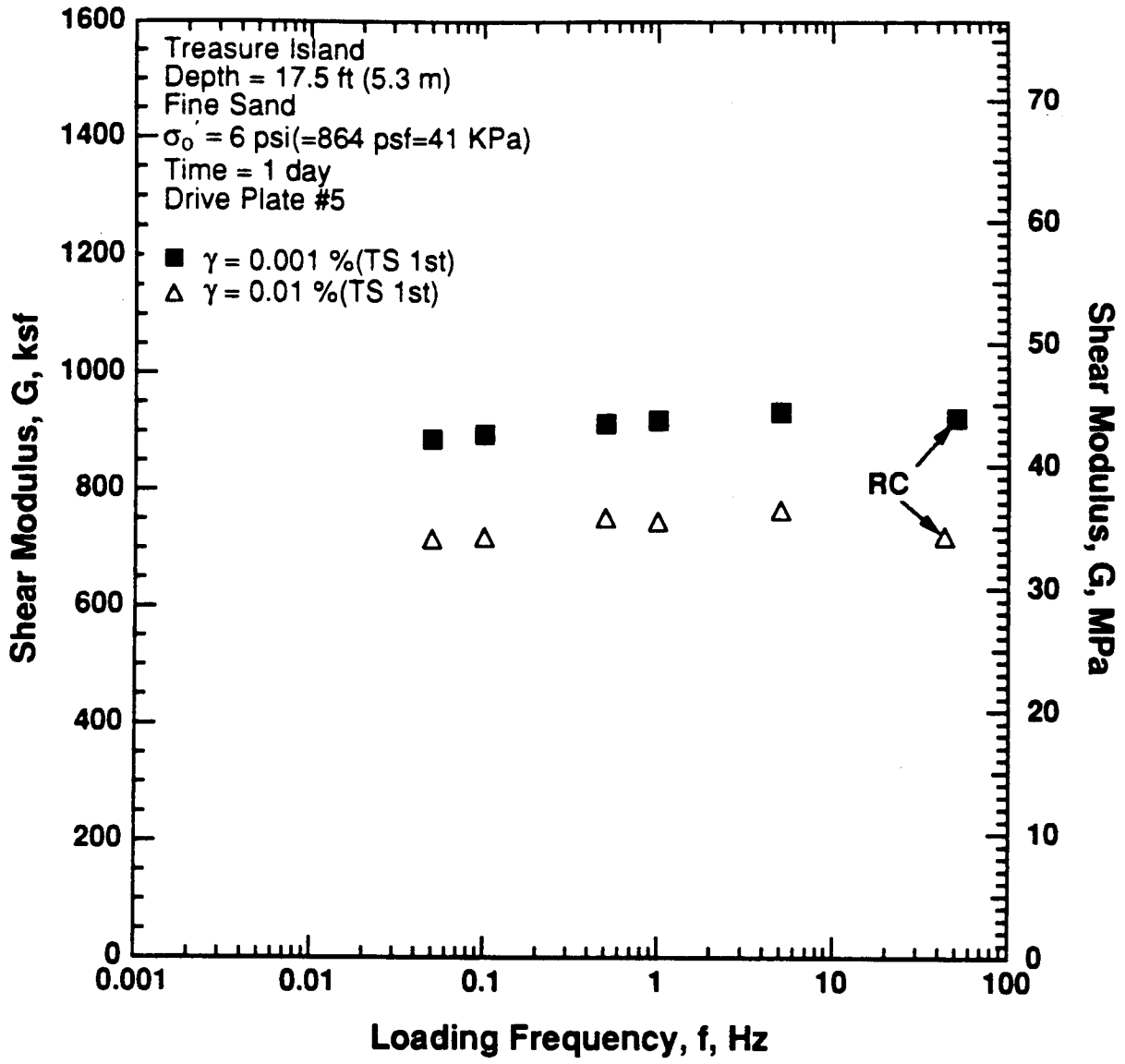

Figure 8.B.1.B-15
Variation in shear modulus with loading frequency and shearing strain at an effective confining pressure of 6 psi (864 psf, 41 kPa) from RCTS tests of sample T1.

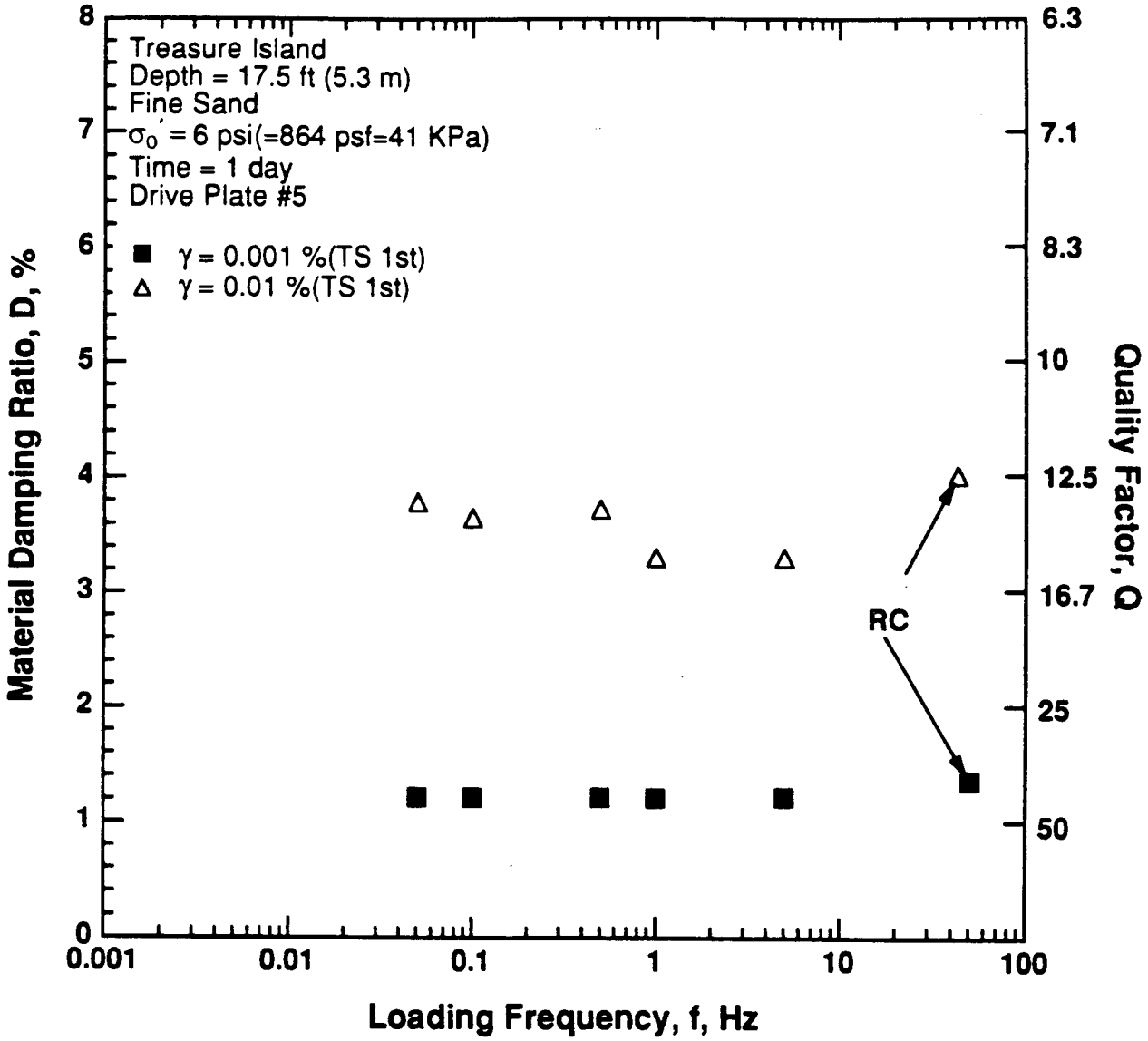

Figure 8.B.1.B-16
Variation in material damping ratio with loading frequency and shearing strain at an effective confining pressure of 6 psi (864 psf, 41 kPa) from RCTS tests of sample T1.

APPENDIX 8.B.1.C
DYNAMIC TESTS OF SAMPLE T2, DEPTH = 30 FT (9.1 M)

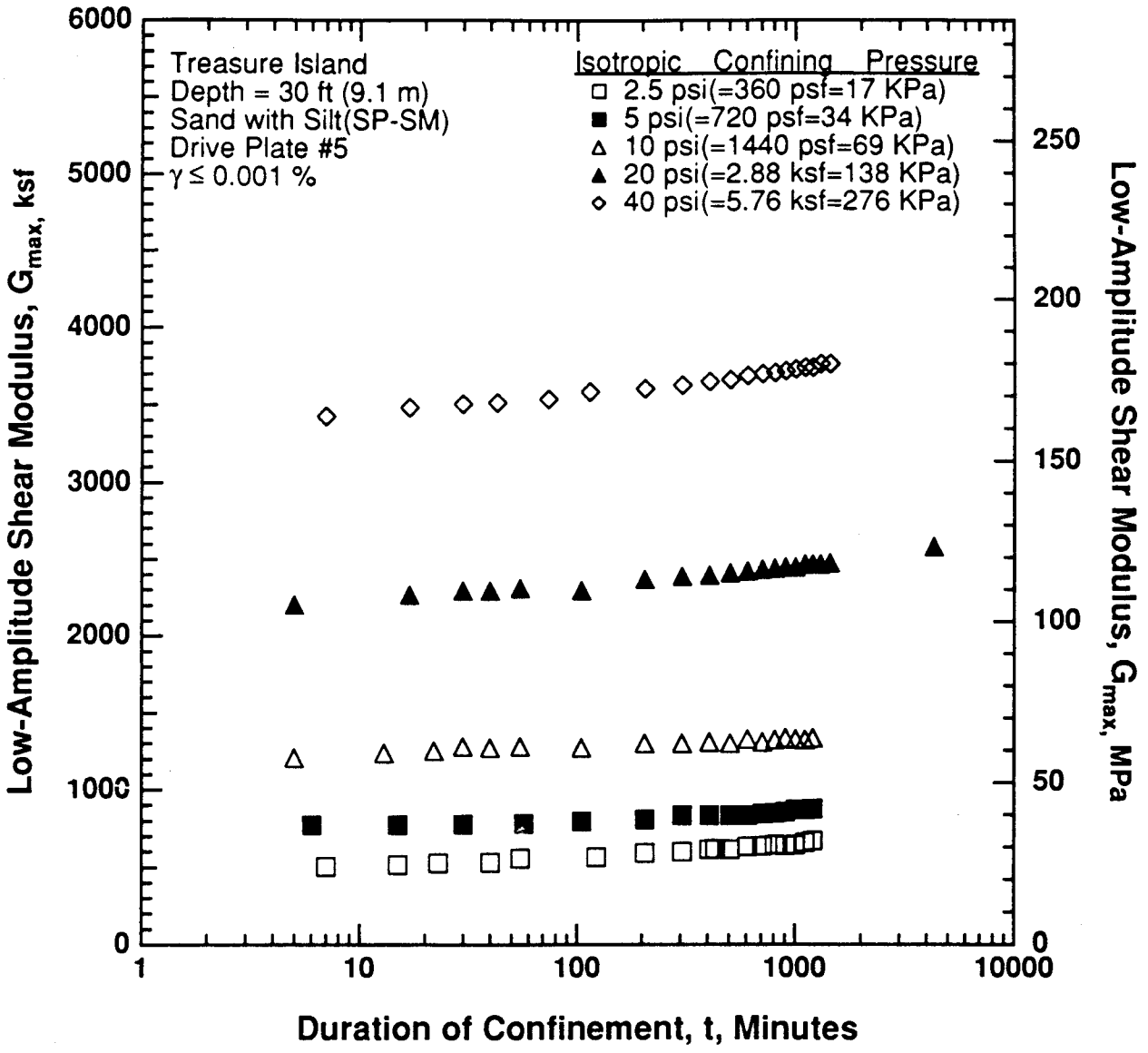

Figure 8.B.1.C-1
Variation in low-amplitude shear modulus with magnitude and duration of isotropic confining pressure from resonant column tests of sample T2.

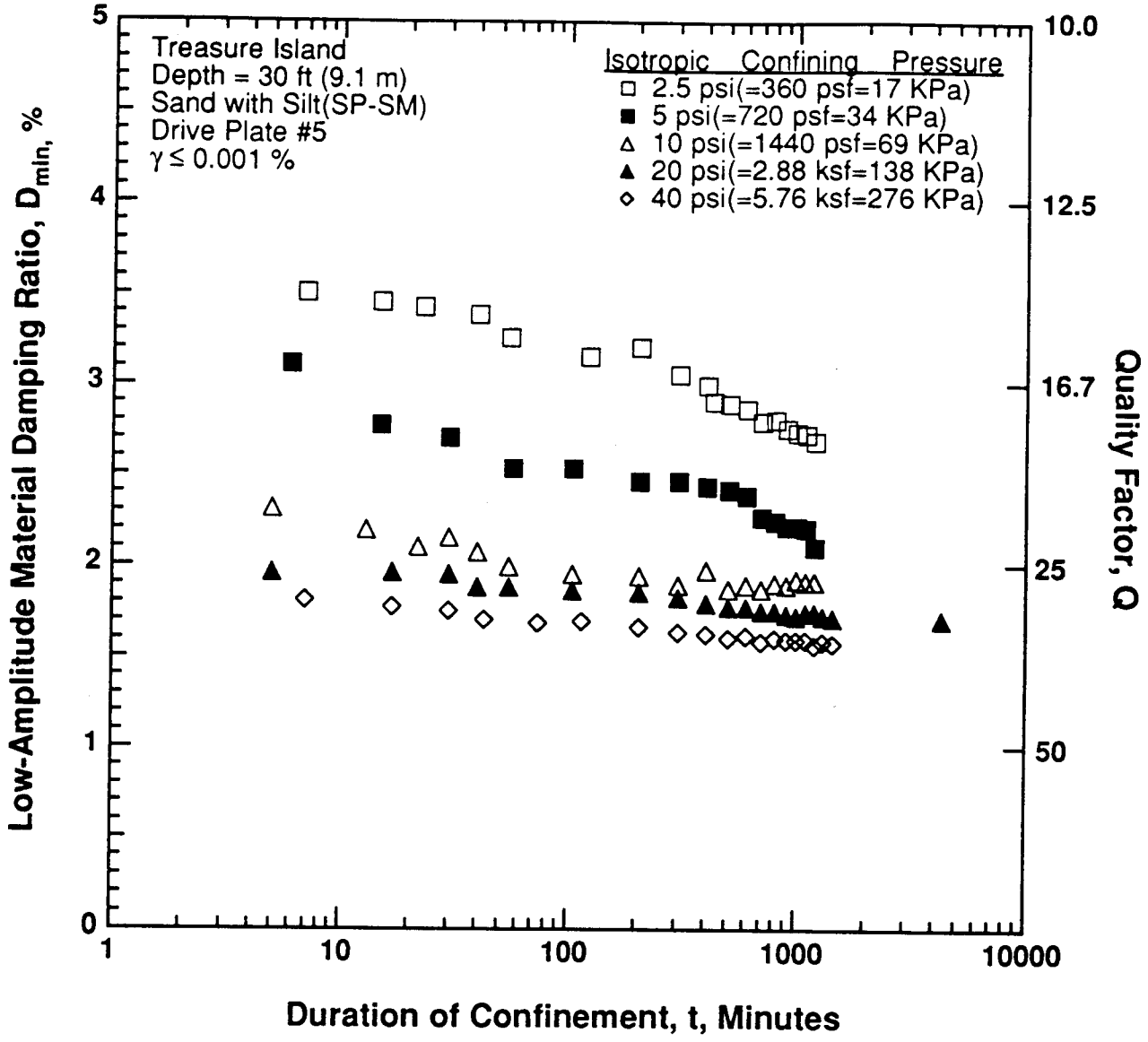

Figure 8.B.1.C-2
Variation in low-amplitude material damping ratio with magnitude and duration of isotropic confining pressure from resonant column tests of sample T2.

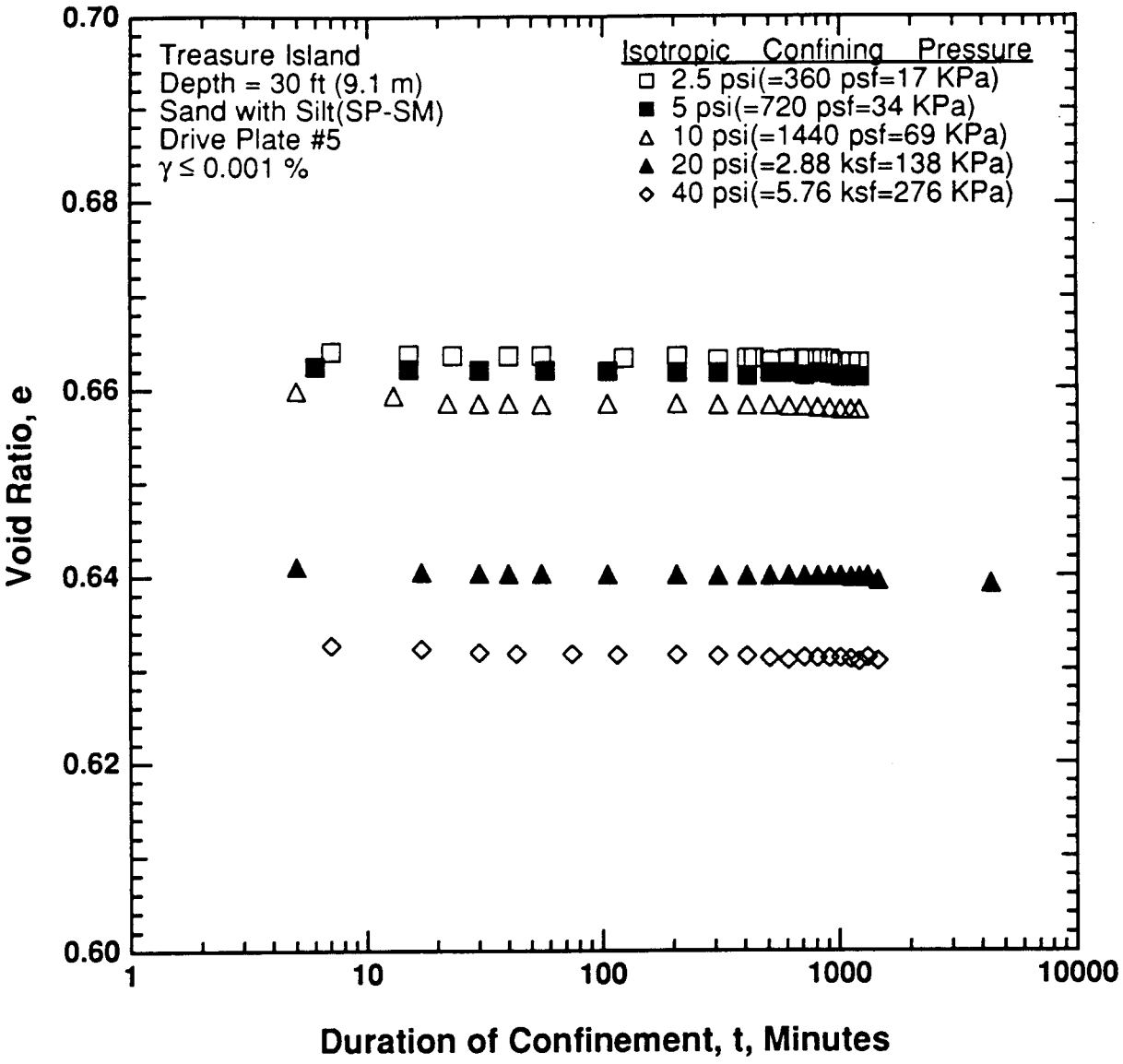

Figure 8.B.1.C-3
Variation in void ratio with magnitude and duration of isotropic confining pressure from resonant column tests of sample T2.

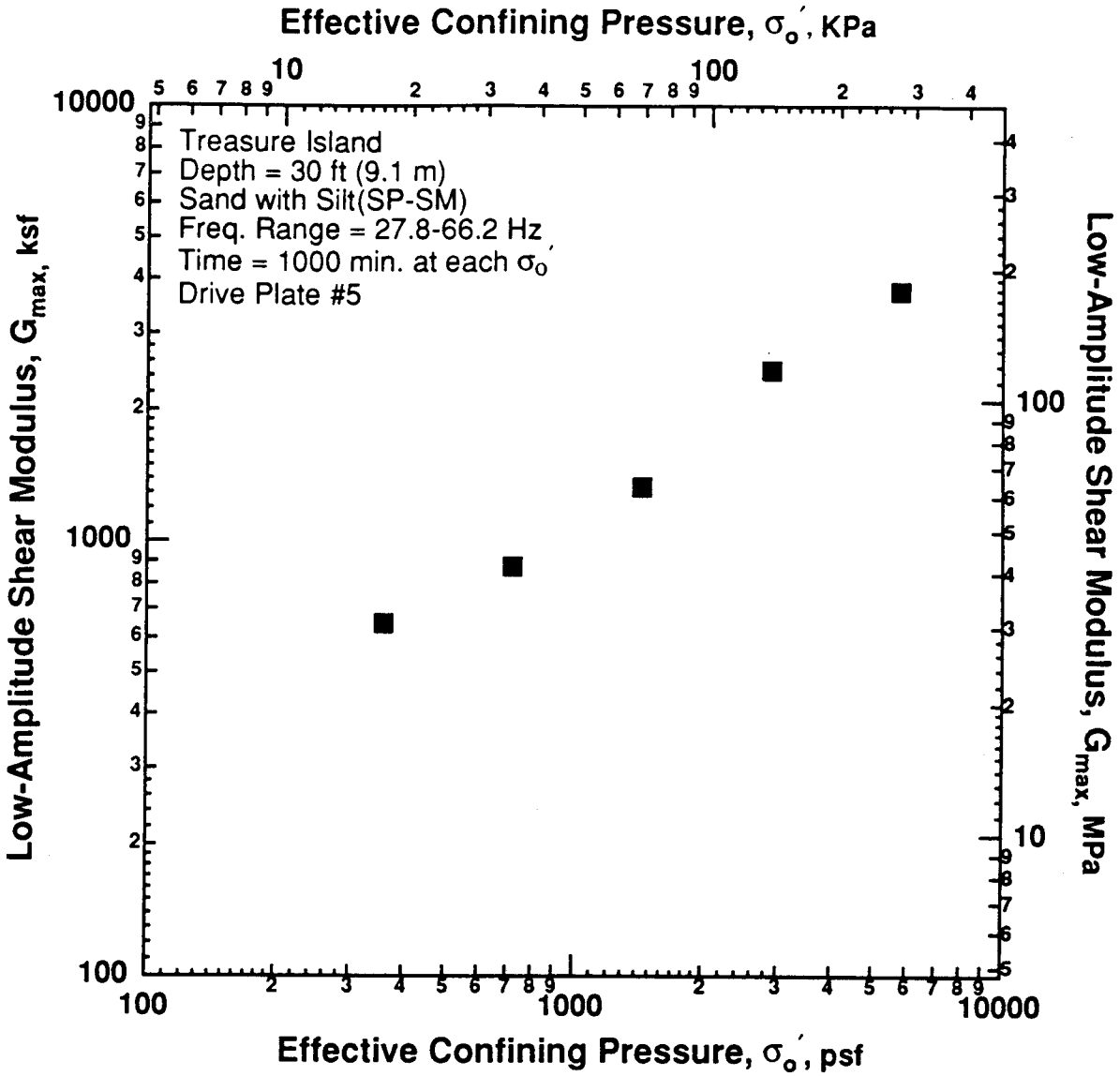

Figure 8.B.1.C-4
Variation in low-amplitude shear modulus with effective confining pressure from resonant column tests of sample T2.

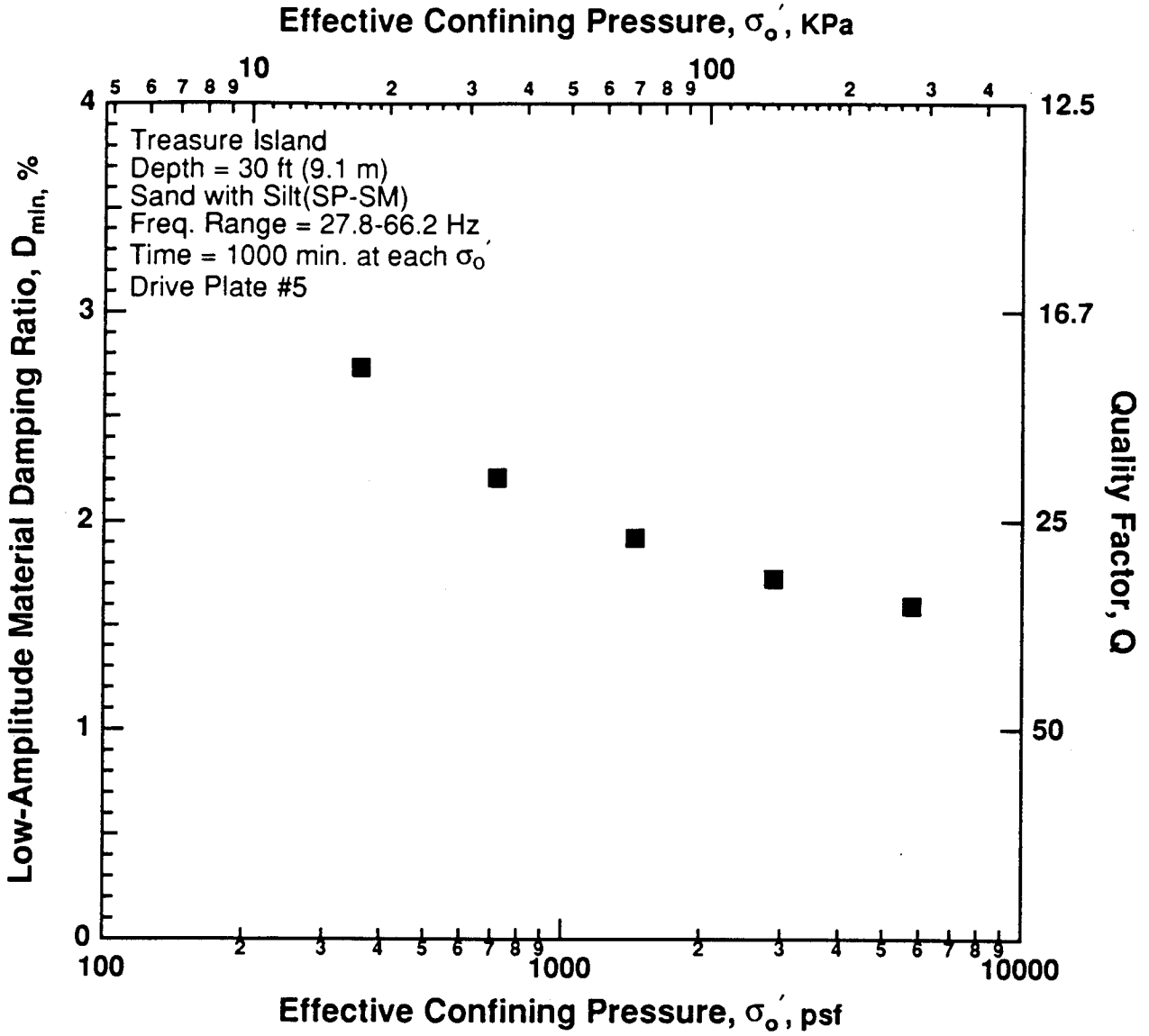

Figure 8.B.1.C-5
Variation in low-amplitude material damping ratio with effective confining pressure from resonant column tests of sample T2.

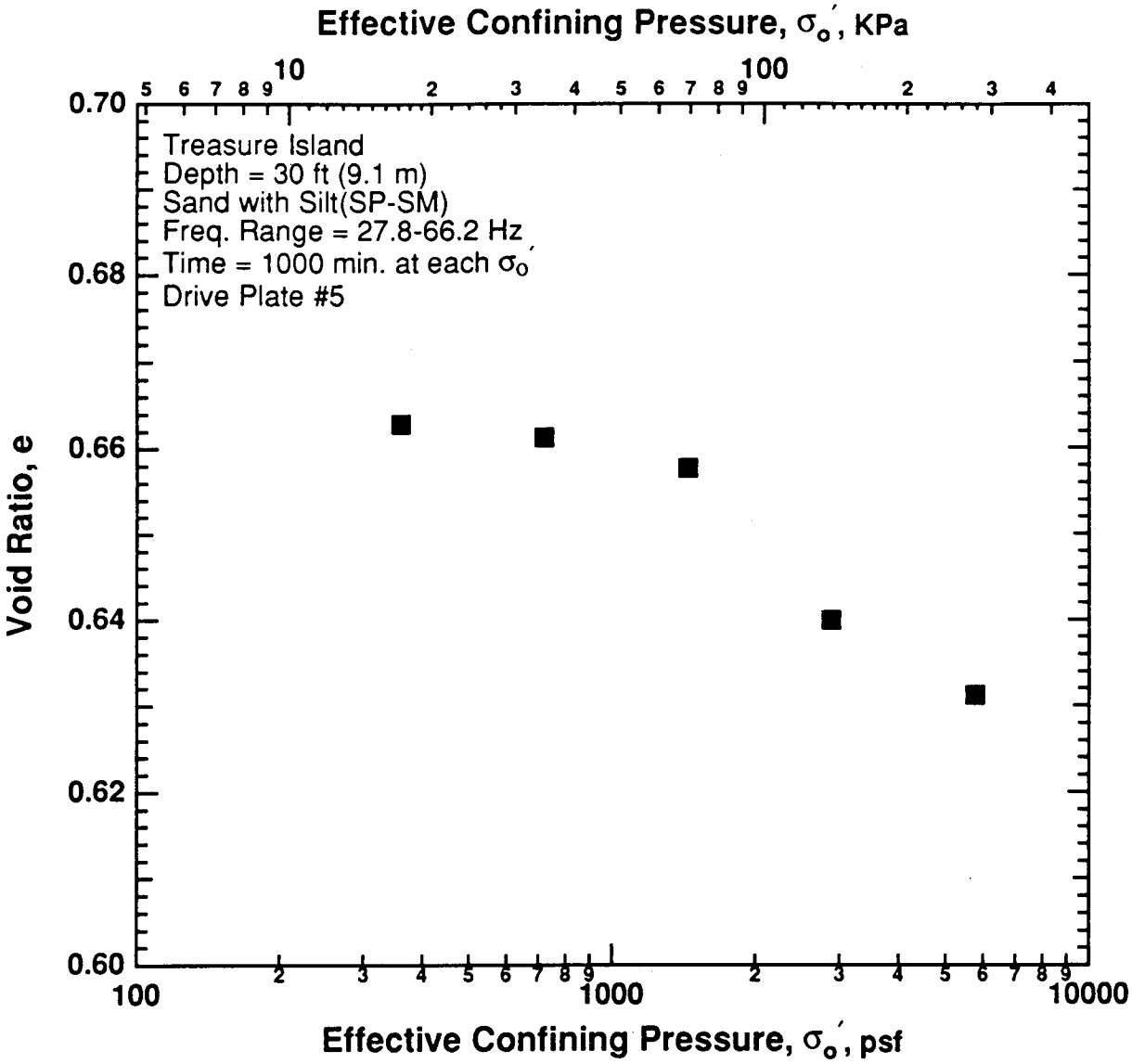

Figure 8.B.1.C-6
Variation in void ratio with effective confining pressure from resonant column tests of sample T2.

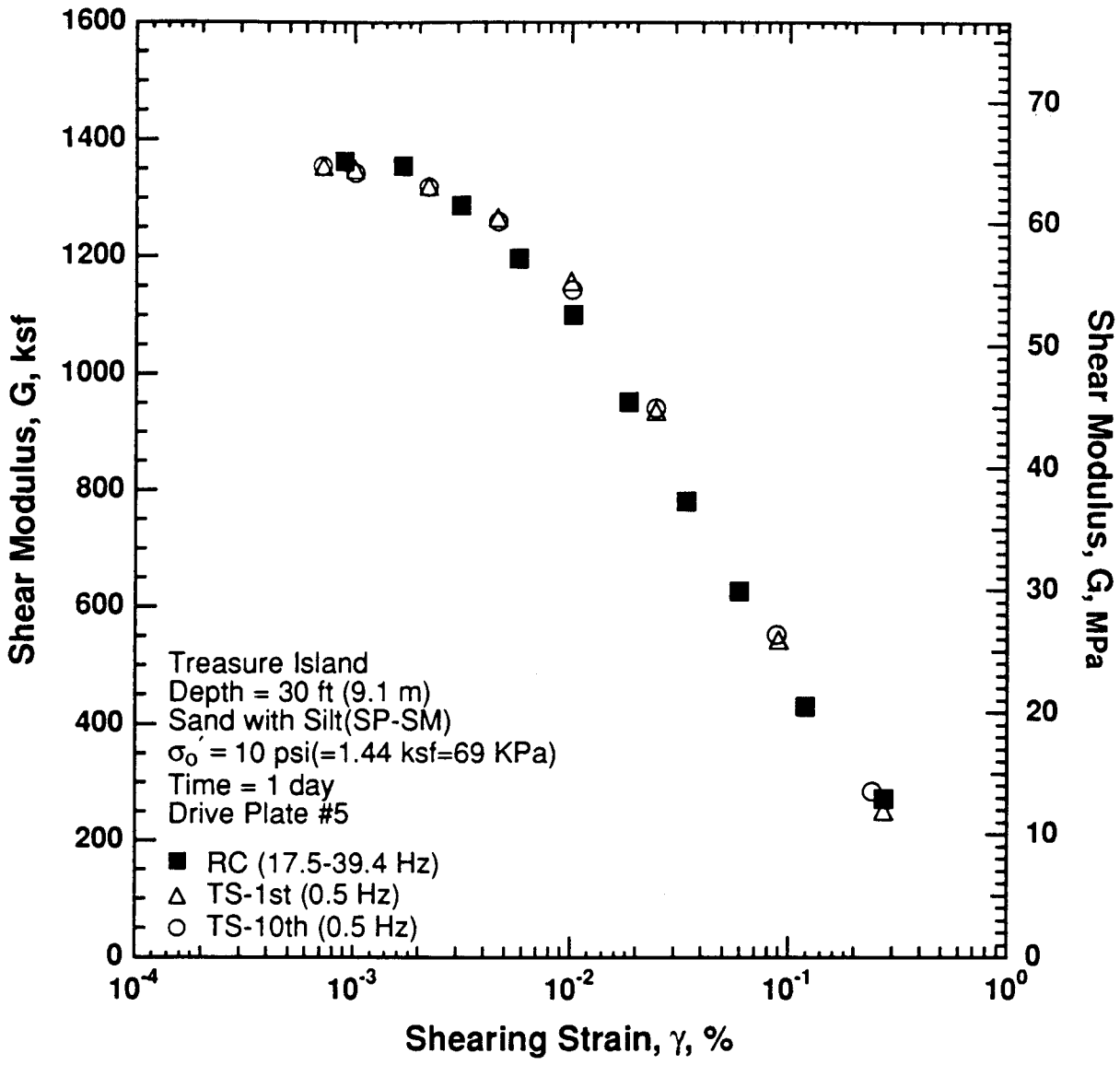

Figure 8.B.1.C-7
Variation in shear modulus with shearing strain at an effective confining pressure of 10 psi (1.44 ksf, 69 kPa) from RCTS tests of sample T2.

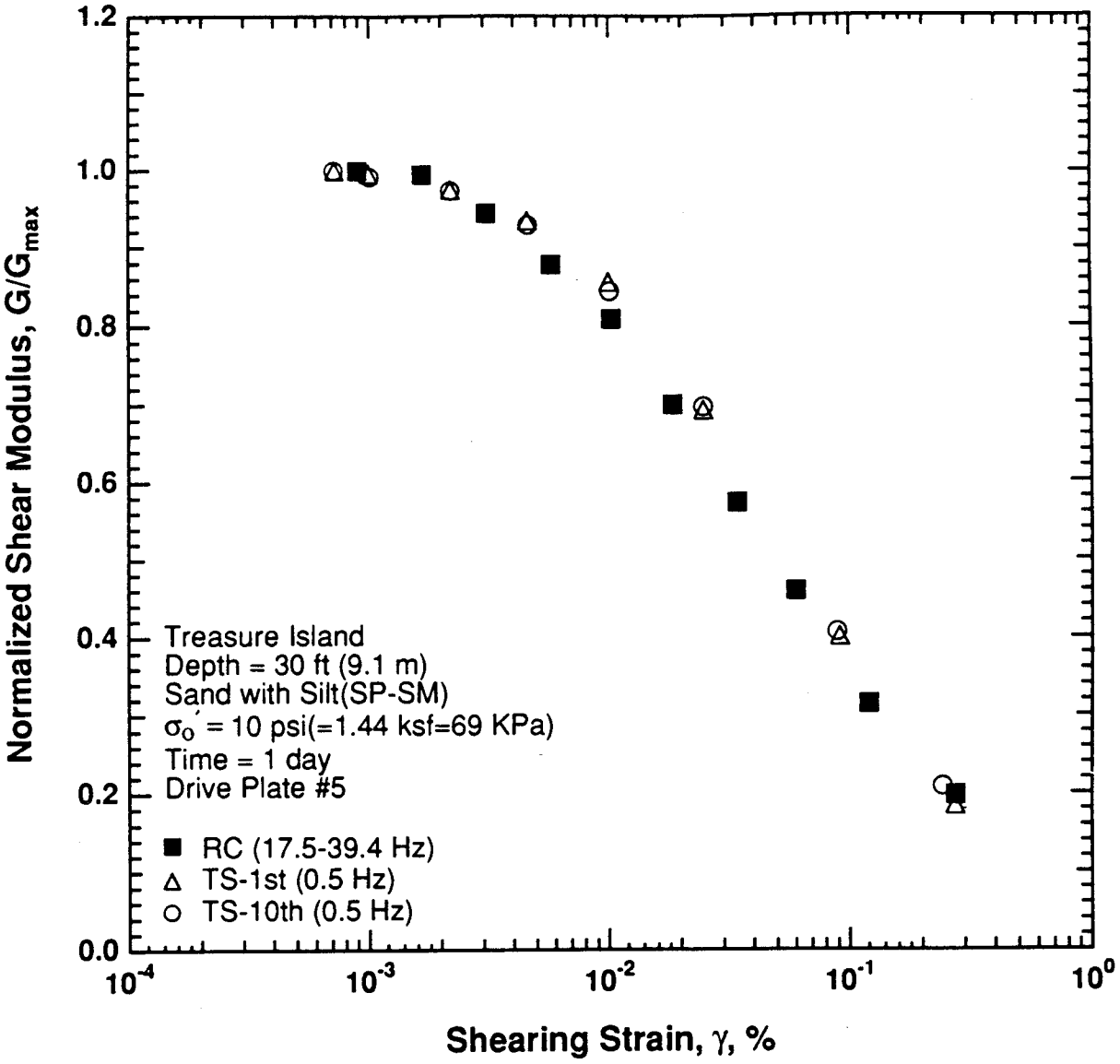

Figure 8.B.1.C-8
Variation in normalized shear modulus with shearing strain at an effective confining pressure of 10 psi (1.44 ksf, 69 kPa) from RCTS tests of sample T2.

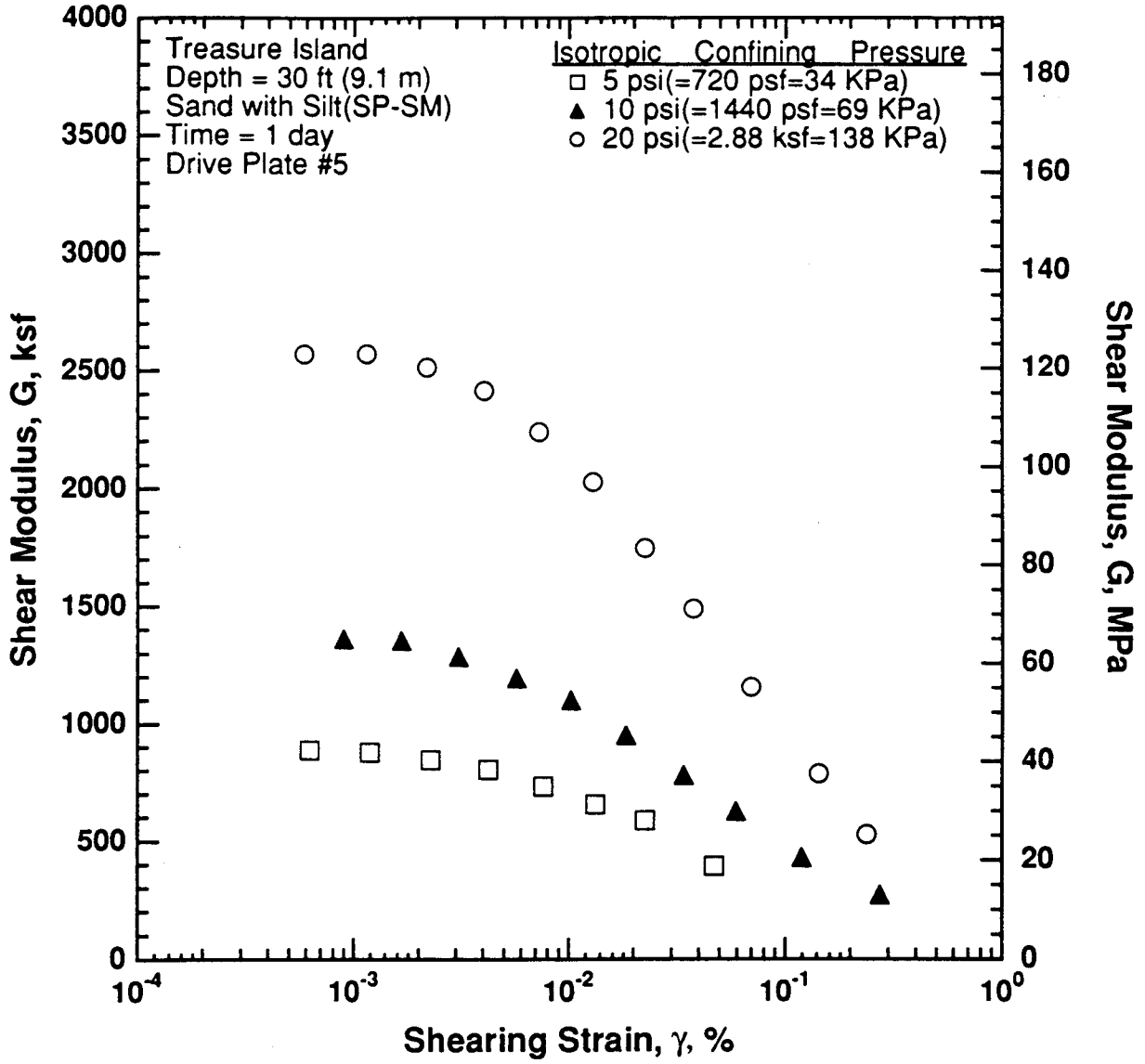

Figure 8.B.1.C-9
Variation in shear modulus with shearing strain and effective confining pressure from resonant column tests of sample T2.

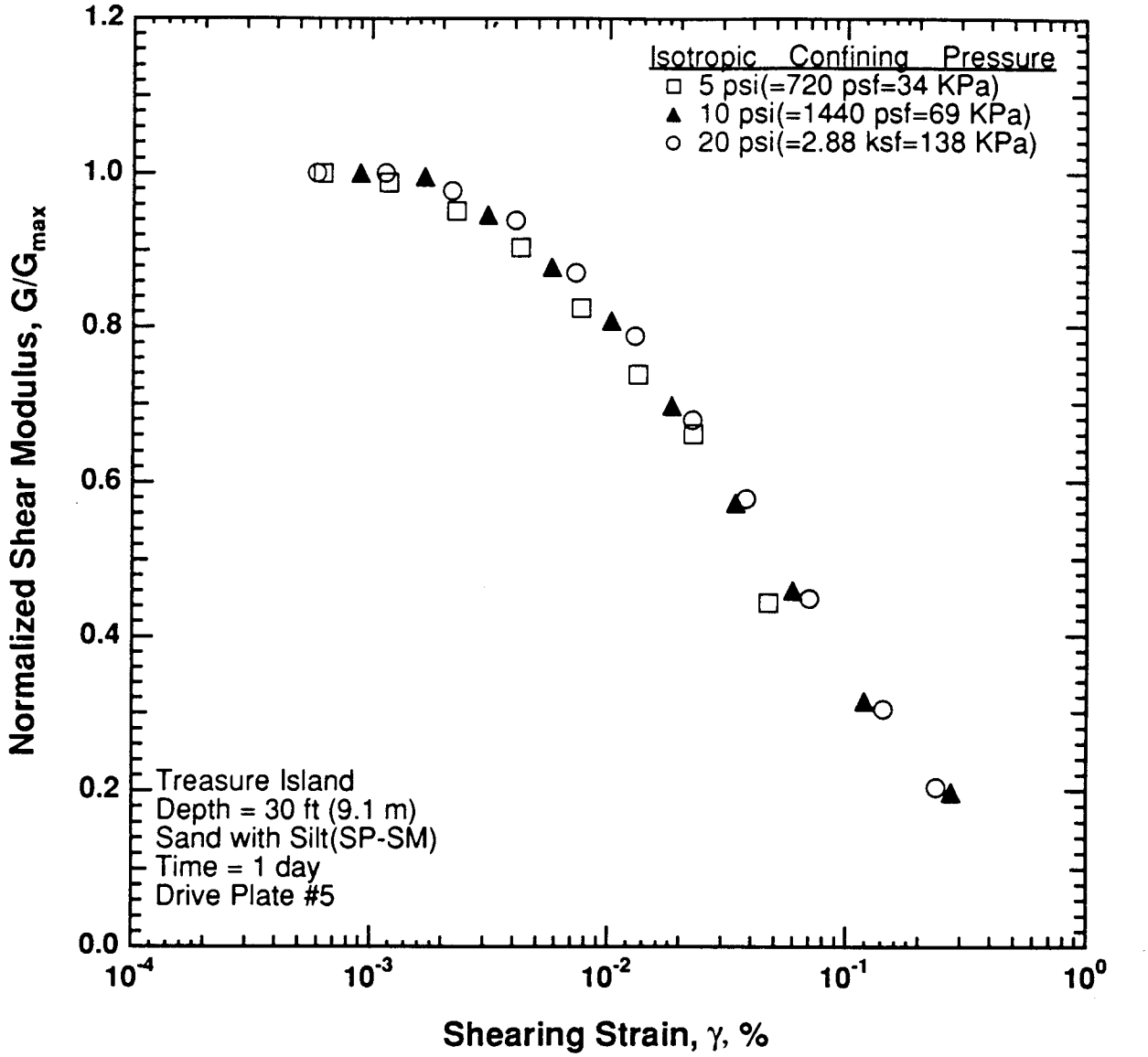

Figure 8.B.1.C-10
Comparison of the variation in normalized shear modulus with shearing strain and effective confining pressure from resonant column tests of sample T2.

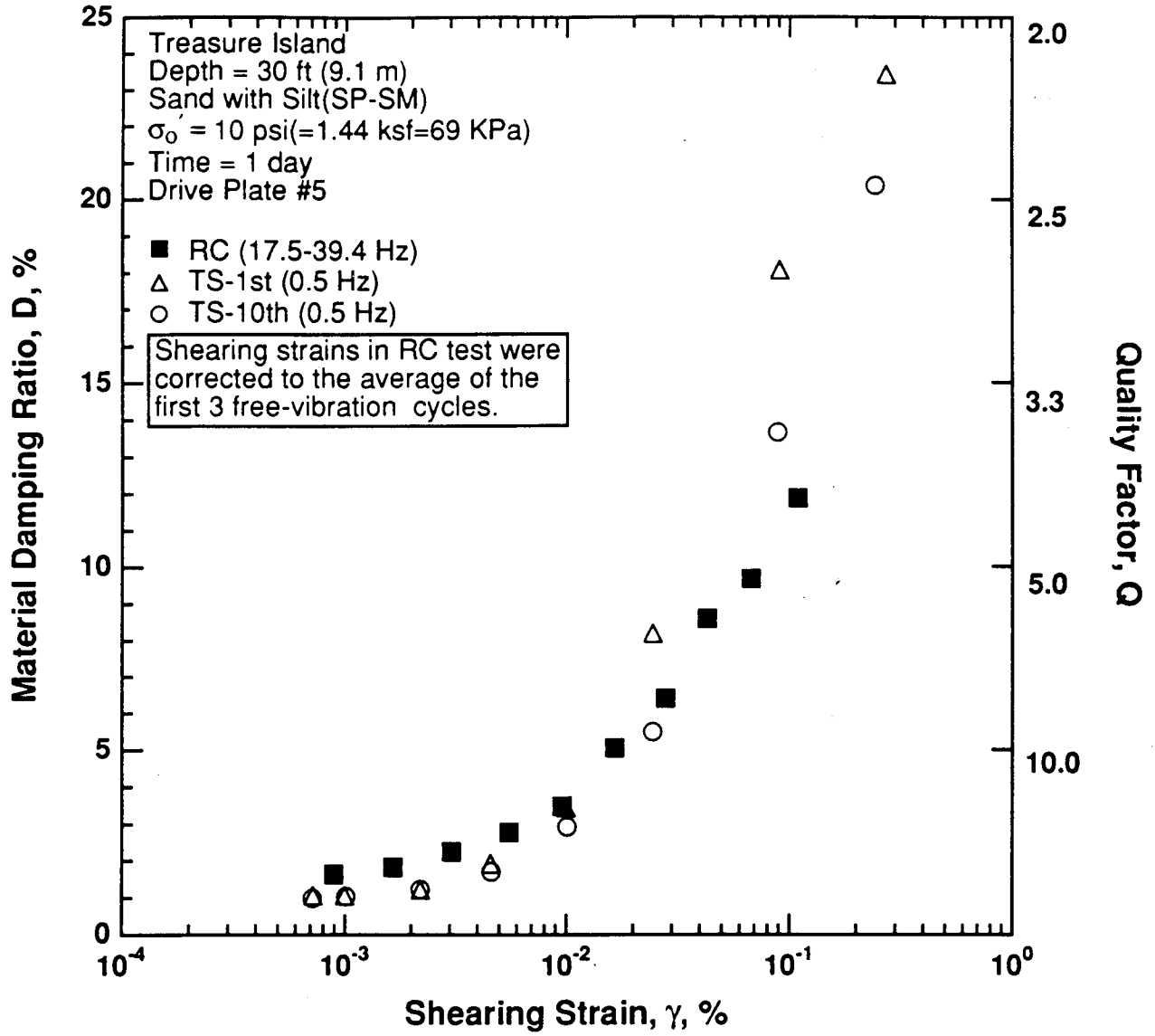

Figure 8.B.1.C-11
Variation in material damping ratio with shearing strain at an effective confining pressure of 10 psi (1.44 ksf, 69 kPa) from RCTS tests of sample T2.

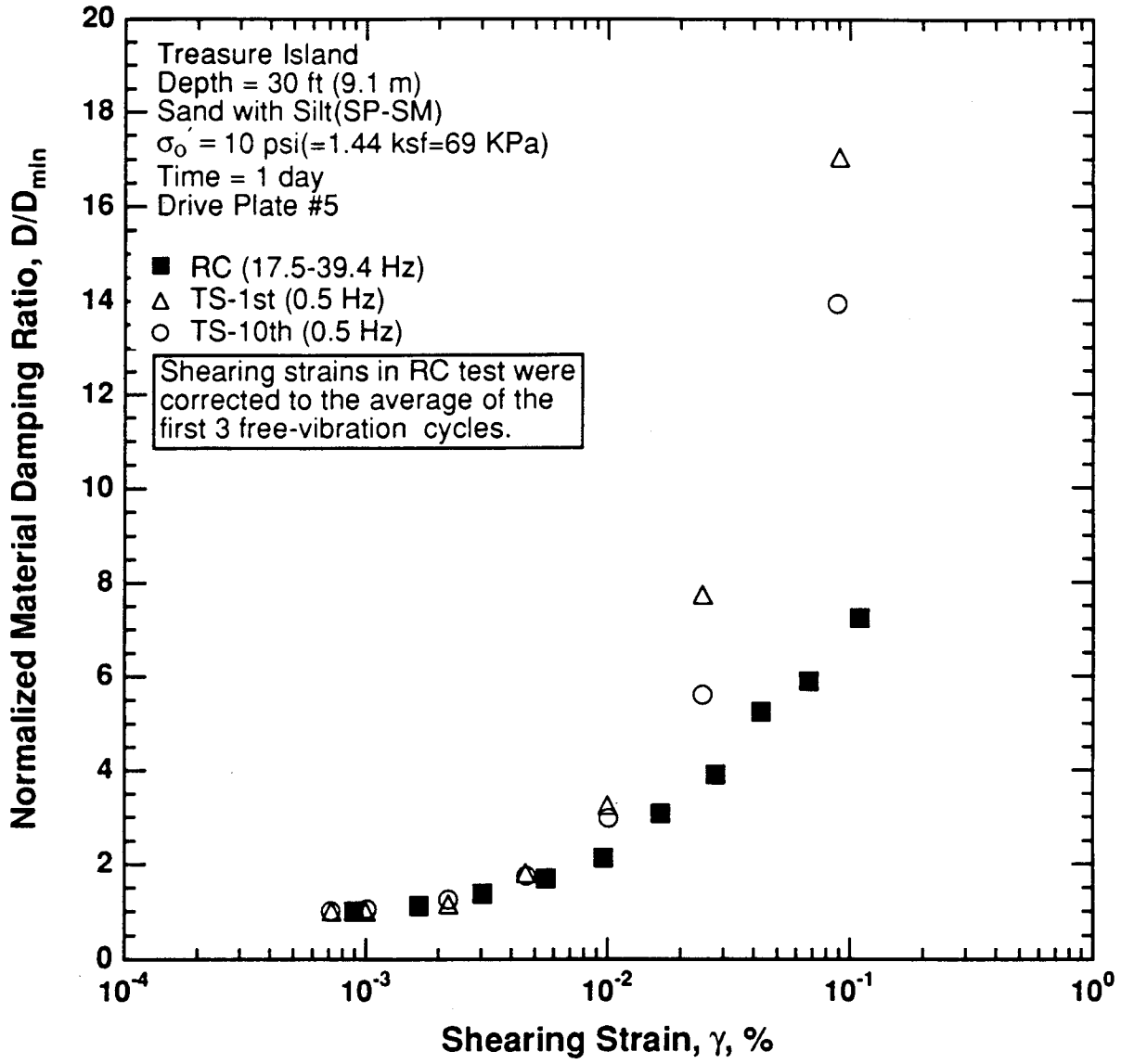

Figure 8.B.1.C-12
Variation in normalized material damping ratio with shearing strain at an effective confining pressure of 10 psi (1.44 ksf, 69 kPa) from RCTS tests of sample T2.

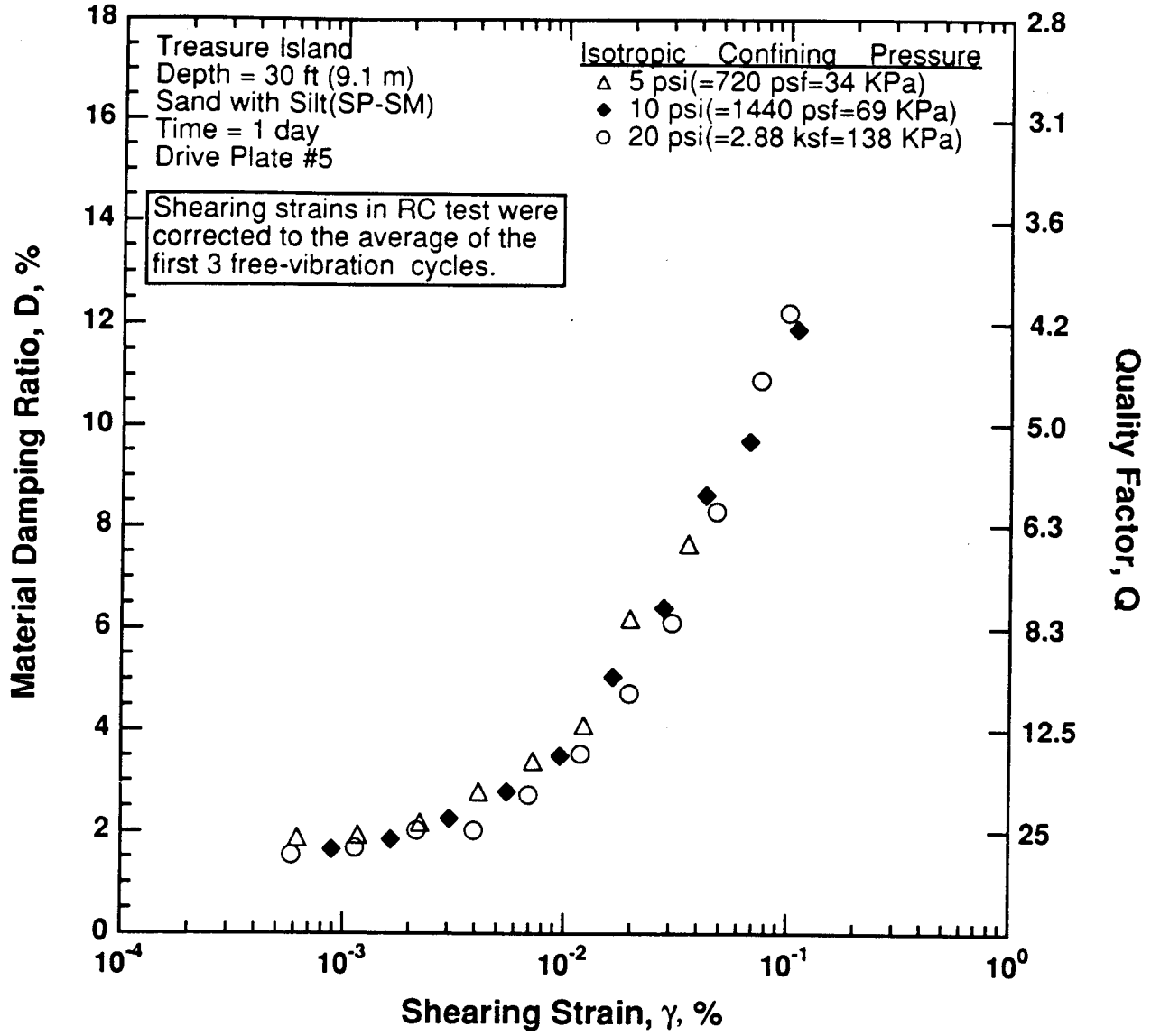

Figure 8.B.1.C-13
Variation in material damping ratio with shearing strain and effective confining pressure from resonant column tests of sample T2.

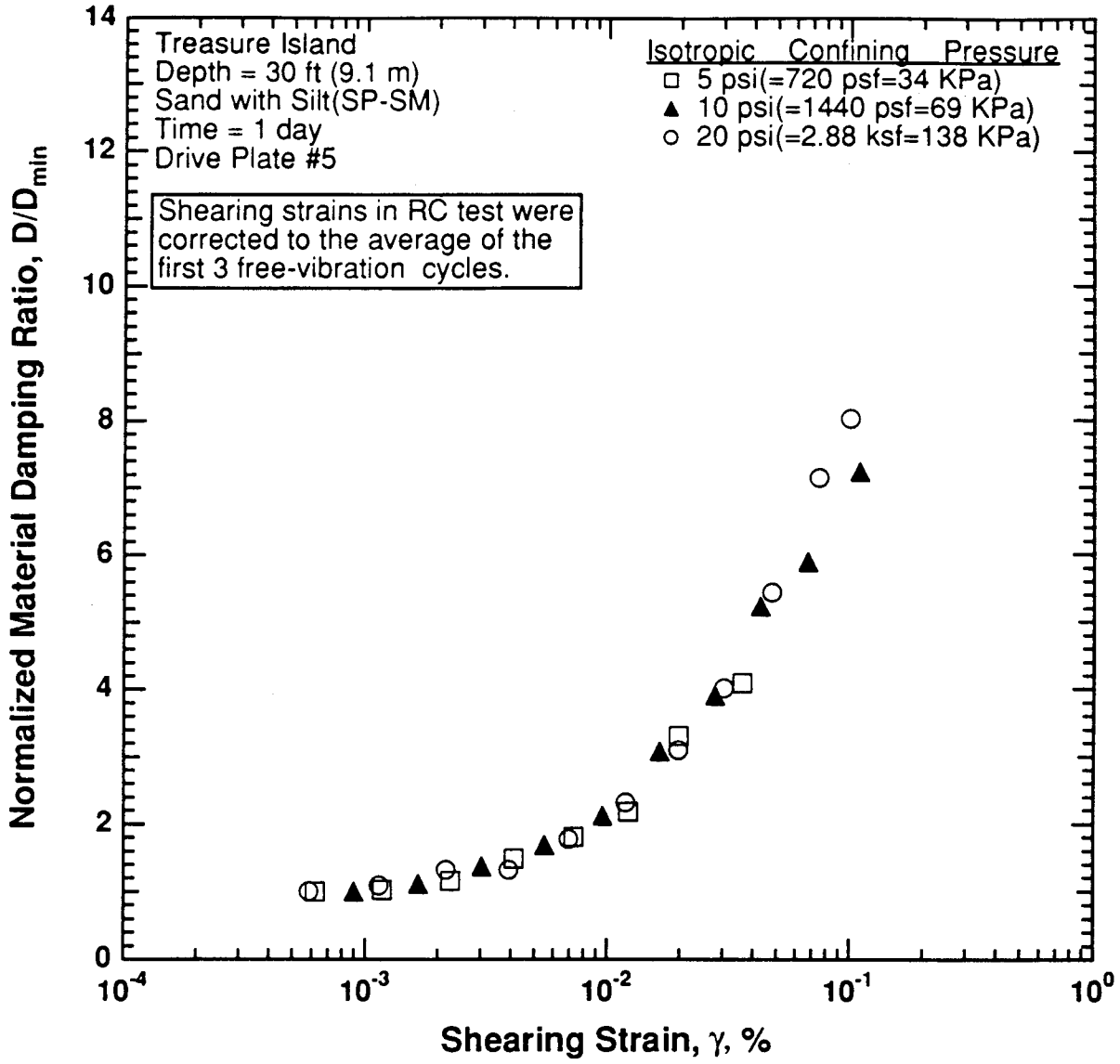

Figure 8.B.1.C-14
Comparison of the variation in normalized material damping ratio with shearing strain and effective confining pressure from resonant column tests of sample T2.

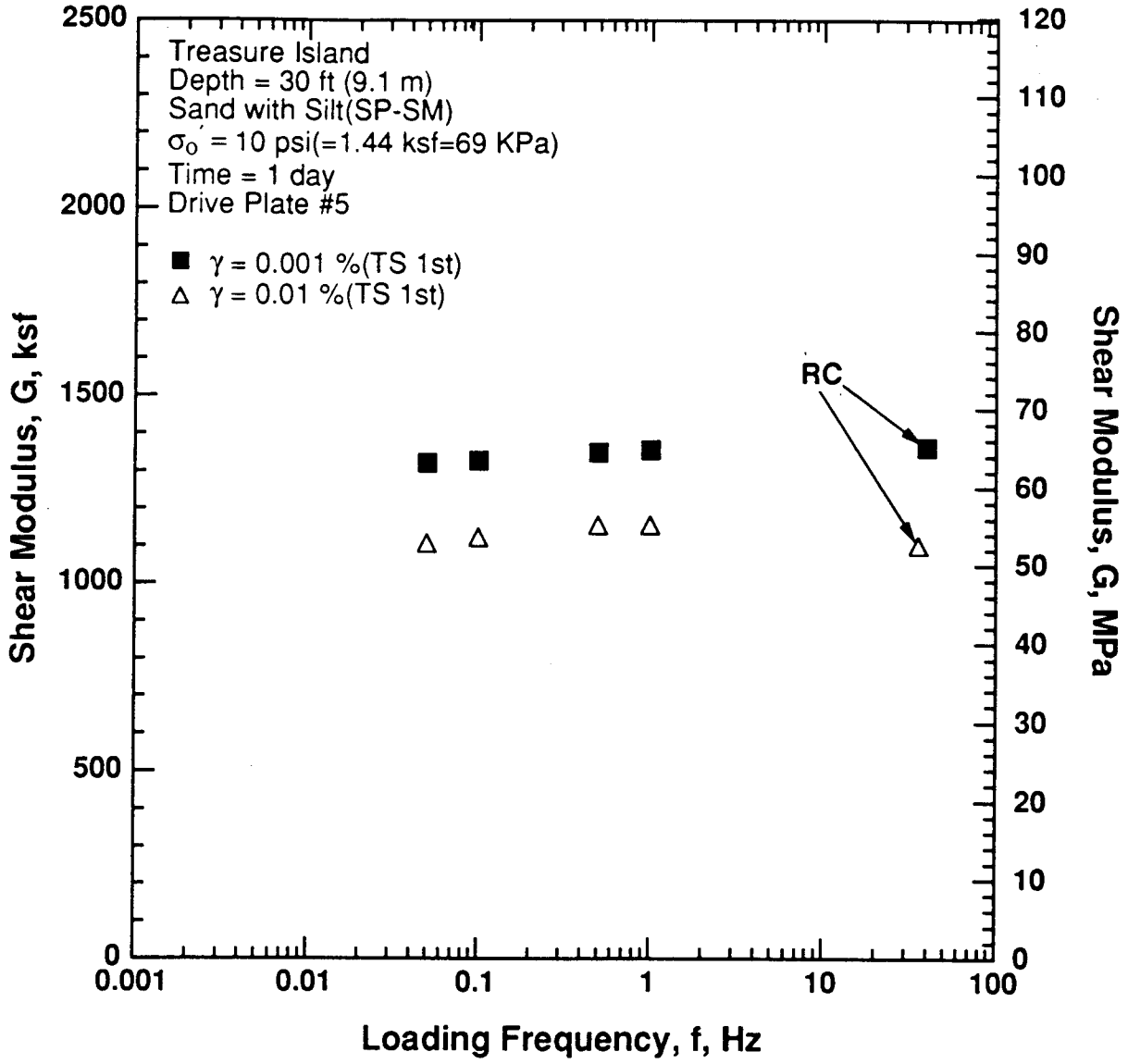

Figure 8.B.1.C-15
Variation in shear modulus with loading frequency and shearing strain at an effective confining pressure of 10 psi (1.44 ksf, 69 kPa) from RCTS tests of sample T2.

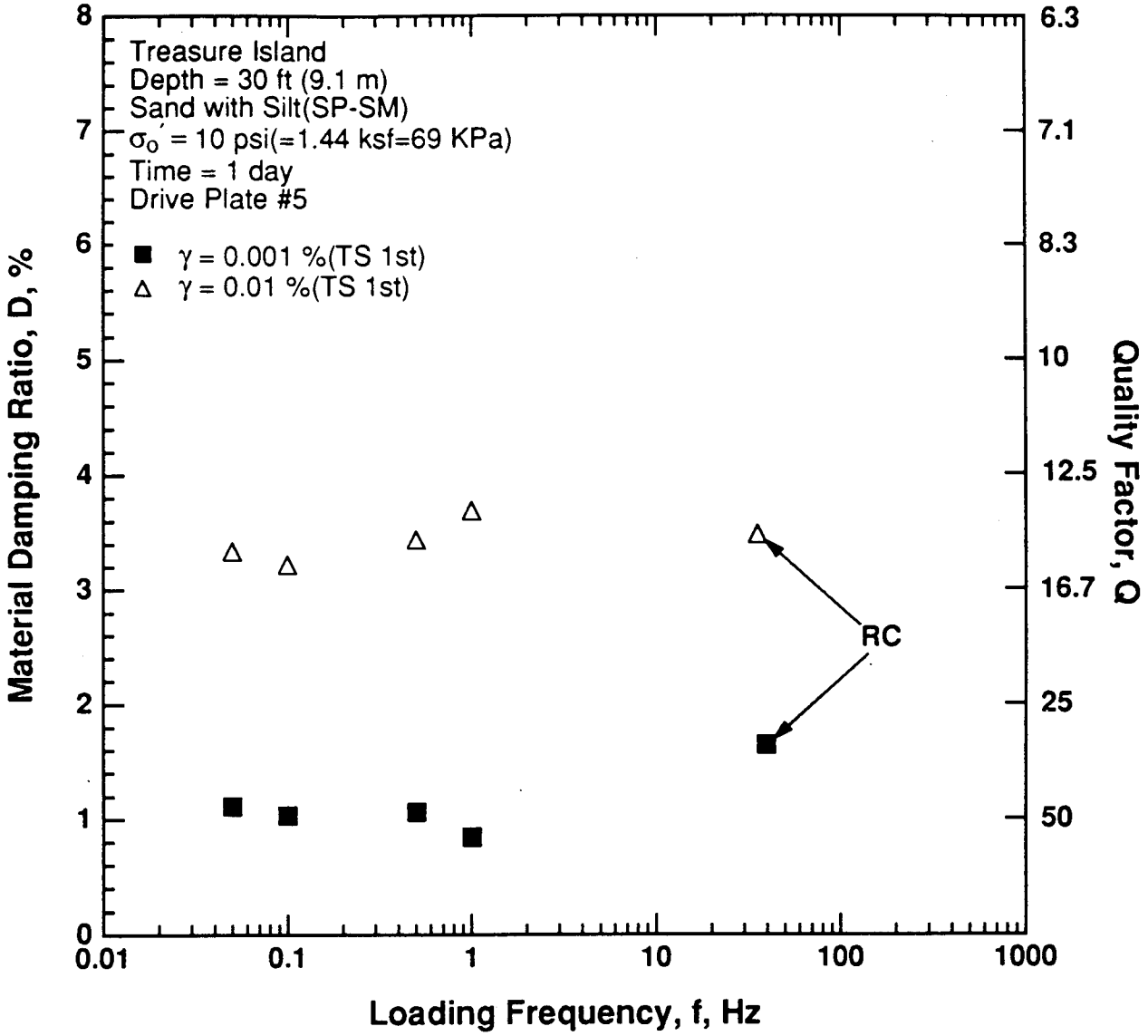

Figure 8.B.1.C-16
Variation in material damping ratio with loading frequency and shearing strain at an effective confining pressure of 10 psi (1.44 ksf, 69 kPa) from RCTS tests of sample T2.

APPENDIX 8.B.1.D
DYNAMIC TESTS OF SAMPLE T3, DEPTH = 60 FT (18.3 M)

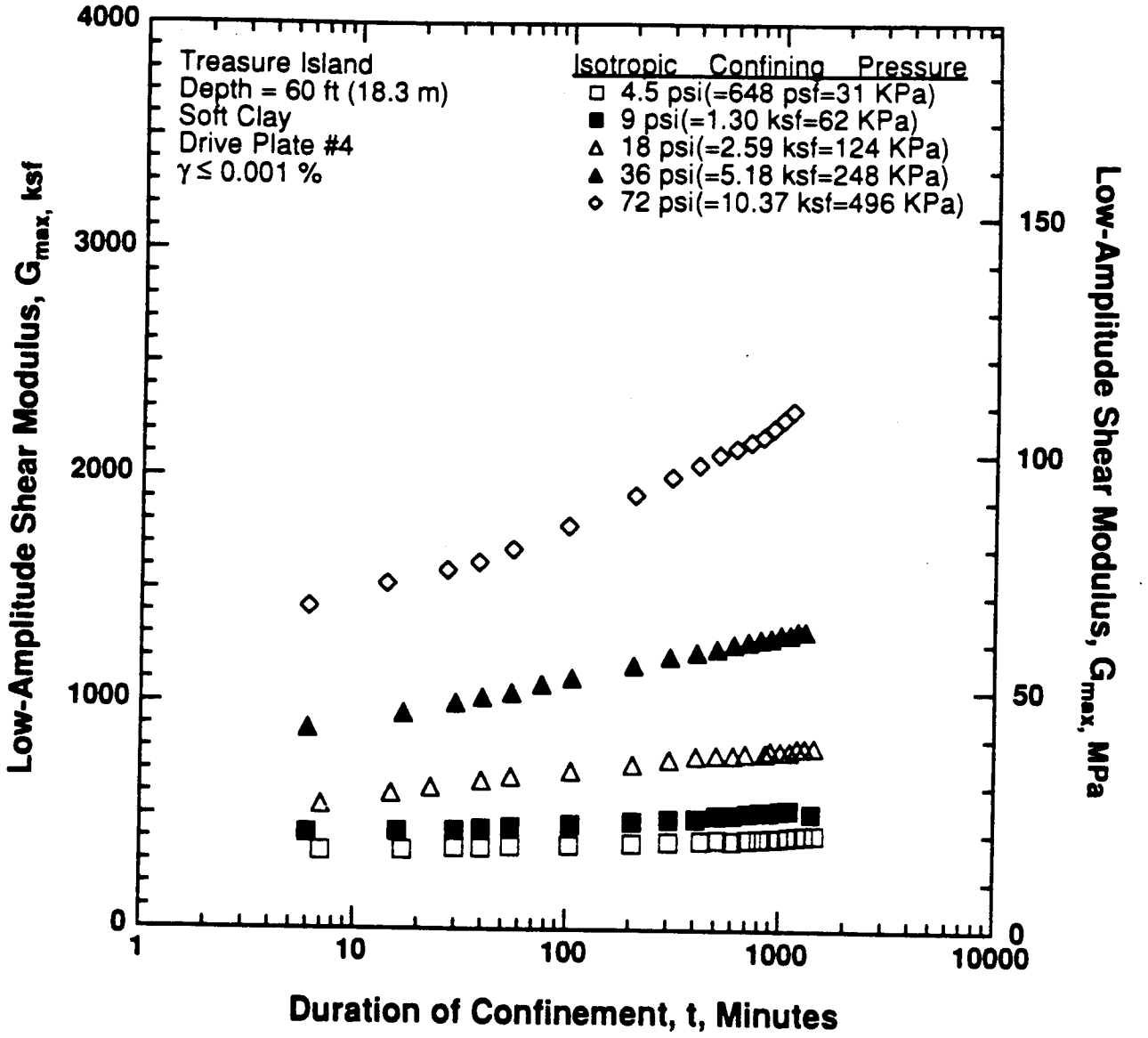

Figure 8.B.1.D-1
Variation in low-amplitude shear modulus with magnitude and duration of isotropic confining pressure from resonant column tests of sample T3.

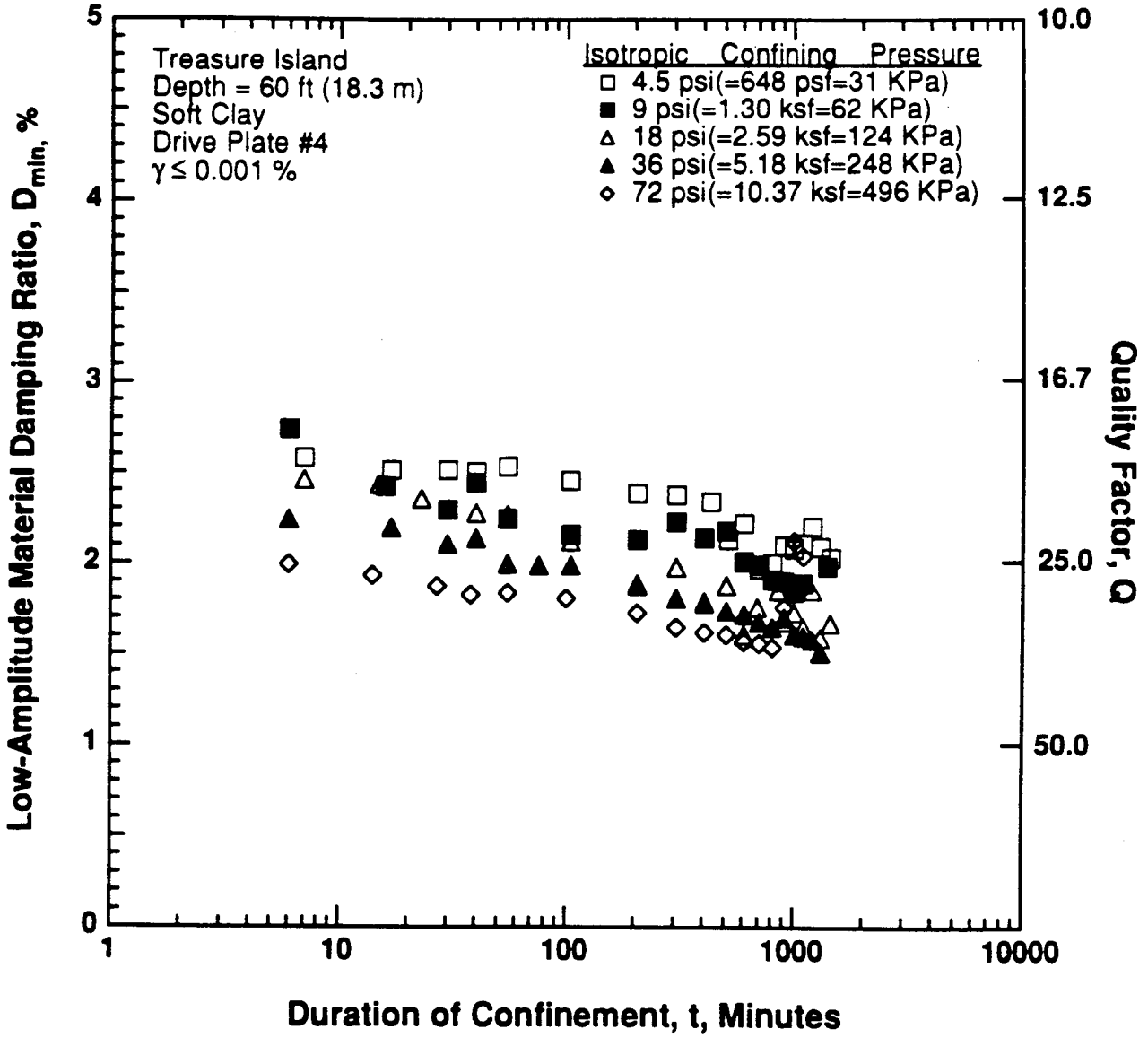

Figure 8.B.1.D-2
Variation in low-amplitude material damping ratio with magnitude and duration of isotropic confining pressure from resonant column tests of sample T3.

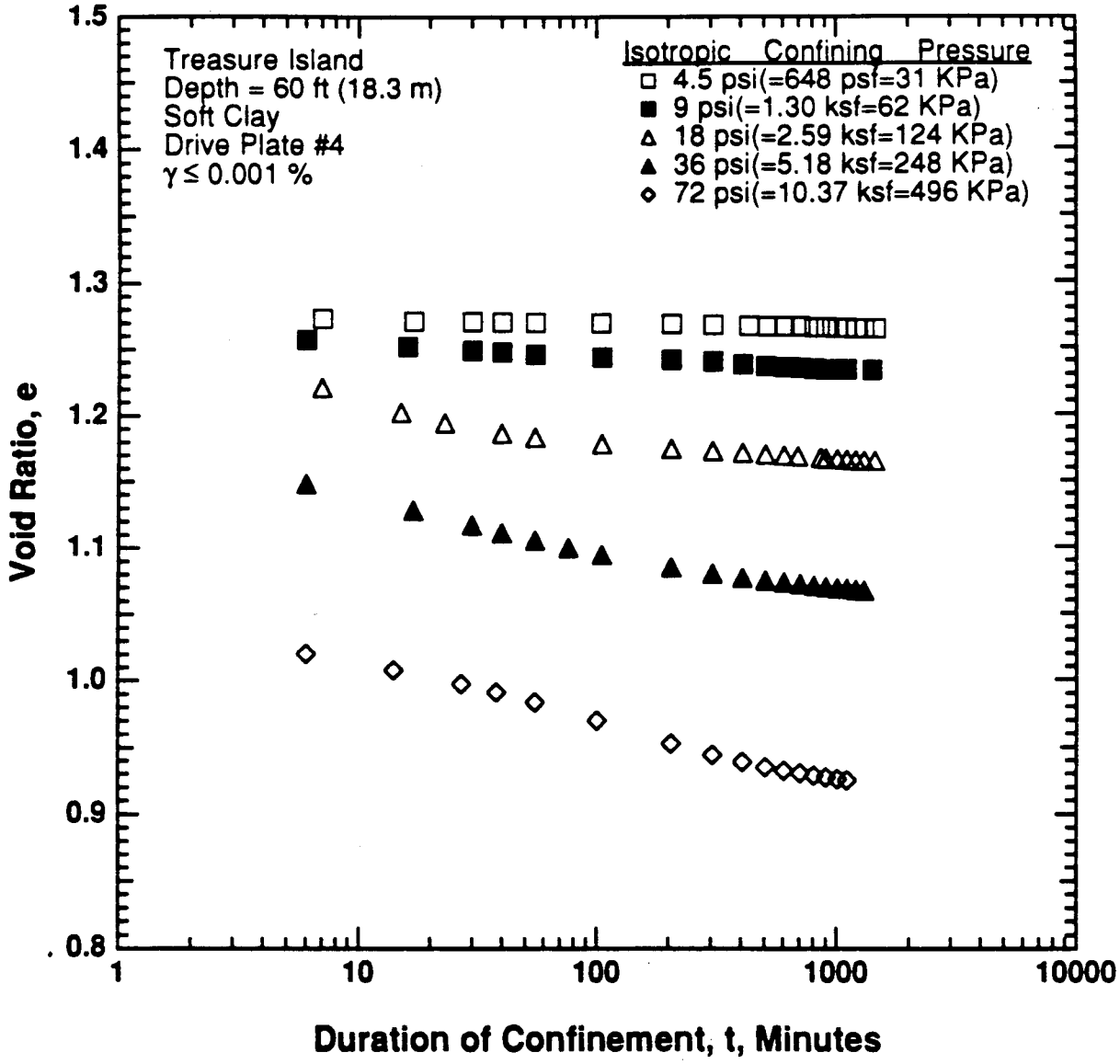

Figure 8.B.1.D-3
Variation in void ratio with magnitude and duration of isotropic confining pressure from resonant column tests of sample T3.

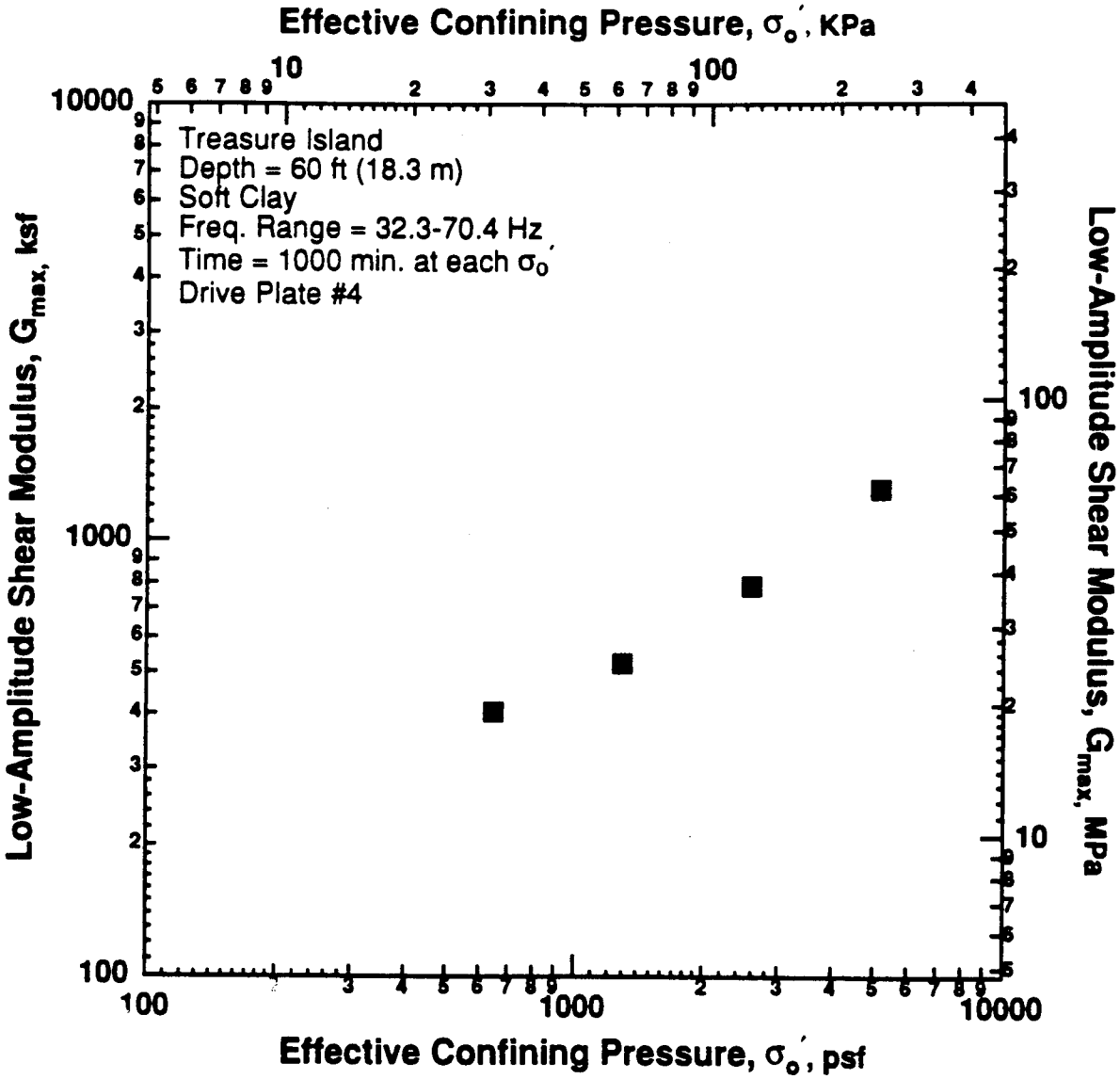

Figure 8.B.1.D-4
Variation in low-amplitude shear modulus with effective confining pressure from resonant column tests of sample T3.

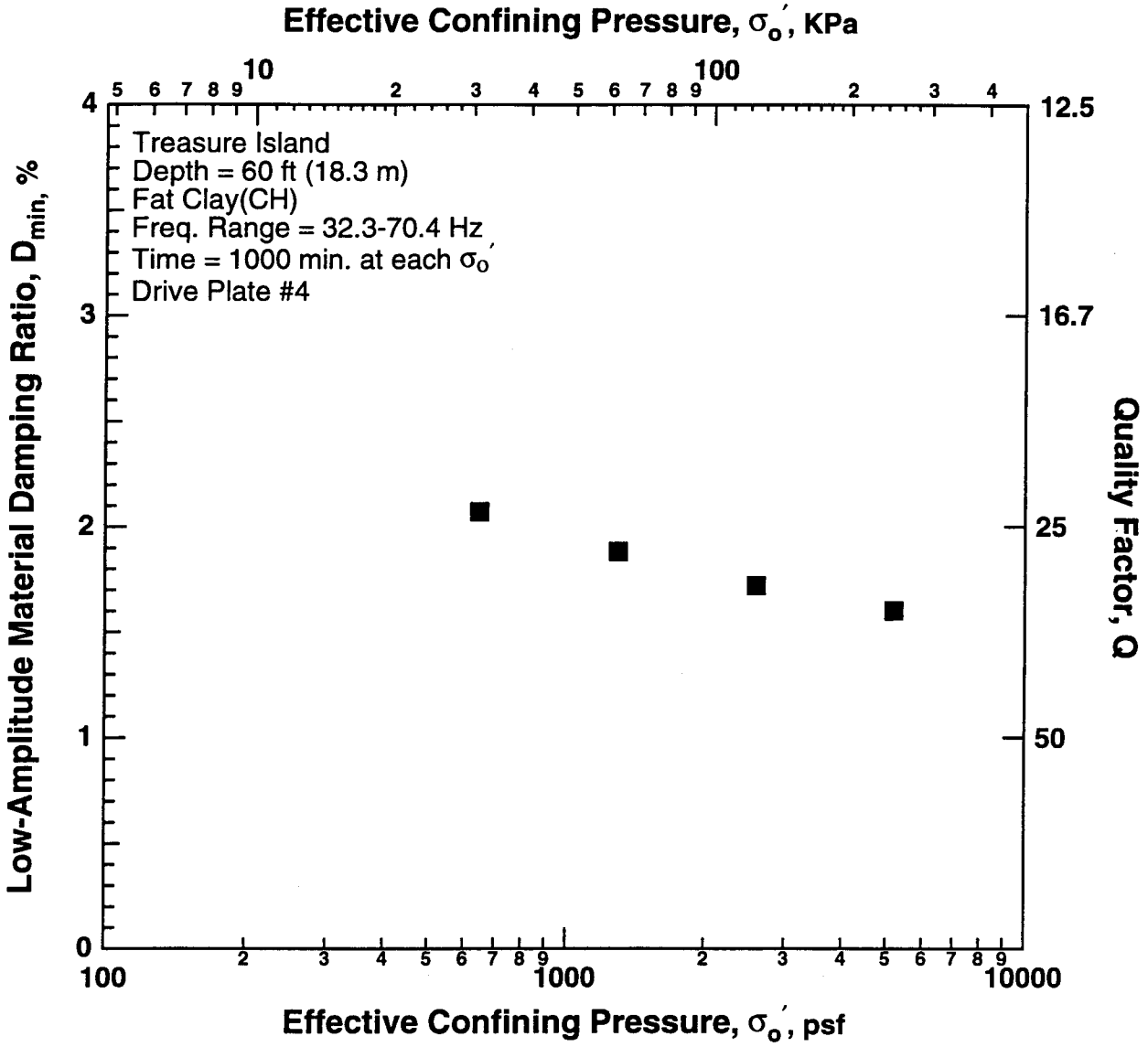

Figure 8.B.1.D-5
Variation in low-amplitude material damping ratio with effective confining pressure from resonant column tests of sample T3.

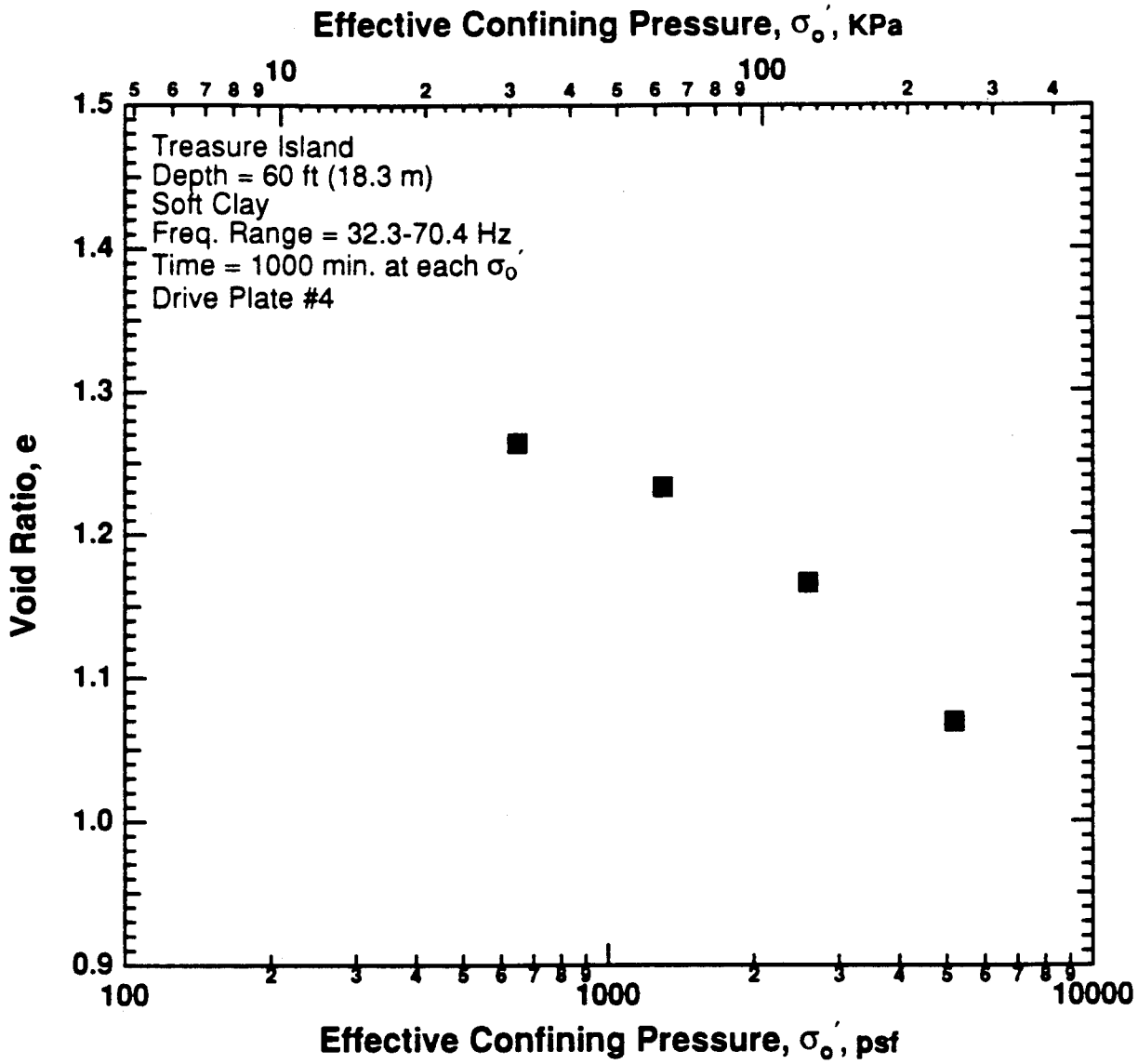

Figure 8.B.1.D-6
Variation in void ratio with effective confining pressure from resonant column tests of sample T3.

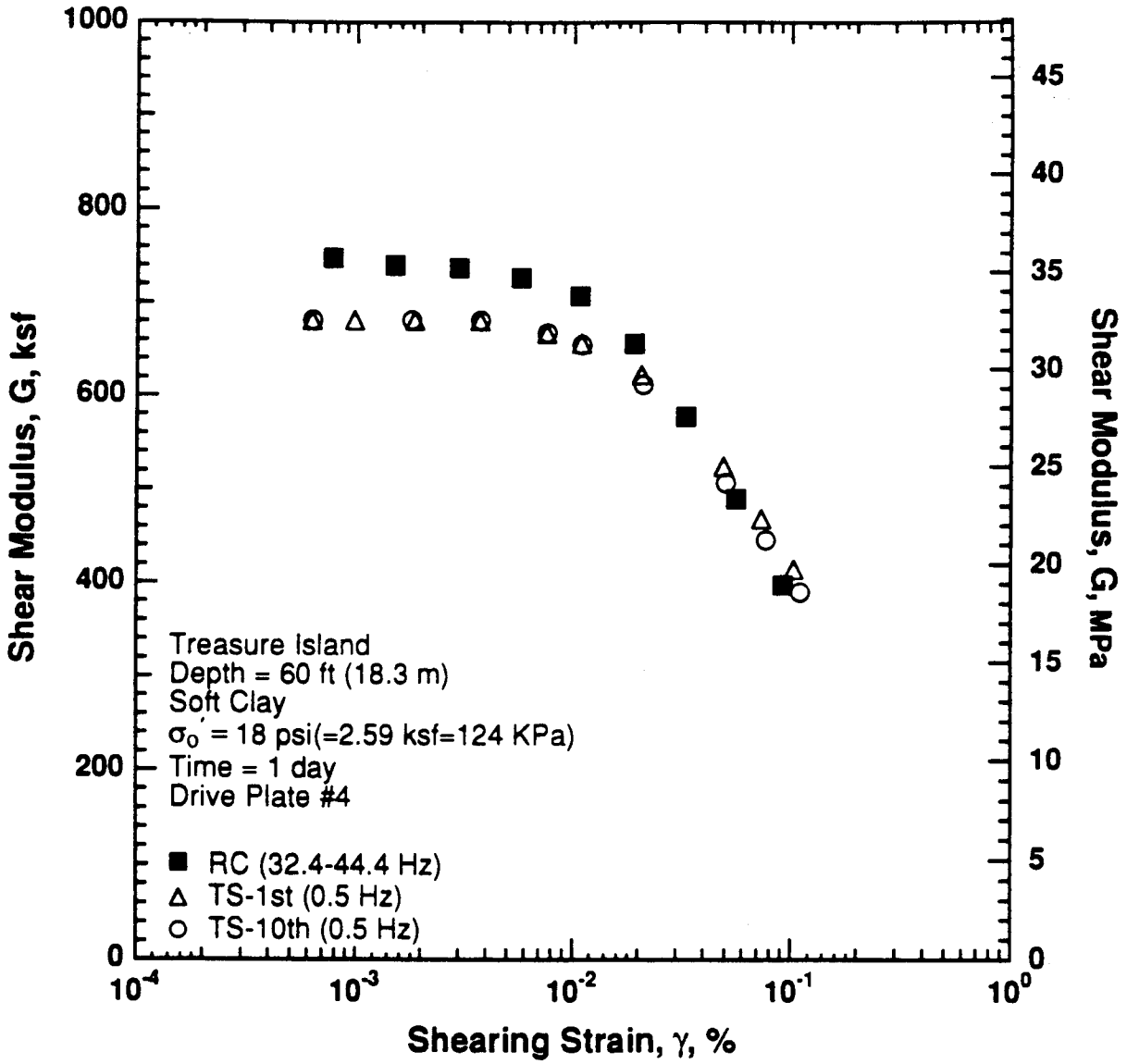

Figure 8.B.1.D-7
Variation in shear modulus with shearing strain at an effective confining pressure of 18 psi (2.59 ksf, 124 kPa) from RCTS tests of sample T3.

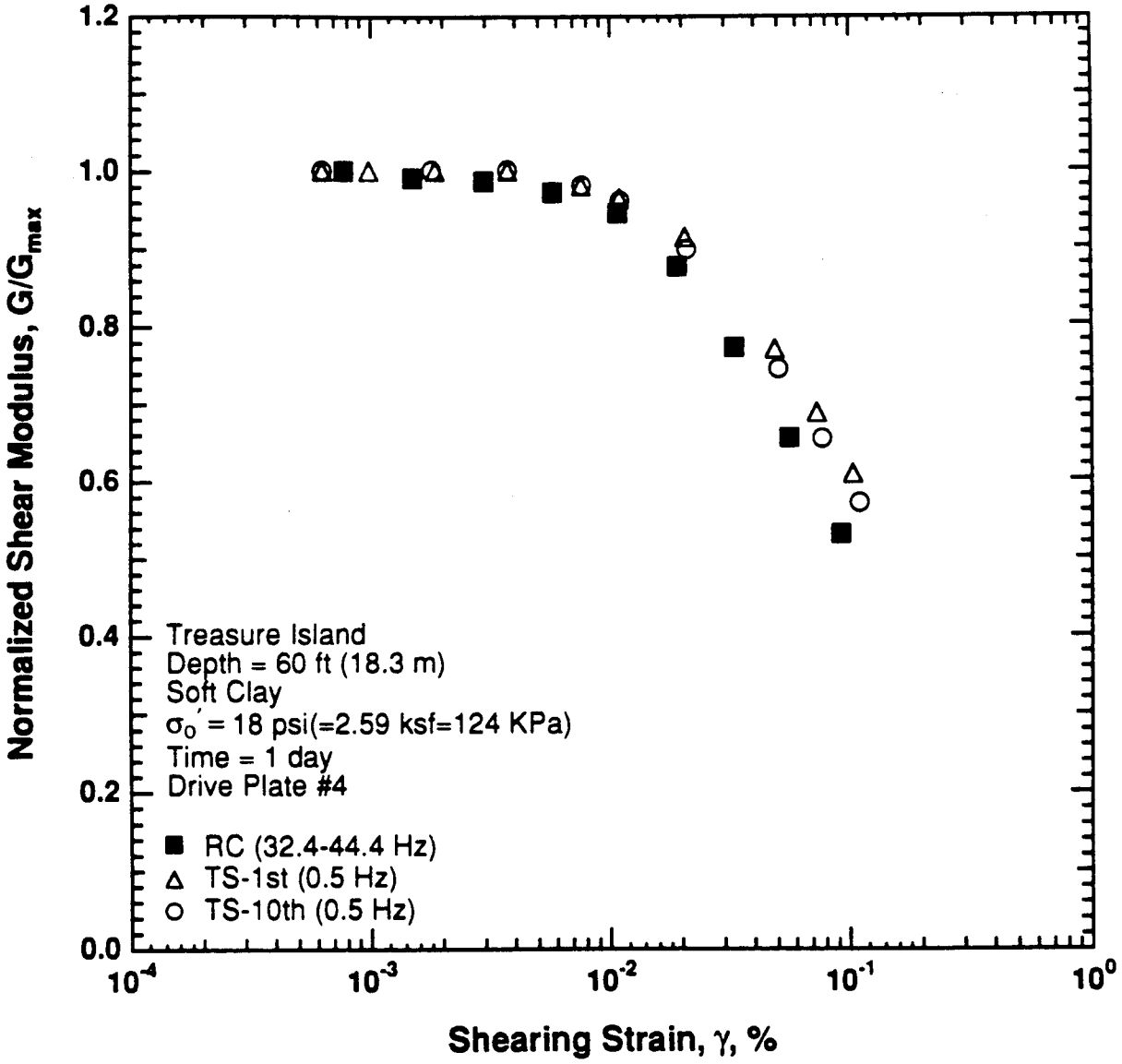

Figure 8.B.1.D-8
Variation in normalized shear modulus with shearing strain at an effective confining pressure of 18 psi (2.59 ksf, 124 kPa) from RCTS tests of sample T3.

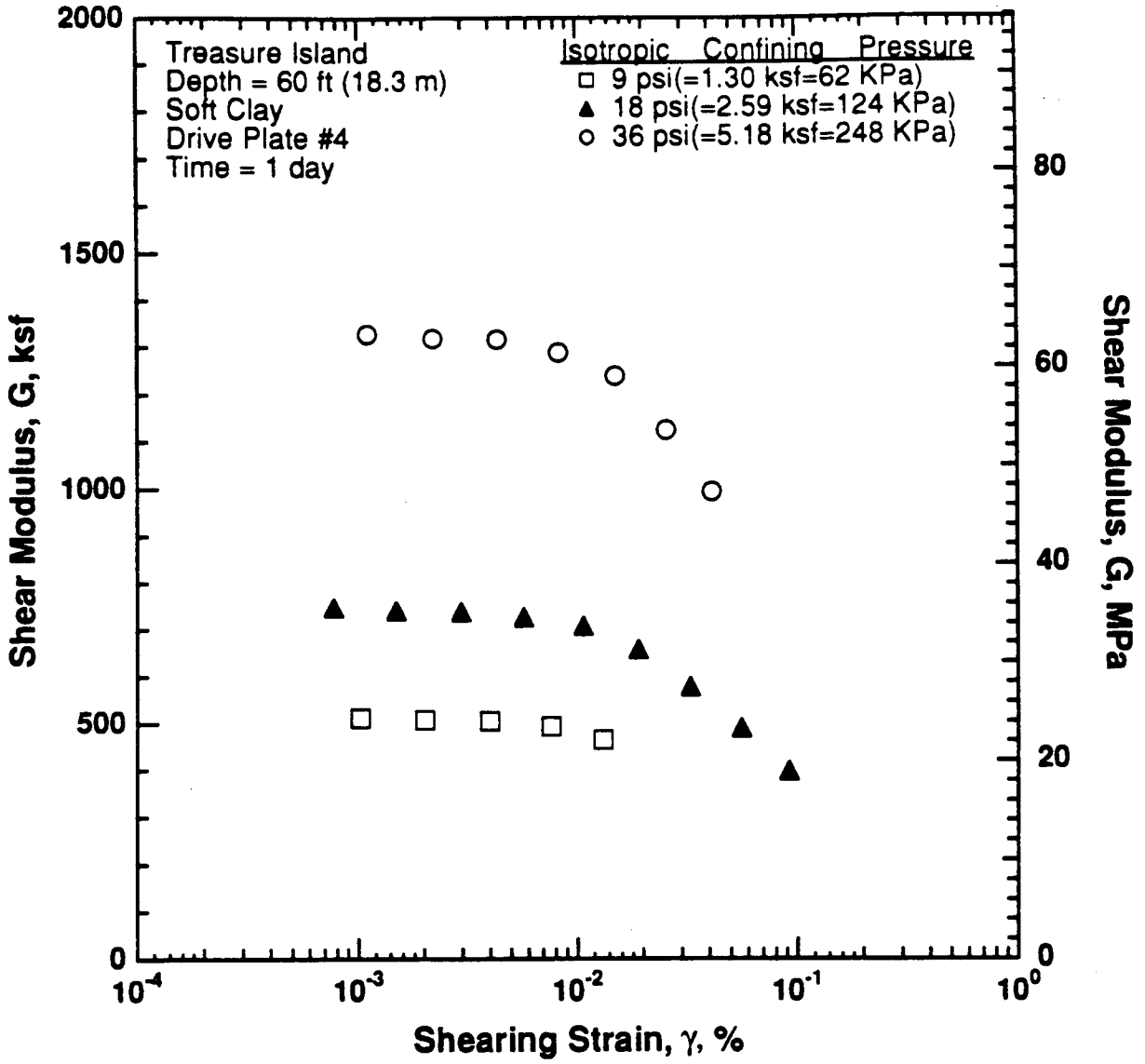

Figure 8.B.1.D-9
Variation in shear modulus with shearing strain and effective confining pressure from resonant column tests of sample T3.

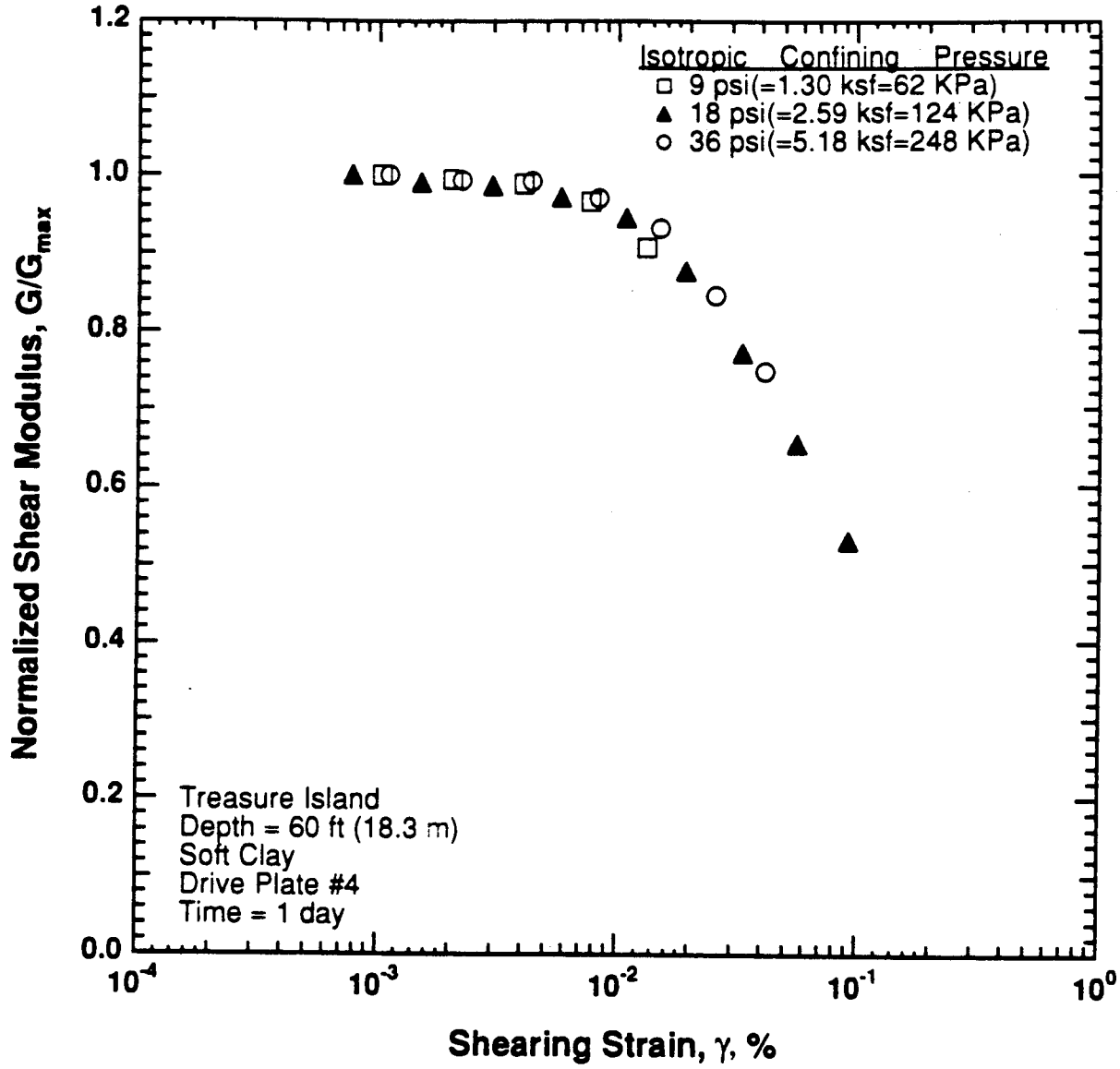

Figure 8.B.1.D-10
Comparison of the variation in normalized shear modulus with shearing strain and effective confining pressure from resonant column tests of sample T3.

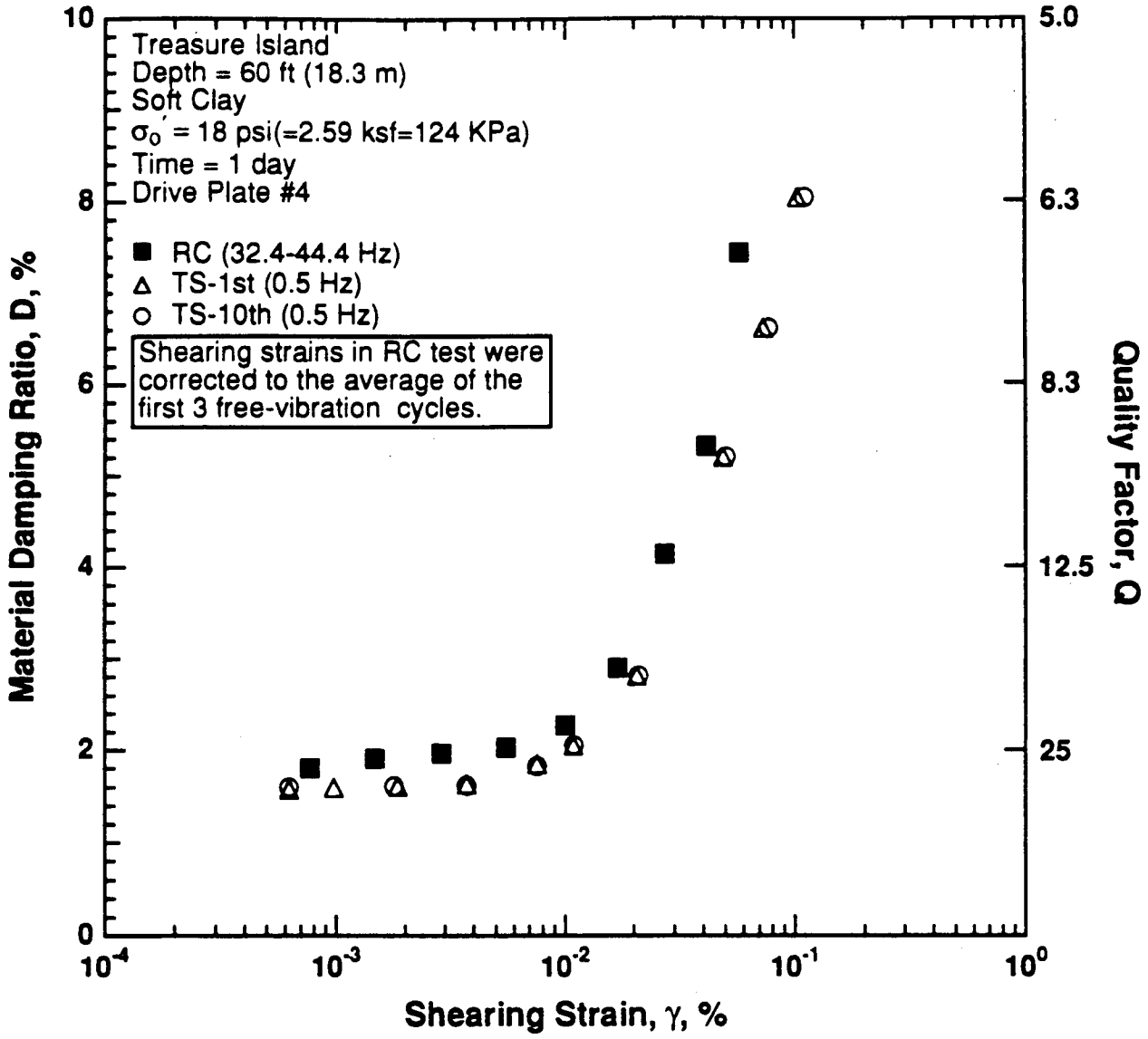

Figure 8.B.1.D-11
Variation in material damping ratio with shearing strain at an effective confining pressure of 18 psi (2.59 ksf, 124 kPa) from RCTS tests of sample T3.

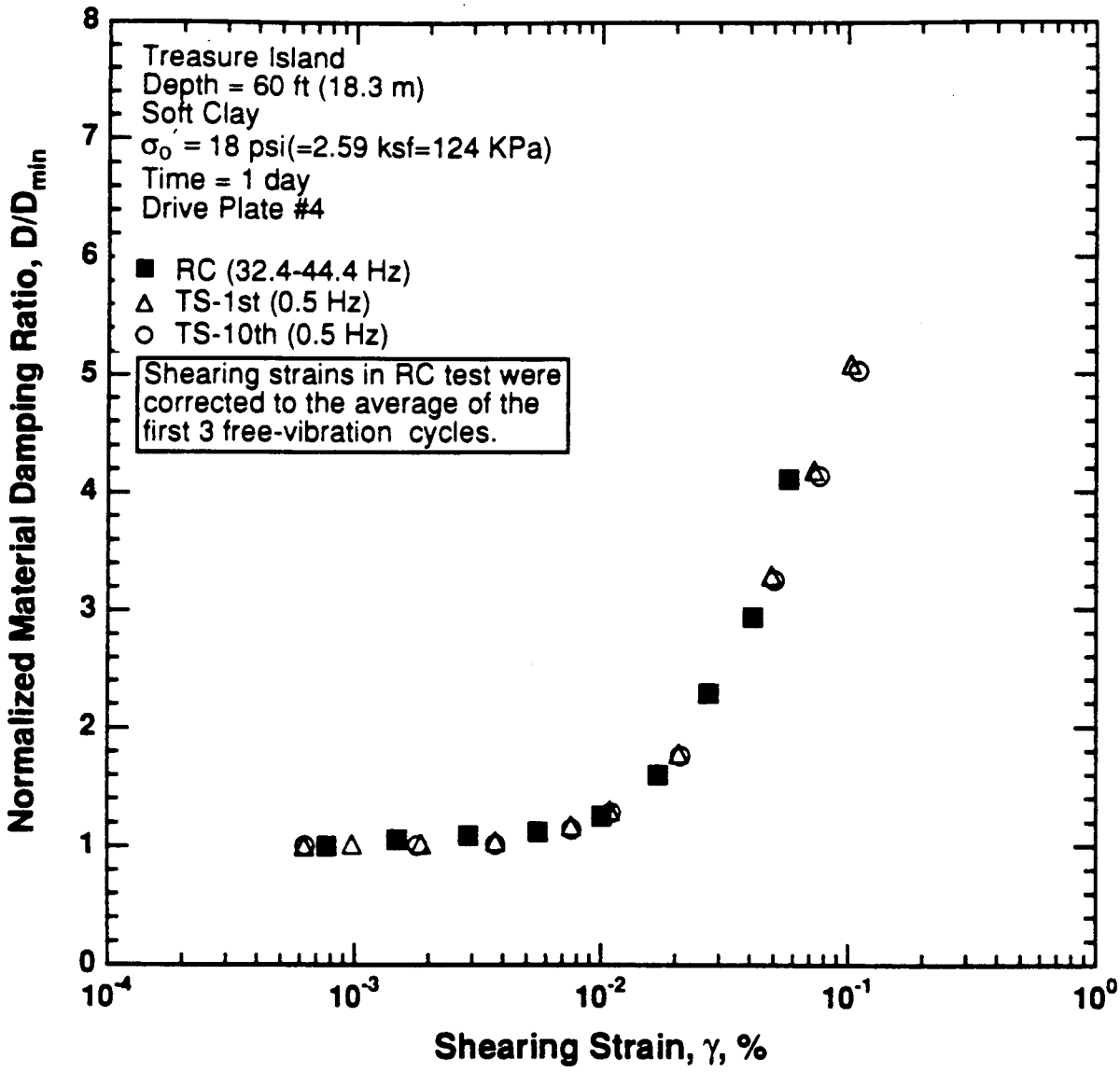

Figure 8.B.1.D-12
Variation in normalized material damping ratio with shearing strain at an effective confining pressure of 18 psi (2.59 ksf, 124 kPa) from RCTS tests of sample T3.

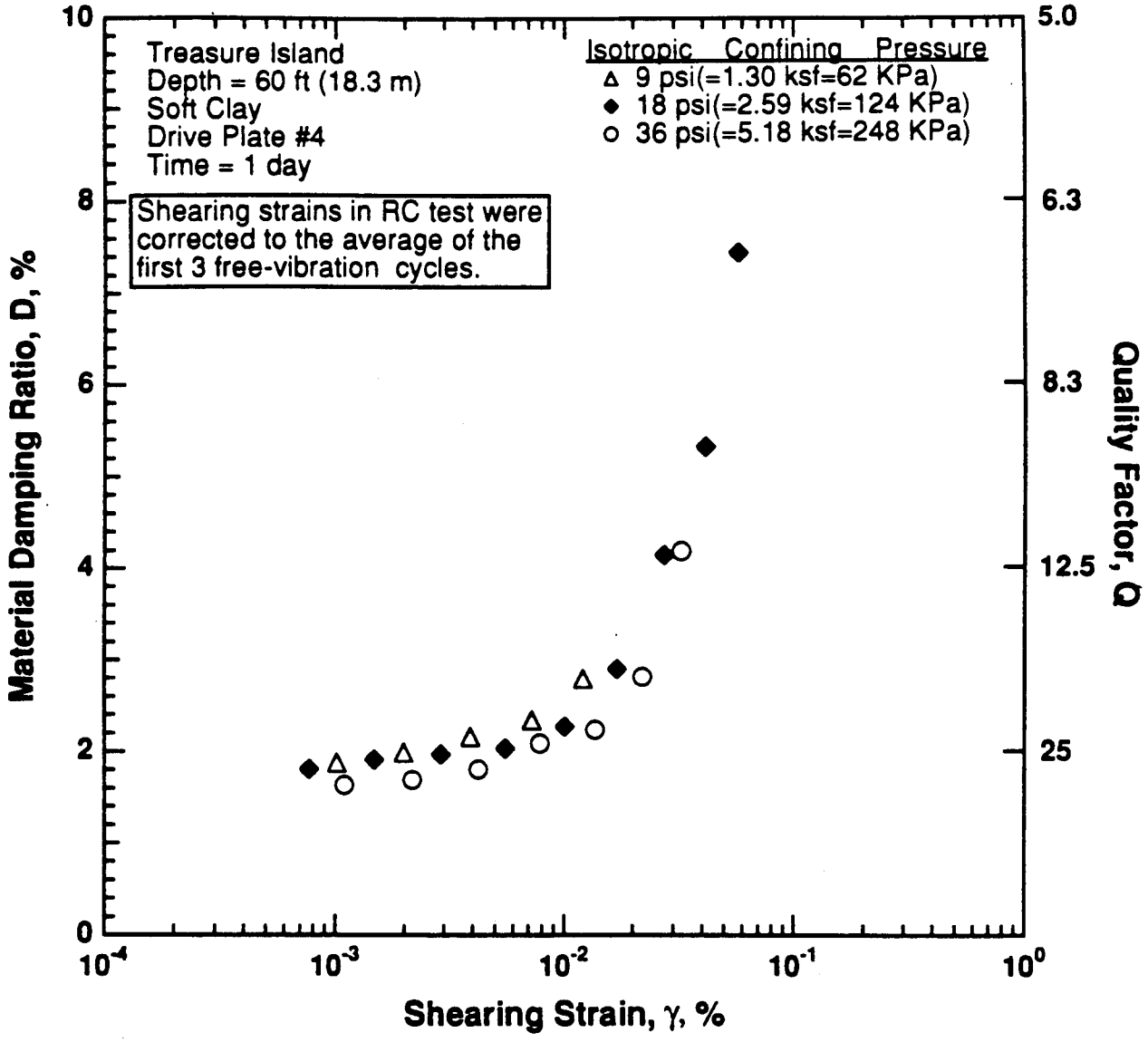

Figure 8.B.1.D-13
Variation in material damping ratio with shearing strain and effective confining pressure from resonant column tests of sample T3.

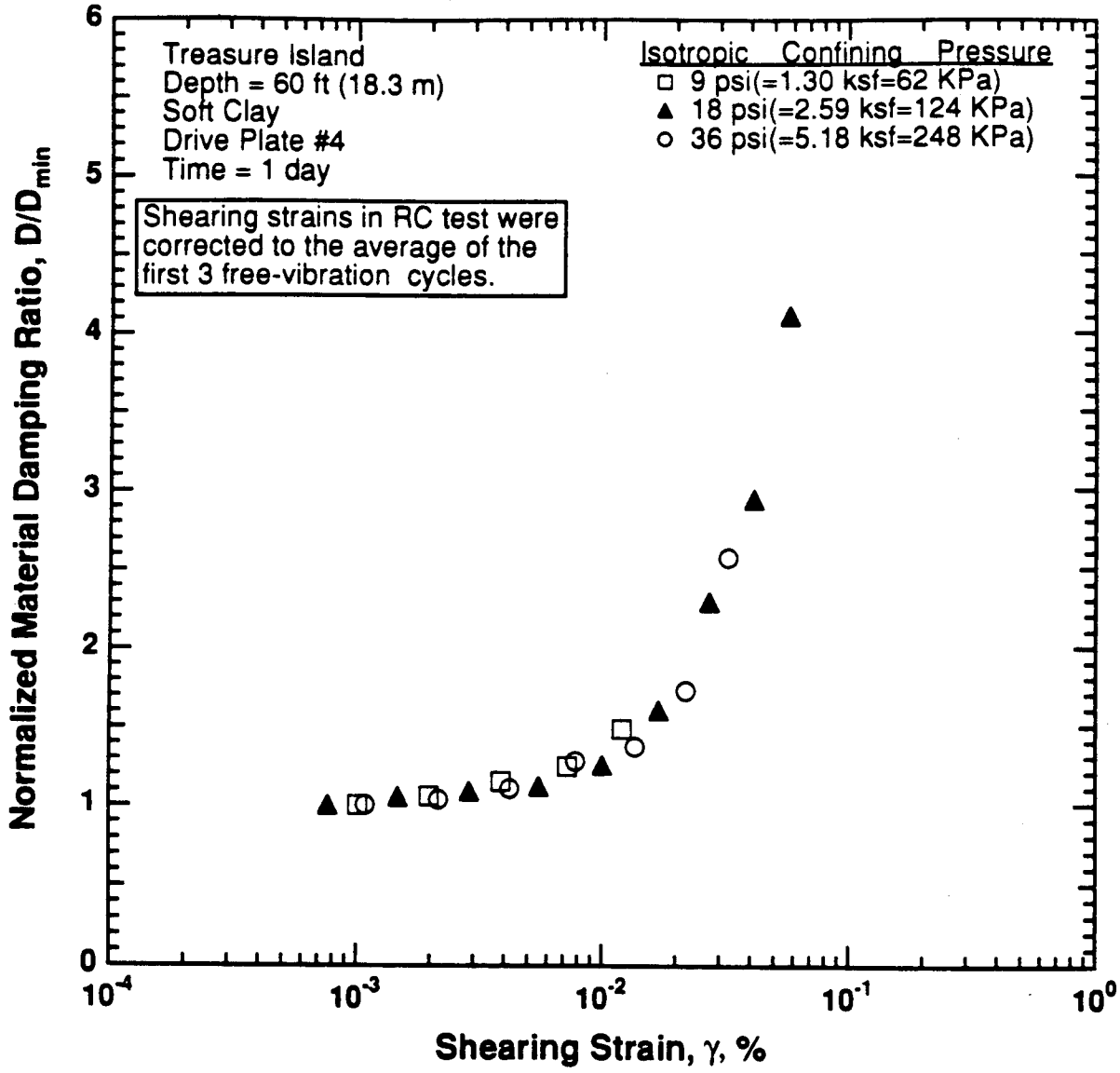

Figure 8.B.1.D-14
Comparison of the variation in normalized material damping ratio with shearing strain and effective confining pressure from resonant column tests of sample T3.

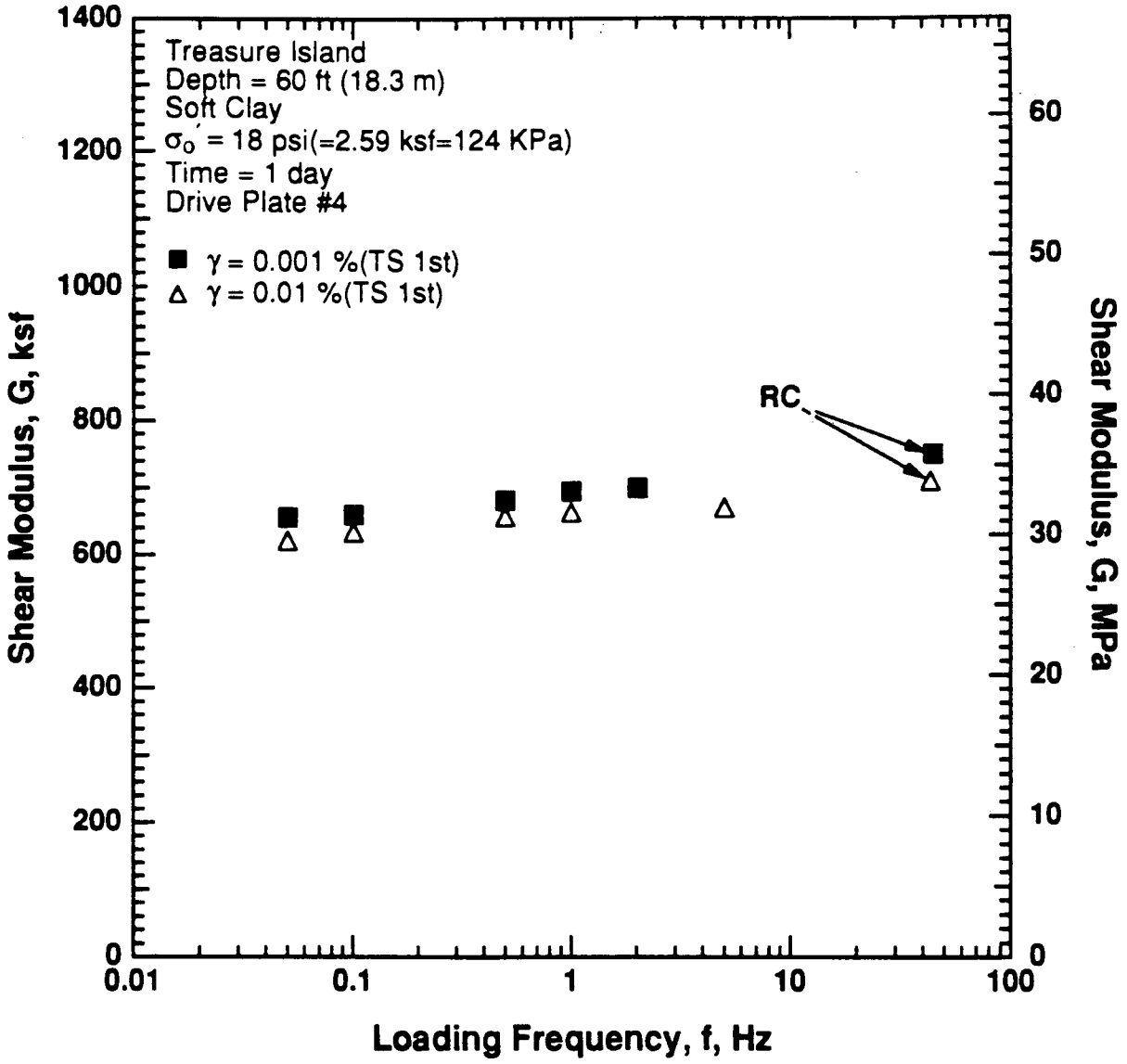

Figure 8.B.1.D-15
Variation in shear modulus with loading frequency and shearing strain at an effective confining pressure of 18 psi (2.59 ksf, 124 kPa) from RCTS tests of sample T3.

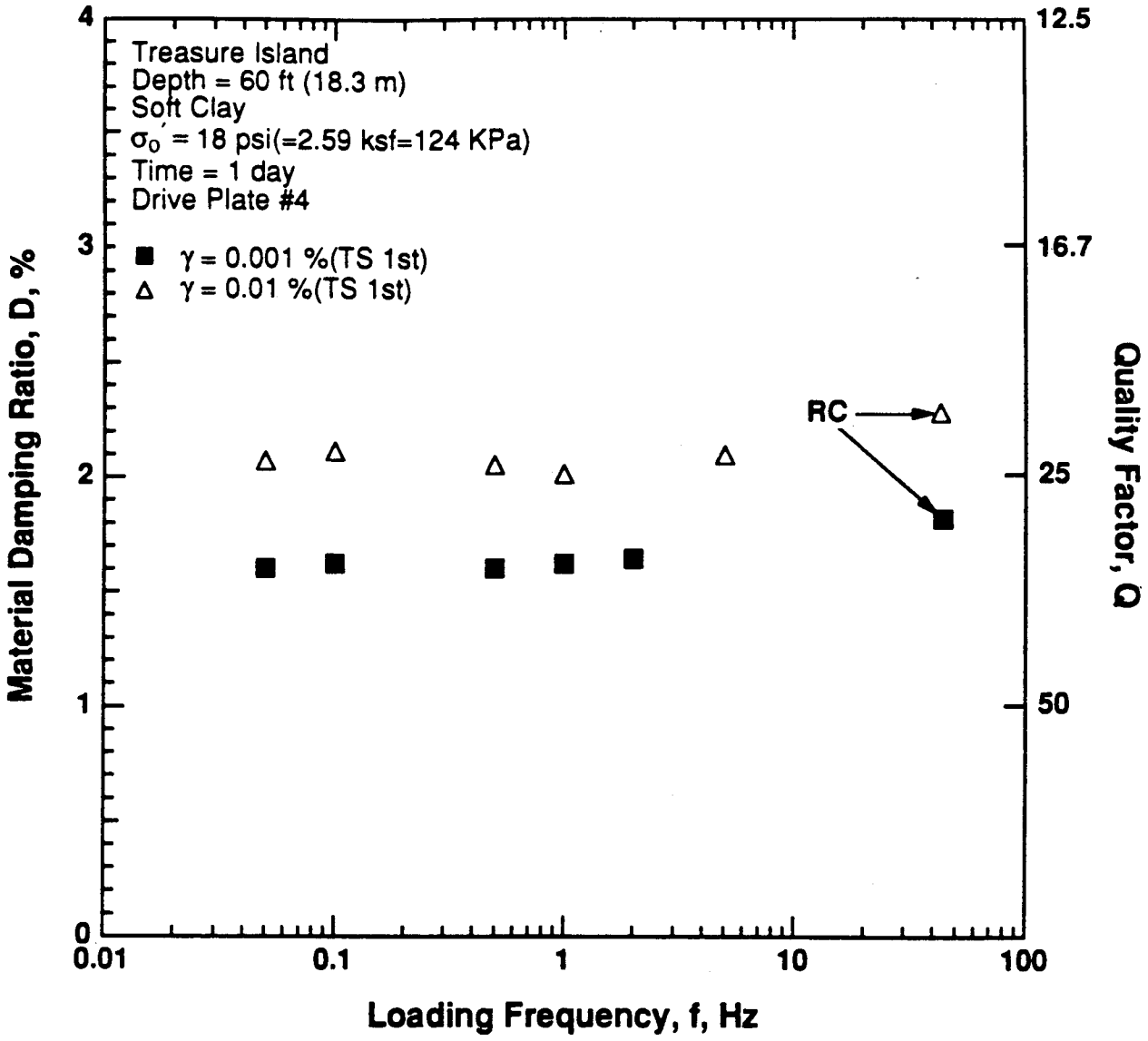

Figure 8.B.1.D-16
Variation in material damping ratio with loading frequency and shearing strain at an effective confining pressure of 181 psi (2.59 ksf, 124 kPa) from RCTS tests of sample T3.

APPENDIX 8.B.1.E
DYNAMIC TESTS OF SAMPLE T4, DEPTH = 90 FT (27.4 M)

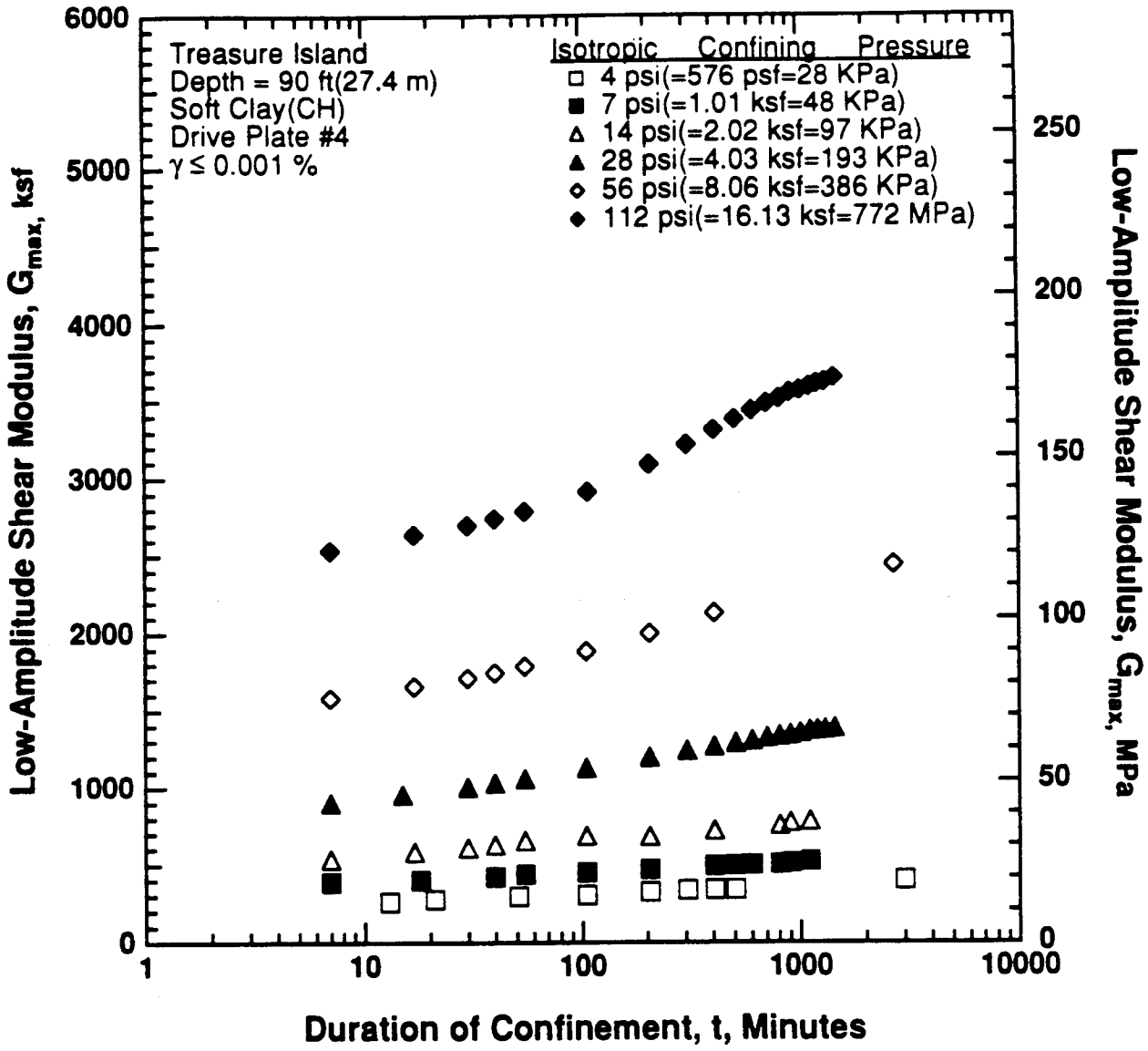

Figure 8.B.1.E-1
Variation in low-amplitude shear modulus with magnitude and duration of isotropic confining pressure from resonant column tests of sample T4.

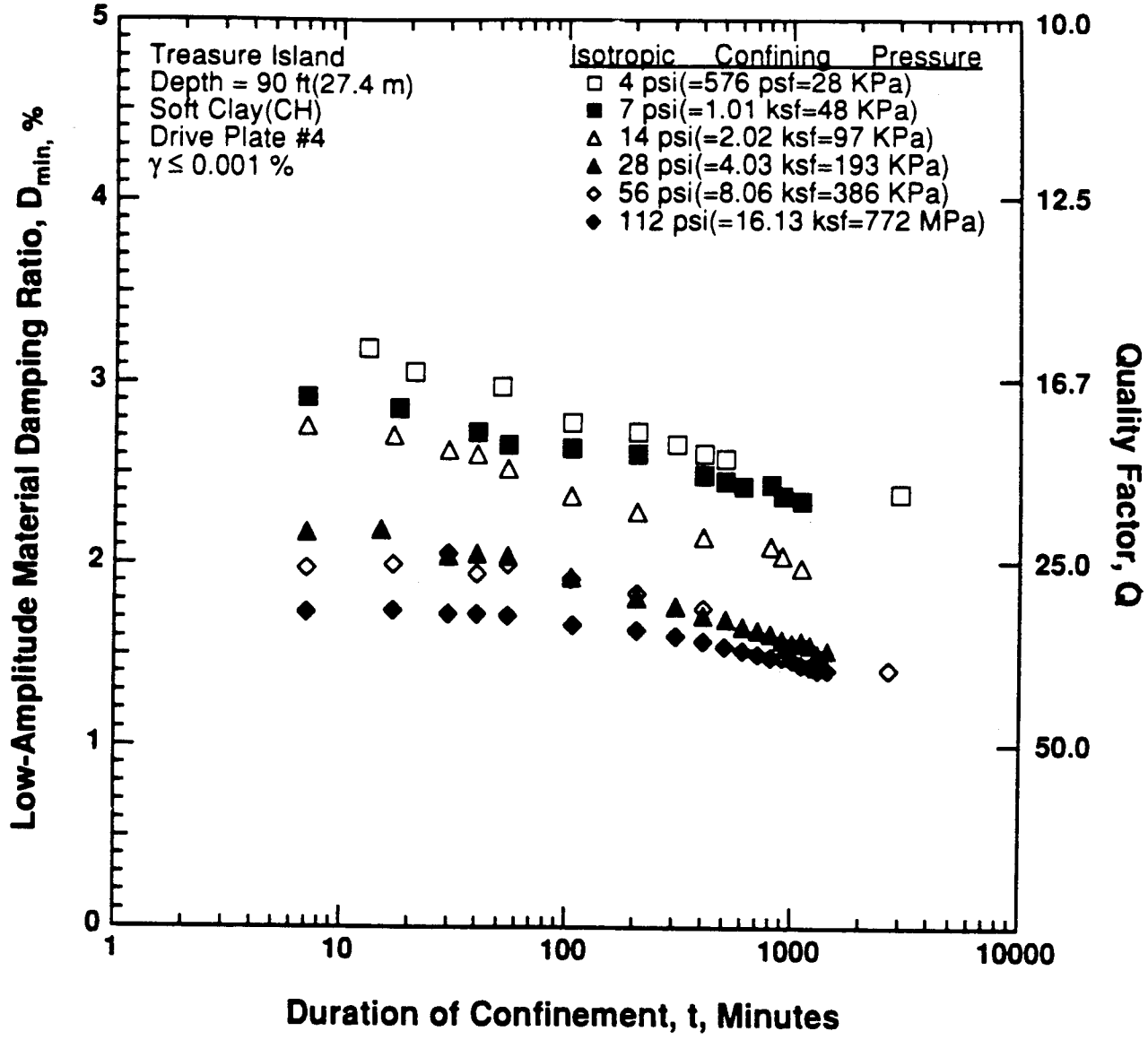

Figure 8.B.1.E-2
Variation in low-amplitude material damping ratio with magnitude and duration of isotropic confining pressure from resonant column tests of sample T4.

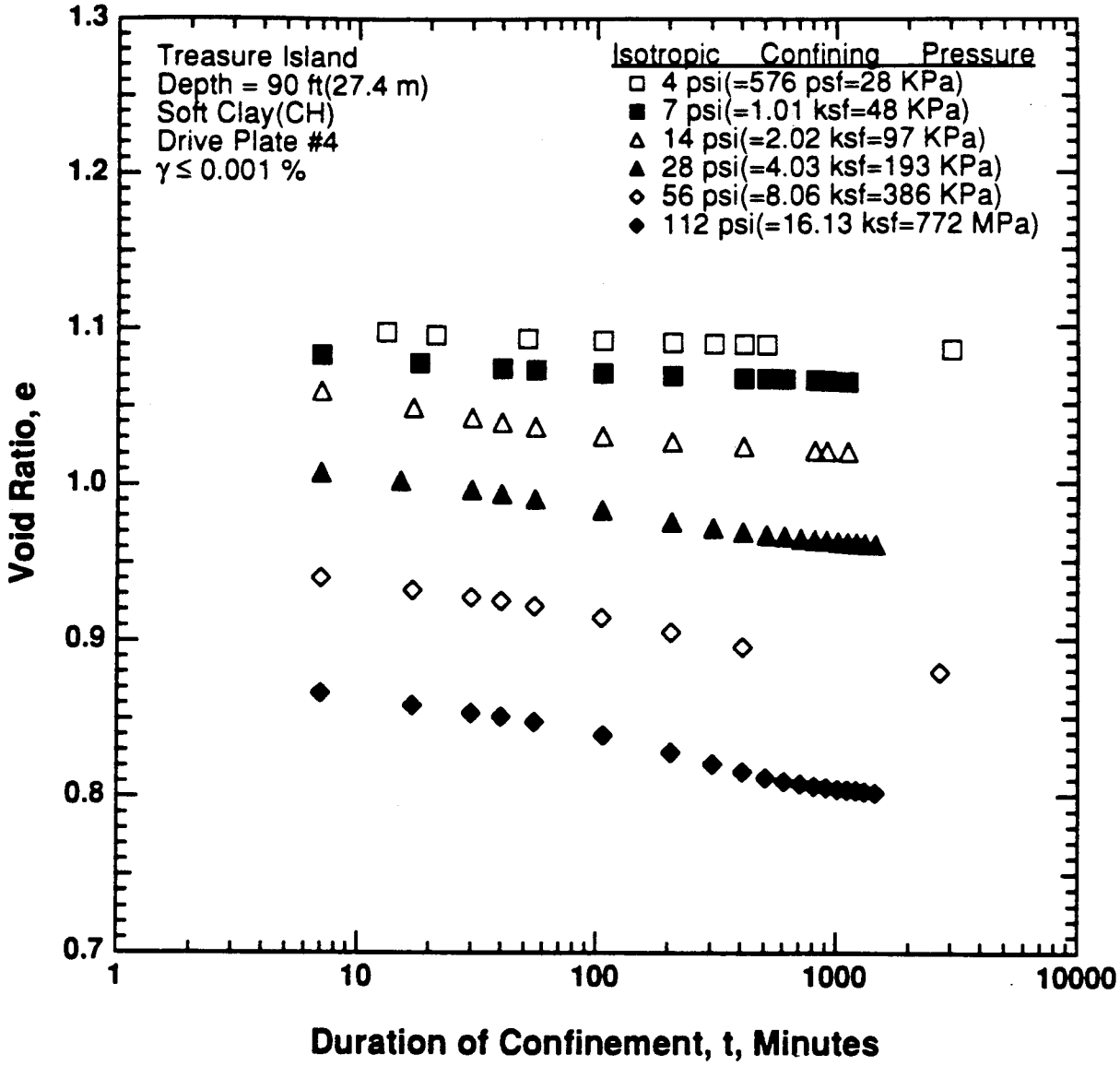

Figure 8.B.1.E-3
Variation in void ratio with magnitude and duration of isotropic confining pressure from resonant column tests of sample T4.

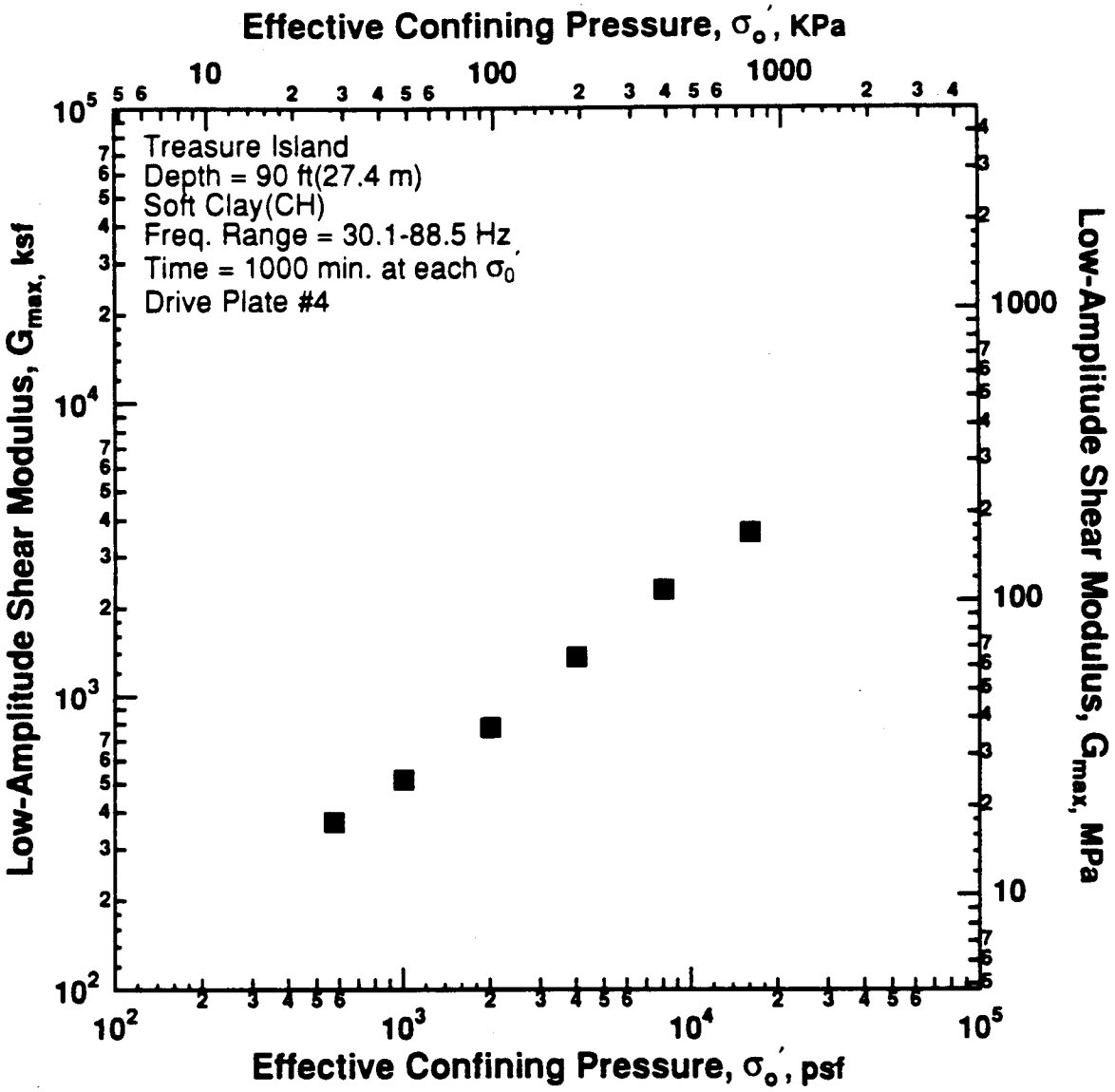

Figure 8.B.1.E-4
Variation in low-amplitude shear modulus with effective confining pressure from resonant column tests of sample T4.

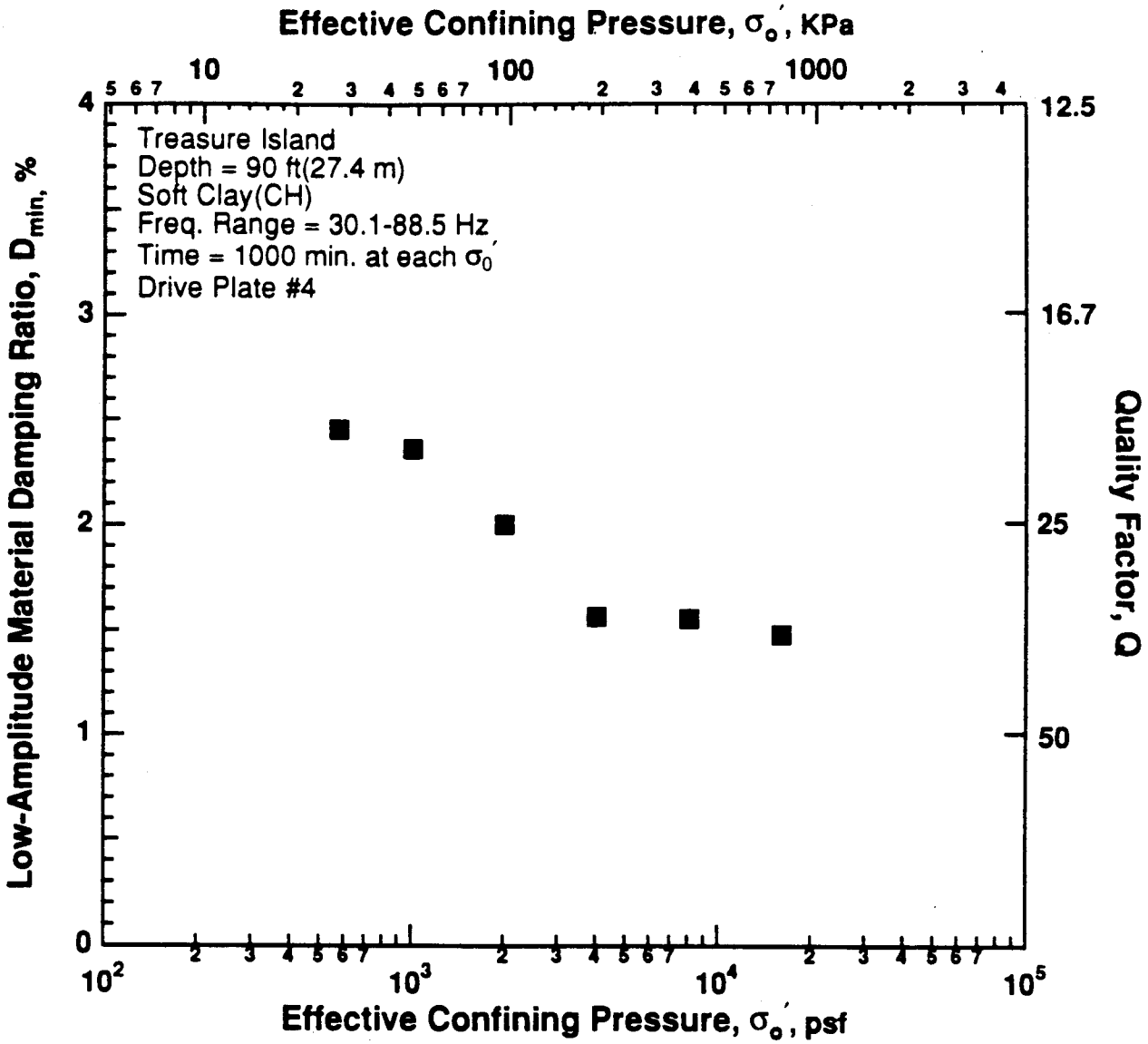

Figure 8.B.1.E-5
Variation in low-amplitude material damping ratio with effective confining pressure from resonant column tests of sample T4.

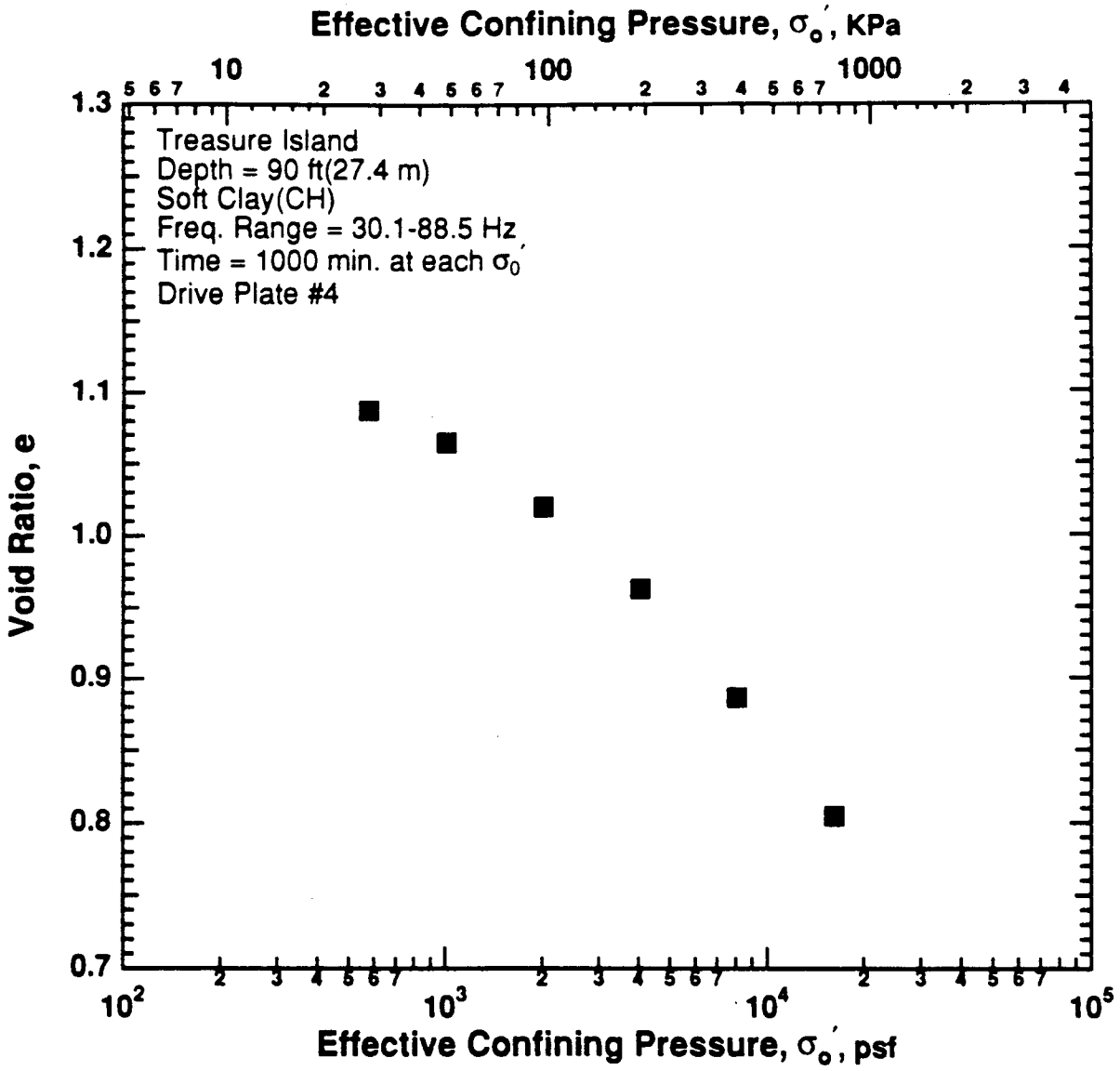

Figure 8.B.1.E-6
Variation in void ratio with effective confining pressure from resonant column tests of sample T4.

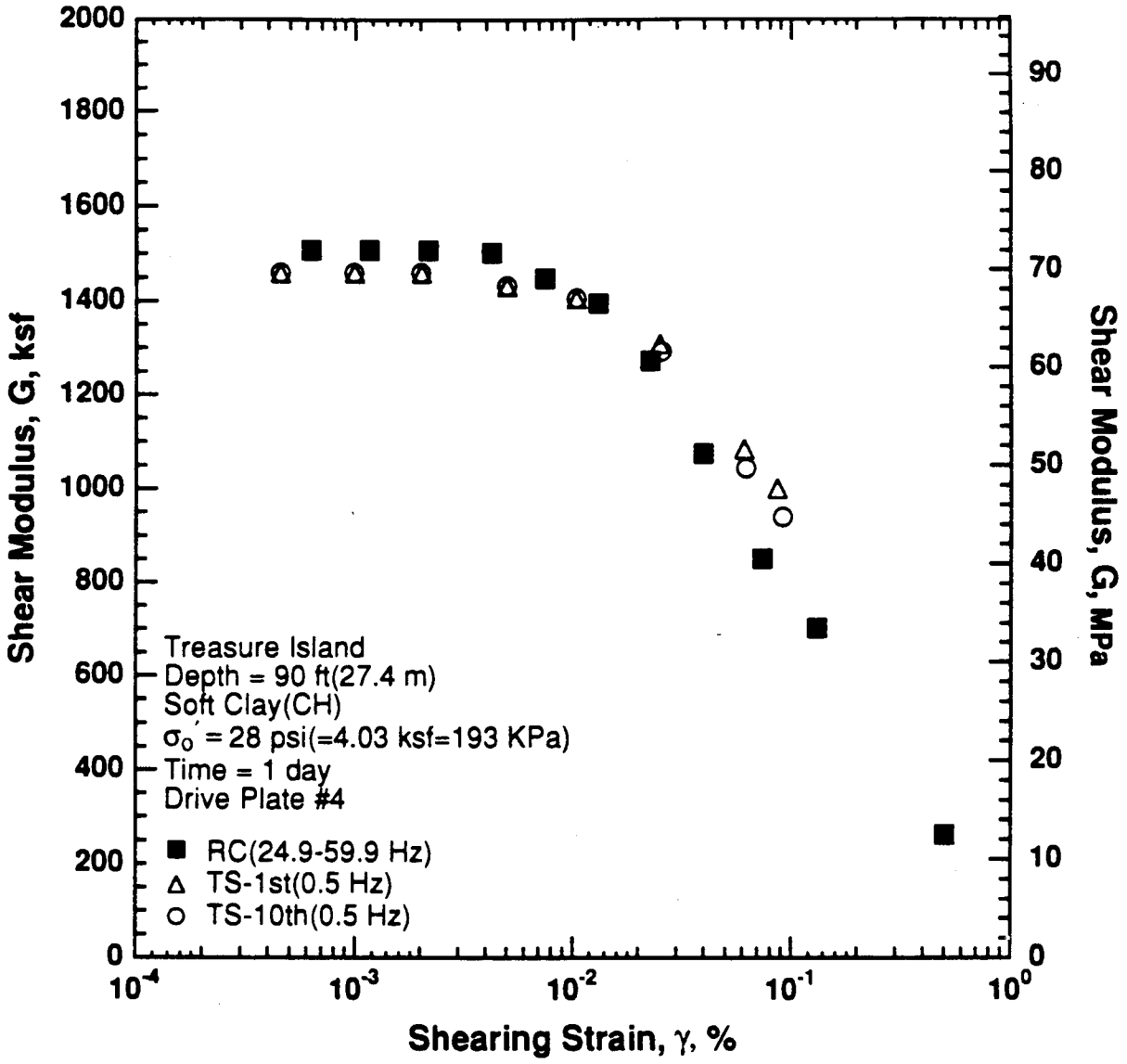

Figure 8.B.1.E-7
Variation in shear modulus with shearing strain at an effective confining pressure of 28 psi (4.03 ksf, 193 kPa) from RCTS tests of sample T4.

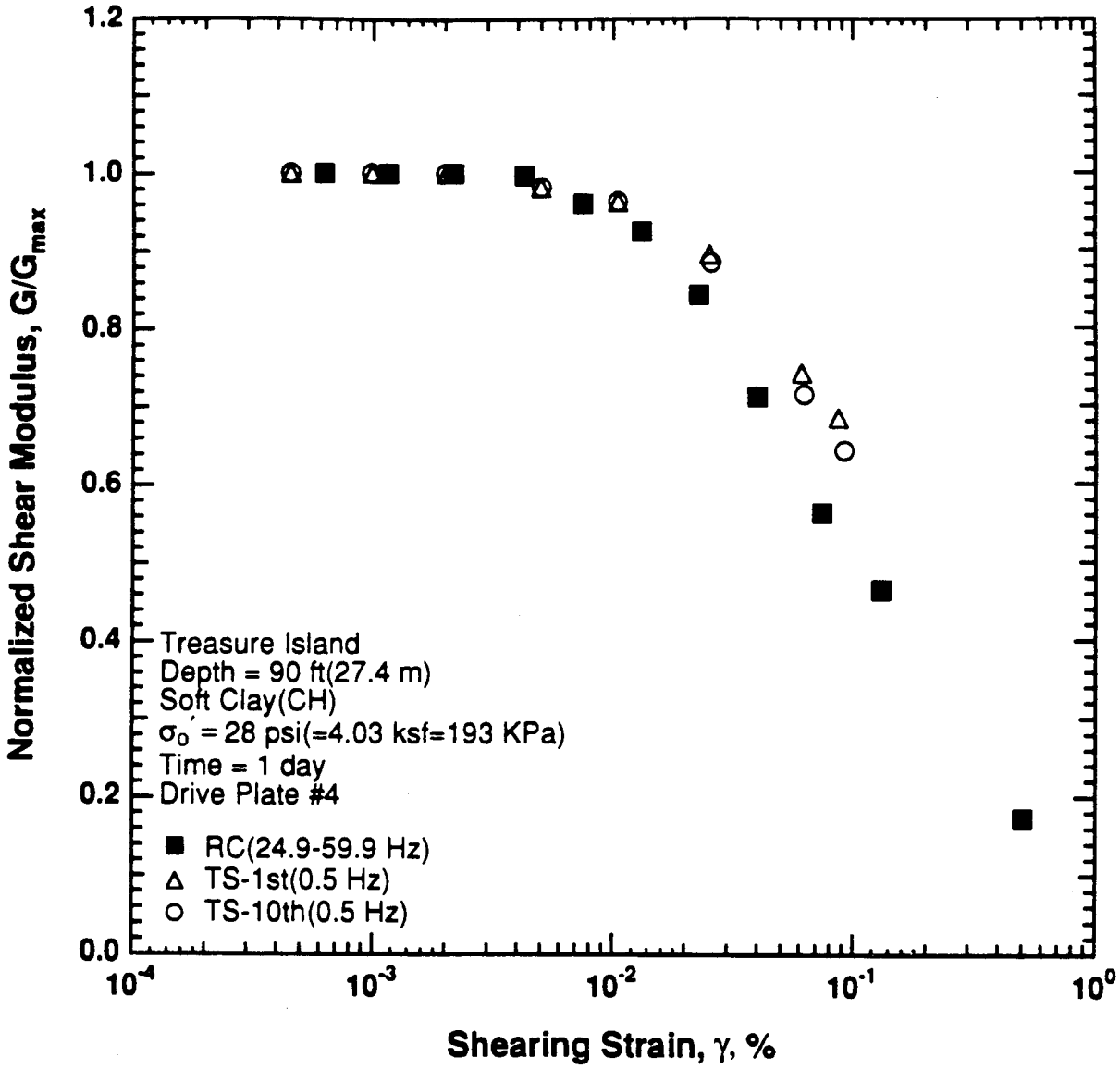

Figure 8.B.1.E-8
Variation in normalized shear modulus with shearing strain at an effective confining pressure of 28 psi (4.03 ksf, 193 kPa) from RCTS tests of sample T4.

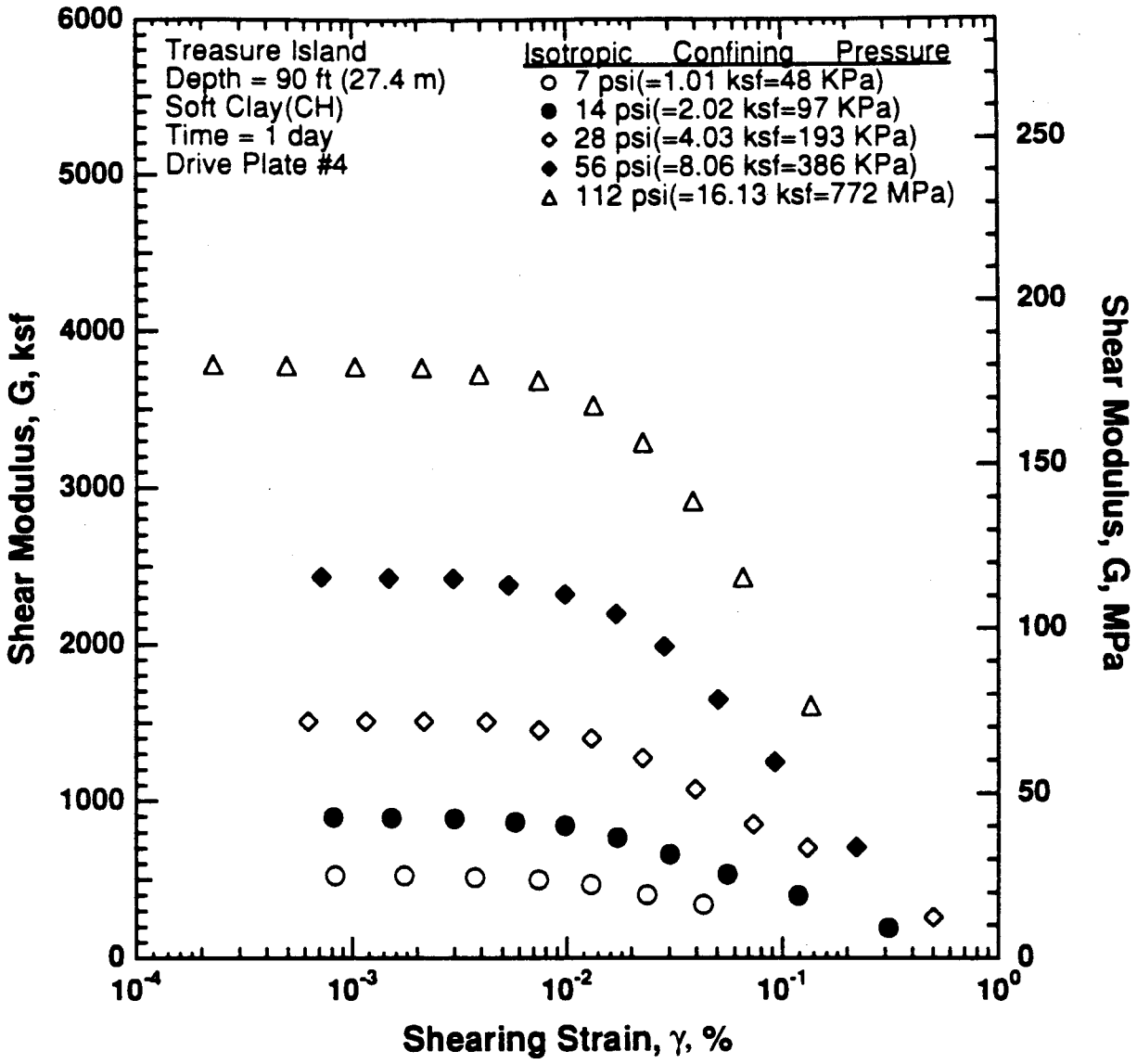

Figure 8.B.1.E-9
Variation in shear modulus with shearing strain and effective confining pressure from resonant column tests of sample T4.

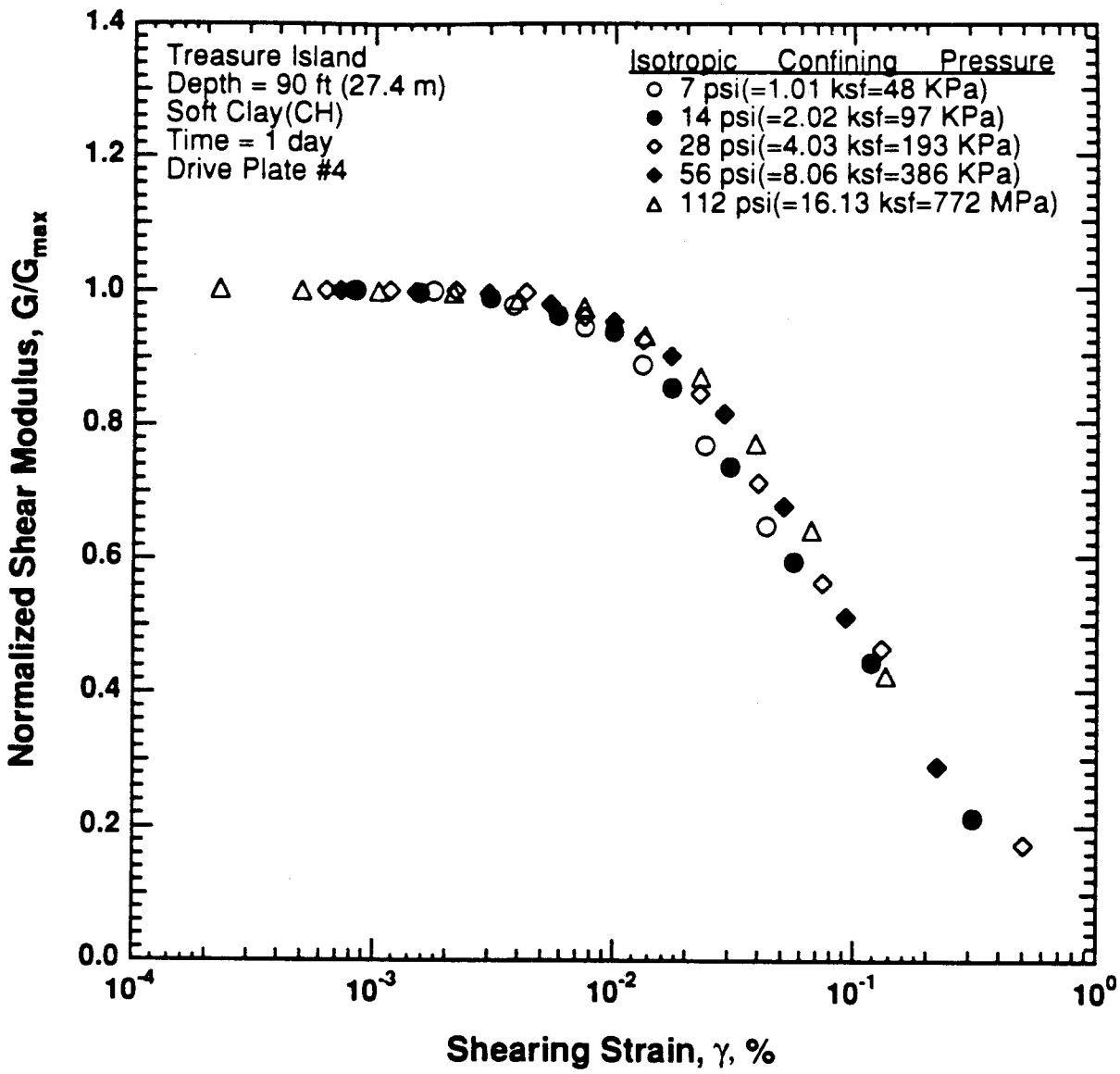

Figure 8.B.1.E-10
Comparison of the variation in normalized shear modulus with shearing strain and effective confining pressure from resonant column tests of sample T4.

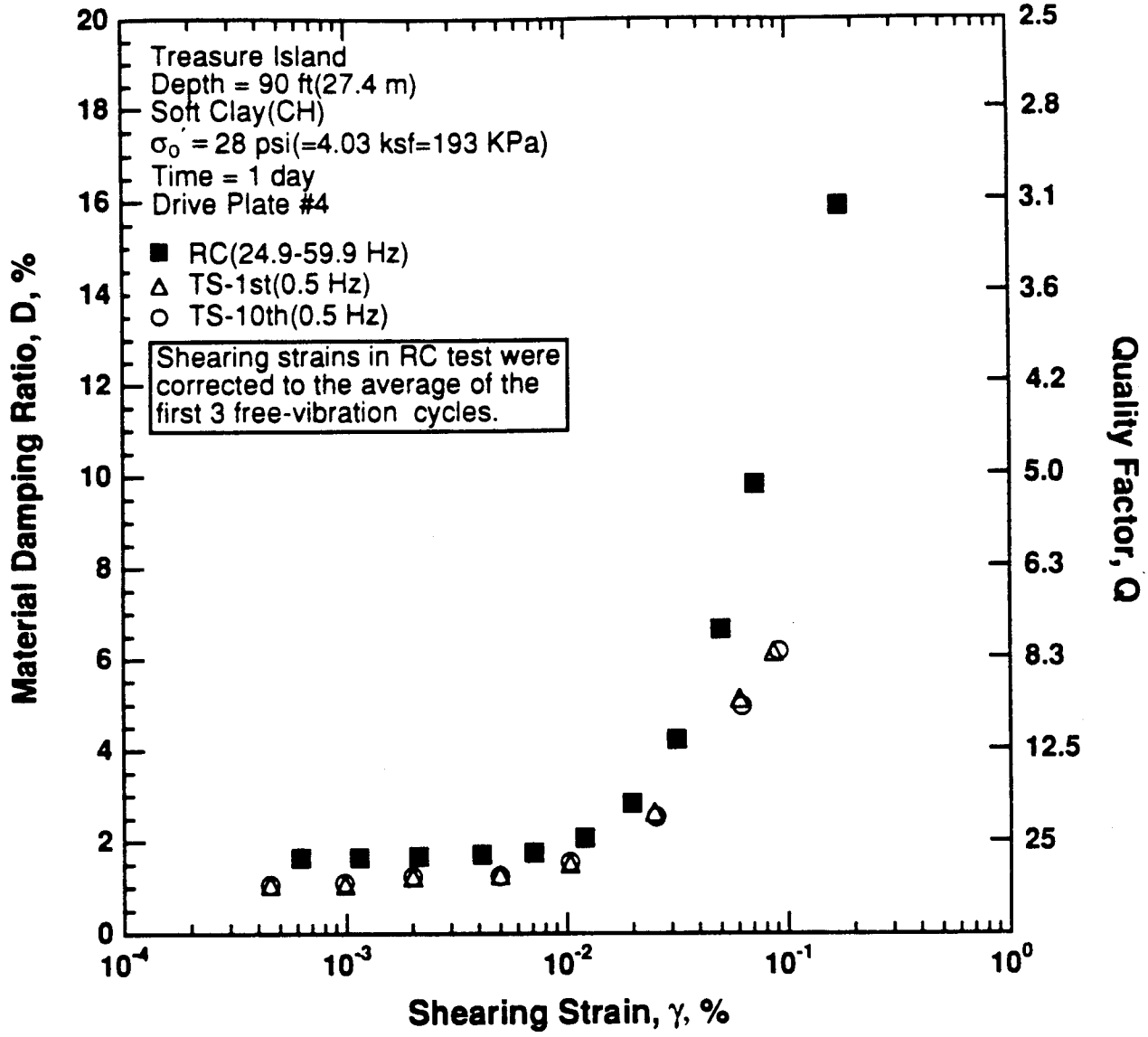

Figure 8.B.1.E-11
Variation in material damping ratio with shearing strain at an effective confining pressure of 28 psi (4.03 ksf, 193 kPa) from RCTS tests of sample T4.

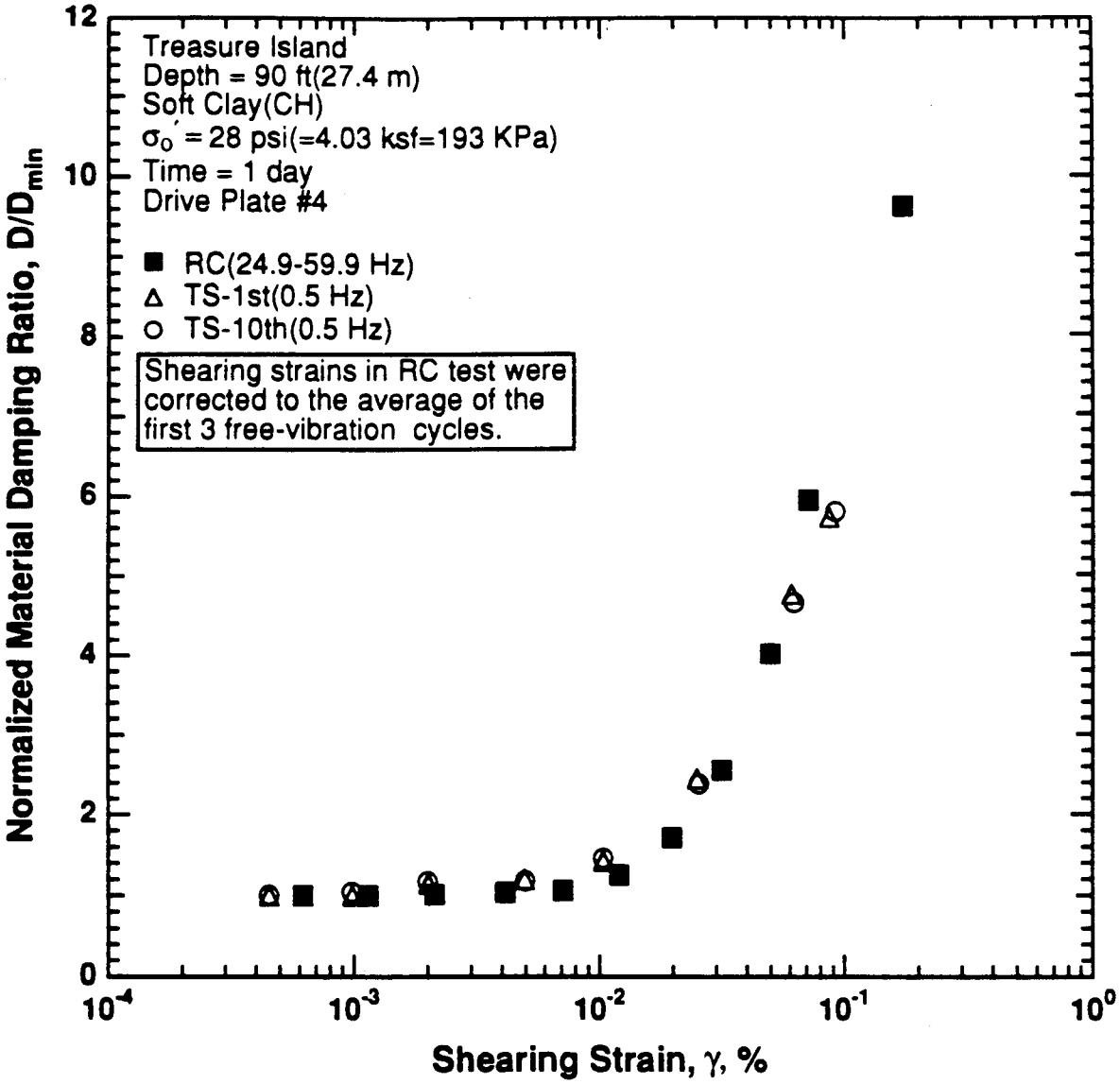

Figure 8.B.1.E-12
Variation in normalized material damping ratio with shearing strain at an effective confining pressure of 28 psi (4.03 ksf, 193 kPa) from RCTS tests of sample T4.

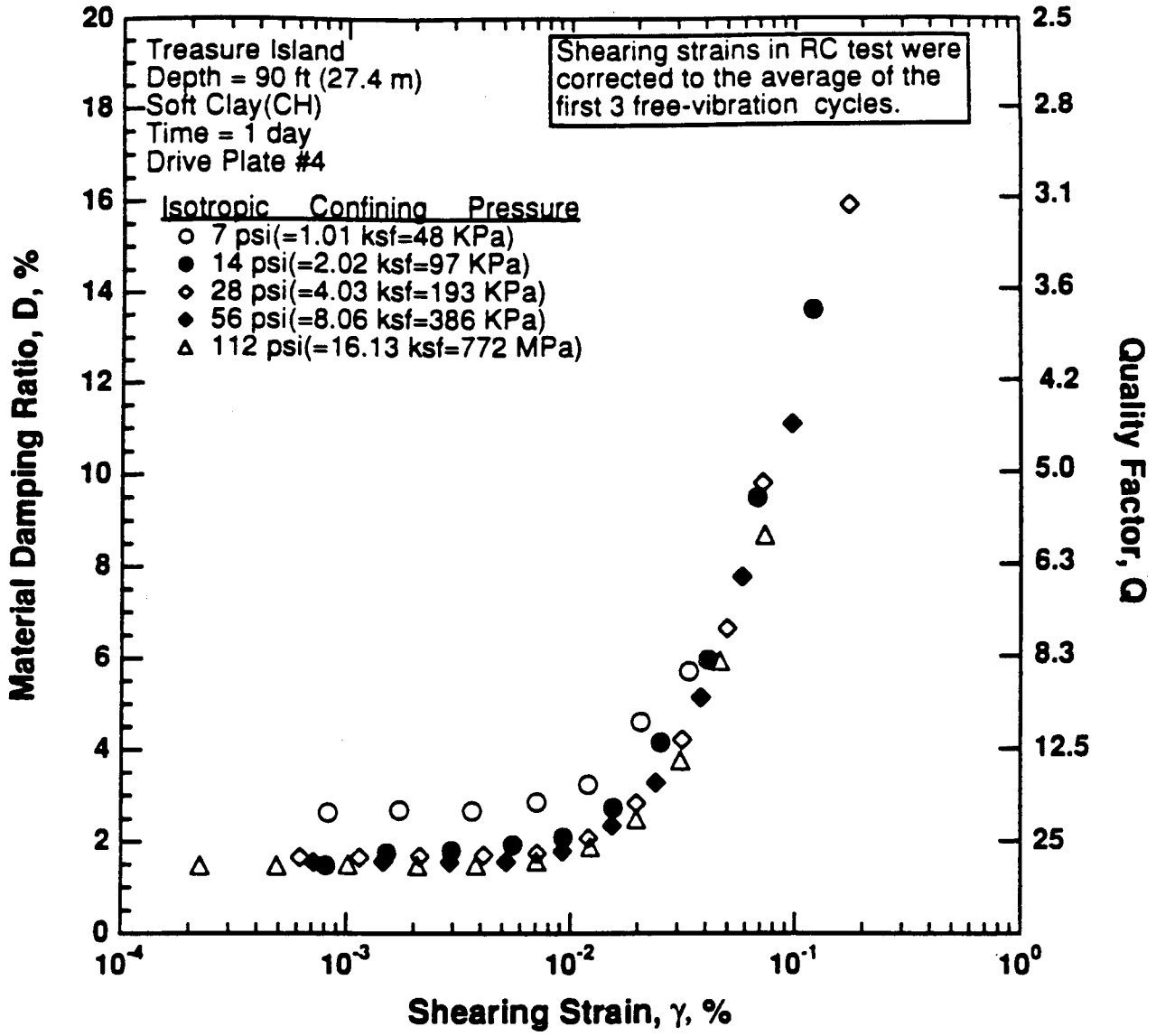

Figure 8.B.1.E-13
Variation in material damping ratio with shearing strain and effective confining pressure from resonant column tests of sample T4.

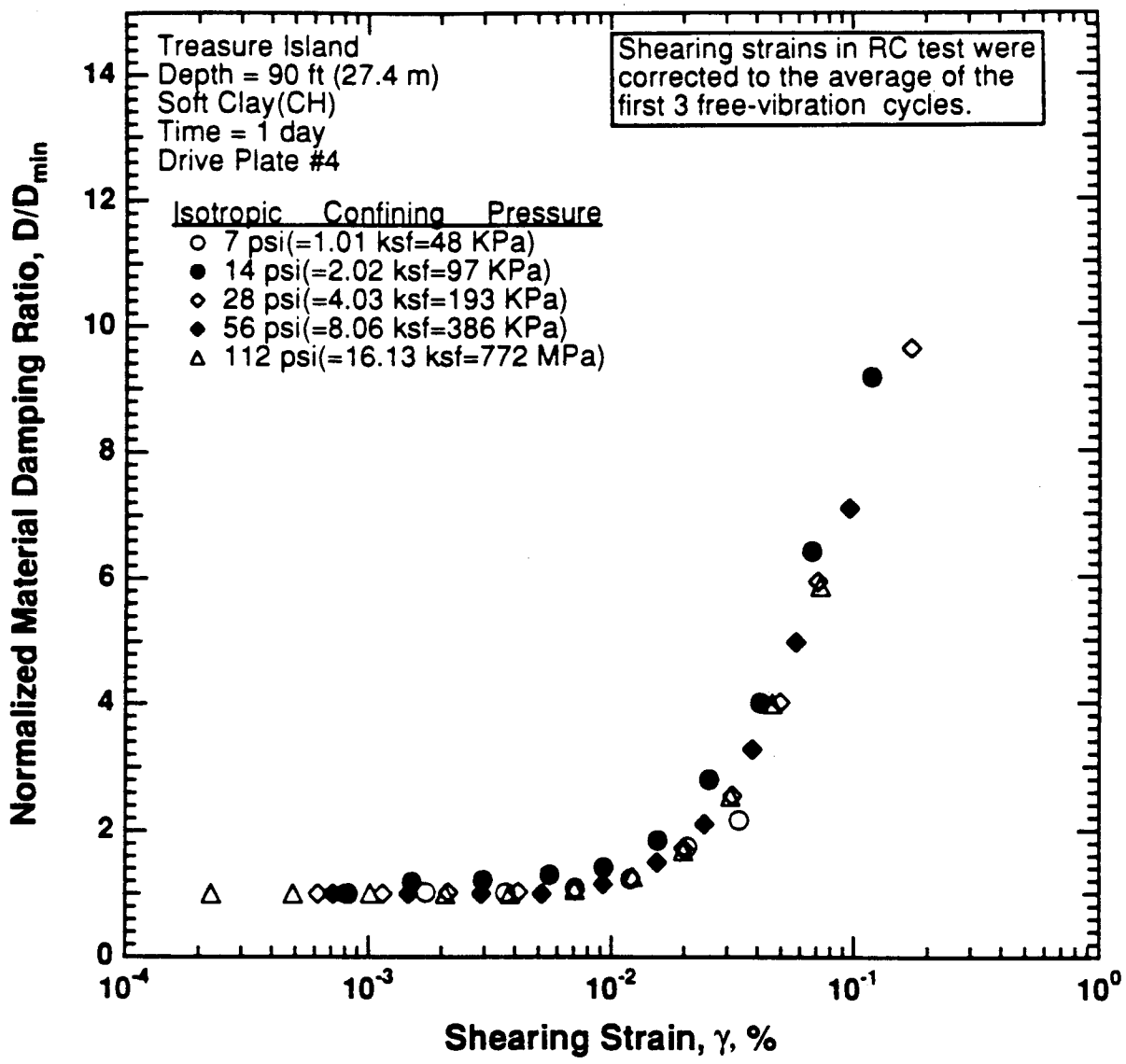

Figure 8.B.1.E-14
Comparison of the variation in normalized material damping ratio with shearing strain and effective confining pressure from resonant column tests of sample T4.

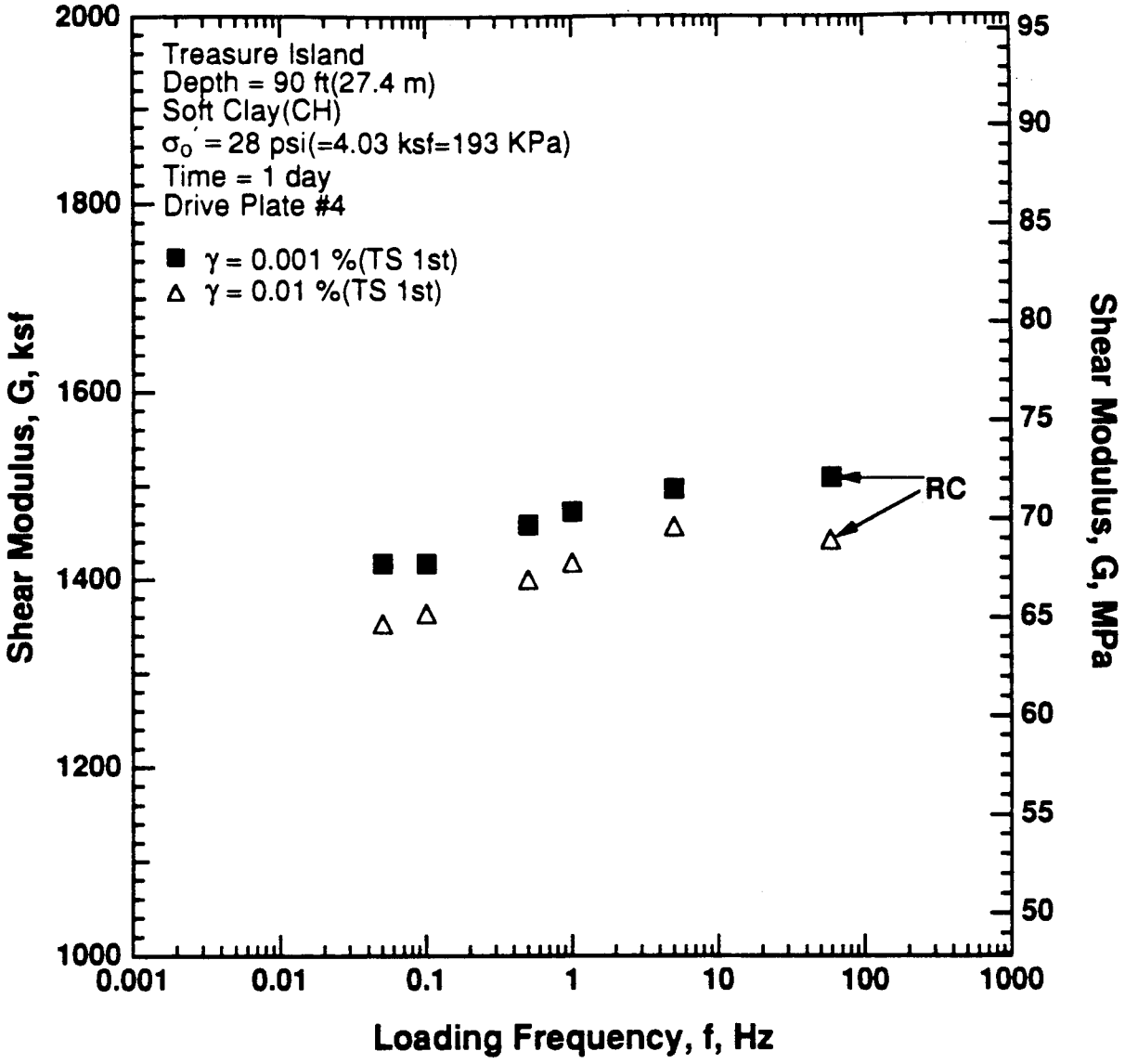

Figure 8.B.1.E-15
Variation in shear modulus with loading frequency and shearing strain at an effective confining pressure of 28 psi (4.03 ksf, 193 kPa) from RCTS tests of sample T4.

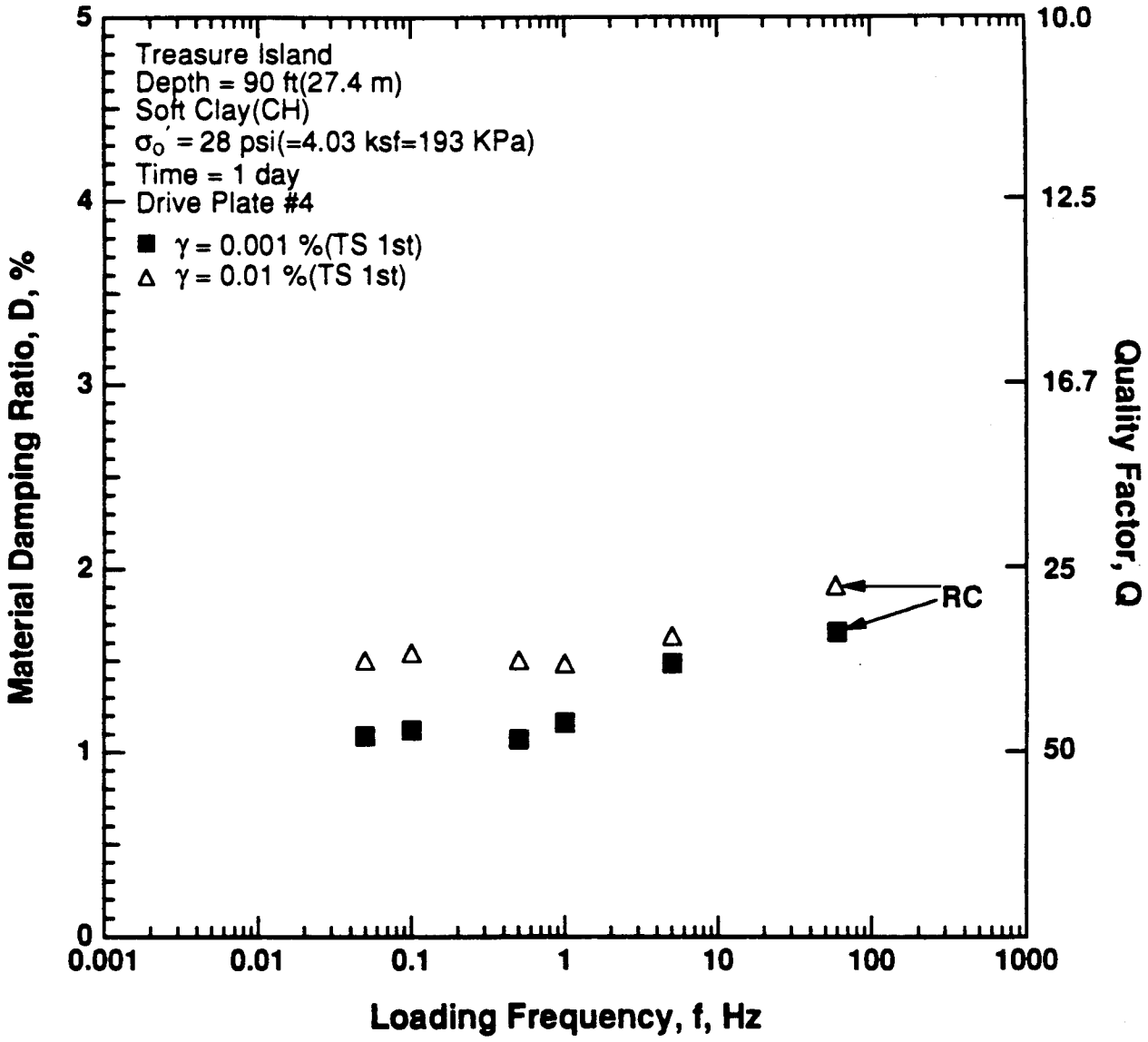

Figure 8.B.1.E-16
Variation in material damping ratio with loading frequency and shearing strain at an effective confining pressure of 28 psi (4.03 ksf, 193 kPa) from RCTS tests of sample T4.

APPENDIX 8.B.1.F
DYNAMIC TESTS OF SAMPLE T5, DEPTH = 110 FT (33.5 M)

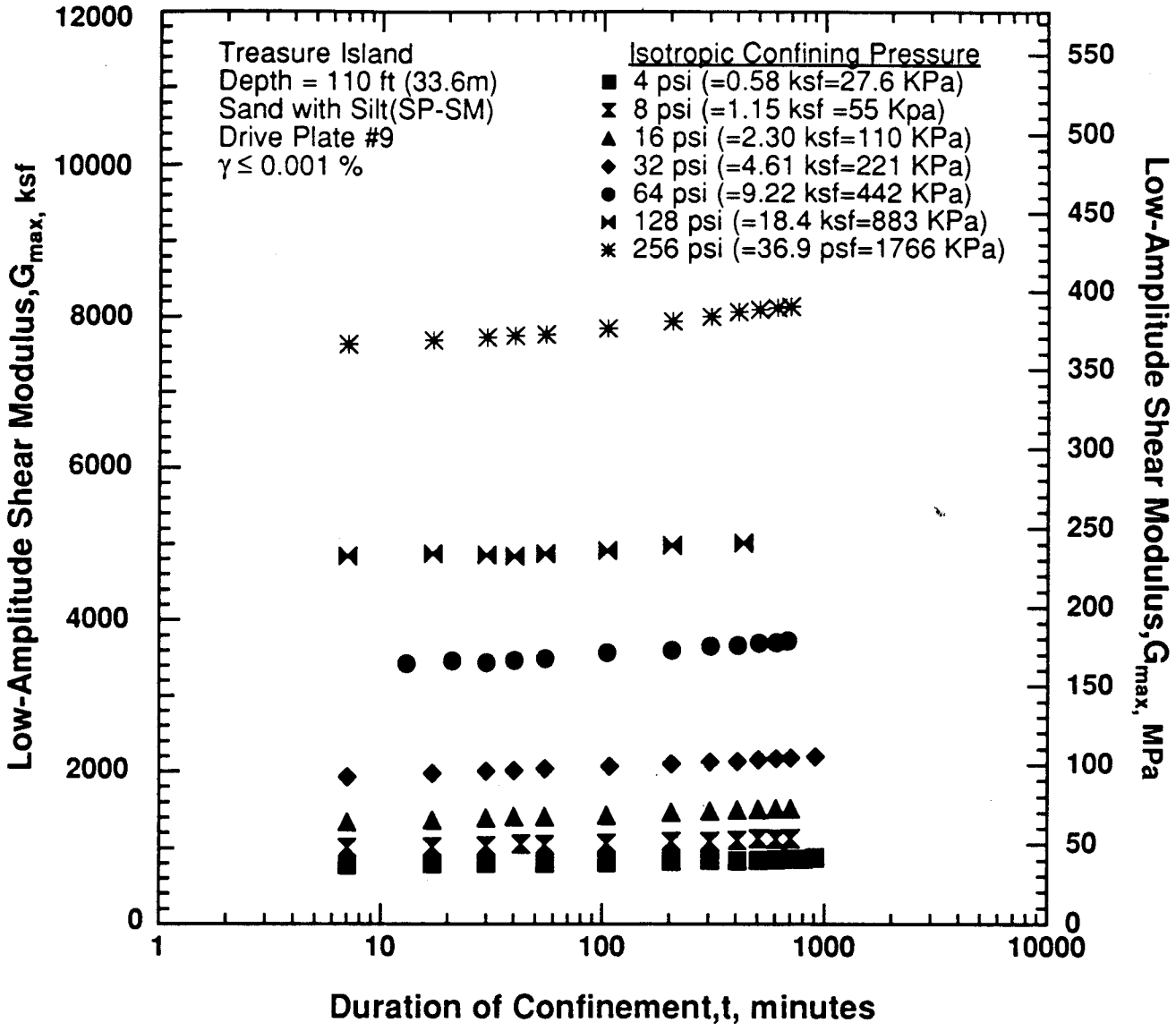

Figure 8.B.1.F-1
Variation in low-amplitude shear modulus with magnitude and duration of isotropic confining pressure from resonant column testing of sample T5.

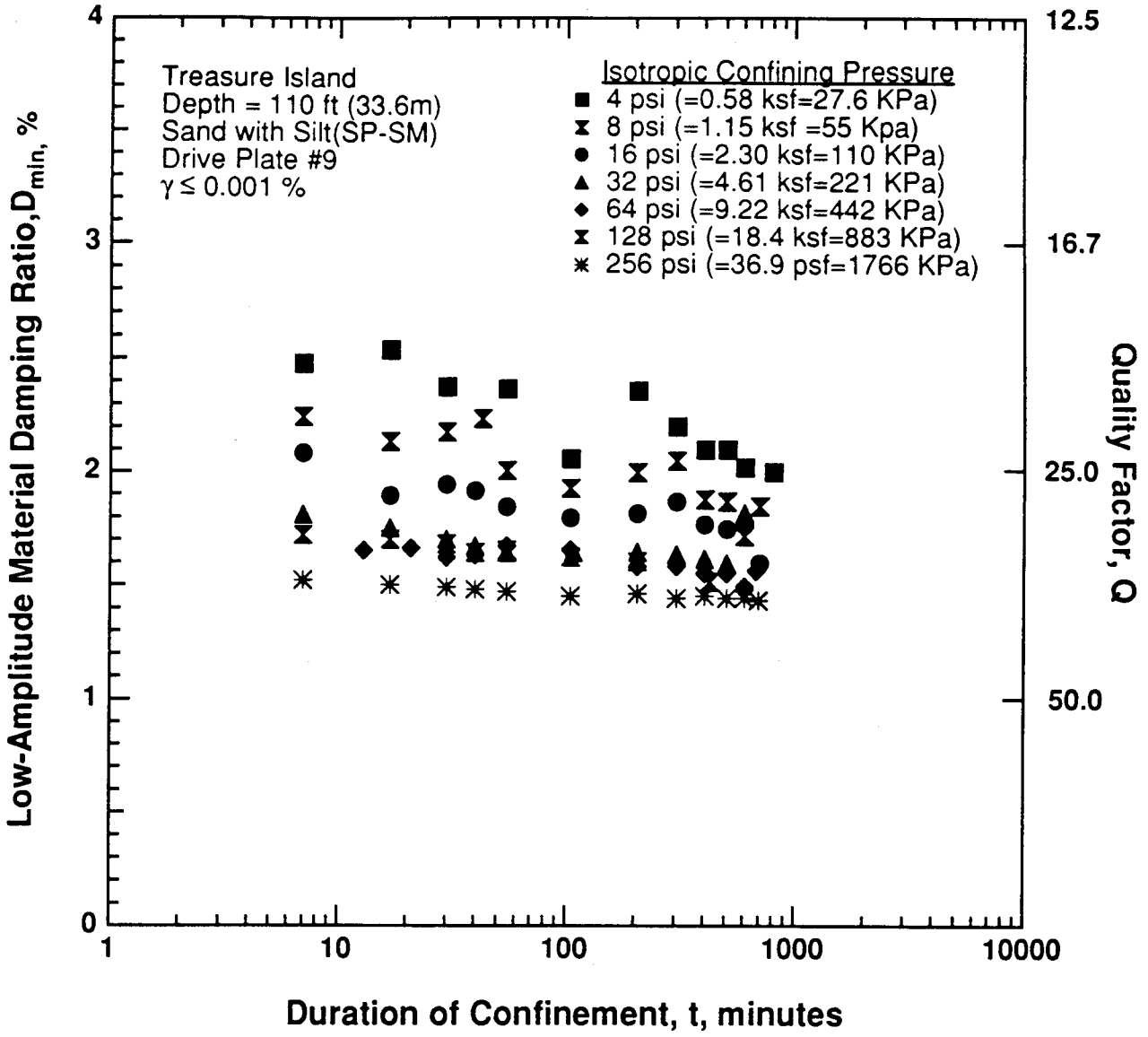

Figure 8.B.1.F-2
Variation in low-amplitude material damping ratio with magnitude and duration of isotropic confining pressure from resonant column testing of sample T5.

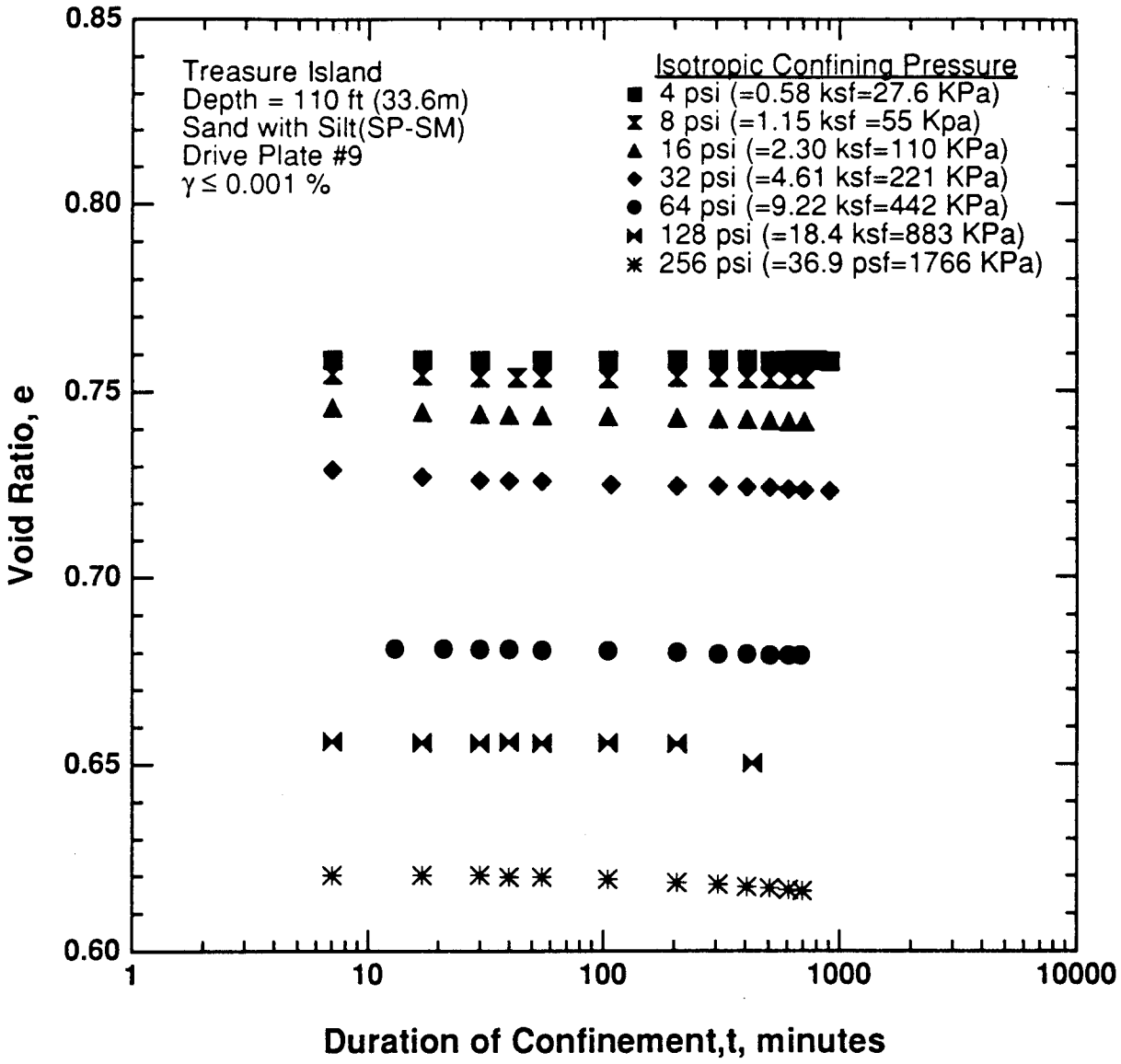

Figure 8.B.1.F-3
Variation in void ratio with magnitude and duration of isotropic confining pressure from resonant column testing of sample T5.

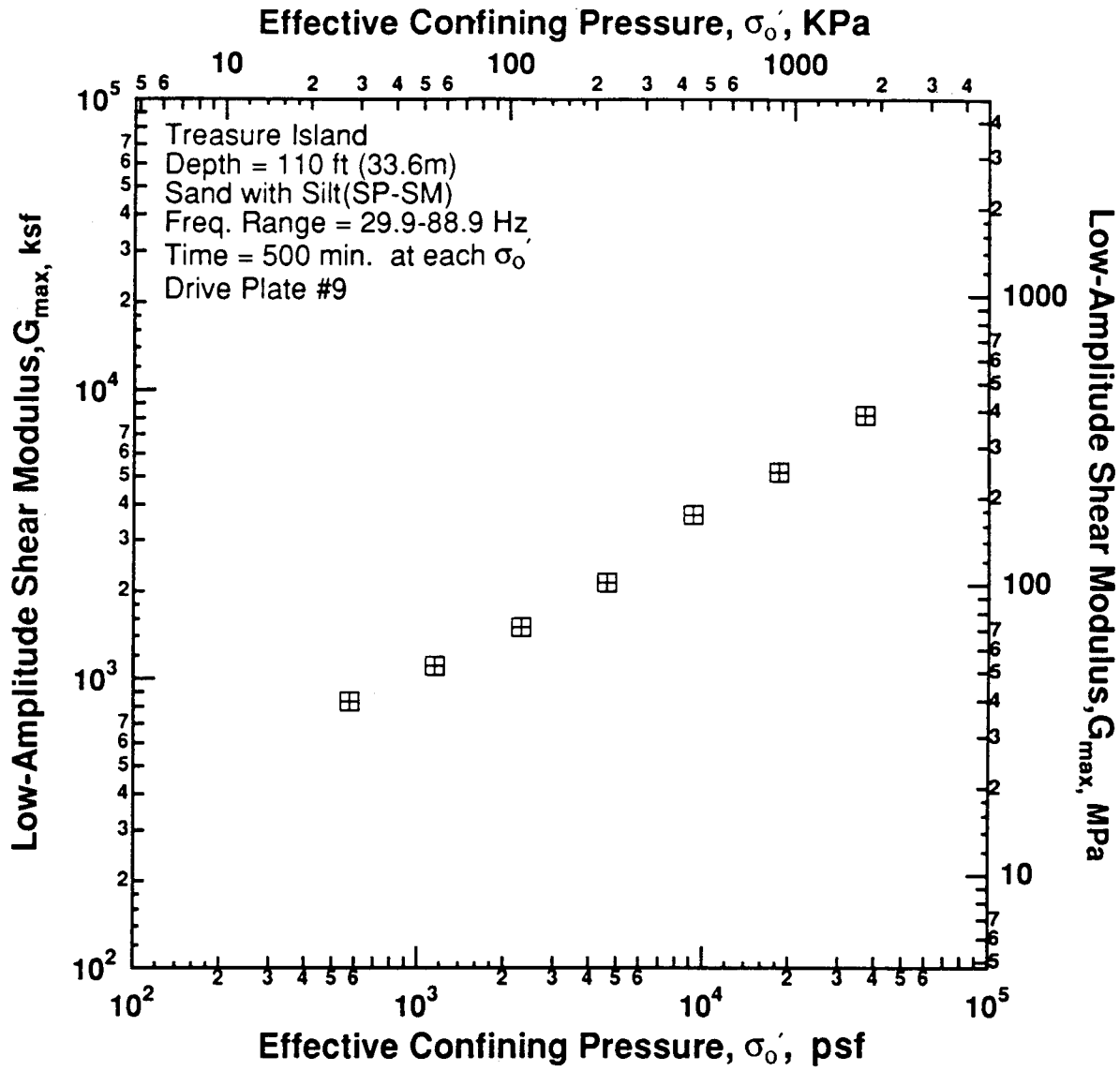

Figure 8.B.1.F-4
Variation in low-amplitude shear modulus with effective confining pressure from resonant column testing of sample T5.

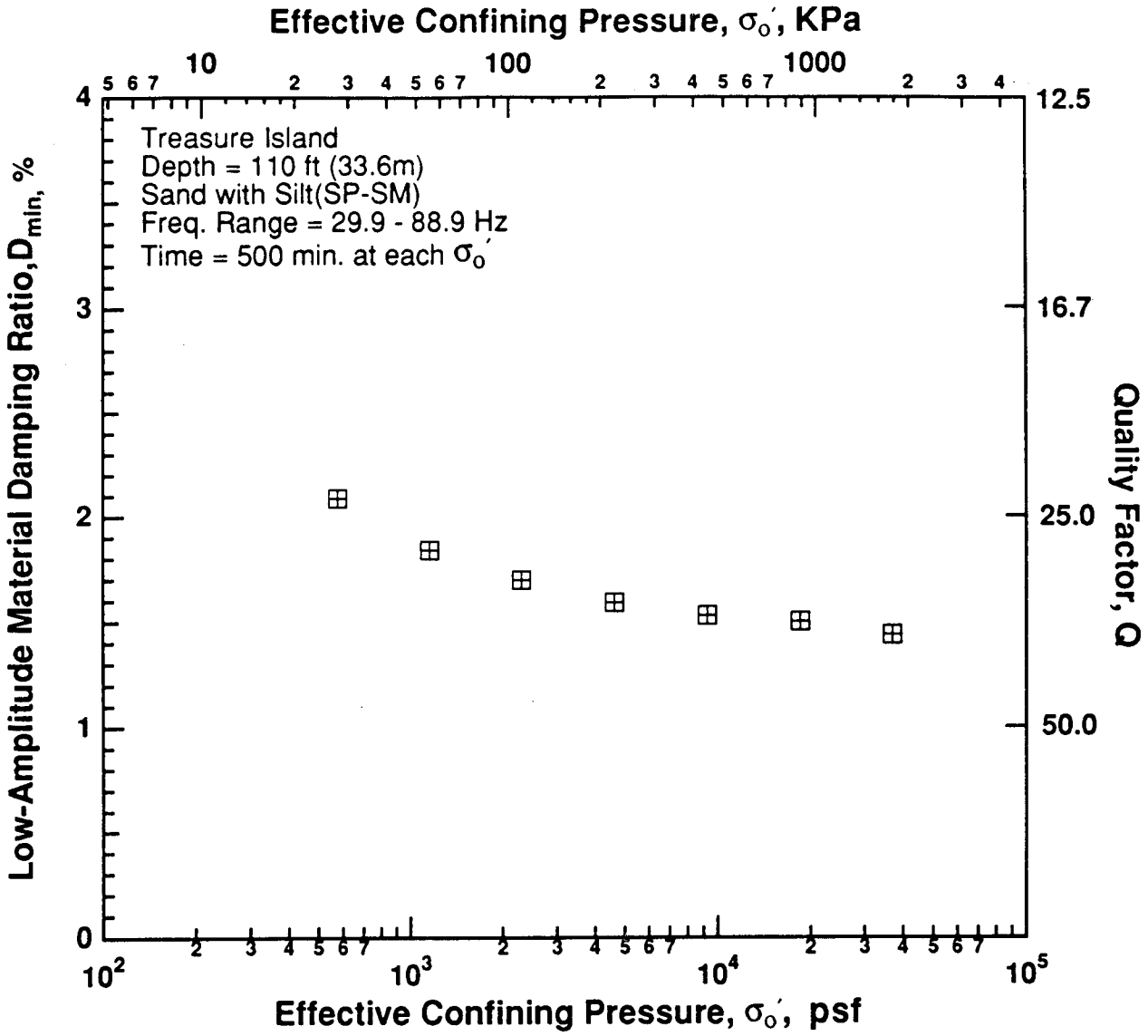

Figure 8.B.1.F-5
Variation in low-amplitude material damping ratio with effective confining pressure from resonant column testing of sample T5.

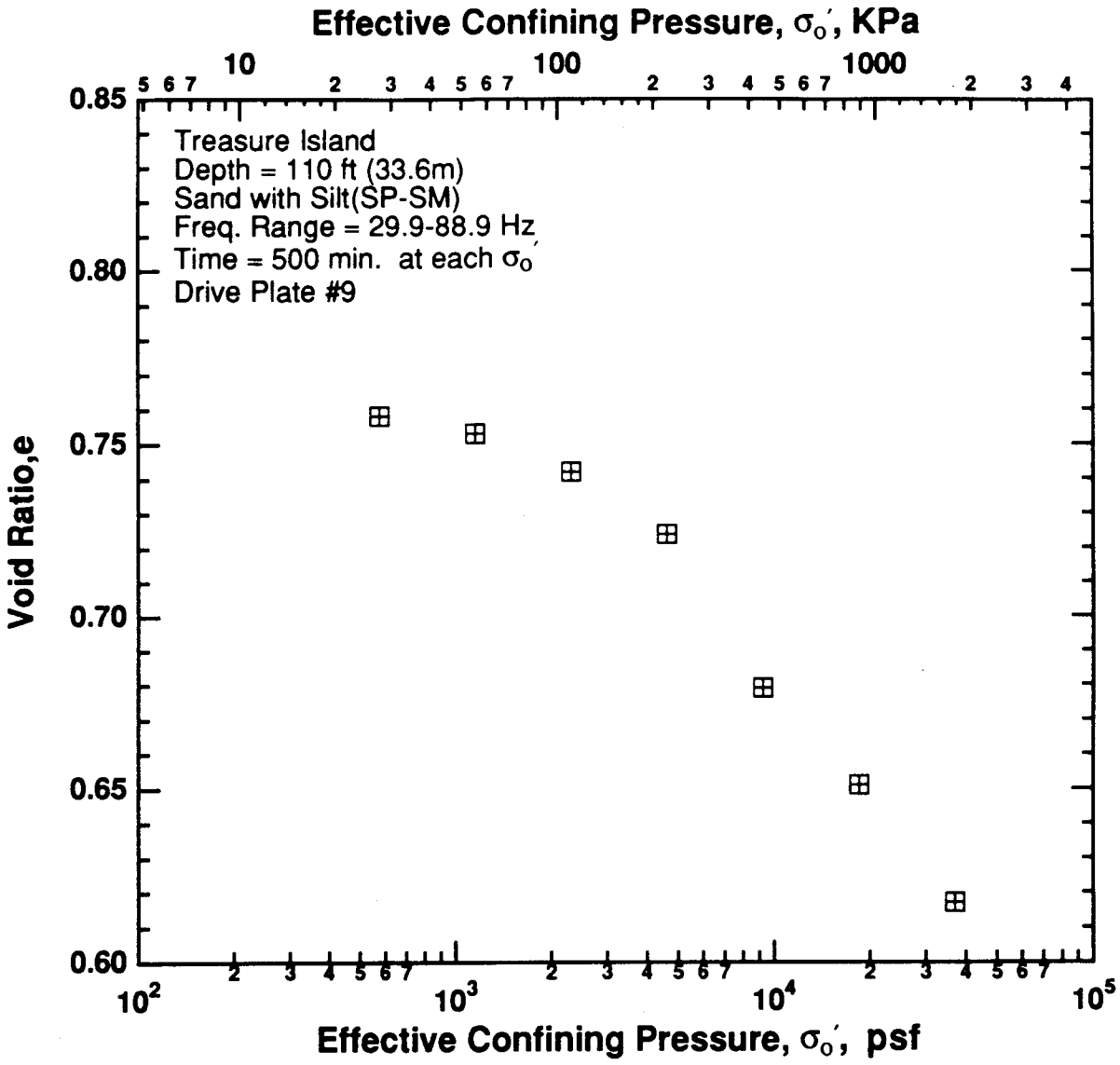

Figure 8.B.1.F-6
Variation in void ratio with effective confining pressure from resonant column testing of sample T5.

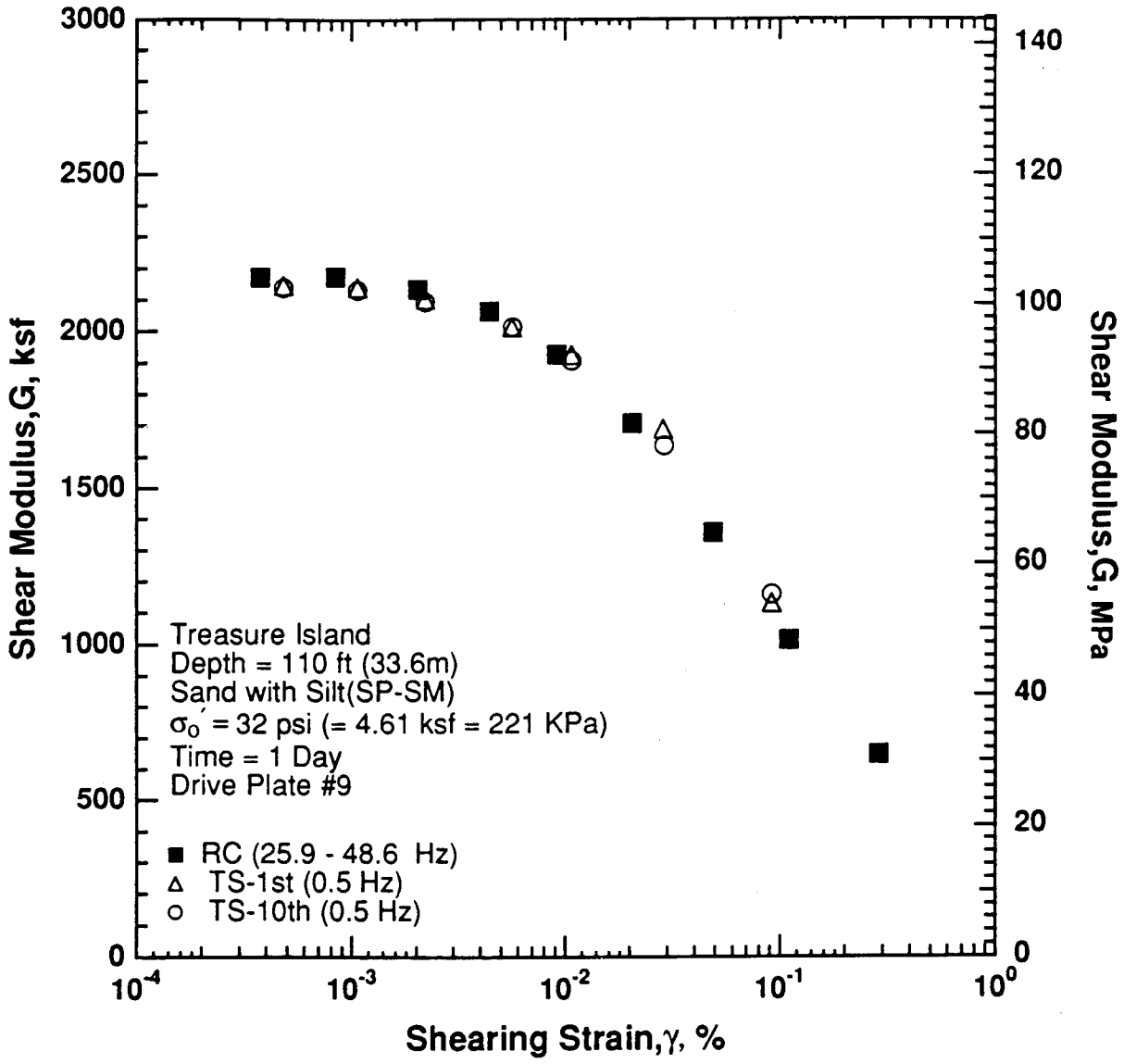

Figure 8.B.1.F-7
Variation in shear modulus with shearing strain at an effective confining pressure of 32 psi (4.61 ksf, 221 kPa) from RCTS testing of sample T5.

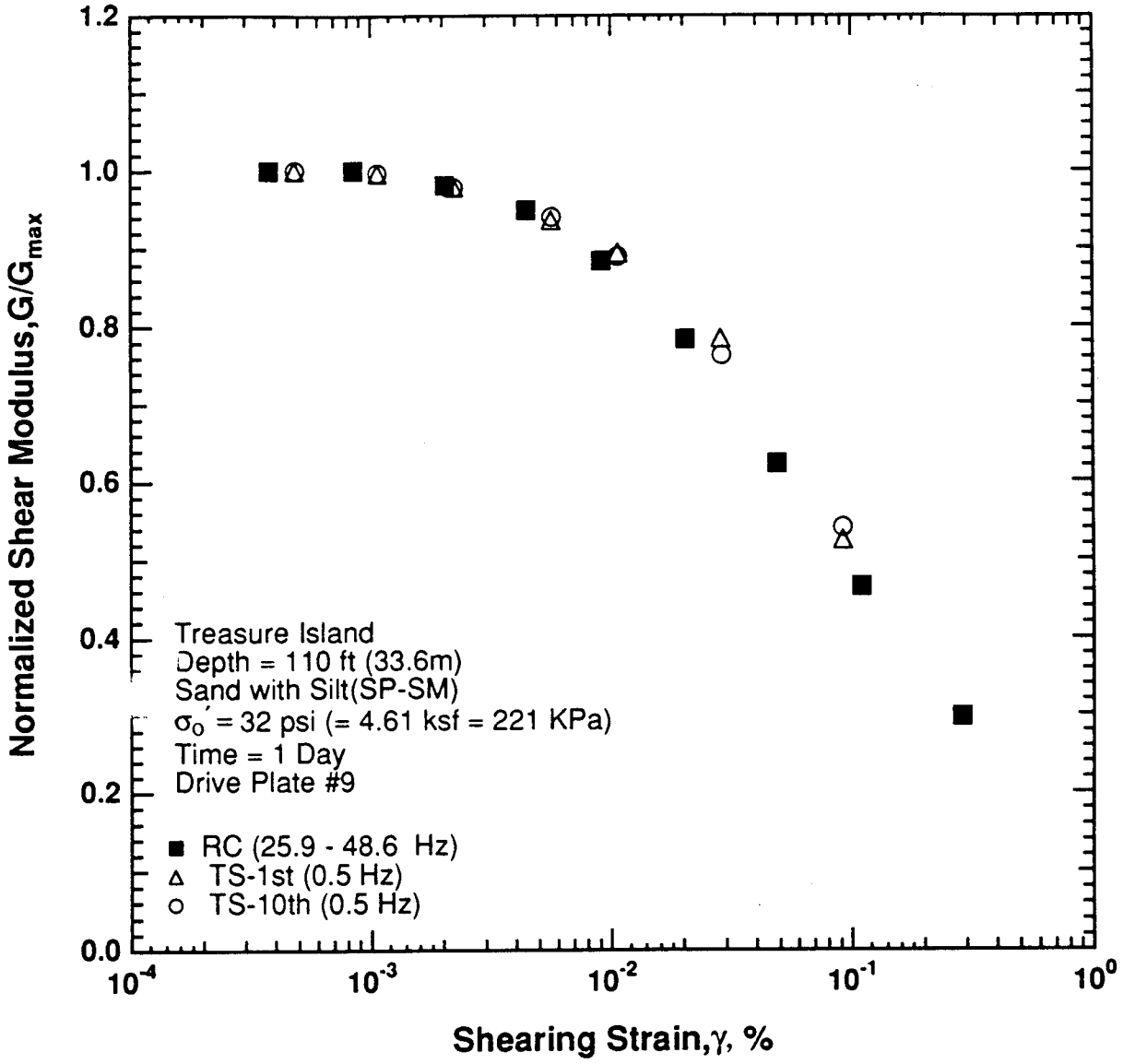

Figure 8.B.1.F-8
Variation in normalized shear modulus with shearing strain at an effective confining pressure of 32 psi (4.61 ksf, 221 kPa) from RCTS testing of sample T5.

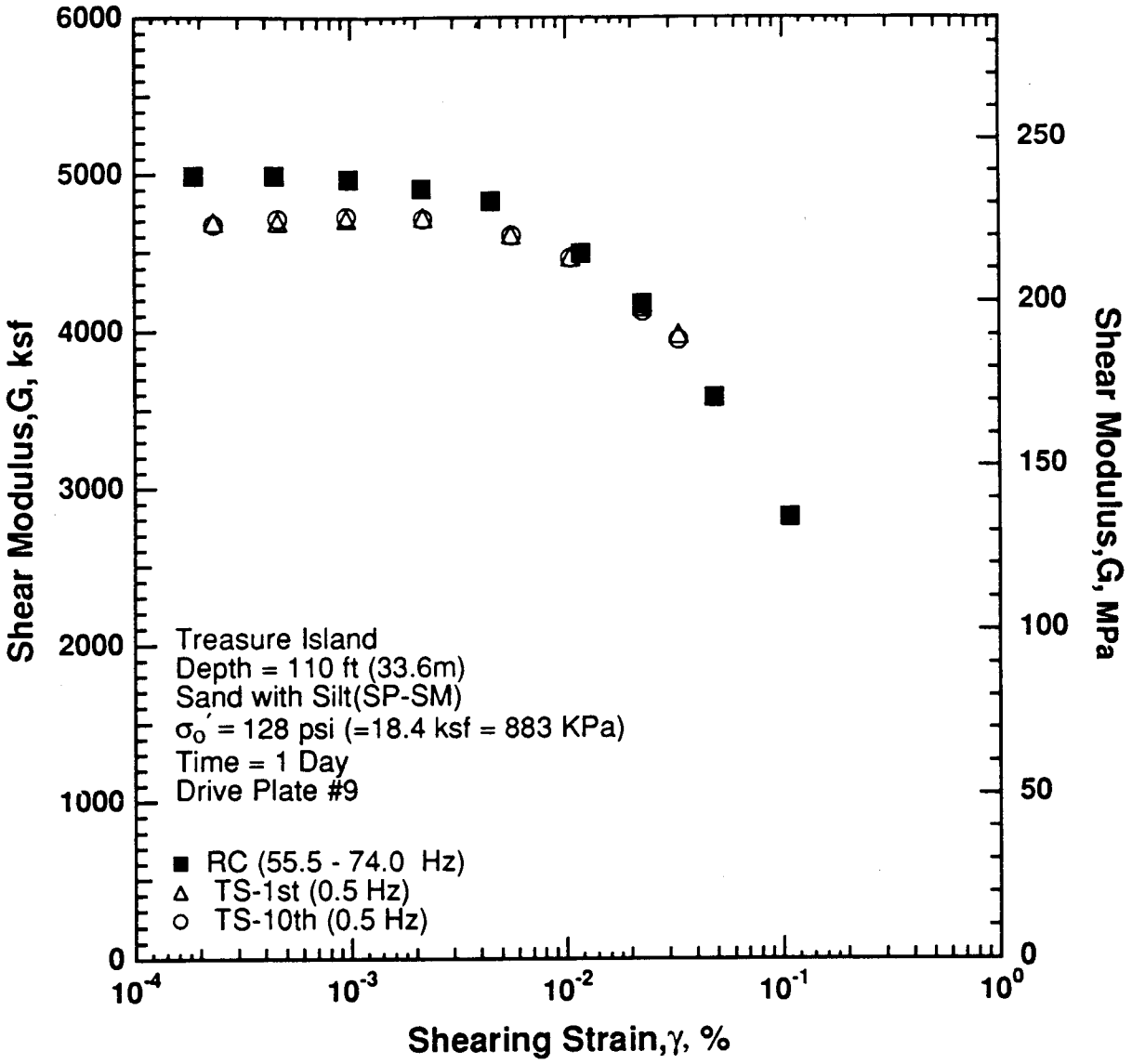

Figure 8.B.1.F-9
Variation in shear modulus with shearing strain at an effective confining pressure of 128 psi (18.4 ksf, 883 kPa) from RCTS testing of sample T5.

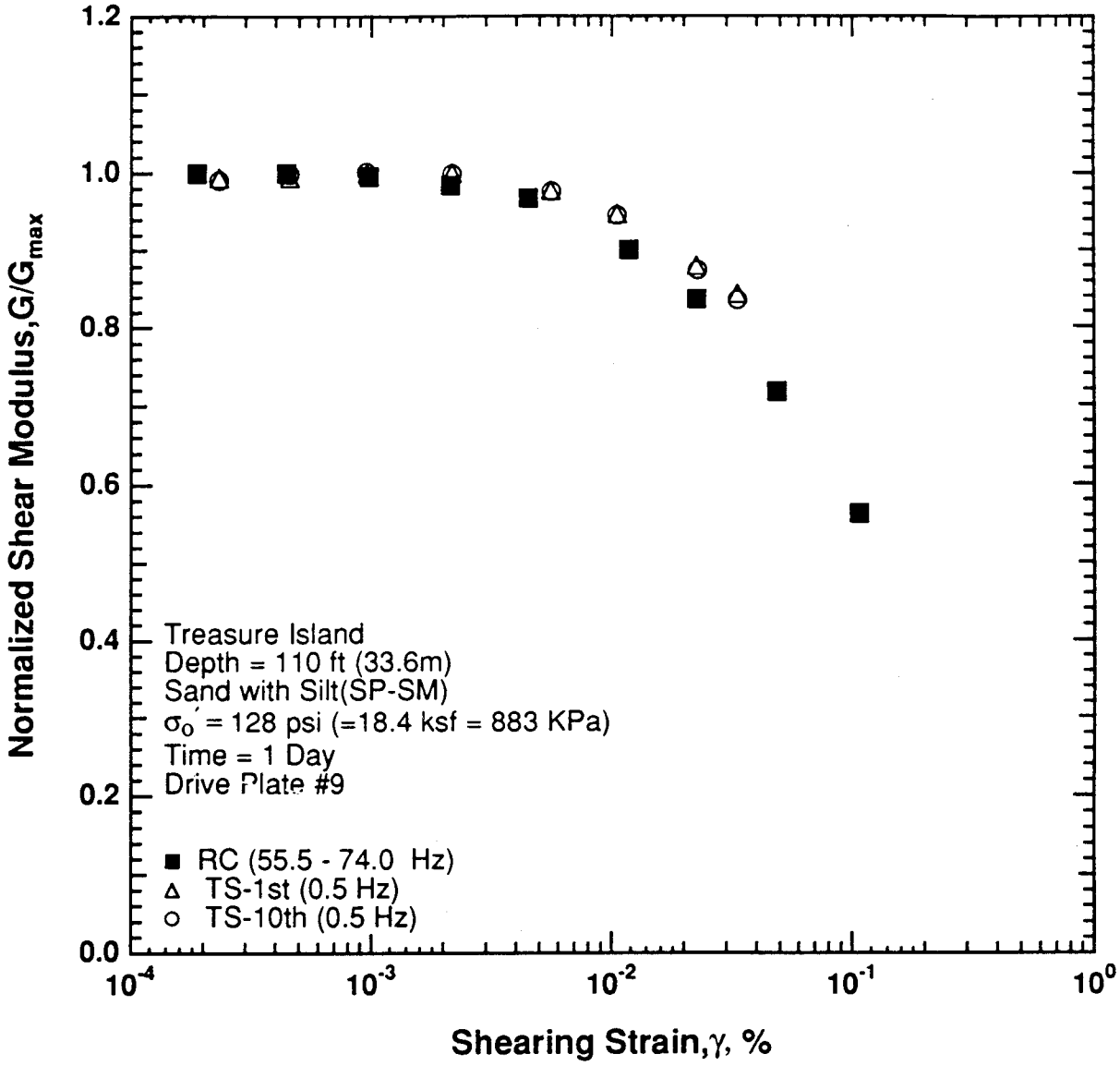

Figure 8.B.1.F-10
Variation in normalized shear modulus with shearing strain at an effective confining pressure of 128 psi (18.4 ksf, 883 kPa) from RCTS testing of sample T5.

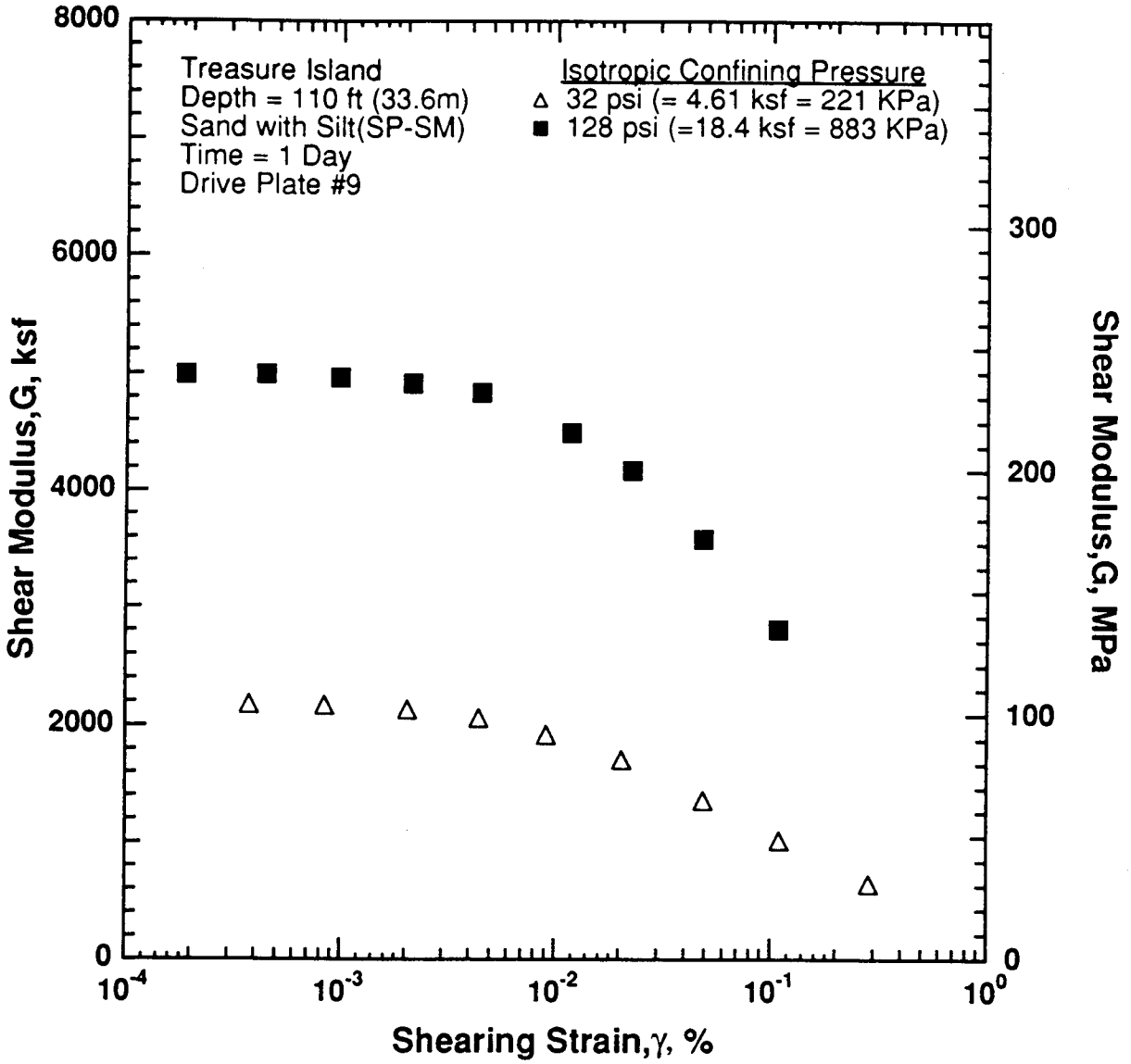

Figure 8.B.1.F-11
Variation in shear modulus with shearing strain and effective confining pressure from resonant column testing of sample T5.

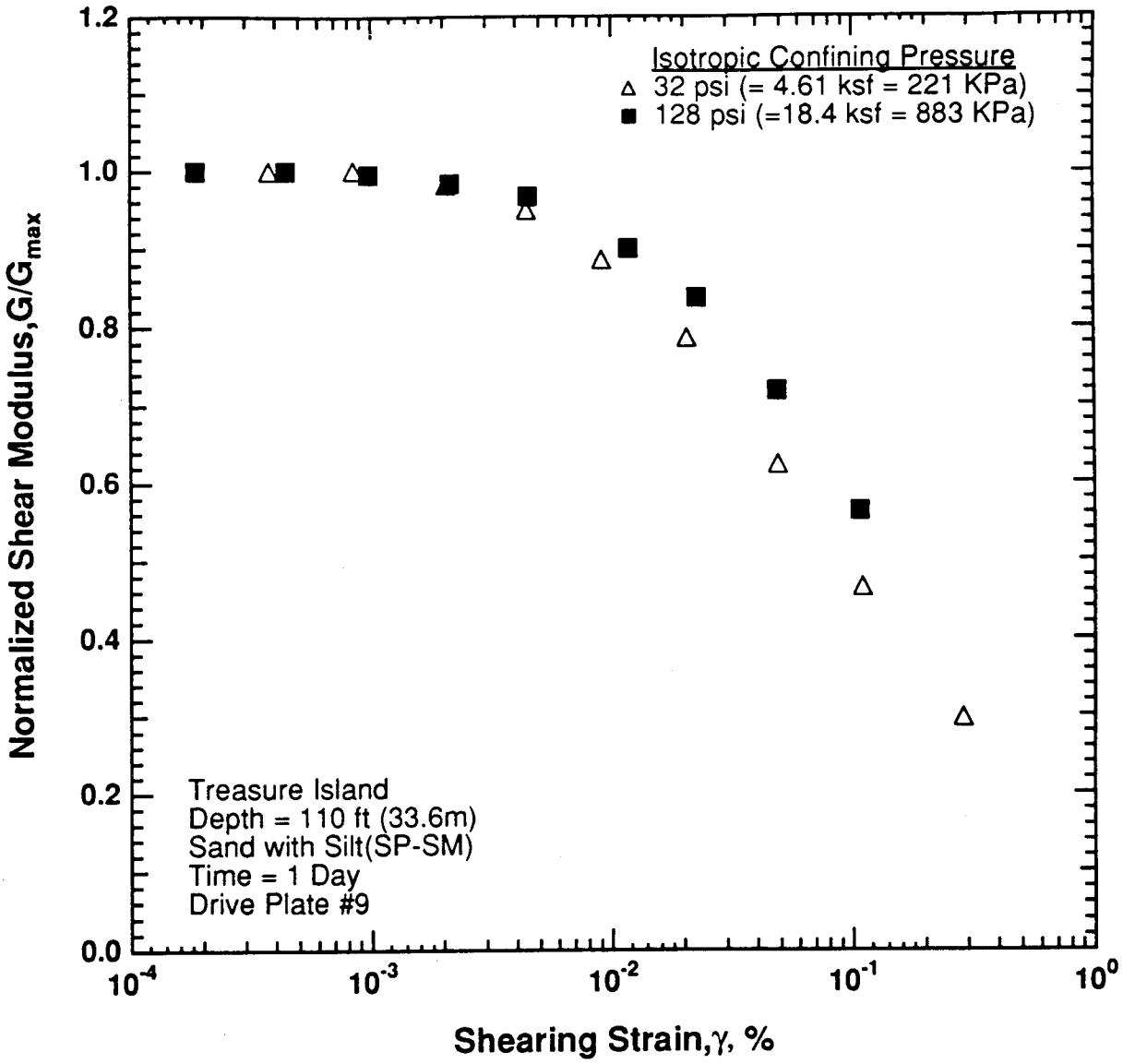

Figure 8.B.1.F-12
Comparison of the variation in normalized shear modulus with shearing strain and effective confining pressure from resonant column tests.

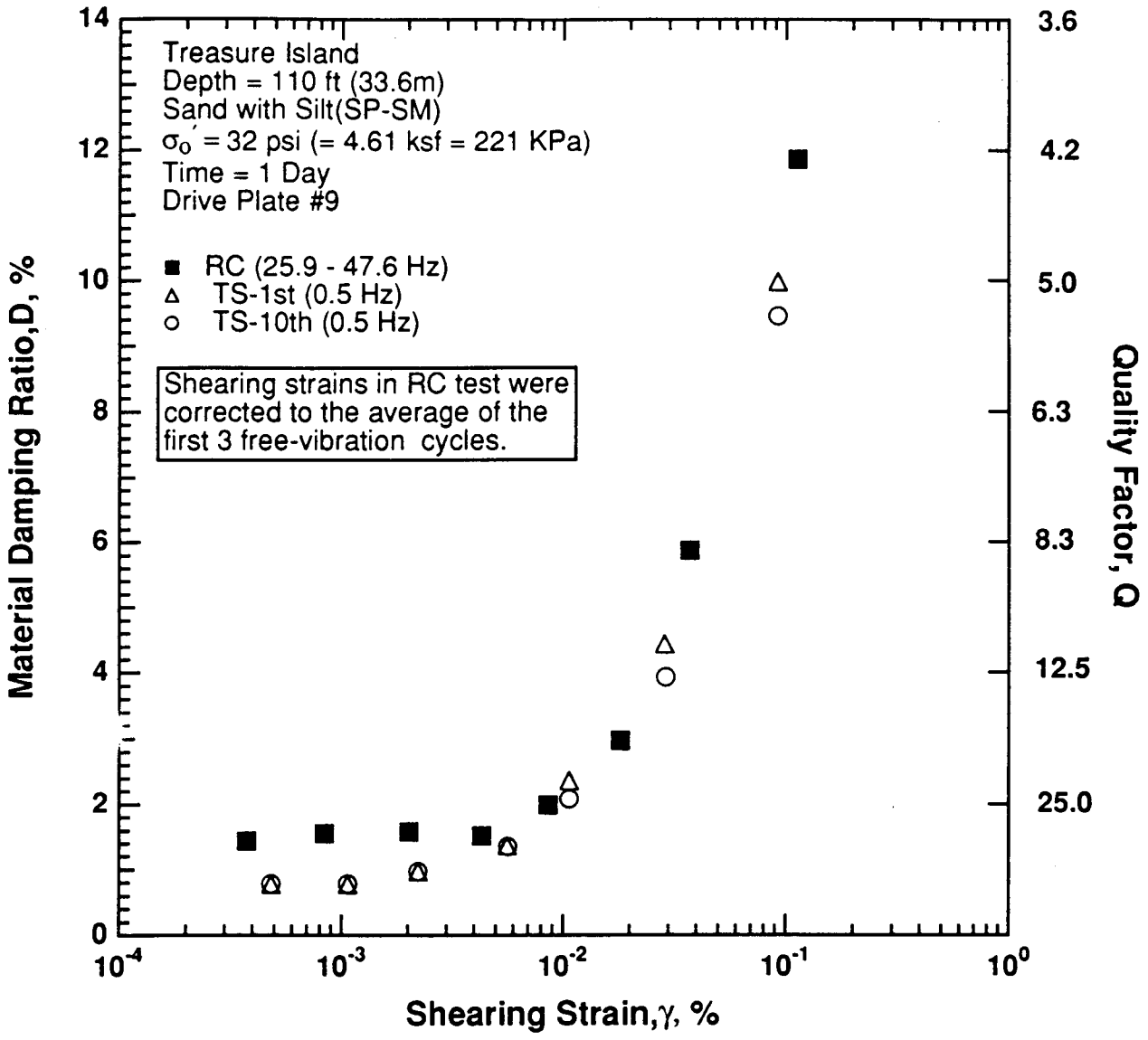

Figure 8.B.1.F-13
Variation in material damping ratio with shearing strain at an effective confining pressure of 32 psi (4.61 ksf, 221 kPa) from RCTS testing of sample T5.

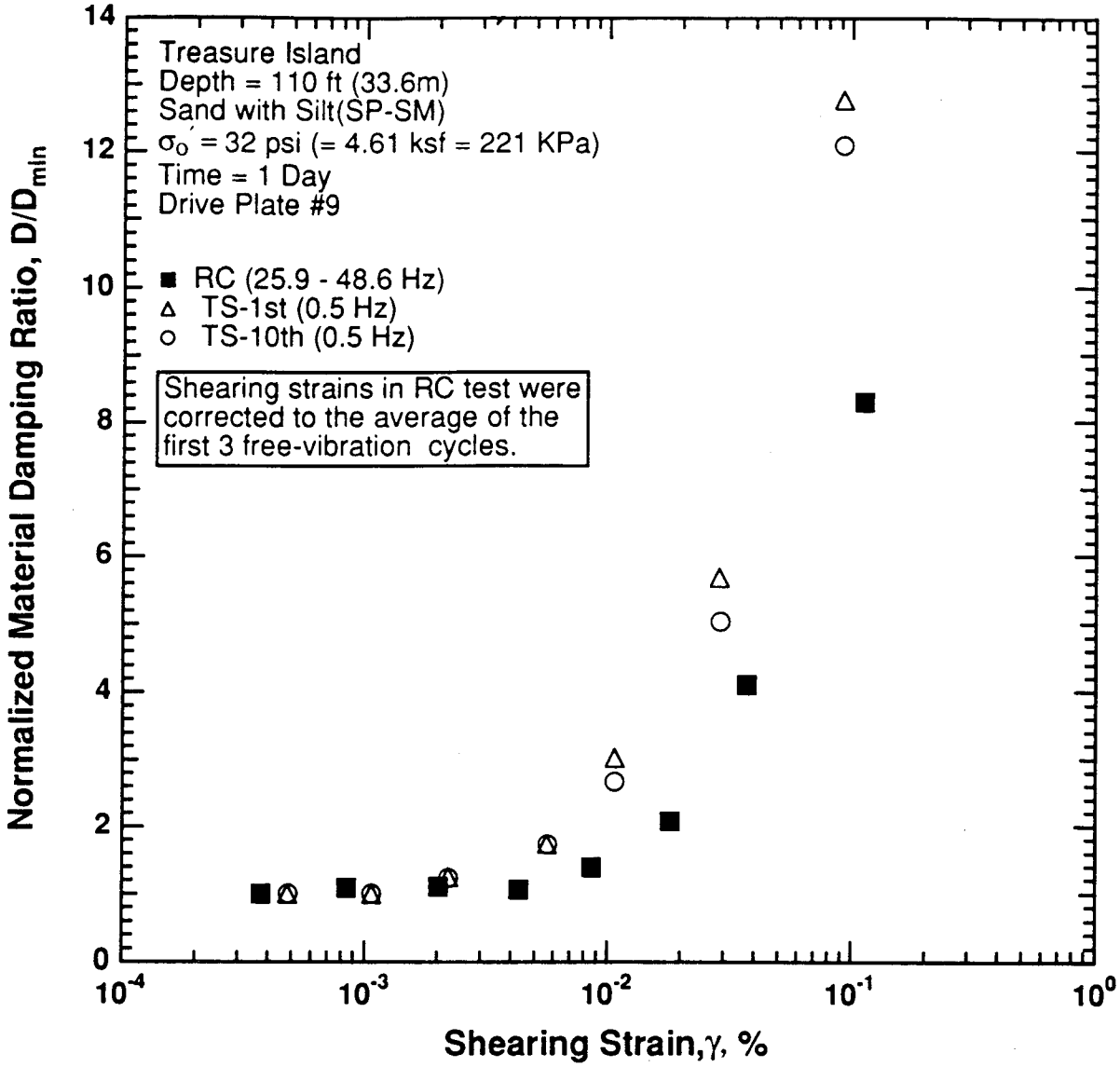

Figure 8.B.1.F-14
Variation in normalized material damping ratio with shearing strain at an effective confining pressure of 32 psi (4.61 ksf, 221 kPa) from RCTS testing of sample T5.

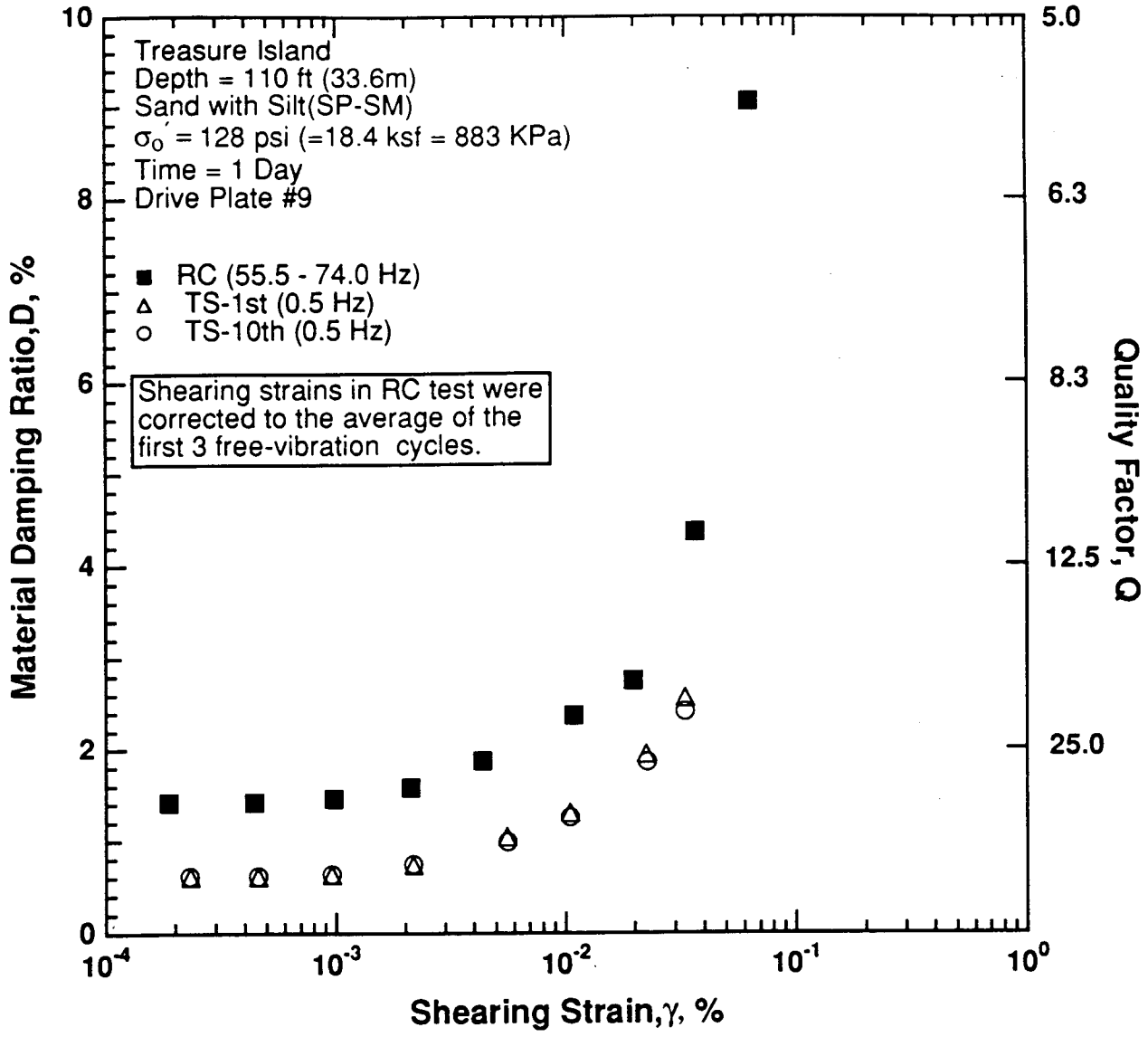

Figure 8.B.1.F-15
Variation in material damping ratio with shearing strain at an effective confining pressure of 128 psi (18.4 ksf, 883 kPa) from RCTS tests of sample T5.

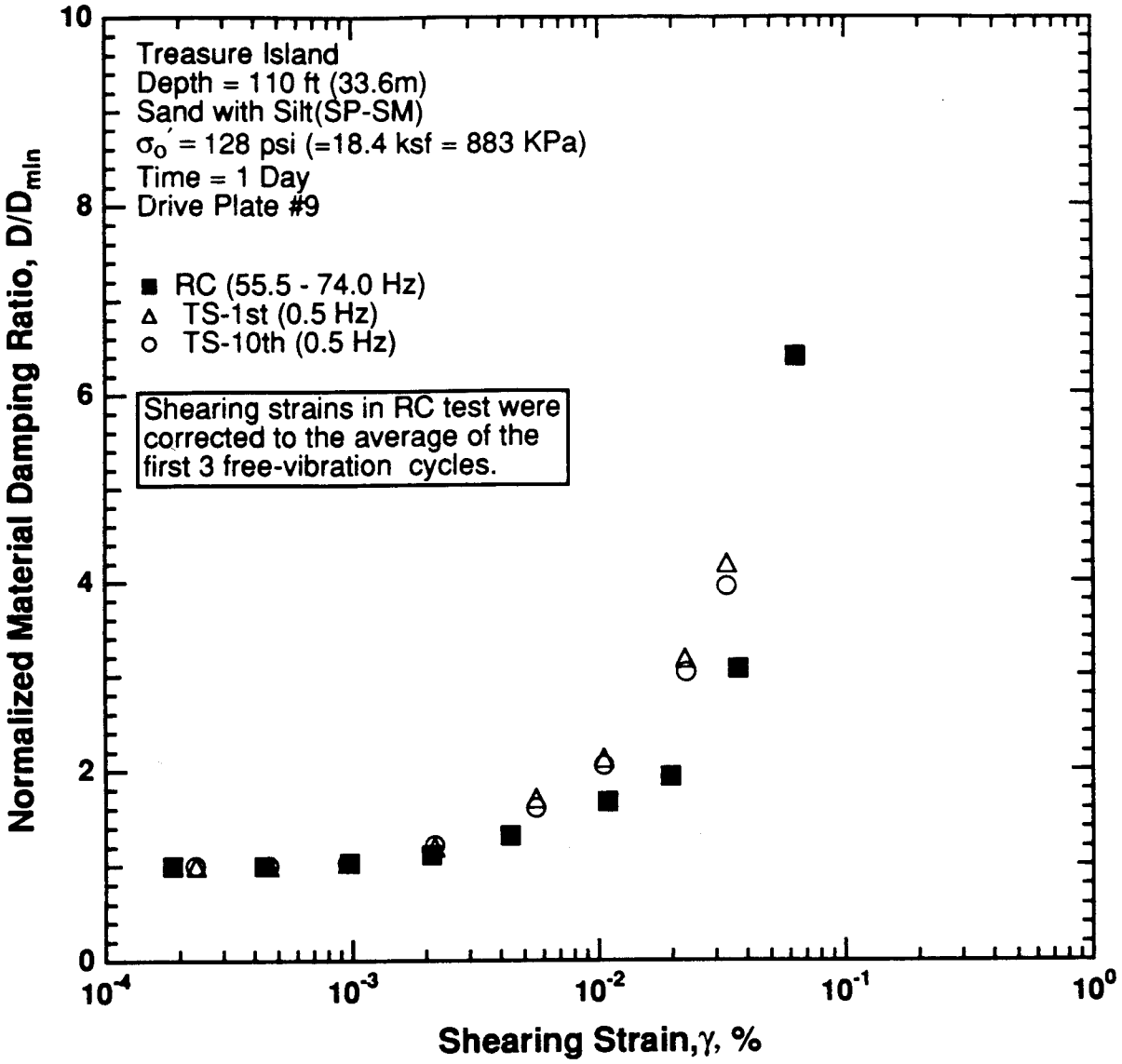

Figure 8.B.1.F-16
Variation in normalized material damping ratio with shearing strain at an effective confining pressure of 128 psi (18.4 ksf, 883 kPa) from RCTS testing of sample T5.

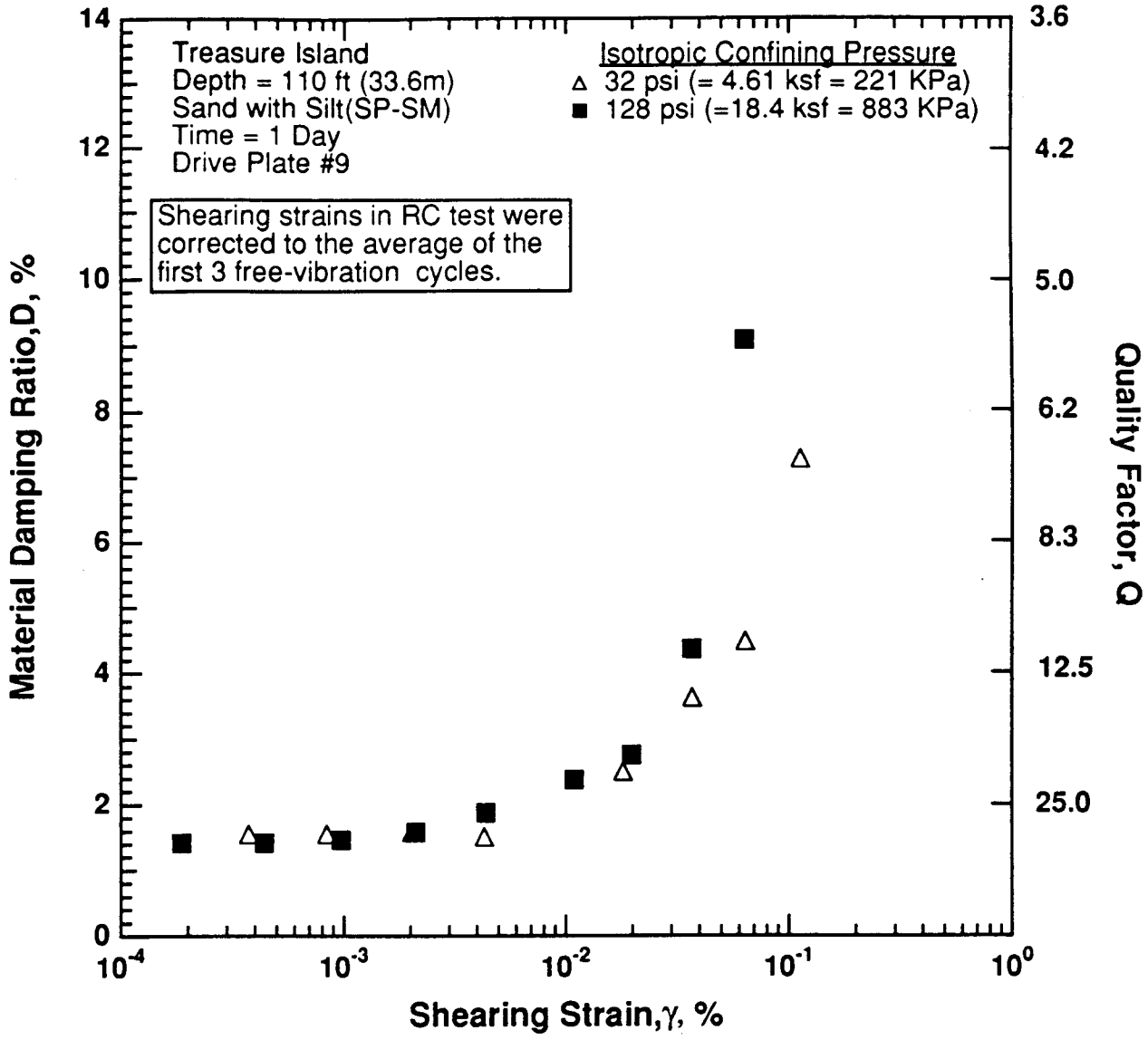

Figure 8.B.1.F-17
Variation in material damping ratio with shearing strain and effective confining pressure from resonant column testing of sample T5.

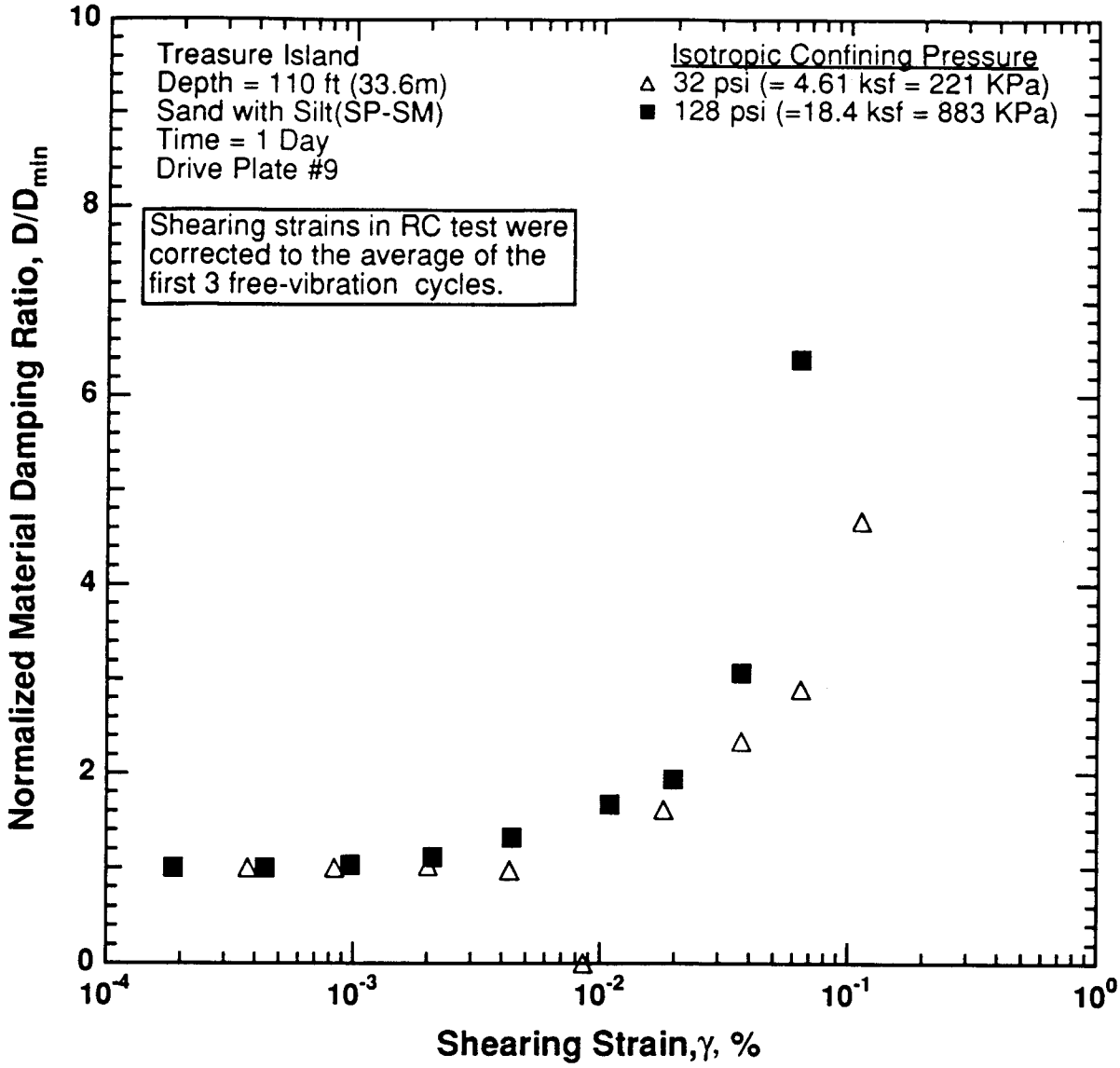

Figure 8.B.1.F-18
Comparison of the variation in normalized material damping ratio with shearing strain and effective confining pressure for resonant column testing of sample T5.

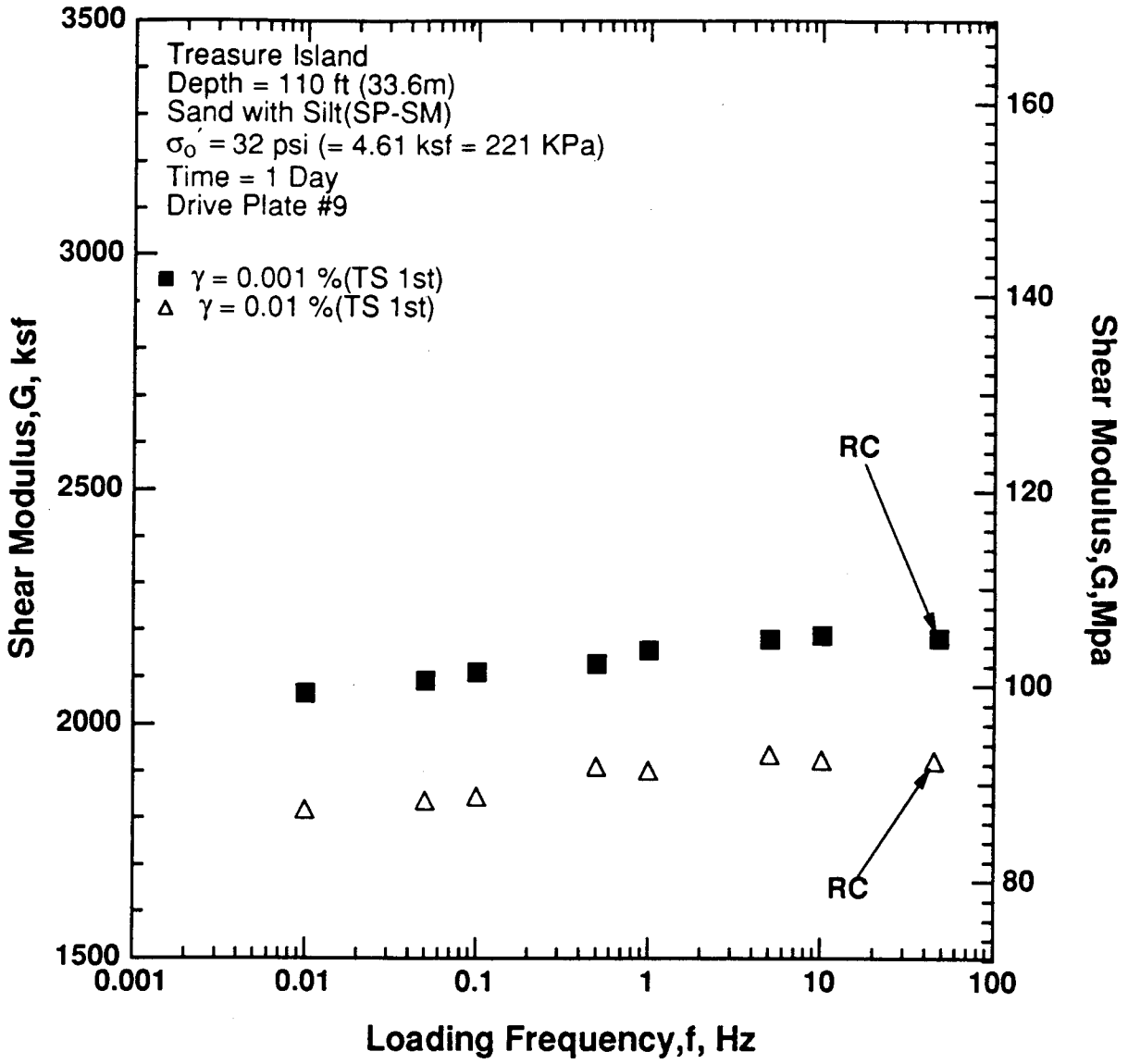

Figure 8.B.1.F-19
Variation in shear modulus with loading frequency and shearing strain at an effective confining pressure of 32 psi (4.61 ksf, 221 kPa) from RCTS testing of sample T5.

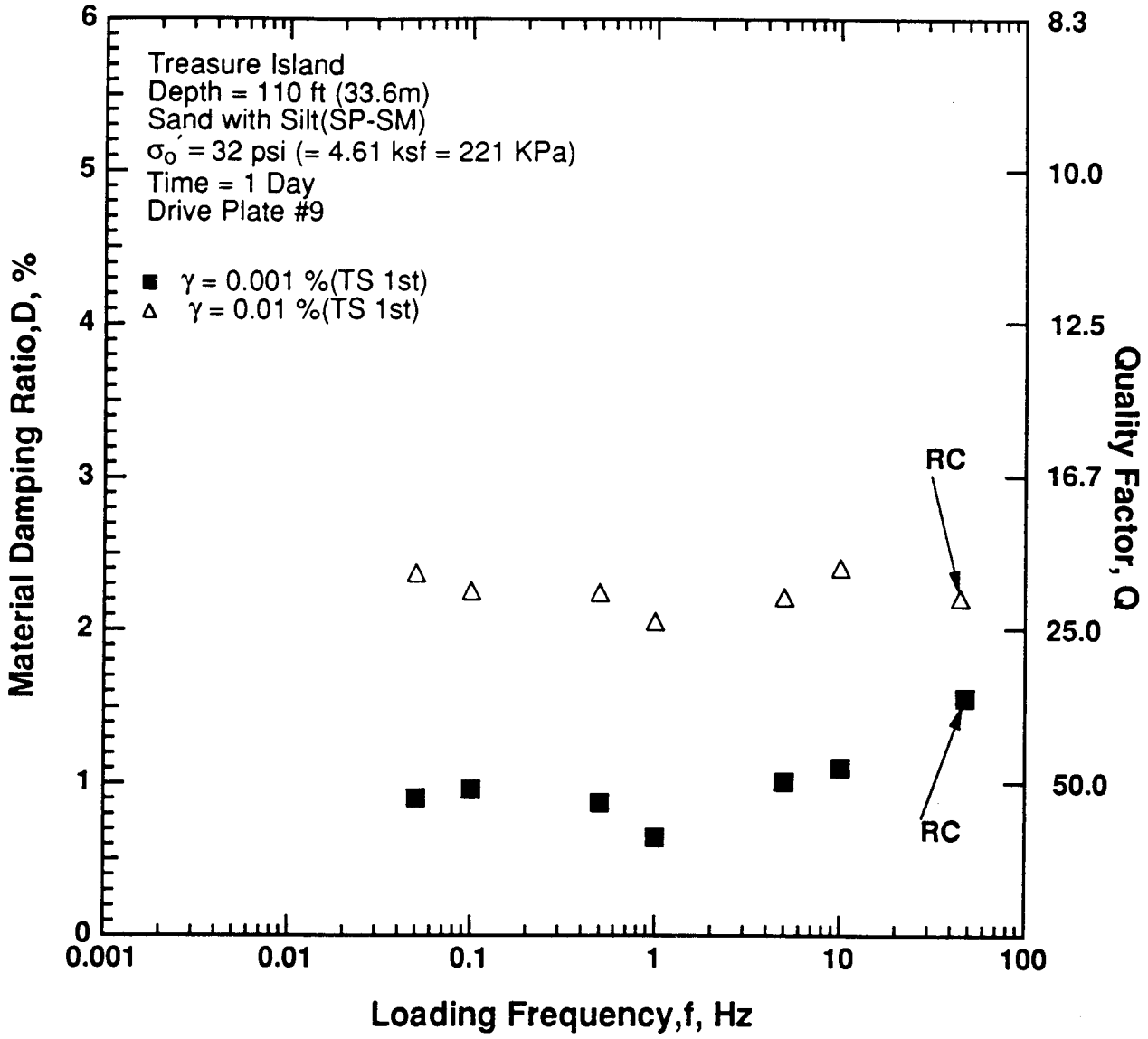

Figure 8.B.1.F-20
Variation in material damping ratio with loading frequency and shearing strain at an effective confining pressure of 32 psi (4.61 ksf, 221 kPa) from RCTS testing of sample T5.

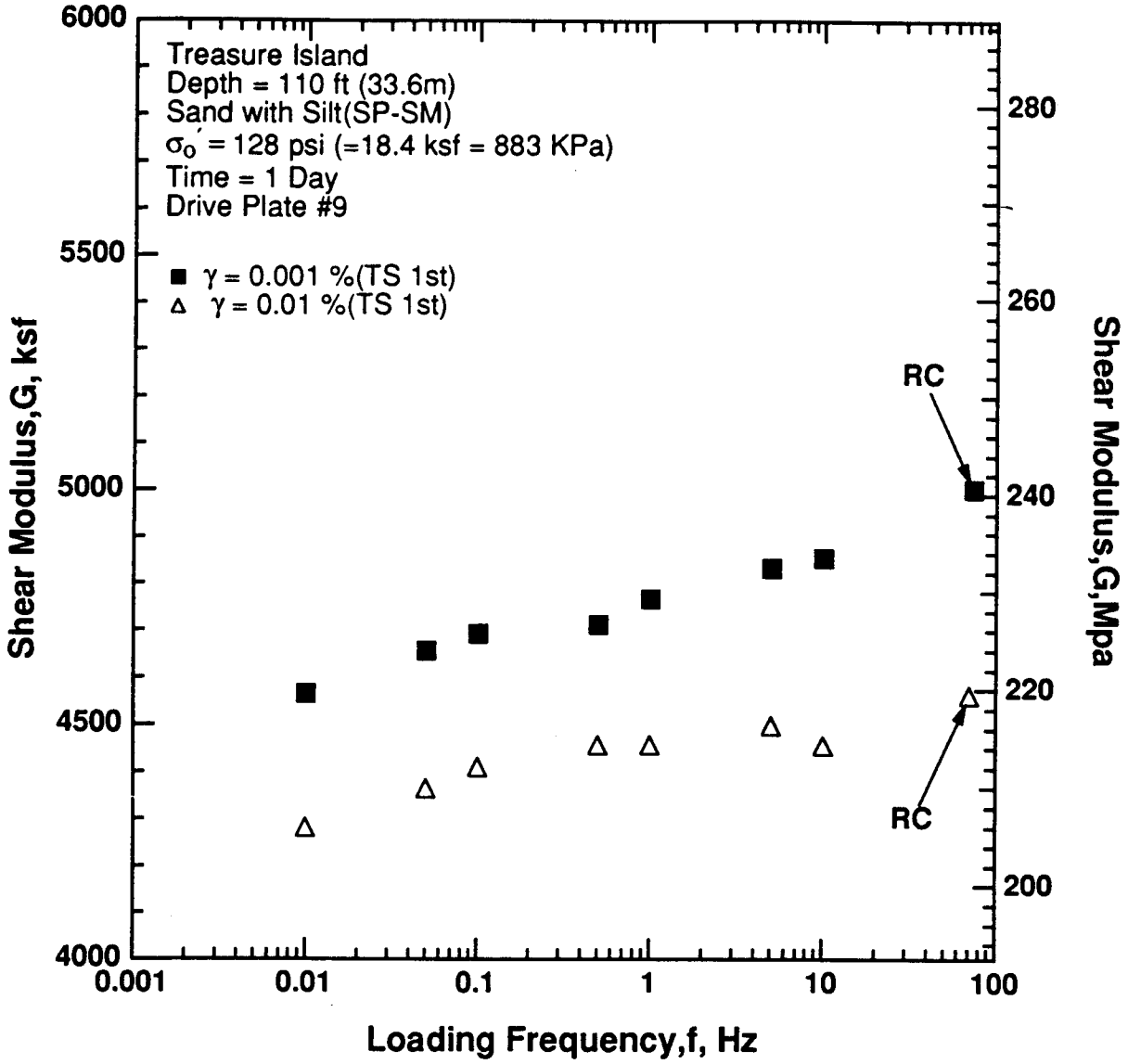

Figure 8.B.1.F-21
Variation in shear modulus with loading frequency and shearing strain at an effective confining pressure of 128 psi (18.4 ksf, 883 kPa) from RCTS testing of sample T5.

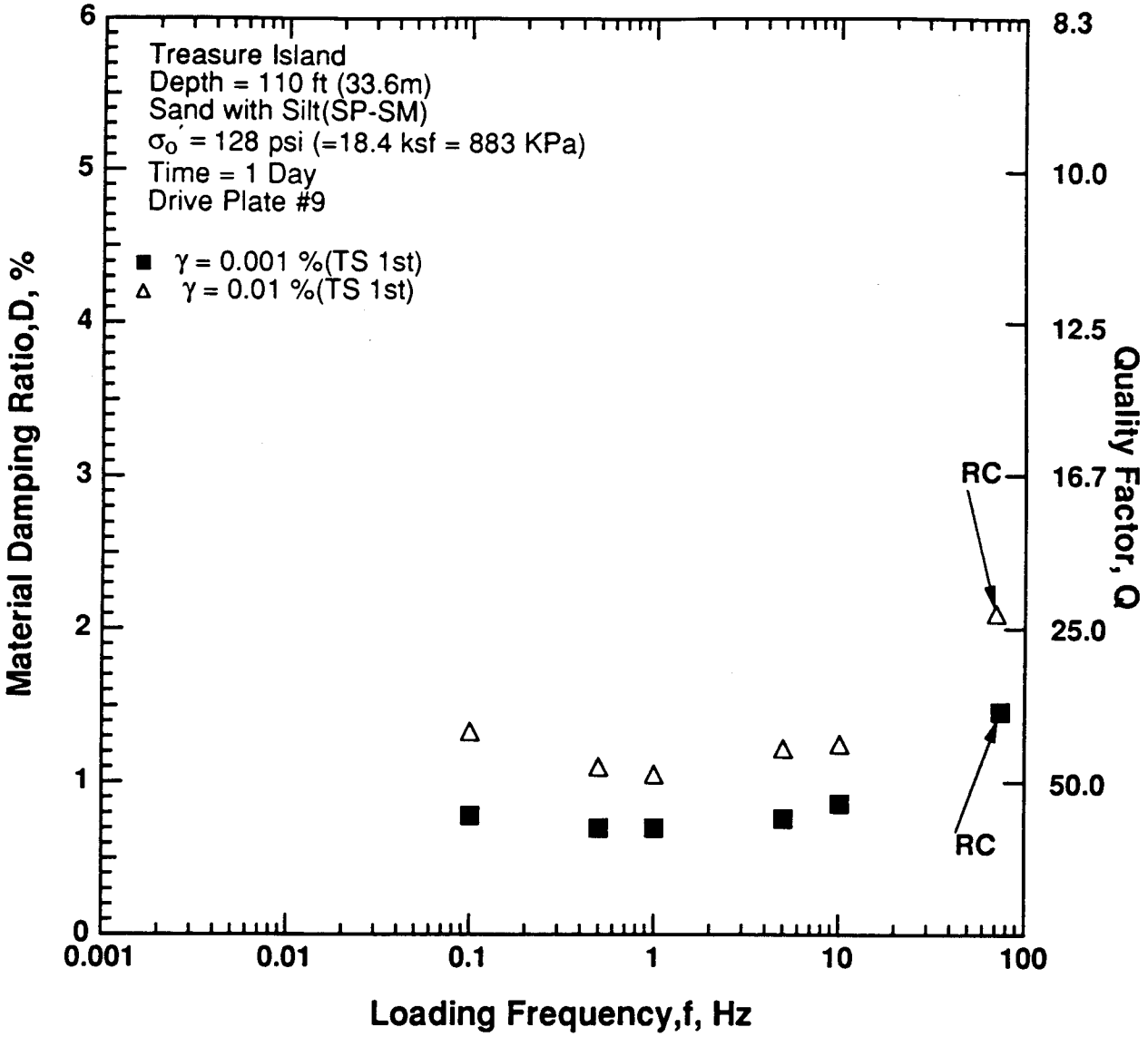

Figure 8.B.1.F-22
Variation in material damping ratio with loading frequency and shearing strain at an effective confining pressure of 128 psi (18.43 ksf, 883 kPa) from RCTS testing of sample T5.

APPENDIX 8.B.1.G
DYNAMIC TESTS OF SAMPLE T6, DEPTH = 130 FT (39.6 M)

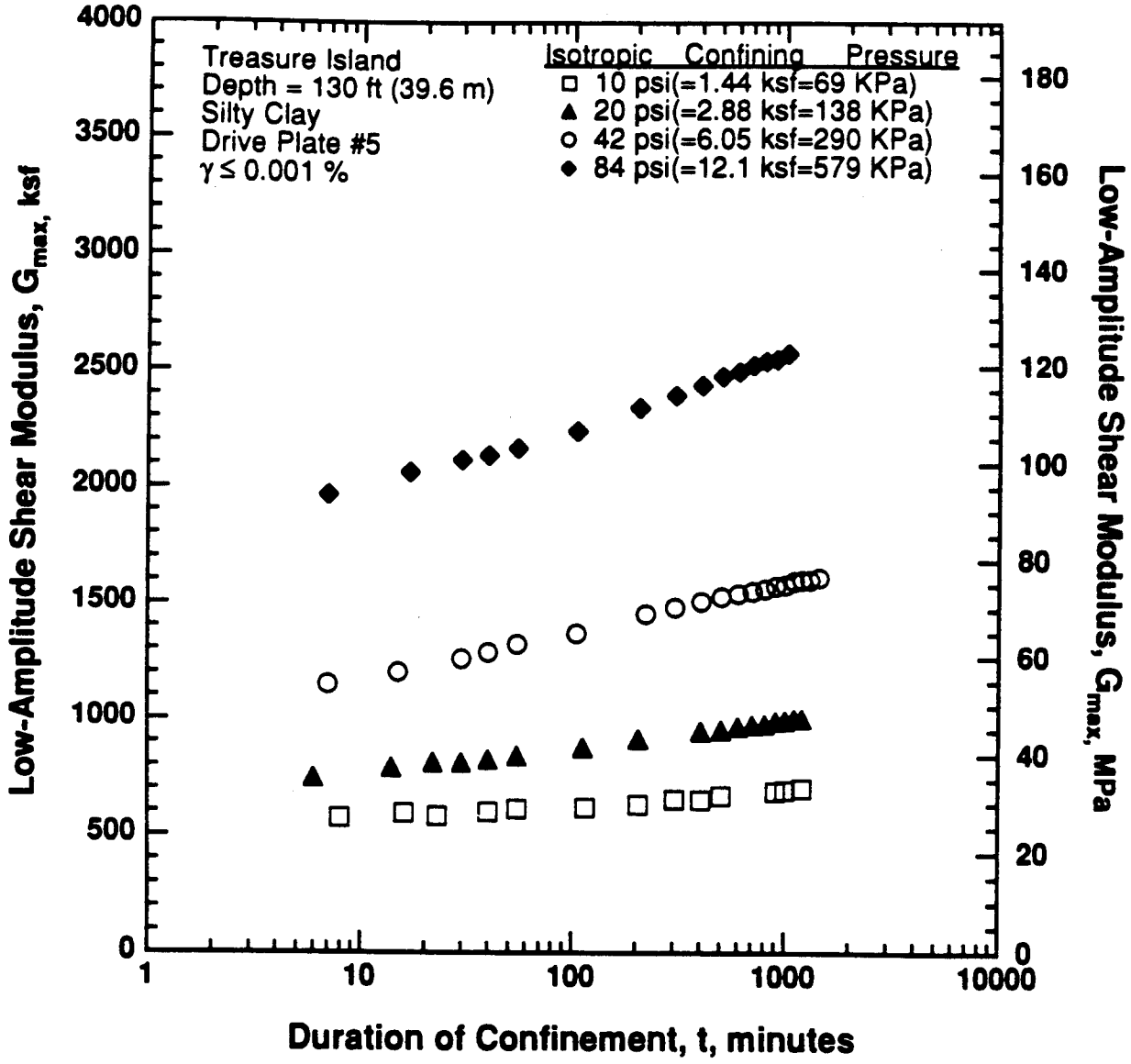

Figure 8.B.1.G-1
Variation in low-amplitude shear modulus with magnitude and duration of isotropic confining pressure from resonant column tests of sample T6.

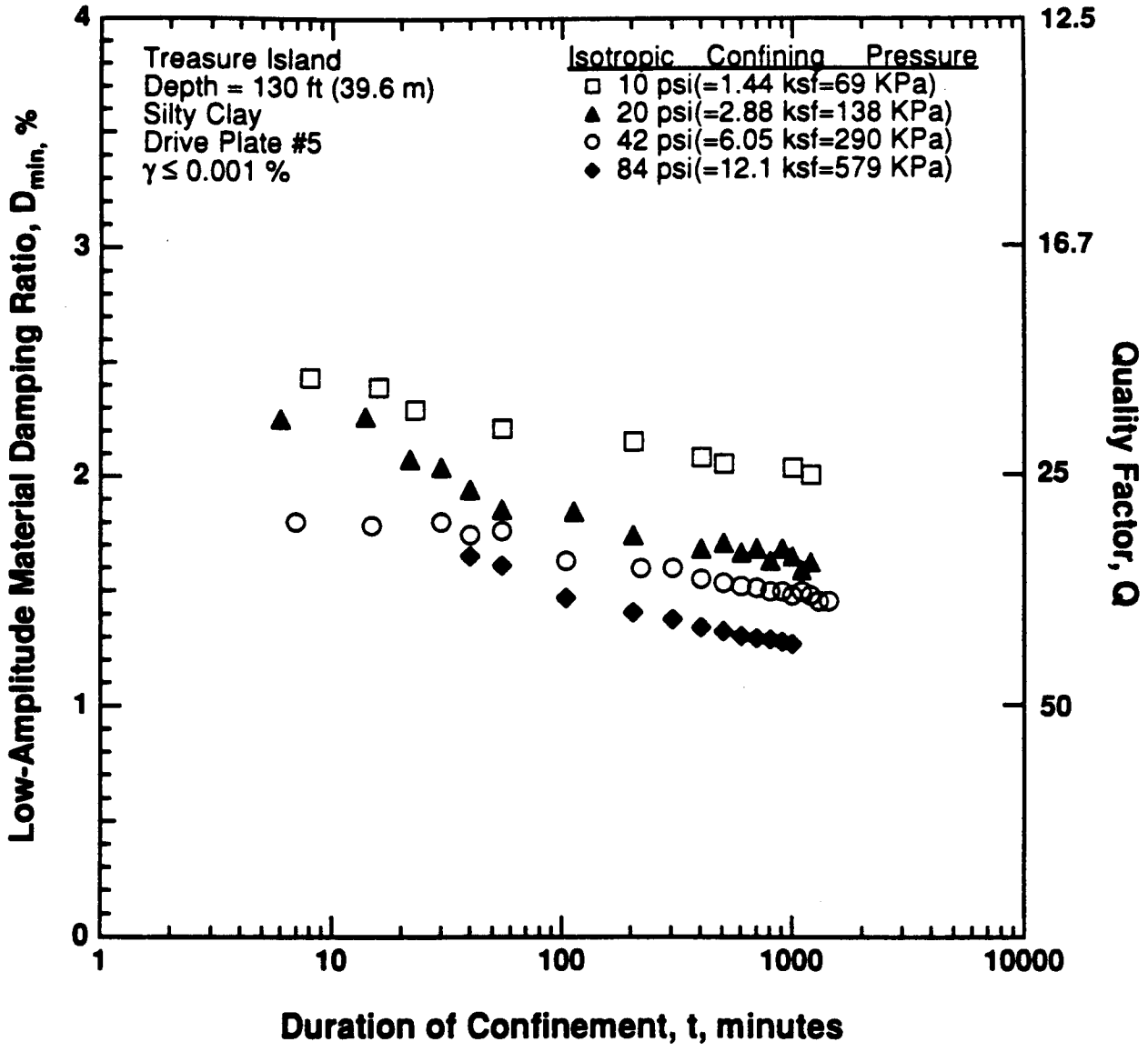

Figure 8.B.1.G-2
Variation in low-amplitude material damping ratio with magnitude and duration of isotropic confining pressure from resonant column tests of sample T6.

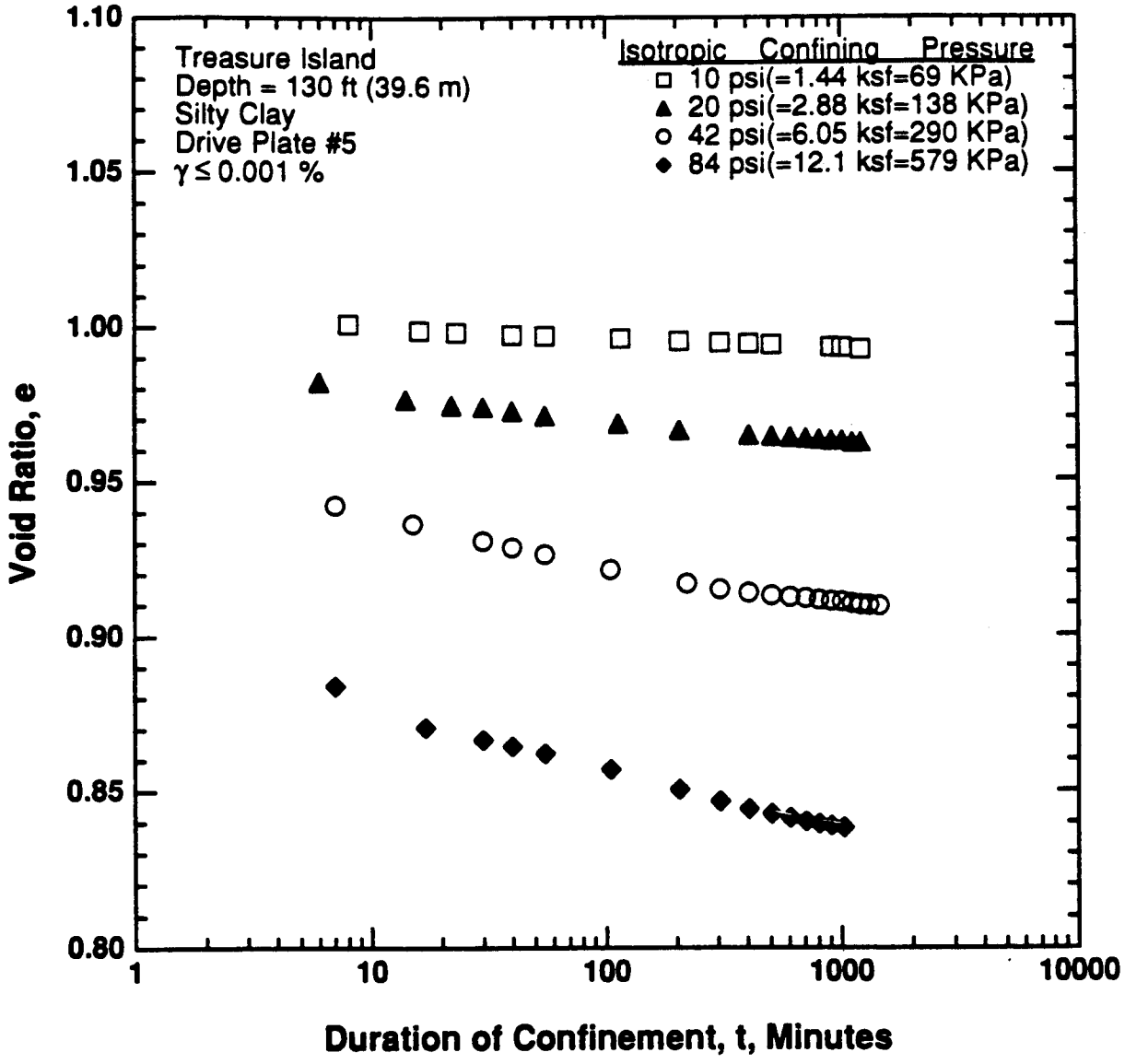

Figure 8.B.1.G-3
Variation in void ratio with magnitude and duration of isotropic confining pressure from resonant column tests of sample T6.

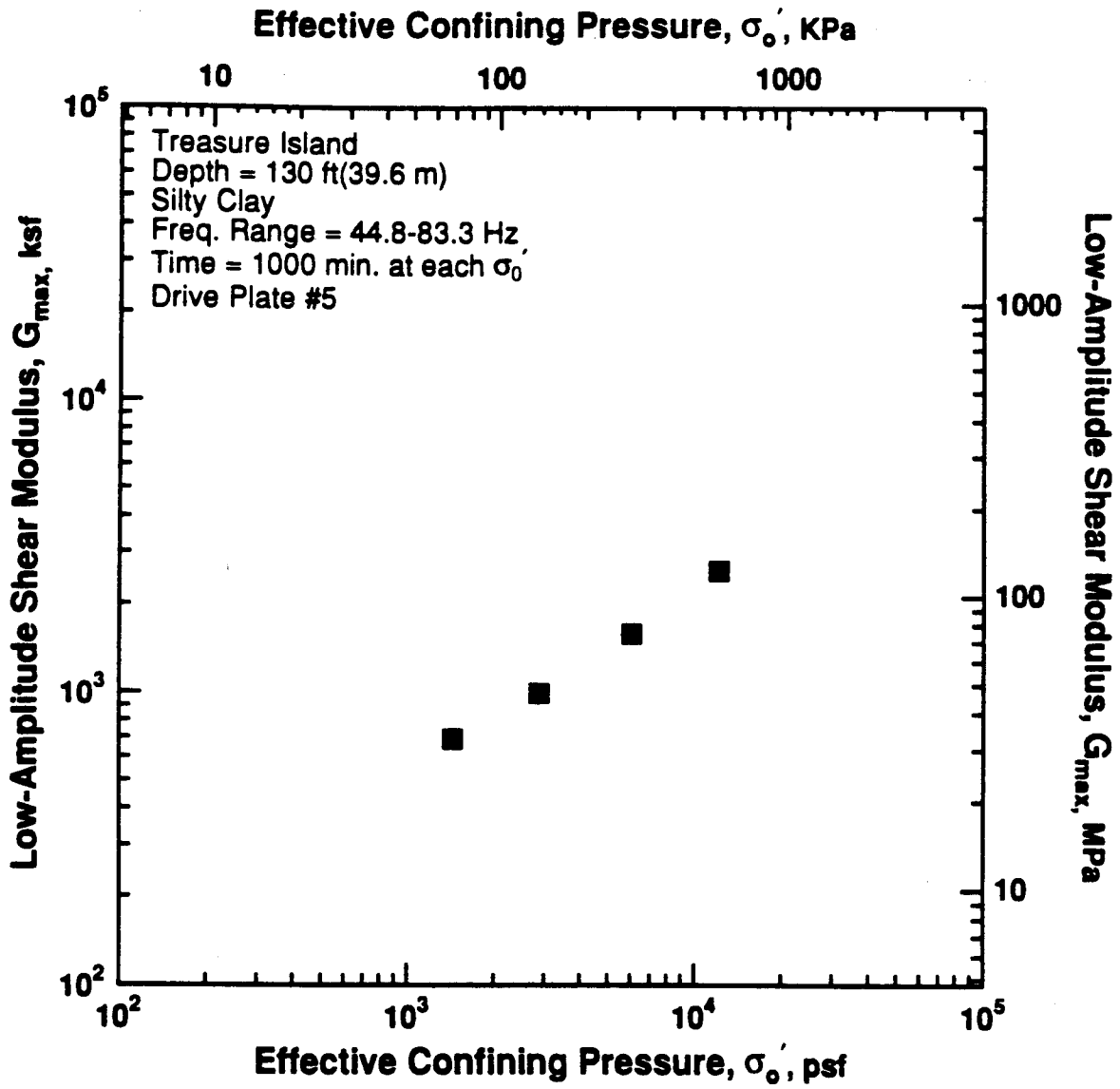

Figure 8.B.1.G-4
Variation in low-amplitude shear modulus with effective confining pressure from resonant column tests of sample T6.

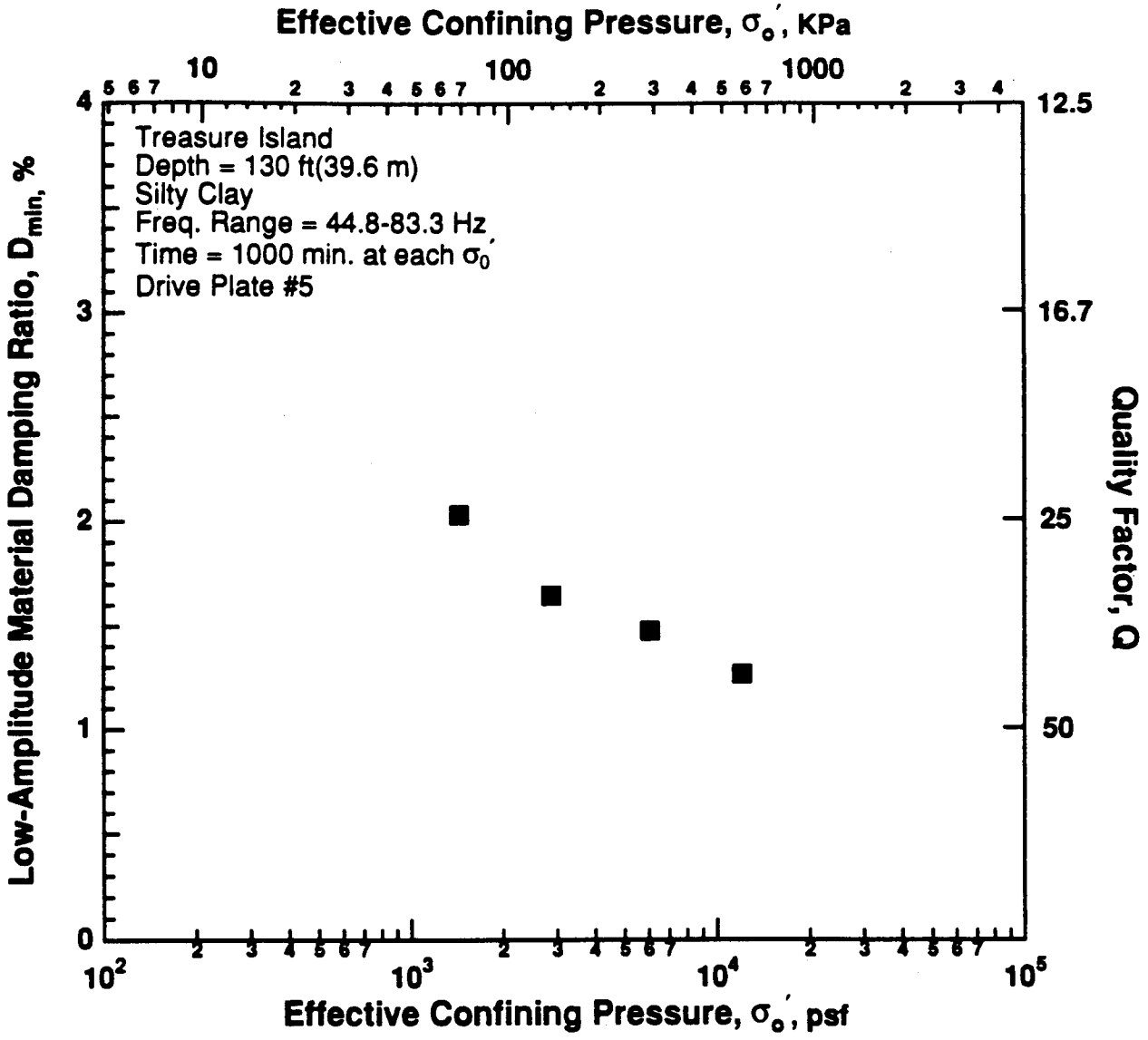

Figure 8.B.1.G-5
Variation in low-amplitude material damping ratio with effective confining pressure from resonant column tests of sample T6.

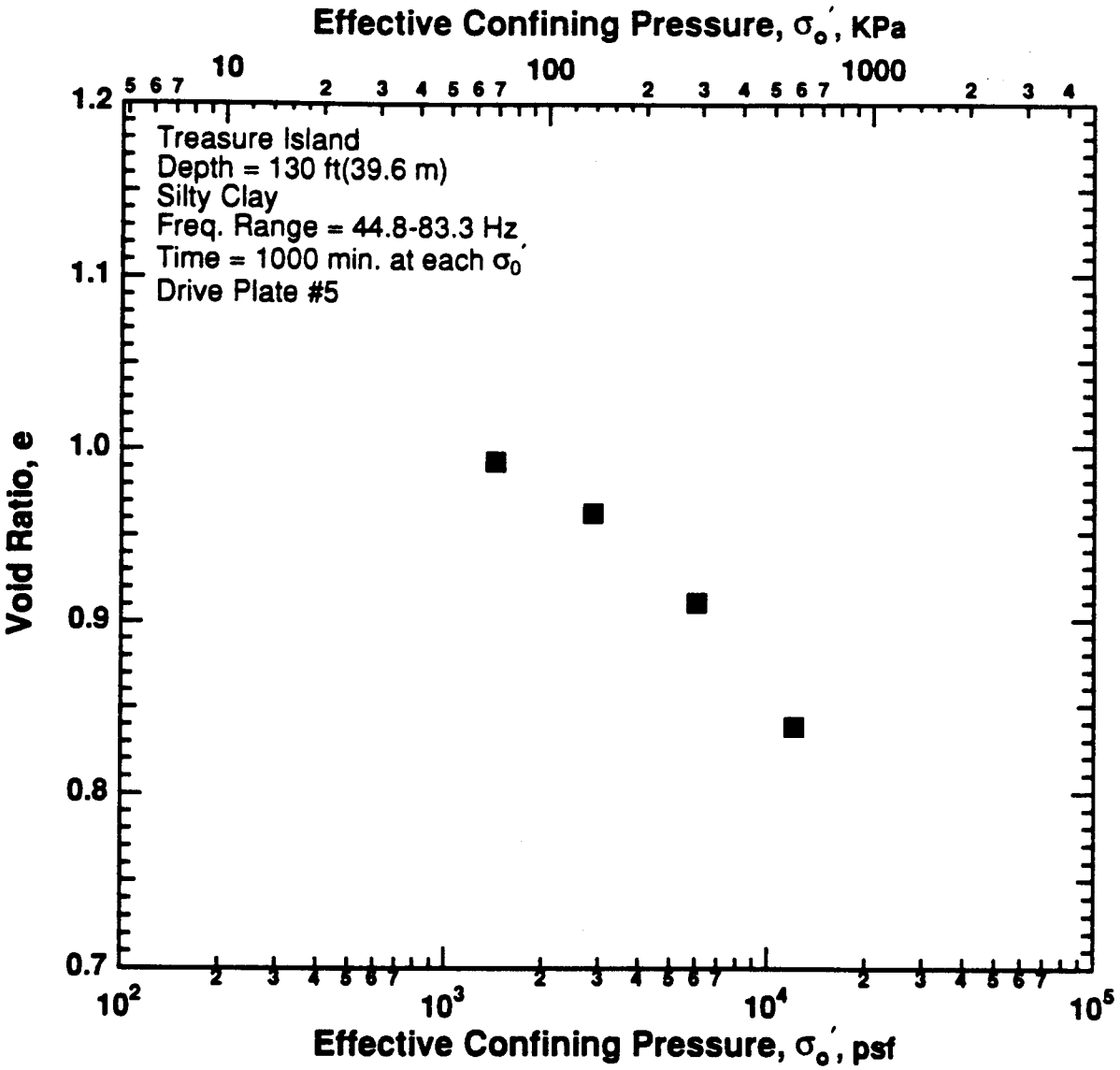

Figure 8.B.1.G-6
Variation in void ratio with effective confining pressure from resonant column tests of sample T6.

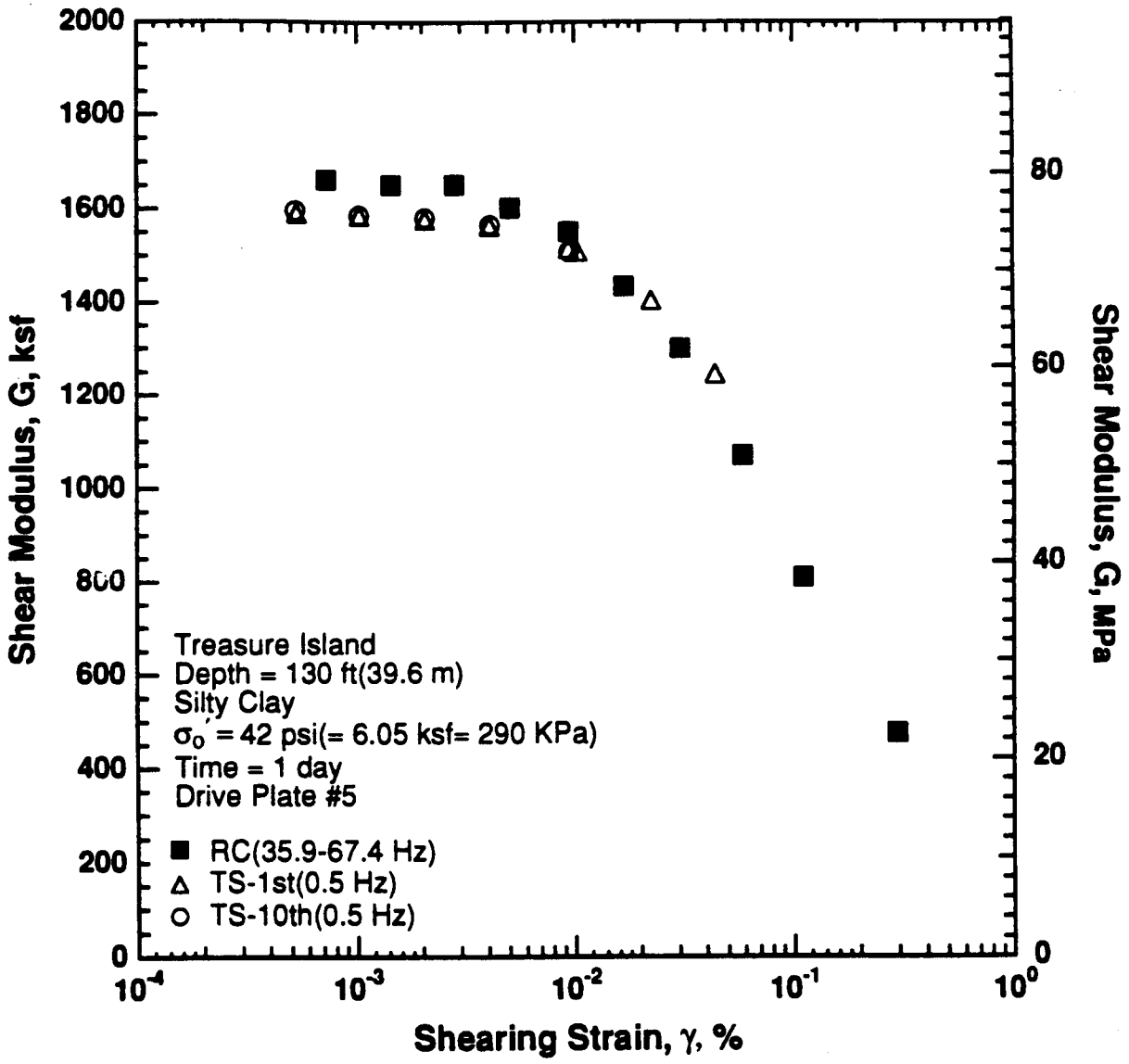

Figure 8.B.1.G-7
Variation in shear modulus with shearing strain at an effective confining pressure of 42 psi (6.05 ksf, 290 kPa) from RCTS tests of sample T6.

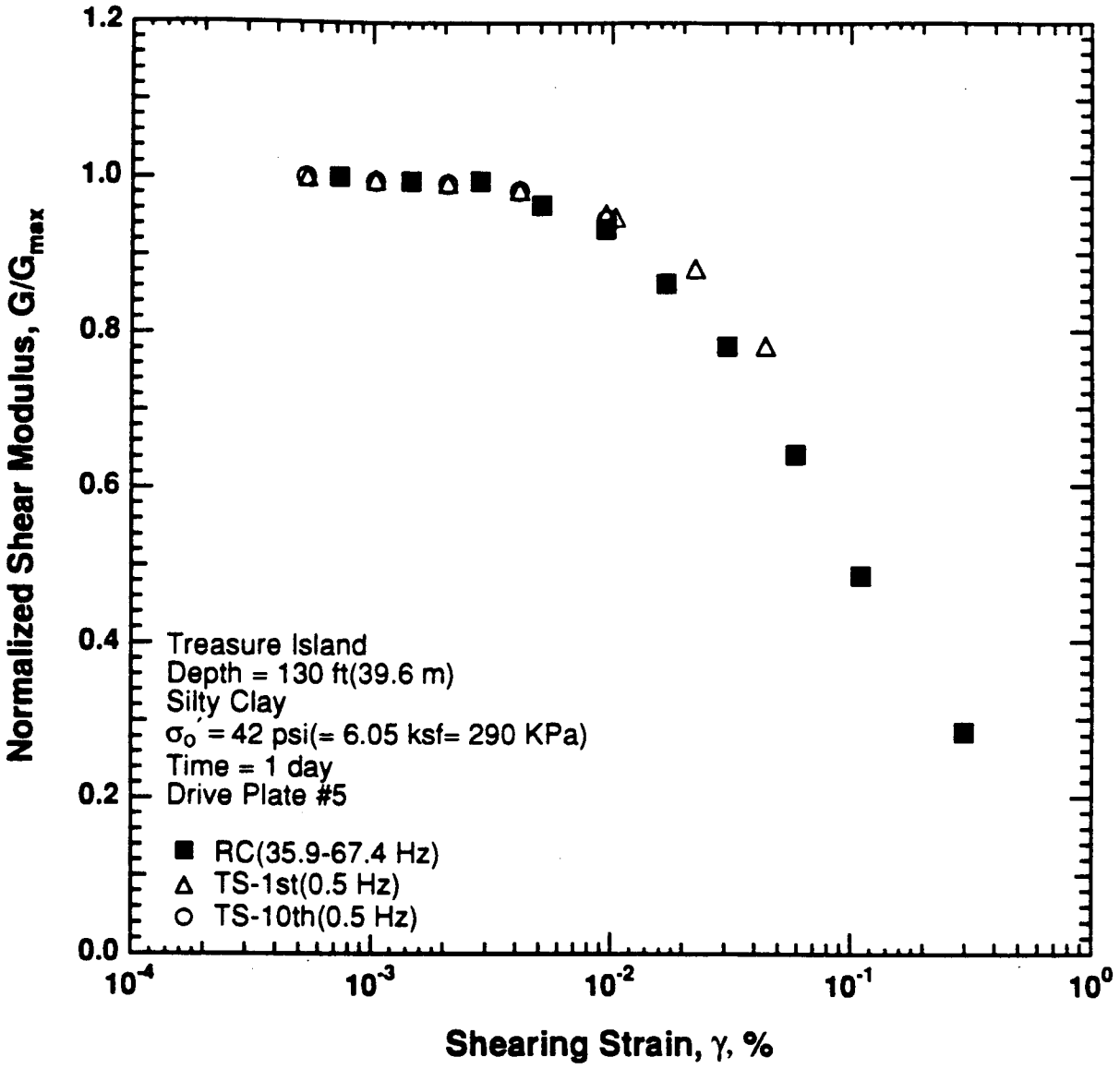

Figure 8.B.1.G-8
Variation in normalized shear modulus with shearing strain at an effective confining pressure of 42 psi (6.05 ksf, 290 kPa) from RCTS tests of sample T6.

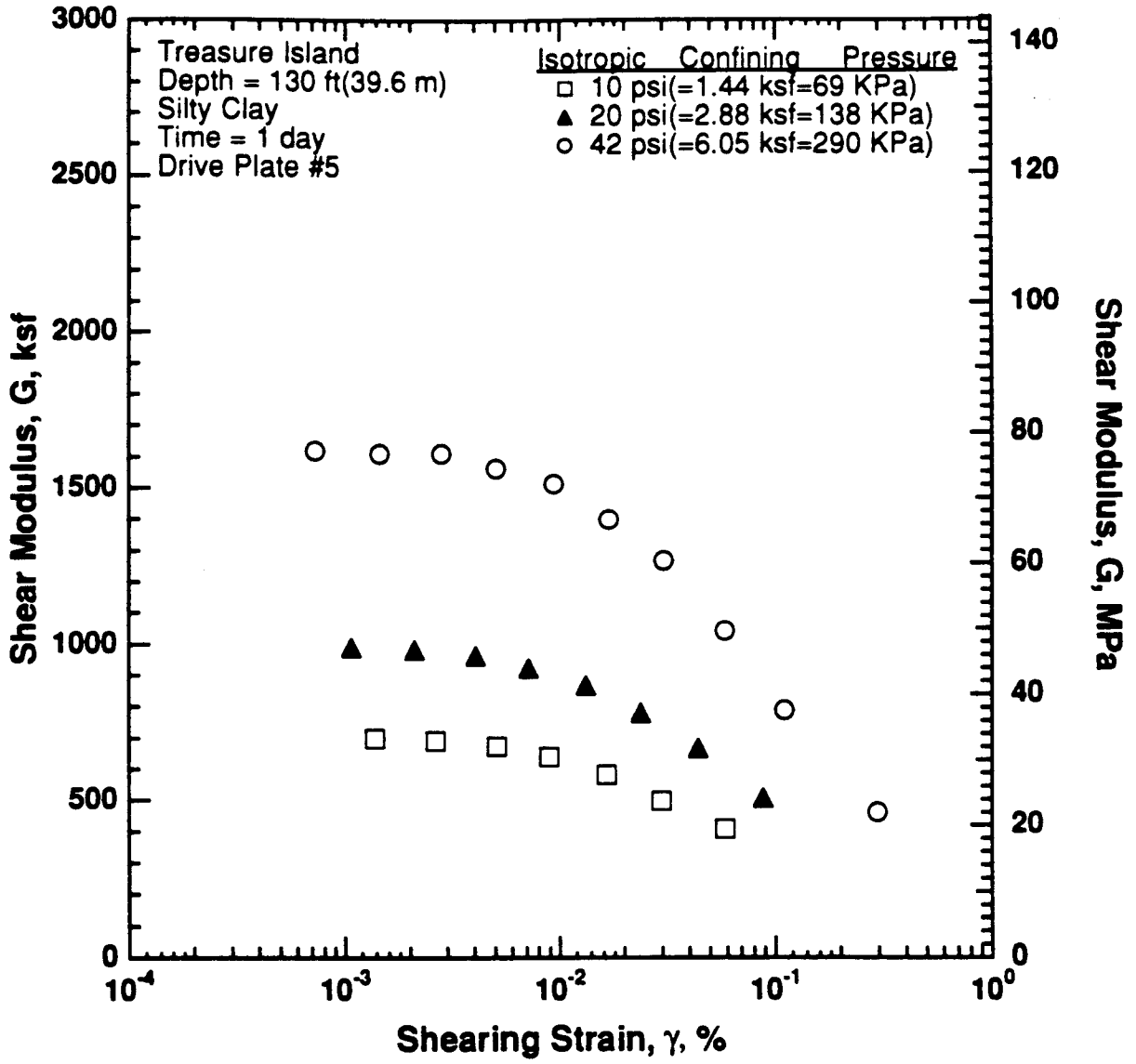

Figure 8.B.1.G-9
Variation in shear modulus with shearing strain and effective confining pressure from resonant column tests of sample T6.

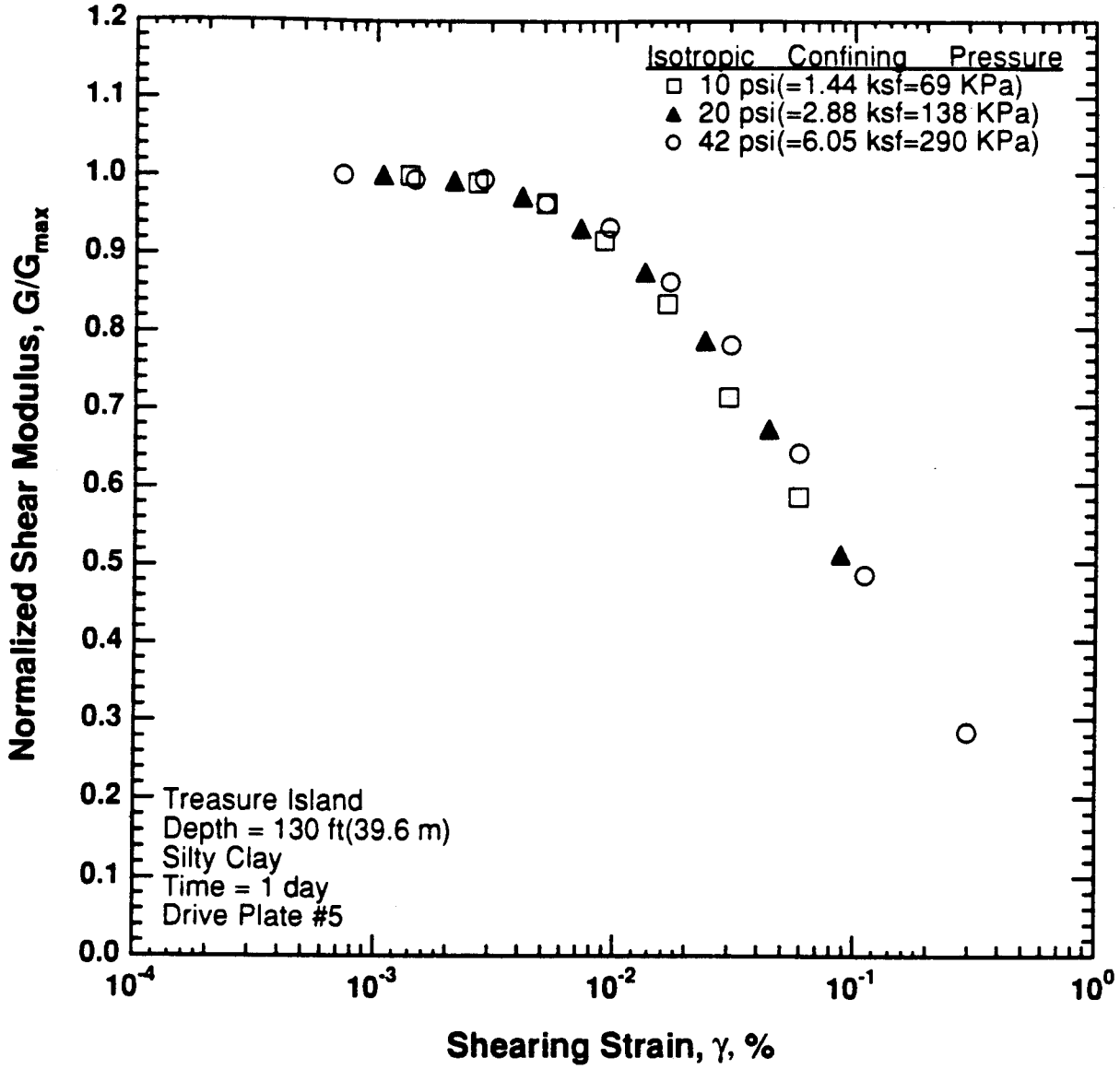

Figure 8.B.1.G-10
Comparison of the variation in normalized shear modulus with shearing strain and effective confining pressure from resonant column tests of sample T6.

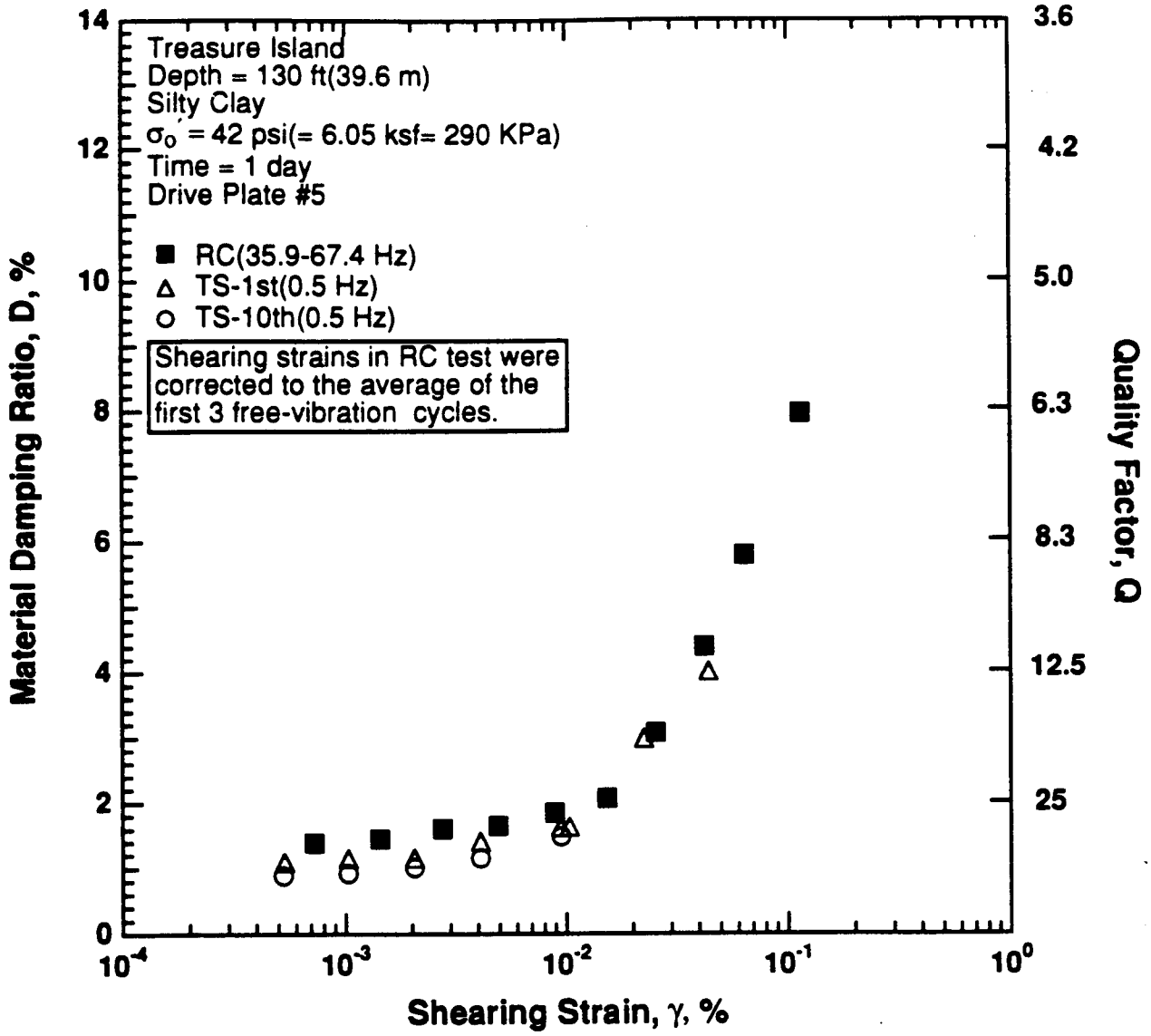

Figure 8.B.1.G-11
Variation in material damping ratio with shearing strain at an effective confining pressure of 42 psi (6.05 ksf, 290 kPa) from RCTS tests of sample T6.

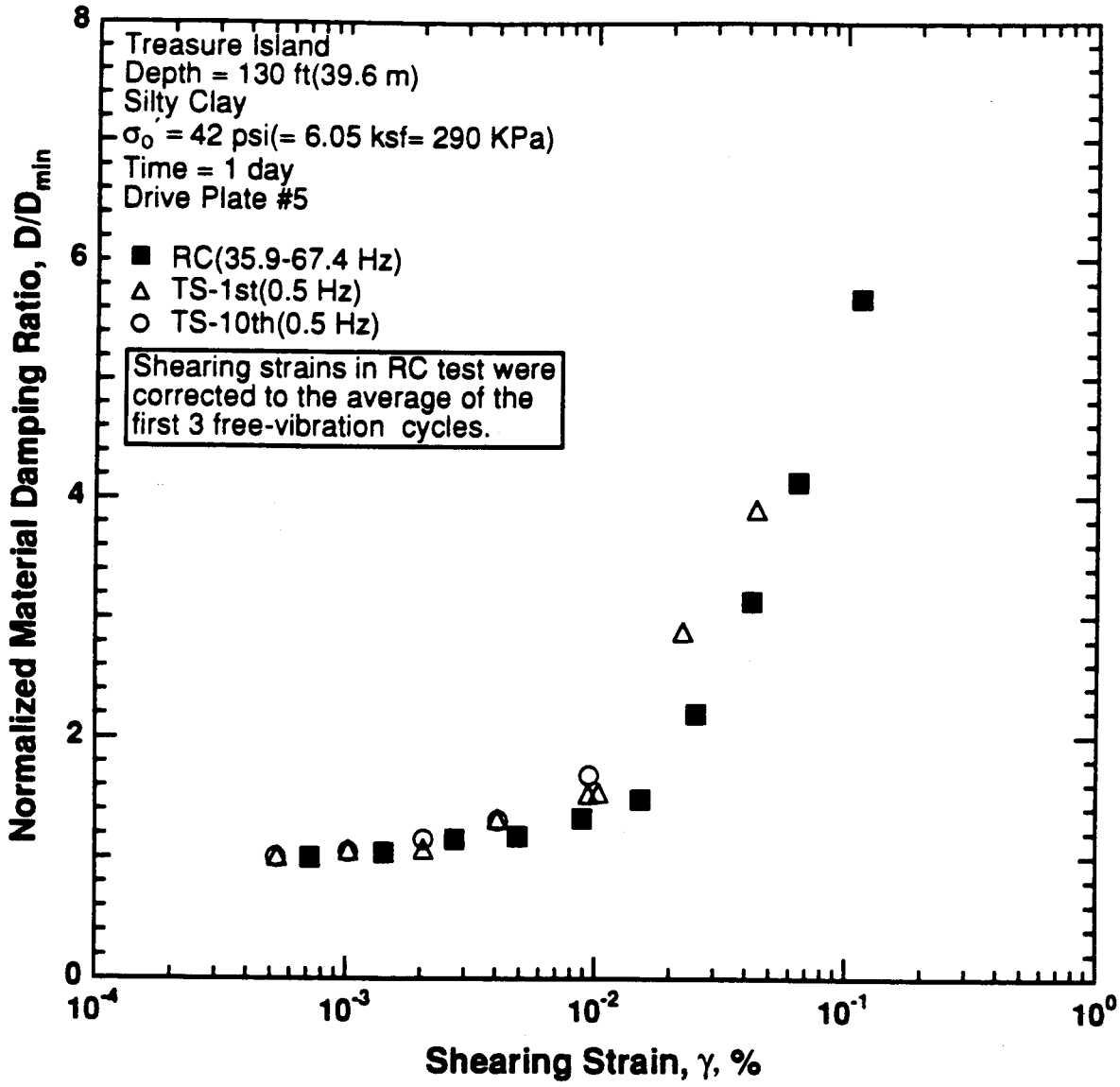

Figure 8.B.1.G-12
Variation in normalized material damping ratio with shearing strain at an effective confining pressure of 42 psi (6.05 ksf, 290 kPa) from RCTS tests of sample T6.

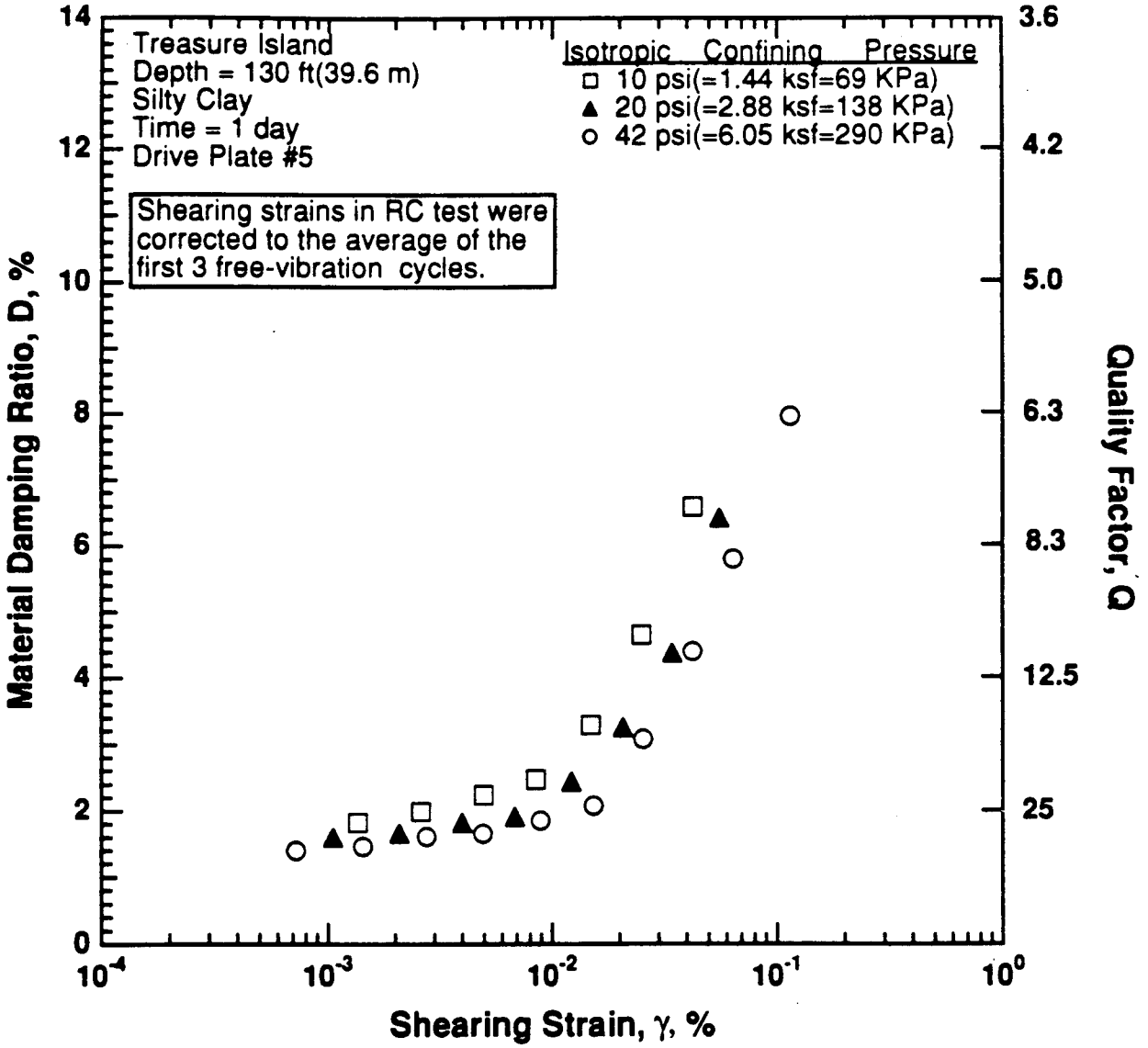

Figure 8.B.1.G-13
Variation in material damping ratio with shearing strain and effective confining pressure from resonant column tests of sample T6.

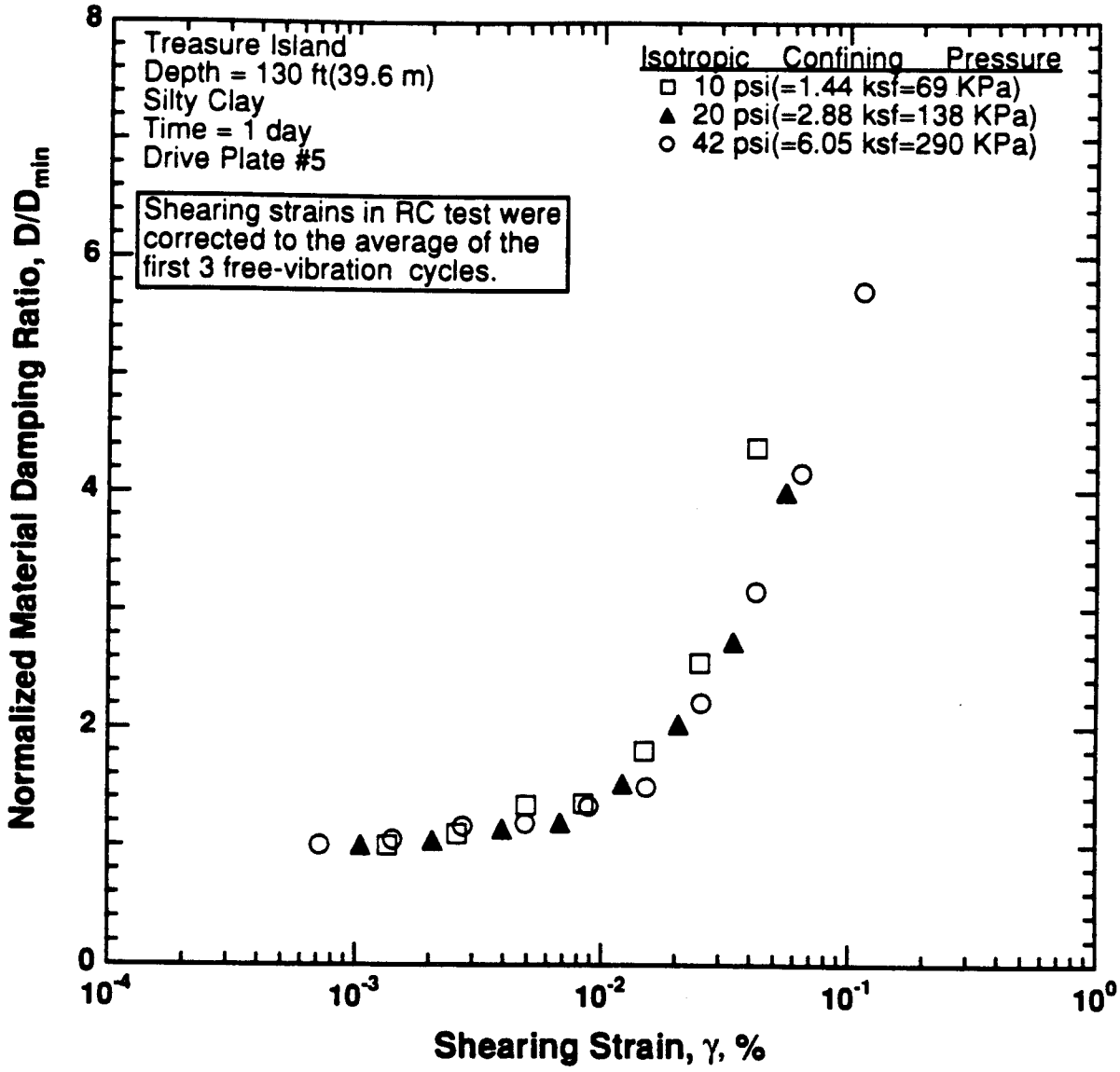

Figure 8.B.1.G-14
Comparison of the variation in normalized material damping ratio with shearing strain and effective confining pressure from resonant column tests of sample T6.

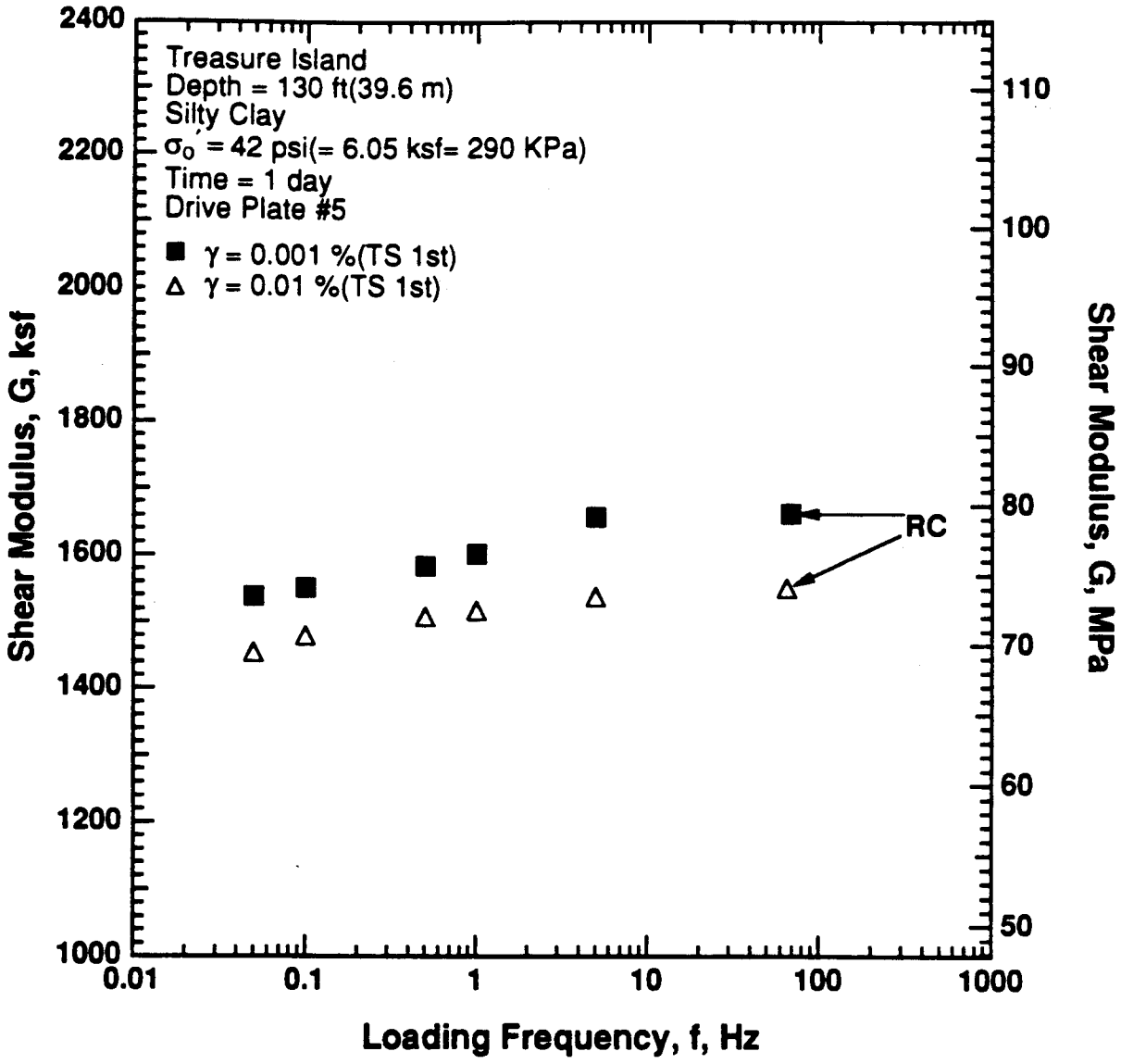

Figure 8.B.1.G-15
Variation in shear modulus with loading frequency and shearing strain at an effective confining pressure of 42 psi (6.05 ksf, 290 kPa) from RCTS tests of sample T6.

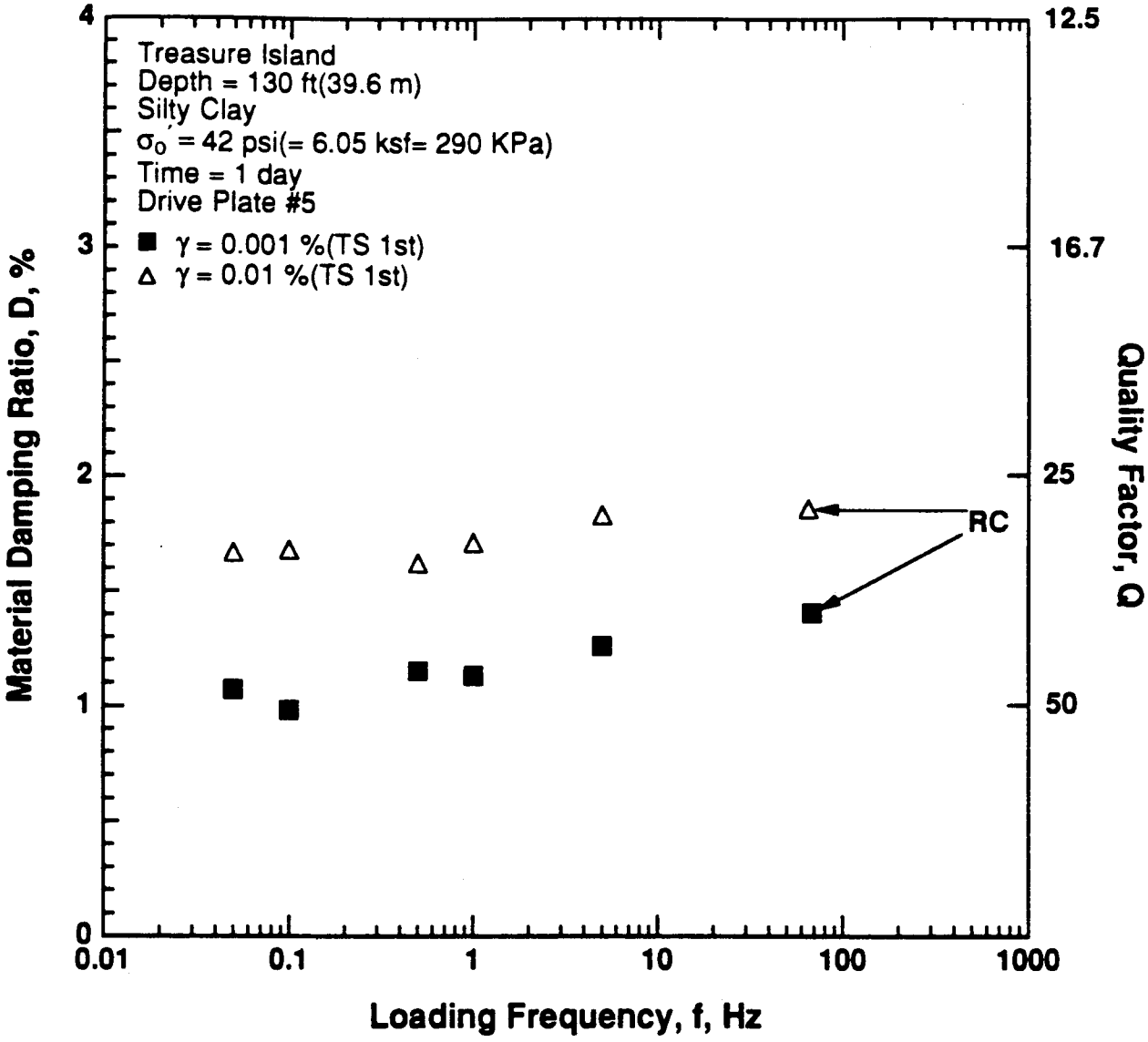

Figure 8.B.1.G-16
Variation in material damping ratio with loading frequency and shearing strain at an effective confining pressure of 42 psi (6.05 ksf, 290 kPa) from RCTS tests of sample T6.

APPENDIX 8.B.1.H
DYNAMIC TESTS OF SAMPLE T7, DEPTH = 170 FT (51.8 M)

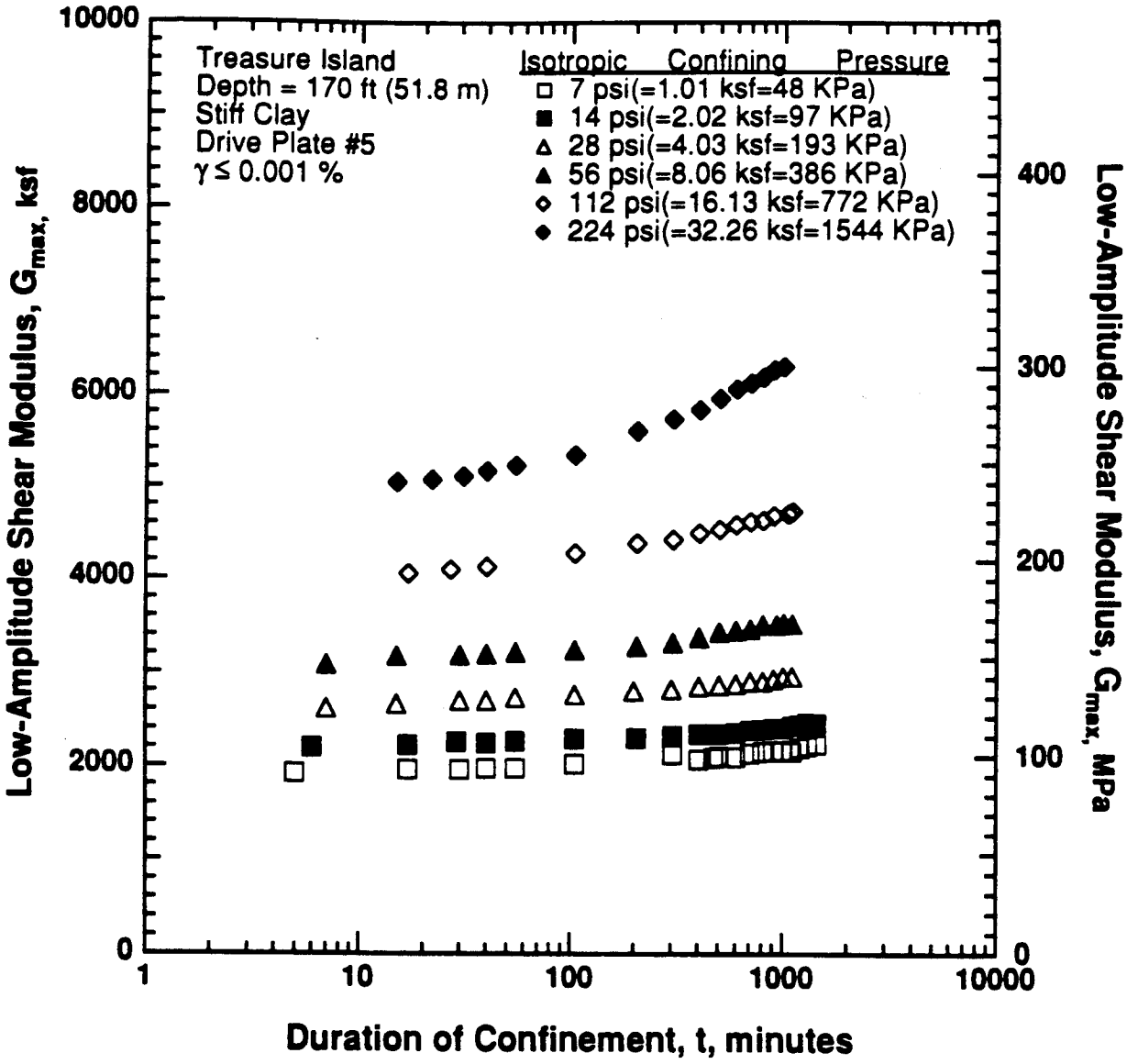

Figure 8.B.1.H-1
Variation in low-amplitude shear modulus with magnitude and duration of isotropic confining pressure from resonant column tests of sample T7.

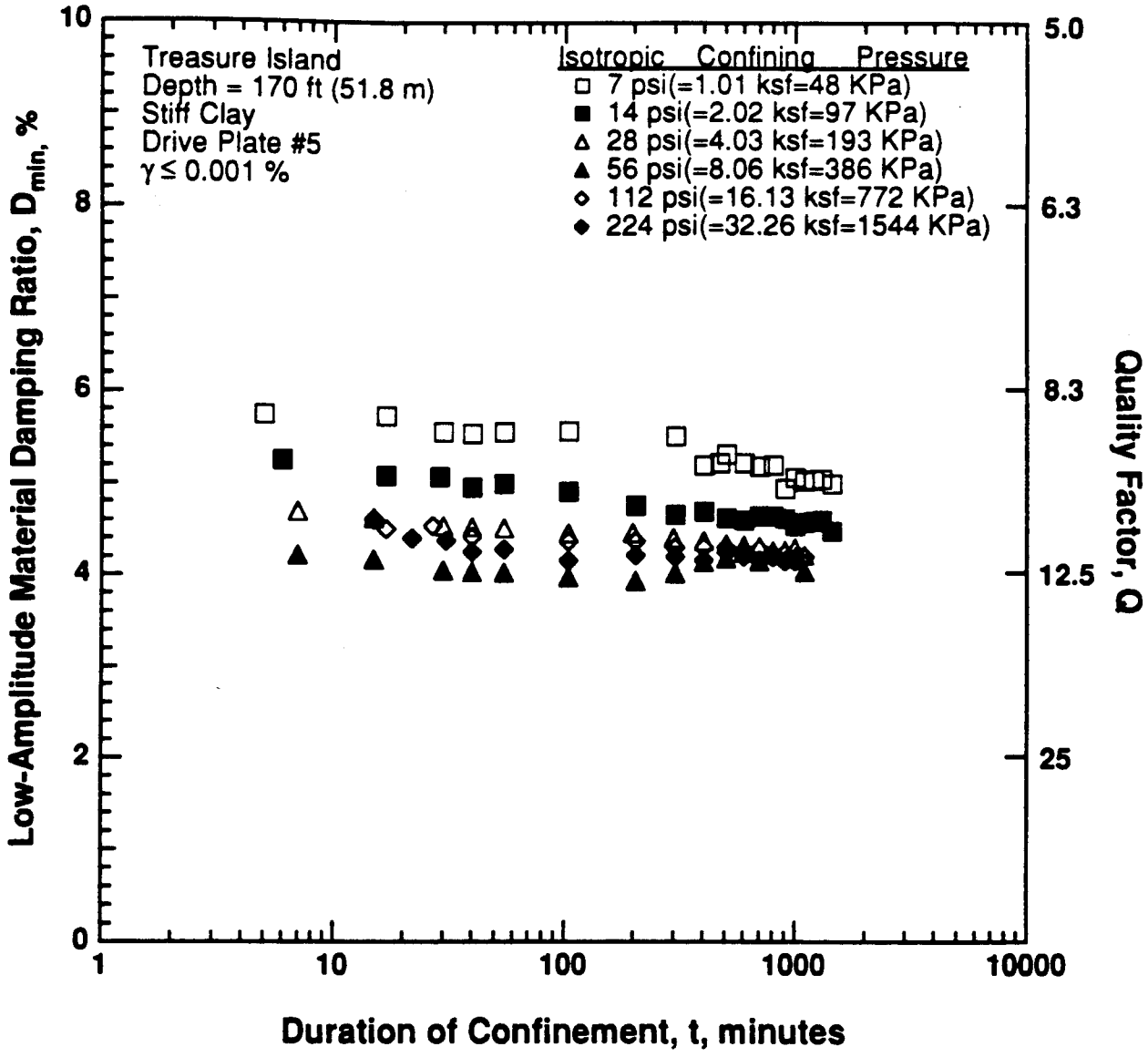

Figure 8.B.1.H-2
Variation in low-amplitude material damping ratio with magnitude and duration of isotropic confining pressure from resonant column tests of sample T7.

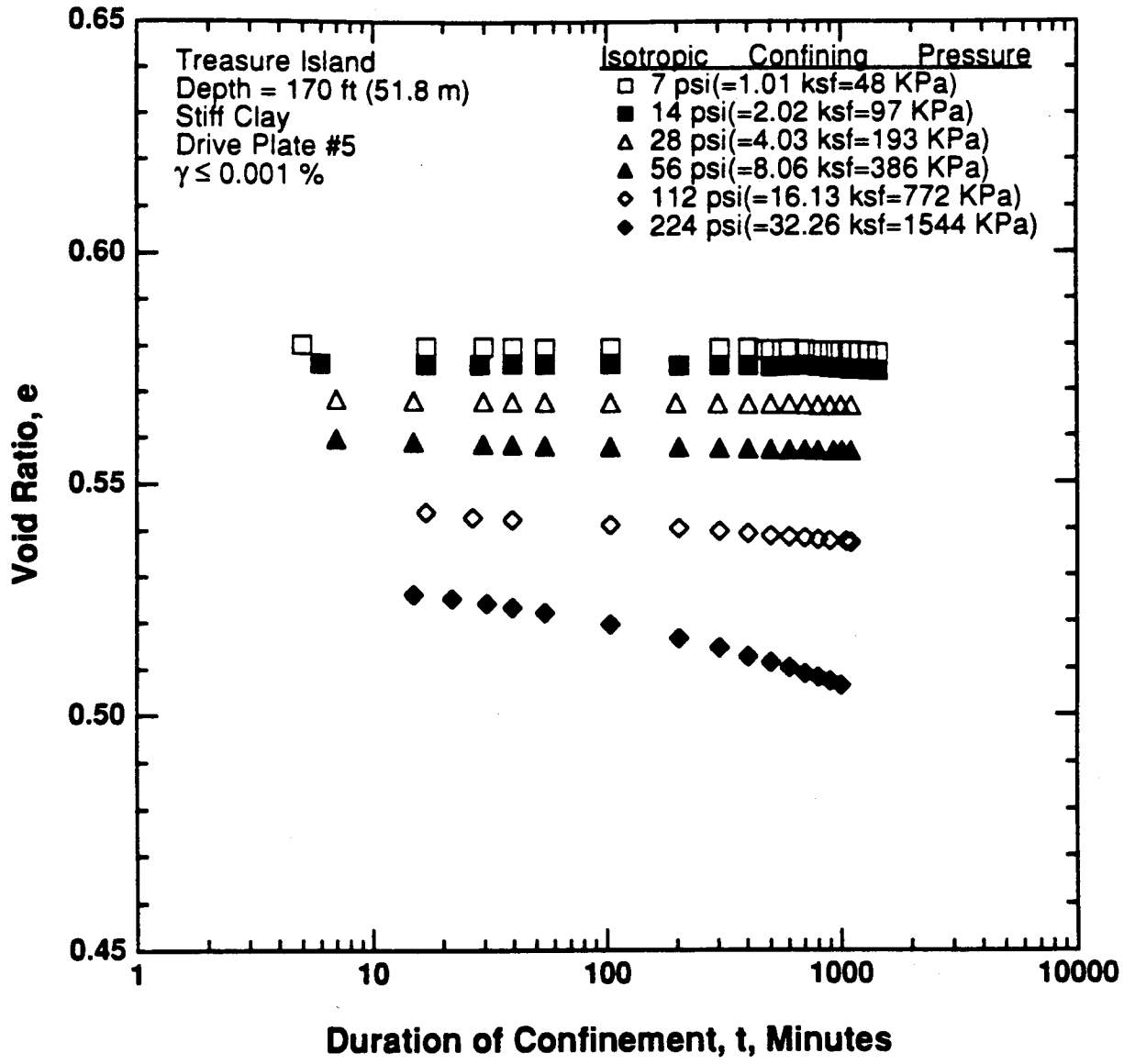

Figure 8.B.1.H-3
Variation in void ratio with magnitude and duration of isotropic confining pressure from resonant column tests of sample T7.

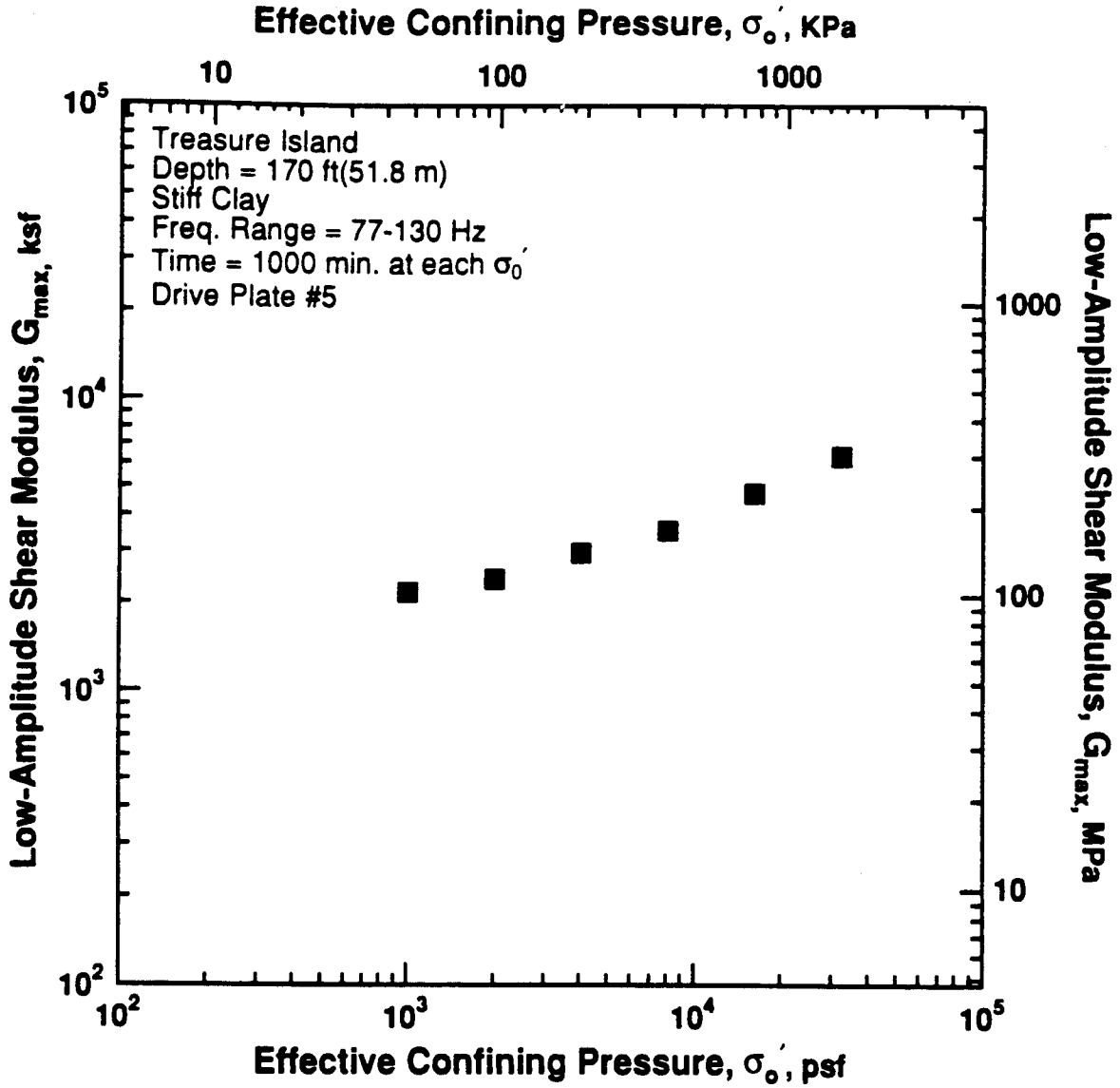

Figure 8.B.1.H-4
Variation in low-amplitude shear modulus with effective confining pressure from resonant column tests of sample T7.

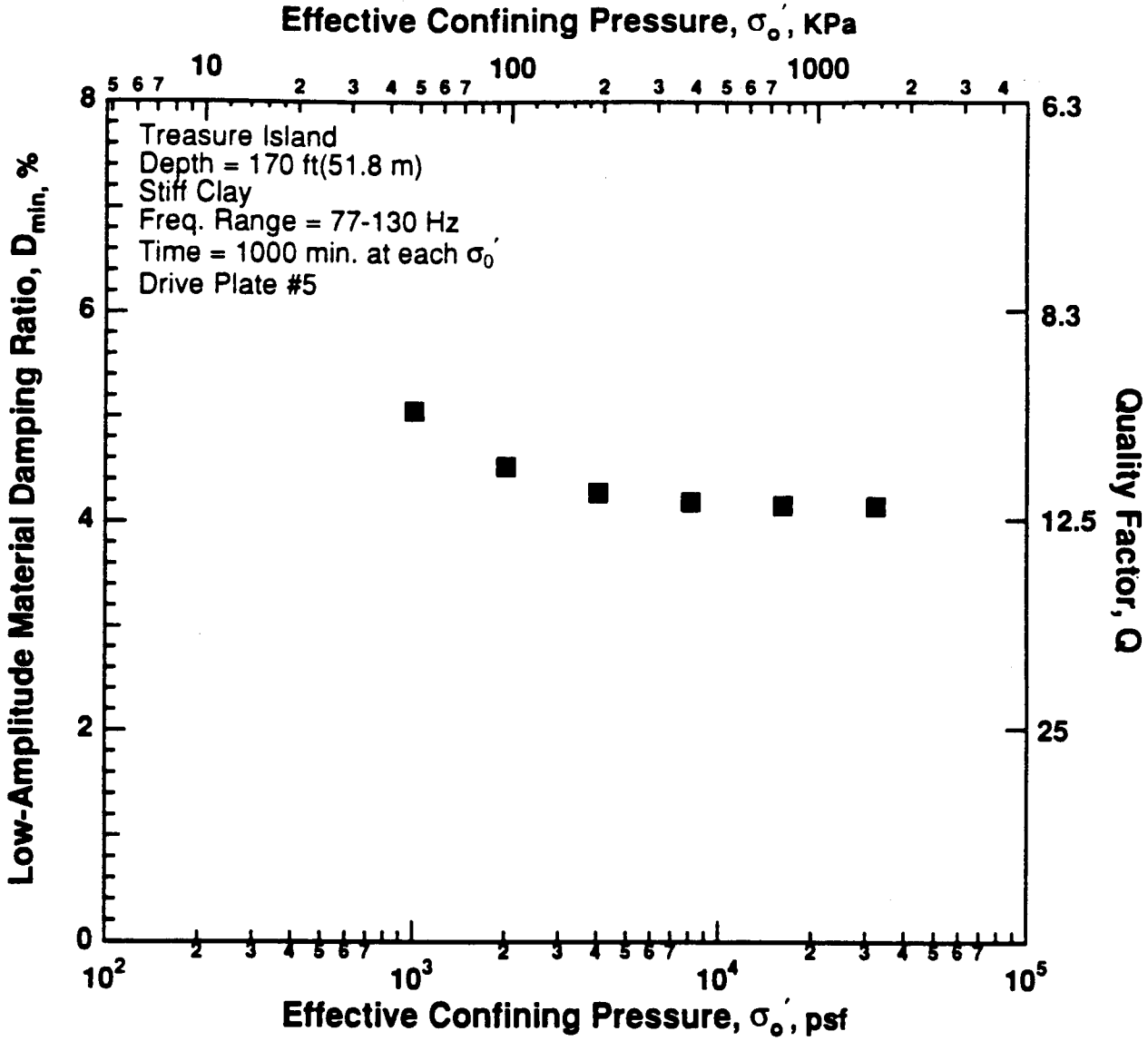

Figure 8.B.1.H-5
Variation in low-amplitude material damping ratio with effective confining pressure from resonant column tests of sample T7.

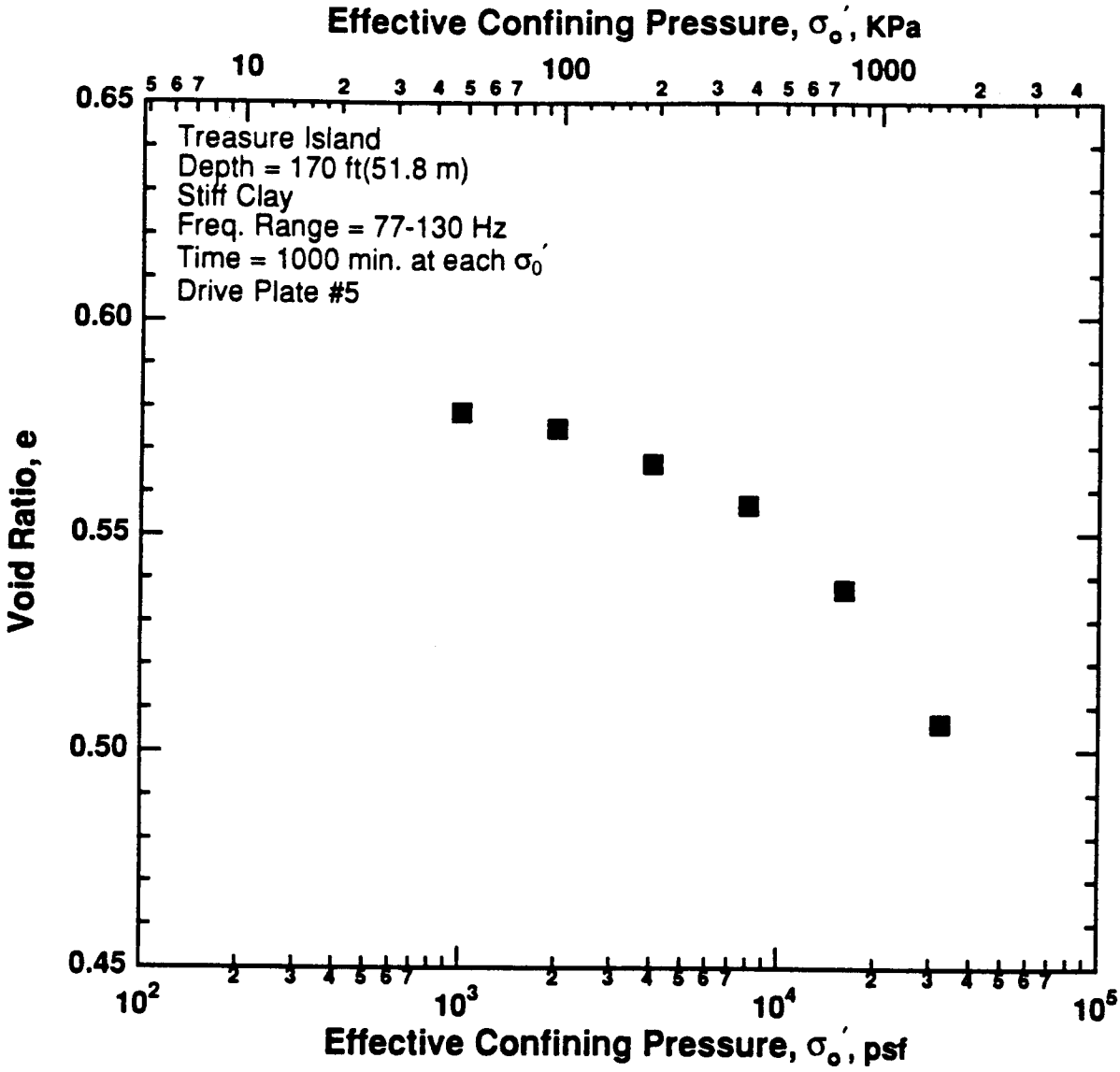

Figure 8.B.1.H-6
Variation in void ratio with effective confining pressure from resonant column tests of sample T7.

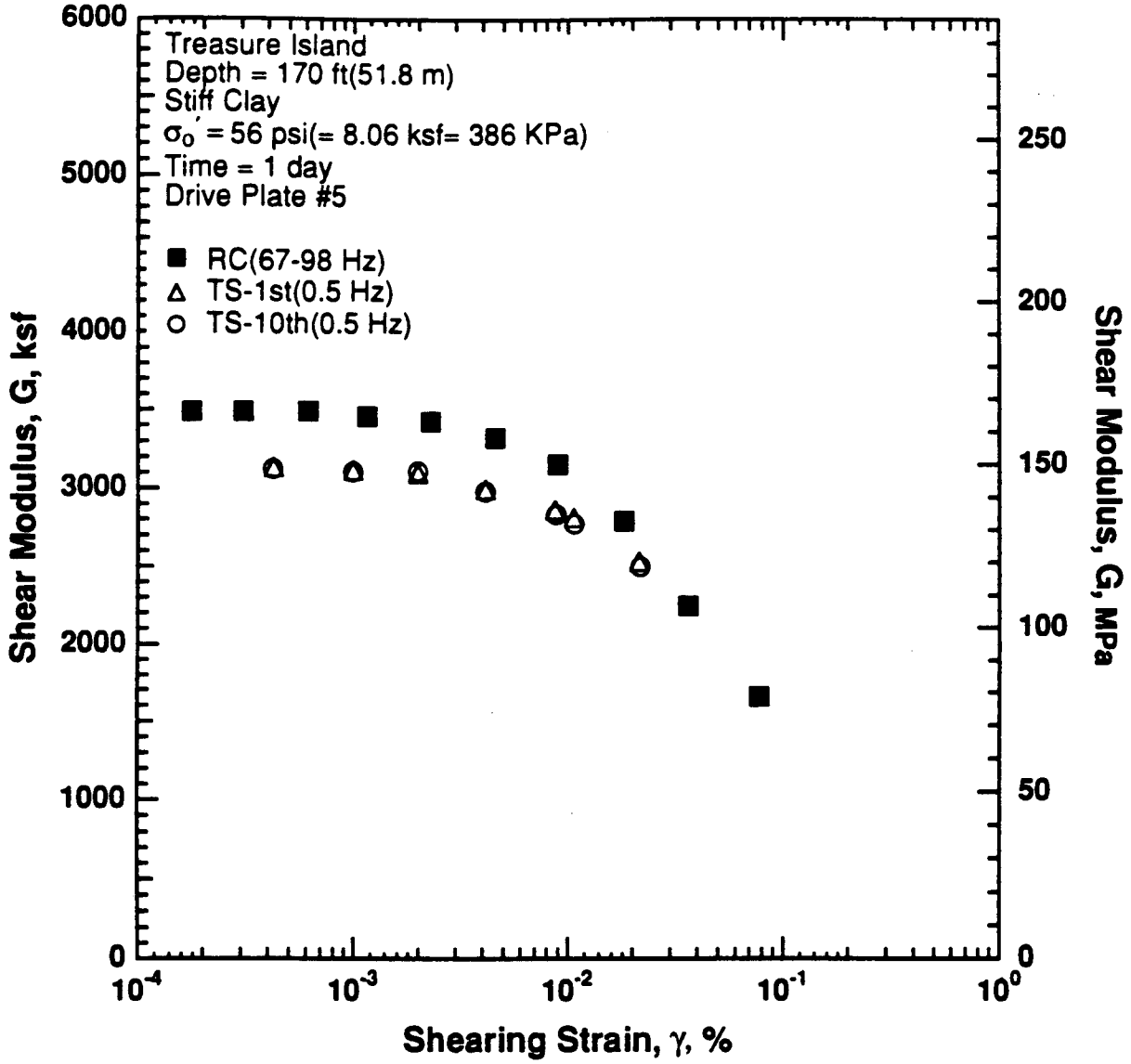

Figure 8.B.1.H-7
Variation in shear modulus with shearing strain at an effective confining pressure of 56 psi (8.06 ksf, 386 kPa) from RCTS tests of sample T7.

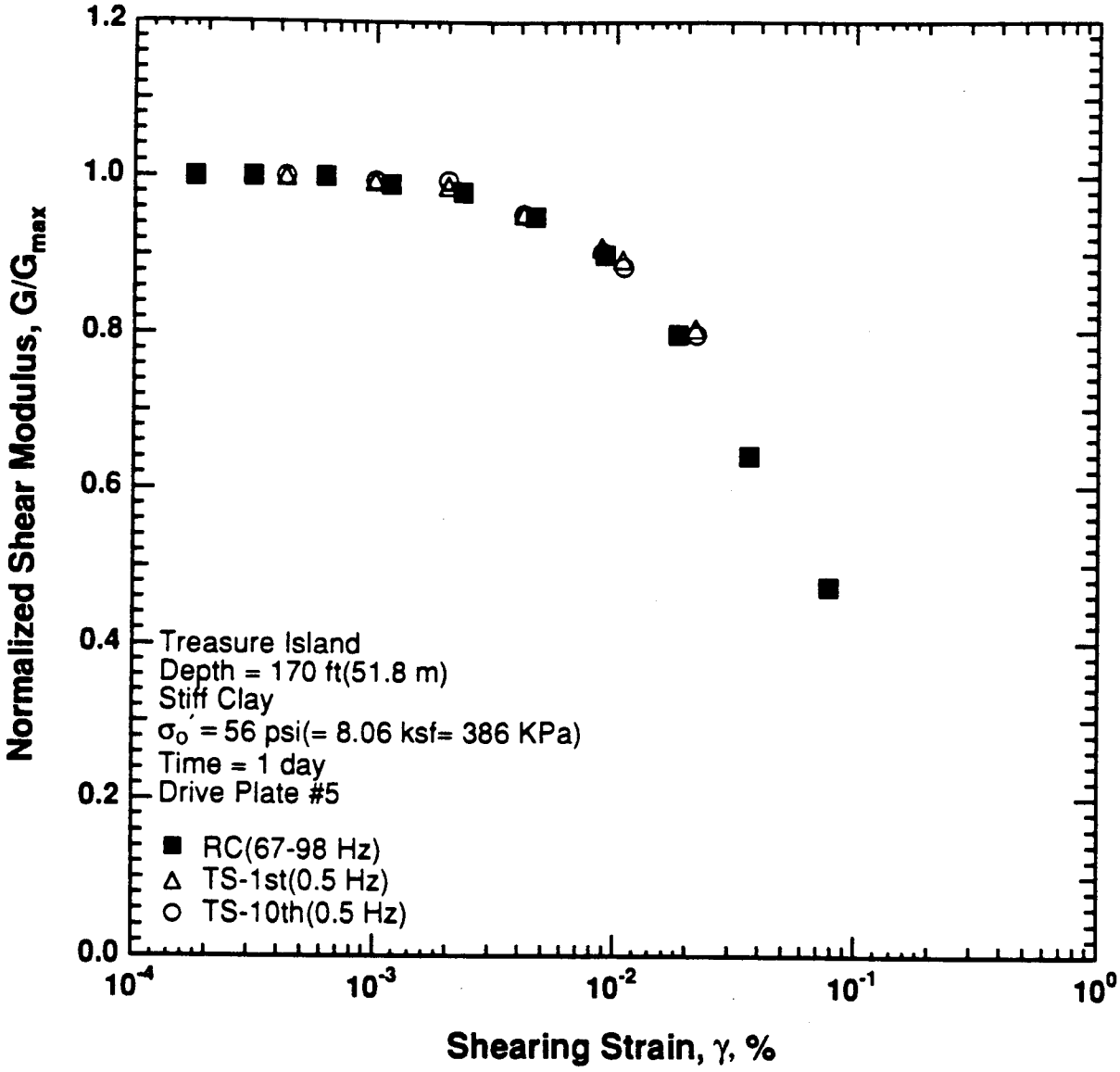

Figure 8.B.1.H-8
Variation in normalized shear modulus with shearing strain at an effective confining pressure of 56 psi (8.06 ksf, 386 kPa) from RCTS tests of sample T7.

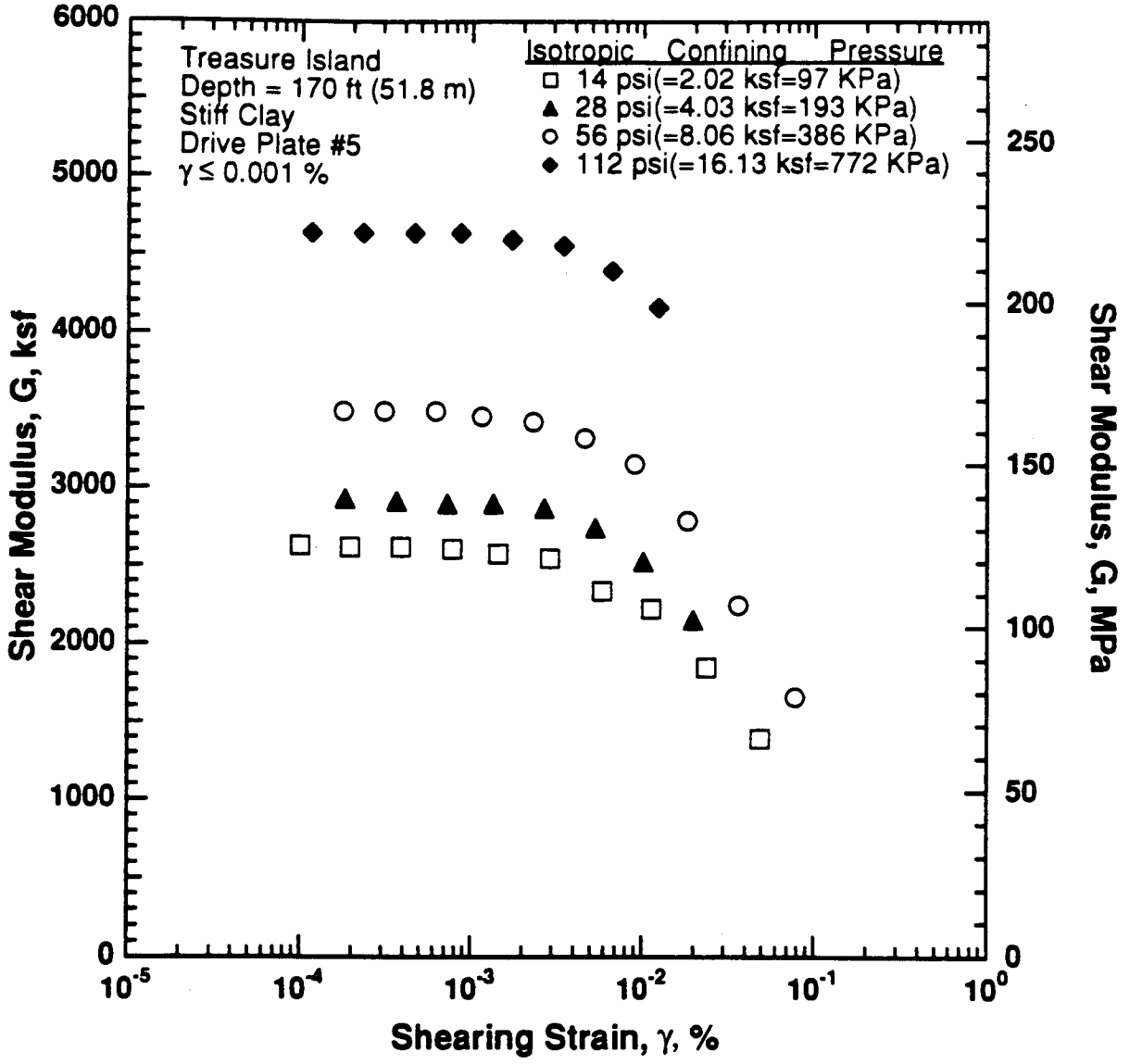

Figure 8.B.1.H-9
Variation in shear modulus with shearing strain and effective confining pressure from resonant column tests of sample T7.

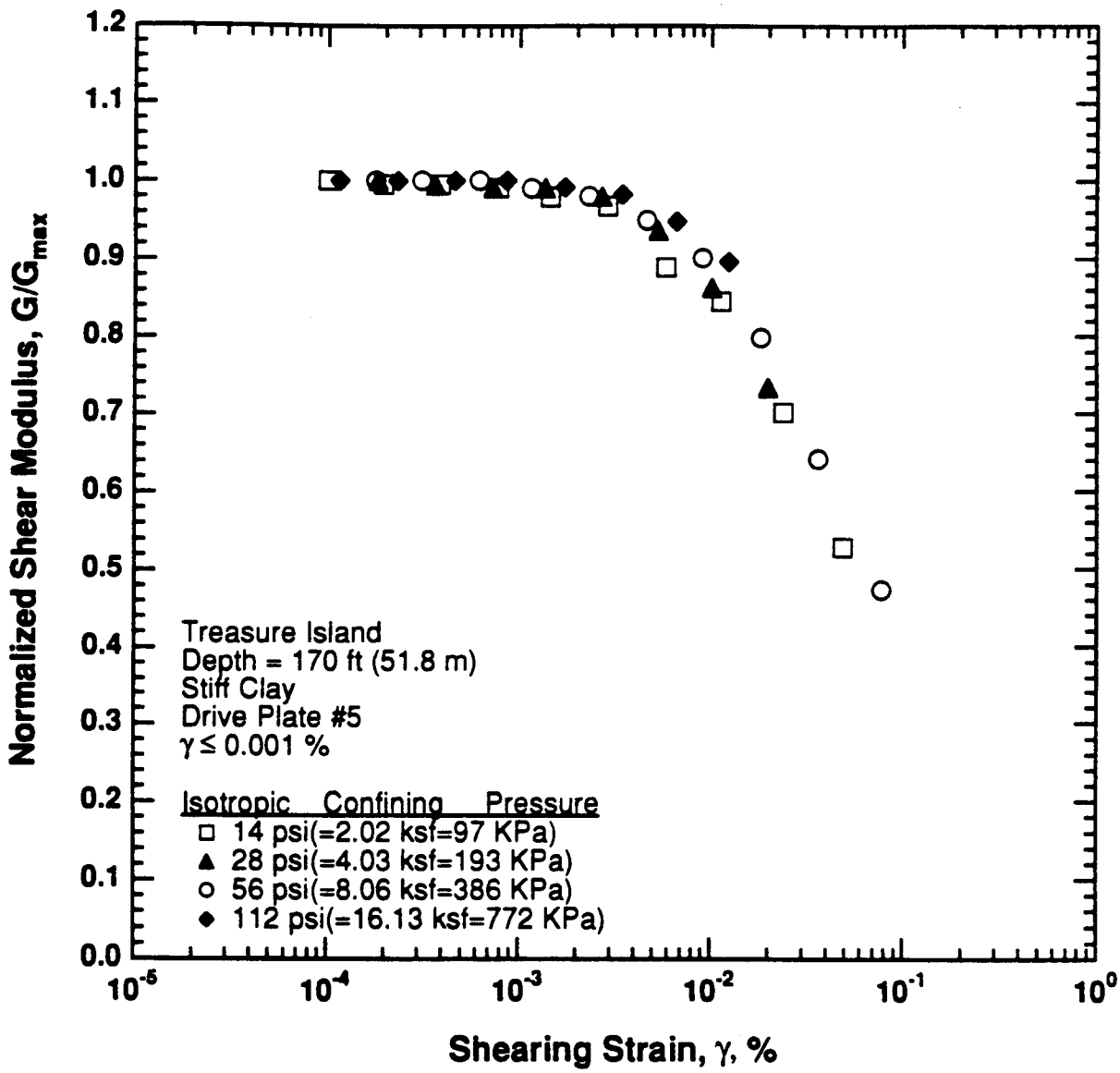

Figure 8.B.1.H-10
Comparison of the variation in normalized shear modulus with shearing strain and effective confining pressure from resonant column tests of sample T7.

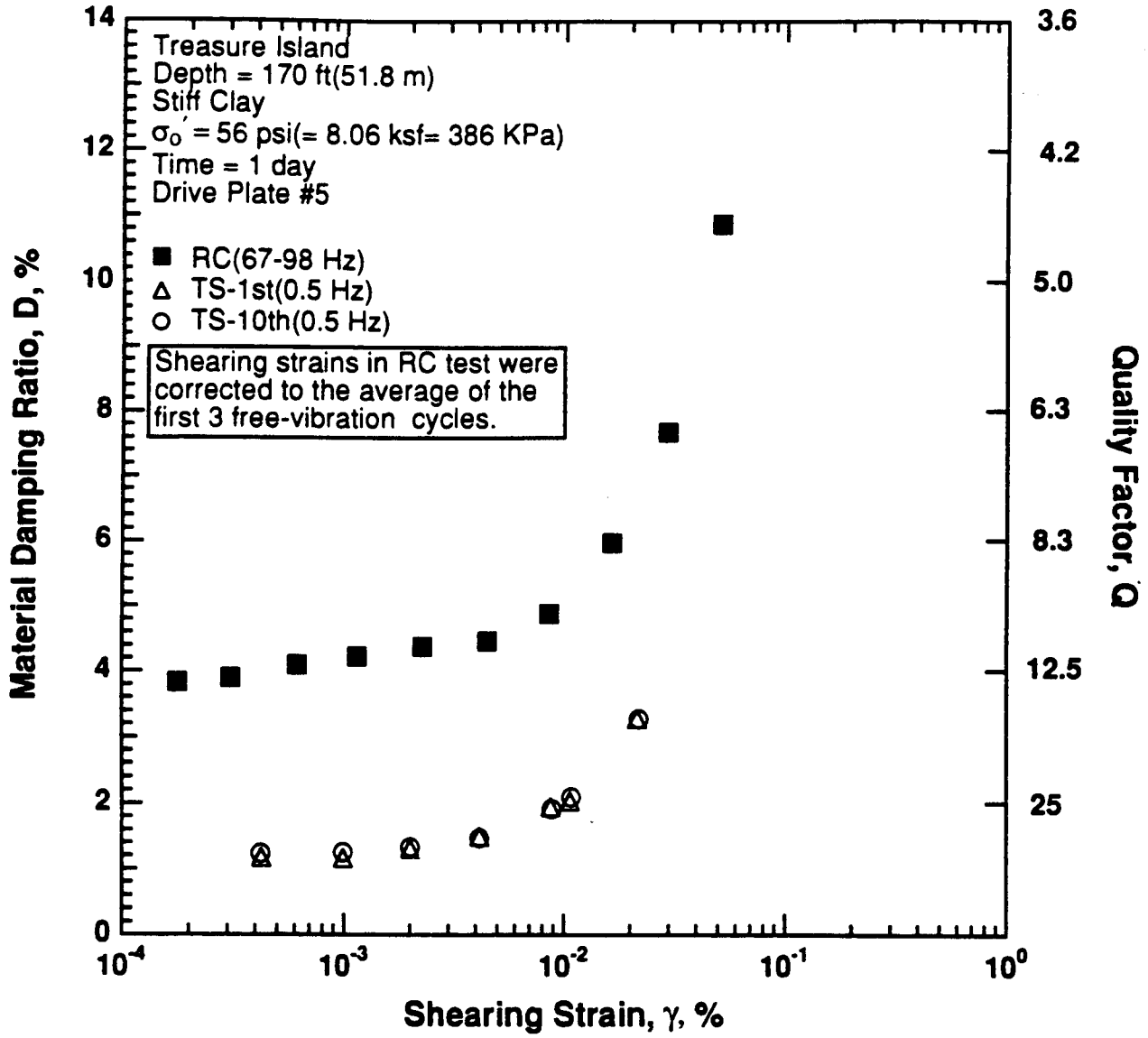

Figure 8.B.1.H-11
Variation in material damping ratio with shearing strain at an effective confining pressure of 56 psi (8.06 ksf, 386 kPa) from RCTS tests of sample T7.

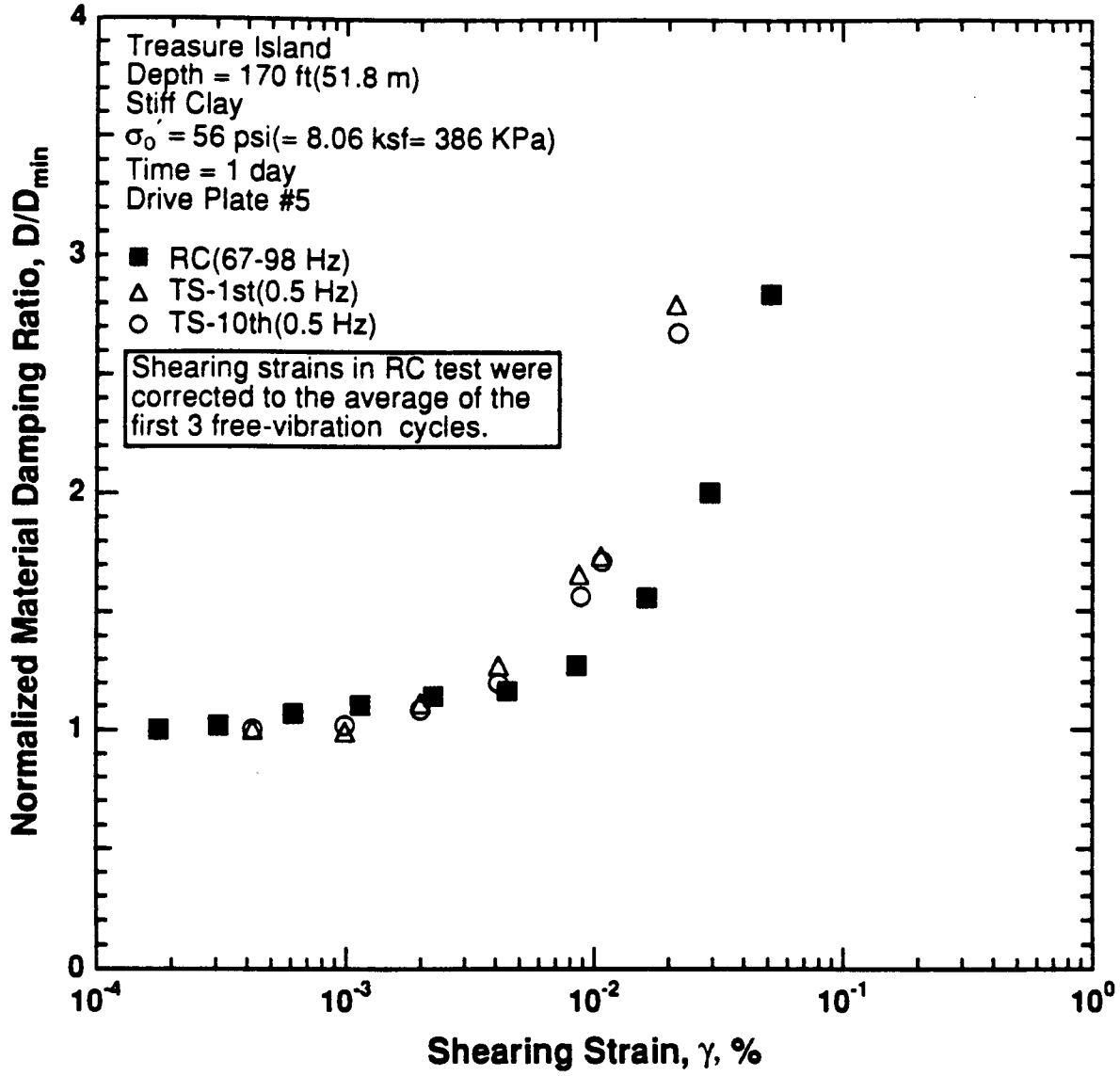

Figure 8.B.1.H-12
Variation in normalized material damping ratio with shearing strain at an effective confining pressure of 56 psi (8.06 ksf, 386 kPa) from RCTS tests of sample T7.

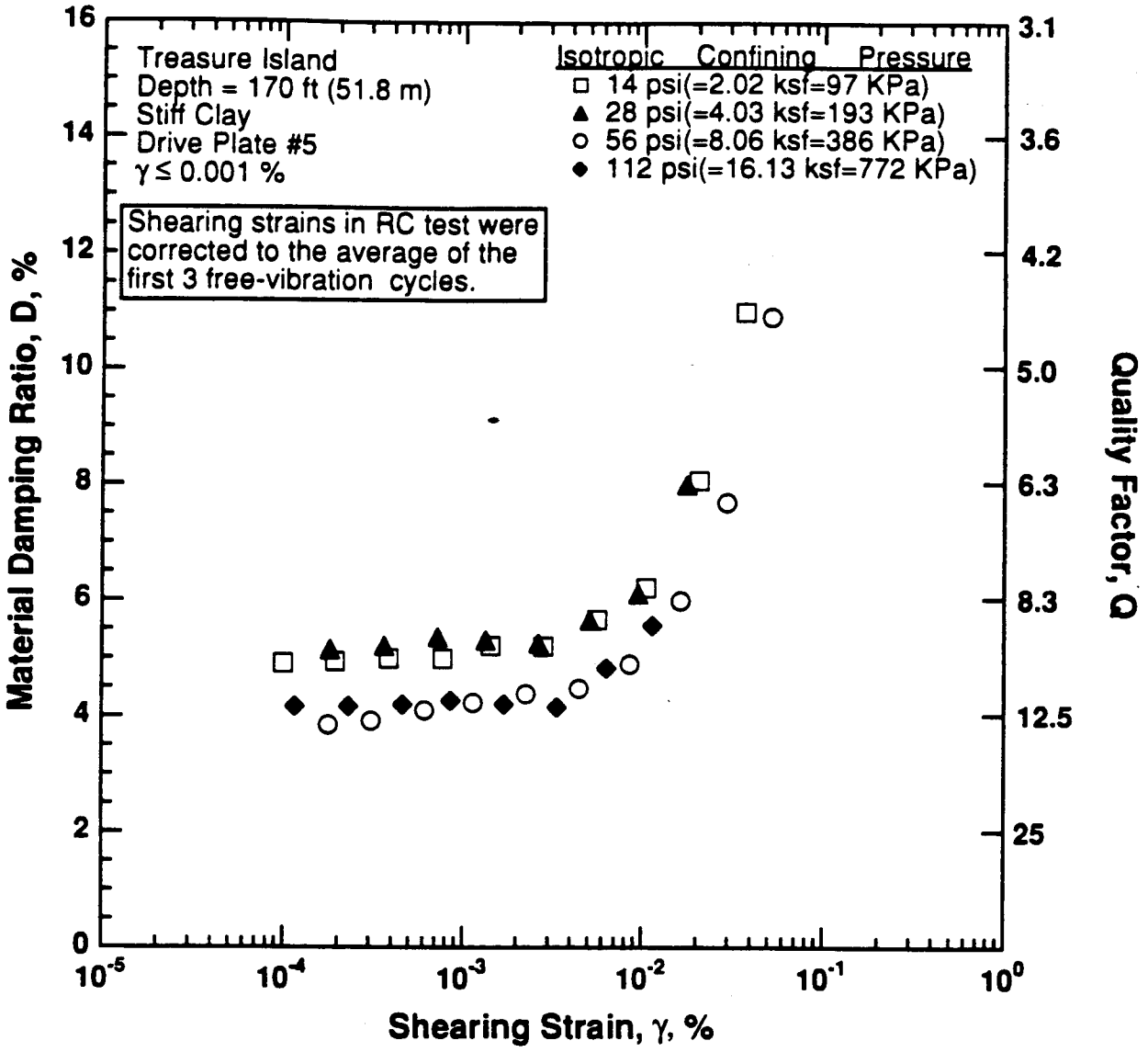

Figure 8.B.1.H-13
Variation in material damping ratio with shearing strain and effective confining pressure from resonant column tests of sample T7.

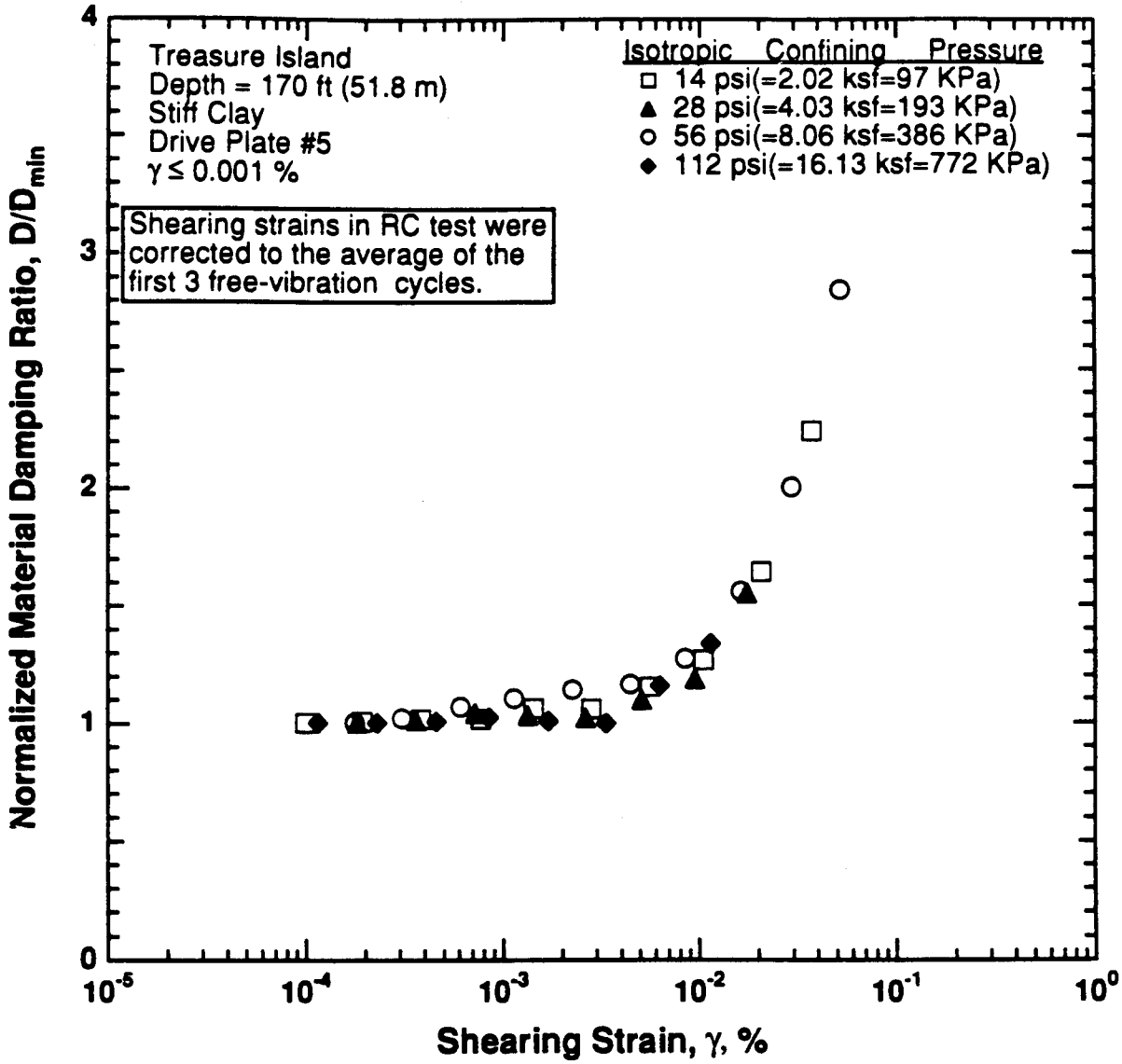

Figure 8.B.1.H-14
Comparison of the variation in normalized material damping ratio with shearing strain and effective confining pressure from resonant column tests of sample T7.

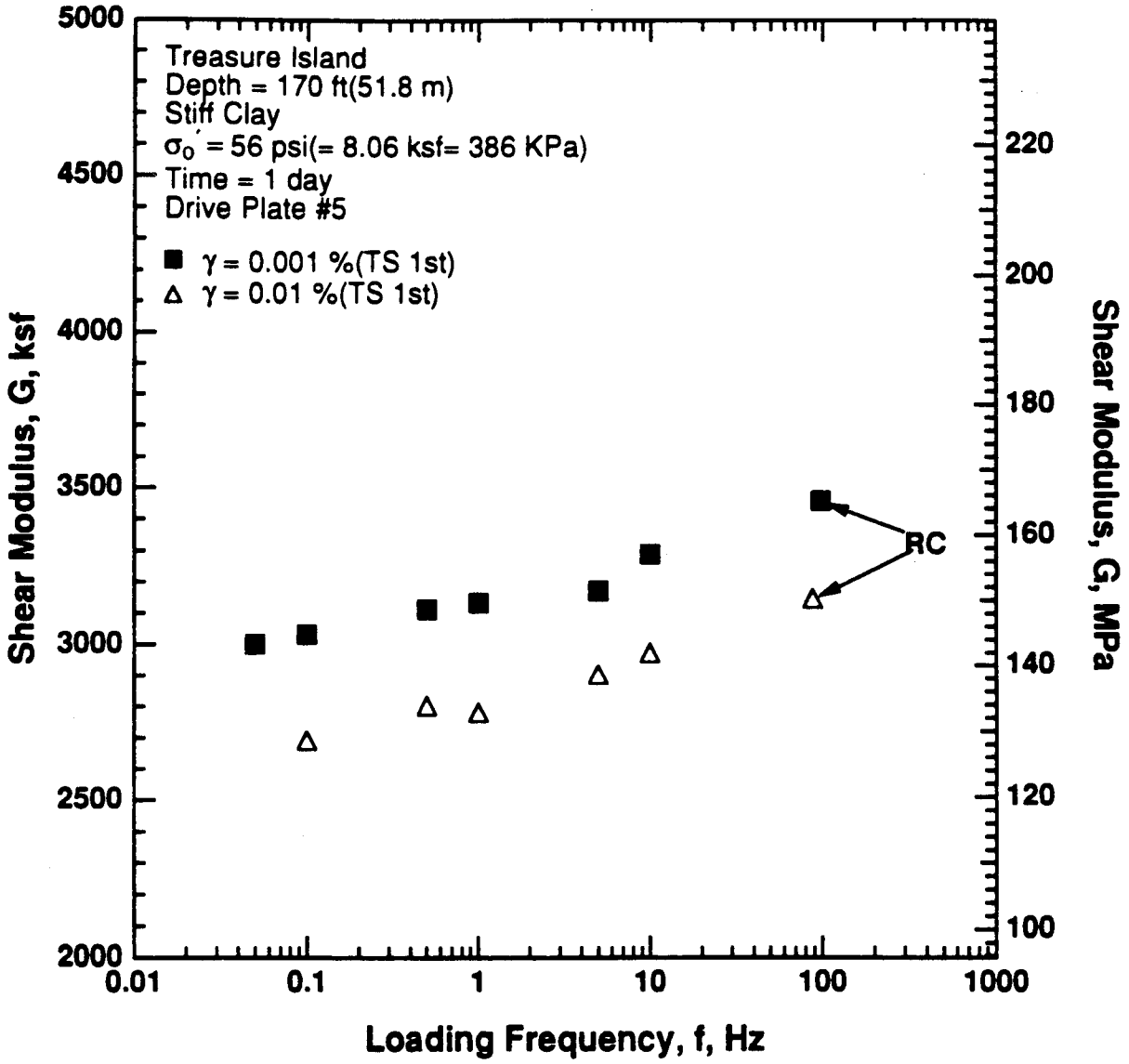

Figure 8.B.1.H-15
Variation in shear modulus with loading frequency and shearing strain at an effective confining pressure of 56 psi (8.06 psf, 386 kPa) from RCTS tests of sample T7.

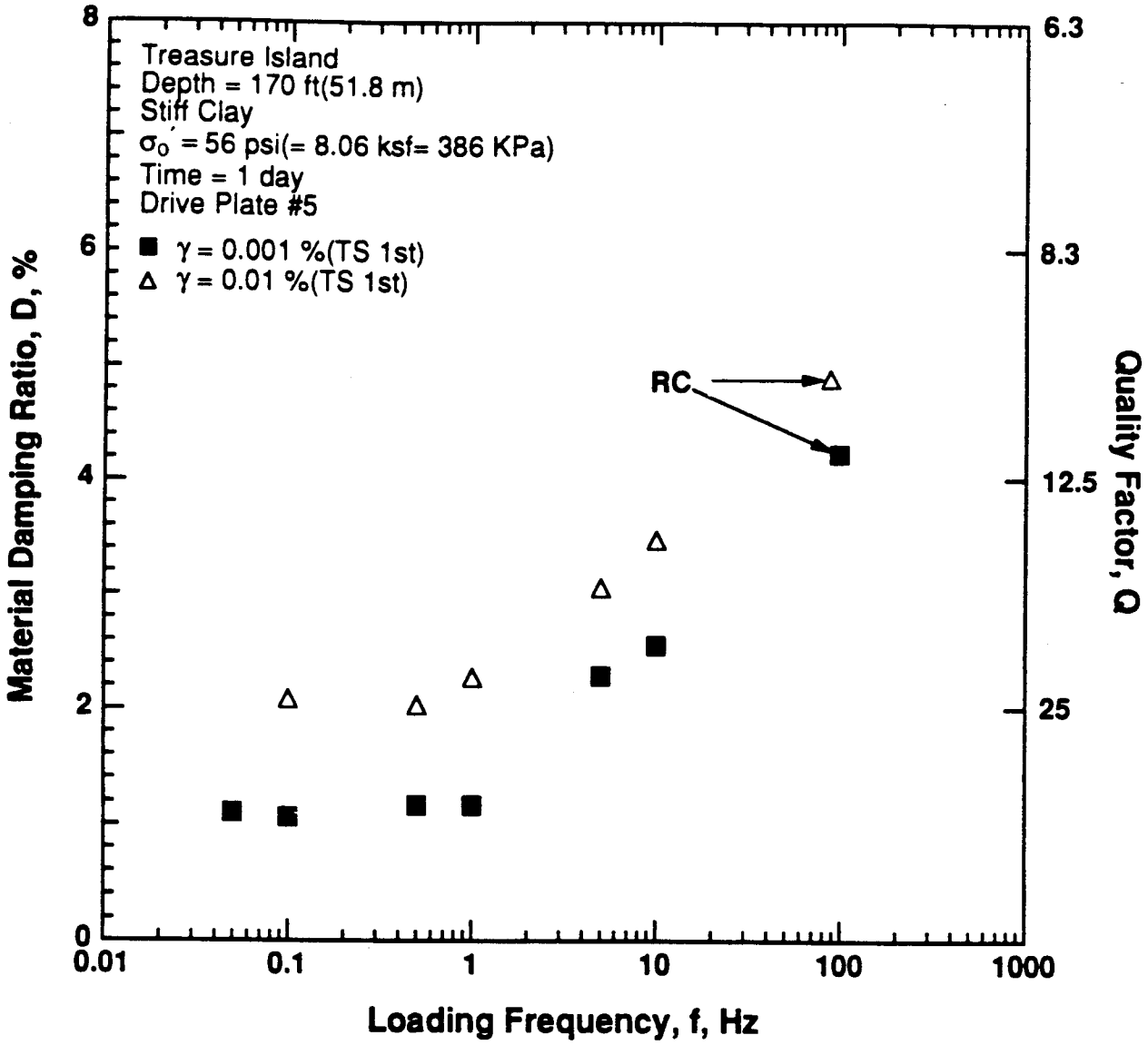

Figure 8.B.1.H-16
Variation in material damping ratio with loading frequency and shearing strain at an effective confining pressure of 56 psi (8.06 psf, 386 kPa) from RCTS tests of sample T7.

APPENDIX 8.B.1.I
DYNAMIC TESTS OF SAMPLE T8, DEPTH = 232 FT (70.7 M)

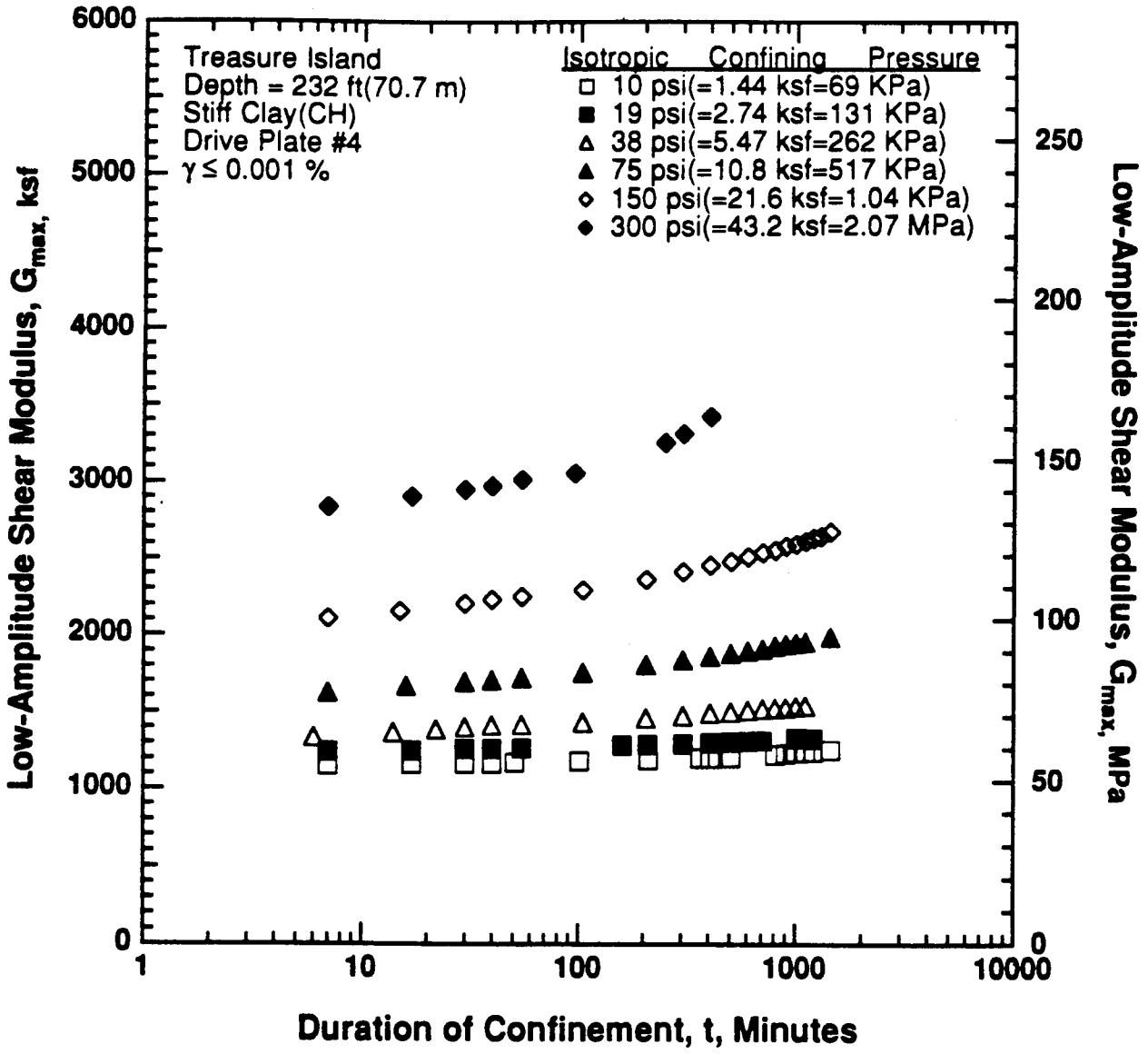

Figure 8.B.1.I-1
Variation in low-amplitude shear modulus with magnitude and duration of isotropic confining pressure from resonant column tests of sample T8.

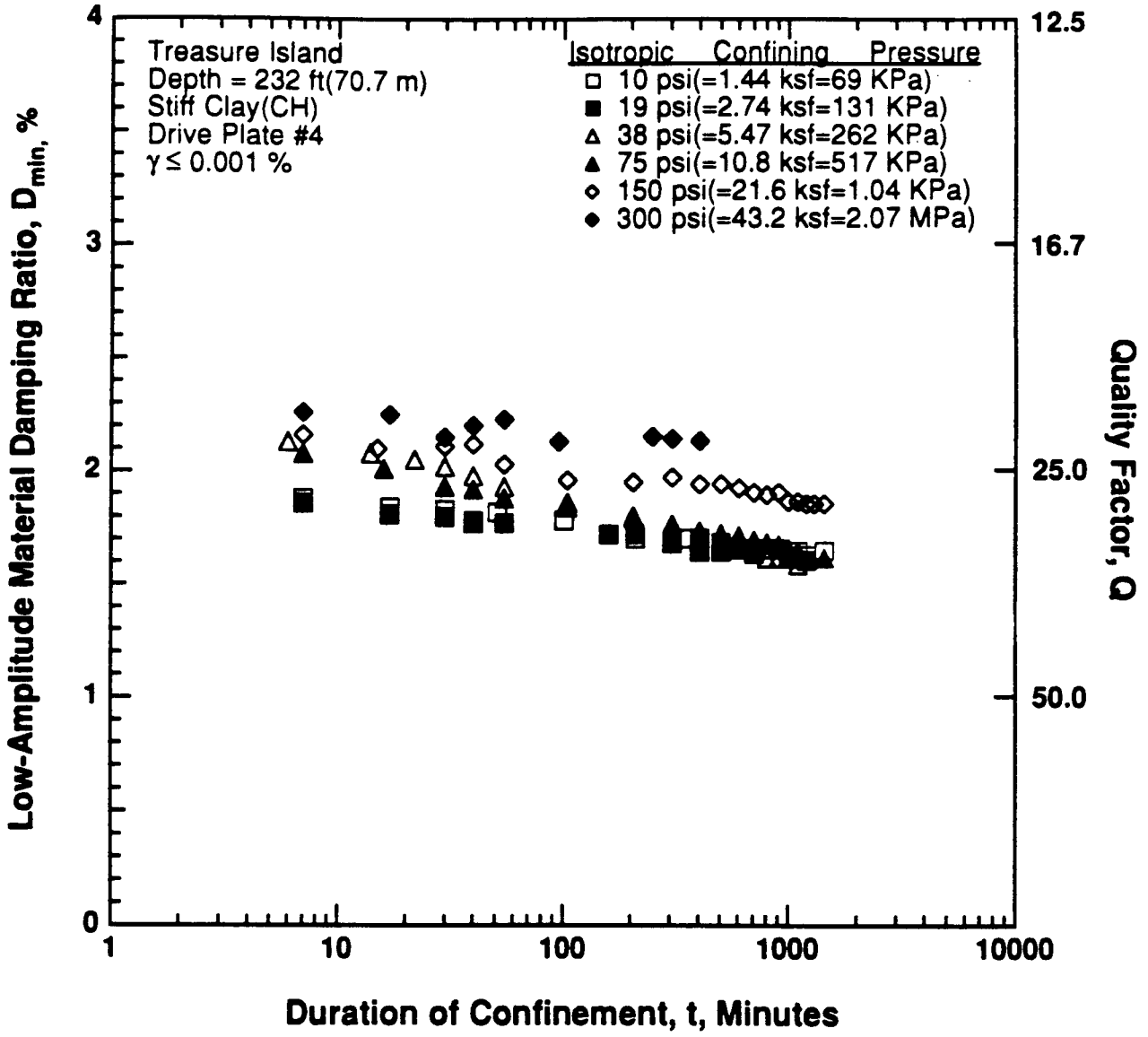

Figure 8.B.1.I-2
Variation in low-amplitude material damping ratio with magnitude and duration of isotropic confining pressure from resonant column tests of sample T8.

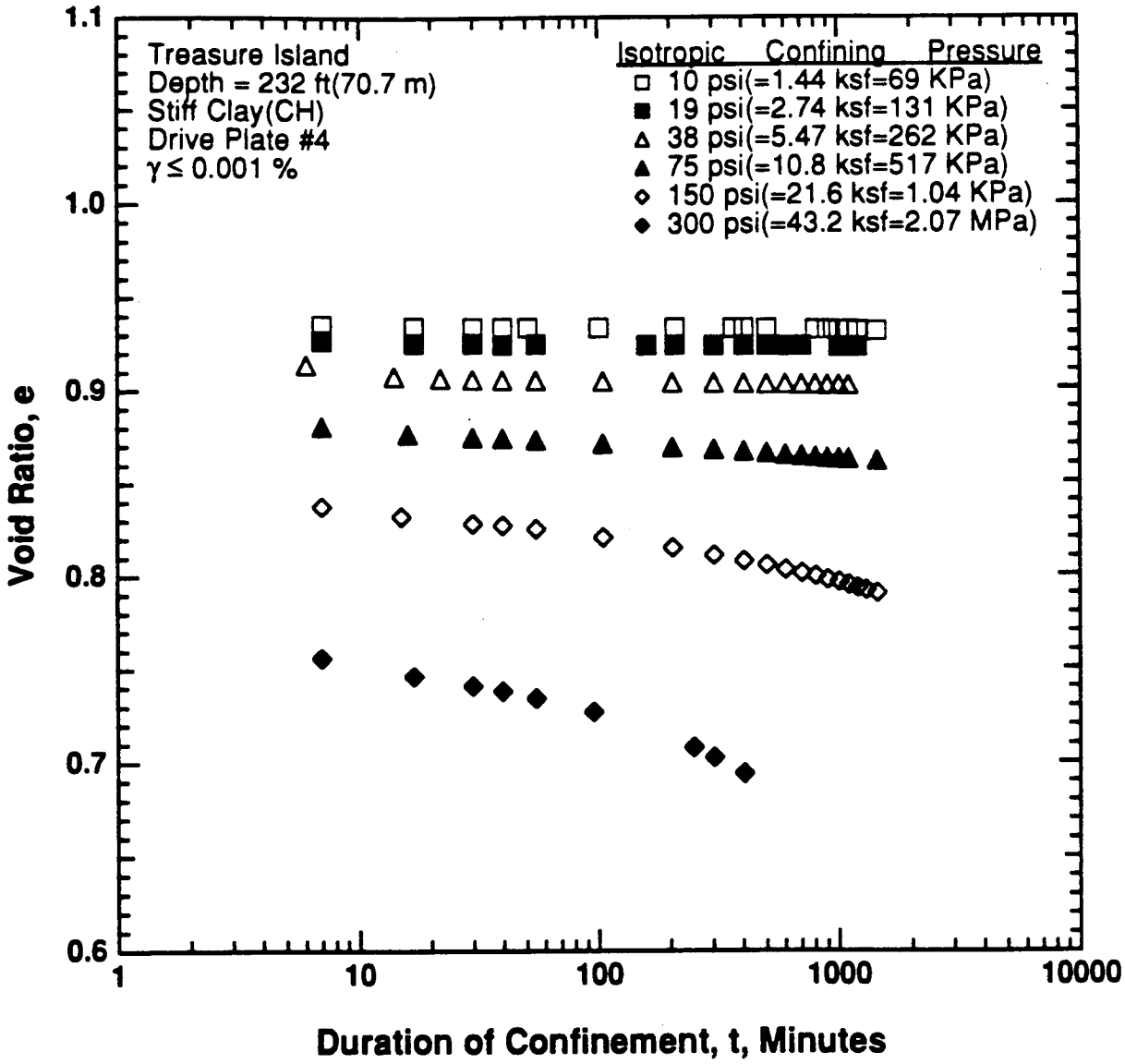

Figure 8.B.1.I-3
Variation in void ratio with magnitude and duration of isotropic confining pressure from resonant column tests of sample T8.

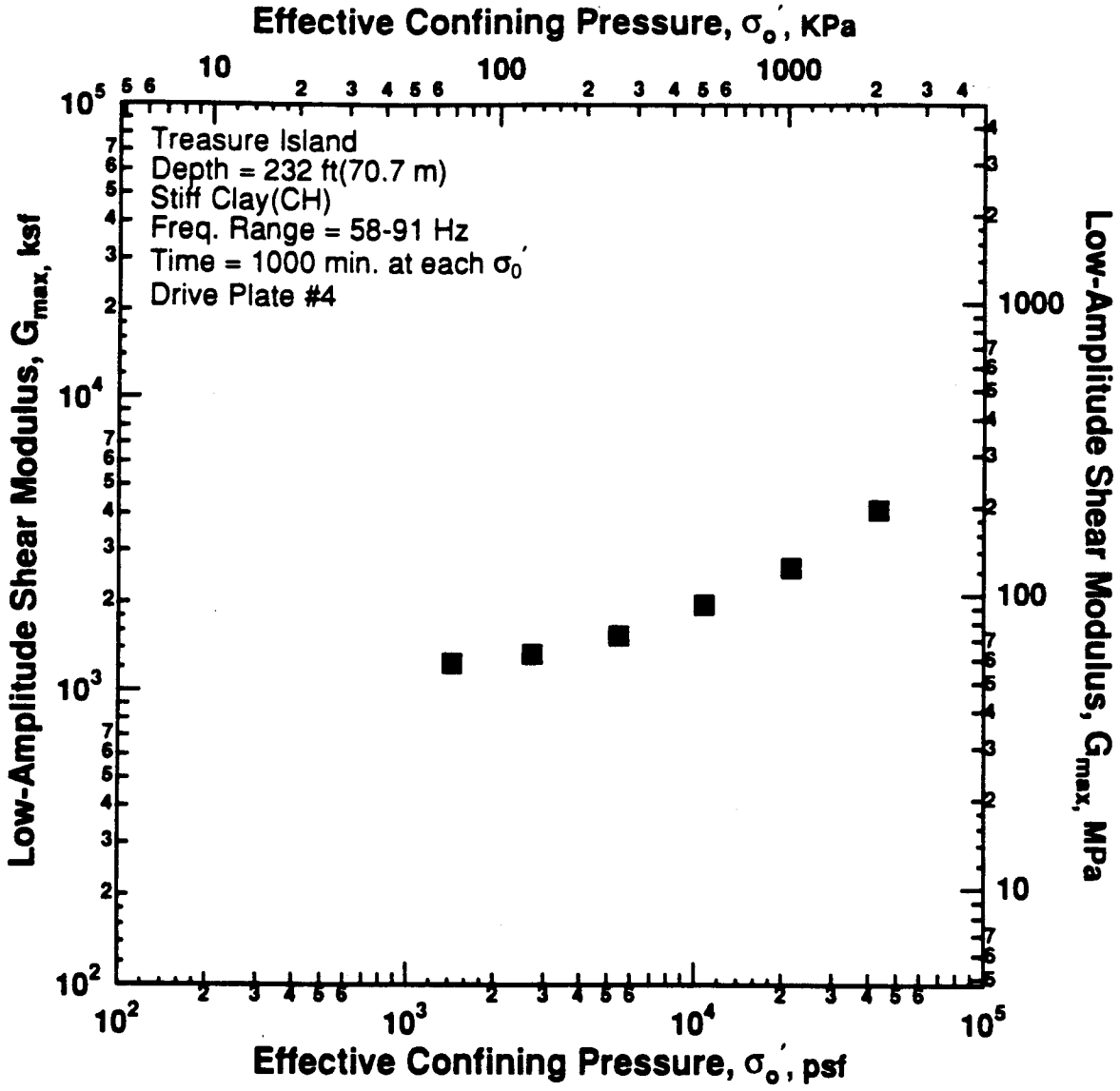

Figure 8.B.1.I-4
Variation in low-amplitude shear modulus with effective confining pressure from resonant column tests of sample T8.

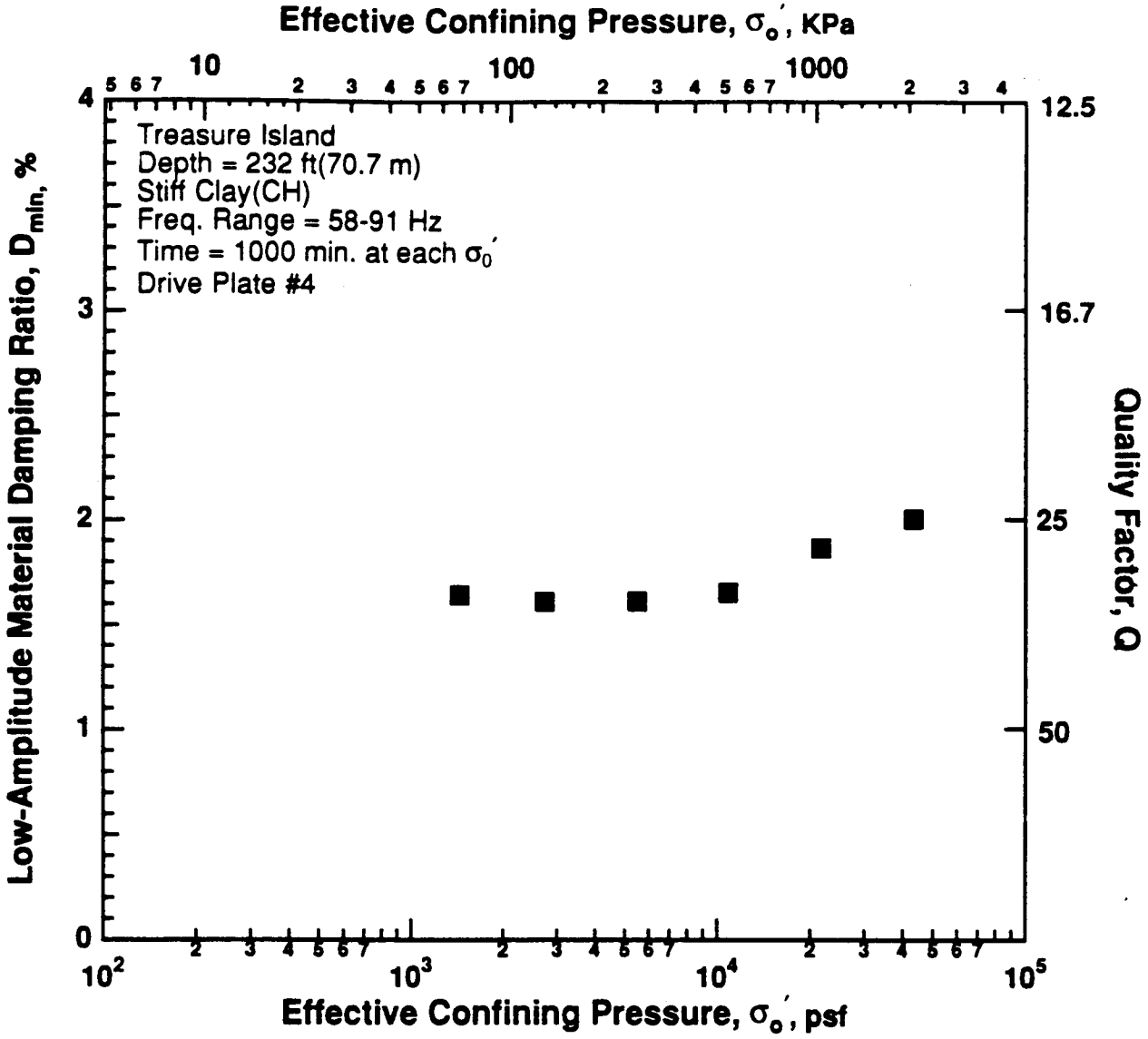

Figure 8.B.1.I-5
Variation in low-amplitude material damping ratio with effective confining pressure from resonant column tests of sample T8.

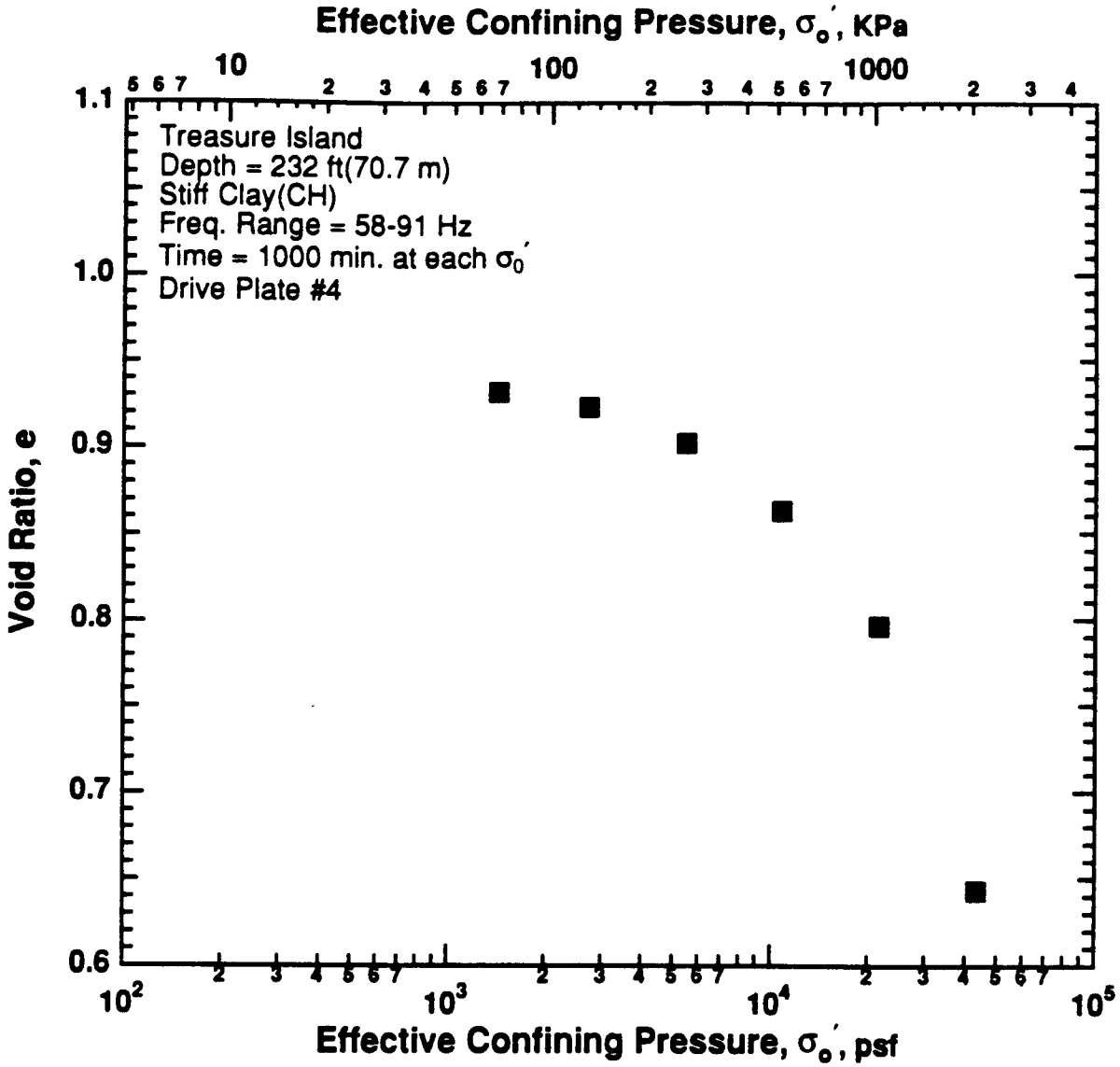

Figure 8.B.1.I-6
Variation in void ratio with effective confining pressure from resonant column tests of sample T8.

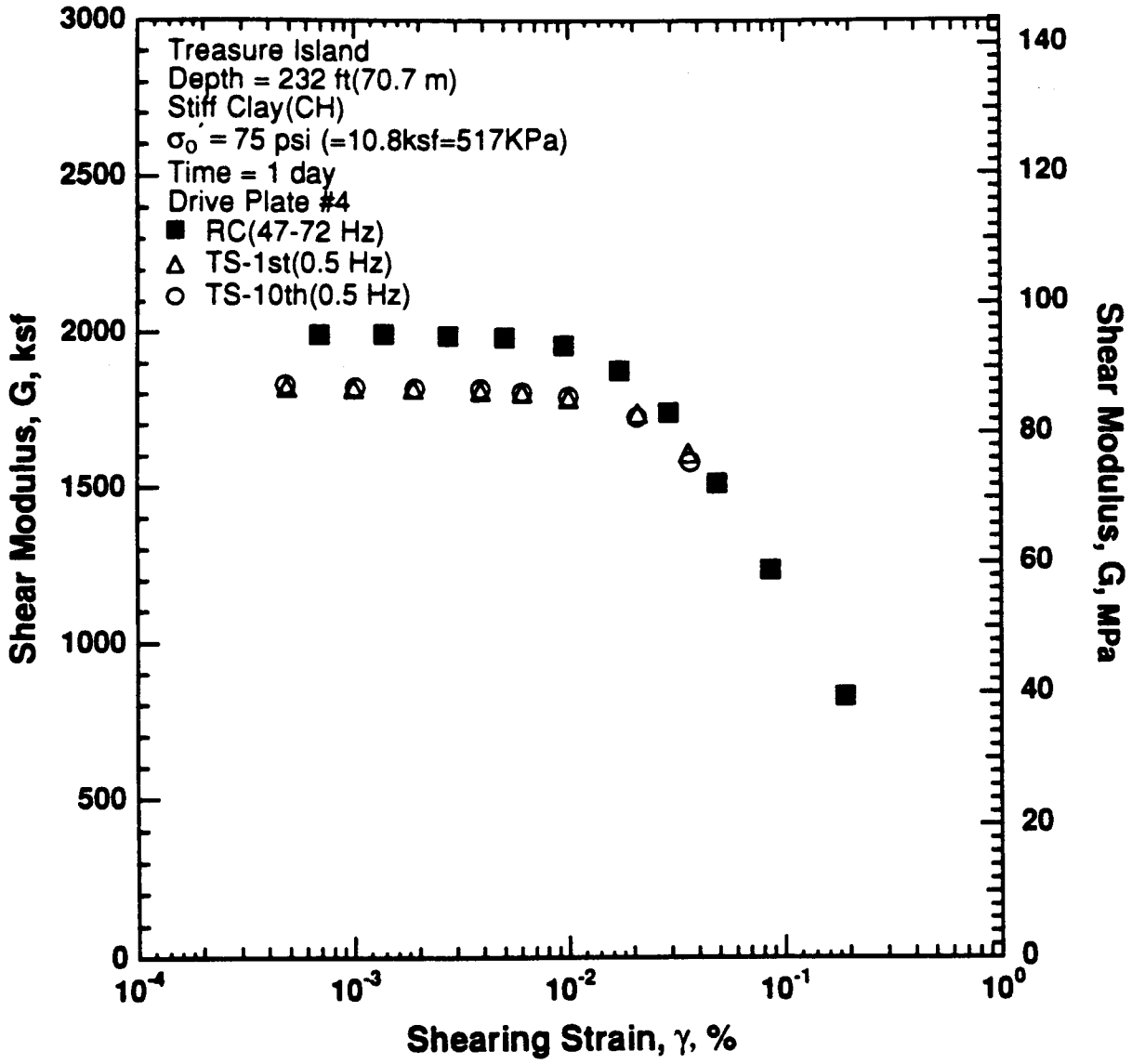

Figure 8.B.1.I-7
Variation in shear modulus with shearing strain at an effective confining pressure of 75 psi (10.8 ksf, 517 kPa) from RCTS tests of sample T8.

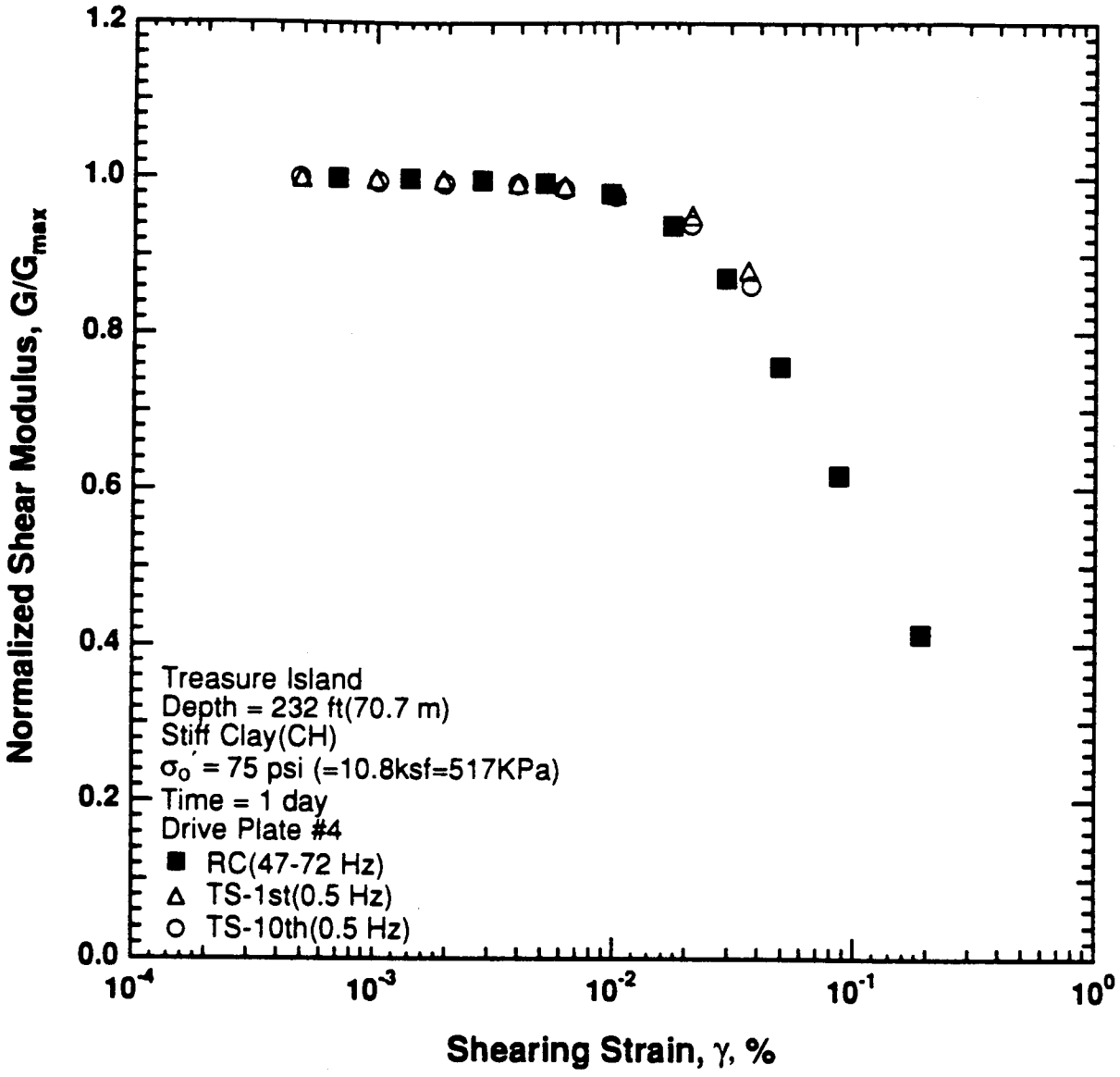

Figure 8.B.1.I-8
Variation in normalized shear modulus with shearing strain at an effective confining pressure of 75 psi (10.8 ksf, 517 kPa) from RCTS tests of sample T8.

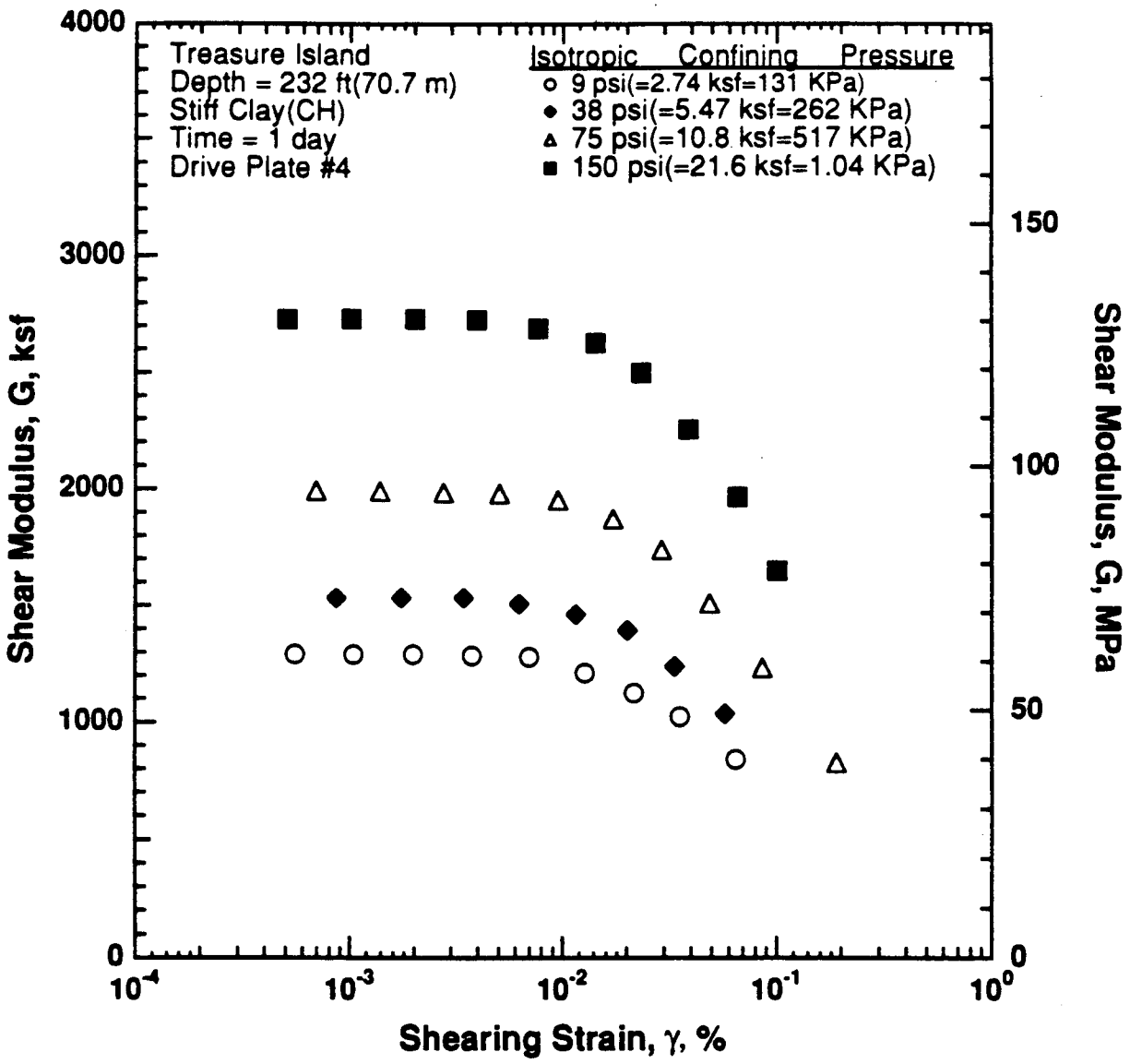

Figure 8.B.1.I-9
Variation in shear modulus with shearing strain and effective confining pressure from resonant column tests of sample T8.

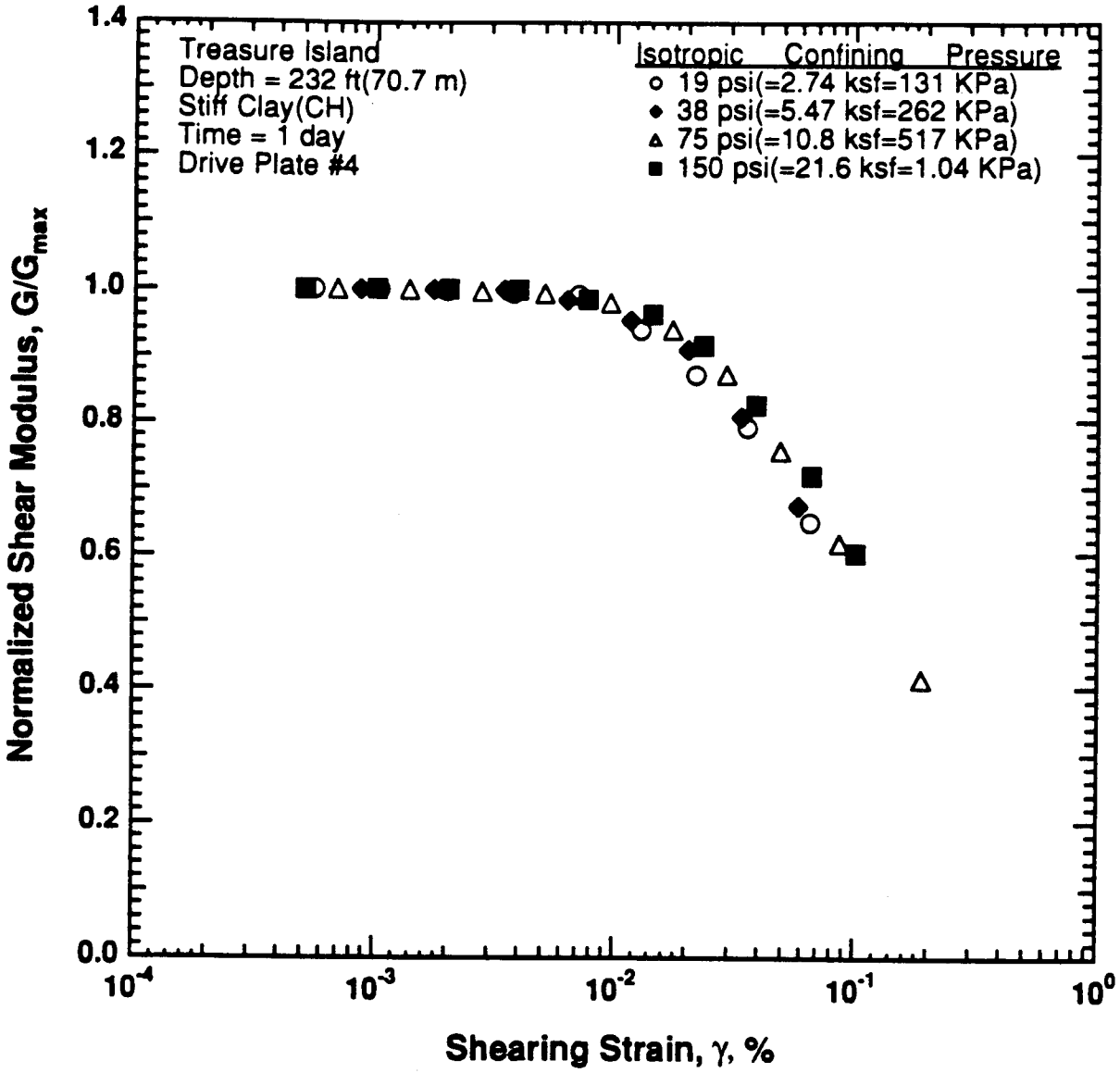

Figure 8.B.1.I-10
Comparison of the variation in normalized shear modulus with shearing strain and effective confining pressure from resonant column tests of sample T8.

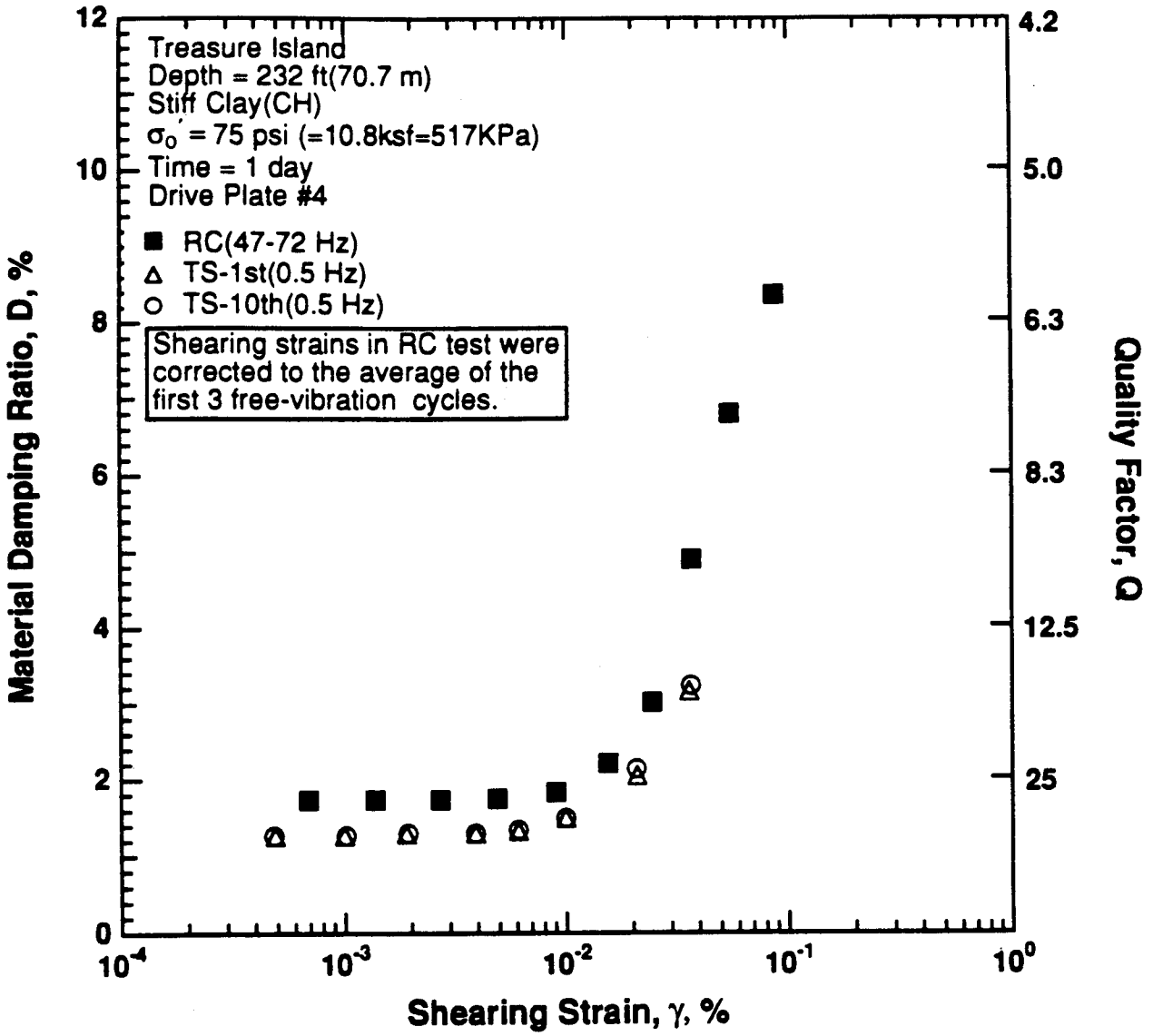

Figure 8.B.1.I-11
Variation in material damping ratio with shearing strain at an effective confining pressure of 75 psi (10.8 ksf, 517 kPa) from RCTS tests of sample T8.

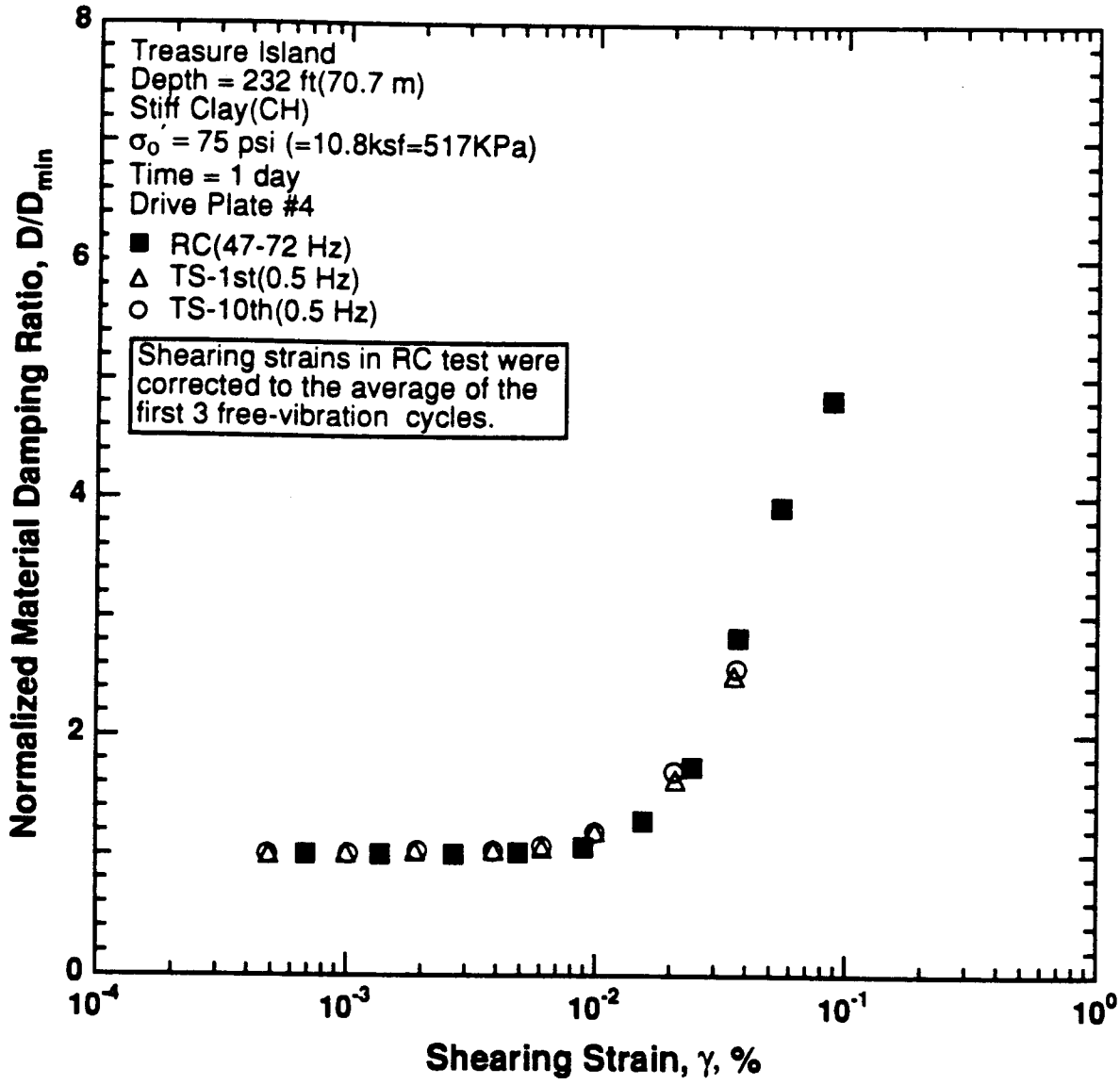

Figure 8.B.1.I-12
Variation in normalized material damping ratio with shearing strain at an effective confining pressure of 75 psi (10.8 ksf, 517 kPa) from RCTS tests of sample T8.

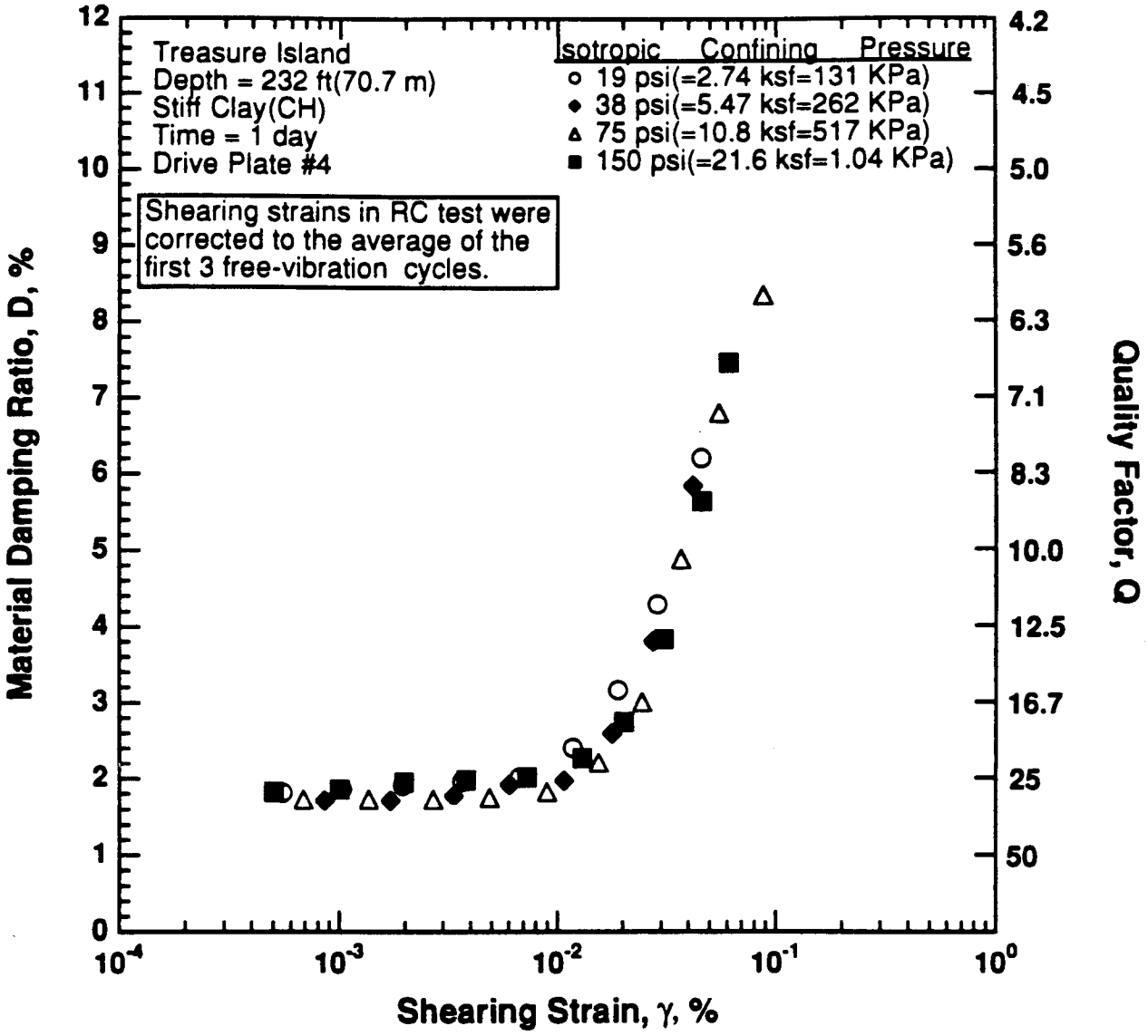

Figure 8.B.1.I-13
Variation in material damping ratio with shearing strain and effective confining pressure from resonant column tests of sample T8.

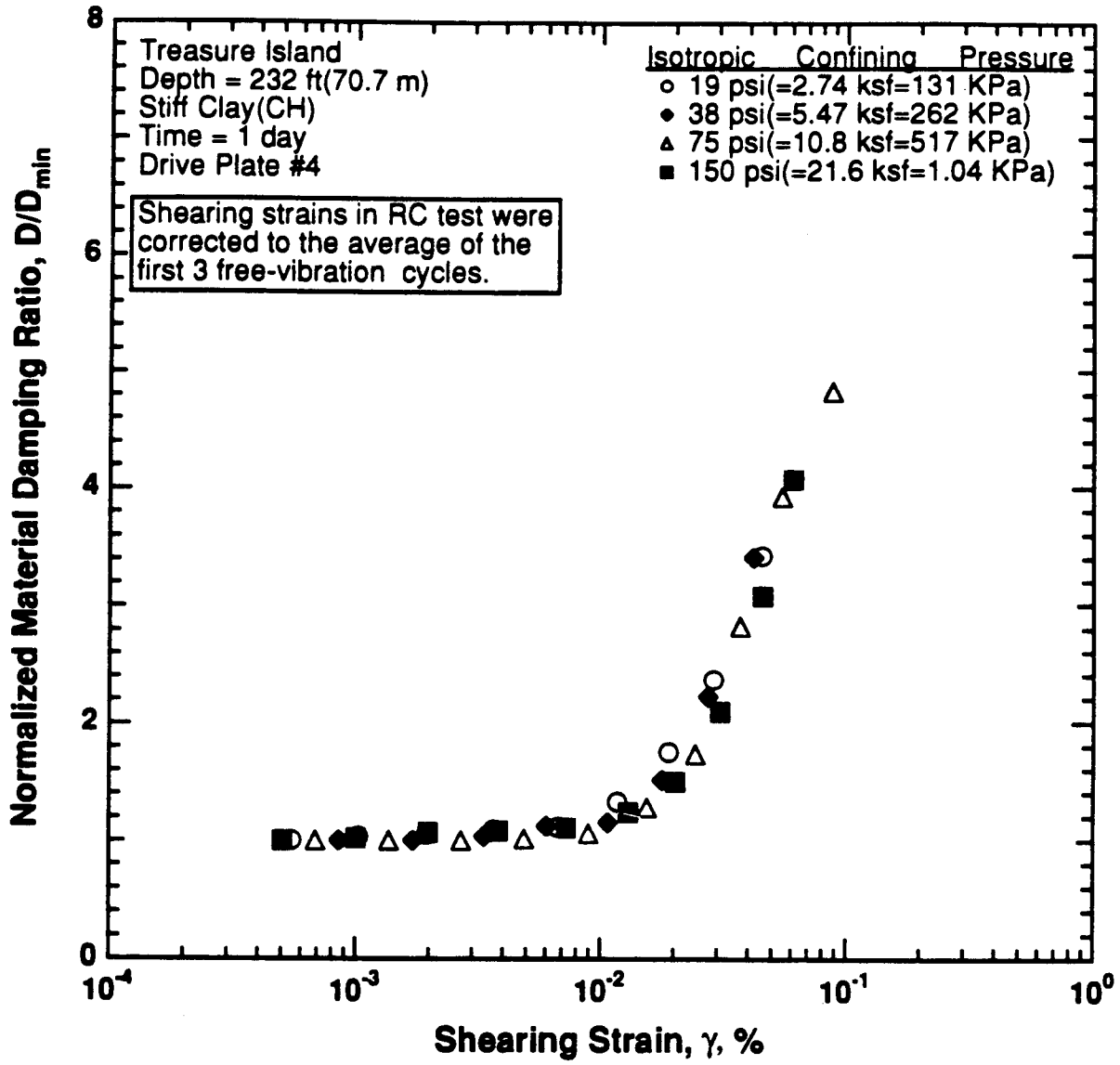

Figure 8.B.1.I-14
Comparison of the variation in normalized material damping ratio with shearing strain and effective confining pressure from resonant column tests of sample T8.

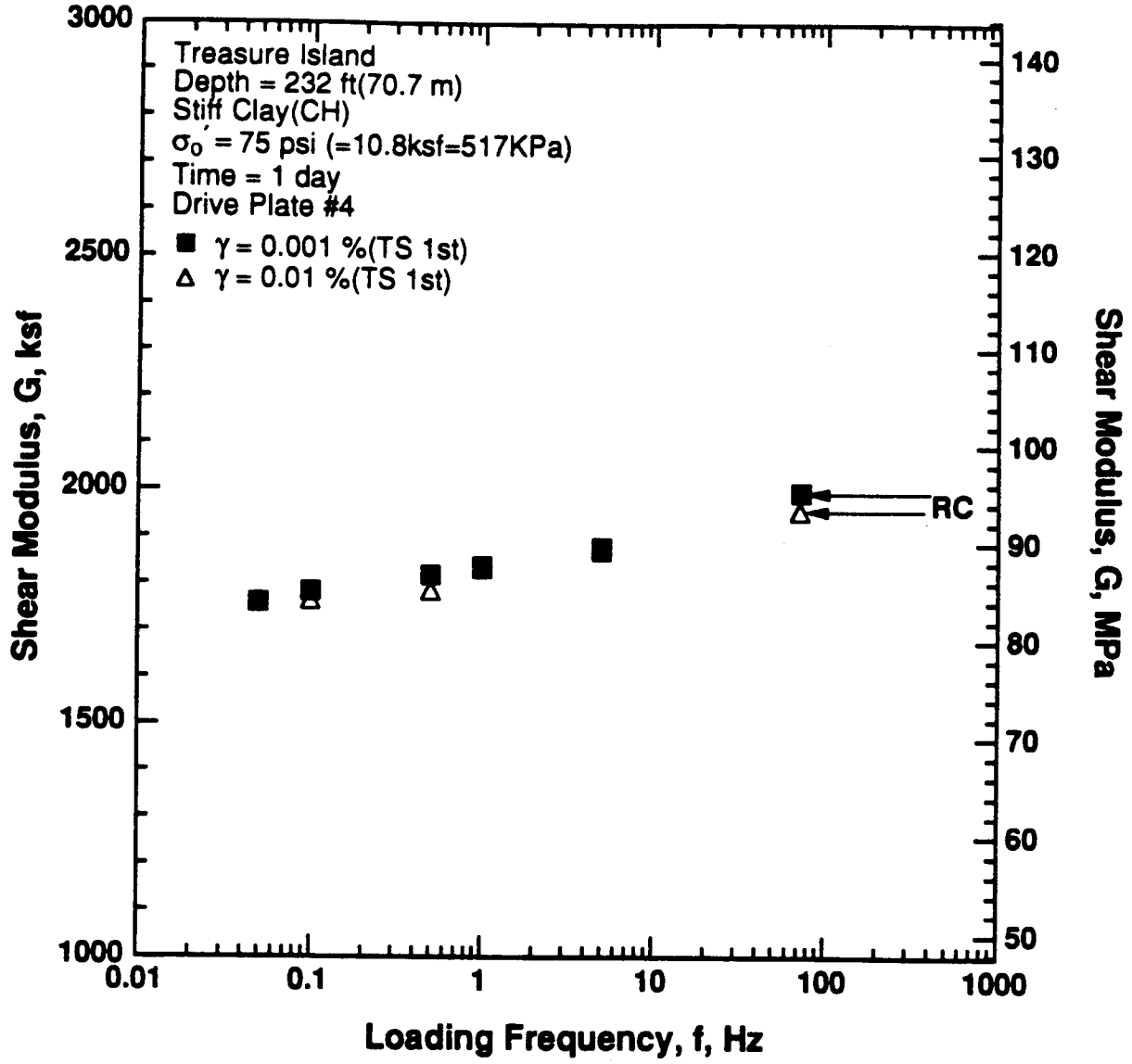

Figure 8.B.1.I-15
Variation in shear modulus with loading frequency and shearing strain at an effective confining pressure of 75 psi (10.8 ksf, 517 kPa) from RCTS tests of sample T8.

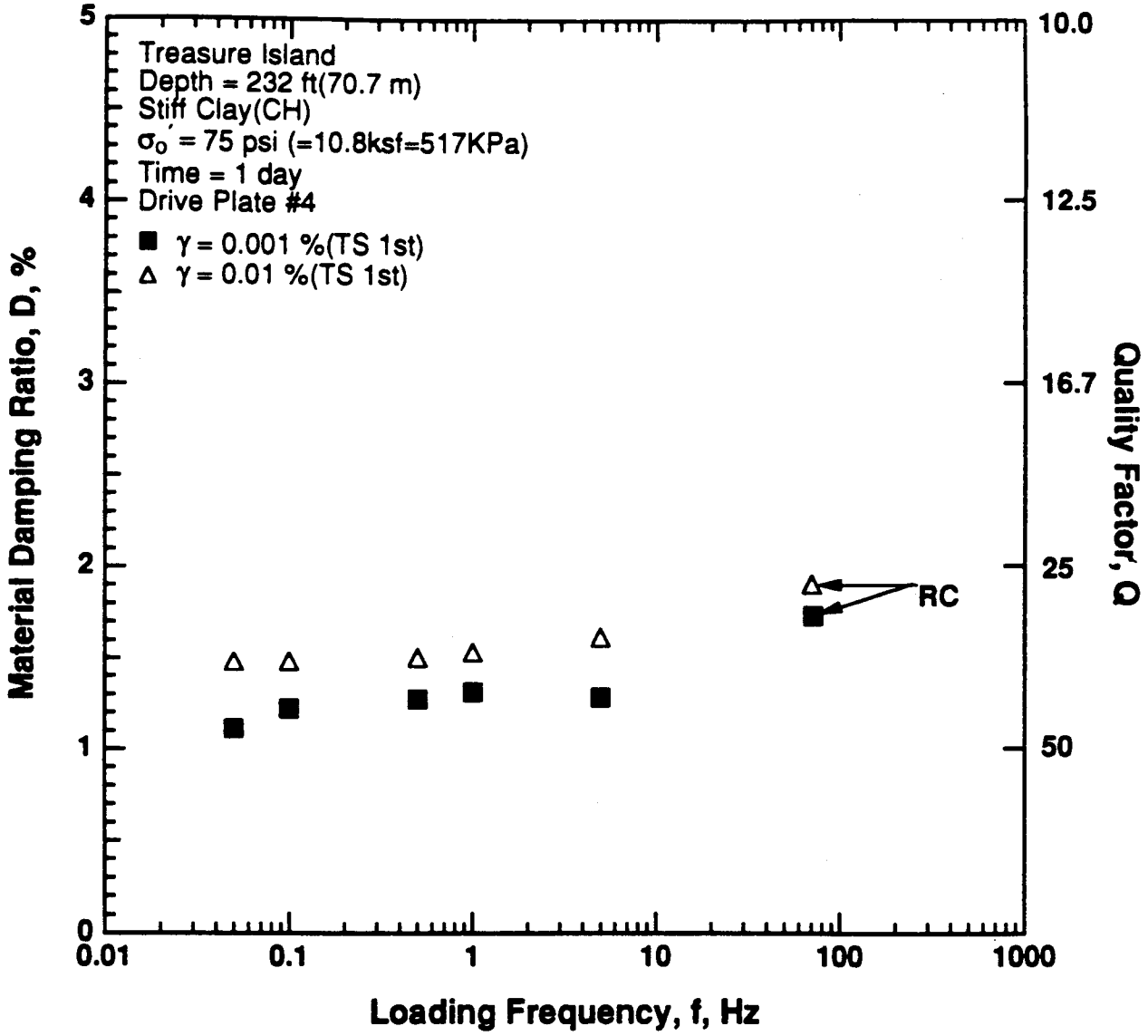

Figure 8.B.1.I-16
Variation in material damping ratio with loading frequency and shearing strain at an effective confining pressure of 75 psi (10.8 ksf, 517 kPa) from RCTS tests of sample T8.

APPENDIX 8.B.2
DYNAMIC PROPERTIES OF UNDISTURBED SOIL SAMPLES FROM GILROY 2, CALIFORNIA

CONTENTS

APPENDIX 8.B.2
DYNAMIC PROPERTIES OF UNDISTURBED SOIL SAMPLES FROM GILROY 2, CALIFORNIA

8.B.2.1 Introduction

An investigation of the dynamic properties in shear of undistributed soil samples from the Gilroy 2 Array in California was conducted. This work was part of an Earthquake Ground Motion Project sponsored by the Electric Power Research Institute (EPRI) and the U.S. Department of Energy (DOE). The dynamic laboratory study was also initiated as part of an earlier EPRI study, No. 3014-14. The soil samples were obtained in late, 1990. The samples were sealed in steel Shelby tubes and transported by automobile to the University of Texas at Austin in December, 1990. Dynamic laboratory testing of the undisturbed samples performed between January, 1991 and October, 1992.

A total of 12 samples was tested. The samples were obtained from depths ranging from 10 ft (3 m) to 420 ft (128 m). Initial properties of the samples are listed in Table 8.B.2-1. The samples range from a silty sand with gravel (SM) to a lean clay (CL). Grain size distribution curves for four of the nonplastic samples are given in Figure 8.B.2-1.

To minimize disturbance effects, eight samples were extruded from the 3-in. (7.6 cm) diameter sampling tubes and hand trimmed to the final specimen dimensions. Three samples were tested "as extruded," without hand trimming due to difficulty in trimming. These three samples were very stiff, and hydrostone was used to attach the samples to the end platens. One reconstituted sample was tested because no intact sample could be extruded.

The dimensions of the hand-carved samples were nominally either 2 in. (5.1 cm) in diameter and 4 in. (10.2 cm) in height or 1.5 in. (3.8 cm) in diameter and 3 in. (7.6 cm) in height. The smaller of the two specimen sizes was used to obtain the larger dynamic strains in testing. With the exception of the three stiff samples, no significant problems were encountered in preparation and testing of the hand-carved specimens.

8.B.2.2 Dynamic Laboratory Tests

Resonant column and torsional shear (RCTS) equipment was used to investigate the dynamic characteristics of the intact and a reconstituted Gilroy 2 samples. This equipment is described in detail in Appendix 8.B.2.A. The dynamic characteristics of concern are the shear modulus, G, and the material damping ratio in shear, D. These parameters were evaluated to determine the influence on them of the following variables:

1. magnitude of isotropic state of stress. Four to six isotropic pressures were used which ranged from below to above the estimated in situ mean effective stress.
2. time of confinement at each isotropic state of stress. Confinement times at each pressure ranged from 1 to about 3 days.
3. shearing strain amplitude. Strains ranged from the small-strain range, less than 0.001%, to rather large strain amplitudes, strains slightly above 0.2%.
4. numbers of cycles of loading. One to ten cycles of loading were used in the torsional shear test followed by 500 to 1000 cycles in the resonant column test.
5. excitation frequency. Frequencies ranging from 0.1 Hz to about 10 Hz were used in the torsional shear test while the frequency associated with resonance in the resonant column test varied with soil stiffness and ranged from between 20 Hz to about 370 Hz.

Table 8.B.2-1
Initial Properties of Samples Tested from Gilroy 2 Site

Sample Number	Depth ft (m)	Soil Type (Unified Soil Classification)	LL %	PI %	D_{10} mm	D_{30} mm	D_{60} mm	R_{200}[1] %	Water Content %	Total Unit Weight pcf(g/cm^3)	Void Ratio e	Dia. cm	Height cm	Specific Gravity Gs[2]	Degree of Saturation %
G1	10 (3.0)	Sandy Silty Clay (CL-ML)	29	7	-	-	-	35	26.1	117 (1.87)	0.81	5.01	8.53	2.70	86
G2									30.1	119(1.91)	0.84	4.99	10.06	2.70	96
G2-1	20 (6.1)	Lean Clay (CL)	43	23	-	-	-	14	27.0	121(1.94)	0.76	3.81	7.62	2.70	96
G3[3,4]	50 (15.2)	Poorly Graded Sand(SP)	non-plastic		0.22	0.32	0.48	98	15.8	123(1.97)	0.55	5.07	10.31	2.65	76
G4									30.8	121(1.94)	0.82	5.06	10.16	2.70	100[7]
G4-1	85 (25.9)	Elastic Silt (MH)	47	17	-	-	-	0	29.5	122(1.95)	0.78	3.80	7.62	2.70	100[7]
G5									19.8	132(2.11)	0.48	4.99	10.19	2.65	100[7]
G5-1	120 (36.6)	Sandy Silt (ML)	non-plastic		-	-	-	38	19.1	131(2.10)	0.51	3.82	7.52	2.65	100
G6[5]	170 (51.8)	Silty Sand with Gravel(SM)	non-plastic		-	0.5	2.8	87	7.9	133 (2.13)	0.34	7.38	14.96	2.65	62
G7	210 (64.0)	Sand with Silt, Gravel(SW-SM)	non-plastic		0.14	1.1	7	92	14.8	130 (2.08)	0.46	4.96	10.18	2.65	85
G8[5]	348 (106.1)	Sandy Lean Clay (CL)	35	13	-	-	-	35	23.7	127 (2.04)	0.63	6.18	12.68	2.70	100[7]
G9[5,6]	420 (128.0)	Gravelly Clay	not tested						14.0	136 (2.18)	0.41	5.97	10.40	2.70	92

1. R_{200} = Percent of soil sample by weight remaining on #200 sieve
2. Specific Gravity was assumed.
3. Reconstituted sample
4. Soil sample from 40 ft was used for classification.
5. Sample grouted with hydrostone to the end platens.
6. Stopped during testing due to leakage and Maximum Shear Modulus was estimated by extrapolation.
7. Degree of saturation slightly exceeds 100 %.

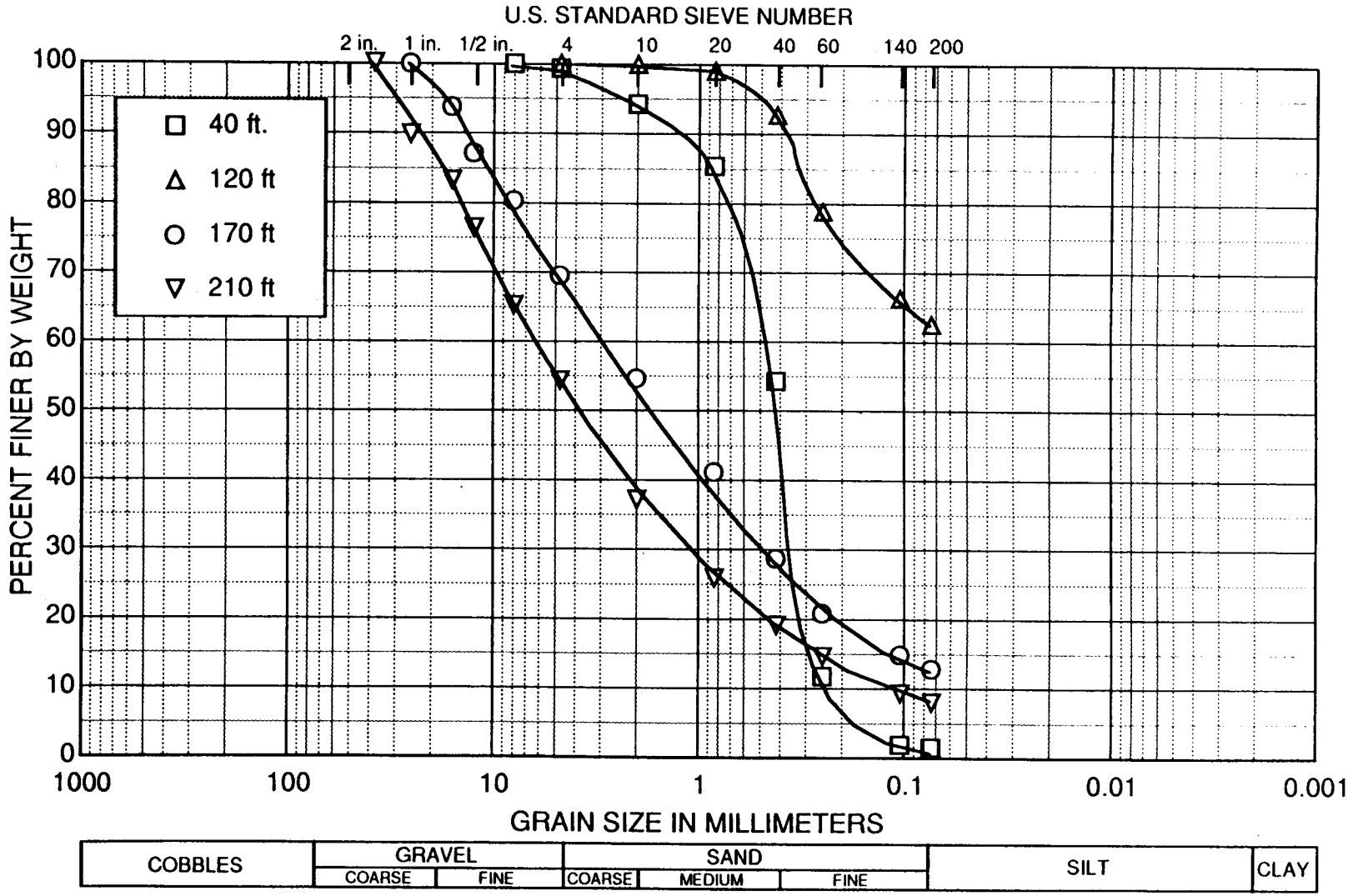

Figure 8.B.2-1
Gradation curves for Gilroy 2 samples.

8.B.2.2.1 Testing Program

Before dynamic testing was started, the in situ mean effective stress, σ_m', had to be estimated. This was done at the Gilroy 2 site by assuming the water table is at a depth of 60 ft (18.3 m), the total unit weight of the soil averages 125 pcf (19.6 kN/m^3), the soil is saturated throughout the profile, and the effective coefficient of earth pressure at rest, K_o', is 0.5. The resulting values of σ_m' for each sample are given in Table 8.B.2-2.

Once σ_m' was estimated, the range in confining pressures over which G and D would be evaluated was determined. Typically, isotropic confining pressures on the order of $0.25\sigma_m'$, $0.5\sigma_m'$, σ_m', $2\sigma_m'$, and $4\sigma_m'$ were selected. Low-amplitude resonant column testing was performed at each confining pressure to determine the influence of time and confining pressure on the small-strain shear modulus, G_{max}, and small-strain material damping ratio, D_{min}. Low-amplitude dynamic tests are defined as those tests in which the resonant amplitude did not exceed 0.001% and typically was considerably below that level.

A summary of all confining pressures at which low-amplitude resonant column tests were performed is given in Table 8.B.2-2. At the estimated in situ mean effective stress, high-amplitude dynamic and cyclic testing was also conducted. This testing is defined as any tests in which the peak shearing strain exceeds 0.001%. This testing was composed of two series of tests. The first involved cyclic torsional (TS) shear testing as illustrated in Figure 8.B.2-2. A complete set of torsional shear tests took about three hours to perform, was performed under drained conditions (although no drainage was observed), and involved shearing strains, γ, from less than 0.001% to above 0.05%, depending on the soil stiffness. The majority of the measurements was performed at 0.5 Hz. These measurements are labeled as TS1 in Figure 8.B.2-2. However, two sets of TS tests, one at $\gamma \approx 0.001\%$ and one at $\gamma \approx 0.01\%$, were conducted to evaluate the effect of excitation frequency on G and D at those strain amplitudes. In these tests (denoted as TS2 in Figure 8.B.2-2), one to four cycles of loading was applied at about five different frequencies ranging from 0.1 Hz to about 10 Hz.

After the TS tests were completed, confinement of the sample was continued at σ_m', and a series of high-amplitude resonant column (RC) tests was performed the next day. However, before high-amplitude RC testing commenced, small-strain RC tests were performed to determine if any changes in the soil skeleton had occurred from the TS tests. In essentially all cases, no changes in G_{max} or D_{min} from the TS tests were measured.

Once the small-strain datum was re-established after the TS tests, high-amplitude resonant column testing was conducted to evaluate the influence of strain amplitude on G and D. This series of tests is illustrated in Figure 8.B.2-3. A complete set of resonant column tests took about one hour to perform, was performed under drained conditions just as in the case of the TS tests, and involved shearing strains from less than 0.001% to above 0.1%, depending on the soil stiffness. In these tests, 500 to 1000 cycles of loading is required at each strain measurement.

Upon completion of the high-amplitude RC tests, low-amplitude RC tests were performed to determine if any changes in the soil skeleton had occurred from the high-amplitude tests. In some cases, changes occurred. At that point, confinement of the sample at σ_m' was continued until G_{max} and D_{min} returned to the values before the high-amplitude tests or the change in values was noted in the next stage of testing.

The confining pressure was then increased to about $2\sigma_m'$, and low-amplitude resonant column testing was performed for one to several days. For eight of the samples, high-amplitude resonant column tests were again performed. Table 8.B.2-2 gives a summary of these tests. In most cases, the pressure was again doubled, and low-amplitude RC testing was repeated.

It should be noted that, in ten cases, high-amplitude RC tests were also performed at confining pressures below σ_m'. This was carefully done with only intermediate strain levels so as not to disturb the sample before testing at σ_m'.

Table 8.B.2-2
Summary of Resonant Column and Torsional Shear Tests Performed for Gilroy 2 Samples

Sample Number	Depth ft (m)	Estimated In Situ Mean EffectiveStress, σ_m', psf	Isotropic Test Pressure , psf		
			Low-Amplitude Resonant Column Tests	High-Amplitude Resonant Column Tests	Torsional Shear Test
G1	10(3.0)	864	432, 864, 1730, 3460	864, 1730	864
G2	20(6.1)	1730	432, 864, 1730, 3460, 6910	864, 1730, 3460	1730
G2-1	20(6.1)	1730	432, 864, 1730, 3460, 6910	864, 1730, 3460	1730
G3	50(15.2)	4167	576, 1152, 2160, 4320, 8640, 17280, 28800	4320, 8640, 17280	4320
G4	85(25.9)	5180	648, 1300, 2590, 5180, 10370, 20450	2590, 5180, 10370	5180
G4-1	85(25.9)	5180	648, 1300, 2590, 5180, 10370, 20450	2590, 5180, 10370	5180
G5	120(36.6)	6910	864, 1730, 3460, 6910, 14400, 28800	1730, 3460, 6910, 14400	6910
G5-1	120(36.6)	6910	864, 1730, 3460, 6910, 14400, 28800	1730, 3460, 6910, 14400	6910
G6	170(51.8)	9967	1300, 2590, 5040, 10080, 18720	5040, 10080	none
G7	210(64.0)	15600	1296, 2592, 5184, 10368, 20160	2592, 5184, 10368	10368
G8	348(106.1)	18179	4608, 9072, 18144, 36000	9072, 18144	18144
G9	420(128.0)	199133	2304, 4608, 9216	9216	none

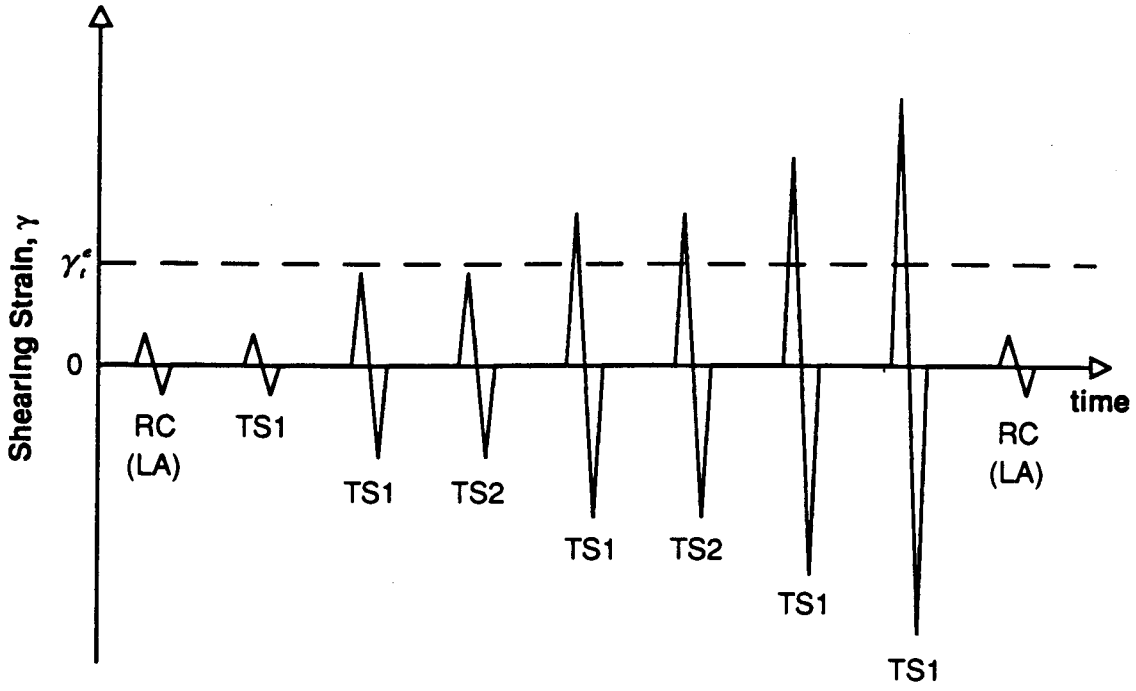

γ_t^e = elastic threshold strain; below γ_t^e, G is constant and equal to G_{max}

RC (LA) = resonant column test at low-amplitudes (strains < 0.001%)

TS1 = torsional shear test in which 1 to 10 cycles are applied at 0.5 Hz

TS2 = torsional shear test in which 4 cycles are applied at each of approximately 5 frequencies between 0.1 to 10 Hz

Figure 8.B.2-2
Testing procedure used in the torsional shear test to investigate the effects of strain amplitude, number of loading cycles, and excitation frequency on G and D of Gilroy 2 samples.

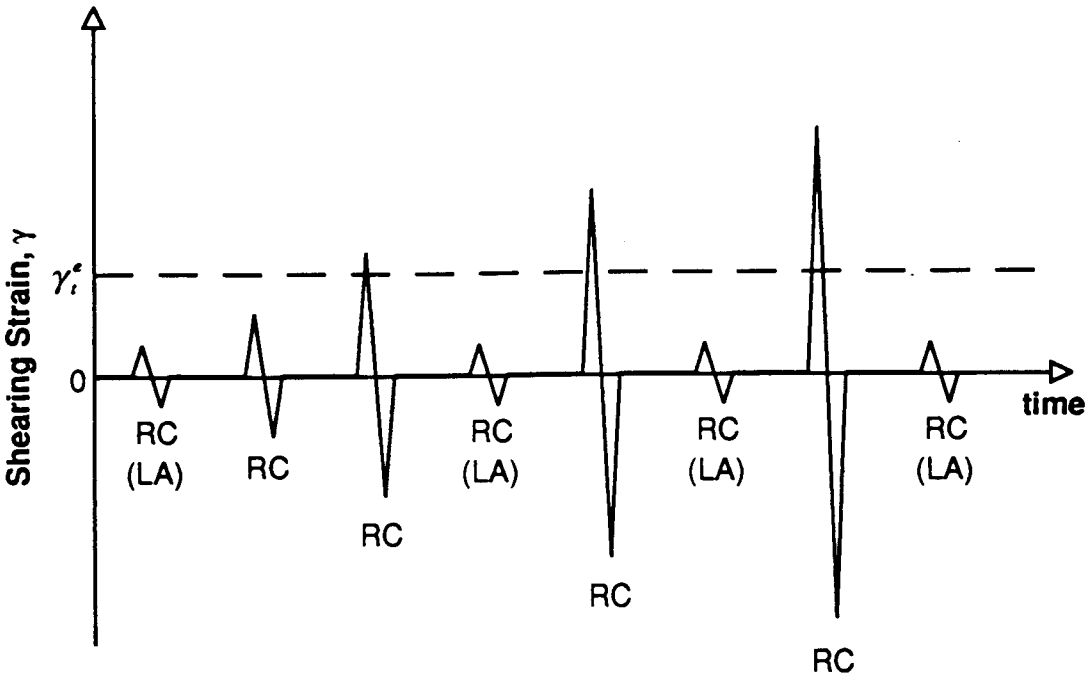

γ_t^e = elastic threshold strain; below γ_t^e, G is constant and equal to G_{max}

RC (LA) = resonant column test at low-amplitudes (strains < 0.001%)

RC = resonant column test in which 500 to 1000 cycles of loading is applied during each measurement

Figure 8.B.2-3
Testing procedure used in the resonant column test to investigate the effects of strain amplitude on G and D of Gilroy 2 samples.

8.B.2.2.2 Test Results

The results of the RC and TS tests are shown in Appendices 8.B.2.B through 8.B.2.M for the twelve Gilroy 2 samples. Each appendix presents the results for one sample in the following general order (using Appendix 8.B.2.B as the example).

1. Figure 8.B.2.B-1 shows the influence of magnitude and duration of isotropic confining pressure on G_{max} as determined by RC tests.
2. Figure 8.B.2.B-2 shows the influence of magnitude and duration of isotropic confining pressure on D_{min} as determined by RC tests.
3. Figure 8.B.2.B-3 shows the change in void ratio of the sample with magnitude and duration of isotropic confining pressure.
4. Figure 8.B.2.B-4 shows the variation in G_{max} at a confinement time of 1000 minute with effective confining pressure from the RC tests.
5. Figure 8.B.2.B-5 shows the variation in D_{min} at a confinement time of 1000 minutes with effective confining pressure from the RC tests.
6. Figure 8.B.2.B-6 shows the variation in void ratio of the sample at a confinement time of 1000 minutes with effective confining pressure.
7. Figure 8.B.2.B-7 shows the variation in G with log γ at σ_m' from the high-amplitude RC and TS tests.
8. Figure 8.B.2.B-8 shows the variation in G/G_{max} with log γ at σ_m' from the high-amplitude RC and TS tests.
9. Figure 8.B.2.B-9 shows the variation in G with log γ at all tests pressures where high-amplitude RC tests were performed.
10. Figure 8.B.2.B-10 is the normalized (G/G_{max}) version of Figure 8.B.2.B-9.
11. Figures 8.B.2.B-11 through 8.B.2.B-14 are simply the damping ratio curves which are the companions to the modulus curves given in Figures 8.B.2.B-7 through 8.B.2.B-10.
12. Figure 8.B.2.B-15 shows the effect of excitation frequency on G at $\gamma \approx 0.001\%$ and $\gamma \approx 0.01\%$.
13. Figure 8.B.2.B-16 shows the effect of excitation frequency on D at $\gamma \approx 0.001\%$ and $\gamma \approx 0.01\%$.

8.B.2.3 Discussion of Results

The variation in G_{max} with σ_o' for ten of the undisturbed samples tested in this study at the estimated σ_m' and above is shown in Figure 8.B.2-4. (Sample G9 was only tested below σ_m' due to leakage of the membrane.) The samples should be normally consolidated samples in the pressure range shown if K_o' is reasonably close to 0.5. In fact, the results from most of the samples show the proper trend of increasing G_{max} with increasing σ_o' for normally consolidated material. These trends are more easily seen by separating the results into sandy samples and fine-grained samples as shown in Figures 8.B.2-5 and 8.B.2-6, respectively. In an attempt to further improve the trends, void ratio variations were taken into accounted using the Hardin (1978) equation as shown in Figures 8.B.2-7 and 8.B.2-8. However, little improvement in the trends occurred by accounting for void ratio variations.

The same set of comparisons for the variation in small-strain material damping ratio, D_{min}, with σ_o' is presented in Figures 8.B.2-9, -10 and -11. In this case, the results show a general decrease in D_{min} with an increase in σ_o'. However, D_{min} exhibits more scatter than in the case of G_{max}. Also, in the case of three samples (G6, G7 and G8), the values of D_{min} are not as low as the other soils tested in this study as well as the samples from Treasure Island and Lotung which all exhibited values of D_{min} less than 4% (or $Q > 12.5$).

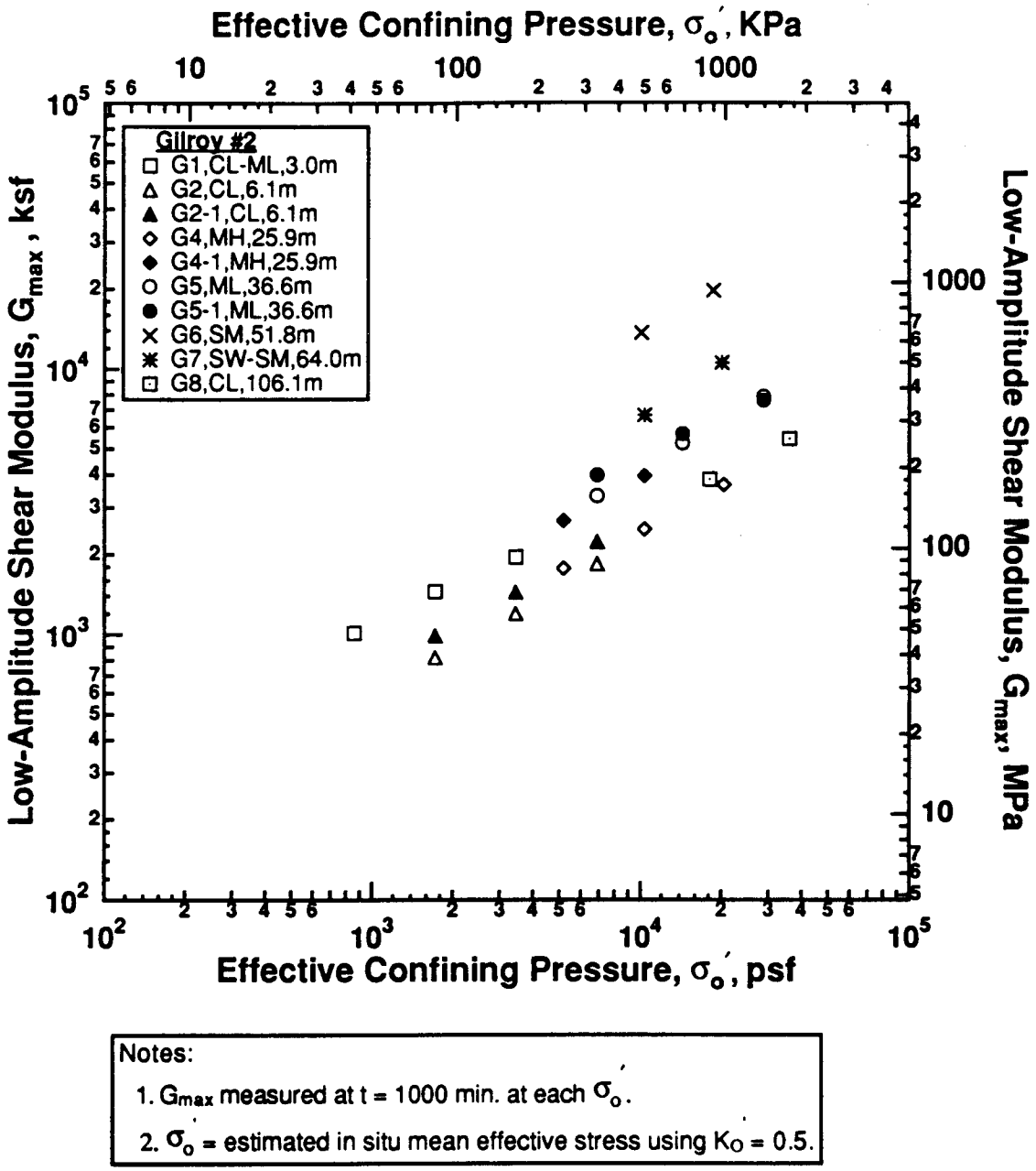

Figure 8.B.2-4
Variation in low-amplitude shear modulus with effective confining pressure from resonant column tests at $\sigma_o' \geq \sigma_m'$ of undisturbed samples from Gilroy 2

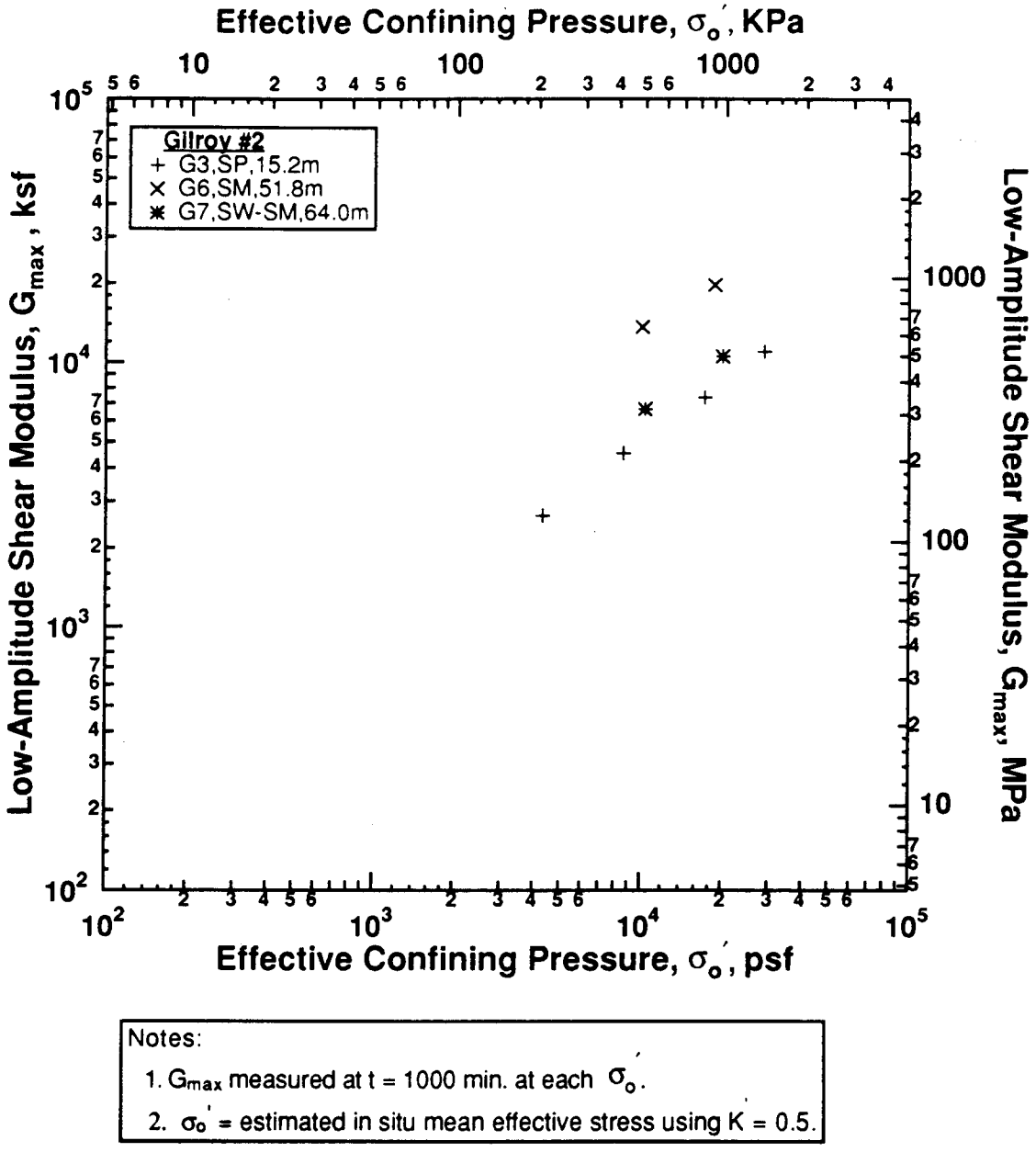

Figure 8.B.2-5
Variation in low-amplitude shear modulus with effective confining pressure from resonant column tests at $\sigma_o' \geq \sigma_m'$ of undisturbed and reconstituted sandy samples from Gilroy 2.

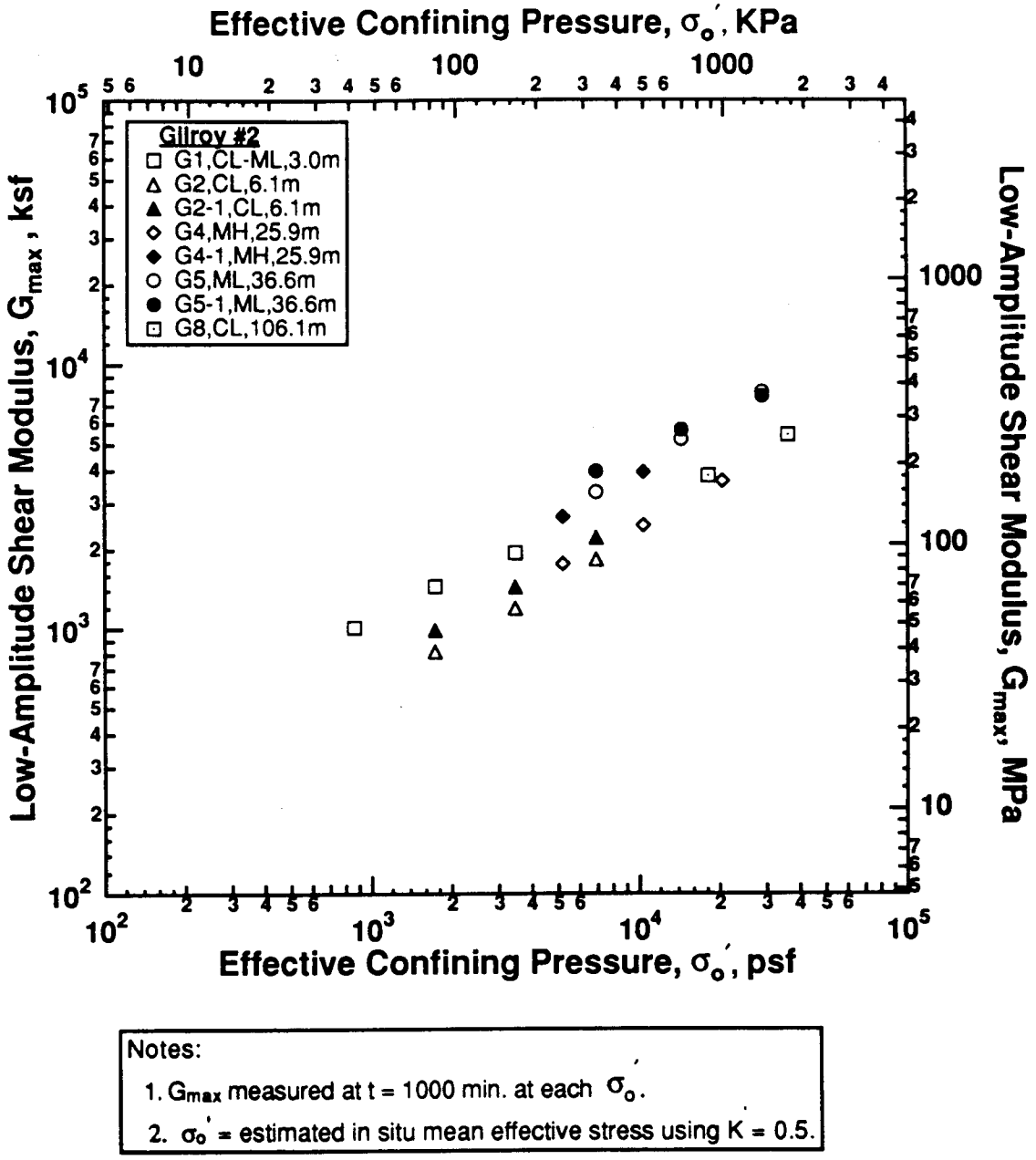

Figure 8.B.2-6
Variation in low-amplitude shear modulus with effective confining pressure from resonant column tests at $\sigma_o' \geq \sigma_m'$ of undisturbed fine-grained samples from Gilroy 2.

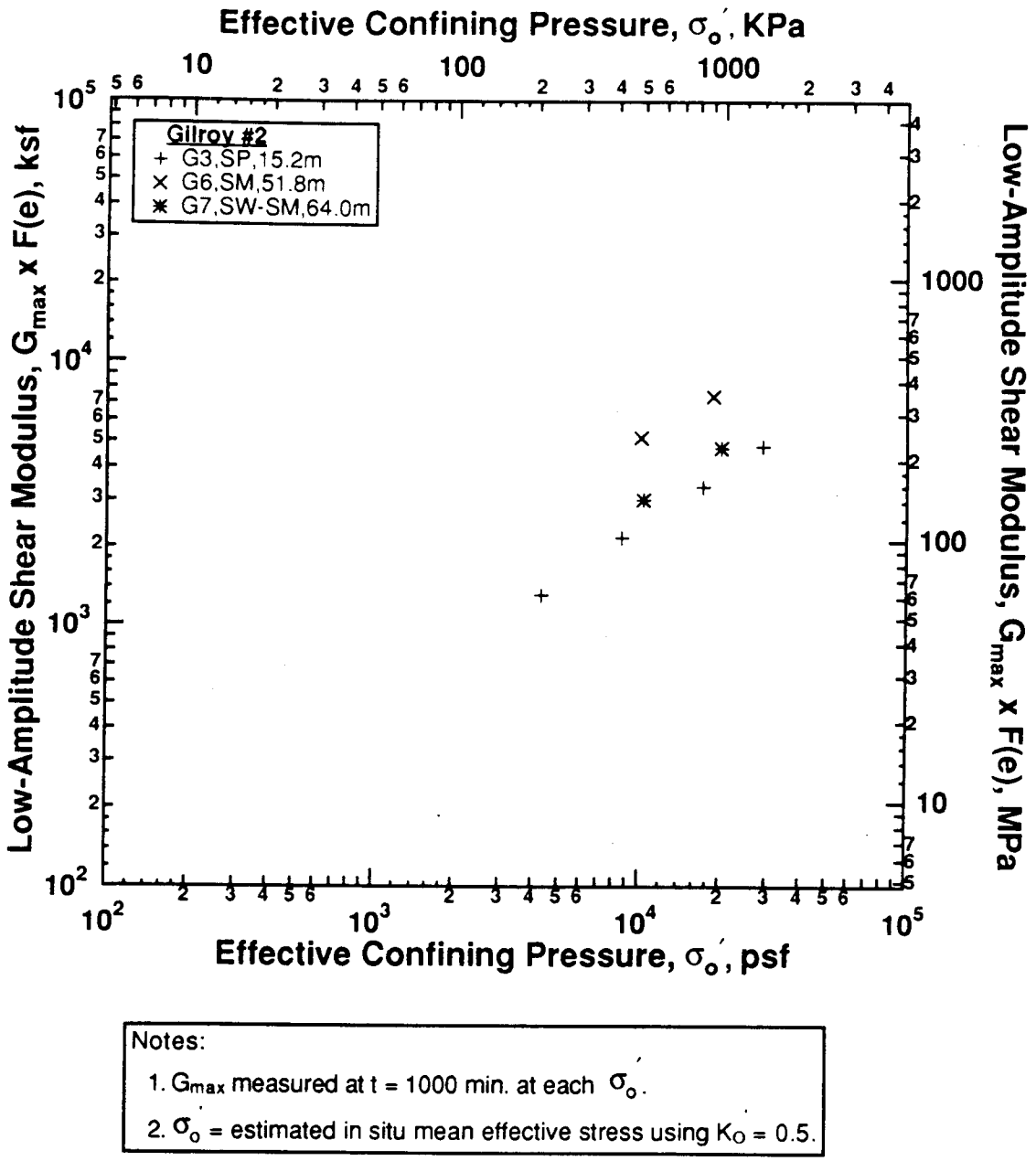

Figure 8.B.2-7
Best-fit curve to log $G_{max} \times F(e)$ – log σ_o' relationship from resonant column tests at $\sigma_o' \geq \sigma_m'$ of undisturbed and reconstituted sandy samples from Gilroy 2.

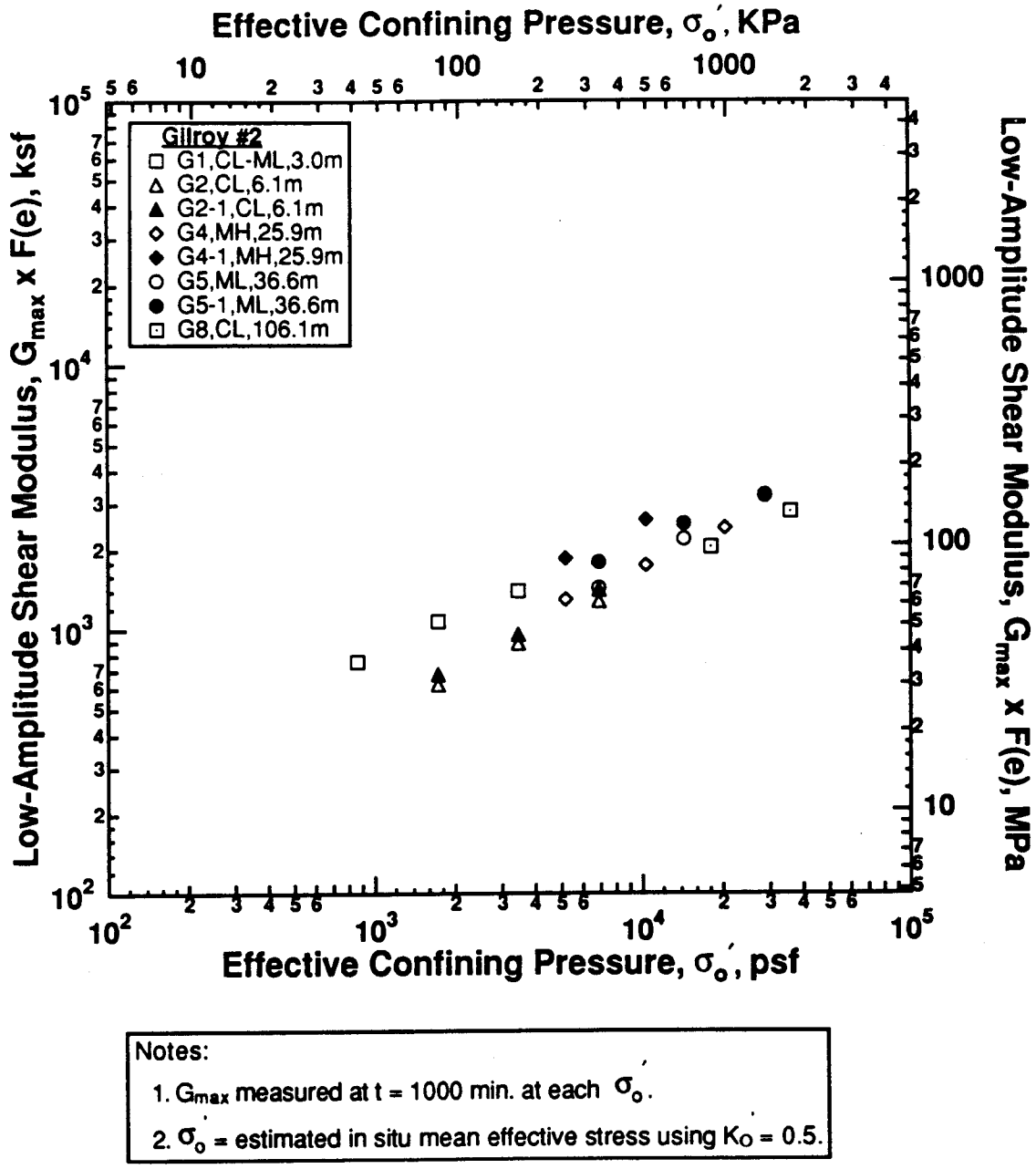

Figure 8.B.2-8
Best-fit curve to log $G_{max} \times F(e)$ – log σ_o' relationship from resonant column tests at $\sigma_o' \geq \sigma_m'$ of undisturbed fine-grained samples from Gilroy 2.

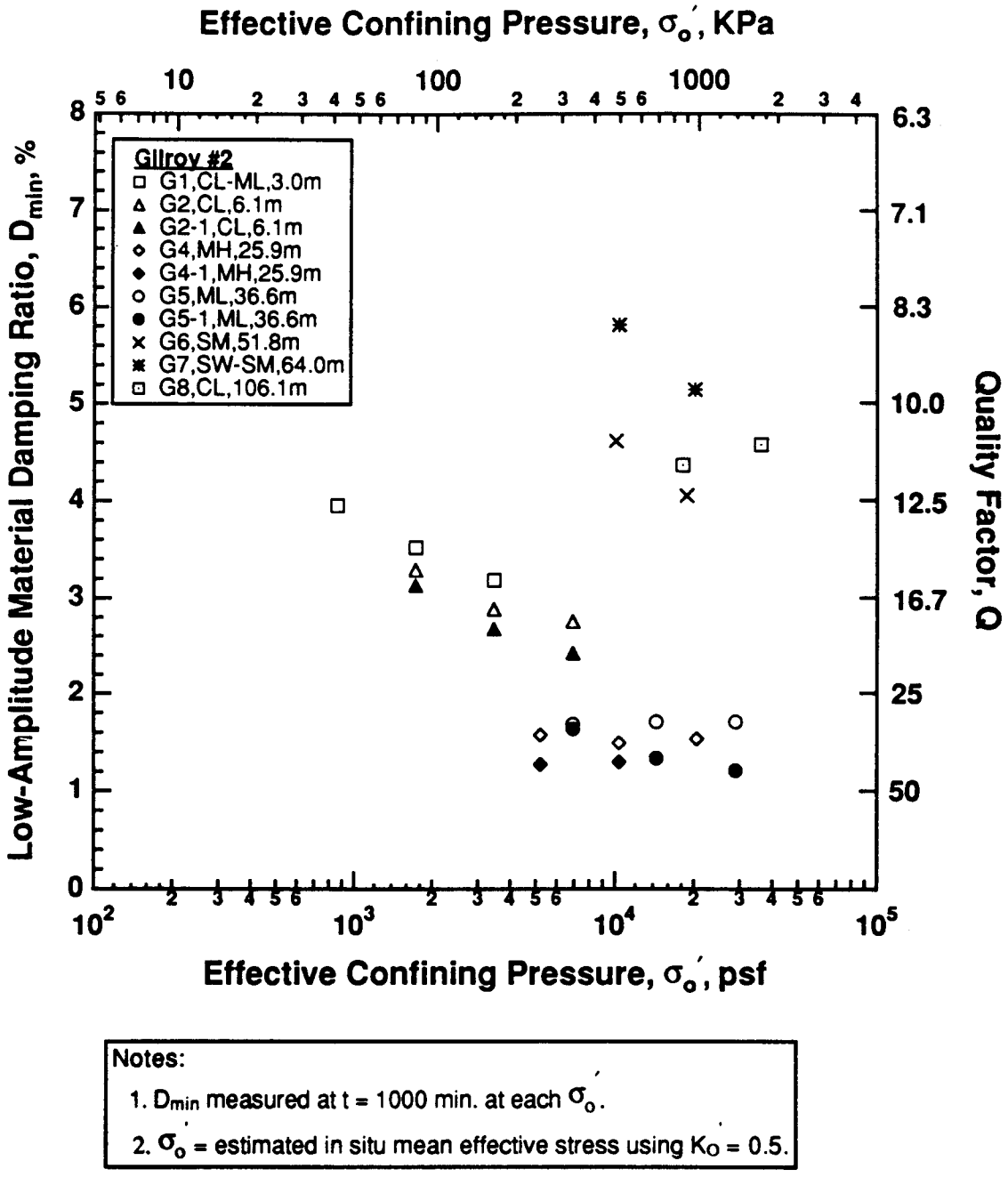

Notes:

1. D_{min} measured at t = 1000 min. at each σ_o'.
2. σ_o' = estimated in situ mean effective stress using K_O = 0.5.

Figure 8.B.2-9
Variation in low-amplitude material damping ratio with effective confining pressure from resonant column tests at $\sigma_o' \geq \sigma_m'$ of undisturbed samples from Gilroy 2.

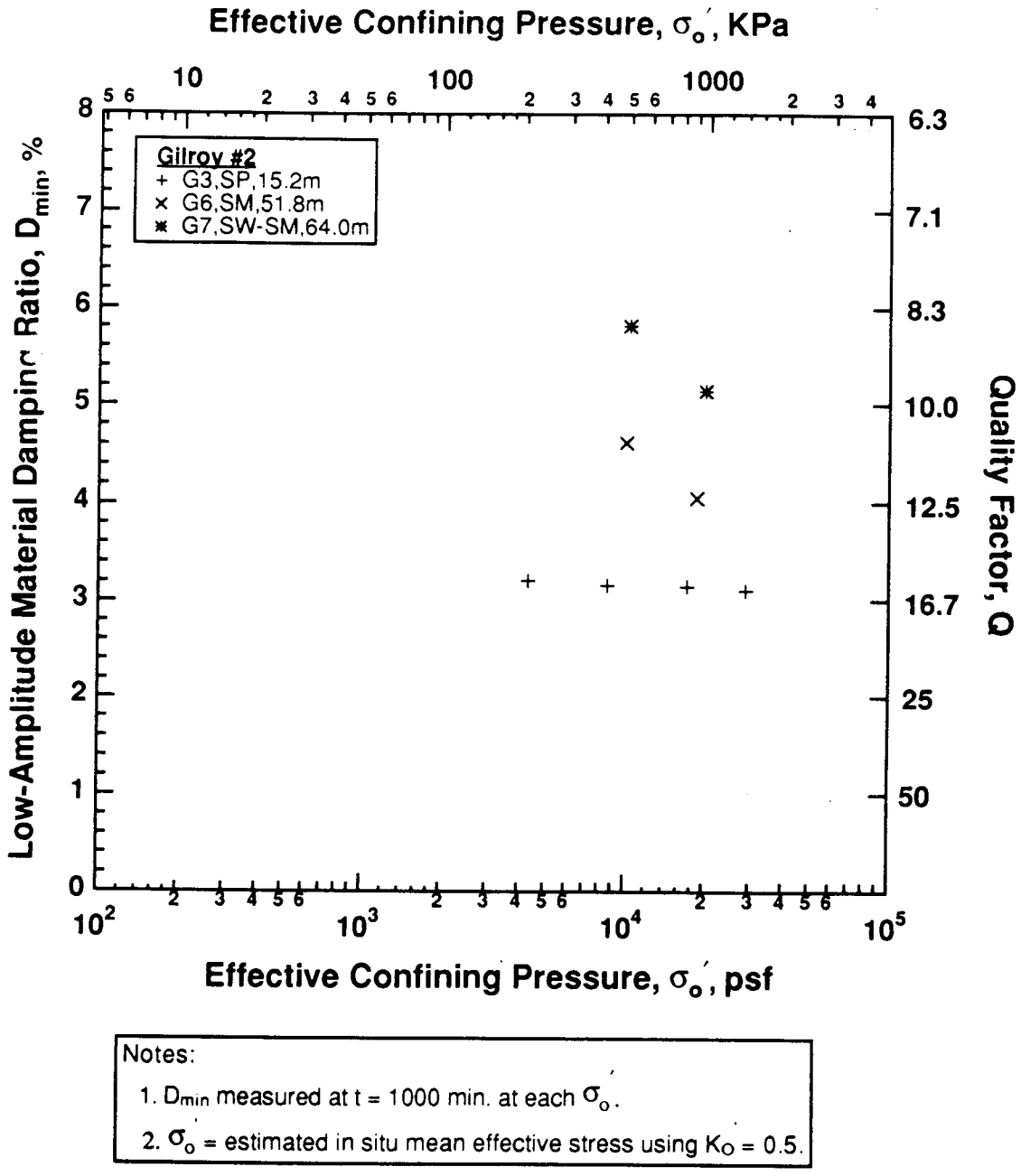

Figure 8.B.2-10
Variation in low-amplitude material damping ratio with effective confining pressure from resonant column tests at $\sigma_o' \geq \sigma_m'$ of undisturbed and reconstituted sandy samples from Gilroy 2.

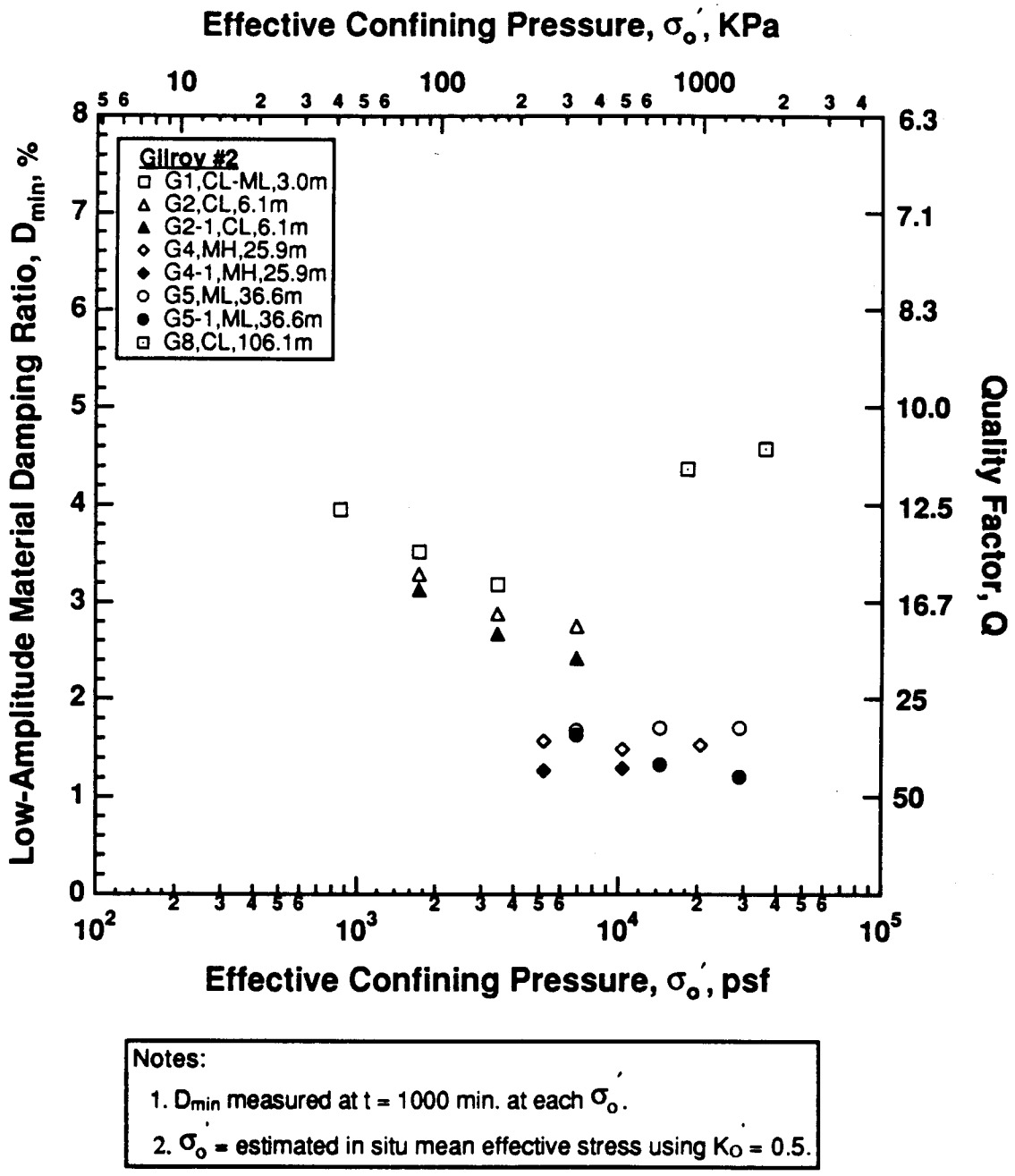

Figure 8.B.2-11
Variation in low-amplitude material damping ratio with effective confining pressure from resonant column tests at $\sigma_o' \geq \sigma_m'$ of undisturbed fine-grained samples from Gilroy 2.

The variation in normalized modulus, G/G_{max}, with log γ for all undisturbed samples tested at the estimated in situ mean effective stress, σ_m', is presented in Figure 8.B.2-12 for the RC tests, in Figure 8.B.2-13 for the first cycle in the TS test, and in Figure 8.B.2-14 for the combined results. In each case, the results for all samples form a wide band which is in the area of the upper range proposed by Seed and Idriss (1970) for sands. It should be noted at this point that all samples are unsaturated and hence any development in pore water pressure due to cyclic loading is significantly inhibited. Therefore, values of G determined at strains above amplitudes on the order of 0.05% do not reflect any reduction which would occur if pore pressures were generated.

The variation in normalized modulus, G/G_{max}, with log γ is divided into sandy samples and fine-grained soils in Figures 8.B.2-15 through 8.B.2-17 and Figures 8.B.2-18 through 8.B.2-20, respectively. It can be seen that the general trends are: (1) for the fine-grained soils to exhibit somewhat less degradation with strain amplitude than the sandy soils and (2) for the torsional shear results to plot somewhat above the resonant column results at larger strains.

Similar results for the variation in material damping ratio with strain amplitude are shown in the remaining figures. Figure 8.B.2-21 shows the variation in D with log γ as determined by RC tests for all ten intact samples. The results fall in a rather wide band which ranges from well above the upper range proposed by Seed and Idriss (1970) for sands at small strains to nearly at the lower range proposed by Seed and Idriss at large strains. The effect of frequency seems to be quite important on some of the samples as shown by comparing the RC results in Figure 8.B.2-21 with the results from TS tests in Figure 8.B.2-22. This comparison of damping measurements is presented in Figure 8.B.2-23. In this case, material damping values are slightly lower in the TS tests than those determined in the RC tests. These results are shown in expanded form in Figures 8.B.2-24 through 8.B.2-26.

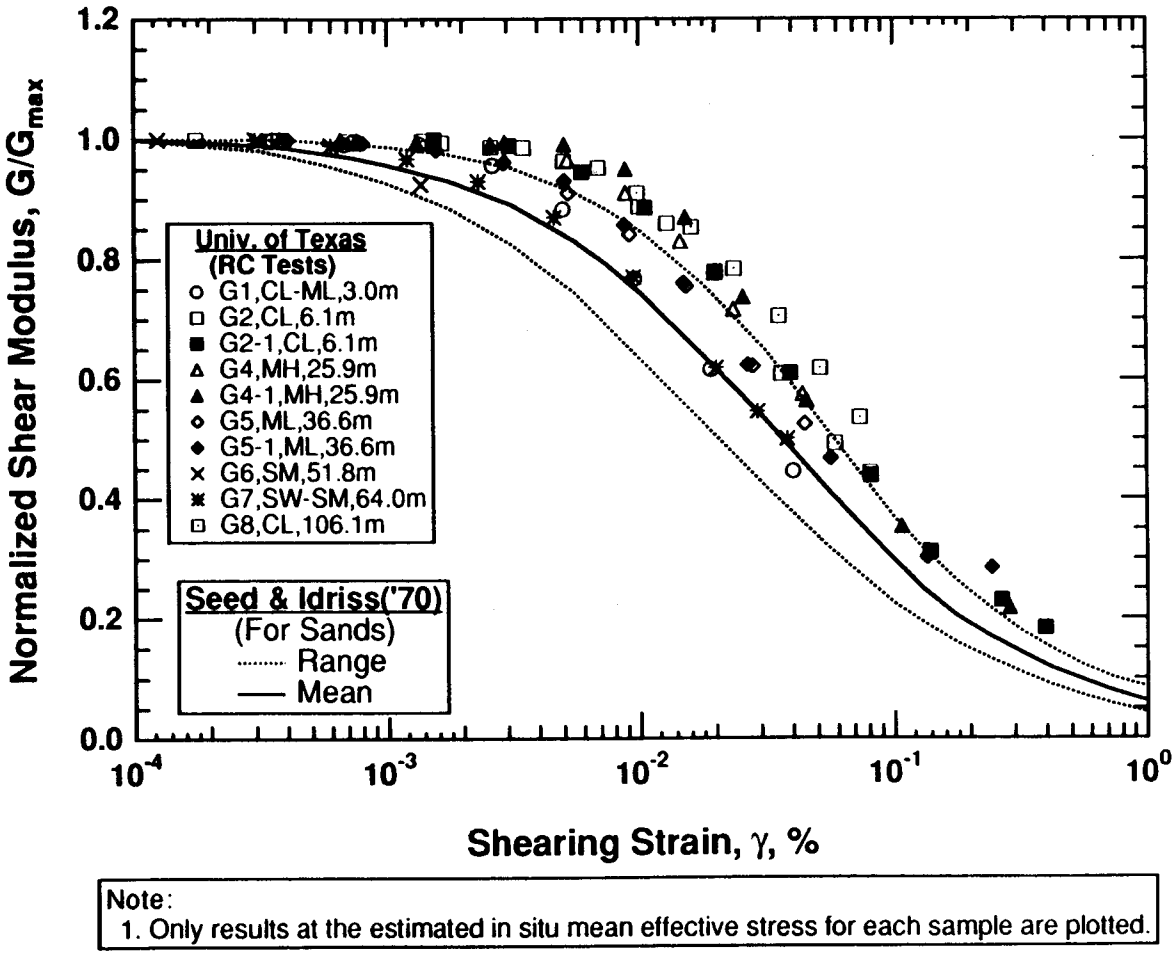

Figure 8.B.2-12
Variation in normalized shear modulus with shearing strain from resonant column tests of undisturbed samples from Gilroy 2.

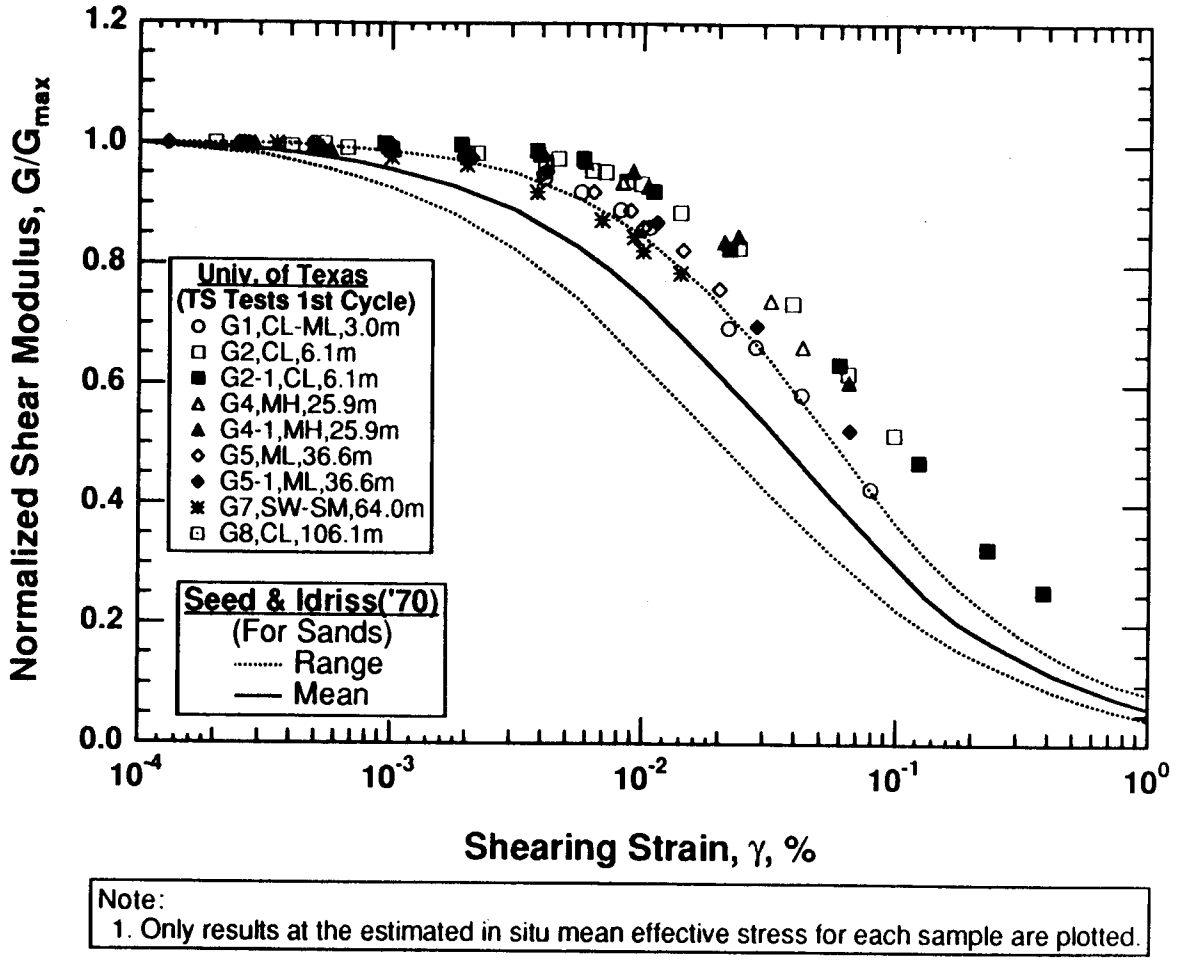

Figure 8.B.2-13
Variation in normalized shear modulus with shearing strain from torsional shear tests of undisturbed samples from Gilroy 2.

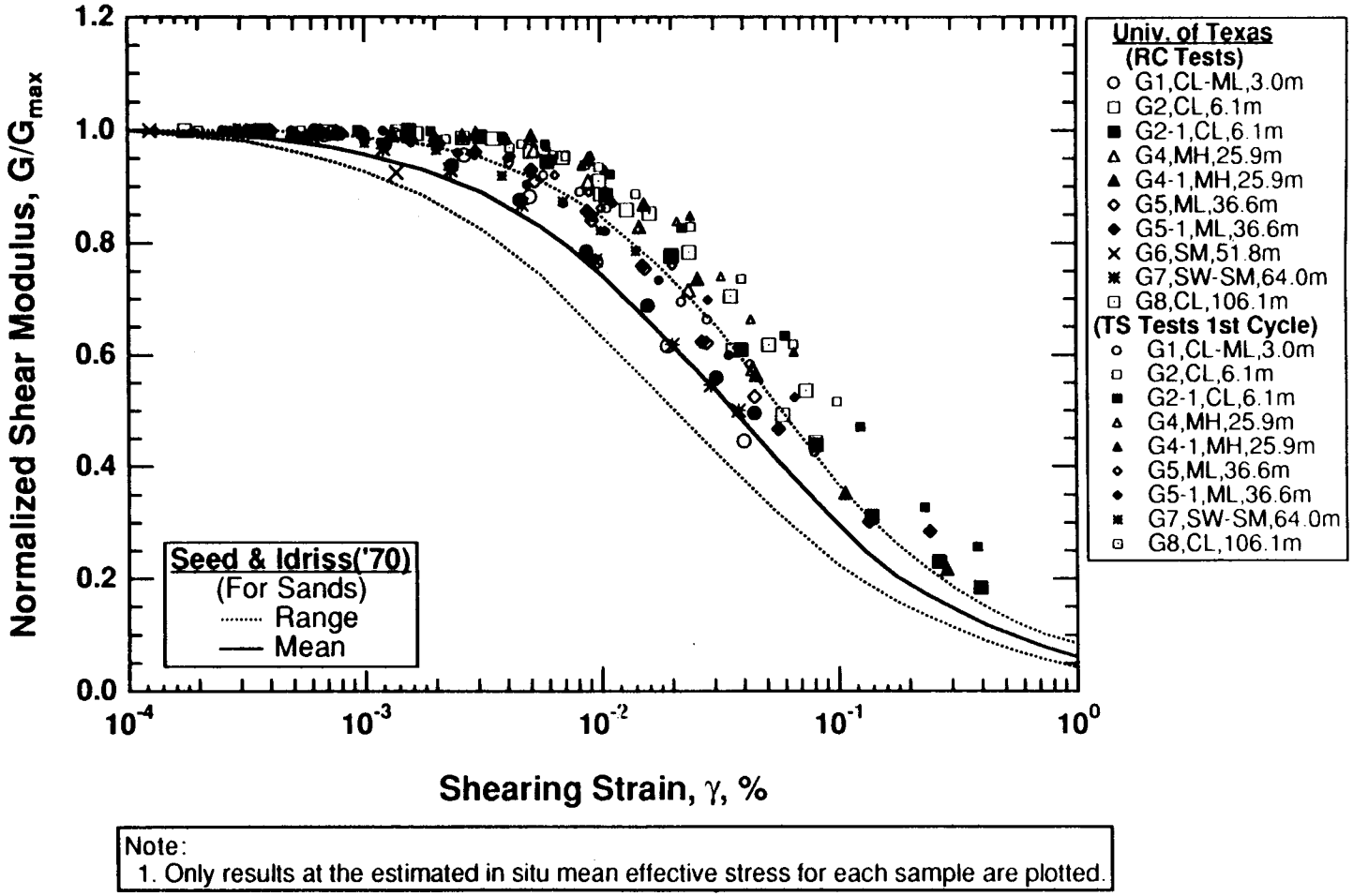

Figure 8.B.2-14
Variation in normalized shear modulus with shearing strain from resonant column and torsional shear tests of undisturbed samples from Gilroy 2.

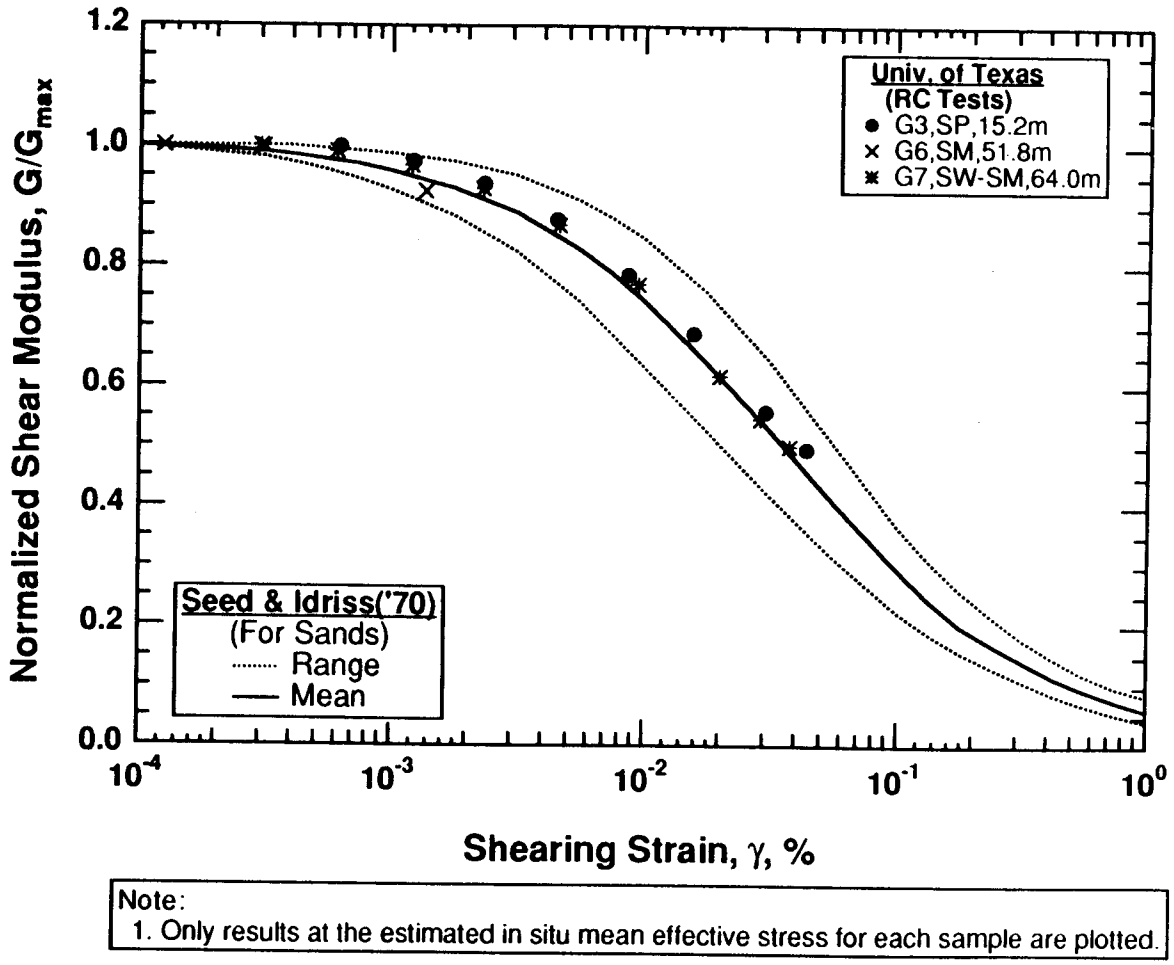

Figure 8.B.2-15
Variation in normalized shear modulus with shearing strain from resonant column tests of undisturbed and reconstituted sandy samples from Gilroy 2.

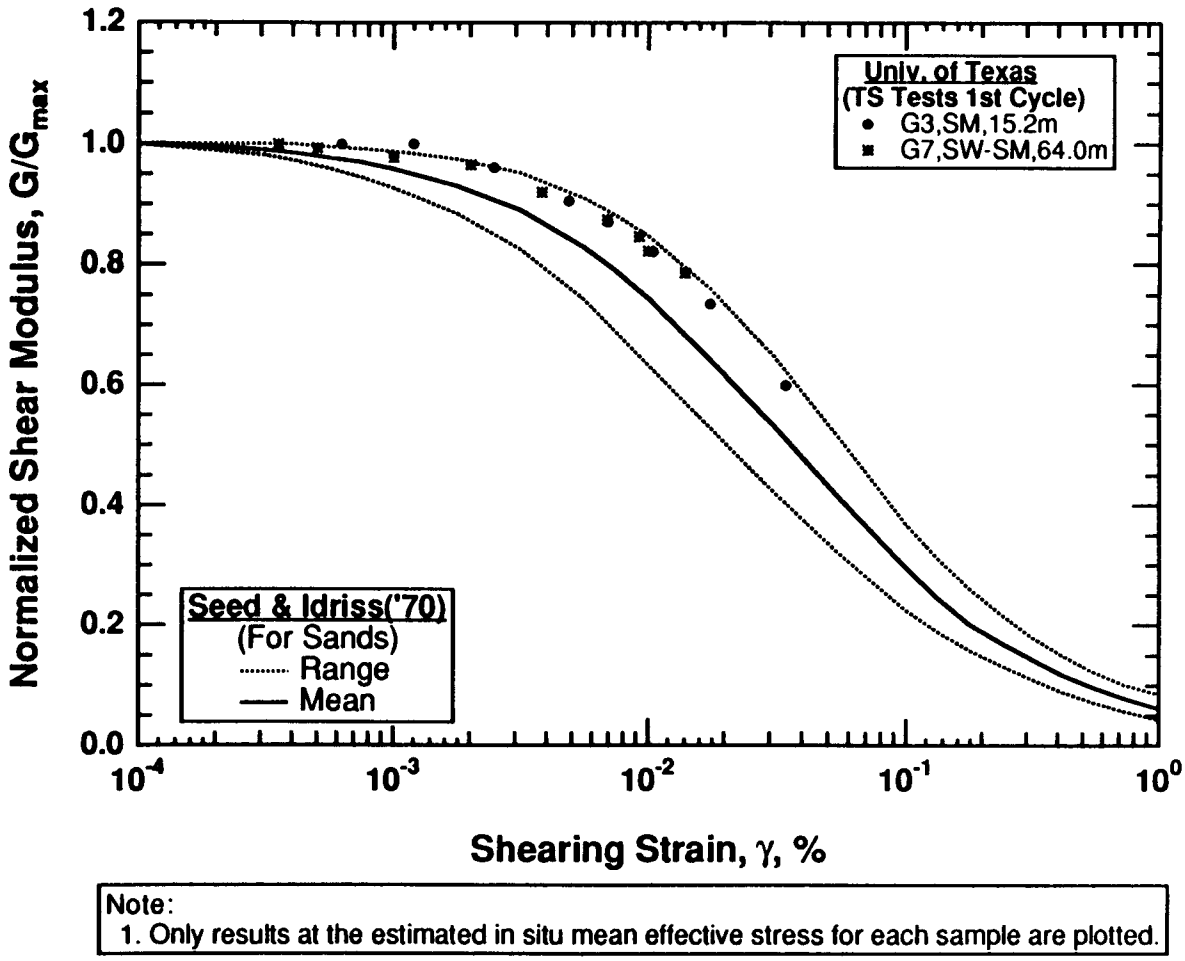

Figure 8.B.2-16
Variation in normalized shear modulus with shearing strain from torsional shear tests of undisturbed sandy samples from Gilroy 2.

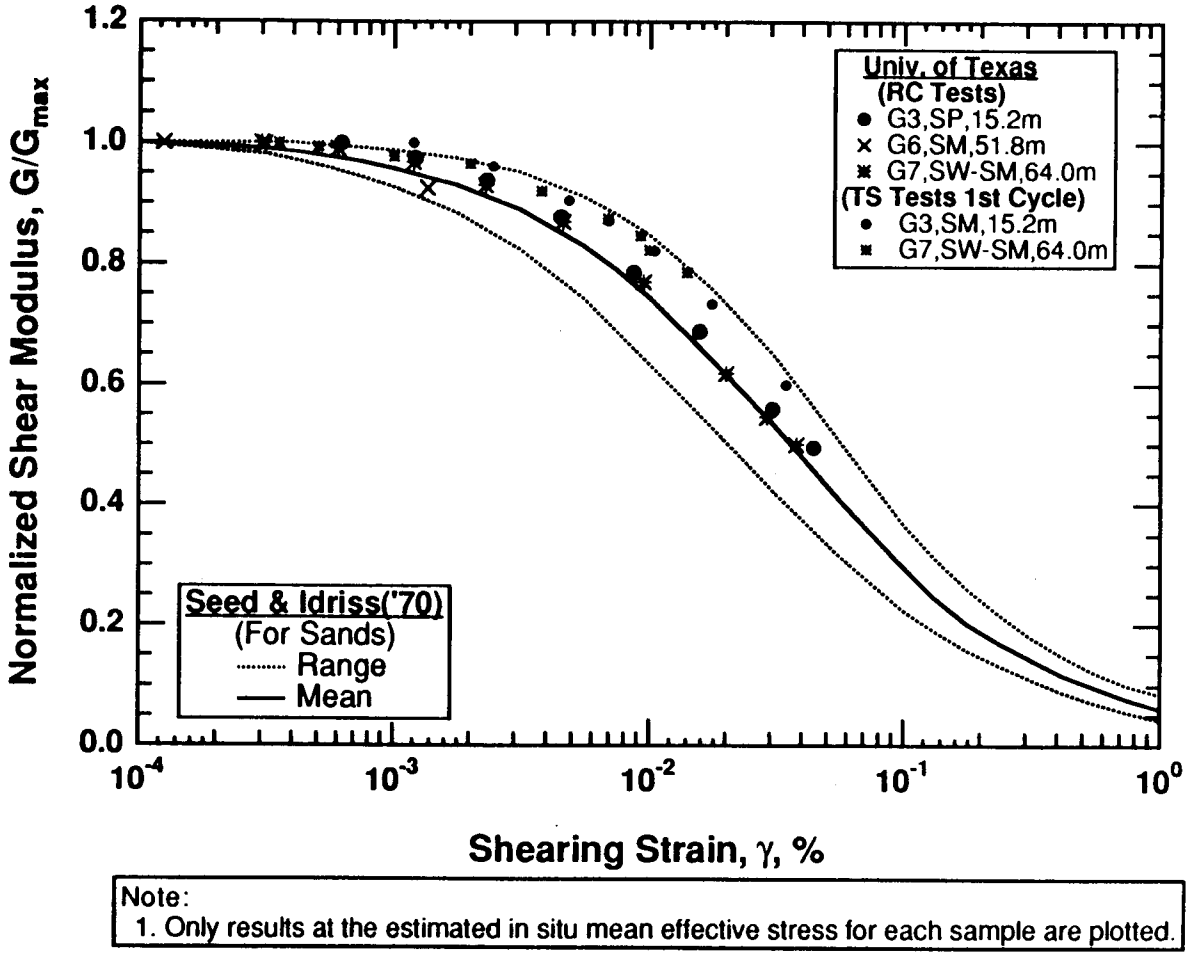

Figure 8.B.2-17
Variation in normalized shear modulus with shearing strain from resonant column and torsional shear tests of undisturbed and reconstituted sandy samples from Gilroy 2.

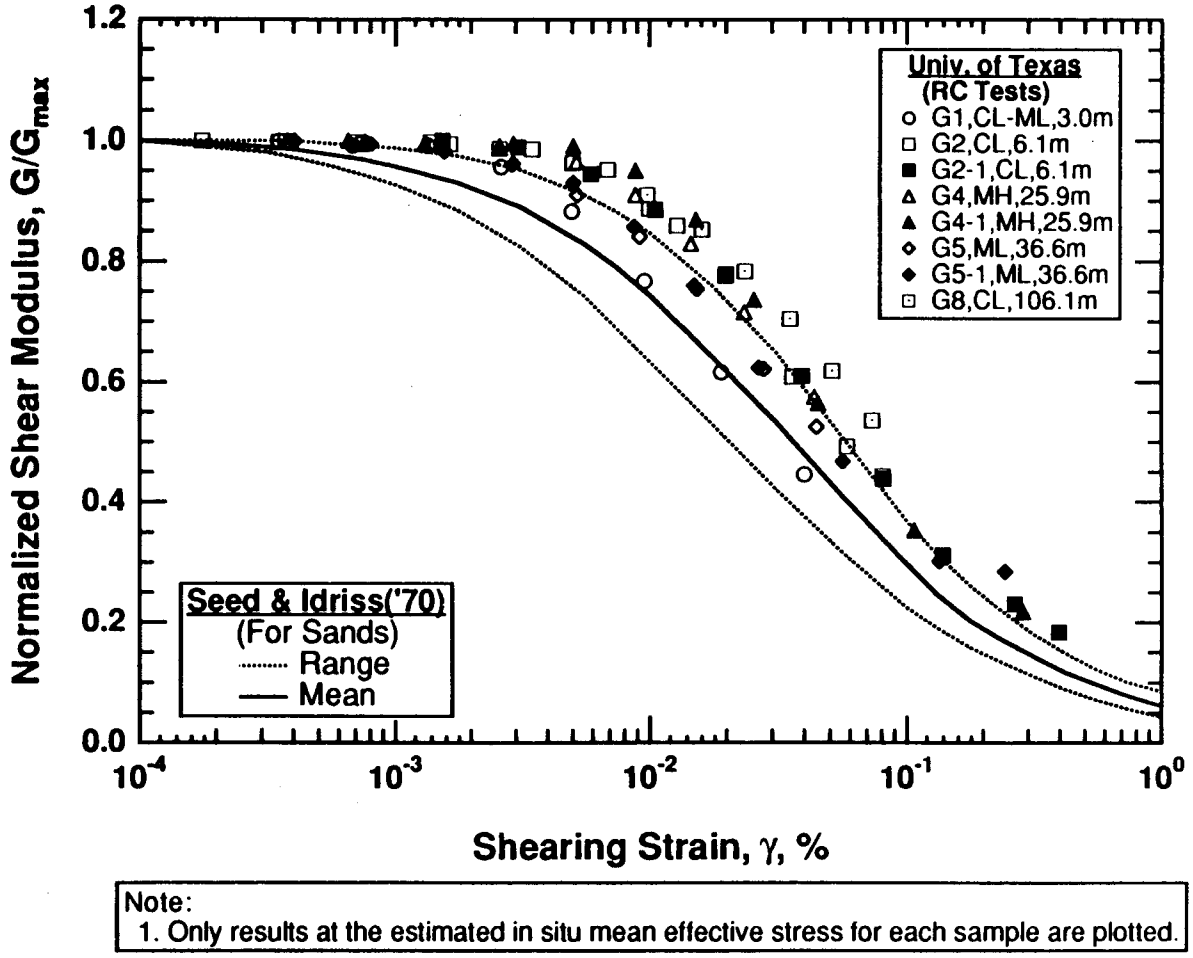

Figure 8.B.2-18
Variation in normalized shear modulus with shearing strain from resonant column tests of undisturbed fine-grained samples from Gilroy 2.

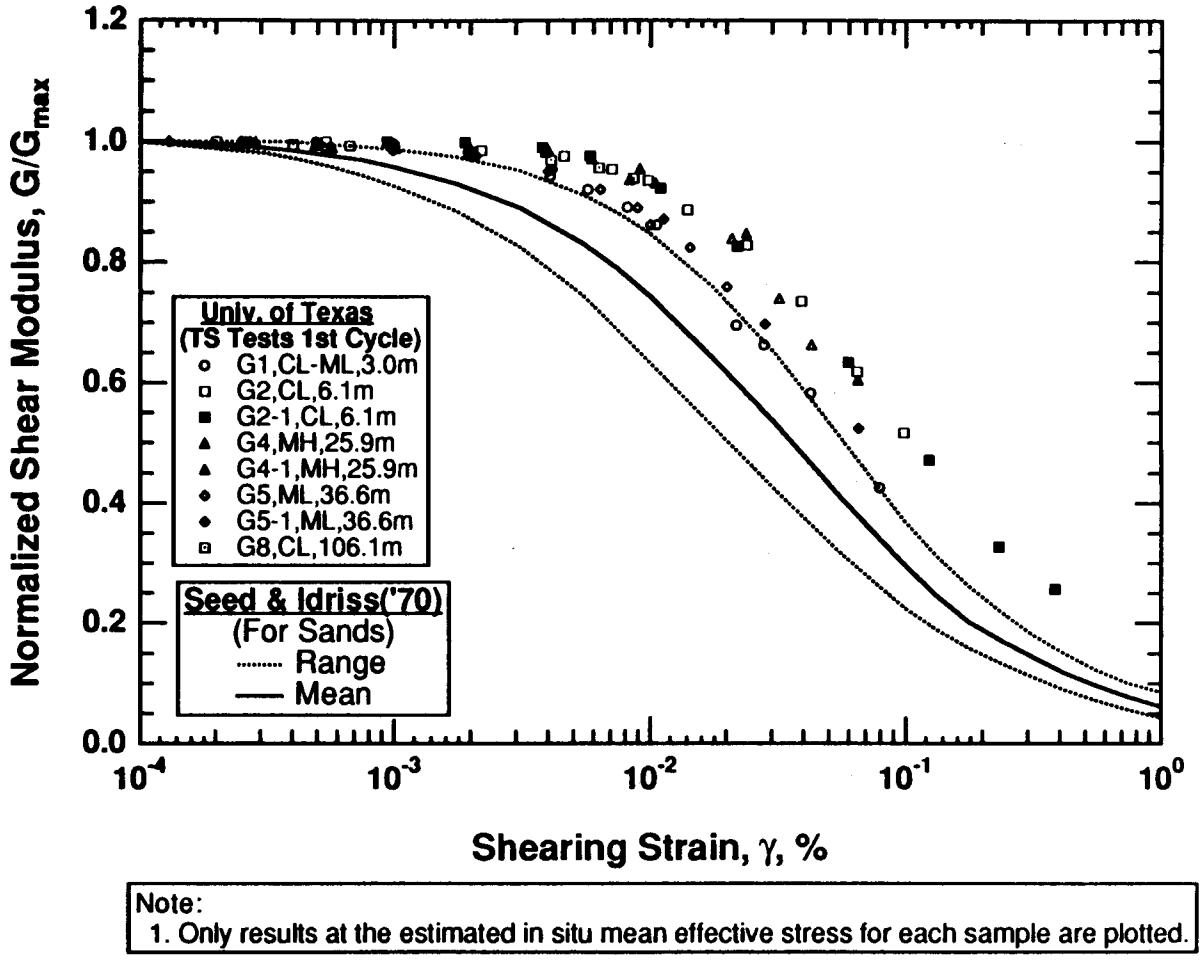

Figure 8.B.2-19
Variation in normalized shear modulus with shearing strain from torsional shear tests of undisturbed fine-grained samples from Gilroy 2.

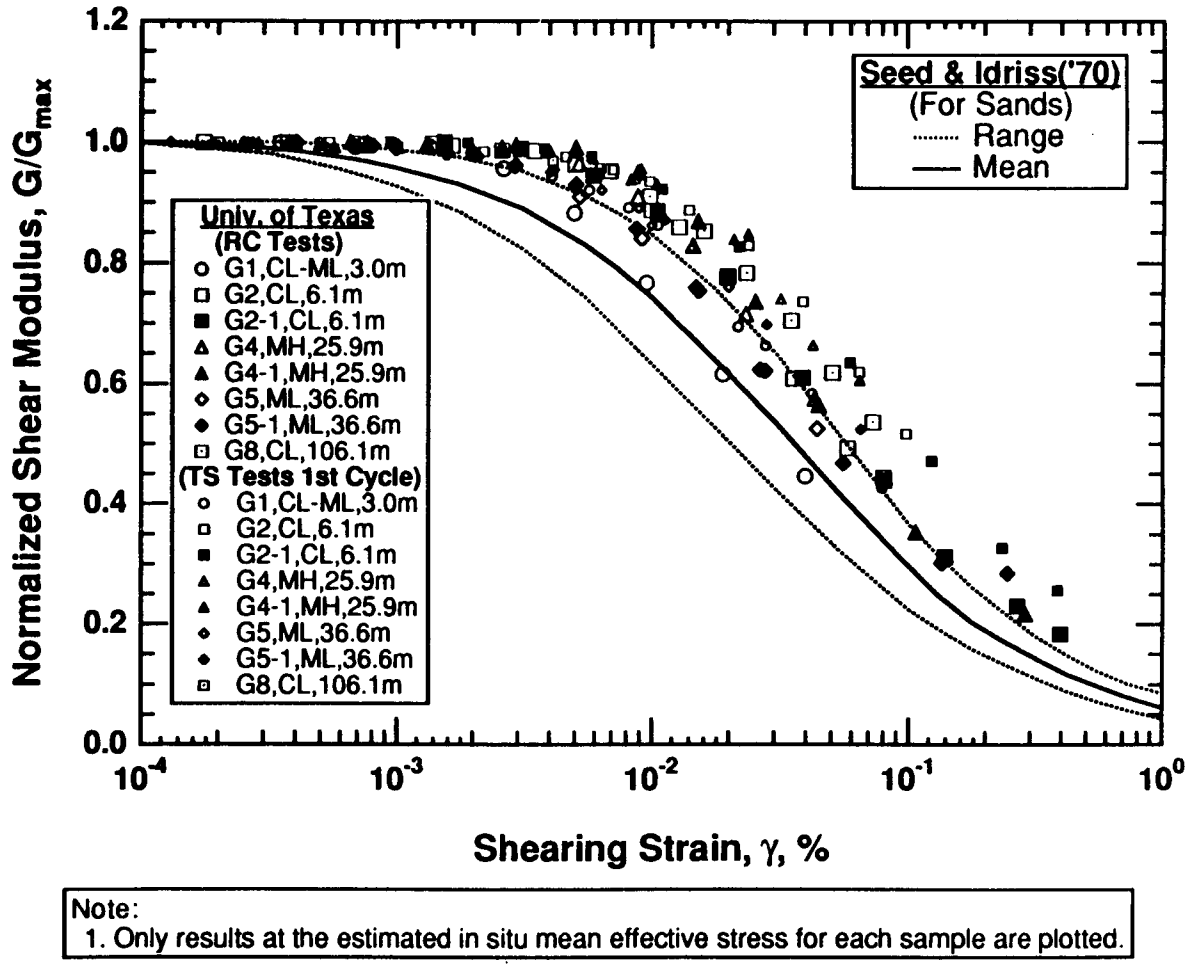

Figure 8.B.2-20
Variation in normalized shear modulus with shearing strain from resonant column and torsional shear tests of undisturbed fine-grained samples from Gilroy 2.

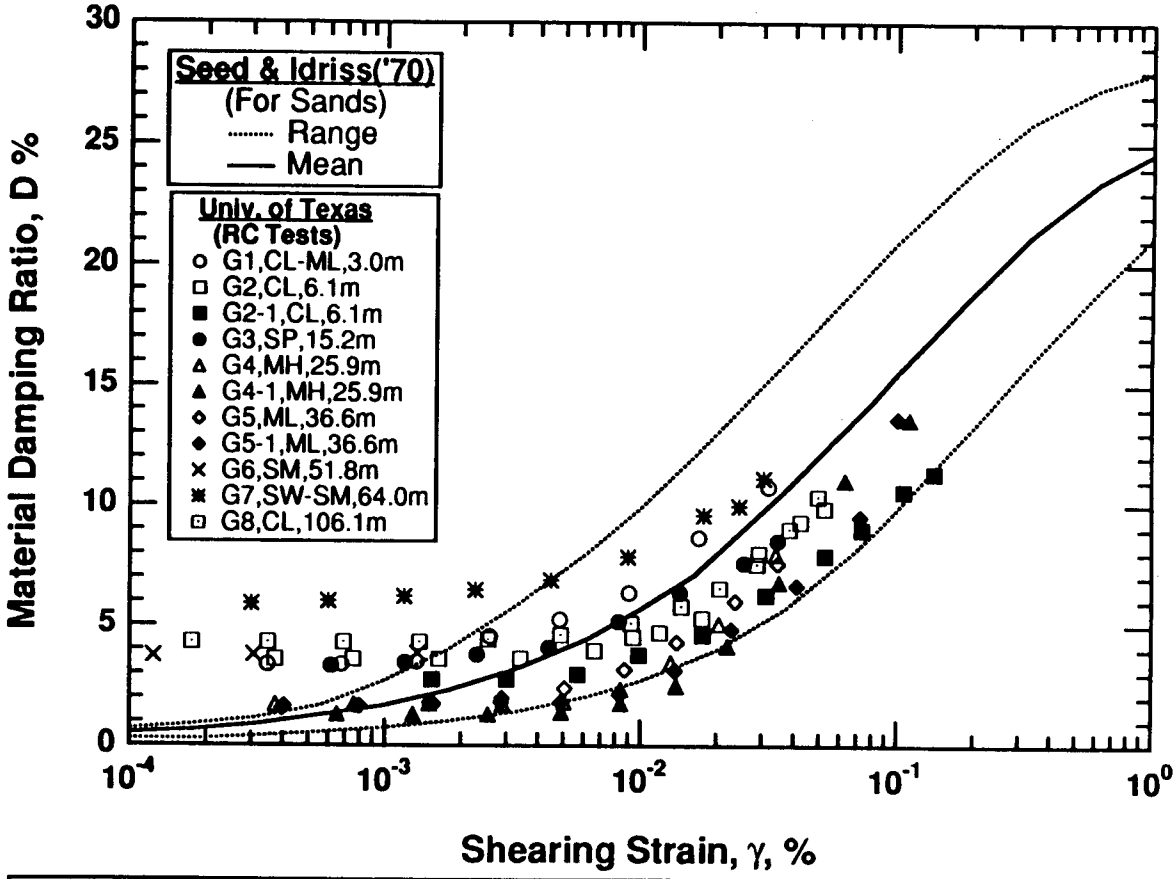

Note:
1. Only results at the estimated in situ mean effective stress for each sample are plotted.
2. Shearing strains in RC test were corrected to the average of the first 3 free-vibration cycles.

Figure 8.B.2-21
Variation in material damping ratio with shearing strain from resonant column tests of undisturbed and reconstituted samples from Gilroy 2.

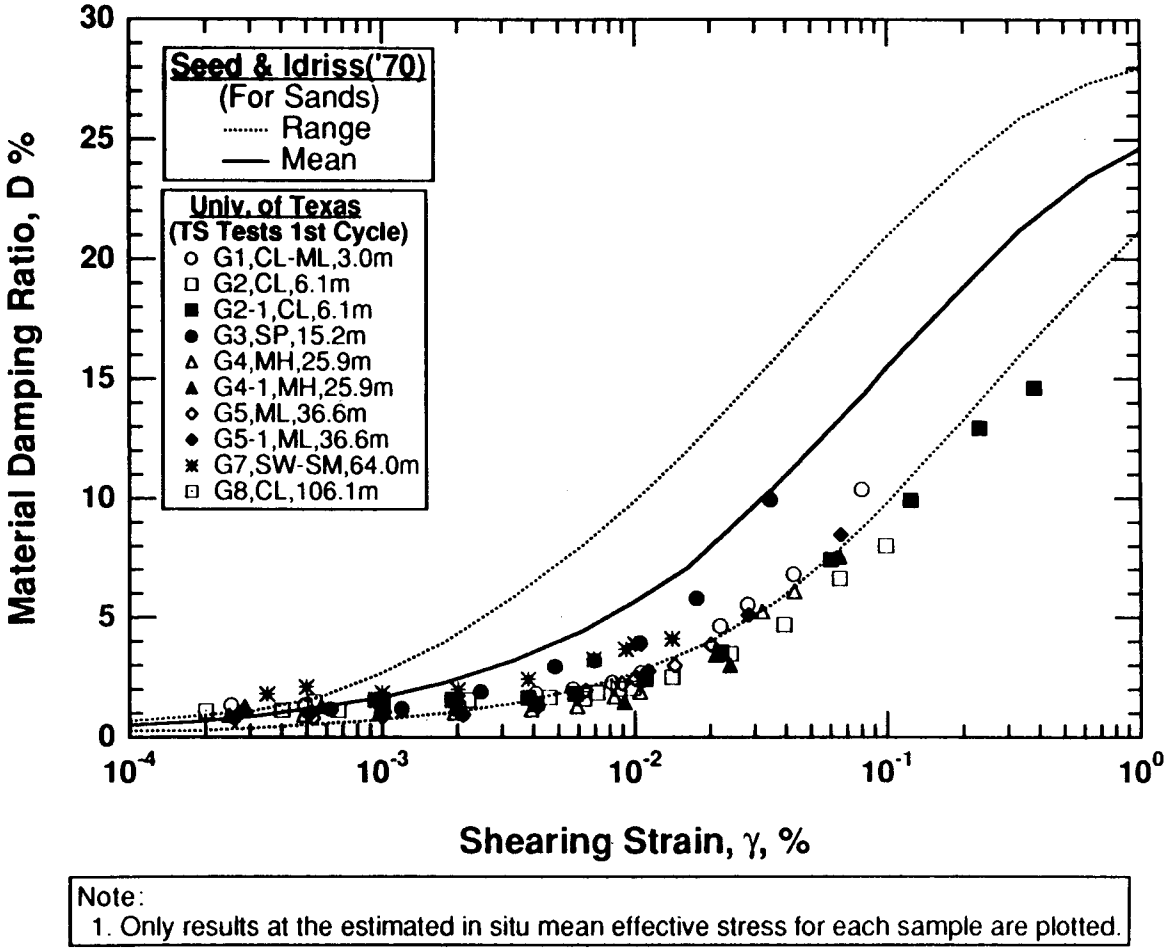

Figure 8.B.2-22
Variation in material damping ratio with shearing strain from torsional shear tests of undisturbed and reconstituted samples from Gilroy 2.

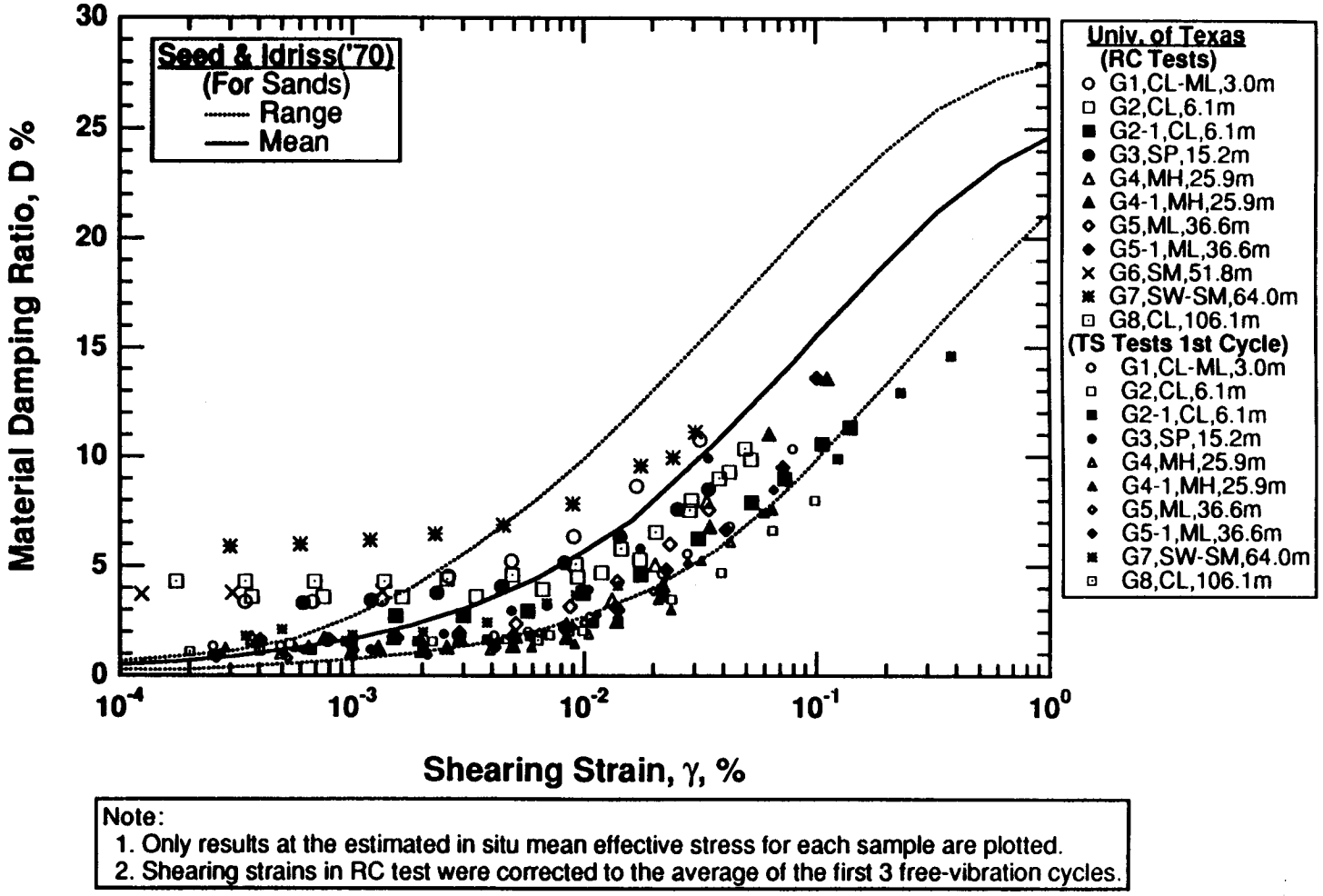

Figure 8.B.2-23
Variation in material damping ratio with shearing strain from resonant column and torsional shear tests of undisturbed and reconstituted samples from Gilroy 2.

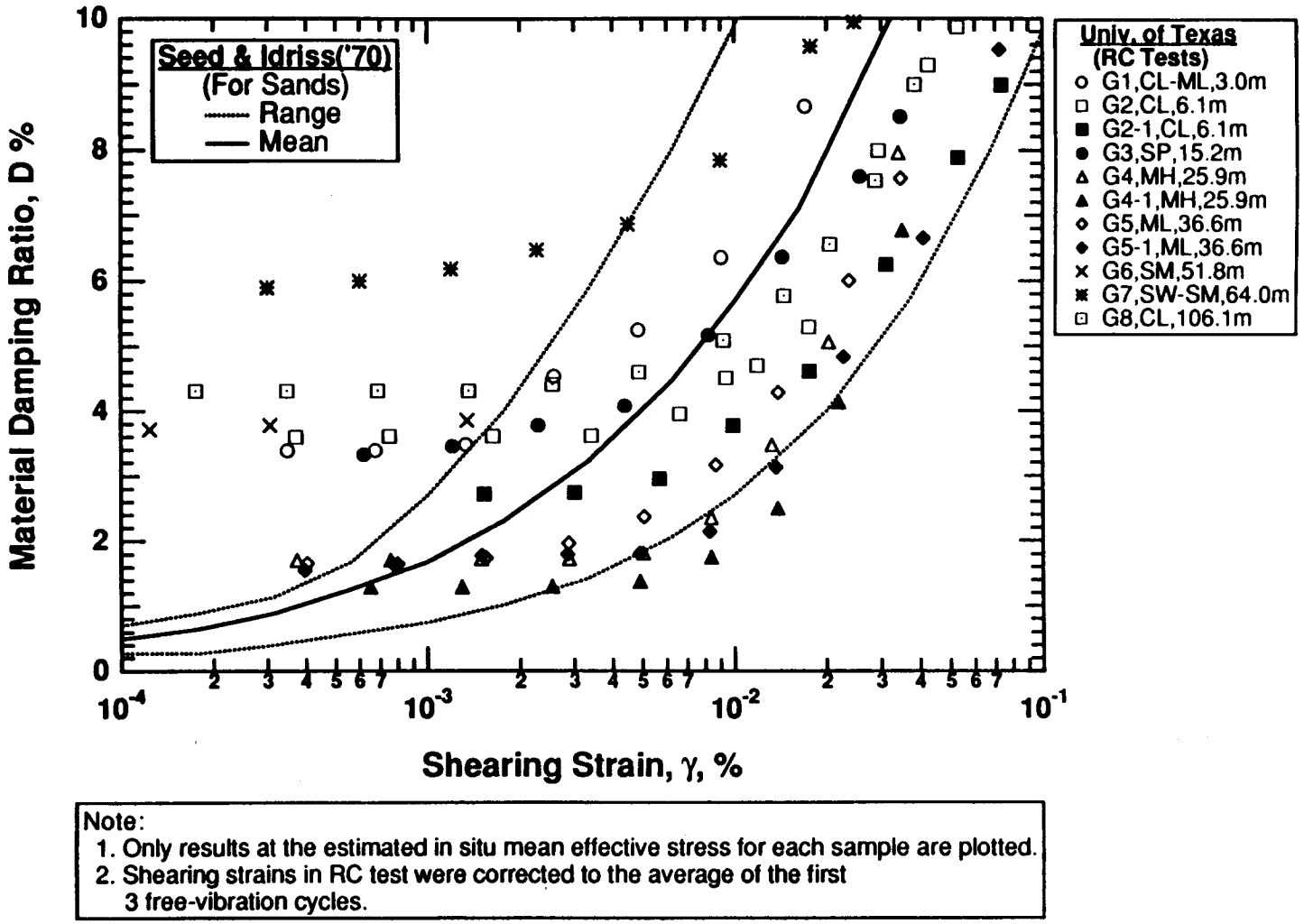

Figure 8.B.2-24
Variation in material damping ratio with shearing strain for $\gamma < 0.1\%$ from resonant column tests of undisturbed and reconstituted samples from Gilroy 2.

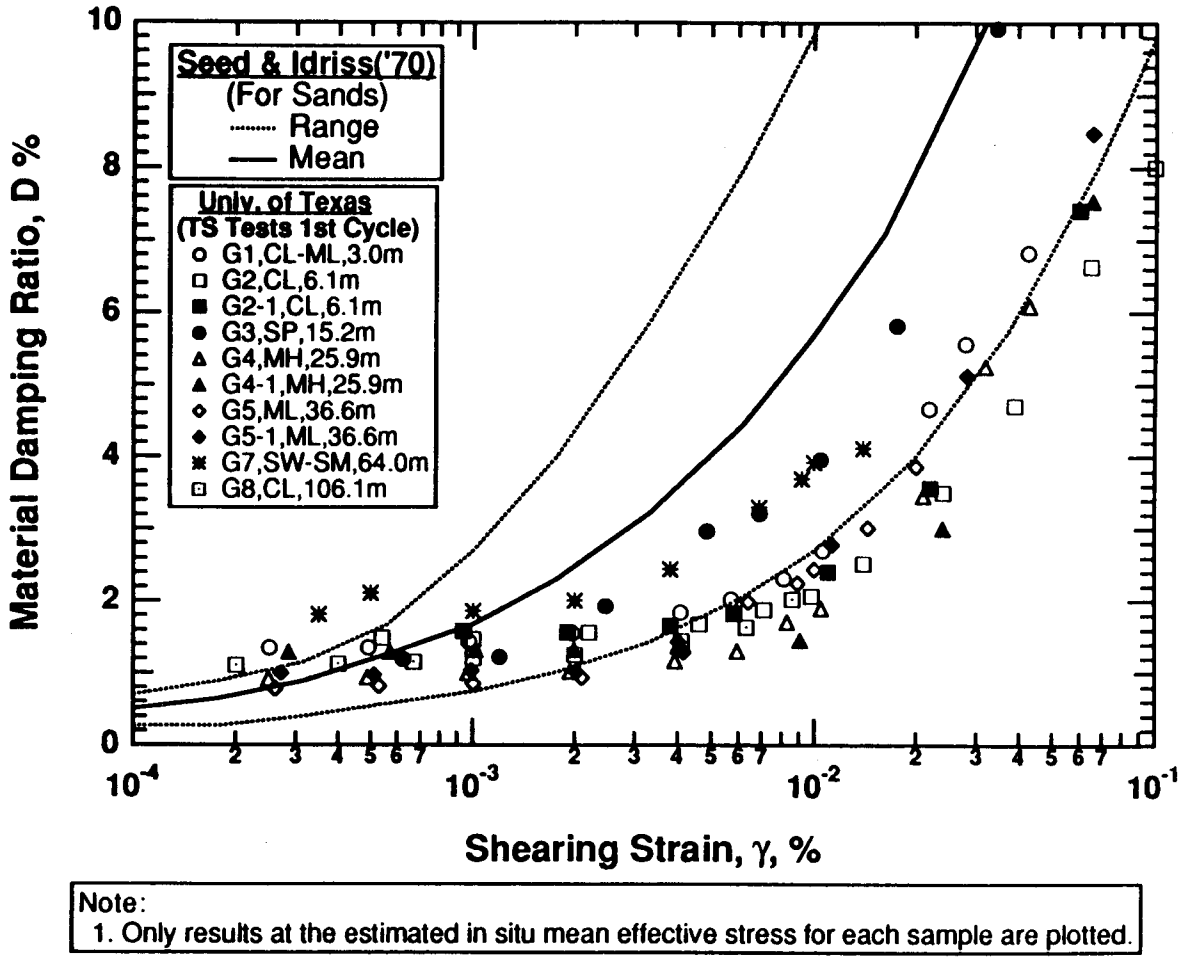

Figure 8.B.2-25
Variation in material damping ratio with shearing strain for $\gamma < 0.1\%$ from the first cycle of torsional shear tests of undisturbed and reconstituted samples from Gilroy 2.

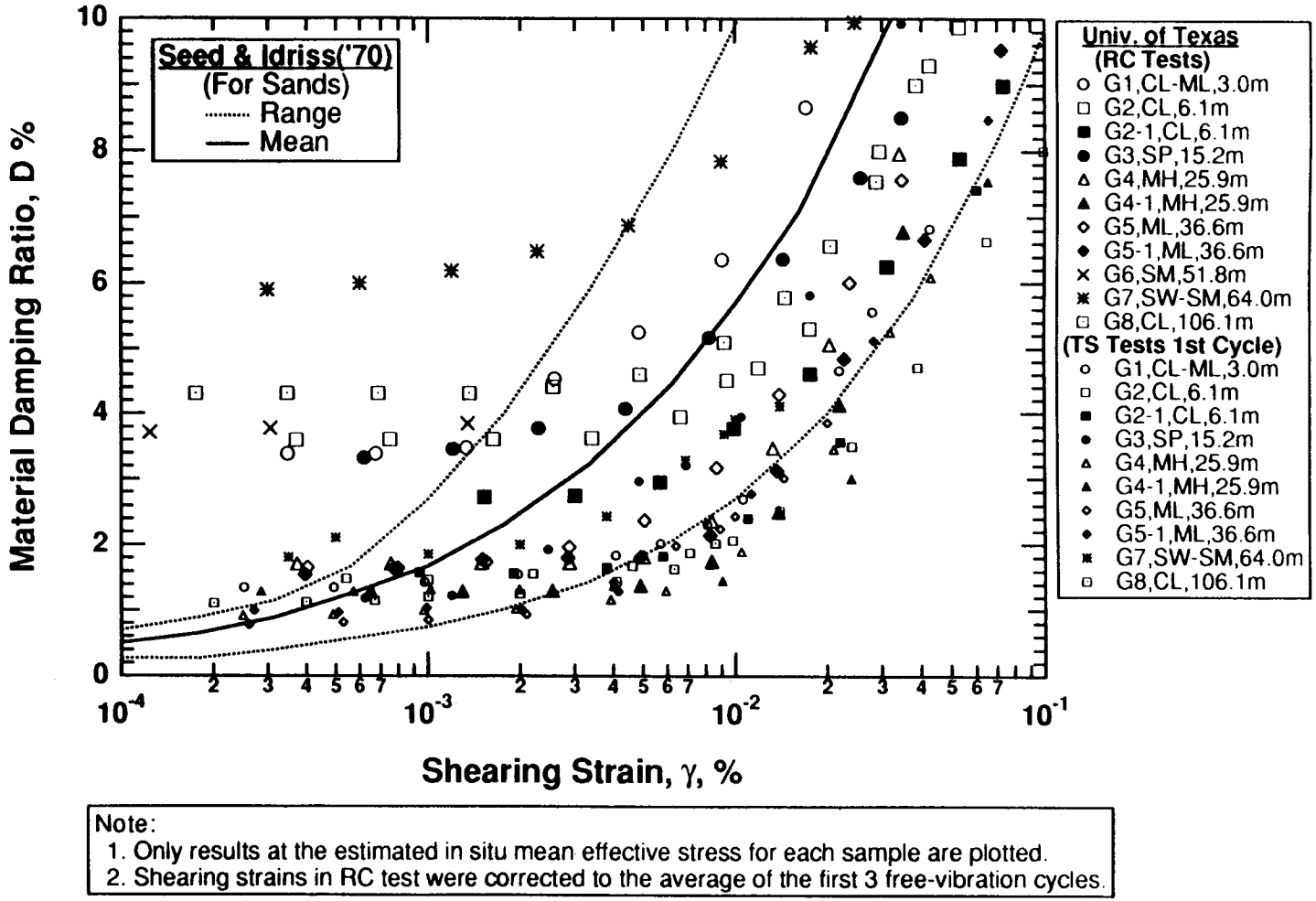

Figure 8.B.2-26
Variation in material damping ratio with shearing strain for $\gamma < 0.1\%$ from resonant column and torsional shear tests of undisturbed and reconstituted samples from Gilroy 2.

References

Hardin, B.O. (1978), "The Nature of Stress-Strain Behavior for Soils," Proceedings, Geotechnical Engineering Division Specialty Conference on Earthquake Engineering and Soil Dynamics, Vol. 1, ASCE, Pasadena, CA, June, pp. 3–90.

Seed, H.B., and Idriss, I.M. (1970), "Soil Moduli and Damping Factors for Dynamic Response Analysis," Report No. EERC 70-10, Earthquake Engineering Research Center, University of California, Berkeley, September, p. 37.

APPENDIX 8.B.2.A
TEST EQUIPMENT AND MEASUREMENT TECHNIQUES

8.B.2.A.1 Introduction

Resonant column and torsional shear (RCTS) equipment has been employed in this investigation for measurement of the deformational characteristics (shear modulus and material damping) of intact soil specimens. This equipment has been developed at The University of Texas at Austin over the past two decades (Isenhower, 1979; Lodde, 1982; Ni, 1987; and Kim, 1991). The equipment is of the fixed-free type, with the bottom of the specimen fixed and torsional excitation applied to the top. Both resonant column (RC) and torsional shear (TS) tests can be performed in a sequential series on the same specimen over a shearing strain range from about 10^{-4}% to slightly more than 10^{-1}%. The primary difference between the two types of tests is the excitation frequency. In the RC test, frequencies above 20 Hz are required and inertia of the specimen and drive system are needed to analyze the measurements. On the other hand, slow cyclic loading involving frequencies generally below 5 Hz is performed in the TS test and inertia does not enter data analysis.

8.B.2.A.2 Resonant Column and Torsional Shear Equipment

8.B.2.A.2.1 Overview of RCTS Equipment

The RCTS apparatus can be idealized as a fixed-free system as shown in Figure 8.B.2.A-1. The bottom end of the specimen is fixed against rotation at the base pedestal, and top end of the specimen is connected to the driving system. The driving system, which consists of a top cap and drive plate, can rotate freely to excite the specimen in cyclic torsion.

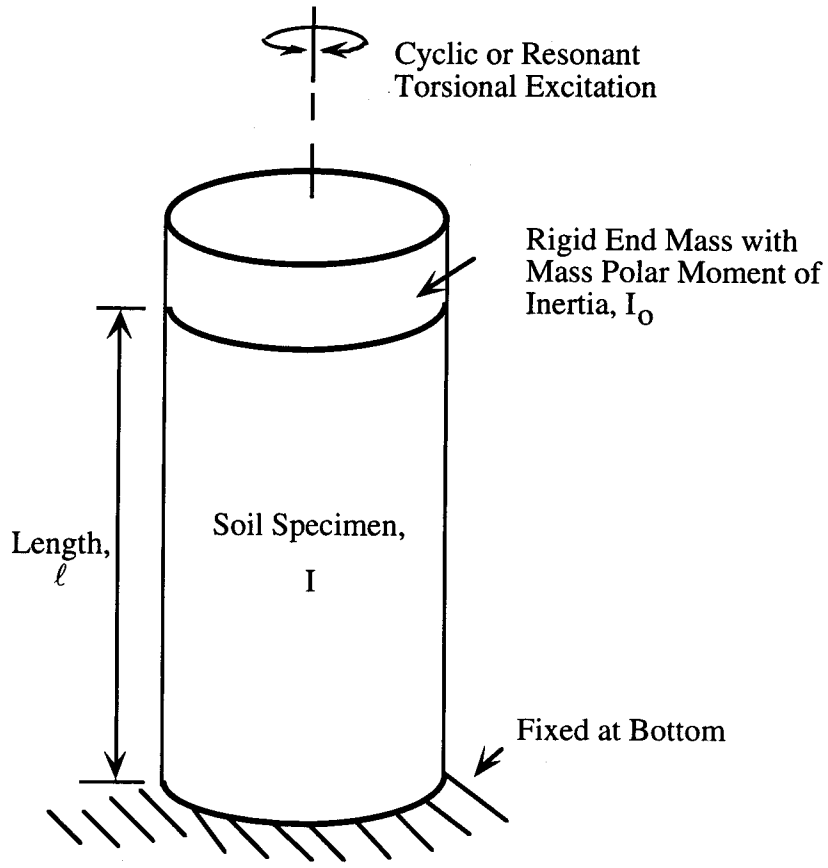

Figure 8.B.2.A-1
Idealized fixed-free RCTS equipment.

A simplified diagram of a fixed-free resonant column (RC) test is shown in Figure 8.B.2.A-2. The basic operational principle is to vibrate the cylindrical specimen in first-mode torsional motion. Harmonic torsional excitation is applied to the top of the specimen over a range in frequencies, and the variation of the acceleration amplitude of the specimen with frequency is obtained. Once first-mode resonance is established, measurements of the resonant frequency and amplitude of vibration are made. These measurements are then combined with equipment characteristics and specimen size to calculate shear wave velocity and shear modulus based on elastic wave propagation. Material damping is determined either from the width of the frequency response curve or from the free-vibration decay curve.

The torsional shear (TS) test is another method of determining shear modulus and material damping using the same RCTS equipment but operating it in a different manner. The simplified configuration of the torsional shear test is shown in Figure 8.B.2.A-3. A cyclic torsional force with a given frequency, generally below 10 Hz, is applied at the top of the specimen. Instead of determining the resonant frequency, the stress-strain hysteresis loop is determined from measuring the torque-twist response of the specimen. Proximitors are used to measure the angle of twist while the voltage applied to the coil is calibrated to yield torque. Shear modulus is calculated from the slope of a line through the end points of the hysteresis loop, and material damping is obtained from the area of the hysteresis loop as shown in Figure 8.B.2.A-3.

The RCTS apparatus used in this study has three advantages. First, both resonant column and torsional shear tests can be performed with the same set-up simply by changing (outside the apparatus) the frequency of the forcing function. Variability due to preparing "identical" samples is eliminated so that both test results can be compared effectively. Second, the torsional shear test can be performed over a shearing strain range between 10^{-4}% and about 10^{-1}%. Common types of torsional shear tests, which generate torque by a mechanical motor outside of the confining chamber, are usually performed at strains above 0.01% because of system compliance. However, the RCTS apparatus used in this study generates torque with an electrical coil-magnet system inside the confining chamber, thus eliminating the problem with an external motor. The torsional shear test can be performed at the same low-strain amplitudes as the resonant column test, and results between torsional shear and resonant column testing can be easily compared over a wide range of strains. Third, the loading frequency in the torsional shear test can be changed easily from 0.01 Hz to 10 Hz. Therefore, the effect of frequency on deformational characteristics can be conveniently investigated using this apparatus.

The RCTS apparatus consists of four basic subsystems which are: (1) a confinement system, (2) a drive system, (3) a height-change measurement system, and (4) a motion monitoring system. The general configuration of the RCTS apparatus (without the confinement system) is shown in Figure 8.B.2.A-4. The RCTS apparatus was automated by Ni (1987) so that a microcomputer controls the test, collects the data, and reduces results. Computer-aided subsystems are discussed briefly in the following sections.

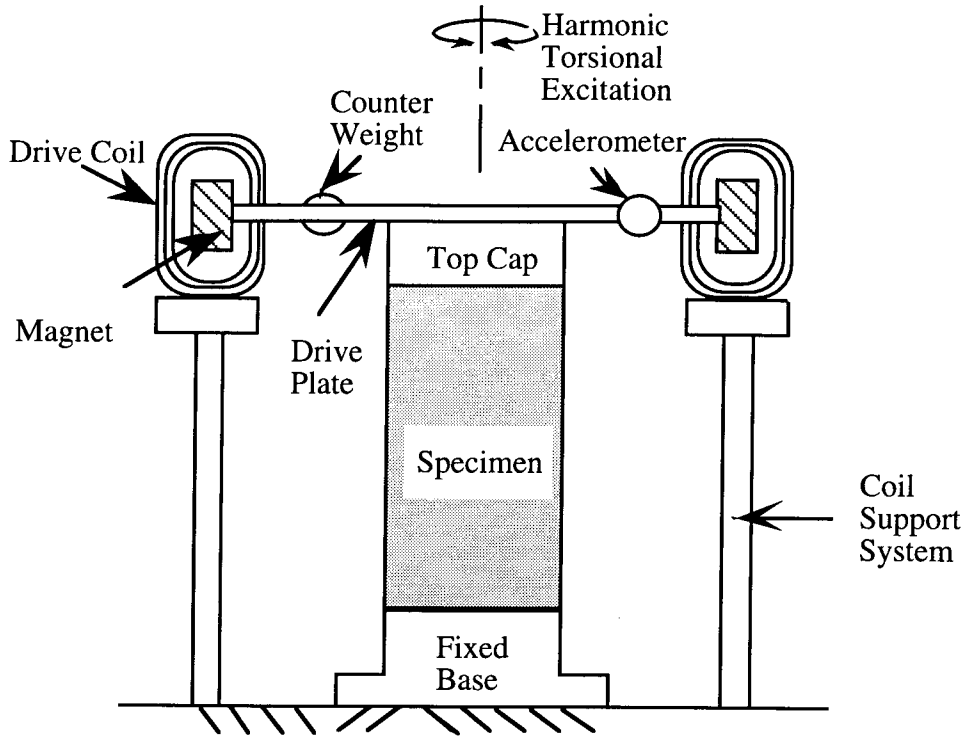

a) Specimen in the Resonant Column Apparatus
(Confinement Chamber Not Shown)

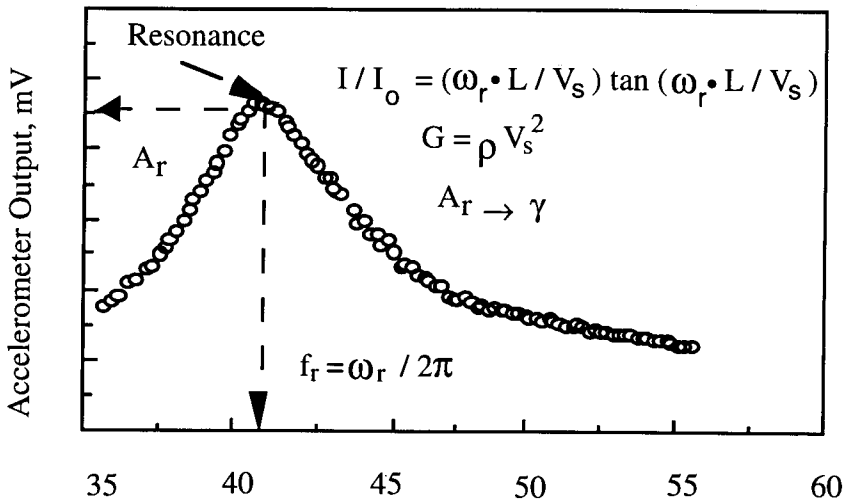

b) Typical Frequency Response Curve

Figure 8.B.2.A-2
Simplified diagram of a fixed-free resonant column test and an associated frequency response curve.

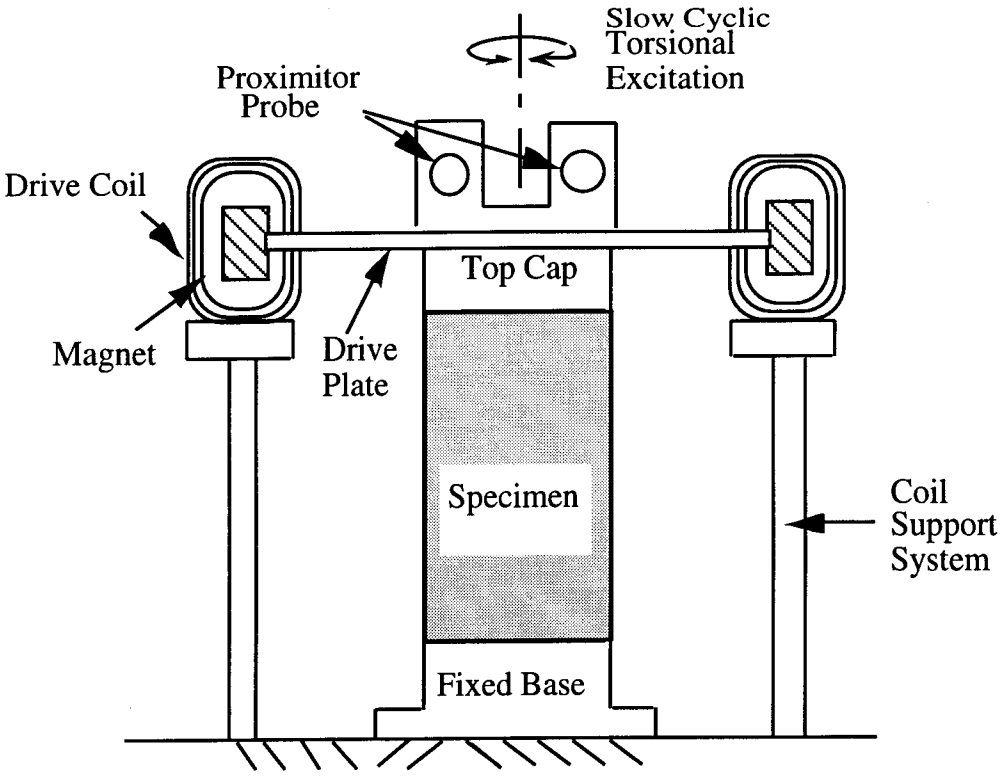

a) Specimen in the Torsional Shear Test Apparatus
(Confinement Chamber Not Shown)

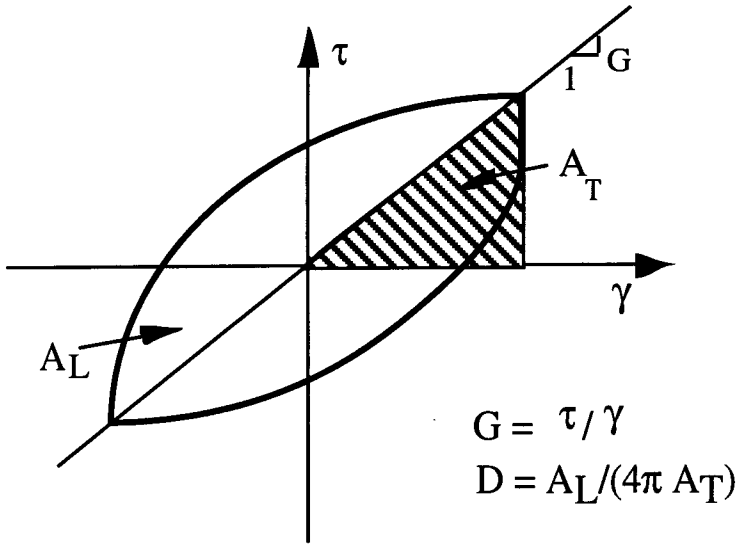

b) Measurement of Shear Modulus and Damping Ratio

Figure 8.B.2.A-3
Configuration of a torsional shear test and evaluation of shear modulus and material damping ratio.

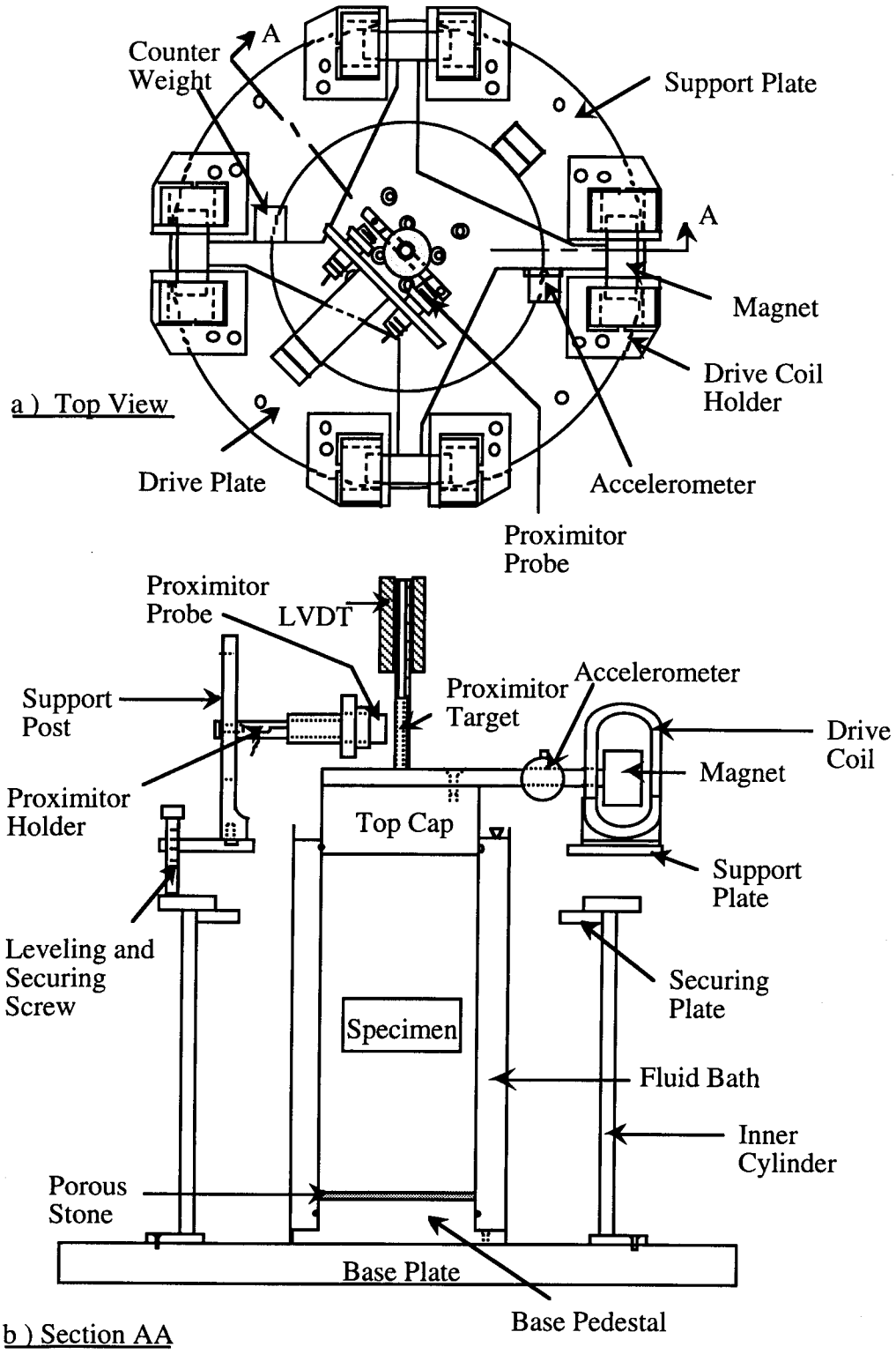

Figure 8.B.2.A-4
General configuration of RCTS equipment (from Ni, 1987).

8.B.2.A.2.2 RCTS Confinement System

The confining chamber is made of stainless steel. A thin-walled (0.6 cm in thickness) hollow cylinder fits into circular grooves machined in 2.5 cm thick base and top plates. Four stainless steel connecting rods (1.28 cm in diameter) are used to secure the base and top plates to the hollow cylinder, and O-rings in the circular grooves are used to seal the chamber. In this configuration, the chamber has been designed to withstand a maximum air pressure of about 200 psi (1379 kPa). To safely test samples at higher confining pressures (pressures on the order of 600 psi (4137 kPa)), the confinement system was modified by adding additional stainless steel rods to secure the cylinder to the top and base plates and reinforcement to the top and base plates.

Compressed air is used to confine isotropically the specimen in the RCTS device. The air pressure to the chamber generally is regulated by a Fairchild M 30 regulator and air supplied to the regulator is filtered. At high confining pressures, additional regulators are used. The soil specimen is sealed in a membrane and pore pressure in the specimen is normally vented to atmospheric pressure.

Inside the confining chamber, the air pressure acts upon a silicon fluid bath which surrounds the sides of the soil specimen. The purpose of the silicon fluid bath is to retard air migration through the membrane and into the specimen to prevent drying of the specimen. Figure 8.B.2.A-5 shows the simplified configuration of the confinement system.

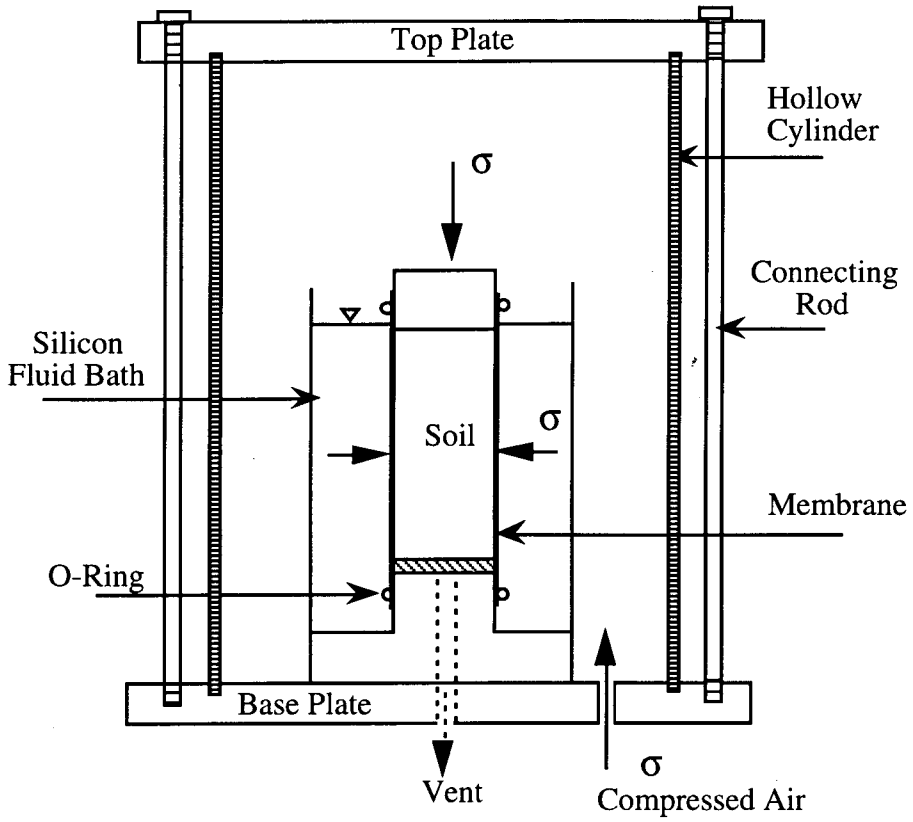

Figure 8.B.2.A-5
Simplified configuration of confinement system.

8.B.2.A.2.3 Drive System

The drive system consists of a four-armed drive plate, four magnets, eight drive coils, a power amplifier, and a function generator. Each magnet is rigidly attached to the end of one arm of the drive plate as shown in Figure 8.B.2.A-4. Eight drive coils encircle the ends of the four magnets so that the drive plate excites the soil specimen in torsional motion when a current is passed through the coils. The maximum torque that the drive system can develop depends on the strength of the magnets, size of the drive coils, resistance of the drive coils, size of the space between the magnets and drive coils, length of the arms of the drive plate, and the electrical characteristics of the function generator and power amplifier. For the three drive systems used in this work, the maximum torque was about 0.60 lb-ft (82 N-cm).

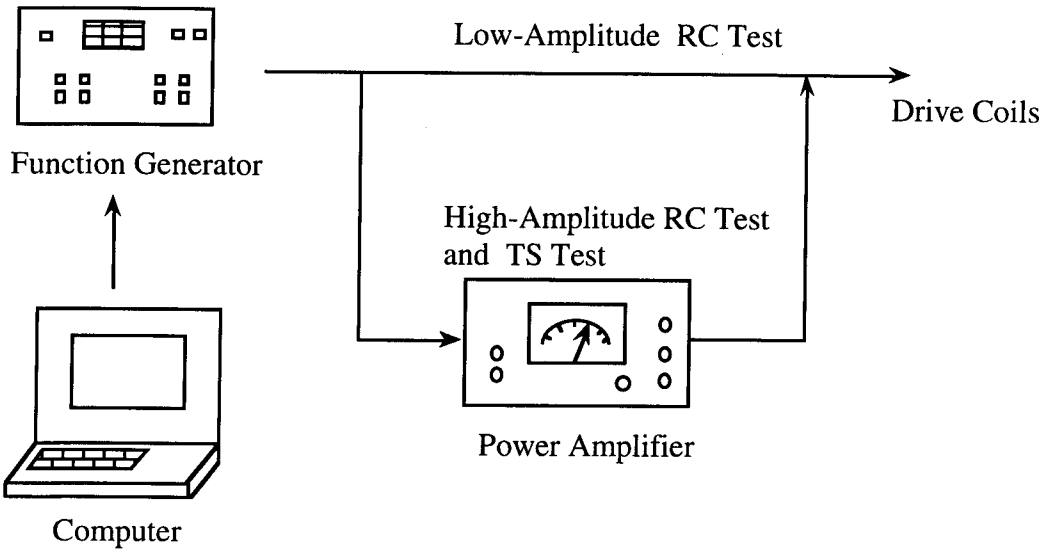

Figure 8.B.2.A-6
Schematic diagram of the drive system.

A schematic diagram of the drive system is shown in Figure 8.B.2.A-6. The micro-computer activates a function generator (HP 3314A) to input sinusoidal voltage to the drive coils. In the resonant column (RC) test, the function generator performs frequency sweeps with a constant amplitude while in the torsional shear test, a fixed-frequency N-cycle mode is used. For high-amplitude resonant column and torsional shear (TS) tests, the sinusoidal input current is amplified by a power amplifier (HP 6824A) before going to the drive coils.

8.B.2.A.2.4 Height-Change Measurement System

The height change of the soil specimen is measured to account for the changes in the length and mass of the specimen during consolidation or swell. This measurement is also used to calculate change in the mass moment of inertia, mass density, and void ratio during testing (by assuming isotropic strain under isotropic confinement and constant degree of saturation). The height change is measured by a linear variable differential transformer (LVDT). The height change measurement system consists of an LVDT (CRL Model SH-200-53R), a function generator (HP 3314A), and a digital voltmeter (HP 3456A). The LVDT core is not in contact with the LVDT coil housing so that no friction occurs during RCTS testing.

The output and calibration factor of an LVDT depend on both the frequency and magnitude of the excitation voltage. In this test the computer activates the function generator to generate the input signal in the LVDT coil at a frequency of 500 Hz and a voltage level of 4.77 RMS volts. The output from the LVDT is read with a digital voltmeter. The height change is calculated from the output voltage combined with the calibration factor. The schematic diagram of the height change measuring system is shown in Figure 8.B.2.A-7.

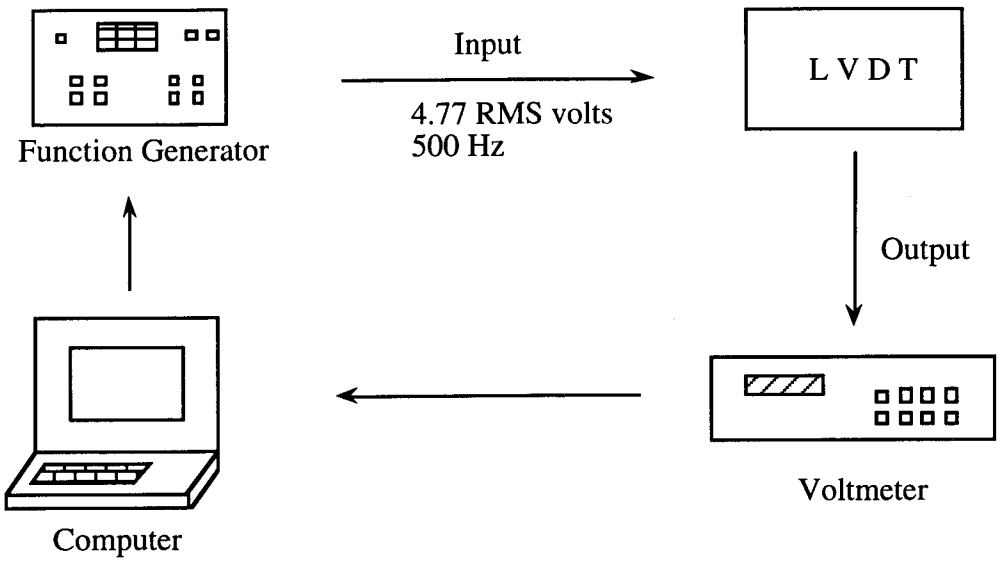

Figure 8.B.2.A-7
Schematic diagram of the height-change measuring system.

8.B.2.A.2.5 Motion Monitoring System

Dynamic soil properties are obtained in the RC test at the resonant frequency which is usually above 20 Hz while torsional shear testing is used to measure the low-frequency (below 10 Hz) cyclic stress-strain relationship of soil. Because of the different frequencies applied in the resonant column and torsional shear tests, different motion monitoring systems are used.

Resonant Column (RC) Test. The motion monitoring system in the RC test is designed to measure the resonant frequency, shearing strain, and free-vibration decay curve. This system consists of an accelerometer (Columbia Research Laboratory Model 3021), a charge amplifier (Columbia Research Laboratory Model 4102M), a frequency counter (HP 5334A), a digital voltmeter (HP 3456A), and a digital oscilloscope (Nicolet 20929-01). The schematic diagram of the motion monitoring system is shown in Figure 8.B.2.A-8.

The accelerometer is oriented to be sensitive to torsional vibrations of the drive plate. The charge amplifier conditions the accelerometer output to be linear for all levels of acceleration in the test. The digital voltmeter reads the output voltage from the accelerometer at each frequency which is measured by the frequency counter. The resonant frequency is obtained from the frequency response curve. Once the resonant frequency is obtained, the computer activates the function generator to excite the specimen at the resonant frequency and then suddenly stops the current so that the free-vibration decay curve is recorded by the digital oscilloscope.

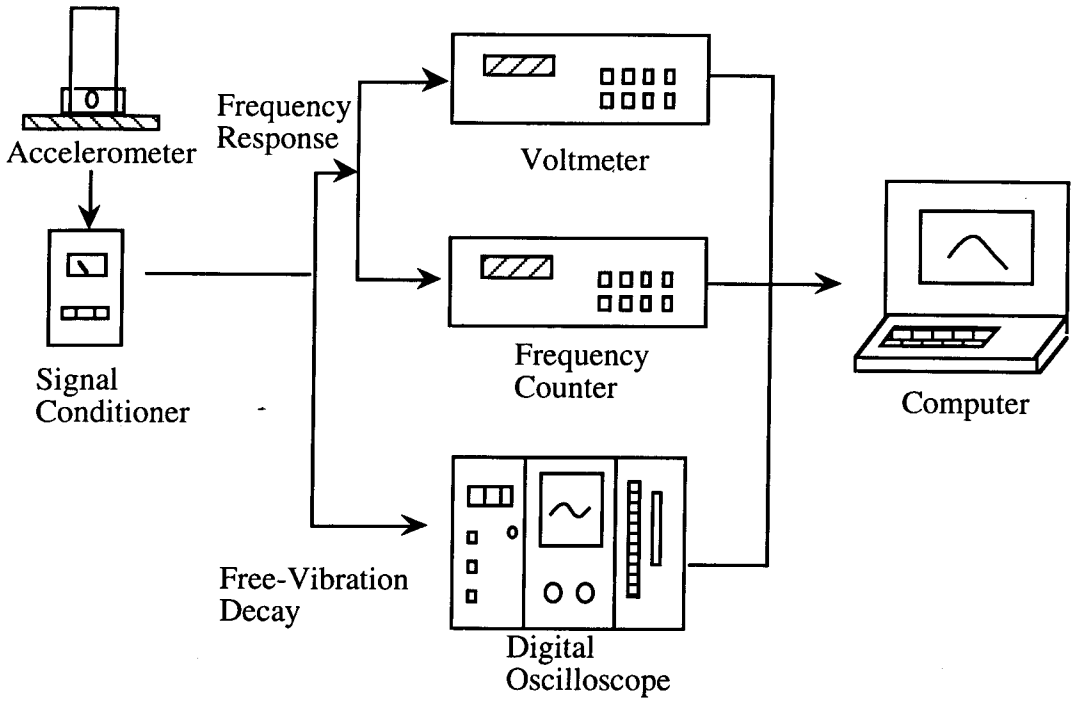

Figure 8.B.2.A-8
Schematic diagram of the motion monitoring system in the resonant column test.

The resonant frequency of soils are typically in the range of 20 Hz to 300 Hz with this equipment. To test soils effectively over a wide range of stiffnesses, the search for the resonant frequency is performed in two stages, a rough sweep and a fine sweep. During the rough sweep, a fast logarithmic-linear frequency sweep (16 seconds to sweep from 1 to 170 Hz) is used. The fine sweep is then performed to determine an accurate resonant frequency in the neighborhood where the resonant frequency was found in the rough sweep.

Torsional Shear (TS) Test. The motion monitoring system in the TS test (3000 Proximitor System) is used to monitor torque-twist hysteresis loops of the specimen. This system consists of two proximitors (Bentry Nevada M 20929-01), two proximitor probes (Bentry Nevada M 300-00), an operational amplifier (Tektronix TM 504 with AM501), a DC power supply (Lambda M-11-902), a U-shaped target and a digital oscilloscope (Nicolet 20929-01). The U-shaped target is secured to the top of the drive plate, and the two proximitor probes are rigidly attached to the support stand. A schematic diagram of the motion monitoring system in the torsional shear test is shown in Figure 8.B.2.A-9.

The function of the proximitor probes is to measure the width of the air gap between the target and the probe tip. Because the proximitor probes do not touch the drive plate, no compliance problems are introduced into the measurement. Two probes are used and the operational amplifier subtracts the signal from one probe from the other so that the effect of bending in the specimen toward the probes can be eliminated. The proximitor system is a very effective low-frequency motion monitoring system which does not introduce any compliance problems into the measurement. With the simultaneous measurement of torque, load-displacement hysteresis loops can be determined.

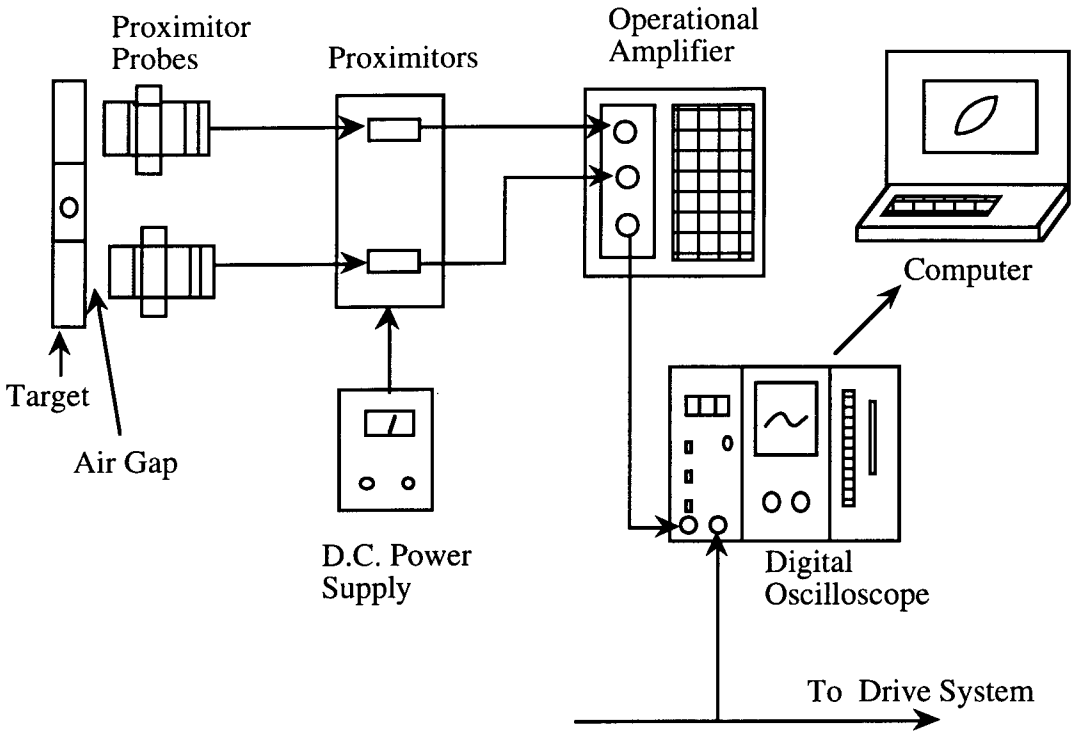

Figure 8.B.2.A-9
Schematic diagram of the motion monitoring system in the torsional shear test (3000 Proximitor System).

8.B.2.A.3 Method of Analysis in the Resonant Column Test

The resonant column test is based on the one-dimensional wave equation derived from the theory of elasticity. The shear modulus is obtained by measuring the first-mode resonant frequency while material damping is evaluated from either the free-vibration decay curve or from the width of the frequency response curve assuming viscous damping.

8.B.2.A.3.1 Shear Modulus

The governing equation of motion for the fixed-free torsional resonant column test is:

$$\frac{\Sigma I}{I_o} = \frac{\omega_n \bullet l}{V_s} \bullet \tan\left(\frac{\omega_n \bullet l}{V_s}\right) \qquad (8.B.2.A\text{-}1)$$

Where,

ΣI = $I_s + I_m$ + ---
I_s = mass moment of inertia of soil,
I_m = mass moment of inertia of membrane,
I_o = mass moment of inertia of rigid end mass at the top of the specimen,
l = length of the specimen,
V_s = shear wave velocity of the specimen, and
ω_n = undamped natural circular frequency of the system.

The value of I_o is known from the calibration of the drive plate. The values of I_s and l are easily determined from the specimen size and weight. Once the first-mode resonant frequency is determined, the shear wave velocity can be calculated from Eq. 8.B.2.A-1 by assuming that the resonant circular frequency and ω_n are equal.

As noted above and shown in Figure 8.B.2.A-2 the resonant circular frequency, ω_r,is measured instead of undamped natural frequency, ω_n, and ω_r is used to calculate shear wave velocity. If the damping in the system is zero, ω_r and ω_n are equal. The relationship between ω_r and ω_n is:

$$\omega_r = \omega_n \sqrt{1-2D^2} \qquad \text{(8.B.2.A-2)}$$

A typical damping ratio encountered in the resonant column test is less than 20 percent, which corresponds to a difference of less than 5 percent between ω_r and ω_n. In this study, the damping measured in the resonant column test was usually less than 10 percent, and ω_r can be used instead of ω_n with less than a two percent error.

Once the shear wave velocity is determined, shear modulus is calculated from the relationship:

$$G = \rho \bullet V_s^2 \qquad \text{(8.B.2.A-3)}$$

where ρ is the total mass density of the soil (total unit weight divided by gravity).

8.B.2.A.3.2 Shearing Strain

The shearing strain varies radially within the specimen and may be expressed as a function of the distance from the longitudinal axis as illustrated in Figure 8.B.2.A-10. The equivalent shearing strain, γ_{eq} or γ, is represented by:

$$\gamma = r_{eq} * \theta_{max} / l \qquad \text{(8.B.2.A-4)}$$

Where,

r_{eq} = equivalent radius,
θ_{max} = angle of twist at the top of the specimen, and
l = length of the specimen.

Chen and Stokoe (1979) studied the radial distribution in shearing strain to find a value of r_{eq} for the specimen tested in the RCTS equipment to evaluate an effective strain. They found that the value of r_{eq} varied from $0.82*r_0$ for a peak shearing strain amplitude below 0.001% to $0.79*r_0$ for a peak shearing strain of 0.1% for a solid specimen. These values of r_{eq} have been adopted in this study.

In the resonant column test, the resonant period (T_r, seconds), and output voltage of accelerometer (A_c, volts (RMS)) at resonance are measured. Accelerometer output is changed to the displacement by using the accelerometer calibration factor (CF, volts (RMS)/in./sec^2) assuming harmonic motion. The accelerometer displacement is divided by the distance (D_{ac}, inches) between the location of accelerometer and the axis of the specimen to calculate the angle of twist at the top of the specimen (θ_{max}). The shearing strain is then calculated by:

$$\gamma = r_{eq} \frac{A_c \bullet Tr^2}{4\pi^2 \bullet CF} \bullet \frac{1}{D_{ac}} \bullet \frac{1}{l} \qquad \text{(8.B.2.A-5)}$$

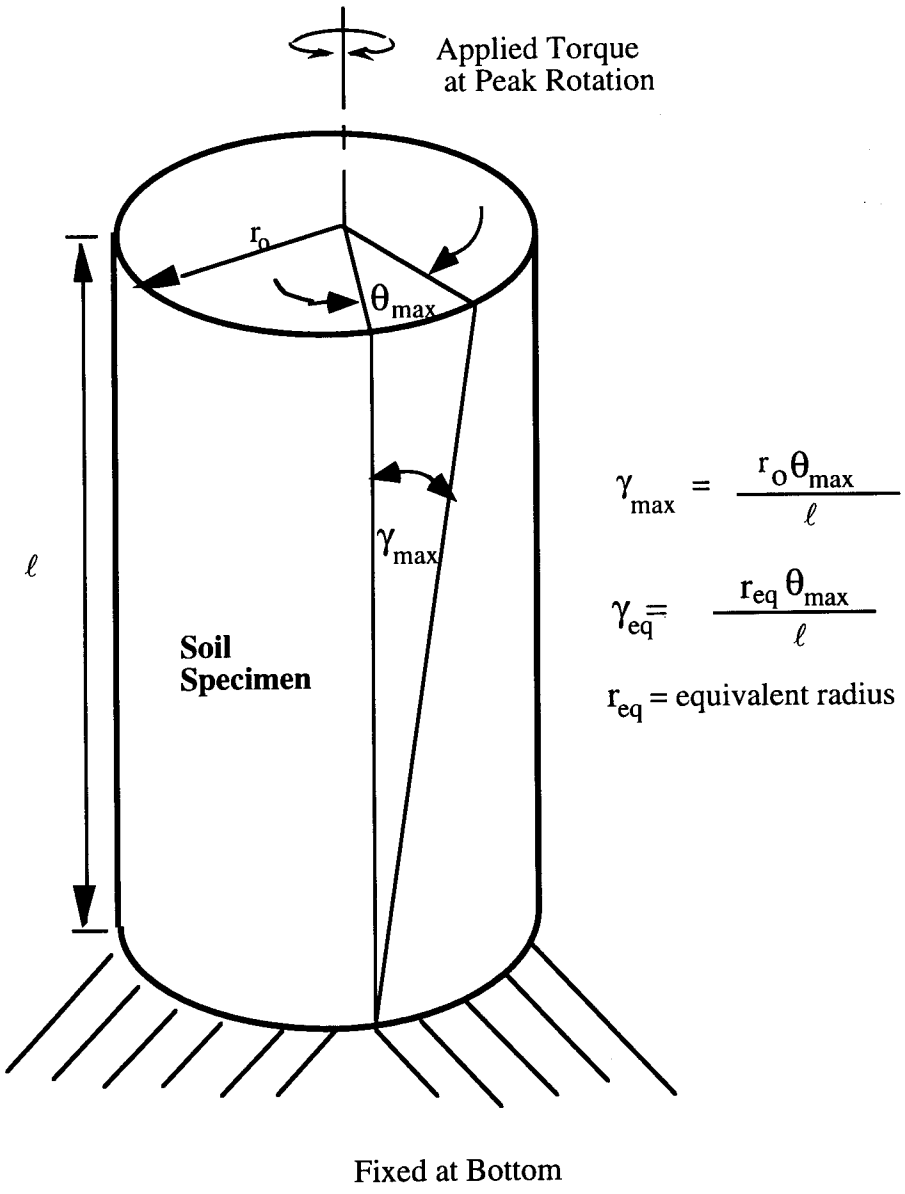

Figure 8.B.2.A-10
Shearing strain in soil column.

8.B.2.A.3.3 Material Damping

In the resonant column test, material damping ratio can be evaluated from either the free-vibration decay method or from the half-power bandwidth method. Each of these methods is discussed below. It is important to note that, in these measurements, the damping measurement includes material damping in the soil plus any damping in the equipment. Calibration of equipment damping is discussed in Section 8.B.2.A.5.

Free-Vibration Decay Method. Material damping in soils can be quite complex to define. However, the theory for a single-degree-of-freedom system with viscous damping is a useful framework for describing the effect of damping which occurs in soil (Richart et al., 1970). The decay of free vibrations of a single-degree-of-freedom system with viscous damping is described by the logarithmic decrement, δ, which is the ratio of the natural logarithm of two successive amplitudes of motion as:

$$\delta = \ln\left(\frac{Z_1}{Z_2}\right) = \frac{2\pi D}{\sqrt{1-D^2}} \qquad \text{(8.B.2.A-6)}$$

Where,

Z_1 and Z_2 = two successive strain amplitudes of motion, and
D = material damping ratio.

The free-vibration decay curve is recorded using an oscilloscope by shutting off the driving force while the specimen is vibrating at the resonant frequency. The amplitude of each cycle is measured from the decay curve, and the logarithmic decrement is then calculated using Eq. 8.B.2.A-6. Material damping ratio is calculated from logarithmic decrement according to:

$$D = \sqrt{\frac{\delta^2}{4\pi^2 + \delta^2}} \qquad \text{(8.B.2.A-7)}$$

A typical damping measurement from a free-vibration decay curve (from a metal calibration specimen) is shown in Figure 8.B.2.A-11.

In this method, it is not certain which strain amplitude is a representative strain for damping ratio calculated by Eq. 8.B.2.A-7 because strain amplitude decreases during free-vibration decay. In this study, a representative strain amplitude was used as the peak strain amplitude during steady-state vibration for shearing strains below 0.001%. However, at larger strains, the representative strain is smaller than the peak strain, and the average strain determined for the first three cycles of free vibration was used.

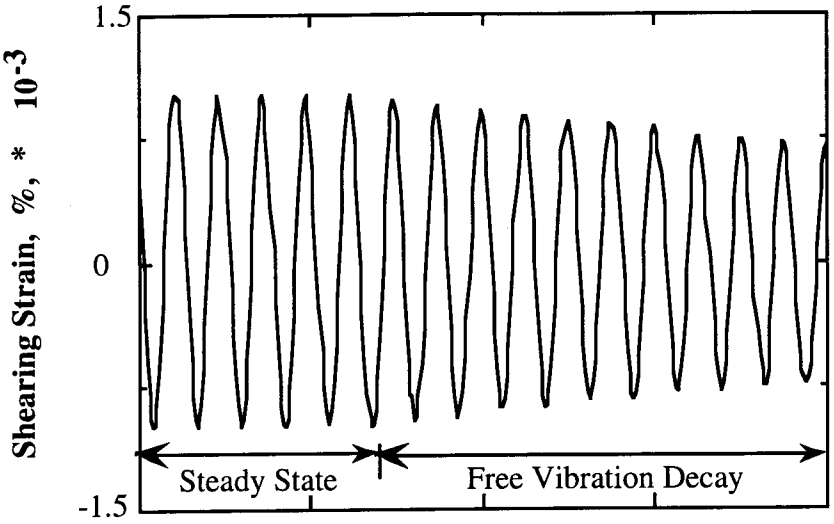

a) Free-Vibration Decay Curve

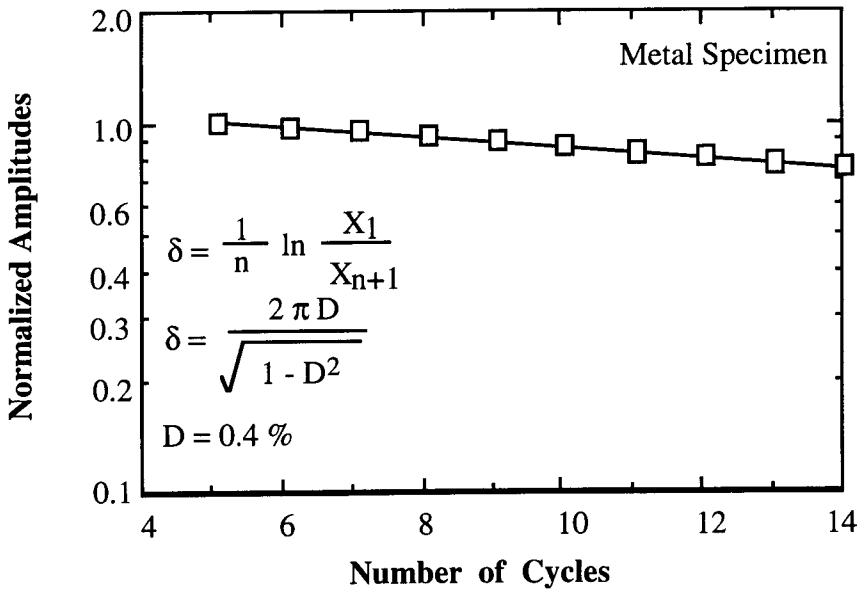

b) Analysis of Free-Vibration Decay Curve

Figure 8.B.2.A-11
Determination of material damping ratio from the free-vibration decay curve using a metal specimen.

Half-Power Bandwidth Method. Another method of measuring damping in the resonant column test is the half-power bandwidth method, which is based on measurement of the width of the frequency response curve near resonance. From the frequency response curve, the logarithmic decrement can be calculated from:

$$\delta = \frac{\pi}{2}\frac{f_2^2 - f_1^2}{f_r^2}\sqrt{\frac{A^2}{A_{max}^2 - A^2}\frac{\sqrt{1-2D^2}}{1-D^2}} \qquad \text{(8.B.2.A-8)}$$

Where,

f_1 = frequency below the resonance where the strain amplitude is A,
f_2 = frequency above the resonance where the strain amplitude is A,
f_r = resonant frequency, and
D = material damping ratio.

If the damping ratio is small and A is chosen as 0.707 A_{max}, which is called the half-power point, Eq. 8.B.2.A-8 can be simplified as:

$$\delta \equiv \pi \bullet \frac{f_2 - f_1}{f_r} \qquad \text{(8.B.2.A-9)}$$

Therefore, the damping ratio can be expressed as:

$$D \equiv \frac{f_2 - f_1}{2f_r} \qquad \text{(8.B.2.A-10)}$$

A typical damping measurement by the half-power bandwidth method (for a metal calibration specimen) is shown in Figure 8.B.2.A-12.

Background noise can be a problem in measuring material damping using the free-vibration decay method at strains less than about 0.001%. On the other hand, background noise generally has a smaller effect on the frequency response curve at strains below 0.001%. Therefore, the half-power bandwidth method is preferred to the free-vibration decay method for making small-strain damping measurements. However, at large strains, symmetry in the frequency response curve is no longer maintained, and a serious error can be introduced in the half-power bandwidth method (Ni, 1987). In this study, both types of damping measurements were made at small-strains in an attempt to obtain good data sets while only the free-vibration decay method was used at larger strains (above 0.001%).

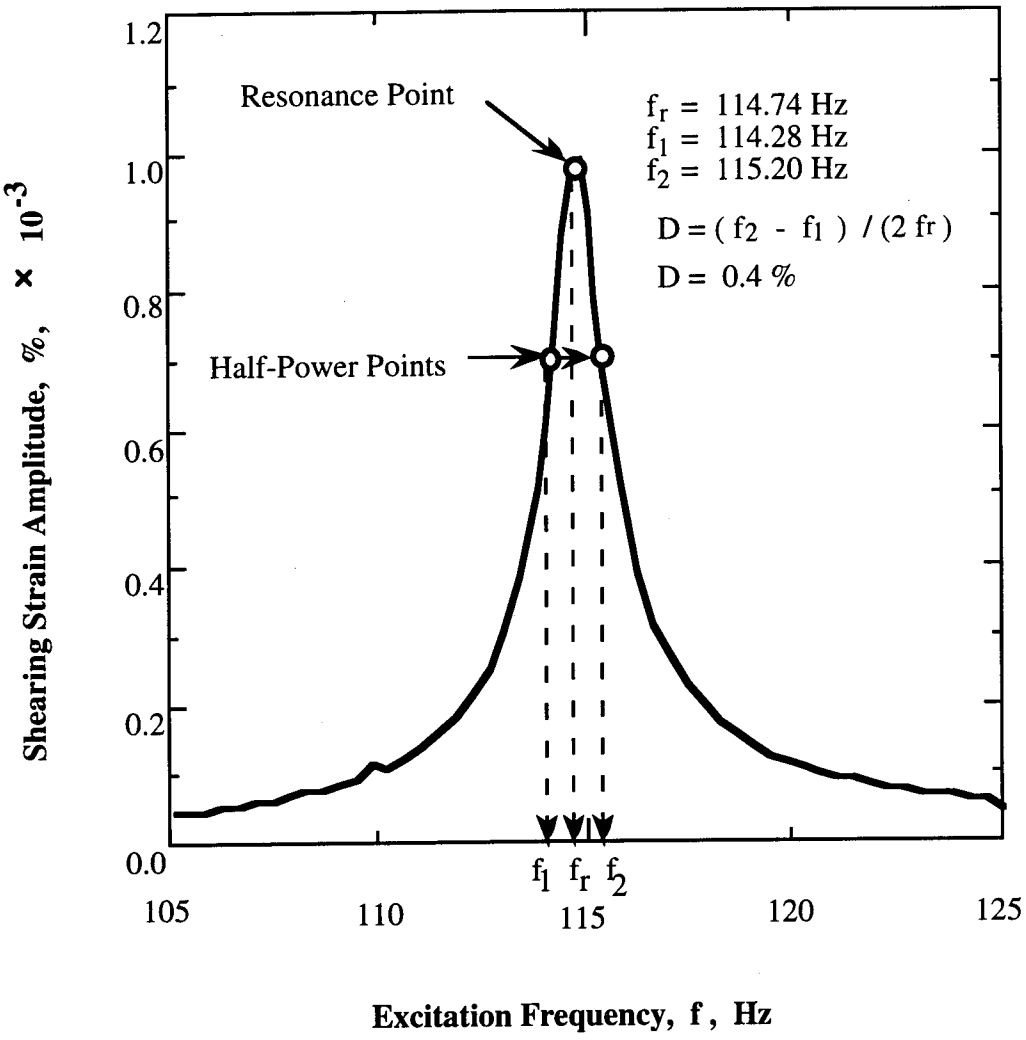

Figure 8.B.2.A-12
Determination of material damping from the half-power bandwidth method using a metal specimen.

8.B.2.A.4 Method of Analysis in the Torsional Shear Test

The torsional shear test is another method of determining the deformational characteristics (modulus and damping) of soil using the same RCTS device. Rather than measuring the dynamic response of the specimen, the actual stress-strain hysteresis loop is determined by means of measuring the torque-twist curve. Shear modulus is calculated from the slope of the hysteresis loop, and the hysteric damping ratio is calculated using the area of the hysteresis loop.

8.B.2.A.4.1 Shear Modulus

Because shear modulus is calculated from the stress-strain hysteresis loop, shearing stress and shearing strain in the torsional shear test need to be defined.

Shearing Stress. Determination of shearing stress in the torsional shear test is based on the theory of elasticity for circular or tubular rods in pure torsion. Assume that pure torque, T, is applied to the top of the specimen. The torque can be calculated from:

$$T = \int_{r_i}^{r_o} \tau_r (2\pi\ r)\ r\ dr \qquad \text{(8.B.2.A-11)}$$

where τ_r is the shearing stress at a distance r from the axis of specimen and, r_o and r_i are outside and inside radii, respectively. If the shearing stress is assumed to vary linearly across the radius:

$$\tau_r = \tau_m \bullet (r / r_o) \qquad \text{(8.B.2.A-12)}$$

where τ_m is the maximum shearing stress at $r = r_o$. Eq. 8.B.2.A-12 can be rewritten as:

$$T = \frac{\tau_m}{r_o} \bullet \frac{\pi}{2} \bullet (r_o^4 - r_i^4) = \frac{\tau_m}{r_o} \bullet J_p \qquad \text{(8.B.2.A-13)}$$

where J_p is the area polar moment of inertia. From Eq. 8.B.2.A-13, one can write:

$$\tau_m = r_o \bullet \frac{T}{J_p} \qquad \text{(8.B.2.A-14)}$$

Because shearing stress is assumed to vary linearly across the radius, the average torsional shearing stress is defined as:

$$\tau_{avg} = r_{eq} \bullet \frac{T}{J_p} \qquad \text{(8.B.2.A-15)}$$

The value of r_{eq} is the same value as used in the resonant column analysis for calculation of shearing strain (Section 8.B.2.A.3.2).

The value of applied torque, T, is calculated from the input voltage applied to the drive system, V_T (Volts), and the torque calibration factor, K_T (torque / Volts). Thus, average shearing stress becomes:

$$\tau_{avg} = r_{eq} \bullet K_T \bullet V_T / J_p \qquad \text{(8.B.2.A-16)}$$

Shearing Strain. Calculation of shearing strain in the torsional shear test follows the same procedure used in the resonant column test. The proximitor system directly measures the displacement (instead of acceleration measured in the resonant test). Hence, the angle of twist (θ) is calculated from the proximitor output voltage, V_P (volts), and the proximitor calibration factor, K_P (rad / volt). Shearing strain, γ, is then calculated from:

$$\gamma = r_{eq}\ \Sigma\ K_P \bullet V_P / l \qquad \text{(8.B.2.A-17)}$$

Shear Modulus. Once the stress-strain hysteresis loop is measured, the shear modulus, G, is calculated from the slope of a line through the end points of the hysteresis loop as shown in Figure 8.B.2.A-13. Thus, the shear modulus is calculated from:

$$G = \tau / \gamma \qquad \text{(8.B.2.A-18)}$$

where τ is peak shearing stress and γ is peak shearing strain.

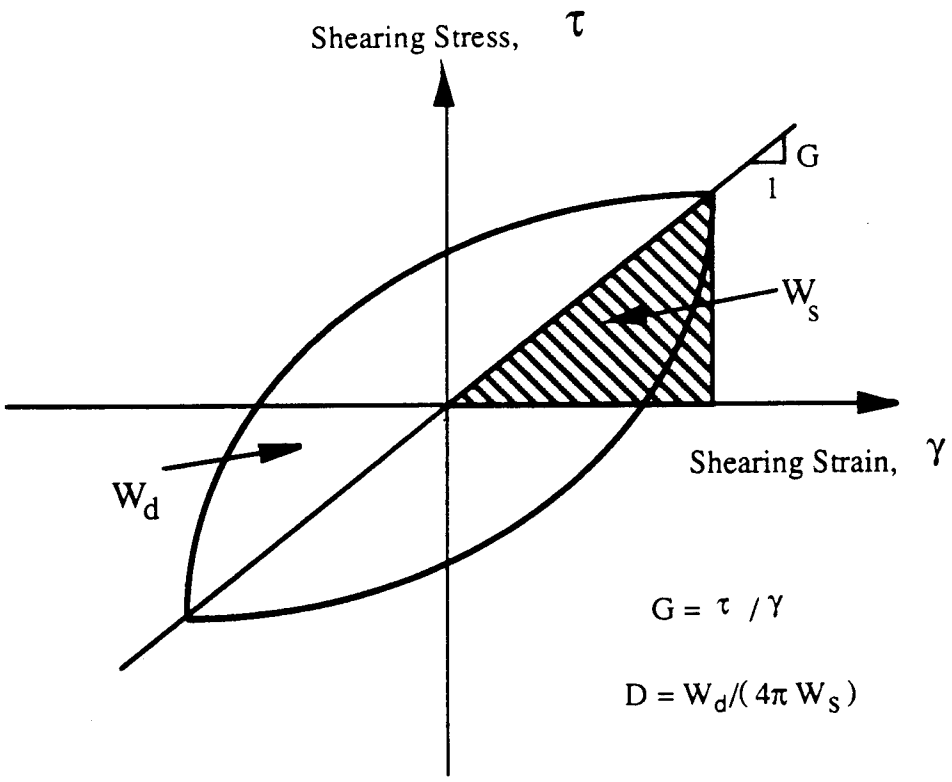

Figure 8.B.2.A-13
Determination of shear modulus and damping ratio in the torsional shear test.

8.B.2.A.4.2 Hysteretic Damping Ratio

Hysteretic damping ratio in the torsional shear test is measured using the amount of energy dissipated in one complete cycle of loading and the peak strain energy stored in the specimen during the cycle.

In the torsional shear test, the dissipated energy is measured from the area of the stress-strain hysteresis loop. The energy per cycle, W_d, due to a viscous damping force, F_d, is:

$$W_d = \int_o^T F_d \bullet \dot{x}\, dt \qquad (8.B.2.A\text{-}19)$$

where $\dot{x}$ is a velocity and T is a period. For simple harmonic motion with frequency of ω, i.e. x = A Cos (ωt–ϕ), W_d become:

$$W_d = \pi\, c\, \omega\, A^2 \qquad (8.B.2.A\text{-}20)$$

From the Eq. 8.B.2.A-20, the viscous damping coefficient can be expressed as:

$$c = W_d / (\pi\, \omega\, A^2) \qquad (8.B.2.A\text{-}21)$$

The peak strain energy, W_s, stored by the spring is equal to the area under the secant modulus line in Figure 8.B.2.A-13 and can be written as:

$$W_s = k\, A^2 / 2 \qquad (8.B.2.A\text{-}22)$$

The critical damping coefficient, C_c, is

$$C_c = 2 \bullet \sqrt{k\,m} = 2\,k / \omega_n \qquad \text{(8.B.2.A-23)}$$

where k is an elastic spring constant, m is a mass, and ω_n is a natural frequency of system. Using Eq. 8.B.2.A-22, Eq. 8.B.2.A-23 can be rewritten as:

$$C_c = 4\,W_s / (\omega_n A^2) \qquad \text{(8.B.2.A-24)}$$

Therefore, the damping ratio, D, can be expressed as:

$$D = C / C_c = W_d / (4\,\pi\,W_s) * (\omega_n / \omega) \qquad \text{(8.B.2.A-25)}$$

For soils, material damping is often assumed to be frequency independent. Therefore, ω_n / ω is ignored and hysteretic damping is written as:

$$D = \frac{1}{4\pi} * \frac{W_d}{W_s} \qquad \text{(8.B.2.A-26)}$$

where W_d is the area of the hysteresis loop and W_s is the area of the triangle as shown in Figure 8.B.2.A-13.

8.B.2.A.5 Evaluation of RCTS Equipment Compliance with Metal Specimens

To evaluate the RCTS equipment for system compliance, metal specimens were used. The metal specimens were made of brass and aluminum tubes. Eighteen metal specimens of different sizes and materials were used to obtain different resonant frequencies. Details of the metal specimens are presented in Table 8.B.2.A-1. It was assumed that the metal specimens should have (essentially) zero damping and that these specimens should exhibit no effect of frequency on stiffness or damping over the complete range of frequencies used in these tests (from about 0.05 Hz to 400 Hz).

Table 8.B.2.A-1
Metal Specimens Used to Evaluate Equipment Damping Ratio

Specimen Number	Outside Diameter		Inside Diameter		Height		Weight
	inch	cm	inch	cm	inch	cm	gram
1(Brass Tube)	1.000	2.540	0.875	2.223	4.98	12.65	132.35
2(Brass Tube)	0.875	2.223	0.813	2.064	6.96	17.68	79.96
3(Brass Tube)	0.875	2.223	0.813	2.064	8.49	21.56	97.07
4(Brass Tube)	0.750	1.905	0.688	1.746	6.97	17.70	70.72
5(Brass Tube)	0.750	1.905	0.688	1.746	8.49	21.57	85.87
6(Brass Tube)	0.625	1.588	0.563	1.429	6.96	17.68	58.45
7(Brass Tube)	0.625	1.588	0.563	1.429	8.49	21.57	70.94
8(Brass Tube)	0.375	0.953	0.313	0.794	6.94	17.63	33.69
9(Brass Tube)	0.375	0.953	0.313	0.794	8.44	21.45	40.86
10(Brass Rod)	0.313	0.794	0	0	6.92	17.57	74.46
11(Brass Rod)	0.313	0.794	0	0	8.44	21.44	90.30
12(Brass Rod)	0.500	1.270	0	0	7.00	17.78	191.22
13(Brass Rod)	0.750	1.905	0	0	7.00	17.75	429.52
14(Brass Rod)	0.250	0.635	0	0	6.96	17.67	47.53
15(Brass Rod)	1.500	3.810	0	0	7.00	17.78	1731.64
16(Brass Tube)	0.500	1.270	0.438	1.111	6.97	17.71	44.63
17(Brass Tube)	0.500	1.270	0.438	1.111	8.48	21.53	54.29
18(Brass Tube)	1.000	2.540	0.875	2.223	6.97	17.70	178.50

Unit Weight of Brass = 8.49 g/cm^3 (=0.316 lbs/in^3)

Hysteresis loops with one metal specimen measured at a frequency of 0.5 Hz are shown in Figure 8.B.2.A-14. The stress-strain curve is linear, resulting in no damping as expected. On the other hand, Figures 8.B.2.A-11 and 8.B.2.A-12 show the damping measurements with the same metal specimen in the resonant column test predict an apparent damping of 0.4% from both the free-vibration decay and half-power bandwidth methods.

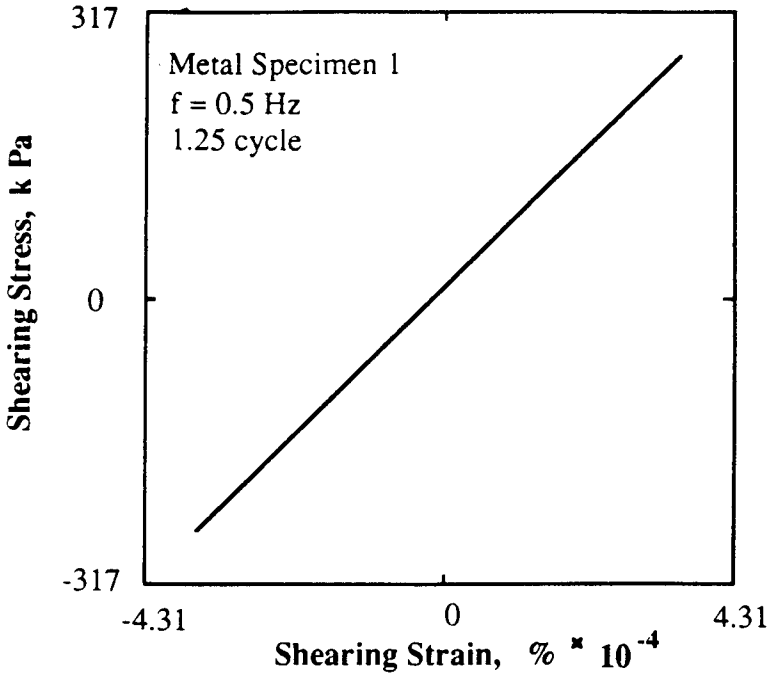

Figure 8.B.2.A-14
Hysteresis loops of metal specimen determined by torsional shear testing at a frequency of 0.5 Hz.

The variations in shear modulus and damping ratio with loading frequency for four of the metal specimens are plotted in Figure 8.B.2.A-15. The shear modulus of each metal specimen determined from the RCTS equipment is independent of loading frequency as expected. Therefore, shear modulus can be measured properly with RCTS equipment over a wide frequency range without any compliance problem.

On the other hand, the damping ratio measured by the RCTS equipment is affected by the loading frequency. For frequencies less than or equal to 0.5 Hz, damping ratio evaluated by the torsional shear test is essentially zero as expected. In this frequency range, material damping can be evaluated without any equipment correction. For higher frequencies, however, non-zero damping values are obtained with all metal specimens in the torsional shear as shown in Figures 8.B.2.A-15b and 8.B.2.A-16. In this case the apparent material damping increases significantly as the excitation frequency increases from 1 to 10 Hz. Strain amplitude has little effect on the damping values as shown in Figure 8.B.2.A-16. These values of apparent material damping are considered to be due to a compliance problem with the complete RCTS system (back-EMF generated by the drive system) and are, therefore, subtracted from all damping measurements in the torsional shear test at the same frequencies when soil specimens are tested.

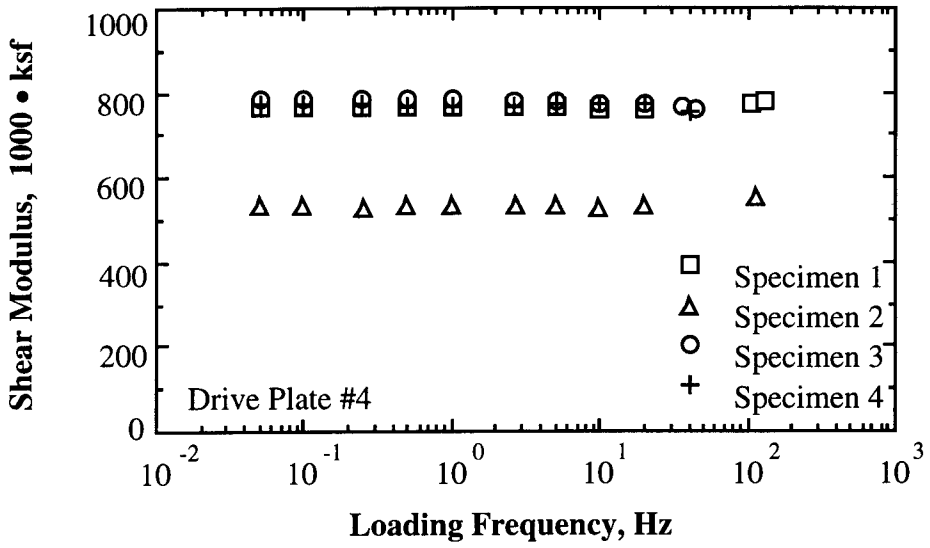

a) Variation in Shear Modulus

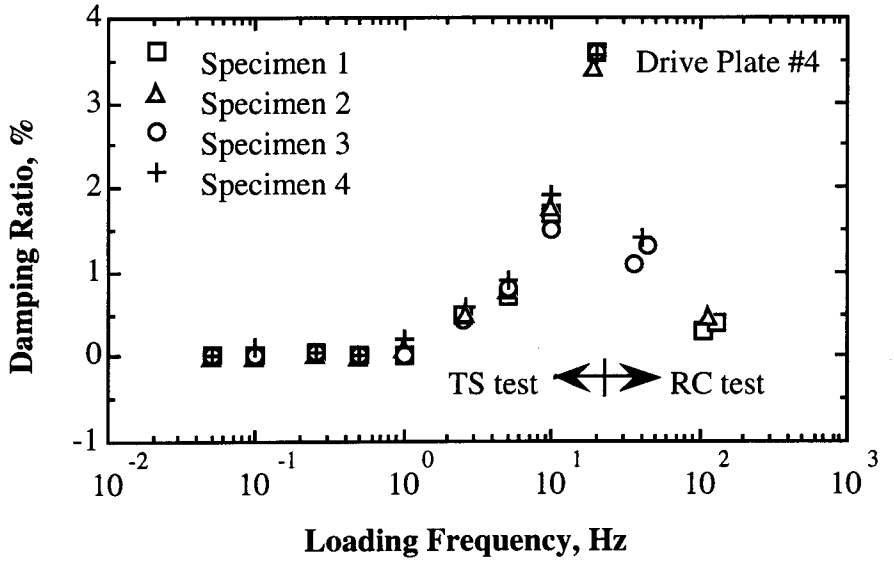

Figure 8.B.2.A-15
Variation in shear modulus and material damping ratio with loading frequency determined for metal specimens (from Kim, 1991).

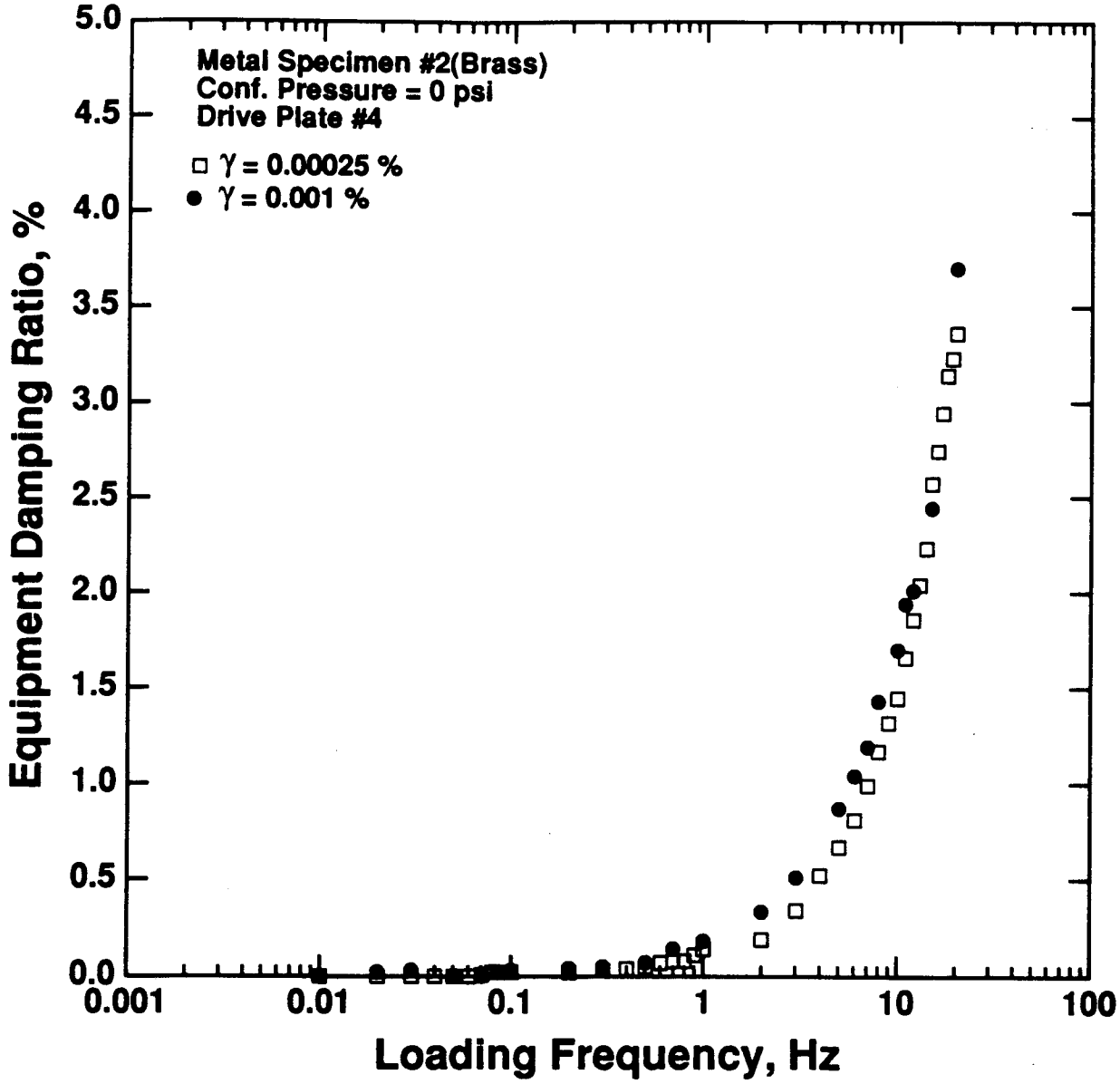

Figure 8.B.2.A-16
Measured damping ratio for metal specimen #2 in the torsional shear test.

It should be noted that excitation frequencies in the torsional shear test never exceeded 0.1 times the resonant frequency of the soil specimen. This approach was followed so that dynamic amplification did not affect the TS measurements. Even in this case, however, corrections were made for minor dynamic amplification which occurs near 0.1 times the resonant frequency.

In the resonant column test, non-zero damping values were obtained at all resonant frequencies as seen in Figures 8.B.2.A-15b and 8.B.2.A-17. Equipment damping values ranged from about 3.5% at 20 Hz to about 0.4% at 200 Hz. These resonant frequencies are in the frequency range where all soil testing was conducted. Just as in the TS test, the values of equipment damping measured with the metal specimens were subtracted from the damping measurements in all RC tests with soil specimens at the same resonant frequencies. Strain amplitude had a negligible effect on equipment damping as shown in Figure 8.B.2.A-18.

Finally, to be sure that coil-magnet interaction was the cause of the equipment damping problem, free-vibration tests were conducted with the RC equipment. In this case, however, all coils were removed which required that the drive plate be excited by hand in free vibration. The resulting tests with drive plate #4 are given in Figure 8.B.2.A-19 by the solid square symbols. As seen, damping values less than 0.1% were measured. These values are considered to equal zero in this work, indicating the coil-magnet interaction is mainly the cause of the equipment damping.

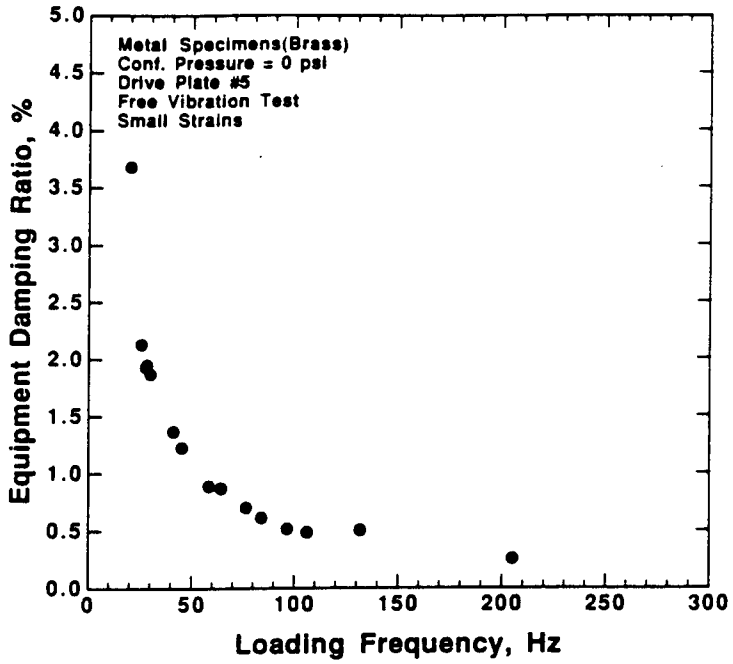

a. Damping from the Free-Vibration Decay Curve

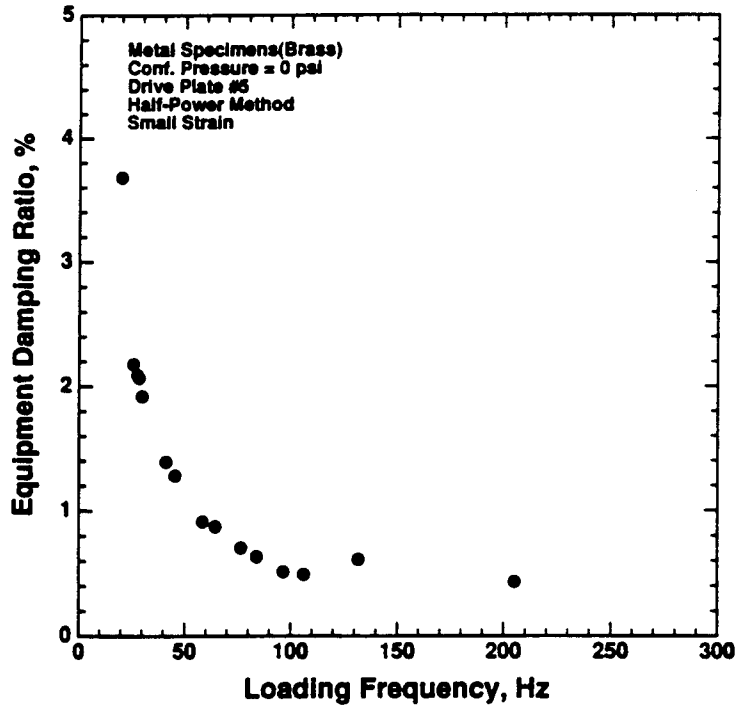

b. Damping from the Half-Power Bandwidth

Figure 8.B.2.A-17
Equipment damping measured in the resonant column test.

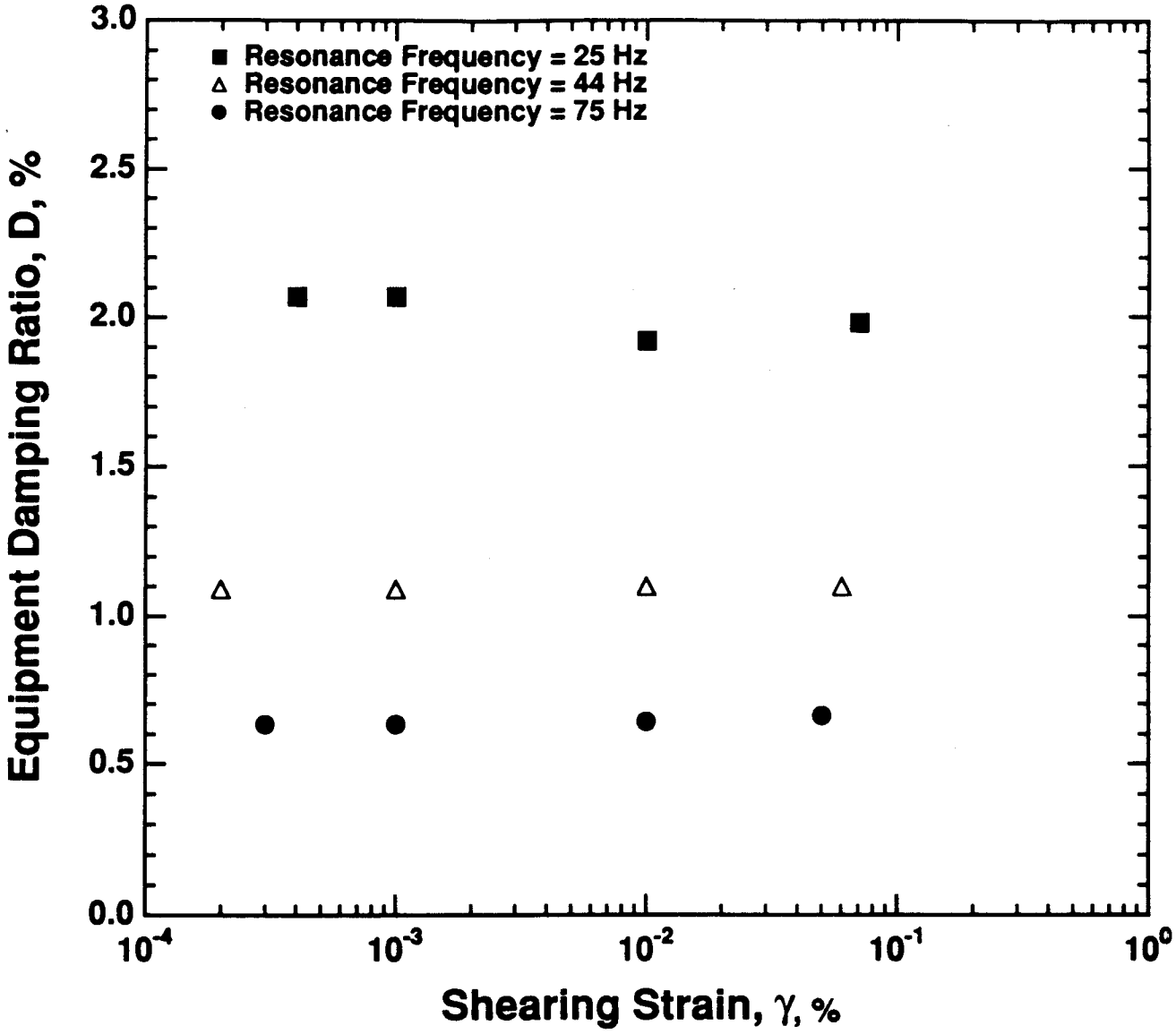

Figure 8.B.2.A-18
Effect of strain amplitude on equipment damping measured in the resonant column test.

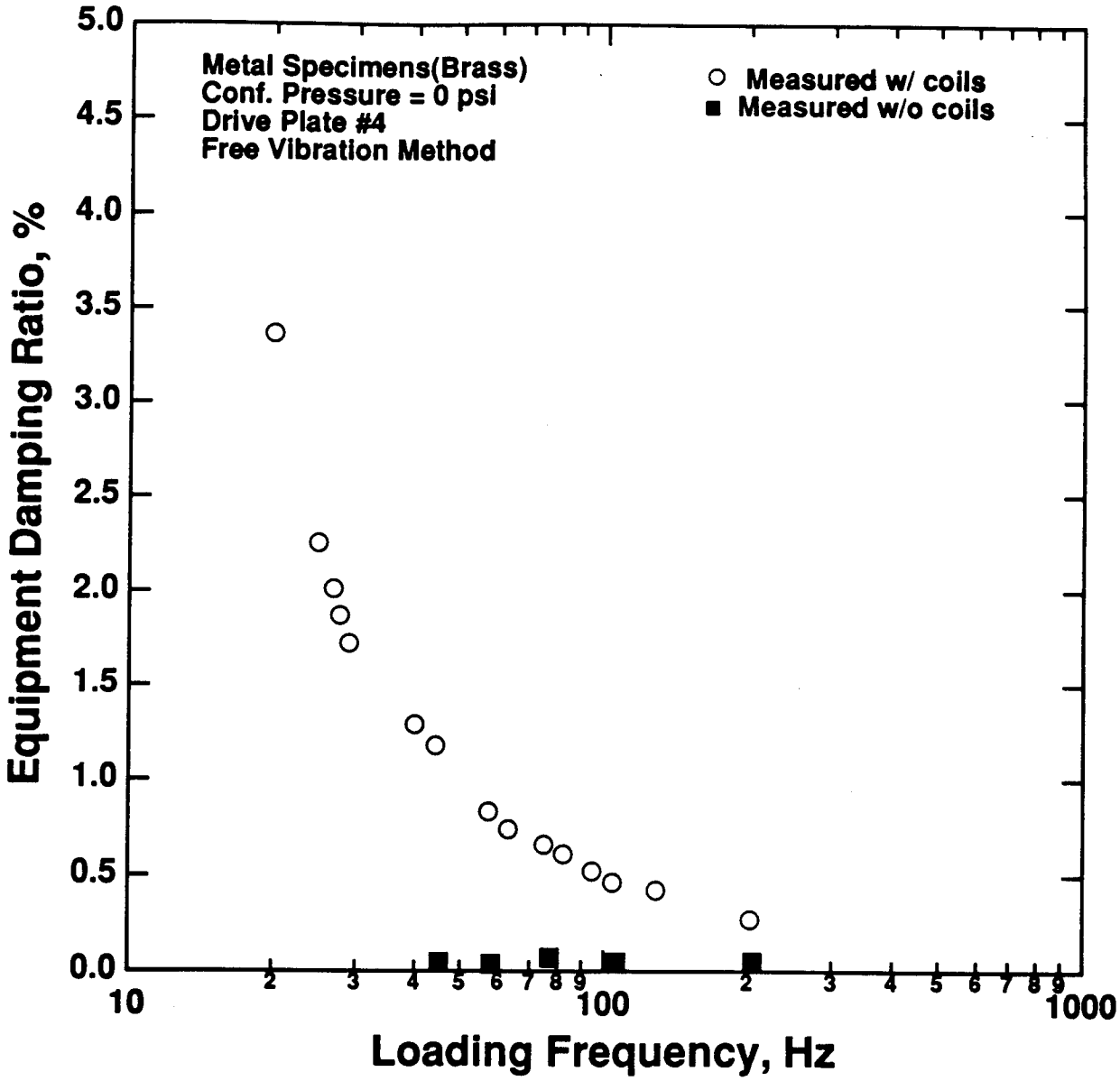

Figure 8.B.2.A-19
Comparison of equipment damping measured in free vibration RC tests with and without the electrical coils.

References

Chen, A.T.F., Stokoe, K.H., II (1979), "Interpretation of Strain Dependent Modulus and Damping from Torsional Soil Tests," Report No. USGS-GD-79-002, *NTIS No. PB-298479*, U.S. Geological Survey, 46 pp.

Isenhower, W.M. (1979), "Torsional Simple Shear/Resonant Column Properties of San Francisco Bay Mud," Geotechnical Engineering Thesis, *GT 80-1*, University of Texas, Dec., 307 pp.

Kim, D.S. (1991), "Deformational Characteristics of Soils at Small to Intermediate Strains from Cyclic Tests," Ph.D. Dissertation, University of Texas at Austin, 341 pp.

Lodde, P.F. (1982), "Shear Moduli and Material Damping of San Francisco Bay Mud," M.S. Thesis, University of Texas at Austin.

Ni, S.H. (1987), "Dynamic Properties of Sand Under True Triaxial Stress States from Resonant Column/Torsional Shear Tests," Ph.D. Dissertation, University of Texas at Austin, 421 pp.

Richart, F.E., Jr., Hall, J.R., Jr. and Woods, R.D. (1970), *Vibrations of Soils and Foundations*, Prentice-Hall Inc., Englewood Cliffs, New Jersey, 414 pp.

APPENDIX 8.B.2.B
DYNAMIC TESTS OF SAMPLE G1, DEPTH = 10 FT (3.0 M)

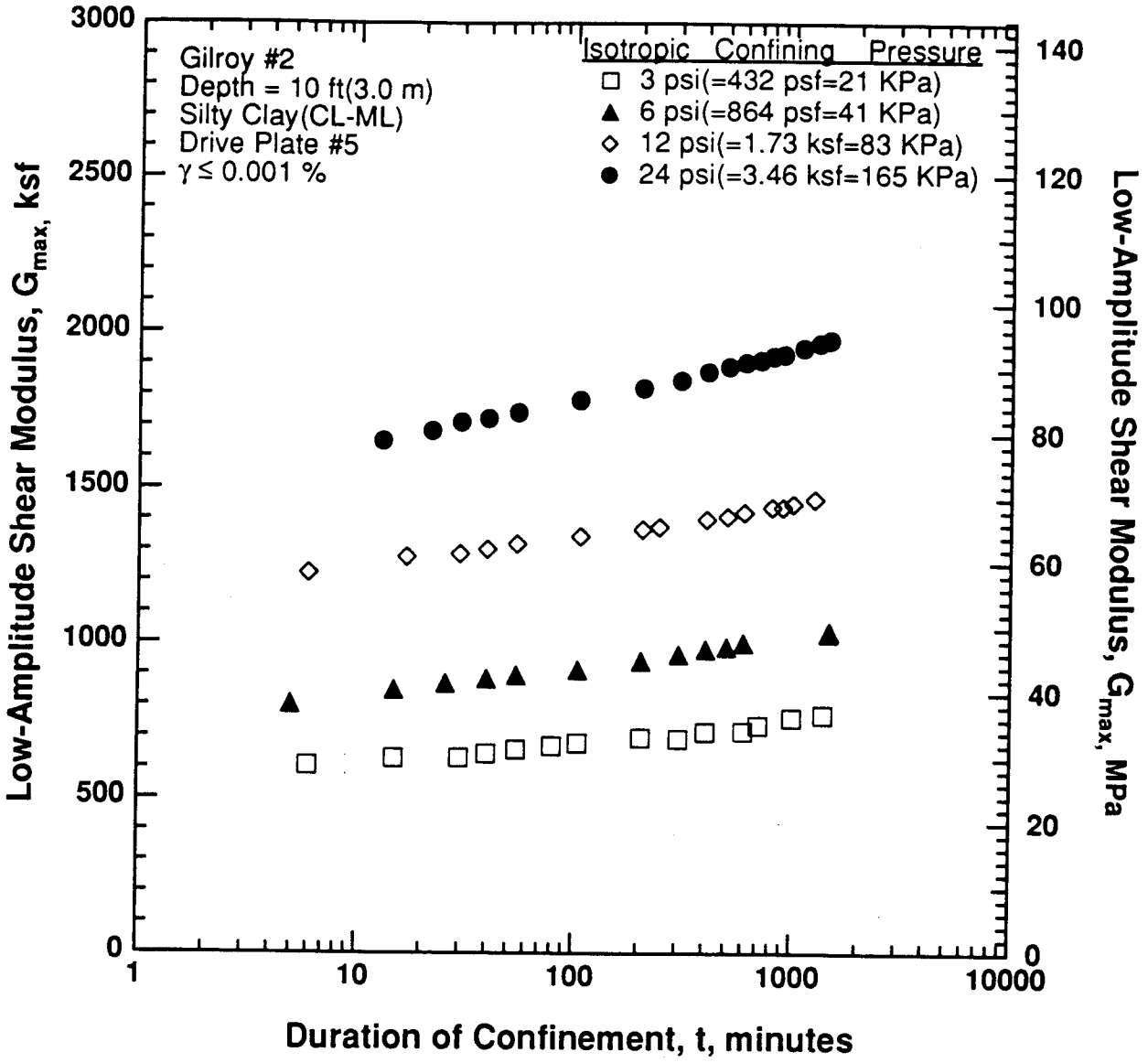

Figure 8.B.2.B-1
Variation in low-amplitude shear modulus with magnitude and duration of isotropic confining pressure from resonant column tests of sample G1.

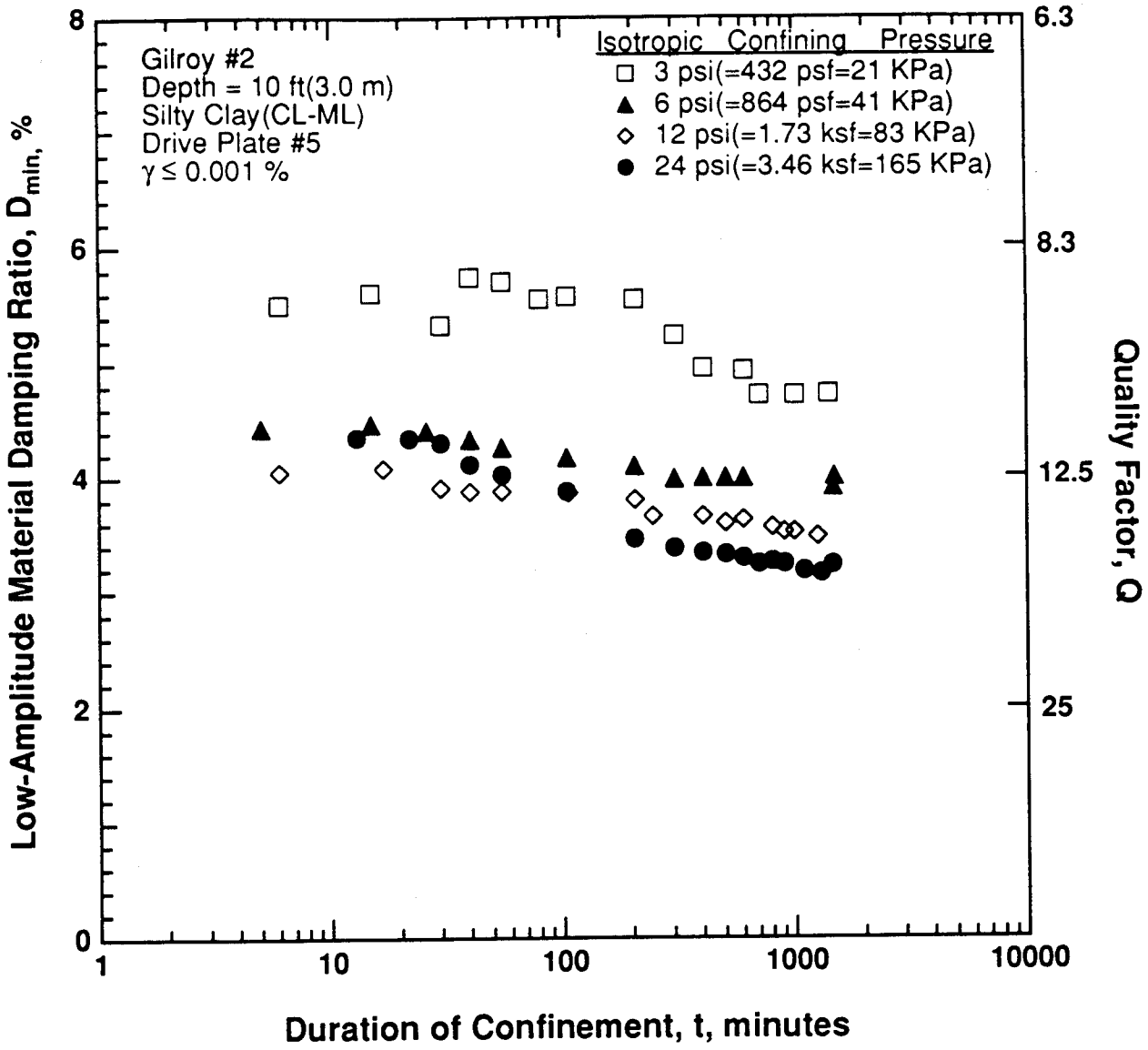

Figure 8.B.2.B-2
Variation in low-amplitude material damping ratio with magnitude and duration of isotropic confining pressure from resonant column tests of sample G1.

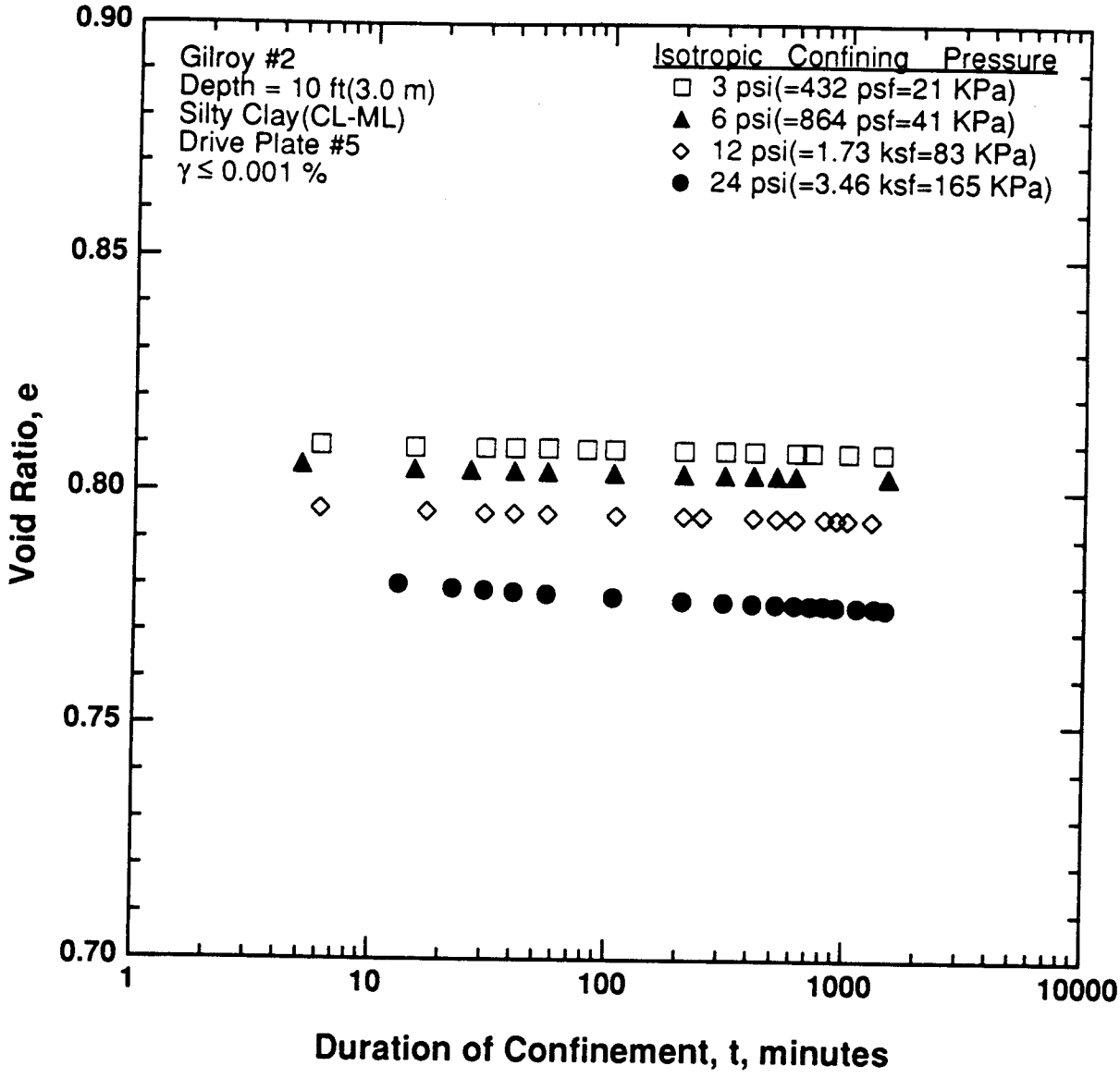

Figure 8.B.2.B-3
Variation in void ratio with magnitude and duration of isotropic confining pressure from resonant column tests of sample G1.

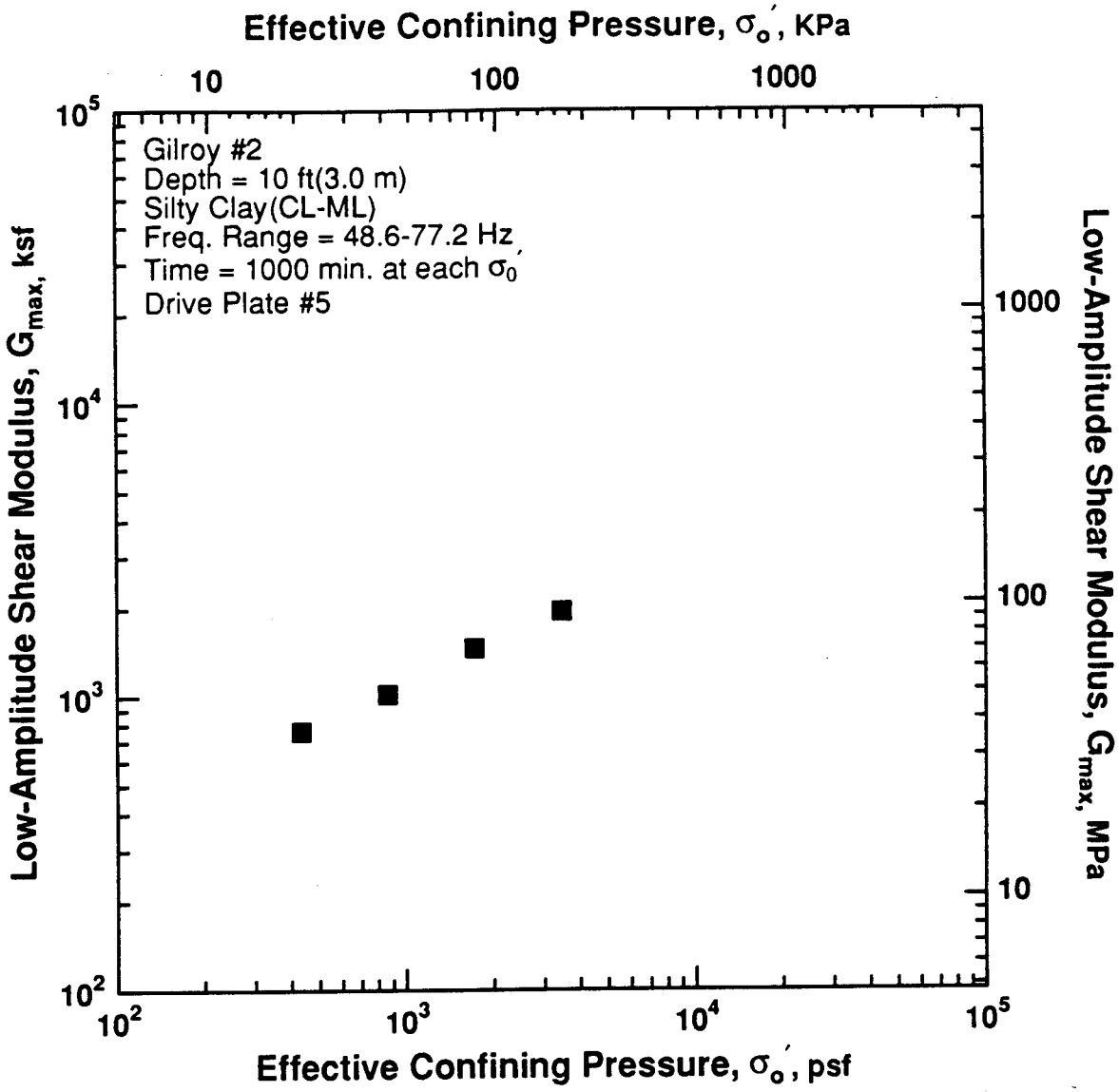

Figure 8.B.2.B-4
Variation in low-amplitude shear modulus with effective confining pressure from resonant column tests of sample G1.

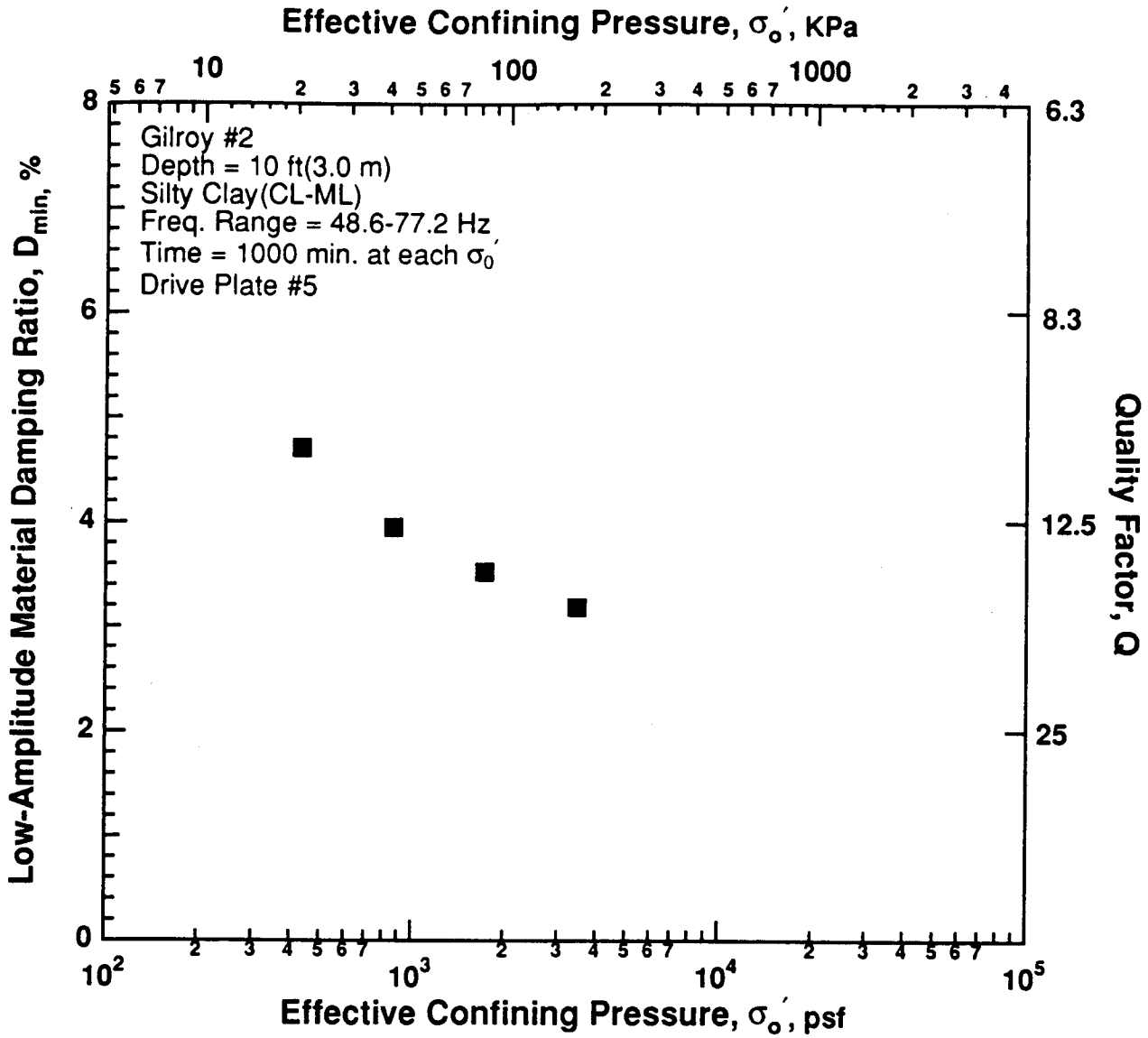

Figure 8.B.2.B-5
Variation in low-amplitude material damping ratio with effective confining pressure from resonant column tests of sample G1.

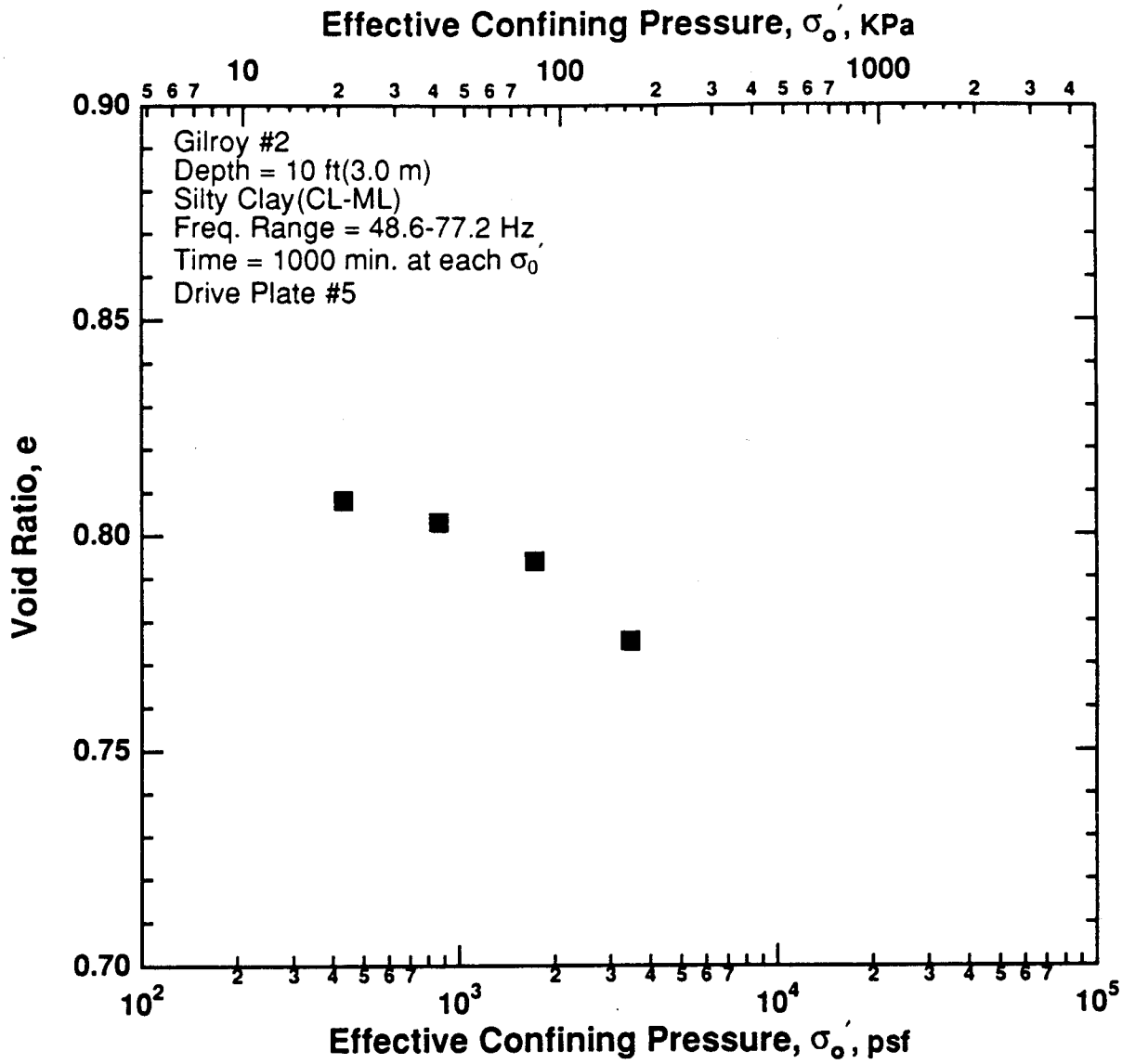

Figure 8.B.2.B-6
Variation in void ratio with effective confining pressure from resonant column tests of sample G1.

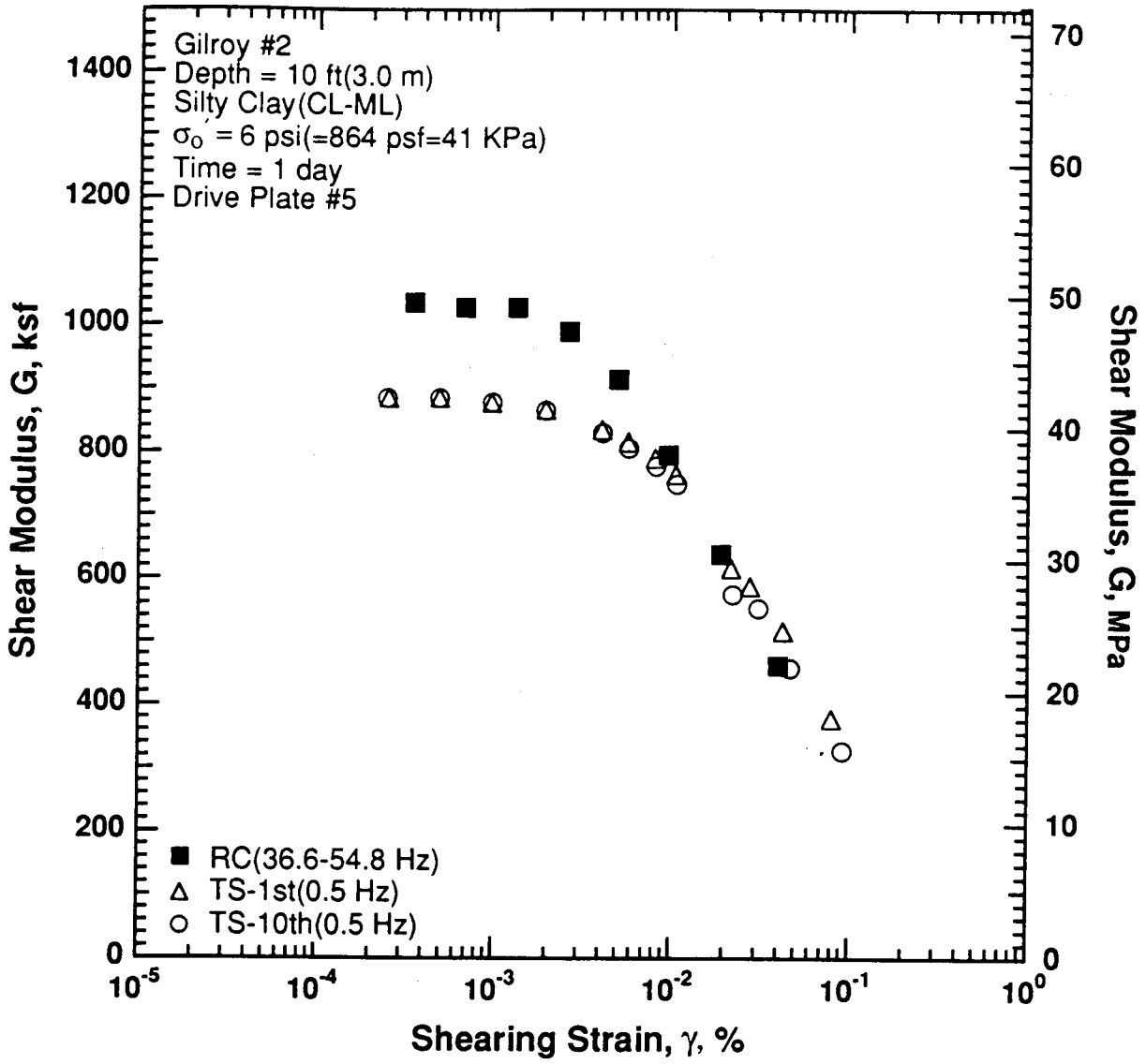

Figure 8.B.2.B-7
Variation in shear modulus with shearing strain at an effective confining pressure of 6 psi (864 psf, 41 kPa) from RCTS tests of sample G1.

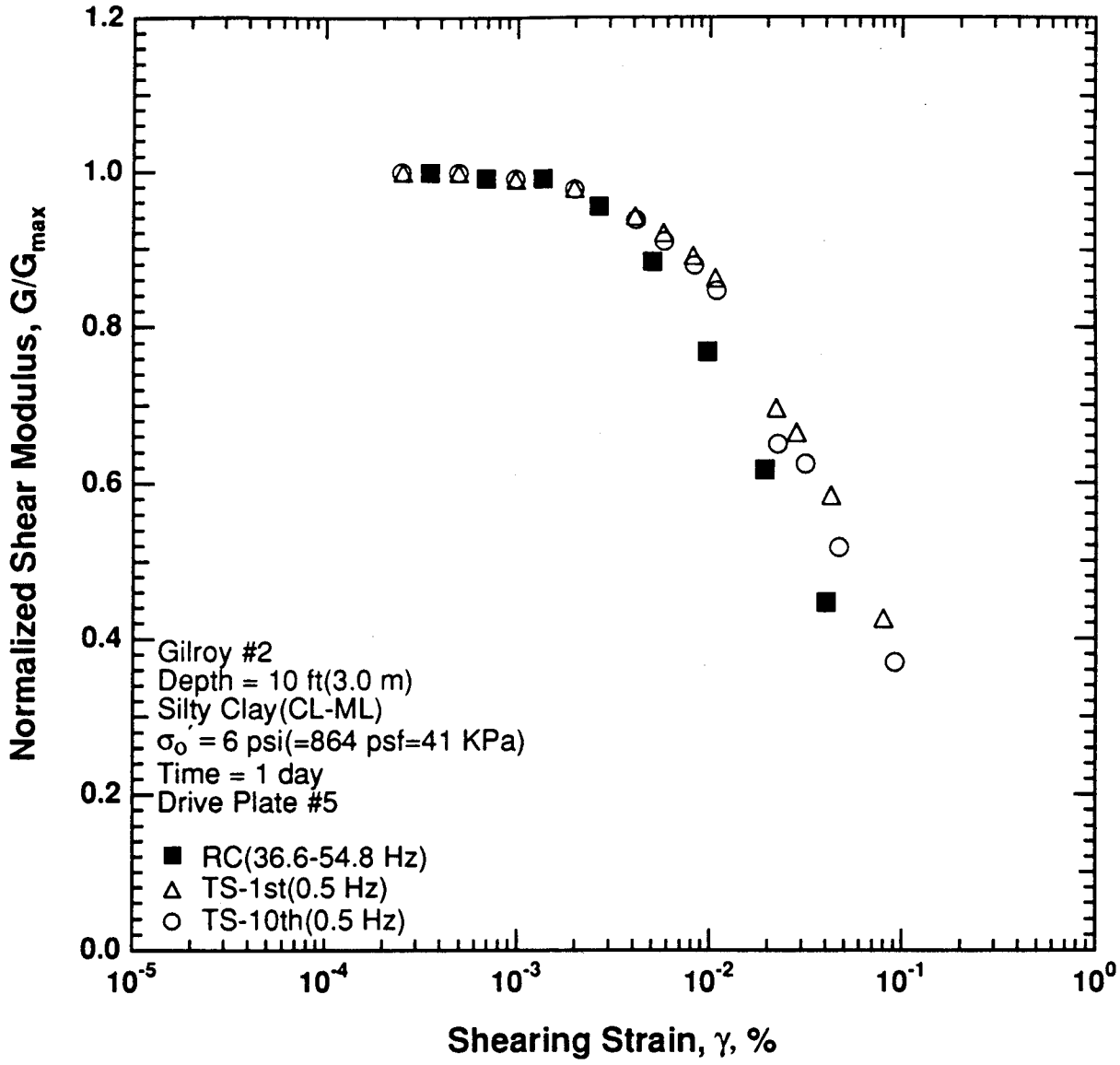

Figure 8.B.2.B-8
Variation in normalized shear modulus with shearing strain at an effective confining pressure of 6 psi (864 psf, 41 kPa) from RCTS tests of sample G1.

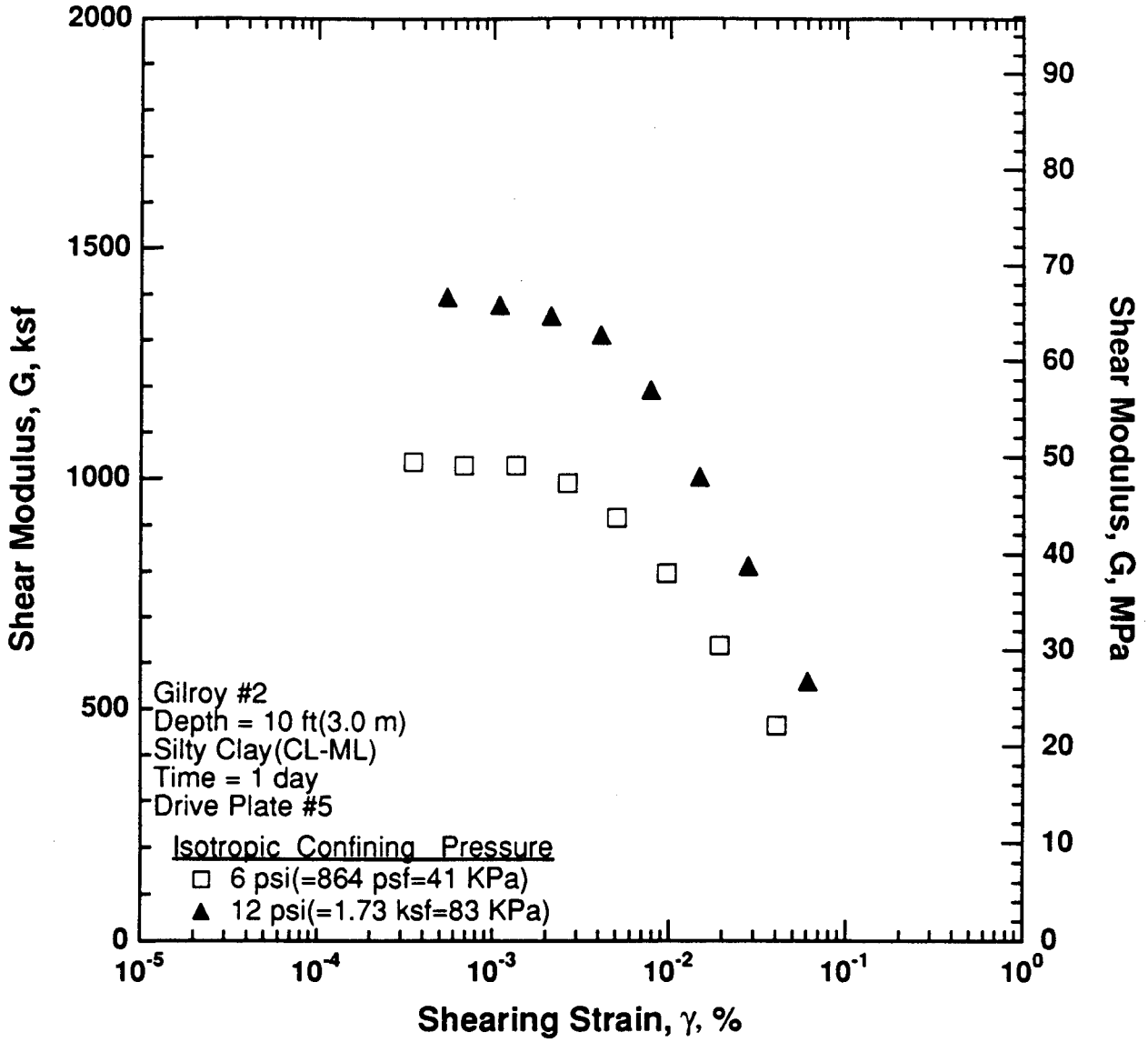

Figure 8.B.2.B-9
Variation in shear modulus with shearing strain and effective confining pressure from resonant column tests of sample G1.

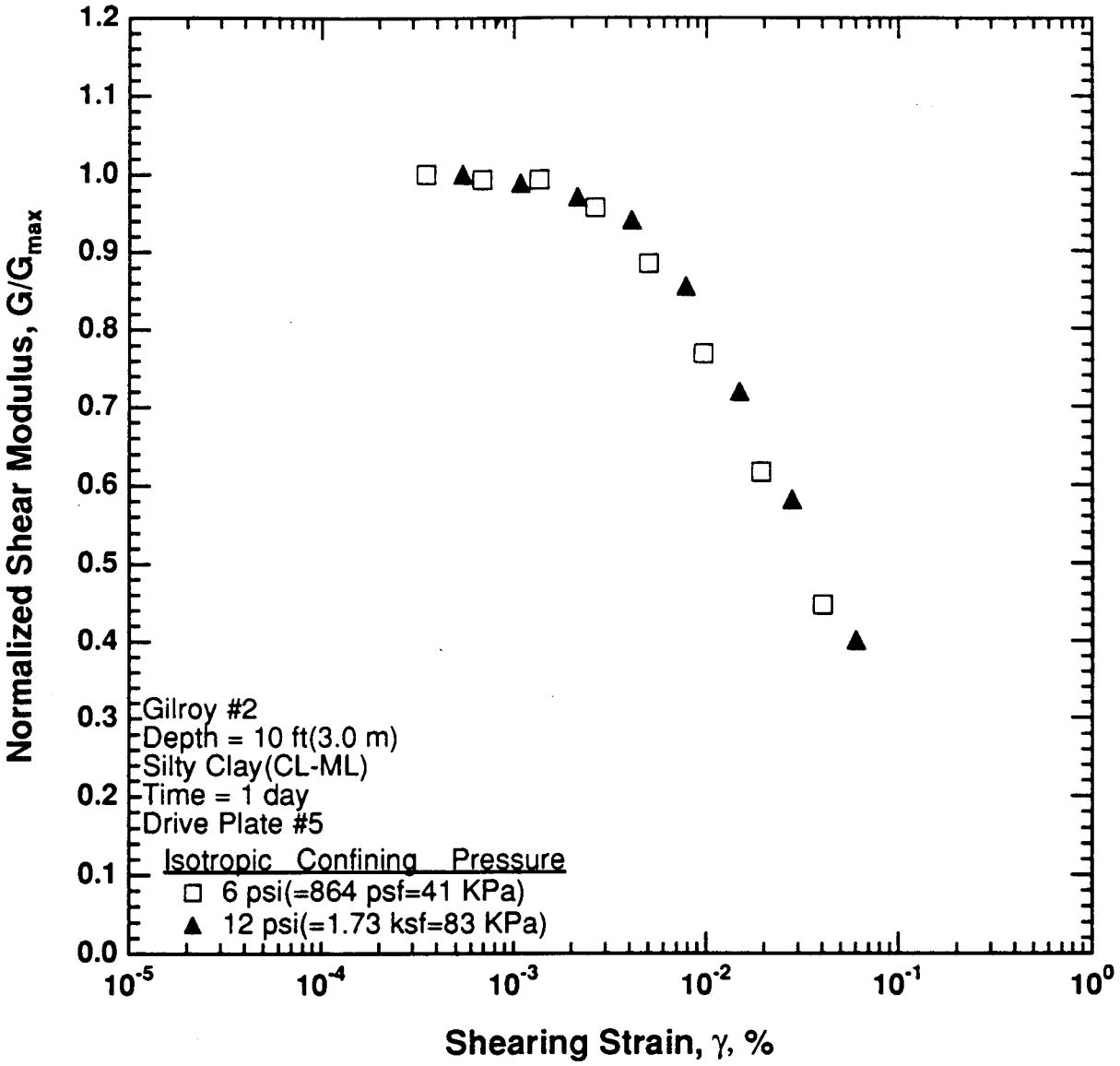

Figure 8.B.2.B-10
Comparison of the variation in normalized shear modulus with shearing strain and effective confining pressure from resonant column tests of sample G1.

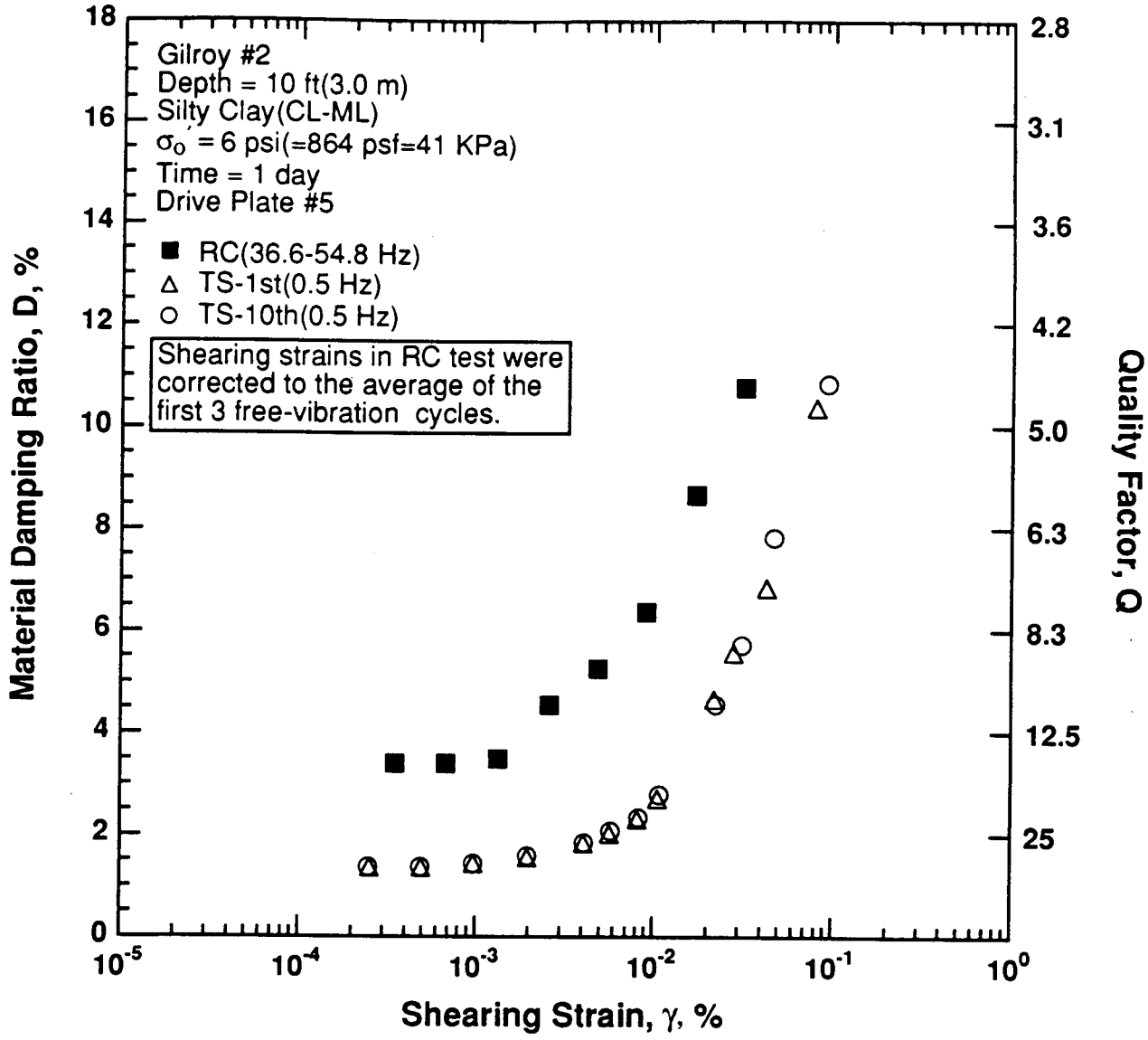

Figure 8.B.2.B-11
Variation in material damping ratio with shearing strain at an effective confining pressure of 6 psi (864 psf, 41 kPa) from RCTS tests of sample G1.

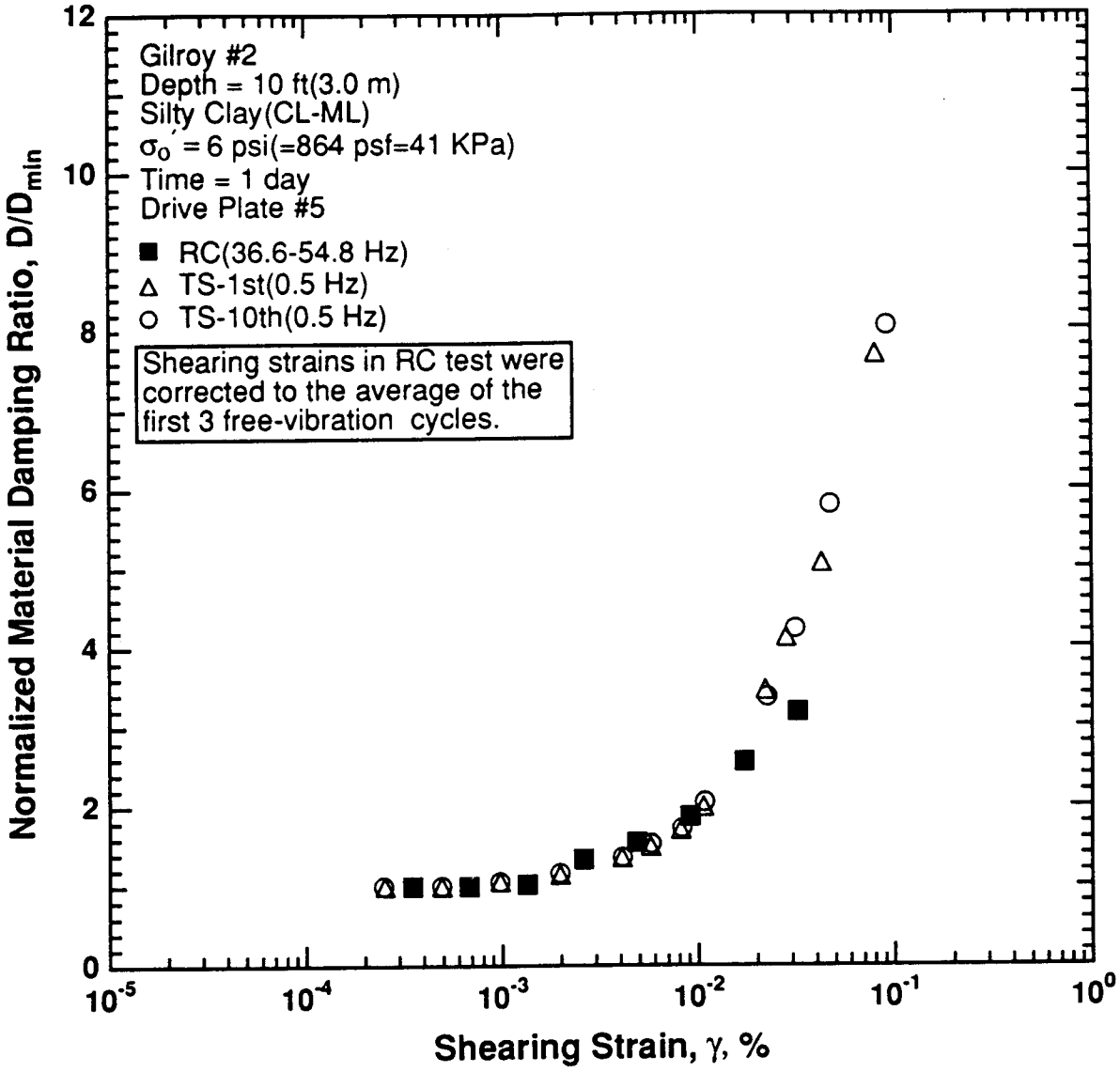

Figure 8.B.2.B-12
Variation in normalized material damping ratio with shearing strain at an effective confining pressure of 6 psi (864 psf, 41 kPa) from RCTS tests of sample G1.

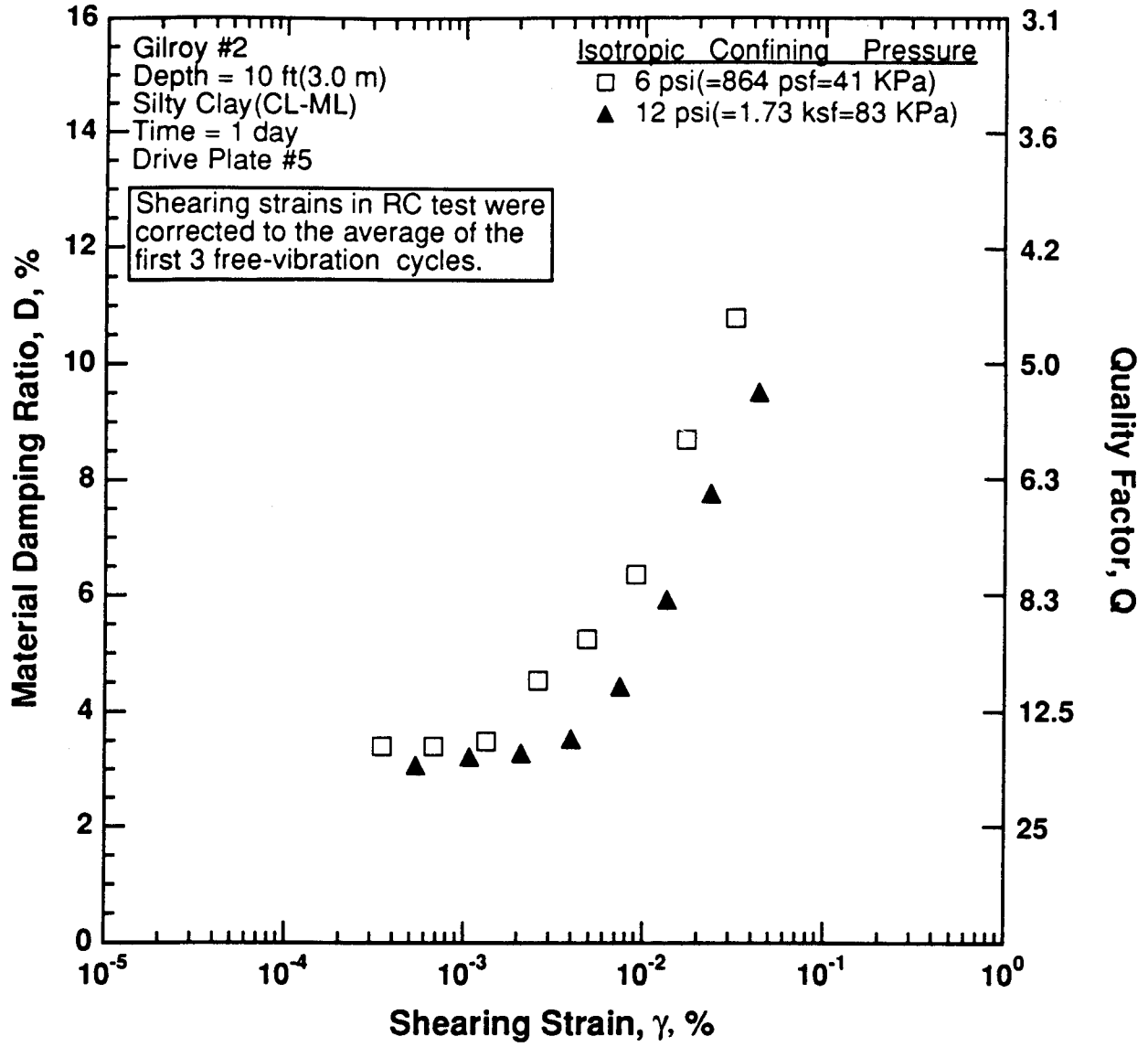

Figure 8.B.2.B-13
Variation in material damping ratio with shearing strain and effective confining pressure from resonant column tests of sample G1.

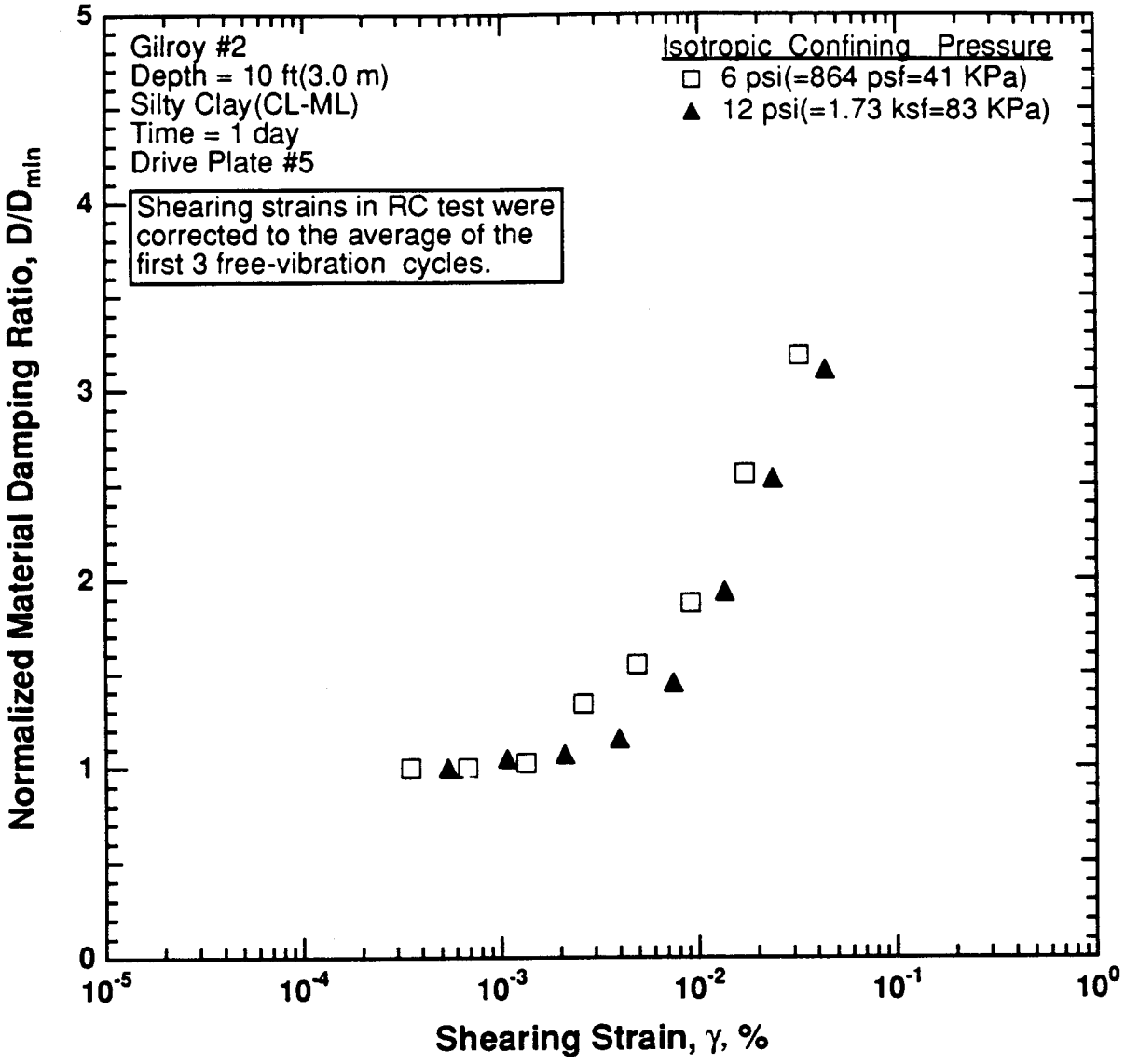

Figure 8.B.2.B-14
Comparison of the variation in normalized material damping ratio with shearing strain and effective confining pressure from resonant column tests of sample G1.

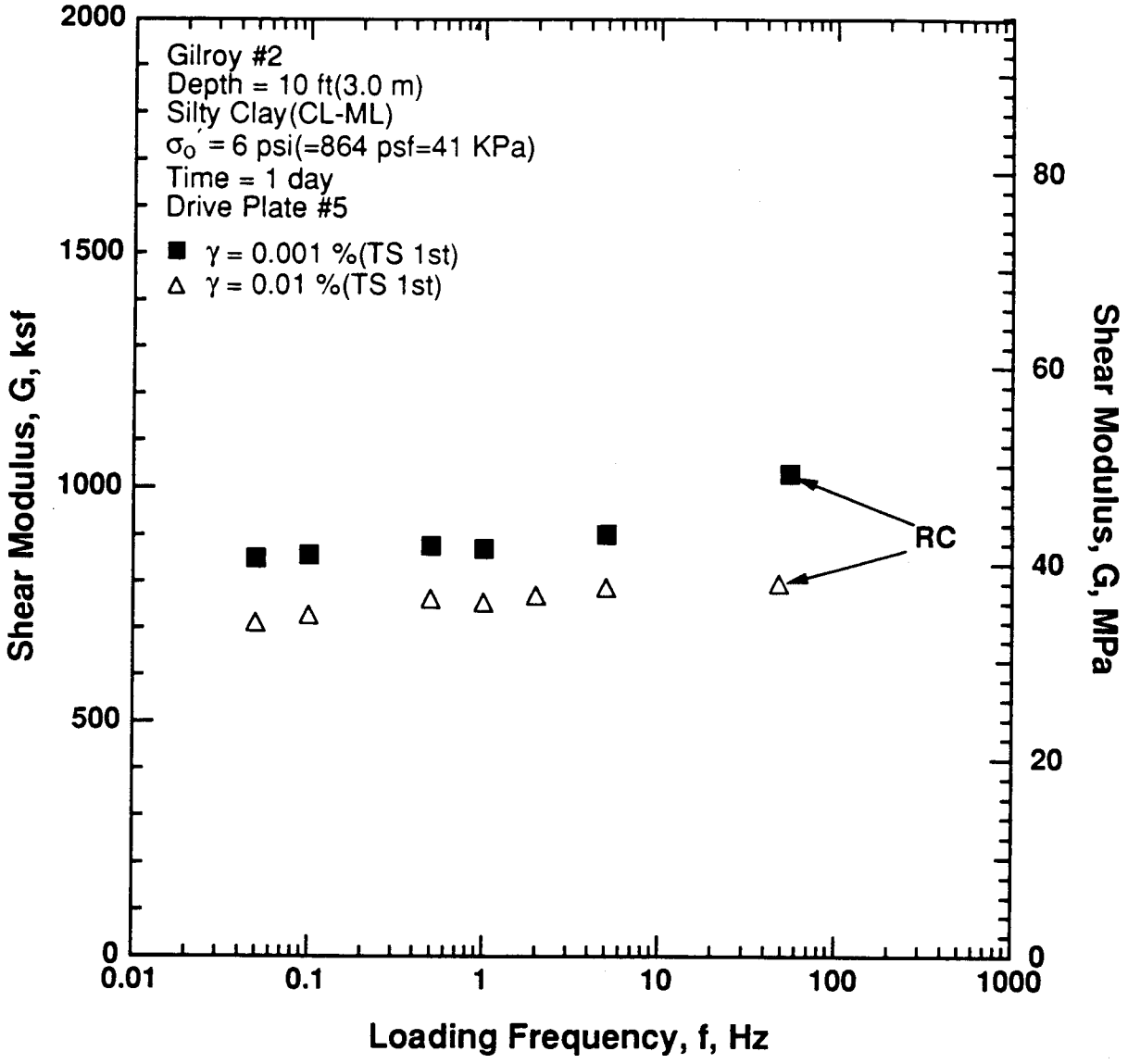

Figure 8.B.2.B-15
Variation in shear modulus with loading frequency and shearing strain at an effective confining pressure of 6 psi (864 psf, 41 kPa) from RCTS tests of sample G1.

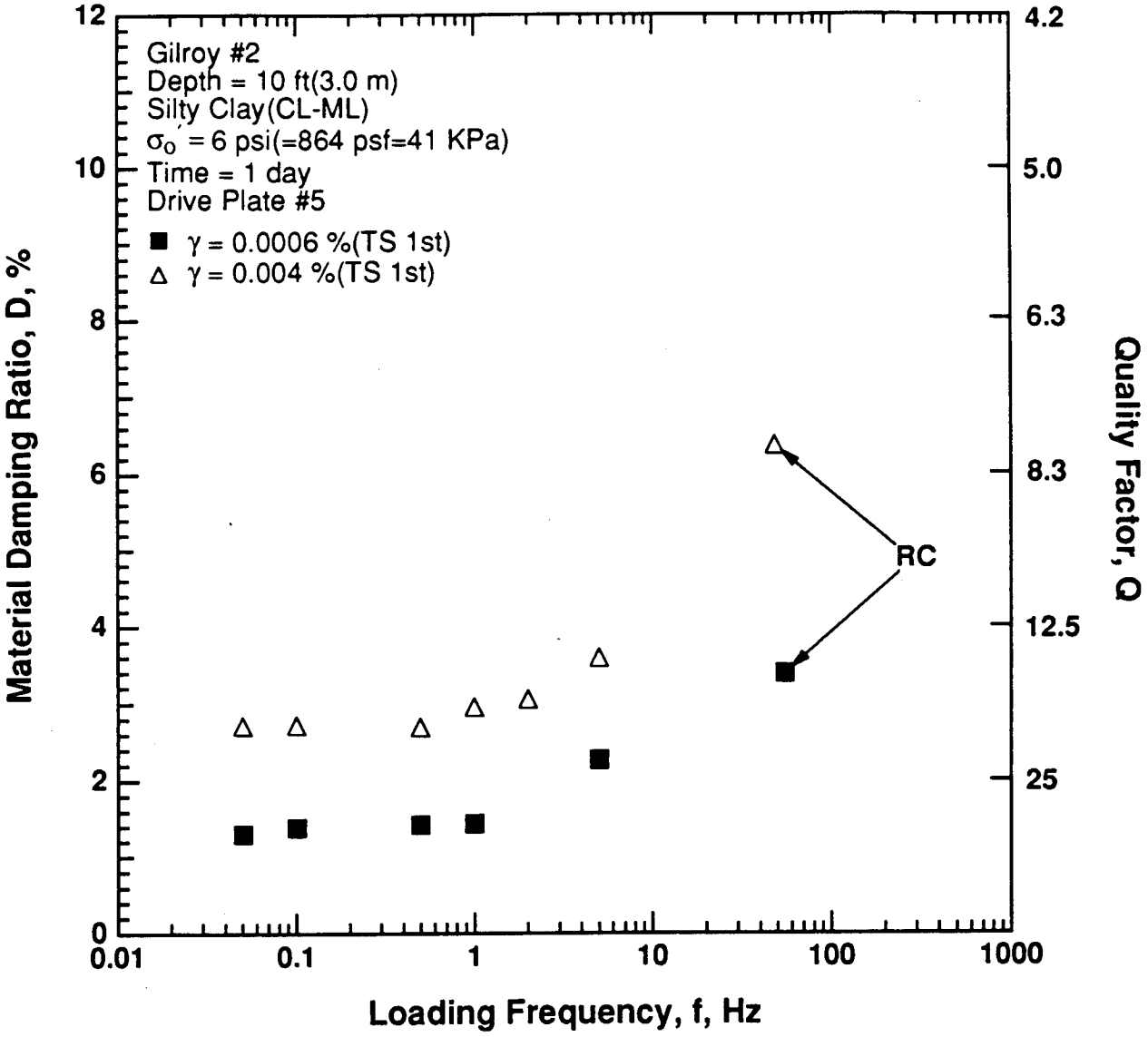

Figure 8.B.2.B-16
Variation in material damping ratio with loading frequency and shearing strain at an effective confining pressure of 6 psi (864 psf, 41 kPa) from RCTS tests of sample G1.

APPENDIX 8.B.2.C
DYNAMIC TESTS OF SAMPLE G2, DEPTH = 20 FT (6.1 M)

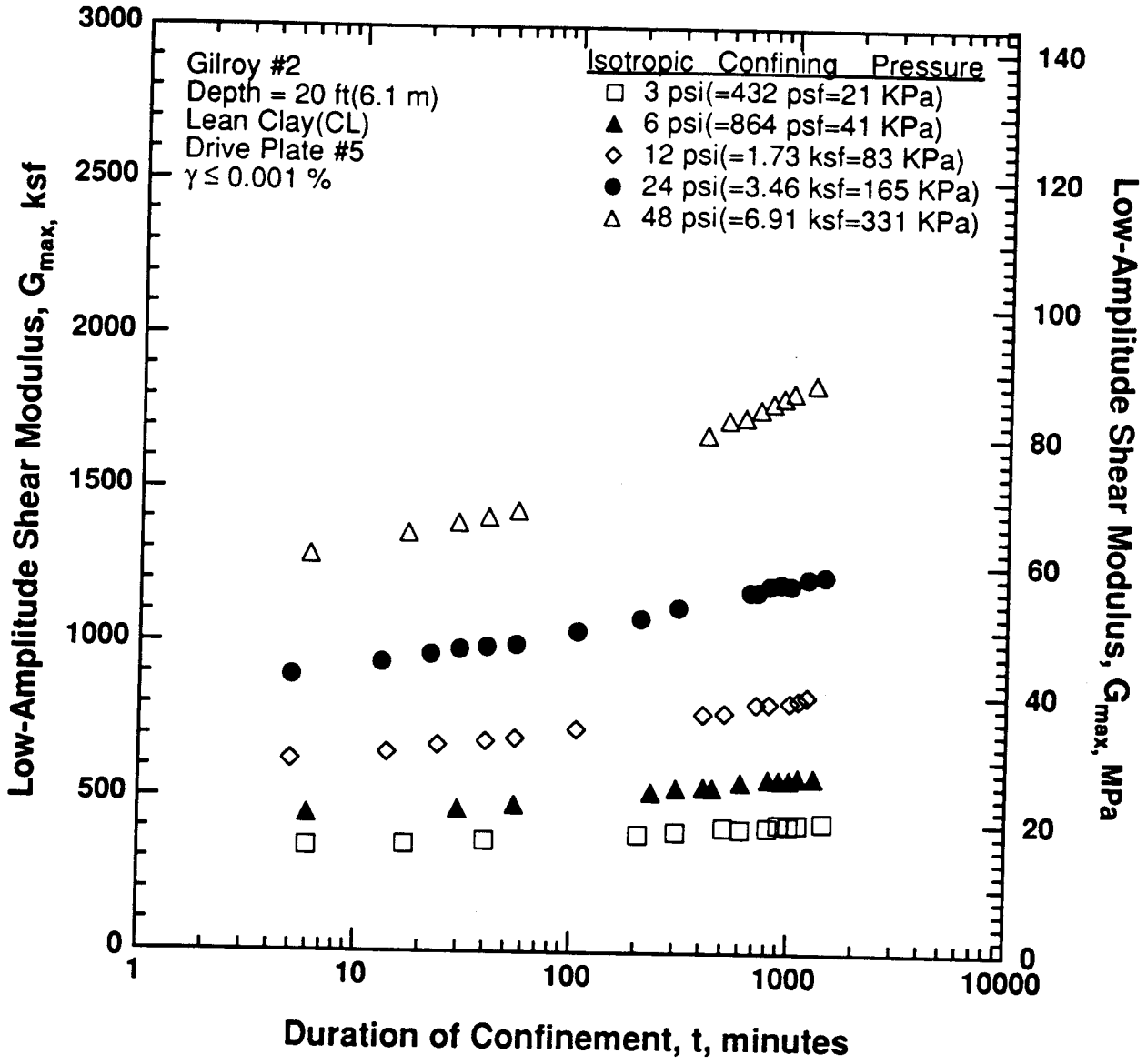

Figure 8.B.2.C-1
Variation in low-amplitude shear modulus with magnitude and duration of isotropic confining pressure from resonant column tests of sample G2.

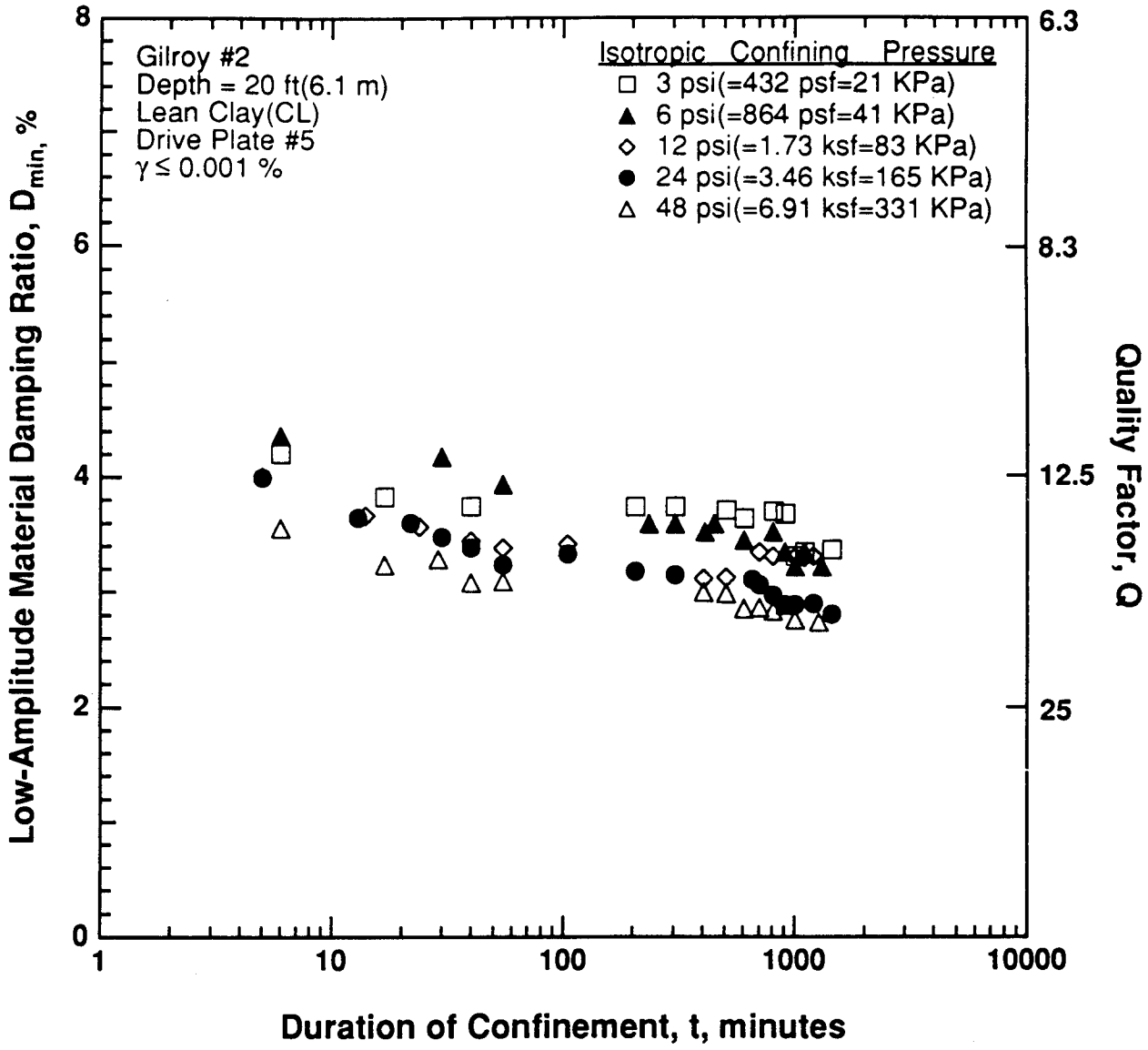

Figure 8.B.2.C-2
Variation in low-amplitude material damping ratio with magnitude and duration of isotropic confining pressure from resonant column tests of sample G2.

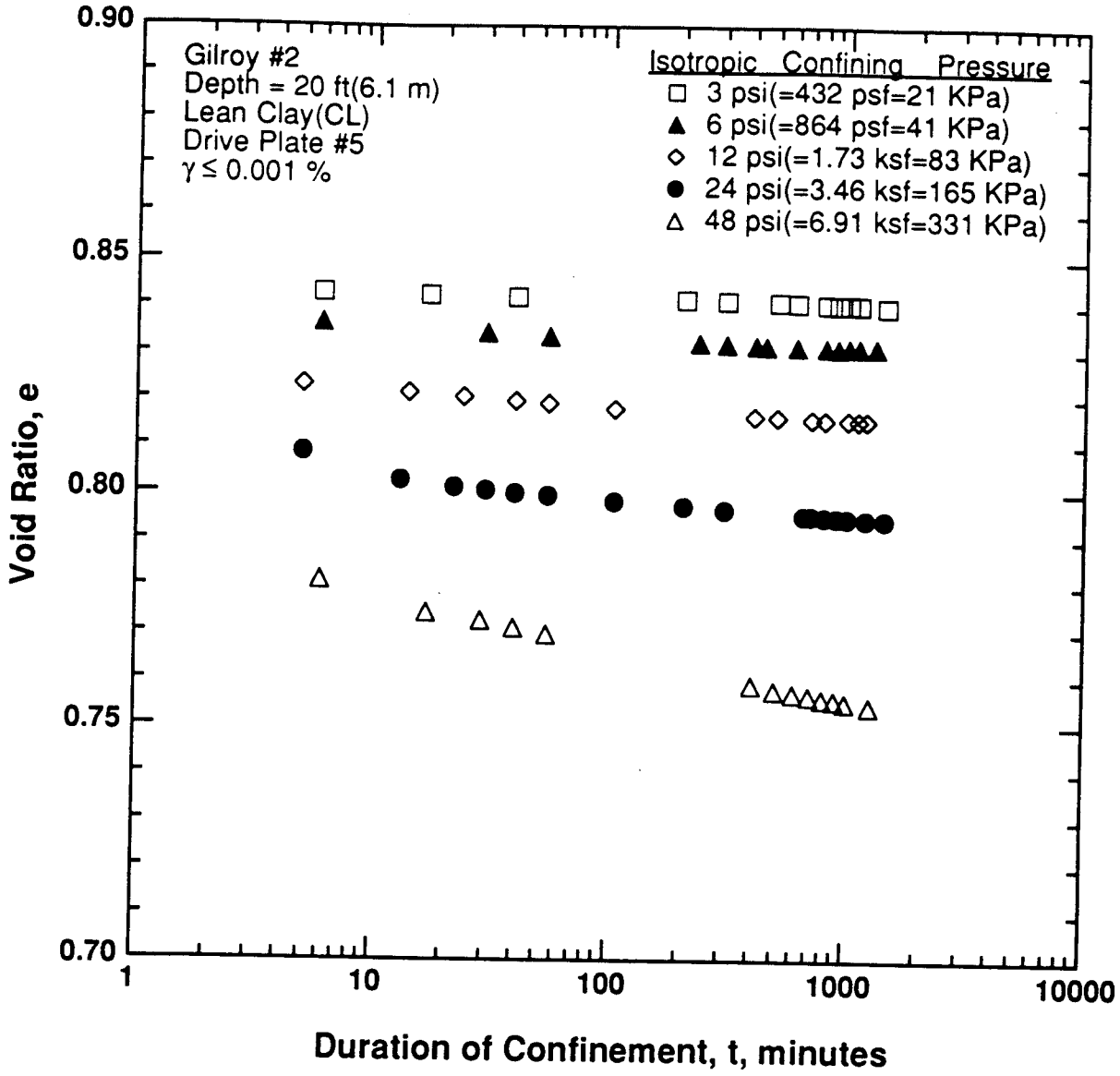

Figure 8.B.2.C-3
Variation in void ratio with magnitude and duration of isotropic confining pressure from resonant column tests of sample G2.

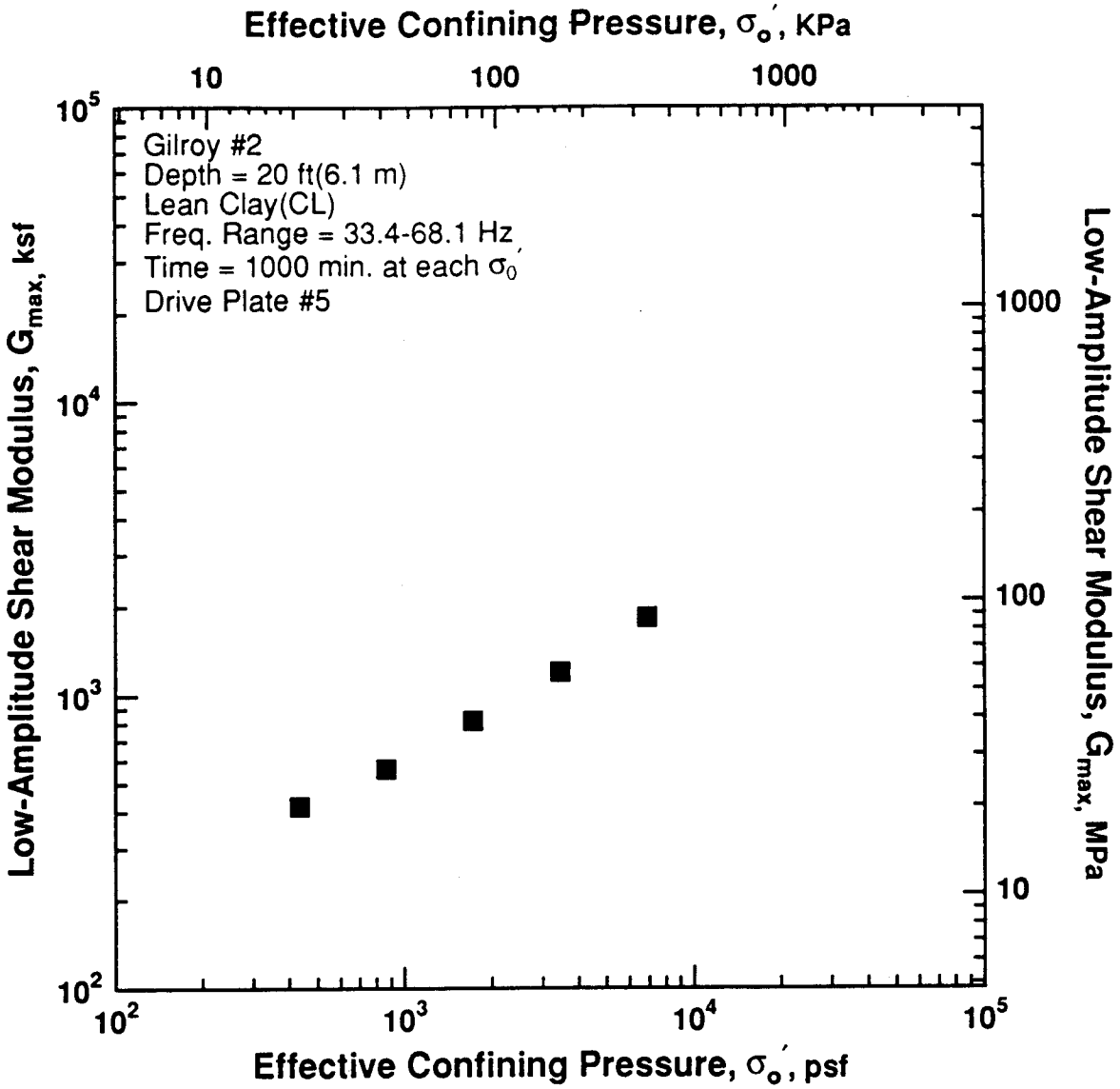

Figure 8.B.2.C-4
Variation in low-amplitude shear modulus with effective confining pressure from resonant column tests of sample G2.

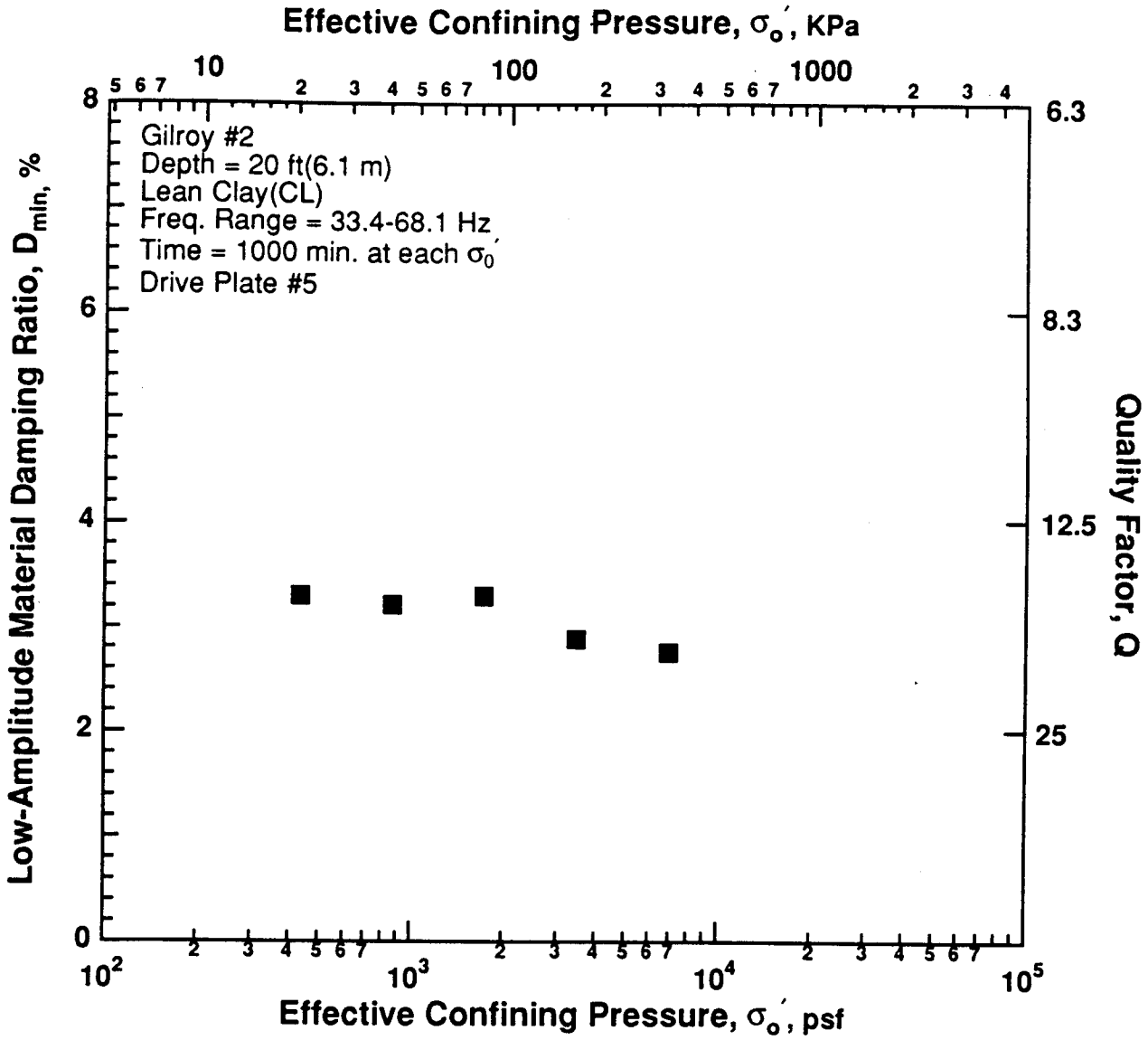

Figure 8.B.2.C-5
Variation in low-amplitude material damping ratio with effective confining pressure from resonant column tests of sample G2.

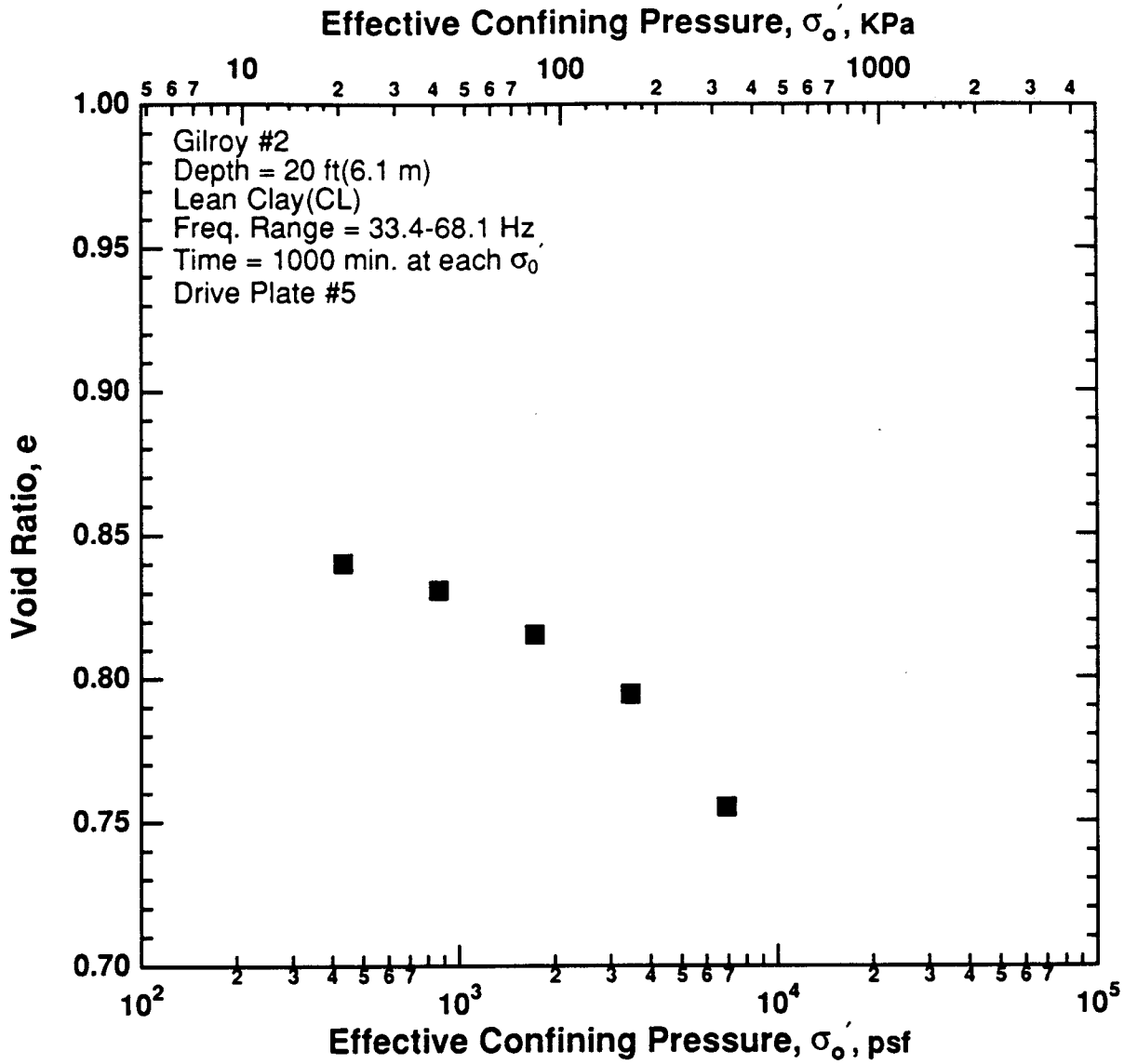

Figure 8.B.2.C-6
Variation in void ratio with effective confining pressure from resonant column tests of sample G2.

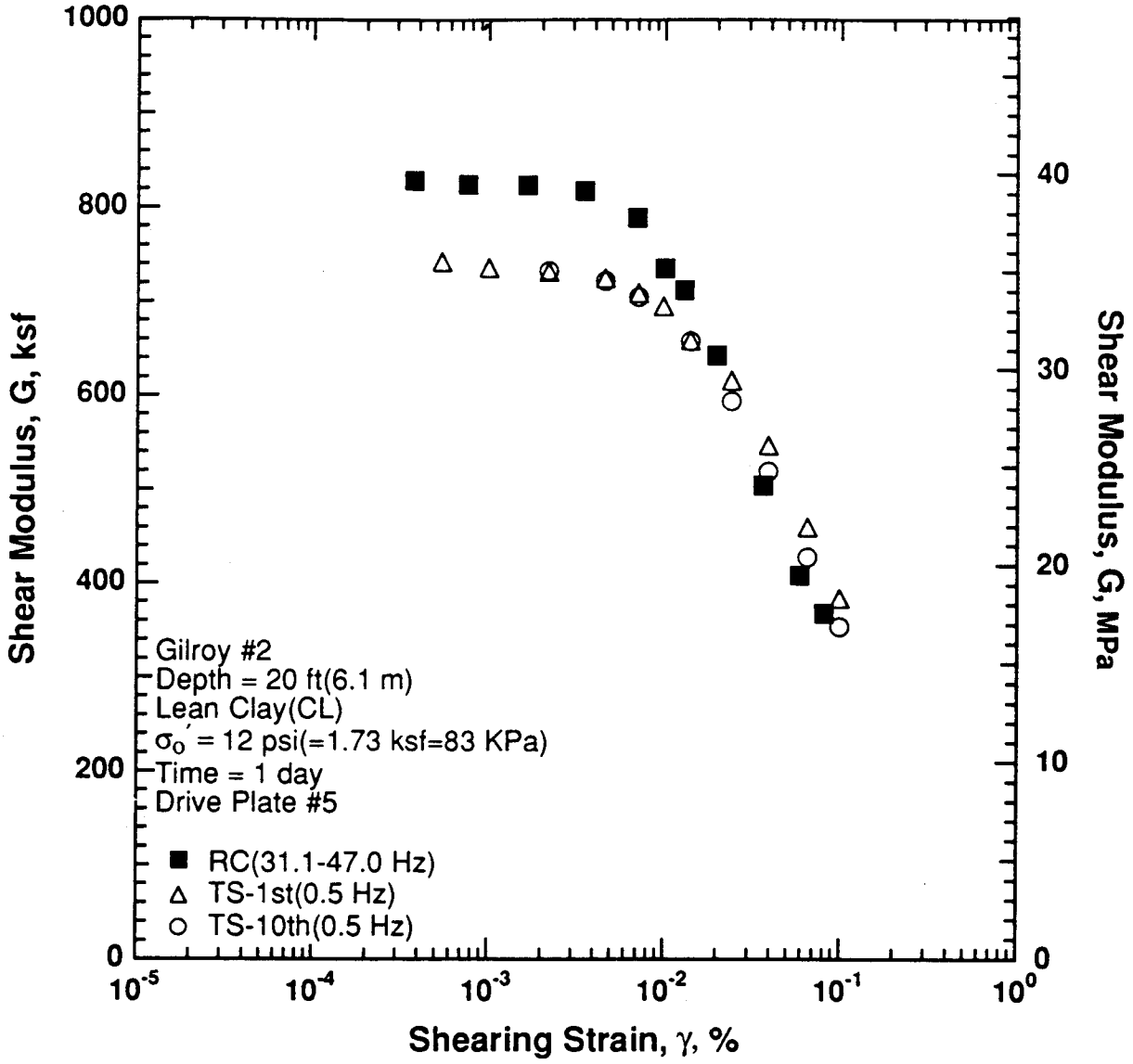

Figure 8.B.2.C-7
Variation in shear modulus with shearing strain at an effective confining pressure of 12 psi (1.73 ksf, 83 kPa) from RCTS tests of sample G2.

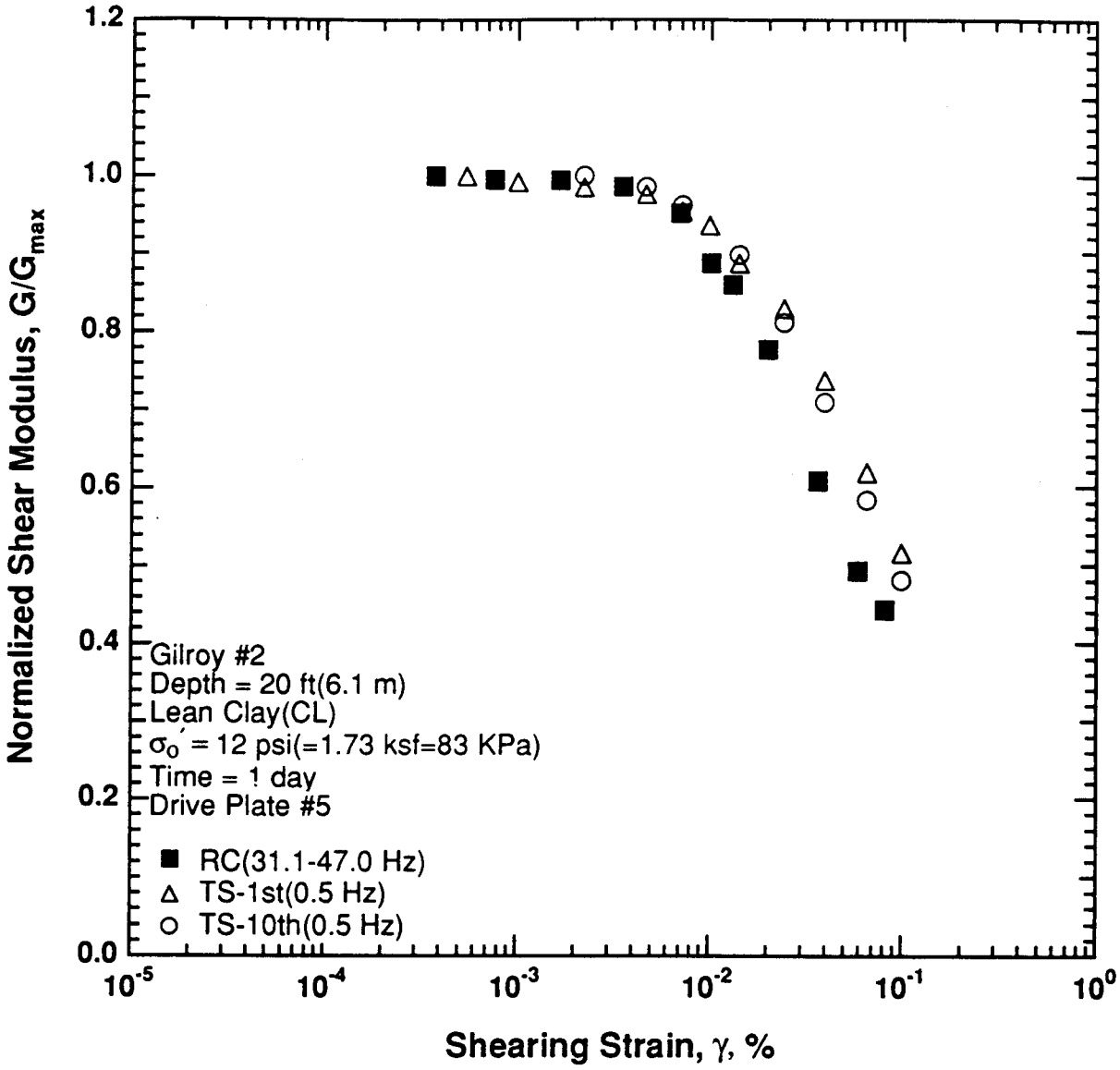

Figure 8.B.1.C-8
Variation in normalized shear modulus with shearing strain at an effective confining pressure of 12 psi (1.73 ksf, 83 kPa) from RCTS tests of sample G2.

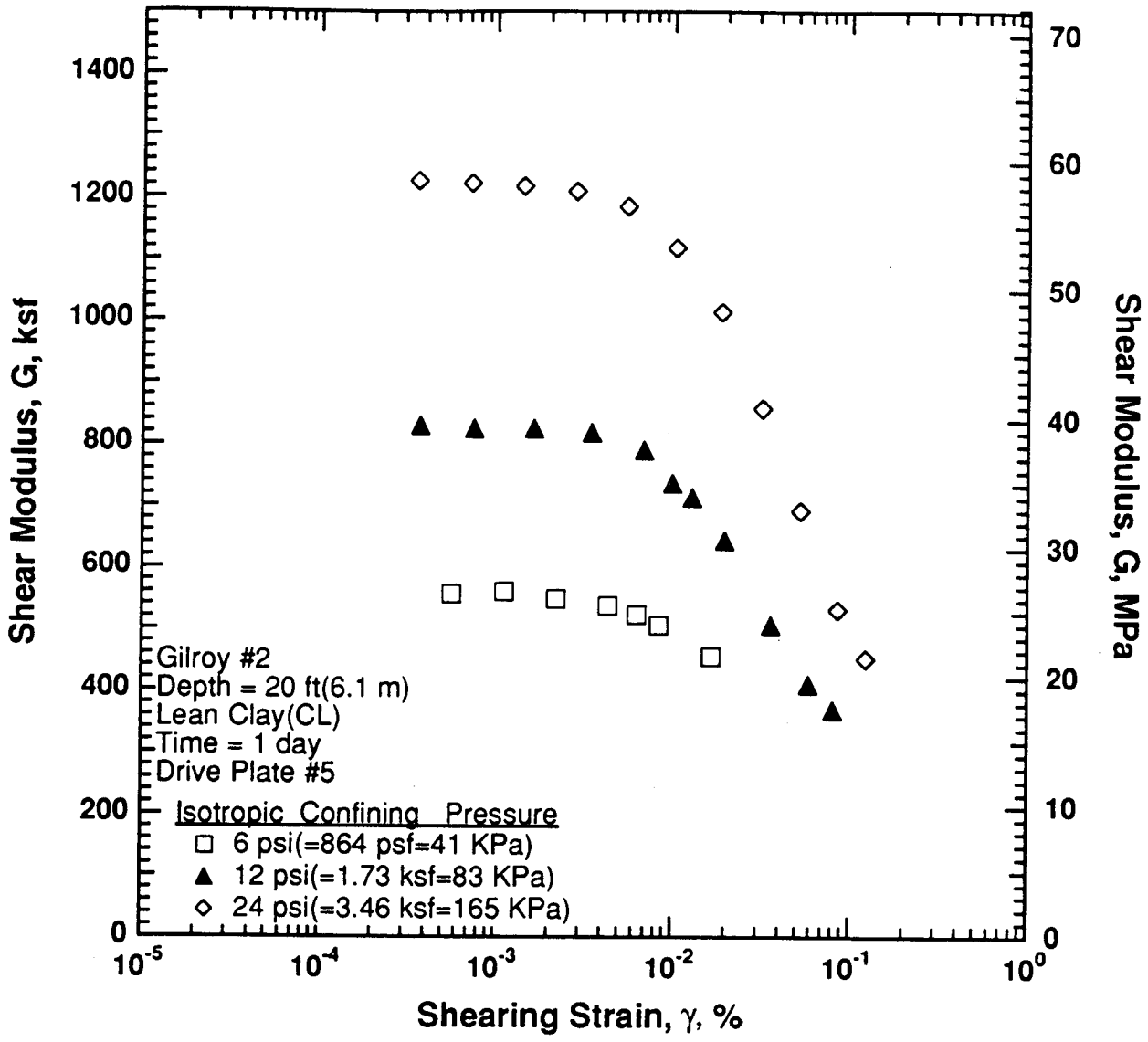

Figure 8.B.2.C-9
Variation in shear modulus with shearing strain and effective confining pressure from resonant column tests of sample G2.

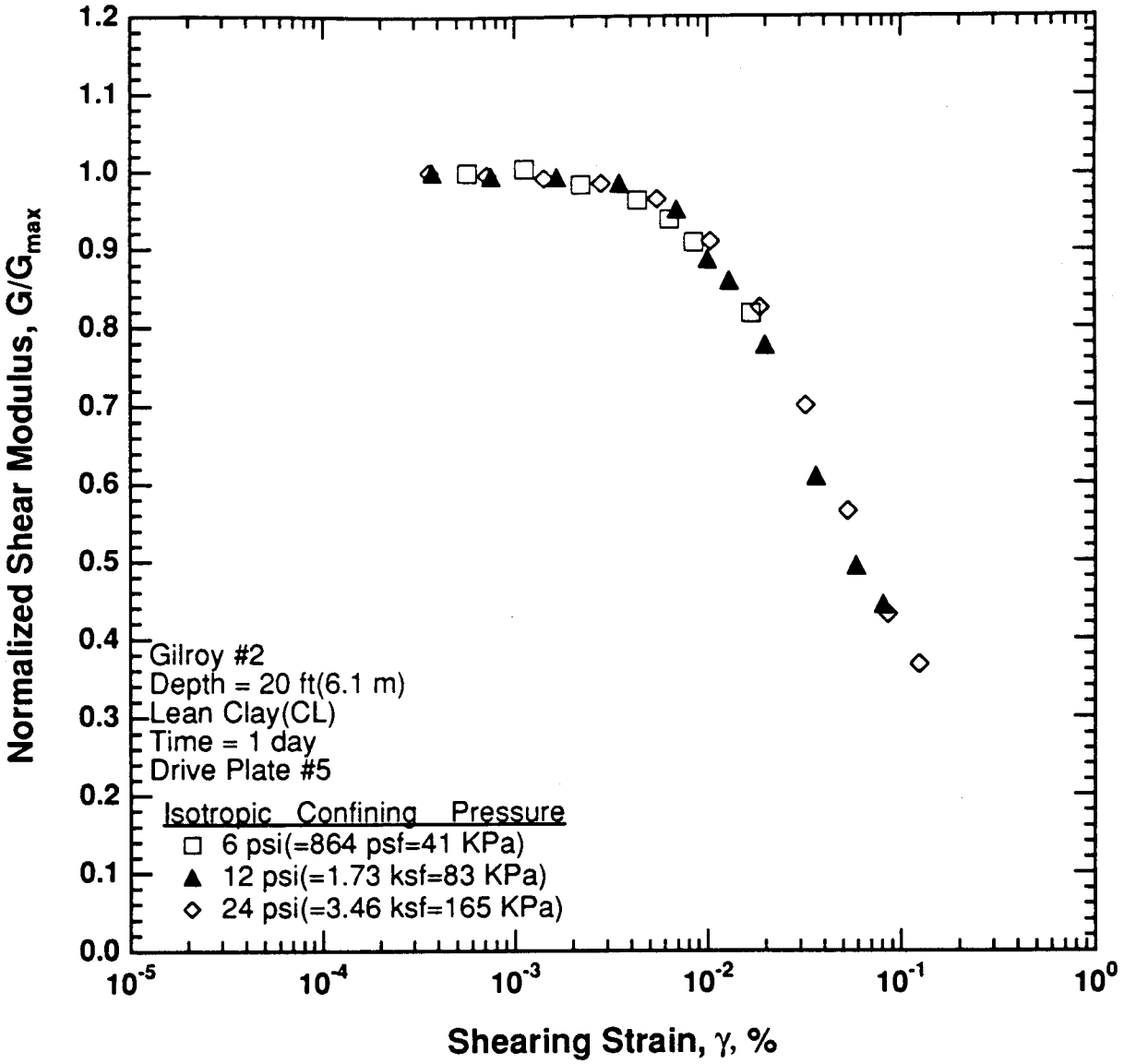

Figure 8.B.2.C-10
Comparison of the variation in normalized shear modulus with shearing strain and effective confining pressure from resonant column tests of sample G2.

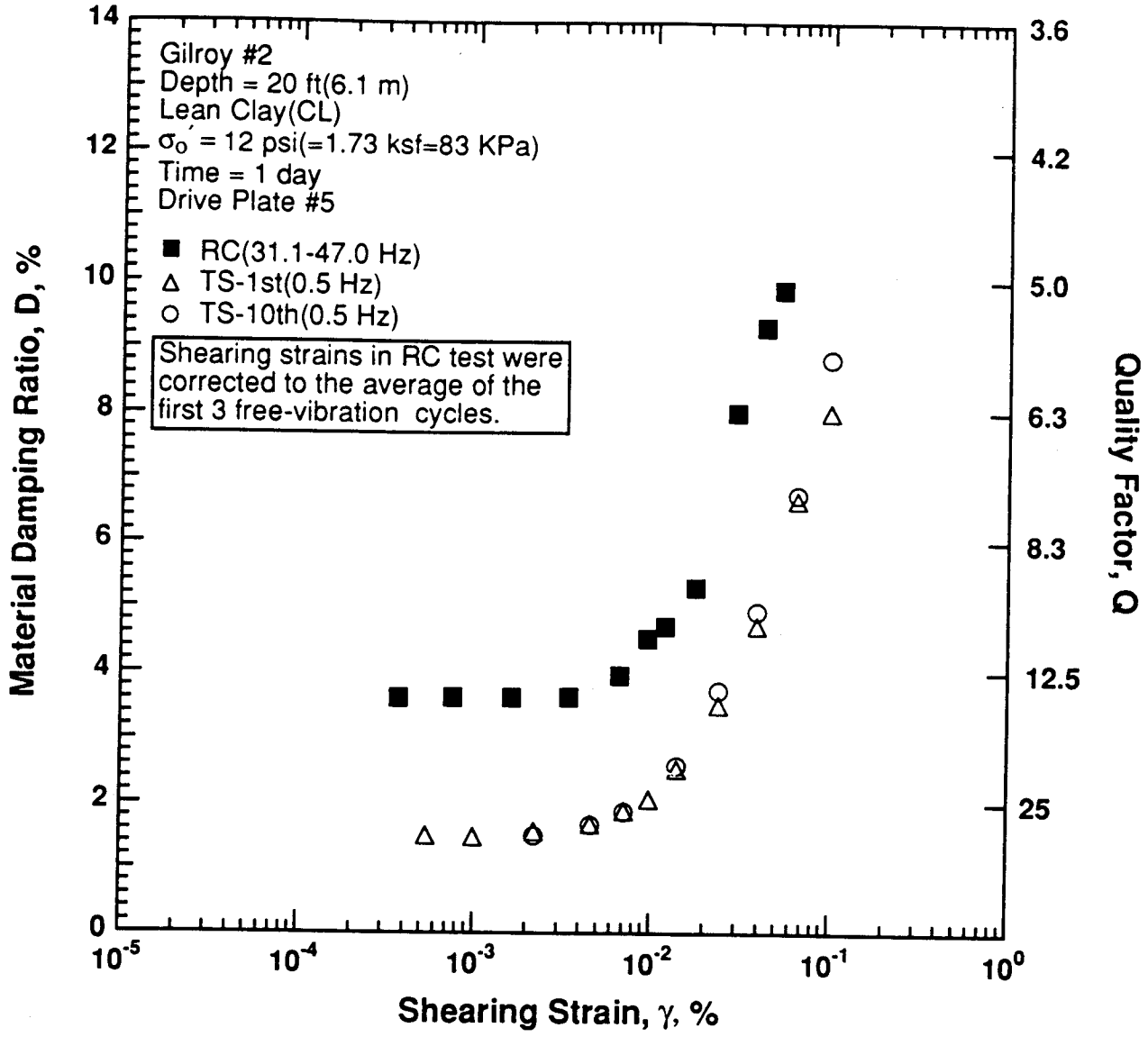

Figure 8.B.2.C-11
Variation in material damping ratio with shearing strain at an effective confining pressure of 12 psi (1.73 ksf, 83 kPa) from RCTS tests of sample G2.

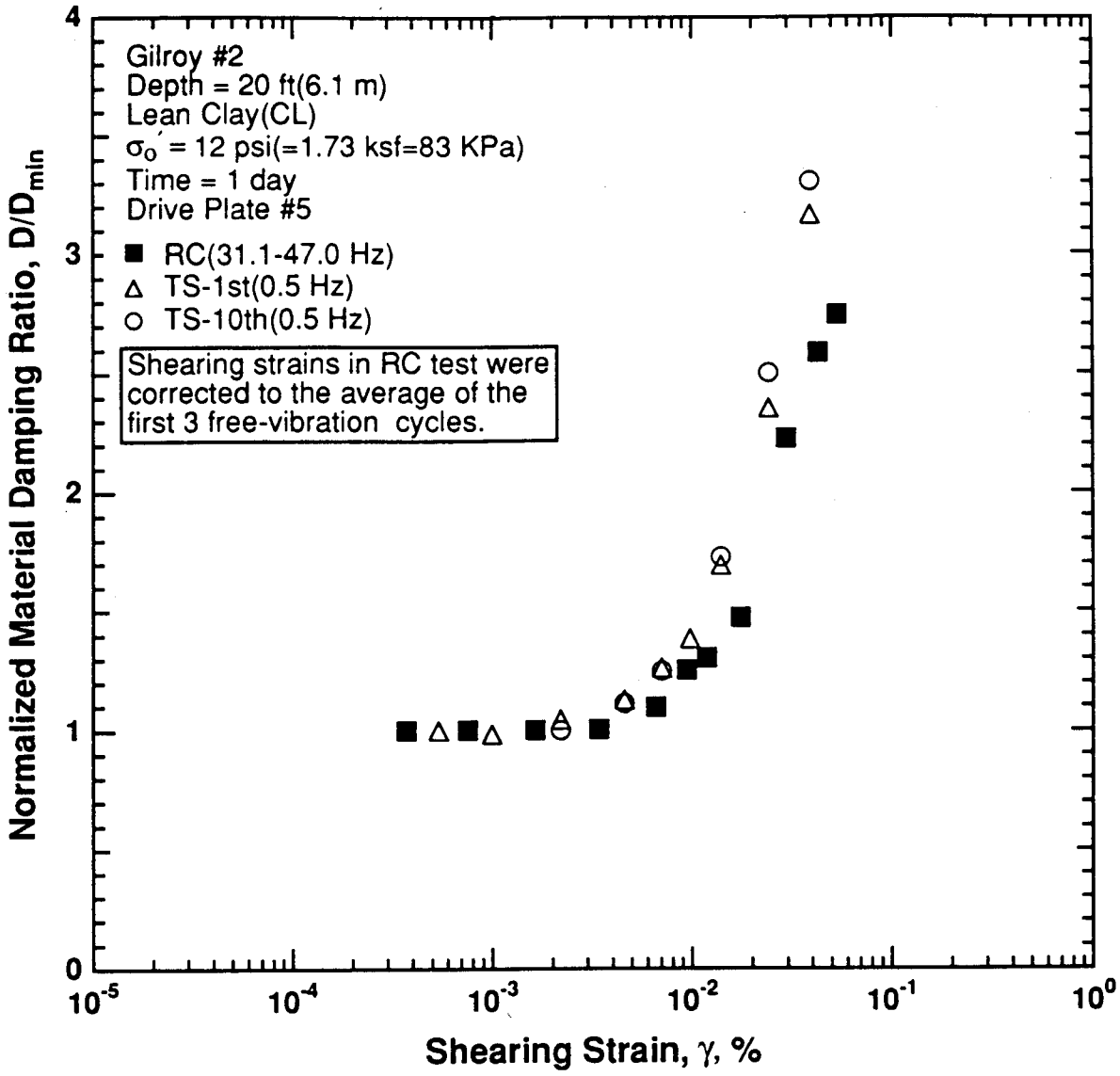

Figure 8.B.2.C-12
Variation in normalized material damping ratio with shearing strain at an effective confining pressure of 12 psi (1.73 ksf, 83 kPa) from RCTS tests of sample G2.

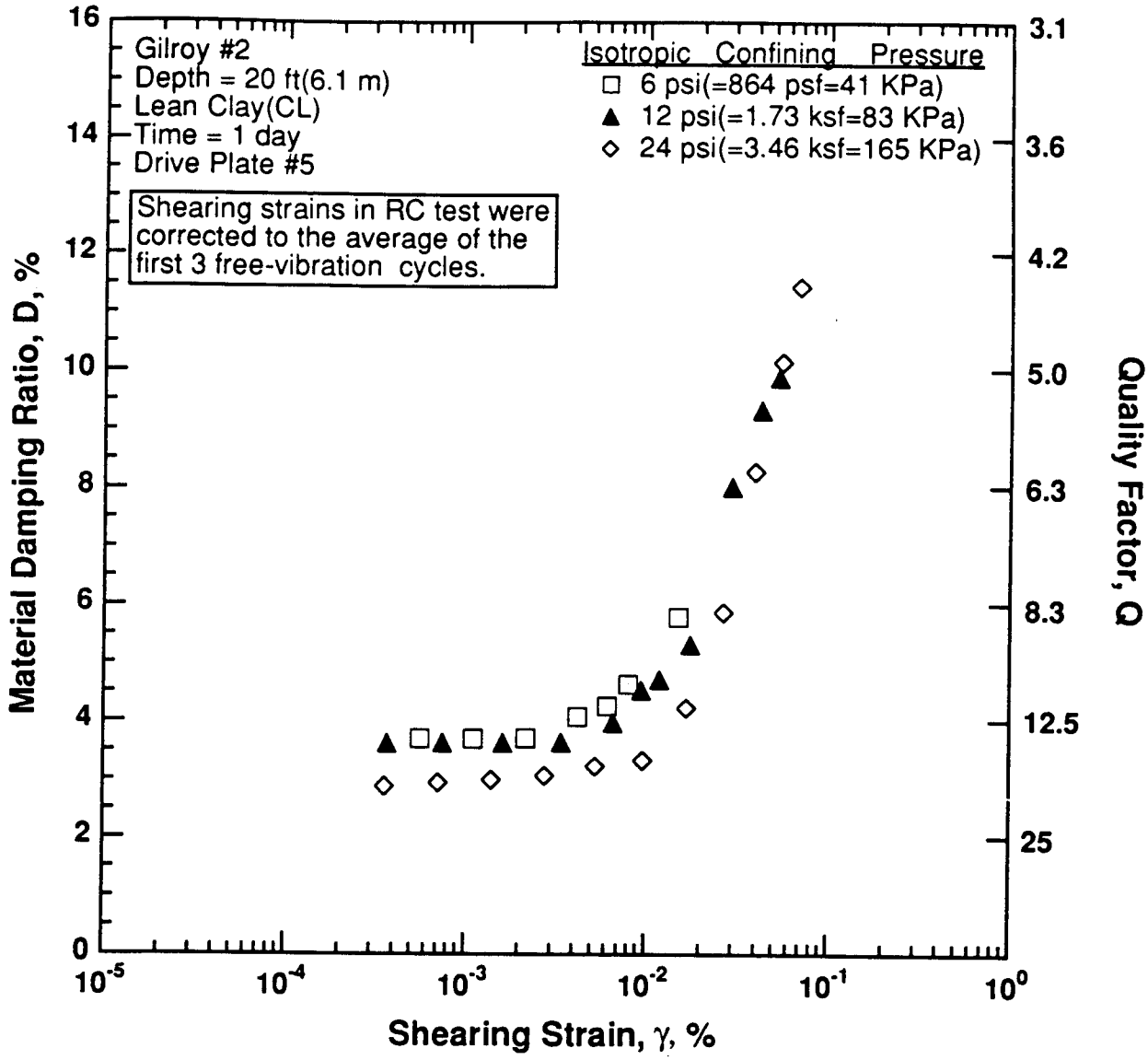

Figure 8.B.2.C-13
Variation in material damping ratio with shearing strain and effective confining pressure from resonant column tests of sample G2.

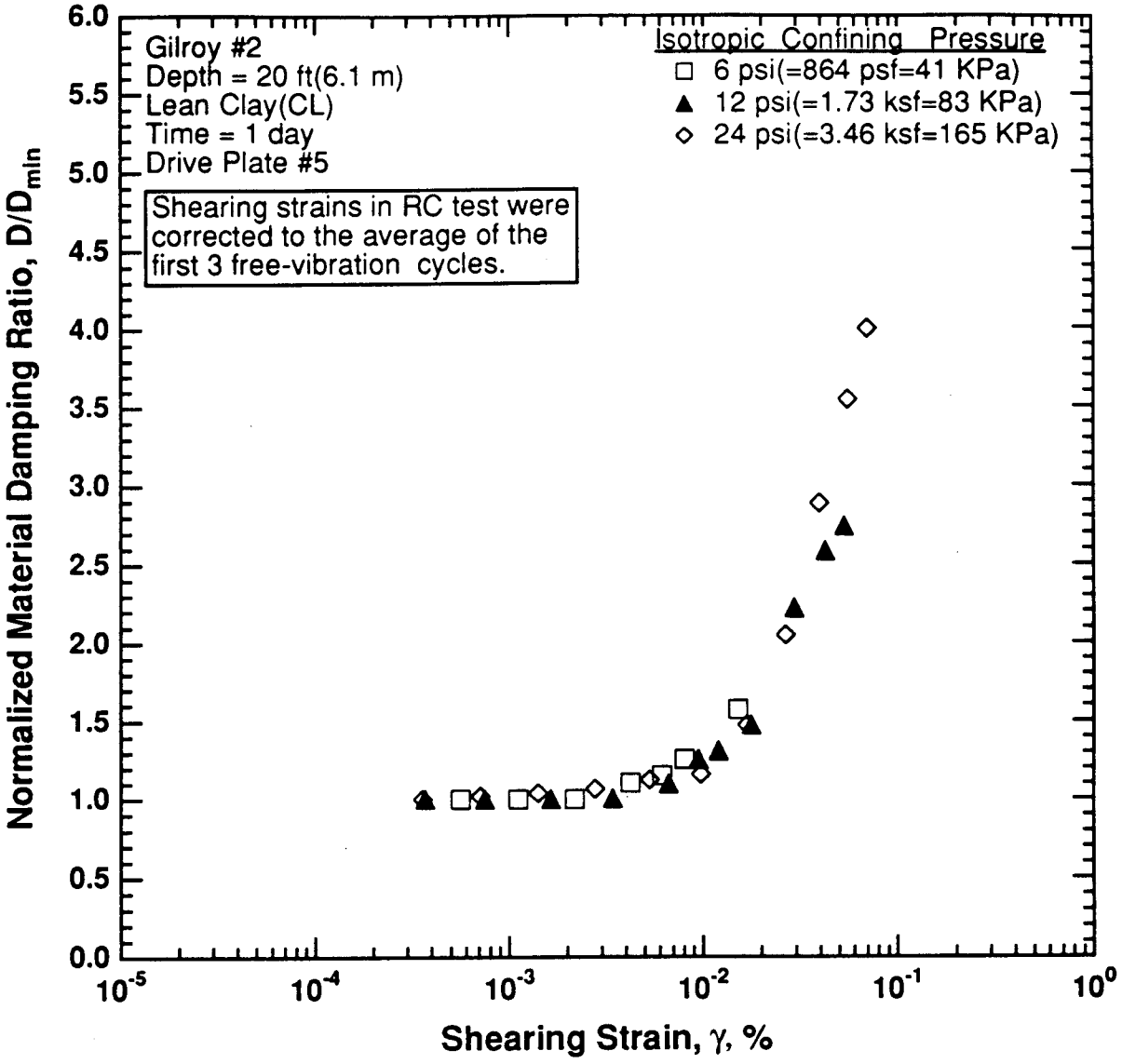

Figure 8.B.2.C-14
Comparison of the variation in normalized material damping ratio with shearing strain and effective confining pressure from resonant column tests of sample G2.

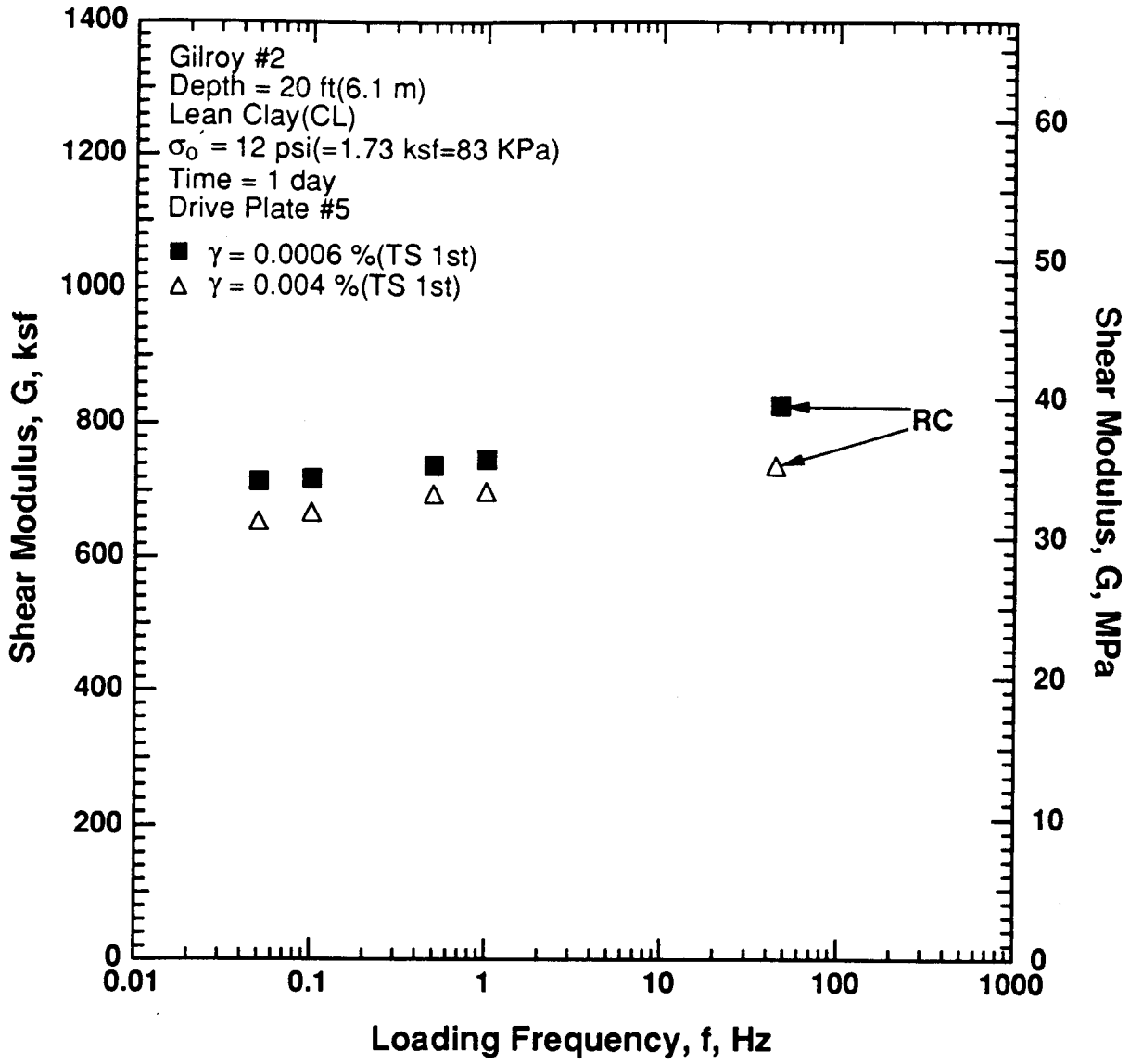

Figure 8.B.2.C-15
Variation in shear modulus with loading frequency and shearing strain at an effective confining pressure of 12 psi (1.73 ksf, 83 kPa) from RCTS tests of sample G2.

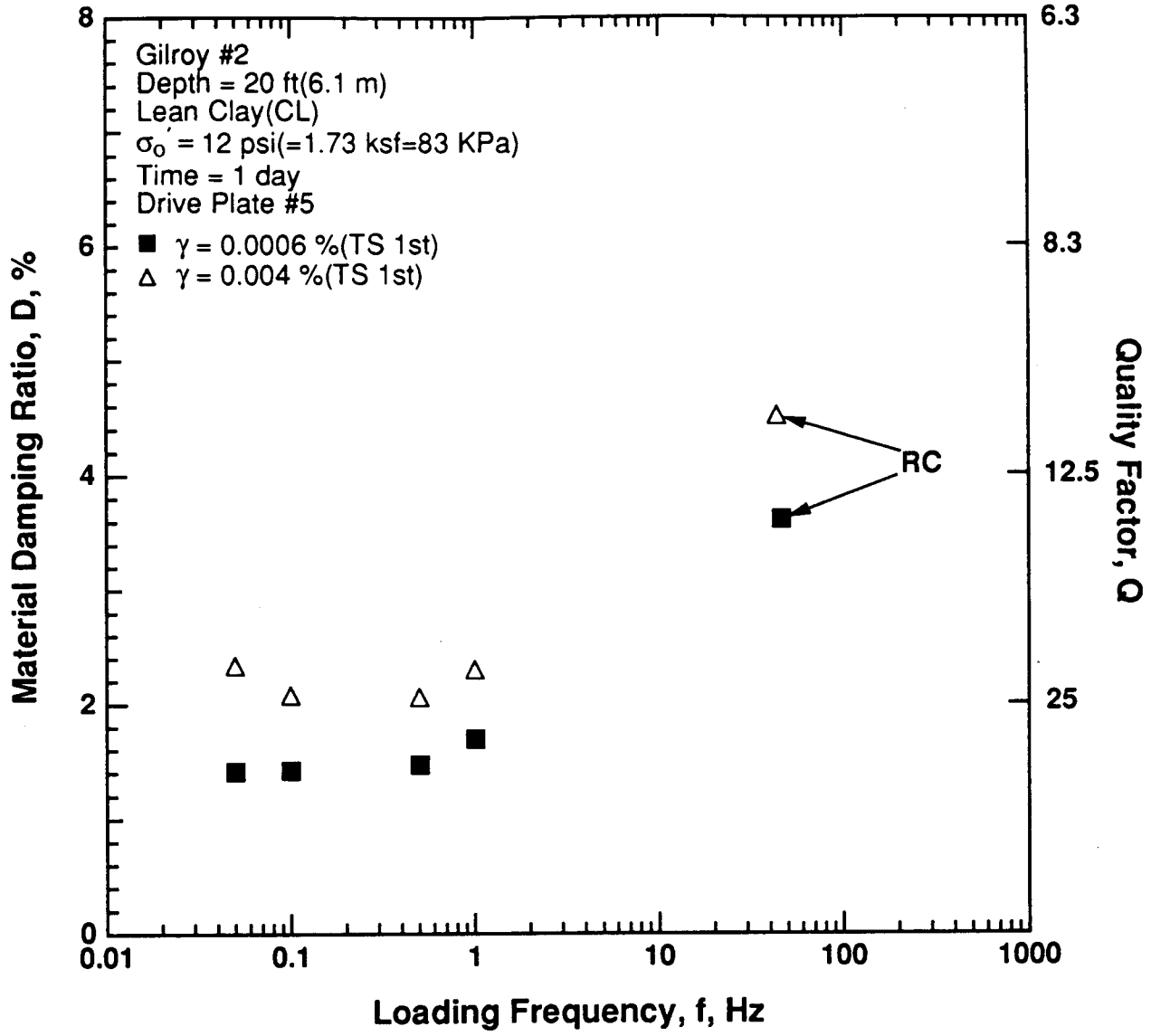

Figure 8.B.2.C-16
Variation in material damping ratio with loading frequency and shearing strain at an effective confining pressure of 12 psi (1.73 ksf, 83 kPa) from RCTS tests of sample G2.

APPENDIX 8.B.2.D
DYNAMIC TESTS OF SAMPLE G2-1, DEPTH = 20 FT (6.1 M)

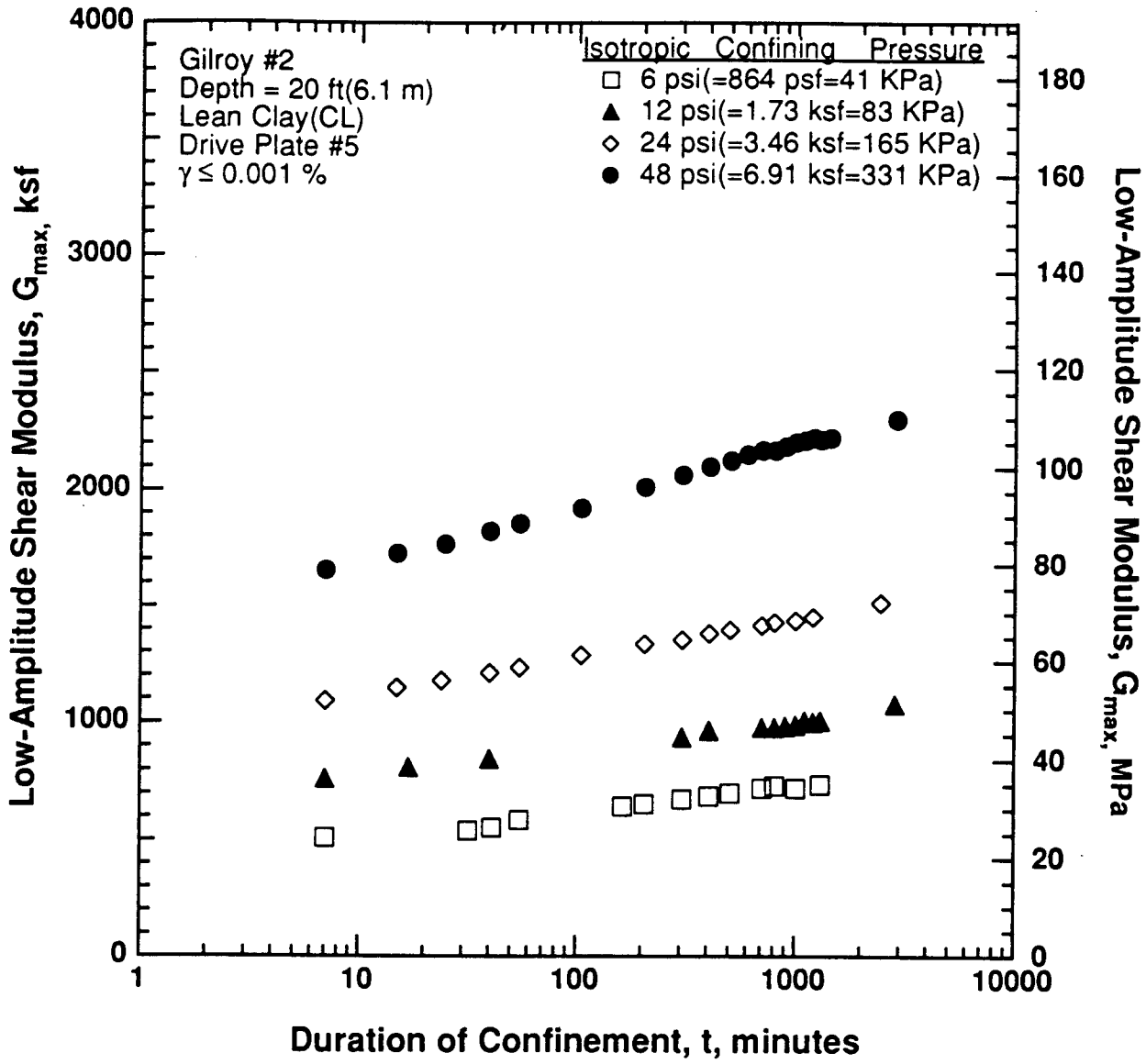

Figure 8.B.2.D-1
Variation in low-amplitude shear modulus with magnitude and duration of isotropic confining pressure from resonant column tests of sample G2-1.

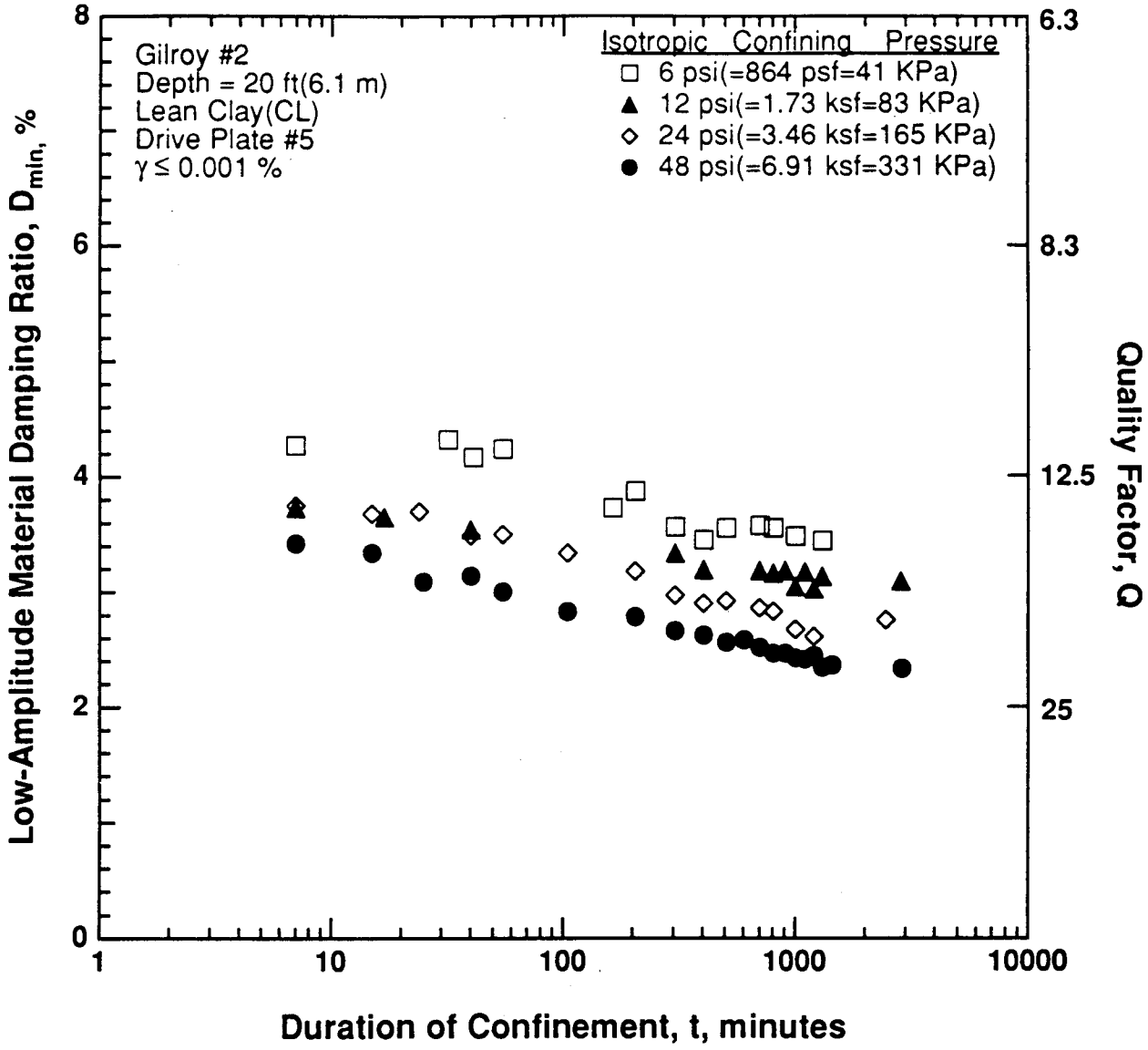

Figure 8.B.2.D-2
Variation in low-amplitude material damping ratio with magnitude and duration of isotropic confining pressure from resonant column tests of sample G2-1.

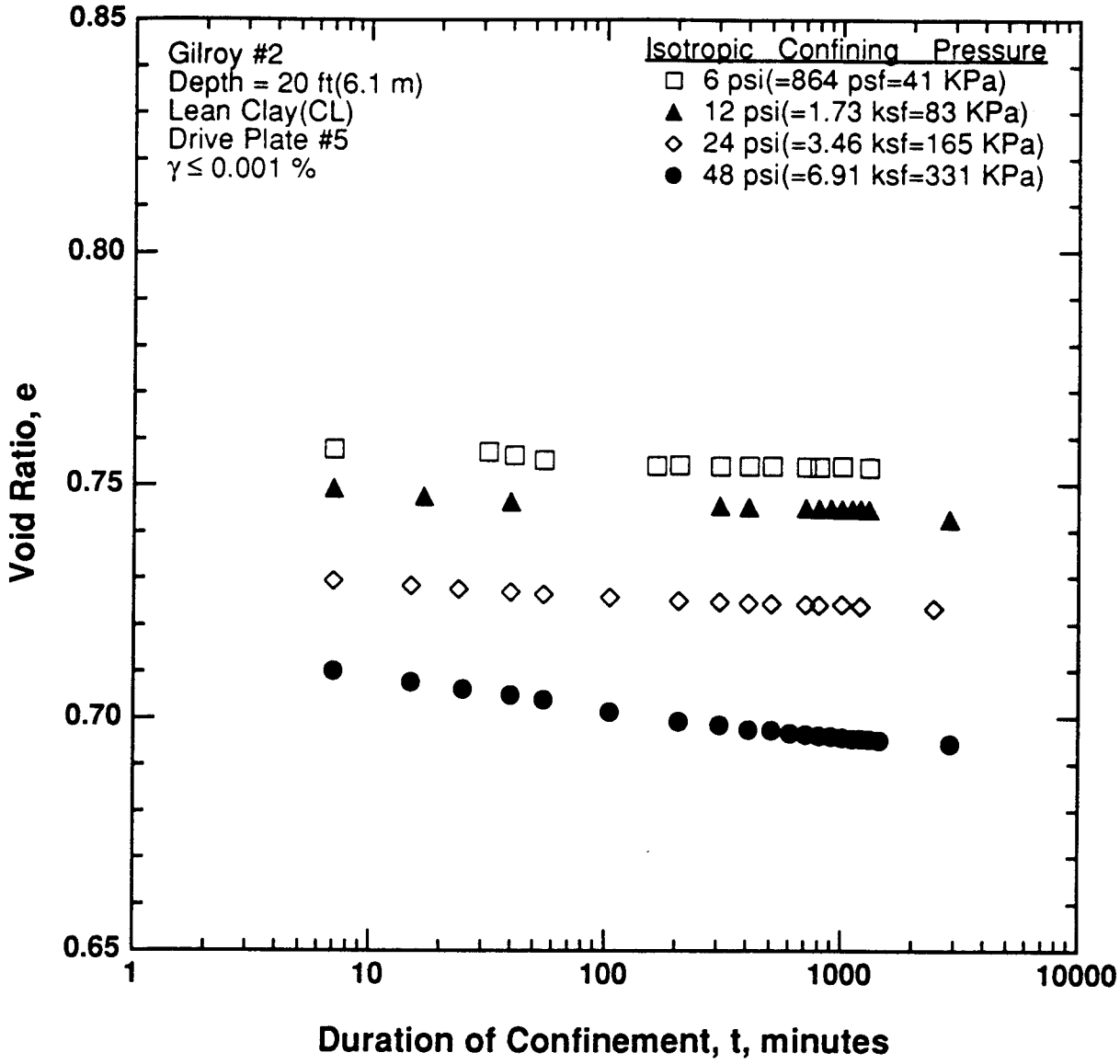

Figure 8.B.2.D-3
Variation in void ratio with magnitude and duration of isotropic confining pressure from resonant column tests of sample G2-1.

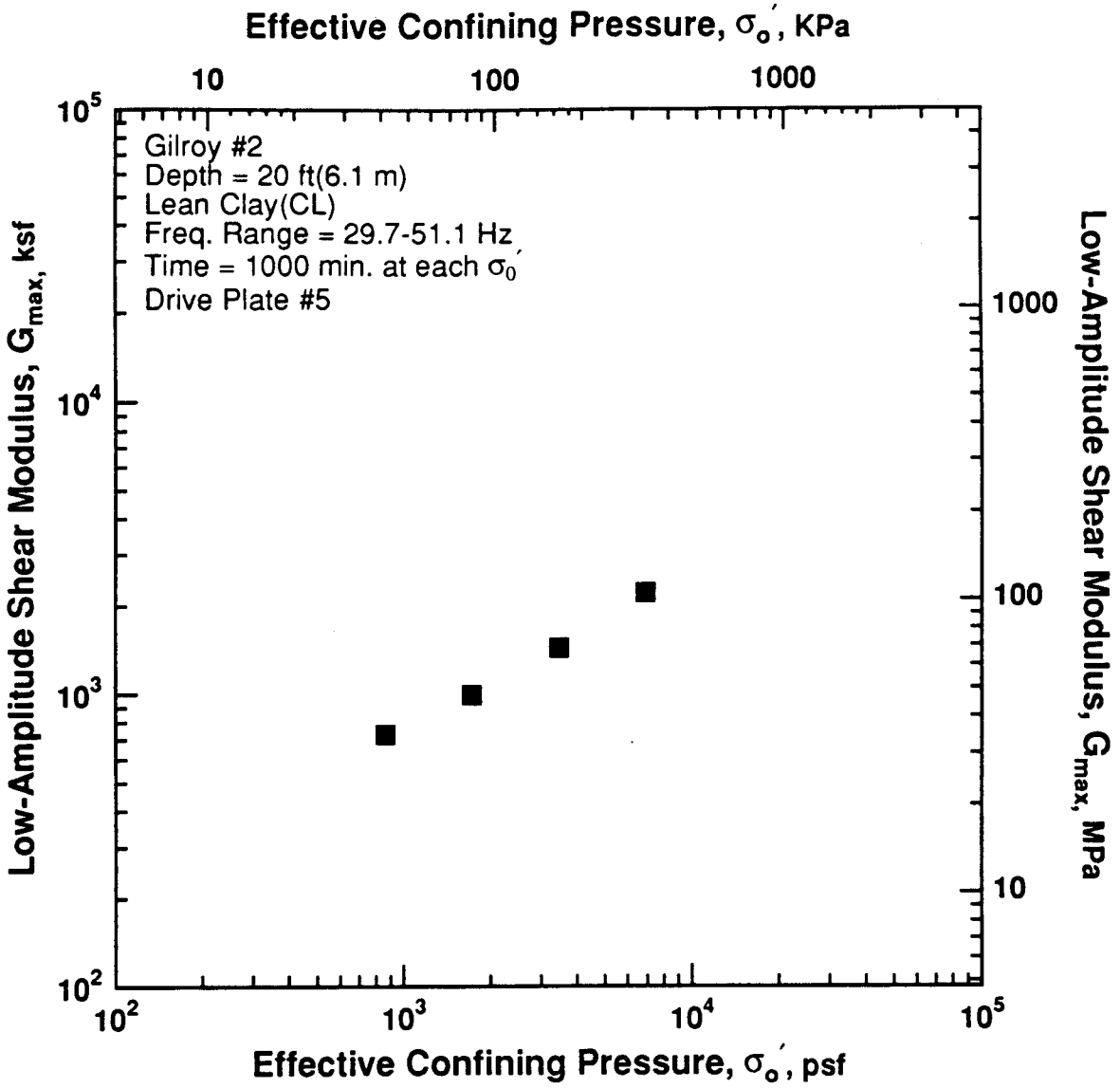

Figure 8.B.2.D-4
Variation in low-amplitude shear modulus with effective confining pressure from resonant column tests of sample G2-1.

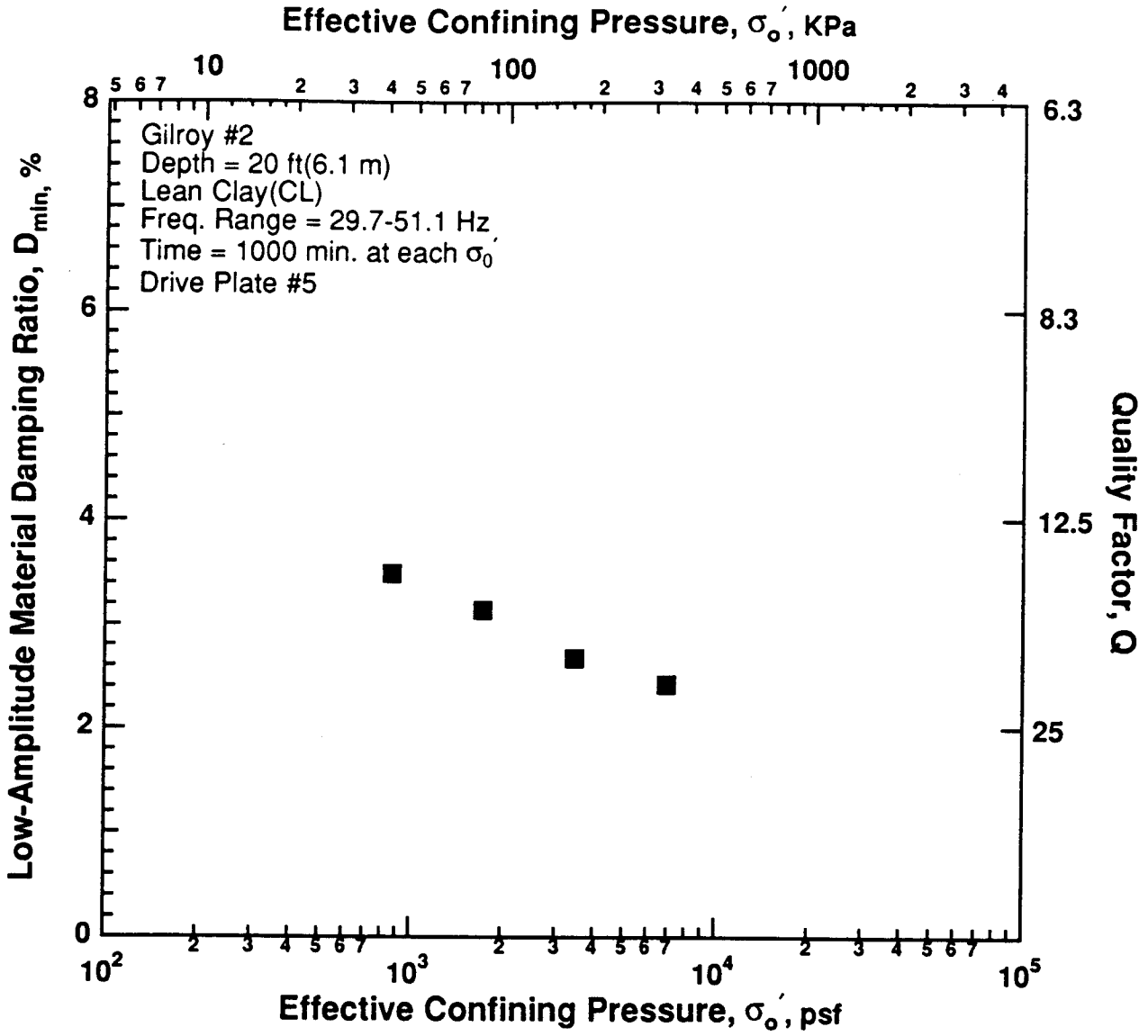

Figure 8.B.2.D-5
Variation in low-amplitude material damping ratio with effective confining pressure from resonant column tests of sample G2-1.

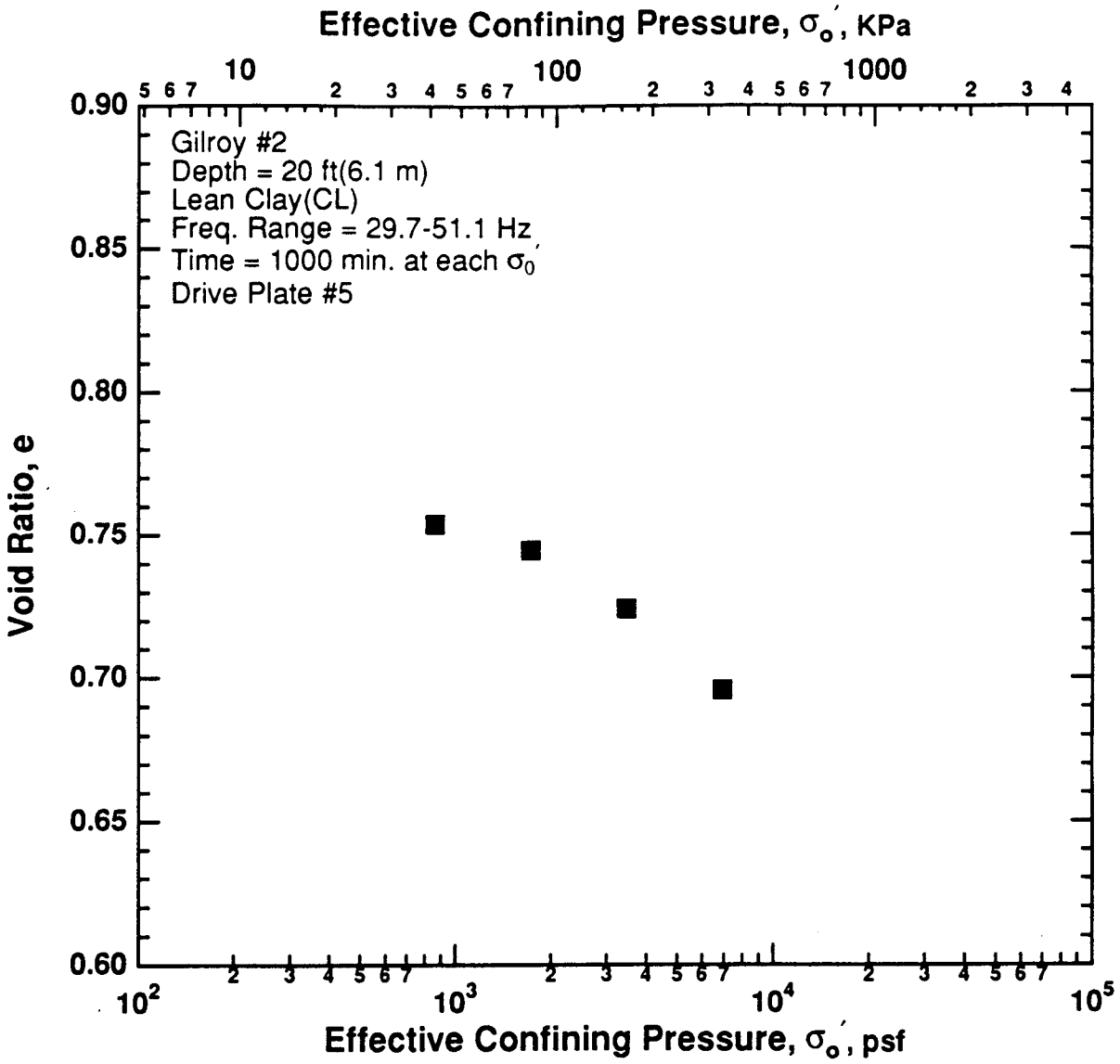

Figure 8.B.2.D-6
Variation in void ratio with effective confining pressure from resonant column tests of sample G2-1.

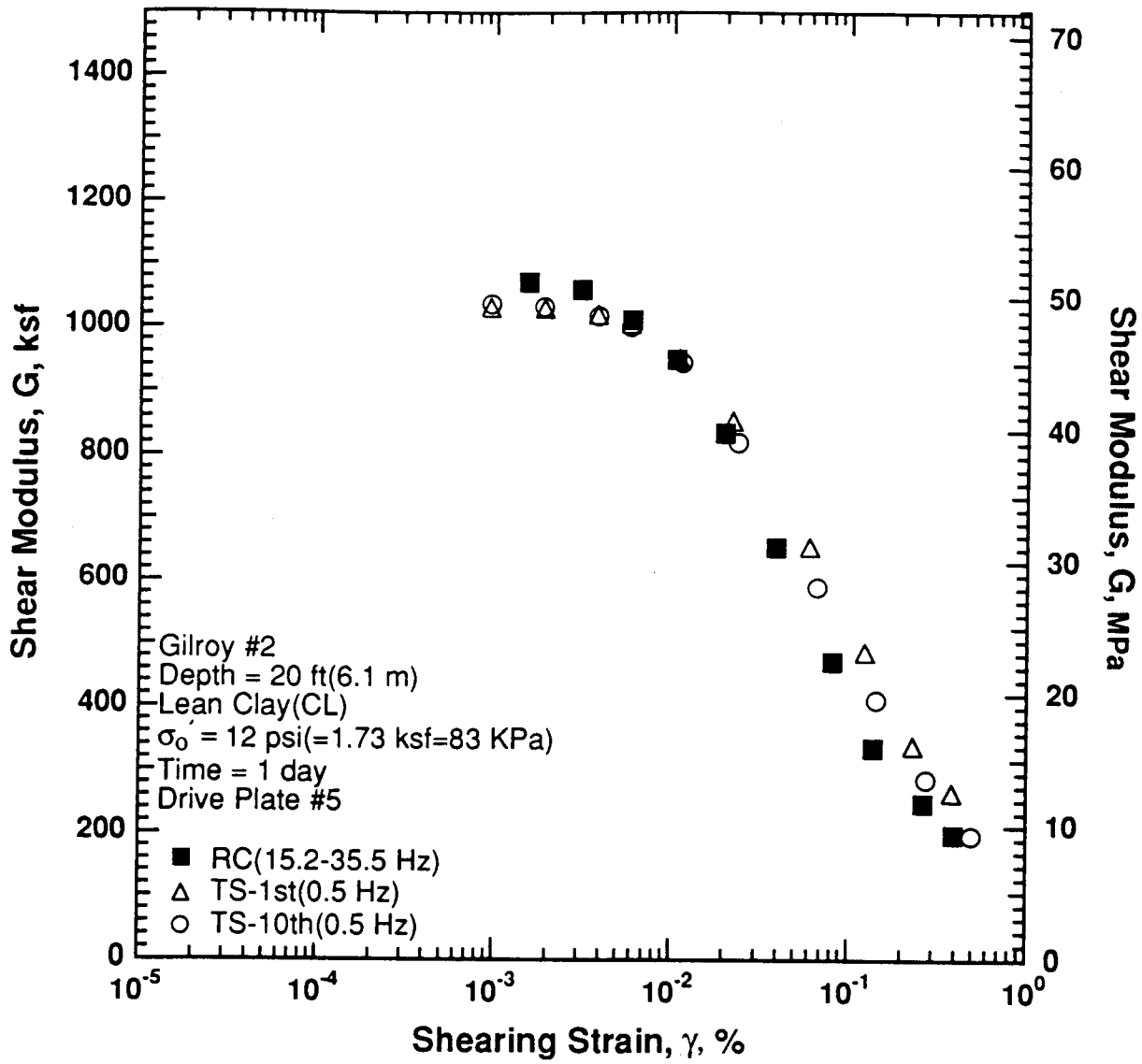

Figure 8.B.2.D-7
Variation in shear modulus with shearing strain at an effective confining pressure of 12 psi (1.73 ksf, 83 kPa) from RCTS tests of sample G2-1.

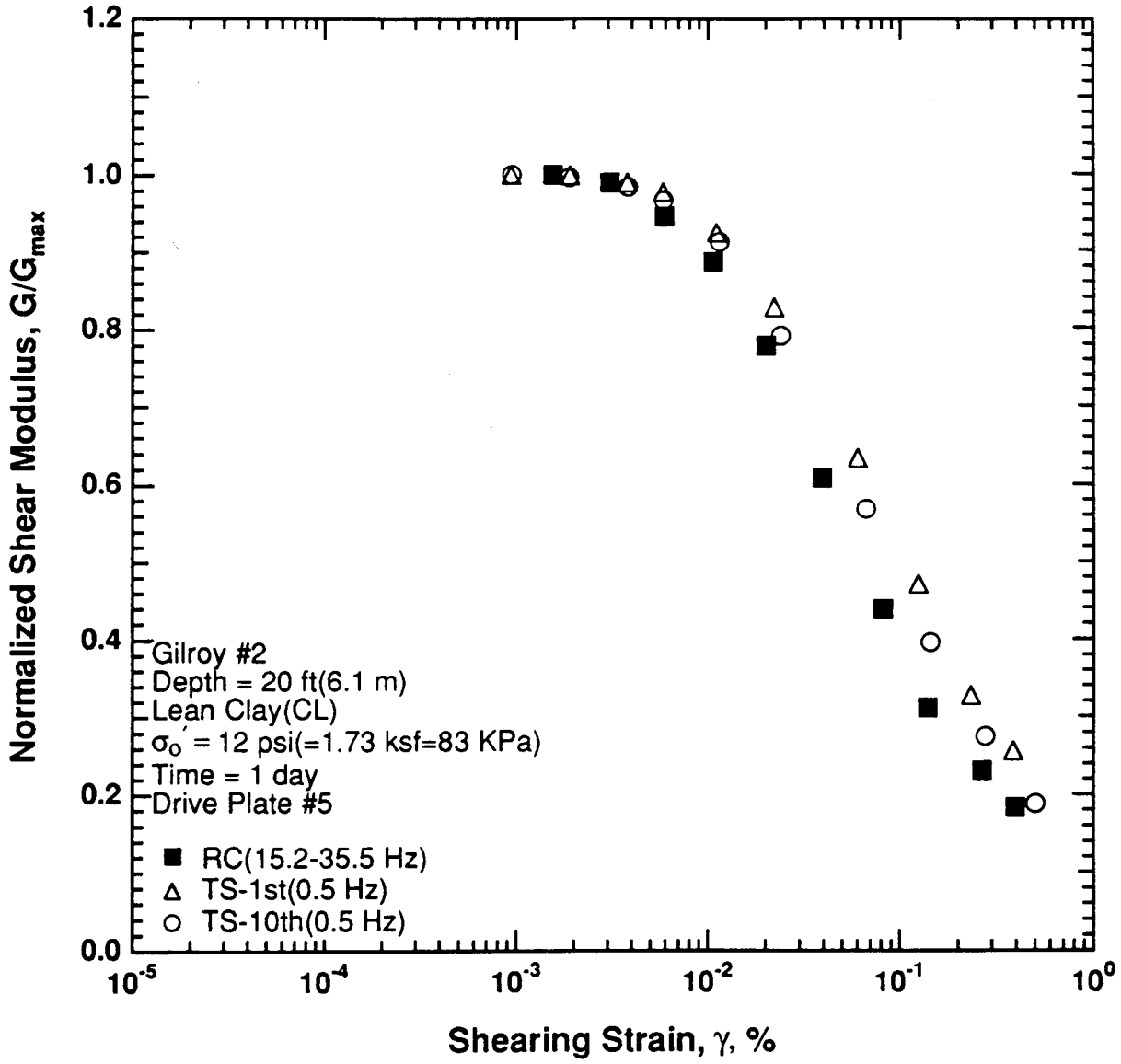

Figure 8.B.1.D-8
Variation in normalized shear modulus with shearing strain at an effective confining pressure of 12 psi (1.73 ksf, 83 kPa) from RCTS tests of sample G2-1.

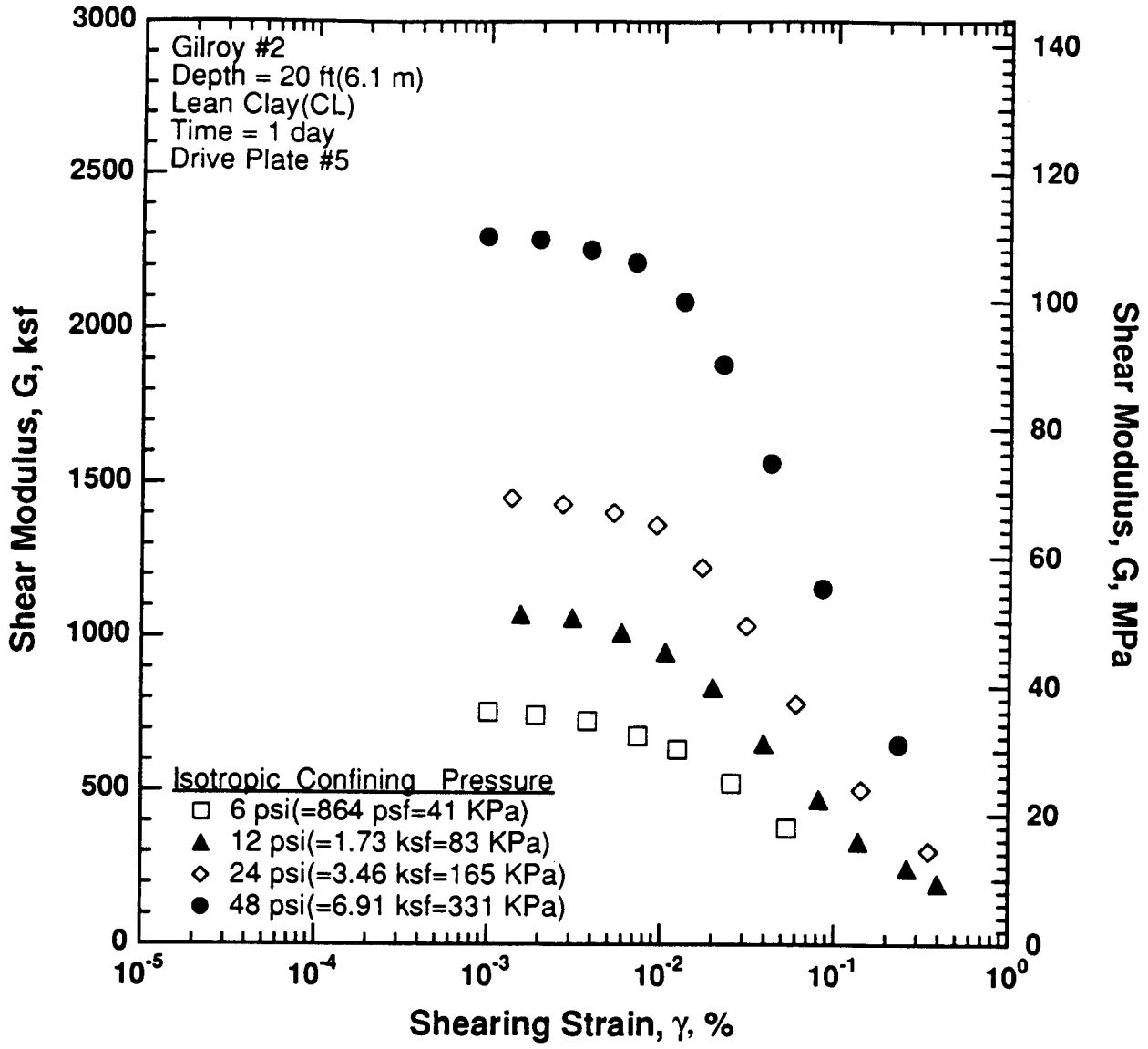

Figure 8.B.2.D-9
Variation in shear modulus with shearing strain and effective confining pressure from resonant column tests of sample G2-1.

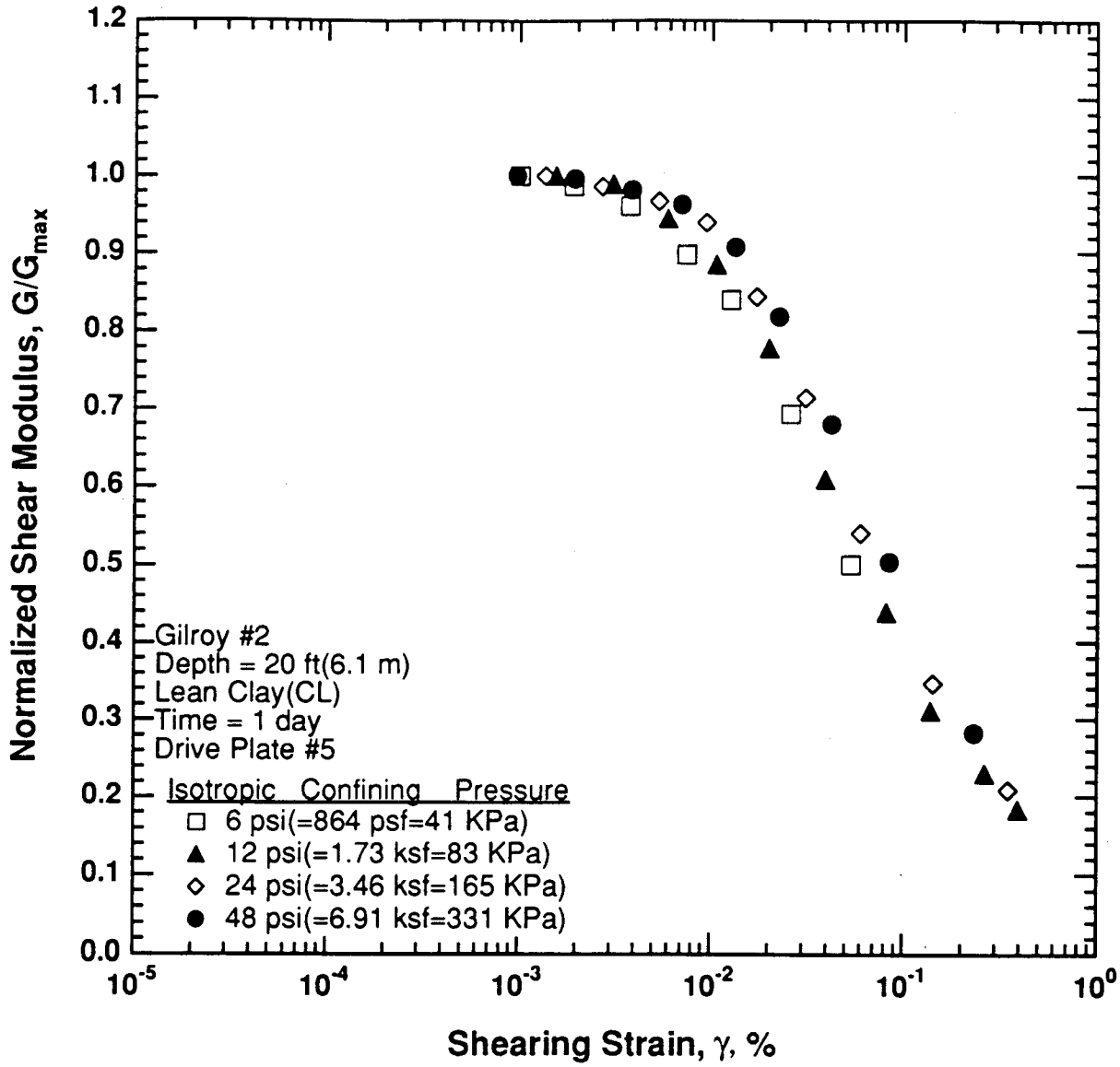

Figure 8.B.2.D-10
Comparison of the variation in normalized shear modulus with shearing strain and effective confining pressure from resonant column tests of sample G2-1.

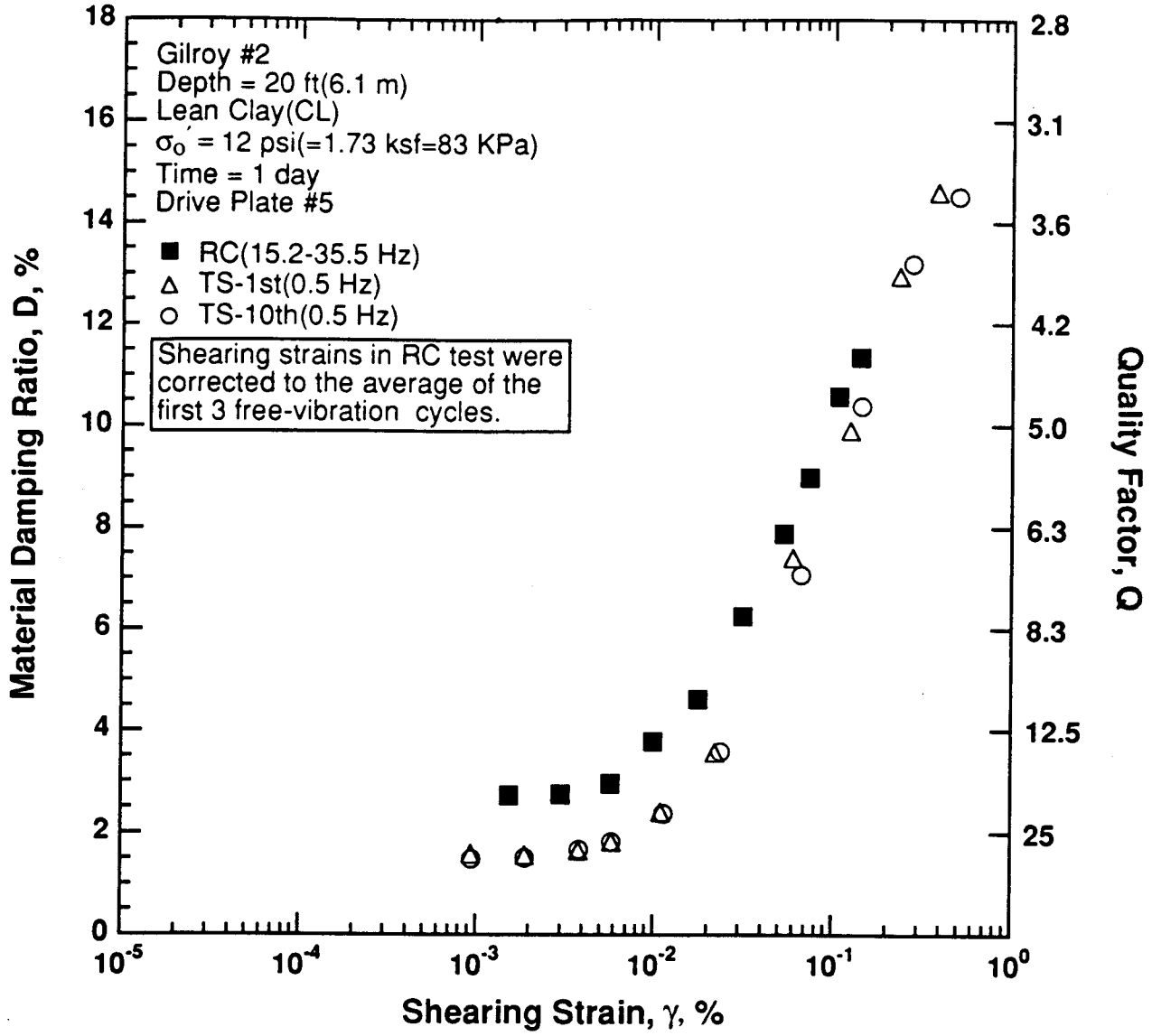

Figure 8.B.2.D-11
Variation in material damping ratio with shearing strain at an effective confining pressure of 12 psi (1.73 ksf, 83 kPa) from RCTS tests of sample G2-1.

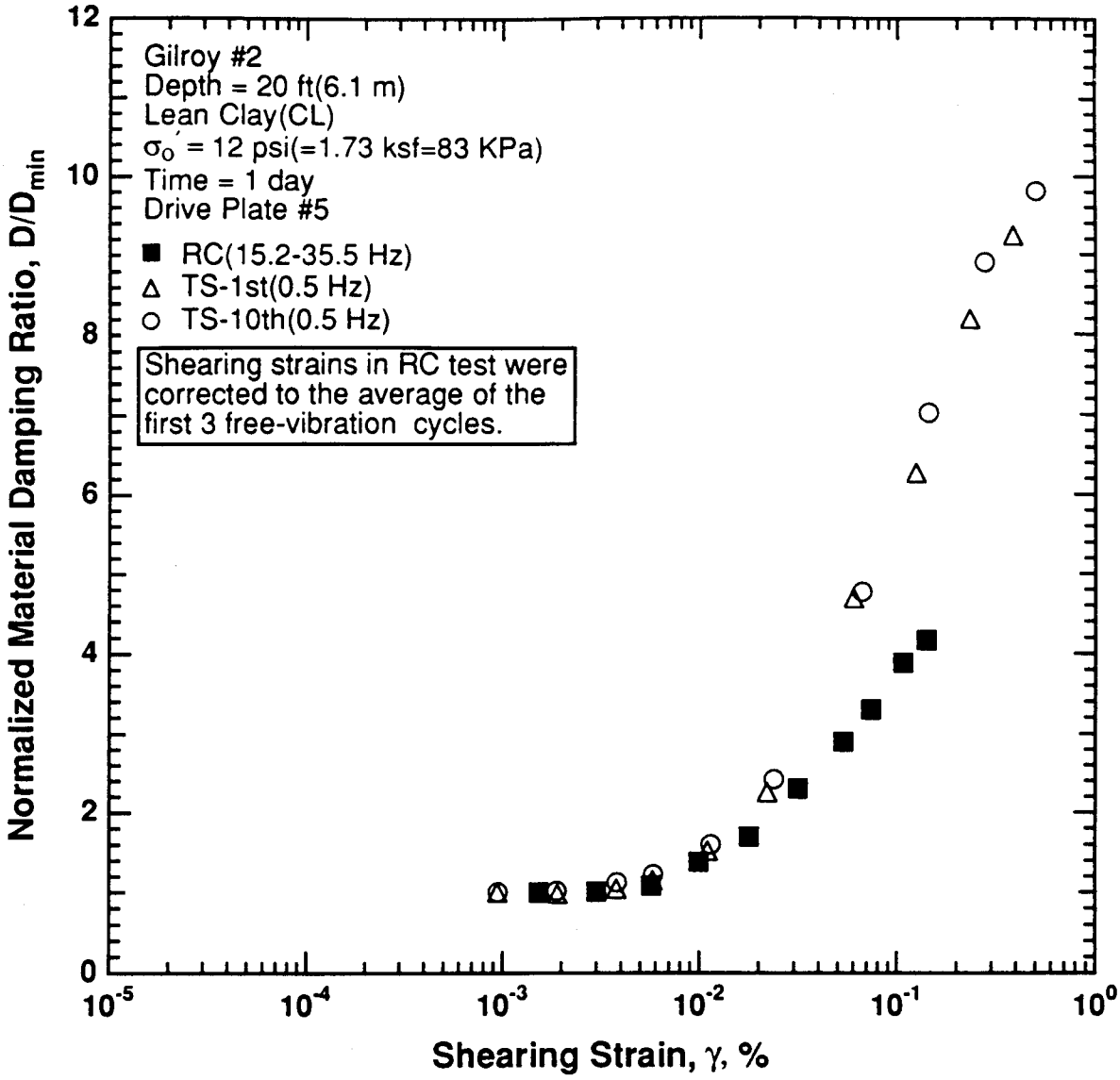

Figure 8.B.2.D-12
Variation in normalized material damping ratio with shearing strain at an effective confining pressure of 12 psi (1.73 ksf, 83 kPa) from RCTS tests of sample G2-1.

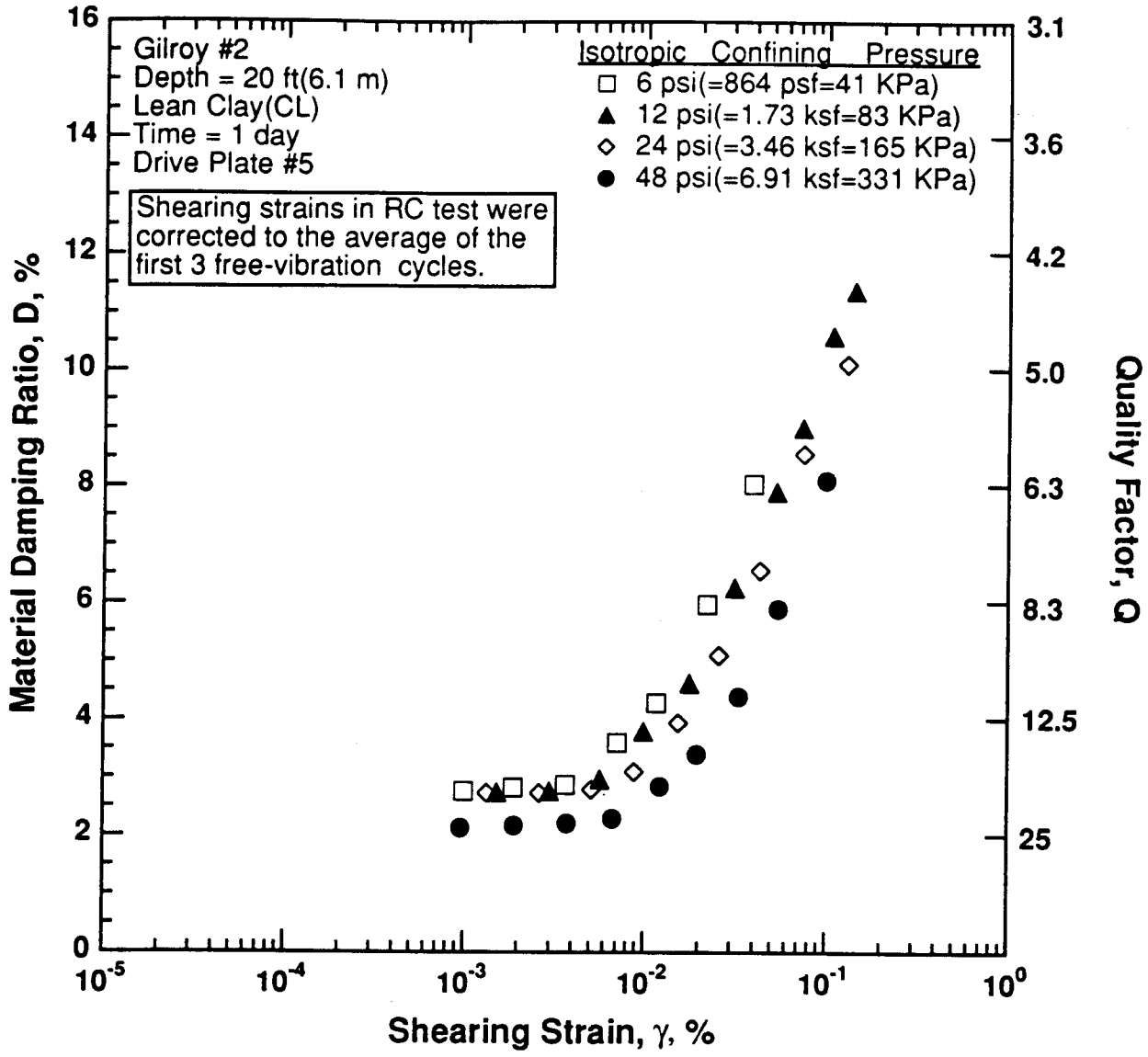

Figure 8.B.2.D-13
Variation in material damping ratio with shearing strain and effective confining pressure from resonant column tests of sample G2-1.

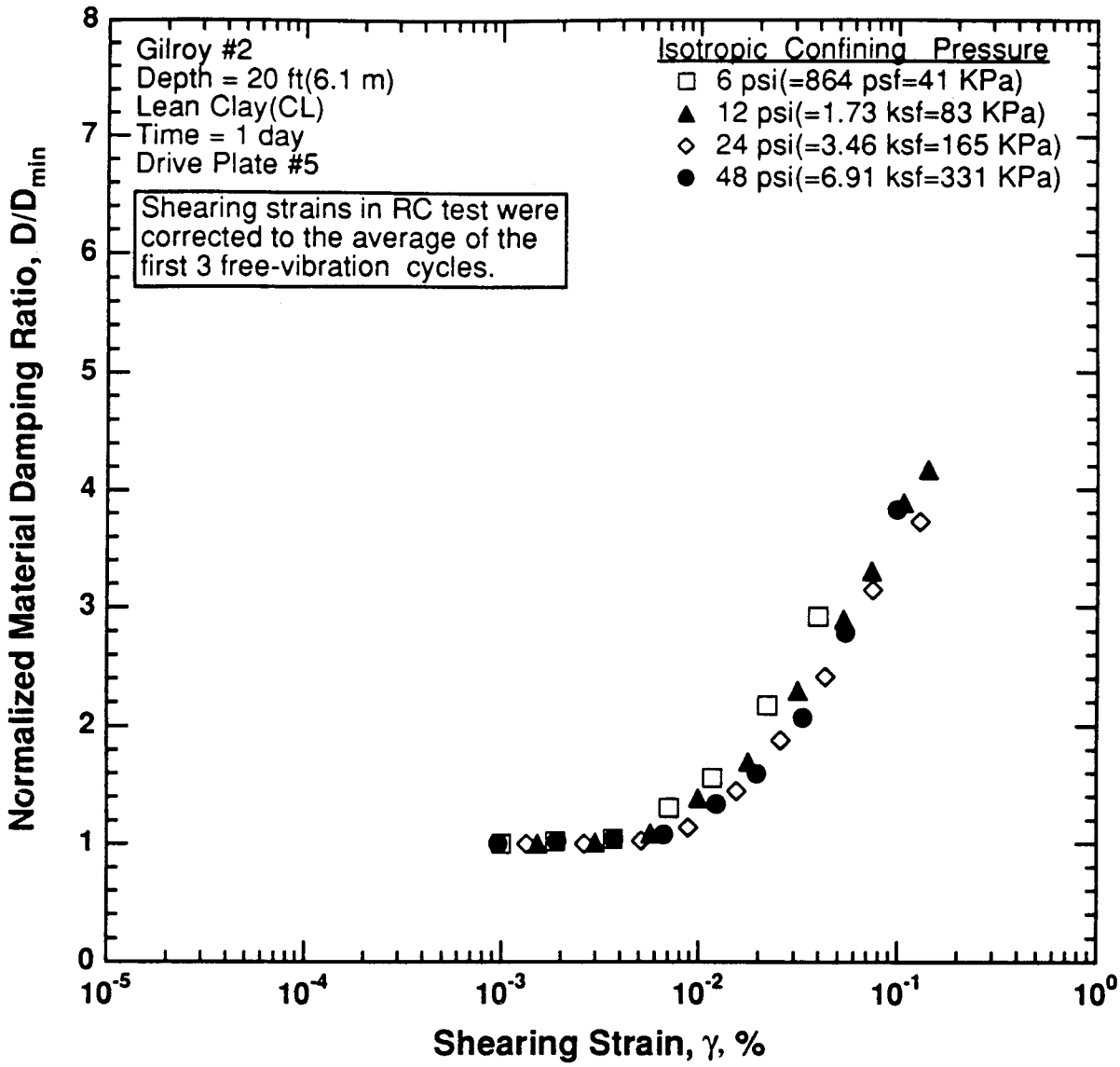

Figure 8.B.2.D-14
Comparison of the variation in normalized material damping ratio with shearing strain and effective confining pressure from resonant column tests of sample G2-1.

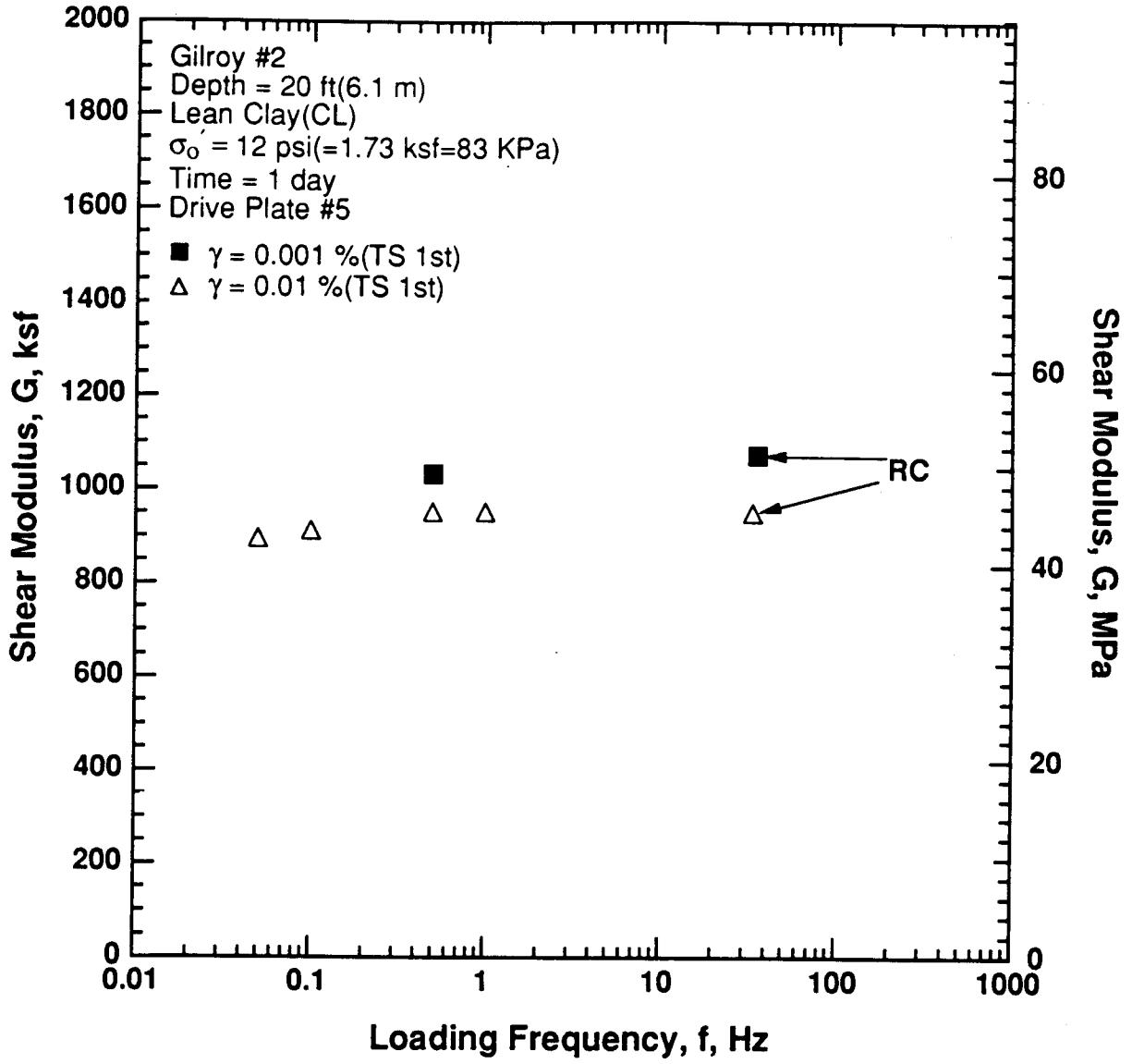

Figure 8.B.2.D-15
Variation in shear modulus with loading frequency and shearing strain at an effective confining pressure of 12 psi (1.73 ksf, 83 kPa) from RCTS tests of sample G2-1.

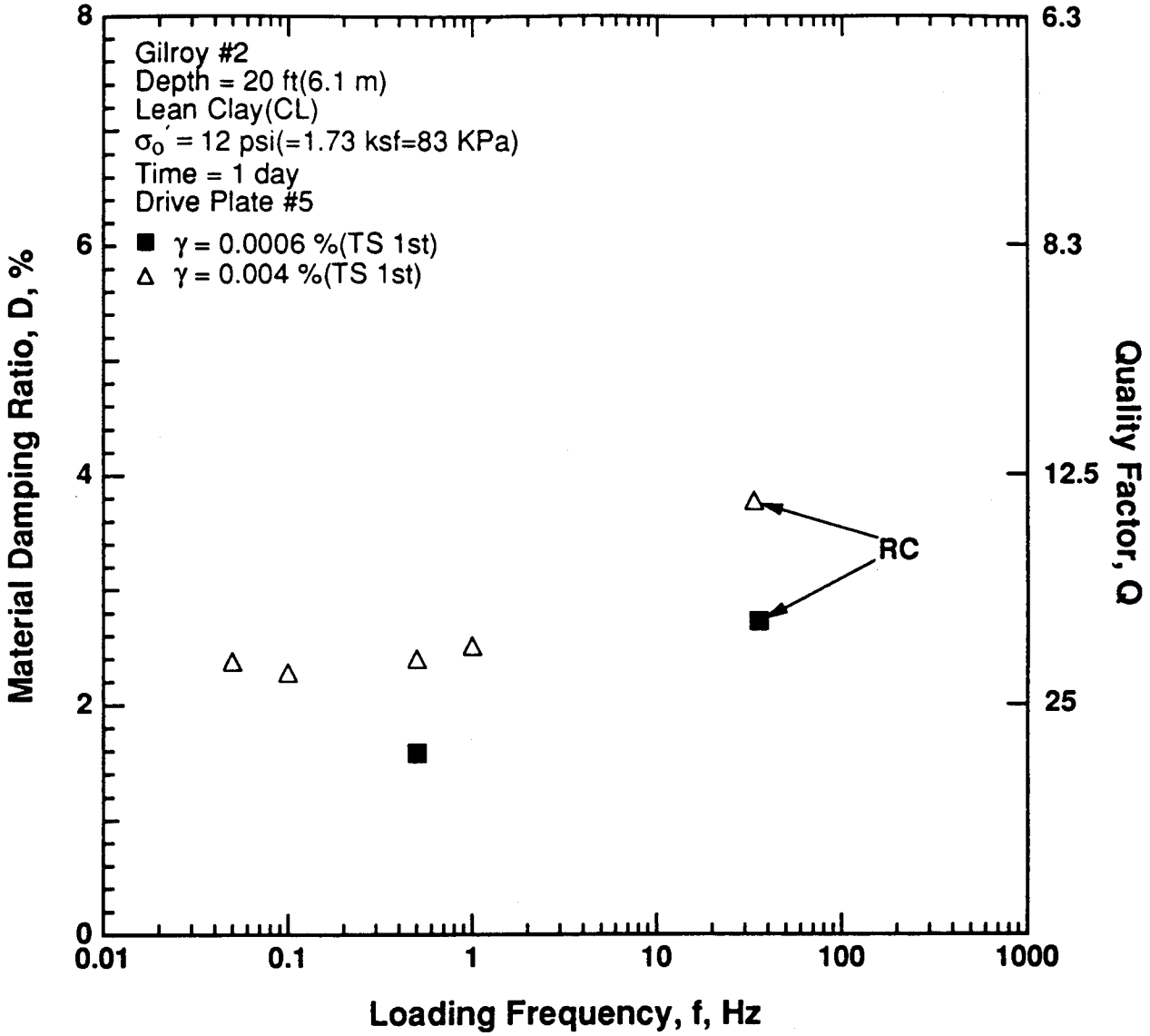

Figure 8.B.2.D-16
Variation in material damping ratio with loading frequency and shearing strain at an effective confining pressure of 12 psi (1.73 ksf, 83 kPa) from RCTS tests of sample G2-1.

APPENDIX 8.B.2.E
DYNAMIC TESTS OF SAMPLE G3, DEPTH = 50 FT (15.2 M)

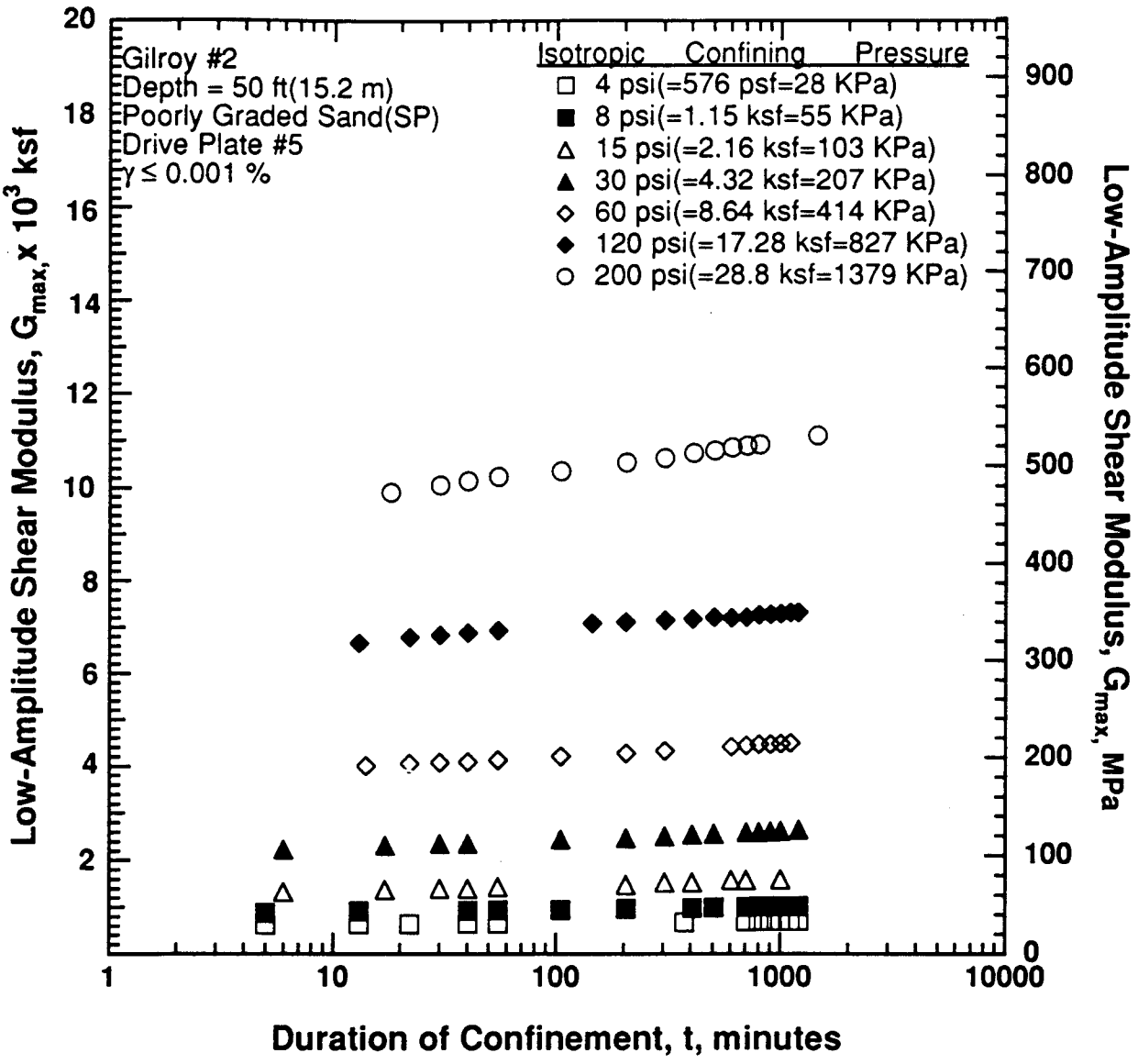

Figure 8.B.2.E-1
Variation in low-amplitude shear modulus with magnitude and duration of isotropic confining pressure from resonant column tests of sample G3.

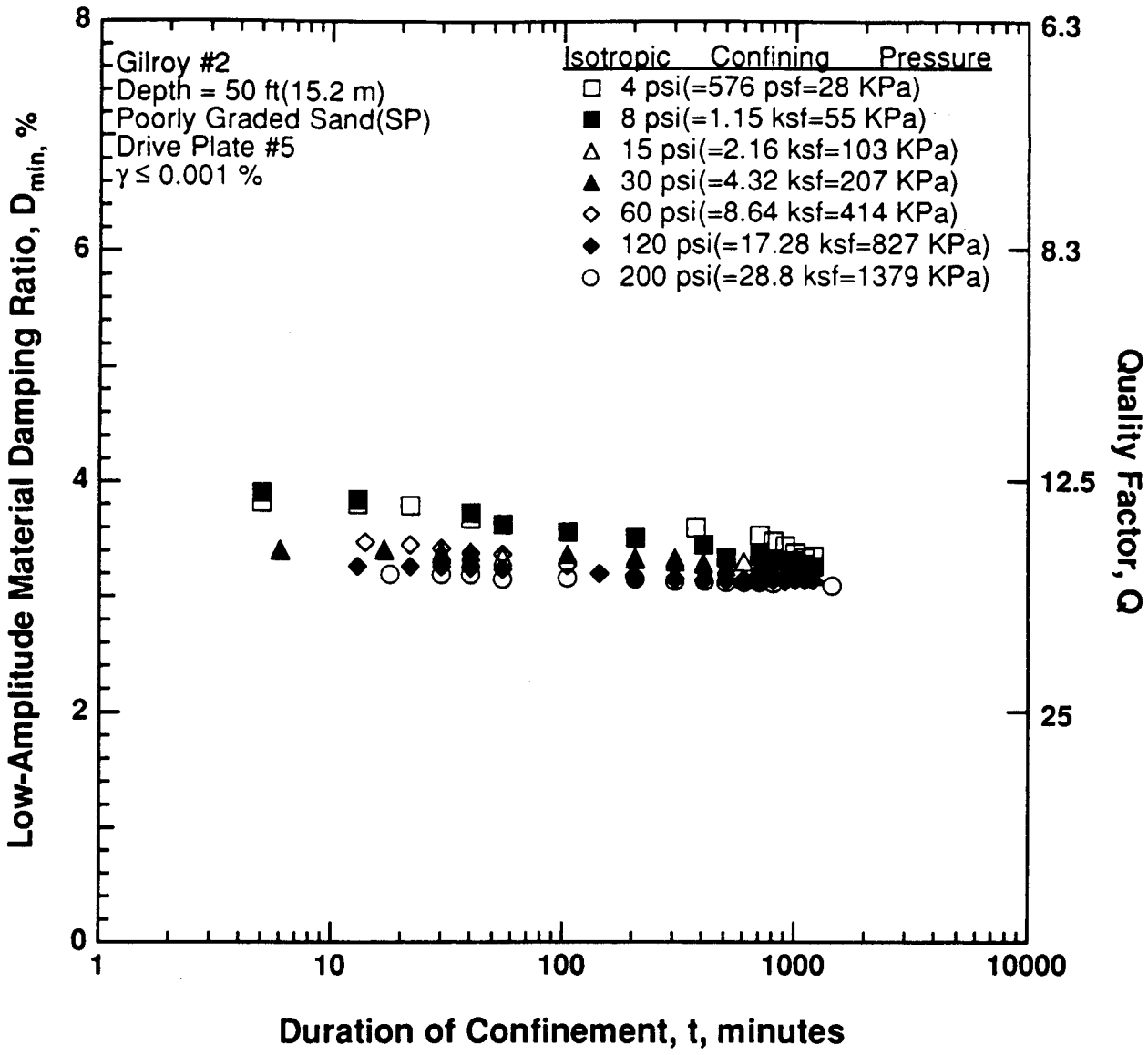

Figure 8.B.2.E-2
Variation in low-amplitude material damping ratio with magnitude and duration of isotropic confining pressure from resonant column tests of sample G3.

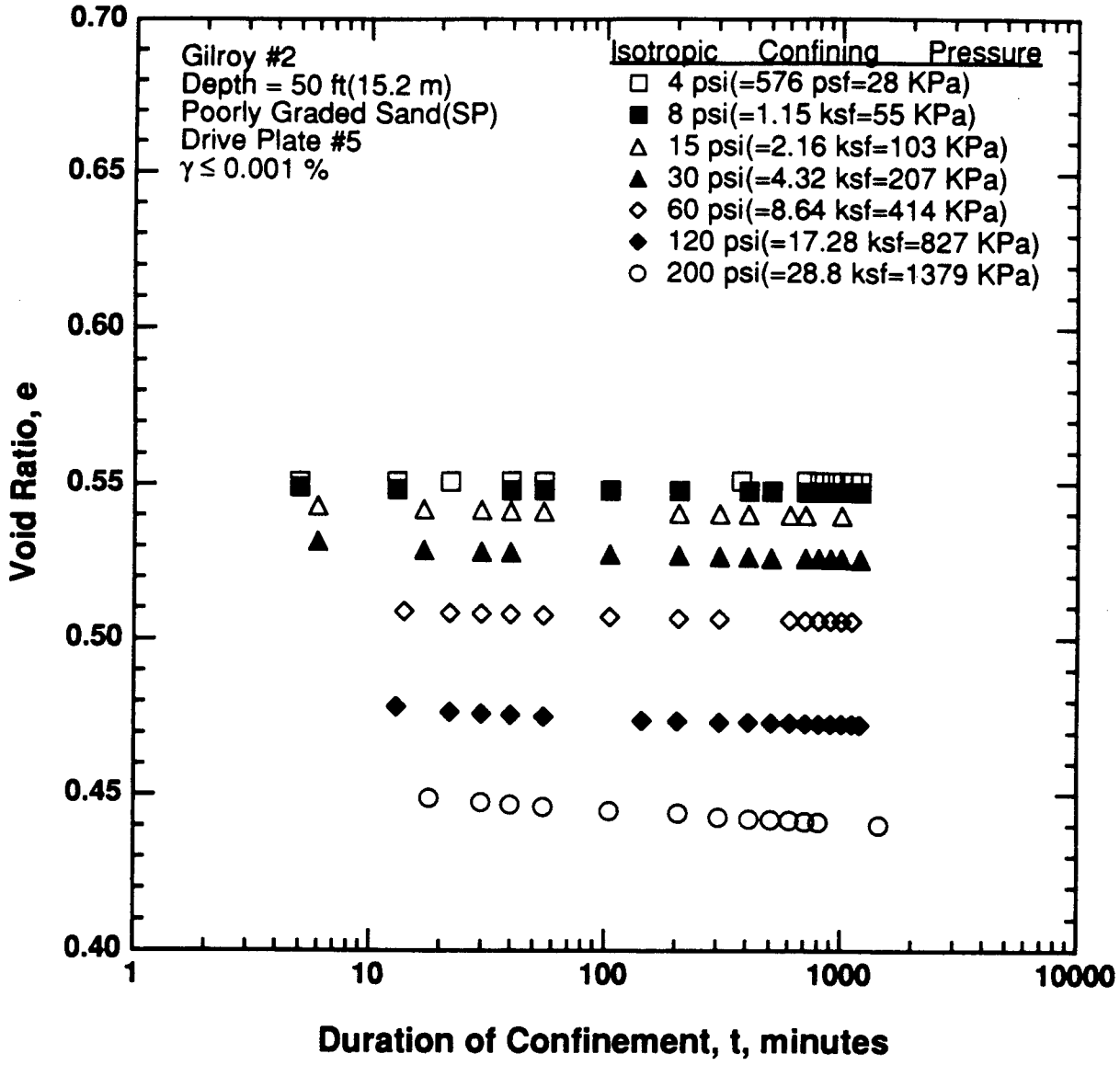

Figure 8.B.2.E-3
Variation in void ratio with magnitude and duration of isotropic confining pressure from resonant column tests of sample G3.

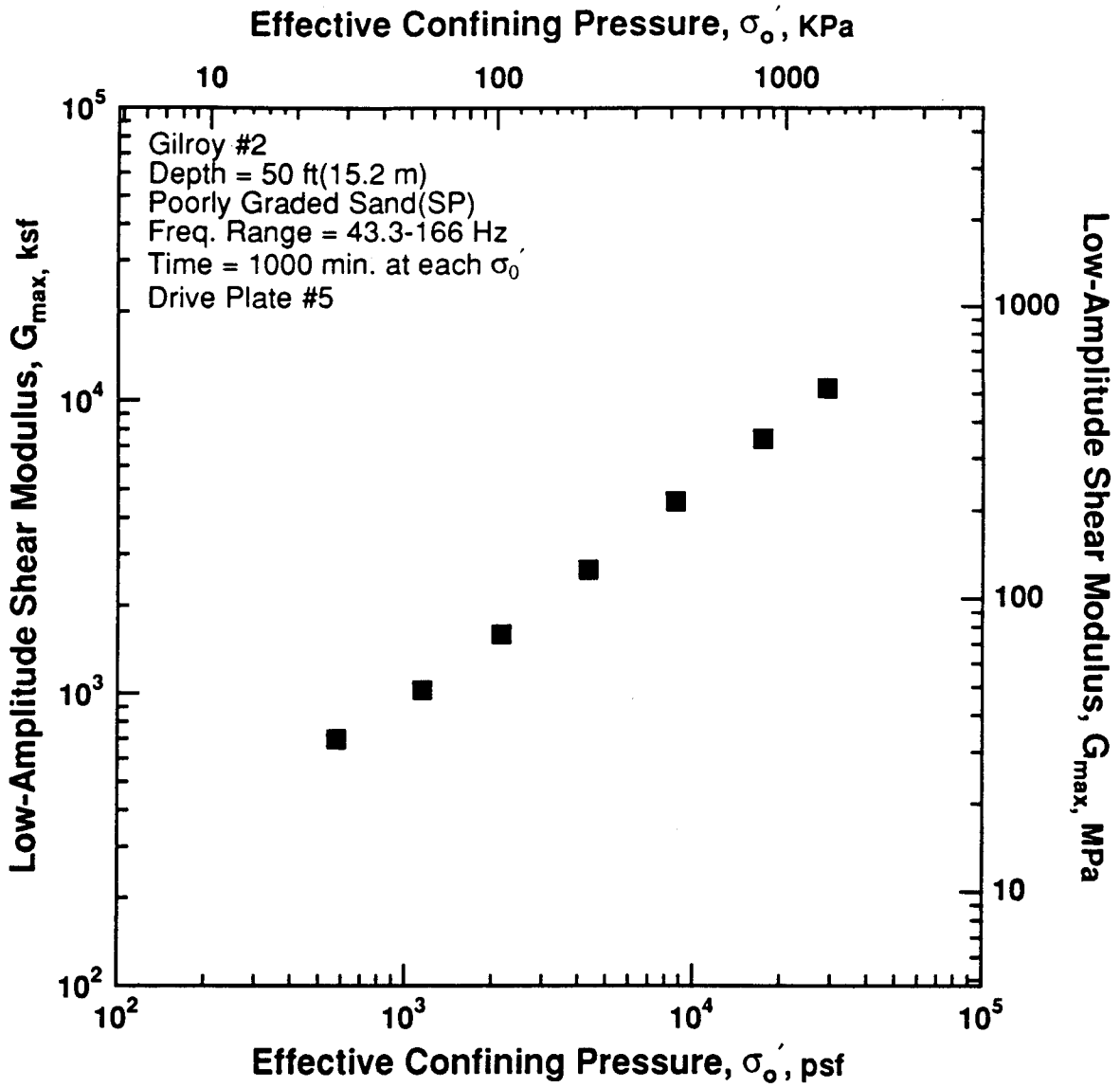

Figure 8.B.2.E-4
Variation in low-amplitude shear modulus with effective confining pressure from resonant column tests of sample G3.

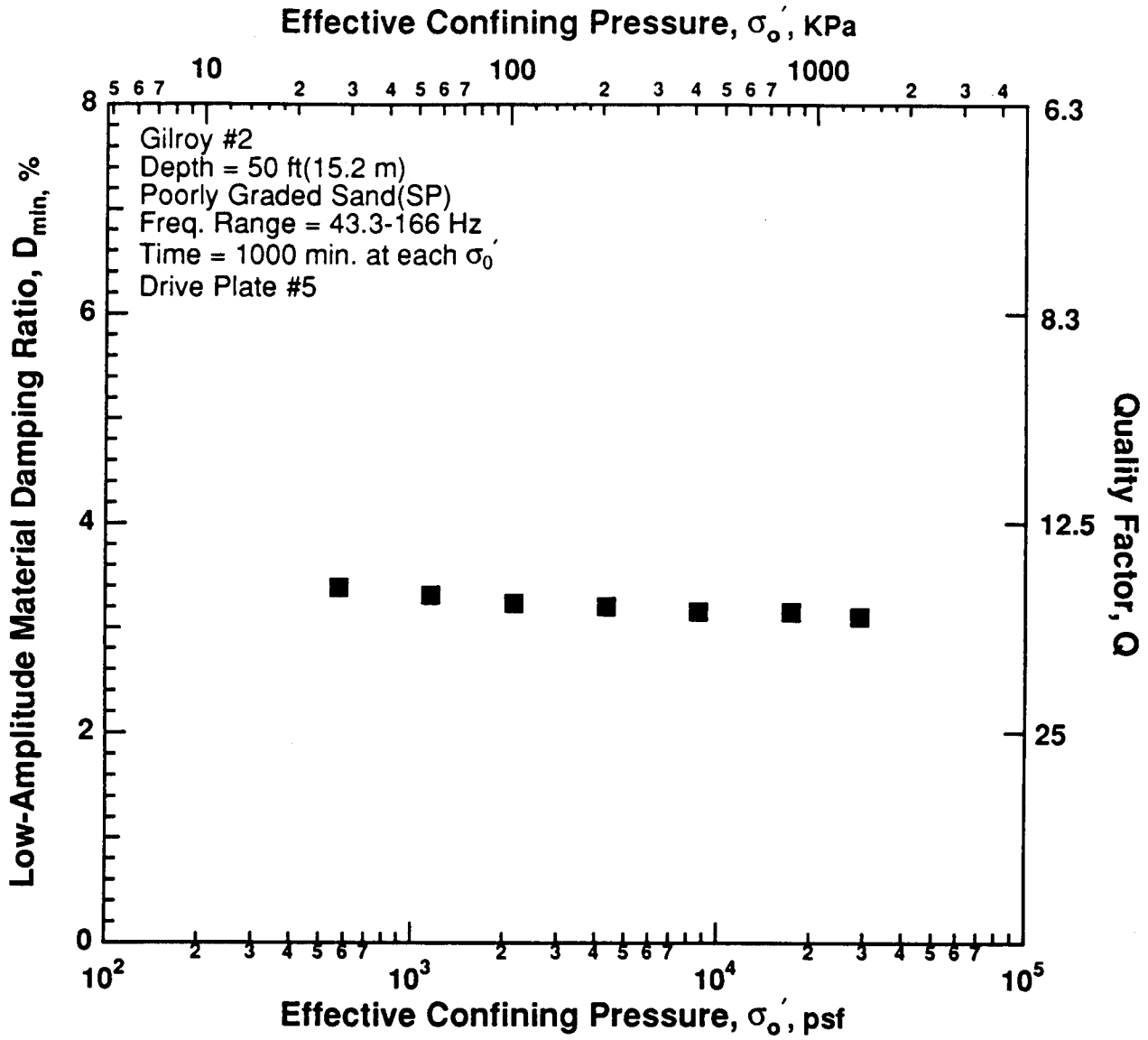

Figure 8.B.2.E-5
Variation in low-amplitude material damping ratio with effective confining pressure from resonant column tests of sample G3.

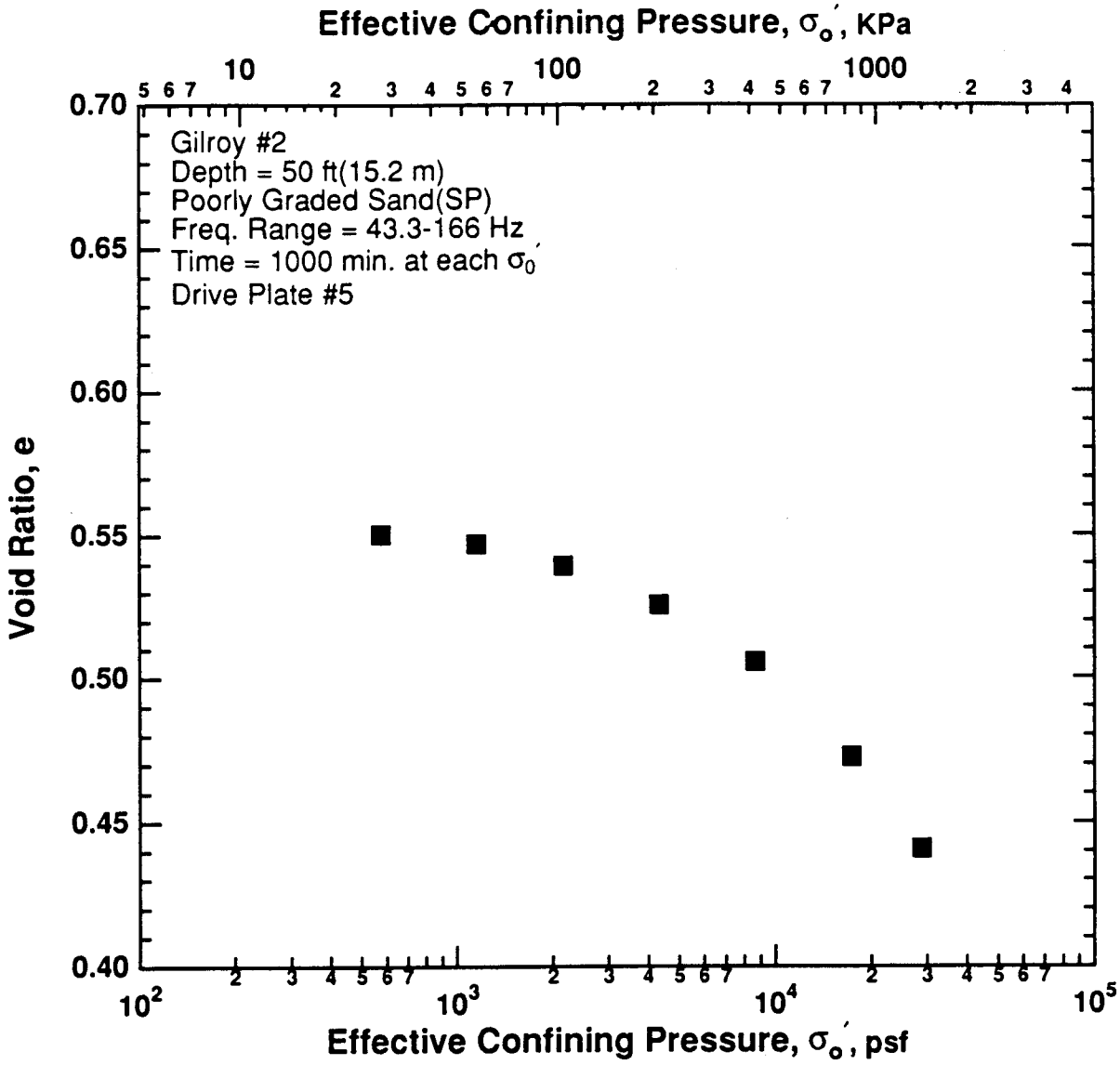

Figure 8.B.2.E-6
Variation in void ratio with effective confining pressure from resonant column tests of sample G3.

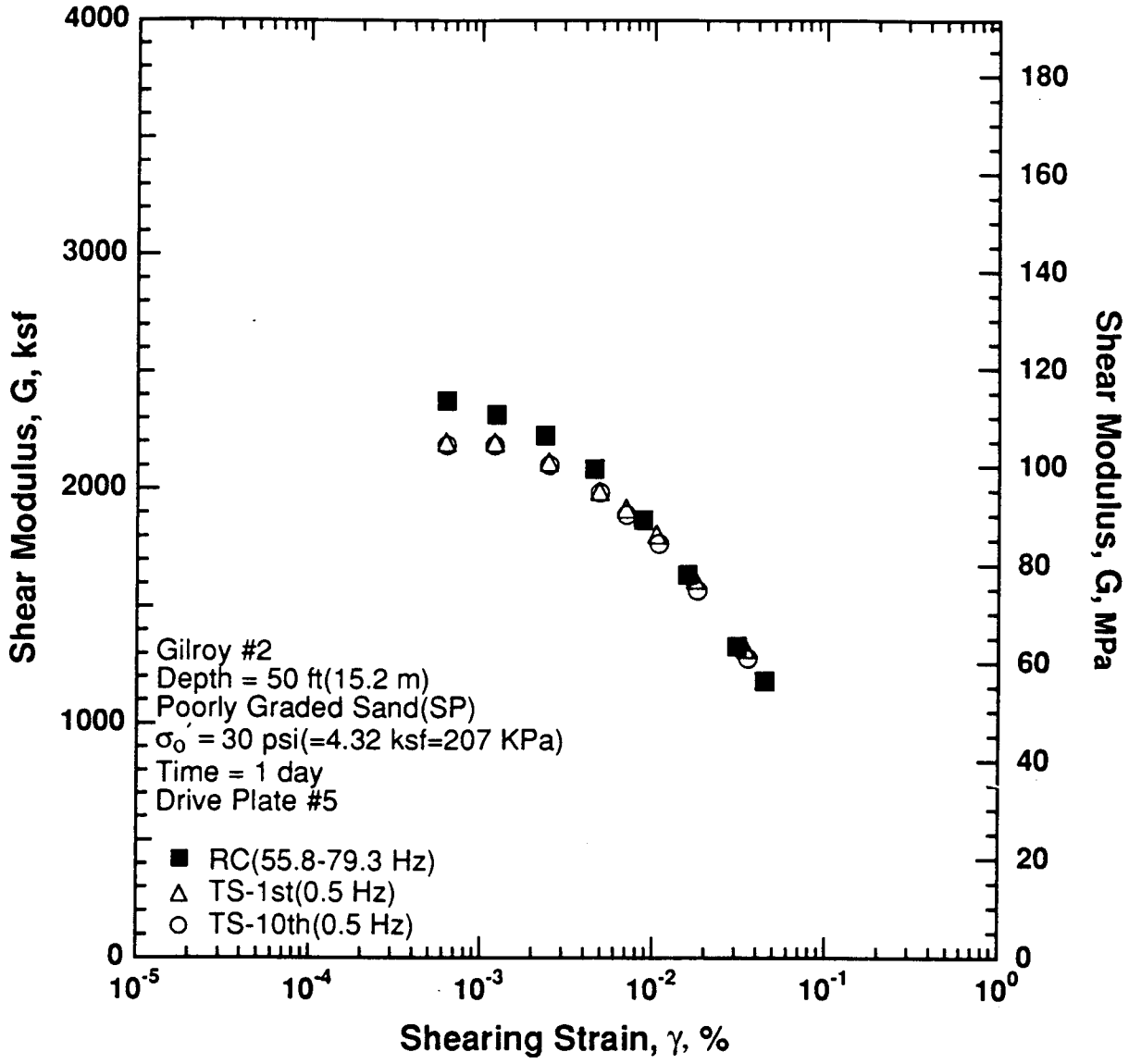

Figure 8.B.2.E-7
Variation in shear modulus with shearing strain at an effective confining pressure of 30 psi (4.32 ksf, 207 kPa) from RCTS tests of sample G3.

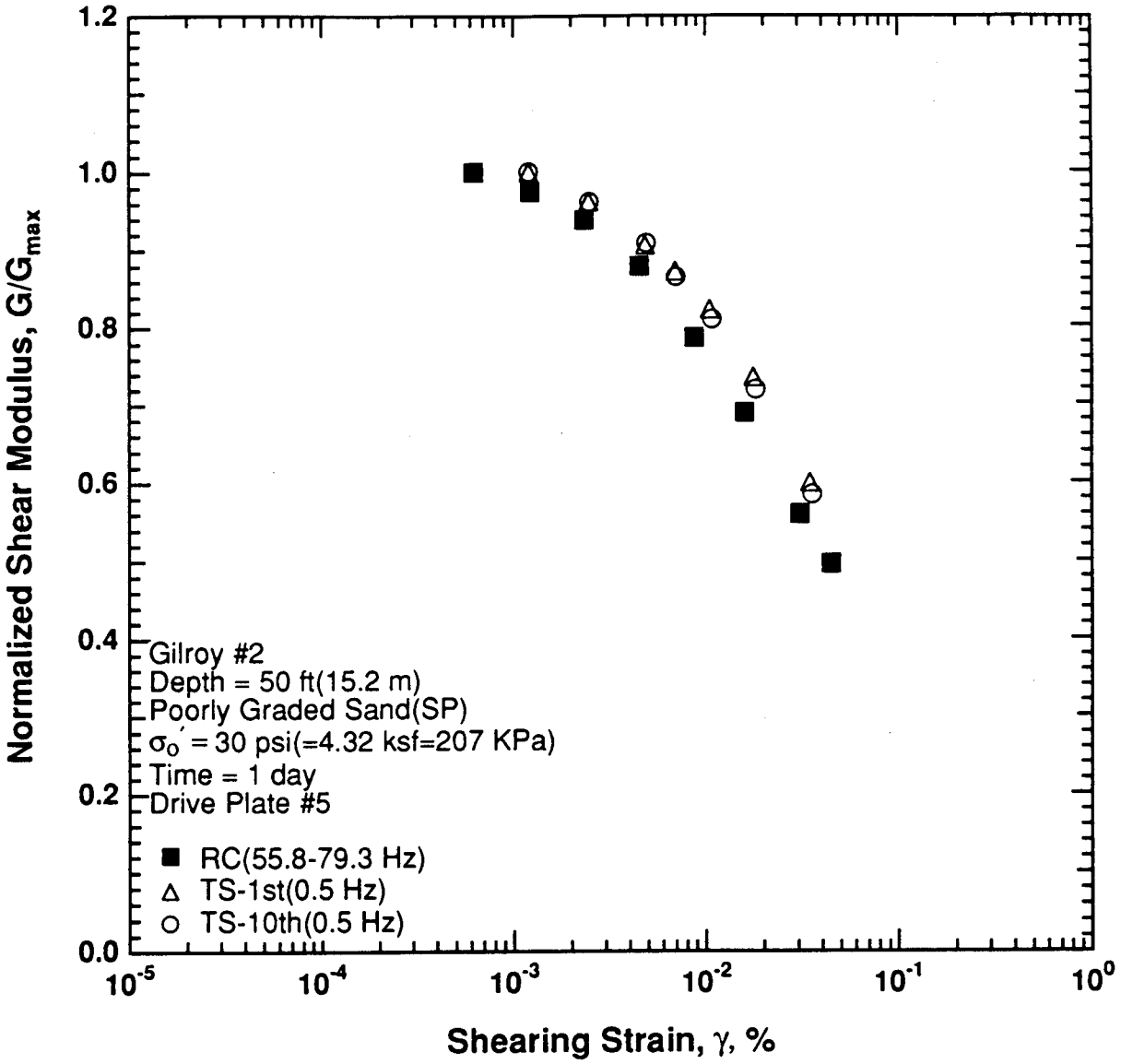

Figure 8.B.2.E-8
Variation in normalized shear modulus with shearing strain at an effective confining pressure of 30 psi (4.32 ksf, 207 kPa) from RCTS tests of sample G3.

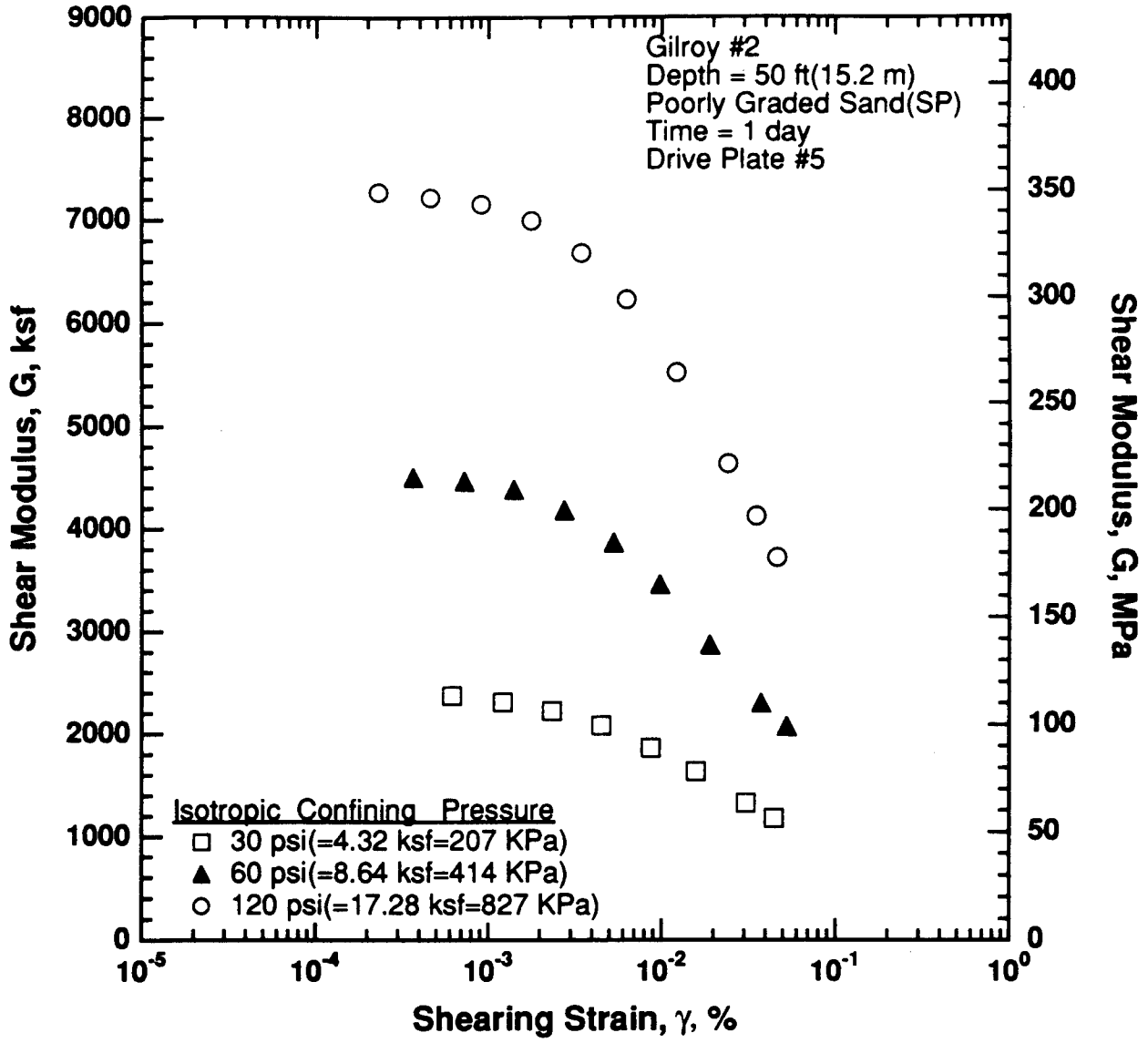

Figure 8.B.2.E-9
Variation in shear modulus with shearing strain and effective confining pressure from resonant column tests of sample G3.

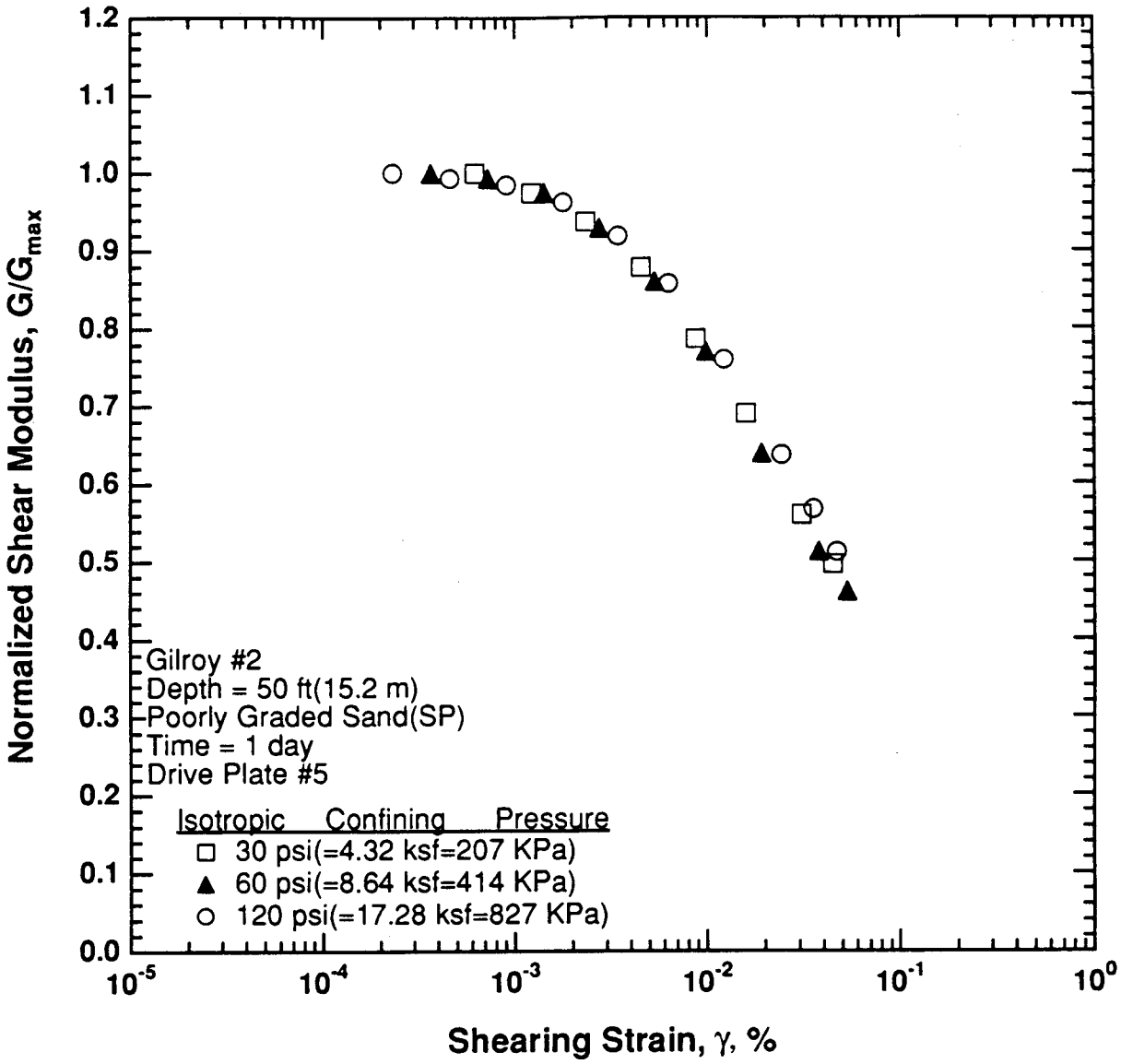

Figure 8.B.2.E-10
Comparison of the variation in normalized shear modulus with shearing strain and effective confining pressure from resonant column tests of sample G3.

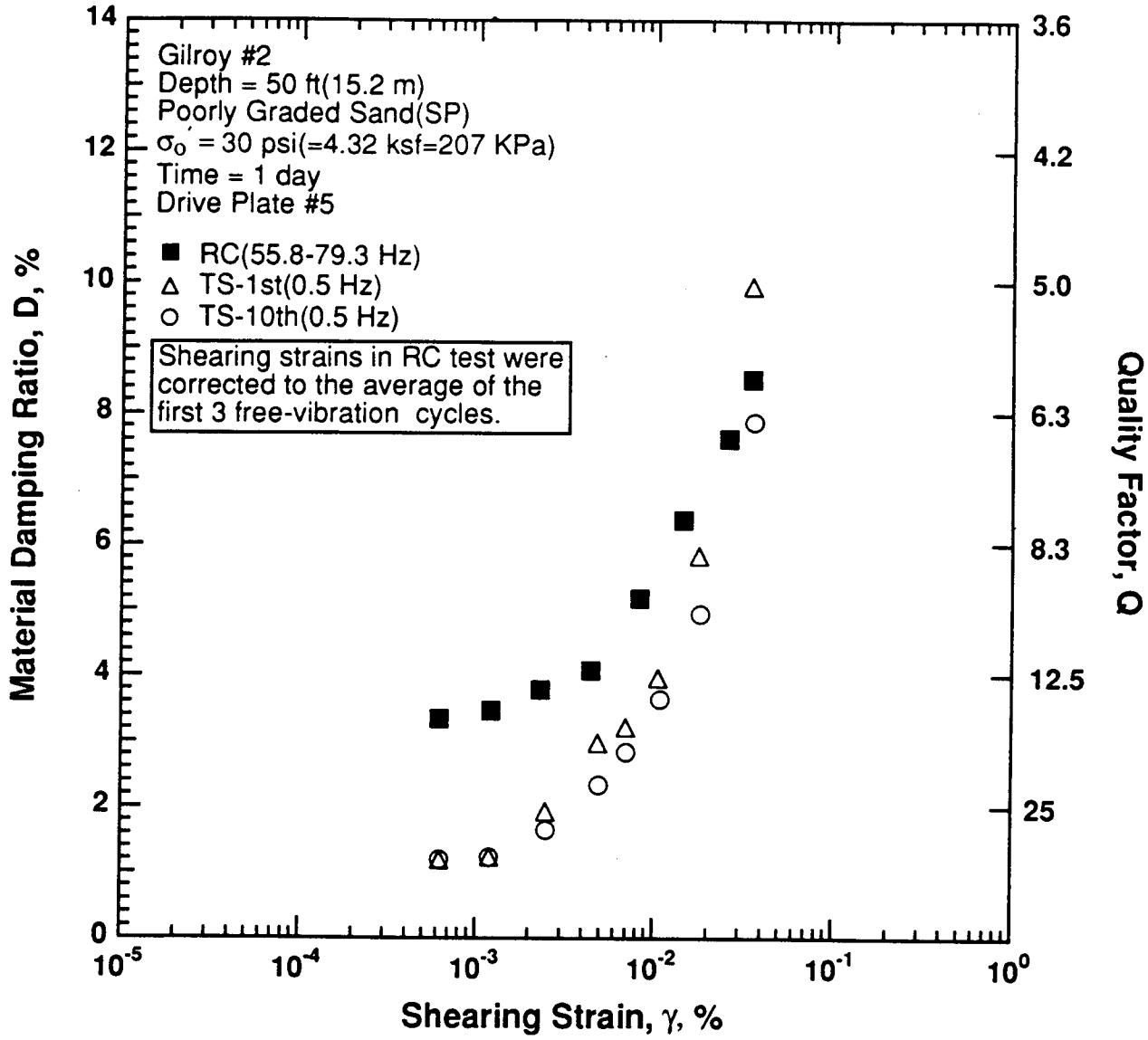

Figure 8.B.2.E-11
Variation in material damping ratio with shearing strain at an effective confining pressure of 30 psi (4.32 ksf, 207 kPa) from RCTS tests of sample G3.

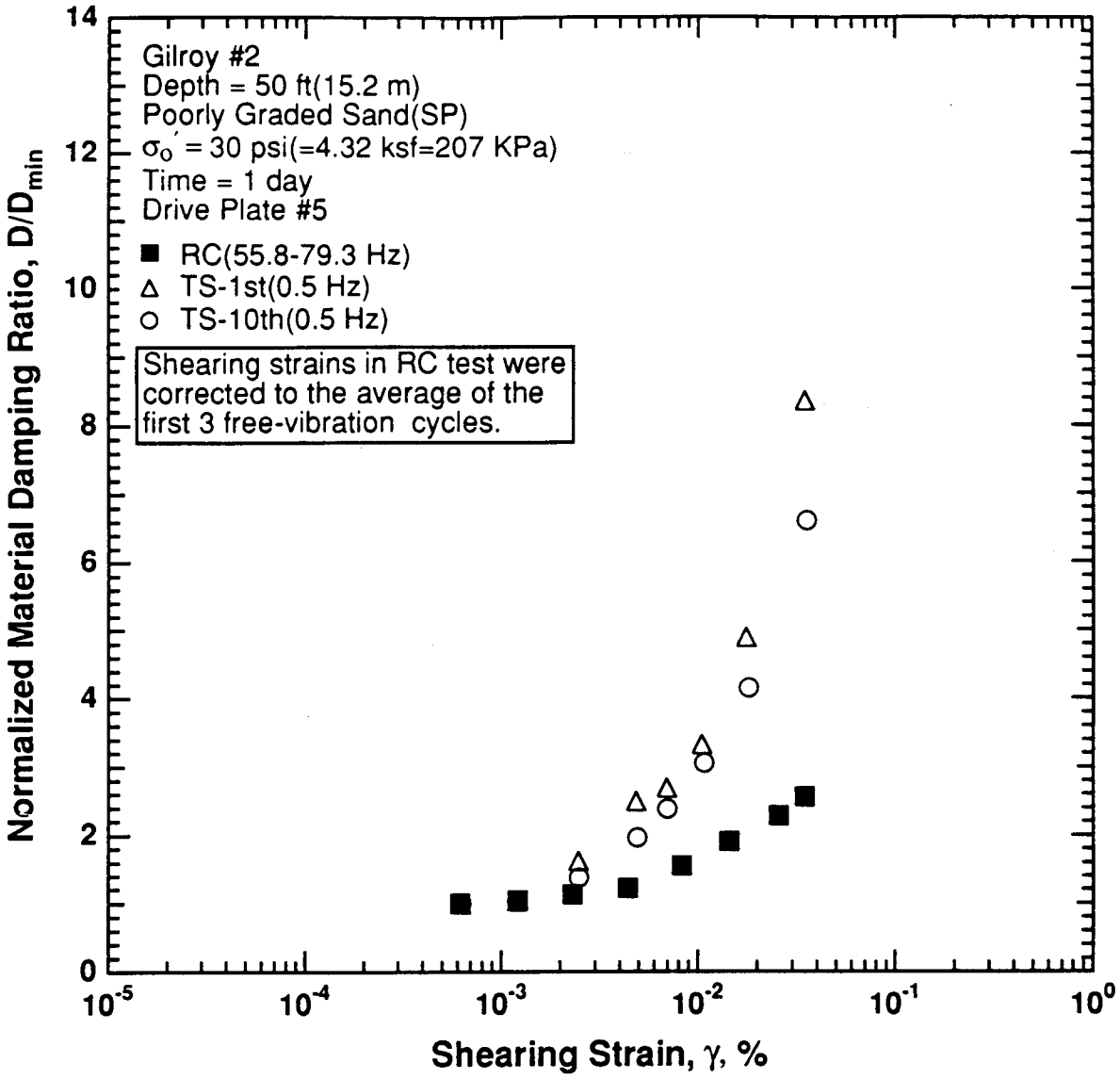

Figure 8.B.2.E-12
Variation in normalized material damping ratio with shearing strain at an effective confining pressure of 30 psi (4.32 ksf, 207 kPa) from RCTS tests of sample G3.

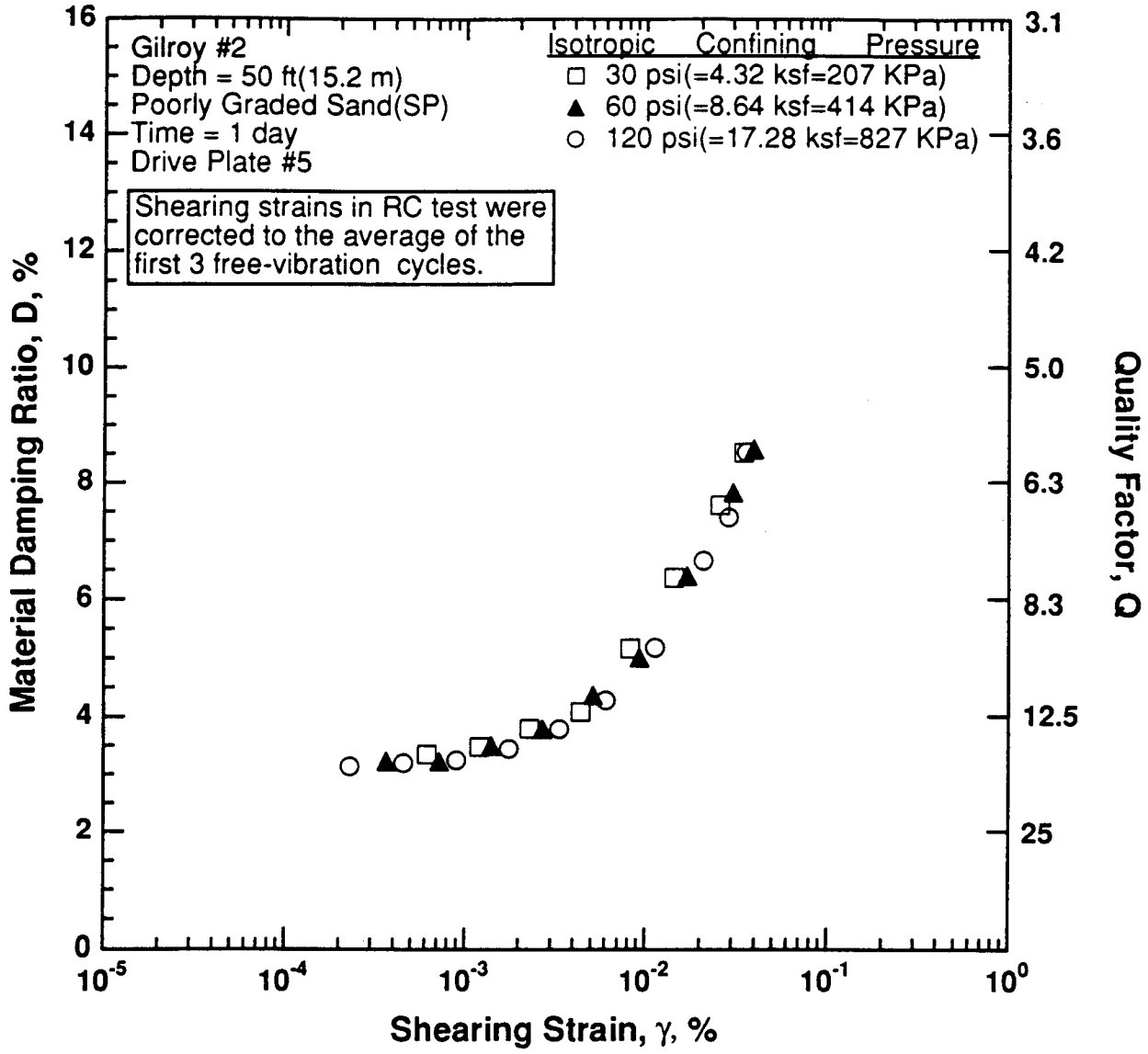

Figure 8.B.2.E-13
Variation in material damping ratio with shearing strain and effective confining pressure from resonant column tests of sample G3.

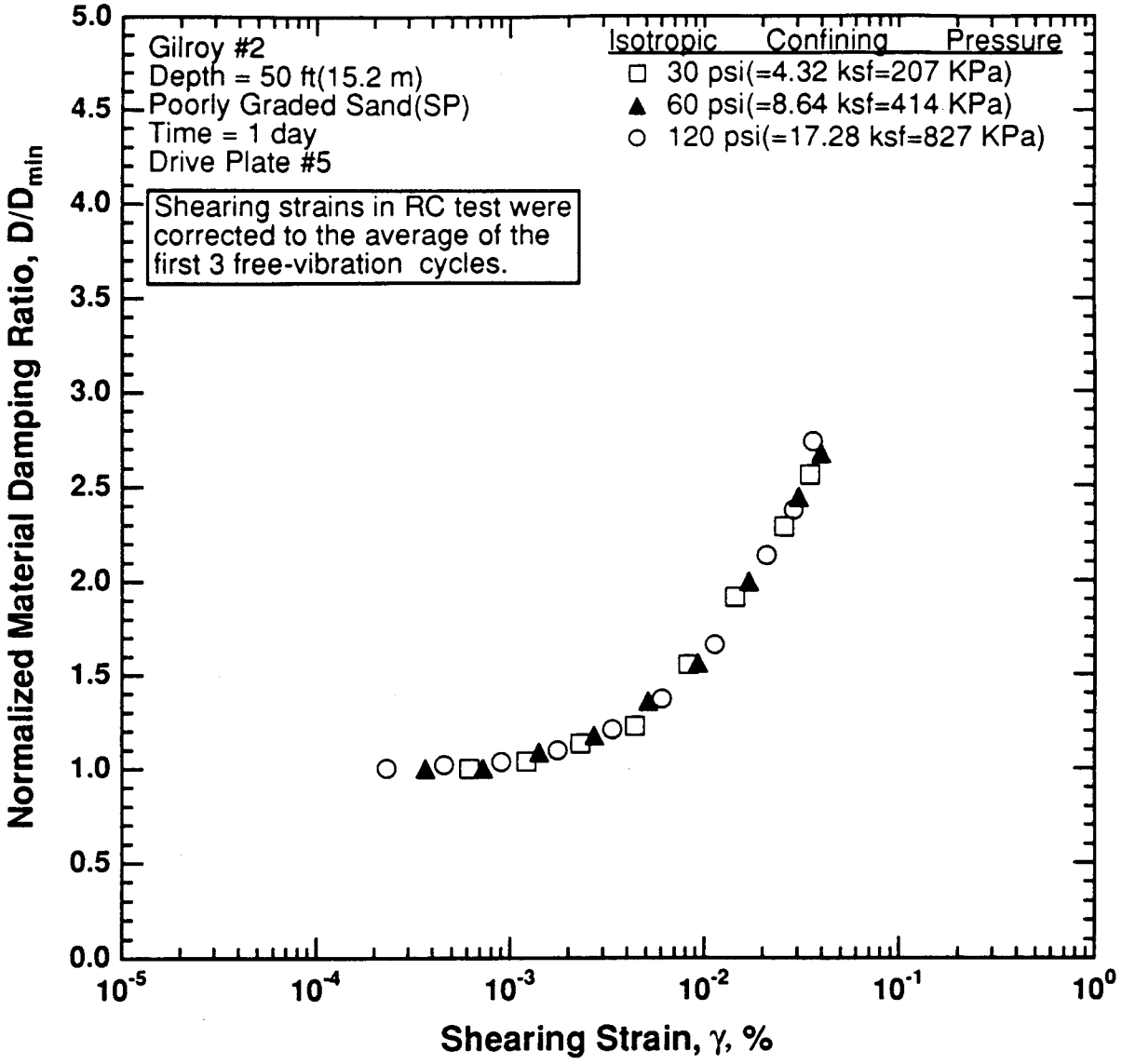

Figure 8.B.2.E-14
Comparison of the variation in normalized material damping ratio with shearing strain and effective confining pressure from resonant column tests of sample G3.

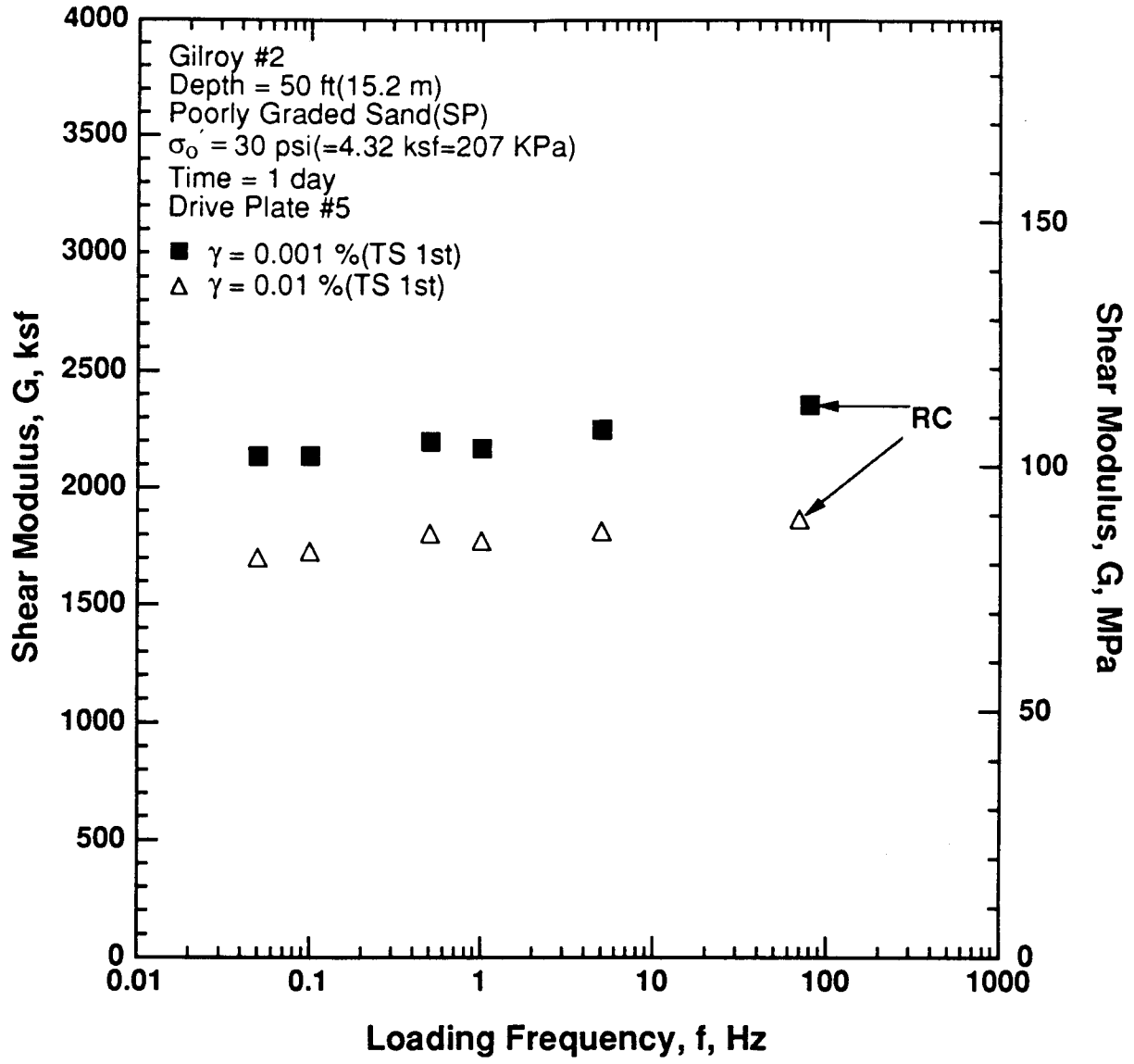

Figure 8.B.2.E-15
Variation in shear modulus with loading frequency and shearing strain at an effective confining pressure of 30 psi (4.32 ksf, 207 kPa) from RCTS tests of sample G3.

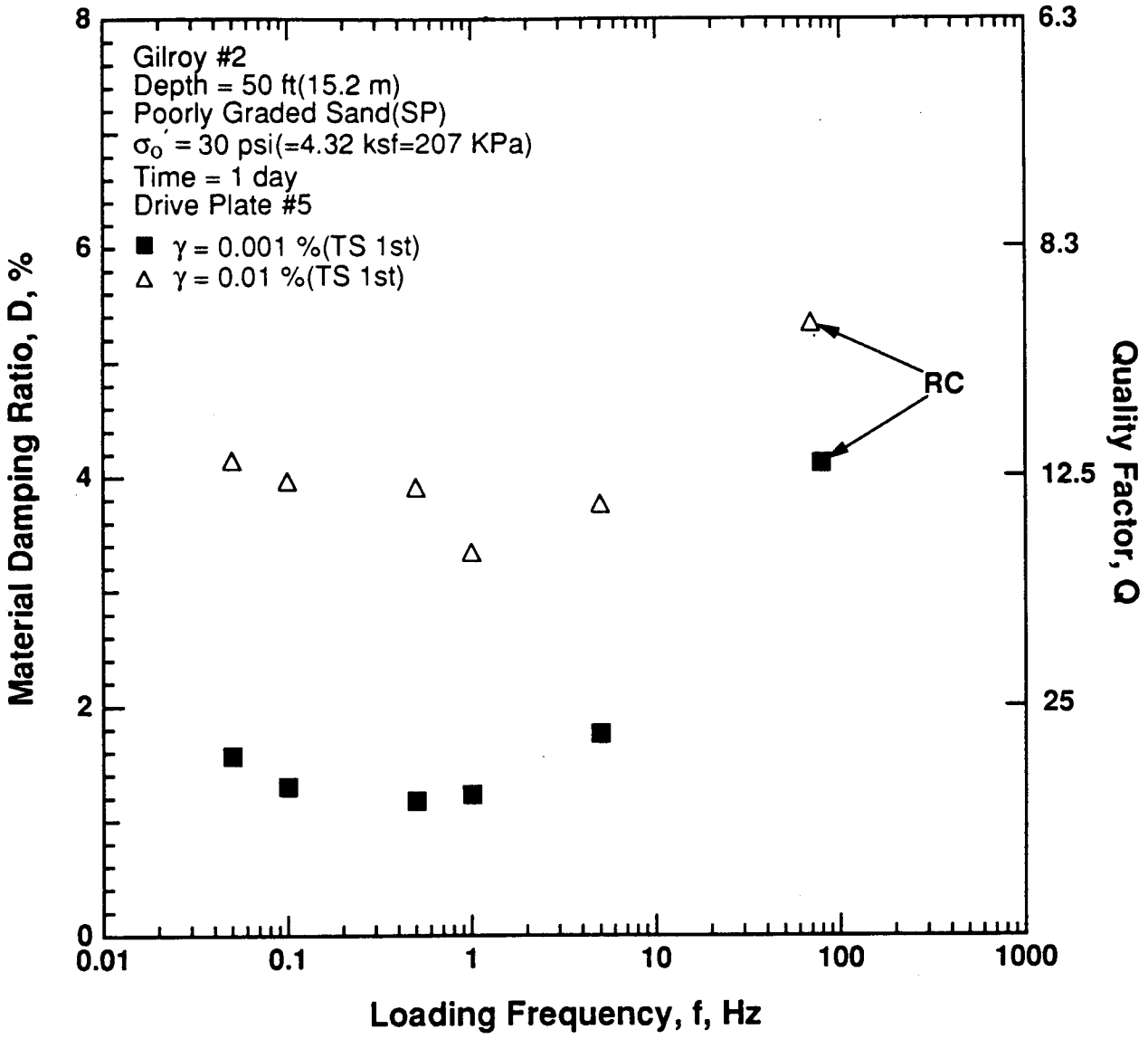

Figure 8.B.2.E-16
Variation in material damping ratio with loading frequency and shearing strain at an effective confining pressure of 30 psi (4.32 ksf, 207 kPa) from RCTS tests of sample G3.

APPENDIX 8.B.2.F
DYNAMIC TESTS OF SAMPLE G4, DEPTH = 85 FT (25.9 M)

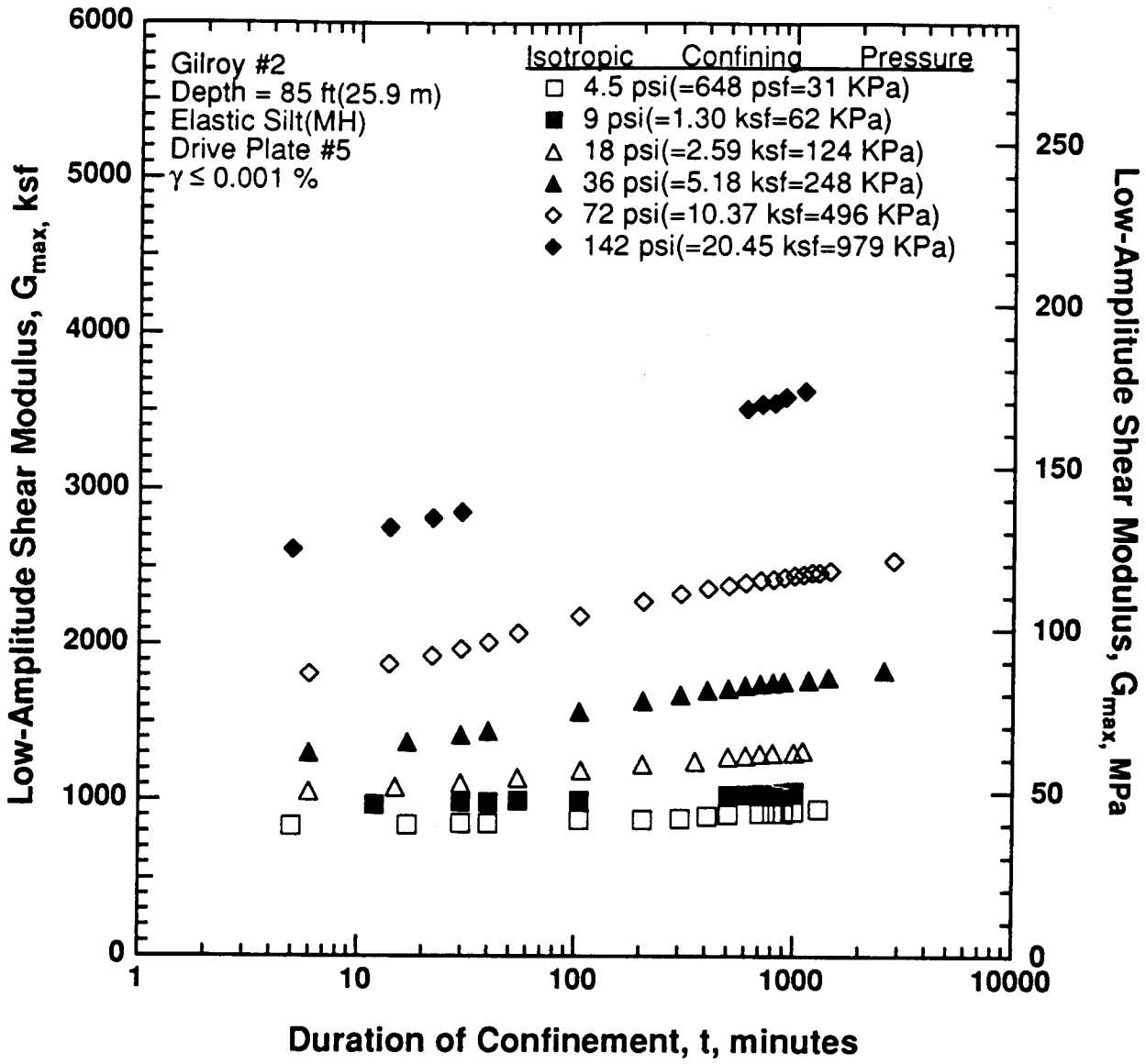

Figure 8.B.2.F-1
Variation in low-amplitude shear modulus with magnitude and duration of isotropic confining pressure from resonant column tests of sample G4.

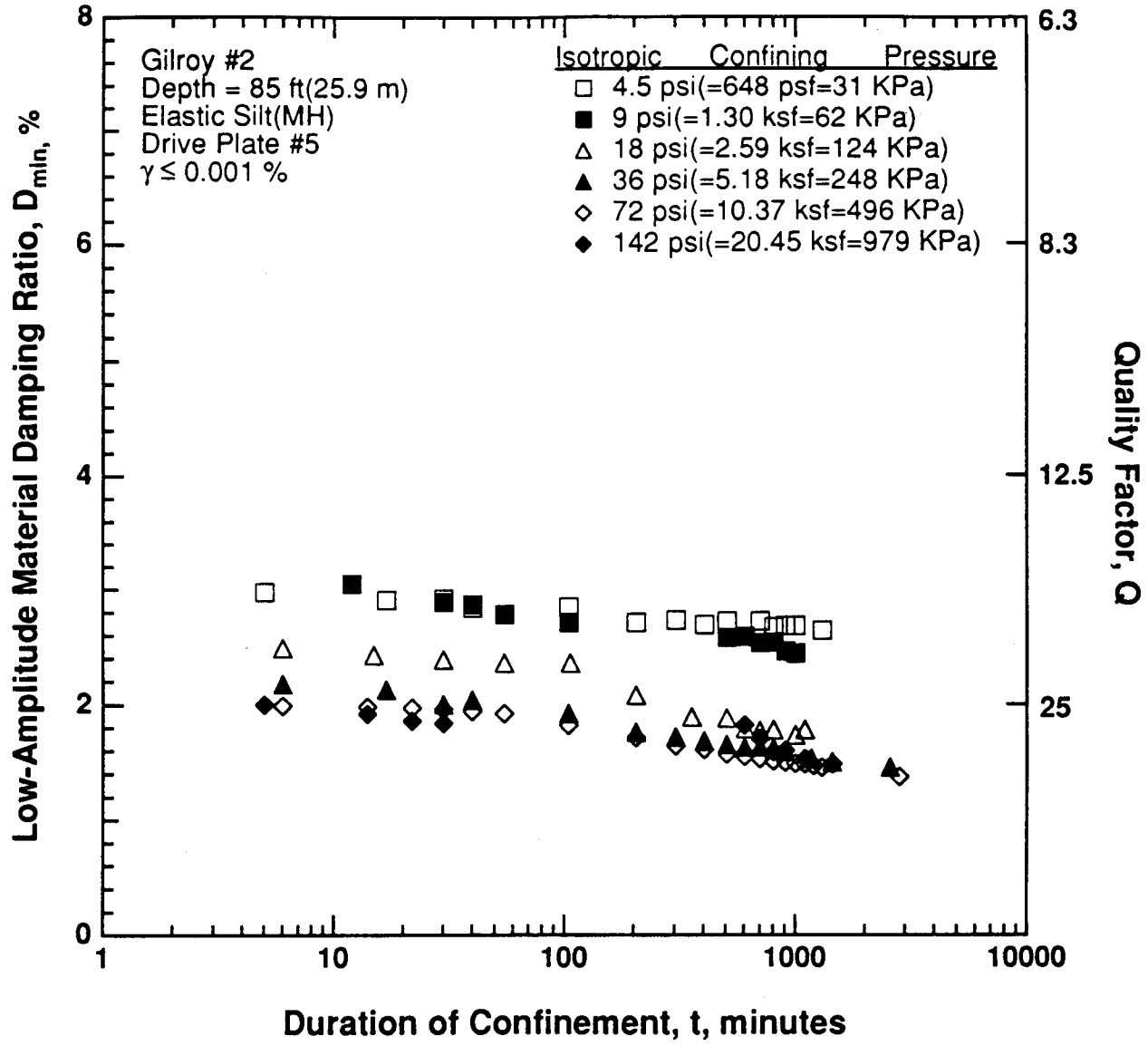

Figure 8.B.2.F-2
Variation in low-amplitude material damping ratio with magnitude and duration of isotropic confining pressure from resonant column tests of sample G4.

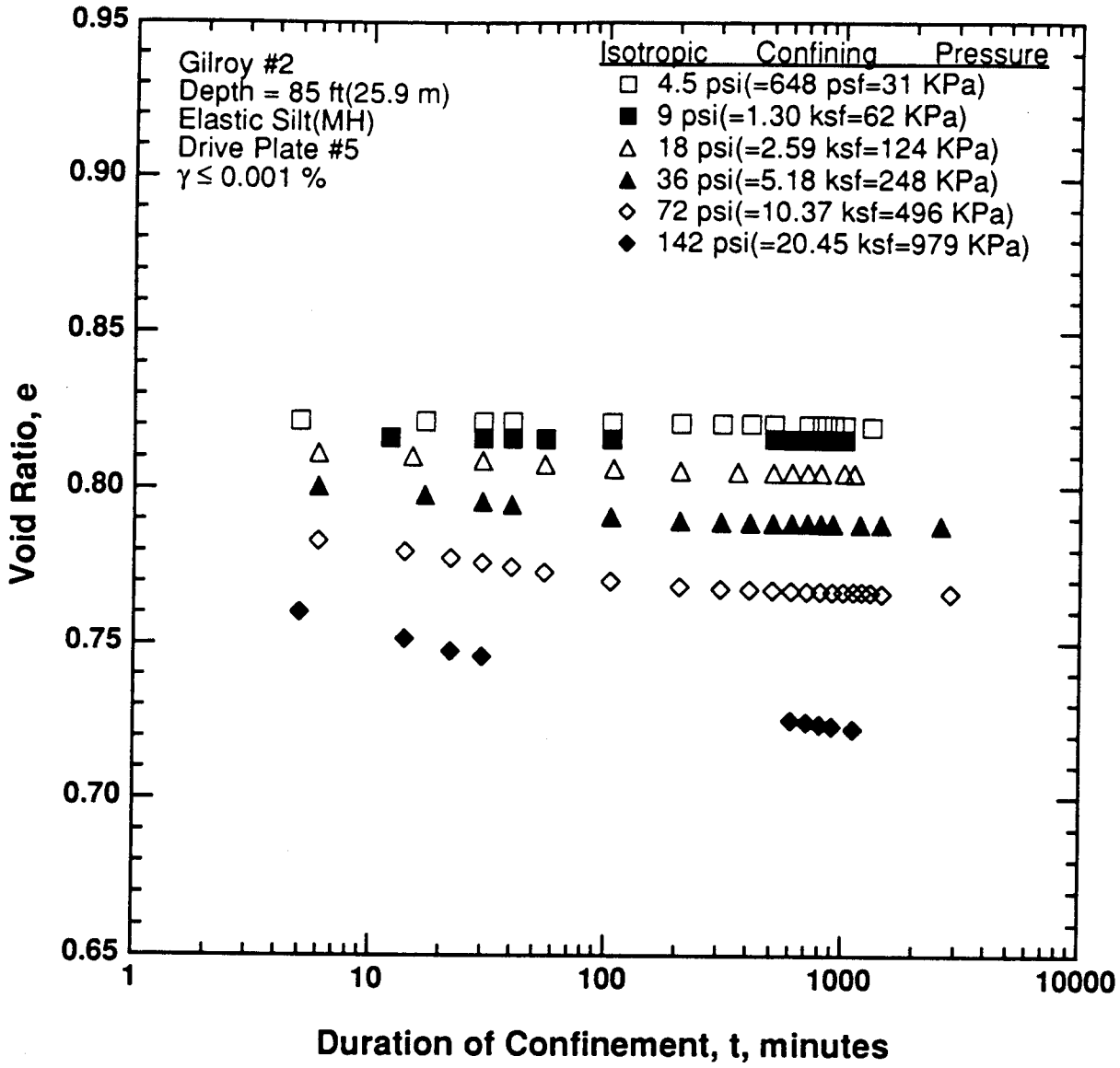

Figure 8.B.2.F-3
Variation in void ratio with magnitude and duration of isotropic confining pressure from resonant column tests of sample G4.

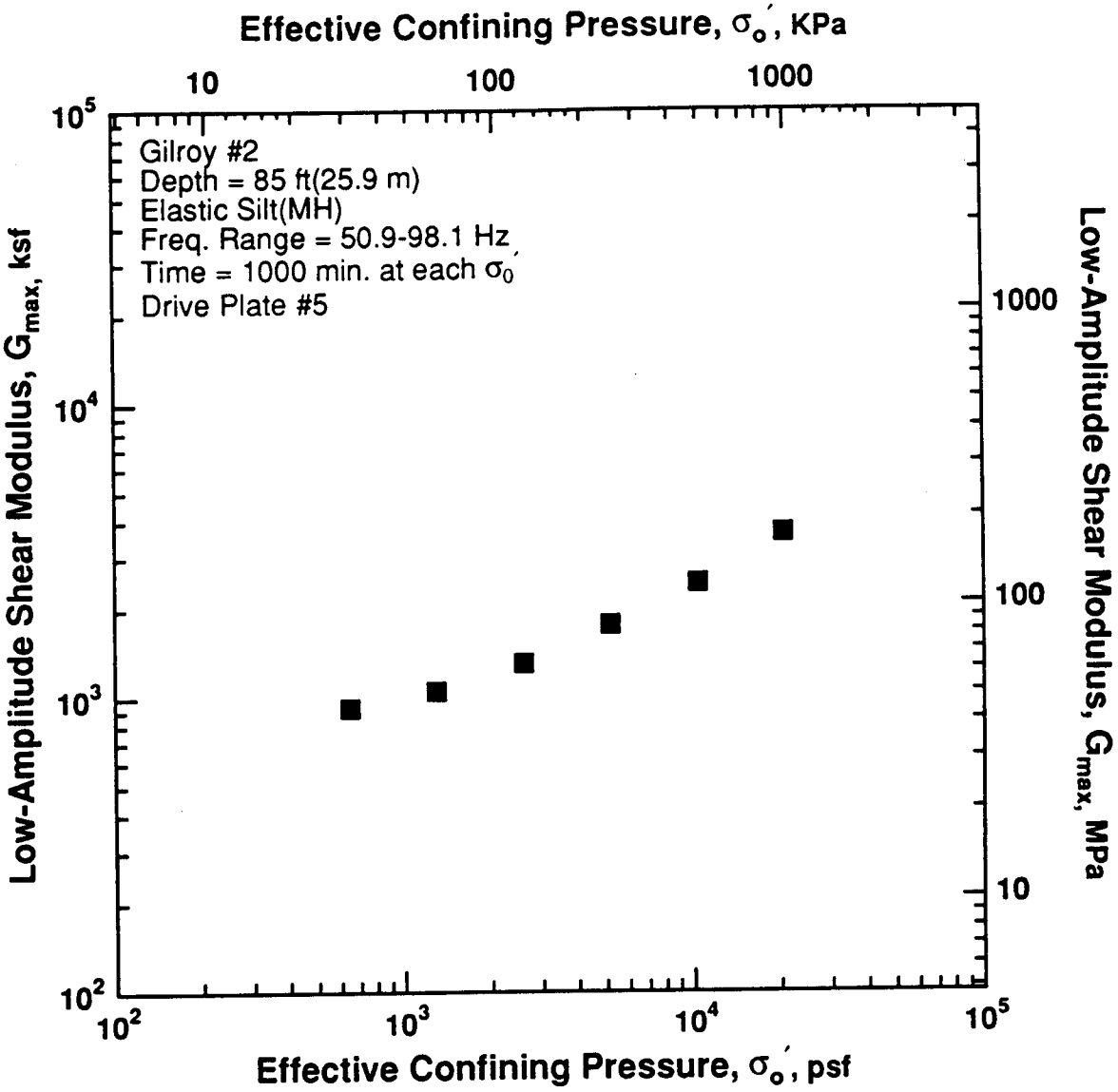

Figure 8.B.2.F-4
Variation in low-amplitude shear modulus with effective confining pressure from resonant column tests of sample G4.

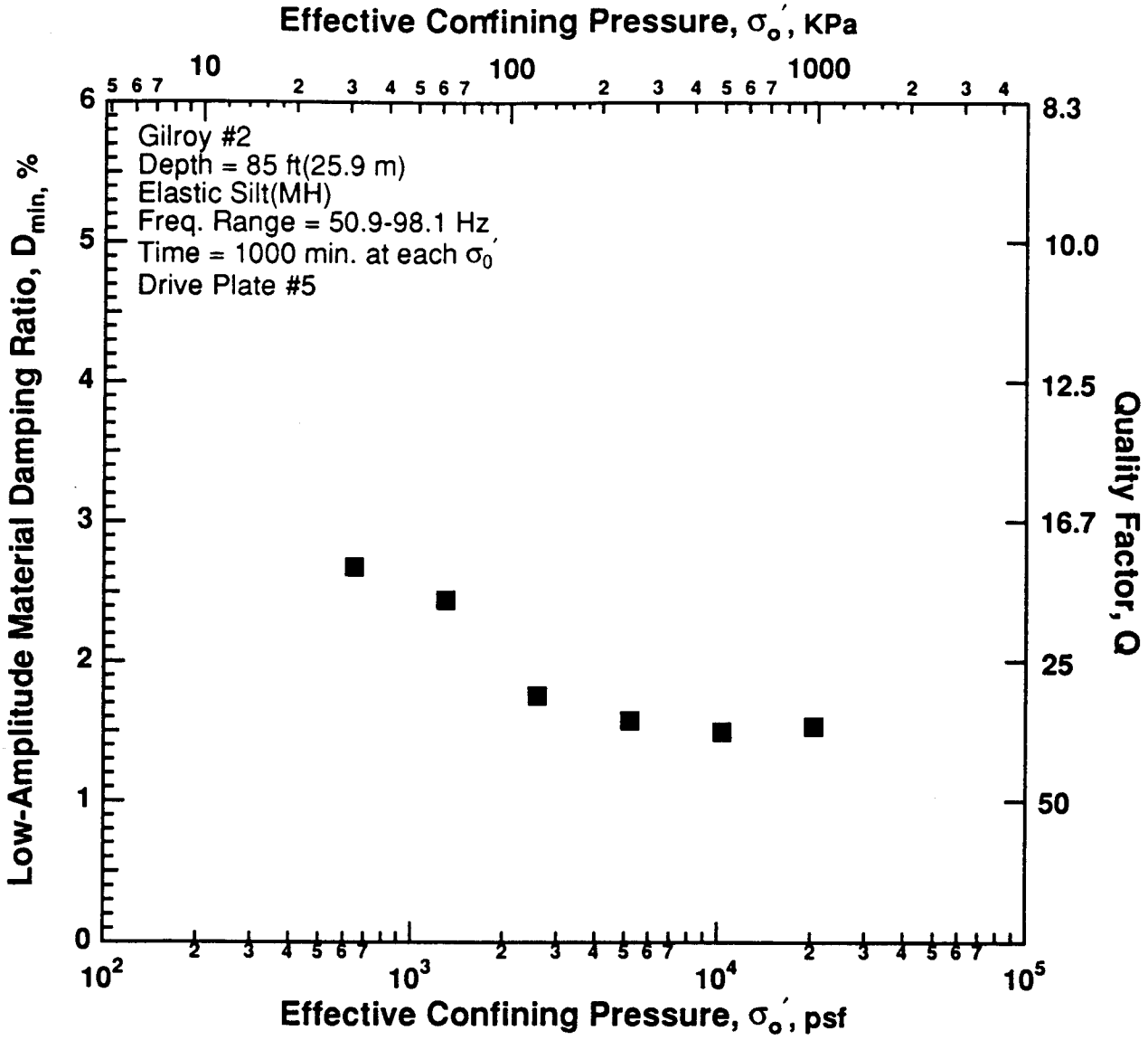

Figure 8.B.2.F-5
Variation in low-amplitude material damping ratio with effective confining pressure from resonant column tests of sample G4.

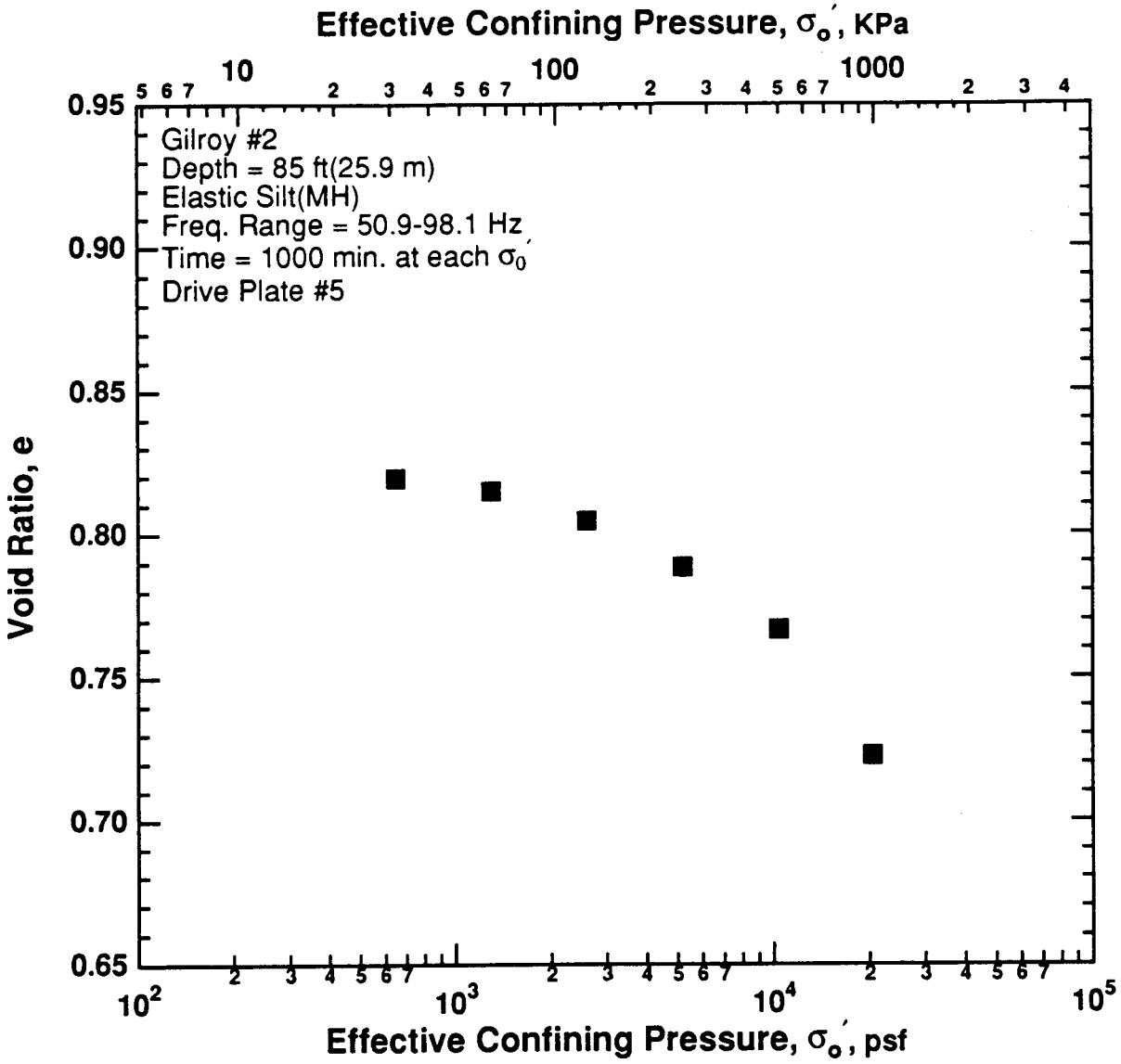

Figure 8.B.2.F-6
Variation in void ratio with effective confining pressure from resonant column tests of sample G4.

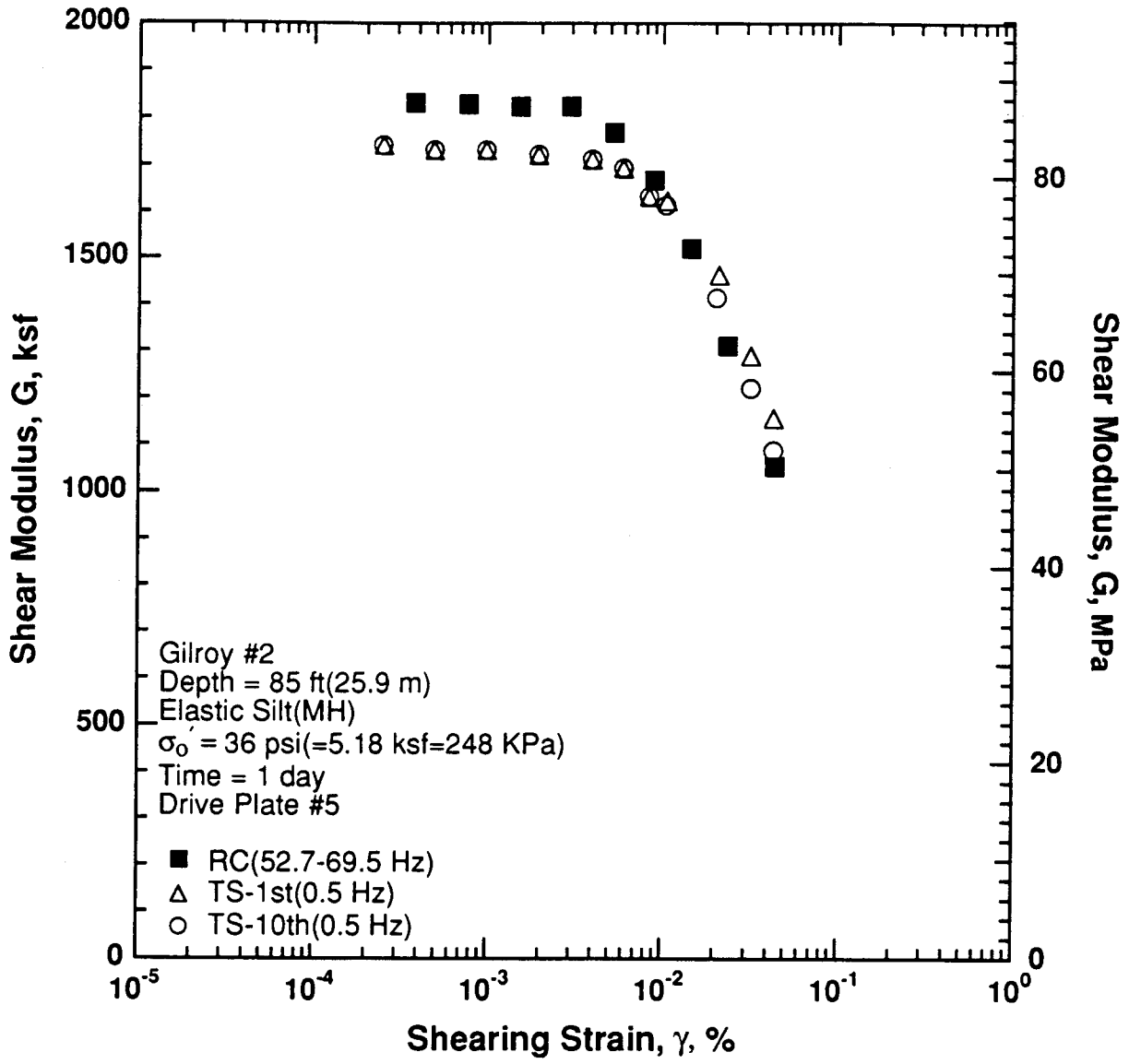

Figure 8.B.2.F-7
Variation in shear modulus with shearing strain at an effective confining pressure of 36 psi (5.18 ksf, 248 kPa) from RCTS tests of sample G4.

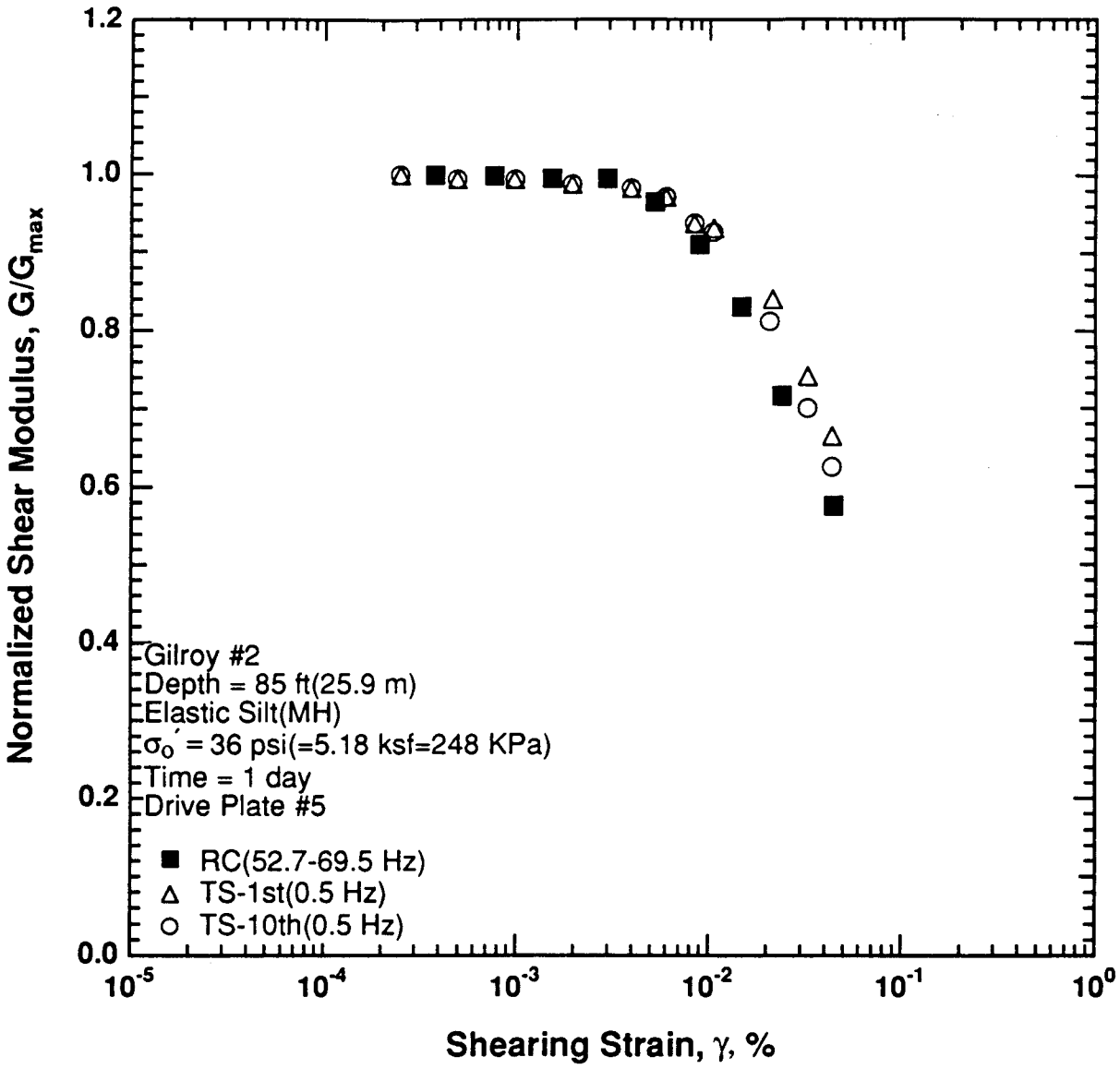

Figure 8.B.2.F-8
Variation in normalized shear modulus with shearing strain at an effective confining pressure of 36 psi (5.18 ksf, 248 kPa) from RCTS tests of sample G4.

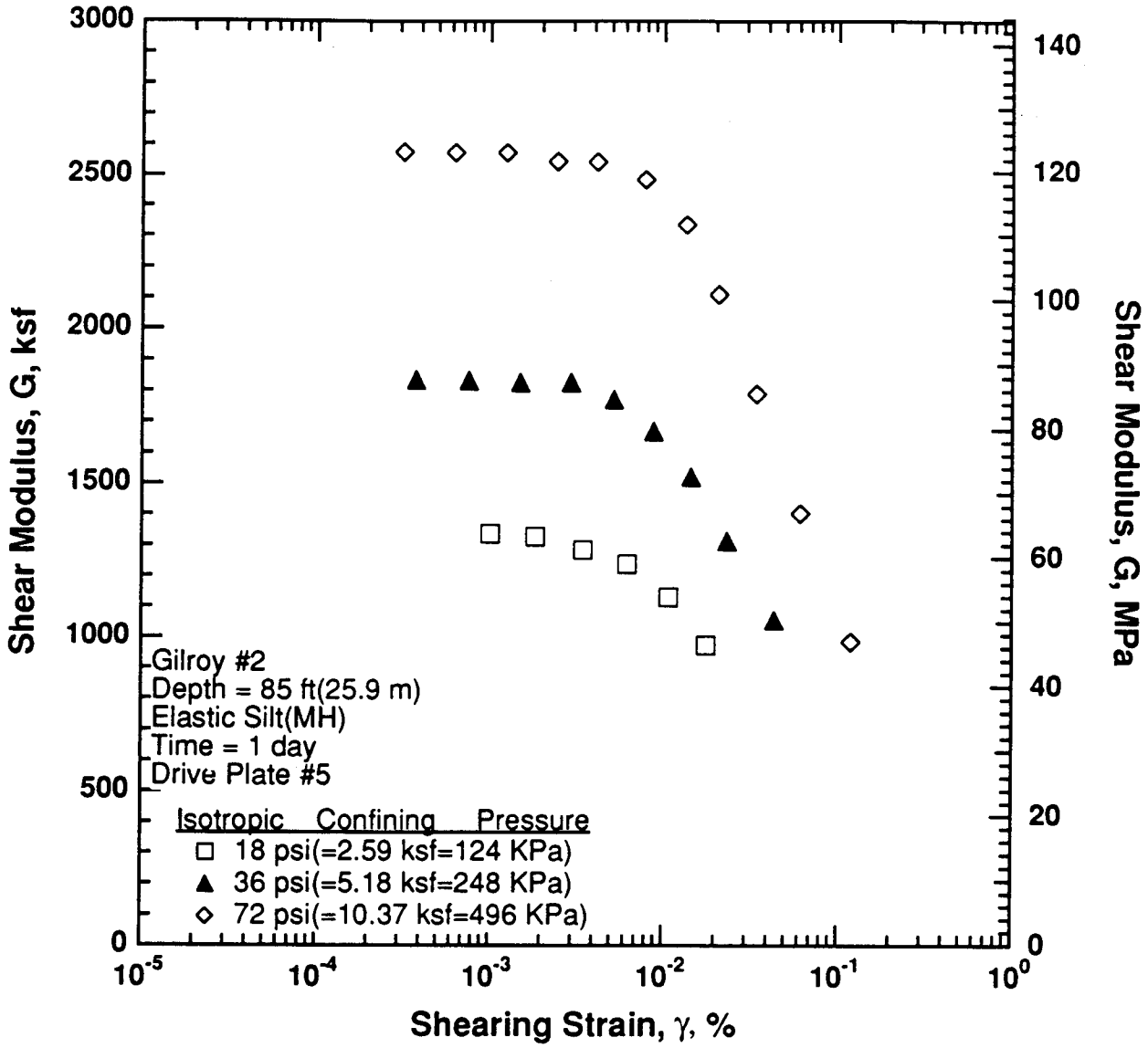

Figure 8.B.2.F-9
Variation in shear modulus with shearing strain and effective confining pressure from resonant column tests of sample G4.

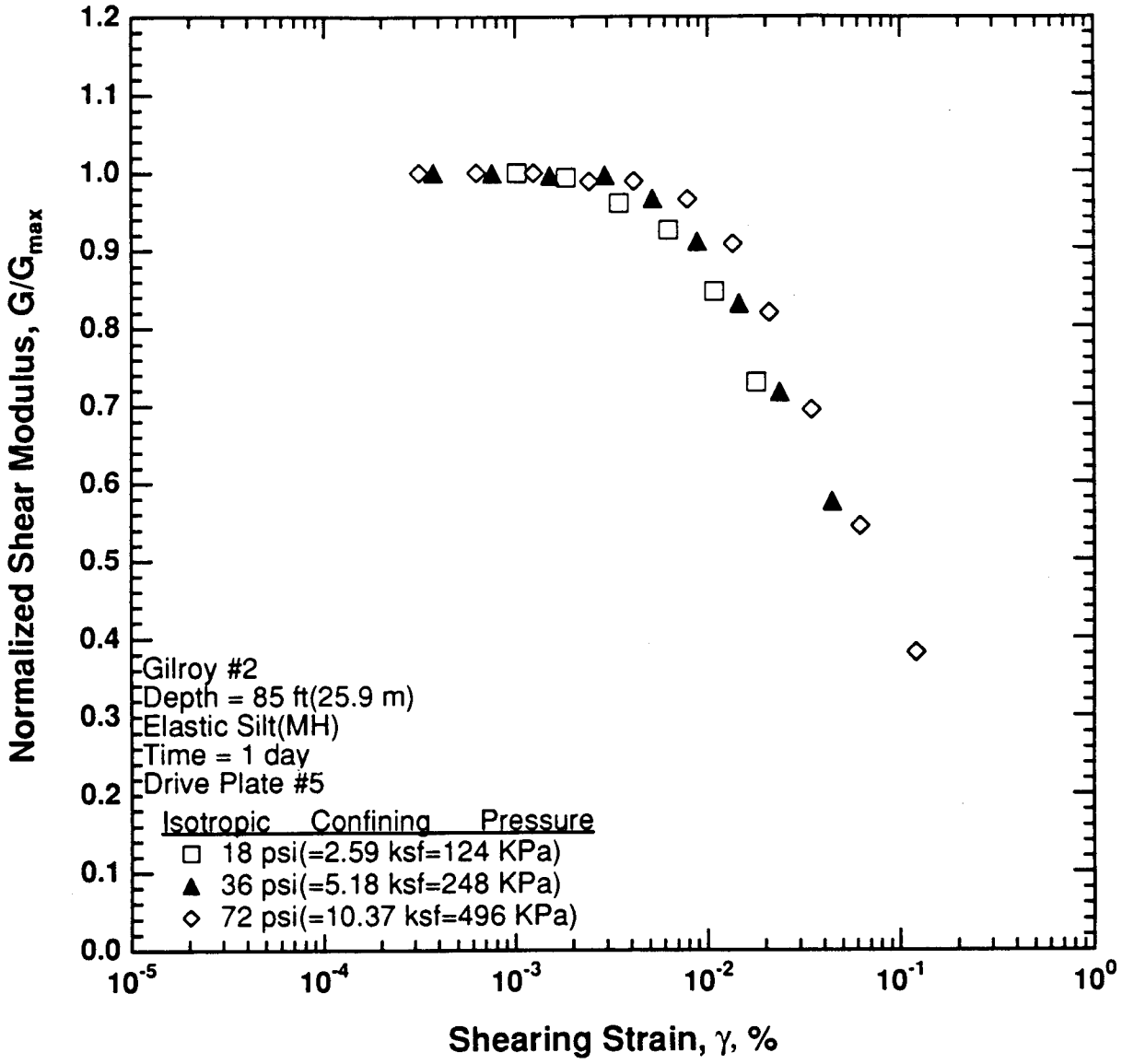

Figure 8.B.2.F-10
Comparison of the variation in normalized shear modulus with shearing strain and effective confining pressure from resonant column tests of sample G4.

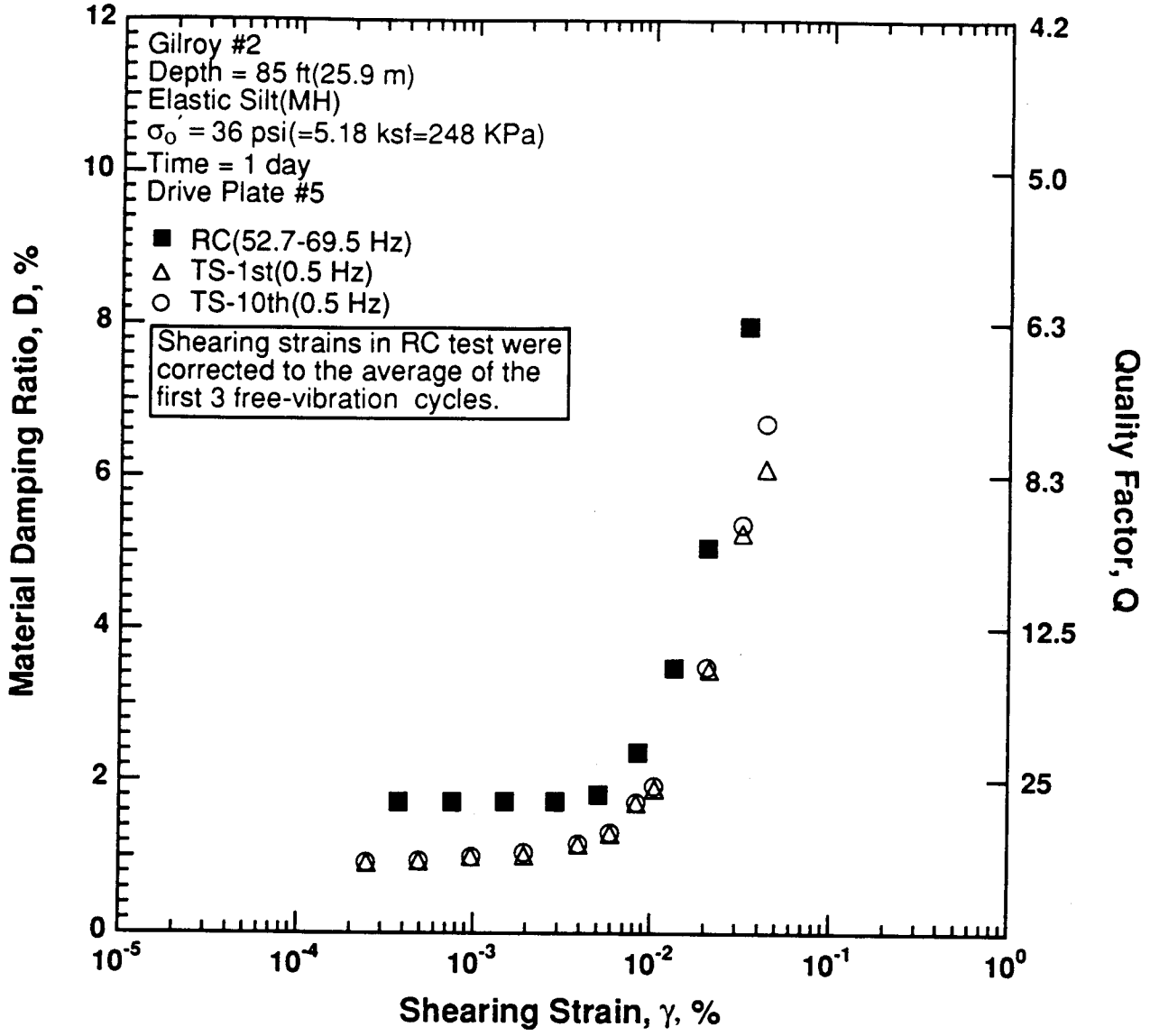

Figure 8.B.2.F-11
Variation in material damping ratio with shearing strain at an effective confining pressure of 36 psi (5.18 ksf, 248 kPa) from RCTS tests of sample G4.

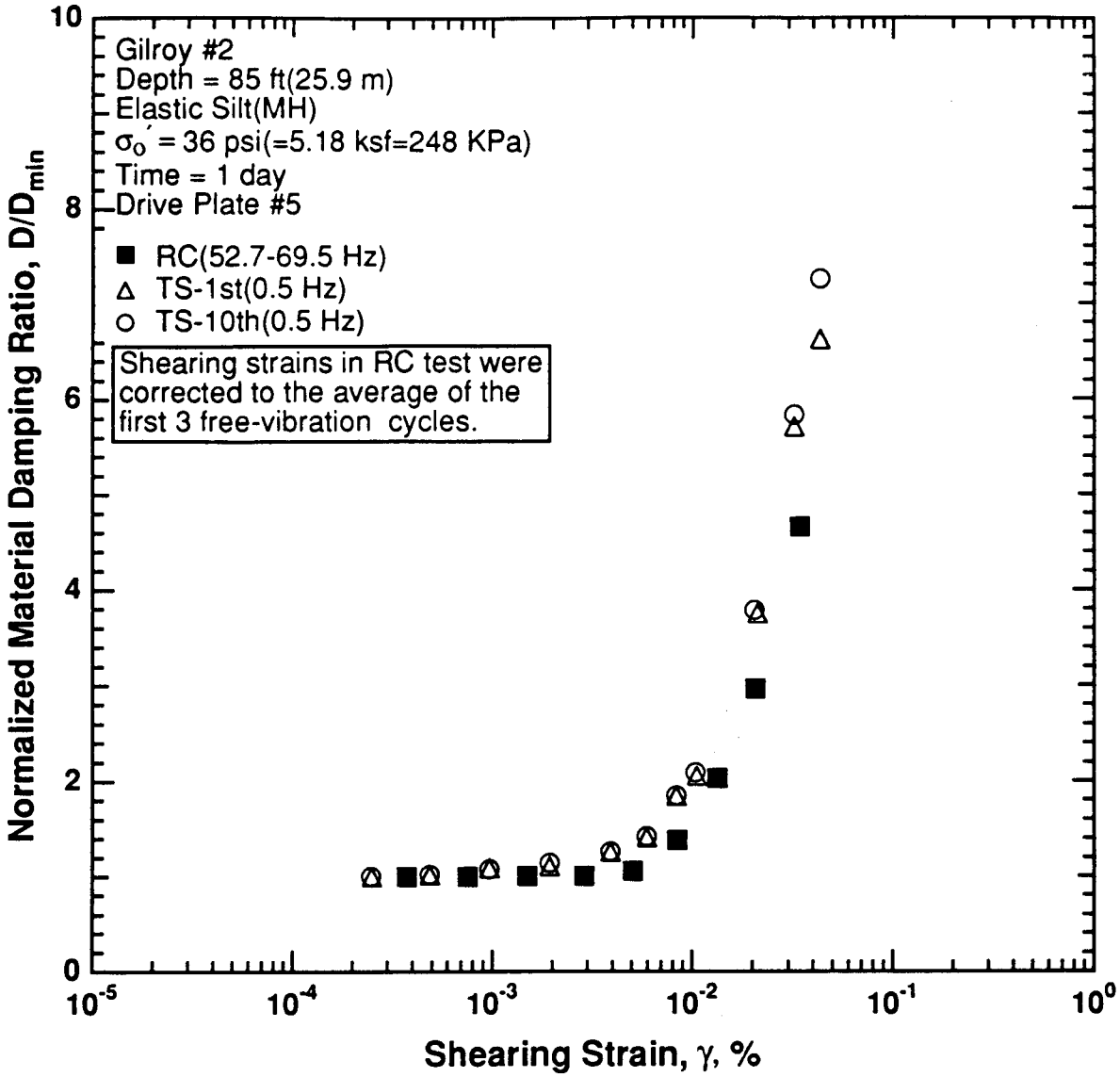

Figure 8.B.2.F-12
Variation in normalized material damping ratio with shearing strain at an effective confining pressure of 36 psi (5.18 ksf, 248 kPa) from RCTS tests of sample G4.

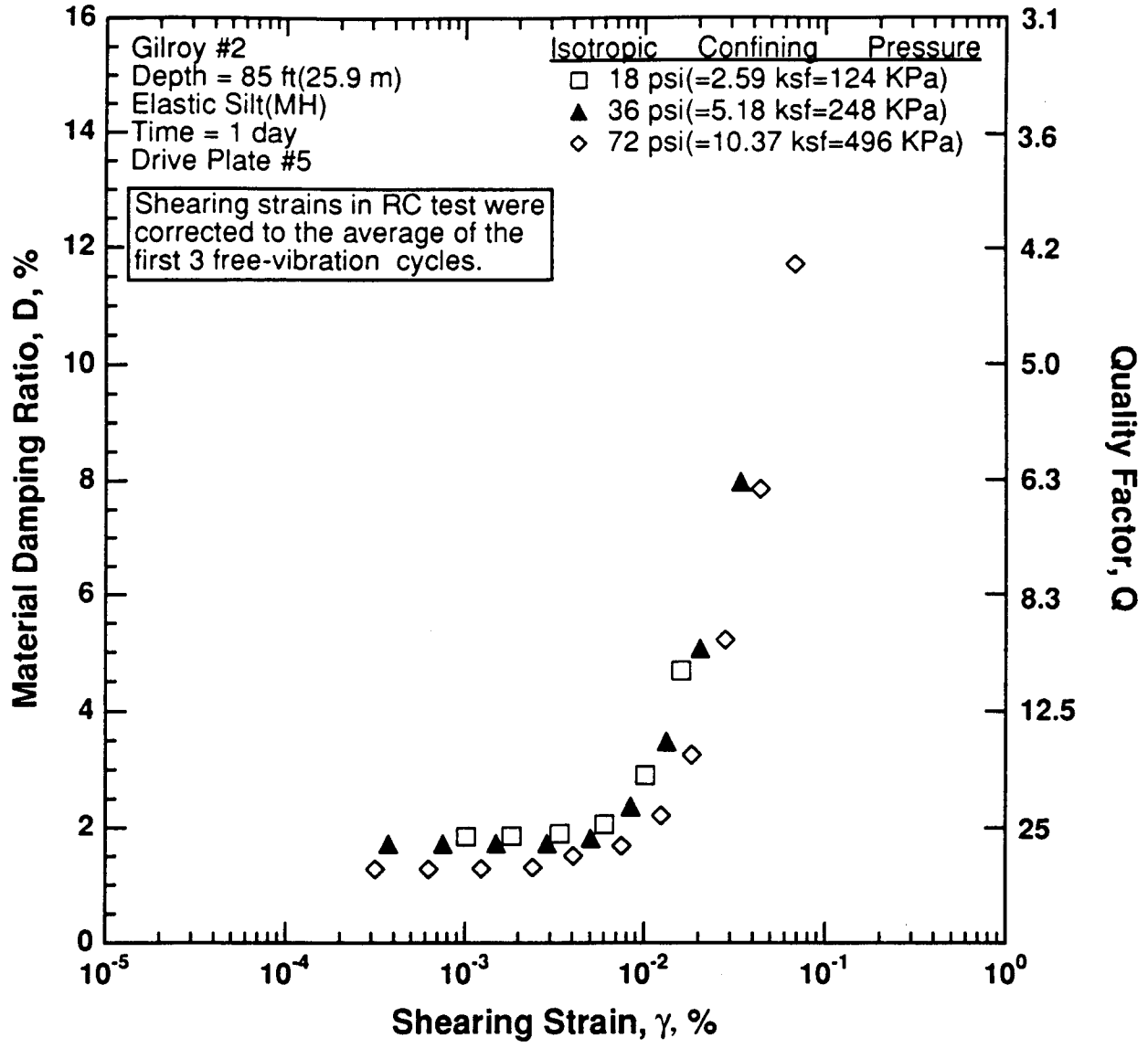

Figure 8.B.2.F-13
Variation in material damping ratio with shearing strain and effective confining pressure from resonant column tests of sample G4.

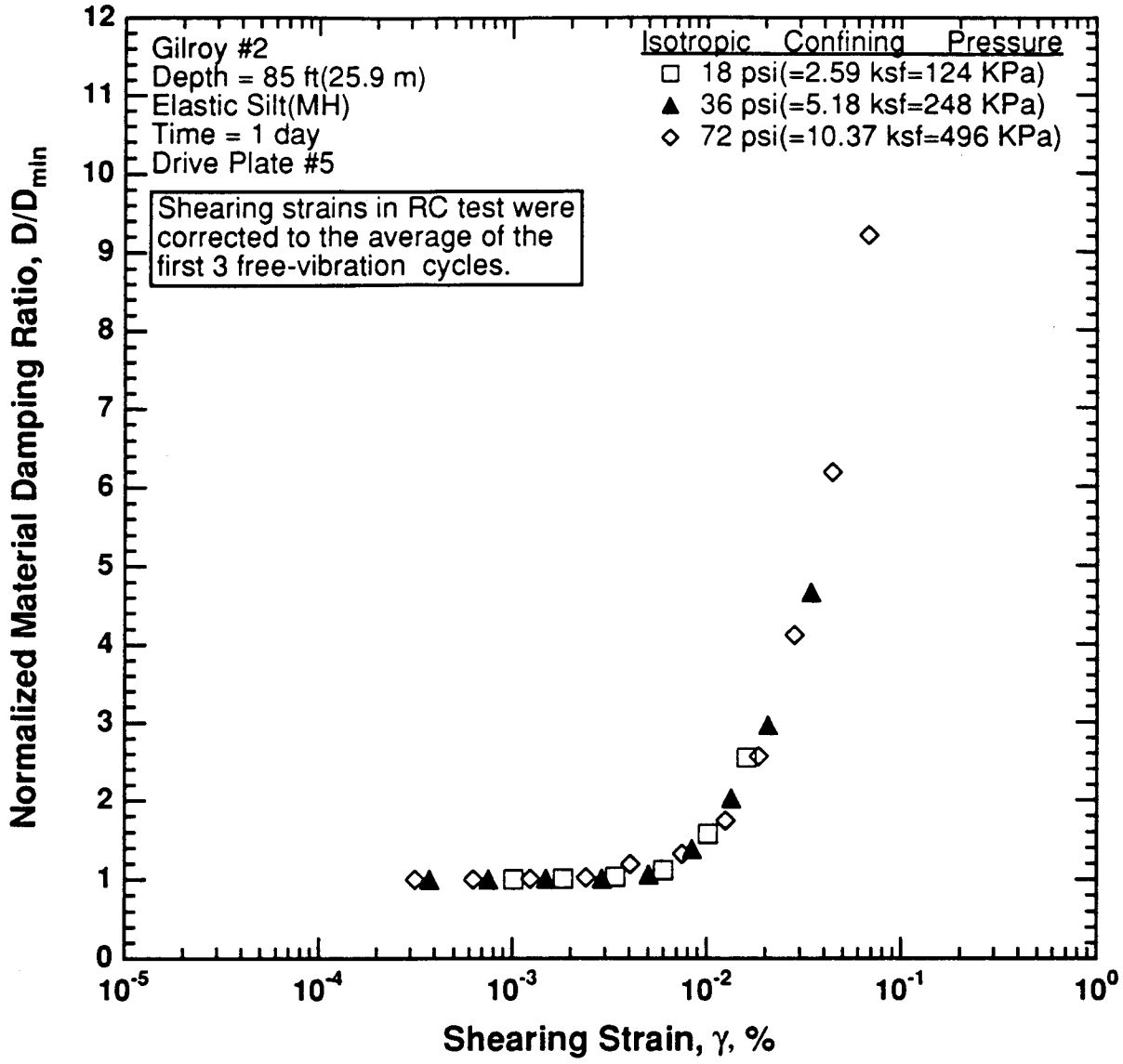

Figure 8.B.2.F-14
Comparison of the variation in normalized material damping ratio with shearing strain and effective confining pressure from resonant column tests of sample G4.

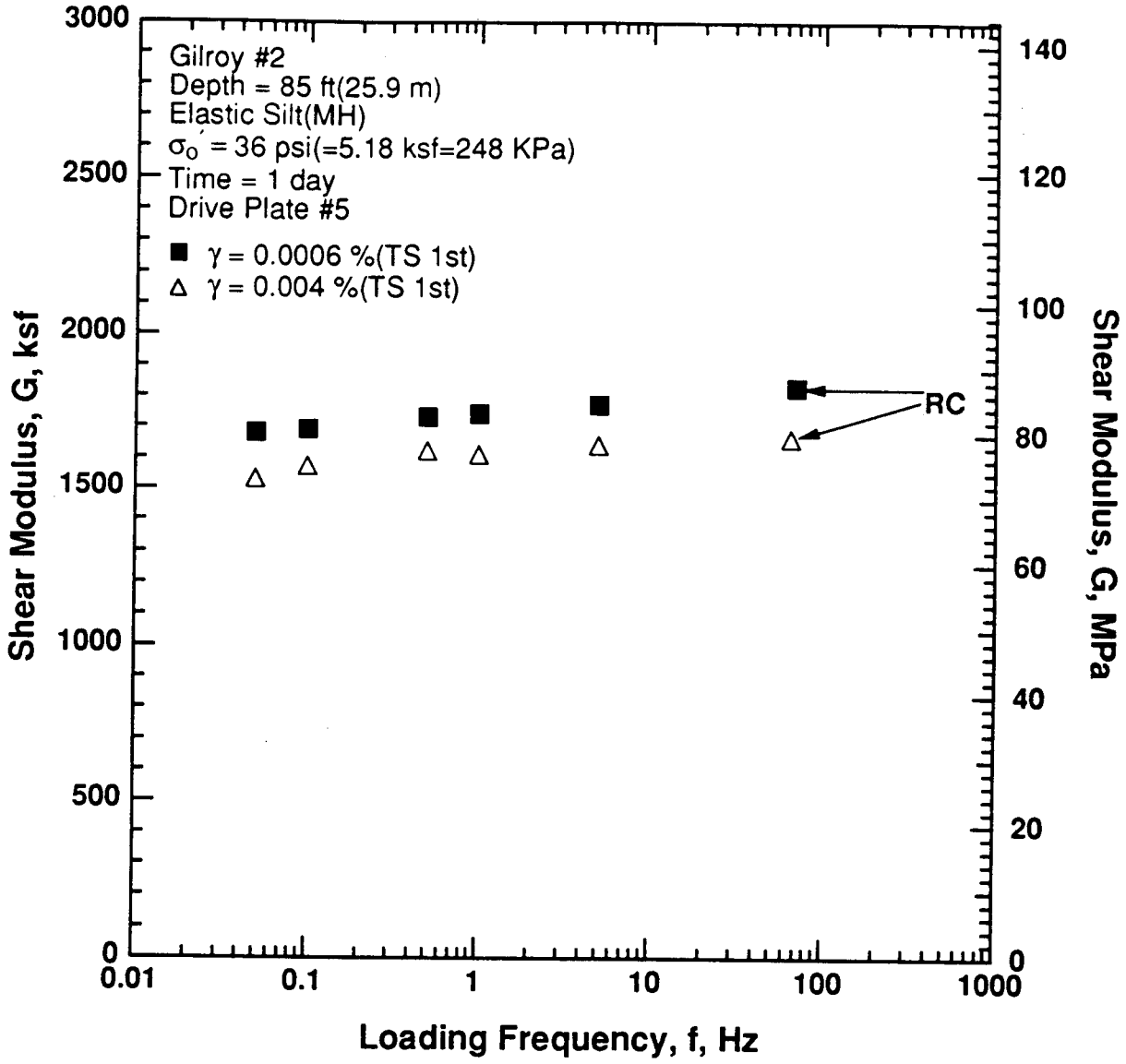

Figure 8.B.2.F-15
Variation in shear modulus with loading frequency and shearing strain at an effective confining pressure of 36 psi (5.18 ksf, 248 kPa) from RCTS tests of sample G4.

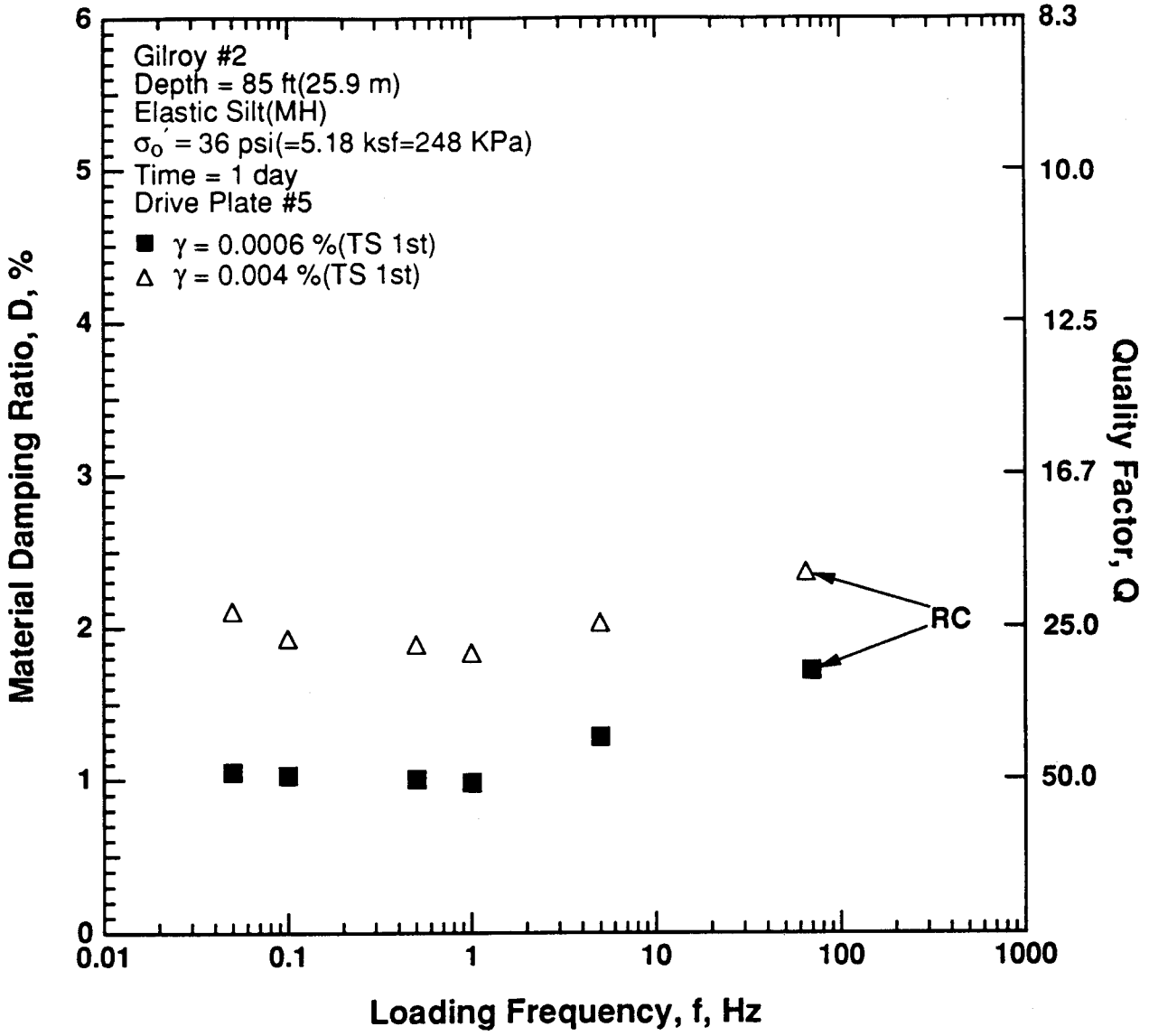

Figure 8.B.2.F-16
Variation in material damping ratio with loading frequency and shearing strain at an effective confining pressure of 36 psi (5.18 ksf, 248 kPa) from RCTS tests of sample G4.

APPENDIX 8.B.2.G
DYNAMIC TESTS OF SAMPLE G4-1, DEPTH = 85 FT (25.9 M)

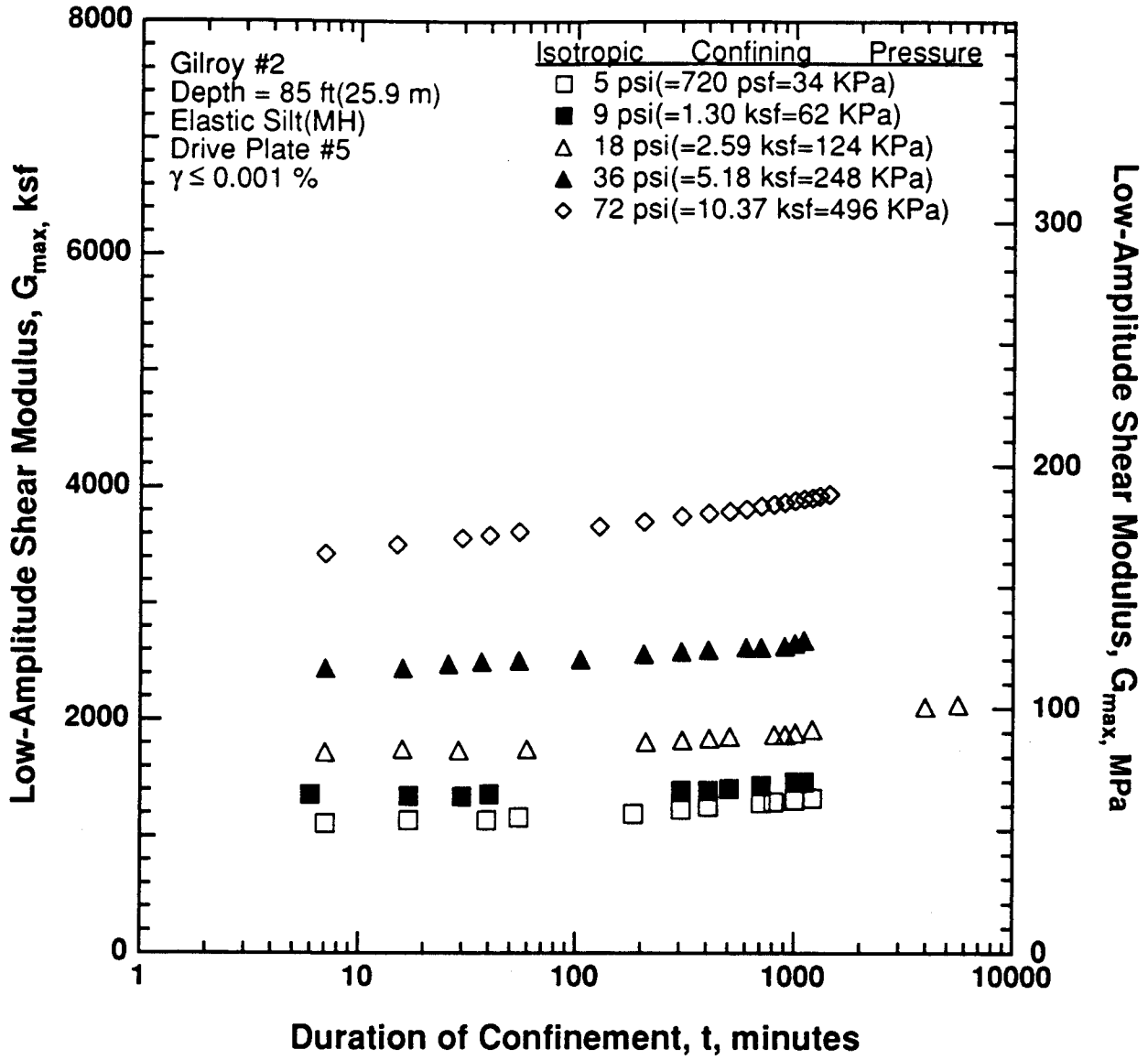

Figure 8.B.2.G-1
Variation in low-amplitude shear modulus with magnitude and duration of isotropic confining pressure from resonant column tests of sample G4-1.

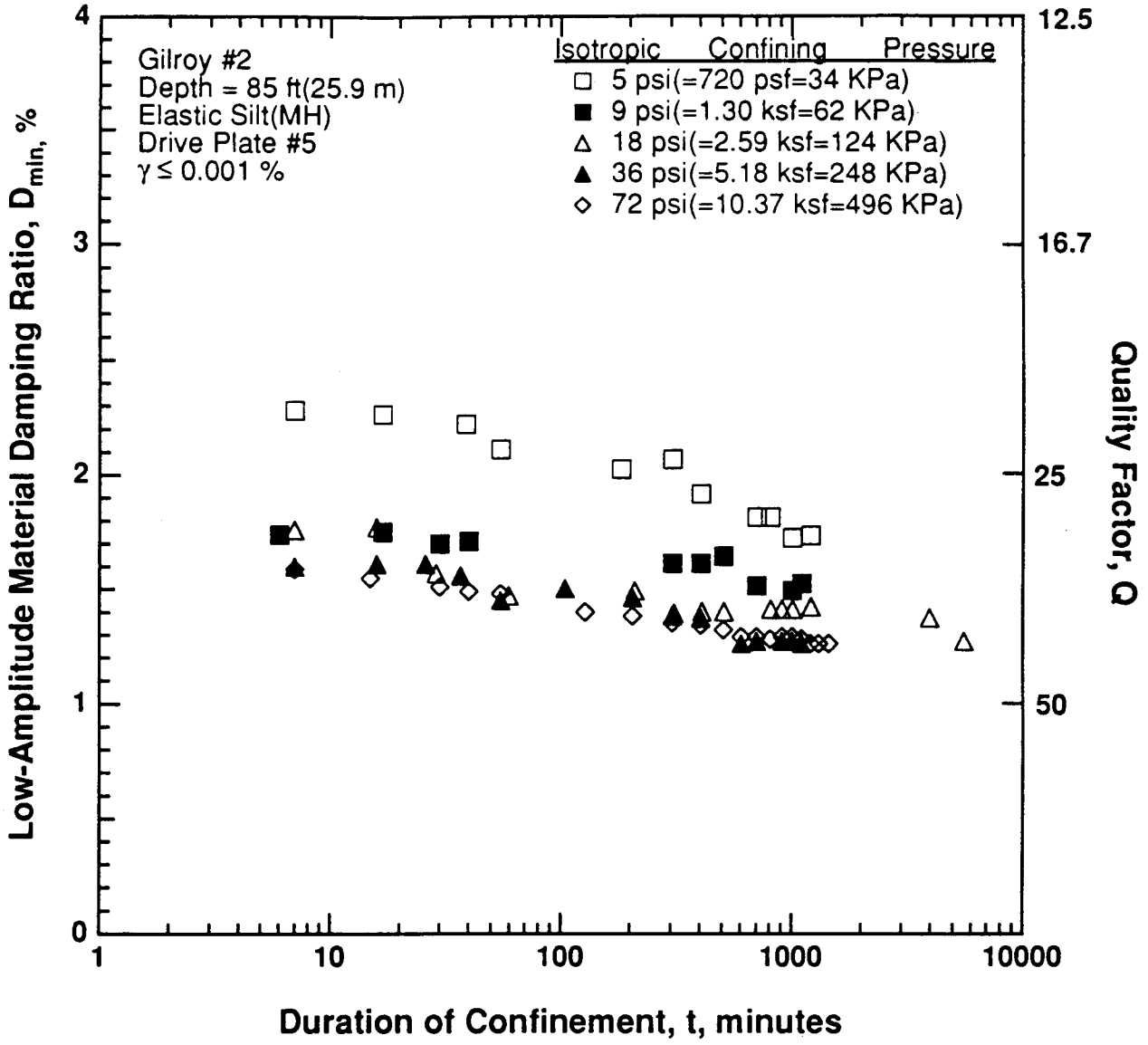

Figure 8.B.2.G-2
Variation in low-amplitude material damping ratio with magnitude and duration of isotropic confining pressure from resonant column tests of sample G4-1.

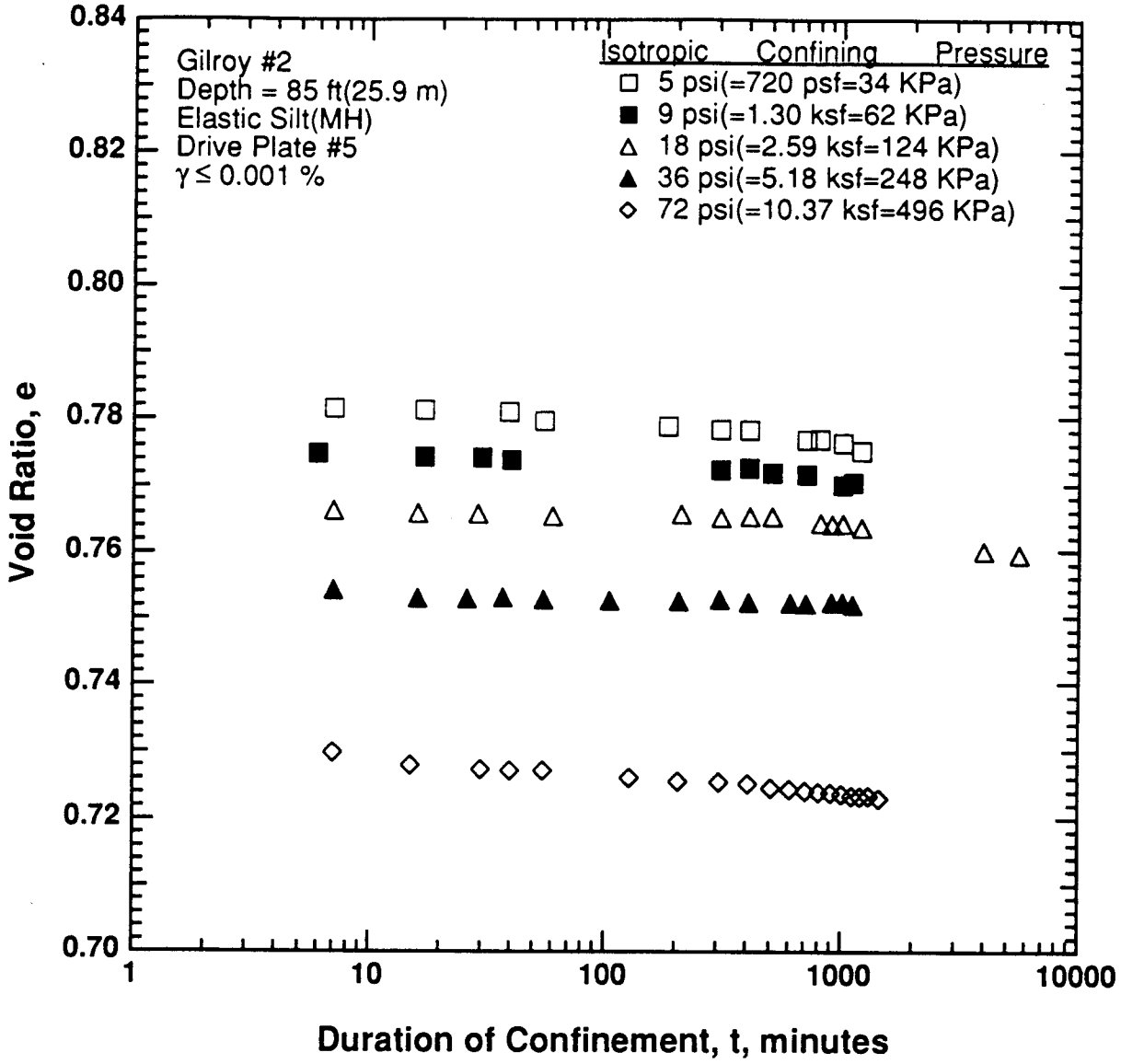

Figure 8.B.2.G-3
Variation in void ratio with magnitude and duration of isotropic confining pressure from resonant column tests of sample G4-1.

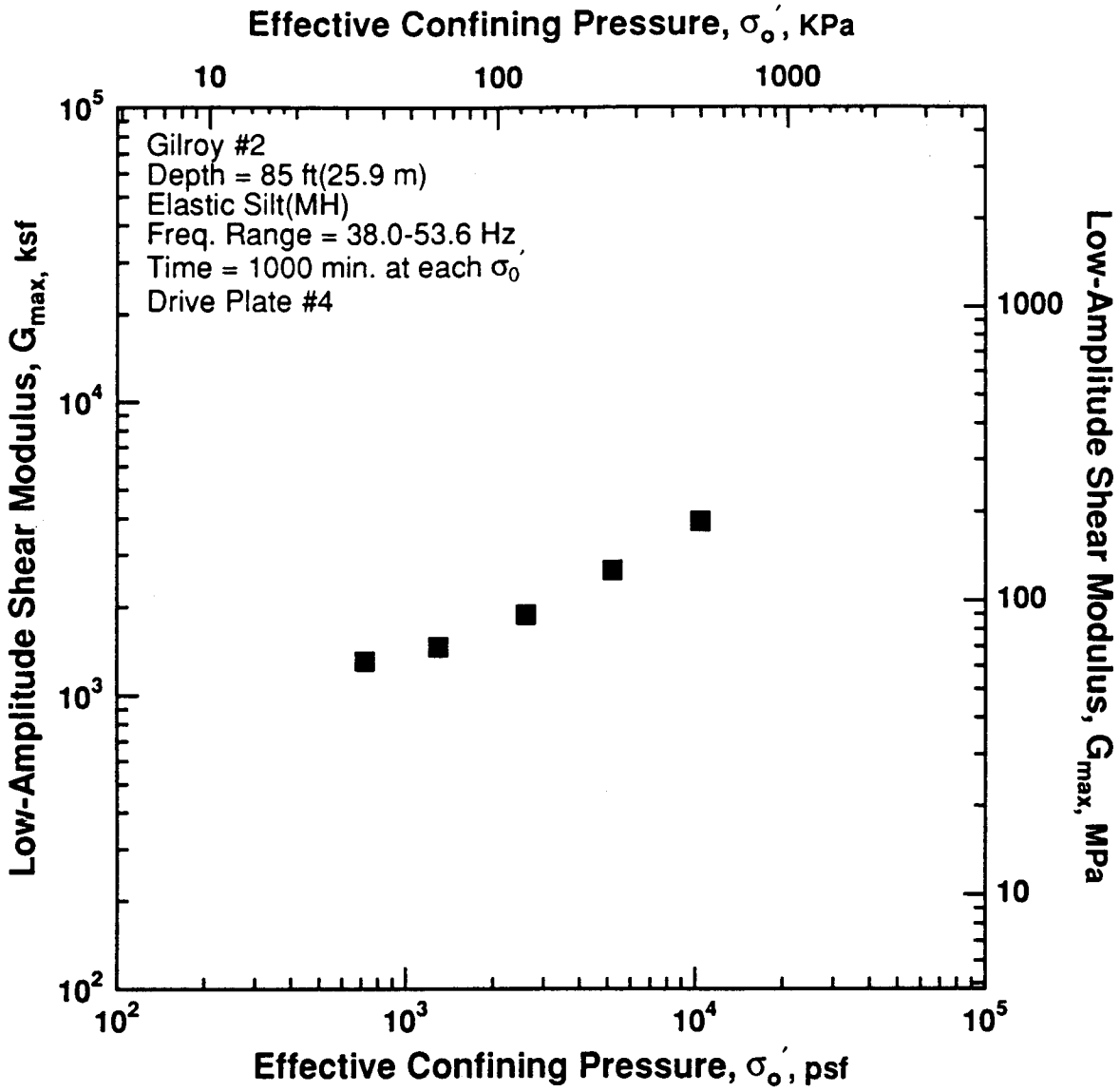

Figure 8.B.2.G-4
Variation in low-amplitude shear modulus with effective confining pressure from resonant column tests of sample G4-1.

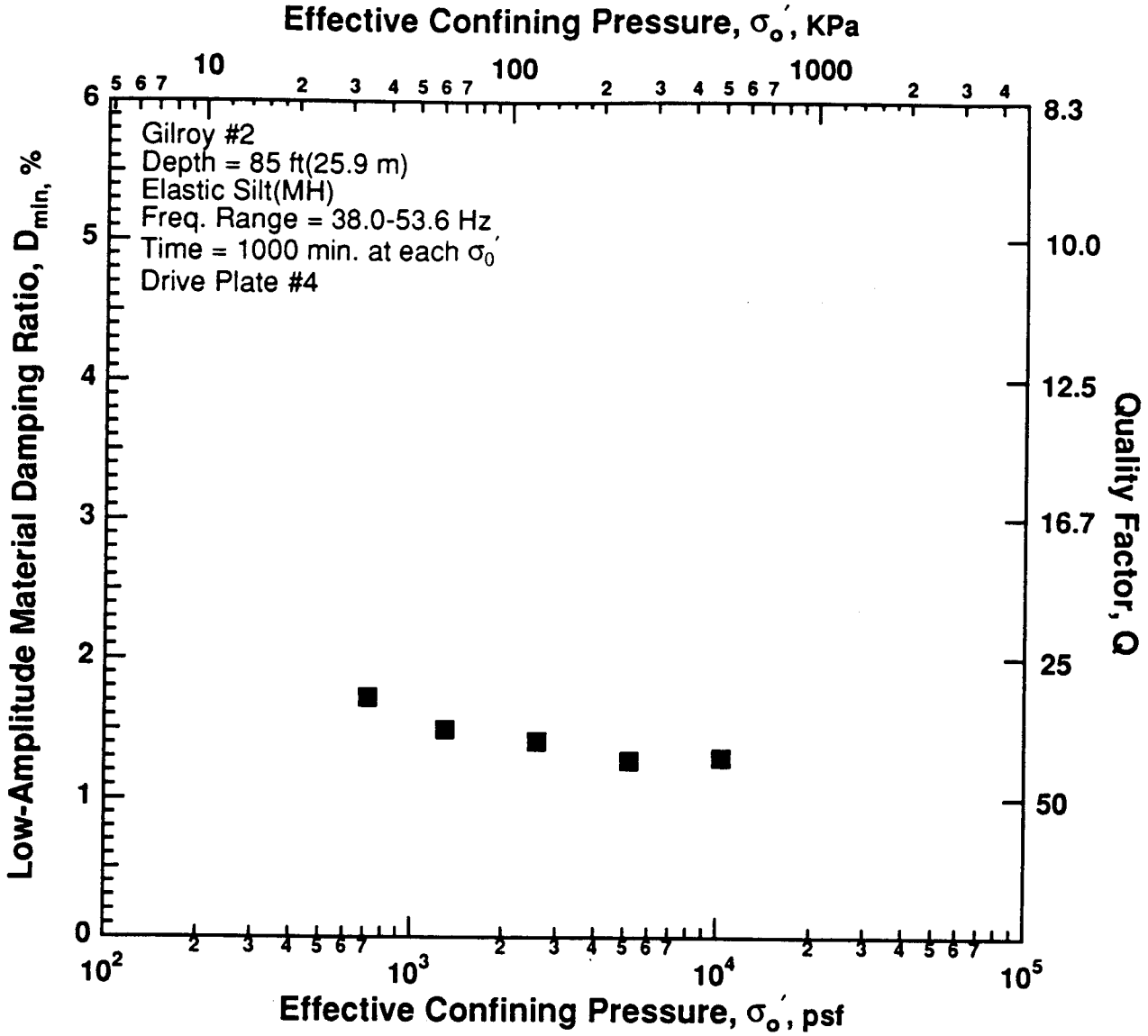

Figure 8.B.2.G-5
Variation in low-amplitude material damping ratio with effective confining pressure from resonant column tests of sample G4-1.

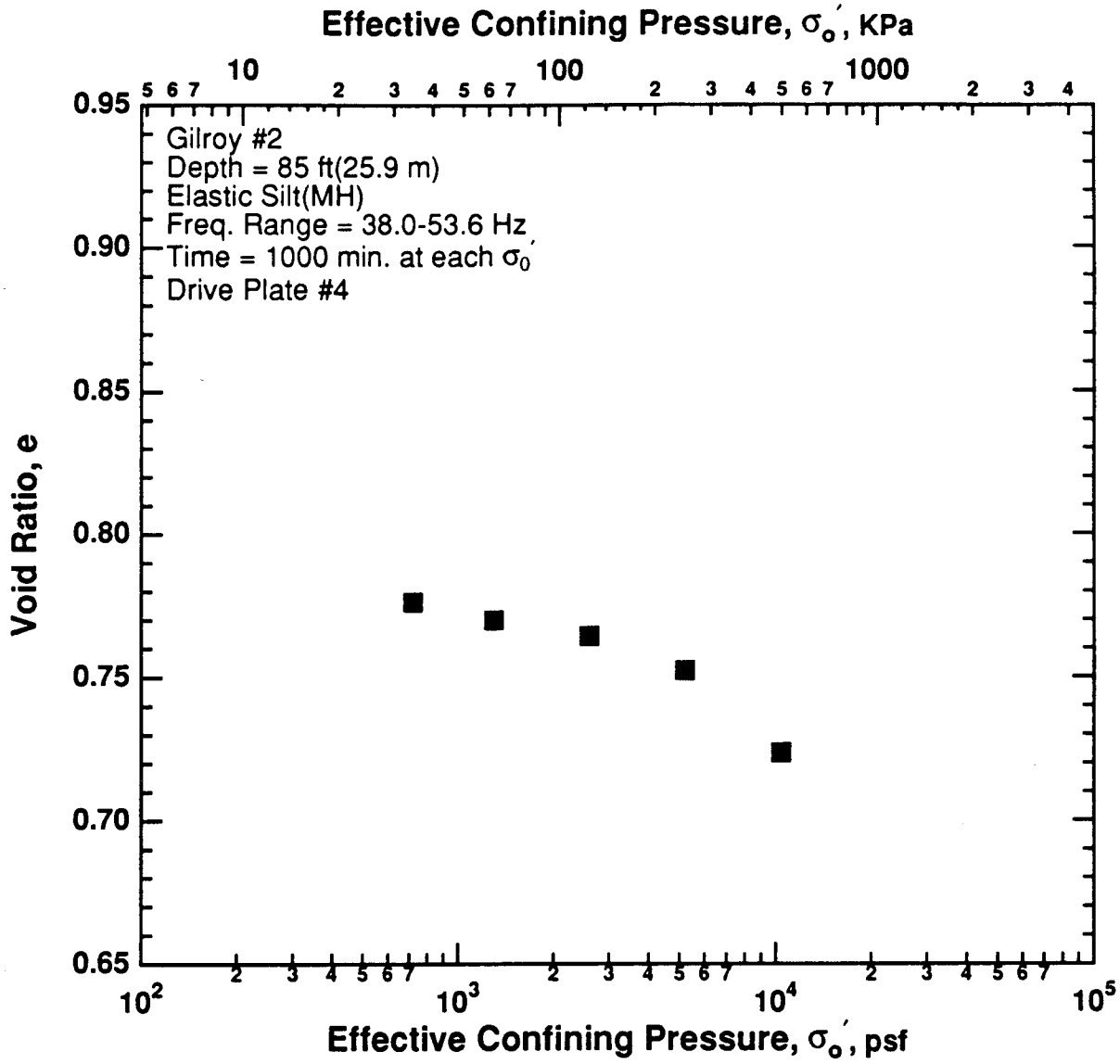

Figure 8.B.2.G-6
Variation in void ratio with effective confining pressure from resonant column tests of sample G4-1.

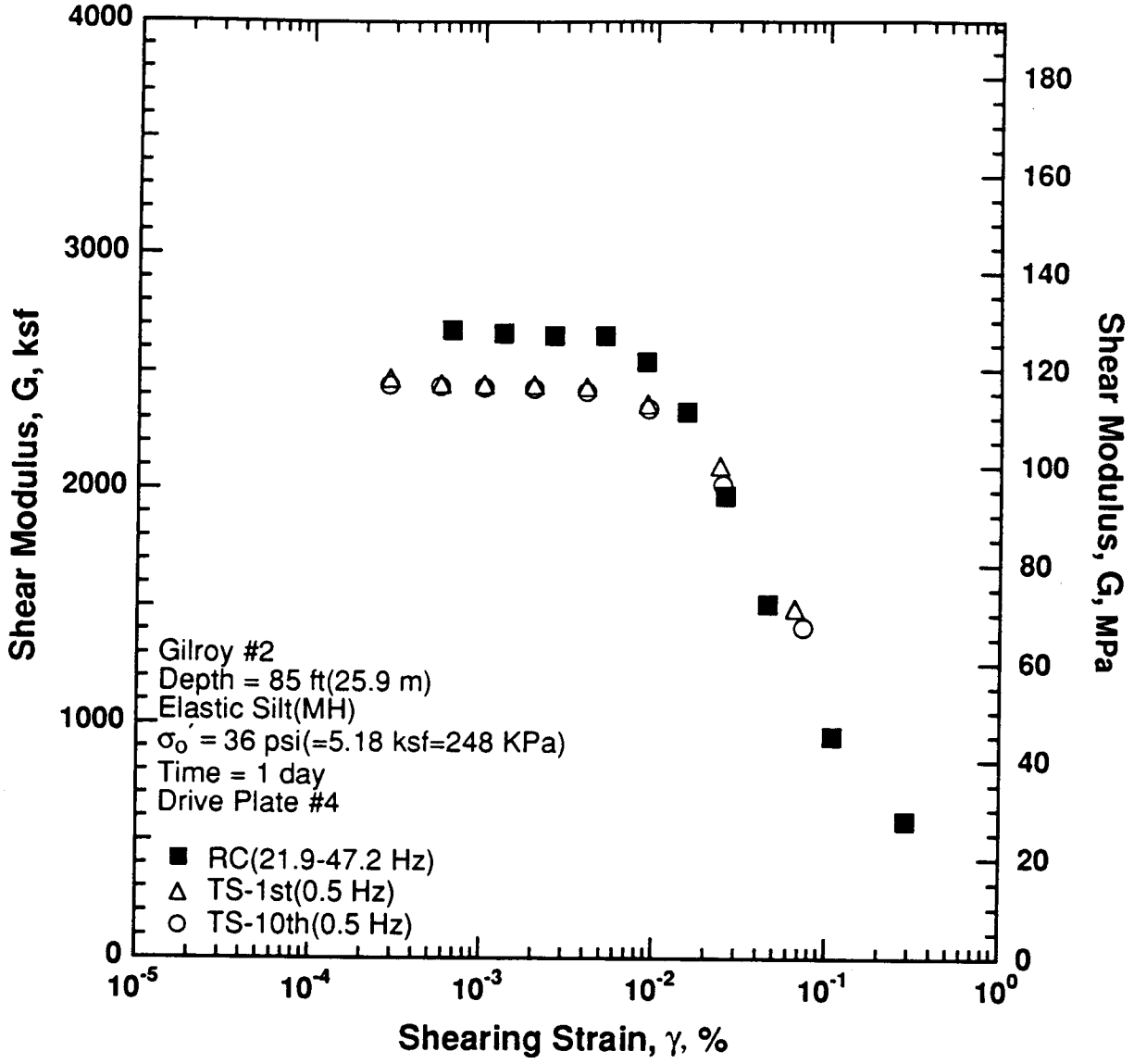

Figure 8.B.2.G-7
Variation in shear modulus with shearing strain at an effective confining pressure of 36 psi (5.18 ksf, 248 kPa) from RCTS tests of sample G4-1.

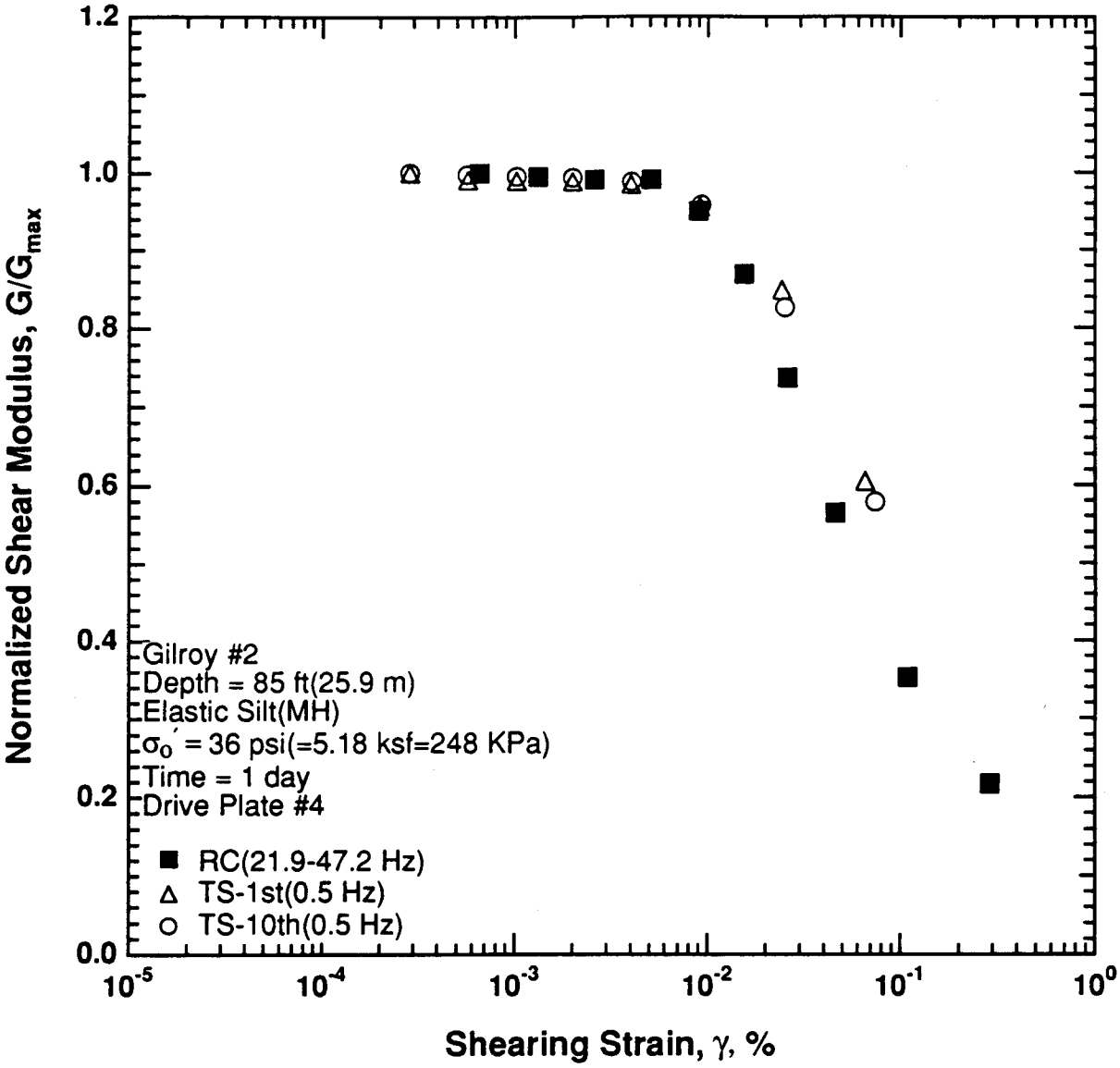

Figure 8.B.2.G-8
Variation in normalized shear modulus with shearing strain at an effective confining pressure of 36 psi (5.18 ksf, 248 kPa) from RCTS tests of sample G4-1.

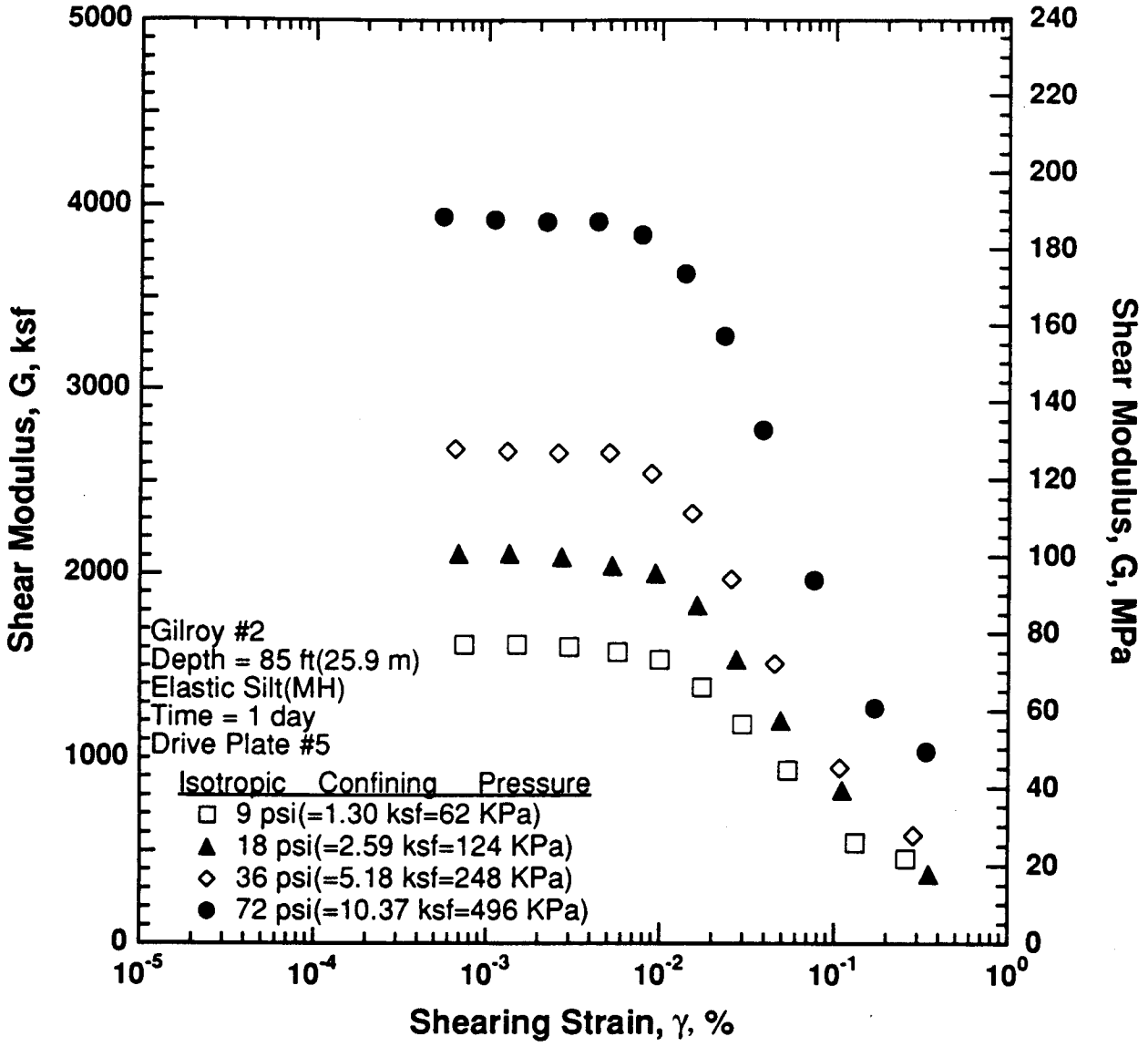

Figure 8.B.2.G-9
Variation in shear modulus with shearing strain and effective confining pressure from resonant column tests of sample G4-1.

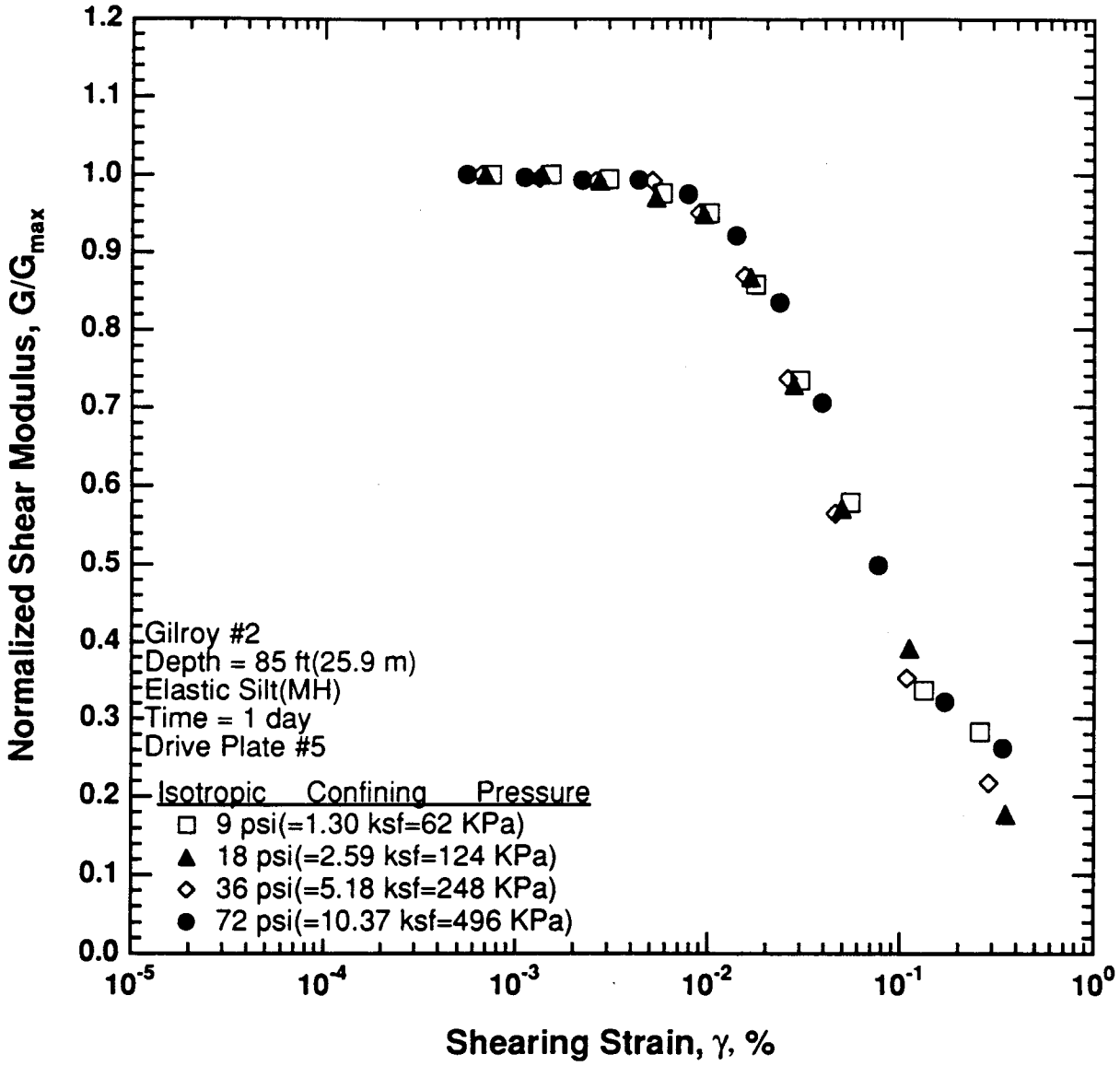

Figure 8.B.2.G-10
Comparison of the variation in normalized shear modulus with shearing strain and effective confining pressure from resonant column tests of sample G4-1.

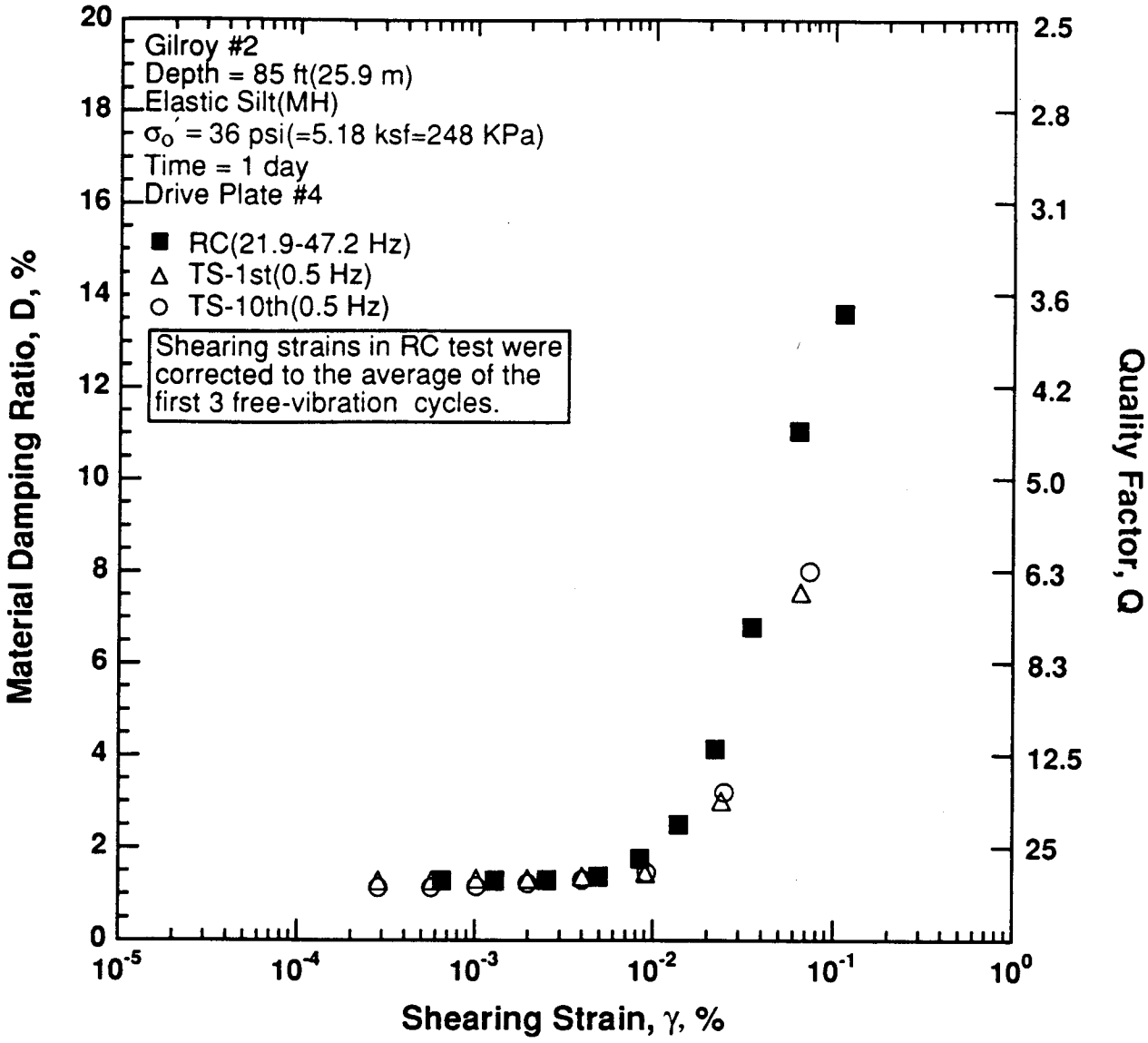

Figure 8.B.2.G-11
Variation in material damping ratio with shearing strain at an effective confining pressure of 36 psi (5.18 ksf, 248 kPa) from RCTS tests of sample G4-1.

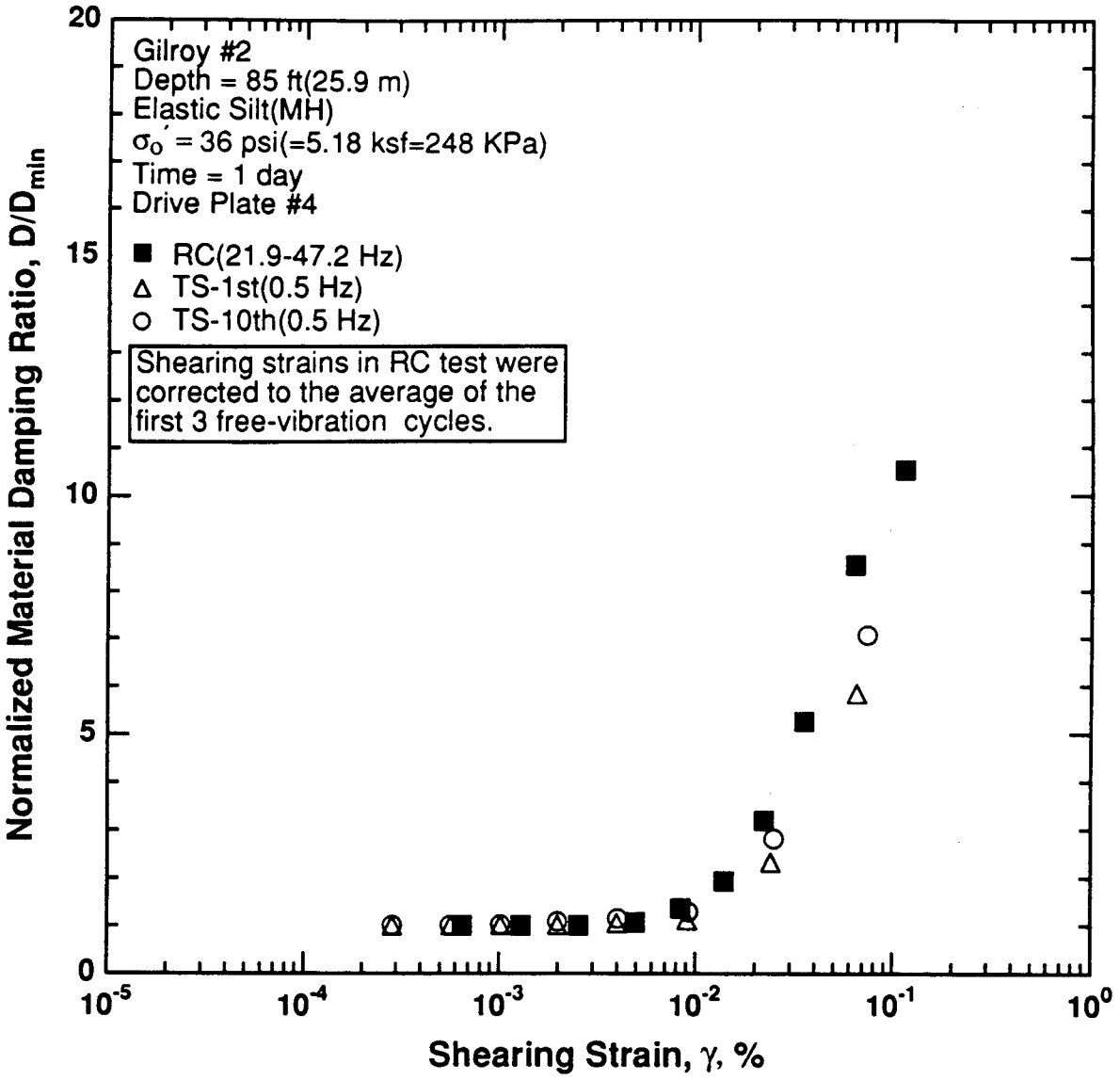

Figure 8.B.2.G-12
Variation in normalized material damping ratio with shearing strain at an effective confining pressure of 36 psi (5.18 ksf, 248 kPa) from RCTS tests of sample G4-1.

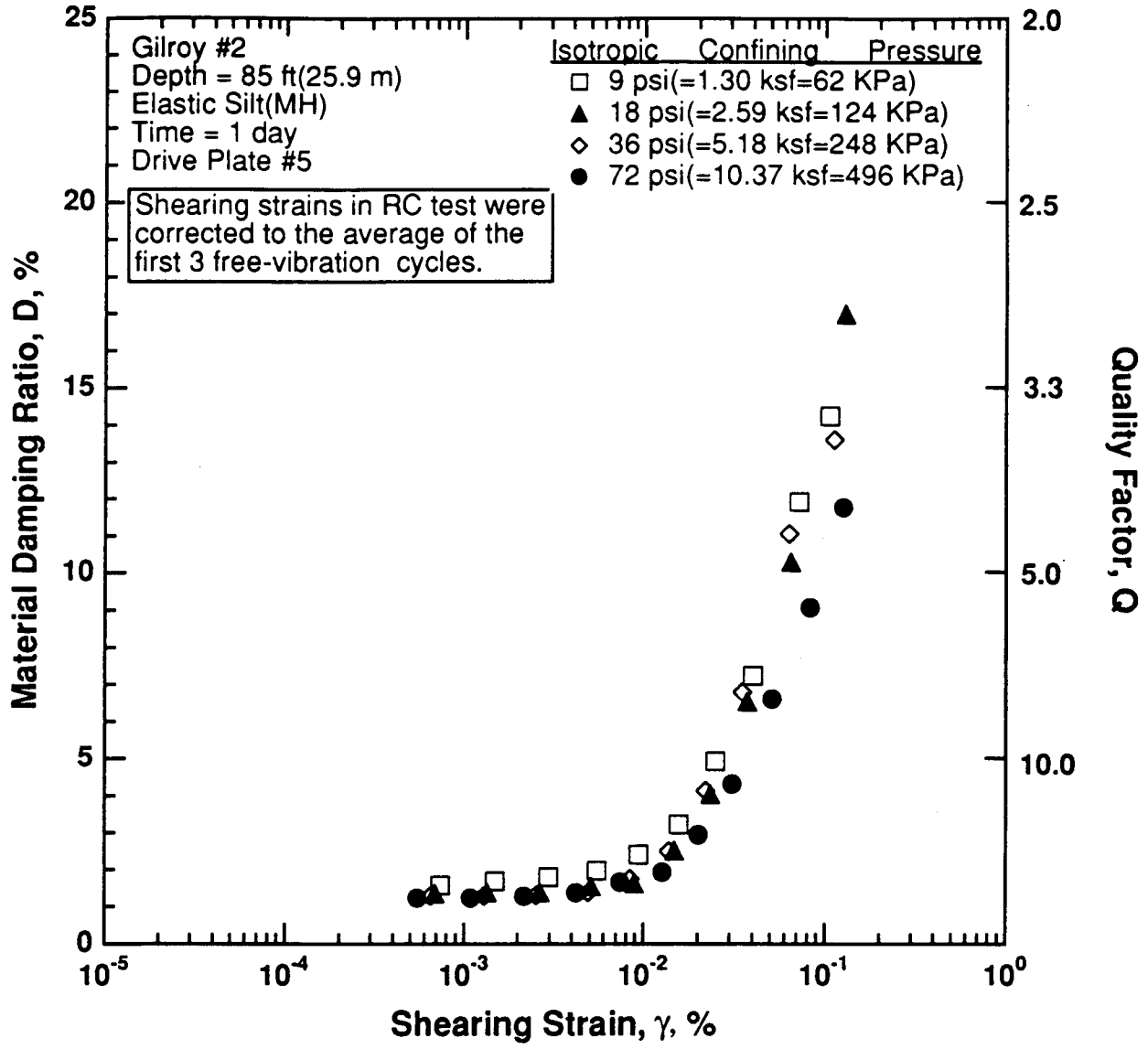

Figure 8.B.2.G-13
Variation in material damping ratio with shearing strain and effective confining pressure from resonant column tests of sample G4-1.

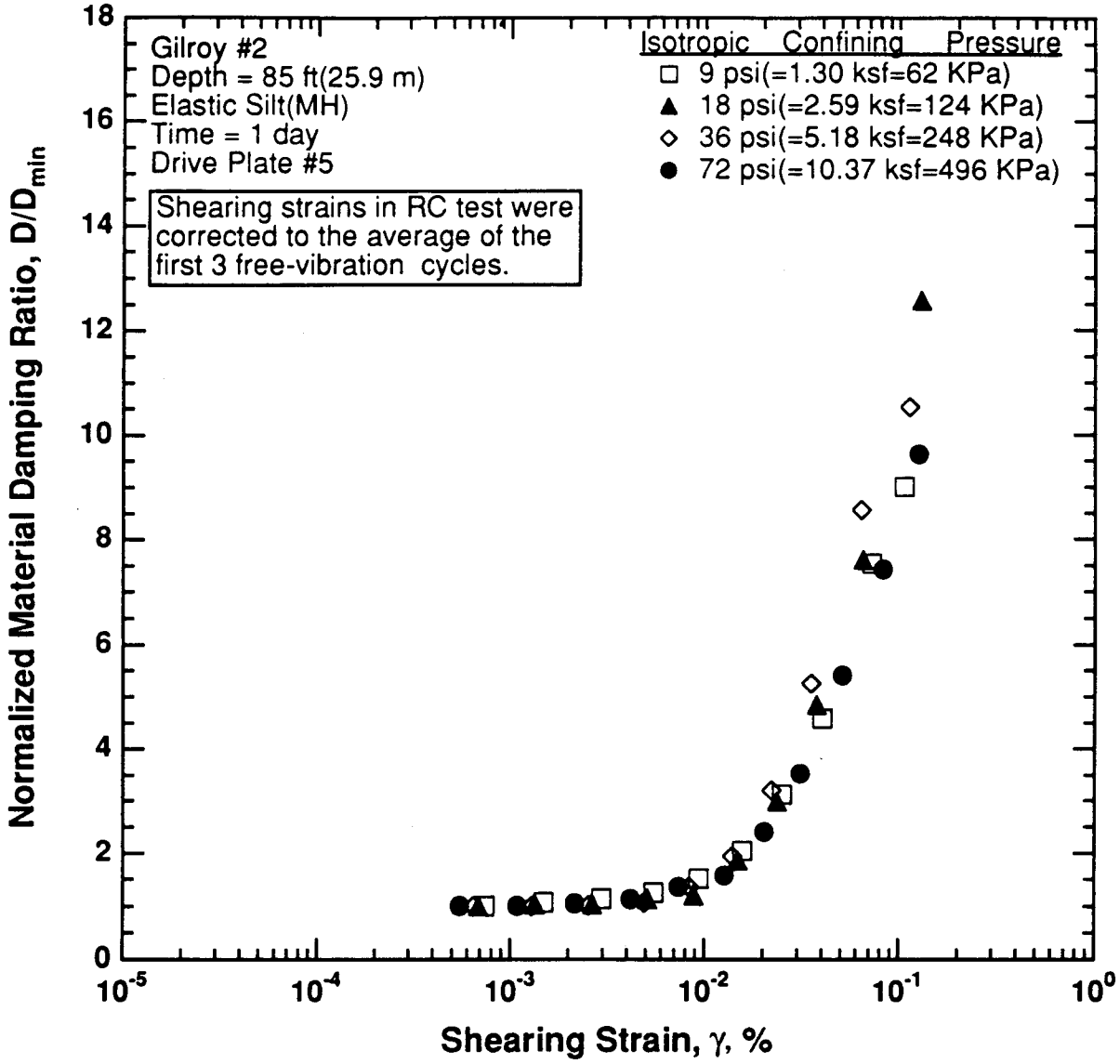

Figure 8.B.2.G-14
Comparison of the variation in normalized material damping ratio with shearing strain and effective confining pressure from resonant column tests of sample G4-1.

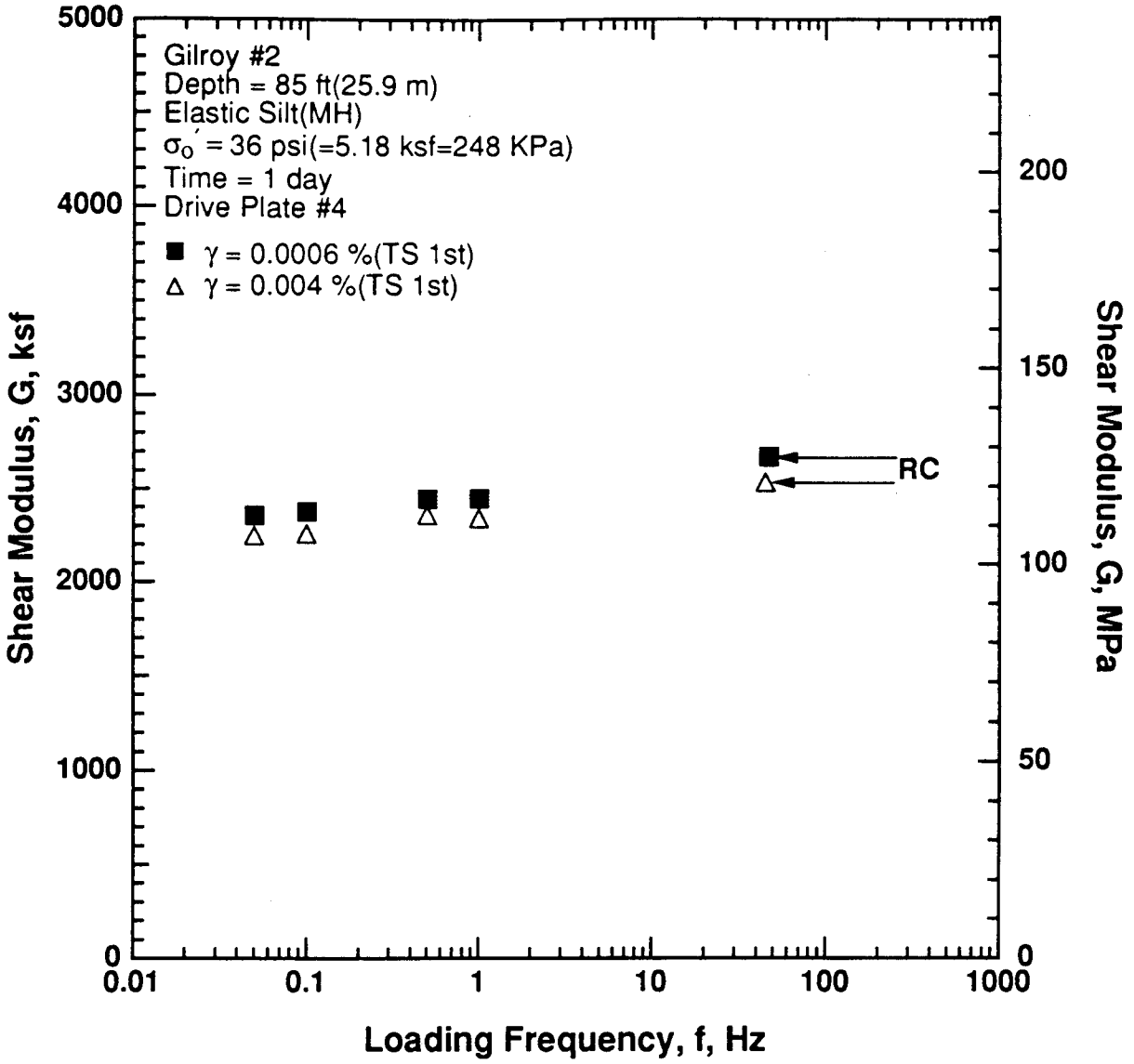

Figure 8.B.2.G-15
Variation in shear modulus with loading frequency and shearing strain at an effective confining pressure of 36 psi (5.18 ksf, 248 kPa) from RCTS tests of sample G4-1.

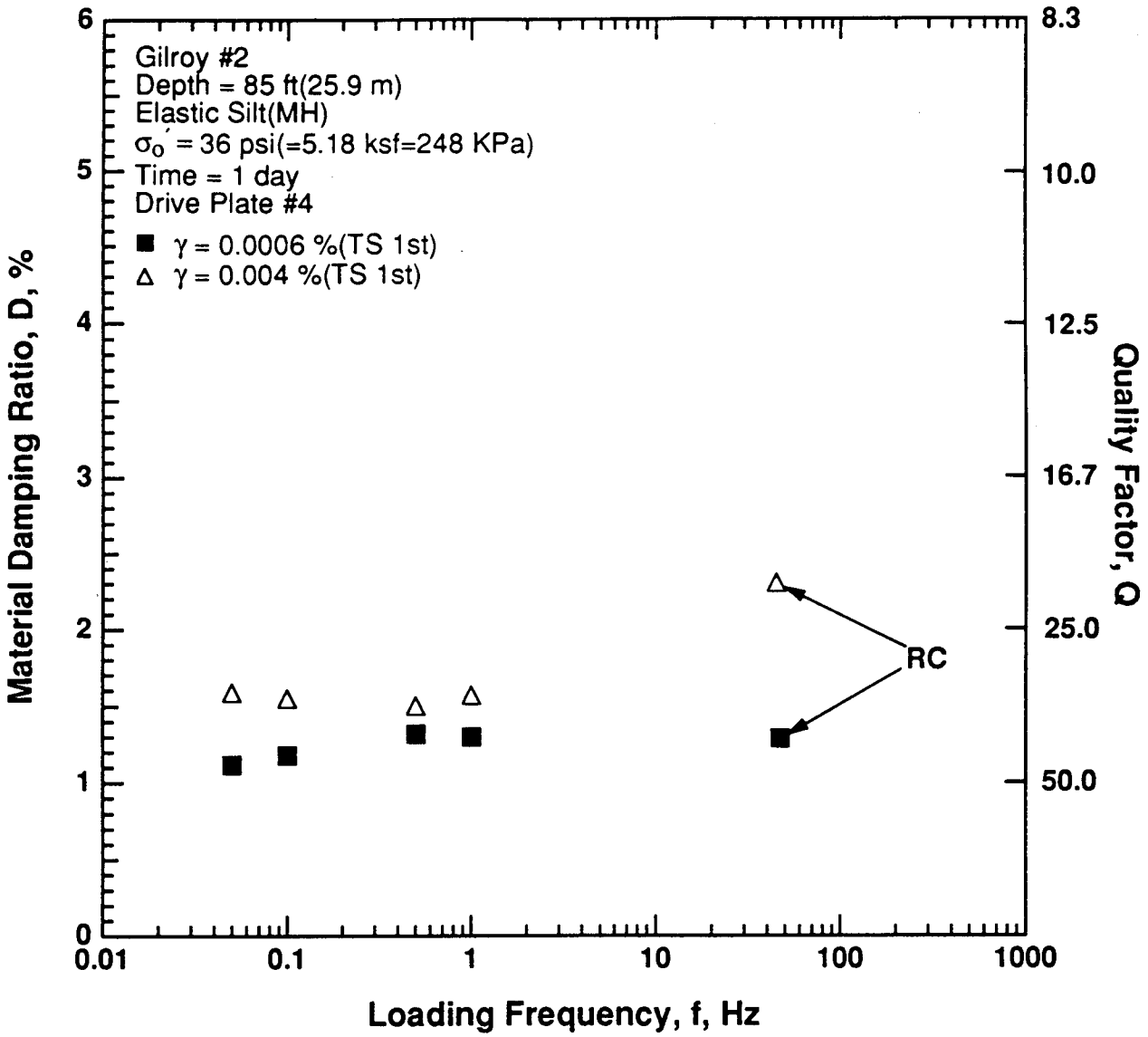

Figure 8.B.2.G-16
Variation in material damping ratio with loading frequency and shearing strain at an effective confining pressure of 36 psi (5.18 ksf, 248 kPa) from RCTS tests of sample G4-1.

APPENDIX 8.B.2.H
DYNAMIC TESTS OF SAMPLE G5, DEPTH = 120 FT (36.6 M)

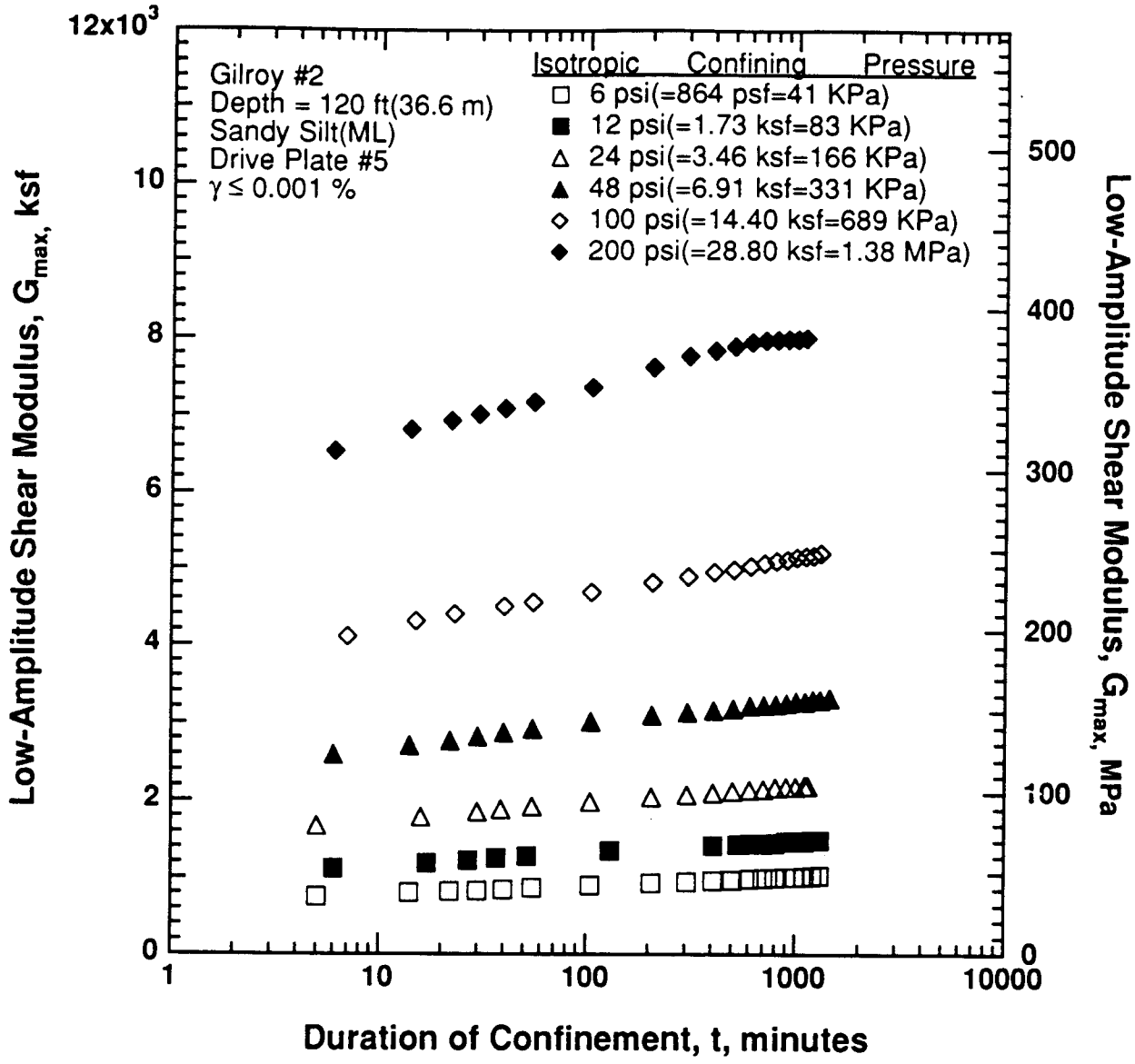

Figure 8.B.2.H-1
Variation in low-amplitude shear modulus with magnitude and duration of isotropic confining pressure from resonant column tests of sample G5.

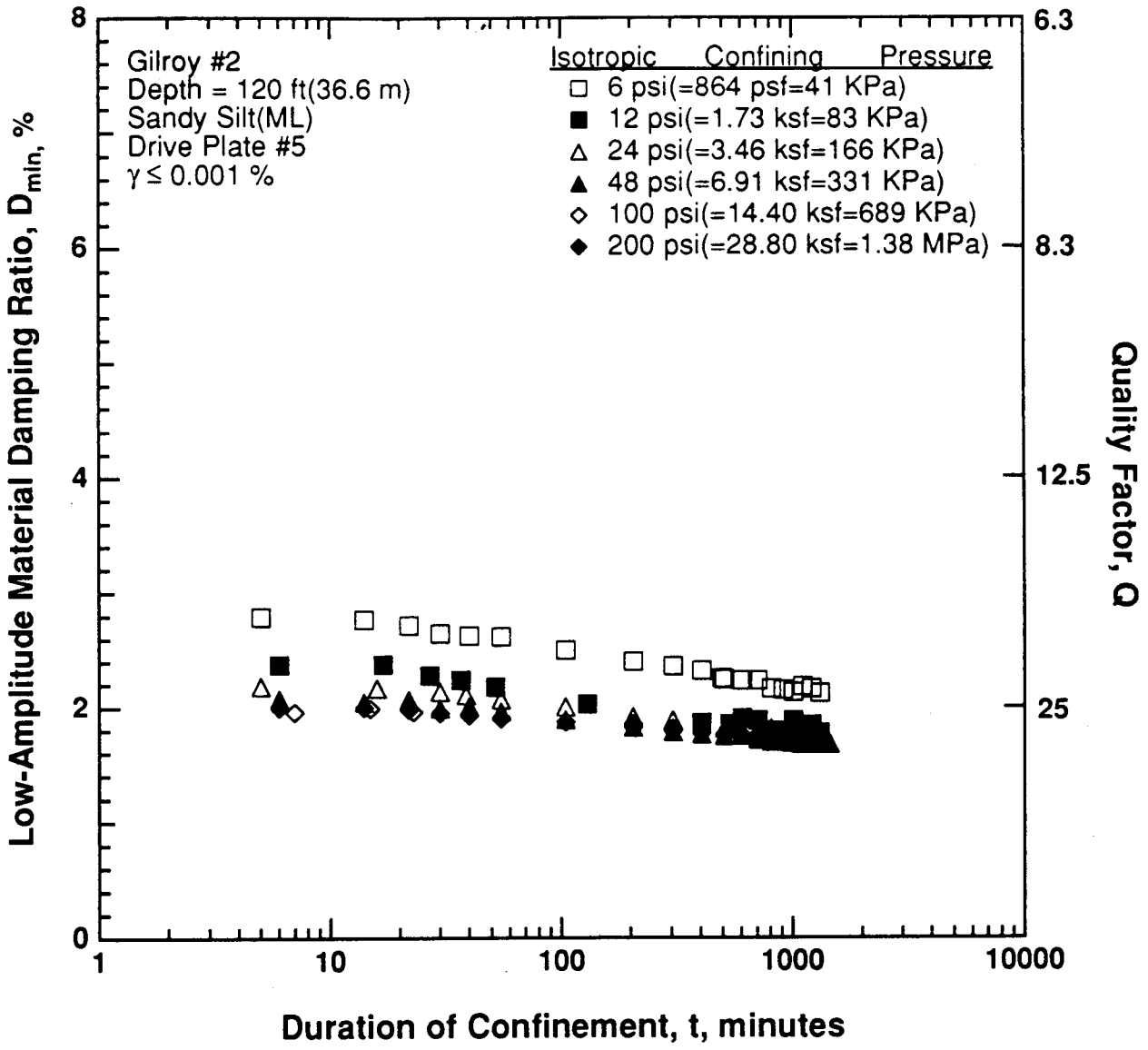

Figure 8.B.2.H-2
Variation in low-amplitude material damping ratio with magnitude and duration of isotropic confining pressure from resonant column tests of sample G5.

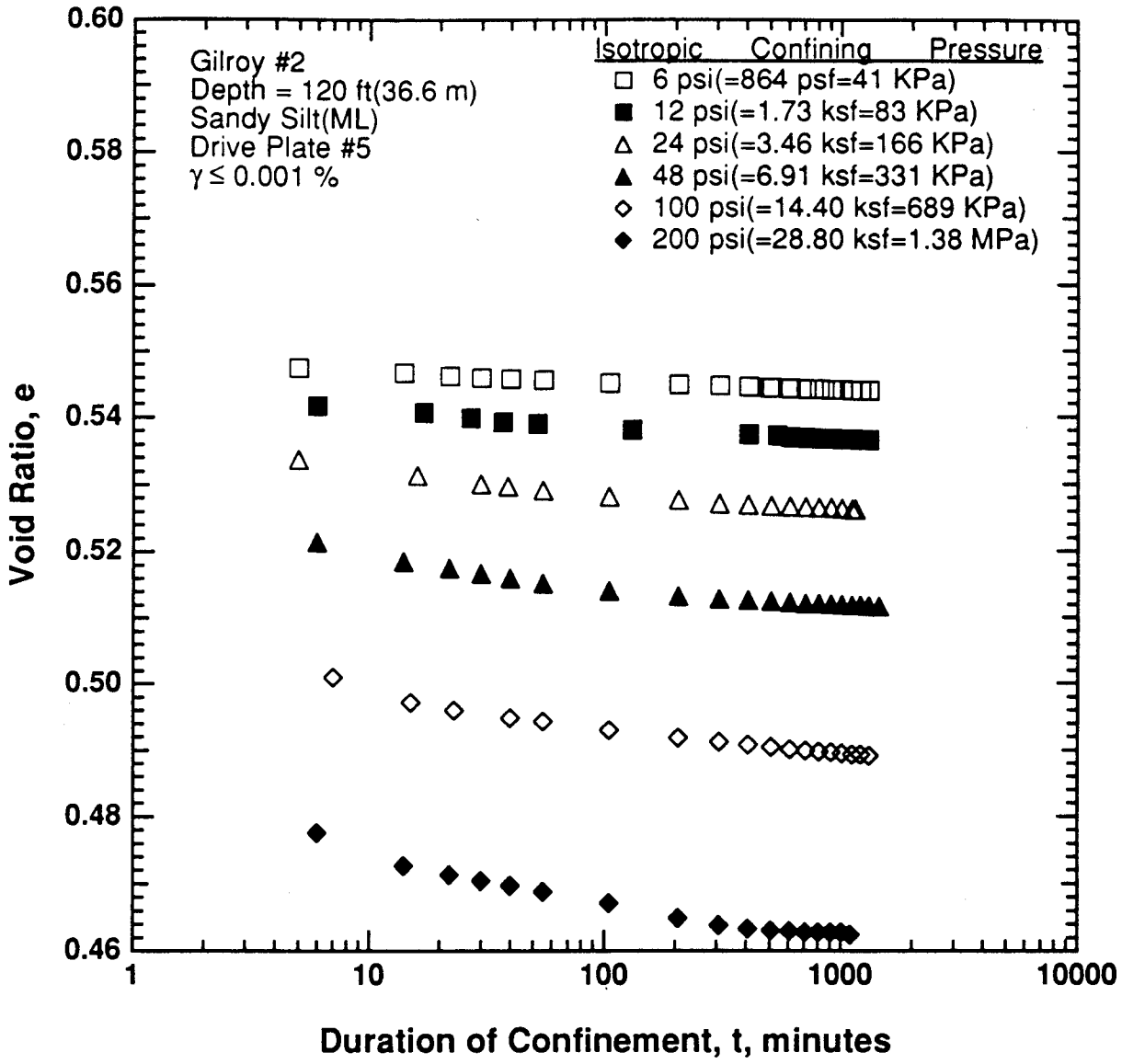

Figure 8.B.2.H-3
Variation in void ratio with magnitude and duration of isotropic confining pressure from resonant column tests of sample G5.

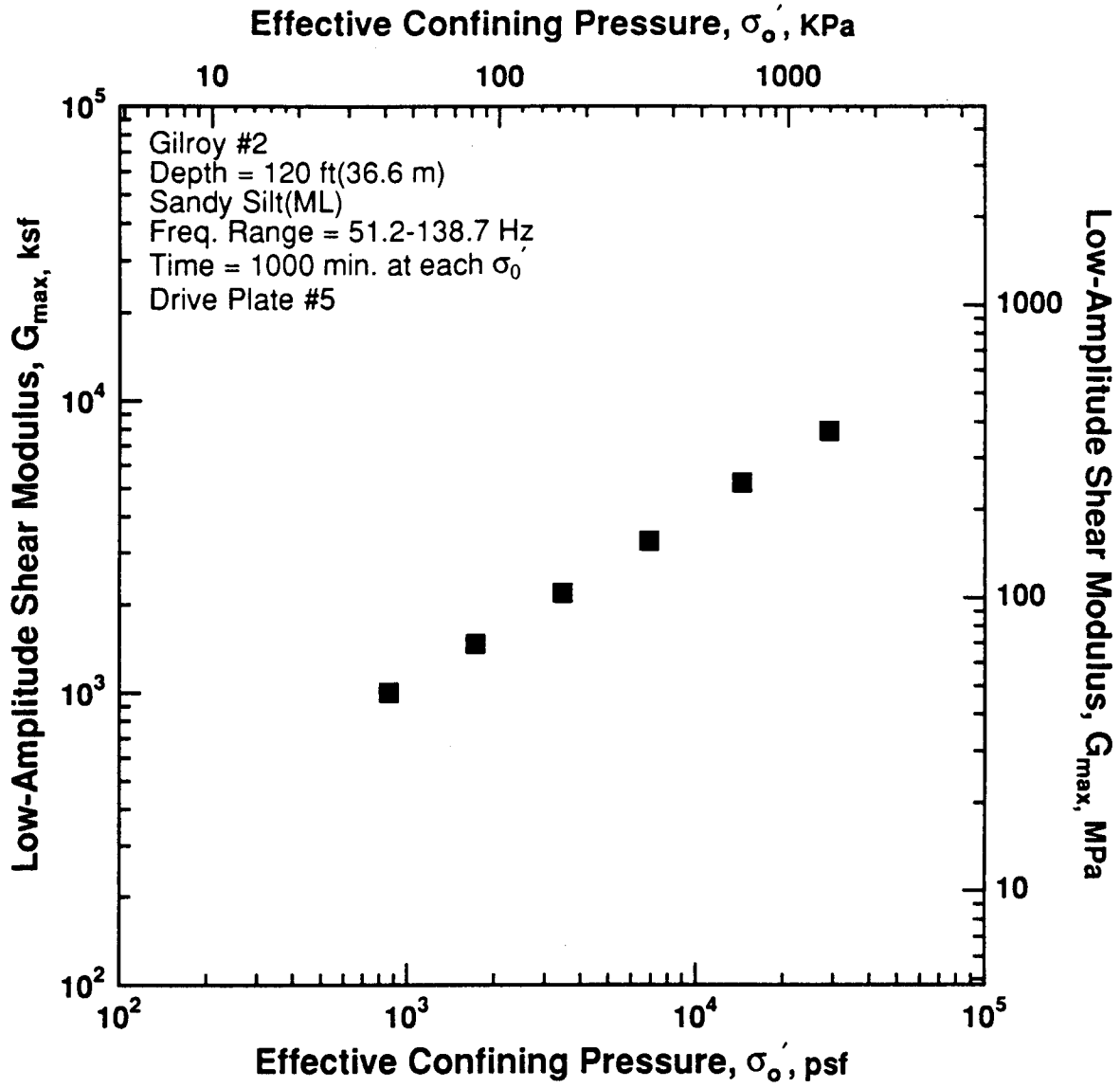

Figure 8.B.2.H-4
Variation in low-amplitude shear modulus with effective confining pressure from resonant column tests of sample G5.

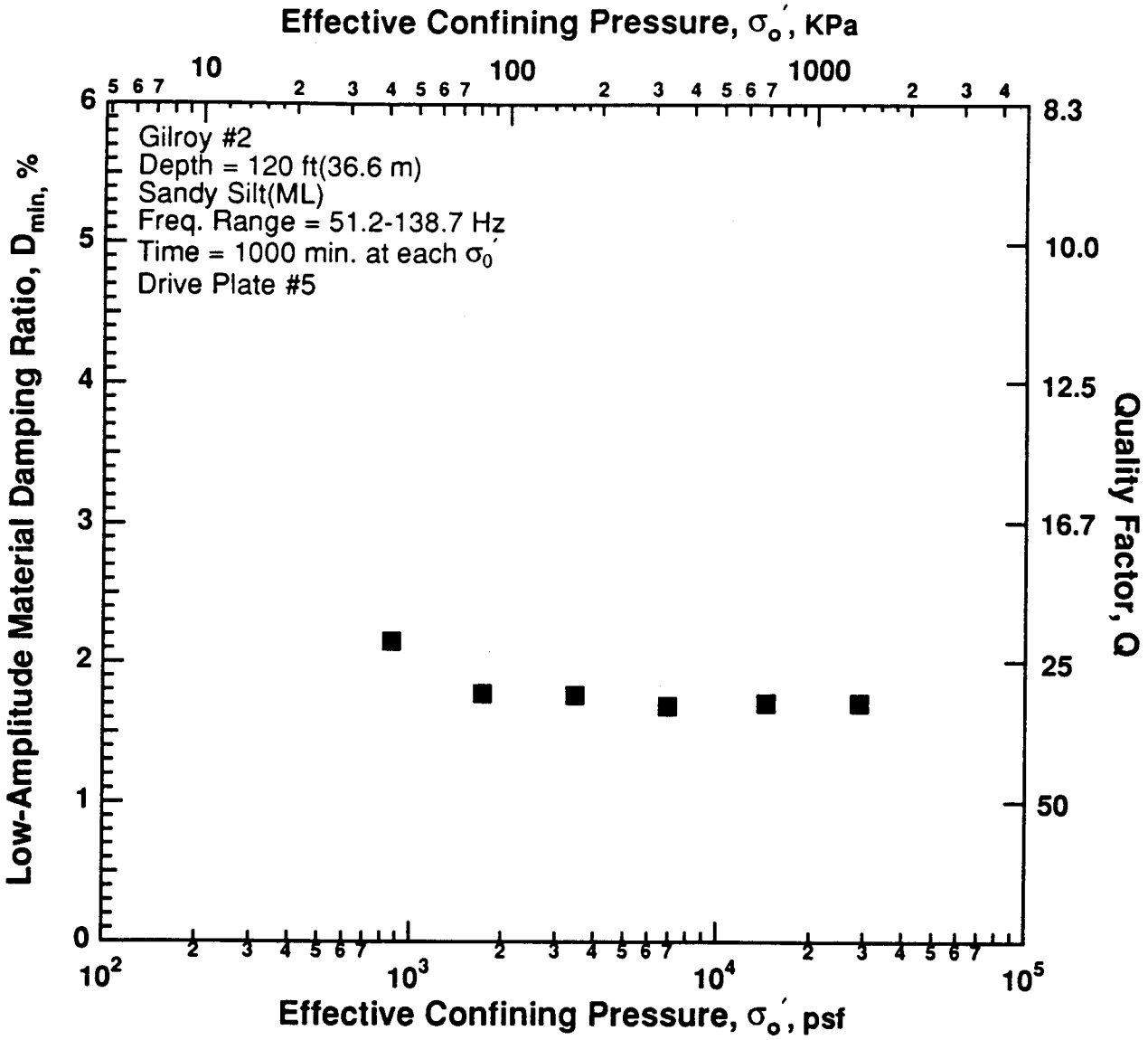

Figure 8.B.2.H-5
Variation in low-amplitude material damping ratio with effective confining pressure from resonant column tests of sample G5.

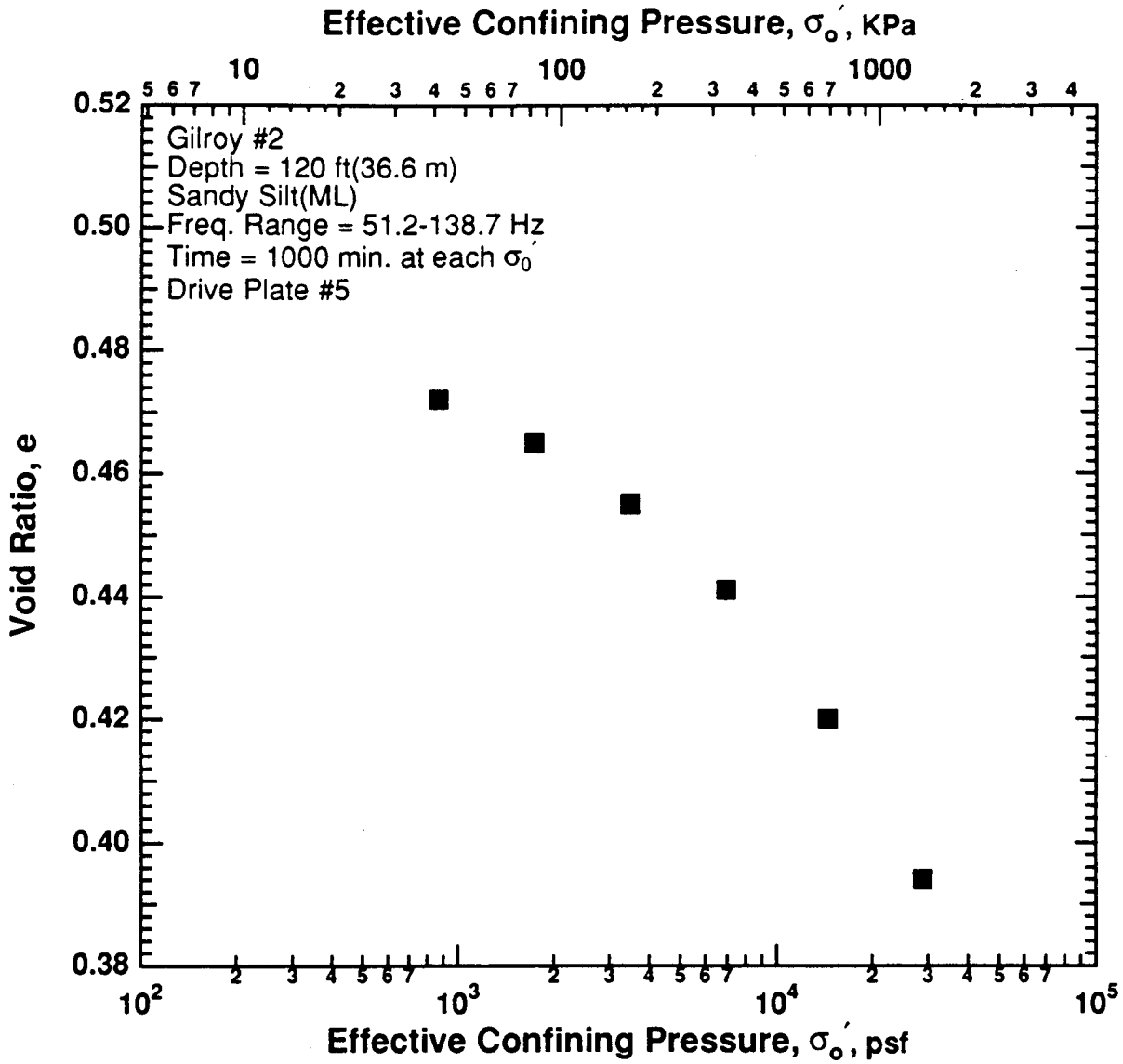

Figure 8.B.2.H-6
Variation in void ratio with effective confining pressure from resonant column tests of sample G5

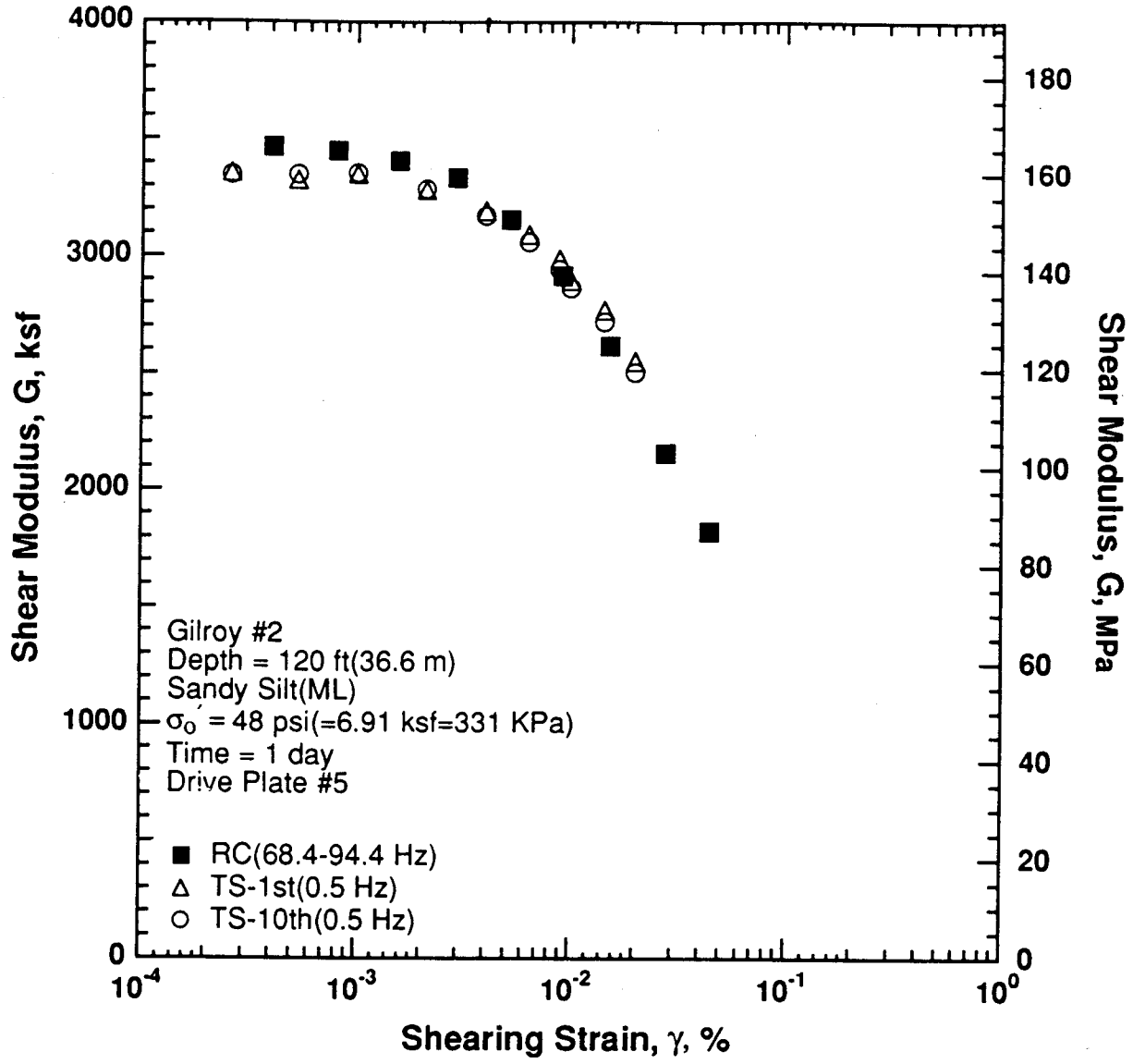

Figure 8.B.2.H-7
Variation in shear modulus with shearing strain at an effective confining pressure of 48 psi (6.91 ksf, 331 kPa) from RCTS tests of sample G5

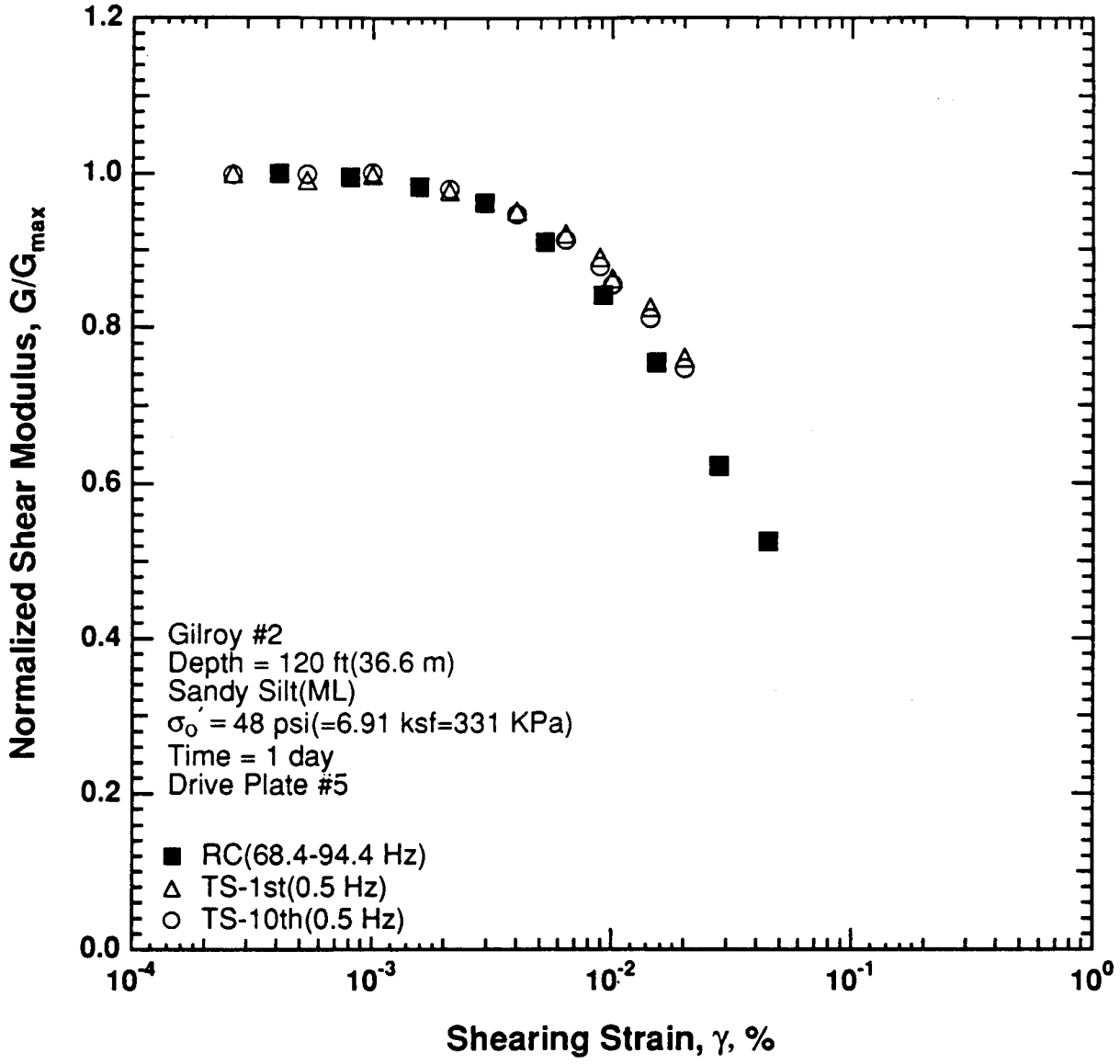

Figure 8.B.2.H-8
Variation in normalized shear modulus with shearing strain at an effective confining pressure of 48 psi (6.91 ksf, 331 kPa) from RCTS tests of sample G5

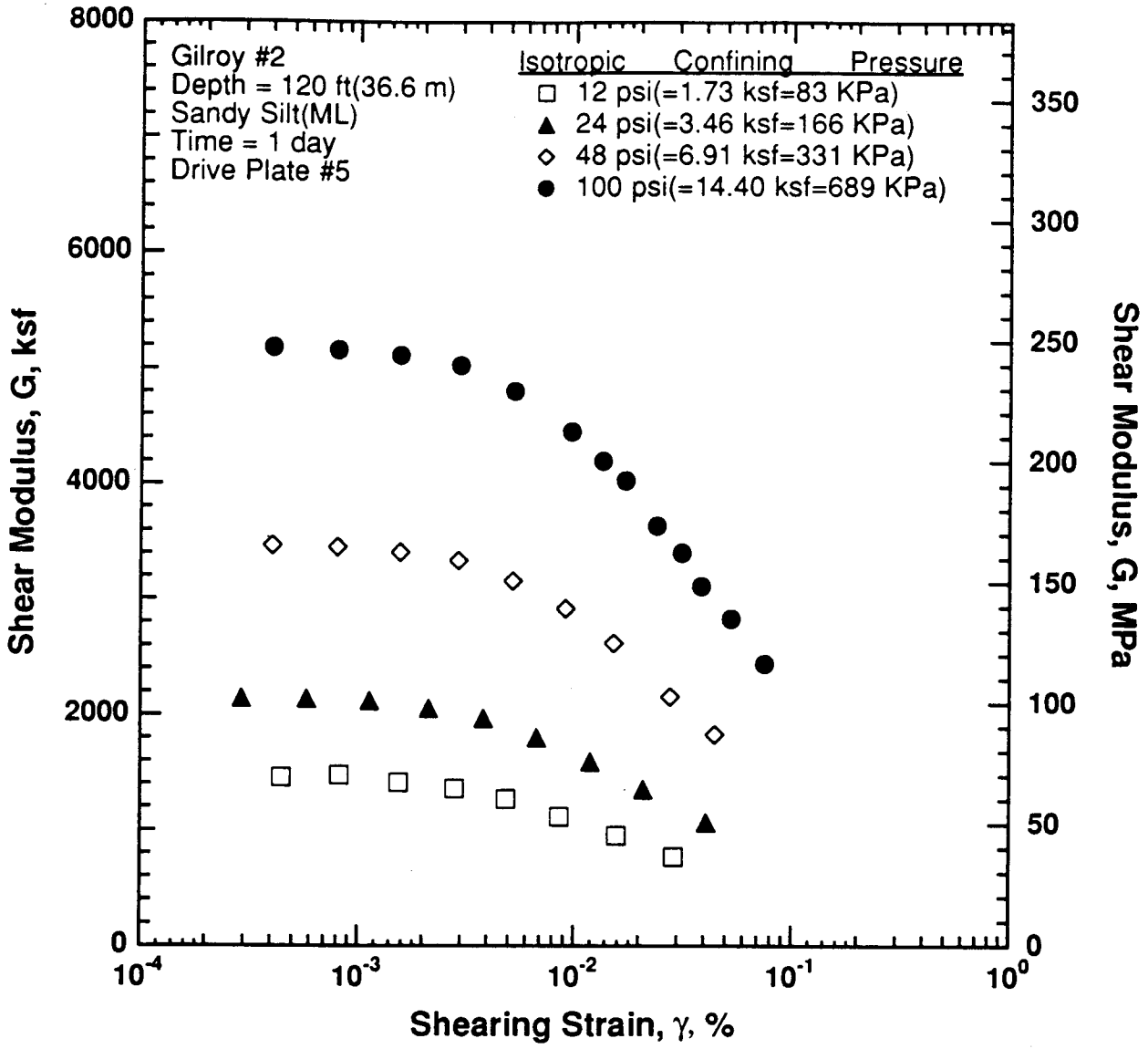

Figure 8.B.2.H-9
Variation in shear modulus with shearing strain and effective confining pressure from resonant column tests of sample G5

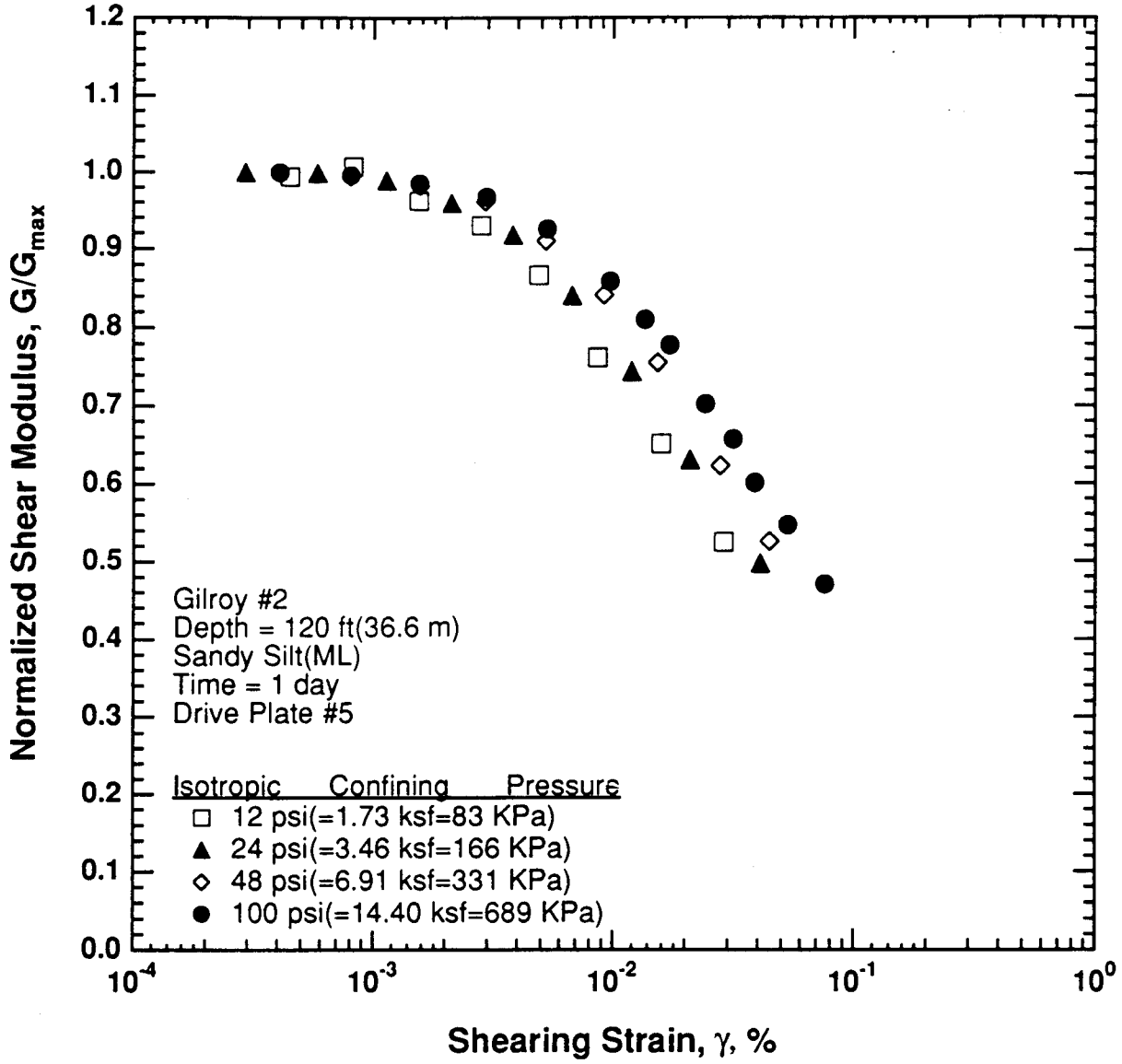

Figure 8.B.2.H-10
Comparison of the variation in normalized shear modulus with shearing strain and effective confining pressure from resonant column tests of sample G5

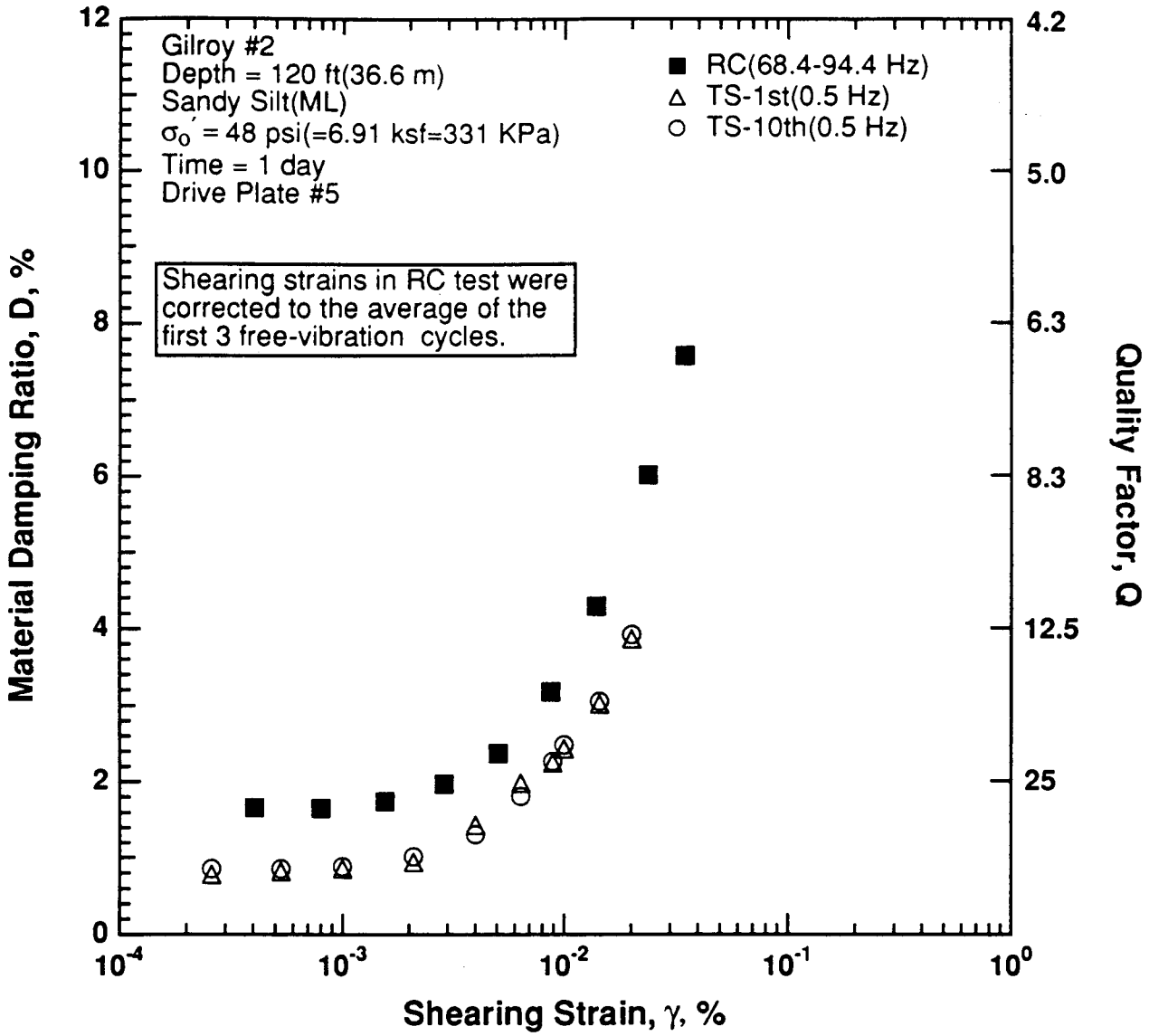

Figure 8.B.2.H-11
Variation in material damping ratio with shearing strain at an effective confining pressure of 48 psi (6.91 ksf, 331 kPa) from RCTS tests of sample G5.

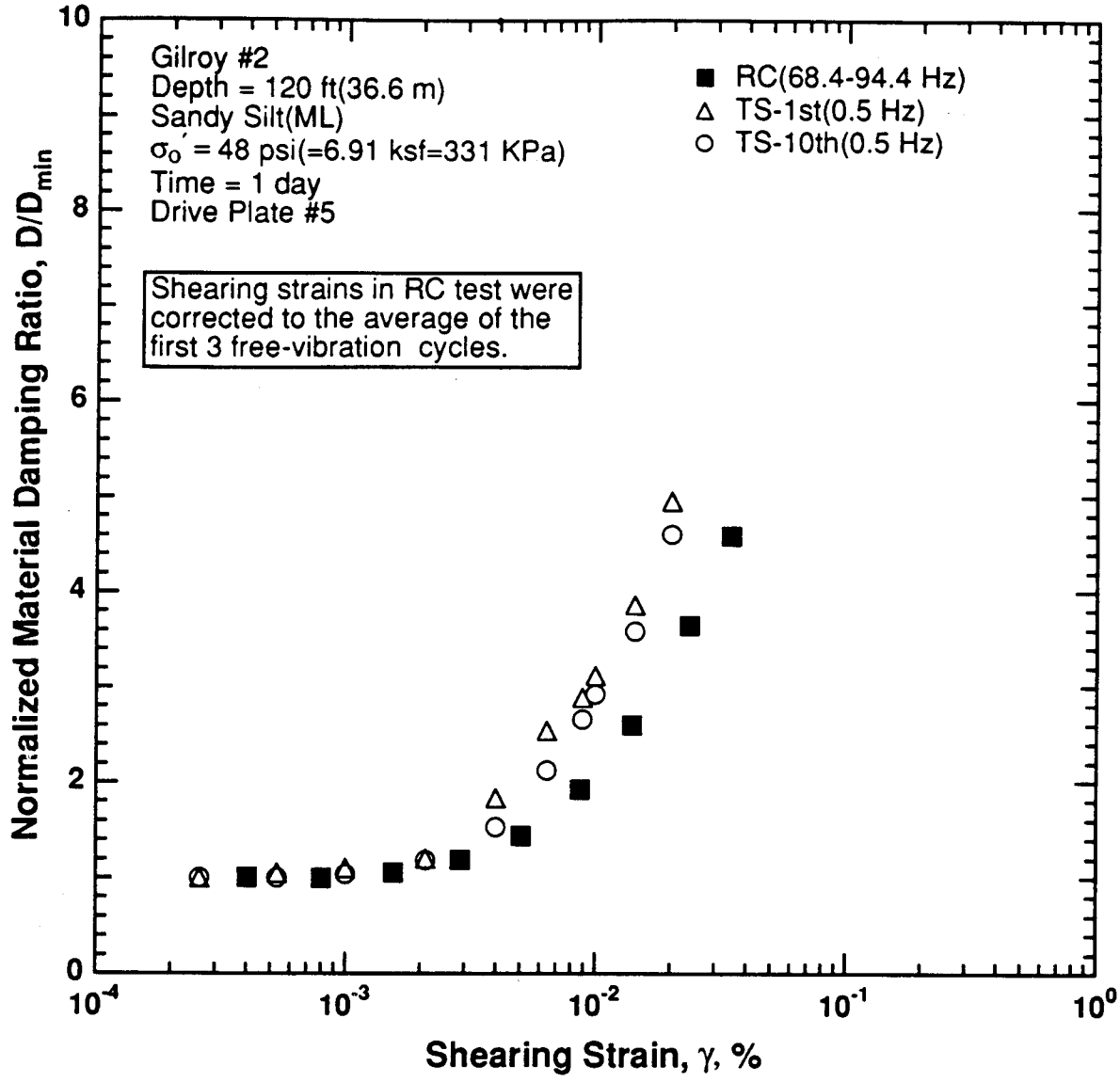

Figure 8.B.2.H-12
Variation in normalized material damping ratio with shearing strain at an effective confining pressure of 48 psi (6.91 ksf, 331 kPa) from RCTS tests of sample G5

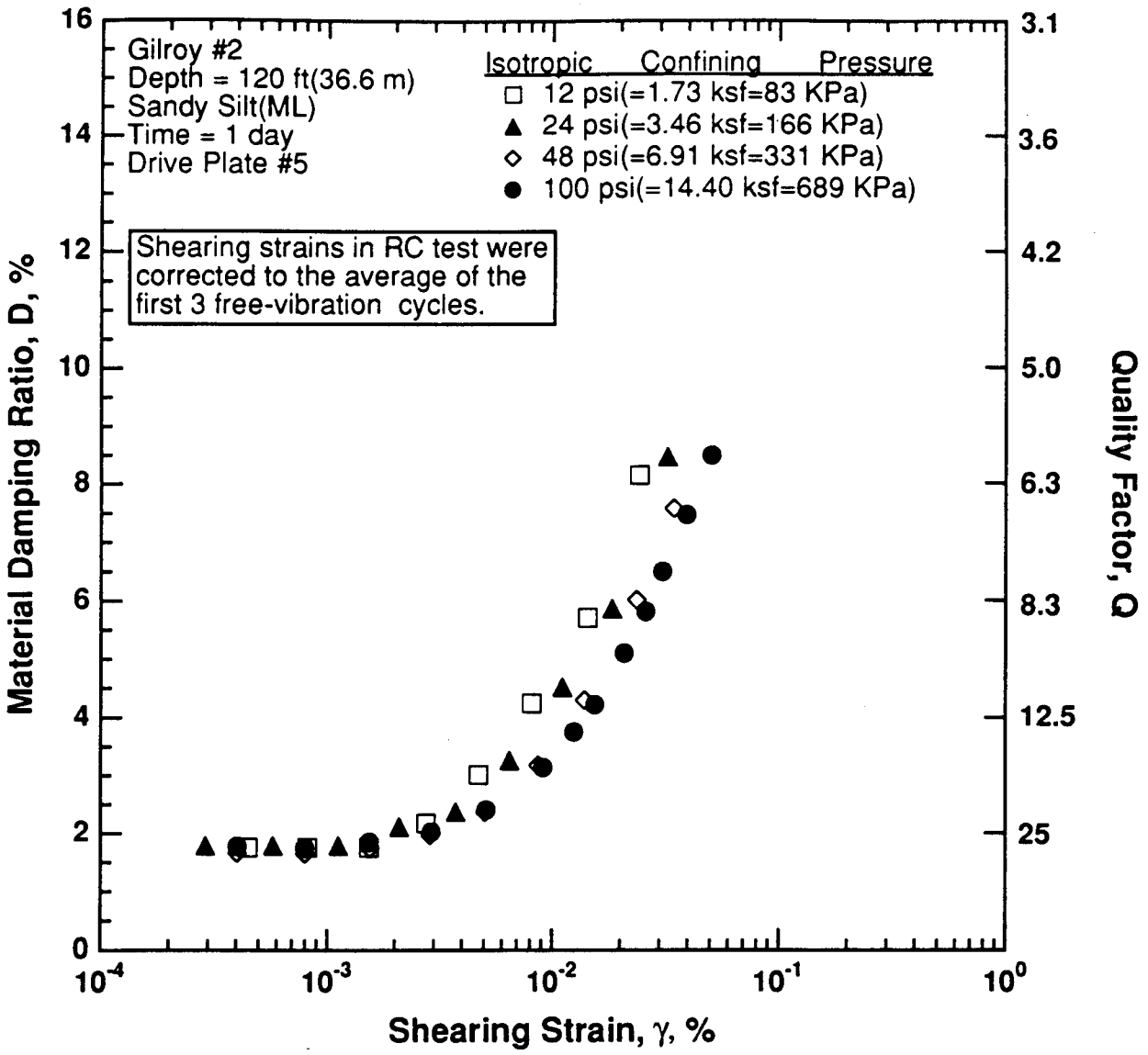

Figure 8.B.2.H-13
Variation in material damping ratio with shearing strain and effective confining pressure from resonant column tests of sample G5

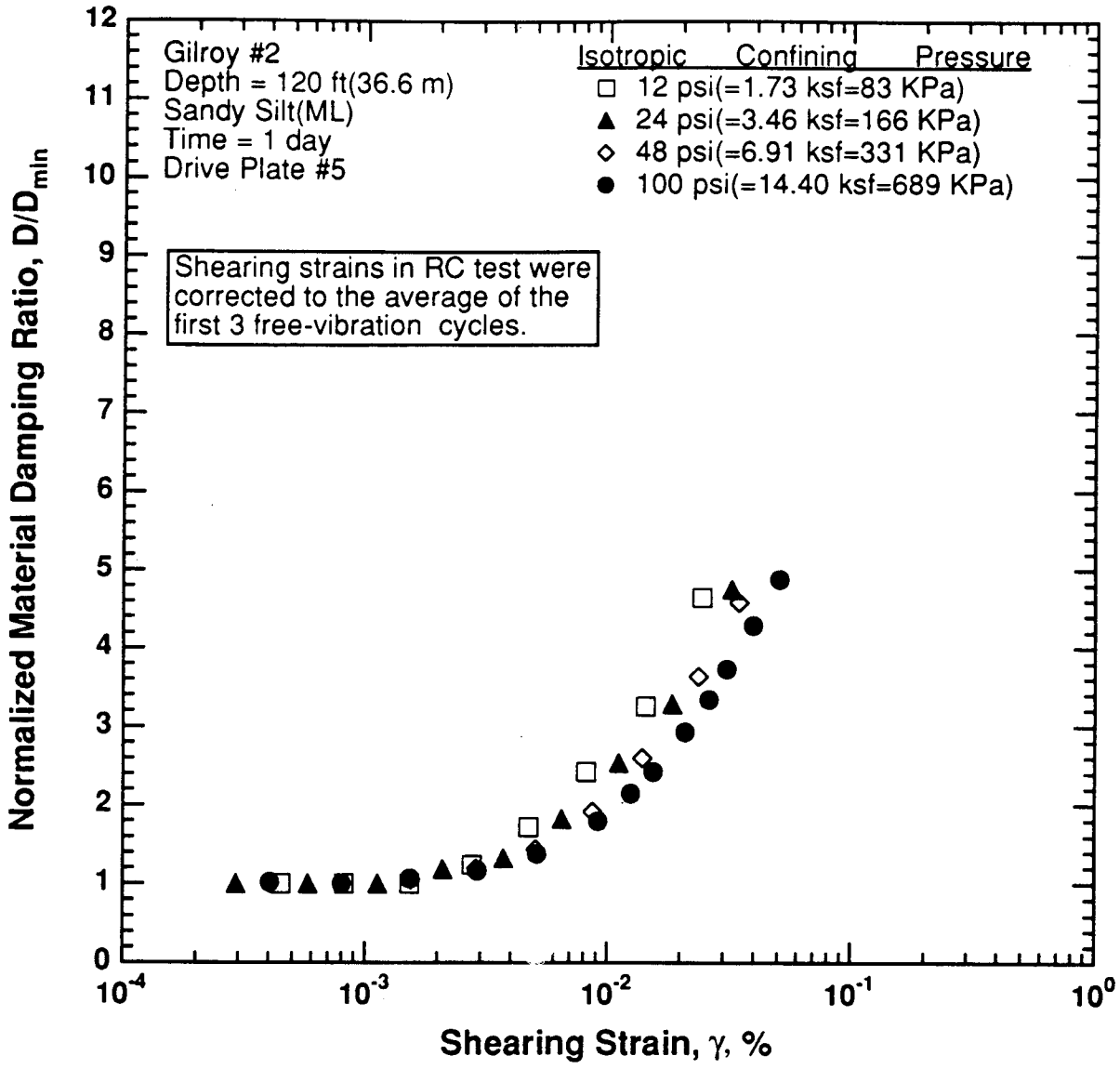

Figure 8.B.2.H-14
Comparison of the variation in normalized material damping ratio with shearing strain and effective confining pressure from resonant column tests of sample G5

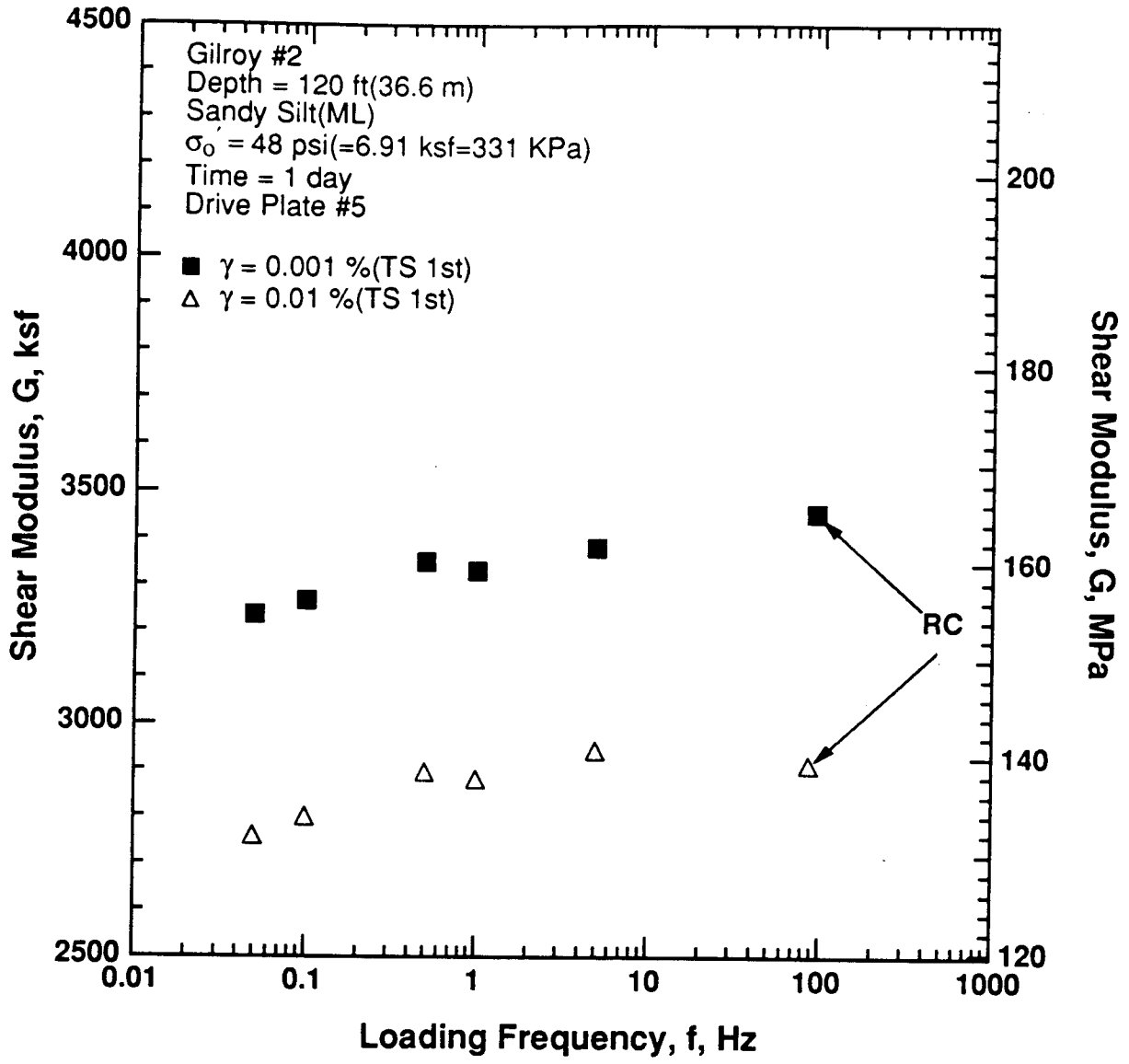

Figure 8.B.2.H-15
Variation in shear modulus with loading frequency and shearing strain at an effective confining pressure of 48 psi (6.91 ksf, 331 kPa) from RCTS tests of sample G5.

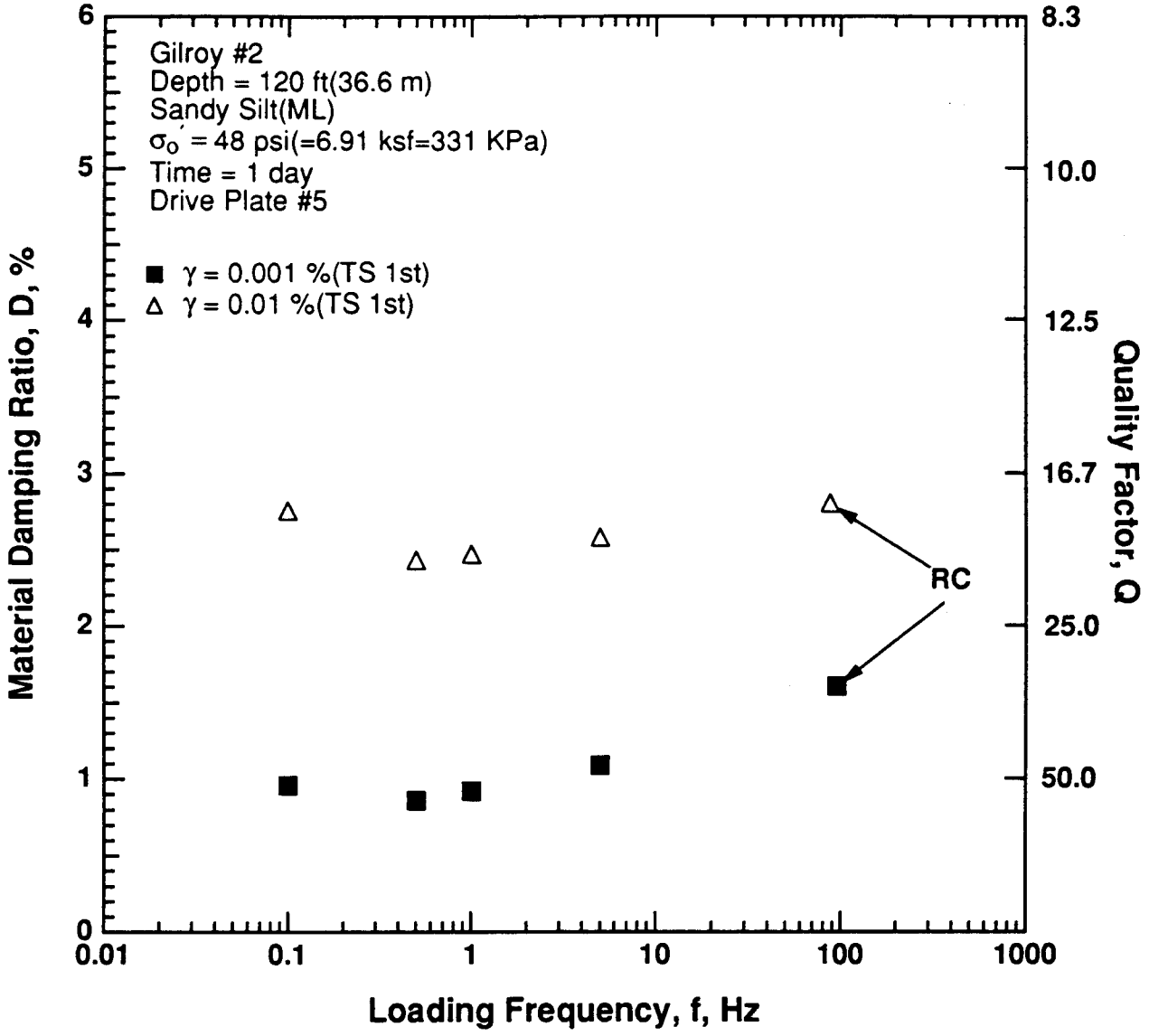

Figure 8.B.1.H-16
Variation in material damping ratio with loading frequency and shearing strain at an effective confining pressure of 48 psi (6.91 ksf, 331 kPa) from RCTS tests of sample G5.

APPENDIX 8.B.2.I
DYNAMIC TESTS OF SAMPLE G5-1, DEPTH = 120 FT (36.6 M)

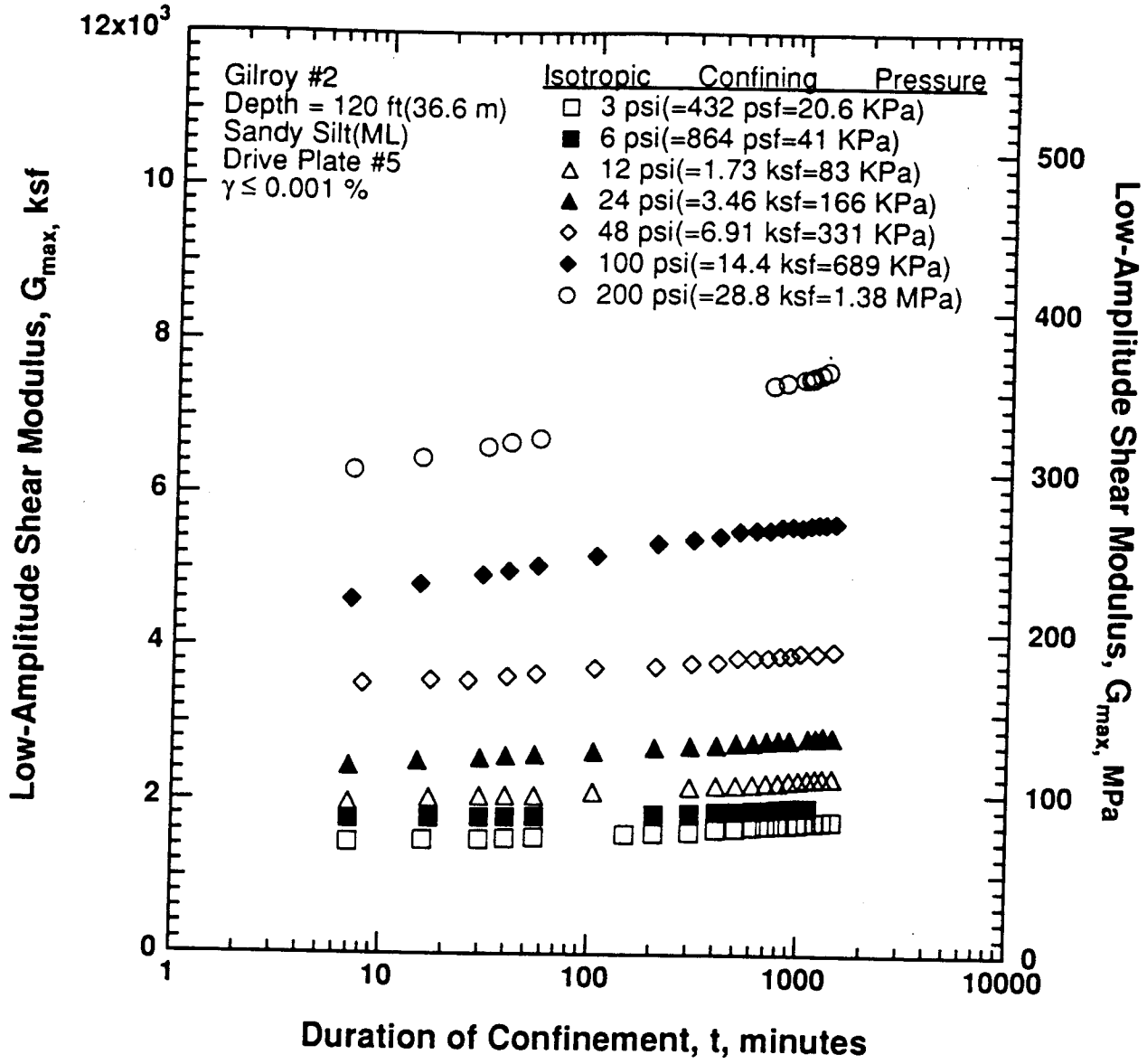

Figure 8.B.2.I-1
Variation in low-amplitude shear modulus with magnitude and duration of isotropic confining pressure from resonant column tests of sample G5-1.

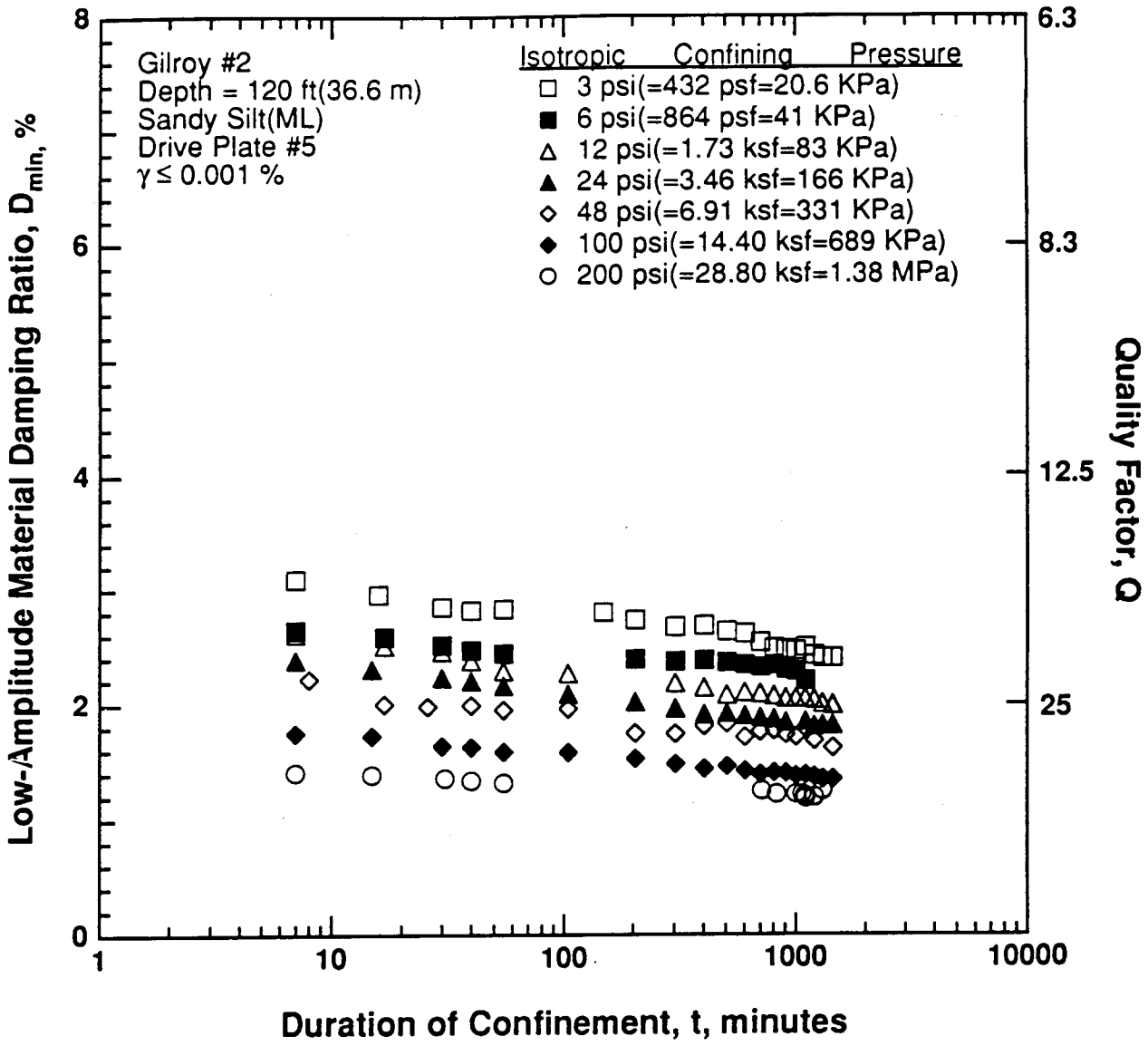

Figure 8.B.2.I-2
Variation in low-amplitude material damping ratio with magnitude and duration of isotropic confining pressure from resonant column tests of sample G5-1.

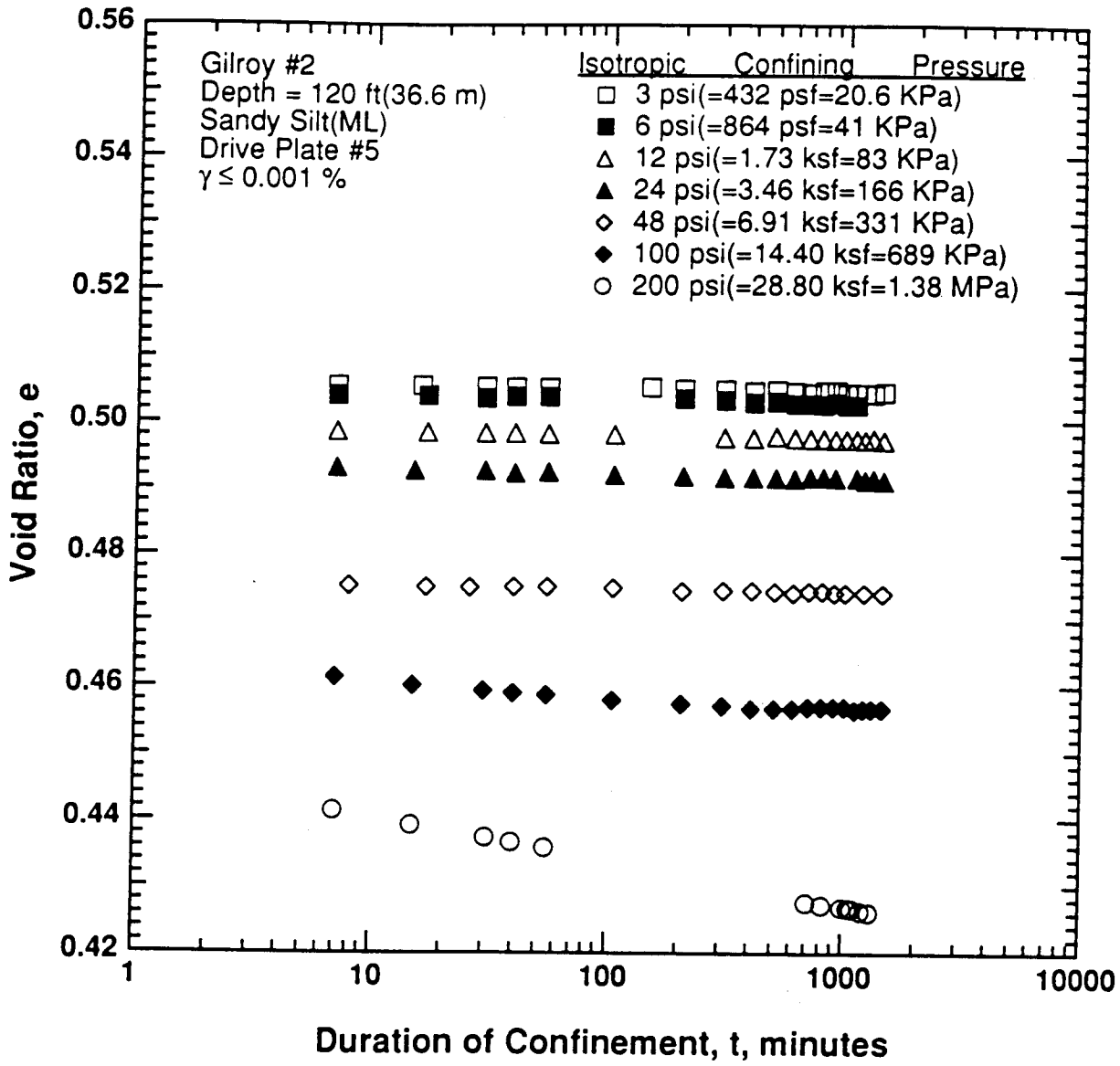

Figure 8.B.2.I-3
Variation in void ratio with magnitude and duration of isotropic confining pressure from resonant column tests of sample G5-1.

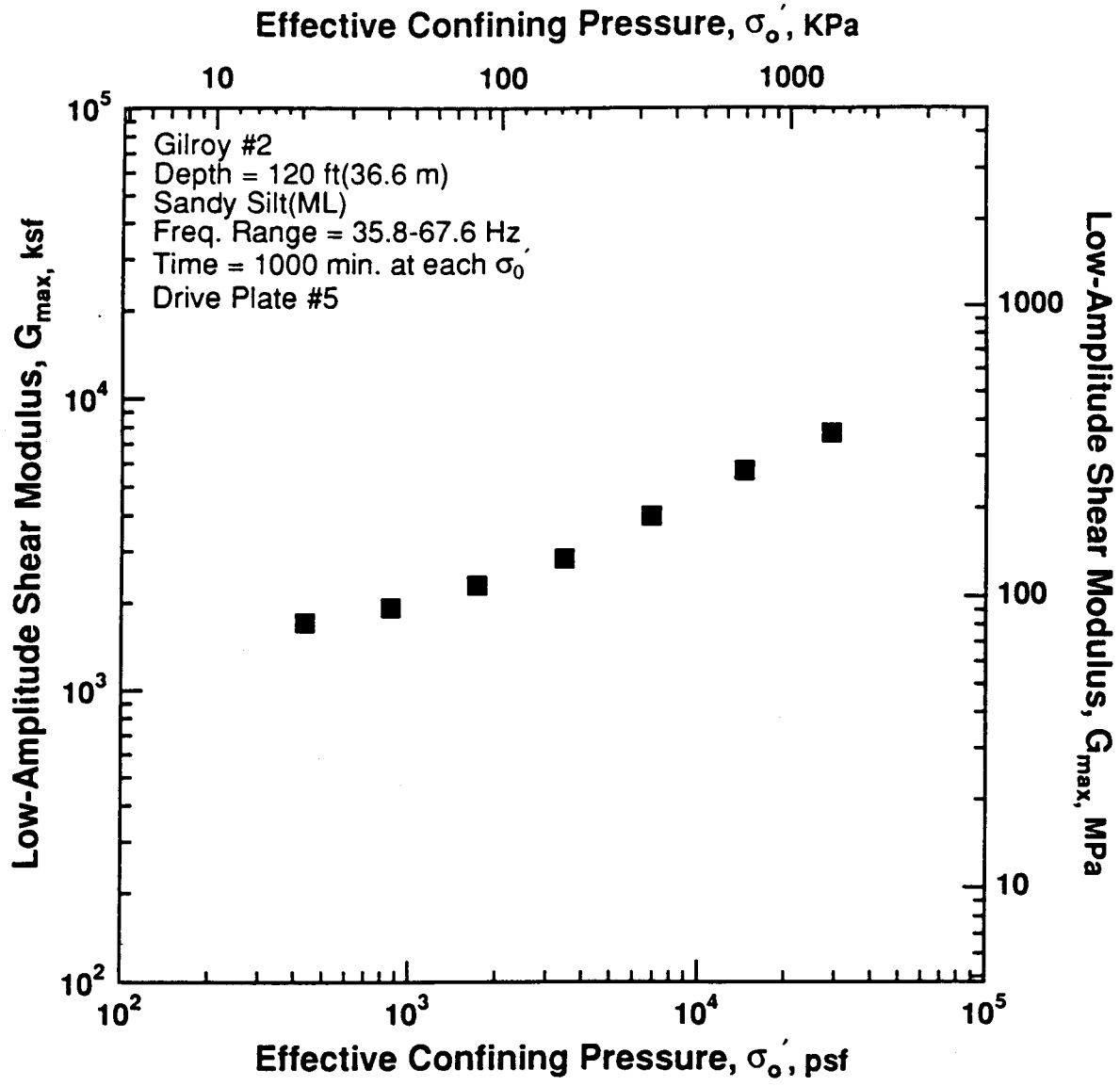

Figure 8.B.2.I-4
Variation in low-amplitude shear modulus with effective confining pressure from resonant column tests of sample G5-1.

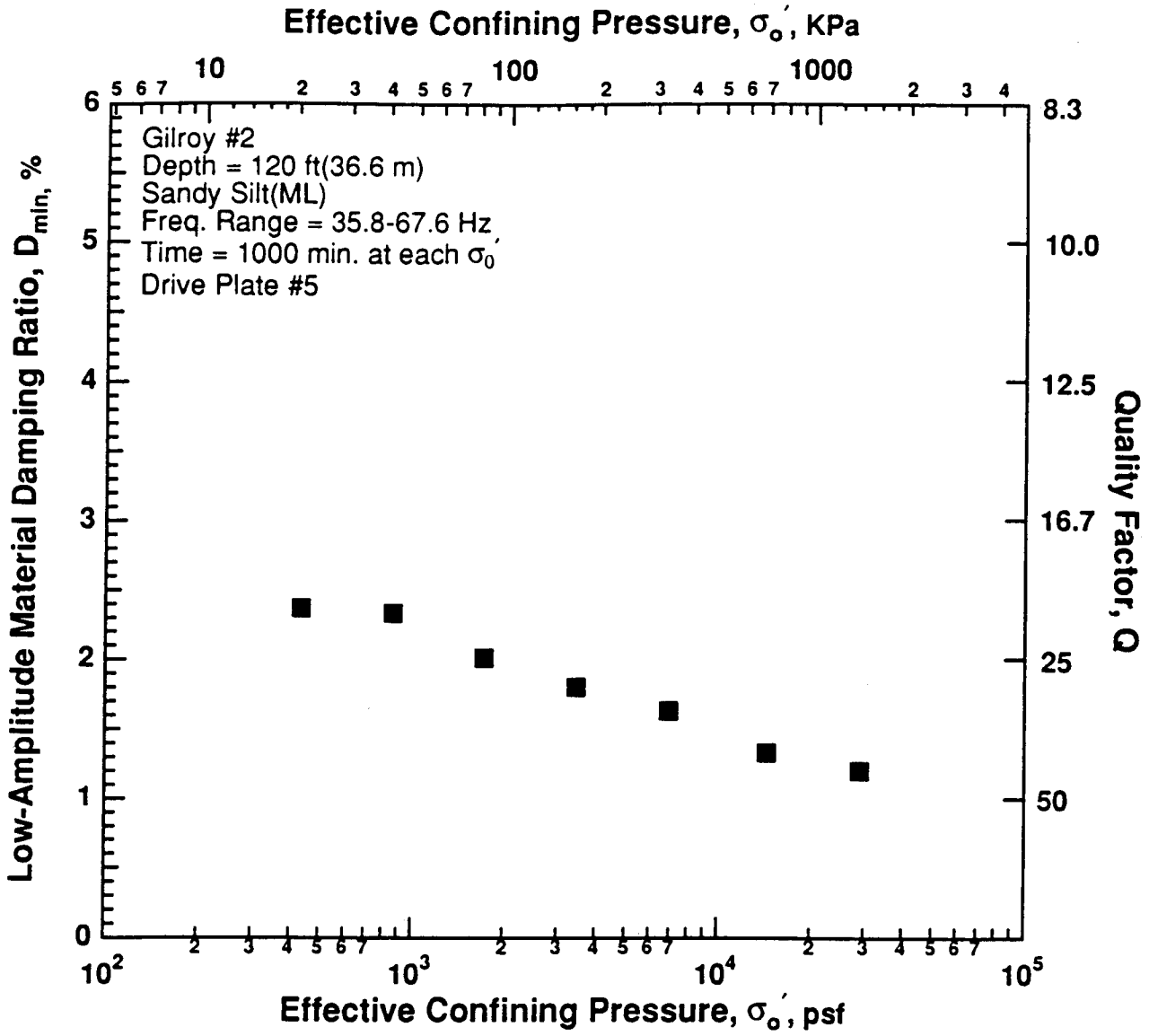

Figure 8.B.2.I-5
Variation in low-amplitude material damping ratio with effective confining pressure from resonant column tests of sample G5-1.

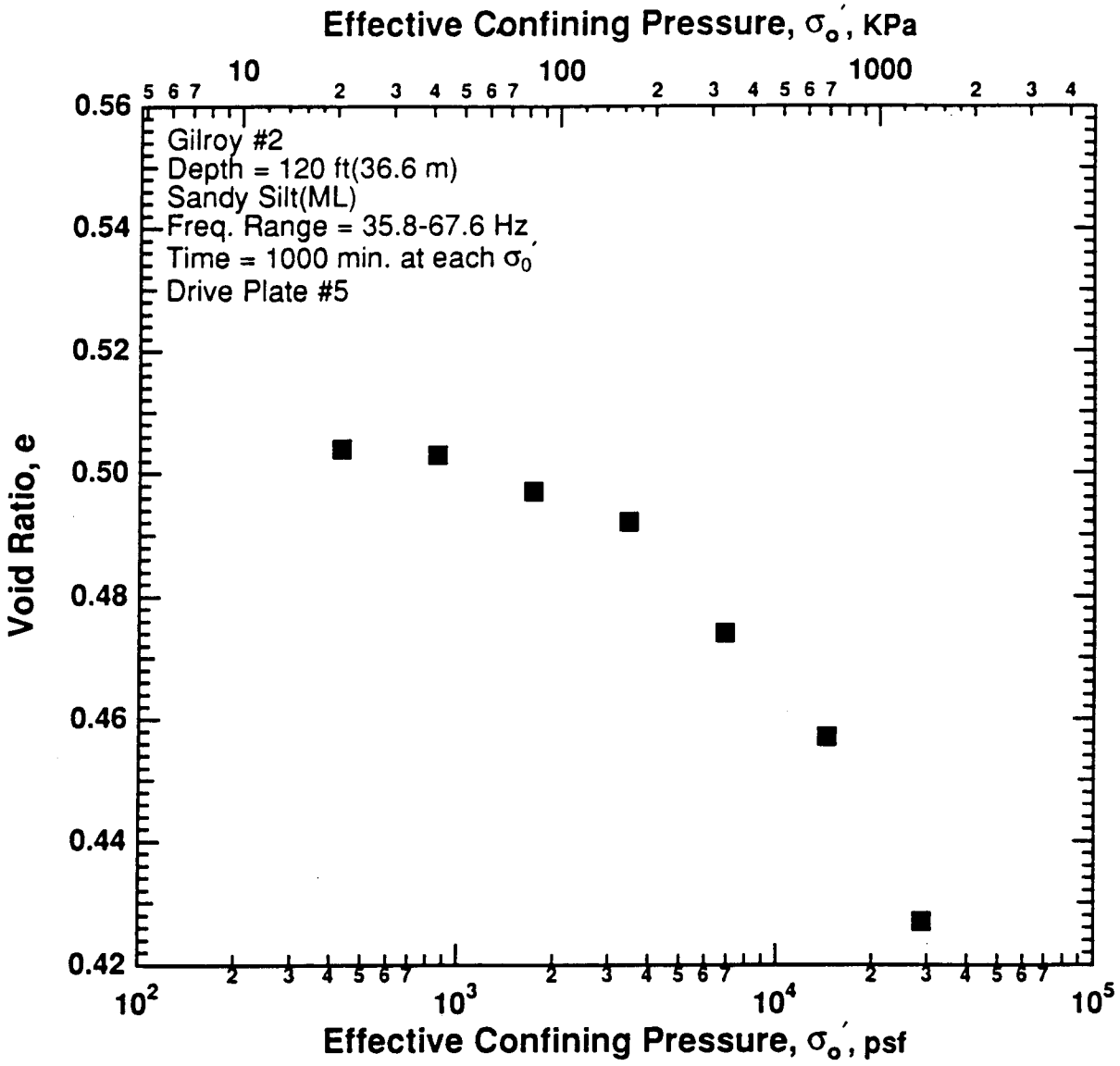

Figure 8.B.2.I-6
Variation in void ratio with effective confining pressure from resonant column tests of sample G5-1.

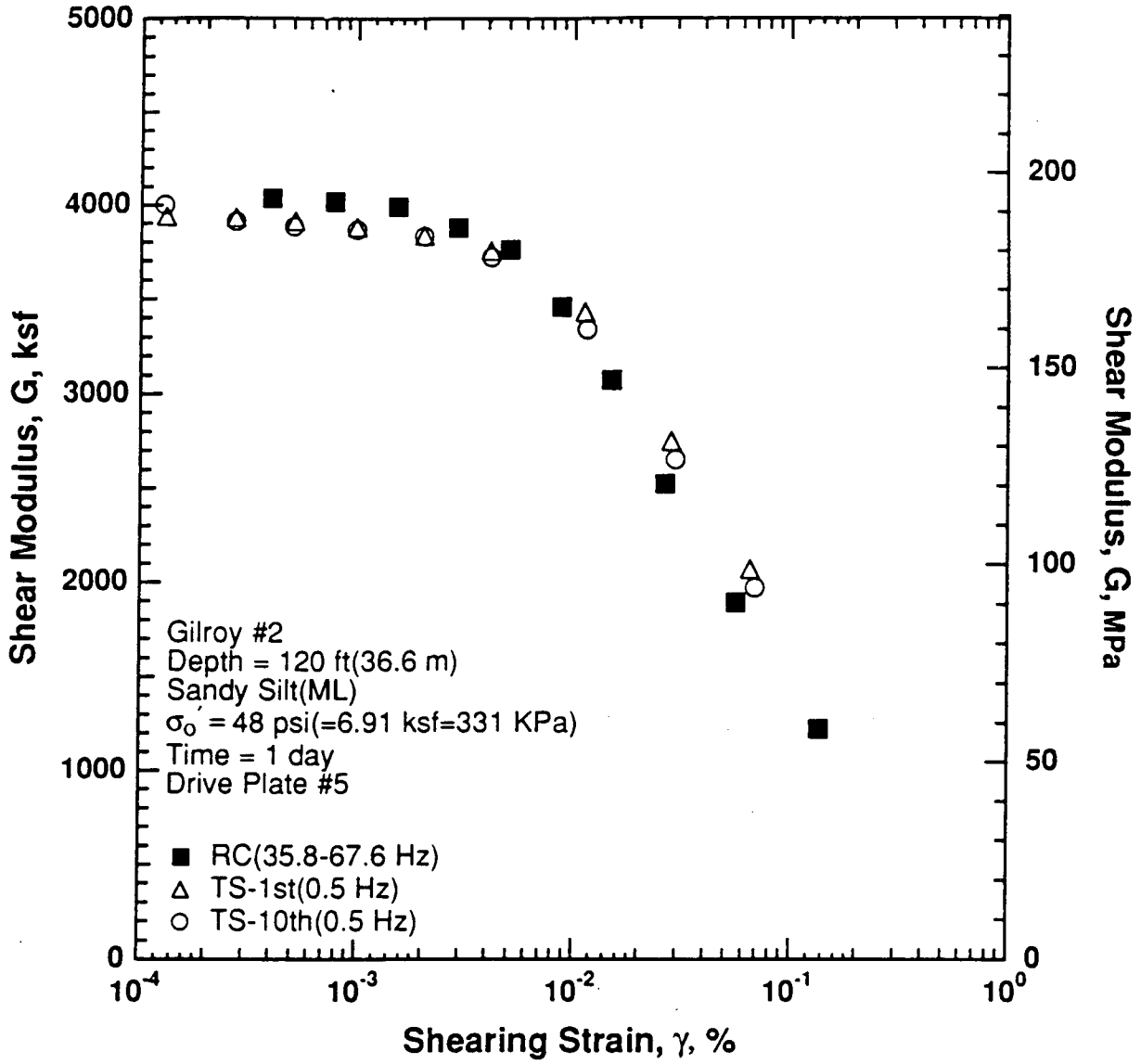

Figure 8.B.2.I-7
Variation in shear modulus with shearing strain at an effective confining pressure of 48 psi (6.91 ksf, 331 kPa) from RCTS tests of sample G5-1.

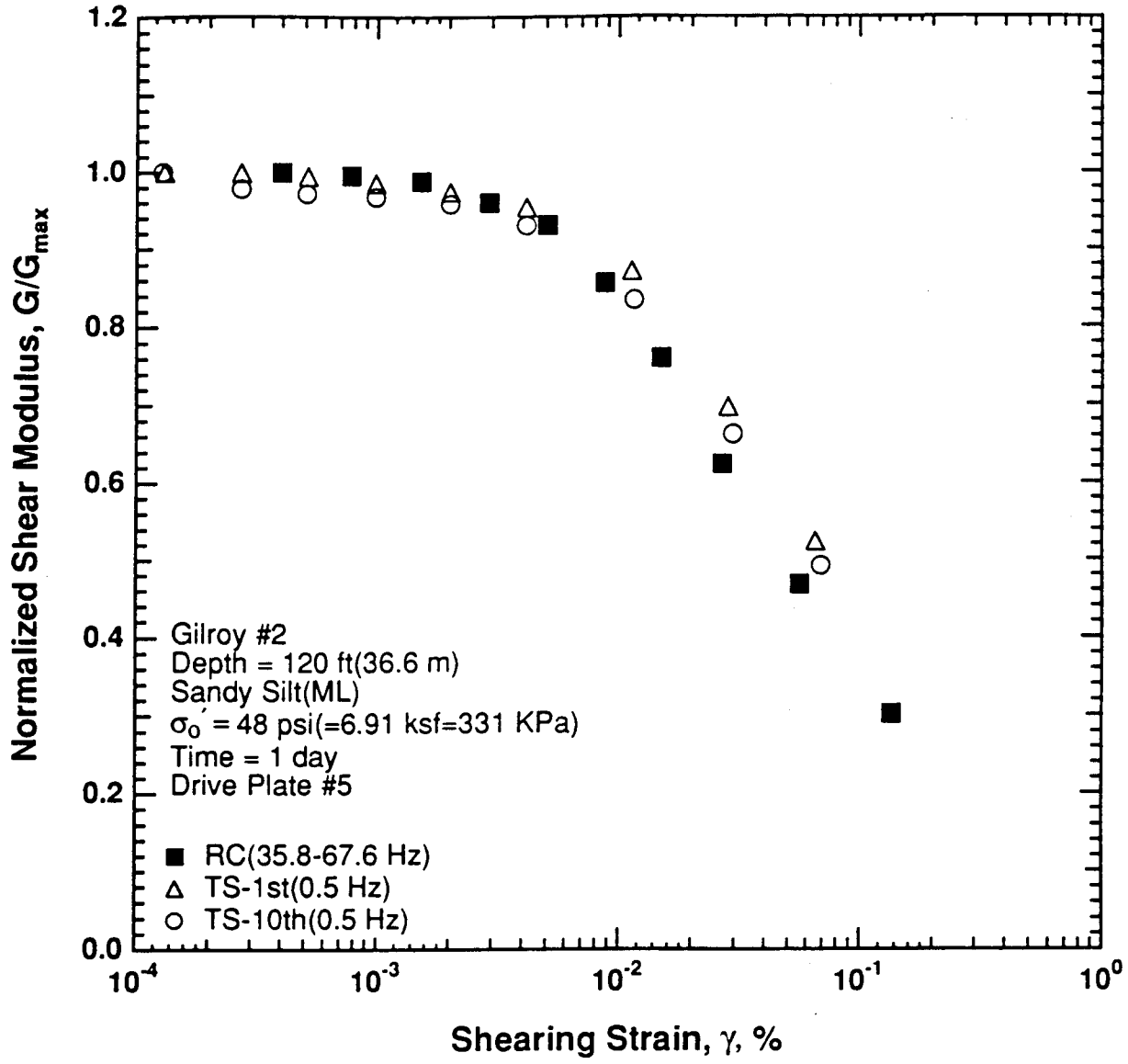

Figure 8.B.2.I-8
Variation in normalized shear modulus with shearing strain at an effective confining pressure of 48 psi (6.91 ksf, 331 kPa) from RCTS tests of sample G5-1.

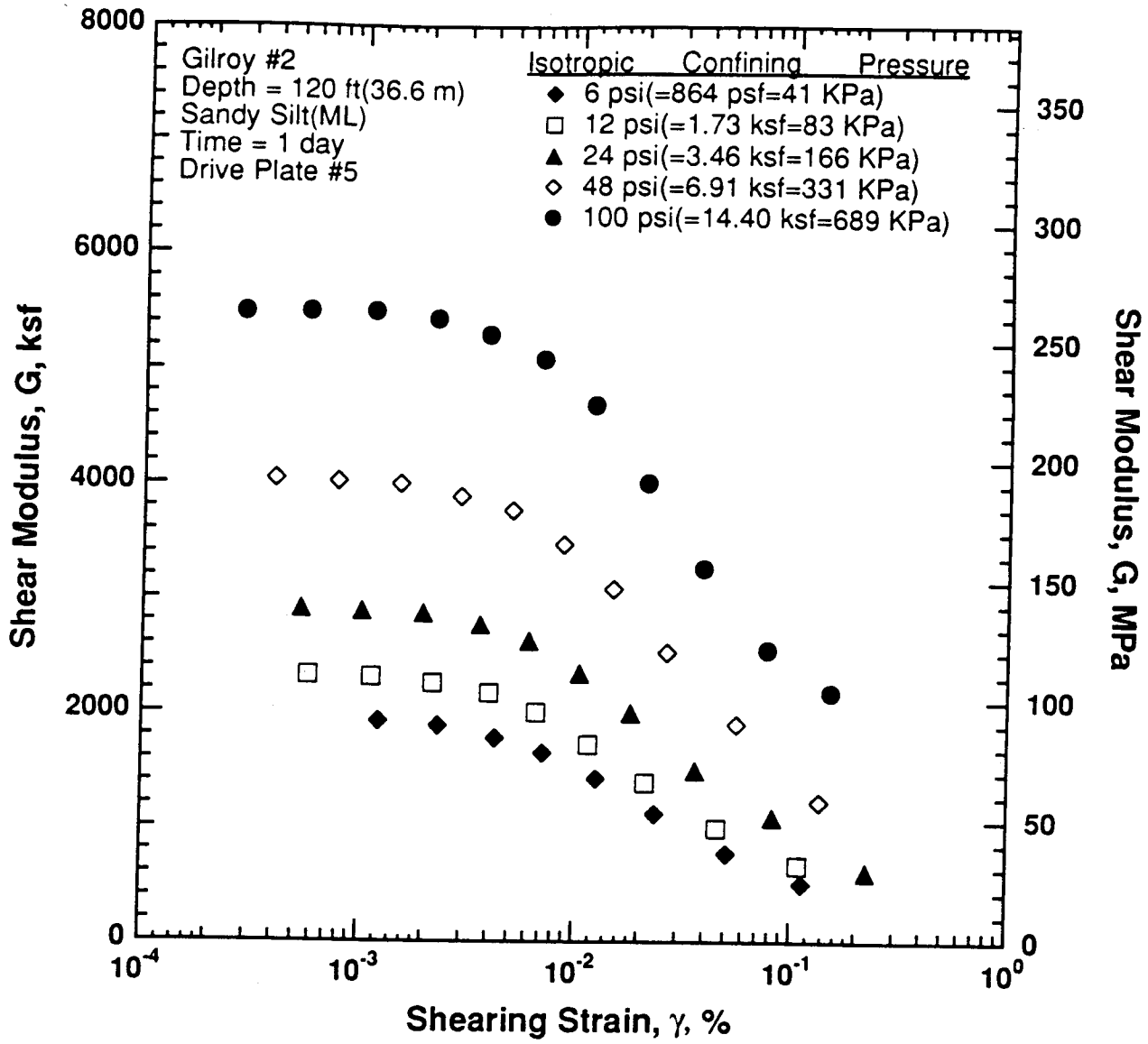

Figure 8.B.2.I-9
Variation in shear modulus with shearing strain and effective confining pressure from resonant column tests of sample G5-1.

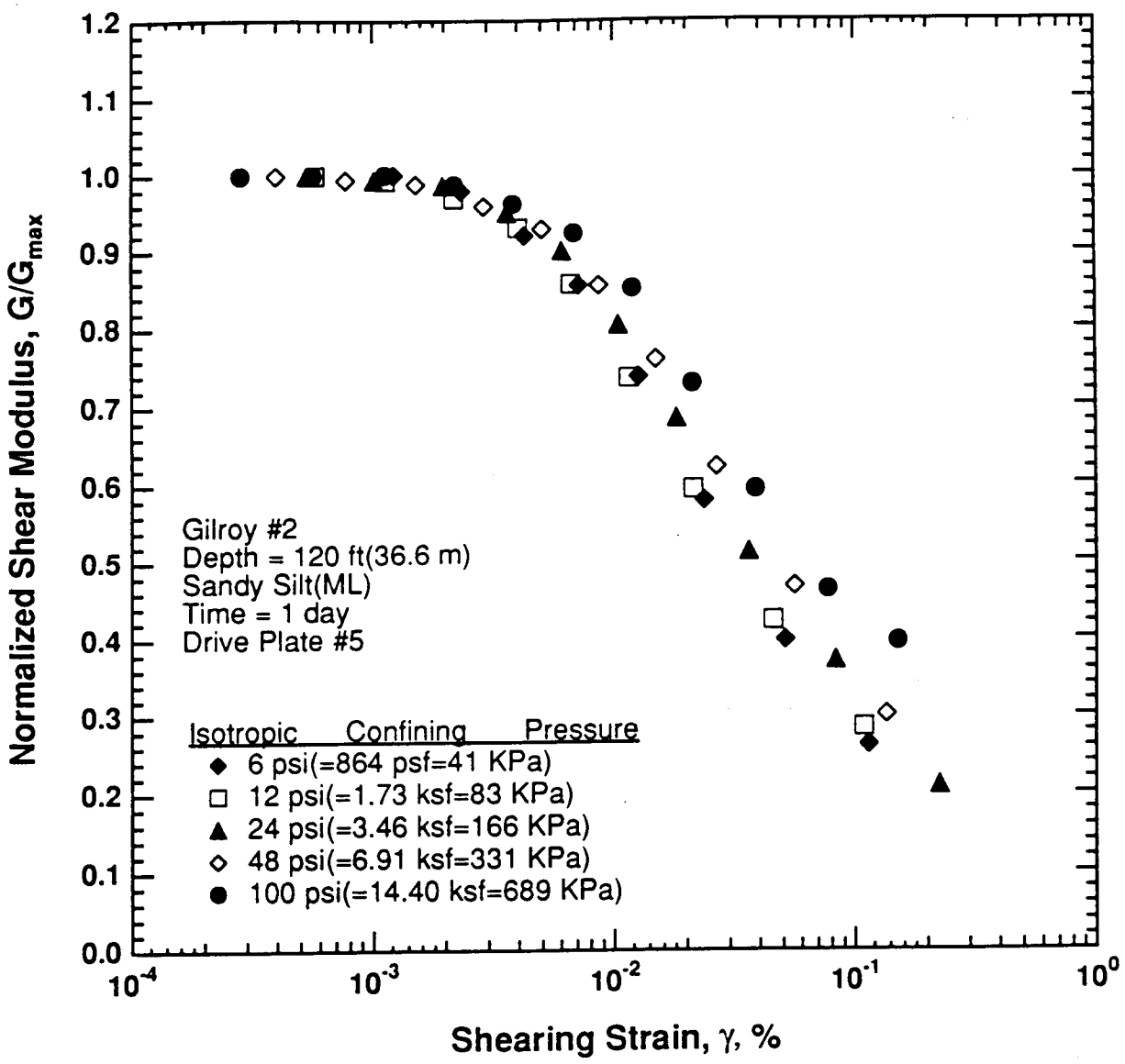

Figure 8.B.2.I-10
Comparison of the variation in normalized shear modulus with shearing strain and effective confining pressure from resonant column tests of sample G5-1.

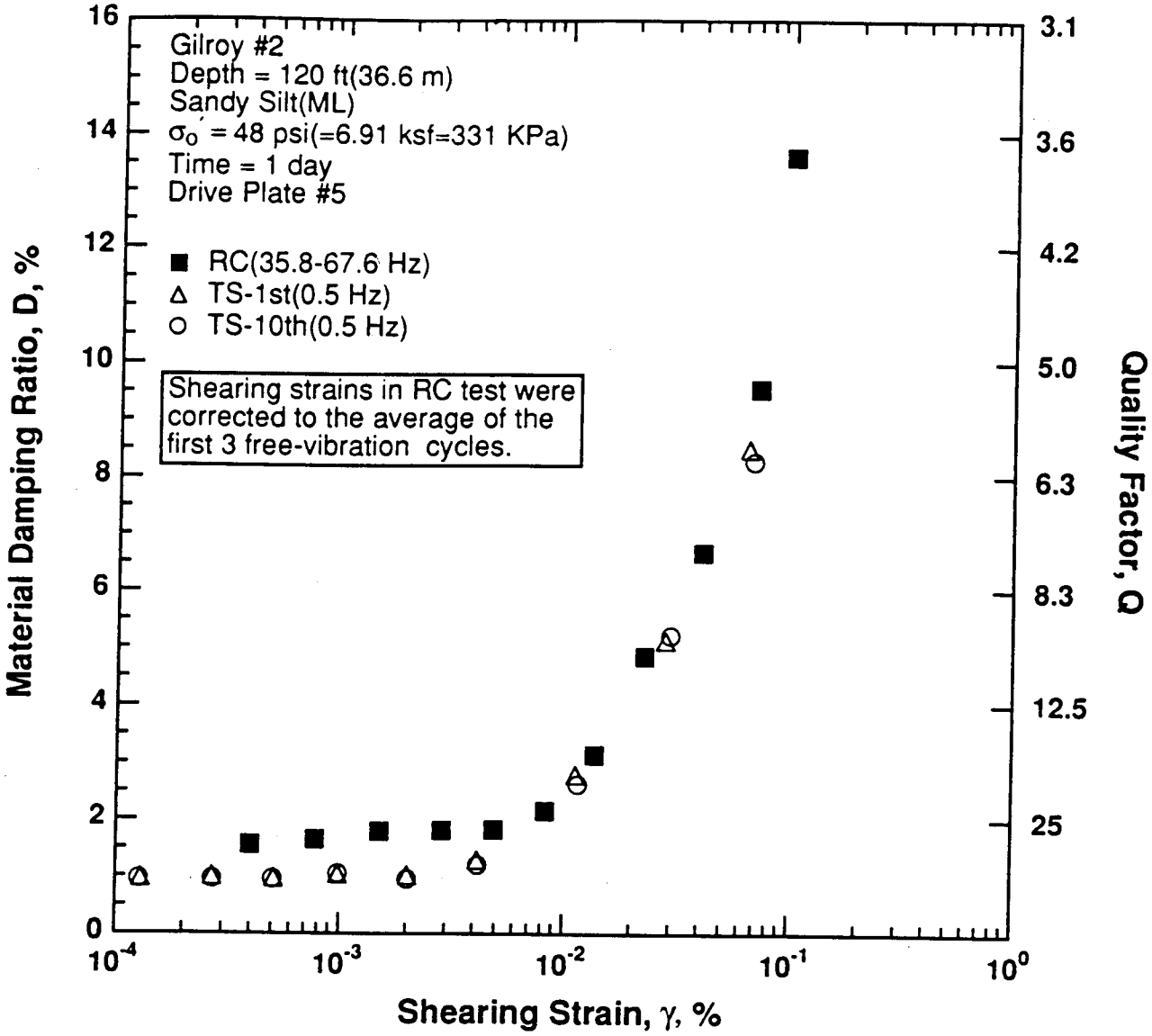

Figure 8.B.2.I-11
Variation in material damping ratio with shearing strain at an effective confining pressure of 48 psi (6.91 ksf, 331 kPa) from RCTS tests of sample G5-1.

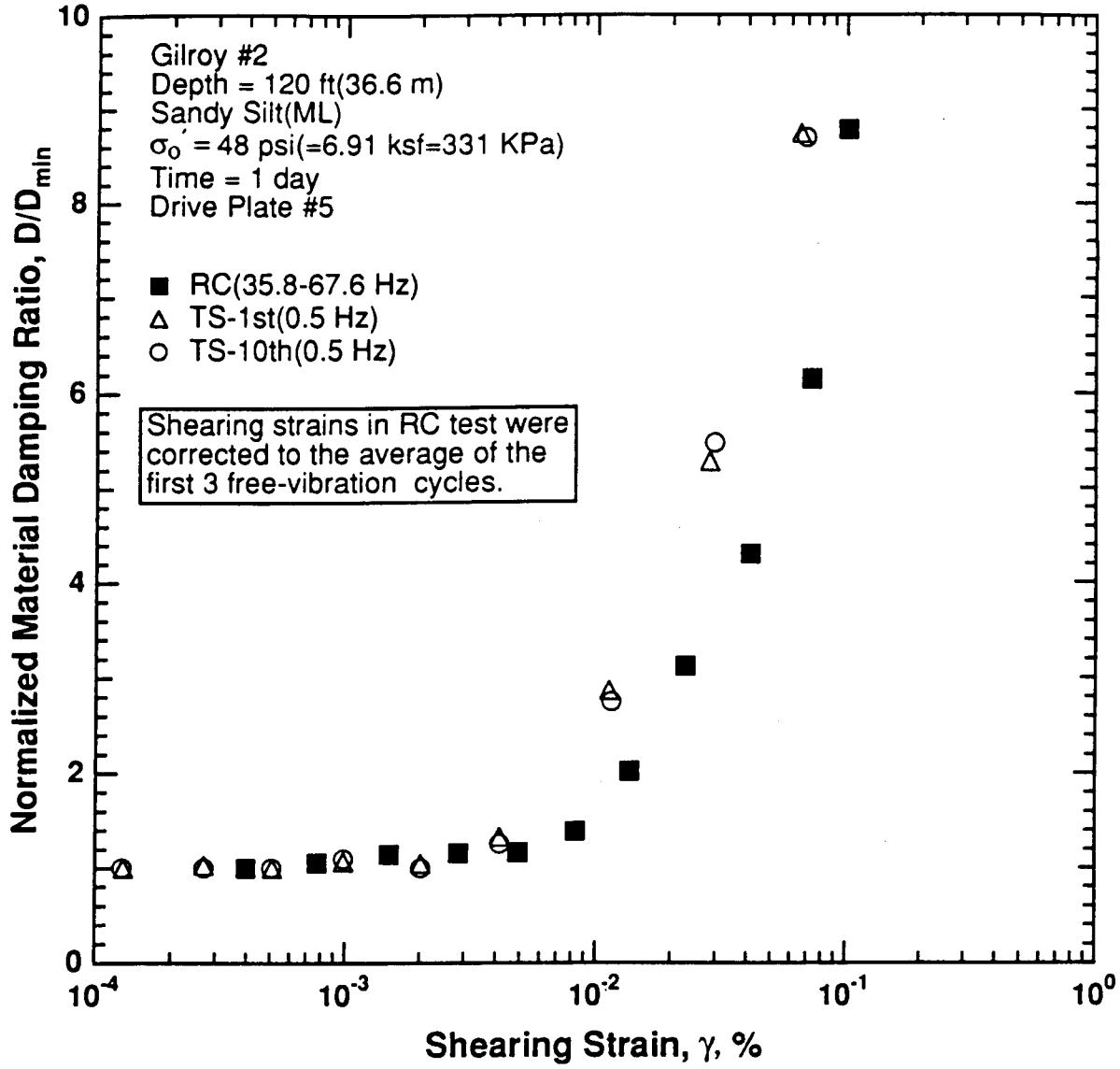

Figure 8.B.2.I-12
Variation in normalized material damping ratio with shearing strain at an effective confining pressure of 48 psi (6.91 ksf, 331 kPa) from RCTS tests of sample G5-1.

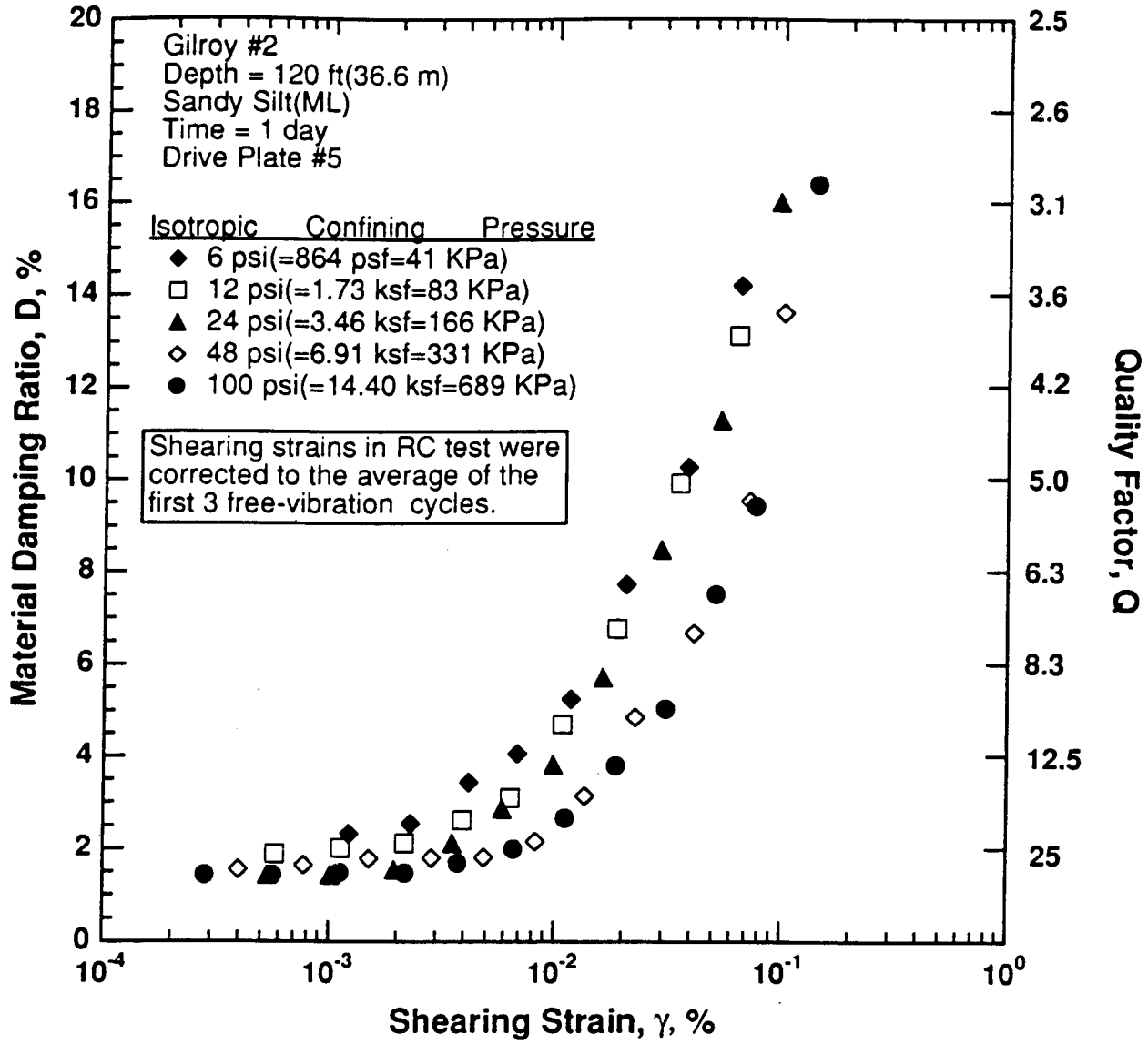

Figure 8.B.2.I-13
Variation in material damping ratio with shearing strain and effective confining pressure from resonant column tests of sample G5-1.

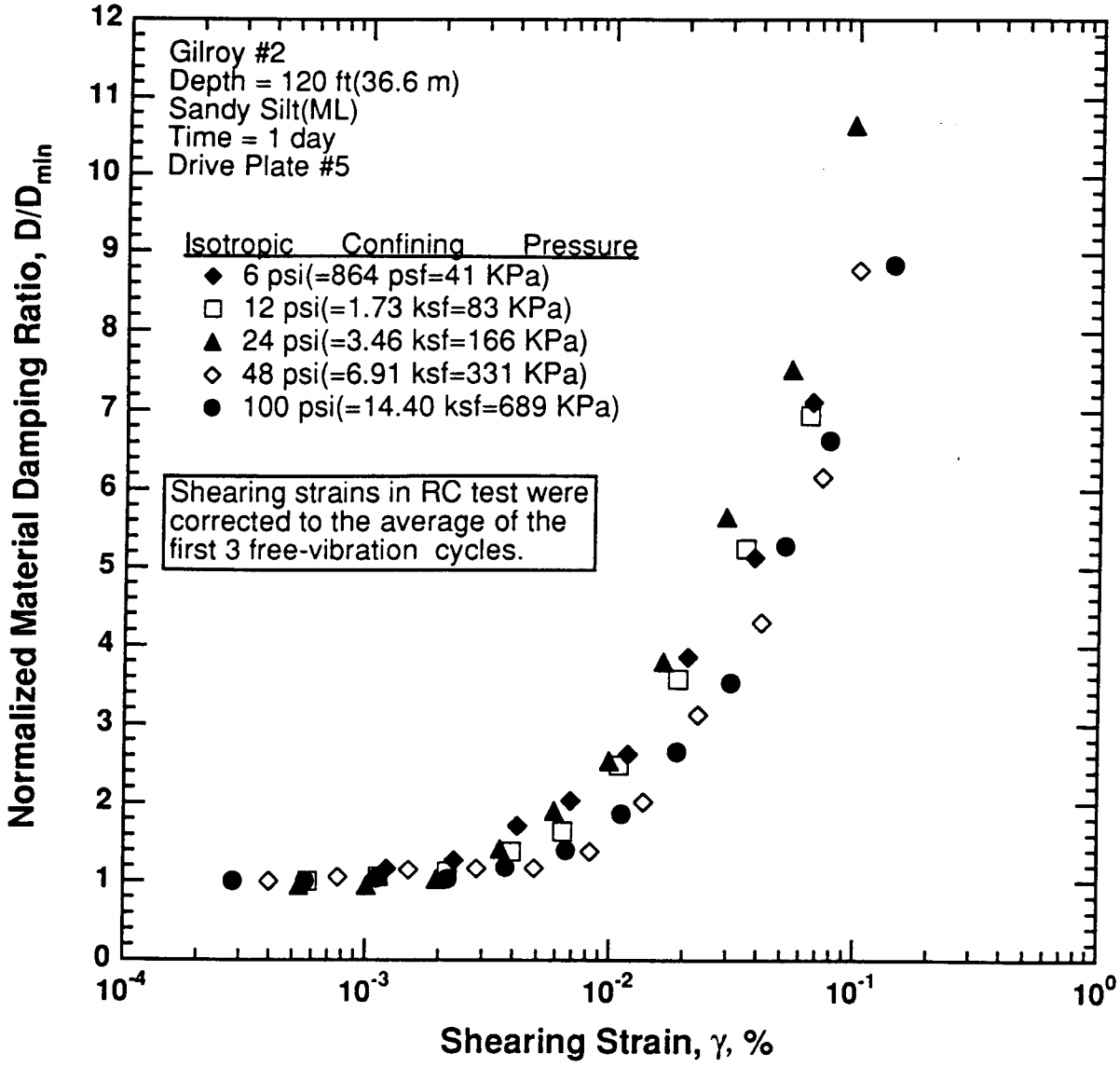

Figure 8.B.2.I-14
Comparison of the variation in normalized material damping ratio with shearing strain and effective confining pressure from resonant column tests of sample G5-1.

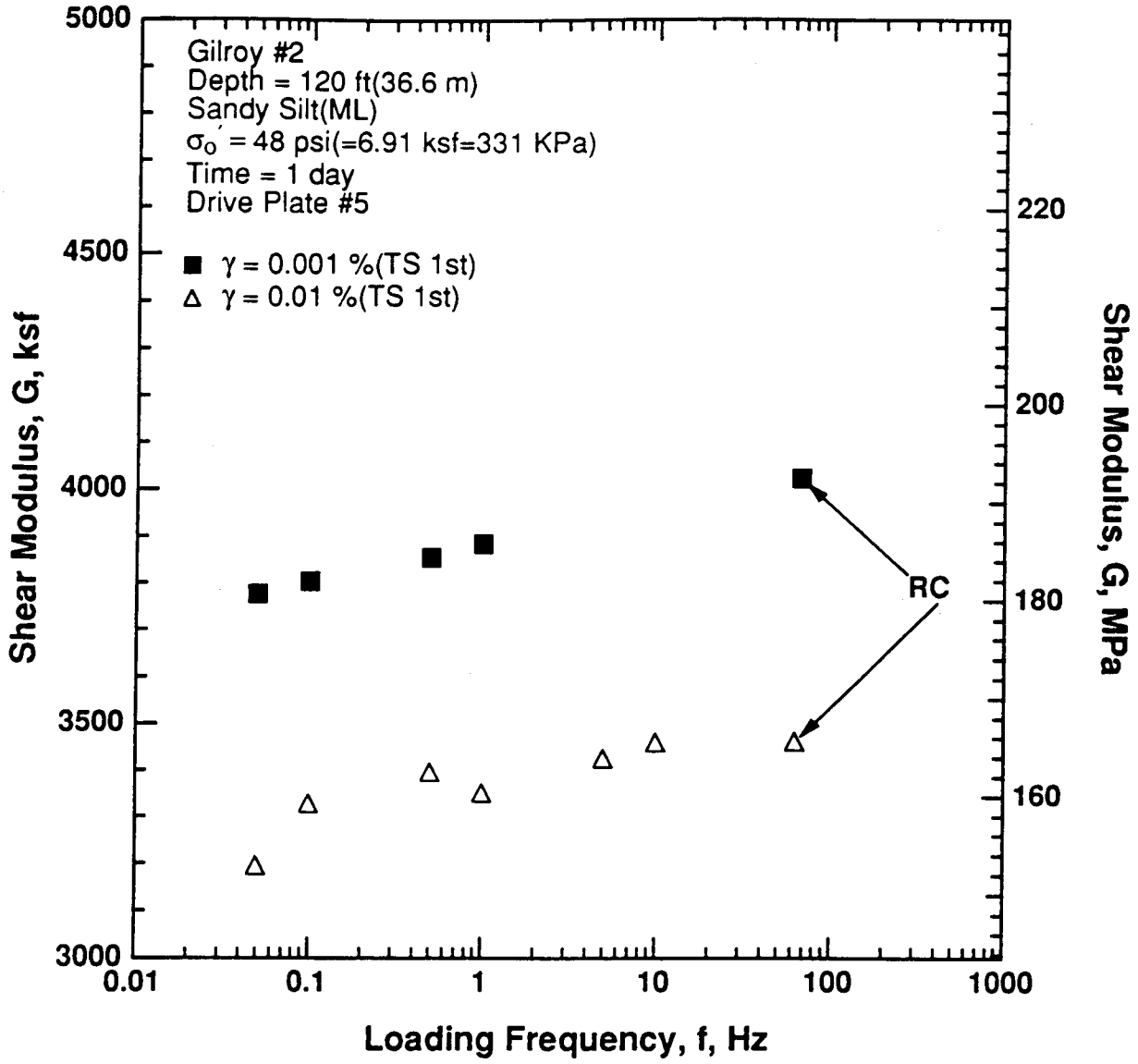

Figure 8.B.2.I-15
Variation in shear modulus with loading frequency and shearing strain at an effective confining pressure of 48 psi (6.91 ksf, 331 kPa) from RCTS tests of sample G5-1.

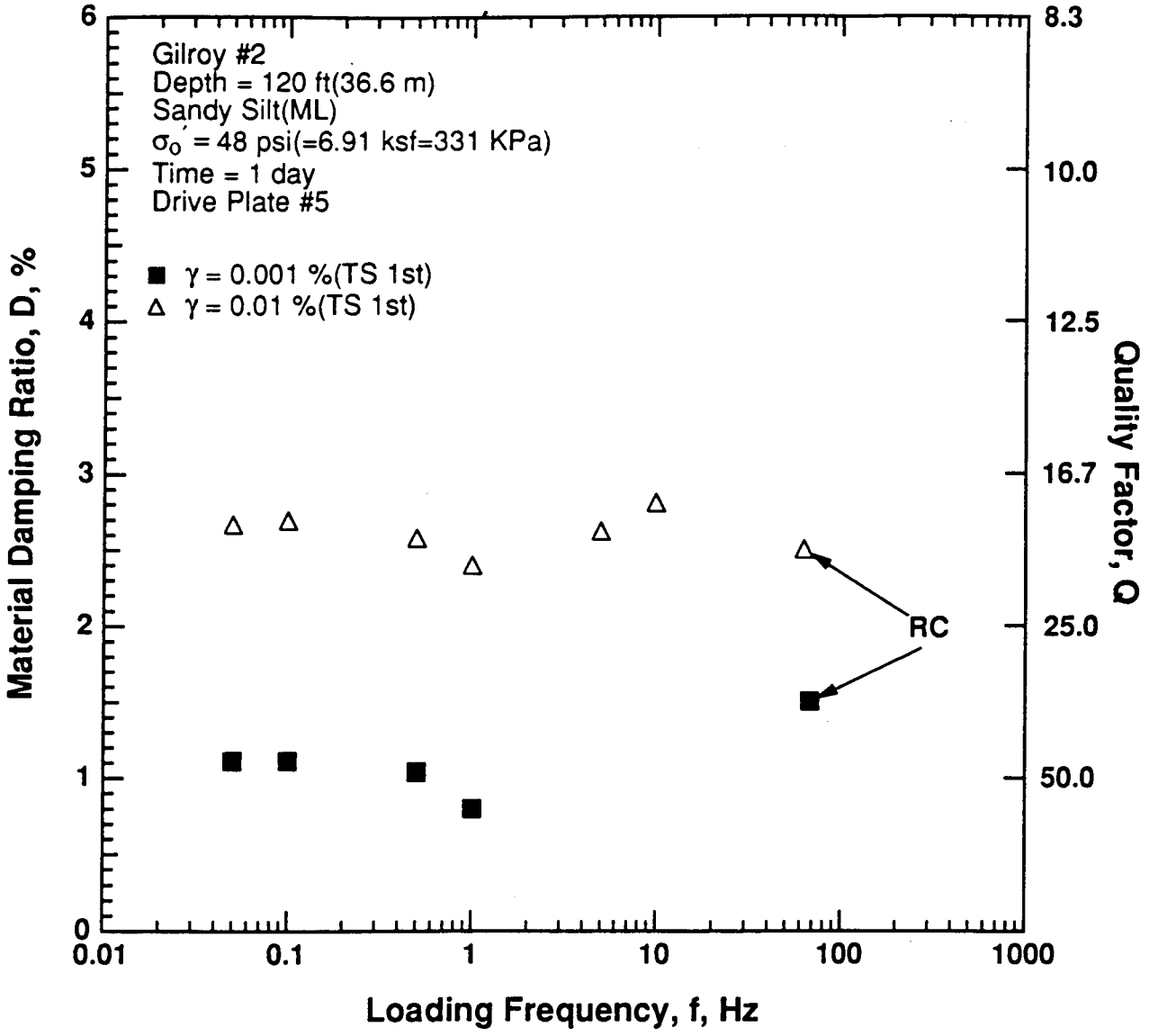

Figure 8.B.1.I-16
Variation in material damping ratio with loading frequency and shearing strain at an effective confining pressure of 48 psi (6.91 ksf, 331 kPa) from RCTS tests of sample G5-1.

APPENDIX 8.B.2.J
DYNAMIC TESTS OF SAMPLE G6, DEPTH = 170 FT (51.8 M)

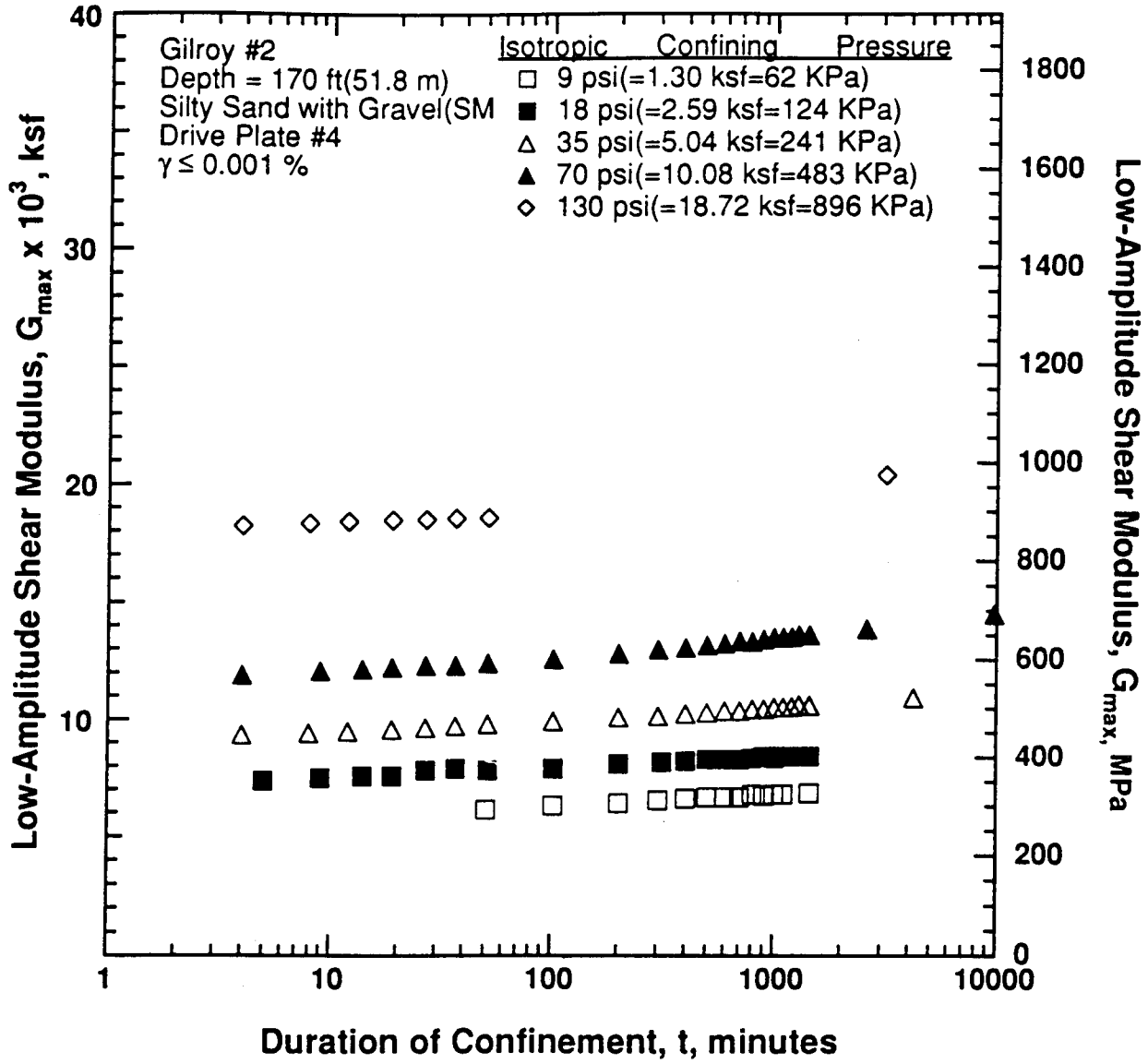

Figure 8.B.2.J-1
Variation in low-amplitude shear modulus with magnitude and duration of isotropic confining pressure from resonant column tests of sample G6.

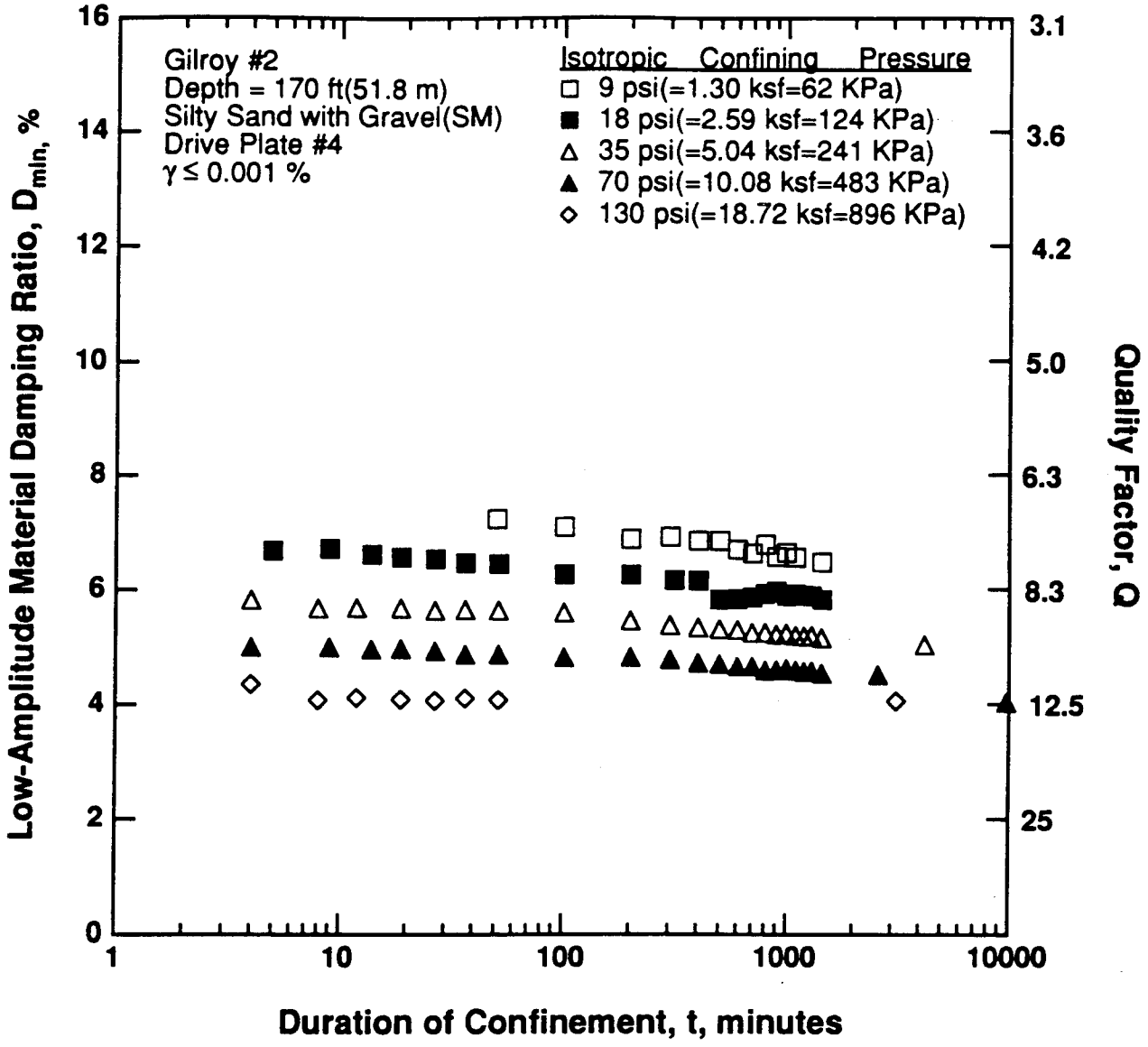

Figure 8.B.2.J-2
Variation in low-amplitude material damping ratio with magnitude and duration of isotropic confining pressure from resonant column tests of sample G6.

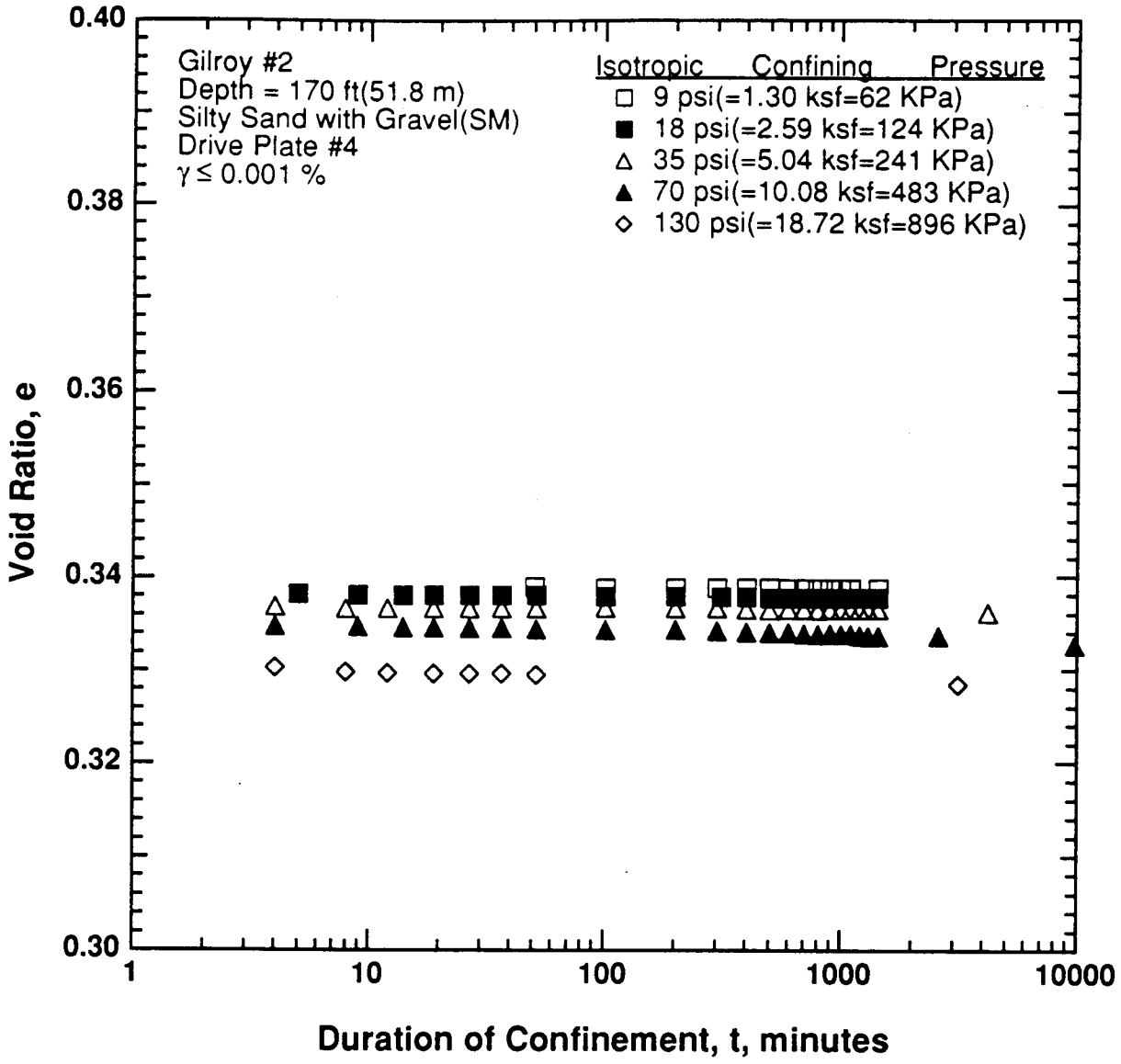

Figure 8.B.2.J-3
Variation in void ratio with magnitude and duration of isotropic confining pressure from resonant column tests of sample G6.

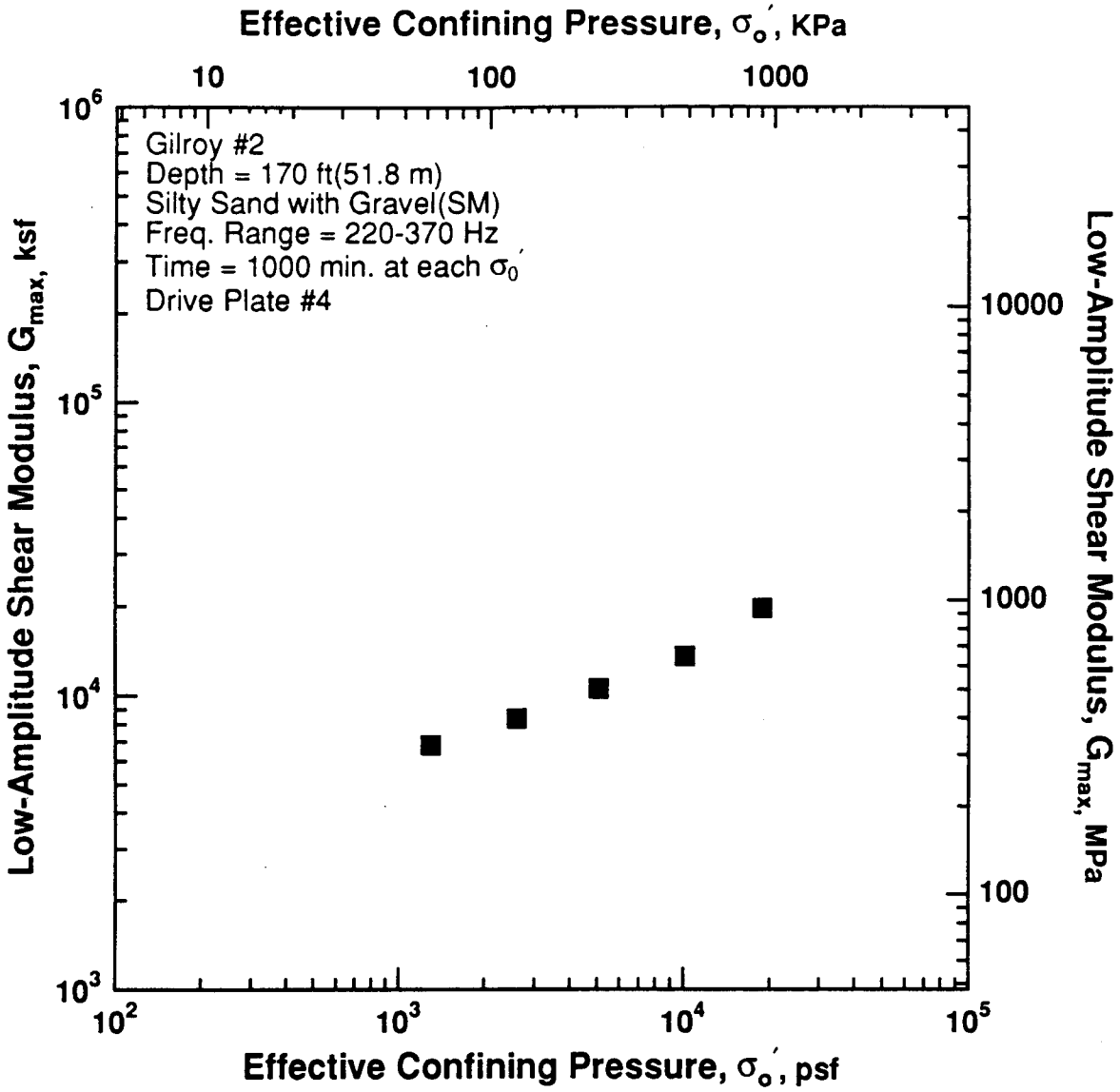

Figure 8.B.2.J-4
Variation in low-amplitude shear modulus with effective confining pressure from resonant column tests of sample G6.

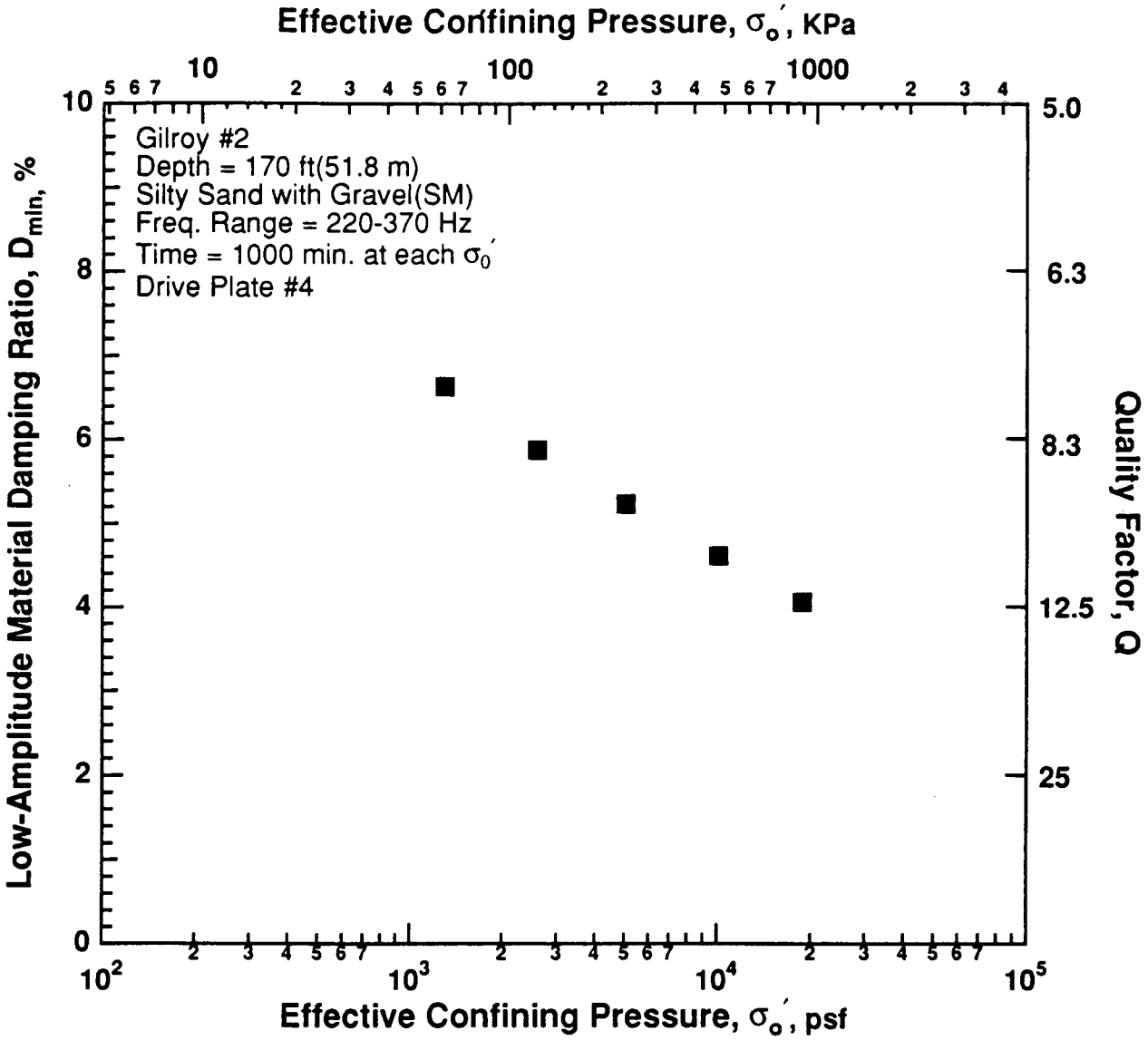

Figure 8.B.2.J-5
Variation in low-amplitude material damping ratio with effective confining pressure from resonant column tests of sample G6.

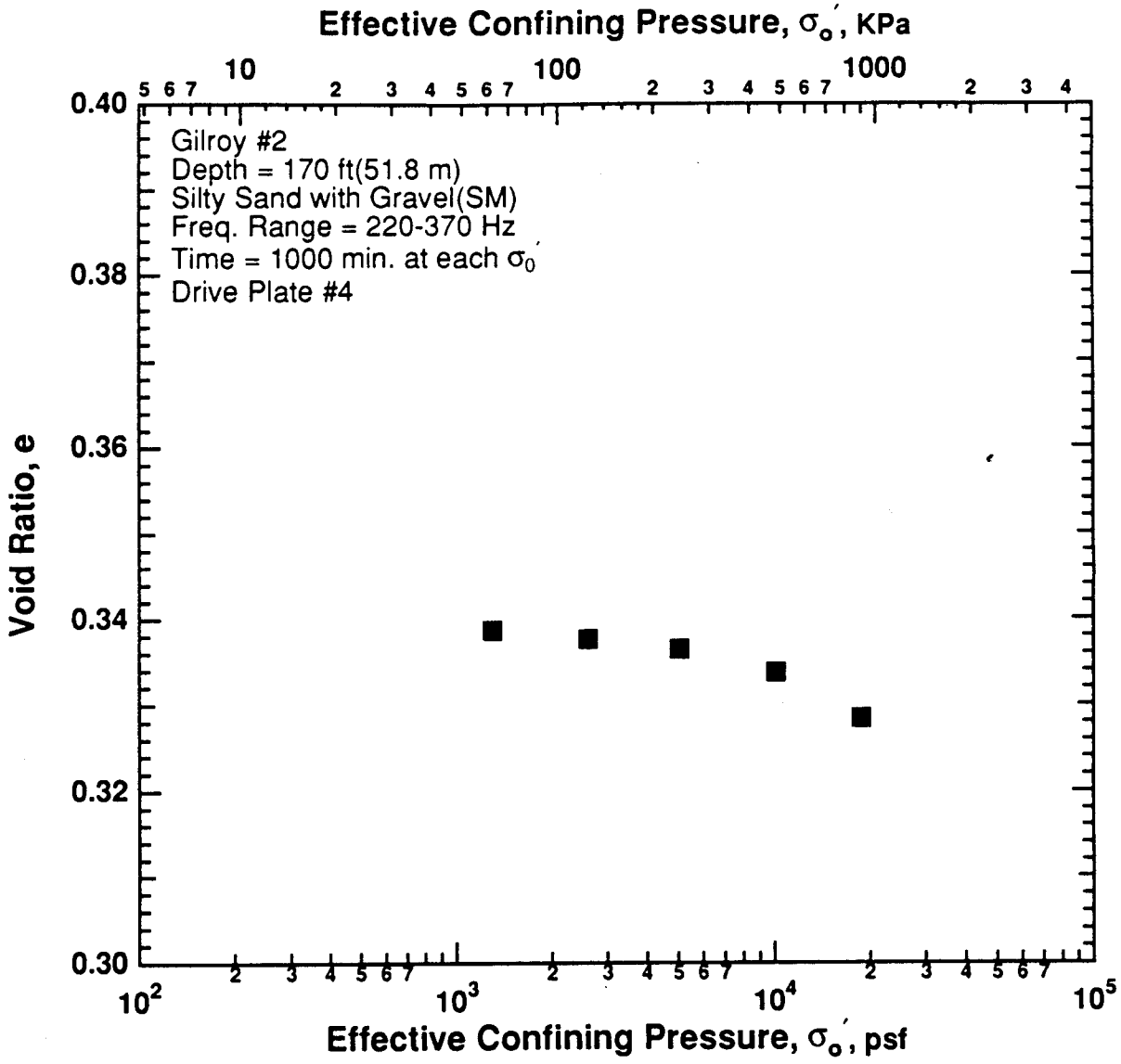

Figure 8.B.2.J-6
Variation in void ratio with effective confining pressure from resonant column tests of sample G6.

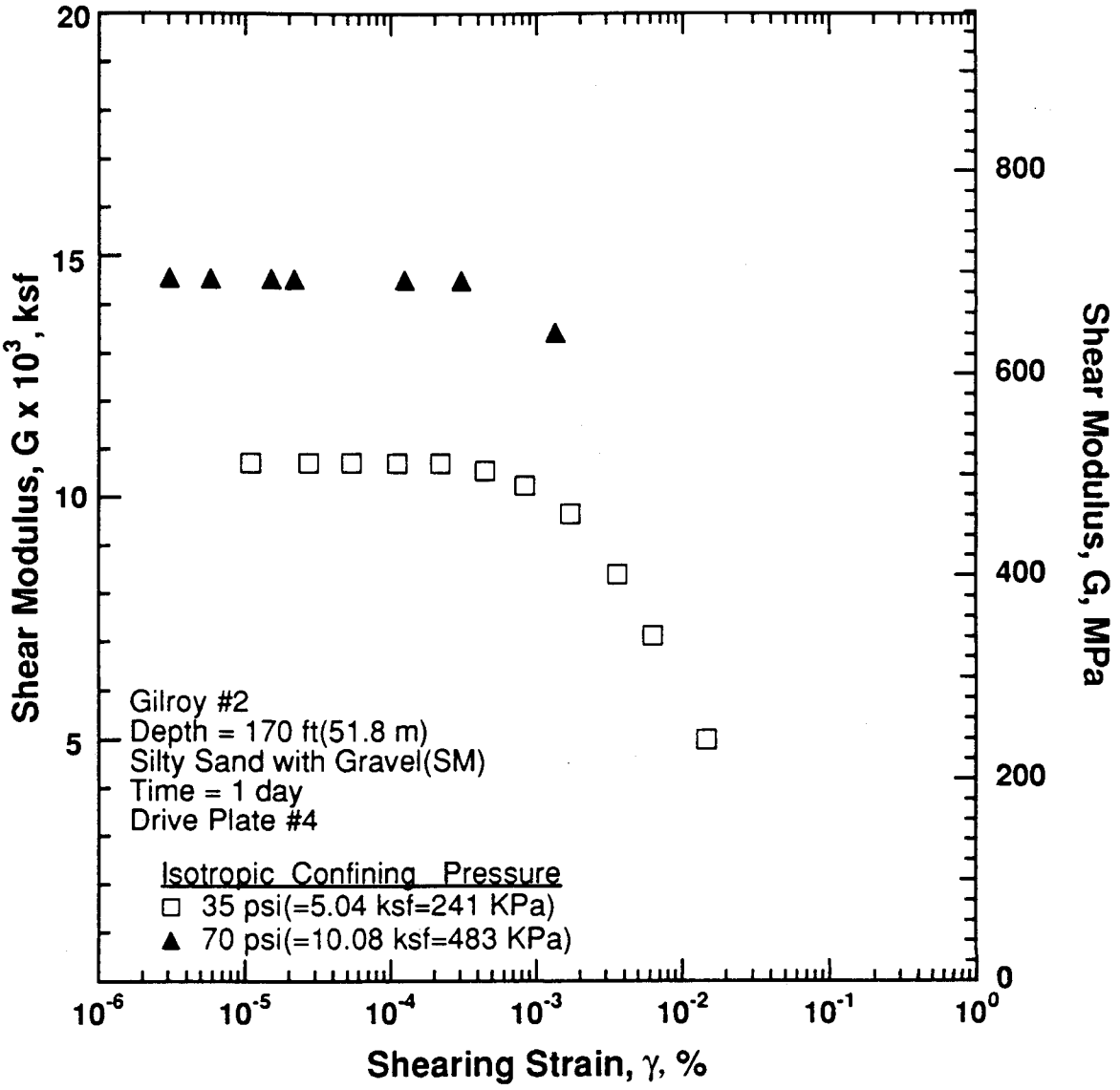

Figure 8.B.2.J-7
Variation in shear modulus with shearing strain and effective confining pressure from resonant column tests of sample G6.

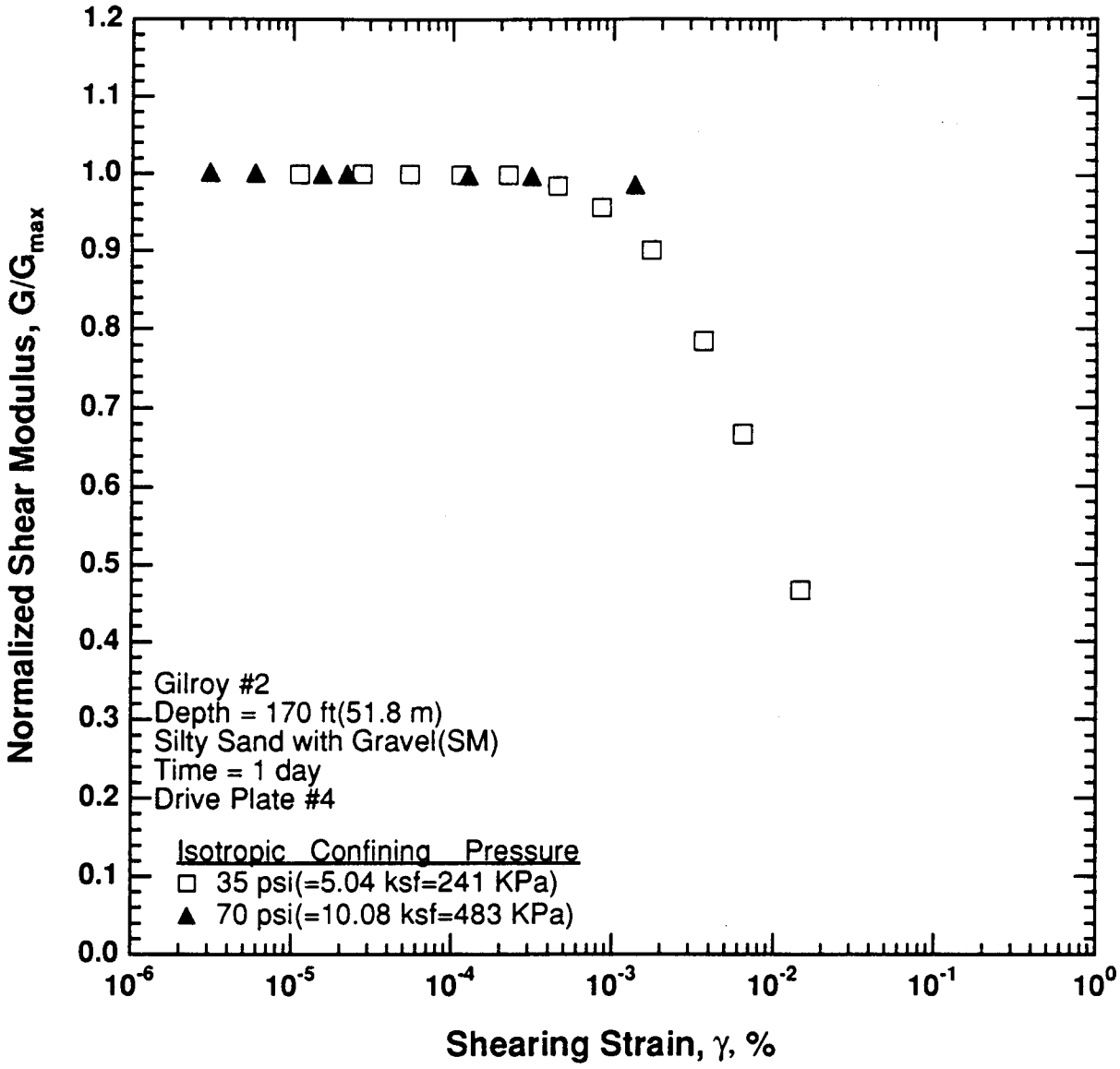

Figure 8.B.2.J-8
Comparison of the variation in normalized shear modulus with shearing strain and effective confining pressure from resonant column tests of sample G6.

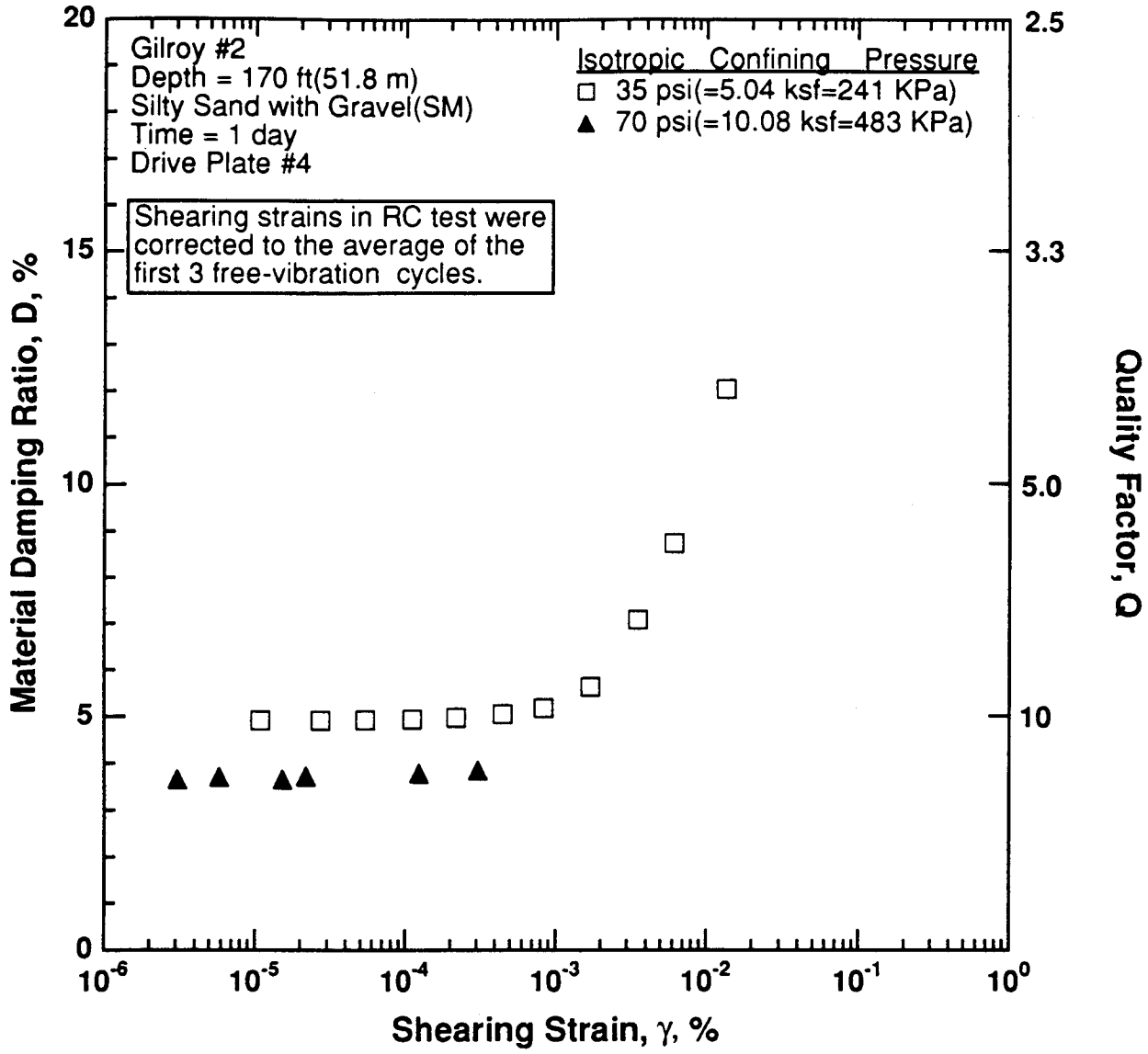

Figure 8.B.2.J-9
Variation in material damping ratio with shearing strain and effective confining pressure from resonant column tests of sample G6.

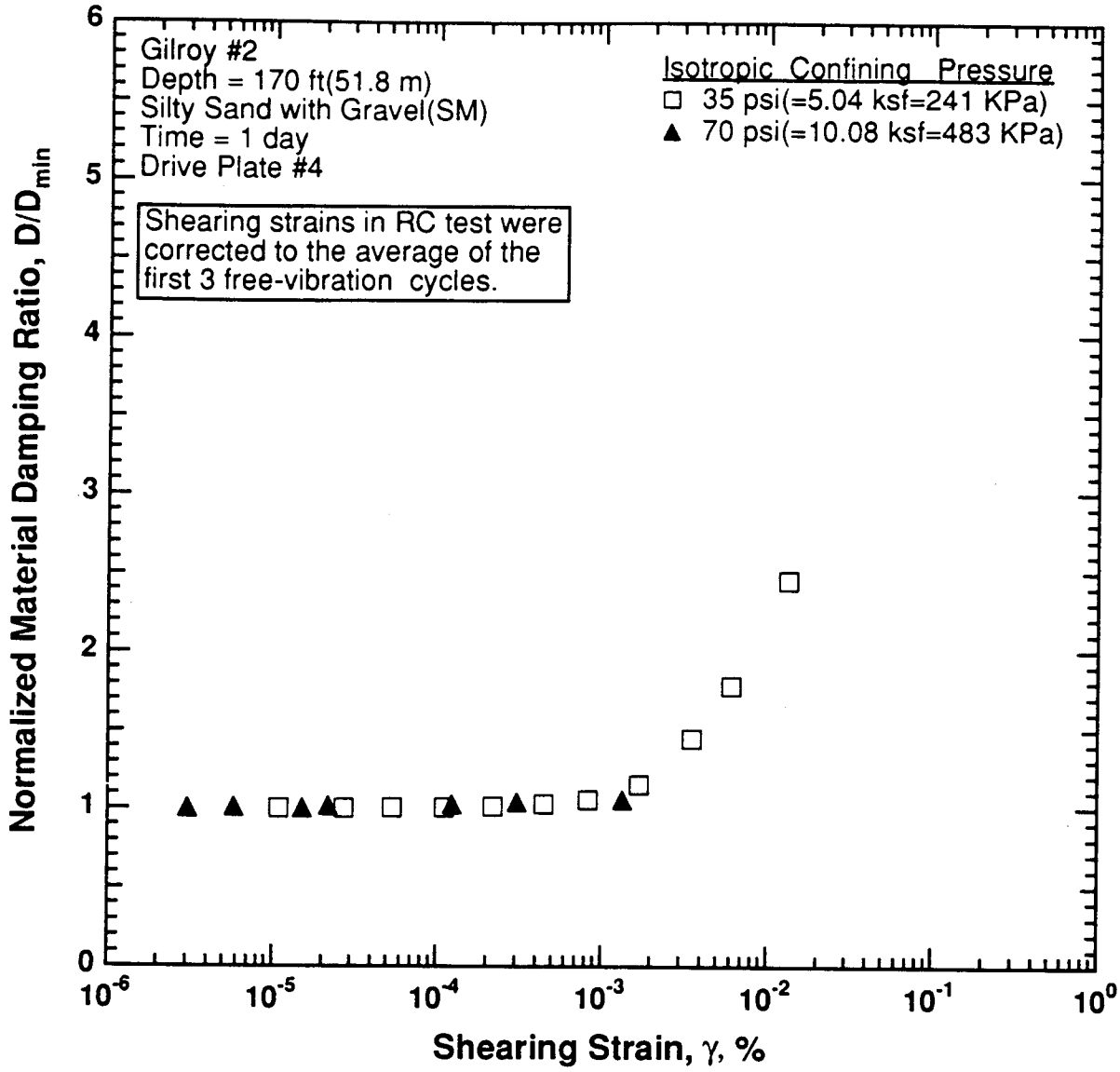

Figure 8.B.2.J-10
Comparison of the variation in normalized material damping ratio with shearing strain and effective confining pressure from resonant column tests of sample G6.

APPENDIX 8.B.2.K
DYNAMIC TESTS OF SAMPLE G7, DEPTH = 210 FT (64.0 M)

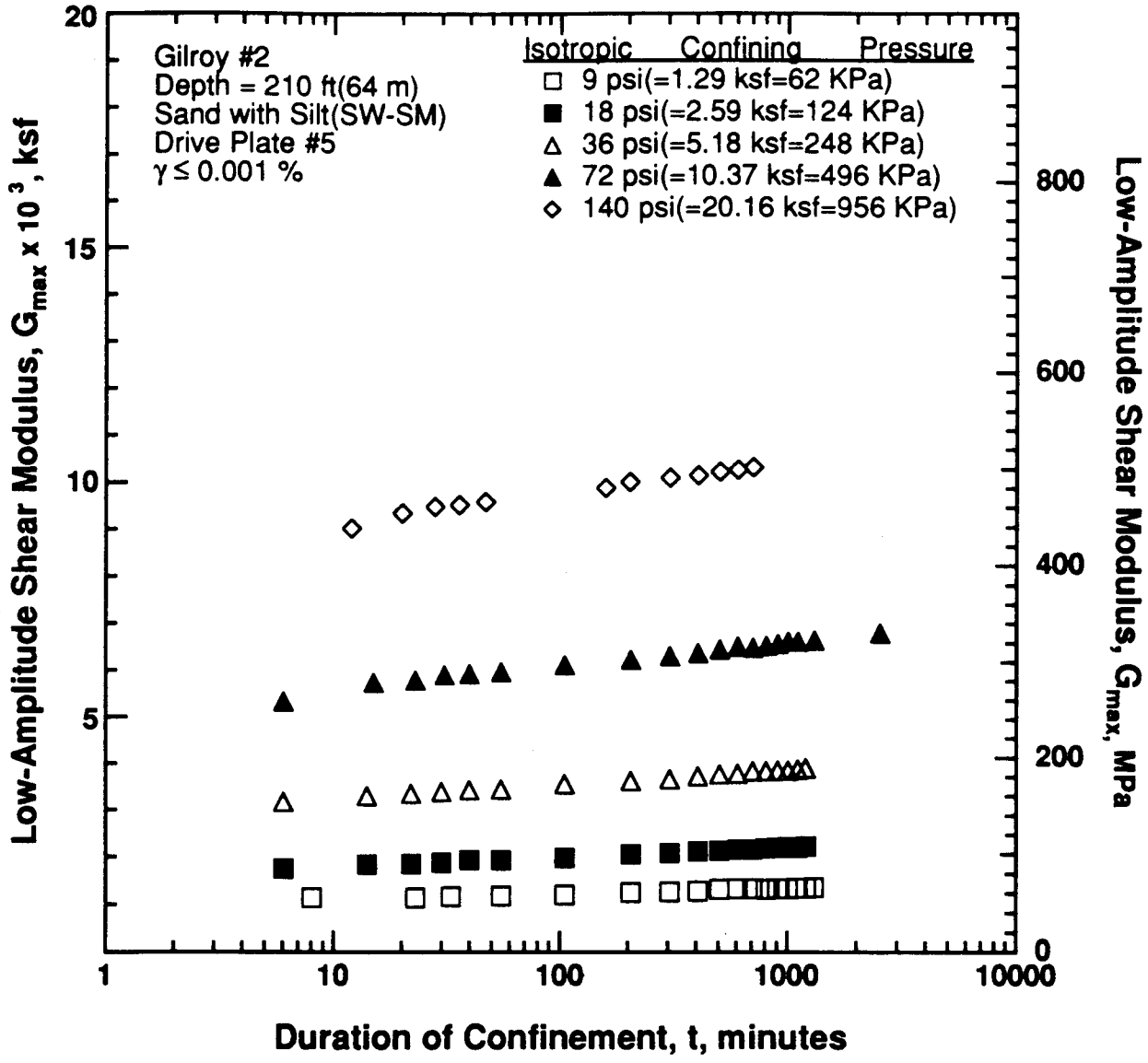

Figure 8.B.2.K-1
Variation in low-amplitude shear modulus with magnitude and duration of isotropic confining pressure from resonant column tests of sample G7.

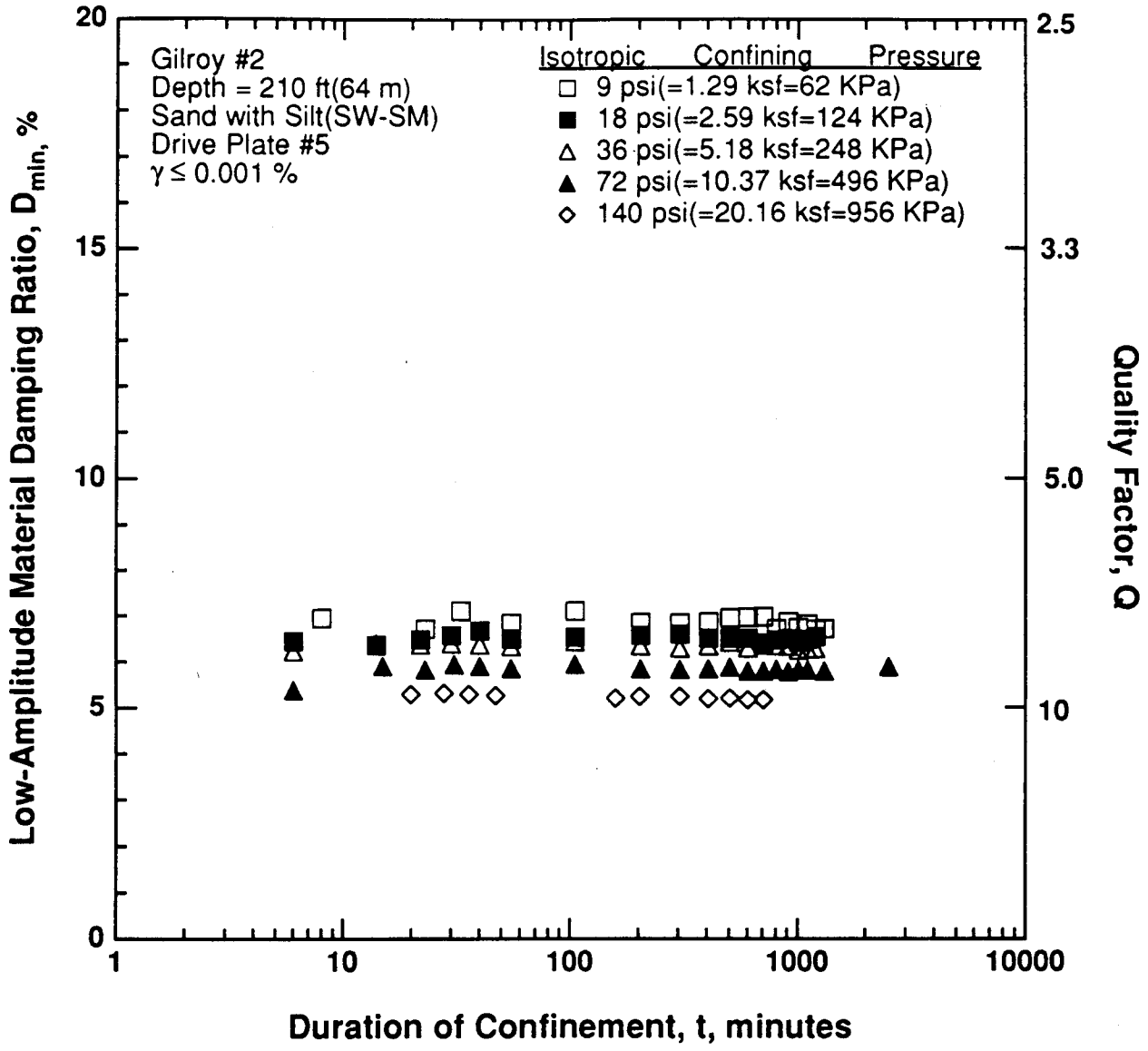

Figure 8.B.2.K-2
Variation in low-amplitude material damping ratio with magnitude and duration of isotropic confining pressure from resonant column tests of sample G7.

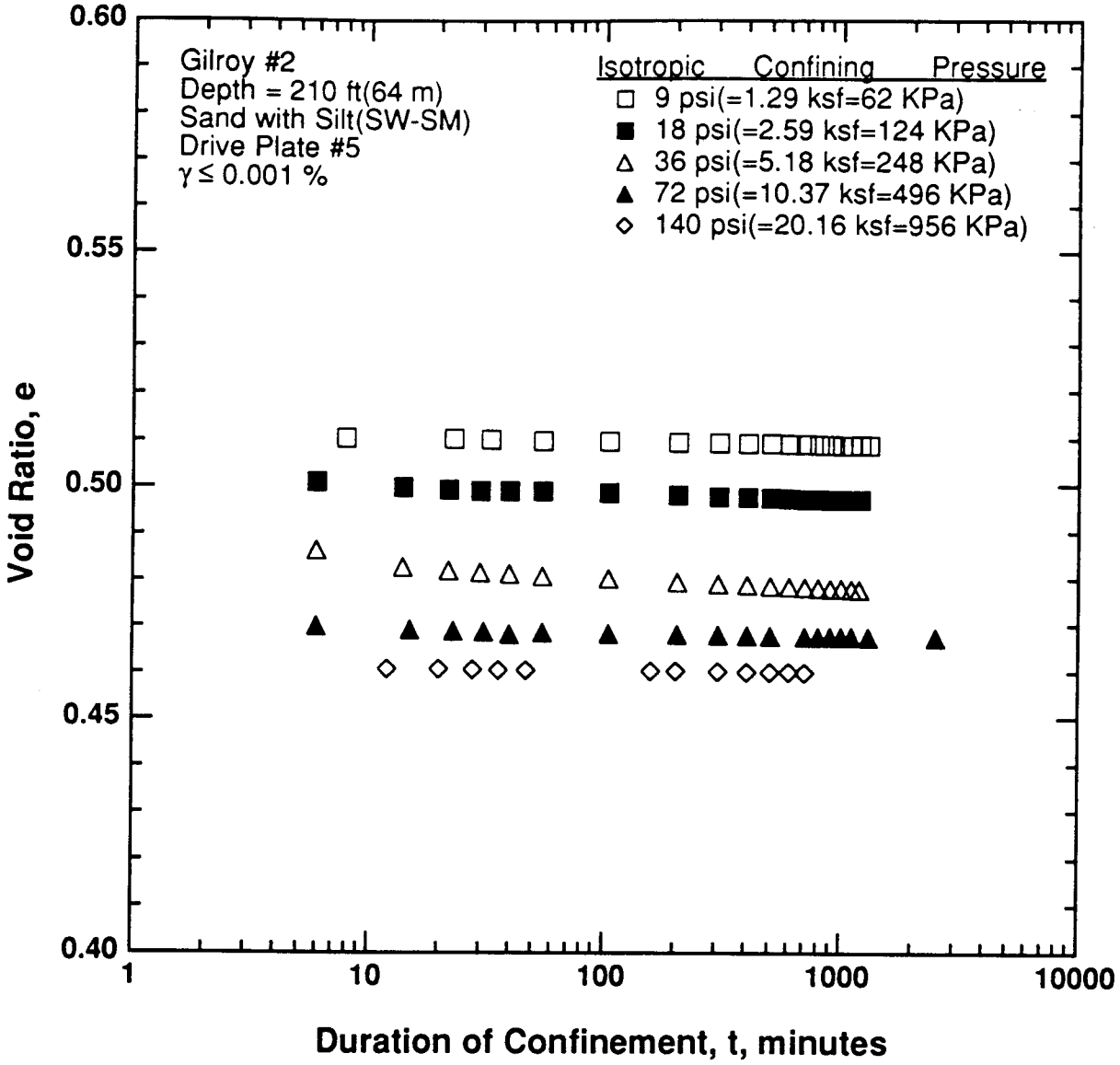

Figure 8.B.2.K-3
Variation in void ratio with magnitude and duration of isotropic confining pressure from resonant column tests of sample G7.

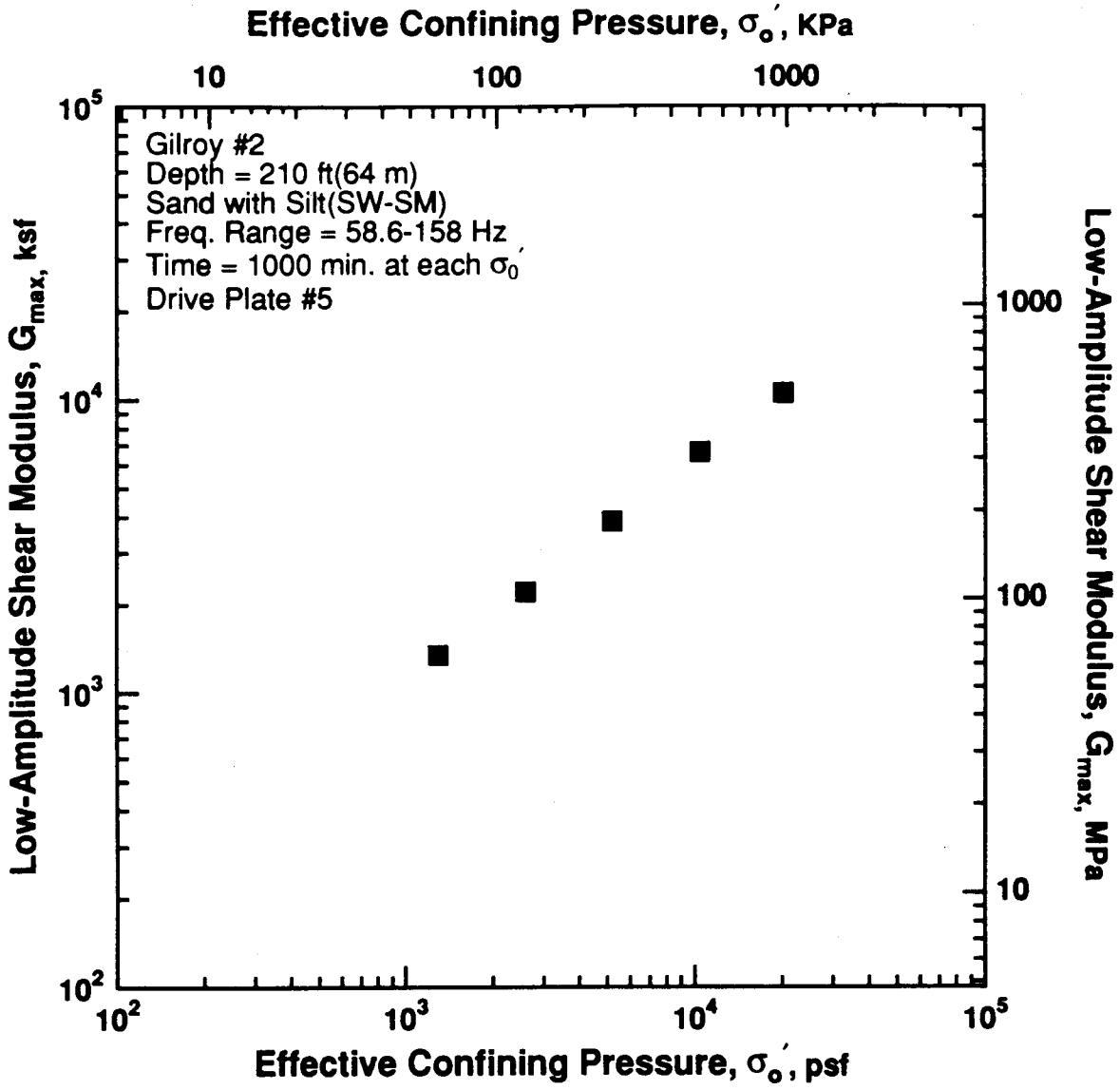

Figure 8.B.2.K-4
Variation in low-amplitude shear modulus with effective confining pressure from resonant column tests of sample G7.

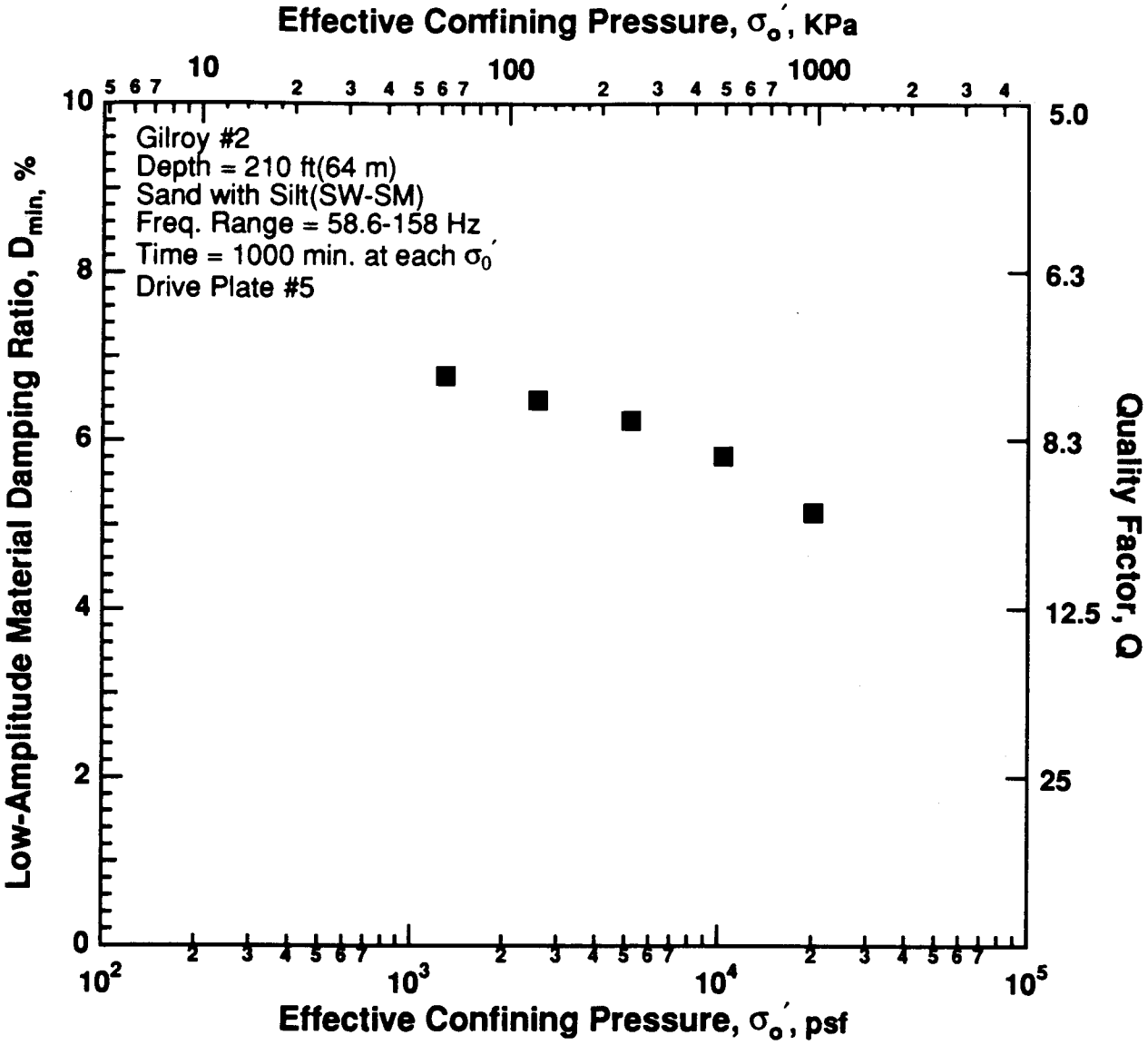

Figure 8.B.2.K-5
Variation in low-amplitude material damping ratio with effective confining pressure from resonant column tests of sample G7.

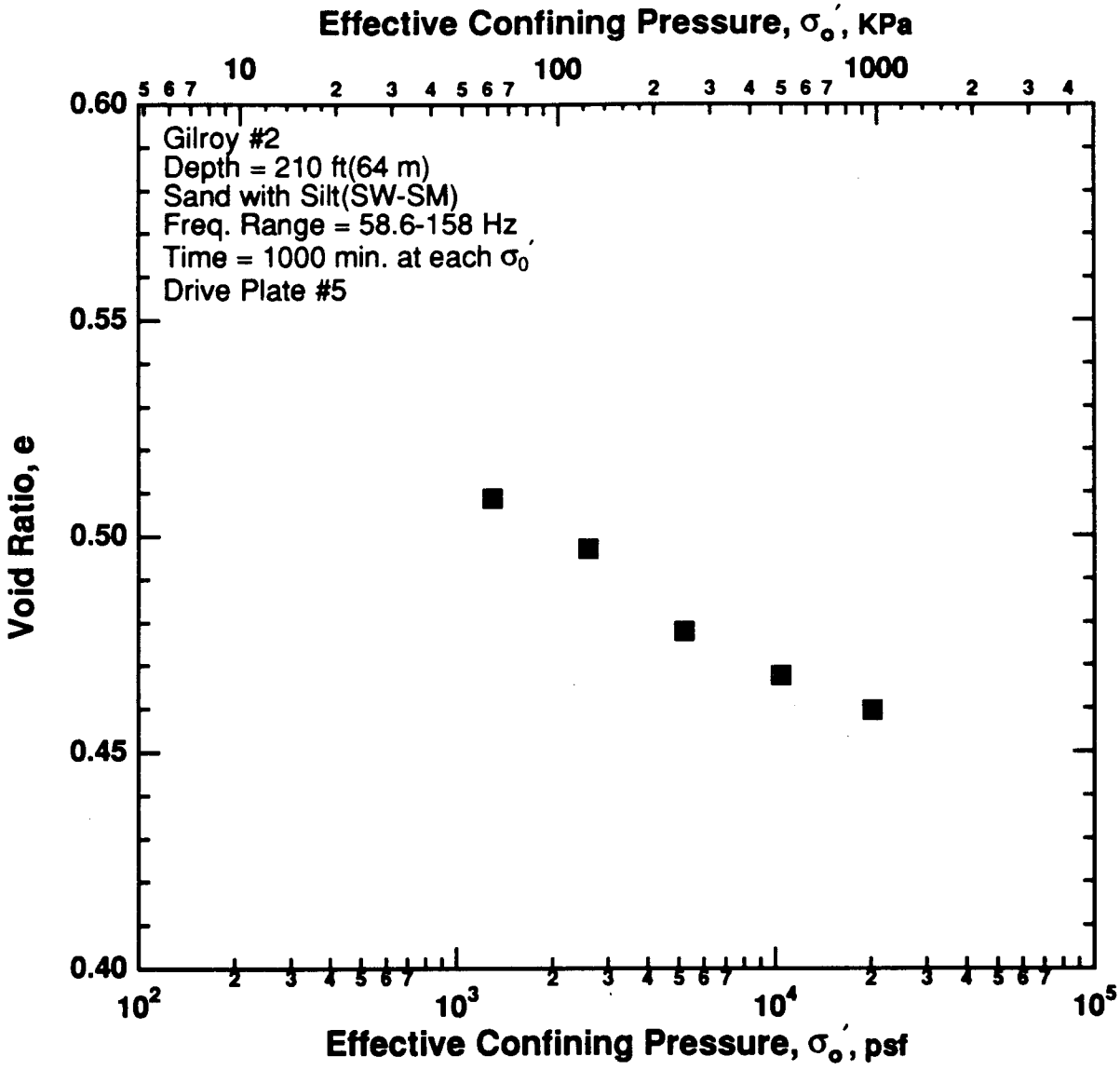

Figure 8.B.2.K-6
Variation in void ratio with effective confining pressure from resonant column tests of sample G7.

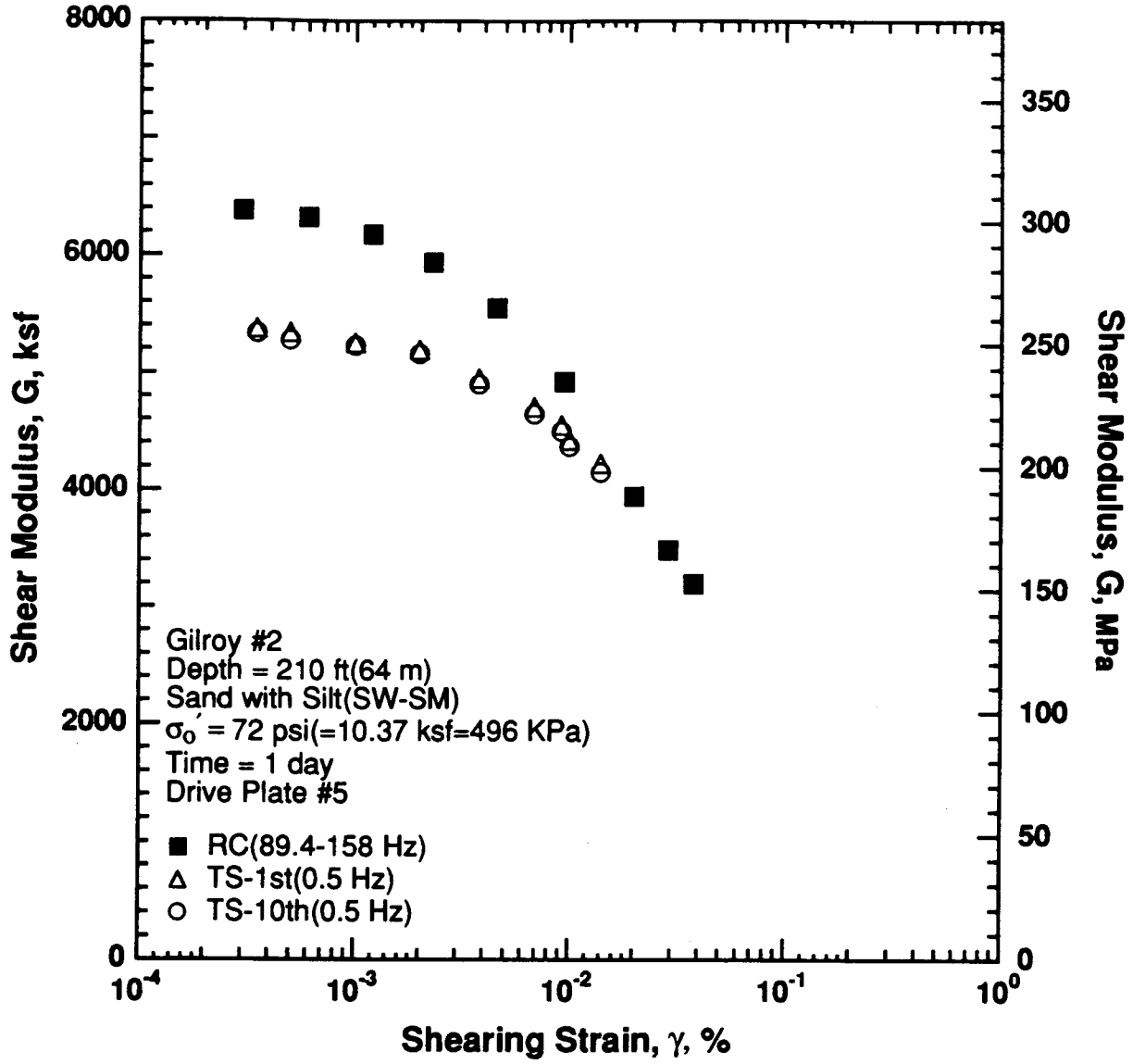

Figure 8.B.2.K-7
Variation in shear modulus with shearing strain at an effective confining pressure of 72 psi (10.37 ksf, 496 kPa) from RCTS tests of sample G7.

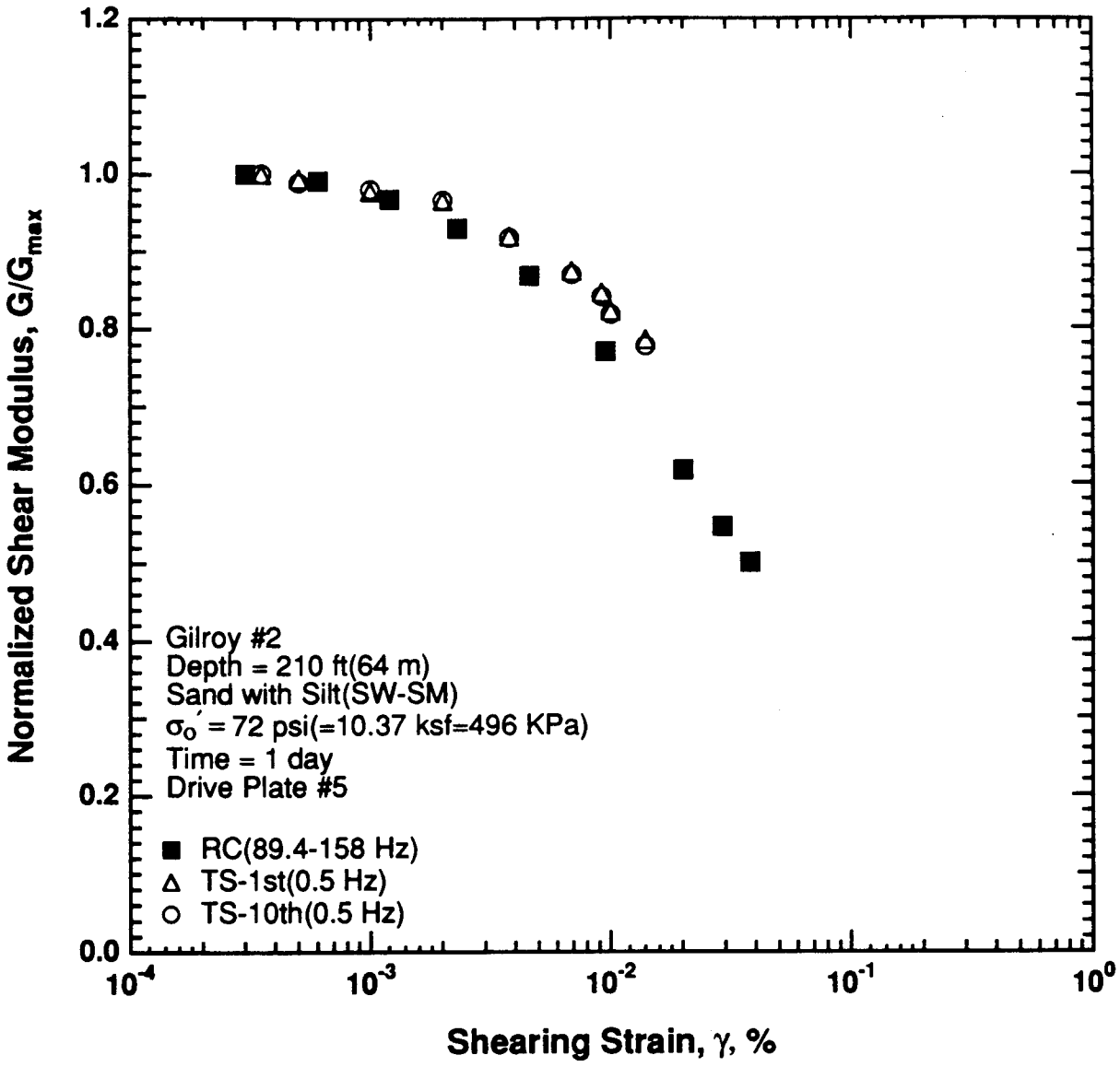

Figure 8.B.2.K-8
Variation in normalized shear modulus with shearing strain at an effective confining pressure of 72 psi (10.37 ksf, 496 kPa) from RCTS tests of sample G7.

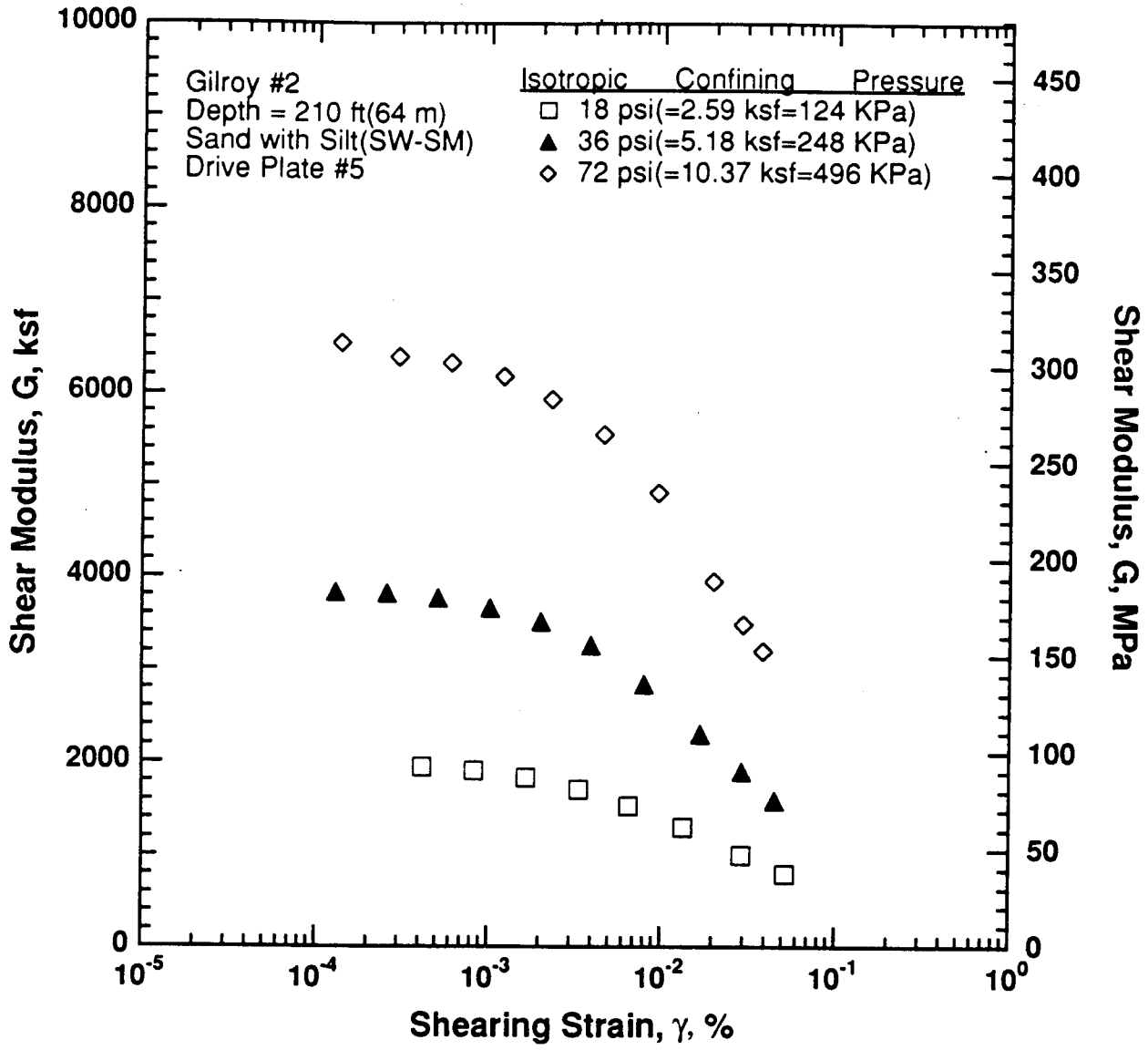

Figure 8.B.2.K-9
Variation in shear modulus with shearing strain and effective confining pressure from resonant column tests of sample G7.

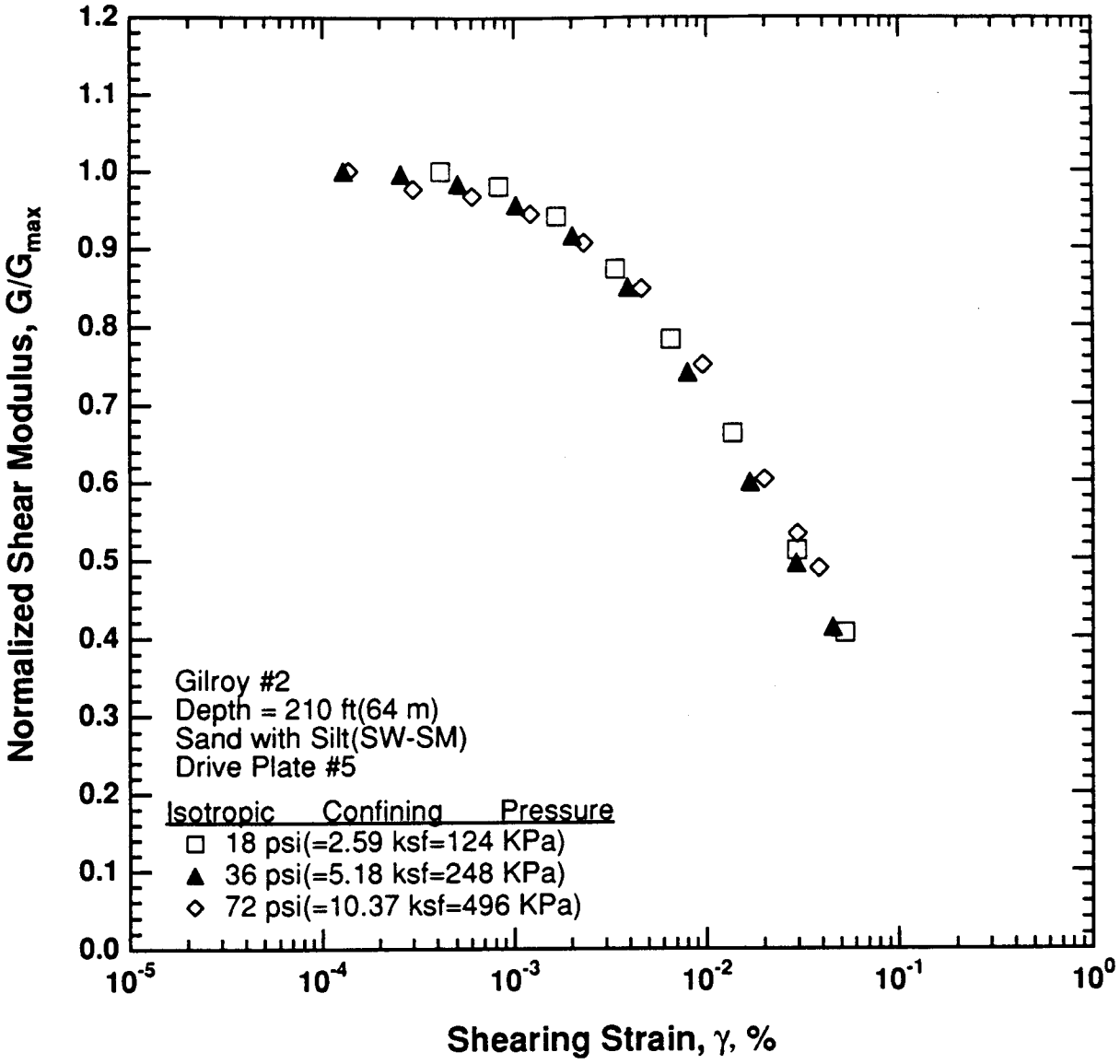

Figure 8.B.2.K-10
Comparison of the variation in normalized shear modulus with shearing strain and effective confining pressure from resonant column tests of sample G7.

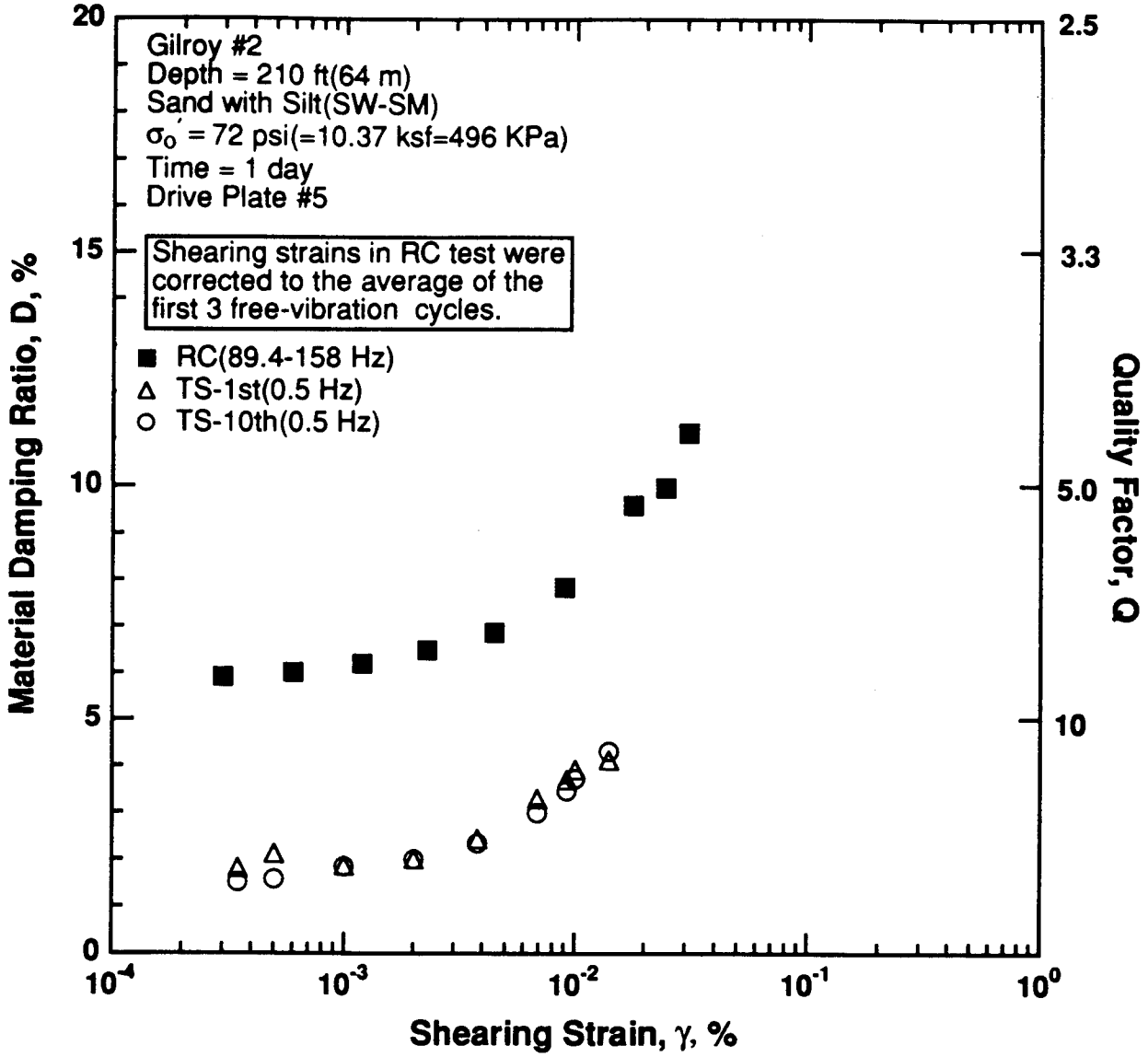

Figure 8.B.2.K-11
Variation in material damping ratio with shearing strain at an effective confining pressure of 72 psi (10.37 ksf, 496 kPa) from RCTS tests of sample G7.

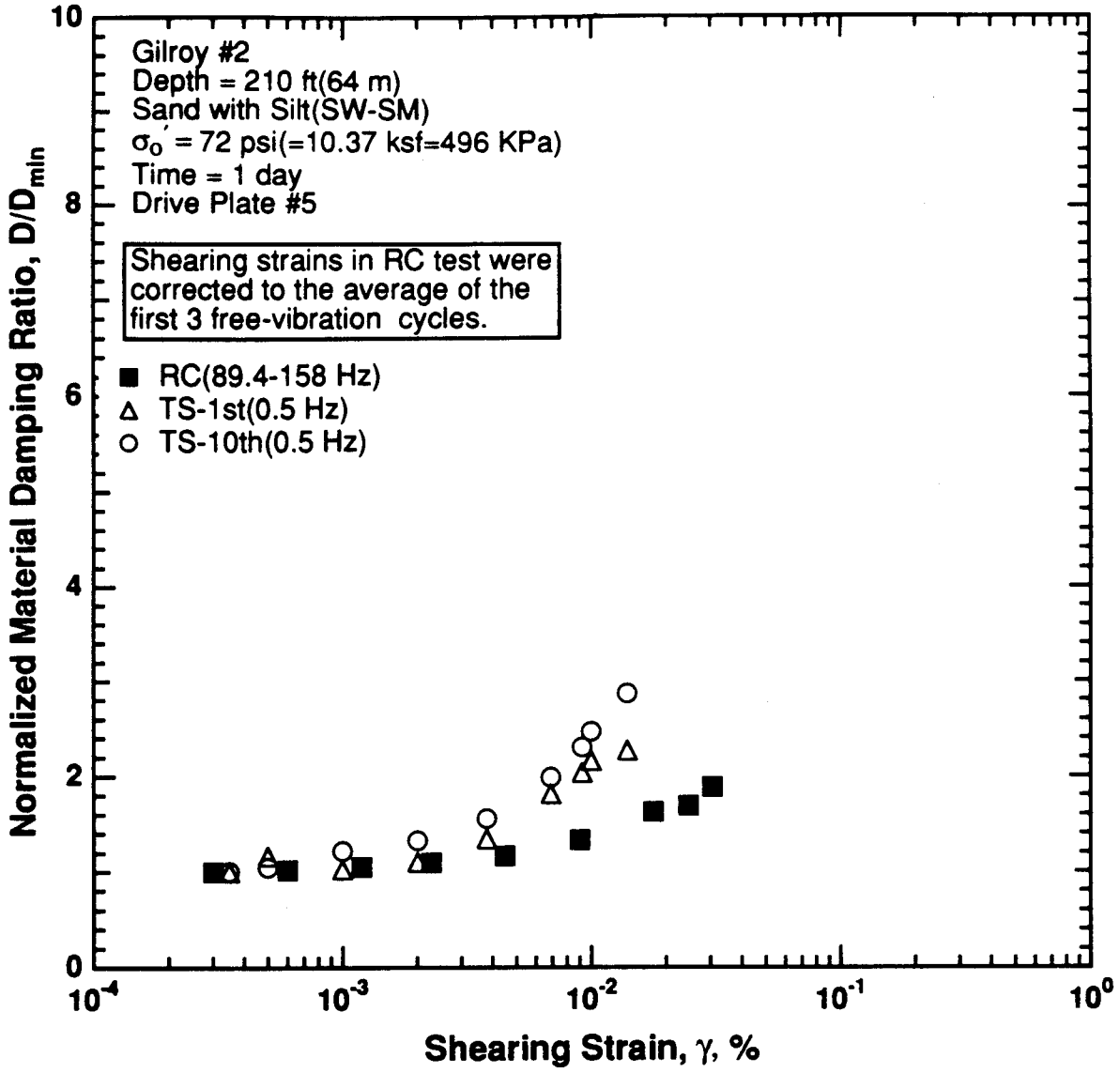

Figure 8.B.2.K-12
Variation in normalized material damping ratio with shearing strain at an effective confining pressure of 72 psi (10.37 ksf, 496 kPa) from RCTS tests of sample G7.

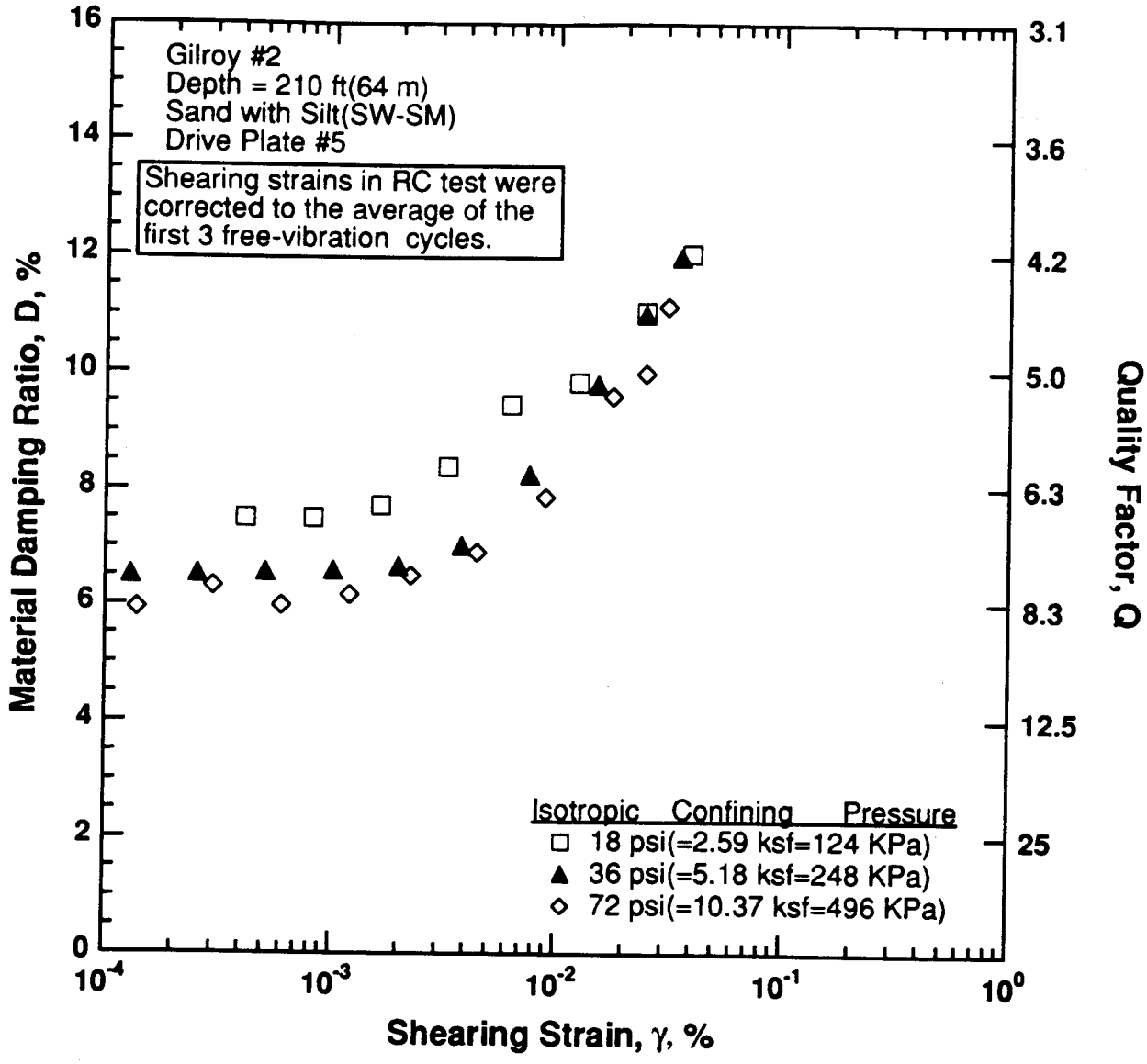

Figure 8.B.2.K-13
Variation in material damping ratio with shearing strain and effective confining pressure from resonant column tests of sample G7.

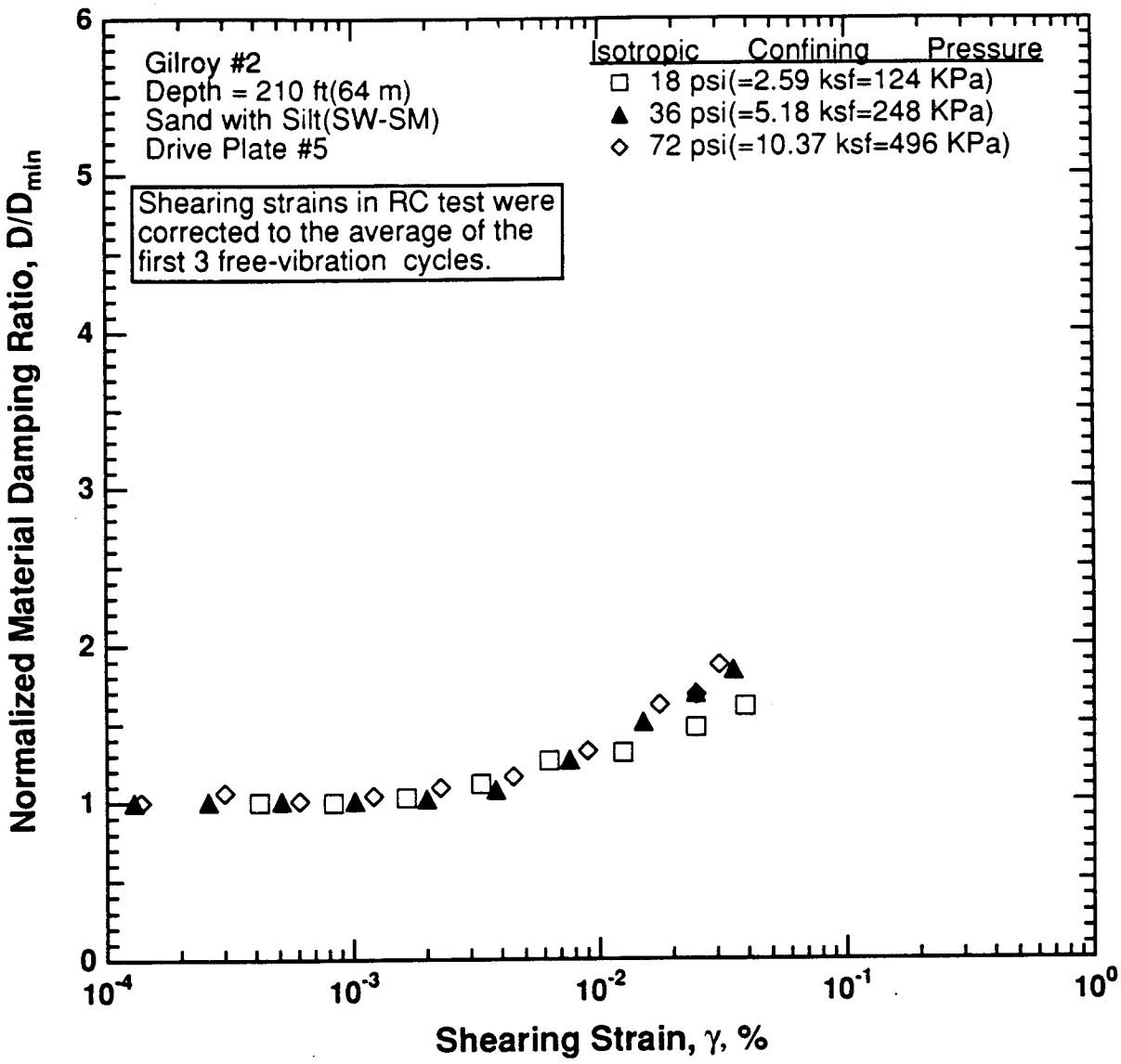

Figure 8.B.2.K-14
Comparison of the variation in normalized material damping ratio with shearing strain and effective confining pressure from resonant column tests of sample G7.

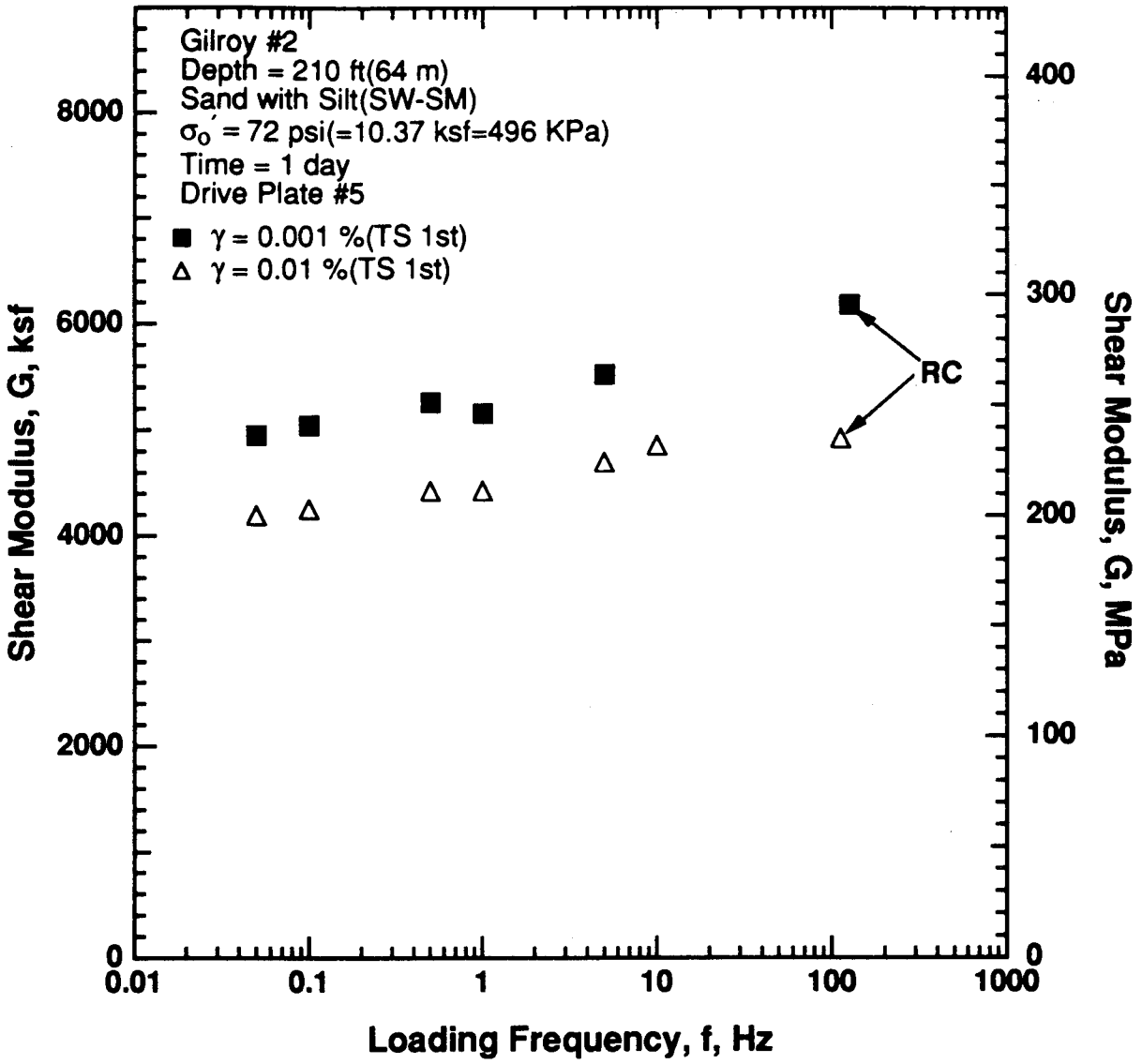

Figure 8.B.2.K-15
Variation in shear modulus with loading frequency and shearing strain at an effective confining pressure of 72 psi (10.37 ksf, 496 kPa) from RCTS tests of sample G7.

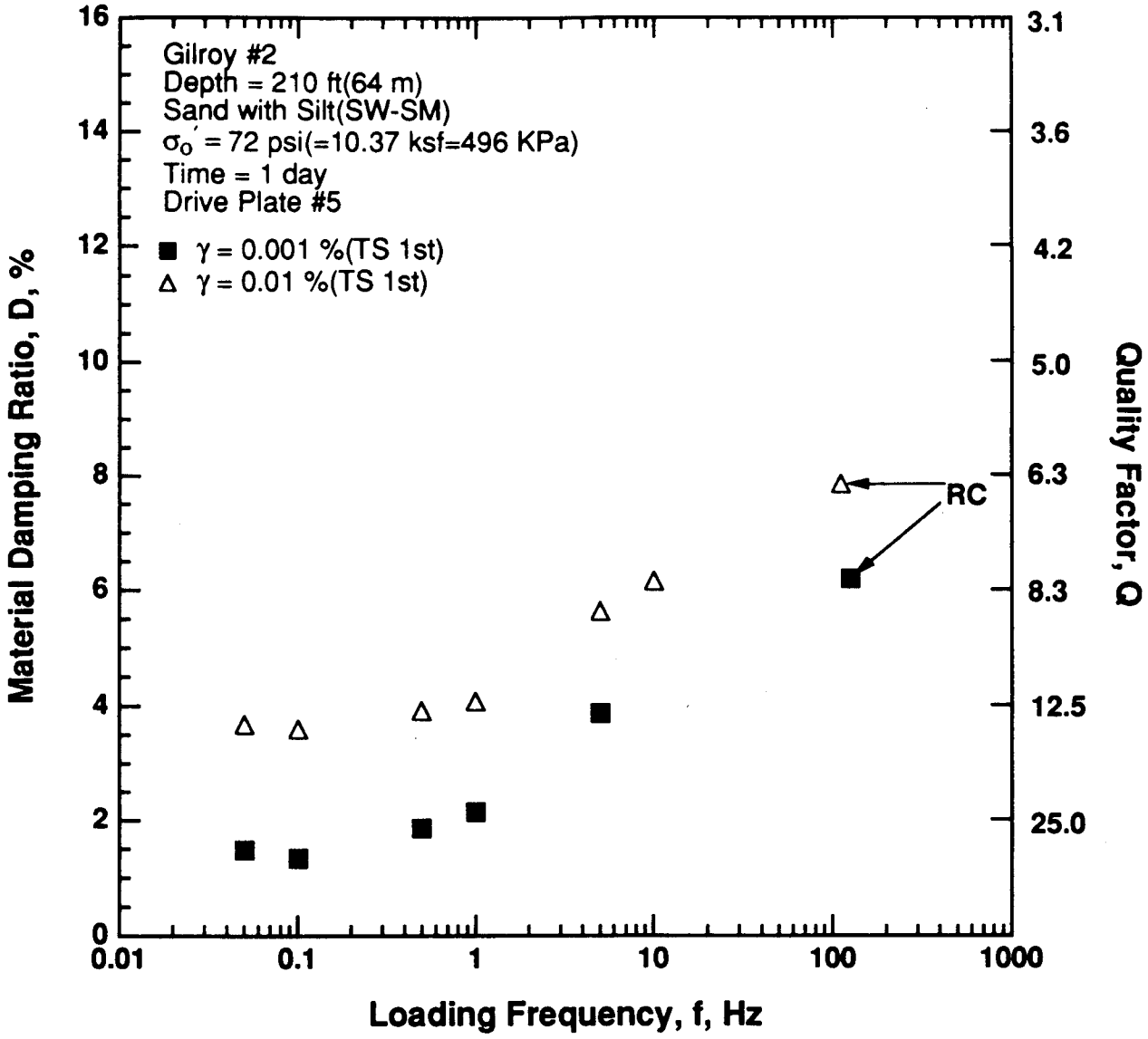

Figure 8.B.1.K-16
Variation in material damping ratio with loading frequency and shearing strain at an effective confining pressure of 72 psi (10.37 ksf, 496 kPa) from RCTS tests of sample G7.

APPENDIX 8.B.2.L
DYNAMIC TESTS OF SAMPLE G8, DEPTH = 348 FT (106.0 M)

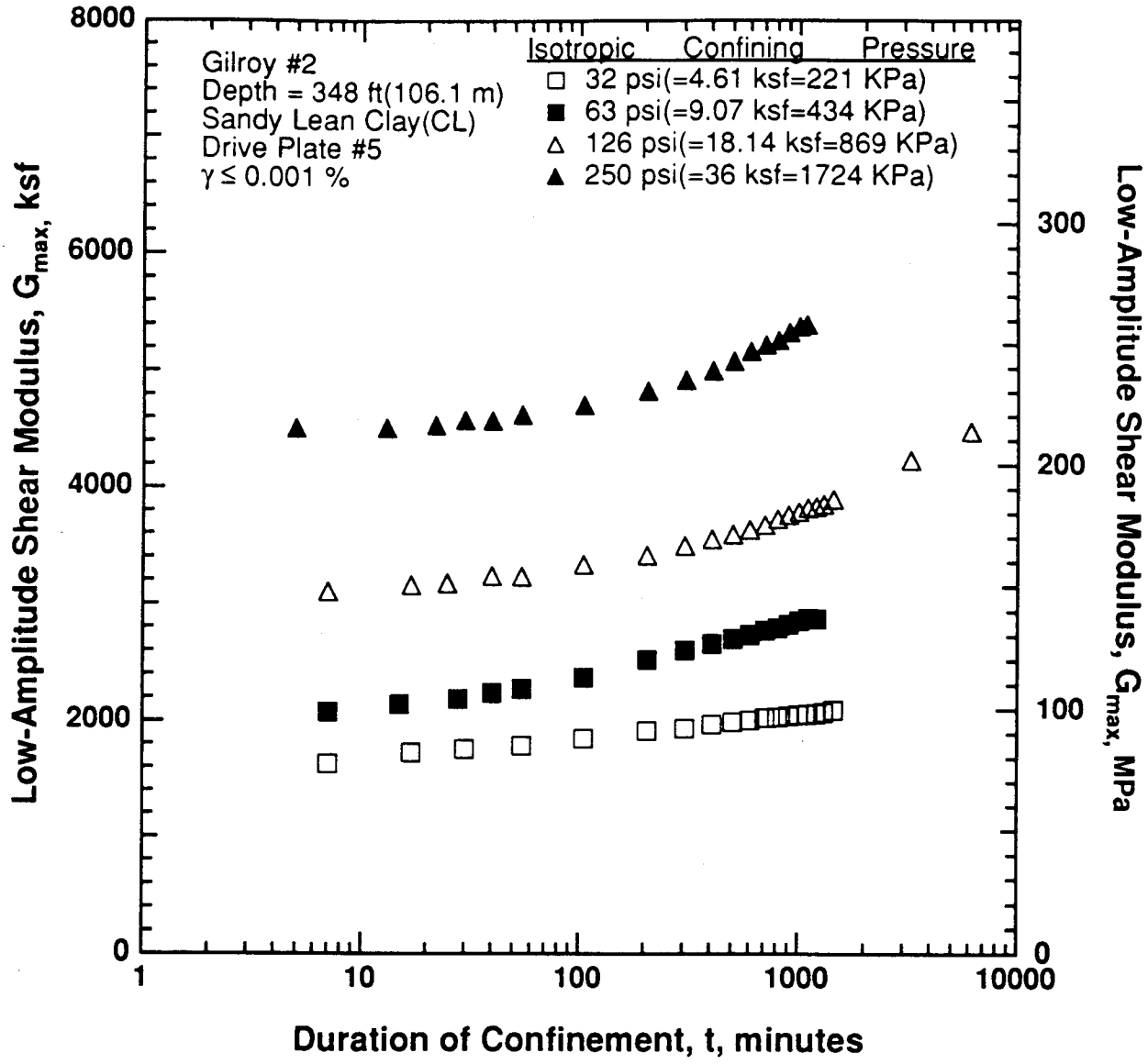

Figure 8.B.2.L-1
Variation in low-amplitude shear modulus with magnitude and duration of isotropic confining pressure from resonant column tests of sample G8.

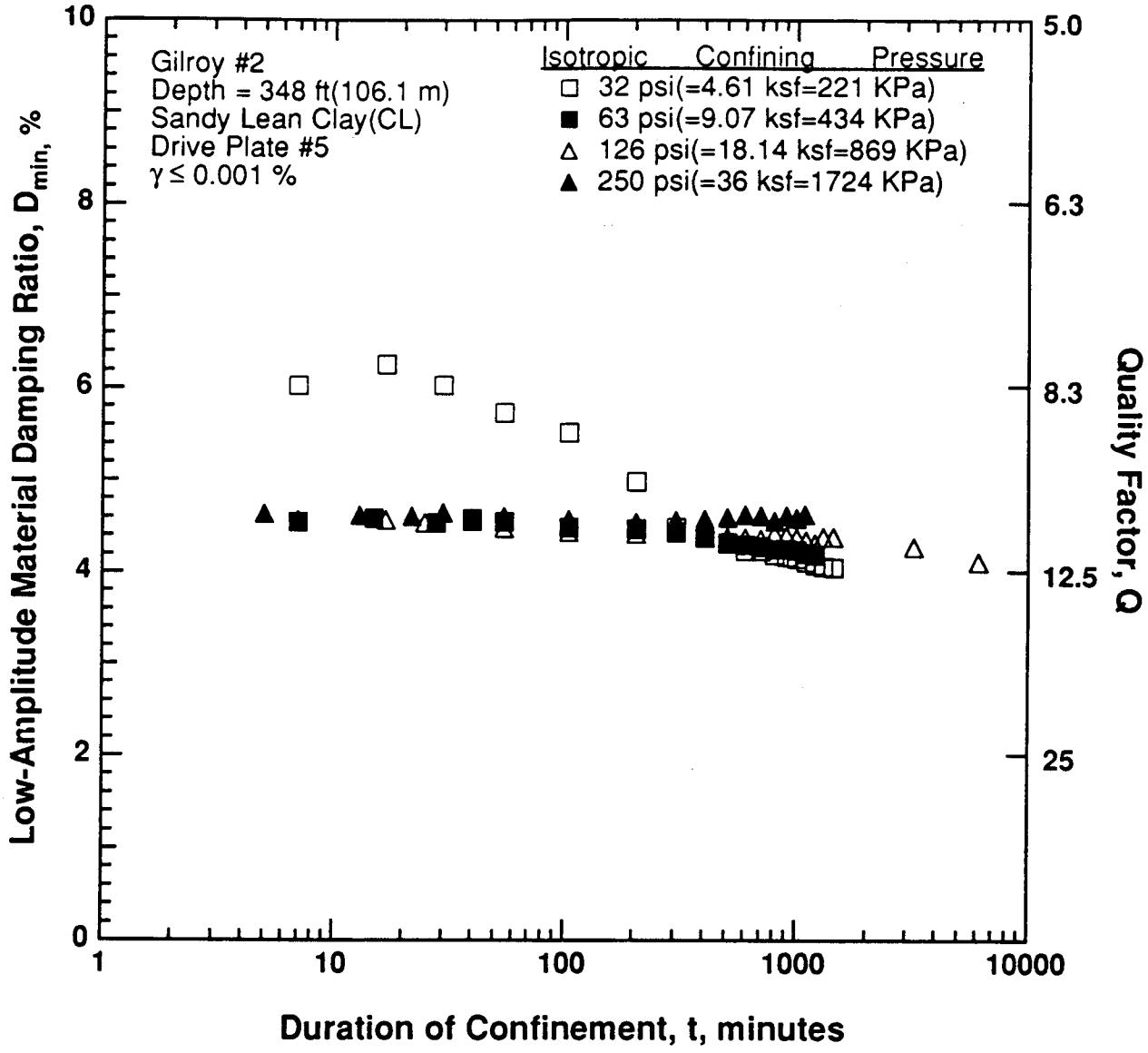

Figure 8.B.2.L-2
Variation in low-amplitude material damping ratio with magnitude and duration of isotropic confining pressure from resonant column tests of sample G8.

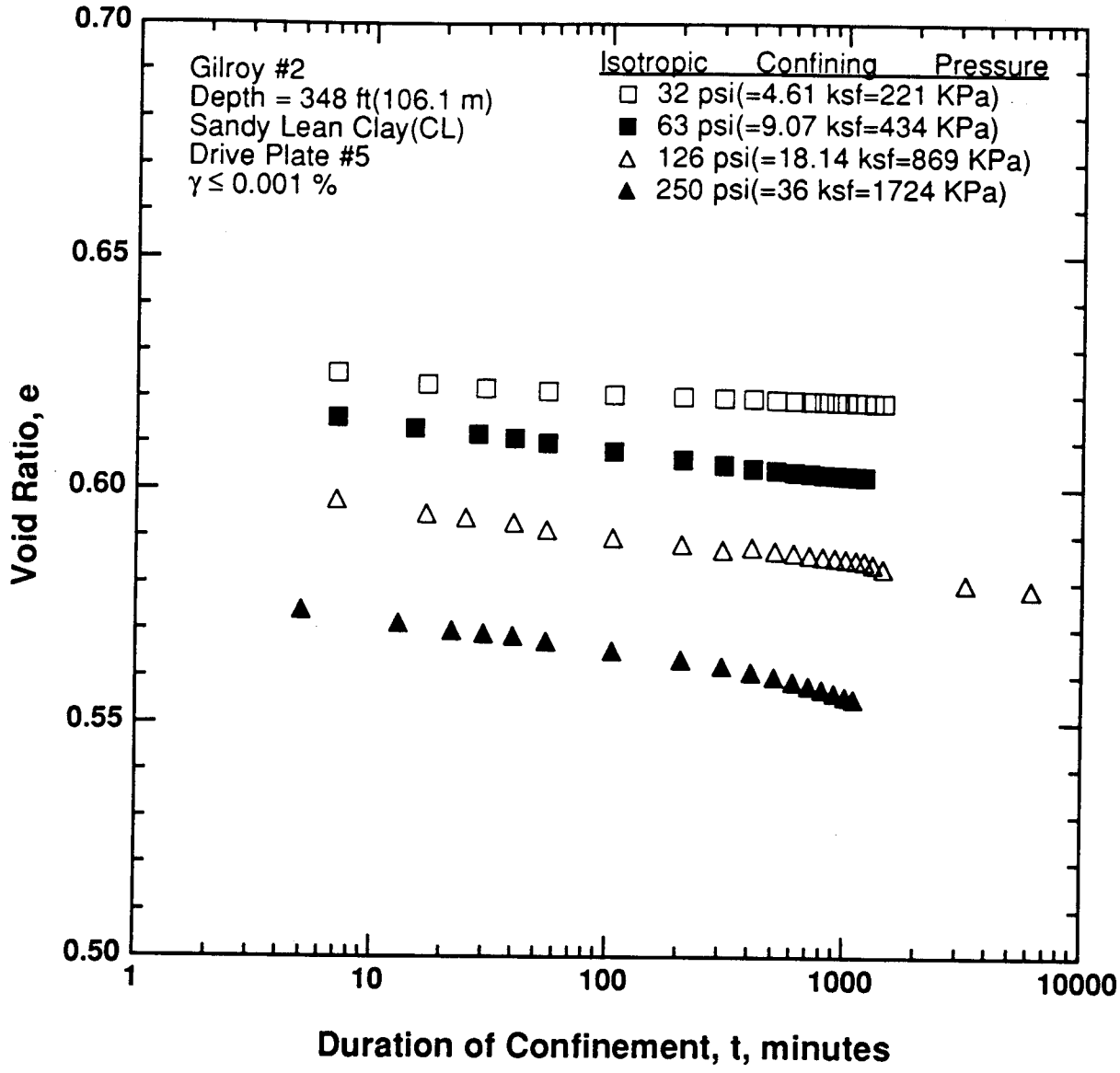

Figure 8.B.2.L-3
Variation in void ratio with magnitude and duration of isotropic confining pressure from resonant column tests of sample G8.

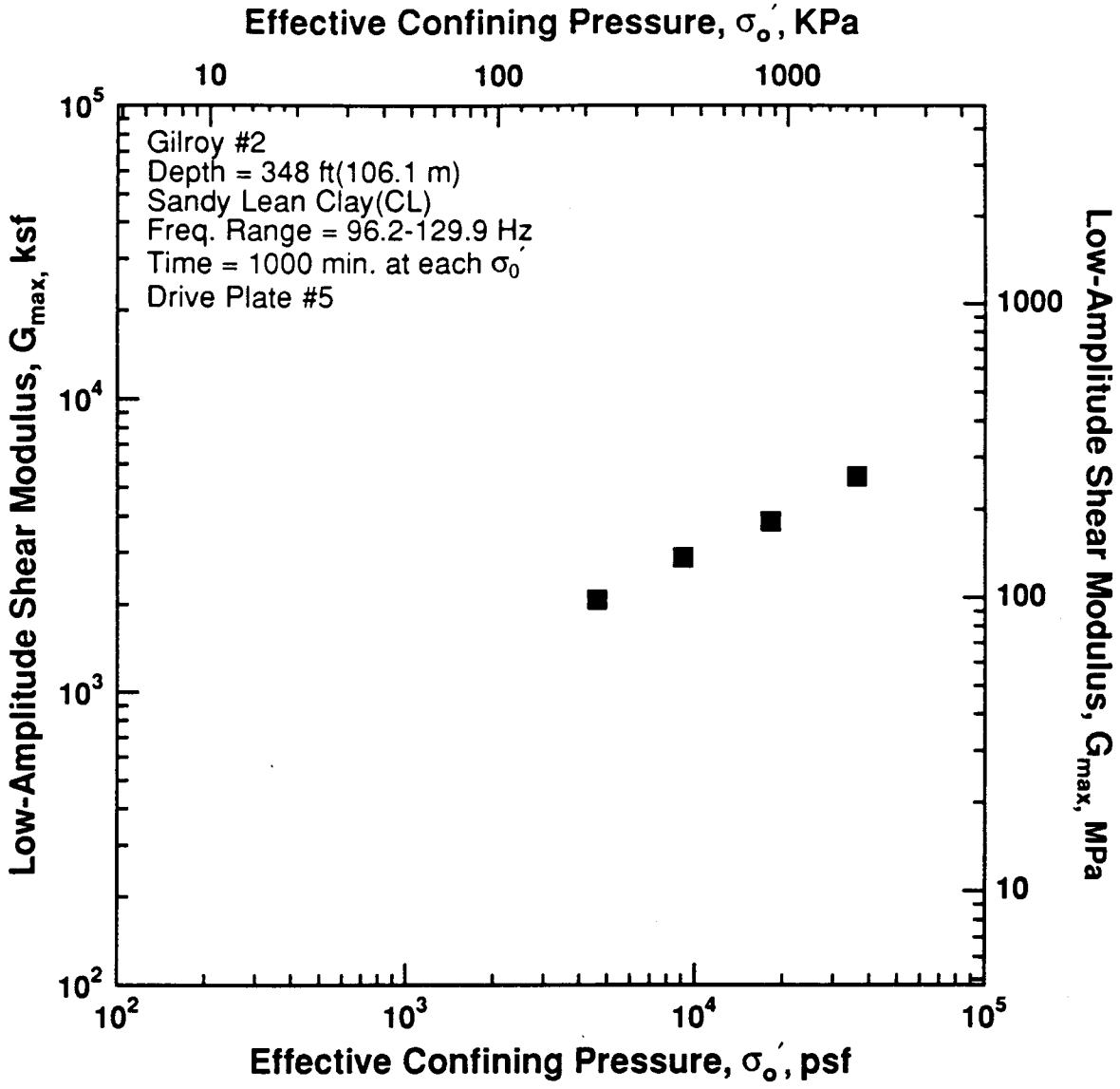

Figure 8.B.2.L-4
Variation in low-amplitude shear modulus with effective confining pressure from resonant column tests of sample G8.

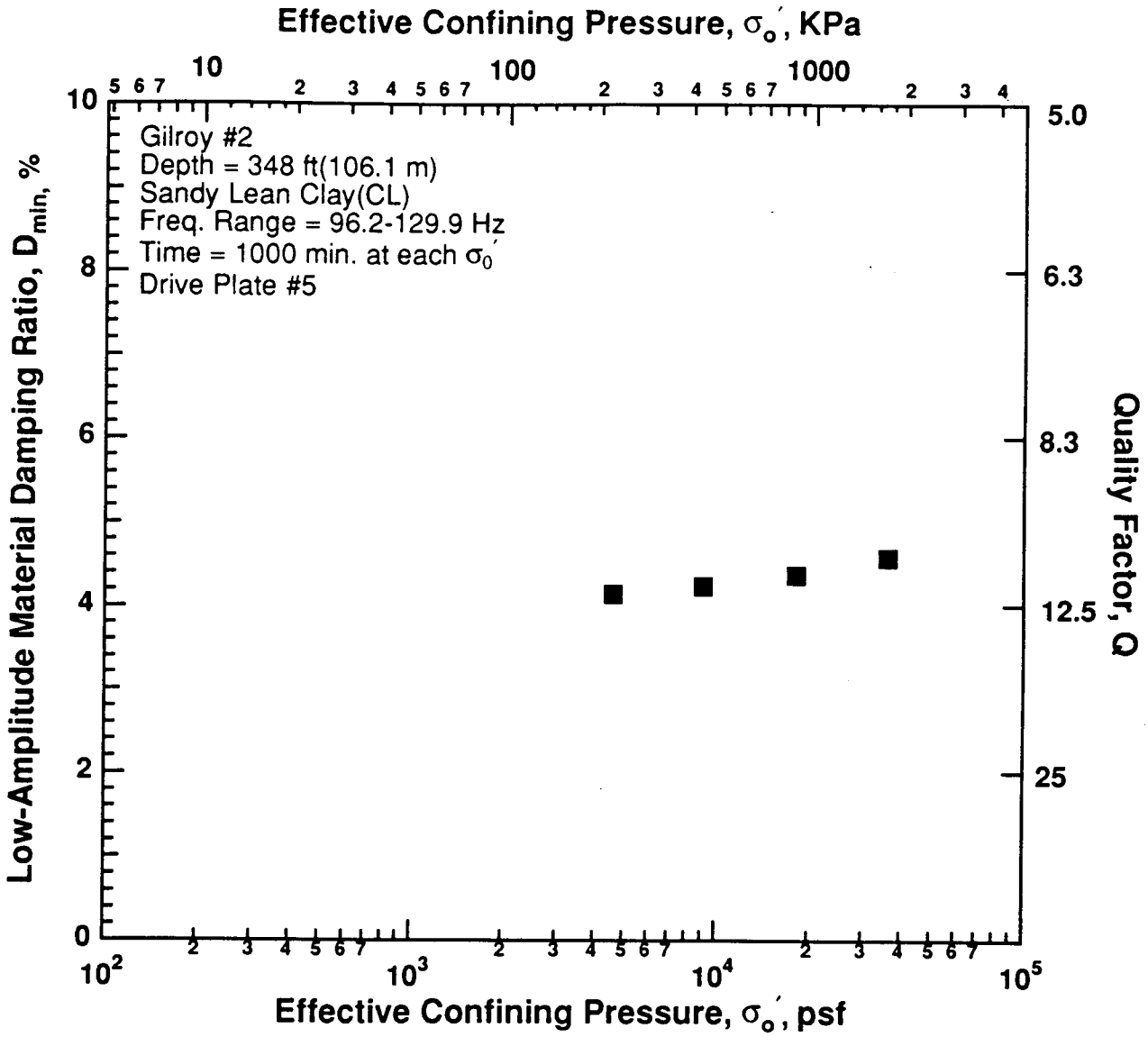

Figure 8.B.2.L-5
Variation in low-amplitude material damping ratio with effective confining pressure from resonant column tests of sample G8.

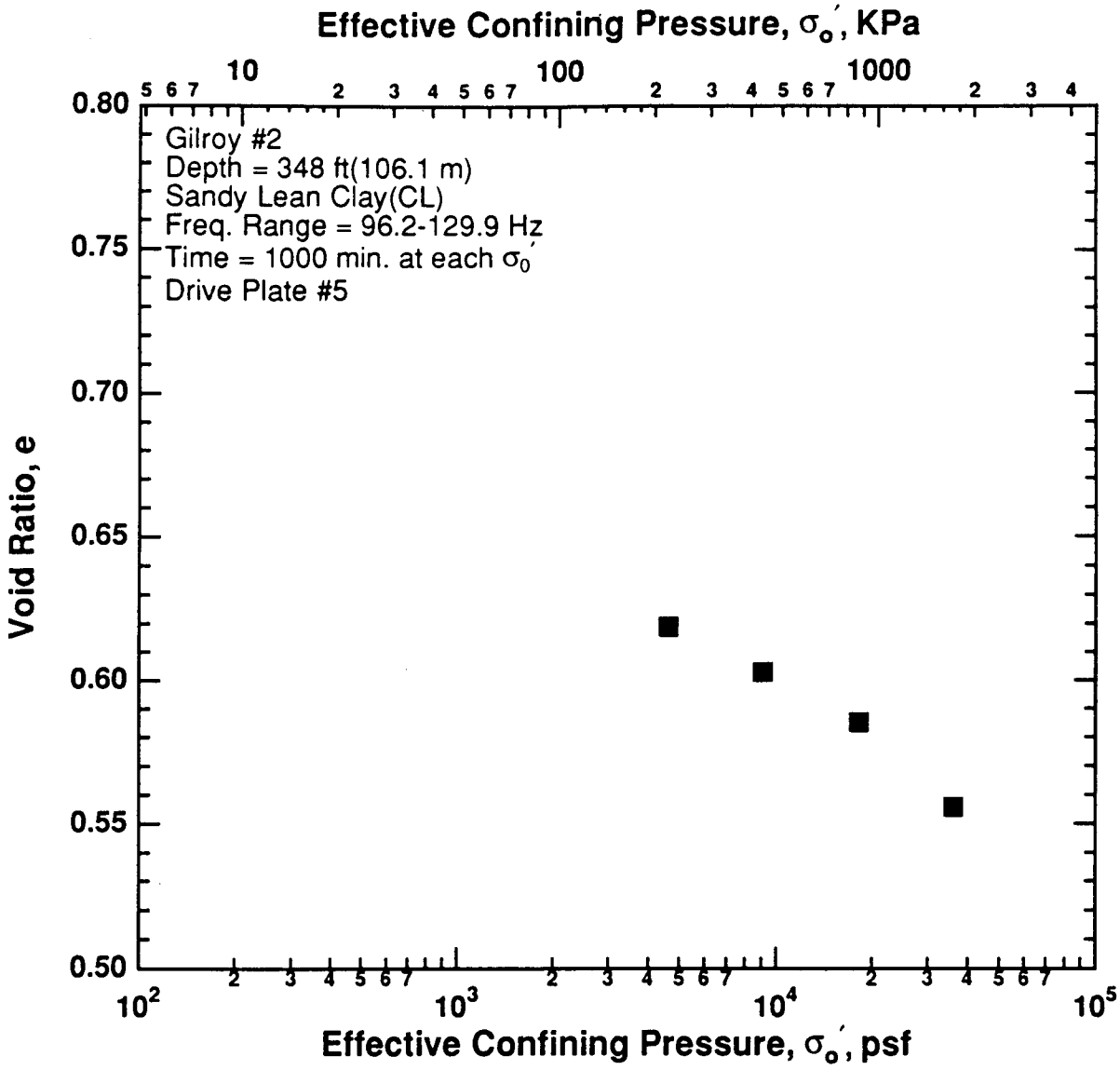

Figure 8.B.2.L-6
Variation in void ratio with effective confining pressure from resonant column tests of sample G8.

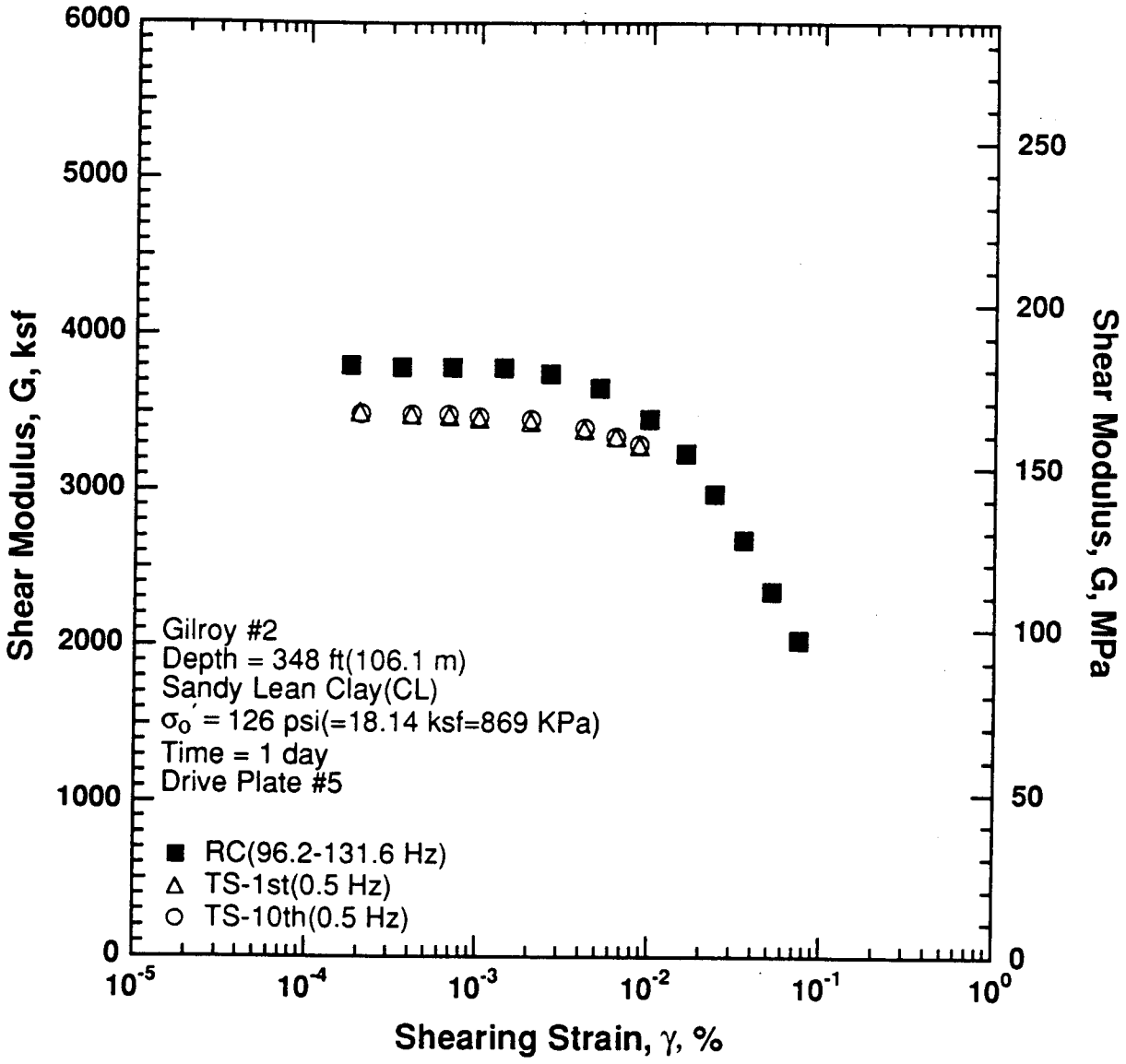

Figure 8.B.2.L-7
Variation in shear modulus with shearing strain at an effective confining pressure of 126 psi (18.14 ksf, 869 kPa) from RCTS tests of sample G8.

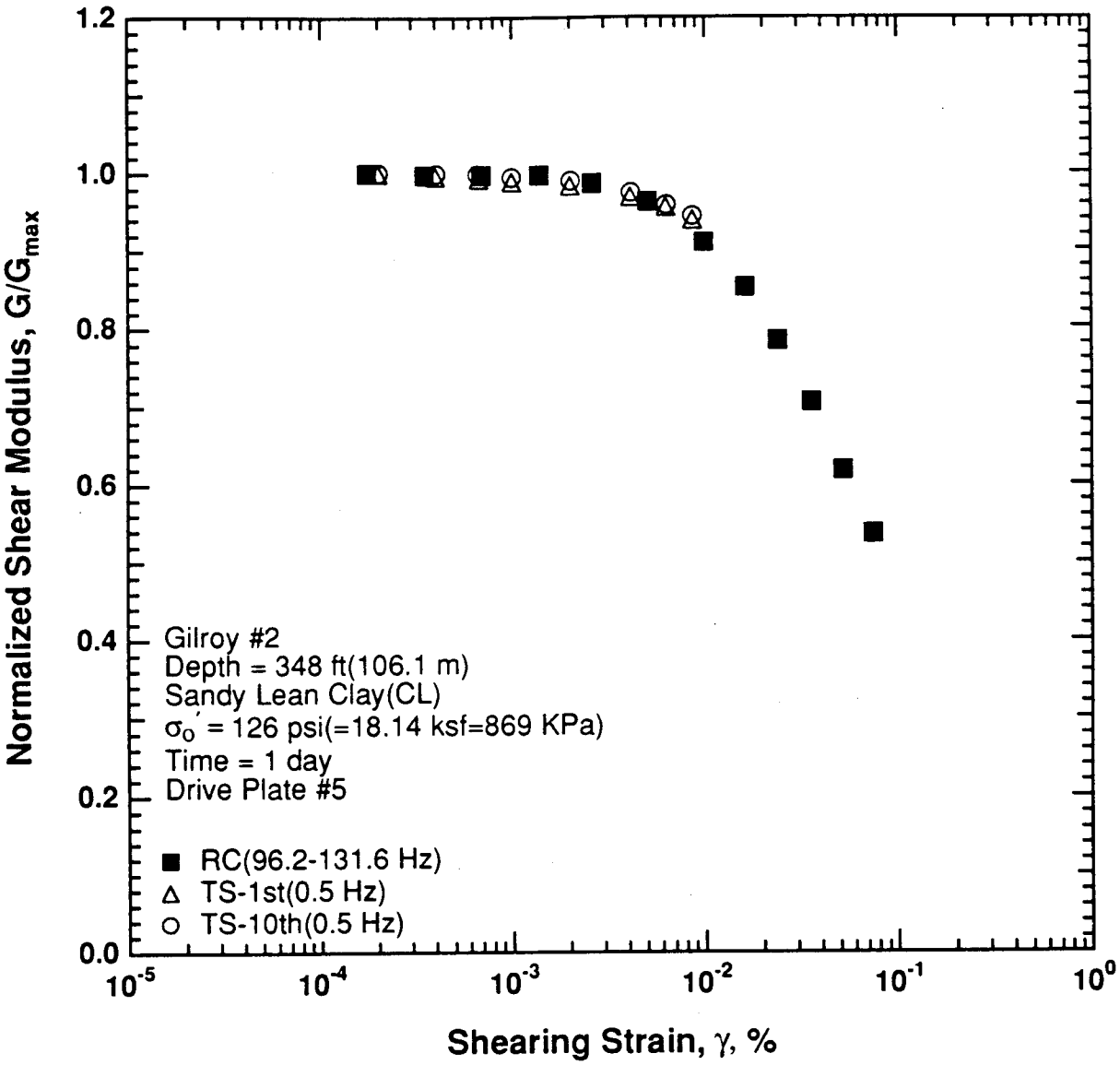

Figure 8.B.2.L-8
Variation in normalized shear modulus with shearing strain at an effective confining pressure of 126 psi (18.14 ksf, 869 kPa) from RCTS tests of sample G8.

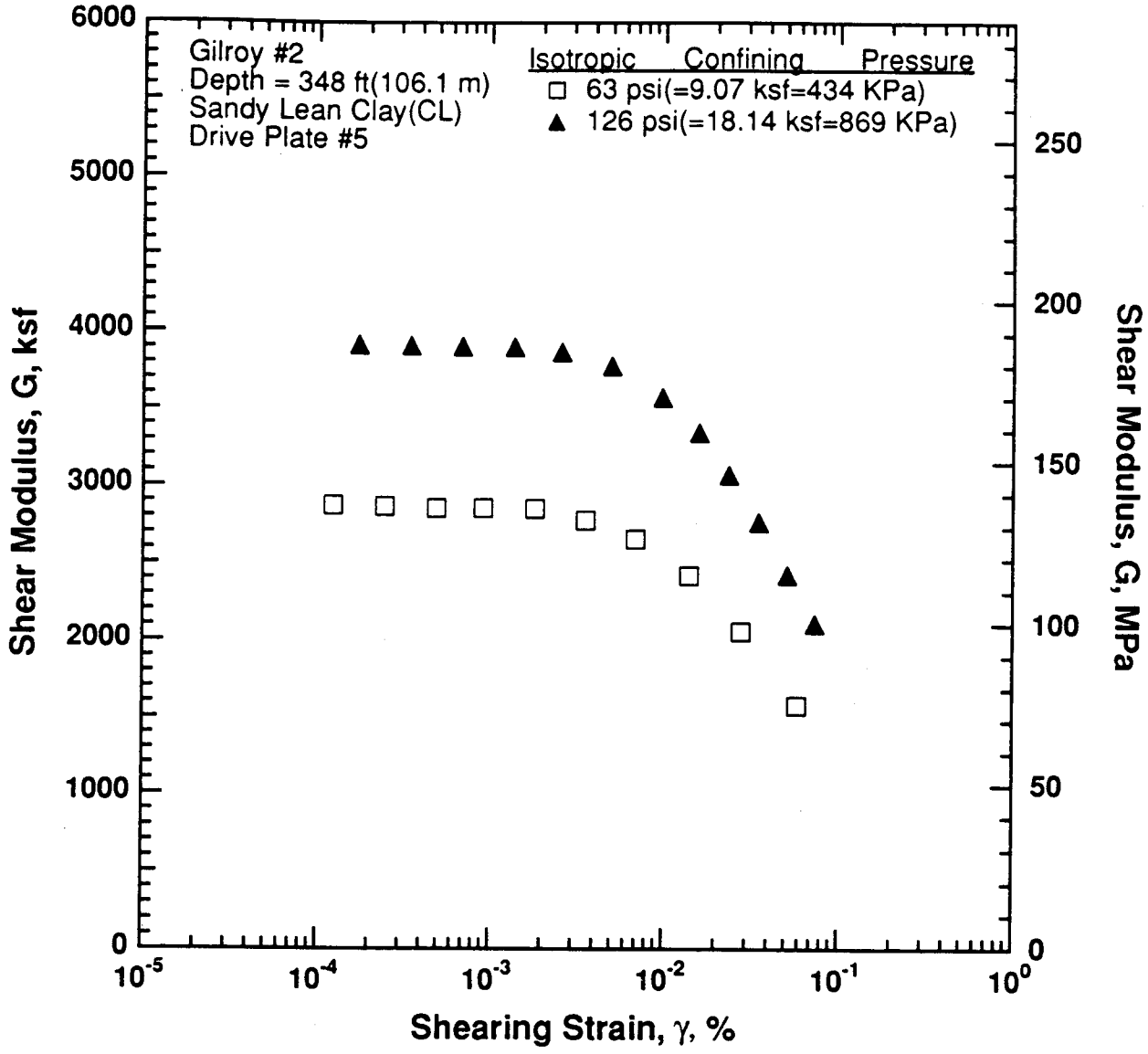

Figure 8.B.2.L-9
Variation in shear modulus with shearing strain and effective confining pressure from resonant column tests of sample G8.

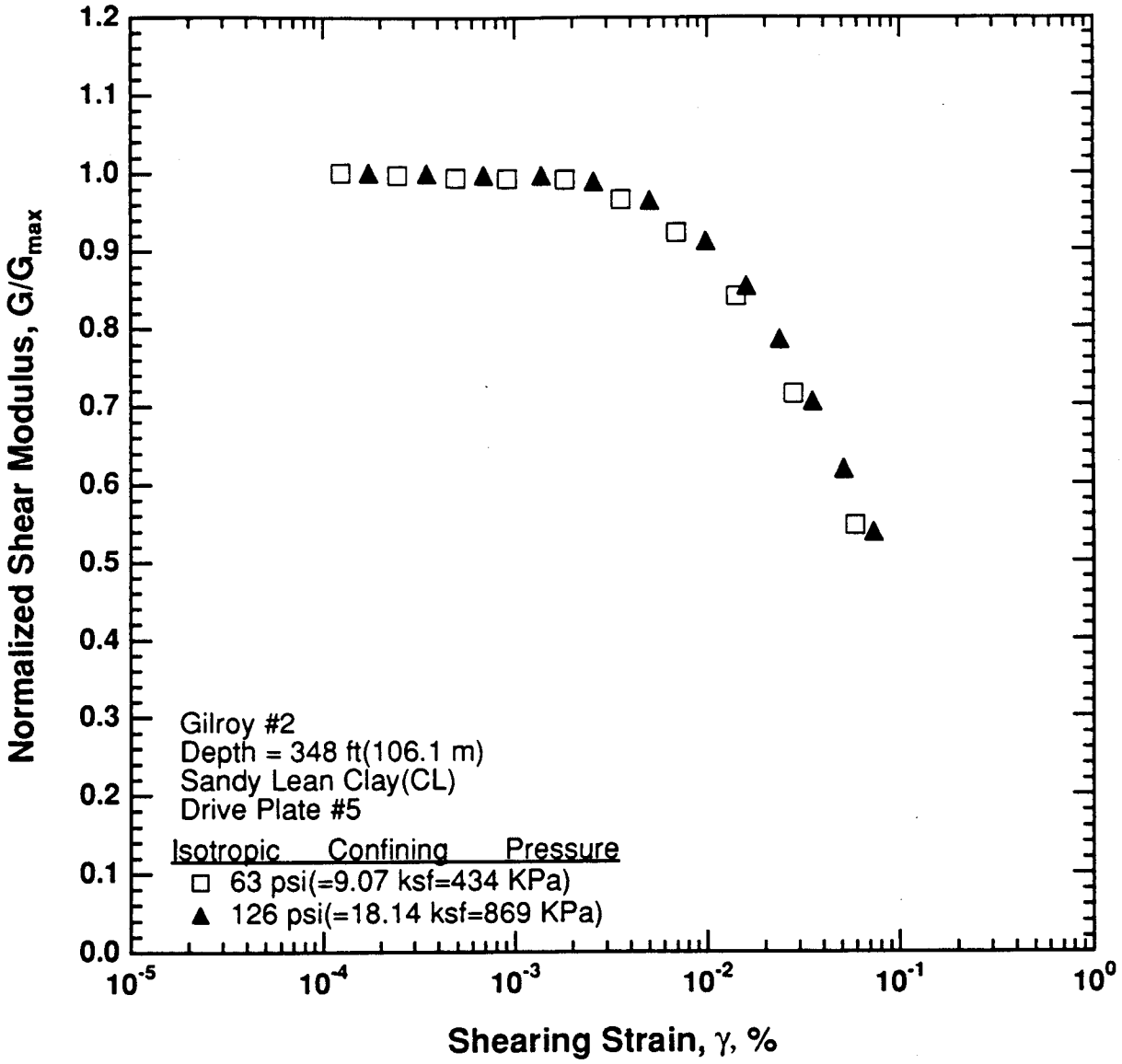

Figure 8.B.2.L-10
Comparison of the variation in normalized shear modulus with shearing strain and effective confining pressure from resonant column tests of sample G8.

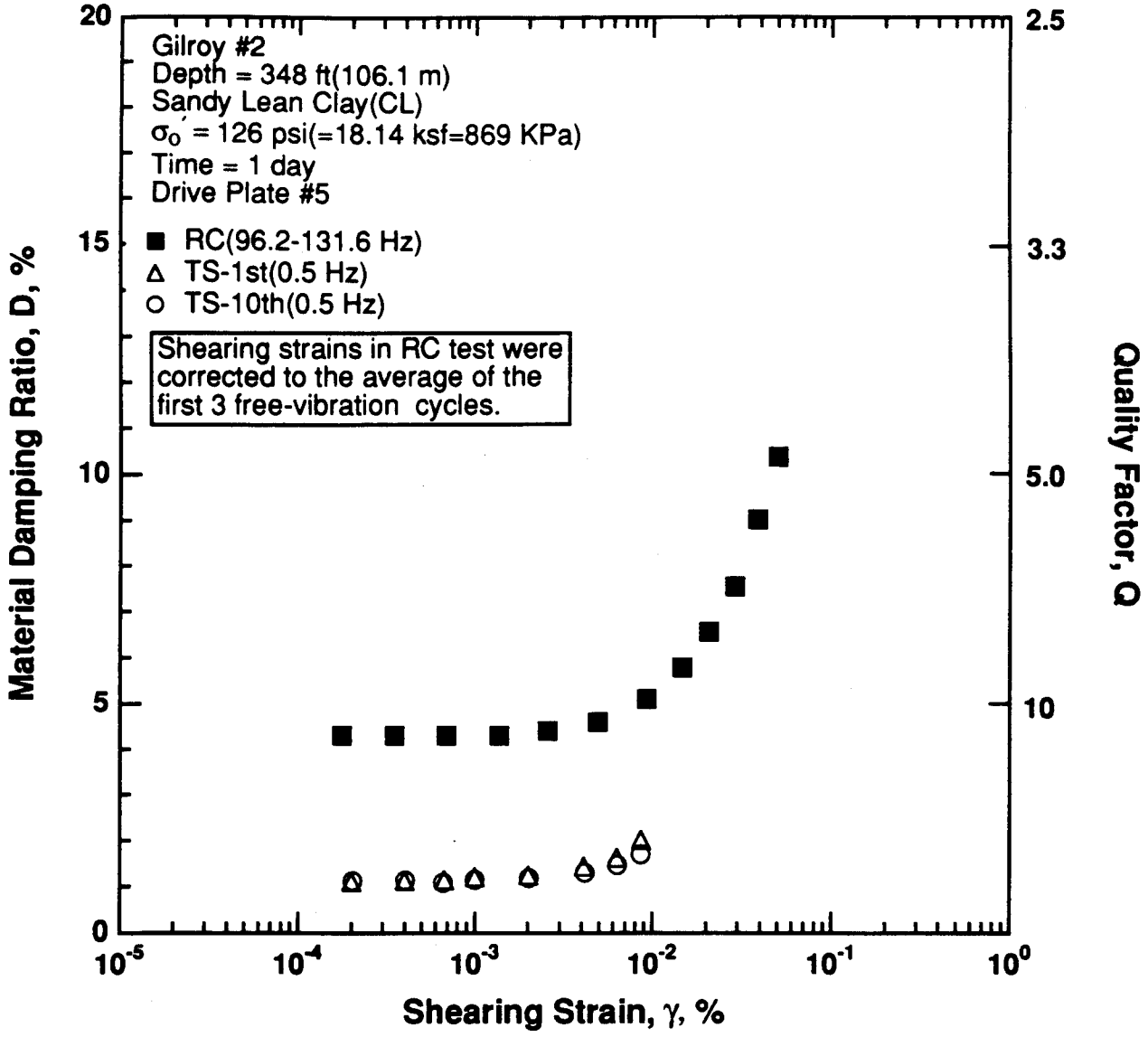

Figure 8.B.2.L-11
Variation in material damping ratio with shearing strain at an effective confining pressure of 126 psi (18.14 ksf, 869 kPa) from RCTS tests of sample G8.

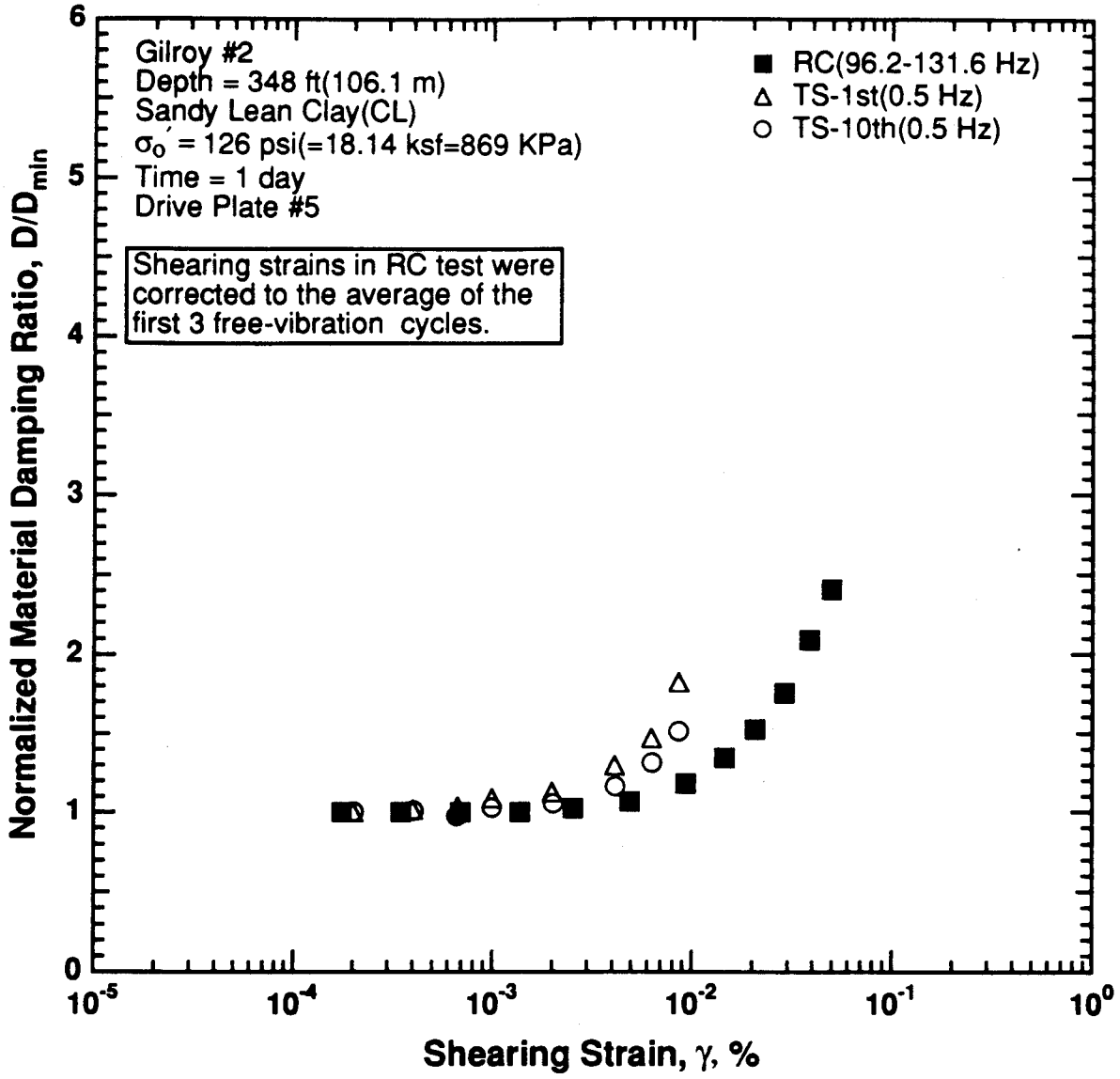

Figure 8.B.2.L-12
Variation in normalized material damping ratio with shearing strain at an effective confining pressure of 126 psi (18.14 ksf, 869 kPa) from RCTS tests of sample G8.

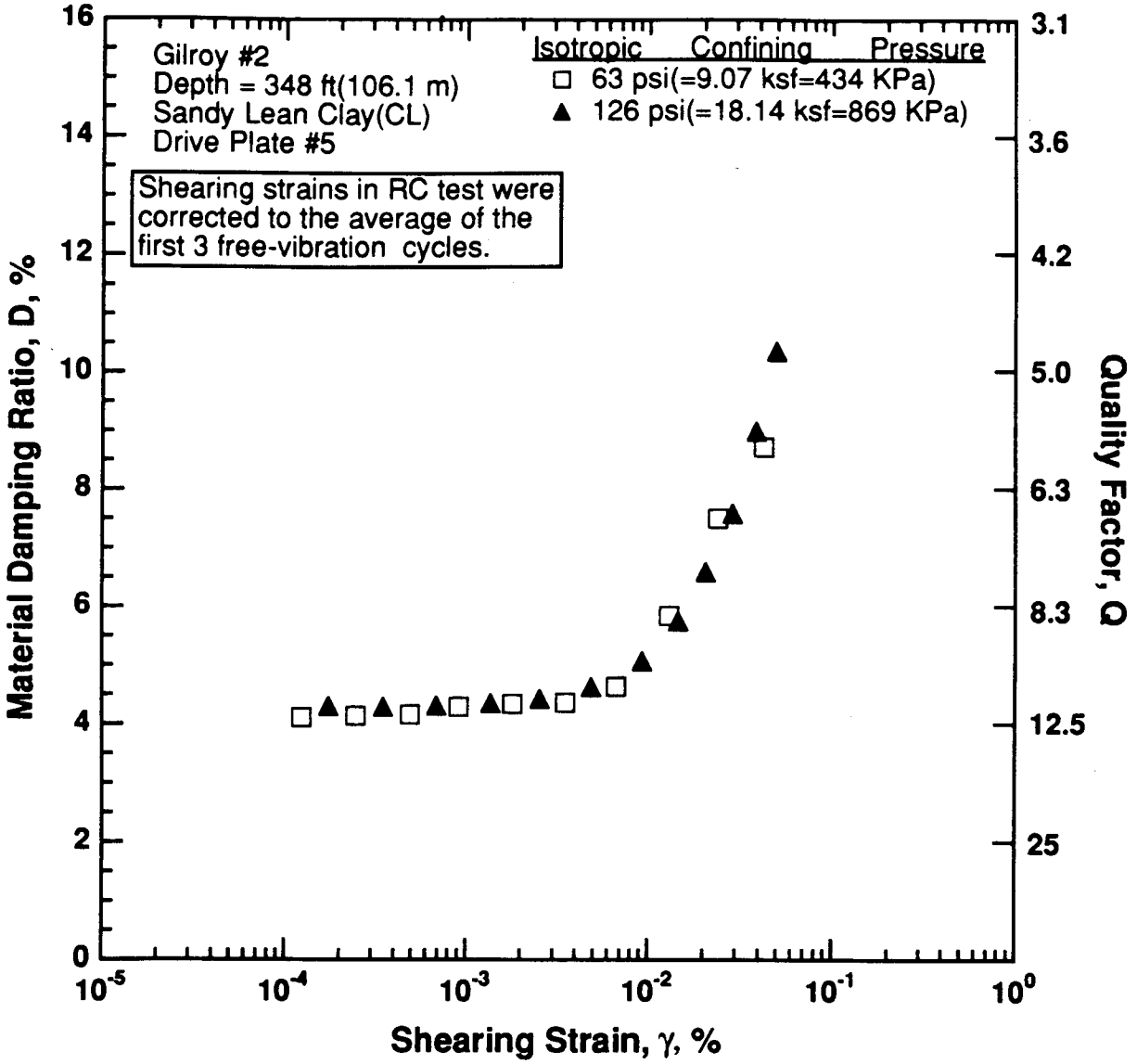

Figure 8.B.2.L-13
Variation in material damping ratio with shearing strain and effective confining pressure from resonant column tests of sample G8.

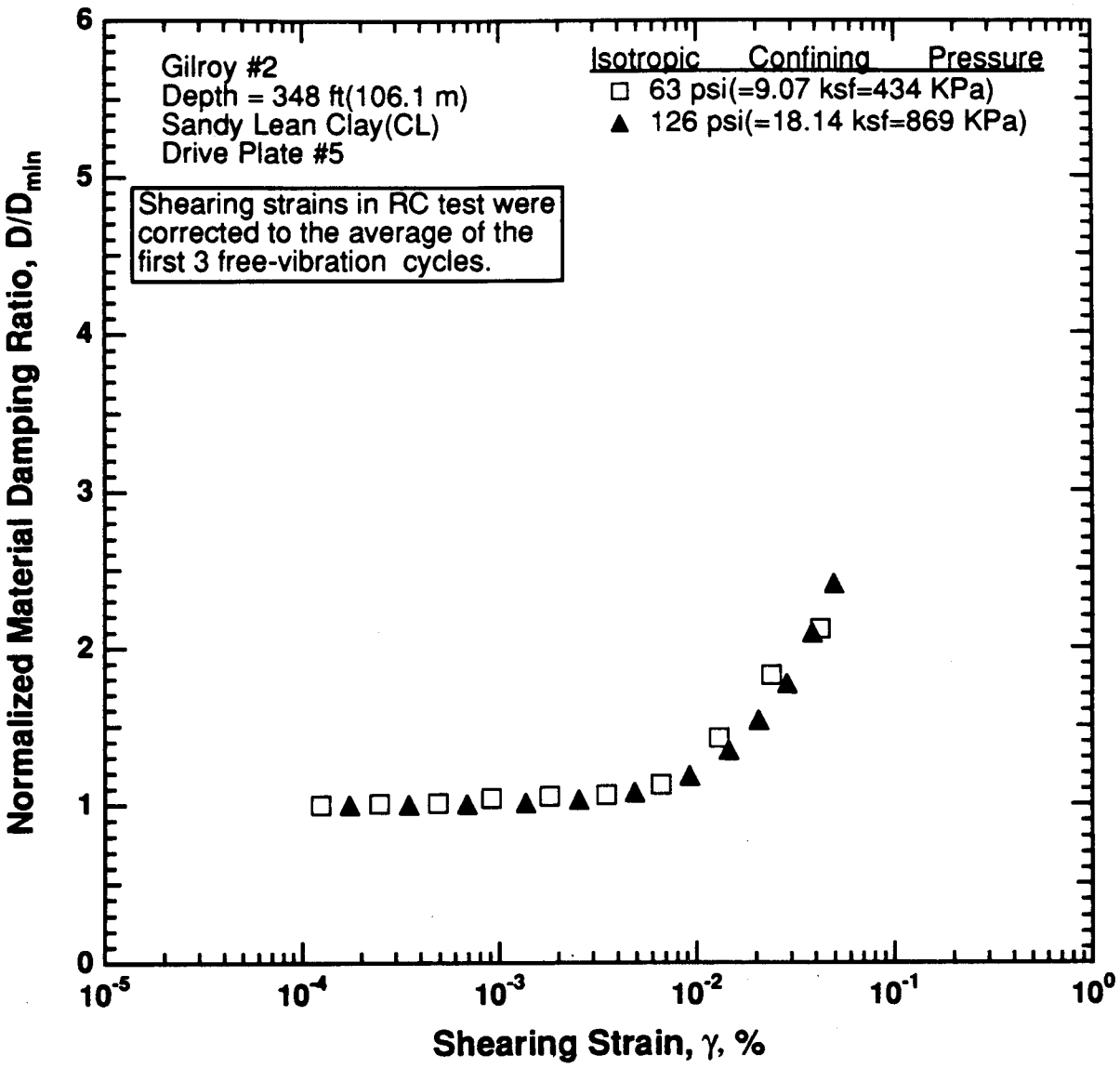

Figure 8.B.2.L-14
Comparison of the variation in normalized material damping ratio with shearing strain and effective confining pressure from resonant column tests of sample G8.

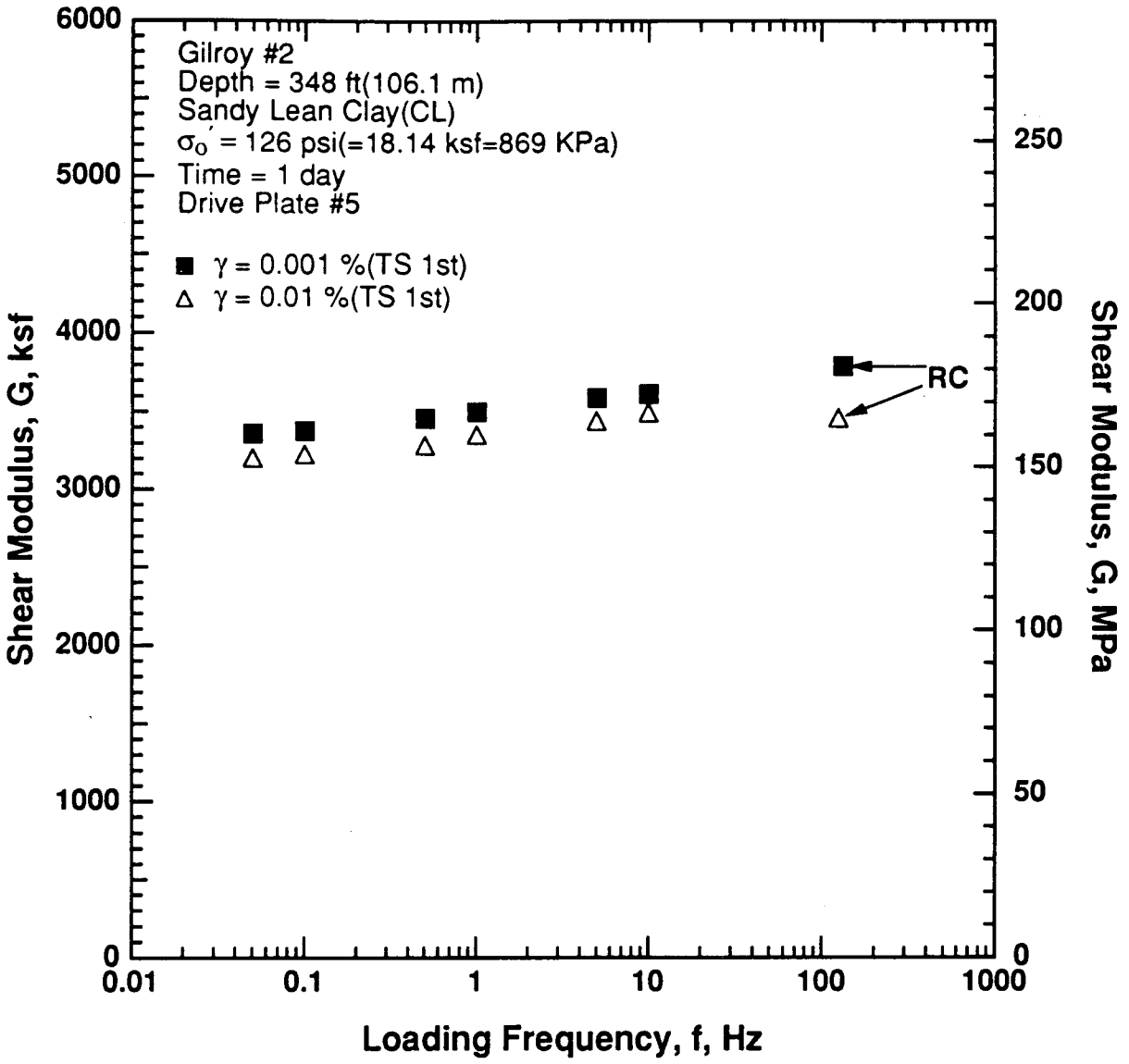

Figure 8.B.2.L-15
Variation in shear modulus with loading frequency and shearing strain at an effective confining pressure of 126 psi (18.14 ksf, 869 kPa) from RCTS tests of sample G8.

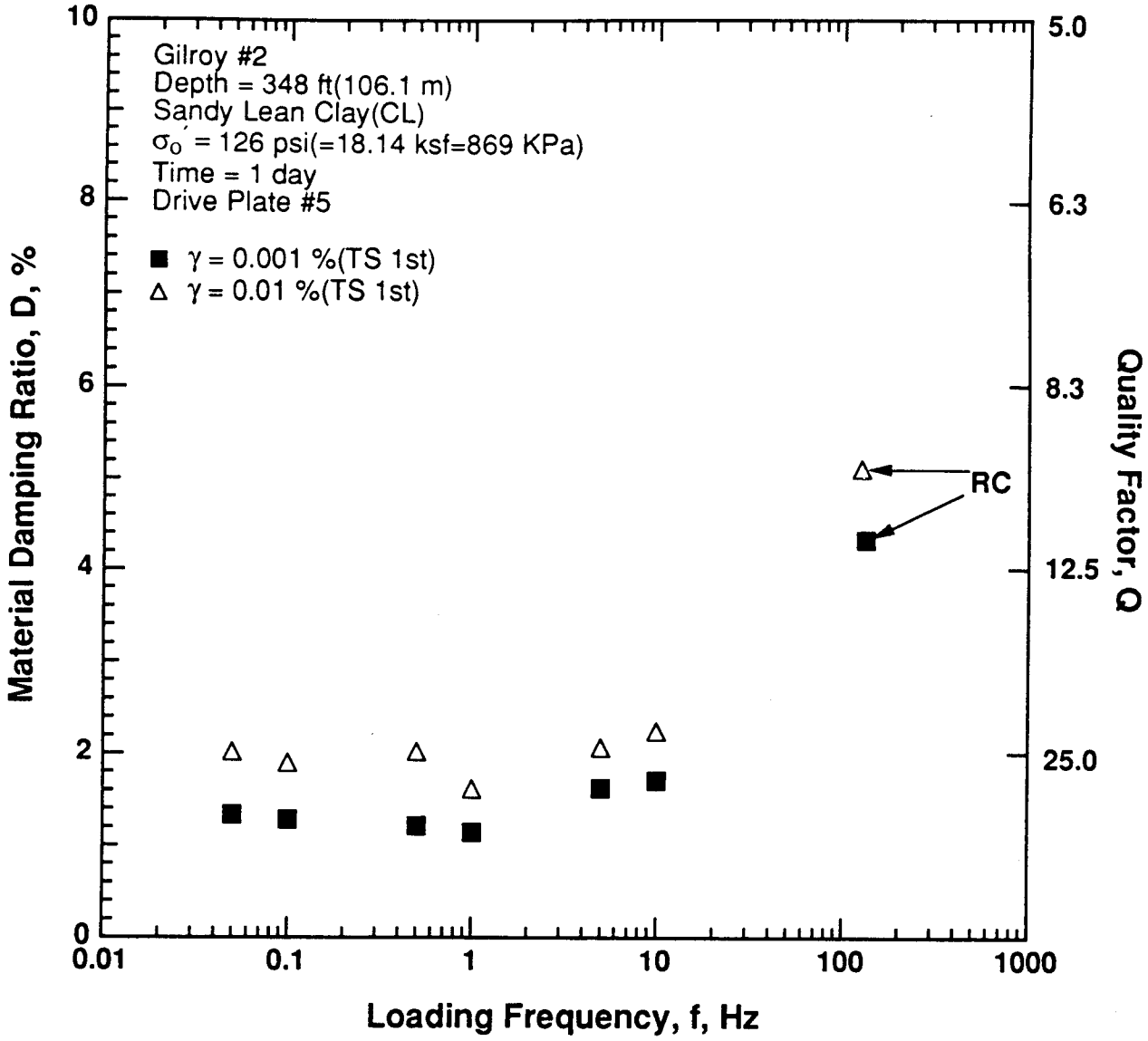

Figure 8.B.1.L-16
Variation in material damping ratio with loading frequency and shearing strain at an effective confining pressure of 126 psi (18.14 ksf, 869 kPa) from RCTS tests of sample G8.

APPENDIX 8.B.2.M
DYNAMIC TESTS OF SAMPLE G9, DEPTH = 410 FT (138.0 M)

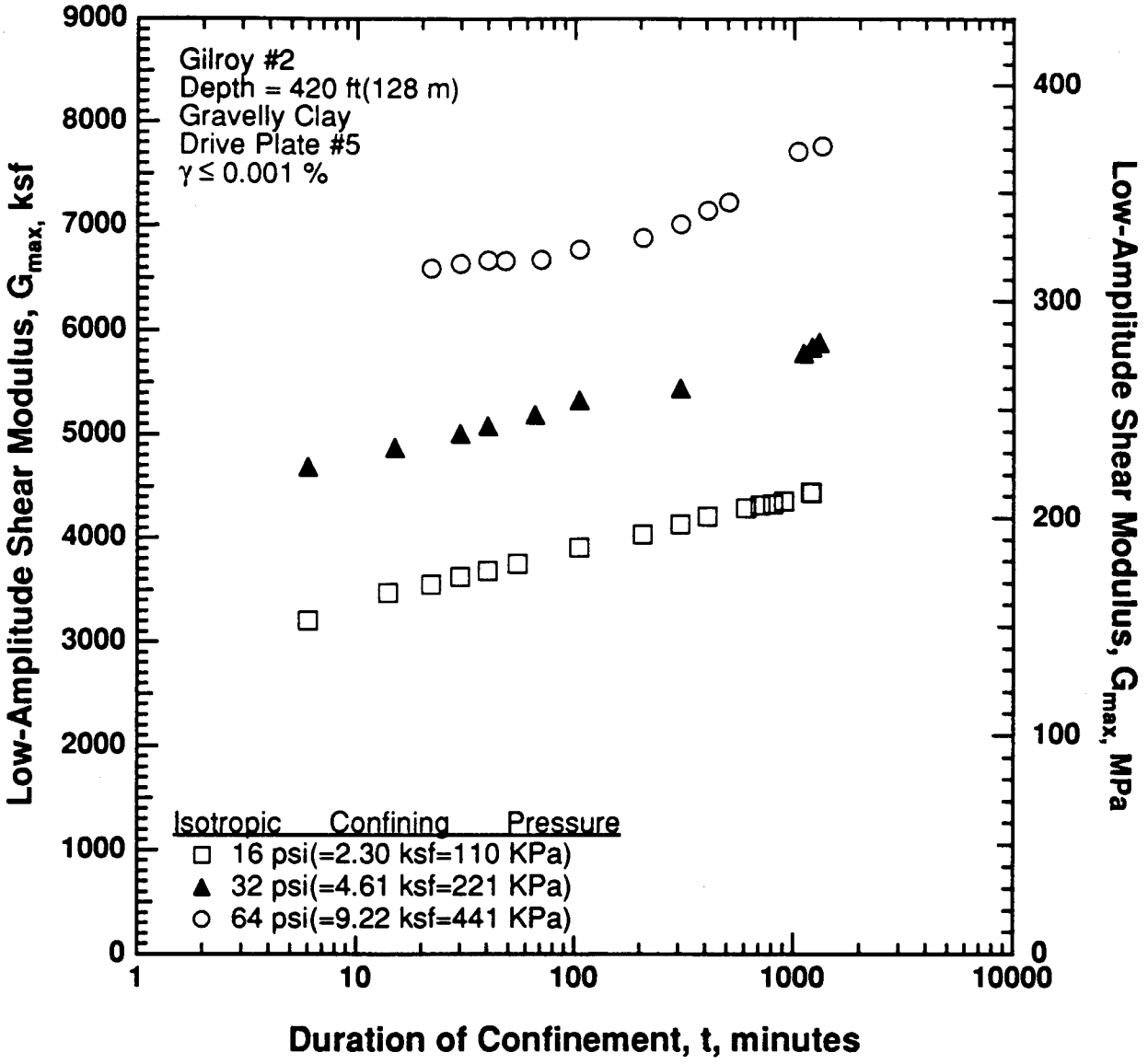

Figure 8.B.2.G-1
Variation in low-amplitude shear modulus with magnitude and duration of isotropic confining pressure from resonant column tests of sample G9.

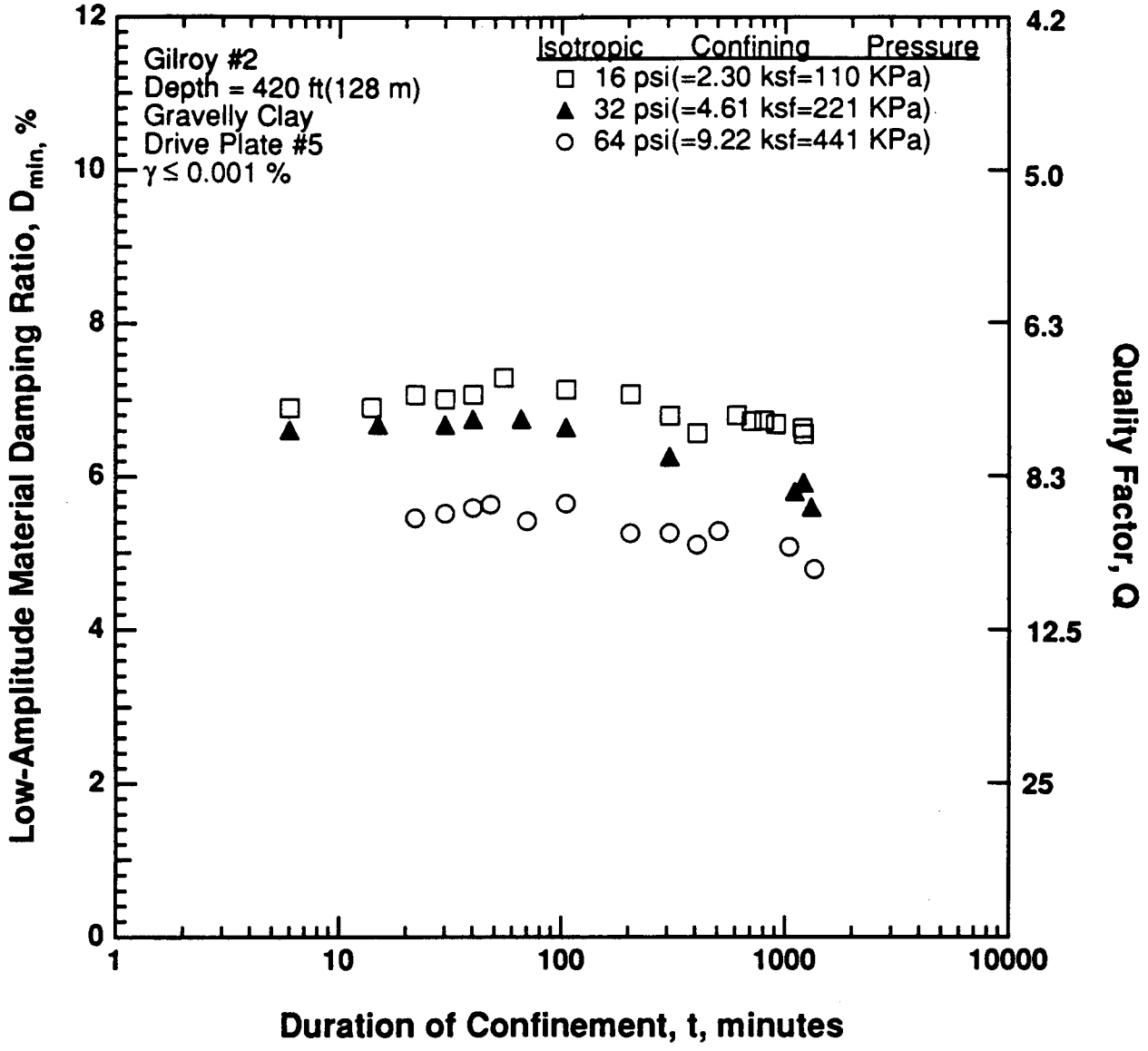

Figure 8.B.2.M-2
Variation in low-amplitude material damping ratio with magnitude and duration of isotropic confining pressure from resonant column tests of sample G9.

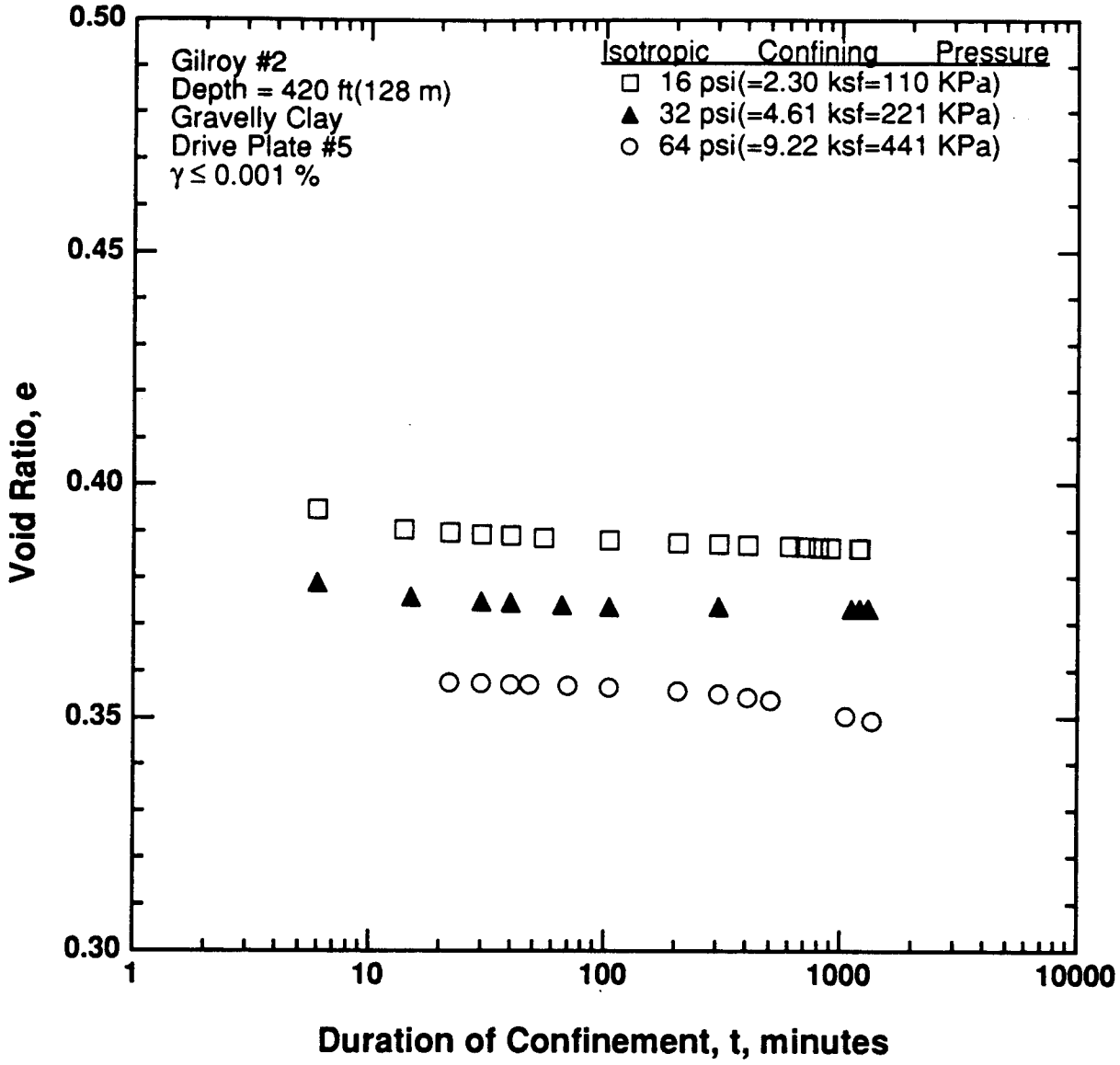

Figure 8.B.2.M-3
Variation in void ratio with magnitude and duration of isotropic confining pressure from resonant column tests of sample G9.

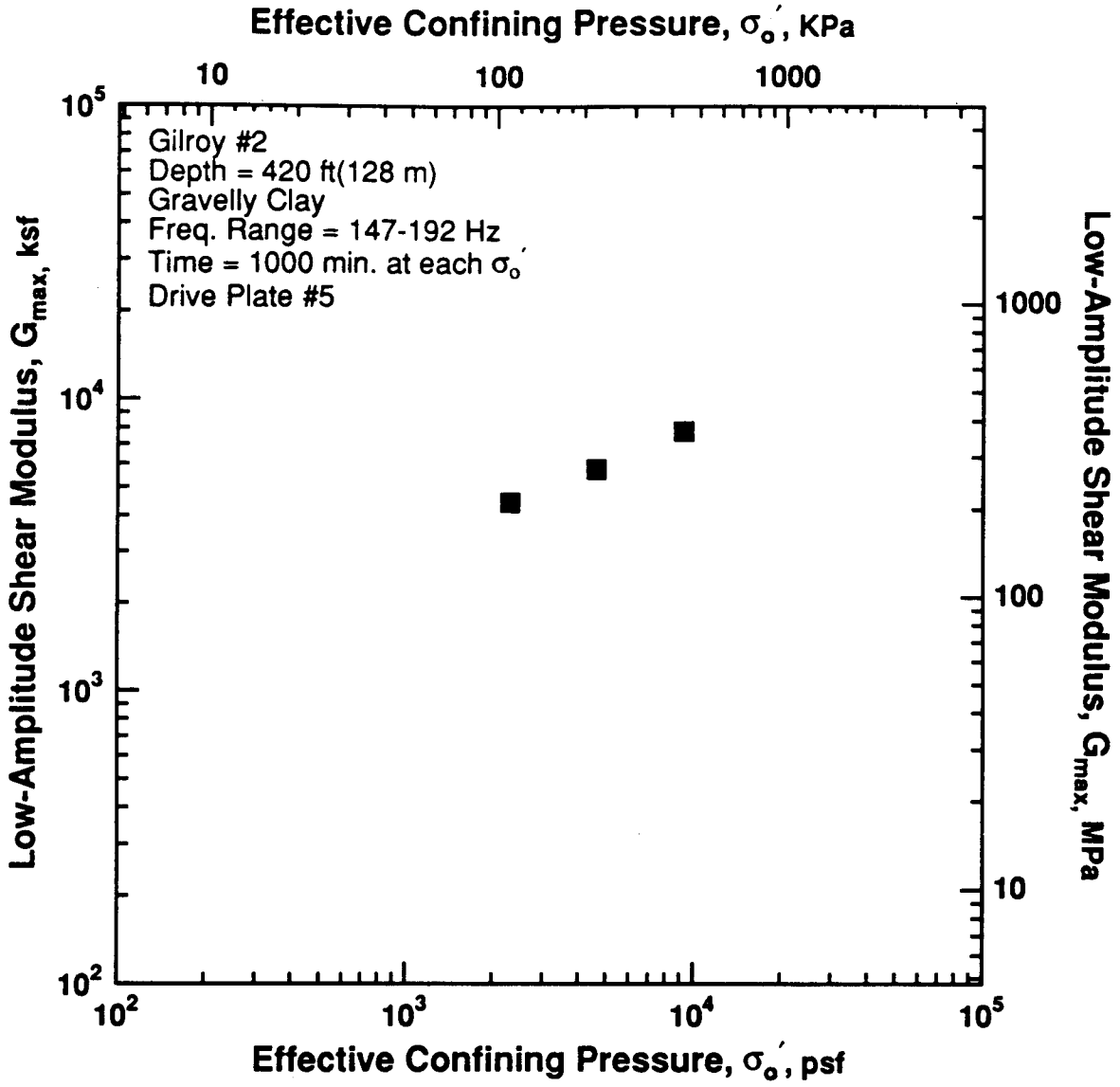

Figure 8.B.2.M-4
Variation in low-amplitude shear modulus with effective confining pressure from resonant column tests of sample G9.

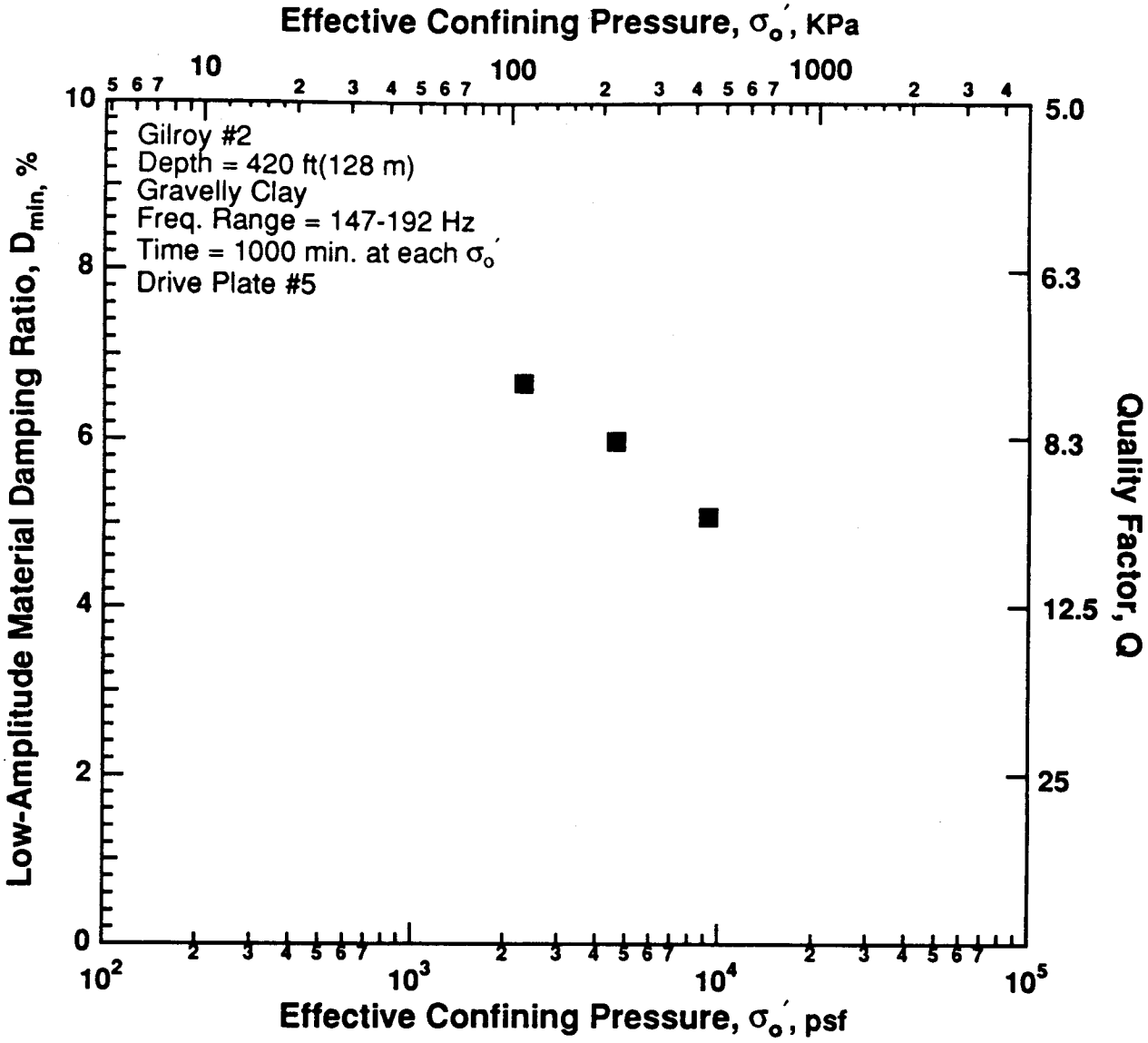

Figure 8.B.2.M-5
Variation in low-amplitude material damping ratio with effective confining pressure from resonant column tests of sample G9.

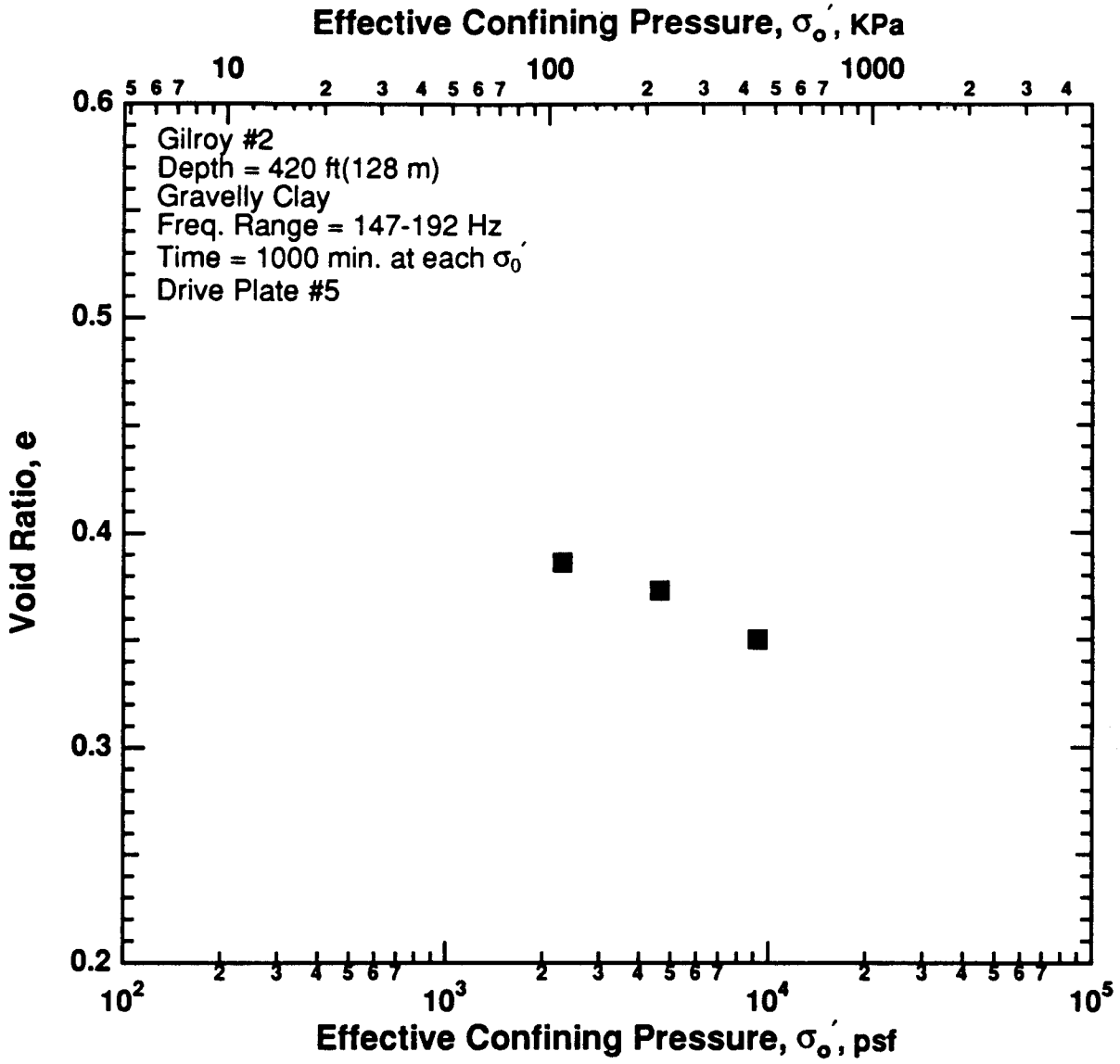

Figure 8.B.2.M-6
Variation in void ratio with effective confining pressure from resonant column tests of sample G9.

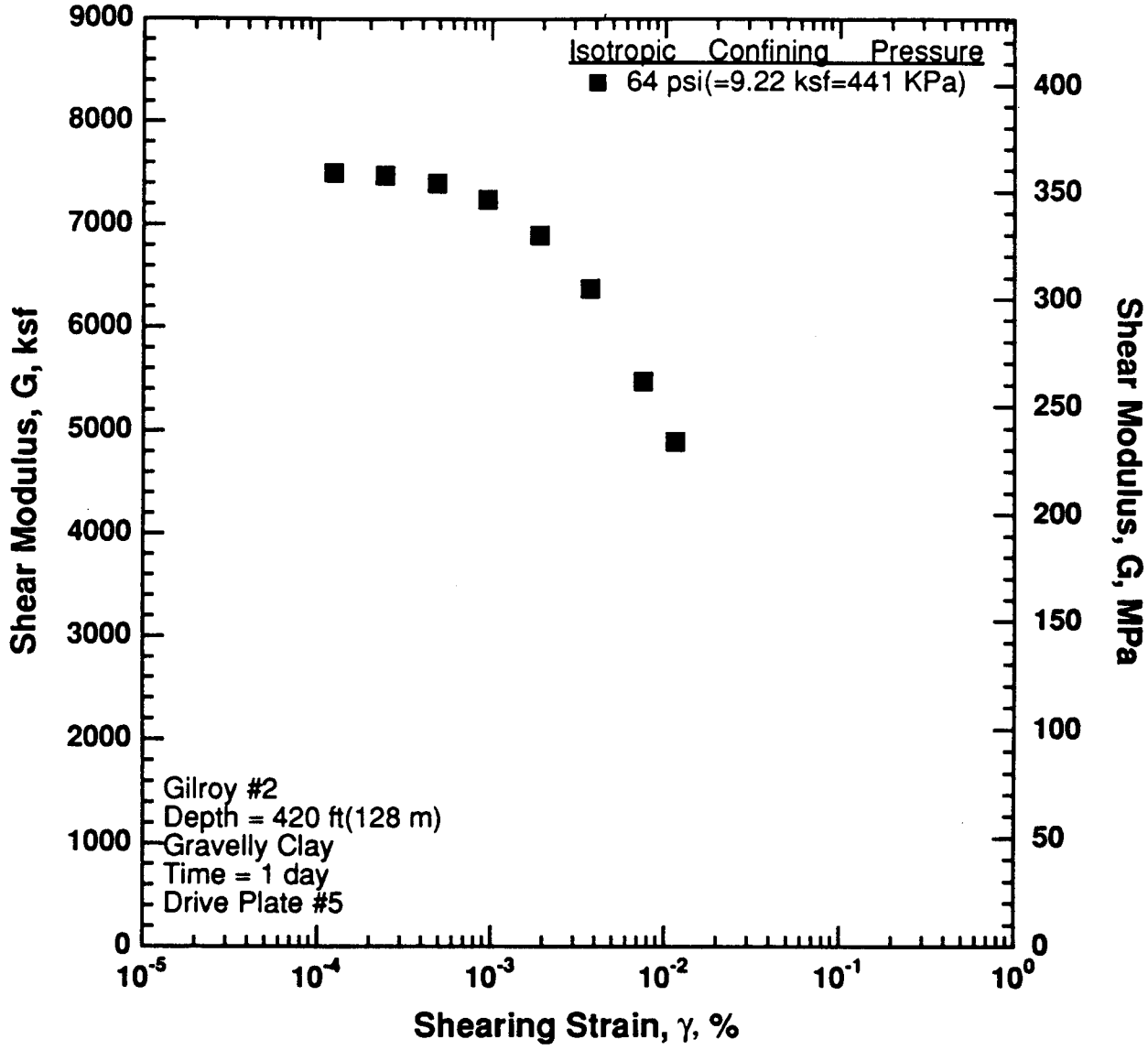

Figure 8.B.2.M-7
Variation in shear modulus with shearing strain and effective confining pressure from resonant column tests of sample G9.

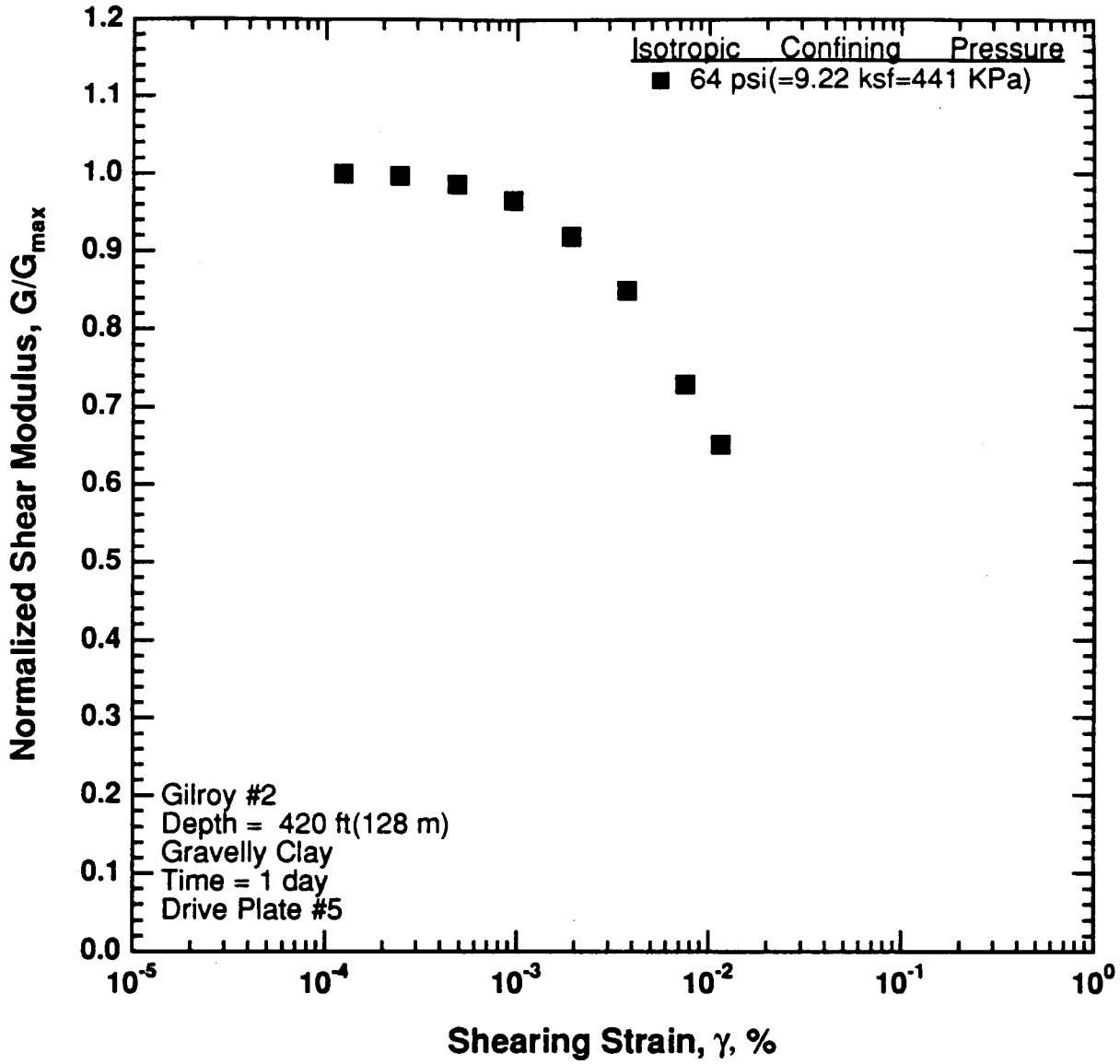

Figure 8.B.2.M-8
Comparison of the variation in normalized shear modulus with shearing strain and effective confining pressure from resonant column tests of sample G9.

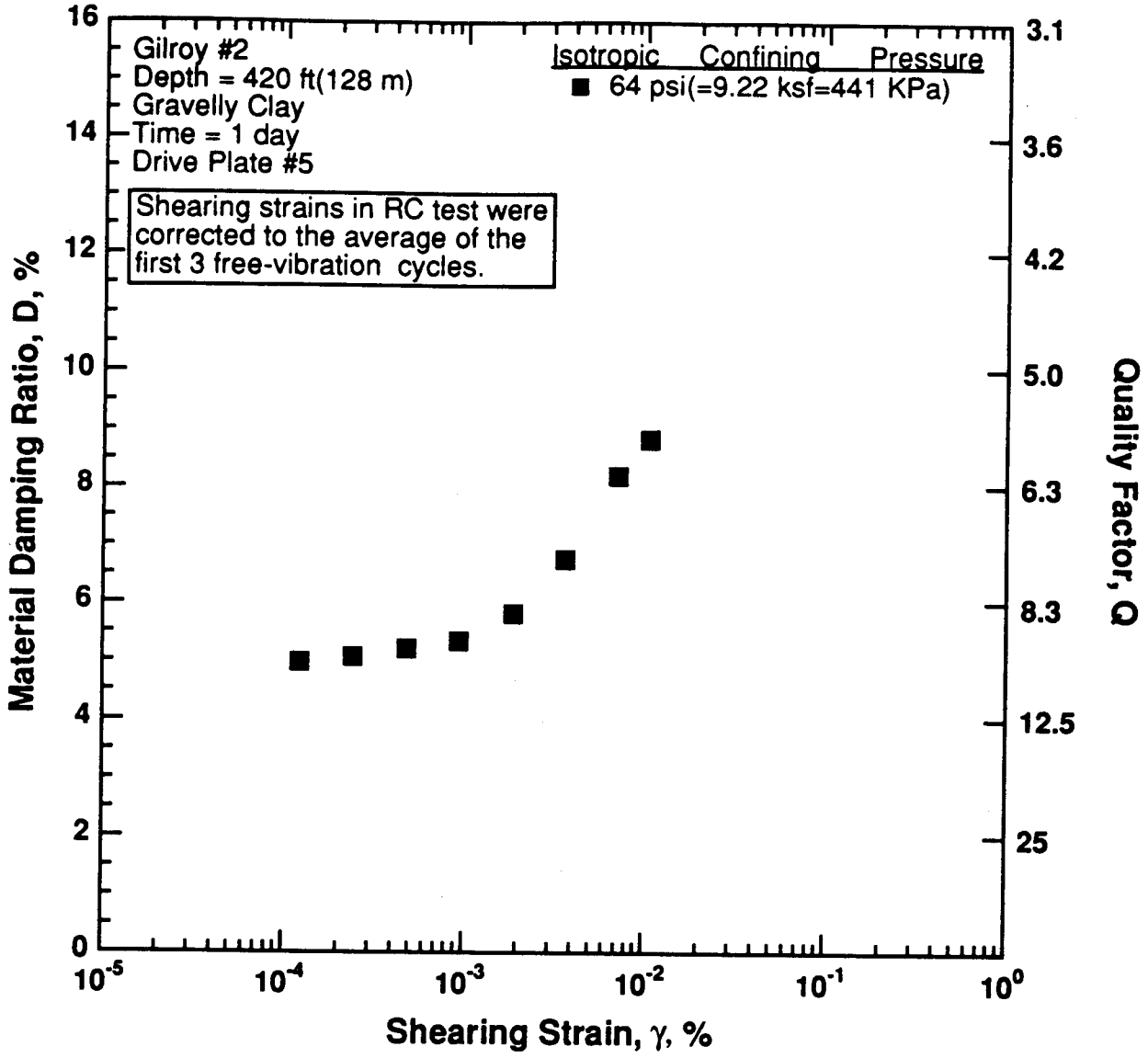

Figure 8.B.2.M-9
Variation in material damping ratio with shearing strain and effective confining pressure from resonant column tests of sample G9.

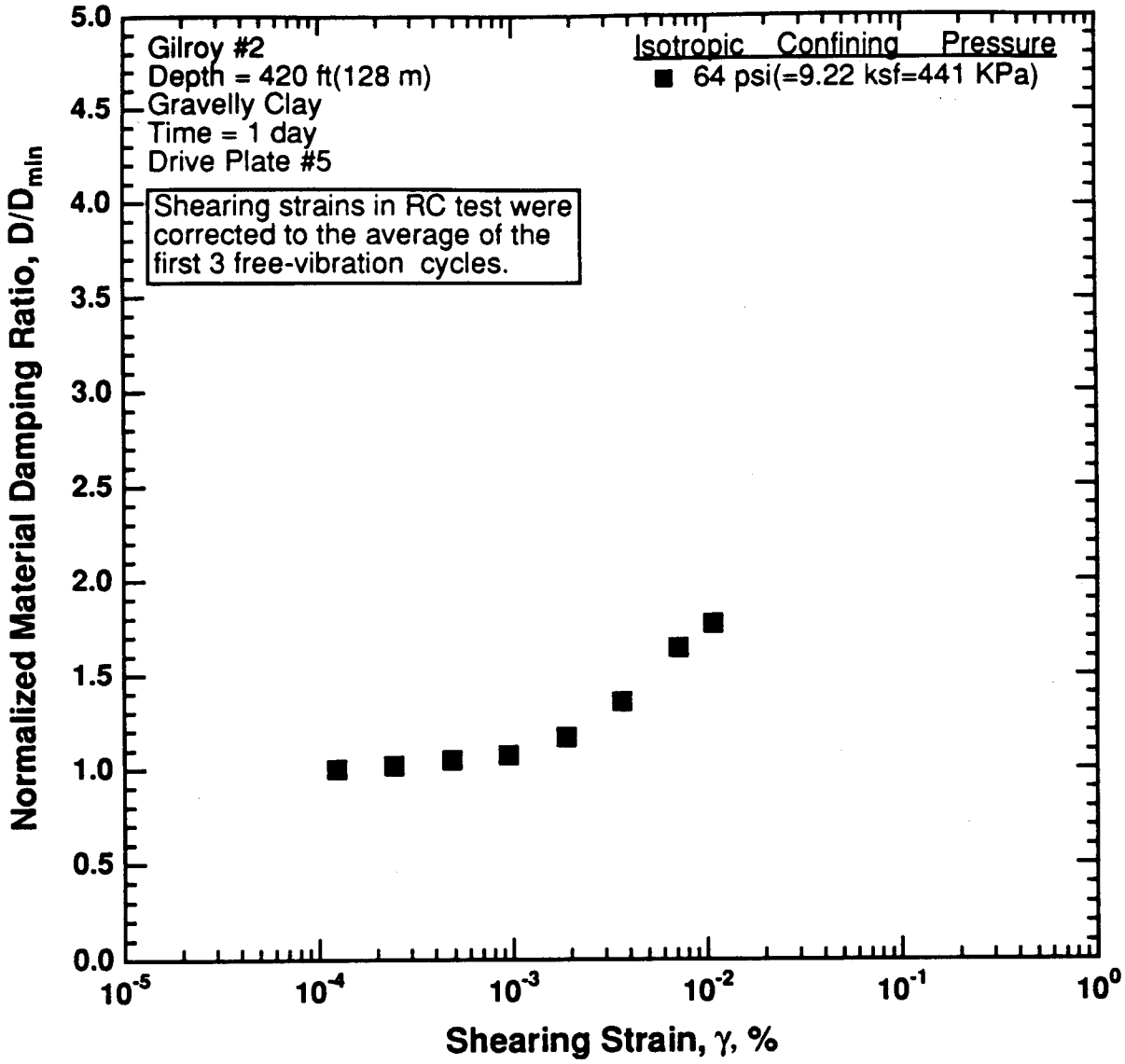

Figure 8.B.2.M-10
Comparison of the variation in normalized material damping ratio with shearing strain and effective confining pressure from resonant column tests of sample G9.

APPENDIX 8.B.3
DYNAMIC PROPERTIES OF UNDISTURBED SOIL SAMPLES FROM LOTUNG, TAIWAN

CONTENTS

APPENDIX 8.B.3
DYNAMIC PROPERTIES OF UNDISTURBED SOIL SAMPLES FROM LOTUNG, TAIWAN

8.B.3.1 Introduction

An investigation of the dynamic properties in shear of undistributed soil samples from the Lotung experiment in Taiwan was conducted as part of the EPRI/DOE Ground Motion Project. The soil samples were obtained in February 1992 as described in the report by Moh and Associates (1992). The samples were sealed in steel Shelby tubes and shipped to the University of Texas at Austin in mid-March. Dynamic laboratory testing of the undisturbed samples occurred between May and October 1992.

A total of eight samples was tested. The samples were obtained from depths ranging from 18 ft (5.5 m) to 146 ft (44.5 m). Initial properties of the samples are listed in Table 8.B.3-1. The samples range from silty sands (SM) to silts (ML). Samples in the upper 133 ft (40.5 m) of the profile exhibit a rather narrow range in water contents (31% to 37%), void ratios (0.82 to 1.02) and total unit weights (109 to 119 pcf (17.1 to 18.7 kN/m^3)). Grain size distribution curves for the five, nonplastic samples are given in Figure 8.B.3-1.

To minimize disturbance effects, each sample was extruded from the 3 in. (7.6 cm) diameter sampling tube and hand trimmed to the final specimen dimensions. The dimensions were nominally either 2 in. (5.1 cm) in diameter and 4 in. (10.2 cm) in height or 1.5 in. (3.8 cm) in diameter and 3 in. (7.6 cm) in height. The smaller of the two specimen sizes was used to obtain the larger dynamic strains in testing. No significant problems were encountered in preparation and testing of the undisturbed specimens. The key in the preparation process was cutting the sampling tubes using a high-speed (25,000 rpm) rotary bit used by hobby enthusiasts. The tubes were cut into approximately 6 in. (15.2 cm) lengths before extruding the samples.

8.B.3.2 Dynamic Laboratory Tests

Resonant column and torsional shear (RCTS) equipment was used to investigate the dynamic characteristics of the intact Lotung samples. This equipment is described in detail in Appendix 8.B.3.A. The dynamic characteristics of concern are the shear modulus, G, and the material damping ratio in shear, D. These parameters were evaluated to determine the influence on them of the following variables:

- magnitude of isotropic state of stress. Four to six isotropic pressures were used which ranged from below to above the estimated in situ mean effective stress.
- time of confinement at each isotropic state of stress. Confinement times at each pressure ranged from 1 to about 3 days.
- shearing strain amplitude. Strains ranged from the small-strain range, less than 0.001%, to rather large strain amplitudes, strains slightly above 0.2%.
- numbers of cycles of loading. One to ten cycles of loading were used in the torsional shear test followed by 500 to 1000 cycles in the resonant column test.
- excitation frequency. Frequencies ranging from 0.1 Hz to about 10 Hz were used in the torsional shear test while the frequency associated with resonance in the resonant column test varied with soil stiffness and ranged from 20 Hz to about 130 Hz.

Table 8.B.3-1
Initial Properties of Samples Tested from Lotung, Taiwan

Sample Number	Depth ft (m)	Soil Type (Unified Soil Classification)	LL %	PI %	D_{10} mm	D_{30} mm	D_{60} mm	R_{200}[1] %	Water Content %	Total Unit Weight pcf(g/cm³)	Void Ratio e	Dia. cm	Height cm	Specific Gravity Gs[2]	Degree of Saturation %
CH1(T1)	18 (5.5)	Sandy Silt (ML)	non-plastic		0.009	0.035	0.080	48	31.0	112 (1.80)	0.965	5.10	10.12	2.70	87
CH2(T5)	34.5 (10.5)	Silt (ML)	non-plastic		0.003	0.017	0.036	15	32.5	118 (1.89)	0.914	5.05	10.09	2.73	97
CH1(T4)	59 (18.0)	Silty Sand (SM)	non-plastic		0.007	0.036	0.100	60	33.3	109 (1.75)	1.08	5.18	10.19	2.73	84
CH1(T7)	82 (25.0)	Silt (ML)	38	12	-	-	-	2	37.2	117 (1.87)	0.996	4.98	10.23	2.72	100[3]
CH2(T9)	93.5 (28.5)	Silty Sand (SM)	non-plastic		0.010	0.072	0.150	70	31.2	119 (1.91)	0.875	5.00	10.11	2.73	97
CH1(T8)	113 (34.4)	Silt (ML)	32	7	-	-	-	1	35.3	118 (1.88)	0.92	3.60	7.56	2.70	100[3]
CH2(T11)	133 (40.5)	Silt (ML)	33	8	-	-	-	2	31.1	117 (1.87)	0.928	5.10	10.18	2.75	92
CH1(T10)	146 (44.5)	Sandy Silt (ML)	non-plastic		0.002	0.015	0.042	22	24.0	128 (2.06)	0.637	5.01	10.11	2.72	100[3]

1. R_{200} = Percent of soil sample by weight remaining on #200 sieve
2. Specific Gravity was taken from National Taiwan University (1987).
3. Degree of saturation slightly exceeds 100 %.

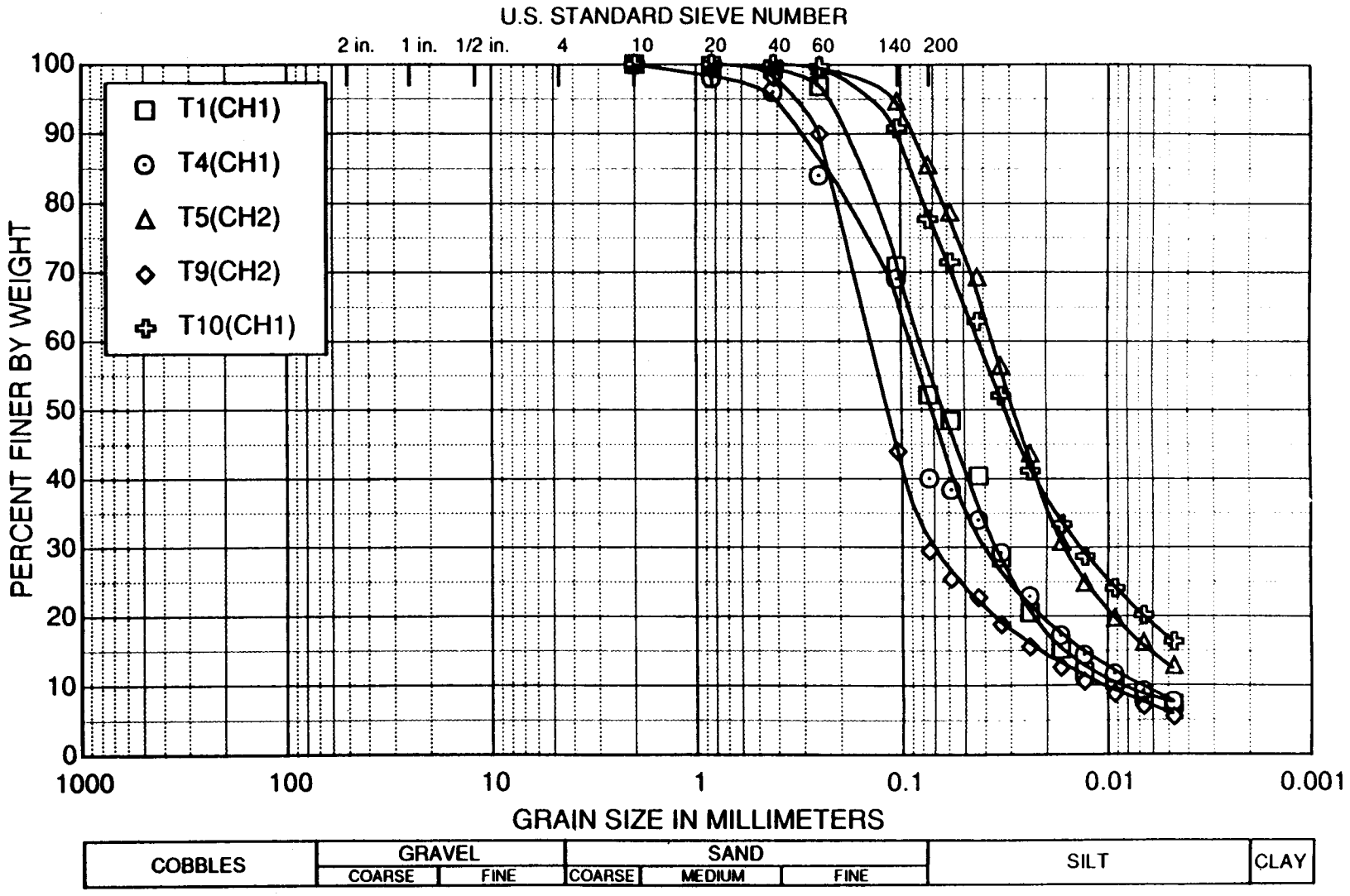

Figure 8.B.3-1
Gradation curves for Lotung samples.

8.B.3.2.1. Testing Program

Before dynamic testing was started, the in situ mean effective stress, σ_m', had to be estimated. This was done at the Lotung site by assuming the water table is at a depth of 1.2 ft (0.4 m), the total unit weight of the soil averages 120 pcf (18.8 kN/m^3), the soil is saturated throughout the profile, and the effective coefficient of earth pressure at rest, K_o', is 0.5. The resulting values of σ_m' for each sample are given in Table 8.B.3-2.

Once σ_m' was estimated, the range in confining pressures over which G and D would be evaluated was determined. Typically, isotropic confining pressures on the order of $0.25\sigma_m'$, $0.5\sigma_m'$, σ_m'' $2\sigma_m'$ and $4\sigma_m'$ were selected. Low-amplitude resonant column testing was performed at each confining pressure to determine the influence of time and confining pressure on the small-strain shear modulus, G_{max}, and small-strain material damping ratio, D_{min}. Low-amplitude dynamic tests are defined as those tests in which the resonant amplitude did not exceed 0.001% and typically was considerably below that level.

A summary of all confining pressures at which low-amplitude resonant column tests were performed is given in Table 8.B.3-2. At the estimated in situ mean effective stress, high-amplitude dynamic and cyclic testing was also conducted. This testing is defined as any tests in which the peak shearing strain exceeds 0.001%. This testing was composed of two series of tests. The first involved cyclic torsional (TS) shear testing as illustrated in Figure 8.B.3-2. A complete set of torsional shear tests took about three hours to perform, was performed under drained conditions although no drainage was observed, and involved shearing strains, γ, from less than 0.001% to above 0.05%, depending on the soil stiffness. The majority of the measurements were performed at 0.5 Hz and are labeled as TS1 in Figure 8.B.3-2. However, two sets of TS tests, one at $\gamma \approx 0.001\%$ and one at $\gamma \approx 0.01\%$, were conducted to evaluate the effect of excitation frequency on G and D at those strain amplitudes. In these tests, (denoted as TS2 in Figure 8.B.3-2) one to four cycles of loading was applied at about five different frequencies ranging from 0.1 Hz to about 10 Hz.

After the TS tests were completed, confinement of the sample was continued at σ_m', and a series of high-amplitude resonant column (RC) tests was performed the next day. However, before high-amplitude RC testing commenced, small-strain RC tests were performed to determine if any changes in the soil skeleton had occurred from the TS tests. In essentially all cases, no changes in G_{max} or D_{min} from the TS tests were measured.

Once the small-strain datum was re-established after the TS tests, high-amplitude resonant column testing was conducted to evaluate the influence of strain amplitude on G and D. This series of tests is illustrated in Figure 8.B.3-3. A complete set of resonant column tests took about one hour to perform, was performed under drained conditions just as in the case of the TS tests, and involved shearing strains from less than 0.001% to above 0.1%, depending on the soil stiffness. In these tests, 500 to 1000 cycles of loading is required at each strain measurement.

Upon completion of the high-amplitude RC tests, low-amplitude RC tests were performed to determine if any changes in the soil skeleton had occurred from the high-amplitude tests. In some cases, changes occurred. At that point, confinement of the sample at σ_m' was continued until G_{max} and D_{min} returned to the values before the high-amplitude tests or the change in values was noted in the next stage of testing.

The confining pressure was then increased to about $2\sigma_m'$, and low-amplitude resonant column testing was performed for one to several days. For six of the samples, high-amplitude resonant column tests were again performed. Table 8.B.3-2 gives a summary of these tests. In most cases, the pressure was again doubled, and low-amplitude RC testing was repeated.

It should be noted that, in three cases (samples CH1(T7), CH2(T11) and CH1(T10)), high-amplitude RC tests were also performed at one confining pressure below σ_m'. This was carefully done with only intermediate strain levels so as not to disturb the sample before testing at σ_m'.

Table 8.B.3-2
Summary of Resonant Column and Torsional Shear Tests Performed for Lotung Samples

Sample Number	Depth ft (m)	Estimated In Situ Mean EffectiveStress, σ_m', psf	Isotropic Test Pressure, psf		
			Low-Amplitude Resonant Column Tests	High-Amplitude Resonant Column Tests	Torsional Shear Test
CH1 (T1)	18 (5.5)	733	432, 720, 1440, 2880	720, 1440, 2880	720
CH2 (T5)	34.5 (10.5)	1366	432, 720, 1440, 2880, 5760	1440, 2880	1440
CH1 (T4)	59 (18.0)	2322	576, 1152, 2304, 4608	2304	2304
CH1 (T7)	82 (25.0)	3168	720, 1440, 3168, 6480, 12960, 25920	1440, 3168, 6480, 12960, 25920	3168
CH2 (T9)	93.5 (28.5)	3629	864, 1728, 3600, 7200, 14400	3600, 7200, 14400	3600
CH1 (T8)	113 (34.4)	4401	1080, 2160, 4320, 8640	4320	4320
CH2 (T11)	133 (40.5)	5155	720, 1296, 2592, 5184, 10368, 20736	2592, 5184, 10368	5184
CH1 (T10)	146 (44.5)	5648	720, 1440, 2880, 5760, 11520, 23040	2880, 5760, 11520	5760

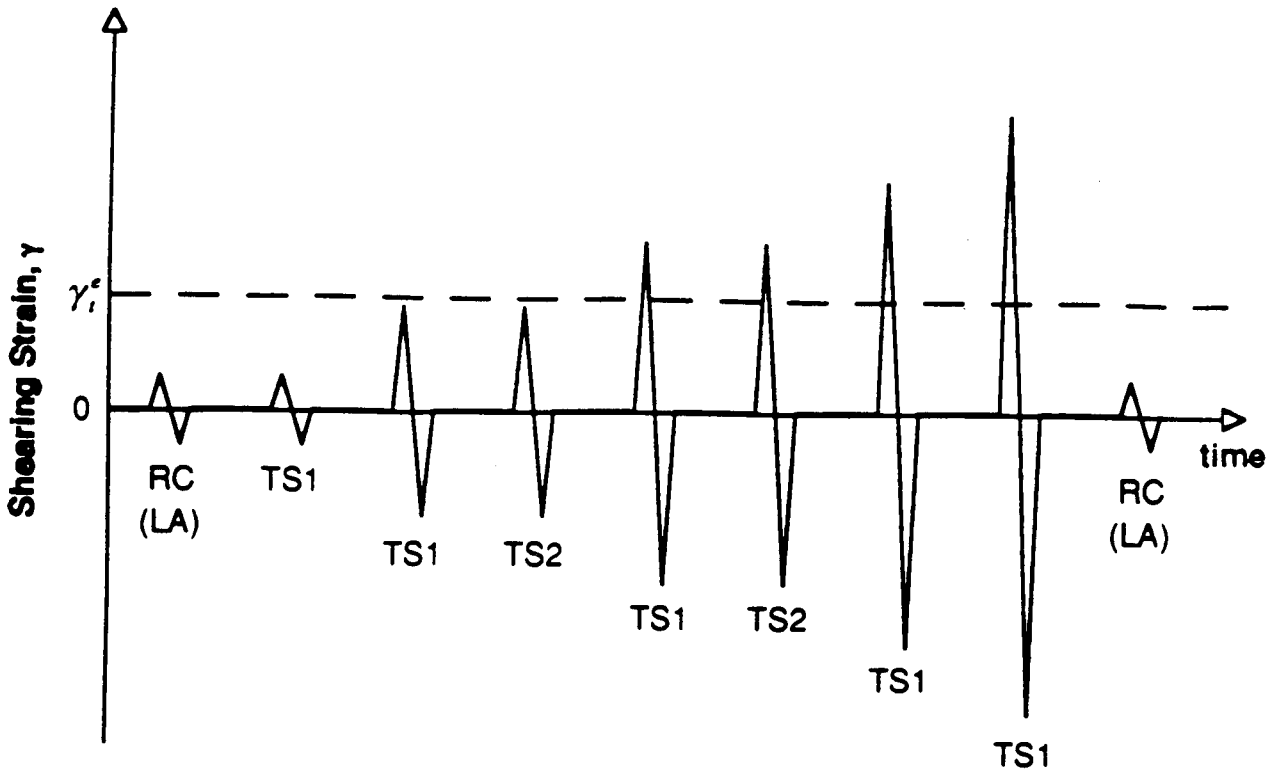

γ_t^e = elastic threshold strain; below γ_t^e, G is constant and equal to G_{max}

RC (LA) = resonant column test at low-amplitudes (strains < 0.001%)

TS1 = torsional shear test in which 1 to 10 cycles are applied at 0.5 Hz

TS2 = torsional shear test in which 4 cycles are applied at each of approximately 5 frequencies between 0.1 to 10 Hz

Figure 8.B.3-2
Testing procedure used in the torsional shear test to investigate the effects of strain amplitude, number of loading cycles, and excitation frequency of undisturbed Lotung samples.

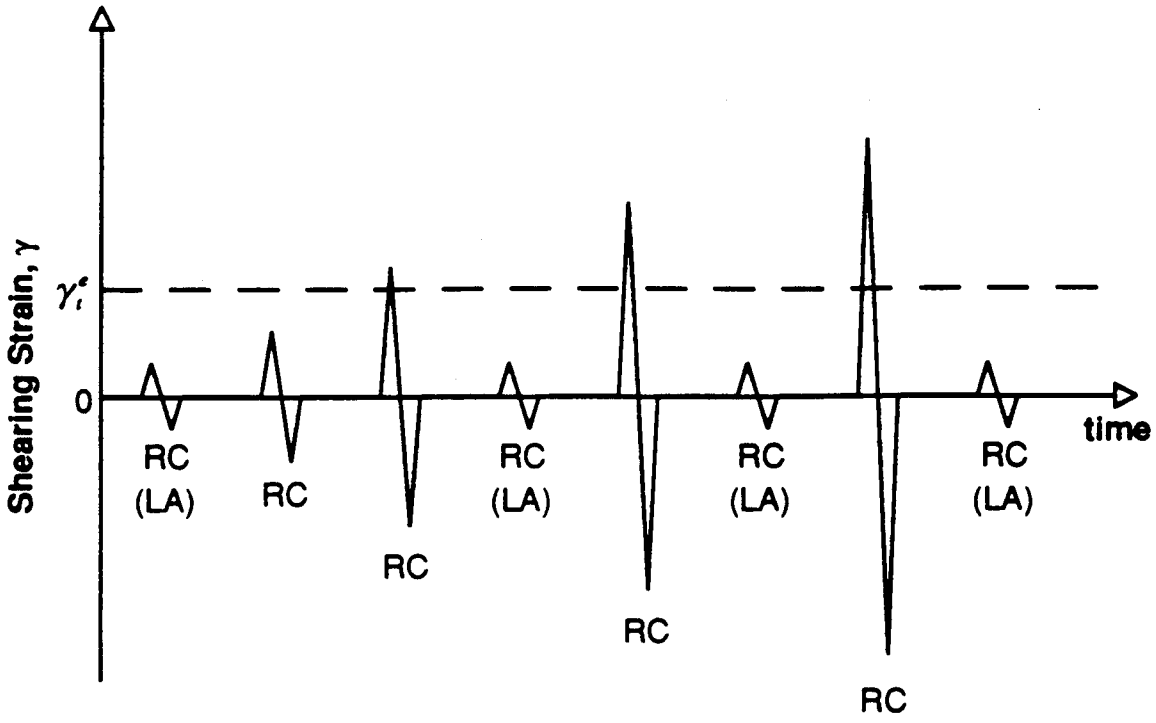

γ_t^e = elastic threshold strain; below γ_t^e, G is constant and equal to G_{max}

RC (LA) = resonant column test at low-amplitudes (strains < 0.001%)

RC = resonant column test in which 500 to 1000 cycles of loading is applied during each measurement

Figure 8.B.3-3
Testing procedure used in the resonant column test to investigate the effect of strain amplitude on G and D of undisturbed Lotung samples.

8.B.3.2.2 Test Results

The results of the RC and TS tests are shown in Appendices 8.B.3.B through 8.B.3.I for the eight Lotung samples. Each appendix presents the results for one sample in the following general order (using Appendix 8.B.3.B as the example).

1. Figure 8.B.3.B-1 shows the influence of magnitude and duration of isotropic confining pressure on G_{max} as determined by RC tests.
2. Figure 8.B.3.B-2 shows the influence of magnitude and duration of isotropic confining pressure on D_{min} as determined by RC tests.
3. Figure 8.B.3.B-3 shows the change in void ratio of the sample with magnitude and duration of isotropic confining pressure.
4. Figure 8.B.3.B-4 shows the variation in G_{max} at a confinement time of 1000 minute with effective confining pressure from the RC tests.
5. Figure 8.B.3.B-5 shows the variation in D_{min} at a confinement time of 1000 minutes with effective confining pressure from the RC tests.
6. Figure 8.B.3.B-6 shows the variation in void ratio of the sample at a confinement time of 1000 minutes with effective confining pressure.
7. Figure 8.B.3.B-7 shows the variation in G with log γ at σ_m' from the high-amplitude RC and TS tests.
8. Figure 8.B.3.B-8 shows the variation in G/G_{max} with log γ at σ_m' from the high-amplitude RC and TS tests.
9. Figure 8.B.3.B-9 shows the variation in G with log γ at all tests pressures where high-amplitude RC tests were performed.
10. Figure 8.B.3.B-10 is the normalized (G/G_{max}) version of Figure 8.B.3.B-9.
11. Figures 8.B.3.B-11 through 8.B.3.B-14 are simply the damping ratio curves which are the companions to the modulus curves given in Figures 8.B.3.B-7 through 8.B.3.B-10.
12. Figure 8.B.3.B-15 shows the effect of excitation frequency on G at $\gamma \approx 0.001\%$ and $\gamma \approx 0.01\%$.
13. Figure 8.B.3.B-16 shows the effect of excitation frequency on D at $\gamma \approx 0.001\%$ and $\gamma \approx 0.01\%$.

8.B.3.3 Comparison of Results

The variation in G_{max} with σ_o' for all undisturbed samples tested in this study at the σ_m' and above is shown in Figure 8.B.3-4. (Therefore, the samples should be normally consolidated samples in the pressure range shown.) The results fall in a narrow band which can be fit with the Hardin (1978) equation as shown in Figure 8.B.3-5. In Figure 8.B.3-5, the void ratio associated with each confining pressure has been used in plotting the results. Moduli from earlier resonant column tests performed at the National Taiwan University (1978) are shown in Figure 8.B.3-6 and are fit with the Hardin (1978) equation in Figure 8.B.3-7. In Figure 8.B.3-7, only the void ratio at the start of testing was available for use in these results. Moduli determined at the University of Texas (UT) and at the National Taiwan University (NTU) are compared in Figure 8.B.3-8 without accounting for variation in void ratio and in Figure 8.B.3-9 by accounting for void ratio variations. The G_{max} values determined at UT and NTU compared very favorably.

The same set of comparisons for the variation in small-strain material damping ratio, D_{min}, with σ_o' is presented in Figures 8.B.3-10,-11 and -12. In this case, the UT results again fall in a rather narrow range. But D_{min} exhibits more scatter than in the case with G_{max}. The values of D_{min} are also quite low, all less than 2% (or $Q > 25$). The NTU results, on the other hand, exhibit more scatter and are equal to or greater than the values determined in this study.

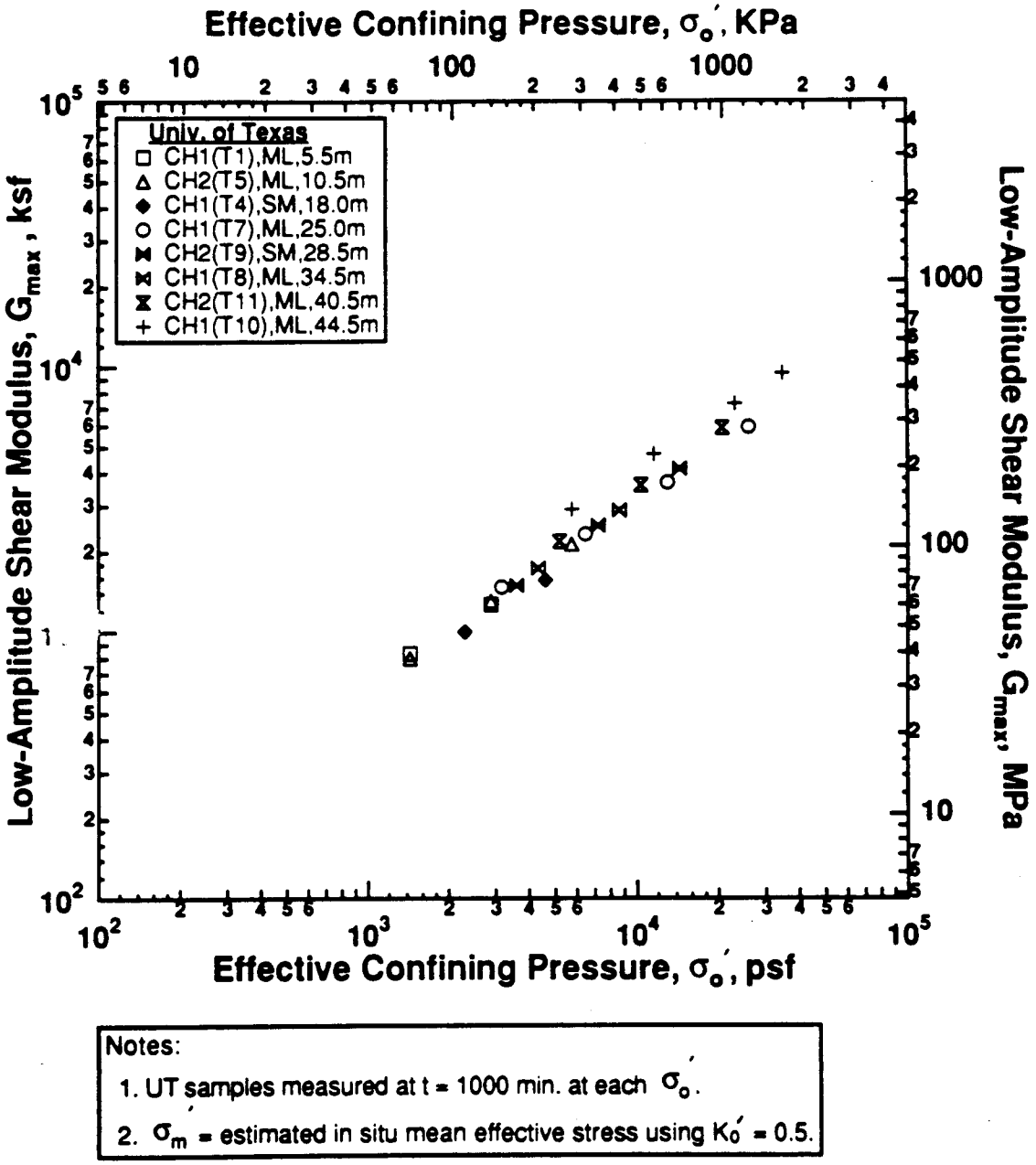

Figure 8.B.3-4
Variation in low-amplitude shear modulus with effective confining pressure from resonant column tests at $\sigma_o' \geq \sigma_m'$ of undisturbed samples from Lotung site; UT tests.

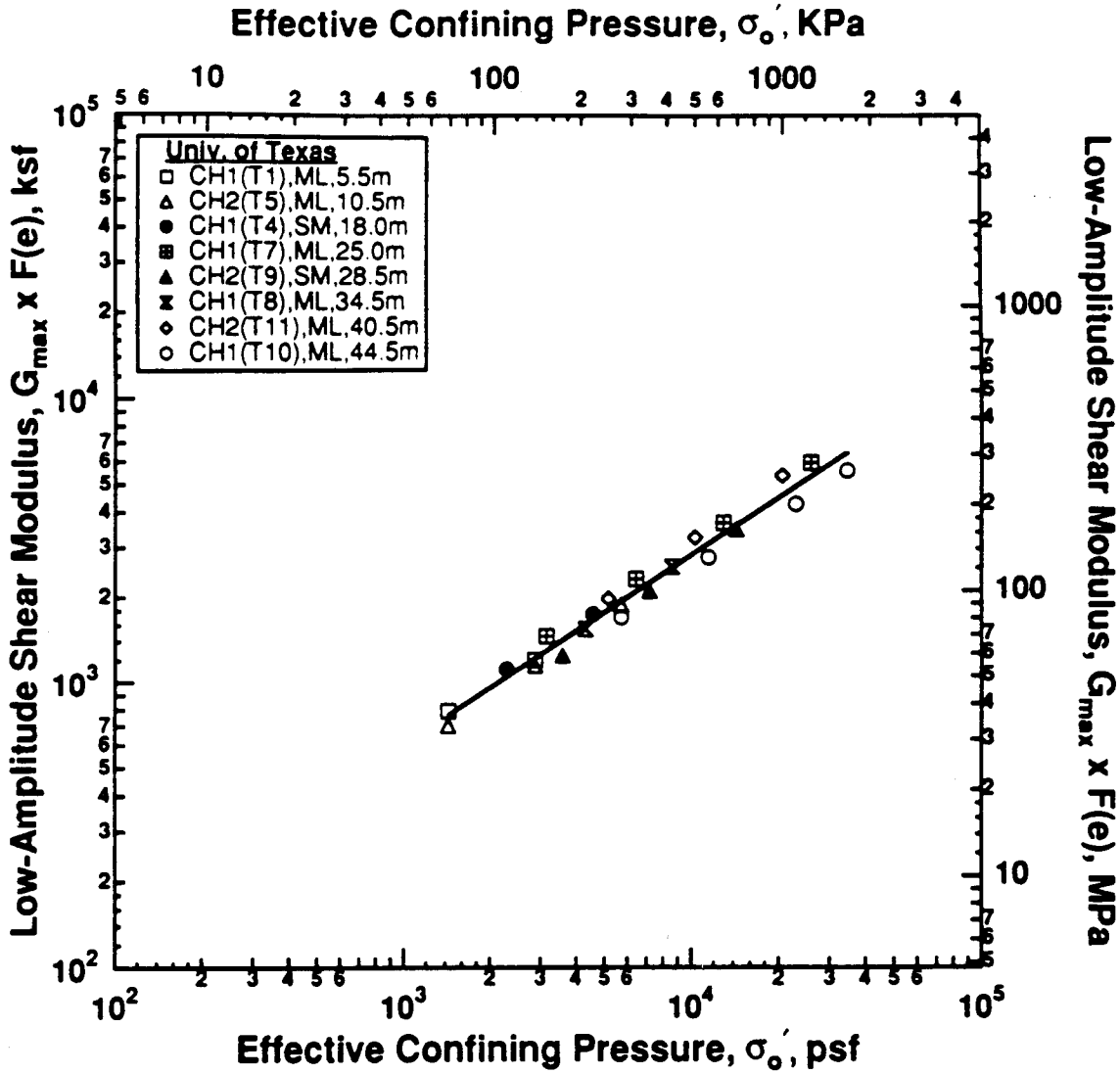

Notes:

1. UT samples measured at t = 1000 min. at each σ_o'.
2. Best-Fit Curve:

$G_{max} \times F(e) = A \times P_a^{(1-n)} \times \sigma_o'^{(n)}$

$F(e) = 0.3 + 0.7 \times e^2$, $P_a = 2117$ psf

$n = 0.665$, $A = 466$

Figure 8.B.3-5
Best-fit curve to log G_{max} x F(e) – log σ_o' relationship from resonant column tests at $\sigma_o' \geq \sigma_m'$ of undisturbed samples from Lotung site; UT tests.

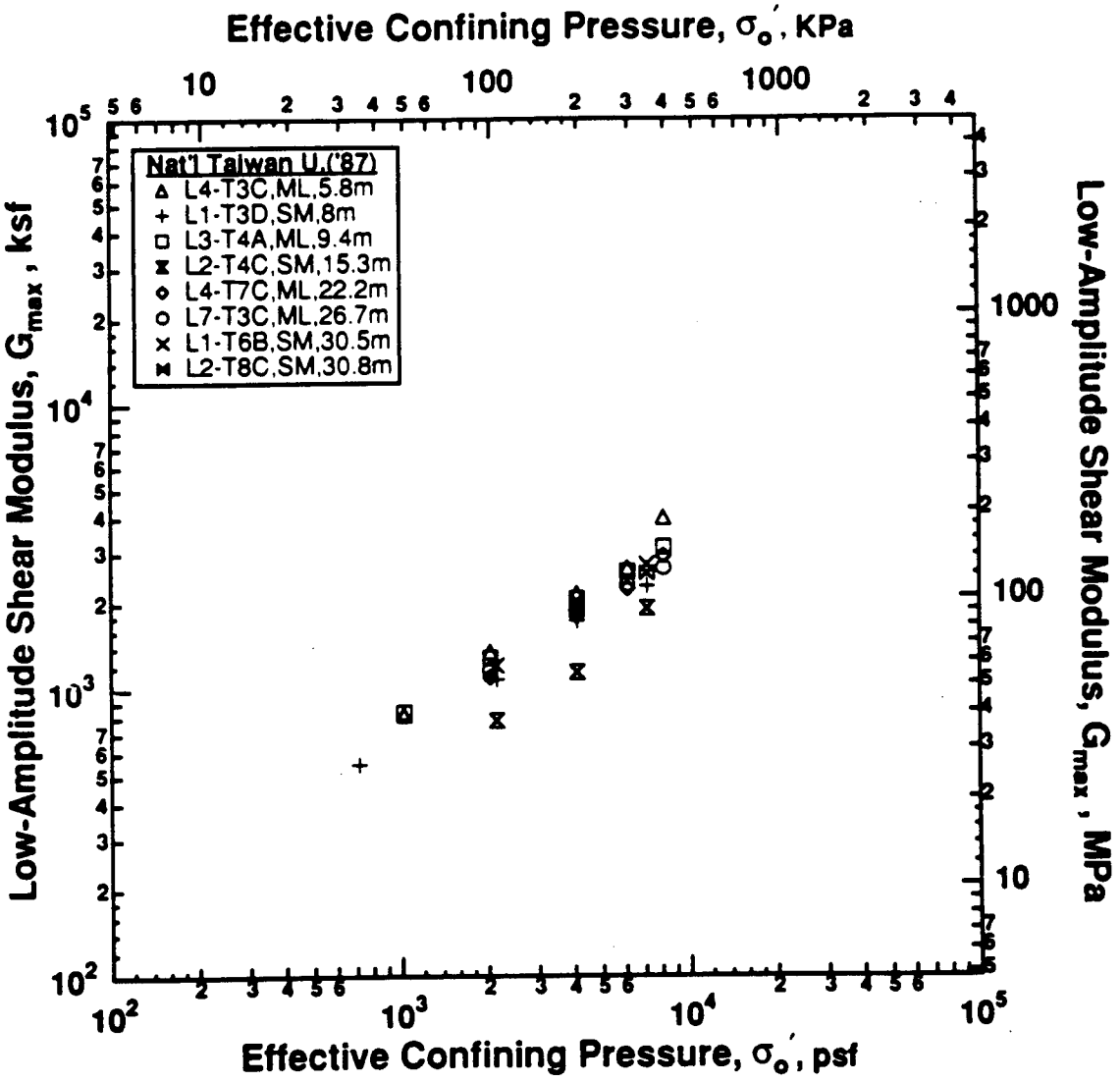

Figure 8.B.3-6
Variation in low-amplitude shear modulus with effective confining pressure from resonant column tests at $\sigma_o' \geq \sigma_m'$ of undisturbed samples from Lotung site; NTU tests.

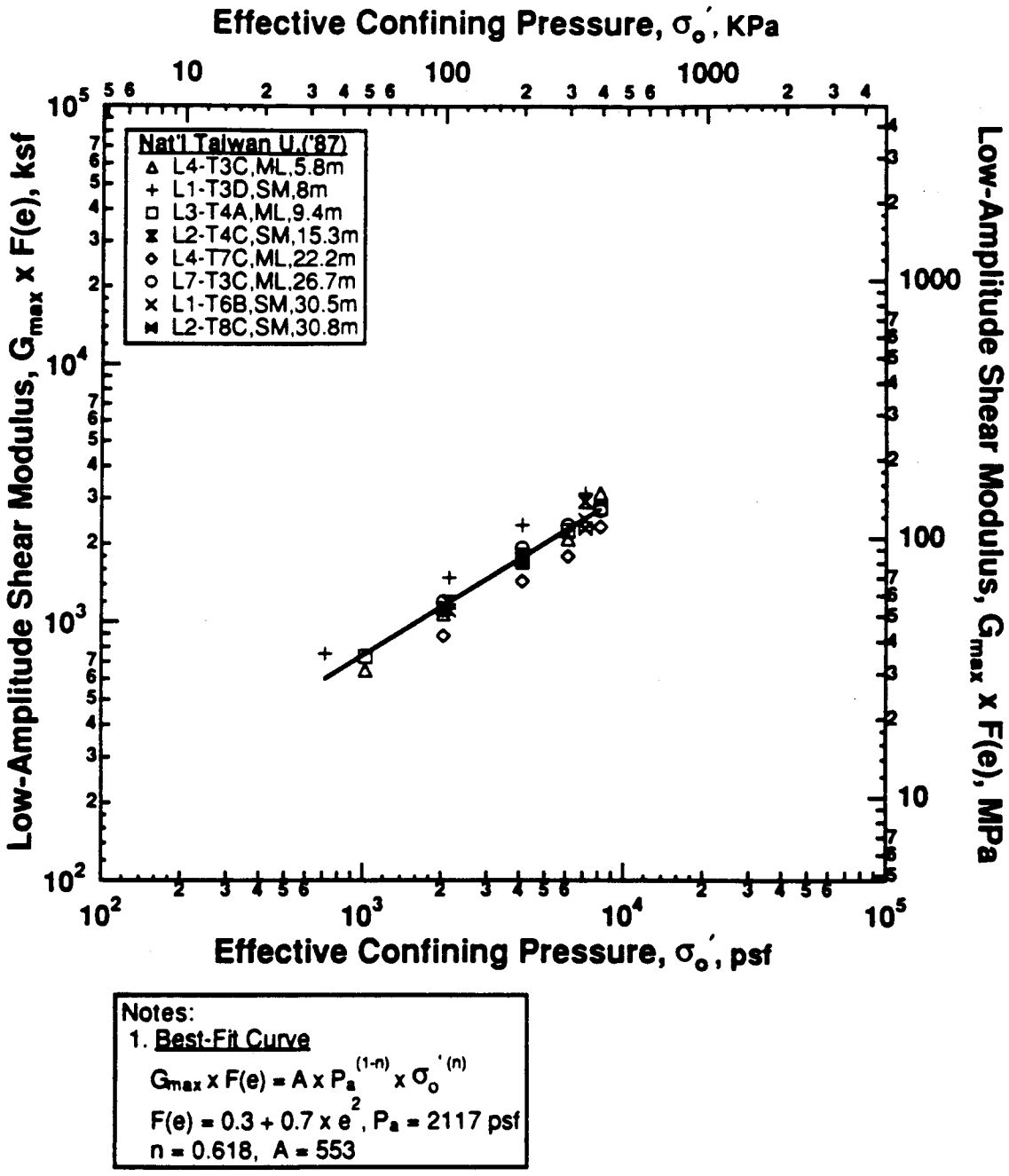

Figure 8.B.3-7
Best-fit curve to log G_{max} x F(e) – log σ_O' relationship from resonant column tests at $\sigma_O' \geq \sigma_m'$ of undisturbed samples from Lotung site; NTU tests.

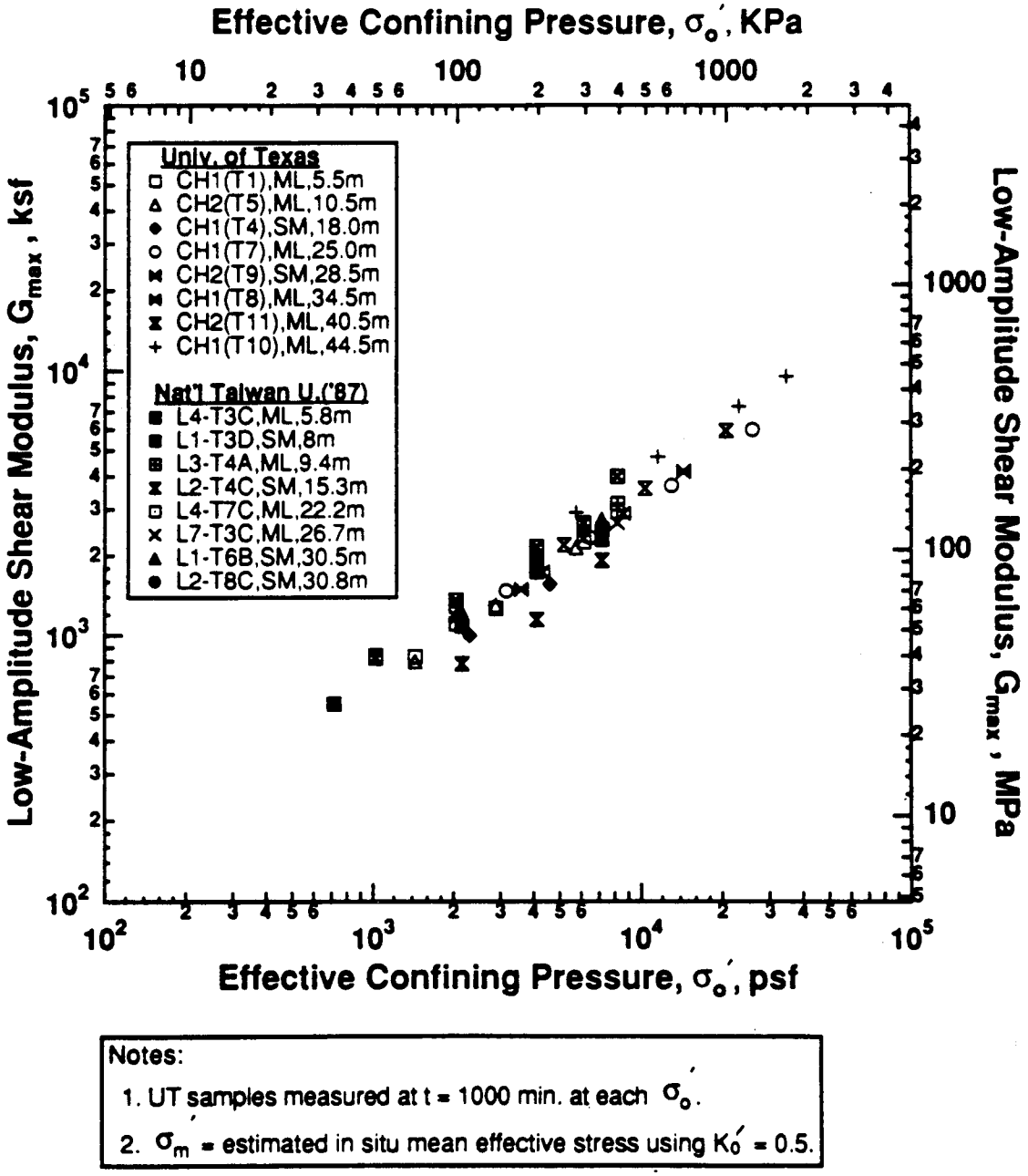

Figure 8.B.3-8
Comparison of log G_{max} – log σ_o' relationships from resonant column tests at $\sigma_o' \geq \sigma_m'$ of undisturbed samples from Lotung site; UT and NTU tests.

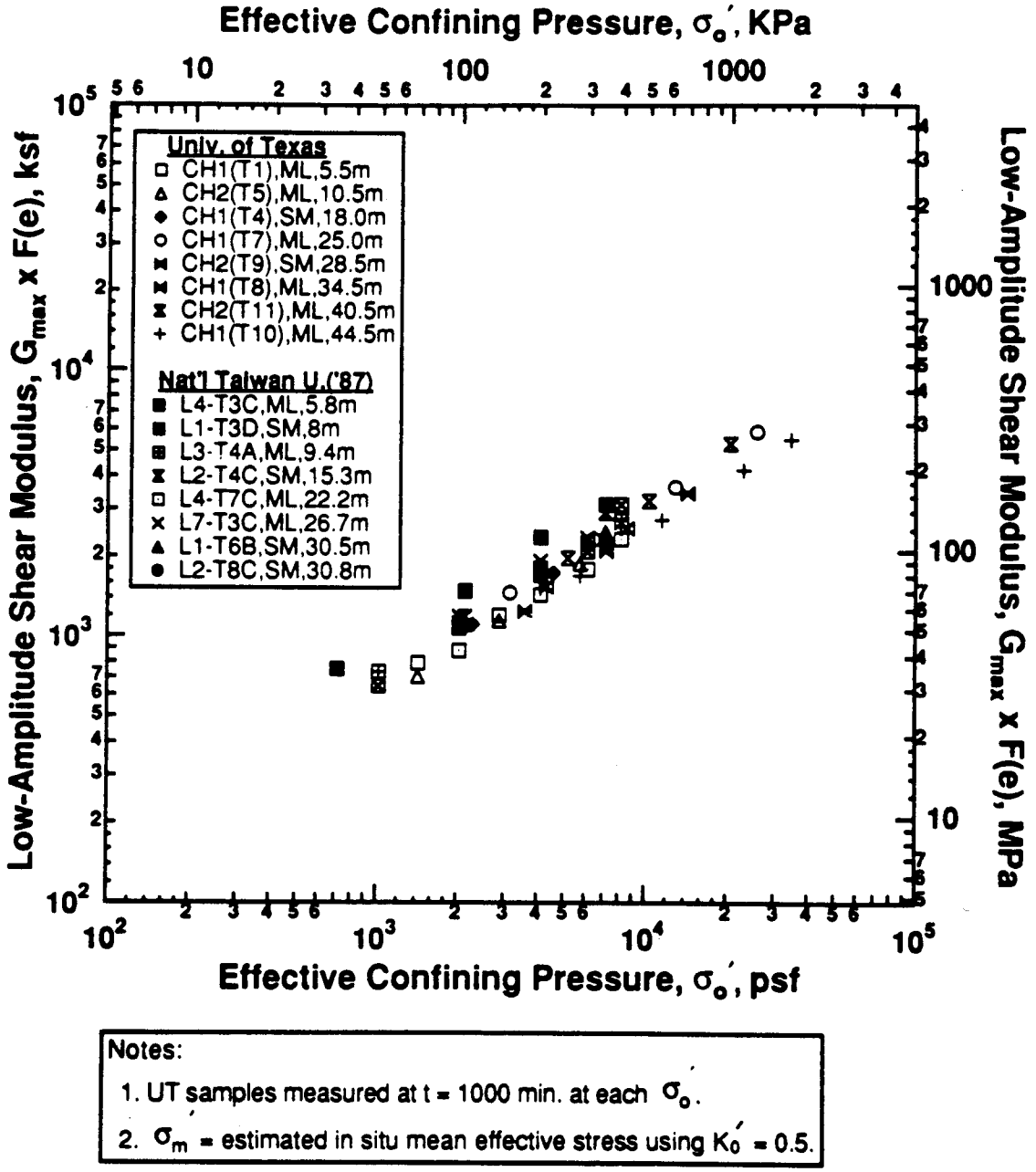

Notes:

1. UT samples measured at t = 1000 min. at each σ_o'.
2. σ_m' = estimated in situ mean effective stress using K_o' = 0.5.

Figure 8.B.3-9
Comparison of log G_{max} x F(e) – log σ_o' relationships from resonant column tests at $\sigma_o' \geq \sigma_m'$ of undisturbed samples from Lotung site; UT and NTU tests.

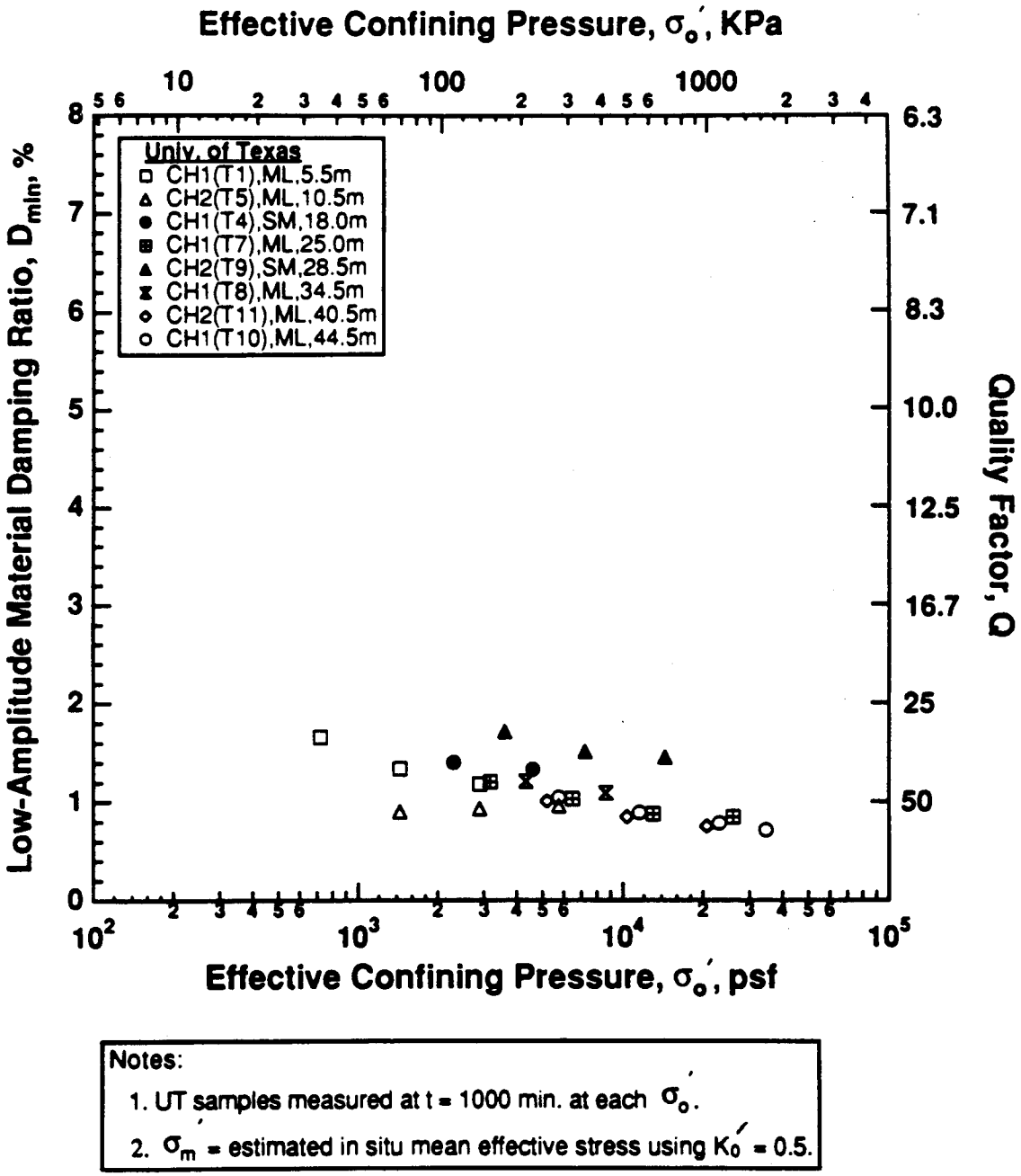

Figure 8.B.3-10
Variation in low-amplitude material damping ratio with effective confining pressure from resonant column tests at $\sigma_O' \geq \sigma_m'$ of undisturbed samples from Lotung site; UT tests.

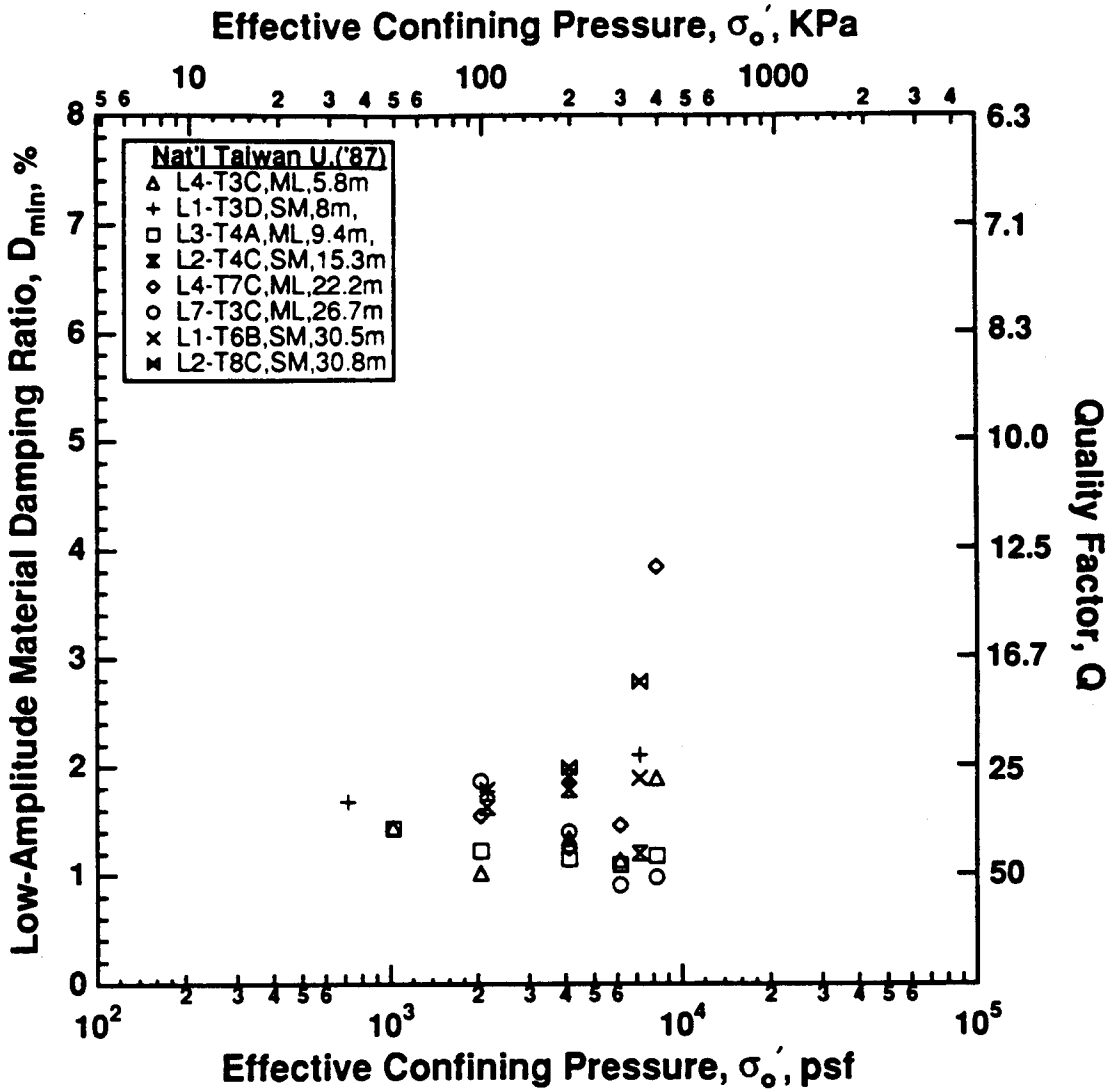

Figure 8.B.3-11
Variation in low-amplitude material damping ratio with effective confining pressure from resonant column tests at $\sigma_o' \geq \sigma_m'$ of undisturbed samples from Lotung site; NTU tests.

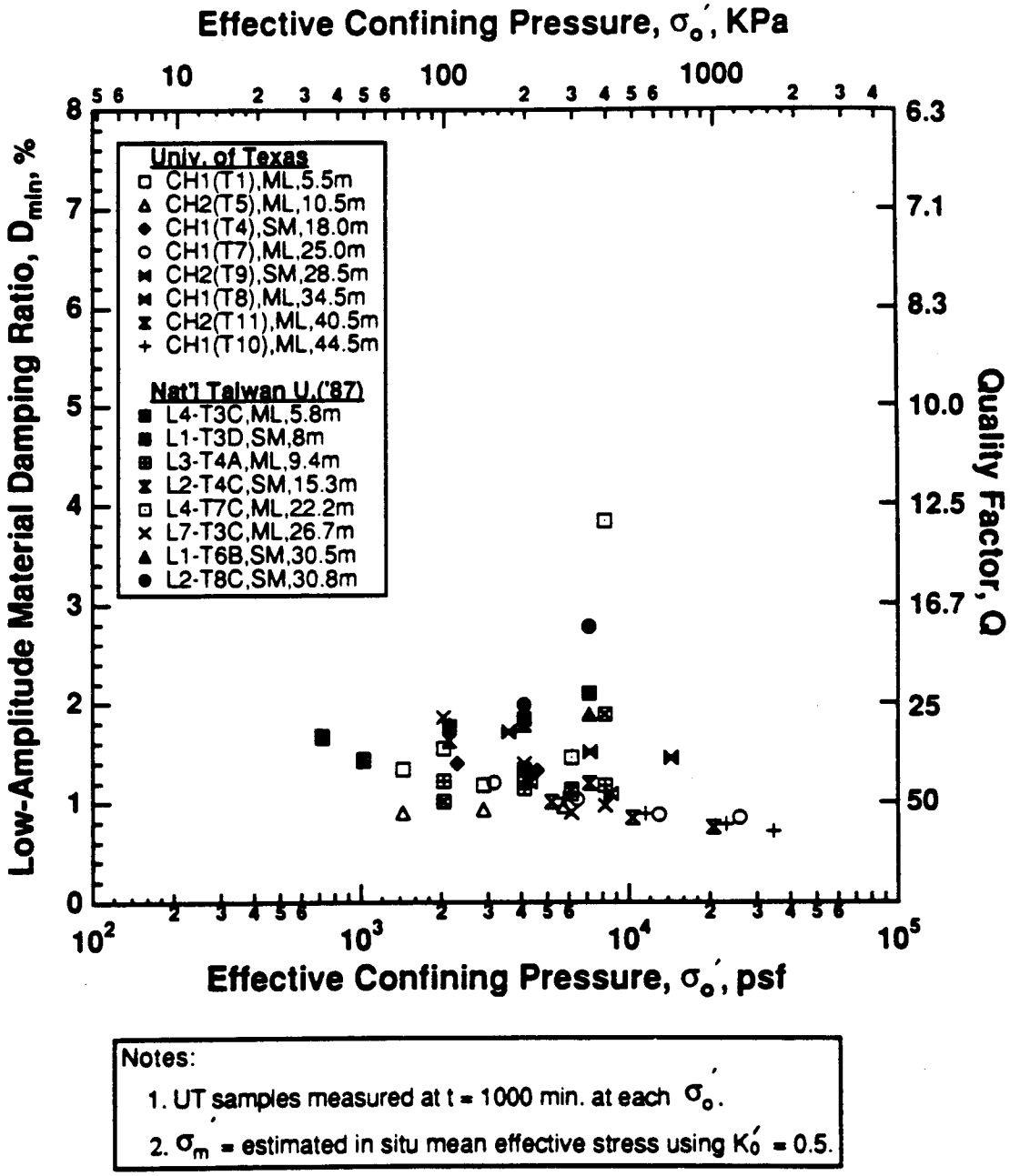

Figure 8.B.3-12
Comparison of D_{min} – log σ_o' relationships from resonant column tests at $\sigma_o' \geq \sigma_m'$ of undisturbed samples from Lotung site; UT and NTU tests.

The variation in normalized modulus, G/G_{max}, with log γ for all samples tested in this study at the estimated in situ means effective stress, σ_m', is presented in Figure 8.B.3-13 for the RC tests and in Figure 8.B.3-14 for the first cycle in the TS test. In each case, the results for all samples form a narrow band which is very close to the upper range proposed by Seed and Idriss (1970) for sands. The results from both the RC and TS tests are compared in Figure 8.B.3-15 and are essentially the same. It should be noted at this point that all samples are essentially unsaturated and hence any development in pore water pressure due to cyclic loading is significantly inhibited. Therefore, values of G determined at strains above amplitudes on the order of 0.05% do not reflect any reduction which would occur if pore pressures were generated.

A comparison of G/G_{max} versus log γ from the resonant column tests performed at σ_m' by UT and NTU is presented in Figure 8.B.3-16. With the exception of the results from one or two samples, the comparison is quite reasonable. The results from additional cyclic triaxial (CT) tests performed at the National Taiwan University (1987 and 1989) and the University of California at Davis (UCD) (1991) combined with the resonant column tests from NTU are presented in Figure 8.B.3-17. These results are compared with the results from this study in Figure 8.B.3-18. In Figure 8.B.3-18, considerable scatter can be seen.

Similar results for the variation in material damping ratio with strain amplitude are shown in the remaining figures. Figure 8.B.3-19 shows the variation in D with log γ as determined by RC tests in this study. The results fall in a rather narrow band which is closest to the lower range proposed by Seed and Idriss (1970) for sands. Figure 8.B.3-20 shows the same results determined in the first cycle in the TS test. In this case, material damping values are slightly higher in the TS tests than those determined in the RC test at all strains above about 0.003%. This behavior is typical of sandy material with few fines (Kim, 1991). Both results are compared in Figure 8.B.3-21 and expanded versions of Figures 8.B.3-19 through 8.B.3-21 are presented in Figures 8.B.3-22 through 8.B.3-24.

The variation in D with log γ determined by NTU and UCD with resonant column and cyclic triaxial tests is shown in Figures 8.B.3-25 and 8.B.3-26. The results from the previous studies and this study are compared in Figures 8.B.3-27 and 8.B.3-28. In general, material damping values determined in the previous studies are equal to or greater than the values determined in this study, especially at small strains.

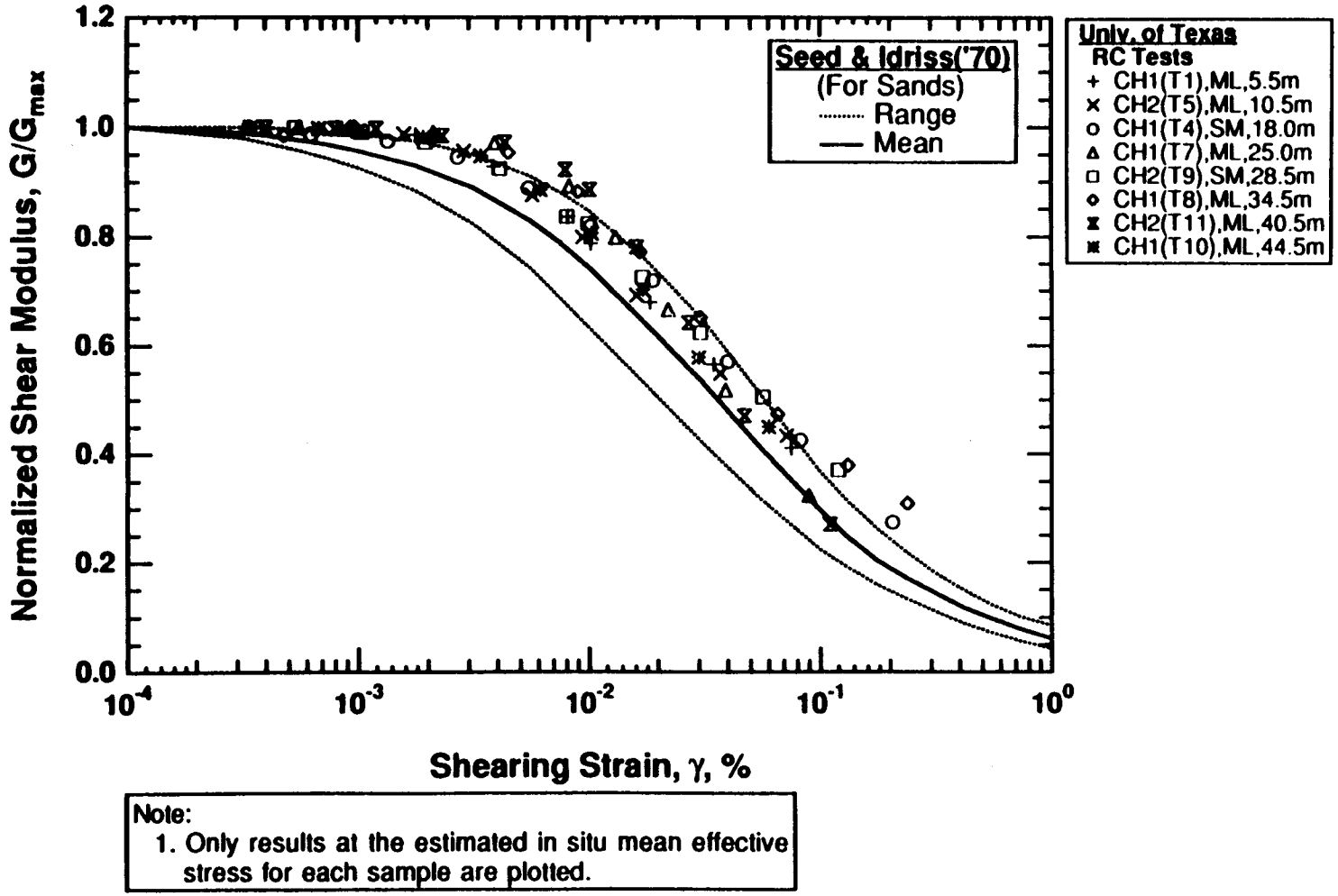

Figure 8.B.3-13
Variation in normalized shear modulus with shearing strain from resonant column tests of undisturbed samples from Lotung site; UT tests.

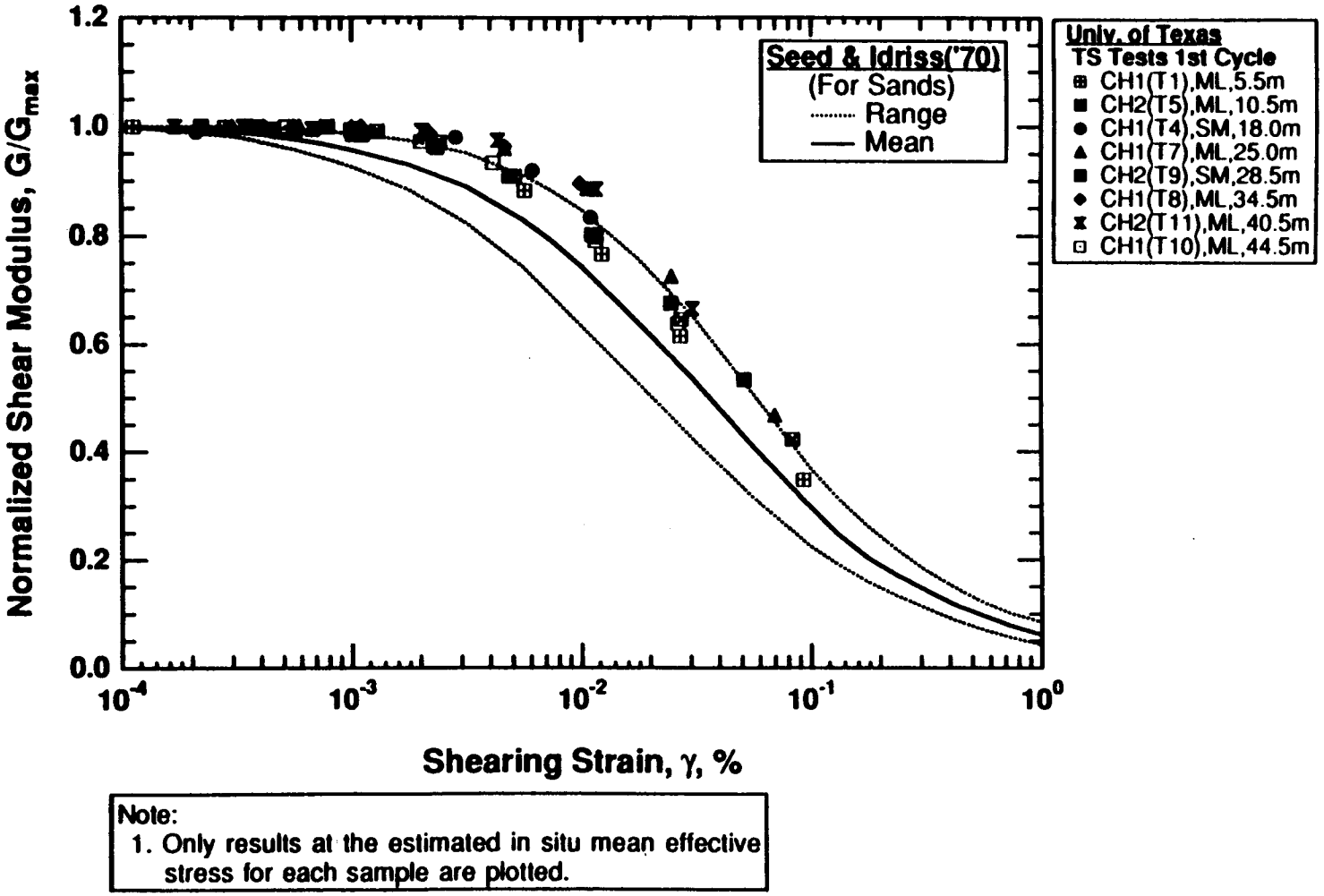

Figure 8.B.3-14
Variation in normalized shear modulus with shearing strain from torsional shear tests of undisturbed samples from Lotung site; UT tests.

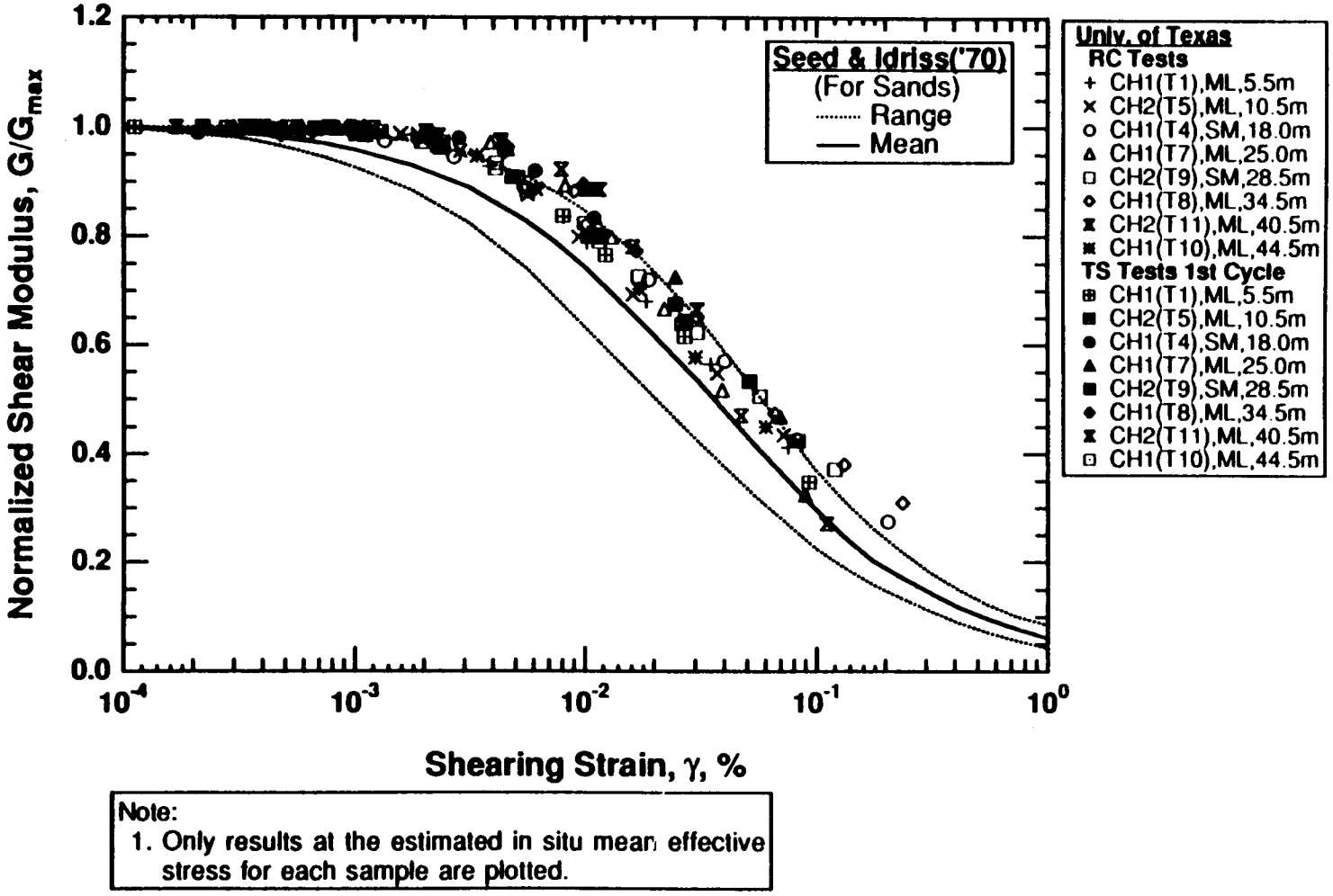

Figure 8.B.3-15
Variation in normalized shear modulus with shearing strain from resonant column and torsional shear tests of undisturbed samples from Lotung site; UT tests.

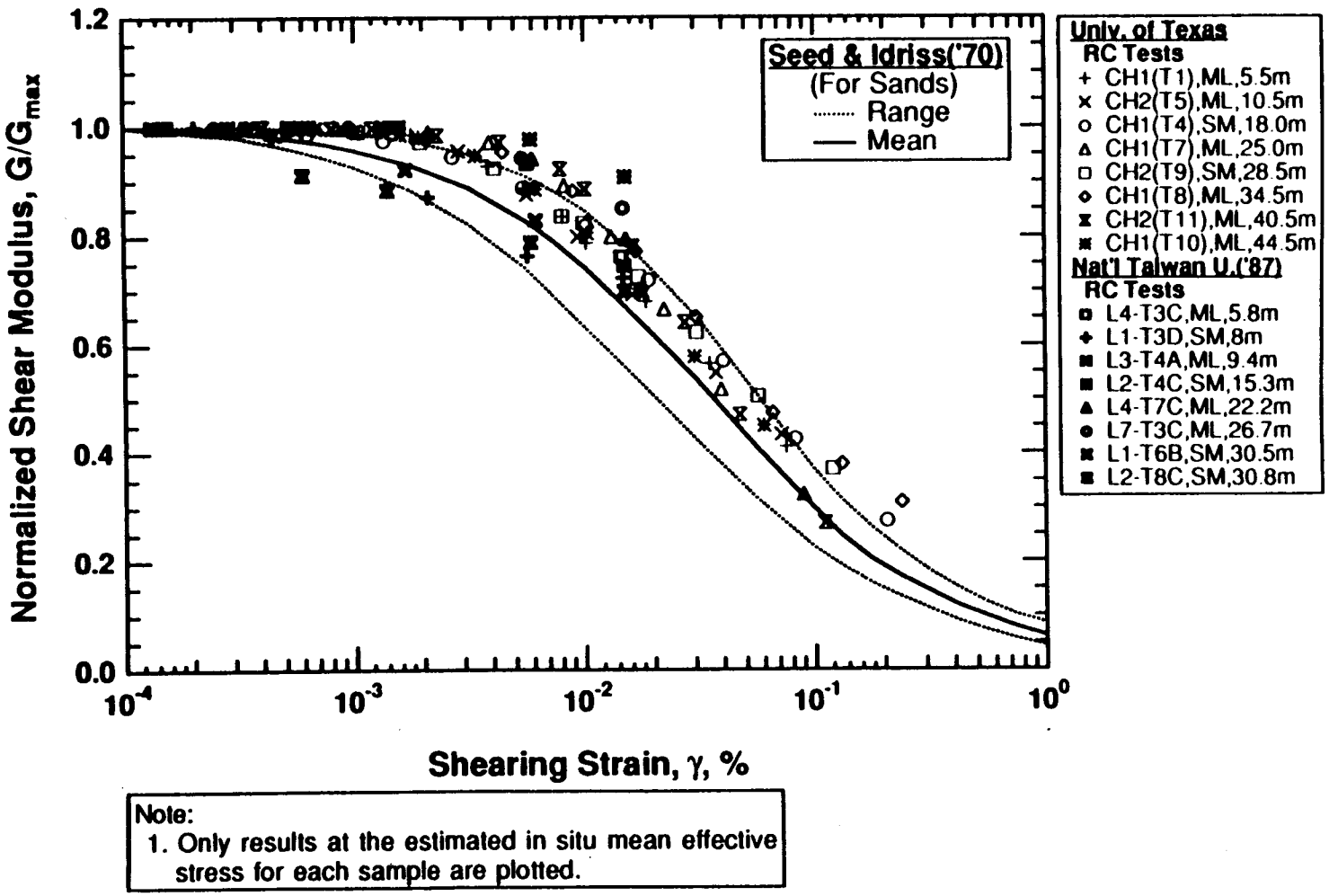

Figure 8.B.3-16
Variation in normalized shear modulus with shearing strain from resonant column tests of undisturbed samples from Lotung site; UT and NTU tests.

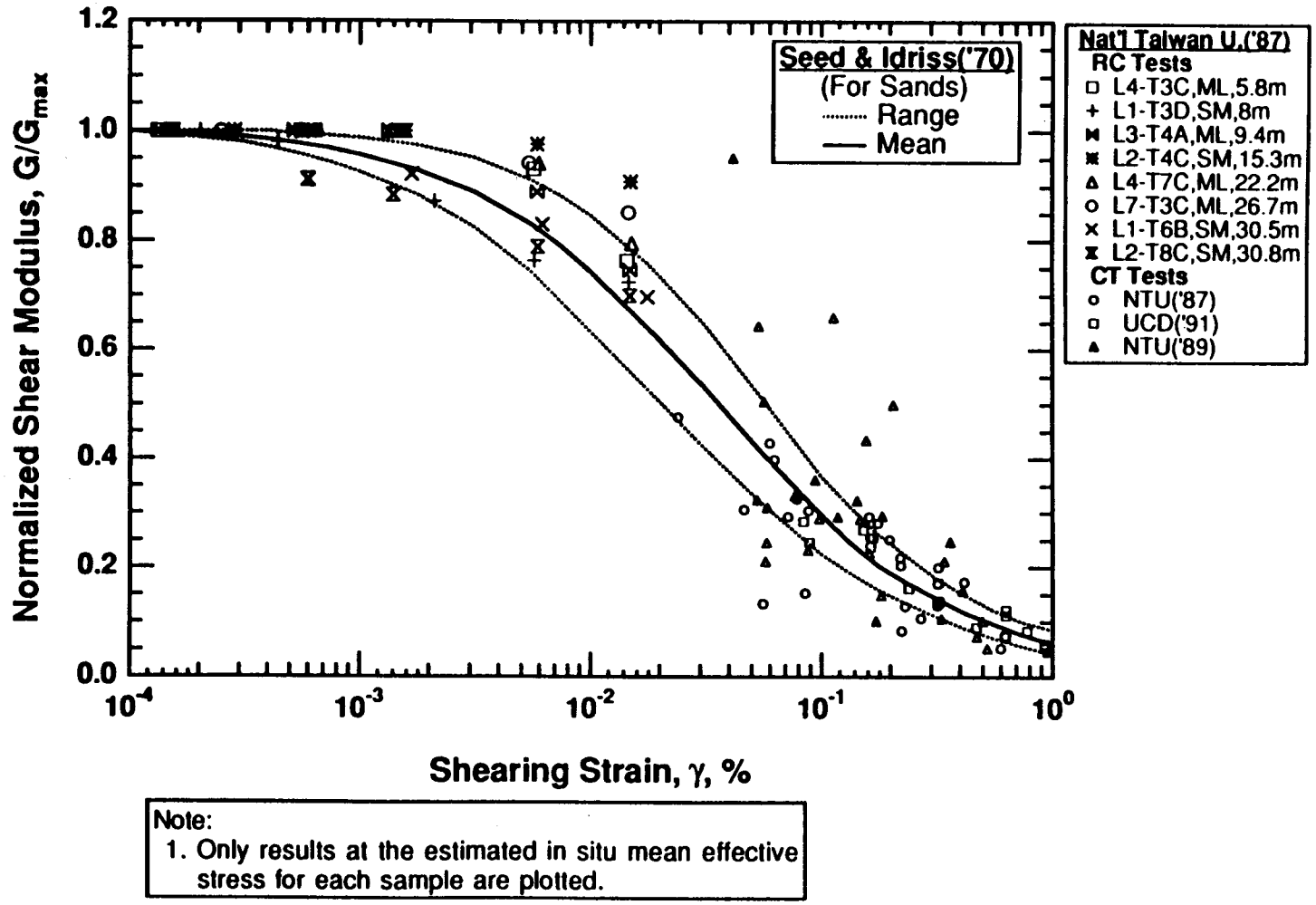

Figure 8.B.3-17
Variation in normalized shear modulus with shearing strain from resonant column and cyclic triaxial tests of undisturbed samples from Lotung site; NTU and UCD tests.

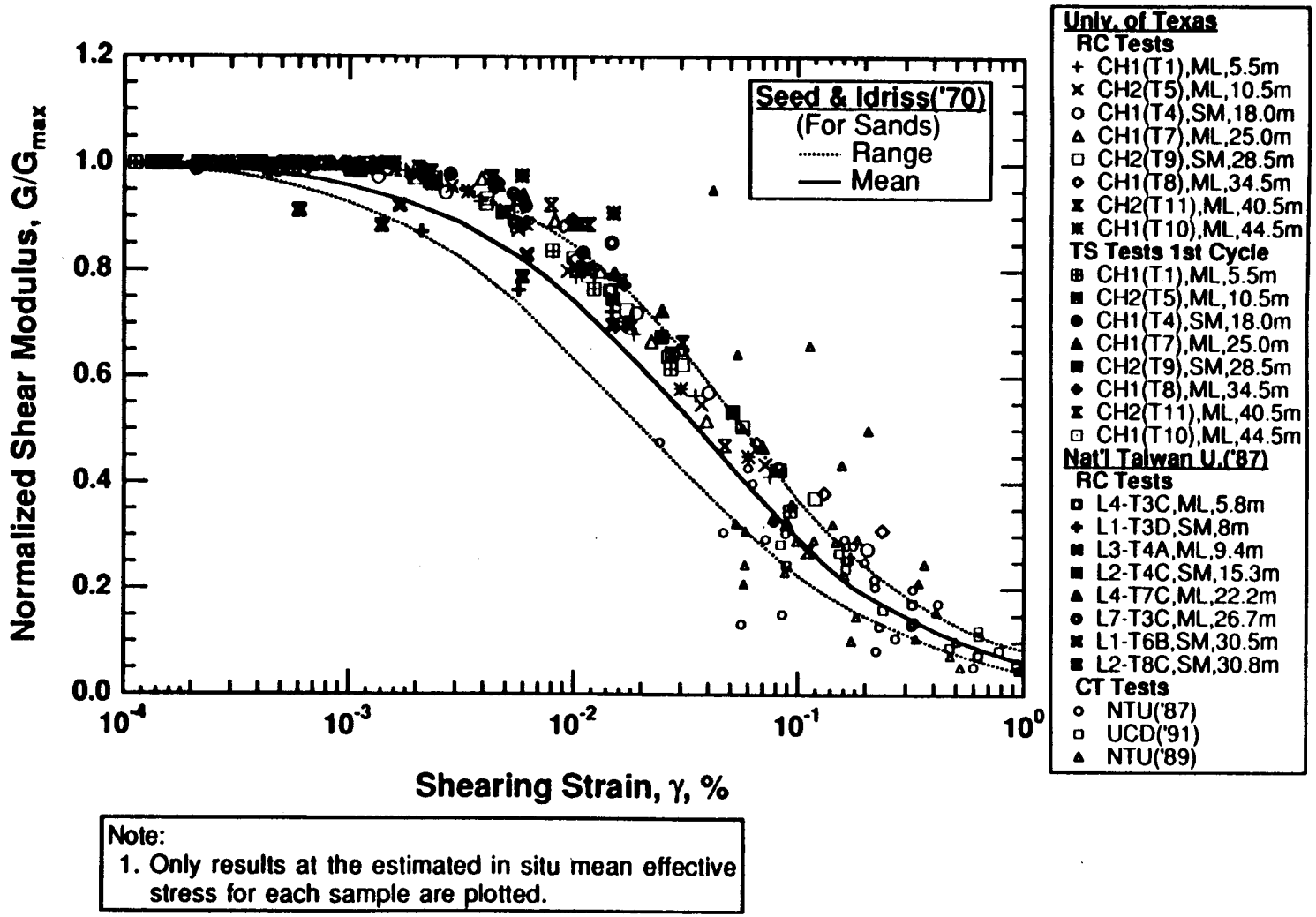

Figure 8.B.3-18
Comparison of all normalized modulus-strain data from resonant column, torsional shear and cyclic triaxial tests of undisturbed samples from Lotung site.

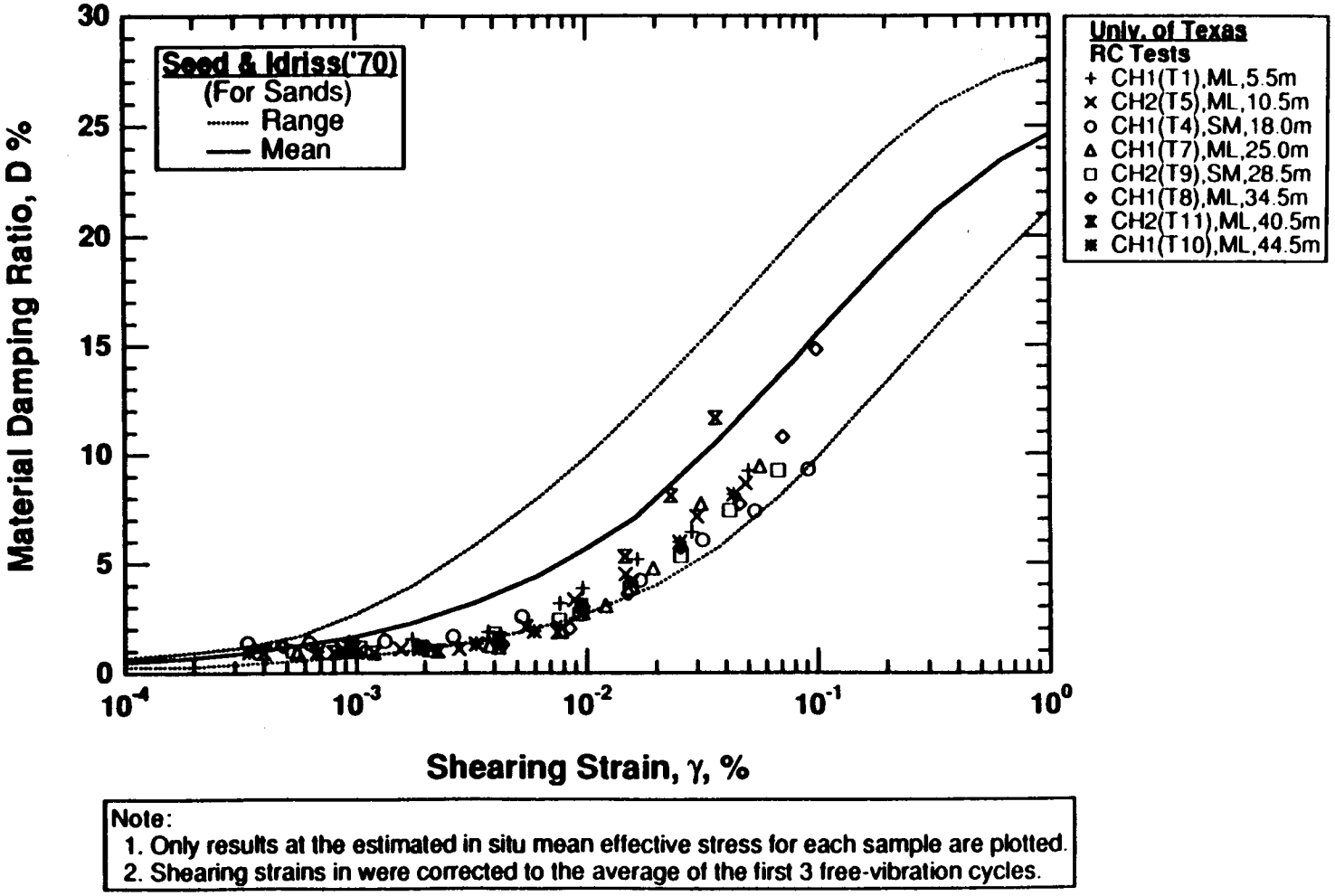

Figure 8.B.3-19
Variation in material damping ratio with shearing strain from resonant column tests of undisturbed samples from Lotung site; UT tests.

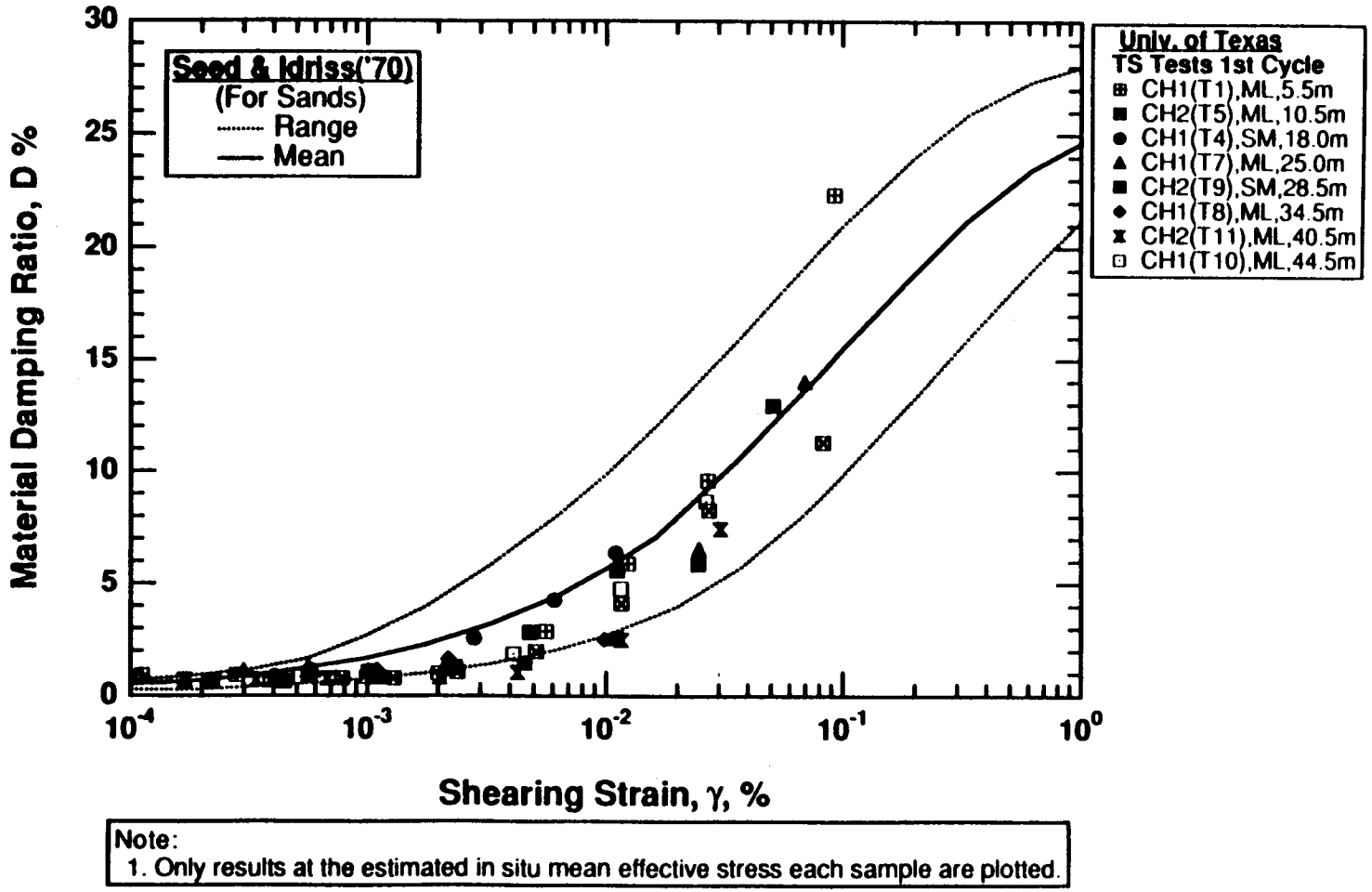

Figure 8.B.3-20
Variation in material damping ratio with shearing strain from torsional shear tests of undisturbed samples from Lotung site; UT tests.

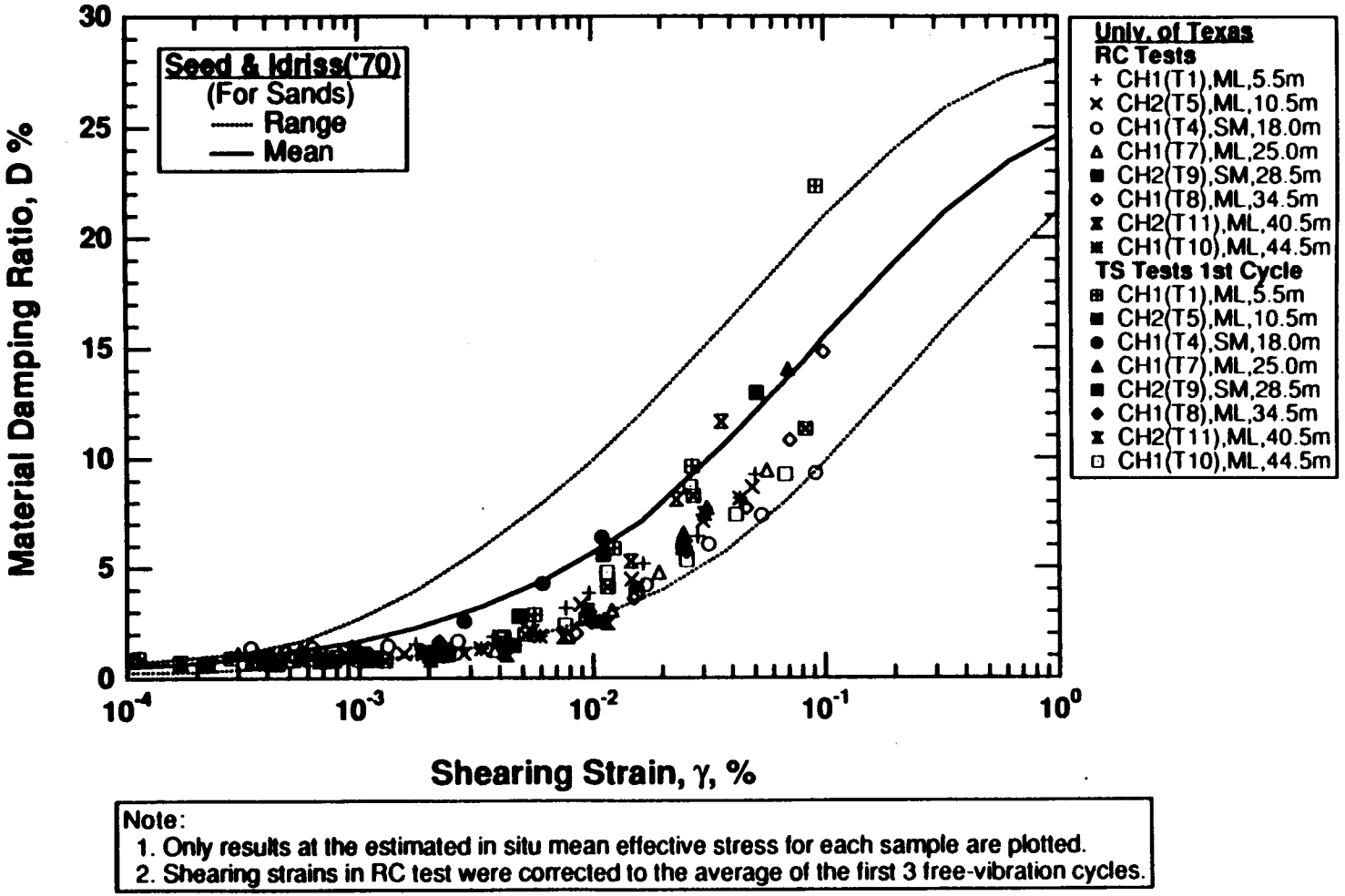

Figure 8.B.3-21
Variation in material damping ratio with shearing strain from resonant column and torsional shear tests of undisturbed samples from Lotung site; UT tests.

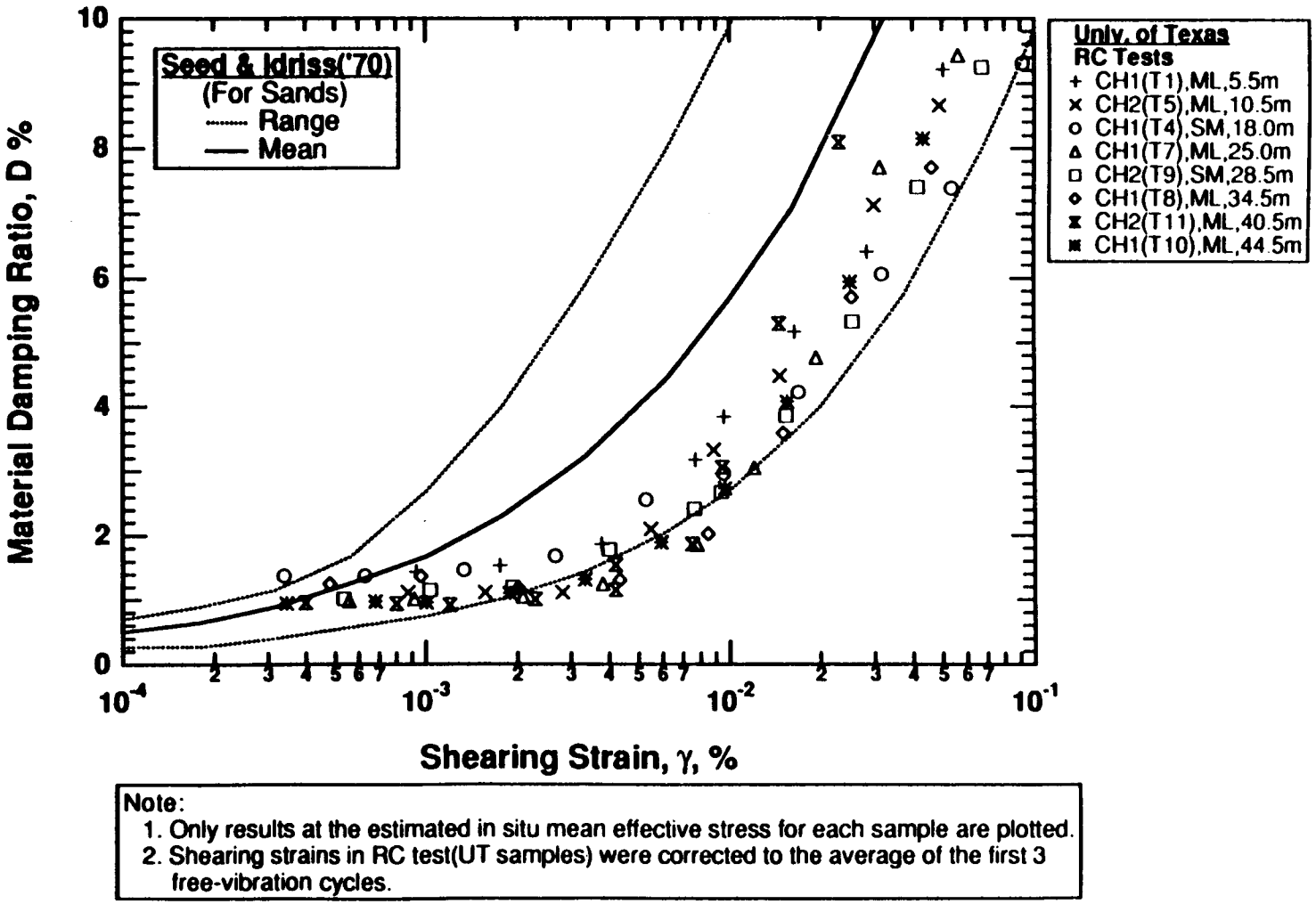

Figure 8.B.3-22
Variation in material damping ratio with shearing strain for $\gamma < 0.1\%$ from resonant column tests of undisturbed samples from Lotung site; UT tests.

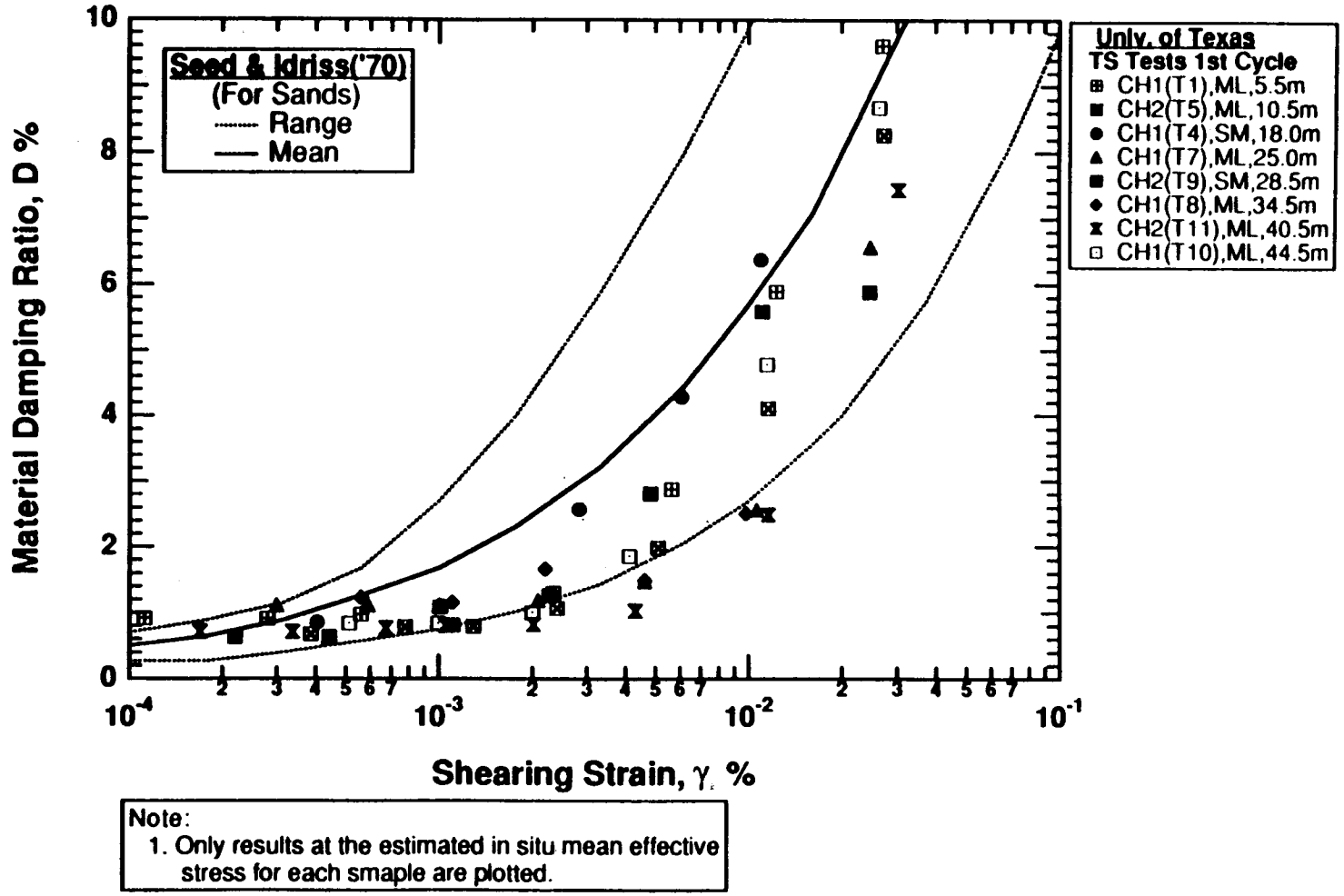

Figure 8.B.3-23
Variation in material damping ratio with shearing strain for $\gamma < 0.1\%$ from torsional shear tests of undisturbed samples from Lotung site; UT tests.

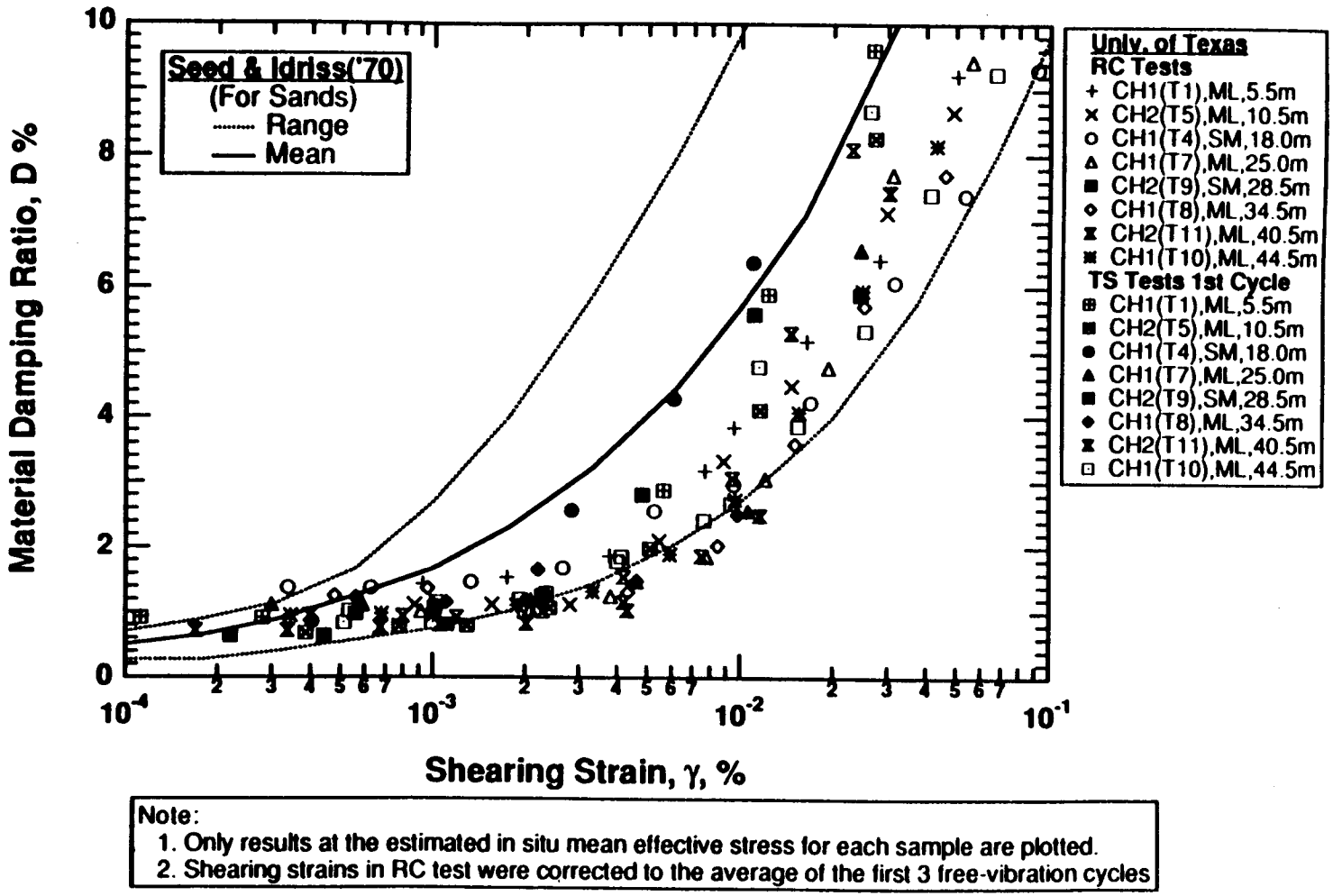

Figure 8.B.3-24
Variation in material damping ratio with shearing strain for $\gamma < 0.1\%$ from resonant column and torsional shear tests of undisturbed samples from Lotung site; UT tests.

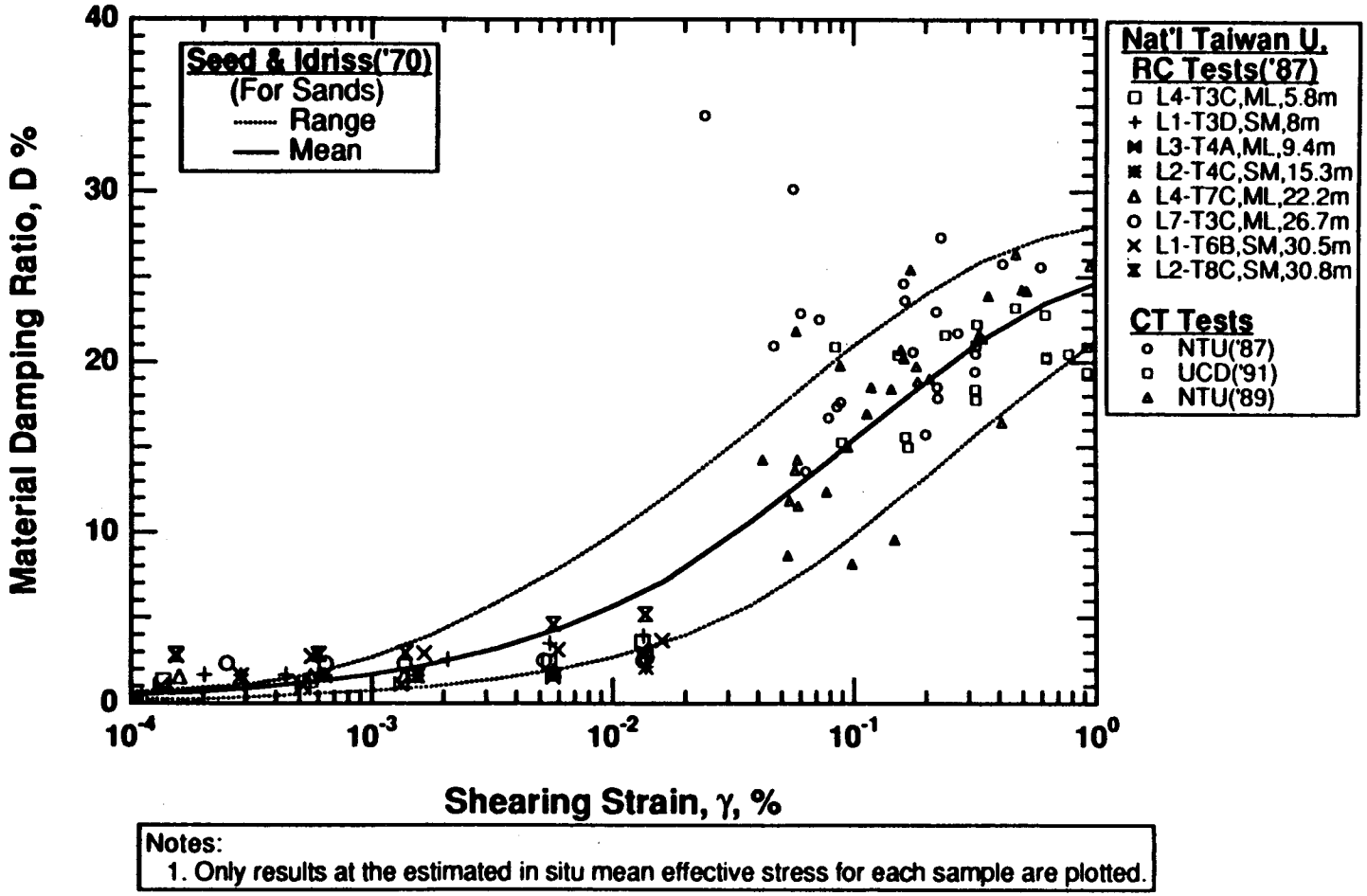

Figure 8.B.3-25
Variation in material damping ratio with shearing strain from resonant column and cyclic triaxial tests of samples from Lotung site; NTU and UCD tests.

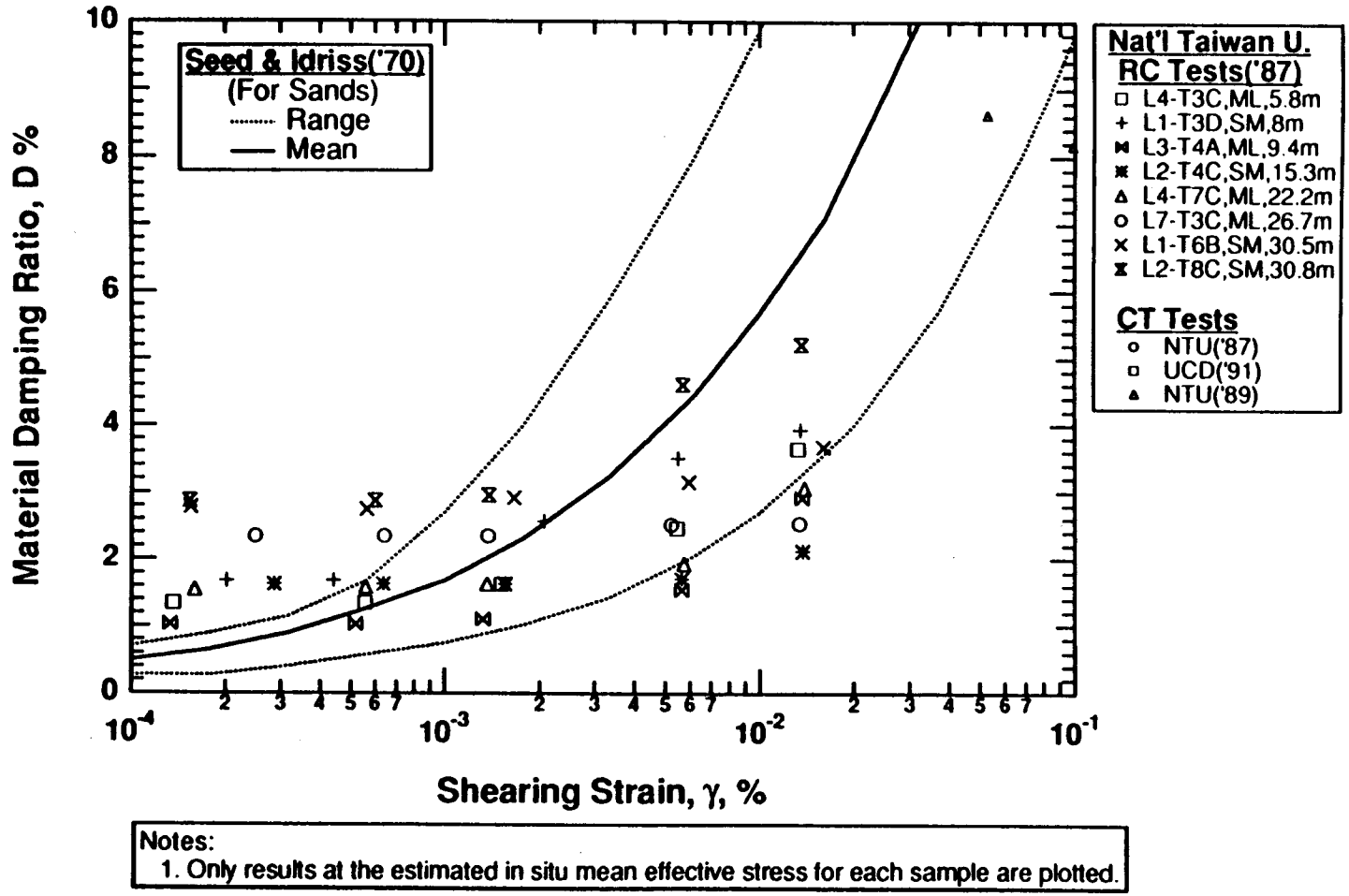

Figure 8.B.3-26
Variation in material damping ratio with shearing strain for $\gamma < 0.1\%$ from resonant column and cyclic triaxial tests of samples from Lotung site; NTU and UCD tests.

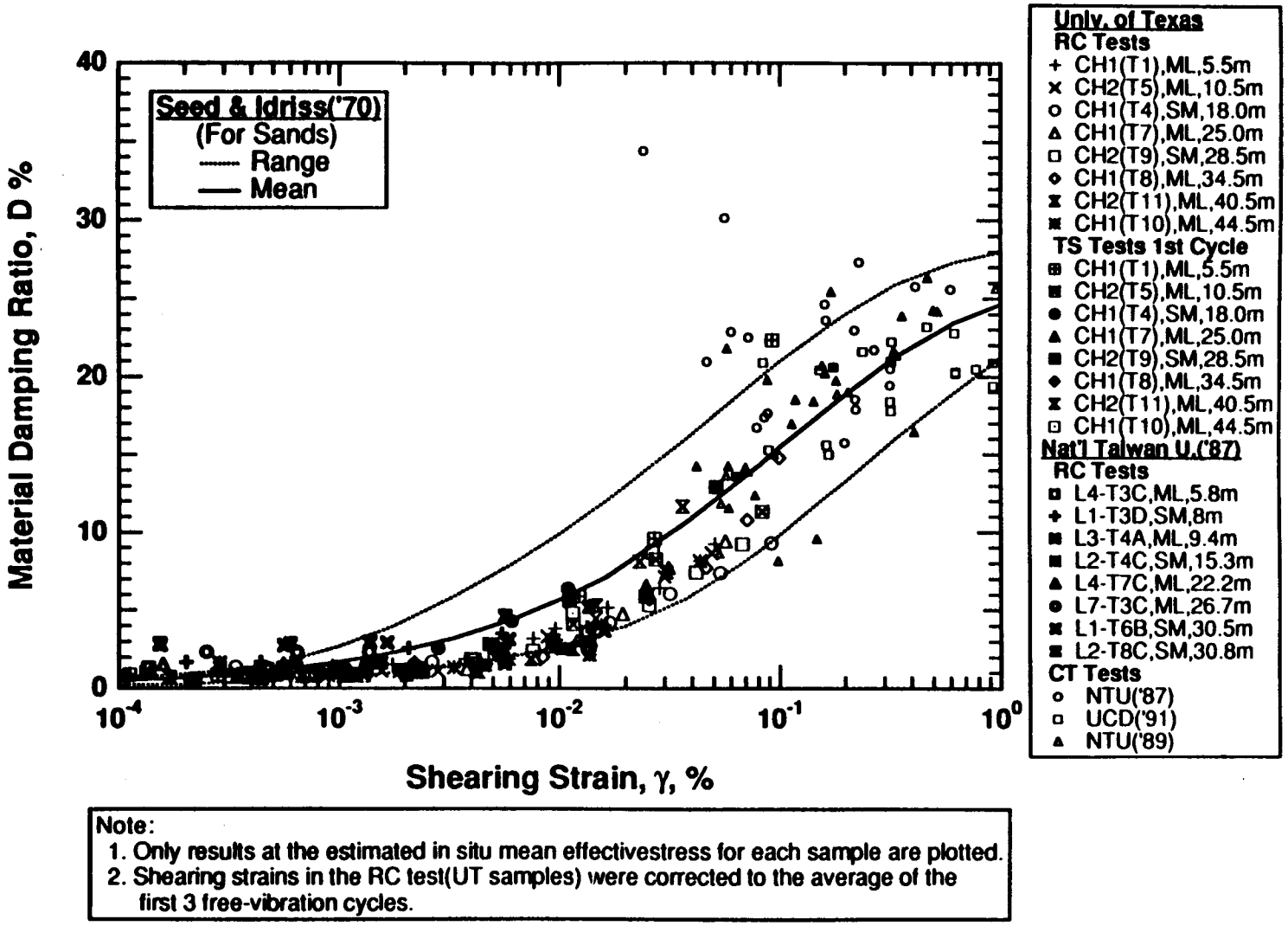

Figure 8.B.3-27
Comparison of all damping-strain data from resonant column, torsional shear and cyclic shear tests of undisturbed samples from Lotung site.

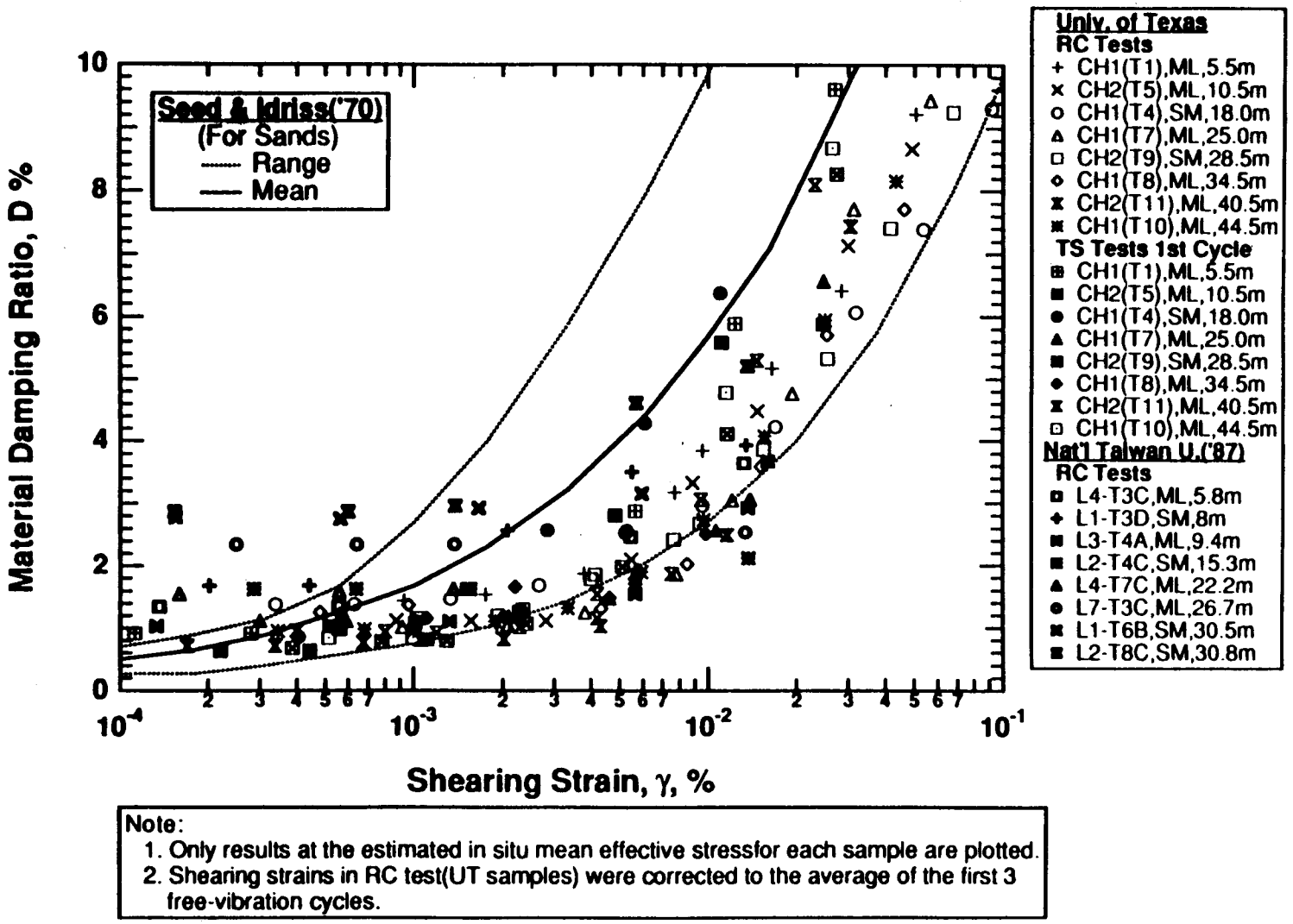

Figure 8.B.3-28
Variation in material damping ratio with shearing strain for $\gamma < 0.1\%$ from resonant column and torsional shear tests of undisturbed samples from Lotung site; UT and NTU tests.

References

Hardin, B.O. (1978), "The Nature of Stress-Strain Behavior for Soils," Proceedings, Geotechnical Engineering Division Specialty Conference on Earthquake Engineering and Soil Dynamics, Vol. 1, ASCE, Pasadena, CA, June, pp. 3–90.

Kim, D.S. (1991), *Deformational Characteristic of Soils at Small to Intermediate Strains from Cyclic Tests*, Ph.D. Dissertation, Geotechnical Engineering, Department of Civil Engineering, University of Texas at Austin, August.

Moh and Associates (1992), "Report for the Lotung Exploration Program," Report 527-2.

National Taiwan (1987), "Final Testing Reports of Foundation Soils for Lotung Nuclear Power Plant Model," prepared for Taiwan Power Company by W.T. Wu, S.-L. Foo, C.-C. Chang and L.-Y. Cheng.

National Taiwan University (1989), "Final Testing Reports of Foundation Soils Phase 3 Lotung LSST Site," prepared for Taiwan Power Company by W.-T. Wu, W.-Y. Chang and C.-Y. Wang.

Seed, H.B., and Idriss, I.M. (1970), "Soil Moduli and Damping Factors for Dynamics Response Analysis," Report No. EERC 70-10, Earthquake Engineering Research Center, University of California, Berkeley, September, p. 37.

University of California at Davis (1991), "Phase III Soil Laboratory Testing Program Report for the Lotung LSST Site," prepared for the Electric Power Research Institute by C.K. Shen and H.W. Wang.

APPENDIX 8.B.3.A
TEST EQUIPMENT AND MEASUREMENT TECHNIQUES

8.B.3.A.1 Introduction

Resonant column and torsional shear (RCTS) equipment has been employed in this investigation for measurement of the deformational characteristics (shear modulus and material damping) of intact soil specimens. This equipment has been developed at The University of Texas at Austin over the past two decades (Isenhower, 1979; Lodde, 1982; Ni, 1987; and Kim, 1991). The equipment is of the fixed-free type, with the bottom of the specimen fixed and torsional excitation applied to the top. Both resonant column (RC) and torsional shear (TS) tests can be performed in a sequential series on the same specimen over a shearing strain range from about 10^{-4}% to slightly more than 10^{-1}%. The primary difference between the two types of tests is the excitation frequency. In the RC test, frequencies above 20 Hz are required and inertia of the specimen and drive system are needed to analyze the measurements. On the other hand, slow cyclic loading involving frequencies generally below 5 Hz is performed in the TS test and inertia does not enter data analysis.

8.B.3.A.2 Resonant Column and Torsional Shear Equipment

8.B.3.A.2.1 Overview of RCTS Equipment

The RCTS apparatus can be idealized as a fixed-free system as shown in Figure 8.B.3.A-1. The bottom end of the specimen is fixed against rotation at the base pedestal, and top end of the specimen is connected to the driving system. The driving system, which consists of a top cap and drive plate, can rotate freely to excite the specimen in cyclic torsion.

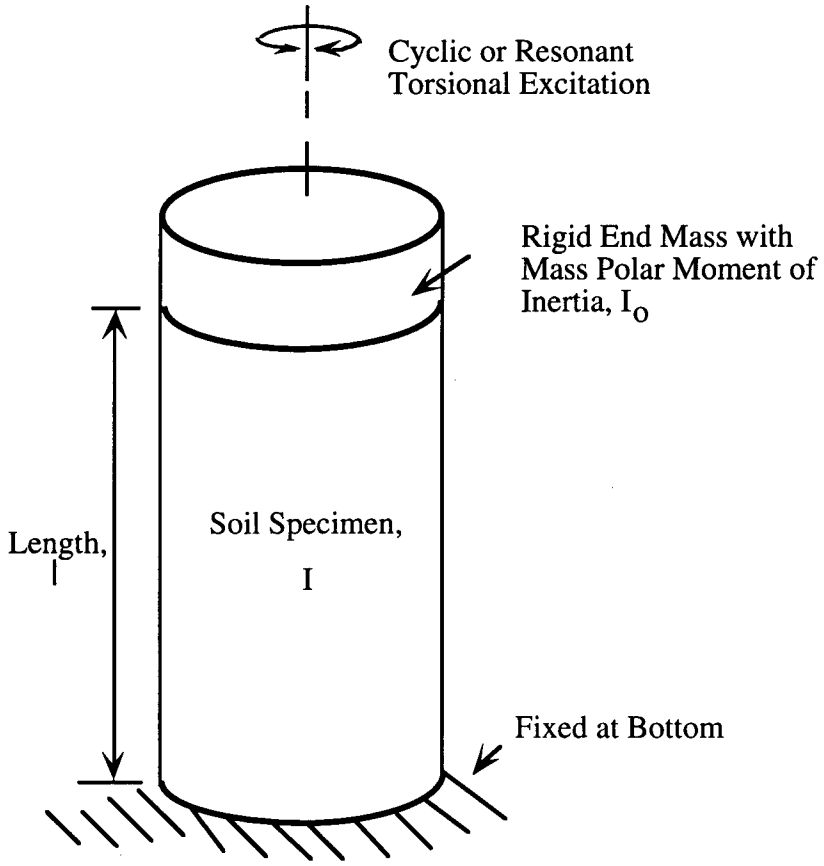

Figure 8.B.3.A-1
Idealized fixed-free RCTS equipment.

A simplified diagram of a fixed-free resonant column (RC) test is shown in Figure 8.B.3.A-2 The basic operational principle is to vibrate the cylindrical specimen in first-mode torsional motion. Harmonic torsional excitation is applied to the top of the specimen over a range in frequencies, and the variation of the acceleration amplitude of the specimen with frequency is obtained. Once first-mode resonance is established, measurements of the resonant frequency and amplitude of vibration are made. These measurements are then combined with equipment characteristics and specimen size to calculate shear wave velocity and shear modulus based on elastic wave propagation. Material damping is determined either from the width of the frequency response curve or from the free-vibration decay curve.

The torsional shear (TS) test is another method of determining shear modulus and material damping using the same RCTS equipment but operating it in a different manner. The simplified configuration of the torsional shear test is shown in Figure 8.B.3.A-3. A cyclic torsional force with a given frequency, generally below 10 Hz, is applied at the top of the specimen. Instead of determining the resonant frequency, the stress-strain hysteresis loop is determined from measuring the torque-twist response of the specimen. Proximitors are used to measure the angle of twist while the voltage applied to the coil is calibrated to yield torque. Shear modulus is calculated from the slope of a line through the end points of the hysteresis loop, and material damping is obtained from the area of the hysteresis loop as shown in Figure 8.B.3.A-3.

The RCTS apparatus used in this study has three advantages. First, both resonant column and torsional shear tests can be performed with the same set-up simply by changing (outside the apparatus) the frequency of the forcing function. Variability due to preparing "identical" samples is eliminated so that both test results can be compared effectively. Second, the torsional shear test can be performed over a shearing strain range between 10^{-4}% and about 10^{-1}%. Common types of torsional shear tests, which generate torque by a mechanical motor outside of the confining chamber, are usually performed at strains above 0.01% because of system compliance. However, the RCTS apparatus used in this study generates torque with an electrical coil-magnet system inside the confining chamber, thus eliminating the problem with an external motor. The torsional shear test can be performed at the same low-strain amplitudes as the resonant column test, and results between torsional shear and resonant column testing can be easily compared over a wide range of strains. Third, the loading frequency in the torsional shear test can be changed easily from 0.01 Hz to 10 Hz. Therefore, the effect of frequency on deformational characteristics can be conveniently investigated using this apparatus.

The RCTS apparatus consists of four basic subsystems which are: (1) a confinement system, (2) a drive system, (3) a height-change measurement system, and (4) a motion monitoring system. The general configuration of the RCTS apparatus (without the confinement system) is shown in Figure 8.B.3.A-4. The RCTS apparatus was automated by Ni (1987) so that a microcomputer controls the test, collects the data, and reduces results. Computer-aided subsystems are discussed briefly in the following sections.

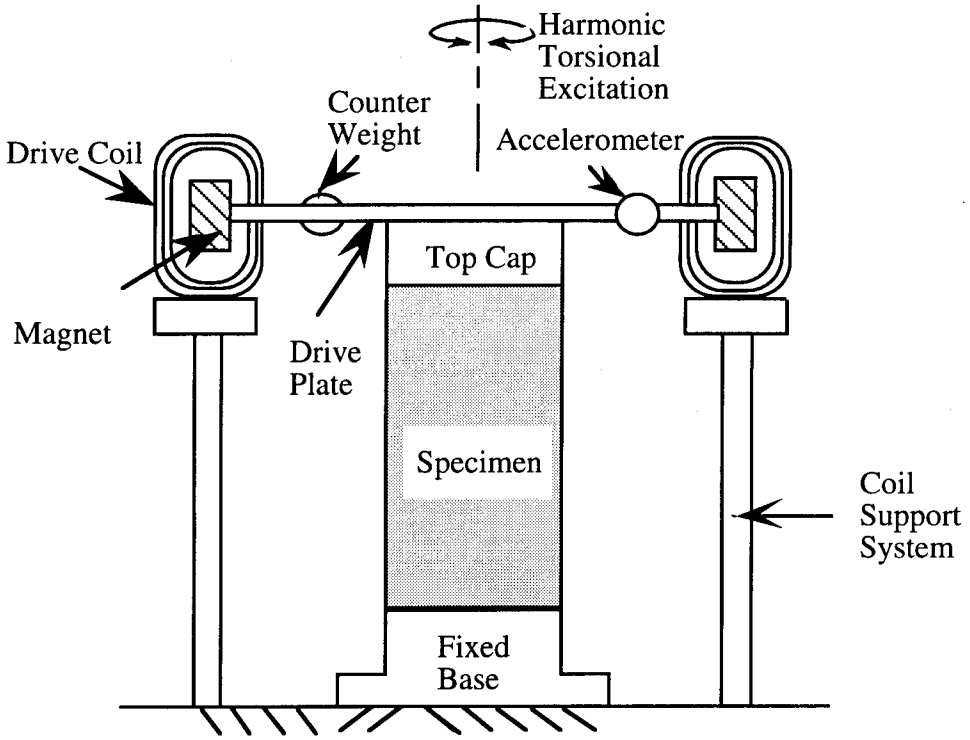

a) Specimen in the Resonant Column Apparatus
(Confinement Chamber Not Shown)

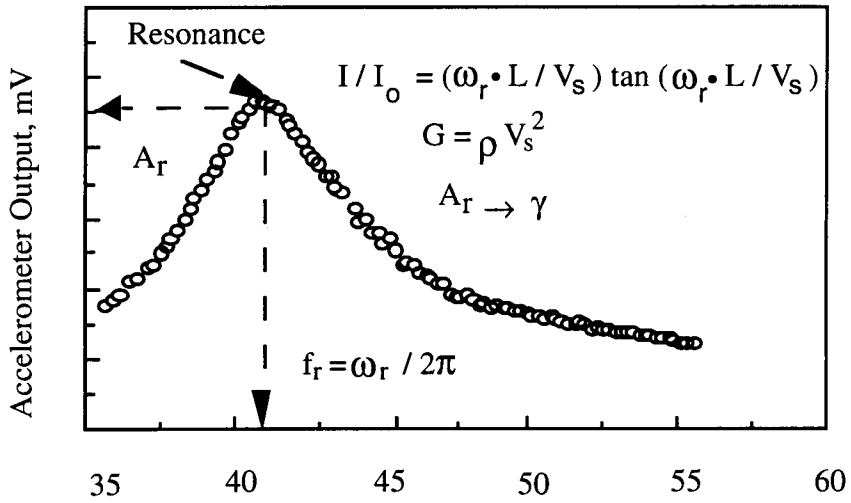

b) Typical Frequency Response Curve

Figure 8.B.3.A-2
Simplified diagram of a fixed-free resonant column test and an associated frequency response curve.

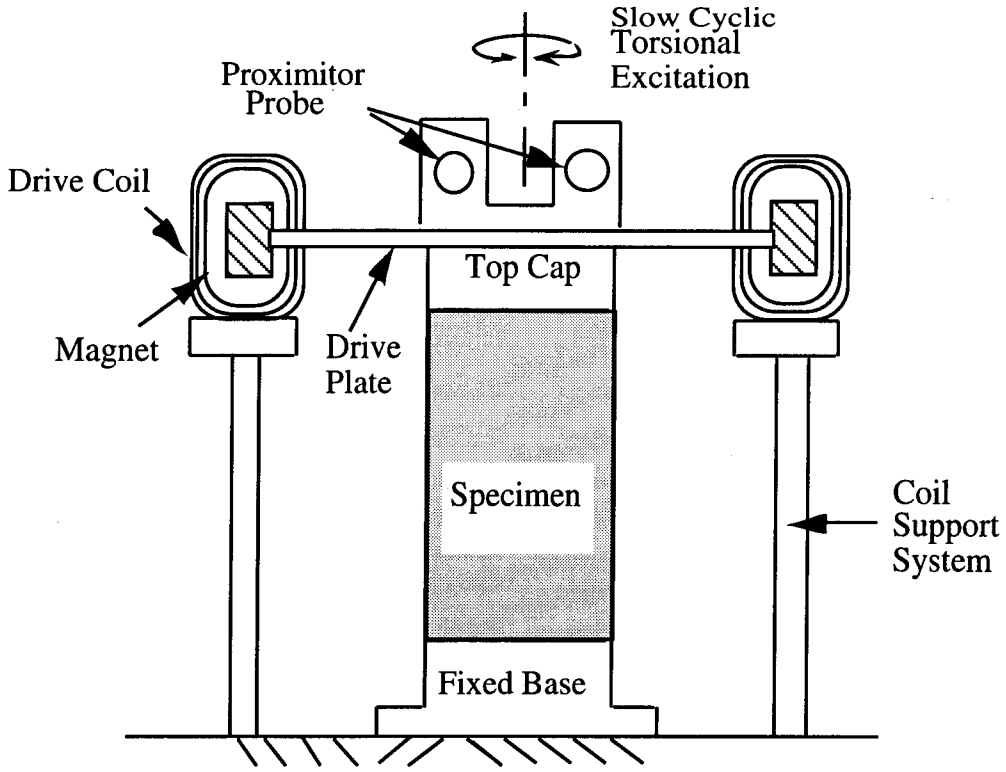

a) Specimen in the Torsional Shear Test Apparatus
(Confinement Chamber Not Shown)

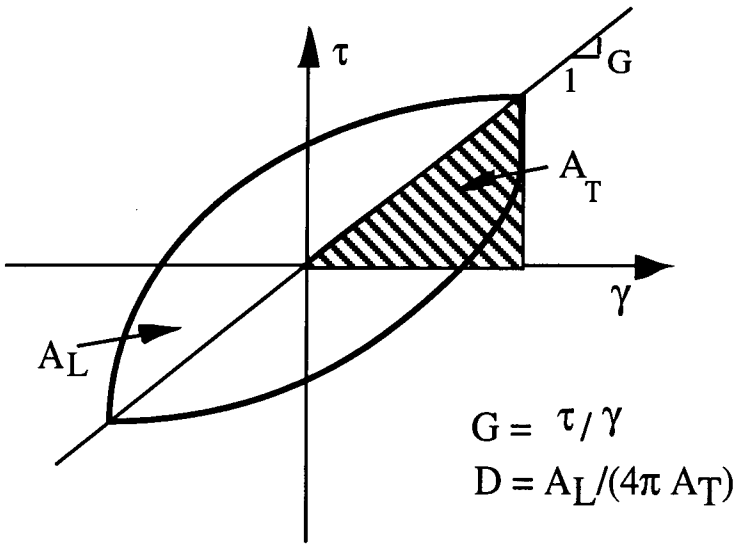

b) Measurement of Shear Modulus and Damping Ratio

Figure 8.B.3.A-3
Configuration of a torsional shear test and evaluation of shear modulus and material damping ratio.

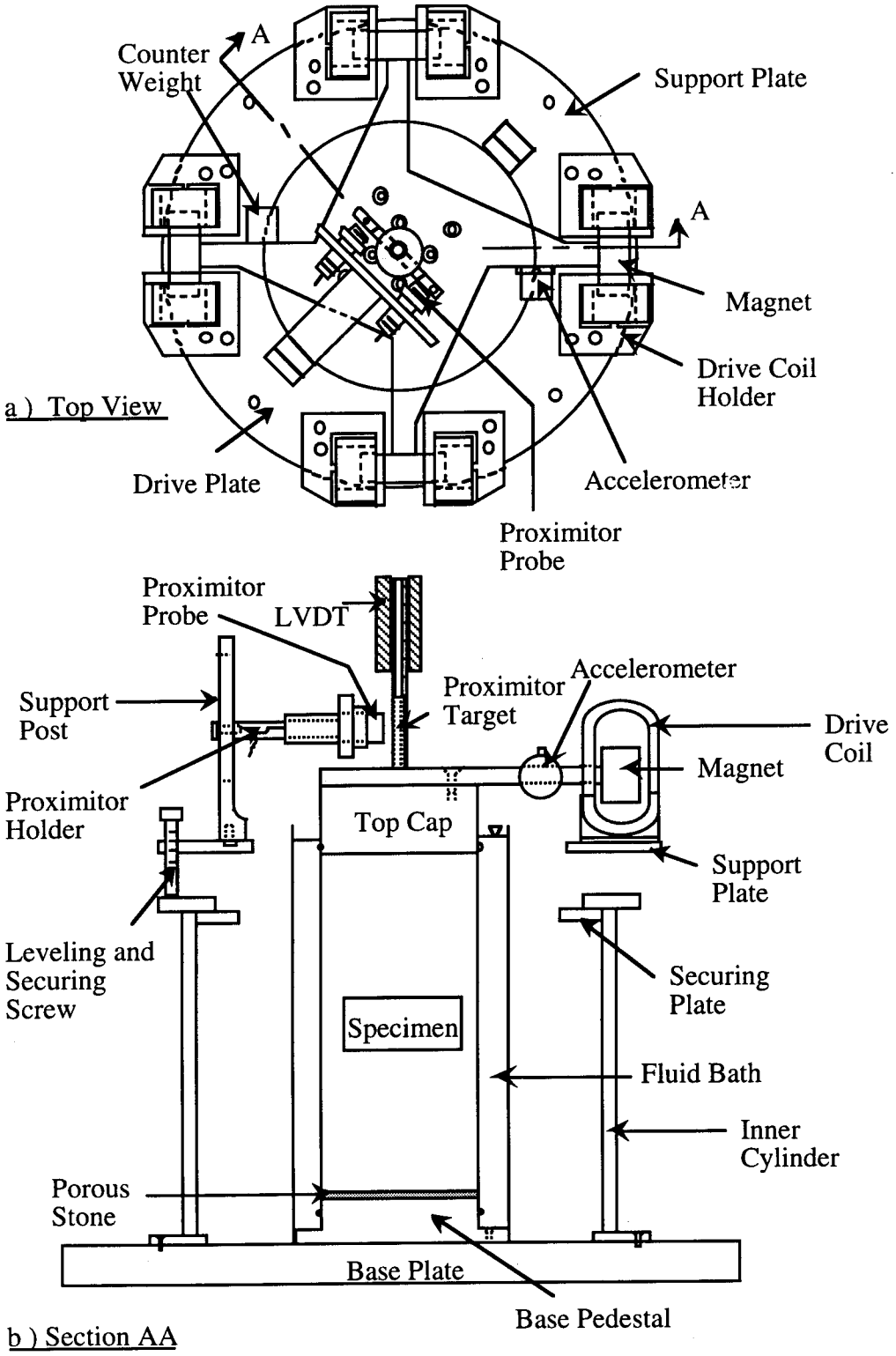

Figure 8.B.3.A-4
General configuration of RCTS equipment (from Ni, 1987).

8.B.3.A.2.2 RCTS Confinement System

The confining chamber is made of stainless steel. A thin-walled (0.6 cm in thickness) hollow cylinder fits into circular grooves machined in 2.5 cm thick base and top plates. Four stainless steel connecting rods (1.28 cm in diameter) are used to secure the base and top plates to the hollow cylinder, and O-rings in the circular grooves are used to seal the chamber. In this configuration, the chamber has been designed to withstand a maximum air pressure of about 200 psi (1379 kPa). To safely test samples at higher confining pressures (pressures on the order of 600 psi (4137 kPa)), the confinement system was modified by adding additional stainless steel rods to secure the cylinder to the top and base plates and reinforcement to the top and base plates.

Compressed air is used to confine isotropically the specimen in the RCTS device. The air pressure to the chamber generally is regulated by a Fairchild M 30 regulator and air supplied to the regulator is filtered. At high confining pressures, additional regulators are used. The soil specimen is sealed in a membrane and pore pressure in the specimen is normally vented to atmospheric pressure.

Inside the confining chamber, the air pressure acts upon a silicon fluid bath which surrounds the sides of the soil specimen. The purpose of the silicon fluid bath is to retard air migration through the membrane and into the specimen to prevent drying of the specimen. Figure 8.B.3.A-5 shows the simplified configuration of the confinement system.

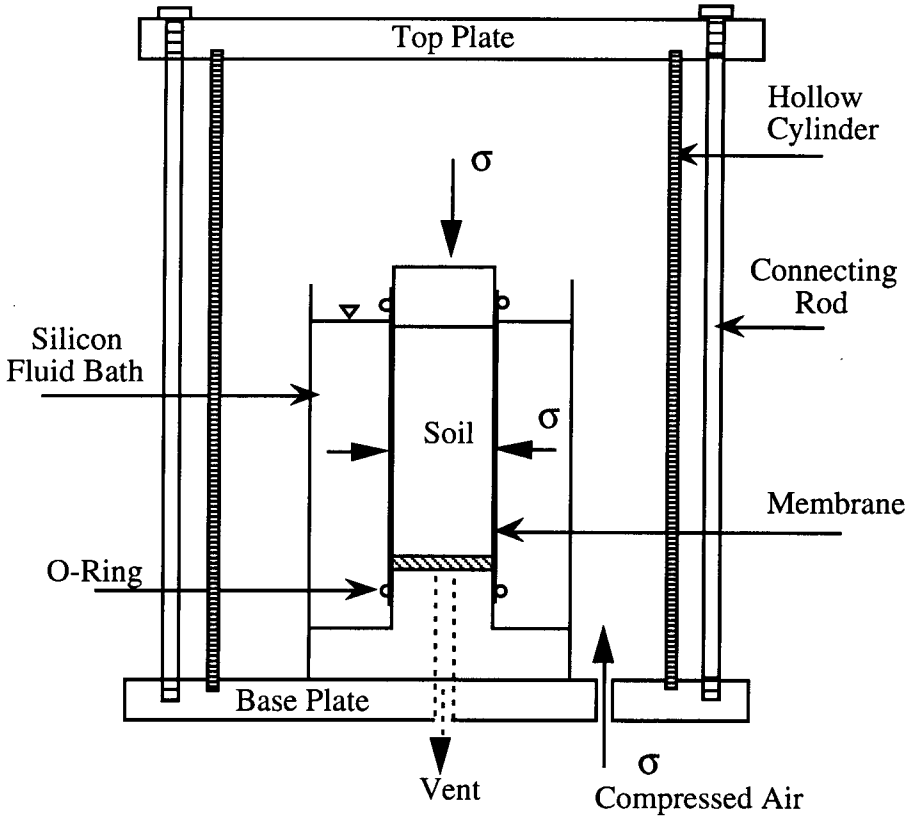

Figure 8.B.3.A-5
Simplified configuration of confinement system.

8.B.3.A.2.3 Drive System

The drive system consists of a four-armed drive plate, four magnets, eight drive coils, a power amplifier, and a function generator. Each magnet is rigidly attached to the end of one arm of the drive plate as shown in Figure 8.B.3.A-4. Eight drive coils encircle the ends of the four magnets so that the drive plate excites the soil specimen in torsional motion when a current is passed through the coils. The maximum torque that the drive system can develop depends on the strength of the magnets, size of the drive coils, resistance of the drive coils, size of the space between the magnets and drive coils, length of the arms of the drive plate, and the electrical characteristics of the function generator and power amplifier. For the three drive systems used in this work, the maximum torque was about 0.60 lb-ft (82 N-cm).

A schematic diagram of the drive system is shown in Figure 8.B.3.A-6. The micro-computer activates a function generator (HP 3314A) to input sinusoidal voltage to the drive coils. In the resonant column (RC) test, the function generator performs frequency sweeps with a constant amplitude while in the torsional shear test, a fixed-frequency N-cycle mode is used. For high-amplitude resonant column and torsional shear (TS) tests, the sinusoidal input current is amplified by a power amplifier (HP 6824A) before going to the drive coils.

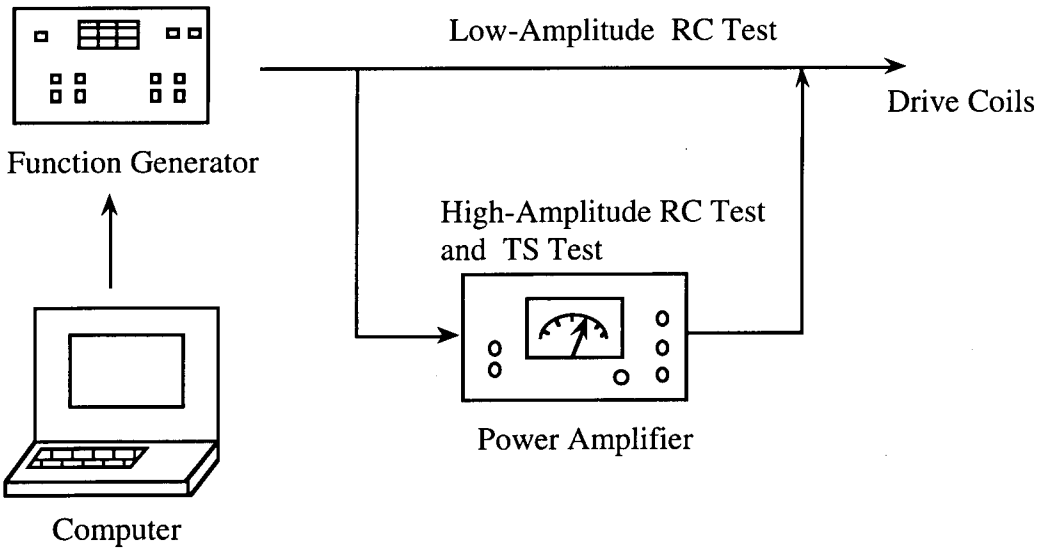

Figure 8.B.3.A-6
Schematic diagram of the drive system.

8.B.3.A.2.4 Height-Change Measurement System

The height change of the soil specimen is measured to account for the changes in the length and mass of the specimen during consolidation or swell. This measurement is also used to calculate change in the mass moment of inertia, mass density, and void ratio during testing (by assuming isotropic strain under isotropic confinement and constant degree of saturation). The height change is measured by a linear variable differential transformer (LVDT). The height change measurement system consists of an LVDT (CRL Model SH-200-53R), a function generator (HP 3314A), and a digital voltmeter (HP 3456A). The LVDT core is not in contact with the LVDT coil housing so that no friction occurs during RCTS testing.

The output and calibration factor of an LVDT depend on both the frequency and magnitude of the excitation voltage. In this test the computer activates the function generator to generate the input signal in the LVDT coil at a frequency of 500 Hz and a voltage level of 4.77 RMS volts. The output from the LVDT is read with a digital voltmeter. The height change is calculated from the output voltage combined with

the calibration factor. The schematic diagram of the height change measuring system is shown in Figure 8.B.3.A-7.

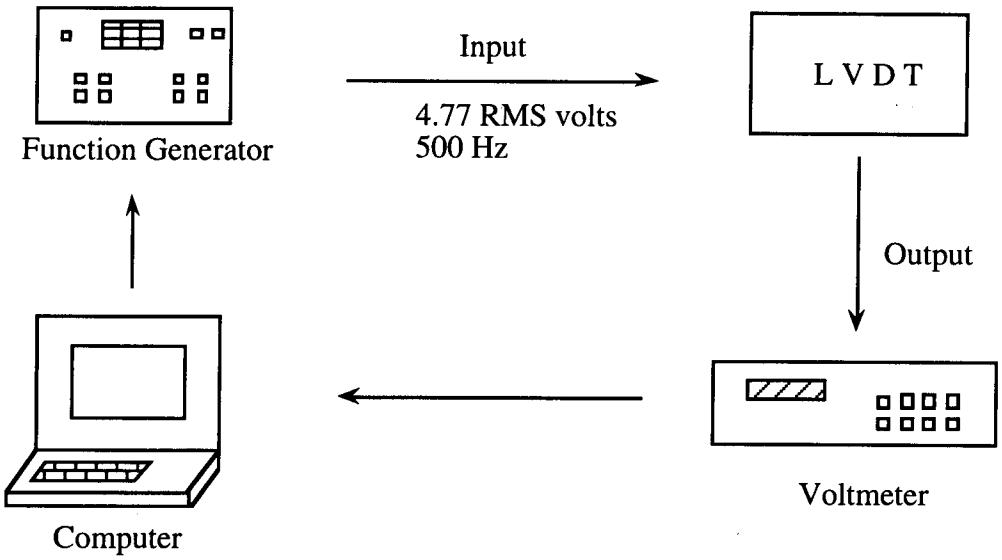

Figure 8.B.3.A-7
Schematic diagram of the height-change measuring system.

8.B.3.A.2.5 Motion Monitoring System

Dynamic soil properties are obtained in the RC test at the resonant frequency which is usually above 20 Hz while torsional shear testing is used to measure the low-frequency (below 10 Hz) cyclic stress-strain relationship of soil. Because of the different frequencies applied in the resonant column and torsional shear tests, different motion monitoring systems are used.

Resonant Column (RC) Test. The motion monitoring system in the RC test is designed to measure the resonant frequency, shearing strain, and free-vibration decay curve. This system consists of an accelerometer (Columbia Research Laboratory Model 3021), a charge amplifier (Columbia Research Laboratory Model 4102M), a frequency counter (HP 5334A), a digital voltmeter (HP 3456A), and a digital oscilloscope (Nicolet 20929-01). The schematic diagram of the motion monitoring system is shown in Figure 8.B.3.A-8.

The accelerometer is oriented to be sensitive to torsional vibrations of the drive plate. The charge amplifier conditions the accelerometer output to be linear for all levels of acceleration in the test. The digital voltmeter reads the output voltage from the accelerometer at each frequency which is measured by the frequency counter. The resonant frequency is obtained from the frequency response curve. Once the resonant frequency is obtained, the computer activates the function generator to excite the specimen at the resonant frequency and then suddenly stops the current so that the free-vibration decay curve is recorded by the digital oscilloscope.

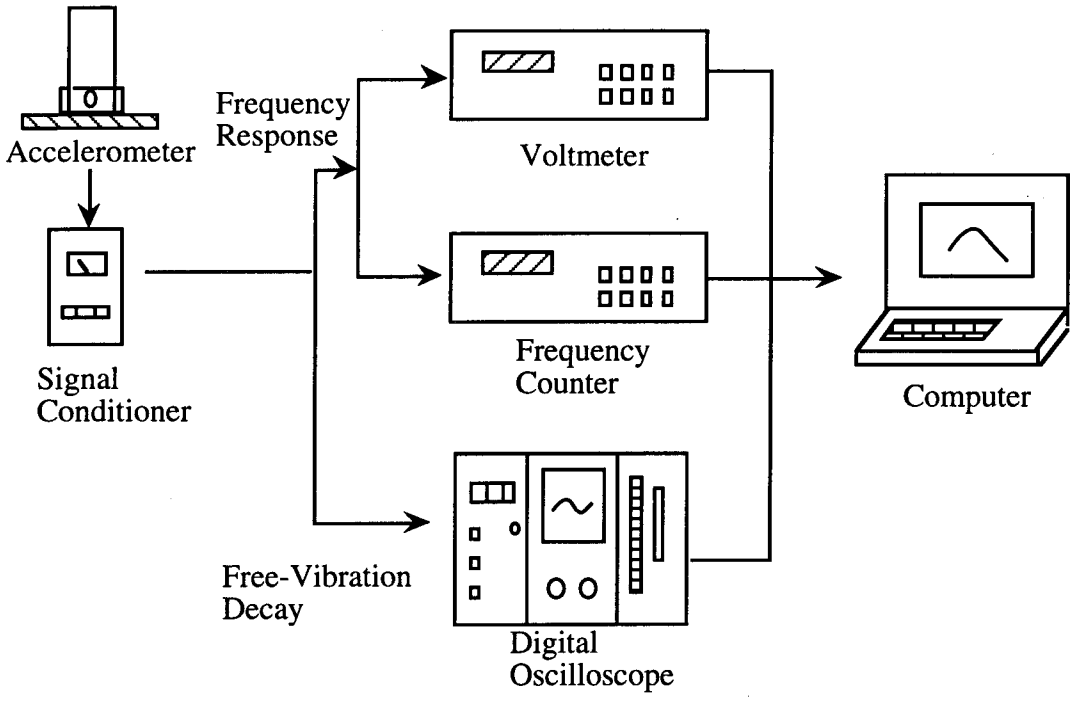

Figure 8.B.3.A-8
Schematic diagram of the motion monitoring system in the resonant column test.

The resonant frequency of soils are typically in the range of 20 Hz to 300 Hz with this equipment. To test soils effectively over a wide range of stiffnesses, the search for the resonant frequency is performed in two stages, a rough sweep and a fine sweep. During the rough sweep, a fast logarithmic-linear frequency sweep (16 seconds to sweep from 1 to 170 Hz) is used. The fine sweep is then performed to determine an accurate resonant frequency in the neighborhood where the resonant frequency was found in the rough sweep.

Torsional Shear (TS) Test. The motion monitoring system in the TS test (3000 Proximitor System) is used to monitor torque-twist hysteresis loops of the specimen. This system consists of two proximitors (Bentry Nevada M 20929-01), two proximitor probes (Bentry Nevada M 300-00), an operational amplifier (Tektronix TM 504 with AM501), a DC power supply (Lambda M-11-902), a U-shaped target and a digital oscilloscope (Nicolet 20929-01). The U-shaped target is secured to the top of the drive plate, and the two proximitor probes are rigidly attached to the support stand. A schematic diagram of the motion monitoring system in the torsional shear test is shown in Figure 8.B.3.A-9.

The function of the proximitor probes is to measure the width of the air gap between the target and the probe tip. Because the proximitor probes do not touch the drive plate, no compliance problems are introduced into the measurement. Two probes are used and the operational amplifier subtracts the signal from one probe from the other so that the effect of bending in the specimen toward the probes can be eliminated. The proximitor system is a very effective low-frequency motion monitoring system which does not introduce any compliance problems into the measurement. With the simultaneous measurement of torque, load-displacement hysteresis loops can be determined.

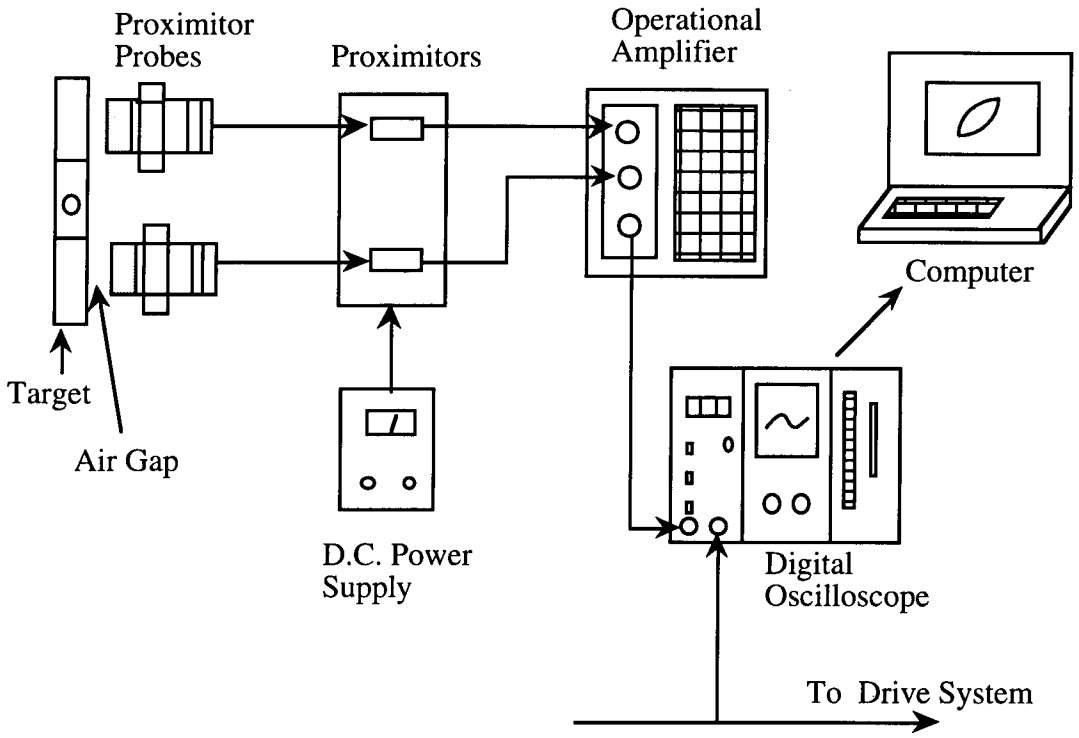

Figure 8.B.3.A-9
Schematic diagram of the motion monitoring system in the torsional shear test (3000 Proximitor System).

8.B.3.A.3 Method of Analysis in the Resonant Column Test

The resonant column test is based on the one-dimensional wave equation derived from the theory of elasticity. The shear modulus is obtained by measuring the first-mode resonant frequency while material damping is evaluated from either the free-vibration decay curve or from the width of the frequency response curve assuming viscous damping.

8.B.3.A.3.1 Shear Modulus

The governing equation of motion for the fixed-free torsional resonant column test is:

$$\frac{\Sigma I}{I_o} = \frac{\omega_n \bullet l}{V_s} \bullet \tan\left(\frac{\omega_n \bullet l}{V_s}\right) \qquad (8.B.3.A\text{-}1)$$

where $\Sigma I = I_s + I_m + \cdots$

I_s = mass moment of inertia of soil,
I_m = mass moment of inertia of membrane,
I_o = mass moment of inertia of rigid end mass at the top of the specimen,
l = length of the specimen,
V_s = shear wave velocity of the specimen, and
ω_n = undamped natural circular frequency of the system.

The value of I_o is known from the calibration of the drive plate. The values of I_s and l are easily determined from the specimen size and weight. Once the first-mode resonant frequency is determined, the shear wave velocity can be calculated from Eq. 8.B.3.A-1 by assuming that the resonant circular frequency and ω_n are equal.

As noted above and shown in Figure 8.B.3.A-2 the resonant circular frequency, ω_r,is measured instead of undamped natural frequency, ω_n, and ω_r is used to calculate shear wave velocity. If the damping in the system is zero, ω_r and ω_n are equal. The relationship between ω_r and ω_n is:

$$\omega_r = \omega_n \sqrt{1-2D^2} \qquad \text{(8.B.3.A-2)}$$

A typical damping ratio encountered in the resonant column test is less than 20 percent, which corresponds to a difference of less than 5 percent between ω_r and ω_n. In this study, the damping measured in the resonant column test was usually less than 10 percent, and ω_r can be used instead of ω_n with less than a two percent error.

Once the shear wave velocity is determined, shear modulus is calculated from the relationship:

$$G = \rho \bullet V_s^2 \qquad \text{(8.B.3.A-3)}$$

where ρ is the total mass density of the soil (total unit weight divided by gravity).

8.B.3.A.3.2 Shearing Strain

The shearing strain varies radially within the specimen and may be expressed as a function of the distance from the longitudinal axis as illustrated in Figure 8.B.3.A-10. The equivalent shearing strain, γ_{eq} or γ, is represented by:

$$\gamma = r_{eq} * \theta_{max} / l \qquad \text{(8.B.3.A-4)}$$

Where

r_{eq} = equivalent radius,
θ_{max} = angle of twist at the top of the specimen, and
l = length of the specimen.

Chen and Stokoe (1979) studied the radial distribution in shearing strain to find a value of r_{eq} for the specimen tested in the RCTS equipment to evaluate an effective strain. They found that the value of r_{eq} varied from $0.82*r_0$ for a peak shearing strain amplitude below 0.001% to $0.79*r_0$ for a peak shearing strain of 0.1% for a solid specimen. These values of r_{eq} have been adopted in this study.

In the resonant column test, the resonant period (T_r, seconds), and output voltage of accelerometer (A_c, volts(RMS)) at resonance are measured. Accelerometer output is changed to the displacement by using the accelerometer calibration factor (CF, volts(RMS)/in./sec^2) assuming harmonic motion. The accelerometer displacement is divided by the distance (D_{ac}, inches) between the location of accelerometer and the axis of the specimen to calculate the angle of twist at the top of the specimen(θ_{max}). The shearing strain is then calculated by:

$$\gamma = r_{eq} \frac{A_c \bullet Tr^2}{4\pi^2 \bullet CF} \bullet \frac{1}{D_{ac}} \bullet \frac{1}{l} \qquad \text{(8.B.3.A-5)}$$

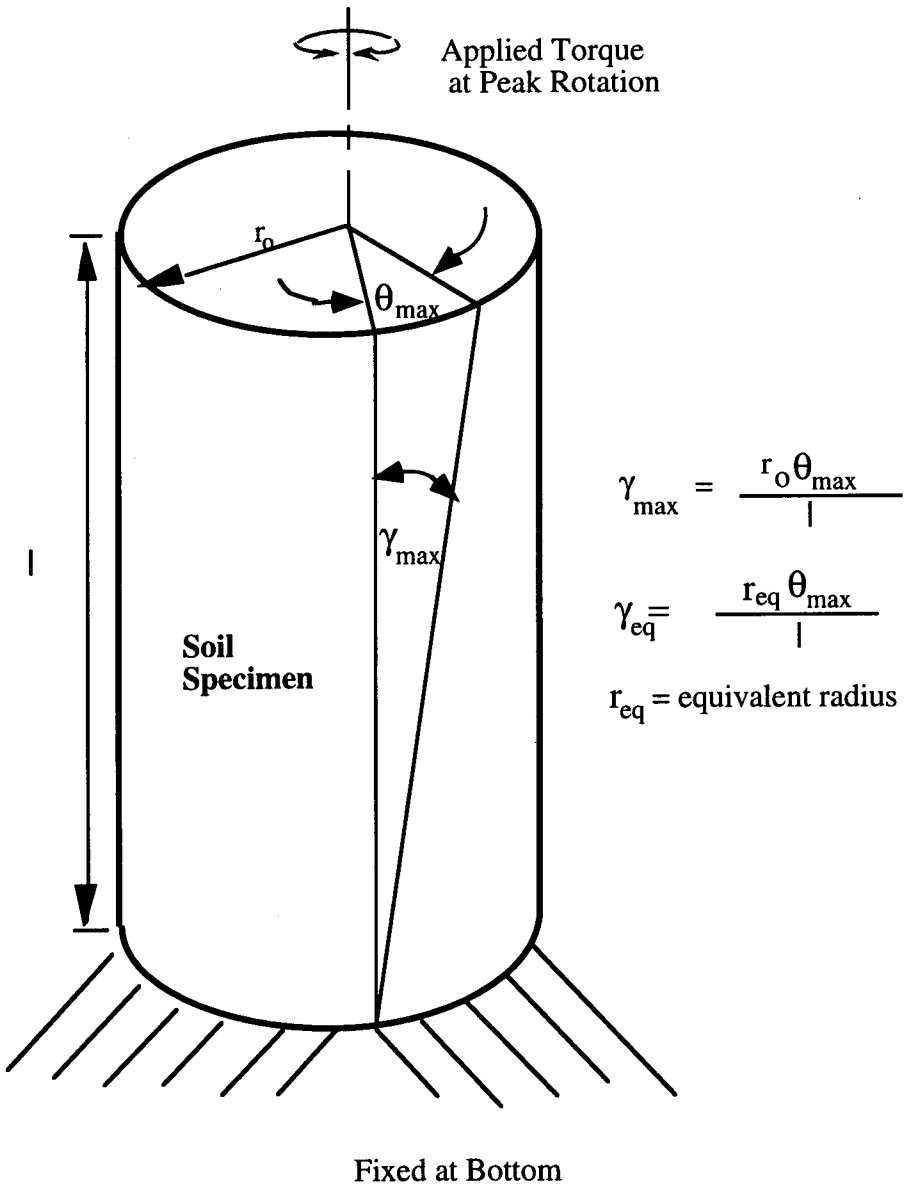

Figure 8.B.3.A-10
Shearing strain in soil column.

8.B.3.A.3.3 Material Damping

In the resonant column test, material damping ratio can be evaluated from either the free-vibration decay method or from the half-power bandwidth method. Each of these methods is discussed below. It is important to note that, in these measurements, the damping measurement includes material damping in the soil plus any damping in the equipment. Calibration of equipment damping is discussed in Section 8.B.3.A.5.

Free-Vibration Decay Method. Material damping in soils can be quite complex to define. However, the theory for a single-degree-of-freedom system with viscous damping is a useful framework for describing the effect of damping which occurs in soil (Richart et al., 1970). The decay of free vibrations of a single-degree-of-freedom system with viscous damping is described by the logarithmic decrement, δ, which is the ratio of the natural logarithm of two successive amplitudes of motion as:

$$\delta = \ln\left(\frac{Z_1}{Z_2}\right) = \frac{2\pi D}{\sqrt{1-D^2}} \qquad \text{(8.B.3.A-6)}$$

Where

Z_1 and Z_2 = two successive strain amplitudes of motion, and
D = material damping ratio.

The free-vibration decay curve is recorded using an oscilloscope by shutting off the driving force while the specimen is vibrating at the resonant frequency. The amplitude of each cycle is measured from the decay curve, and the logarithmic decrement is then calculated using Eq. 8.B.3.A-6. Material damping ratio is calculated from logarithmic decrement according to:

$$D = \sqrt{\frac{\delta^2}{4\pi^2 + \delta^2}} \qquad \text{(8.B.3.A-7)}$$

A typical damping measurement from a free-vibration decay curve (from a metal calibration specimen) is shown in Figure 8.B.3.A-11.

In this method, it is not certain which strain amplitude is a representative strain for damping ratio calculated by Eq. 8.B.3.A-7 because strain amplitude decreases during free-vibration decay. In this study, a representative strain amplitude was used as the peak strain amplitude during steady-state vibration for shearing strains below 0.001%. However, at larger strains, the representative strain is smaller than the peak strain, and the average strain determined for the first three cycles of free vibration was used.

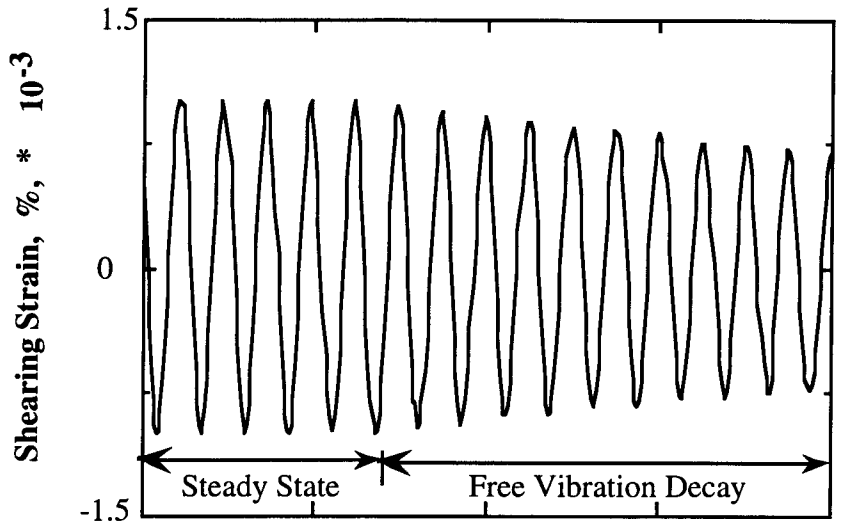

a) Free-Vibration Decay Curve

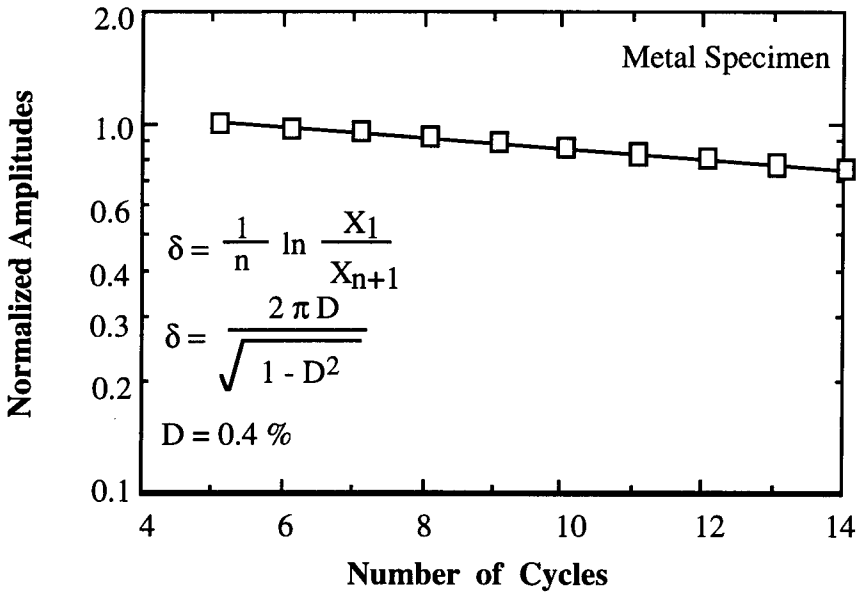

b) Analysis of Free-Vibration Decay Curve

Figure 8.B.3.A-11
Determination of material damping ratio from the free-vibration decay curve using a metal specimen.

Half-Power Bandwidth Method. Another method of measuring damping in the resonant column test is the half-power bandwidth method, which is based on measurement of the width of the frequency response curve near resonance. From the frequency response curve, the logarithmic decrement can be calculated from:

$$\delta = \frac{\pi}{2}\frac{f_2^2 - f_1^2}{f_r^2}\sqrt{\frac{A^2}{A_{max}^2 - A^2}}\frac{\sqrt{1-2D^2}}{1-D^2} \qquad (8.B.3.A\text{-}8)$$

Where

f_1 = frequency below the resonance where the strain amplitude is A,
f_2 = frequency above the resonance where the strain amplitude is A,
f_r = resonant frequency, and
D = material damping ratio.

If the damping ratio is small and A is chosen as 0.707 A_{max}, which is called the half-power point, Eq. 8.B.3.A-8 can be simplified as:

$$\delta \cong \pi \bullet \frac{f_2 - f_1}{f_r} \qquad (8.B.3.A\text{-}9)$$

Therefore, the damping ratio can be expressed as:

$$D \cong \frac{f_2 - f_1}{2f_r} \qquad (8.B.3.A\text{-}10)$$

A typical damping measurement by the half-power bandwidth method (for a metal calibration specimen) is shown in Figure 8.B.3.A-12.

Background noise can be a problem in measuring material damping using the free-vibration decay method at strains less than about 0.001%. On the other hand, background noise generally has a smaller effect on the frequency response curve at strains below 0.001%. Therefore, the half-power bandwidth method is preferred to the free-vibration decay method for making small-strain damping measurements. However, at large strains, symmetry in the frequency response curve is no longer maintained, and a serious error can be introduced in the half-power bandwidth method (Ni, 1987). In this study, both types of damping measurements were made at small-strains in an attempt to obtain good data sets while only the free-vibration decay method was used at larger strains (above 0.001%).

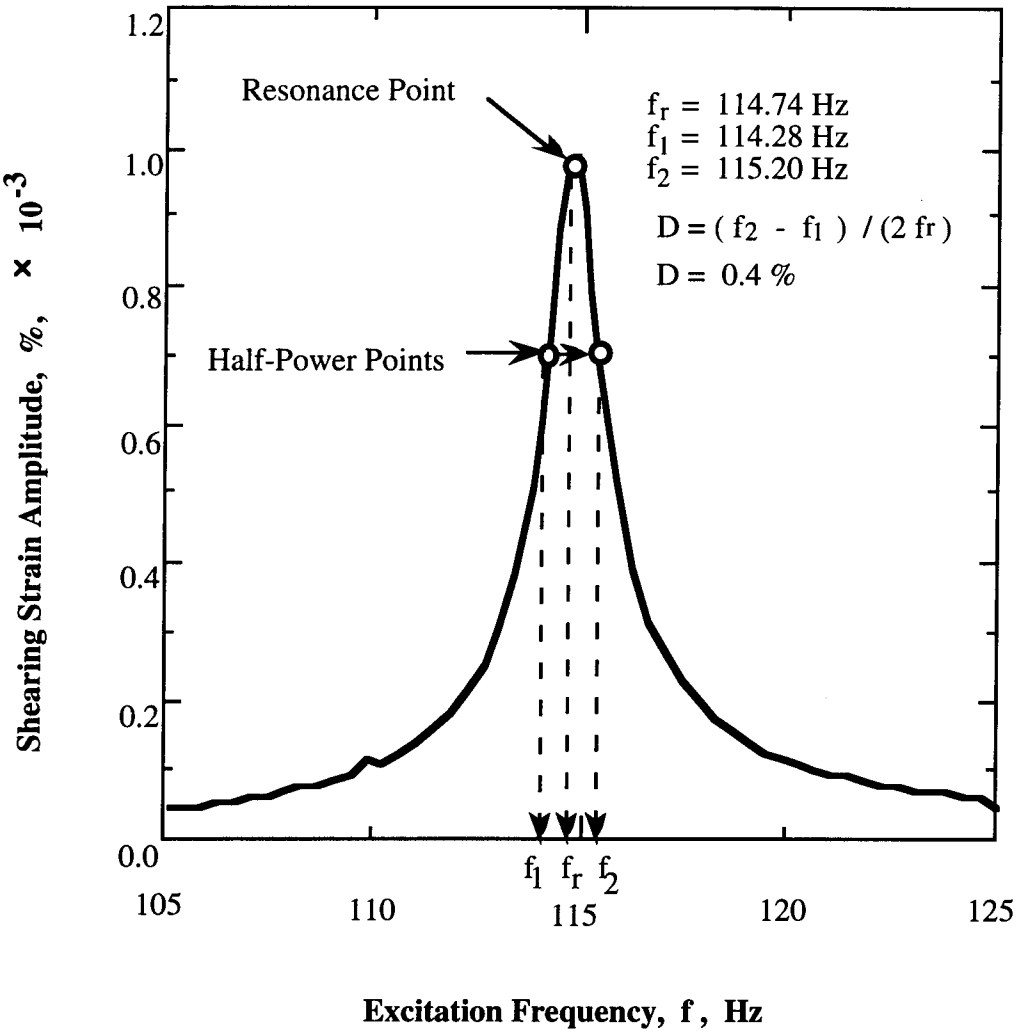

Figure 8.B.3.A-12
Determination of material damping from the half-power bandwidth method using a metal specimen.

8.B.3.A.4 Method of Analysis in the Torsional Shear Test

The torsional shear test is another method of determining the deformational characteristics (modulus and damping) of soil using the same RCTS device. Rather than measuring the dynamic response of the specimen, the actual stress-strain hysteresis loop is determined by means of measuring the torque-twist curve. Shear modulus is calculated from the slope of the hysteresis loop, and the hysteric damping ratio is calculated using the area of the hysteresis loop.

8.B.3.A.4.1 Shear Modulus

Because shear modulus is calculated from the stress-strain hysteresis loop, shearing stress and shearing strain in the torsional shear test need to be defined.

Shearing Stress. Determination of shearing stress in the torsional shear test is based on the theory of elasticity for circular or tubular rods in pure torsion. Assume that pure torque, T, is applied to the top of the specimen. The torque can be calculated from:

$$T = \int_{r_i}^{r_o} \tau_r (2\pi\ r)\ r\ dr \qquad \text{(8.B.3.A-11)}$$

where τ_r is the shearing stress at a distance r from the axis of specimen and, r_o and r_i are outside and inside radii, respectively. If the shearing stress is assumed to vary linearly across the radius:

$$\tau_r = \tau_m \bullet (r / r_o) \qquad \text{(8.B.3.A-12)}$$

where τ_m is the maximum shearing stress at $r = r_o$. Eq. 8.B.3.A-12 can be rewritten as:

$$T = \frac{\tau_m}{r_o} \bullet \frac{\pi}{2} \bullet (r_o^4 - r_i^4) = \frac{\tau_m}{r_o} \bullet J_p \qquad \text{(8.B.3.A-13)}$$

where J_p is the area polar moment of inertia. From Eq. 8.B.3.A-13, one can write:

$$\tau_m = r_o \bullet \frac{T}{J_p} \qquad \text{(8.B.3.A-14)}$$

Because shearing stress is assumed to vary linearly across the radius, the average torsional shearing stress is defined as:

$$\tau_{avg} = r_{eq} \bullet \frac{T}{J_p} \qquad \text{(8.B.3.A-15)}$$

The value of r_{eq} is the same value as used in the resonant column analysis for calculation of shearing strain (Section 8.B.3.A.3.2).

The value of applied torque, T, is calculated from the input voltage applied to the drive system, V_T (Volts), and the torque calibration factor, K_T (torque / Volts). Thus, average shearing stress becomes:

$$\tau_{avg} = r_{eq} \bullet K_T \bullet V_T / J_p \qquad \text{(8.B.3.A-16)}$$

Shearing Strain. Calculation of shearing strain in the torsional shear test follows the same procedure used in the resonant column test. The proximitor system directly measures the displacement (instead of acceleration measured in the resonant test). Hence, the angle of twist (θ) is calculated from the proximitor output voltage, V_P (volts), and the proximitor calibration factor, K_P (rad / volt). Shearing strain, γ, is then calculated from:

$$\gamma = r_{eq} \Sigma K_P \bullet V_P / l \qquad \text{(8.B.3.A-17)}$$

Shear Modulus. Once the stress-strain hysteresis loop is measured, the shear modulus, G, is calculated from the slope of a line through the end points of the hysteresis loop as shown in Figure 8.B.3.A-13. Thus, the shear modulus is calculated from:

$$G = \tau / \gamma \qquad \text{(8.B.3.A-18)}$$

where τ is peak shearing stress and γ is peak shearing strain.

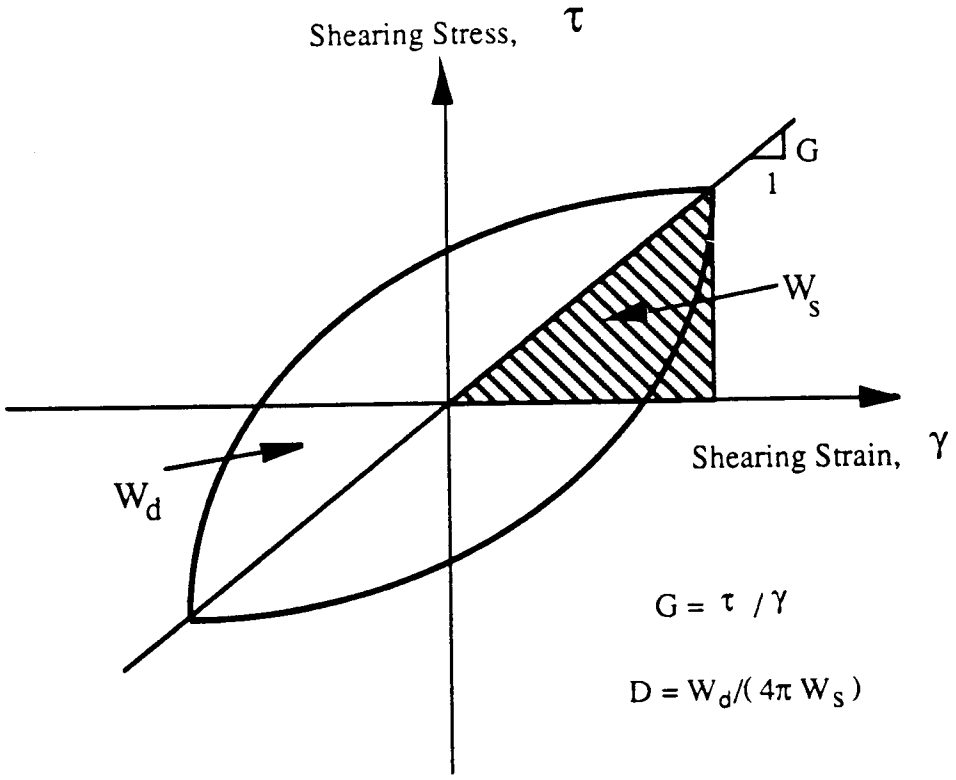

Figure 8.B.3.A-13
Determination of shear modulus and damping ratio in the torsional shear test.

8.B.3.A.4.2 Hysteretic Damping Ratio

Hysteretic damping ratio in the torsional shear test is measured using the amount of energy dissipated in one complete cycle of loading and the peak strain energy stored in the specimen during the cycle.

In the torsional shear test, the dissipated energy is measured from the area of the stress-strain hysteresis loop. The energy per cycle, W_d, due to a viscous damping force, F_d, is:

$$W_d = \int_o^T F_d \bullet \dot{x}\, dt \qquad \text{(8.B.3.A-19)}$$

where $\dot{x}$ is a velocity and T is a period. For simple harmonic motion with frequency of ω, i.e. $x = A\,\text{Cos}(\omega t - \phi)$, W_d become:

$$W_d = \pi\, c\, \omega\, A^2 \qquad \text{(8.B.3.A-20)}$$

From the Eq. 8.B.3.A-20, the viscous damping coefficient can be expressed as:

$$c = W_d / (\pi \omega A^2) \quad (8.B.3.A\text{-}21)$$

The peak strain energy, W_s, stored by the spring is equal to the area under the secant modulus line in Figure 8.B.3.A-13 and can be written as:

$$W_s = k A^2 / 2 \quad (8.B.3.A\text{-}22)$$

The critical damping coefficient, C_c, is

$$C_c = 2 \bullet \sqrt{k m} = 2 k / \omega_n \quad (8.B.3.A\text{-}23)$$

where k is an elastic spring constant, m is a mass, and ω_n is a natural frequency of system. Using Eq. 8.B.3.A-22, Eq. 8.B.3.A-23 can be rewritten as:

$$C_c = 4 W_s / (\omega_n A^2) \quad (8.B.3.A\text{-}24)$$

Therefore, the damping ratio, D, can be expressed as:

$$D = C / C_c = W_d / (4 \pi W_s) * (\omega_n / \omega) \quad (8.B.3.A\text{-}25)$$

For soils, material damping is often assumed to be frequency independent. Therefore, ω_n / ω is ignored and hysteretic damping is written as:

$$D = \frac{1}{4\pi} * \frac{W_d}{W_s} \quad (8.B.3.A\text{-}26)$$

where W_d is the area of the hysteresis loop and W_s is the area of the triangle as shown in Figure 8.B.3.A-13.

8.B.3.A.5 Evaluation of RCTS Equipment Compliance with Metal Specimens

To evaluate the RCTS equipment for system compliance, metal specimens were used. The metal specimens were made of brass and aluminum tubes. Eighteen metal specimens of different sizes and materials were used to obtain different resonant frequencies. Details of the metal specimens are presented in Table 8.B.3.A-1. It was assumed that the metal specimens should have (essentially) zero damping and that these specimens should exhibit no effect of frequency on stiffness or damping over the complete range of frequencies used in these tests (from about 0.05 Hz to 400 Hz).

Table 8.B.3.A-1
Metal Specimens Used to Evaluate Equipment Damping Ratio

Specimen Number	Outside Diameter		Inside Diameter		Height		Weight
	inch	cm	inch	cm	inch	cm	gram
1(Brass Tube)	1.000	2.540	0.875	2.223	4.98	12.65	132.35
2(Brass Tube)	0.875	2.223	0.813	2.064	6.96	17.68	79.96
3(Brass Tube)	0.875	2.223	0.813	2.064	8.49	21.56	97.07
4(Brass Tube)	0.750	1.905	0.688	1.746	6.97	17.70	70.72
5(Brass Tube)	0.750	1.905	0.688	1.746	8.49	21.57	85.87
6(Brass Tube)	0.625	1.588	0.563	1.429	6.96	17.68	58.45
7(Brass Tube)	0.625	1.588	0.563	1.429	8.49	21.57	70.94
8(Brass Tube)	0.375	0.953	0.313	0.794	6.94	17.63	33.69
9(Brass Tube)	0.375	0.953	0.313	0.794	8.44	21.45	40.86
10(Brass Rod)	0.313	0.794	0	0	6.92	17.57	74.46
11(Brass Rod)	0.313	0.794	0	0	8.44	21.44	90.30
12(Brass Rod)	0.500	1.270	0	0	7.00	17.78	191.22
13(Brass Rod)	0.750	1.905	0	0	7.00	17.75	429.52
14(Brass Rod)	0.250	0.635	0	0	6.96	17.67	47.53
15(Brass Rod)	1.500	3.810	0	0	7.00	17.78	1731.64
16(Brass Tube)	0.500	1.270	0.438	1.111	6.97	17.71	44.63
17(Brass Tube)	0.500	1.270	0.438	1.111	8.48	21.53	54.29
18(Brass Tube)	1.000	2.540	0.875	2.223	6.97	17.70	178.50

Unit Weight of Brass = 8.49 g/cm^3 (=0.316 lbs/in^3)

Hysteresis loops with one metal specimen measured at a frequency of 0.5 Hz are shown in Figure 8.B.3.A-14. The stress-strain curve is linear, resulting in no damping as expected. On the other hand, Figure 8.B.3.A-11 and 8.B.3.A-12 show the damping measurements with the same metal specimen in the resonant column test predict an apparent damping of 0.4% from both the free-vibration decay and half-power bandwidth methods.

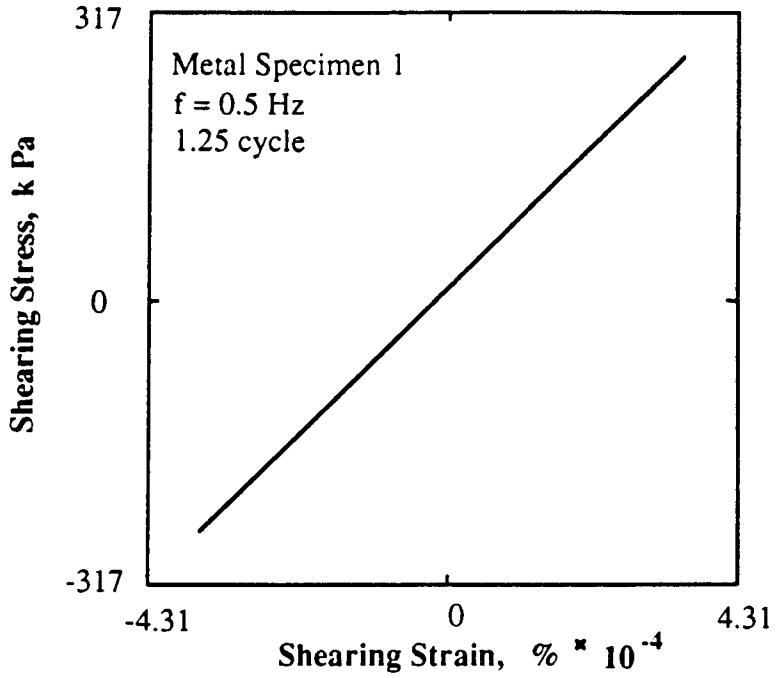

Figure 8.B.3.A-14
Hysteresis loops of metal specimen determined by torsional shear testing at a frequency of 0.5 Hz.

The variations in shear modulus and damping ratio with loading frequency for four of the metal specimens are plotted in Figure 8.B.3.A-15. The shear modulus of each metal specimen determined from the RCTS equipment is independent of loading frequency as expected. Therefore, shear modulus can be measured properly with RCTS equipment over a wide frequency range without any compliance problem.

On the other hand, the damping ratio measured by the RCTS equipment is affected by the loading frequency. For frequencies less than or equal to 0.5 Hz, damping ratio evaluated by the torsional shear test is essentially zero as expected. In this frequency range, material damping can be evaluated without any equipment correction. For higher frequencies, however, non-zero damping values are obtained with all metal specimens in the torsional shear as shown in Figures 8.B.3.A-15b and 8.B.3.A-16. In this case the apparent material damping increases significantly as the excitation frequency increases from 1 to 10 Hz. Strain amplitude has little effect on the damping values as shown in Figure 8.B.3.A-16. These values of apparent material damping are considered to be due to a compliance problem with the complete RCTS system (back-EMF generated by the drive system) and are, therefore, subtracted from all damping measurements in the torsional shear test at the same frequencies when soil specimens are tested.

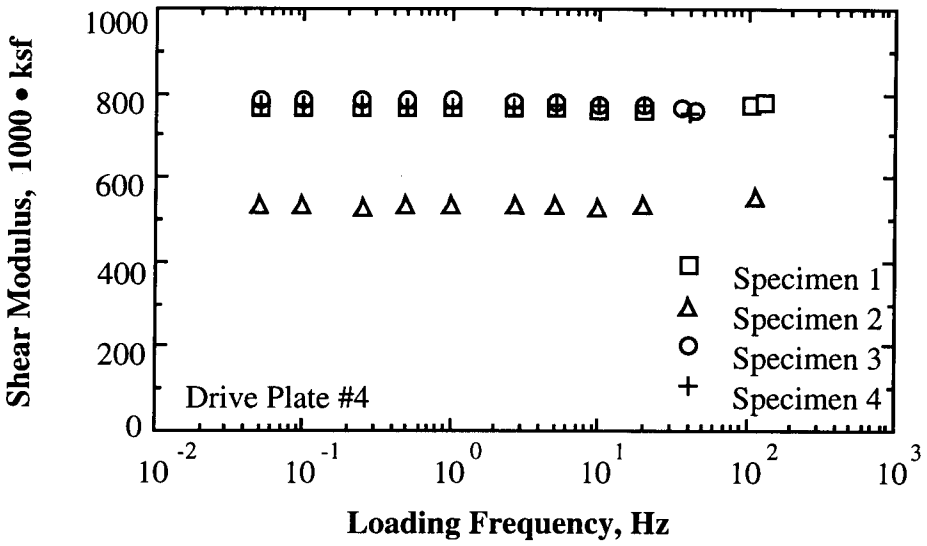

a) Variation in Shear Modulus

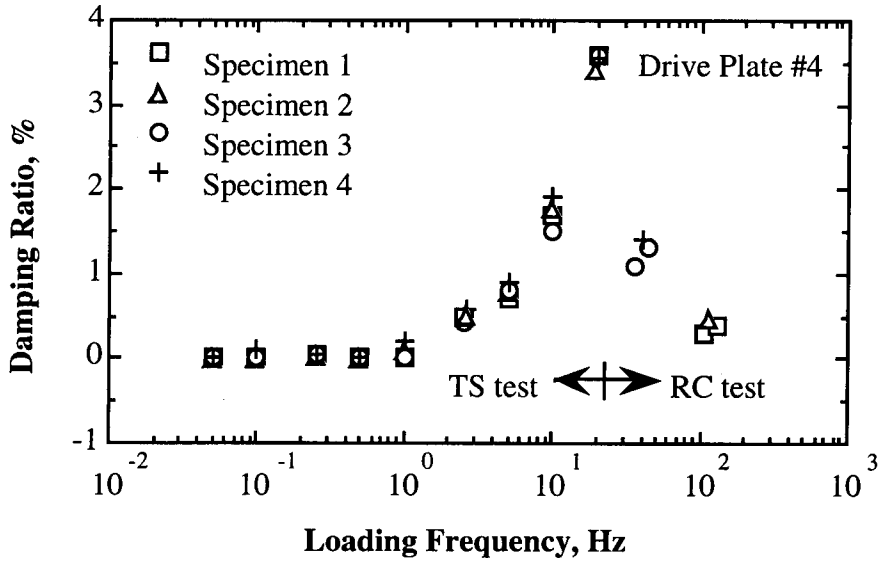

b) Variation in Material Damping Ratio

Figure 8.B.3.A-15
Variation in shear modulus and material damping ratio with loading frequency determined for metal specimens (from Kim, 1991).

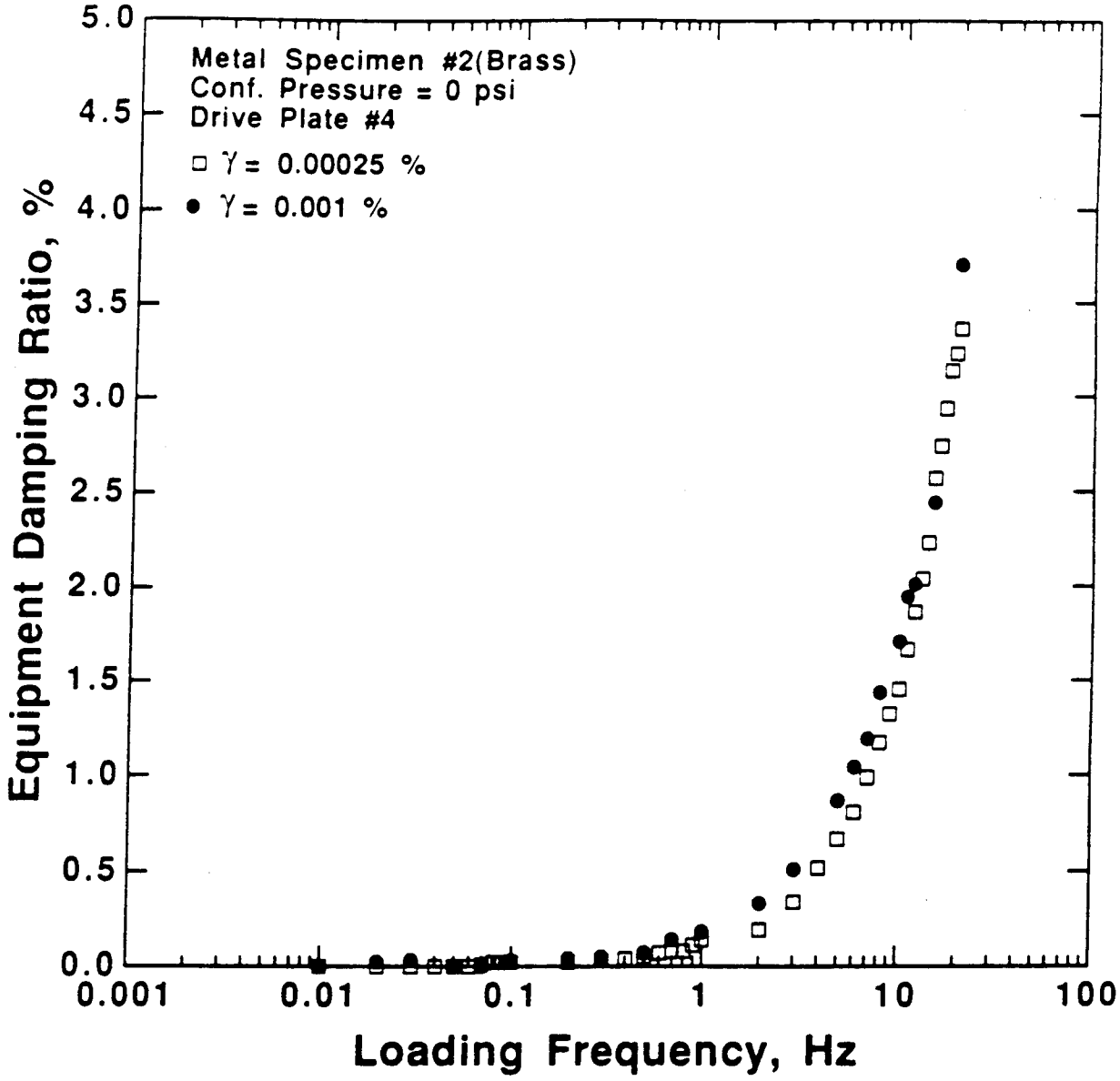

Figure 8.B.3.A-16
Measured damping ratio for metal specimen #2 in the torsional shear test.

It should be noted that excitation frequencies in the torsional shear test never exceeded 0.1 times the resonant frequency of the soil specimen. This approach was followed so that dynamic amplification did not affect the TS measurements. Even in this case, however, corrections were made for minor dynamic amplification which occurs near 0.1 times the resonant frequency.

In the resonant column test, non-zero damping values were obtained at all resonant frequencies as seen in Figures 8.B.3.A-15b and 8.B.3.A-17 Equipment damping values ranged from about 3.5% at 20 Hz to about 0.4% at 200 Hz. These resonant frequencies are in the frequency range where all soil testing was conducted. Just as in the TS test, the values of equipment damping measured with the metal specimens were subtracted from the damping measurements in all RC tests with soil specimens at the same resonant frequencies. Strain amplitude had a negligible effect on equipment damping as shown in Figure 8.B.3.A-18.

Finally, to be sure that coil-magnet interaction was the cause of the equipment damping problem, free-vibration tests were conducted with the RC equipment. In this case, however, all coils were removed which required that the drive plate be excited by hand in free vibration. The resulting tests with drive plate #4 are given in Figure 8.B.3.A-19 by the solid square symbols. As seen, damping values less than 0.1% were measured. These values are considered to equal zero in this work, indicating the coil-magnet interaction is mainly the cause of the equipment damping.

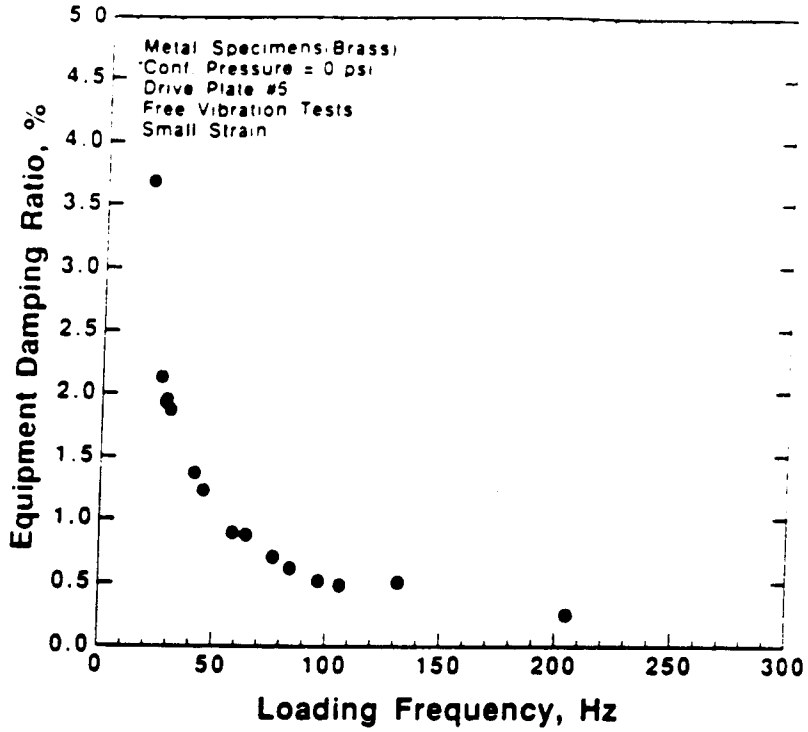

a. Damping from the Free-Vibration Decay Curve

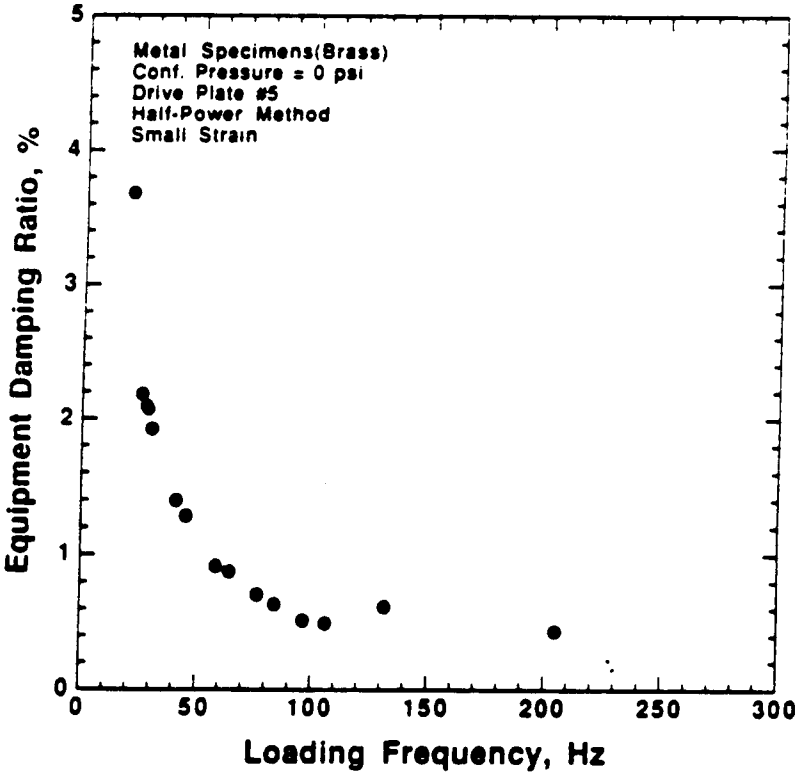

b. Damping from the Half-Power Bandwidth

Figure 8.B.3.A-17
Equipment damping measured in the resonant column test.

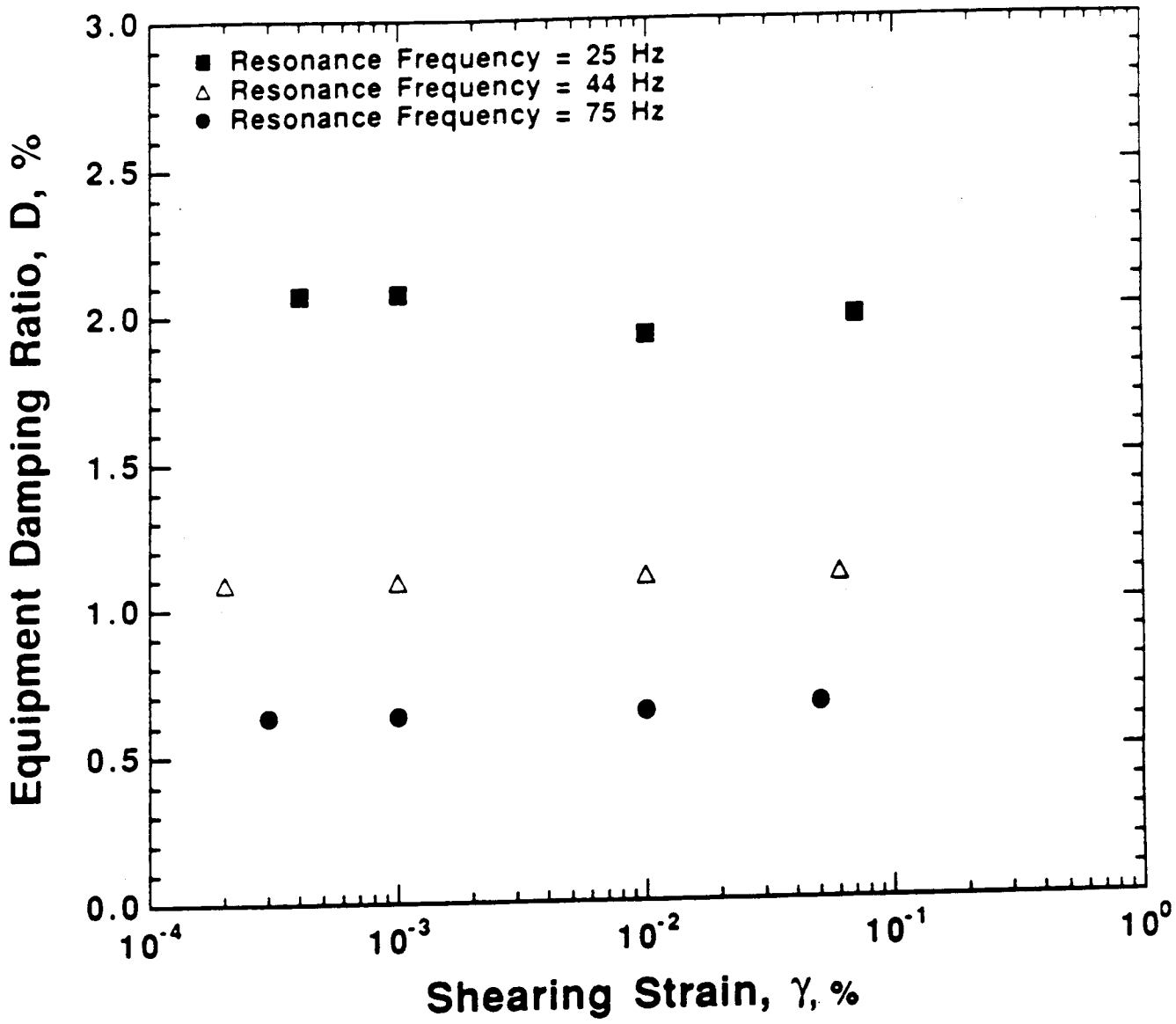

Figure 8.B.3.A-18
Effect of strain amplitude on equipment damping measured in the resonant column test.

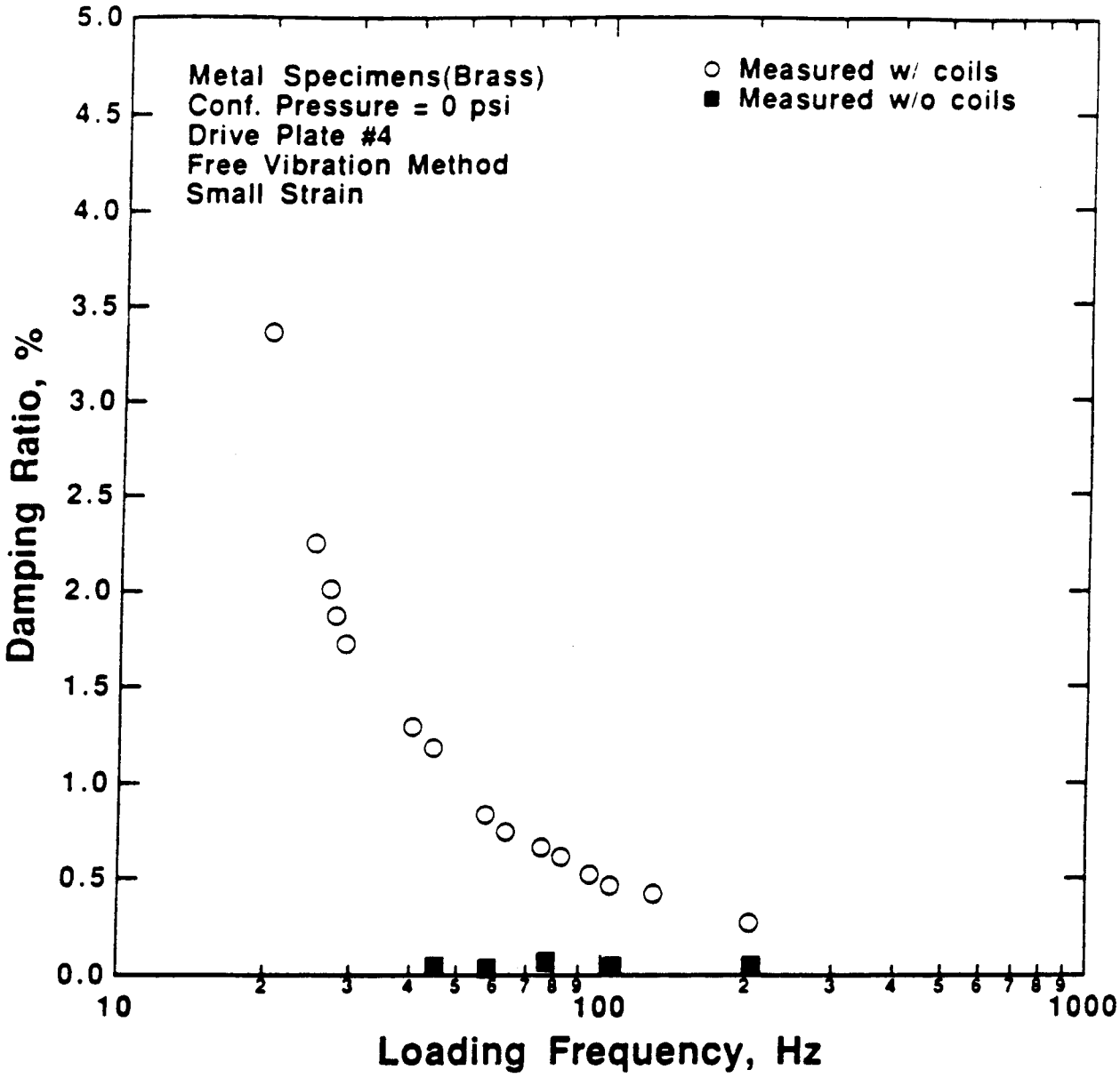

Figure 8.B.3.A-19
Comparison of equipment damping measured in free vibration RC tests with and without the electrical coils.

References

Chen, A.T.F., Stokoe, K.H., II (1979), "Interpretation of Strain Dependent Modulus and Damping from Torsional Soil Tests," Report No. USGS-GD-79-002, NTIS No. PB-298479, U.S. Geological Survey, 46 pp.

Isenhower, W.M. (1979), *Torsional Simple Shear/Resonant Column Properties of San Francisco Bay Mud,* Geotechnical Engineering Thesis, GT 80-1, University of Texas, Dec., 307 pp.

Kim, D.-S. (1991), *Deformational Characteristics of Soils at Small to Intermediate Strains from Cyclic Tests,* Ph.D. Dissertation, The University of Texas at Austin, 341 pp.

Lodde, P.F. (1982), *Shear Moduli and Material Damping of San Francisco Bay Mud,* M.S. Thesis, The University of Texas at Austin.

Ni, S.-H. (1987), *Dynamic Properties of Sand Under True Triaxial Stress States from Resonant Column/Torsional Shear Tests,* Ph.D. Dissertation, The University of Texas at Austin, 421 pp.

Richart, F.E.,Jr., Hall, J.R.,Jr. and Woods, R.D. (1970), *Vibrations of Soils and Foundations,* Prentice-Hall Inc., Englewood Cliffs, New Jersey, 414 pp.

APPENDIX 8.B.3.B
DYNAMIC TESTS OF SAMPLE T1 FROM BOREHOLE CH1, DEPTH = 18 FT (5.5 M)

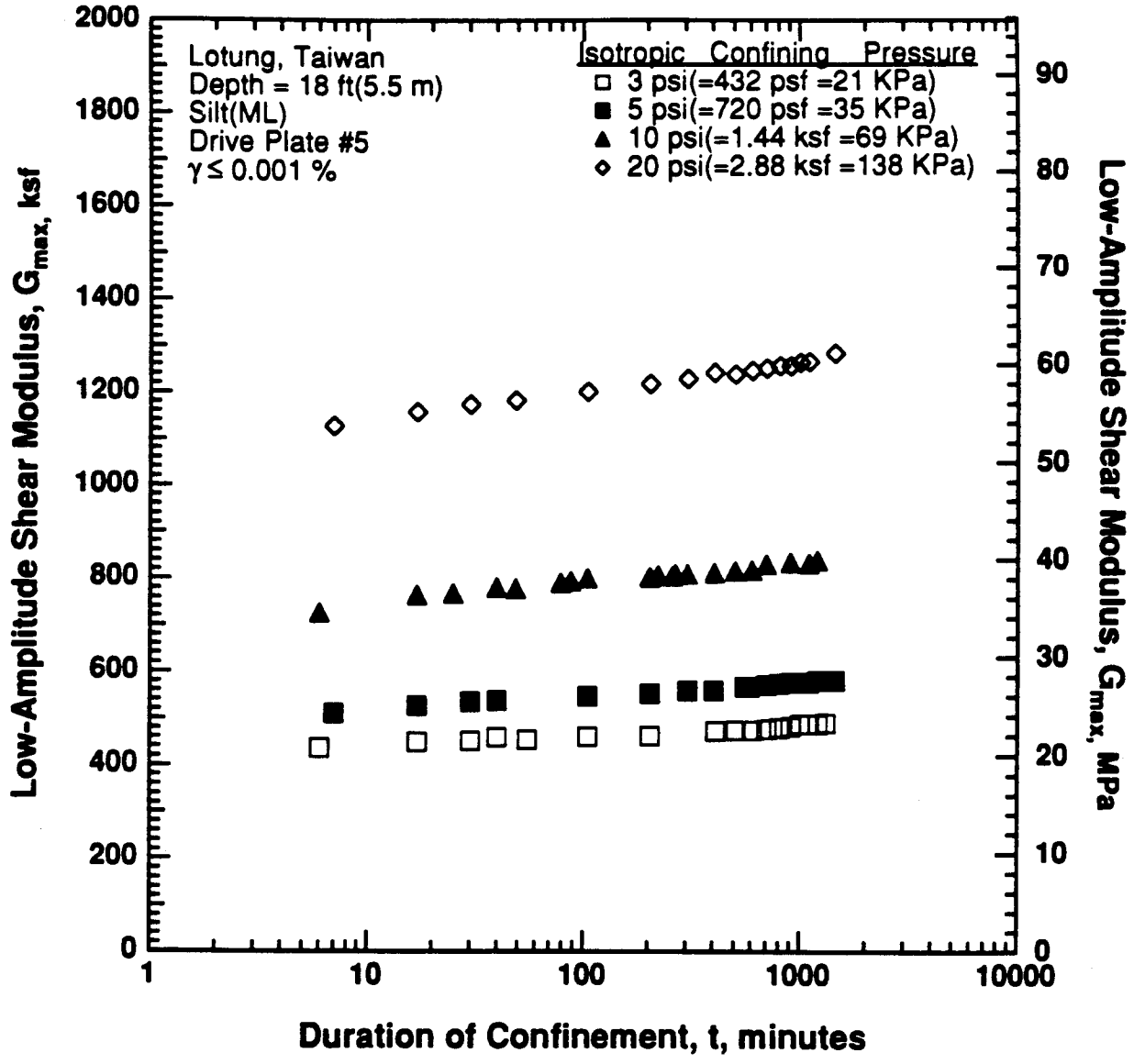

Figure 8.B.3.B-1
Variation in low-amplitude shear modulus with magnitude and duration of isotropic pressure from resonant column tests of sample T1 from borehole CH2.

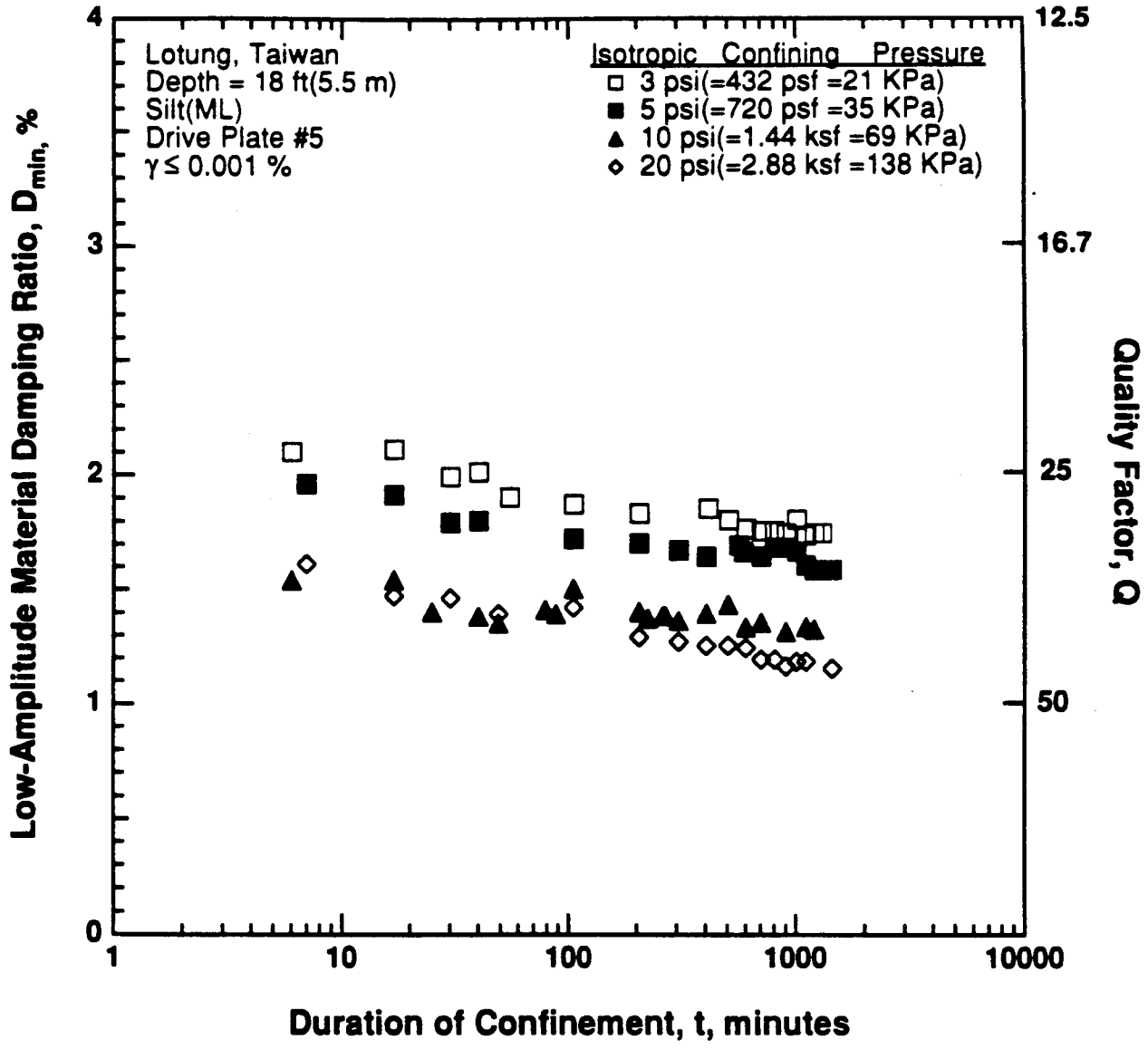

Figure 8.B.3.B-2
Variation in low-amplitude material damping ratio with magnitude and duration of isotropic confining pressure from resonant column tests of sample T1 from borehole CH2.

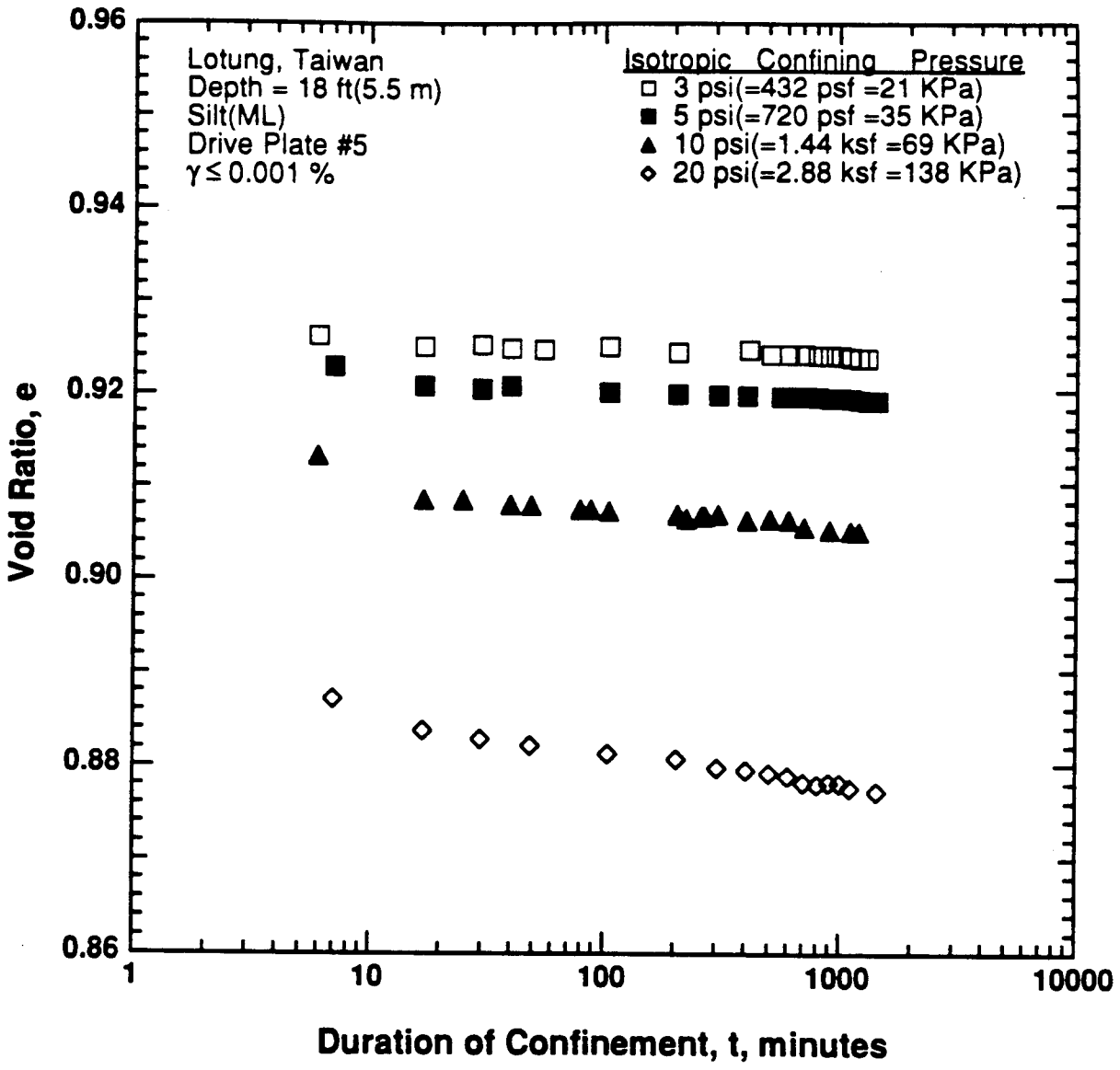

Figure 8.B.3.B-3
Variation in void ratio with magnitude and duration of isotropic confining pressure from resonant column tests of sample T1 from borehole CH2.

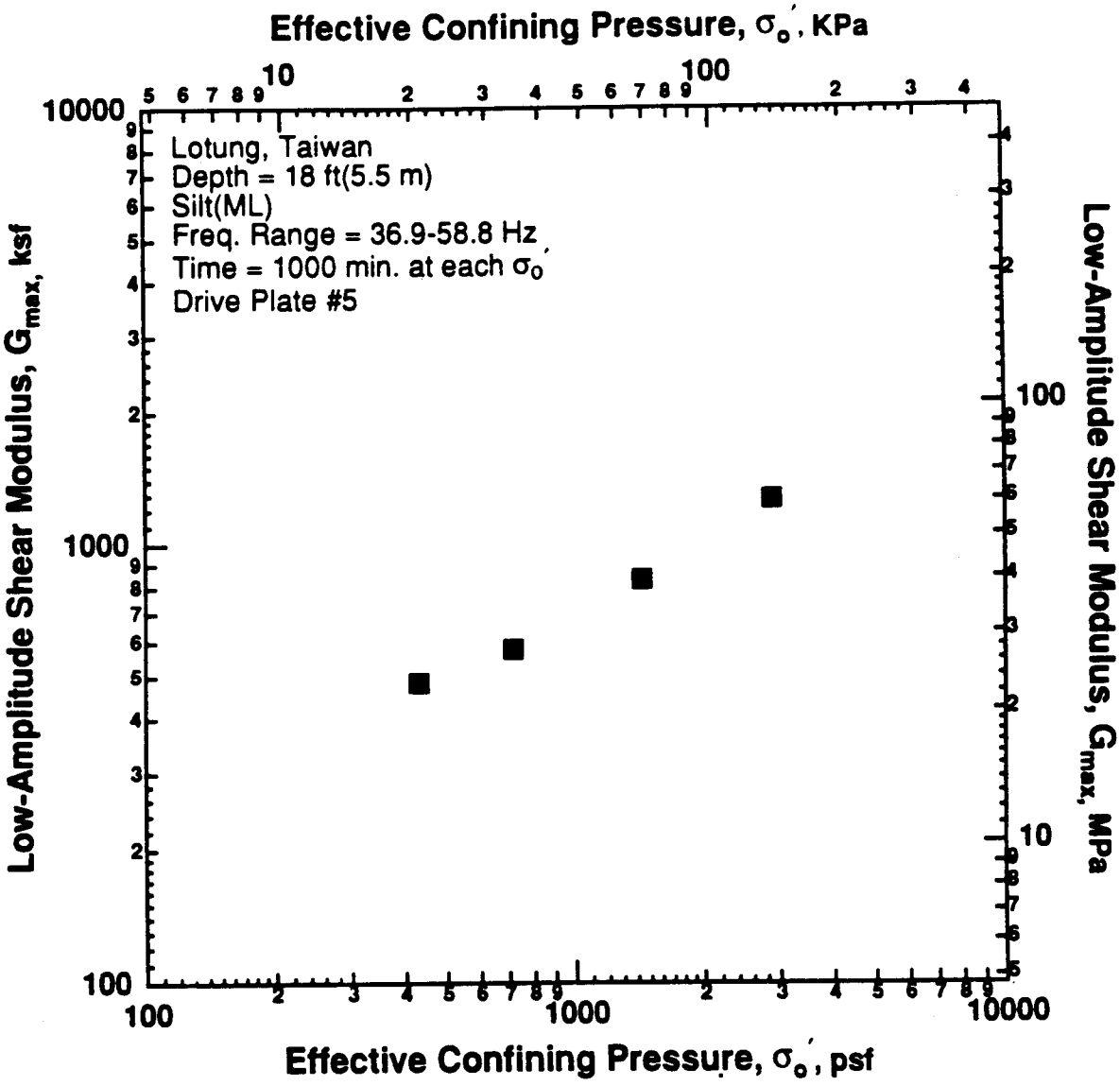

Figure 8.B.3.B-4
Variation in low-amplitude shear modulus with effective confining pressure from resonant column tests of sample T1 from borehole CH2.

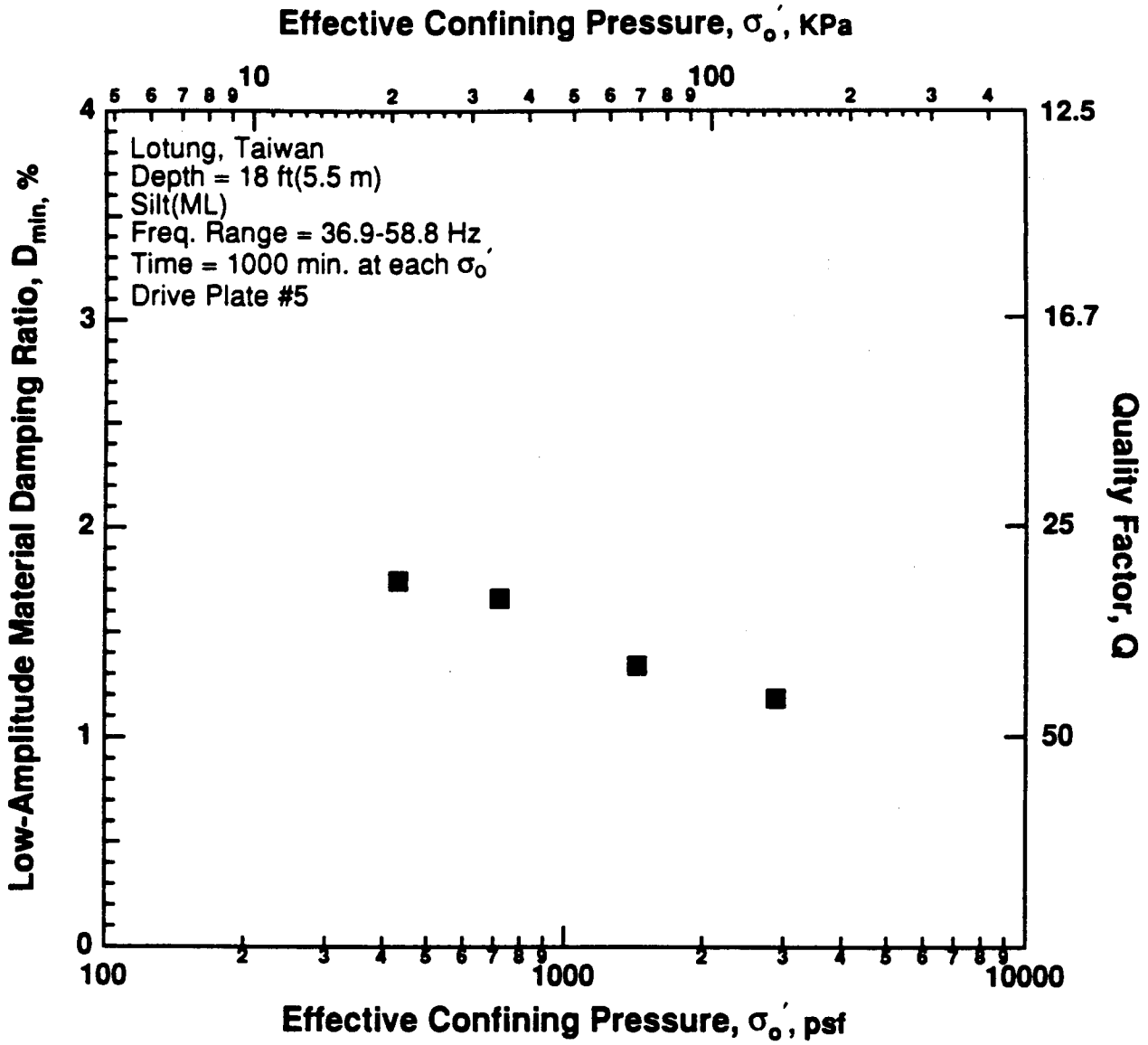

Figure 8.B.3.B-5
Variation in low-amplitude material damping ratio with effective confining pressure from resonant column tests of sample T1 from borehole CH2.

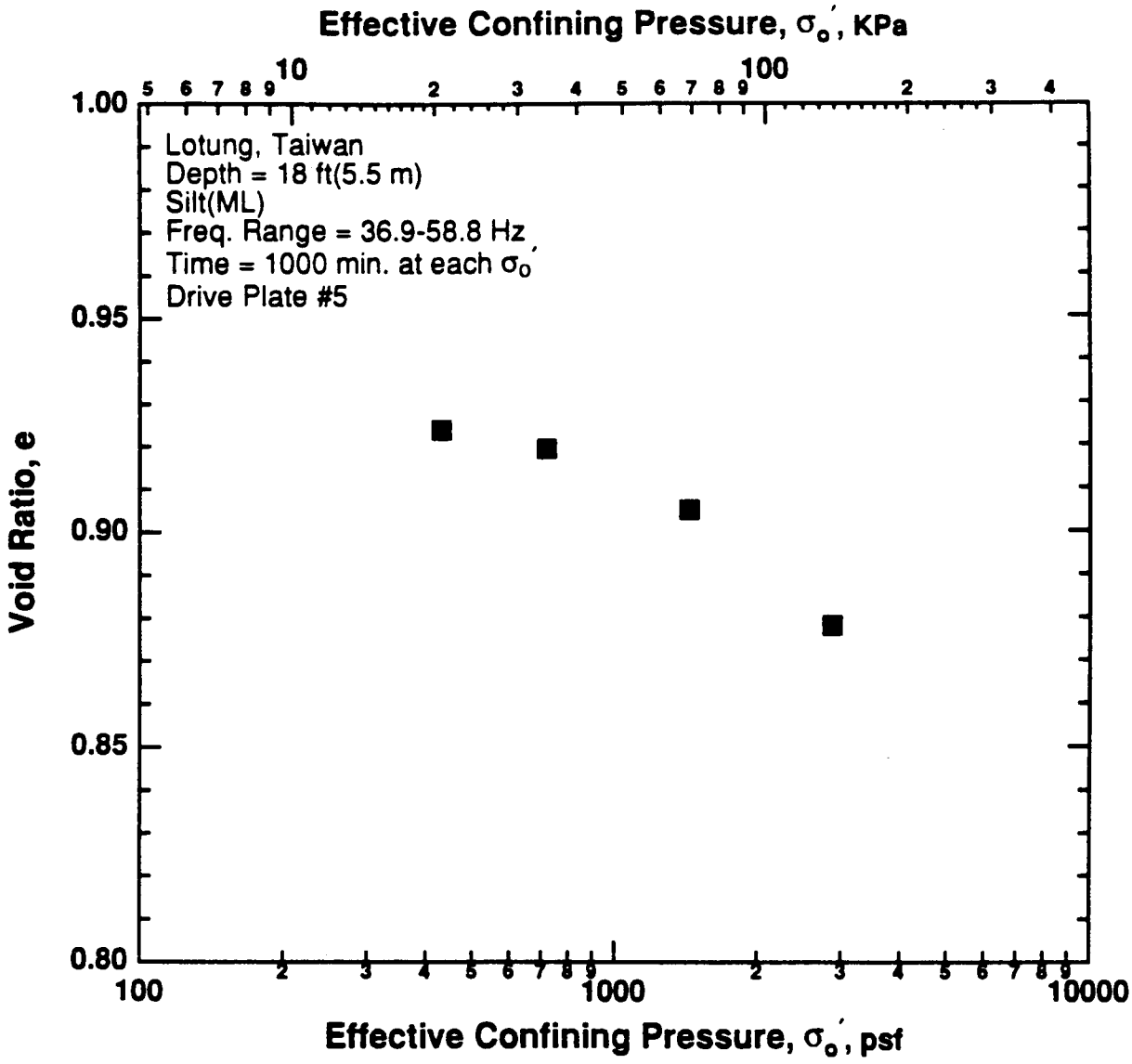

Figure 8.B.3.B-6
Variation in void ratio with effective confining pressure from resonant column tests of sample T1 from borehole CH2.

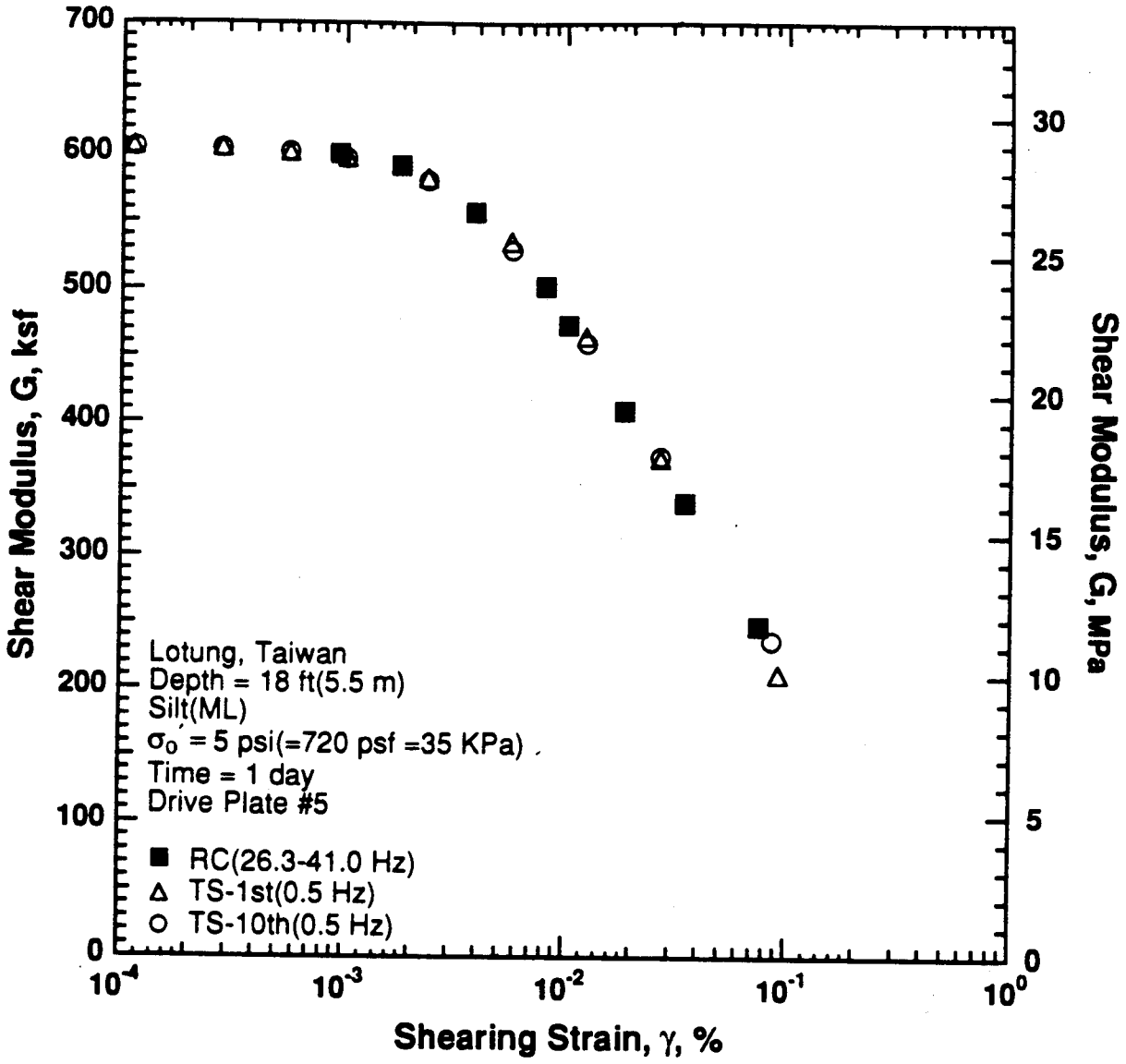

Figure 8.B.3.B-7
Variation in shear modulus with shearing strain at an effective confining pressure of 5 psi (720 psf, 35 kPa) from RCTS tests of sample T1 from borehole CH2.

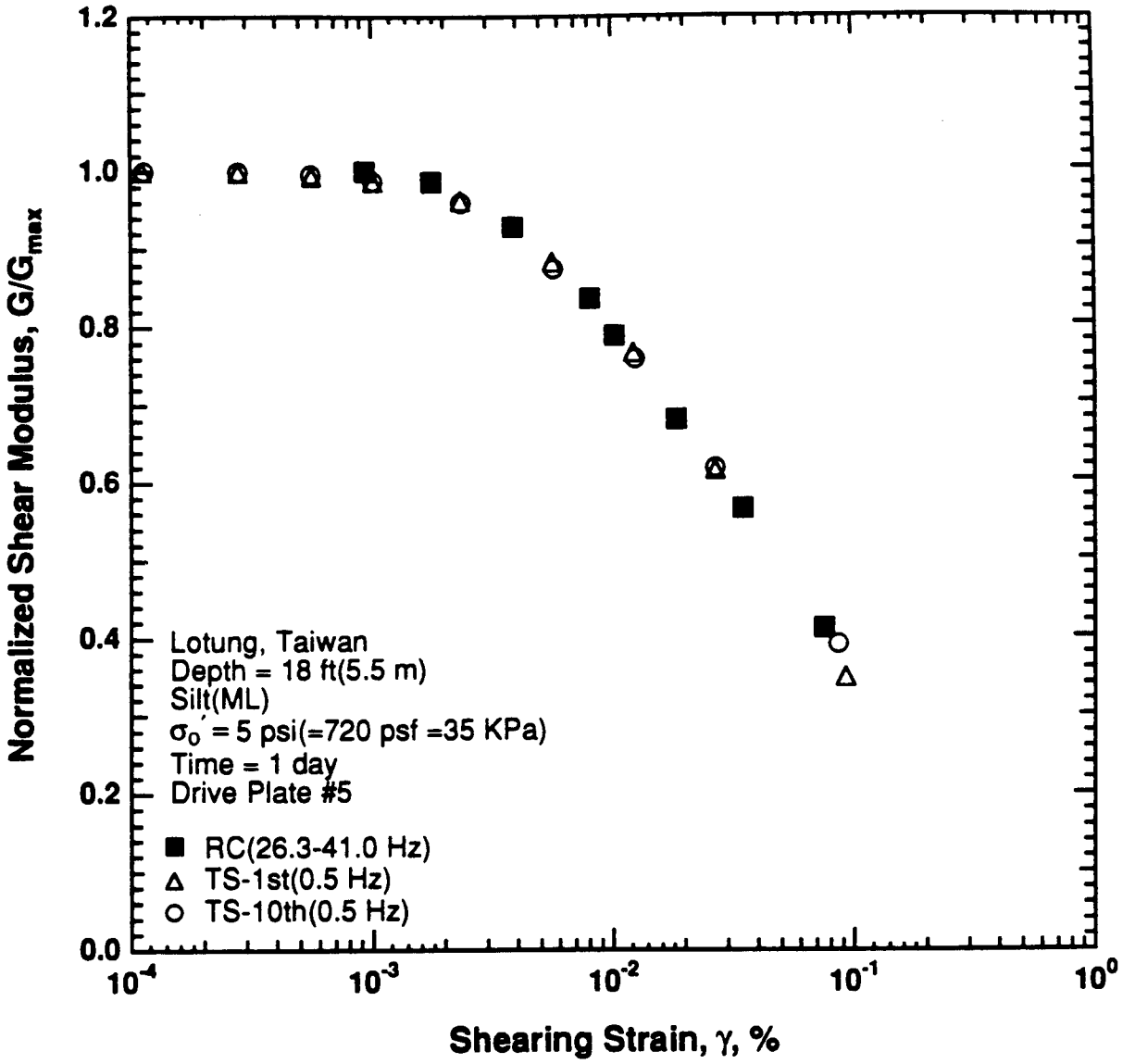

Figure 8.B.3.B-8
Variation in normalized shear modulus with shearing strain at an effective confining pressure of 5 psi (720 psf, 35 kPa) from RCTS tests of sample T1 from borehole CH2.

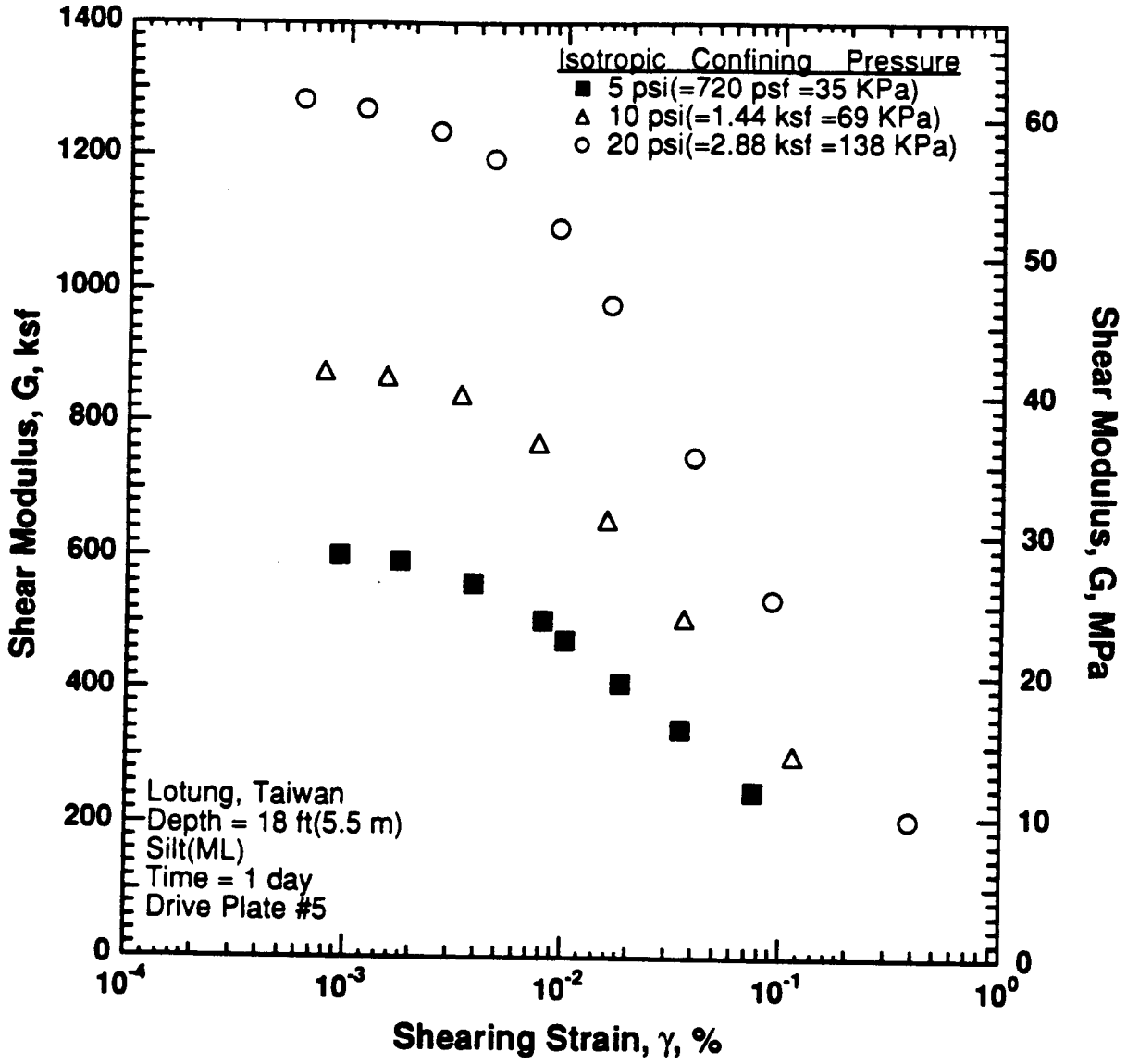

Figure 8.B.3.B-9
Variation in shear modulus with shearing strain and effective confining pressure from resonant column tests of sample T1 from borehole CH2.

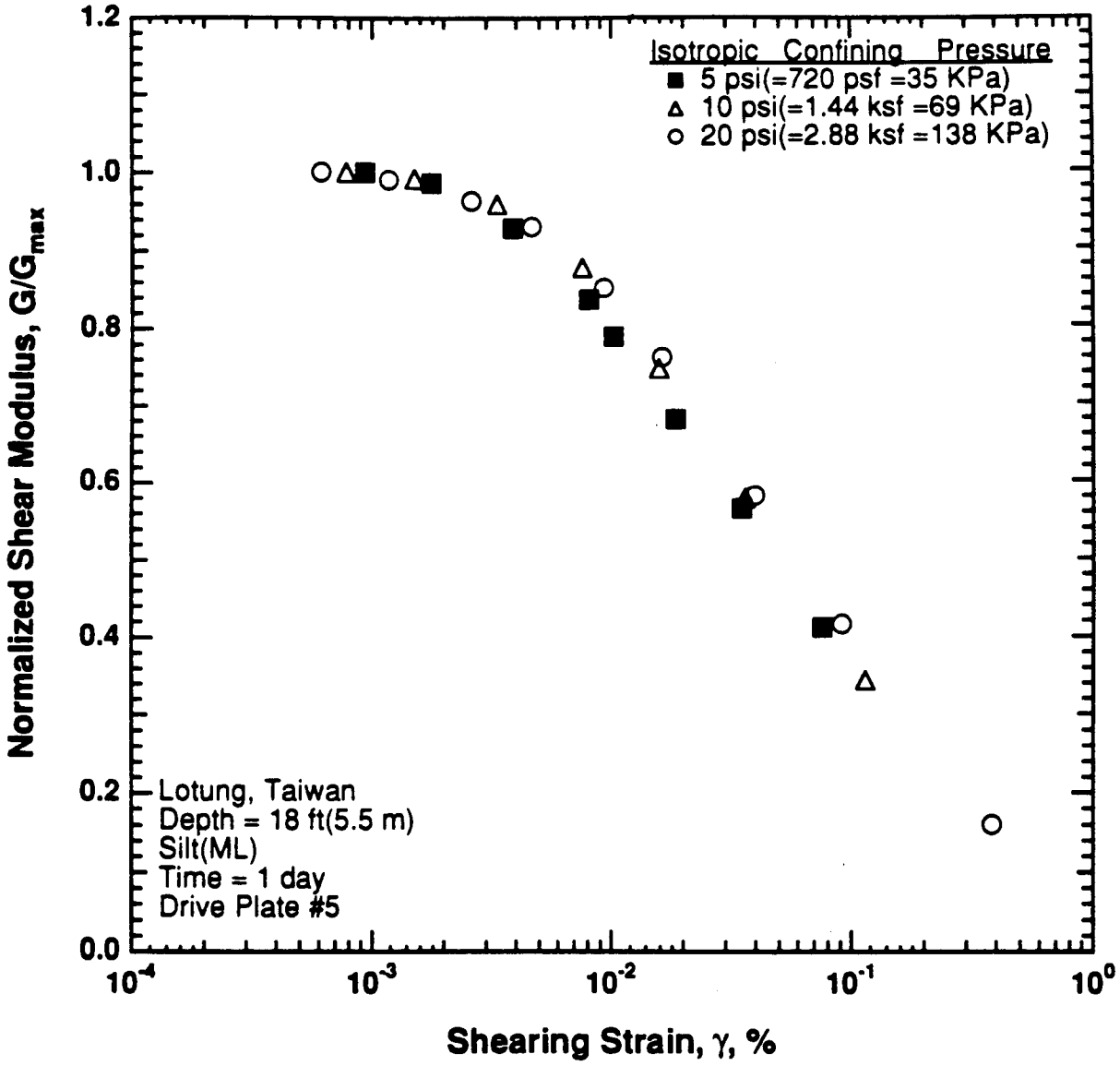

Figure 8.B.3.B-10
Comparison of the variation in normalized shear modulus with shearing strain and effective confining pressure from resonant column tests of sample T1 from borehole CH2.

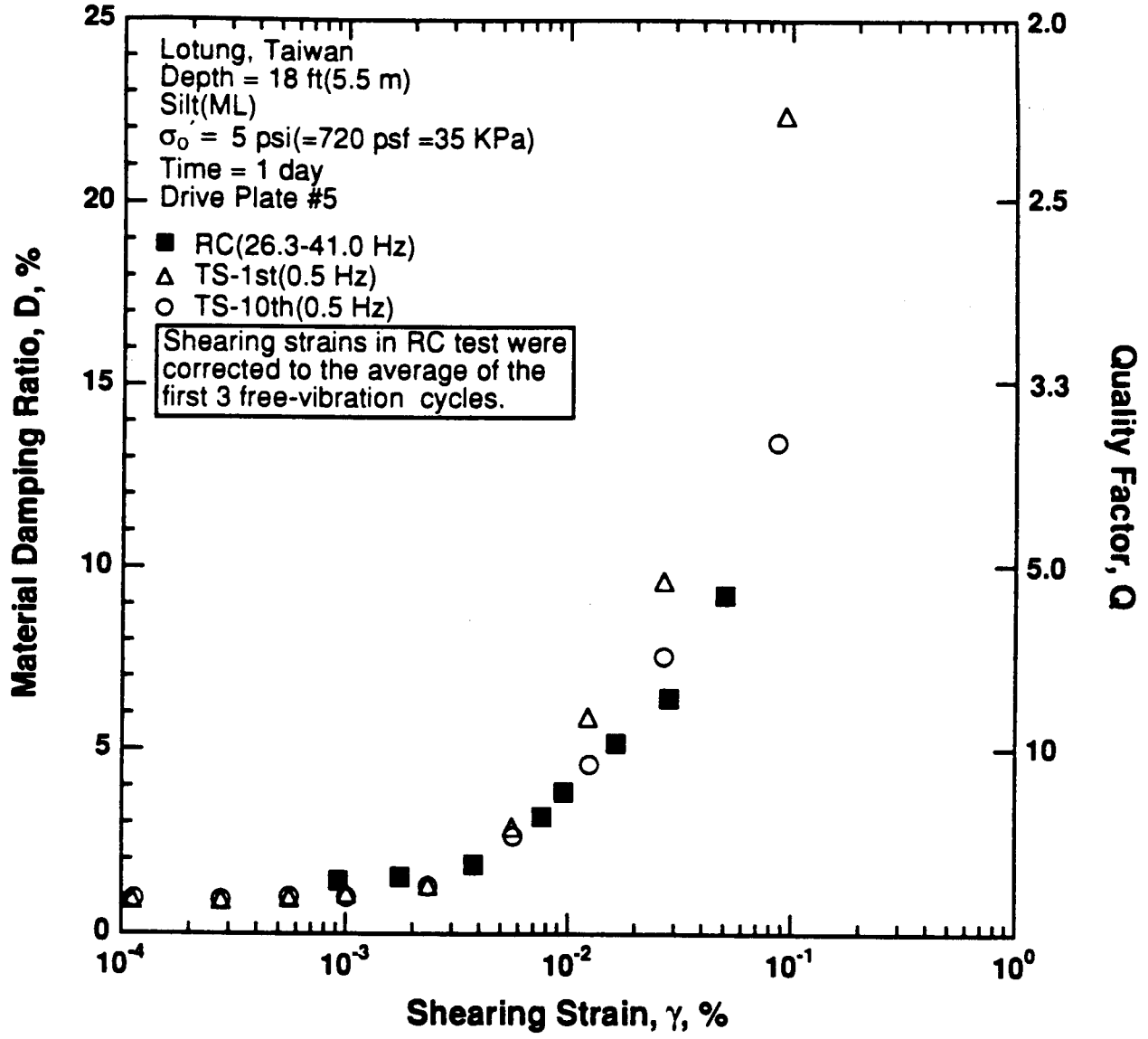

Figure 8.B.3.B-11
Variation in material damping ratio with shearing strain at an effective confining pressure of 5 psi (720 psf, 35 kPa) from RCTS tests of sample T1 from borehole CH2.

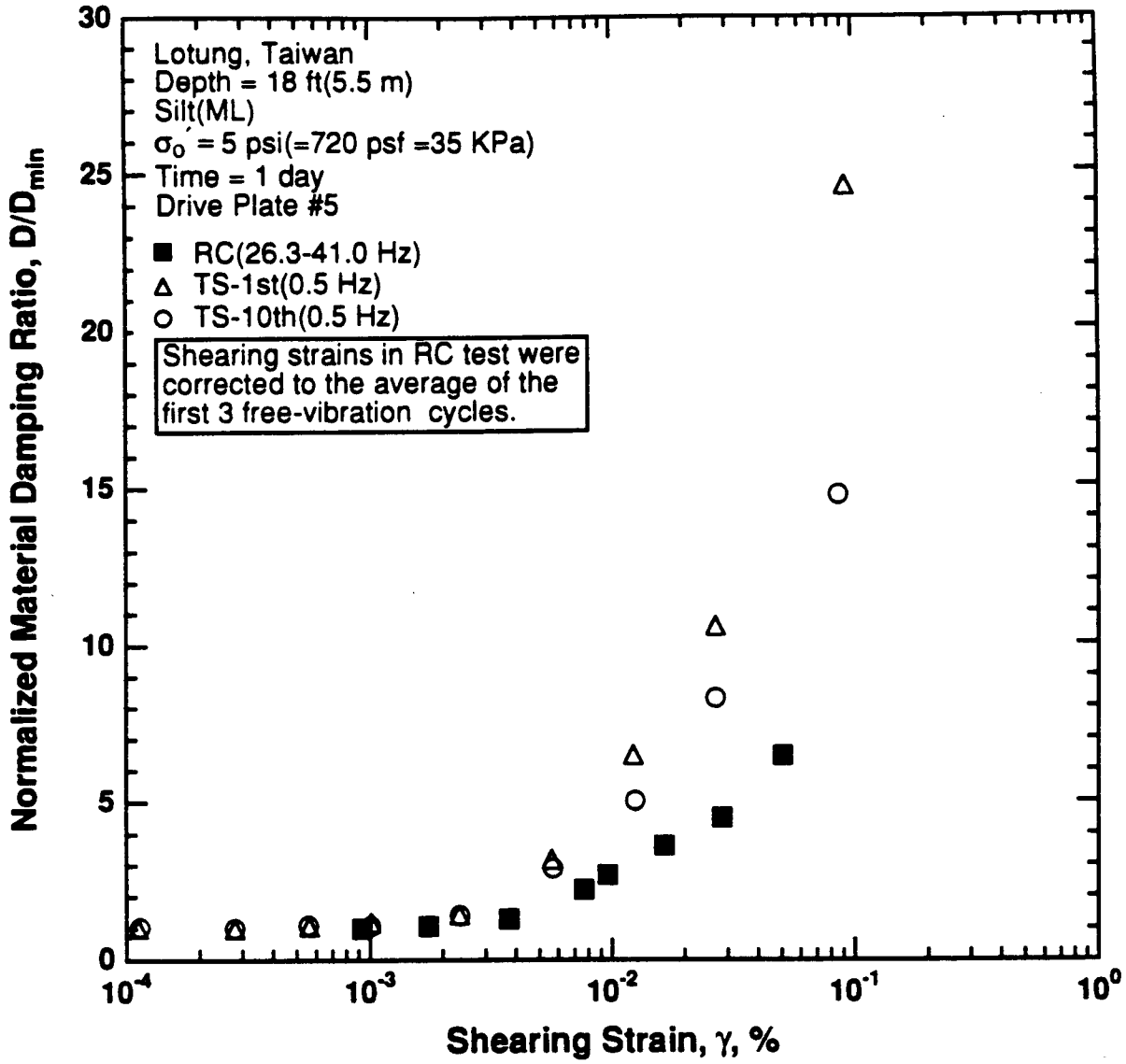

Figure 8.B.3.B-12
Variation in normalized material damping ratio with shearing strain at an effective confining pressure of 5 psi (720 psf, 35 kPa) from RCTS tests of sample T1 from borehole CH2.

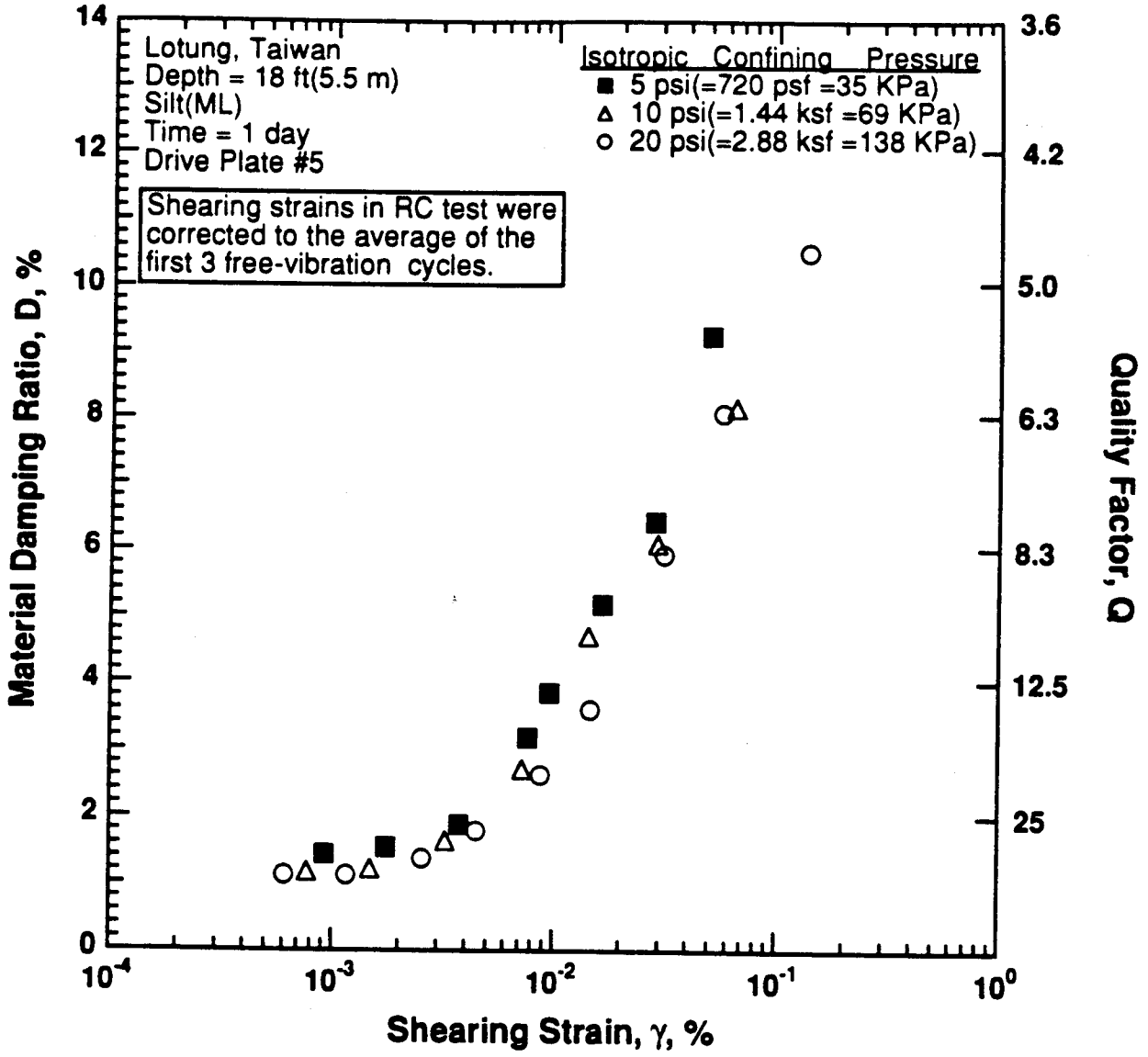

Figure 8.B.3.B-13
Variation in material damping ratio with shearing strain and effective confining pressure from resonant column tests of sample T1 from borehole CH2.

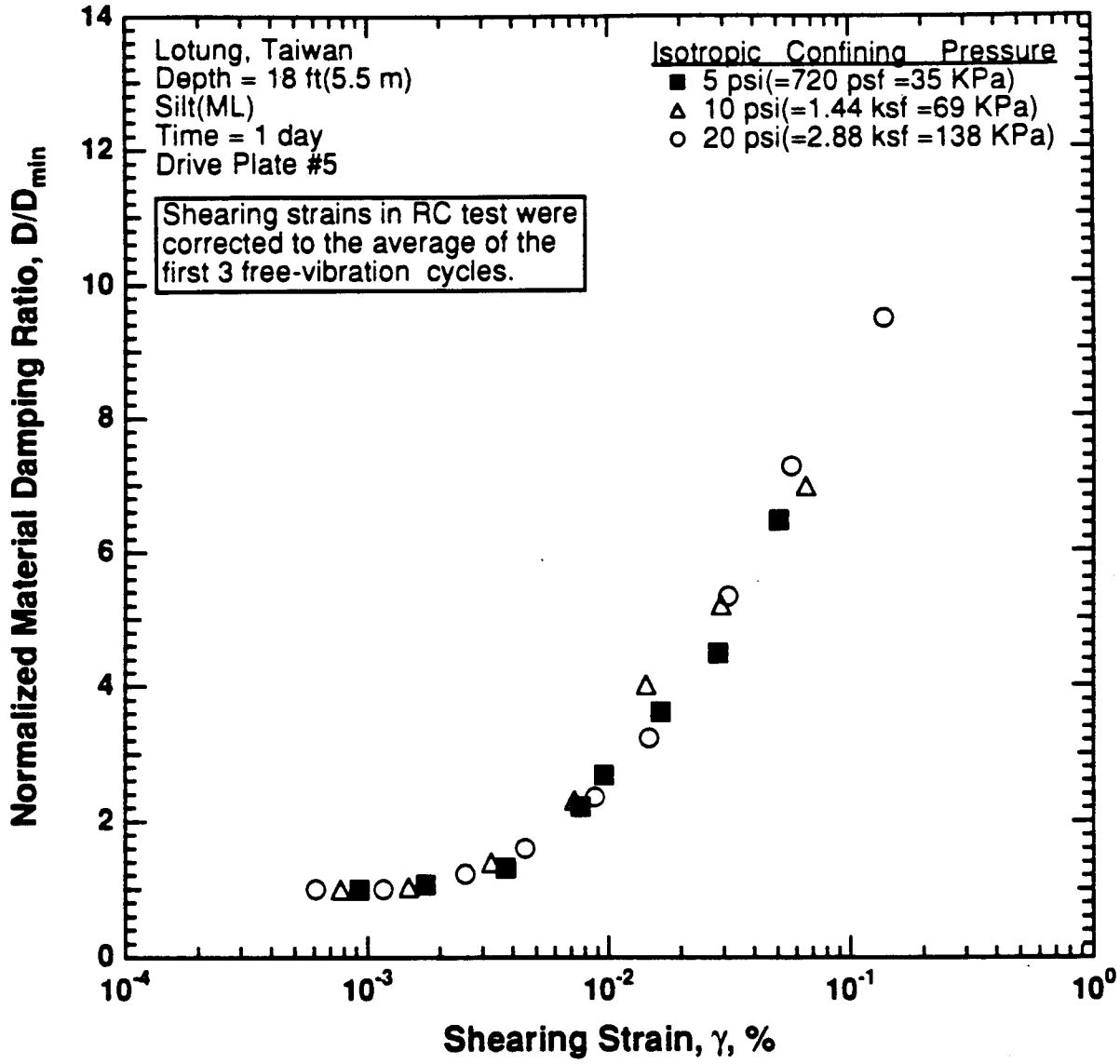

Figure 8.B.3.B-14
Comparison of the variation in normalized material damping ratio with shearing strain and effective confining pressure from resonant column tests of sample T1 from borehole CH2.

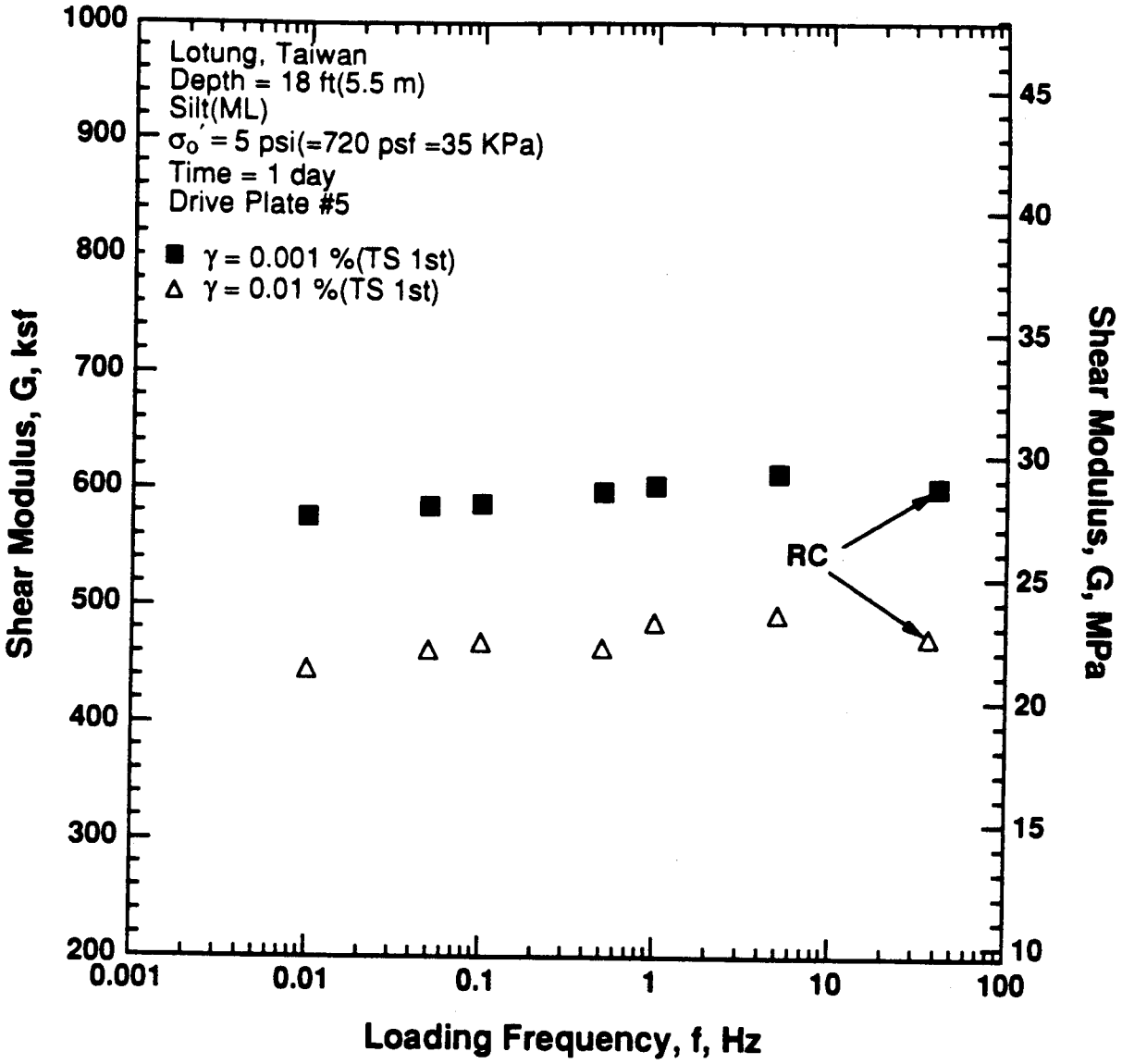

Figure 8.B.3.B-15
Variation in shear modulus with loading frequency and shearing strain at an effective confining pressure of 5 psi (720 psf, 35 kPa) from RCTS tests of sample T1 from borehole CH2.

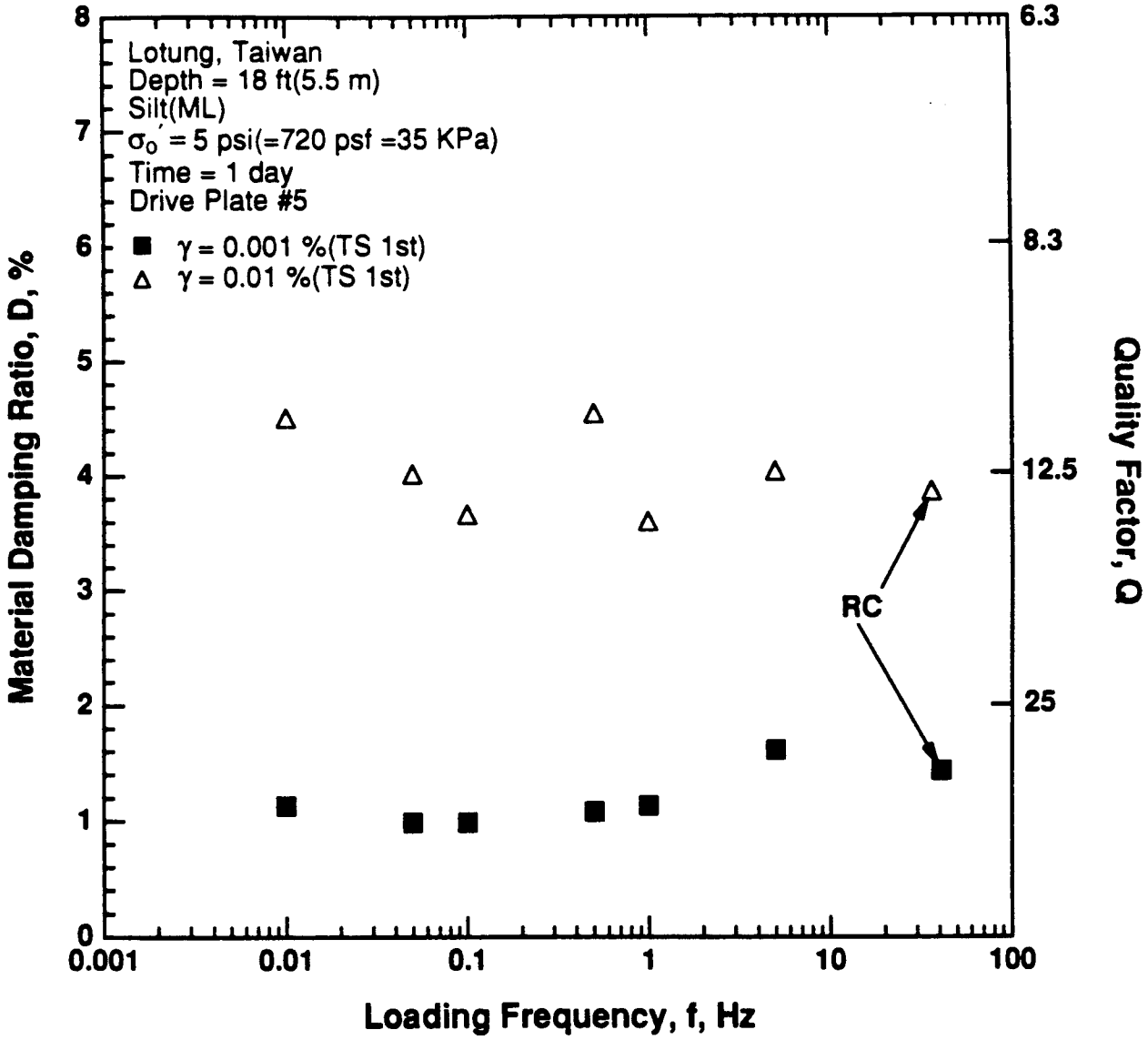

Figure 8.B.3.B-16
Variation in material damping ratio with loading frequency and shearing strain at an effective confining pressure of 5 psi (720 psf, 35 kPa) from RCTS tests of sample T1 from borehole CH2.

APPENDIX 8.B.3.C
DYNAMIC TESTS OF SAMPLE T5 FROM BOREHOLE CH2, DEPTH = 34.5 FT (10.5 M)

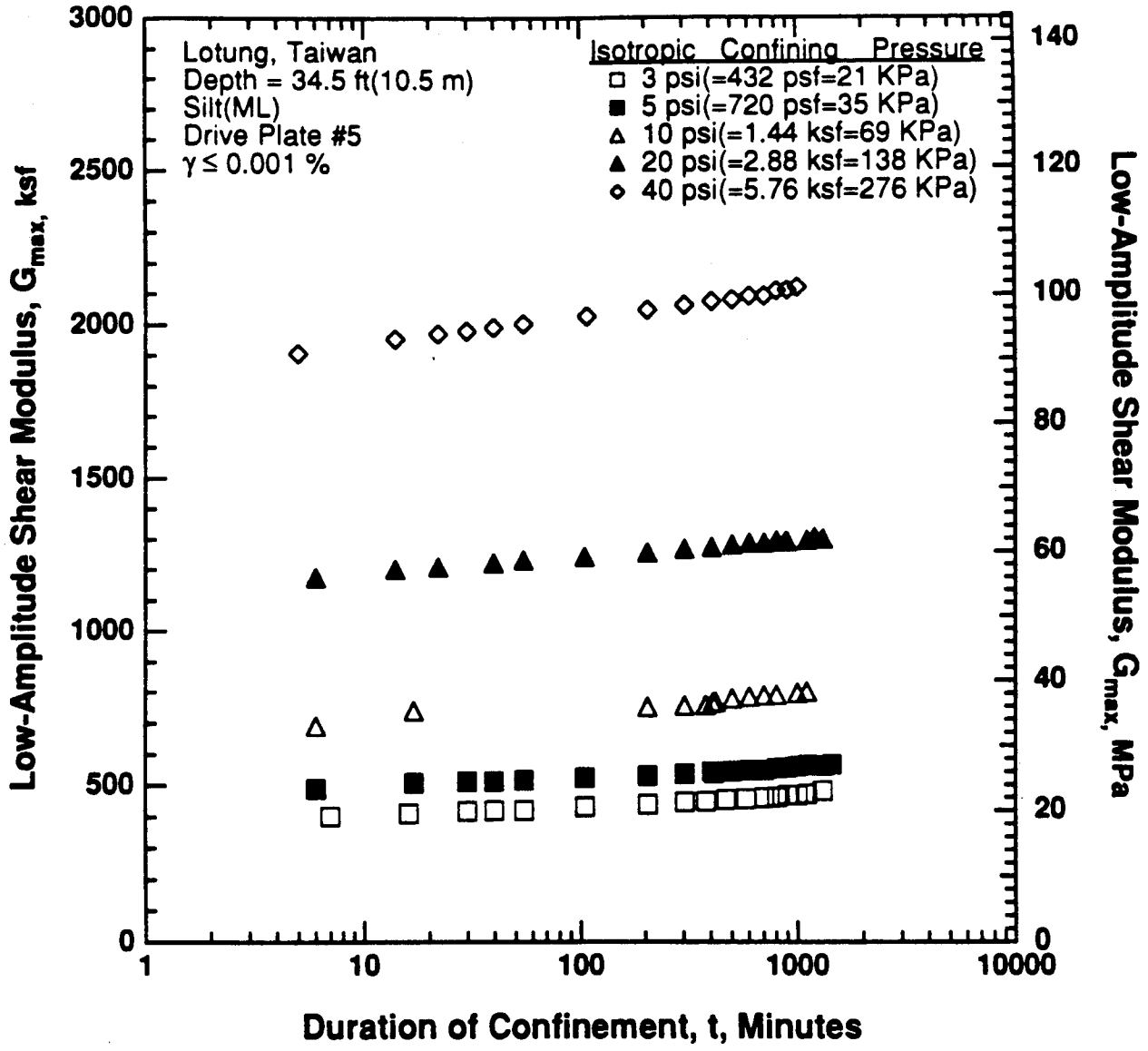

Figure 8.B.3.C-1
Variation in low-amplitude shear modulus with magnitude and duration of isotropic confining pressure from resonant column tests of sample T5 from borehole CH2.

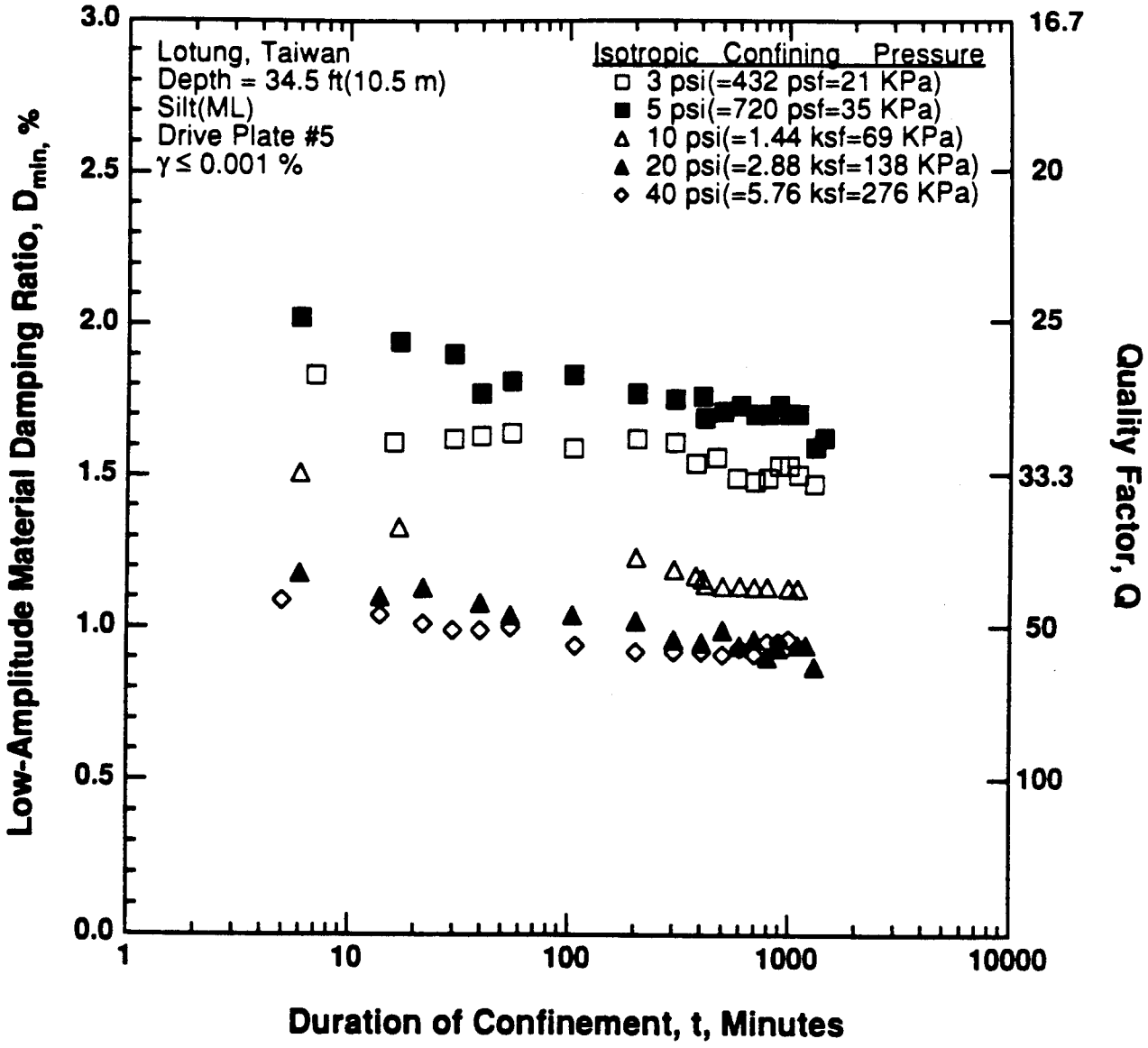

Figure 8.B.3.C-2
Variation in low-amplitude material damping ratio with magnitude and duration of isotropic confining pressure from resonant column tests of sample T5 from borehole CH2.

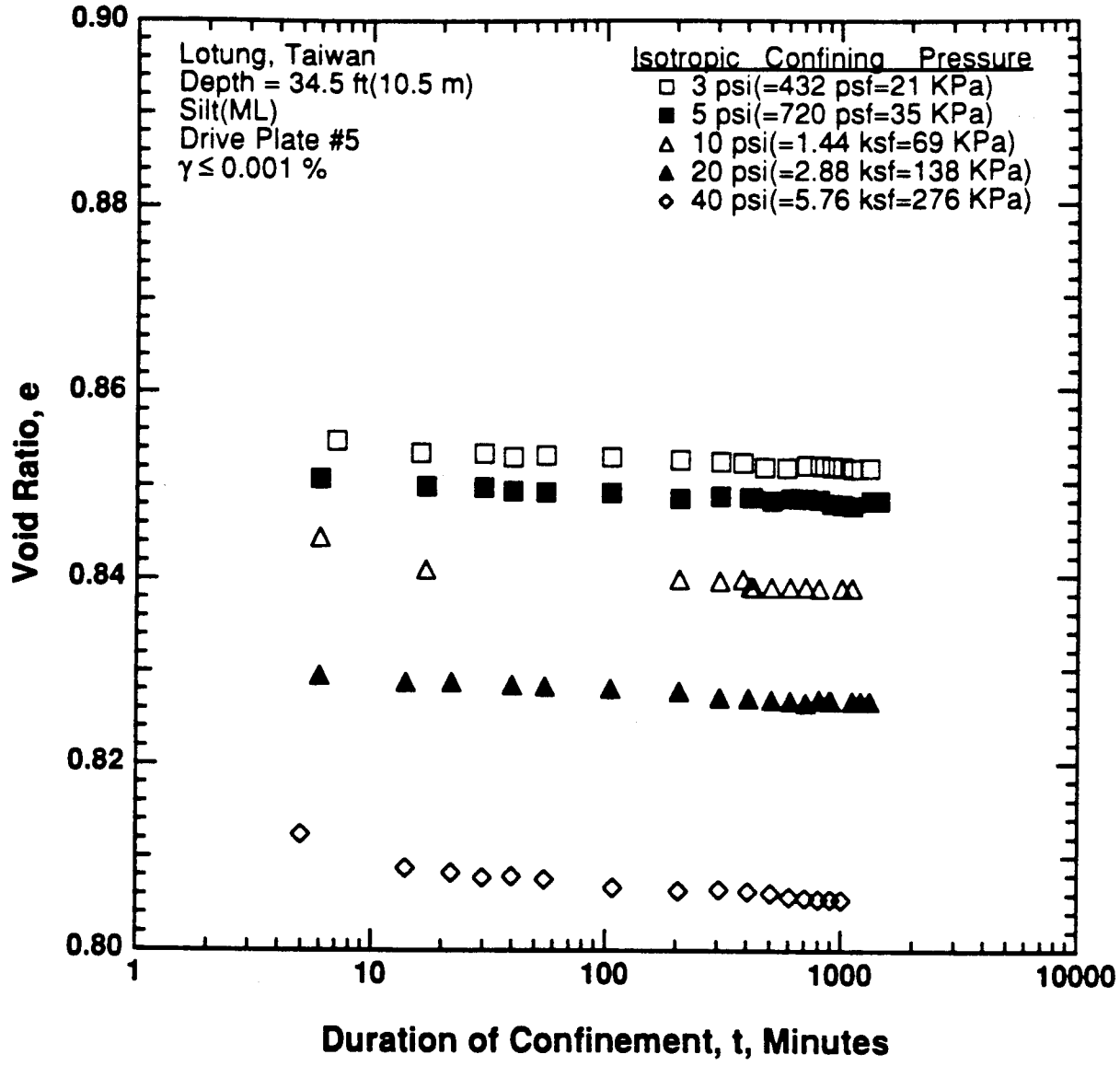

Figure 8.B.3.C-3
Variation in void ratio with magnitude and duration of isotropic confining pressure from resonant column tests of sample T5 from borehole CH2.

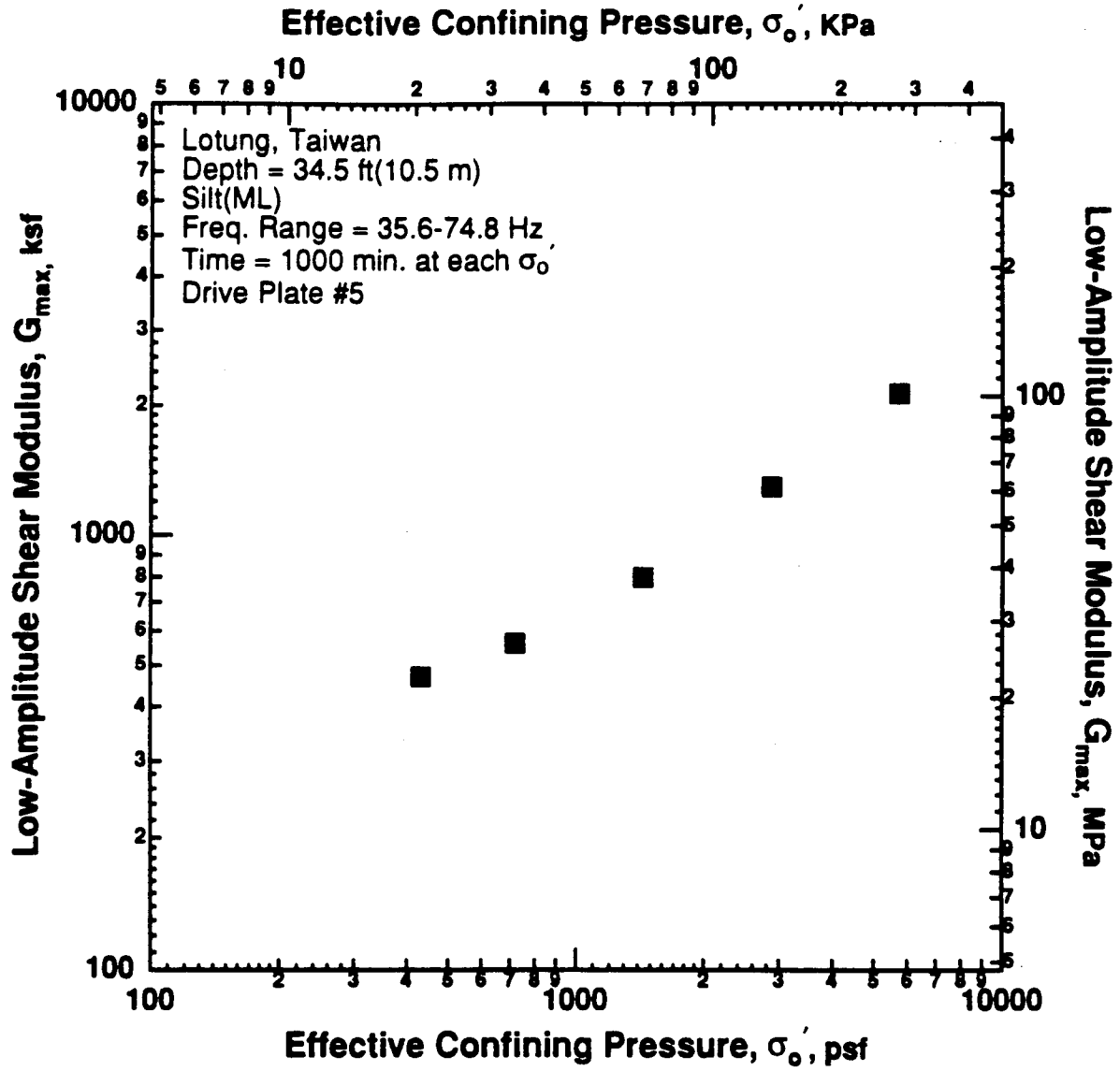

Figure 8.B.3.C-4
Variation in low-amplitude shear modulus with effective confining pressure from resonant column tests of sample T5 from borehole CH2.

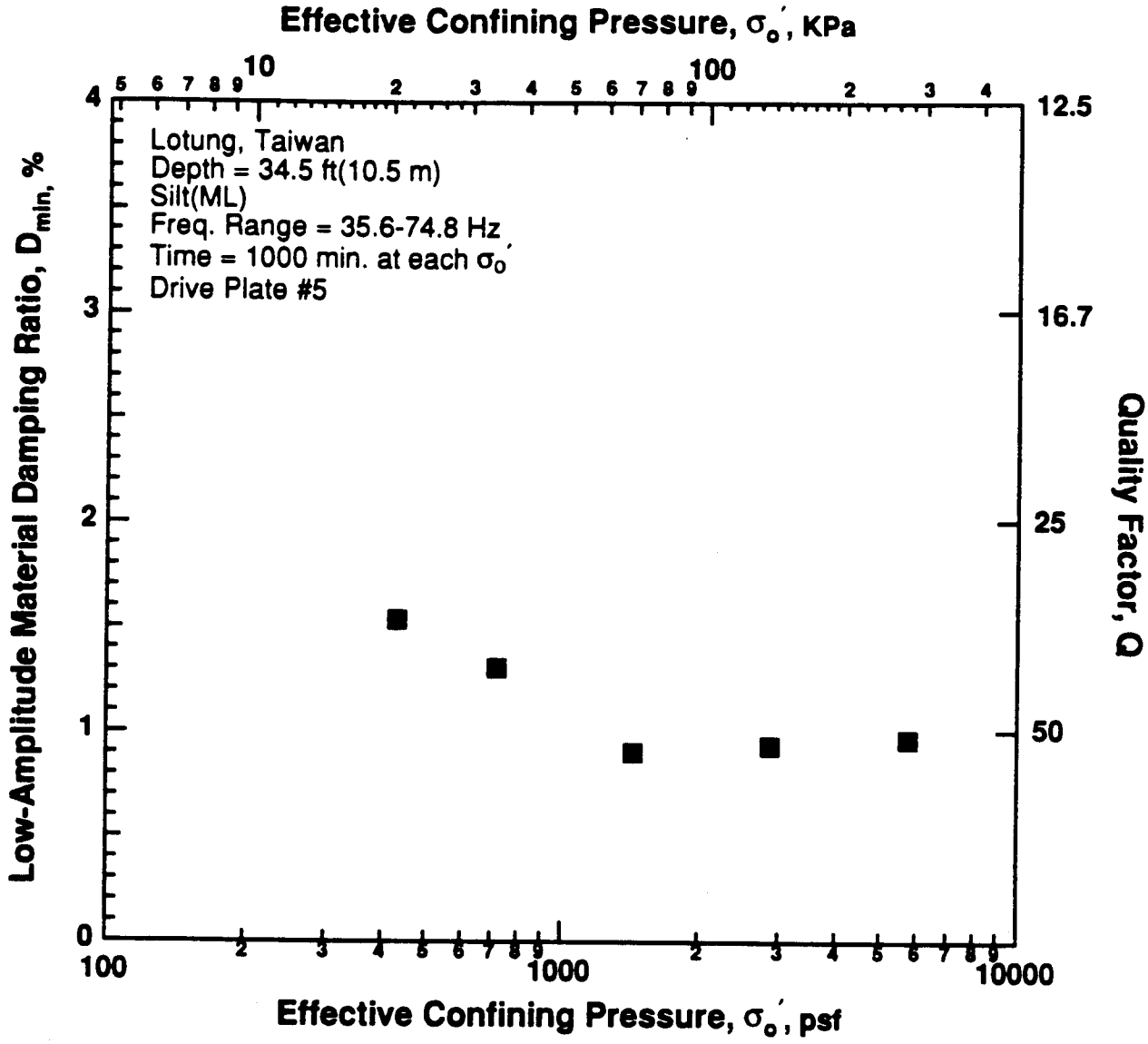

Figure 8.B.3.C-5
Variation in low-amplitude material damping ratio with effective confining pressure from resonant column tests of sample T5 from borehole CH2.

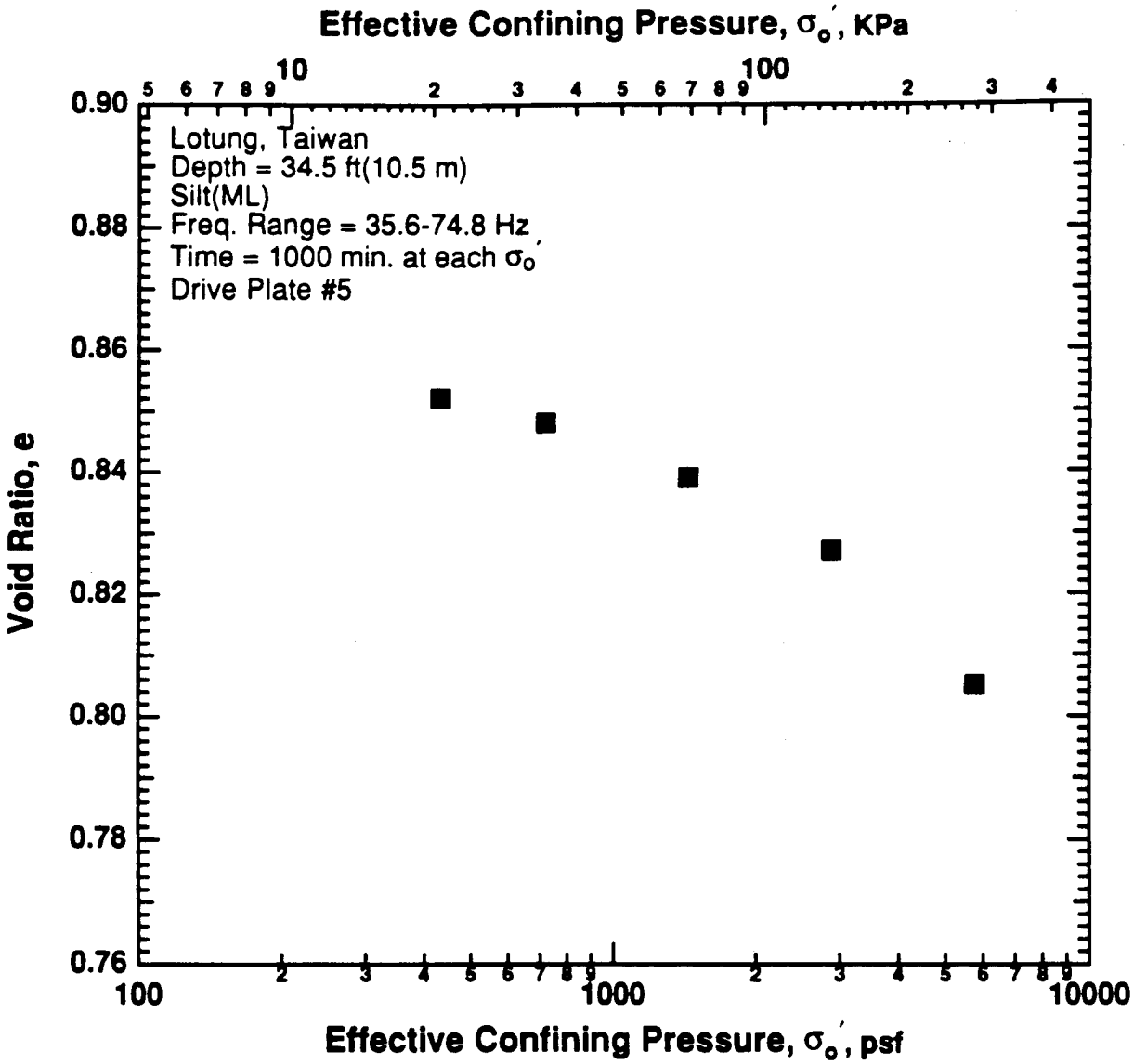

Figure 8.B.3.C-6
Variation in void ratio with effective confining pressure from resonant column tests of sample T5 from borehole CH2.

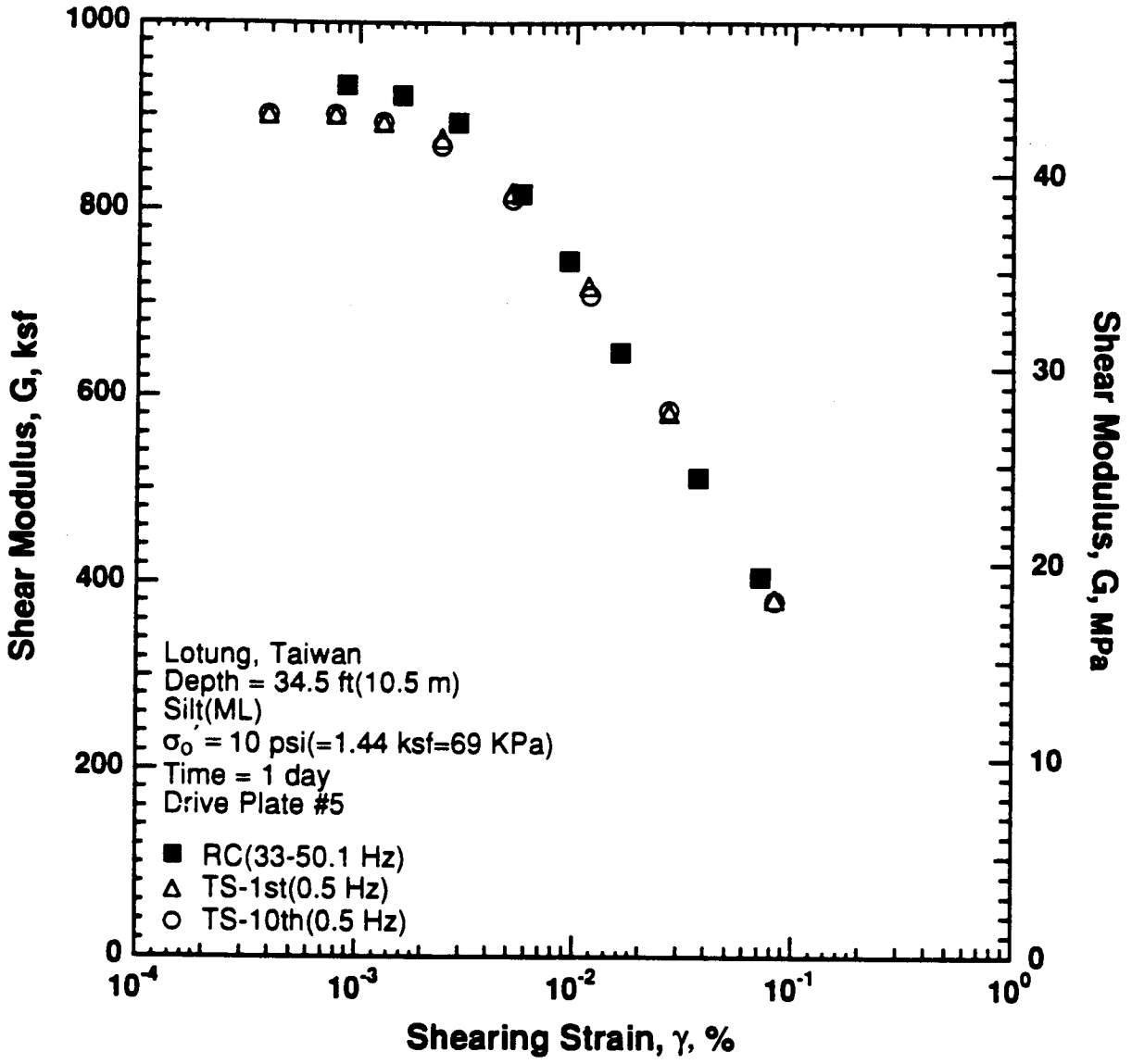

Figure 8.B.3.C-7
Variation in shear modulus with shearing strain at an effective confining pressure of 10 psi (1.44 ksf, 69 kPa) from RCTS tests of sample T5 from borehole CH2.

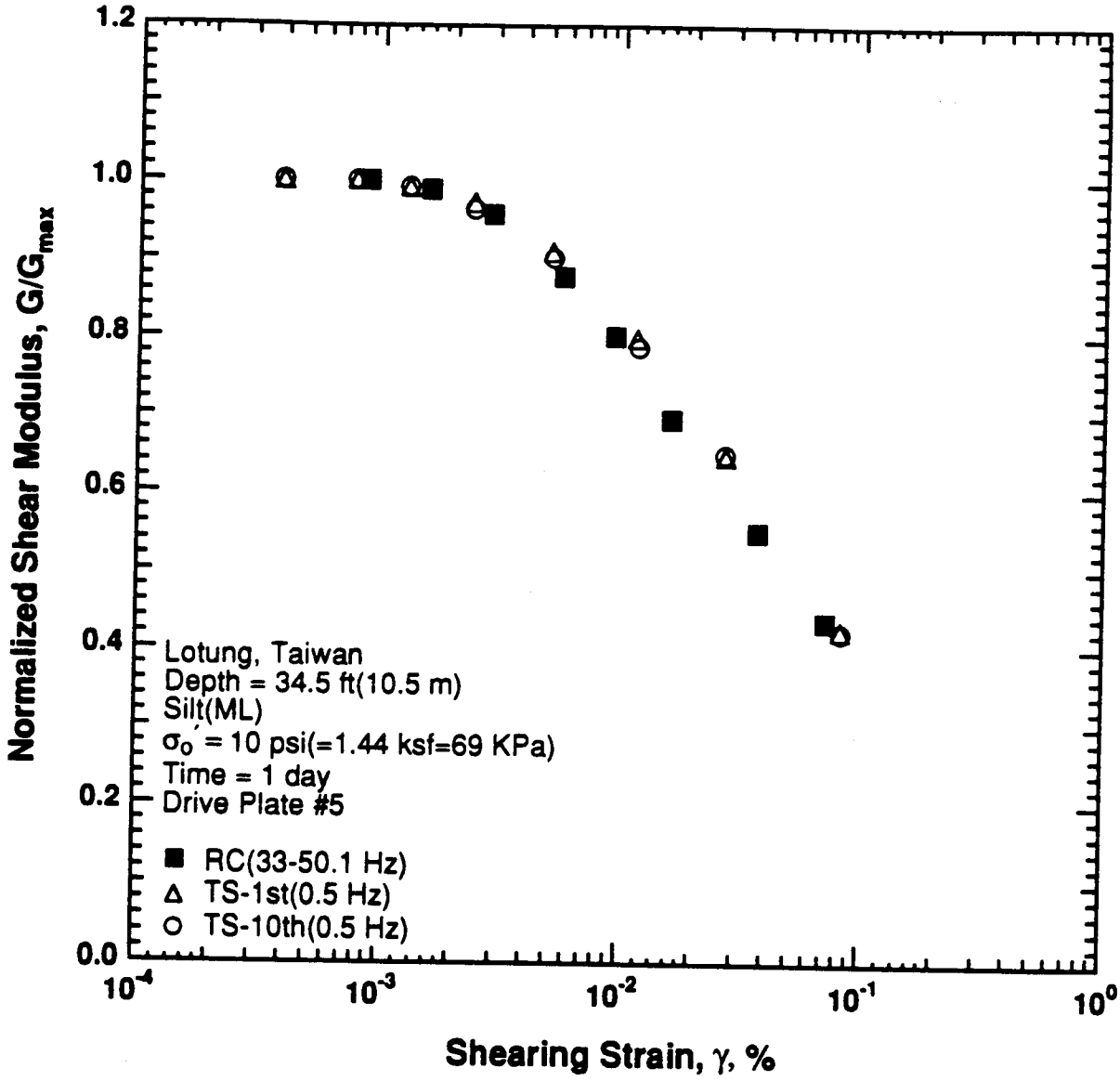

Figure 8.B.3.C-8
Variation in normalized shear modulus with shearing strain at an effective confining pressure of 10 psi (1.44 ksf, 69 kPa) from RCTS tests of sample T5 from borehole CH2.

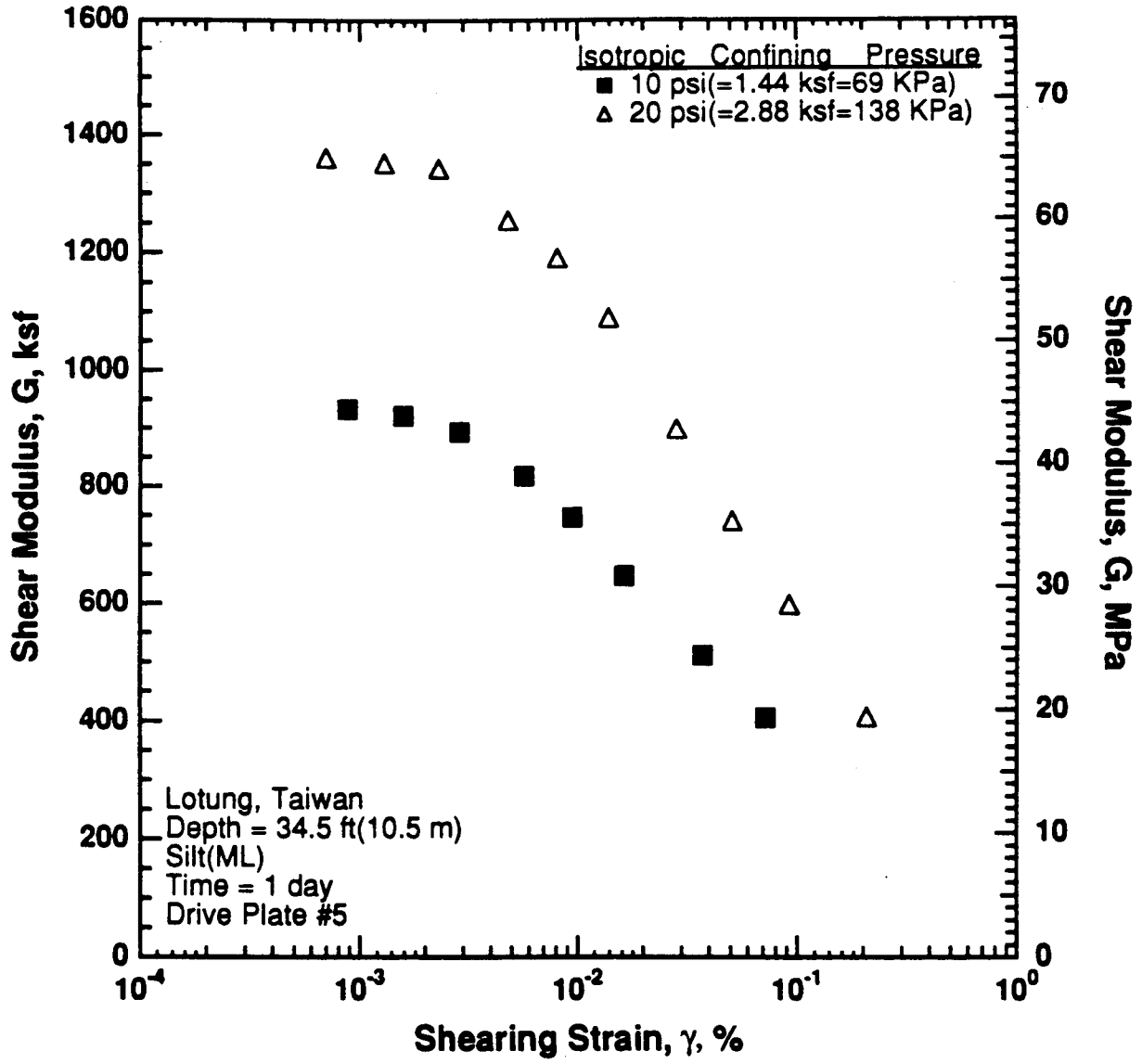

Figure 8.B.3.C-9
Variation in shear modulus with shearing strain and effective confining pressure from resonant column tests of sample T5 from borehole CH2.

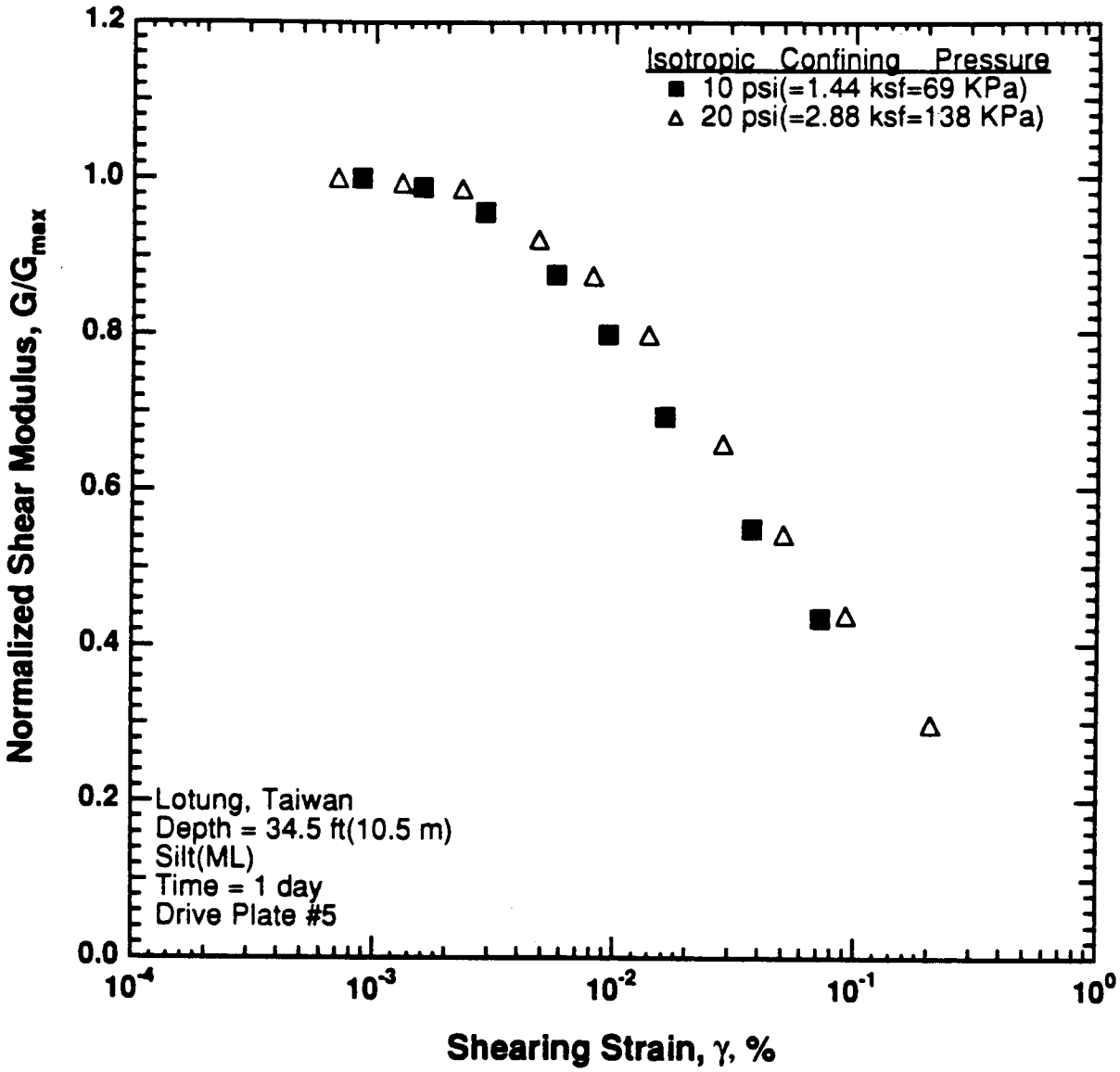

Figure 8.B.3.C-10
Comparison of the variation in normalized shear modulus with shearing strain and effective confining pressure from resonant column tests of sample T5 from borehole CH2.

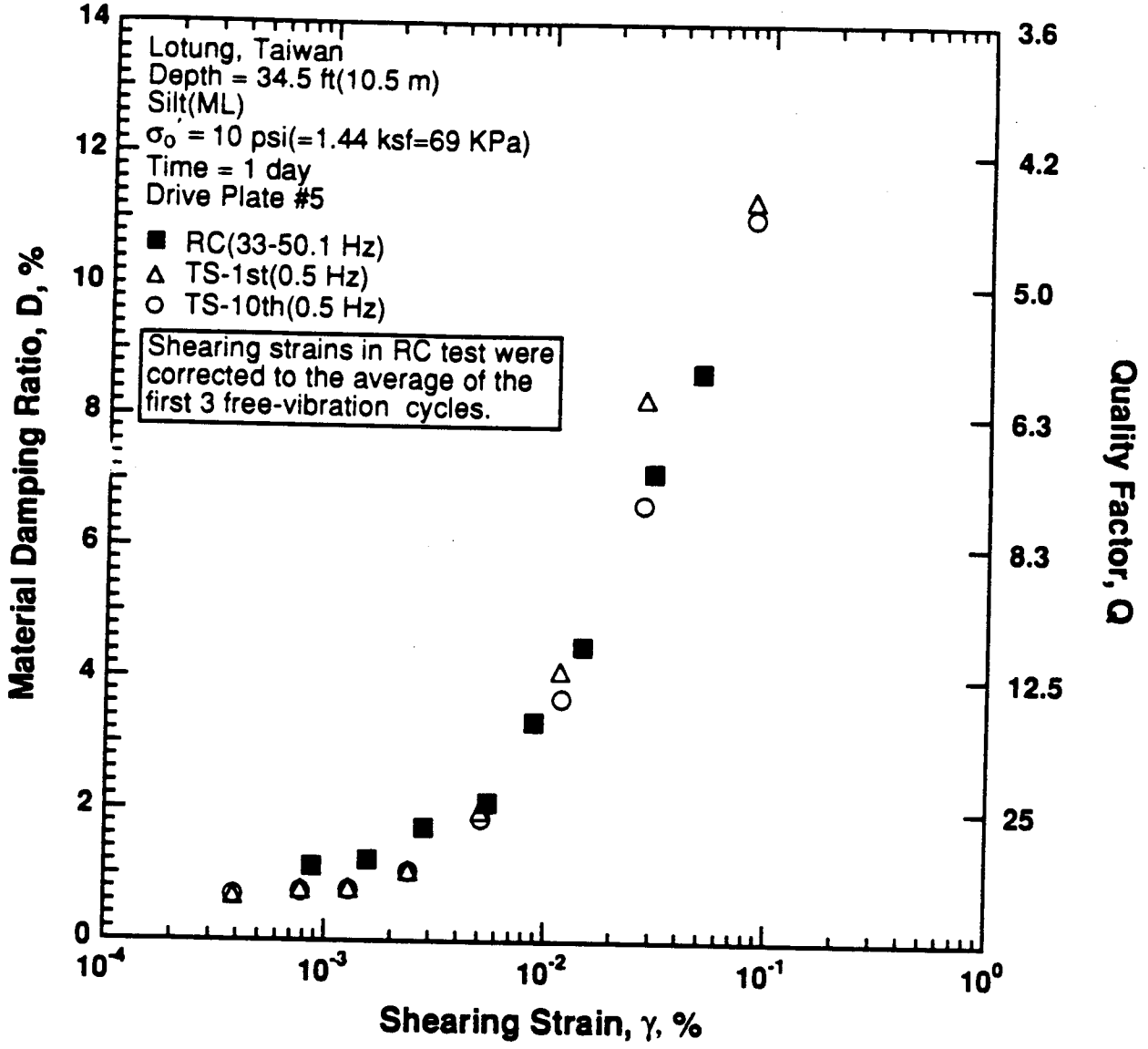

Figure 8.B.3.C-11
Variation in material damping ratio with shearing strain at an effective confining pressure of 10 psi (1.44 ksf, 69 kPa) from RCTS tests of sample T5 from borehole CH2.

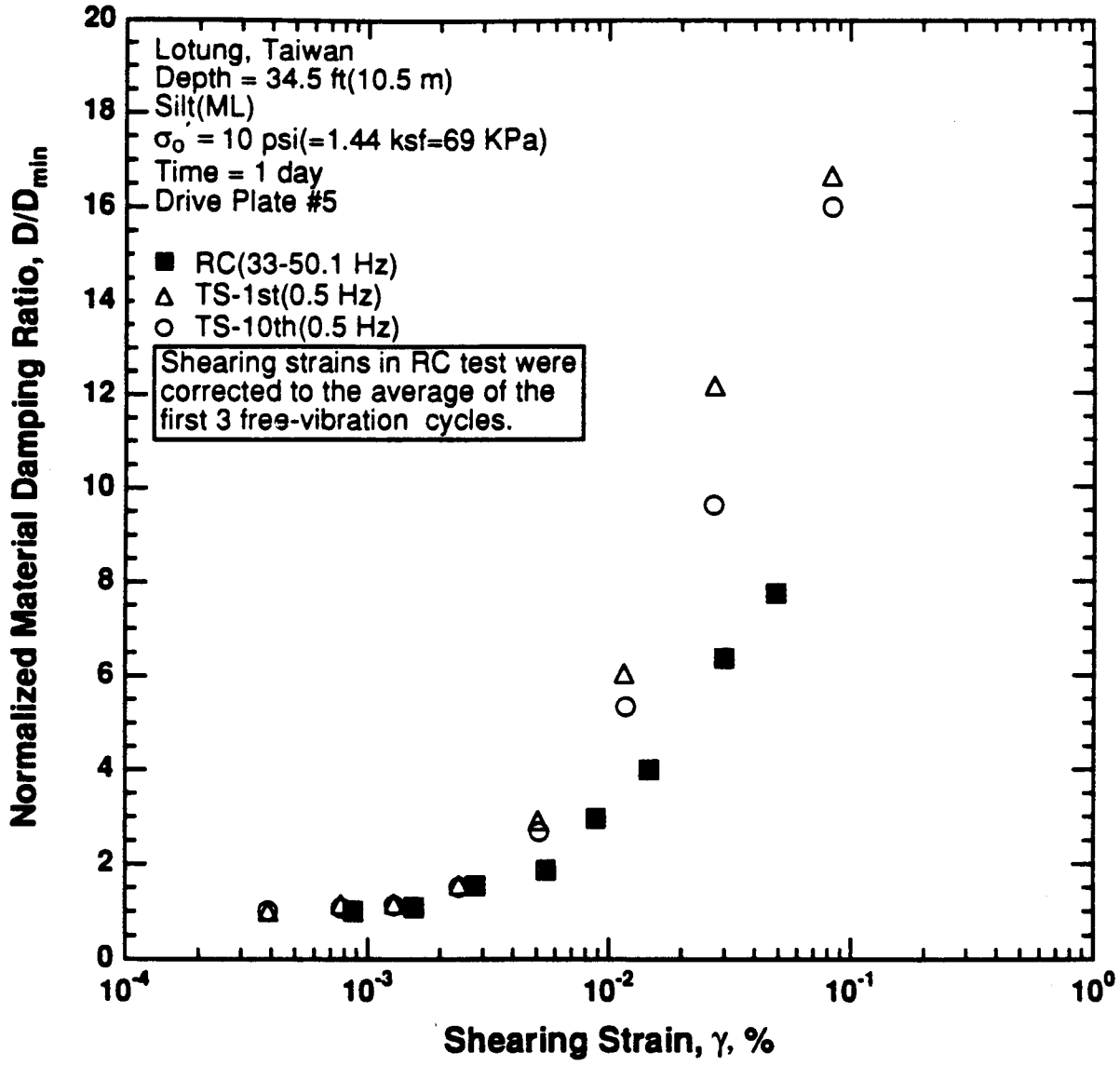

Figure 8.B.3.C-12
Variation in normalized material damping ratio with shearing strain at an effective confining pressure of 10 psi (1.44 ksf, 69 kPa) from RCTS tests of sample T5 from borehole CH2.

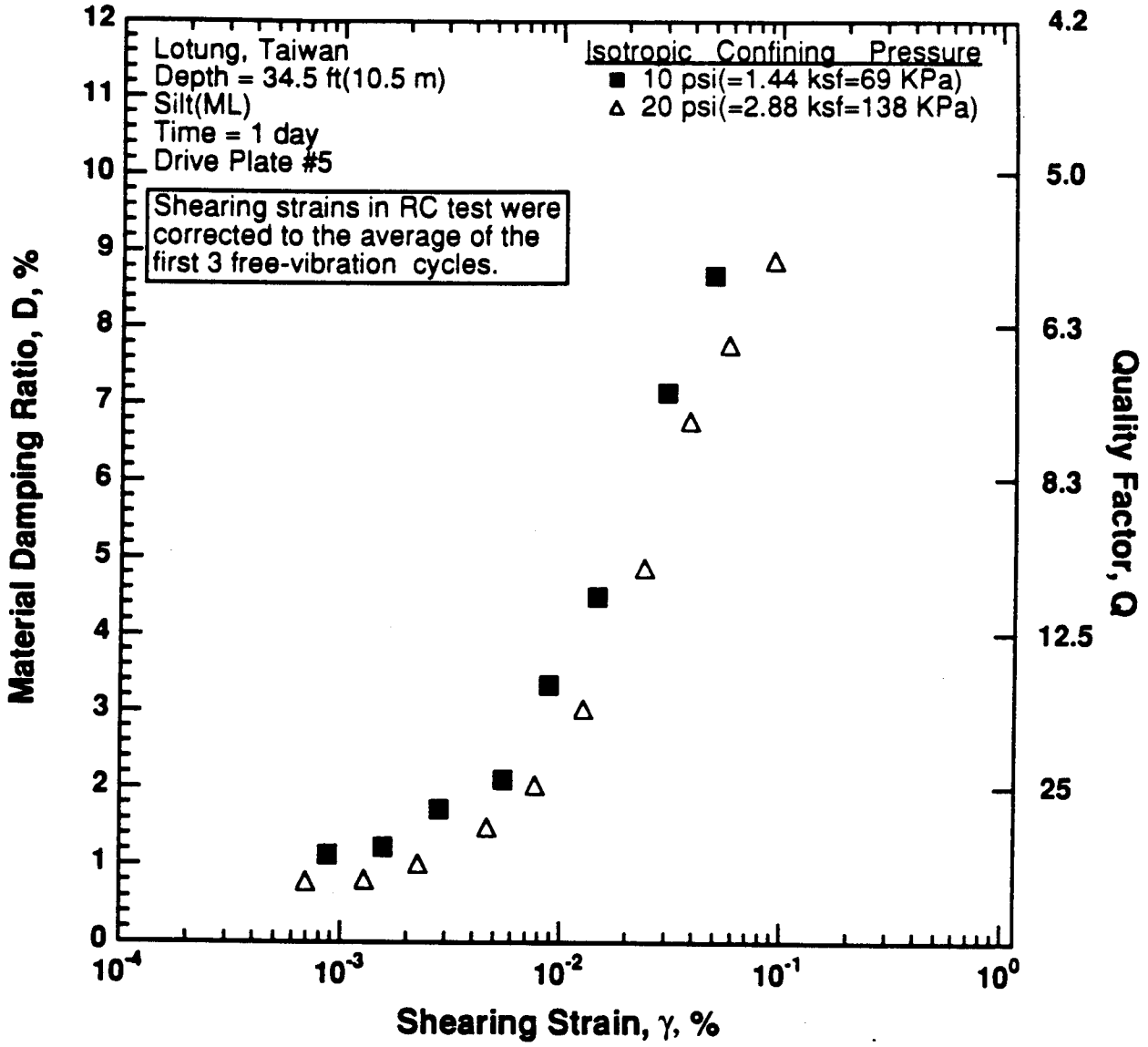

Figure 8.B.3.C-13
Variation in material damping ratio with shearing strain and effective confining pressure from resonant column tests of sample T5 from borehole CH2.

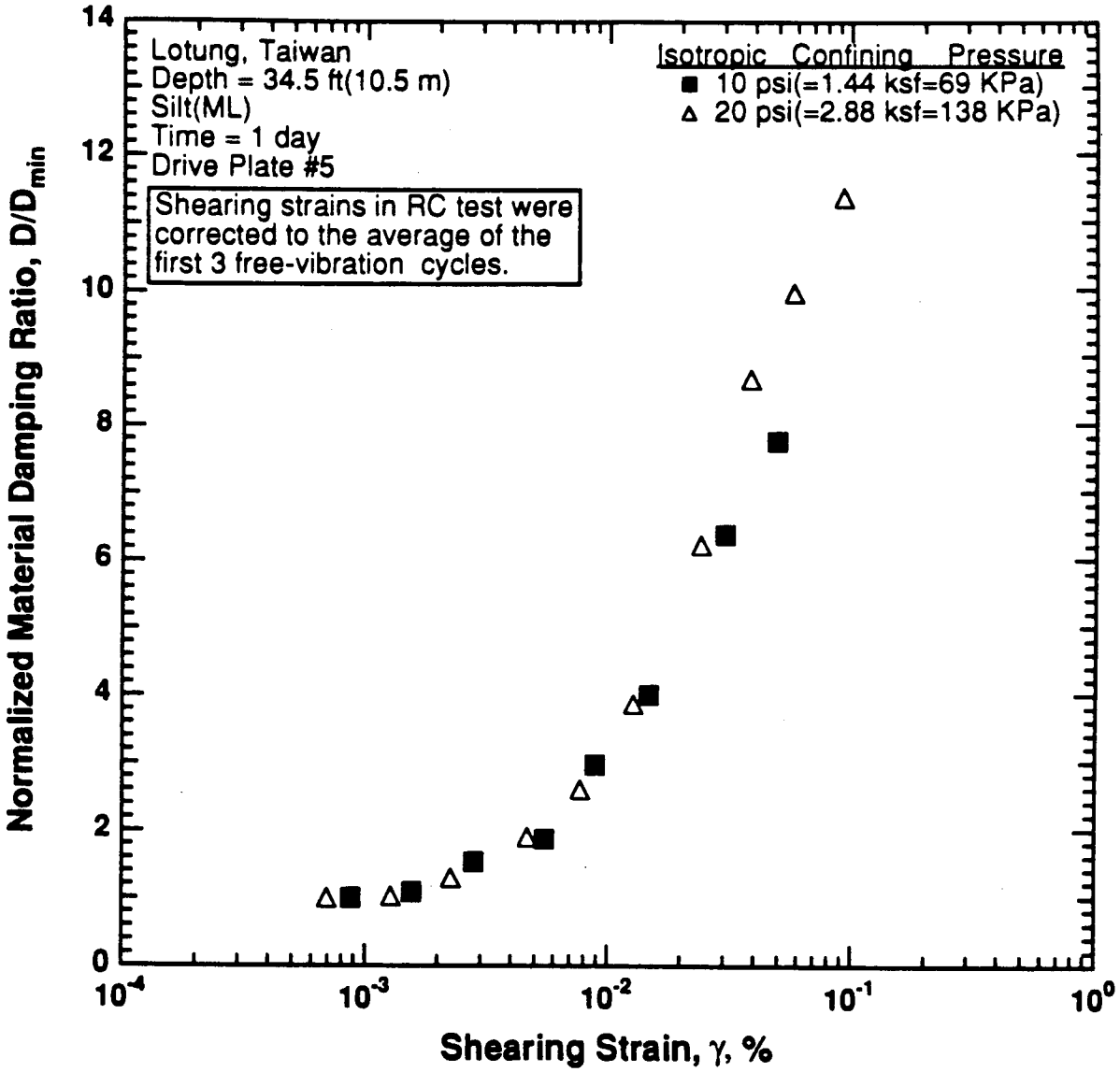

Figure 8.B.3.C-14
Comparison of the variation in normalized material damping ratio with shearing strain and effective confining pressure from resonant column tests of sample T5 from borehole CH2.

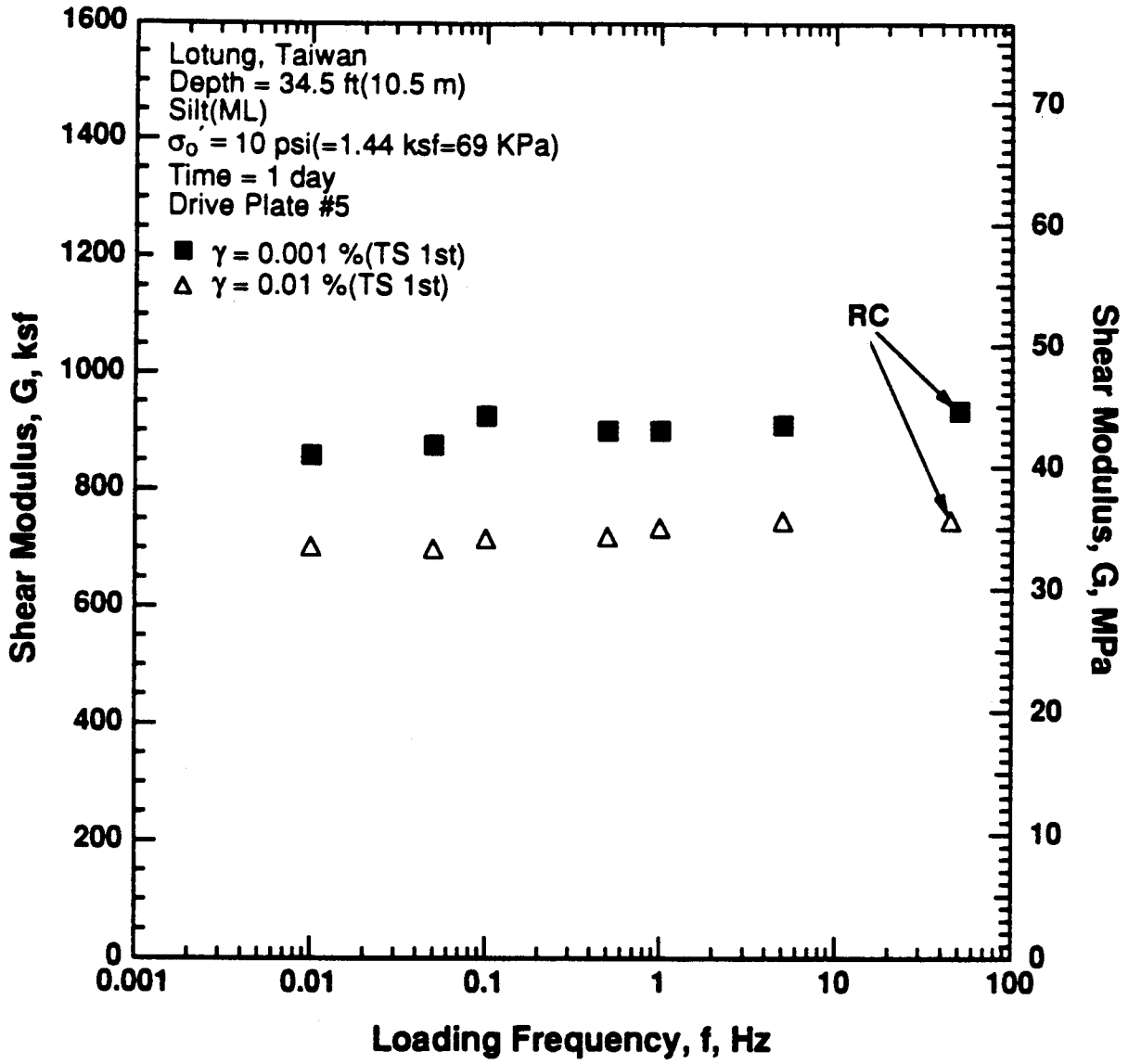

Figure 8.B.3.C-15
Variation in shear modulus with loading frequency and shearing strain at an effective confining pressure of 10 psi (1.44 ksf, 69 kPa) from RCTS tests of sample T5 from borehole CH2.

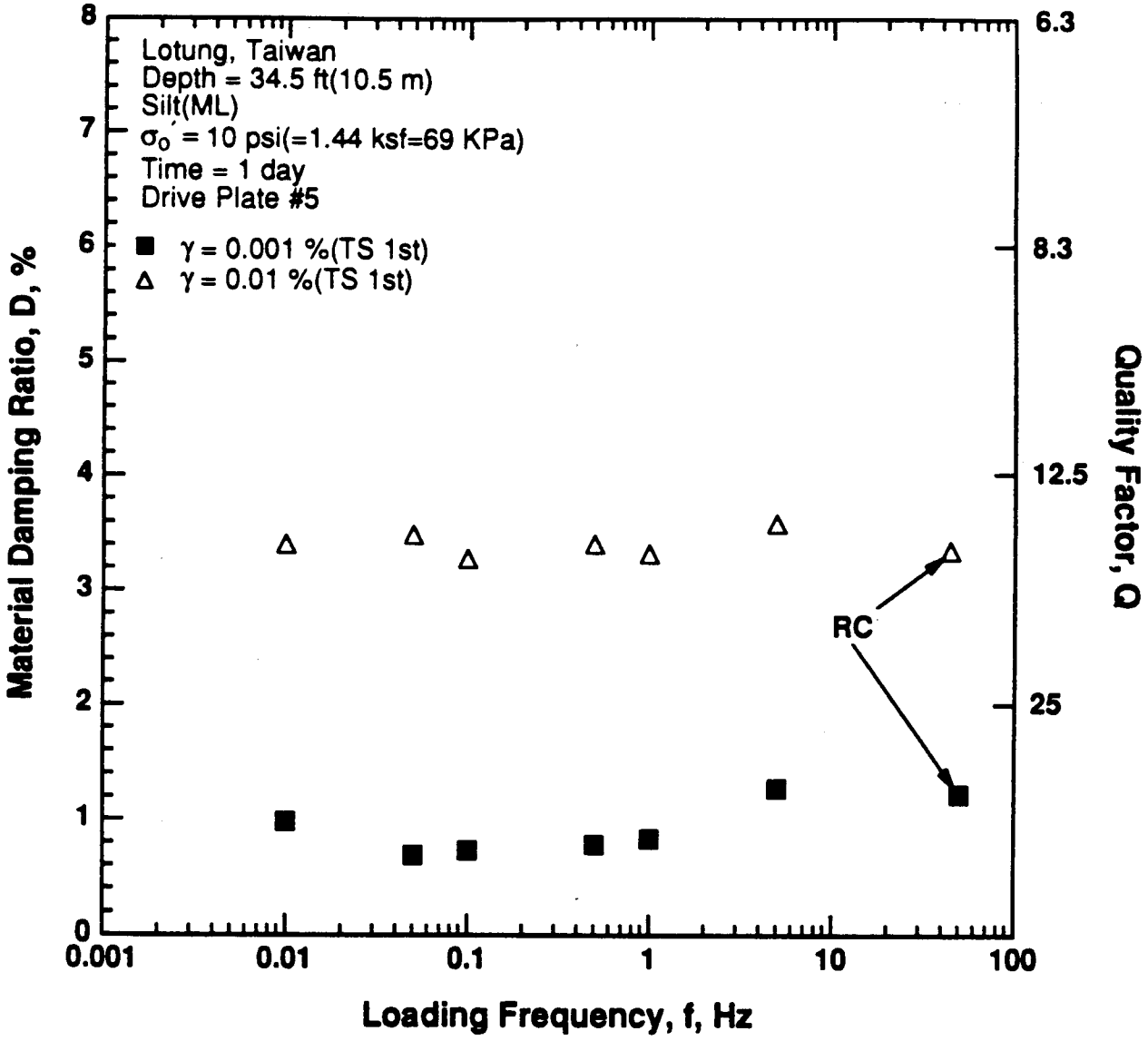

Figure 8.B.3.C-16
Variation in material damping ratio with loading frequency and shearing strain at an effective confining pressure of 10 psi (1.44 ksf, 69 kPa) from RCTS tests of sample T5 from borehole CH2.

APPENDIX 8.B.3.D
DYNAMIC TESTS OF SAMPLE T4 FROM BOREHOLE CH1, DEPTH = 59 FT (18.0 M)

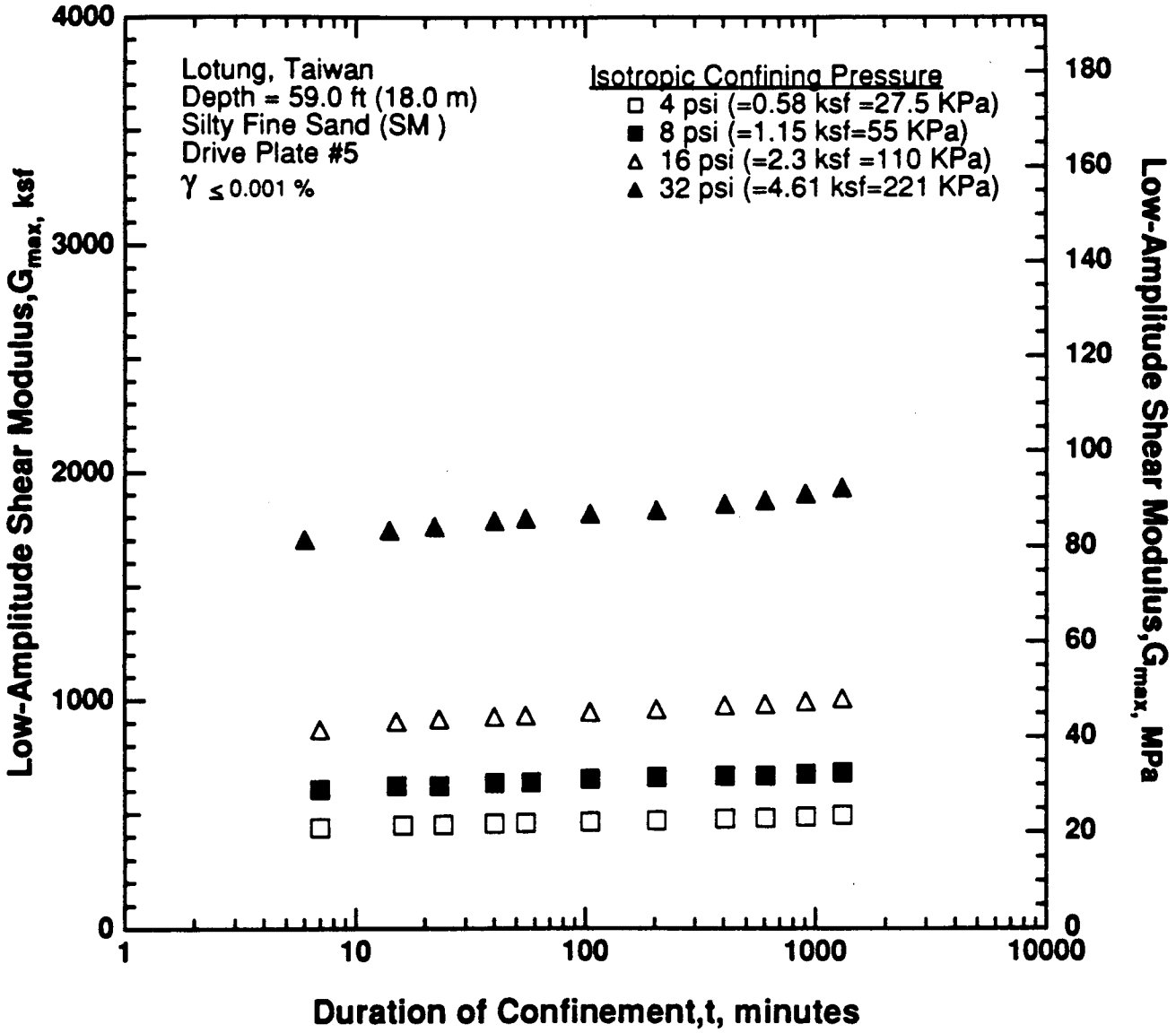

Figure 8.B.3.D-1
Variation in low-amplitude shear modulus with magnitude and duration of isotropic confining pressure from resonant column tests of sample T4 from borehole CH1.

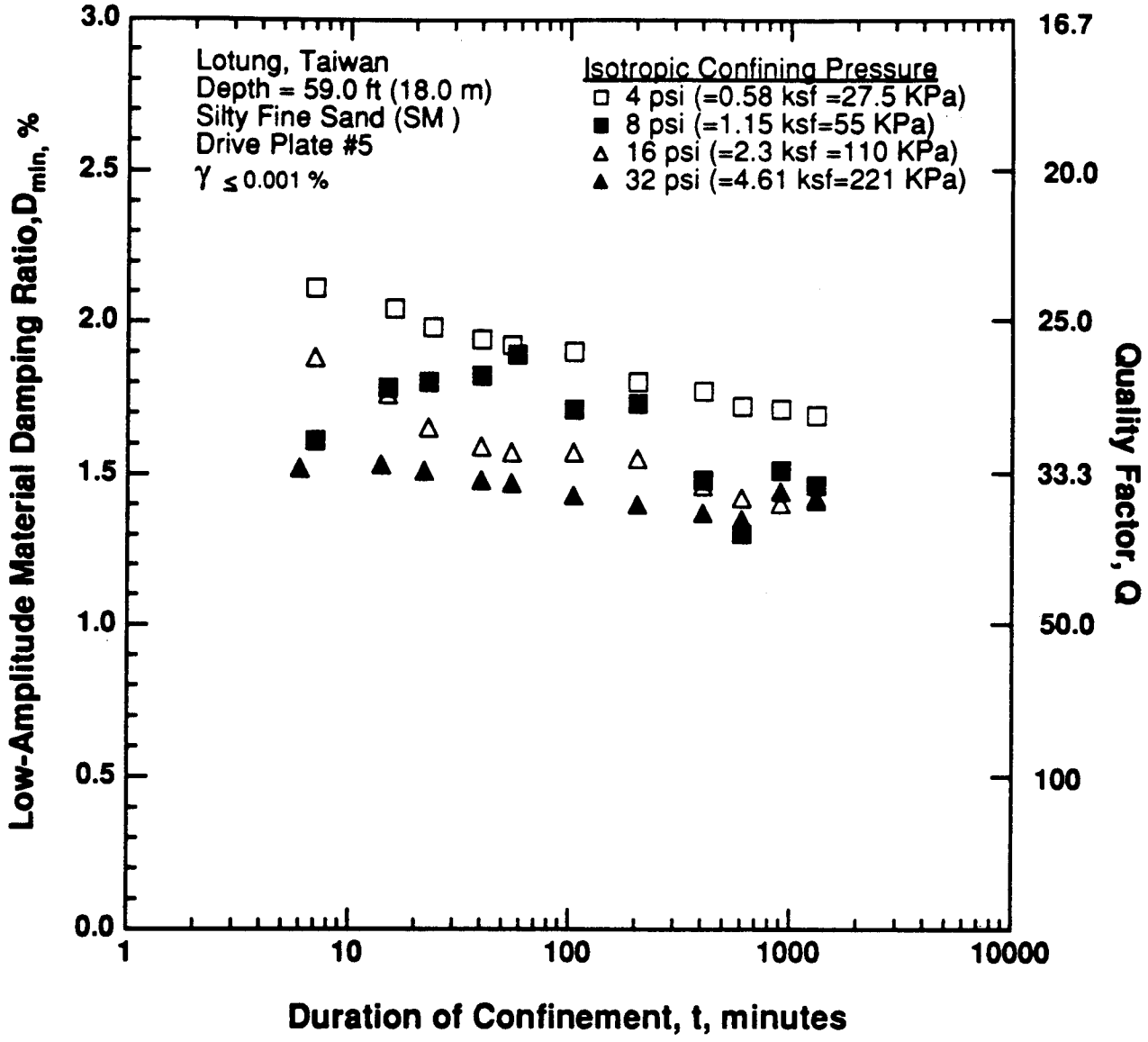

Figure 8.B.3.D-2
Variation in low-amplitude material damping ratio with magnitude and duration of isotropic confining pressure from resonant column tests of sample T4 from borehole CH1.

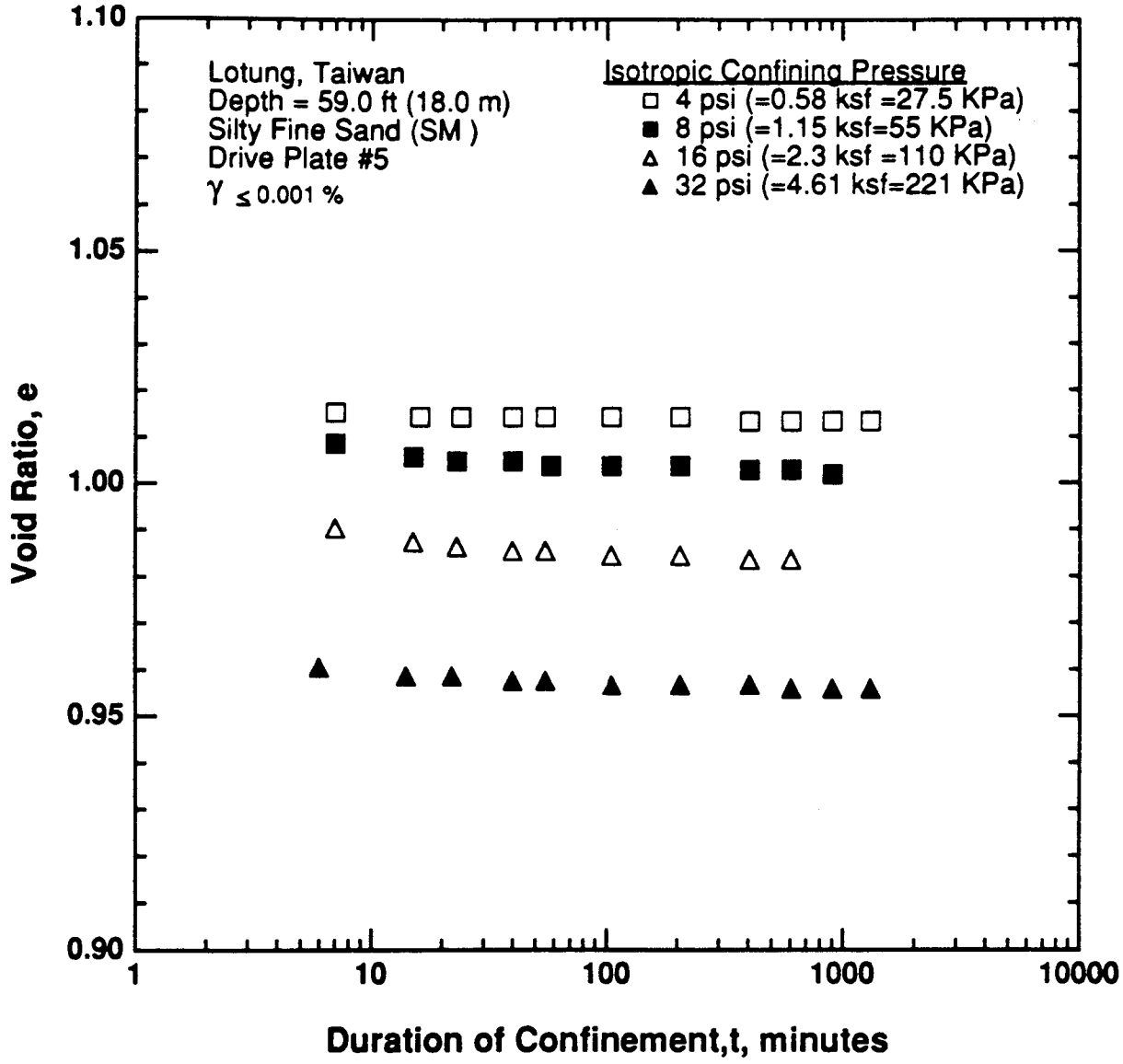

Figure 8.B.3.D-3
Variation in void ratio with magnitude and duration of isotropic confining pressure from resonant column tests of sample T4 from borehole CH1.

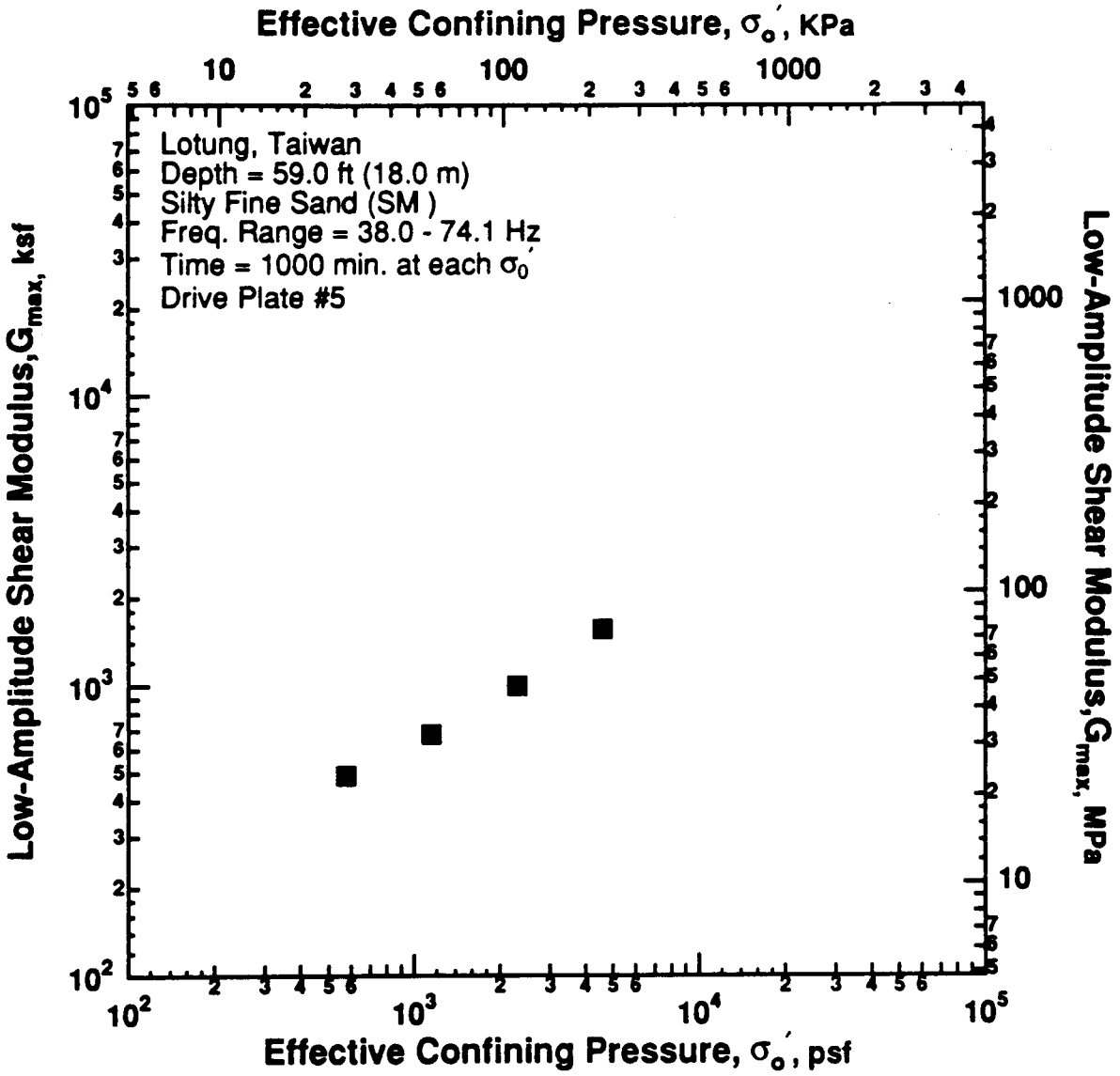

Figure 8.B.3.D-4
Variation in low-amplitude shear modulus with effective confining pressure from resonant column tests of sample T4 from borehole CH1.

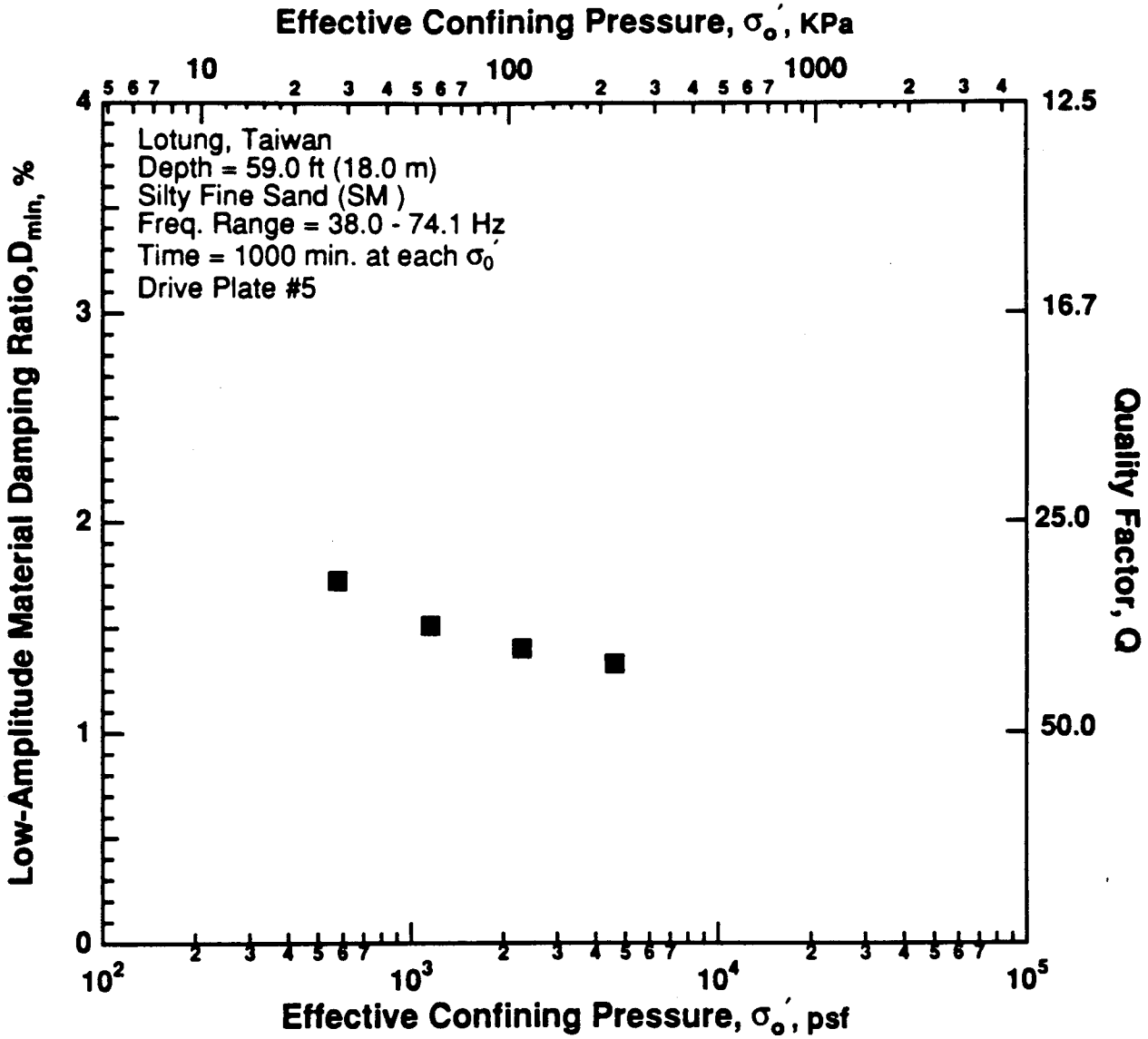

Figure 8.B.3.D-5
Variation in low-amplitude material damping ratio with effective confining pressure from resonant column tests of sample T4 from borehole CH1.

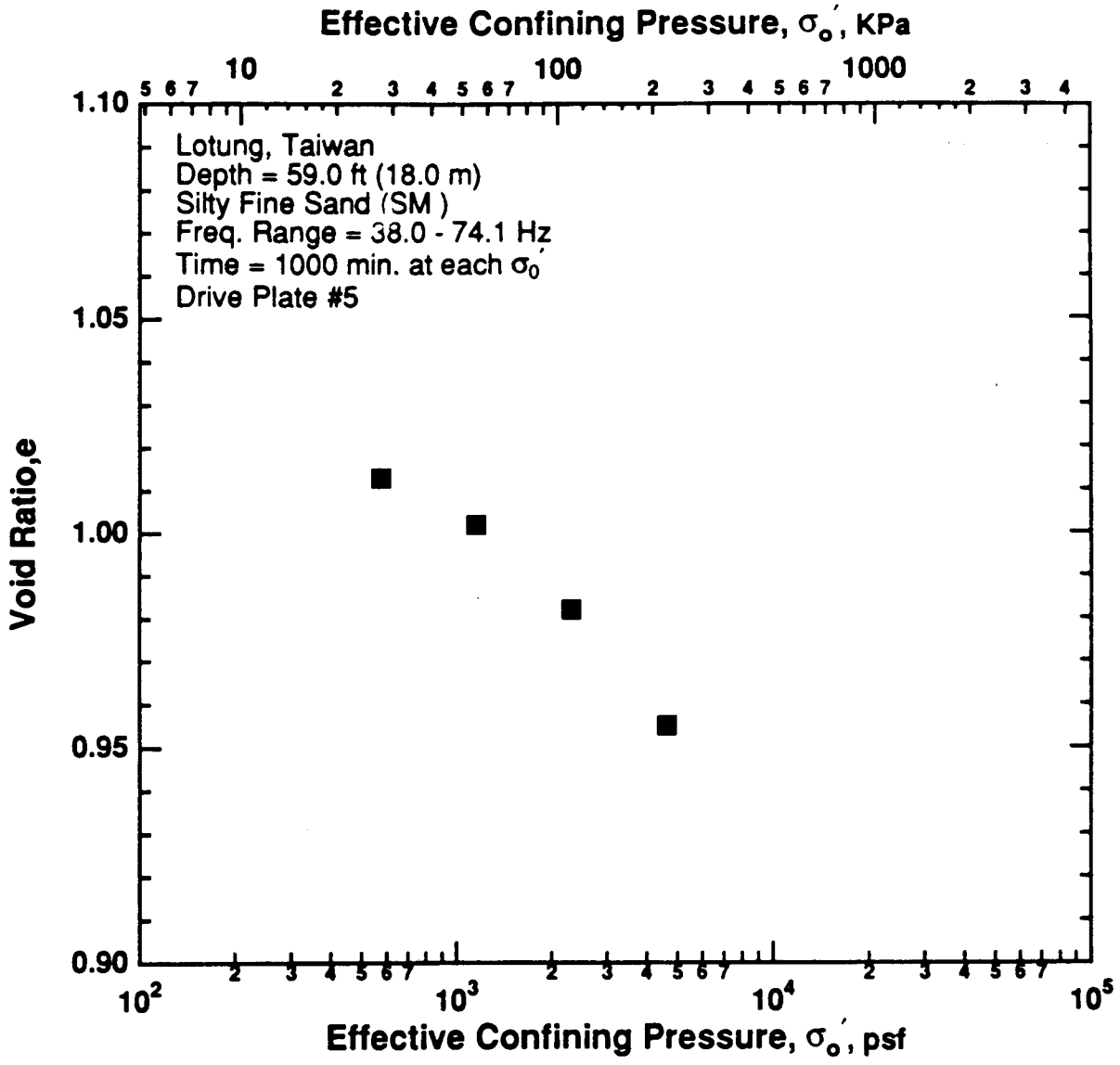

Figure 8.B.3.D-6
Variation in void ratio with effective confining pressure from resonant column tests of sample T4 from borehole CH1.

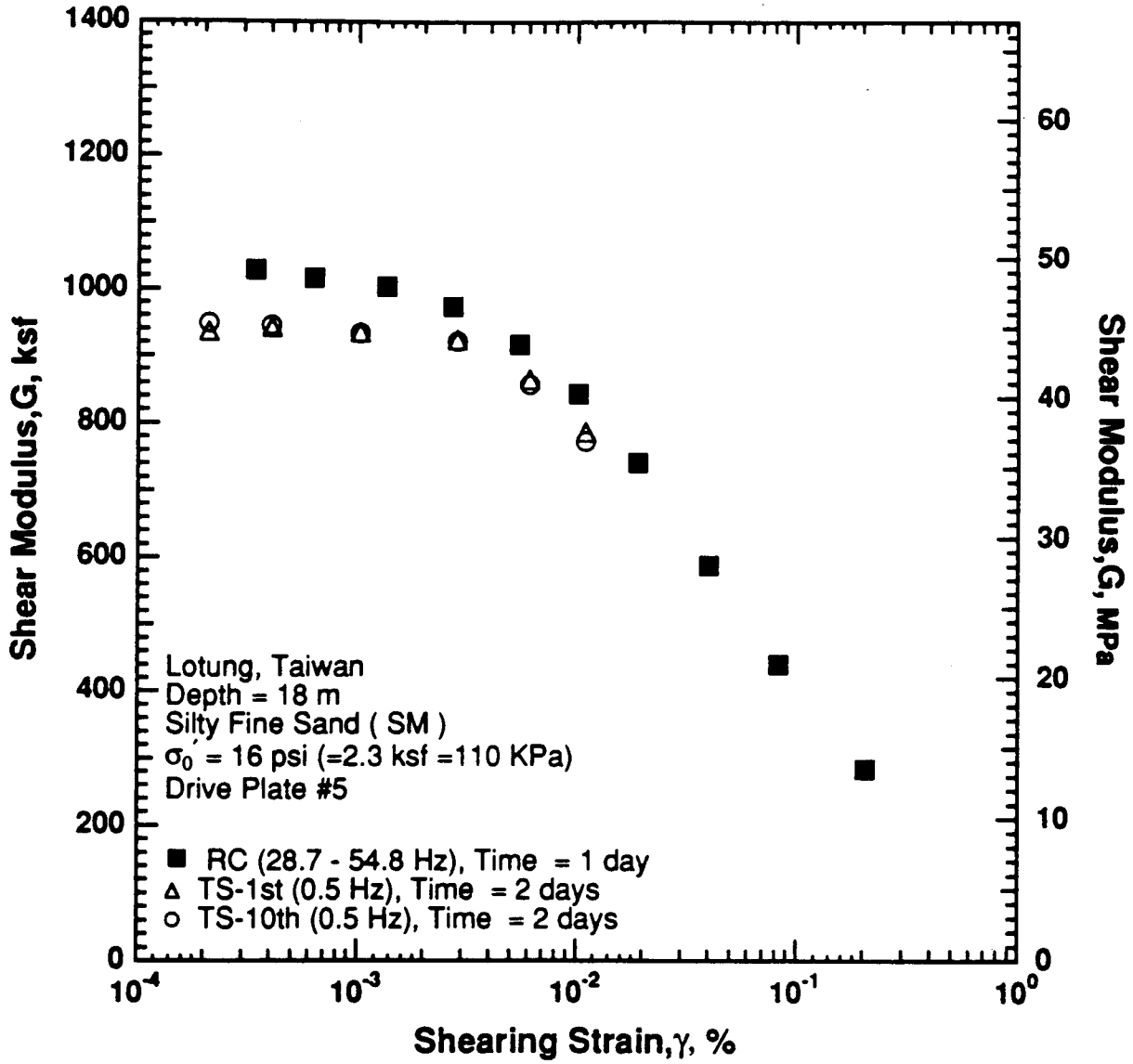

Figure 8.B.3.D-7
Variation in shear modulus with shearing strain at an effective confining pressure of 16 psi (2.3 ksf, 110 kPa) from RCTS tests of sample T4 from borehole CH1.

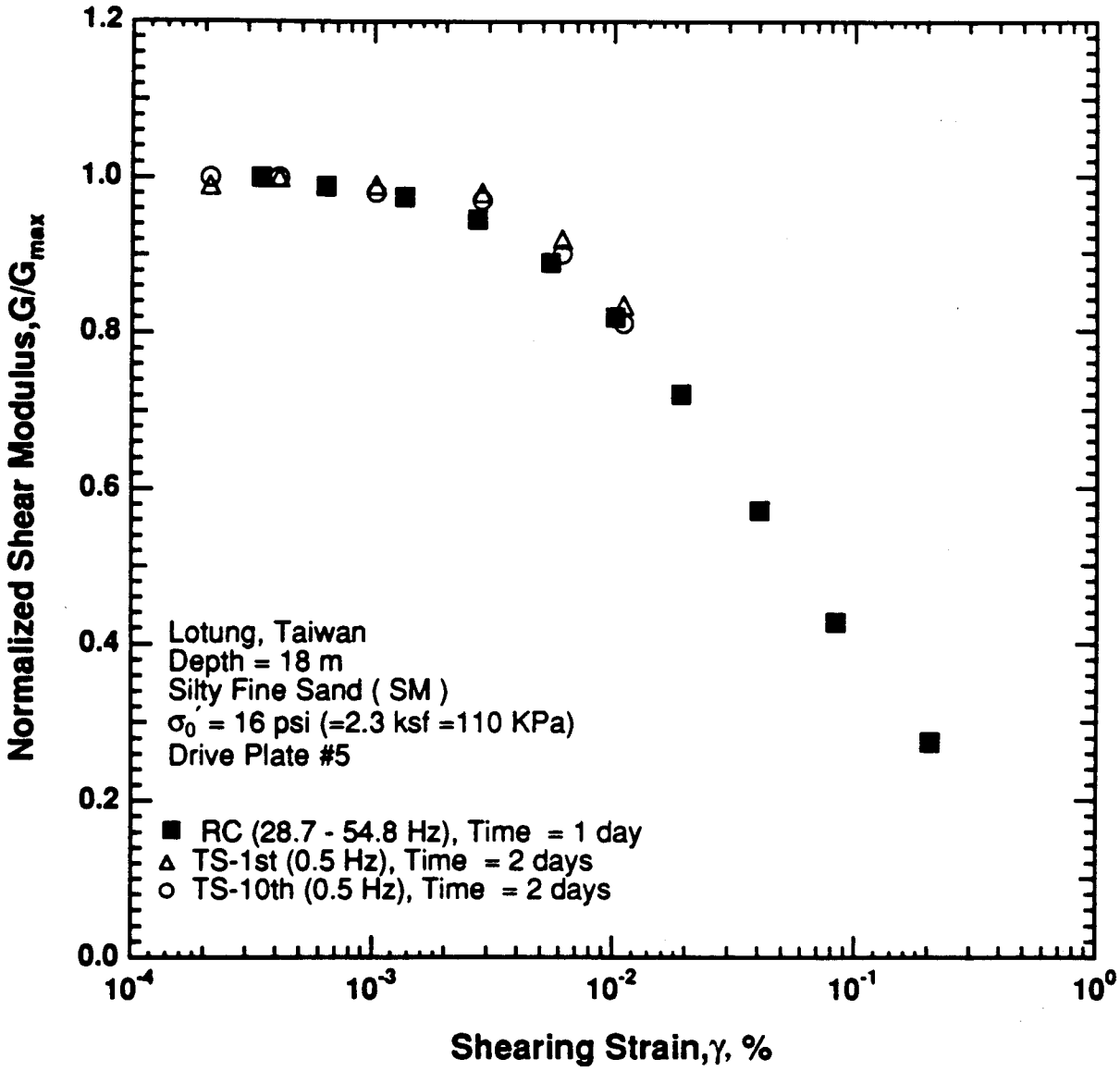

Figure 8.B.3.D-8
Variation in normalized shear modulus with shearing strain at an effective confining pressure of 16 psi (2.3 ksf, 110 kPa) from RCTS tests of sample T4 from borehole CH1.

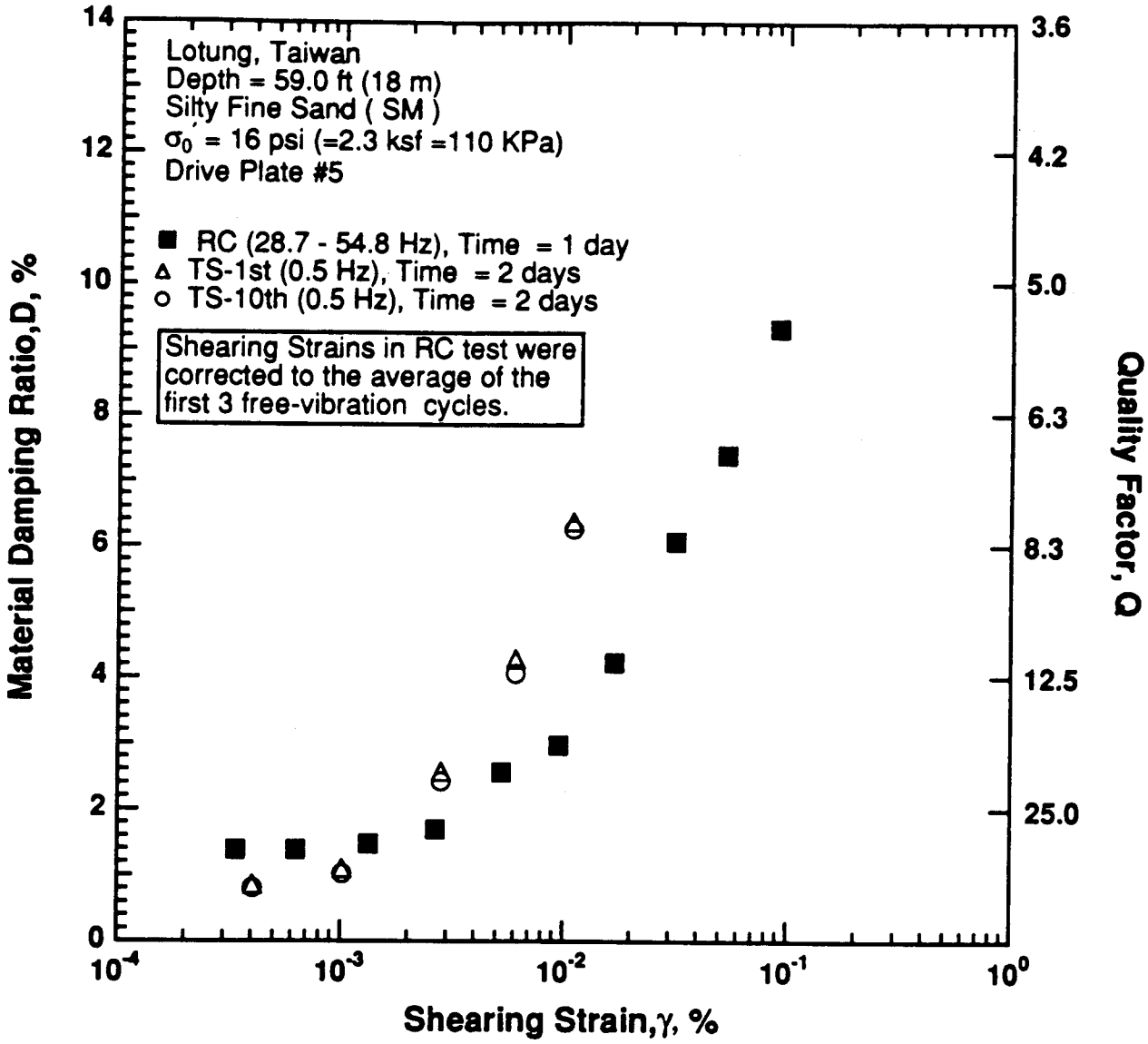

Figure 8.B.3.D-9
Variation in material damping ratio with shearing strain at an effective confining pressure of 16 psi (2.3 ksf, 110 kPa) from RCTS tests of sample T4 from borehole CH1.

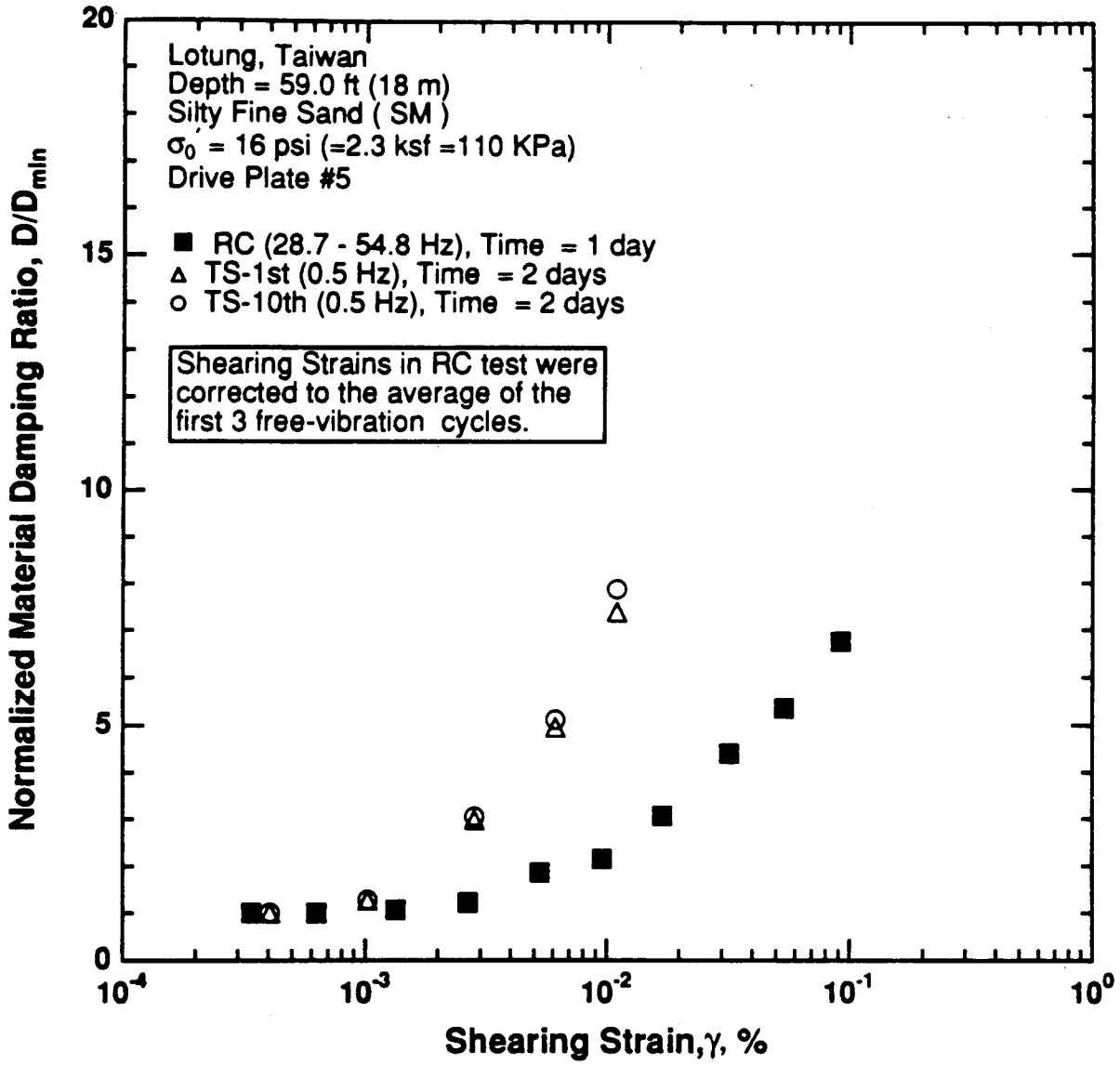

Figure 8.B.3.D-10
Variation in normalized material damping ratio with shearing strain at an effective confining pressure of 16 psi (2.3 ksf, 110 kPa) from RCTS tests of sample T4 from borehole CH1.

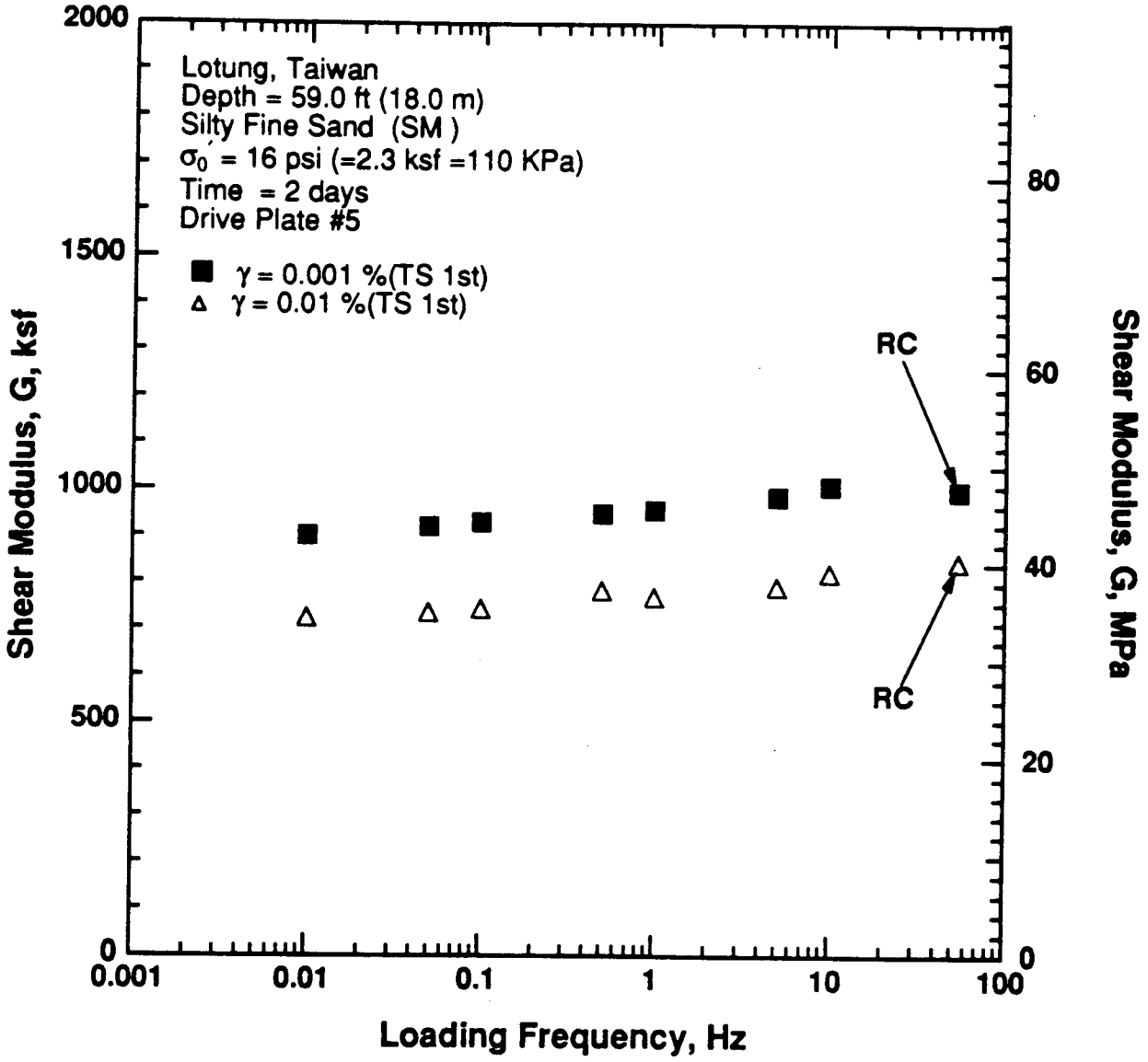

Figure 8.B.3.D-11
Variation in shear modulus with loading frequency and shearing strain at an effective confining pressure of 16 psi (2.3 ksf, 110 kPa) from RCTS tests of sample T4 from borehole CH1.

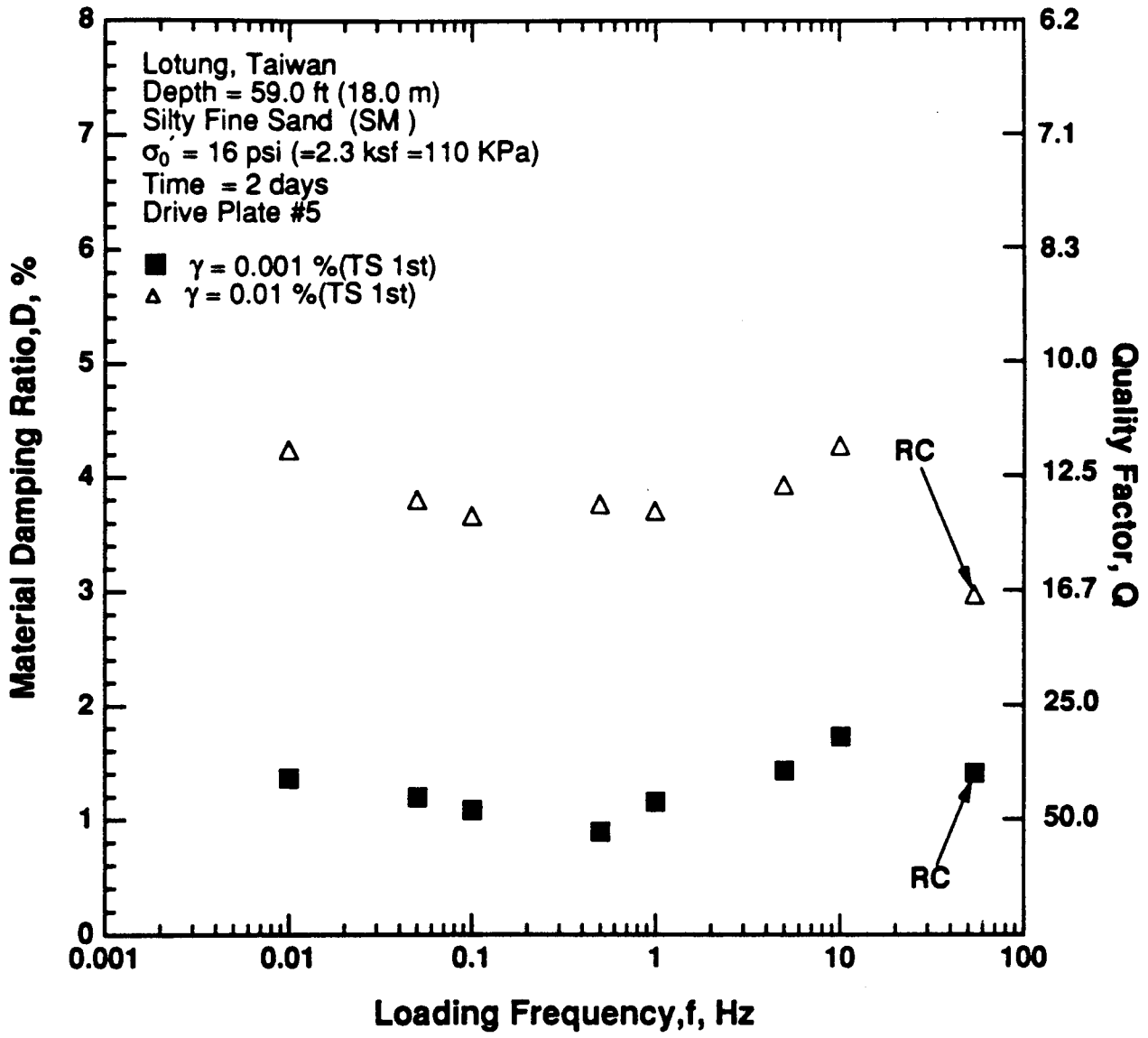

Figure 8.B.3.D-12
Variation in material damping ratio with loading frequency and shearing strain at an effective confining pressure of 16 psi (2.3 ksf, 110 kPa) from TCTS tests of sample T4 from borehole CH1.

APPENDIX 8.B.3.E
DYNAMIC TESTS OF SAMPLE T7 FROM BOREHOLE CH1, DEPTH = 82 FT (25.0 M)

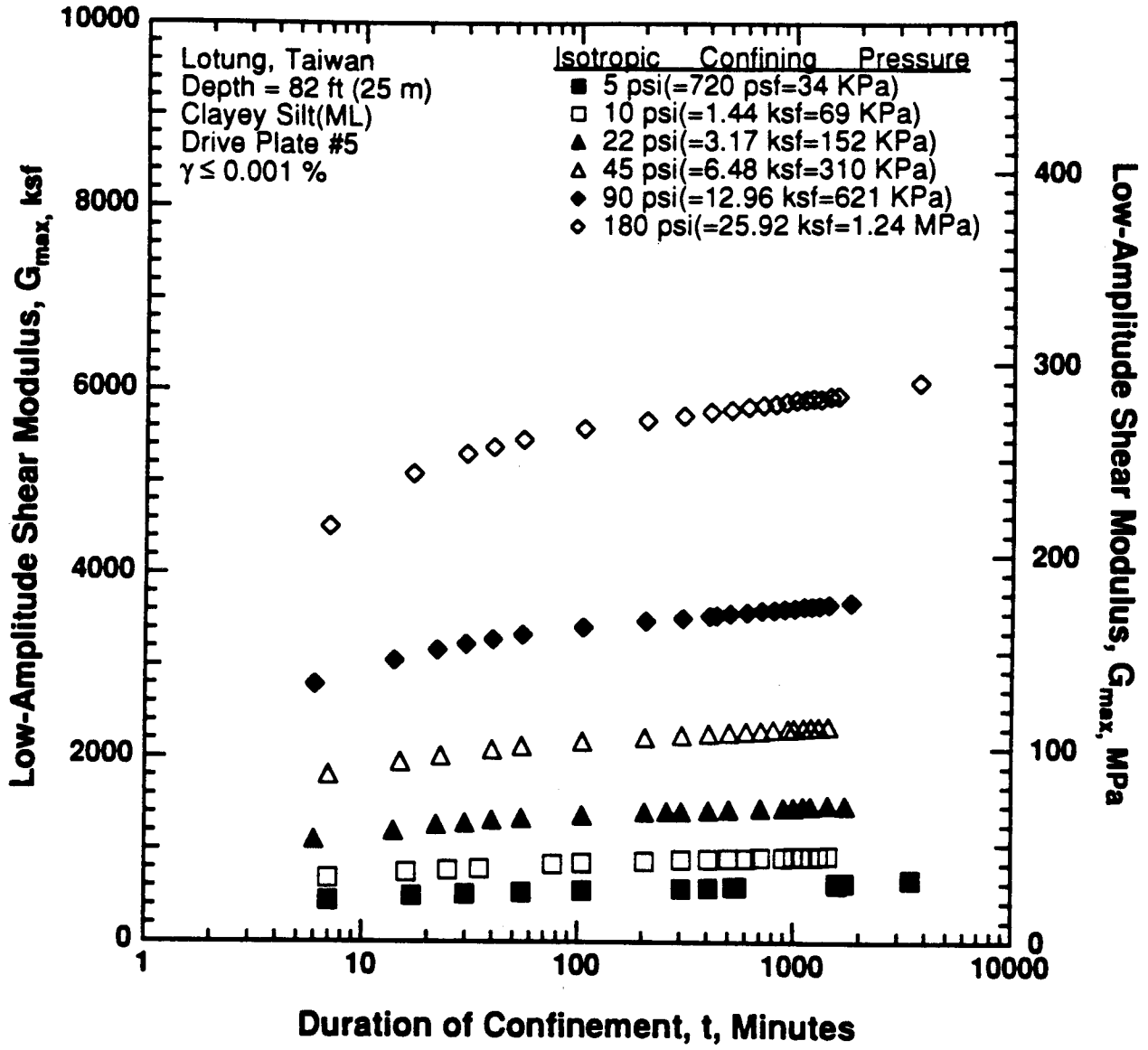

Figure 8.B.3.E-1
Variation in low-amplitude shear modulus with magnitude and duration of isotropic confining pressure from resonant column tests of sample T7 from borehole CH1.

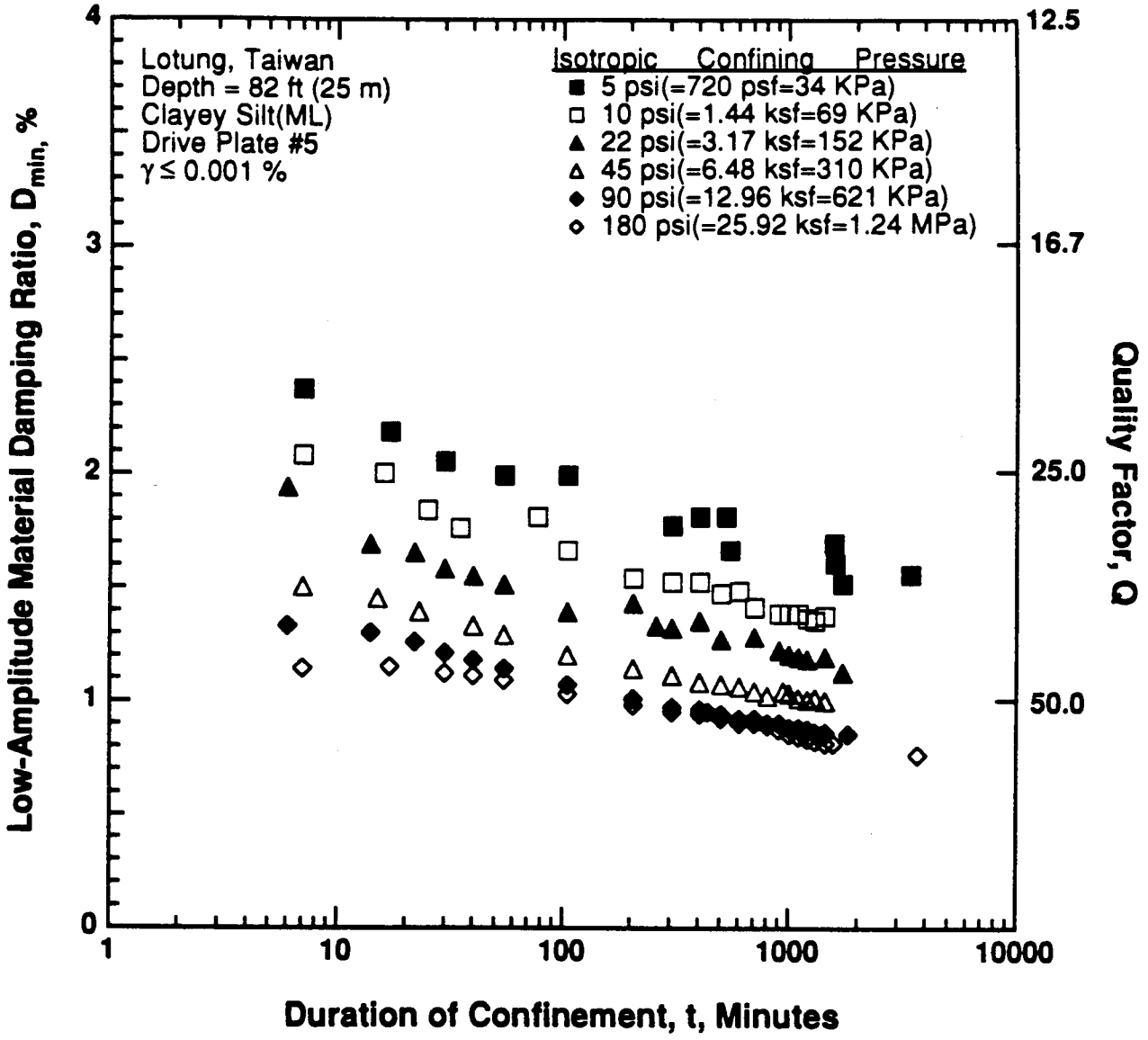

Figure 8.B.3.E-2
Variation in low-amplitude material damping ratio with magnitude and duration of isotropic confining pressure from resonant column tests of sample T7 from borehole CH1.

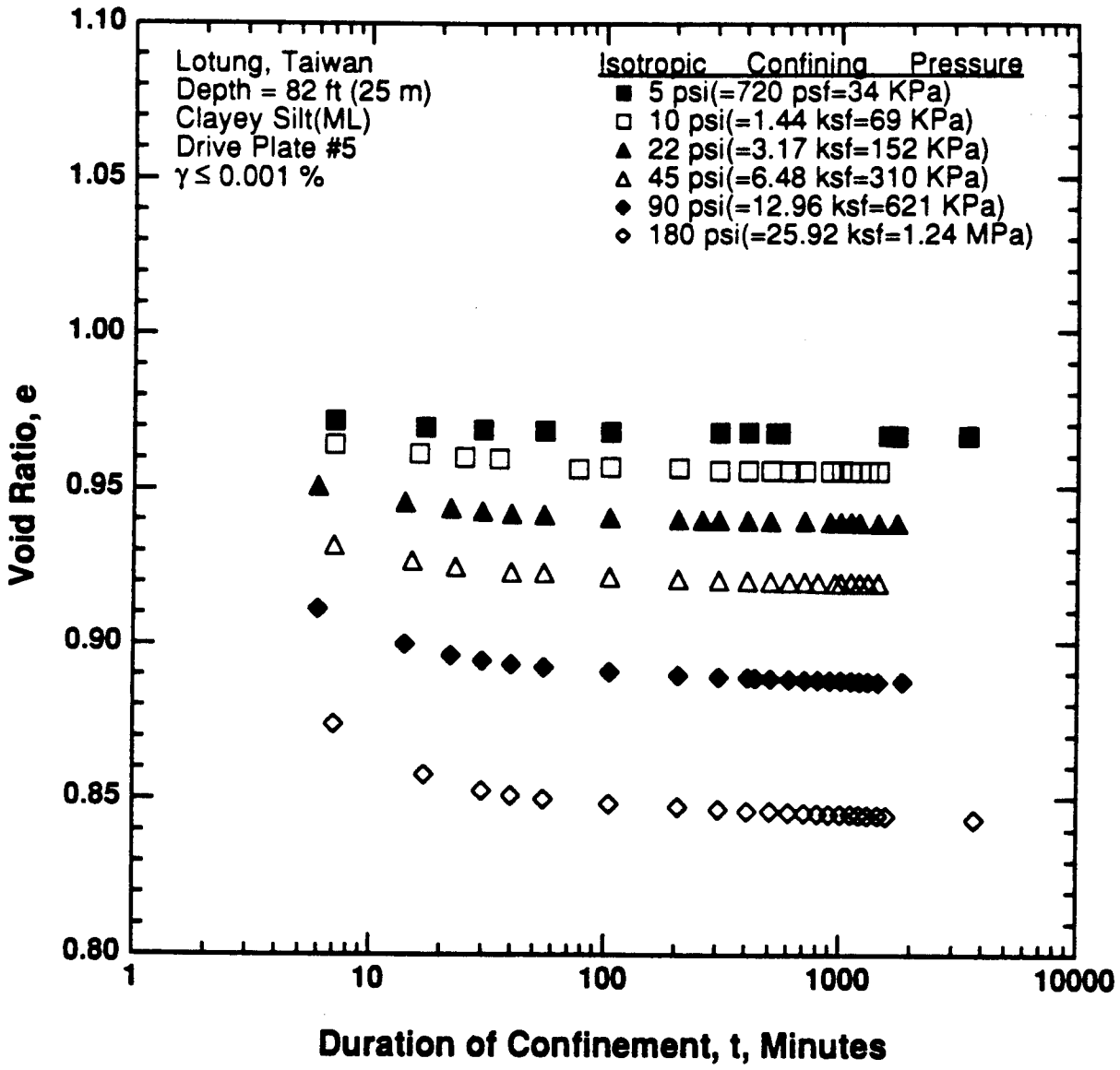

Figure 8.B.3.E-3
Variation in void ratio with magnitude and duration of isotropic confining pressure from resonant column tests of sample T7 from borehole CH1.

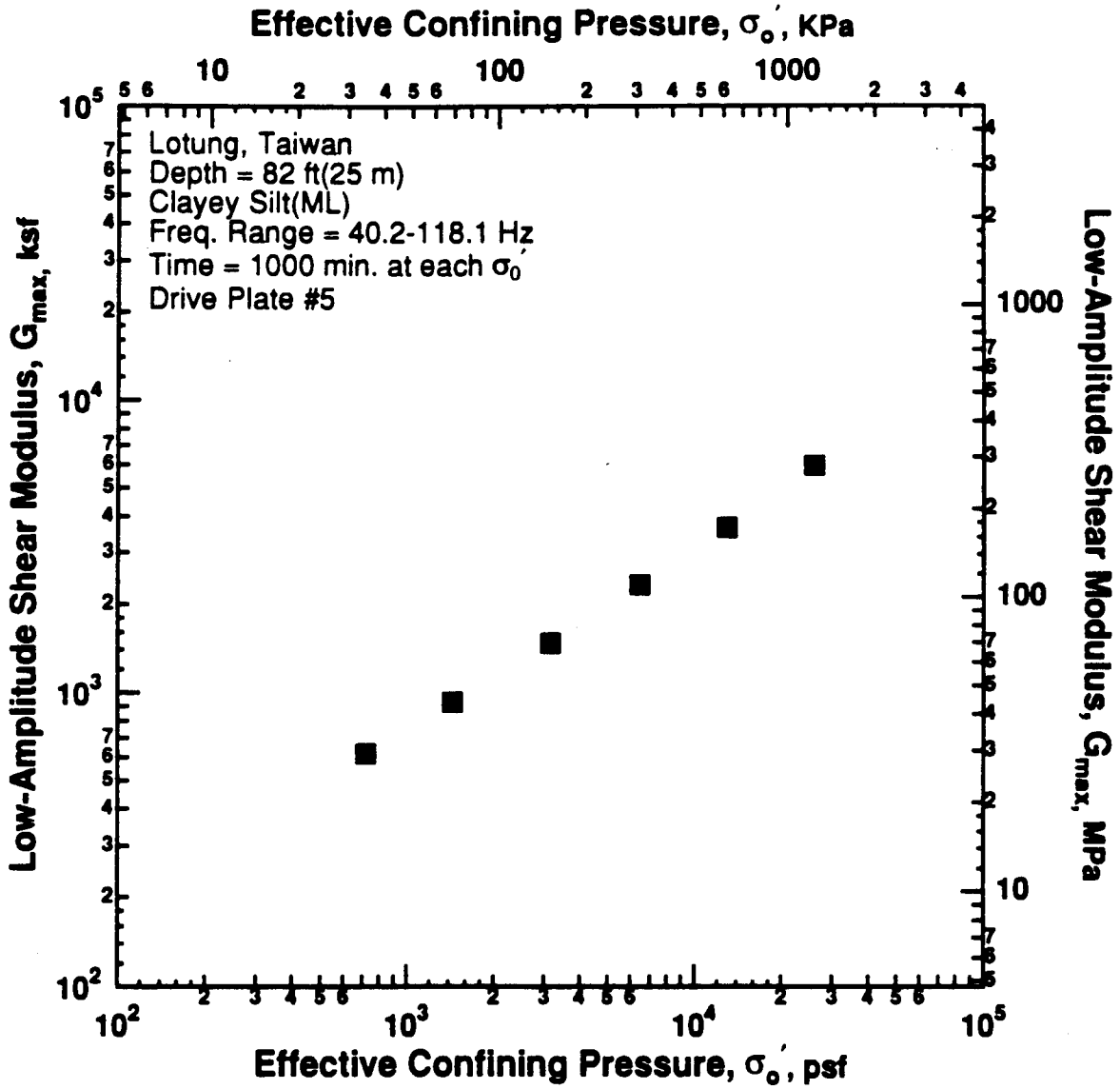

Figure 8.B.3.E-4
Variation in low-amplitude shear modulus with effective confining pressure from resonant column tests of sample T7 from borehole CH1.

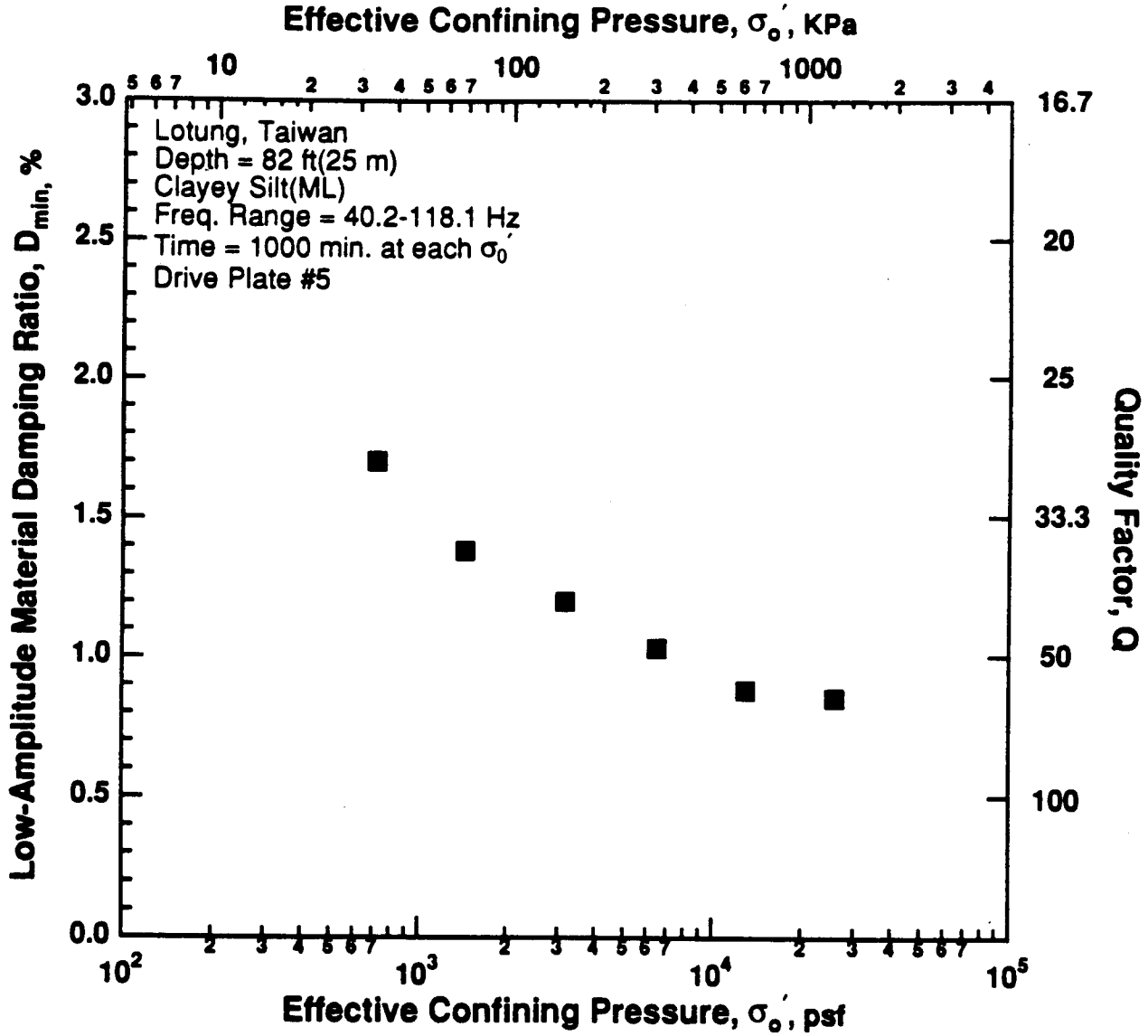

Figure 8.B.3.E-5
Variation in low-amplitude material damping ratio with effective confining pressure from resonant column tests of sample T7 from borehole CH1.

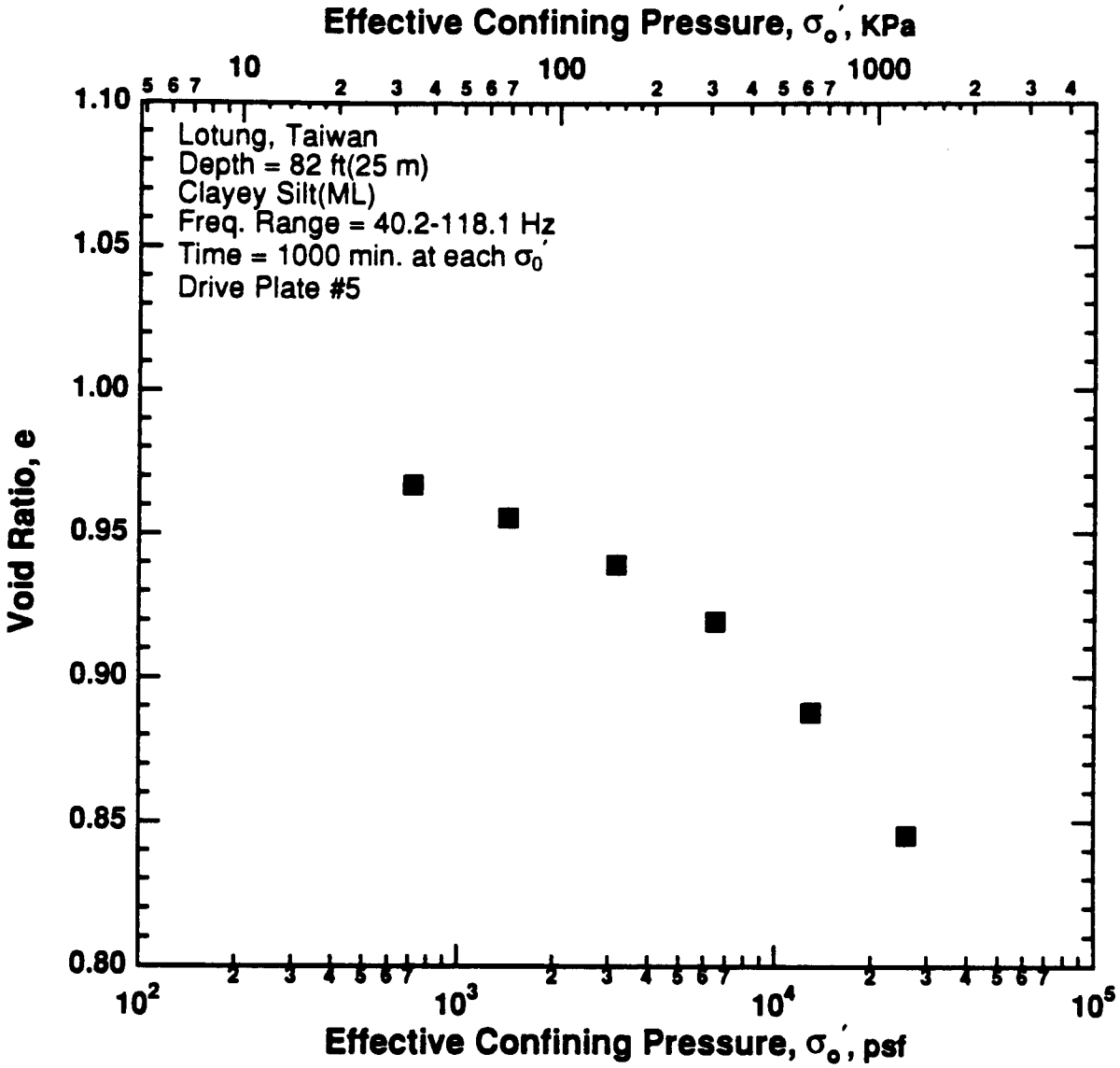

Figure 8.B.3.E-6
Variation in void ratio with effective confining pressure from resonant column tests of sample T7 from borehole CH1.

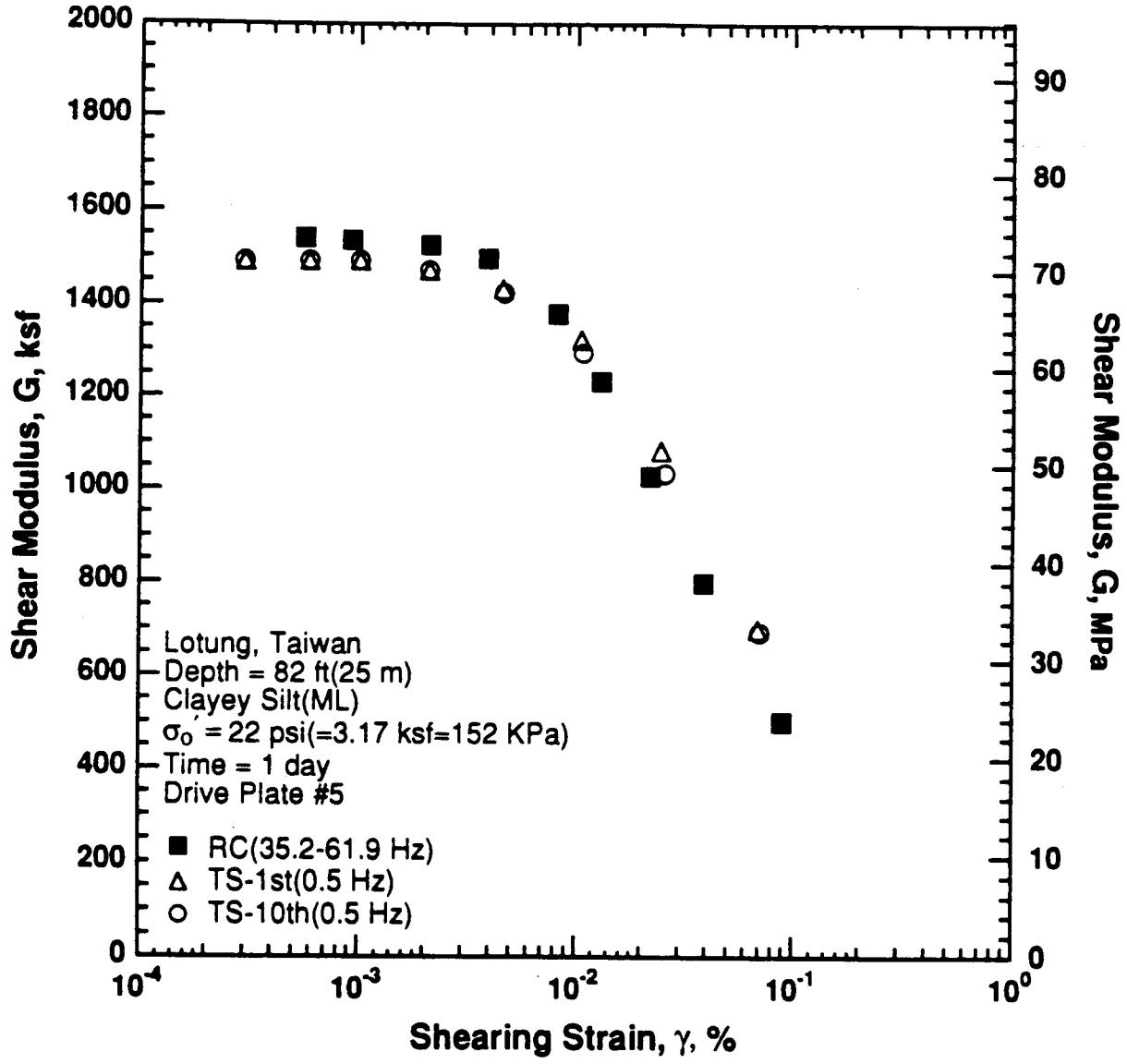

Figure 8.B.3.E-7
Variation in shear modulus with shearing strain at an effective confining pressure of 22 psi (3.17 ksf, 152 kPa) from RCTS tests of sample T7 from borehole CH1.

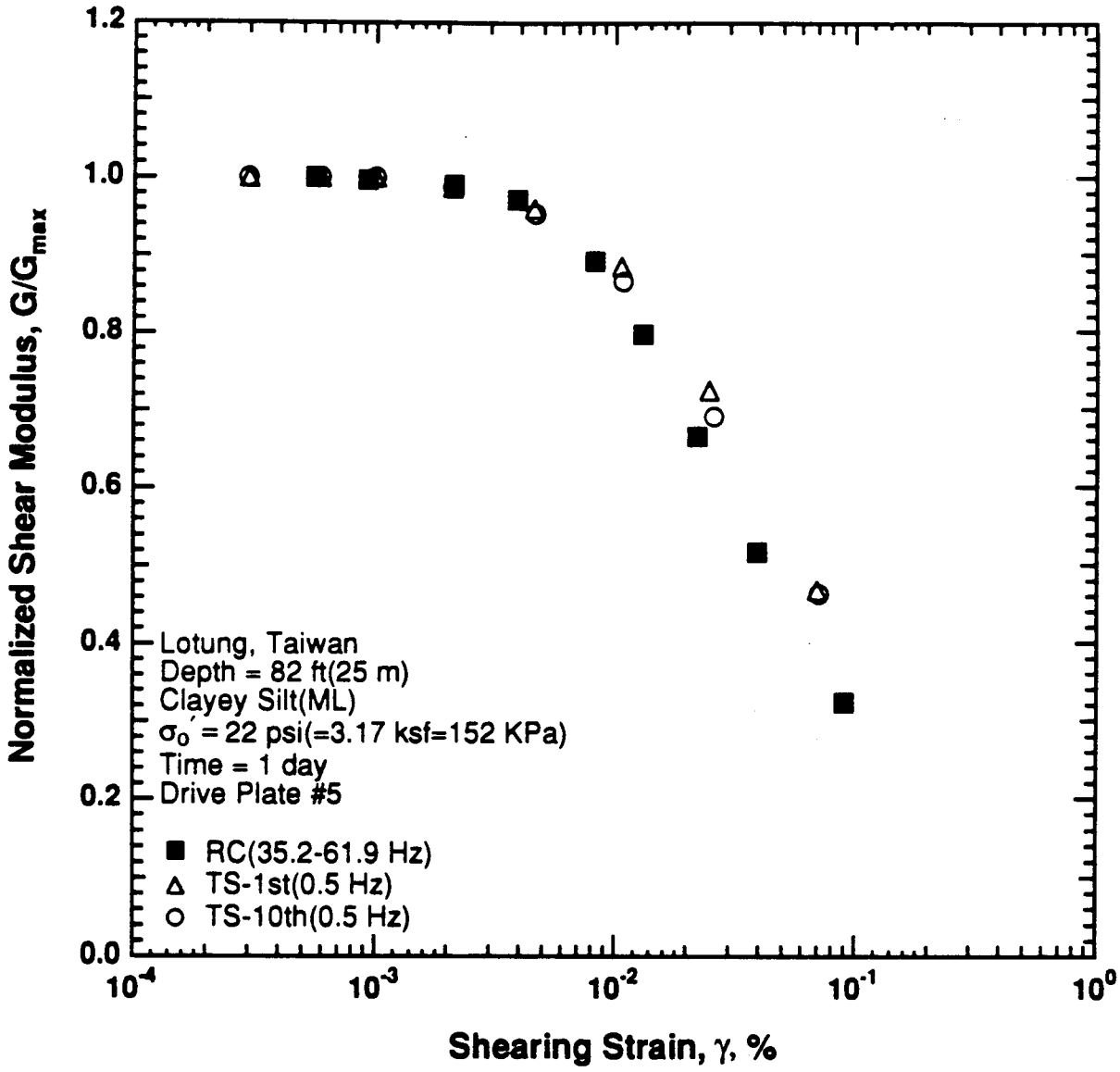

Figure 8.B.3.E-8
Variation in normalized shear modulus with shearing strain at an effective confining pressure of 22 psi (3.17 ksf, 152 kPa) from RCTS tests of sample T7 from borehole CH1.

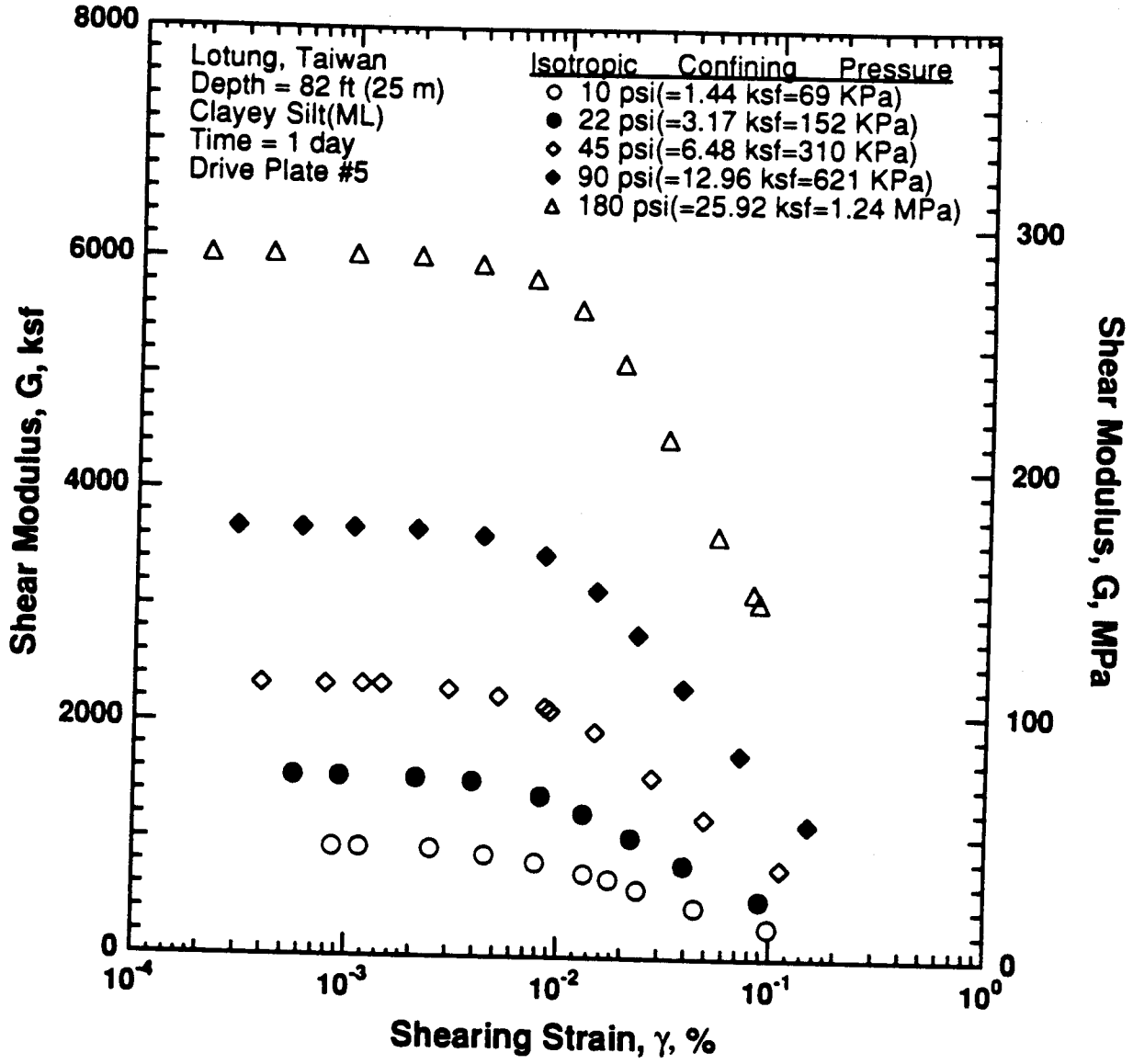

Figure 8.B.3.E-9
Variation in shear modulus with shearing strain and effective confining pressure from resonant column tests of sample T7 from borehole CH1.

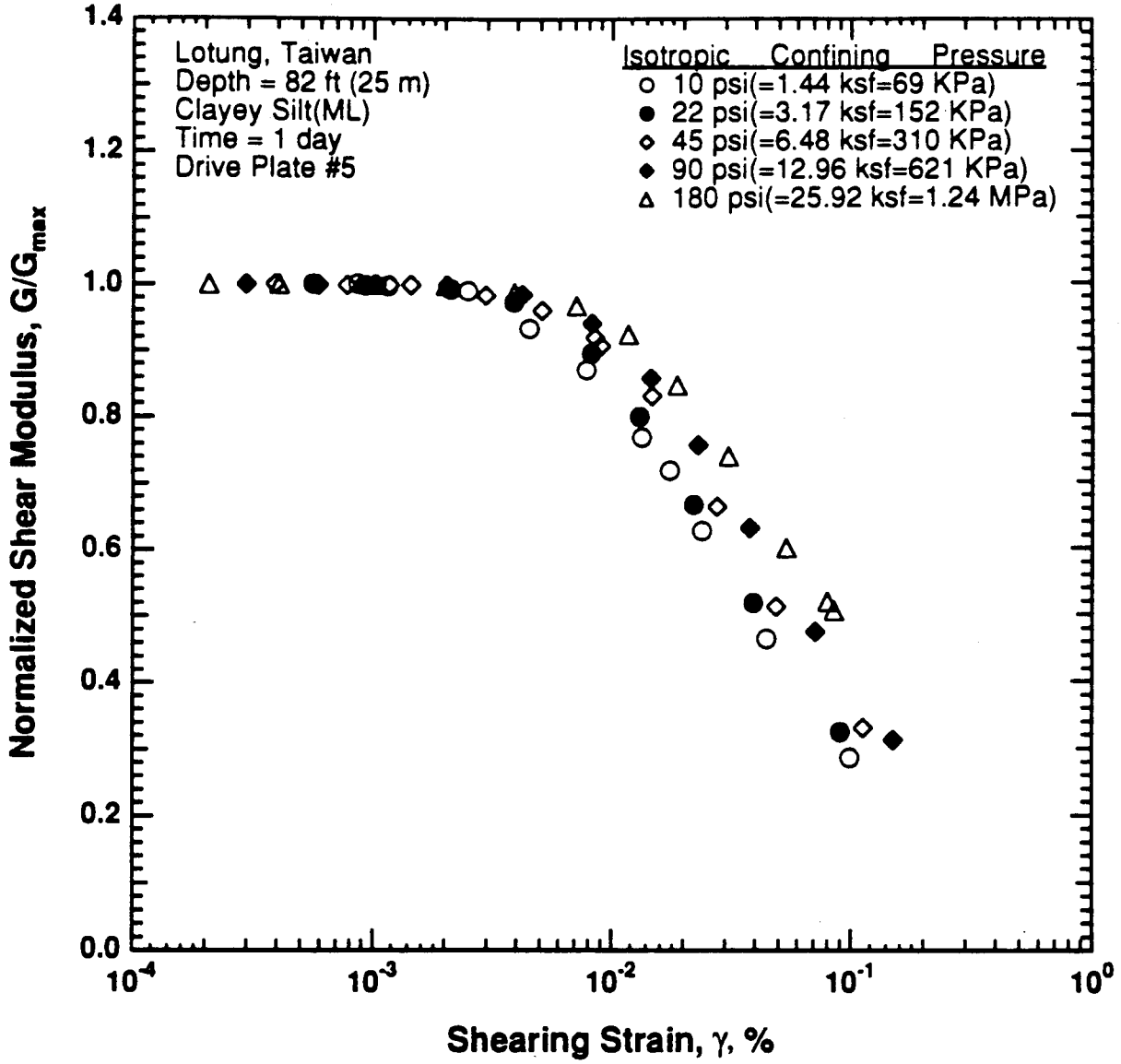

Figure 8.B.3.E-10
Comparison of the variation in normalized shear modulus with shearing strain and effective confining pressure from resonant column tests of sample T7 from borehole CH1.

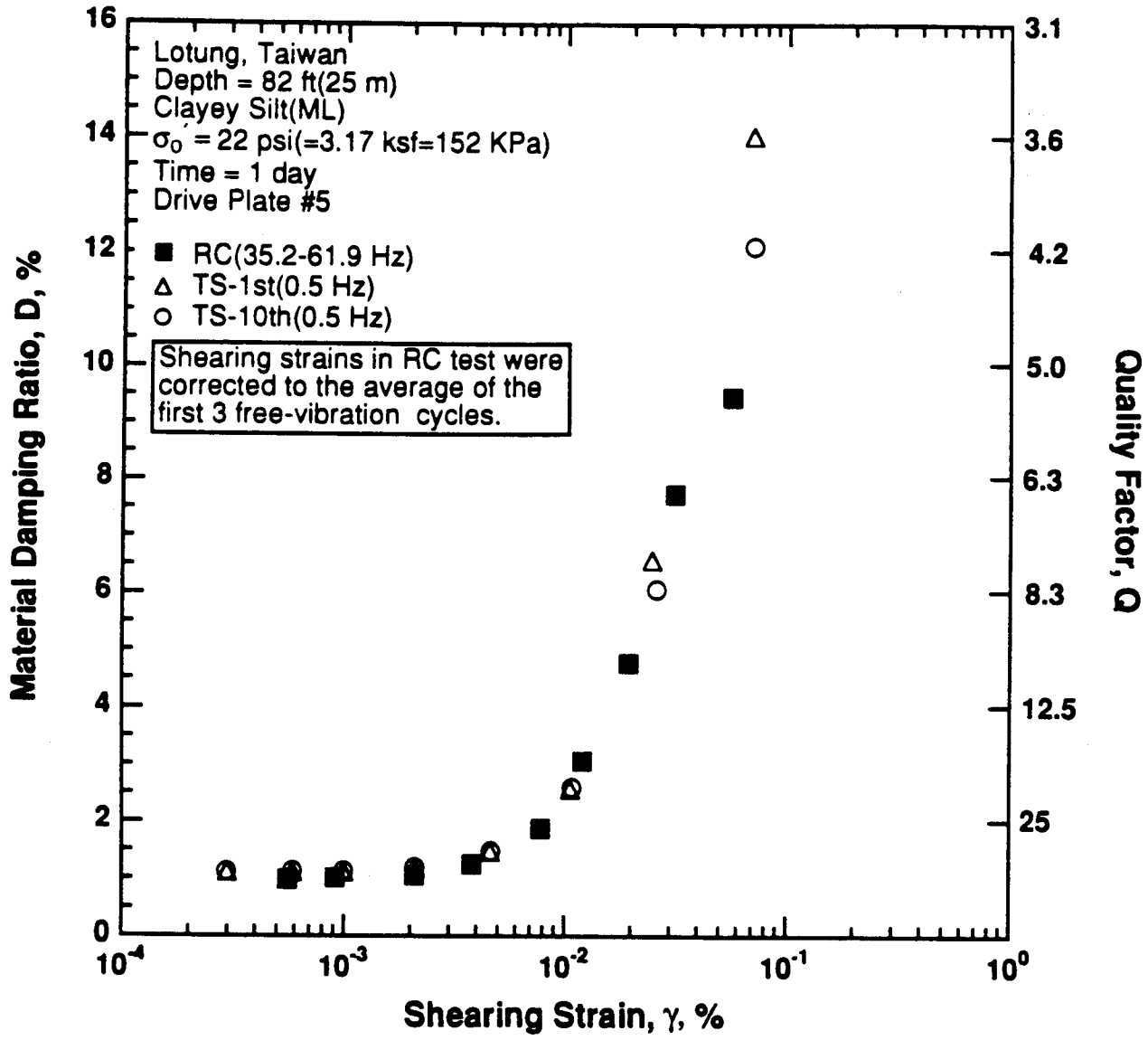

Figure 8.B.3.E-11
Variation in material damping ratio with shearing strain at an effective confining pressure of 22 psi (3.17 ksf, 152 kPa) from RCTS tests of sample T7 from borehole CH1.

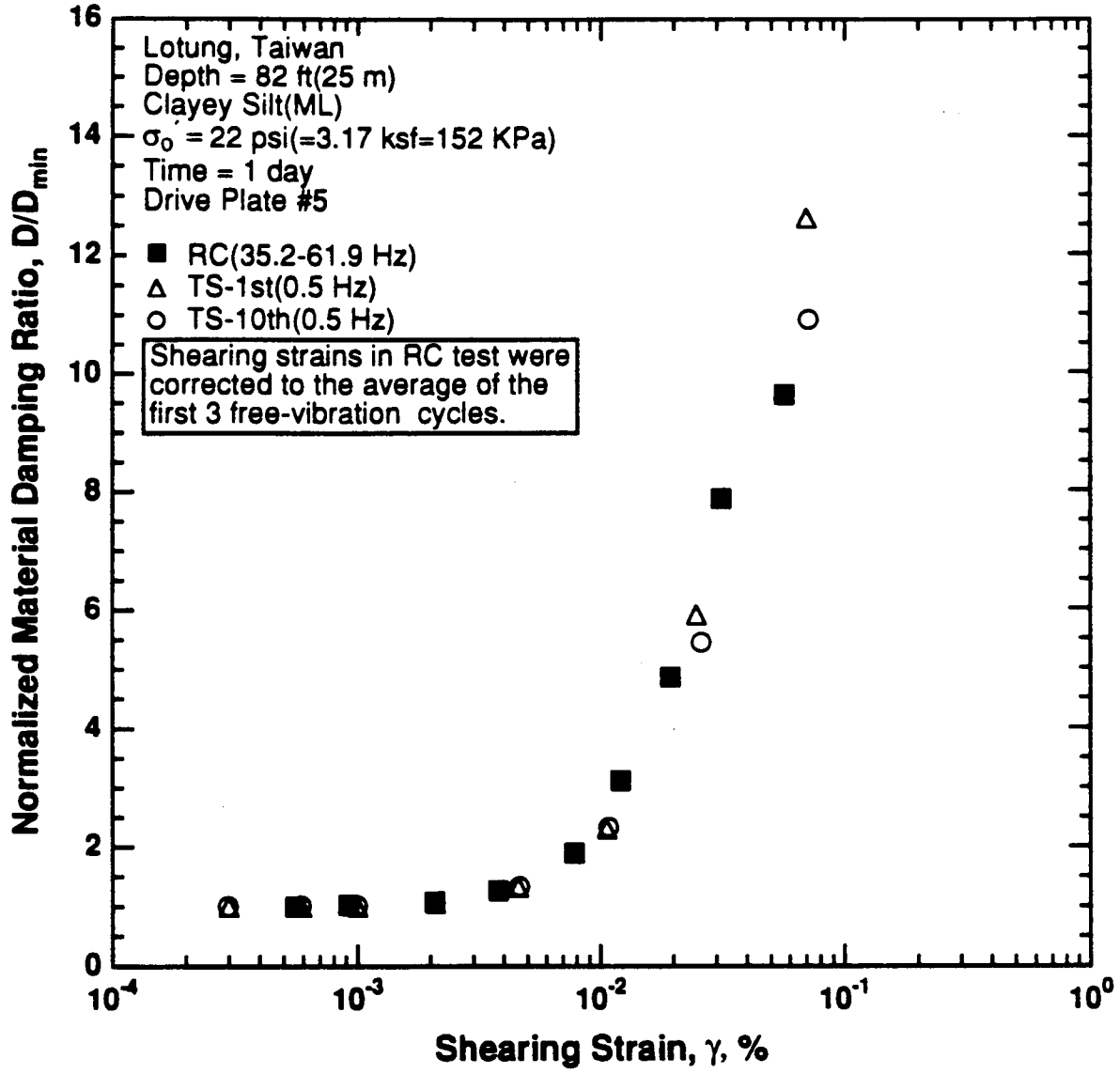

Figure 8.B.3.E-12
Variation in normalized material damping ratio with shearing strain at an effective confining pressure of 22 psi (3.17 ksf, 152 kPa) from RCTS tests of sample T7 from borehole CH1.

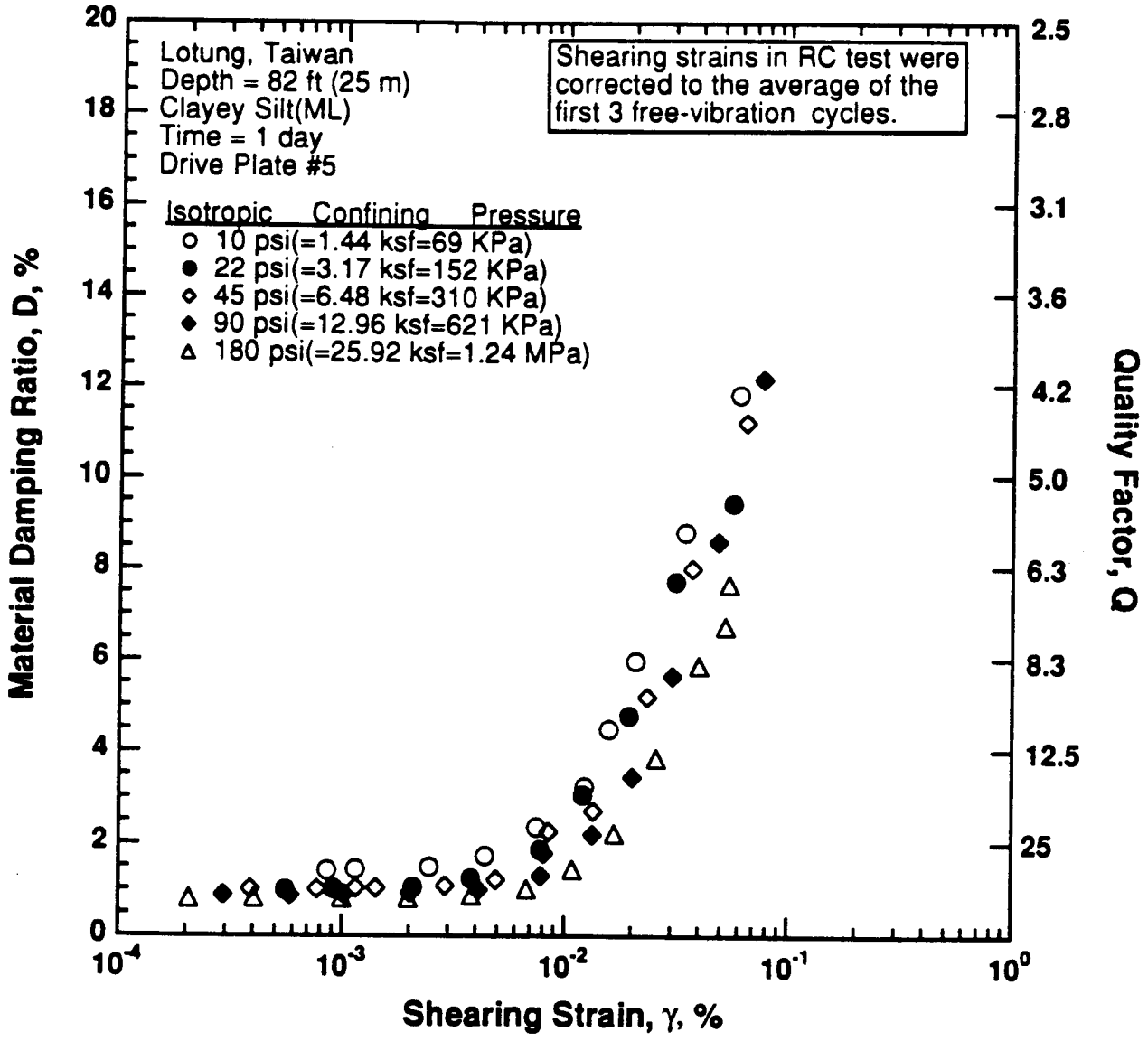

Figure 8.B.3.E-13
Variation in material damping ratio with shearing strain and effective confining pressure from resonant column tests of sample T7 from borehole CH1.

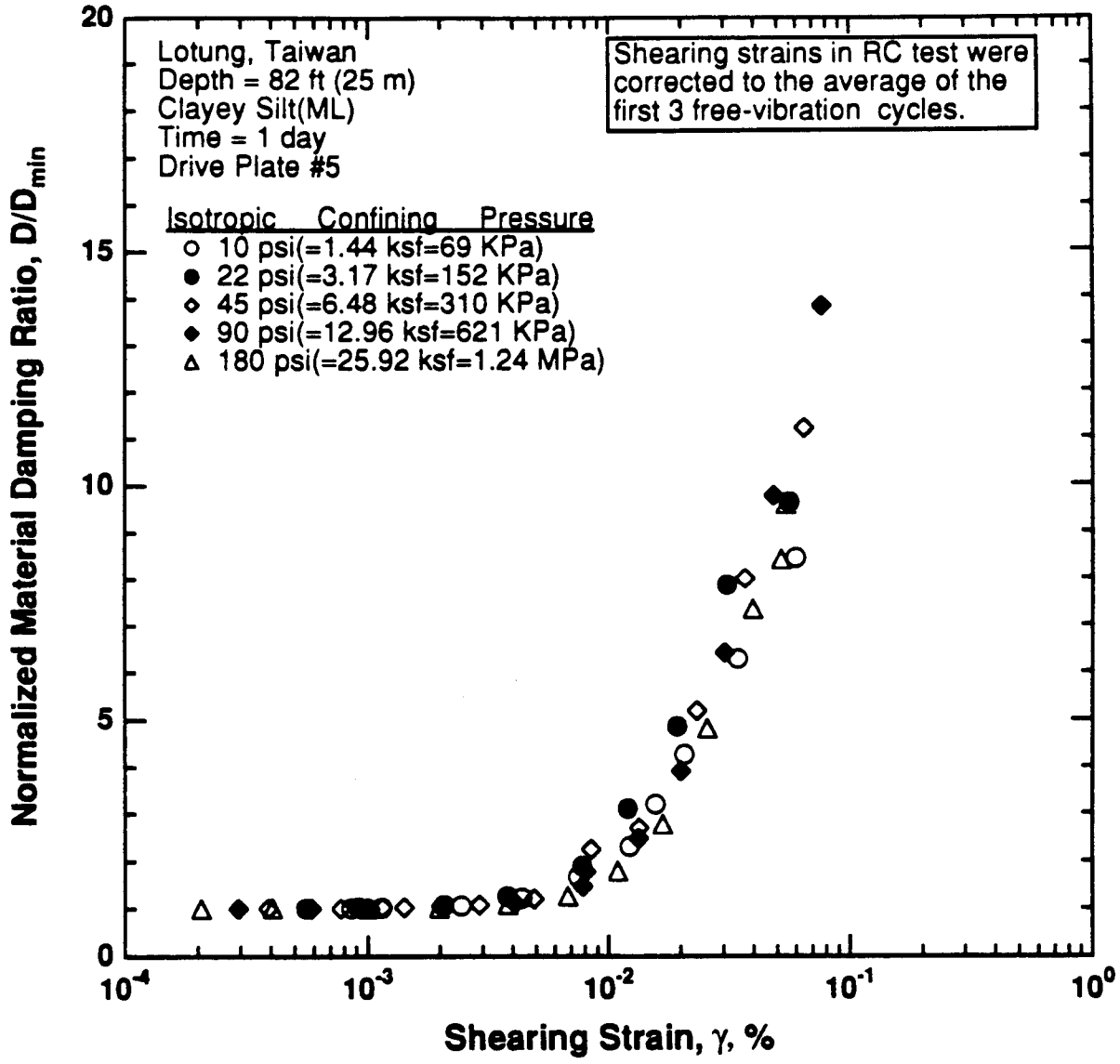

Figure 8.B.3.E-14
Comparison of the variation in normalized material damping ratio with shearing strain and effective confining pressure from resonant column tests of sample T7 from borehole CH1.

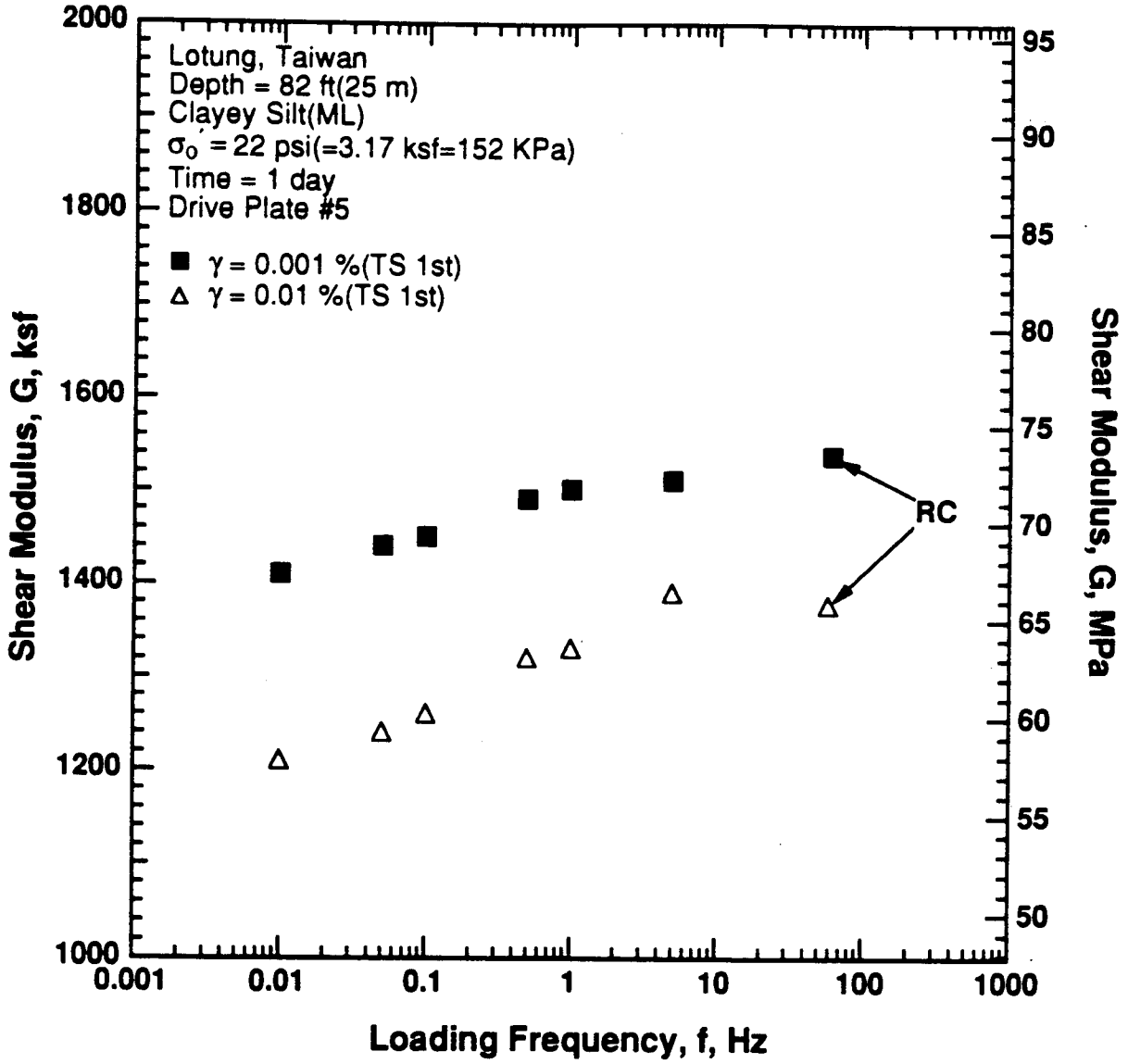

Figure 8.B.3.E-15
Variation in shear modulus with loading frequency and shearing strain at an effective confining pressure of 22 psi (3.17 ksf, 152 kPa) from RCTS tests of sample T7 from borehole CH1.

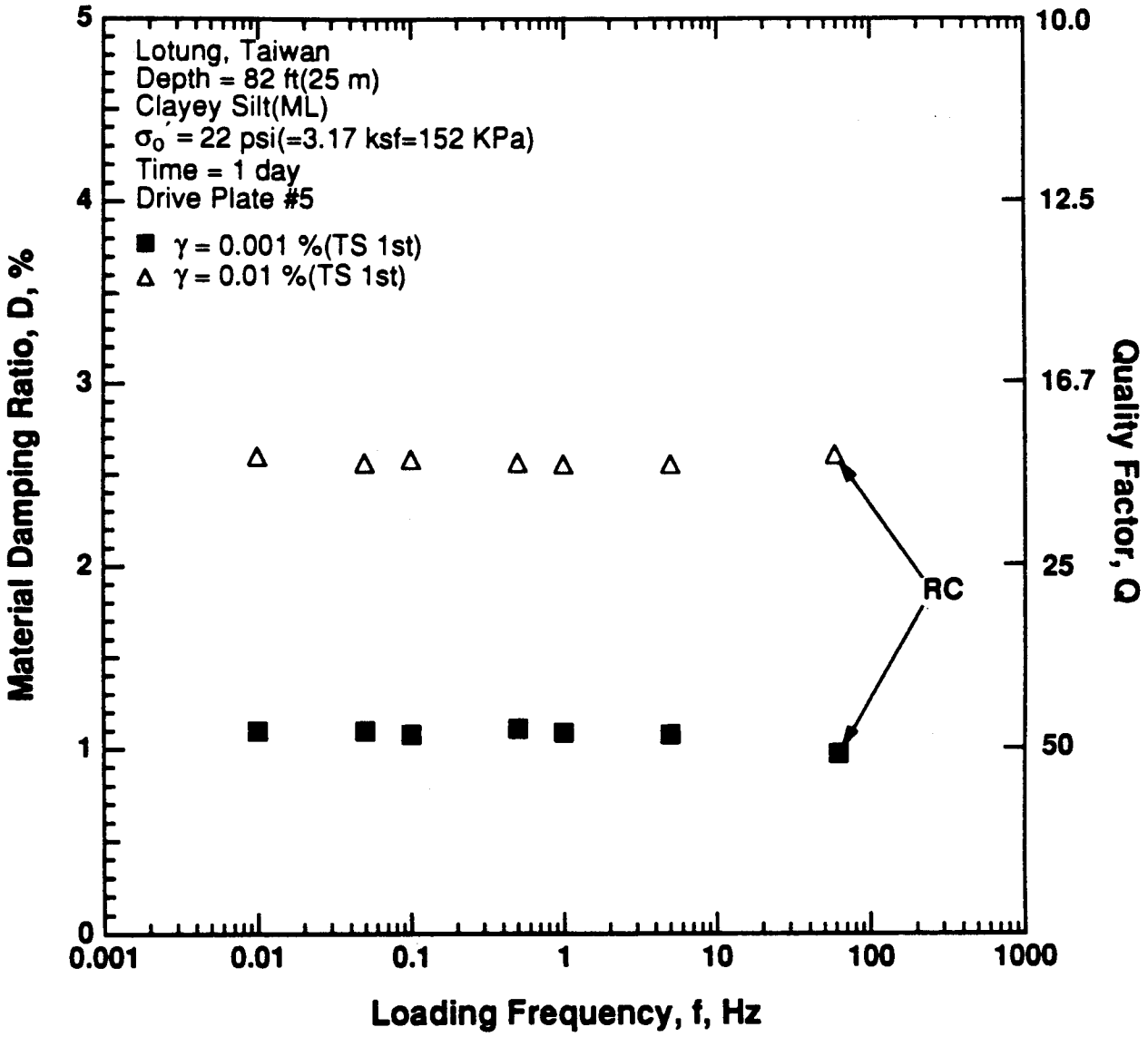

Figure 8.B.3.E-16
Variation in material damping ratio with loading frequency and shearing strain at an effective confining pressure of 22 psi (3.17 ksf, 152 kPa) from RCTS tests of sample T7 from borehole CH1.

APPENDIX 8.B.3.F
DYNAMIC TESTS OF SAMPLE T9 FROM BOREHOLE CH2, DEPTH = 93.5 FT (28.5 M)

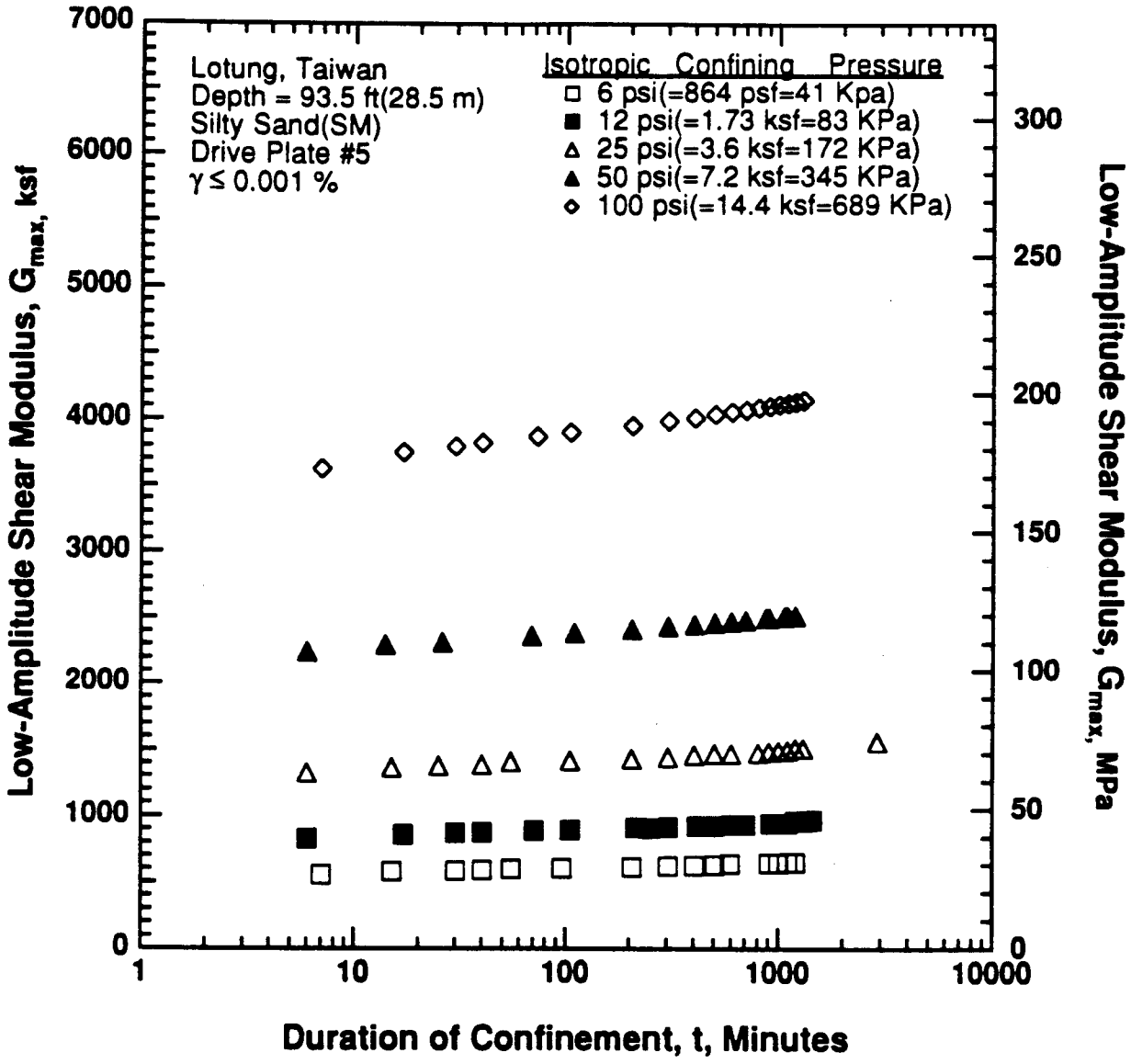

Figure 8.B.3.F-1
Variation in low-amplitude shear modulus with magnitude and duration of isotropic confining pressure from resonant column tests of sample T9 from borehole CH2.

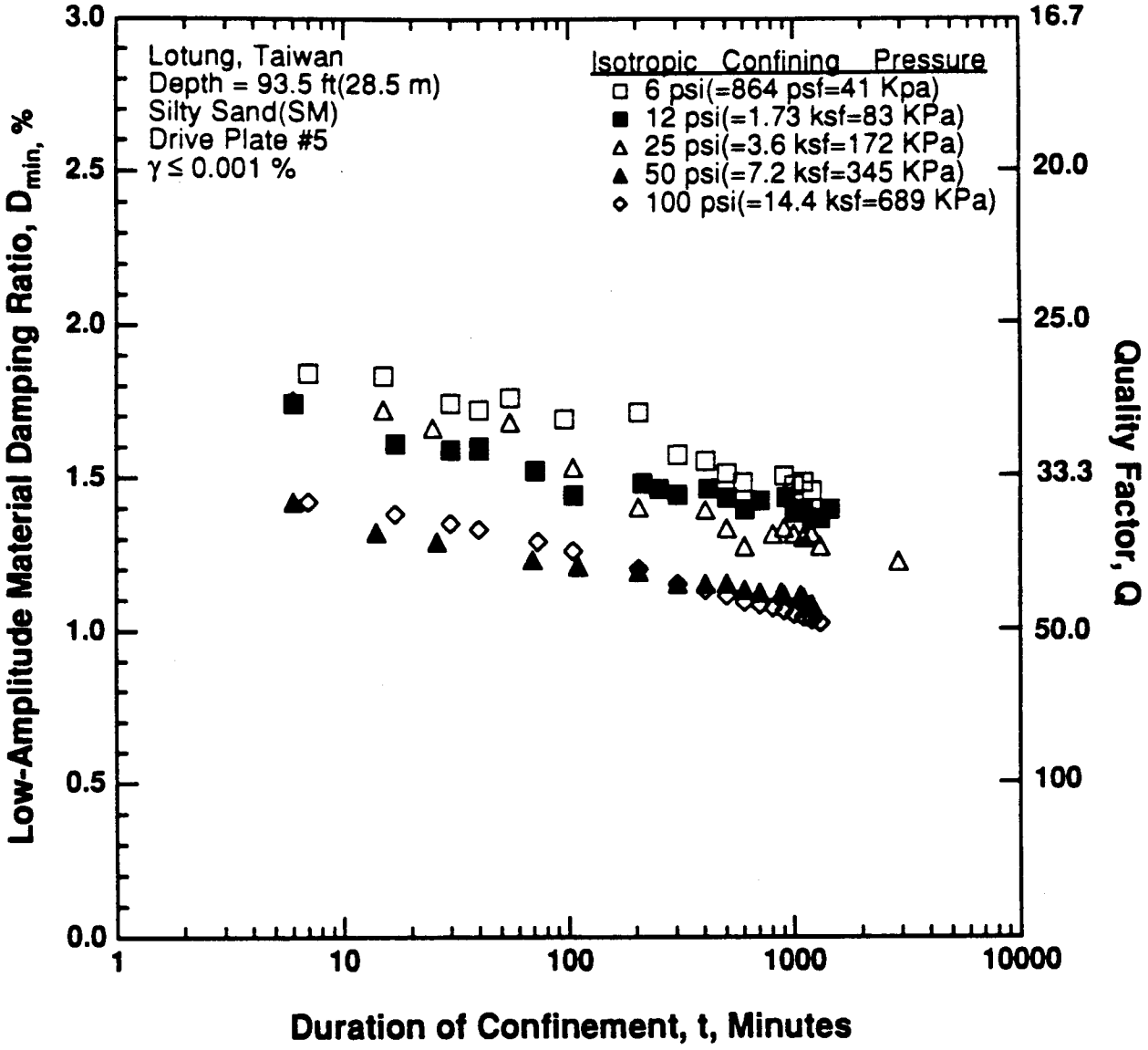

Figure 8.B.3.F-2
Variation in low-amplitude material damping ratio with magnitude and duration of isotropic confining pressure from resonant column tests of sample T9 from borehole CH2.

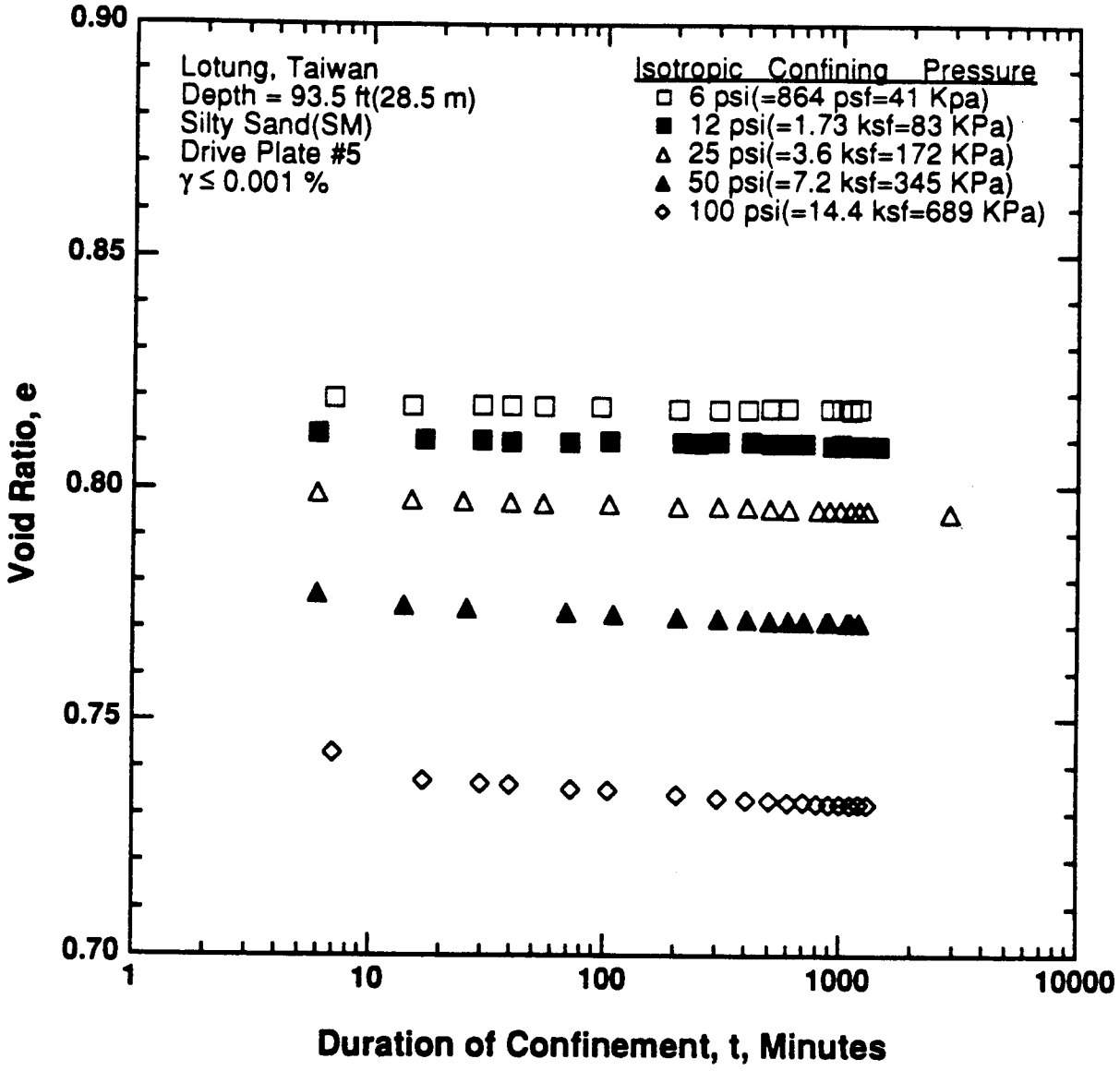

Figure 8.B.3.F-3
Variation in void ratio with magnitude and duration of isotropic confining pressure from resonant column tests of sample T9 from borehole CH2.

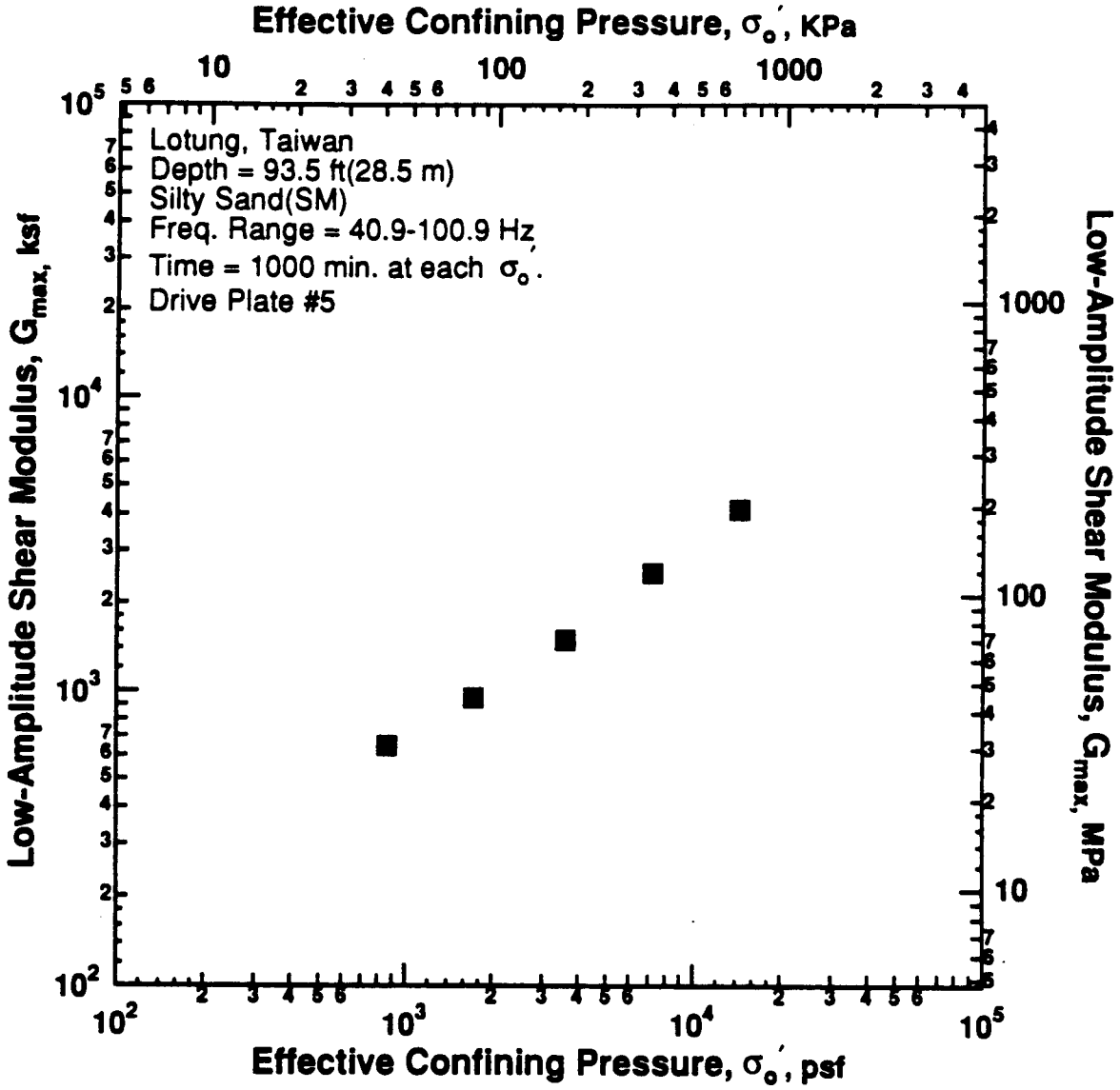

Figure 8.B.3.F-4
Variation in low-amplitude shear modulus with effective confining pressure from resonant column tests of sample T9 from borehole CH2.

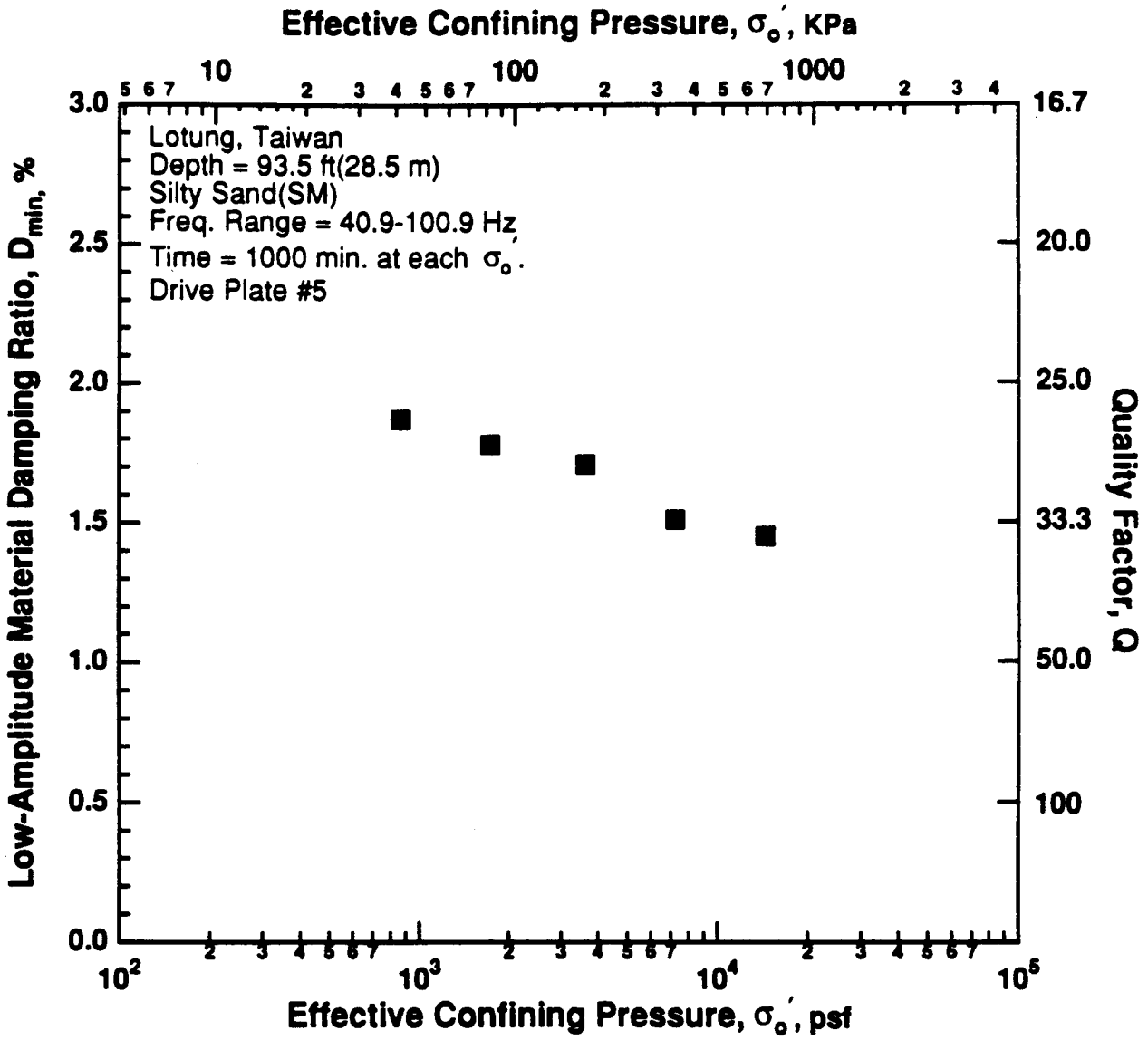

Figure 8.B.3.F-5
Variation in low-amplitude material damping ratio with effective confining pressure from resonant column tests of sample T9 from borehole CH2.

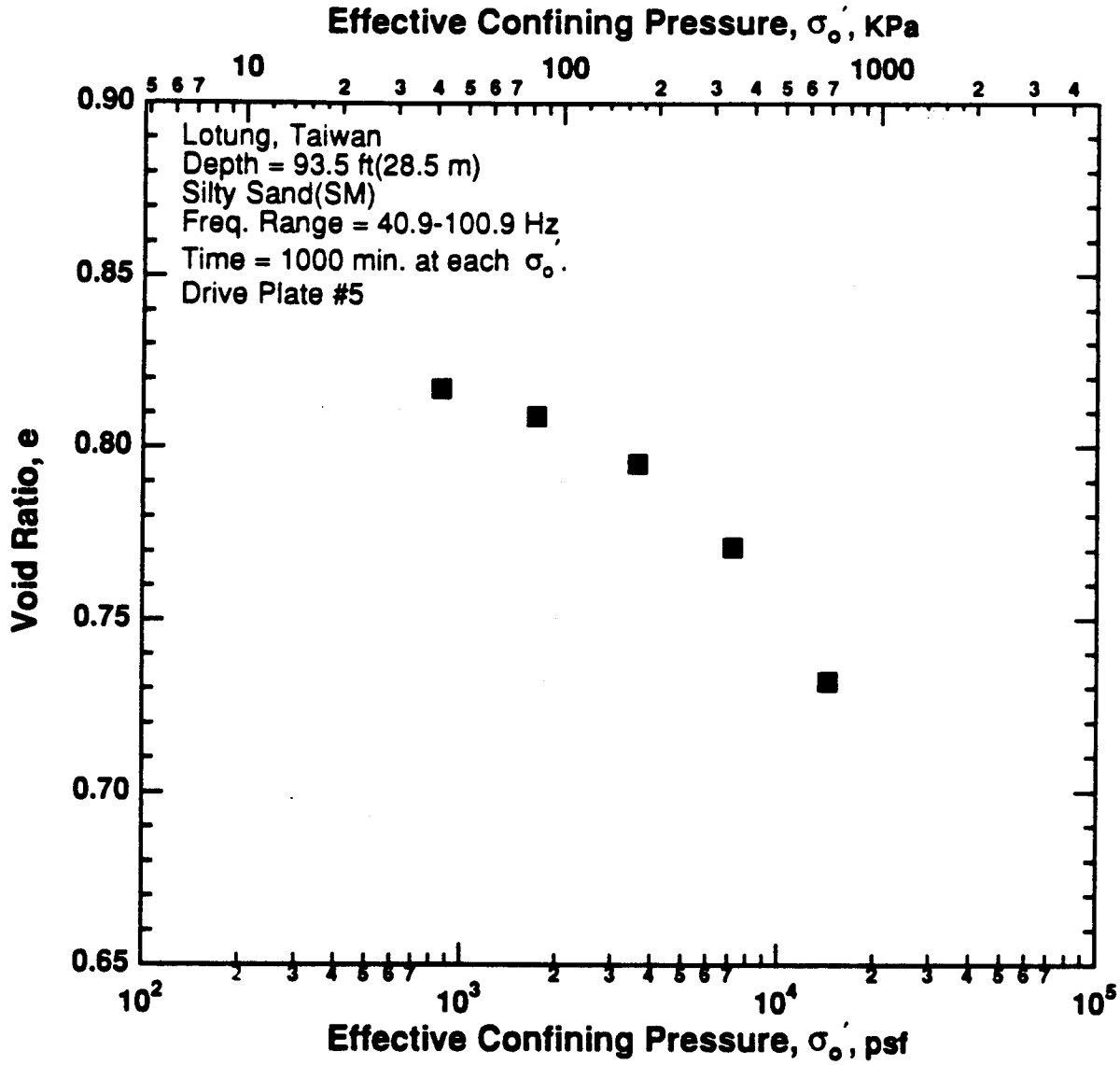

Figure 8.B.3.F-6
Variation in void ratio with effective confining pressure from resonant column tests of sample T9 from borehole CH2.

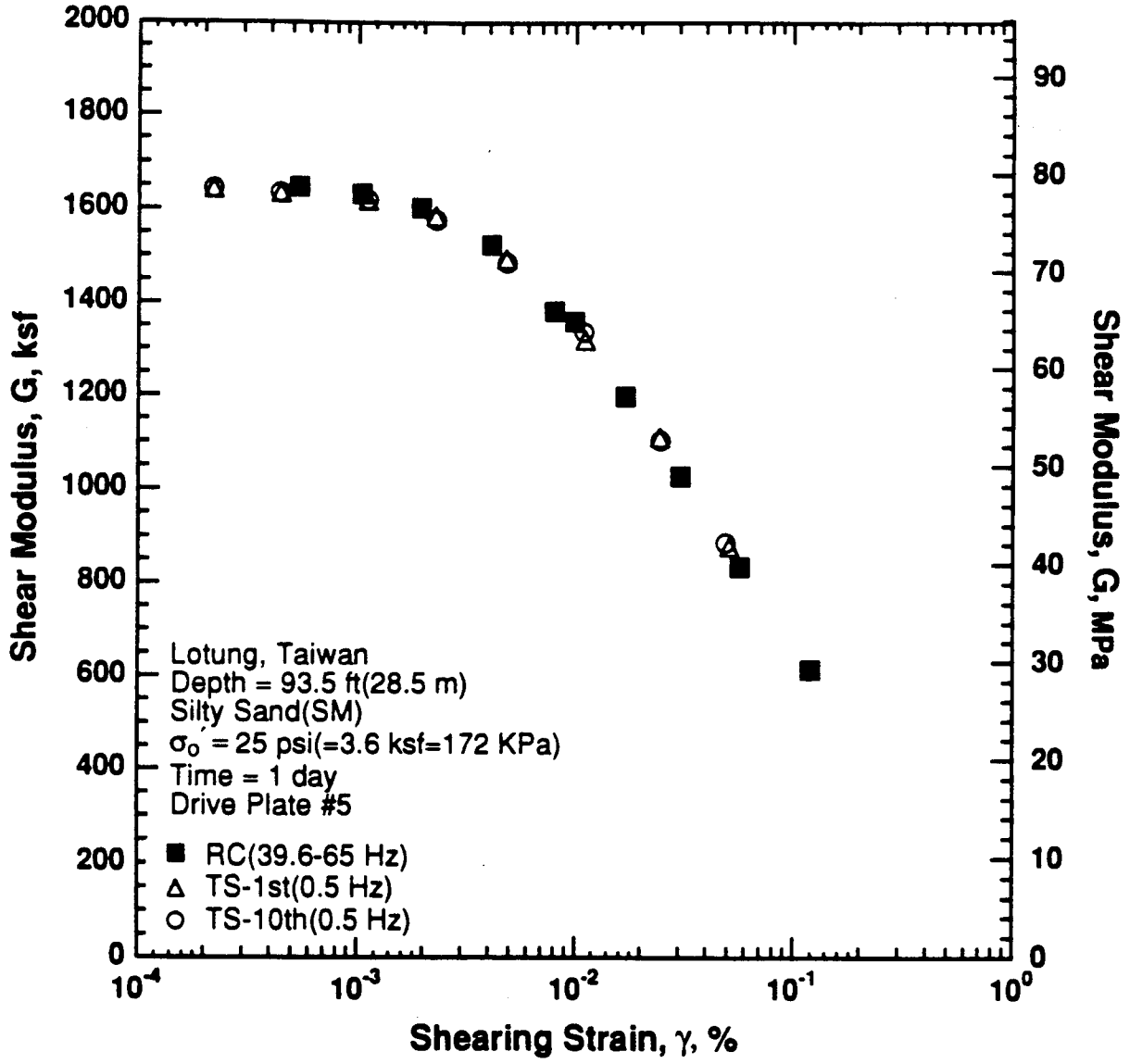

Figure 8.B.3.F-7
Variation in shear modulus with shearing strain at an effective confining pressure of 25 psi (3.6 ksf, 172 kPa) from RCTS tests of sample T9 from borehole CH2.

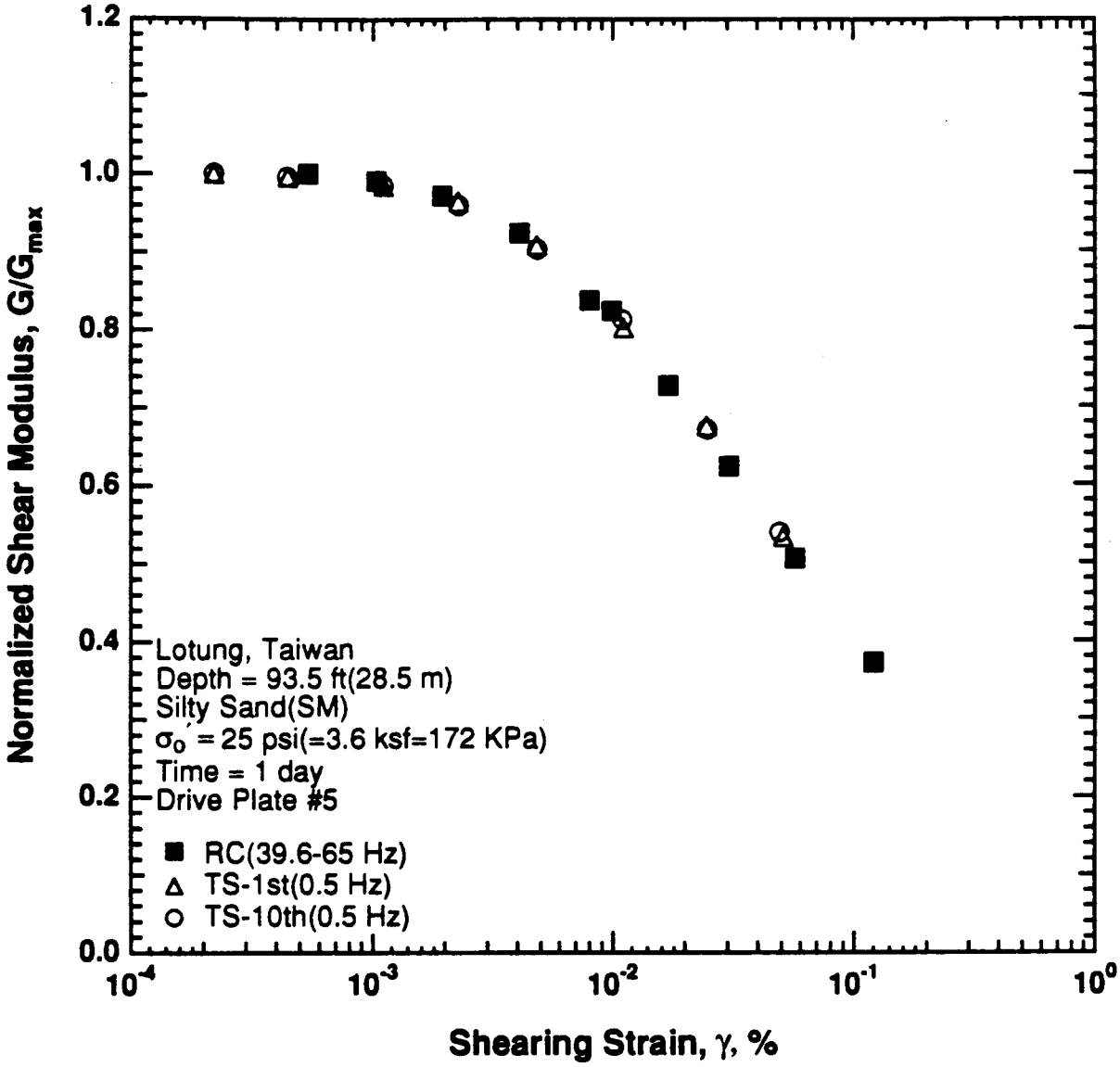

Figure 8.B.3.F-8
Variation in normalized shear modulus with shearing strain at an effective confining pressure of 25 psi (3.6 ksf, 172 kPa) from RCTS tests of sample T9 from borehole CH2.

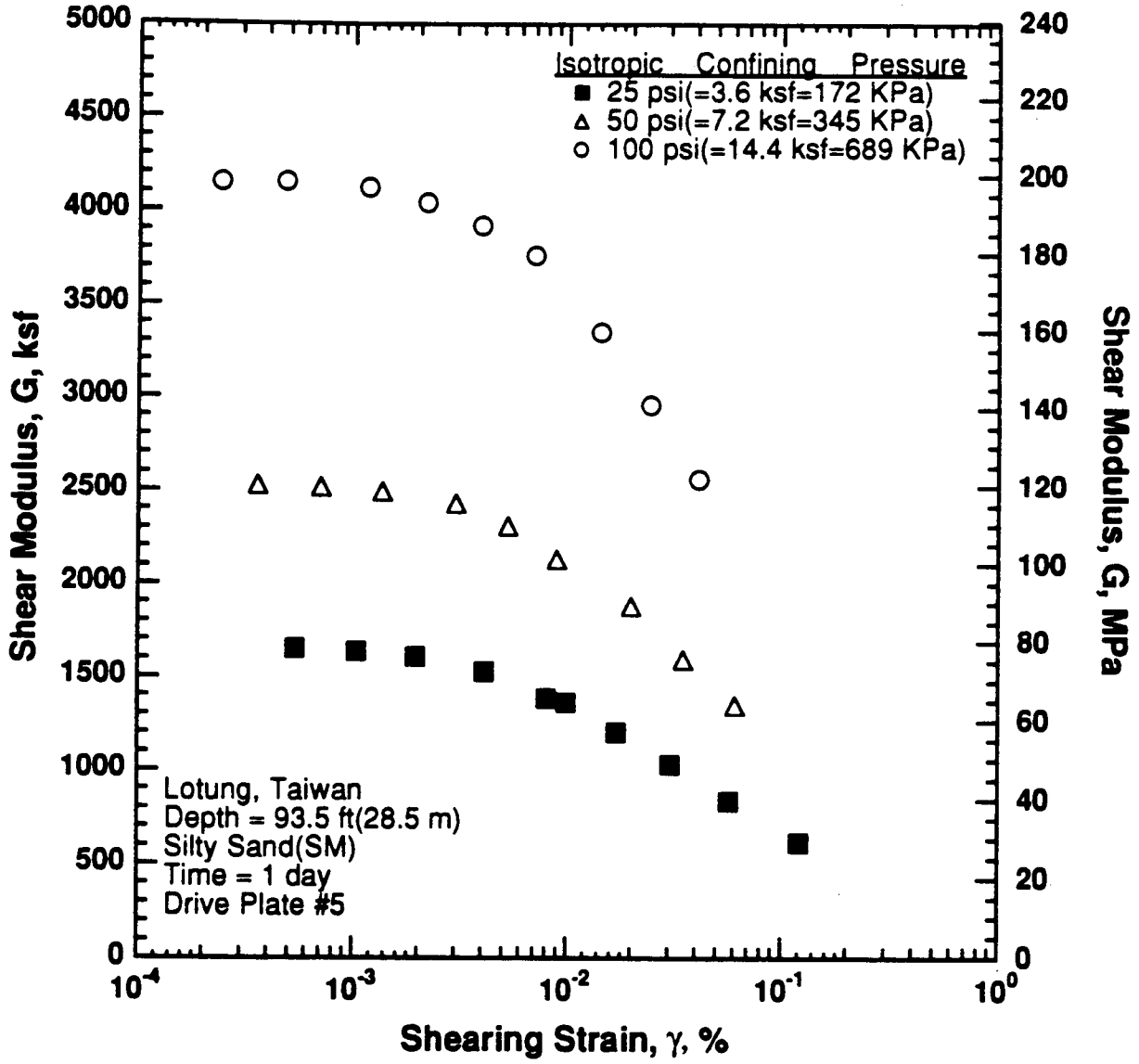

Figure 8.B.3.F-9
Variation in shear modulus with shearing strain and effective confining pressure from resonant column tests of sample T9 from borehole CH2.

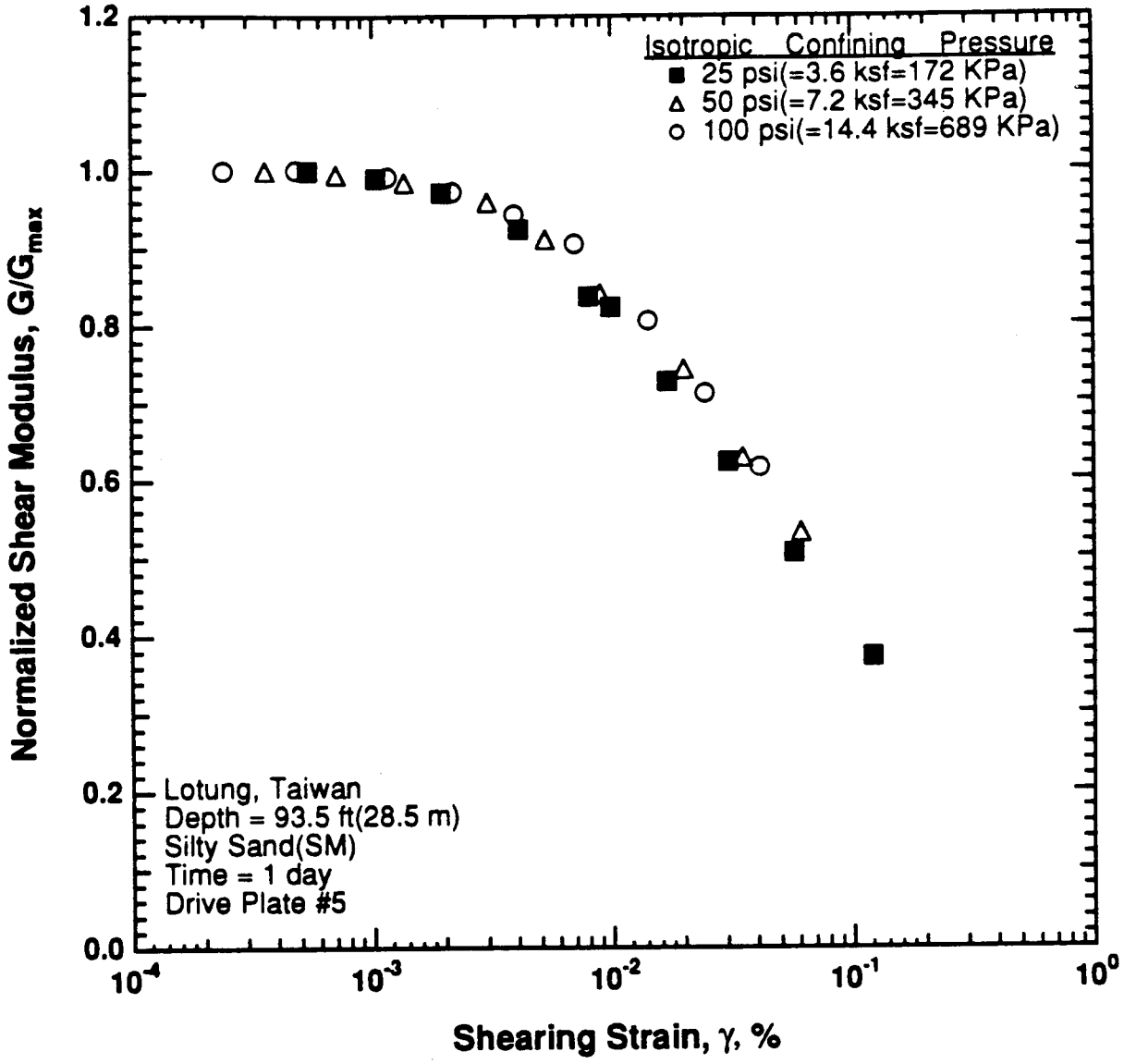

Figure 8.B.3.F-10
Comparison of variation in normalized shear modulus with shearing strain and effective confining pressure from resonant column tests of sample T9 from borehole CH2.

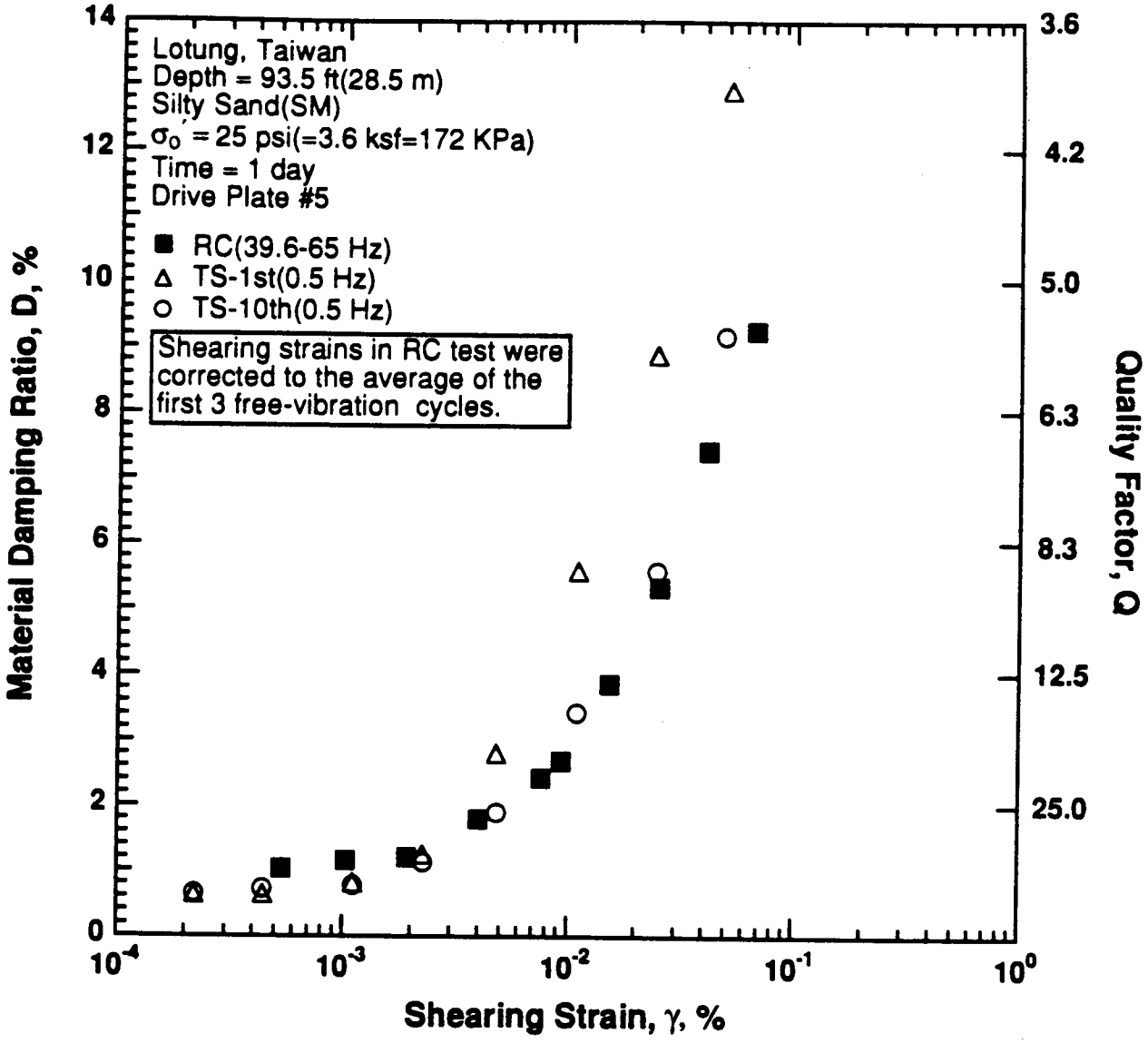

Figure 8.B.3.F-11
Variation in material damping ratio with shearing strain at an effective confining pressure of 25 psi (3.6 ksf, 172 kPa) from RCTS tests of sample T9 from borehole CH2.

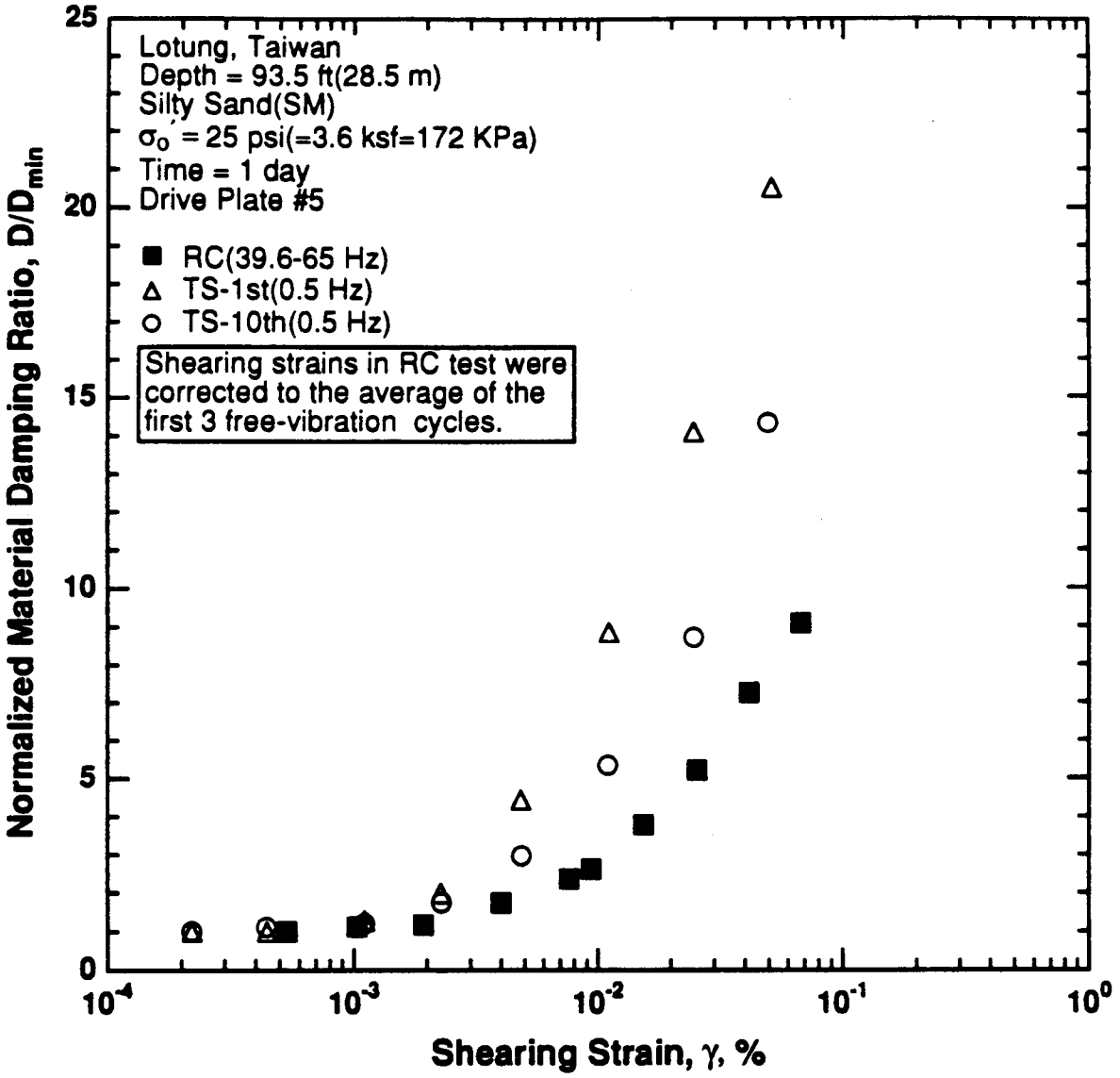

Figure 8.B.3.F-12
Variation in normalized material damping ratio with shearing strain at an effective confining pressure of 25 psi (3.6 ksf, 172 kPa) from RCTS tests of sample T9 from borehole CH2.

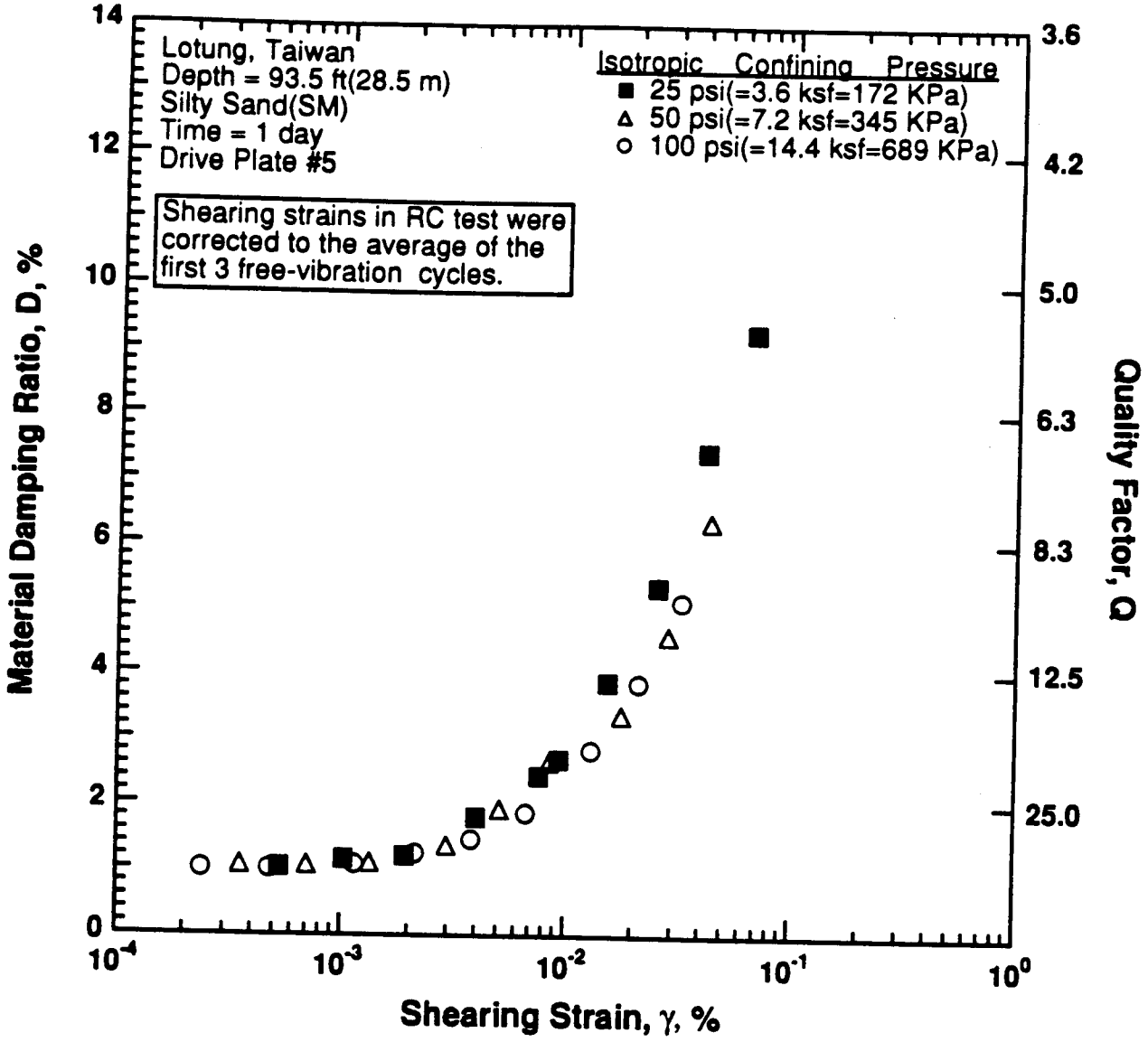

Figure 8.B.3.F-13
Variation in material damping ratio with shearing strain and effective confining pressure from resonant column tests of sample T9 from borehole CH2.

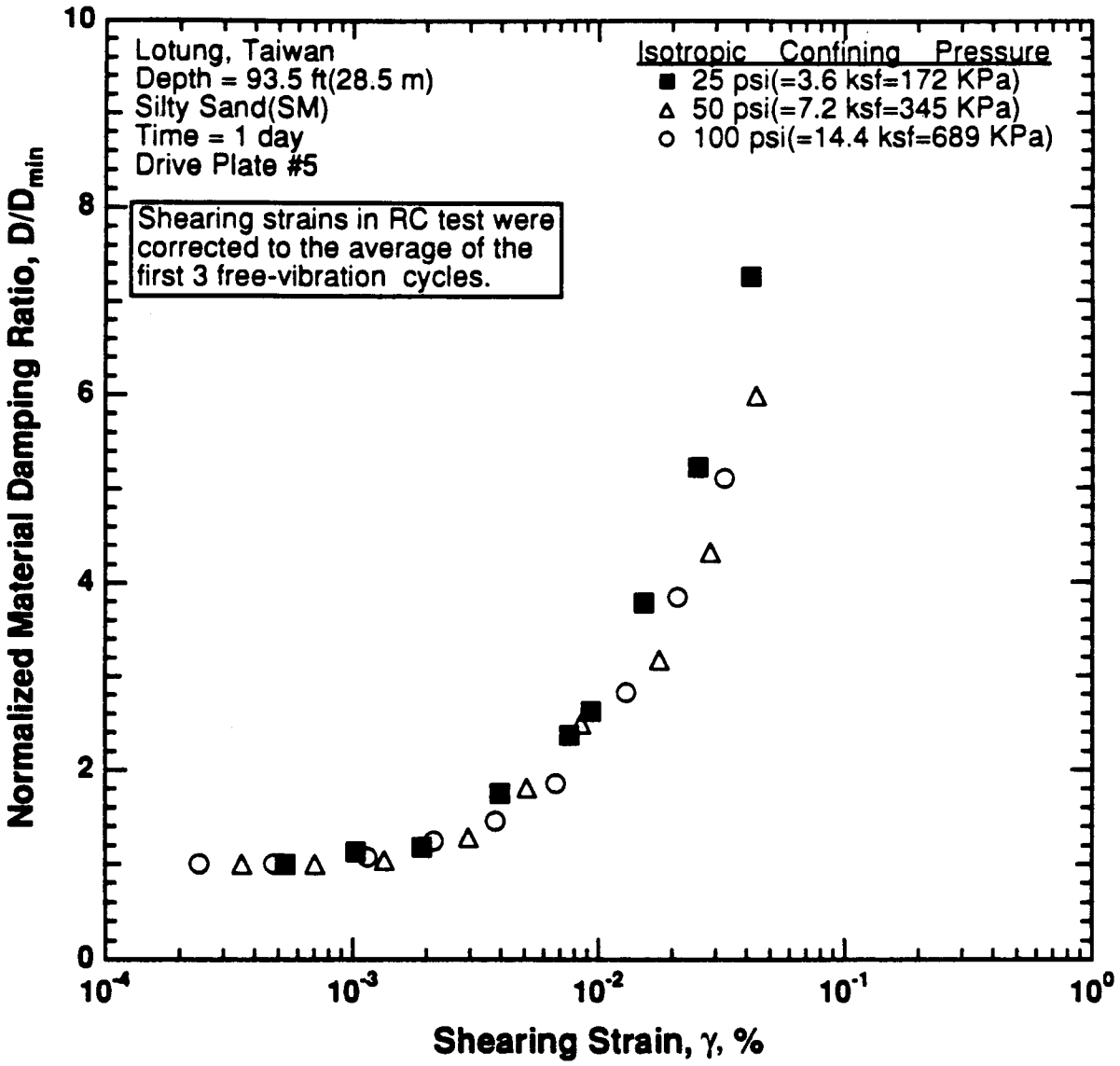

Figure 8.B.3.F-14
Comparison of the variation in normalized material damping ratio with shearing strain and effective confining pressure from resonant column tests of sample T9 from borehole CH2.

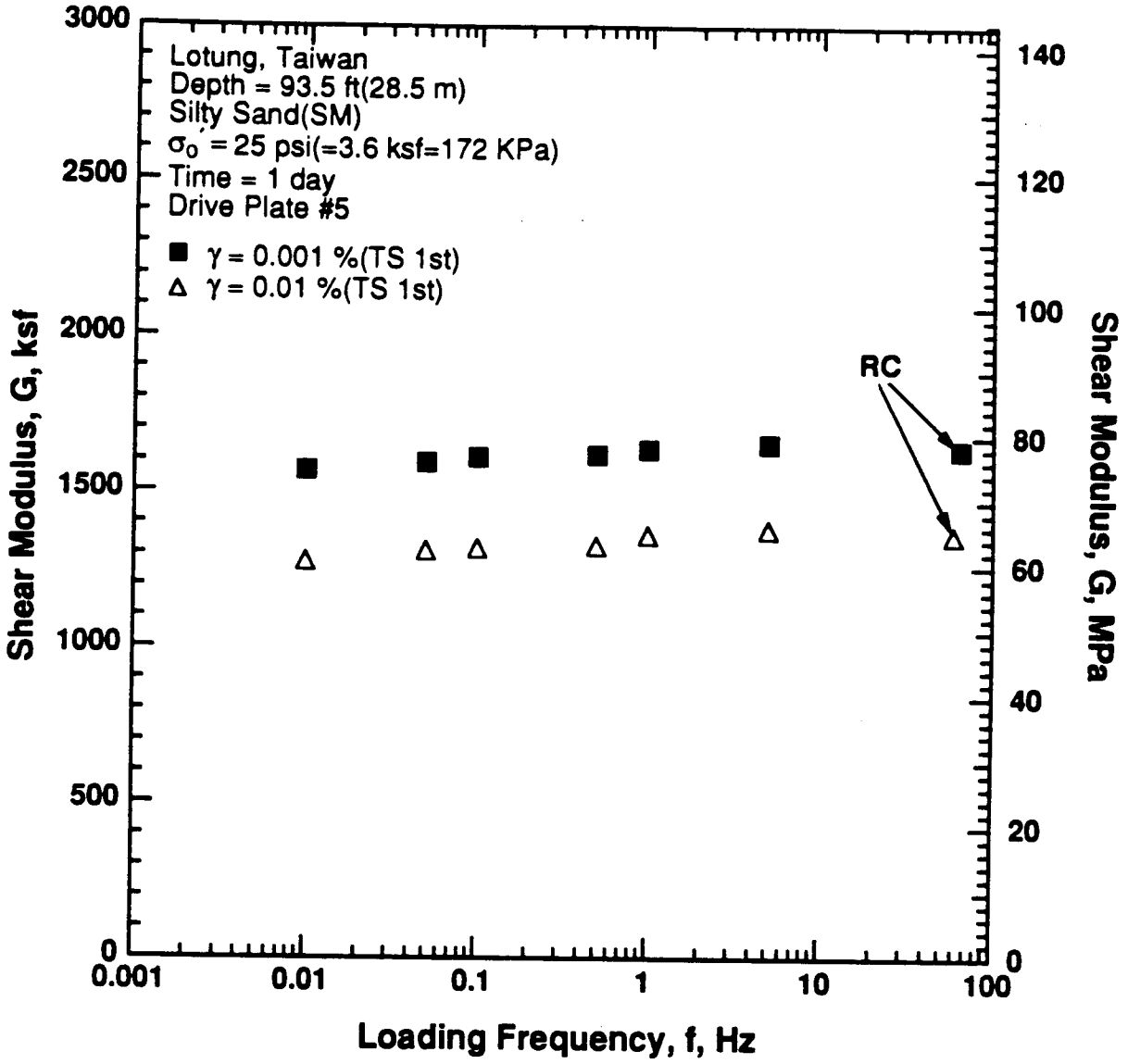

Figure 8.B.3.F-15
Variation in shear modulus with loading frequency and shearing strain at an effective confining pressure of 25 psi (3.6 ksf, 172 kPa) from RCTS tests of sample T9 from borehole CH2.

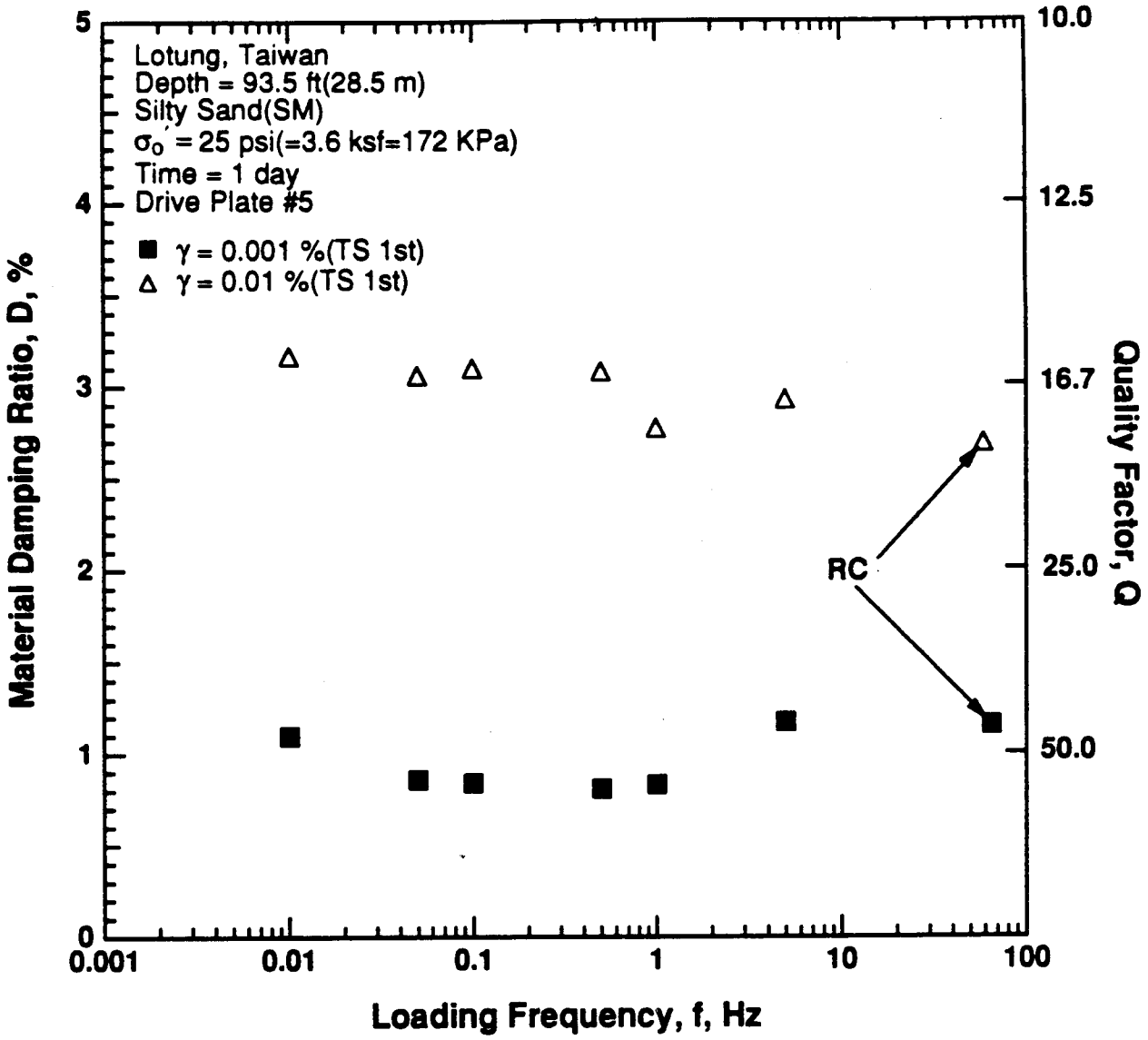

Figure 8.B.3.F-16
Variation in material damping ratio with loading frequency and shearing strain at an effective confining pressure of 25 psi (3.6 ksf, 172 kPa) from RCTS tests of sample T9 from borehole CH2.

APPENDIX 8.B.3.G
DYNAMIC TESTS OF SAMPLE T8 FROM BOREHOLE CH1, DEPTH = 113 FT (34.4 M)

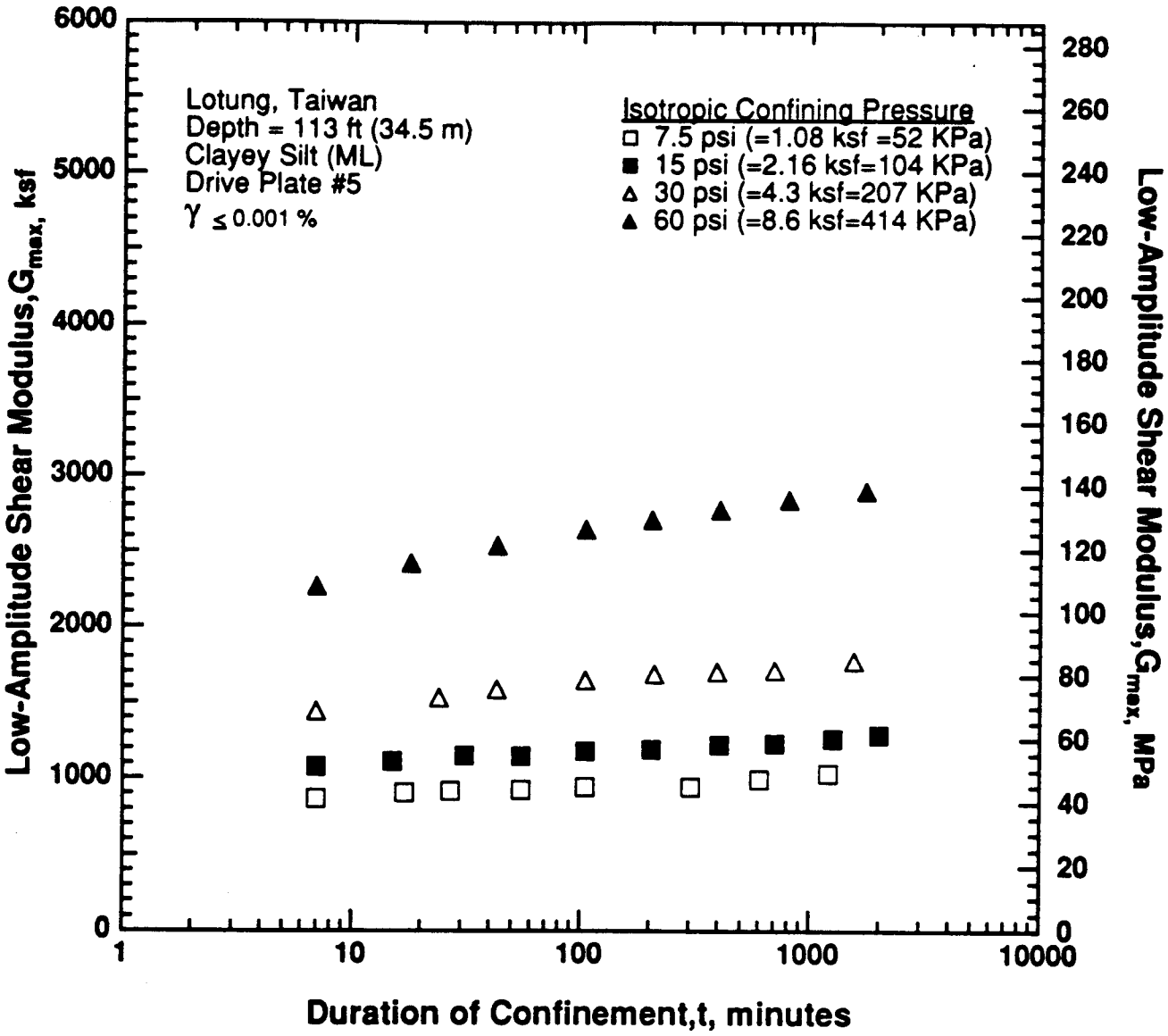

Figure 8.B.3.G-1
Variation in low-amplitude shear modulus with magnitude and duration of isotropic confining pressure from resonant column tests of sample T8 from borehole CH1.

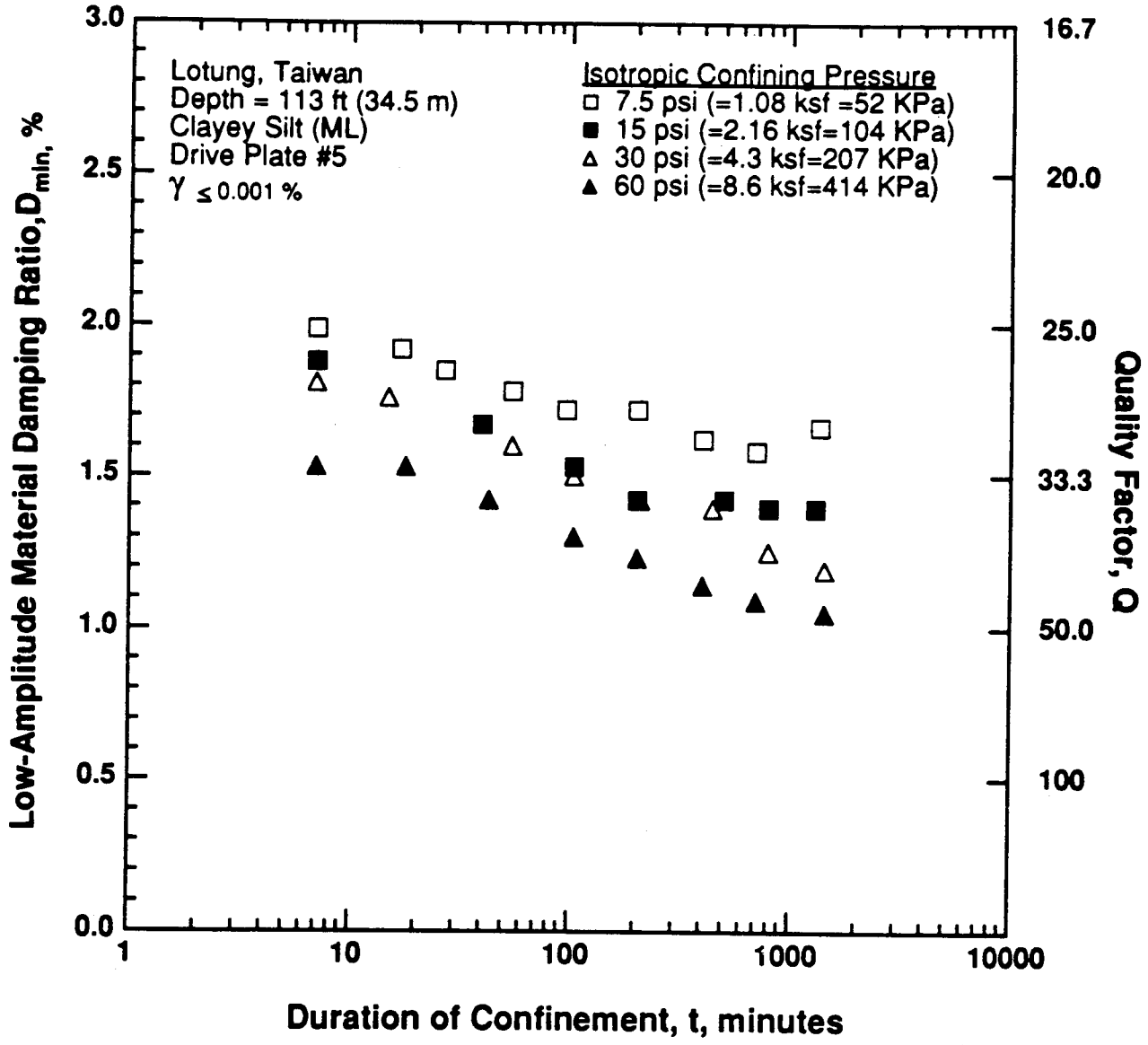

Figure 8.B.3.G-2
Variation in low-amplitude material damping ratio with magnitude and duration of isotropic confining pressure from resonant column tests of sample T8 from borehole CH1.

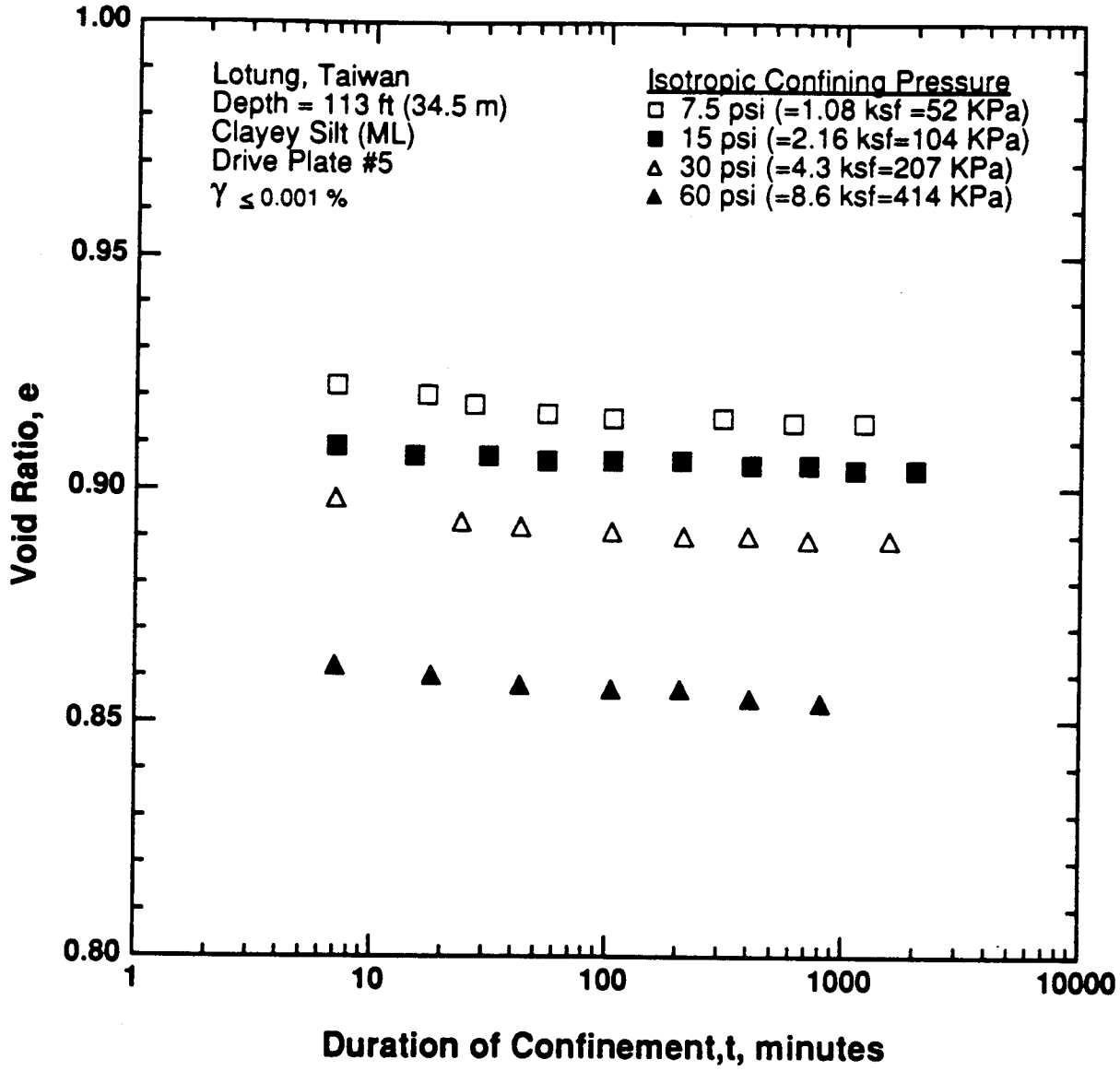

Figure 8.B.3.G-3
Variation in void ratio with magnitude and duration of isotropic confining pressure from resonant column tests of sample T8 from borehole CH1.

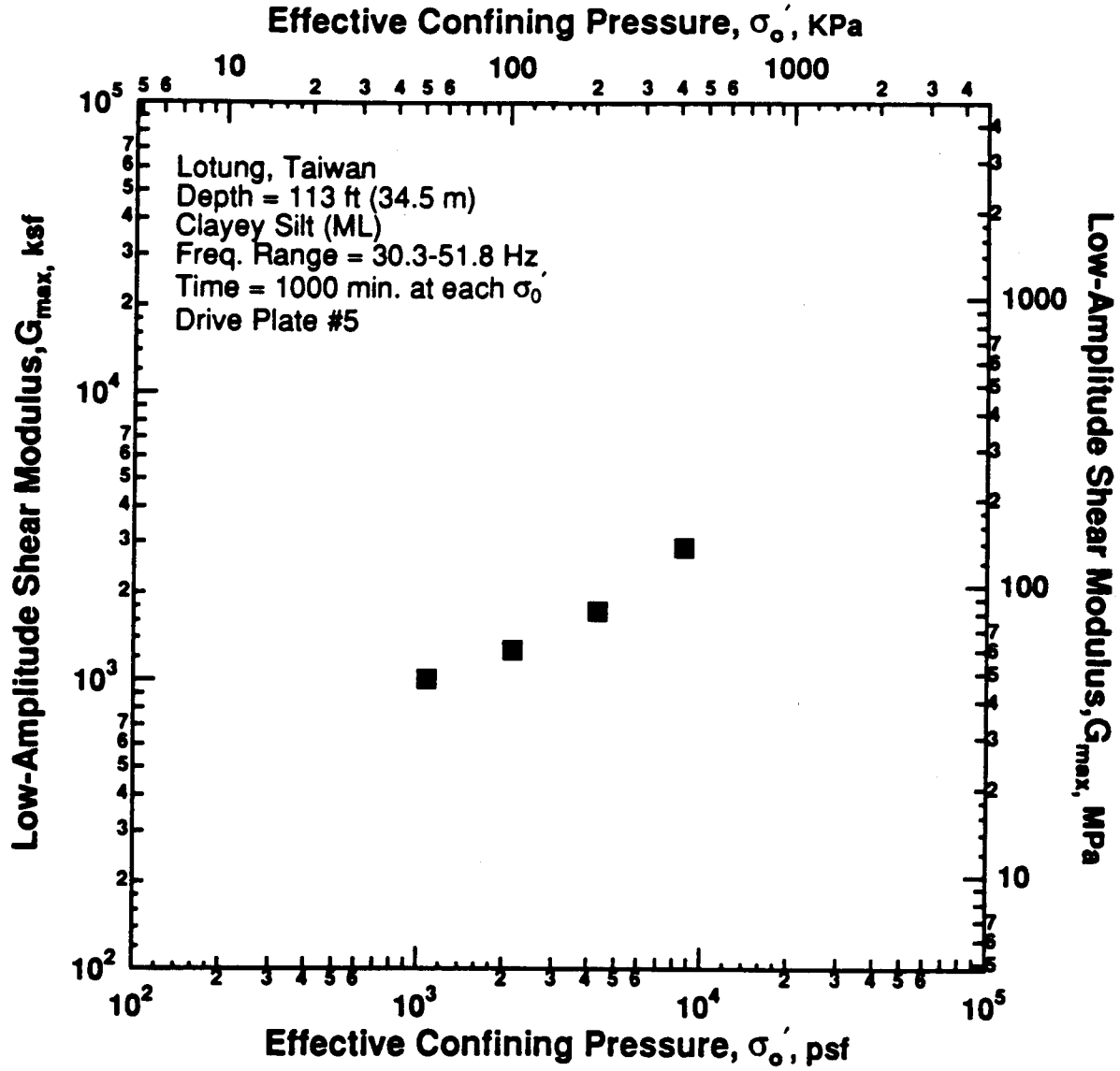

Figure 8.B.3.G-4
Variation in low-amplitude shear modulus with effective confining pressure from resonant column tests of sample T8 from borehole CH1.

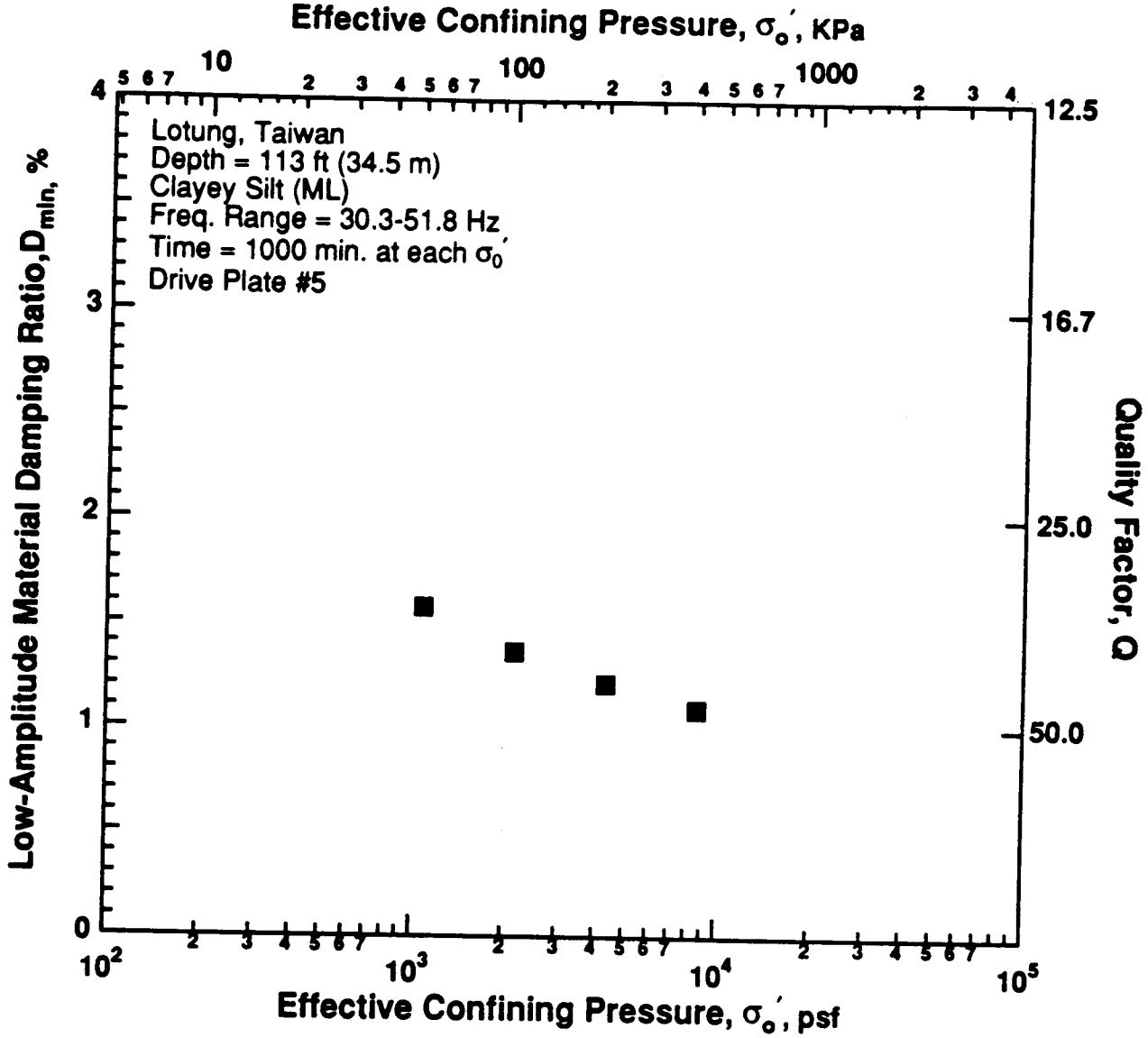

Figure 8.B.3.G-5
Variation in low-amplitude material damping ratio with effective confining pressure from resonant column tests of sample T8 from borehole CH1.

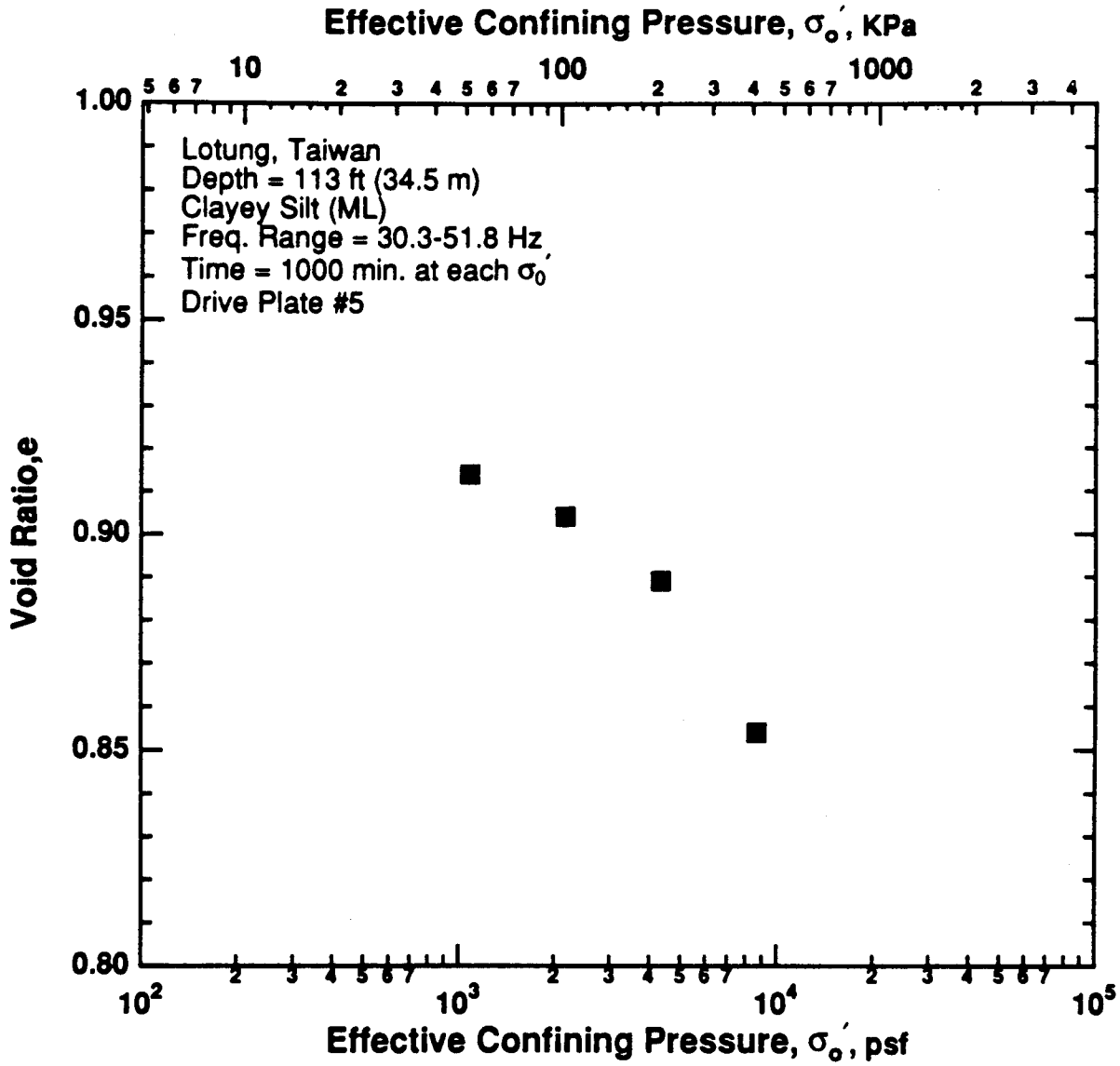

Figure 8.B.3.G-6
Variation in void ratio with effective confining pressure from resonant column tests of sample T8 from borehole CH1.

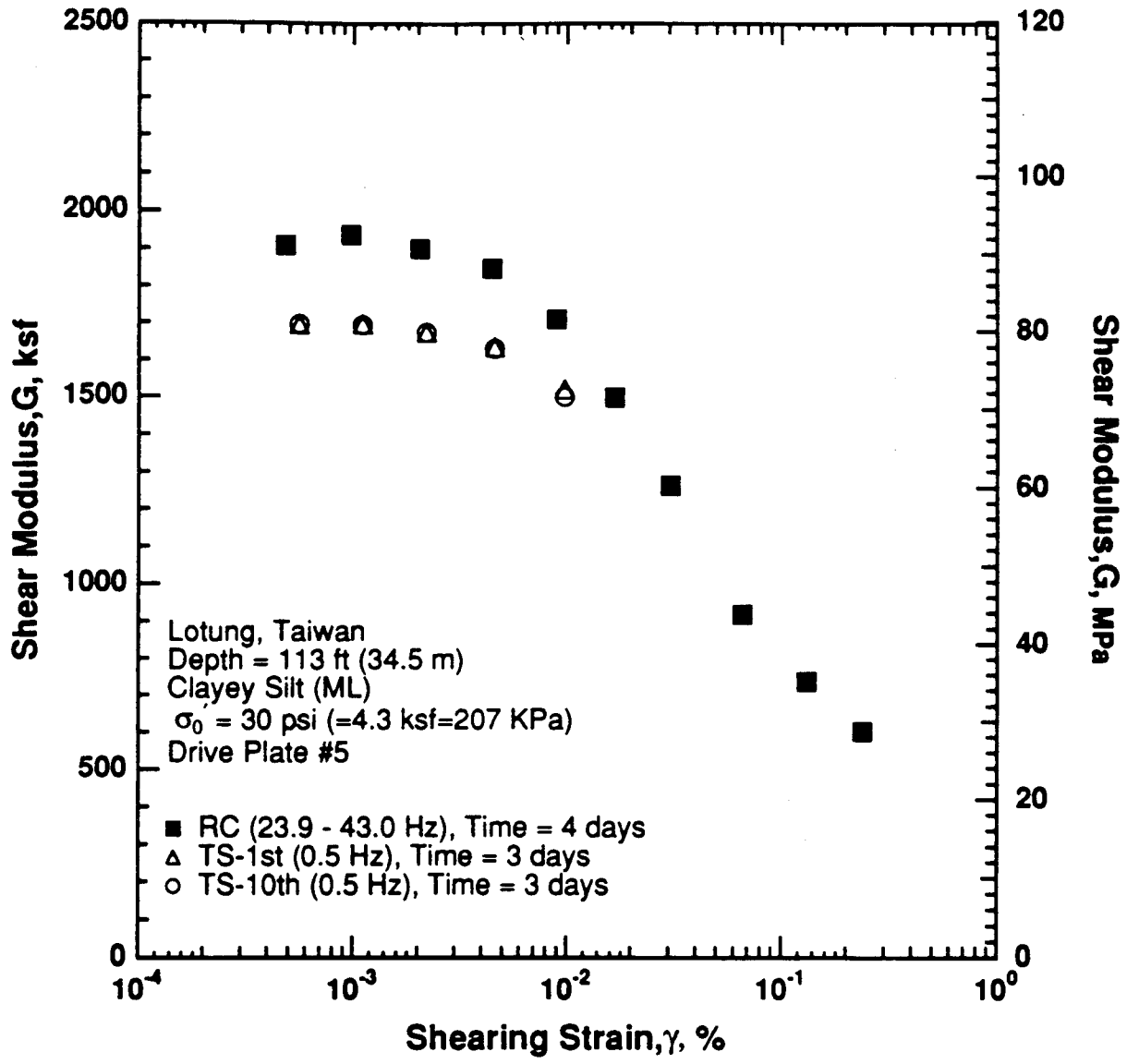

Figure 8.B.3.G-7
Variation in shear modulus with shearing strain at an effective confining pressure of 30 psi (4.3 ksf, 207 kPa) from RCTS tests of sample T8 from borehole CH1.

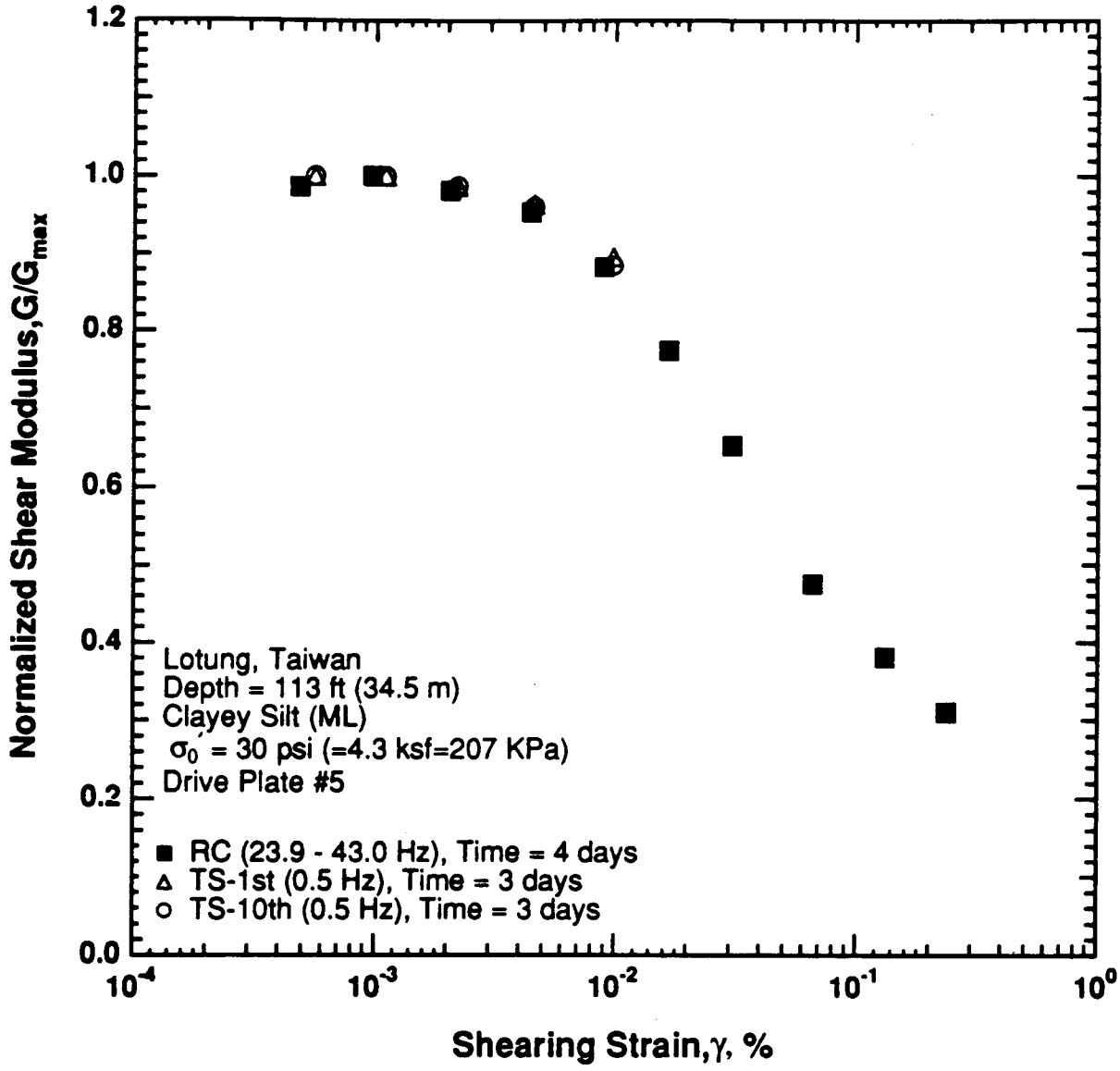

Figure 8.B.3.G-8
Variation in normalized shear modulus with shearing strain at an effective confining pressure of 30 psi (4.3 ksf, 207 kPa) from RCTS tests of sample T8 from borehole CH1.

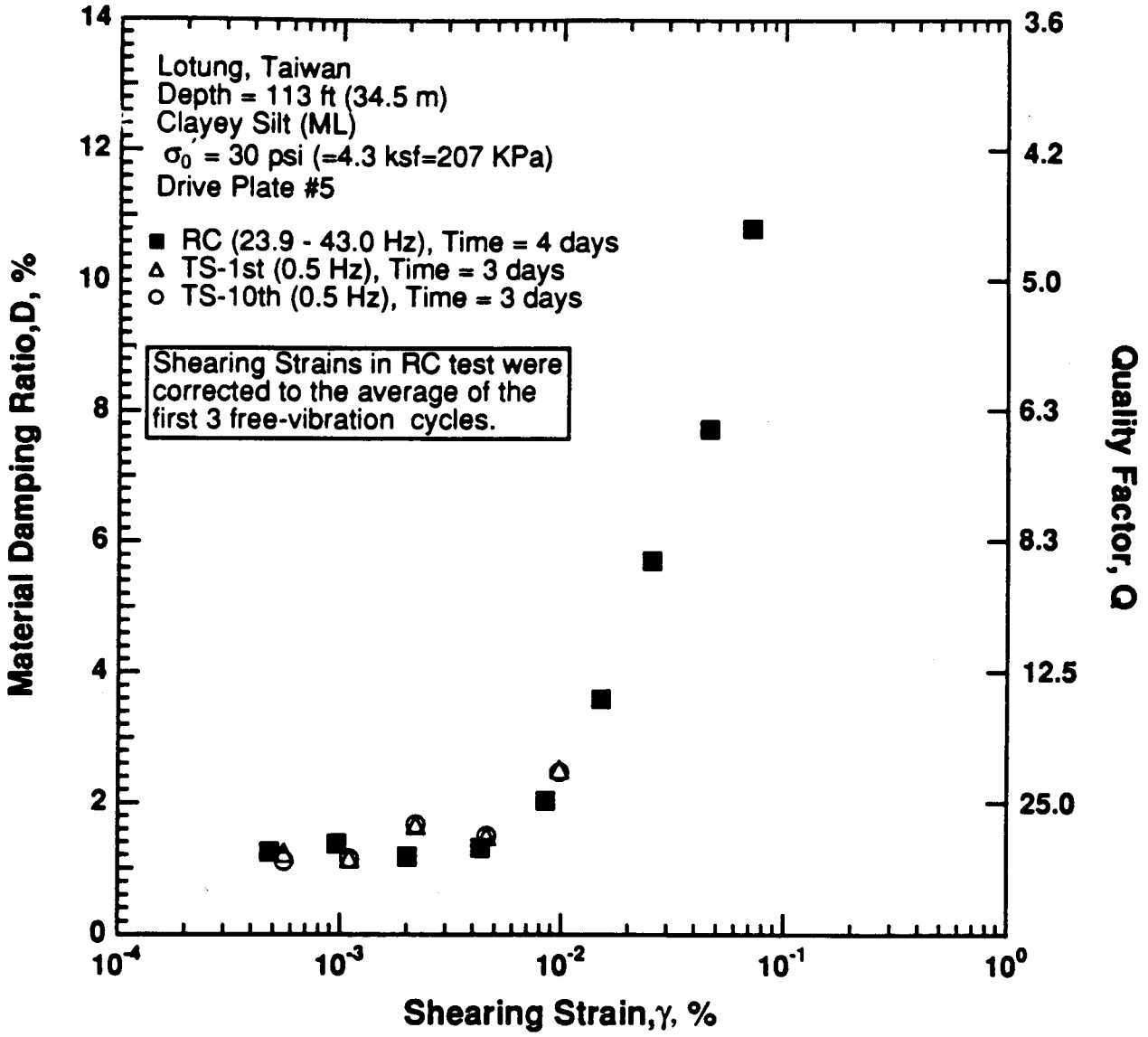

Figure 8.B.3.G-9
Variation in material damping ratio with shearing strain at an effective confining pressure of 30 psi (4.3 ksf, 207 kPa) from RCTS tests of sample T8 from borehole CH1.

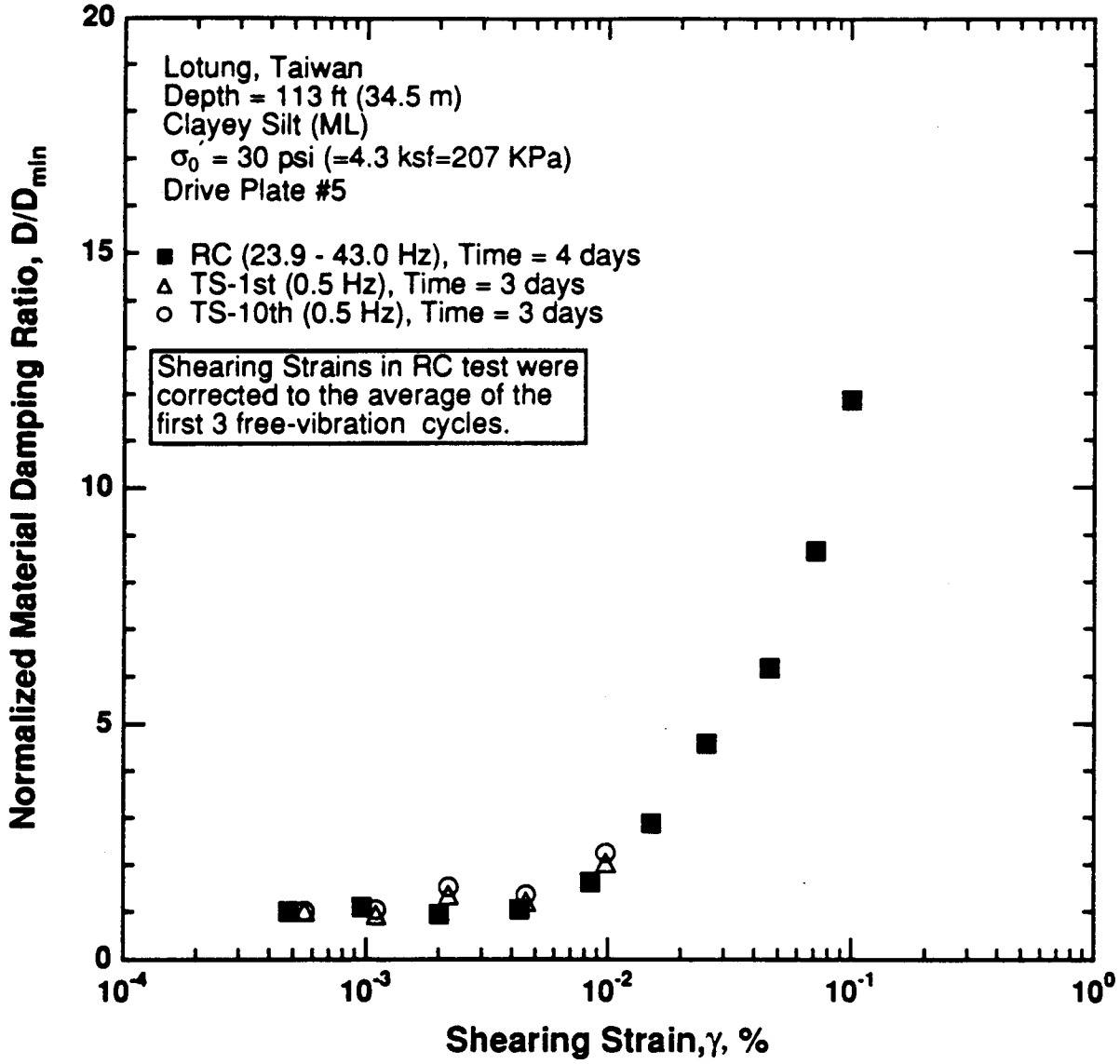

Figure 8.B.3.G-10
Variation in normalized material damping ratio with shearing strain at an effective confining pressure of 30 psi (4.3 ksf, 207 kPa) from RCTS tests of sample T8 from borehole CH1.

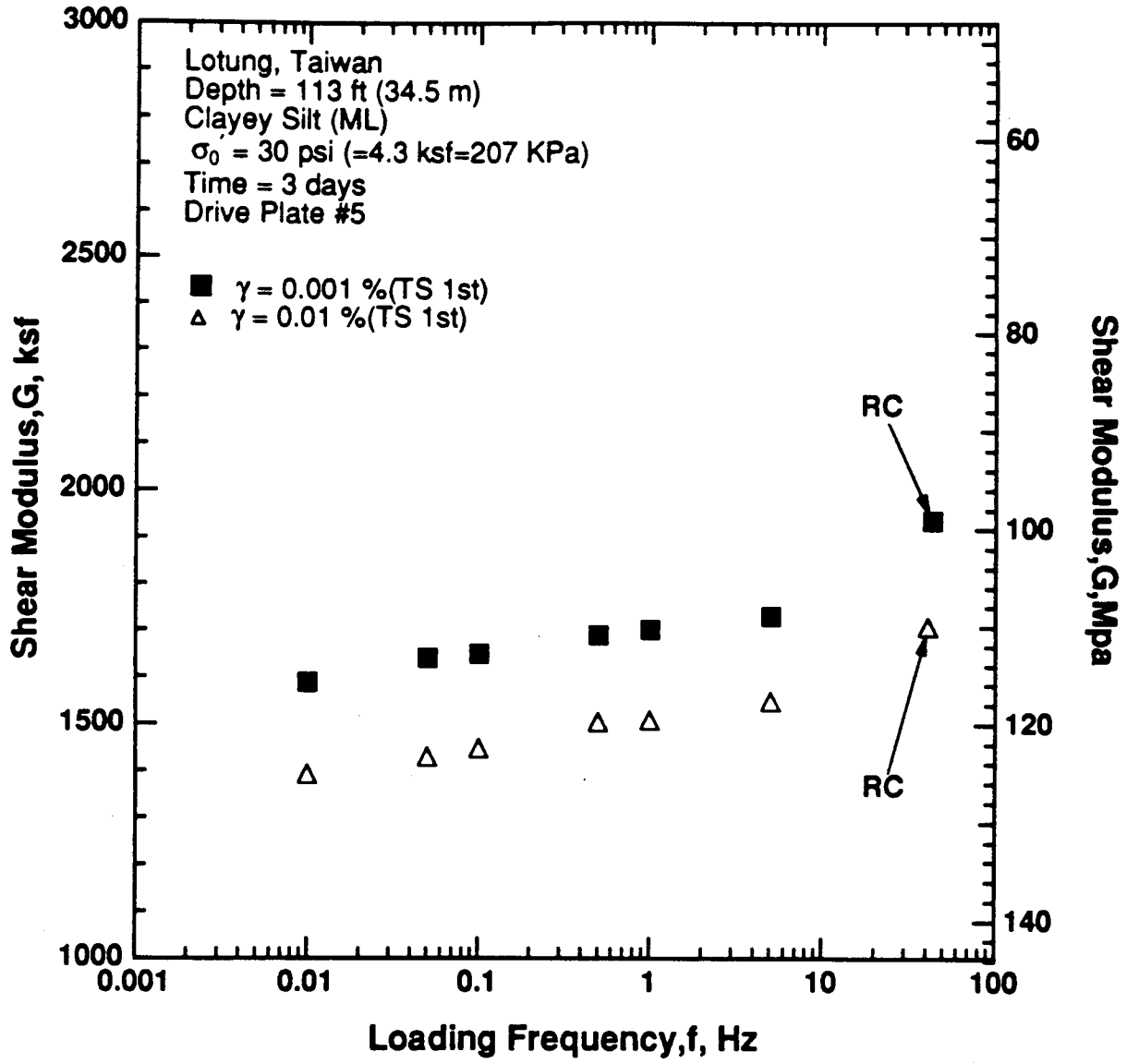

Figure 8.B.G-11
Variation in shear modulus with loading frequency and shearing strain at an effective confining pressure of 30 psi (4.3 ksf, 207 kPa) from RCTS tests of sample T8 from borehole CH1.

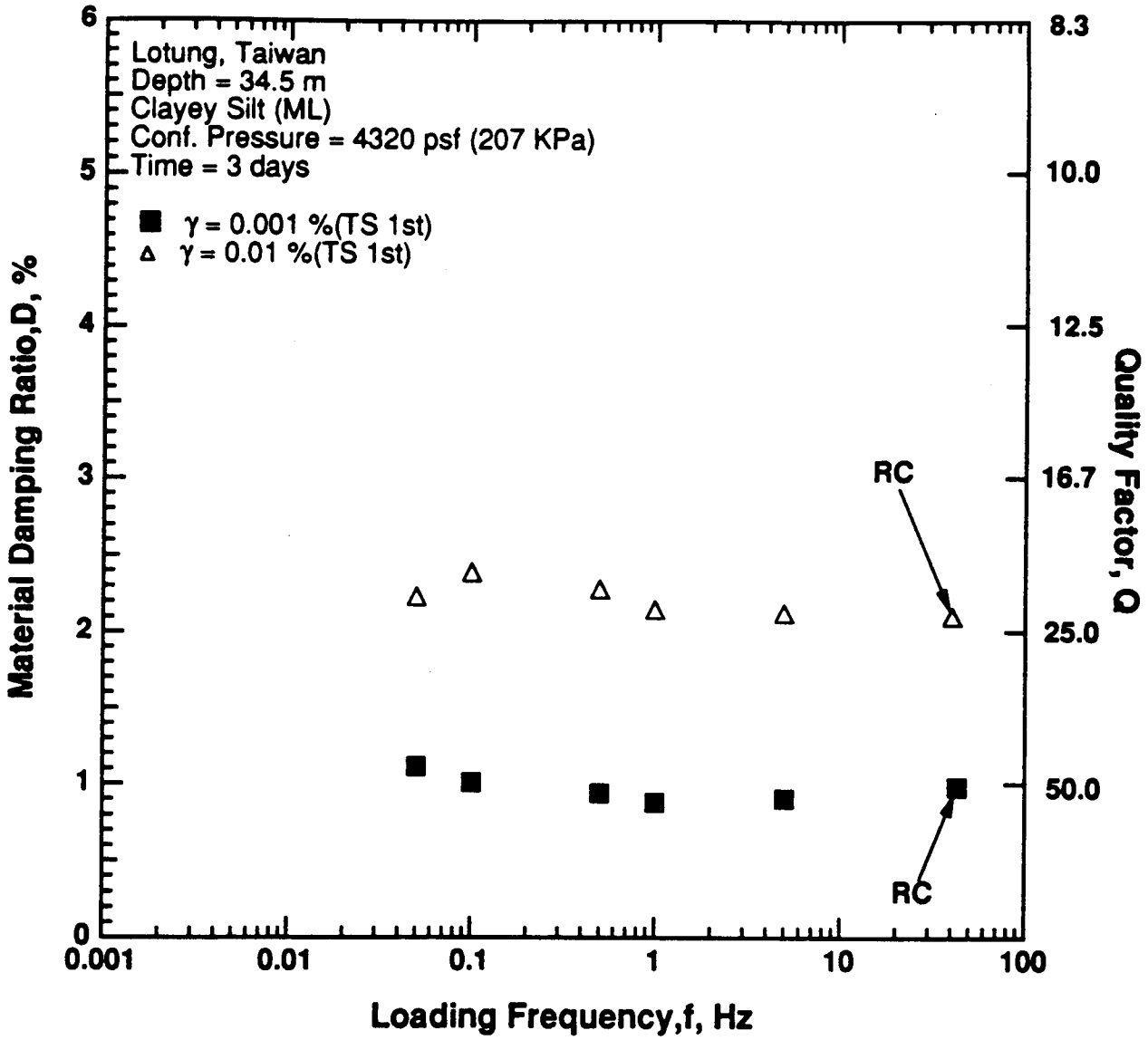

Figure 8.B.3.G-12
Variation in material damping ratio with loading frequency and shearing strain at an effective confining pressure of 30 psi (4.3 ksf, 207 kPa) from RCTS tests of sample T8 from borehole CH1.

APPENDIX 8.B.3.H
DYNAMIC TESTS OF SAMPLE T11 FROM BOREHOLE CH2, DEPTH = 133 FT (40.5 M)

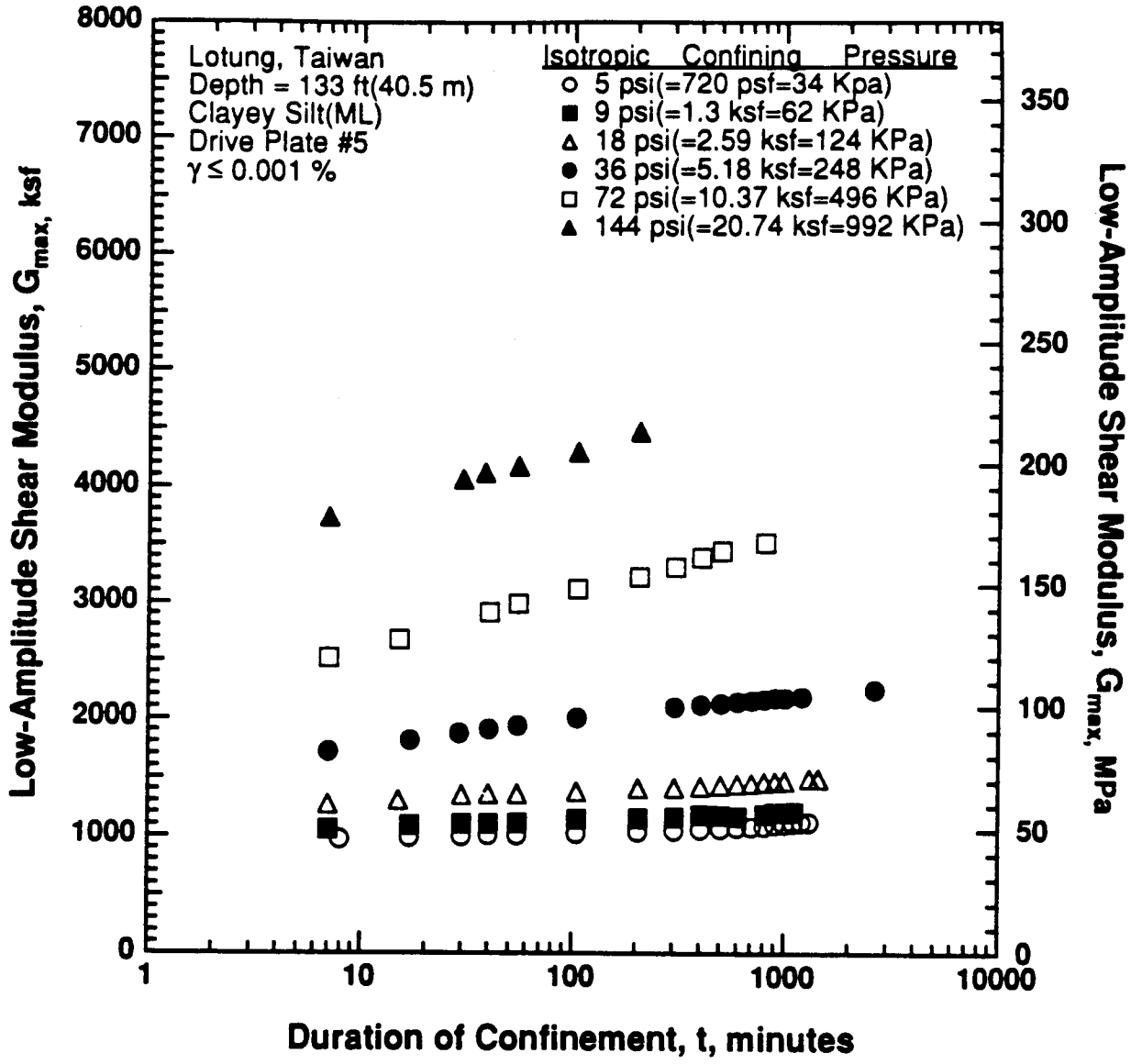

Figure 8.B.3.H-1
Variation in low-amplitude shear modulus with magnitude and duration of isotropic confining pressure from resonant column tests of sample T11 from borehole CH2.

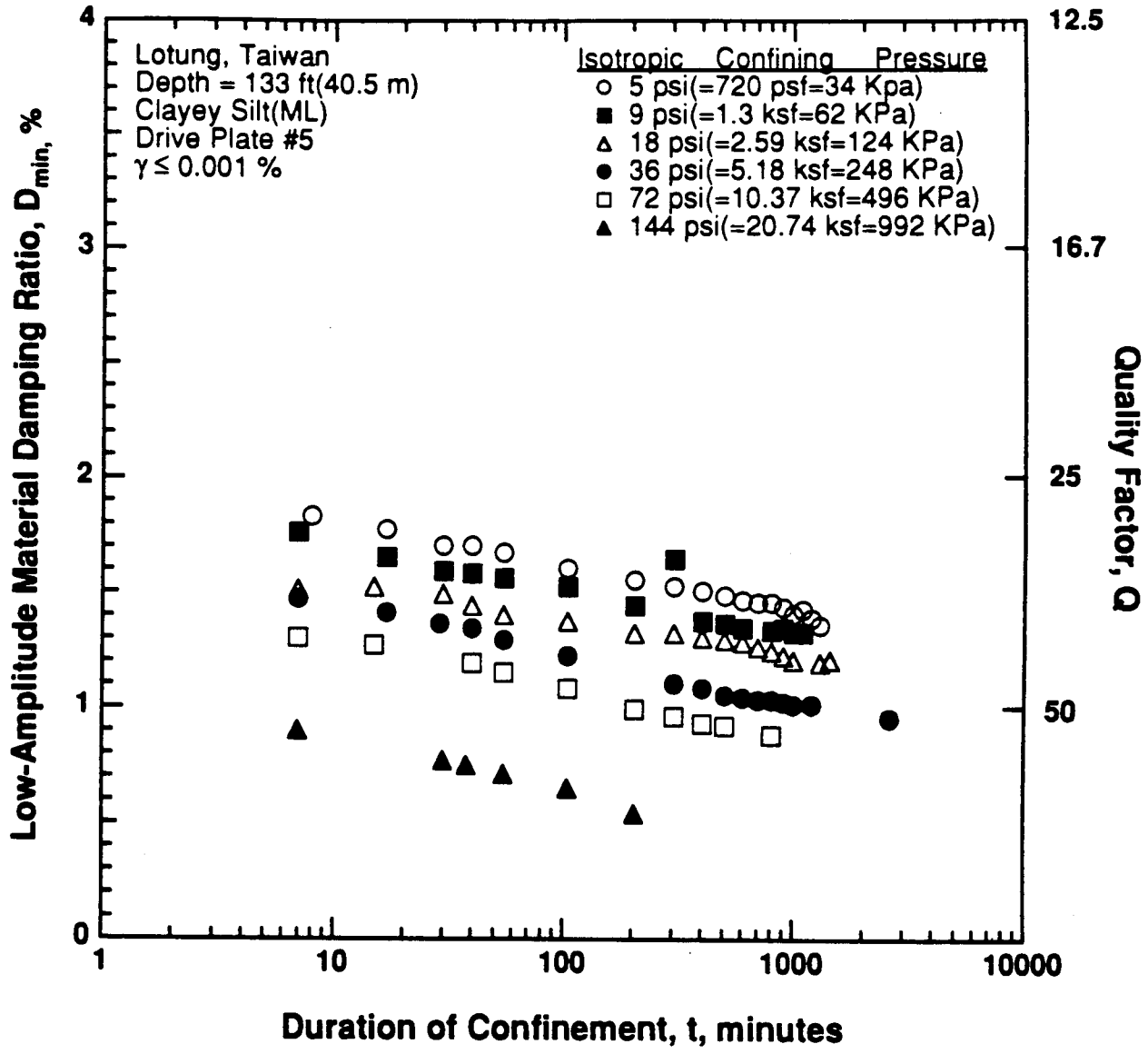

Figure 8.B.3.H-2
Variation in low-amplitude material damping ratio with magnitude and duration of isotropic confining pressure from resonant column tests of sample T11 from borehole CH2.

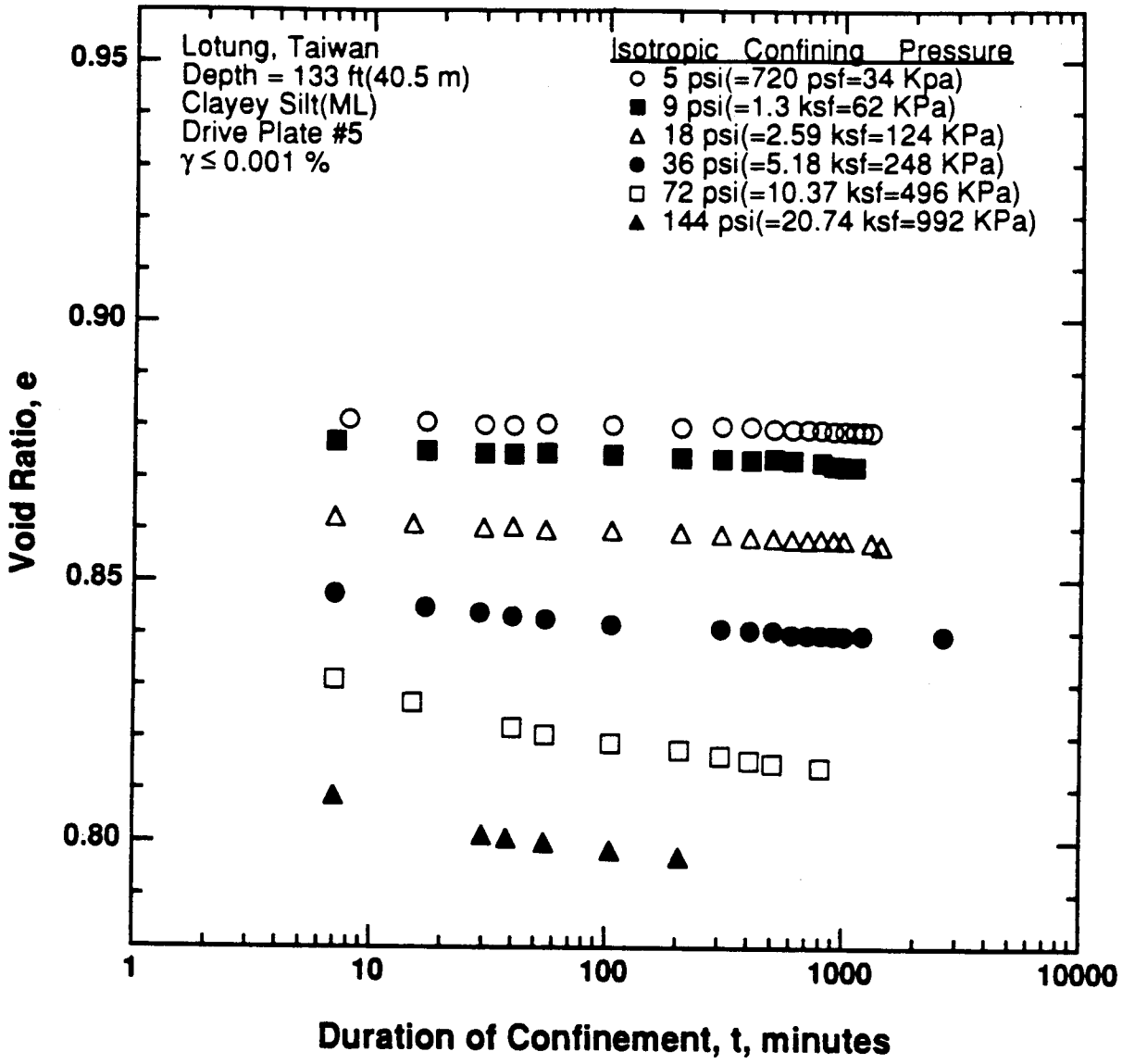

Figure 8.B.3.H-3
Variation in void ratio with magnitude and duration of isotropic confining pressure from resonant column tests of sample T11 from borehole CH2.

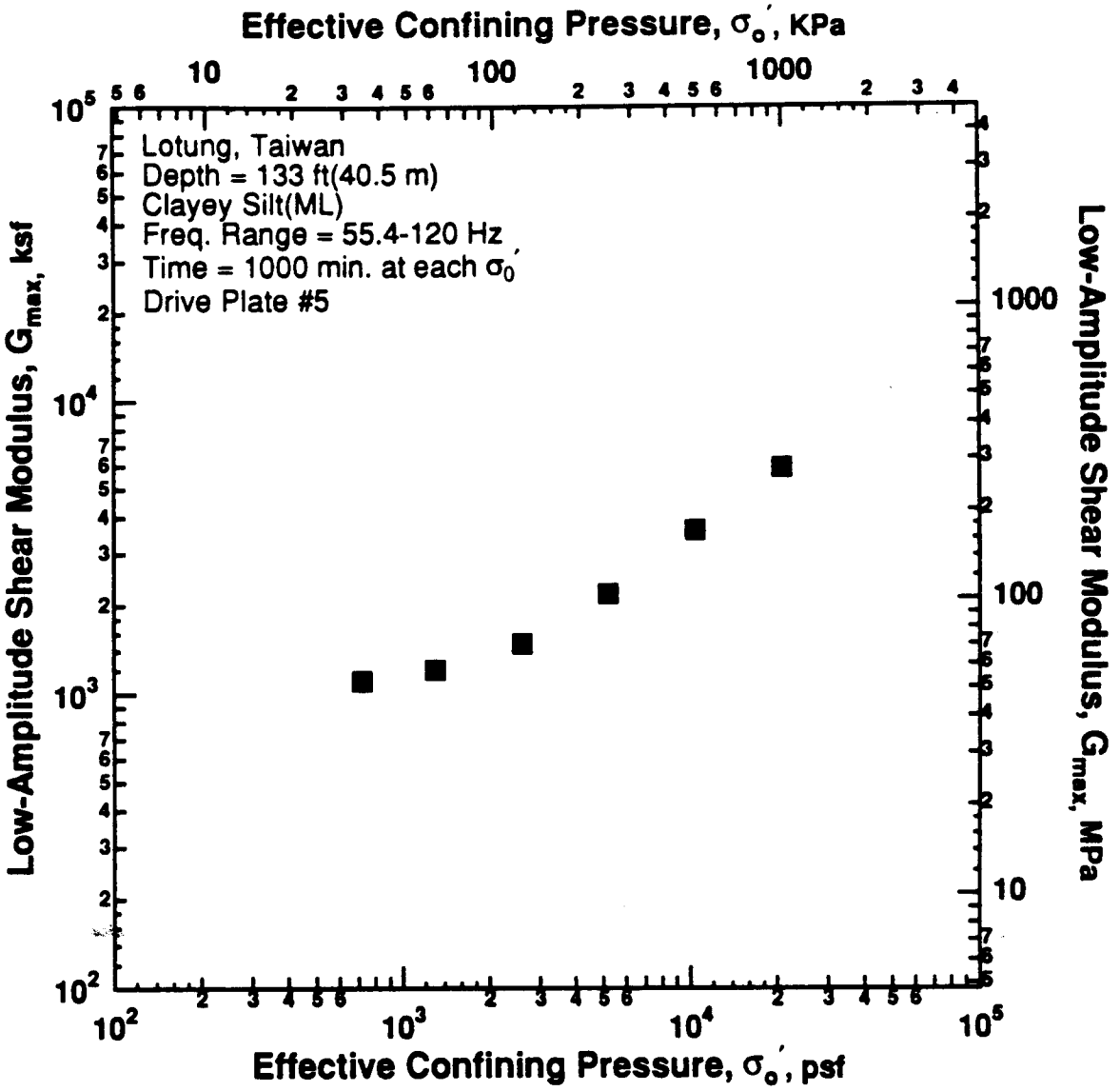

Figure 8.B.3.H-4
Variation in low-amplitude shear modulus with effective confining pressure from resonant column tests of sample T11 from borehole CH2.

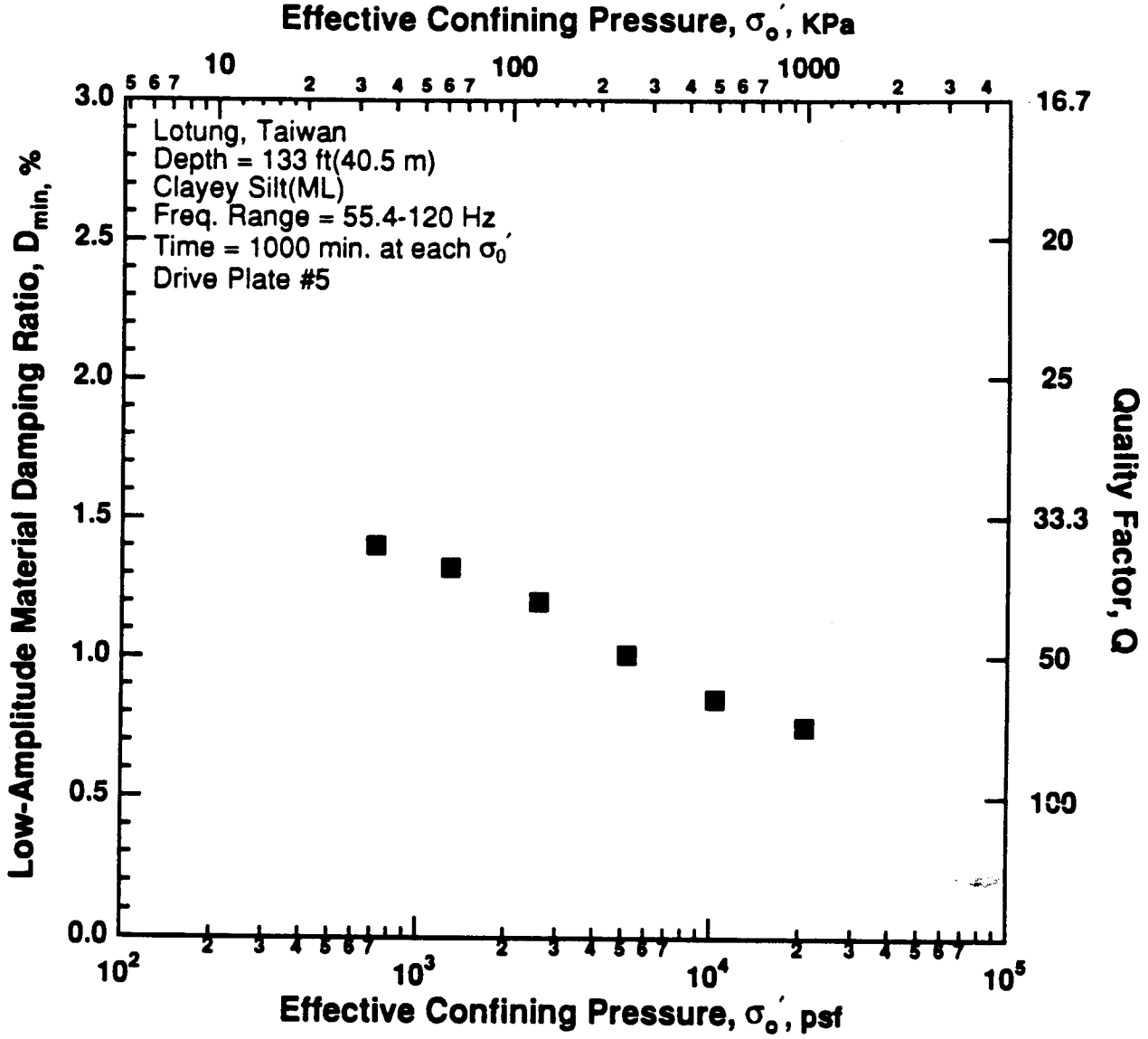

Figure 8.B.3.H-5
Variation in low-amplitude material damping ratio with effective confining pressure from resonant column tests of sample T11 from borehole CH2.

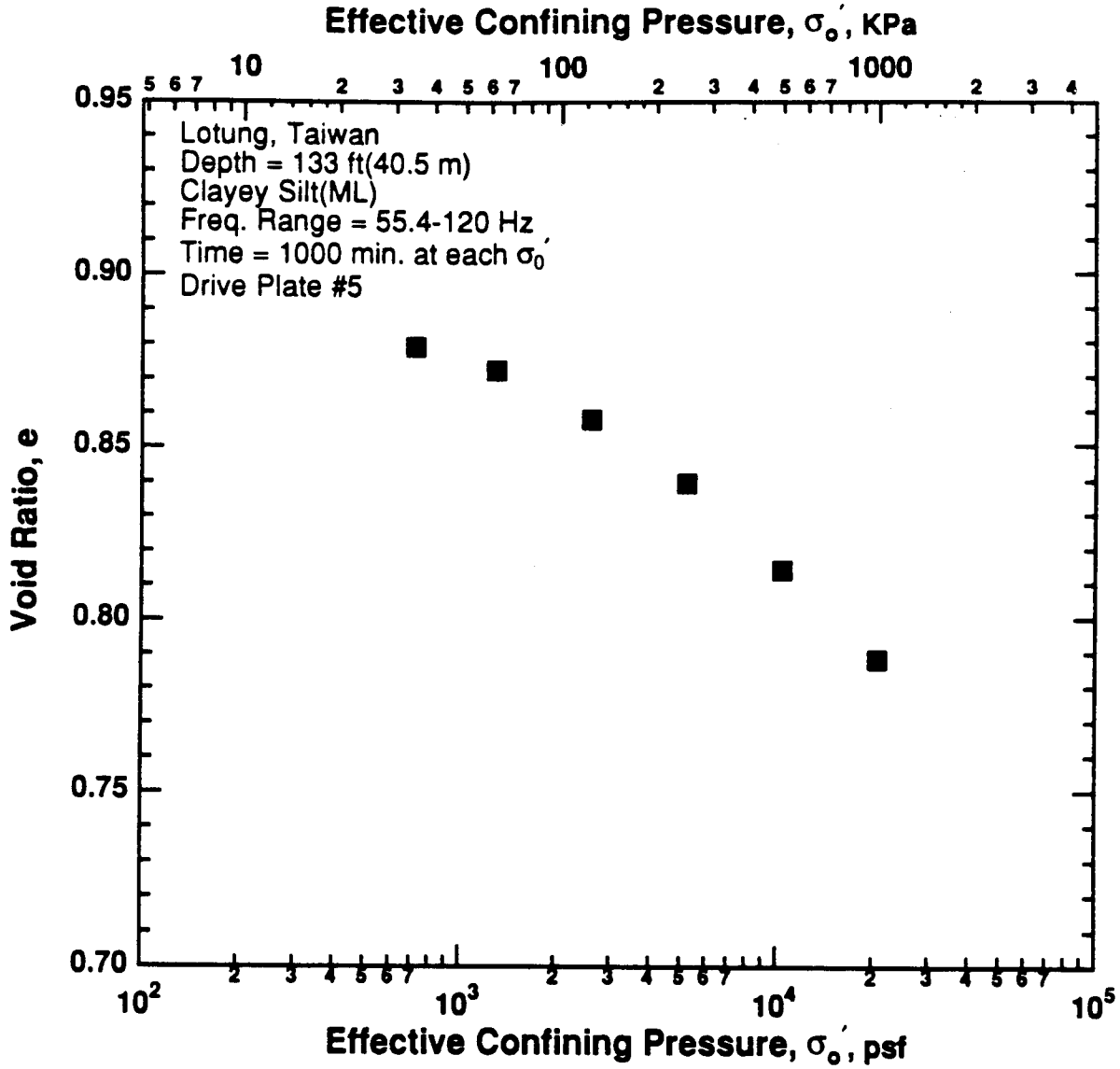

Figure 8.B.3.H-6
Variation in void ratio with effective confining pressure from resonant column tests of sample T11 from borehole CH2.

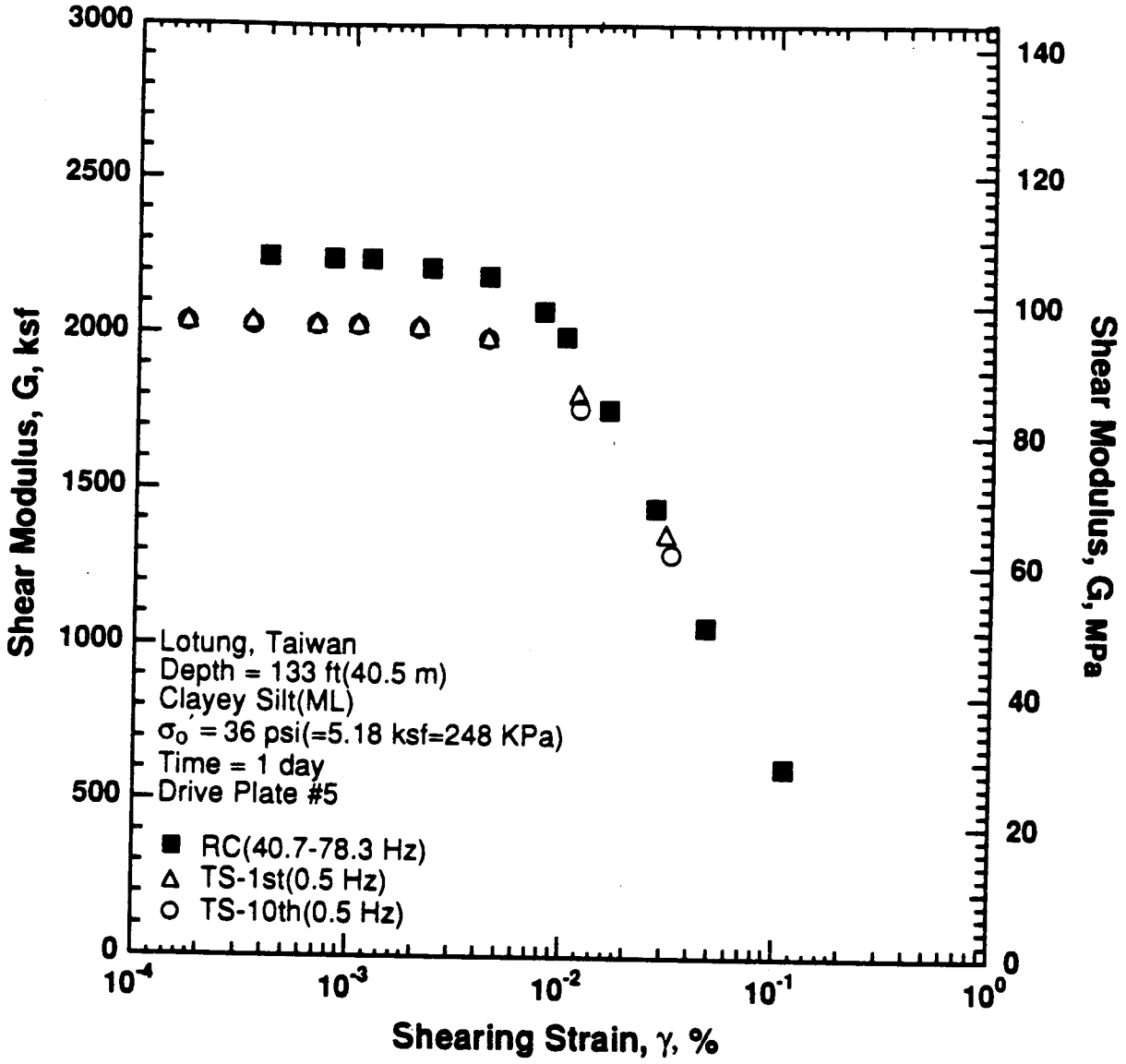

Figure 8.B.3.H-7
Variation in shear modulus with shearing strain at an effective confining pressure of 36 psi (5.18 ksf, 248 kPa) from RCTS tests of sample T11 from borehole CH2.

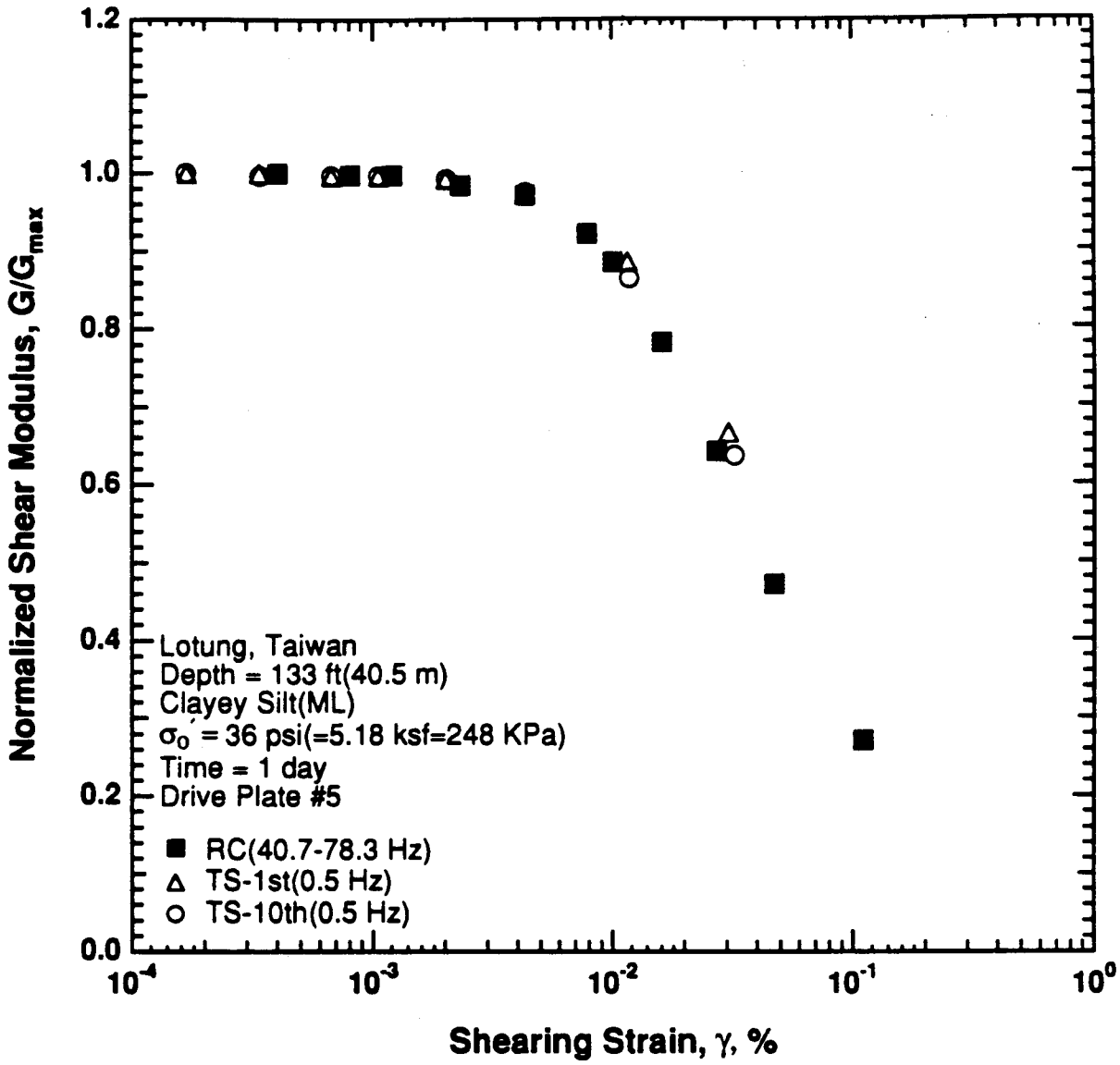

Figure 8.B.3.H-8
Variation in normalized shear modulus with shearing strain at an effective confining pressure of 36 psi (5.18 ksf, 248 kPa) from RCTS tests of sample T11 from borehole CH2.

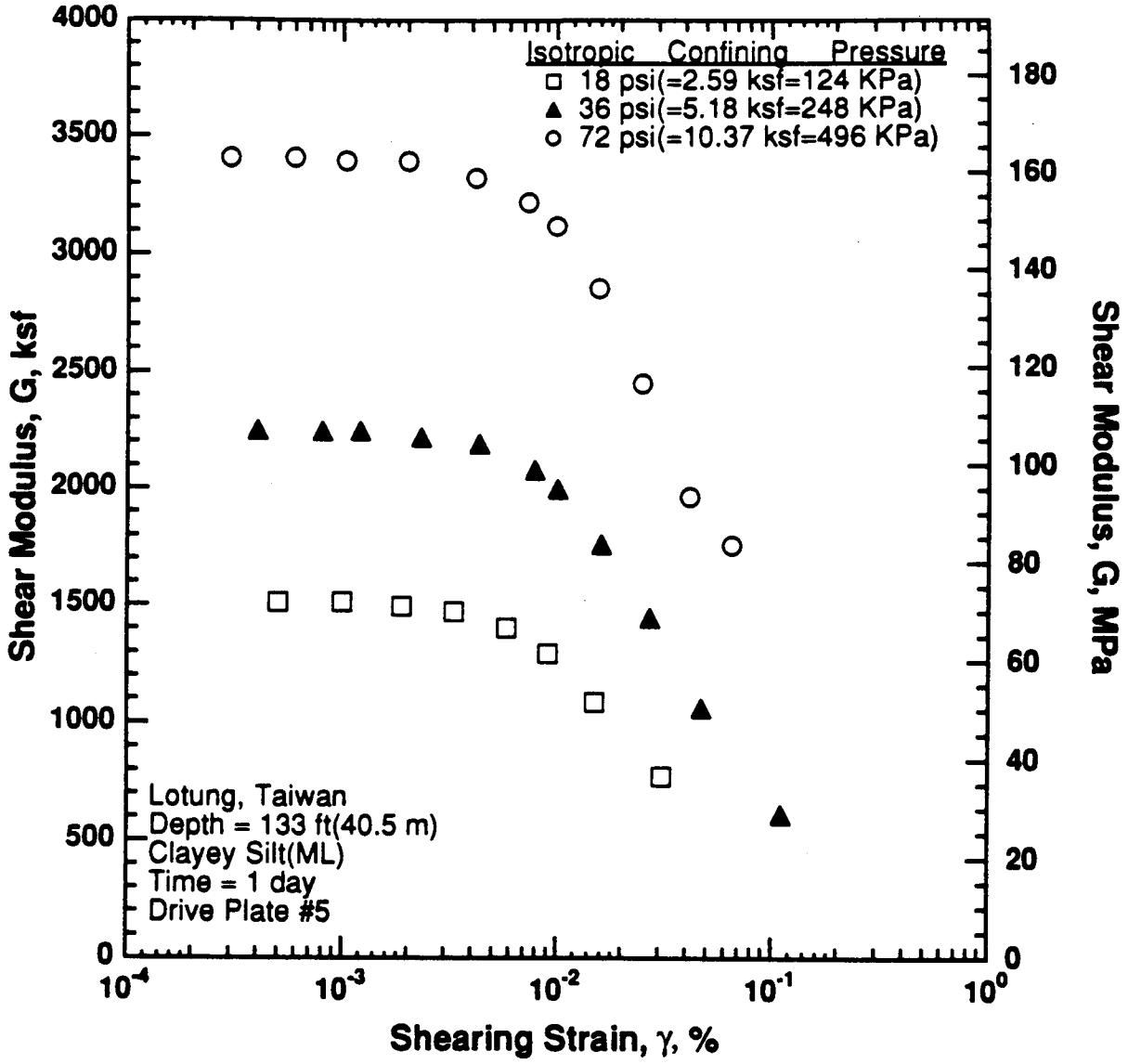

Figure 8.B.3.H-9
Variation in shear modulus with shearing strain and effective confining pressure from resonant column tests of sample T11 from borehole CH2.

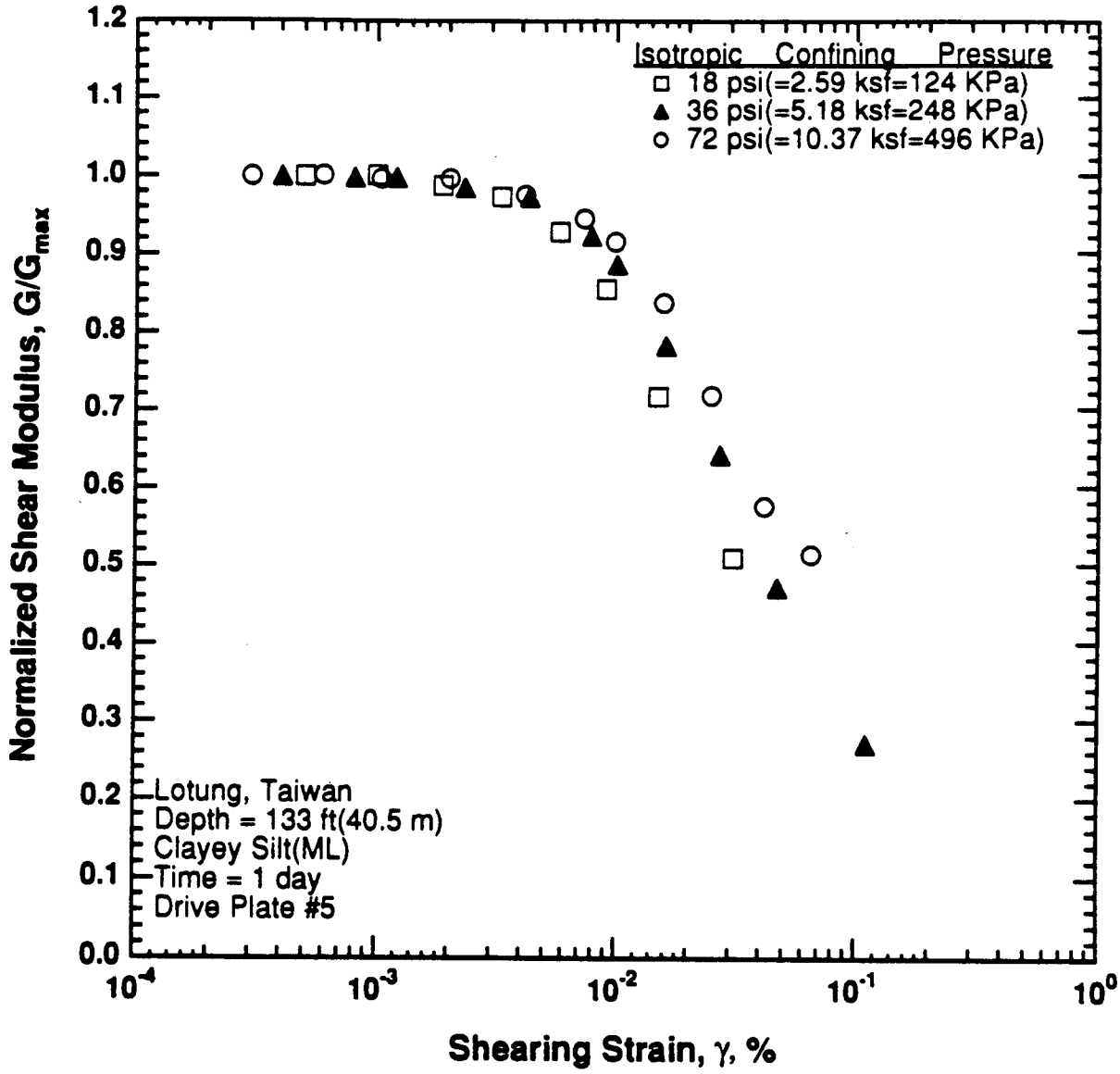

Figure 8.B.3.H-10
Comparison of the variation in normalized shear modulus with shearing strain and effective confining pressure from resonant column tests of sample T11 from borehole CH2.

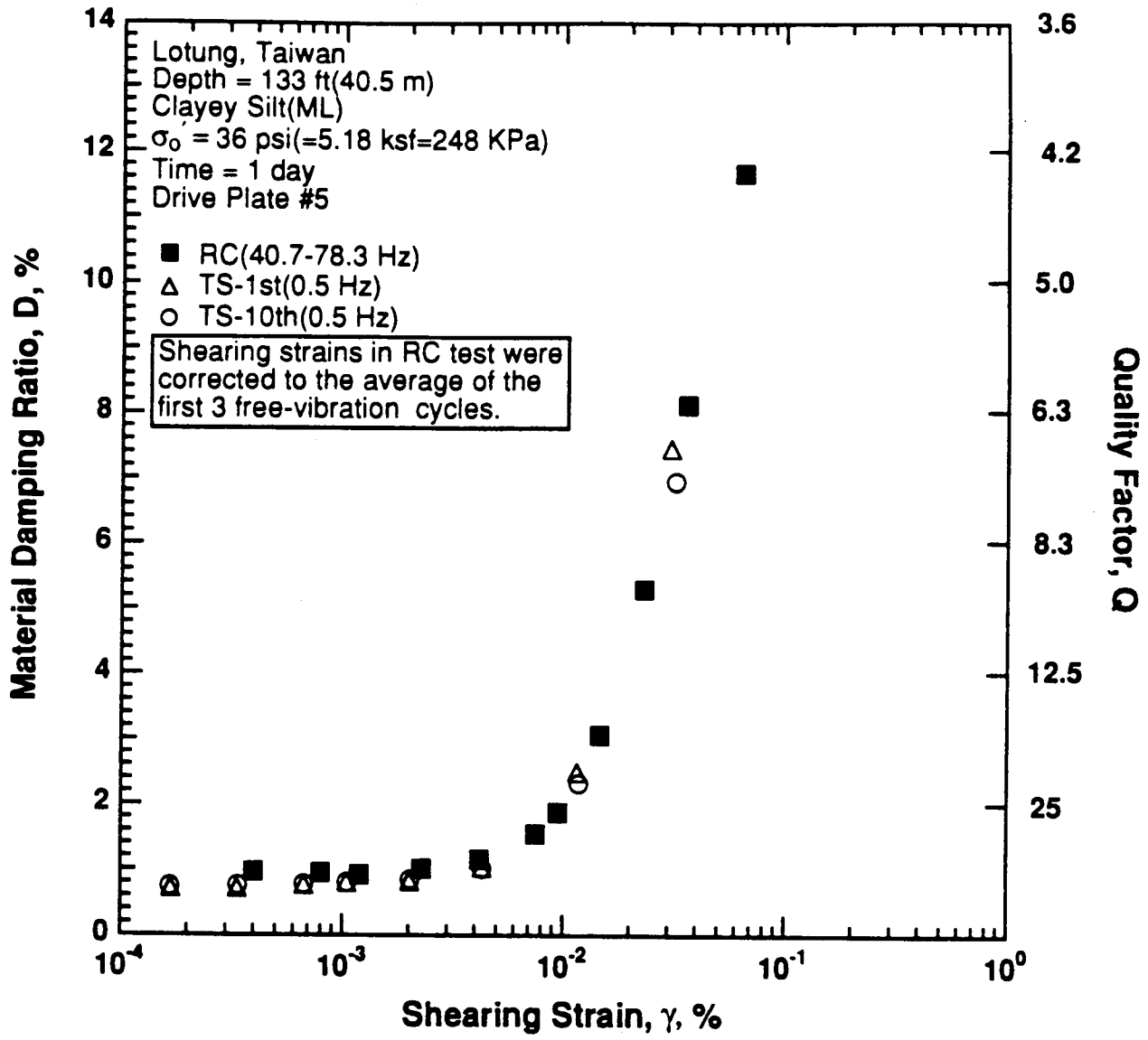

Figure 8.B.3.H-11
Variation in material damping ratio with shearing strain at an effective confining pressure of 36 psi (5.18 ksf, 248 kPa) from RCTS tests of sample T11 from borehole CH2.

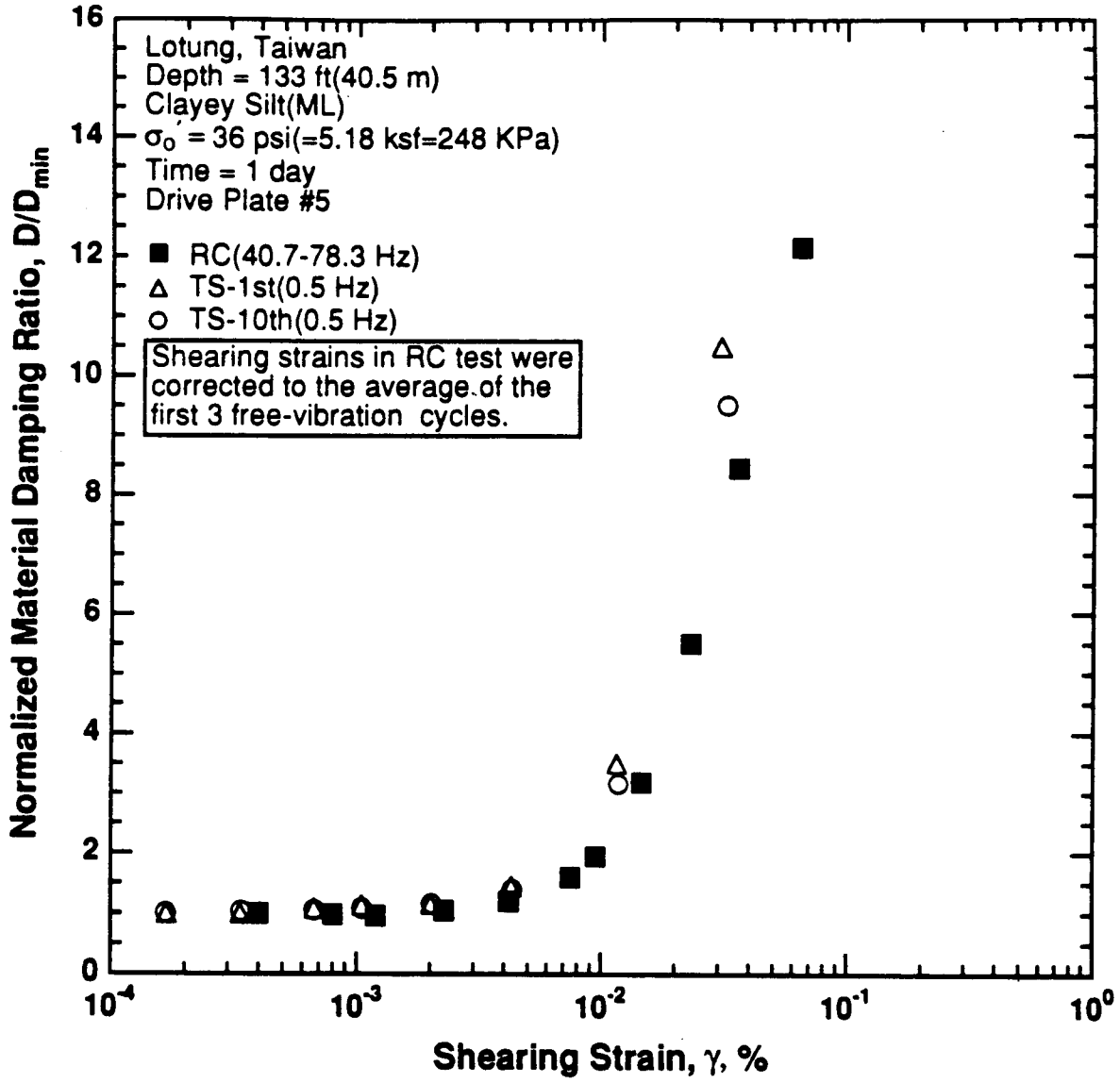

Figure 8.B.3.H-12
Variation in normalized material damping ratio with shearing strain at an effective confining pressure of 36 psi (5.18 ksf, 248 kPa) from RCTS tests of sample T11 from borehole CH2.

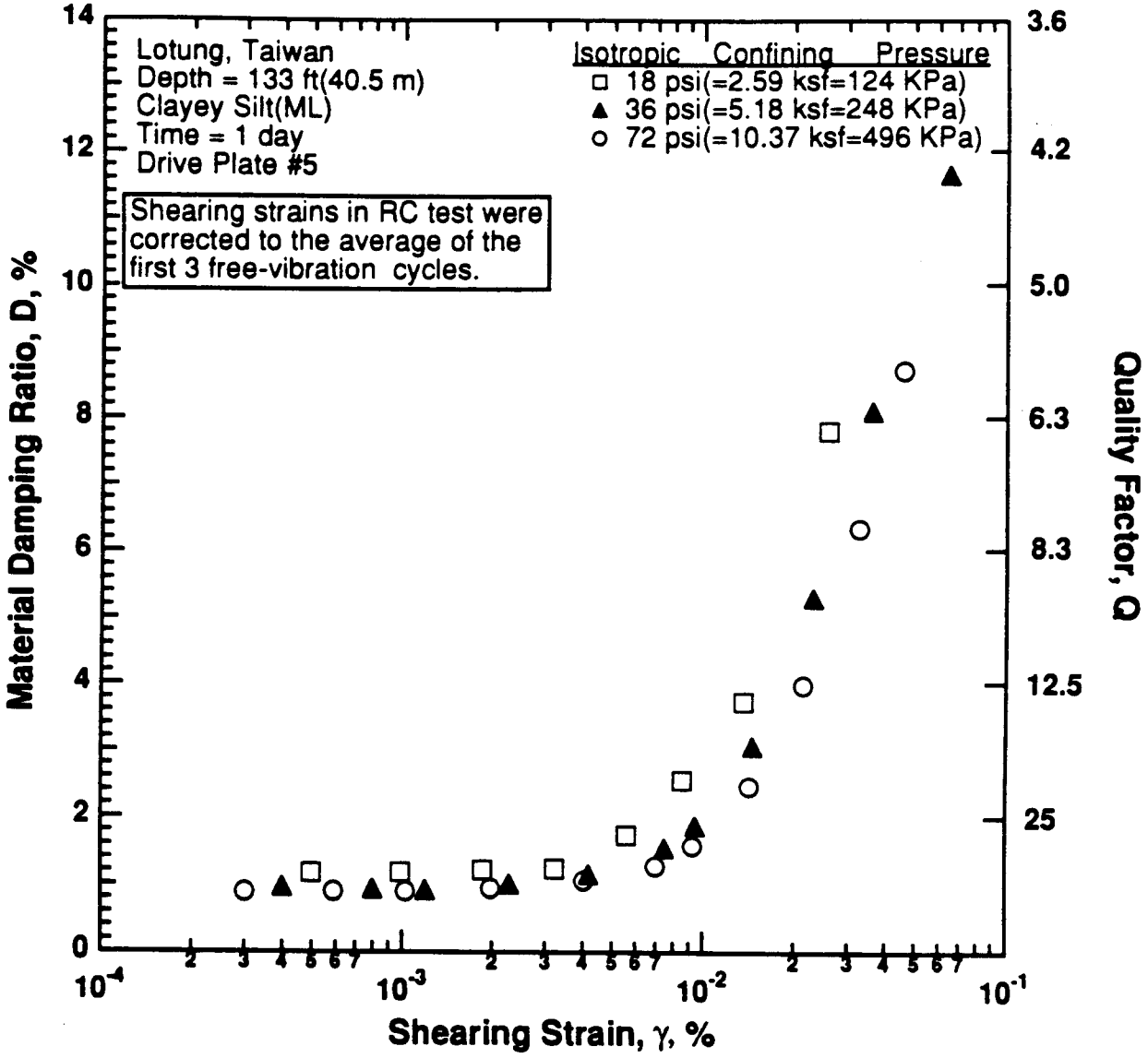

Figure 8.B.3.H-13
Variation in material damping ratio with shearing strain and effective confining pressure from resonant column tests of sample T11 from borehole CH2.

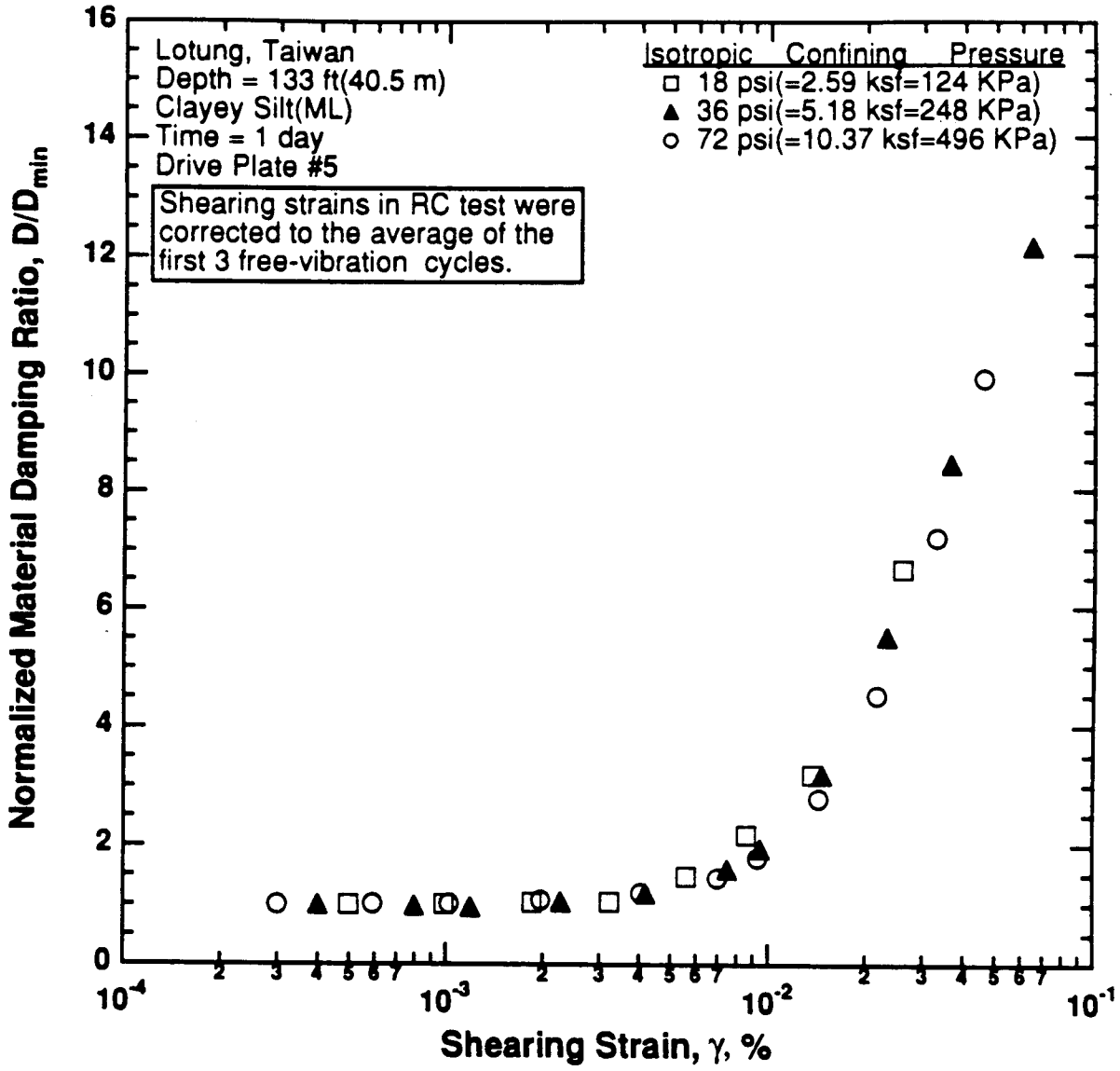

Figure 8.B.3.H-14
Comparison of the variation in normalized material damping ratio with shearing strain and effective confining pressure from resonant column tests of sample T11 from borehole CH2.

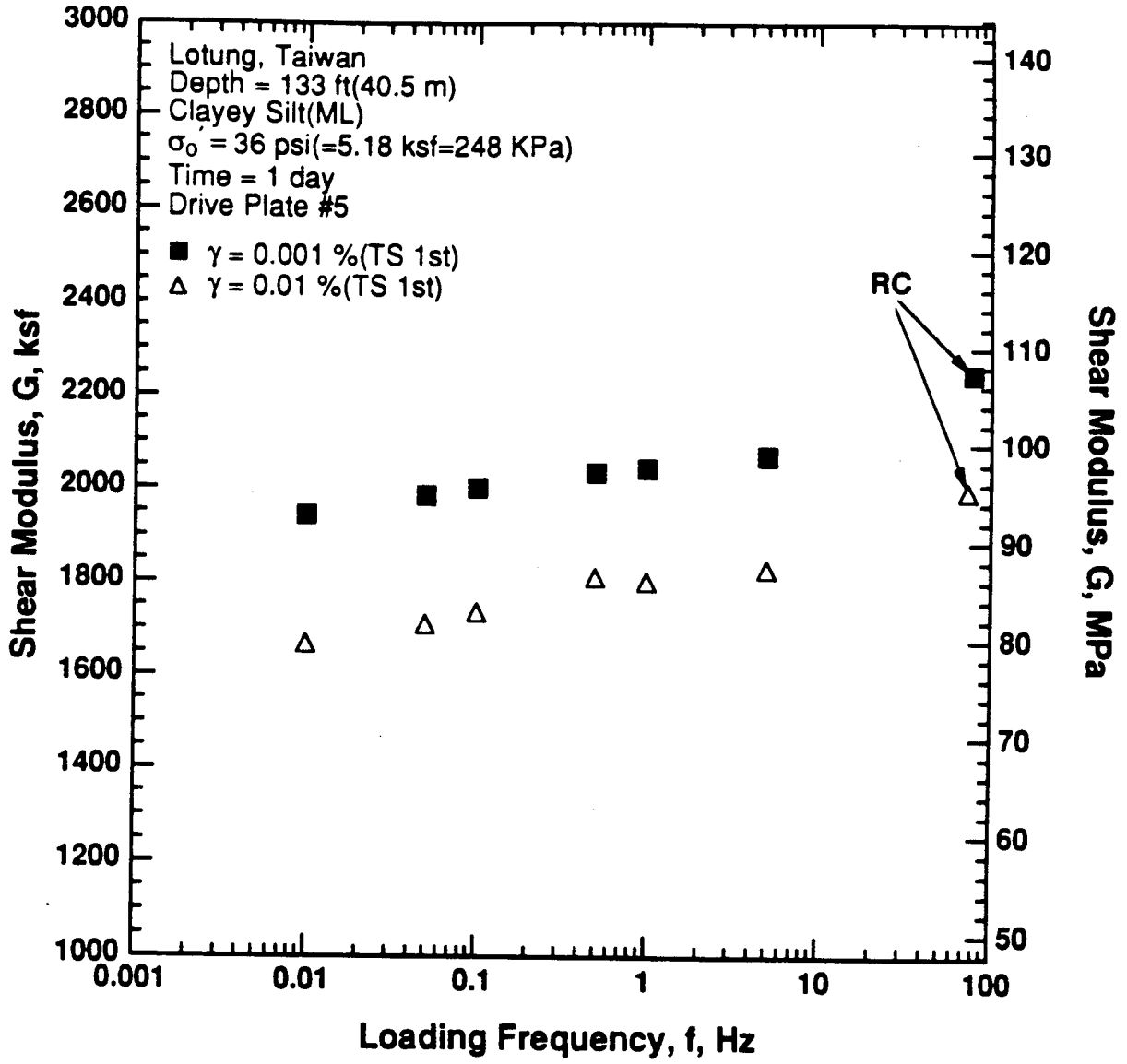

Figure 8.B.3.H-15
Variation in shear modulus with loading frequency and shearing strain at an effective confining pressure of 36 psi (5.18 ksf, 248 kPa) from RCTS tests of sample T11 from borehole CH2.

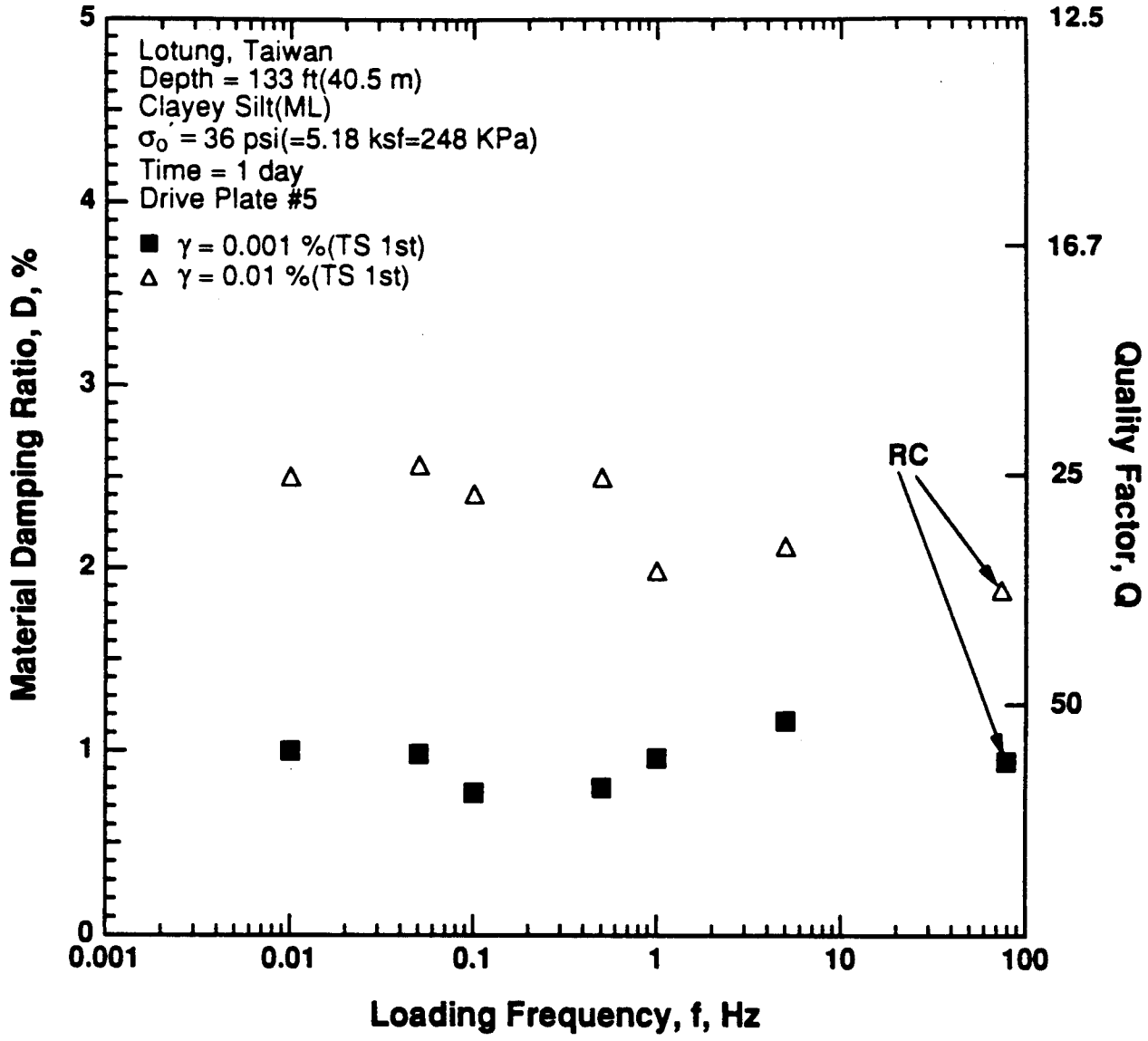

Figure 8.B.3.H-16
Variation in material damping ratio with loading frequency and shearing strain at an effective confining pressure of 36 psi (5.18 ksf, 248 kPa) from RCTS tests of sample T11 from borehole CH2.

APPENDIX 8.B.3.I
DYNAMIC TESTS OF SAMPLE T10 FROM BOREHOLE CH1, DEPTH = 146 FT (44.5 M)

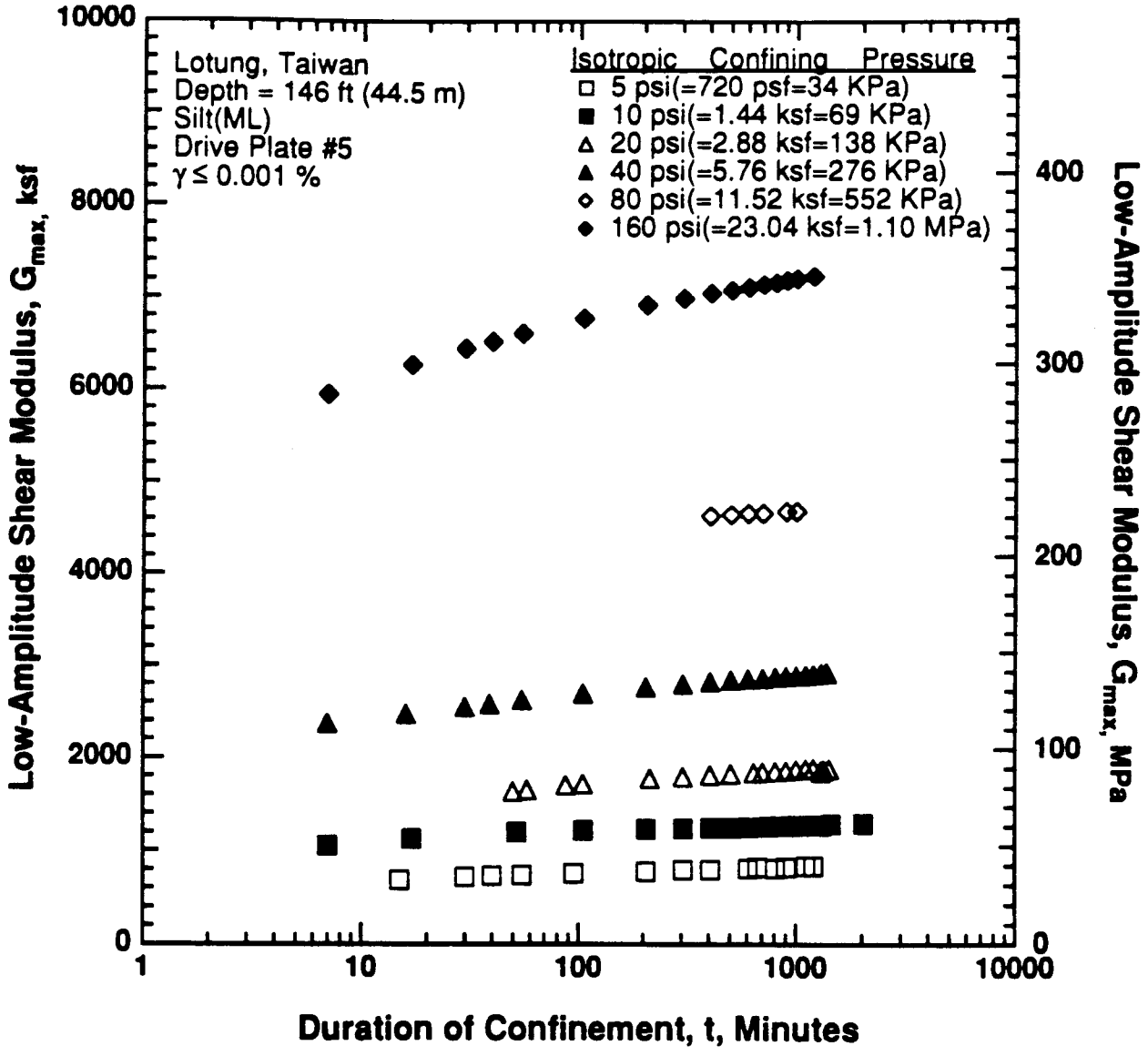

Figure 8.B.3.I-1
Variation in low-amplitude shear modulus with magnitude and duration of isotropic confining pressure from resonant column tests of sample T10 from borehole CH1.

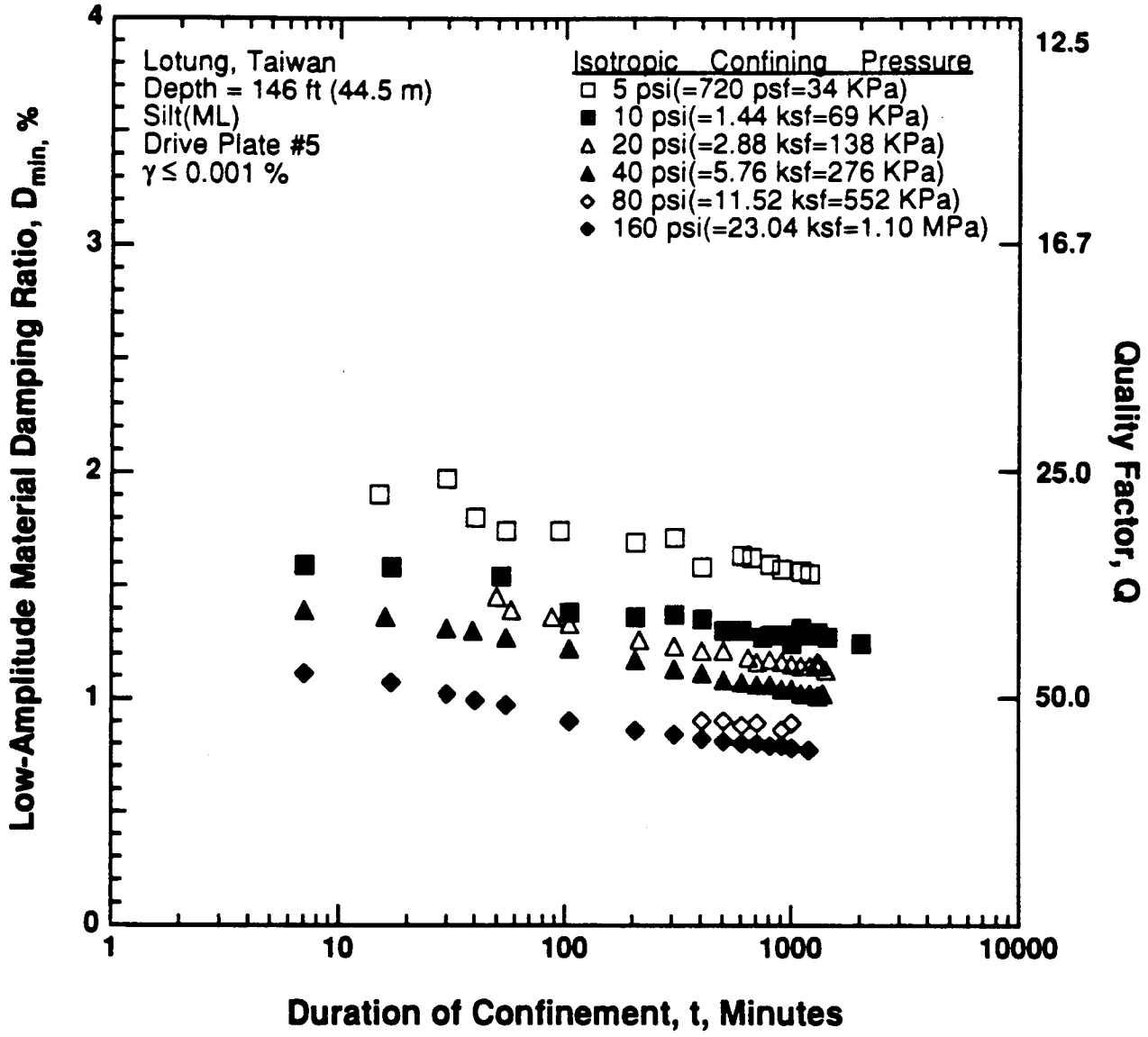

Figure 8.B.3.I-2
Variation in low-amplitude material damping ratio with magnitude and duration of isotropic confining pressure from resonant column tests of sample T10 from borehole CH1.

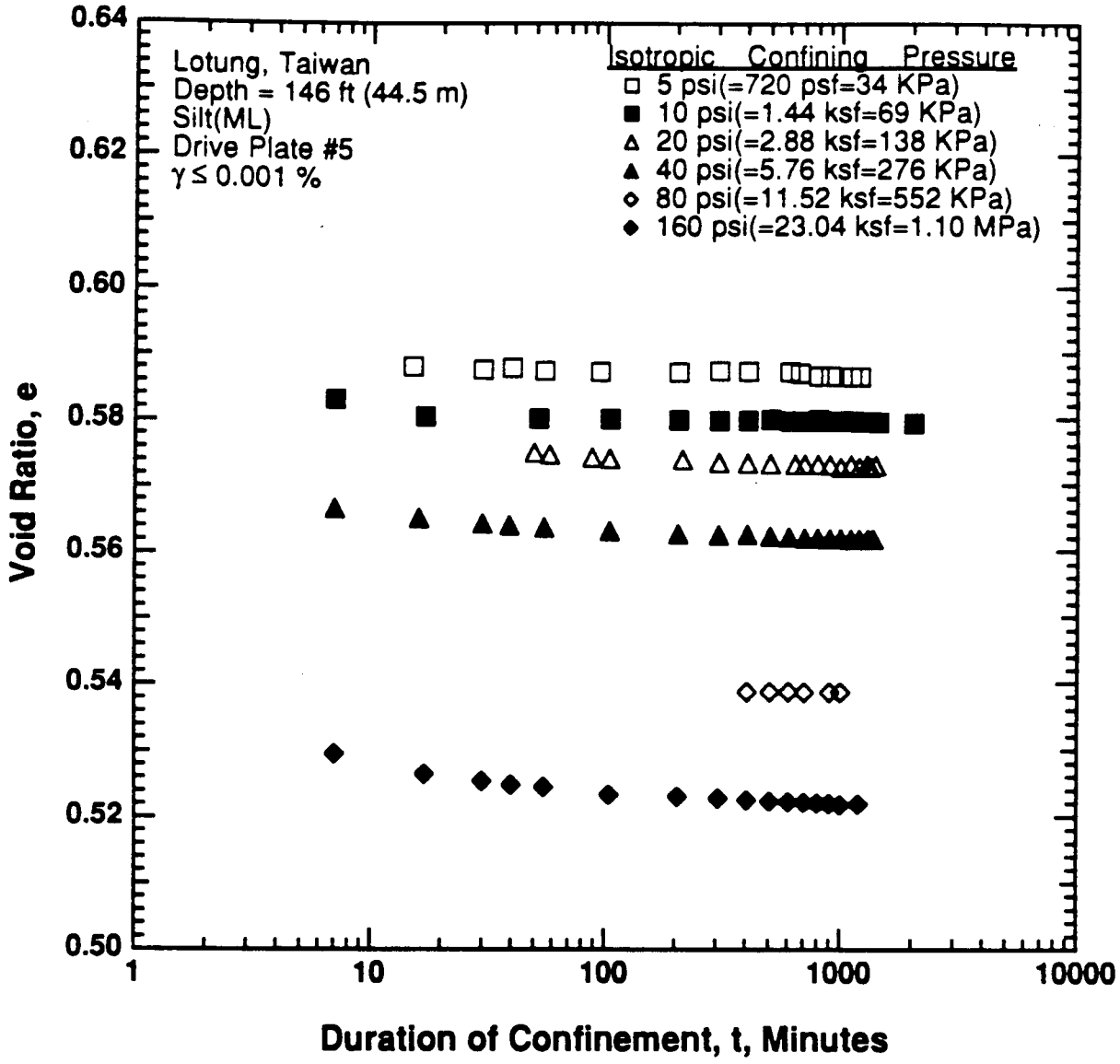

Figure 8.B.3.I-3
Variation in void ratio with magnitude and duration of isotropic confining pressure from resonant column tests of sample T10 from borehole CH1.

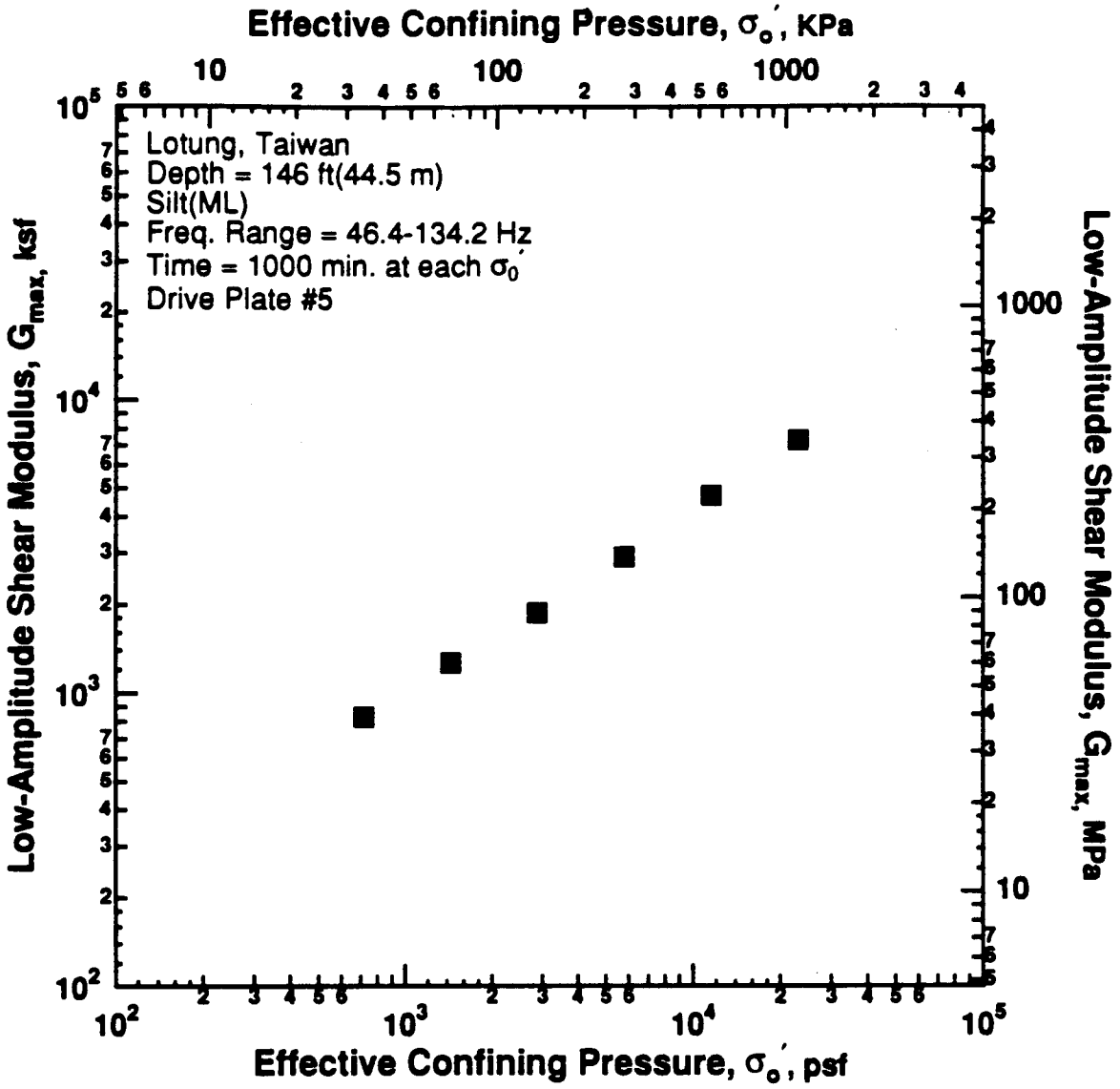

Figure 8.B.3.I-4
Variation in low-amplitude shear modulus with effective confining pressure from resonant column tests of sample T10 from borehole CH1.

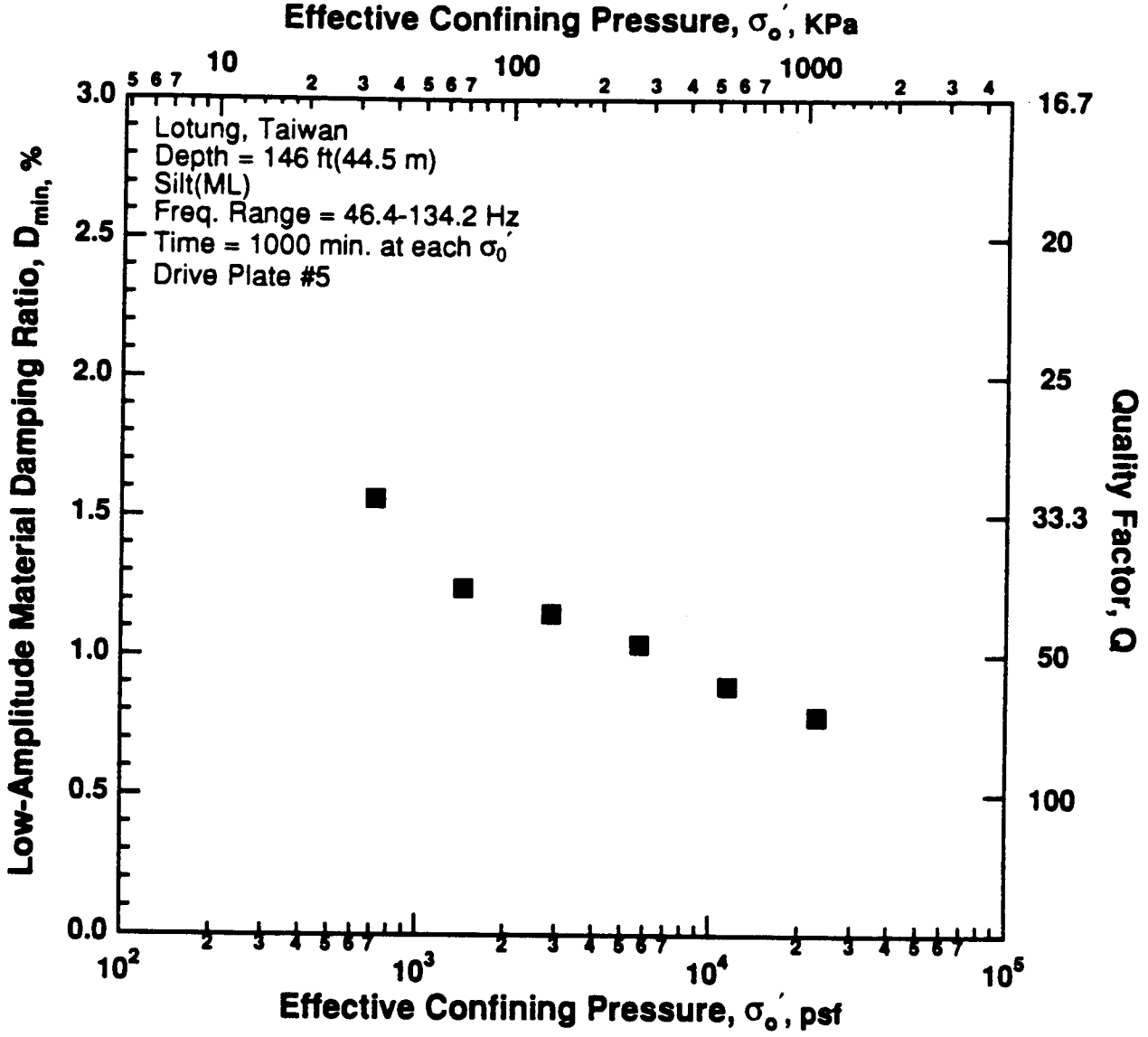

Figure 8.B.3.I-5
Variation in low-amplitude material damping ratio with effective confining pressure from resonant column tests of sample T10 from borehole CH1.

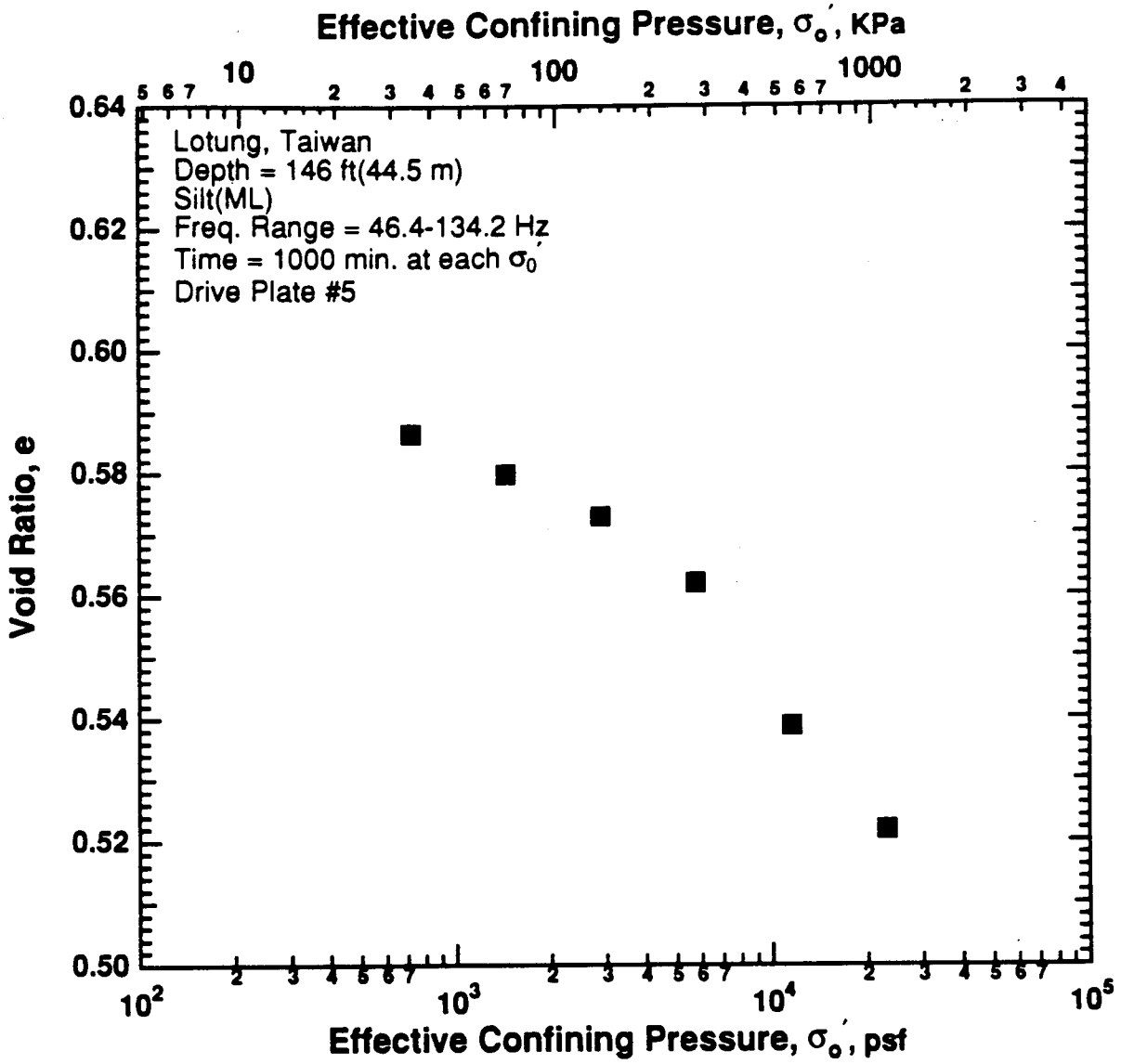

Figure 8.B.3.I-6
Variation in void ratio with effective confining pressure from resonant column tests of sample T10 from borehole CH1.

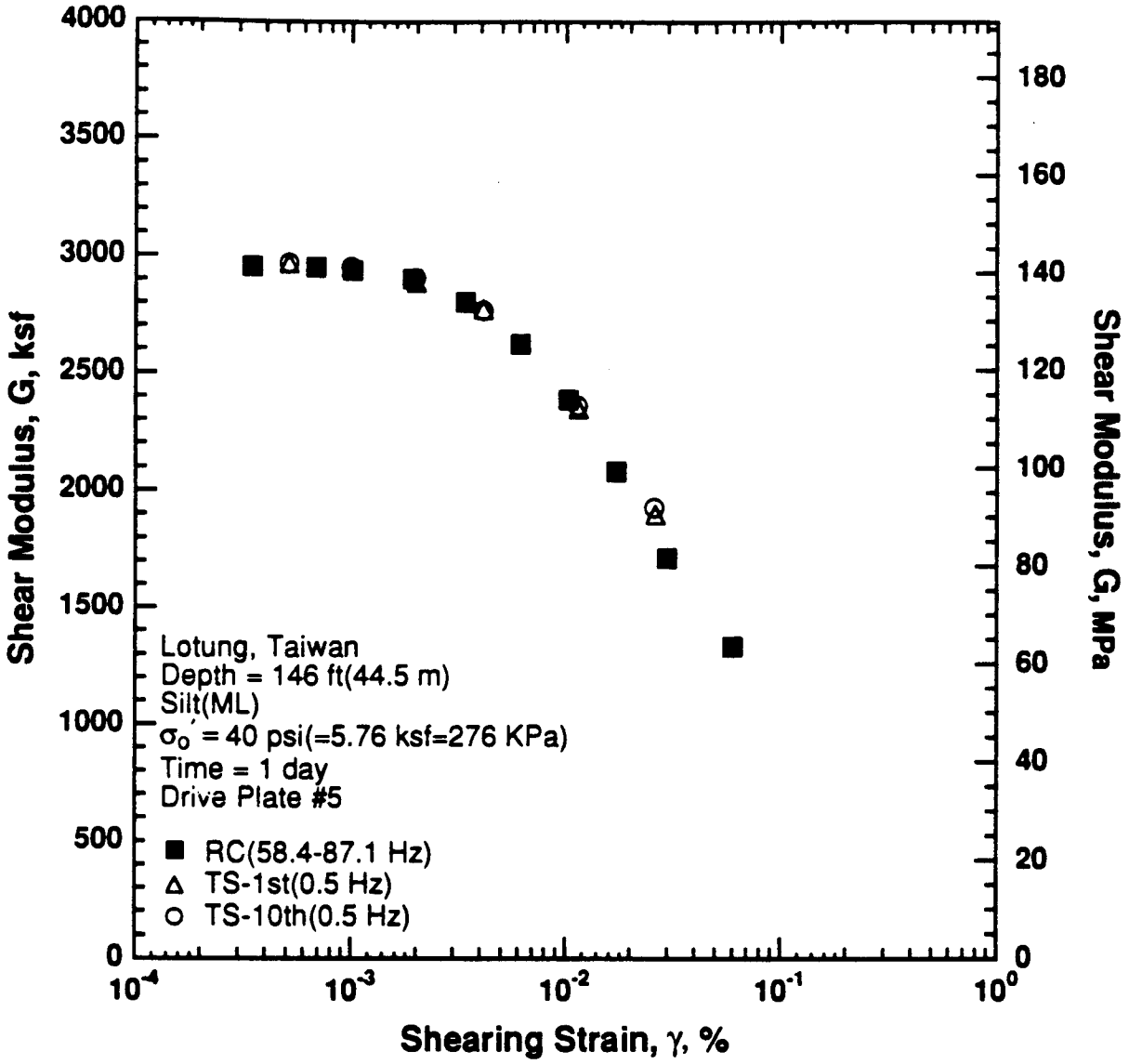

Figure 8.B.3.I-7
Variation in shear modulus with shearing strain at an effective confining pressure of 40 psi (5.76 ksf, 276 kPa) from RCTS tests of sample T10 from borehole CH1.

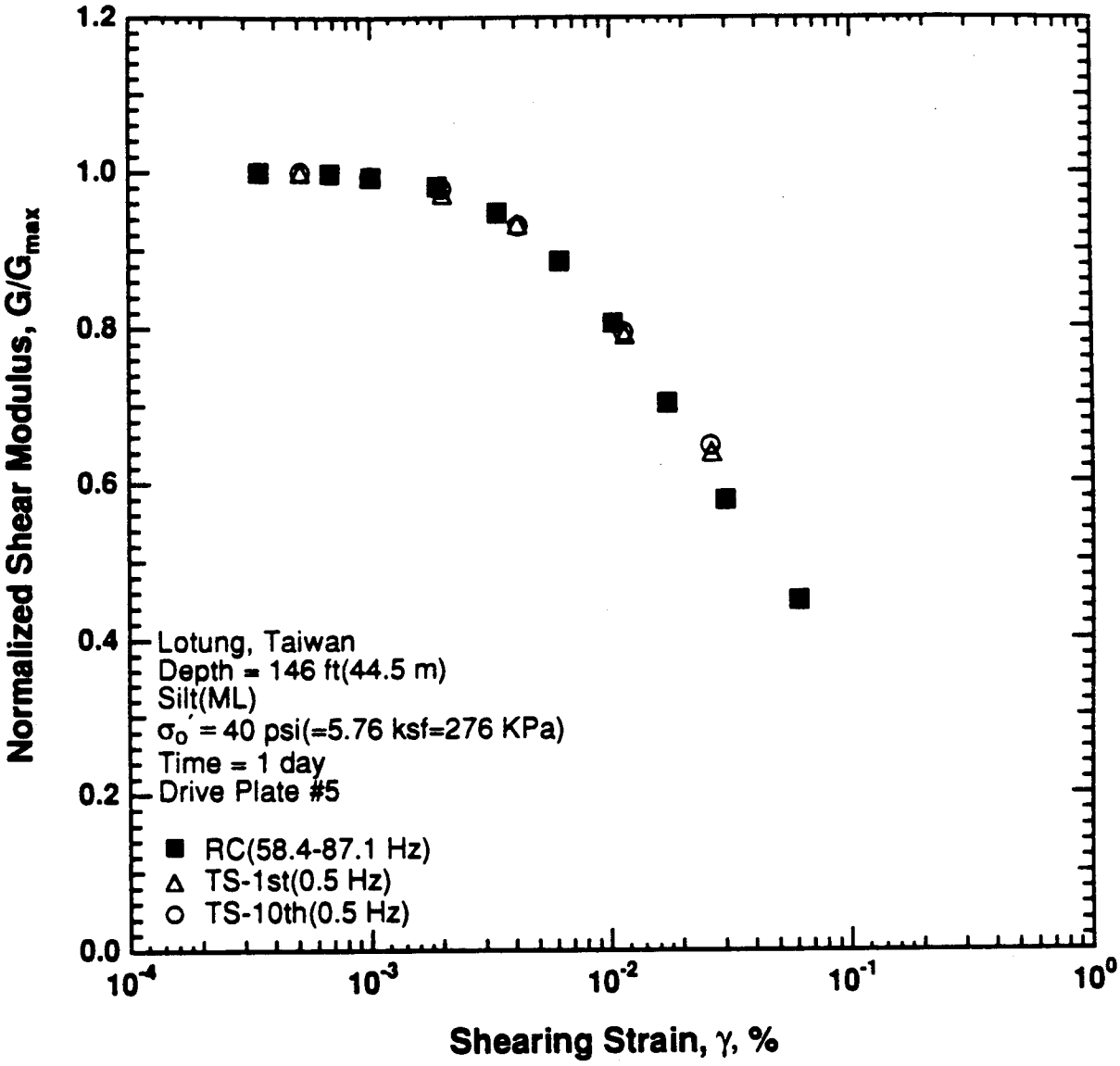

Figure 8.B.3.I-8
Variation in normalized shear modulus with shearing strain at an effective confining pressure of 40 psi (5.76 ksf, 276 kPa) from RCTS tests of sample T10 from borehole CH1.

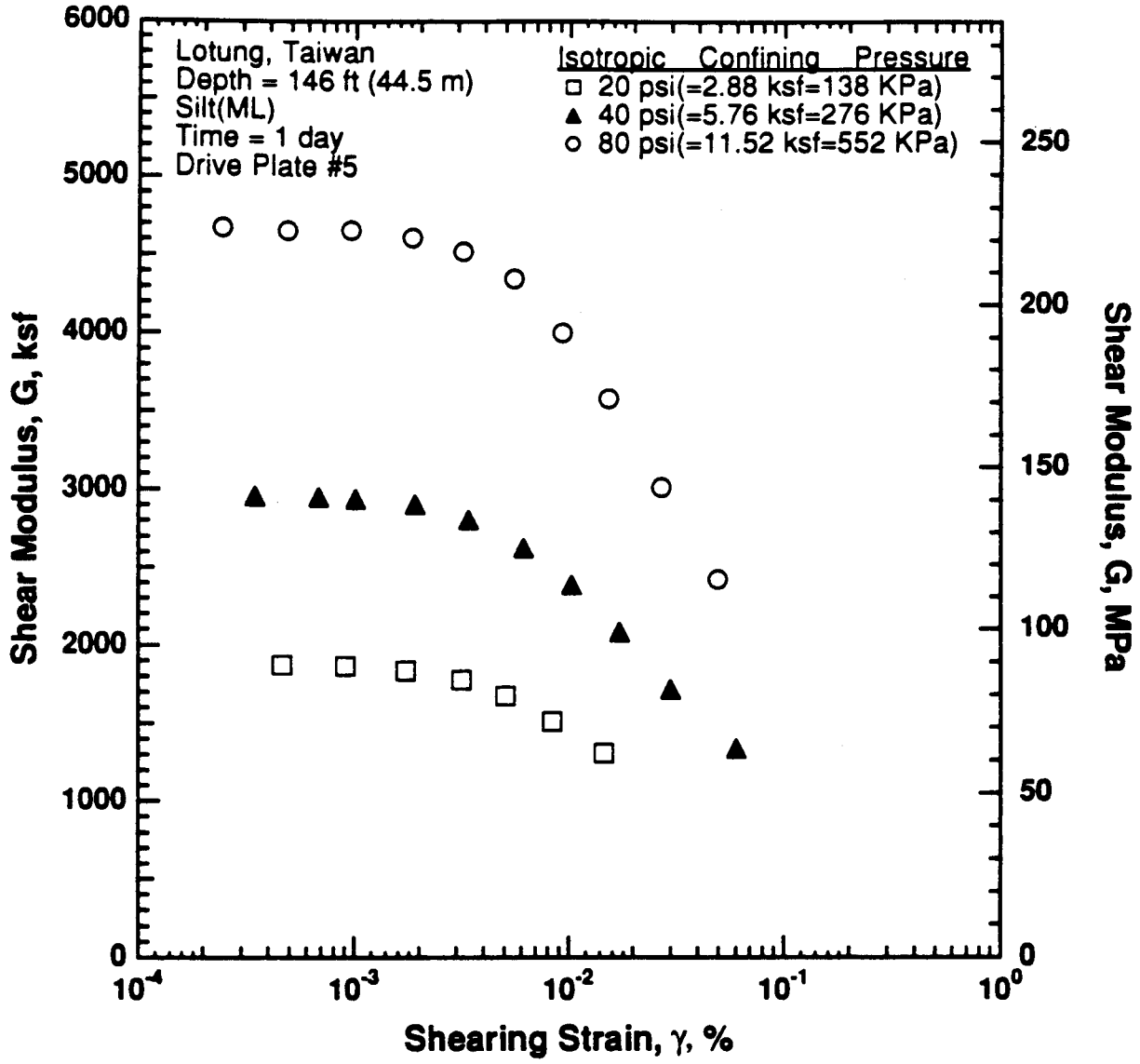

Figure 8.B.3.I-9
Variation in shear modulus with shearing strain and effective confining pressure from resonant column tests of sample T10 from borehole CH1.

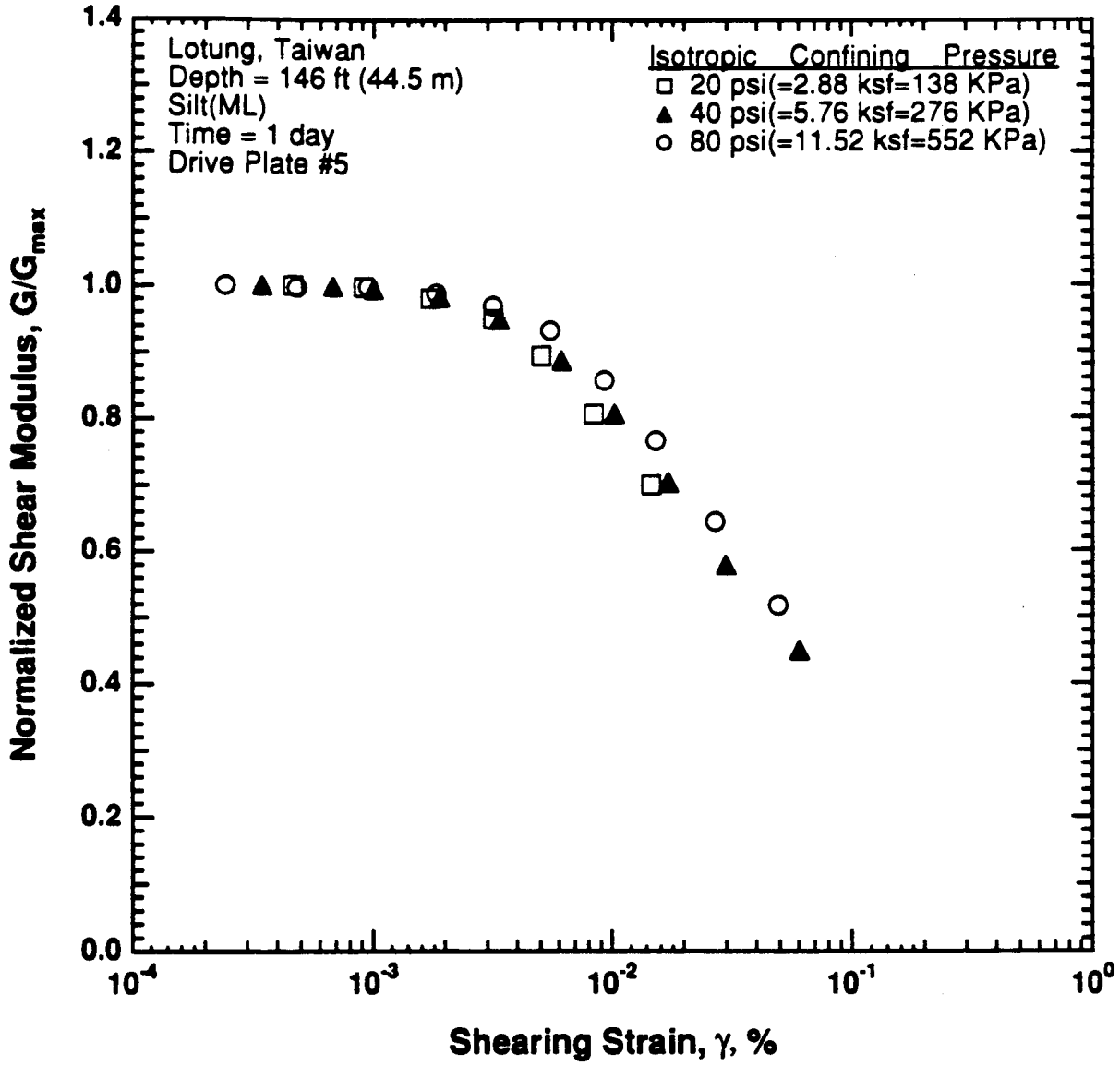

Figure 8.B.3.I-10
Comparison of the variation in normalized shear modulus with shearing strain and effective confining pressure from resonant column tests of sample T10 from borehole CH1.

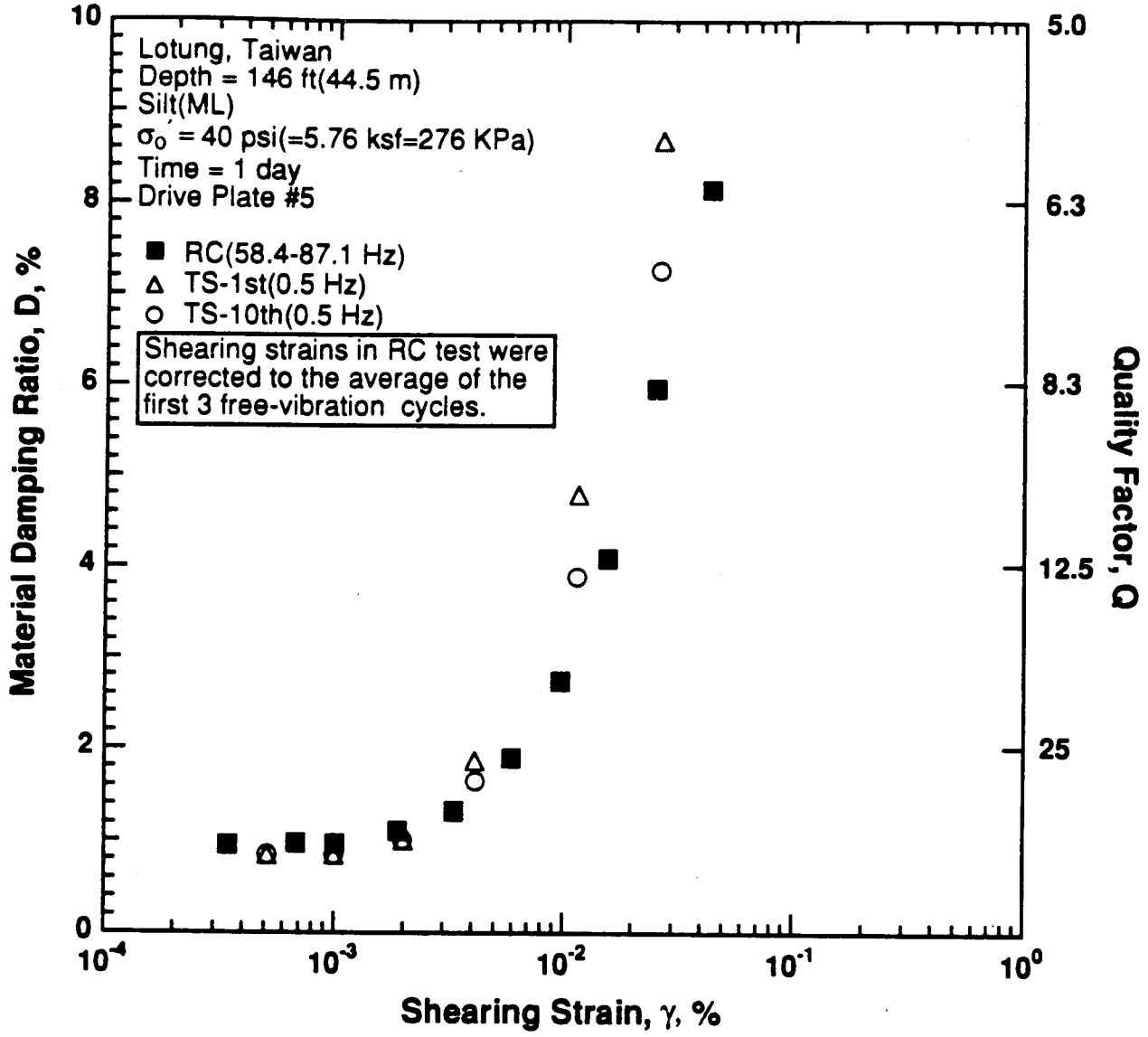

Figure 8.B.3.I-11
Variation in material damping ratio with shearing strain at an effective confining pressure of 40 psi (5.76 ksf, 276 kPa) from RCTS tests of sample T10 from borehole CH1.

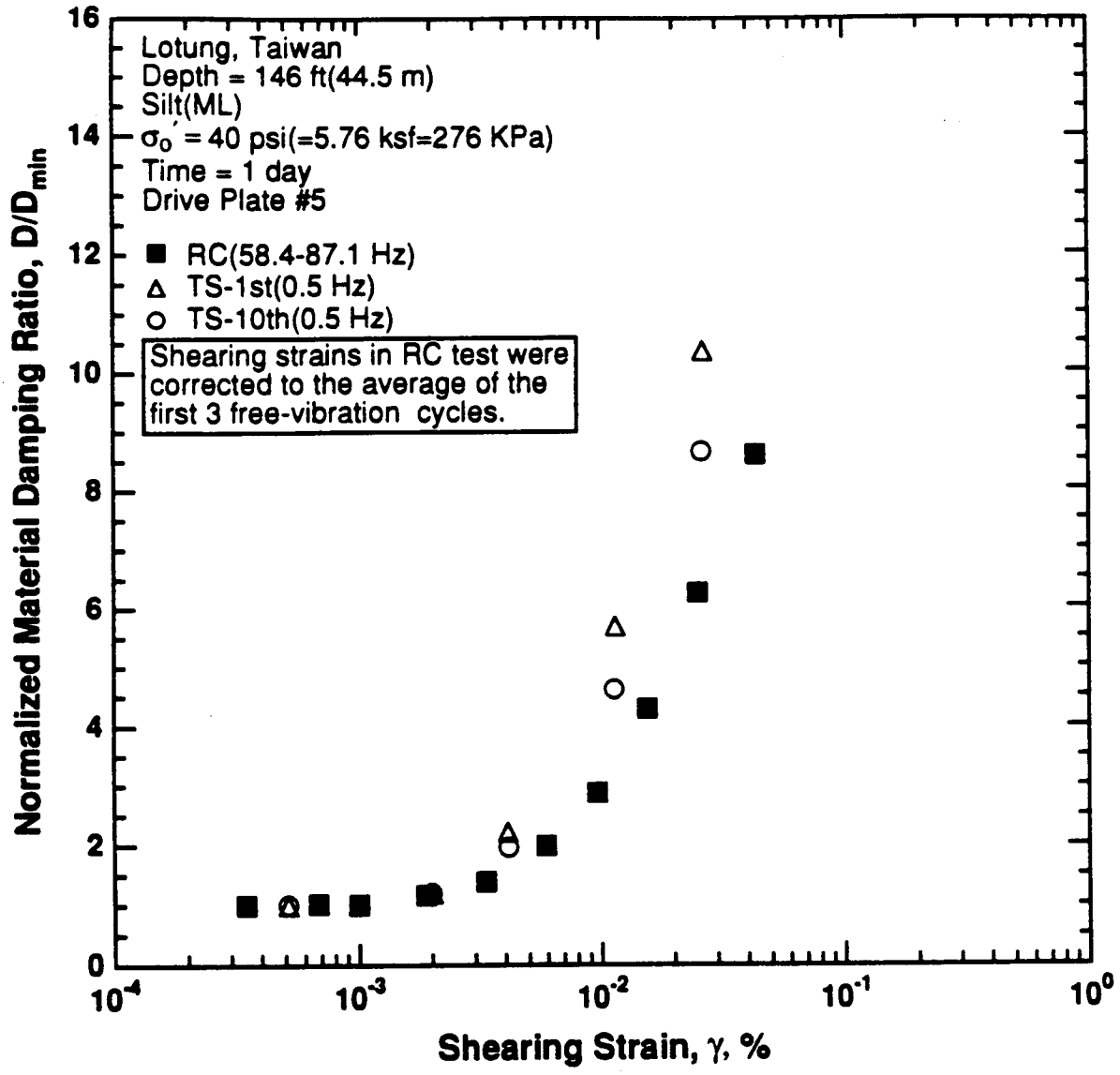

Figure 8.B.3.I-12
Variation in normalized material damping ratio with shearing strain at an effective confining pressure of 40 psi (5.76 ksf, 276 kPa) from RCTS tests of sample T10 from borehole CH1.

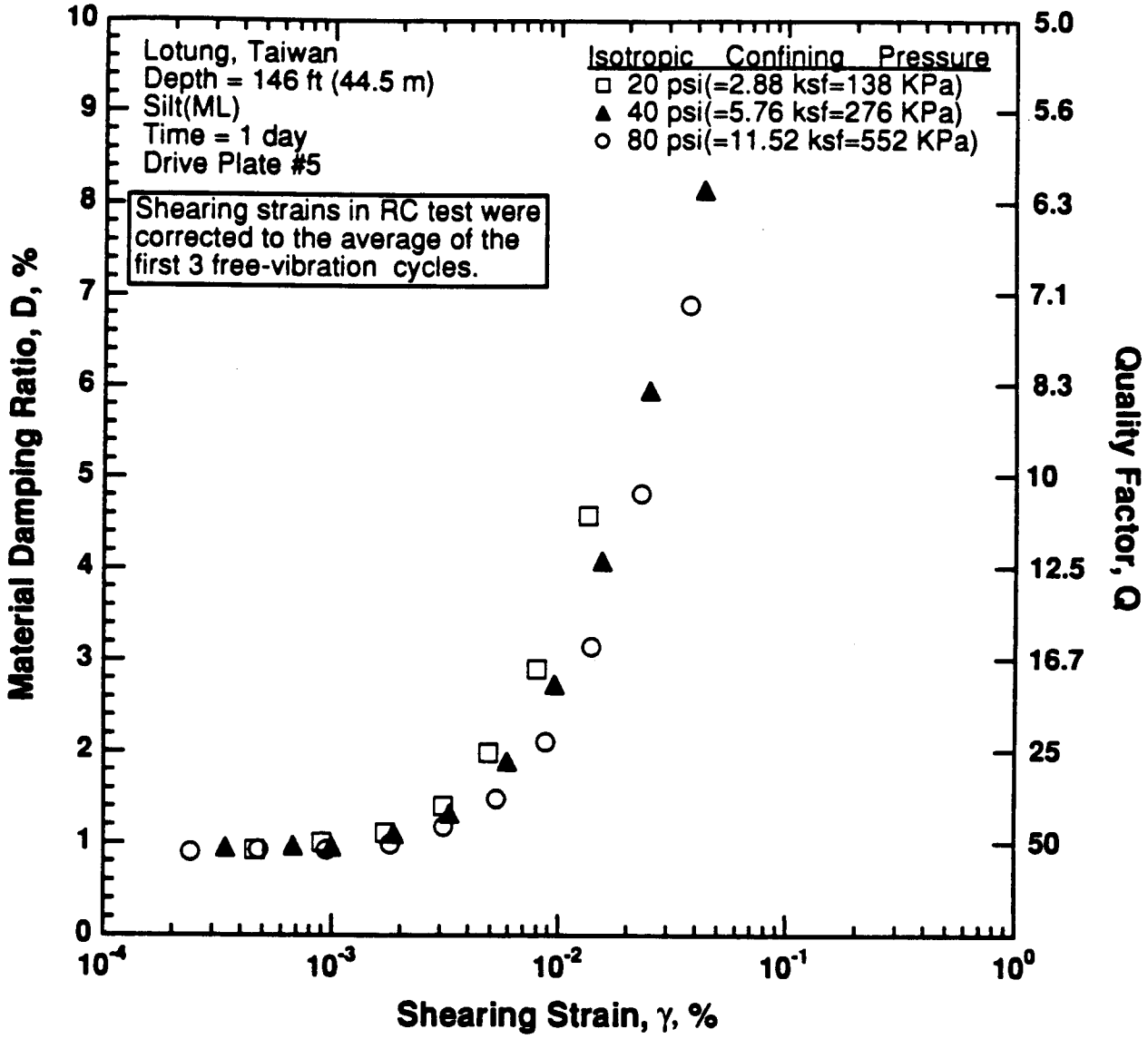

Figure 8.B.3.I-13
Variation in material damping ratio with shearing strain and effective confining pressure from resonant column tests of sample T10 from borehole CH1.

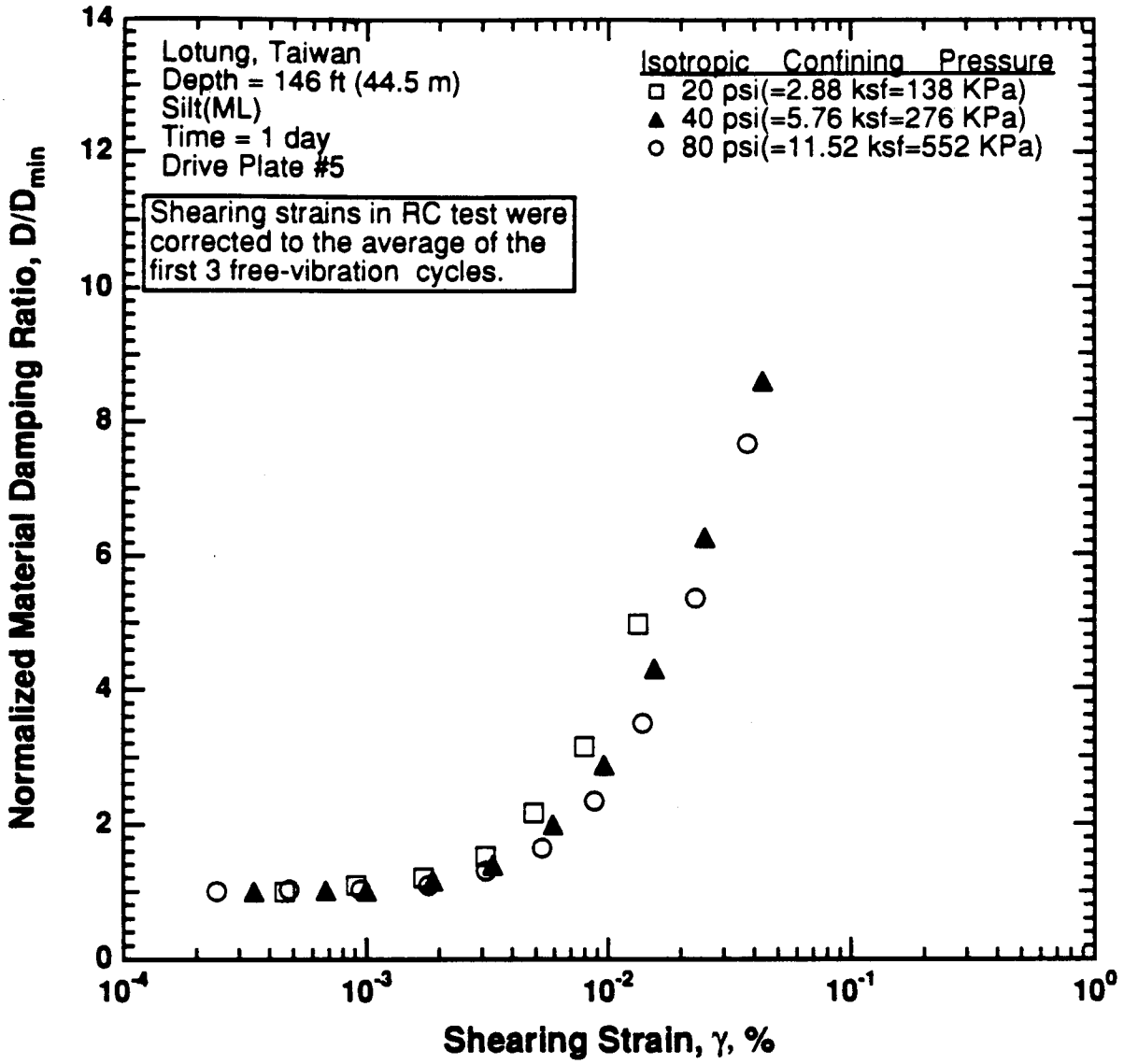

Figure 8.B.3.I-14
Comparison of the variation in normalized material damping ratio with shearing strain and effective confining pressure from resonant column tests of sample T10 from borehole CH1.

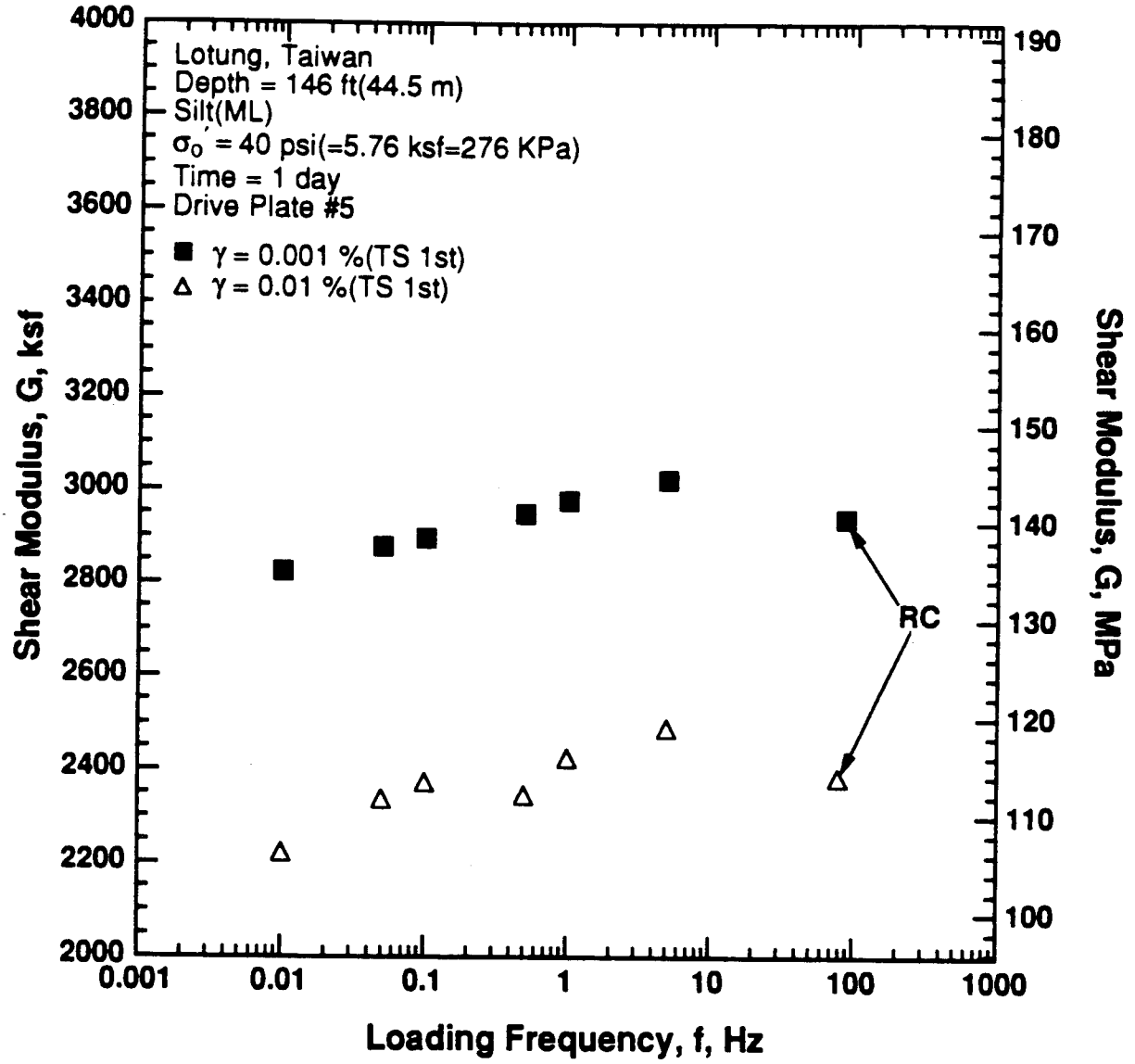

Figure 8.B.3.I-15
Variation in shear modulus with loading frequency and shearing strain at an effective confining pressure of 40 psi (5.76 ksf, 276 kPa) from RCTS tests of sample T10 from borehole CH1.

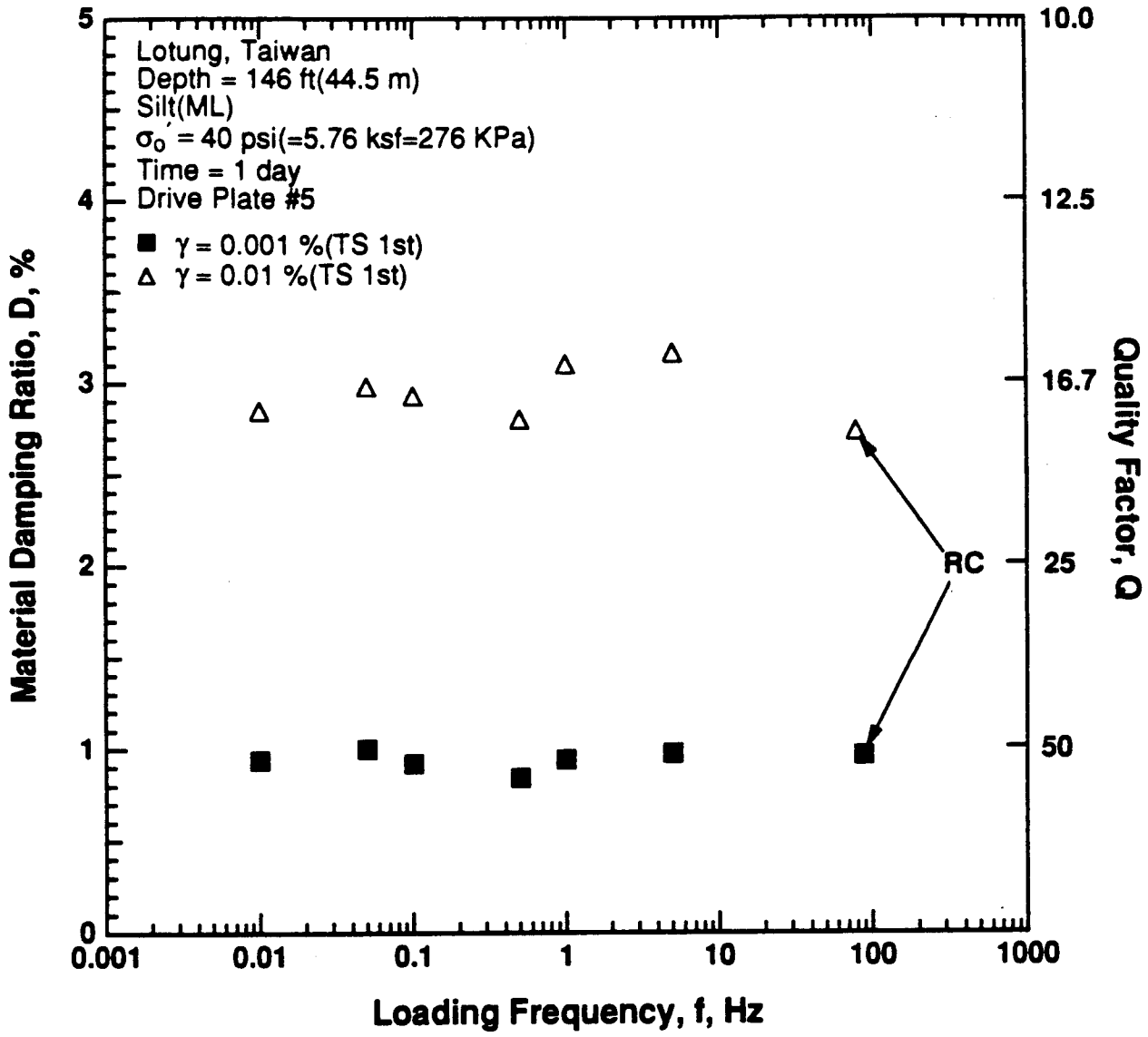

Figure 8.B.3.I-16
Variation in material damping ratio with loading frequency and shearing strain at an effective confining pressure of 40 psi (5.76 ksf, 276 kPa) from RCTS tests of sample T10 from borehole CH1.

APPENDIX 8.B.4
DYNAMIC PROPERTIES OF REMOLDED AND UNDISTURBED SOIL SAMPLES TESTED AT HIGH CONFINING PRESSURES

CONTENTS

APPENDIX 8.B.4
DYNAMIC PROPERTIES OF REMOLDED AND UNDISTURBED SOIL SAMPLES TESTED AT HIGH CONFINING PRESSURES

8.B.4.1 Introduction

To determine the dynamic properties of soils at significant depths, depths on the order of 500 ft to 2000 ft (150 m to 600 m), laboratory tests at high confining pressures were performed. Both remolded and undisturbed specimens were tested to achieve this goal. The dynamic testing was performed between March 1992, and March 1993, as part of the EPRI/DOE Ground Motion Project.

Washed mortar sand was used to build remolded sand specimens. This sand has been used at the University of Texas at Austin in several previous studies (Lee, S.H.H., 1985; Ni, S.H., 1987; Lewis, 1990; Kim, 1991; Lee, J.N. 1993; and Khwaja and Stokoe, 1993). The sand is poorly-graded, with a medium to fine grain size, and classifies as (SP) in the Unified Soil Classification System. The grain size curve of washed mortar sand is shown in Figure 8.B.4-1.

Six remolded sand specimens were constructed in the laboratory. The undercompaction method (Ladd, 1978) was used to constructed each specimens so that all specimens were constructed in the same manner. Initial properties of the specimens are presented in Table 8.B.4-1. The void ratio of the remolded specimens ranged from 0.66 to 0.77. Five samples were constructed dry and also tested dry. In addition, one sample was saturated before testing. The specimen size was either 2 in. (5.1 cm) in diameter and 4 in. (10.2 cm) in height or 2.8 in. (7.2 cm) in diameter and 5.6 in. (14.3 cm) in height.

In addition to the remolded specimens, four undisturbed specimens, two from Treasure Island and two from Lotung, were tested at high confining pressures. The samples from Treasure Island were obtained from depths of 33 ft (10.1 m) and 110 ft (33.6 m) and are classified as a sand with silt (SP-SM). The Lotung samples include a silty sand (SM) from a depth of 59 ft (18.0 m) and a silt (ML) from a depth of 146 ft (44.5 m). The initial properties of the intact samples and the grain size curves for these samples are presented in Table 8.B.4-1 and Figure 8.B.4-1, respectively.

To minimize disturbance effects, each intact sample was extruded from the 3-in. (7.6 cm) diameter sampling tube and hand trimmed to the final specimen dimensions. The dimensions were nominally either 2 in. (5.1 cm) in diameter and 4 in. (10.2 cm) in height or 1.5 in. (3.8 cm) in diameter and 3 in. (7.6 cm) in height. The smaller of the two specimen sizes was used to obtain the larger dynamic strains in testing. No significant problems were encountered in preparation and testing of the undisturbed specimens. The key in the preparation process was cutting the sampling tubes using a high-speed (25,000 rpm) rotary bit used by hobby enthusiasts. The tubes were cut into approximately 6-in. (15.2 cm) lengths before extruding the samples.

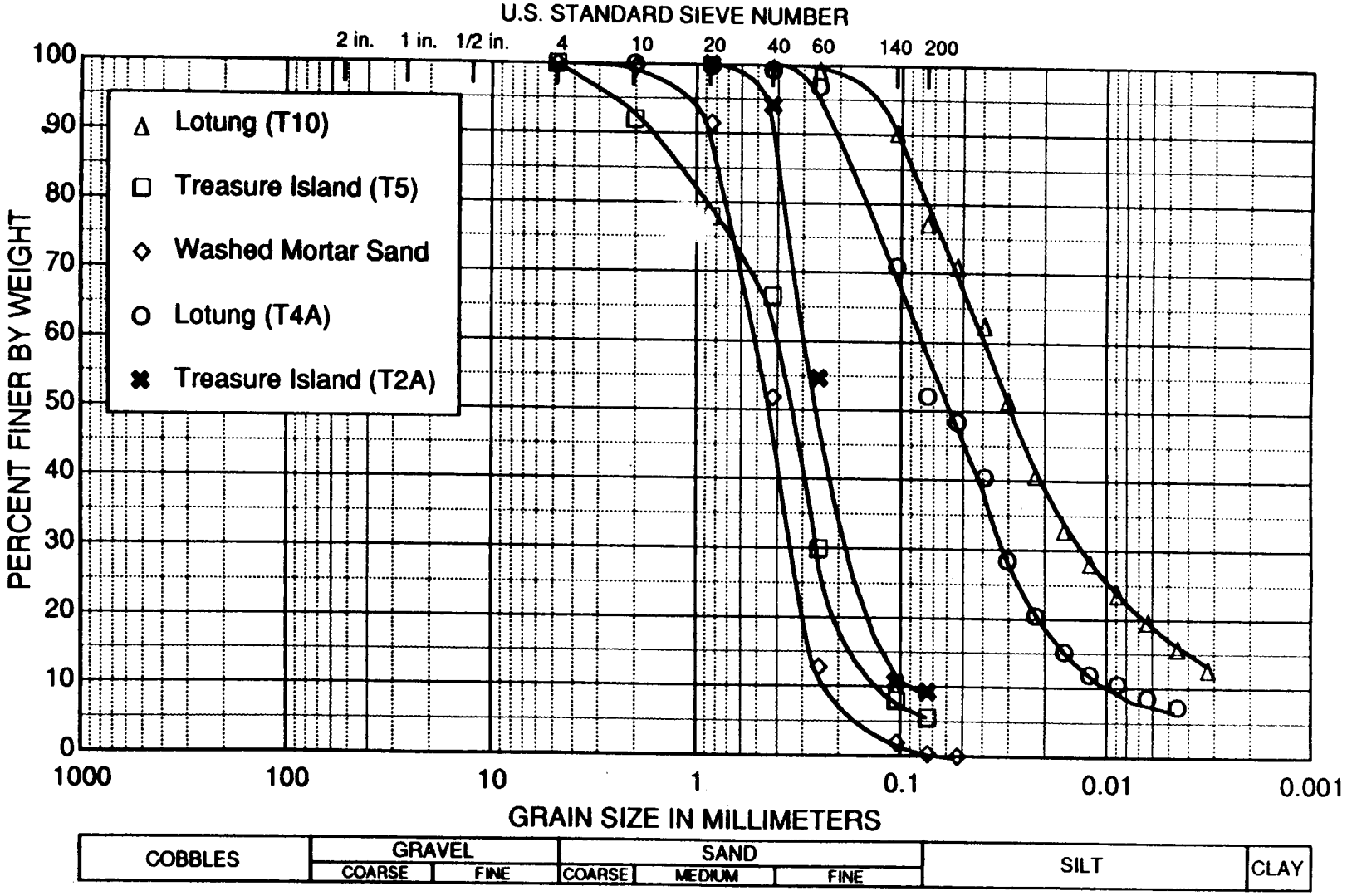

Figure 8.B.4-1
Gradation curves for samples used in high confining pressure tests.

Table 8.B.4-1
Initial Properties of Samples Tested at High Confining Pressures

Sample Number	Depth ft (m)	Soil Type (Unified Soil Classification)	LL %	PI %	D10 (mm)	D30 (mm)	D60 (mm)	Water Content %	Total Unit Weight pcf(g/cm^3)	Void Ratio e	Dia. cm	Height cm	Specific Gravity Gs	Degree of Satuaration %
RS1	-	Sand (SP)	non-plastic		0.23	0.37	0.45	0	100 (1.60)	0.66	5.08	10.16	2.65	0
RS2	-	Sand (SP)	non-plastic		0.23	0.37	0.45	0	99 (1.59)	0.66	5.14	9.96	2.65	0
RS3	-	Sand (SP)	non-plastic		0.23	0.37	0.45	0	96 (1.54)	0.73	5.24	9.98	2.65	0
RS4	-	Sand (SP)	non-plastic		0.23	0.37	0.45	0	94 (1.51)	0.77	5.20	10.36	2.65	0
RS5	-	Sand (SP)	non-plastic		0.23	0.37	0.45	0	97 (1.55)	0.71	7.22	14.30	2.65	0
RS6	-	Sand (SP)	non-plastic		0.23	0.37	0.45	27.0	122 (1.96)	0.72	7.25	14.28	2.65	100
Treasure Island(T5)	110 (33.6)	Sand with Silt (SP-SM)	non-plastic		0.13	0.35	0.46	21.8	114 (1.83)	0.76	3.75	7.61	2.65	76
Lotung CH1(T10)	146 (44.5)	Silt (ML)	non-plastic		0.003	0.013	0.04	24.0	128 (2.06)	0.64	5.01	10.11	2.72[1]	100[2]
Lotung CH1(T4A)	59 (18.0)	Silty Sand (SM)	non-plastic		0.007	0.036	0.100	37.3	110 (1.76)	1.12	3.80	7.63	2.73[1]	90
Treasure Isl.(T2A)	33 (10.1)	Sand with Silt (SP-SM)	non-plastic		0.10	0.18	0.26	20.9	124 (1.98)	0.62	3.75	7.63	2.65	89

1. Specific Gravity was taken from National Taiwan University (1987).
2. Calculated degree of saturation slighty exceeds 100%.

8.B.4.2 Dynamic Laboratory Tests

Resonant column and torsional shear (RCTS) equipment was used to investigate the dynamic characteristics of the samples tested at high confining pressures. This equipment is described in detail in Appendix 8.B.4.A. The dynamic characteristics of concern are the shear modulus, G, and the material damping ratio in shear, D. These parameters were evaluated to determine the influence on them of the following variables:

- magnitude of isotropic state of stress. Six to eight isotropic pressures were used which ranged from below to above the estimated in situ mean effective stress, for the undisturbed samples.
- time of confinement at each isotropic state of stress. Confinement times at each pressure ranged from 1 to about 3 days for undisturbed samples, and from 15–50 minutes for the remolded specimens since previous studies have shown that time of confinement has minimal effect on shear modulus and damping ratio for washed mortar sand.
- shearing strain amplitude. Strains ranged from the small-strain range, less than 0.001%, to rather large strain amplitudes, strains slightly above 0.2%.
- numbers of cycles of loading. One to ten cycles of loading were used in the torsional shear test followed by 500 to 1000 cycles in the resonant column test.
- excitation frequency. Frequencies ranging from 0.1 Hz to about 10 Hz were used in the torsional shear test while the frequency associated with resonance in the resonant column test varied with soil stiffness and ranged from between 20 Hz to about 225 Hz.

8.B.4.2.1. Testing Program

For dynamic testing of the remolded sand samples, G and D were evaluated over a range of confining pressures. Typically, the confining pressure was doubled upon completing the required tests at the previous level. Low-amplitude resonant column testing was performed at each confining pressure to determine the influence of time and confining pressure on the small-strain shear modulus, G_{max}, and small-strain material damping ratio, D_{min}. Low-amplitude dynamic tests are defined as those tests in which the resonant amplitude did not exceed 0.001% and typically was considerably below that level.

For the undisturbed specimens, the confining pressures tested were based on the estimated in situ mean effective stress, σ_m'. For example, this was done at the Lotung site by assuming the water table is at a depth of 1.2 ft (0.4 m), the total unit weight of the soil averages 120 pcf (18.8 kN/m^3), the soil is saturated throughout the profile, and the effective coefficient of earth pressure at rest, K_o', is 0.5. The resulting values of σ_m' for each sample are given in Table 8.B.4-2. Once σ_m' was estimated, the range in confining pressures over which G and D would be evaluated was determined. Typically, isotropic confining pressures on the order of $0.25\sigma_m'$, $0.5\sigma_m'$, σ_m', $2\sigma_m'$ and $4\sigma_m'$ were selected, as well as additional confining pressures up to about 500 psi.

A summary of all confining pressures at which low-amplitude resonant column tests were performed is given in Table 8.B.4-2. In addition to small-strain testing, high-amplitude tests were performed on four of the six remolded sand specimens. For the remolded sand specimens, high-amplitude tests were typically performed only up to shearing strains, γ, of 0.01% at selected confining pressures, and only after all low-amplitude testing was completed at the given pressure. High-amplitude testing, with the largest strains possible was then attempted at one of the highest confining pressures. For the undisturbed specimens, high-amplitude testing was completed at one or more confining pressures, including the estimated in situ mean effective stress.

Table 8.B.4-2
Summary of Resonant Column and Torsional Shear Tests Performed for Samples Tested at High Confining Pressures

Sample Number	Depth ft (m)	Estimated In Situ Mean EffectiveStress, σ_m', psf	Isotropic Test Pressure, psf		
			Low-Amplitude Resonant Column Tests	High-Amplitude Resonant Column Tests	Torsional Shear Test
RS1	N/A	N/A	576, 1152, 2304, 4608, 9216, 2304, 576, 2304, 9216, 18432, 36864, 9216, 2304, 1152, 4608, 18432, 36864, 73728, 18432, 4608, 1152	None	None
RS2	N/A	N/A	576, 1152, 2304, 4608, 9216, 18432, 36864, 72000	576, 1152, 2304, 4608, 9216, 18432, 36864, 72000	None
RS3	N/A	N/A	864, 1440, 2592, 4896, 9504, 18720, 37152, 72288	864, 1440, 2592, 4896, 9504, 18720, 37152, 72288	None
RS4	N/A	N/A	576, 1152, 2304, 4608, 9216, 18432, 36864, 72000	None	None
RS5	N/A	N/A	576, 1152, 2160, 4320, 8640, 17280, 34560	1152, 4320, 17280	1152, 4320, 17280
RS6	N/A	N/A	576, 1152, 2160, 4320, 8640, 17280, 34560	1152, 4320, 17280	1152, 4320, 17280
Treasure Island(T5)	110(33.6)	4392	576, 1152, 2304, 4608, 9216, 18432, 36864	4608, 18432	4608, 18432
Lotung CH1(T10)	146(44.5)	5648	720, 1440, 2880, 5760, 11520, 23040, 34560, 11520, 5760	2880, 5760, 11520, 23040, 34560, 11520, 5760	5760, 34560
Lotung CH1(T4A)	59(18.0)	2318	2304, 4608, 9216, 18000, 36000, 72000	72000	72000
Treasure Isl.(T2A)	33(10.1)	1434	2880, 5760, 9360, 18720, 36000, 72000	72000	72000

High-amplitude testing is defined as any test in which the peak shearing strain exceeds 0.001%. This testing was composed of two series of tests. The first involved cyclic torsional (TS) shear testing as illustrated in Figure 8.B.4-2. A complete set of torsional shear tests took about three hours to perform, was performed under drained conditions although no drainage was observed, and involved shearing strains, γ, from less than 0.001% to above 0.05%, depending on the soil stiffness. The majority of the measurements were performed at 0.5 Hz and are labeled as TS1 in Figure 8.B.4-2. However, two sets of TS tests, one at $\gamma \approx 0.001\%$ and one at $\gamma \approx 0.01\%$, were conducted to evaluate the effect of excitation frequency on G and D at those strain amplitudes. In these tests, (denoted as TS2 in Figure 8.B.4-2) one to four cycles of loading was applied at about five different frequencies ranging from 0.1 Hz to about 10 Hz.

After the TS tests were completed, confinement of the sample was continued at the given confining pressure, and a series of high-amplitude resonant column (RC) tests was performed the next day. However, before high-amplitude RC testing commenced, small-strain RC tests were performed to determine if any changes in the soil skeleton had occurred from the TS tests. In essentially all cases, no changes in G_{max} or D_{min} from the TS tests were measured.

Once the small-strain datum was re-established after the TS tests, high-amplitude resonant column testing was conducted to evaluate the influence of strain amplitude on G and D. This series of tests is illustrated in Figure 8.B.4-3. A complete set of resonant column tests took about one hour to perform, was performed under drained conditions just as in the case of the TS tests, and involved shearing strains from less than 0.001% to above 0.1%, depending on the soil stiffness. In these tests, 500 to 1000 cycles of loading is required at each strain measurement.

Upon completion of the high-amplitude RC tests, low-amplitude RC tests were performed to determine if any changes in the soil skeleton had occurred from the high-amplitude tests. In some cases, changes occurred. At that point, confinement of the sample at σ_m' was continued until G_{max} and D_{min} returned to the values before the high-amplitude tests or the change in values was noted in the next stage of testing.

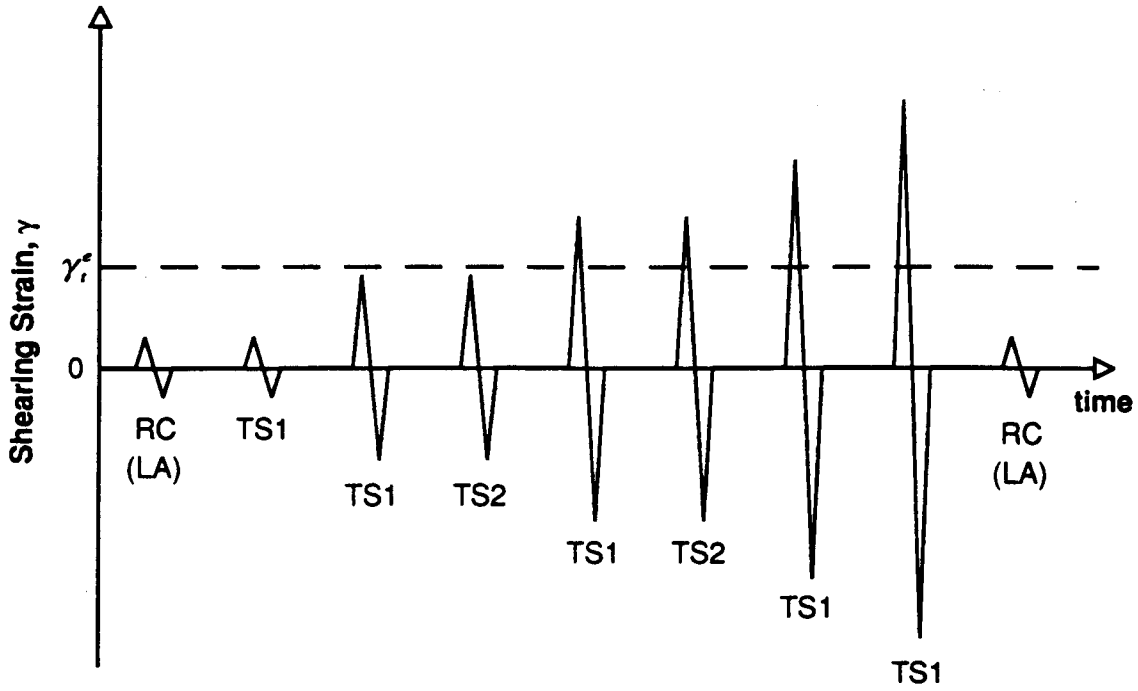

γ_t^e = elastic threshold strain; below γ_t^e, G is constant and equal to G_{max}

RC (LA) = resonant column test at low-amplitudes (strains < 0.001%)

TS1 = torsional shear test in which 1 to 10 cycles are applied at 0.5 Hz

TS2 = torsional shear test in which 4 cycles are applied at each of approximately 5 frequencies between 0.1 to 10 Hz

Figure 8.B.4-2
Testing procedure used in the torsional shear test to investigate the effects of strain amplitude, number of loading cycles, and excitation frequency on G and D of the remolded sand and undisturbed samples.

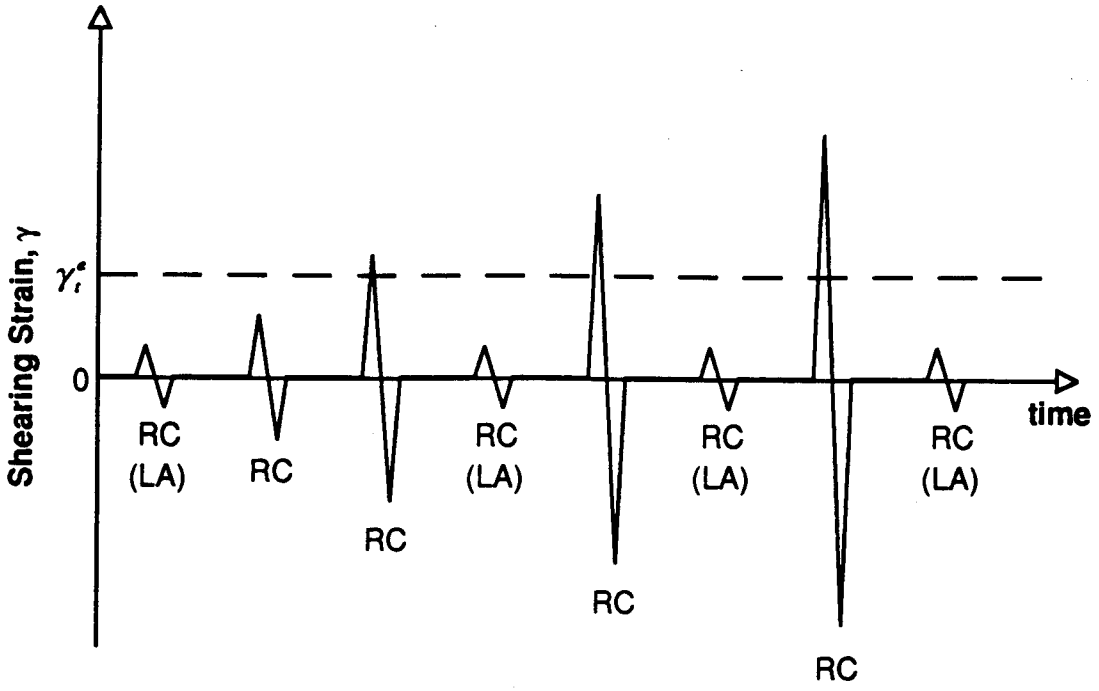

γ_t^e = elastic threshold strain; below γ_t^e, G is constant and equal to G_{max}

RC (LA) = resonant column test at low-amplitudes (strains < 0.001%)

RC = resonant column test in which 500 to 1000 cycles of loading is applied during each measurement

Figure 8.B.4-3
Testing procedure used in the resonant column test to investigate the effects of strain amplitude on G and D of remolded sand and undisturbed samples.

8.B.4.2.2. Test Results

The results of the RC and TS tests are shown in Appendices 8.B.4.B through 8.B.4.K for the term samples tested at high confining pressures. Each appendix presents the results for one sample. Although testing of the samples at high confining pressures varied somewhat between samples, Appendix 8.B.4.F is presented as an example of general results.

The results are presented in Appendix 8.B.4.F as follows.

1. Figure 8.B.4.F-1 shows the variation in G_{max} at a confinement time of 15 minutes with effective confining pressure from the RC tests.
2. Figure 8.B.4.F-2 shows the variation in normalized G_{max} at a confinement time of 15 minutes with effective confining pressure from the RC tests.
3. Figure 8.B.4.F-3 shows the variation in D_{min} at a confining time of 15 minutes with effective confining pressure from the RC tests.
4. Figure 8.B.4.F-4 shows the variation in void ratio of the sample at a confinement time of 15 minutes with effective confinement pressure.
5. Figure 8.B.4.F-5 shows the variation in G with log γ at a specific confining pressure from the high-amplitude RC and TS tests.
6. Figure 8.B.4.F-6 shows the variation in G/G_{max} with log γ at a specific confining pressure from the high-amplitude RC and TS tests.
7. Figure 8.B.4.F-7 shows the variation in G with log γ at all tests pressures where high-amplitude RC tests were performed.
8. Figure 8.B.4.F-8 is the normalized (G/G_{max}) version of Figure 8.B.4.F-7.
9. Figures 8.B.4.F-9 through 8.B.4.F-12 are simply the damping ratio curves which are companions to the modulus curves given in Figures 8.B.4.F-5 through 8.B.4.F-8.
10. Figure 8.B.4.F-13 shows the effect of excitation frequency on G at two strain amplitudes.
11. Figure 8.B.4.F-14 shows the effect of excitation frequency on D at two strain amplitudes.

8.B.4.3 Comparison of Results

The variation of small-strain shear modulus, G_{max}, with effective confining pressure, σ_o', for the ten samples tested in this study are presented in Figure 8.B.4-4. For the undisturbed samples, only pressures which are assumed to be in the normally consolidated range are plotted. Results from the remolded samples form a narrow band in which log G_{max} linearly increases with log σ_o'. However, the results from the undisturbed samples vary in slope and magnitude, but appear to converge at very high confining pressures. The remolded specimens are fit with the Hardin (1978) equation to account for the variation in void ratio, as shown in Figure 8.B.4-5.

In Figure 8.B.4-6, the variation of small-strain material damping ratio, D_{min}, with effective confining pressure, σ_o', for the ten samples tested in this study are presented. In this case, there is a significant decrease in D_{min} as σ_o' is raised to high confining pressures. In addition, the material damping ratio obtained from the undisturbed samples is significantly higher than that of the remolded specimens. However, it should be noted that the values of D_{min} at high confining pressures are still quite low, less than 2% (or $Q > 25$).

Results of normalized shear modulus, G/G_{max}, versus shearing strain, γ, are compared in Figures 8.B.4-7 through 8.B.4-10. In Figure 8.B.4-7, it can be seen that the trend is quite dependent on the σ_o' at which the sample is tested. At high confining pressures, the G/G_{max} versus log γ curves are located to the right of the upper bound of the Seed and Idriss (1970) curve for sands. A comparison of G/G_{max} versus log γ for undisturbed and remolded specimens at similar effective confining pressures is presented in Figures 8.B.4-8 and 8.B.4-9. The shifting of the G/G_{max} versus log γ curve to the right of the Seed and Idriss (1970) curve is clearly shown at σ_o' of 500 psi (3.45 MPa) in Figure 8.B.4-9. The results of a saturated remolded specimen and a dry remolded specimen are compared in Figure 8.B.4-10.

Figures 8.B.4-11 through 8.B.4-15 are the damping ratio curves which are companions to the modulus curves given in Figures 8.B.4-7 through 8.B.4-10. It may be noted that the material damping ratios obtained for the remolded samples are always less than those of the undisturbed samples at essentially all shearing strains.

The damping ratios of the remolded specimens are close to the lower bound proposed by Seed and Idriss (1970) for sands at γ less than 0.001%. On the other hand, the damping ratios of the intact specimens range from above the upper bound proposed by Seed an Idriss (1970) at γ of about 0.0001% to within the range proposed by Seed and Idriss at γ of 0.001%.

As shearing strain exceeds 0.01%, material damping ratios of the remolded and intact samples are generally less than those give by the lower-bound Seed and Idriss (1970) curve for sands. At a confining pressure of 500 psi (3.45 MPa), the damping valves of the intact specimens are considerably less than the Seed-Idriss curve (Fig. 14). However, as shown in the testing of the Lotung and Treasure Island specimens, material damping in the first few cycles of torsional shear is considerably above that measured in the resonant column test for granular specimens. Thus, these specimens should be expected to exhibit higher damping in the first few cycles of loading at $\gamma > 0.01\%$.

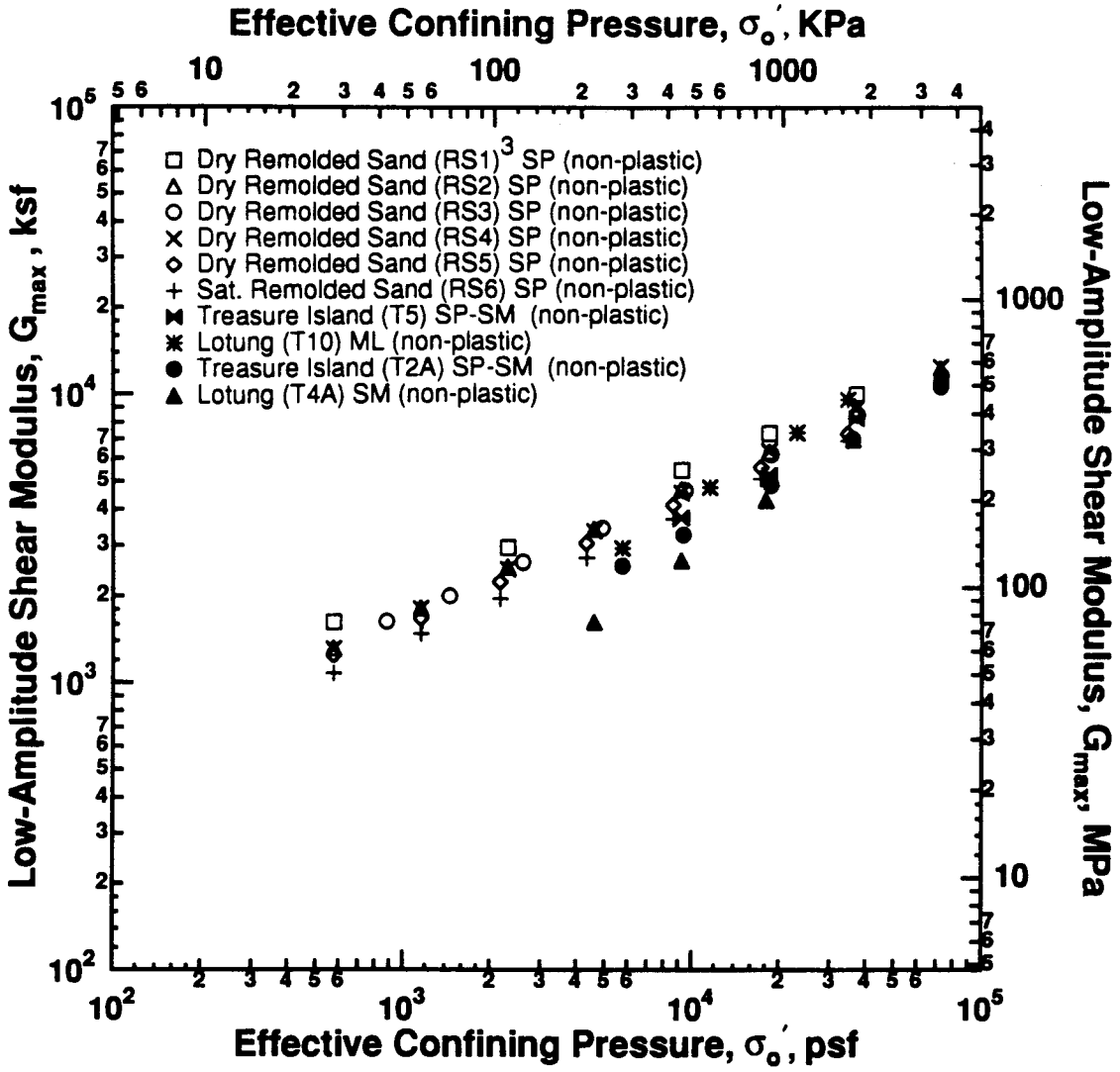

Notes:

1. G_{max} measured at t = 15-50 min. at each σ_o' for remolded sand samples of washed mortar sand.
2. G_{max} measured at t = 1000 min. at each $\sigma_o' \geq \sigma_m'$ for undisturbed samples from Lotung and Treasure Island.
3. Second Loading Cycle (B) is plotted.
4. σ_m' = estimated in situ mean effective stress using K_o = 0.5.

Figure 8.B.4-4
Variation in low-amplitude shear modulus with effective confining pressure from resonant column tests of remolded sand samples and undisturbed samples tested at $\sigma_o' \geq \sigma_m'$.

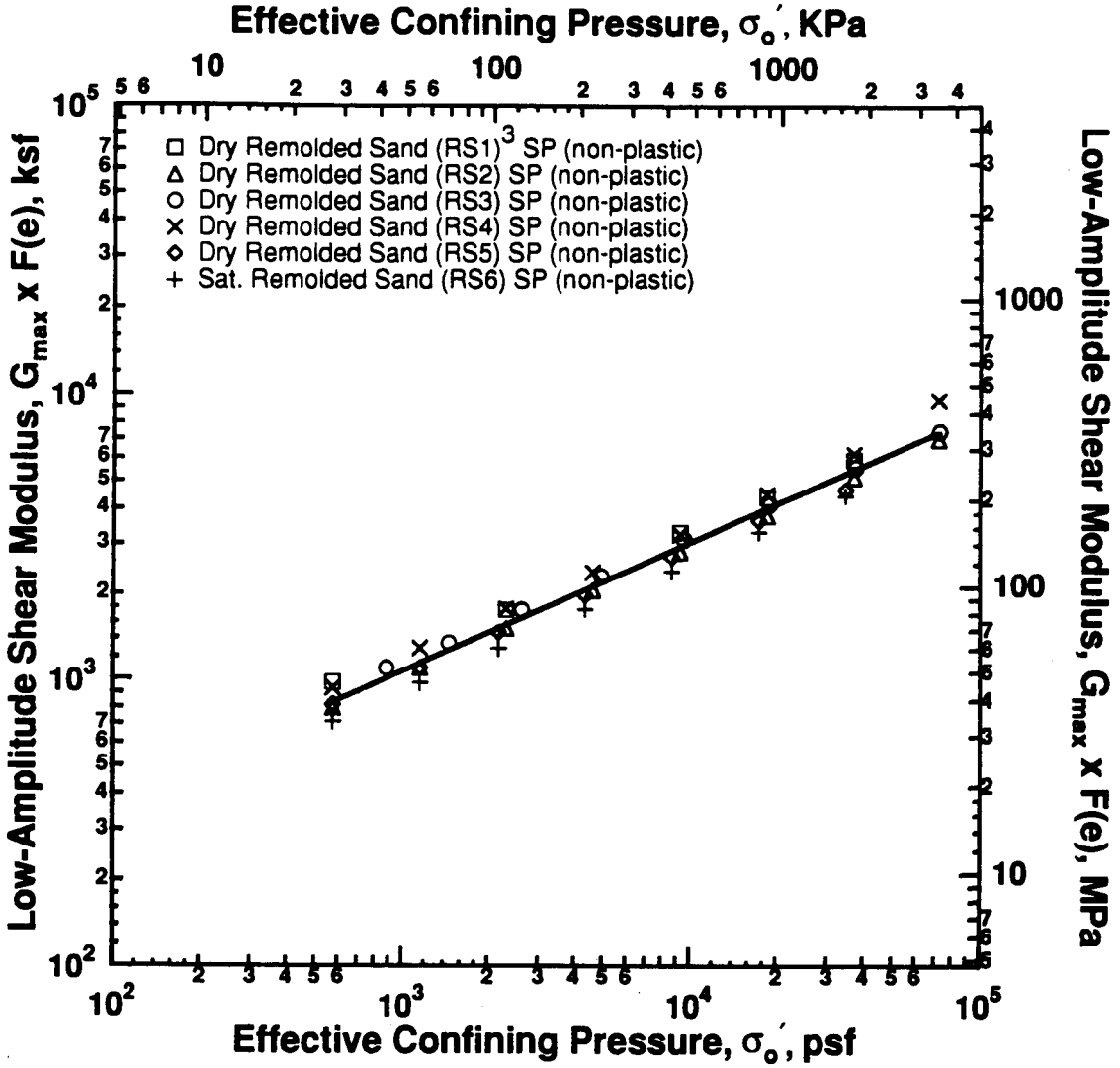

Notes:

1. G_{max} measured at t = 15-50 min. at each σ_o' for remolded sand samples of washed mortar sand.
2. Best-Fit Curve:
   $G_{max} \times F(e) = A \times P_a^{(1-n)} \times \sigma_o'^{(n)}$
   $F(e) = 0.3 + 0.7 \times e^2$, P_a = 2117 psf
   n = 0.445, A = 703
3. Second Loading Cycle (B) is plotted.

Figure 8.B.4-5
Best-fit curve to log G_{max} x F(e) – log σ_O' relationship from resonant column tests of remolded sand samples.

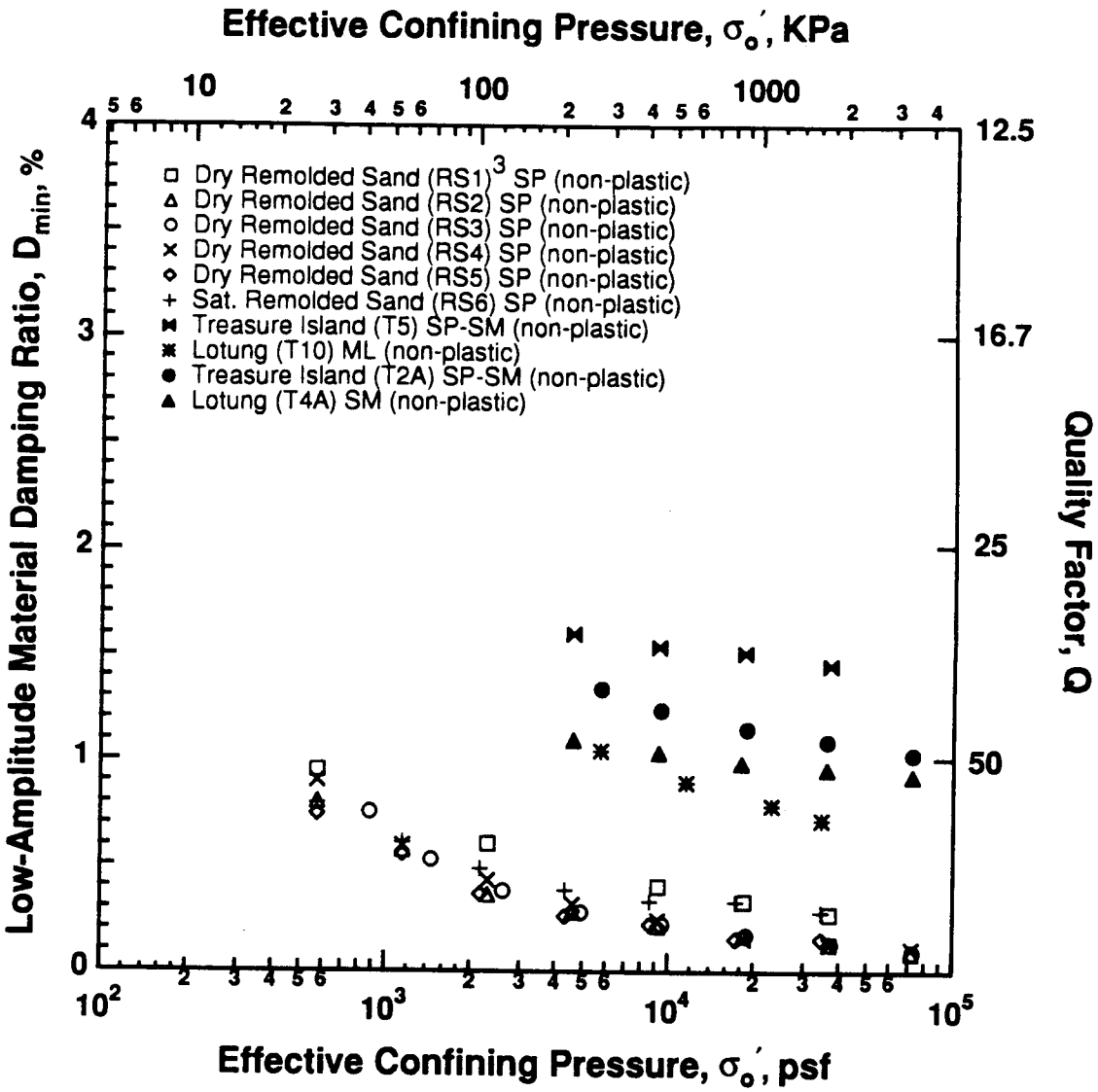

Notes:

1. D_{min} measured at t = 15-50 min. at each σ_o' for remolded sand samples of washed mortar sand.
2. D_{min} measured at t = 1000 min. at each $\sigma_o' \geq \sigma_m'$ for undisturbed samples from Lotung and Treasure Island.
3. Second Loading Cycle (B) is plotted.
4. σ_m' = estimated in situ mean effective stress using K_o = 0.5.

Figure 8.B.4-6
Variation in low-amplitude material damping ratio with effective confining pressure from resonant column tests of remolded sand samples and undisturbed samples tested at $\sigma_o' \geq \sigma_m'$.

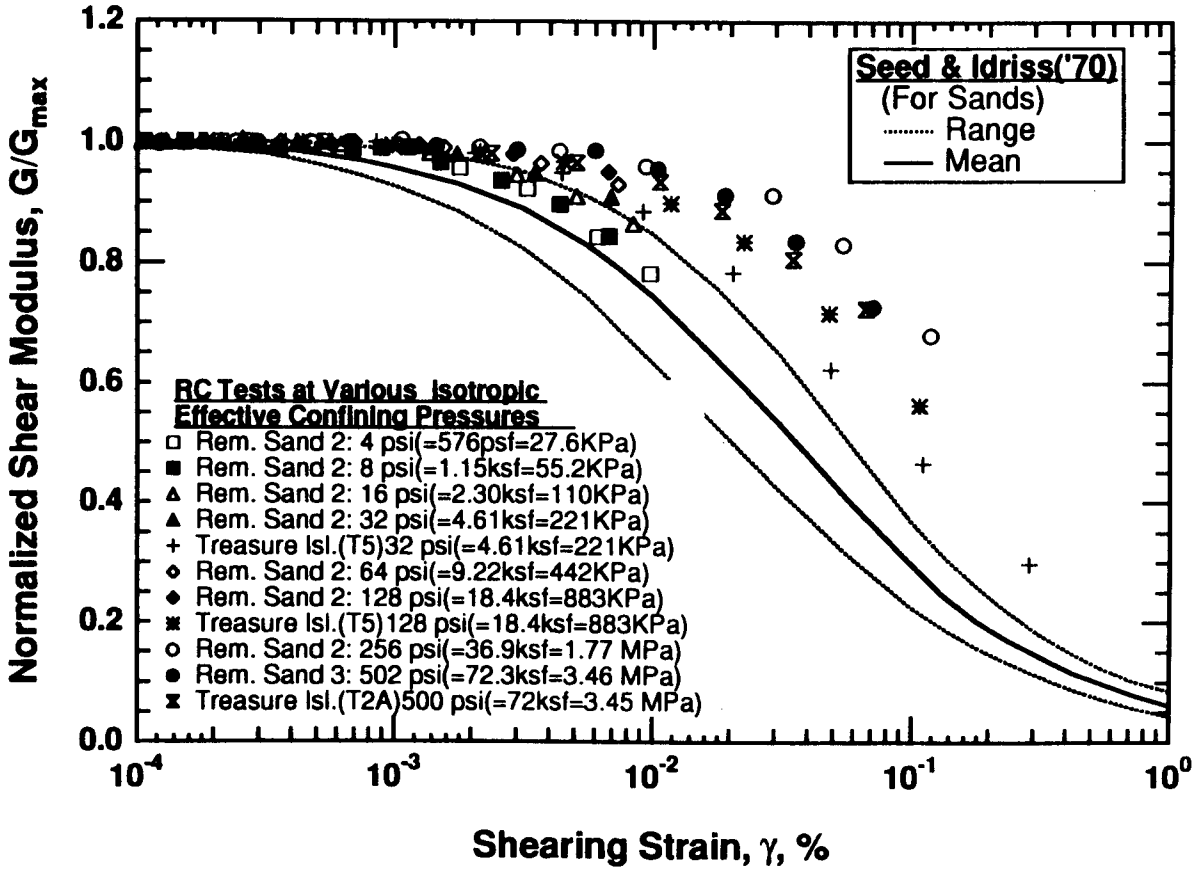

Figure 8.B.4-7
Variation in normalized shear modulus with shearing strain and isotropic effective confining pressure from resonant column tests of remolded sand samples of washed mortar sand and undisturbed samples from Treasure Island.

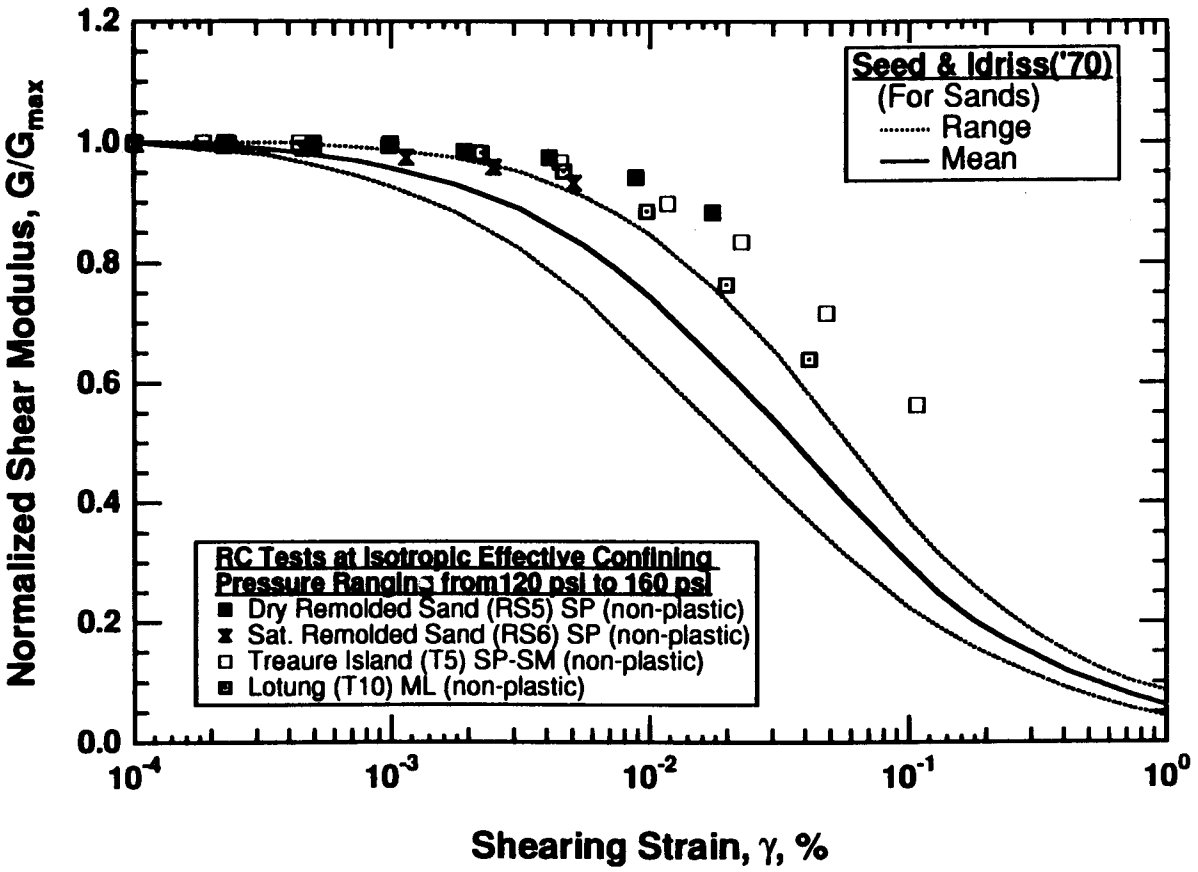

Figure 8.B.4-8
Variation in normalized shear modulus with shearing strain from resonant column tests of remolded samples of washed mortar sand and undisturbed samples from Lotung and Treasure Island at an effective confining pressure ranging from 120 psi (17.3 ksf, 828 kPa) to 160 psi (23.0 ksf, 1.10 MPa).

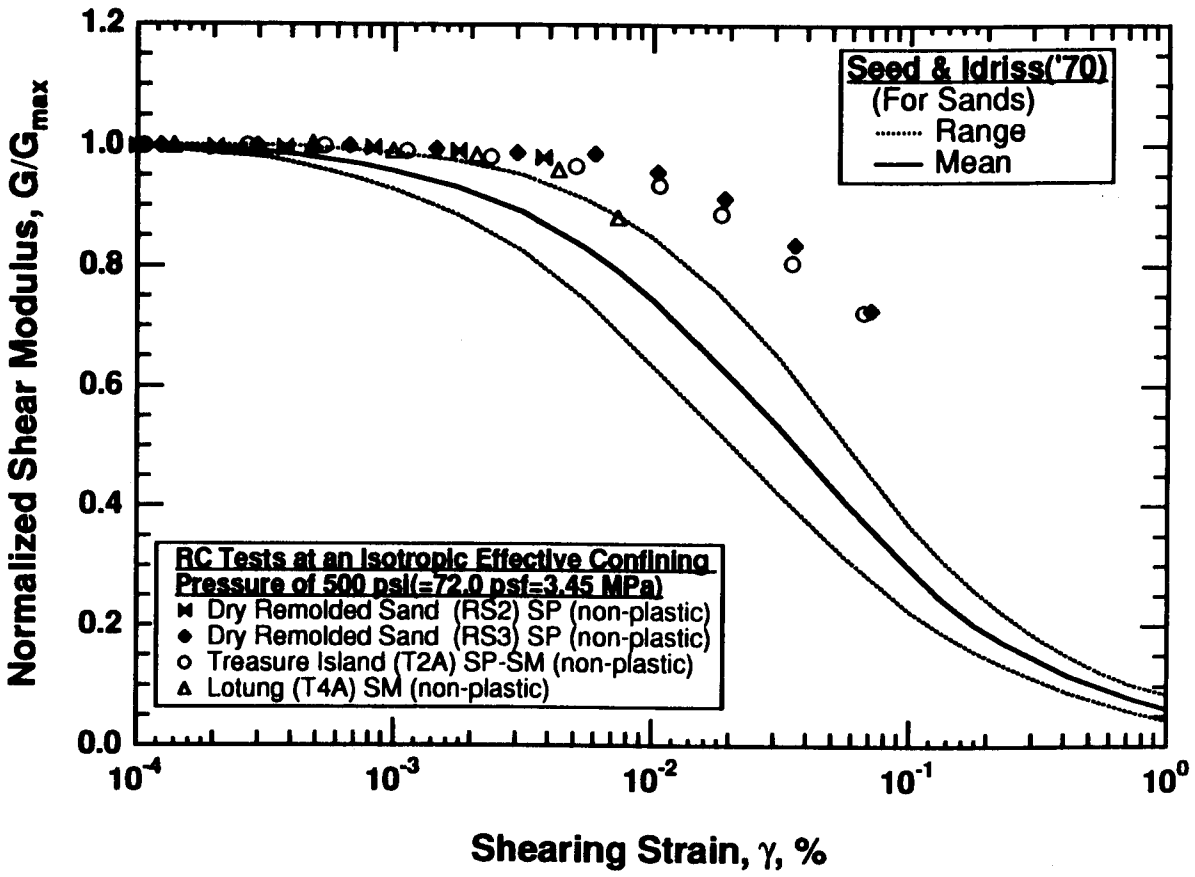

Figure 8.B.4-9
Variation in normalized shear modulus with shearing strain from resonant column tests of remolded samples of washed mortar sand and undisturbed samples from Lotung and Treasure Island at an effective confining pressure of 500 psi (72.0 psf, 3.45 MPa) .

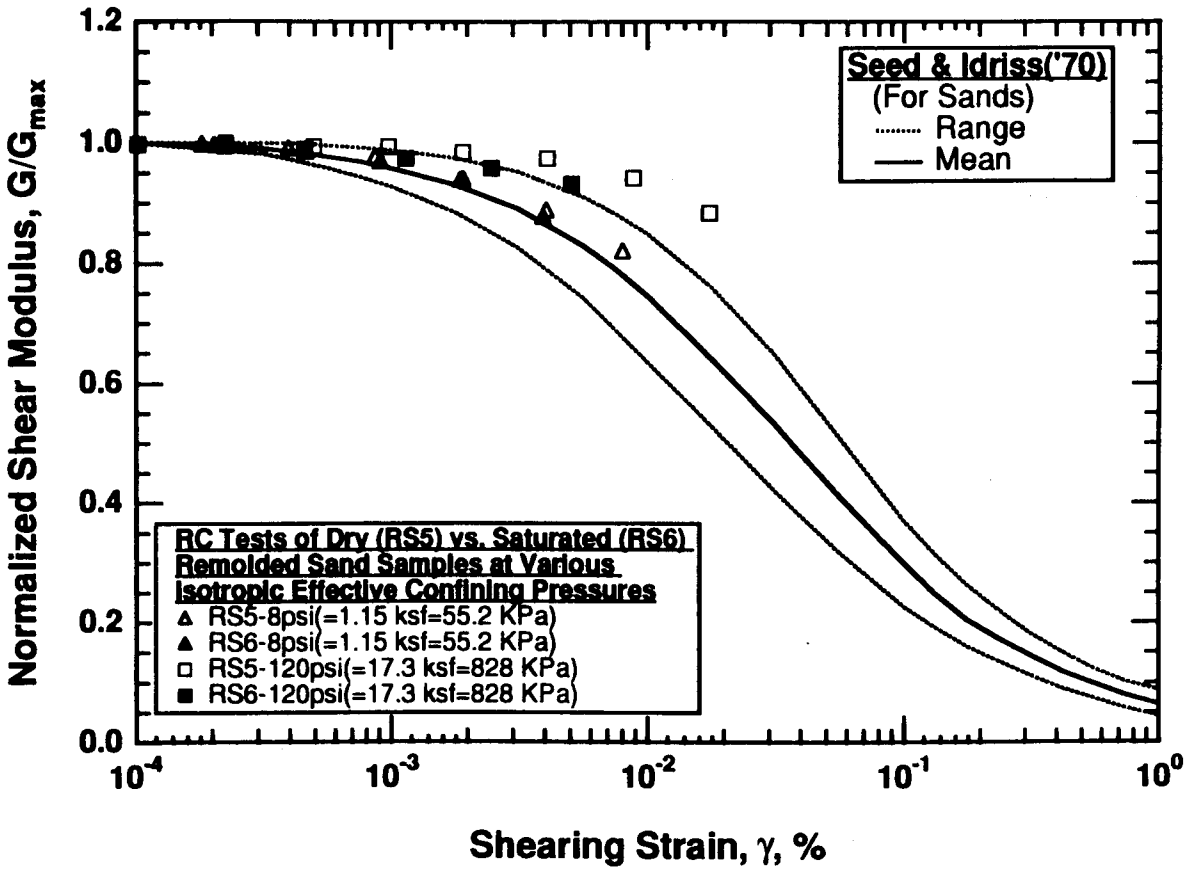

Figure 8.B.4-10
Variation in normalized shear modulus with shearing strain from resonant column tests of a dry and saturated remolded sand sample.

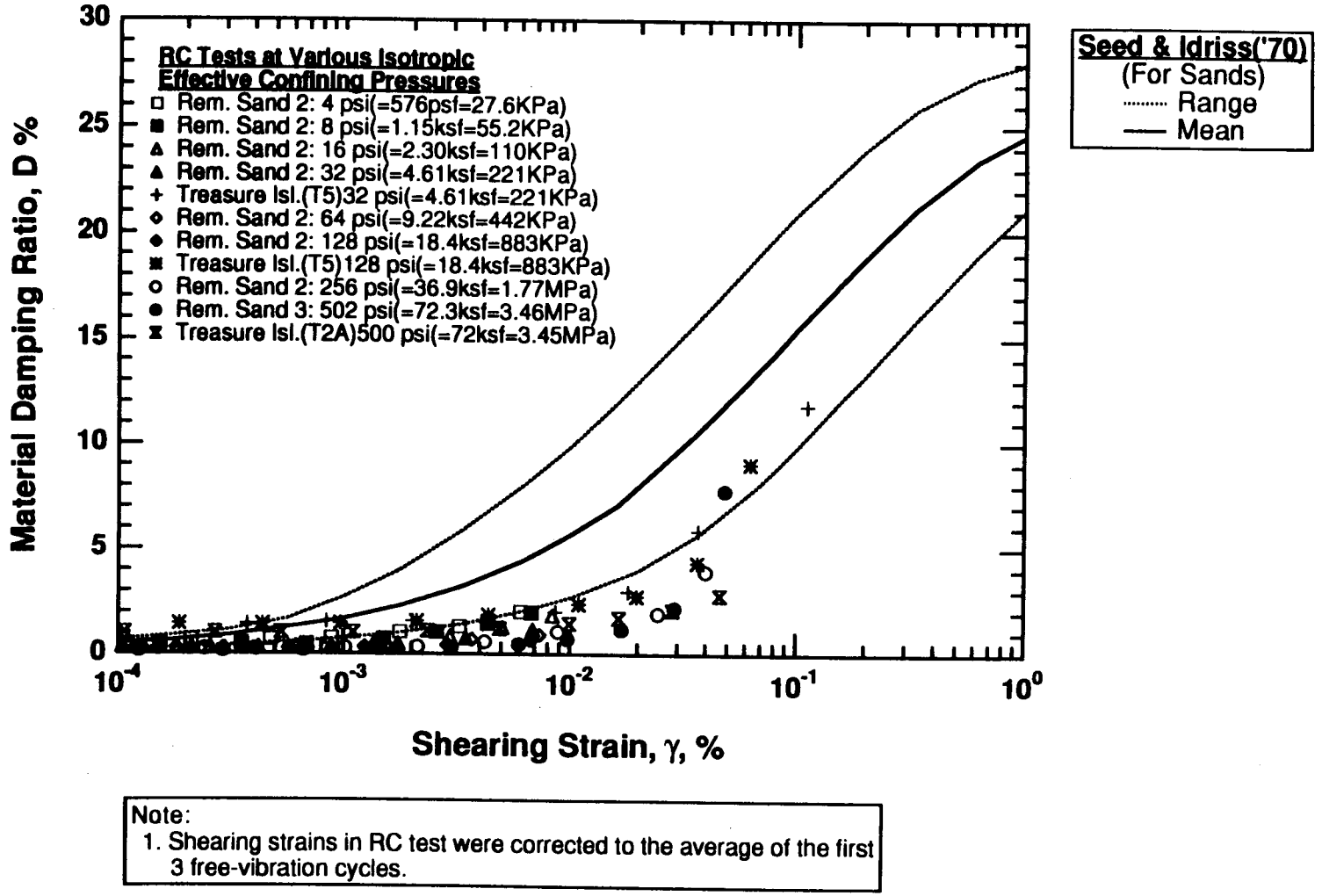

Note:
1. Shearing strains in RC test were corrected to the average of the first 3 free-vibration cycles.

Figure 8.B.4-11
Variation in material damping ratio with shearing strain and isotropic effective confining pressure from resonant column tests of remolded sand samples of washed mortar sand and undisturbed samples from Treasure Island.

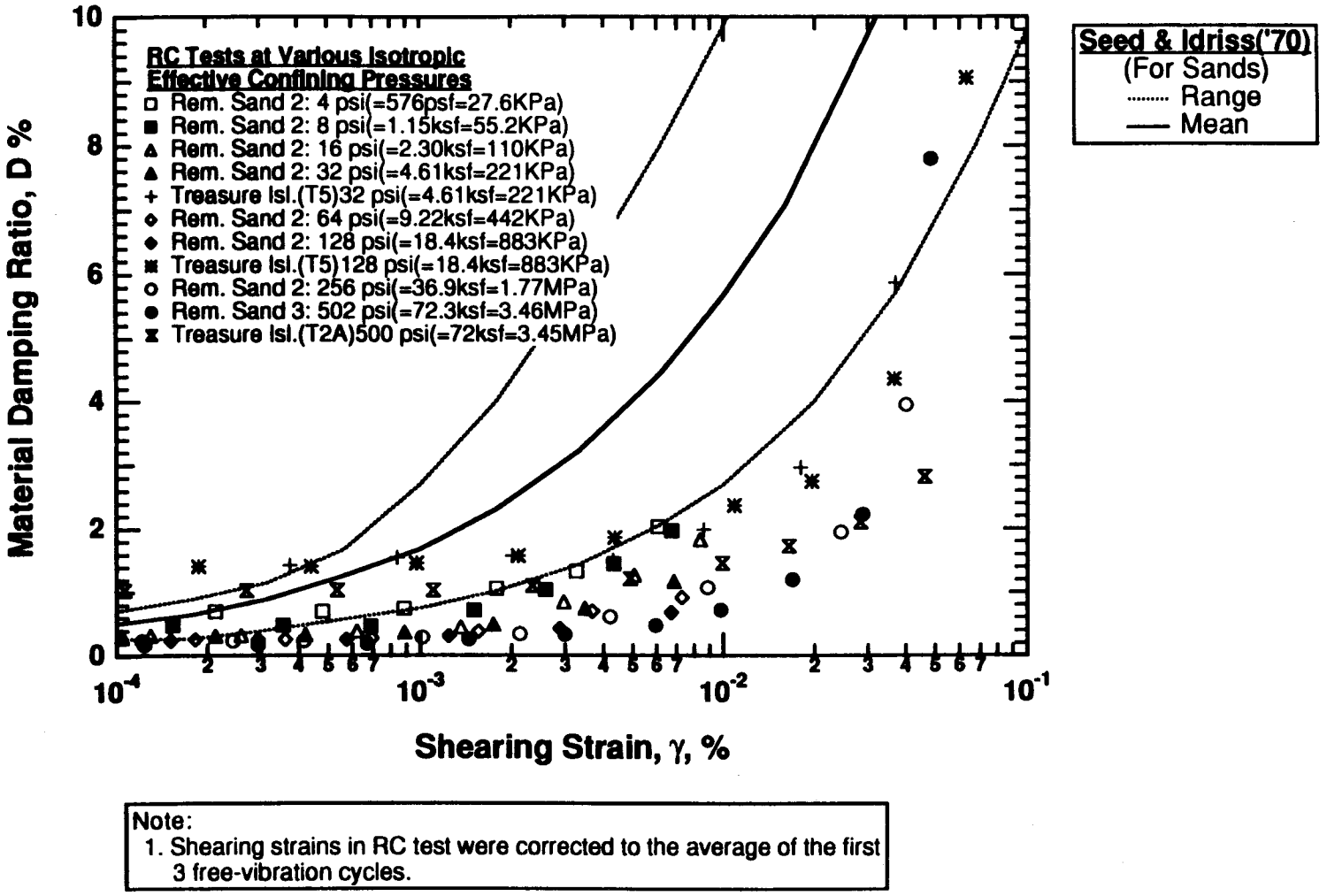

Figure 8.B.4-12
Variation in material damping ratio with shearing strain and isotropic effective confining pressure from resonant column tests of remolded sand samples of washed mortar sand and undisturbed samples from Treasure Island.

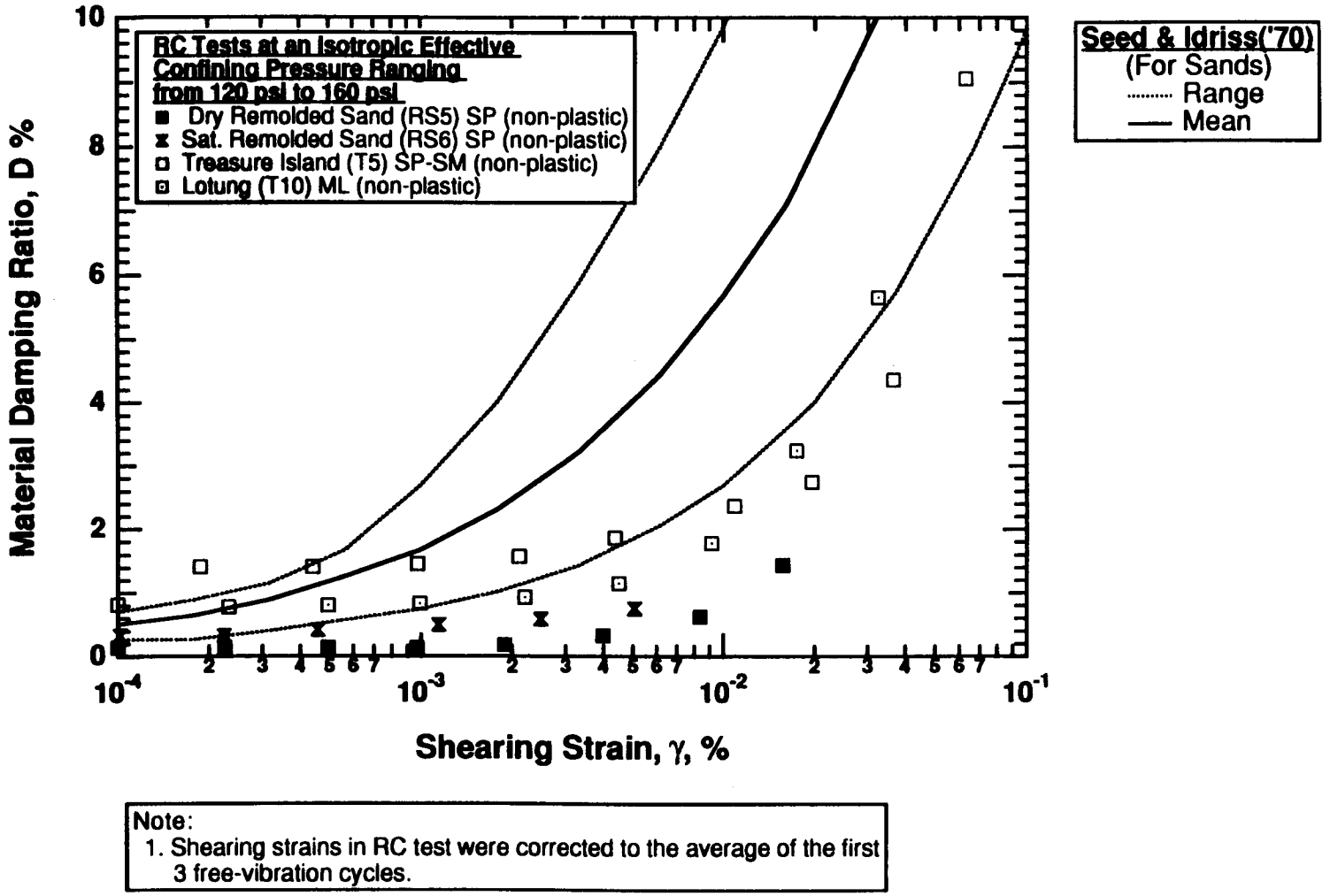

Figure 8.B.4-13
Variation in material damping ratio with shearing strain from resonant column tests of remolded specimens of washed mortar sand and undisturbed samples from Treasure Island and Lotung at an isotropic effective confining pressure ranging from 120 psi (17.3 ksf, 828 kPa) to 160 psi (23.0 ksf, 1.10 MPa).

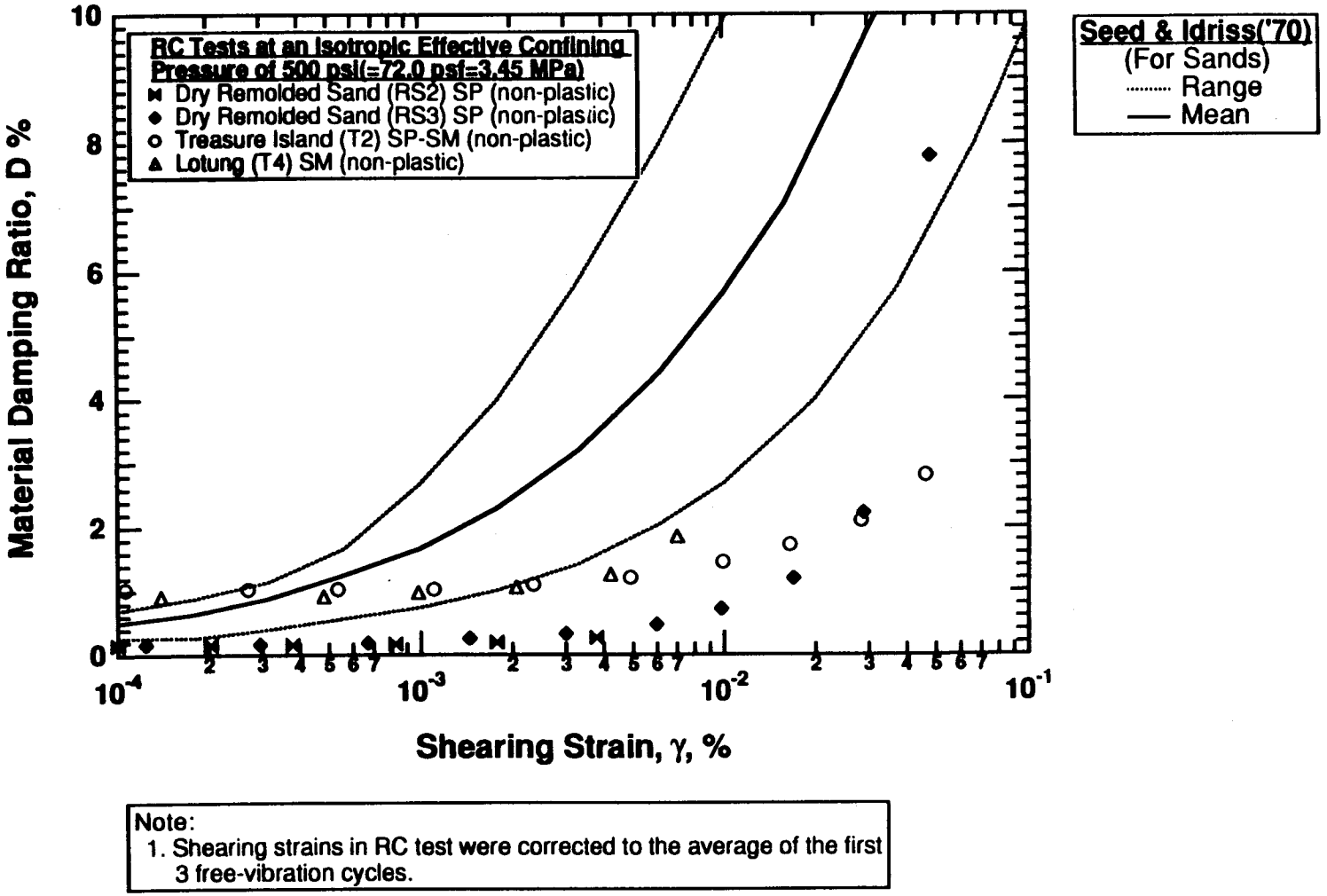

Figure 8.B.4-14
Variation in material damping ratio with shearing strain from resonant column tests of remolded specimens of washed mortar sand and undisturbed samples from Treasure Island and Lotung at an isotropic effective confining pressure of 500 psi (72.0 psf, 3.45 MPa) .

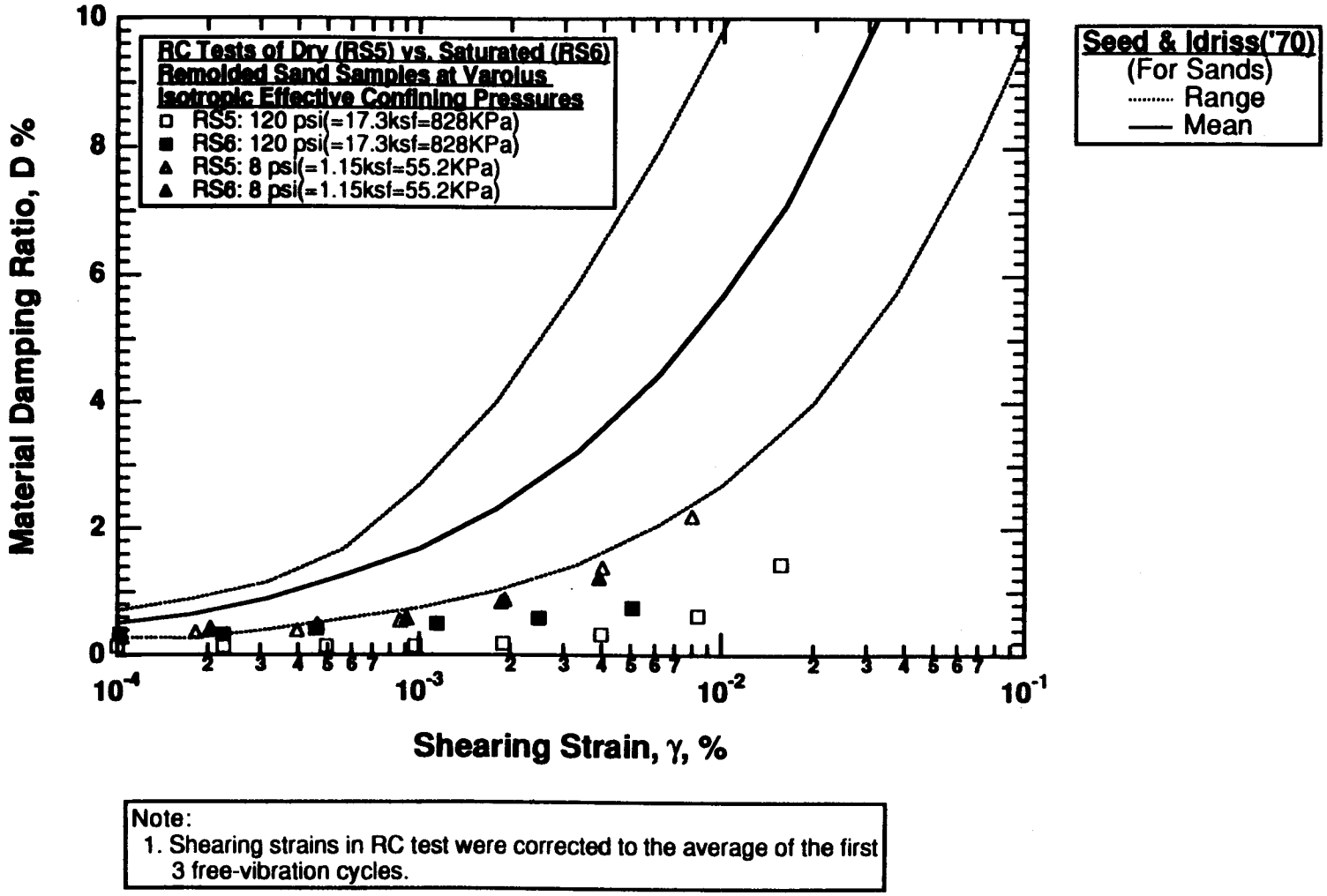

Figure 8.B.4-15
Variation in material damping ratio with shearing strain from resonant column tests of dry and saturated remolded samples of washed mortar sand.

References

Hardin B.O. (1978), "The Nature of Stress-Strain Behavior for Soils," Proceedings, Geotechnical Engineering Division Specialty Conference on Earthquake Engineering and Soil Dynamics, Vol. I, ASCE, Pasadena, CA., June, pp. 3–90.

Kim, D.S. (1991), *Deformational Characteristics of Soils at Small to Intermediate Strains from Cyclic Tests*, Ph.D. Dissertation, Geotechnical Engineering, Department of Civil Engineering, University of Texas at Austin, August.

Khwaja, A.S. and Stokoe, K.S.,II (1993), "Damping Ratios from Compression and Shear Wave Measurements in the Large-scale Triaxial Chamber," Geotechnical Engineering Report GR93-2, Geotechnical Engineering Center, Department of Civil Engineering, University of Texas at Austin, January.

Ladd, R.S. (1978), "Preparing Test Specimens Using Undercompaction" *Geotechnical Testing Journal*, ASTM, Vol. 1, No.1, March, pp. 16–23.

Lee, J.N. (1993), *Inherent and Stress-Induced Anisotropy of Sand Determined by Body Wave Velocities*, Ph.D. Dissertation, Geotechnical Engineering, Department of Civil Engineering, University of Texas at Austin, December.

Lee, S.H.H (1985), *Investigation of Low-Amplitude Shear Wave Velocity in Anisotropic Material*, Ph.D. Dissertation, Geotechnical Engineering, Department of Civil Engineering, University of Texas at Austin, December.

Lewis, M.D. (1990), *A Laboratory Study of The Effect of Stress State on the Elastic Moduli of Sand*, Ph.D. Dissertation, Geotechnical Engineering, Department of Civil Engineering, University of Texas at Austin, December.

Ni, S.H. (1987), *Dynamic Properties of Sand under True Triaxial Stress States from Resonant Column/Torsional Shear Tests*, Ph.D. Dissertation, Geotechnical Engineering, Department of Civil Engineering, University of Texas at Austin, August.

Seed, H.B., and Idriss, I.M. (1970), "Soil Moduli and Damping Factors for Dynamic Response Analysis," Report No. EERC 70-10, Earthquake Engineering Research Center, University of California, Berkeley, September, p. 37.

APPENDIX 8.B.4.A
TEST EQUIPMENT AND MEASUREMENT TECHNIQUES

8.B.4.A.1 Introduction

Resonant column and torsional shear (RCTS) equipment has been employed in this investigation for measurement of the deformational characteristics (shear modulus and material damping) of intact soil specimens. This equipment has been developed at The University of Texas at Austin over the past two decades (Isenhower, 1979; Lodde, 1982; Ni, 1987; and Kim, 1991). The equipment is of the fixed-free type, with the bottom of the specimen fixed and torsional excitation applied to the top. Both resonant column (RC) and torsional shear (TS) tests can be performed in a sequential series on the same specimen over a shearing strain range from about 10^{-4}% to slightly more than 10^{-1}%. The primary difference between the two types of tests is the excitation frequency. In the RC test, frequencies above 20 Hz are required and inertia of the specimen and drive system are needed to analyze the measurements. On the other hand, slow cyclic loading involving frequencies generally below 5 Hz is performed in the TS test and inertia does not enter data analysis.

8.B.4.A.2 Resonant Column and Torsional Shear Equipment

8.B.4.A.2.1 Overview of RCTS Equipment

The RCTS apparatus can be idealized as a fixed-free system as shown in Figure 8.B.4.A-1. The bottom end of the specimen is fixed against rotation at the base pedestal, and top end of the specimen is connected to the driving system. The driving system, which consists of a top cap and drive plate, can rotate freely to excite the specimen in cyclic torsion.

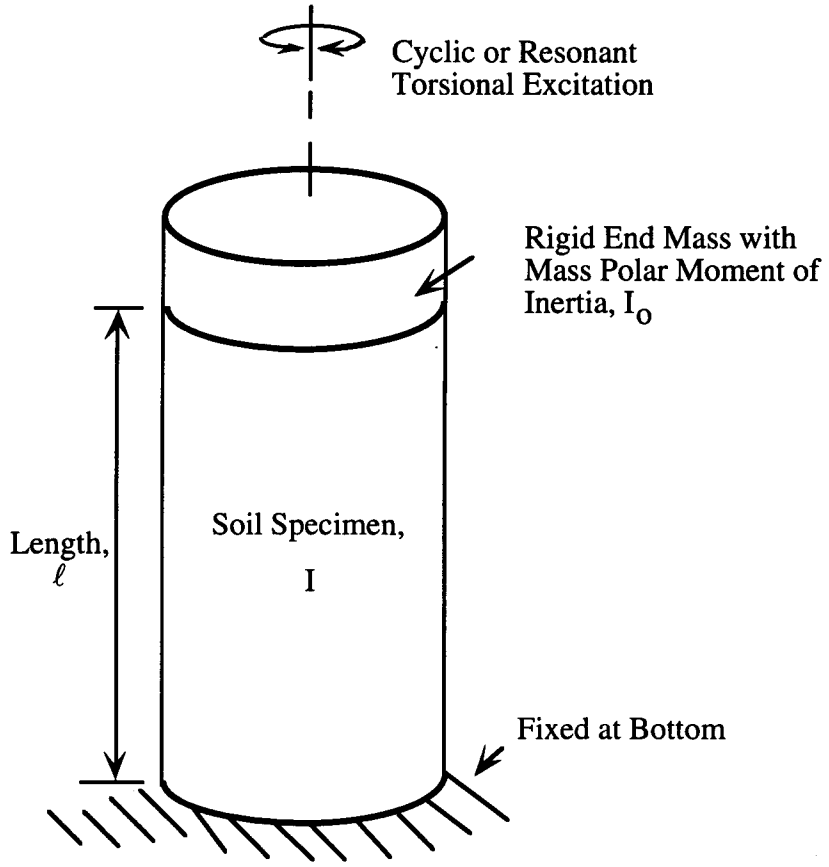

Figure 8.B.4.A-1
Idealized fixed-free RCTS equipment.

A simplified diagram of a fixed-free resonant column (RC) test is shown in Figure 8.B.4.A-2. The basic operational principle is to vibrate the cylindrical specimen in first-mode torsional motion. Harmonic torsional excitation is applied to the top of the specimen over a range in frequencies, and the variation of the acceleration amplitude of the specimen with frequency is obtained. Once first-mode resonance is established, measurements of the resonant frequency and amplitude of vibration are made. These measurements are then combined with equipment characteristics and specimen size to calculate shear wave velocity and shear modulus based on elastic wave propagation. Material damping is determined either from the width of the frequency response curve or from the free-vibration decay curve.

The torsional shear (TS) test is another method of determining shear modulus and material damping using the same RCTS equipment but operating it in a different manner. The simplified configuration of the torsional shear test is shown in Figure 8.B.4.A-3. A cyclic torsional force with a given frequency, generally below 10 Hz, is applied at the top of the specimen. Instead of determining the resonant frequency, the stress-strain hysteresis loop is determined from measuring the torque-twist response of the specimen. Proximitors are used to measure the angle of twist while the voltage applied to the coil is calibrated to yield torque. Shear modulus is calculated from the slope of a line through the end points of the hysteresis loop, and material damping is obtained from the area of the hysteresis loop as shown in Figure 8.B.4.A-3.

The RCTS apparatus used in this study has three advantages. First, both resonant column and torsional shear tests can be performed with the same set-up simply by changing (outside the apparatus) the frequency of the forcing function. Variability due to preparing "identical" samples is eliminated so that both test results can be compared effectively. Second, the torsional shear test can be performed over a shearing strain range between 10^{-4}% and about 10^{-1}%. Common types of torsional shear tests, which generate torque by a mechanical motor outside of the confining chamber, are usually performed at strains above 0.01% because of system compliance. However, the RCTS apparatus used in this study generates torque with an electrical coil-magnet system inside the confining chamber, thus eliminating the problem with an external motor. The torsional shear test can be performed at the same low-strain amplitudes as the resonant column test, and results between torsional shear and resonant column testing can be easily compared over a wide range of strains. Third, the loading frequency in the torsional shear test can be changed easily from 0.01 Hz to 10 Hz. Therefore, the effect of frequency on deformational characteristics can be conveniently investigated using this apparatus.

The RCTS apparatus consists of four basic subsystems which are: (1) a confinement system, (2) a drive system, (3) a height-change measurement system, and (4) a motion monitoring system. The general configuration of the RCTS apparatus (without the confinement system) is shown in Figure 8.B.4.A-4. The RCTS apparatus was automated by Ni (1987) so that a microcomputer controls the test, collects the data, and reduces results. Computer-aided subsystems are discussed briefly in the following sections.

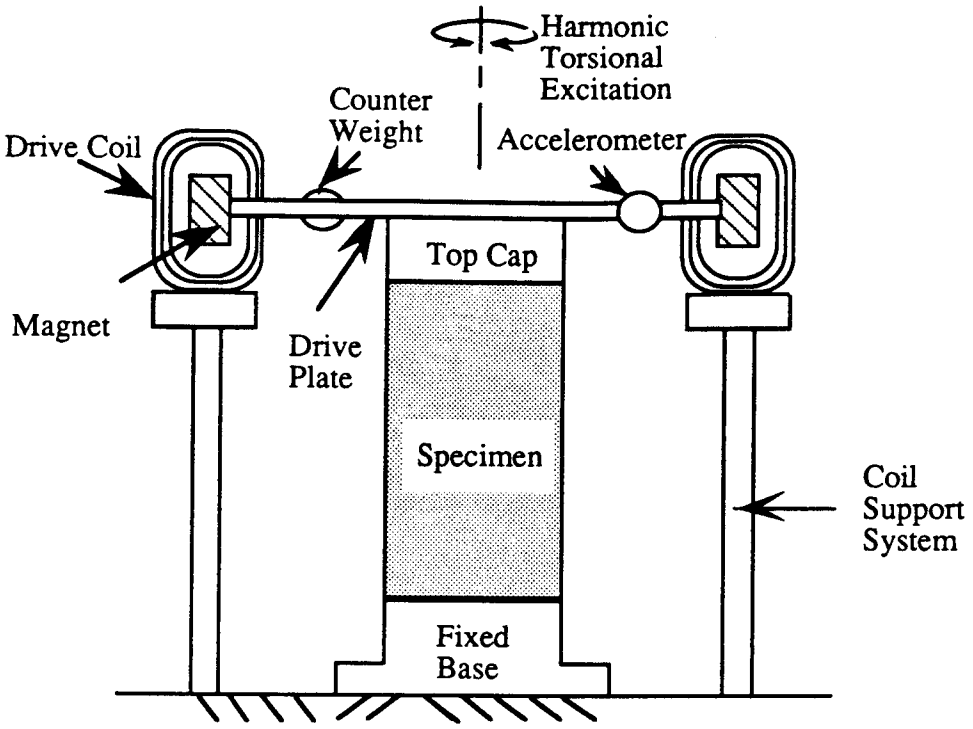

a) Specimen in the Resonant Column Apparatus
(Confinement Chamber Not Shown)

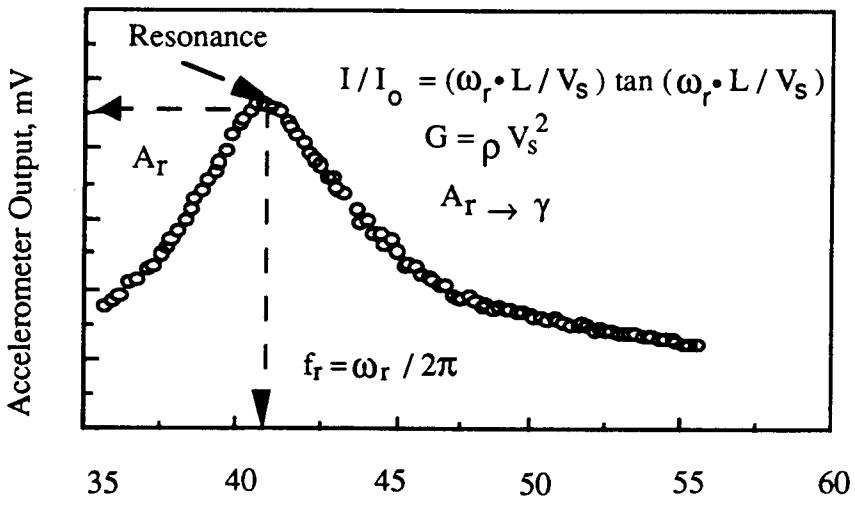

b) Typical Frequency Response Curve

Figure 8.B.4.A-2
Simplified diagram of a fixed-free resonant column test and an associated frequency response curve.

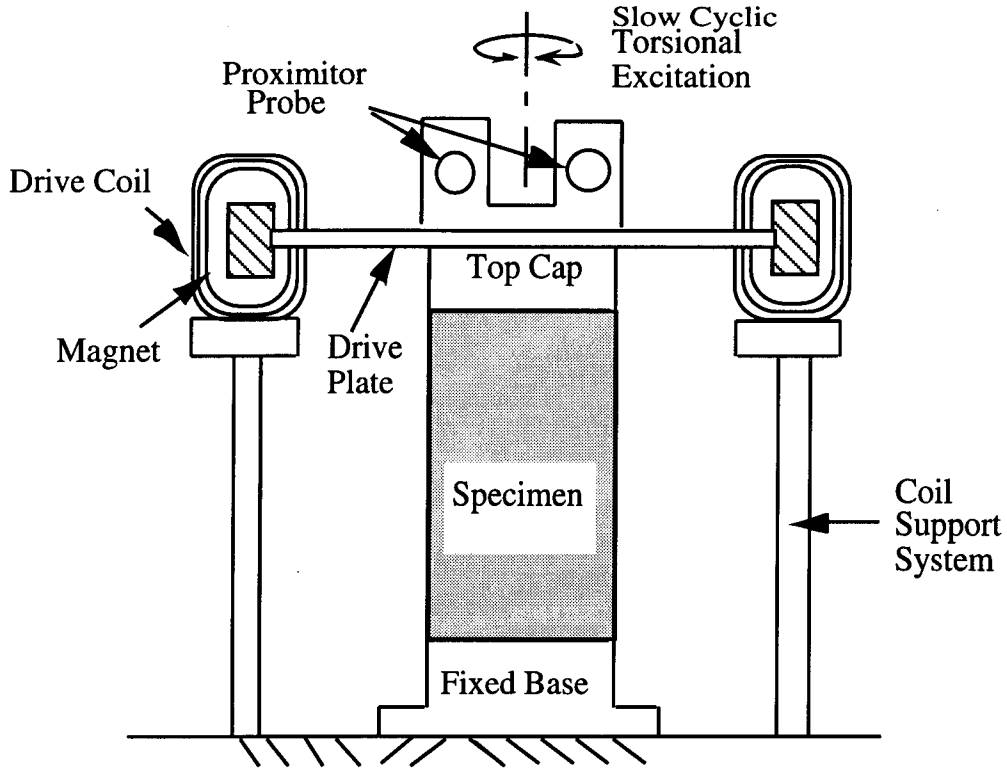

a) Specimen in the Torsional Shear Test Apparatus
(Confinement Chamber Not Shown)

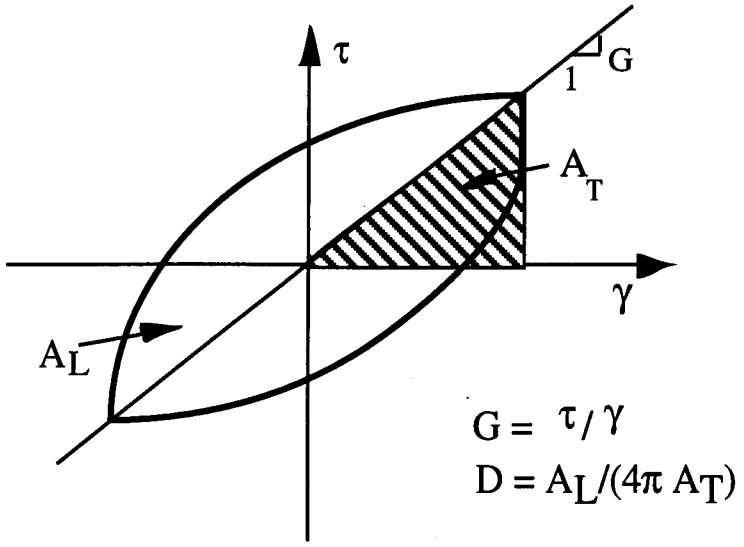

b) Measurement of Shear Modulus and Damping Ratio

Figure 8.B.4.A-3
Configuration of a torsional shear test and evaluation of shear modulus and material damping ratio.

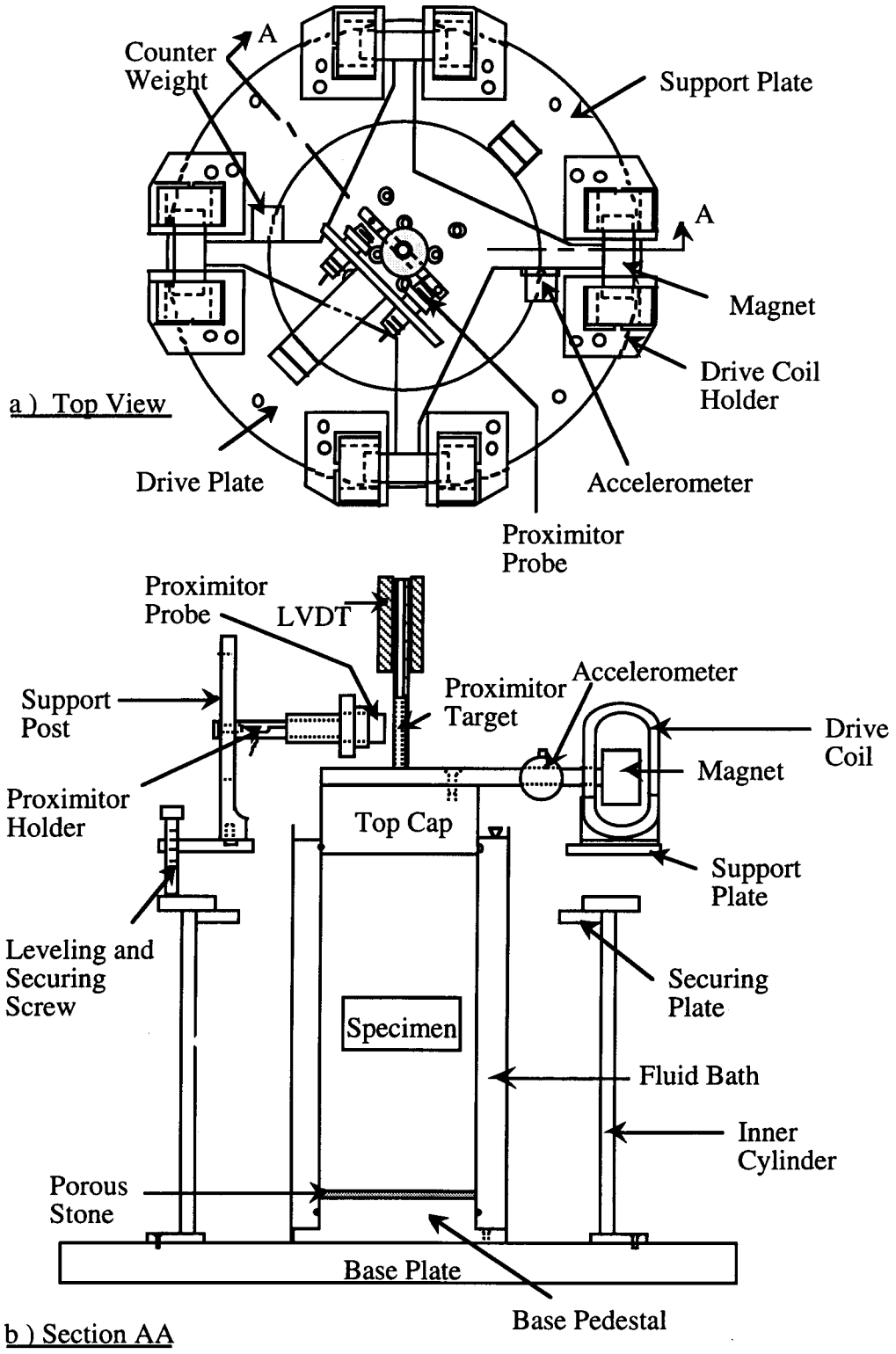

Figure 8.B.4.A-4
General configuration of RCTS equipment (from Ni, 1987).

8.B.4.A.2.2. RCTS Confinement System

The confining chamber is made of stainless steel. A thin-walled (0.6 cm in thickness) hollow cylinder fits into circular grooves machined in 2.5 cm thick base and top plates. Four stainless steel connecting rods (1.28 cm in diameter) are used to secure the base and top plates to the hollow cylinder, and O-rings in the circular grooves are used to seal the chamber. In this configuration, the chamber has been designed to withstand a maximum air pressure of about 200 psi (1379 kPa). To safely test samples at higher confining pressures (pressures on the order of 600 psi (4137 kPa)), the confinement system was modified by adding additional stainless steel rods to secure the cylinder to the top and base plates and reinforcement to the top and base plates.

Compressed air is used to confine isotropically the specimen in the RCTS device. The air pressure to the chamber generally is regulated by a Fairchild M 30 regulator and air supplied to the regulator is filtered. At high confining pressures, additional regulators are used. The soil specimen is sealed in a membrane and pore pressure in the specimen is normally vented to atmospheric pressure.

Inside the confining chamber, the air pressure acts upon a silicon fluid bath which surrounds the sides of the soil specimen. The purpose of the silicon fluid bath is to retard air migration through the membrane and into the specimen to prevent drying of the specimen. Figure 8.B.4.A-5 shows the simplified configuration of the confinement system.

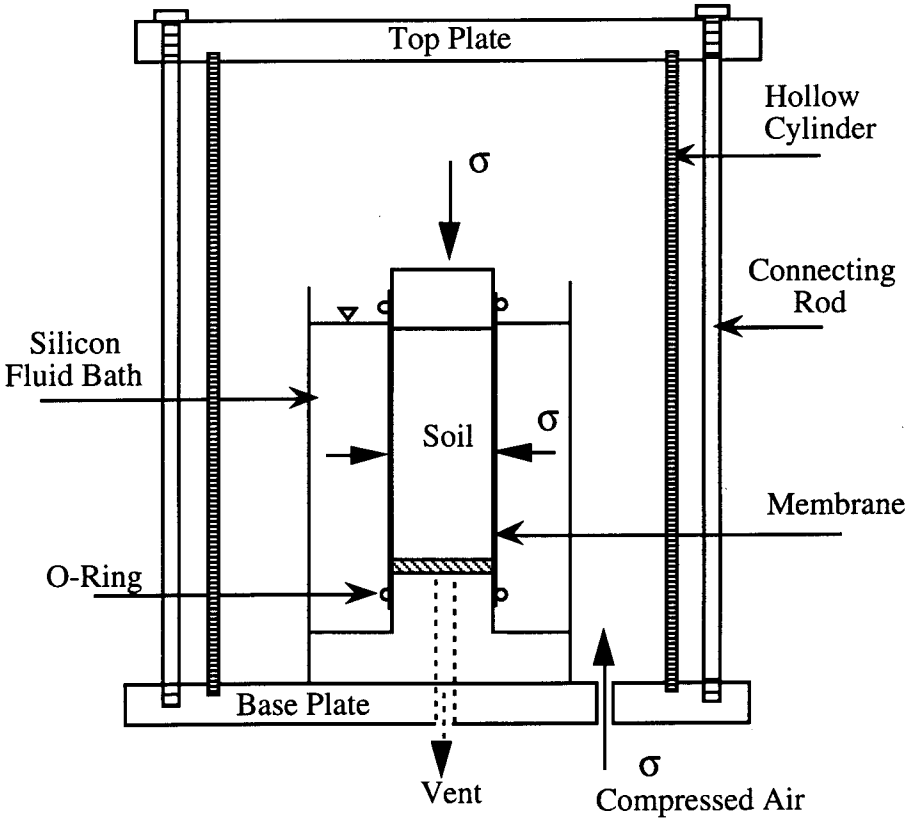

Figure 8.B.4.A-5
Simplified configuration of confinement system.

8.B.4.A.2.3 Drive System

The drive system consists of a four-armed drive plate, four magnets, eight drive coils, a power amplifier, and a function generator. Each magnet is rigidly attached to the end of one arm of the drive plate as shown in Figure 8.B.4.A-4. Eight drive coils encircle the ends of the four magnets so that the drive plate excites the soil specimen in torsional motion when a current is passed through the coils. The maximum torque that the drive system can develop depends on the strength of the magnets, size of the drive coils, resistance of the drive coils, size of the space between the magnets and drive coils, length of the arms of the drive plate, and the electrical characteristics of the function generator and power amplifier. For the three drive systems used in this work, the maximum torque was about 0.60 lb-ft (82 N-cm).

A schematic diagram of the drive system is shown in Figure 8.B.4.A-6. The micro-computer activates a function generator (HP 3314A) to input sinusoidal voltage to the drive coils. In the resonant column (RC) test, the function generator performs frequency sweeps with a constant amplitude while in the torsional shear test, a fixed-frequency N-cycle mode is used. For high-amplitude resonant column and torsional shear (TS) tests, the sinusoidal input current is amplified by a power amplifier (HP 6824A) before going to the drive coils.

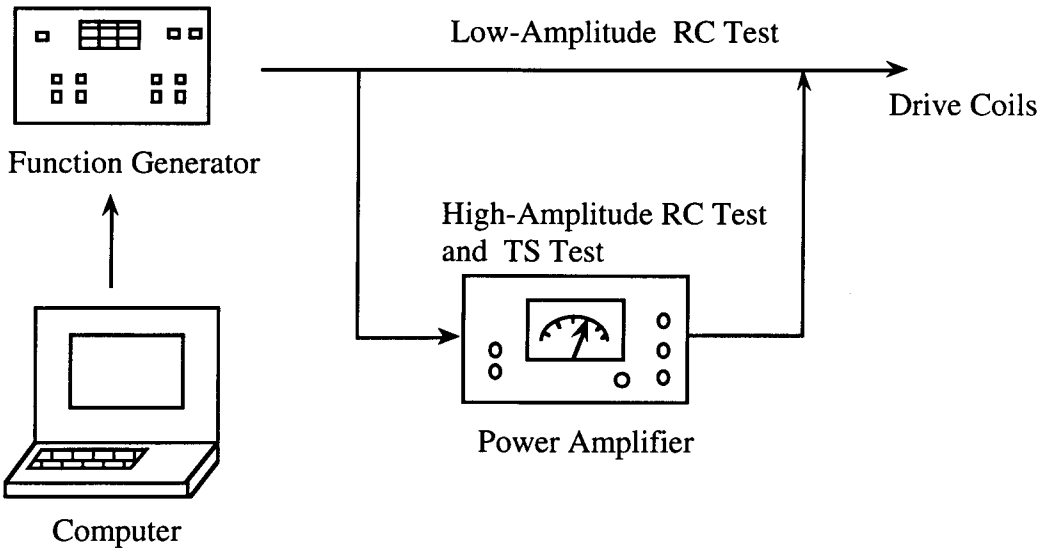

Figure 8.B.4.A-6
Schematic diagram of the drive system

8.B.4.A.2.4 Height-Change Measurement System

The height change of the soil specimen is measured to account for the changes in the length and mass of the specimen during consolidation or swell. This measurement is also used to calculate change in the mass moment of inertia, mass density, and void ratio during testing (by assuming isotropic strain under isotropic confinement and constant degree of saturation). The height change is measured by a linear variable differential transformer (LVDT). The height change measurement system consists of an LVDT (CRL Model SH-200-53R), a function generator (HP 3314A), and a digital voltmeter (HP 3456A). The LVDT core is not in contact with the LVDT coil housing so that no friction occurs during RCTS testing.

The output and calibration factor of an LVDT depend on both the frequency and magnitude of the excitation voltage. In this test the computer activates the function generator to generate the input signal in the LVDT coil at a frequency of 500 Hz and a voltage level of 4.77 RMS volts. The output from the LVDT is read with a digital voltmeter. The height change is calculated from the output voltage combined with

the calibration factor. The schematic diagram of the height change measuring system is shown in Figure 8.B.4.A-7.

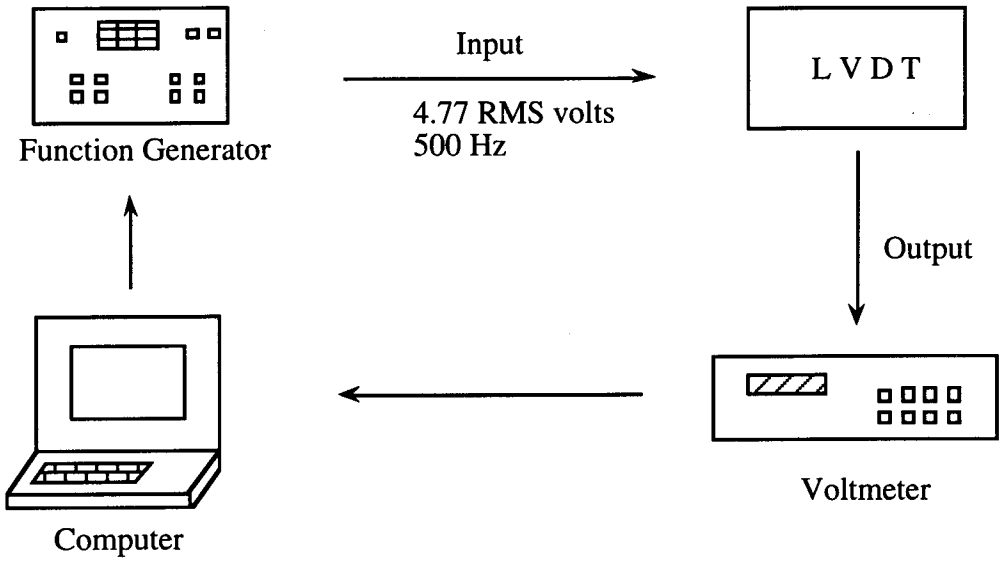

Figure 8.B.4.A-7
Schematic diagram of the height-change measuring system.

8.B.4.A.2.5 Motion Monitoring System

Dynamic soil properties are obtained in the RC test at the resonant frequency which is usually above 20 Hz while torsional shear testing is used to measure the low-frequency (below 10 Hz) cyclic stress-strain relationship of soil. Because of the different frequencies applied in the resonant column and torsional shear tests, different motion monitoring systems are used.

Resonant Column (RC) Test. The motion monitoring system in the RC test is designed to measure the resonant frequency, shearing strain, and free-vibration decay curve. This system consists of an accelerometer (Columbia Research Laboratory Model 3021), a charge amplifier (Columbia Research Laboratory Model 4102M), a frequency counter (HP 5334A), a digital voltmeter (HP 3456A), and a digital oscilloscope (Nicolet 20929-01). The schematic diagram of the motion monitoring system is shown in Figure 8.B.4.A-8.

The accelerometer is oriented to be sensitive to torsional vibrations of the drive plate. The charge amplifier conditions the accelerometer output to be linear for all levels of acceleration in the test. The digital voltmeter reads the output voltage from the accelerometer at each frequency which is measured by the frequency counter. The resonant frequency is obtained from the frequency response curve. Once the resonant frequency is obtained, the computer activates the function generator to excite the specimen at the resonant frequency and then suddenly stops the current so that the free-vibration decay curve is recorded by the digital oscilloscope.

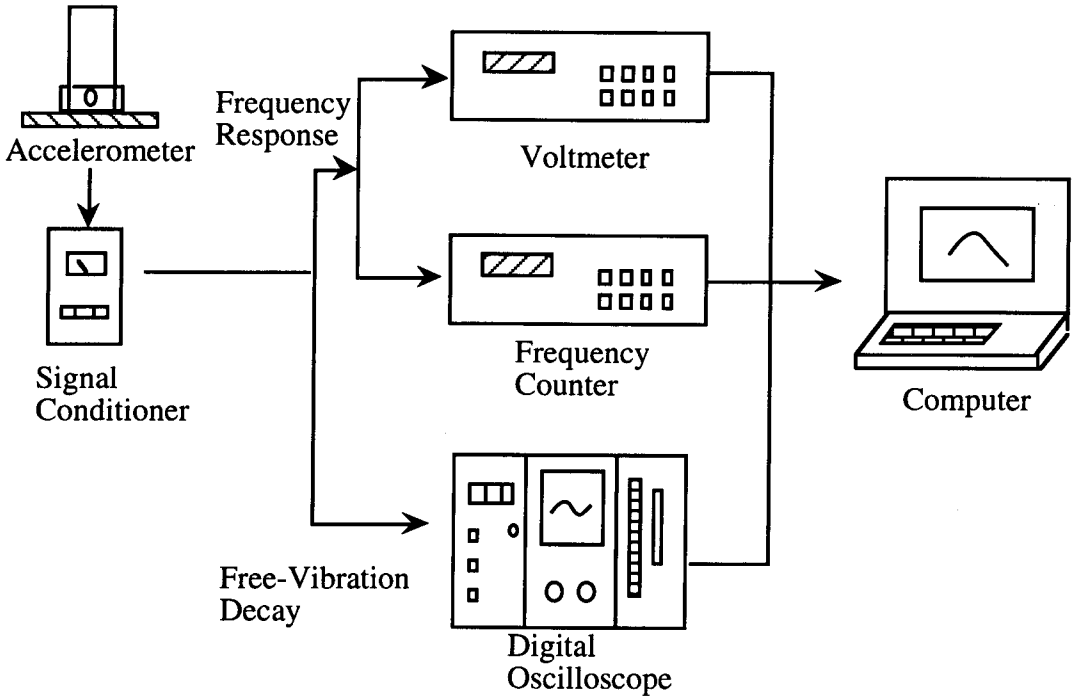

Figure 8.B.4.A-8
Schematic diagram of the motion monitoring system in the resonant column test.

The resonant frequency of soils are typically in the range of 20 Hz to 300 Hz with this equipment. To test soils effectively over a wide range of stiffnesses, the search for the resonant frequency is performed in two stages, a rough sweep and a fine sweep. During the rough sweep, a fast logarithmic-linear frequency sweep (16 seconds to sweep from 1 to 170 Hz) is used. The fine sweep is then performed to determine an accurate resonant frequency in the neighborhood where the resonant frequency was found in the rough sweep.

Torsional Shear (TS) Test. The motion monitoring system in the TS test (3000 Proximitor System) is used to monitor torque-twist hysteresis loops of the specimen. This system consists of two proximitors (Bentry Nevada M 20929-01), two proximitor probes (Bentry Nevada M 300-00), an operational amplifier (Tektronix TM 504 with AM501), a DC power supply (Lambda M-11-902), a U-shaped target and a digital oscilloscope (Nicolet 20929-01). The U-shaped target is secured to the top of the drive plate, and the two proximitor probes are rigidly attached to the support stand. A schematic diagram of the motion monitoring system in the torsional shear test is shown in Figure 8.B.4.A-9.

The function of the proximitor probes is to measure the width of the air gap between the target and the probe tip. Because the proximitor probes do not touch the drive plate, no compliance problems are introduced into the measurement. Two probes are used and the operational amplifier subtracts the signal from one probe from the other so that the effect of bending in the specimen toward the probes can be eliminated. The proximitor system is a very effective low-frequency motion monitoring system which does not introduce any compliance problems into the measurement. With the simultaneous measurement of torque, load-displacement hysteresis loops can be determined.

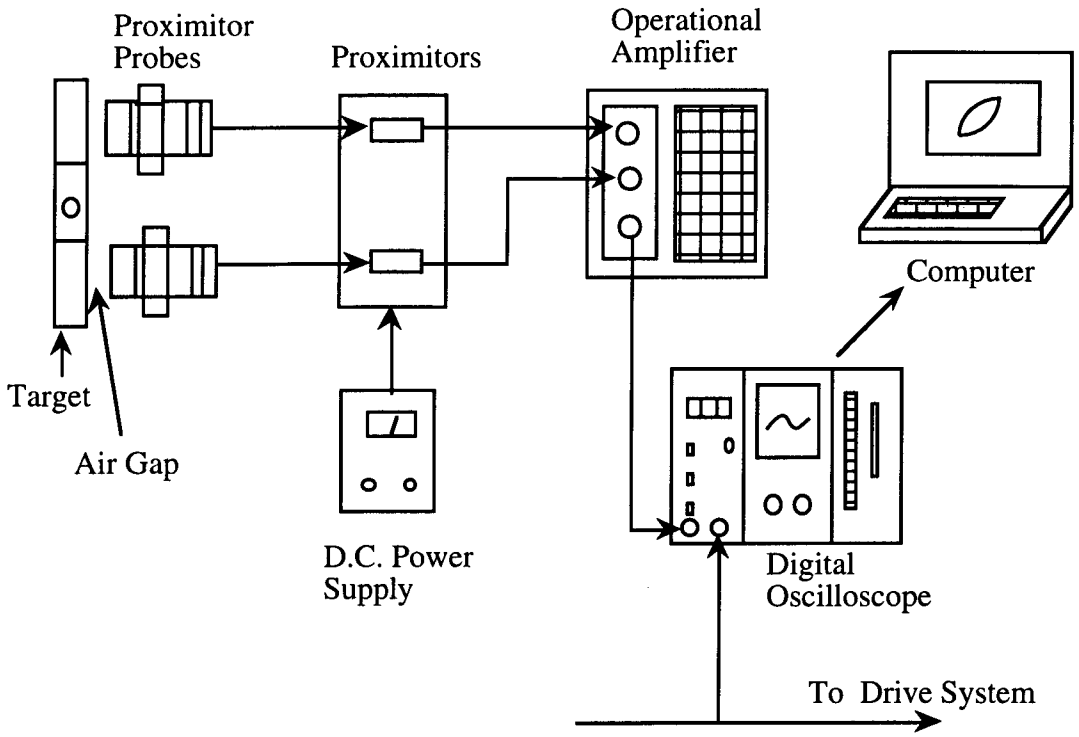

Figure 8.B.4.A-9
Schematic diagram of the motion monitoring system in the torsional shear test (3000 Proximitor System).

8.B.4.A.3 Method of Analysis in the Resonant Column Test

The resonant column test is based on the one-dimensional wave equation derived from the theory of elasticity. The shear modulus is obtained by measuring the first-mode resonant frequency while material damping is evaluated from either the free-vibration decay curve or from the width of the frequency response curve assuming viscous damping.

8.B.4.A.3.1 Shear Modulus

The governing equation of motion for the fixed-free torsional resonant column test is:

$$\frac{\Sigma I}{I_o} = \frac{\omega_n \bullet l}{V_s} \bullet \tan\left(\frac{\omega_n \bullet l}{V_s}\right) \qquad \text{(8.B.4.A-1)}$$

where $\Sigma I = I_s + I_m + \cdots$

I_s = mass moment of inertia of soil,
I_m = mass moment of inertia of membrane,
I_o = mass moment of inertia of rigid end mass at the top of the specimen,
l = length of the specimen,
V_s = shear wave velocity of the specimen, and
ω_n = undamped natural circular frequency of the system.

The value of I_o is known from the calibration of the drive plate. The values of I_s and l are easily determined from the specimen size and weight. Once the first-mode resonant frequency is determined, the shear wave velocity can be calculated from Eq. 8.B.4.A-1 by assuming that the resonant circular frequency and ω_n are equal.

As noted above and shown in Figure 8.B.4.A-2 the resonant circular frequency, ω_r ,is measured instead of undamped natural frequency, ω_n, and ω_r is used to calculate shear wave velocity. If the damping in the system is zero, ω_r and ω_n are equal. The relationship between ω_r and ω_n is:

$$\omega_r = \omega_n \sqrt{1-2D^2} \qquad (8.B.4.A\text{-}2)$$

A typical damping ratio encountered in the resonant column test is less than 20 percent, which corresponds to a difference of less than 5 percent between ω_r and ω_n. In this study, the damping measured in the resonant column test was usually less than 10 percent, and ω_r can be used instead of ω_n with less than a two percent error.

Once the shear wave velocity is determined, shear modulus is calculated from the relationship:

$$G = \rho \bullet V_s^2 \qquad (8.B.4.A\text{-}3)$$

where ρ is the total mass density of the soil (total unit weight divided by gravity).

8.B.4.A.3.2 Shearing Strain

The shearing strain varies radially within the specimen and may be expressed as a function of the distance from the longitudinal axis as illustrated in Figure 8.B.4.A-10. The equivalent shearing strain, γ_{eq} or γ, is represented by:

$$\gamma = r_{eq} * \theta_{max} / l \qquad (8.B.4.A\text{-}4)$$

where

r_{eq} = equivalent radius,
θ_{max} = angle of twist at the top of the specimen, and
l = length of the specimen.

Chen and Stokoe (1979) studied the radial distribution in shearing strain to find a value of r_{eq} for the specimen tested in the RCTS equipment to evaluate an effective strain. They found that the value of r_{eq} varied from $0.82*r_0$ for a peak shearing strain amplitude below 0.001% to $0.79*r_0$ for a peak shearing strain of 0.1% for a solid specimen. These values of r_{eq} have been adopted in this study.

In the resonant column test, the resonant period (T_r, seconds), and output voltage of accelerometer (A_c, volts(RMS)) at resonance are measured. Accelerometer output is changed to the displacement by using the accelerometer calibration factor (CF, volts(RMS)/in./sec^2) assuming harmonic motion. The accelerometer displacement is divided by the distance (D_{ac}, inches) between the location of accelerometer and the axis of the specimen to calculate the angle of twist at the top of the specimen(θ_{max}). The shearing strain is then calculated by:

$$\gamma = r_{eq} \frac{A_c \bullet Tr^2}{4\pi^2 \bullet CF} \bullet \frac{1}{D_{ac}} \bullet \frac{1}{l} \qquad (8.B.4.A\text{-}5)$$

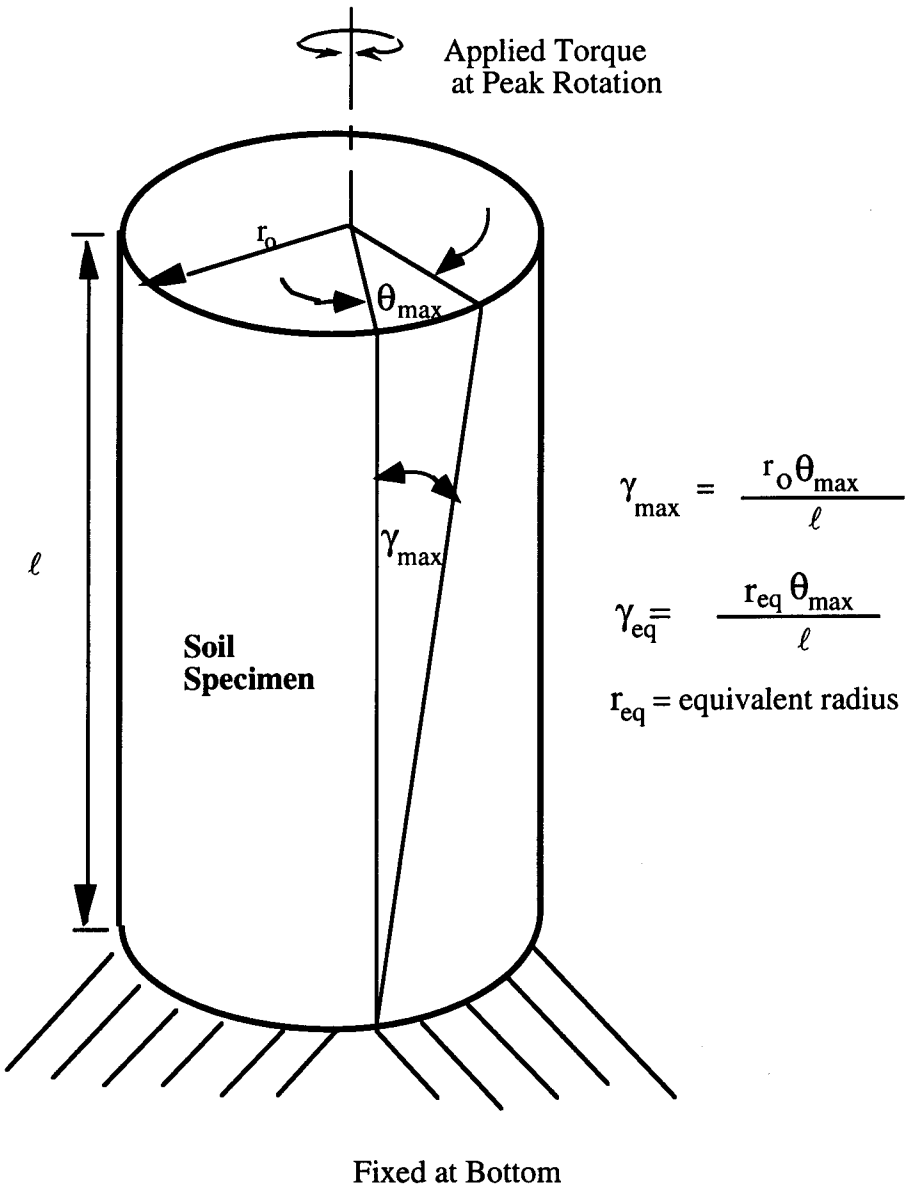

Figure 8.B.4.A-10
Shearing strain in soil column.

8.B.4.A.3.3 Material Damping

In the resonant column test, material damping ratio can be evaluated from either the free-vibration decay method or from the half-power bandwidth method. Each of these methods is discussed below. It is important to note that, in these measurements, the damping measurement includes material damping in the soil plus any damping in the equipment. Calibration of equipment damping is discussed in Section 8.B.4.A.5.

Free-Vibration Decay Method. Material damping in soils can be quite complex to define. However, the theory for a single-degree-of-freedom system with viscous damping is a useful framework for describing the effect of damping which occurs in soil (Richart et al., 1970). The decay of free vibrations of a single-degree-of-freedom system with viscous damping is described by the logarithmic decrement, δ, which is the ratio of the natural logarithm of two successive amplitudes of motion as:

$$\delta = \ln\left(\frac{Z_1}{Z_2}\right) = \frac{2\pi D}{\sqrt{1-D^2}} \qquad \text{(8.B.4.A-6)}$$

where

Z_1 and Z_2 = two successive strain amplitudes of motion, and
D = material damping ratio.

The free-vibration decay curve is recorded using an oscilloscope by shutting off the driving force while the specimen is vibrating at the resonant frequency. The amplitude of each cycle is measured from the decay curve, and the logarithmic decrement is then calculated using Eq. 8.B.4.A-6. Material damping ratio is calculated from logarithmic decrement according to:

$$D = \sqrt{\frac{\delta^2}{4\pi^2 + \delta^2}} \qquad \text{(8.B.4.A-7)}$$

A typical damping measurement from a free-vibration decay curve (from a metal calibration specimen) is shown in Figure 8.B.4.A-11.

In this method, it is not certain which strain amplitude is a representative strain for damping ratio calculated by Eq. 8.B.4.A-7 because strain amplitude decreases during free-vibration decay. In this study, a representative strain amplitude was used as the peak strain amplitude during steady-state vibration for shearing strains below 0.001%. However, at larger strains, the representative strain is smaller than the peak strain, and the average strain determined for the first three cycles of free vibration was used.

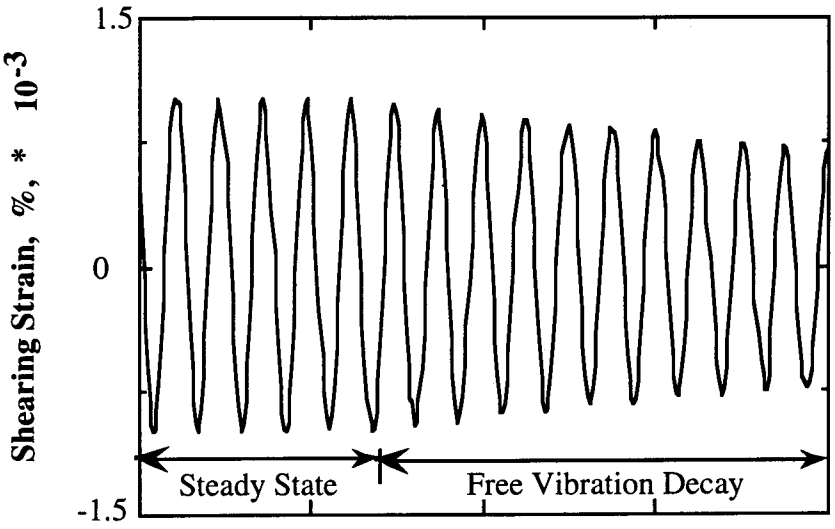

a) Free-Vibration Decay Curve

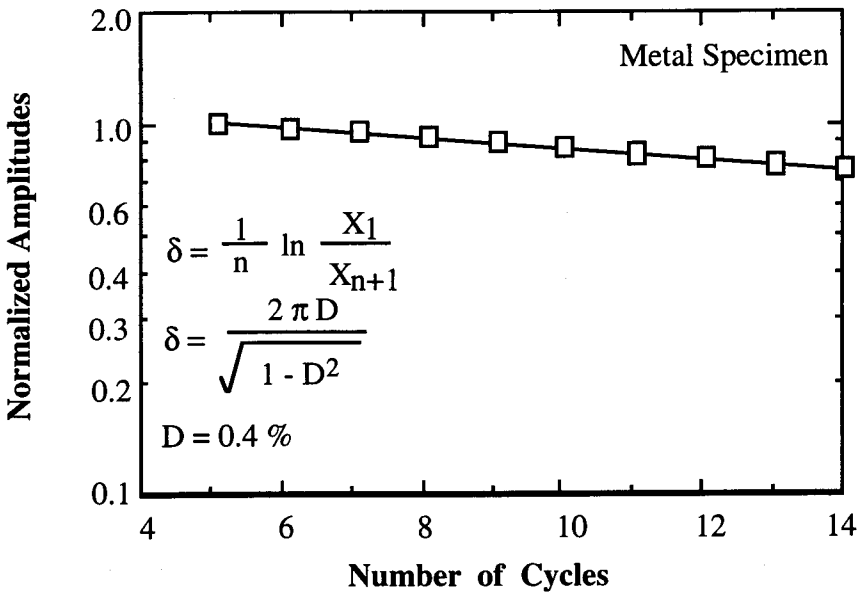

b) Analysis of Free-Vibration Decay Curve

Figure 8.B.4.A-11
Determination of material damping ratio from the free-vibration decay curve using a metal specimen.

Half-Power Bandwidth Method. Another method of measuring damping in the resonant column test is the half-power bandwidth method, which is based on measurement of the width of the frequency response curve near resonance. From the frequency response curve, the logarithmic decrement can be calculated from:

$$\delta = \frac{\pi}{2}\frac{f_2^2 - f_1^2}{f_r^2}\sqrt{\frac{A^2}{A_{max}^2 - A^2}\frac{\sqrt{1-2D^2}}{1-D^2}} \qquad \text{(8.B.4.A-8)}$$

where

f_1 = frequency below the resonance where the strain amplitude is A,
f_2 = frequency above the resonance where the strain amplitude is A,
f_r = resonant frequency, and
D = material damping ratio.

If the damping ratio is small and A is chosen as 0.707 A_{max}, which is called the half-power point, Eq. 8.B.4.A-8 can be simplified as:

$$\delta \cong \pi \bullet \frac{f_2 - f_1}{f_r} \qquad \text{(8.B.4.A-9)}$$

Therefore, the damping ratio can be expressed as:

$$D \cong \frac{f_2 - f_1}{2f_r} \qquad \text{(8.B.4.A-10)}$$

A typical damping measurement by the half-power bandwidth method (for a metal calibration specimen) is shown in Figure 8.B.4.A-12.

Background noise can be a problem in measuring material damping using the free-vibration decay method at strains less than about 0.001%. On the other hand, background noise generally has a smaller effect on the frequency response curve at strains below 0.001%. Therefore, the half-power bandwidth method is preferred to the free-vibration decay method for making small-strain damping measurements. However, at large strains, symmetry in the frequency response curve is no longer maintained, and a serious error can be introduced in the half-power bandwidth method (Ni, 1987). In this study, both types of damping measurements were made at small-strains in an attempt to obtain good data sets while only the free-vibration decay method was used at larger strains (above 0.001%).

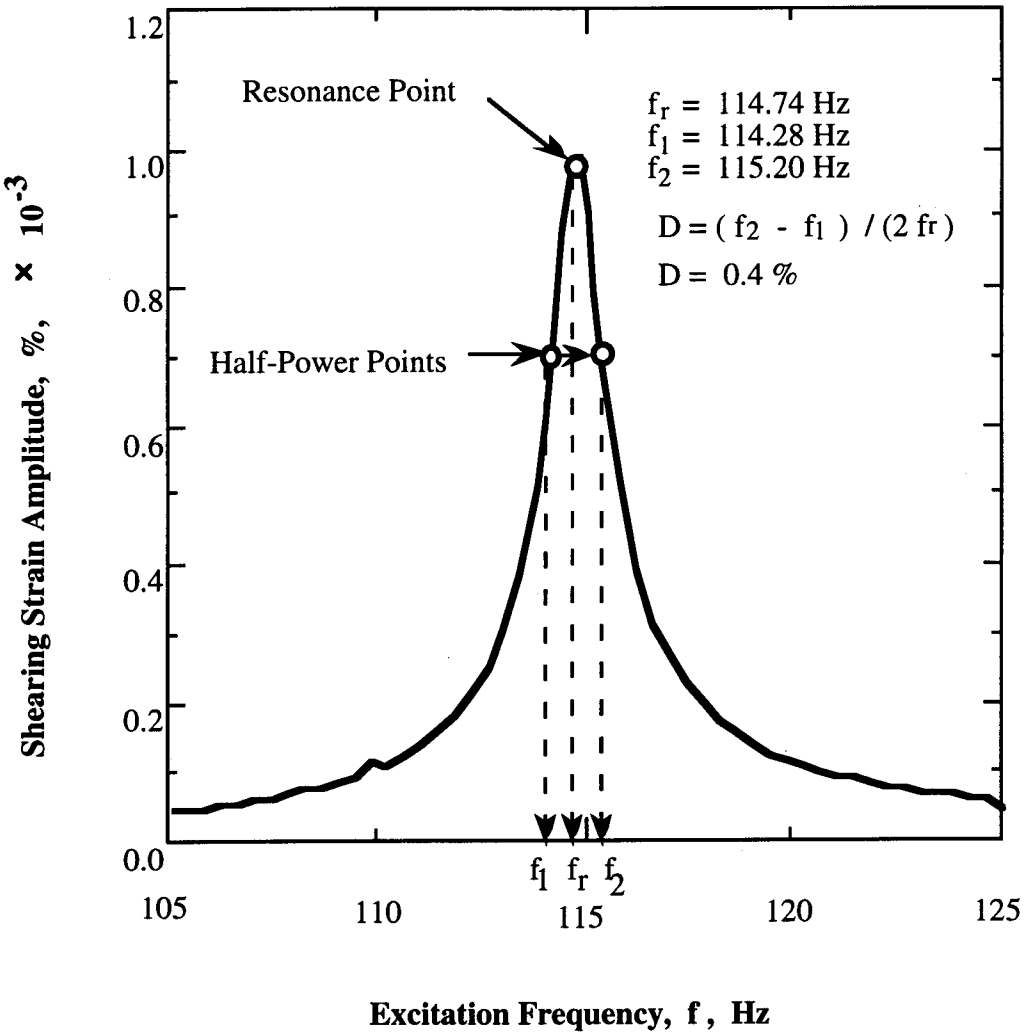

Figure 8.B.4.A-12
Determination of material damping from the half-power bandwidth method using a metal specimen.

8.B.4.A.4 Method of Analysis in the Torsional Shear Test

The torsional shear test is another method of determining the deformational characteristics (modulus and damping) of soil using the same RCTS device. Rather than measuring the dynamic response of the specimen, the actual stress-strain hysteresis loop is determined by means of measuring the torque-twist curve. Shear modulus is calculated from the slope of the hysteresis loop, and the hysteric damping ratio is calculated using the area of the hysteresis loop.

8.B.4.A.4.1 Shear Modulus

Because shear modulus is calculated from the stress-strain hysteresis loop, shearing stress and shearing strain in the torsional shear test need to be defined.

Shearing Stress. Determination of shearing stress in the torsional shear test is based on the theory of elasticity for circular or tubular rods in pure torsion. Assume that pure torque, T, is applied to the top of the specimen. The torque can be calculated from:

$$T = \int_{r_i}^{r_o} \tau_r (2\pi\ r)\ r\ dr \qquad \text{(8.B.4.A-11)}$$

where τ_r is the shearing stress at a distance r from the axis of specimen and, r_o and r_i are outside and inside radii, respectively. If the shearing stress is assumed to vary linearly across the radius:

$$\tau_r = \tau_m \bullet (r / r_o) \qquad \text{(8.B.4.A-12)}$$

where τ_m is the maximum shearing stress at $r = r_o$. Eq. 8.B.4.A-12 can be rewritten as:

$$T = \frac{\tau_m}{r_o} \bullet \frac{\pi}{2} \bullet (r_o^4 - r_i^4) = \frac{\tau_m}{r_o} \bullet J_p \qquad \text{(8.B.4.A-13)}$$

where J_p is the area polar moment of inertia. From Eq. 8.B.4.A-13, one can write:

$$\tau_m = r_o \bullet \frac{T}{J_p} \qquad \text{(8.B.4.A-14)}$$

Because shearing stress is assumed to vary linearly across the radius, the average torsional shearing stress is defined as:

$$\tau_{avg} = r_{eq} \bullet \frac{T}{J_p} \qquad \text{(8.B.4.A-15)}$$

The value of r_{eq} is the same value as used in the resonant column analysis for calculation of shearing strain (Section 8.B.4.A.3.2).

The value of applied torque, T, is calculated from the input voltage applied to the drive system, V_T (Volts), and the torque calibration factor, K_T (torque / Volts). Thus, average shearing stress becomes:

$$\tau_{avg} = r_{eq} \bullet K_T \bullet V_T / J_p \qquad \text{(8.B.4.A-16)}$$

Shearing Strain. Calculation of shearing strain in the torsional shear test follows the same procedure used in the resonant column test. The proximitor system directly measures the displacement (instead of acceleration measured in the resonant test). Hence, the angle of twist (θ) is calculated from the proximitor output voltage ,V_P (volts), and the proximitor calibration factor, K_P (rad / volt). Shearing strain, γ, is then calculated from:

$$\gamma = r_{eq} \Sigma K_P \bullet V_P / l \qquad \text{(8.B.4.A-17)}$$

Shear Modulus. Once the stress-strain hysteresis loop is measured, the shear modulus, G, is calculated from the slope of a line through the end points of the hysteresis loop as shown in Figure 8.B.4.A-13. Thus, the shear modulus is calculated from:

$$G = \tau / \gamma \qquad \text{(8.B.4.A-18)}$$

where τ is peak shearing stress and γ is peak shearing strain.

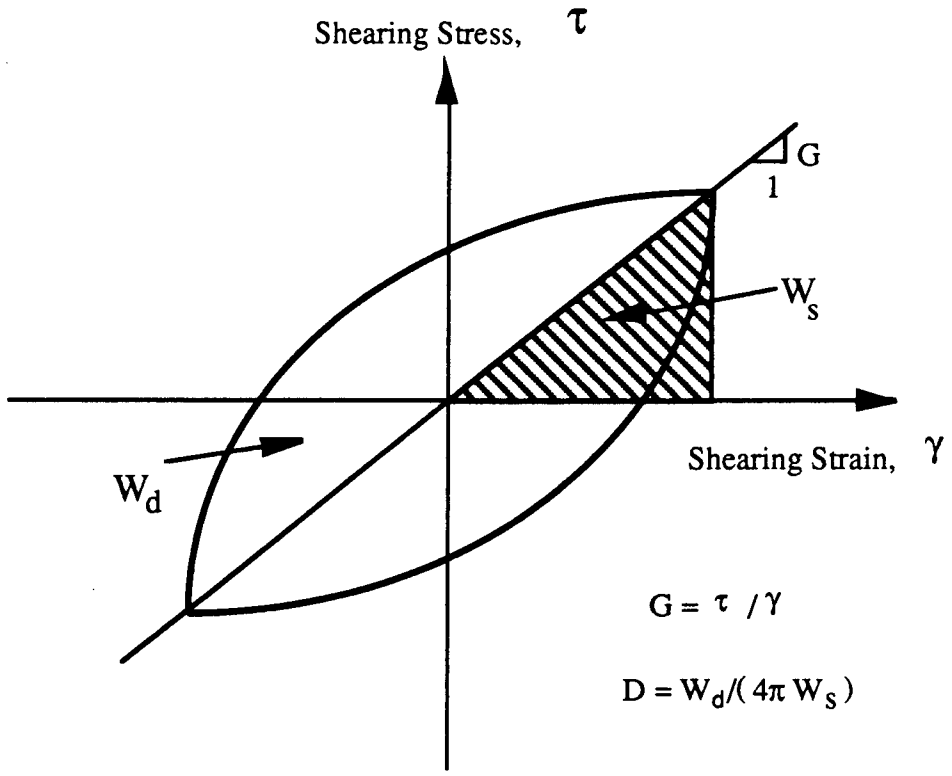

Figure 8.B.4.A-13
Determination of shear modulus and damping ratio in the torsional shear test.

8.B.4.A.4.2 Hysteretic Damping Ratio

Hysteretic damping ratio in the torsional shear test is measured using the amount of energy dissipated in one complete cycle of loading and the peak strain energy stored in the specimen during the cycle.

In the torsional shear test, the dissipated energy is measured from the area of the stress-strain hysteresis loop. The energy per cycle, W_d, due to a viscous damping force, F_d, is:

$$W_d = \int_o^T F_d \bullet \dot{x}\, dt \qquad \text{(8.B.4.A-19)}$$

where $\dot{x}$ is a velocity and T is a period. For simple harmonic motion with frequency of ω, i.e. $x = A\,\mathrm{Cos}(\omega t - \phi)$, W_d become:

$$W_d = \pi\, c\, \omega\, A^2 \qquad \text{(8.B.4.A-20)}$$

From the Eq. 8.B.4.A-20, the viscous damping coefficient can be expressed as:

$$c = W_d / (\pi \omega A^2) \quad (8.B.4.A\text{-}21)$$

The peak strain energy, W_s, stored by the spring is equal to the area under the secant modulus line in Figure 8.B.4.A-13 and can be written as:

$$W_s = k A^2 / 2 \quad (8.B.4.A\text{-}22)$$

The critical damping coefficient, C_c, is

$$C_c = 2 \bullet \sqrt{k m} = 2 k / \omega_n \quad (8.B.4.A\text{-}23)$$

where k is an elastic spring constant, m is a mass, and ω_n is a natural frequency of system. Using Eq. 8.B.4.A-22, Eq. 8.B.4.A-23 can be rewritten as:

$$C_c = 4 W_s / (\omega_n A^2) \quad (8.B.4.A\text{-}24)$$

Therefore, the damping ratio, D, can be expressed as:

$$D = C / C_c = W_d / (4 \pi W_s) * (\omega_n / \omega) \quad (8.B.4.A\text{-}25)$$

For soils, material damping is often assumed to be frequency independent. Therefore, ω_n / ω is ignored and hysteretic damping is written as:

$$D = \frac{1}{4\pi} * \frac{W_d}{W_s} \quad (8.B.4.A\text{-}26)$$

where W_d is the area of the hysteresis loop and W_s is the area of the triangle as shown in Figure 8.B.4.A-13.

8.B.4.A.5 Evaluation of RCTS Equipment Compliance with Metal Specimens

To evaluate the RCTS equipment for system compliance, metal specimens were used. The metal specimens were made of brass and aluminum tubes. Eighteen metal specimens of different sizes and materials were used to obtain different resonant frequencies. Details of the metal specimens are presented in Table 8.B.4.A-1. It was assumed that the metal specimens should have (essentially) zero damping and that these specimens should exhibit no effect of frequency on stiffness or damping over the complete range of frequencies used in these tests (from about 0.05 Hz to 400 Hz).

Table 8.B.4.A-1
Metal Specimens Used to Evaluate Equipment Damping Ratio

Specimen Number	Outside Diameter		Inside Diameter		Height		Weight
	Inch	cm	Inch	cm	Inch	cm	gram
1(Brass Tube)	1.000	2.540	0.875	2.223	4.98	12.65	132.35
2(Brass Tube)	0.875	2.223	0.813	2.064	6.96	17.68	79.96
3(Brass Tube)	0.875	2.223	0.813	2.064	8.49	21.56	97.07
4(Brass Tube)	0.750	1.905	0.688	1.746	6.97	17.70	70.72
5(Brass Tube)	0.750	1.905	0.688	1.746	8.49	21.57	85.87
6(Brass Tube)	0.625	1.588	0.563	1.429	6.96	17.68	58.45
7(Brass Tube)	0.625	1.588	0.563	1.429	8.49	21.57	70.94
8(Brass Tube)	0.375	0.953	0.313	0.794	6.94	17.63	33.69
9(Brass Tube)	0.375	0.953	0.313	0.794	8.44	21.45	40.86
10(Brass Rod)	0.313	0.794	0	0	6.92	17.57	74.46
11(Brass Rod)	0.313	0.794	0	0	8.44	21.44	90.30
12(Brass Rod)	0.500	1.270	0	0	7.00	17.78	191.22
13(Brass Rod)	0.750	1.905	0	0	7.00	17.75	429.52
14(Brass Rod)	0.250	0.635	0	0	6.96	17.67	47.53
15(Brass Rod)	1.500	3.810	0	0	7.00	17.78	1731.64
16(Brass Tube)	0.500	1.270	0.438	1.111	6.97	17.71	44.63
17(Brass Tube)	0.500	1.270	0.438	1.111	8.48	21.53	54.29
18(Brass Tube)	1.000	2.540	0.875	2.223	6.97	17.70	178 50

Unit Weight of Brass = 8.49 g/cm^3 (=0.316 lbs/in^3)

Hysteresis loops with one metal specimen measured at a frequency of 0.5 Hz are shown in Figure 8.B.4.A-14. The stress-strain curve is linear, resulting in no damping as expected. On the other hand, Figures 8.B.4.A-11 and 8.B.4.A-12 show the damping measurements with the same metal specimen in the resonant column test predict an apparent damping of 0.4% from both the free-vibration decay and half-power bandwidth methods.

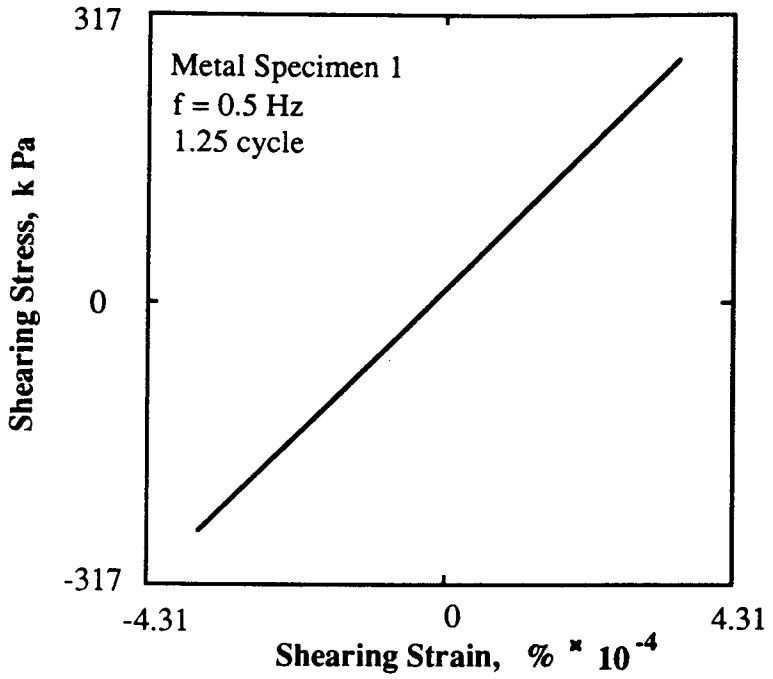

Figure 8.B.4.A-14
Hysteresis loops of metal specimen determined by torsional shear testing at a frequency of 0.5 Hz.

The variations in shear modulus and damping ratio with loading frequency for four of the metal specimens are plotted in Figure 8.B.4.A-15. The shear modulus of each metal specimen determined from the RCTS equipment is independent of loading frequency as expected. Therefore, shear modulus can be measured properly with RCTS equipment over a wide frequency range without any compliance problem.

On the other hand, the damping ratio measured by the RCTS equipment is affected by the loading frequency. For frequencies less than or equal to 0.5 Hz, damping ratio evaluated by the torsional shear test is essentially zero as expected. In this frequency range, material damping can be evaluated without any equipment correction. For higher frequencies, however, non-zero damping values are obtained with all metal specimens in the torsional shear as shown in Figure 8.B.4.A-15b and 8.B.4.A-16. In this case the apparent material damping increases significantly as the excitation frequency increases from 1 to 10 Hz. Strain amplitude has little effect on the damping values as shown in Figure 8.B.4.A-16. These values of apparent material damping are considered to be due to a compliance problem with the complete RCTS system (back-EMF generated by the drive system) and are, therefore, subtracted from all damping measurements in the torsional shear test at the same frequencies when soil specimens are tested.

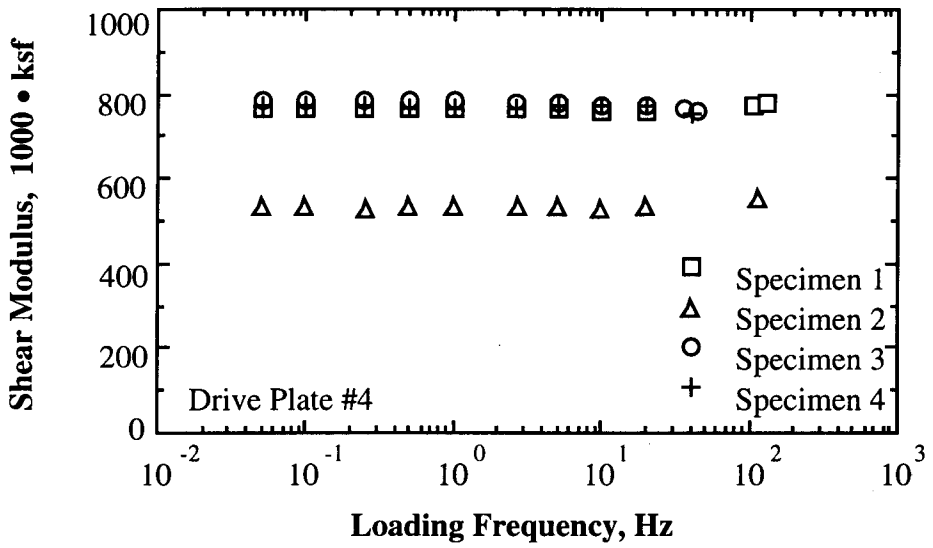

a) Variation in Shear Modulus

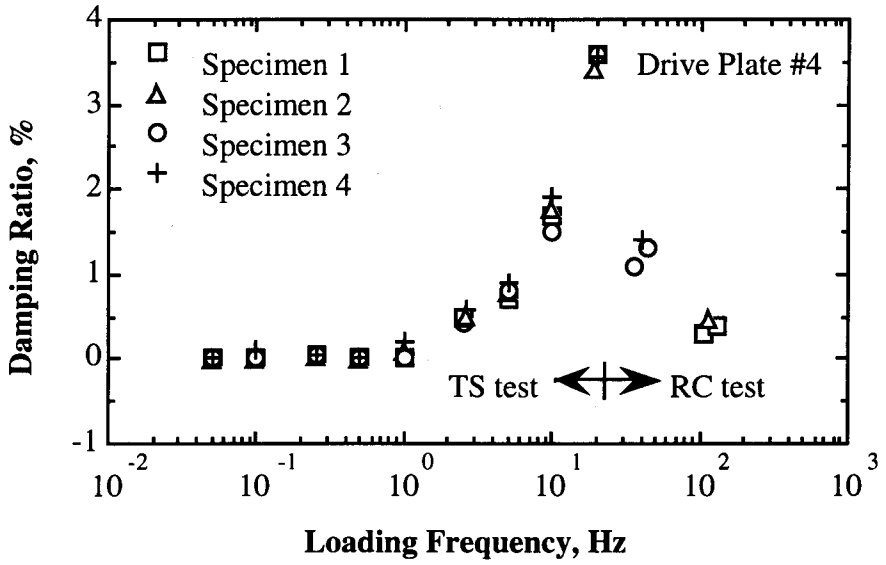

b) Variation in Material Damping Ratio

Figure 8.B.4.A-15
Variation in shear modulus and material damping ratio with loading frequency determined for metal specimens (from Kim, 1991).

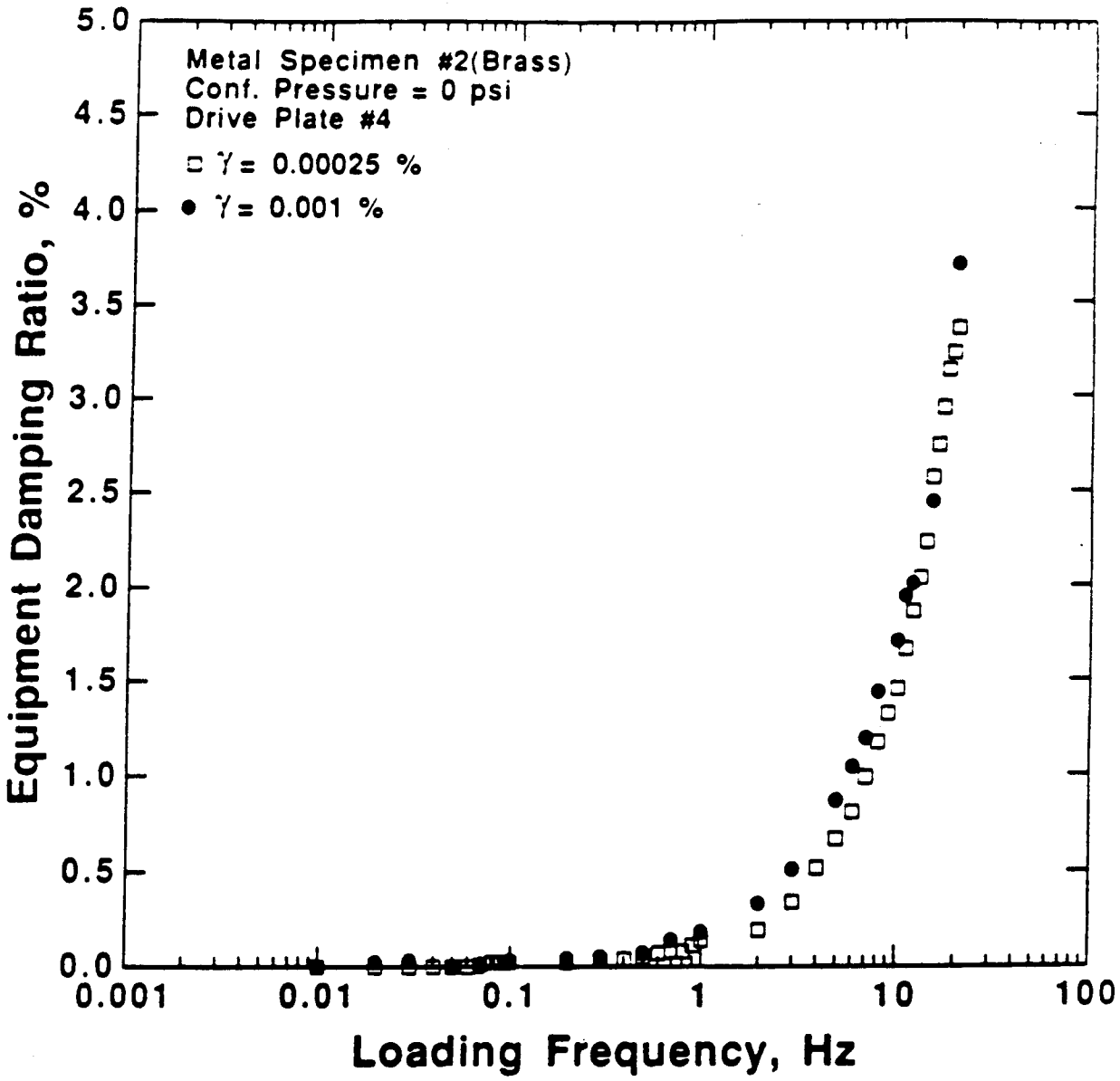

Figure 8.B.4.A-16
Measured damping ratio for metal specimen #2 in the torsional shear test.

It should be noted that excitation frequencies in the torsional shear test never exceeded 0.1 times the resonant frequency of the soil specimen. This approach was followed so that dynamic amplification did not affect the TS measurements. Even in this case, however, corrections were made for minor dynamic amplification which occurs near 0.1 times the resonant frequency.

In the resonant column test, non-zero damping values were obtained at all resonant frequencies as seen in Figures 8.B.4.A-15b and 8.B.4.A-17. Equipment damping values ranged from about 3.5% at 20 Hz to about 0.4% at 200 Hz. These resonant frequencies are in the frequency range where all soil testing was conducted. Just as in the TS test, the values of equipment damping measured with the metal specimens were subtracted from the damping measurements in all RC tests with soil specimens at the same resonant frequencies. Strain amplitude had a negligible effect on equipment damping as shown in Figure 8.B.4.A-18.

Finally, to be sure that coil-magnet interaction was the cause of the equipment damping problem, free-vibration tests were conducted with the RC equipment. In this case, however, all coils were removed which required that the drive plate be excited by hand in free vibration. The resulting tests with drive plate #4 are given in Figure 8.B.4.A-19 by the solid square symbols. As seen, damping values less than 0.1% were measured. These values are considered to equal zero in this work, indicating the coil-magnet interaction is mainly the cause of the equipment damping.

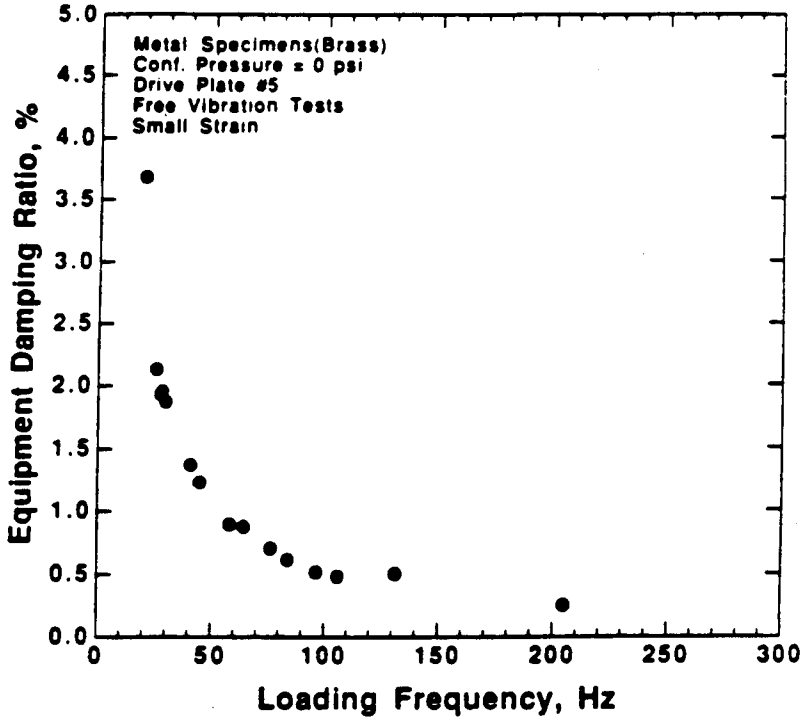

a. Damping from the Free-Vibration Decay Curve

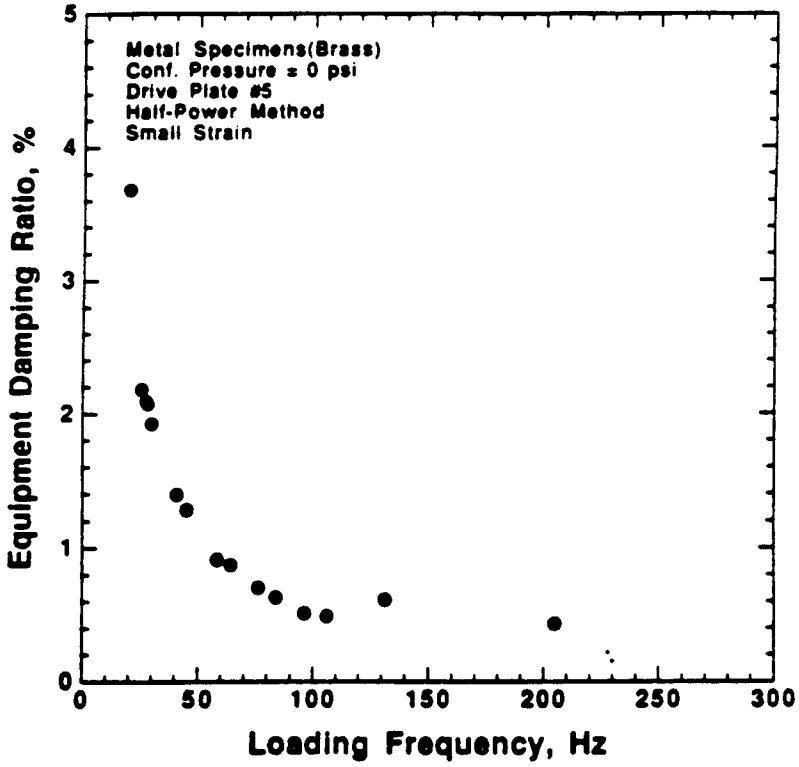

b. Damping from the Half-Power Bandwidth

Figure 8.B.4.A-17
Equipment damping measured in the resonant column test.

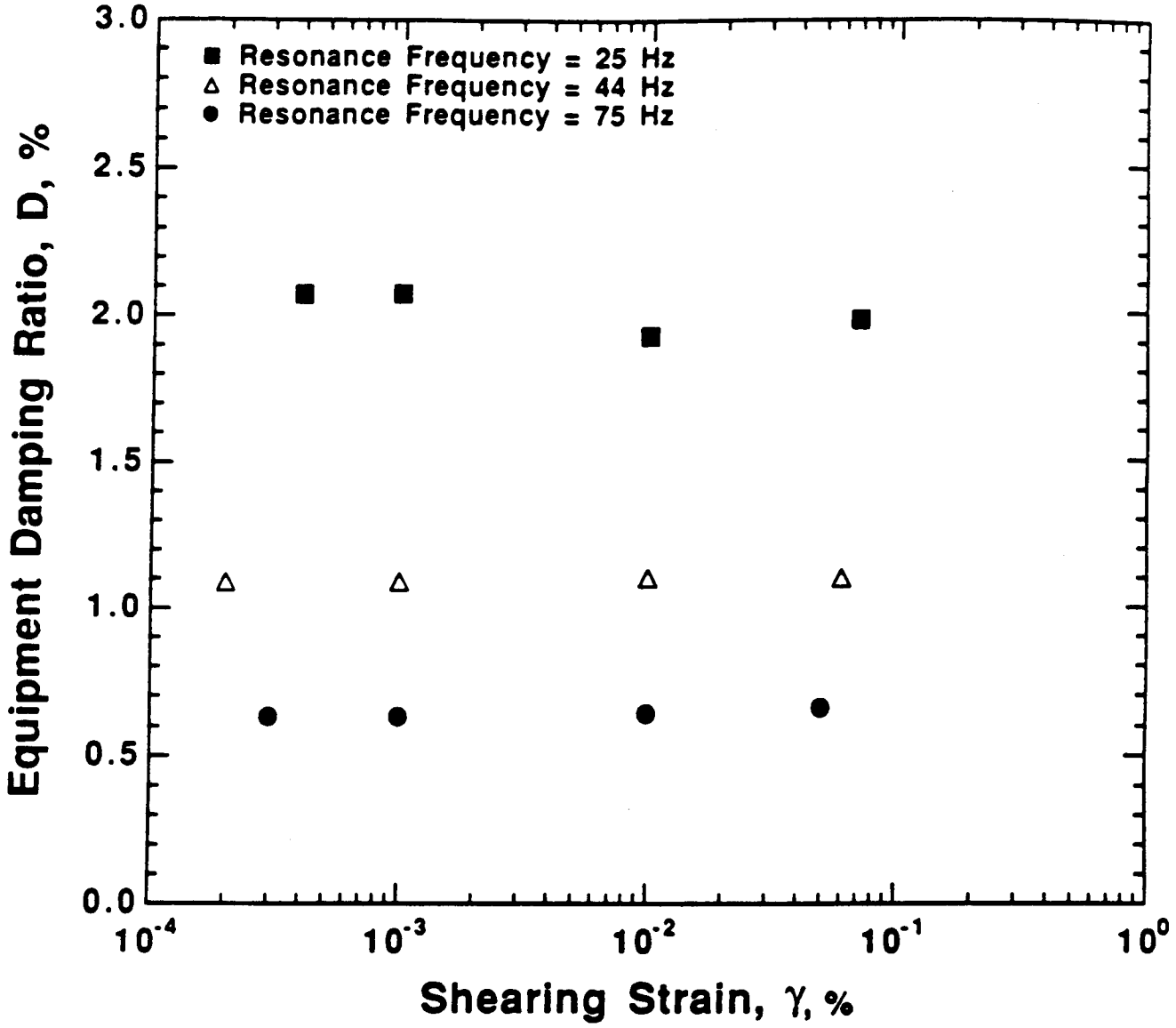

Figure 8.B.4.A-18
Effect of strain amplitude on equipment damping measured in the resonant column test.

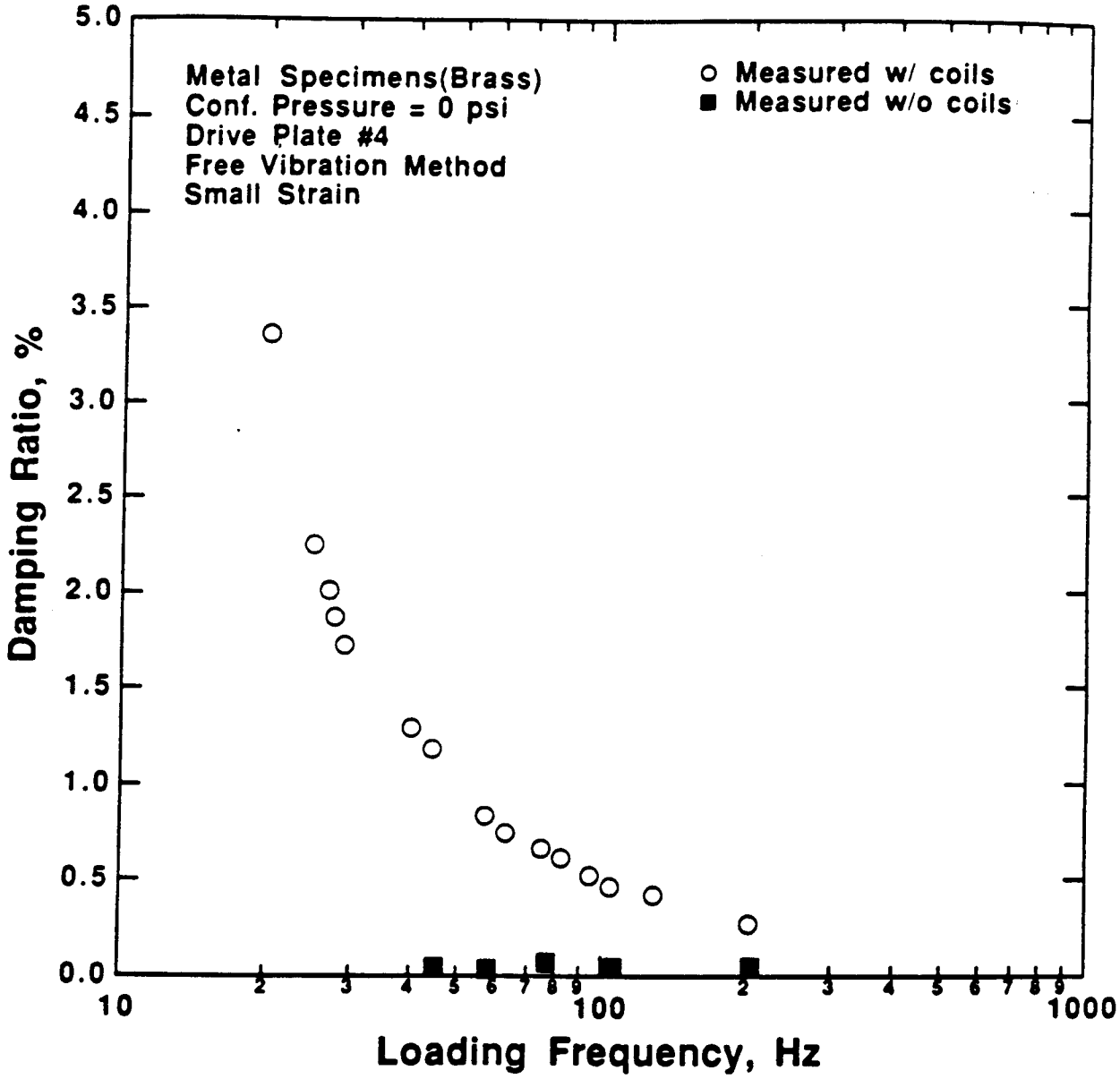

Figure 8.B.4.A-19
Comparison of equipment damping measured in free vibration RC tests with and without the electrical coils.

References

Chen, A.T.F., Stokoe, K.H., II (1979), *Interpretation of Strain Dependent Modulus and Damping from Torsional Soil Tests*, Report No. USGS-GD-79-002, NTIS No. PB-298479, U.S. Geological Survey, 46 pp.

Isenhower, W.M. (1979), *Torsional Simple Shear/Resonant Column Properties of San Francisco Bay Mud*, Geotechnical Engineering Thesis, GT 80-1, University of Texas, Dec., 307 pp.

Kim, D.-S. (1991), *Deformational Characteristics of Soils at Small to Intermediate Strains from Cyclic Tests*, Ph.D. Dissertation, The University of Texas at Austin, 341 pp.

Lodde, P.F. (1982), *Shear Moduli and Material Damping of San Francisco Bay Mud*, M.S. Thesis, The University of Texas at Austin.

Ni, S.-H. (1987), *Dynamic Properties of Sand Under True Triaxial Stress States from Resonant Column/Torsional Shear Tests*, Ph.D. Dissertation, The University of Texas at Austin, 421 pp.

Richart, F.E.,Jr., Hall, J.R.,Jr. and Woods, R.D. (1970), *Vibrations of Soils and Foundations*, Prentice-Hall Inc., Englewood Cliffs, New Jersey, 414 pp.

APPENDIX B
DYNAMIC TESTS OF DRY REMOLDED SAND SAMPLE RS1

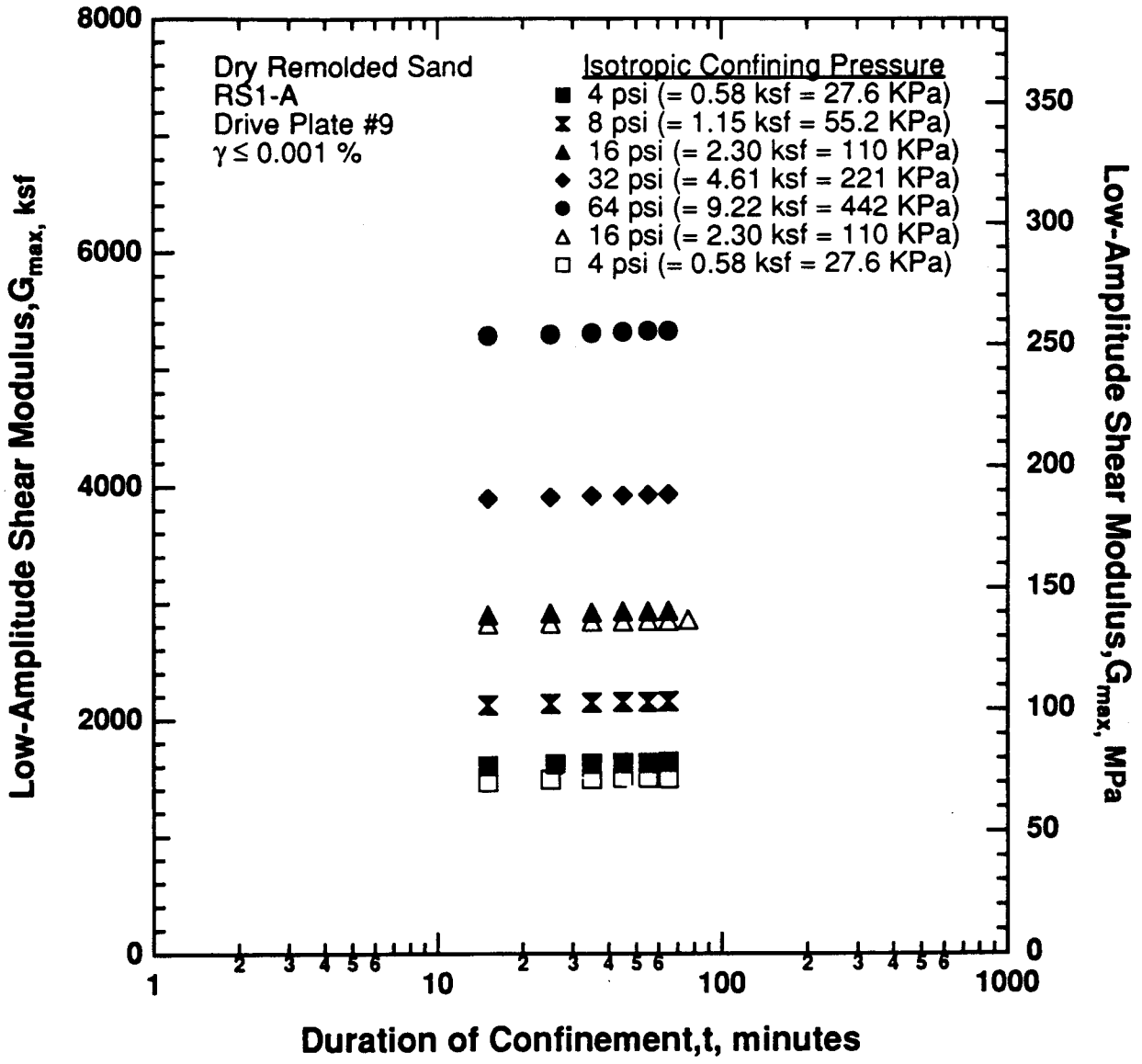

Figure 8.B.4.B-1
Variation in low-amplitude shear modulus with magnitude and duration of isotropic confining pressure for dry sand sample (RS1); initial loading cycle (A).

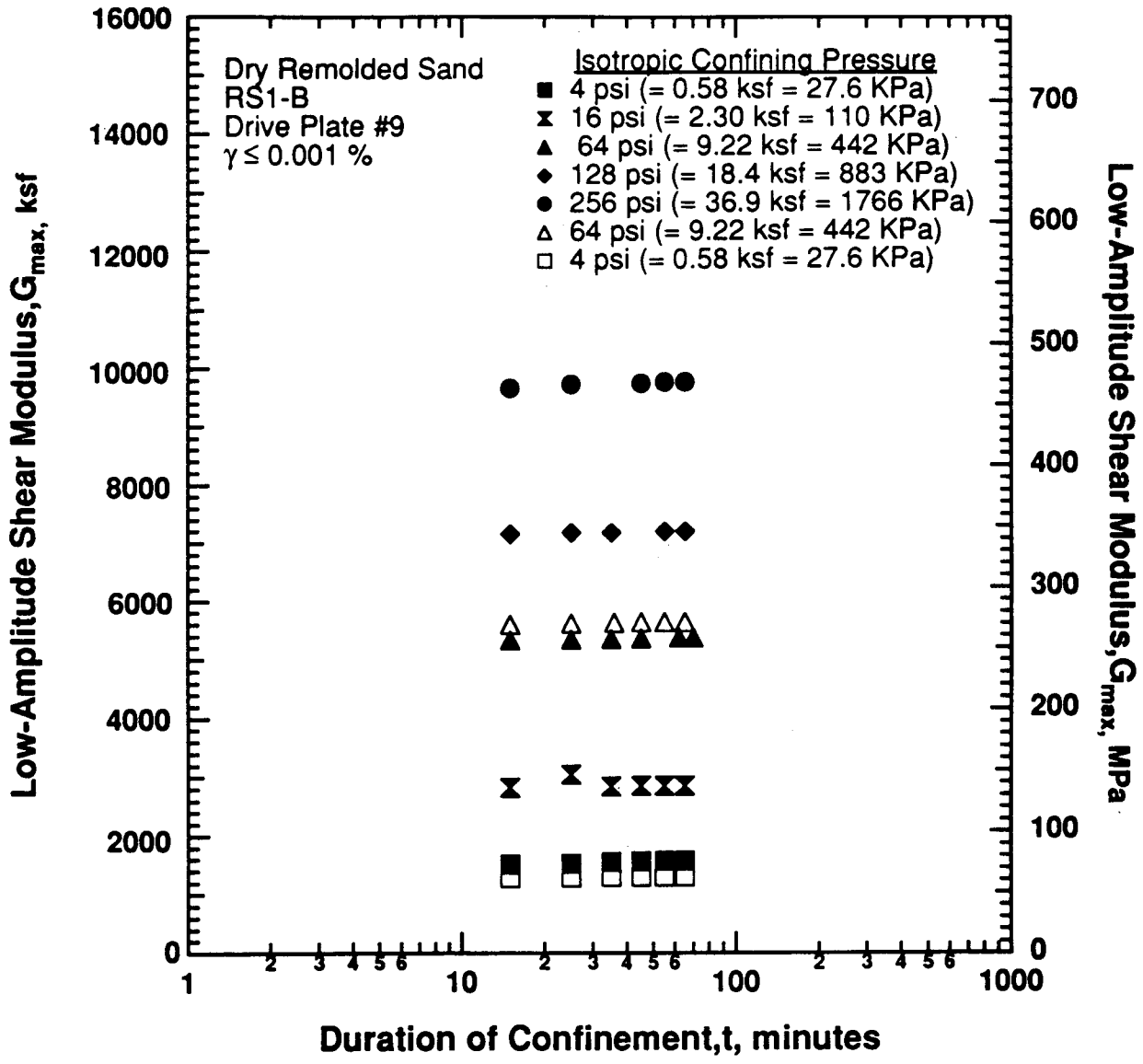

Figure 8.B.4.B-2
Variation in low-amplitude shear modulus with magnitude and duration of isotropic confining pressure for dry sand sample (RS1); second loading cycle (B).

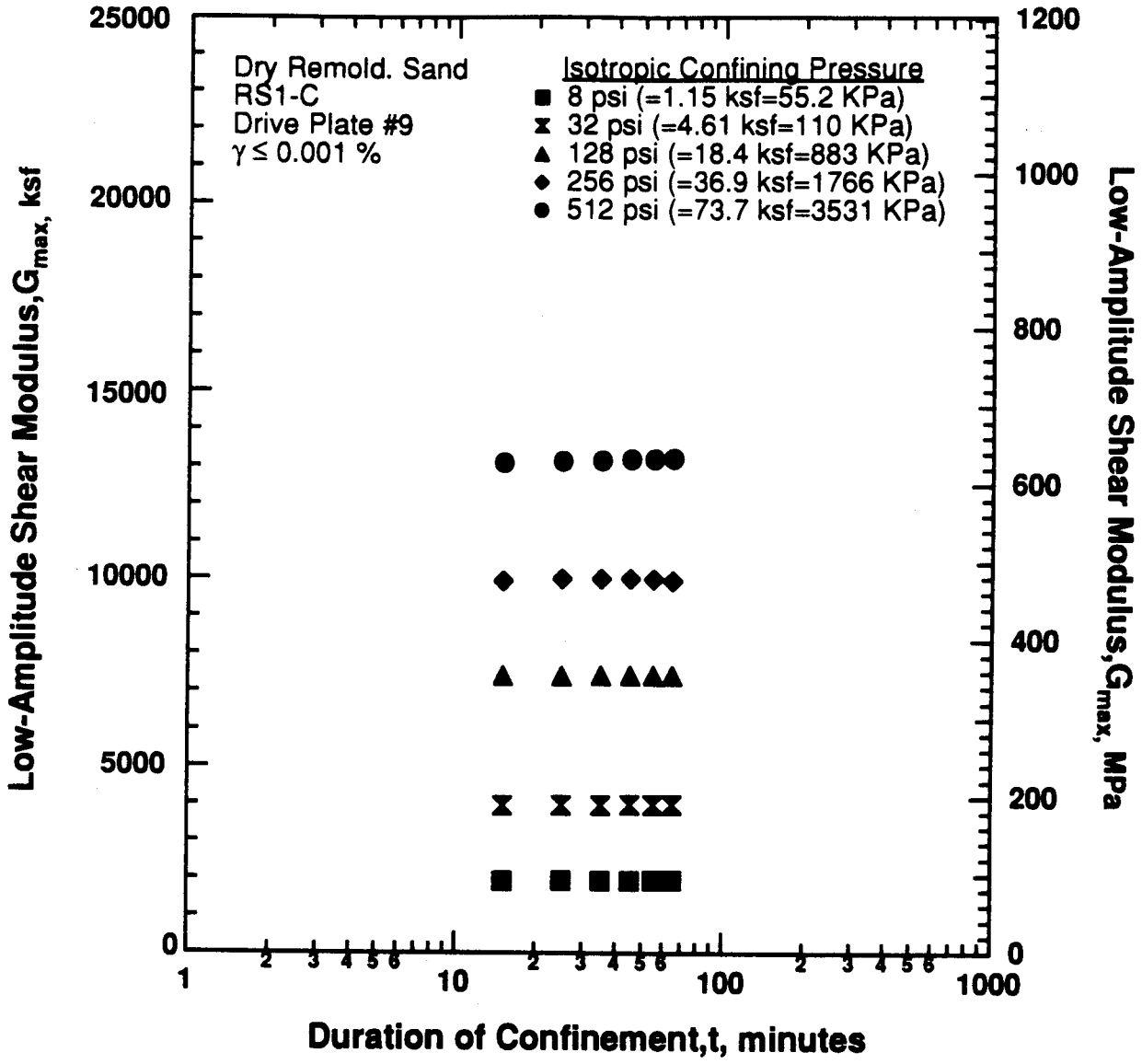

Figure 8.B.4.B-3
Variation in low-amplitude shear modulus with magnitude and duration of isotropic confining pressure for dry sand sample (RS1); third loading cycle (C).

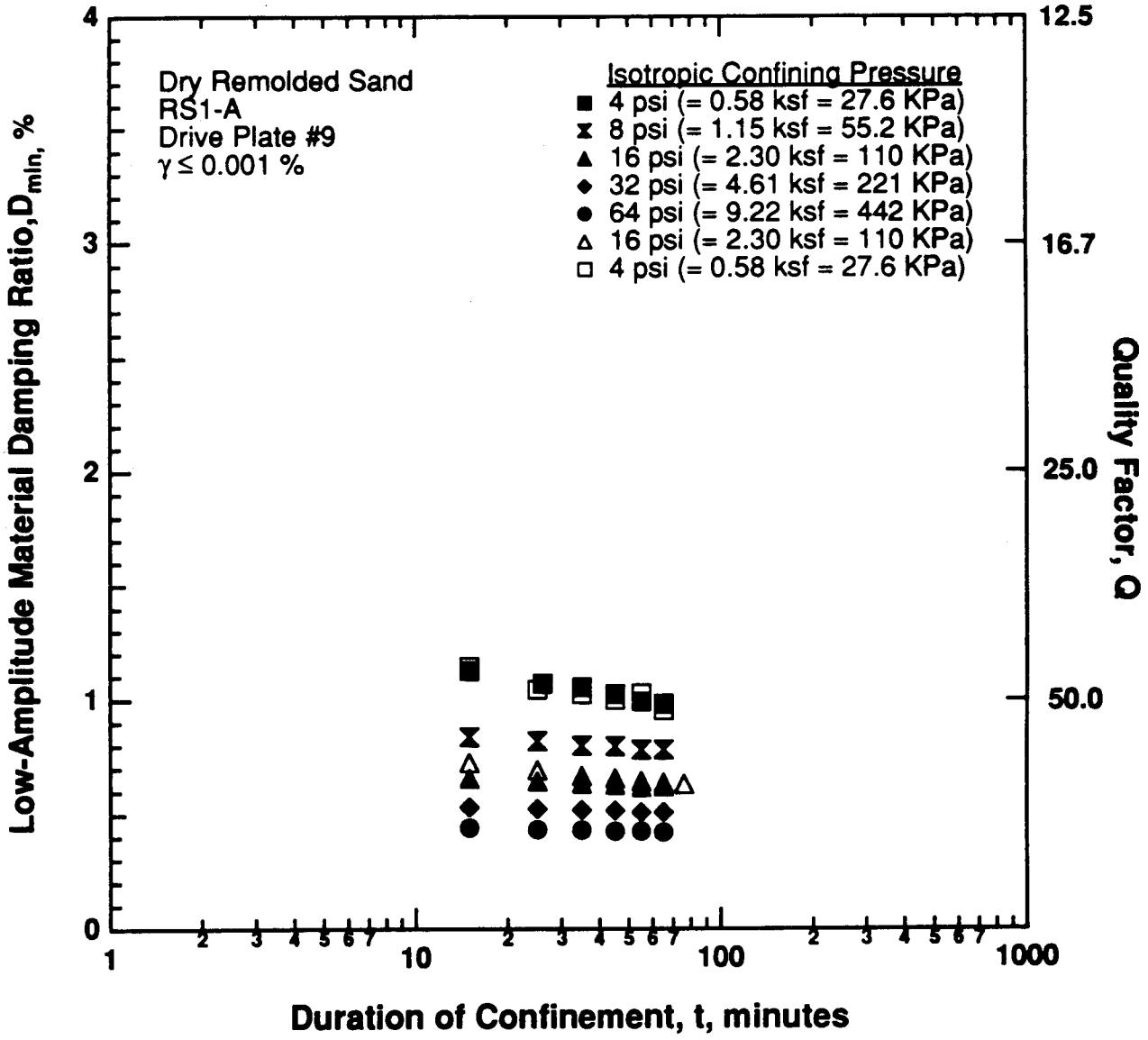

Figure 8.B.4.B-4
Variation in low-amplitude material damping ratio with magnitude and duration of isotropic confining pressure for dry sand sample (RS1); initial loading cycle (A).

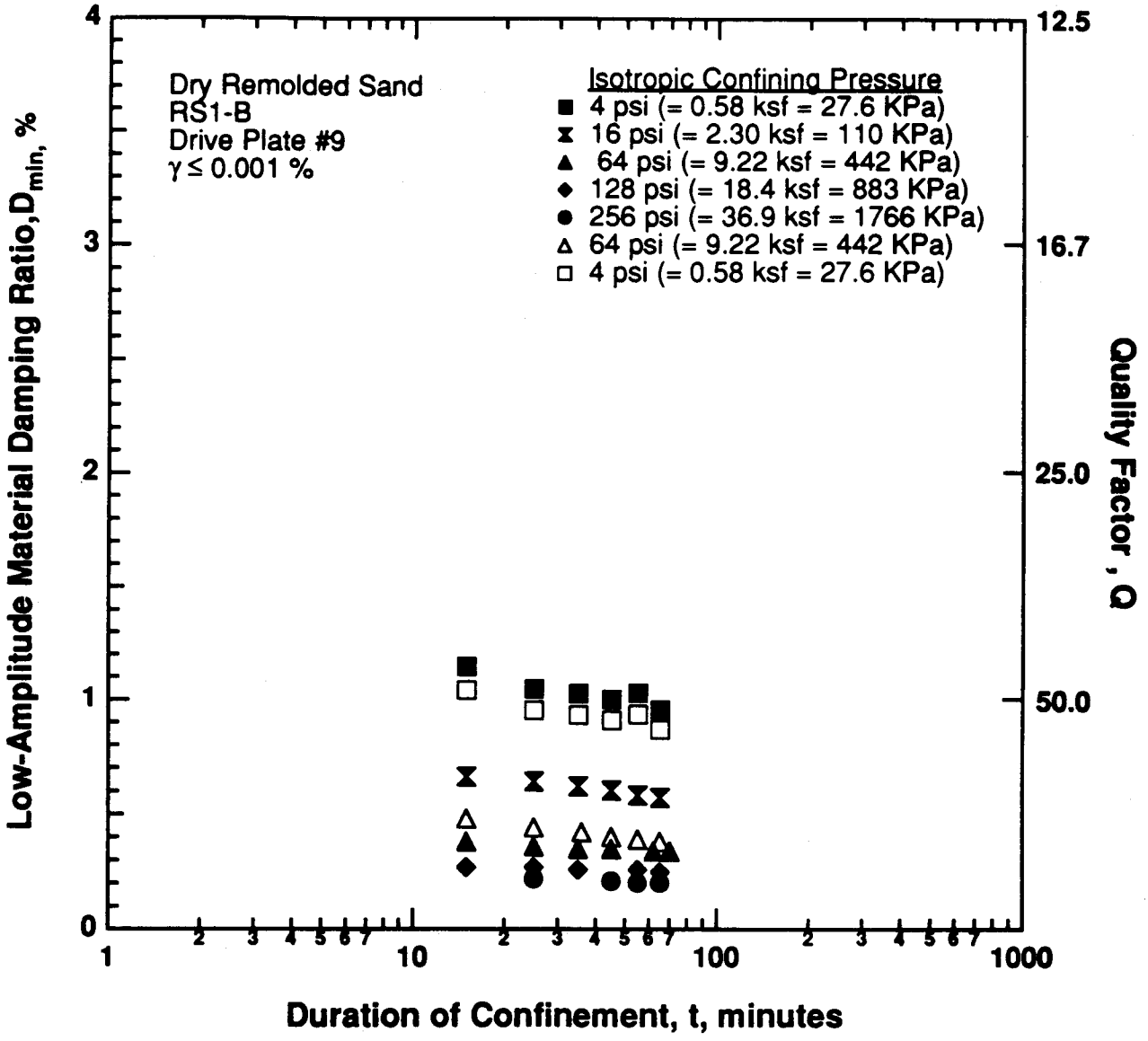

Figure 8.B.4.B-5
Variation in low-amplitude material damping ratio with magnitude and duration of isotropic confining pressure for dry sand sample (RS1); second loading cycle (B).

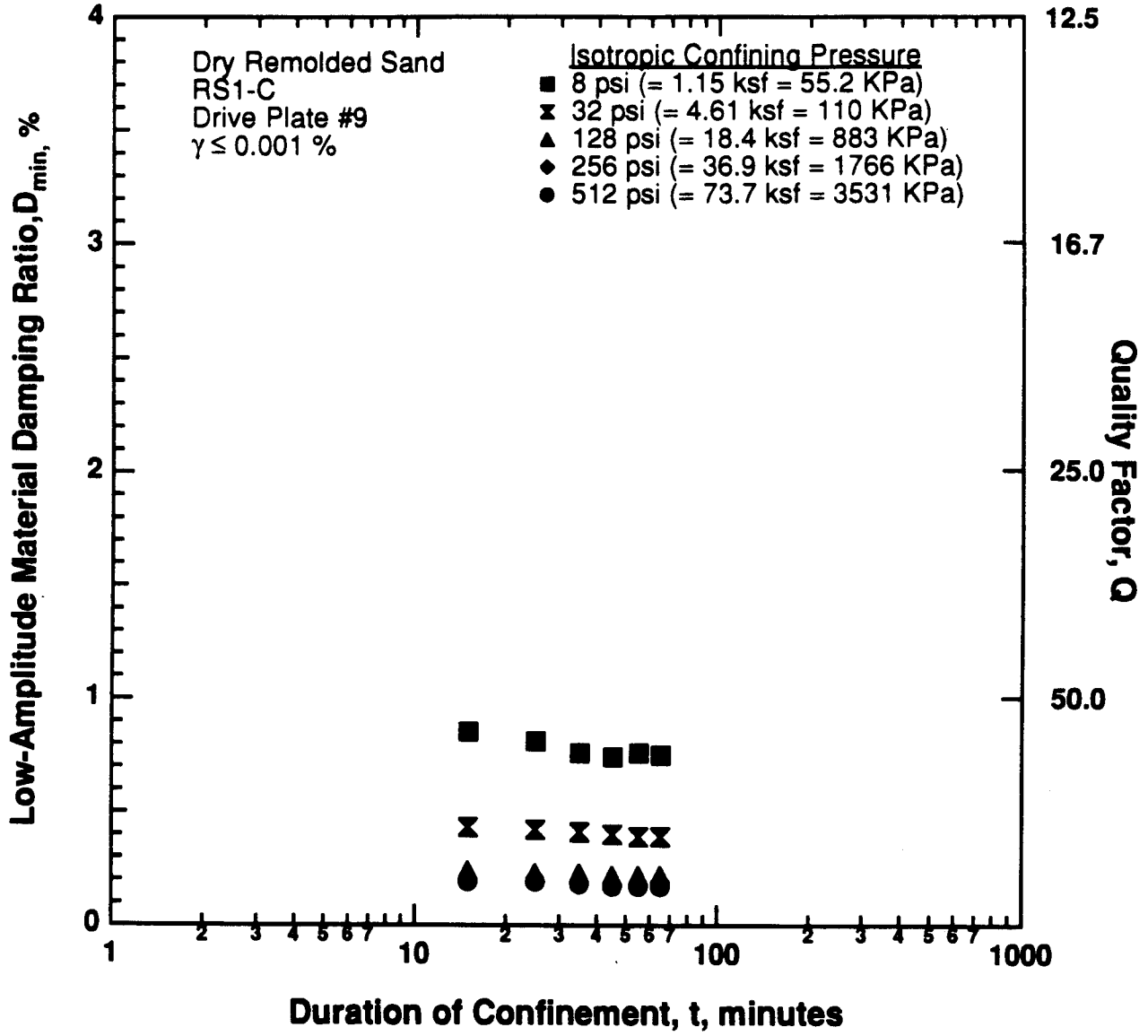

Figure 8.B.4.B-6
Variation in low-amplitude material damping ratio with magnitude and duration of isotropic confining pressure for dry sand sample (RS1); third loading cycle (C).

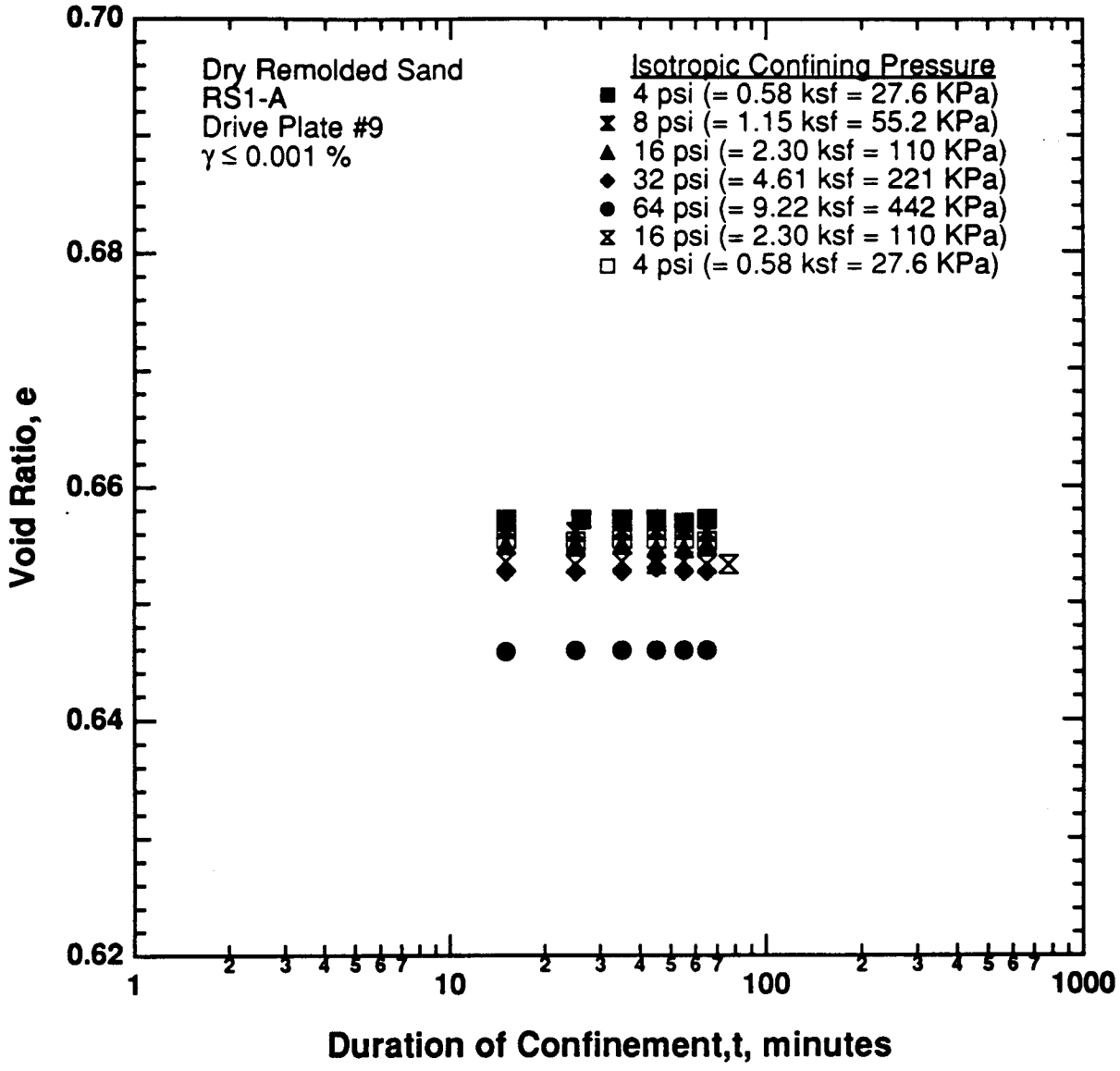

Figure 8.B.4.B-7
Variation in void ratio with magnitude and duration of isotropic confining pressure for dry remolded sand sample (RS1); initial loading cycle (A).

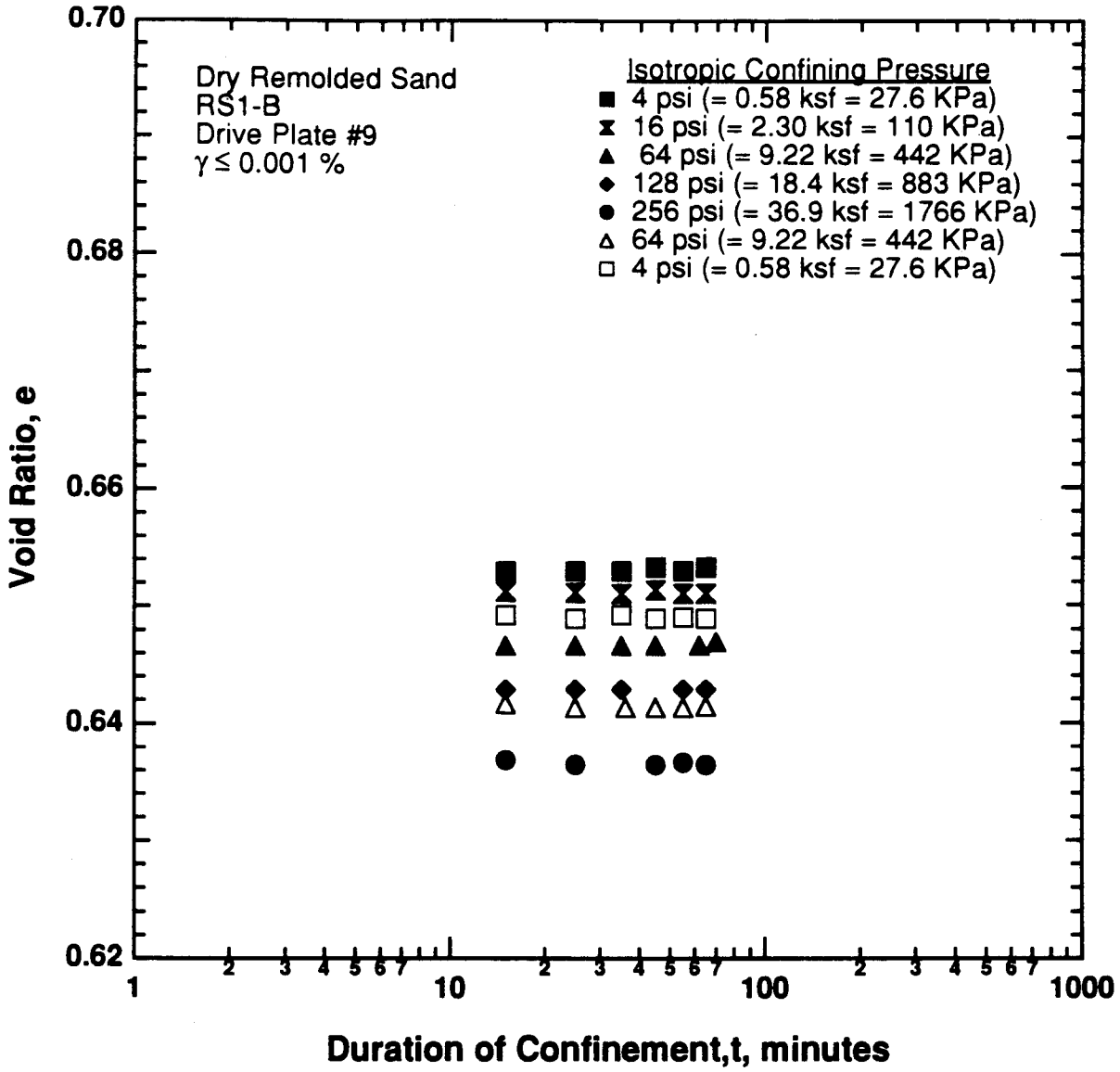

Figure 8.B.4.B-8
Variation in void ratio with magnitude and duration of isotropic confining pressure for dry remolded sand sample (RS1); second loading cycle (B).

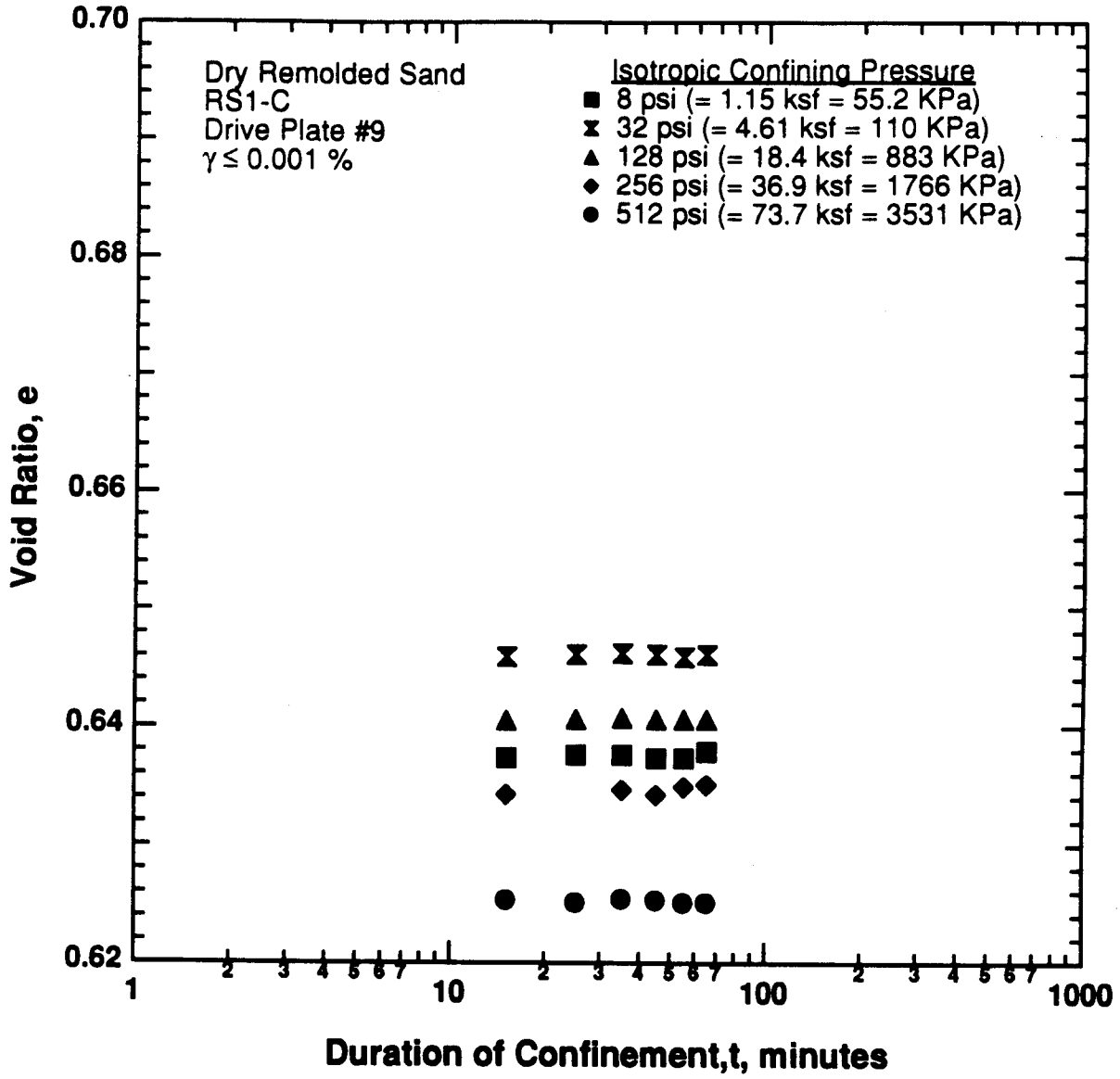

Figure 8.B.4.B-9
Variation in void ratio with magnitude and duration of isotropic confining pressure for dry remolded sand sample (RS1); third loading cycle (C).

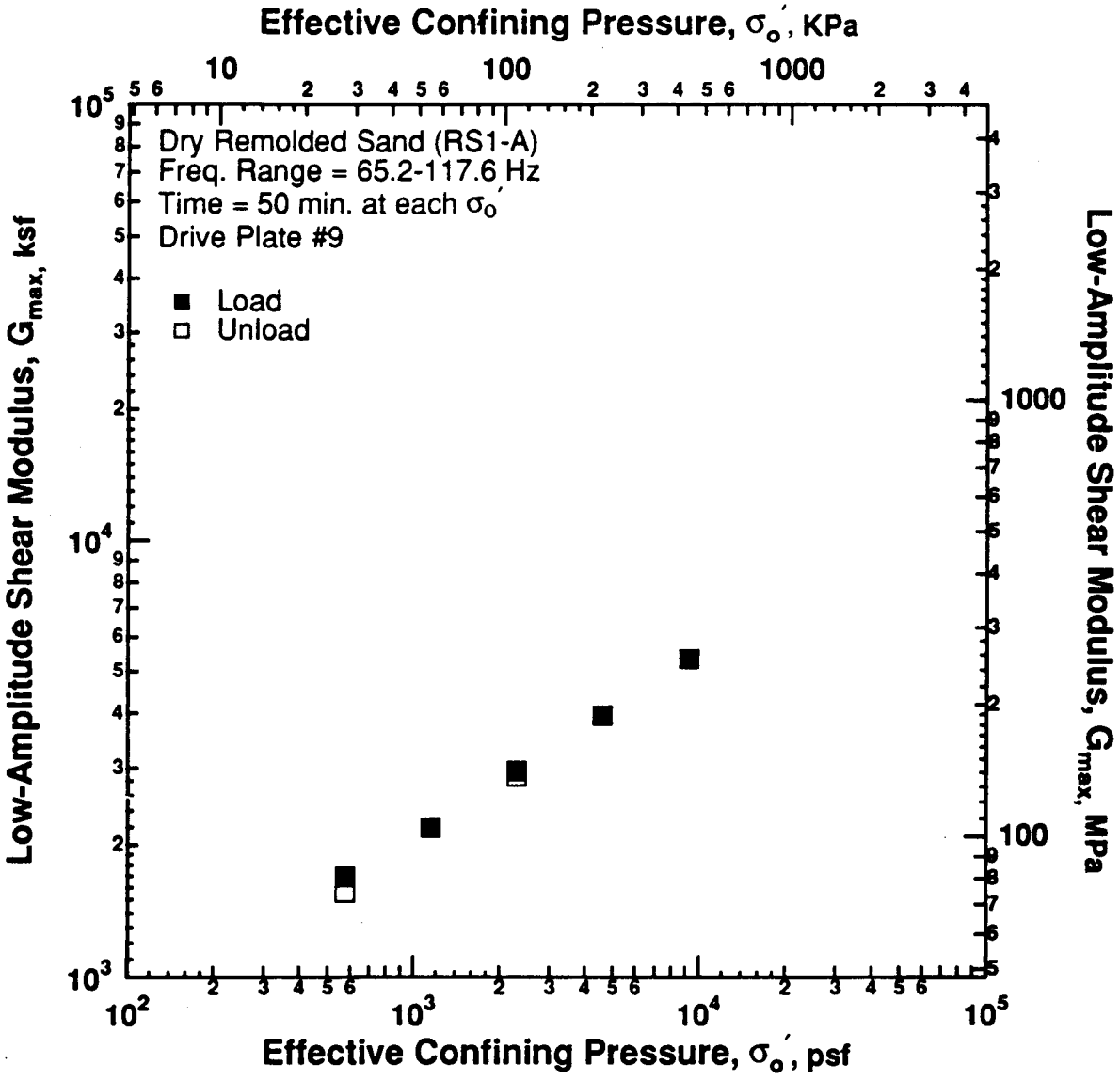

Figure 8.B.4.B-10
Variation in low-amplitude shear modulus with effective confining pressure from resonant column testing of dry remolded sand sample (RS1); initial loading cycle (A).

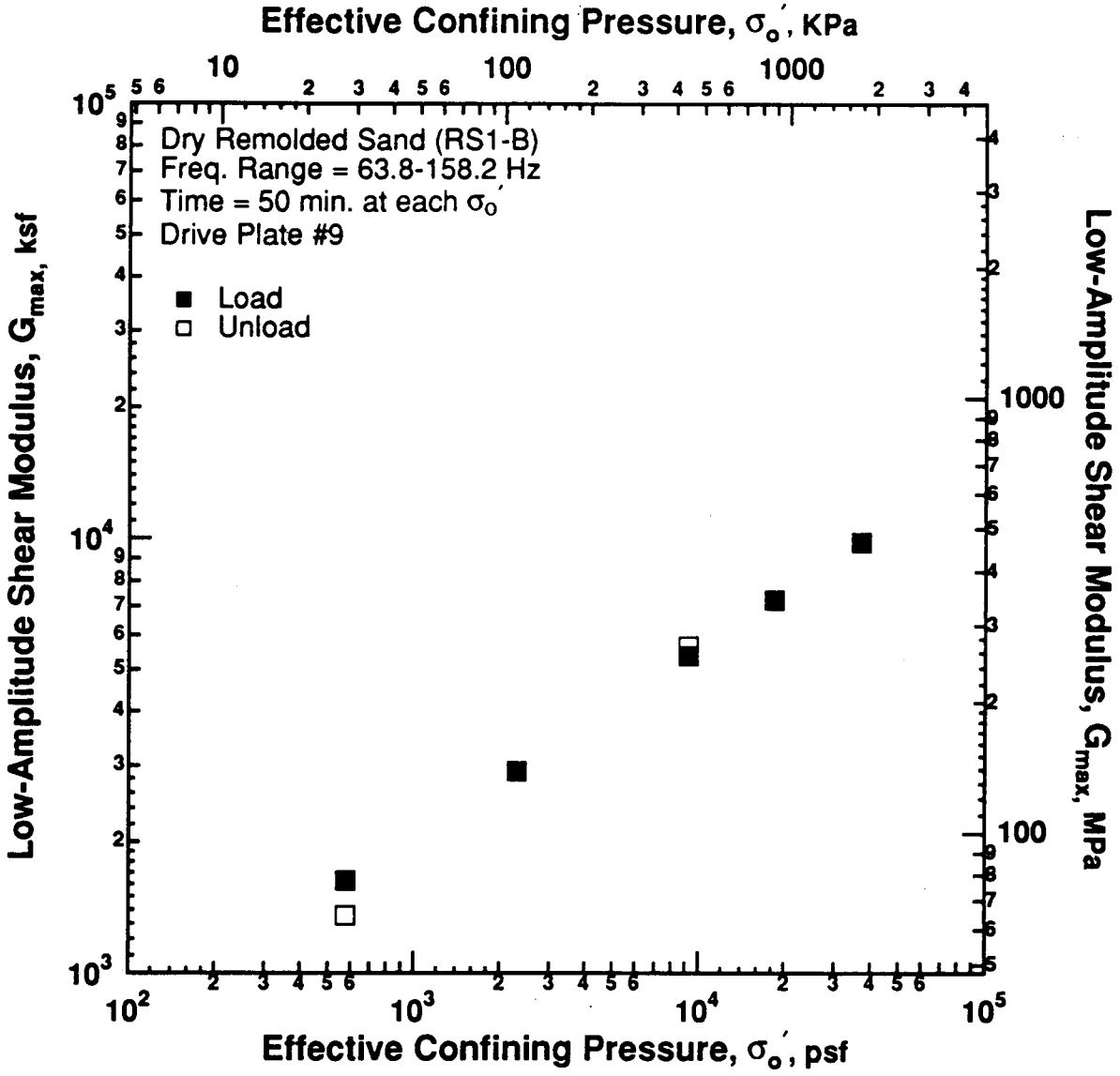

Figure 8.B.4.B-11
Variation in low-amplitude shear modulus with effective confining pressure from resonant column testing of dry remolded sand sample (RS1); second loading cycle (B).

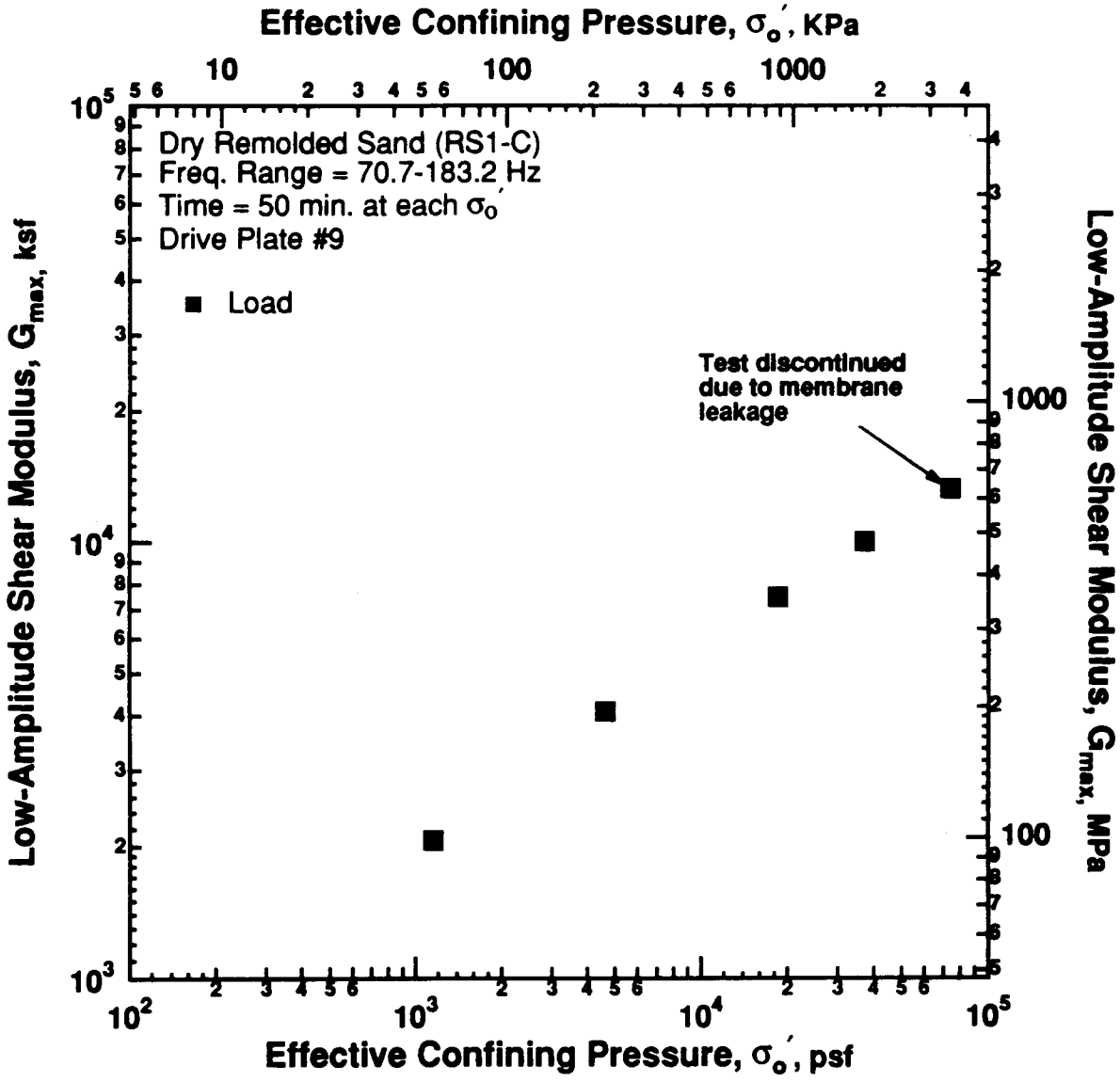

Figure 8.B.4.B-12
Variation in low-amplitude shear modulus with effective confining pressure from resonant column testing of dry remolded sand sample (RS1); third loading cycle (C).

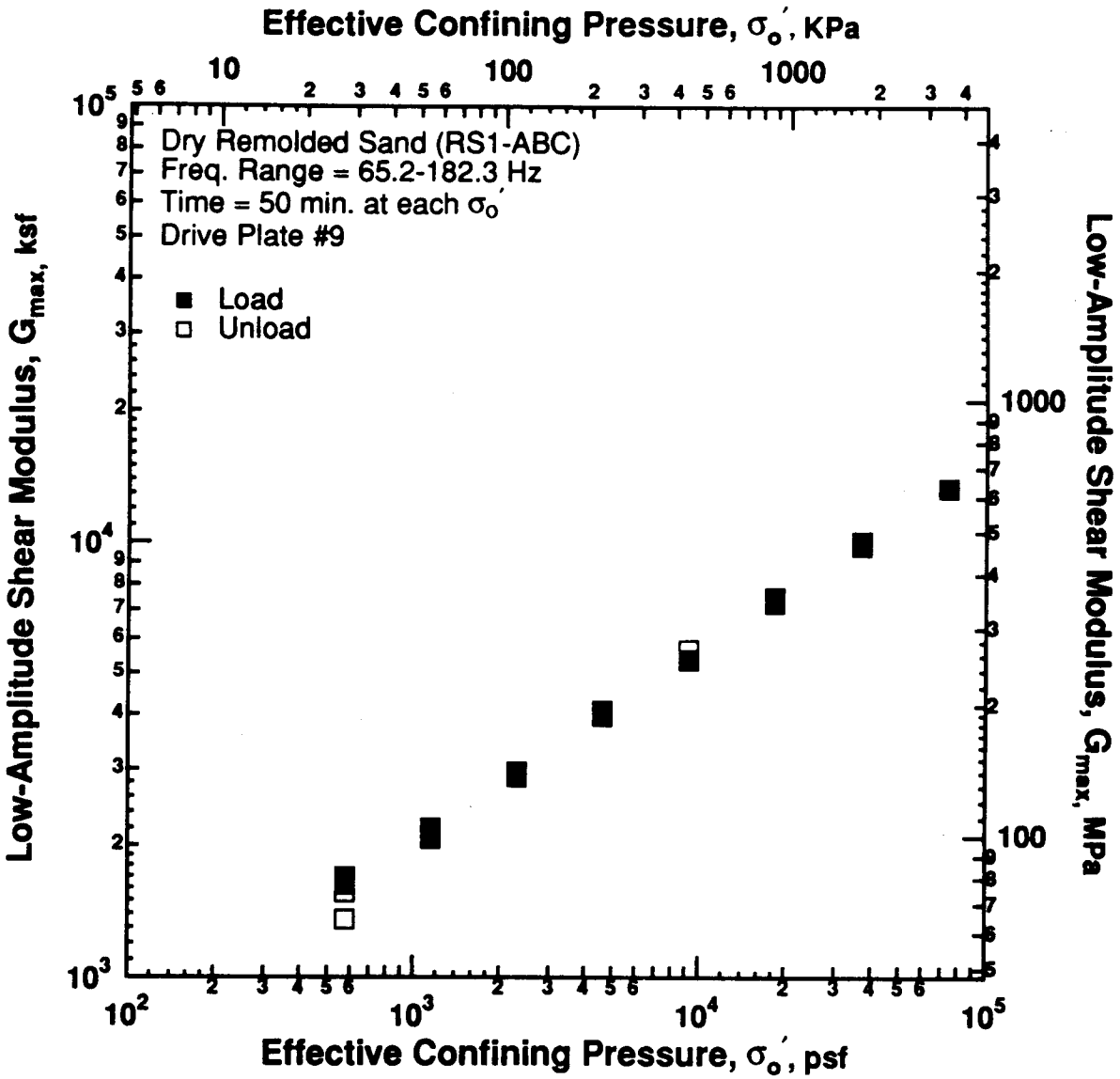

Figure 8.B.4.B-13
Variation in low-amplitude shear modulus with effective confining pressure from resonant column testing of dry remolded sand sample (RS1); initial, second, third loading cycles (ABC).

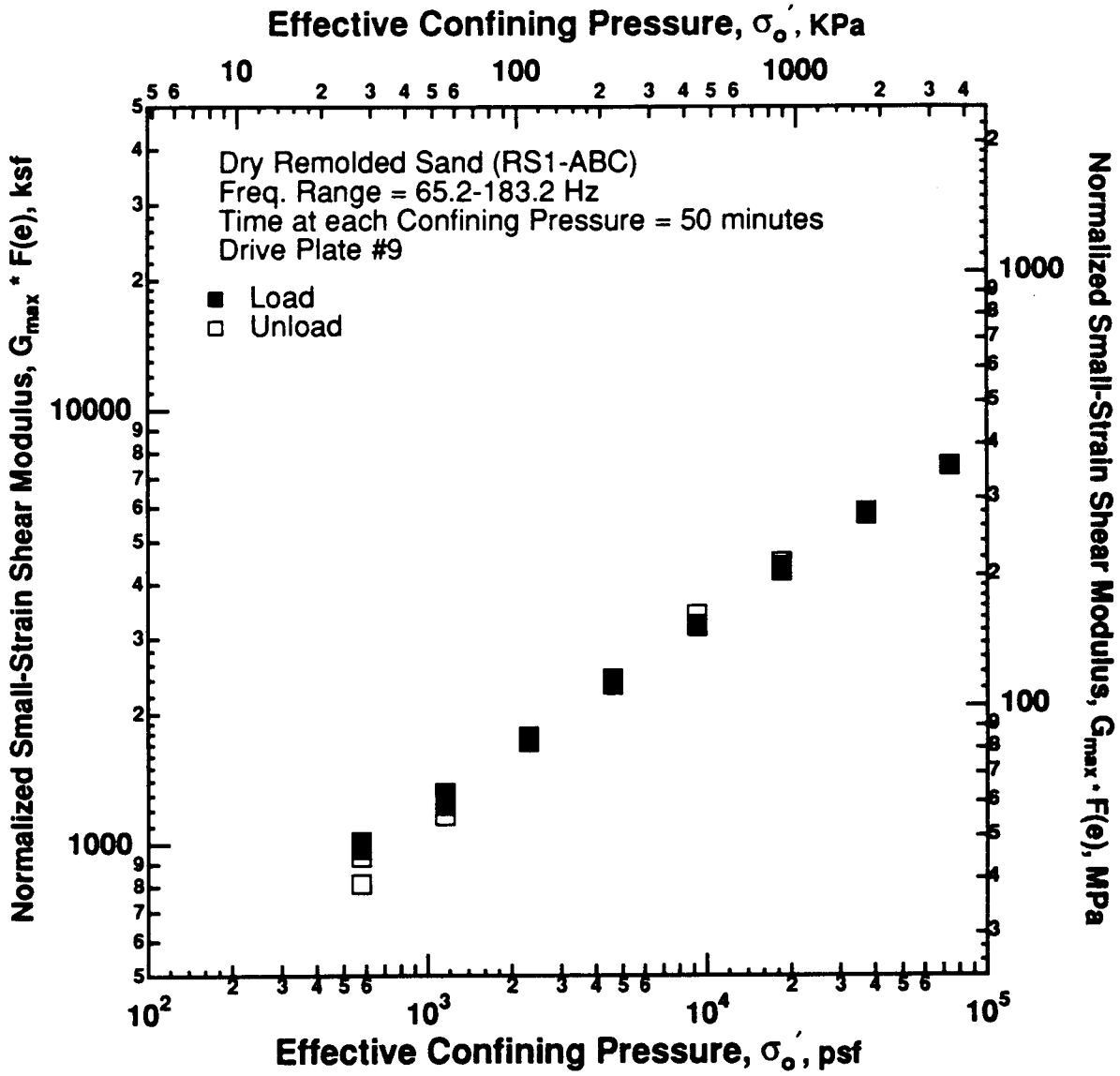

$$G_{max} * F(e), \text{ psf} = A * P_{atm}^{(1-n)} * \sigma_o'^{(n)}, \text{ psf}$$

$$F(e) = 0.3 + 0.7\,(e)^2$$

$A = 801$

$n = 0.428$

$P_{atm} = 2117$ psf

Figure 8.B.4.B-14
Variation in normalized low-amplitude shear modulus with effective confining pressure from resonant column testing of dry remolded sand sample (RS1); initial, second, third loading cycles (ABC).

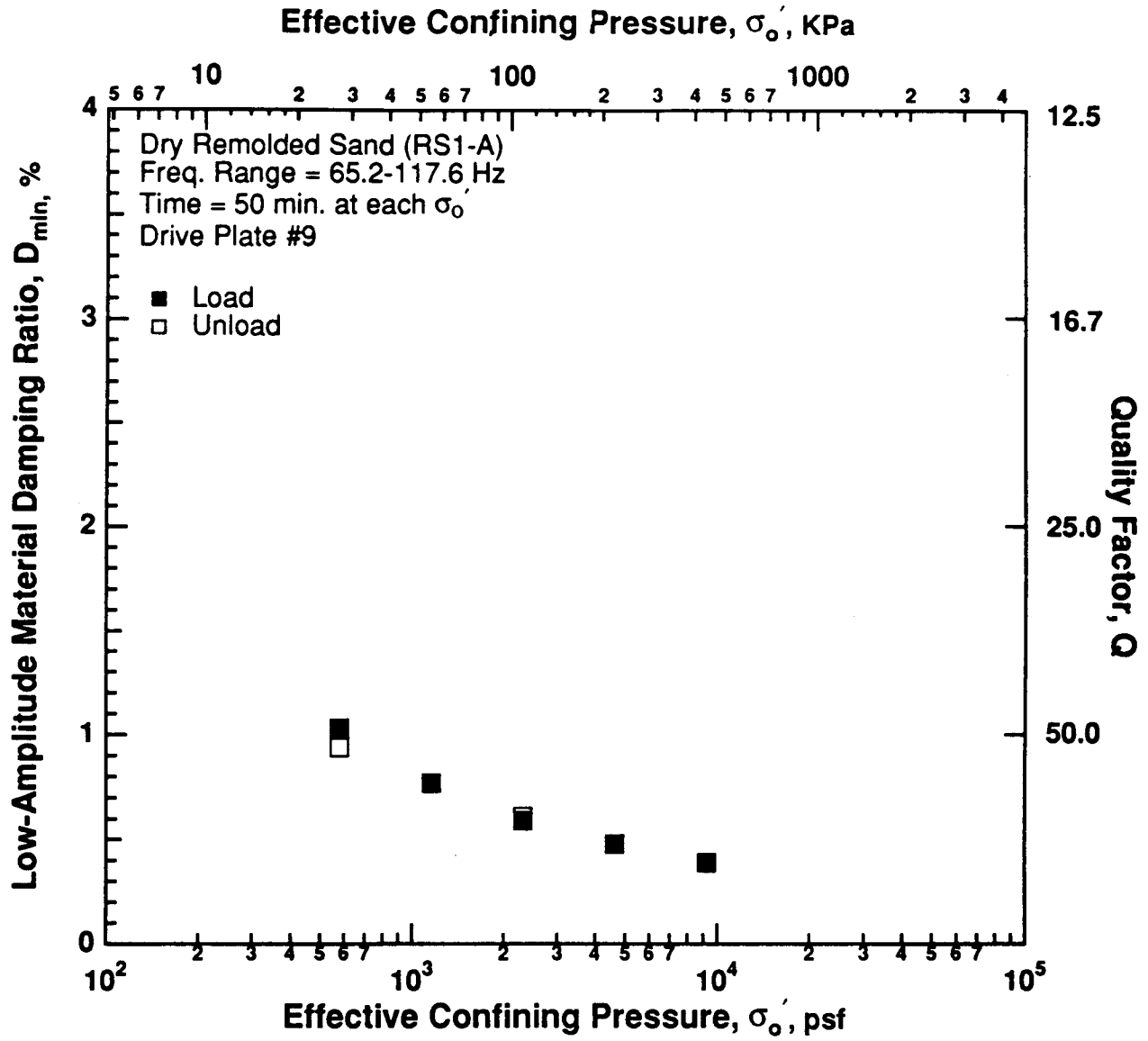

Figure 8.B.4.B-15
Variation in low-amplitude material damping ratio with effective confining pressure from resonant column testing of dry remolded sand sample (RS1); initial loading cycle (A).

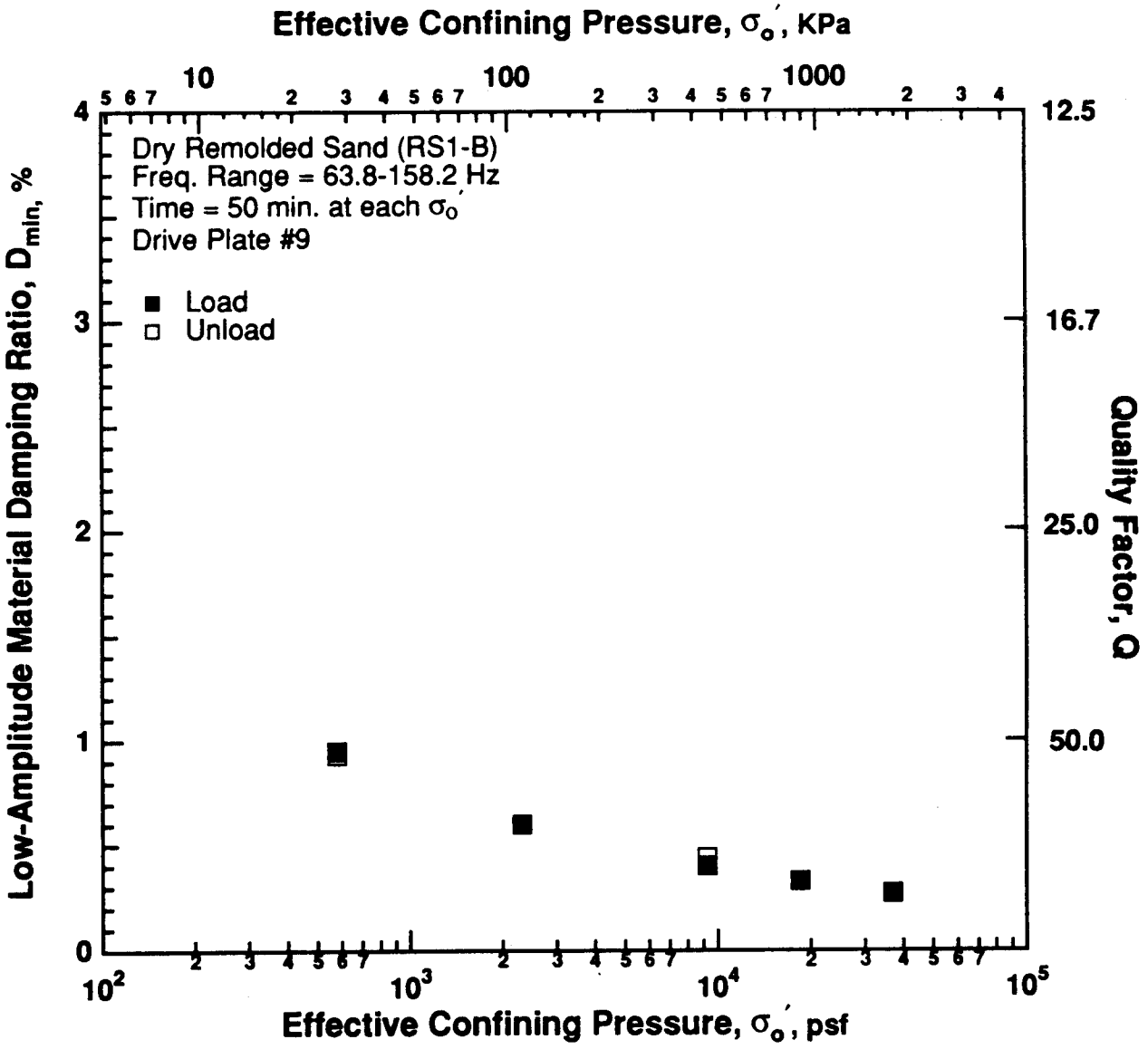

Figure 8.B.4.B-16
Variation in low-amplitude material damping ratio with effective confining pressure from resonant column testing of dry remolded sand sample (RS1); second loading cycle (B).

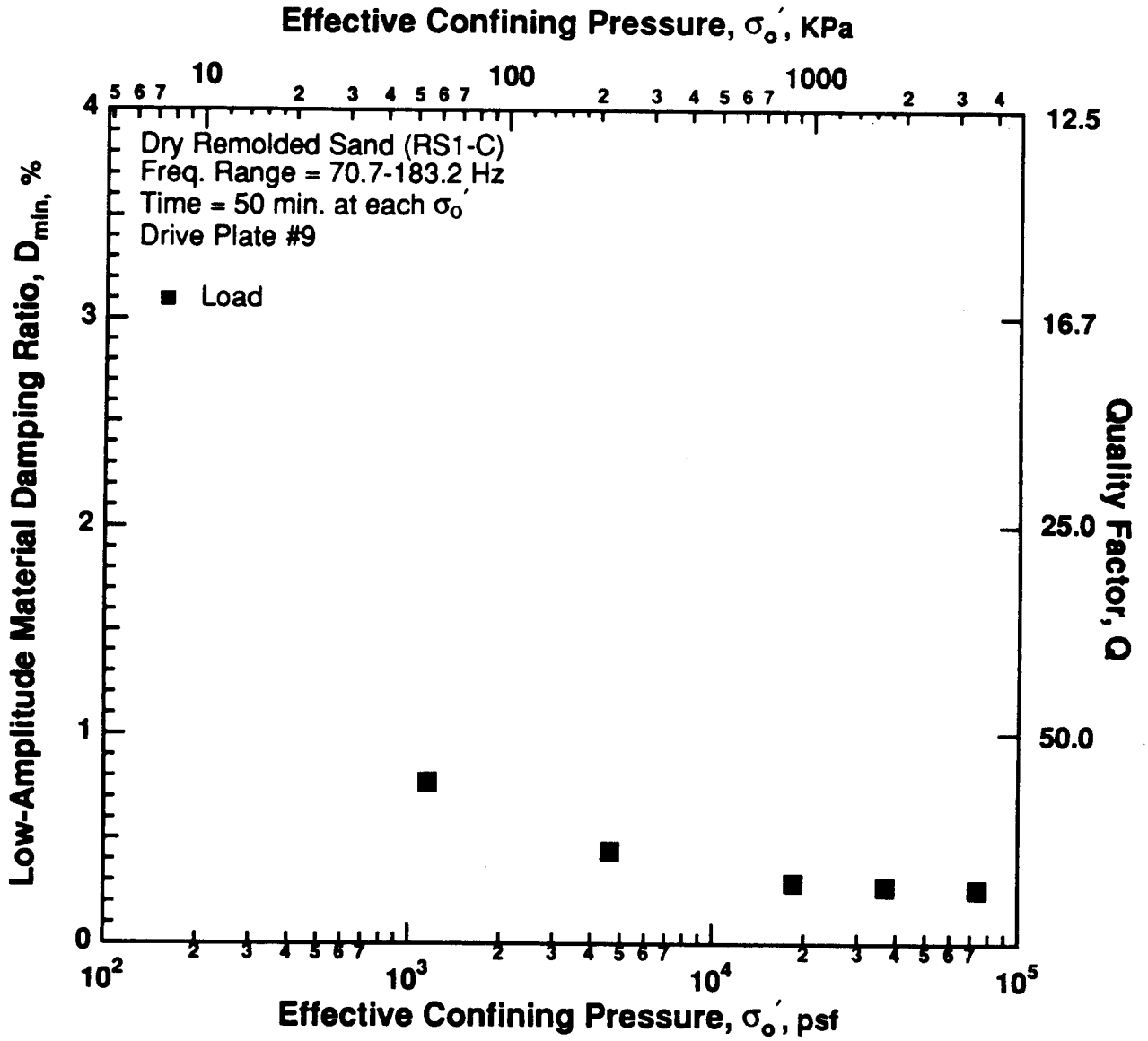

Figure 8.B.4.B-17
Variation in low-amplitude material damping ratio with effective confining pressure from resonant column testing of dry remolded sand sample (RS1); third loading cycle (C).

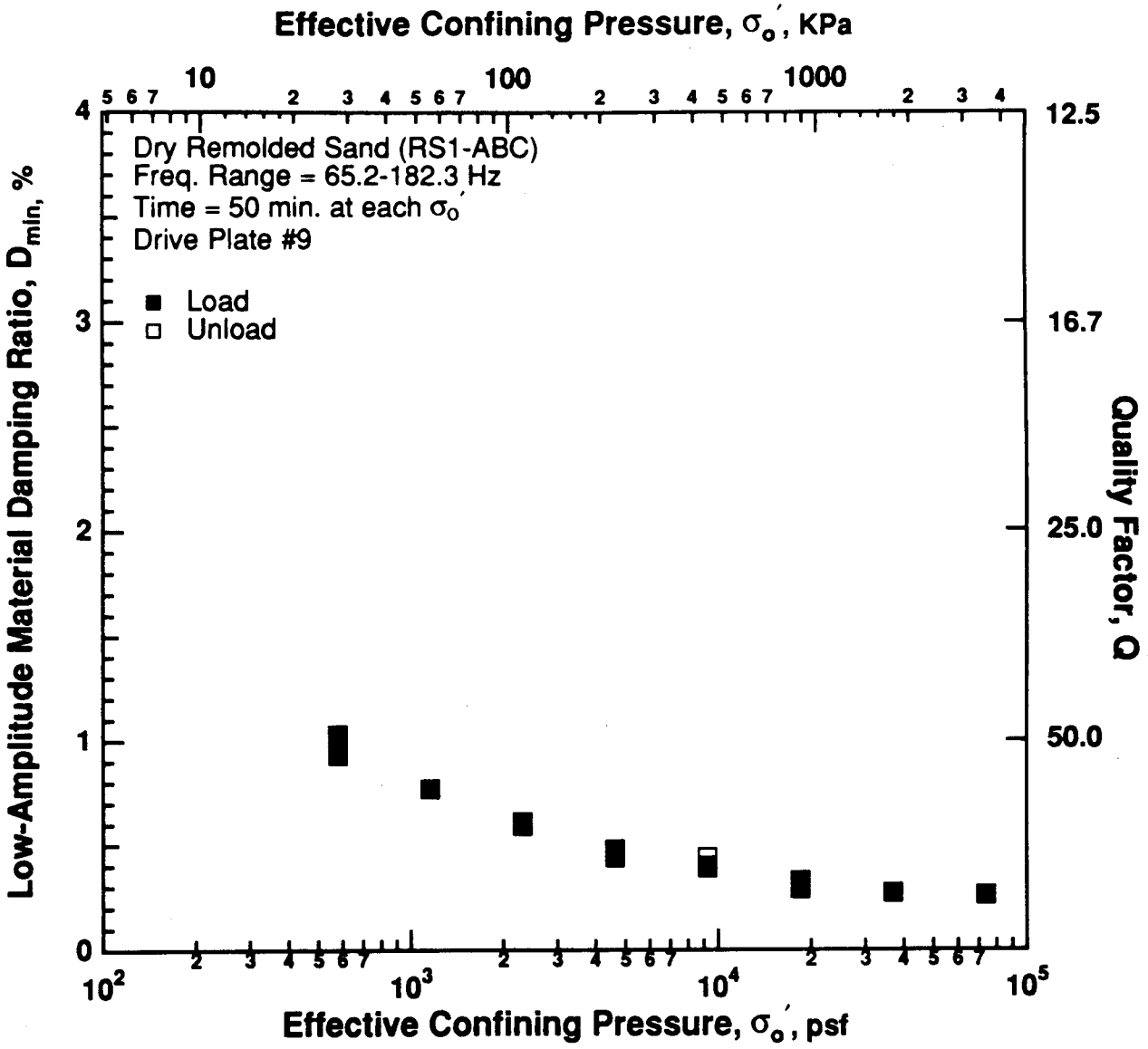

Figure 8.B.4.B-18
Variation in low-amplitude material damping ratio with effective confining pressure from resonant column testing of dry remolded sand sample (RS1); initial, second, third loading cycles (ABC).

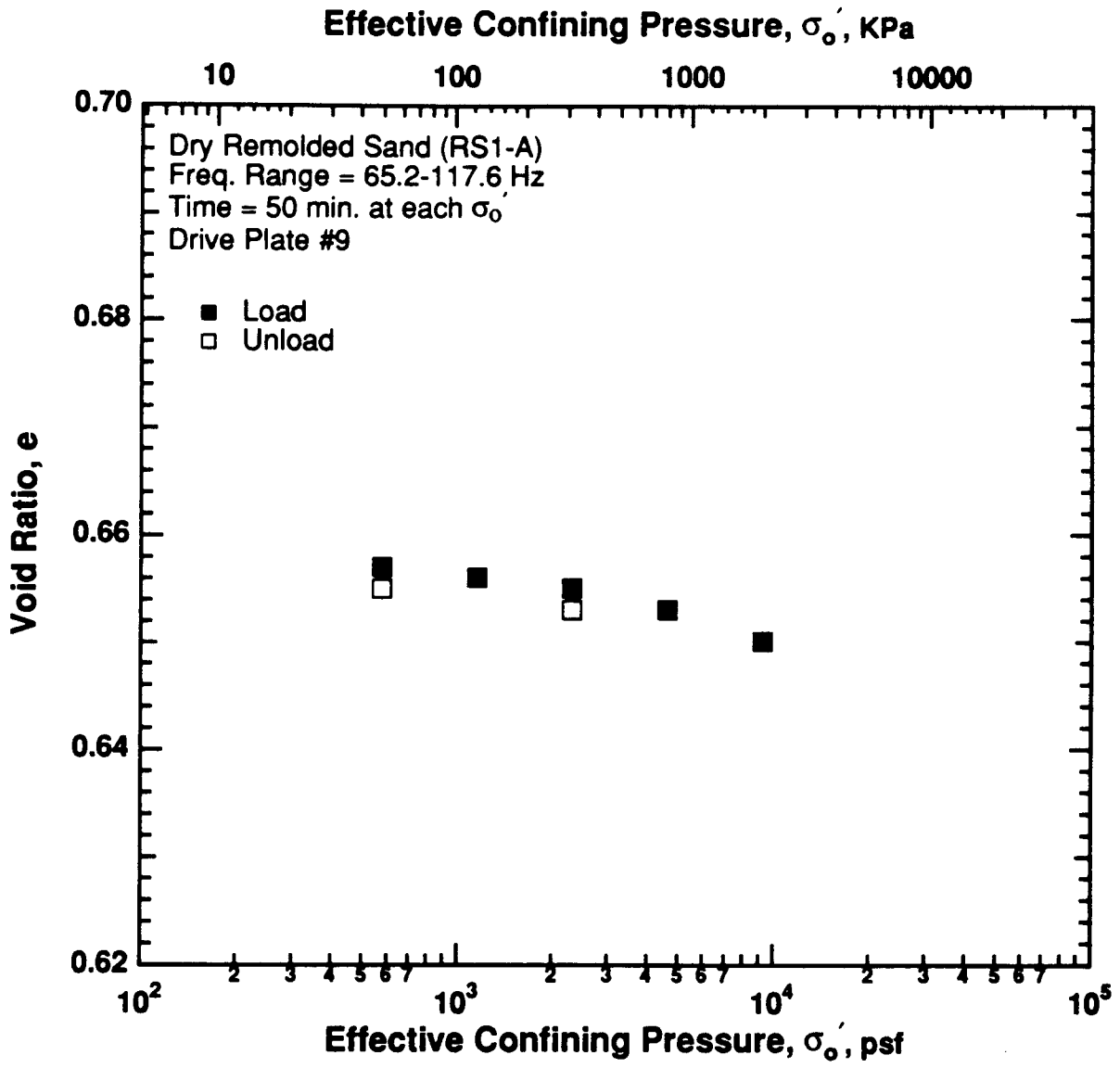

Figure 8.B.4.B-19
Variation in void ratio with effective confining pressure from resonant column testing of dry remolded sand sample (RS1); initial loading cycle (A).

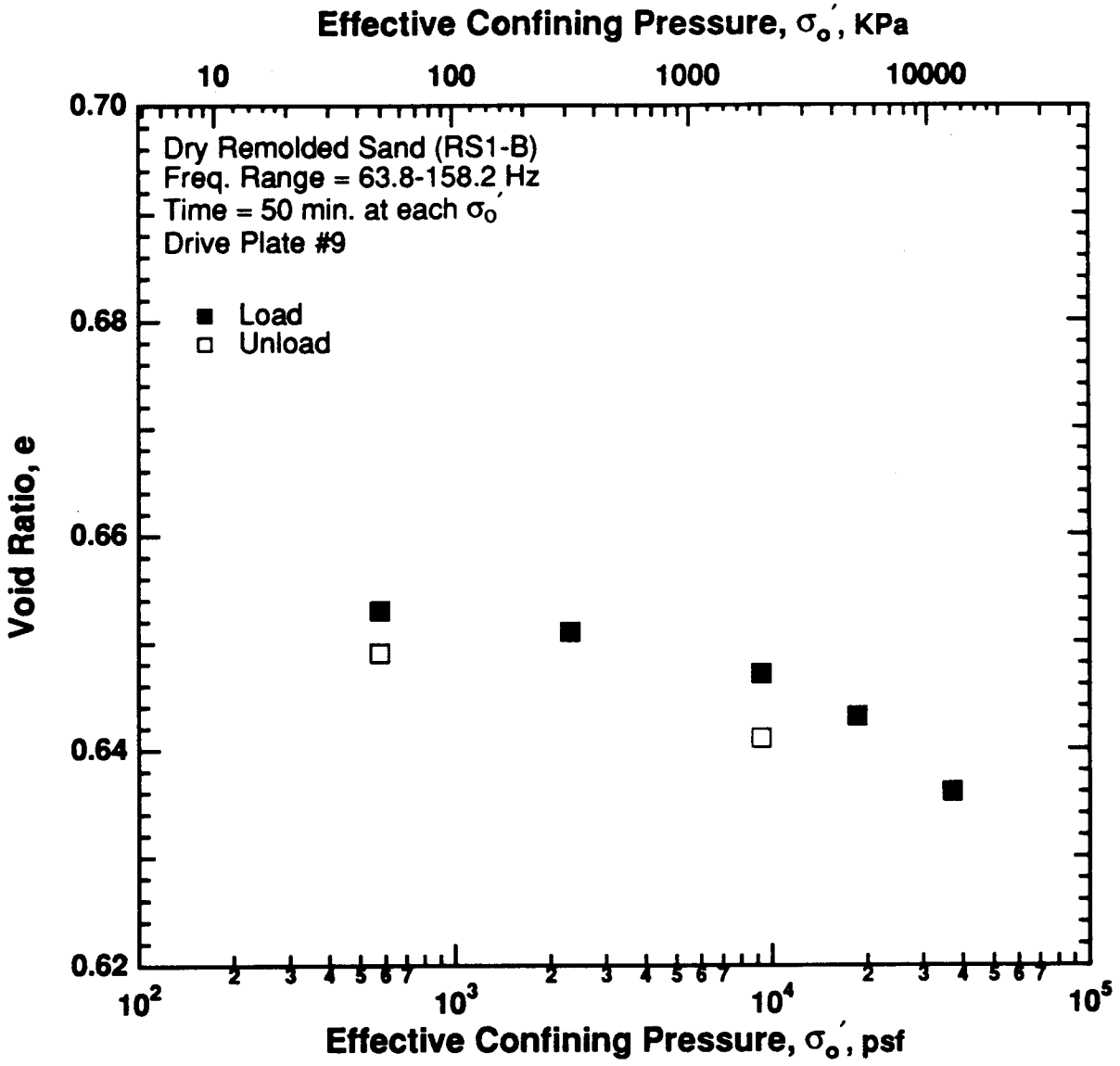

Figure 8.B.4.B-20
Variation in void ratio with effective confining pressure from resonant column testing of dry remolded sand sample (RS1); second loading cycle (B).

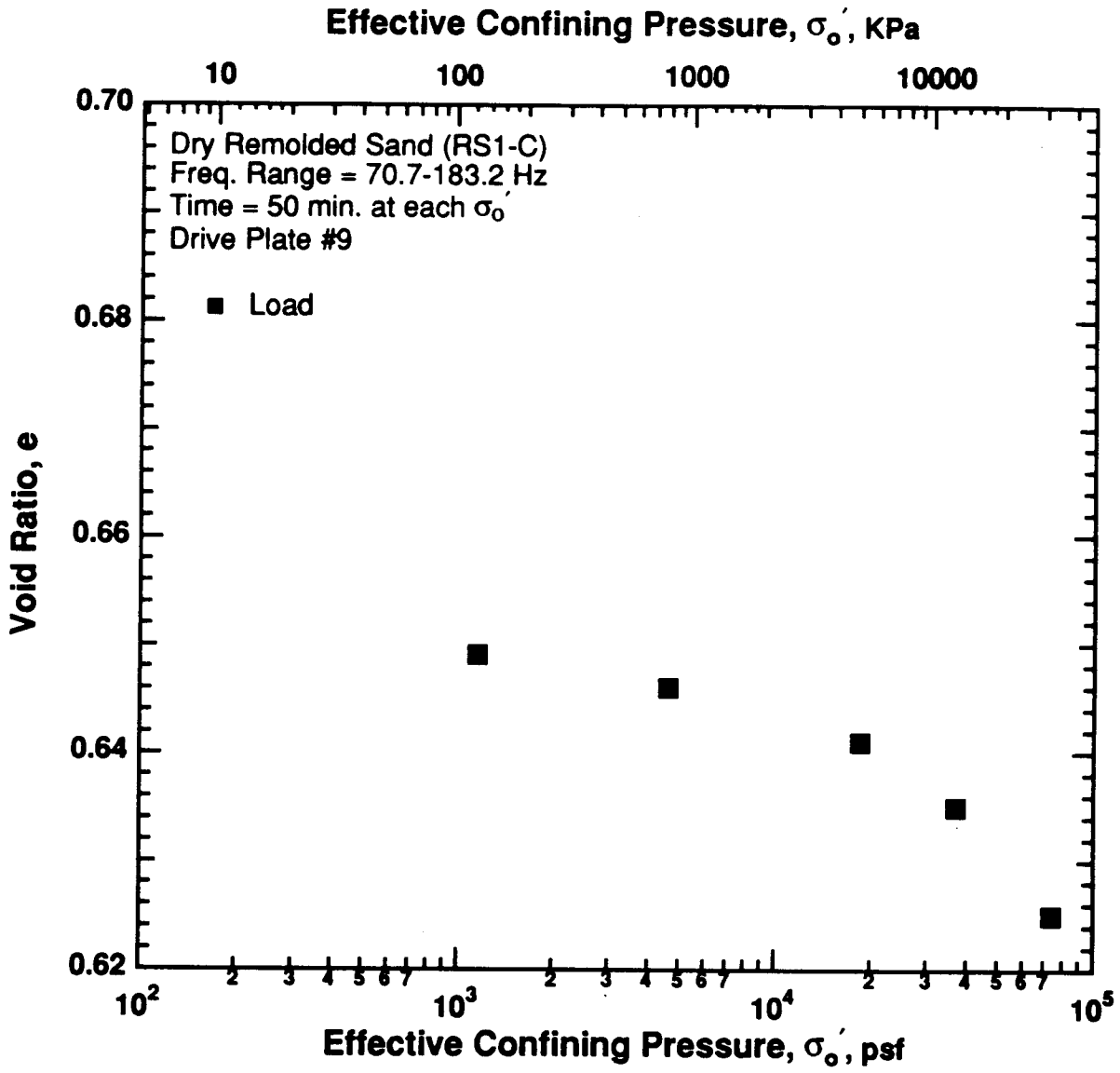

Figure 8.B.4.B-21
Variation in void ratio with effective confining pressure from resonant column testing of dry remolded sand sample (RS1); third loading cycle (C).

APPENDIX C
DYNAMIC TESTS OF DRY REMOLDED SAND SAMPLE RS2

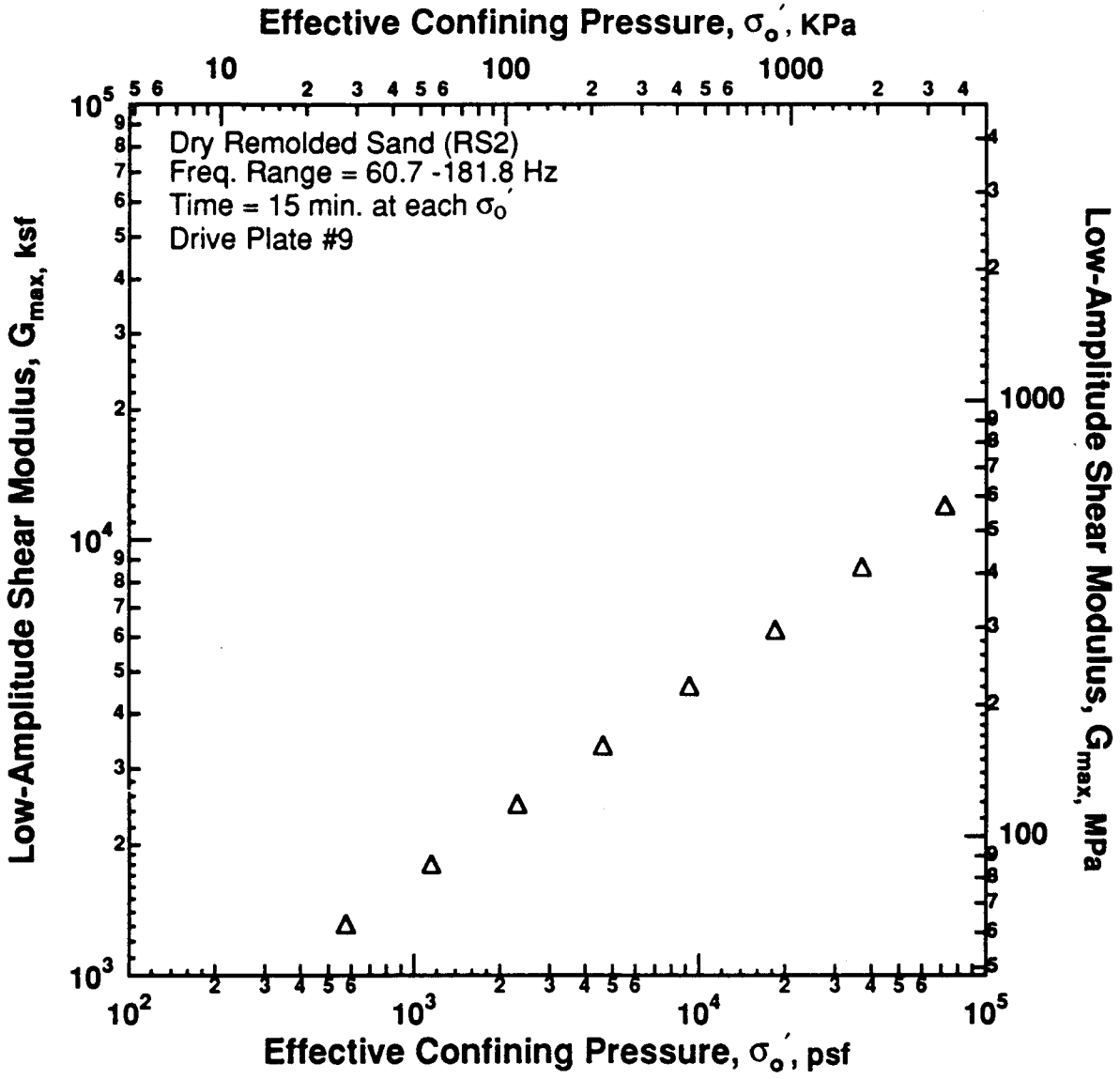

Figure 8.B.4.C-1
Variation in low-amplitude shear modulus with effective confining pressure from resonant column testing of dry remolded sand sample (RS2).

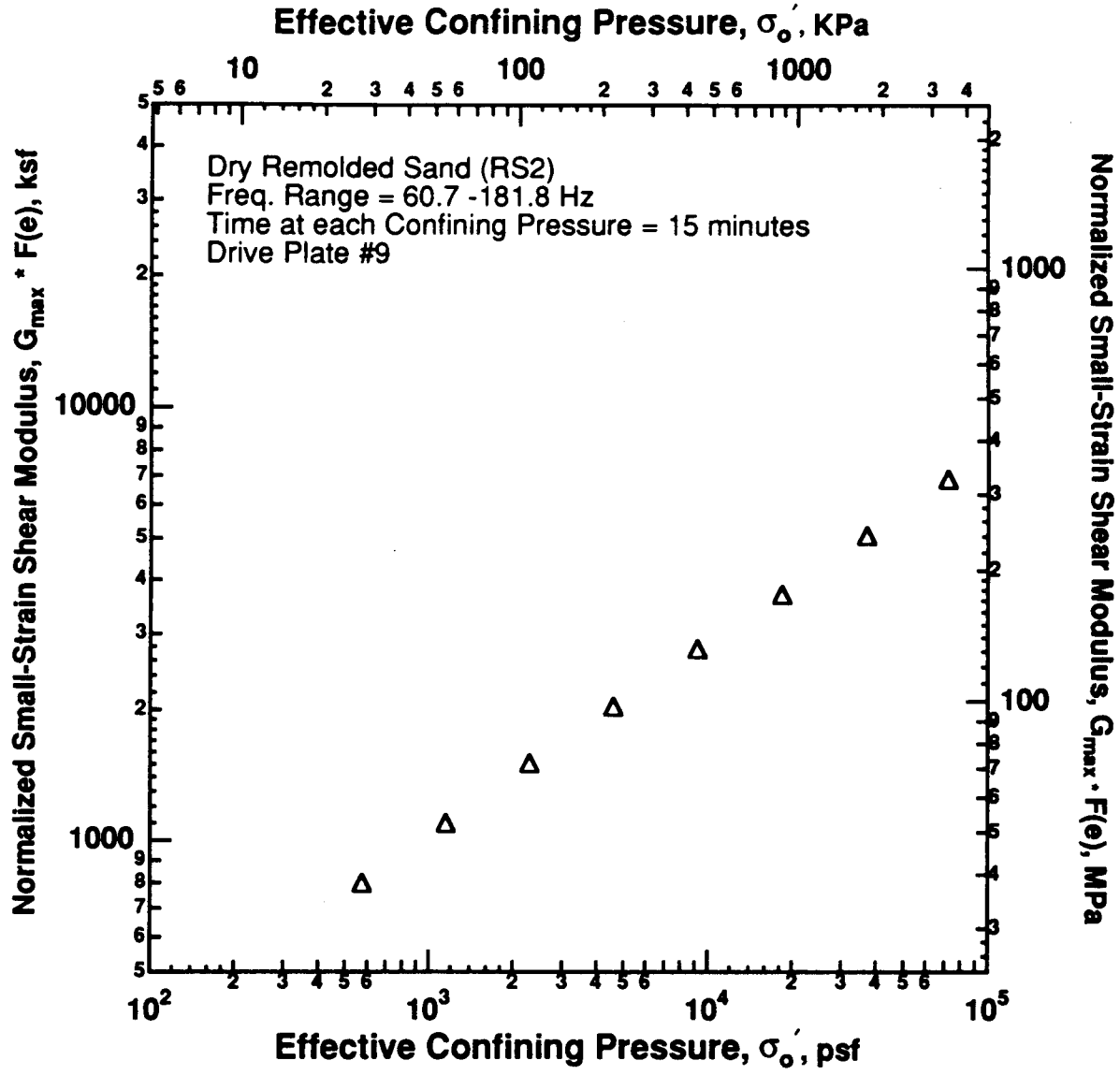

$$G_{max} * F(e), psf = A * P_{atm}^{(1-n)} * \sigma_o'^{(n)}, psf$$

$$F(e) = 0.3 + 0.7\,(e)^2$$

$$A = 675$$

$$n = 0.441$$

$$P_{atm} = 2117\ psf$$

Figure 8.B.4.C-2
Variation in normalized low-amplitude shear modulus with effective confining pressure from resonant column testing of dry remolded sand sample (RS2).

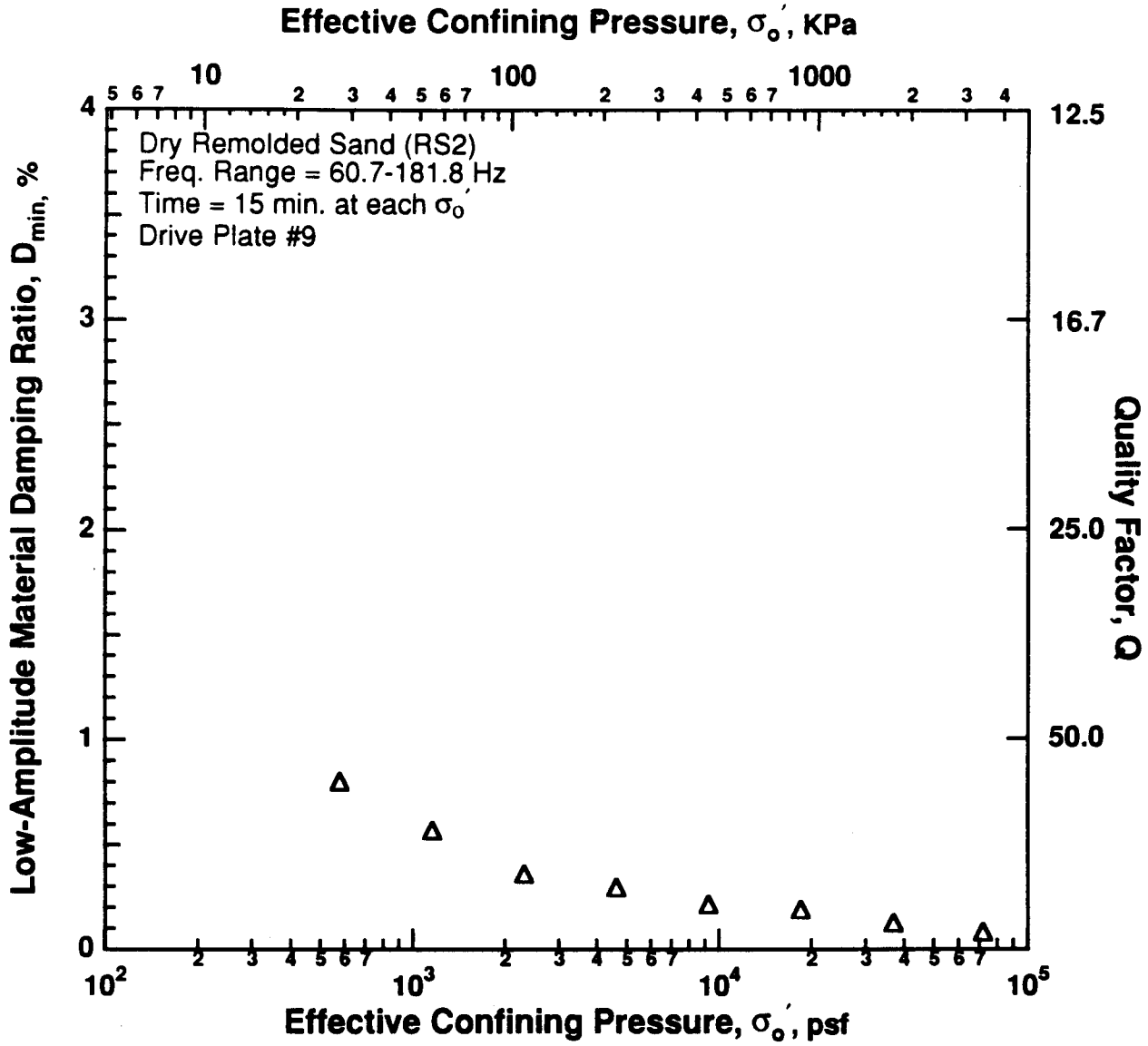

Figure 8.B.4.C-3
Variation in low-amplitude material damping ratio with effective confining pressure from resonant column testing of dry remolded sand sample (RS2).

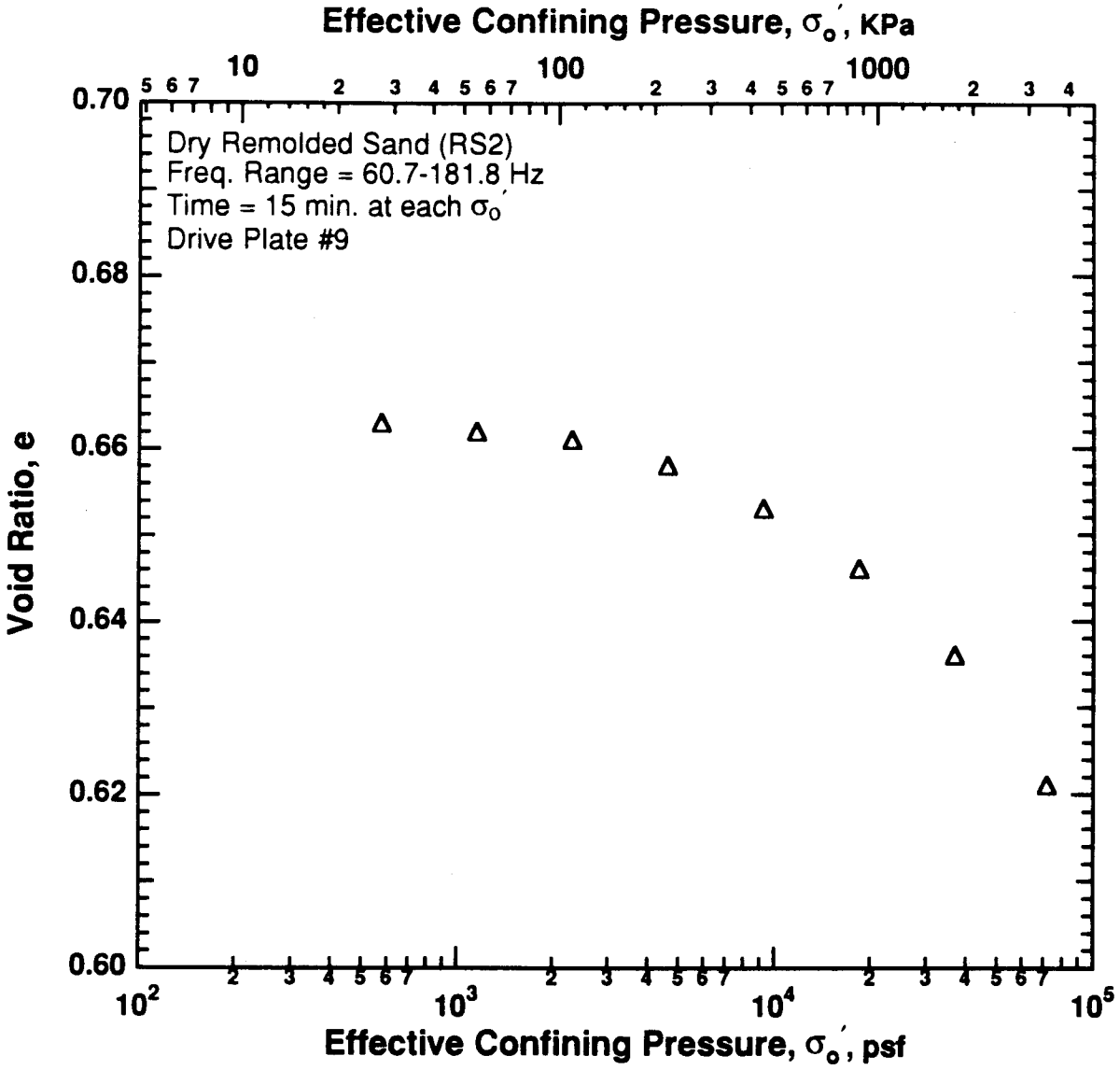

Figure 8.B.4.C-4
Variation in low-amplitude void ratio with effective confining pressure from resonant column testing of dry remolded sand sample (RS2).

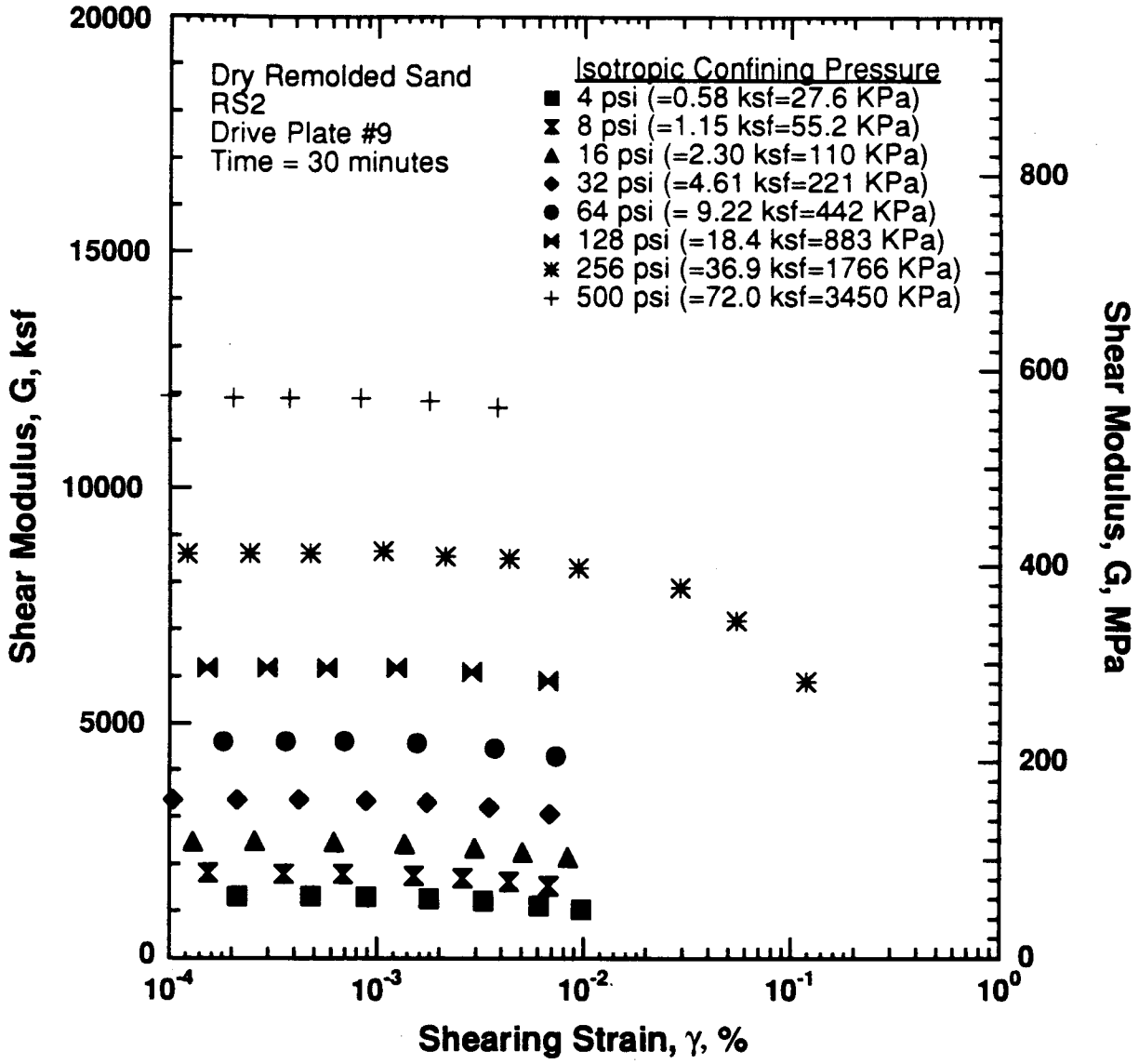

Figure 8.B.4.C-5
Variation in shear modulus with shearing strain and effective confining pressure from resonant column testing of dry remolded sand sample (RS2).

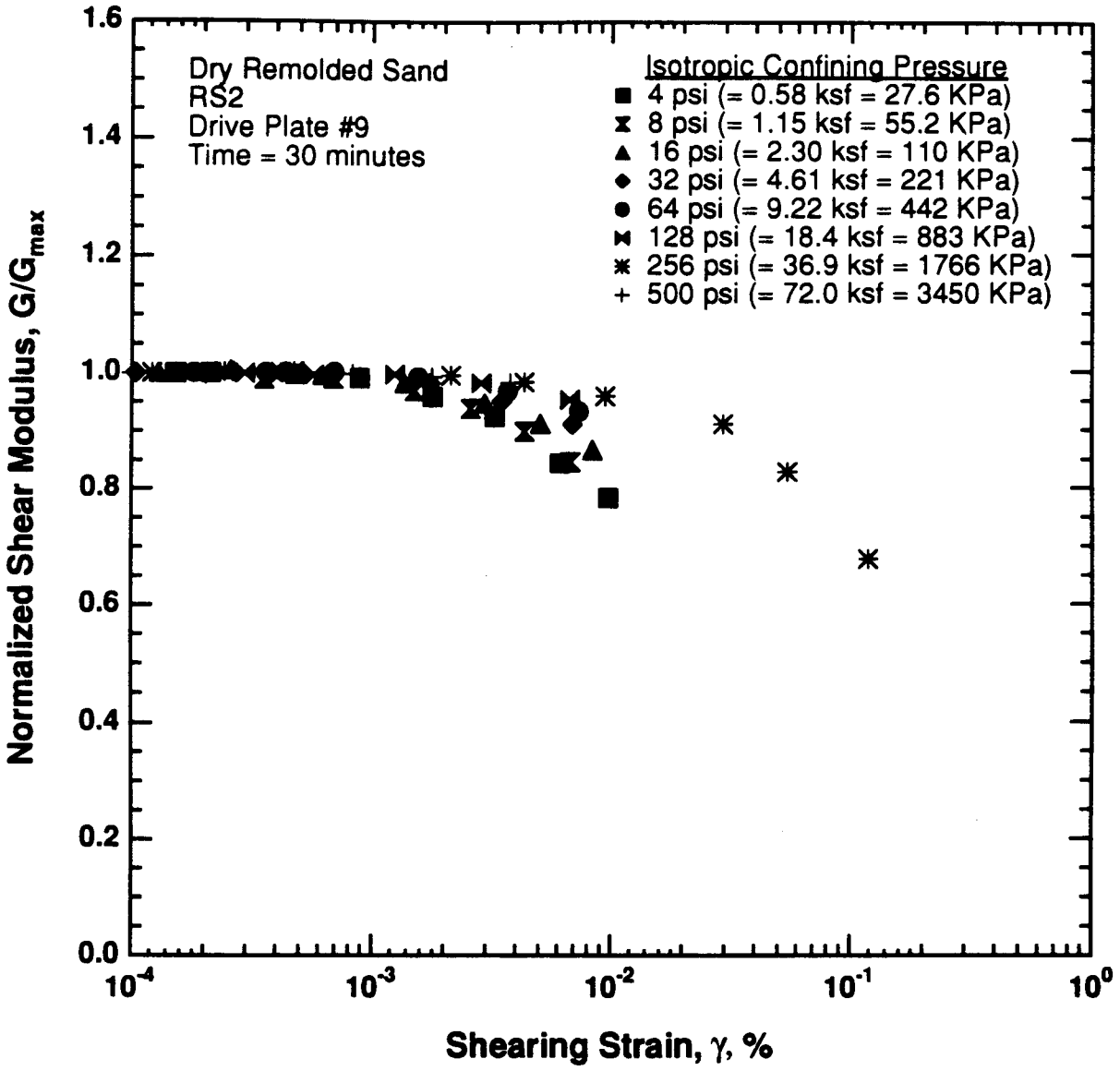

Figure 8.B.4.C-6
Comparison of the variation in normalized shear modulus with shearing strain and effective confining pressure from resonant column testing of dry remolded sand sample (RS2).

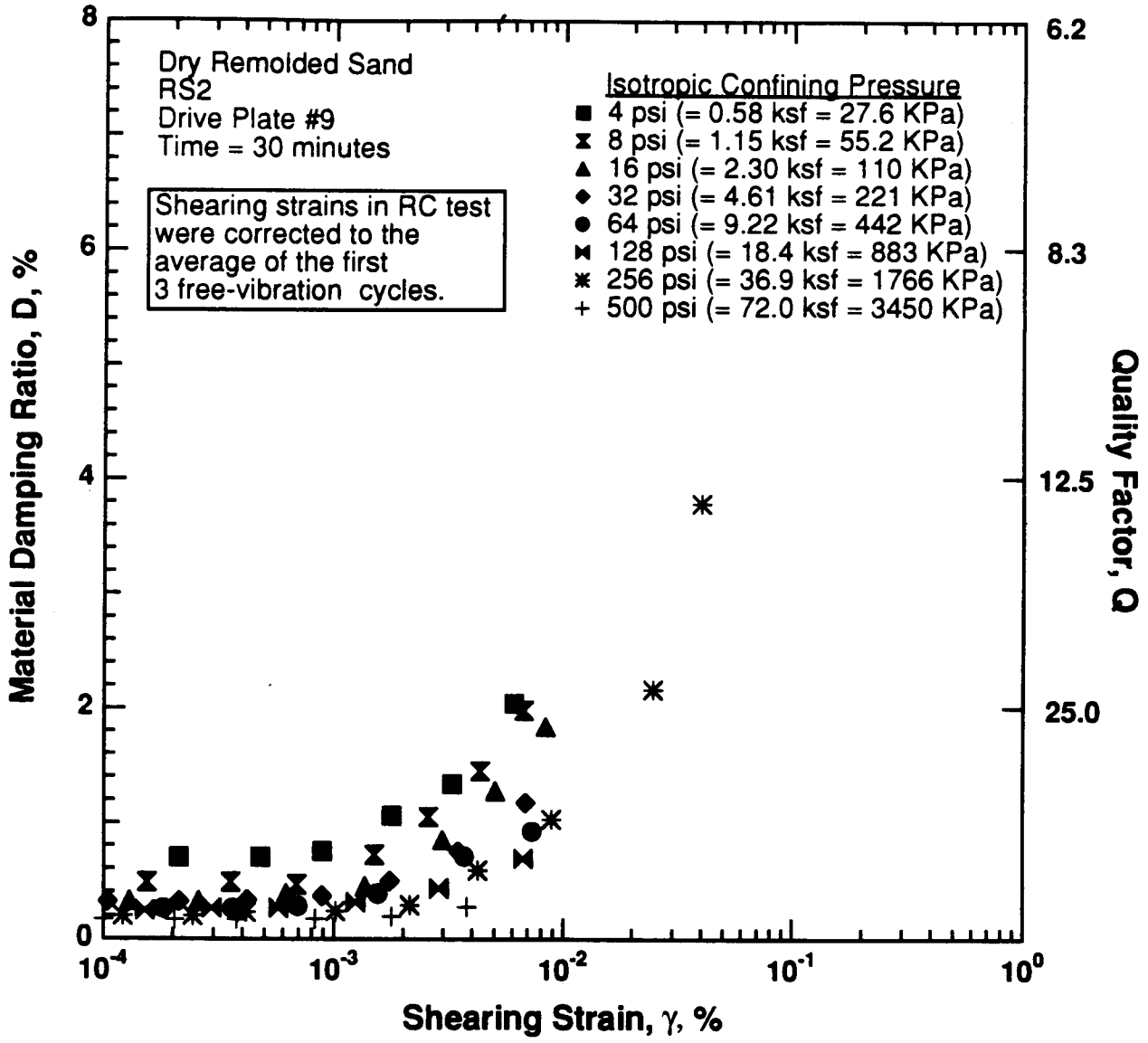

Figure 8.B.4.C-7
Variation in material damping ratio with shearing strain and effective confining pressure from resonant column testing of dry remolded sand sample (RS2).

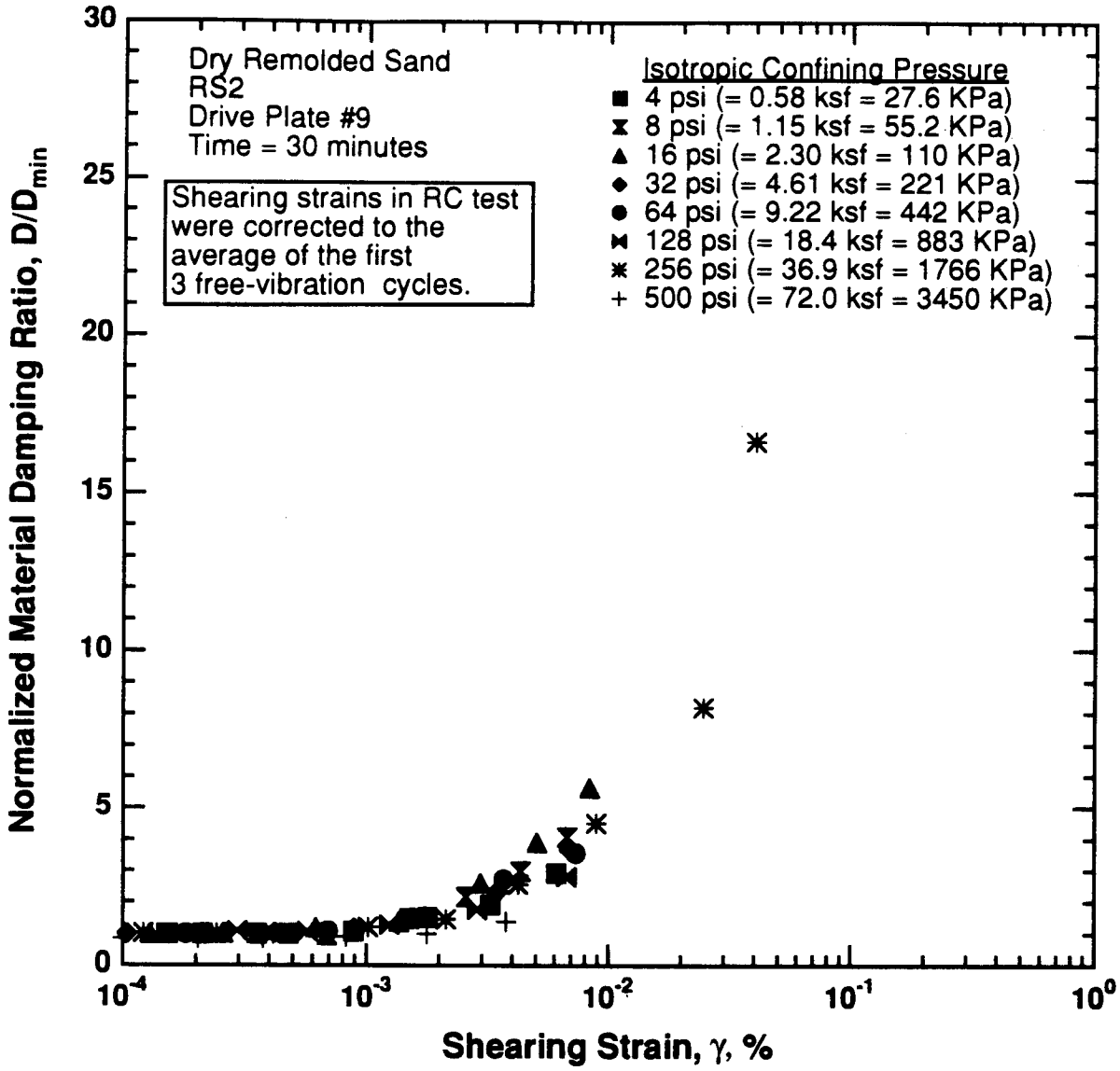

Figure 8.B.4.C-8
Comparison of the variation in normalized material damping ratio with shearing strain and effective confining pressure from resonant column testing of dry remolded sand sample (RS2).

APPENDIX D
DYNAMIC TESTS OF DRY REMOLDED SAND SAMPLE RS3

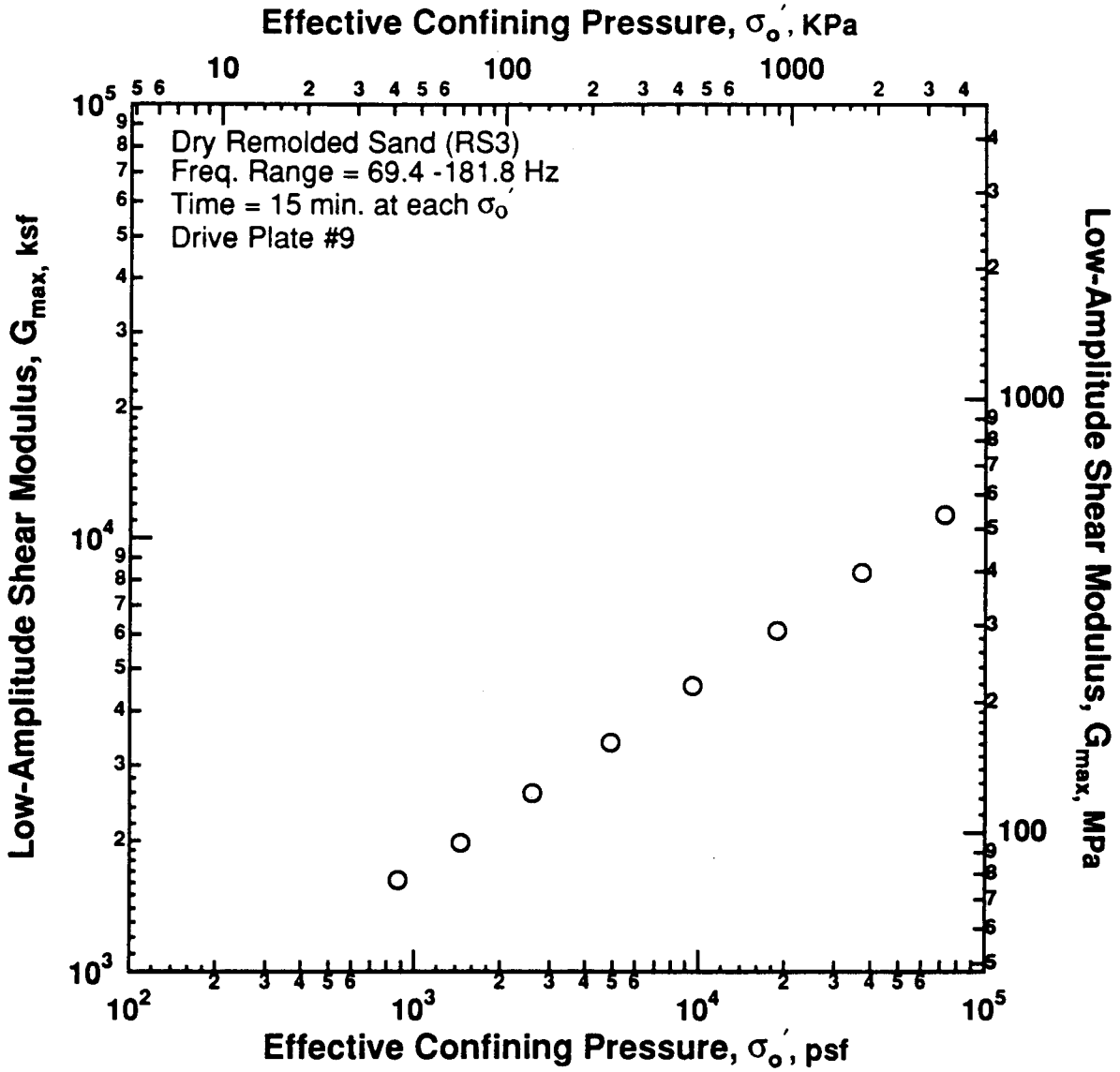

Figure 8.B.4.D-1
Variation in low-amplitude shear modulus with effective confining pressure from resonant column testing of dry remolded sand sample (RS3).

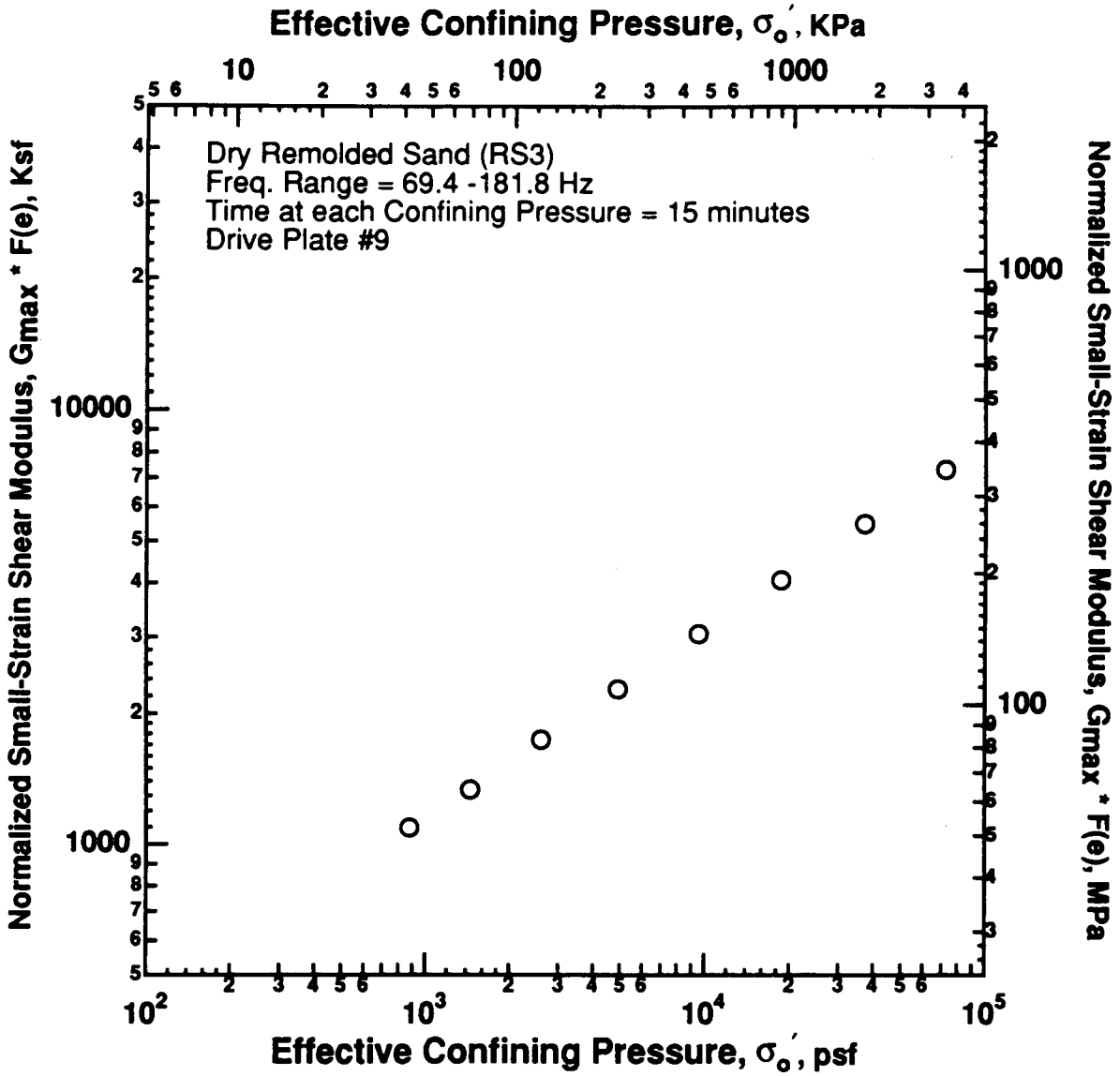

$$G_{max} * F(e), psf = A * P_{atm}^{(1-n)} * \sigma_o'^{(n)}, psf$$

$$F(e) = 0.3 + 0.7\,(e)^2$$

$$A = 747$$

$$n = 0.429$$

$$P_a = 2117\ psf$$

Figure 8.B.4.D-2
Variation in normalized low-amplitude shear modulus with effective confining pressure from resonant column testing of dry remolded sand sample (RS3).

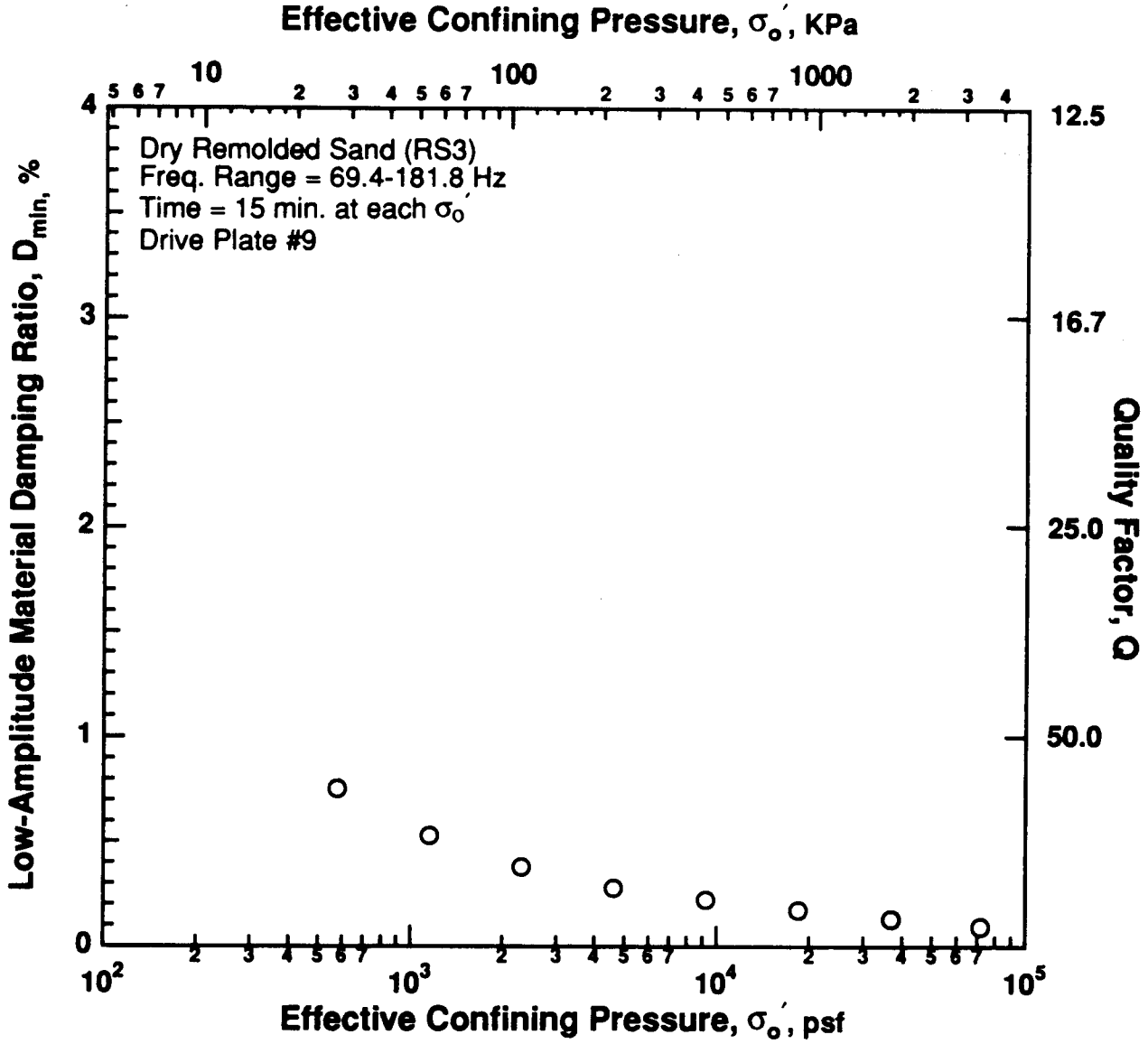

Figure 8.B.4.D-3
Variation in low-amplitude material damping ratio with effective confining pressure from resonant column testing of dry remolded sand sample (RS3).

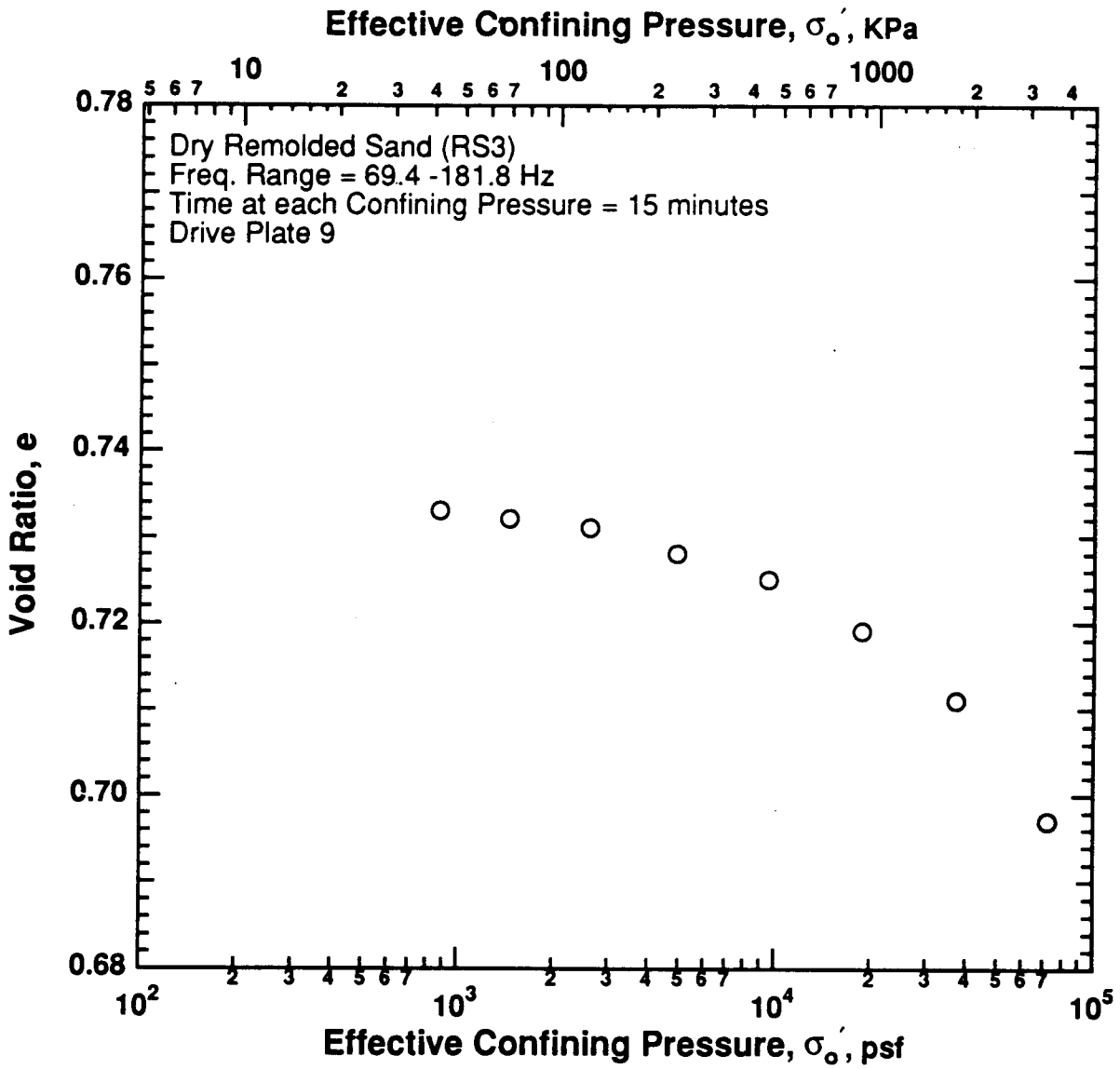

Figure 8.B.4.D-4
Variation in void ratio with effective confining pressure from resonant column testing of dry remolded sand sample (RS3).

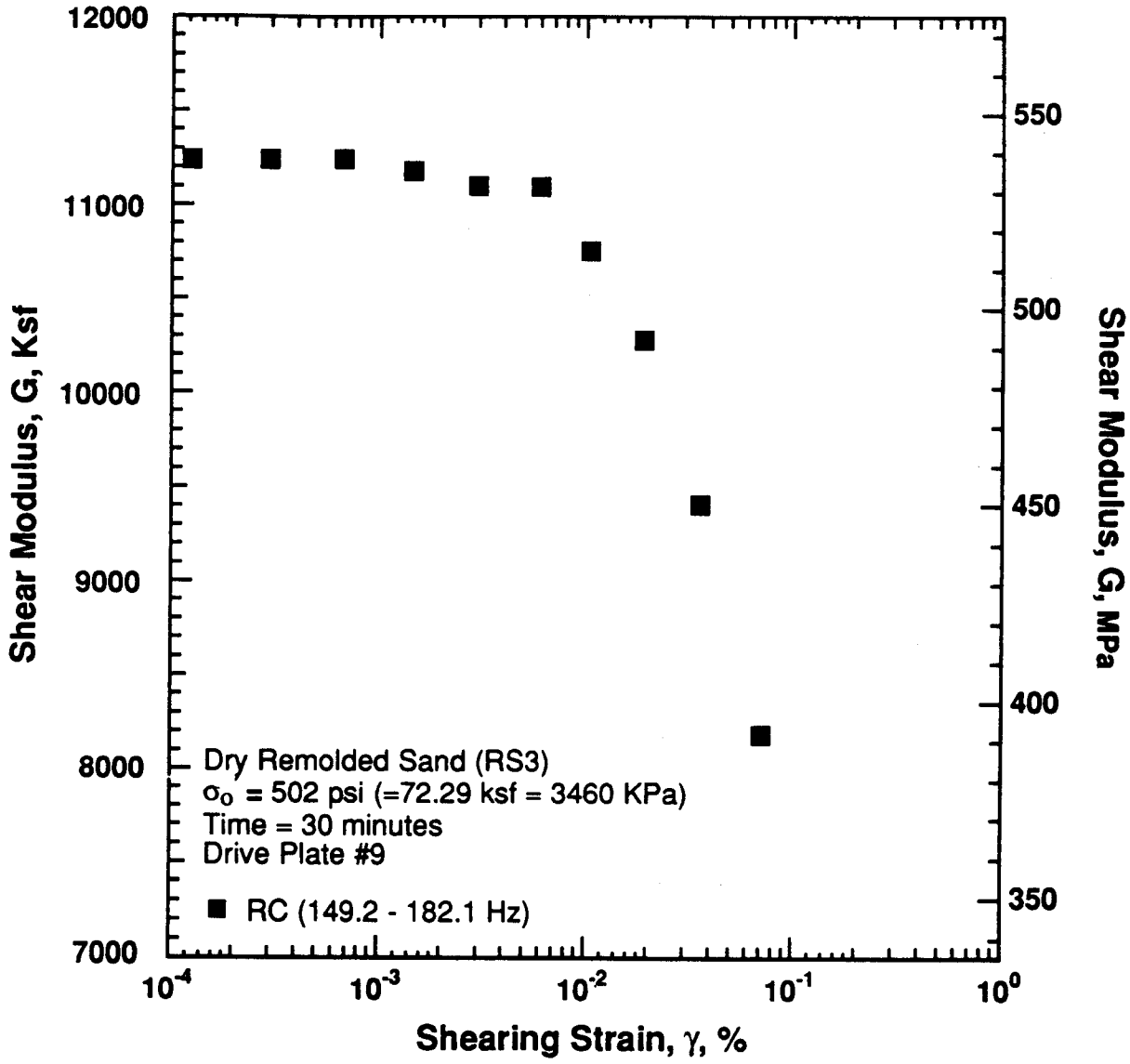

Figure 8.B.4.D-5
Variation in shear modulus with shearing strain at an effective confining pressure of 502 psi (72.29 ksf, 3460 kPa) from resonant column testing of dry remolded sand sample (RS3).

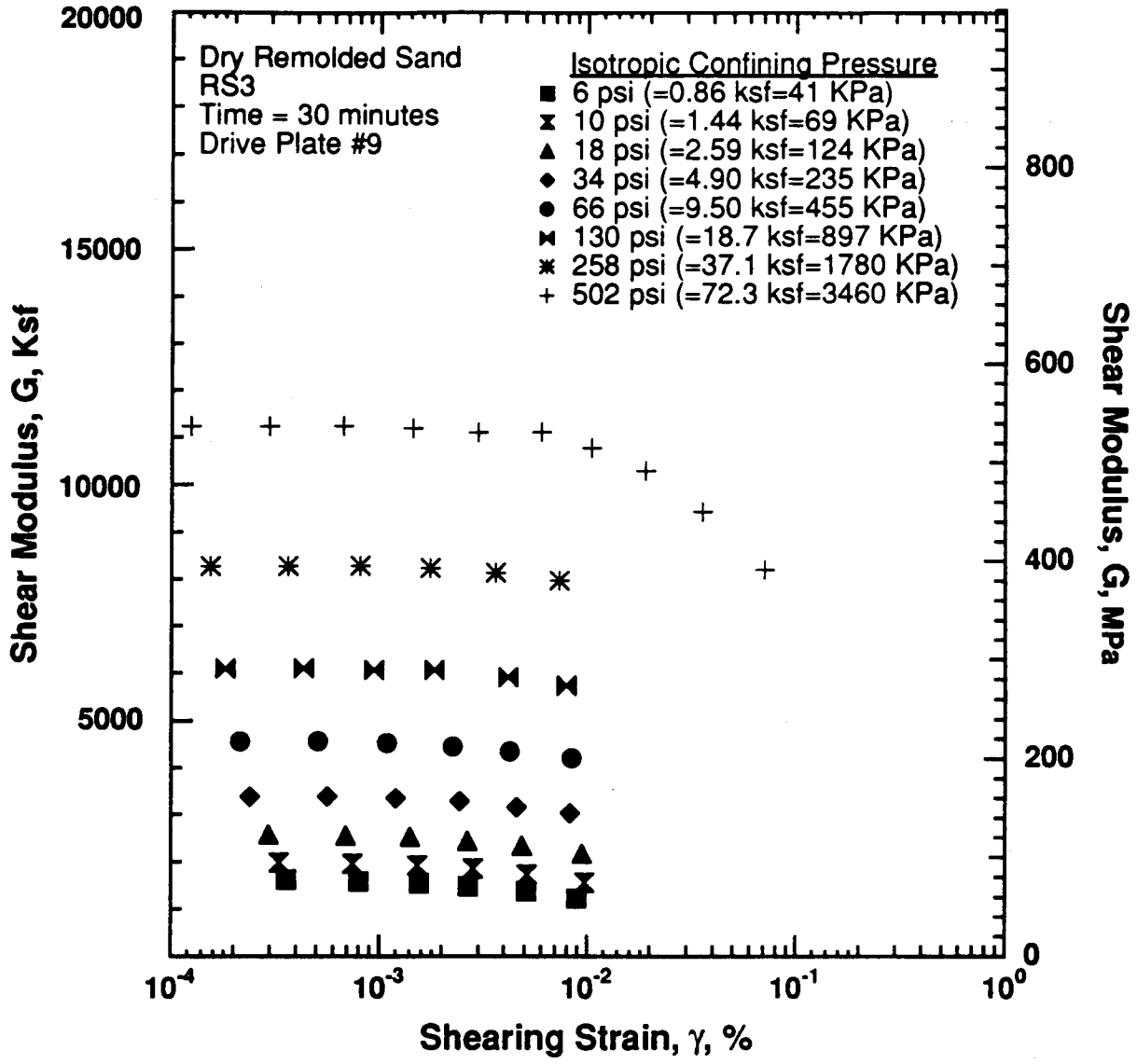

Figure 8.B.4.D-6
Variation in normalized shear modulus with shearing strain and effective confining pressure from resonant column testing of dry remolded sand sample (RS3).

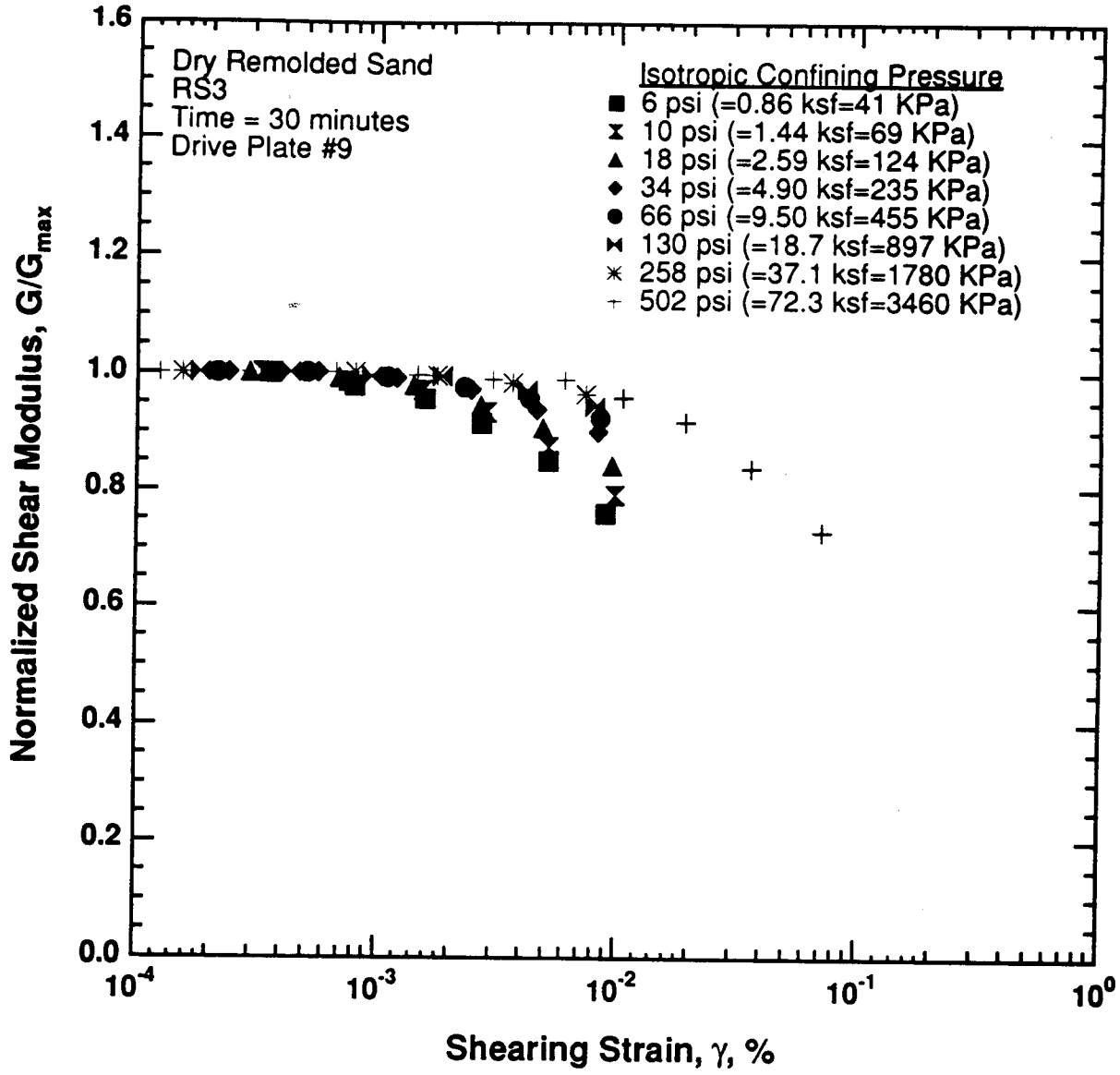

Figure 8.B.4.D-7
Variation in normalized shear modulus with shearing strain and effective confining pressure from resonant column testing of dry remolded sand sample (RS3).

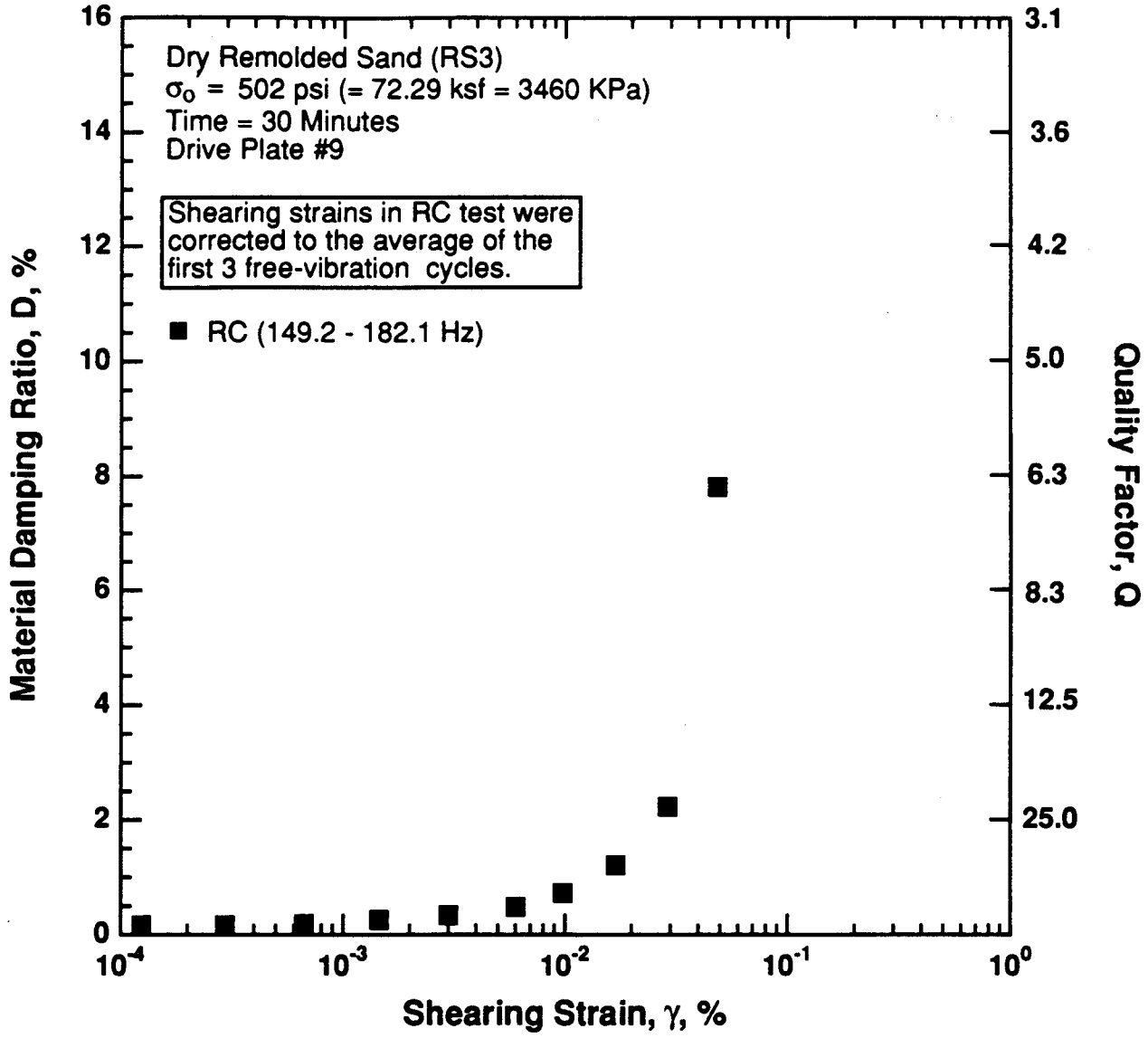

Figure 8.B.4.D-8
Variation in shear modulus with shearing strain at an effective confining pressure of 502 psi (72.29 ksf, 3460 kPa) from resonant column testing of dry remolded sand sample (RS3).

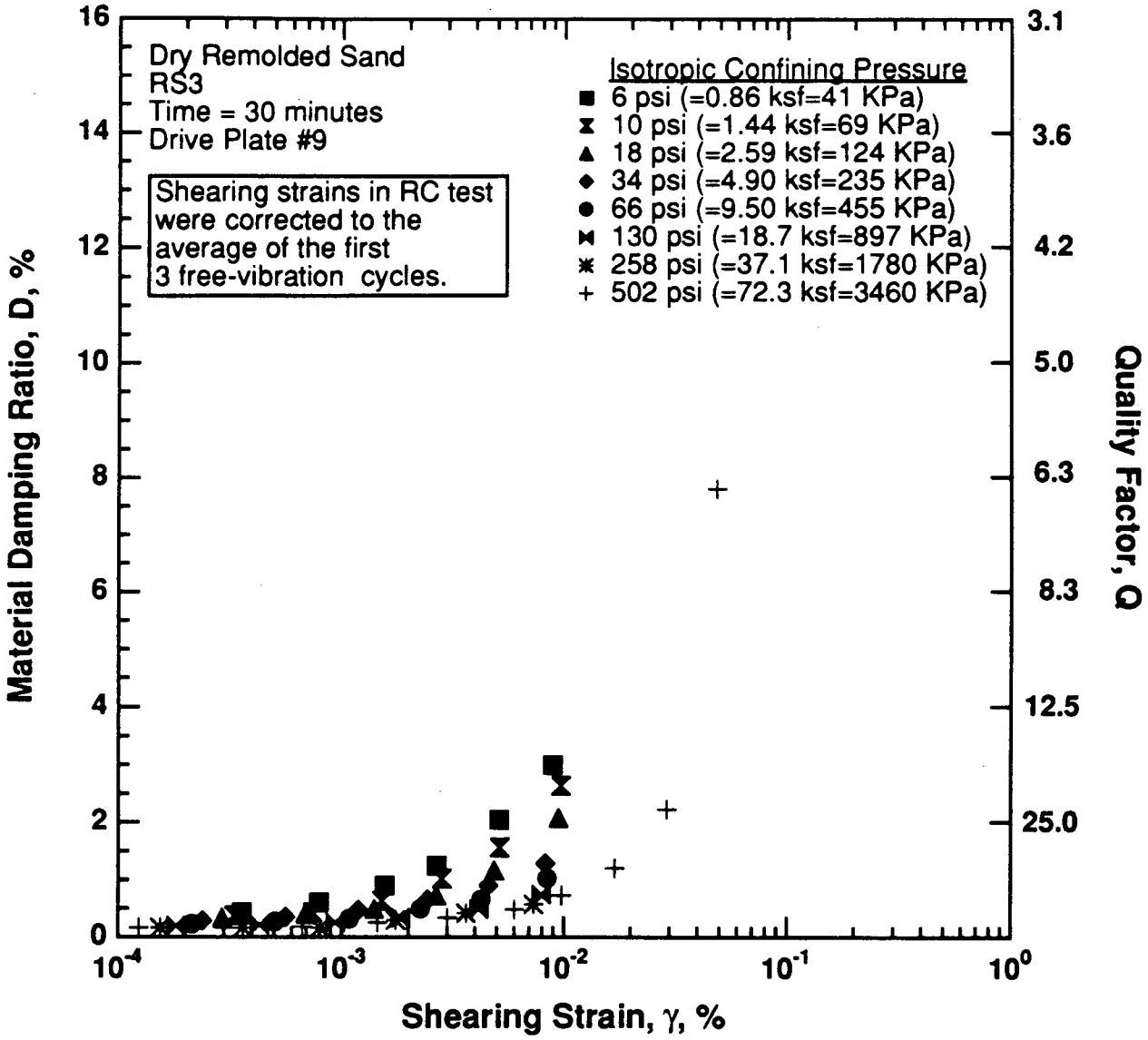

Figure 8.B.4.D-9
Variation in material damping ratio and shearing strain at an effective confining pressure from resonant column testing of dry remolded sand sample (RS3).

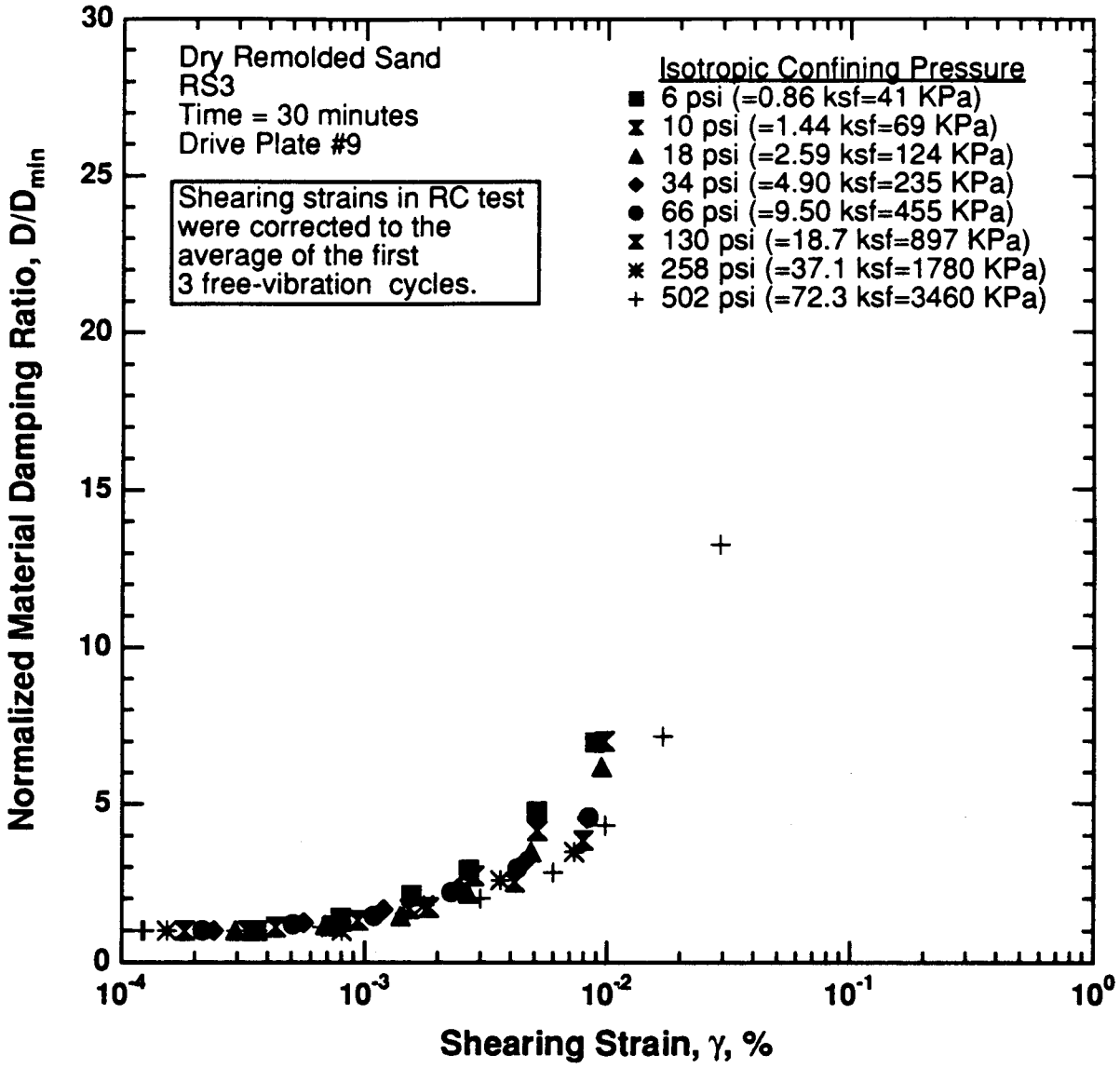

Figure 8.B.4.D-10
Variation in normalized material damping ratio with shearing strain and effective confining pressure from resonant column testing of dry remolded sand sample (RS3).

APPENDIX E
DYNAMIC TESTS OF DRY REMOLDED SAND SAMPLE RS4

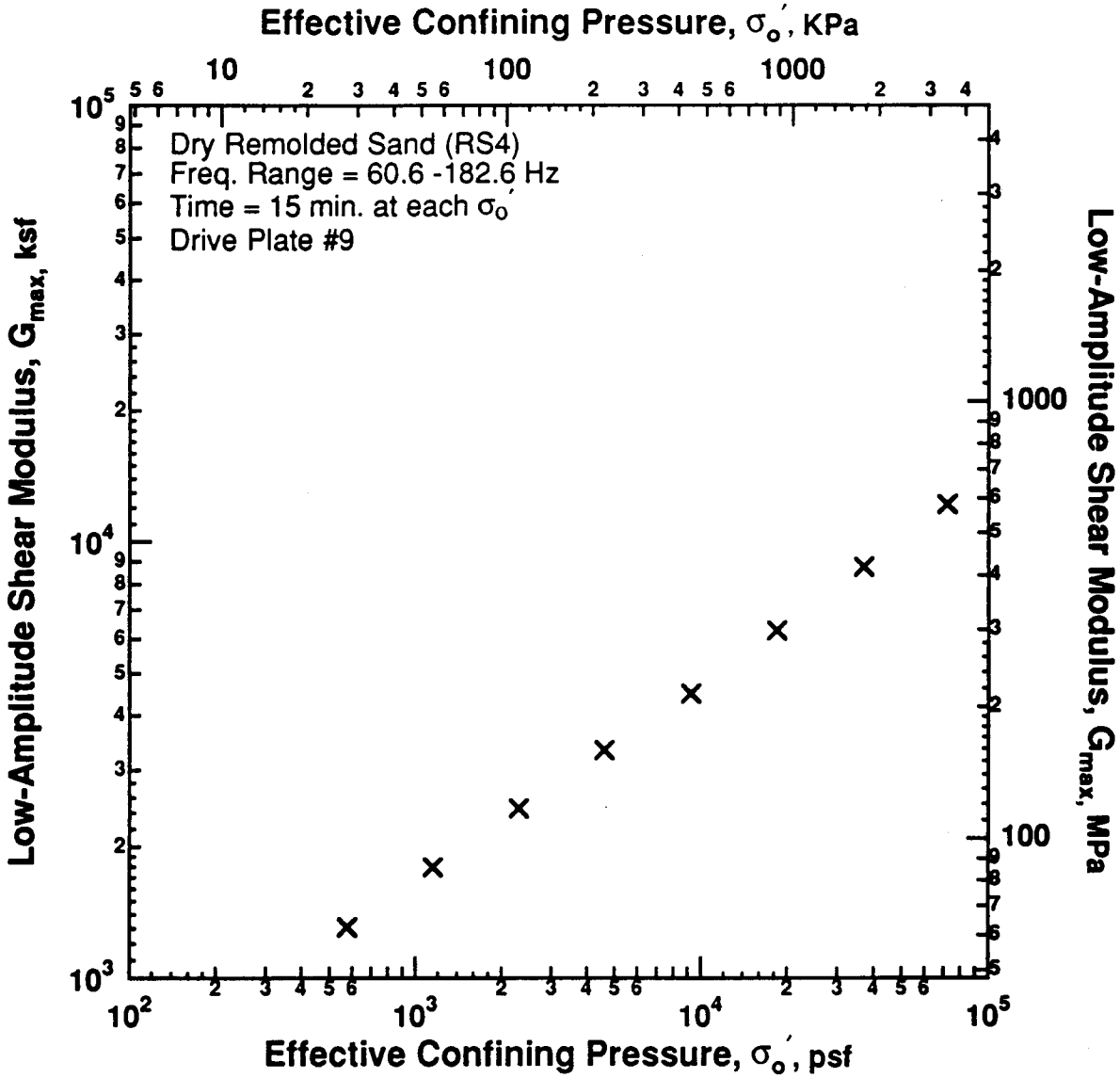

Figure 8.B.4.E-1
Variation in low-amplitude shear modulus with effective confining pressure from resonant column testing of dry remolded sand sample (RS4).

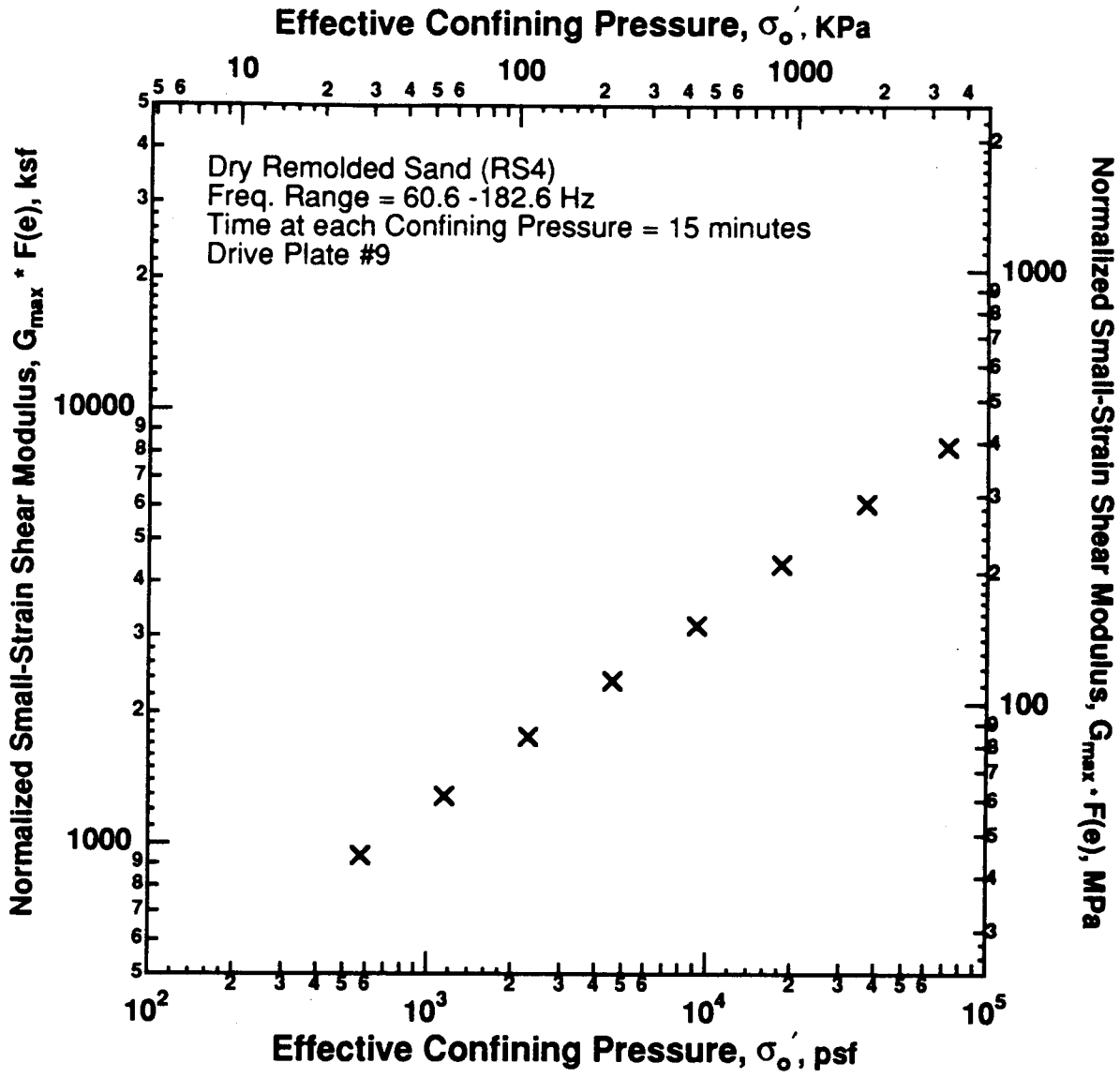

$$G_{max} * F(e), psf = A * P_{atm}^{(1-n)} * \sigma_o'^{(n)}, psf$$

$$F(e) = 0.3 + 0.7\,(e)^2$$

$$A = 787$$

$$n = 0.446$$

$$P_{atm} = 2117 \text{ psf}$$

Figure 8.B.4.E-2
Variation in normalized low-amplitude shear modulus with effective confining pressure for dry remolded sand sample (RS4).

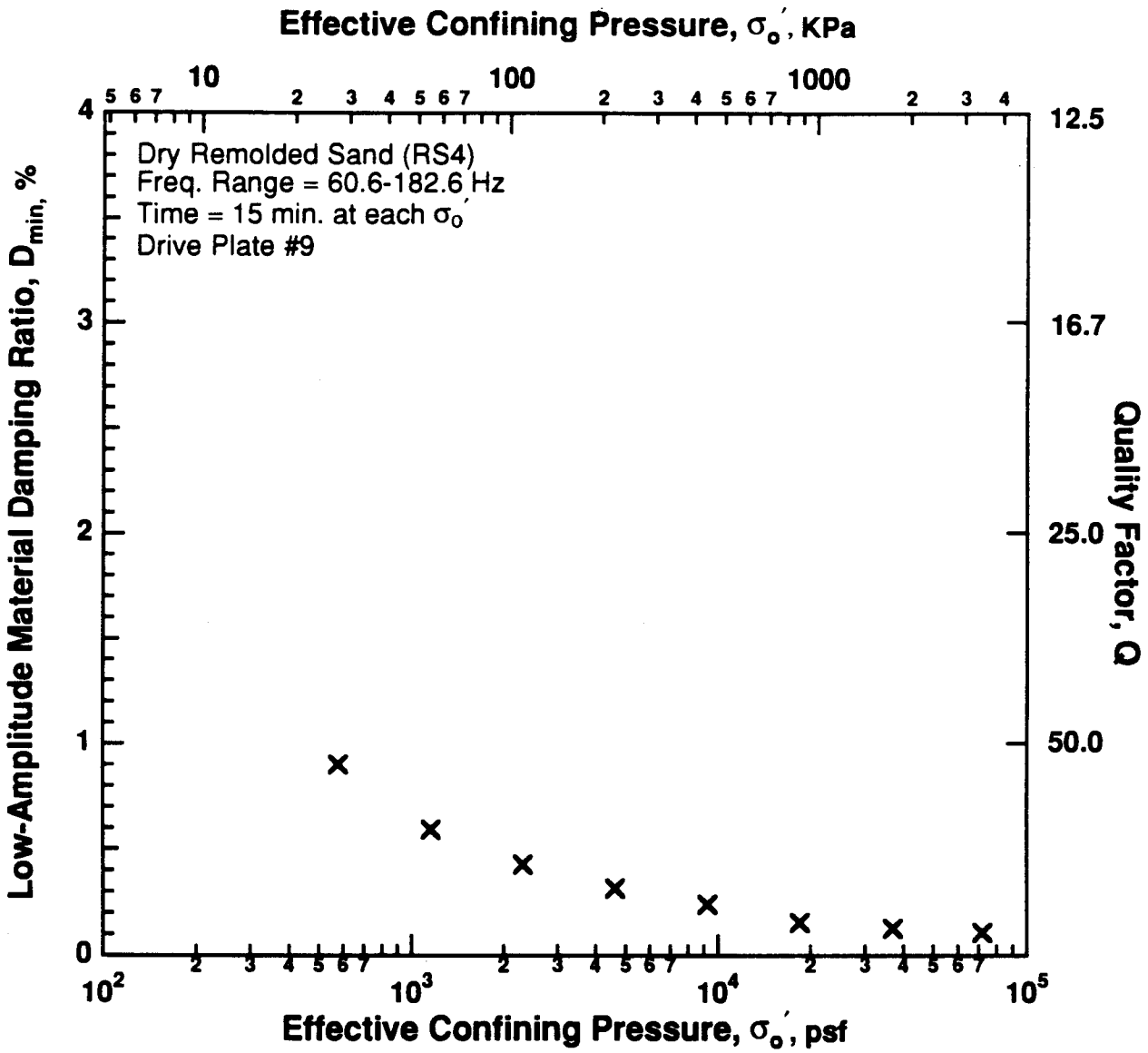

Figure 8.B.4.E-3
Variation in low-amplitude material damping ratio with effective confining pressure from resonant column testing of dry remolded sand (RS4).

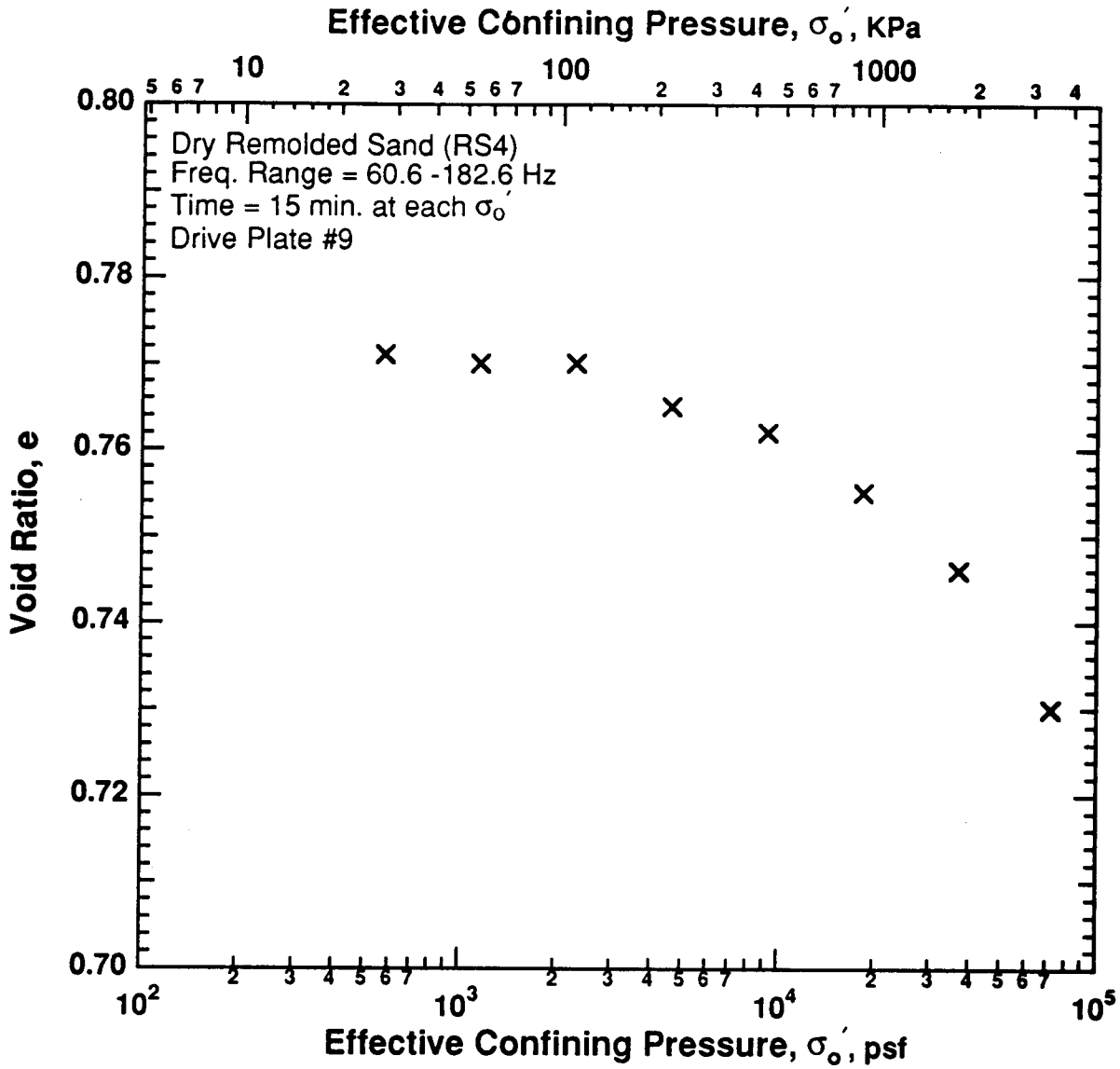

Figure 8.B.4.E-4
Variation in low-amplitude void ratio with effective confining pressure from resonant column testing of dry remolded sand sample (RS4).

APPENDIX F
DYNAMIC TESTS OF DRY REMOLDED SAND SAMPLE RS5

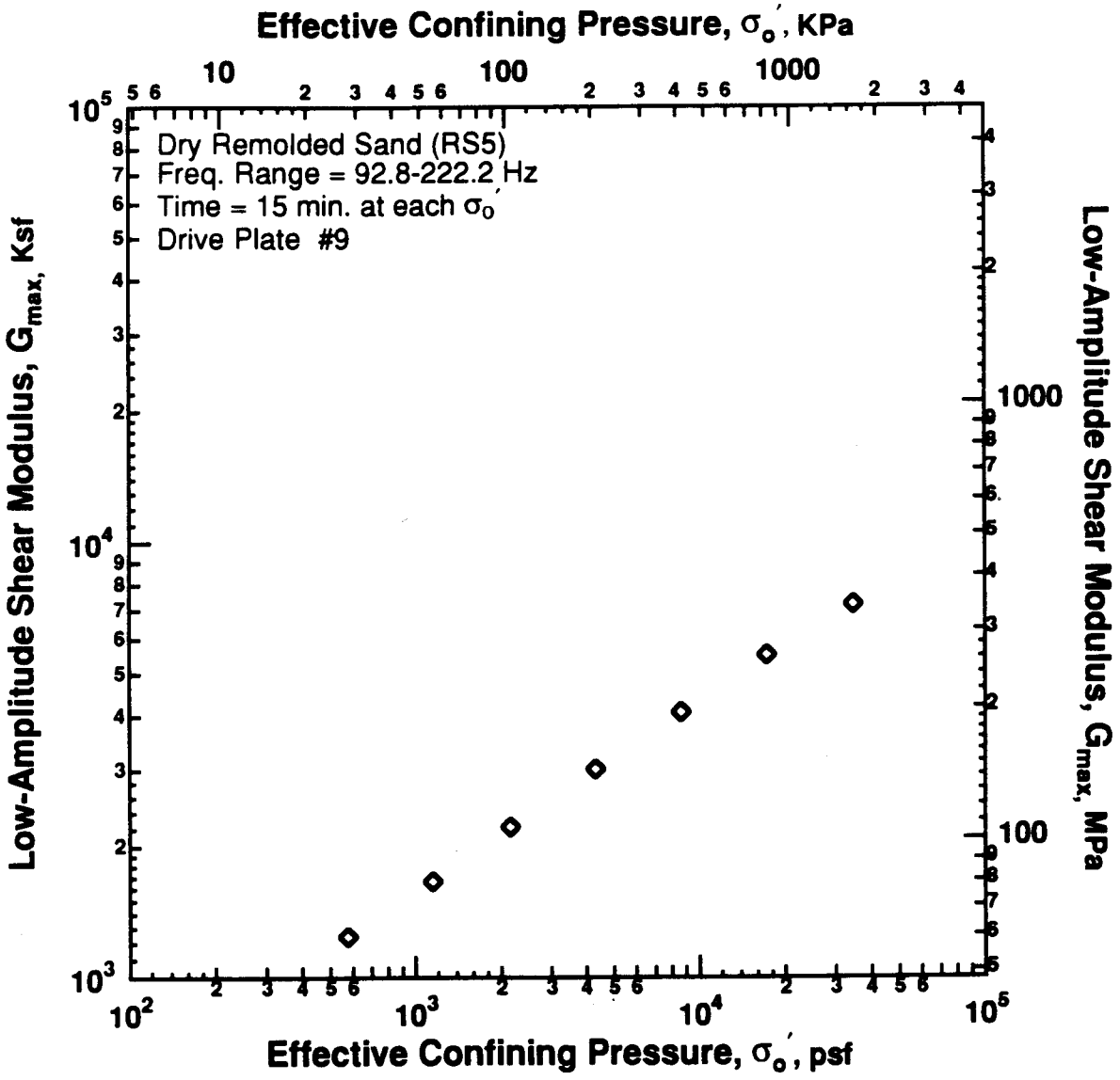

Figure 8.B.4.F-1
Variation in low-amplitude shear modulus with effective confining pressure from resonant column testing of dry remolded sand sample (RS5).

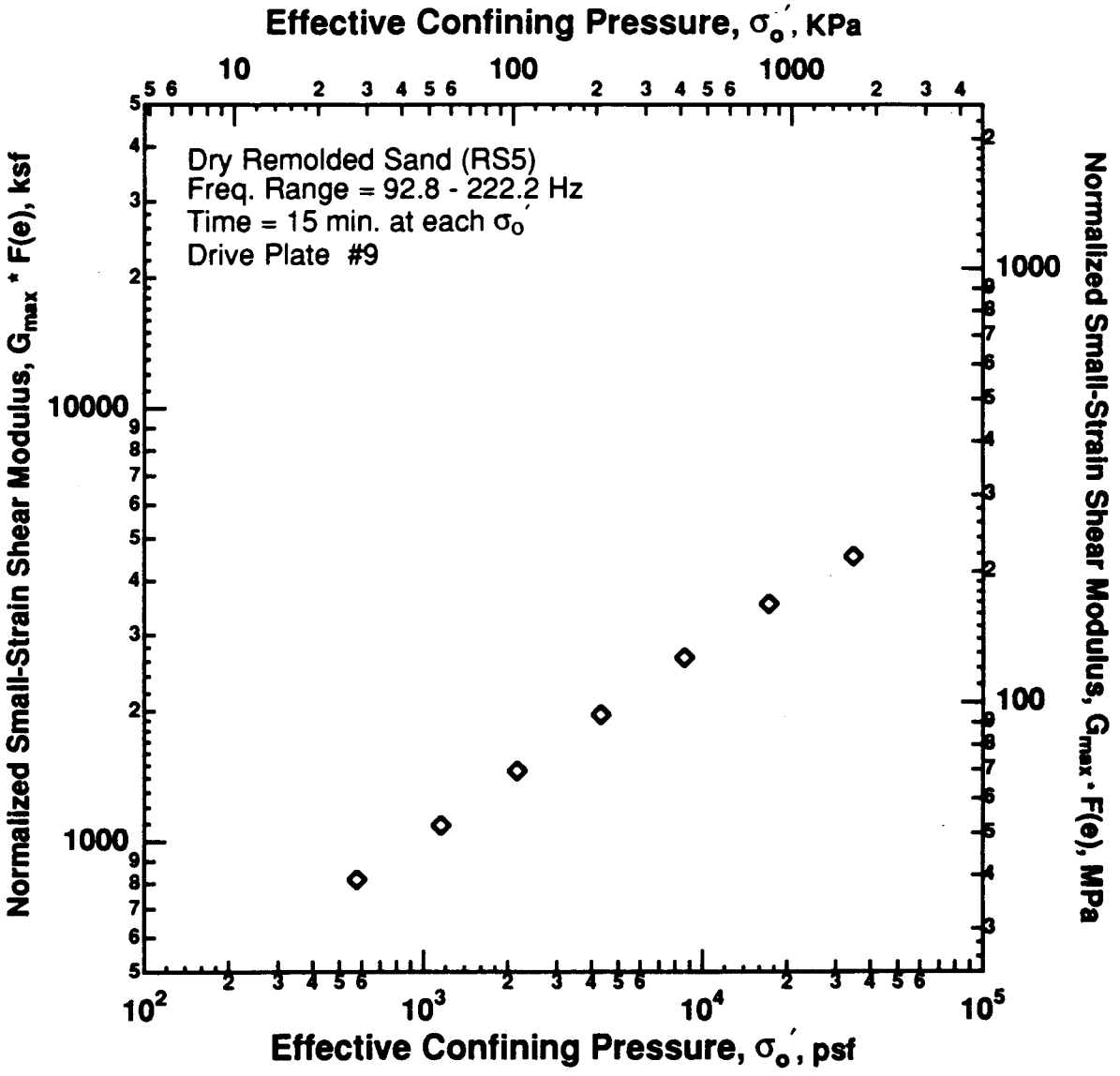

$$G_{max} * F(e), psf = A * P_{atm}^{(1-n)} * \sigma_o'^{(n)}, psf$$

$$F(e) = 0.3 + 0.7\,(e)^2$$

$A = 674$

$n = 0.423$

$P_{atm} = 2117$ psf

Figure 8.B.4.F-2
Variation in normalized low-amplitude shear modulus with effective confining pressure from resonant column testing of dry remolded sand sample (RS5).

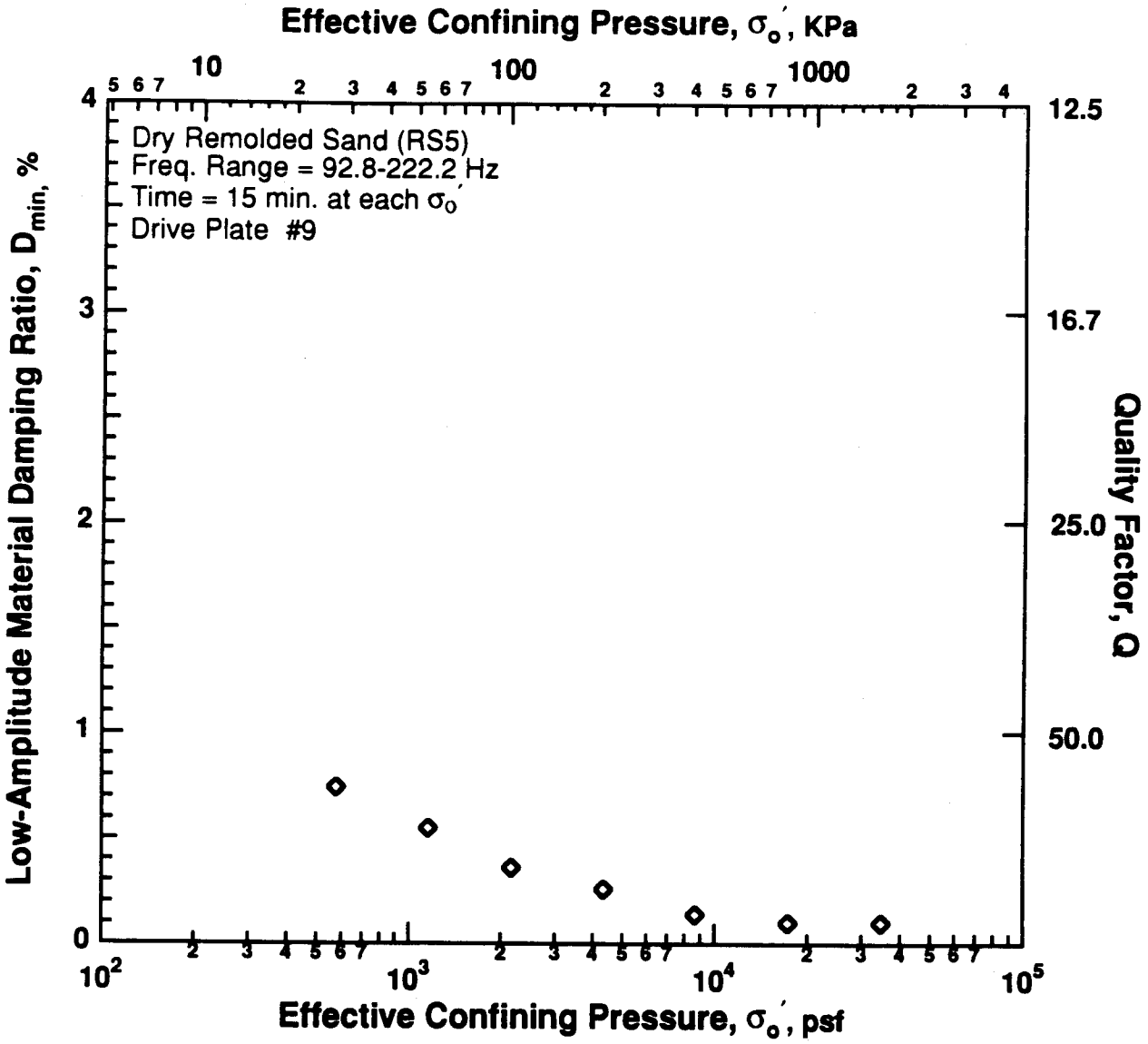

Figure 8.B.4.F-3
Variation in low-amplitude material damping ratio with effective confining pressure from resonant column testing of dry remolded sand sample (RS5).

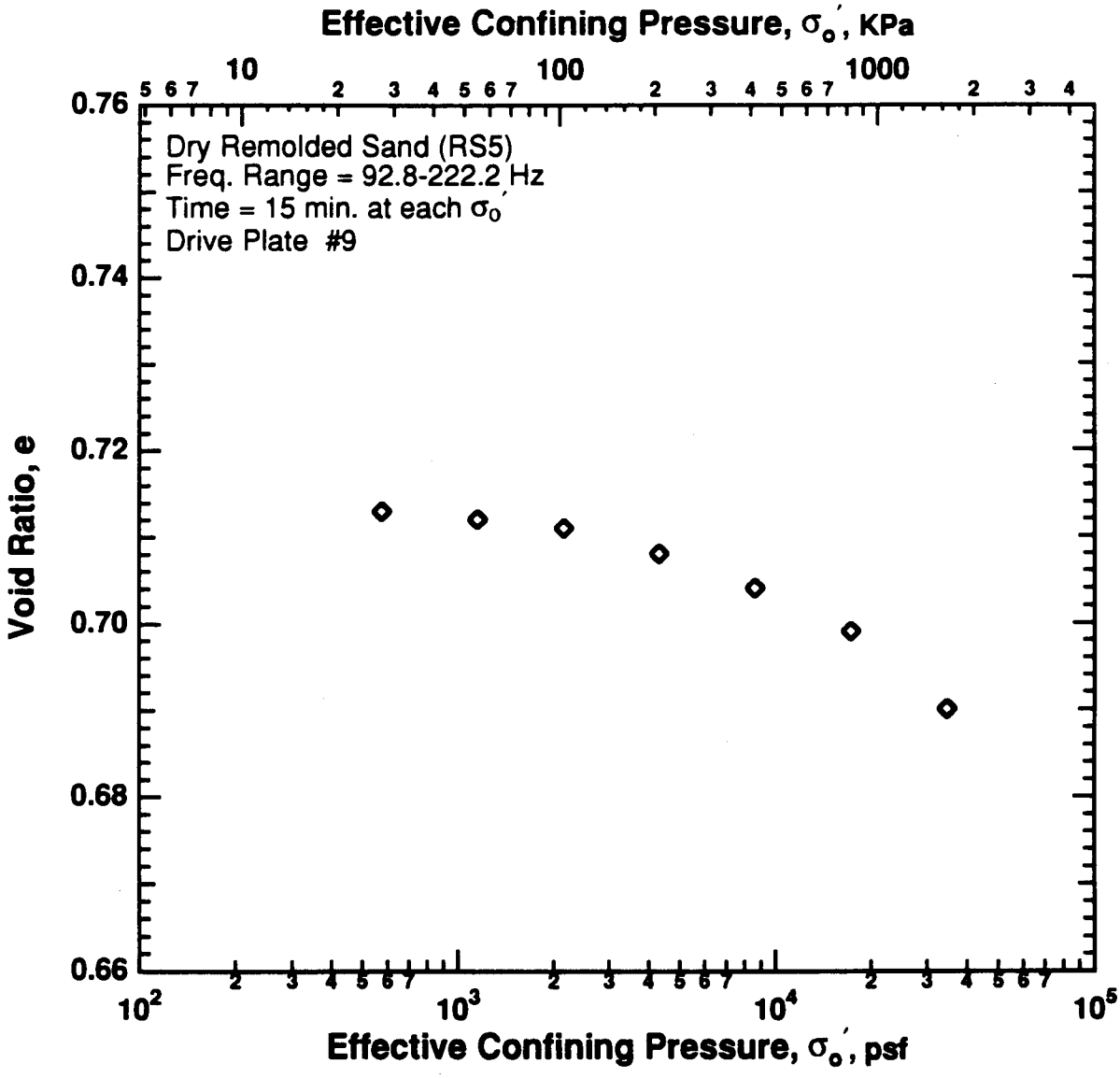

Figure 8.B.4.F-4
Variation in void ratio with effective confining pressure from resonant column testing of dry remolded sand sample (RS5).

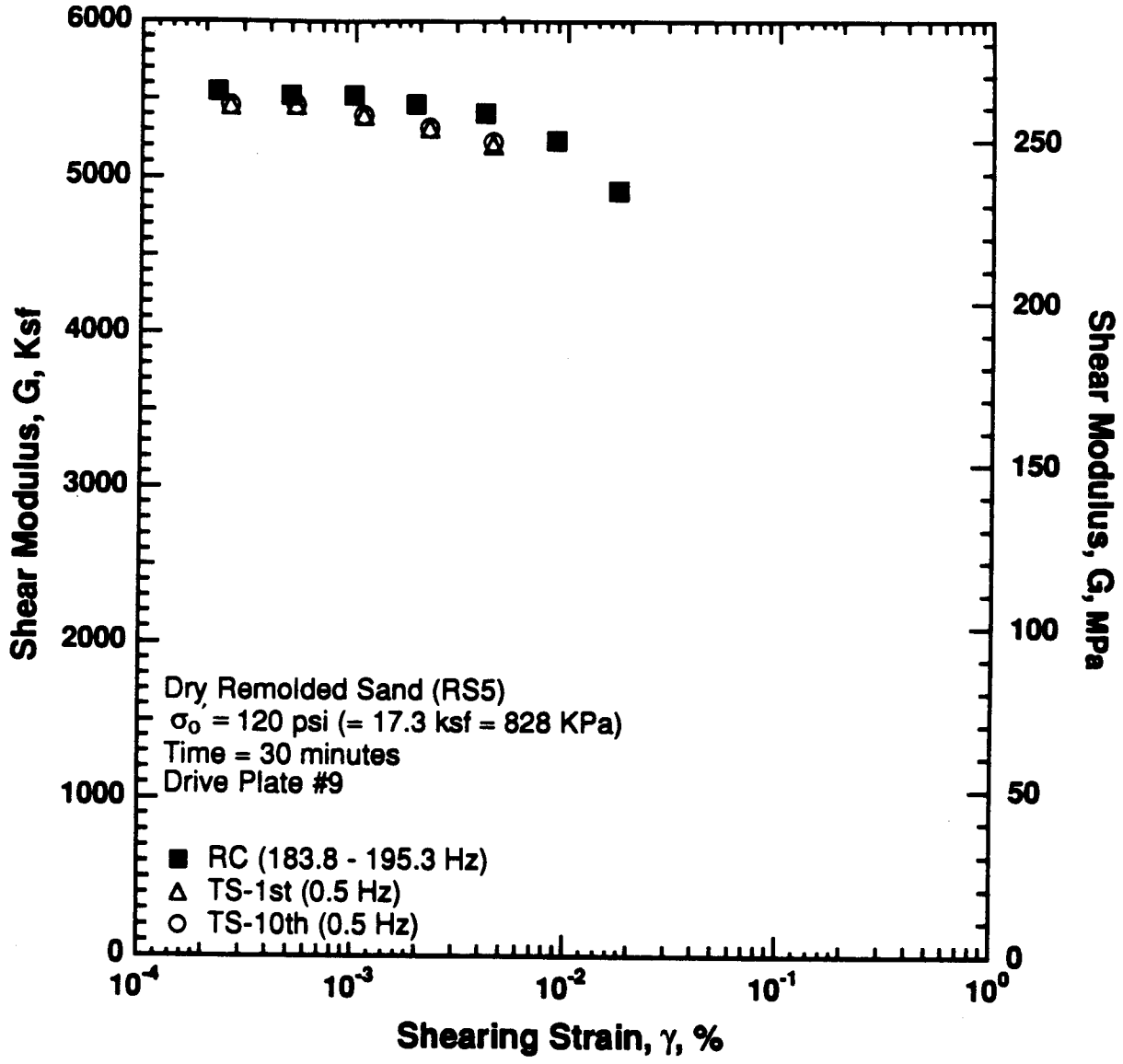

Figure 8.B.4.F-5
Variation in shear modulus with shearing strain at an effective confining pressure of 120 psi (17.3 ksf, 828 kPa) from RCTS testing of dry remolded sand sample (RS5).

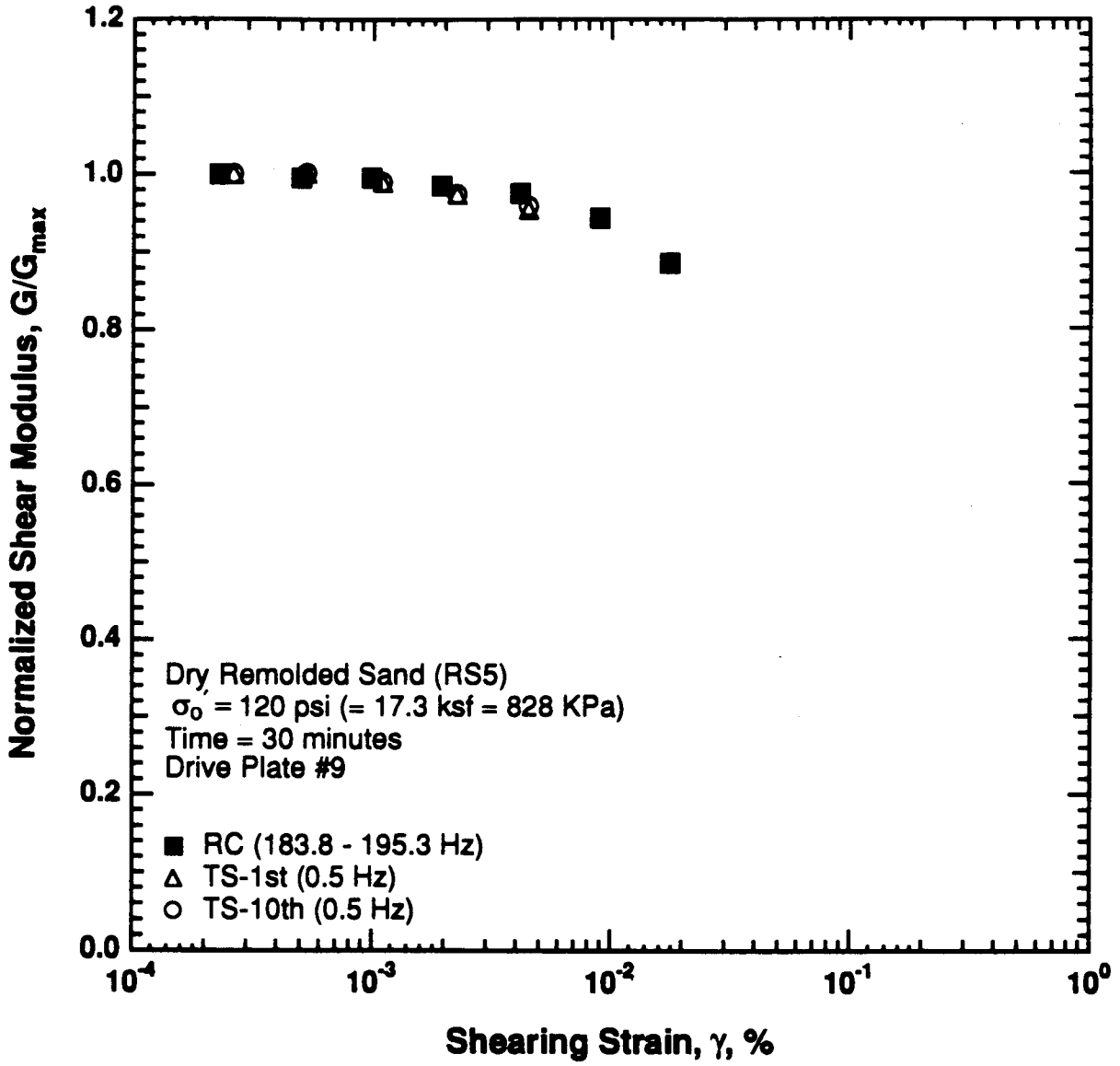

Figure 8.B.4.F-6
Variation in normalized shear modulus with shearing strain at an effective confining pressure of 120 psi (17.3 ksf, 828 kPa) from RCTS testing of dry remolded sand sample (RS5).

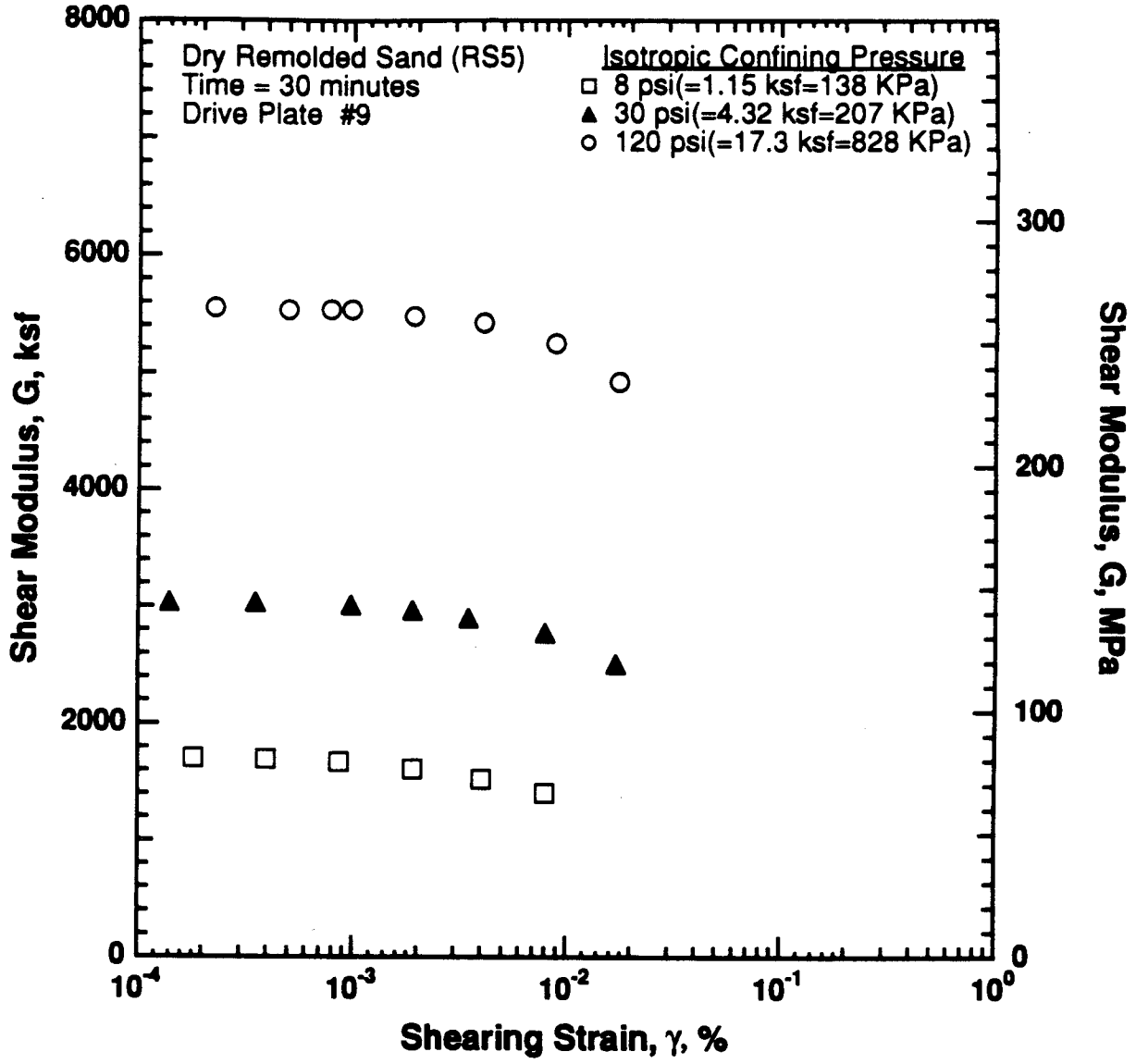

Figure 8.B.4.F-7
Variation in shear modulus with shearing strain and effective confining pressure from resonant column testing of dry remolded sand sample (RS5).

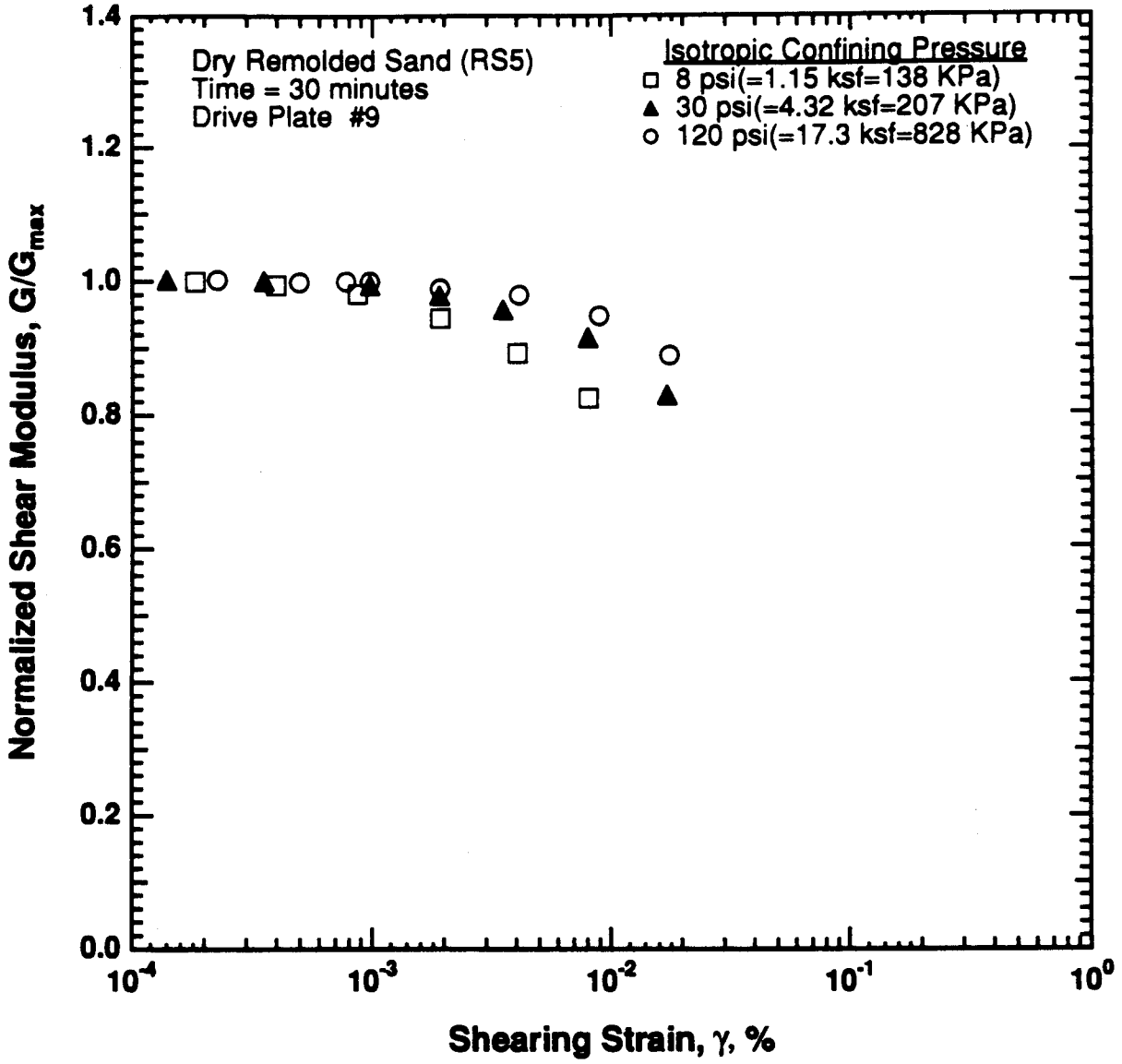

Figure 8.B.4.F-8
Comparison of the variation in normalized shear modulus with shearing strain and effective confining pressure from resonant column testing of dry remolded sand sample (RS5).

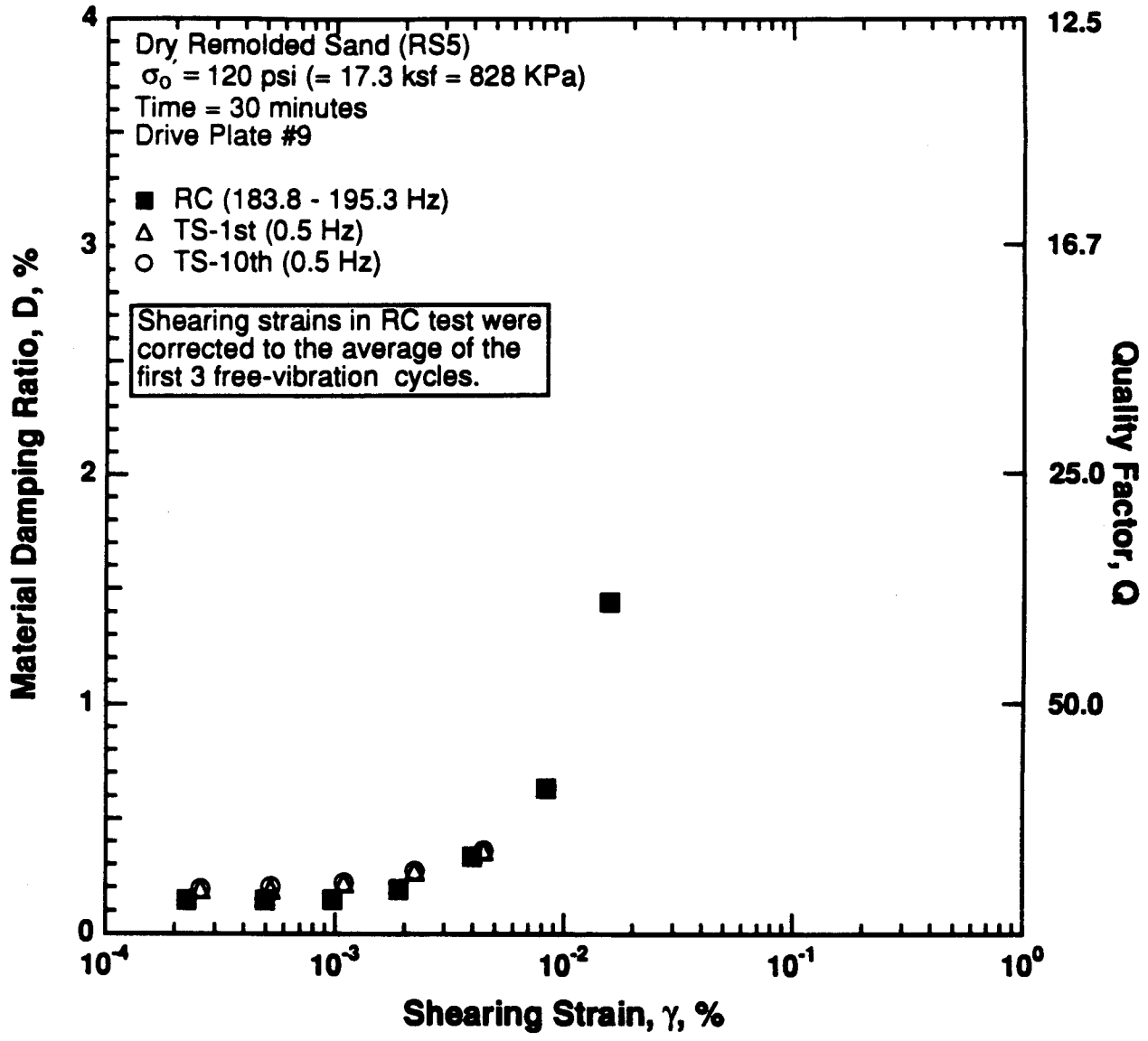

Figure 8.B.4.F-9
Variation in material damping ratio with shearing strain at an effective confining pressure of 120 psi (17.3 ksf, 828 kPa) from RCTS testing of dry remolded sand sample (RS5).

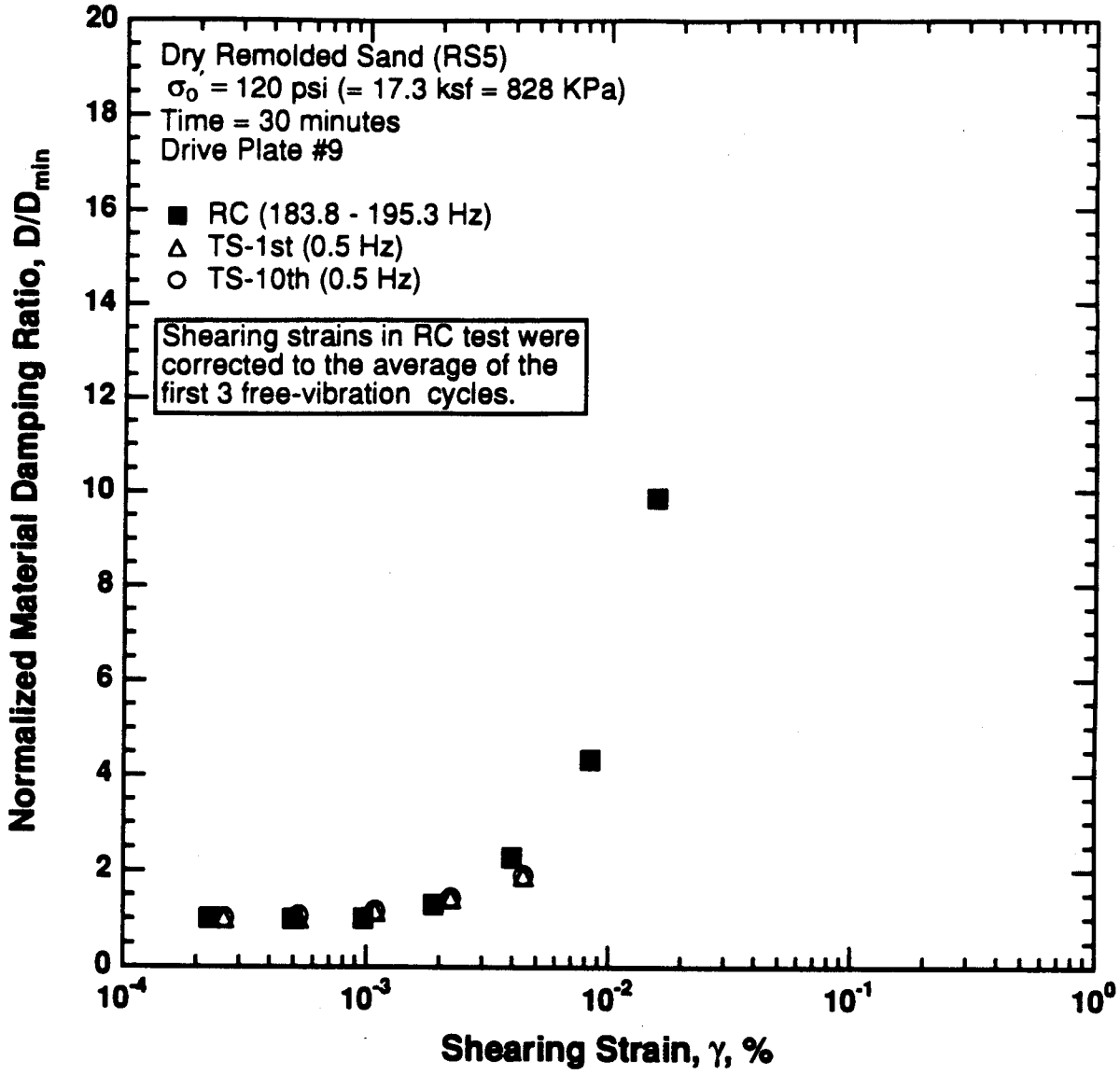

Figure 8.B.4.F-10
Variation in normalized material damping ratio with shearing strain at an effective confining pressure of 120 psi (17.3 ksf, 828 kPa) from RCTS testing of dry remolded sand sample (RS5).

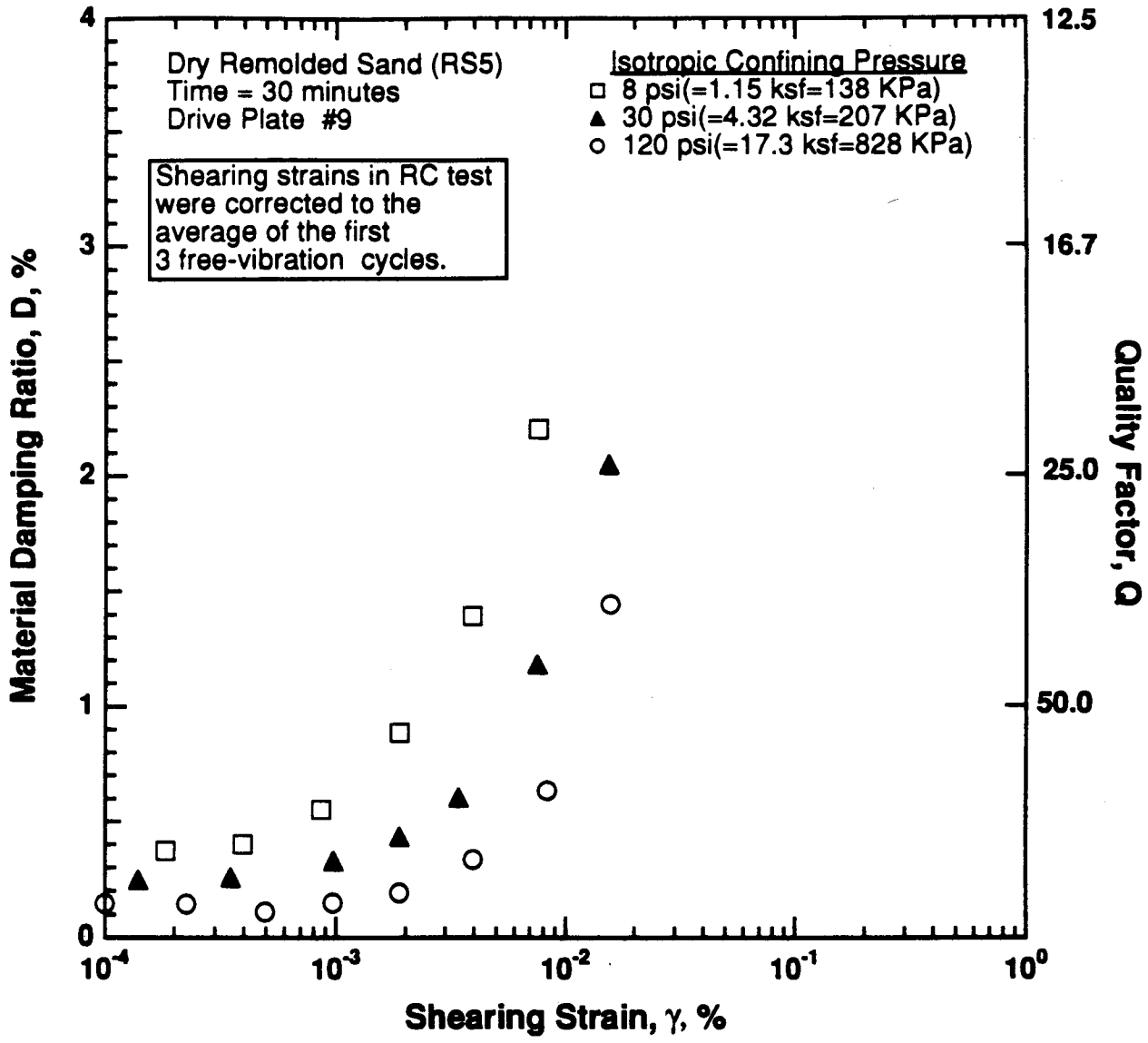

Figure 8.B.4.F-11
Variation in material damping ratio with shearing strain and effective confining pressure from resonant column testing of dry remolded sand sample (RS5).

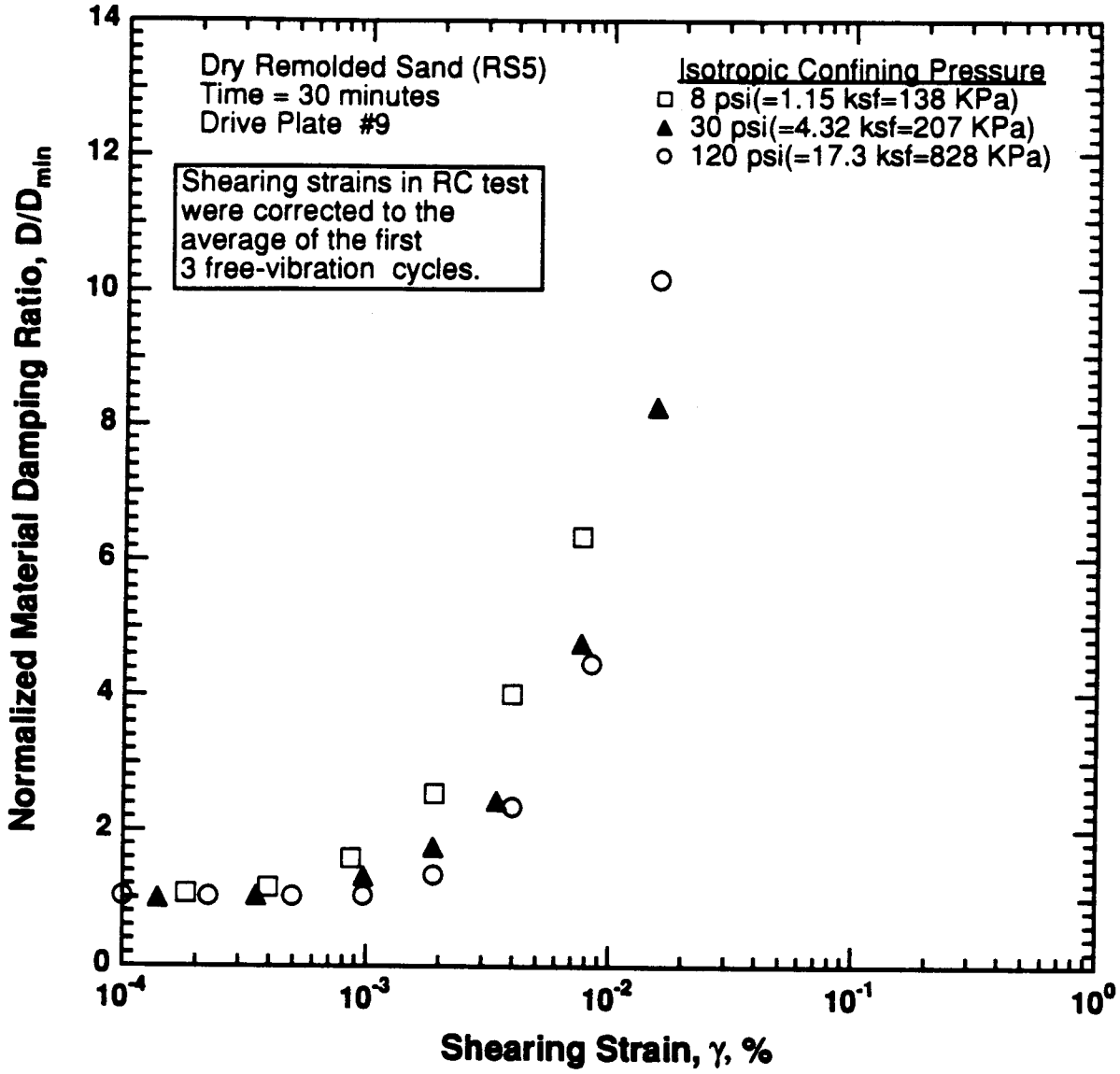

Figure 8.B.4.F-12
Comparison of the variation in normalized material damping ratio with shearing strain and effective confining pressure from resonant column testing of dry remolded sand sample (RS5).

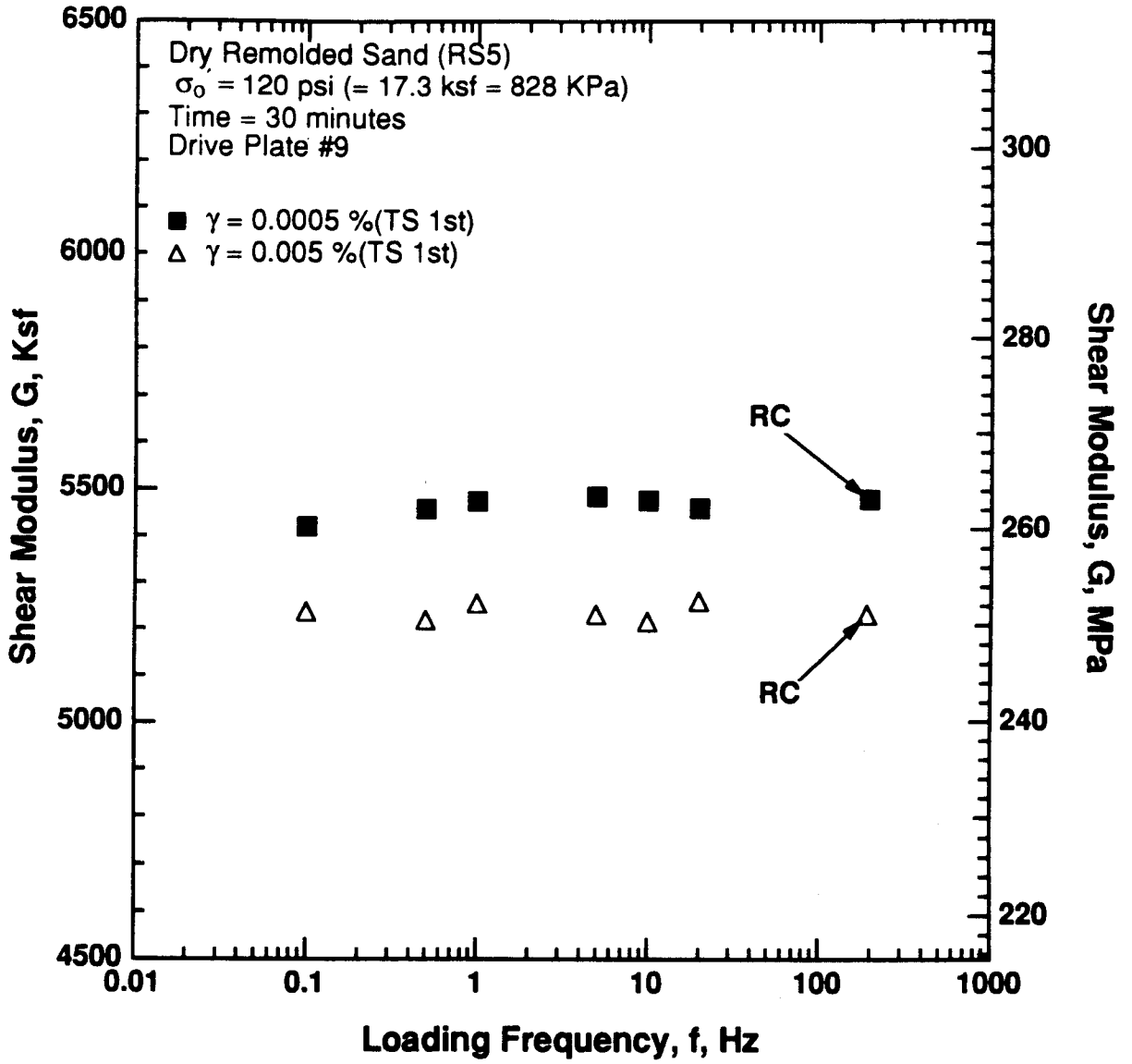

Figure 8.B.4.F-13
Variation in shear modulus with loading frequency and shearing strain at an effective confining pressure of 120 psi (17.3 ksf, 828 kPa) from RCTS testing of dry remolded sand sample (RS5).

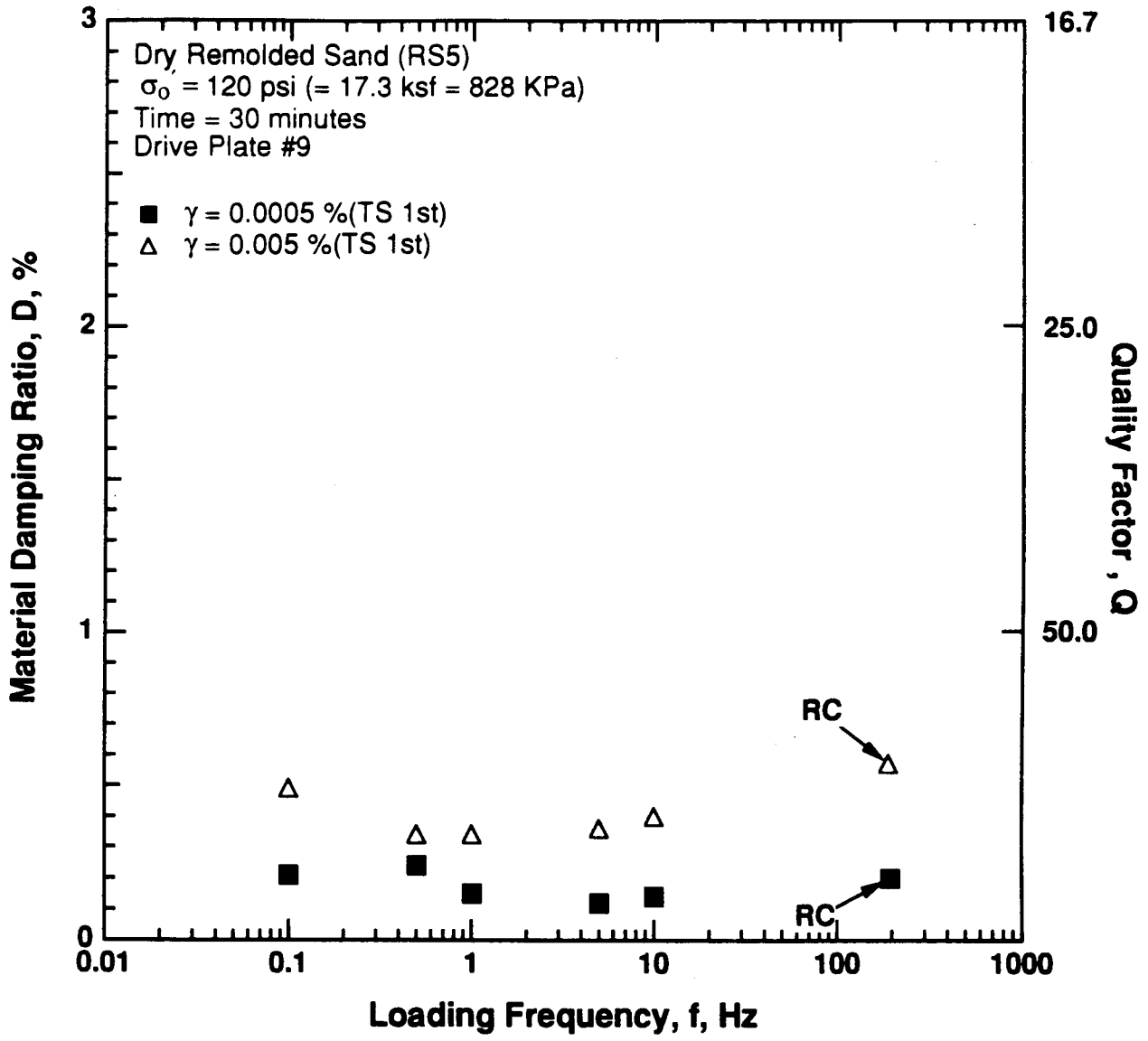

Figure 8.B.4.F-14
Variation in material damping ratio with loading frequency and shearing strain at an effective confining pressure of 120 psi (17.3 ksf, 828 kPa) from RCTS testing of dry remolded sand sample (RS5).

APPENDIX G
DYNAMIC TESTS OF SATURATED REMOLDED SAND SAMPLE RS6

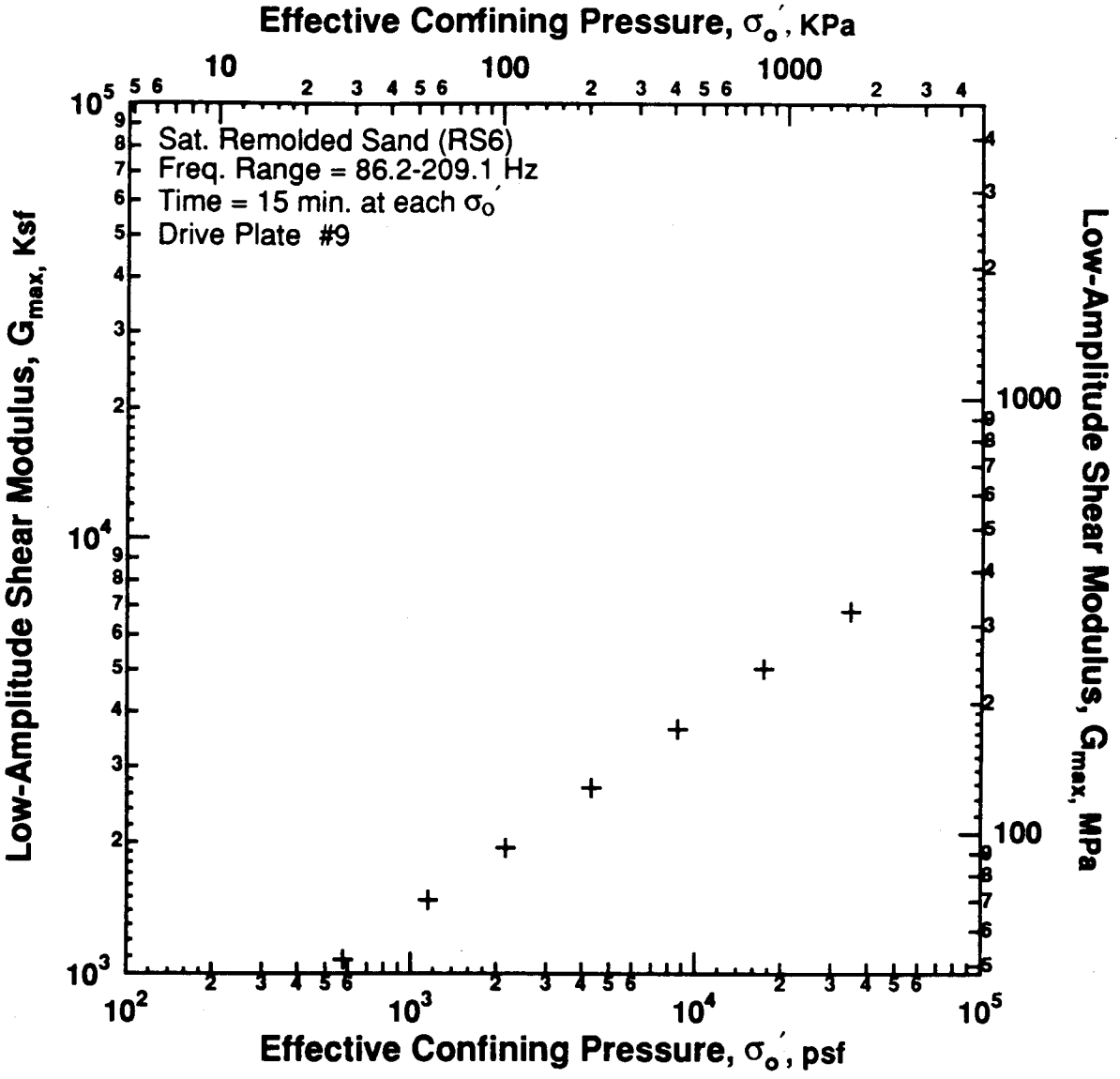

Figure 8.B.4.G-1
Variation in low-amplitude shear modulus with effective confining pressure from resonant column testing of saturated remolded sand sample (RS6).

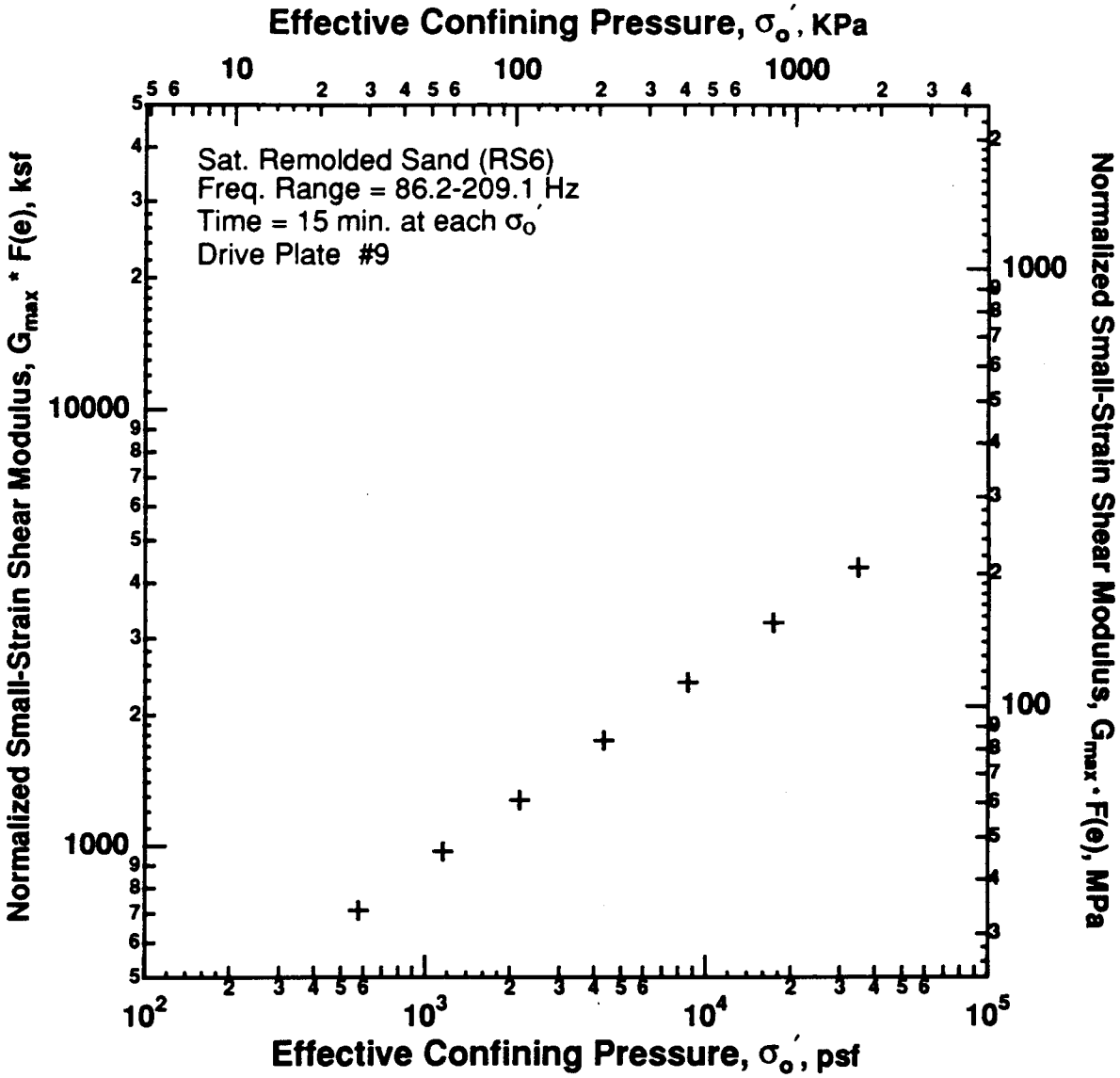

$$G_{max} * F(e), psf = A * Patm^{(1-n)} * \sigma_o'^{(n)}, psf$$

$$F(e) = 0.3 + 0.7\,(e)^2$$

$$A = 597$$

$$n = 0.443$$

$$Patm = 2117\ psf$$

Figure 8.B.4.G-2
Variation in normalized low-amplitude shear modulus with effective confining pressure for saturated remolded sand sample (RS6).

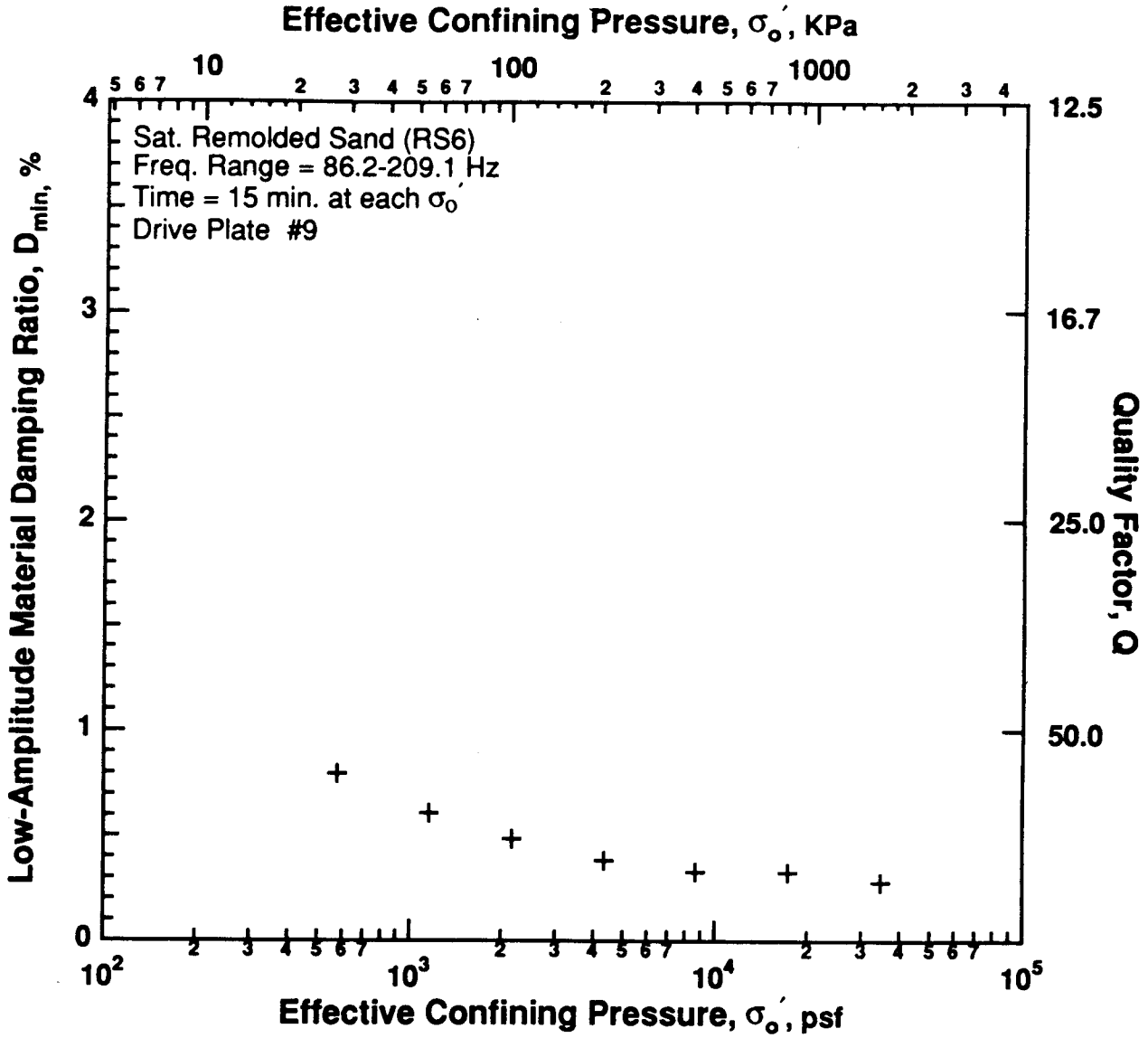

Figure 8.B.4.G-3
Variation in low-amplitude material damping ratio with effective confining pressure from resonant column testing of saturated remolded sand sample (RS6).

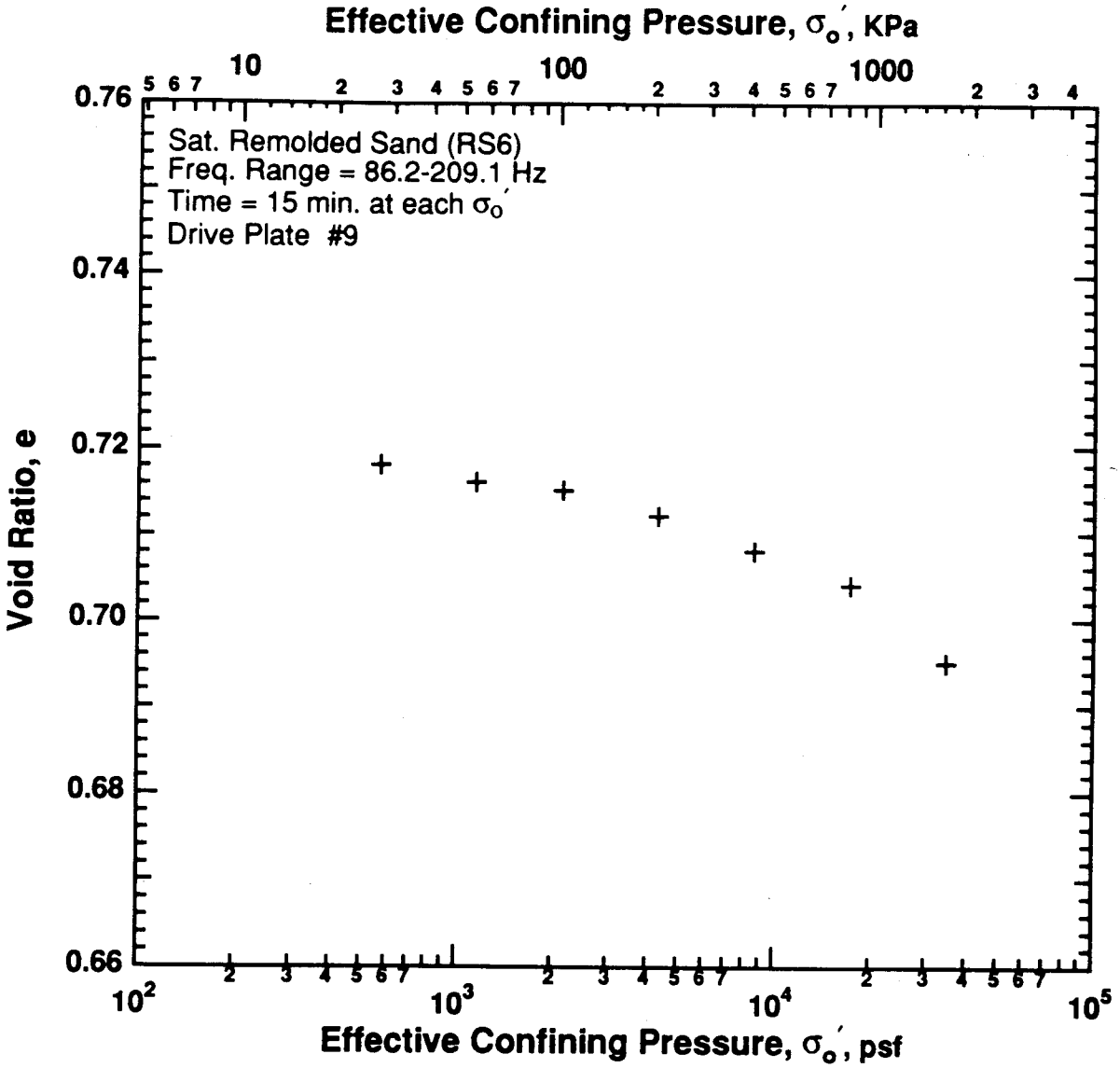

Figure 8.B.4.G-4
Variation in void ratio with effective confining pressure from resonant column testing of saturated remolded sand sample (RS6).

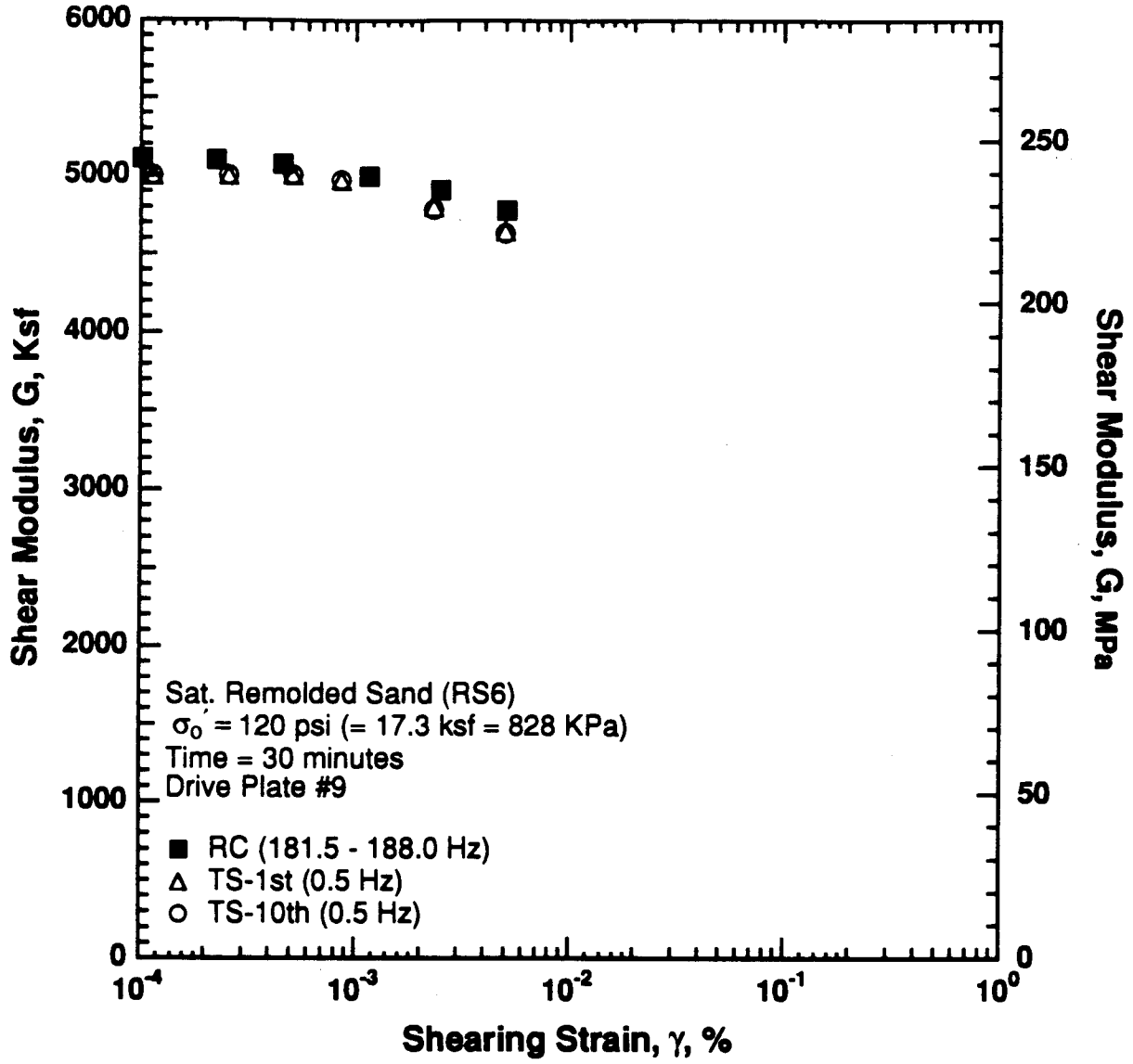

Figure 8.B.4.G-5
Variation in shear modulus with shearing strain at an effective confining pressure of 120 psi (17.3 ksf, 828 kPa) from RCTS testing of saturated remolded sand sample (RS6).

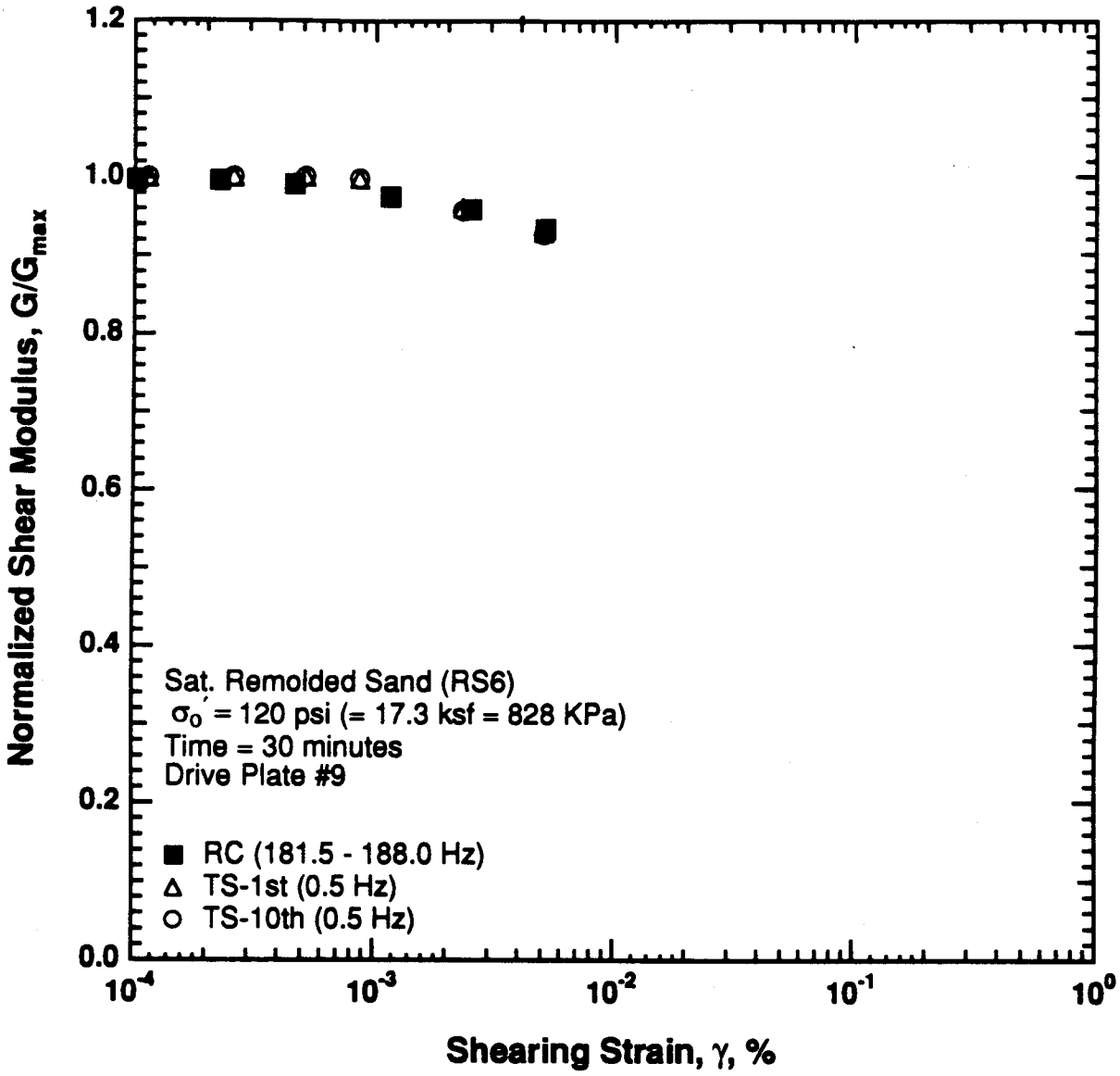

Figure 8.B.4.G-6
Variation in normalized shear modulus with shearing strain at an effective confining pressure of 120 psi (17.3 ksf, 828 kPa) from RCTS testing of saturated remolded sand sample (RS6).

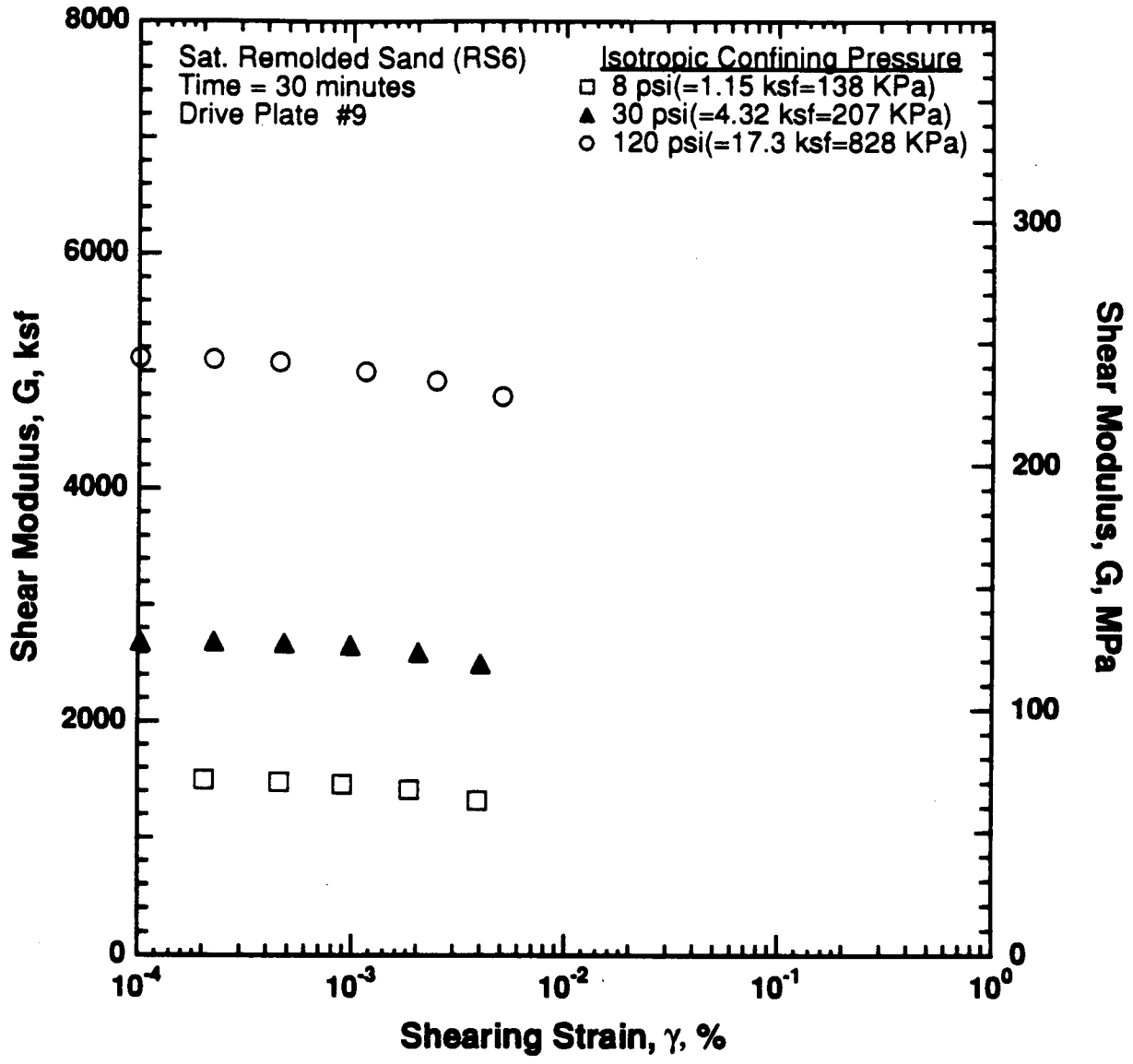

Figure 8.B.4.G-7
Variation in shear modulus with shearing strain and effective confining pressure from resonant column testing of saturated remolded sand sample (RS6).

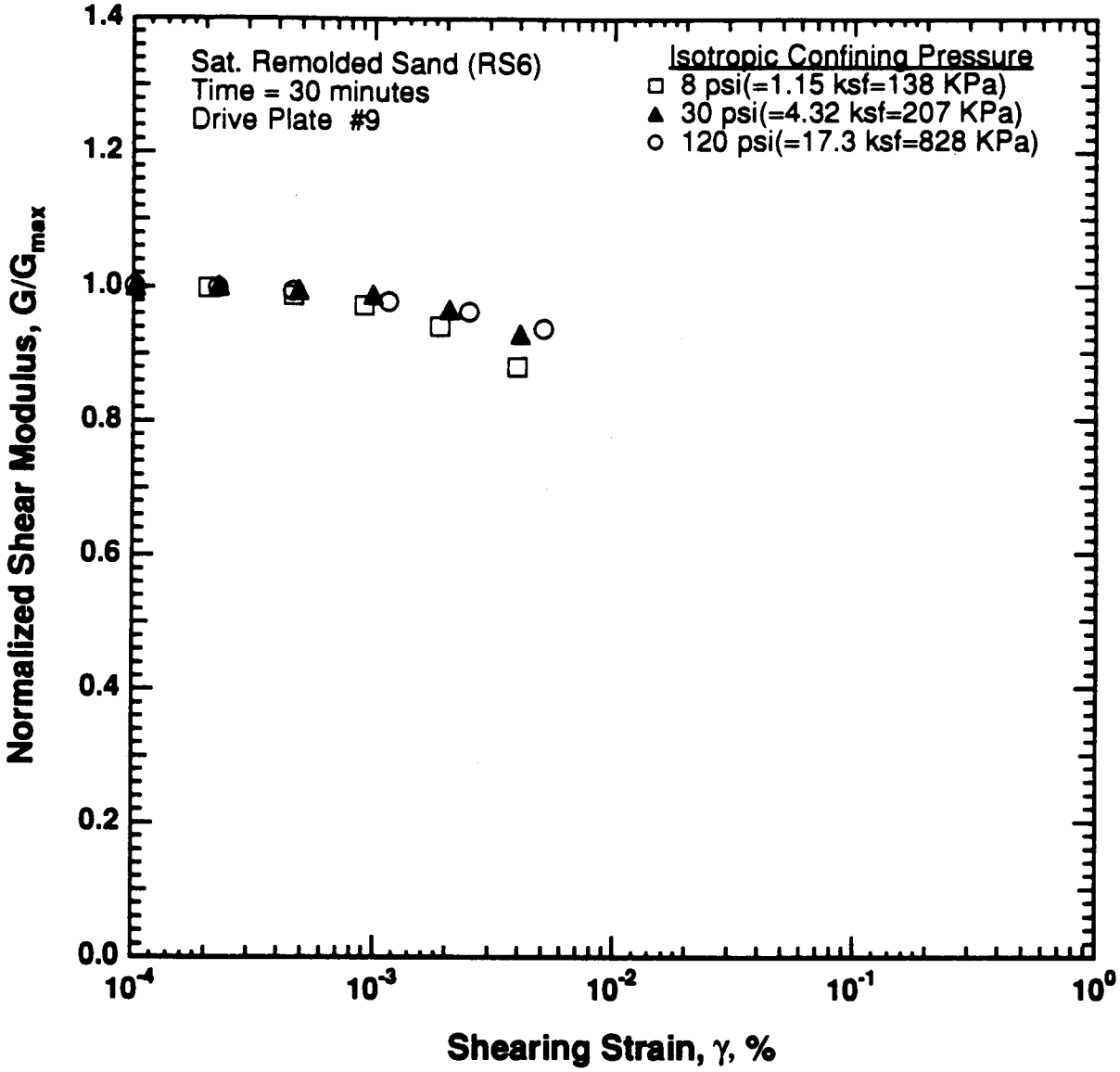

Figure 8.B.4.G-8
Comparison of the variation in normalized shear modulus with shearing strain and effective confining pressure from resonant column testing of saturated remolded sand sample (RS6).

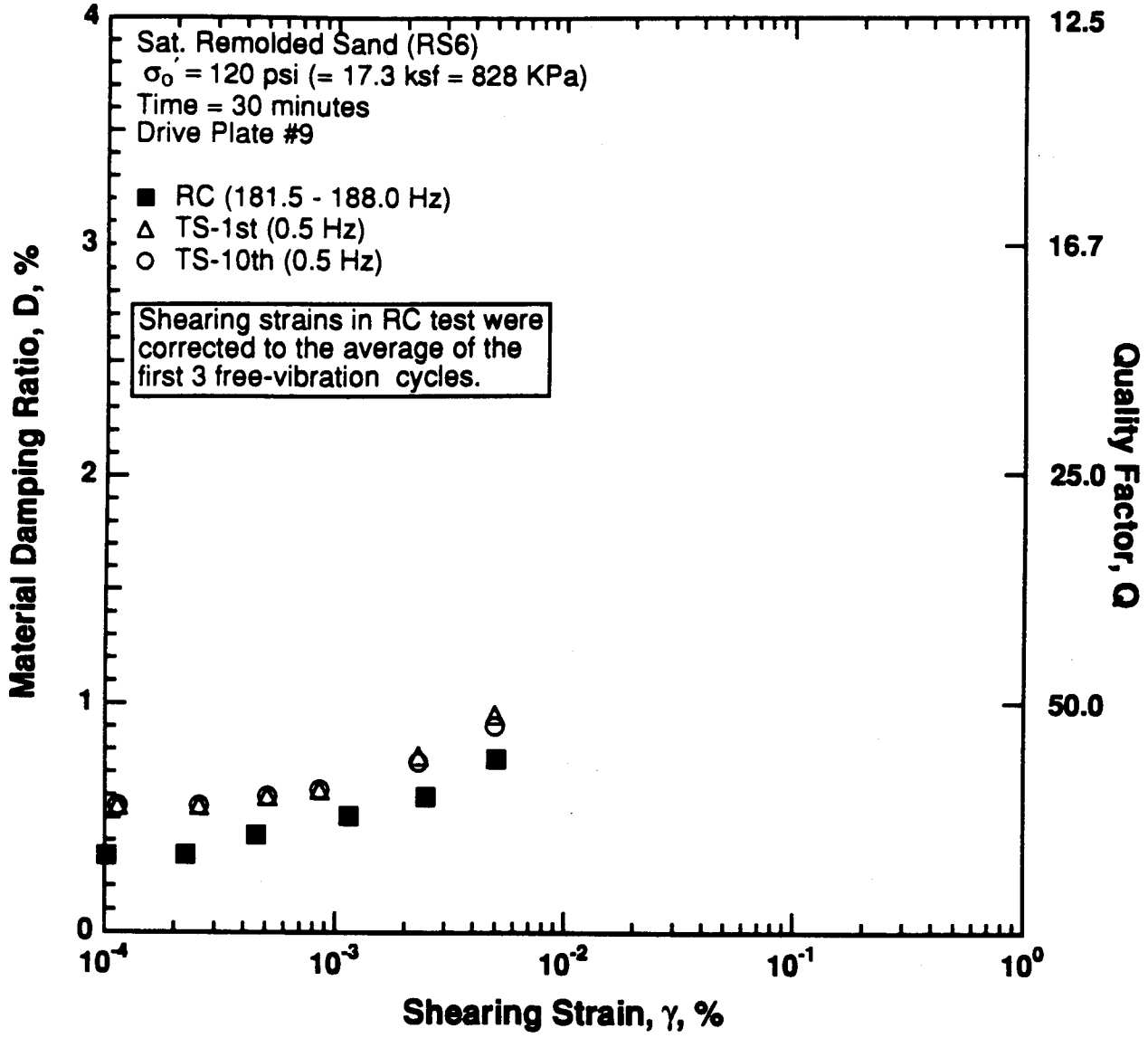

Figure 8.B.4.G-9
Variation in material damping ratio with shearing strain at an effective confining pressure of 120 psi (17.3 ksf, 828 kPa) from RCTS testing of saturated remolded sand sample (RS6).

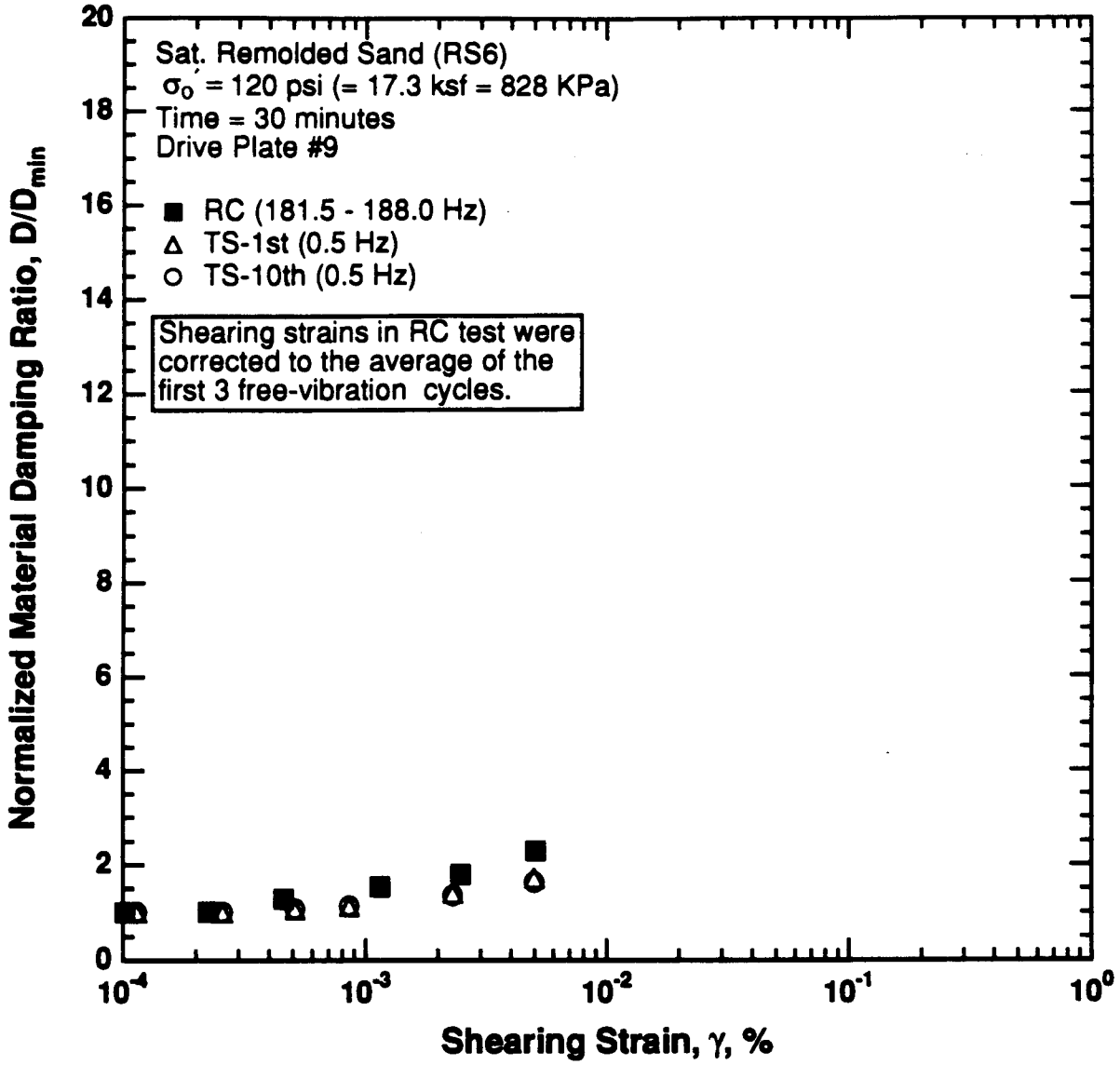

Figure 8.B.4.G-10
Variation in normalized material damping ratio with shearing strain at an effective confining pressure of 120 psi (17.3 ksf, 828 kPa) from RCTS testing of saturated remolded sand sample (RS6).

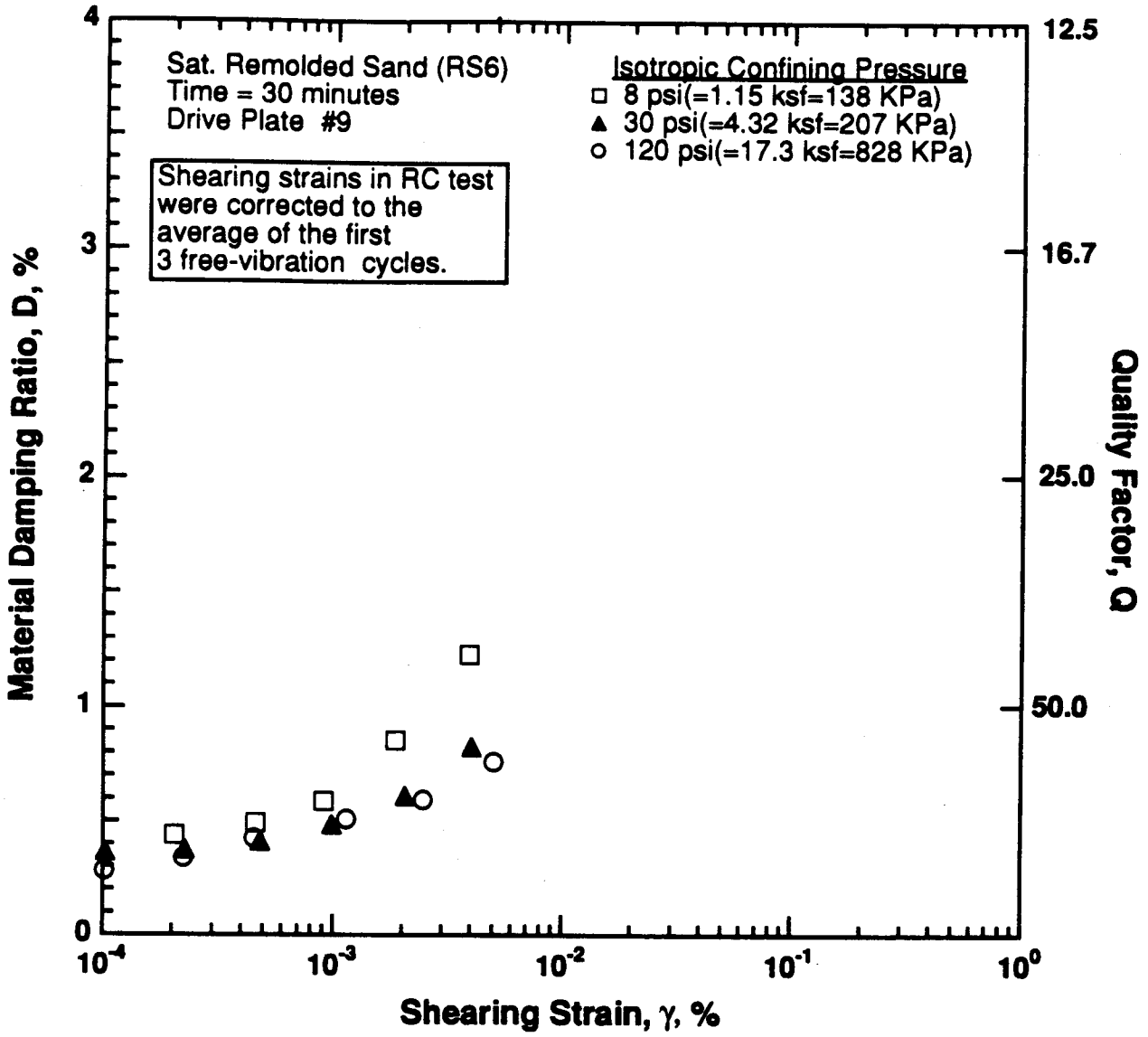

Figure 8.B.4.G-11
Variation in material damping ratio with shearing strain and effective confining pressure from resonant column testing of saturated remolded sand sample (RS6).

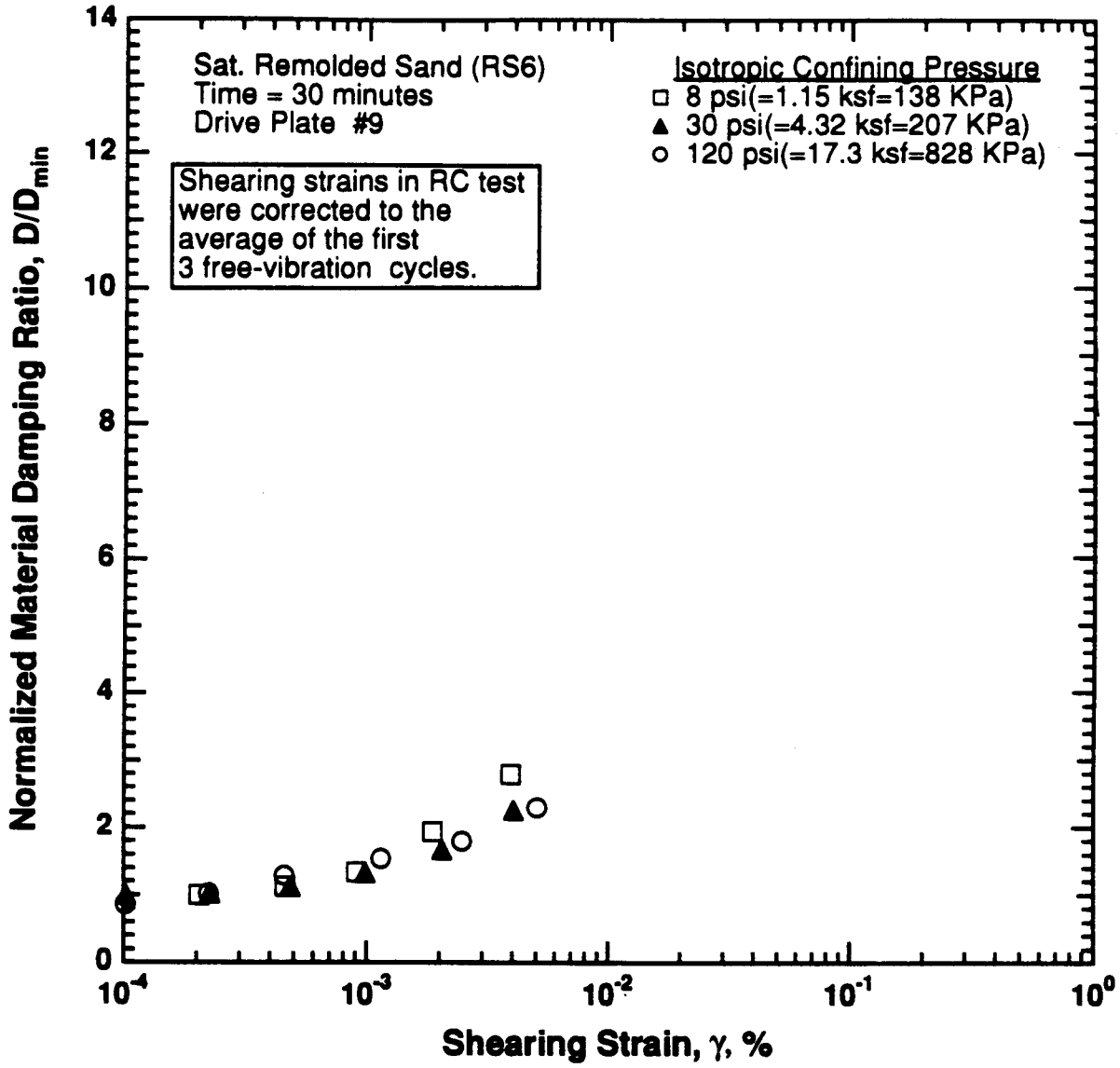

Figure 8.B.4.G-12
Comparison of the variation in normalized material damping ratio with shearing strain and effective confining pressure from resonant column testing of saturated remolded sand sample (RS6).

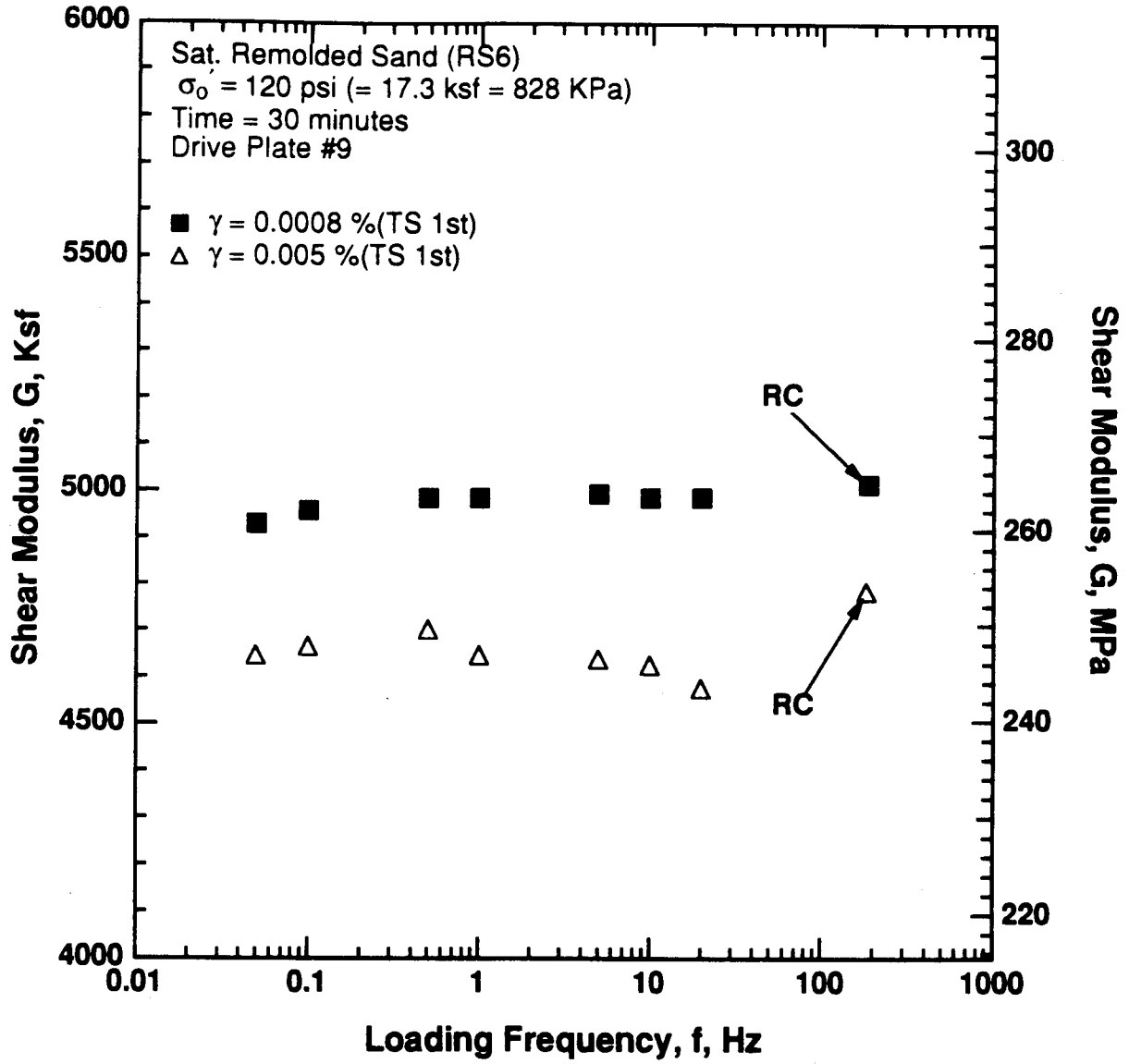

Figure 8.B.4.G-13
Variation in shear modulus with loading frequency and shearing strain at an effective confining pressure of 120 psi (17.3 ksf, 828 kPa) from RCTS testing of saturated remolded sand sample (RS6).

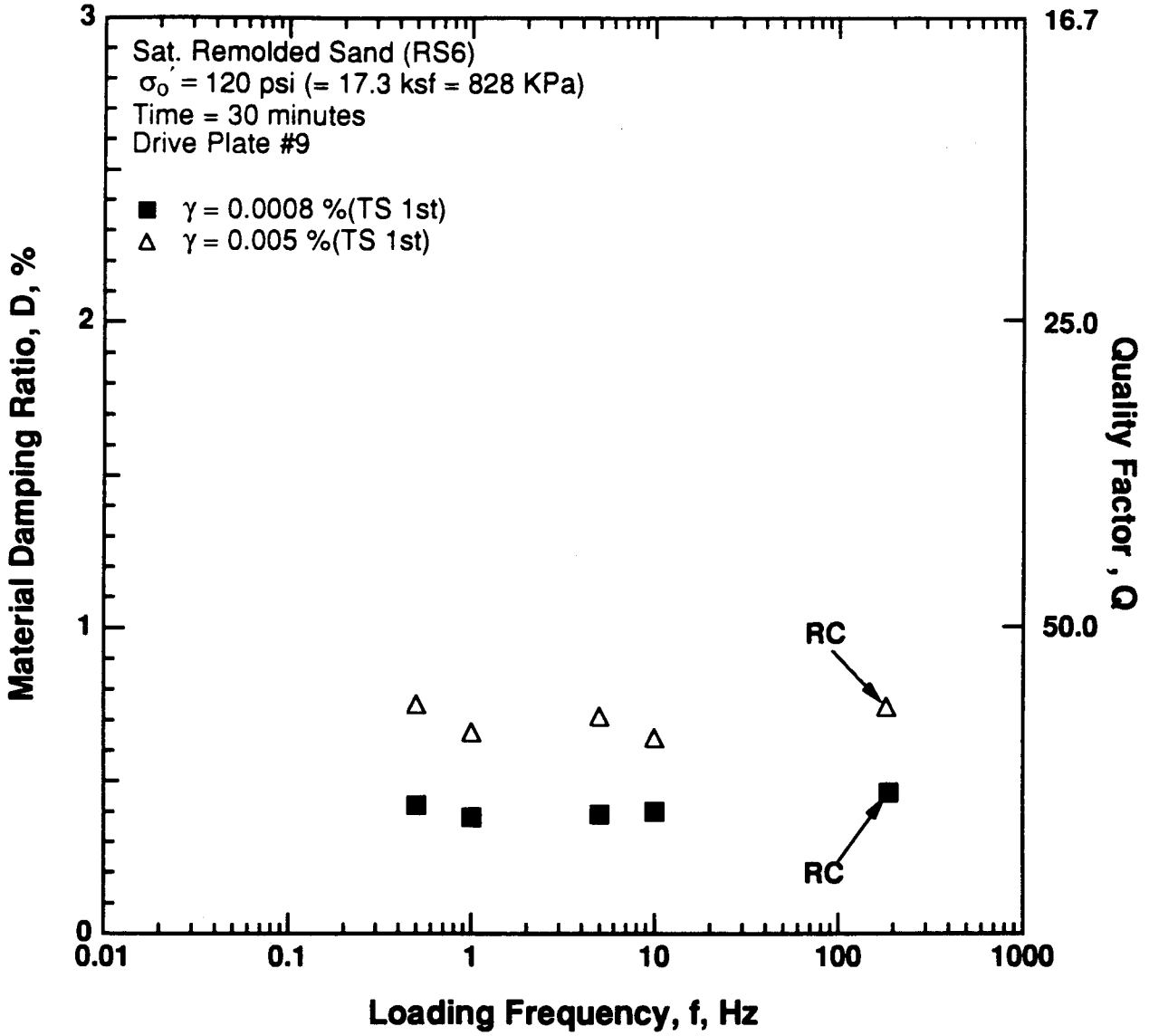

Figure 8.B.4.G-14
Variation in material damping ratio with loading frequency and shearing strain at an effective confining pressure of 120 psi (17.3 ksf, 828 kPa) from RCTS tests of saturated remolded sand sample (RS6).

APPENDIX H
DYNAMIC TESTS OF TREASURE ISLAND SAMPLE T5, DEPTH = 110 FT (33.6 M)

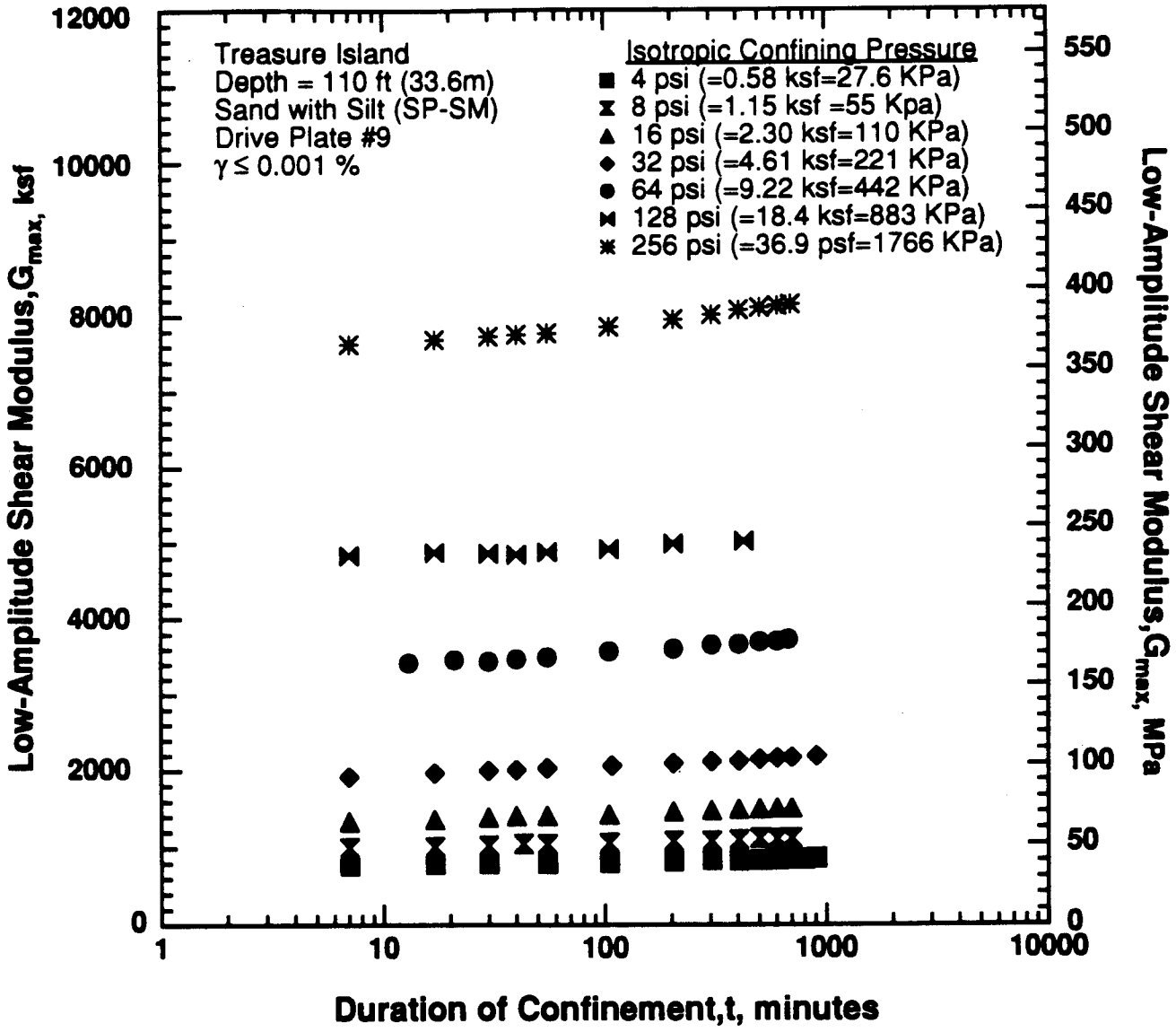

Figure 8.B.4.H-1
Variation in low-amplitude shear modulus with magnitude and duration of isotropic confining pressure from resonant column testing of sample T5.

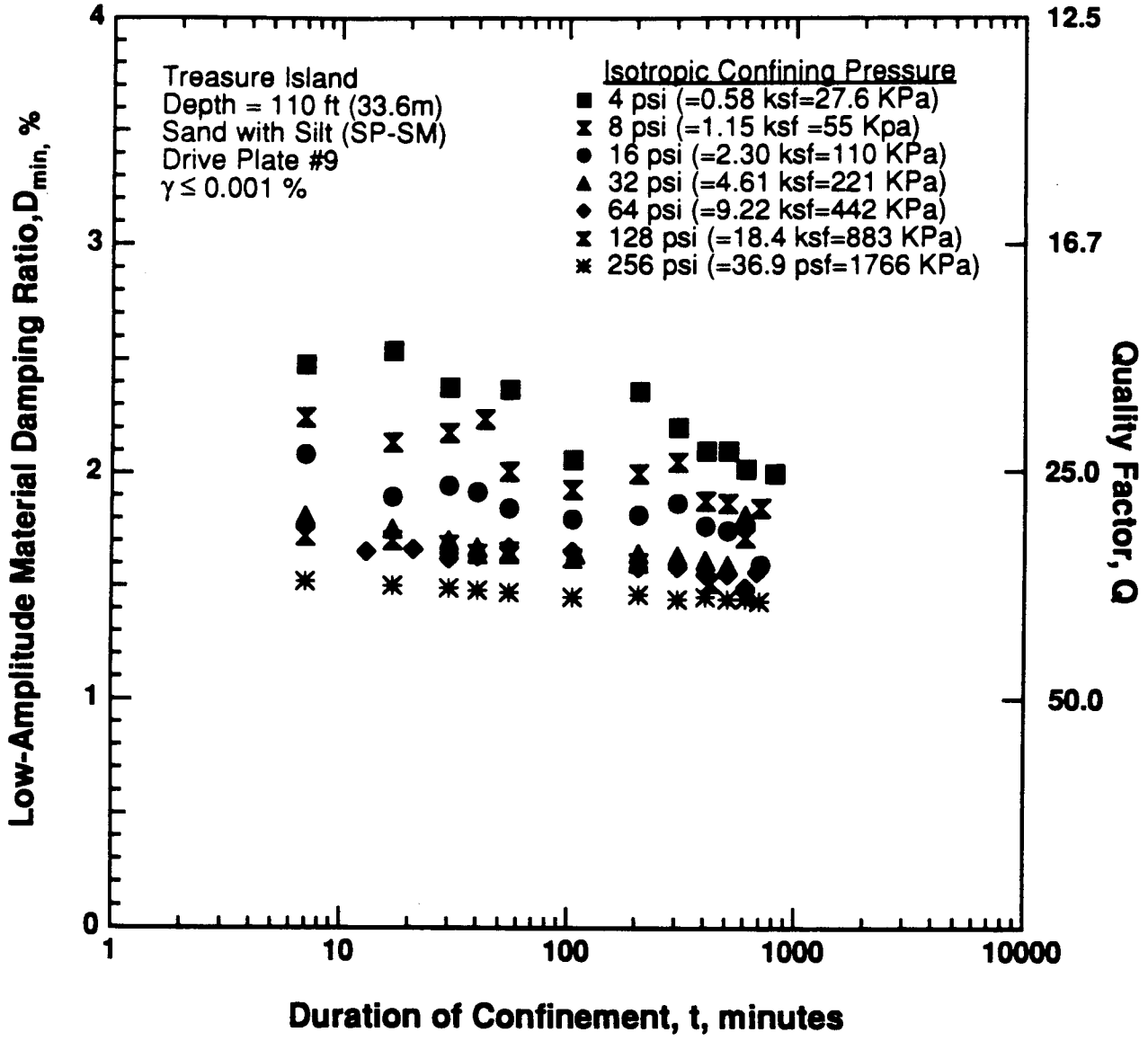

Figure 8.B.4.H-2
Variation in low-amplitude material damping ratio with magnitude and duration of isotropic confining pressure from resonant column testing of sample T5.

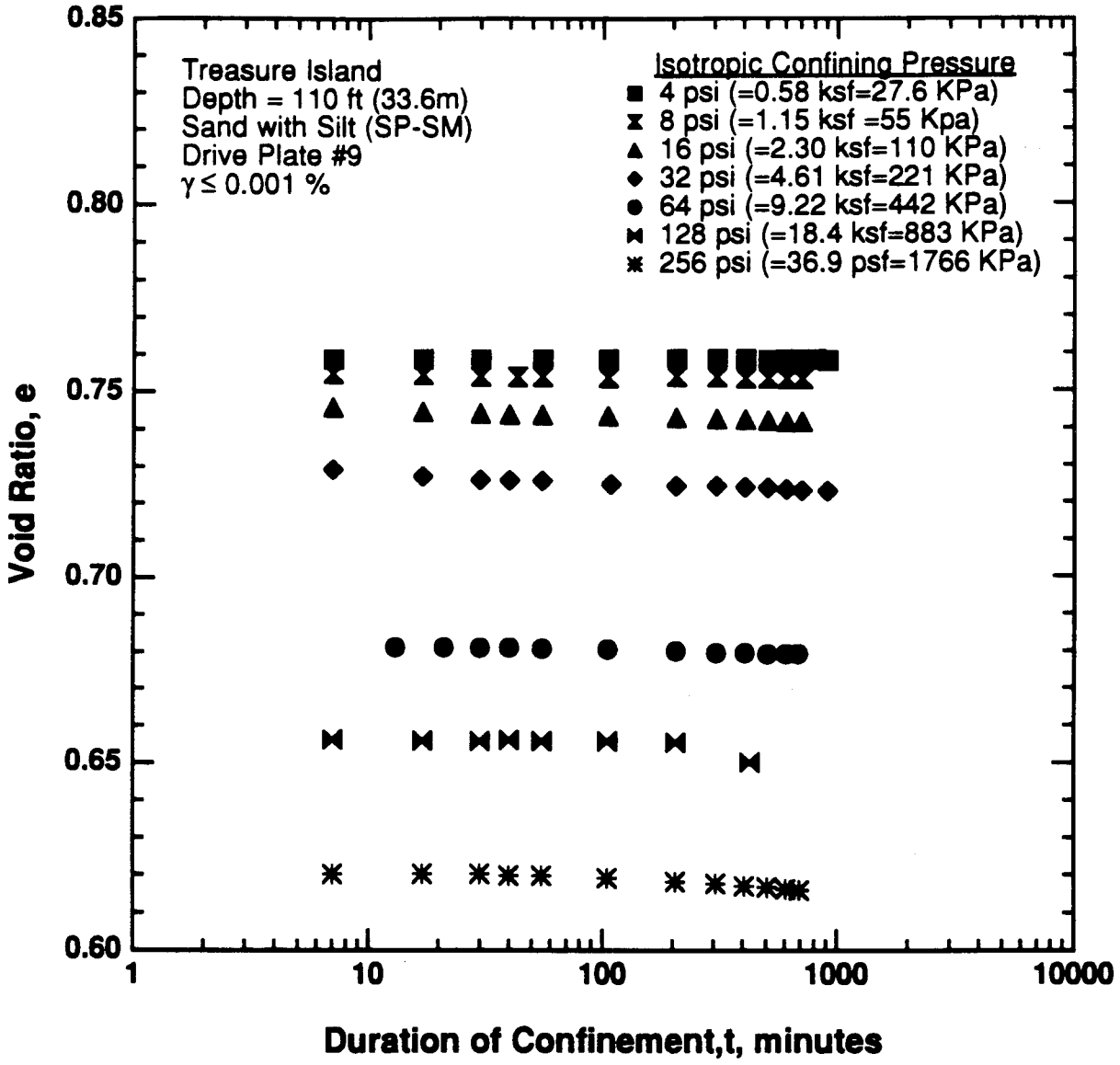

Figure 8.B.4.H-3
Variation in void ratio with magnitude and duration of isotropic confining pressure from resonant column testing of sample T5.

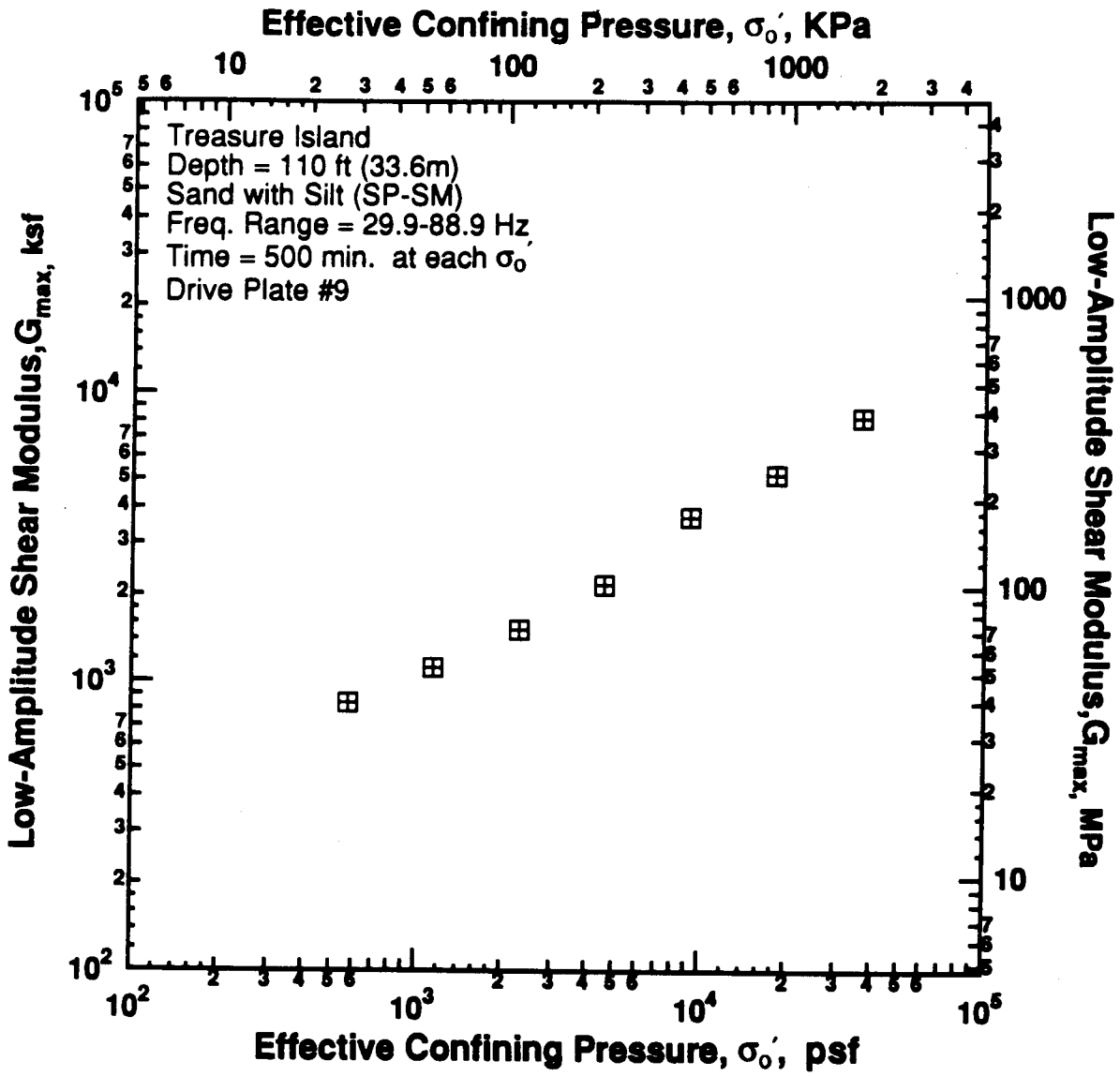

Figure 8.B.4.H-4
Variation in low-amplitude shear modulus with effective confining pressure from resonant column testing of sample T5.

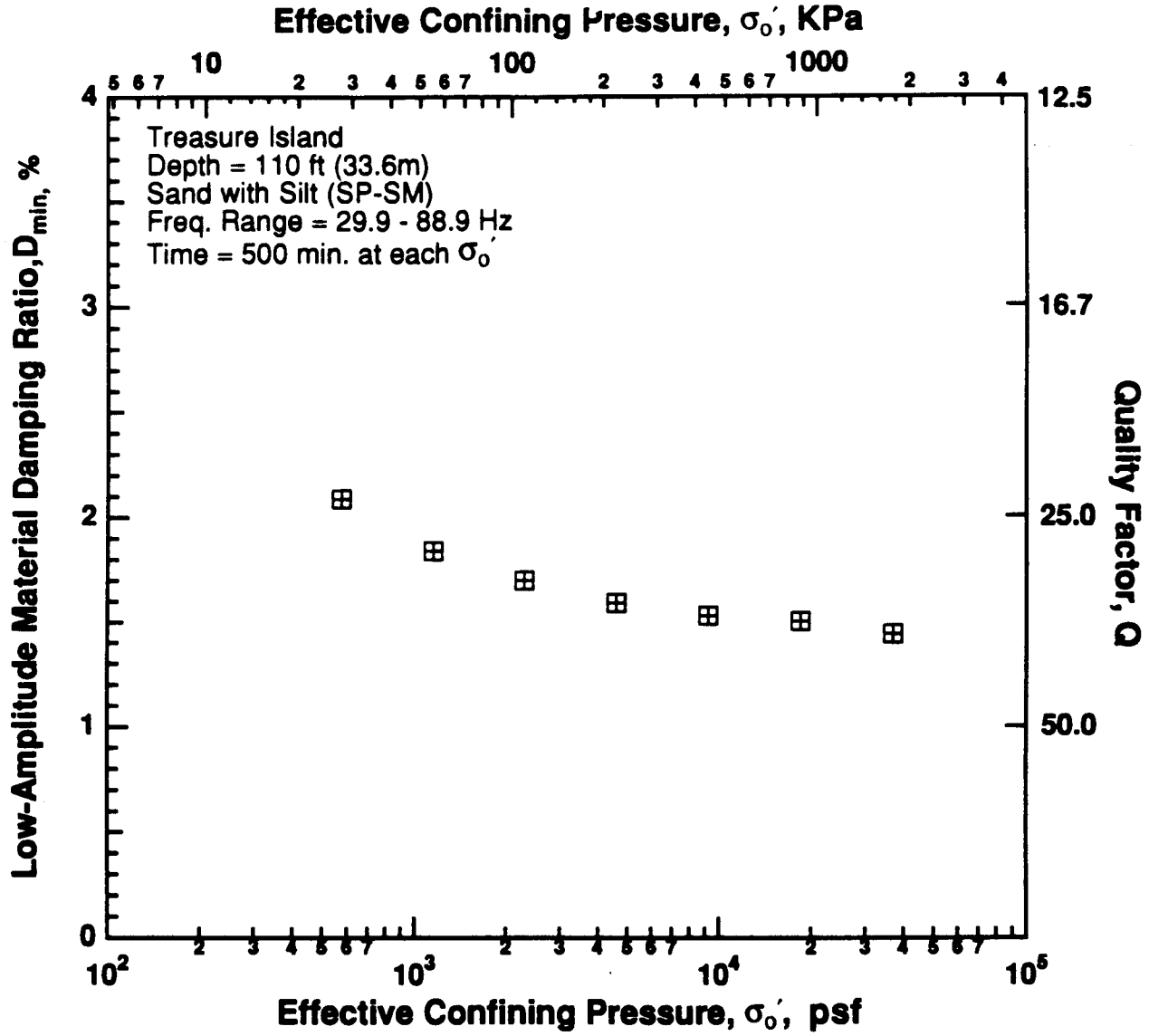

Figure 8.B.4.H-5
Variation in low-amplitude material damping ratio with effective confining pressure from resonant column testing of sample T5.

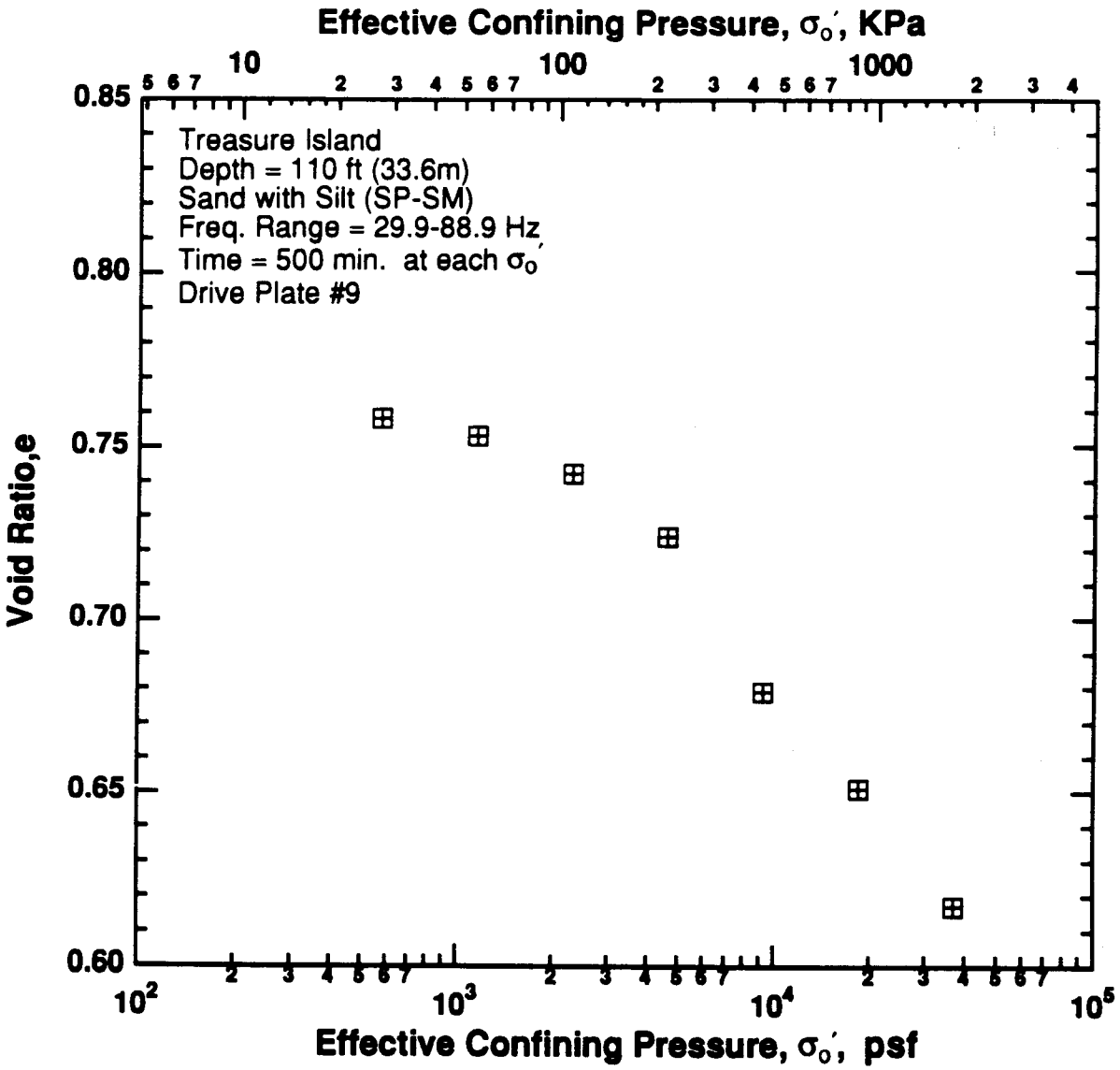

Figure 8.B.4.H-6
Variation in void ratio with effective confining pressure from resonant column testing of sample T5.

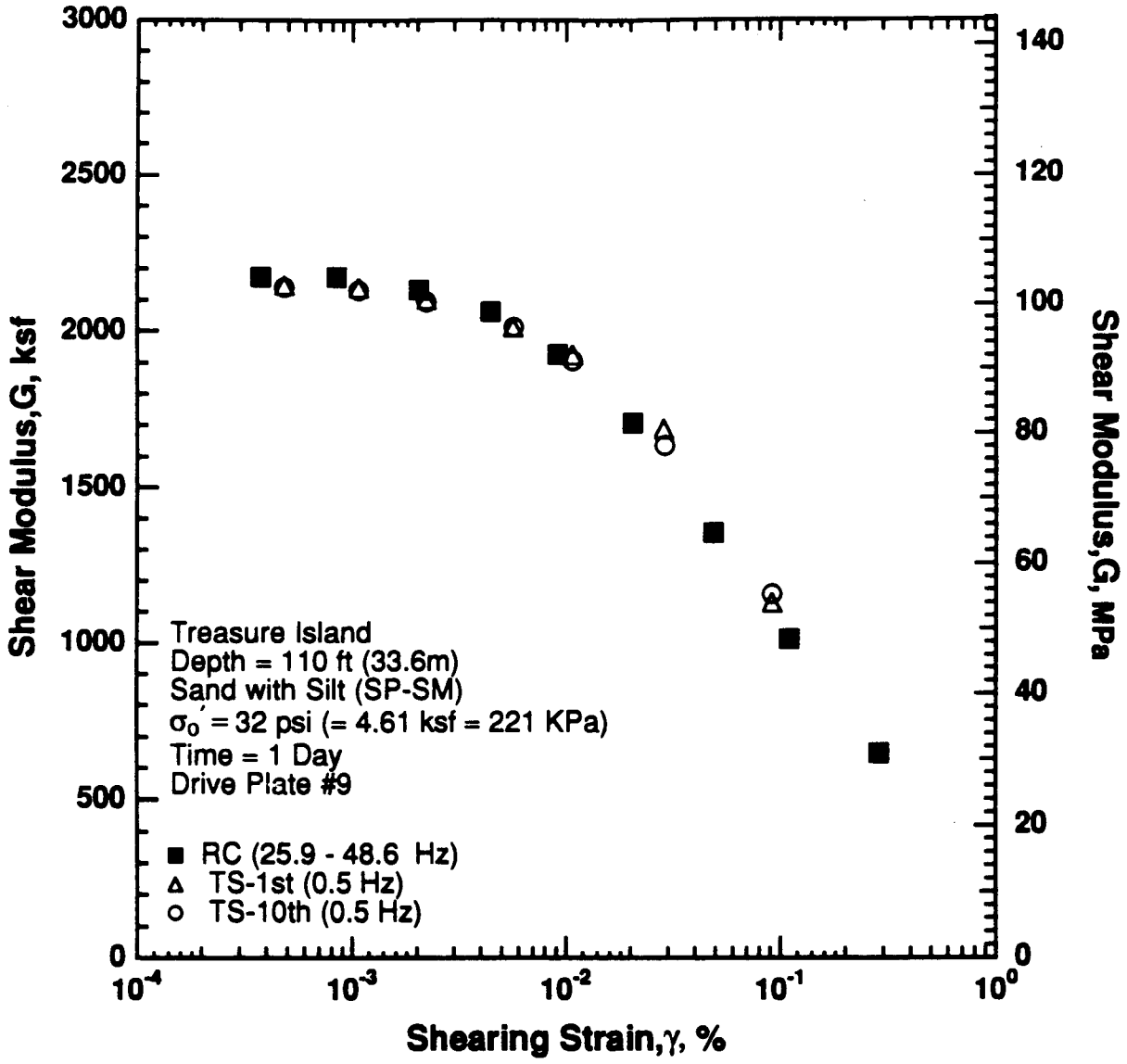

Figure 8.B.4.H-7
Variation in shear modulus with shearing strain at an effective confining pressure of 32 psi (4.61 ksf, 221 kPa) from RCTS testing of sample T5.

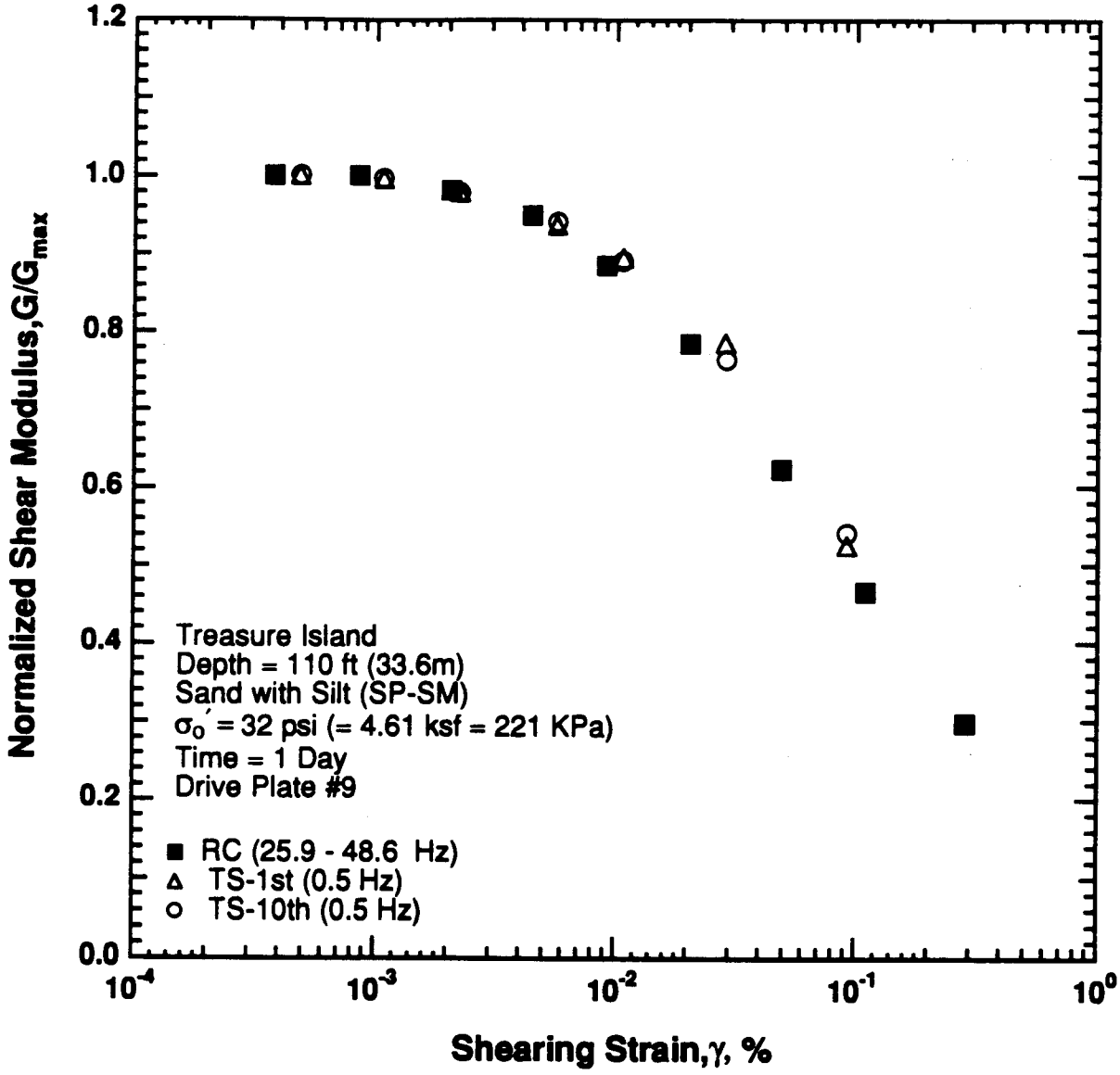

Figure 8.B.4.H-8
Variation in normalized shear modulus with shearing strain at an effective confining pressure of 32 psi (4.61 ksf, 221 kPa) from RCTS testing of sample T5.

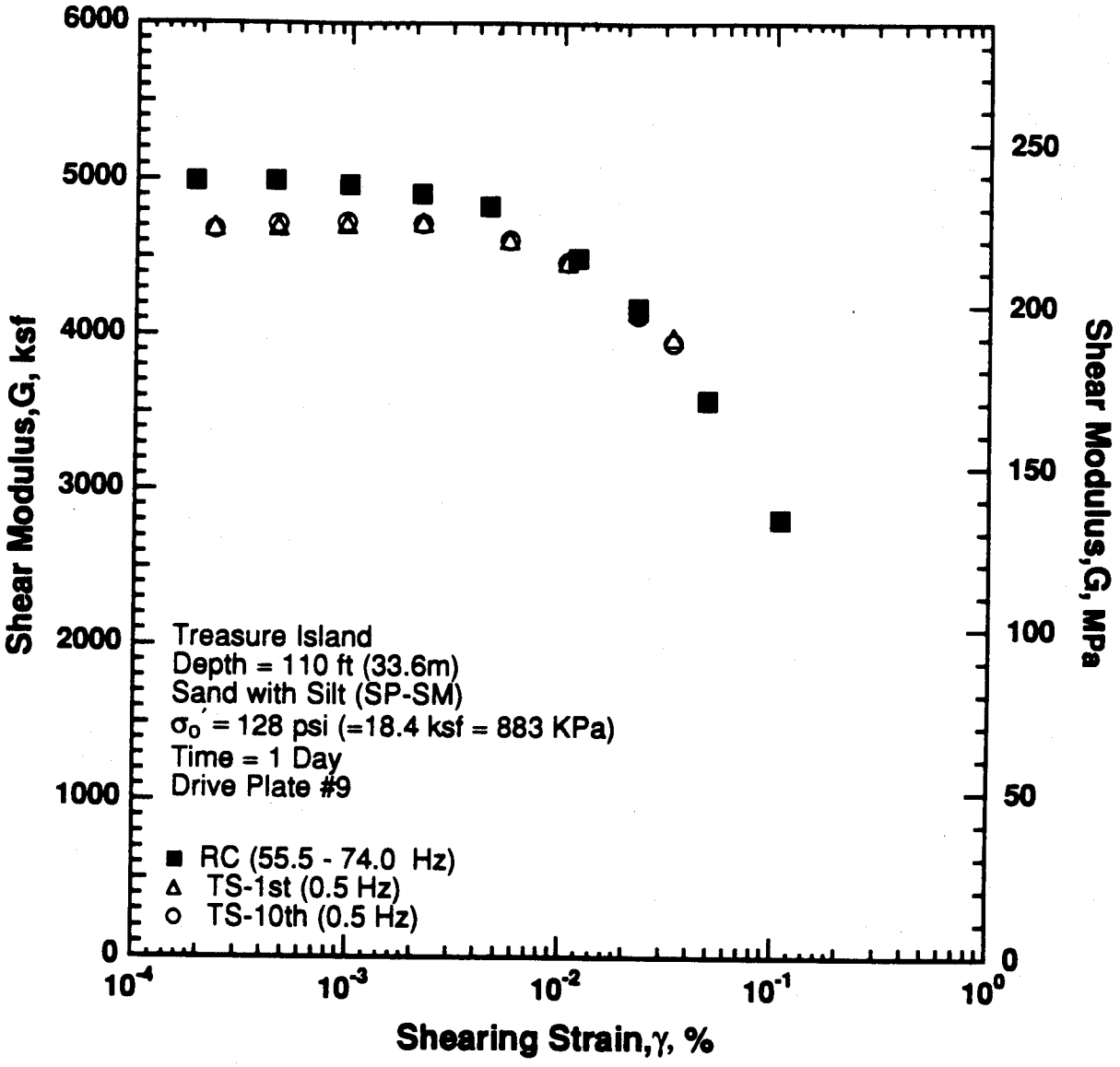

Figure 8.B.4.H-9
Variation in shear modulus with shearing strain at an effective confining pressure of 128 psi (18.4 ksf, 883 kPa) from RCTS testing of sample T5.

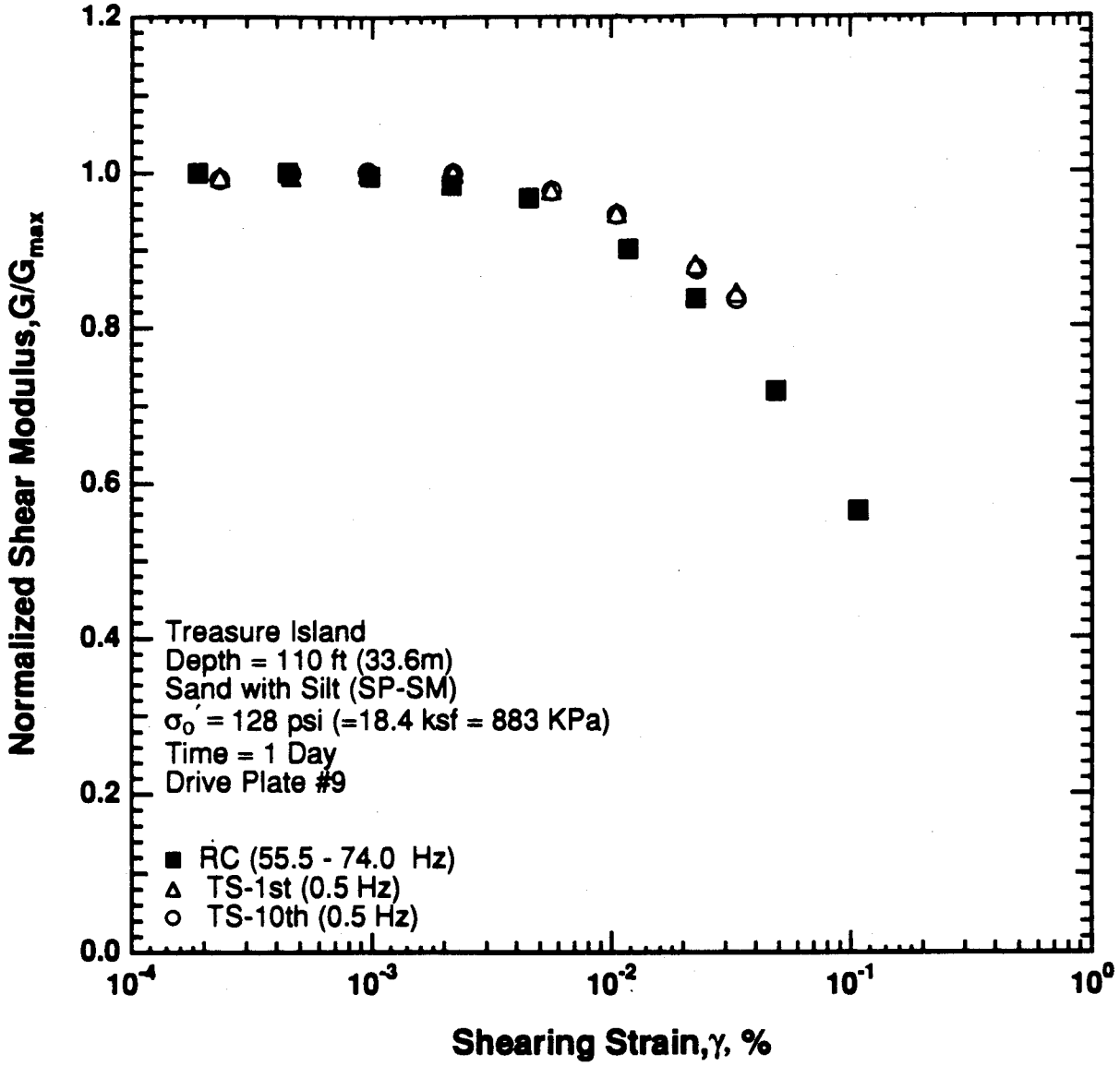

Figure 8.B.4.H-10
Variation in normalized shear modulus with shearing strain at an effective confining pressure of 128 psi (18.4 ksf, 883 kPa) from RCTS testing of sample T5.

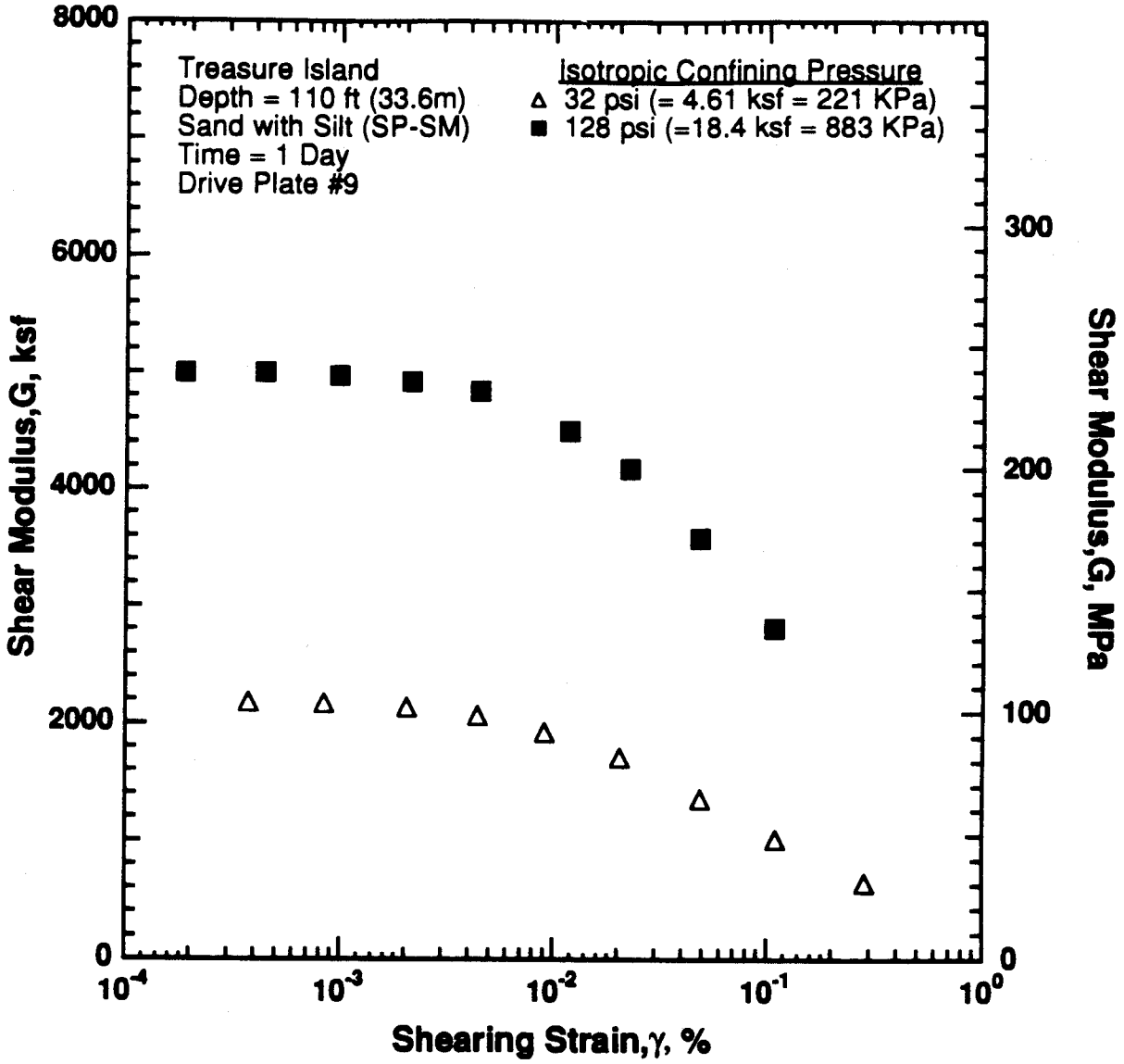

Figure 8.B.4.H-11
Variation in shear modulus with shearing strain and effective confining pressure from resonant column testing of sample T5.

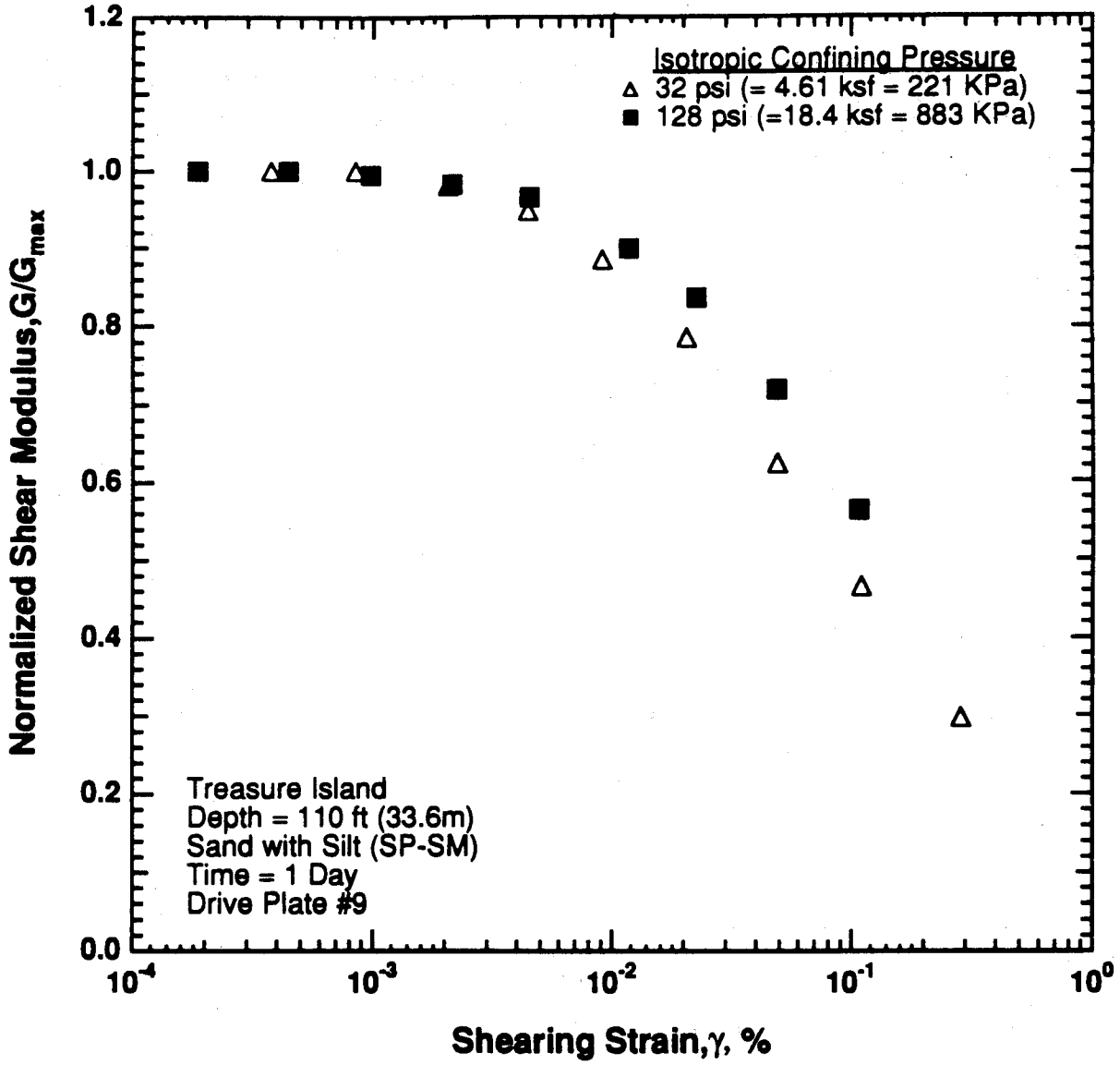

Figure 8.B.4.H-12
Comparison of the variation in normalized shear modulus with shearing strain and effective confining pressure from resonant column tests.

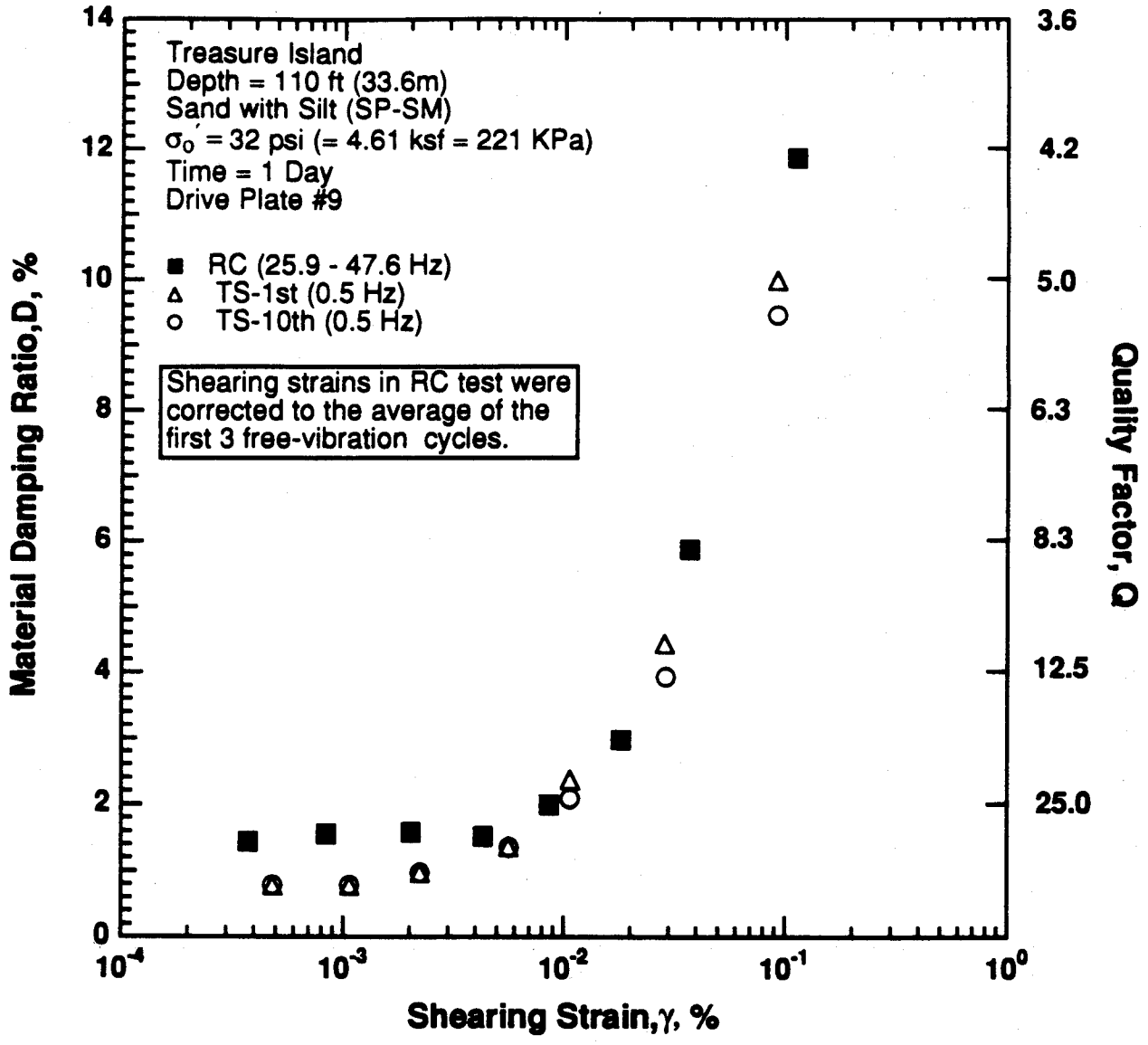

Figure 8.B.4.H-13
Variation in material damping ratio with shearing strain at an effective confining pressure of 32 psi (4.61 ksf, 221 kPa) from RCTS testing of sample T5.

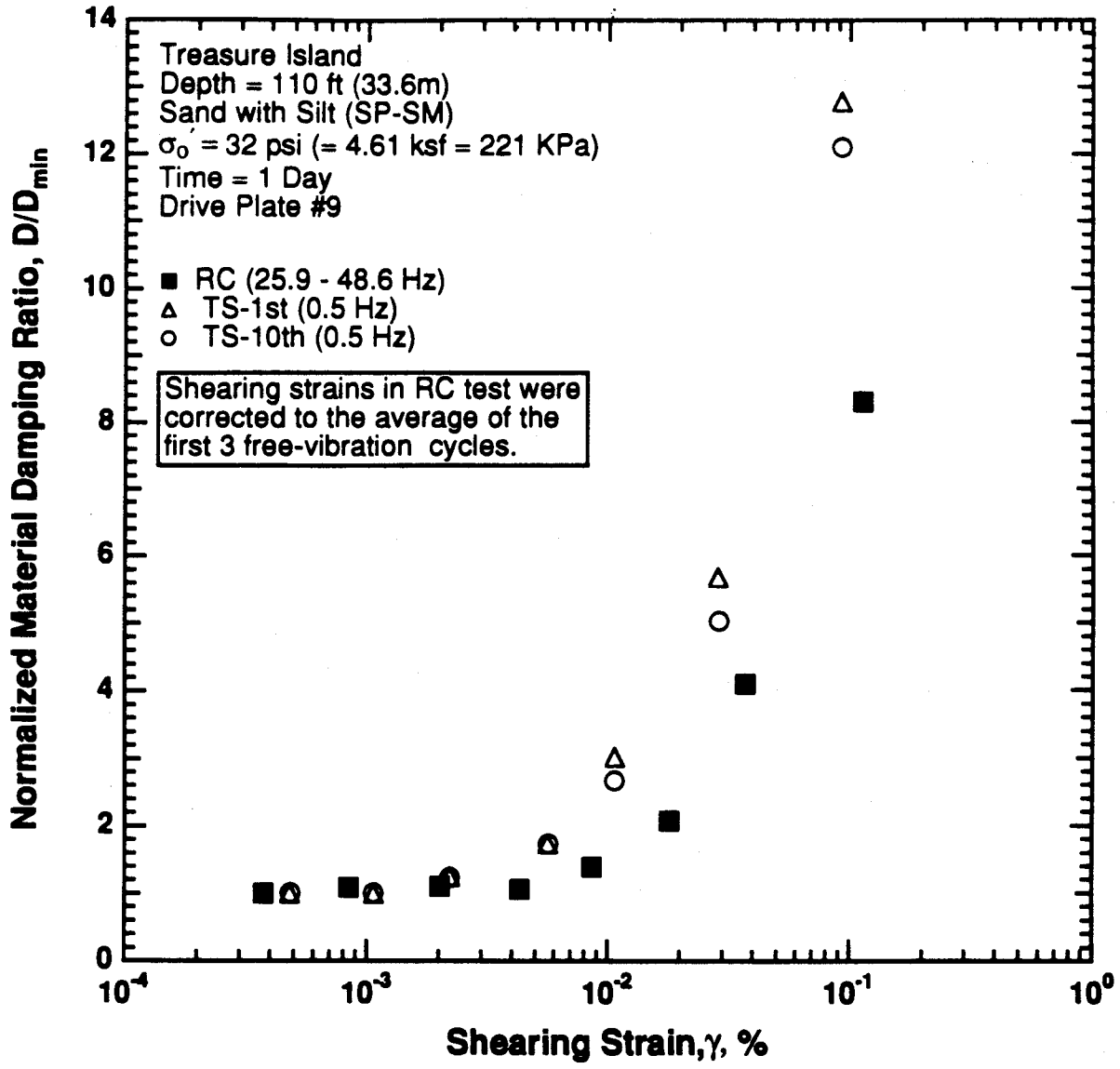

Figure 8.B.4.H-14
Variation in normalized material damping ratio with shearing strain at an effective confining pressure of 32 psi (4.61 ksf, 221 kPa) from RCTS testing of sample T5.

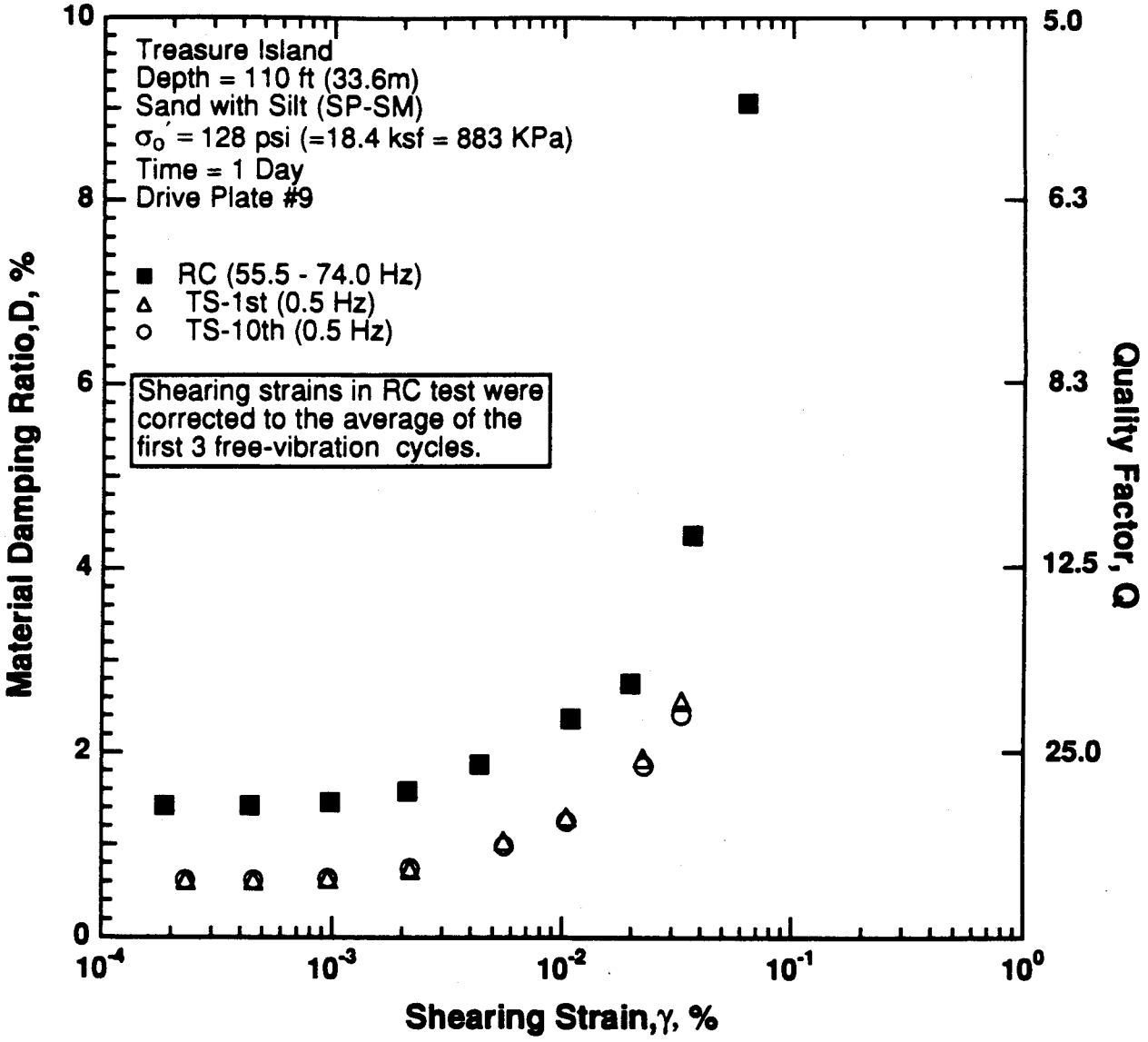

Figure 8.B.4.H-15
Variation in material damping ratio with shearing strain at an effective confining pressure of 128 psi (18.4 ksf, 883 kPa) from RCTS testing of sample T5.

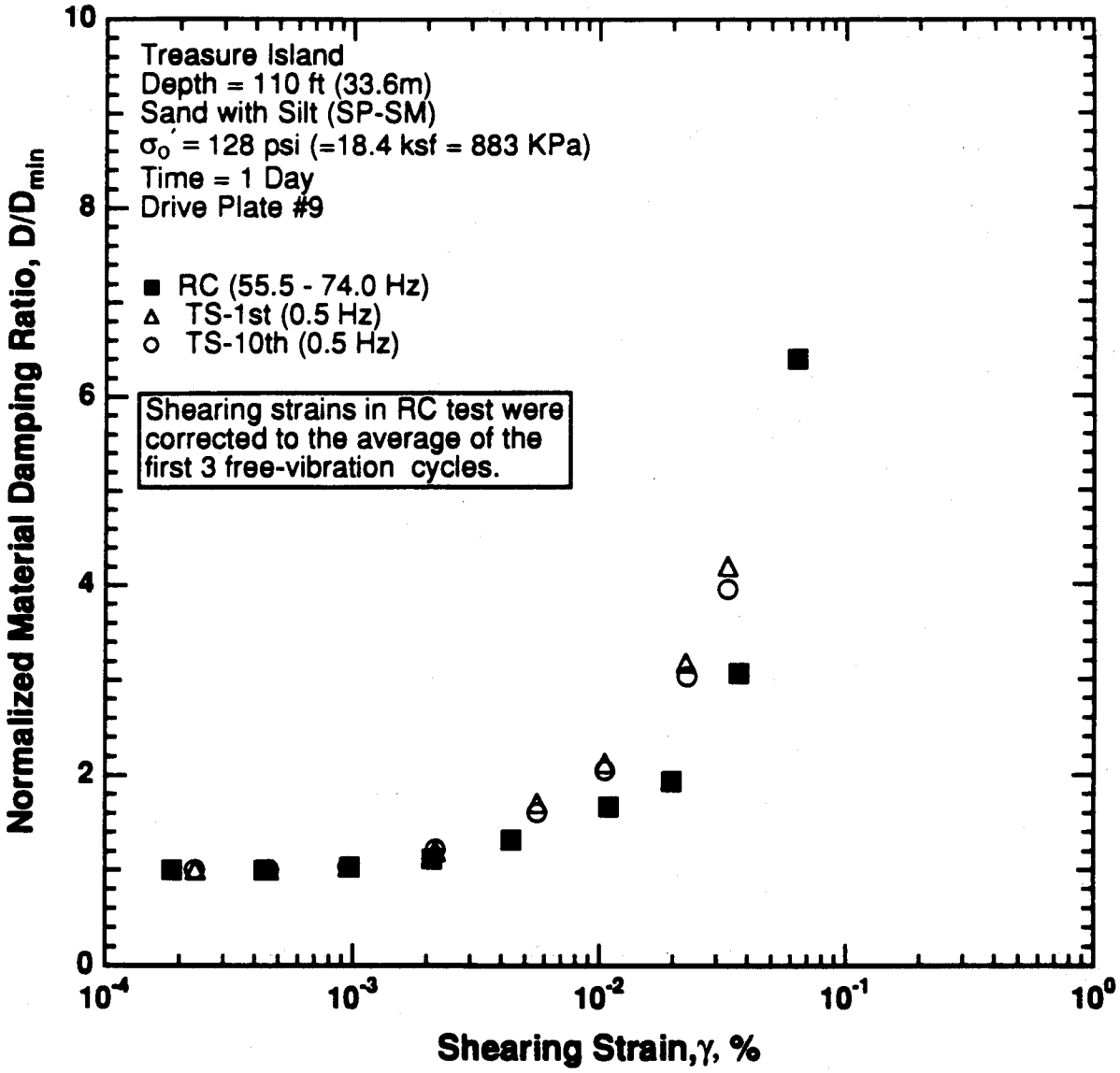

Figure 8.B.4.H-16
Variation in normalized material damping ratio with shearing strain at an effective confining pressure of 128 psi (18.4 ksf, 883 kPa) from RCTS testing of sample T5.

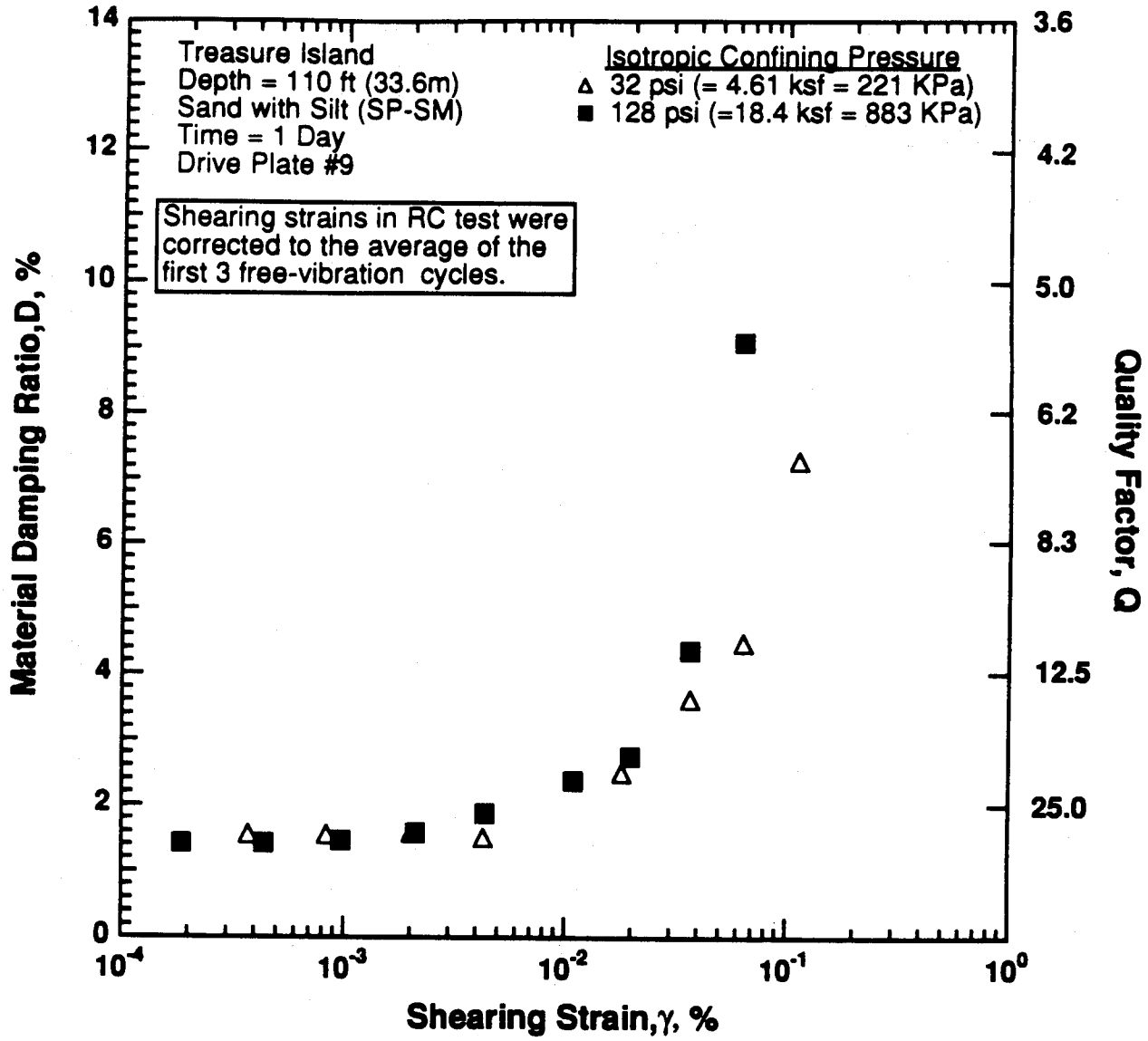

Figure 8.B.4.H-17
Variation in material damping ratio with shearing strain and effective confining pressure from resonant column testing of sample T5.

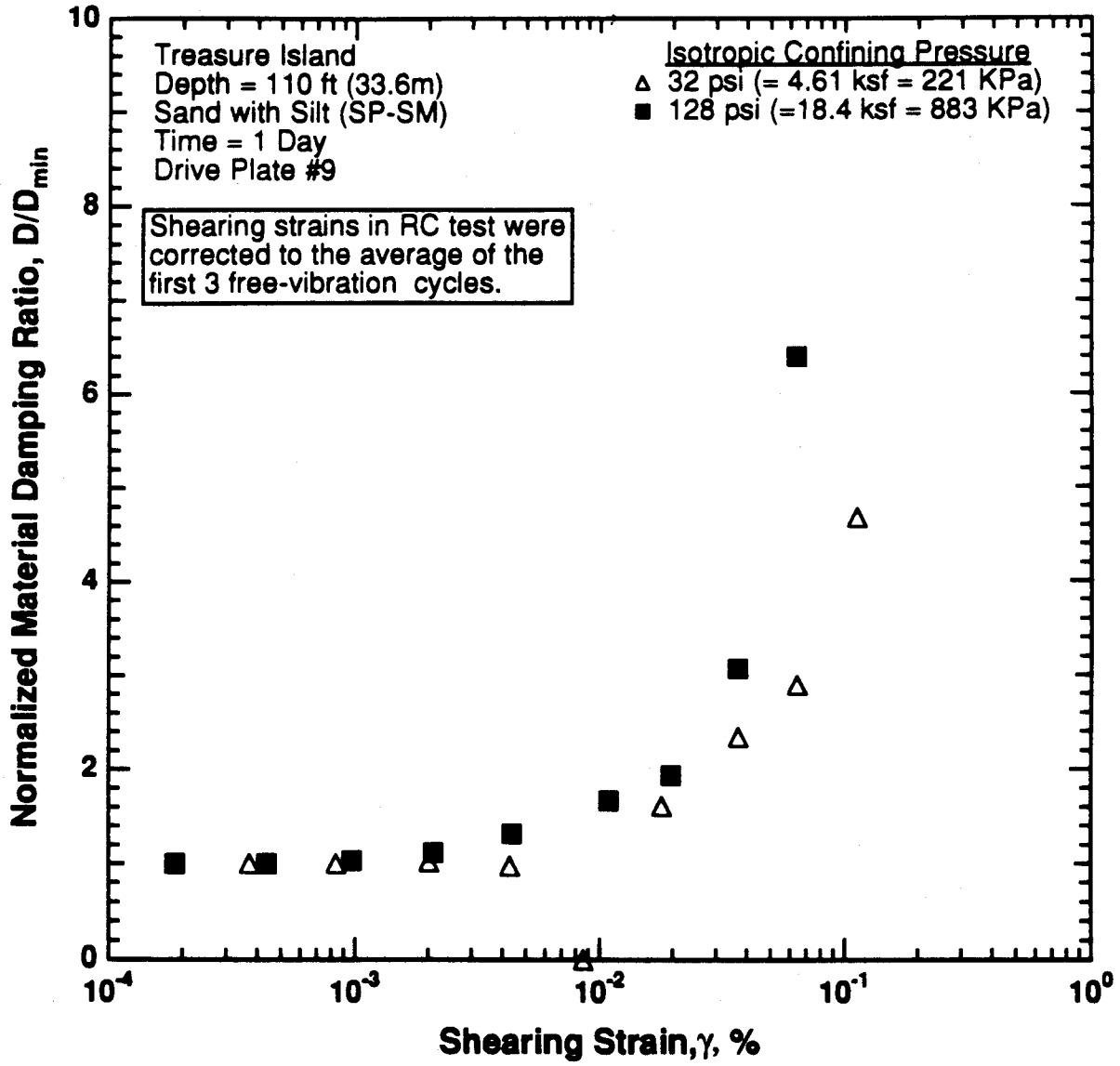

Figure 8.B.4.H-18
Comparison of the variation in normalized material damping ratio with shearing strain and effective confining pressure for resonant column testing of sample T5.

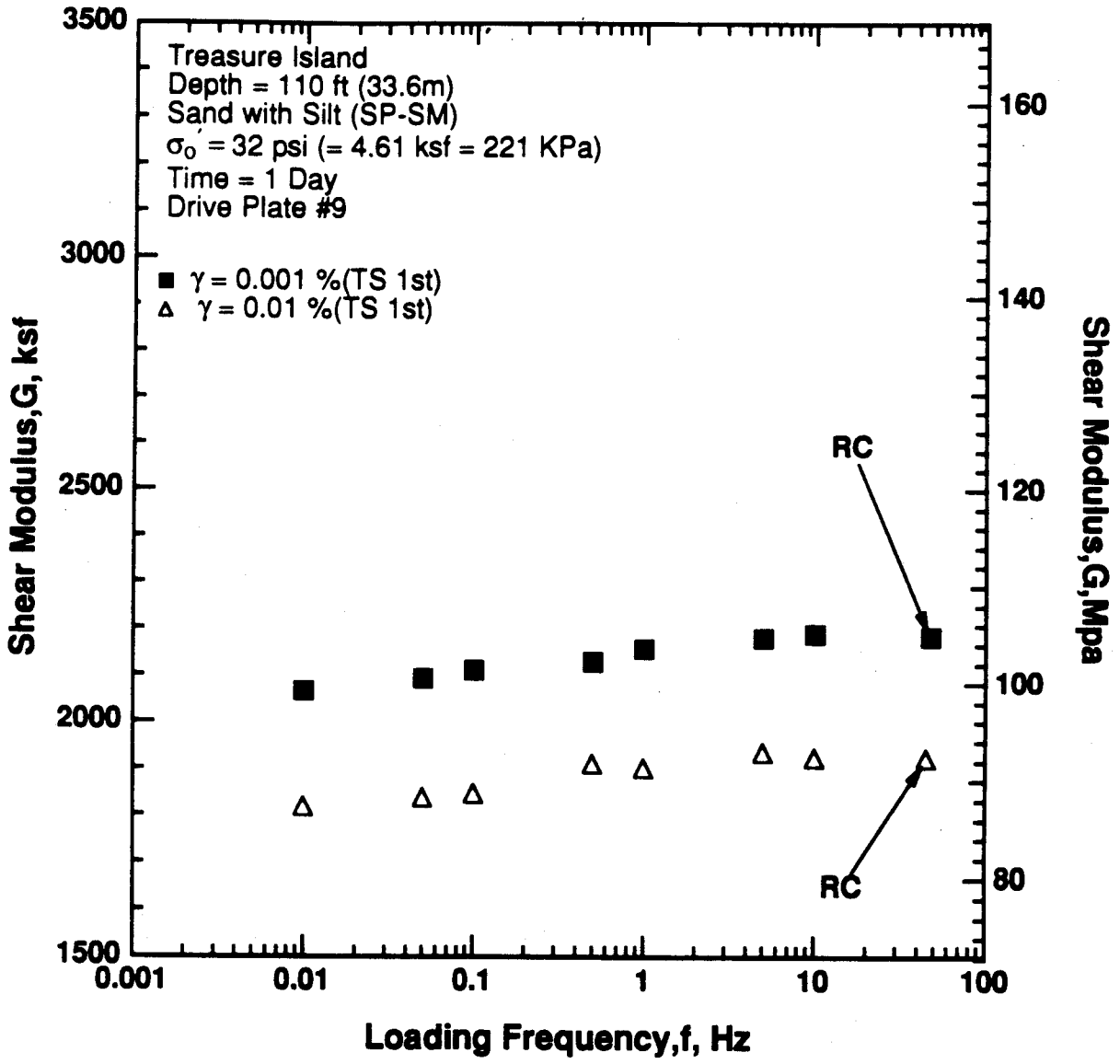

Figure 8.B.4.H-19
Variation in shear modulus with loading frequency and shearing strain at an effective confining pressure of 32 psi (4.61 ksf, 221 kPa) from RCTS testing of sample T5.

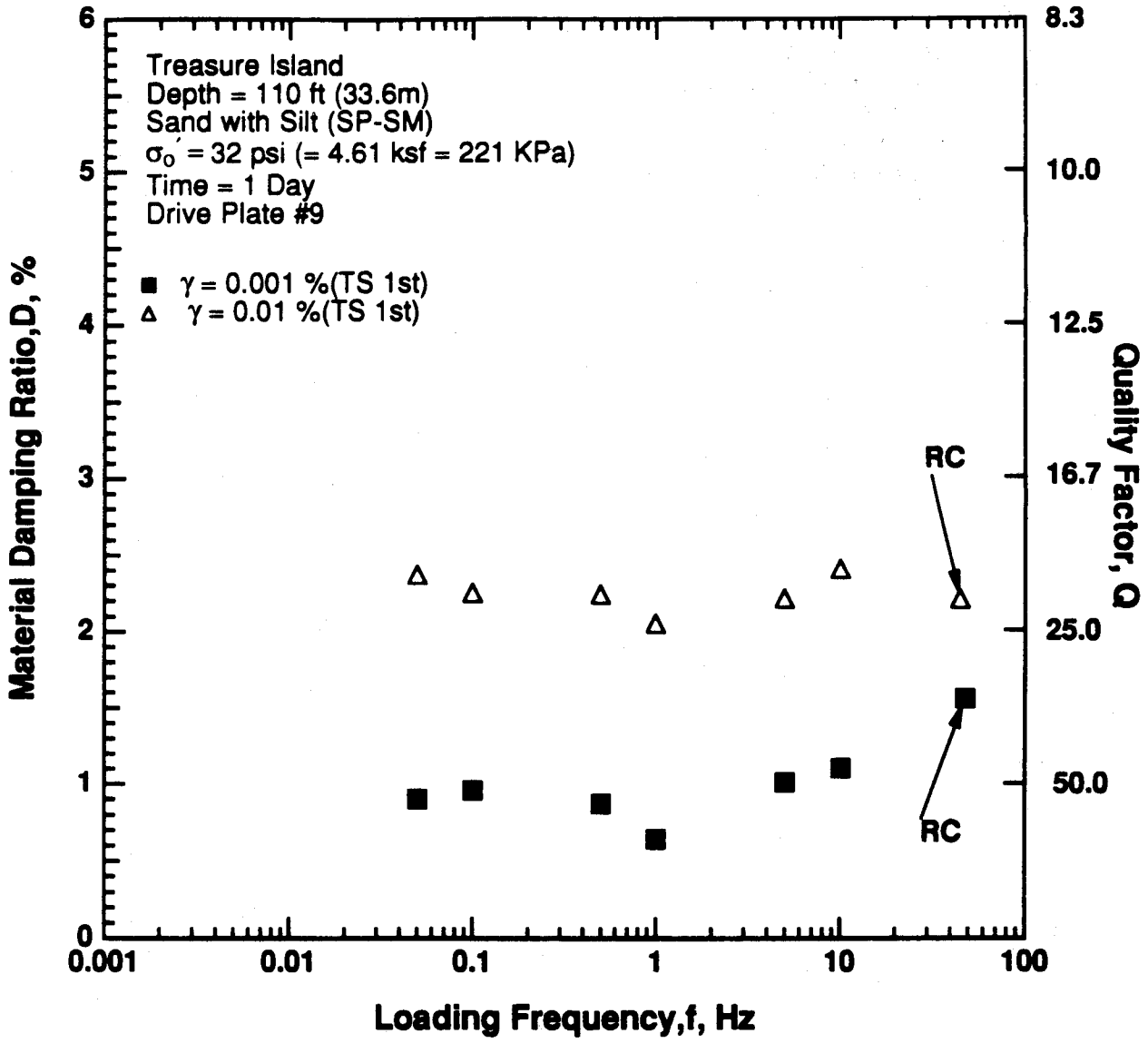

Figure 8.B.4.H-20
Variation in material damping ratio with loading frequency and shearing strain at an effective confining pressure of 32 psi (4.61 ksf, 221 kPa) from RCTS testing of sample T5.

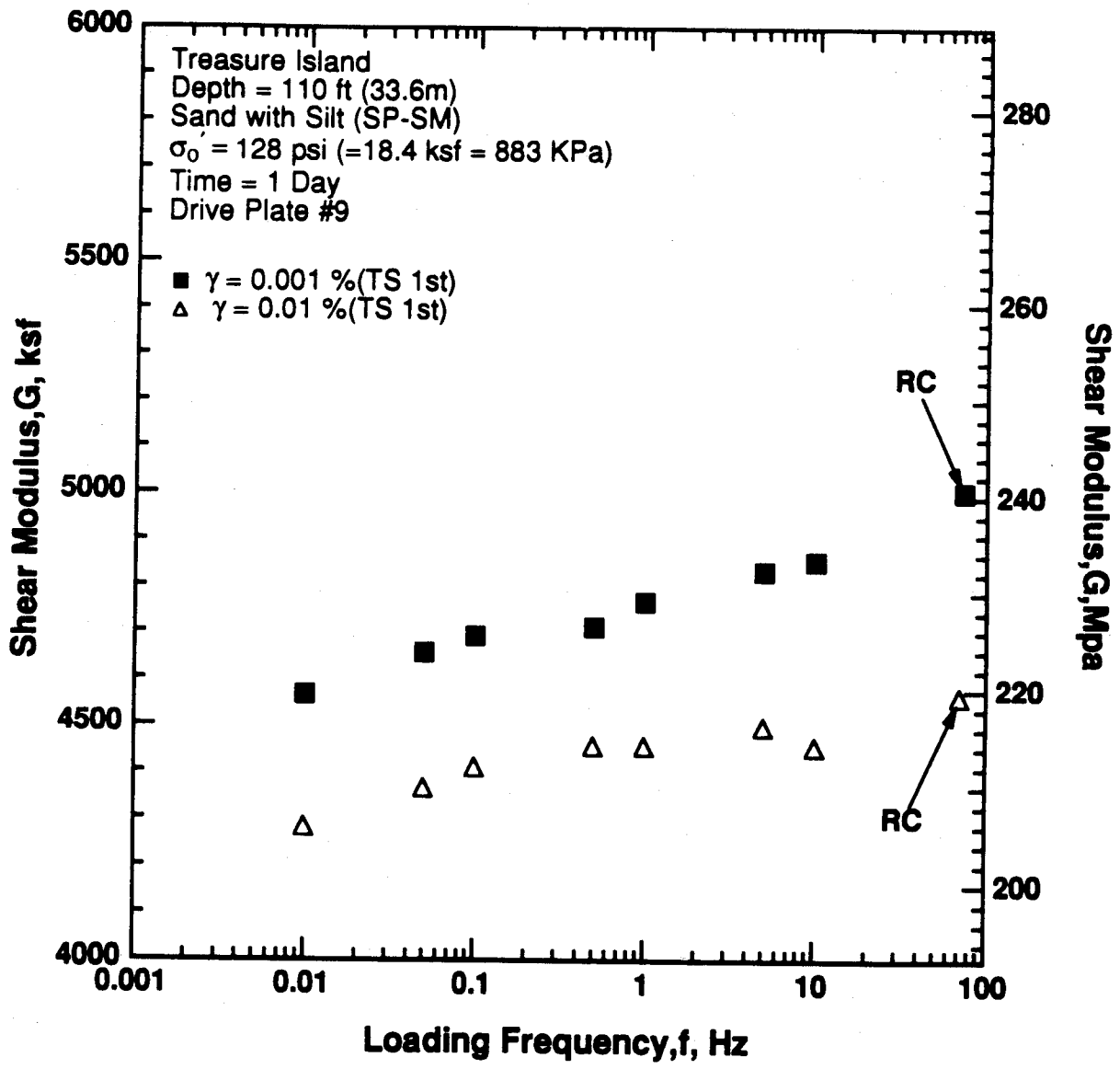

Figure 8.B.4.H-21
Variation in shear modulus with loading frequency and shearing strain at an effective confining pressure of 128 psi (18.4 ksf, 883 kPa) from RCTS testing of sample T5.

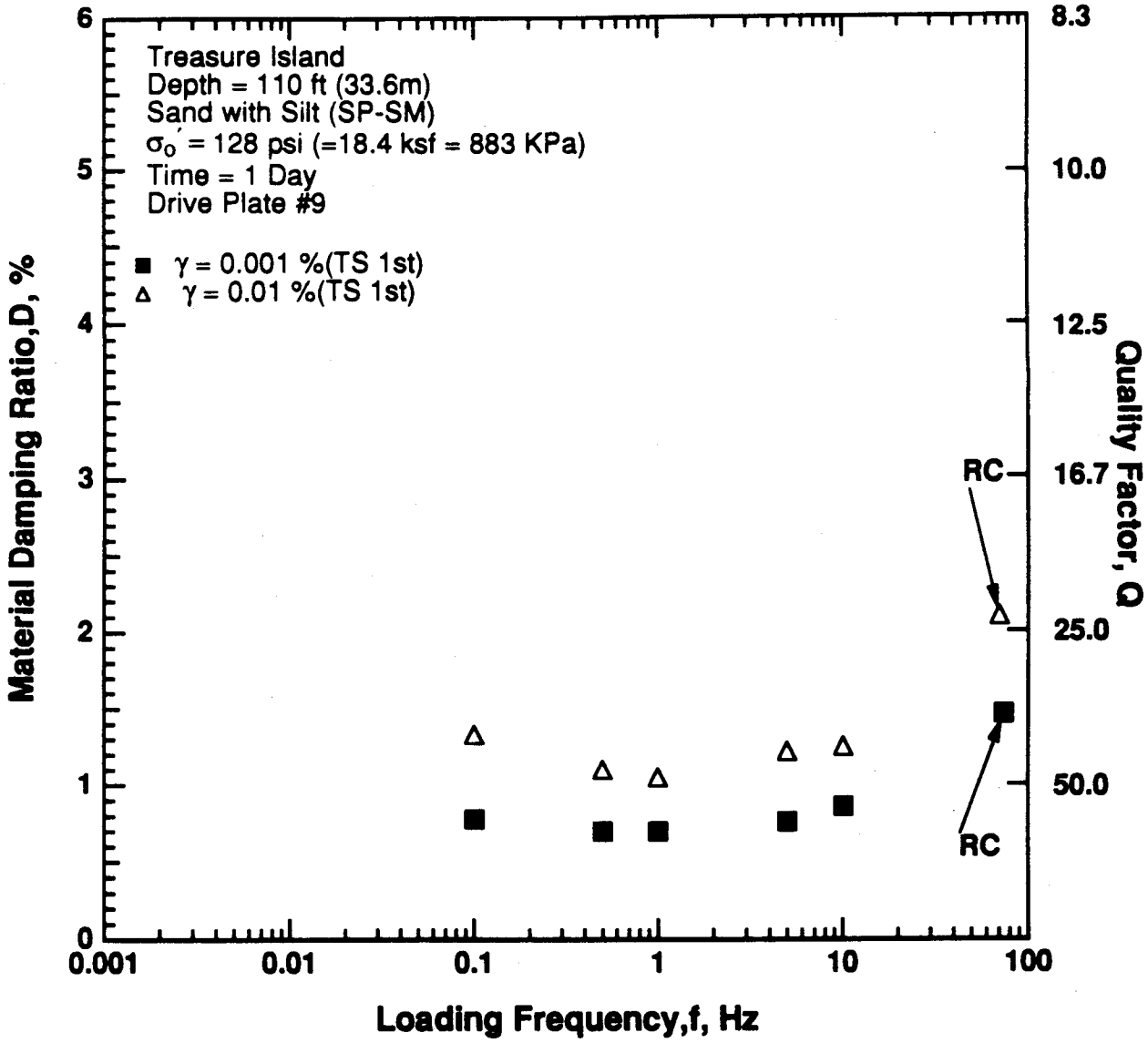

Figure 8.B.4.H-22
Variation in material damping ratio with loading frequency and shearing strain at an effective confining pressure of 128 psi (18.4 ksf, 883 kPa) from RCTS testing of sample T5.

APPENDIX I
DYNAMIC TESTS OF LOTUNG SAMPLE T10 FROM BOREHOLE CH1, DEPTH = 146 FT (44.5 M)

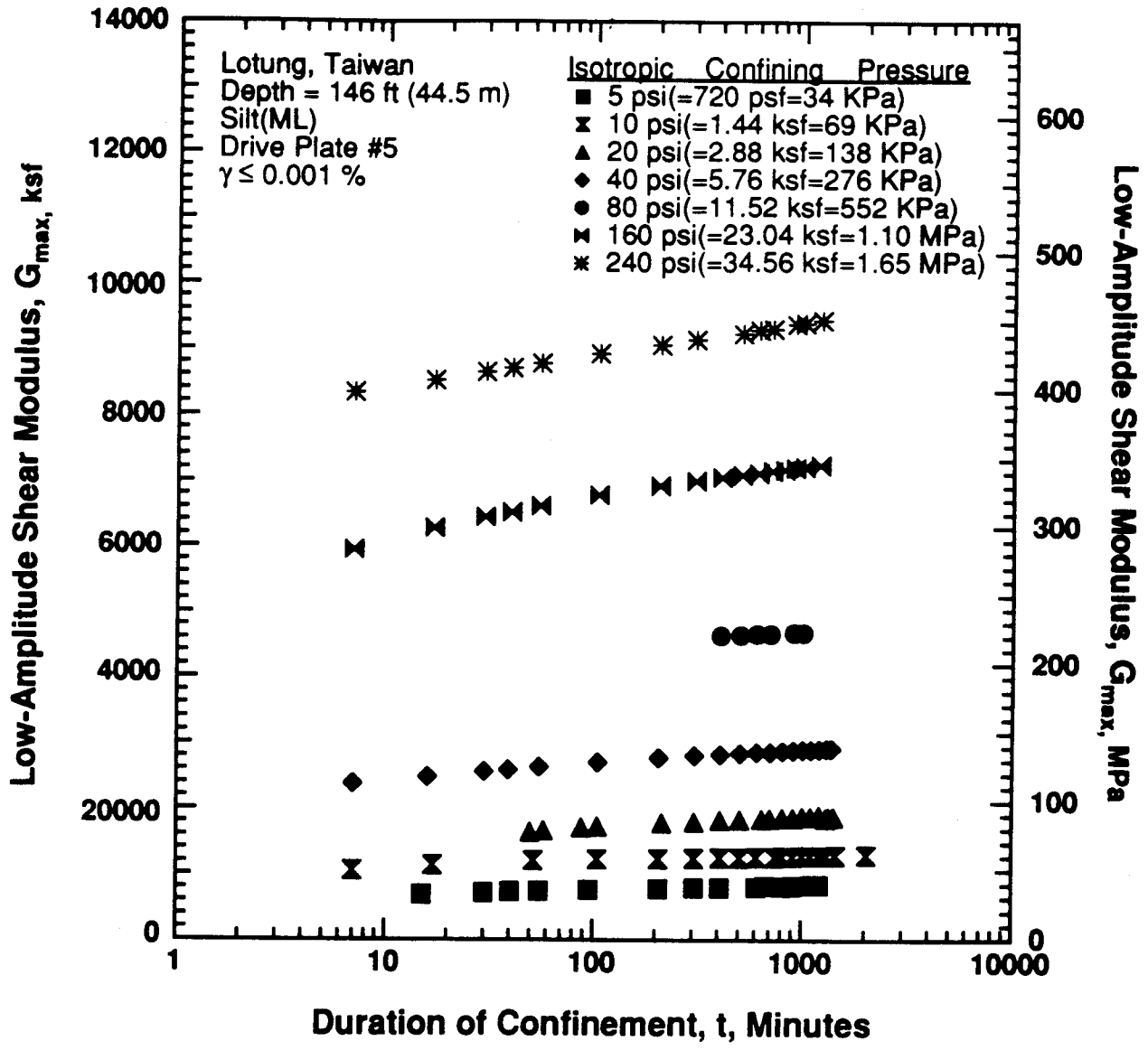

Figure 8.B.4.I-1
Variation in low-amplitude shear modulus with magnitude and duration of isotropic confining pressure from resonant column testing of sample T10 from borehole CH1 for loading pressure sequence.

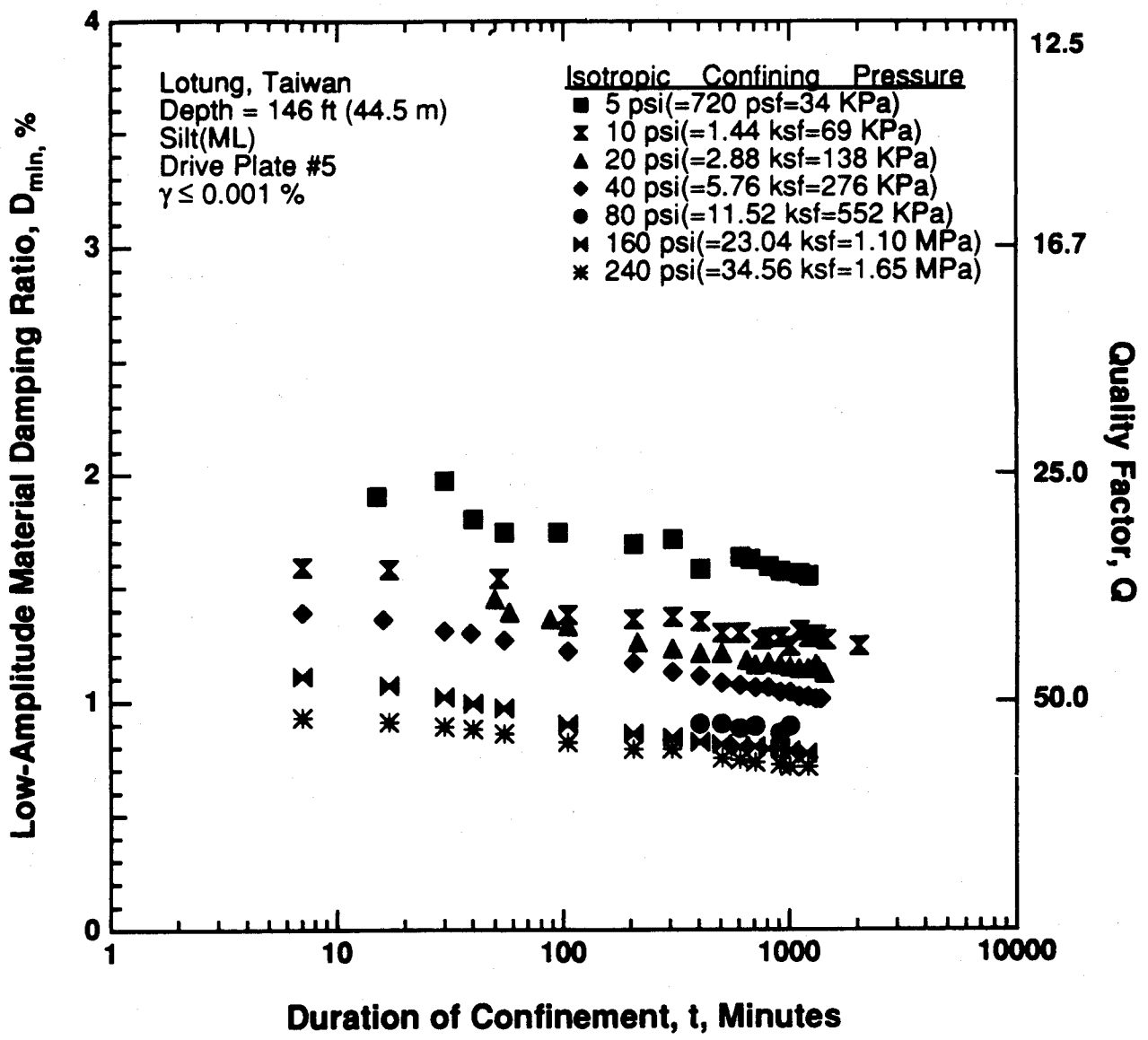

Figure 8.B.4.I-2
Variation in low-amplitude material damping ratio with magnitude and duration of isotropic confining pressure from resonant column testing of sample T10 from borehole CH1 for loading pressure sequence.

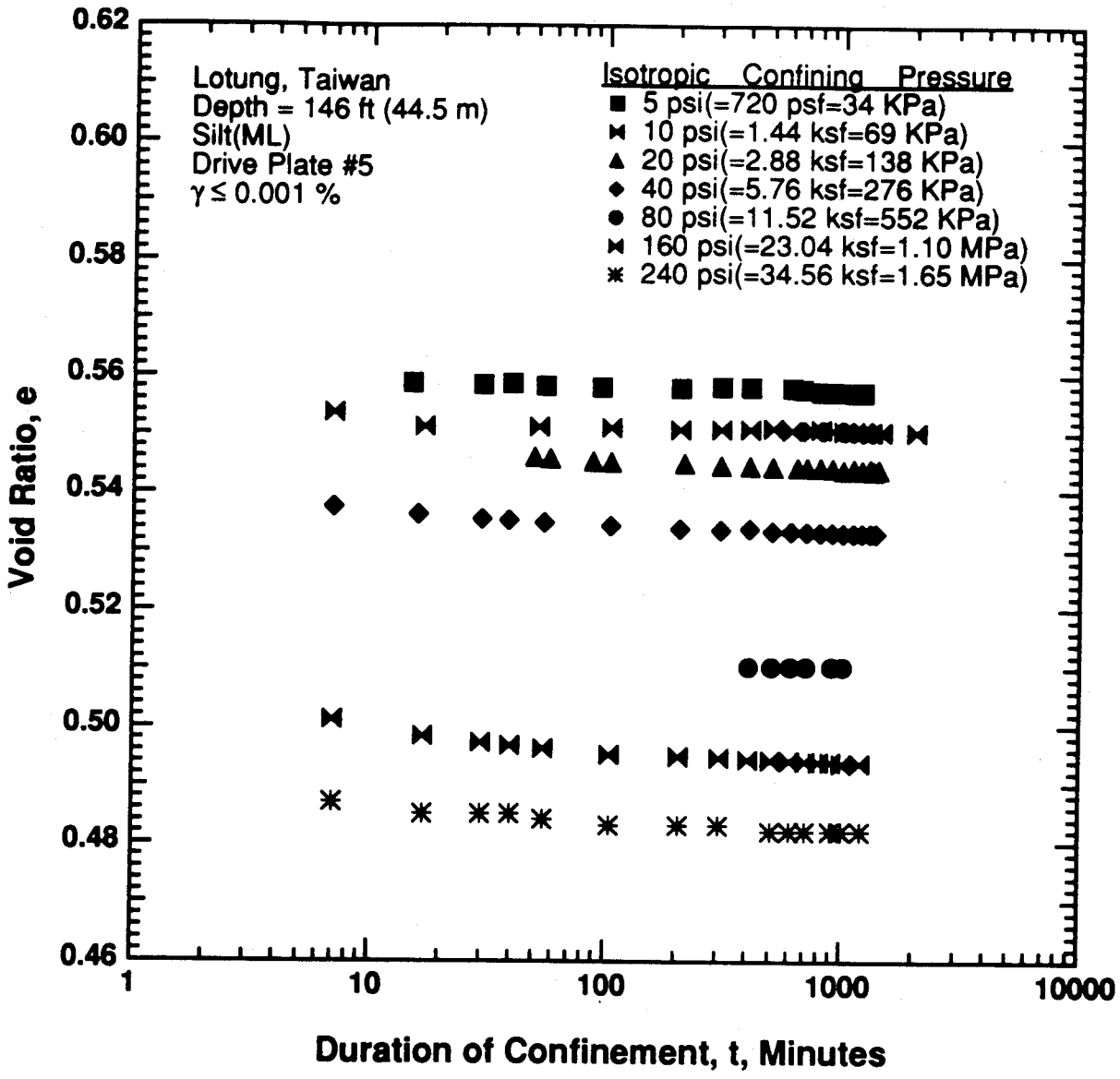

Figure 8.B.4.I-3
Variation in void ratio with magnitude and duration of isotropic confining pressure from resonant column testing of sample T10 from borehole CH1 for loading pressure sequence.

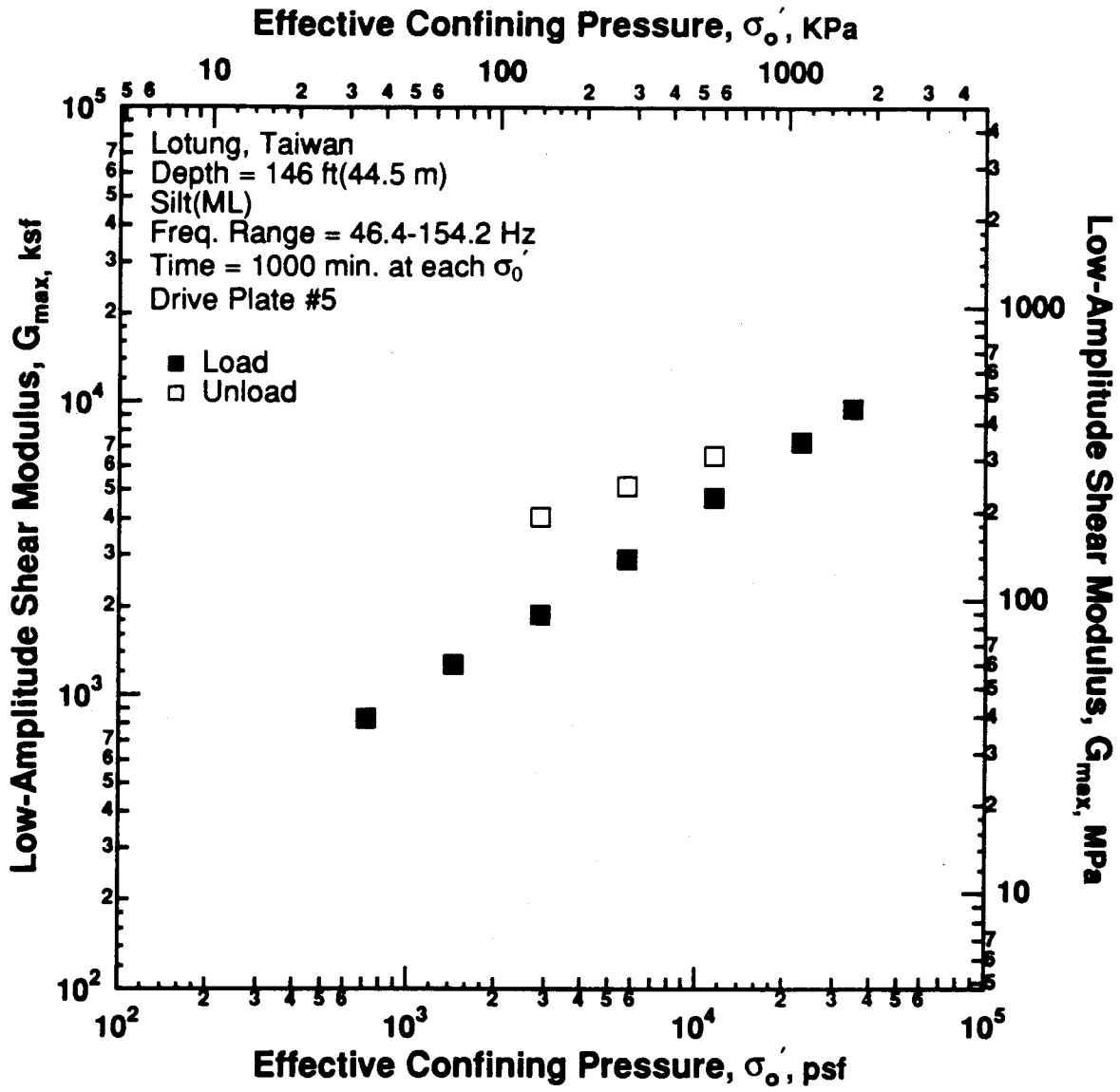

Figure 8.B.4.I-4
Variation in low-amplitude shear modulus with effective confining pressure from resonant column testing of sample T10 from borehole CH1 for loading and unloading pressure sequences.

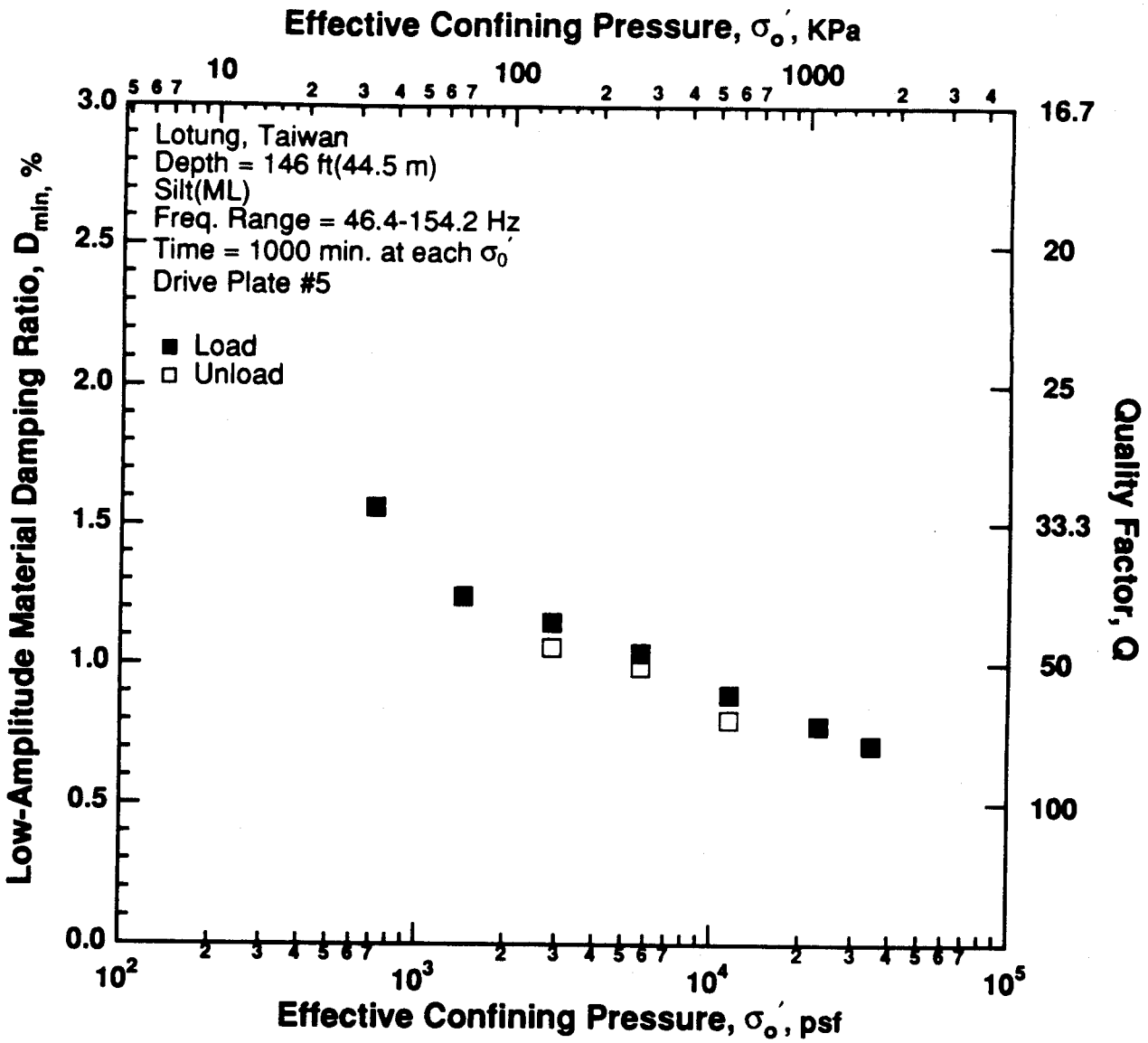

Figure 8.B.4.I-5
Variation in low-amplitude material damping ratio with effective confining pressure from resonant column testing of sample T10 from borehole CH1 for loading and unloading pressure sequences.

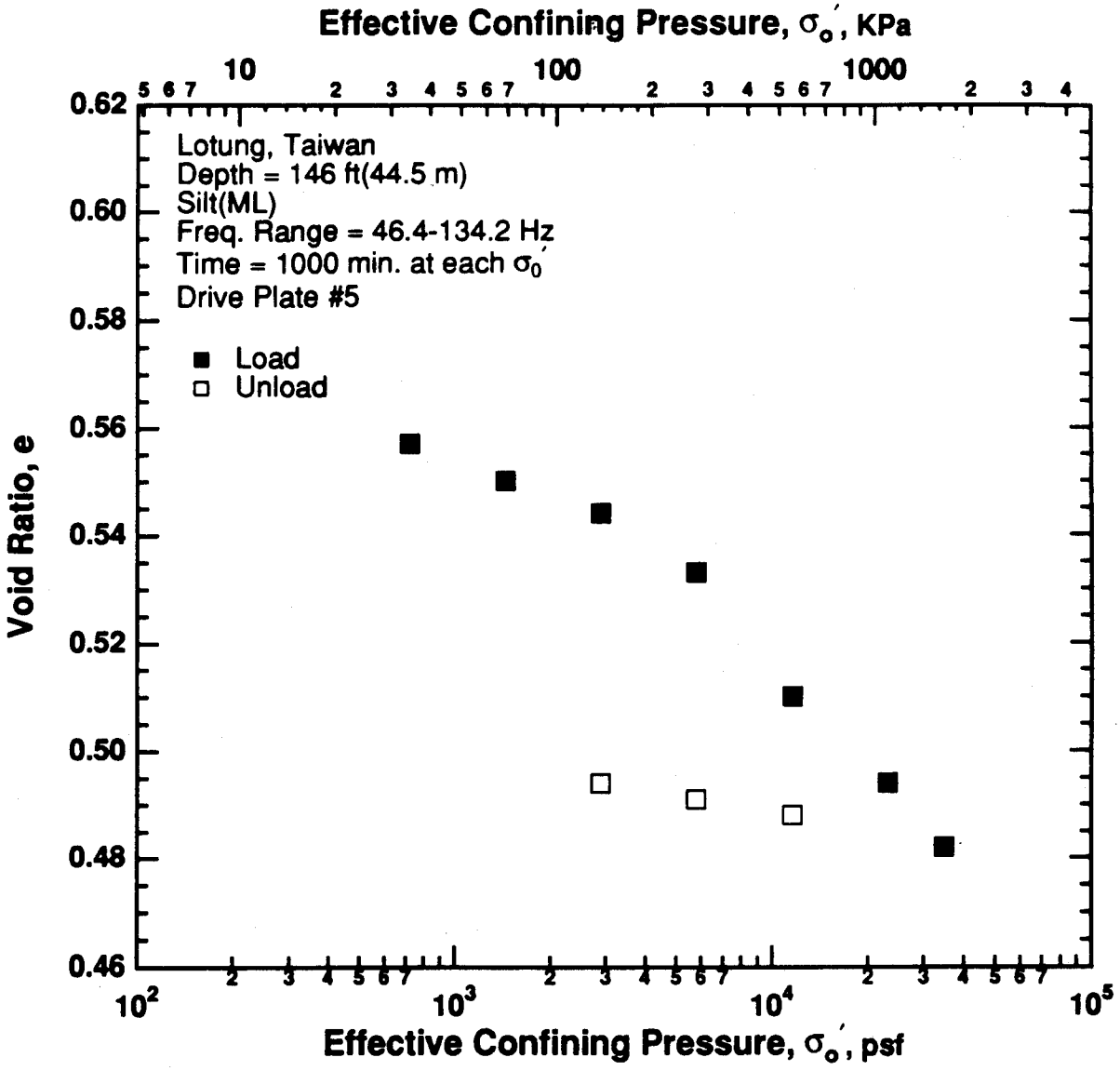

Figure 8.B.4.I-6
Variation in void ratio with effective confining pressure from resonant column testing of sample T10 from borehole CH1 for loading and unloading pressure sequences.

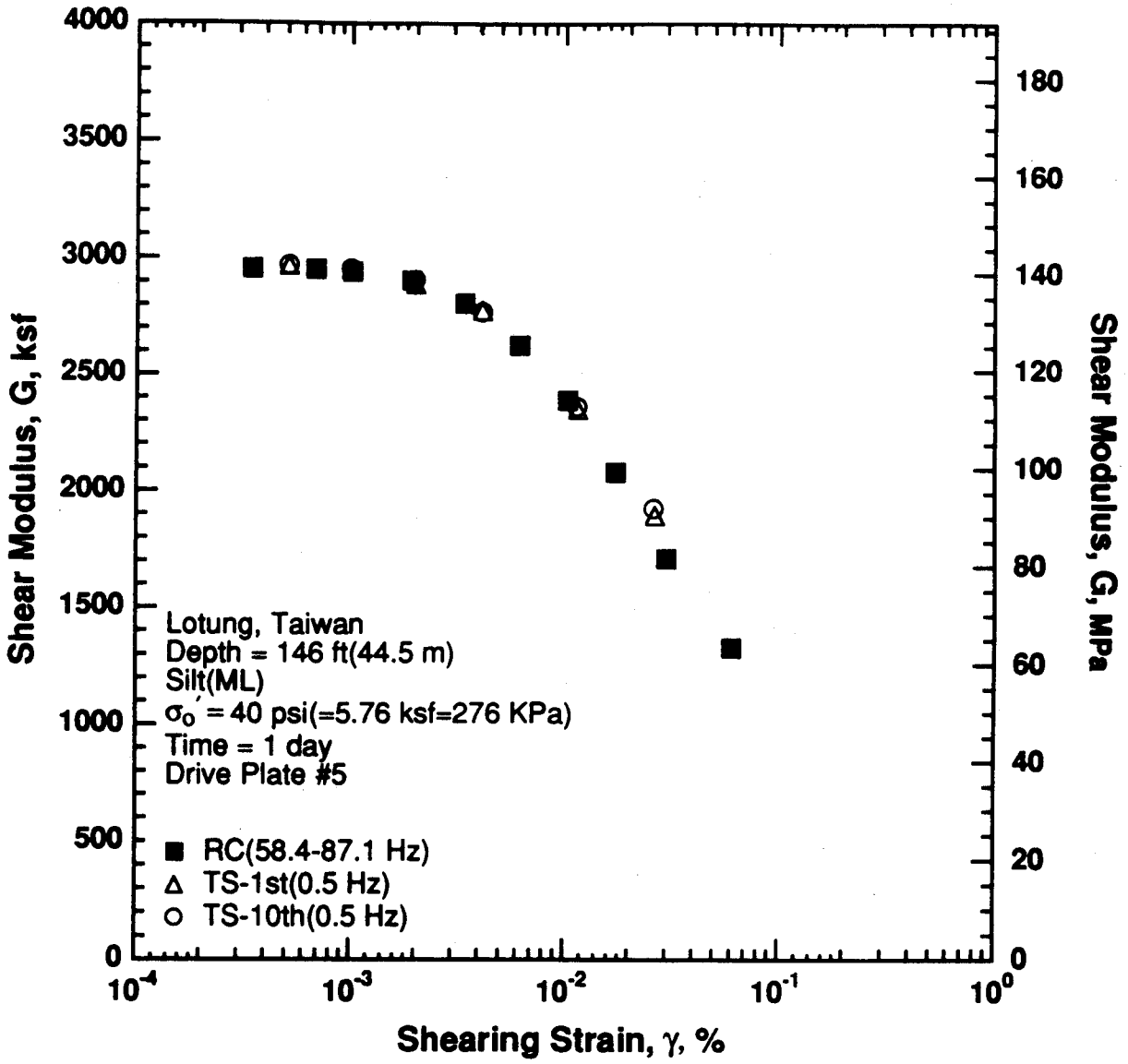

Figure 8.B.4.I-7
Variation in shear modulus with shearing strain at an effective confining pressure of 40 psi (5.76 ksf, 276 kPa) from RCTS tests of sample T10 from borehole CH1; determined on the loading pressure sequence.

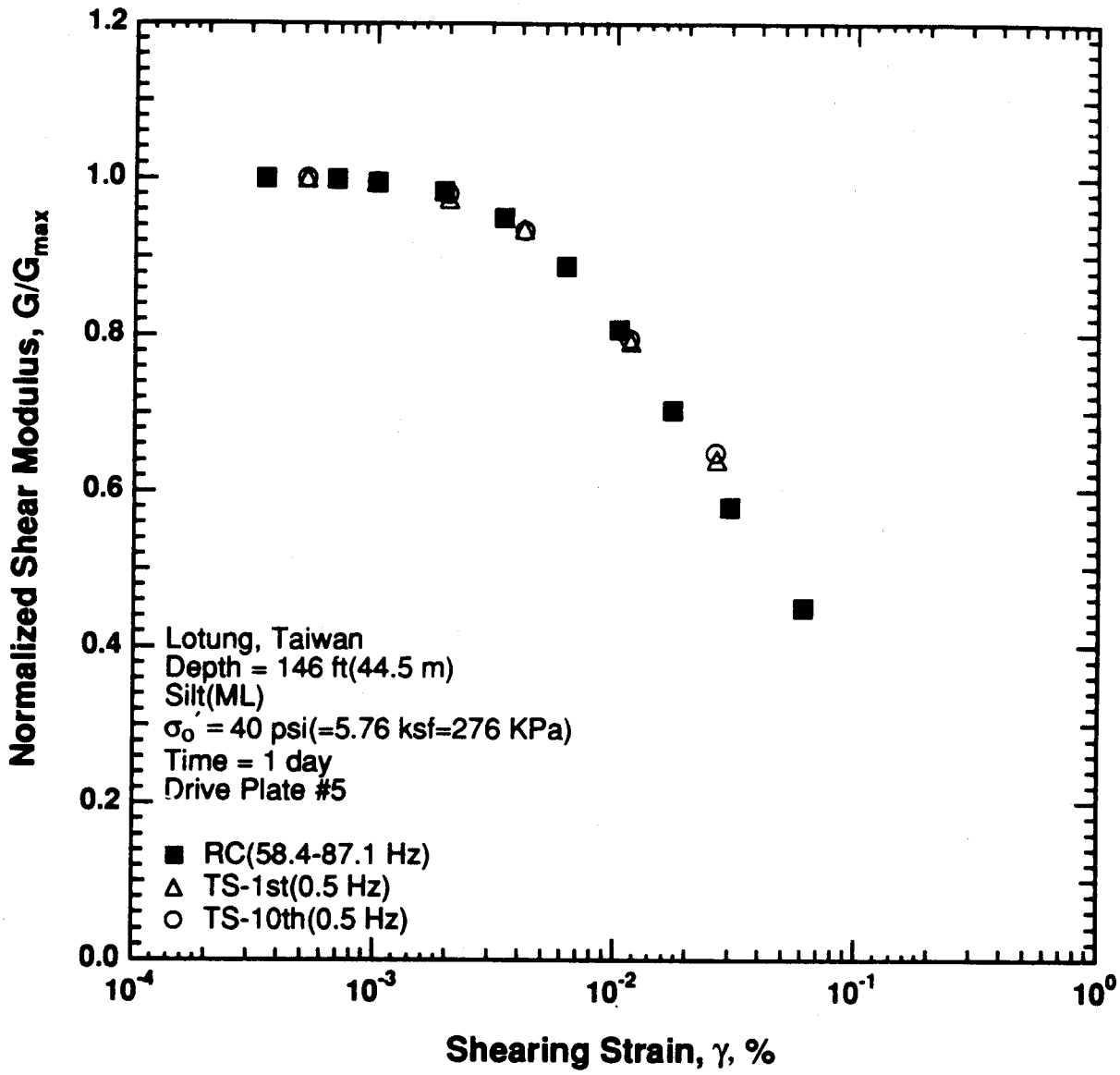

Figure 8.B.4.I-8
Variation in normalized shear modulus with shearing strain at an effective confining pressure of 40 psi (5.76 ksf, 276 kPa) from RCTS tests of sample T10 from borehole CH1; determined on the loading pressure sequence.

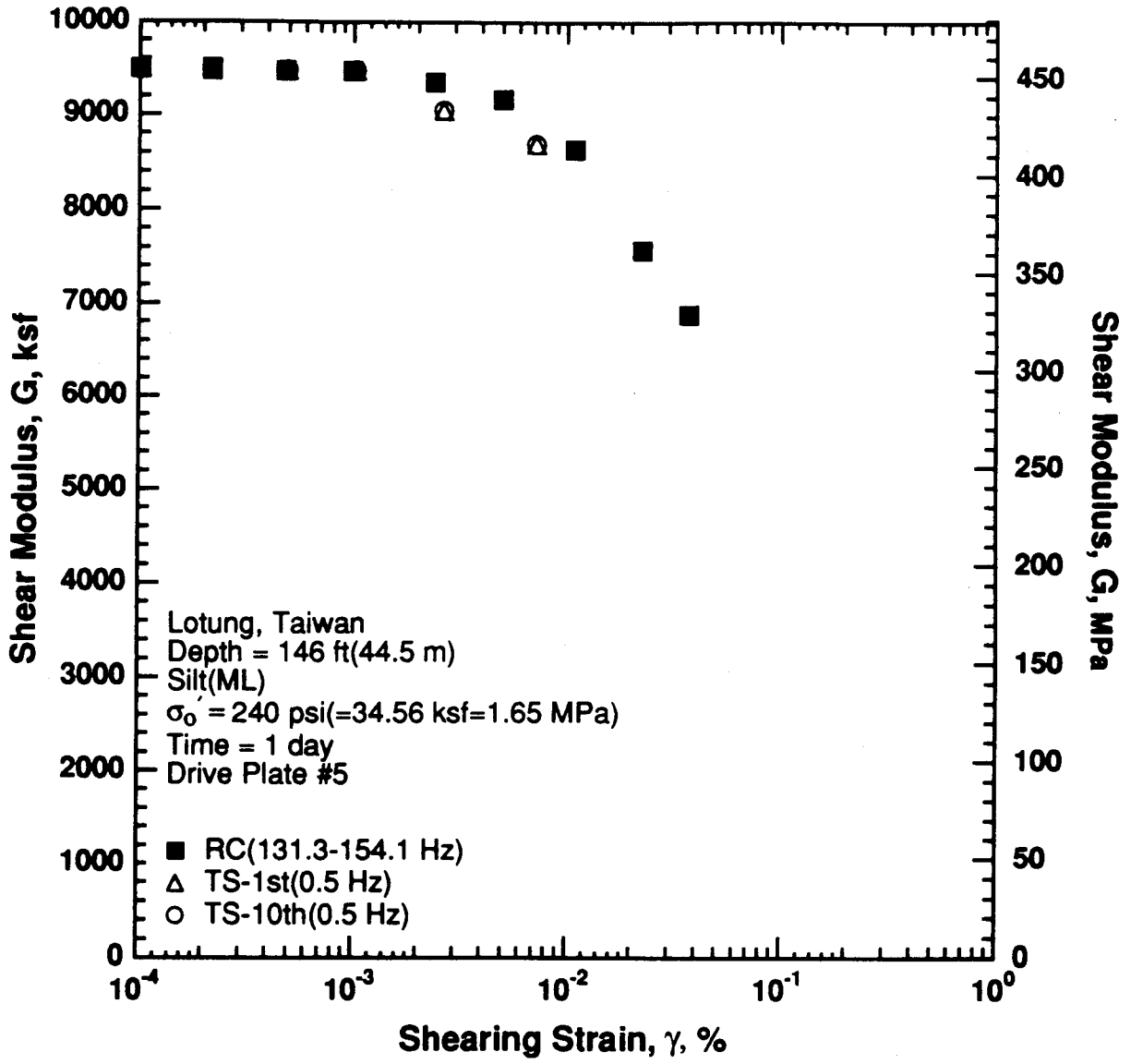

Figure 8.B.4.I-9
Variation in shear modulus with shearing strain at an effective confining pressure of 240 psi (34.56 ksf, 1.65 MPa) from RCTS tests of sample T10 from borehole CH1; determined on the loading pressure sequence.

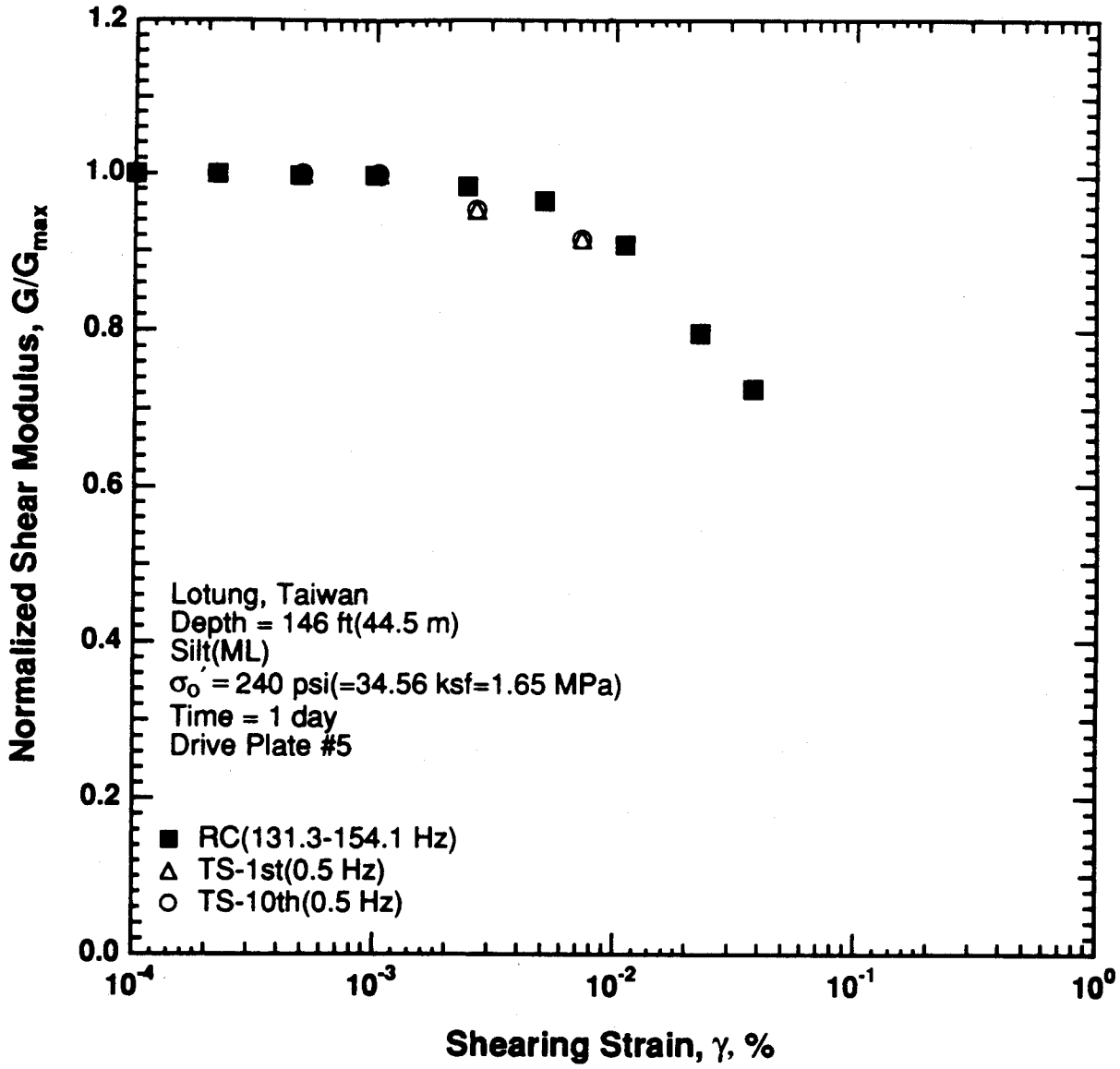

Figure 8.B.4.I-10
Variation in normalized shear modulus with shearing strain at an effective confining pressure of 240 psi (34.56 ksf, 1.65 MPa) from RCTS tests of sample T10 from borehole CH1; determined on the loading pressure sequence

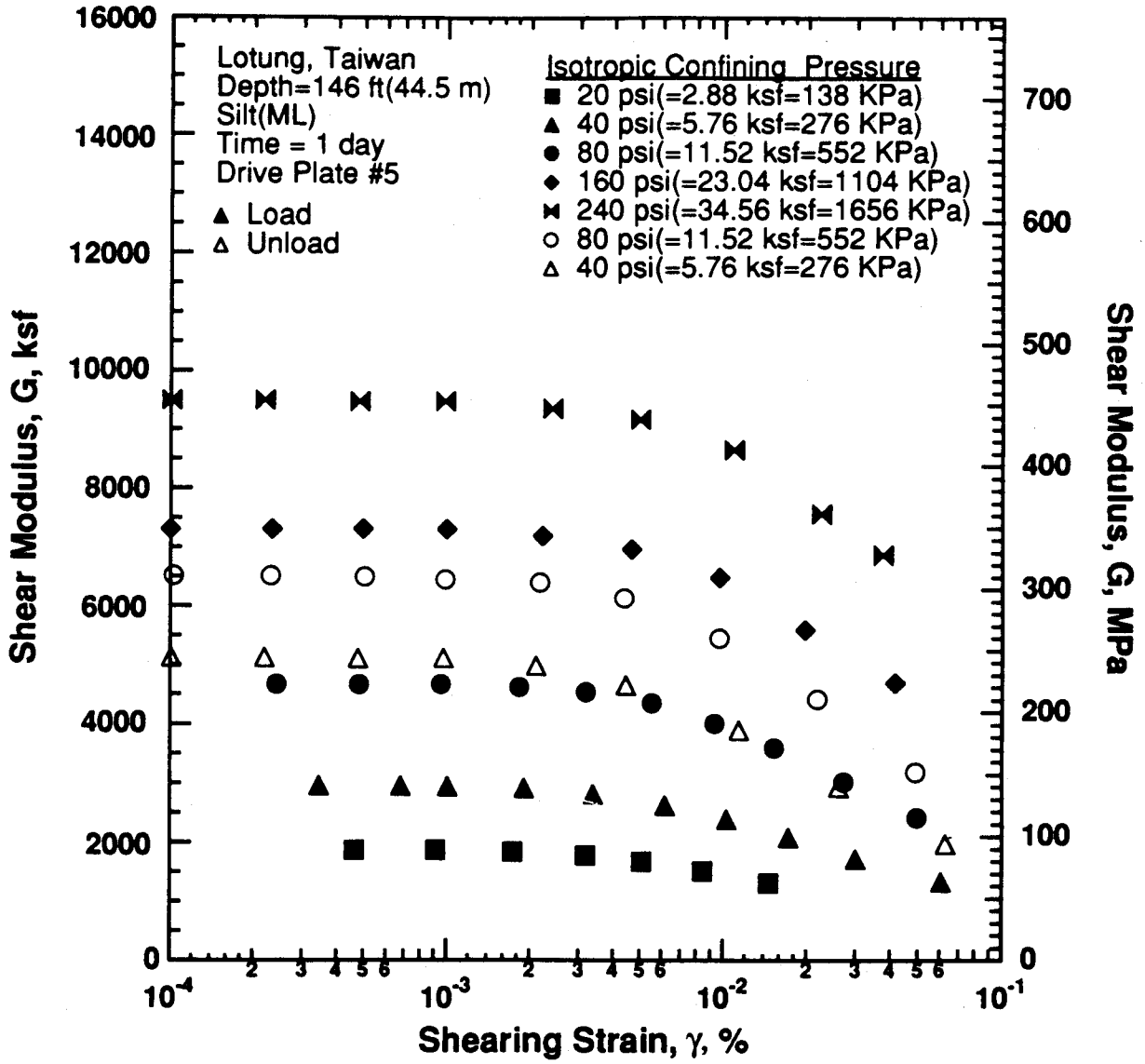

Figure 8.B.4.I-11
Variation in shear modulus with shearing strain and effective confining pressure from RC tests of sample T10 from borehole CH1; performed on the loading and unloading sequences.

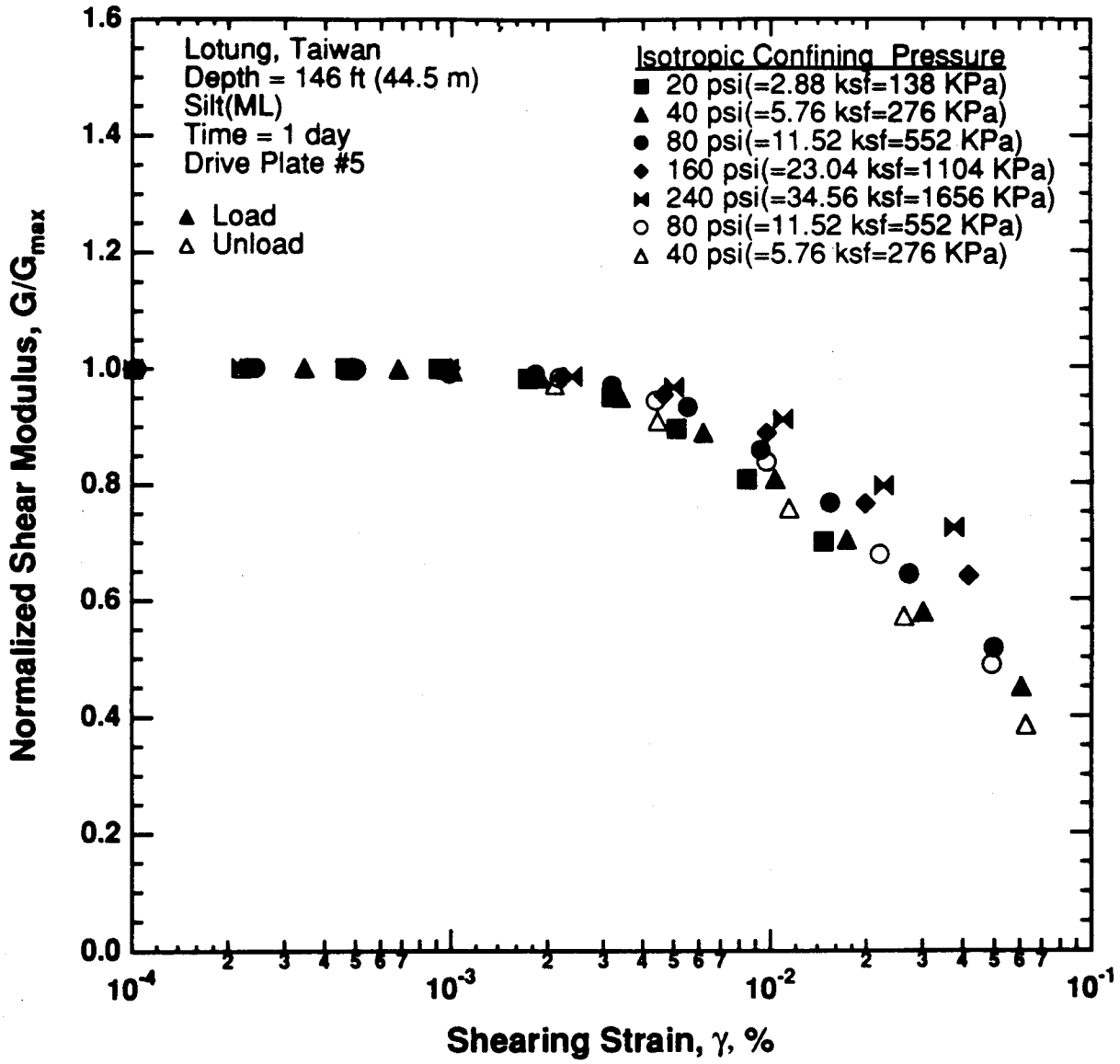

Figure 8.B.4.I-12
Comparison of the variation in normalized shear modulus with shearing strain and effective confining pressure from RC tests of sample T10 from borehole CH1; performed on the loading and unloading sequences.

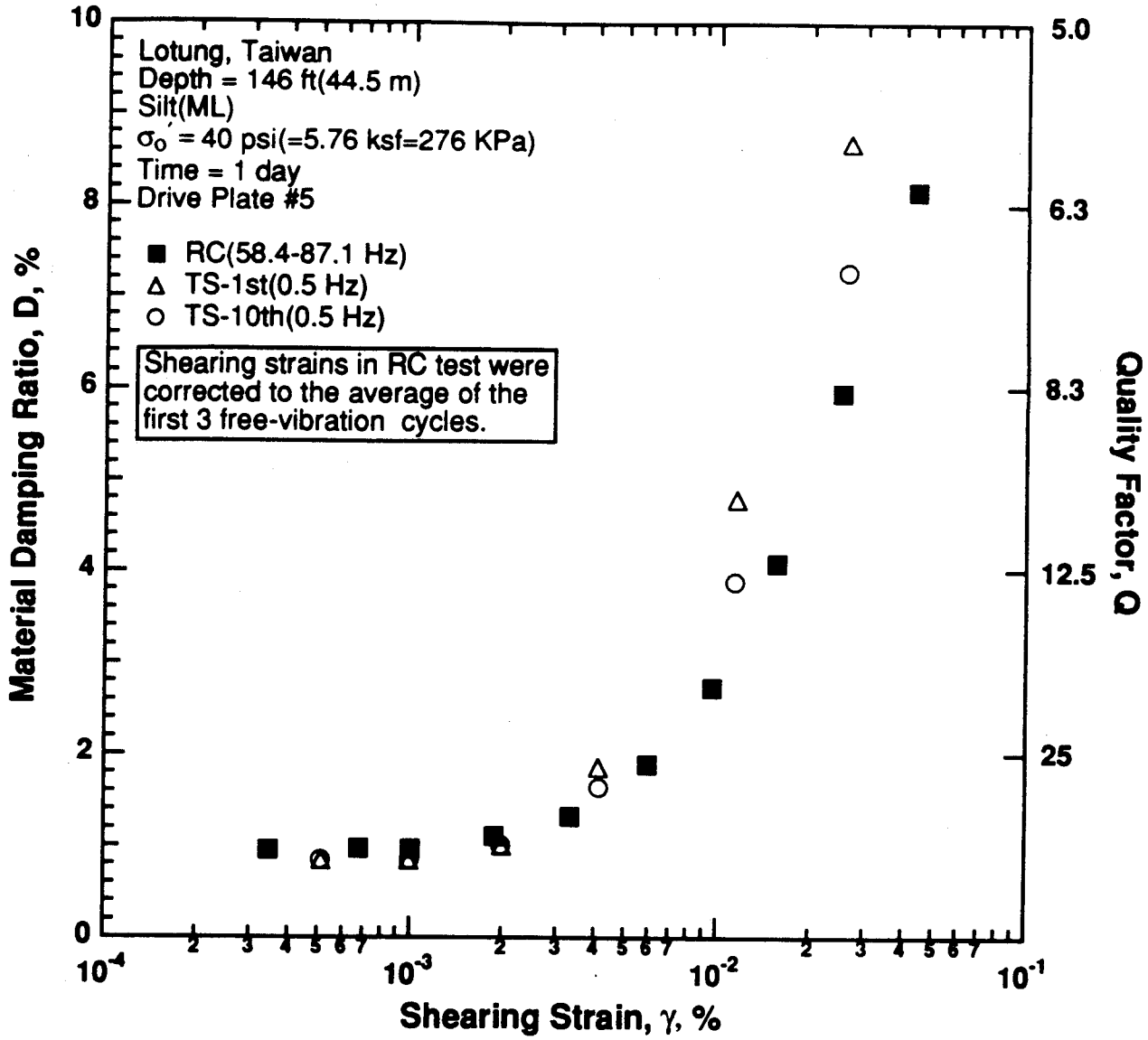

Figure 8.B.4.I-13
Variation in material damping ratio with shearing strain at an effective confining pressure of 40 psi (5.76 ksf, 276 kPa) from RCTS tests of sample T10 from borehole CH1; determined on the loading pressure sequence.

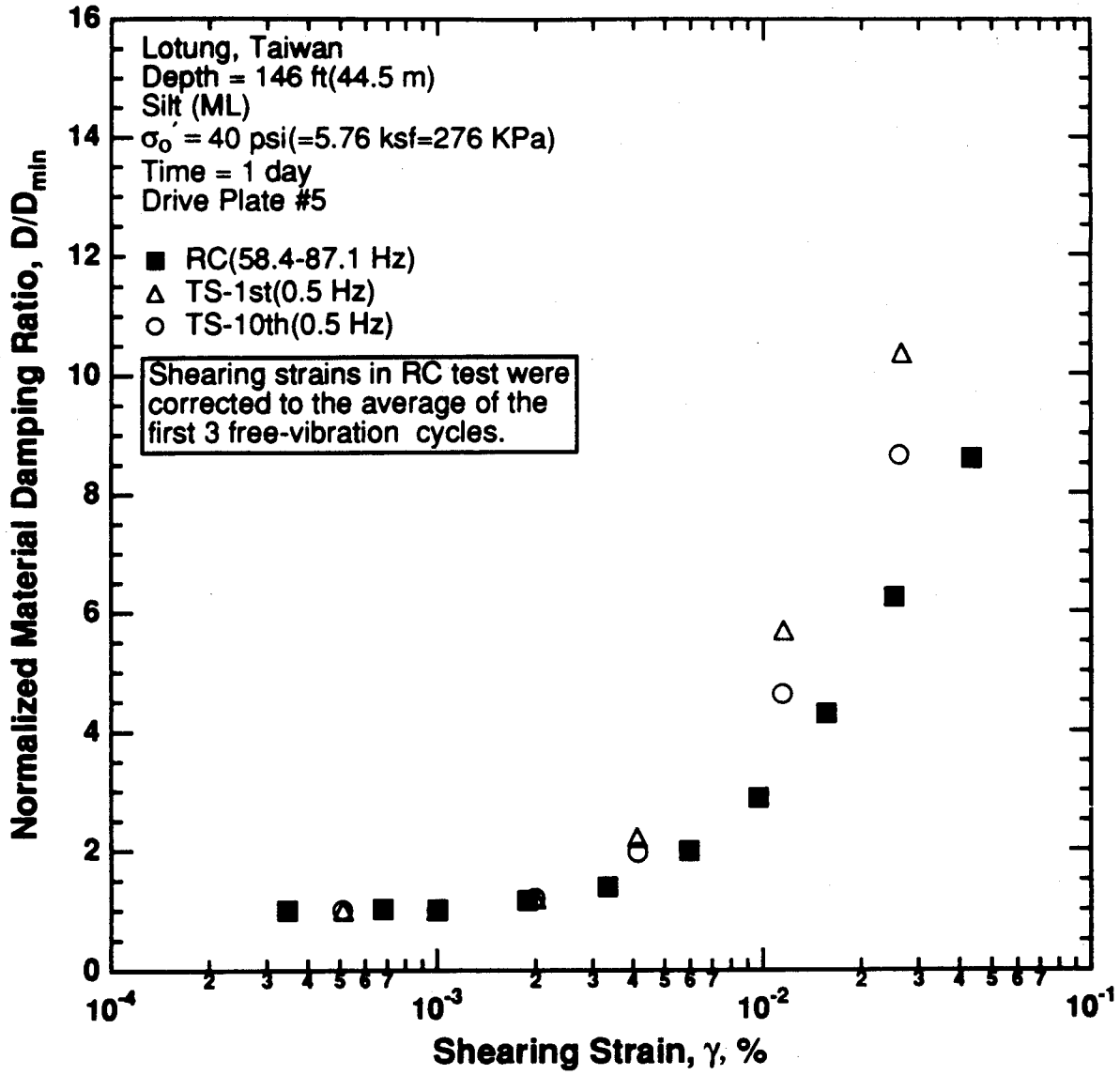

Figure 8.B.4.I-14
Variation in normalized material damping ratio with shearing strain at an effective confining pressure of 40 psi (5.76 ksf, 276 kPa) from RCTS tests of sample T10 from borehole CH1; determined on the loading pressure sequence.

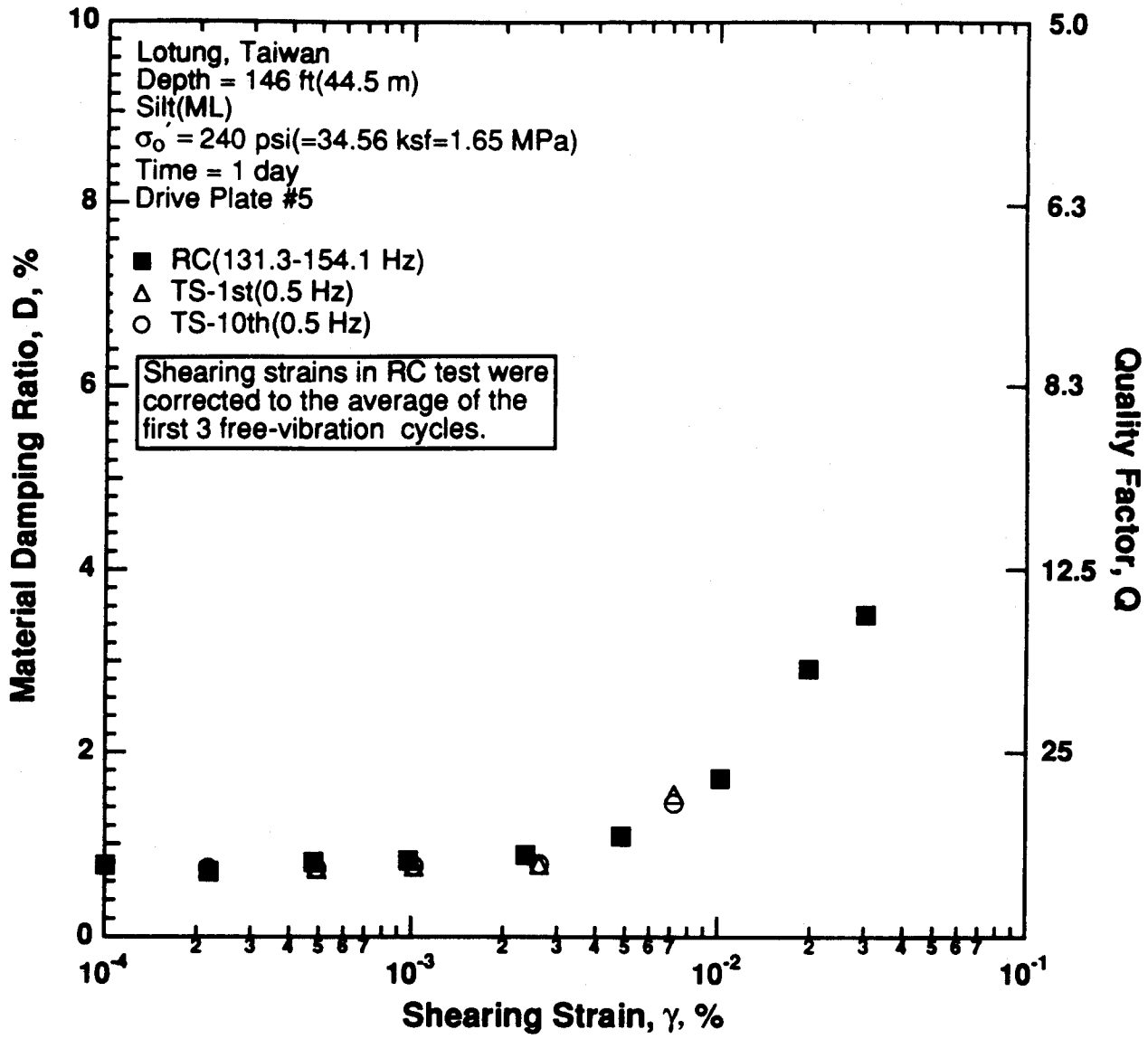

Figure 8.B.4.I-15
Variation in material damping ratio with shearing strain at an effective confining pressure of 240 psi (34.56 ksf, 1.65 MPa) from RCTS tests of sample T10 from borehole CH1; determined on the loading pressure sequence.

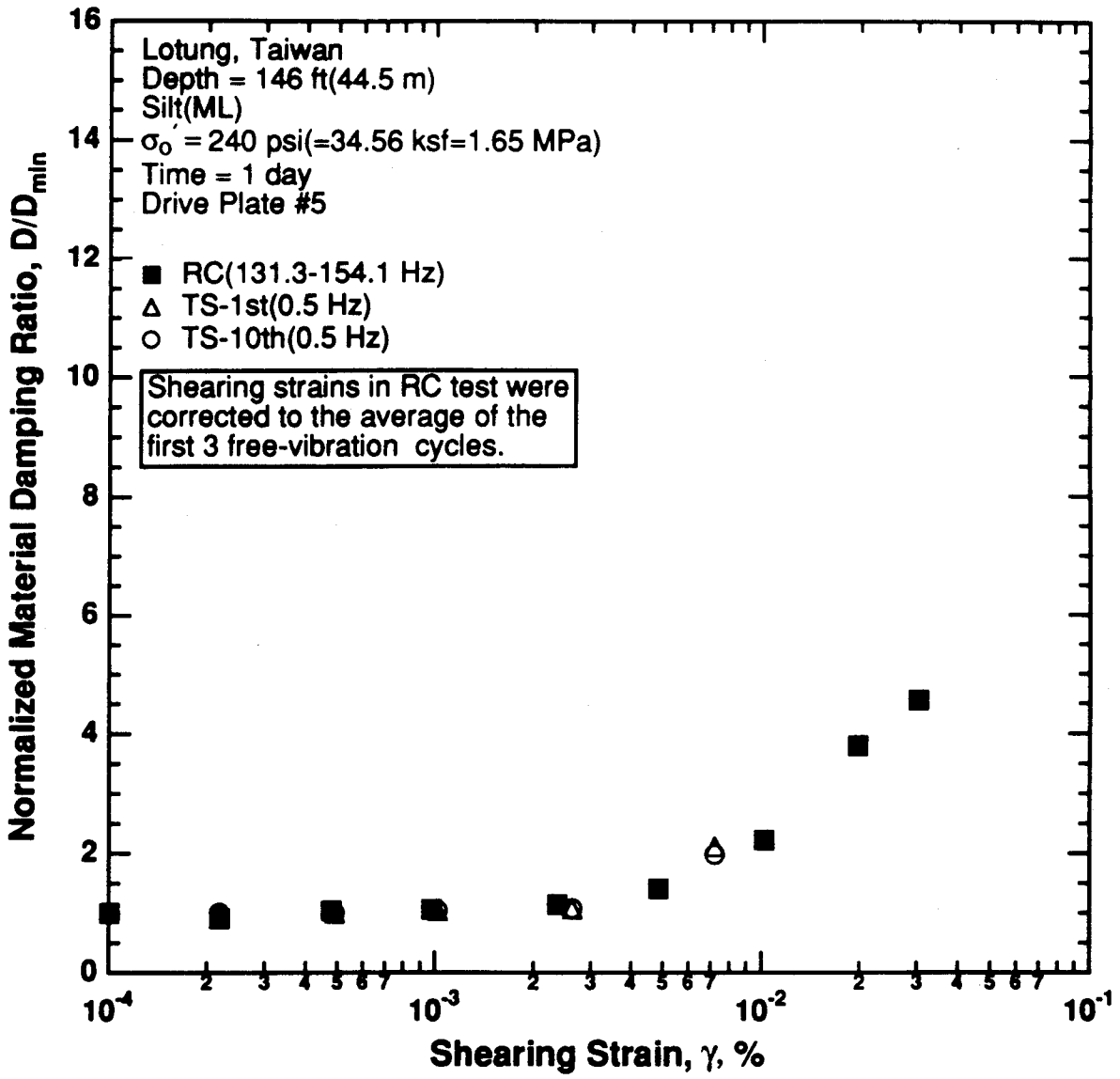

Figure 8.B.4.I-16
Variation in normalized material damping ratio with shearing strain at an effective confining pressure of 240 psi (34.56 ksf, 1.65 MPa) from RCTS tests of sample T10 from borehole CH1; determined on the loading pressure sequence.

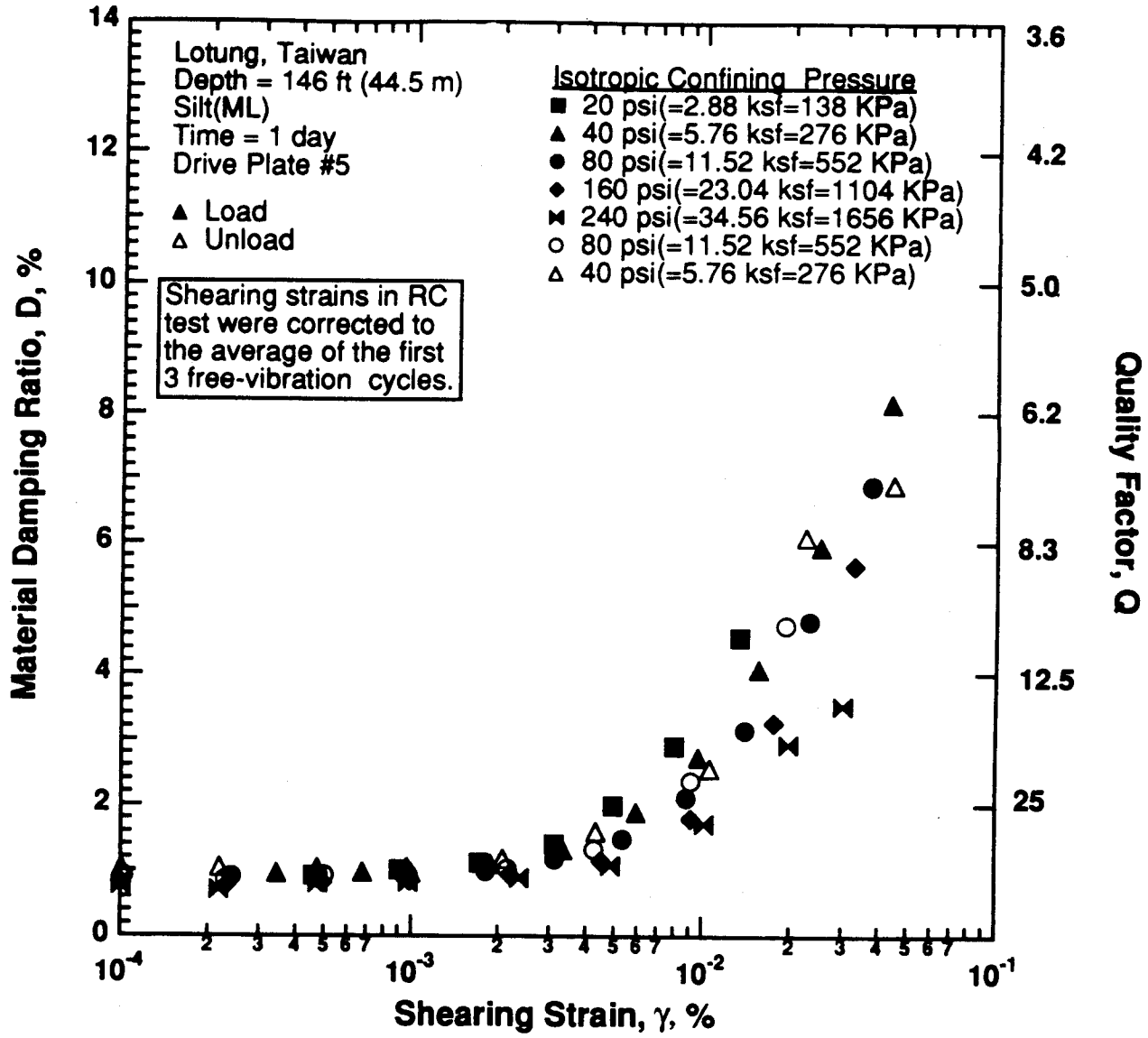

Figure 8.B.4.I-17
Variation in material damping ratio with shearing strain and effective confining pressure from RC tests of sample T10 from borehole CH1; performed on the loading and unloading sequences.

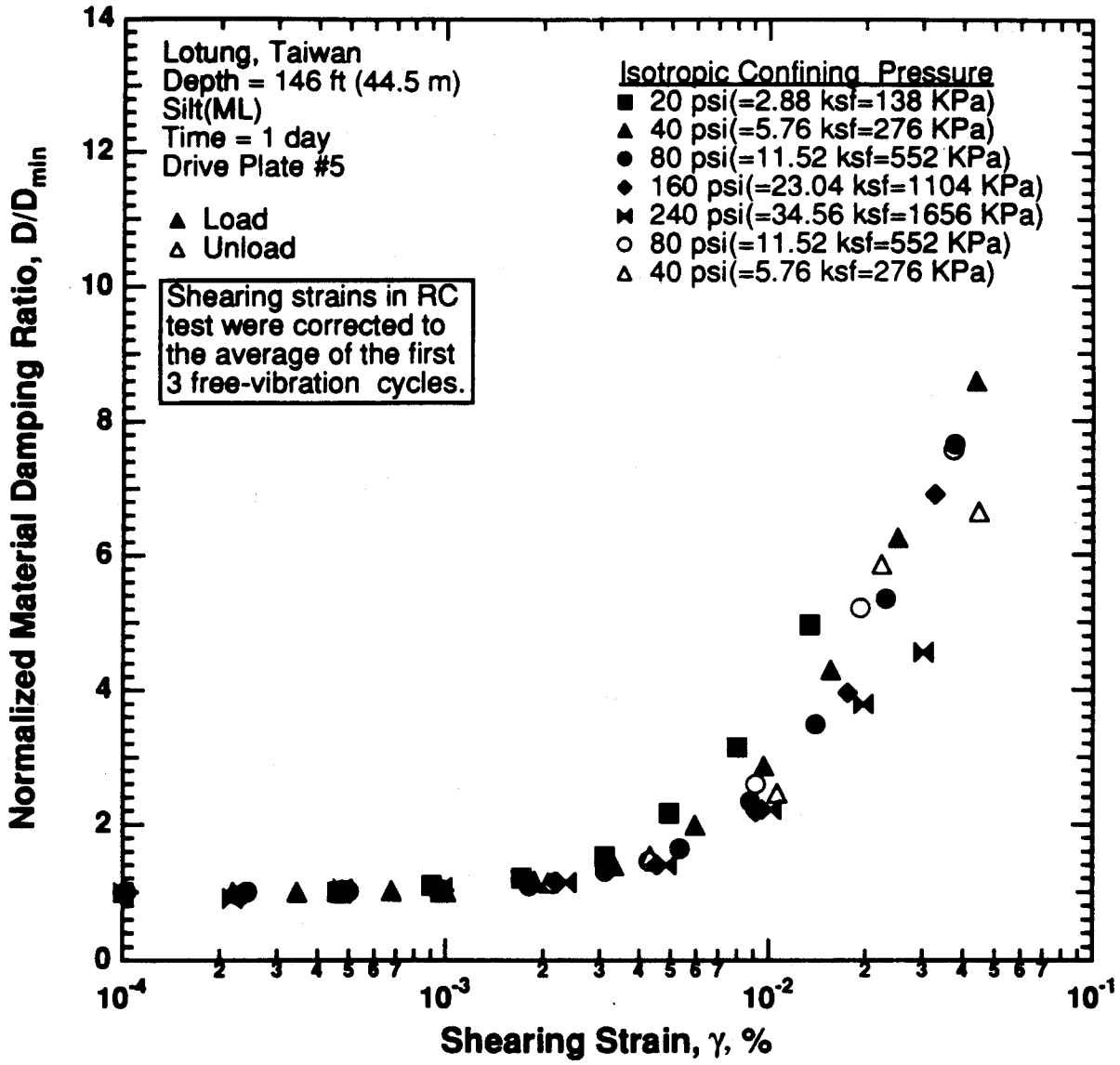

Figure 8.B.4.I-18
Comparison of the variation in normalized material damping ratio with shearing strain and effective confining pressure from RC tests of sample T10 from borehole CH1; performed on the loading and unloading sequences.

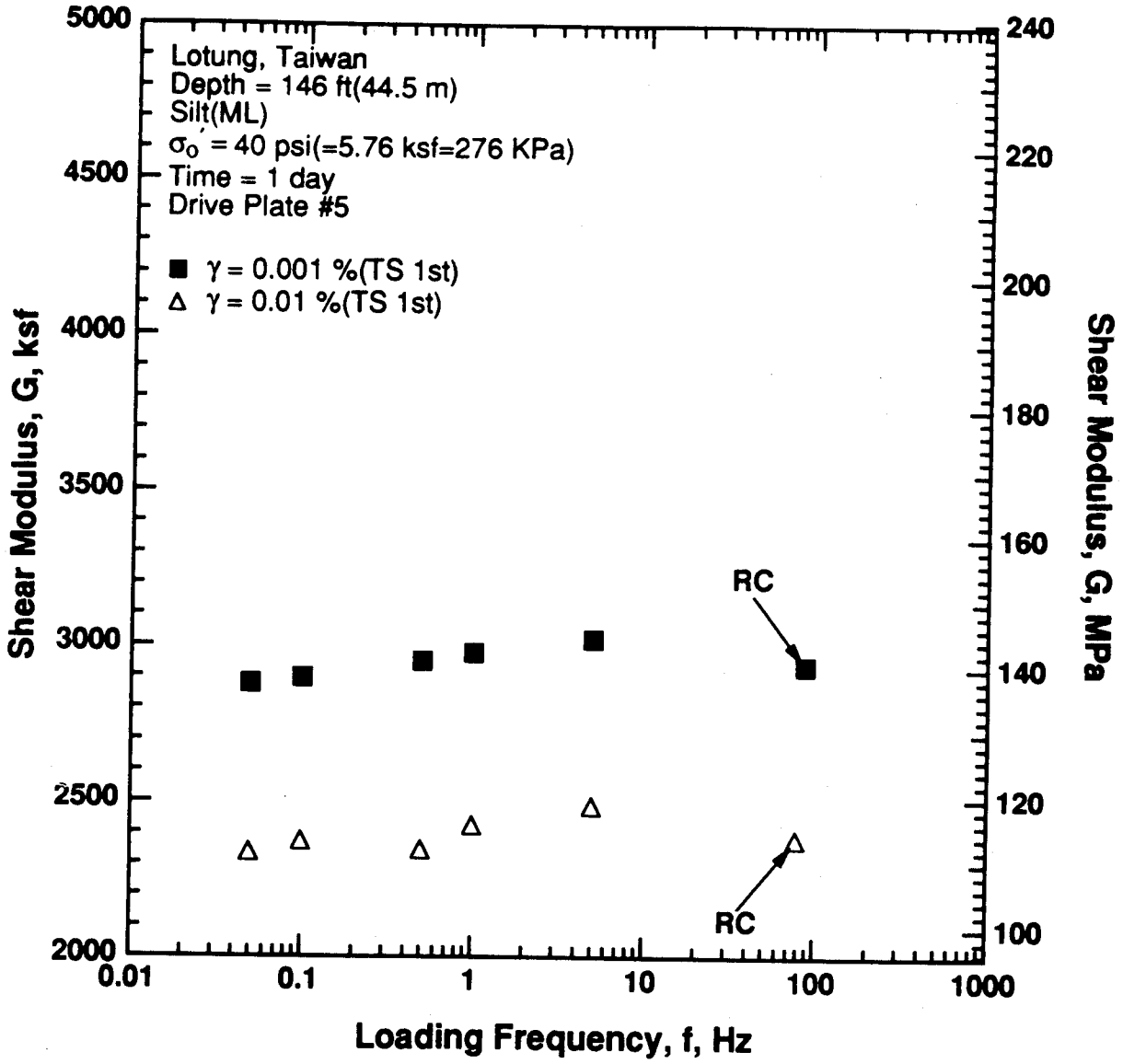

Figure 8.B.4.I-19
Variation in shear modulus with loading frequency and shearing strain at an effective confining pressure of 40 psi (5.76 ksf, 276 kPa) from RCTS tests of sample T10 from borehole CH1; determined on the loading pressure sequence.

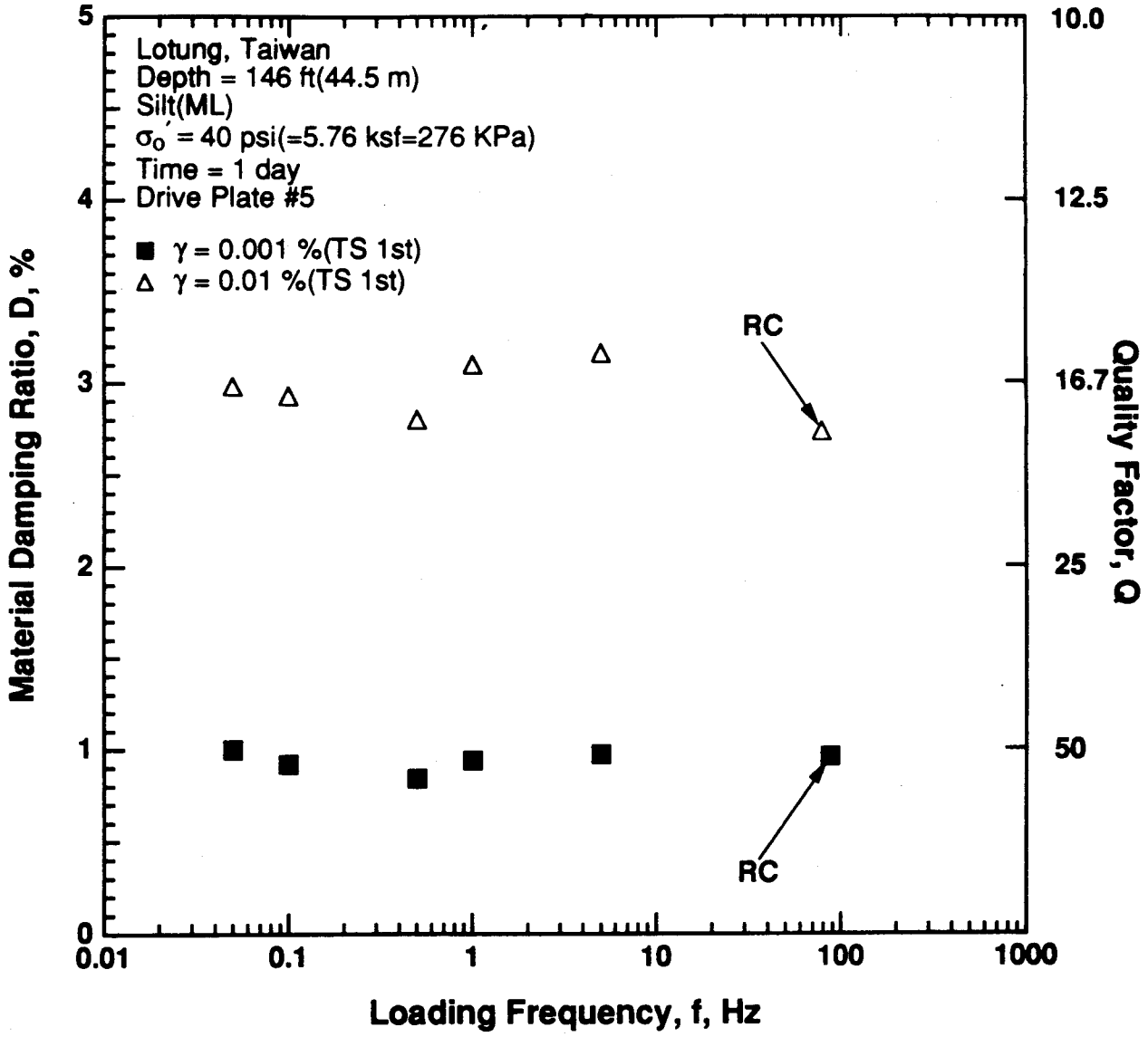

Figure 8.B.4.I-20
Variation in material damping ratio with loading frequency and shearing strain at an effective confining pressure of 40 psi (5.76 ksf, 276 kPa) from RCTS tests of sample T10 from borehole CH1; determined on the loading pressure sequence.

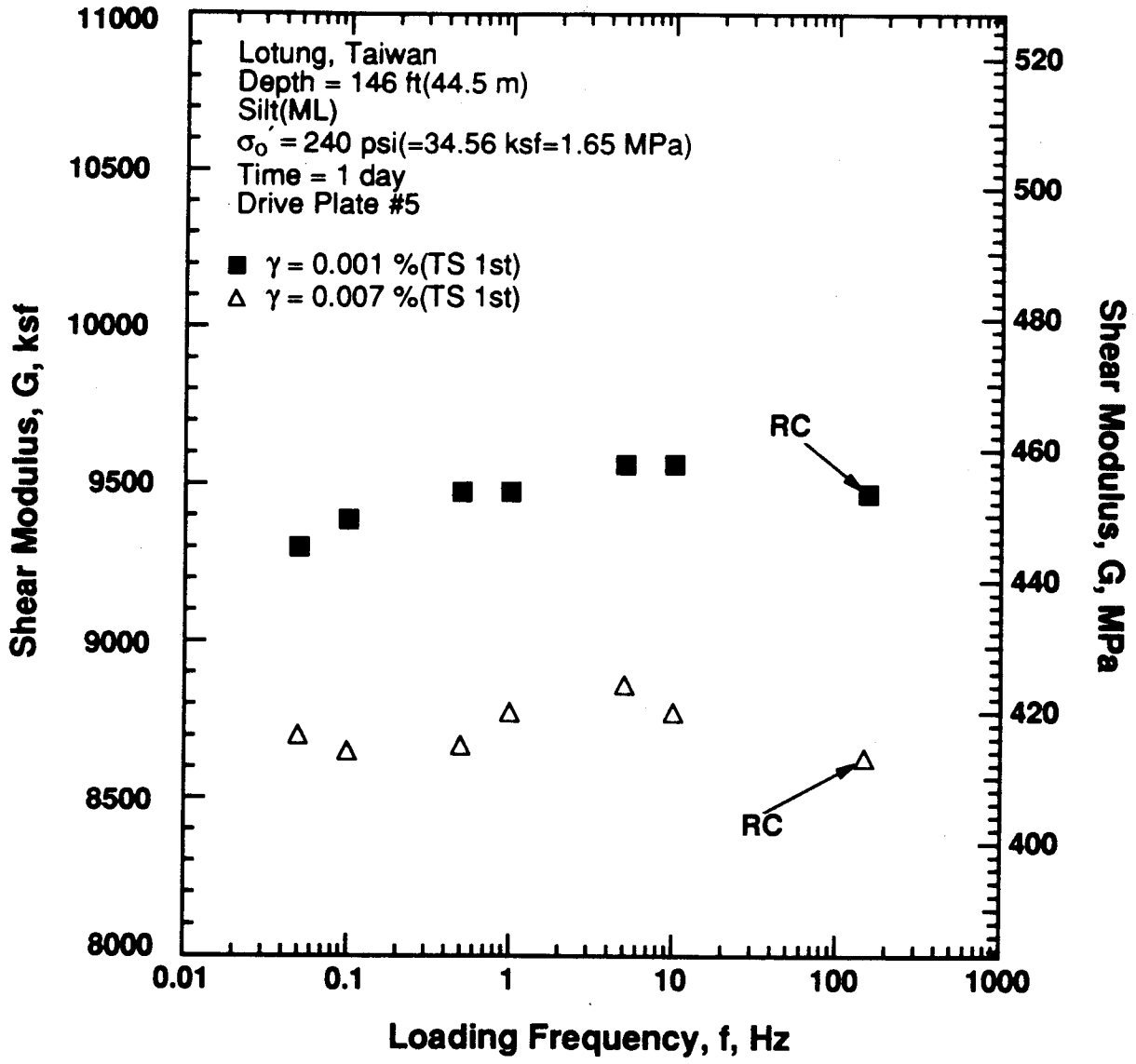

Figure 8.B.4.I-21
Variation in shear modulus with loading frequency and shearing strain at an effective confining pressure of 240 psi (34.56 ksf, 1.65 MPa) from RCTS tests of sample T10 from borehole CH1; determined on the loading pressure sequence.

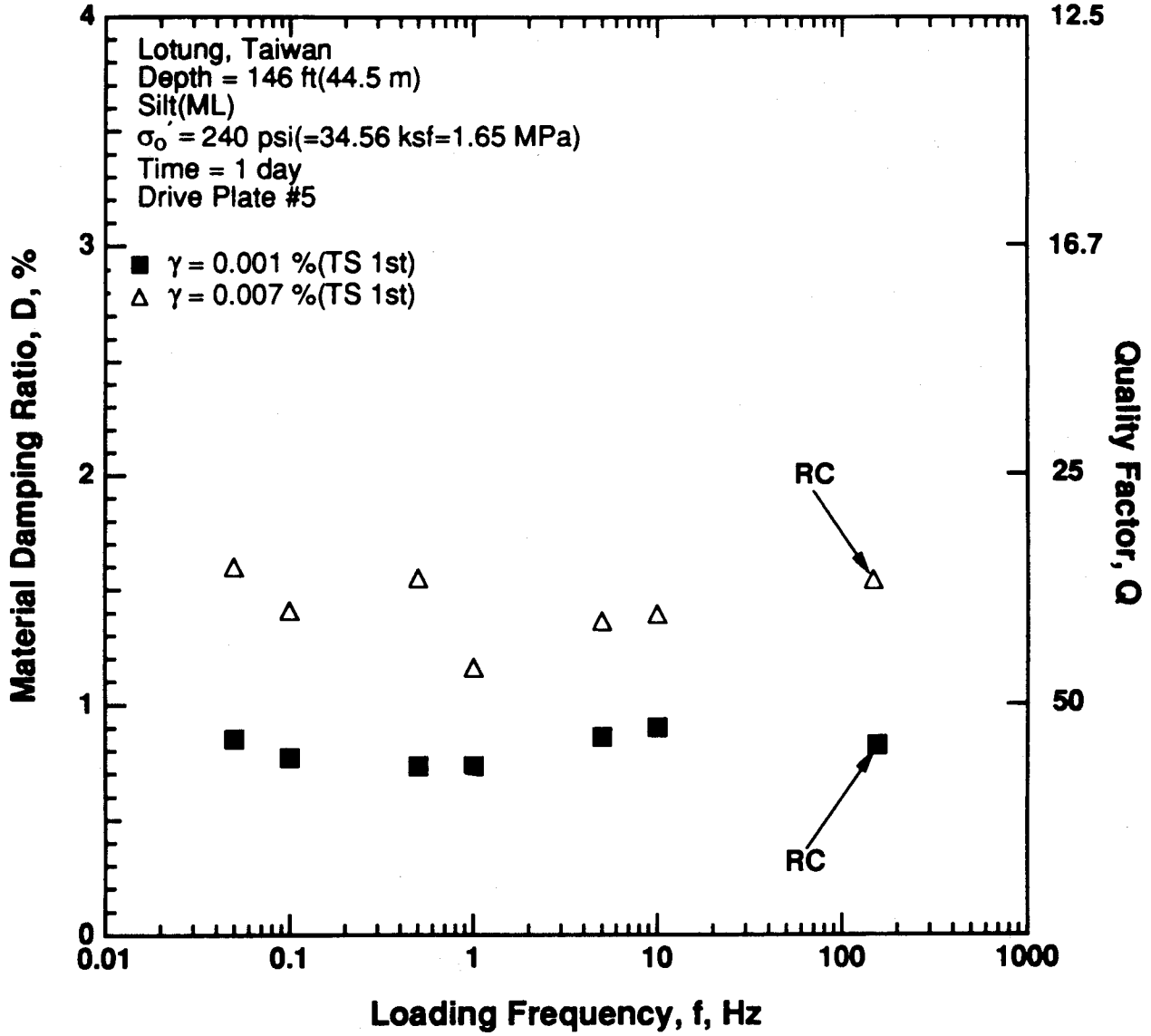

Figure 8.B.4.I-22
Variation in material damping ratio with loading frequency and shearing strain at an effective confining pressure of 240 psi (34.56 ksf, 1.65 MPa) from RCTS tests of sample T10 from borehole CH1; determined on the loading pressure sequence.

APPENDIX J
DYNAMIC TESTS OF LOTUNG SAMPLE T4A FROM BOREHOLE CH1, DEPTH = 59 FT (18.0 M)

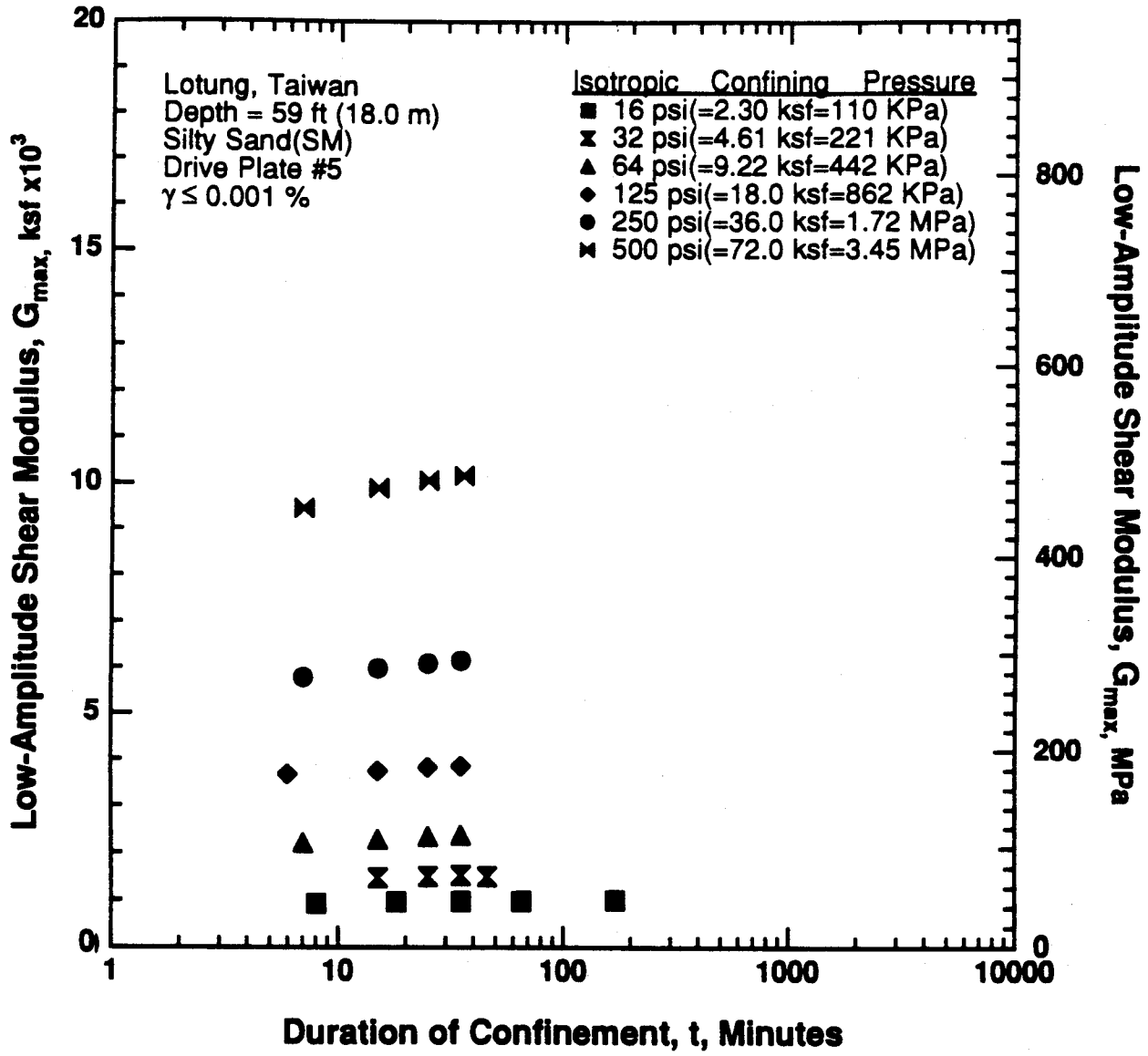

Figure 8.B.4.J-1
Variation in low-amplitude shear modulus with magnitude and duration of isotropic confining pressure from resonant column testing of sample T4A from borehole CH1.

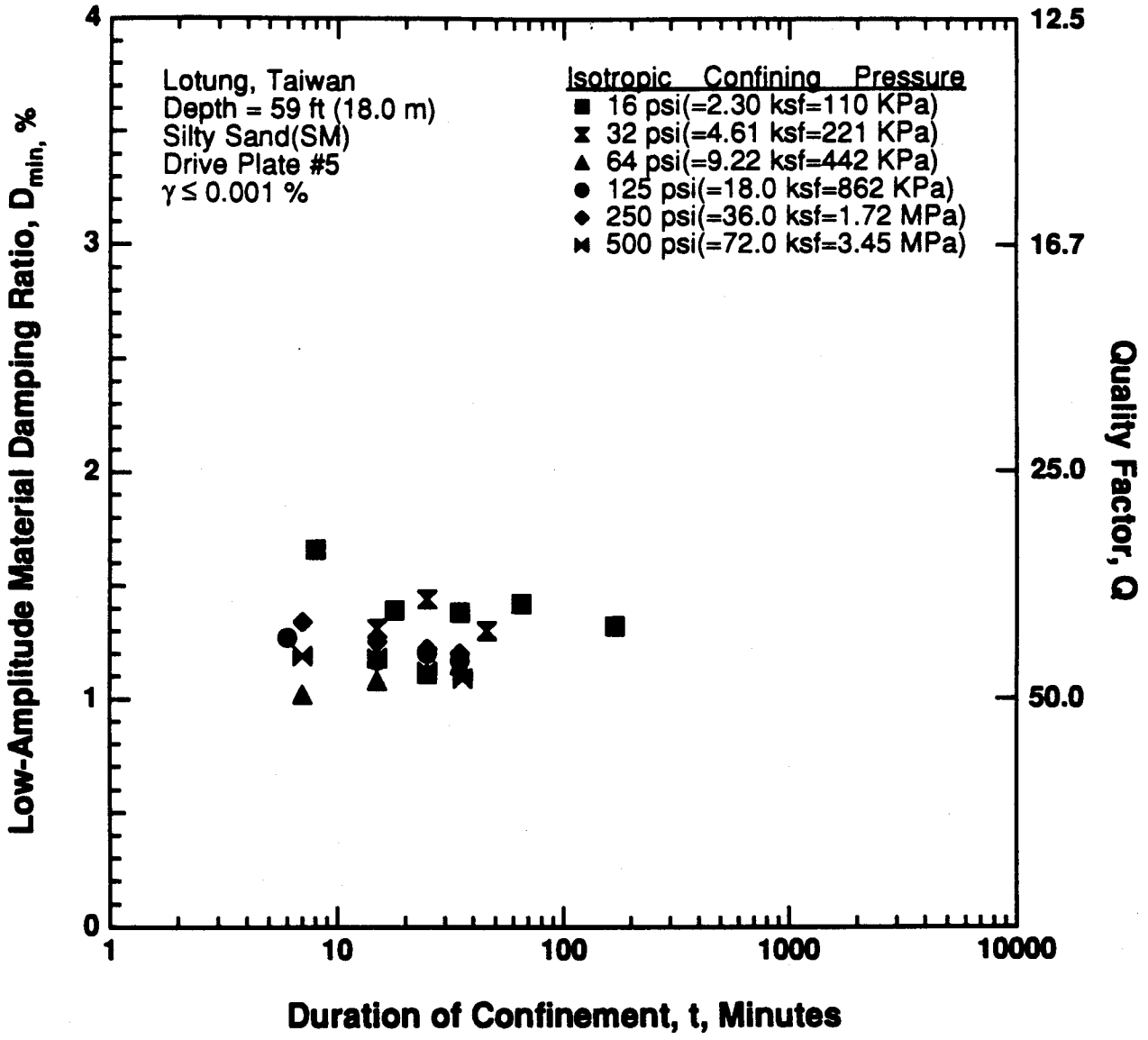

Figure 8.B.4.J-2
Variation in low-amplitude material damping ratio with magnitude and duration of isotropic confining pressure from resonant column testing of sample T4A from borehole CH1.

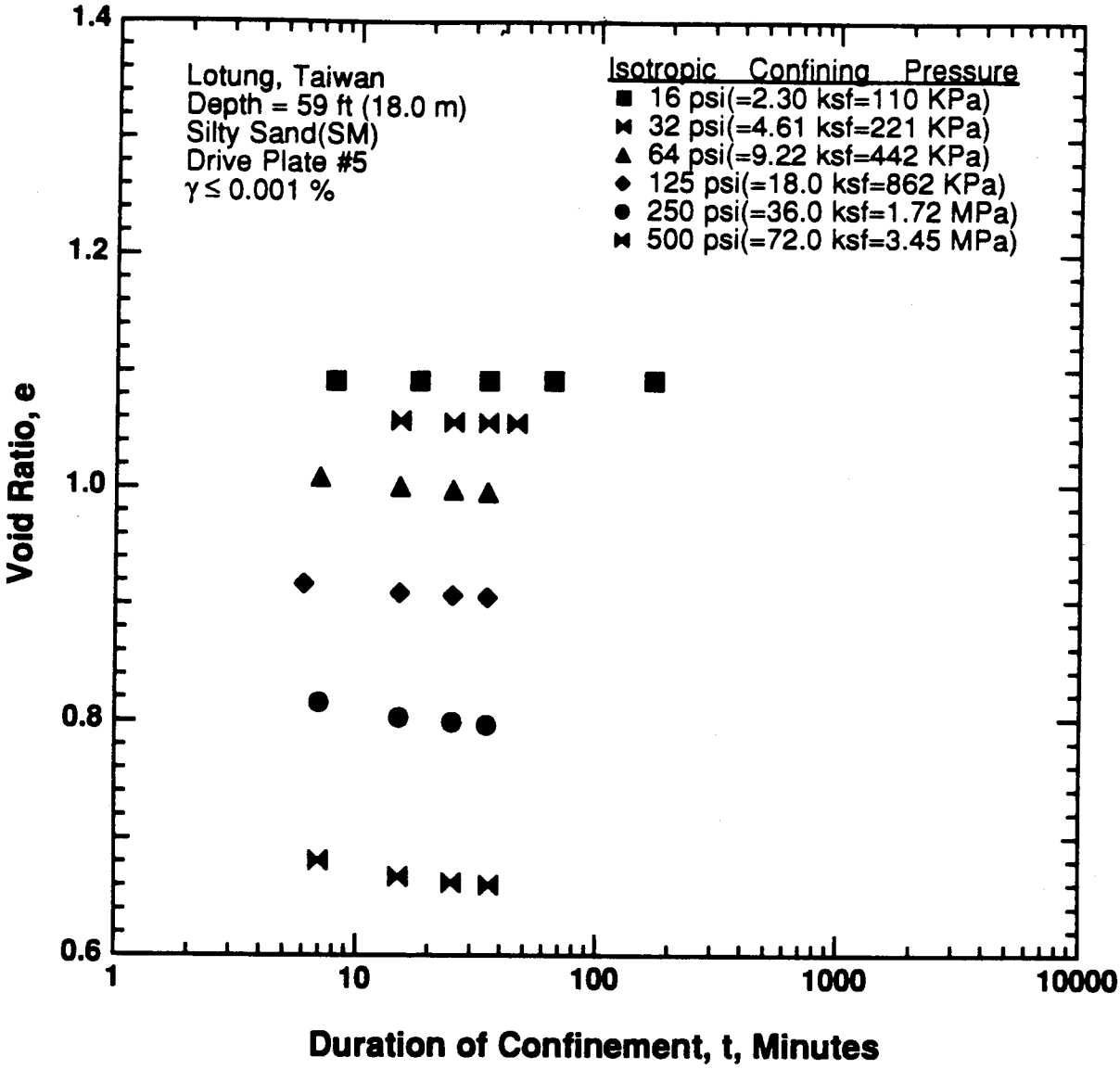

Figure 8.B.4.J-3
Variation in void ratio with magnitude and duration of isotropic confining pressure from resonant column testing of sample T4A from borehole CH1.

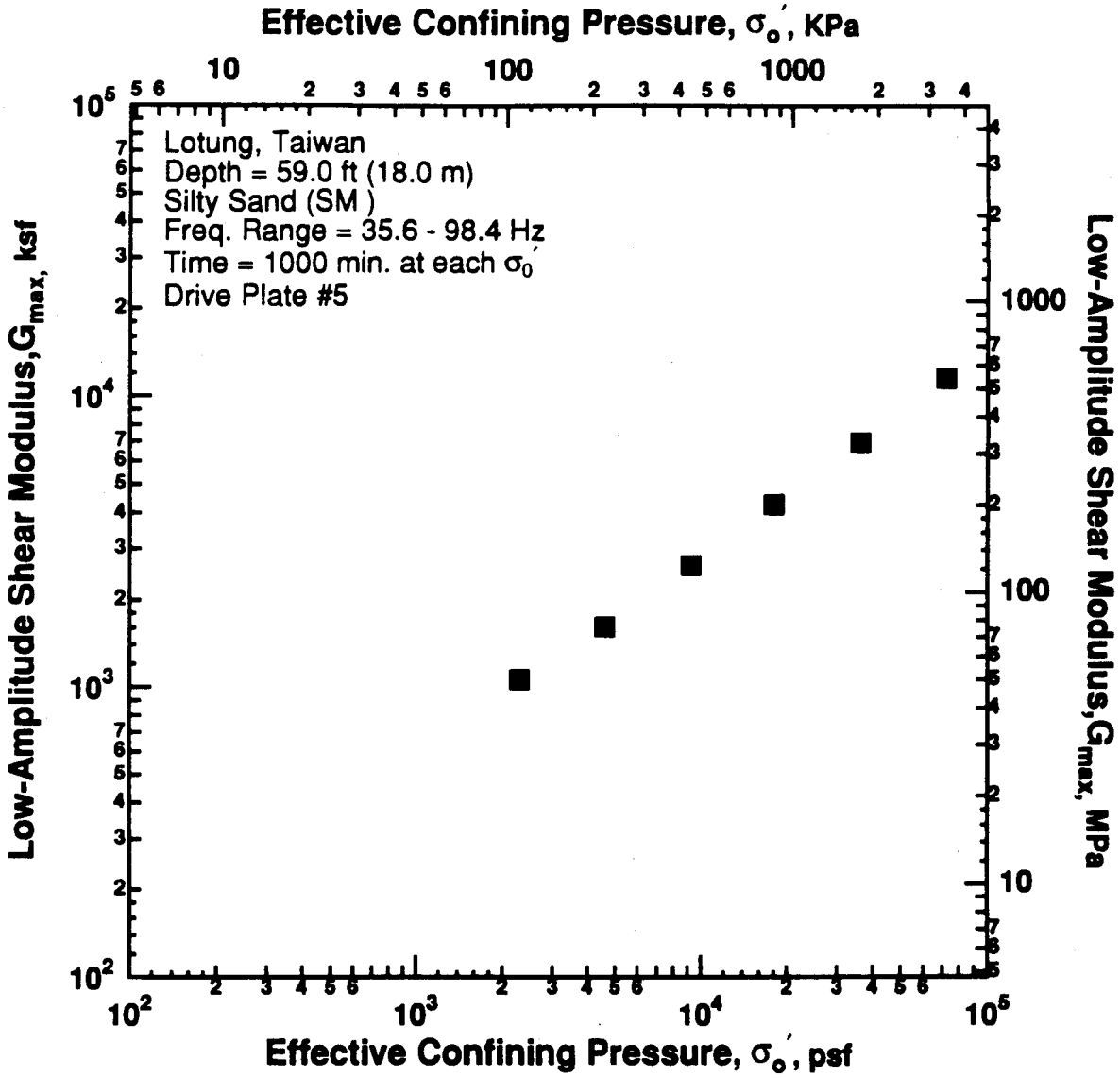

1. Shear modulus values at 1000 minutes were obtained by using linear interpolation from data presented in Figure J.1.

Figure 8.B.4.J-4
Variation in low-amplitude shear modulus with effective confining pressure from resonant column tests of sample T4A from borehole CH1.

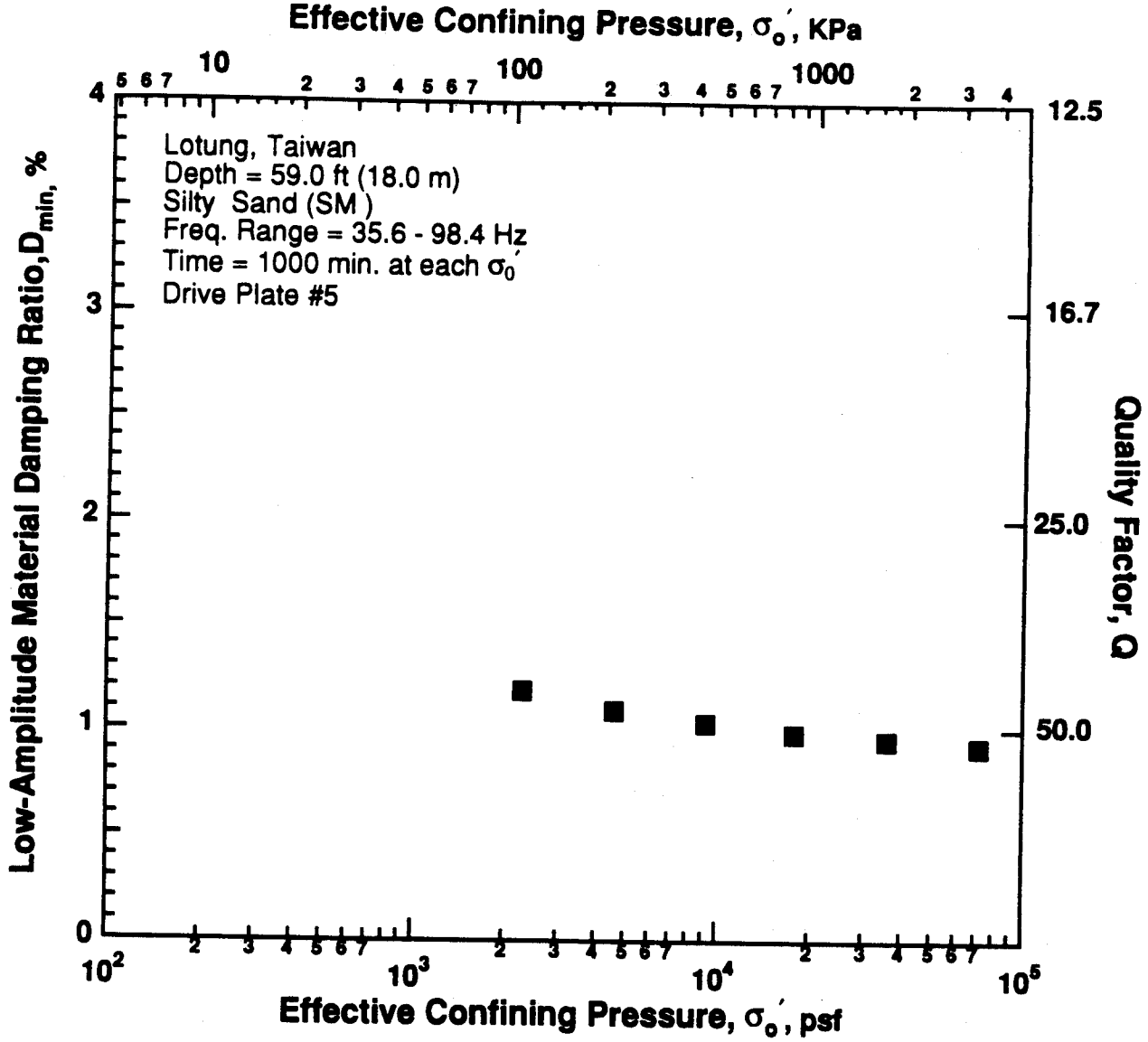

1. Damping ratio values at 1000 minutes were obtained by using linear interpolation from data presented in Figure J.2.

Figure 8.B.4.J-5
Variation in low-amplitude material damping ratio with effective confining pressure from resonant column tests of sample T4A from borehole CH1.

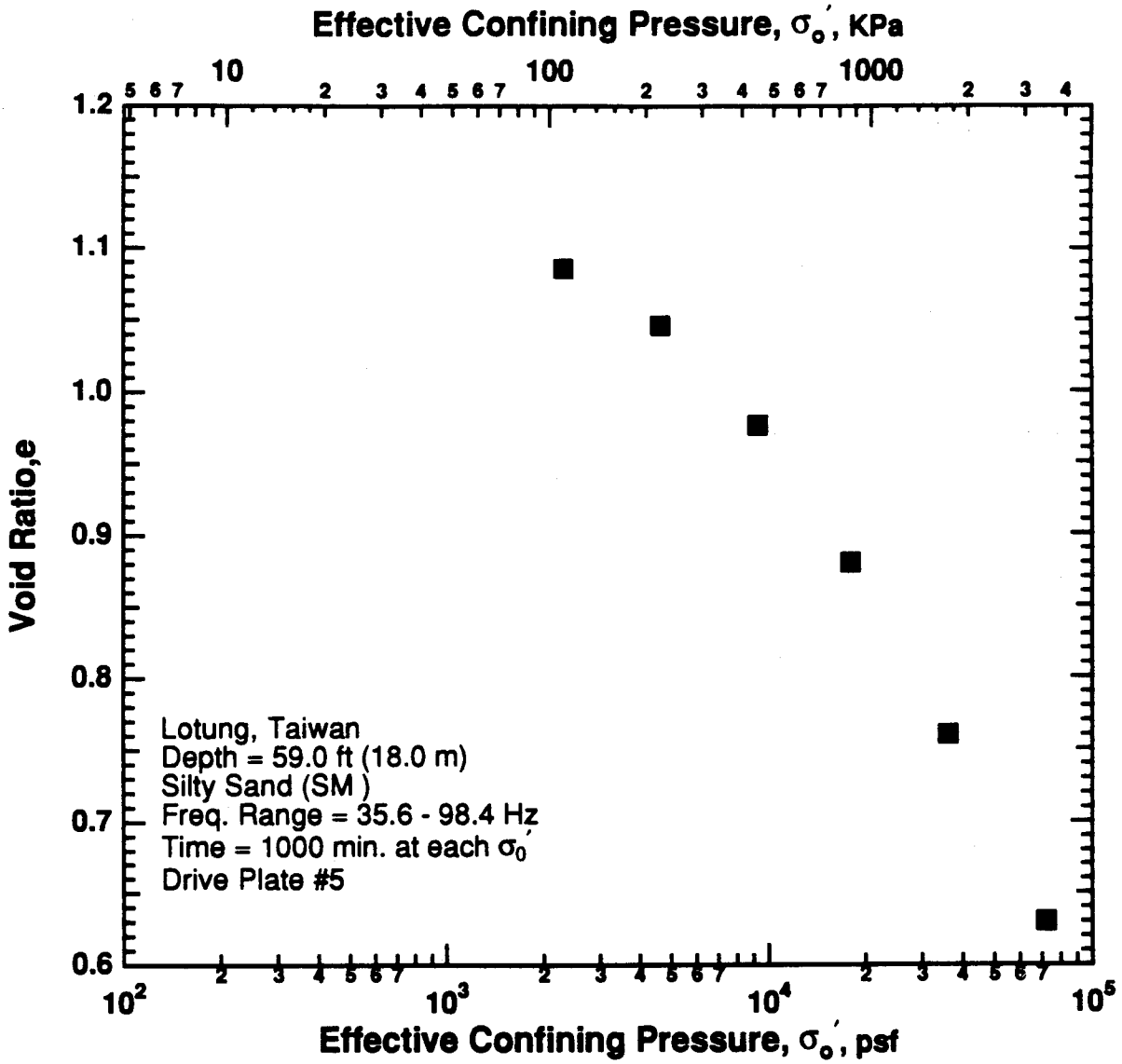

1. Void ratio values at 1000 minutes were obtained by using linear interpolation from data presented in Figure J.3.

Figure 8.B.4.J-6
Variation in void ratio with effective confining pressure from resonant column tests of sample T4A from borehole CH1.

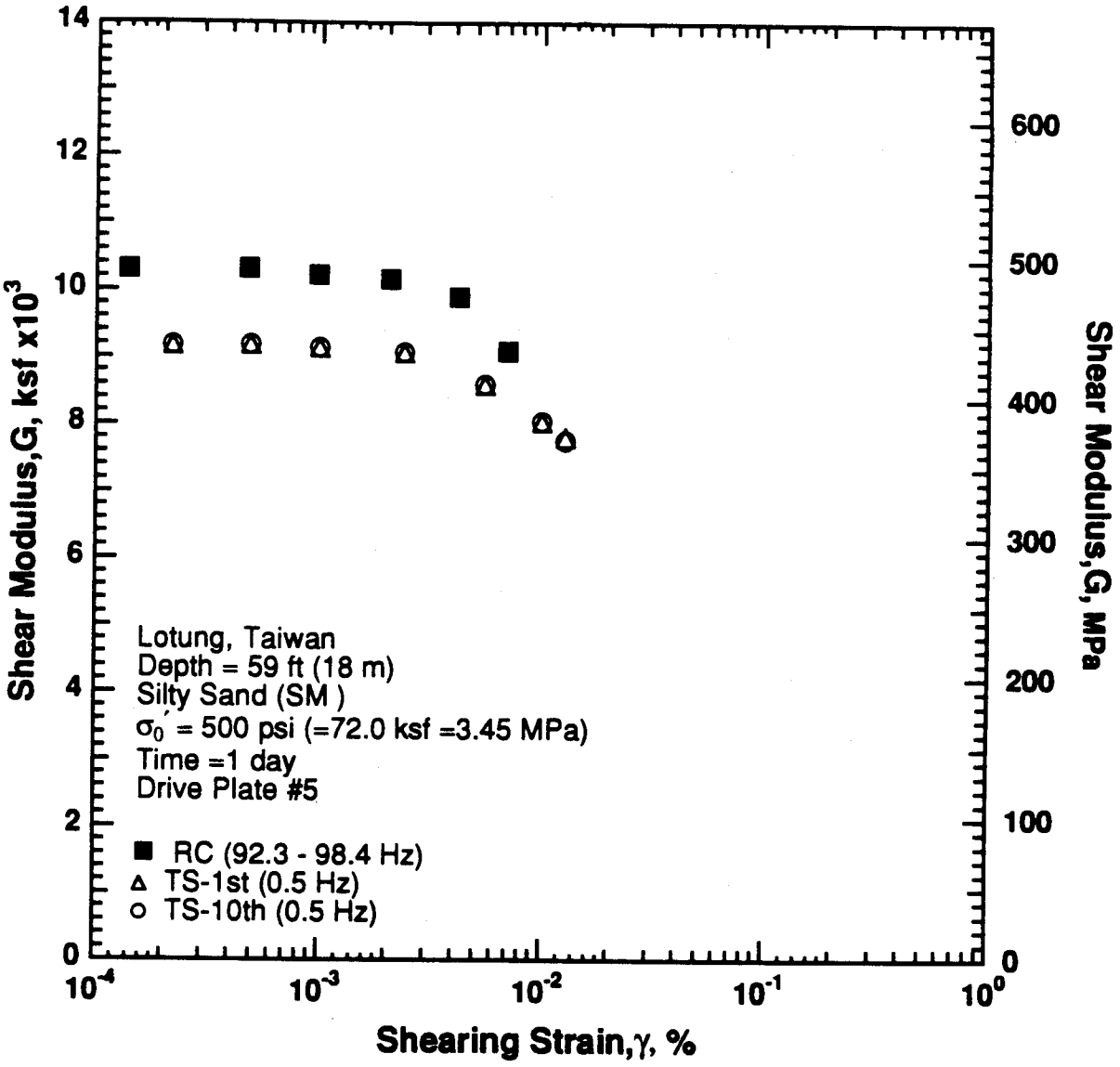

Figure 8.B.4.J-7
Variation in shear modulus with shearing strain at an effective confining pressure of 500 psi (72.0 ksf, 3.45 MPa) from RCTS tests of sample T4A from borehole CH1.

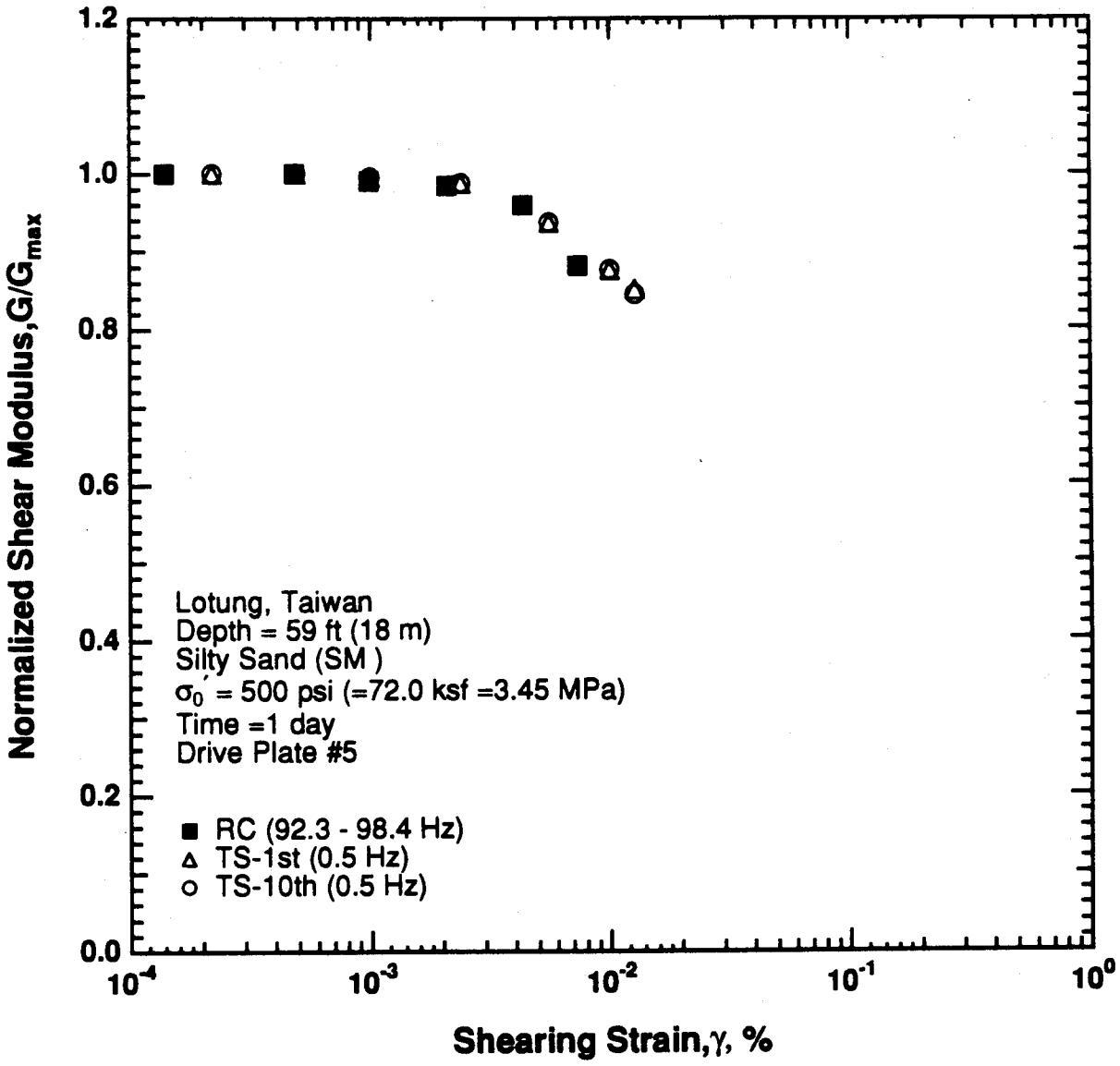

Figure 8.B.4.J-8
Variation in normalized shear modulus with shearing strain at an effective confining pressure of 500 psi (72.0 ksf, 3.45 MPa) from RCTS tests of sample T4A from borehole CH1.

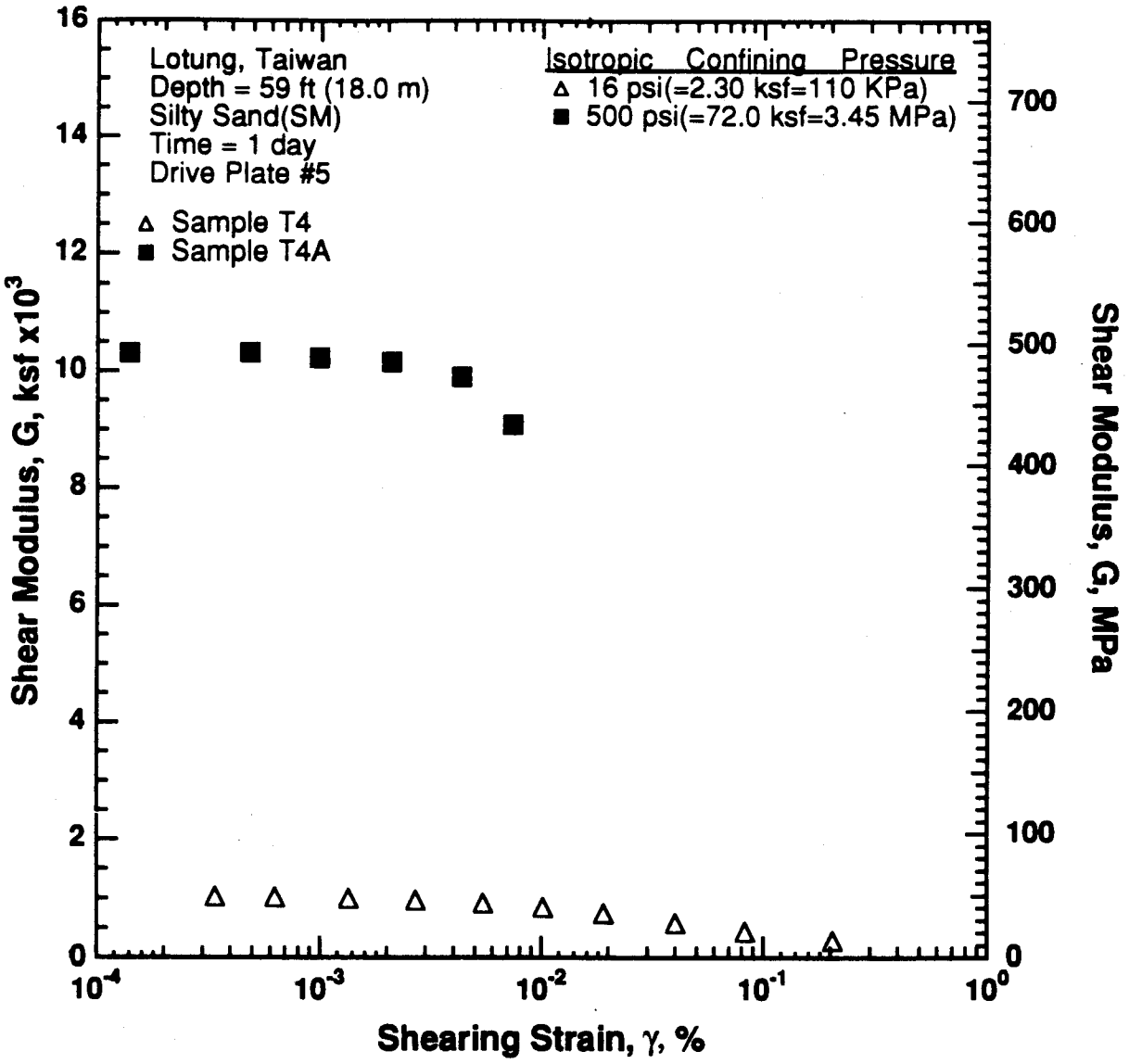

Figure 8.B.4.J-9
Variation in shear modulus with shearing strain and effective confining pressure from RC tests of samples T4 and T4A from borehole CH1.

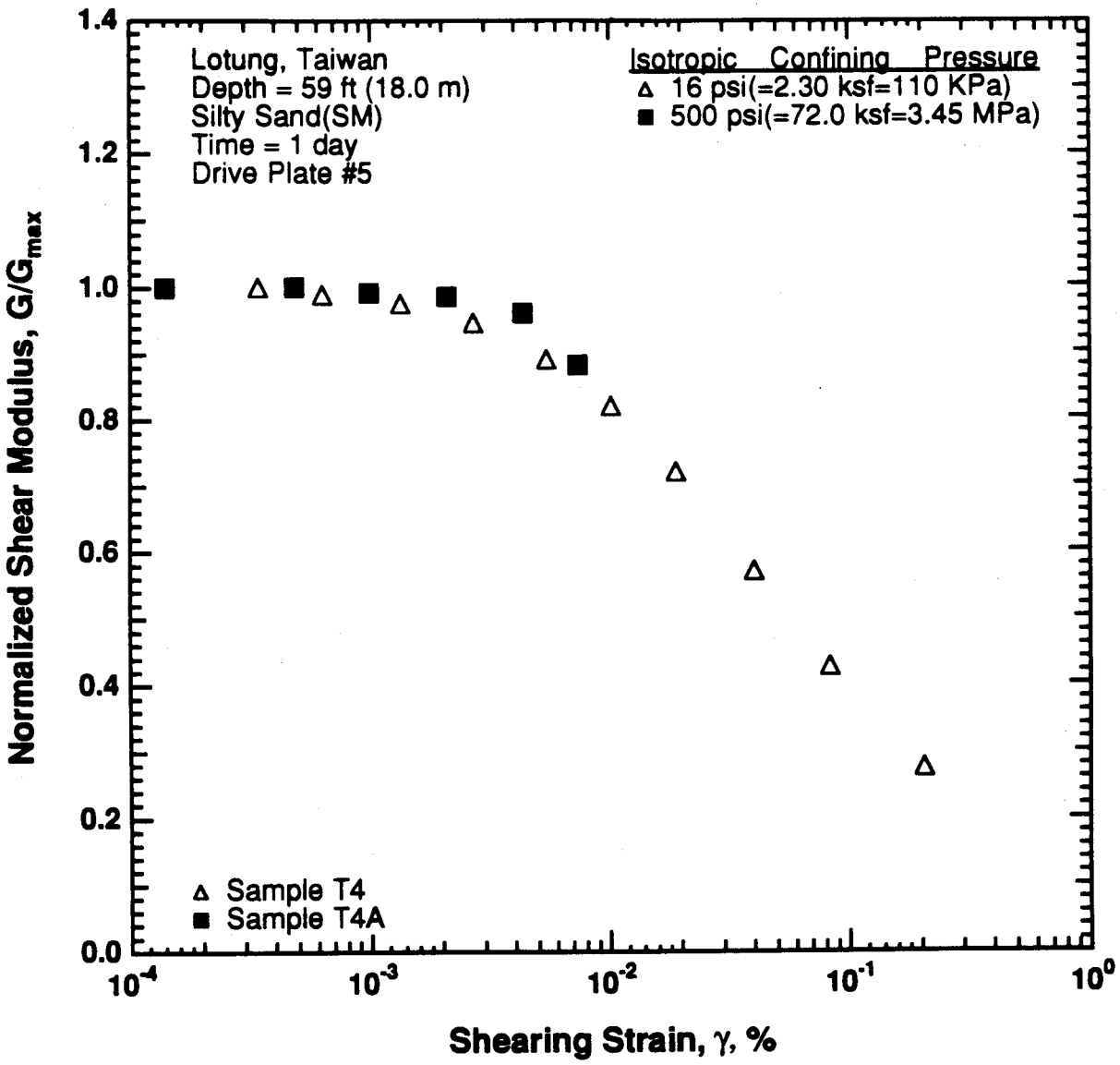

Figure 8.B.4.J-10
Comparison of the variation in normalized shear modulus with shearing strain and effective confining pressure from RC tests of samples T4 and T4A from borehole CH1.

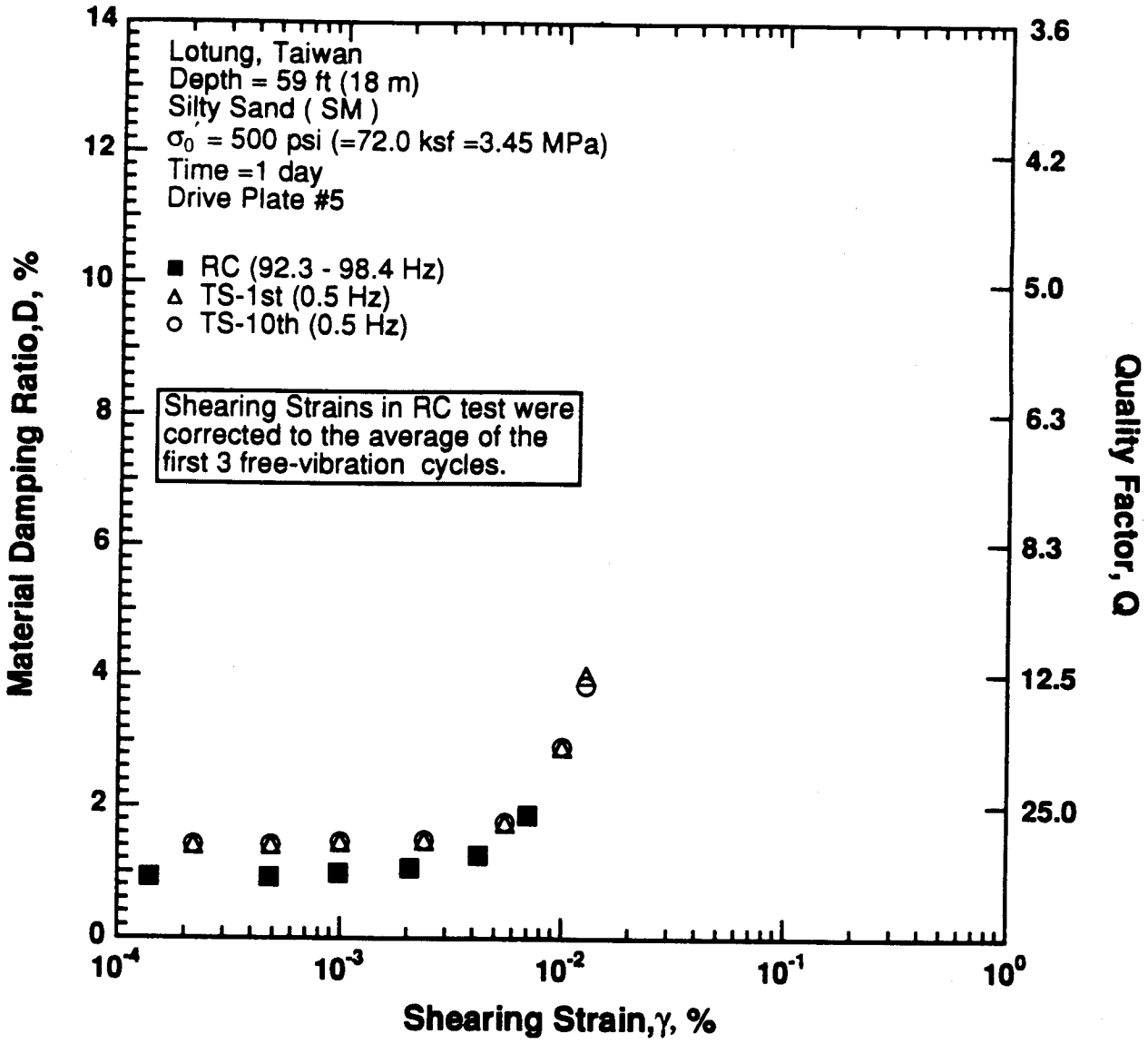

Figure 8.B.4.J-11
Variation in material damping ratio with shearing strain at an effective confining pressure of 500 psi (72.0 ksf, 3.45 MPa) from RCTS tests of sample T4A from borehole CH1.

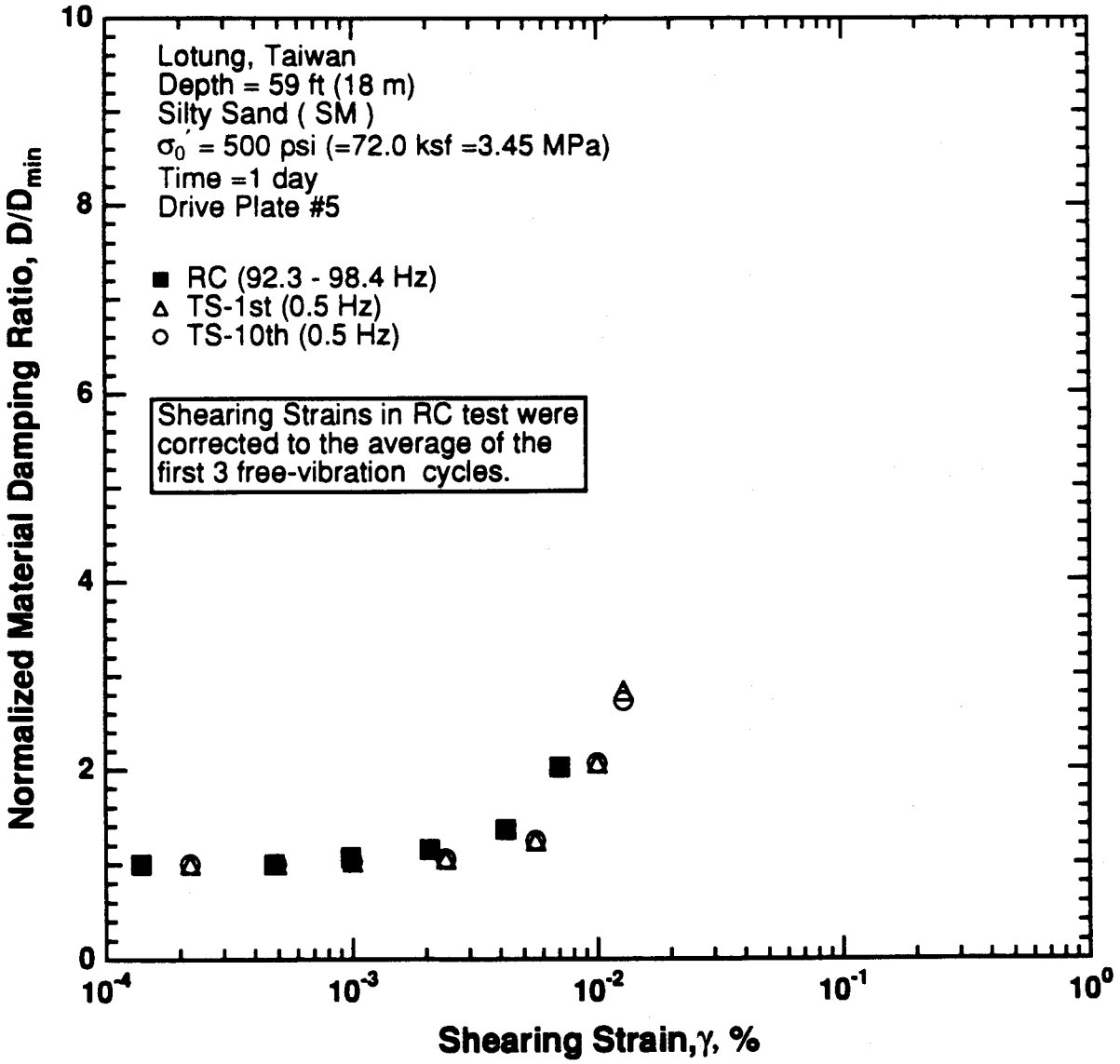

Figure 8.B.4.J-12
Variation in normalized material damping ratio with shearing strain at an effective confining pressure of 500 psi (72.0 ksf, 3.45 MPa) from RCTS tests of sample T4A from borehole CH1.

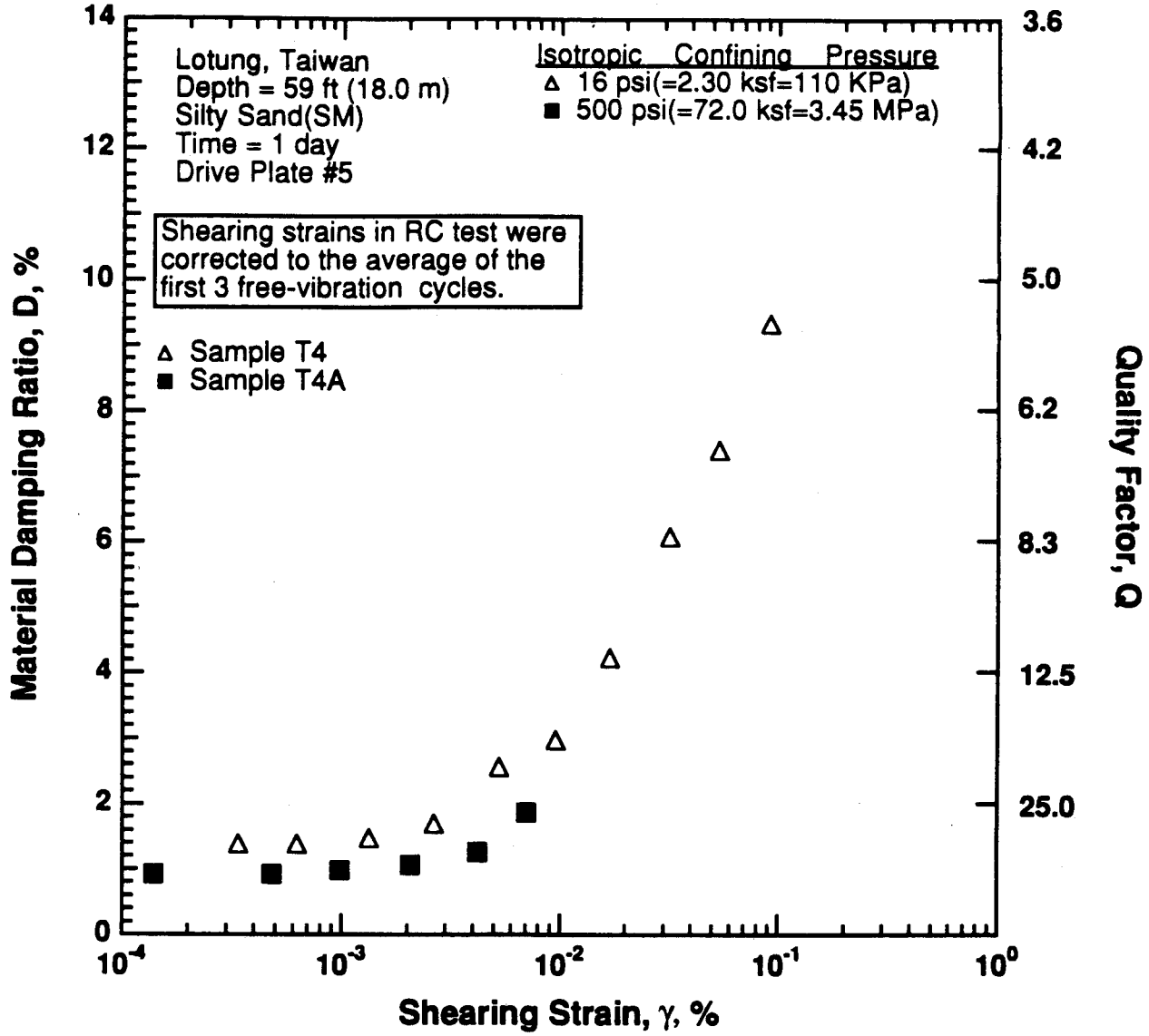

Figure 8.B.4.J-13
Variation in material damping ratio with shearing strain and effective confining pressure from RC tests of samples T4 and T4A from borehole CH1.

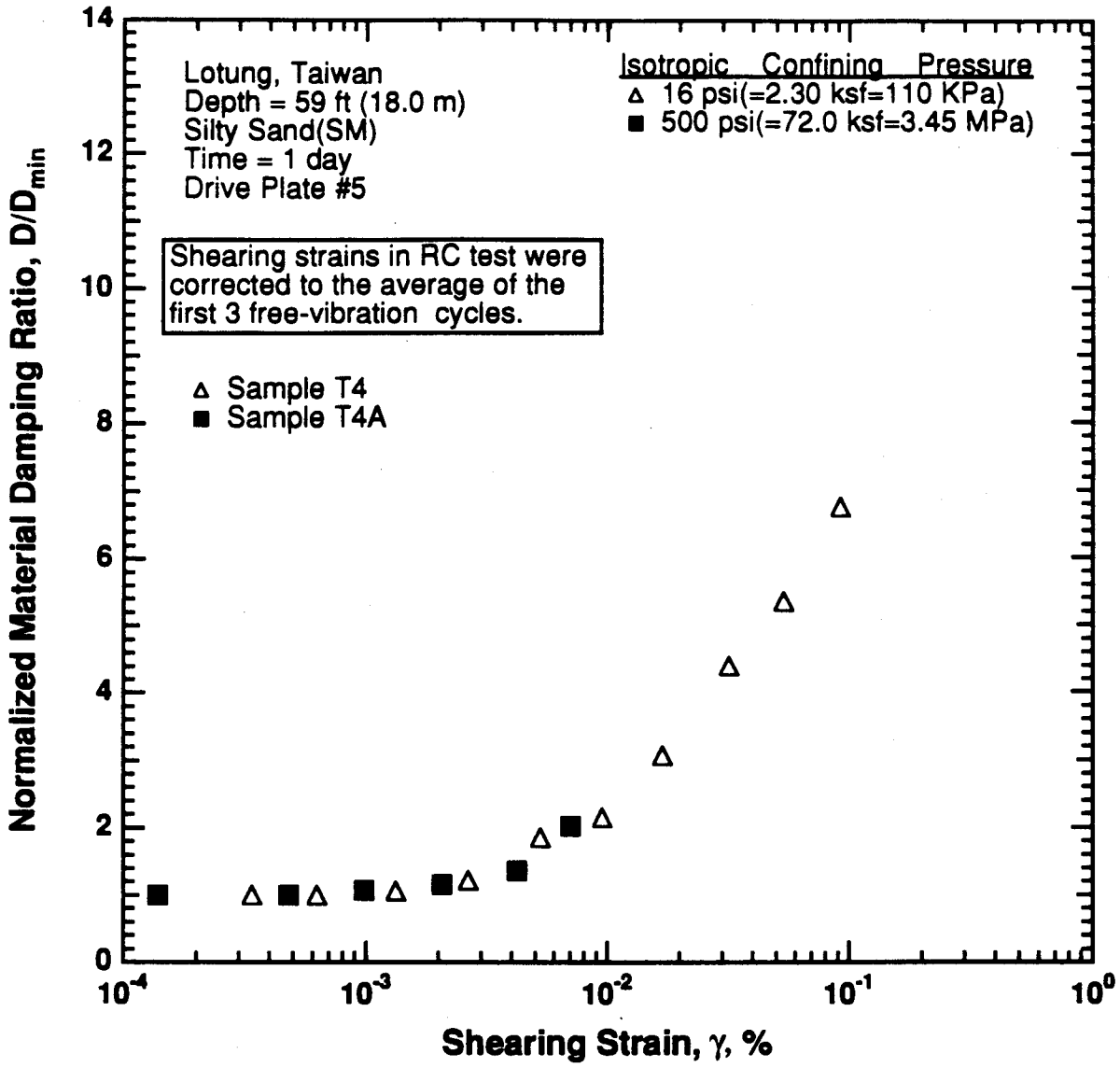

Figure 8.B.4.J-14
Comparison of the variation in normalized material damping ratio with shearing strain and effective confining pressure from RC tests of samples T4 and T4A from borehole CH1.

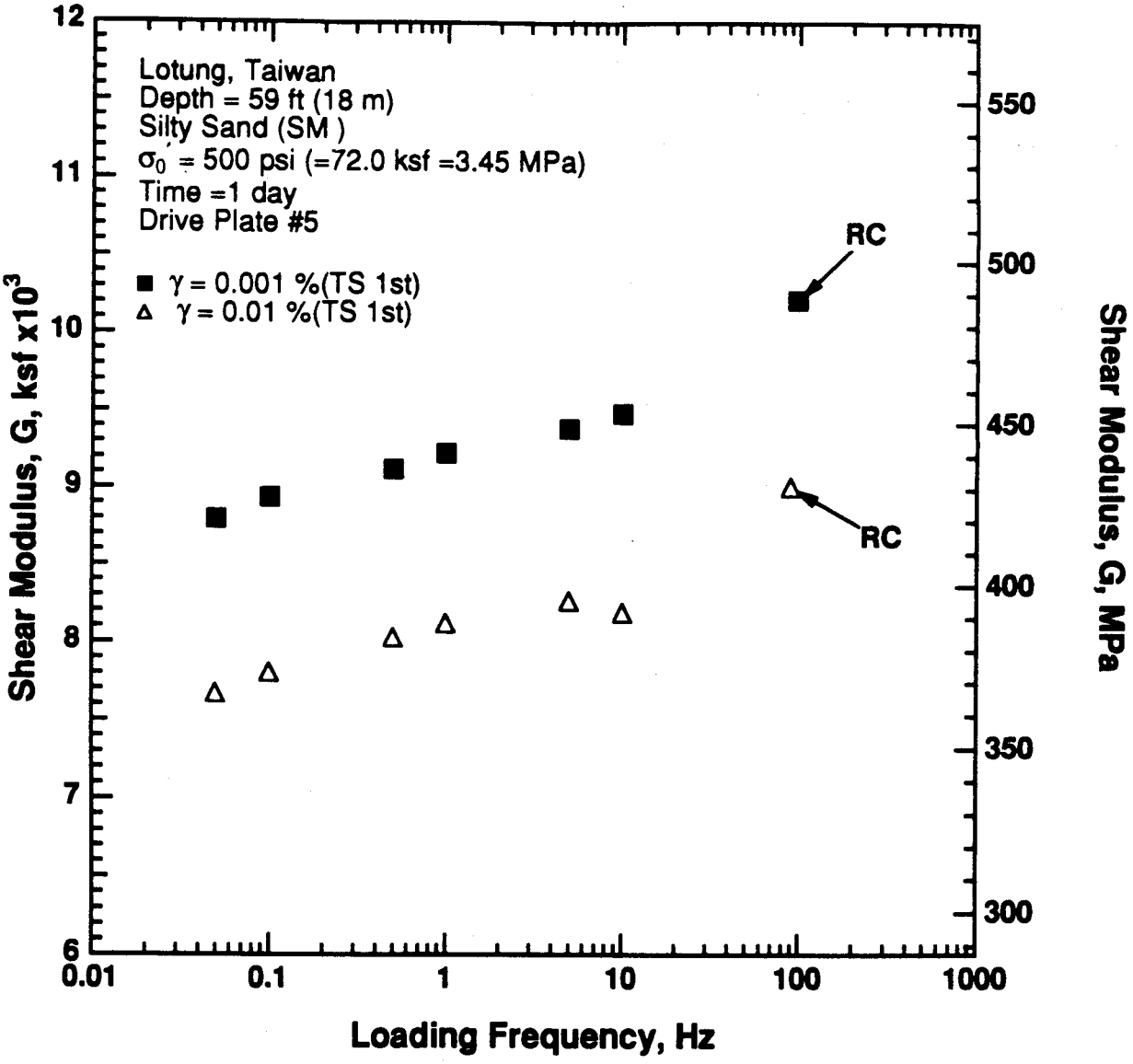

Figure 8.B.4.J-15
Variation in shear modulus with loading frequency and shearing strain at an effective confining pressure of 500 psi (72.0 ksf, 3.45 MPa) from RCTS tests of sample T4A from borehole CH1.

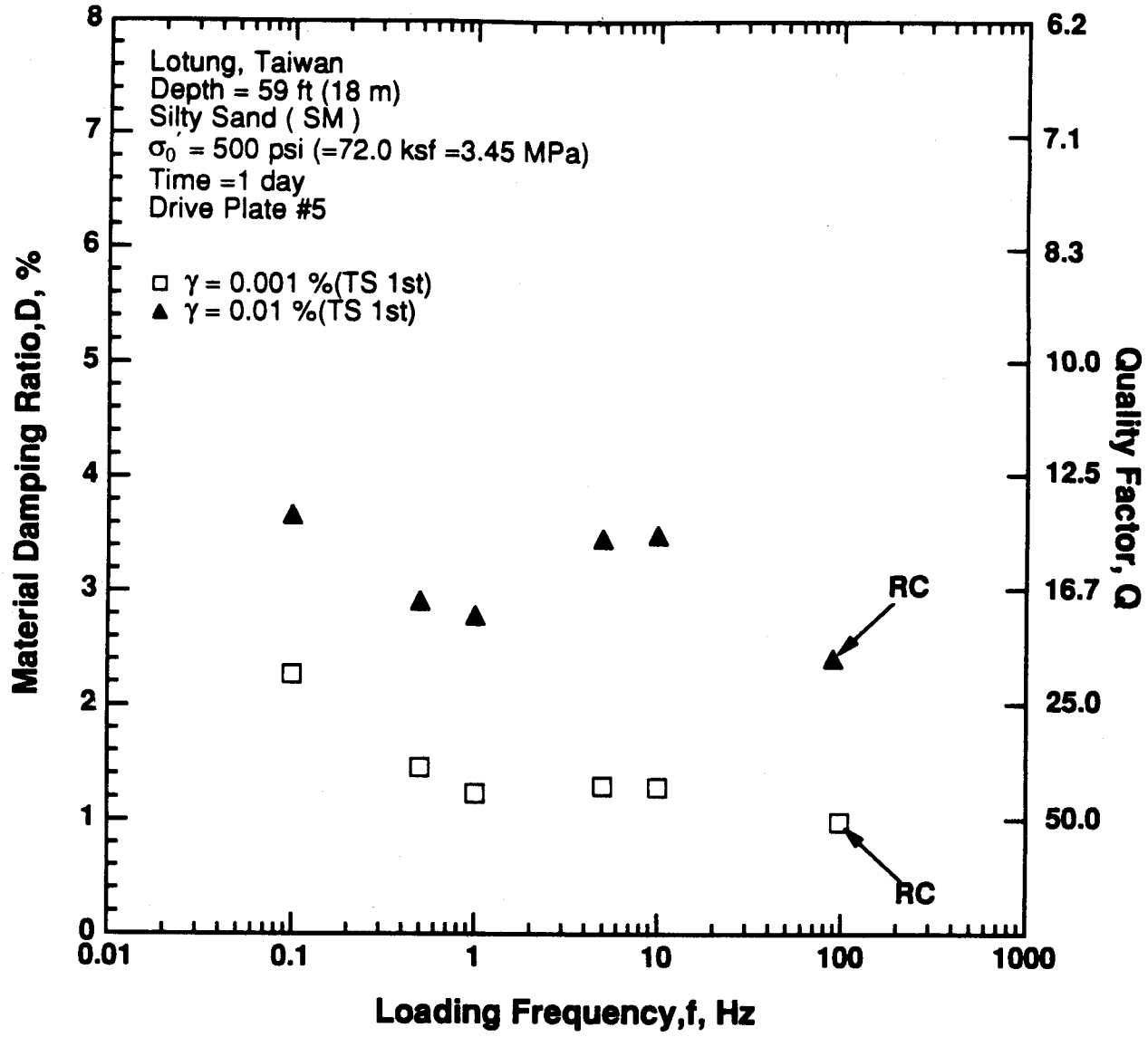

Figure 8.B.4.J-16
Variation in material damping ratio with loading frequency and shearing strain at an effective confining pressure of 500 psi (72.0 ksf, 3.45 MPa) from RCTS tests of sample T4A from borehole CH1.

APPENDIX K
DYNAMIC TESTS OF TREASURE ISLAND SAMPLE T2A, DEPTH = 33 FT (10.1 M)

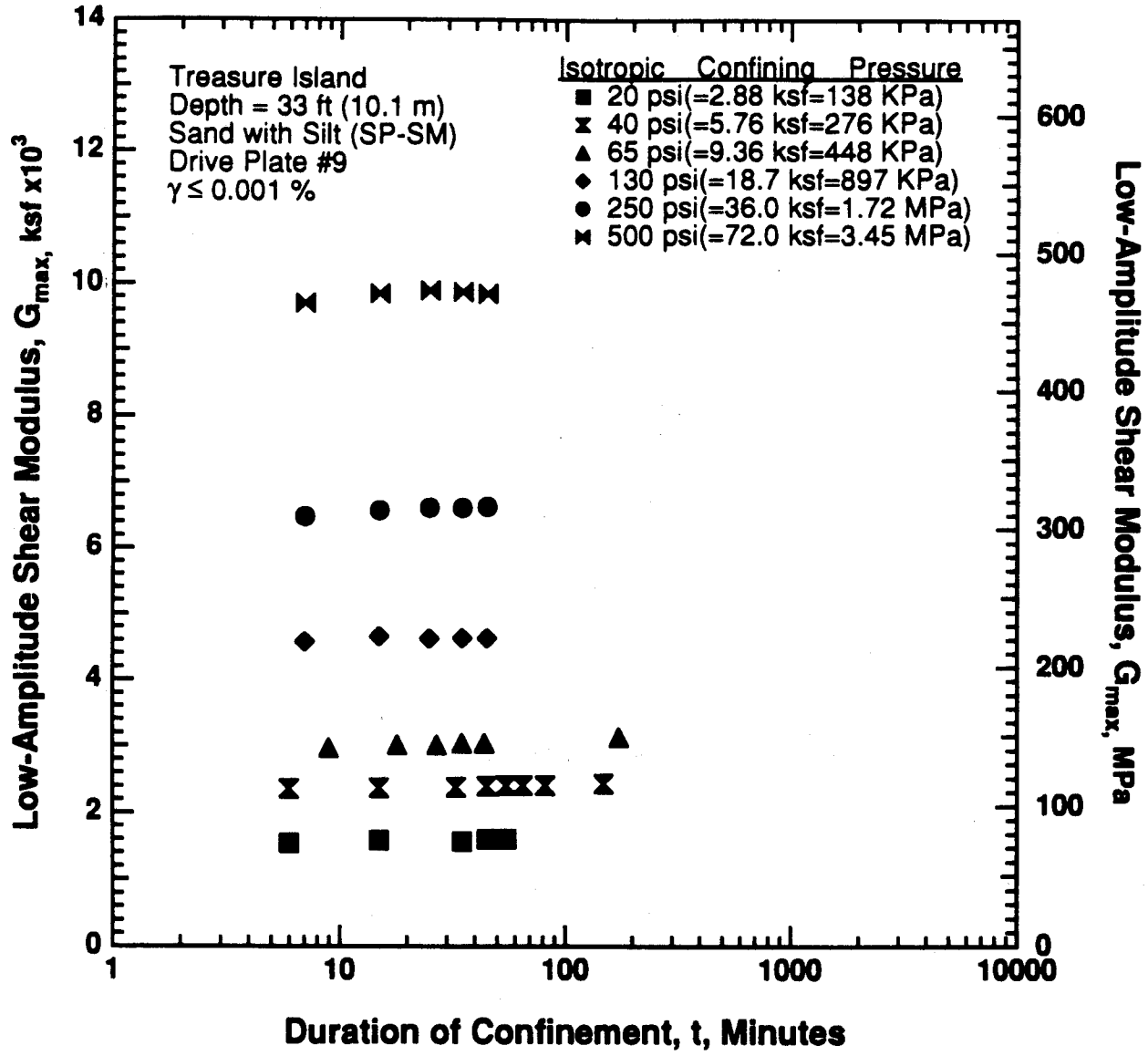

Figure 8.B.4.K-1
Variation in low-amplitude shear modulus with magnitude and duration of isotropic confining pressure from resonant column tests of sample T2A.

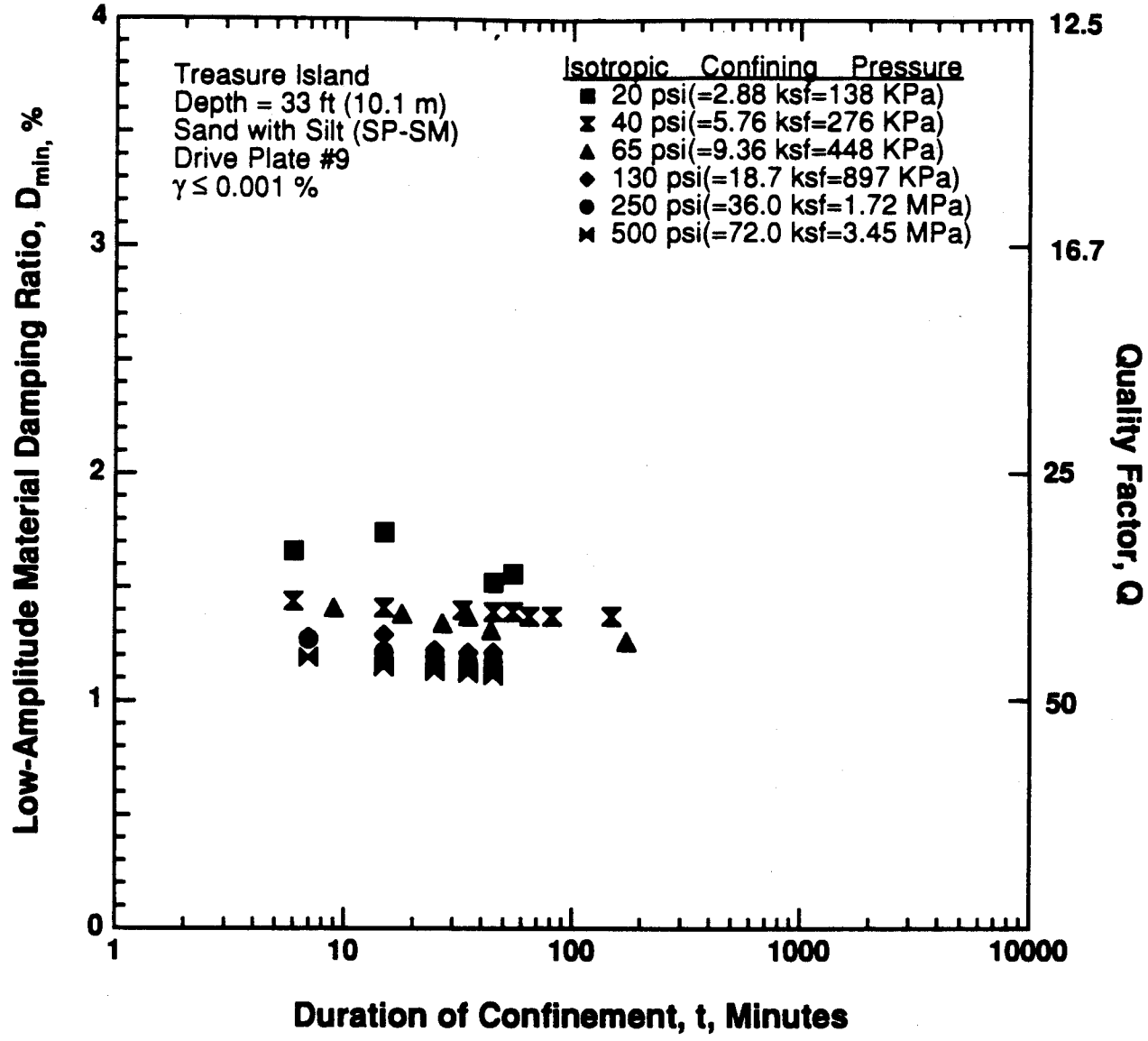

Figure 8.B.4.K-2
Variation in low-amplitude material damping ratio with magnitude and duration of isotropic confining pressure from resonant column tests of sample T2A.

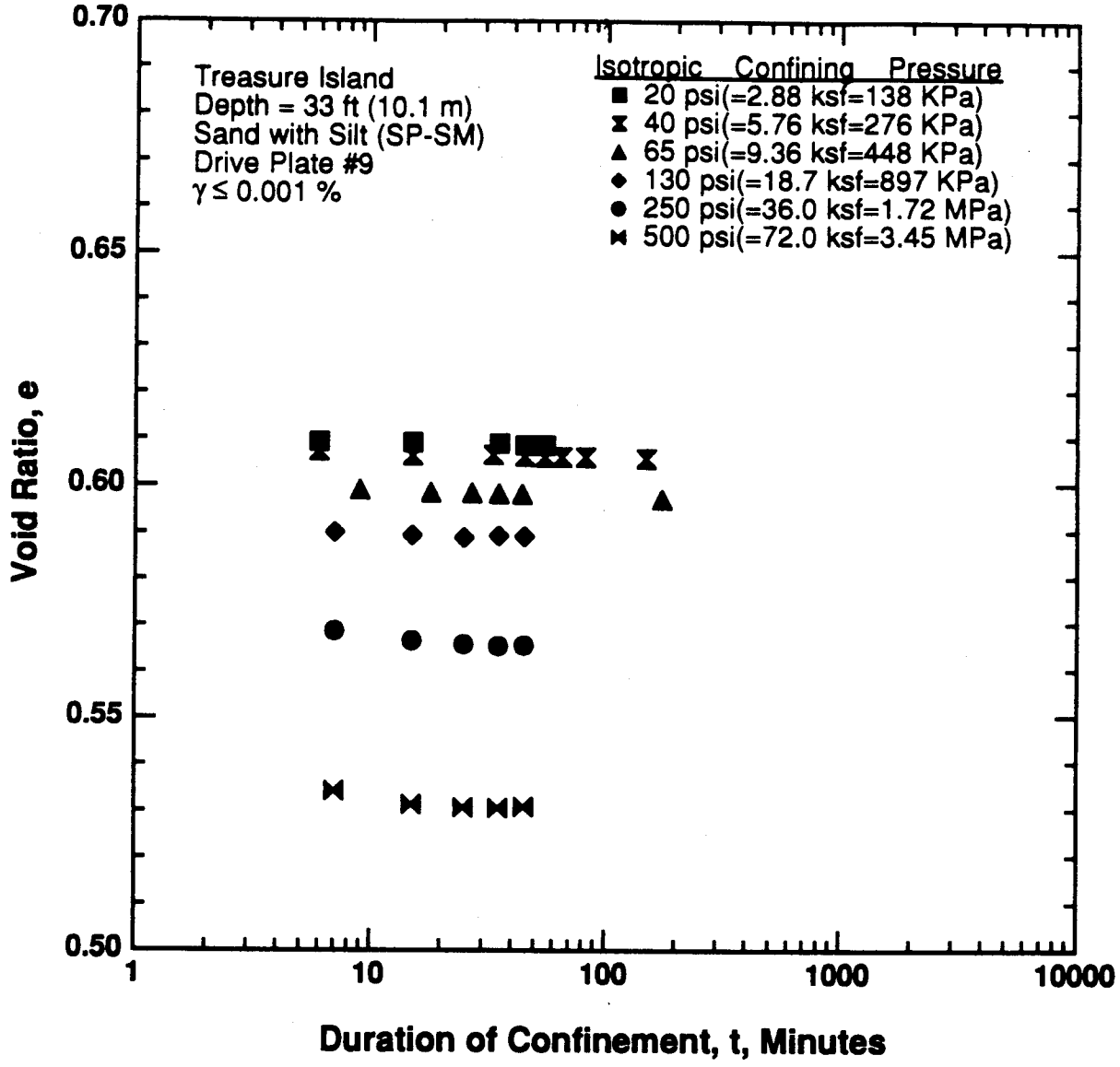

Figure 8.B.4.K-3
Variation in void ratio with magnitude and duration of isotropic confining pressure from resonant column tests of sample T2A.

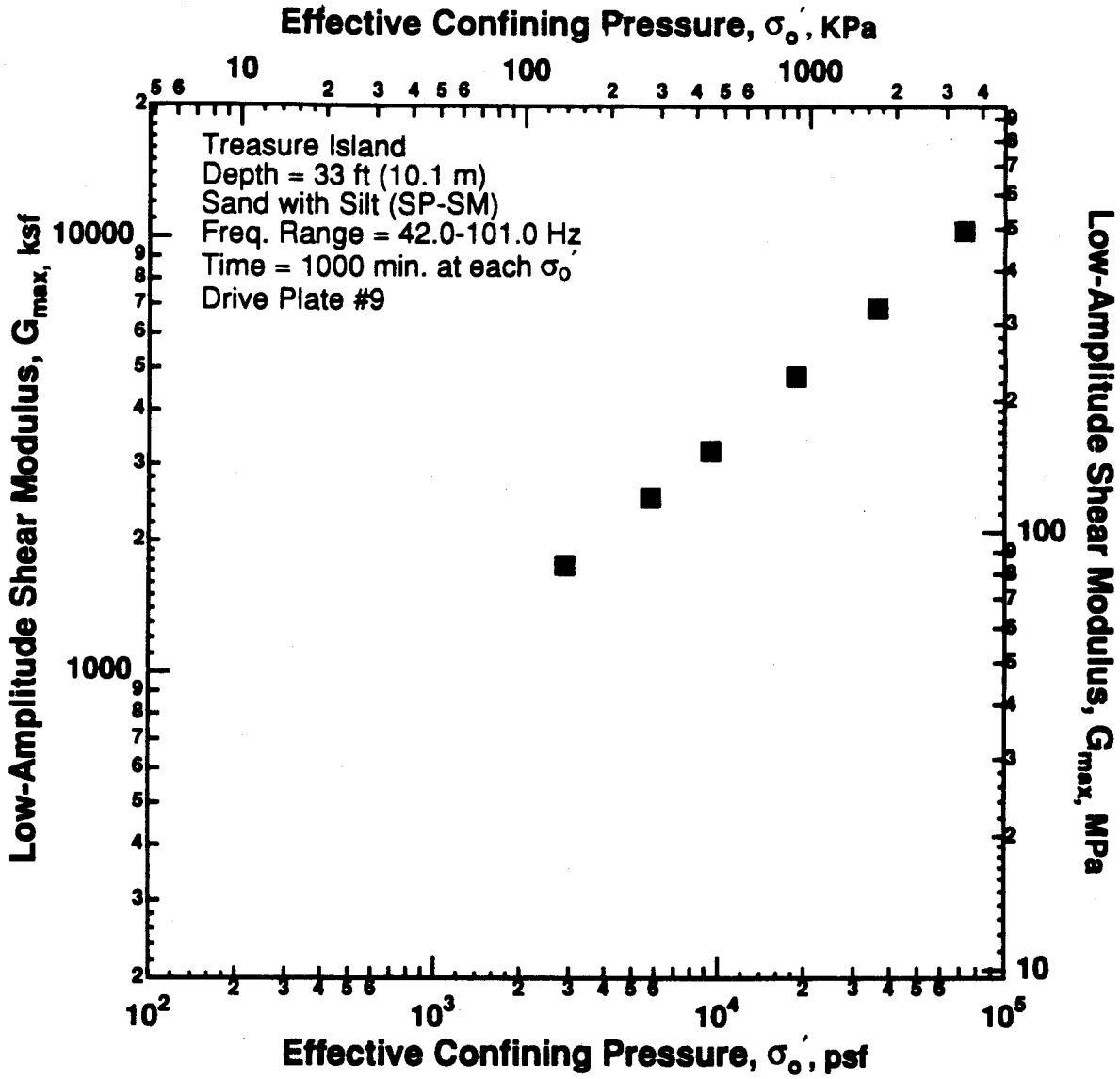

1. Shear modulus values at 1000 minutes were obtained by using linear interpolation from data presented in Figure K.1.

Figure 8.B.4.K-4
Variation in low-amplitude shear modulus with effective confining pressure from resonant column tests of sample T2A.

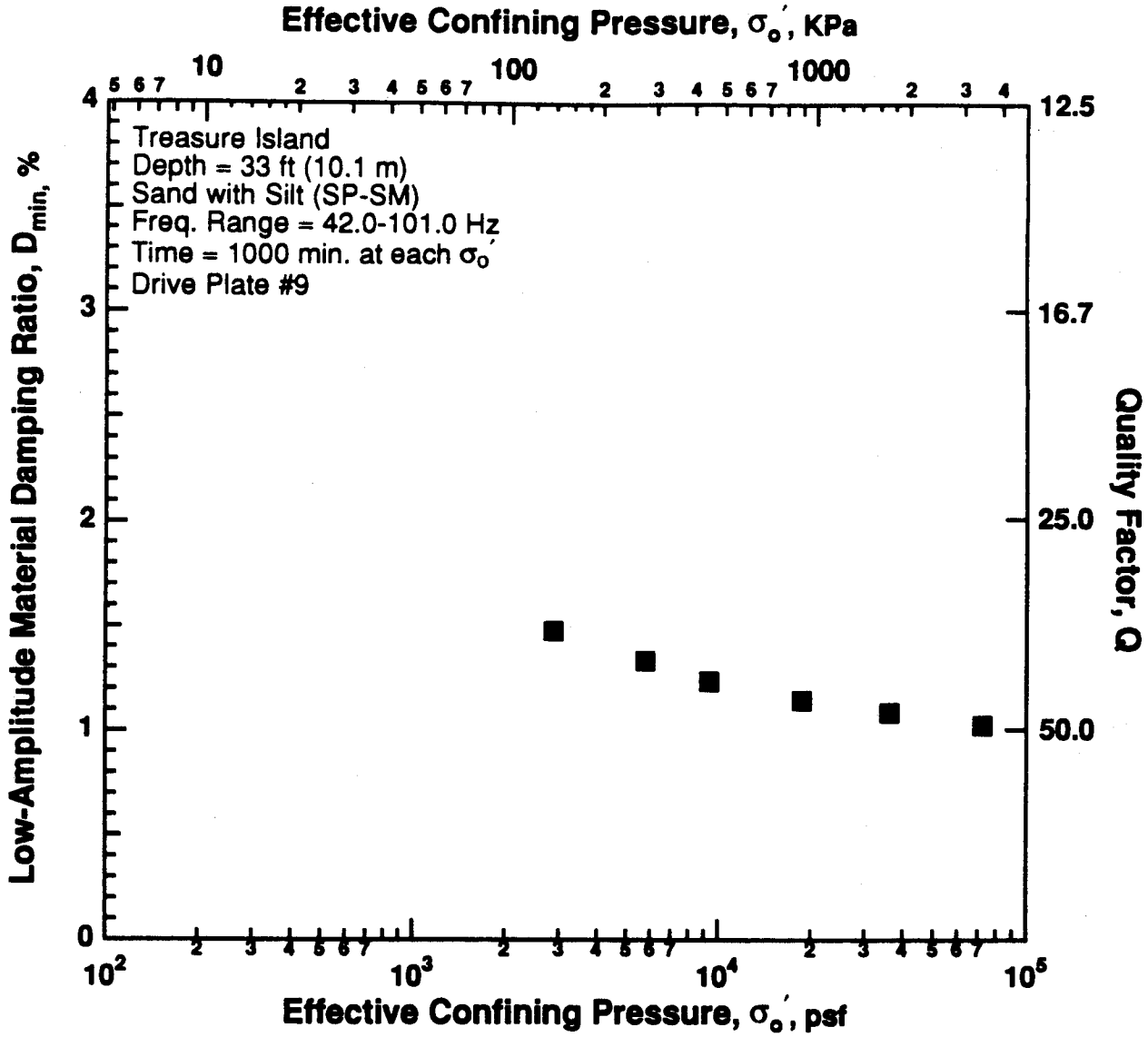

1. Damping Ratio values at 1000 minutes were obtained by using linear interpolation from data presented in Figure K.2.

Figure 8.B.4.K-5
Variation in low-amplitude material damping ratio with effective confining pressure from resonant column tests of sample T2A.

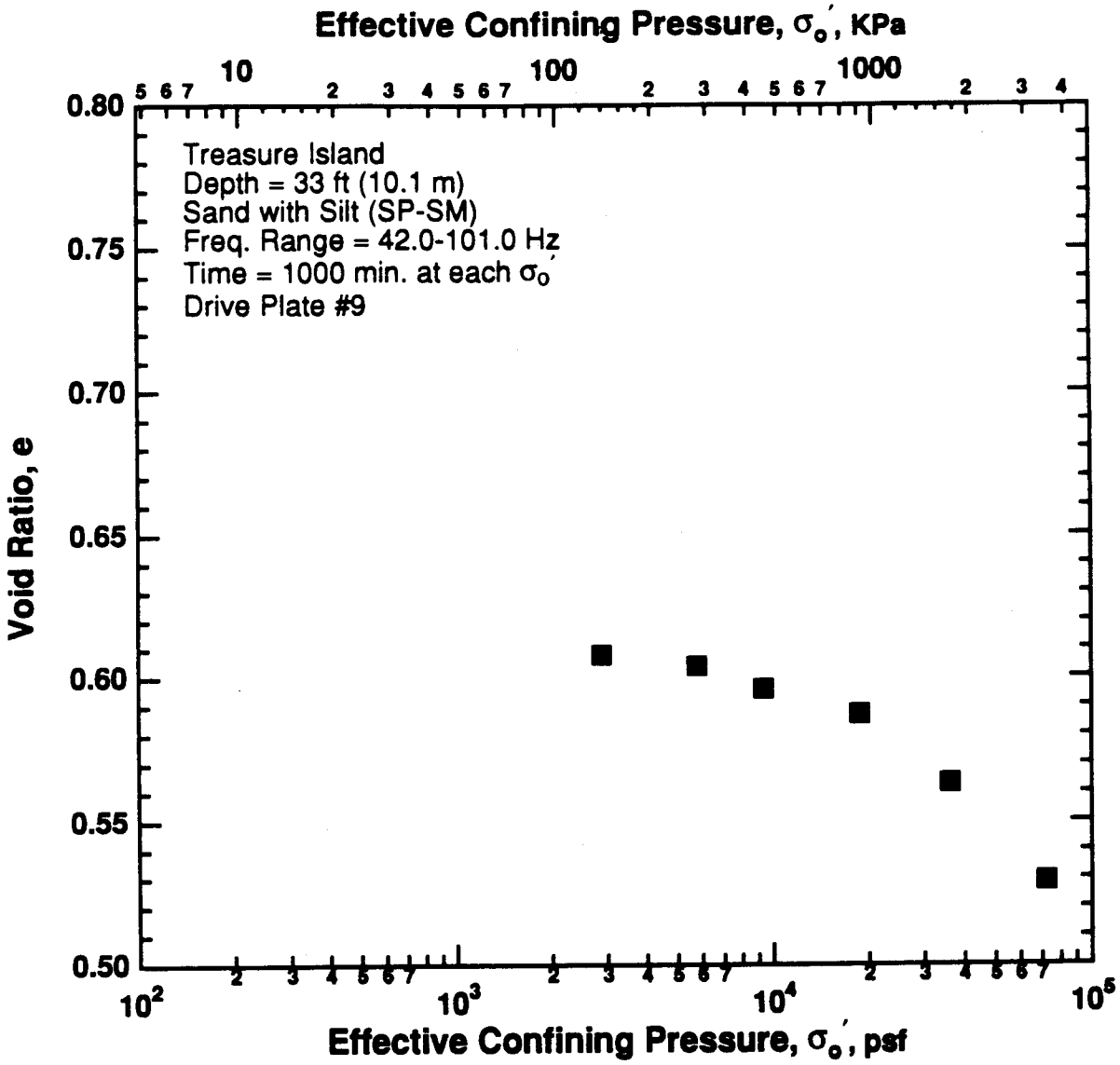

1. Void ratio values at 1000 minutes were obtained by using linear interpolation from data presented in Figure K.3.

Figure 8.B.4.K-6
Variation in void ratio with effective confining pressure from resonant column tests of sample T2A.

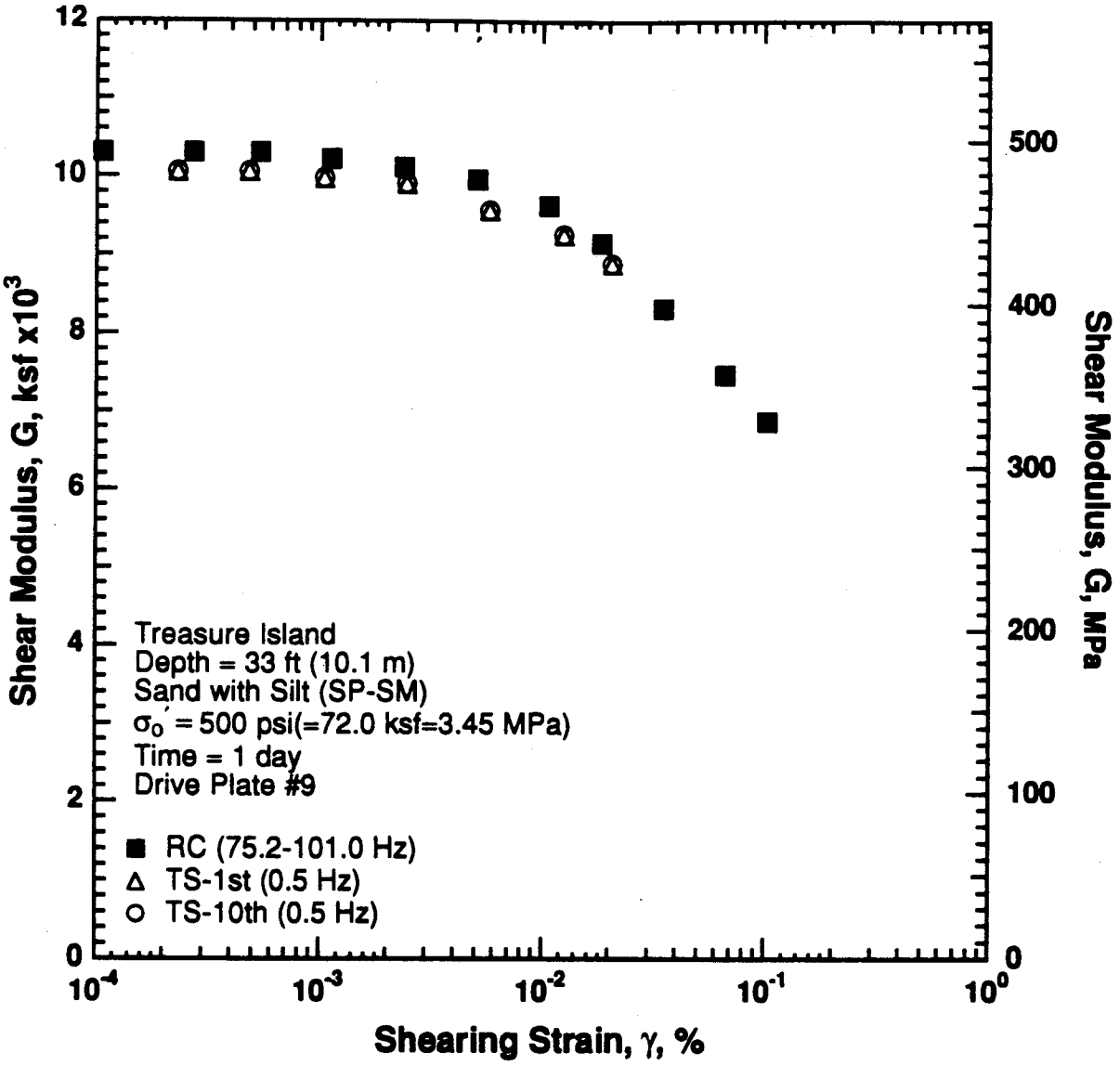

Figure 8.B.4.K-7
Variation in shear modulus with shearing strain at an effective confining pressure of 500 psi (72.0 ksf, 3.45 MPa) from RCTS tests of sample T2A.

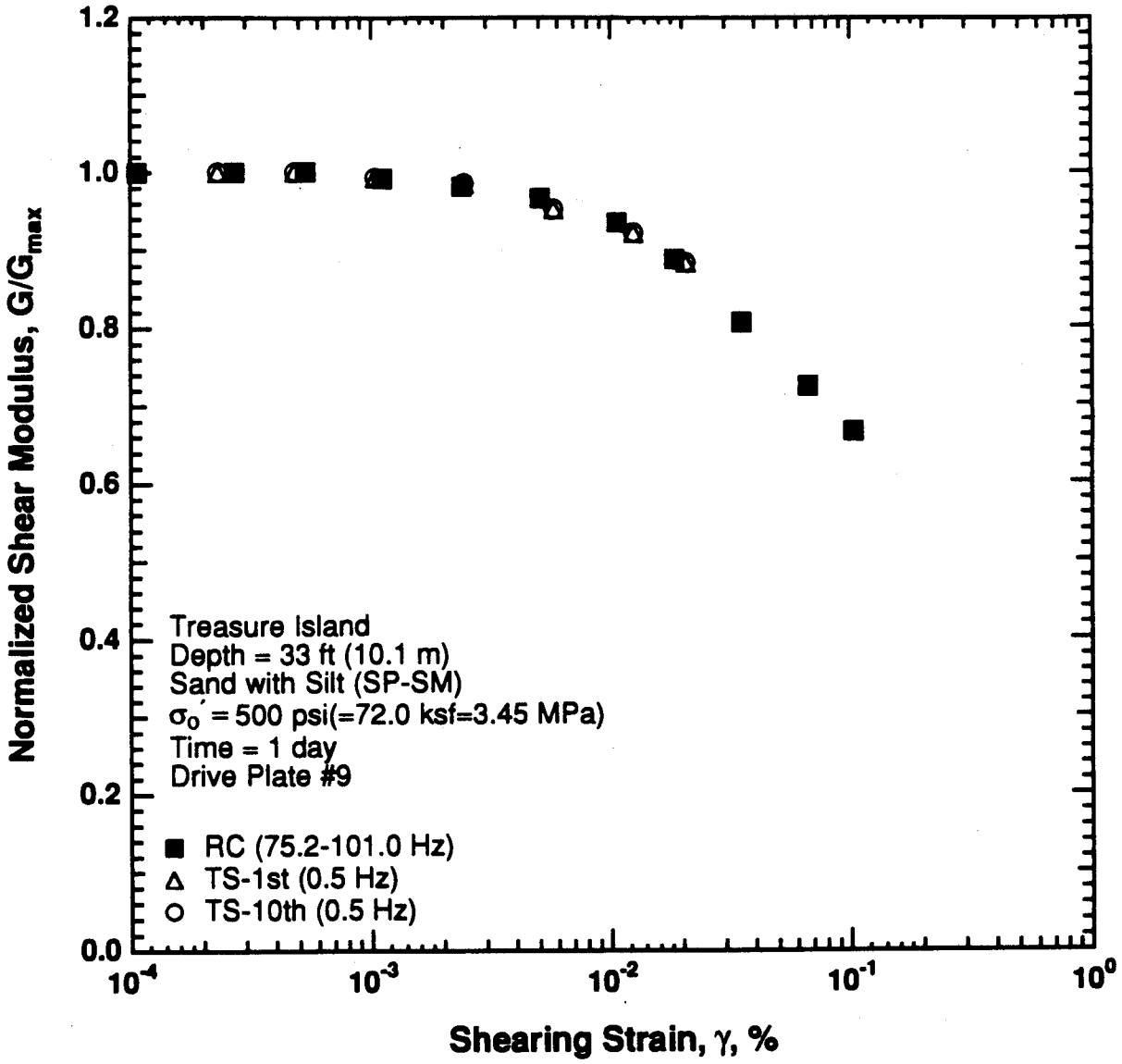

Figure 8.B.4.K-8
Variation in normalized shear modulus with shearing strain at an effective confining pressure of 500 psi (72.0 ksf, 3.45 MPa) from RCTS tests of sample T2A.

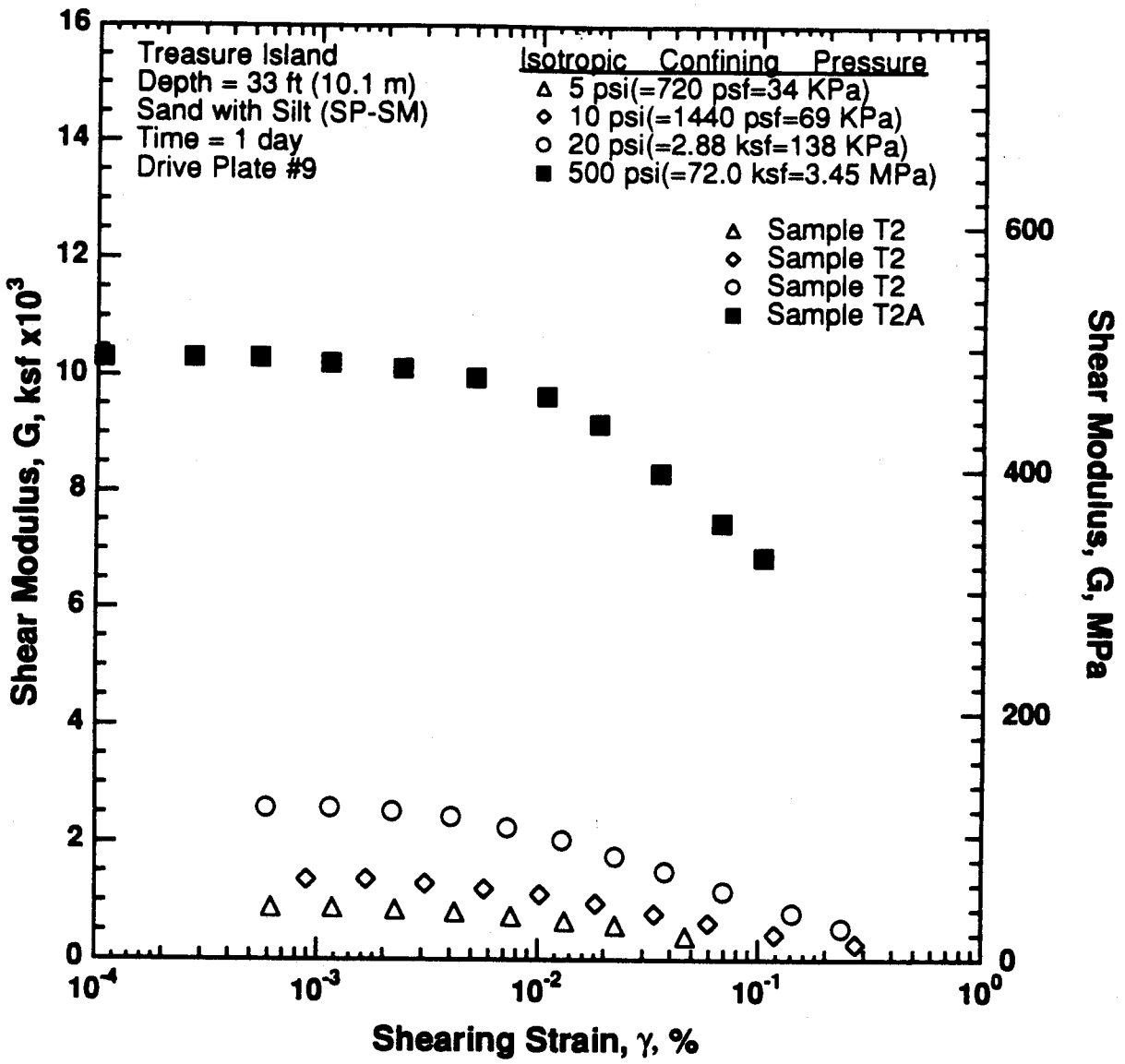

Figure 8.B.4.K-9
Variation in shear modulus with shearing strain and effective confining pressure from resonant column tests of samples T2 and T2A.

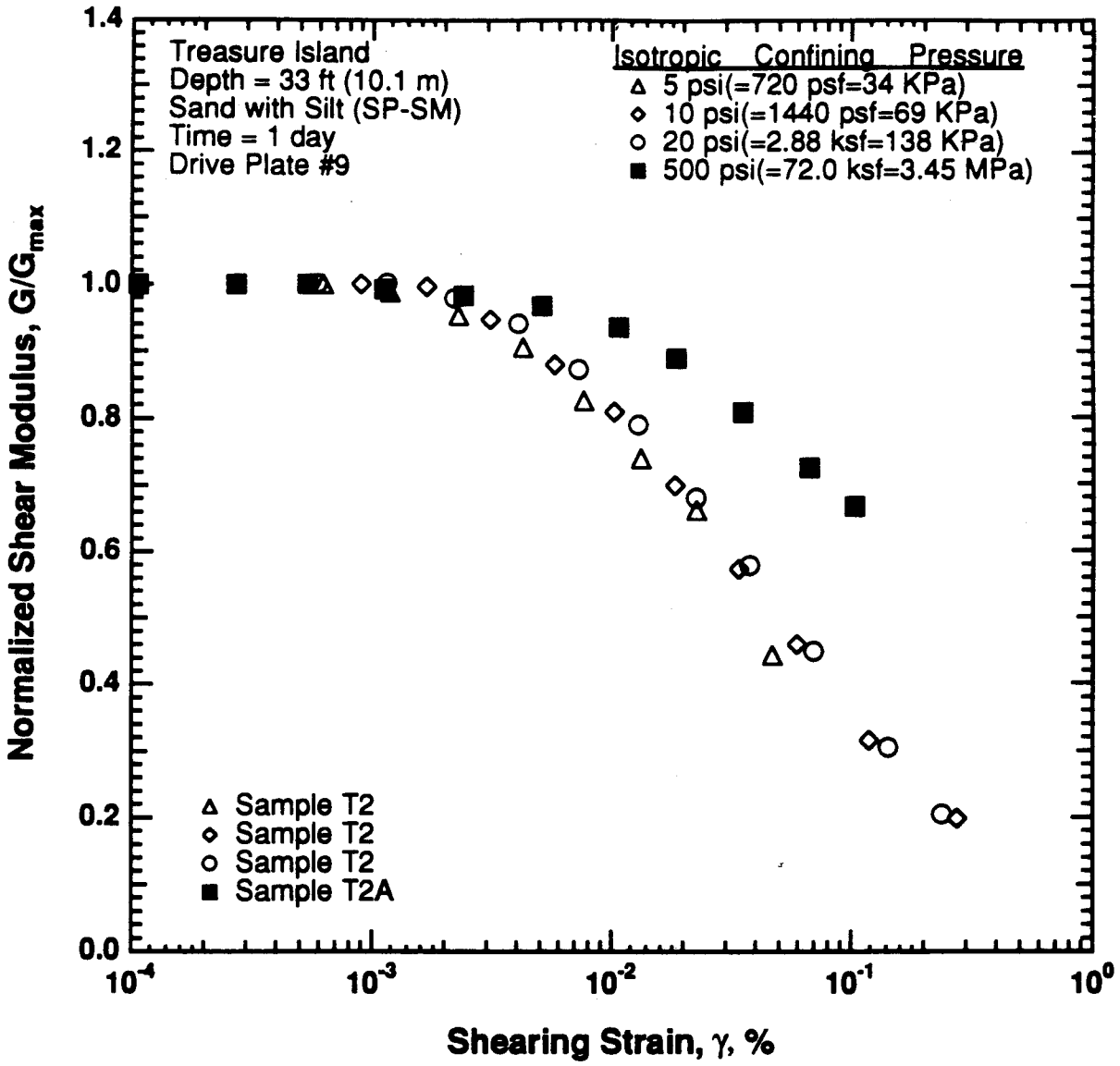

Figure 8.B.4.K-10
Comparison of the variation in normalized shear modulus with shearing strain and effective confining pressure from resonant column tests of samples T2 and T2A.

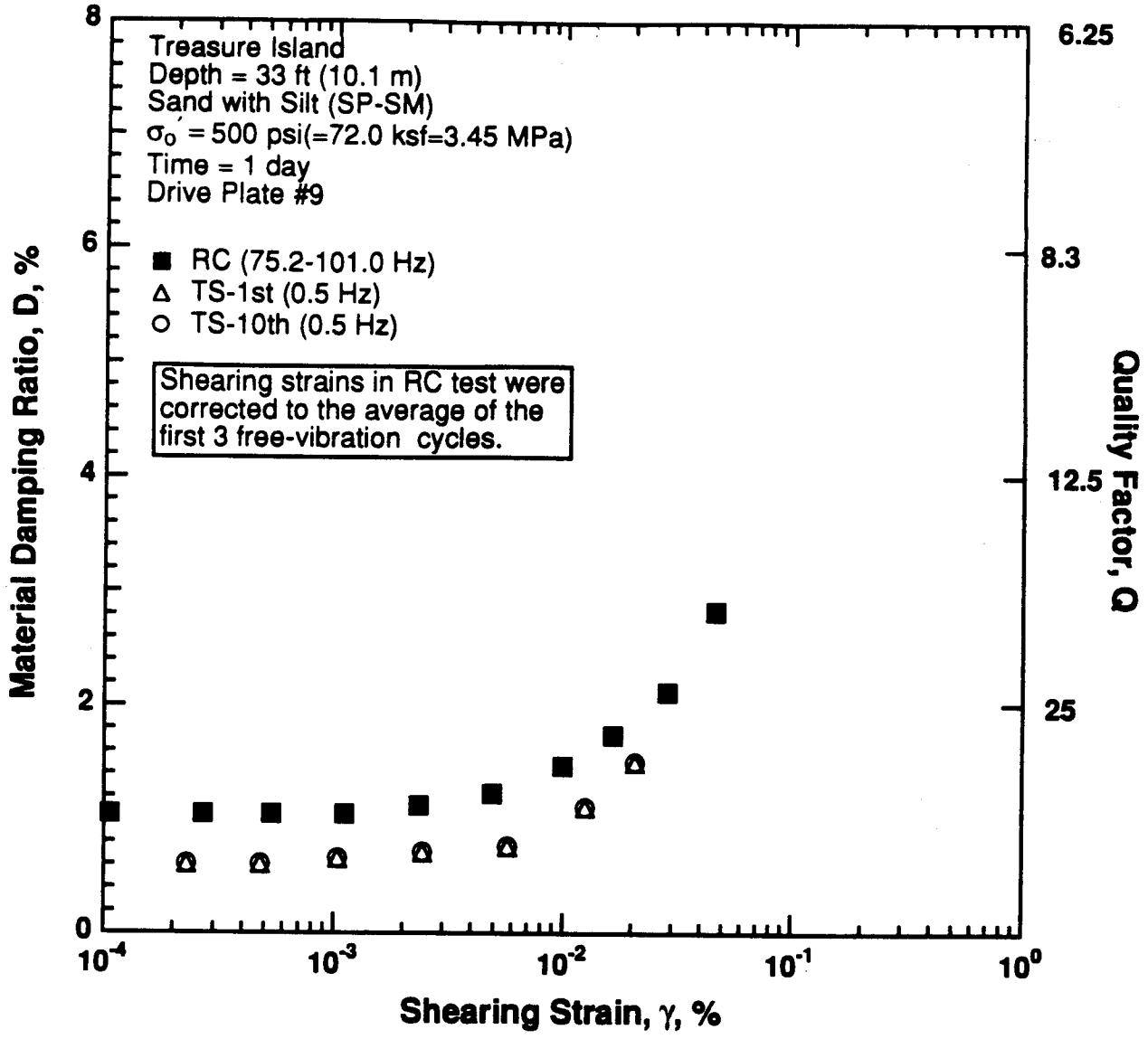

Figure 8.B.4.K-11
Variation in material damping ratio with shearing strain at an effective confining pressure of 500 psi (72.0 ksf, 3.45 MPa) from RCTS tests of sample T2A.

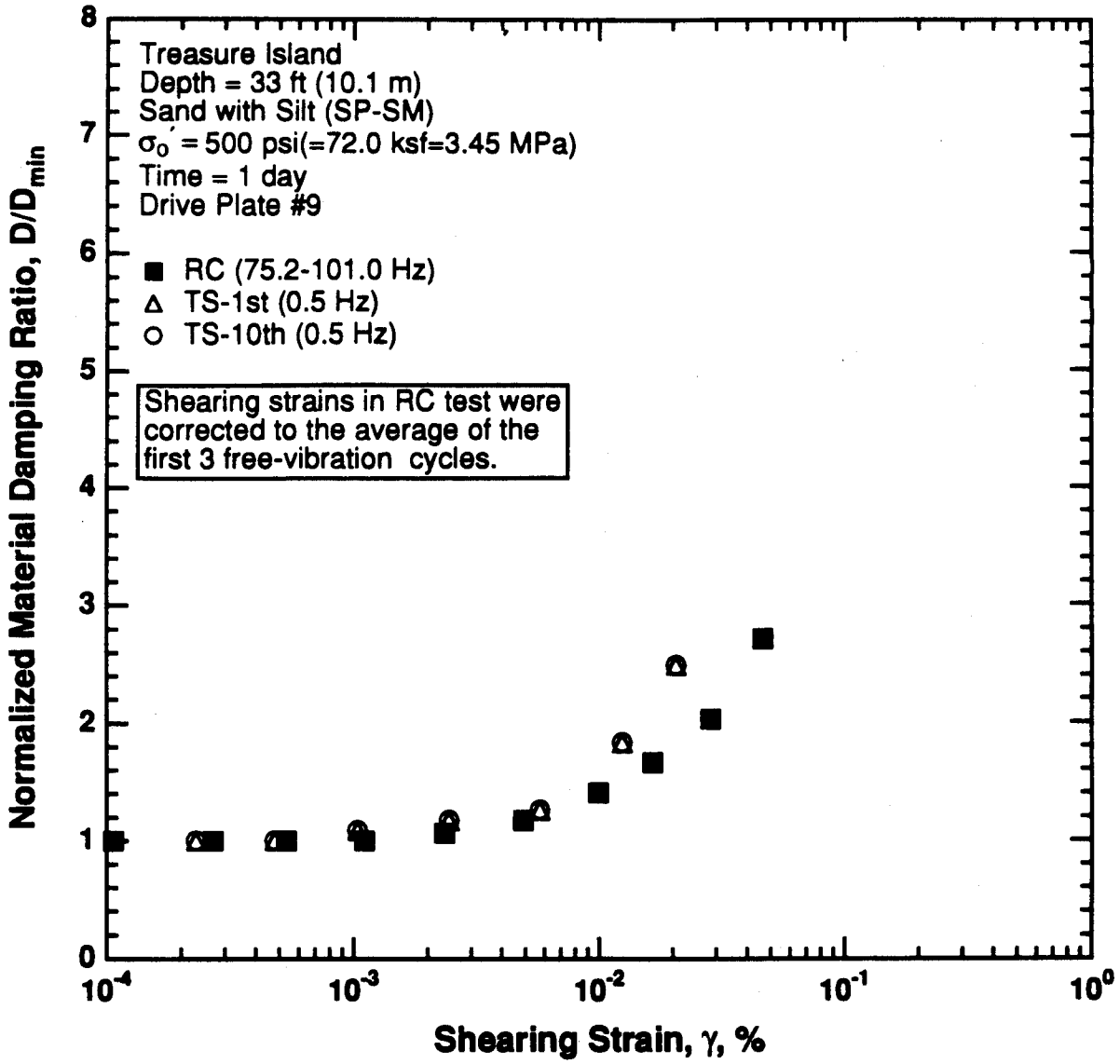

Figure 8.B.4.K-12
Variation in normalized material damping ratio with shearing strain at an effective confining pressure of 500 psi (72.0 ksf, 3.45 MPa) from RCTS tests of sample T2A.

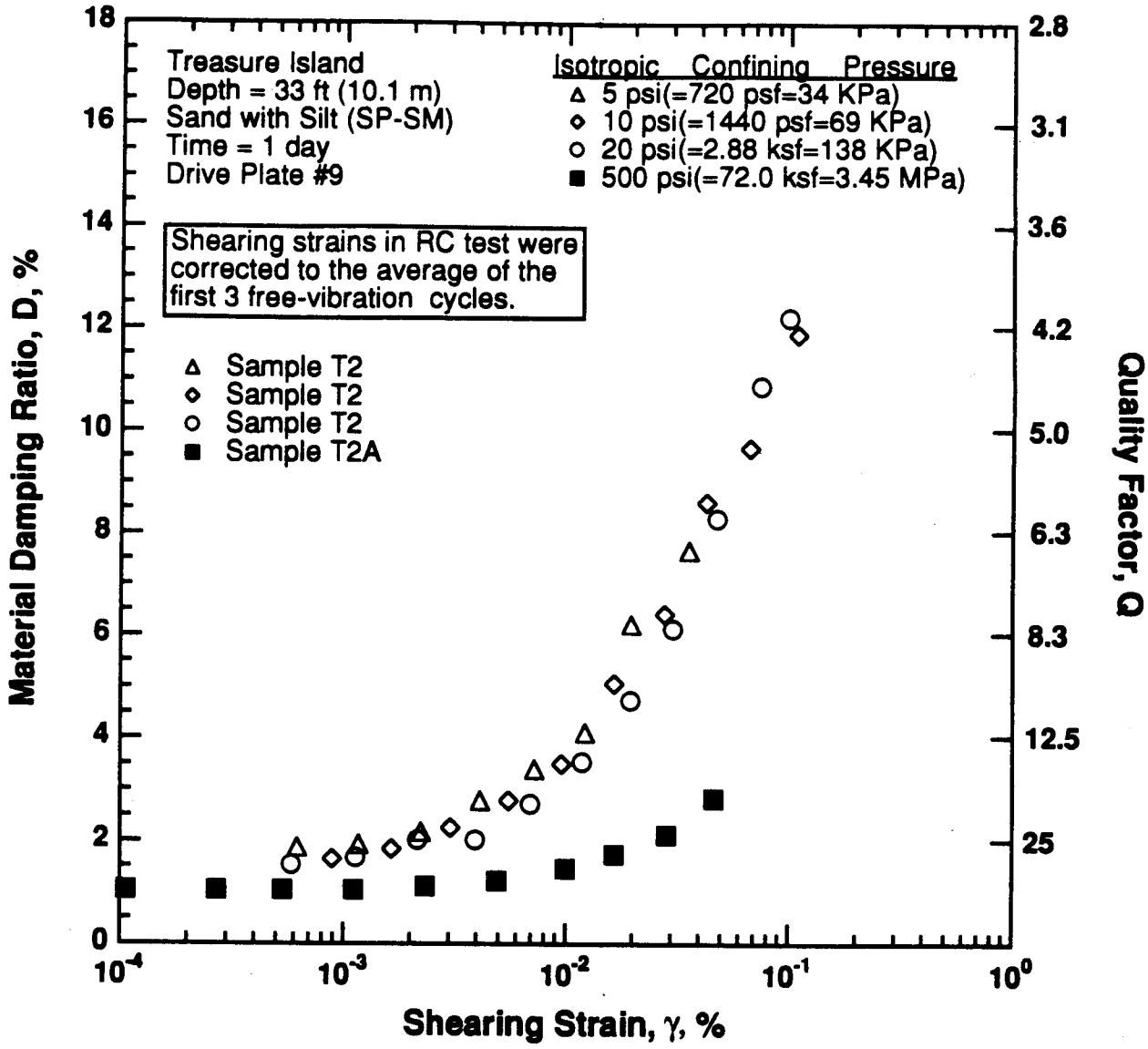

Figure 8.B.4.K-13
Variation in material damping ratio with shearing strain and effective confining pressure from resonant column tests of samples T2 and T2A.

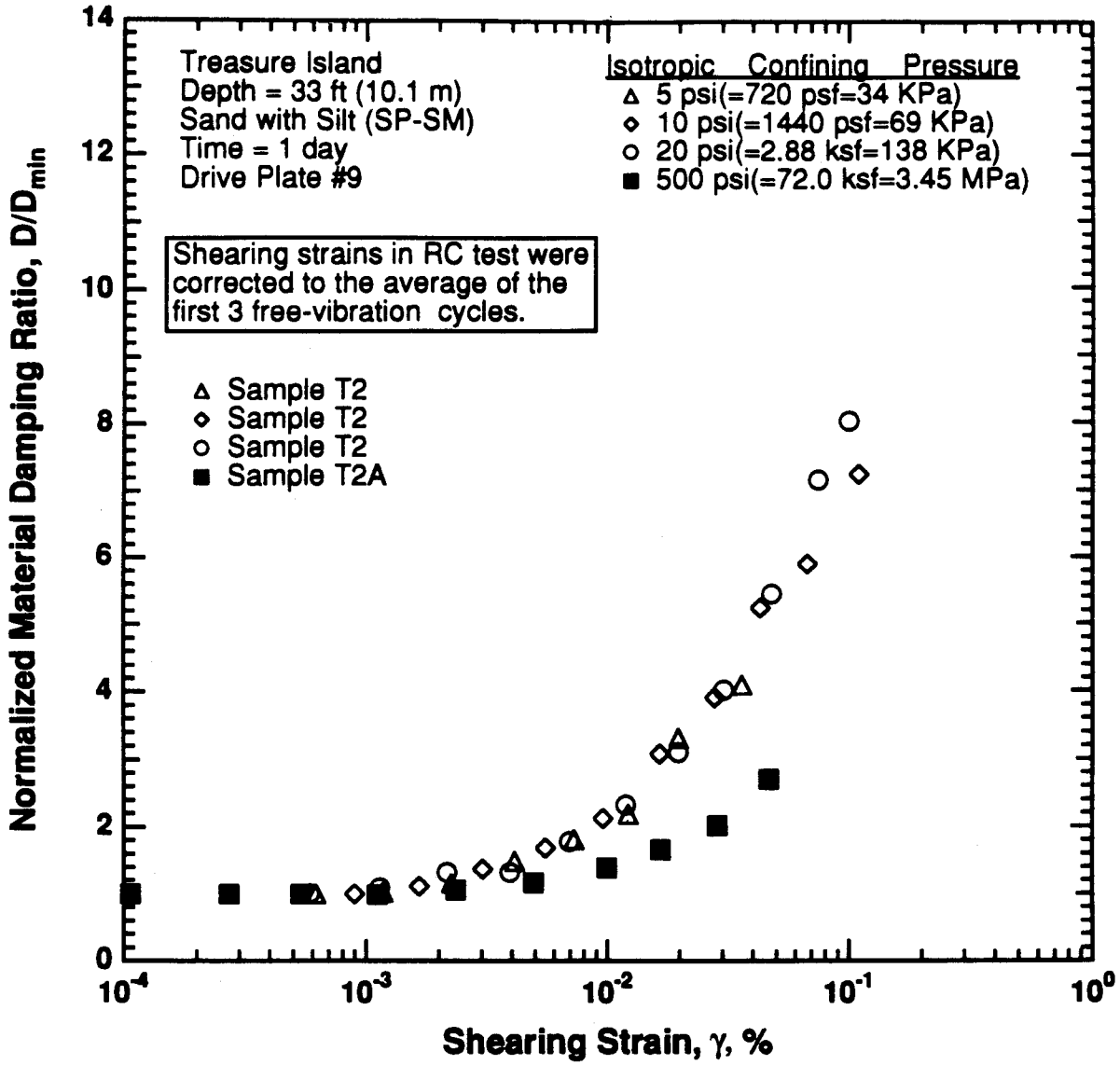

Figure 8.B.4.K-14
Comparison of the variation in normalized material damping ratio with shearing strain and effective confining pressure from resonant column tests of samples T2 and T2A.

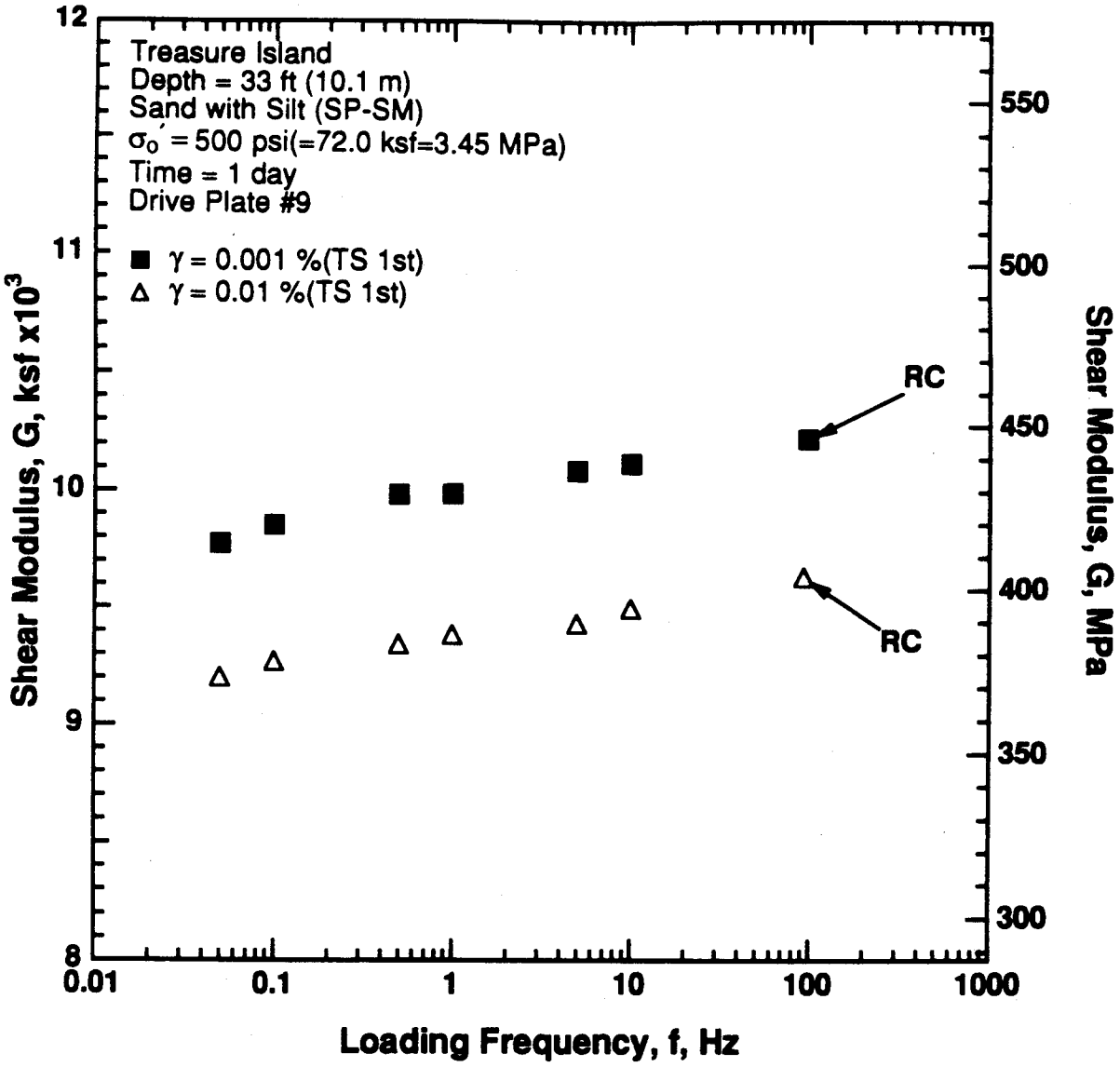

Figure 8.B.4.K-15
Variation in shear modulus with loading frequency and shearing strain at an effective confining pressure of 500 psi (72.0 ksf, 3.45 MPa) from RCTS tests of sample T2A.

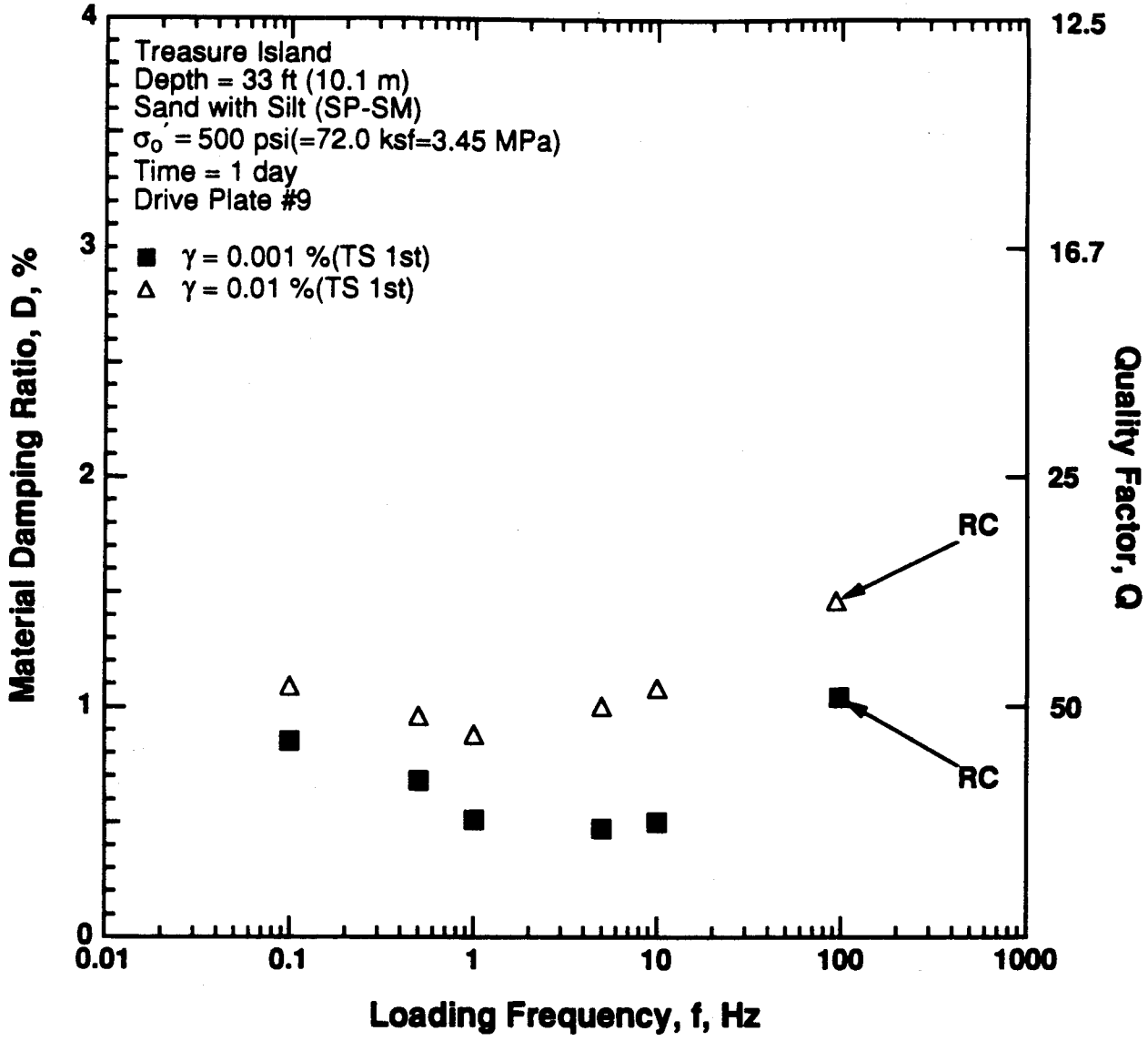

Figure 8.B.4.K-16
Variation in material damping ratio with loading frequency and shearing strain at an effective confining pressure of 500 psi (72.0 ksf, 3.45 MPa) from RCTS tests of sample T2A.

APPENDIX 8.B.5
DAMPING RATIOS FROM COMPRESSION AND SHEAR WAVE MEASUREMENTS IN THE LARGE-SCALE TRIAXIAL CHAMBER

CONTENTS

APPENDIX 8.B.5
DAMPING RATIOS FROM COMPRESSION AND SHEAR WAVE MEASUREMENTS IN THE LARGE-SCALE TRIAXIAL CHAMBER

1—INTRODUCTION

8.B.5.1.1 Background

To predict dynamic ground response accurately, models of the sub-surface soils at a site are needed. Values of material damping (attenuation) and shear modulus are almost always required. Typically the variation in these parameters with strain is also required. However, values at small strains are important reference points which optimally are determined in situ by seismic techniques such as the crosshole or downhole. These measurements are straightforward for evaluating moduli by measuring wave velocities. These measurements are not as straightforward for evaluating material damping. Therefore as part of an EPRI supported study, a large-scale laboratory experiment was conducted under carefully controlled conditions to investigate: (1) material damping measurements, and (2) material damping in shear and compression of dry sand at small strains.

8.B.5.1.2 Purpose and Objectives

A large-scale triaxial chamber constructed by Kopperman et al (1982) was used in these seismic studies. The chamber, referred to as the LSTC, was constructed to emulate crosshole and downhole seismic tests in the laboratory. The chamber is a cubical box with interior dimensions of 7 ft (2.1 m) on a side. The LSTC was designed to confine dry sand under

isotropic $(\bar{\sigma}_1 = \bar{\sigma}_2 = \bar{\sigma}_3)$, biaxial $(\bar{\sigma}_1 > \bar{\sigma}_2 = \bar{\sigma}_3$ or $\bar{\sigma}_1 = \bar{\sigma}_2 > \bar{\sigma}_3)$,

and true triaxial states of stress $(\bar{\sigma}_1 > \bar{\sigma}_2 > \bar{\sigma}_3)$.

The purpose of the LSTC is to allow wave propagation studies to be conducted in soil systems such as the dry sand used in these tests.

Lee (1993) conducted a comprehensive study of compression (P) and shear(S) wave velocity measurements in anisotropic material. He used sand confined in the LSTC. In conjunction with his work, he developed numerous records of wave propagation in the sand under various states of stress which were only analyzed for wave velocity. Therefore, this study was undertaken with the primary purpose of evaluating material damping in the sand from these existing records. Measurements under the following two states of stress were considered: (1) isotropic and (2) biaxial with $\bar{\sigma}_v$= constant and $\bar{\sigma}_{h1} = \bar{\sigma}_{h2}$ and varying.

Lee (1993) performed compression and shear wave measurements in the dry sand at small strains. The measurements were obtained with velocity transducers and accelerometers buried in the sand. These measurement were also collected by performing forward- and reverse-array measurements in an attempt to eliminate some variables that might adversely effect the records. The objectives of this study are then to use Lee's measurements:

1. to investigate simulated downhole and crosshole measurements of material damping,
2. to study the scatter that could be present in such measurements,
3. to evaluate material damping in constrained compression (P) in the sand skeleton under isotropic and anisotropic conditions, and
4. to evaluate material damping in shear (S) in the sand skeleton under isotropic and anisotropic conditions.

8.B.5.1.3 Organization

A brief review and general background of dynamic soil properties measured at low strains is presented in Section 8.B.5.2. Methods involved in determination of compressional and shear wave velocities are also briefly discussed in this section as well as in Section 8.B.5.4.

In Section 8.B.5.3, the equipment setup used to obtain compression (P) and shear (S) wave records under isotropic and biaxial confinement states is described. Effective confining pressures of 4 to 37.4 psi (27.5 to 257 KPa) were used for the isotropic confinement, while for biaxial confinement the vertical pressure was kept constant at 12 psi (82.5 KPa) and both horizontal confining pressures were kept equal and ranged from 6 to 21.4 psi (41.4 to 147 KPa). Also discussed in Section 8.B.5.3 are the soil sample properties and the preparation of sample in the LSTC.

A discussion of the attenuation mechanisms involved in soils, different methods of calculating material damping in soils, and techniques and assumptions applied in calculating material damping in this research are presented in Section 8.B.5.4. Also reviewed are the methods used for calculating the P- and S-wave velocities by Lee (1993).

The damping results are divided into two sections. The first section is a presentation of the results obtained under isotropic loading and is presented in Section 8.B.5.5. The second section is a discussion of the results obtained under biaxial confinement. These results are presented in Section 8.B.5.6. The majority of the tests were conducted with isotropic states of stress and involved compression wave measurements.

Section 8.B.5.7 is a concluding section and contains a brief summary of the findings.

2—GENERAL BACKGROUND

8.B.5.2.1 Introduction

Dynamic soil behavior can be described by the stiffness, damping and volume change characteristics of the soil. Soil stiffness is generally described in terms of shear and constrained moduli. Soil damping is typically expressed in terms of hysteretic damping in shear and compression, and volume change is expressed in terms of changes during shear and compressional motions. In this research, material damping in the soil skeleton at small strains is of concern.

8.B.5.2.2 Stress-Strain Behavior in Shear

Soils exhibit non-linear stress-strain behavior when loaded to failure. The dynamic response in shear is usually of most concern in the case of ground motions involving no residual displacements. This non-linear behavior can be shown by the initial loading curve (backbone curve) of the soil when loaded monotonically in simple shear to failure (Fig. 8.B.5-1). The curve is represented by an initial tangent modulus, G_{max}, and a failure shearing stress, τ_{max}. It is apparent that shear modulus and material damping must be determined as functions of induced strain in the soil. A typical modulus-strain relationship is shown in Fig. 8.B.5-2 while the companion damping-strain relationship is shown in Fig. 8.B.5-3.

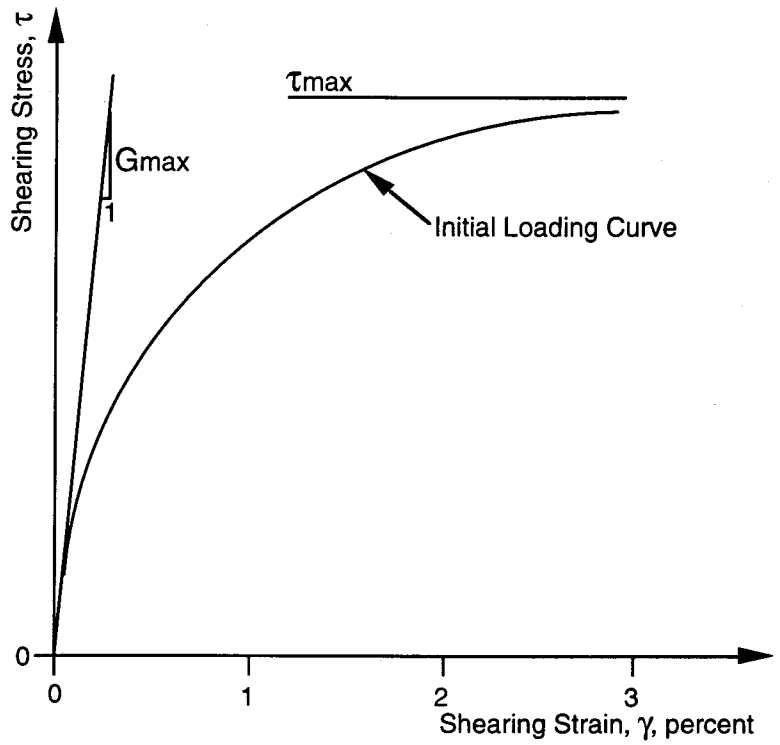

Figure 8.B.5-1
Generalized stress-strain behavior in shear for monotonic loading of soil.

As seen from Figs. 8.B.5-2 and 8.B.5-3, there is a threshold strain on the order of 0.001% below which shear modulus can be considered constant and equal to the initial tangent modulus. This is the value of strain below which most seismic tests are performed in the field. Below the threshold strain, material damping can also be considered as constant and equal to a minimum value. It is material damping at small strains which is of concern in this study.

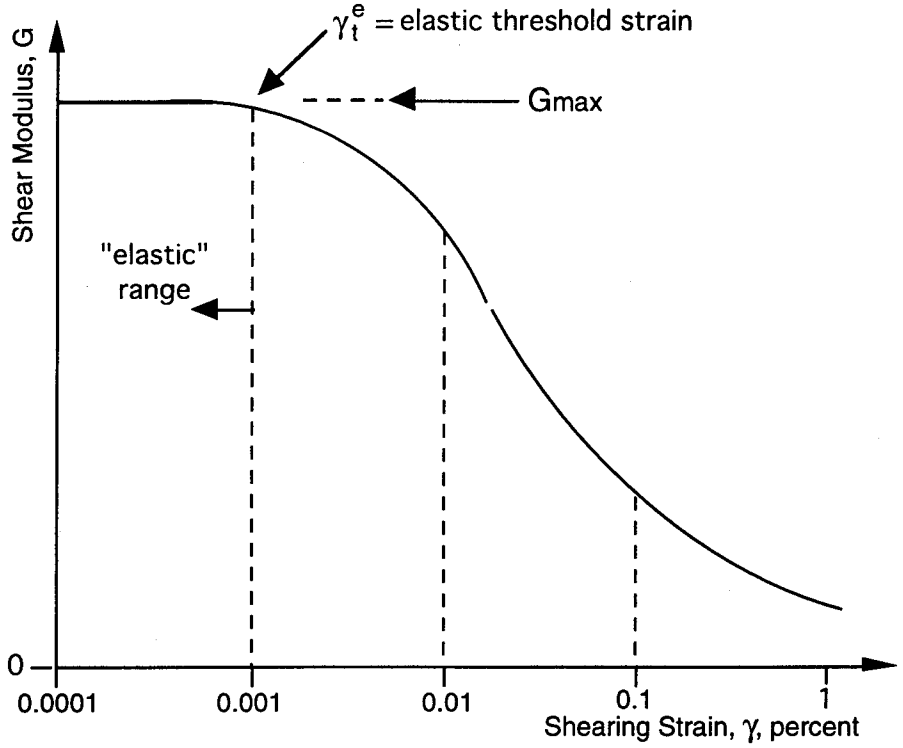

Figure 8.B.5-2
Generalized variation in shear modulus with shearing strain for soil.

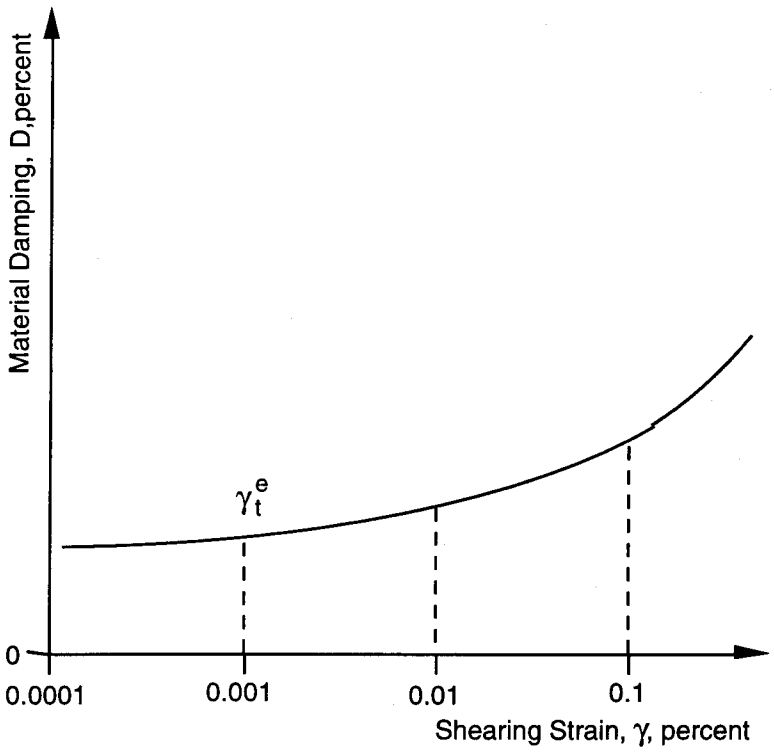

Figure 8.B.5-3
Generalized variation in material damping in shear with shearing strain.

8.B.5.2.3 Methods for Determining Dynamic Soil Properties

8.B.5.2.3.1 In Situ Seismic Methods

In situ methods allow evaluation of dynamic soil properties under actual, in situ conditions. Field methods which are used for these measurements at small strains (less than 0.001 percent) are seismic methods. These methods are briefly discussed below.

Crosshole Seismic Method. This is one of the most widely used methods for the measurement of dynamic soil properties. Seismic wave records are collected for body waves traveling horizontally from a source borehole to one or more receiver boreholes at the same depth. From the wave records, arrival times for P- and S-waves are determined; hence, wave velocities and moduli are determined. Material damping can be calculated by obtaining the amplitude of the spectra at the receivers and using one of several procedures (refer to Section 8.B.5.4). In this study, the spectral ratio method has been utilized. The field procedures for the crosshole method have been discussed in detail by various authors including Woods (1978), Stokoe (1980), Hoar (1982), Woods and Stokoe (1985) and the American Society for Testing and Materials (ASTM) has developed a standard for the crosshole method (ASTM D 4428M-84).

Downhole Seismic Method. The downhole method is the other in situ seismic method which is widely used for measurement of dynamic soil properties. With this method, seismic records for body waves traveling vertically from a source on the surface to one or more receivers at different depths in a single borehole are obtained. Field procedures for this method are discussed in Woods (1978), Stokoe (1980), Mok (1987) and Liu et at. (1988). In recent years, this method has received considerable attention for downhole damping measurements (Redpath and Lee, 1986) and is presently the most widely used method for in situ measurements of S-wave damping.

Logging Tool. Recently, a logging tool has been developed for P- and S-wave velocity measurements in soil and rock (Ohya et al., 1984). With this tool, vertically propagating shear waves are measured between horizontal receivers spaced about 1 m apart. The shear waves are generated in the walls of uncased boreholes using a horizontal exciter located about 3 m below the receivers. The advantages of the logging tool is that it can be used at significant depths, say 500 to 2000 ft (150 to 600 m), to measure shear wave velocities over short vertical travel paths. This tool was employed for just a purpose on the general EPRI study at the Gilroy 2 site over the depth range of 100 to 800 ft (30 to 240 m).

8.B.5.2.3.2 Laboratory Methods

There are two basic groups of laboratory tests available for the determination of dynamic soil properties. These are slow cyclic tests which are based on measurement of the stress-strain behavior at low frequencies and dynamic tests which are based on wave propagation and involve either resonance or pulse measurements.

8.B.5.2.3.2.1 Cyclic Tests

These include the cyclic triaxial tests, cyclic simple shear tests, and cyclic torsional shear tests. These tests yield stress-strain relationships from which modulus and material damping at frequencies below about 5 Hz are obtained. These characteristics are evaluated typically by varying confinement states, cyclic loads and number of loading cycles. Only the cyclic torsional shear test will be is discussed below.

Cyclic Torsional Tests. Cyclic torsional shear devices using either solid or hollow soil specimens have been developed (Drnevich 1972, Ishibashi and Sherif, 1974 and Isenhower (1979). In these tests, a solid or hollow cylindrical specimen is loaded by applying cyclic torsional shear about the vertical axis of the specimen. One disadvantage of using solid specimens is that the shearing stress and shearing strain vary along the diameter of the specimen from zero at the axis to a maximum at the outside radius. For this reason, hollow specimens have also been used.

8.B.5.2.3.2.2 Dynamic Tests

These tests involve high frequency tests. There are two groups of dynamic laboratory tests, one based on resonant methods and the other based on pulse methods. Generally, strain amplitudes involved in dynamic tests are lower than those associated with cyclic tests.

Resonant Testing Devices. The most widely used resonant testing device for soils is the torsional resonant column. In this resonant device, a cylindrical soil specimen is excited in first-mode torsional resonance. The soil specimen is typically confined under isotropic stress conditions. A torsional vibration is applied to the top of the soil column. The exciting frequency is adjusted until resonance is obtained. The modulus is then computed from the resonant frequency and the geometric properties of the specimen and driving apparatus. Damping is generally determined by turning of the driving power at resonance and recording the decaying vibrations from which a logarithmic decrement is calculated. However the shape of the resonance curve or a resonant factor from the driving-current measurements can also be used to evaluate material damping. Resonant column devices have been described in detail by Woods (1978), Drnevich (1985) and Ni (1987). The American Society for Testing and Materials has developed standard ASTM D4015-87 for dynamic testing of soils.

Pulse Testing Devices. In laboratory pulse tests, a seismic disturbance is generated by a source i.e. a mechanical, electro-mechanical, or piezoelectric source, at one point. Sensors are then used to detect the signal at various distances from the source. The sensors are typically velocity (geophones) and/or acceleration (accelerometers) transducers which convert physical motion into electrical signals that can then be amplified and recorded. The seismic records are then used to find the travel time for the motion and hence calculate velocity and modulus. The damping measurements are made by measuring the amplitudes and utilizing either the rise time, spectral ratio, or spectral slope method (Redpath and Lee (1986)) to calculate material damping in the specimen as discussed in Section 8.B.5.4.

Pulse tests can be used to measure compressional and shear wave velocities. The use of polarized waves is the basis of all pulse testing, i.e., the sources and receivers are oriented in such a manner that maximum energy is propagated for any one type of wave at an instant.

Pulse devices employ samples which are either in the shape of a right circular cylinder or a cube. In cylindrical specimens, only isotropic or biaxial loadings are generally applied while for cubic devices all three orthogonal stresses can be varied individually. Lawrence (1963), Schmertmann (1978), Roesler (1979), Dyvik and Madshus (1985) all built and used various types of devices. Lewis (1990) developed a multi-moduli testing device (MTD) to determine independently constrained, rod and shear wave velocities in the same specimen. Knox et al. (1982) constructed a large-scale triaxial chamber (LSTC) in which 7-ft (2.1-m) cubical samples could be loaded in true triaxial states of stress. The LSTC is discussed in detail in Section 8.B.5.3. The LSTC was used by Chu et al. (1984), Lee (1986), and Lee (1993) to study: (1) the effects of stress states on compressional and shear wave velocities (and hence, constrained and shear moduli), and (2) the influence of structural anisotropy on compression and shear wave velocities. The seismic wave records collected by Lee (1993) for his research form the basis for this study in the evaluation of material damping in the sand skeleton.

8.B.5.2.4 Factors Affecting Modulus and Damping

From previous studies, Hardin and Drnevich (1972a) and Hardin (1978) presented the following as the primary factors affecting moduli and damping of soil:

a. strain amplitude,
b. effective mean principal stress,
c. void ratio,
d. number of cycles of loading, and
e. degree of saturation for cohesive soils.

They presented the less important factors to include:

f. octahedral shear stress,
g. over-consolidation ratio,
h. effective stress parameter,
i. loading frequency, and
j. time effects.

Since material damping is of concern in this work, only a brief review of some of the factors affecting material damping are presented below.

8.B.5.2.4.1 Material Damping or Attenuation

Studies have shown that factors such as grain size characteristics, degree of saturation, void ratio, lateral earth pressure coefficient, angle of internal friction, and number of stress cycles have reasonably minor effects on the material damping of sands. The main factors affecting material damping are the strain level induced in the sand and the effective confining pressure to which it is subjected.

Strain Amplitude. The effect of strain amplitude and other factors on the damping ratios of sand is shown in Fig. 8.B.5-4. Much of this work is based on Hardin and Drnevich (1972a and 1972b). For strains associated with in situ seismic testing, attenuation is independent of strain amplitude as the material is considered to be in the small-strain range. The most common relationship used in geotechnical engineering between strain amplitude and material damping for soils is that shown in Fig. 8.B.5-5 (Seed and Idriss, 1970).This figure shows a wide scatter in the damping ratios obtained for sands. Approximate lower and upper bounds for damping ratios versus shear strain are shown by the dashed lines. The solid line in Fig. 8.B.5-5 shows an average strain-damping relationship for sands. The scatter in the data is clearly shown in the figure.

For rocks, attenuation increases rapidly above strains of about 10^{-6} just as for sands (Winkler and Nur, 1978; and Johnston and Toksoz, 1978).

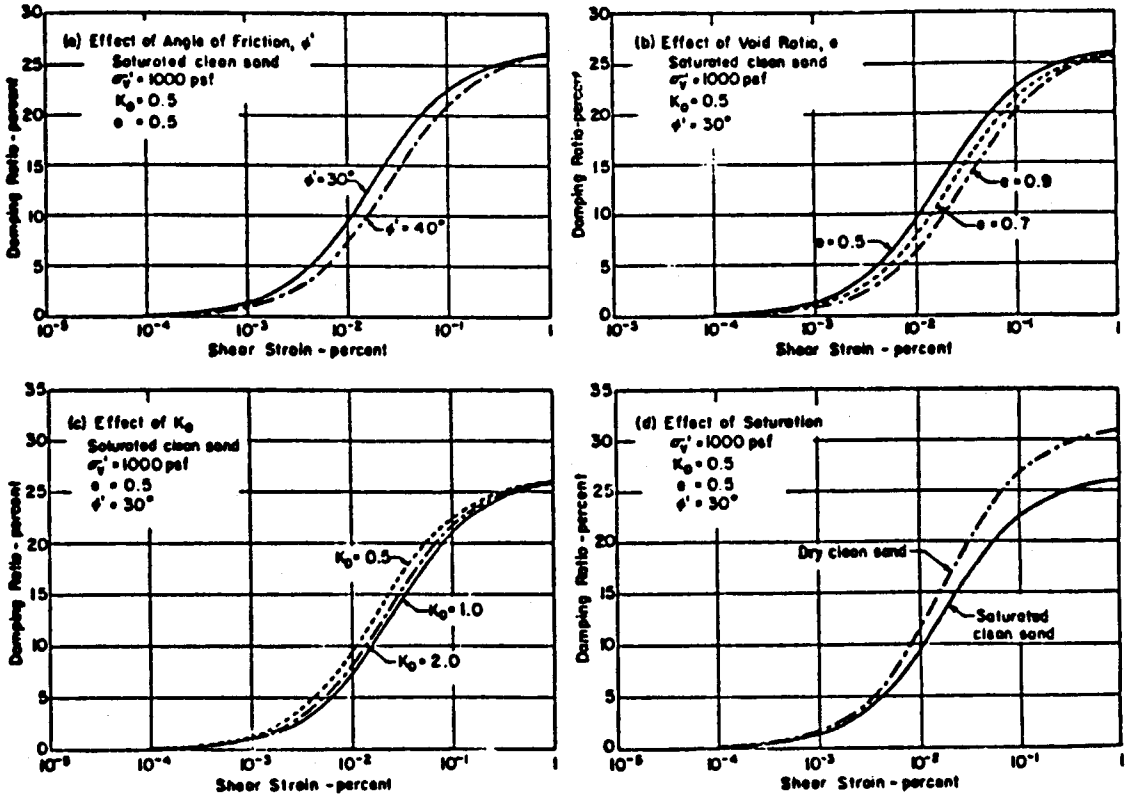

Figure 8.B.5-4
Effects of various factors on the material damping ratios in shear of sand (from Seed and Idriss, 1970).

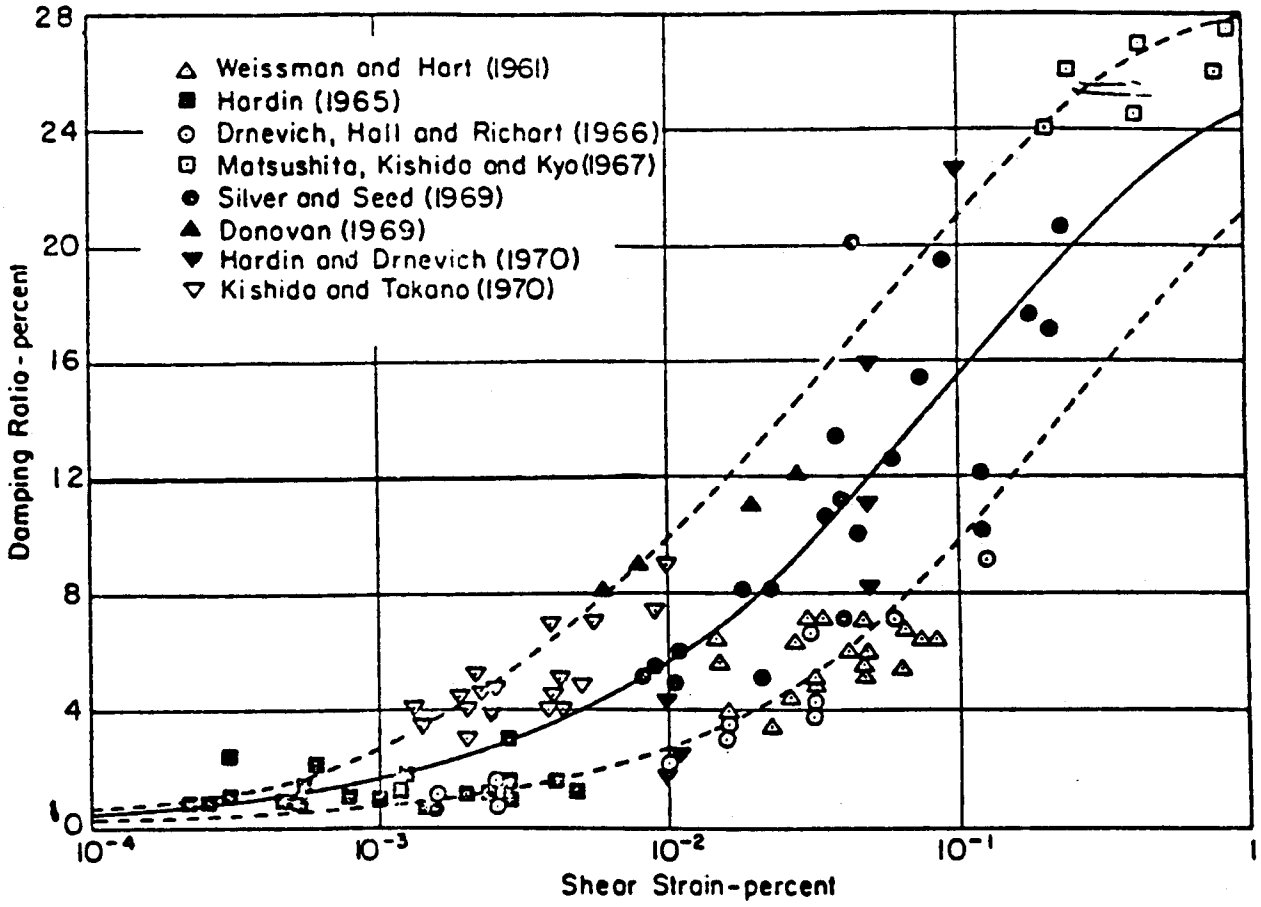

Figure 8.B.5-5
Influence of strain amplitude on the damping ratios of sands (from Seed and Idriss, 1970).

Pressure and Stress Dependence. Using resonant column tests, Laird (1993) has shown that there is a decrease in low-amplitude material damping with increasing stress (Fig. 8.B.5-23) on the same sand as was used in this study. This can be seen in Fig. 8.B.5-6 from Toksoz et al. (1979). The quality factors Q_P and Q_S (in compression and shear, respectively) increase with increasing pressure and level off at very high pressures (Q is defined in Section 8.B.5.4). These values were calculated using dry sandstone samples at ultrasonic frequencies in the laboratory.

Frequency Dependence. Kim (1991) has demonstrated using a combination of cyclic and resonant tests that damping is independent of frequency for the sand used in this study. This is discussed further in Section 8.B.5.4. Figures 8.B.5-7 and 8.B.5-8 show the same effect as discussed above, but for compressional and shear wave motions determined in situ for Pierre shale. The signals were generated using explosive and mechanical devices (McDonal et al., 1958). These figures show that attenuation has a linear relationship with frequency.

Fluid Saturation. In the frequency range of seismic tests, attenuation has been shown to be higher for fluid-saturated material and to depend on the degree of saturation, fluid type and frequency (Fig. 8.B.5-9).

Attenuation Q_E^{-1} is defined as $\Delta f/f$ here, i.e. the resonance peak. As noticed the attenuation increases as the Berea sandstone becomes more saturated (Winkler et al., 1979). Water is thought to most probably change the frictional properties of the sliding interfaces of the sandstone.

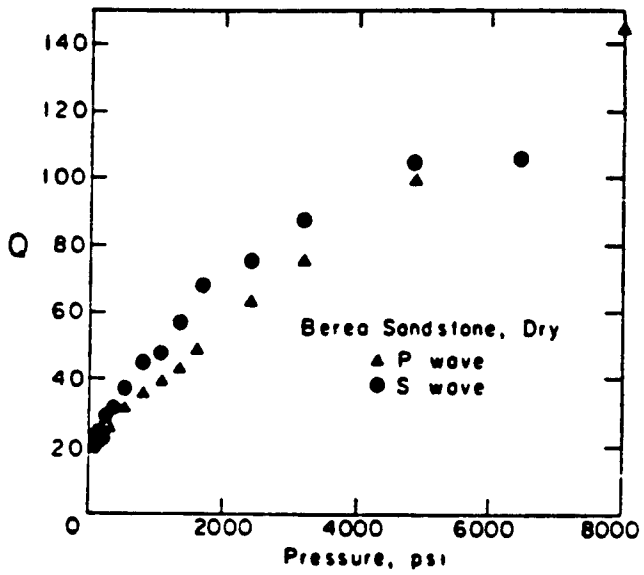

Figure 8.B.5-6
Q values of P- and S-waves as a function of confining pressure in dry Berea sandstone (from Toksoz et al, 1979).

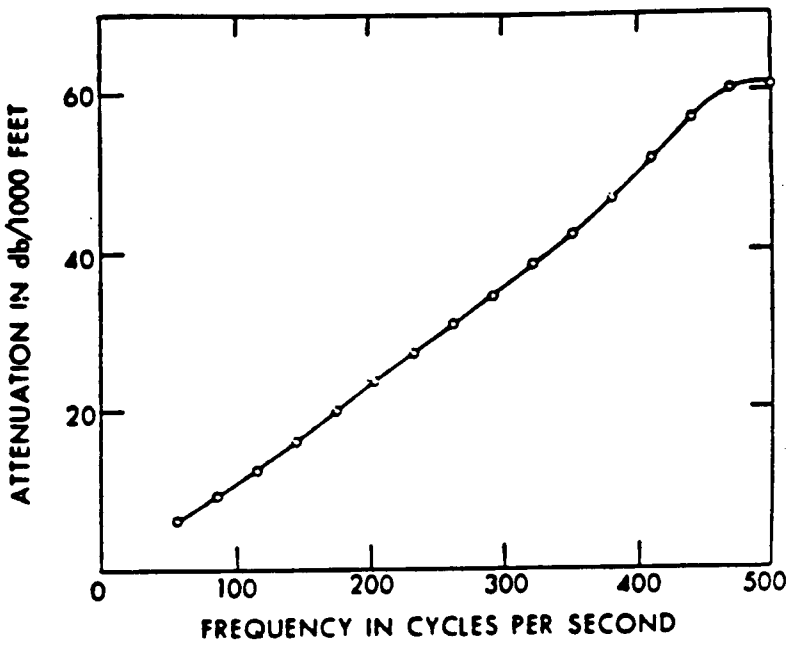

Figure 8.B.5-7
Attenuation of vertically traveling compressional waves generated by a charge of one pound of dynamite at a depth of 260 ft (from McDonal et al., 1958).

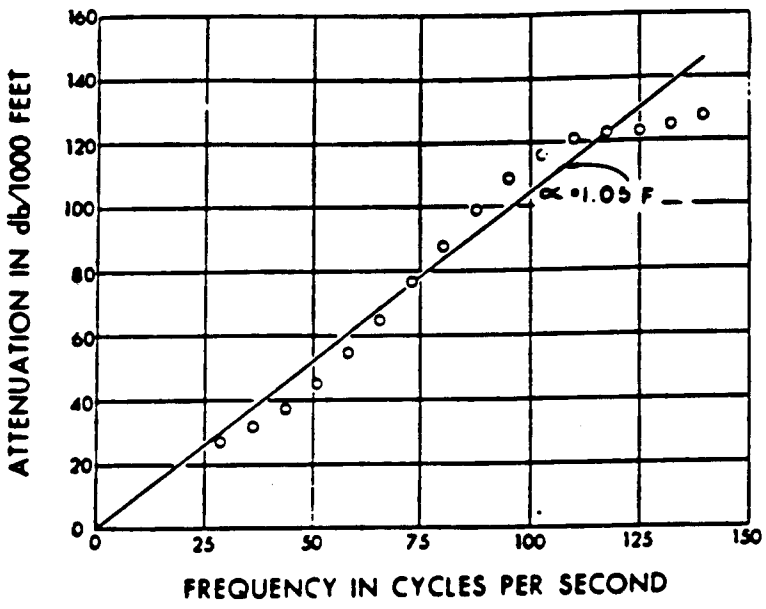

Figure 8.B.5-8
Attenuation of horizontally traveling shear waves with vertical particle motion generated by dropping a weight on the bottom of a 500-ft borehole (from McDonal et. al., 1958).

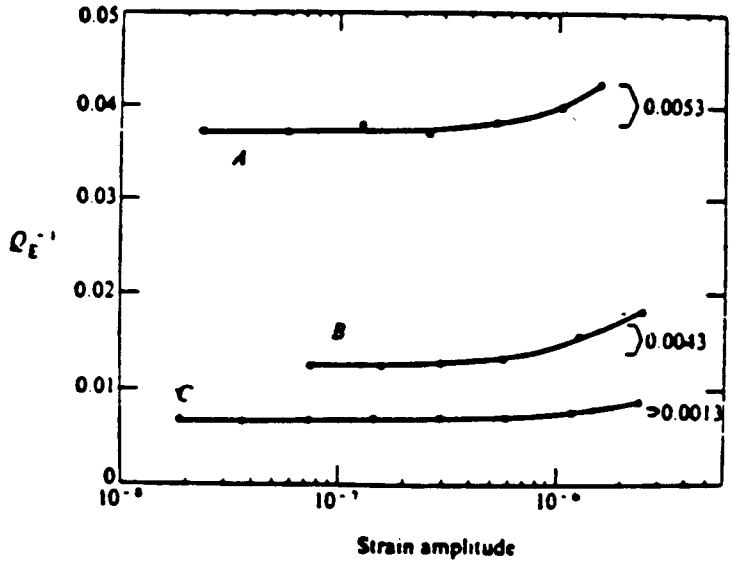

Figure 8.B.5-9
Attenuation in Berea sandstone at various degrees of saturation as a function of strain amplitude (A, saturated; B, partially saturated; C, dry) (from Winkler et al, 1979).

8.B.5.2.5 Summary

Based on review of previous work, the vast majority of research on dynamic soil properties at small strains has been directed towards moduli. Very little effort has been directed towards studying material damping. This is especially true for material damping in the soil skeleton with compression and shear waves at stress states comparable to the upper 100 ft (30 m) at soil sites. Therefore this study was undertaken to study this problem.

3—EXPERIMENTAL EQUIPMENT, ARRANGEMENT AND PROCEDURES

8.B.5.3.1 Introduction

In this section, the experimental setup used by Lee (1993) to perform compression and shear wave velocity measurements in the large-scale triaxial chamber, LSTC, is briefly discussed. The purpose of Lee's work was to study body wave velocities in the soil skeleton under isotropic, biaxial and triaxial states of stress. Measurements were performed with body waves polarized along the principal stress directions and also with body waves propagating at oblique angles to the principal stress directions. The discussion in this section is presented because Lee's data is reanalyzed herein to evaluate material damping of the dry sand in compression and in shear.

Only the essentials of the LSTC and associated equipment are discussed. A more detailed discussion has been presented by Lee (1993) in his dissertation. Details of sample preparation as well as the properties of the washed mortar sand used to construct the sample are also discussed in this section.

8.B.5.3.2 Large-Scale Triaxial Chamber

The large-scale triaxial chamber, LSTC, is a steel cubical chamber. The LSTC and associated equipment is shown in Fig. 8.B.5-10. The Chamber is designed to confine dry sand under true triaxial states of stress. The LSTC can stress dry sand up to a maximum confining pressure of about 50 psi (343.5 kPa).

Isotropic $\left(\bar{\sigma}_1 = \bar{\sigma}_2 = \bar{\sigma}_3\right)$, biaxial $\left(\bar{\sigma}_1 > \bar{\sigma}_2 = \bar{\sigma}_3 \text{ or } \bar{\sigma}_1 = \bar{\sigma}_2 > \bar{\sigma}_3\right)$,

and true triaxial $\left(\bar{\sigma}_1 \neq \bar{\sigma}_2 \neq \bar{\sigma}_3\right)$

stress states as illustrated in Fig. 8.B.5-11. These stress states are applied by controlling the pressures applied to all six sides of the chamber. Pressure membranes on all each side of the chamber permit this control to be exercised. These membranes, which can be controlled independently, are filled with water and then pressurized with air until the necessary stress state is obtained.

Basically three planes of seismic instrumentation were constructed in the chamber during placement of the sand by Lee (1993). This was done by stopping the filling operation and placing the seismic instrumentation. There were two horizontal and one vertical instrumentation planes. These instrumentation planes were constructed in the middle portion of the sand specimen. This was done because any induced shear stresses are minimized in the central portion of the sand mass as the central portion exhibits minimal displacements upon loading and unloading.

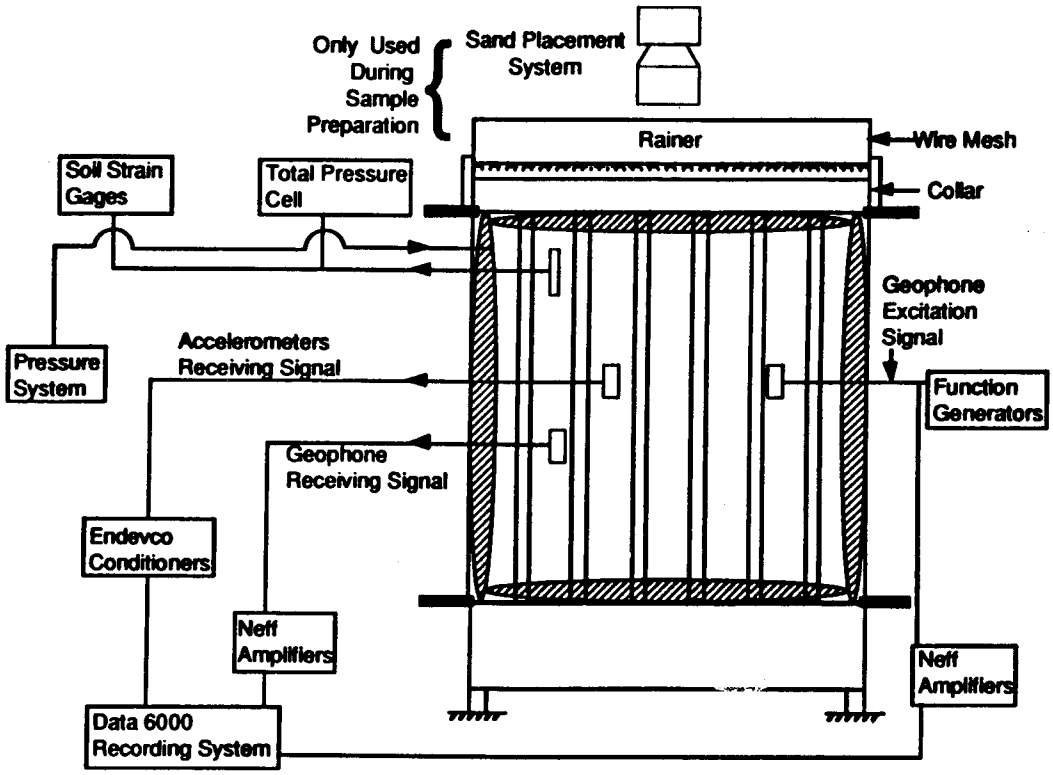

Fig 8.B.5-10
Sketch of the large-scale triaxial chamber (LSTC) and associated equipment.

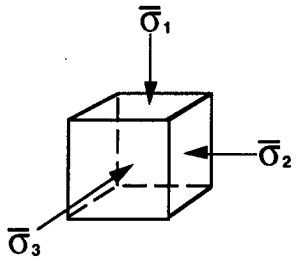

a. Isotropic State of Stress $(\overline{\sigma}_1 = \overline{\sigma}_2 = \overline{\sigma}_3)$

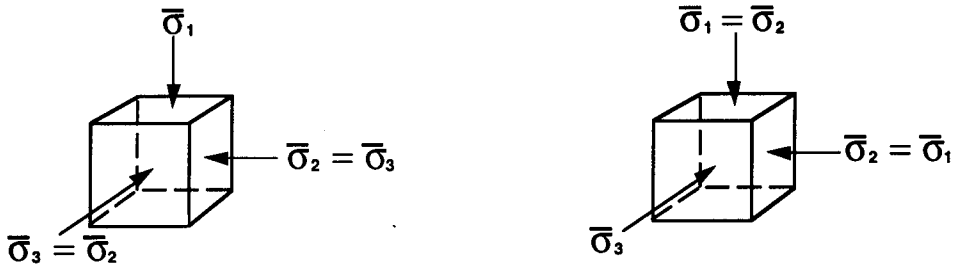

b. Biaxial State of Stress $(\overline{\sigma}_1 > \overline{\sigma}_2 = \overline{\sigma}_3$ **or** $\overline{\sigma}_1 = \overline{\sigma}_2 > \overline{\sigma}_3)$

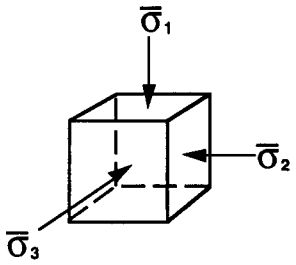

c. True Triaxial State of Stress $(\overline{\sigma}_1 > \overline{\sigma}_2 > \overline{\sigma}_3)$

Figure 8.B.5-11
Possible principal stress states applied to the dry sand sample in the LSTC.

8.B.5.3.2.1 Zone of Induced Shear Stresses

As pressure is increased in the pressure membranes, the membranes bulge nonuniformly and the amount of translational movement is not constant across each membrane. As a result, shear stresses are induced in the sand. Also, when membranes from opposite sides of the chamber are pressurized, the central plane does not move while sand away from the central plane moves. This movement also introduces shear stresses along the sides of the LSTC. Studies (Finn, 1985) have shown that these boundary effects can be essentially avoided if instrumentation is kept within about the middle two thirds of the sample. This is

about 4.7 ft (1.43 m) for the LSTC. The measurement portion of each instrumentation array was 2 ft (0.61 m) long and in the central portion of the LSTC. As a result, the principal effective stress states illustrated in Fig. 8.B.5-11 were assumed to exist in the zone where the seismic measurements were performed.

8.B.5.3.3 Instrumentation

8.B.5.3.3.1 Sources and Receivers

As illustrated in Fig. 8.B.5-12, a total of four distinct planes of instrumentation were developed in the sand in the LSTC. Of these planes, the top horizontal plane was used for placement of stress and strain sensors. The remaining three instrumentation planes were used for seismic measurements. One vertical plane and another horizontal plane were used for placement of instruments to generate and measure compression waves. In addition, some instrumentation for measurement of shear waves was placed in the vertical plane. Finally, the fourth instrumentation plane was horizontal and was used for placement of instrumentation to generate and measure shear waves. In the three seismic instrumentation planes, a total of eighteen lines or arrays for stress wave generation and monitoring were deployed.

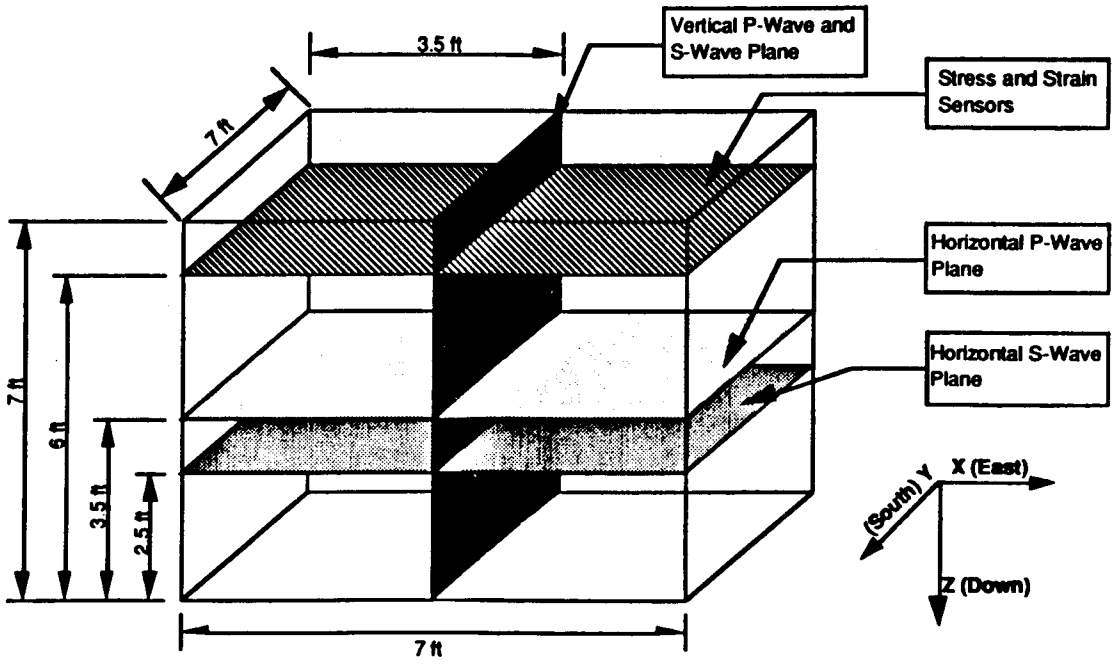

Figure 8.B.5-12
Layout of instrumentation planes in the LSTC (from Lee, 1993).

In both P-wave measurement planes, geophones were used as the sources, and accelerometers were used as receivers. Figs. 8.B.5-13 and 8.B.5-14 show these horizontal and vertical planes, respectively. There were seven seismic arrays in each P-wave measurement plane. Each array consisted of a linear arrangement of a geophone source, two accelerometer receivers and another geophone source. As there were two sources in each array, time records were obtained in both the forward and reverse directions.

For example, in the array G7A7A8G8 in Fig. 8.B.5-13, measurements in the forward direction were conducted using G7 as the source and accelerometers A7 and A8 as the near and far receivers, respectively. The reverse direction was represented by using G8 as the source and accelerometers A8 and A7 as the near and far receivers, respectively.

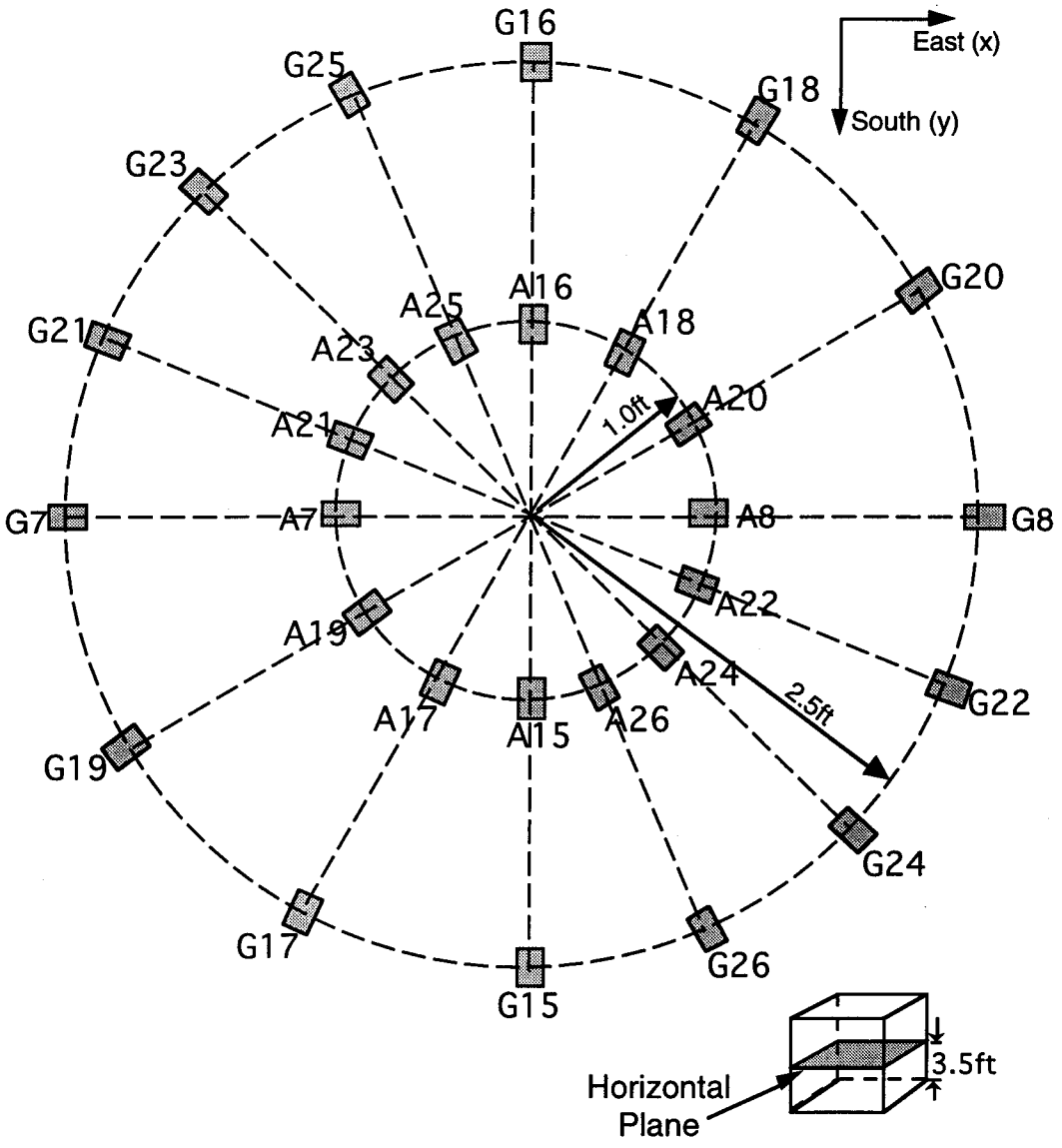

Note: G-denotes location of geophone source
A-denotes location of accelerometer receiver

Figure 8.B.5-13
Layout of instrumentation arrays for P-waves propagating in the horizontal plane (after Lee, 1993).

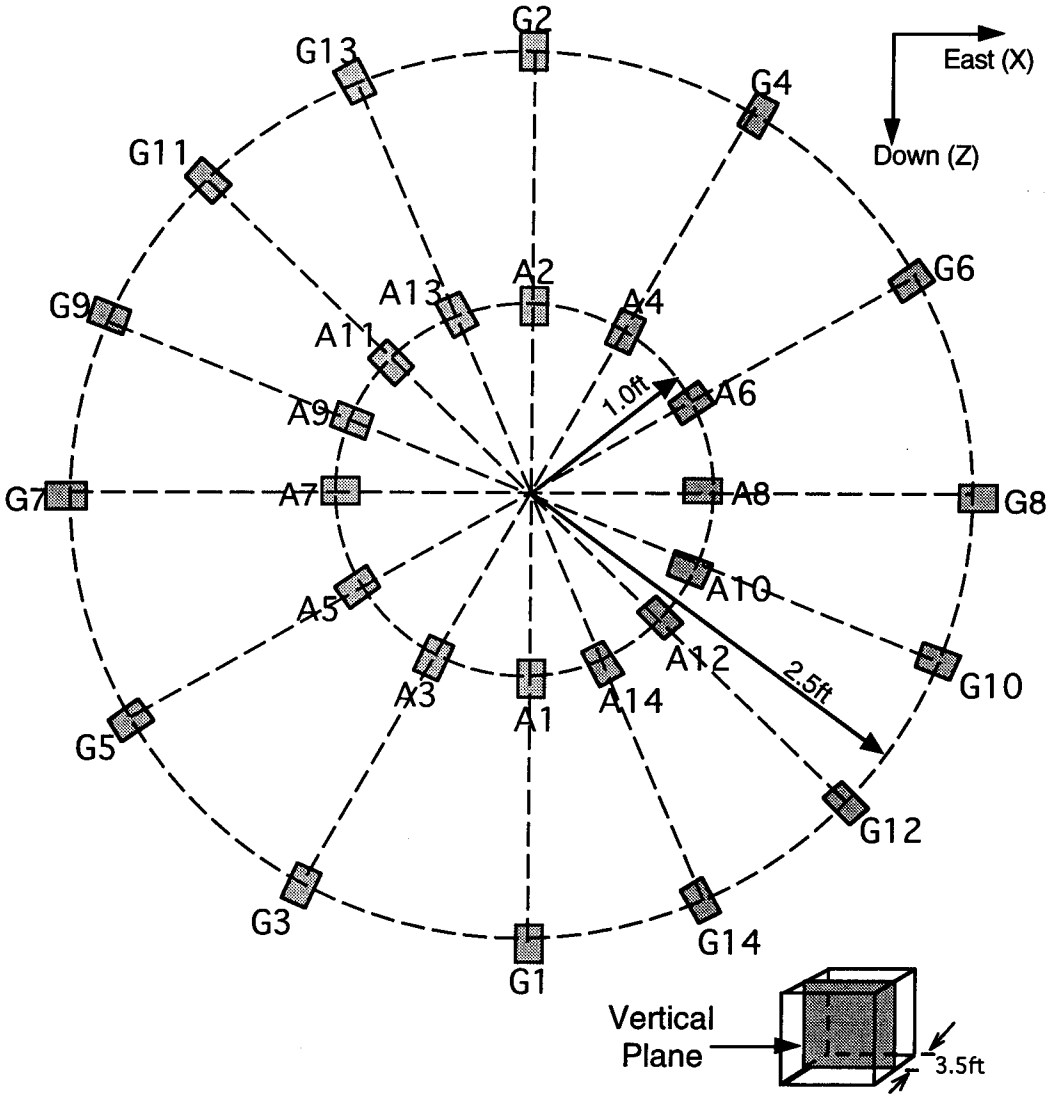

Note: G-denotes location of geophone source
A-denotes location of accelerometer receiver

Figure 8.B.5-14
Layout of instrumentation arrays for P-waves propagating in the vertical plane (after Lee, 1993).

In the S-wave measurement planes, geophones were used as both sources and receivers. Only one array was placed in the vertical S-wave plane as illustrated in Fig. 8.B.5-15. This is an SH-wave because the direction of particle motion is horizontal. However SH-waves and SV-waves are identical when the direction of wave propagation is vertical. In the horizontal S-wave plane, two arrays were constructed to obtain SH-wave records while another two arrays were constructed to obtain SV-wave records. In the horizontal plane, these two waves are different. All four sets of arrays in the horizontal plane are shown in Fig. 8.B.5-16. As in the P-wave planes, two sources and two receivers were utilized for the S-wave plane so that wave records in both the forward and reverse directions could be obtained.

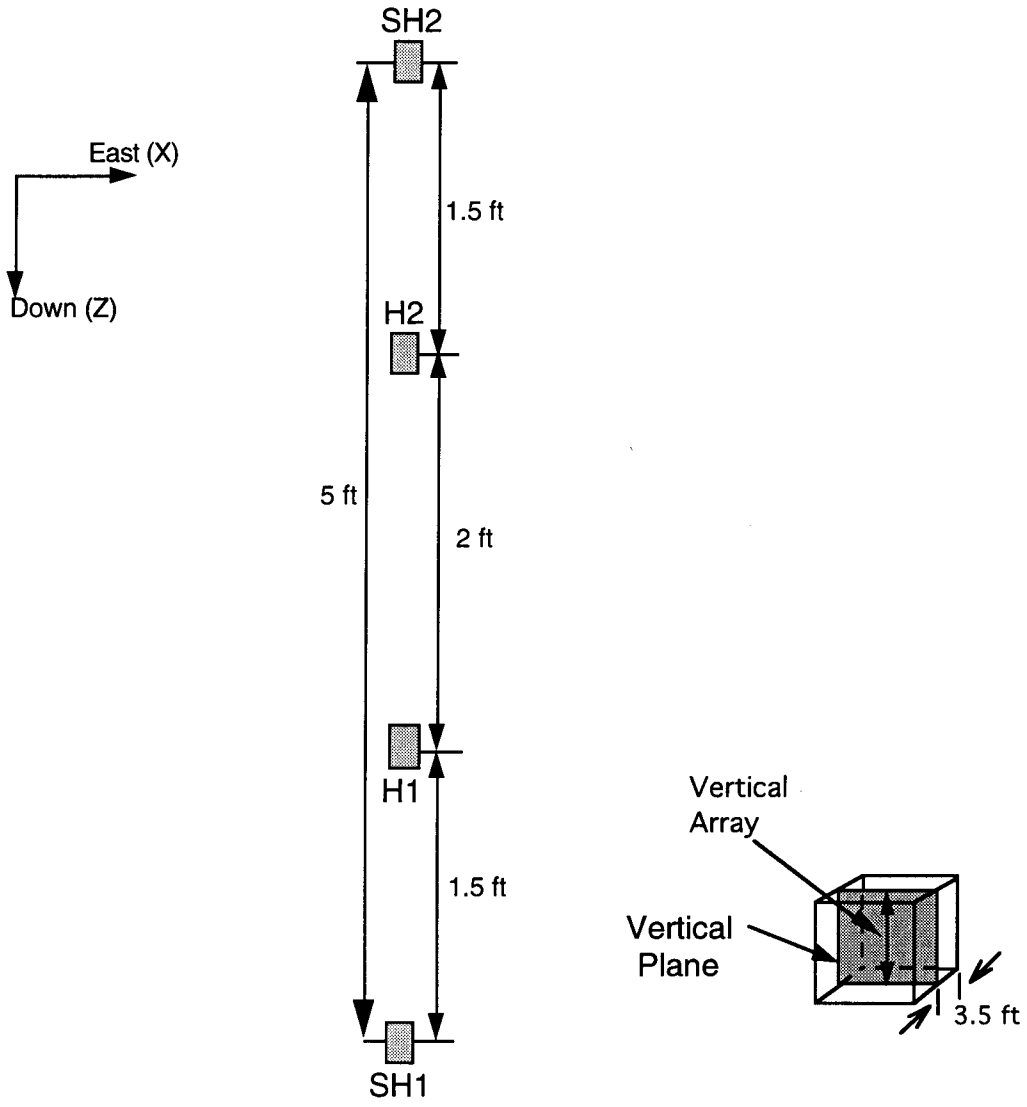

Note: G-denotes location of geophone source
A-denotes location of accelerometer receiver

Figure 8.B.5-15
Layout of instrumentation array for SH-waves propagating in the vertical plane (after Lee, 1993).

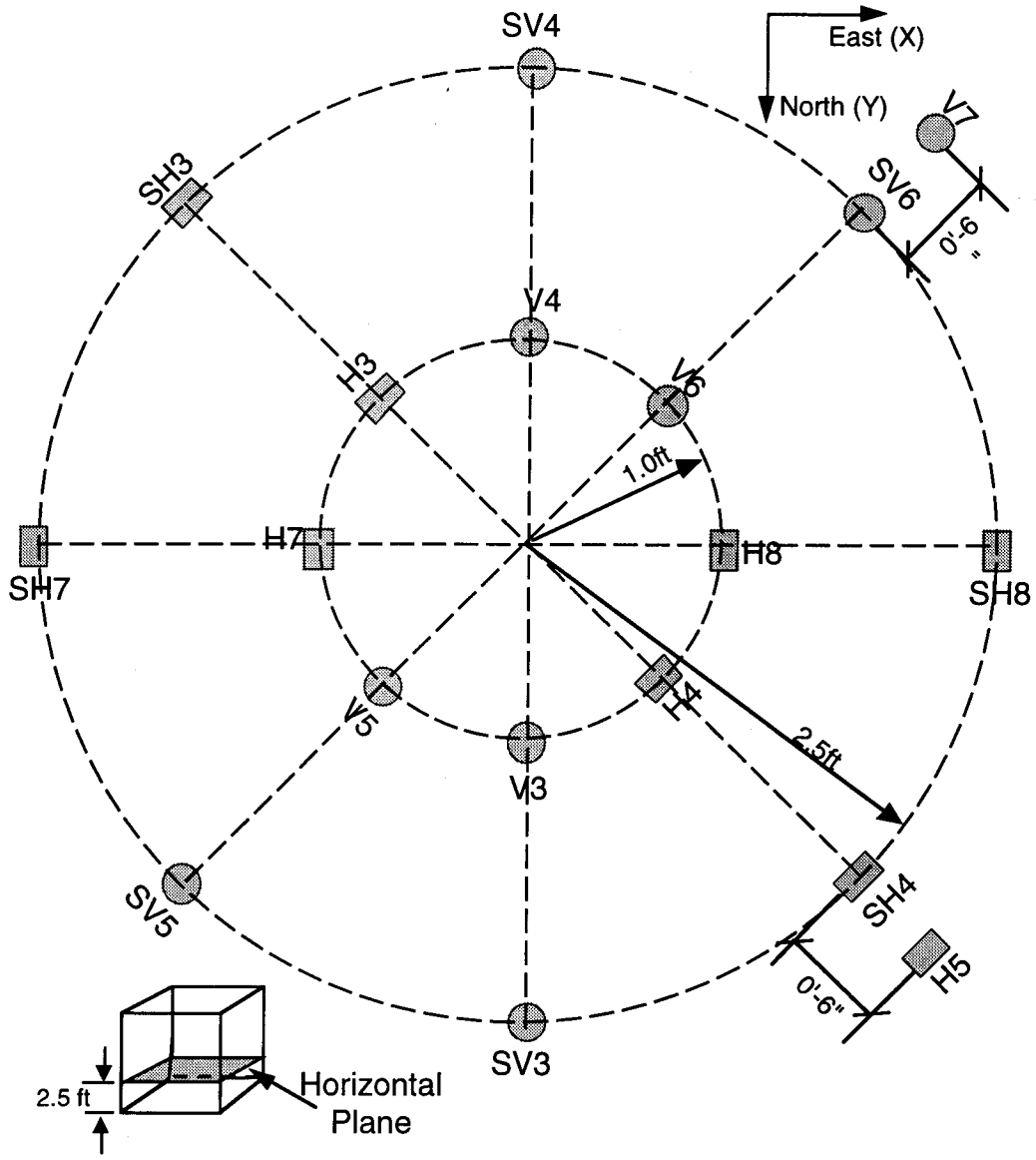

Note: SV-denotes location of geophone sources
SH-denotes location of geophone sources
V-denotes location of accelerometer receivers
H-denotes location of accelerometer receivers

Figure 8.B.5-16
Layout of instrumentation arrays for S-waves (SH and SV) propagating in the horizontal plane (after Lee, 1993).

The geophones and accelerometers in each of the P-wave measurement planes were aligned so that the direction of sensitivity of the receiver was parallel to the direction of particle motion as shown in Fig. 8.B.5-17a for P-wave measurements in the horizontal plane. This was done in an attempt to obtain the maximum wave signal. To obtain SV-wave records in the horizontal shear wave plane, the instruments were placed so that the direction of receiver sensitivity was perpendicular to the direction of propagation of wave and parallel to the direction of particle motion as illustrated in Fig. 8.B.5-17b for an SV-wave.

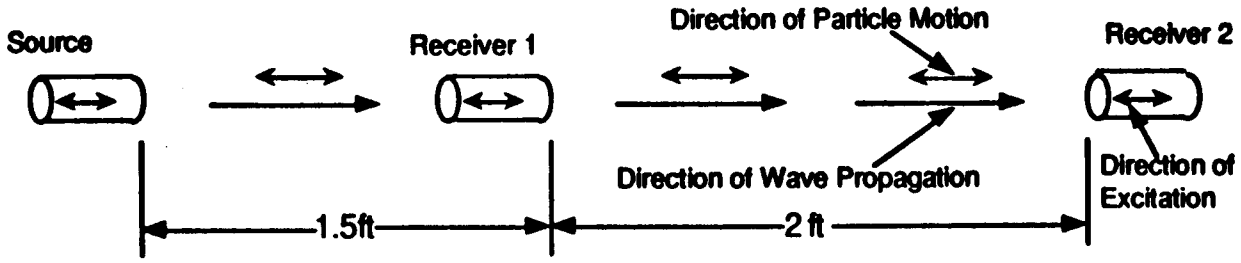

a. Compression Waves (P-Waves)

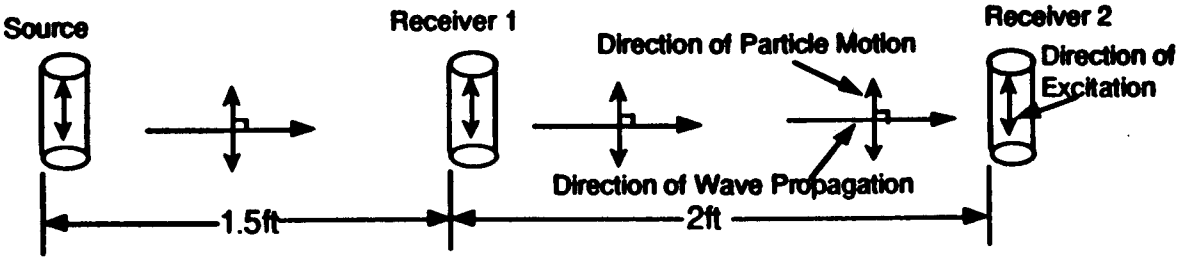

b. Shear Waves with Vertical Particle Motion (SV-Waves)

Figure 8.B.5-17
Arrangement of sources and receivers used to obtain seismic wave records in the horizontal plane.

Care must be taken when analyzing wave propagation in anisotropic material, however. In an infinite isotropic medium, spherical wavefronts spread out from a mechanical disturbance, and the direction of the group velocity is the same as the direction of movement of the wavefront (ray path) as illustrated in Fig. 8.B.5-18a. This implies that the maximum particle motion occurs along the ray path and hence we are able to obtain the correct velocities and particle amplitudes by orienting transducers parallel to the ray path. In an anisotropic medium, however, the wavefront is not spherical but elliptical as illustrated in Fig. 8.B.5-18b. Hence, a key point in measuring particle motion in an anisotropic medium is that the direction of the wavefront normal is not in the direction of the ray path. This means that the receivers should not be placed in the direction of the ray path as was done for measurements in an isotropic material, but they should be placed with their axes perpendicular or parallel to the wavefront normal. As the receivers were placed to measure the maximum wave signals for the sand under isotropic loading (when the material is nearly isotropic), they were not positioned to measure the maximum wave signal when conducting tests under anisotropic states of stress. However, one assumes that the component of particle motion which was measured in this study under anisotropic conditions was the same at both receiver locations and, hence, valid for attenuation measurements.

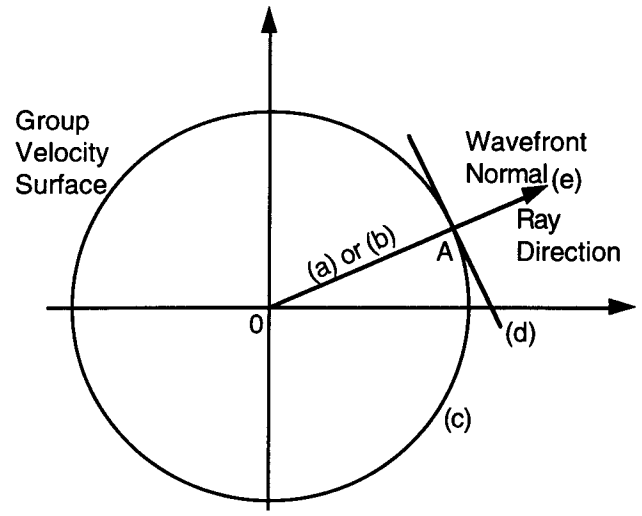

a. Spherical Wavefront in an Isotropic Medium

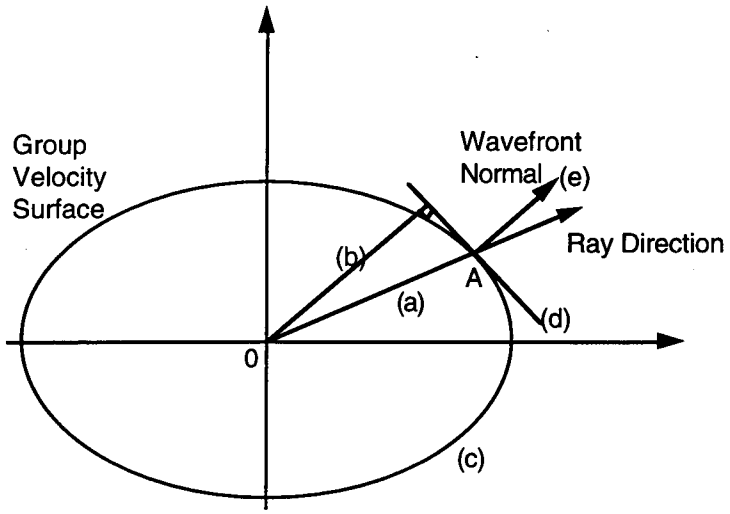

b. Elliptical Wavefront in an Anisotropic Medium

where: a = ray (group) velocity
b = phase velocity
c = group velocity surface,
d = tangent line to the ray velocity vector at point A, and
e = normal to the tangent line at point A.

Figure 8.B.5-18
Sketch showing that the direction of the ray path is oblique to the wavefront normal for a non-spherical wavefront (from Lee, 1993).

The geophones used in this study were manufactured by Mark Products, Model L40. The natural frequency of the geophones was 60 Hz, and the frequencies used in testing ranged from 1 kHz. to 4 kHz. A typical frequency response curve for these geophones is shown in Fig. 8.B.5-19. From the response curve, it is evident that the geophones do not show a flat response curve over the frequency range of concern in this work. However, since only interval measurements are being recorded, the variations in the response curve are of little significance as long as all geophones respond similarly. Also, it should be remembered, that geophones were only used for a limited number of S-wave measurements and accelerometers were used for the bulk of the measurements.

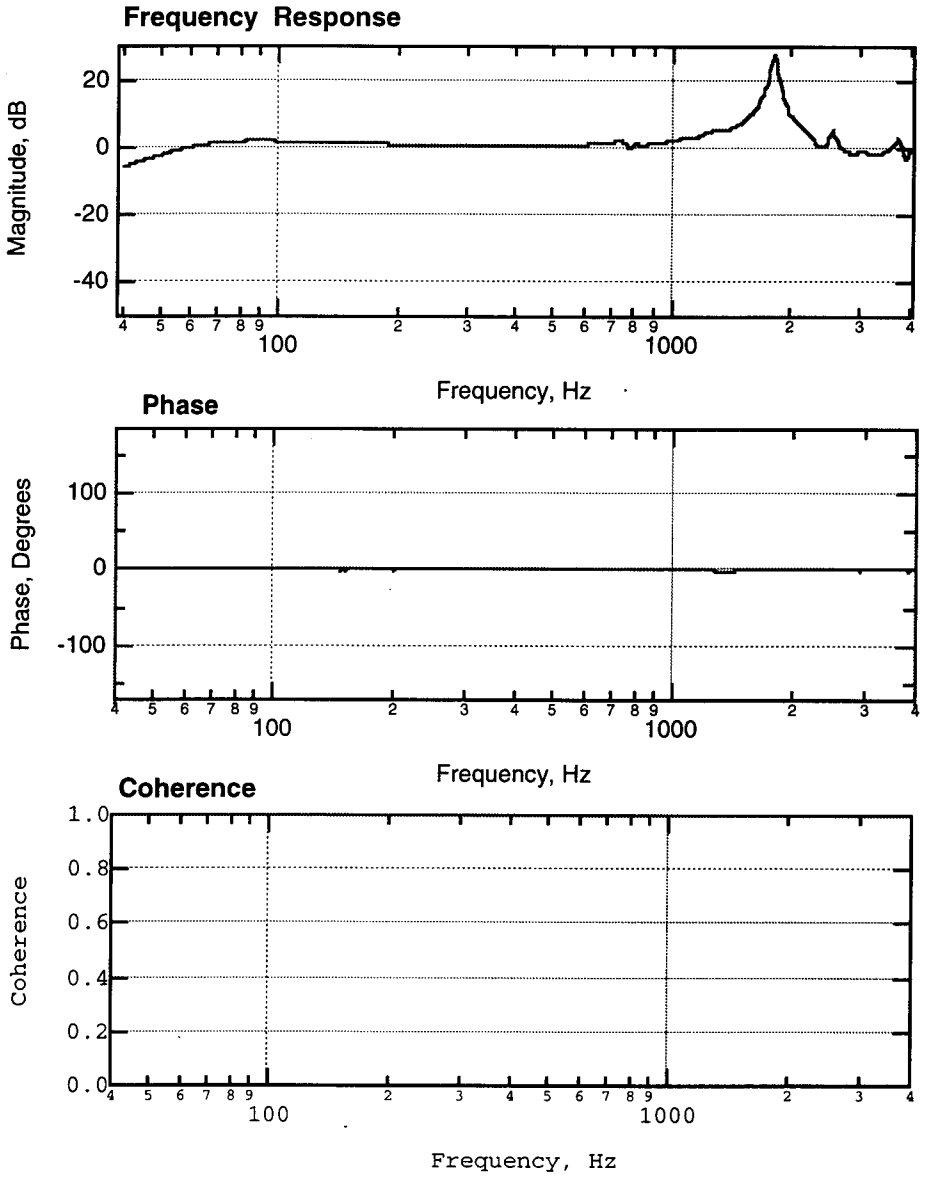

Figure 8.B.5-19
Typical frequency response, curve from calibration of mark products L40, 60-Hz geophones (from Lee, 1993).

The accelerometers used as receivers were Endevco Model 7701-100. Since the frequency range used in the tests was from 1 kHz to 4 kHz and the resonant frequency of the accelerometers was about 20 kHz, a linear response curve for these receivers was assumed (Lee, 1986). The major difference between the geophones and accelerometers is that the geophone measures particle motion in terms of particle velocity while the accelerometer measures particle motion in terms of acceleration. A 90-degree phase shift exists between the accelerometer and geophone signals. Once again, since only interval measurements of like receivers were performed, differences between receivers had a minimal effect in these tests.

8.B.5.3.3.2 Important Source Characteristics

Geophones were used as seismic sources in all tests. The advantages of using a geophone as a source in the LSTC are that geophones are small in size and can be easily embedded in the sand. In addition, a repeatable signal can be obtained with a controlled input (Lee, 1993). Some other important characteristics of a source in seismic testing are the following.

Output Magnitude. The source signal should be of such a magnitude that it produces a recognizable signal yet also remains in the small-strain range in these short-travel-path tests. Geophone sources can easily be kept in the small-strain range because they are excited by introducing small voltages across the coil of the geophone. The coil is attached to the casing and is suspended in a magnetic field. When a voltage is applied to the coil, it cuts the magnetic field and causes a force on the case. The case in turn reacts against the soil. The signal which is ultimately generated in the soil is recognized by the way the geophone has been oriented and excited as discussed below.

Source Direction and Polarization. The source should generate a high signal-to-noise ratio. All motion other than the required signal is considered as noise. The source must have a distinctive energy pattern so that a particular type of seismic energy can be generated in a given direction. This pattern is especially necessary in S-wave generation so that minimal P-wave energy propagates in the direction of the S-wave. In this fashion, one is able to identify distinctively the shear wave arrival.

To obtain distinctive wave patterns, the source has to be oriented in such a way that the principal axis of the source is parallel to the direction of particle motion of the required wave type as illustrated in Fig. 8.B.5-17. This orientation produces a signal which is rich in the type of energy required.

Frequency Content. The source must be able to generate a wide range of frequencies. It is necessary to vary the frequency of the source as the confining pressure is increased so as to be able to reduce the near-field effect (Sanchez-Salinero et al., 1986). The frequencies used should be in the linear frequency response range of the source. In this study, signals were generated at 0.25, 0.5, 1, 2, 3, and 4 kHz, but only data from 1, 2, 3, and 4 kHz were used to calculate material damping. These frequencies were selected such that the source-receiver spacing was greater than two times the wavelength.

Coupling and Impedance. Good coupling between the source and the sand in the LSTC is necessary to generate a strong signal. This was developed by burying the geophone sources in the sand. It is beneficial if the source has a similar stiffness and unit weight to the soil so as to reduce any impedance mismatch (Hoar, 1982 and Mok et al., 1987). In these tests, the unit weight of the geophone was about twice that of the soil. Additionally, the geophone was much stiffer than the soil. As a result the impedance matching was only marginal.

8.B.5.3.3.3 Important Receiver Characteristics

A receiver is used to monitor the amplitudes of particle motion at selected locations relative to the source. Two types of receivers were used, geophones and accelerometers. Some requirements for a good receiver are discussed below.

Receiver Orientation. For body wave propagation measurements, receivers must be placed with their sensitive axis in the direction of maximum particle motion. This orientation depends on the type of wave being propagated. In this work, orientation of the receivers (and sources) was done during sample construction.

Frequency Range. For the LSTC, the geophone must have a reasonably flat frequency response curve from about 1 kHz to 4 kHz. The lower limit of 1 kHz was established to satisfy the near-field criterion as discussed in Section 8.B.5.4. The upper limit comes from satisfying the receiver size versus wavelength criterion as discussed below.

Receiver Size. Suddhipraken et al. (1983) noted that the ratio of size of receiver to the wavelength should be less than one third. For studies in the LSTC, Suddhipraken et al. found that the receiver would have little effect on the amplitude of motion as long as this criterion was followed. The receiver size did not effect the arrival time or time interval, but had a significant effect on amplitude of motion at high frequencies. However, since interval measurements were made, this effect was assumed to be minimal. The geophone receivers used during testing in this study were 1.37 in. (3.48 cm) long. A minimum wavelength of about 3.5 in. (8.9 cm) was used in this study. The accelerometers used in this study also satisfied this criterion as they were smaller in dimensions than the geophones.

Impedance Match. To minimize compliance problems between the sand mass and receivers, the density and stiffness of the sand and receivers should be approximately the same. It was impossible to match the stiffnesses of the sand and receivers. However it was possible to closely match the densities. The accelerometers were embedded in wooden blocks to alter their density. The density of the sand was about 101 pcf (14.9 kN/m^3), while for the package containing the accelerometer and wooden block it was about 110 pcf (16.2 kN/m^3). The geophones receivers used were comparatively large and have a gross unit weight of about 245 pcf (36.2 kN/m^3). Their densities could not be easily altered without making them too large, and therefore no more matching was done.

8.B.5.3.3.4 Function Generators

An impulse or a steady-state signal is required to drive the source geophones. Two, Hewlett-Packard model 3310B function generators were used in series to produce the source signal. The first generator was used to produce a square waveform which was used to trigger the second generator. Once triggered, the second function generator was used to produce a sine wave of a particular frequency, amplitude, and number of cycles (as illustrated in Fig. 8.B.5-20). This arrangement allowed repetitive signals to be generated. A diagrammatic sketch of the electronic equipment used in the LSTC is shown in Fig. 8.B.5-10, and some typical source and receiver signals are presented in Section 8.B.5.4 (Figs. 8.B.5-37 and 8.B.5-38).

8.B.5.3.3.5 Amplifiers

Neff amplifiers (model 128) were used to amplify the voltage from the geophone receivers to a level which could be more easily recorded with the waveform analyzer described below. The gain varied from 1 to 1000 times the original signal generated by the receiver. Neff amplifiers were also used to amplify signals from the accelerometer receivers. As with the geophones, the accelerometer signals were amplified before being sent to the data acquisition unit.

The amplifiers also served as low-pass filters to remove noise which had a frequency above 100 kHz.

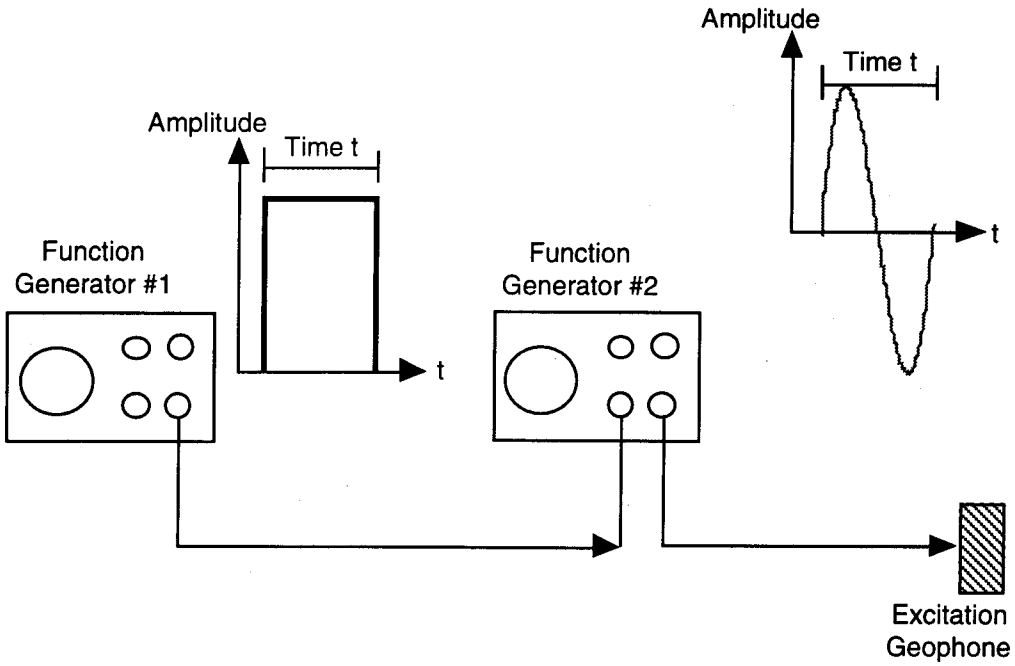

Figure 8.B.5-20
Function generators used to drive the source geophones.

8.B.5.3.3.6 Digital Recorder

A Data 6000 Universal Waveform Analyzer built by Analogic Corporation was used to collect and analyze the data. The Data 6000 has four sampling channels with a maximum sampling rate of 250 kHz (40 msec) for all four channels. The analyzer has a 9 in. (22.9 cm) display unit. Digital signals can be stored on a dual floppy disk drive.

An analog signal is first sent to the acquisition unit which is then converted to a digital signal after being filtered by an anti-aliasing filter. The anti-aliasing filter removes frequency components which are higher than the Nyquist frequency. A multiplexer or A/D converter samples the incoming signal voltage (analog signal) and converts it to a binary (digital) output. A 16-bit output can be obtained from the sampler.

8.B.5.3.4 Sand Sample Preparation

All seismic testing was performed in dry sand confined in the LSTC. Proper placement of the sand in the LSTC is very important to produce as homogeneous a sample as possible. This means that, throughout the depth of the sand sample, a uniform density is desired. If the density is not uniform, density contrasts within the sample can adversely effect the amplitudes of body waves by reflecting, refracting and scattering wave energy. Such effects generally cause a decrease in amplitude and hence adversely affect the damping measurements.

In the LSTC, a reasonably uniform density was achieved throughout the soil sample by raining sand through air from a maximum height of 9.5 ft (2.90 m) at the start of the filling operation to a minimum height of 2.5 ft (0.76 m) at the end. The filling operation satisfied the minimum drop height criterion of 2.5 ft (0.76 m) suggested by Beiganousky and Marcusson (1976) for development of uniform samples of dry sand.

8.B.5.3.5 Sand Properties

Some properties of the dry sand used in the LSTC as determined by Lee (1993) and previous investigators are discussed below.

8.B.5.3.5.1 Soil Type

The soil is a uniform, medium-to-fine washed mortar sand. The sand classifies as SP in the Unified Soil Classification system. Various properties of the sand are summarized in Table 8.B.5-1.

Table 8.B.5-1
Summary of Soil Properties and Characteristics of Washed Mortar Sand (From Lee, 1993)

	Previous Samples	**This Sample**
Soil Type	Washed Mortar Sand	Washed Mortar Sand
Unified Soil Classification	SP	SP
Mean Grain Diameter D_{50}	0.35	0.40
D_{10}	0.25	0.23
Cu	1.71	2.17
%Passing #200 sieve	<1%	0.1 to 0.4%
Specific Gravity	2.67	–
Maximum Dry Density	106.6 pcf	–
Minimum Dry Density	90.6 pcf	–
Maximum Void Ratio	0.839	–
Minimum Void Ratio	0.563	–
Grain Shape	Sub-angular to Sub-rounded	Sub-angular to Sub-rounded
Total Density (pcf),	$98.6 < g_t < 104.8$	$98.6 < g_t < 104.9$
Average Total Density (pcf), g_t	101.8 pcf	101.3 pcf
Water Content (w)	0.05%	0.01% to 0.04%
Void Ratio, e	0.70 > e > 0.62	0.70 > e > 0.61
Relative Density, Dr	50.4% < RD < 79.3%	50.4% <RD< 79.3%
Soil Composition		40% of Quartz 30% of Feldspar 20% of Other Minerals 10% of Sea Shell Fragments

8.B.5.3.5.2 Dry Density

Total densities of sand samples measured in the LSTC ranged from 98.3 pcf (14.5 kN/m^3) to 104.9 pcf (15.4 kN/m^3) and averaged 101.3 pcf (14.9 kN/m^3). The void ratio ranged from 0.70 to 0.59 and averaged 0.65. The relative density (D_r) of the sand sample ranged from 50% to 79% and averaged 72%.

The sand used in the LSTC was treated as dry because the water content ranged from 0.01% to 0.04%.

8.B.5.3.6 Soil Properties Obtained From Static Triaxial Tests

8.B.5.3.6.1 Friction Angle

Summarized in Table 8.B.5-2 are results from drained triaxial tests performed on samples of the washed mortar sand (Knox et al, 1982). From the results it can be seen that the angle of internal friction increases as the void ratio decreases and varies from 37 degrees to 44 degrees for medium and medium dense samples, respectively.

Table 8.B.5-2.
Friction Angle of Washed Mortar Sand (From Knox Et Al, 1982)

Void Ratio e	Total Unit Weight γ_t, pcf (kN/m^3)	Effective Angle of Internal Friction (ϕ'), degree
0.82	91.4 (2.47x10^6)	34.5
0.81	92.0 (2.49x10^6)	34.5
0.79	92.3 (2.50x10^6)	36.5
0.78	93.8 (2.54x10^6)	38.5
0.72	99.0 (2.68x10^6)	42.0
0.51	109.3 (2.96x10^6)	44.1

8.B.5.3.6.2 Stress-Strain Curves

Multi-staged isotropically consolidated, drained compression tests on medium dense specimens of washed mortar sand were performed to evaluate the stress-strain relationships at low strains. The stress-strain curves were then used to evaluate Young's modulus at these strain levels. The results are shown in Fig. 8.B.5-21. As can be seen in Fig. 8.B.5-21 for axial strains below 0.001%, Young's modulus is essentially independent of strain amplitude. Average values of Young's modulus obtained from static triaxial tests at strains less than 0.001% are presented in Table 8.B.5-3.

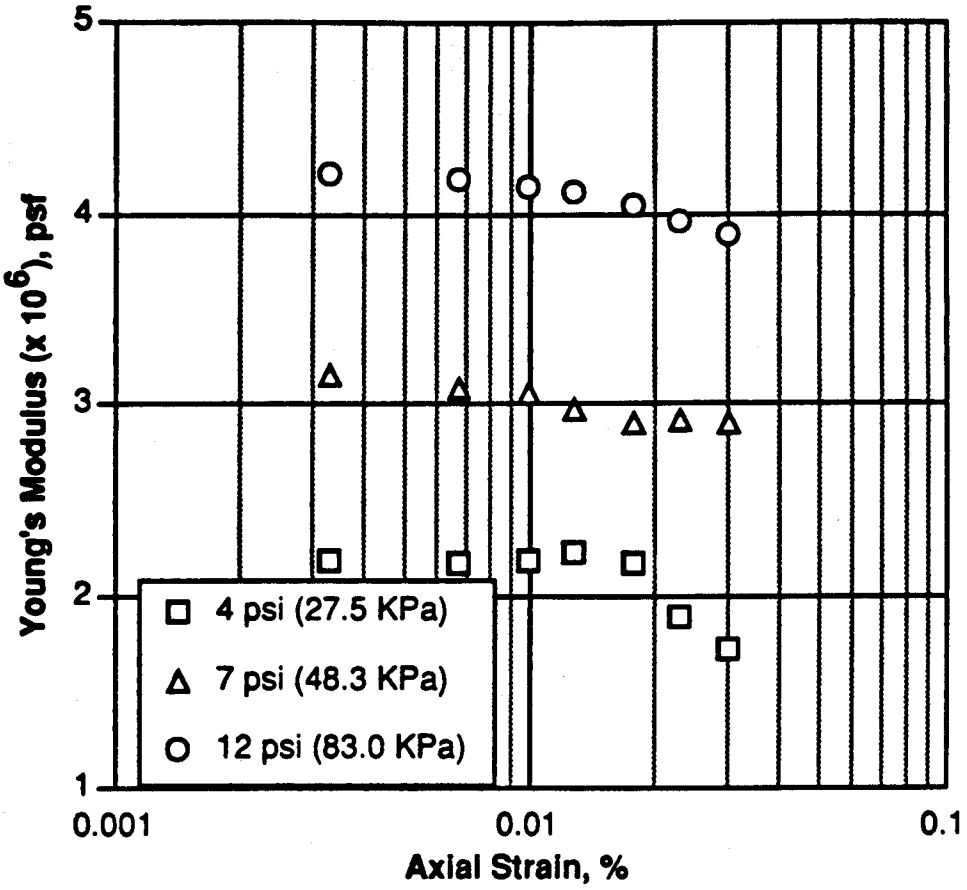

Figure 8.B.5-21
Variation in Young's modulus with strain amplitude from static triaxial tests (from Lee, 1993).

Table 8.B.5-3
Average values of Young's modulus obtained from static triaxial tests at strains $\leq 0.001\%$ (from Lee 1993).

Isotropic Confining Pressure, psi (kN/m^2)	Young's Modulus (Loading), psf (kN/m^2)	Young's Modulus (Unloading), psf (kN/m^2)
4 (28)	1.45×10^6 (10.0×10^6)	–
7 (48)	2.21×10^6 (15.25×10^6)	–
12 (82.8)	4.024×10^6 (27.76×10^6)	4.38×10^6 (30.2×10^6)

8.B.5.3.7 Dynamic Properties of Washed Mortar Sand

8.B.5.3.7.1 Shear Modulus

Torsional resonant column tests were performed on the same sand as that used in the LSTC by Laird (1993). A typical shear modulus versus effective confining pressure relationship is shown in Fig. 8.B.5-22. This relationship can be expressed using the approach suggested by Hardin (1978) as:

$$G_{max} = \frac{A}{F(e)} P_a^{1-n} \bar{\sigma}_o^n \qquad (8.B.5\text{-}1)$$

Where:

G_{max} = small-strain shear modulus,
A = stiffness coefficient,
F(e) = $0.3+0.7(e)^2$,
P_a = atmospheric pressure (14.7 psi),
n = stress exponent,
$\bar{\sigma}_o$ = effective isotropic confining pressure (psi), and
e = void ratio

When Hardin's equation is fit to the data in Fig. 8.B.5-22, A = 661 and n = 0.44.

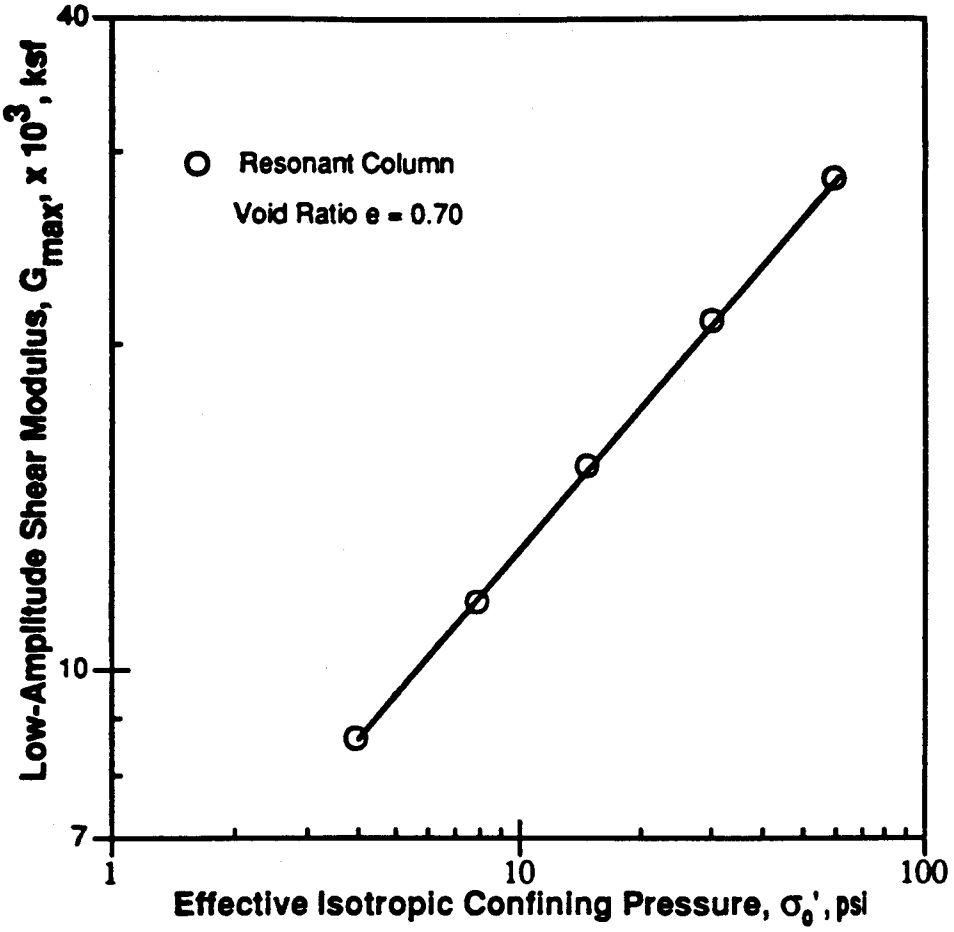

Figure 8.B.5-22
Variation in low-amplitude shear modulus with effective isotropic confining pressure from resonant column tests (from Laird, 1993).

8.B.5.3.7.2 Material Damping in Shear

Torsional resonant column tests were also used to evaluate material damping at small strains (Laird, 1993). Typical results are shown in Fig. 8.B.5-23 where it can be seen that damping ratio decreases as isotropic confining pressure increases.

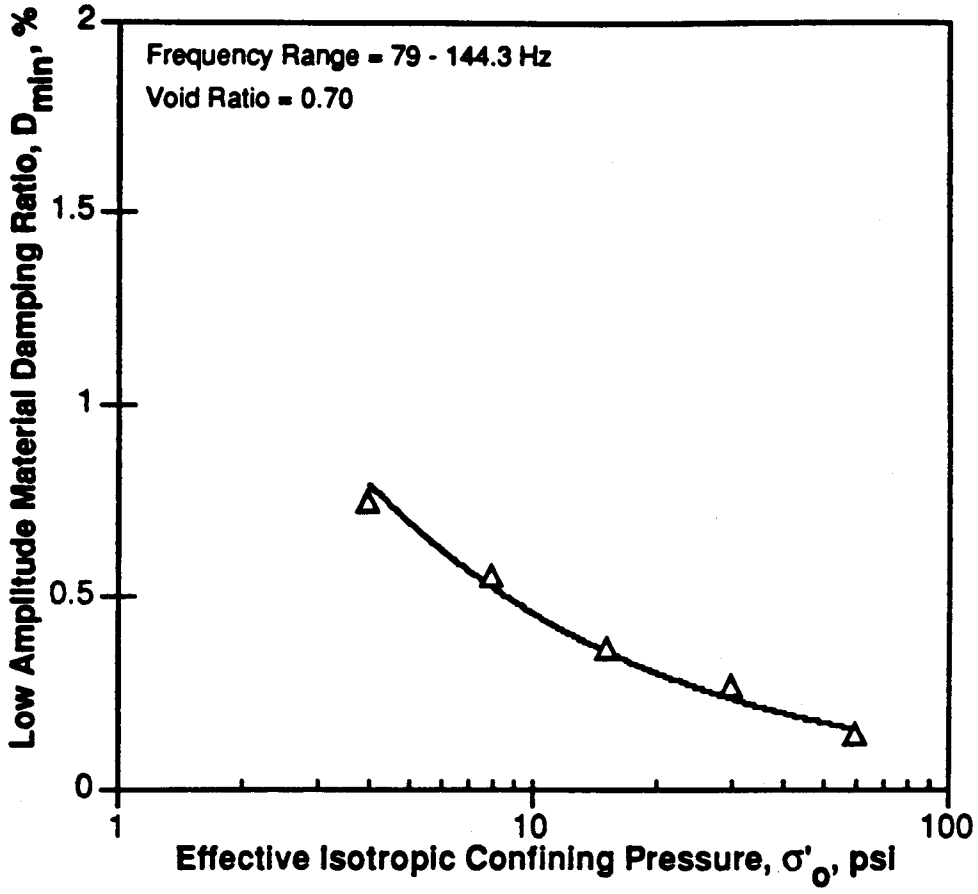

Figure 8.B.5-23
Variation in low-amplitude material damping ratio in shear with effective isotropic confining pressure from resonant column tests (from Laird, 1993).

8.B.5.3.7.3 Time of Confinement

The effect on shear modulus and material damping of time of confinement at a constant effective stress was also investigated. Laird (1993) found that modulus was essentially constant with time at a constant isotropic confining pressure as shown in Fig. 8.B.5-24. This result agrees with previous research (Lee, 1985). Hence, the effect of confinement time on modulus was neglected in this study.

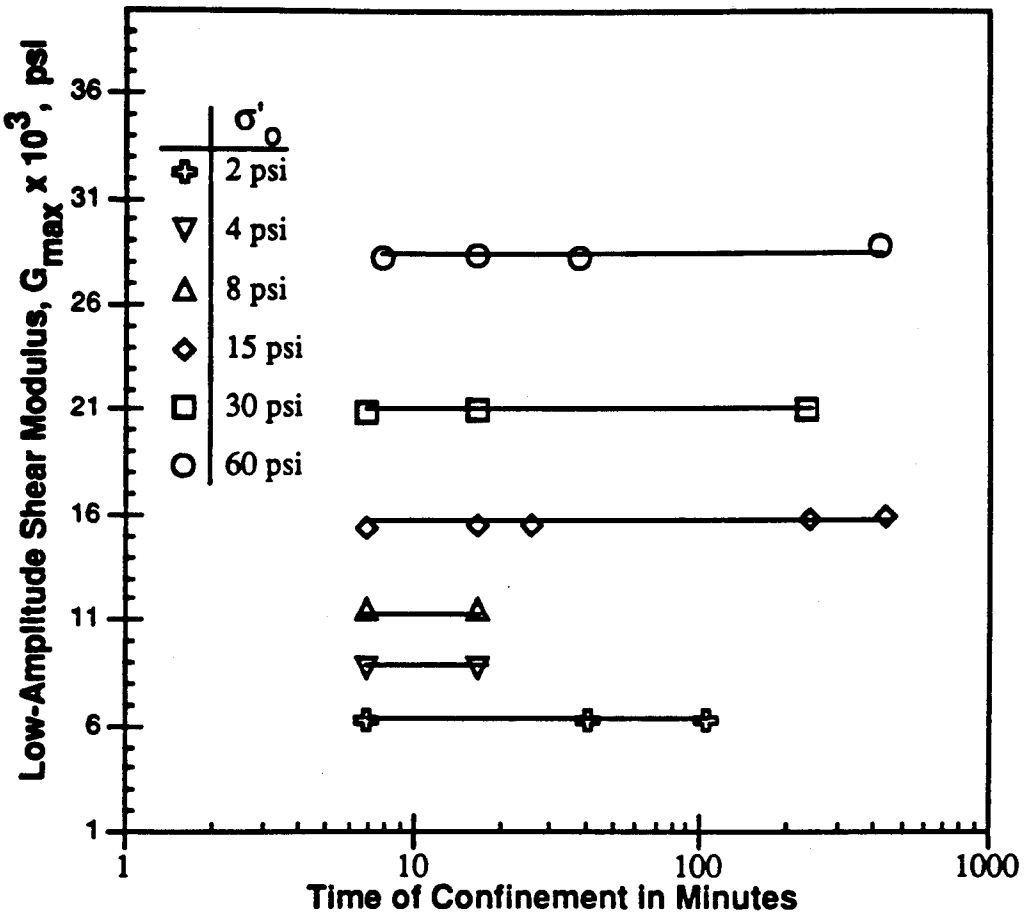

Figure 8.B.5-24
Variation in low-amplitude shear modulus with time of confinement at a constant effective stress (from Laird, 1993).

Laird (1993) also studied the effect of time of confinement on material damping and found that material damping is essentially independent of time at a constant effective stress (Fig. 8.B.5-25). Any slight effect might appear could be because measurements are being carried out at small strains and calculated values of the damping ratio show some scatter.

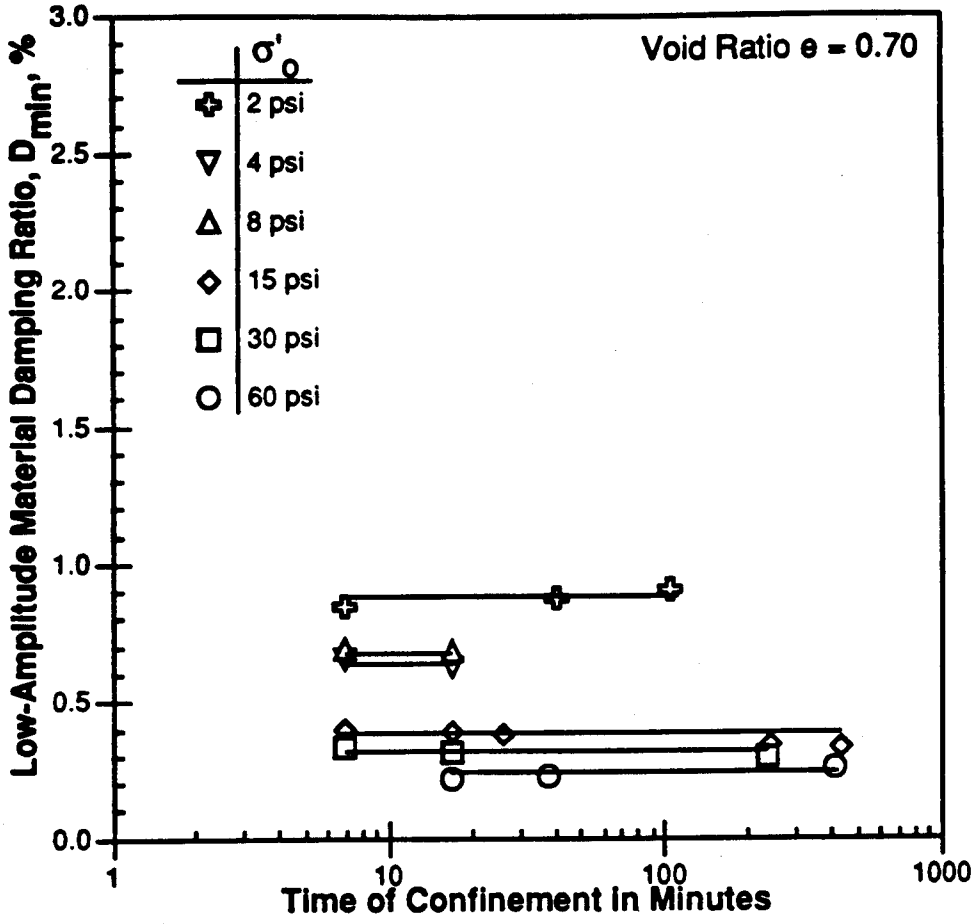

Figure 8.B.5-25
Variation in low-amplitude material damping ratio in shear with time of confinement at a constant effective stress (from Laird 1993).

8.B.5.3.7.4 Effects of Frequency

Kim (1991) showed shear modulus and damping were independent of frequency from tests performed on samples of washed mortar sand. The resonant column and torsional shear tests were used to obtain the properties at a void ratio of 0.70. Fig. 8.B.5-26 shows the variation in shear modulus with frequency and confining pressure. The variation of damping ratio with frequency at confining pressures of 3, 5, 10 and 20 (21, 34, 69 and 138 kPa) is shown in Fig. 8.B.5-27.

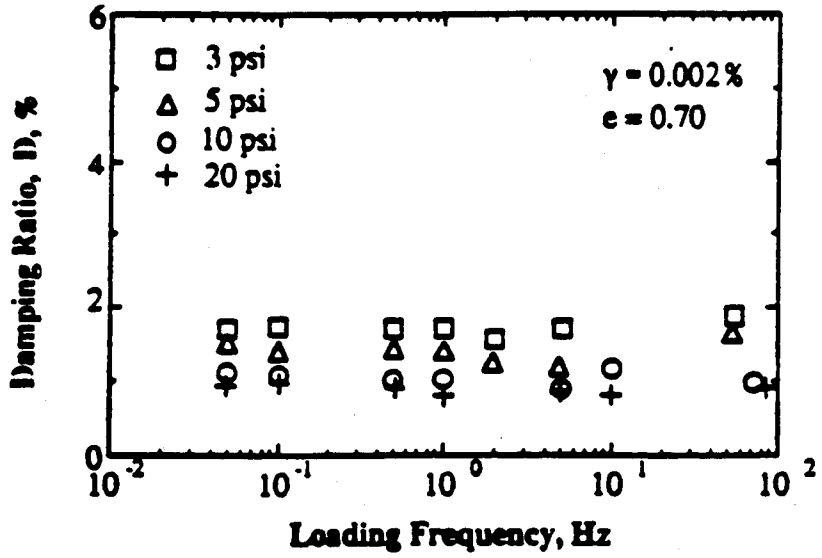

Figure 8.B.5-26
Variation in low-amplitude shear modulus at a constant effective confining stress with frequency (from Kim, 1991).

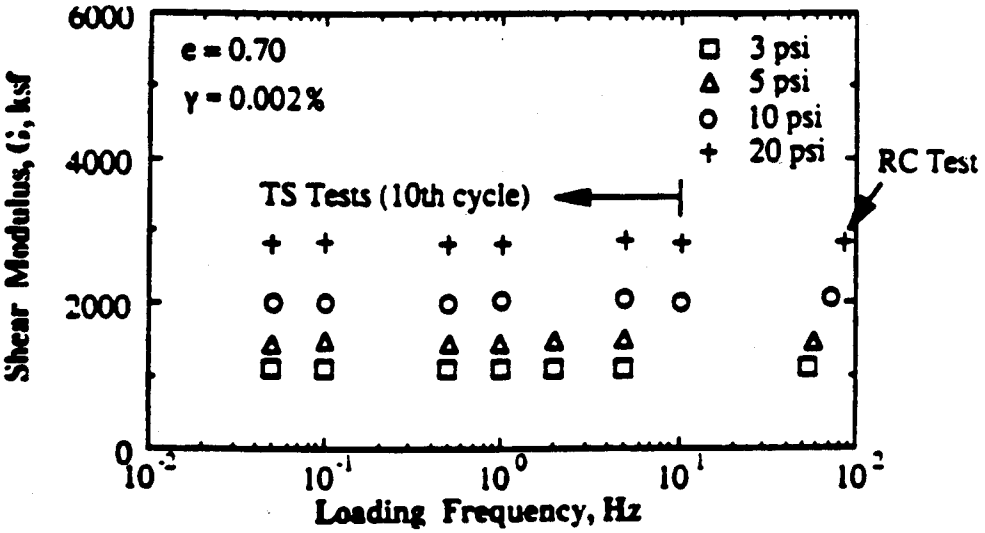

Figure 8.B.5-27
Variation in low-amplitude material damping ratio at a constant effective confining stress with frequency (from Kim, 1991).

8.B.5.3.7.5 Young's Modulus and Constrained Modulus

A series of resonant longitudinal tests by Lewis (1990) on the washed mortar sand for determination of Young's modulus yielded the results shown in Fig. 8.B.5-28. The void ratio for the medium-dense test series was 0.71 while for the dense test series was 0.62. From the graphs, a straight-line fit could be made on a log–log plot of modulus versus strain. The slopes of the lines for both series of tests are almost the same and are about 1300 (i.e. strain = 0.0008%). The dynamic stiffness equation representing Young's modulus as a function of mean effective stress is as below:

$$E = \frac{C_E}{F(e)} P_a^{1-nm} \bar{\sigma}_o^{nm} \qquad (8.B.5\text{-}2)$$

Where:

E = Young's modulus,
C_E = stiffness coefficient,
$F(e)$ = $0.3+0.7(e)^2$,
P_a = atmospheric pressure (14.7 psi),
nm = stress exponent,
$\bar{\sigma}_o$ = effective isotropic confining pressure (psi), and
e = void ratio

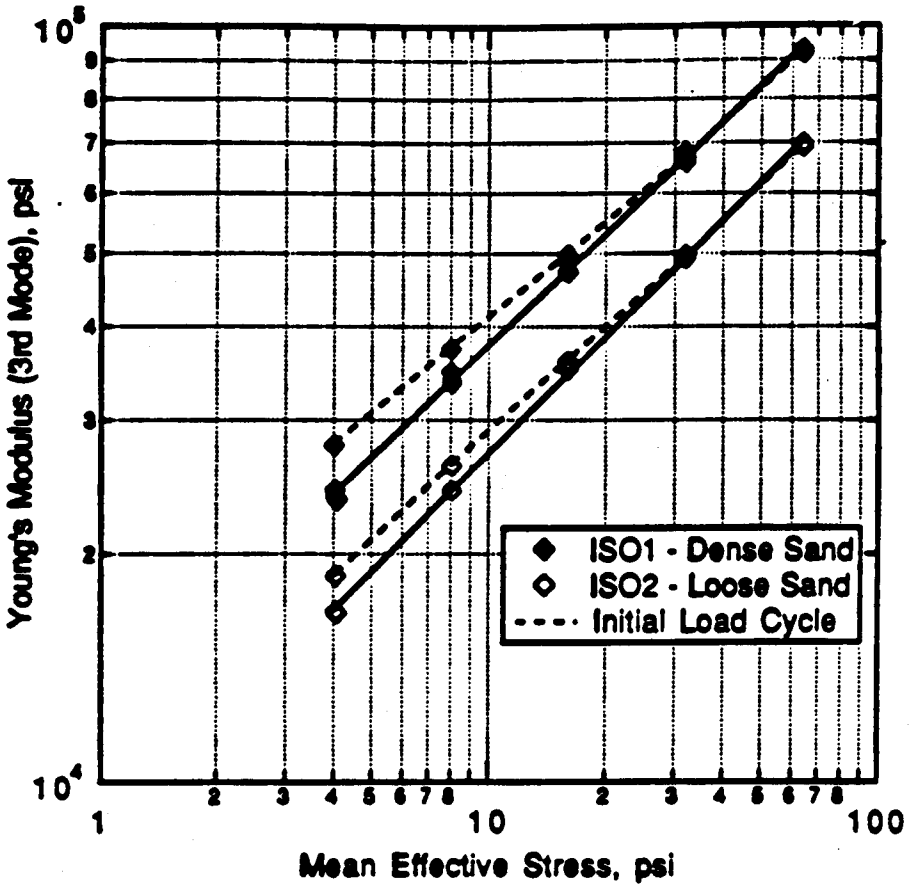

Figure 8.B.5-28
Variation of Young's modulus with mean effective stress (from Lewis, 1990).

Lewis also measured the values of constrained modulus with mean effective stress (Fig. 8.B.5-29). It was observed that the sand exhibits a similar variation in constrained modulus with effective as found for shear modulus. The dynamic stiffness equation representing constrained modulus as a function of mean effective stress is as below

$$M = \frac{C_M}{F(e)} P_a^{1-nm} \bar{\sigma}_o^{nm} \qquad (8.B.5\text{-}3)$$

Where:

M = Young's modulus,
C_M = stiffness coefficient,
$F(e)$ = $0.3+0.7(e)^2$,
P_a = atmospheric pressure (14.7 psi),
nm = stress exponent,
$\bar{\sigma}_o$ = effective isotropic confining pressure (psi), and
e = void ratio

The slope of these tests are similar to those obtained from the shear modulus (G_{max}) tests performed by Laird (1993).

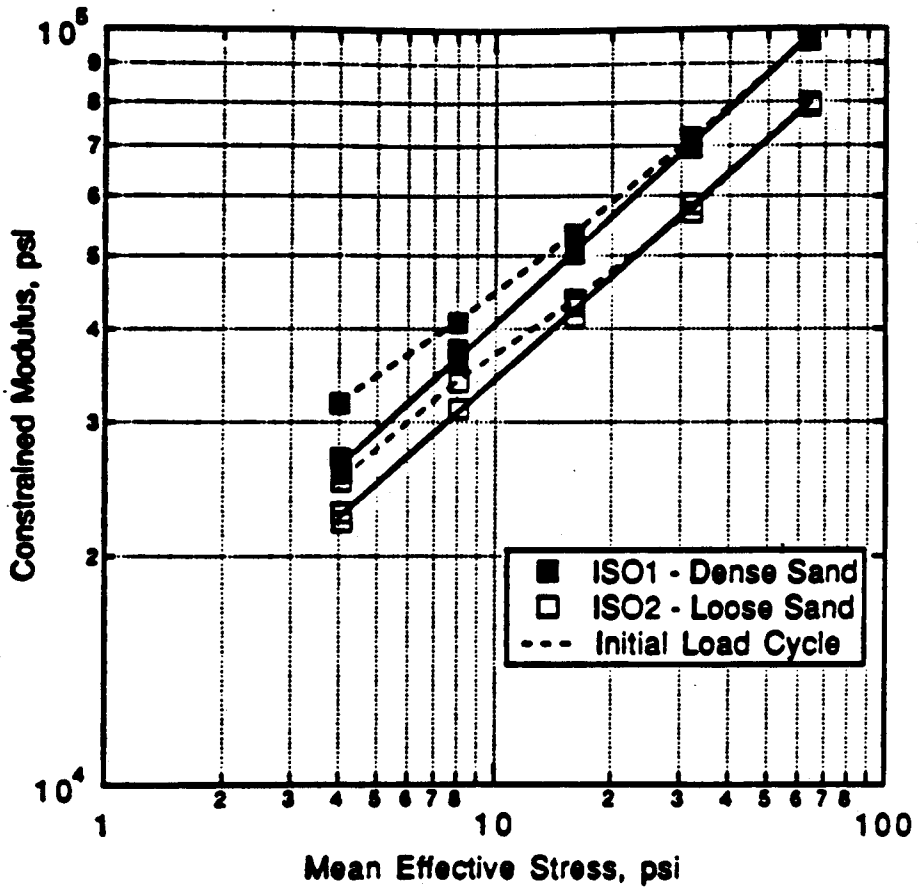

Figure 8.B.5-29
Variation of constrained modulus with mean effective stress (from Lewis, 1990).

8.B.5.3.8 Conclusions

A brief discussion of the equipment and instrumentation used in performing seismic tests in the LSTC is presented in this section.

Washed mortar sand was used as the soil medium for testing. A summary of the properties of the washed mortar sand is presented along with a discussion of the method of sand placement in the LSTC.

The washed mortar sand exhibits a linear log–log relationship for shear modulus with effective stress. The material damping ratios, D_{min} of the washed mortar sand as obtained from resonant column test range between 1.3% to 0.3% and decrease with increasing confining pressure. From the resonant column and torsional shear results, it is obvious that time of confinement and frequency have little to no effect on the damping values of the sand.

The properties of most concern to this study are wave velocities, V_S and V_P, and material damping ratios. Torsional resonant column tests were used to obtain V_S and D_S, while longitudinal resonant column test were used to evaluate V_C and pulse tests were used to evaluate V_P.

4—ANALYTICAL PROCEDURES FOR EVALUATING MATERIAL DAMPING FROM WAVE ATTENUATION MEASUREMENTS

8.B.5.4.1 Introduction

The rise time, spectral ratio and the spectral slope methods for material damping measurements are briefly discussed in this section. The spectral slope method was the only method that could be used in this study because of the way in which the P- and S-wave measurements were recorded (Lee, 1993). However measurements were performed in both forward and reverse directions. Therefore, equations for measurements in the combined directions (forward and reverse array directions) are developed herein. The range of frequencies used in the tests and the typical data reduction techniques are also briefly discussed.

8.B.5.4.2 Nature of Damping

The basic mechanisms involved in the attenuation of seismic waves propagating away from a point source and through an infinite soil medium can be divided into the following two categories:

1. geometrical spreading which results from a fixed amount of energy along the wavefront expanding into larger volumes; i.e. for each wave the energy density decreases with distance from the source and hence a decrease in wave amplitude takes place. This type of energy dissipation is known as geometrical damping or radiation damping.
2. material damping which results from dissipation of energy within the material elements and is due to: (1) frictional mechanisms which involve friction at cracks and grain boundaries, and (2) fluid-flow mechanisms which involve the movement of fluids in the pores and cracks of saturated and unsaturated materials (Winkler and Nur, 1982). This type of energy dissipation is also known as internal damping.

Geometrical or radiation damping for P- and S-waves in an elastic infinite medium decreases in proportion to the ratio

$$(1/R),$$

where R equals the distance from the energy source. This type of damping is easily understood at least for simple geometrical systems. Material damping, on the other hand, is still a topic deserving much research.

In this study, evaluation of material damping is the topic of concern. Material damping is evaluated by measuring the decay in amplitude of a seismic wave after taking into account geometrical spreading. Material damping in geotechnical earthquake engineering can be represented by the energy dissipation within a soil element during cyclic (dynamic) loading. As soils are not perfectly elastic, the stress-strain curves are not the same during cyclic loading and unloading as shown in Fig. 8.B.5-30. Hence the loading and unloading curves define a hysteresis loop. For this loop, damping capacity,

$$\Delta_{CS},$$

is represented as the ratio of the area enclosed by the hysteresis loop to the area representing the peak energy stored in each cycle as:

$$\Delta_{CS} = \frac{\Delta E_\sigma}{E_\sigma} \qquad (8.B.5\text{-}4)$$

where,

ΔE_σ = area of hysteresis loop, and

E_σ = total strain energy.

This behavior implies that the amount of dissipated energy increases as the number of cycles increases.

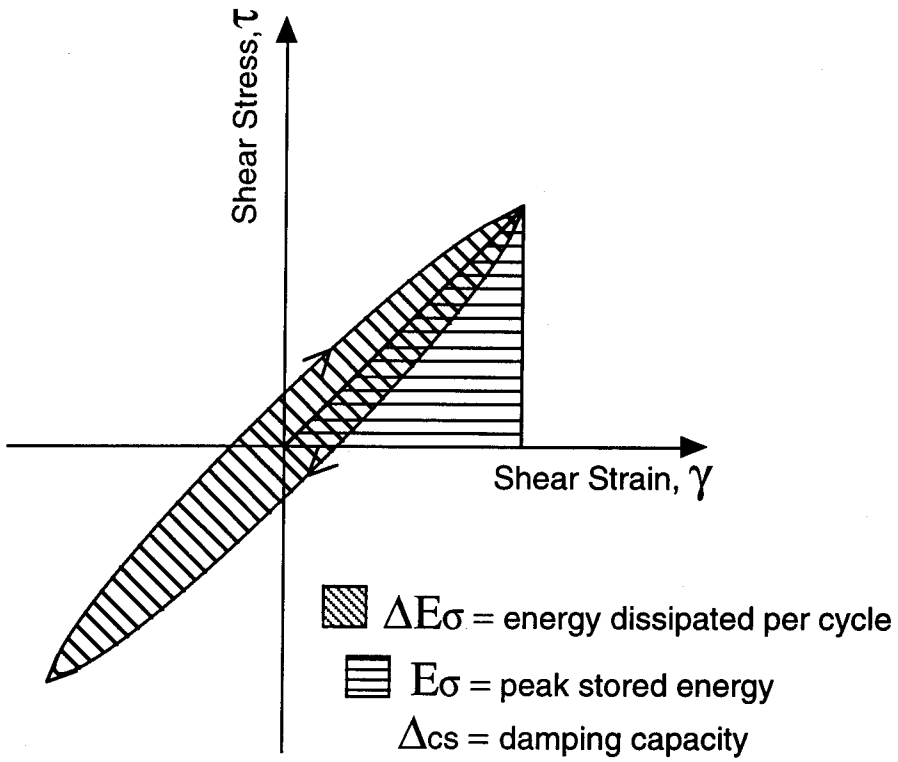

Figure 8.B.5-30
Stress-strain diagram for a simple dynamic system with hysteretic damping.

8.B.5.4.3 Definitions and Terminology

In geotechnical engineering, wave attenuation is typically expressed in terms of material damping ratio, D. In seismology, wave attenuation is expressed in terms of a dimensionless quality factor, Q, or as the dissipation factor,

$$1/Q.$$

The quality factor is defined as the ratio of stored energy to dissipated energy as:

$$\frac{1}{Q} = \frac{\Delta E_\sigma}{2\pi E_\sigma} \qquad (8.B.5\text{-}5)$$

where,

ΔE_σ = the amount of energy dissipated per cycle in a certain volume of material,
E_σ = the peak elastic energy stored in the same volume, and
Π = 3.14159.....

Damping ratio, D, is related to quality factor, Q, for measurements at small strains in the following form:

$$D = \frac{1}{2Q} \tag{8.B.5-6}$$

There are several other measures of attenuation which are defined and related to each other as follows:

$$\frac{1}{Q} = \frac{\alpha V}{\Pi f} = \frac{\delta}{\Pi} = \frac{\Delta f}{f} \tag{8.B.5-7}$$

where,

Q–1 = dissipation factor,
α = attenuation factor,
δ = logarithmic decrement,
Δf = resonance width,
V = propagation velocity, and
f = frequency.

8.B.5.4.4 Measurement Methods

8.B.5.4.4.1 Rise Time Method

One seismic method of evaluating damping utilizes the fact that the width of the seismic wave broadens with distance and is due to material damping. It is also assumed that material damping is independent of geometrical spreading and that Q is independent of frequency. Using this method, interference in the seismic signals (noise) can be minimized because measurements are made from the first quarter-cycle of the P- or S-wave event. This approach is especially applicable to P-waves which are the first arrivals in the waveform. This method is less easily applied to S-waves because they are never the first arrival so that the S-wave is superimposed on other wave energy.

The broadening of the seismic wave is measured by the rise time. The rise time is defined as the time interval between two intercepts determined by the tangent to the point of maximum gradient of the initial pulse. The intercepts are for the zero crossing and peak amplitude as illustrated in Fig. 8.B.5-31.

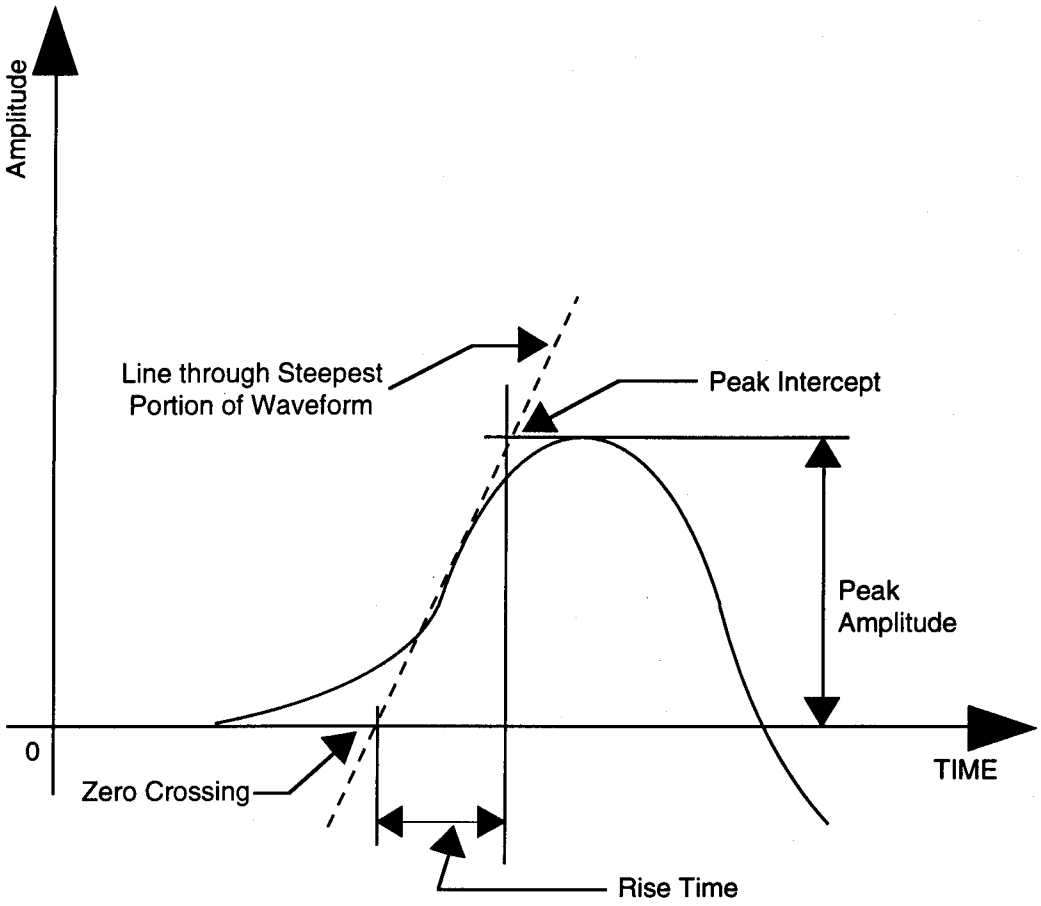

Figure 8.B.5-31
Definition of rise time as used in seismic attenuation measurements.

Travel time is directly proportional to rise time and is related to Q by (Gladwin and Stacy, 1974; and Kjartansson, 1979):

$$T = T_0 + \frac{c\,t}{Q} \qquad (8.B.5\text{-}8)$$

where,

T = rise time,
c = a constant, with a value of 0.53 ± 0.04 (Gladwin and Stacy, 1974),
T_0 = rise time of the source,
t = travel time, and
Q = Quality factor.

To find the value of Q, the rise time from the waveforms recorded at progressively larger distances from a source are plotted against their corresponding travel times, and the slope of the plot at any point results in the value of Q at the distance corresponding to that travel time. A typical plot is shown in Fig. 8.B.5-32.

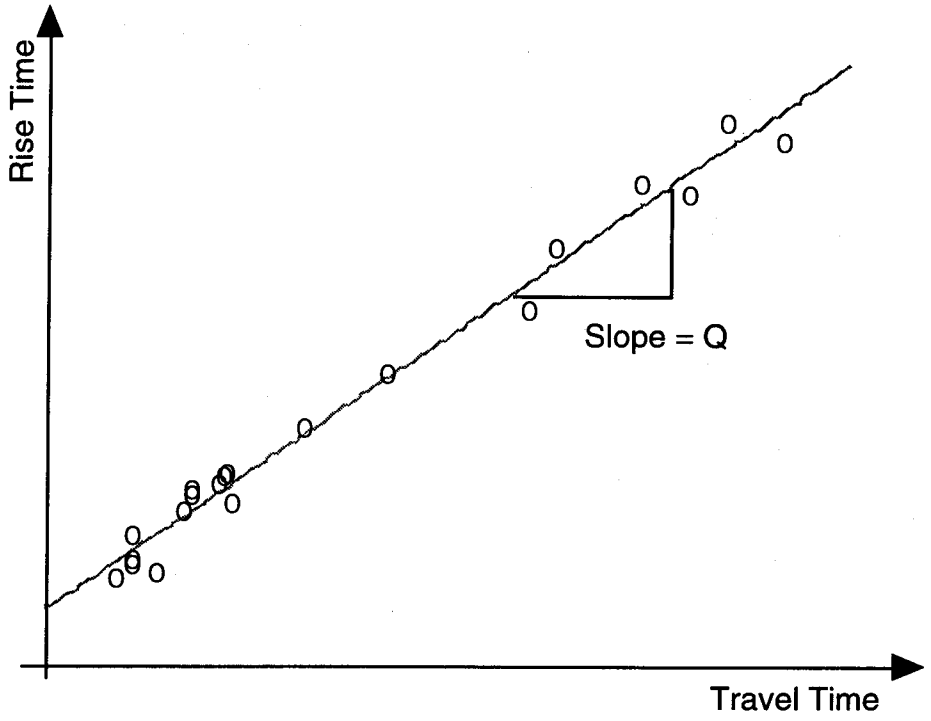

Figure 8.B.5-32
Plot of rise time versus travel time for calculation of material damping using the rise time method.

8.B.5.4.4.2 Spectral Ratio Method

In this method, the decay in amplitude of seismic waves propagating through a medium is utilized (Mok et al, 1988 and White 1965). A typical arrangement of source and receivers for such a measurement is shown in Fig. 8.B.5-33. For a harmonic wave propagating in an infinite homogeneous medium and measured as in Fig. 8.B.5-33, the change in body wave amplitude with distance from the source due to both geometrical and material damping can be described by:

$$A_R = S\frac{1}{R} I \exp^{(-\alpha R)} \qquad (8.B.5\text{-}9)$$

where,

I = soil-receiver interaction function,
exp. = base of natural logarithm,
α = attenuation coefficient,
S = wave amplitude at the source,
A_R = wave amplitude at the receiver, and
R = distance from source to receiver.

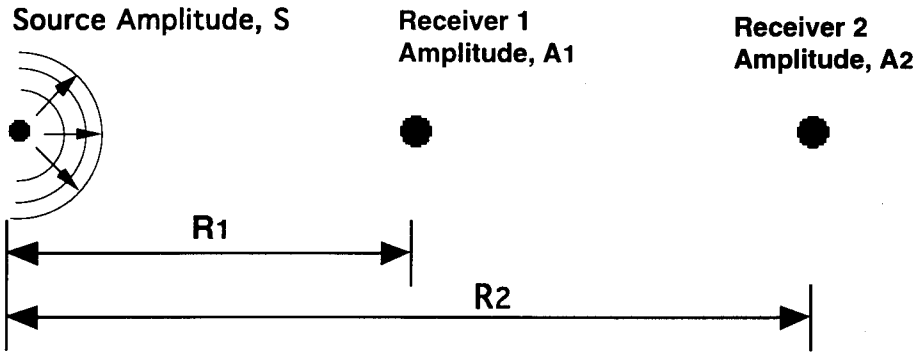

Figure 8.B.5-33
Arrangement of source and receivers in a three-point array for measurement of wavefront attenuation.

In Eq. 8.B.5-9, the term

$$1/R$$

accounts for geometrical or radiation damping, and the exponential term accounts for material damping. This equation ignores the near-field terms and, therefore, is referred to as a far-field expression. The term I is called the interaction function and accounts for the response of the receivers modified by the medium and boreholes.

For calculations, the amplitudes of the seismic wave at two different distances (R_1 and R_2) from the source are measured as:

$$A_1 = S\frac{1}{R_1} I_1 \exp^{(-\alpha R_1)} \qquad (8.B.5\text{-}10)$$

and

$$A_2 = S\frac{1}{R_2} I_2 \exp^{(-\alpha R_2)} \qquad (8.B.5\text{-}11)$$

The ratio of the two amplitudes is obtained from Eqs. 8.B.5-10 and 8.B.5-11 as:

$$\frac{A_2}{A_1} = SR_{21} = \frac{R_1}{R_2}\frac{I_1}{I_2}\exp^{-\alpha(R_2-R_1)} \qquad (8.B.5\text{-}12)$$

where,

SR_{21} = spectral ratio,
A_1 = body wave amplitude at distance R_1 from the source,
A_2 = body wave amplitude at distance R_2 from the source,
I_1 = soil-receiver interaction function for receiver 1, and
I_2 = soil-receiver interaction function for receiver 2.

The assumption is generally made in applying Eq. 8.B.5-12 that the response of both receivers is the same (i.e. $I_1 = I_2$).

A measure of material damping is the attenuation coefficient, α, which can be expressed as:

$$\alpha = \frac{-\ln\left(SR_{21}\frac{R_2}{R_1}\right)}{(R_2 - R_1)} \qquad (8.B.5\text{-}13)$$

From Eq. 8.B.5-7, the attenuation coefficient becomes:

$$\alpha = \frac{2\pi Df}{V} \qquad (8.B.5\text{-}14)$$

where,

D = material damping,
f = frequency, and
V = wave velocity.

The phase difference between receivers 1 and 2 is:

$$\phi_{21} = \frac{R_2 - R_1}{V} 2\pi f \qquad (8.B.5\text{-}15)$$

where, ϕ_{21} = phase difference between receivers 1 and 2. Then from Eqs. 8.B.5-12, -13, -14 and -15, material damping ratio can simply be calculated by:

$$D = \frac{-\ln\left(SR_{21}\frac{R_2}{R_1}\right)}{\phi_{21}} \qquad (8.B.5\text{-}16)$$

8.B.5.4.4.3 Spectral Slope Method

In this method, the basic assumptions are that (Redpath, and Lee, 1986):

1. Q is independent of frequency (hence D is also frequency independent),
2. geometrical damping is constant (does not depend on frequency),
3. scattering is not a "major effect" so that a straight-line fit passes through the appropriate data,
4. transmission losses across boundaries are independent of frequency, and
5. damping can be calculated using two receivers, i.e. a two-point measurement.

For a harmonic wave propagating in an infinite homogeneous medium, the change in body wave amplitude with distance from the source due to material damping can be described by as:

$$A_1 = S\frac{1}{R_1} I_1 \exp^{-KfR_1} \qquad (8.B.5\text{-}17)$$

$$A_2 = S\frac{1}{R_2} I_2 \exp^{-KfR_2} \qquad (8.B.5\text{-}18)$$

where,

A_1 = amplitude spectrum of the signal at the first receiver,
A_2 = amplitude spectrum of the signal at the second receiver,
S = wave amplitude of the source,
R_1 = distance of first receiver from the source,
R_2 = distance of second receiver from the source,
I_1, I_2 = interaction of the receivers with the medium,
K = spectral slope (change in spectral ratio with frequency),
f = frequency, and
exp. = base of natural logarithm.

A typical array arrangement is shown in Fig. 8.B.5-33. The spectral ratio can be obtained by dividing Eq. (8.B.5-17) by Eq. (8.B.5-18) as:

$$SR_{21} = \frac{A_2}{A_1} = \frac{R_1}{R_2}\frac{I_2}{I_1}\exp^{-Kf(R_2-R_1)} \tag{8.B.5-19}$$

where, SR_{21} = spectral ratio.

It could also be expressed in the form:

$$\ln SR_{21} = \ln\left[\frac{R_1}{R_2}\frac{I_2}{I_1}\right] - Kf(R_2 - R_1) \tag{8.B.5-20}$$

The assumption that $I_1 = I_2$ is not necessary here, hence the interaction functions are not as important as in the spectral ratio method. As K is defined as the change in spectral ratio with frequency, the term

$$\Delta \ln\left[\frac{R_1}{R_2}\frac{I_1}{I_2}\right]$$

becomes zero as the change in a constant is zero. Therefore, defines K as:

$$K = -\frac{\Delta \ln SR_{21}}{\Delta f(\Delta R)} \tag{8.B.5-21}$$

and

$$\delta = KV \tag{8.B.5-22}$$

where,

$\Delta R = R_2 - R_1$
δ = logarithmic decrement,
K = spectral slope,
V = wave velocity.

From Eq. 8.B.5-7, Q can be defined as:

$$Q = \frac{\Pi}{\delta} \tag{8.B.5-23}$$

$$\therefore Q = \frac{\Pi}{KV} \tag{8.B.5-24}$$

So, the spectral slope, K, will be

$$K = -\frac{\Delta \ln SR_{21}}{\Delta f \Delta R} = \frac{\Pi}{QV} \tag{8.B.5-25}$$

Hence by definition,

$$-\frac{\Delta \ln SR_{21}}{\Delta f \Delta R} = \frac{2\Pi D}{V} \tag{8.B.5-26}$$

$$-\frac{\Delta \ln SR_{21}}{\Delta f} = 2\Pi D \Delta t \tag{8.B.5-27}$$

The material damping ratio is given by:

$$D = -\frac{\Delta \ln SR_{21}}{\Delta f} \cdot \frac{1}{2\Pi \Delta t} \tag{8.B.5-28}$$

$$D = -K \frac{1}{2\Pi \Delta t} \tag{8.B.5-29}$$

From this method a straight line fit should pass through the data when lnSR is plotted against frequency, the slope of the line is called the spectral slope and is constant for a given soil type as illustrated in Fig. 8.B.5-34.

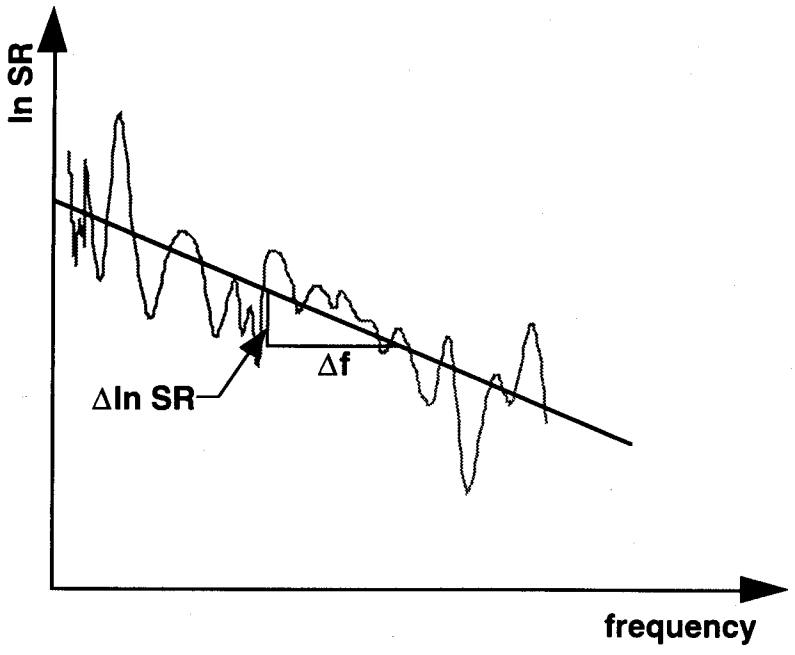

Figure 8.B.5-34
Figure illustrating the idea behind the spectral slope method.

8.B.5.4.4.4 Spectral Ratio Method using Combined Directions

During sample construction in the LSTC, sources were placed at both ends of each array as shown in Figs. 8.B.5-13 and 8.B.5-15. This arrangement made it possible for the seismic wave records to be obtained for wave propagation in both the forward and reverse directions as illustrated in Fig. 8.B.5-35. This arrangement was used in order to minimize many of the variables which can adversely affect the amplitude spectra.

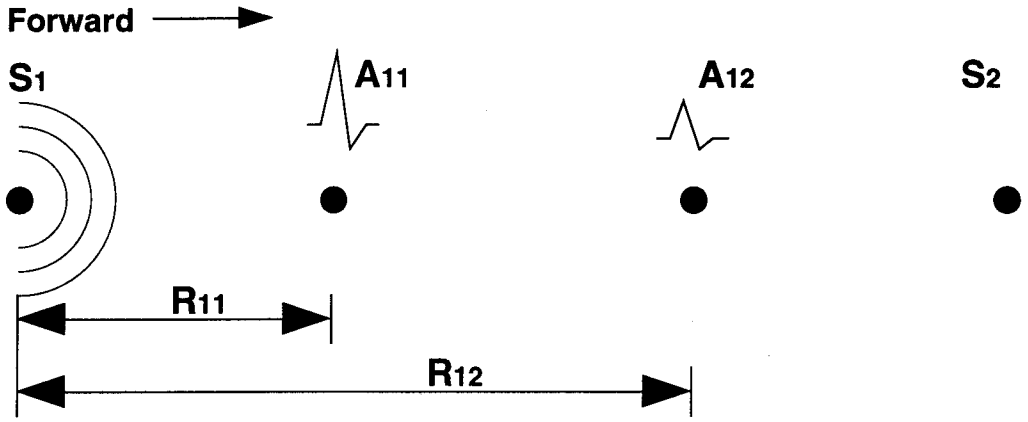

a. Forward Testing

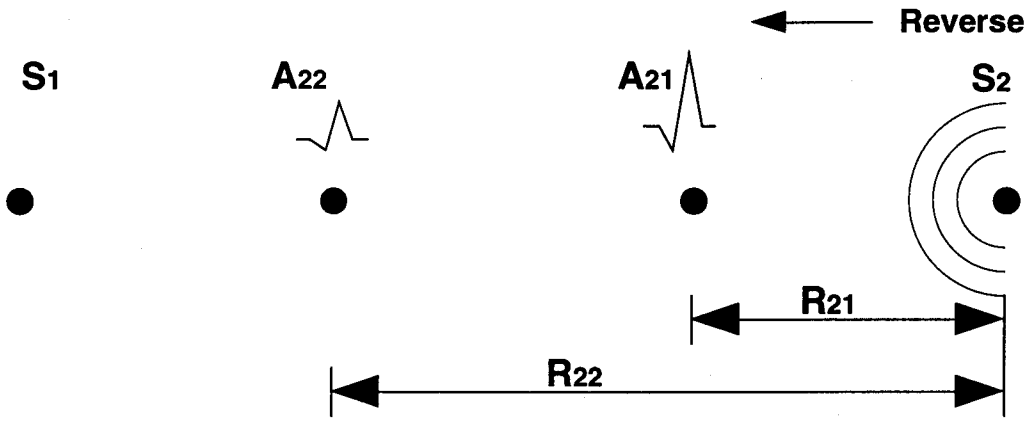

b. Reverse Testing

Figure 8.B.5-35
Arrangement of sources and receivers in an array for seismic testing in both forward and reverse directions.

For the forward array, signals at each receiver are recorded and the amplitude of each signal is described by modifying Eqs. 8.B.5- 10 and 8.B.5-11 as follows:

$$A_{11} = S_1 \frac{1}{R_{11}} I_1 \exp^{(-\alpha R_{11})} \quad \text{(8.B.5-30)}$$

and

$$A_{12} = S_1 \frac{1}{R_{12}} I_2 \exp^{(-\alpha R_{12})} \quad \text{(8.B.5-31)}$$

Where,

A_{11} = amplitude spectrum of the signal at the first receiver,
A_{12} = amplitude spectrum of the signal at the second receiver,
R_{11} = distance of first receiver from the source,
R_{12} = distance of second receiver from the source,
I_1 = soil-receiver interaction function for receiver 1, and
I_2 = soil-receiver interaction function for receiver 2.
S_1 = amplitude spectrum of the source, and
α_2 = attenuation coefficient.

The spectral ratio in the forward direction is then defined as:

$$\frac{A_{12}}{A_{11}} = SR_f = \frac{R_{11}}{R_{12}} \frac{I_1}{I_2} \exp^{-\alpha(R_{12}-R_{11})} \quad \text{(8.B.5-32)}$$

where,

SR_f = spectral ratio in the forward direction.

Signals from tests in the reverse direction are recorded using the second source, and the amplitude of each signal is described as:

$$A_{21} = S_2 \frac{1}{R_{21}} I_2 \exp^{(-\alpha R_{21})} \quad \text{(8.B.5-33)}$$

and

$$A_{22} = S_2 \frac{1}{R_{22}} I_1 \exp^{(-\alpha R_{22})} \quad \text{(8.B.5-34)}$$

Where,

A_{21} = amplitude spectrum of the signal at the first receiver,
A_{22} = amplitude spectrum of the signal at the second receiver,
R_{21} = distance of first receiver from the source,
R_{22} = distance of second receiver from the source,
I_1 = soil-receiver interaction function for receiver 1,
I_2 = soil-receiver interaction function for receiver 2.
S_2 = amplitude spectrum of the source, and
α = attenuation coefficient.

The spectral ratio from the reverse array is:

$$\frac{A_{22}}{A_{21}} = SR_r = \frac{R_{21}}{R_{22}}\frac{I_2}{I_1}\exp^{-\alpha(R_{22}-R_{21})} \quad (8.B.5\text{-}35)$$

where,

SR_r = spectral ratio in the reverse direction.

By multiplying Eqs. (8.B.5-32) and (8.B.5-35), the result is:

$$SR_f SR_r = \frac{R_{11}}{R_{12}}\frac{R_{21}}{R_{22}}\frac{I_1}{I_2}\frac{I_2}{I_1}\exp^{[-\alpha_1(R_{12}-R_{11})-\alpha_2(R_{22}-R_{21})]} \quad (8.B.5\text{-}36)$$

The phase difference associated with each frequency for the forward and reverse directions can be defined as:

$$\phi_{12} = \frac{R_{12}-R_{11}}{V_1}2\Pi f \quad (8.B.5\text{-}37)$$

and

$$\phi_{21} = \frac{R_{22}-R_{21}}{V_2}2\Pi f \quad (8.B.5\text{-}38)$$

where,

f = frequency at which wave record obtained,
V_1 = velocity in the forward direction,
V_2 = velocity in the reverse direction,
ϕ_{12} = phase difference in the forward direction, and
ϕ_{21} = phase difference in the reverse direction,
Π = 3.14159.....

The combined material damping ratio D for both the forward and reverse directions can be calculated as follows:

$$D = \frac{\ln\left(SR_f SR_r \frac{R_{12}}{R_{11}}\frac{R_{22}}{R_{21}}\right)}{\left(\phi_{21}+\phi_{12}\right)} \times 100\% \quad (8.B.5\text{-}39)$$

where,

D = material damping ratio in percent.

The following assumptions are made in applying this method:

1. material damping ratio is independent of strain amplitude for the small strains (less than 0.001%) generated in these tests,
2. measured wave amplitudes are not affected by reflected or refracted waves, and
3. any near-field effects are negligible.

To utilize these equation for waves generated from a point source. The wave records at distances R_{11}, R_{12}, and R_{21}, R_{22} for the forward and reverse directions, respectively, are used to obtain the amplitudes at each frequency. The spectral ratio's are calculated for the forward and reverse directions, and, using Eq. 8.B.5-39, the material damping ratio is calculated.

8.B.5.4.5 Data Analysis

By simultaneously monitoring the two receivers in an array for the same source impulse, amplitude spectrums were collected at each frequency.

8.B.5.4.5.1 Selection of Frequency Limits

Two criteria were used in the selection of the frequency bandwidth for computing material damping ratios. First, the wavelength associated with the source-receiver spacing must be considered. Wavelength, frequency, and wave velocity are related by:

$$f = \frac{V}{\lambda} \tag{8.B.5-40}$$

where,

f = frequency,
V = wave velocity, and
λ = wavelength.

The wavelength should be less than $\frac{R_{11}}{2}$ or $\frac{R_{21}}{2}$. Therefore the lower-limit of the frequency, f_{lower} is given by:

$$f_{lower} \geq \frac{2V}{R_{11}} \text{ for forward array,} \tag{8.B.5-41}$$

$$f_{lower} \geq \frac{2V}{R_{21}} \text{ for reverse array.} \tag{8.B.5-42}$$

The upper limit was based on the receiver size versus wavelength ratio criteria. The receiver size was 1.37 in. (2.9 cm) and the wavelength should be greater than 2.5× receiver size. Therefore the upper limit of the frequency, f_{upper}, is given by:

$$f_{upper} \leq \frac{V}{2.5R_S} \tag{8.B.5-43}$$

The upper limit is also bounded by the upper-bound frequencies from the autopower spectrum of the wave sources.

The complete bandwidth for the forward and reverse directions can be expressed as:

$$\frac{2V}{R_{11}} \leq f \leq \frac{V}{2.5R_S} \text{ for forward array,} \quad (8.B.5\text{-}44)$$

$$\frac{2V}{R_{21}} \leq f \leq \frac{V}{2.5R_S} \text{ for reverse array.} \quad (8.B.5\text{-}45)$$

where,

R_{11} = distance of first receiver from source,
R_{21} = distance of second receiver from source,
R_S = receiver size.

This bandwidth applies to both S- and P-waves.

8.B.5.4.5.2 Data Reduction

Typical S- and P-wave records are shown in Figs. 8.B.5-36 and 8.B.5-37, respectively. Peak-to-peak displacement amplitudes or double amplitudes were measured from the seismic waves recorded at the receivers. The amplitude was averaged by taking an average peak-to-peak value of a number of peaks and taking an average peak value of a number of troughs from the mean position of zero. A typical measurement is illustrated in Fig. 8.B.5-38. The values were recorded in the data form shown in Fig. 8.B.5.B-1, presented in Appendix 8.B.5.B.

Equation 8.B.5-16 was used to calculate material damping in either the forward and reverse directions while Eq. 8.B.5-39 was used to calculate material damping from a combination of the measurements in both directions. These values were recorded in the data form of the type presented in Fig. 8.B.5.B-2 in Appendix 8.B.5.B. The material damping ratios were either rejected or selected based on the criteria discussed earlier in Section 8.B.5.4.5.1.

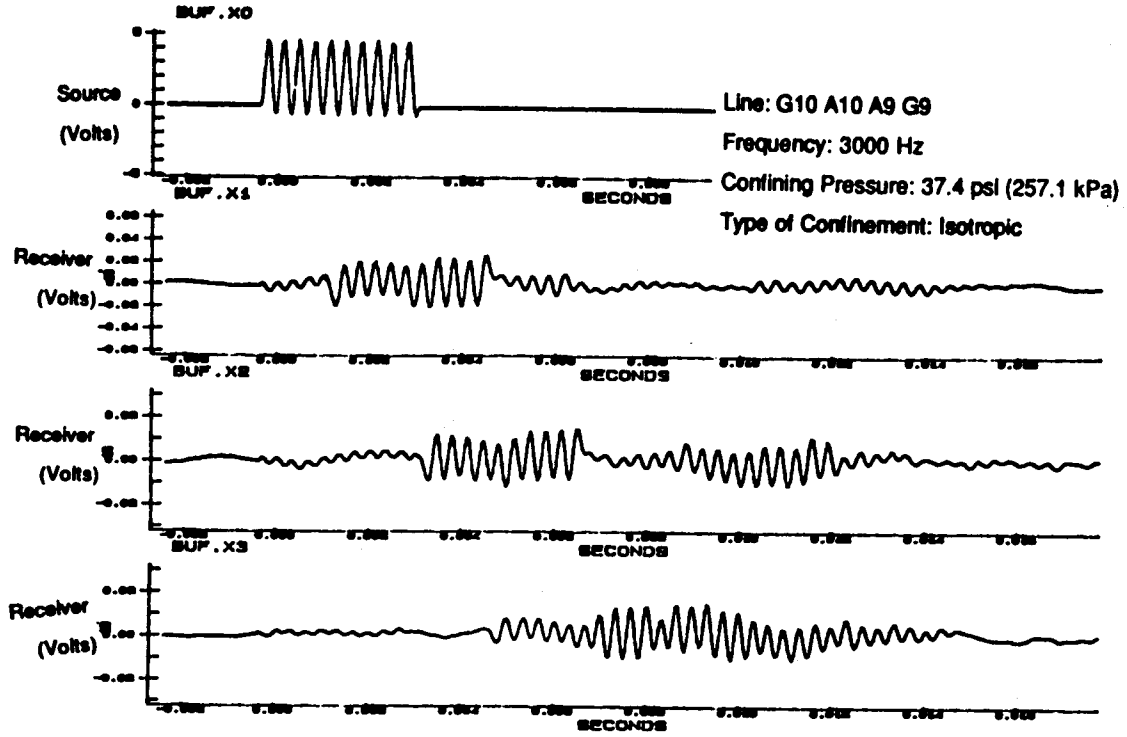

Figure 8.B.5-36
A typical S-wave record.

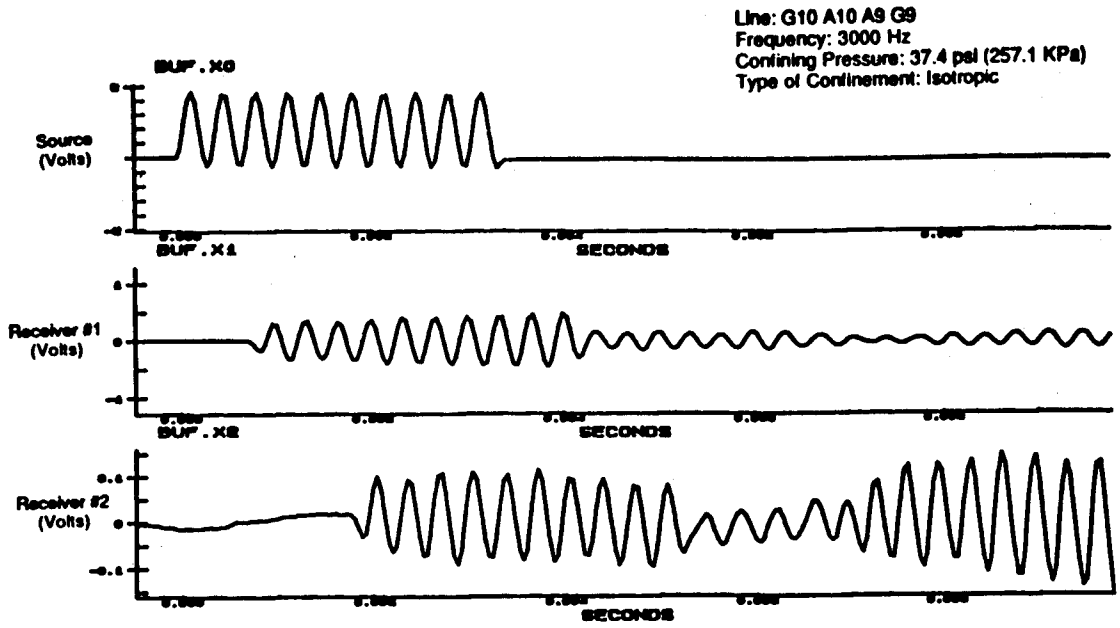

Figure 8.B.5-37
A typical P-wave record.

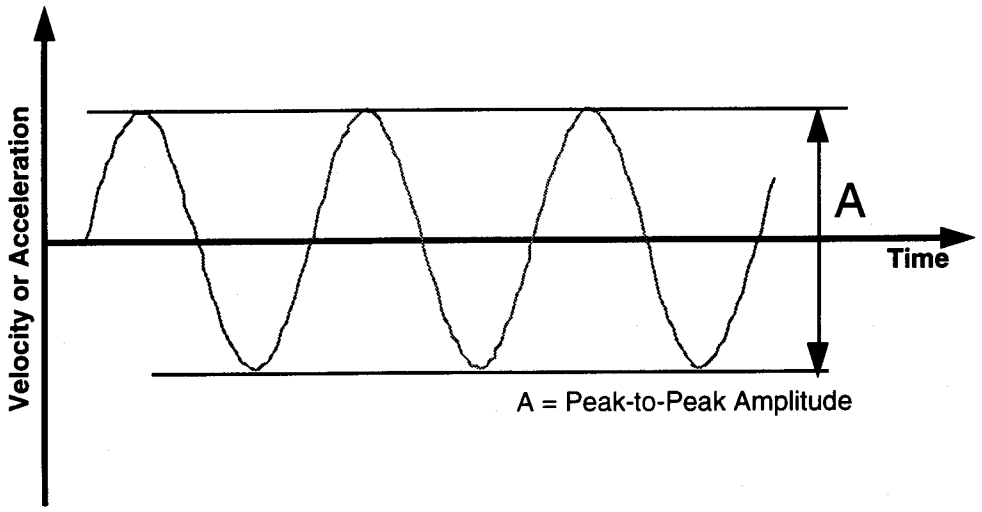

Figure 8.B.5-38
Figure illustrating peak-to-peak measurement of particle amplitude.

8.B.5.4.6 Velocity Determination

For the determination of seismic velocity, the distance traveled by the wave as well as the time of travel should be available. For the determination of velocity, center-to-center distances between the two receivers were used. These distances were determined during sample construction (Lee, 1993).

In his work, Lee (1993) utilized the interval time method for determination of wave velocities. His travel times were generally based on first arrivals.

8.B.5.4.7 Summary

There are two mechanisms of damping involved in soil systems; namely geometrical and material damping. To calculate material damping in soils using wave propagation, the spectral ratio method was employed in this study. The spectral ratio method, as well as the rise time and spectral slope methods, are briefly discussed herein.

The frequency limits for the damping calculations were selected on the basis of the source-receiver spacing and the receiver size compared to the wavelengths involved in the measurement. These limits are defined by Eqs. 8.B.5-44 and 8.B.5-45.

Also discussed in the section are the typical data reduction techniques utilized.

5—P-WAVE AND S-WAVE MEASUREMENTS UNDER ISOTROPIC STATES OF STRESS

8.B.5.5.1 Introduction

Results of material damping measurements from P-wave and S-wave measurements in the LSTC are presented in this section. Only measurements under isotropic states of stress are discussed. The section is divided into two parts; the first dealing with P-waves and the second dealing with S-waves. The part dealing with P-wave damping is more extensive because the bulk of the testing performed by Lee (1993) involved P-waves. A comparison of P- and S-wave measurements is then made with material damping values determined with torsional resonant column equipment on remolded samples.

Isotropic confining pressures of 4, 7, 12, 21.4 and 37.4 psi (27.5, 48.1, 82.5, 147.1 and 257.1 kPa) were used. The minimum pressure of 4 psi (27.5 kPa) was selected because this was the lowest pressure that could accurately be measured in the LSTC. The upper limit was selected so as to remain within the design limit of the LSTC.

All damping calculations were made taking into account the wavelength limit of at least two wavelengths between the source and first receiver. Each data point represents the average of measurements at 2 or 3 frequencies which generally were 2, 3 and 4 kHz. The damping values were calculated for the forward, reverse and combined directions using equations presented in Section 8.B.5.4.

8.B.5.5.2 General Comments about P-Wave Measurements

Thirteen arrays were employed in the measurement of P-wave attenuation. Seven of these arrays were located in the horizontal plane while six arrays were located in the vertical plane as shown in Figs. 8.B.5-13 and 8.B.5-14, respectively.

The notation used to identify the P-wave array has been changed in this section for ease in identification. The new notation is based on the location of the array relative to the direction of movement of the rainer during placement of the sand. The rainer was moved in the east–west direction. Array G7A7A8G8 is in the horizontal plane and is parallel to the movement of the rainer. This array was named C7. The north–south direction which is along array G15A15A16G16 was taken to be at zero degrees (0°) in the horizontal plane and array G1A1A2G2 to be at zero degrees (0°) in the vertical plane. By taking the clockwise direction as positive, the new notation for the arrays is presented in Table 8.B.5-4. The C7 array (G7A7A8G8) is common to both the horizontal and vertical planes as it lies in the east–west direction at the intersection of the planes.

Damping calculations were performed for each array in the forward, reverse and combined directions, at two or three frequencies (2, 3 and 4 kHz). These results are presented in tables as well as plotted for each individual array. The results are presented in Appendix 8.B.5.B for the horizontal plane and in Appendix 8.B.5.C for the vertical plane. In these tables, damping values which fell outside the established wavelength limits were not calculated. Also damping values for the combined directions could be calculated only if damping values in both the forward and reverse direction could be calculated. A typical table (Table 8.B.5.C-4) is presented in Table 8.B.5-5 to illustrate the results. This table is discussed below to illustrate how the measurements and the scatter in the results were evaluated.

Table 8.B.5-4
New Notation for Compression Wave Arrays

Original Array Notation (Figs. 8.B.5-13 and 8.B.5-14)	Angles from Zero Array	New Array Notation
Horizontal Plane		
G15A15A16G16	0°	C1
G25A25A26G26	22.5°	C2
G17A17A18G18	30°	C3
G23A23A24G24	45°	C4
G19A19A20G0	60°	C5
G21A21A22G22	67.5°	C6
G7A7A8G8	90°	C7
Vertical Plane		
G1A1A2G2	0° (vert.)	C13
G13A13A14G14	22.5°	C12
G3A3A4G4	30°	C11
G11A11A12G12	45°	C10
G5A5A6G6	60°	C9
G9A9A10G10	67.5°	C8
G7A7A8G8	90° (horz.)	C7

Typical Results. As seen in Table 8.B.5-5, there is significant scatter for damping measurements evaluated in any one direction. For the forward measurements, damping ratios ranged from –2.91% to 9.48%. On the other hand, damping ratios in the reverse direction ranged from –2.17% to 6.16% for the same arrays. It is interesting to note that if the measured damping ratio is low in one direction, then it is usually on the high side in the other direction. For instance, the measurements at 2 kHz under a 12 psi (82.5 kPa) pressure along array C10 were –2.91% and 9.48% in the forward and reverse directions, respectively. But the combined measurement does an excellent job of reducing the scatter which most likely comes from the effects of the receivers and their interaction with the surrounding sand.

Table 8.B.5-5
Values of Material Damping in Compression for Forward, Reverse and Combined Directions Along Array C10 in the Vertical Plane for Isotropic Loading Conditions.

Excitation Frequency	Confining Pressure, psi, (kPa)	D(%) Measured in Test Direction Forward	Reverse	Combined
2000 Hz	4 (27.5)	2.73	3.33	3.03
	7 (48.1)	2.09	2.26	2.18
	12 (82.5)	–2.91	9.48	3.39
	21.4 (147.1)	**	**	**
	37.4 (257.1)	**	**	**
3000 Hz	4 (27.5)	2.12	2.57	2.35
	7 (48.1)	2.14	1.08	1.61
	12 (82.5)	–2.27	6.16	2.03
	21.4 (147.1)	1.96	1.90	1.93
	37.4 (257.1)	1.93	2.17	2.05
4000 Hz	4 (27.5)	2.70	1.70	2.20
	7 (48.1)	2.51	2.52	2.52
	12 (82.5)	–0.45	3.67	1.69
	21.4 (147.1)	2.48	1.42	1.95
	37.4 (257.1)	1.49	1.87	1.49

* One or both record(s) were missing or could not be interpreted.
** Damping value not calculated because outside established wavelength limits.

For P-wave measurements along array C10 at 2 kHz under isotropic pressures of 21.4 and 37.4 psi (147.1 and 37.4 kPa), no values of damping are listed. At these confining pressures, the velocity of propagation was 1508 ft/sec and 1599 ft/sec (459.5 m/sec and 487.3 m/sec), respectively. Using equations presented in Section 8.B.5.4 for the established wavelength limits, the wavelengths turn out to be greater than 0.75 ft (0.228 m), and hence the data were rejected.

Measurements obtained from the C10 array have also been presented in graphical form in Fig. 8.B.5-39. In the graphs, damping values which were negative were not plotted. Also the upper limit of the damping ratios plotted in the graphs was set at 4% so that values of 9.48% and 6.16% were not plotted. This approach of using a graph with limits of 0 to 4% was used because most of the data fit within these limits and a larger scale would tend to obscure potentially meaningful variations. These graphs show that although there is large scatter in the damping measurements as obtained from the forward and reverse directions, the values obtained by combining both directions narrows the band significantly. The graphs show that there is a general trend of decreasing damping with increasing confining pressure for all three frequencies used.

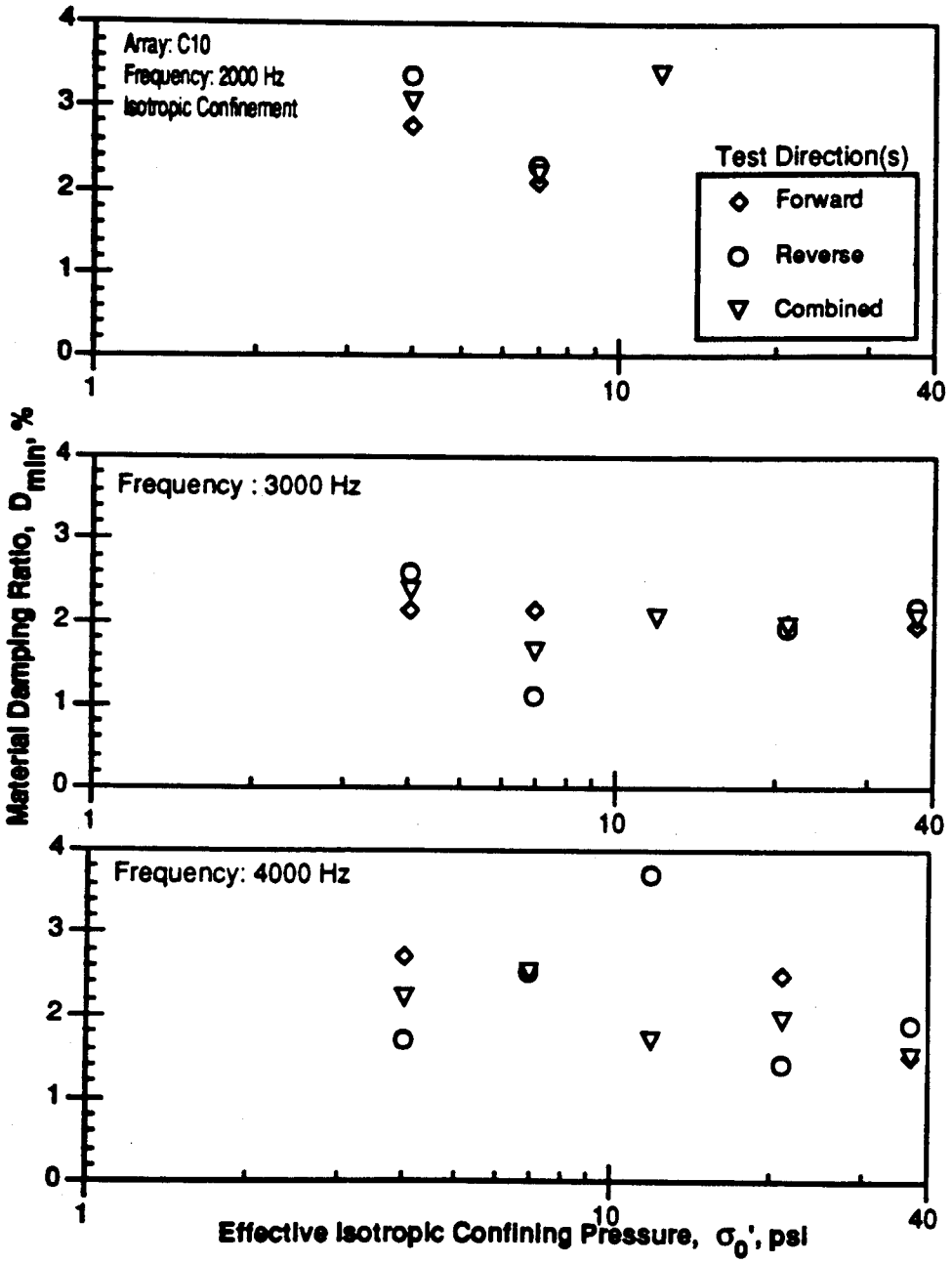

Figure 8.B.5-39
Material damping measurements in compression for forward, reverse and combined directions along array C10 in the vertical plane during isotropic loading.

Measurements at all frequencies for the C10 array have been combined and are presented in Fig. 8.B.5-40. From the figure, it can be observed that damping ratio decreases with increasing pressure. By using this approach, any effect of frequency has been neglected and the combined measurements have been used by assuming them to be the most representative values.

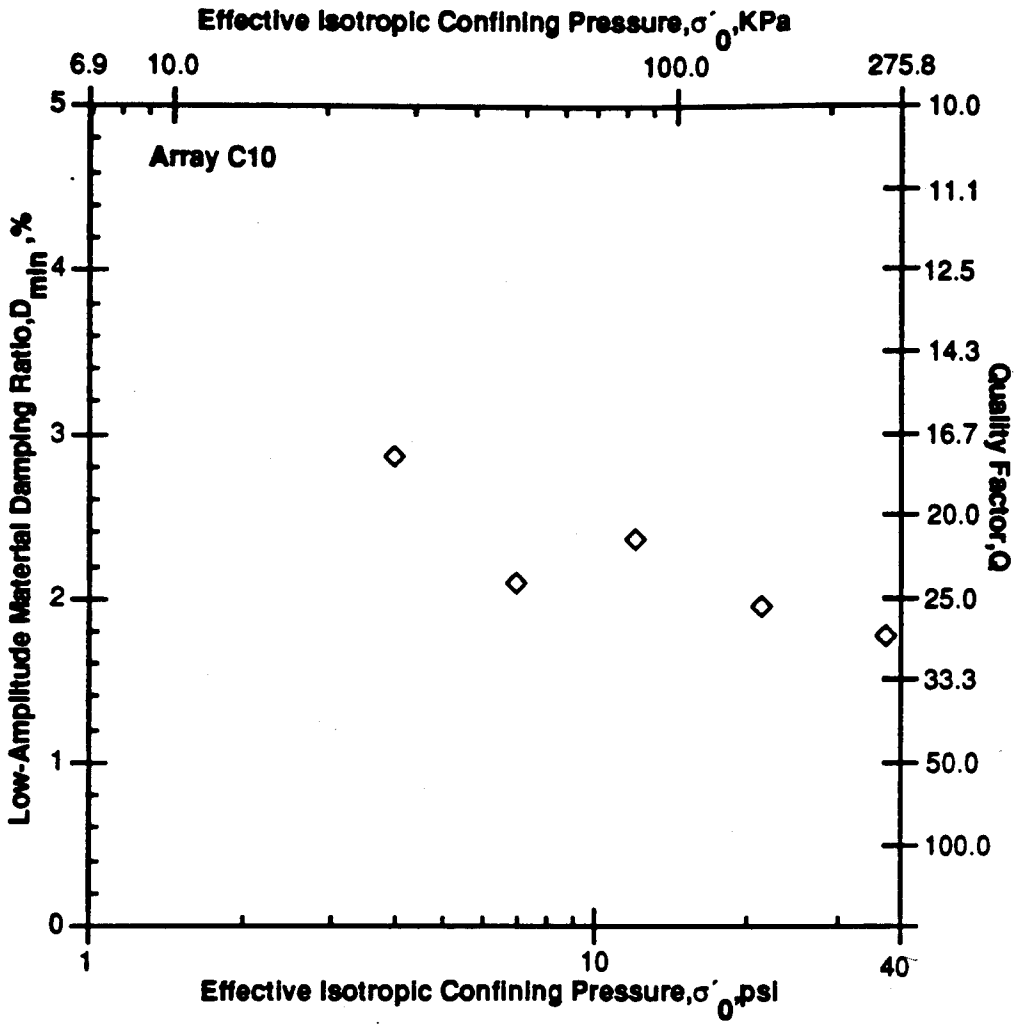

Notes:

1. Each data point represents the average of measurements at 2 or 3 frequencies (2000, 3000 and 4000 Hz were typically used).
2. Each data point was calculated using waves propagating in both the forward and reverse directions.
3. All measurements were made with accelerometer receivers.

Figure 8.B.5-40
Average material damping ratios in compression from combined measurements along array C10 in the vertical plane during isotropic loading.

8.B.5.5.3 P-Wave Measurements in the Horizontal Plane

Material damping ratios measured in the horizontal plane are tabulated in Table 8.B.5-6 by neglecting any effect of frequency and averaging the combined damping measurements for all arrays, at 2, 3, and 4 kHz. Each data point in this table represents the average of 2 or more measurements at 2, 3, and 4 KHz. Also each data point was calculated using both forward and reverse measurements, i.e. the combined directions. Measurements were not recorded if the wave amplitude could not be evaluated at one or more receivers in these records. If negative values were obtained even after combining the forward and reverse directions, these values were neglected when averaging the results.

Fig. 8.B.5-41 represents the average measurements obtained from each array in the horizontal plane. Damping values ranged from a high of 3.67% at a confining pressure of 4 psi (27.5 kPa) to a low of 0.64% at a confining pressure of 21.4 psi (147.1 kPa). By taking the average of all of the array measurements, the variation in material damping is significantly reduced and a nice trend is observed as shown in Fig. 8.B.5-42. In this figure, material damping decreases with increasing confining pressure. The standard deviation for these averages varies from 0.79 to 0.48 and decreases with increasing confining pressure. The average values of material damping range from a maximum of 2.24% to a minimum of 1.31%, and generally decrease with increasing pressure. The curve fit to the data was fit by eye and generally follows the trend obtained from the resonant column tests in shear (Fig. 8.B.5-23).

To obtain a general feel for the scatter in the damping measurements, histograms have been plotted. First, they were plotted ignoring any effects of the confining pressure and frequency. In this case, the average measurements at all pressures for the forward, reverse and combined directions are shown in Figs. 8.B.5-43, 8.B.5-44 and 8.B.5-45, respectively. The wide variation in values is quite apparent in the damping measurements in the forward and reverse directions from Figs. 8.B.5-43 and 8.B.5-44. It can be seen that by combining both directions the scatter is significantly reduced and the majority of the measurements fall between 0 and 3% as shown in Fig. 8.B.5-45 The total number of measurements that could be obtained were 66, and the number of measurements between 0 and 3% is 58. Hence the vast majority of the data falls in this range.

Table 8.B.5-6
Average Values of Material Damping Ratios from P-Waves Propagating in the Horizontal Plane During Isotropic Confinement

Pressure psi (KPa)	Material Damping Ratio, D_{min}, %								
	Array Number								
	C7	C1	C3	C5	C6	C4	C2	Average	Standard Deviation
4.0(27.5)	3.66	1.49	*	1.81	2.33	2.47	1.70	2.24	±0.79
7.0(48.1)	*	*	*	*	1.53	2.86	1.88	2.09	±0.69
12.0(82.5)	1.80	0.97	*	1.56	2.62	2.04	1.27	1.71	±0.58
21.4(147.1)	1.92	1.46	0.64	1.16	1.73	*	0.97	1.31	±0.48
37.4(257.1)	2.12	*	1.92	*	1.56	*	1.02	1.66	±0.48

*Unable to evaluate wave amplitudes at one or more receivers in these records.

Notes:

1. Each data point represents the average of measurements at 2 or 3 frequencies (2000, 3000 and 4000 Hz were typically used).
2. Each data point was calculated using waves propagating in both the forward and reverse directions.
3. All measurements were made with accelerometer receivers.

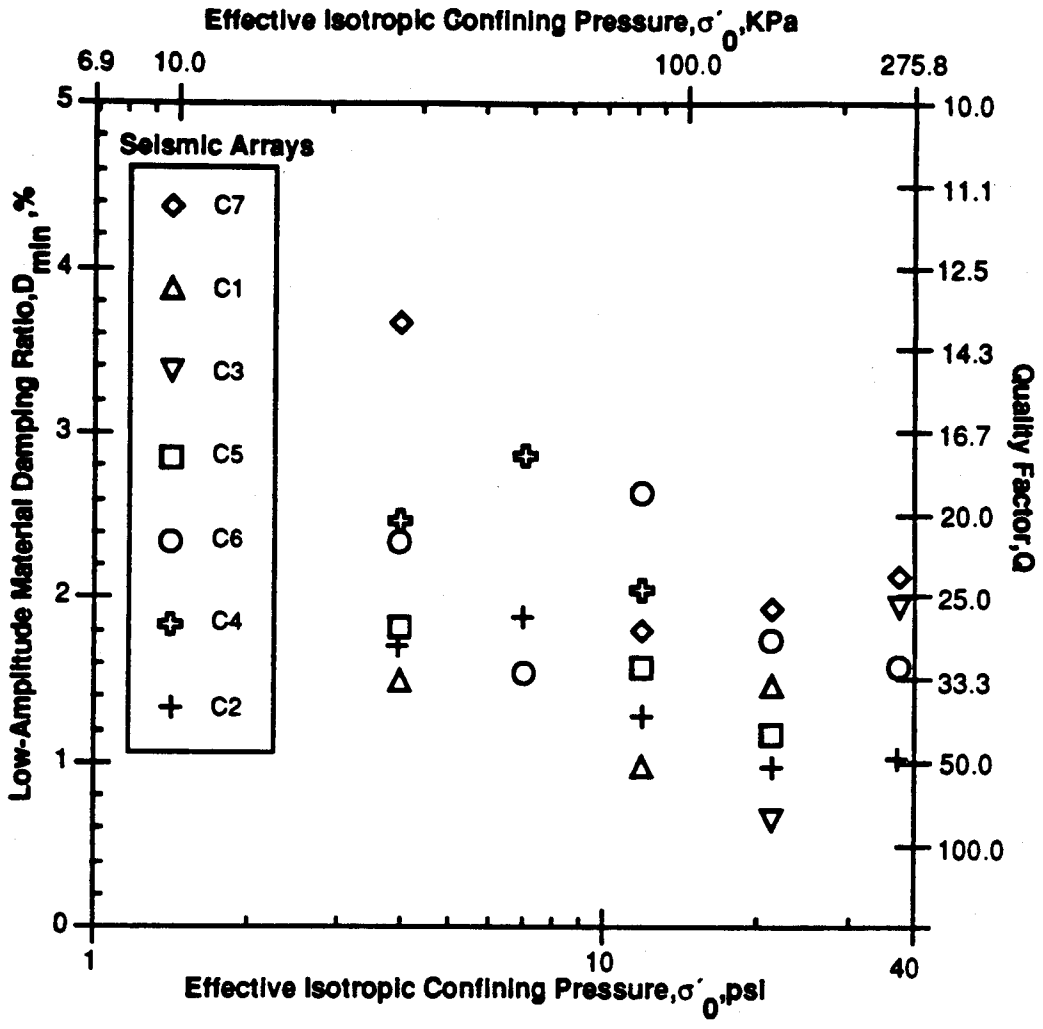

Notes:

1. Each data point represents the average of measurements at 2 or 3 frequencies (2000, 3000 and 4000 Hz were typically used).
2. Each data point was calculated using waves propagating in both the forward and reverse directions.
3. All measurements were made with accelerometer receivers.

Figure 8.B.5-41
Average values of material damping ratio from P-wave measurements along each seismic array in the horizontal plane during isotropic loading.

To obtain a general feel for the scatter in the damping measurements, histograms have been plotted. First, they were plotted ignoring any effects of the confining pressure and frequency. In this case, the average measurements at all pressures for the forward, reverse and combined directions are shown in Figs. 8.B.5-43, 8.B.5-44 and 8.B.5-45, respectively. The wide variation in values is quite apparent in the damping measurements in the forward and reverse directions from Figs. 8.B.5-43 and 8.B.5-44. It can be seen that by combining both directions the scatter is significantly reduced and the majority of the measurements fall between 0 and 3% as shown in Fig. 8.B.5-45 The total number of measurements that could be obtained were 66, and the number of measurements between 0 and 3% is 58. Hence the vast majority of the data falls in this range.

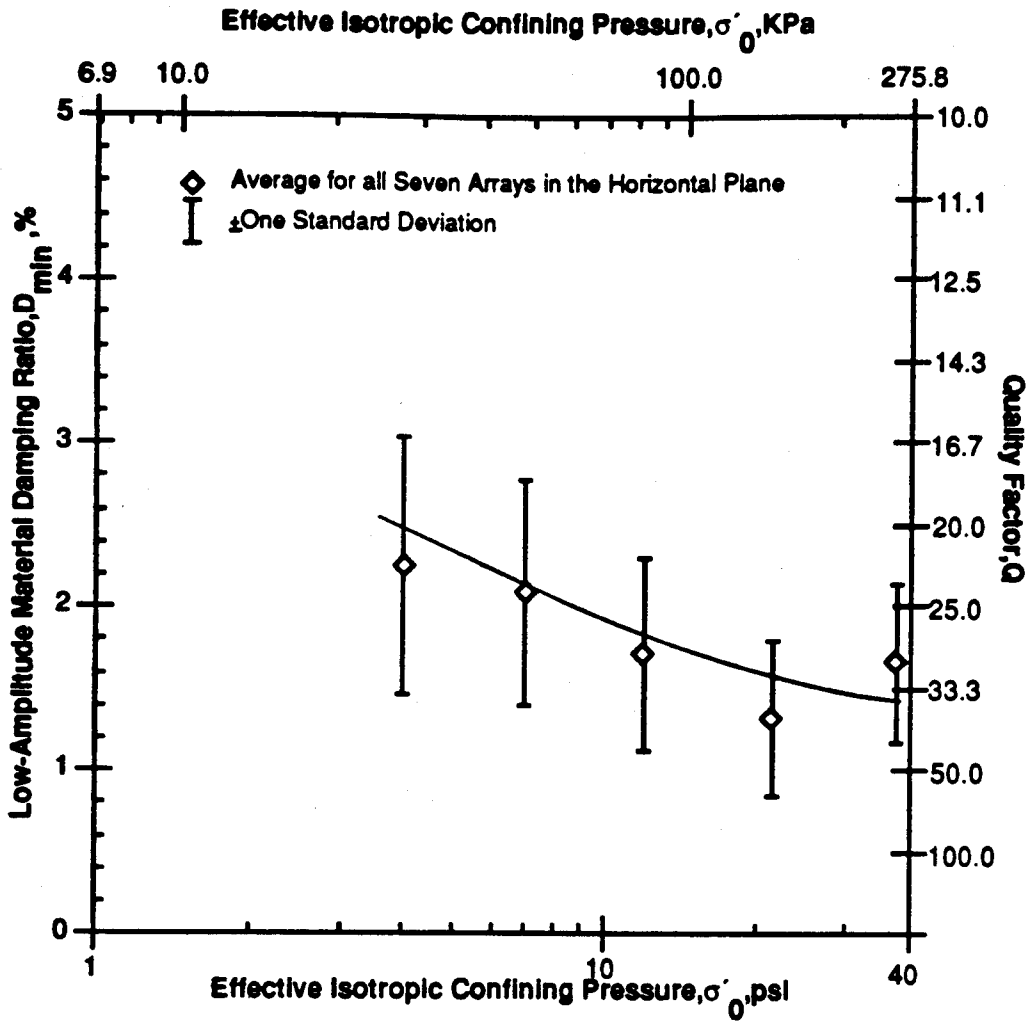

Notes:

1. Average measurements from all 7 instrumentation lines.
2. Each data point represents the average of measurements at 2 or 3 frequencies (2000, 3000 and 4000 Hz were typically used).
3. Each data point was calculated using waves propagating in both the forward and reverse directions.
4. All measurements were made with accelerometer receivers.

Figure 8.B.5-42
Average values of material damping ratio from all P-wave measurements in the horizontal plane during isotropic loading.

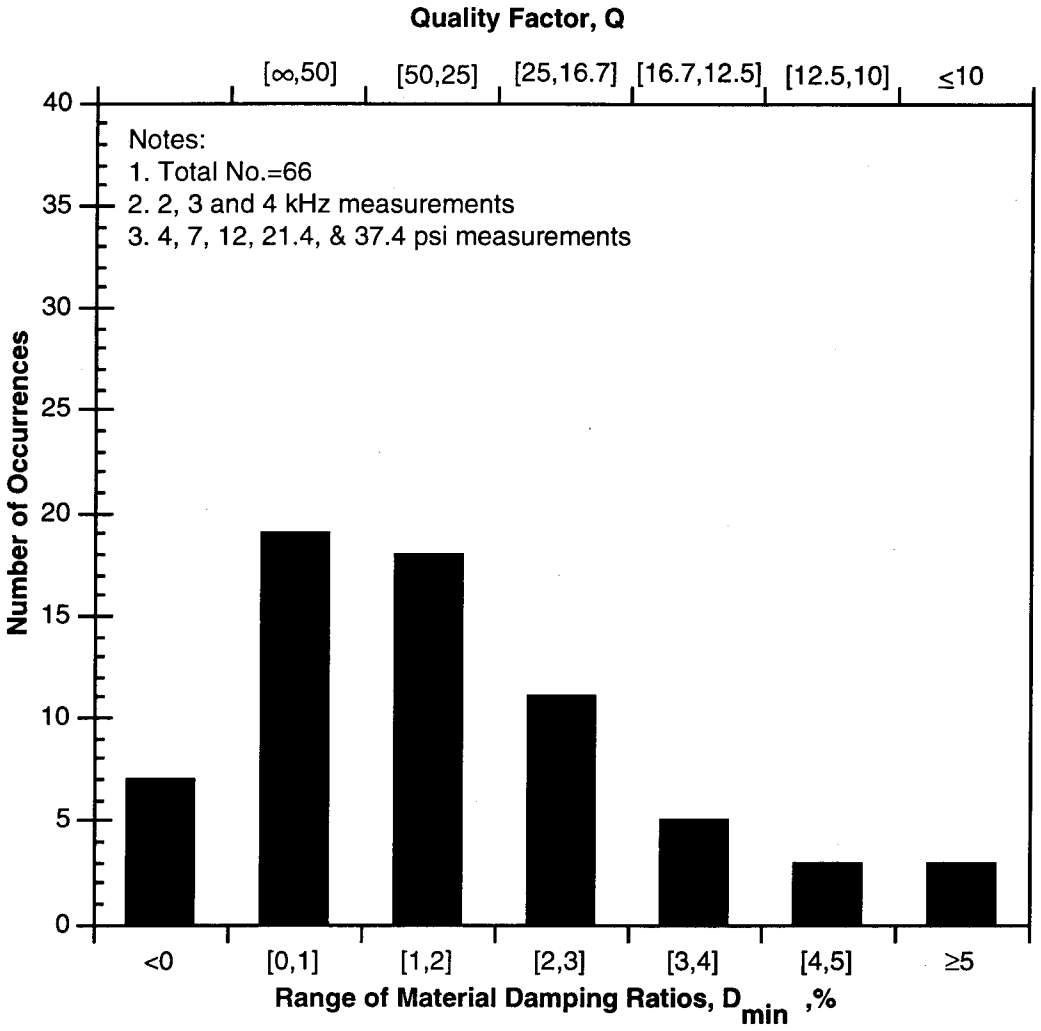

Figure 8.B.5-43
Histogram of all material damping measurements for P-waves propagating in the forward direction in the horizontal plane during isotropic confinement.

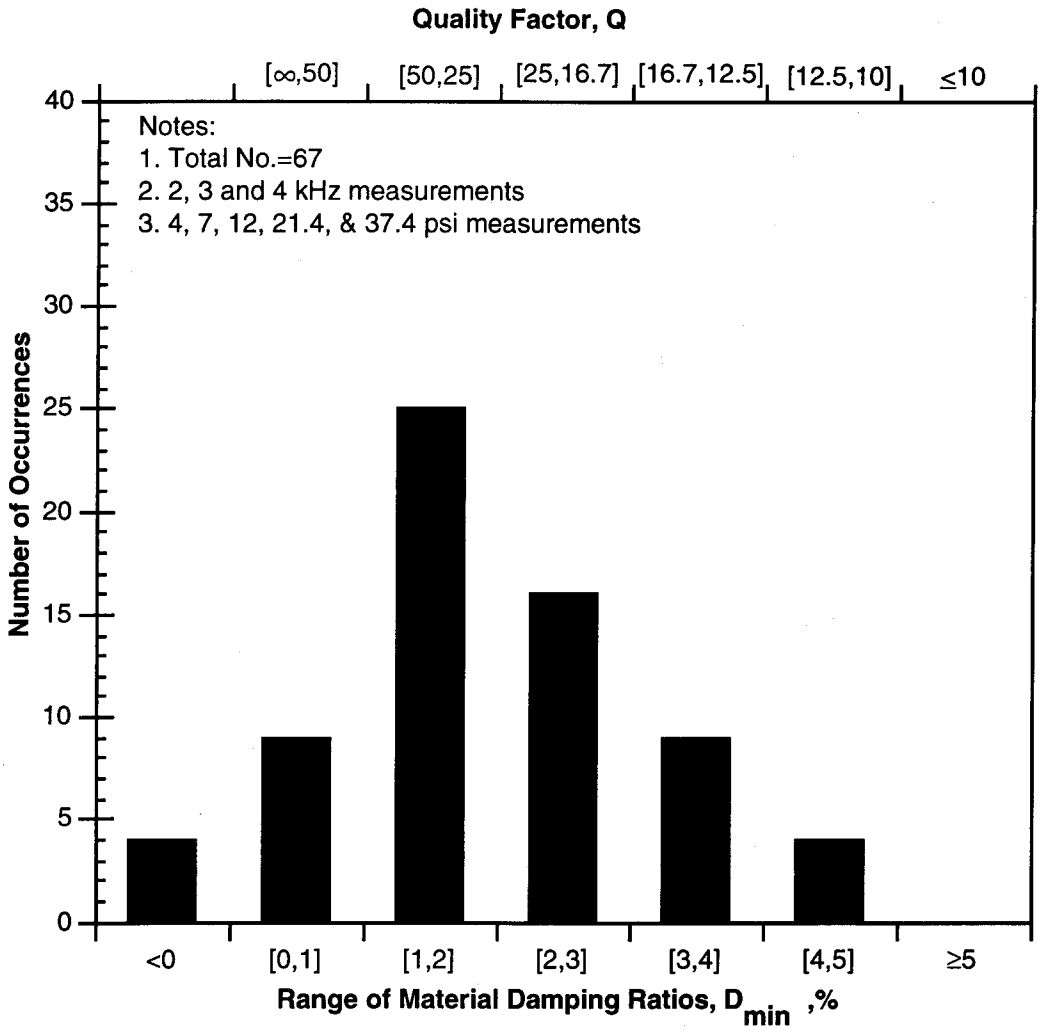

Figure **8.B.5-44**
Histogram of all material damping measurements for P-waves propagating in the reverse direction in the horizontal plane during isotropic confinement.

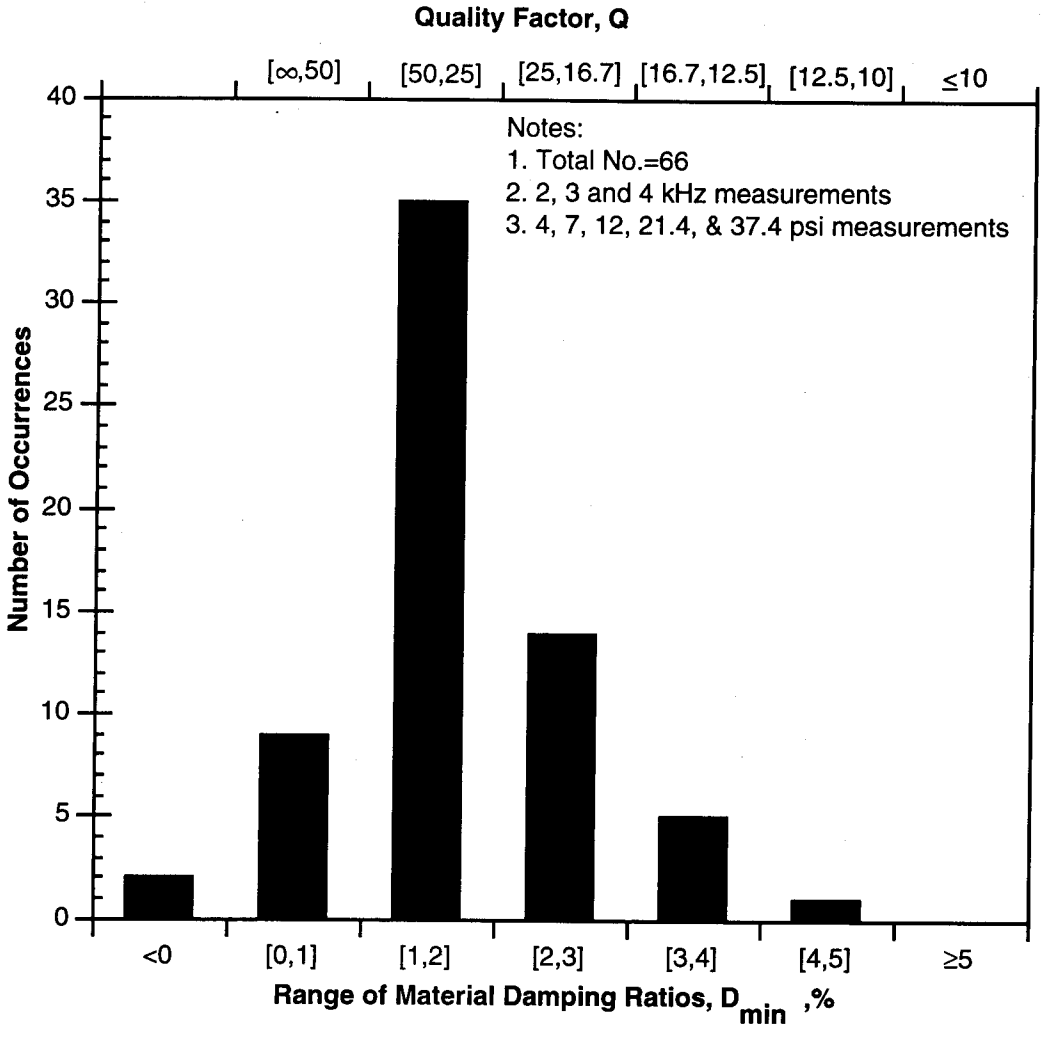

Figure 8.B.5-45
Histogram of all material damping measurements for P-waves propagating in the horizontal plane during isotropic confinement for combined directions.

By presenting the damping values in the form of histograms for each pressure an attempt has been made to show how the damping values decrease with pressure. These results are shown by the histograms in Figs. 8.B.5-46 through 8.B.5-50. In Fig. 8.B.5-46, all the measurements fall between 1 and 5% (18 measurements), and 84 percent are between 1% and 3%. From Fig. 8.B.5-47 (7 psi (48.1 kPa)), 67 percent of the total measurements fall between 1 and 2%. At 12 psi (82.5 kPa) (Fig. 8.B.5-48), 71 percent of the total measurements fall between 0 to 2%. At 21.4 psi (147.1 kPa) (Fig 8.B.5-49) 50% of the total measurements fall between 0 and 1%, while at 37.4 psi (257.1 kPa) (Fig. 8.B.5-50) 75 percent of the damping values fall between 1 and 2%. These results show a general trend of decreasing material damping with increasing confining pressure. However, they also show the significant scatter that is present in the data.

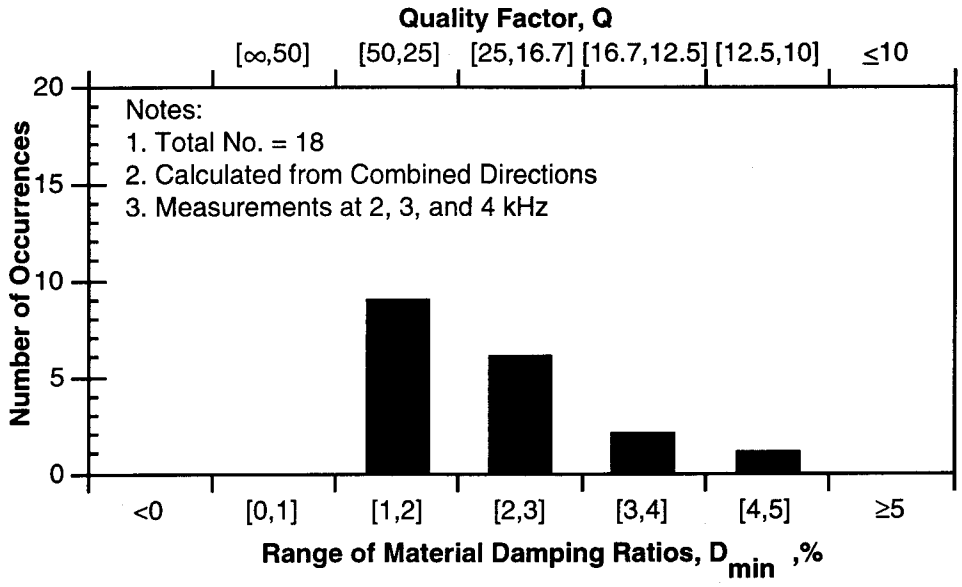

Figure 8.B.5-46
Histogram of material damping measurements for P-waves propagating in the horizontal plane under an isotropic pressure of 4 psi.

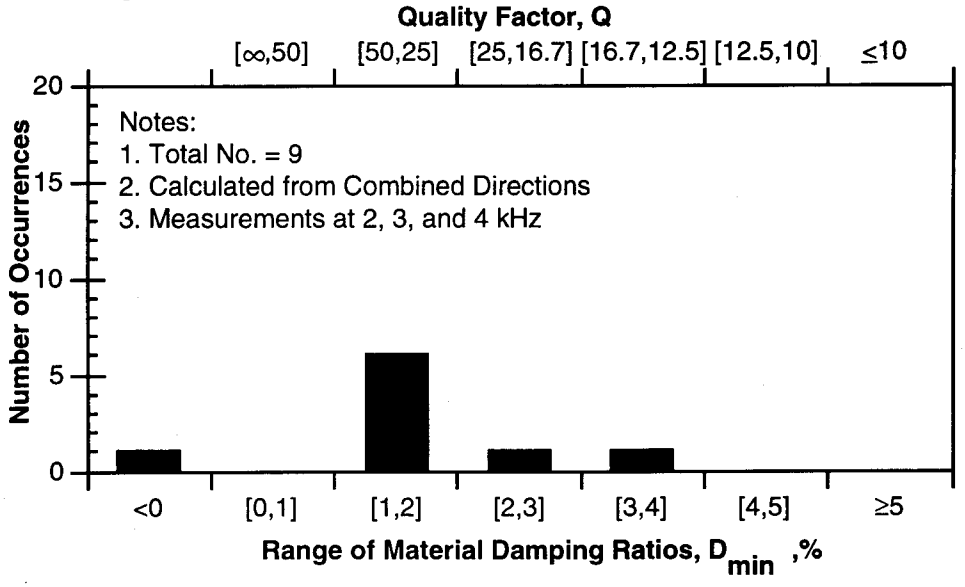

Figure 8.B.5-47
Histogram of material damping measurements for P-waves propagating in the horizontal plane under an isotropic pressure of 7 psi.

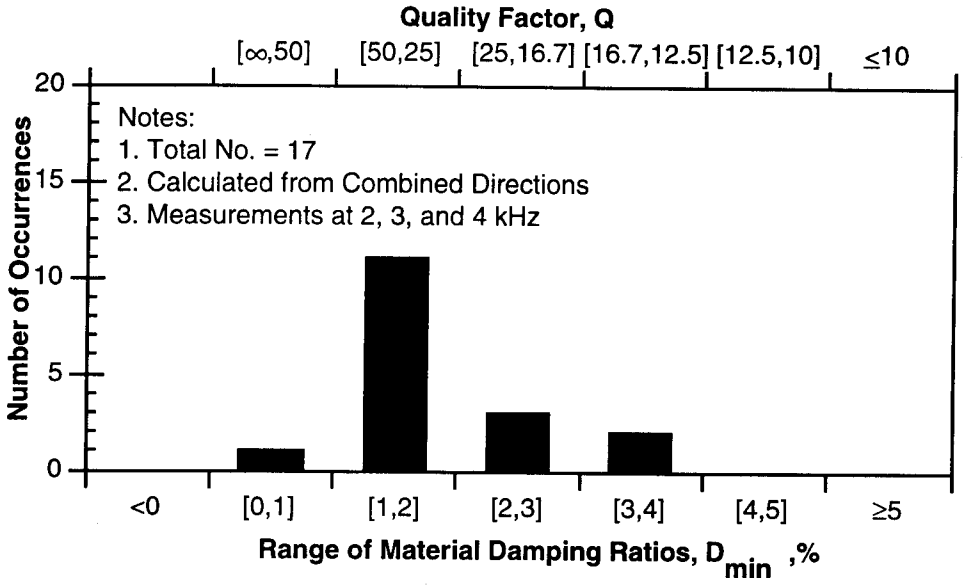

Figure 8.B.5-48
Histogram of material damping measurements for P-waves propagating in the horizontal plane under an isotropic pressure of 12 psi.

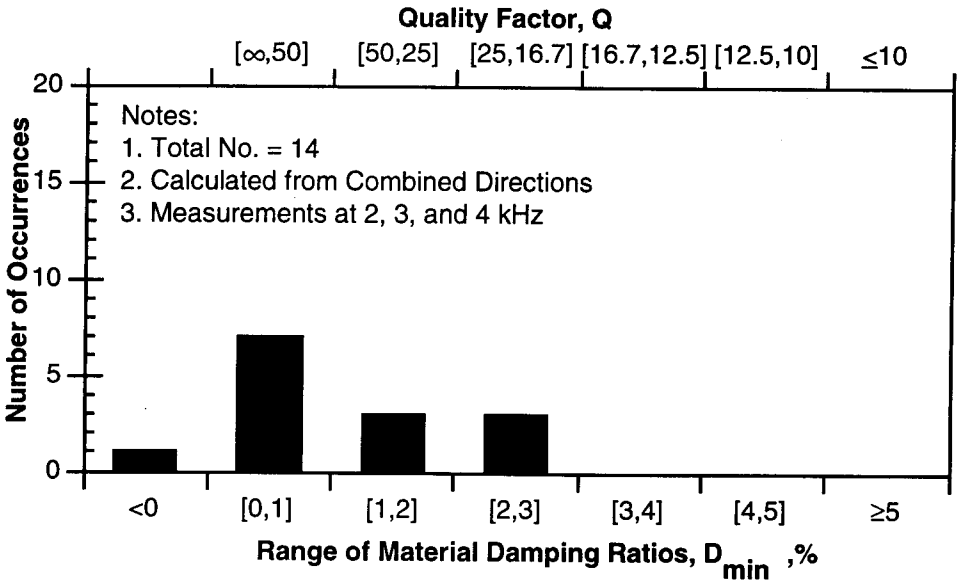

Figure 8.B.5-49
Histogram of material damping measurements for P-waves propagating in the horizontal plane under an isotropic pressure of 21.4 psi.

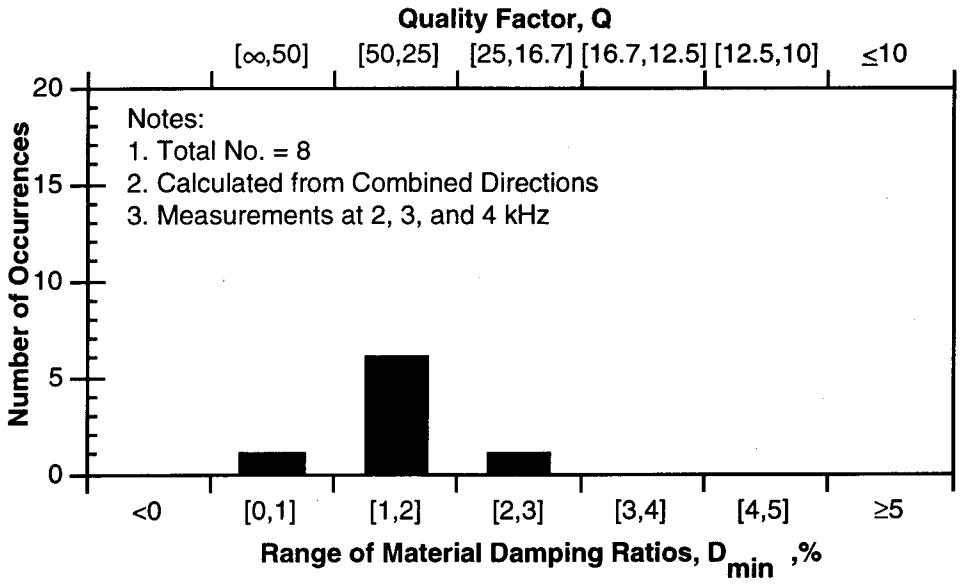

Figure 8.B.5-50
Histogram of material damping measurements for P-waves propagating in the horizontal plane under an isotropic pressure of 37.4 psi.

8.B.5.5.4 P-Wave Measurements in the Vertical Plane

In the vertical plane, no damping values could be obtained from the C12 array The remaining damping measurements are tabulated in Table 8.B.5-7 by neglecting any effect of frequency and averaging all measurements for a given array at 2, 3 and 4 kHz (just as was done in the horizontal plane). Damping values range from 3.66% to 1.30%. These average to a maximum of 2.88% and a minimum of 1.52% when taken at each confining pressure. Damping values measured with each array are plotted versus isotropic confining pressure in Fig. 8.B.5-51, and the average of all six arrays is presented in Fig. 8.B.5-52 with error bars for one standard deviation from the average also shown. The standard deviation varied from 0.67 to 0.35 for the averages at the lowest and highest pressures, respectively.

The same point noted for measurements in the horizontal plane can be noted for these measurements; that is, there is lot of scatter in the damping measurements. However, when the average is calculated, a trend is evident which shows a general decrease in D with increase in $\overline{\sigma}_0$. This is the same trend that has been observed in other research. However, the scatter is greater in the vertical plane than was noted for measurements in the horizontal plane. This trend is the same as the trend found by Lee (1993) for P-wave velocities in the horizontal and vertical planes.

Table 8.B.5-7
Average Values of Material Damping Ratios from P-Waves Propagating in the Vertical Plane During Isotropic Confinement

Pressure psi (KPa)	Material Damping Ratio, D_{min}, %							
	Array Number						Average	Standard Deviation
	C13	C11	C9	C7	C8	C10		
4.0(27.5)	3.15	1.83	*	3.66	2.92	2.86	2.88	±0.67
7.0(48.1)	1.37	1.10	*	*	*	2.10	1.52	±0.52
12.0(82.5)	2.39	1.85	*	1.80	1.44	2.36	1.97	±0.40
21.4(147.1)	2.27	1.17	*	1.92	2.36	1.94	1.93	±0.47
37.4(257.1)	1.79	1.30	1.77	2.12	2.33	1.77	1.85	±0.35

*Unable to evaluate wave amplitudes at one or more receivers in these records.

Notes:

1. Each data point represents the average of measurements at 2 or 3 frequencies (2000, 3000 and 4000 Hz were typically used).
2. Each data point was calculated using waves propagating in both the forward and reverse directions.
3. All measurements were made with accelerometer receivers.

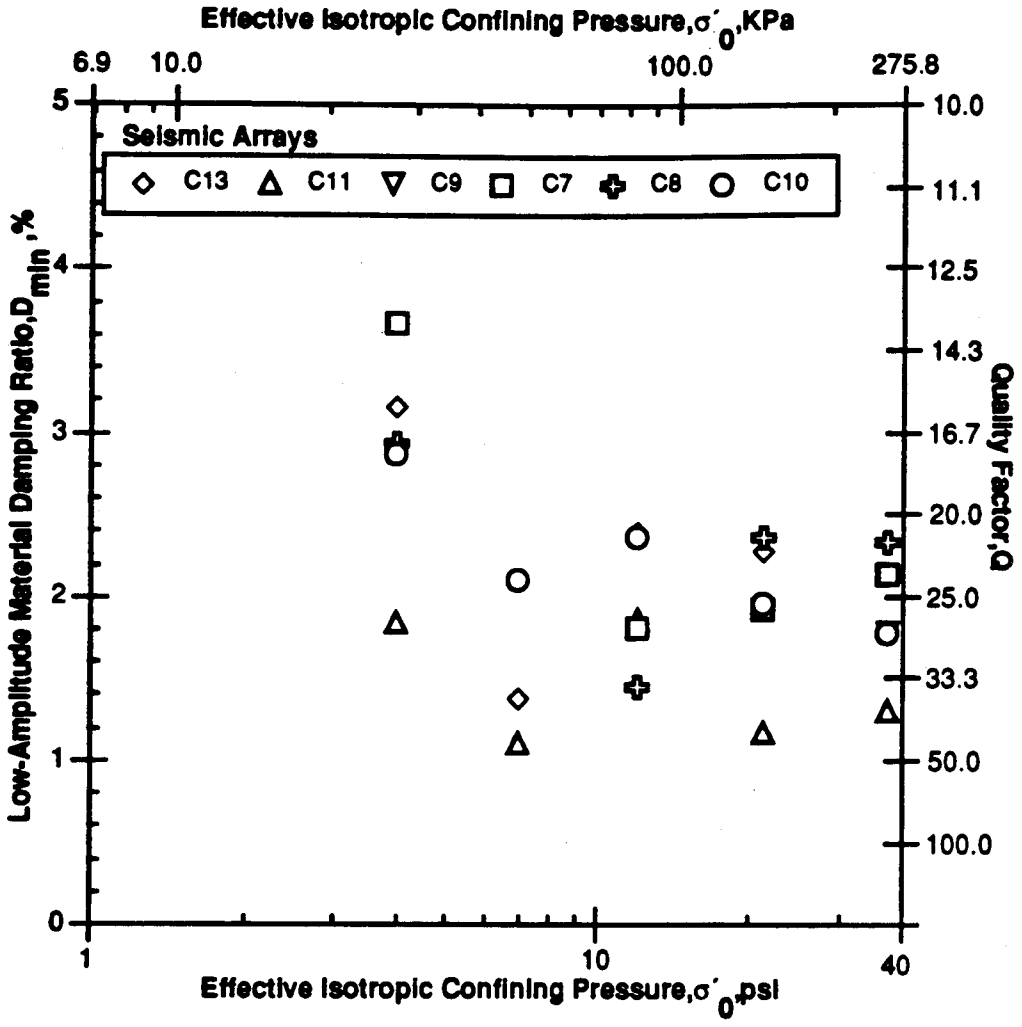

Notes:

1. Each data point represents the average of measurements at 2 or 3 frequencies (2000, 3000 and 4000 Hz were typically used).
2. Each data point was calculated using waves propagating in both the forward and reverse directions.
3. All measurements were made with accelerometer receivers.

Figure 8.B.5-51
Average values of material damping ratio from P-wave measurements along each seismic array in the vertical plane during isotropic loading.

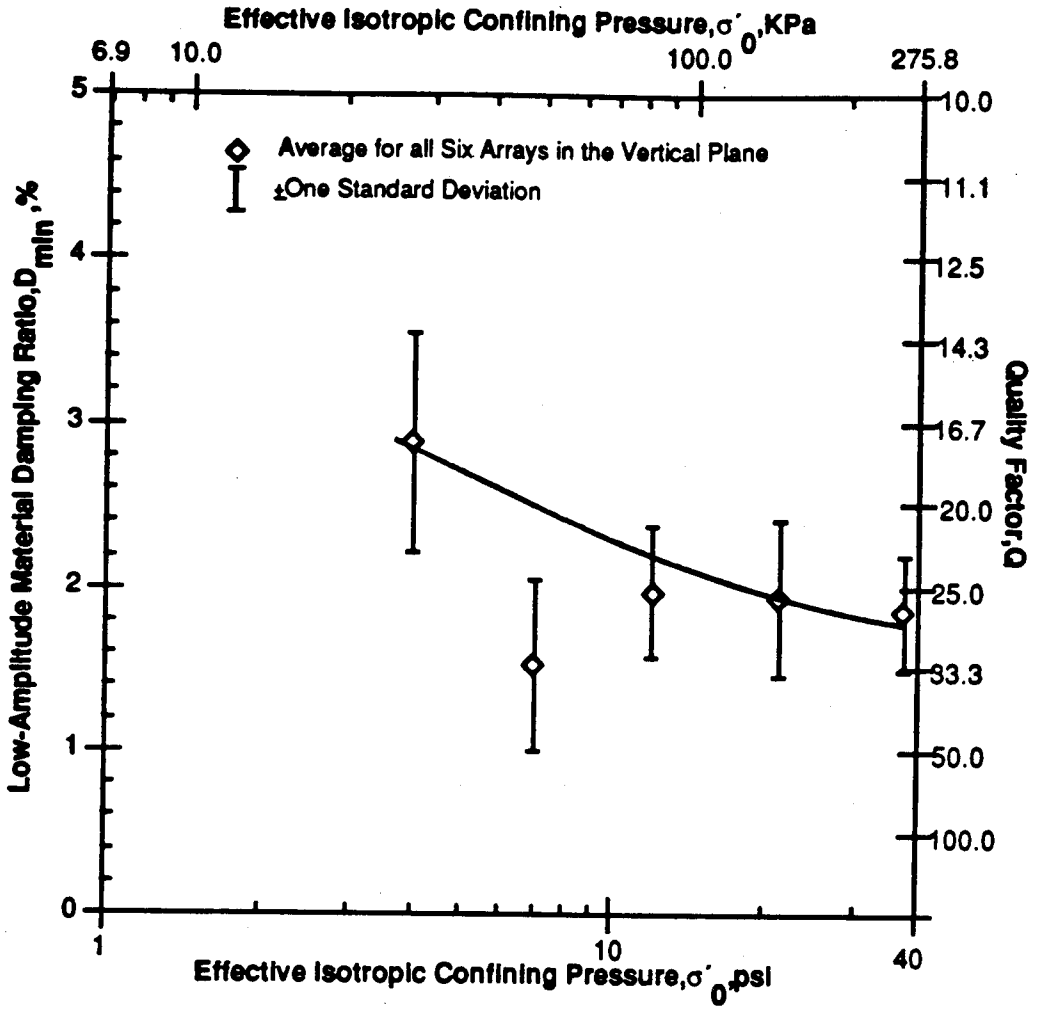

Notes:

1. Average measurements from all 6 instrumentation lines.
2. Each data point represents the average of measurements at 2 or 3 frequencies (2000, 3000 and 4000 Hz were typically used).
3. Each data point was calculated using waves propagating in both the forward and reverse directions.
4. All measurements were made with accelerometer receivers.

Figure 8.B.5-52
Average values of material damping ratio from all P-wave measurements in the vertical plane during isotropic loading.

The histograms for the forward and reverse directions (Figs. 8.B.5-53 and 8.B.5-54) show even more scatter than for measurements in the horizontal plane. However, the combined measurements (Fig. 8.B.5-55) again significantly narrow the band of damping values and the majority of the values lie between 0% and 3%. From a total of 61 measurements, 45 measurements lie between damping ratios of 1% and 3%. When looking at the distribution of measurements for each pressure individually (Figs. 8.B.5-56 through 8.B.5-60), it can be seen that the damping values generally scatter quite evenly, but, just like measurements in the horizontal plane, the trend is for decreasing damping with increasing confining pressure.

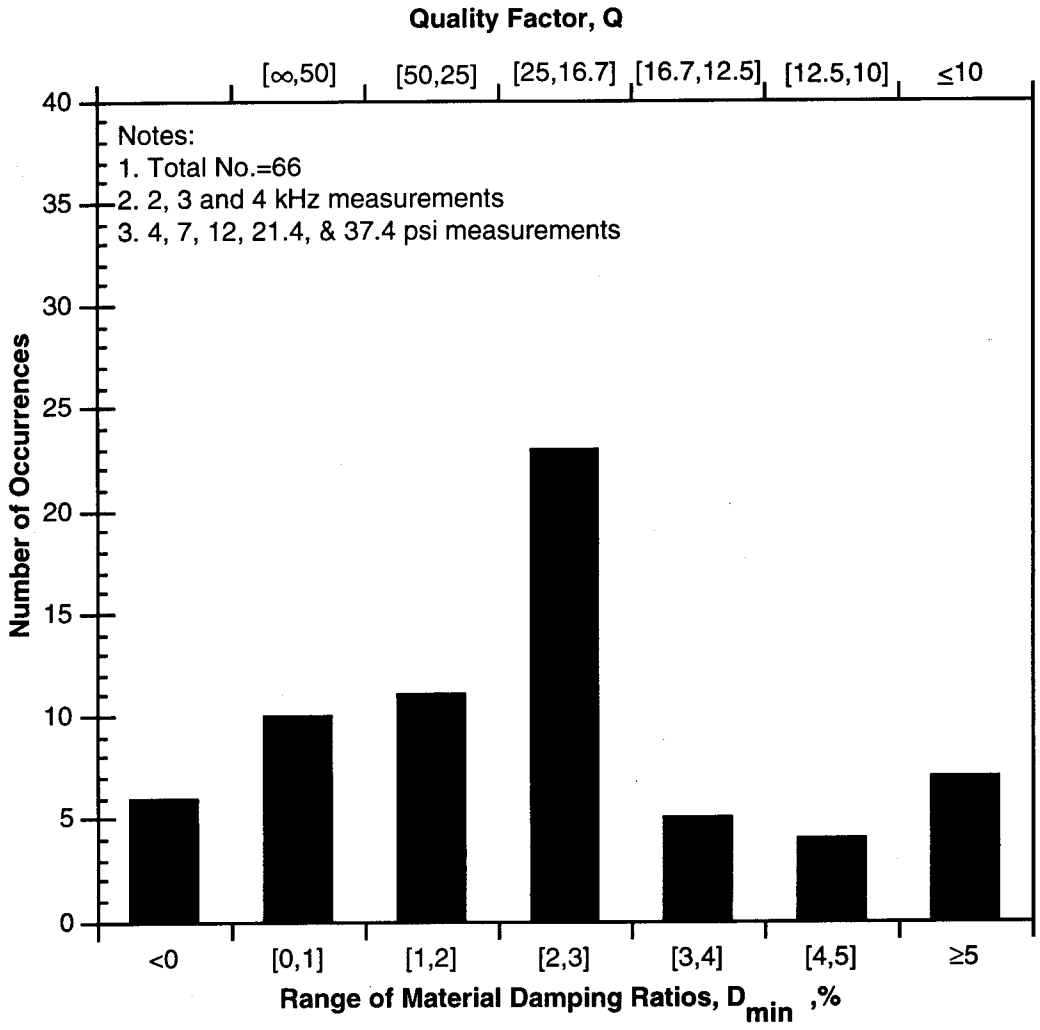

Figure 8.B.5-53
Histogram of all material damping measurements for P-waves propagating in the forward direction in the vertical plane during isotropic confinement.

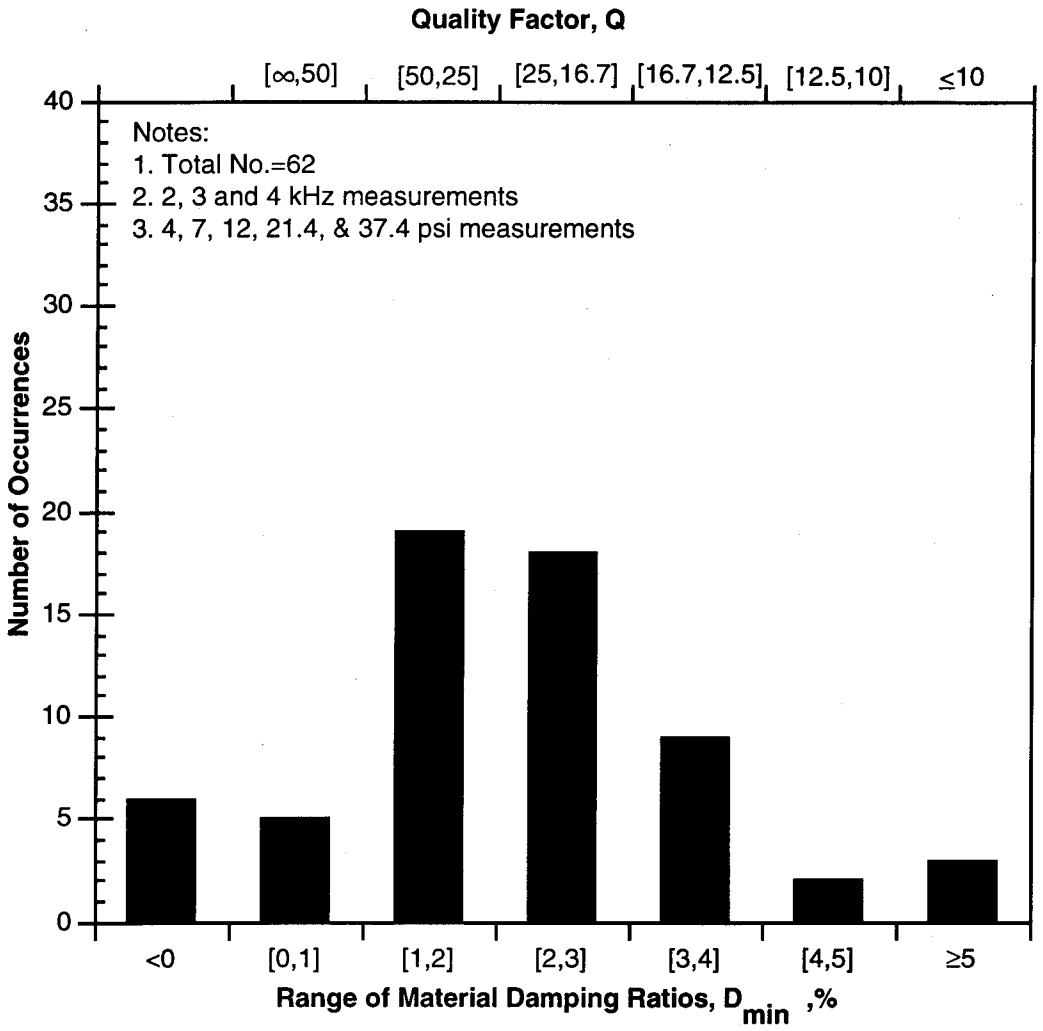

Figure 8.B.5-54
Histogram of all material damping measurements for P-waves propagating in the reverse direction in the vertical plane during isotropic confinement.

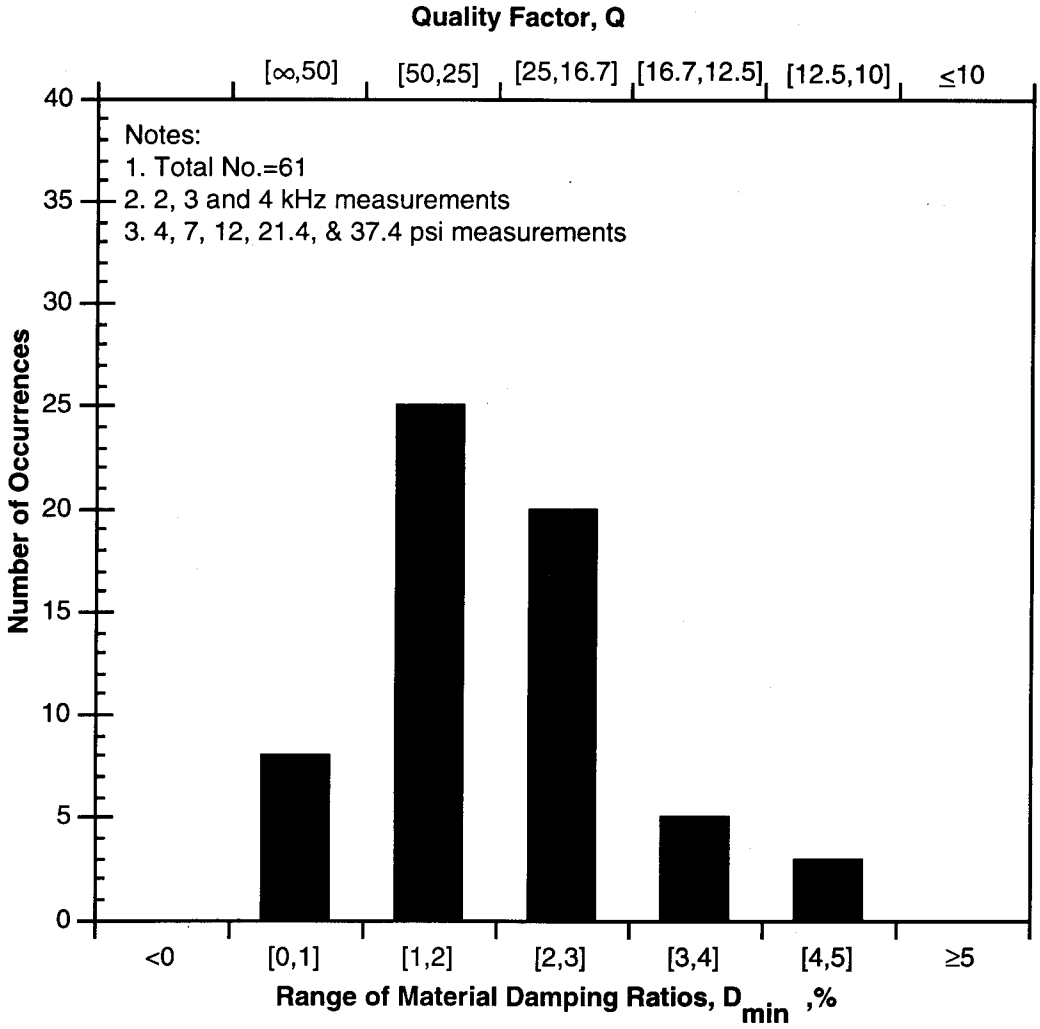

Figure 8.B.5-55
Histogram of all material damping measurements for P-waves propagating in the vertical plane during isotropic confinement for combined direction.

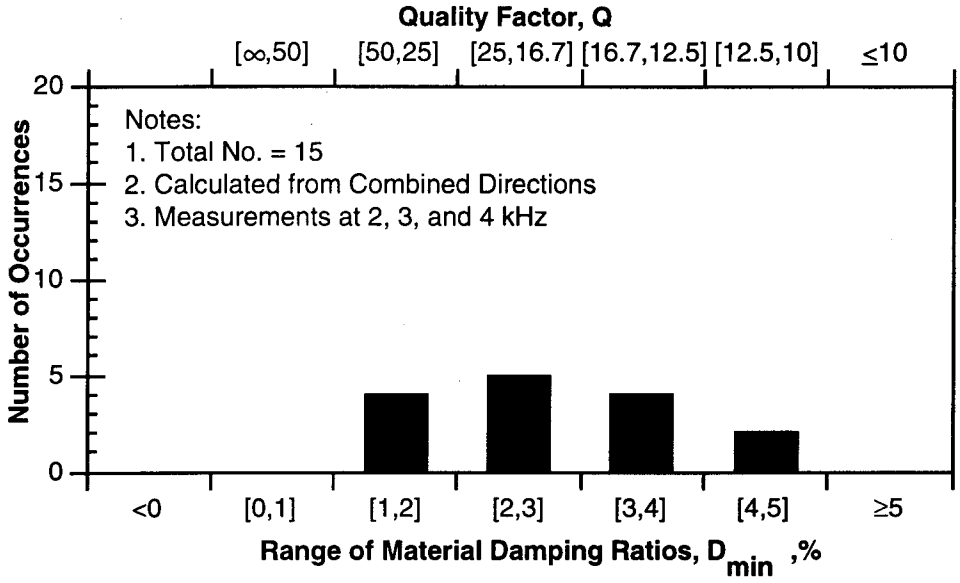

Figure 8.B.5-56
Histogram of material damping measurements for P-waves propagating in the vertical plane under an isotropic pressure of 4 psi.

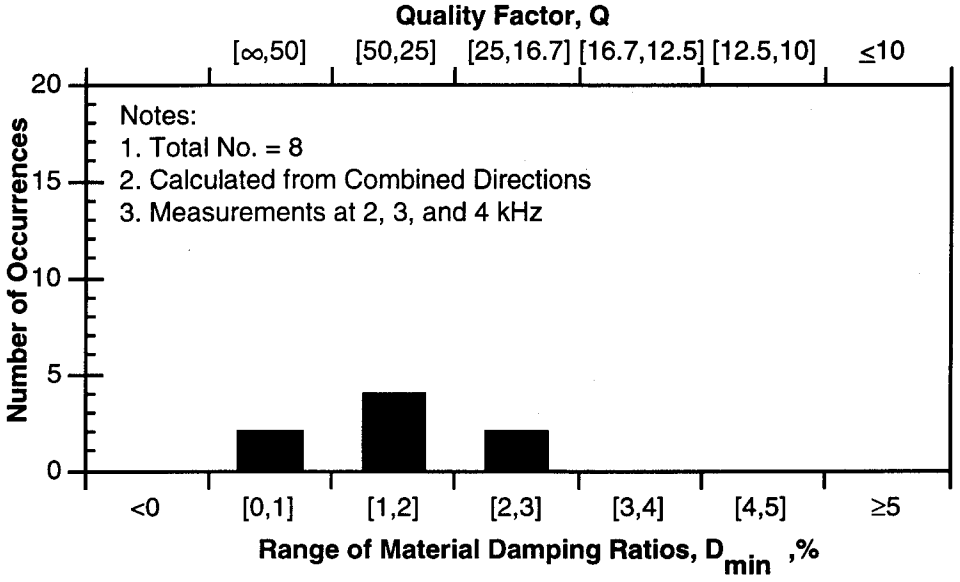

Figure 8.B.5-57
Histogram of material damping measurements for P-waves propagating in the vertical plane under an isotropic pressure of 7 psi.

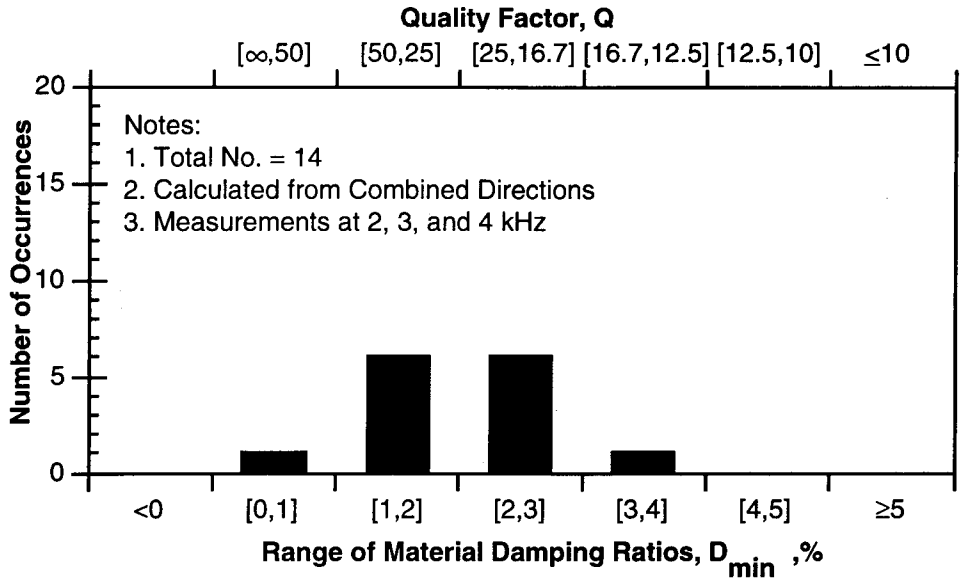

Figure 8.B.5-58
Histogram of material damping measurements for P-waves propagating in the vertical plane under an isotropic pressure of 12 psi.

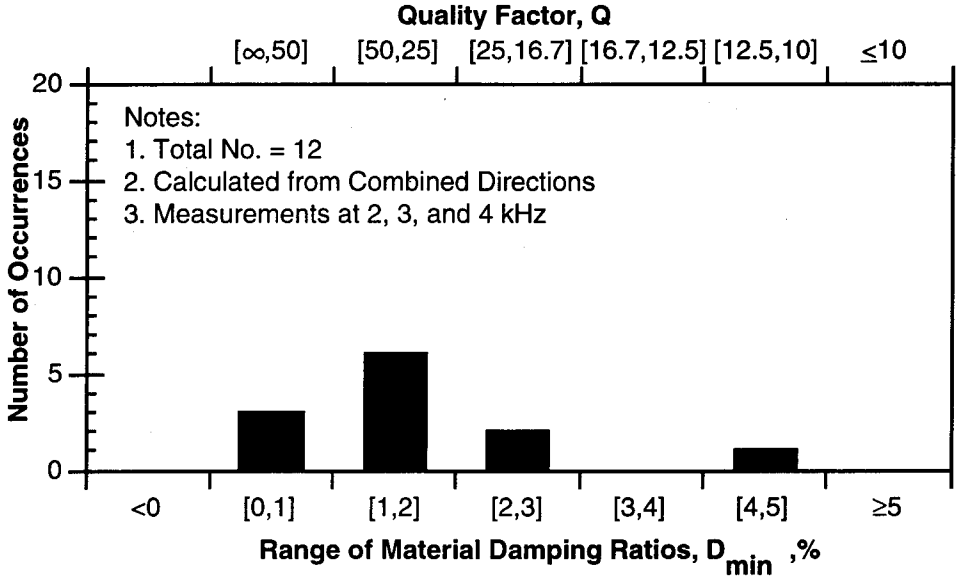

Figure 8.B.5-59
Histogram of material damping measurements for P-waves propagating in the vertical plane under an isotropic pressure of 21.4 psi.

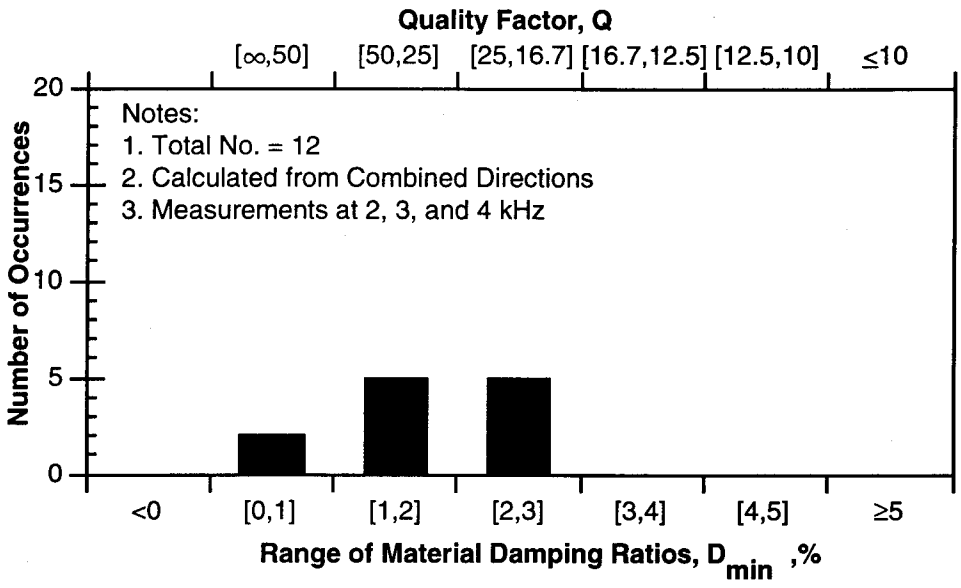

Figure 8.B.5-60
Histogram of material damping measurements for P-waves propagating in the vertical plane under an isotropic pressure of 37.4 psi.

8.B.5.5.5 Horizontal and Vertical P-Wave Planes Combined

Measured damping values in the vertical plane are somewhat higher than those measured in the horizontal plane, with the ratio varying from about 1.1 to 1.5. Under isotropic loading, the horizontal plane is considered to be the plane of isotropy (Lee, 1993). The vertical plane, on the other hand, is suppose to be isotropic, but because of structural anisotropy this plane is actually slightly anisotropic (Lee, 1993). This anisotropy is due to the depositional characteristics of the sand particles, grain size and grain shape so that the vertical plane is anisotropic even under isotropic loading conditions.

The higher damping values measured in the vertical plane may result from the anisotropic nature of this plane. However, it seems that considering the scatter of damping values obtained in the vertical plane from oblique arrays, the damping values fall generally within the range obtained from those in the horizontal plane. This would imply that anisotropy is not a major contributor in this case. The damping values from both the horizontal and vertical planes are thus plotted in Fig. 8.B.5-61.

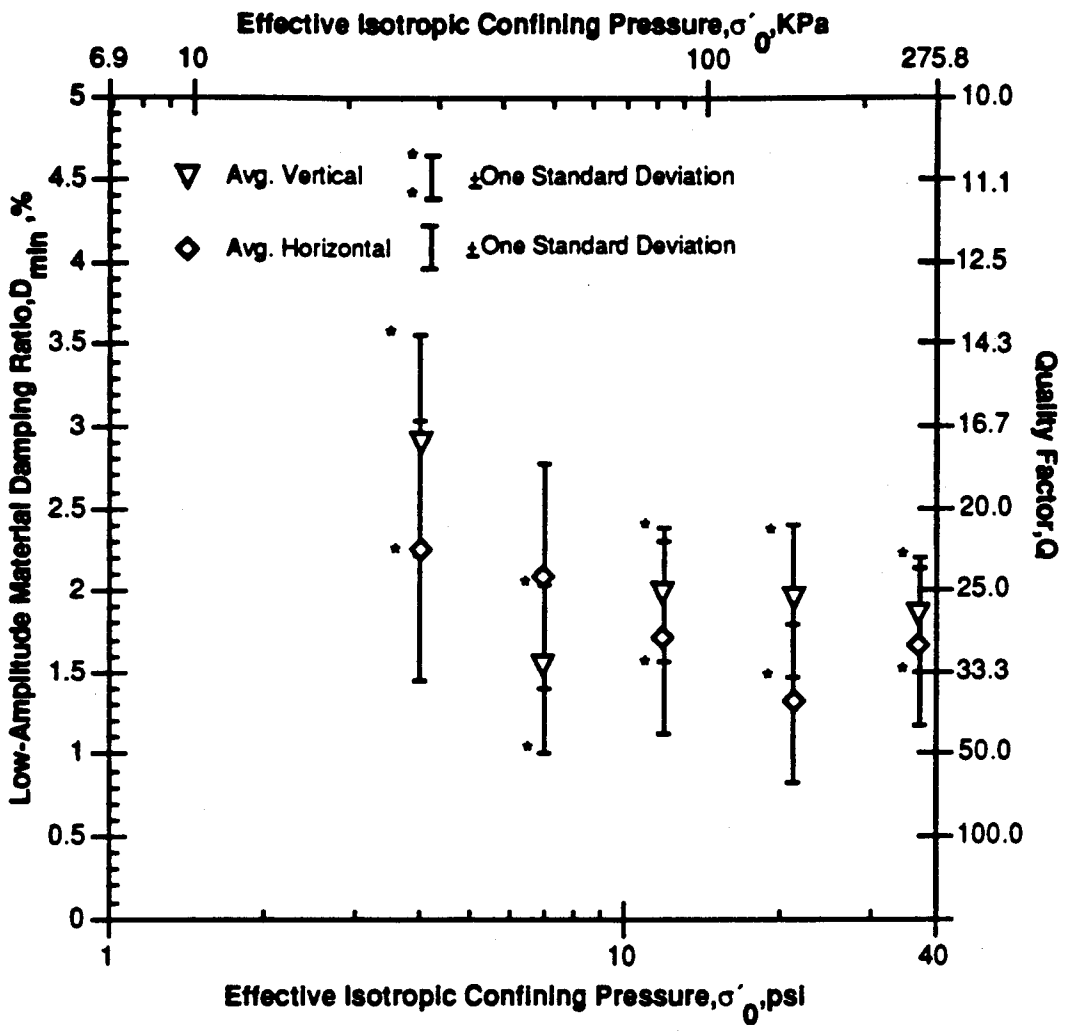

Figure 8.B.5-61
Average values of material damping ratio from all P-wave measurements in the vertical and horizontal planes during isotropic loading.

These values fall within one standard deviation of each other. The average values obtained from the horizontal plane are generally less than those from the vertical except at a confining pressure of 7 psi (48.1 kPa) where the opposite trend happens.

8.B.5.5.6 S-Wave Measurements

Five arrays of geophones and accelerometer for measurement of shear waves were installed in the LSTC (Figs. 8.B.5-16 and 8.B.5-17). One array was in the vertical plane (S5) for the measurement of vertically propagating SH-waves. Four arrays were located in the horizontal plane, two of which were for the measurement of horizontally propagating SV-waves (S1 and S2), while the other two were for the measurement of horizontally propagating SH-waves (S3 and S4). The two arrays for the measurement of horizontally propagating SH-waves could not be utilized to obtain any data. So essentially only three arrays were available for the measurement of S-waves. The array notation for the shear waves has also been changed for ease of identification. The new notation is presented in Table 8.B.5-8.

Table 8.B.5-8
New Notation for Shear Wave Arrays

Original Array Notation (Fig. 8.B.5-15 and 8.B.5-16)	New Array Notation
Horizontal Plane	
SV3V3V4SV4	S1
SV5V5V6SV6V7	S2
SH3H3H4H5	S4
SH6H6H7SH7	S3
Vertical Plane	
SH1H1H2SH2	S5

As in the case of P-waves, the same data reduction techniques were employed. Tables 8.B.5-9, 8.B.5-10 and 8.B.5-11 show the damping values obtained from S5, S1 and S2 Arrays respectively. These tables show values for the forward, reverse and combined directions individually for measurements at 1, 2, 3 and 4 kHz for each pressure. Similar to the P-wave damping measurements, damping values were not calculated if they were not within the established wavelength limits (a minimum of two wavelengths between the source and first receiver).

Averages of these damping measurements are presented in Table 8.B.5-12. Each average represents the average of measurements at 1, 2, 3 and 4 kHz using waves propagating in both the forward and reverse directions. In these arrays since all the sources and receivers were geophones, damping values were calculated using only the middle two receivers so as to maintain a consistency between the P-wave and S-wave results.

Table 8.B.5-9
Values Of Material Damping in Shear for Forward, Reverse and Combined Directions Along Array S5 in the Vertical Plane for Isotropic Loading Conditions

Excitation Frequency	Confining Pressure, psi, (kPa)	D(%) Measured in Test Direction Forward	Reverse	Combined
1000 Hz	7 (48.1)	1.18	1.30	1.24
	12 (82.5)	**	**	**
	21.4 (147.1)	**	**	**
	37.4 (257.1)	**	**	**
2000 Hz	4 (27.5)	1.55	0.71	1.13
	7 (48.1)	2.60	0.33	1.47
	12 (82.5)	2.12	2.02	2.07
	21.4 (147.1)	2.41	1.75	2.08
	37.4 (257.1)	1.07	1.27	1.18
3000 Hz	4 (27.5)	0.94	1.75	1.35
	7 (48.1)	2.30	2.16	2.23
	12 (82.5)	1.51	1.24	1.38
	21.4 (147.1)	1.38	0.48	0.93
	37.4 (257.1)	1.42	1.20	1.31
4000 Hz	4 (27.5)	**	**	**
	7 (48.1)	*	*	*
	12 (82.5)	**	**	**
	21.4 (147.1)	**	**	**
	37.4 (257.1)	1.02	1.46	1.25

* One or both record(s) were missing or could not be interpreted.
** Damping value not calculated because outside established wavelength limits.

Table 8.B.5-10
Values of Material Damping in Shear for Forward, Reverse and Combined Directions Along Array S1 in the Horizontal Plane for Isotropic Loading Conditions

Excitation Frequency	Confining Pressure, psi, (kPa)	D(%) Measured in Test Direction Forward	Reverse	Combined
1000 Hz	4 (27.5)	0.49	0.40	0.45
	7 (48.1)	*	*	*
	12 (82.5)	**	**	**
	21.4 (147.1)	**	**	**
	37.4 (257.1)	**	**	**
2000 Hz	4 (27.5)	*	–0.75	*
	7 (48.1)	*	*	*
	12 (82.5)	0.98	0.69	0.84
	21.4 (147.1)	0.52	–1.47	–0.48
	37.4 (257.1)	1.12	0.68	0.90
3000 Hz	4 (27.5)	0.34	0.44	0.39
	7 (48.1)	*	*	*
	12 (82.5)	0.15	0.33	0.24
	21.4 (147.1)	0.69	0.32	0.42
	37.4 (257.1)	0.82	0.79	0.81
4000 Hz	4 (27.5)	**	**	**
	7 (48.1)	*	*	*
	12 (82.5)	**	**	**
	21.4 (147.1)	0.35	0.35	0.35
	37.4 (257.1)	0.59	0.30	0.45

* One or both record(s) were missing or could not be interpreted.
** Damping value not calculated because outside established wavelength limits.

Table 8.B.5-11
Values of Material Damping in Shear for Forward, Reverse and Combined Directions Along Array S2 in the Horizontal Plane for Isotropic Loading Conditions

Excitation Frequency	Confining Pressure, psi, (kPa)	D(%) Measured in Test Direction Forward	Reverse	Combined
1000 Hz	4 (27.5)	4.27	2.35	3.32
	7 (48.1)	**	**	**
	12 (82.5)	**	**	**
	21.4 (147.1)	**	**	**
	37.4 (257.1)	**	**	**
2000 Hz	4 (27.5)	2.48	1.51	2.00
	7 (48.1)	2.99	1.21	2.10
	12 (82.5)	2.09	1.43	1.76
	21.4 (147.1)	0.84	0.34	0.59
	37.4 (257.1)	1.98	1.32	1.65
3000 Hz	4 (27.5)	0.50	0.46	0.48
	7 (48.1)	1.03	0.14	0.59
	12 (82.5)	1.67	0.18	0.93
	21.4 (147.1)	1.51	0.28	0.90
	37.4 (257.1)	1.77	1.47	1.62
4000 Hz	4 (27.5)	**	**	**
	7 (48.1)	**	**	**
	12 (82.5)	**	**	**
	21.4 (147.1)	**	**	**
	37.4 (257.1)	1.47	0.97	1.22

* One or both record(s) were missing or could not be interpreted.
** Damping value not calculated because outside established wavelength limits.

Table 8.B.5-12
Average Values of Material Damping Ratios from SH-Waves and SV-Waves Propagating in the Horizontal and Vertical Planes During Isotropic Confinement

Pressure psi (KPa)	Material Damping Ratio, D_{min}, %			Average	Standard Deviation
	Array Number				
	S5 (Vertical Plane)	S1 (Horizontal Plane)	S2 (Horizontal Plane)		
4.0(27.5)	1.45	0.50	1.93	1.29	±0.73
7.0(48.1)	1.65	*	1.35	1.50	±0.21
12.0(82.5)	1.73	0.54	1.35	1.21	±0.61
21.4(147.1)	1.51	0.39	0.75	0.88	±0.57
37.4(257.1)	1.25	0.72	1.50	1.16	±0.40

*Unable to evaluate wave amplitudes at one or more receivers in these records.

Notes:

1. Each data point represents the average of measurements at 2 or 3 frequencies (1000, 2000, 3000 and 4000 Hz were typically used).
2. Each data point was calculated using waves propagating in both the forward and reverse directions.
3. All measurements were made with geophone receivers.

The results are presented by combining all data available in the horizontal and vertical planes because there are only three arrays available for S-waves. The damping ratios vary from a maximum of 1.93% to a minimum of 0.39% as shown in Fig. 8.B.5-62. The average varies from 1.50% to 0.88% (Fig. 8.B.5-63). The standard deviation varies from 0.73 to 0.21, but for this limited data set the standard deviation does not mean much. The damping values do show a general trend of decreasing value with increasing confining pressure.

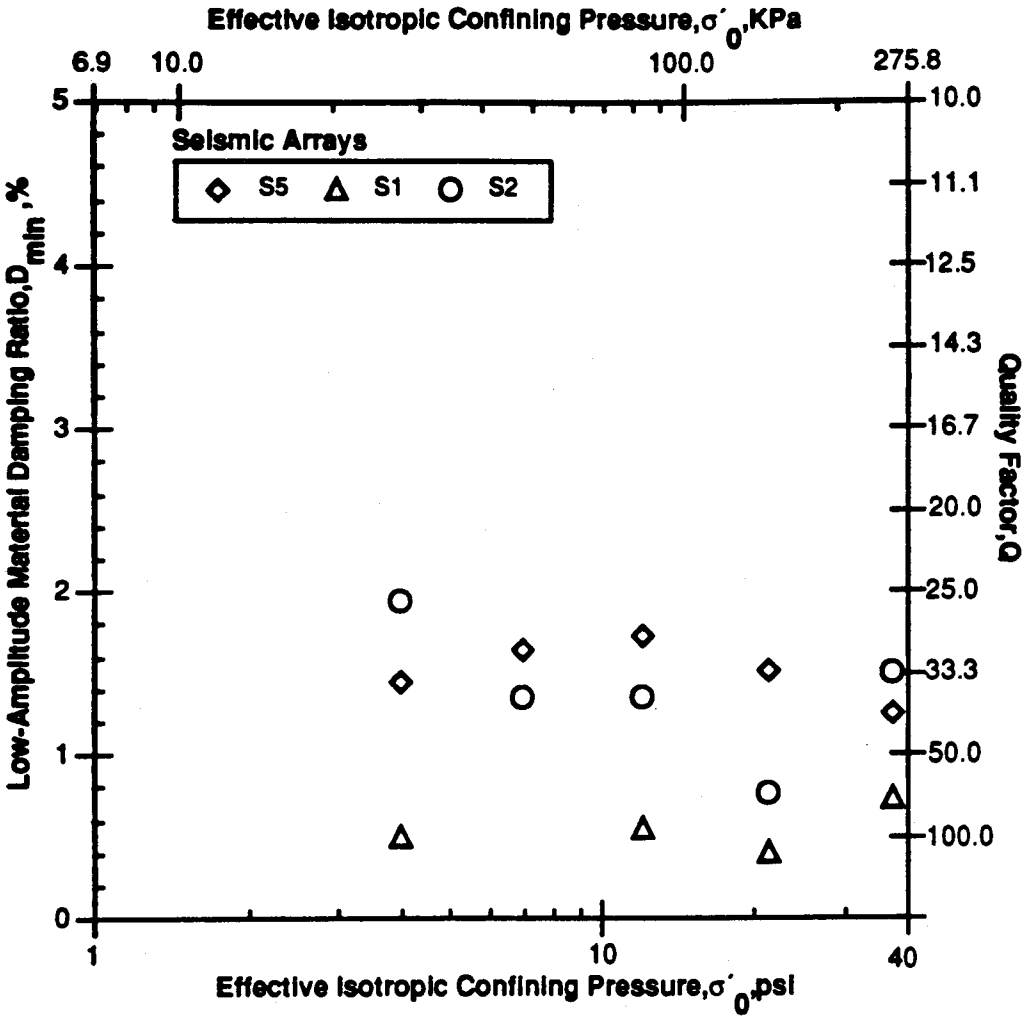

Notes:

1. Each data point represents the average of measurements at 2 or 3 frequencies (1000, 2000, 3000 and 4000 Hz were typically used).
2. Each data point was calculated using waves propagating in both the forward and reverse directions.
3. All measurements were made with geophone receivers.

Figure 8.B.5-62
Average values of material damping ratio from SH- and SV-wave measurements along each seismic array in the vertical and horizontal planes during isotropic loading.

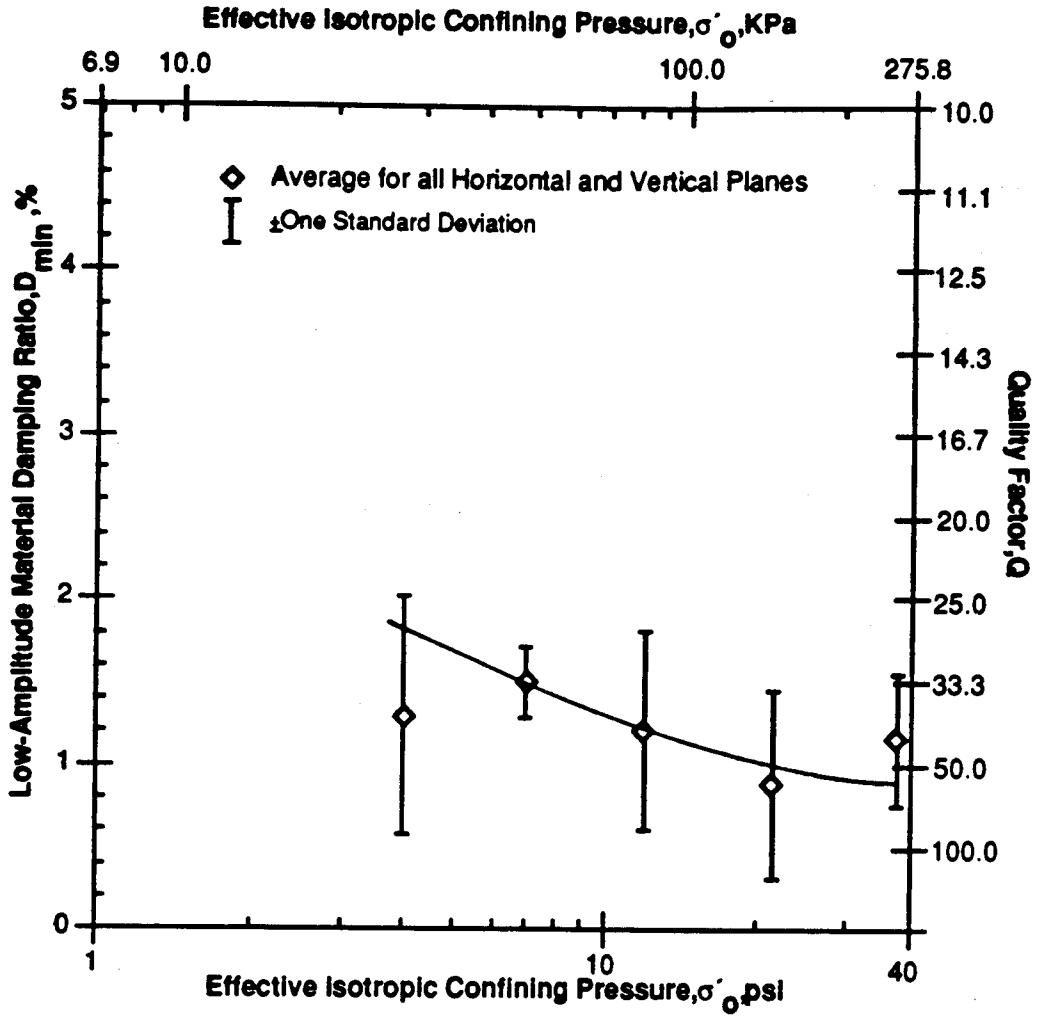

Notes:

1. Average measurements from all 3 instrumentation lines.
2. Each data point represents the average of measurements at 2 or 3 frequencies (1000, 2000, 3000 and 4000 Hz were typically used).
3. Each data point was calculated using waves propagating in both the forward and reverse directions.
4. All measurements were made with geophone receivers.

Figure 8.B.5-63
Average values of material damping ratio from all SH- and SV-wave measurements in the vertical and horizontal planes during isotropic loading.

The histograms representing the measurements in the forward, reverse and combined directions are shown in Fig. 8.B.5-64, 8.B.5-65 and 8.B.5-66, respectively. These also do not mean a lot as the number of measurements is quite small.

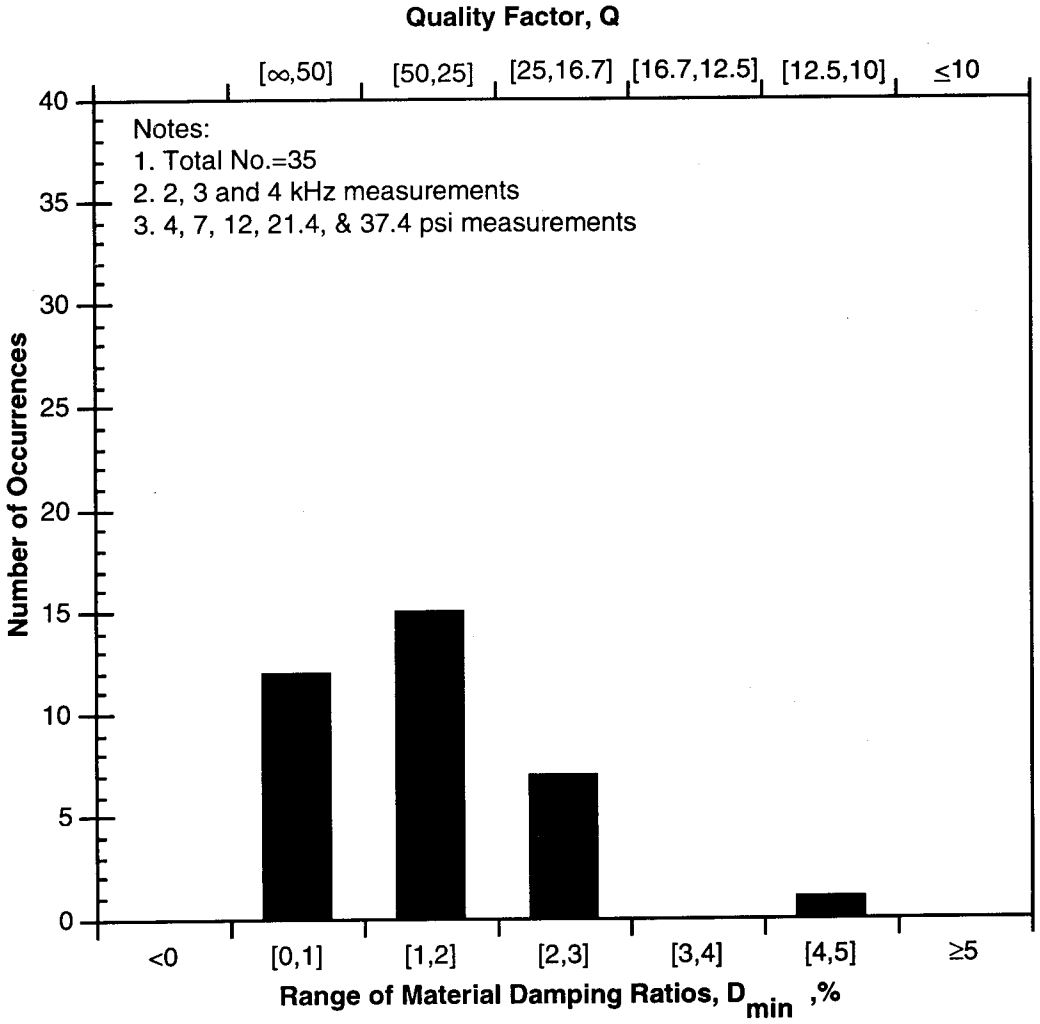

Figure 8.B.5-64
Histogram of all material damping measurements for SV-waves and SH-waves propagating in the forward direction in the horizontal and vertical planes during isotropic confinement.

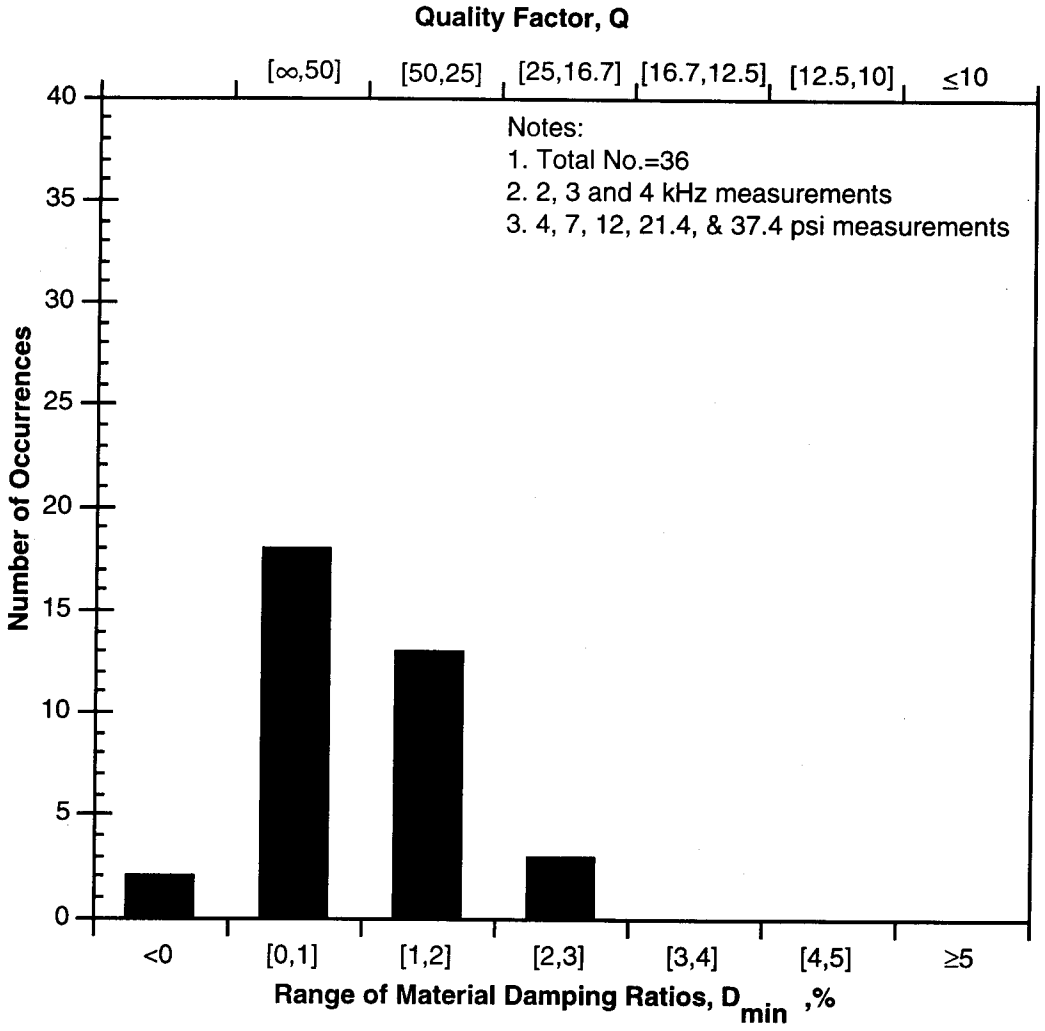

Figure 8.B.5-65
Histogram of all material damping measurements for SV-waves and SH-waves propagating in the reverse direction in the horizontal and vertical planes during isotropic confinement.

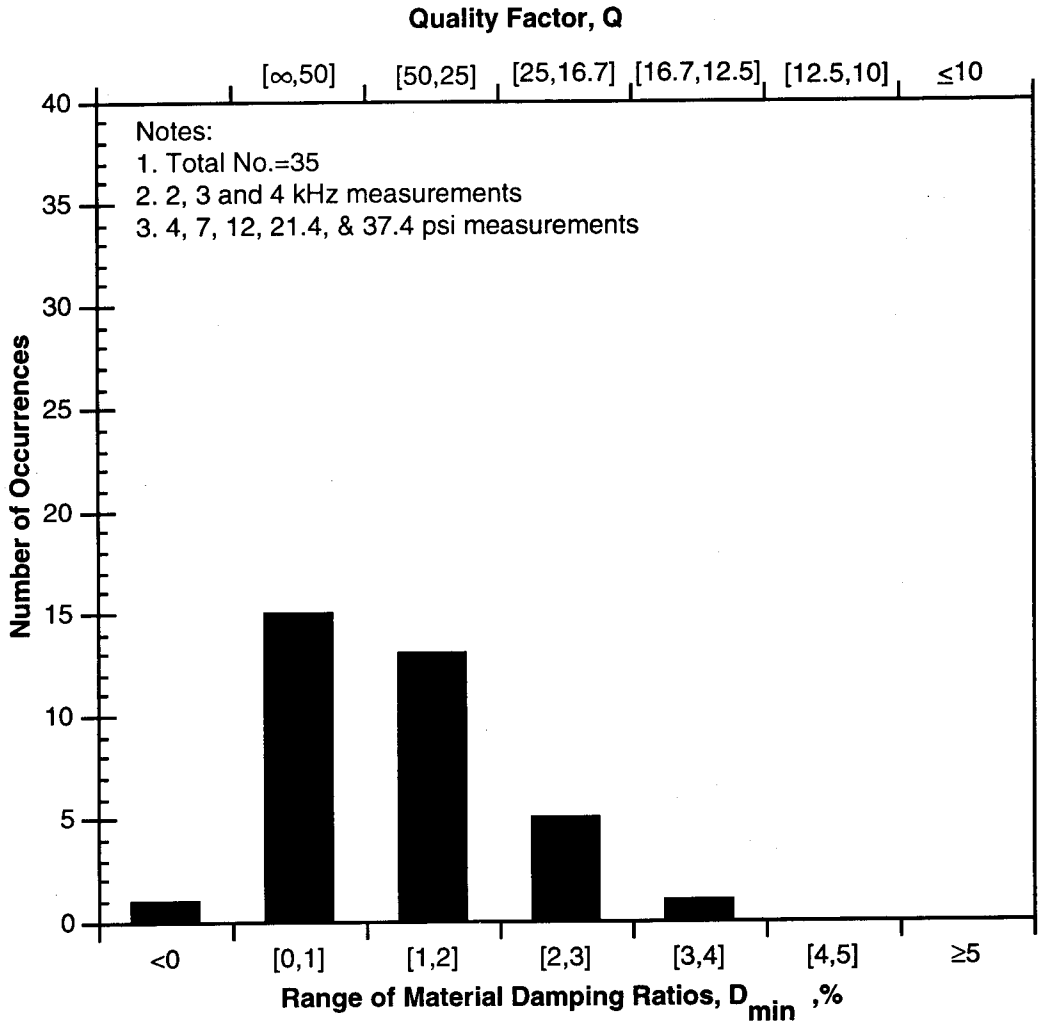

Figure 8.B.5-66
Histogram of all material damping measurements for SV-waves and SH-waves propagating in the horizontal and vertical planes during isotropic confinement for combined directions.

8.B.5.5.7 Comparison of All Results

Average damping values obtained from both compression wave planes and the shear wave measurements are plotted in Fig. 8.B.5-67. It is evident that the damping measurements obtained from the shear waves are lower than those for the compression waves. However, the P- and S-wave ranges overlap in terms of one standard deviation and exhibit the same trend. When compared to the torsional resonant column tests, the damping values obtained from measurements in the LSTC are considerably higher. This could be due to the range of frequencies used in the resonant column test which were less than about 100 Hz compared with the 1 to 4 kHz used in the LSTC. However, the exact reason(s) is unclear at this time.

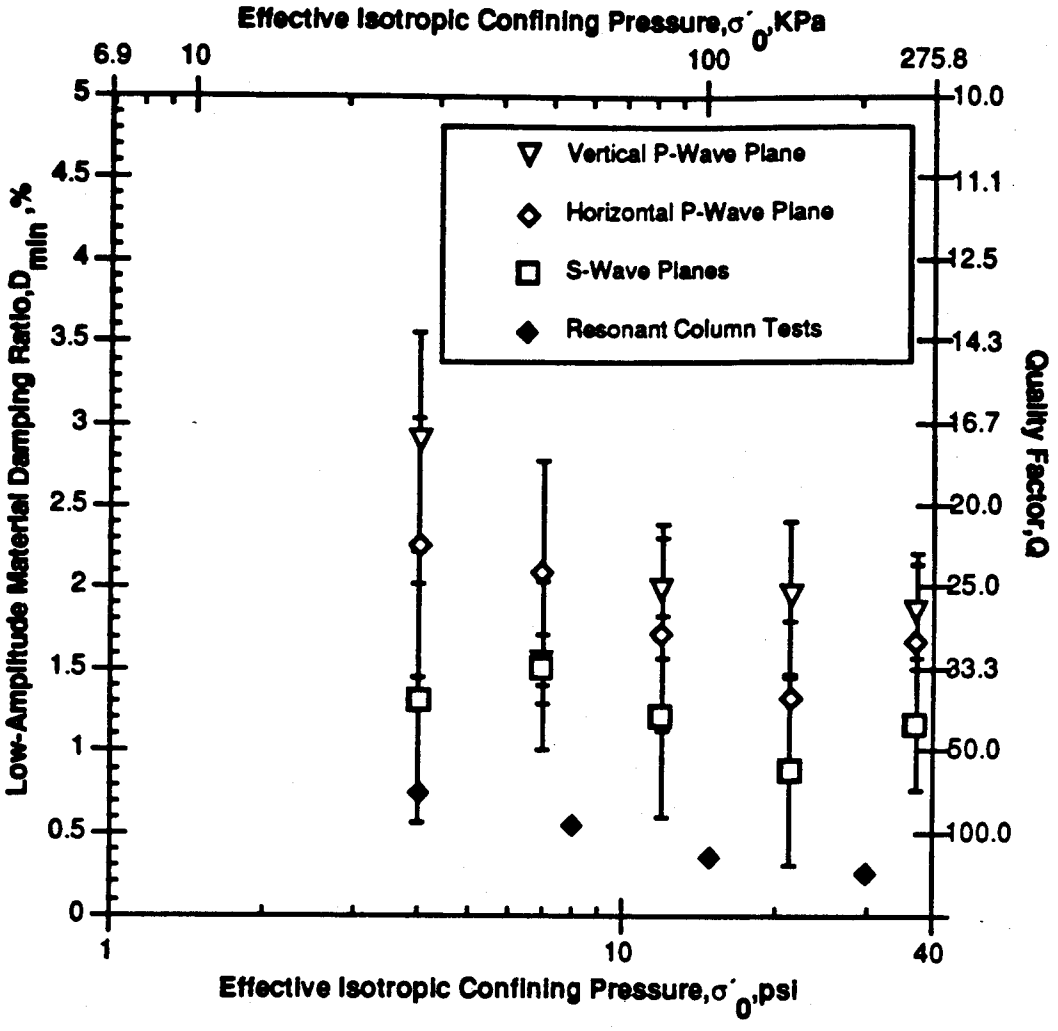

Figure 8.B.5-67
Average values of material damping from all P- and S-waves measured in the vertical and horizontal planes under isotropic confinement compared with results from resonant column tests.

8.B.5.5.8 Conclusions

There are several important conclusions from these tests performed under carefully controlled laboratory conditions. The first is that damping measurements as performed herein exhibited considerable scatter. This scatter is typical of the scatter found at the Gilroy 2 site by Fuhriman and Stokoe (1993). This scatter becomes more apparent when the directions of testing were kept separate as in tests in either the forward or reverse directions. When the two directions are taken together and presented in combined form, the scatter is reduced significantly. The reduction in scatter for the combined measurements likely comes from reducing the effects of the individual receivers and their interaction with the surrounding sand.

Based on these measurements, material damping in the soil skeleton seems to be about equal in compression and shear. If there is any difference, these measurements indicate that damping in shear is slightly less than damping in compression. In addition, these damping values averaged about 1% to 1.5% above material damping measurements in the torsional resonant column.

6—P-WAVE AND S-WAVE MEASUREMENTS UNDER BIAXIAL STATES OF STRESS

8.B.5.6.1 Introduction

In this section, material damping measurements obtained from P-wave and S-wave measurements under a biaxial state of stress in the LSTC are presented. In Section 8.B.5.5, only measurements under isotropic states of stress were discussed. Just as in Section 8.B.5.5, this section is divided into two parts; the first part dealing with P-wave results and the second dealing with the S-wave measurements. A comparison of the P- and S-wave results is then made with material damping values obtained from the isotropic tests.

For these biaxial loads, the stress in the vertical direction was kept constant at 12 psi, while both principal stresses in the horizontal plane were varied equally. Horizontal stresses of 6, 7, 9.5, 12 and 21.4 psi (41.4, 48.1, 65.3, 82.5 and 147.1 kPa) were employed. The state of stress is shown in Fig. 8.B.5-68 and further listed in Table 8.B.5-13.

All damping calculations were made taking into account the wavelength limit of at least two wavelengths between the source and first receiver. Each data point represents the average of measurements at 2 or 3 frequencies which generally were 2, 3 and 4 kHz. The damping values were calculated for the forward, reverse and combined directions using equations presented in Section 8.B.5.4.

Table 8.B.5-13
Principal Stresses Used in the Biaxial Stress Series

Testing Sequence	Pressure 1(σ'_x)	Pressure 2(σ'_y)	Pressure 3(σ'_z)
1	12	12	12
2	21.4	21.4	12
3	6	6	12
4	7	7	12
5	9.5	9.5	12

8.B.5.6.2 Typical Damping Results

The damping results have been computed in a manner similar to Section 8.B.5.5 (Section 8.B.5.5.2). The same notation was used for the arrays as was employed in Section 8.B.5.5. These results are presented in tables as well as plotted for each individual array. The results are presented in Appendix 8.B.5.C for the horizontal plane and in Appendix 8.B.5.D for the vertical plane.

Typical damping measurements are presented for the C10 array in Table 8.B.5-14. Again, significant scatter occurs for the forward and reverse directions which is significantly reduced upon combining the measurements. By comparing the results obtained from the C10 array in Section 8.B.5.5.2 to those obtained for the biaxial state of stress for the same array, one can see that in general the damping values for the biaxial state are a bit higher for that particular array (Table 8.B.5-14). The averages for the C10 array are plotted in Fig. 8.B.5-69. From this, scatter for the biaxial state of stress seems to be even a bit greater than that for the isotropic state of stress.

Table 8.B.5-14
Values of Material Damping in Compression for Forward, Reverse and Combined Directions Along Array C10 in the Vertical Plane for Biaxial Loading Conditions

Excitation Frequency	Confining Pressure, psi, (kPa)	D(%) Measured in Test Direction Forward	Reverse	Combined
2000 Hz	6 (41.4)	4.71	2.44	3.57
	7 (48.1)	5.18	3.18	4.18
	9.5 (65.3)	17.18	–3.48	4.45
	12 (82.5)	–2.91	9.48	3.39
	21.4 (147.1)	**	**	**
3000 Hz	6 (41.4)	3.67	1.62	3.57
	7 (48.1)	3.21	1.84	2.52
	9.5 (65.3)	2.50	2.08	2.29
	12 (82.5)	–2.27	6.16	2.03
	21.4 (147.1)	4.96	4.63	4.80
4000 Hz	6 (41.4)	3.89	2.44	3.16
	7 (48.1)	3.14	2.49	2.80
	9.5 (65.3)	2.62	2.96	2.79
	12 (82.5)	–0.45	3.67	1.67
	21.4 (147.1)	2.59	2.78	2.69

* One or both record(s) were missing or could not be interpreted.
** Damping value not calculated because outside established frequency limits.

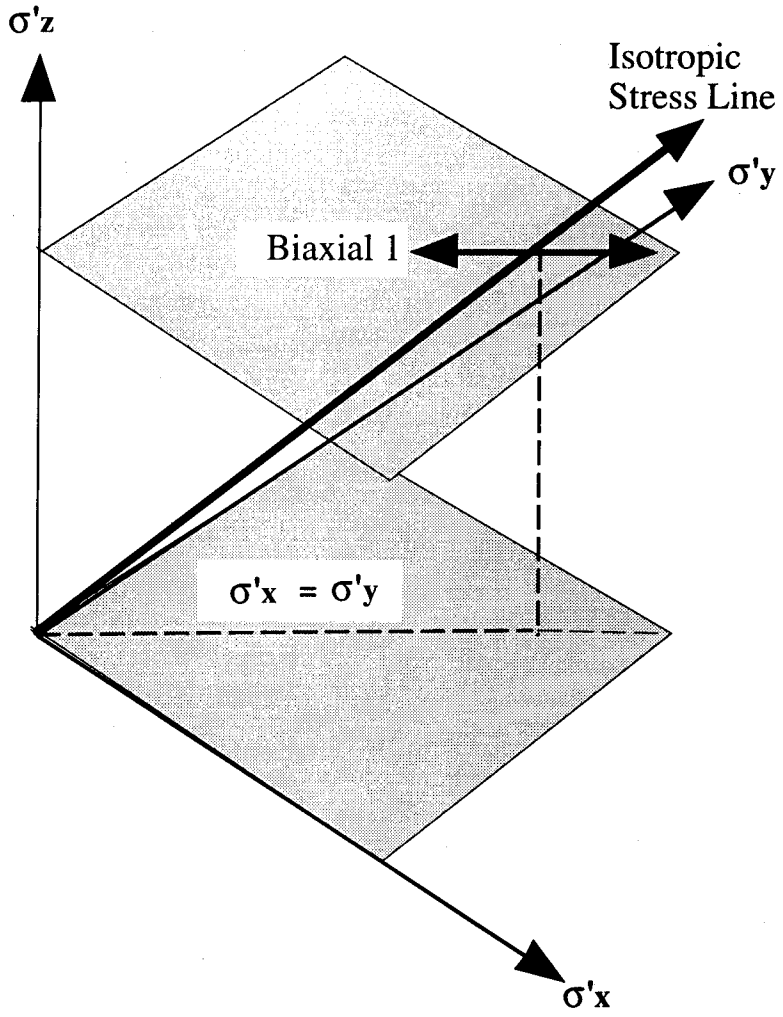

Figure 8.B.5-68
Stress condition in the biaxial stress series plotted in three-dimensional stress space (from Lee, 1993).

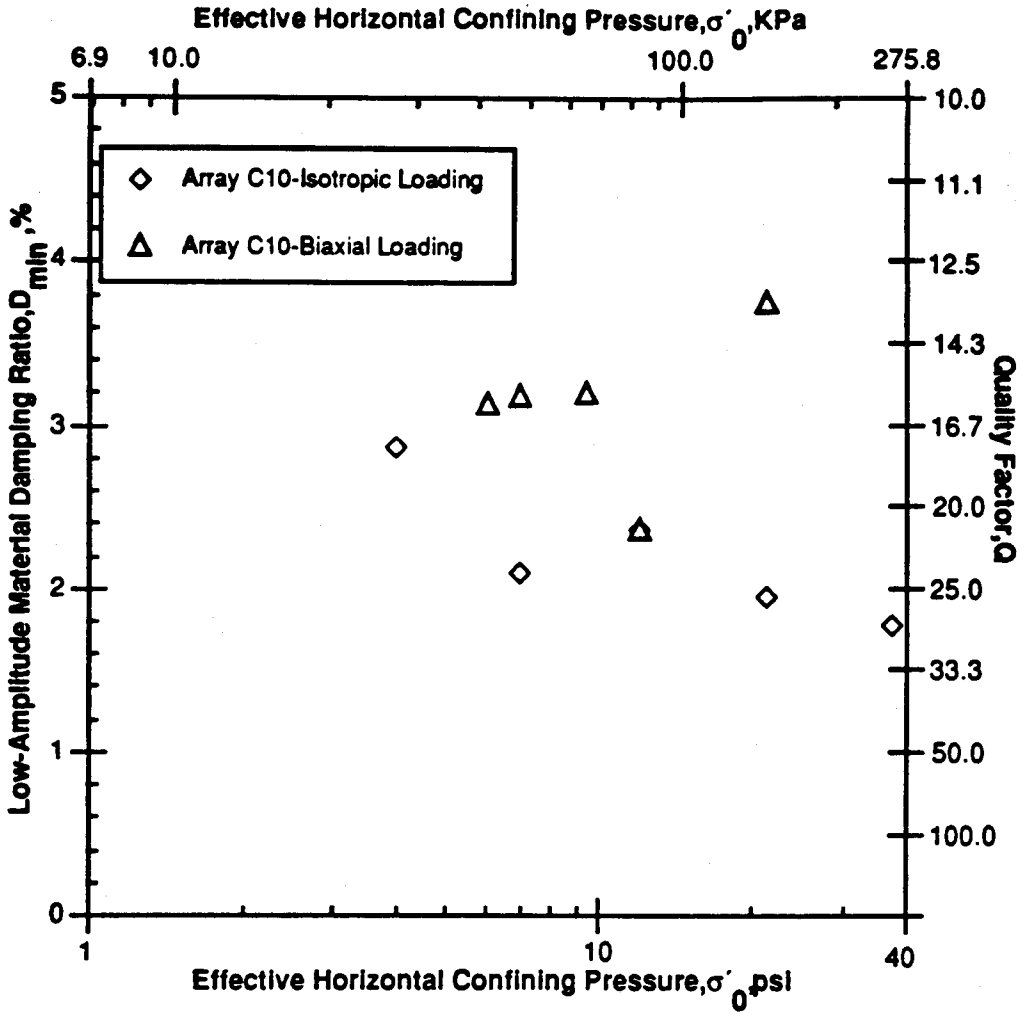

Notes:

1. Each data point represents the average of measurements at 2 or 3 frequencies (2000, 3000 and 4000 Hz were typically used).
2. Each data point was calculated using waves propagating in both the forward and reverse directions.
3. All measurements were made with accelerometer receivers.

Figure 8.B.5-69
Average material damping ratios in compression from combined measurements along array C10 in the vertical plane during isotropic and biaxial loading conditions.

8.B.5.6.3 P-Wave Measurements in the Horizontal Plane

Material damping ratios measured in the horizontal plane are tabulated in Table 8.B.5-15 by neglecting any effect of frequency and averaging the combined damping measurements for all arrays at 2, 3, and 4 kHz. Each data point in this table represents the average of 2 or more measurements at 2, 3, and 4 kHz. Also each data point was calculated using both forward and reverse measurements i.e. the combined directions. Measurements were not recorded if the wave amplitude could not be evaluated at one or more receivers in these records. If negative values were obtained even after combining the forward and reverse directions, these values were neglected when averaging the results.

Table 8.B.5-15
Average Values of Material Damping Ratios from P-Waves Propagating in the Horizontal Plane During Biaxial Confinement

Pressure psi (KPa)	Material Damping Ratio, D_{min}, % Array Number							Average	Standard Deviation
	C7	C1	C3	C5	C6	C4	C2		
6.0(41.4)	3.33	1.08	*	*	1.44	2.30	1.22	1.87	±0.94
7.0(48.1)	3.34	0.24	*	1.25	1.93	2.41	1.68	1.81	±1.05
9.5(65.3)	3.09	0.39	*	*	1.93	2.52	1.74	1.93	±1.01
12.0(82.5)	*	0.97	*	1.16	2.24	1.57	1.27	1.44	±0.50
21.4(147.1)	*	1.06	0.26	0.88	2.19	1.98	1.02	1.23	±0.72

*Unable to evaluate wave amplitudes at one or more receivers in these record.

Notes:

1. Each data point represents the average of measurements at 2 or 3 frequencies (2000, 3000 and 4000 Hz were typically used).
2. Each data point was calculated using waves propagating in both the forward and reverse directions.
3. All measurements were made with accelerometer receivers.

Figure 8.B.5-70 presents the average measurements obtained from each the array in the horizontal plane. Damping values ranged from a high of 3.34% at a confining pressure of 7 psi (48.1 kPa) to a low of 0.24% at the same pressure. By taking the average of all array measurements, the variation in the damping value is significantly reduced and a nice trend is observed of reducing damping with increasing pressure as shown in Fig. 8.B.5-71. The standard deviations for the average values of D at each pressure vary from 1.01 to 0.50, with the average material damping ratios ranging from a maximum of 1.93% to a minimum of 1.23%. The curve fit to the data was fit by eye and generally follows the trend obtained from the resonant column tests in shear (Fig. 8.B.5-23). It is interesting to note that the average damping values are essentially the same as those determined under isotropic loading in the horizontal plane (Fig. 8.B.5-42).

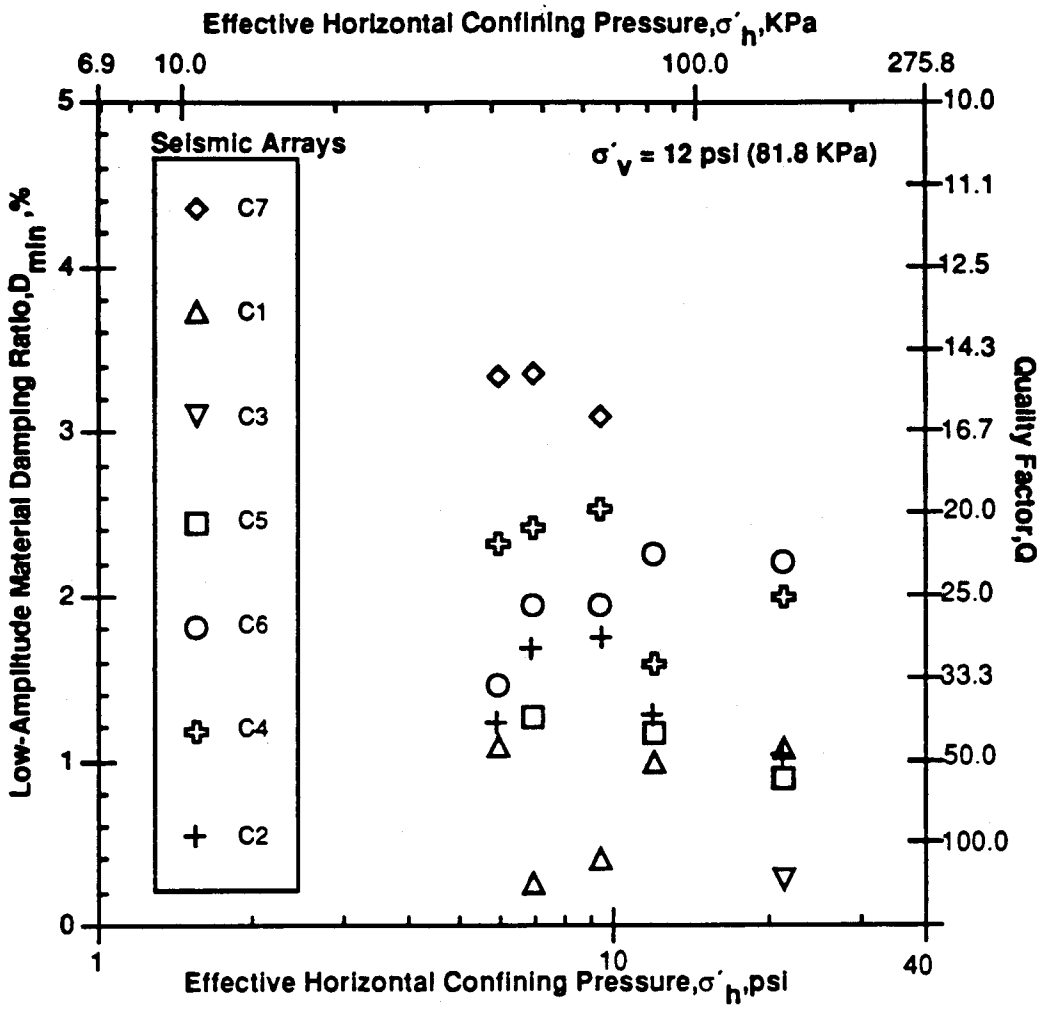

Notes:

1. Each data point represents the average of measurements at 2 or 3 frequencies (2000, 3000 and 4000 Hz were typically used).
2. Each data point was calculated using waves propagating in both the forward and reverse directions.
3. All measurements were made with accelerometer receivers.

Figure 8.B.5-70
Average values of material damping ratio from P-wave measurements along each seismic array in the horizontal plane during biaxial loading.

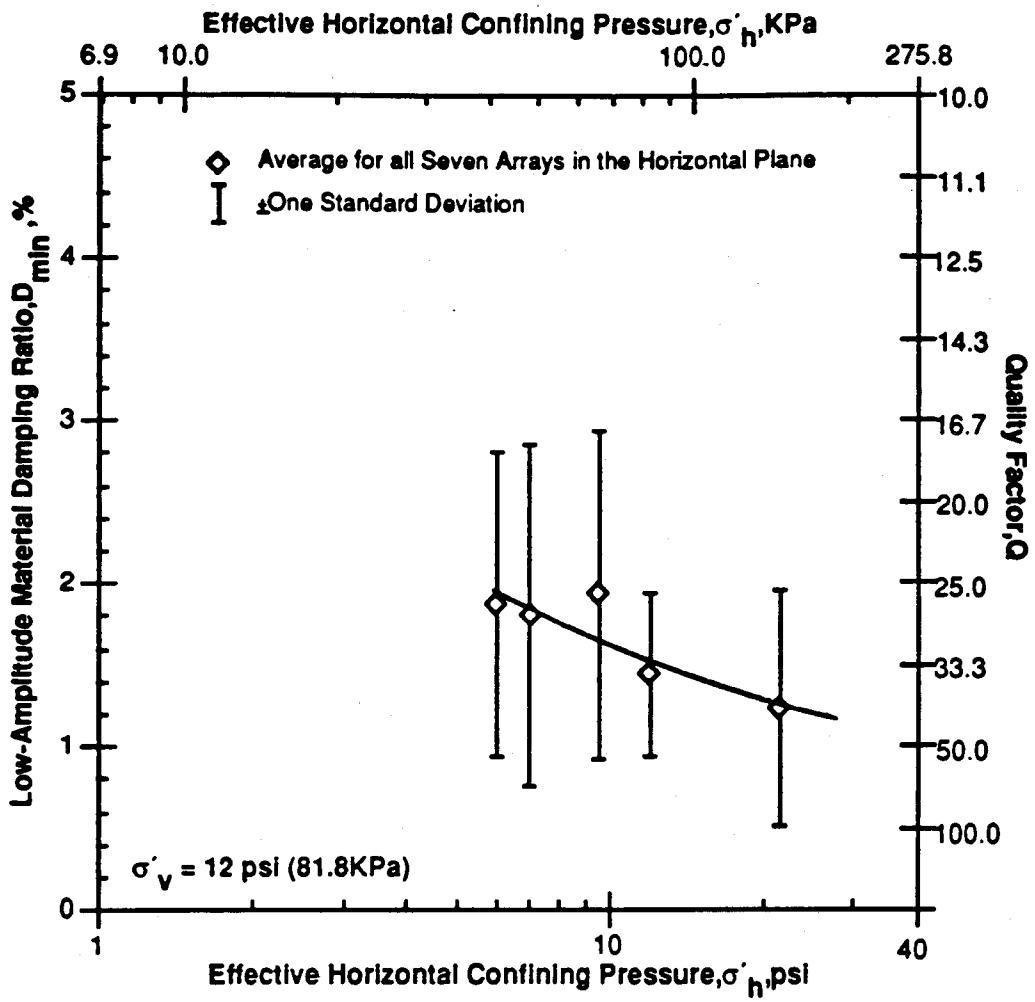

Notes:

1. Average measurements from all 7 instrumentation lines.
2. Each data point represents the average of measurements at 2 or 3 frequencies (2000, 3000 and 4000 Hz were typically used).
3. Each data point was calculated using waves propagating in both the forward and reverse directions.
4. All measurements were made with accelerometer receivers.

Figure 8.B.5-71
Average values of material damping ratio from all P-wave measurements in the horizontal plane during biaxial loading.

Histograms were initially plotted by combining all data and ignoring any effects of confining pressure and frequency. In this case the average measurements at all pressures for the forward, reverse and combined directions are shown in Figs. 8.B.5-72, 8.B.5-73 and 8.B.5-74 respectively. The scatter in damping measurements in the forward and reverse directions from Figs. 8.B.5-72 and 8.B.5-73 is not quite as apparent as it was in the isotropic case. It can be seen that, by using the combined damping values, the scatter is reduced and the majority of the values fall between 0 and 3% in Fig. 8.B.5-74. The total number of measurements that could be obtained was 79, and the number of measurements between 0 and 3% is 61; hence, 77% of the data falls in this range.

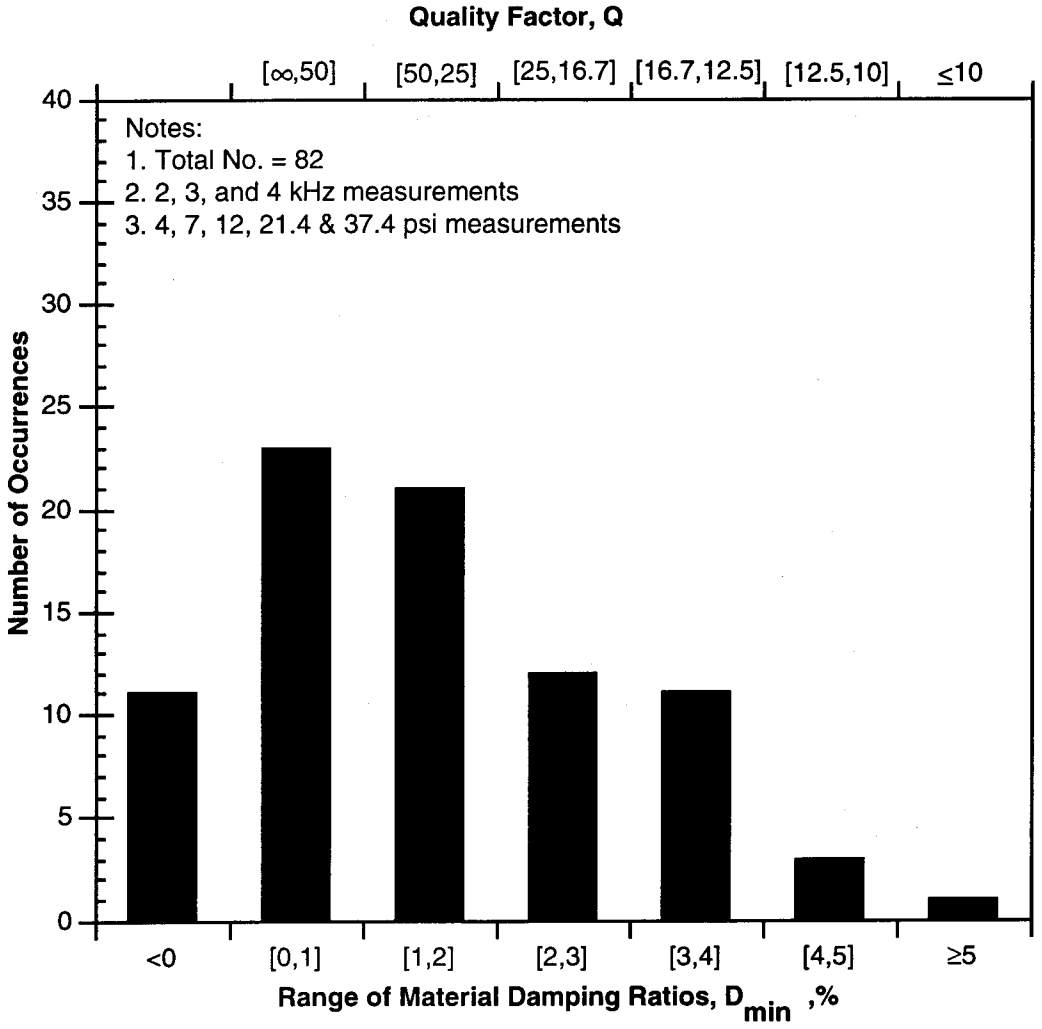

Figure 8.B.5-72
Histogram of all material damping measurements for P-waves propagating in the forward direction in the horizontal plane during biaxial confinement.

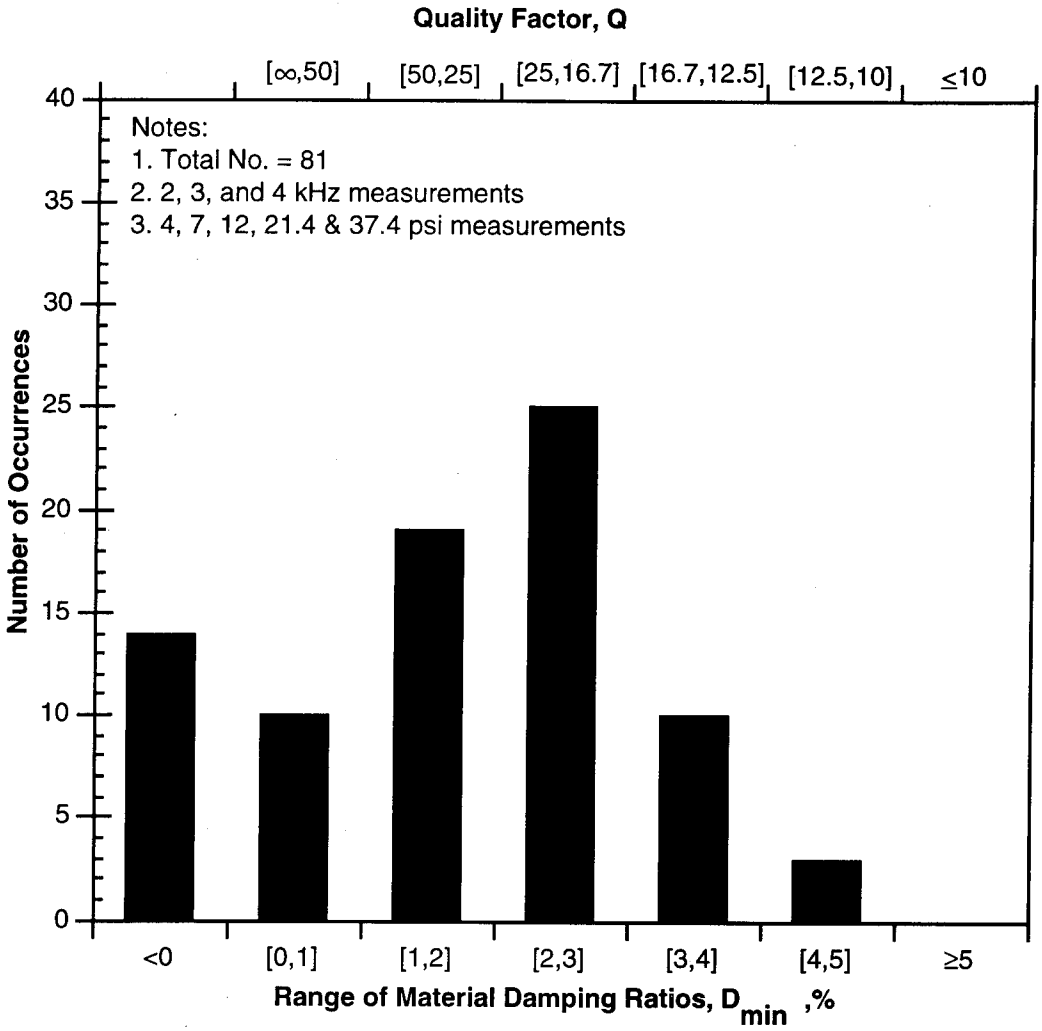

Figure 8.B.5-73
Histogram of all material damping measurements for P-waves propagating in the reverse direction in the horizontal plane during biaxial confinement.

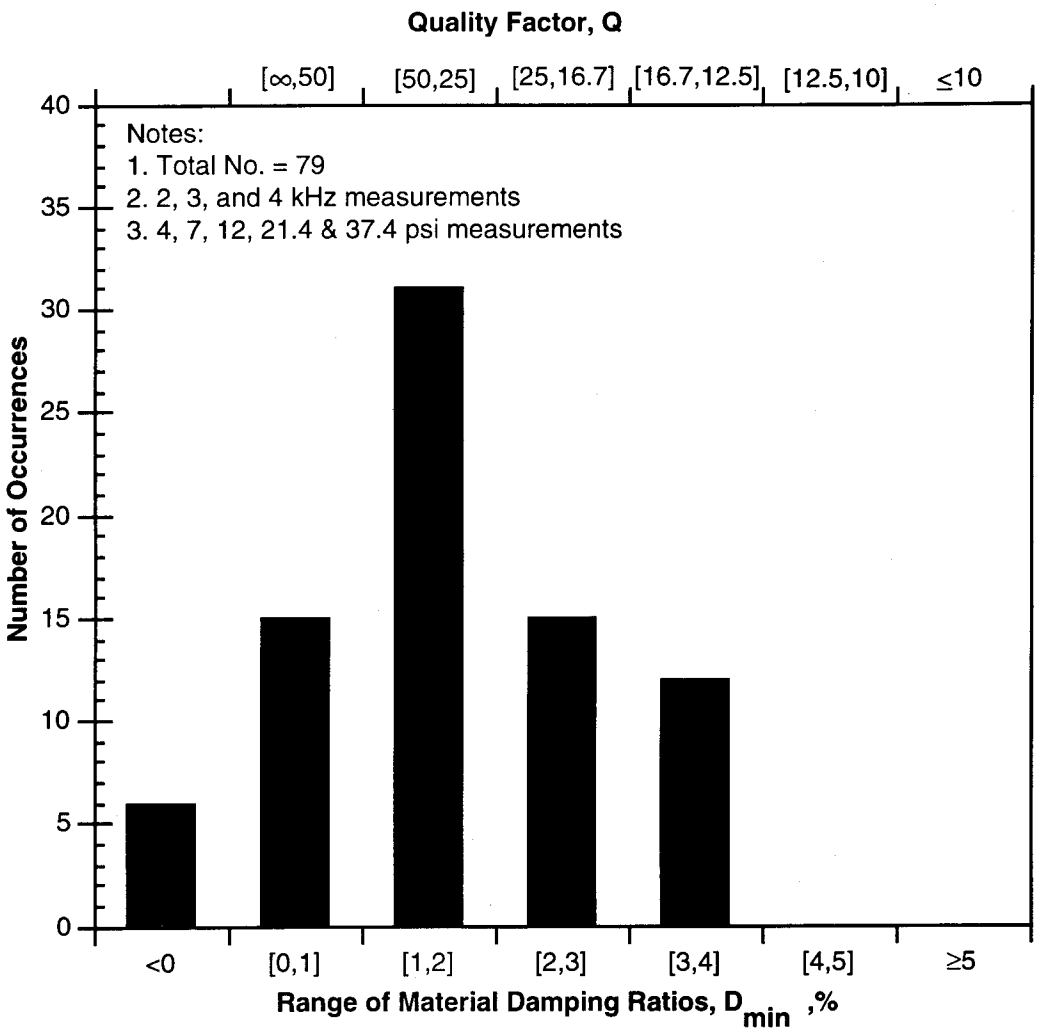

Figure 8.B.5-74
Histogram of all material damping measurements for P-waves propagating in the horizontal plane during biaxial confinement for combined directions.

By presenting the damping values in the form of histograms for each pressure, an attempt was again made to show the scatter in the damping values and how the damping values change (decrease) with pressure. These results are shown by the histograms in Figs. 8.B.5-75 through 8.B.5-79. From these figures, a slight trend of decreasing damping ratios with increasing confining pressure is observed. However, when compared to Figs. 8.B.5-46 through 8.B.5-50, there seems to be significantly more scatter in these results.

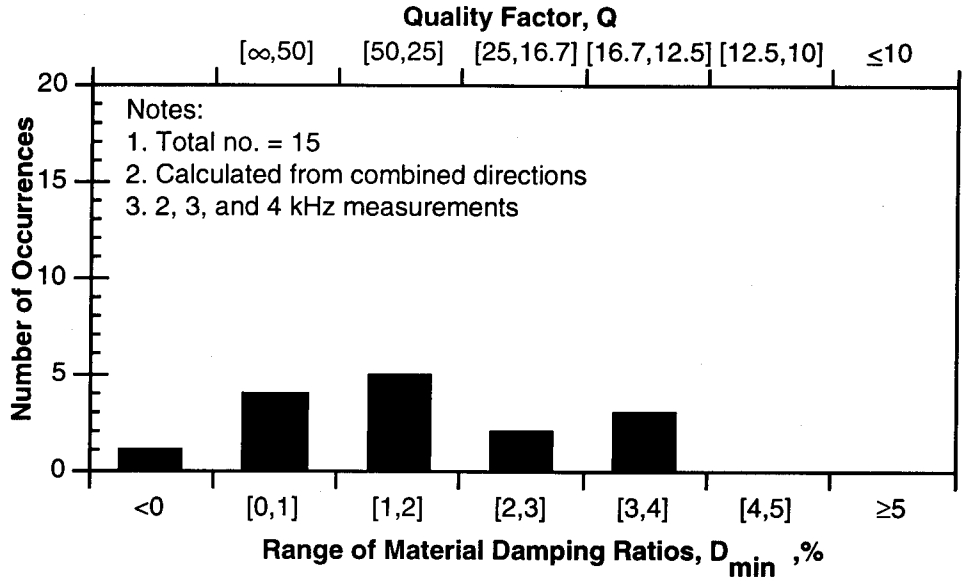

Figure 8.B.5-75
Histogram of material damping measurements for P-waves propagating in the horizontal plane under a biaxial pressure of 6 psi.

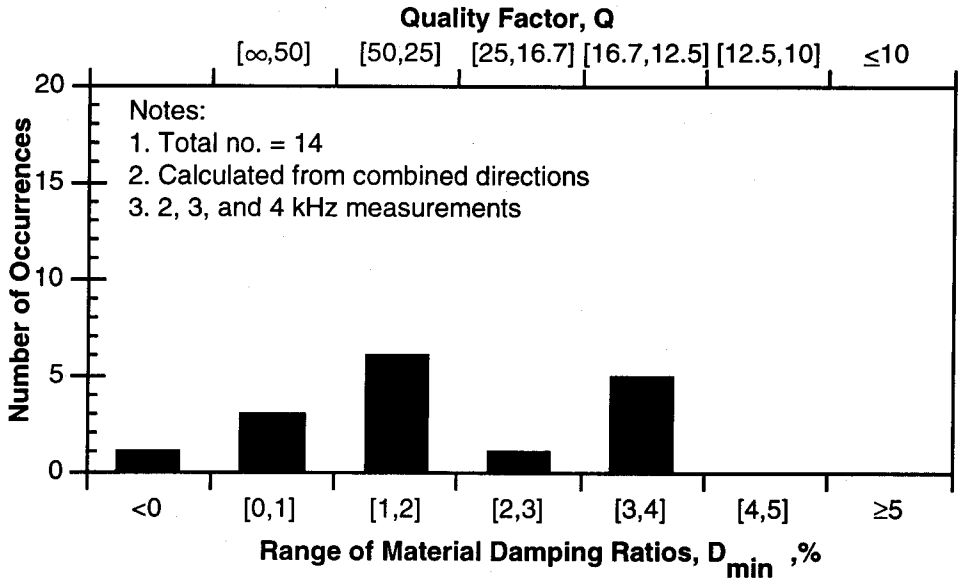

Figure 8.B.5-76
Histogram of material damping measurements for P-waves propagating in the horizontal plane under a biaxial pressure of 7 psi.

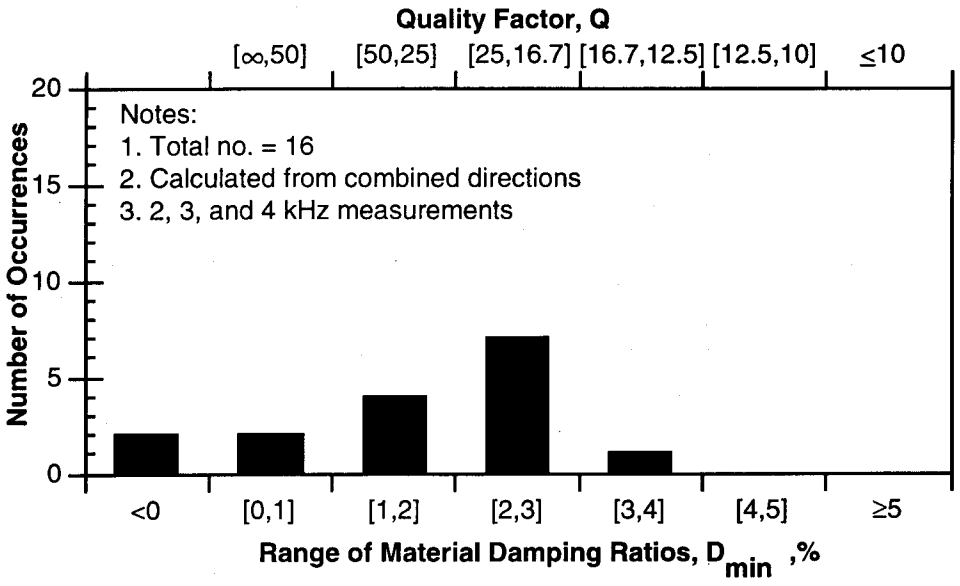

Figure 8.B.5-77
Histogram of material damping measurements for P-waves propagating in the horizontal plane under a biaxial pressure of 9.5 psi.

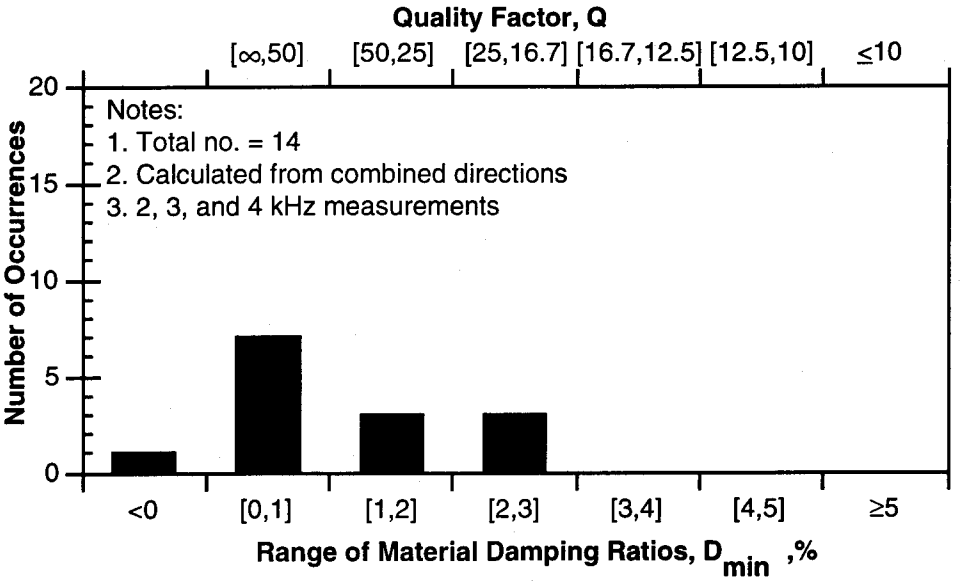

Figure 8.B.5-78
Histogram of material damping measurements for P-waves propagating in the horizontal plane under a biaxial pressure of 12 psi.

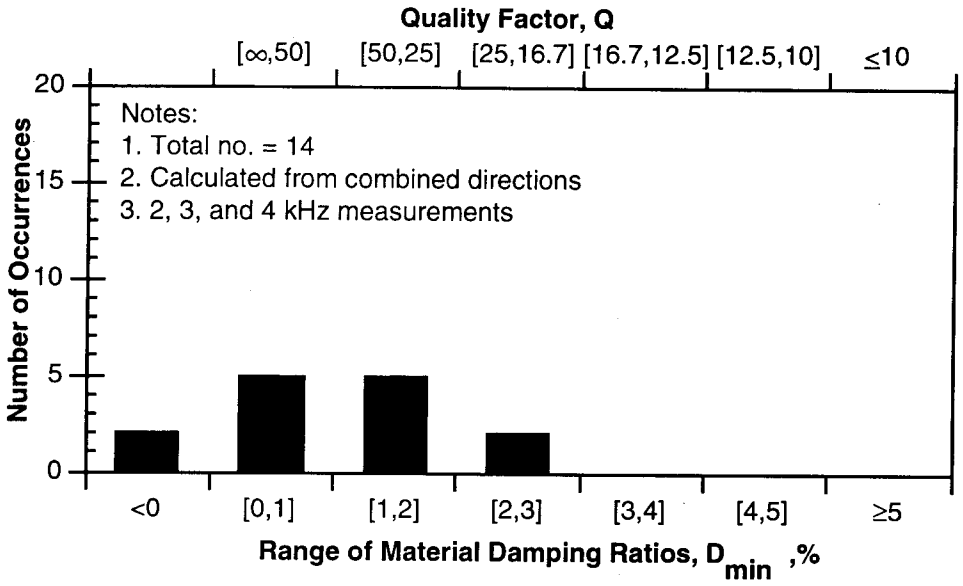

Figure 8.B.5-79
Histogram of material damping measurements for P-waves propagating in the horizontal plane under a biaxial pressure of 21.4 psi.

8.B.5.6.4 P-Wave Measurements in the Vertical Plane

In the vertical plane, no damping values could be obtained from array C9. The measurements along the C7 array were also deleted from this comparison because the values are from horizontally propagating P-waves. The remaining damping measurements are tabulated in Table 8.B.5-16 by neglecting any effect of frequency and averaging all measurements for any given array at 2, 3 and 4 kHz. These measurements are all from waves whose propagation direction ranges from vertical to 45 degrees from vertical.

The damping values obtained along each array are plotted in Fig. 8.B.5-80 at the normal effective pressure in the direction of wave propagation during biaxial confinement. The effective normal stresses in the direction of wave propagation in this biaxial series are tabulated in Table 8.B.5-17. Measured damping values range from 3.75% at a horizontal pressure of 21.4 psi (147.1 kPa) and a normal effective stress of 16.90 psi (116.5 kPa) to 0.91% at a horizontal pressure of 21.4 psi (147.1 kPa) and a normal effective stress of 19.05 psi (131.3 kPa).

Average material damping values for these arrays were calculated by taking the following ranges in normal effective pressures in the direction of wave propagation: 9.0 ± 0.5 psi, 10.0 ± 3.4 psi, 11.0 ± 3.4 psi, 12.0 ± 0.5 psi, 16.5 ± 0.5 psi, 19.5 ± 0.5 psi (62.1 ± 0.5 kPa, 68.9 ± 0.5 kPa, 75.9 ± 3.4 kPa, 82.7 ± 3.4 kPa, 113.8 ± 3.4 kPa, 134.5 ± 3.4 kPa). The averages are shown in Table 8.B.5-18. When these averages are taken at each confining pressure, the values range from a maximum of 2.25% to a minimum of 1.99%. These average values are plotted versus the normal effective stress in Fig. 8.B.5-80, and the average of all six arrays is presented in Fig. 8.B.5-81 with error bars for one standard deviation from the average also shown. The standard deviation varied from 1.58 to 0.31 for the averages involving two or more measurements.

From Fig. 8.B.5-80 it can be observed that there is significantly more scatter in the damping ratios in the vertical plane than in the horizontal plane. In this case averages of all measurements do not show a trend of decreasing damping with increasing $\overline{\sigma}_h$. However, if the two data points with only one measurement (values of 3.12% and 3.75%) are deleted, the scatter is reduced and the results do reasonably define a trend of decreasing damping, with increasing pressure.

Table 8.B.5-16
Average Values of Material Damping Ratios from P-Waves Propagating in the Vertical Plane During Biaxial Confinement

Pressure psi (KPa)	Material Damping Ratio, D_{min}, %						
	Array Number					Average	Standard Deviation
	C13	C11	C9	C10	C12		
6.0(41.4)	1.06	0.93	*	3.12	1.56	1.67	±1.01
7.0(48.1)	1.10	1.58	*	3.17	1.45	1.83	±0.92
9.5(65.3)	1.06	0.92	*	3.18	1.71	1.72	±1.03
12.0(82.5)	2.39	1.99	*	2.36	*	2.25	±0.22
21.4(147.1)	2.20	0.91	*	3.75	2.04	2.23	±1.02

*Unable to evaluate wave amplitudes at one or more receivers in these record.

Notes:

1. Each data point represents the average of measurements at 2 or 3 frequencies (2000, 3000 and 4000 Hz were typically used).
2. Each data point was calculated using waves propagating in both the forward and reverse directions.
3. All measurements were made with accelerometer receivers.

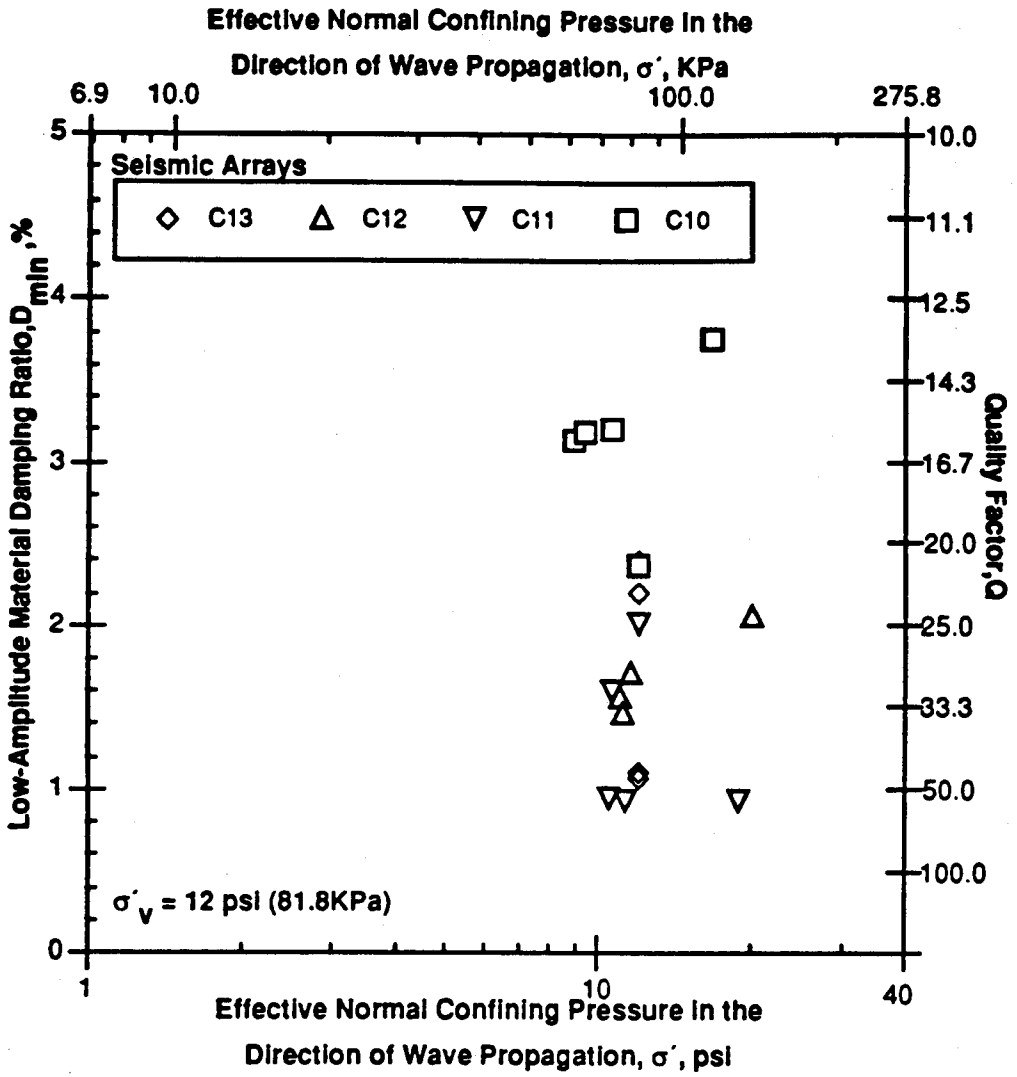

Notes:

1. Each data point represents the average of measurements at 2 or 3 frequencies (2000, 3000 and 4000 Hz were typically used).
2. Each data point was calculated using waves propagating in both the forward and reverse directions.
3. All measurements were made with accelerometer receivers.

Figure 8.B.5-80
Average values of material damping ratio from P-wave measurements along each seismic array in the vertical plane during biaxial loading.

Table 8.B.5-17
Effective Normal Stress in the Vertical Plane in the Direction of P-Wave Propagation During Biaxial Loading

$\bar{\sigma}_h$=	6 psi	7 psi	9.5 psi	12 psi	21.4 psi
Array	Effective Normal Confining Pressure in the Direction of Wave Propagation (psi)				
C13	12.00	12.00	12.00	12.00	12.00
C12	11.12	11.27	11.63	12.00	20.02
C11	10.5	10.75	11.38	12.00	19.05
C10	9.00	9.50	10.75	12.00	16.70

Table 8.B.5-18
Averages of all Material Damping Values for P-Waves Propagating in the Vertical Plane and Associated Normal Effective Pressures in the Direction Wave Propagation

Pressure	No. of Measurements	Average Damping%
9.00± 0.5	1	3.12
10.0 ± 0.5	2	2.05
11.0 ± 0.5	4	1.38
12.0 ± 0.5	8	1.73
16.5 ± 0.5	1	3.75
19.5 ± 0.5	2	1.48

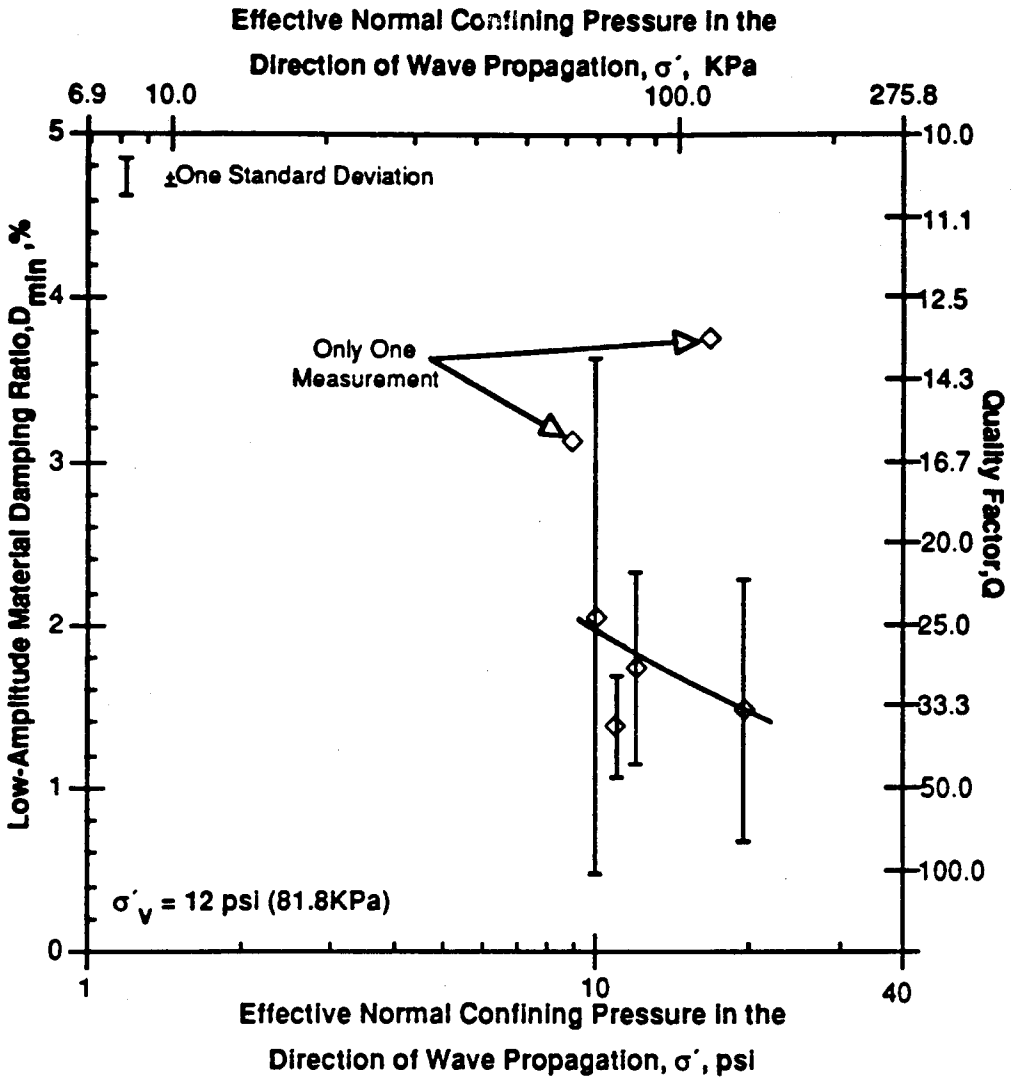

Notes:

1. Average measurements from all 6 instrumentation lines.
2. Each data point represents the average of measurements at 2 or 3 frequencies (2000, 3000 and 4000 Hz were typically used).
3. Each data point was calculated using waves propagating in both the forward and reverse directions.
4. All measurements were made with accelerometer receivers.

Figure 8.B.5-81
Average Values of Material Damping Ratio from all P-Wave Measurements in the Vertical Plane During Biaxial Loading.

The histograms for the forward and reverse directions (Figs. 8.B.5-82 and 8.B.5-83) show even more scatter than that obtained in the horizontal plane, but the combined direction (Fig. 8.B.5-84) again does a good job of getting the values down into a narrower band and the majority of damping values lie between 1% and 3%. From a total of 52 measurements, 39 measurements lie between 1% and 3%. When looking at the distribution of measurements for every pressure individually (Figs. 8.B.5-85 through 8.B.5-89), it can be seen that the damping values are quite evenly spread out. There is no easily observable trend of decreasing damping with increasing pressure.

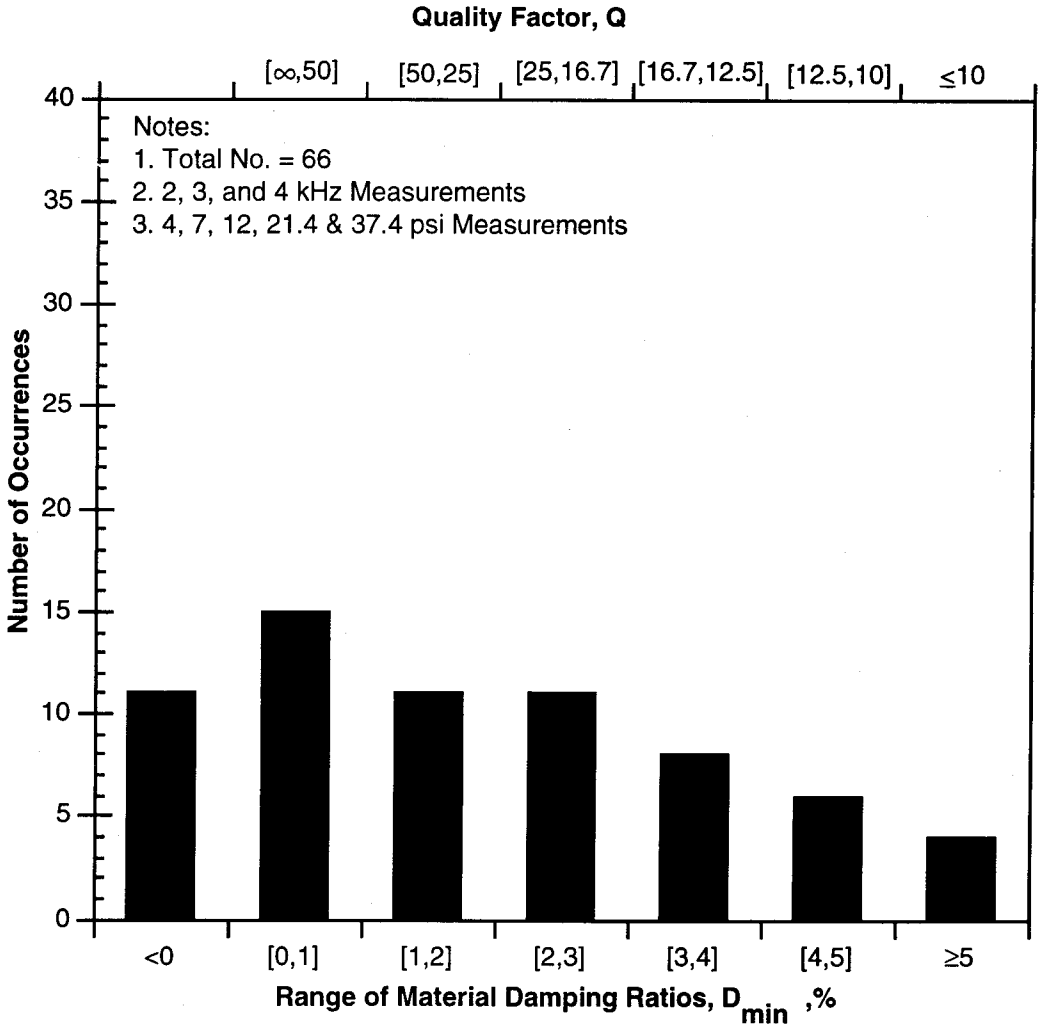

Figure 8.B.5-82
Histogram of all material damping measurements for P-waves propagating in the forward direction in the vertical plane during biaxial confinement.

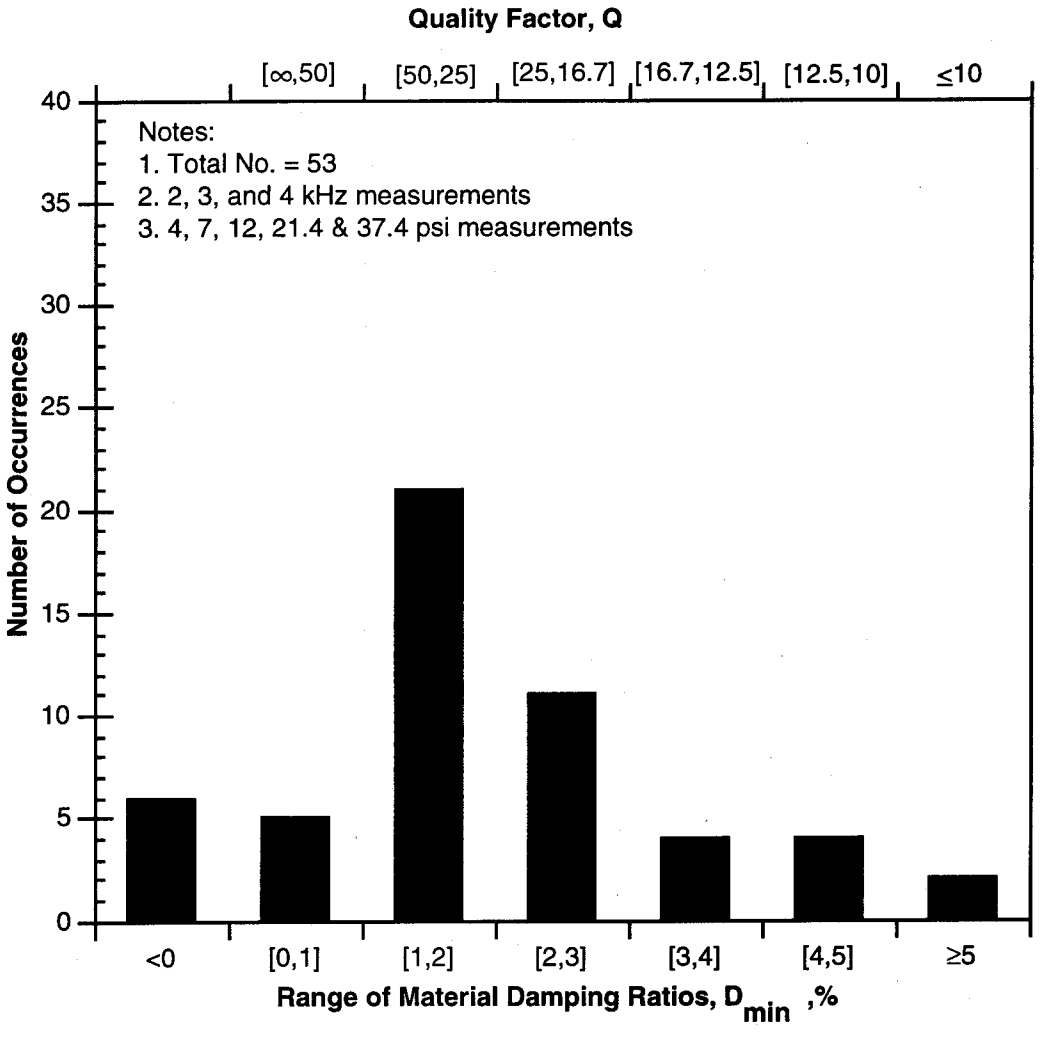

Figure 8.B.5-83
Histogram of all material damping measurements for P-waves propagating in the reverse direction in the vertical plane during biaxial confinement.

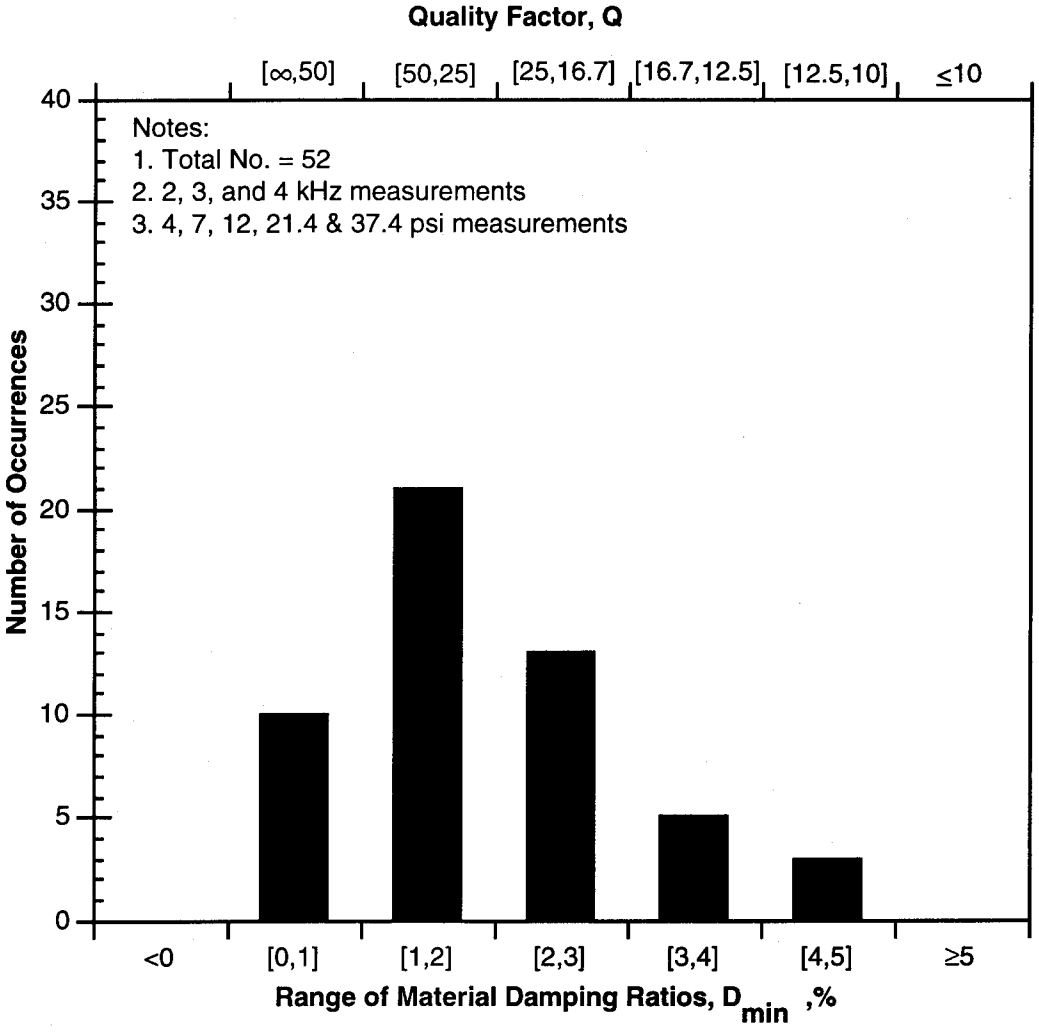

Figure 8.B.5-84
Histogram of all material damping measurements for P-waves propagating in the vertical plane during biaxial confinement for combined direction.

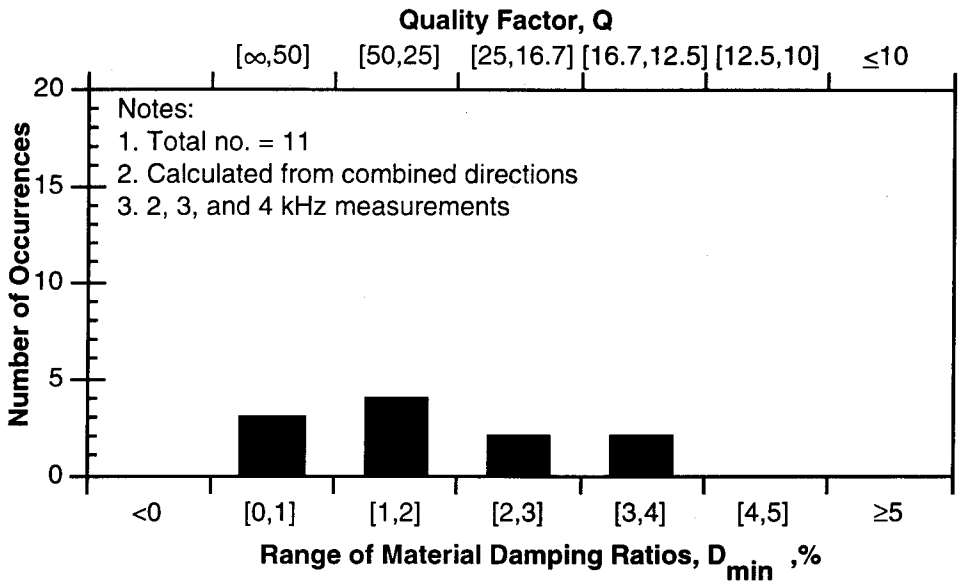

Figure 8.B.5-85
Histogram of material damping measurements for P-waves propagating in the vertical plane under a biaxial pressure of 6 psi.

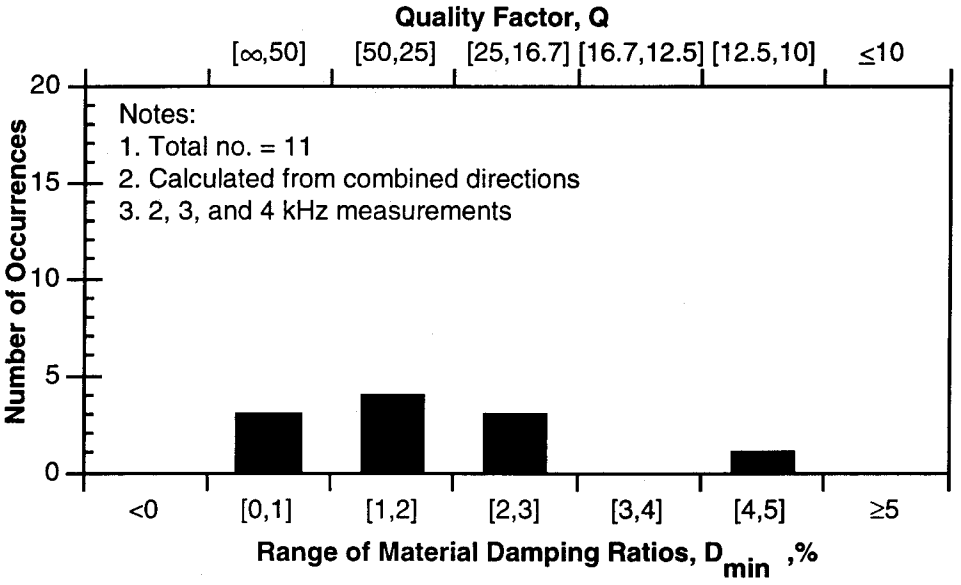

Figure 8.B.5-86
Histogram of material damping measurements for P-waves propagating in the vertical plane under a biaxial pressure of 7 psi.

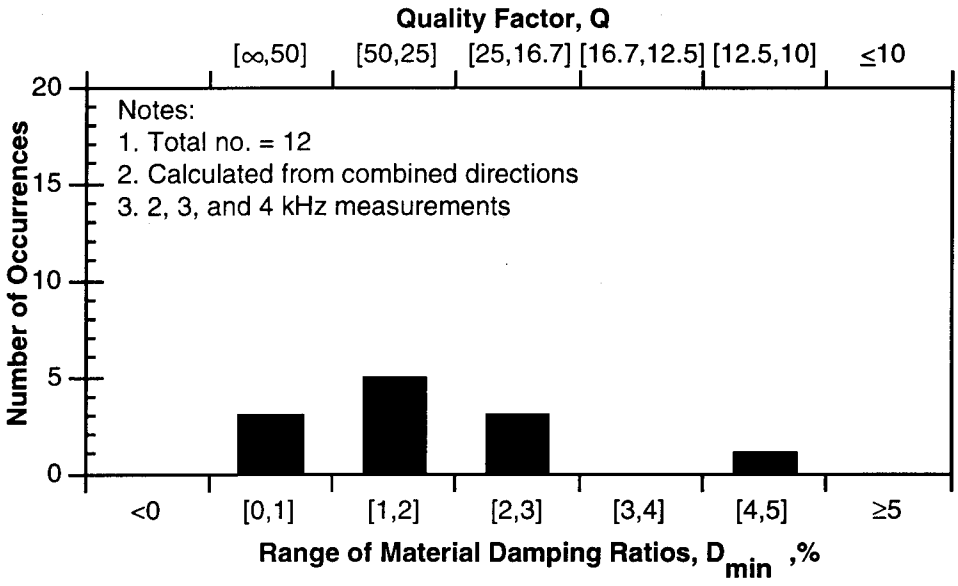

Figure 8.B.5-87
Histogram of material damping measurements for P-waves propagating in the vertical plane under a biaxial pressure of 9.5 psi.

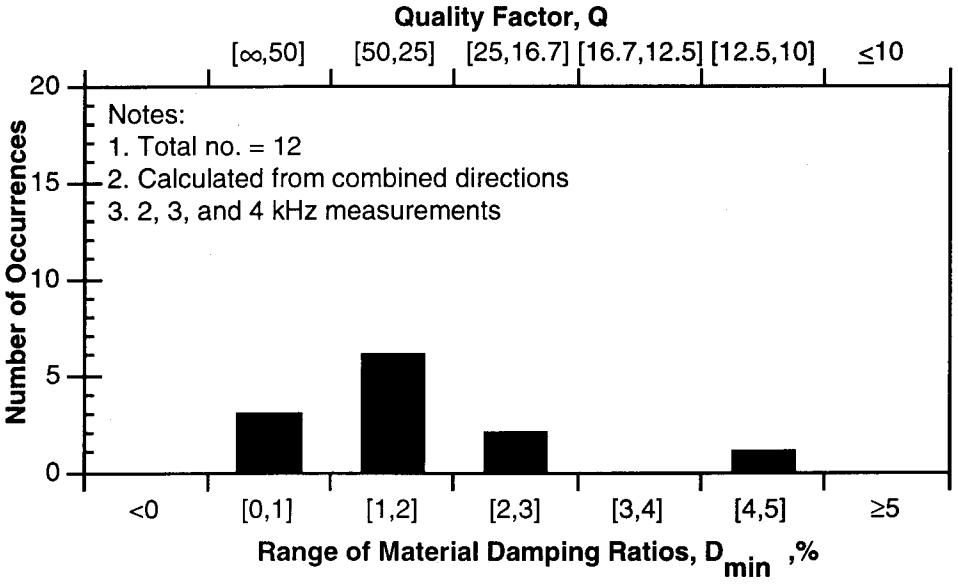

Figure 8.B.5-88
Histogram of material damping measurements for P-waves propagating in the vertical plane under a biaxial pressure of 12 psi.

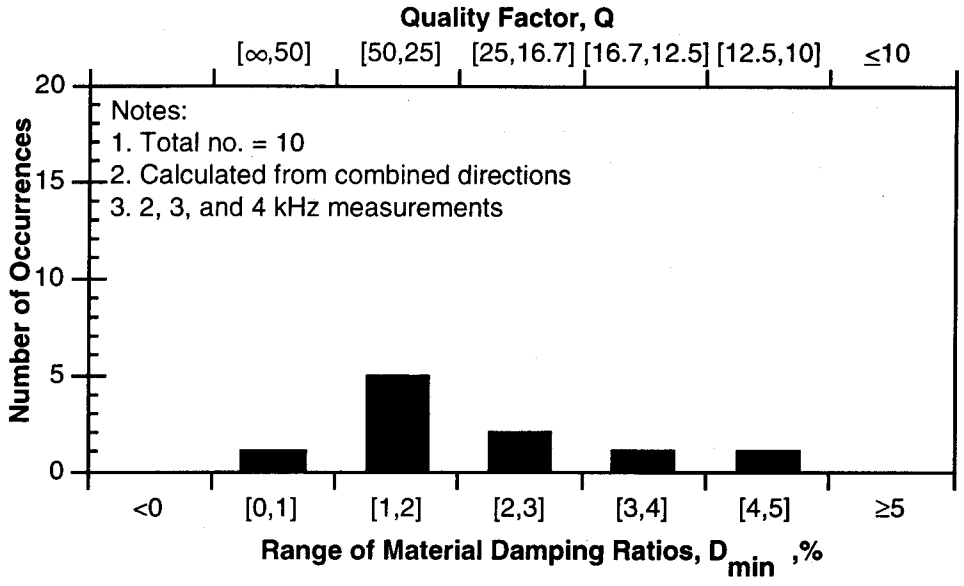

Figure 8.B.5-89
Histogram of material damping measurements for P-waves propagating in the vertical plane under a biaxial pressure of 21.4 psi.

8.B.5.6.5 Horizontal and Vertical P-Wave Planes Combined

Damping values in the vertical plane are presented in Fig. 8.B.5-90. These values are for the arrays that are either vertical or nearly vertical (within 30 degrees of vertical). From this figure, it can be noticed that the damping measurements scatter over a wide range. A trend of increasing damping with increasing stress is not observed, however.

The damping values measured in the vertical plane with arrays within 30 degrees of vertical are generally about the same as those in the horizontal plane, with the ratio ranging from 0.89 to 1.81. The damping values from both the horizontal and vertical planes are plotted in Fig. 8.B.5-91 (only arrays within 30 degrees of vertical are used in the vertical plane). These values fall within one standard deviation of each other. The average values obtained from the horizontal plane are about the same as those from the vertical plane. The horizontal plane is considered as the plane of isotropy, while the vertical plane shows stress-induced and structural anisotropy.

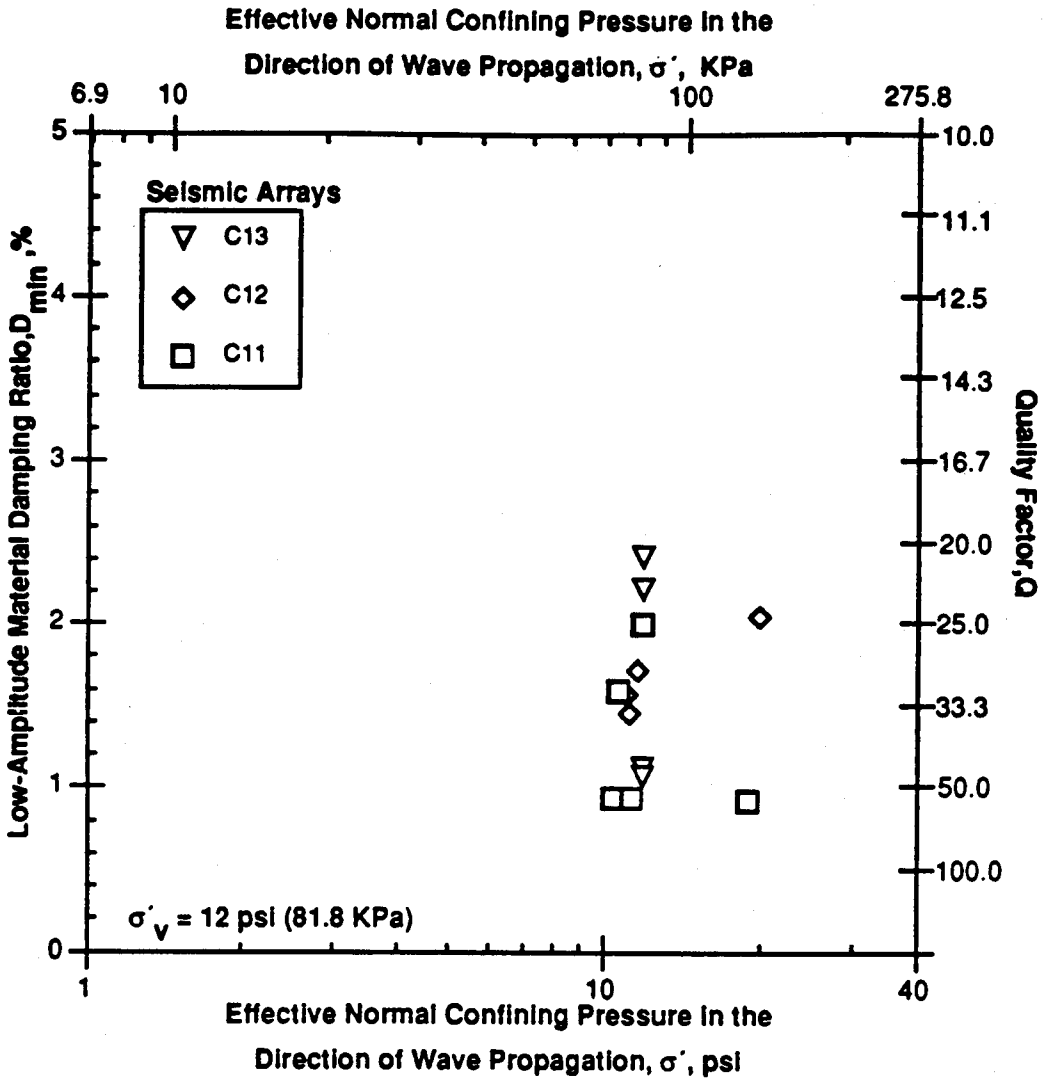

Notes:

1. Each data point represents the average of measurements at 2 or 3 frequencies (2000, 3000 and 4000 Hz were typically used).
2. Each data point was calculated using waves propagating in both the forward and reverse directions.
3. All measurements were made with accelerometer receivers.

Figure 8.B.5-90
Average values of material damping ratio from P-wave measurements along vertical or nearly vertical arrays (C11, C12 and C13) in the vertical plane during biaxial loading.

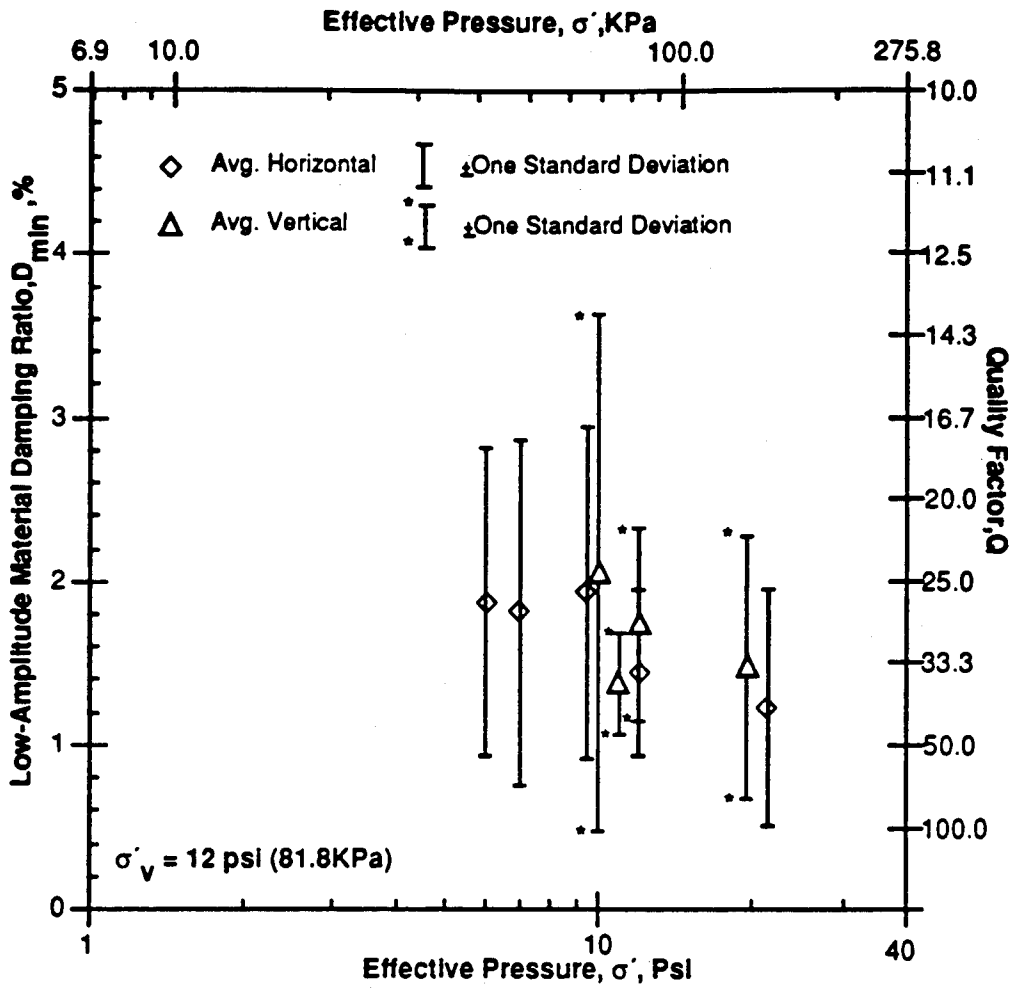

Figure 8.B.5-91
Average values of material damping ratio from all P-wave measurements in the vertical and horizontal planes during isotropic loading.

8.B.5.6.6 S-Wave Measurements

Five arrays of geophones for measurement of shear waves were installed in the LSTC (Figs. 8.B.5-15 and 8.B.5-16). One array was in the vertical plane (S5) for the measurement of vertically propagating SH-waves. Four arrays were in the horizontal plane. Two of these were for measurement of horizontally propagating SV-waves (S1 and S2) while the other two were for the measurement of horizontally propagating SH-waves (S3 and S4). The two arrays for the measurement of horizontally propagating SH-waves could not be utilized to obtain any data. So essentially only three arrays were available for the measurement of S-wave attenuation. The array notation for the shear waves has also been changed for ease of identification. The new notation is presented in Table 8.B.5-19.

Table 8.B.5-19
New Notation for Shear Wave Arrays

Original Array Notation (Fig. 8.B.5-15 and 8.B.5-16)	New Array Notation
Horizontal Plane	
SV3V3V4SV4	S1
SV5V5V6SV6V7	S2
SH3H3H4H5	S4
SH6H6H7SH7	S3
Vertical Plane	
SH1H1H2SH2	S5

Just like the case of P-waves, the same data reduction techniques were employed. Tables 8.B.5-20, 8.B.5-21 and 8.B.5-22 give the damping values obtained from S5, S1 and S2 Arrays, respectively. These tables show values for the forward, reverse and combined directions for each array at 1, 2, 3 and 4 kHz for each pressure. Similar to the P-wave damping measurements, values were not recorded if they were not within the established wavelength limits (a minimum of two wavelengths between the source and first receiver).

Average values for all damping measurements are presented in Table 8.B.5-23. Each value represents the average values of measurements at 1, 2, 3 and 4 kHz using waves propagating in both the forward and reverse directions. In these arrays since all the sources and receivers were geophones, damping values were calculated using only the middle two receivers so as maintain a consistency between the P- and S-wave results.

Table 8.B.5-20
Values of Material Damping in Shear for Forward, Reverse and Combined Directions Along Array S5 in the Vertical Plane for Biaxial Loading Conditions

Excitation Frequency	Confining Pressure, psi, (kPa)	D(%) Measured in Test Direction Forward	Reverse	Combined
2000 Hz	6 (41.4)	1.36	0.32	0.84
	7 (48.1)	1.45	0.55	1.00
	9.5 (65.3)	1.07	0.20	0.64
	12 (82.5)	2.12	2.02	2.07
	21.4 (147.1)	2.07	0.56	1.32
3000 Hz	6 (41.4)	0.51	0.32	1.32
	7 (48.1)	1.01	0.12	0.57
	9.5 (65.3)	1.00	0.85	0.93
	12 (82.5)	1.51	1.24	1.38
	21.4 (147.1)	0.89	0.31	0.6
4000 Hz	6 (41.4)	**	**	**
	7 (48.1)	*	*	*
	9.5 (65.3)	*	*	*
	12 (82.5)	**	**	**
	21.4 (147.1)	**	**	**

* One or both record(s) were missing or could not be interpreted.
** Damping value not calculated because outside established frequency limits.

Table 8.B.5-21
Values of Material Damping in Shear for Forward, Reverse and Combined Directions Along Array S1 in the Horizontal Plane for Biaxial Loading Conditions

Excitation Frequency	Confining Pressure, psi, (kPa)	D(%) Measured in Test Direction Forward	Reverse	Combined
2000 Hz	6 (41.4)	4.06	–1.48	1.3
	7 (48.1)	0.57	–1.36	–0.39
	9.5 (65.3)	0.37	–1.26	–0.45
	12 (82.5)	0.98	0.69	0.84
	21.4 (147.1)	–0.87	–0.47	–0.67
3000 Hz	6 (41.4)	–0.48	–0.09	–0.29
	7 (48.1)	–0.21	–0.45	–0.32
	9.5 (65.3)	–0.42	–0.60	–0.51
	12 (82.5)	0.15	0.33	0.24
	21.4 (147.1)	–1.16	–0.11	–0.64
4000 Hz	6 (41.4)	**	**	**
	7 (48.1)	*	*	*
	9.5 (65.3)	**	**	**
	12 (82.5)	**	**	**
	21.4 (147.1)	**	**	**

* One or both record(s) were missing or could not be interpreted.
** Damping value not calculated because outside established frequency limits.

Table 8.B.5-22
Values of Material Damping in Shear for Forward, Reverse and Combined Directions Along Array S2 in the Horizontal Plane for Biaxial Loading Conditions

Excitation Frequency	Confining Pressure, psi, (kPa)	D(%) Measured in Test Direction Forward	Reverse	Combined
2000 Hz	6 (41.4)	1.83	1.85	1.84
	7 (48.1)	2.29	2.15	2.22
	9.5 (65.3)	2.69	1.53	2.11
	12 (82.5)	2.09	1.43	1.76
	21.4 (147.1)	2.82	2.02	2.42
3000 Hz	6 (41.4)	1.07	0.98	1.03
	7 (48.1)	1.51	2.44	2.22
	9.5 (65.3)	1.59	0.23	0.91
	12 (82.5)	1.67	0.18	0.93
	21.4 (147.1)	2.05	0.65	1.35
4000 Hz	6 (41.4)	**	**	**
	7 (48.1)	**	**	**
	9.5 (65.3)	**	**	**
	12 (82.5)	**	**	**
	21.4 (147.1)	**	**	**

* One or both record(s) were missing or could not be interpreted.
** Damping value not calculated because outside established frequency limits.

Table 8.B.5-23
Average Values of Material Damping Ratios from SH-Waves and SV-Waves Propagating in the Horizontal and Vertical Planes Respectively During Biaxial Confinement

Pressure psi (KPa)	Material Damping Ratio, D_{min}, % Array Number S5 (Vertical Plane)	S1 (Horizontal Plane)	S2 (Horizontal Plane)	Average	Standard Deviation
6.0(41.4)	1.08	1.30	1.43	1.27	±0.18
7.0(48.1)	0.79	-*	2.10	1.45	±0.93
9.5(65.3)	0.79	-*	1.51	1.15	±0.51
12.0(82.5)	1.65	-*	1.35	1.50	±0.21
21.4(147.1)	0.96	-*	1.89	1.43	±0.66

*Unable to evaluate wave amplitudes at one or more receivers in these record.

Notes:

1. Each data point represents the average of measurements at 2 or 3 frequencies (2000, 3000 and 4000 Hz were typically used).
2. Each data point was calculated using waves propagating in both the forward and reverse directions.
3. All measurements were made with geophone receivers.

All data available in the horizontal and vertical planes have been combined because there are only three arrays available for S-waves. Additionally, this combination is reasonable because all of the shear waves create distortions in the vertical plane and therefore are similar waves (in contrast to a horizontally propagating SH-wave which creates distortions in the horizontal plane). The damping ratios vary from a maximum of 1.89% to a minimum of 0.79% as shown in Fig. 8.B.5-92 in which the values are simply plotted versus the effective horizontal stress. The average damping values vary from 1.50% to 1.15% as shown in Fig. 8.B.5-93. The standard deviation varies from 0.93 to 0.18, but for this limited data set the standard deviation does not mean a whole lot.

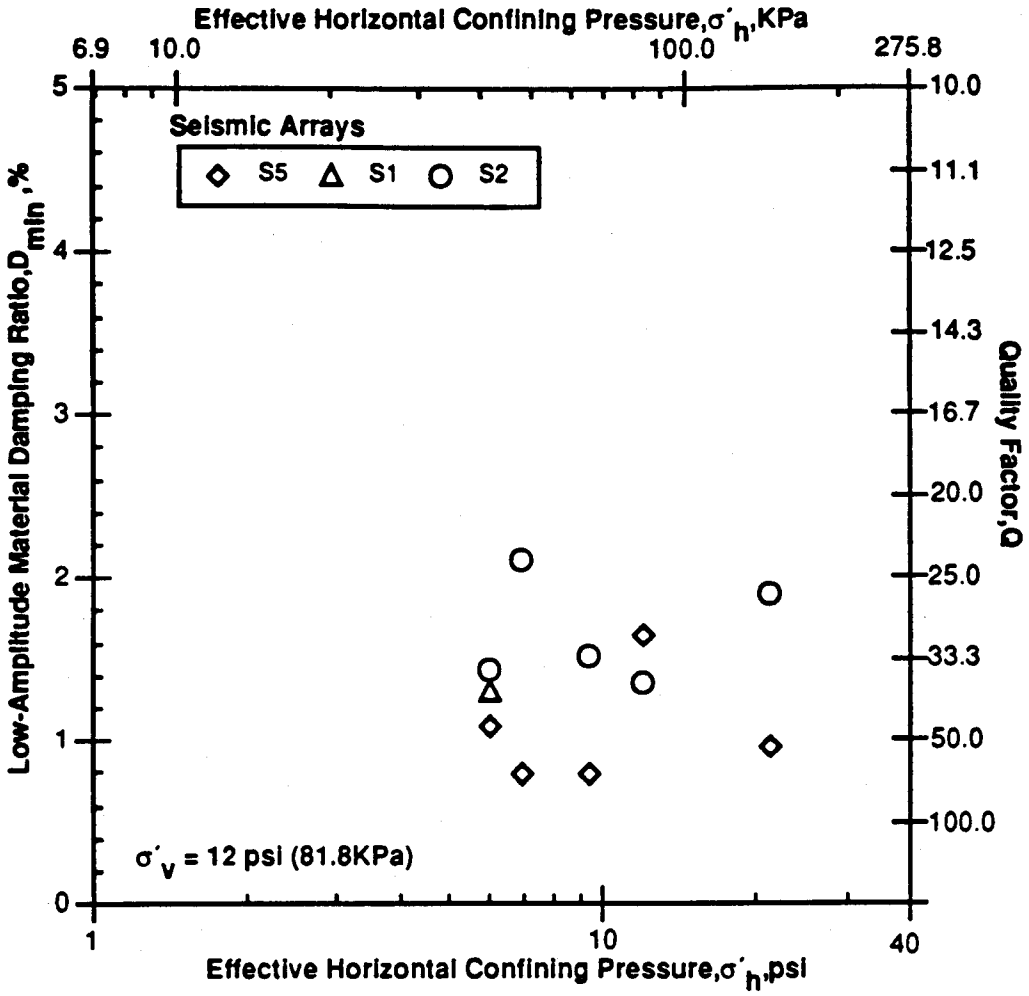

Notes:

1. Each data point represents the average of measurements at 2 or 3 frequencies (2000, 3000 and 4000 Hz were typically used).
2. Each data point was calculated using waves propagating in both the forward and reverse directions.
3. All measurements were made with geophone receivers.

Figure 8.B.5-92
Average values of material damping versus $\log \bar{\sigma}_{li}$ from SH- and SV-wave measurements along each seismic array in the vertical and horizontal planes during biaxial loading.

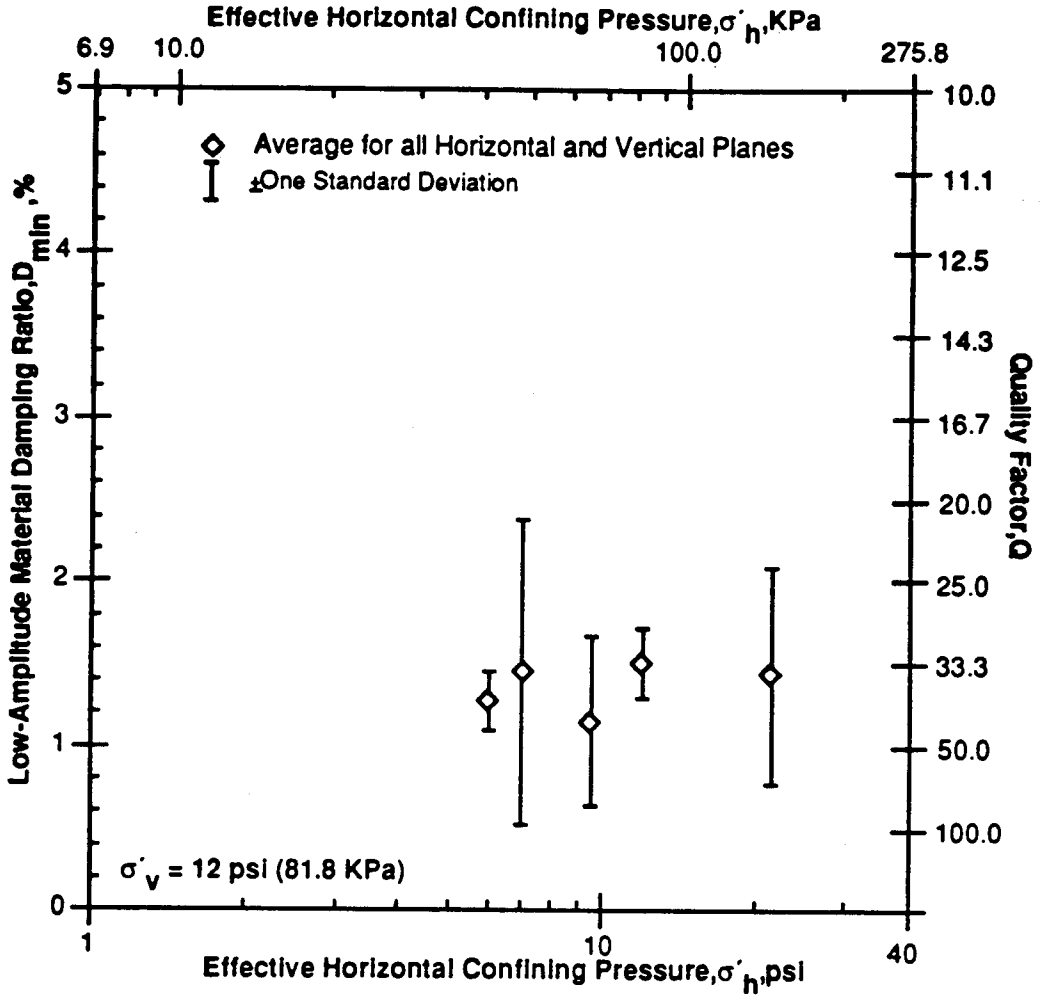

Notes:

1. Average measurements from all 3 instrumentation lines.
2. Each data point represents the average of measurements at 2 or 3 frequencies (2000, 3000 and 4000 Hz were typically used).
3. Each data point was calculated using waves propagating in both the forward and reverse directions.
4. All measurements were made with geophone receivers.

Figure 8.B.5-93
Average values of material damping ratio versus log $\overline{\sigma}_h$ from all SH- and SV-wave measurements in the vertical and horizontal planes during biaxial loading.

The trend in the damping should not be evaluated from Figs. 8.B.5-92 and 8.B.5-93. This is the case because the horizontal stress is not the only principal stress affecting these shear waves in biaxial loading. Shear waves are affected by the principal stress in the direction of wave propagation, σ'_a, and the principal stress in the direction of particle motion, σ'_b. A correct plot according to Lee (1986) is to use log

$$\sqrt{\sigma'_a \times \sigma'_b}$$

as shown in Fig. 8.B.5-94. The average damping values are then shown correctly plotted in Fig. 8.B.5-95. As seen in this figure damping seems to be essentially independent of confining pressure. However, the pressure range is so small that it is difficult to draw any firm conclusions. More importantly, the values are only slightly less than those found for the P-waves in this test series.

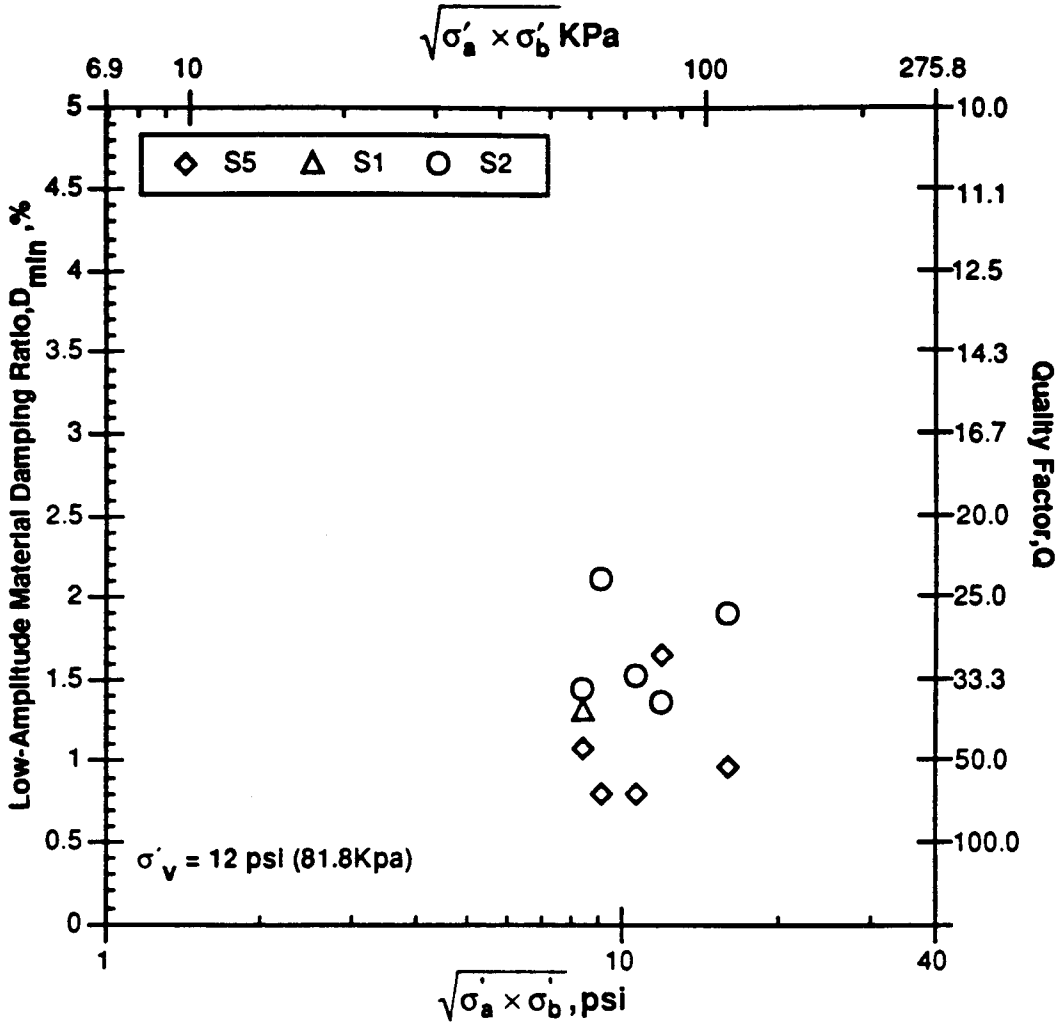

Figure 8.B.5-94

Average values of material damping versus $\log\sqrt{\sigma'_a \times \sigma'_b}$ from SH- and SV-wave measurements along each seismic array in the vertical and horizontal planes during biaxial loading.

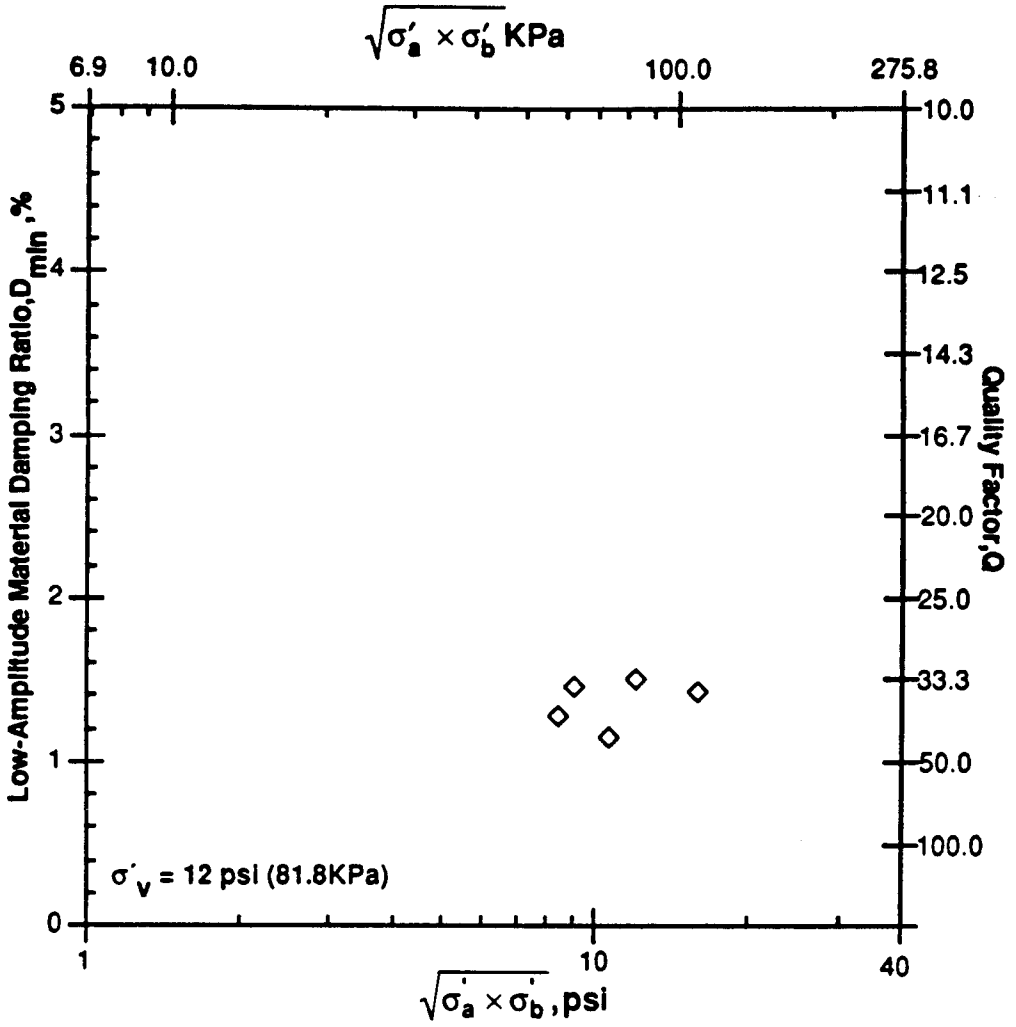

Figure 8.B.5-95

Average values of material damping ratio versus $\log\sqrt{\sigma'_a \times \sigma'_b}$ from all SH- and SV-wave measurements in the vertical and horizontal planes during biaxial loading.

The histograms representing the measurements in the forward, reverse and combined directions are shown in Figs. 8.B.5-96, 8.B.5-97 and 8.B.5-98, respectively. These also do not mean a lot as the number of measurements is quite small. They do show, however, the significant scatter in the measurements.

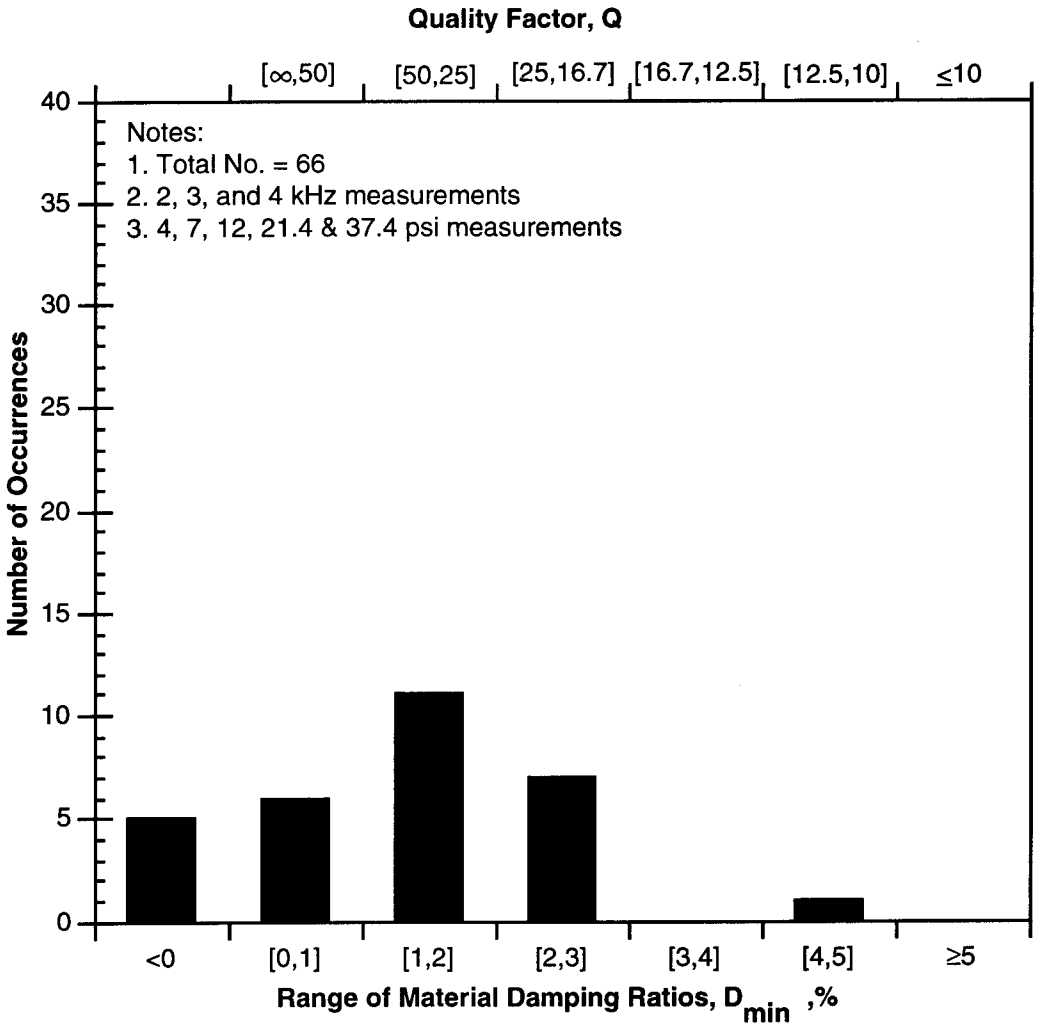

Figure 8.B.5-96
Histogram of all material damping measurements for SV- and SH-waves propagating in the forward direction in the horizontal and vertical planes during biaxial confinement.

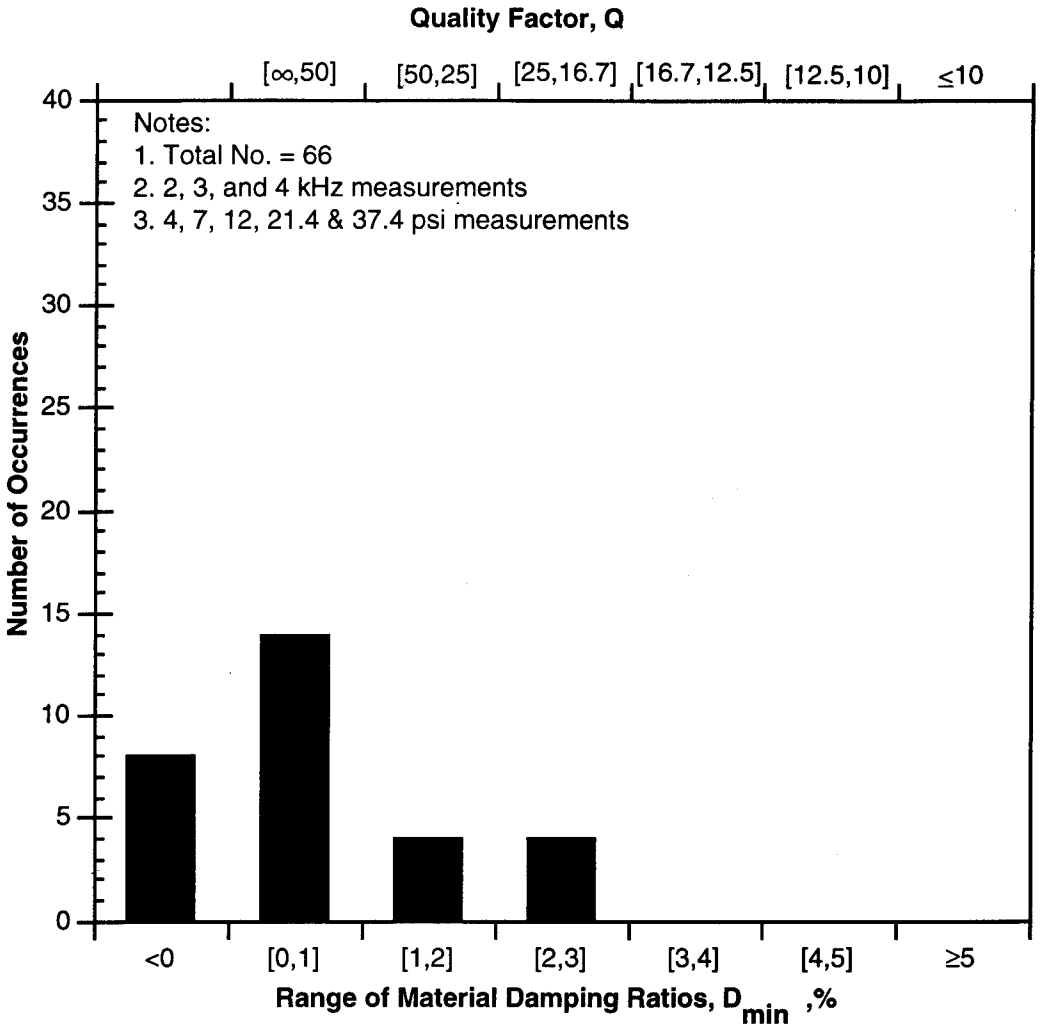

Figure 8.B.5-97
Histogram of all material damping measurements for SV- and SH-waves propagating in the reverse direction in the horizontal and vertical planes during biaxial confinement.

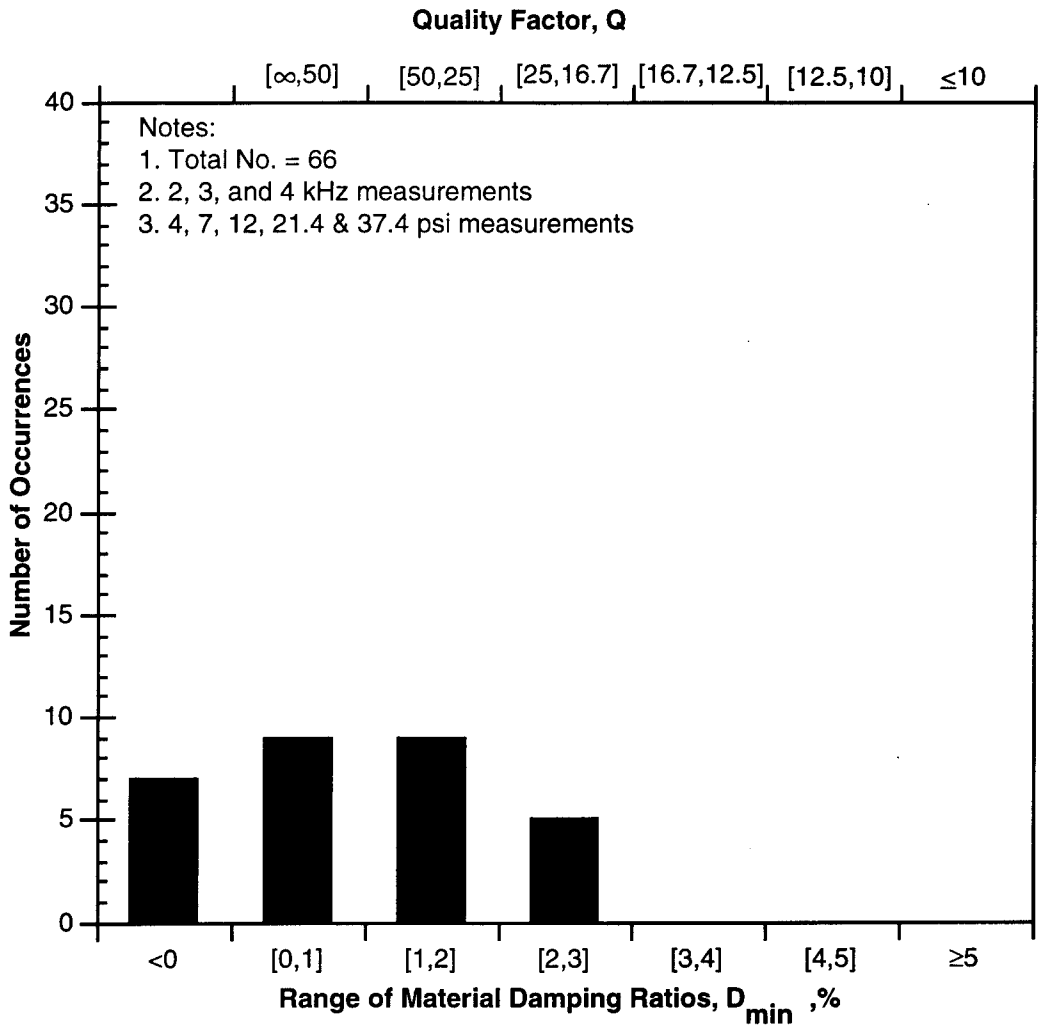

Figure 8.B.5-98
Histogram of all material damping measurements for SV- and SH-waves propagating in the horizontal and vertical planes during biaxial confinement in the combined directions.

8.B.5.6.7 Comparison of All Results

The average damping values obtained from both the compression wave planes and the shear wave planes are plotted in Fig. 8.B.5-99. It is evident that the damping measurements obtained from the shear wave planes are generally lower than those for the compression wave planes but are still within one standard deviation and exhibit the same trend. Compared to the resonant column tests, the damping measurements obtained from the LSTC are considerably higher. This could be due to the range of frequencies in the resonant column which was only up to a maximum of about 100 Hz. In the biaxial stress series only the horizontal P-wave damping measurements show an obvious trend of decreasing values with increasing confining pressures. This is most likely due to the small range of stress which occurred in the other tests.

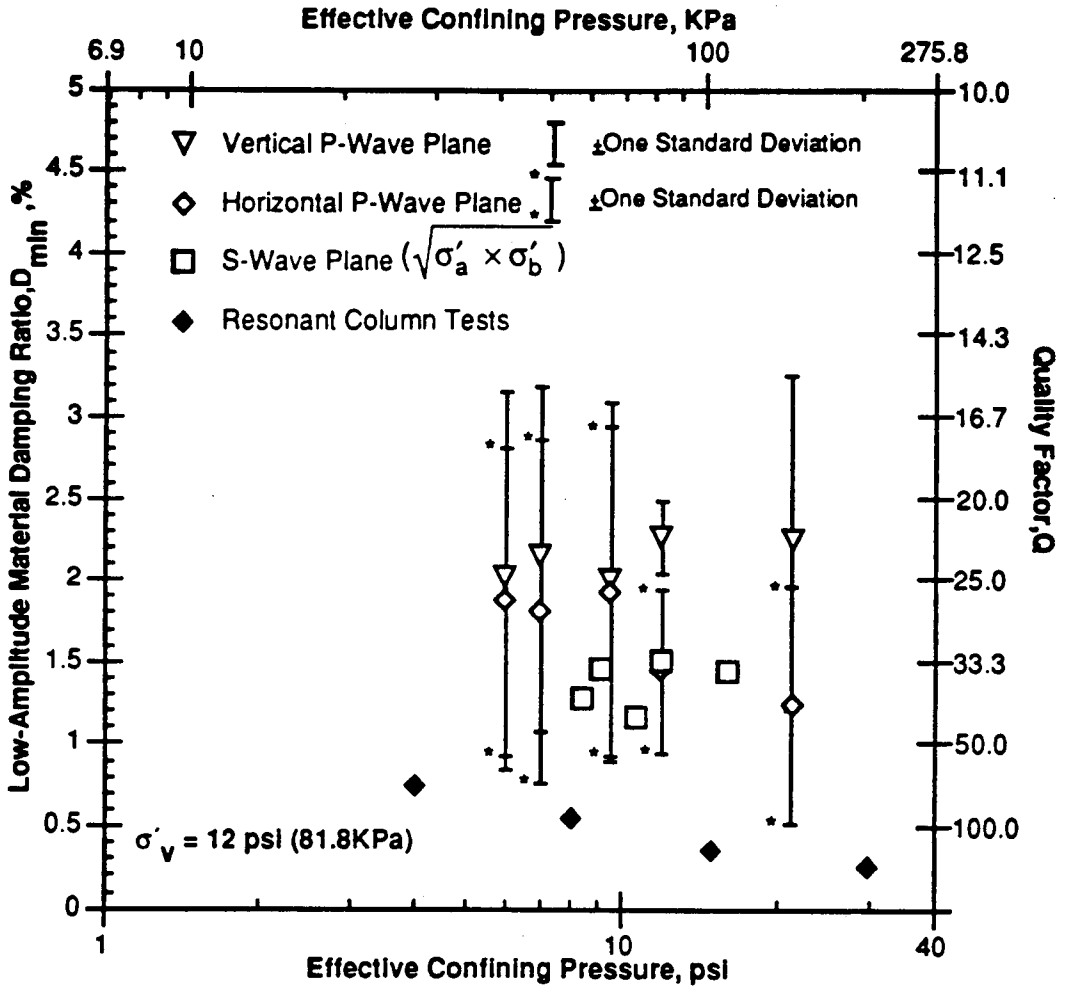

Figure 8.B.5-99
Average values of material damping from all P- and S-waves measured in the vertical and horizontal planes under biaxial confinement compared with results from torsional resonant column tests.

8.B.5.6.8 Conclusions

From the damping measurements, there again is a lot of scatter in the carefully controlled measurements. This scatter becomes more apparent when the directions of testing are kept separate; forward and reverse measurements. When the two directions are taken together and presented in combined form, the scatter is significantly reduced. The combined direction does a good job of reducing scatter probably because the scatter comes from the effects of the receivers and their interaction with the surrounding sand, which is minimized in the combined measurement. For the biaxial state of stress, there seems to be more scatter which could be attributed to the fact that the vertical plane is now a plane of anisotropy from both structural and stress-induced contributions.

7—SUMMARY AND CONCLUSIONS

8.B.5.7.1 Summary

A comprehensive study of material damping measurements of soils at small strains was carried out. This work was performed using seismic records generated in an experimental study by Lee (1993). He performed compression and shear wave measurements in dry sand confined under isotropic and anistropic conditions. Lee's work concentrated on wave velocities, and the influence of structural and stress-induced anisotropy on these velocities. These records were, therefore, available for additional evaluations of material damping in the soil skeleton under isotropic and biaxial loading conditions.

In this study, many more compression wave records than shear wave records were analyzed. This happened because Lee's work involved mostly compression wave measurements. As a result, the emphasis in this work has been placed on P-wave attenuation.

8.B.5.7.2 Conclusions

This study can be divided into two parts. The first part had to do with investigating wave attenuation measurements performed in the laboratory under carefully controlled conditions. Conclusions from this part of the study can be summarized as follows.

1. For material damping measurements using the spectral ratio method, a wide range in scatter occurred if measurements were performed using a linear source-receiver array and propagating waves in only one direction. For instance, if the material damping ratio is actually 1.7%, it would not be unusual to measure damping ratios ranging from about –0.5% to 3.7%.
2. Scatter in the damping values reduced considerably when material damping values for combined directions (forward and reverse arrays) were calculated. For instance, if the material damping ratio is actually 1.7%, it would not be unusual to measure damping ratios ranging from 1.0% to 2.4%.
3. By calculating material damping from the combined directions, the scatter in damping was most probably reduced because of a reduction in the effects of individual receivers and their interaction with the surrounding sand.

The second part of the study was concerned with the actual values of material damping measured in the dry sand. This part of the study can be subdivided into two parts; the first dealing with measurements under isotropic states of a stress and the second dealing with measurements under biaxial states of stress. The conclusions from this work are as follows.

Under isotropic states of stress ranging from 4 to 37.4 psi (27.5 to 257.1 KPa):

1. Average damping ratios for compression waves measured in the horizontal plane in dry sand ranged from 2.2% to 1.3%. There was a general decrease in damping with increase in isotropic stress. Also, it should be noted that, based on the work of Lee (1993), the horizontal plane under isotropic loading is a plane of isotropy.
2. The damping measurements from compression in the vertical plane under isotropic stress conditions were slightly higher than those measured in the horizontal plane. These values ranged from 2.9% to 1.5% and also exhibited a general decrease with increasing pressure. Based on the work by Lee (1993), the vertical plane is an anisotropic plane under isotropic loading due to structural anisotropy.
3. Values of material damping for shear waves were only measured for waves creating distortions in the vertical plane. Values of material damping for these waves were less than for the compression waves and ranged from 1.5% to 0.9%. Material damping in shear exhibited a general decrease in value with increasing pressure similar to that observed with the P-waves.

4. Material damping values in the sand in the LSTC averaged about 1% to 2% above material damping measurements in the torsional resonant column. In other words, at an isotropic pressure of 4 psi (27.5 KPa), damping in compression and shear ranged from about 1.3% to 2.9% while material damping from the torsional resonant column was about 0.7%. The seismic measurements in the LSTC were performed in the frequency range of 1 kHz to 4 kHz. On the other hand, the torsional resonant column tests were conducted at frequencies less than 100 Hz. Frequency may be the reason for the difference in damping ratios measured by the two methods.

Under biaxial states of stress with σ_v' = constant = 12 psi (82.5 KPa and $\sigma_{h1} = \sigma_{h2}$ and varying from 4 to 21.4 psi (27.5 to 147.1 KPa):

1. Material damping values calculated for the horizontal plane for the biaxial stress condition were within the same range as those obtained from the horizontal plane during isotropic loading. These values ranged from 1.9% to 1.2% under the anistropic stress states and exhibited a general decrease with increasing in pressure. As in the case of isotropic loading, the horizontal plane is a plane of isotropy under this type of biaxial loading.
2. Damping ratios for compression waves measured in the vertical plane in dry sand ranged from 2.1% to 1.4%. There was a general decrease in damping with increase in normal stress. The vertical plane is an anisotropic plane under the this type of biaxial loading.
3. Values of material damping of shear waves for the biaxial stress condition were only measured for waves creating distortions in the vertical plane. Values of material damping for these waves were less than for the compression waves and ranged from 1.5% to 1.1%. A general decrease with increasing stress state was also observed with the shear waves.
4. Damping values measured in the sand averaged about 1% to 2.2% above material damping measurements in the torsional resonant column, just as observed in the isotropic loading tests.
5. On the whole, values of material damping calculated under the biaxial state of stress were comparable to those values measured in the isotropic loading tests.

APPENDIX 8.B.5.A
TYPICAL DATA REDUCTION FORMS

BOX # DISK # PAGE#

Confining pressure psi	Frequency Hz						
		mV	mV	mV	mV	mV	mV
	4000						
	3000						
	2000						
	1000						
	500						
	250						
	250						
	500						
	1000						
	2000						
	3000						
	4000						

Figure 8.B.5.A-1
Typical data reduction form #1.

Confining Pressure:
Line Type:

Frequency (Hz)	Velocity (Ft/Sec)	Damping, D,%		
		R1–R2	R1–R3	R2–R3

WAVES PROPAGATING IN ONE DIRECTION

FORWARD DIRECTION				
500				
1000				
2000				
3000				
4000				
Average Damping				

REVERSE DIRECTION				
500				
1000				
2000				
3000				
4000				
Average Damping				

WAVES PROPAGATING IN BOTH DIRECTIONS

Frequency (Hz)	Velocity (Ft/Sec)	Damping (Both Directions), D,%		
		R1–R2	R1–R3	R2–R3
500				
1000				
2000				
3000				
4000				
Average Damping				

Figure 8.B.5.A-2
Typical data form #2.

APPENDIX 8.B.5.B
MATERIAL DAMPING IN COMPRESSION FOR MEASUREMENTS IN THE HORIZONTAL PLANE UNDER ISOTROPIC LOADING CONDITIONS

Table 8.B.5.B-1
Values of Material Damping in Compression for Forward, Reverse and Combined Directions Along Array C1 in the Horizontal Plane for Isotropic Loading Conditions

Excitation Frequency	Confining Pressure, psi, (kPa)	D(%) Measured in Test Direction Forward	Reverse	Combined
2000 Hz	4 (27.5)	1.46	1.38	1.42
	7 (48.1)	*	*	*
	12 (82.5)	1.31	0.99	1.15
	21.4 (147.1)	3.15	2.74	2.95
	37.4 (257.1)	*	*	*
3000 Hz	4 (27.5)	1.05	1.26	1.16
	7 (48.1)	*	*	*
	12 (82.5)	0.99	1.09	1.04
	21.4 (147.1)	1.08	0.58	0.83
	37.4 (257.1)	*	*	*
4000 Hz	4 (27.5)	1.80	1.98	1.89
	7 (48.1)	*	*	*
	12 (82.5)	0.83	0.60	0.72
	21.4 (147.1)	0.94	0.23	0.59
	37.4 (257.1)	*	*	*

* One or both record(s) were missing or could not be interpreted.
** Damping value not calculated because outside established wavelength limits.

Table 8.B.5.B-2
Values of Material Damping In Compression for Forward, Reverse and Combined Directions Along Array C2 in the Horizontal Plane for Isotropic Loading Conditions

Excitation Frequency	Confining Pressure, psi, (kPa)	D(%) Measured in Test Direction Forward	Reverse	Combined
2000 Hz	4 (27.5)	0.71	3.20	1.96
	7 (48.1)	3.34	2.15	2.75
	12 (82.5)	**	**	**
	21.4 (147.1)	**	**	**
	37.4 (257.1)	**	**	**
3000 Hz	4 (27.5)	0.64	2.48	1.56
	7 (48.1)	1.25	1.01	1.13
	12 (82.5)	0.56	1.89	1.23
	21.4 (147.1)	–0.68	1.18	0.31
	37.4 (257.1)	0.78	1.68	1.23
4000 Hz	4 (27.5)	0.96	2.19	1.58
	7 (48.1)	1.83	1.69	1.76
	12 (82.5)	0.80	1.82	1.31
	21.4 (147.1)	–0.36	0.90	0.30
	37.4 (257.1)	0.58	1.04	0.81

* One or both record(s) were missing or could not be interpreted.
** Damping value not calculated because outside established wavelength limits.

Table 8.B.5.B-3
Values of Material Damping In Compression for Forward, Reverse and Combined Directions Along Array C3 in the Horizontal Plane for Isotropic Loading Conditions

Excitation Frequency	Confining Pressure, psi, (kPa)	D(%) Measured in Test Direction Forward	Reverse	Combined
2000 Hz	4 (27.5)	*	*	*
	7 (48.1)	*	*	*
	12 (82.5)	*	*	*
	21.4 (147.1)	0.62	–1.70	–0.57
	37.4 (257.1)	*	*	*
3000 Hz	4 (27.5)	*	*	*
	7 (48.1)	*	*	*
	12 (82.5)	*	*	*
	21.4 (147.1)	1.11	0.00	0.53
	37.4 (257.1)	5.01	–1.03	1.98
4000 Hz	4 (27.5)	*	*	*
	7 (48.1)	*	*	*
	12 (82.5)	*	*	*
	21.4 (147.1)	1.33	0.00	0.74
	37.4 (257.1)	5.10	–1.40	1.86

* One or both record(s) were missing or could not be interpreted.
** Damping value not calculated because outside established wavelength limits.

Table 8.B.5.B-4
Values of Material Damping in Compression for Forward, Reverse and Combined Directions Along Array C4 in the Horizontal Plane for Isotropic Loading Conditions

Excitation Frequency	Confining Pressure, psi, (kPa)	D(%) Measured in Test Direction Forward	Reverse	Combined
2000 Hz	4 (27.5)	2.19	2.70	2.45
	7 (48.1)	2.87	4.66	3.77
	12 (82.5)	4.46	1.99	3.23
	21.4 (147.1)	*	*	*
	37.4 (257.1)	*	*	*
3000 Hz	4 (27.5)	2.41	3.11	2.76
	7 (48.1)	–2.87	–1.66	–2.27
	12 (82.5)	0.62	1.59	1.11
	21.4 (147.1)	*	*	*
	37.4 (257.1)	*	*	*
4000 Hz	4 (27.5)	2.21	2.18	2.20
	7 (48.1)	0.27	3.61	1.94
	12 (82.5)	2.41	1.12	1.77
	21.4 (147.1)	*	*	*
	37.4 (257.1)	*	*	*

* One or both record(s) were missing or could not be interpreted.
** Damping value not calculated because outside established wavelength limits.

Table 8.B.5.B-5
Values of Material Damping in Compression for Forward, Reverse and Combined Directions Along Array C5 in the Horizontal Plane for Isotropic Loading Conditions

Excitation Frequency	Confining Pressure, psi, (kPa)	D(%) Measured in Test Direction Forward	Reverse	Combined
2000 Hz	4 (27.5)	2.97	2.09	2.54
	7 (48.1)	*	*	*
	12 (82.5)	1.17	2.09	1.60
	21.4 (147.1)	**	**	**
	37.4 (257.1)	*	*	*
3000 Hz	4 (27.5)	1.95	1.05	1.51
	7 (48.1)	*	*	*
	12 (82.5)	1.57	1.45	1.51
	21.4 (147.1)	–0.28	3.83	1.86
	37.4 (257.1)	*	*	*
4000 Hz	4 (27.5)	1.53	1.25	1.39
	7 (48.1)	*	*	*
	12 (82.5)	1.36	1.79	1.57
	21.4 (147.1)	–1.62	2.43	0.45
	37.4 (257.1)	*	*	*

* One or both record(s) were missing or could not be interpreted.
** Damping value not calculated because outside established wavelength limits.

Table 8.B.5.B-6
Values of Material Damping in Compression for Forward, Reverse and Combined Directions Along Array C6 in the Horizontal Plane for Isotropic Loading Conditions

Excitation Frequency	Confining Pressure, psi, (kPa)	D(%) Measured in Test Direction Forward	Reverse	Combined
2000 Hz	4 (27.5)	2.66	3.39	3.02
	7 (48.1)	0.97	2.16	1.55
	12 (82.5)	3.79	1.55	2.62
	21.4 (147.1)	**	**	**
	37.4 (257.1)	**	**	**
3000 Hz	4 (27.5)	1.30	3.10	2.16
	7 (48.1)	–1.63	4.53	1.37
	12 (82.5)	3.71	3.83	3.77
	21.4 (147.1)	0.44	2.15	1.29
	37.4 (257.1)	1.06	1.66	1.36
4000 Hz	4 (27.5)	1.81	1.80	1.81
	7 (48.1)	0.98	2.39	1.67
	12 (82.5)	0.19	2.82	1.47
	21.4 (147.1)	2.15	2.17	2.16
	37.4 (257.1)	–0.61	4.21	1.75

* One or both record(s) were missing or could not be interpreted.
** Damping value not calculated because outside established wavelength limits.

Table 8.B.5.B-7
Values of Material Damping in Compression for Forward, Reverse and Combined Directions Along Array C7 in The Horizontal Plane for Isotropic Loading Conditions

Excitation Frequency	Confining Pressure, psi, (kPa)	D(%) Measured in Test Direction Forward	Reverse	Combined
2000 Hz	4 (27.5)	5.80	3.40	4.6
	7 (48.1)	*	*	*
	12 (82.5)	4.30	0.10	2.20
	21.4 (147.1)	2.90	0.49	1.73
	37.4 (257.1)	**	**	**
3000 Hz	4 (27.5)	0.35	4.66	2.50
	7 (48.1)	*	*	*
	12 (82.5)	0.76	1.32	1.04
	21.4 (147.1)	3.08	1.24	2.11
	37.4 (257.1)	1.33	1.87	1.60
4000 Hz	4 (27.5)	4.48	3.28	3.88
	7 (48.1)	*	*	*
	12 (82.5)	2.69	1.64	2.17
	21.4 (147.1)	**	2.21	**
	37.4 (257.1)	2.92	2.34	2.63

* One or both record(s) were missing or could not be interpreted.
** Damping value not calculated because outside established wavelength limits.

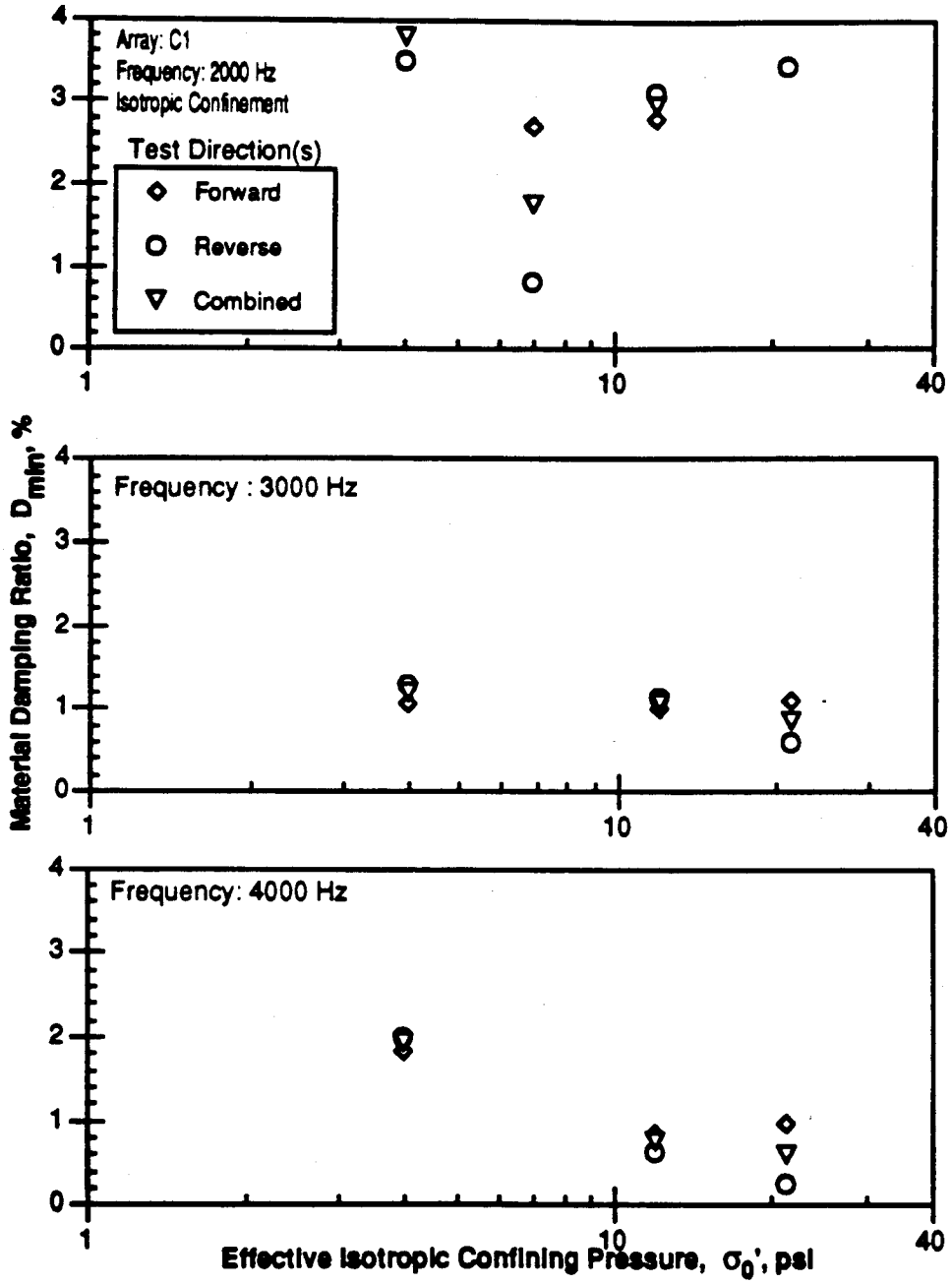

Figure 8.B.5.B-1
Material damping measurements in compression for forward, reverse and combined directions along array C1 in the horizontal plane during isotropic loading.

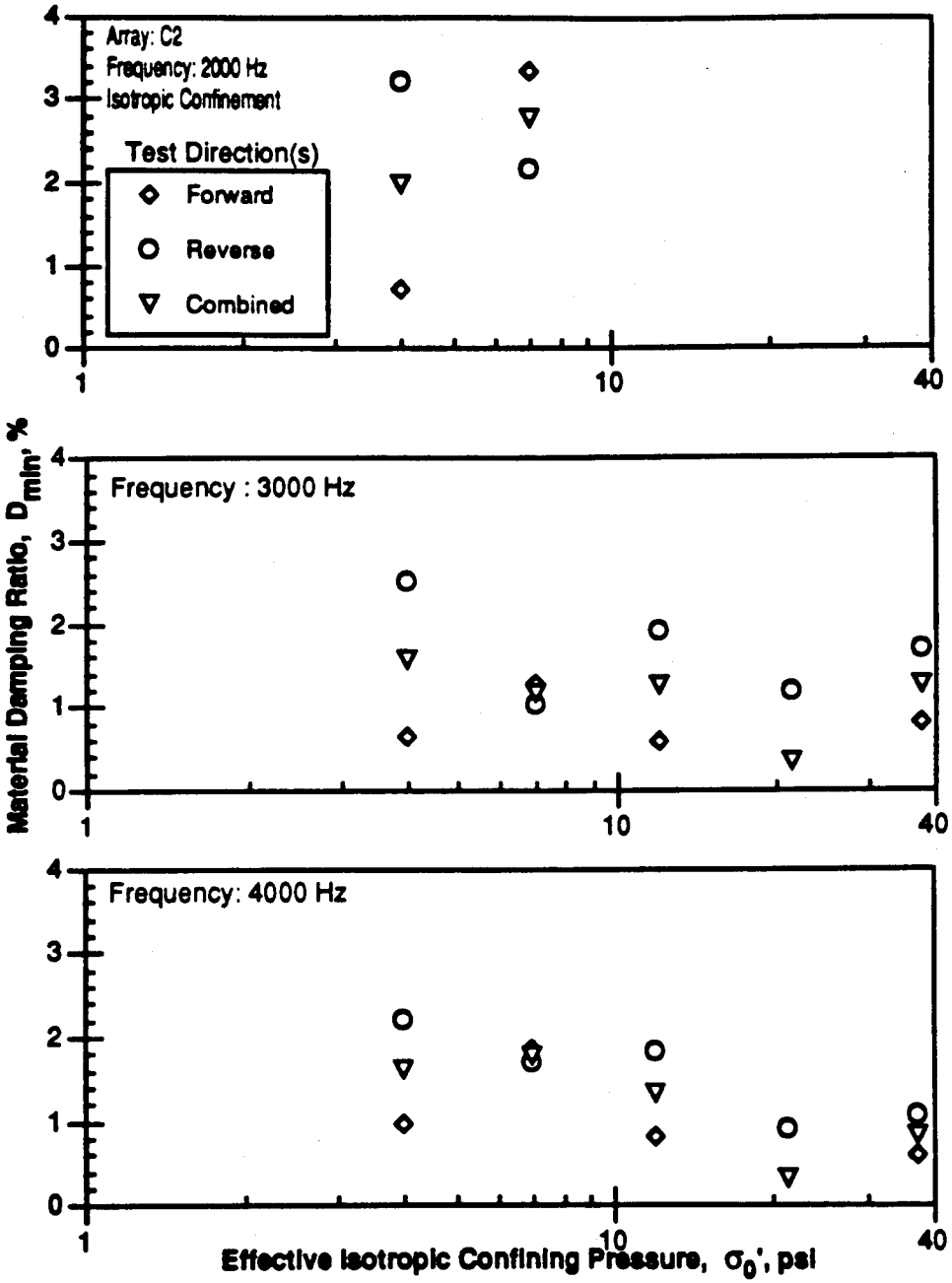

Figure 8.B.5.B-2
Material damping measurements in compression for forward, reverse and combined directions along array C2 in the horizontal plane during isotropic loading.

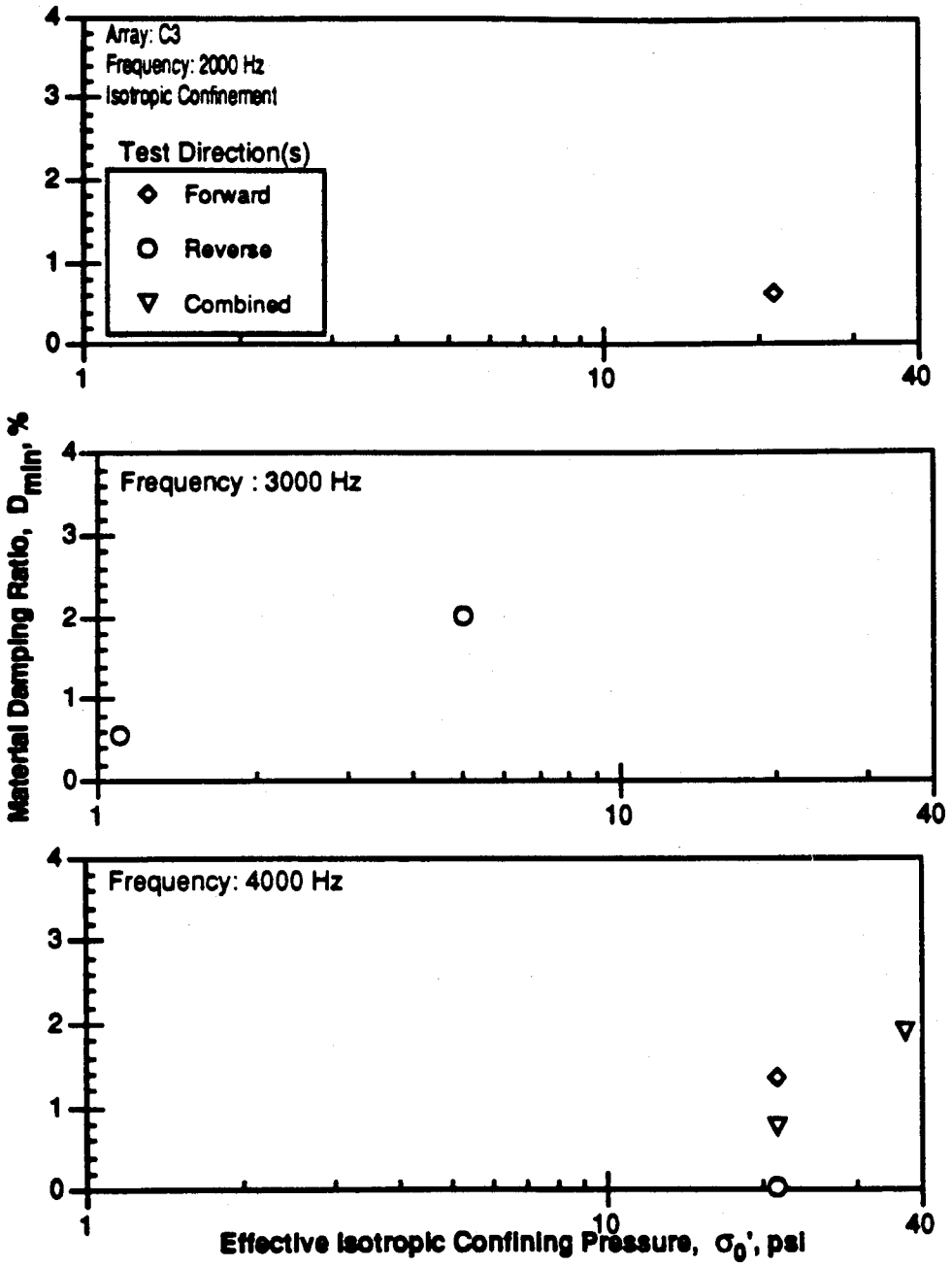

Figure 8.B.5.B-3
Material damping measurements in compression for forward, reverse and combined directions along array C3 in the vertical plane during isotropic loading.

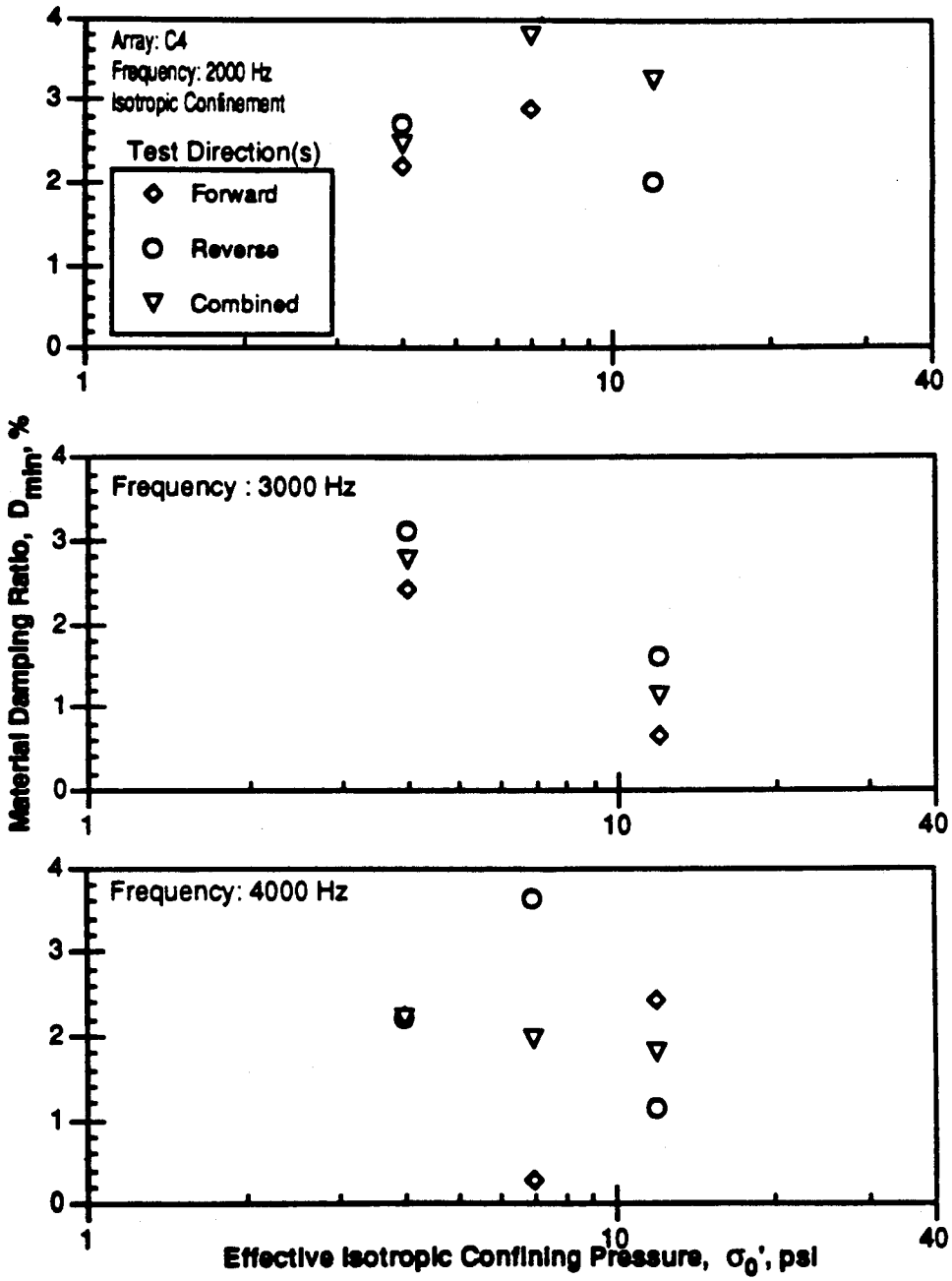

Figure 8.B.5.B-4
Material damping measurements in compression for forward, reverse and combined directions along array C4 in the horizontal plane during isotropic loading.

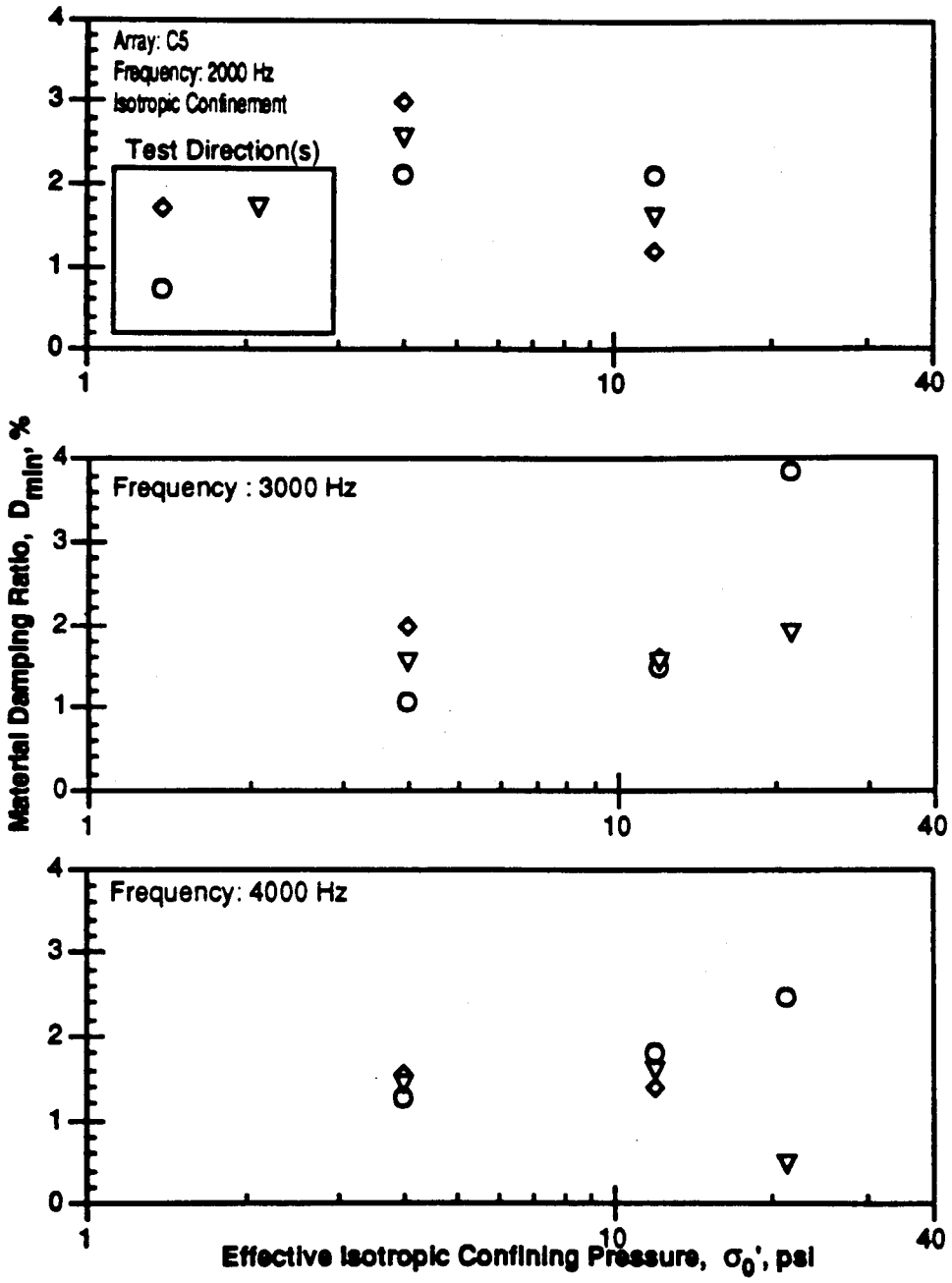

Figure 8.B.5.B-5
Material damping measurements in compression for forward, reverse and combined directions along array C5 in the horizontal plane during isotropic loading.

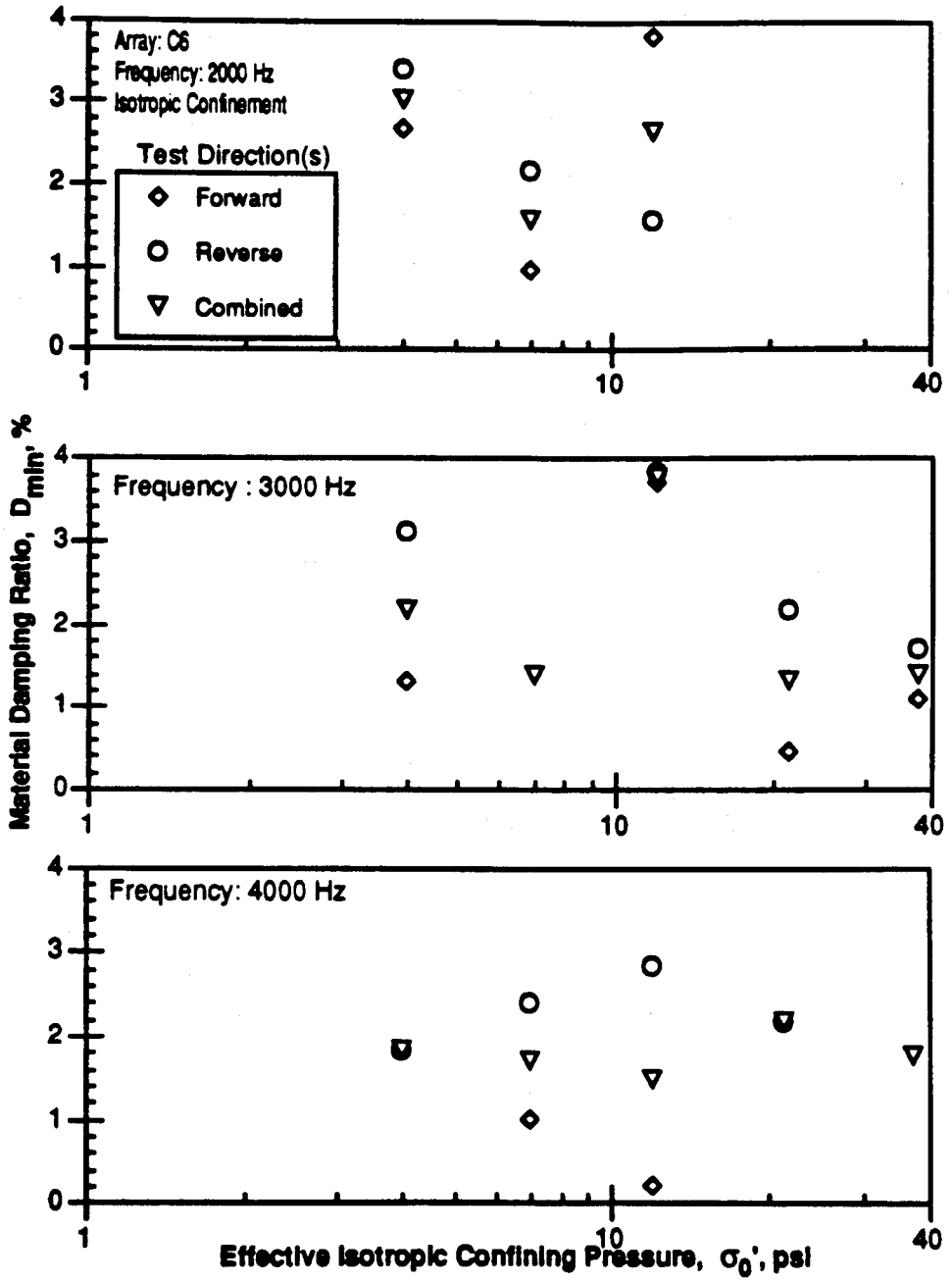

Figure 8.B.5.B-6
Material damping measurements in compression for forward, reverse and combined directions along array C6 in the horizontal plane during isotropic loading.

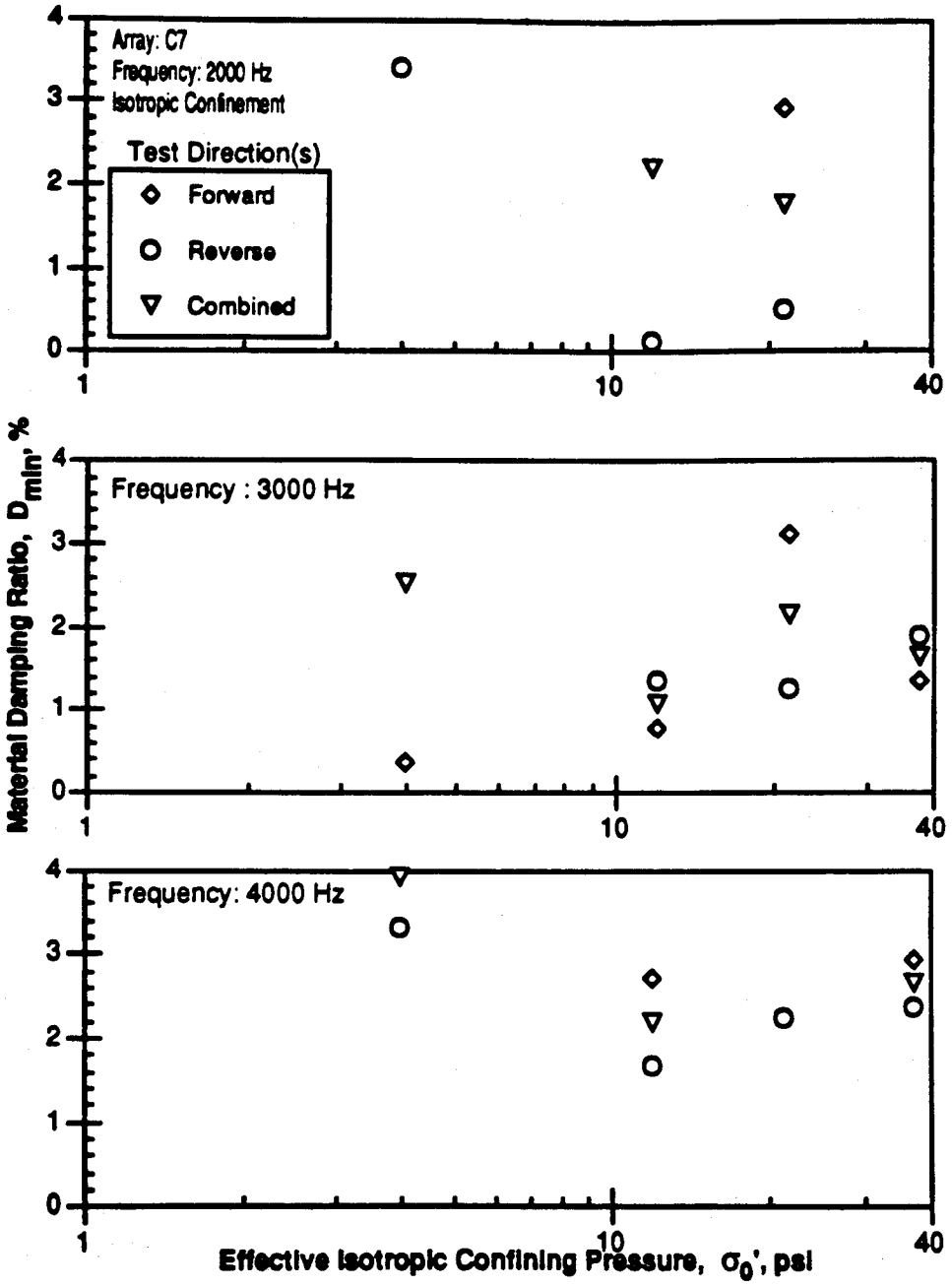

Figure 8.B.5.B-7
Material damping measurements in compression for forward, reverse and combined directions along array C7 in the horizontal plane during isotropic loading.

APPENDIX 8.B.5.C
MATERIAL DAMPING IN COMPRESSION FOR MEASUREMENTS IN THE VERTICAL PLANE UNDER ISOTROPIC LOADING CONDITIONS

Table 8.B.5.C-1
Values of Material Damping in Compression for Forward, Reverse and Combined Directions Along Array C7 in the Vertical Plane for Isotropic Loading Conditions

Excitation Frequency	Confining Pressure, psi, (kPa)	D(%) Measured in Test Direction Forward	Reverse	Combined
2000 Hz	4 (27.5)	5.80	3.40	4.6
	7 (48.1)	*	*	*
	12 (82.5)	4.30	0.10	2.20
	21.4 (147.1)	2.90	0.49	1.73
	37.4 (257.1)	**	**	**
3000 Hz	4 (27.5)	0.35	4.66	2.50
	7 (48.1)	*	*	*
	12 (82.5)	0.76	1.32	1.04
	21.4 (147.1)	3.08	1.24	2.11
	37.4 (257.1)	1.33	1.87	1.60
4000 Hz	4 (27.5)	4.48	3.28	3.88
	7 (48.1)	*	*	*
	12 (82.5)	2.69	1.64	2.17
	21.4 (147.1)	**	2.21	**
	37.4 (257.1)	2.92	2.34	2.63

* One or both record(s) were missing or could not be interpreted.
** Damping value not calculated because outside established wavelength limits.

Table 8.B.5.C-2
Values of Material Damping in Compression for Forward, Reverse and Combined Directions Along Array C8 in the Vertical Plane for Isotropic Loading Conditions

Excitation Frequency	Confining Pressure, psi, (kPa)	D(%) Measured in Test Direction Forward	Reverse	Combined
2000 Hz	4 (27.5)	3.37	5.17	4.27
	7 (48.1)	*	*	*
	12 (82.5)	3.36	–2.10	0.54
	21.4 (147.1)	**	**	**
	37.4 (257.1)	**	**	**
3000 Hz	4 (27.5)	3.06	2.06	2.56
	7 (48.1)	*	*	*
	12 (82.5)	2.12	1.20	1.66
	21.4 (147.1)	2.42	3.01	2.76
	37.4 (257.1)	1.93	2.51	2.22
4000 Hz	4 (27.5)	2.81	1.04	1.93
	7 (48.1)	*	*	*
	12 (82.5)	2.02	2.21	2.11
	21.4 (147.1)	2.10	1.79	1.95
	37.4 (257.1)	2.11	2.77	2.44

* One or both record(s) were missing or could not be interpreted.
** Damping value not calculated because outside established wavelength limits.

Table 8.B.5.C-3
Values of Material Damping in Compression for Forward, Reverse and Combined Directions Along Array C9 in the Vertical Plane for Isotropic Loading Conditions

Excitation Frequency	Confining Pressure, psi, (kPa)	D(%) Measured in Test Direction Forward	Reverse	Combined
2000 Hz	4 (27.5)	2.37	*	**
	7 (48.1)	*	*	*
	12 (82.5)	*	*	*
	21.4 (147.1)	*	*	*
	37.4 (257.1)	**	**	**
3000 Hz	4 (27.5)	2.04	*	**
	7 (48.1)	*	*	*
	12 (82.5)	*	*	*
	21.4 (147.1)	*	*	*
	37.4 (257.1)	2.71	2.51	2.61
4000 Hz	4 (27.5)	0.78	*	**
	7 (48.1)	*	*	*
	12 (82.5)	*	*	*
	21.4 (147.1)	*	*	*
	37.4 (257.1)	0.82	1.03	0.93

* One or both record(s) were missing or could not be interpreted.
** Damping value not calculated because outside established wavelength limits.

Table 8.B.5.C-4
Values of Material Damping in Compression for Forward, Reverse and Combined Directions Along Array C10 in the Vertical Plane for Isotropic Loading Conditions

Excitation Frequency	Confining Pressure, psi, (kPa)	D(%) Measured in Test Direction Forward	Reverse	Combined
2000 Hz	4 (27.5)	2.73	3.33	3.03
	7 (48.1)	2.09	2.26	2.18
	12 (82.5)	–2.91	9.48	3.39
	21.4 (147.1)	**	**	**
	37.4 (257.1)	**	**	**
3000 Hz	4 (27.5)	2.12	2.57	2.35
	7 (48.1)	2.14	1.08	1.61
	12 (82.5)	–2.27	6.16	2.03
	21.4 (147.1)	1.96	1.90	1.93
	37.4 (257.1)	1.93	2.17	2.05
4000 Hz	4 (27.5)	2.70	1.70	2.20
	7 (48.1)	2.51	2.52	2.52
	12 (82.5)	–0.45	3.67	1.69
	21.4 (147.1)	2.48	1.42	1.95
	37.4 (257.1)	1.49	1.87	1.49

* One or both record(s) were missing or could not be interpreted.
** Damping value not calculated because outside established wavelength limits.

Table 8.B.5.C-5
Values of Material Damping in Compression for Forward, Reverse and Combined Directions Along Array C11 in the Vertical Plane for Isotropic Loading Conditions

Excitation Frequency	Confining Pressure, psi, (kPa)	D(%) Measured in Test Direction Forward	Reverse	Combined
2000 Hz	4 (27.5)	5.53	–0.70	2.26
	7 (48.1)	6.26	–3.69	1.27
	12 (82.5)	14.32	–9.43	1.71
	21.4 (147.1)	6.37	–1.68	1.97
	37.4 (257.1)	**	**	**
3000 Hz	4 (27.5)	1.32	2.12	1.72
	7 (48.1)	0.59	1.25	0.92
	12 (82.5)	3.76	0.45	1.98
	21.4 (147.1)	1.72	0.26	0.99
	37.4 (257.1)	4.71	–1.68	1.68
4000 Hz	4 (27.5)	1.45	1.54	1.50
	7 (48.1)	0.93	*	**
	12 (82.5)	2.27	*	**
	21.4 (147.1)	–1.39	2.25	0.54
	37.4 (257.1)	–0.41	2.33	0.92

* One or both record(s) were missing or could not be interpreted.
** Damping value not calculated because outside established wavelength limits.

Table 8.B.5.C-6
Values of Material Damping in Compression for Forward, Reverse and Combined Directions Along Array C13 in the Vertical Plane for Isotropic Loading Conditions

Excitation Frequency	Confining Pressure, psi, (kPa)	D(%) Measured in Test Direction Forward	Reverse	Combined
2000 Hz	4 (27.5)	4.05	3.47	3.76
	7 (48.1)	2.69	0.80	1.74
	12 (82.5)	2.80	3.10	2.95
	21.4 (147.1)	5.15	3.41	4.35
	37.4 (257.1)	*	*	*
3000 Hz	4 (27.5)	5.39	2.06	3.73
	7 (48.1)	0.77	1.02	0.90
	12 (82.5)	0.60	4.71	2.66
	21.4 (147.1)	1.23	2.02	1.64
	37.4 (257.1)	2.21	1.58	1.90
4000 Hz	4 (27.5)	1.22	2.70	1.96
	7 (48.1)	1.56	1.40	1.48
	12 (82.5)	–0.83	3.83	1.55
	21.4 (147.1)	0.20	1.47	0.83
	37.4 (257.1)	0.96	2.37	1.67

* One or both record(s) were missing or could not be interpreted.
** Damping value not calculated because outside established wavelength limits.

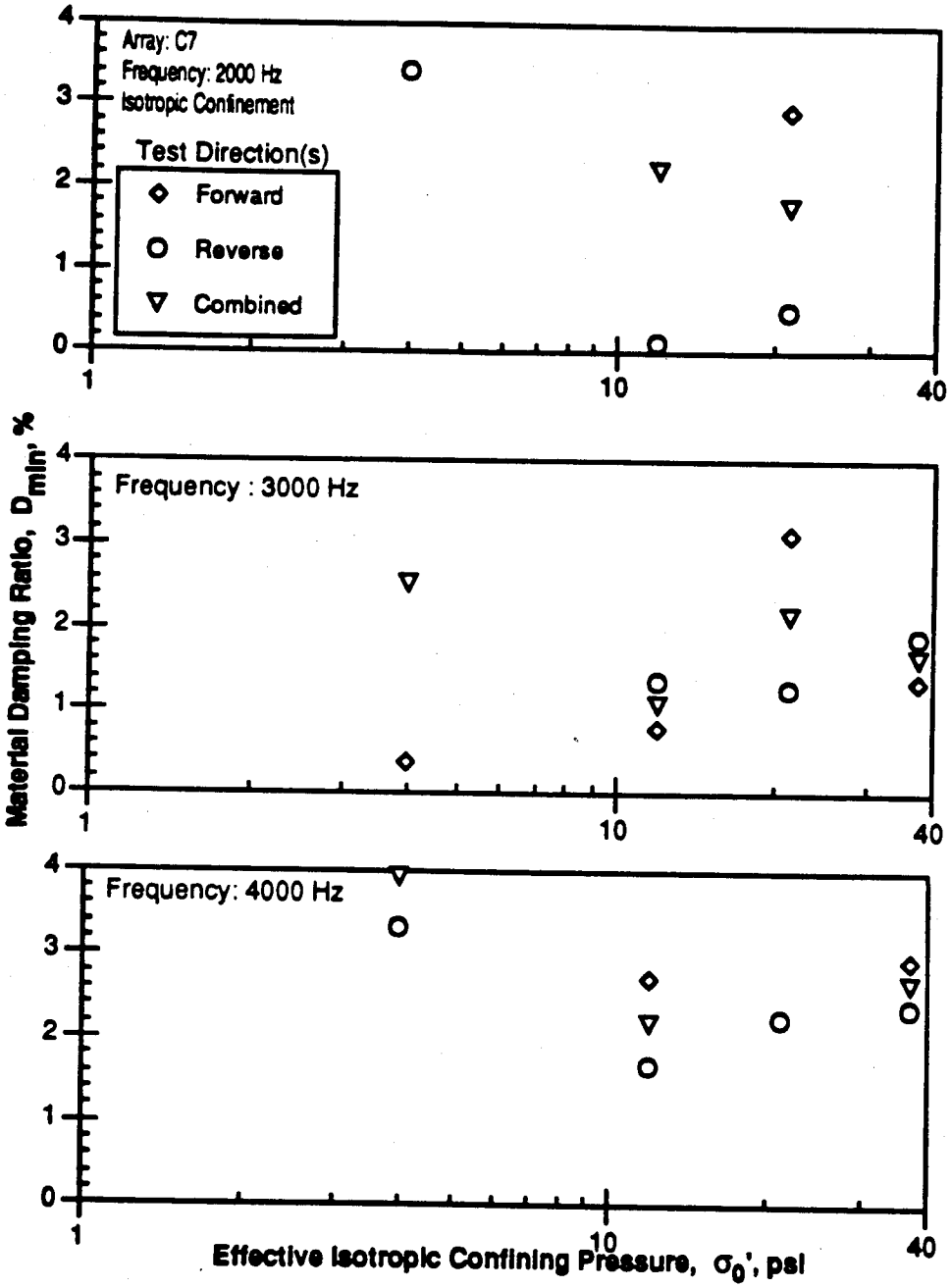

Figure 8.B.5.C-1
Material damping measurements in compression for forward, reverse and combined directions along array C7 in the vertical plane during isotropic loading.

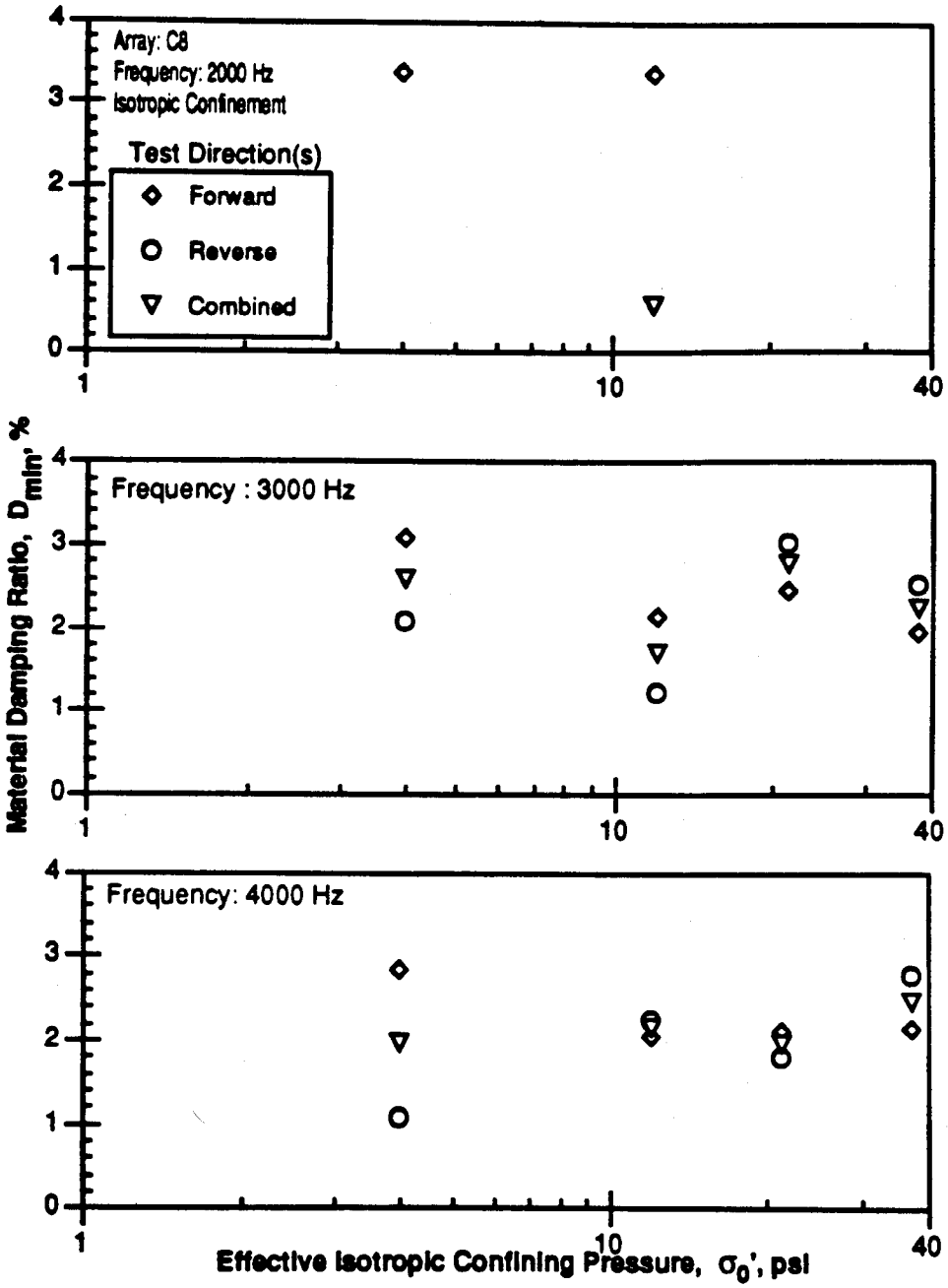

Figure 8.B.5.C-2
Material damping measurements in compression for forward, reverse and combined directions along array C8 in the vertical plane during isotropic loading.

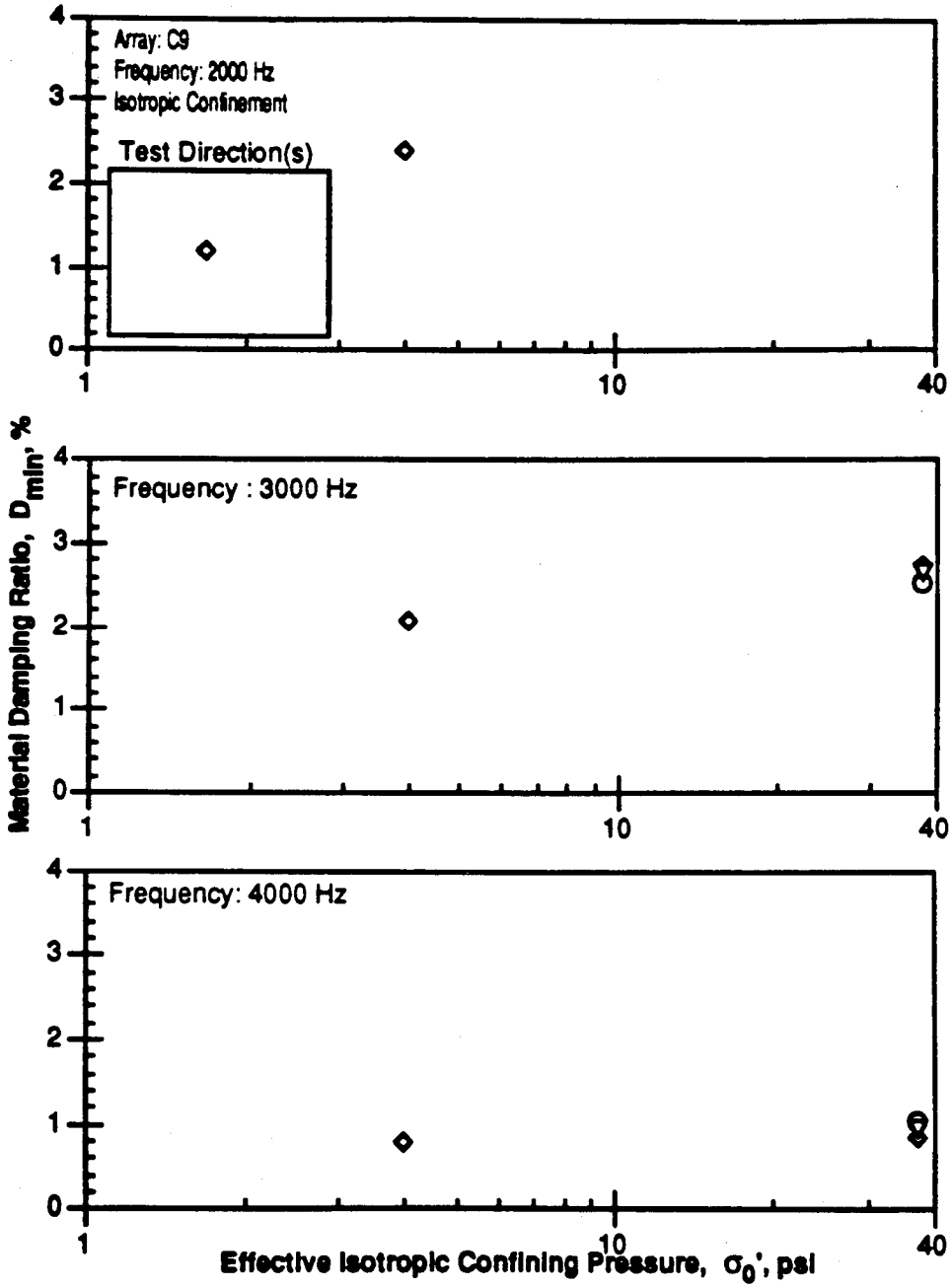

Figure 8.B.5.C-3
Material damping measurements in compression for forward, reverse and combined directions along array C9 in the vertical plane during isotropic loading.

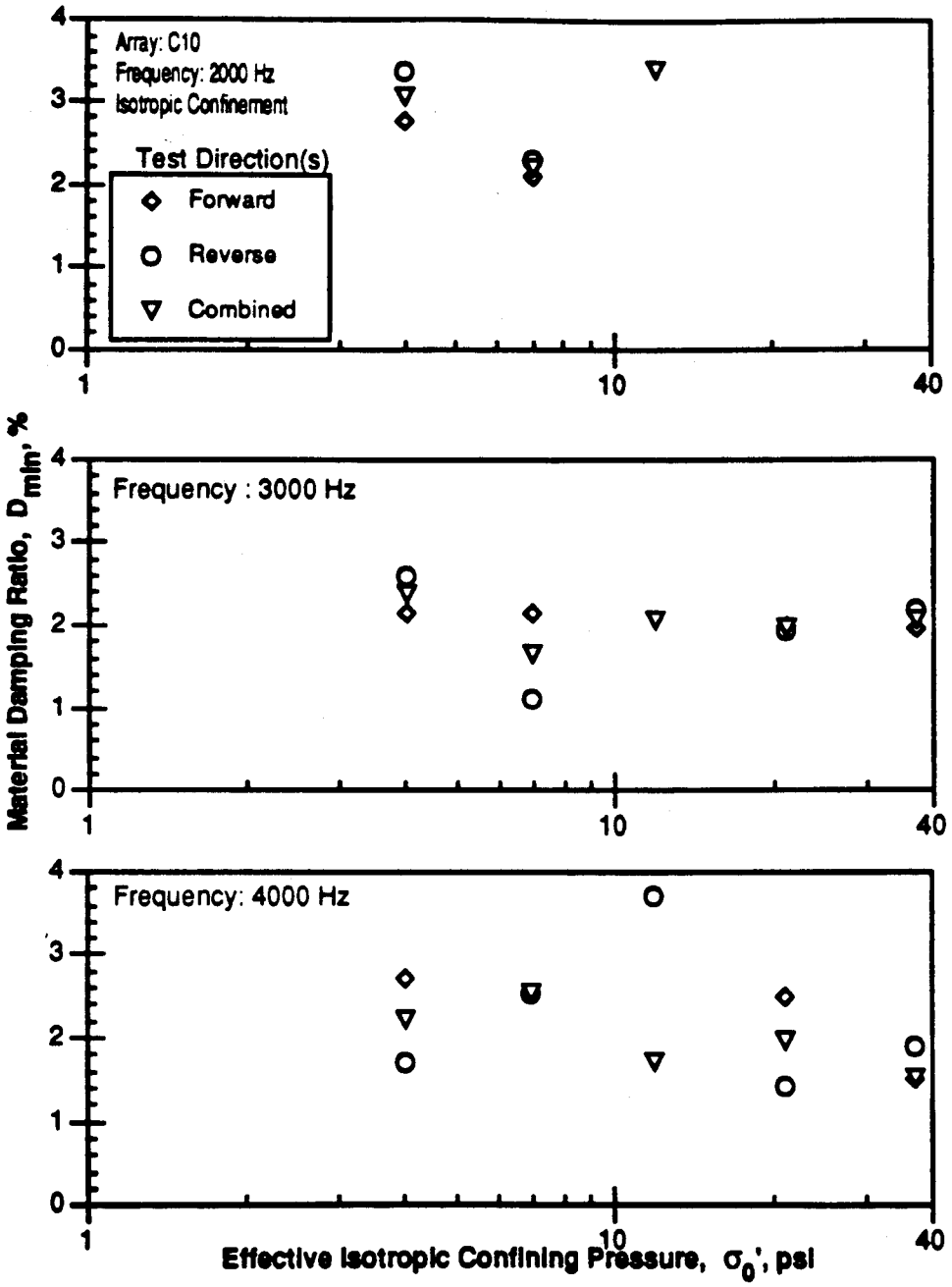

Figure 8.B.5.C-4
Material damping measurements in compression for forward, reverse and combined directions along array C10 in the vertical plane during isotropic loading.

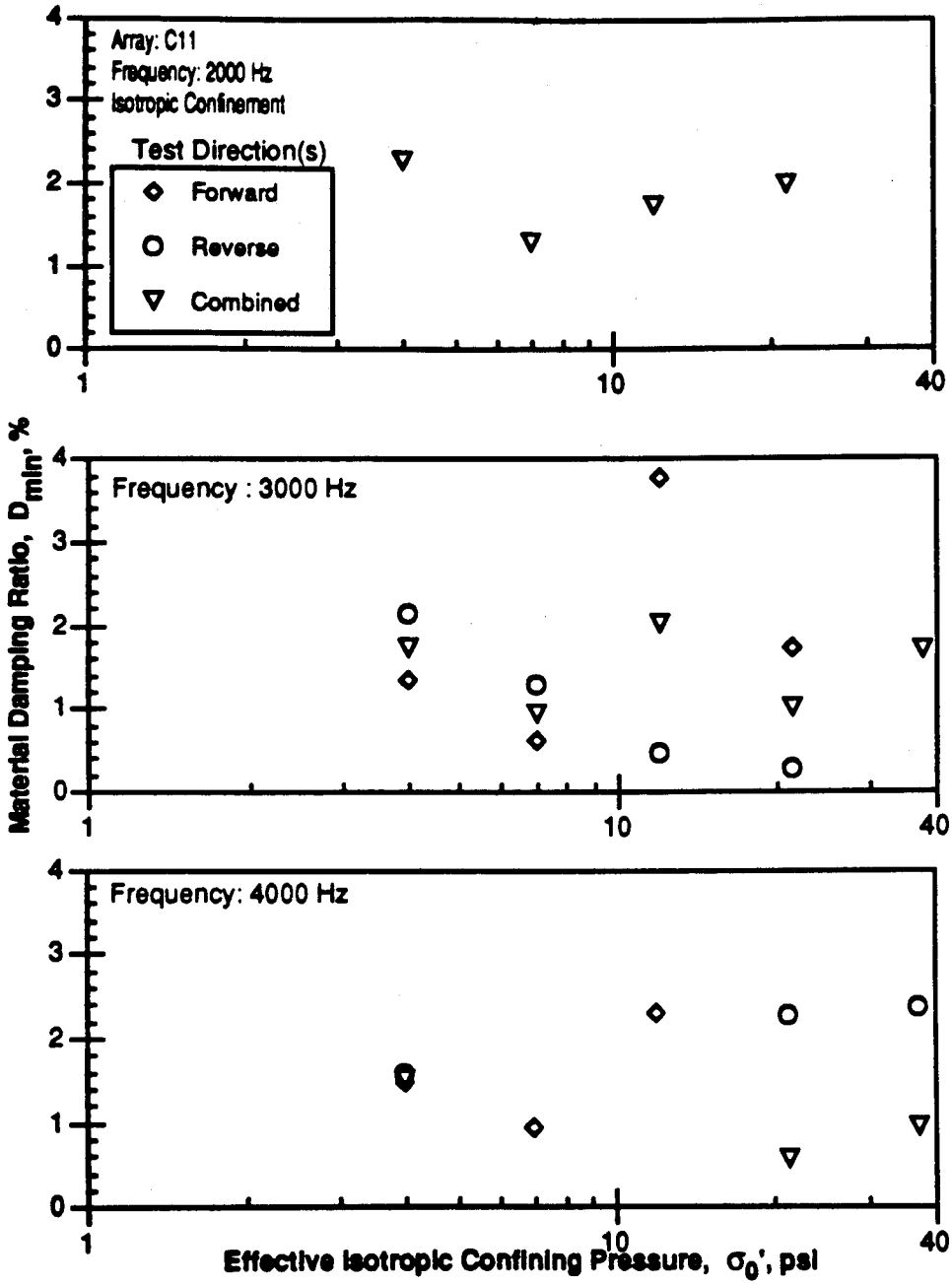

Figure 8.B.5.C-5
Material damping measurements in compression for forward, reverse and combined directions along array C11 in the vertical plane during isotropic loading.

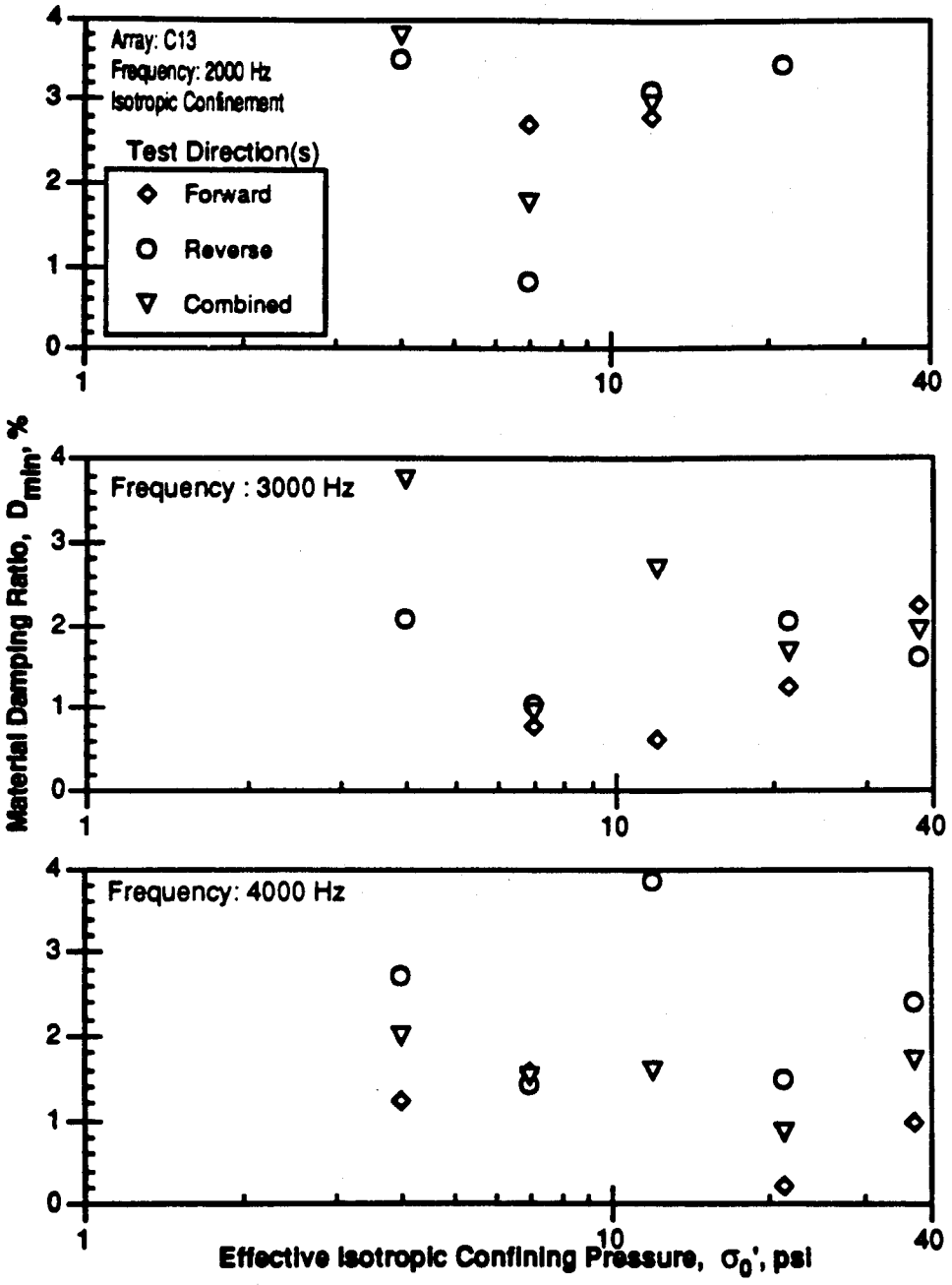

Figure 8.B.5.C-6
Material damping measurements in compression for forward, reverse and combined directions along array C13 in the vertical plane during isotropic loading.

APPENDIX 8.B.5.D
MATERIAL DAMPING IN COMPRESSION FOR MEASUREMENTS IN THE HORIZONTAL PLANE UNDER BIAXIAL LOADING CONDITIONS

Table 8.B.5.D-1
Values of Material Damping in Compression for Forward, Reverse and Combined Directions Along Array C1 in the Horizontal Plane for Biaxial Loading Conditions

Excitation Frequency	Confining Pressure, psi, (kPa)	D(%) Measured in Test Direction Forward	Reverse	Combined
2000 Hz	6 (41.4)	1.79	–0.68	0.56
	7 (48.1)	0.63	0.25	0.44
	9.5 (65.3)	1.22	0.17	0.69
	12 (82.5)	1.31	0.99	1.15
	21.4 (147.1)	**	**	**
3000 Hz	6 (41.4)	0.33	–0.06	0.13
	7 (48.1)	–0.31	0.37	0.03
	9.5 (65.3)	–0.56	0.68	0.06
	12 (82.5)	0.99	1.09	1.04
	21.4 (147.1)	2.21	0.59	1.40
4000 Hz	6 (41.4)	1.12	–0.88	0.12
	7 (48.1)	0.37	–0.53	–0.08
	9.5 (65.3)	–0.01	–0.28	–0.15
	12 (82.5)	0.83	0.60	0.72
	21.4 (147.1)	1.88	–0.46	0.71

* One or both record(s) were missing or could not be interpreted.
** Damping value not calculated because outside established frequency limits.

Table 8.B.5.D-2
Values of Material Damping In Compression for Forward, Reverse and Combined Directions Along Array C2 in the Horizontal Plane for Biaxial Loading Conditions

Excitation Frequency	Confining Pressure, psi, (kPa)	D(%) Measured in Test Direction		
		Forward	Reverse	Combined
2000 Hz	6 (41.4)	1.33	*	*
	7 (48.1)	1.55	4.65	3.10
	9.5 (65.3)	2.15	3.78	2.97
	12 (82.5)	2.18	4.18	3.18
	21.4 (147.1)	**	**	**
3000 Hz	6 (41.4)	0.79	2.46	1.63
	7 (48.1)	0.25	2.13	1.19
	9.5 (65.3)	0.00	2.08	1.04
	12 (82.5)	0.56	1.89	1.23
	21.4 (147.1)	0.53	1.26	0.89
4000 Hz	6 (41.4)	–0.74	2.36	0.81
	7 (48.1)	–0.51	2.00	0.75
	9.5 (65.3)	0.64	1.75	1.20
	12 (82.5)	0.80	1.82	1.31
	21.4 (147.1)	0.43	1.85	1.14

* One or both record(s) were missing or could not be interpreted.
** Damping value not calculated because outside established frequency limits.

Table 8.B.5.D-3
Values of Material Damping in Compression for Forward, Reverse and Combined Directions Along Array C3 in the Horizontal Plane for Biaxial Loading Conditions

Excitation Frequency	Confining Pressure, psi, (kPa)	D(%) Measured in Test Direction Forward	Reverse	Combined
2000 Hz	6 (41.4)	*	*	*
	7 (48.1)	*	*	*
	9.5 (65.3)	*	*	*
	12 (82.5)	*	*	*
	21.4 (147.1)	**	**	**
3000 Hz	6 (41.4)	*	*	*
	7 (48.1)	*	*	*
	9.5 (65.3)	*	*	*
	12 (82.5)	*	*	*
	21.4 (147.1)	–0.89	1.28	0.20
4000 Hz	6 (41.4)	*	*	*
	7 (48.1)	*	*	*
	9.5 (65.3)	*	*	*
	12 (82.5)	*	*	*
	21.4 (147.1)	0.88	–0.24	0.32

* One or both record(s) were missing or could not be interpreted.
** Damping value not calculated because outside established frequency limits.

Table 8.B.5.D-4
Values of Material Damping in Compression for Forward, Reverse and Combined Directions Along Array C4 in the Horizontal Plane for Biaxial Loading Conditions

Excitation Frequency	Confining Pressure, psi, (kPa)	D(%) Measured in Test Direction Forward	Reverse	Combined
2000 Hz	6 (41.4)	2.24	3.88	3.06
	7 (48.1)	3.67	2.64	3.16
	9.5 (65.3)	3.09	2.59	2.84
	12 (82.5)	4.46	1.99	3.23
	21.4 (147.1)	**	**	**
3000 Hz	6 (41.4)	1.47	2.05	1.76
	7 (48.1)	1.74	1.58	1.66
	9.5 (65.3)	1.72	2.36	2.04
	12 (82.5)	0.62	1.59	1.11
	21.4 (147.1)	0.39	2.75	1.57
4000 Hz	6 (41.4)	1.47	2.73	2.10
	7 (48.1)	*	*	*
	9.5 (65.3)	3.13	2.22	2.67
	12 (82.5)	2.41	1.12	1.77
	21.4 (147.1)	2.26	2.51	2.39

* One or both record(s) were missing or could not be interpreted.
** Damping value not calculated because outside established frequency limits.

Table 8.B.5.D-5
Values of Material Damping in Compression for Forward, Reverse and Combined Directions Along Array C5 in the Horizontal Plane for Biaxial Loading Conditions

Excitation Frequency	Confining Pressure, psi, (kPa)	D(%) Measured in Test Direction Forward	Reverse	Combined
2000 Hz	6 (41.4)	–0.73	–1.28	–1.00
	7 (48.1)	1.74	1.01	1.37
	9.5 (65.3)	–0.61	*	*
	12 (82.5)	1.17	2.09	1.60
	21.4 (147.1)	**	**	**
3000 Hz	6 (41.4)	*	–1.13	*
	7 (48.1)	1.88	0.36	1.12
	9.5 (65.3)	–0.12	–0.82	–0.47
	12 (82.5)	1.57	1.45	1.51
	21.4 (147.1)	3.09	–1.78	0.65
4000 Hz	6 (41.4)	*	*	*
	7 (48.1)	*	0.47	*
	9.5 (65.3)	–0.82	*	*
	12 (82.5)	1.36	1.79	1.57
	21.4 (147.1)	2.56	–0.34	1.11

* One or both record(s) were missing or could not be interpreted.
** Damping value not calculated because outside established frequency limits.

Table 8.B.5.D-6
Values of Material Damping in Compression for Forward, Reverse and Combined Directions Along Array C6 in the Horizontal Plane for Biaxial Loading Conditions

Excitation Frequency	Confining Pressure, psi, (kPa)	D(%) Measured in Test Direction Forward	Reverse	Combined
2000 Hz	6 (41.4)	1.65	1.55	1.60
	7 (48.1)	1.63	3.35	2.49
	9.5 (65.3)	2.58	2.32	2.45
	12 (82.5)	3.79	1.55	2.62
	21.4 (147.1)	**	**	**
3000 Hz	6 (41.4)	0.31	2.56	1.44
	7 (48.1)	0.10	3.60	1.85
	9.5 (65.3)	0.23	3.57	1.90
	12 (82.5)	3.71	3.83	3.77
	21.4 (147.1)	1.96	2.84	2.40
4000 Hz	6 (41.4)	1.17	1.36	1.27
	7 (48.1)	0.71	2.20	1.46
	9.5 (65.3)	0.74	2.16	1.45
	12 (82.5)	0.19	2.82	1.47
	21.4 (147.1)	1.89	2.06	1.97

* One or both record(s) were missing or could not be interpreted.
** Damping value not calculated because outside established frequency limits.

Table 8.B.5.D-7
Values of Material Damping in Compression for Forward, Reverse and Combined Directions Along Array C7 in the Horizontal Plane for Biaxial Loading Conditions

Excitation Frequency	Confining Pressure, psi, (kPa)	D(%) Measured in Test Direction		
		Forward	Reverse	Combined
2000 Hz	6 (41.4)	4.07	2.42	3.25
	7 (48.1)	2.82	3.58	3.20
	9.5 (65.3)	3.18	2.04	2.61
	12 (82.5)	4.3	0.1	2.2
	21.4 (147.1)	**	**	**
3000 Hz	6 (41.4)	2.89	2.95	2.92
	7 (48.1)	3.13	3.40	3.26
	9.5 (65.3)	3.01	2.80	2.90
	12 (82.5)	0.76	1.32	1.04
	21.4 (147.1)	–5.73	–7.21	–6.47
4000 Hz	6 (41.4)	3.42	3.83	3.63
	7 (48.1)	2.78	4.31	3.55
	9.5 (65.3)	3.86	3.67	3.77
	12 (82.5)	2.69	1.64	2.17
	21.4 (147.1)	6.17	–6.80	–0.31

* One or both record(s) were missing or could not be interpreted.
** Damping value not calculated because outside established frequency limits.

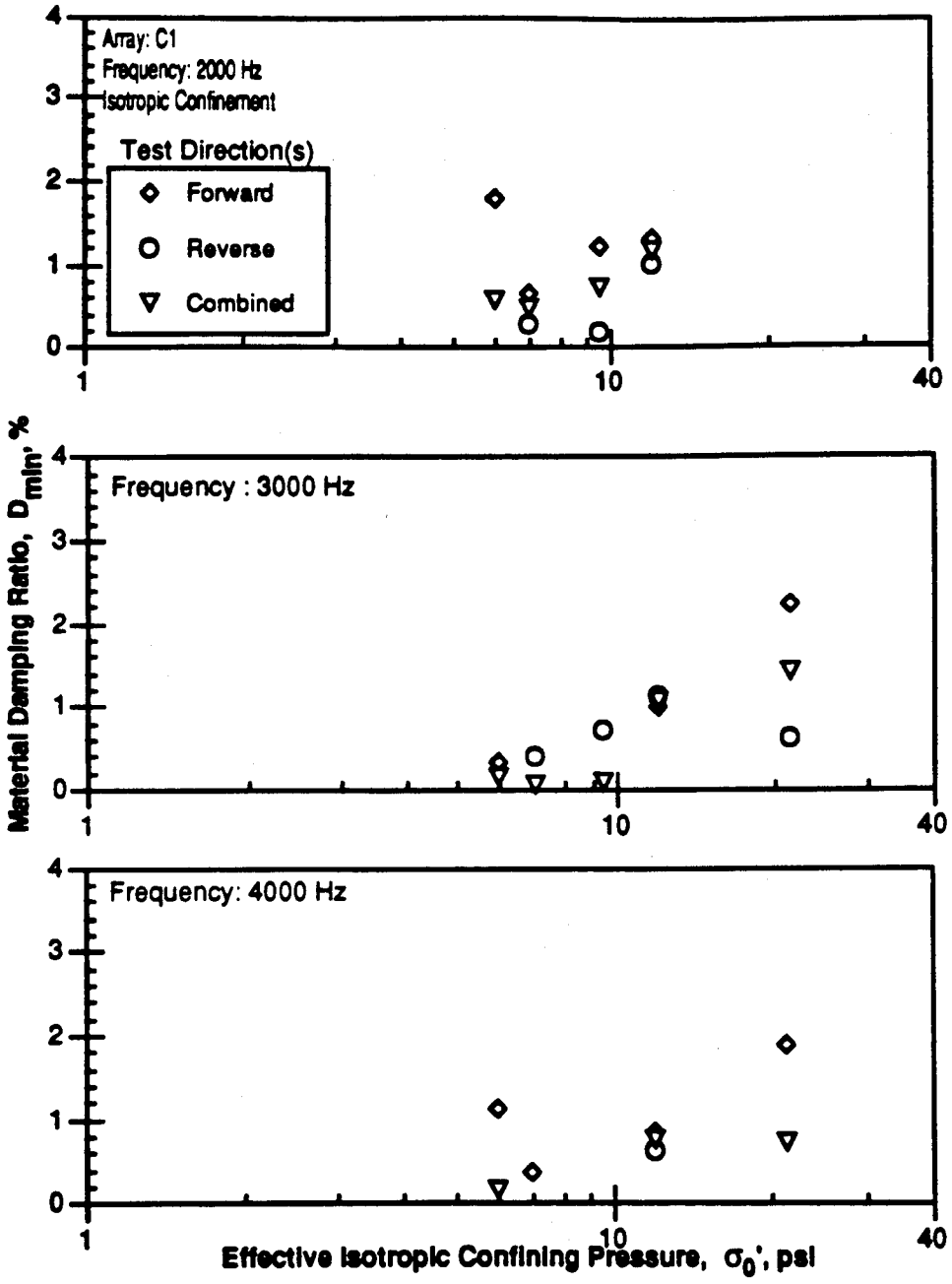

Figure 8.B.5.D-1
Material damping measurements in compression for forward, reverse and combined directions along array C1 in the horizontal plane during biaxial loading.

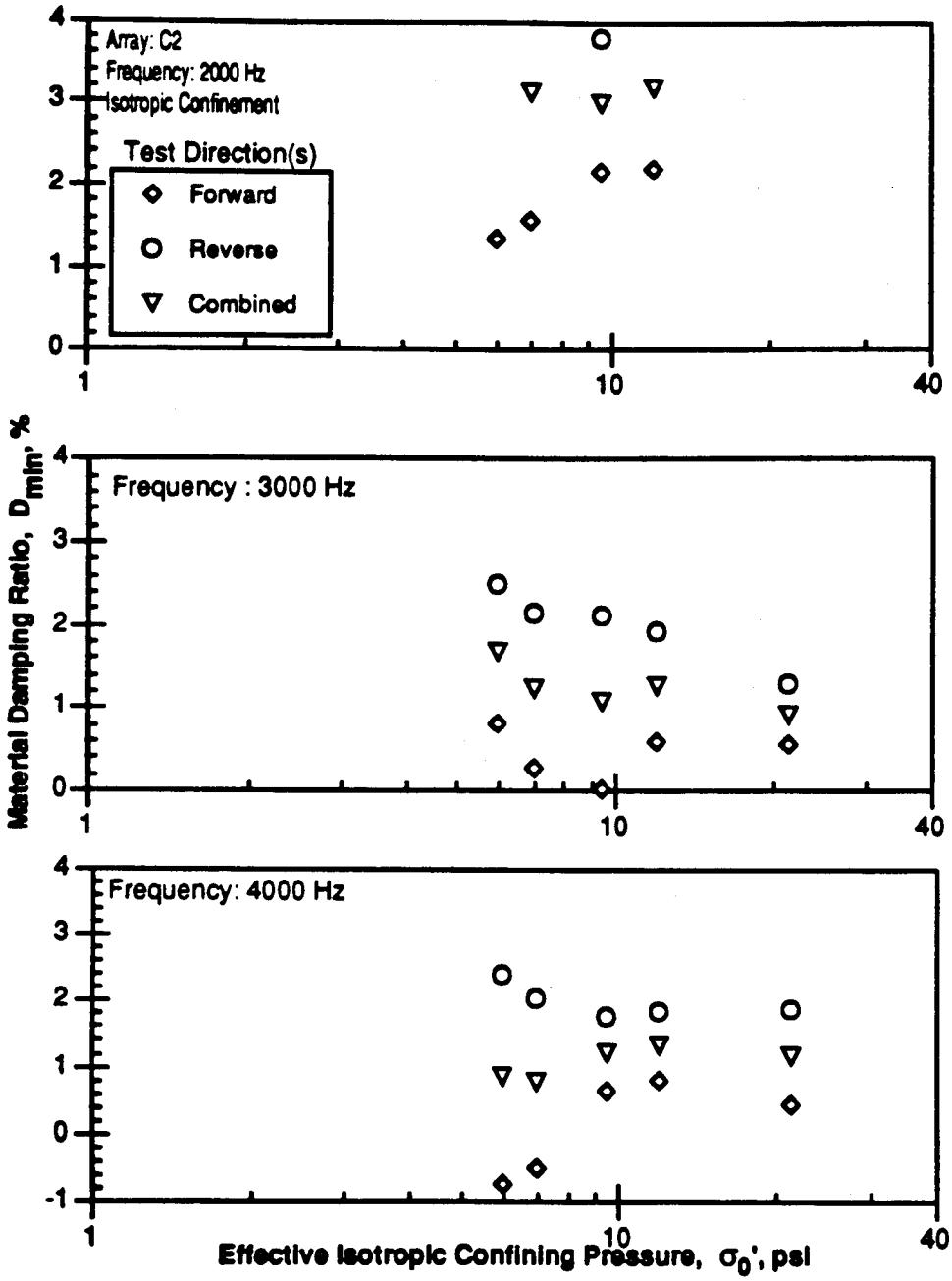

Figure 8.B.5.D-2
Material damping measurements in compression for forward, reverse and combined directions along array C2 in the horizontal plane during biaxial loading.

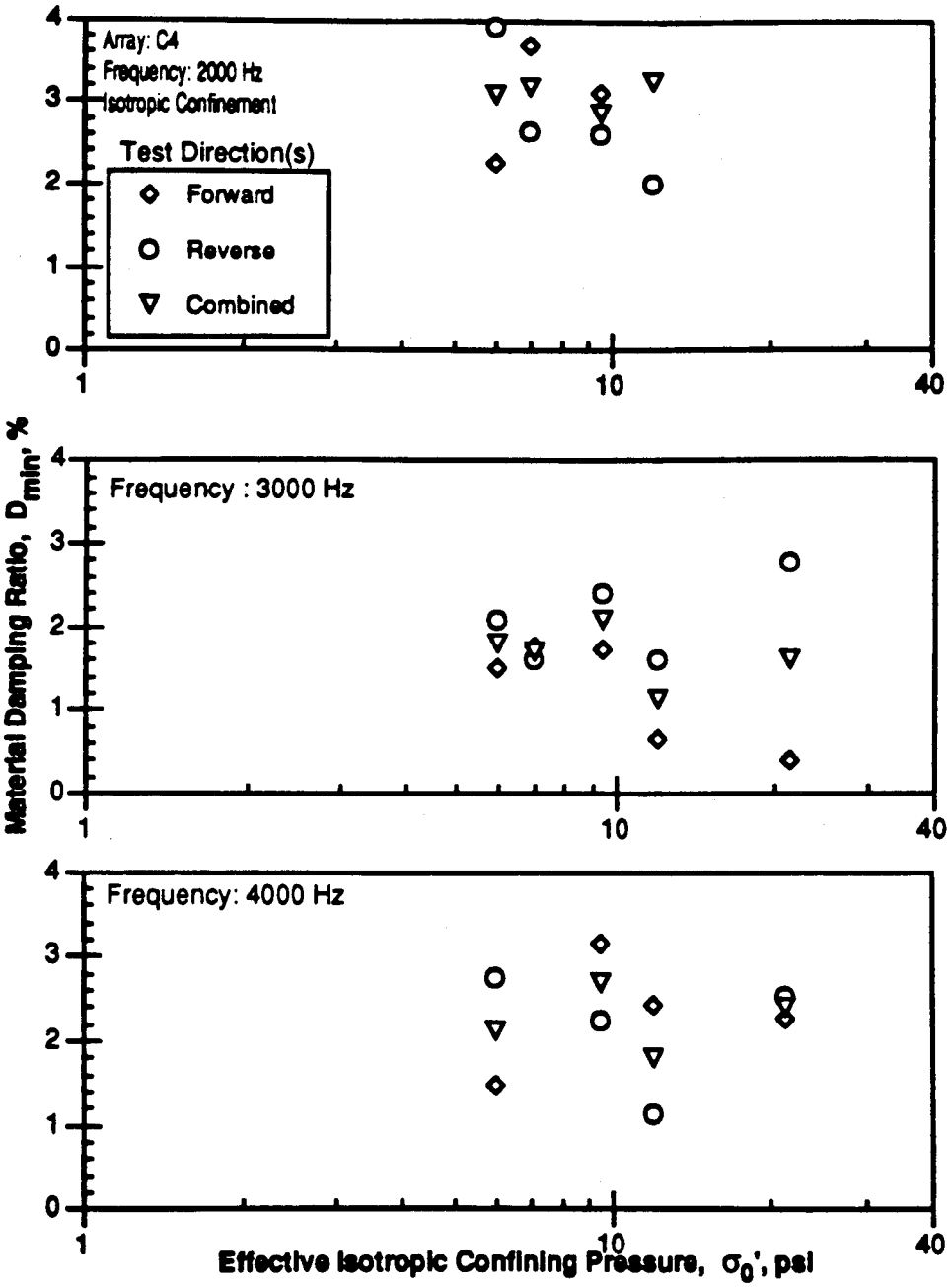

Figure 8.B.5.D-3
Material damping measurements in compression for forward, reverse and combined directions along array C4 in the horizontal plane during biaxial loading.

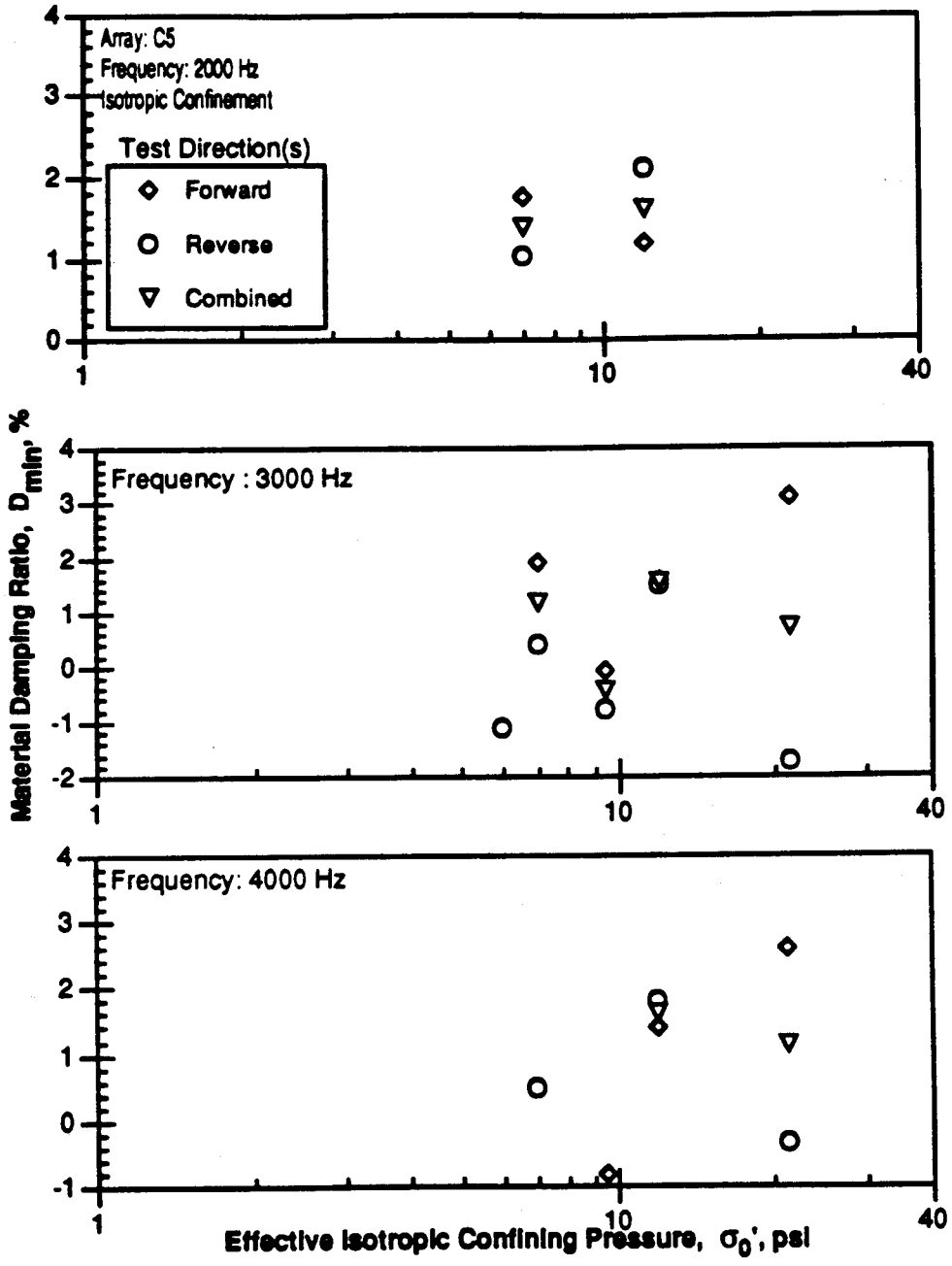

Figure 8.B.5.D-4
Material damping measurements in compression for forward, reverse and combined directions along array C5 in the horizontal plane during biaxial loading.

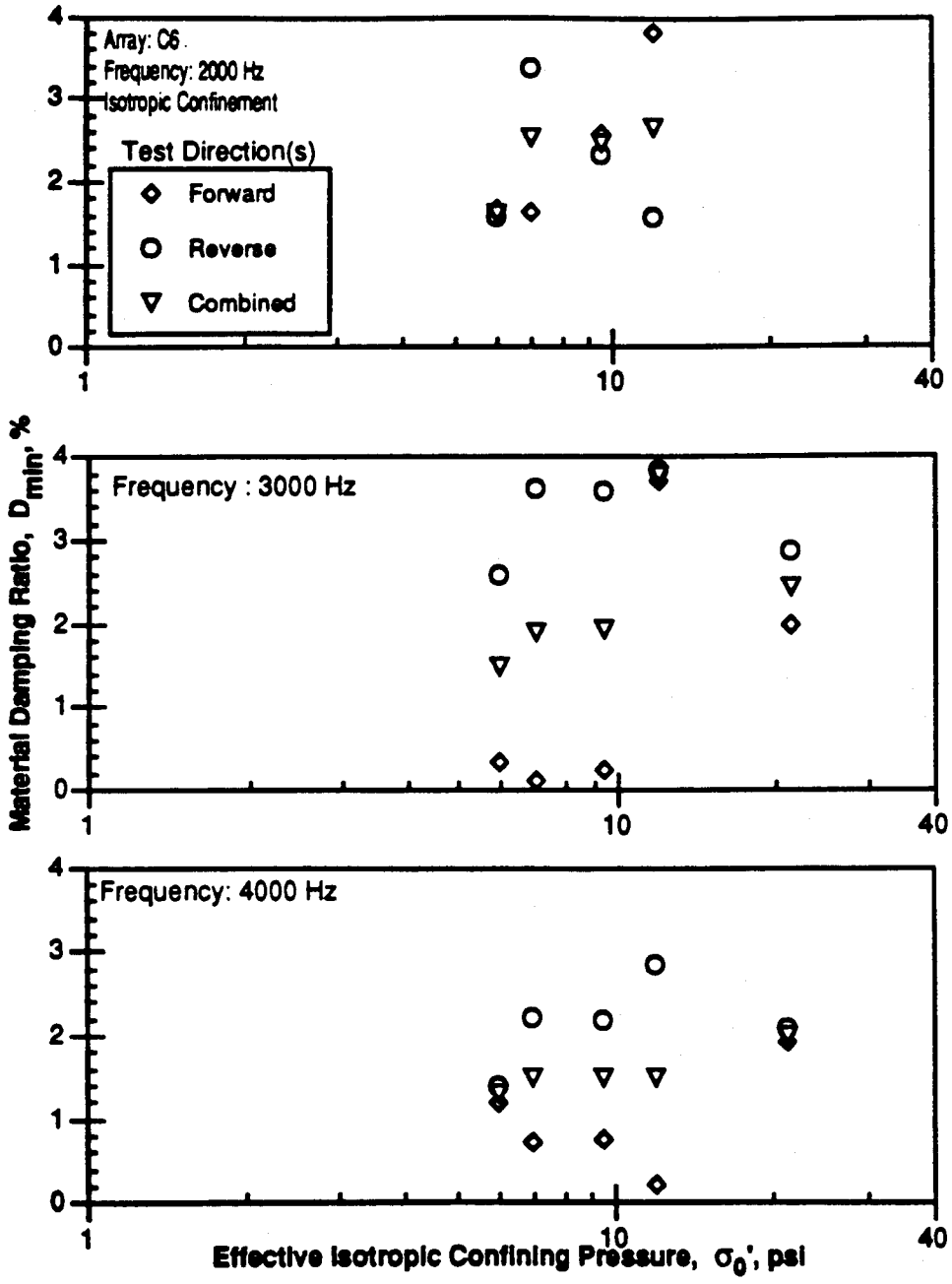

Figure 8.B.5.D-5
Material damping measurements in compression for forward, reverse and combined directions along array C6 in the horizontal plane during biaxial loading.

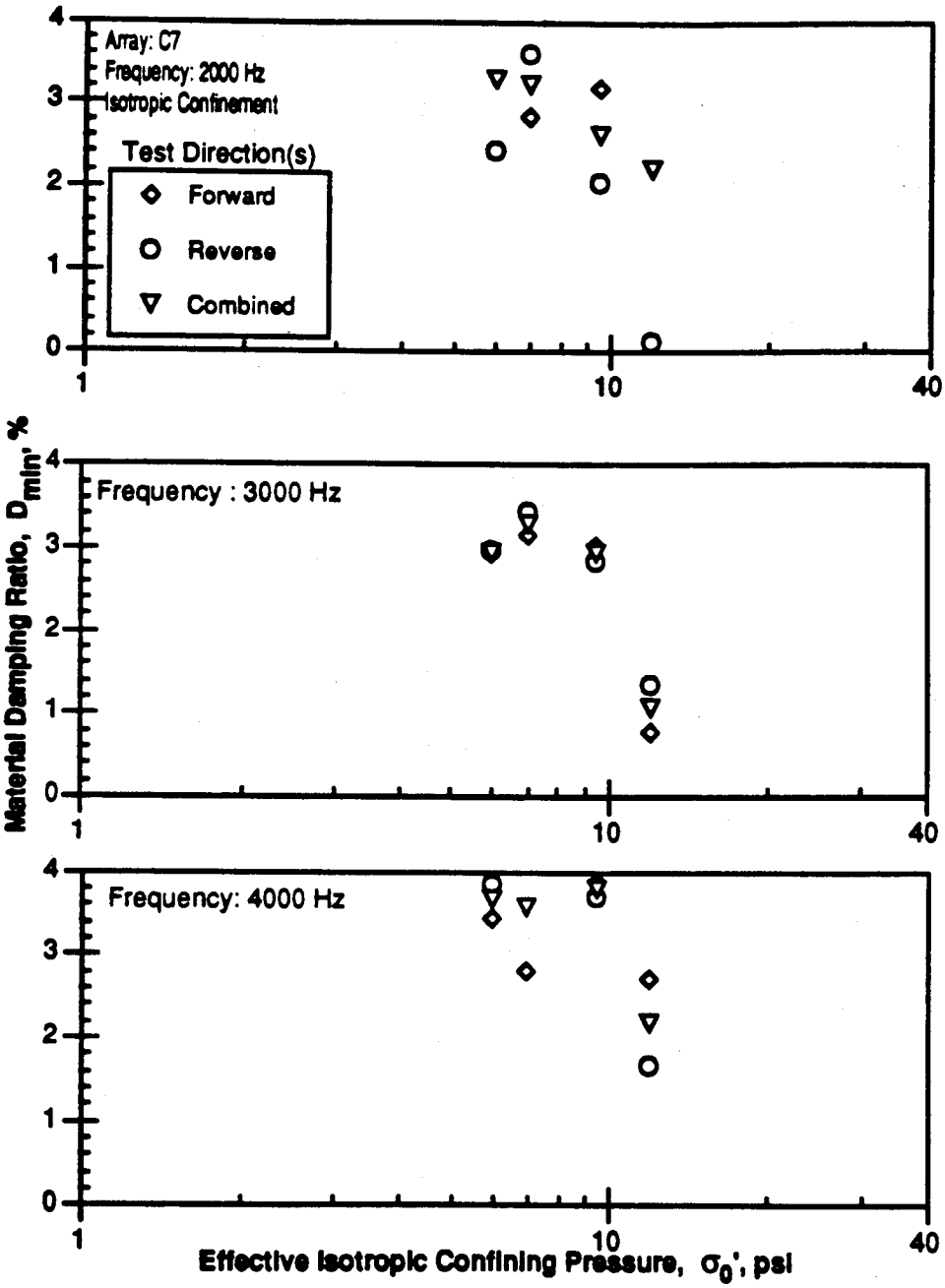

Figure 8.B.5.D-6
Material damping measurements in compression for forward, reverse and combined directions along array C7 in the horizontal plane during biaxial loading.

APPENDIX 8.B.5.E
MATERIAL DAMPING IN COMPRESSION FOR MEASUREMENTS IN THE VERTICAL PLANE UNDER BIAXIAL LOADING CONDITIONS

Table 8.B.5.E-1
Values of Material Damping in Compression for Forward, Reverse and Combined Directions Along Array C7 in the Vertical Plane for Biaxial Loading Conditions

Excitation Frequency	Confining Pressure, psi, (kPa)	D(%) Measured in Test Direction Forward	Reverse	Combined
2000 Hz	6 (41.4)	4.07	2.42	3.25
	7 (48.1)	2.82	3.58	3.20
	9.5 (65.3)	3.18	2.04	2.61
	12 (82.5)	4.3	0.1	2.2
	21.4 (147.1)	**	**	**
3000 Hz	6 (41.4)	2.89	2.95	2.92
	7 (48.1)	3.13	3.40	3.26
	9.5 (65.3)	3.01	2.80	2.90
	12 (82.5)	0.76	1.32	1.04
	21.4 (147.1)	–5.73	–7.21	–6.47
4000 Hz	6 (41.4)	3.42	3.83	3.63
	7 (48.1)	2.78	4.31	3.55
	9.5 (65.3)	3.86	3.67	3.77
	12 (82.5)	2.69	1.64	2.17
	21.4 (147.1)	6.17	–6.80	–0.31

* One or both record(s) were missing or could not be interpreted.
** Damping value not calculated because outside established frequency limits.

Table 8.B.5.E-2
Values of Material Damping in Compression for Forward, Reverse and Combined Directions Along Array C9 in the Vertical Plane for Biaxial Loading Conditions

Excitation Frequency	Confining Pressure, psi, (kPa)	D(%) Measured in Test Direction		
		Forward	Reverse	Combined
2000 Hz	6 (41.4)	3.10	*	*
	7 (48.1)	4.56	*	*
	9.5 (65.3)	4.02	*	*
	12 (82.5)	*	*	*
	21.4 (147.1)	2.65	*	*
3000 Hz	6 (41.4)	–0.62	*	*
	7 (48.1)	0.70	*	*
	9.5 (65.3)	0.30	*	*
	12 (82.5)	*	*	*
	21.4 (147.1)	1.26	*	*
4000 Hz	6 (41.4)	0.60	*	*
	7 (48.1)	1.71	*	*
	9.5 (65.3)	0.71	*	*
	12 (82.5)	*	*	*
	21.4 (147.1)	–0.50	*	*

* One or both record(s) were missing or could not be interpreted.
** Damping value not calculated because outside established frequency limits.

Table 8.B.5.E-3
Values of Material Damping in Compression for Forward, Reverse and Combined Directions Along Array C10 in the Vertical Plane for Biaxial Loading Conditions

Excitation Frequency	Confining Pressure, psi, (kPa)	D(%) Measured in Test Direction Forward	Reverse	Combined
2000 Hz	6 (41.4)	4.71	2.44	3.57
	7 (48.1)	5.18	3.18	4.18
	9.5 (65.3)	17.18	–3.48	4.45
	12 (82.5)	–2.91	9.48	3.39
	21.4 (147.1)	**	**	**
3000 Hz	6 (41.4)	3.67	1.62	3.57
	7 (48.1)	3.21	1.84	2.52
	9.5 (65.3)	2.50	2.08	2.29
	12 (82.5)	–2.27	6.16	2.03
	21.4 (147.1)	4.96	4.63	4.80
4000 Hz	6 (41.4)	3.89	2.44	3.16
	7 (48.1)	3.14	2.49	2.80
	9.5 (65.3)	2.62	2.96	2.79
	12 (82.5)	–0.45	3.67	1.67
	21.4 (147.1)	2.59	2.78	2.69

* One or both record(s) were missing or could not be interpreted.
** Damping value not calculated because outside established frequency limits.

Table 8.B.5.E-4
Values of Material Damping in Compression for Forward, Reverse and Combined Directions Along Array C11 in the Vertical Plane for Biaxial Loading Conditions

Excitation Frequency	Confining Pressure, psi, (kPa)	D(%) Measured in Test Direction Forward	Reverse	Combined
2000 Hz	6 (41.4)	3.68	–1.38	1.24
	7 (48.1)	4.38	–0.62	1.88
	9.5 (65.3)	4.46	–0.99	1.74
	12 (82.5)	14.32	–9.43	1.71
	21.4 (147.1)	5.41	–2.93	1.24
3000 Hz	6 (41.4)	0.75	0.47	0.61
	7 (48.1)	1.20	1.37	1.28
	9.5 (65.3)	0.96	0.61	0.78
	12 (82.5)	3.76	0.45	1.98
	21.4 (147.1)	0.93	1.25	1.09
4000 Hz	6 (41.4)	*	2.31	*
	7 (48.1)	–0.06	*	*
	9.5 (65.3)	–1.13	1.62	0.25
	12 (82.5)	2.27	*	**
	21.4 (147.1)	–0.31	1.08	0.39

* One or both record(s) were missing or could not be interpreted.
** Damping value not calculated because outside established frequency limits.

Table 8.B.5.E-5
Values of Material Damping in Compression for Forward, Reverse and Combined Directions Along Array C12 in the Vertical Plane for Biaxial Loading Conditions

Excitation Frequency	Confining Pressure, psi, (kPa)	D(%) Measured in Test Direction Forward	Reverse	Combined
2000 Hz	6 (41.4)	1.22	1.04	1.13
	7 (48.1)	–0.13	1.62	0.74
	9.5 (65.3)	2.15	1.94	2.04
	12 (82.5)	*	*	*
	21.4 (147.1)	**	**	**
3000 Hz	6 (41.4)	1.08	1.46	1.27
	7 (48.1)	0.36	1.71	1.04
	9.5 (65.3)	1.47	1.14	1.30
	12 (82.5)	*	*	*
	21.4 (147.1)	1.65	1.77	1.71
4000 Hz	6 (41.4)	2.33	2.23	2.28
	7 (48.1)	2.07	3.08	2.57
	9.5 (65.3)	1.91	1.70	1.80
	12 (82.5)	*	*	*
	21.4 (147.1)	2.44	2.30	2.37

* One or both record(s) were missing or could not be interpreted.
** Damping value not calculated because outside established frequency limits.

Table 8.B.5.E-6
Values of Material Damping in Compression for Forward, Reverse and Combined Directions Along Array C13 in the Vertical Plane for Biaxial Loading Conditions

Excitation Frequency	Confining Pressure, psi, (kPa)	D(%) Measured in Test Direction Forward	Reverse	Combined
2000 Hz	6 (41.4)	1.79	1.90	1.85
	7 (48.1)	0.60	2.65	1.62
	9.5 (65.3)	2.31	0.57	1.44
	12 (82.5)	2.80	3.10	2.95
	21.4 (147.1)	3.13	4.07	3.60
3000 Hz	6 (41.4)	0.65	0.59	0.62
	7 (48.1)	0.16	1.36	0.76
	9.5 (65.3)	1.27	1.09	1.18
	12 (82.5)	0.60	4.71	2.66
	21.4 (147.1)	1.52	1.06	1.29
4000 Hz	6 (41.4)	0.32	1.07	0.70
	7 (48.1)	–0.11	1.94	0.92
	9.5 (65.3)	–0.03	1.15	0.56
	12 (82.5)	–0.83	3.83	1.55
	21.4 (147.1)	0.79	2.64	1.71

* One or both record(s) were missing or could not be interpreted.
** Damping value not calculated because outside established frequency limits.

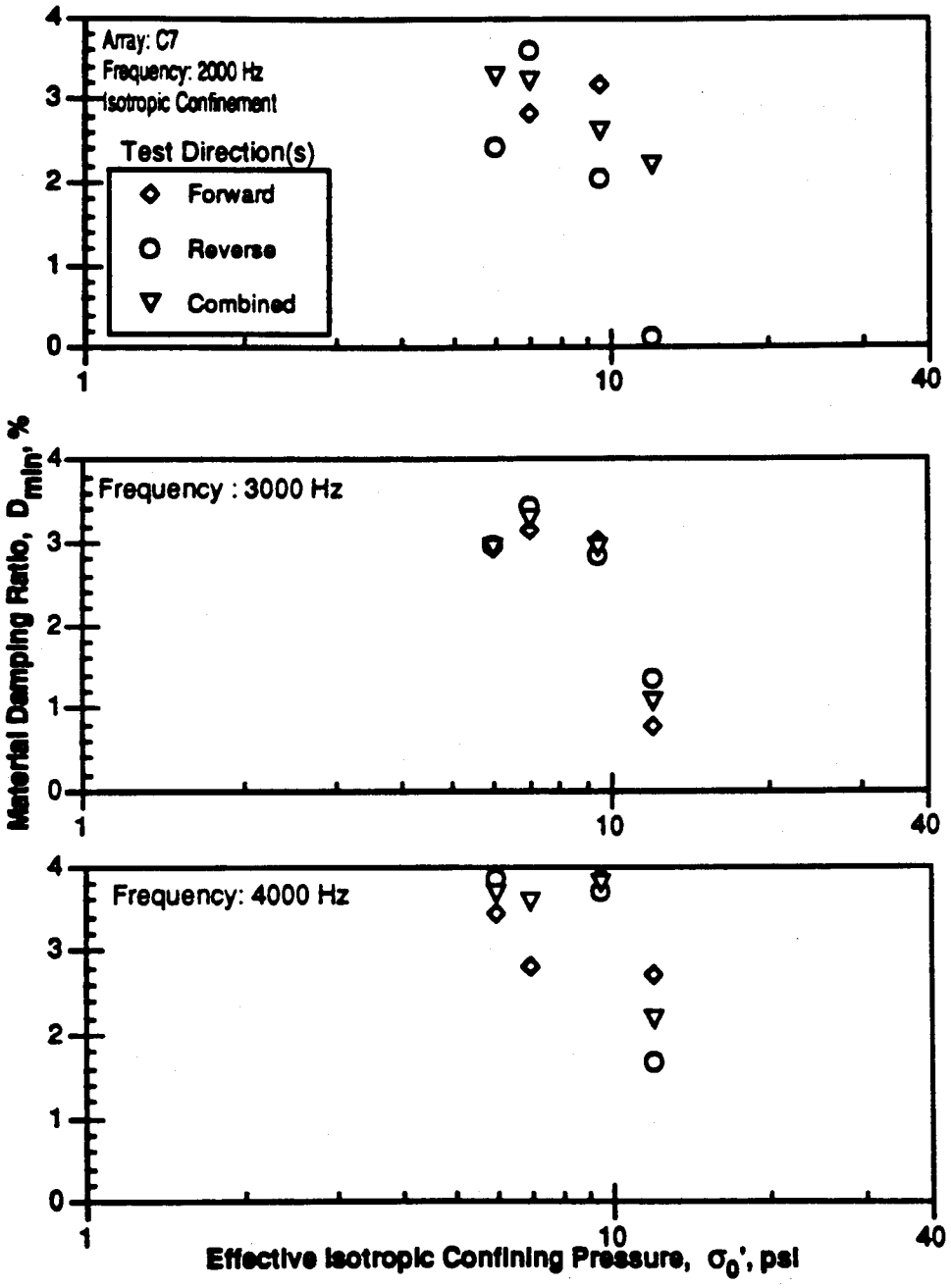

Figure 8.B.5.E-1
Material damping measurements in compression for forward, reverse and combined directions along array C7 in the vertical plane during biaxial loading.

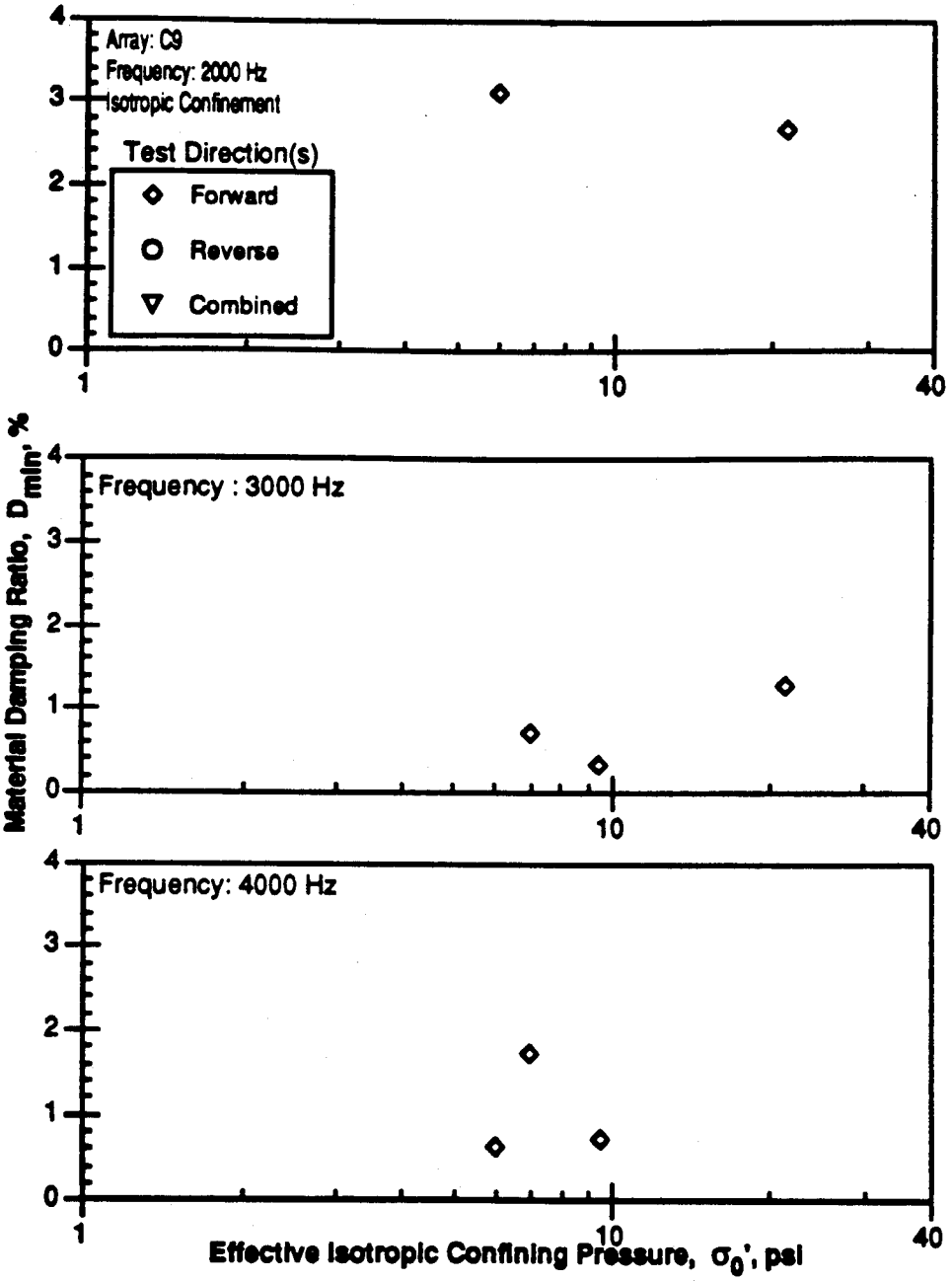

Figure 8.B.5.E-2
Material damping measurements in compression for forward, reverse and combined directions along array C9 in the vertical plane during biaxial loading.

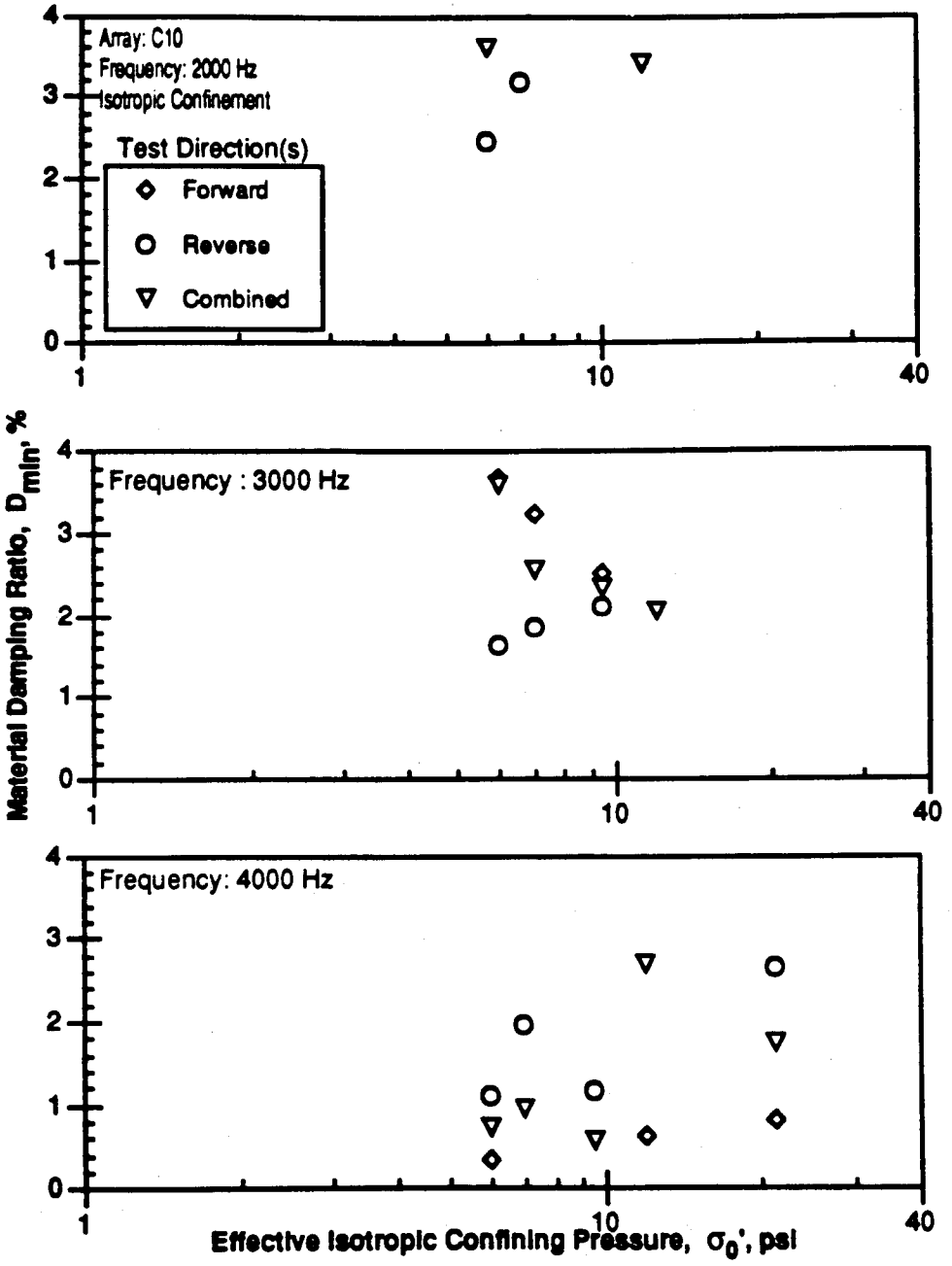

Figure 8.B.5.E-3
Material damping measurements in compression for forward, reverse and combined directions along array C10 in the vertical plane during biaxial loading.

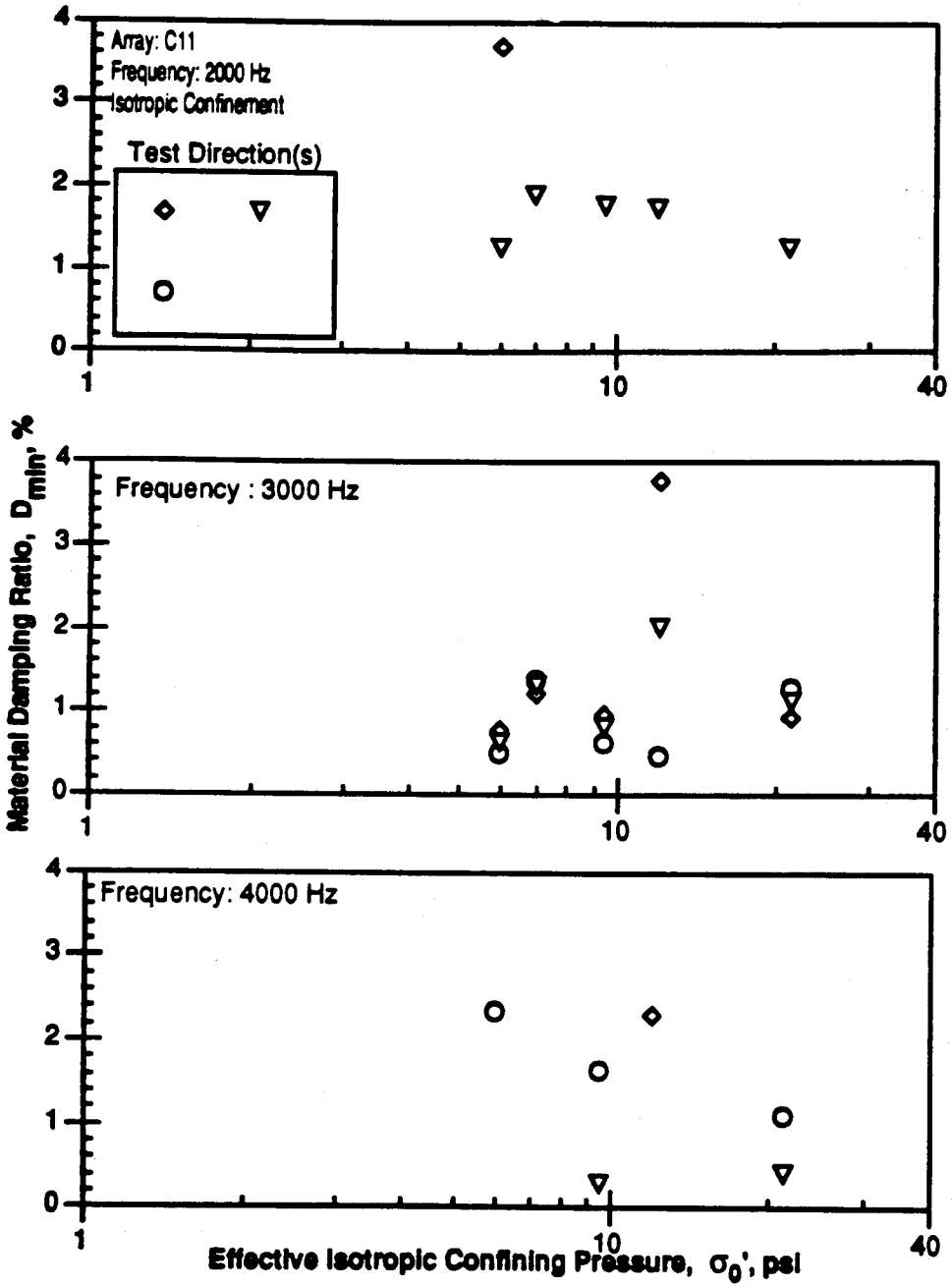

Figure 8.B.5.E-4
Material damping measurements in compression for forward, reverse and combined directions along array C11 in the vertical plane during biaxial loading.

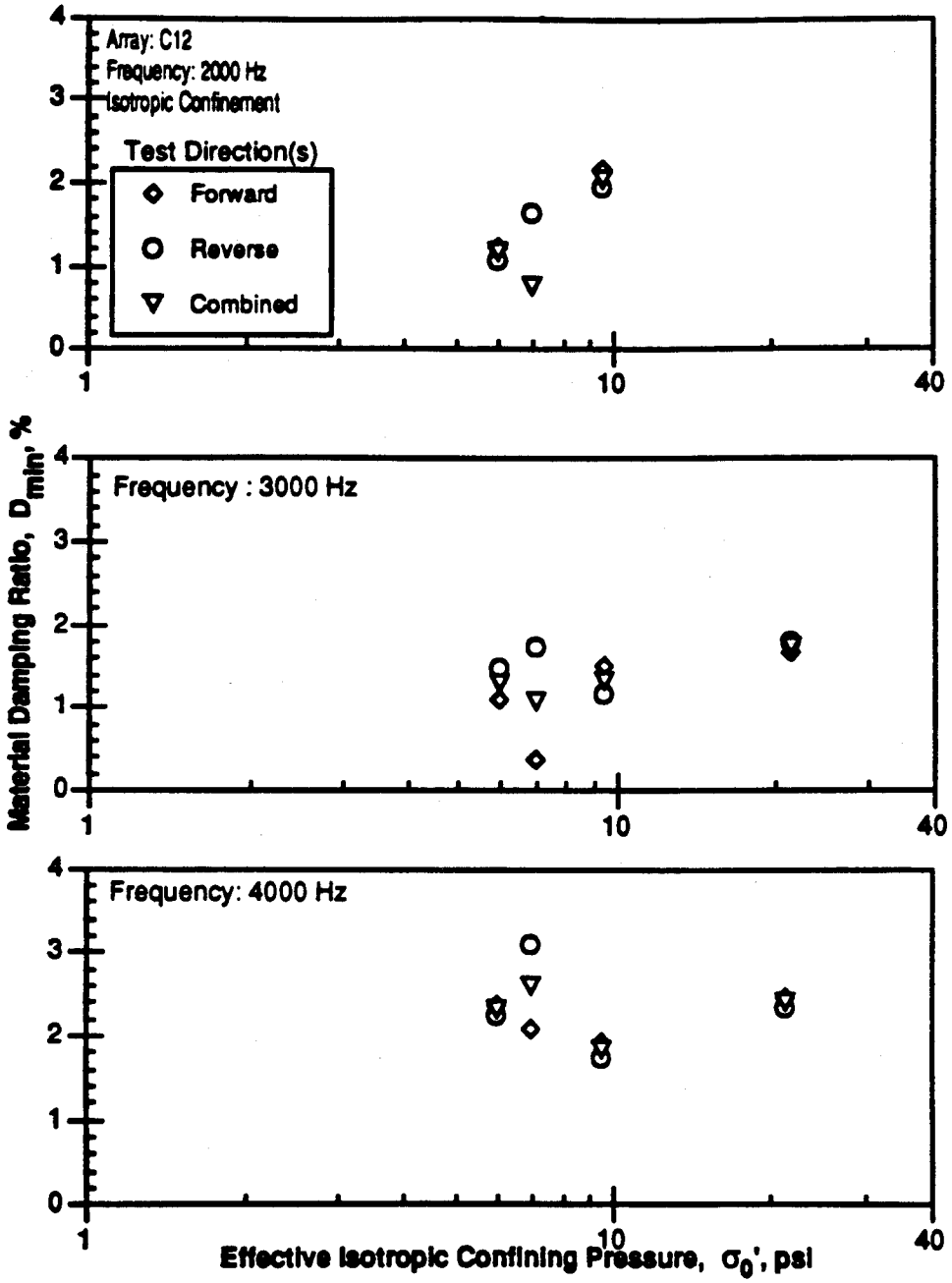

Figure 8.B.5.E-5
Material damping measurements in compression for forward, reverse and combined directions along array C12 in the vertical plane during biaxial loading.

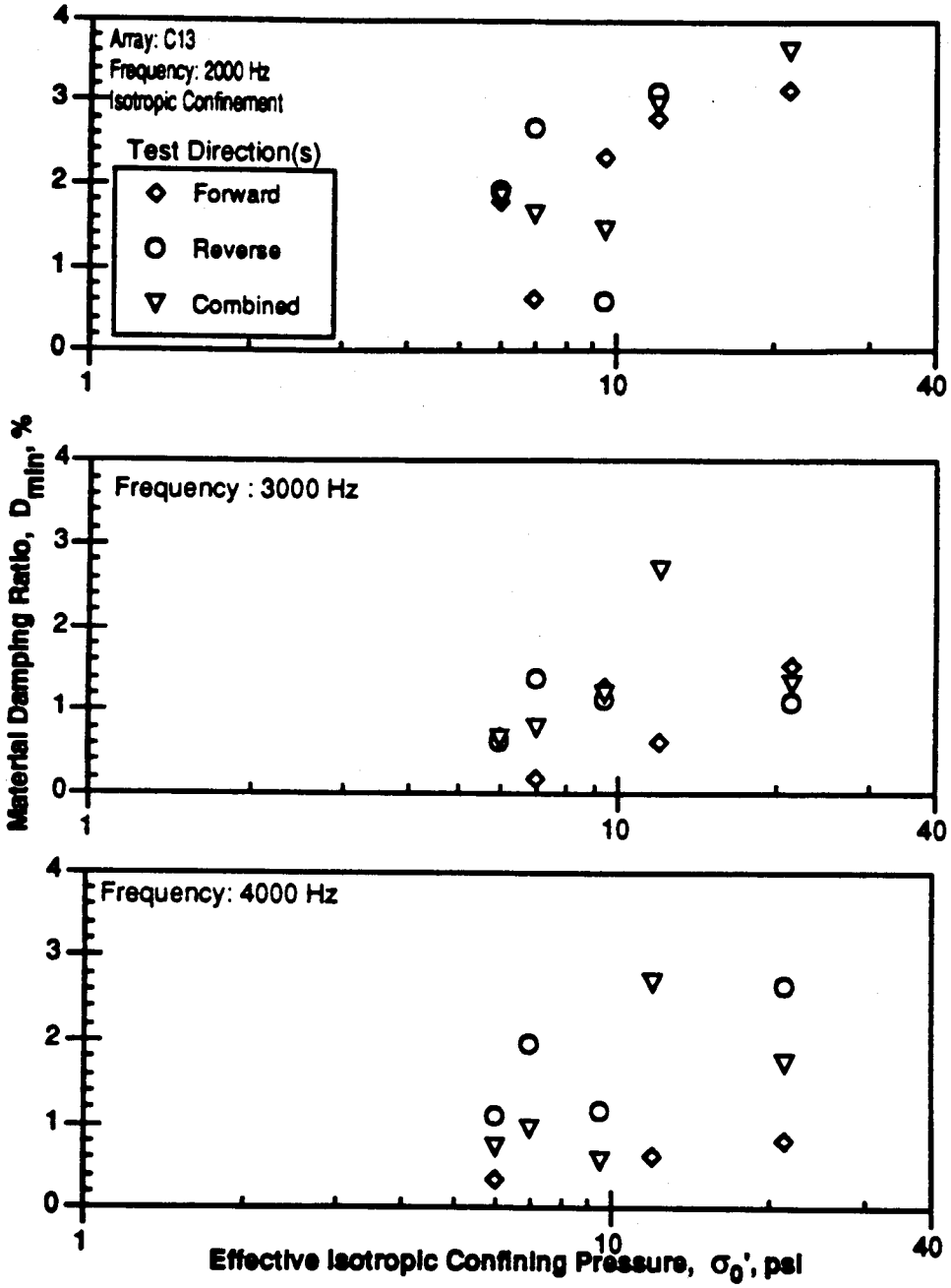

Figure 8.B.5.E-6
Material damping measurements in compression for forward, reverse and combined directions along array C13 in the vertical plane during biaxial loading.

REFERENCES

Bieganousky, W.A. and Marcuson, W.F., III (1976), "Uniform Placement of Sand," *Journal of Geotechnical Engineering Division*, American Society of Civil Engineers, Vol. 102, No. GT3, March, pp. 229–233.

Chu, H.Y.F., Lee, S.H.H., and Stokoe, K.H., II (1984), "Effect of Structural and Stress Anisotropy on Velocity of Low-Amplitude Compression Waves Propagating Along Principal Stress Directions in Dry Sand," Geotechnical Engineering Report GR84-6, Department of Civil Engineering, University of Texas at Austin.

Drnevich, V.P. (1972), "Undrained Cyclic Shear of Saturated Sand," *Journal of the Soil Mechanics and Foundation Division*, American Society of Civil Engineers, Vol. 98, No. SM8, August, pp. 807–825.

Dyvik, R. and Madshus, C. (1985), "Lab Measurements of G_{max} Using Bender Elements," *Advances in the Art of Testing Soils Under Cyclic Conditions*, American Society of Civil Engineers, Detroit, MI October, pp. 186–196.

Fuhriman, M.D. and Stokoe, K.H., II (1993), "Crosshole Seismic Tests at Two Northern California Sites Affected by the 1989 Loma Prieta Earthquake," Geotechnical Engineering Report GR93-1, Department of Civil Engineering, University of Texas at Austin.

Finn, L.W.D. (1985), "Aspects of Constant Volume Cyclic Simple Shear," *Advances in the Art of Testing Soils Under Cyclic Conditions*, American Society of Civil Engineers, Detroit, MI, October, pp. 74–98.

Gladwin, M.T., and Stacey, F.D. (1974), "An Elastic Degradation of Acoustic Pulses in Rock," *Physical Earth Plan International*, Vol. 8, pp. 332–336.

Hamilton, E.L. (1972), "Compressional Wave Attenuation in Marine Sediments," *Geophysics*, Vol. 37, pp. 620–646.

Hardin, B.O. (1978), "The Nature of Stress-Strain Behavior for Soils," Proceedings, Geotechnical Engineering Division Specialty Conference on Earthquake Engineering and Soil Dynamics, Vol. I, ASCE, Pasadena, CA, June, pp. 3–90.

Hardin, B.O., and Drnevich, V.P. (1972a), "Shear Modulus and Damping in Soils: Measurement and Parameter Effects," *Journal of the Soil Mechanics and Foundation Division*, American Society of Civil Engineers, Vol. 98, No. SM6, June, pp. 603–624.

Hardin, B.O., and Drnevich, V.P. (1972b), "Shear Modulus and Damping in Soils: Design Equations and Curves," *Journal of the Soil Mechanics and Foundation Division*, American Society of Civil Engineers, Vol. 98, No. SM7, July, pp. 667–692.

Hoar, R.J. (1982), "Field Measurement of Seismic Wave Velocity and Attenuation," Ph.D. Dissertation, *Geotechnical Engineering*, Department of Civil Engineering, University of Texas at Austin.

Isenhower, W.M. (1979), "Torsional Simple Shear/Resonant Column Properties of San Francisco Bay Mud," Geotechnical Engineering Thesis GT80-1, Department of Civil Engineering, University of Texas at Austin.

Ishibashi, I., and Sherif, M.A. (1974), "Soil Liquefaction by Torsional Simple Shear Device," *Journal of Soil Mechanics and Foundation Division*, American society of Civil Engineers, Vol. 100, No. GT8, August, pp. 871–888.

Kim, D. S. (1991), "Deformational Characteristics of Soils at Small to Intermediate Strains for Cyclic Tests, Ph.D. Dissertation, *Geotechnical Engineering*, Department of Civil Engineering, University of Texas at Austin, August.

Kjartansson, E. (1979), "Constant Q-Wave Propagation and Attenuation," *Journal of Geophysical Research*, Vol. 84, pp. 4737–4748.

Koppermann S.E., Stokoe, K.H., II and Knox, D.P. (1982), "Effect of State of Stress on Velocity of Low-Amplitude Compression Waves Propagating Along Principal Stress Directions in Dry Sand," Geotechnical Engineering Report GR82-22, *Geotechnical Engineering*, Department of Civil Engineering, University of Texas at Austin.

Knox, D.P., Stokoe, K.H., II and Kopperman, S.E. (1986), "Effect of State of Stress on Velocity of Low-Amplitude Shear Wave Propagating Along Principal Directions in Dry sand," Geotechnical Engineering Report GR82-23, Department of Civil Engineering, University of Texas at Austin.

Laird, J. (1993), "Material Damping measurements at High Confining Pressure," M.S. Thesis, Geotechnical Engineering, Department of Civil Engineering, University of Texas at Austin, (in progress).

Lawrence, F.V. (1963), "The Response of Soils to Dynamic Loadings: Report 14: Propagation Velocity of Ultrasonic Waves Through Sand," Research Report R63-8, Department of Civil Engineering, Massachusetts Institute of Technology, March, 54 pp.

Lee, J.N. (1993), "Inherent and Stress-Induced Anisotropy of Sand Determined by Body Wave Velocities," Ph.D. Dissertation, *Geotechnical Engineering*, Department of Civil Engineering, University of Texas at Austin, December.

Lewis, M.D. (1990), "A Laboratory Study of the Effect of Stress State on the Elastic Moduli of Sand," Ph.D. Dissertation, *Geotechnical Engineering*, Department of Civil Engineering, University of Texas at Austin, December.

Lui, H.P., Warrick, R.E., Westerlund, R.E., Fletcher, J.B., and Maxwell, G.L. (1988), "An Air-Powered Impulsive Shear-Wave Source with Repeatable Signals," *Bulletin of the Seismological Society of America*, Vol. 78, pp. 355–369.

McDonal, F.J., Angona, F.A., Mills, R.L., Sengbush, R.L., Van Nostrand, R.G. and White, J.E. (1958), "Attenuation of Shear and Compressional Waves in Pierre Shale," *Geophysics*, Vol. 23, pp. 421–439.

Mok, Y.J. (1987), "Analytical and Experimental Studies of Borehole Seismic Methods," Ph.D. Dissertation, *Geotechnical Engineering*, Department of Civil Engineering, University of Texas at Austin, May.

Mok, Y.J., Sanchez-Salinero, I., Stokoe, K.H., II and Roesset, J.M. (1988), "In Situ Damping Measurement by Crosshole Seismic Methods," Earthquake Engineering and Soil Dynamics II American Society of Civil Engineers, Geotechnical Engineering Specialty Conference, Park City, Utah, pp. 305–320.

Ohya, S., Ogura, K. and Imai, T. (1984), "The Suspension P-S Logging System," Proceedings, Offshore Technology Conference, Paper OTC 4680, Houston, Texas.

Redpath, B.B. and Lee, R.C. (1986), "In Situ Measurement of Shear Wave Attenuation at a Strong-Motion Recording Site," Prepared of USGS Contract No. 14-08-001-21823.

Roesler, K.H (1979), "Anisotropic Shear Modulus Due to Stress Anisotropy," *Journal of the Geotechnical Engineering Division*, American Society of Civil Engineers, Vol. 105,, No. GT5, July, pp. 871–880.

Sanchez-Salinero, I., Roesset, J.M. and Stokoe, K.H., II (1986), "Analytical Studies of Body Wave Propagation and Attenuation," Geotechnical Engineering Report GR86-15, Department of Civil Engineering, University of Texas at Austin.

Schmertmann, J.H. (1978), "Effect of Shear Stress on Dynamic Bulk Modulus of Sand," U.S. Army Engineering Waterways Experiment Station, Technical Report S-78-16, October, pg. 92.

Seed, H.B., Wong, R.T., Idriss, I.M. and Tokimatsu, K. "Moduli and Damping Factors for Dynamic Analyses of Cohesionless Soils," *ASCE Journal of Geotechnical Engineering Division*, American Society of Civil Engineers, Vol. 112, No. 11, November 1986, pp. 1016–1032.

Stokoe, K.H., II and Hoar, R.J. (1980), "Field Measurements of Dynamic Soil Properties," Specialty Conference on Civil Engineering and Nuclear Power, American Society of Civil Engineers, September 15–17, Vol. II, Knoxville, Tennessee.

Stokoe, K.H., II and Hoar, R.J. (1978), "Variables Affecting In Situ Seismic Measurements," Proceedings of the Conference on Earthquake Engineering and Soil Dynamics, American Society of Civil Engineers, Geotechnical Engineering Division, Pasadena, CA, Vol. II, pp. 919–939.

Suddhiprakarn, C. Roesset, J.M., and Stokoe, K.H. II (1983), "Effects of Rigid Inclusions on Wave Propagation," Report GR83-3, Department of Civil Engineering, University of Texas at Austin, pg. 175.

Toksoz, M.N., Johnston, D.H. and Timur, A. (1979), "Attenuation of Seismic Waves in Dry and Saturated Rocks: I. Laboratory Measurements," *Geophysics*, Vol. 44, pp. 681–690.

White, J.E. (1965), *Seismic Waves: Radiation, Transmission and Attenuation*, McGraw-Hill Book Company, pg. 302.

Winkler, K., and Nur, A. (1979), "Pore Fluids and Seismic Attenuation in Rocks," Geophysics Research Letter, Vol. 6, pp. 1–4.

Winkler, K.W., and Nur, A. (1982), "Seismic Attenuation: Effect of Pore Fluid and Frictional Sliding," *Geophysics*, Vol. 47, pp. 1–15.

Woods, R.D. (1978), "Measurements of Dynamic Soil Properties," Proceedings, Earthquake Engineering and Soil Dynamics Conference, American Society of Civil Engineers, Pasadena, CA June 19–21, Vol. I, pp. 91–178.

Woods, R.D. and Stokoe, K.H., II (1985), "Shallow Seismic Exploration in Soil Dynamics," Richart Commemorative Lecture, American Society of Civil Engineers, Detroit MI, October, pp. 120–156.

About EPRI

EPRI creates science and technology solutions for the global energy and energy services industry. U.S. electric utilities established the Electric Power Research Institute in 1973 as a nonprofit research consortium for the benefit of utility members, their customers, and society. Now known simply as EPRI, the company provides a wide range of innovative products and services to more than 1000 energy-related organizations in 40 countries. EPRI's multidisciplinary team of scientists and engineers draws on a worldwide network of technical and business expertise to help solve today's toughest energy and environmental problems.

EPRI. Electrify the World

Printed on recycled paper in the United States of America

EPRI • 3412 Hillview Avenue, Palo Alto, California 94304 • PO Box 10412, Palo Alto, California 94303 • USA
800.313.3774 • 650.855.2121 • askepri@epri.com • www.epri.com